applied mechanics reviews

published by The American Society of Mechanical Engineers

Feature article:

Vibrations of planar curved beams, rings, and arches

Volume 46, Number 9, September 1993

applied mechanics reviews

AN ASSESSMENT OF THE WORLD LITERATURE IN ENGINEERING SCIENCES

Applied Mechanics Reviews (ISSN 0003-6900) is published monthly by the ASME, 345 E 47th St, New York NY 10017. 2nd class postage paid at New York NY and additional mailing offices. POSTMASTER: Send address changes to ASME/AMR, 22 Law Drive, Box 2300, Fairfield NJ 07007-2300. CHANGES OF ADDRESS must be received at ASME seven weeks before they are to be effective. Send old label and new address. SUBSCRIPTION PRICES: \$534 (incl Annual Index and Suppl.), single copies \$57 (Suppl. or Index \$84). Countries outside USA and Canada add \$102 for postage (\$156 airmail). 2nd library subscription \$99. DISCLAIMER: "The Society shall not be responsible for statements or opinions ...printed in its publications" (ASME Bylaws B7.1.3).

Canadian goods and services tax registration #126 148 048.
Printed in the USA. (7/93)

The American Society of Mechanical Engineers

VOLUME 46, NUMBER 9, SEPTEMBER 1993

FEATURE ARTICLE

BOOK REVIEWS AND NOTES

REVIEW OF THE JOURNAL LITERATURE

Information for authors (inside back cover).
Announcement p ii
Advertisement p 484
Abbreviations used in AMR p J969

APPLIED MECHANICS REVIEWS BOARD OF ASSOCIATE EDITORS

ANNOUNCEMENT

First International Symposium on Thermal Stresses and Related Topics

Hamamatsu, JAPAN
June 5-7, 1995
Act City

THERMAL STRESSES '95

The objective of this Symposium is to provide a forum for engineers and scientists in the field of thermal stresses, for industrial applications and basic research, in order to exchange ideas and to effect further cooperation among the participants. The Symposium will enable researchers and engineers to meet at one place, where they will present their papers and conduct discussions.

The Symposium will be comprised of invited lectures, and presentation and discussion of contributed papers. Sessions are planned on stresses, deformations, shock, fracture, fatigue, cracking and ratcheting in thermal environments; thermoelasticity and plasticity; mechanical behaviors of materials and structures at high and low temperatures; dynamic problems; computational and experimental methods; and ceramic, composite and advanced materials.

The official language will be English

The Symposium will be held from Monday, June 5, to Wednesday, June 7, 1995, at the Act City in Hamamatsu, Japan. Hamamatsu City, located halfway between Tokyo and Osaka, is blessed with a mild climate and with surroundings of abundant natural beauty, such as Mt. Fuji and Lake Hamana.

Call for Papers

Participants who wish to contribute a paper are requested to submit two copies of an abstract (about 500 words) by June 30, 1994, to one of the following:

Dr. R.B. Hetnarski
James E. Gleason, Prof of Mech Eng
Rochester Institute of Tech
PO Box 9887
Rochester, NY 14623-0887, USA
Telephone: 716-475-2157
Telefax: 716-475-6879
Bitnet: 632HETNA@RITVAX

Professor N. Noda
Department of Mech Eng
Shizuoka University 5-1
Johoku 3 chome,
Hamamatsu, 432, JAPAN
Telephone: 81/53-471-1171, Ext. 267, 268
Telefax: 81/53-475-4794
E-Mail:tmnnoda@mm.shizuoka.ac.jp

The abstract should include the title, full name, address of the authors, telephone and fax numbers.

Schedule

• Submission of abstract:	June	30, 1994
• Notification of acceptance:	September	30, 1994
• Submission of paper:	December	31, 1994

Vibrations of planar curved beams, rings, and arches

P. Chidamparam and A.W. Leissa
Department of Engineering Mechanics, The Ohio State University, Columbus OH 43210

This work attempts to organize and summarize the extensive published literature on the vibrations of curved bars, beams, rings and arches of arbitrary shape which lie in a plane. In-plane, out-of-plane and coupled vibrations are considered. Various theories that have been developed to model curved beam vibration problems are examined. An overview is presented of the types of problems which are addressed in the literature. Particular attention is given to the effects of initial static loading, nonlinear vibrations and the application of finite element techniques. The significantly different frequencies arising from curved beam theories which either allow or prevent extension of the centerline during vibratory motion are shown. An extensive bibliography of 407 relevant references is included.

CONTENTS

INTRODUCTION

The study of free vibrations of curved bars (or beams) and rings (closed curved bars) assumes great importance in a wide variety of technical applications like spring design, turbomachinery blades, automotive tire dynamics, aircraft structures, design of bridges for dynamic loads and circumferential stiffeners for shells. Real life engineering applications may also be found in interdisciplinary areas such as bioengineering and vibration control. While the dynamics of straight beams is well established, the same cannot be said about curved beams. The initial curvature has been a source of difficulty in developing governing relations between stress resultants and deformations. Thus, many theories have evolved in attempts at refining already existing ones. A similar scenario is seen in the theory of shells. Whereas this hierarchy is well documented in the case of shells [1], the situation is quite different with curved beams.

Interest in this area can be traced back to the nineteenth century. During the past few years there has been a steady growth of publications and at least two survey articles devoted solely to the dynamics of arches and curved bars [2,3] and a book [4] have appeared. The report by Royster [5] and certain review articles on beam vibrations [6-8] also contain some useful information.

The theory of curved bars is an extremely complicated one in the context of the three dimensional theory of nonlinear elasticity. As in the technical theories of straight beams, simplifying assumptions are made in describing the deformation so as to reduce the problem to a one dimensional form. The Euler-Bernoulli hypothesis of plane cross sections remaining plane after deformation is a case in point. It is known that the shear stress distribution across the cross section is nonuniform. Theories that do not account for a nonuniform variation of the through-thickness shear stress use a shear correction factor depending on the cross section in order to compensate for the errors introduced. One drawback of all the theories involving torsion lies in the twisting moment-twist relation which is based on the torsional stiffness obtained from a study of the static torsion problem of a straight cylindrical rod of identical cross section as the bar under consideration. In spite of all these limitations, it has been found that reasonably accurate results can be obtained from the theories developed in the aforementioned fashion.

The most general problem in free vibration of plane curved beams involves in-plane, out-of-plane, coupled motions consisting of extension, flexure, shear and twist. However, if the plane containing the centerline of the undeformed beam axis is a principal plane of the cross section at every point along the bar and also a plane of material symmetry, the in-plane and out-of-plane motions uncouple. In the case of a beam made of laminated composite material, for example, this uncoupling may or may not occur depending on the orientation of the

Transmitted by Associate Editor Patricio AA Laura.

ASME Reprint No AMR132 $18

laminates. The in-plane motion consists primarily of bending-extensional modes, while the out-of-plane motion is essentially bending-twisting dynamics.

Although the spatial motion of planar curved beams involves all the free vibration modes in varying proportions, the lowest natural frequency is predominantly flexural. Thus, many of the early investigators have used the inextensionality condition, wherein the length of the centerline of the beam is assumed to be invariant during deformation. Such a constraint condition typically simplifies the analysis and is acceptable in many practical problems wherein the extensional modes correspond to much higher frequencies. The classical theory ignores the effects of shear deformation and rotary inertia, both of which tend to decrease the natural frequencies. Classical boundary conditions refer to either hinged (simply supported), clamped or free ends.

Because the topic of this compilation is pursued by people with diverse backgrounds, the literature is replete with technical information from allied fields such as wave propagation, thin walled beams, shells, computational methods, mathematical theory of rods and other related areas. It was therefore necessary to present a somewhat restricted view of the field in sufficient detail for the survey to be reasonably comprehensive without being unduly lengthy. Consequently, the scope of this review has been to a large extent influenced by the technical interests of the authors.

IN-PLANE VIBRATIONS

The in-plane vibrations have been studied with theories for thin curved bars as well as ones for thick curved bars. Invariably, the majority of the existing theories are based on the Euler-Bernoulli hypothesis of plane cross-sections remaining plane during deformation, which applies to thin curved bars. It is rather difficult to have a sharp demarcation between thin and thick bars purely on the basis of physical dimensions. It is accepted practice, though, to refer to a ring as thin when the ratio of the radius of curvature to the in-plane thickness is greater than about 10. The thin curved bar approximation has as its essential ingredient the carry over of the moment-curvature relationship used in the technical theory of straight beams. Further, the centroidal axis and the neutral axis are assumed to coincide.

Consider the curved bar shown in Fig 1. The x and z axes are principal axes of the cross section at the centroid, with the z axis lying in the plane of initial curvature. The normal component of the displacement of the centroidal axis is w, while the tangential component is v. Both v and w are functions of s, the arc length measured along the centroidal axis from a fixed reference point as shown in Fig 1. Due to in-plane vibrations, the stress resultants at any cross section consist of a normal force N arising out of the normal stresses at the section, a shearing force Q_z that is the resultant of the distributed shear stresses across the section, and a bending moment M_x that is the moment resultant with respect to the centroidal axis of the normal stresses. The positive senses for all the quantities are as indicated in the figure. The radius of curvature ρ is assumed to be a function of s, i.e., $\rho = \rho(s)$. Further, the area of cross section is denoted by $A=A(s)$, the mass density (mass per unit volume) by $m=m(s)$, and the second moment of the area of cross section about the x axis by $I_x = I_x(s)$. The material of the bar is assumed to be linearly elastic with Young's modulus E and shear modulus G. As in Timoshenko beam theory, the total rotation of the centroidal axis (denoted by ω) is assumed to be composed of a part due to bending (denoted by ψ) and a part due to transverse shear effects.

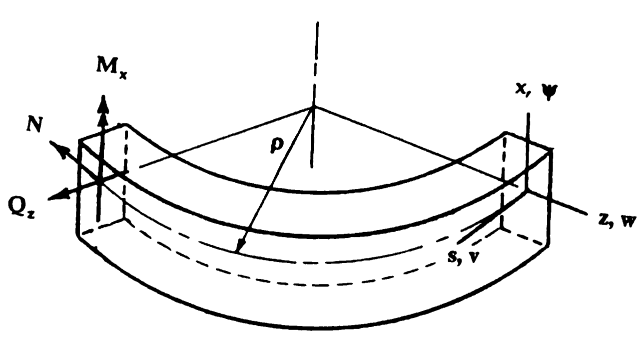

FIG 1. Curved beam coordinates and stress resultants for in-plane vibration.

Application of Newton's second law yields the following three differential equations, with primes denoting derivatives with respect to the arc length s and dots denoting time derivatives:

$$N' + \frac{Q_z}{\rho} = mA\ddot{v}, \tag{1a}$$

$$Q_z' - \frac{N}{\rho} = mA\ddot{w}, \tag{1b}$$

$$M_x' + Q_z = mI_x\ddot{\psi}. \tag{1c}$$

For small motions, the extensional strain (ε) and the rotation (ω) of the centroidal axis are given by:

$$\varepsilon = v' + \frac{w}{\rho}, \quad \omega = w' - \frac{v}{\rho}. \tag{2a, 2b}$$

Assuming a linearly elastic material, the normal force N is linearly related to ε, while the bending moment is proportional to the change in curvature as in the technical theory of beams. The shear force-shear strain relation is the familiar one from Timoshenko beam theory, with κ being the shear coefficient of the cross-section. Thus,

$$N = EA\varepsilon = EA\left(v' + \frac{w}{\rho}\right), \tag{3a}$$

$$Q_z = \kappa AG(\omega - \psi) = \kappa AG\left(w' - \frac{v}{\rho} - \psi\right), \tag{3b}$$

$$M_x = EI_x\psi'. \tag{3c}$$

Bresse [9] derived essentially the same equations as the ones presented above more than a century ago. Most of the work on purely in-plane motions of thin rings and curved beams are based on these equations, and sometimes under more restrictive conditions. Thus, by letting $G \to \infty$ in (3b) (no shear deformation) and $mI_x \to 0$ in (1c) (no rotary inertia), one gets the classical theory of extensional deformations with the equations of motion:

$$N' - \frac{M_x{}'}{\rho} = mA\ddot{v} \tag{4a}$$

$$-M_x{}'' - \frac{N}{\rho} = mA\ddot{w} \tag{4b}$$

where N is related to the displacement components v and w as in (3a), and M_x is given by

$$M_x = EI_x\left(w' - \frac{v}{\rho}\right)' \tag{5}$$

Although $\omega \to \psi$, because $G \to \infty$ in (3b) the shear force Q_z is finite. Waltking [10], obtained the above equations for the symmetric and antisymmetric extensional modes of hinged uniform circular arches. Adding the constraint of inextensionality, viz.,

$$\varepsilon = v' + \frac{w}{\rho} = 0, \tag{6}$$

one gets a sixth order equation in the tangential displacement v identical to the one developed by Hoppe [11], Federhofer [12] and Love [13]:

$$\frac{\partial^6 v}{\partial\theta^6} + 2\frac{\partial^4 v}{\partial\theta^4} + \frac{\partial^2 v}{\partial\theta^2} = \frac{mAR^4}{EI_x}\left(\frac{\partial^2 v}{\partial t^2} - \frac{\partial^4 v}{\partial\theta^2\partial t^2}\right) \tag{7}$$

where $\rho = R$ is the constant circular radius and $s = R\theta$. For a closed ring, displacements must be periodic in θ. Thus, one may assume a solution to (7) as:

$$v = C\cos n\theta \sin(\omega t + \gamma) \tag{8}$$

where n is an integer, ω is the free vibration frequency, C is an amplitude coefficient and γ is an arbitrary phase angle, with C and γ being determined by initial conditions. Substituting (8) into (7), one obtains the frequency equation derived by Hoppe [11],

$$\lambda^2 = \frac{n^2(n^2-1)^2}{n^2+1}, \tag{9}$$

where λ is a nondimensional frequency parameter defined by

$$\lambda = \omega R^2\sqrt{\frac{mA}{EI_x}} \tag{10}$$

Some of the other early works that treat thin rings are those of Rayleigh [14], Love [15] and Lamb [16]. Carver [17] considered bending-extensional coupling and found no significant variation in his results between thin and thick rings. Morley [18] presented the free vibration frequencies of the first ten symmetric and antisymmetric modes of a thin ring neglecting centerline extension. Archer [19] and Clayton and Royster [20] studied the damped inextensional vibrations of thin circular rings and outlined a solution procedure for time dependent displacement end conditions based on the Mindlin Goodman technique [21].

The equations of motion of rings and arches have also been obtained from plate and shell theory [22-28]. Ambati et al [29] analyzed the in-plane vibrations of an annulus of which the thin ring is a special case. Liu and Langhaar [30] examined the dilatationless circumferential ring vibration modes wherein the deformations of all cross sections are identical. Experimental data on circular rings can be found in [31-33]. Based on the eigenvalue problem for rectangular cross section thick rings, Lecoanet and Piranda [34] investigated the frequencies and modes of thick rings whose cross sections can be broken up into rectangles. Support motion problems have also received some attention in the literature [35-38]. A number of other authors have also analyzed thin rings [39-65].

For curved bars which are not complete rings, the inextensional theory is not adequate for determining in-plane vibrational behavior. Consider a circular arch subtended by an angle 2α, having appropriate boundary conditions at the ends $\theta = \pm\alpha$. Using the inextensional theory, one assumes

$$v(\theta, t) = V(\theta)\sin(\omega t + \gamma), \tag{11}$$

obtains a general solution to the ordinary differential equation in V resulting from (7), and applies the boundary conditions to obtain the frequency determinant. The extensional theory is obtained by not assuming $\varepsilon = 0$ in (6), but by substituting (5) into (4) to yield a set of coupled equations of motion in v and w. For circular curvature $\left(\rho = R, \frac{d}{ds} = \frac{1}{R}\frac{d}{d\theta}\right)$, they are [66]:

$$\left(1+k^2\right)\frac{\partial^2 v}{\partial\theta^2} + \left(-k^2\frac{\partial^3}{\partial\theta^3} + \frac{\partial}{\partial\theta}\right)w = \frac{mR^2}{E}\frac{\partial^2 v}{\partial t^2} \tag{12a}$$

$$\left(-k^2\frac{\partial^3}{\partial\theta^3} + \frac{\partial}{\partial\theta}\right)v + \left(k^2\frac{\partial^4}{\partial\theta^4} + 1\right)w = -\frac{mR^2}{E}\frac{\partial^2 w}{\partial t^2} \tag{12b}$$

where $k^2 = I_x/AR^2$. An exact solution of (12) may be obtained, and boundary conditions applied, to yield a proper frequency determinant.

Figure 2 shows nondimensional frequency parameters λ for circular arches of rectangular cross-section having both ends clamped ($v = w = \frac{\partial w}{\partial\theta} = 0$ at $\theta = \pm\alpha$), with varying arc segment half-angle, α. The thickness-to-mean radius ratio (h/R) is 0.1. The first four frequencies are given for both the inextensional and extensional theories described above. This corresponds to two symmetric and two antisymmetric modes for each theory. For the antisymmetric modes, it is seen that the inextensional and extensional results agree closely (but not exactly). Thus, the axial deformation required by the antisymmetric modes is small. However, the frequencies predicted by the two theories are observed to be greatly different for the symmetric modes, for $\alpha < 60°$ in the case of the first

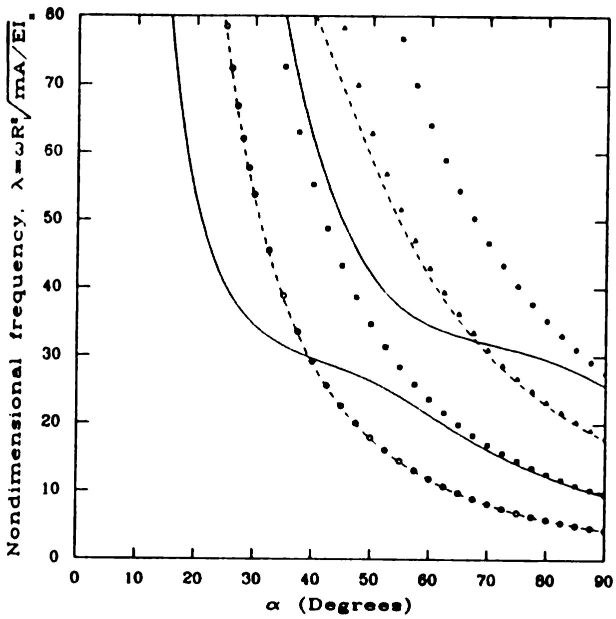

symmetric modes 1 &2 (extensional)
antisymmetric modes 1 &2 (extensional)
modes 1-4 (inextensional)

FIG 2. Nondimensional frequency versus arc segment half-angle for clamped circular arches (h/R=0.1).

mode, and $\alpha < 90°$ (the semicircular arch) for the second mode. As expected, the frequencies from the extensional theory are less than the inextensional ones, for the constraint of no axial deformation is relaxed. However, for $\alpha = 25°$, Fig 2 shows the fundamental (lowest frequency) value of λ for the inextensional theory to be approximately twice that of the more accurate, extensional theory. For shallower arches, and for higher modes, the disparity becomes even greater. For $\alpha > 90°$, frequencies of the two theories approach each other, becoming equal at $\alpha = 180°$ (the full circle).

Figure 3 shows similar results for arches having both ends pinned ($v = w = M_x = 0$ at $\theta = \pm\alpha$). The frequencies are all considerably less than those of the previous clamped arches. Again, the antisymmetric mode frequencies from the two theories agree closely, but the symmetric mode frequencies may differ greatly. The differences are seen to be greater for the pin supported ends than for the clamped ends.

For thinner arches, agreement between the two theories is closer, as may be seen for the data shown in Fig 4 for pinned arches having h/R=0.01. Nevertheless, as the arches become shallower, the symmetric mode frequencies disagree considerably.

It is well known that the effects of shear deformation and rotary inertia are to decrease the natural frequencies and that these effects are very important with a short and stubby bar. Federhofer [67] considered the influence of centerline stretching, she[...]rmation and rotary inertia on the natural freq[...]ing vibrations of circular rings. Philipson [...]e inextensibility assumption for the flexur[...]hin rings by extending Love's [13] ana[...]ne effect of rotary inertia and centerli[...]ound the extensibility effects to be negl[...]] derived the equations of motion for a circular bar considering shear deformation, rotary inertia and stretching of the neutral axis. Austin and Veletsos [70] and others [71-75] examined the influence of shear deformation and rotary inertia on the free vibration characteristics of arches. Based on the numerical results in [70], it was concluded that the free vibration modes can be classified as mainly inextensional with flexural-shearing coupling, mainly extensional with rotary inertia and shear deformation having insignificant participation, and a

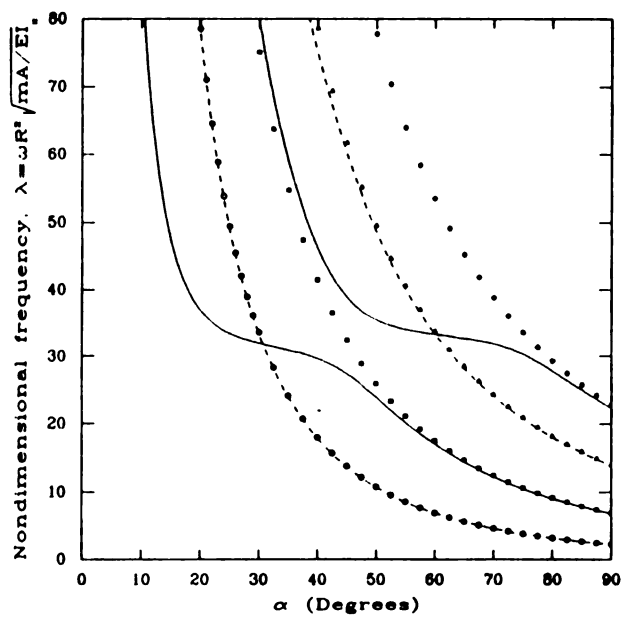

symmetric modes 1 &2 (extensional)
antisymmetric modes 1 &2 (extensional)
modes 1-4 (inextensional)

FIG 3. Nondimensional frequency versus arc segment half-angle for pinned circular arches (h/R=0.1).

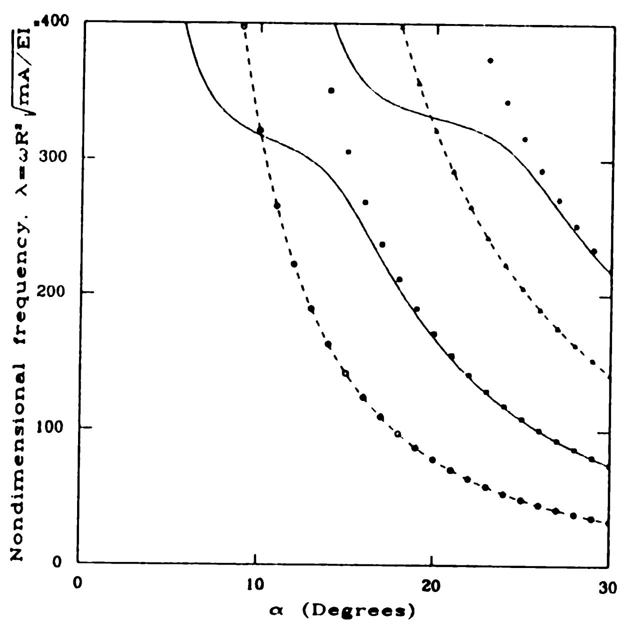

symmetric modes 1 &2 (extensional)
antisymmetric modes 1 &2 (extensional)
modes 1-4 (inextensional)

FIG 4. Nondimensional frequency versus arc segment half-angle for pinned circular arches (h/R=0.01).

combination of these two types of behavior.

The thick ring theories differ from one another with regard to the through-thickness strain distribution. The description of the strain variation across the cross section has in fact been a difficult task even with straight rods [76]. Buckens [77] studied the influence of radial thickness on the natural frequencies of a ring considering the effect of shear and extension and concluded shear to be a significant factor affecting free vibration frequencies compared to rotary inertia and curvature, with extensibility playing a negligible role. Seidel and Erdelyi [78] derived the characteristic equation for the free vibration frequencies of thick rings considering transverse shear, rotary inertia and extensibility effects by formulating the Lagrangian. The normal strain variation across the cross section was assumed to be nonlinear and an average shear angle was used. It was shown that consideration of extensibility effects could lead to certain computational difficulties. Their frequency equation for inextensional deformation reads:

$$k^6\lambda^4 - k^2\left(\frac{e}{R}n^2 + \kappa\frac{G}{E} + \kappa\frac{G}{E}\frac{\left(n^2-1\right)^2}{\left(n^2+1\right)}k^2\right)\lambda^2 + \kappa\frac{G}{E}\frac{n^2\left(n^2-1\right)^2}{\left(n^2+1\right)}\frac{e}{R} = 0 \qquad (13a)$$

$$\text{where}\quad \frac{e}{R} = 1 - \frac{h/R}{\ln\left(2+\frac{h}{R}\right) - \ln\left(2+\frac{h}{R}\right)}, \qquad \frac{h}{R} < 2, \qquad (13b)$$

$$k^2 = \frac{I_x}{AR^2} = \frac{1}{12}\left(\frac{h}{R}\right)^2. \qquad (13c)$$

where h is the radial thickness of the ring, κ is the shear correction factor and λ is as given in (10).

Kirkhope [79] obtained an approximate frequency expression for thick circular rings using the Rayleigh method and assessed its accuracy with the experimental results of Kuhl [80] and Lincoln and Volterra [81]. This simple expression reads:

$$\lambda^2 = \frac{n^2\left(n^2-1\right)^2}{\left(n^2+1\right)}\frac{1}{1+n^2\alpha}, \qquad (14a)$$

$$\text{where}\quad \alpha = \frac{I_y}{AR^2}\frac{E}{G}\frac{1}{\kappa}. \qquad (14b)$$

Kirkhope [82] also derived a cubic frequency equation for the in-plane motion of a thick circular ring, the three roots corresponding to flexural, extensional and shear modes. The computed frequencies were again compared with the experimental results in [80] and [81]. Rao and Sundararajan [83] developed inextensional equations of motion for circular rings considering shear deformation and rotary inertia. Their frequency equation was:

$$\left(n^2+1\right)\frac{E}{\kappa G}k^4\lambda^4 - \left(k^2\left(n^2-1\right)^2 + \frac{E}{\kappa G}k^2n^2\left(n^2+1\right) + \left(n^2+1\right)\right)\lambda^2 + n^2\left(n^2-1\right)^2 = 0 \qquad (15)$$

A comparison of some of the various theories described above for a complete circular ring of rectangular cross section is presented in Fig 5 for the lowest frequency (n=2). The abscissa represents the ratio of thickness to radius of curvature (h/R). Representative values of the shear correction factor $\kappa = 5/6$ and the Poisson ratio $\nu = 0.29$ were used in plotting.

Gardner and Bert [84] proposed another theory for shear deformable rings and curved beams. The through thickness shear strain distribution was chosen to satisfy the zero shear conditions on the inner and outer boundaries of the ring. Natural frequencies predicted by this theory were compared with their own experimental results and also with other analytical and experimental results reported in the literature. Suzuki [85], in an attempt to improve the accuracy of existing solutions, considered the effect of cross section warping on in-plane vibrations. According to his conclusion, it is possible to improve solution accuracy by considering section warping.

A number of studies aimed at computing the natural frequencies of arcs (or ring segments) based on the Rayleigh-Ritz and related methods have been reported [86-96]. Takahashi [97] obtained the equations of motion governing the radial and tangential displacements of a thin circular arc bar by minimizing the Lagrangian of the system. With his coworkers [98] he conducted an analytical and experimental investigation of the in-plane vibration of curved bars of elliptic and sinusoidal

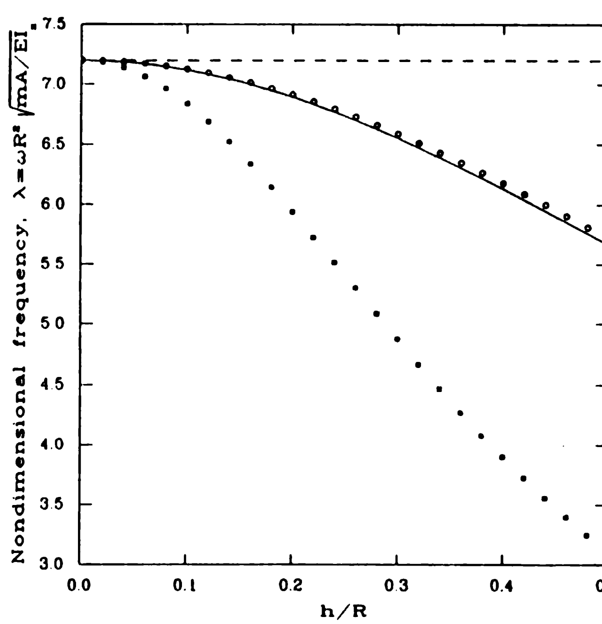

——— Seidel & Erdelyi [78] and Kirkhope [82]
------- Hoppe [11]
o Kirkhope [79] • Rao & Sundararajan [83]

FIG 5. Fundamental vibration frequency of a full circular ring.

centerlines, considering the effects of bending and extension. Suzuki et al [99] studied the free vibration of curved beams neglecting the effect of shear deformation and rotary inertia. Results were presented for clamped symmetric arcs with sinusoidal, catenary, hyperbolic, parabolic and cycloidal centerlines and for an asymmetric elliptic arc bar with both ends clamped. Suzuki and Takahashi [100] in a subsequent publication, used the Timoshenko theory to compute the natural frequencies and modes of clamped and hinged elliptic arc bars. A comparison was made with the classical theory to assess the relative importance of the shear and rotary inertia terms. Lee and Wilson [101] derived governing equations for the in-plane motions of arches of arbitrary centerline accounting for bending, extension and rotary inertia. Shear deformation was neglected. The lowest three natural frequencies of parabolic, sinusoidal and elliptic arcs under hinged and clamped end conditions were presented. The effect of rotary inertia on the frequencies was examined. Experimental data were reported to support the numerically generated results.

Discretization procedures [102-104] have been used to study the in-plane motions of a thin curved rod. Rings on multiple supports are considered in [105-110]. Vibrations of continuous and multisupported curved beams [111-122] have been pursued by some researchers. Finite difference schemes have been employed in the study of in-plane vibrations [123-126]. The vibrations of slightly curved (very shallow) beams were studied [127-132]. Nagaya [133] studied the in-plane vibration of thick-walled pipes and rings of arbitrary shape by solving the equation of motion of elastic solids under plane strain conditions.

The free vibrations of rings and arches with varying cross section has been the subject of numerous investigations [134-148]. Suzuki and Takahashi [134] derived the equations of motion based on classical theory for the in-plane vibrations of a curved bar with varying cross section using the Lagrangian approach. They presented extensive results for the natural frequencies and mode shapes of clamped and hinged symmetric elliptic arc bars, with thickness varying quadratically as $h = h_o(1 + ks^2)$. Lecoanet and Piranda [136] examined the in-plane vibrations of circular rings of radially variable thickness using the Galerkin method. They used the eigenfunctions of a constant thickness ring as trial functions and noticed good agreement with experimental data. Rutledge and Royster [137,138] developed mathematical models for the free vibrations of arcs of arbitrary shape and varying cross section. Royster [139] presented the fundamental extensional frequency of a clamped circular arc with a linear taper normal to the plane of the arc. Suzuki et al [140] deduced the equations of motion of inhomogeneous curved bars with varying cross sections and curvatures from the Lagrangian. Natural frequencies and modes for circular and elliptic arc bars with clamped and clamped-free ends were presented. Extensive studies have been made by Laura and his colleagues [141-155]. A number of these [141-145] use approximate methods to analyze the in-plane vibrations of variable cross section rings and arcs. Others [149-156] deal with the in-plane vibrations of curved beams and arcs with attached concentrated masses. Research has also been conducted on the vibrations of rings with irregularities and deviations [157-161] from perfect axisymmetry. Spline interpolation [162] and transfer matrix techniques [163-166] have been used. Forced vibration problems have also been attempted [167-178]. Vibrations of beams on foundations, and viscoelastic and composite curved beams [180-198] are also studied in the literature.

OUT-OF-PLANE VIBRATIONS

As shown in Fig 6, the out-of-plane motion is described by the displacement u, the bending rotation ς and the twist angle ϕ. Q_x and M_z are the out-of-plane shear force and bending moment, respectively, and M_t is the twisting moment. I_z is the second moment of the cross sectional area about the z axis and J is the polar moment. Newton's Laws give

$$Q_x' = mA\ddot{u}, \tag{16a}$$

$$-M_z' + \frac{M_t}{\rho} - Q_x = mI_z\ddot{\varsigma}, \tag{16b}$$

$$M_t' + \frac{M_z}{\rho} = mJ\ddot{\phi}. \tag{16c}$$

The stress resultants and displacements are related as follows:

$$Q_x = \kappa GA(u' - \varsigma), \tag{17a}$$

$$M_z = -EI_z\left(\varsigma' + \frac{\phi}{\rho}\right), \tag{17b}$$

$$M_t = C\left(\phi' - \frac{\varsigma}{\rho}\right). \tag{17c}$$

where C is the torsional stiffness coefficient.

Michell [199] developed the frequency equation for out-of-plane ring vibrations using classical theory. Love [15] gave frequency formulas for thin rings neglecting rotary inertia and shear deformation. Volterra [200,201] used the method of internal constraints to develop equations of motion of curved bars and discussed a solution methodology [202] for these equations based on that of a straight bar. Federhofer [203] derived an exact frequency equation for the lowest natural frequency of clamped arches. Brown [204] used the Rayleigh method for a clamped arch. Nelson [205] employed the Rayleigh-Ritz method for doubly symmetric thin circular ring segments, neglecting rotary inertia and shear deformation. Ojalvo [206] considered the out-of-plane twisting-bending dynamics of

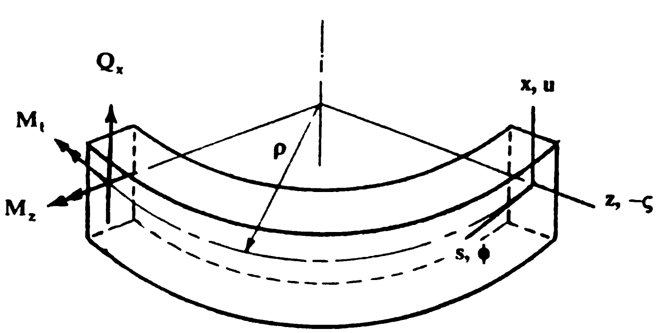

FIG 6. Curved beam coordinates and stress resultants for out-of-plane vibration.

clamped circular ring segments based on classical theory. Takahashi [207] obtained frequency equations for a circular arc with clamped and free ends considering rotary inertia, but not shear deformation. Kirkhope [208] and Rao [209] included shear deformation to develop equations of motion for thick circular rings. Irie et al [210] computed the natural frequencies of circular arcs vibrating out of the plane of curvature, for all combinations of classical boundary conditions, including shear deformation effects. Endo and Taniguchi [211] analyzed the in-plane flexural and out-of-plane twist bending vibrations of rings with cross sections having a single axis of symmetry. All these investigations neglected cross sectional warping and the variation of curvature through the thickness ($\rho^* = \rho + z$). Bickford and Maganty [212] developed equations of motion for symmetric cross section thick rings, accounting for curvature variation through the thickness and supported their frequency predictions with the experimental data of Kuhl [80].

Curved plates and plate-like theories for curved beams have also come under scrutiny [213-215]. Shell theories have been used to model ring vibrations [216,217]. Chang and Volterra [218,219] employed differential operator theory to assess the upper and lower bounds for the first four natural frequencies of elastic clamped and simply supported arcs. They considered centerlines in the form of circles, cycloids, catenaries and parabolas. Takahashi and Suzuki [220] studied the vibrations of elliptic arc bars. Suzuki and coworkers [221,222] obtained governing equations for the out-of-plane vibrations of plane curved bars of arbitrary centerline profile, based on both the classical and the shear deformation theory. Frequencies and mode shapes were given for clamped bars with centerlines in the form of ellipses, sines, catenaries, hyperbolas, parabolas and cycloids. Silva and Urgueira [223] developed tip dynamic stiffness matrices for a free-free curved beam, incorporating shear deformation and rotary inertia in their analysis. Model validation based on experimental results was also discussed. Curved beams with nonuniform cross section [224-226] have been studied. Reddy [227] used a lumped mass approach for out-of-plane vibrations. Free and forced vibration problems have been attempted using the transfer matrix approach [228-232]. Suzuki et al [233] investigated the out-of-plane, steady-state response of curved bars. Impulse response due to dynamic loads on bars and rings have been studied [234-236]. Joseph and Wilson [237] investigated the dynamic response of curved beams with moving loads. Elastically supported curved beams [238-240] and continuous curved beams [241-245] have also received some attention. More information is available in [246-253].

COUPLED VIBRATIONS

The coupled motion between in-plane and out-of-plane displacements gives rise to a twelfth order set of equations of motion and six boundary conditions at each end of the beam. Thus, in general, the free vibration problem yields a twelfth order frequency determinant, whose solution corresponds to two bending modes, a twisting mode, an extensional mode and two shearing modes if the displacements were to uncouple. However, in general, the motion is completely coupled. A derivation of the governing equations for the coupled motions of a thin curved bar are outlined in this section. The coordinate axes along with the displacement and stress resultant components are as indicated in Figs 1 and 6, except that x and z are now principal axes of inertia of the cross section. In general, the z-axis will not lie in the initial plane of curvature. Let the angle between the inward principal normal to the centerline and the z-axis be $\chi = \chi(s)$. Rotation angles about the x, s and z coordinates are ψ, ϕ and $-\varsigma$, respectively, as used in the previous two sections dealing with uncoupled motions. The displacement components u, v and w describe the motion of a point on the centerline (locus of centroids). Displacement and rotation components u, v, w, ψ, ϕ, and ς are functions of s. It is assumed that the displacements are small, and that plane cross sections remain plane during deformation. Thus cross sectional warping due to torsional motions is ignored.

The equations for the coupled motions of a curved and pretwisted bar were obtained by Washizu [254]. In the following, these results are presented for the case of no pretwist. The displacement components of any point in the bar denoted by U, V and W satisfying these requirements are given by:

$$U(s,t) = u(s,t) + z\phi(s,t), \tag{18a}$$
$$V(s,t) = v(s,t) - x\varsigma(s,t) - z\psi(s,t), \tag{18b}$$
$$W(s,t) = w(s,t) - x\phi(s,t). \tag{18c}$$

Based on this, it can be shown that the strain components for small motions are given by:

$$\varepsilon_y = 0,\ \varepsilon_z = 0,\ \varepsilon_{yz} = 0, \tag{19a-19c}$$

$$\varepsilon_s = \left(v' - \frac{\cos\chi}{\rho}w + \frac{\sin\chi}{\rho}u\right) + x\left(-\theta' - \chi'\psi + \frac{\cos\chi}{\rho}\phi\right) - z\left(\psi' - \frac{\sin\chi}{\rho}\phi - \chi'\theta\right) \tag{19d}$$

$$\varepsilon_{xs} = \frac{1}{2}\left[\left(u' - \frac{\sin\chi}{\rho}v + \chi'w - \theta\right) + z\left(\phi' + \frac{\cos\chi}{\rho}\theta + \frac{\sin\chi}{\rho}\psi\right)\right] \tag{19e}$$

$$\varepsilon_{zs} = \frac{1}{2}\left[\left(w' + \frac{\cos\chi}{\rho}v - \chi'u - \psi\right) - x\left(\phi' + \frac{\cos\chi}{\rho}\theta + \frac{\sin\chi}{\rho}\psi\right)\right] \tag{19f}$$

The only nonzero stress components in the case of a linearly elastic material with no Poisson effect are σ_s, σ_{xs} and σ_{zs}. The stress resultants are seen in Figs.1 and 6, and are given in terms of the stresses as:

$$Q_x = \int_A \sigma_{xs}dA, \qquad Q_z = \int_A \sigma_{zs}dA, \tag{20a,20b}$$

$$N = \int_A \sigma_s dA, \qquad M_x = -\int_A z\sigma_s dA, \tag{20c,20d}$$

$$M_z = \int_A x\sigma_s dA, \qquad M_t = \int_A (z\sigma_{xs} - x\sigma_{zs})\, dA. \quad (20e,20f)$$

In order to account for the variation of the shear strain across the cross section, a constant shear correction factor κ is introduced in the shear stress resultants. Evaluating the integrals given by (20a)-(20c) and incorporating the shear correction factor leads to:

$$Q_x = \kappa G A\left(u' + \chi' w - \frac{\sin\chi}{\rho} v - \varsigma\right), \quad (21a)$$

$$Q_z = \kappa G A\left(w' - \chi' u + \frac{\cos\chi}{\rho} v - \psi\right), \quad (21b)$$

$$N = EA\left(v' - \frac{\cos\chi}{\rho} w + \frac{\sin\chi}{\rho} u\right), \quad (21c)$$

The twisting moment-twist relationship, with C denoting the torsional stiffness of the section, and the bending moment-curvature change relations are:

$$M_t = C\left[\phi' + \frac{\cos\chi}{\rho}\varsigma + \frac{\sin\chi}{\rho}\psi\right], \quad (21d)$$

$$M_x = EI_x\left[\psi' - \chi'\varsigma - \frac{\sin\chi}{\rho}\phi\right], \quad (21e)$$

$$M_z = EI_z\left[-\varsigma' - \chi'\psi + \frac{\cos\chi}{\rho}\phi\right]. \quad (21f)$$

The equations of motion can be shown to be:

$$Q_x{}' + \chi' Q_z - \frac{\sin\chi}{\rho} N = mA\ddot{u}, \quad (22a)$$

$$N' + \frac{\sin\chi}{\rho} Q_x - \frac{\cos\chi}{\rho} Q_z = mA\ddot{v}, \quad (22b)$$

$$Q_z{}' - \chi' Q_x + \frac{\cos\chi}{\rho} N = mA\ddot{w}, \quad (22c)$$

$$-M_z{}' + \chi' M_x - \frac{\cos\chi}{\rho} M_t + Q_x = mI_z\ddot{\varsigma}, \quad (22d)$$

$$M_x{}' + \chi' M_z - \frac{\sin\chi}{\rho} M_t + Q_z = mI_x\ddot{\psi}, \quad (22e)$$

$$M_t{}' + \frac{\sin\chi}{\rho} M_x - \frac{\cos\chi}{\rho} M_z = mJ\ddot{\phi}. \quad (22f)$$

Substituting Eqs (21) into (22) yields a twelfth order system of differential equations in terms of the displacement components u, v, w and the rotation components ψ, ϕ and ς. It can be shown that Eqs (22a)-(22f) uncouple when $\chi = 180^\circ$ and the equations of motion for in-plane and out-of-plane vibrations presented previously may be recovered.

Endo [255], Hawking[illegible]6], Kirkhope et al [257] and Hammoud and Arch[illegible] analyzed unsymmetrical cross section ring[illegible] [illegible]lane and out-of-plane motions coupled. [illegible] 259,260] developed a generalized shear [illegible]y valid for thick and thin rings of circular centerline; with the classical thin ring theory and the shear deformation theory as special cases. Williams [261], in a well written paper, deduced the equations of motion for small motions of a circular ring of thin open cross section including the effects of warping deformations. Natural frequencies and mode shapes of both complete and incomplete rings were presented.

VIBRATIONS UNDER INITIAL STRESSES

Figure 7 shows a curved beam or arch subjected to components of normal (q) and tangential (p) static loading distributed along its length. In general, the magnitudes of the loads vary along the length; i.e., q=q(s) and p=p(s). These loads cause a static axial force $N_o = N_o(s)$, which affects the free vibration frequencies and mode shapes. Generally, if N_o is tensile, the frequencies are increased. If it is compressive, they are decreased. At a limiting (critical) value of N_o the fundamental frequency is reduced to zero. This corresponds to bifurcation buckling. Thus, it is possible to predict the fundamental buckling load based on a linearized free vibration analysis about a prestressed equilibrium state, and this procedure forms a convenient means of experimentally determining the buckling load by extrapolating the load-frequency curve.

Although a literature search has uncovered well over 100 published references dealing with the buckling of rings and arches [66], little research has taken place on the vibrations of loaded rings and arches. The theory is more intricate than that for unloaded configurations, for one must derive equations of motion based upon small displacements (to obtain a linear eigenvalue problem) away from an initial, loaded equilibrium state.

For an arch that is free to execute both in-plane and out-of-plane motions, the free vibration frequency and critical load associated with the out-of-plane motions may be considerably lower than those for in-plane motions [262], depending upon the aspect ratio of the cross section and the boundary conditions. Wasserman [263] examined the effect of hydrostatic loads, dead loads and centrally directed pressure loads on the frequencies of in-plane and out-of-plane vibrations of circular rings. Centerline extensibility was not considered. Exact and approximate expressions for the frequencies and critical loads of arches, considering end support flexibility have been obtained [264]. The effect of an elastic foundation on the free vibration frequency of a shallow arch subjected to a thrust load was analyzed by Plaut and Johnson [265]. Perkins [266] used a model for the in-plane behavior that accounts for geometric

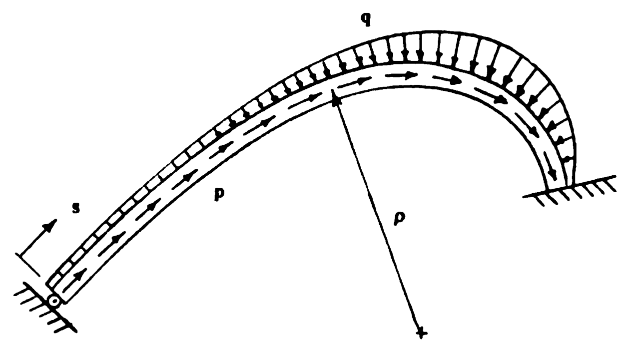

FIG 7. Curved beam under initial stresses.

nonlinearity in the extension and bending terms. The linear vibration problem about the equilibrium configuration was solved numerically for the free vibration frequencies and modes. Comparison of experimental data with theoretical results showed fairly good agreement. Lin and Soedel [267] developed the equations of motion for the general in-plane motion of rotating thick and thin rings on elastic foundations and subjected to initial stresses. They used the nonlinear strain displacement relations to form the energy terms. The simplified ring theories were recovered by imposing constraint conditions and eliminating the Lagrange multiplier. It was also shown that extensional coupling effects could be as significant as shear effects in the case of thick rings.

The effect of extensibility and initial equilibrium rotations on the in-plane stability and free vibrations under static preload, of thin curved beams of arbitrary centerline profile, have recently been analyzed [66]. Normally directed dead loads and gravity loading were considered. The rest of this section takes a closer look at the in-plane free vibration frequencies of loaded circular arches.

Extending the previously described inextensional and extensional theories for curved bars or arches to the loaded situation, it is possible again to obtain exact solutions for the free vibration frequencies and mode shapes of circular arches in the case of uniform normal loading. Fig 8 shows the variation in $\omega R^2\sqrt{mA/EI_x}$ with the nondimensional loading parameter $q_o R^3/EI_x$, where q_o is the uniform normal pressure (force/length) acting constantly in the radial direction, for an arch with both ends clamped, an arc segment $2\alpha = 80^o$ and a rectangular cross-section with a thickness ratio (h/R) of 0.1. The first four vibration frequencies are shown according to both the inextensional and extensional theories. As expected, positive (compressive) loadings cause decreases in the frequencies, and negative (tensile) loadings, which may be caused by uniform pressure on the underside of the arch, cause increases in the frequencies. The great differences previously seen in Fig 2 between the results from inextensional and extensional theories for the unloaded arch, are seen in Fig 8 to be magnified further by the loading.

The problem of the in-plane vibrations of rotating curved beams and rings [268-282] and the out-of plane motions of rotating curved beams [283-288] have also been studied. Additional information on the vibrations of loaded rings and arches can be found in [289-303].

NONLINEAR VIBRATIONS

Nonlinear vibration problems arise when the amplitude of motion cannot be considered to be small, or when the material behavior is nonlinear, or if nonlinear damping is present. Closed form solutions for nonlinear problems of continuous systems are extremely rare. A number of semianalytical techniques are in use that are capable of producing solutions of varied accuracy. One such approach is the assumed modes method that utilizes deflection shapes selected apriori. Alternatively, perturbation based methods are also employed.

Nonlinear free flexural vibrations of circular rings were examined by Federhofer [304]. Attempts have been made to characterize the nonlinear behavior of curved structural elements as having soft or hard spring responses. Many of these investigations were based on approximate solution techniques such as the assumed modes method. These methods can lead to an incomplete description of the frequency-amplitude relationship depending on the nature of the assumed solution. An interesting discussion can be found in [305]. A number of authors have addressed the free vibration of arches and rings [306-317]. Singh and Ali [310] discussed softening and hardening behavior in beams and curved members and also the transition between arches and curved beams. Simmonds [315] developed nonlinear equations for a ring and examined the frequency-amplitude dependence. The effects of extensibility, transverse shear and rotary inertia were found to be negligible and the nonlinearity was identified as a softening one. Maganty and Bickford [316] analyzed the nonlinear motions of thin circular rings by the method of multiple scales, neglecting shear deformation, rotary inertia and centerline stretching. The results for the nonresonant case demonstrated that the frequency of an out-of-plane bending mode is significantly reduced by the presence of a nonzero in-plane bending amplitude, whereas the results for the resonant case indicated the presence of unsteady oscillations with an exchange of energy between the in-plane and the out-of plane modes.

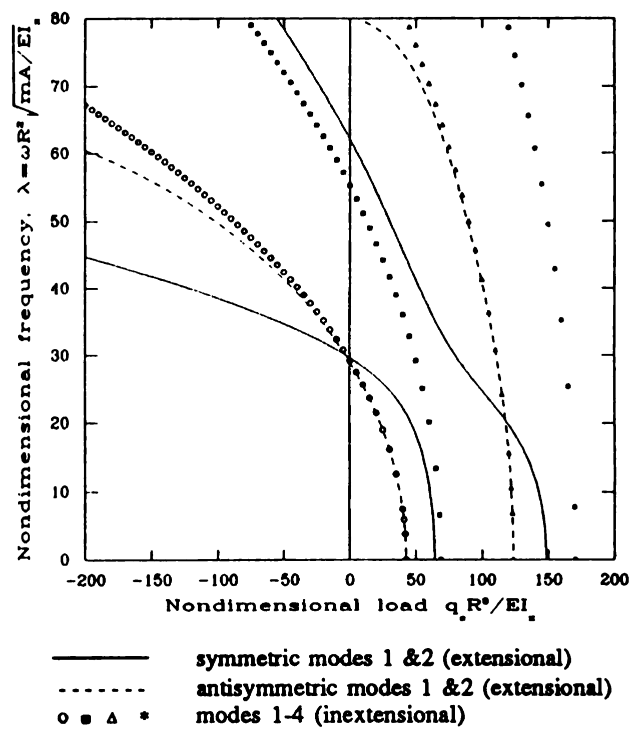

FIG 8. Load-frequency spectrum of a clamped circular arch under normal loading (h/R=0.1, $\alpha=40^o$).

Evensen [318-320] considered the in-plane response of thin circular rings with a nonlinear strain displacement relation to a harmonic excitation, both theoretically and experimentally. The inextensibility condition was used, which was later relaxed by Dowell [321] who found essentially identical results. Further information on nonlinear analysis and response evaluation can be found in [322-342].

FINITE ELEMENTS

The finite element method has been extensively used in the study of curved structures. Interest in developing curved beam elements was increased during the course of synthesizing shell elements. The curved beam element, being a one dimensional counterpart of the more complicated, two dimensional shell element offered simplicity and insight. Most of the investigations were limited to the in-plane motion of arches. It is not intended to describe the various stages in element synthesis that are usually associated with the solution of static problems. Rather, a very brief outline of the various elements that are being used, with particular attention to vibration problems will be presented.

The initial attempts at developing curved beam elements using low order independent interpolations for the in-plane displacements proved unsuccessful. Surprisingly, straight elements which do not account for flexural extensional coupling turned out to be more accurate than the curved elements in certain problems. The failure of these elements were incorrectly attributed to the inability of the assumed displacement fields to represent rigid body modes and constant strain states. Noor and Peters [343] found that the performance of displacement models based on independent low order interpolations (cubic or less) for displacement and rotation components deteriorated as the element became thin, and also in the limit of inextensional deformation. Later studies, however have shown that a spurious mechanism called shear locking was responsible for many such failures. Furthermore, selective integration procedures have been found to alleviate the difficulties. When an element cannot bend without being stretched, undesirable stiffness is added during bending, with subsequent loss of accuracy.

Dawe [344] conducted a numerical evaluation of various curved beam elements for the in-plane static problem. A wide variety of interpolation functions was used, based on both assumed strain distributions and independently interpolated displacement components of up to quintic order polynomials. Based on a study of both shallow and deep arches, it was concluded that the assumed strain models and the quintic-quintic displacement model performed well, while the performance of the low order independently interpolated displacement models degenerated as the arch became thin. Later, Prathap [345] used selective integration to rectify the poor performance of low order displacement models. Nonlinear finite elements, mixed, hybrid and penalty methods and the Timoshenko arch element have also received some attention.

There have been far more articles dealing with the application of finite element analysis for the in-plane vibration of arches [346-358] than with out-of-plane vibration [359,360]. Petyt and Fleischer [346] studied the radial vibrations of curved beams using three different elements. They obtained the most accurate results when both the normal and tangential displacements were approximated using polynomials of the same degree (cubic in their case). In a follow-up study [347], they presented finite element results and supported their findings on the basis of experimentation on multisupported curved beams. Sabir and Ashwell [348] conducted a convergence study on the frequency of free vibrations of thin and thick rings using four different elements. Davis et al [349] included the effects of transverse shear rotary inertia and centerline stretching in their element. An interesting feature of their formulation was that the displacement interpolations were obtained from the governing equations of static equilibrium, instead of assuming them outright. They used a similar technique for analyzing coupled twist bending vibrations [359]. Thomas and Wilson [360] utilized straight beam elements with six degrees of freedom per node to investigate the vibrational behavior of curved beams. Several previously cited research publications also use the finite element method for the vibration analysis of planar curved beams, rings and arches [187, 269, 270, 306, 314]. References [361-365] contain additional useful information.

OTHER RESEARCH ISSUES

During the course of this compilation, pertinent information on certain related topics including vibrations of thin walled curved beams [366-389], optimization problems [390-392], and vibrations of curved beams subjected to a temperature field [393,394] were also gathered. It is felt that this would constitute relevant information worth including for researchers in this field.

CONCLUDING REMARKS

Although the subject of curved beam vibrations had its beginnings in the nineteenth century, it was during the last two decades that the most progress, both in terms of theoretical developments as well as availability of engineering data, has been achieved. In spite of the purely academic motive behind some of the earlier publications, potential areas of engineering applicability do exist as described in the Introduction. Another incentive for such extensive research in this area stems from the interest in furthering the knowledge of the behavior of doubly curved structural elements like shells. The study of curved beams has in fact been thought to be an important first step in developing shell elements for finite element shell analysis as well as for an understanding of their nonlinear behavior.

The in-plane vibration problem has received considerably more attention than the out-of-plane and coupled problems. Most of the studies, have however been directed towards an understanding of the response of circularly curved beams, often under restrictive assumptions and classical boundary conditions. Experimental data is definitely lacking. Less has been accomplished for the vibrations of a general curved bar subjected to static loading, although curved bars with circular centerline have come under scrutiny. No studies have been found on the behavior of curved beams and rings subjected to acoustic excitation, although such studies do exist for shells. Thus, it is felt that research in this area will continue unabated for the near future.

One-dimensional (1-D) analysis of curved beams, rings and arches, upon which the foregoing review is based, requires kinematical assumptions about the behavior of cross-sections. These assumptions will be inaccurate for some situations, such as thick configurations. Further kinematic complications arise when coupling between in-plane and out-of-plane motions occurs. The accuracy of the one-dimensional theories may be tested in certain cases against more accurate 2-D models, such as shells. However, these models also require kinematic assumptions.

More accurate tests are potentially possible using 3-D, continuous system models, such as comparing frequencies with 3-D results for hollow cylinders [395-407]. However, accurate 3-D results are typically difficult to achieve with current numerical computation capabilities. Nonetheless, additional studies comparing numerical results obtained using 3-D elasticity with 1-D and 2-D models are needed to ascertain their ranges of validity.

REFERENCES

[1] Leissa, A W (1973) *Vibration of Shells*, NASA SP-288, U.S. Govt. Printing Office, Washington, D.C.

[2] Markus, S and Nanasi, T (1981) Vibration of curved beams, *Shock Vib Dig* 13(4) p 3-14

[3] Laura, P A A and Maurizi, M J (1987) Recent research on vibrations of arch-type structures, *Shock Vib Dig* 19(1), p 6-9

[4] Henrych, J (1981) *The Dynamics of Arches and Frames*, Elsevier Scientific Publishing Co., New York

[5] Royster, L H (May 1968) *Vibrations of curved beams*, Report, North Carolina State Univ,

[6] Sathyamoorthy, M (1982) Nonlinear analysis of beams; Part I: A survey of recent advances, *Shock Vib Dig* 14(8), p 19-35

[7] Sathyamoorthy, M (1982) Nonlinear analysis of beams; Part II: Finite Element Methods, *Shock Vib Dig* 14(9), p 7-18

[8] Wagner, H and Ramamurti, V (1977) Beam vibrations - a review, *Shock Vib Dig* 9(9), p 17-24

[9] Bresse, J A C (1859) *Cours de Mécanique Appliquée*, Second edition, Gauthier-Villars, Paris

[10] Waltking, F W (1934) Schwingungszahlen und Schwingungsformen von Kreisbogenträgern, *Ing Arch* 5, p 429-449

[11] Hoppe, R (1871) Vibrationen eines Ringes in seiner Ebene, *J für Reine und Angew. Math* (*Crelle's J*) 73, p 158-168

[12] Federhofer, K (1933) Biegungsschwingungen eines Kreisringes bei konstantem aussen- oder Innendrucke, *Ing Arch* Band 4, p 110-120

[13] Love, A E H (1944) *A Treatise on the Mathematical Theory of Elasticity*, Fourth Edition, Dover Publications Inc., New York

[14] Rayleigh, J W S (1945 re-issue) *Theory of Sound* Vol I, Second edition, Dover Publications, New York

[15] Love, A E H (1892-1893) On the vibrations of an elastic circular ring (Abstract), *Proc Lond Math Soc* 24, p 118-120

[16] Lamb, H (1888) On the flexure and the vibrations of a curved bar, *Proc Lond Math Soc* 19, p 365-376

[17] Carver, D R (1955) Extensional vibrations of rings, *Proc Second Midwestern Conf Solid Mech*, Purdue Univ, p 229-235

[18] Morley, L S D (1958) The flexural vibrations of a cut thin ring, *Quart J Mech Appl Math* 11 Part 4, p 491-497

[19] Archer, R R (1960) Small vibrations of thin incomplete circular rings, *Int J Mech Sci* 1(1), p 45-56. Also see *Int J Mech Sci* 1, 1966, p 132

[20] Clayton, M H and Royster, L H (1966) In-plane inextensional vibrations of a circular ring with a time-dependent displacement prescribed at the boundaries, *J Acoust Soc Am* 40(5), p 1039-1044

[21] Mindlin, R D and Goodman, L E (1950) Beam vibrations with time-dependent boundary conditions, *J Appl Mech* 17, p 377-380

[22] Veletsos, A S, Austin, W J, Pereira, C A L and Wung, S-J (1972) Free in-plane vibration of circular arches, *J Eng Mech* 98(EM2), p 311-329

[23] Mau, S T and Williams, A N (1988) Green's function solution for arch vibration, *J Eng Mech* 114(EM7), p 1259-1264

[24] Dym, C L (1980) On the vibration of thin circular rings, *J Sound Vib* 70(4), p 585-588

[25] Hirashima, K-I and Hirano, K (1990) Higher-order theories for free vibration analysis of circular rings, *JSCE* 416(I-13), p 201-204

[26] Callahan, W R (1965) Frequency equations for the normal modes of vibration for an elliptical ring, including transverse shear and rotary inertia, *J Acoust Soc Am* 37, p 480-485

[27] Brigham, G A (1973) Inplane free vibrations of tapered oval rings, *J Acoust Soc Am* 54(2), p 451-460

[28] Soedel, W (1981) *Vibrations of Shells and Plates*, Marcel Decker Inc., New York

[29] Ambati, G, Bell, J F W, and Sharp, J C K (1976) In-plane vibrations of annular rings, *J Sound Vib* 47(3), p 415-432

[30] Liu, C K and Langhaar, H L (1964) Dilatationless circumferential modes of vibration of a ring, *J Acoust Soc Am* 36(2), p 354-356

[31] Kaiser, E R (1953) Acoustical vibrations of rings, *J Acoust Soc Am* 25, p 617-623

[32] Bundy, F P and Bankes, C W (1942) The vibration characteristics of nearly-complete "free-free" circular rings, *J Appl Phys* 13, p 652-662

[33] Pliskin, W A, Edwards, J E and Bundy, F P (1943) The vibration characteristics of "free-free" circularly curved beams, *J Appl Phy* 14, p 410-417

[34] Lecoanet, H and Piranda, J (1979) Inplane vibrations of thick circular rings with T or I cross sections, *J Appl Mech* 46(2), p 470-472

[35] Mau, S T and Williams, A N (1988) Frequency response functions of circular arches for support motions, *Eng Struct* 10(4), p 265-271

[36] Mau, S T and Williams, A N (1987) Base excited motion of circular arches, Research Report No. UHCE 87-9, Dept. Civil Eng., Univ Houston, Houston, Texas

[37] Kim, C S and Dickinson, S M (1986) The flexural vibration of slightly curved slender beams subject to axial end displacement, *J Sound Vib* 104(1), p 170-175

[38] Bellow, D G and Semeniuk, A (1972) Symmetrical and unsymmetrical forced excitation of thin circular arches, *Int J Mech Sci* 14(3), p 185-195

[39] Zhukov, V B (1979) Vibrations of rings with circular cross section, *Str Matls* 10(11), p 1321-1327

[40] Zhukov, V B (1978) Oscillations of circular rings, *Prbl Prcochn* No. 11, p 69-73

[41] Zhukov, V B (1976) Calculation of rings with circular cross section, *Prbl Prcochn* No. 12, p 10-13

[42] Wang, J T S (1976) On the theories of ring vibrations, *J Appl Mech* 43, p 503-504

[43] Teichmann, D (1980) Schwingungen von Kreisringbalken (Vibrations of circular rings), *Z Angew Math Mech* 60(6), p T81-T84

[44] Lazarev, V I and Rushchak, V E (1983) Equations of circular-ring oscillations, *Str Matls* 14(12), p 1683-1687

[45] Endo, M (1971) Flexural vibration of a ring with arbitrary cross section (in Japanese), *Trans JSME* 37, p 1513-1521

[46] Endo, M and Taniguchi, O (1970) Flexural vibration of a ring (in Japanese), *Trans JSME* 36, p 2011-2019

[47] Teichmann, D (1979) Eigenfrequenzen von gekrümmten Balken mit variablem Krümmungsradius und Darstellung der Eigenformen in einem Trickfilm (Eigenfrequencies of curved beams with variable curvature radius and representation of the eigenmodes in a trick film), *Z Angew Math Mech* 59(5), p T155-T158

[48] Wuest, W (1949) Die Biegeschwingungen einseitig eingespannter gekrümmter Stäbe und Rohre (Bending-vibrations of curved rods and pipes clamped on one end), *Ing Arch* 17(4), p 265-272

[49] Lang, T E (July 1962) Vibration of thin circular rings Part I, Solutions for modal characteristics and forced excitation, Jet Propulsion Lab, Pasadena, California, TR No. 32-261

[50] Lang, T E (March 1963) Vibration of thin circular rings Part II, Modal functions and eigenvalues of constrained semicircular rings, Jet Propulsion Lab, Pasadena, California, TR No. 32-261

[51] Charnley, T and Perrin, R (1973) Perturbation studies with a thin circular ring, *Acustica* 28, p 139-146

[52] Federhofer, K (1950) *Dynamik des Bogenträgers und Kreisringes*, Springer-Verlag, Vienna, Austria

[53] Federhofer, K (1950) On the bending-torsion vibrations of circular rings with double-symmetrical cross sections (in German), *Oster Akad Wiss Math-Nat* Kl S.-B. IIa 157, p 299-320

[54] Federhofer, K (1956) Influence of internal damping and of exterior fluid friction on the plane bending vibration of a circular ring (in German), *Ost Ing-Arch* 10(4), p 344-349

[55] Haines, D W (1974) Approximate theories for wave propagation and vibrations in elastic rings and helical coils of small pitch, *Int J Solids Struct* 10(12), p 1405-1416

[56] Kirkhope, J (1971) Vibrations of systems of elastically coupled concentric rings, *J Acoust Soc Am* 49, p 371-373

[57] Fettahlioglu, O A and Mayers, J (1977) Consistent treatment of extensional deformations for the bending of arches curved beams and rings, *J Pressure Vessel Tech* 99, p 2-11

[58] Fettahlioglu, O A (1974) A variationally developed, consistent theory for thin rings and curved beams with applications to laterally and end-loaded arches and cantilevers, Engineer's Thesis, Stanford Univ

[59] Fettahlioglu, O A and Toridis, T G (1976) Elastic-plastic analysis of curved structures subjected to static and dynamic loads, *J Pressure Vessel Tech* 98(2), p 126-134

[60] Okamoto, S (1951) On the bending and the vibration of the arch ring, *Proc First Nat Congr Appl Mech*, p 315-319

[61] Perrin, R (1971) Selection rules for the splitting of the degenerate pairs of natural frequencies of thin circular rings, *Acustica* 25(2), p 69-72

[62] Federhofer, K (1935) Zweidimensionale Theorie der Biegungsschwingungen des Kreisringes mit rechteckigem Querschnitte, *Akademie der Wissenschaften in Wien*,

Mathematisch-naturwissenschaftliche Klasse, Sitzungsberichte 144 Abteilung IIa, p 561-575

[63] Rehfield, L W, Sparrow, C A and Evani, S R M (1975) Influence of boundary restraint and curvature on the vibration of circular ring segments, *Israel J Tech* 13(1-2), p 7-15

[64] Lang, T E and Reed, R E (Oct 1, 1962) A method for determining modal characteristics of nonuniform thin circular rings, Jet Propulsion Lab, Pasadena, California, TR No. 32-252

[65] Stead, K A (1968) A study of the natural vibrations of a set of N elastically connected concentric circular rings, Ph.D. Thesis, South Carolina Univ., Columbia, 92 p

[66] Chidamparam, P (1993) Free vibration and buckling of curved beams subjected to distributed loads, Ph.D. Dissertation, The Ohio State University

[67] Federhofer, K (1935) Über den einfluss der Achsendehnung, der Rotationsträgheit und der Schubkraft auf die Frequenzen der Biegungsschwingungen eines Kreisringes (The influence of median line extension, rotary inertia and shear force on the frequencies of bending vibrations of circular rings), *Akademie der Wissenschaften in Wien, Mathematisch-naturwissenschaftliche Klasse, Sitzungsberichte* 144 Abteilung IIa, p 307-315

[68] Philipson, L L (1956) On the role of extension in the flexural vibrations of rings, *J Appl Mech* 23(3), p 364-366

[69] Morley, L S D (1961) Elastic waves in a naturally curved rod, *Quart J Mech Appl Math*, 14 Part 2, p 155-172

[70] Austin, W J, and Veletsos, A S (1973) Free vibration of arches flexible in shear, *J Eng Mech* 99(EM4), p 735-753

[71] Irie, T, Yamada, G and Tanaka, K (1983) Natural frequencies of in-plane vibration of arcs, *J Appl Mech* 50(2), p 449-452

[72] Pereira, C A L (1968) Free vibration of circular arches, M Sc Thesis, Rice Univ, Houston, Texas

[73] Filipich, C P (1988) Inplane vibrations of arches and rings taking into account shear and rotatory inertia effects, Ph.D. Thesis, Universidad Nacional de Cordoba, Argentina

[74] Gau, W H (1988) Effects of shear deformation and rotary inertia on the dynamics of curved beams, *MSc Thesis*, Dept of Mech Eng, Univ Illinois at Chicago, Chicago, Illinois

[75] Wung, S-J (1967) Vibration of hinged circular arches, M Sc Thesis, Rice Univ

[76] Novozhilov, V V (1953) *Foundations of the Nonlinear Theory of Elasticity*, Graylock Press, Rochester, New York

[77] Buckens, F (1950) Influence of the relative radial thickness of a ring on its natural frequencies, *J Acoust Soc Am* 22(4), p 437-443

[78] Seidel, B S and Erdelyi, E A (1964) On the vibration of a thick ring in its own plane, *J Eng Indust* 86 B(3), p 240-244

[79] Kirkhope, J (1976) Simple frequency expression for the in-plane vibration of thick circular rings, *J Acoust Soc Am* 59(1), p 86-89

[80] Kuhl, W (1942) Messungen zu den Theorien der Eigenschwingungen von Kreisringen beliebiger Wandstarke, *Akustiche Zeitschrift* 7, p 125-152

[81] Lincoln, J W and Volterra, E (1967) Experimental and theoretical determination of frequencies of elastic toroids, *Exp Mech* 7, p 211-217

[82] Kirkhope, J (1977) Inplane vibration of a thick circular ring, *J Sound Vib* 50(2), p 219-227

[83] Rao, S S and Sundararajan, V (1969) Inplane flexural vibrations of circular rings, *J Appl Mech* E36(3), p 620-625

[84] Gardner, T G and Bert, C W (1985) Vibration of shear deformable rings: theory and experiment, *J Sound Vib* 103(4), p 549-565

[85] Suzuki, S-I (1984) Inplane vibrations of circular rings, *J Sound Vib* 97(1), p 101-105

[86] Den Hartog, J P (1928) The lowest natural frequency of circular arcs, *Phil Mag* 5, p 400-408

[87] Hasselgruber, H (1956) Zur Berechnung der Eigenfrequenzen eines in seiner Ebene freischwingenden, nicht geschlossenen Kreisringes konstanten Querschnittes, *Forschung auf dem Gebiete des Ingenieurwesens, Düsseldorf*, Band 22, Heft 5, p 158-166

[88] Nelson, F C (1962) Inplane vibration of a simply supported circular ring segment, *Int J Mech Sci* 4, p 517-527

[89] Nelson, F C (1961) Vibration of circular ring segments, Ph.D. Thesis, Harvard Univ

[90] Volterra, E and Morell, J D (1960) A note on the lowest natural frequency of elastic arcs, *J Appl Mech* 27(4), p 744-746

[91] Volterra, E and [illegible] J D (1961) Lowest natural frequencies of elastic [illegible] *[illegible]coust Soc Am* 33(12), p 1787-1790. Also see [illegible]72) Comments on "Lowest natural frequer[illegible]d arcs" *J Acoust Soc Am* 51(5), p 1483-[illegible]

[92] Wang, [illegible] natural frequency of clamped para[illegible], *Proc ASCE* 98(ST1), p 407-411

[93] Wang, T M (1975) Effect of variable curvature on fundamental frequency of clamped parabolic arcs, *J Sound Vib* 41, p 247-251

[94] Romanelli, E and Laura, P A A (1972) Fundamental frequencies of non-circular elastic hinged arcs, *J Sound Vib* 24(1), p 17-22

[95] Ikebe, T, (Sept 1935) Paper No. 589, p 244-262 and (July 1938) Paper No. 796, p 680-712, *Inst Phys Chem Research*, Tokyo

[96] Wang, T M and Moore, J A (1973) Lowest natural extensional frequency of clamped elliptic arcs, *J Sound Vib* 30(1), p 1-7

[97] Takahashi, S (1963) Vibration of a circular arc bar in its plane: Part I, Both ends built-in, *Bull JSME* 6(24), p 666-673

[98] Takahashi, S, Suzuki, K, Fukazawa, K and Nakamachi, K (1977) In-plane vibrations of elliptic arc bar and sinus curve bar, *Bull JSME* 20(148), p 1236-1243

[99] Suzuki, K, Takahashi, S and Ishiyama, H (1978) In-plane vibrations of curved bars, *Bull JSME* 21(154), p 618-627

[100] Suzuki, K and Takahashi, S (1979) In-plane vibrations of curved bars considering shear deformation and rotatory inertia, *Bull JSME* 22(171), p 1284-1292

[101] Lee, B K and Wilson, J F (1989) Free vibrations of arches with variable curvature, *J Sound Vib* 136(1), p 75-89

[102] Ouellette, P E (1982) In-plane vibration of an extensible and flexible chain of particles: Application to a thin and curved rod, *J Sound Vib* 83(3), p 379-399

[103] Pestel, E C and Leckie, F A (1963) *Matrix Methods in Elastomechanics*, McGraw-Hill Book Co., New York

[104] Raithel, A and Franciosi, C (1984) Dynamic analysis of arches using Lagrangian approach, *J Struct Div, Proc ASCE* 110(4), p 847-858

[105] McDaniel, T J (1971) Dynamics of circular periodic structures, *J Aircraft* 8, p 143-149

[106] Singh, K and Dhoopar, B L (1979) Free vibration of circular rings on radial supports, *J Sound Vib* 65(2), p 297-301

[107] Sahay, K B and Sundararajan, V (1972) Vibration of a stiffened ring considered as a cyclic structure, *J Sound Vib* 22, p 467-473

[108] Filipich, C P and Rosales, M B (1990) In-plane vibration of symmetrically supported circumferential rings, *J Sound Vib* 136(2), p 305-314

[109] Detinko, F M (1989) Free vibration of a thick ring on multiple supports, *Int J Eng Sci* 27(11), p 1429-1438

[110] Mallik, A K and Mead, D J (1977) Free vibration of thin circular rings on periodic radial supports, *J Sound Vib* 54(1), p 13-27

[111] Suzuki, K, Asakura, A and Takahashi, S (1979) Vibrations of a connecting system of curved bars (inplane), *Bull JSME* 22(172), p 1439-1447

[112] Chen, S-S (1973) Inplane vibration of continuous curved beams, *Nucl Eng Des* 25(3), p 413-431

[113] Issa, M S (1983) Effects of rotary inertia and shear deformation on extensional vibrations of continuous circular curved beams, Ph.D. Thesis Univ New Hampshire, 110 p

[114] Issa, M S, Wang, T M and Hsiao, B T (1987) Extensional vibrations of continuous circular curved beams with rotary inertia and shear deformation I: Free vibration, *J Sound Vib* 114(2), p 297-308

[115] Wang, T M and Issa, M S (1987) Extensional vibrations of continuous circular curved beams with rotary inertia and shear deformation II: Forced vibration, *J Sound Vib* 114(2), p 309-323

[116] Wang, T M and Guilbert, M P (1981) Effects of rotary inertia and shear on natural frequencies of continuous circular curved beams, *Int J Solids Struct* 17(3), p 281-289

[117] Issa, M S, Nasr, M E and Naiem, M A (1990) Free vibrations of curved Timoshenko beams on Pasternak foundations, *Int J Solids Struct* 26(11), p 1243-1252

[118] Wang, T M and Lee, J M (1974) Forced vibrations of continuous circular arch frames, *J Sound Vib* 32(2), p 159-173

[119] Wang, T M and Church, D C (1967) Analysis of continuous arch frames, *J Struct Div, Proc ASCE* 93, p 419-433

[120] Wang, T M and Lee, J M (1972) Natural frequencies of multi-span circular curved frames, *Int J Solids Struct* 8, p 791-805

[121] Issa, M S (1988) Natural frequencies of continuous curved beams on Winkler-type foundation, *J Sound Vib* 127(2), p 291-301

[122] Sakiyama, T (1986) Free vibration of three-hinged arches, *J Sound Vib* 111(2), p 343-348

[123] Ball, R E (1967) Dynamic analysis of rings by finite differences, *J Eng Mech* 93(EM1), p 1-10

[124] Eppink, R T and Veletsos, A S (July 1959) Analysis of circular arches, AFSWC-TR-59-9 Vol II, Kirtland Air Force Base, New Mexico

[125] Eppink, R T and Veletsos, A S (1960) Dynamic analysis of circular elastic arches, *Proc Second Conference on Electronic Digital Computation, ASCE*, p 477-502

[126] Eppink, R T and Veletsos A S (Dec 1960) Response of arches under dynamic loads, AFSWC-TR-60-53 Vol II, Kirtland Air Force Base, New Mexico

[127] Reissner, E (1954) Note on the problem of vibrations of slightly curved bars, *J Appl Mech* 21(2), p 195-196

[128] Rossettos, J N (1972) Natural frequencies of clamped and hinged bars having small curvature, *J Acoust Soc Am* 52(1), p 444-445

[129] Rossettos, J N and Squires, D C (1973) Modes and frequencies of transversely isotropic slightly curved Timoshenko beams, *J Appl Mech* 39, p 1029-1034

[130] Nanasi, T and Pust, L (1982) The influence of support compliances on the vibration of slightly curved beams, *Strojnicky Casopis* 33(1), p 49-70

[131] Weidhammer, F (1956) Lateral oscillations of slightly curved rods under axial pulsating load, *Z Angew Math Mech* 36, p 235-238

[132] Oseled'ko, A I (1965) Vibrations of very shallow circular arches, Lockheed Missiles and Space Co., Sunnyvale, Calif., Transl. into English from *Issled. po Teorii Sooruzh* (USSR), no.13, p 127-134

[133] Nagaya, K (1983) Vibrations of a thick-walled pipe or a ring of arbitrary shape in its plane, *J Appl Mech* 50(4a), p 757-764

[134] Suzuki, K and Takahashi, S (1982) Inplane vibrations of curved bars with varying cross-section, *Bull JSME* 25(205), p 1100-1107

[135] Filipich, C P, Laura, P A A, Rosales, M and Valerga, B H (1987) Numerical experiments on inplane vibrations of rings of nonuniform cross-section, *J Sound Vib* 118, p 166-169

[136] Lecoanet, H and Piranda, J (1983) Inplane vibrations of circular rings with a radially variable thickness, *J Vib Acoust Stress Reliab Des* 105(1), p 137-143

[137] Rutledge, J R and Royster, L H (July 1971) An approximate mathematical model for the free vibrations of a smooth arc of arbitrary shape and varying cross-section, Report, North Carolina State Univ, 24 p

[138] Rutledge, J R and Royster, L H (1971) Mathematical model for the free vibration of an arc with varying radius of curvature, *Proc 81st Meeting Acoust Soc Am*, 17p

[139] Royster, L H (1966) Effect of linear taper on the lowest natural extensional frequency of elastic arcs, *J Appl Mech* 33(1), p 211-212

[140] Suzuki, K, Kosawada, T and Takahashi, S (1986) Inplane vibrations of inhomogeneous curved bars having varying cross-section (in Japanese), *Trans JSME* 52(482), p 2593-2599

[141] Laura, P A A, Filipich, C P, Rossi, R E and Reyes, J A (1988) Vibrations of rings of variable cross section, *Appl Acoust* 25(4), p 225-234

[142] Gutierrez, R H, Laura, P A A, Rossi, R E, Bertero, R and Villaggi, A (1989) Inplane vibrations of non-circular arcs of nonuniform cross-section, *J Sound Vib* 129(2), p 181-200

[143] Laura, P A A, Bambill, E, Filipich, C P and Rossi, R E (1988) A note on free flexural vibrations of a non-uniform elliptical ring in its plane, *J Sound Vib* 126(2), p 249-254

[144] Rosales, M B, Filipich, C P and Laura, P A A (1989) A note on free flexural vibrations of a non-uniform ring with fixed supports, *J Sound Vib* 129(1), p 45-49

[145] Cortinez, V H, Laura, P A A, Filipich, C P and Carnicer, R (1986) Numerical experiments on vibrating cantilever arches of varying cross-section, *J Sound Vib* 110(2), p 356-358

[146] Verniere De Irasser, P L and Laura, P A A (1986) A note on the analysis of the first symmetric mode of vibration of circular arches of non-uniform cross section, *J Sound Vib* 116, p 580-584

[147] Laura, P A A and Irassar, P L V d (1983) A note on inplane vibrations of arch-type structures of non-uniform cross-section: The case of linearly varying thickness, *J Sound Vib* 124(1), p 1-12

[148] Laura, P A A, Irassar, P L V d, Carnicer, R and Bertero, R (1988) A note on vibrations of a circumferential arch with thickness varying in a discontinuous fashion, *J Sound Vib* 120(1), p 95-105

[149] Rossi, R E, Laura, P A A and Irassar, P L V d (1989) Inplane vibrations of cantilevered non-circular arc of non-uniform cross-section with a tip mass, *J Sound Vib* 129(2), p 201-213

[150] Laura, P A A, Filipich, C P and Cortinez, V H (1987) Inplane vibrations of an elastically cantilevered circular arc with a tip mass, *J Sound Vib* 115(3), p 437-446

[151] Filipich, C P, Carnicer, R, Cortinez, V H and Laura, P A A (1987) Inplane vibrations of a circumferential arch elastically restrained against rotation at one end and with an intermediate support, *Appl Acoust* 22(4), p 261-270

[152] Filipich, C P, Laura, P A A and Cortinez, V H (1987) Inplane vibrations of an arch of variable cross section elastically restrained against rotation at one end and carrying a concentrated mass at the other, *Appl Acoust* 21(3), p 241-246

[153] Laura, P A A, Filipich, C P and Cortinez V H (1986) Inplane vibrations of a circumferential arch elastically restrained against rotation at one end and carrying a concentrated mass at the other, Inst Appl Mech, Base Naval Puerto Belgrano, Argentina, Publ No. 86-32

[154] Cortinez, V H, Laura, P A A, Filipich, C P and Carnicer, R (1987) Inplane vibrations of a clamped column-arch system carrying a concentrated mass at the free end, *J Sound Vib* 112(2), p 379-383

[155] Ercoli, L, Laura, P A A, Filipich, C P and Cortinez, V H (1986) Analytical and experimental investigation on vibrating arches clamped at one end and carrying a concentrated mass at the other, *J Sound Vib* 111(2), p 349-351

[156] Hoa, S V (1978) Vibration frequency of a curved beam with tip mass, *J Sound Vib* 61(3), p 427-436

[157] Allaei, D, Soedel, W, and Yang, T Y (1986) Natural frequencies and modes of rings that deviate from perfect axisymmetry, *J Sound Vib* 111(1), p 9-27

[158] Hong, J S (1989) Free vibration analysis of circular rings with slight irregularities, *Proc Seventh Int Modal Anal Conf*, Vol I, p 124-130

[159] Palmer, E W (Aug 1967) The influence of a mass on the free flexural vibrations of a circular ring, Rept.-2536; AD-661226, Naval Ship Engineering Center, Washington D.C. Underwater Explosions Research Div., 51p

[160] Gartner, J R and Bhat, S T (1975) Influence of geometric imperfections on vibrational frequencies of thin rings, *J Eng Indust* 97(4), p 1199-1203

[161] Fox, C H J (1990) A simple theory for the analysis and correction of frequency splitting in slightly imperfect rings, *J Sound Vib* 142(2), p 227-243

[162] Irie, T, Yamada, G and Takahashi, I (1980) Inplane vibration of a free-clamped slender arc of varying cross-section, *Bull JSME* 23(178), p 567-573

[163] Murthy, V R and Nigam, N C (1975) Dynamic characteristics of stiffened rings by transfer matrix approach, *J Sound Vib* 39(2), p 237-245

[164] Irie, T and Yamada, G and Fujikawa, Y (1982) Natural frequencies of circular arcs with varying cross section, *Exp Mech* 22(11), p 407-411

[165] Irie, T and Yamada, G and Takahashi, I (1979) Inplane vibration of Timoshenko arcs of variable cross-section, *Ing Arch* 48(5), p 337-346

[166] Lang, T E and Reed, R E (1962) TR 32-252, Jet Propulsion Laboratory, California

[167] Irie, T, Yamada, G and Takahashi, I (1980) The steady state inplane response of a curved Timoshenko beam with internal damping, *Ing Arch* 49(1), p 41-49

[168] Sheinman, I (1979) Forced vibration of a curved beam with viscous damping, *Comput Struct* 10(3), p 499-503

[169] Mittal, R K (1976) Flexure of a thin elastic ring due to a dynamic concentrated load, *Int J Eng Sci* 14, p 247-257

[170] Suzuki, K, Tamura, S and Takahashi, S (1981) Steady-state response of curved bars (inplane) (in Japanese), *Trans JSME*, 1981-2, p 223

[171] Suzuki, K, Miyashita, Y, Kosawada, T and Takahashi, S (1985) Inplane impulse response of a curved bar with varying cross-section, *Bull JSME* 28(240), p 1181-1187

[172] Isenberg, J, Levine, H S and Pang, S H (1977) Numerical simulation of forced vibration tests on a buried arch, Report No. 7712-NNa-4281F, Weidlinger Assoc, Menlo Park, California

[173] Lu, Y P (1976) An analytical formulation of the forced responses of damped rings, *J Sound Vib* 48(1), p 27-33

[174] Suzuki, S (1966) Dynamic elastic response of a ring to transient pressure loading, *J Appl Mech* 33, p 261

[175] Gecha, V Ya and Poznyak, E L (1983) Free and forced vibrations of a circular ring of high curvature, *Sov Appl Mech* 18(7), p 641-644

[176] Federhofer, K (1957) Vibration of a circular arch pivoted in both ends and loaded with a periodically varying force (in German), *Ost Akad Wiss Math-Nat Kl. S. B.* Abt. II 166 6/10, p 125-137

[177] Carver, D R and Parker, W H (1965) Extensional vibrations and dynamic loading of thick elastic rings, *Developments in Mechanics* 3, part 2, p 255-262

[178] Merkle, D H and Merkle, L D (Sept 1986) High frequency analysis of circular arches, Final Report, Applied Research Associates Inc.,Albuquerque, N. Mex., Contract F29601-85-C-0029, 101 p

[179] Federhofer, K (1957) Forced vibration of a circular ring (in German), *S B Math-Nat Kl Bay Akad Wiss* 166(5), p 1-14

[180] Ahmed, K M (1972) Dynamic analysis of sandwich beams, *J Sound Vib* 21, p 263-276

[181] DiTaranto, R (1973) Free and forced response of a laminated ring, *J Acoust Soc Am* 53(3), p 748-757

[182] Reddy, E S and Mallik, A K (1982) Vibration of a two layered ring on periodic radial supports, *J Sound Vib* 84, p 417-430

[183] Reddy, E S and Mallik, A K (1984) Vibration of a three layered ring on periodic radial supports, *AIAA* [illegible] 43-551

[184] Rossettos, J N and Perl, E (1978) On the damped vibratory response of curved viscoelastic beams, *J Sound Vib* 58(4), p 535-544
[185] Sagartz, M J (1974) Response of a three-layered ring to an axisymmetric impulse, *AIAA J* 12(3), p 390-392
[186] Tatemichi, A, Okazaki, A and Hikiyama, M (1977) Damping properties of curved sandwich beams with viscoelastic layer, *Bull Nagaya Inst Tech* 29, p 309-317
[187] Ahmed, K M (1971) Free vibration of curved sandwich beams by the method of finite elements, *J Sound Vib* 18(1), p 61-74
[188] Nelson, F C and Sullivan, D F (1977) The forced vibration of a three-layered damped circular ring, *ASME Paper* No. 77-DET-154
[189] Nagaya, K and Hirano, Y (1977) Inplane vibration of viscoelastic circular rod with consideration of shearing deformation and rotatory inertia, *Bull JSME* 20(143), p 539-547
[190] Ahmed, K M (March 1971) *Free vibrations of curved sandwich beams*, Institute Sound and Vibration Research, Southampton Univ, England, 44 p
[191] Nanasi, T (1984) Free vibration of curved sandwich beams, *Strojnicky Casopis* 35(1/2), p 121-137
[192] Rossettos, J N (1971) Vibration of slightly curved beams of transversely isotropic composite materials, *AIAA J* 9(11), p 2273-2275
[193] Sagartz, M J (1977) Transient response of three-layered rings, *J Appl Mech* 44(2), p 299-304
[194] Stevens, K K (1969) Transverse vibration of a viscoelastic column with initial curvature under periodic axial load, *J Appl Mech* 36, p 814-818
[195] Vaswani, J, Asnani, N T and Nakra, B C (1988) Vibration and damping analysis of curved sandwich beams with a viscoelastic core, *Composite Struct* 10(3), p 231-245
[196] Qatu, M S (1992) Inplane vibration of slightly curved laminated composite beams, *J Sound Vib* 159(2), p 327-338
[197] Bolotin, V V (1965) Vibrations of multilayer curvilinear rods, *Inits Eng J*, p 99-107
[198] Celep, Z (1990) Inplane vibrations of circular rings on a tensionless foundation, *J Sound Vib* 143(3), p 461-471
[199] Michell, J H (1890) The small deformation of curves and surfaces with application to the vibrations of a helix and a circular ring, *Messenger of Mathematics* 19, p 68
[200] Volterra, E (1955) The equation of motion for curved elastic bars deduced by the use of the "method of internal constraints", *Ing Arch* 23(6), p 402-409
[201] Volterra, E (1967) Vibrations of circular elastic rings, *Israel J Tech* 5(4), p 225-233
[202] Volterra, E (1956) Eigenvibrations of curved elastic bars according to the "method of internal constraints", *Ing Arch* 24, p 317-329
[203] Federhofer, K (1936) Über die Eigenschwingungen des senkrecht zu seiner Ebene schwingenden Kreisbogens, *Akademie der Wissenschaften in Wien, Mathematisch-naturwissenschaftliche Klasse, Sitzungsberichte* 145 Abteilung IIa, p 29-50
[204] Brown, F H (1934) Lateral vibration of ring-shaped frames, *J Franklin Institute* 218, p 41
[205] Nelson, F C (1963) Out-of-plane vibration of a clamped circular ring segment, *J Acoust Soc Am* 35(6), p 933-934
[206] Ojalvo, I U (1962) Coupled twist-bending vibrations of incomplete elastic rings, *Inter J Mech Sci* 4, p 53-72
[207] Takahashi, S (1963) Vibration of a circular arc bar: Part 2, Perpendicular to its plane, *Bull JSME* 6(24), p 674-681
[208] Kirkhope, J (1976) Out-of-plane vibration of thick circular ring, *J Eng Mech* 102(EM2), p 239-247
[209] Rao, S S (1971) Effects of transverse shear and rotatory inertia on the coupled twist-bending vibrations of circular rings, *J Sound Vib* 16(4), p 551-566. Also see *J Sound Vib* 21(2), 1972, p 241-243 and *J Sound Vib* 21(2), 1972, p 243-244
[210] Irie, T, Yamada, G and Tanaka, K (1982) Natural frequencies of out-of-plane vibration of arcs, *J Appl Mech* 49(4), p 910-913
[211] Endo, M and Taniguchi, O (1971) Flexural vibrations of a ring, *Bull JSME* 14(74), p 761-771
[212] Bickford, W B and Maganty, S P (1986) Out-of-plane vibrations of thick rings, *J Sound Vib* 108(3), p 503-507
[213] Wilson, J F and Garg, D P (1978) Frequencies of annular plate and curved beam elements, *AIAA J* 16(3), p 270-272
[214] Bakshi, J S, and Callahan, W R (1966) Flexural vibrations of a circular ring when transverse shear and rotary inertia are considered, *J Acoust Soc Am* 40(2), p 372-375
[215] Tang, C S and Bert, C W (1987) Out-of-plane vibrations of thick rings, *Int J Solids Struct* 23(1), p 175-185
[216] Taniguchi, O and Endo, M (1971) An approximate formula for the flexural vibration of a ring of rectangular cross section, *Bull JSME* 14(70), p 348-354
[217] Endo, M and Taniguchi, O (1969) Flexural vibrations of a ring of rectangular cross section, *Bull JSME* 12(52), p 747-755
[218] Chang, T C and Volterra, E (1969) Upper and lower bounds for frequencies of elastic arcs, *J Acoust Soc Am* 46(5) part 2, p 1165-1174
[219] Chang, T C and Volterra, E (1970) Natural frequencies of simply supported arcs, *J Acoust Soc Am* 49(1), p 370-371
[220] Takahashi, S and Suzuki, K (1977) Vibrations of elliptic arc bar perpendicular to its plane, *Bull JSME* 20(149), p 1409-1416
[221] Suzuki, K, Aida, H and Takahashi, I (1978) Vibrations of curved bars perpendicular to their planes, *Bull JSME* 21(162), p 1685-1695
[222] Suzuki, K and Takahashi, S (1981) Out-plane vibrations of curved bars considering shear deformation and rotatory inertia, *Bull JSME* 24(193), p 1206-1213
[223] Silva, J M M and Urgueira, A P V (1988) Out-of-plane dynamic response of curved beams: an analytical model, *Int J Solids Struct* 24(3), p 271-284
[224] Irie, T and Yamada, G and Takahashi, I (1980) Out-of-plane vibration of arc bar of variable cross-section, *Bulletin JSME* 23(181), p 1200-1205
[225] Suzuki, K, Kosawada,T and Takahashi, S (1983) Out-of-plane vibrations of curved bars with varying cross-section, *Bull JSME* 26(212), p 268-275
[226] Sakiyama, T (1985) Free vibrations of arches with variable cross section and non-symmetrical axis, *J Sound Vib* 102(3), p 448-452
[227] Reddy, M N (1968) Lateral vibrations of plane curved bars, *J Struct Div, Proc ASCE* 94(ST10), p 2197
[228] Strom, B T (1971) Vibration of plane curved beams, Ph.D. Thesis, Arizona State Univ, 108 p
[229] Bickford, W B, and Strom, B T (1975) Vibration of plane curved beams, *J Sound Vib* 39(2), p 135-146
[230] Irie, T, Yamada, G and Tanaka, K (1982) Free out-of-plane vibration of arcs, *J Appl Mech* 49(2), p 439-441
[231] Irie, T, Yamada, G and Takahashi, I (1980) The steady state out-of-plane response of a Timoshenko curved beam with internal damping, *J Sound Vib* 71(1), p 145-156
[232] Irie, T, Yamada, G and Koizumi, H (1982) The steady state out-of-plane response of an internally damped ring supported by springs in some bays, *J Sound Vib* 81(2), p 187-197
[233] Suzuki, K, Sato, Y and Takahashi, S (1981) Steady-state response of curved bars (out-of-plane) (in Japanese), *Trans JSME* (1981-2), p 229
[234] Panayotounakos, D E (1983) Forced motions of cantilevered planar-curved bars considered as discrete systems by the flexibility method, *Acta Mech* 50(1/2), p 105-118
[235] Suzuki, K, Sugi, K, Kosawada, T and Takahashi, S (1986) Out-plane impulse response of a curved bar with varying cross-sections, *Bull JSME* 29(258), p 4312-4317
[236] Chen, Y N and Yetman, W R Jr. (July 1975) Dynamic response of an oval ring, Rept No POLY-AE/AM-75-9, Dept. of Aerospace Engrg and Appl Mech, Polytechnic Inst New York, AFOSR-TR-75-1534, 44 p
[237] Joseph, T P and Wilson, J F (1980) Vibrations of curved spans for mass transit, *J Eng Mech* 106(2), p 255-272
[238] Rao, S S (1971) Three-dimensional vibrations of a ring on an elastic foundation, *Aeronaut J* 75(726), p 417-419
[239] Irie, T, Yamada, G and Okada, H (1982) Free out-of-plane vibration of a ring elastically supported at several points, *J Appl Mech* 49(4), p 854-860
[240] Wang, T M and Brannen, W F (1982) Natural frequencies for out-of-plane vibrations of curved beams on elastic foundations, *J Sound Vib* 84(2), p 241-246
[241] Wang, T M, Nettleton, R H and Keita, R (1980) Natural frequencies for out-of-plane vibrations of continuous curved beams, *J Sound Vib* 68(3), p 427-436
[242] Chen, S S (1973) Coupled twist bending waves and natural frequencies of multispan curved beams, *J Acoust Soc Am* 53(4), p 1179-1183
[243] Wang, T M, Laskey, A J and Ahmad, M (1984) Natural frequencies for out-of-plane vibrations of continuous curved beams considering shear and rotary inertia, *Int J Solids Struct* 20(3), p 257-265
[244] Wang, T M, Ahmad, M F and Hsiao, B T (1992) Out-of-plane forced vibrations of multispan circular curved beams, *Comput Struct* 45(3), p 543-551
[245] Suzuki, K and Takahashi, S (1979) Vibrations of a connecting system of curved bar (out-of-plane), *Bull JSME* 22(172), p 1448-1455
[246] Theocaris, P S and Panayotounakos, D E (1983) The differential equations of uniform skew-curved bars in harmonic motion, *J Sound Vib* 89(2), p 195-211
[247] Krahula, J L (1966) Out-of-plane free vibrations of a uniform circular ring, *J Appl Mech* 33(3), p 708-709
[248] Mallik, A K and Murty, G V R (1988) Free out-of-plane vibration of circular rings on identical equi-spaced elastic supports, *J Sound Vib* 122(3), p 433-439
[249] Ojalvo, I U and Newman, M (May 21 1964) Natural frequencies of clamped ring segments, *Mach Des* 36, p 219-222

[250] Ojalvo, I U and Newman, M (March 18 1965) Natural frequencies of cantilevered ring segments, *Mach Des* 37, p 191-195

[251] Volterra, E and Morell, J D (1961) Lowest natural frequency of elastic arc for vibrations outside the plane of initial curvature, *J Appl Mech* 28, p 624-627. Erratum in J *Appl Mech* 34, 1967, p 1046

[252] Fettahlioglu, O A and Tabi, R (1978) Effect of transverse shearing deformations on the coupled twist-bending of curved beams, *Proc Joint ASME/CSME Pressure Vessels and Piping Conf*, Montreal, Canada, June 25-30 1978, Paper No. 78-PVP-102

[253] Wang, T M (1975) Fundamental frequency of clamped elliptic arcs for vibrations outside the plane of initial curvature, *J Sound Vib* 42, p 515-519

[254] Washizu, K (1964) Some considerations on a naturally curved and twisted slender beam, *J Math and Phy* XLIII(2), p 111-116

[255] Endo, M (1972) Flexural vibrations of a ring with arbitrary cross section, *Bull JSME* 15(82), p 446-454

[256] Hawkings, D L (1977) A generalized analysis of the vibration of circular rings, *J Sound Vib* 54(1), p 67-74

[257] Kirkhope, J, Bell, R and Olmstead, J L D (1984) The vibration of rings of unsymmetrical cross-section, *J Sound Vib* 96(4), p 495-504

[258] Hammoud, A S and Archer, R R (1963) On the free vibration of complete and incomplete rings, *Developments in Mechanics* 2, p 489-524

[259] Bhimaraddi, A, Moss, P J, and Carr, A J (1989) Out-of-plane vibrations of thick rings, *Thin-Walled Struct* 8(1), p 73-79

[260] Bhimaraddi, A (1988) Generalized analysis of shear deformable rings and curved beams, *Int J Solids Struct* 24(4), p 363-373

[261] Williams, H E (1973) On the equations of motion of thin rings, *J Sound Vib* 26(4), p 465-488

[262] Wasserman, E B (1961) The effect of the behavior of the load on the frequency of the free vibrations of a ring, NASA TT F-52

[263] Wasserman, Y (1978) Spatial symmetrical vibrations and stability of circular arches with flexibly supported ends, *J Sound Vib* 59(2), p 181-194

[264] Wasserman, Y (1977) The influence of the behavior of the load on the frequencies and critical loads of arches with flexibly supported ends, *J Sound Vib* 54(4), p 515-526

[265] Plaut, R H and Johnson, E R (1981) The effects of initial thrust and elastic foundation on the vibration frequencies of a shallow arch, *J Sound Vib* 78(4), p 565-571

[266] Perkins, N C (1990) Planar vibration of an elastica arch: theory and experiment, *J Vib Acoust* 112(3), p 374-379

[267] Lin, J L and Soedel, W (1988) General in-plane vibrations of rotating thick and thin rings, *J Sound Vib* 122(3), p 547-570

[268] Wang, J T S and Mahrenholtz, O (1975) Bending frequencies of a rotating curved beam, *Ing Arch* 44(6), p 399-407

[269] Singh, K and Singh, B P (1984) In-plane vibrations of rotating sectors and rings with and without radial supports by finite element method, *Comput Struct* 19(4), p 545-554

[270] Singh, K and Singh, B P (1985) Finite element method for inplane vibrations of rotating Timoshenko rings and sectors, *Int J Numer Methods Eng* 21(8), p 1521-1533

[271] Bickford, W B and Reddy, E S (1985) On the inplane vibrations of rotating rings, *J Sound Vib* 101(1), p 13-22

[272] Huang, S C and Soedel, W (1987) Effects of Coriolis acceleration on the free and forced inplane vibrations of rotating rings on elastic foundation, *J Sound Vib* 115(2), p 253-274

[273] Lin, J L (1987) Vibrations of rotating thick or thin rings, Ph.D. Thesis, Purdue Univ, 262 p

[274] Lin, J L and Soedel, W (1988) Dynamic response of a rotating thick ring to force or displacement excitation, *J Sound Vib* 121(2), p 317-337

[275] Gau, W-H and Shabana, A A (1990) Effects of shear deformation and rotary inertia on the nonlinear dynamics of rotating curved beams, *J Vib Acoust* 112(2), p 183-193

[276] Carrier, G (1945) On the vibrations of the rotating ring, *Quart Appl Math* 3, p 235-245

[277] Ghosh, J (1924) Transverse vibrations of a thin rotating rod and of a rotating circular ring, *Bull Calcutta Math Soc* 14, p 161-172

[278] Endo, M, Hatamura, K, Sakata, M and Taniguchi, O (1984) Flexural vibration of a thin rotating ring, *J Sound Vib* 92, p 261-272

[279] Huang, S C and Soedel, W (1987) Response of rotating rings to harmonic and periodic loading and comparison with the inverted problem, *J Sound Vib* 118(2), p 253-270

[280] Johnson, D C (1952) Free vibrations of a rotating elastic body, *Aircraft Eng* 24, p 234-236

[281] Pelchen, C and Wauer, J (1992) Small vibrations of rotating ring segments and full rings under external or internal pressure, *J Appl Mech* 59(4), p 1038-1040

[282] Reddy, E S and Bickford, W B (1985) On the inplane vibrations of a rotating ring with equi-spaced spokes, *J Sound Vib* 103(4), p 533-544

[283] Bert, C W and Chen, T L C (1978) On vibration of a thick flexible ring rotating at high speed, *J Sound Vib* 61(4), p 517-530

[284] Lallman, F J (Dec 1980) Vibration characteristics of a steadily rotating slender ring, NASA Langley Research Center, Rept No NASA-TP-1775: L13386, 100 p

[285] Williams, H E (1987) On the inplane motion of thin rotating, ring segments, *J Sound Vib* 115(1), p 65-81

[286] Bickford, W B and Maganty, S P (1986) Out-of-plane vibrations of thick rotating rings, *J Sound Vib* 110(1), p 121-127

[287] Rosen, A and Rand, O (1985) A general model of the dynamics of moving and rotating rods, *Comput Struct* 21(3), p 543-561

[288] Chen, D C and Shabana, A A (1989) Effect of the coupling between the longitudinal and transverse displacements on the dynamics of rotating curved beams, *J Appl Mech* 56(4), p 979-981

[289] Huang, Y (1988) New matrix method for solving buckling and free vibration problems of circular arches with variable rigidity, *Mech Struct Machines* 15(4), p 463-479

[290] Johnson, E R and Plaut, R H (Feb 1980) Load frequency relationships for shallow elastic arches, College of Engineering, Virginia Polytechnic Institute and State University, Rept No VPI-E-80-4, 70 p

[291] Sakiyama, T (1979) Free inplane vibration of nonuniform arches with various shapes of axis and initial load, *Proc JSCE* 287, p 33-44

[292] Ilanko, S and Dickinson, S M (1986) Linearization of the strain energy expressions for a vibrating slightly curved beam subjected to an axial load, J *Sound Vib* 108(2), p 357-359

[293] Reed, F E (1965) The natural frequency of a ring subjected to external pressure, *J Appl Mech* 32 E(2), p 431-432

[294] Aydin, A (1980) Free vibration of arches with axial loading, *Proc Seventh World Conf on Earthquake Eng*, Istanbul, 5, p 577-589

[295] Federhofer, K (1933) Berechnung der niedrigsten Eigenschwingzahl des radial belasteten Kreisbogens, *Ing Arch* 4, p 276-286

[296] Vaserman, E B (1957) Three-dimensional vibrations of a circular arch under variable behavior of the load in the process of deformation (in Russian), *Uch. Zap. Latv. In-ta* 13, p 7-31

[297] Vysochin, B M (1959) The free vibrations of loaded parabolic arches (in Russian), *Nauchn Soobshch Dnepropetr Inzh Stroit In-ta* 46, 7p

[298] Wasserman, Y (1983) Vibrations, and static and dynamic stability of circular arches subjected to uniform vertical loads, *Israel J Tech* 21(4), p 171-180

[299] Wasserman, E B (1956) The free oscillations of loaded elastic circular arches and rings, Thesis, Latvian Univ, Riga

[300] Wasserman, Y (1979) Spatial antisymmetrical vibrations and stability of circular arches with flexibly supported ends, *Israel J Tech* 16 5/6, p 224-233

[301] Johnson, E R, Plaut, R H and Deel, C C (July 1980) Load frequency relationships for shallow elastic structures, *Proc Int Conf on Recent Advances in Structural Dynamics*, editor Petyt, M, Univ Southampton, England, p 611-620

[302] Plaut, R H (May 1979) Vibration frequencies of an arch model under various loading conditions, Report No. VPI-E-79-19, Virginia Polytechnic Institute and State Univ, Blacksburg, Virginia

[303] Farshad, M (1980) Wave Propagation in Prestressed Curved Rods, *J Eng Mech* 106(2), p 395-408

[304] Federhofer, K (1959) Nicht-lineare Biegungsschwingungen des Kreisringes, *Ing Arch* 28, p 53-58

[305] Prathap, G and Pandalai, K A V (1978) The role of median surface curvature in large amplitude flexural vibrations of thin shells, *J Sound Vib* 60(1), p 119-131

[306] Sabir, A B and Lock, A C (1973) Large deflection, geometrically nonlinear finite element analysis of circular arches, *Int J Mech Sci* 15(1), p 37-47

[307] Kovrigin, D A and Potapov, A I (1989) Nonlinear vibrations of a thin ring, *Soviet J Appl Mech* 25, p 281-286

[308] Rehfield, L W (1974) Nonlinear flexural oscillations of shallow arches, *AIAA J* 12(1), p 91-93

[309] Sato, K (1975) Free flexural vibrations of an elliptical ring in its plane, *J Acoust Soc Am* 57(1), p 113-115

[310] Singh, P N and Ali, S M J (1975) Non-linear vibration of a moderately thick shallow clamped arch, *J Sound Vib* 41(3), p 275-282

[311] Maewal, A (1978) Nonlinear flexural vibration of an elastic ring, *J Appl Mech* 45(2), p 428-429

[312] Kudva, N J, Nayfeh, A H and Kamat, M P (1978) Natural frequencies of curved elastic arcs, *J Acoust Soc Am* 64(6), p 1700-1702

[313] Valkering, T P and Charnley, T (1983) Radial vibrations of eccentric rings, *J Sound Vib* 86(3), p 369-393

[314] Fried, I (1983) Nonlinear finite element computation of the equilibrium, stability and motion of the extensional beam and ring, *Comput Methods Appl Mech Eng* 38(1), p 29-44

[315] Simmonds, J G (1979) Accurate nonlinear equations and a perturbation solution for the free vibrations of a circular elastic ring, *J Appl Mech* 46(1), p 156-160

[316] Maganty, S P and Bickford, W B (1987) Large amplitude oscillations of thin circular rings, *J Appl Mech* 54(2), p 315-322

[317] Shkenev, Y S (1960) Nelineyniye kolebaniya krugovogo kol'tsa. Non-linear vibrations of circular rings, *Inzhener Sbornik* 28, Akad Nauk USSR, 1960, p 82-86

[318] Evensen, D A (Dec 1965) A theoretical and experimental study of the nonlinear flexural vibrations of thin circular rings, NASA TR R-227, 58 p

[319] Evensen, D A (1966) Nonlinear flexural vibrations of thin circular rings, *J Appl Mech* 33(3), p 553-560

[320] Evensen, D A (1964) Nonlinear flexural vibrations of thin circular rings, Ph.D. Thesis, California Institute of Technology, Pasadena, California

[321] Dowell, E H (1967) On the nonlinear flexural vibrations of rings, *AIAA J* 5(8), p 1508-1509

[322] Sathyamoorthy, M and Pandalai, K A V (1971) Nonlinear flexural vibrations of oval rings, *J Aeronaut Soc India* 23(1), p 1-12

[323] Boresi, A P and Reichenbach, H C (1967) Energy methods in parametric excitation of rings, *Nucl Eng Des* 6, p 196-202

[324] Crespo Da Silva, M R M and Zaretzky, C L (1990) Non-linear modal coupling in planar and non-planar responses of inextensional beams, *Int J Non-Linear Mech* 25(2/3), p 227-239

[325] Piszczek, K (1957) The influence of the curvature of an originally curved bar on the resonance regions of plane form of bending, *Arch Mech Stos* 9(2), p 155-190

[326] Hitchings, D and Ward, P (1977) The steady state response of geometrically non-linear shallow arches, *Int J Numer Methods Eng* 11(8), p 1261-1269

[327] Sheinman, I (1980) Dynamic large-displacement analysis of curved beams involving shear deformation, *Int J Solids Struct* 16(11), p 1037-1049

[328] Reddy, J N and Singh, I R (1981) Large deflections and large-amplitude free vibrations of straight and curved beams, *Int J Numer Methods Eng* 17(6), p 829-852

[329] Crespo Da Silva, M R M (1982) Vibrations of shallow arches, including the effect of geometric non-linearities, *J Sound Vib* 84(2), p 161-172

[330] Pilipchuk, V N (1983) On essentially nonlinear dynamics of arches and rings, *J Appl Math Mech* 46(3), p 360-364

[331] Nayfeh, A H (1984) On the low frequency drumming of bowed structures, *J Sound Vib* 94(4), p 551-562

[332] Plaut, R H and Hsieh, J C (1985) Oscillations and instability of a shallow arch under two-frequency excitation, *J Sound Vib* 102(2), p 189-201

[333] Chow, S-L and Herrmann, G (1988) Dynamic response of a ring fabricated from a non-linear elastic material, *J Sound Vib* 124(3), p 397-413

[334] Maganty, S P and Bickford, W B (1988) Influence of internal resonance on the nonlinear oscillations of a circular ring under primary resonance conditions, *J Sound Vib*, 122(3), p 507-521

[335] Leung, A Y T and Fung, T C (1990) Nonlinear steady state vibration and dynamic snap through of shallow arch beams, *Earthquake Eng Struct Dyn* 19(3), p 409-430

[336] Sabir, A B and Lock, A C (1972) Large amplitude, free vibration of geometrically nonlinear circular arches, *Symp Nonlinear Dynamics*, Loughborough Univ Tech, England, 21 p

[337] Glynn, C C and Maxwell, T L (1981) On the non-linear vibration of a thin ring with steady pressurization, *Int J Non-Linear Mech* 16(2), p 105-116

[338] Pandalai, K A V and Sathyamoorthy, M (1973) On the modal equations of large amplitude flexural vibrations of beams, plates, rings and shells, *Int J Non-Linear Mech* 18, p 213-218

[339] Thomsen, J J (1992) Chaotic vibrations of non-shallow arches, *J Sound Vib* 153(2), p 239-258

[340] Woinowsky-Krieger, S (1942) Über die Biegeschwingungen eines Kreisringes unter gleichmässig verteiltem pulsierendem radialem Druck (On the bending vibrations of circular rings under uniformly distributed pulsating radial pressure), *Ing Arch* 13, p 90-96

[341] Rutkowski, M J (1976) A variationally developed, consistent nonlinear theory for the buckling and vibration of thin rings, arches and curved beams under conservative and nonconservative loading, Stanford Univ., California, 127 p

[342] Mushenkov, Ju A and Bichuk, A I (1977) Free vibrations of a nonlinear parabolical arc (in Russian), *Prikl Mech* 13(1), p 131-134

[343] Noor, A K and Peters, J M (1981) Mixed models and reduced/selective integration displacement models for nonlinear analysis of curved beams, *Int J Numer Methods Eng* 17(4), p 615-631

[344] Dawe, D J (1974) Curved finite elements for the analysis of shallow and deep arches, *Comput Struct* 4, p 559-580

[345] Prathap, G (1985) The curved beam/deep arch/finite ring element revisited, *Int J Numer Methods Eng* 21, p 389-407

[346] Petyt, M and Fleischer, C C (1971) Free vibration of a curved beam, *J Sound Vib* 18(1), p 17-30

[347] Petyt, M and Fleischer, C C (1974) Vibration of multi-supported curved beams, *J Sound Vib* 32(3), p 359-365

[348] Sabir, A B and Ashwell, D G (1971) A comparison of curved beam finite elements when used in vibration problems, *J Sound Vib* 18(4), p 555-563

[349] Davis, R, Henshell, R D and Warburton, G B (1972) Constant curvature beam finite elements for in-plane vibration, *J Sound Vib* 25(4), p 561-576

[350] Wolf, J A Jr. (1971) Natural frequencies of circular arches, *J Struct Div, Proc ASCE* 97(9), p 2337-2350

[351] Dawe, D J (1971) The transverse vibration of shallow arches using the displacement method, *Int J Mech Sci* 13(8), p 713-720

[352] Dong, S B and Wolf, J A (1973) Effect of transverse shear deformation on vibrations of planar structures composed of beam type elements, *J Acoust Soc Am* 53(1), p 120-127

[353] Hoa, S V (1979) Finite element method for the vibration frequency of a curved beam with tip mass, *Proc Fifth World Congress Theory Machines Mechanisms* Vol I, p 90-93

[354] Balasubramanian, T S and Prathap, G (1989) A field consistent higher order curved beam element for static and dynamic analysis of stepped arches, *Comput Struct* 33(1), p 281-288

[355] Rossi, R E (1989) Inplane vibrations of circular rings of non-uniform cross-section with account taken of shear and rotatory inertia effects, *J Sound Vib* 135(3), p 443-452

[356] Rossi, R E and Laura, P A A (1989) Free inplane vibrations of circular rings with radial supports taking into account shear and rotary inertia effects, *J Acoust Soc Am* 86(6), p 2237-2243

[357] Davis, R, Henshell, R D and Warburton, G B (March 1971) New beam elements, British Acoustical Soc Paper 71/11 presented at the *Symp Finite Element Techniques in Structural Vibration*, Southampton

[358] Zhang, Z (1992) A note on the hybrid-mixed C^0 curved beam elements, *Comput Methods Appl Mech Eng* 95(2), p 243-252

[359] Davis, R, Henshell, R D and Warburton, G B (1972) Curved beam finite elements for coupled bending and torsional vibration, *Int J Earthquake Eng Struct Dyn* 1(2), p 165-175

[360] Thomas, D L and Wilson, R R (1973) The use of straight beam finite elements for analysis of vibrations of curved beams, *J Sound Vib* 26(1), p 155-158

[361] Pantazopoulou, S J (1992) Low order interpolation functions for curved beams, *J Eng Mech* 118(2), p 329-350

[362] Heppler, G R (1992) An element for studying the vibration of unrestrained curved Timoshenko beams, *J Sound Vib* 158(3), p 387-404

[363] Trompette, P and Gaertner, R (May 1983) Dynamic behavior of composite layered beams by the finite element method, *Shock and Vib Bull* part 2, p 151-157

[364] Reddy, B D and Volpi, M B (1992) Mixed finite element methods for the circular arch problem, *Comput Methods Appl Mech Eng* 97(1), p 125-145

[365] Noor, A K and Anderson, C M (1992) Hybrid analytical technique for the nonlinear analysis of curved beams, *Comput Struct* 43(5), p 823-830

[366] Ali, S A (1983) Parametric instability of curved girders, *J Struct Div, Proc ASCE* 109(4), p 829-842

[367] Ali, S A (1984) Stability of bending-torsional vibrations of curved thin-walled beams, *J Sound Vib* 95(3), p 341-350

[368] Tan, C P and Shore, S (1968) Dynamic response of a horizontally curved bridge, *J Struct Div, Proc ASCE* 94(ST3), p 761-781

[369] Tan, C P and Shore, S (1968) Response of horizontally curved bridge to moving load, *J Struct Div, Proc ASCE* 94(ST9), 1968, p 2135-2151. Discussions on this paper in *J Struct Div, Proc ASCE* 95(ST11), 1969, p 2523-2525 and *J Struct Div, Proc ASCE* 96(ST4), 1970, p 861-863

[370] Shore, S and Chaudhuri, S (1972) Free vibration of horizontally curved beams, *J Struct Div, Proc ASCE* 98(ST3), p 793-796

[371] Bhattacharya, B (1975) Coupled vibrations of thin-walled open section curved beams, *J Struct Div, Proc ASCE* 3(1), p 29-35

[372] Christiano, P P and Culver, C G (1969) Horizontally curved bridges subject to moving load, *J Struct Div, Proc ASCE* 95(ST8), p 1615-1643

[373] Culver, C G and Oestel, D J (1969) Natural frequencies of multispan curved beams, *J Sound Vib* 10(3), p 380-389

[374] Culver, C G (1967) Natural frequencies of horizontally curved beams, *J Struct Div, Proc ASCE* 93(ST2), p 189-203. Also see *J Struct Div, Proc ASCE* 94(ST2), 1968, p 614-615

[375] Fam, A R M (1973) Static and free vibration analysis of curved box bridges, Ph.D. Thesis, McGill Univ, Montreal, Canada

[376] Komatsu, S and Nakai, H (1970) Fundamental study on forced vibrations of curved girder bridges, *JSCE* **2** part 1

[377] Rutenberg, A (1979) Vibration properties of curved thin-walled beams, *J Struct Div, Proc ASCE* **105**(ST7), p 1445-1455

[378] Tabba, M M and Turkstra, C J (1977) Free vibrations of curved box girders, *J Sound Vib* **54**(4), p 501-514

[379] Yoo, C H and Fehrenbach, J P (1981) Natural frequencies of curved girders, *J Eng Mech* **107**(EM2), p 339-354

[380] Chaudhuri, S K (1975) Dynamic response of horizontally curved I-girder bridges due to a moving vehicle, Ph.D. Thesis, Univ Pennsylvania, Philadelphia

[381] Chaudhuri, S K and Shore, S (1977) Thin-walled curved beam finite element, *J Eng Mech* **103**(EM5), p 921-937

[382] Christiano, P P and Culver, C G (1969) Horizontally curved bridges subjected to moving load, *J Struct Div, Proc ASCE* **95**(ST8), p 1615-1643

[383] Christiano, P P (1967) The dynamic response of horizontally curved bridges subject to moving loads, Ph.D. Thesis, Carnegie-Mellon University

[384] Komatsu, S and Nakai, H (May 1964) Study on free vibration of curved girder bridges, *Nineteenth Annual Conf JSCE*, p 35-60

[385] Maddox, N R (1969) Free oscillations of thin-walled open section circular rings, Ph.D. Thesis, Georgia Institute of Technology, Atlanta, Georgia, 166 p

[386] Oestel, D J (1968) Dynamic response of multi-span curved bridges, M Sc Thesis, Carnegie-Mellon Univ

[387] Rabizadeh, R O and Shore, S (1975) Dynamic analysis of curved box-girder bridges, *J Struct Div, Proc ASCE* **101**, p 1899-1912

[388] Yonezawa, H (1962) Moments and free vibrations in curved girder bridges, *J Eng Mech* **88**(EM1), p 1-21

[389] Gendy, A S and Saleeb, A F (1992) Finite element analysis of the spatial response of curved beams with arbitrary thin-walled sections, *Comput Struct* **44**(3), p 639

[390] Smirnov, A B and Trockij, V A (1978) Determination of the curved axis of a thin elastic beam having optimal in-plane eigenfrequencies (in Russian), *Leningrad polit in-t* 9(C), Dep No. 3, p 46-79

[391] Olhoff, N and Plaut, R H (1983) Bimodal optimization of vibrating shallow arches, *Int J Solids Struct* **19**(6), p 553-570

[392] Plaut, R H and Olhoff, N (1983) Optimal forms of shallow arches with respect to vibration and stability, *J Struct Mech* **11**(1), p 81-100

[393] Kil'chinskaya, G A (1986) Vibrations in the plane of curvature of curved elastic rods during heating, *Sov Appl Mech* **22**(3), p 251-256

[394] Fettahlioglu, O A and Steele, T K (1988) Thermal deformations and stresses in circularly curved thin beams and rings, *J Thermal Stresses* **11**(3), p 233-255

[395] Singal, R K, Williams, K and Wang, H (1991) Effect of radial thickness on the in-plane free vibrations of circular annular discs, *J Vib Acoust* **113**(4), p 455-460

[396] Gladwell, G M L and Tahbildar, U C (1972) Finite element analysis of the axisymmetric vibrations of cylinders, *J Sound Vib* **22**, p 143-157

[397] Gladwell, G M L and Vijay, D K (1975) Natural frequencies of free finite length circular cylinders, *J Sound Vib* **42**, p 387-397

[398] Hutchinson, J R and El-Azhari, S A (1986) Vibrations of free hollow circular cylinders, *J Appl Mech* **53**, p 641-646

[399] Girgis, R S and Verma, S P (1981) Method for accurate determination of resonant frequencies and vibration behavior of stators of electrical machines, *IEE Proc B Electr Power Appl* **128**, p 1-11

[400] Singal, R K and Williams, K (1988) A theoretical and experimental study of vibrations of thick circular cylindrical shells and rings, *J Vib Acoust Stress Reliab Des* **110**, p 533-537

[401] So, J (1993) Three-dimensional vibration analysis of elastic bodies of revolution, Ph.D. Dissertation, The Ohio State University, Columbus Ohio, 312 p

[402] Gladwell, G M L and Vijay, D K (1975) Errors in shell finite element models for the vibration of circular cylinders, *J Sound Vib* **43**, p 511-528

[403] Hutchinson, J R and El-Azhari, S A (1986) On the vibration of thick annular plates, *Proc Euromech Colloq 219 on Refined Dynamical Theories of Beams, Plates and Shells and their Applications*, p 102-111

[404] Verma, S P and Girgis, R S (1981) Experimental verification of resonant frequencies and vibration behavior of stators of electrical machines, Part I: Models, experimental procedure and apparatus, *IEE Proc B Electr Power Appl* **128**, p 12-21

[405] Verma, S P and Girgis, R S (1981) Experimental verification of resonant frequencies and vibration behavior of stators of electrical machines, Part II: Experimental investigations and results, *IEE Proc B Electr Power Appl* **128**, p 22-32

[406] Verma, S P, Singal, R K and Williams, K (1987) Vibration behavior of stators of electrical machines, Part I: Theoretical study, *J Sound Vib* **115**, p 1-12

[407] Verma, S P, Singal, R K and Williams, K (1987) Vibration behavior of stators of electrical machines, Part II: Experimental study, *J Sound Vib* **115**, p 13-23

P. Chidamparam received his B. Tech. in Mechanical Engineering from the Indian Institute of Technology Madras, India, in 1987 and his M.S. in Mechanical Engineering from the Ohio State University, in 1989. He was awarded the Alcan Scholarship in 1989 to pursue doctoral studies at the Ohio State University, where he is currently a doctoral candidate in Engineering Mechanics. He has been an active participant in the development and instruction of undergraduate courses in Mechanical Engineering and Engineering Mechanics at Ohio State. His research interests are in the general areas of structural vibrations, machinery dynamics and acoustics. He is a member of the Phi Kappa Phi Honor Society and the American Society of Mechanical Engineers.

After earning two degrees in Mechanical Engineering, Arthur W Leissa received his PhD degree in Engineering Mechanics in 1958 from Ohio State University, and remained there as Assistant Professor. He became Professor of Engineering Mechanics at Ohio State in 1964, and currently holds that position. The academic year 1972-73 was spent as Visiting Professor at the Federal Institute of Technology in Zurich, Switzerland, teaching graduate courses and doing research. Subsequently, 1985-86 was given to a Visiting Professorship at the Air Force Academy in Colorado Springs. He is the author of two books, Vibration of Plates and Vibration of Shells, which summarize the literature in these fields, as well as approximately 180 other publications dealing primarily with elasticity, plates, shells, vibrations and buckling of continuous systems, composite materials, and approximate methods of solving boundary value problems. A former Associate Editor for Applied Mechanics Reviews, *he recently was appointed Editor-in-Chief. He is on the editorial advisory boards of* Composite Structures, *the* Journal of Sound and Vibration, *and the* International Journal of Mechanical Sciences. *He is a Fellow of ASME and of the American Academy of Mechanics, and is a past President of the American Academy of Mechanics. The Pan American Congress of Applied Mechanics (PACAM) was conceived by him, and he was the general chairman of the first one, in 1989. His technical expertise includes employment by Sperry Gyroscope, Boeing Airplane, North American Aviation, Battelle Memorial Institute, and Kaman Nuclear as an engineer or consultant. In his spare time, he climbs mounta*

BOOK REVIEWS

Items with a reviewer byline (coded R) are by AMR's corps of dedicated outside volunteer reviewers. AMR will attempt to get critical reviews of all relevant textbooks, professional books, reference works, and handbooks. Items without a reviewer byline (coded N) are prepared by AMR in-house staff and are largely based on material such as a book's table of contents and editor's preface or foreword. In the interest of timeliness most conference proceedings and multi-author contributed volumes will receive descriptive notes in this fashion. Books deemed to be somewhat peripheral to AMR's basic scope may simply be listed by title (no code; not included in annual index). Also listed by title when first received are books under review.

I. FOUNDATIONS & BASIC METHODS

9R3. Numerical Recipes in Fortran; (Second Edition). The Art of Scientific Computing. - William H Press *(Harvard-Smithsonian Center for Astrophys)*, Saul A Teukolsky *(Dept of Phys, Cornell)*, William T Vetterling *(Polaroid)*, Brian P Flannery *(Exxon Res and Eng)*. Cambridge UP, New York. 1992. 963 pp. ISBN 0-521-43064-X.

Reviewed by Ben H Thacker (Struct Eng, PO Drawer 28510, SWRI).

This book will be appreciated by anyone involved in the numerical solution of engineering problems. Continuing in the tradition of their first edition, the authors have successfully blended tutorial discussion, fundamental mathematics, explanation of algorithms, and working computer programs into neatly packaged chapters covering all of the basic topics in numerical methods. What sets this book apart, in the reviewer's opinion, is the versatility of the book. It can be used as a textbook in a classroom environment, as an engineer or scientist's "toolkit" for development of a numerical application, or even as a *black-box* in which the computer programs are used as is without an understanding of the inner-workings of the methods. Simply using the programs as black-boxes, however, short-circuits this book's main strength, which is to demystify the traditional algorithms used in numeric computations.

Because Fortran coding is included in the manuscript, chapter 1 is devoted to preliminaries such as programming style, conventions, and machine accuracy. With the exception of chapter 20, which deals with "less-numerical algorithms," the remaining 18 chapters are divided into the traditional topics on numerical methods: solution of linear algebraic equations; interpolation and extrapolation; integration of functions; evaluation of functions; special functions; random numbers; sorting; root finding and nonlinear sets of equations; minimization or maximization of functions; eigensystems; fast Fourier transform; Fourier and spectral applications; statistical description of data; modeling of data; integration of ordinary differential equations; two point boundary value problems; integral equations and inverse theory; and partical differential equations.

Although the second edition is about 50% larger than the first edition, with over 300 included programs, the size is still quite manageable. The authors have (wisely) chosen to expand the book in breadth, not depth, so all of the topics are presented at the same accessible level used in the first edition. A partical list of some of the new topics covered are: integral equations, elliptic partial differential equations, linear algebra on sparse and banded matrices, Cholesky and QR decomposition, numerical derivatives, adaptive and recursive Monte Carlo integration, globally convergent methods for nonlinear equations simulated annealing minimization, FFT's, wavelet transforms, smoothing filters, statistical bootstrap method, and several new methods for solving differential equations. Thus, current owners of the first edition should seriously consider adding this second edition to their library.

Finding information in the book is very easy. The table of contents is well organized, extensive, but not cluttered. The index spans 30 pages, so the reader should have no trouble finding a quick route to the needed section. The reference list is complete, and even includes a "nucleus" of the author's recommended personal references. Finally, an index of programs and program dependencies is listed.

Numerical Recipes is also available in C, for those more familiar with the C programming language (Basic and Pascal versions of the programs are available only in the first edition). An example book and diskette containing the programs are also available in both programming languages. The reviewer highly recommends at least purchasing the diskette - hours of tedious keyboarding will be saved. Moreover, the example driver routines and several handy utilities are supplied with the disk, which are also quite helpful.

In short, *Numerical Recipes in Fortran* is indispensable. Having used the first edition for several years and this second edition for several months, the reviewer can recommend from experience that this book be kept within reach by anyone doing scientific computing.

Correction: The preceeding review appeared with inaccurate reviewer information in the July issue. Our apologies to Dr. Thacker.

9N1. BETA Mathematics Handbook, 2nd ed. - Lennart Rade and Bertil Westergren. CRC Press, Boca Raton FL. 1992. 494 pp. ISBN 0-8493-7758-7. $39.95. Outside US, $49.95.

BETA Mathematics Handbook is a comprehensive, accessible reference compilation of basic facts and information for pure and applied mathematics, probability and statistics, and numerical analysis and basic applications. It offers a blend of classical areas of mathematics such as algebra, geometry, and analysis with new, modern topics. As a result, the book is up to date with the latest math information frequently used in science and engineering.

Contents include: fundamentals; algebra; geometry and trigonometry; linear algebra; the elementary functions; differential calculus (one variable); integral calculus; sequences and series; ordinary differential equations (ODE); multidimensional calculus; vector analysis; orthogonal series and special functions; transforms; complex analysis; optimization; numerical analysis and programming; probability theory; and statistics.

9N2. Pocket Book of Integrals and Mathematical Formulas, 2nd ed. - RJ Tallarida *(Temple Univ, Philadelphia PA)*. CRC Press, Boca Raton FL. 1992. 240 pp. ISBN 0-8493-0142-4. $14.95. Outside US, $17.95.

This book is a handy, compact reference work containing concise discussions of mathematical concepts and formulas frequently needed by students and professionals in engineering, science, applied math and statistics. One of the book's special features is its comprehensive table of integrals arranged and formatted to facilitate the rapid location of the right form. Tables of derivitives; calculus applications; graphs of important Cartesian and polar curves; and formulas from algebra, geometry, trigonometry, calculus and statistics have also been arranged with convenience in mind. The book also lists infinite series and includes discussions and formula listings in differential equations and in advanced topics such as Fourier series, Laplace and z-transforms, vector analysis, and orthogonal polynomials. Important physical constants and numerical tables of probability distributions such as normal, Poisson, t, chi square, and F are provided.

Contents include: elementary algebra and geometry; determinants, matrices and systems of equations; trigonometry; analytical geometry; differential calculus; integral calculus; vector analysis; special functions; differential equations; statistics; table of derivatives and table of integrals.

The Avoidance of Cavitation Damage. - W Tillner. ASME, New York. 1993. 268 pp. ISBN 0-85298-807-9. $134.00. (Under review)

Control of Scale and Corrosion in Building Water Systems. - Russell W Lane *(water treatment consultant, PE, Illinois State Water Survey IL)*. McGraw-Hill, New York. 1993. 270 pp. ISBN 0-07-036217-3. (Under review)

II. DYNAMICS & VIBRATION

9R5. Detonation of Condensed Explosives. - Roger Cheret *(Commissariat a l'Energie Atomique, Paris, France).* Springer, New York. 1993. 425 pp. ISBN 0-387-97898-4.

Reviewed by Alfred Carmichael Buckingham (Comput Phys Div; Phys Dept, LLNL, Mail Code L-321, PO Box 808, Livermore CA 94551).

This is a well written, amply cross-referenced monograph on the physics and dynamics governing the initiation, evolution, and propagation of explosive detonation fronts, and the underlying detonation process itself. It provides a clear exposition of the fundamentally important current theoretical findings and remaining questions on detonation processes. The book is a comprehensive, theoretically well-grounded reference work for specialists working in a broad range of explosive technology topics such as: energetic propellant chemical composition, ignition and detonation onset criticality, analysis of detonation instabilities, their evolution and possible consequences, transient, multidimensional detonation wave growth and propagation influences on building structures, explosive vulnerability, and hazards related to outside shock stimuli. It provides a basis for evaluating and predicting potential biological hazards and safety requirements.

In introducing the subject, the author leads the reader from the origins of understanding detonation processes and applications in early Chinese innovations with black power, to the important thermodynamic state and fluidynamic discontinuous interface concepts developed and studied in the late 19th and early 20th centuries. The author next extends the description to the more recent progress in theoretical and experimental analysis and characterization of the macroscopic connection between the kinetic influences of the detonation process and the fluid motions that advect and mix the reactants and products. He completes his survey with descriptions on the dynamic and kinetic structure of the detonation process extended down to digital computer-aided simulation of microscopic molecular and electronic configuration scale interaction dynamics.

The author supports his development of the physical concepts by providing a compact but usefully comprehensive mathematical foundation based on integral relations, function theory, and singular perturbation methods. These provide both insight and guidance for the reader in developing an understanding of the interaction between thermodynamic and thermokinetic fields, fluid stress force and acceleration fields, and fluid motion fields. The frequent use of illustrations and diagrams complements the text and mathematical constructions. The reader is provided with timely reminders and guidance on physical concepts and mathematical constructions through a number of brief, but quite useful, appendices at the end of the book. These supply helpful notes on operator theory, singular matrix operations, treatments of critical phenomena, integral methods, asymptotic theory and, conveniently, a summary of the notation used and applied consistently. References are provided on most of the major background literature, including seminal work extending over almost two centuries. References are conveniently placed at the end of individual chapters in which they appear, or at the end of each of the four major sections into which the author divides the book.

Within this division, the first three chapters make up Part I. It consists of a review and fundamental theoretical framework for the discussion of the mechanical and thermodynamic concepts defining the development and propagation of detonation waves. It begins with a review of the relations governing basic fluid motion, arbitrary equation of state constructions valid at very high pressures, discontinuities of continuum motion, discontinuities leading to molecular constituent changes and ends with an examination of the detailed structure of the detonation process in the neighborhood of the reaction front aided by asymptotic singular perturbation analysis.

Part II (chapters four through six), moves from the macroscopic to the microscopic descriptive framework. Initially, the reader is provided with background information developed from atomic/molecular group interaction dynamics techniques followed by an extension to analysis of the influence of electron energetic distributions and configurations. Subsequently, the reader is provided with a discussion of reaction mechanism on an atomic/molecular scale, including explosive molecular/atomic decomposition.

Part III, consisting of chapters seven, eight, and nine, contains discussions on the macroscopic mechanisms generating detonation. These give the reader detailed insight on reaction mechanisms, explosive decomposition, cooperative mechanisms, propagation of chemical reactions, compositional changes, connections to (advective) fluid motion, and plane shock initiated detonations.

The final part, exclusive of the appendices and index mentioned previously, is devoted to the dynamic characterization of explosives. In chapters ten through twelve most of the emphasis is placed on experimental techniques, experimental diagnostics and specialized numerical methods for prediction and simulation of process evolution. It includes discussions of the basic principles of prompt measurement (μ-second time scale realizations), numerical "forecasting" simulations, and the computation of state surface detonation processes.

Generally, the book places emphasis on thermodynamical and thermo kinetic-reaction kinetic processes with considerable and very suitable attention to microscopic structure, microscopic scale interactions, and high pressure quantum mechanical dynamic interactions, with less emphasis on the continuum fluid motion influences. For example, background material is supplied on the important role of both reactive and inert discontinuous wave front propagation and interaction with reactive media, but little emphasis is given to the generally well recognized (but imperfectly understood) role of statistically chaotic (turbulent) transport and reactant mixing in the initiation and evolution of the detonation process. This and somewhat abbreviated attention given to more recent advances and applications of numerical simulation methods to isolate and test the influence of sub resolution (temporal and spatial) scale mechanisms are the only (minor) weaknesses I find in the author's otherwise interesting and comprehensive presentation. the author's careful step-by-step development of the subject, supported by systematic buildup of the mathematical foundation, makes necessary the reading of the book from beginning to end in order to develop a proper appreciation of the material. Fortunately, the book is well-written and eminently readable so that this cover-to-cover inspection becomes an interesting, rewarding, and enjoyable exercise.

In summary, *Detonation of Condensed Explosives* is a very good reference work which should be of particular interest and use to chemists, physicists, applied mathematicians, and engineers involved in many aspects of explosive tehcnology. It is also sufficiently self contained and possesses a systematically developed theoretical foundation and substantial references adequate to provide background material for preparation of either formal academic course work or less formal instructional material for industrial laboratory usage. It is recommended for personal acquisition and retention, as well as for more general library purchase.

9R6. Elastiche Mehrkorpersysteme. (Elastic Multibody Systems). (German). - Hartmut Bremer and Friedrich Pfeiffer *(Tech Univ Munchen).* B G Teubner, FRG. 1992. 283 pp. Paper. ISBN 3-519-02374-1.

Reviewed by Frederick V Pohle (61 Kilburn Rd, Garden City NY 11530).

This text of less than 300 pages, moderately priced, is a remarkably complete and comprehensive coverage of elastic multibody systems. Both authors have been active in many areas of this wide field, and this is evident in the detailed coverage which pays attention to the theoretical fundamentals, as well as to numerical and approximate methods, through the fullest use of computers. Their presentation is compact and not a word is wasted.

After a brief introduction on the nature of model building and its relation to engineering practice, the 2nd chapter presents the broad theory of elastic bodies, all in modern vector-matrix formulation. This material is then generalized in the 3rd chapter to multi-body systems and their decompositions, and then, in the 4th chapter, methods of solution (for example, to beams, plates, shells, finite elements, and related topics). Specific applications of current interest are treated in chapter 5 (dynamics of satellites), and in chapter 7 (the dynamics of robotics). In all, there are approximately 200 selected references to the literature, particularly to modern applications, but also to the classical literature as well.

Although some remarks are made on specific applications, there are not detailed discussions of problems and no exercises of any kind; this has made it possible to cover a vast amount of material comprehensively and fully. *Elastische Mehrkorpersysteme*, written in German, is suitable at the senior-graduate level for general and specific applications (particularly to satellites and robotics), and is an important addition not only to research libraries but also to individual libraries, since so much of the material is simply not readily available in one volume.

9R7. Mechanical Measurements, 3rd ed. - RS Sirohi and HC Radha Krishna *(Eng Des Center, Indian IT, Madras, India)*. Wiley, New York. 1991. 285 pp. ISBN 0-470-21953-X. $34.95.

Reviewed by Larry Zavodney (Dept of Engineering, Cedarville Col, Cedarville OH 45314-0601).

The authors advertise this book as a "text for both graduate and post-graduate classes and as a constant reference to a researcher." The book is 290 pages long, including a one-page appendix, 19 references, and a four-page index. There are 10 chapters - three devoted to generalized topics related to measurement and seven devoted to the specific measurement of some physical quantity or methodology. The title of the book accurately reflects the contents of the book. It is a brief summary of some current methods used to make measurements of physical quantities. Since it is so brief, it is an incomplete reference.

Chapter 1 is devoted to the concepts of measurements and uses a few transducer systems for illustration. Chapter 2 discusses performance characteristics of measuring instruments and static and dynamic systems. The discussion of the transfer function and frequency response function is at the undergraduate level as found in a discrete vibration or feedback control course; however, the nature of the exercises has little correlation with the chapter. Chapter 3 has a good but brief discussion on measurement inaccuracy, probability, and statistics; the eight exercises are good.

Chapter 4 summarizes some direct and indirect methods of measuring force and torque by measuring deformation of elastic members such as springs, bars, and rings, and discusses the load cell and dynamometer; there are five exercises at the end of the chapter. Chapter 5 discusses the measurement of strain and the subsequent calculation of stress from appropriate equations. Strain is measured by mechanical methods, opto-mechanical methods, and electrical methods that include capacitive, inductive, and resistive gauges. Basic equations and circuits for the most common applications are given. Grid techniques and Moire fringes and interferometric methods are mentioned.

Chapter 6 is devoted to the measurement of pressure and discusses manometers, the McLeod gauge, and the dead-weight tester. Deformation of elastic members as measured by mechanical devices (such as strain gages, piezoelectric crystals, and the Knudsen gauge) is used to measure pressure. Chapter 7 summarizes methods to measure flow and visualize flow fields. Popular flow meters that include obstruction meters and velocity probes, and specialized methods that include turbine, magnetic, and sonic flow meters, are discussed. Schlieren and interferometric techniques are mentioned. Chapter 8 discusses temperature measurement using the basic types of mechanical and electrical thermometers. Compensation methods for temperature-induced errors in leadwires for Wheatstone bridges are introduced here (instead of earlier when strain gauges and bridges are first mentioned). Radiation methods using optical pyrometers concludes the chapter.

Chapter 9 discusses optical methods, how the laser is used to measure displacement and velocity, and how the diffraction strain gauge and laser doppler anemometer work. The chapter includes a discussion on holography. Chapter 10 introduces fiber optics and discusses basic properties, emitters, detectors, methods of modulation and demodulation, incoherent and coherent sensors, and polarization modulation.

Because the book is brief and quite broad in its topics, it lacks depth in any one topic; hence, this book might be suitable for someone offering a low-budget survey course in mechanical measurements; equations are given--not derived. The book is basically a collection of how selected transducers work and focuses on the physics. There are no worked examples in the text. It is not suitable for undergraduate classes in instrumentation because it does not include some of the more popular transducers, such as dynamic load cells using piezoelectric crystals, LVDT's, or accelerometers (the only mention of an accelerometer is in reference to a method of measuring force). There is no discussion of computers, data acquisition techniques, analogue-to-digital conversion and vice-versa, or processing of analogue or digital signals. The book is organized around particular physical quantities rather than principles; eg, the description of how a piezoelectric crystal works is contained entirely within a discussion of pressure transducers. The book has a British flavor as evidenced in word spellings; noise is that which occurs at 50 Hz (instead of 60 Hz), and there are many articles missing. One would have expected that by the third edition the authors would have corrected the grammar. It is not well written. The qulity of the printing and figures is poor and appears related to the low cost of the book (which was printed in India). Given the availability of better texts suitable for both graduate and undergraduate classes and for reference, I would not recommend *Mechanical Measurements*.

9N8. Seismic Applications of Acoustic Reciprocity. - JT Fokkema *(Pet Eng and Tech Geophys, Univ of Tech, Delft, Netherlands)* and PM van den Berg *(Lab for Electromagnetic Res, Univ of Tech, Delft, Netherlands)*. Elsevier, UK. 1993. 350 pp. ISBN 0-444-89044-0. $156.50.

Progress in seismic data processing requires the knowledge of all the theoretical aspects of the acoustic wave theory. The reciprocity theorum was chosen as the central theme of this book as it constitutes the fundamentals of the seismic wave theory.

Contents of the book include: integral transformations; iterative solution of integral equations; basic equations in acoustics; radiation in an unbounded, homogeneous medium; reciprocity theorums; field reciprocity between transmitter and receiver; radiation in an unbounded, homogeneous medium; scattering by a bounded contrasting domain; scattering by disk; wavefield decomposition; deghosting; removal of surface related wave phenomena; boundary imaging; domain imaging, and seismic inversion.

III. AUTOMATIC CONTROL

9N9. Identification and Control in Systems Governed by Partial Differential Equations. Proceedings in Applied Mathematics 68. - Edited by HT Banks, RH Fabiano, K Ito. SIAM. 1993. 272 pp. ISBN 0-89871-317-X. $48.50.

Written on a graduate research level, this collection of invited papers presented at the 1992 AMS-IMS-SIAM Joint Summer Research Conference focuses on issues related to modeling (including design), parameter estimation and system identification, and feedback control problems described by partial differential equations. It includes applications of flow control (in high pressure vapor transport reactors, airfoil design, and noise suppression), as well as control of structures (beams, plates, robot arms and smart material structures).

Contents include: Modeling of flow dynamics and its impact on the optimal reactor design prob-

lem by HT Tran, JF Scroggs, and KJ Bachmann; Sensitivity calculations for a 2D, inviscid, supersonic forebody problem by J Borggaard, J Burns, E Cliff and M Gunzberger; Models for control in smart structures by HT Banks and RC Smith; Bootstrap methods for inference in least squares identification problems by BG Fitzpatrick and G Yin; MATLAB-software for parameter estimation in two-point boundary value problems by M Kroller and K Kunisch; Some stability estimates for the identification of conductivity in the one-dimensional heat equation by G Crosta; Estimation of material parameters in a dynamic nonlinear plate model with norm constraints by L White; Global stabilization of a von Karman plate without geometric conditions by ME Bradley and I Lasiecka; The standard problem of H∞ optimal control for infinite dimensional systems by A Bensoussan and P Bernhard; Perturbation of well-posed systems by state feedback by KA Morris; Point observation in linear-quadratic elliptic distributed control systems by L Ji and G Chen; Boundary control for a viscous Burgers' equation by CI Byrnes, DS Gilliam and VI Shubov; Feedback control of singular integro-differential systems: An input-output approach by H Ozbay and J Turi; Stable and unstable zero dynamics of infinite dimensional systems by TJ Tarn, AK Bejczy and C Guo; Covariance based control of linear hereditary systems by JA Reneke.

Measurement Errors: Theory and Practice. - Semyon Rabinovich. AIP. 1993. 270 pp. ISBN 0-88318-866-X. $100.00. (Under review)

IV. MECHANICS OF SOLIDS

9R10. Applied Elasticity. - Zhilun Xu *(Hohai Univ, PRC)*. Wiley, New York. 1992. 373 pp. ISBN 0-470-21868-1. $34.95.

Reviewed by Dimitris Lagoudas (Dept of Aerospace Eng, Texas A&M Univ, College Station TX 77843-3141).

This book is intended as a textbook on the theory and solution techniques of linear elasticity. The first chapter briefly introduces the concept of stress, emphasizing operational details rather than fundamental physical understanding. Chapters 2, 3, and 4 cover plane (2D) elasticity problems in rectangular and polar coordinates. Most of the material covered in these chapters can be found in classical texts in elasticity, eg, Timoshenko and Goodier. Unconventional terminology, like geometrical equations and physical equations, used in these chapters and repeated in later chapters renders the book somewhat difficult to follow, especially for a student without a global view of the subject. The inclusion of the complex variable method in chapter 5 (for the solution of plane problems in elasticity and the demonstration of the method to the elliptic hole and crack problems) is a positive step. Plane thermal stress problems are discussed in chapter 6, and the finite difference method for plane problems is introduced in chapter 7. Three-dimensional deformations are first introduced in chapter 8, with displacement potentials used for solving some fundamental problems in 3D elasticity. The theory of torsion of prismatic bars is discussed in chapter 8, where the finite difference method is again used as a numerical tool. Variational methods are introduced in chapter 11, while classical theory of plates and numerical applications using the finite difference scheme are covered in chapters 12 and 13, respectively. The last three chapters of the book are devoted to the general theory of shells, cylindrical shells, and shells of revolution.

Xu's book is a compilation of special topics in elasticity as presented by classical books on the subject, without a personal style other than a detailed account of the finite difference method. The author exclusively uses the finite difference method to obtain numerical solutions, even though the current trend in engineering education and industrial practice is to use the FE and/or the BEMs. Another key omission is the absence of any discussion on constitutive equations beyond the linearly elastic isotropic solid, especially the concept of material symmetries and applications to composites. The author also did not attempt to connect elasticity with continuum mechanics by excluding references to conservation principles, kinematics of deformations, and measures of strain. The book does not introduce tensorial notation, even as an additional alternative formulation, missing the opportunity to prepare students for advanced theoretical or numerical courses in solid mechanics. Treatment of elastodynamics is completely left out of the book.

Based on the above observations, the reviewer concludes that *Applied Elasticity* is out of touch with the current curriculum demands in the area of solid mechanics in the USA and does not recommend it as a textbook for an applied elasticity course. It might be of some use, however, as a reference book to the practicing engineer who does not have access to a FE code.

9R11. Metallurgical Failures in Fossil Fired Boilers; (2nd ed). - David N French *(David N French, Inc, Northborough MA)*. Wiley, New York. 1993. 560 pp. ISBN 0-471-55839-7. $69.95.

Reviewed by William J D Shaw (Mech Eng Dept, Univ of Calgary, 2500 Univ Dr NW, Calgary, T2N 1N4, AB, Canada).

This book is targeted toward those working with boilers and covers an extremely broad range of failures occurring under very diverse circumstances. It is a good documentation of microstructures and failures with excellent illustrative photographs. The book tackles this subject from an integrated approach, bringing in areas as far-reaching as statistics of boiler failures. It provides a general but limited basis of the various design considerations, such as stress analysis (ASME Codes), mass and heat transfer, specific fuel types, and material selections.

Coverage also extends through the metallurgical area, looking at the fundamentals of materials science with respect to atomic structure, phase diagrams, and time temperature transformation diagrams. Also covered is the mechanical behavior of materials; more specifically, the creep and fatigue areas. The metallurgy evolves from ferritic steels through stainless steels. However, what is missing in general is that of welding behavior and microstructure-property relationships and how these are affected by high temperature operation. Additionally, the stainless steel coverage is very weak and does not look at the broader range of stainless materials, which would give a more complete picture for designers using this book as a reference.

Other aspects that are looked at are failures that occur due to material-environment interaction, eg, failures taking place on both the stream side and the fire side of the heat exchanger. Similarly, corrosion is also explored, but due to the complex nature of this subject, it is somewhat weak in presentation. Weld failures are presented in fairly good detail, with the prevention of failures based primarily upon furnace design and creep relationships. Some aspects of remaining life assessment are also covered.

The main strength of the book is that many case studies are presented throughout which offer practical information and guidance to boiler designers. The book is well-referenced, with useful appendices and a fairly comprehensive index. It is definitely a major and important reference book for designers involved in the boiler industry. Years of invaluable information and failure feedback are contained within *Metallurgical Failures in Fossil Fired Boilers*. This, combined with the integrated approach, far exceeds any shortcomings that were mentioned above.

9R12. Stability Design of Steel Frames. - W F Chen *(Sch of Civ Eng, Purdue)* and E M Lui *(Dept of Civ and Env Eng, Syracuse Univ, Syracuse NY)*. CRC Press, Boca Raton FL. 1991. 392 pp. ISBN 0-8493-8606-3. $75.00. $90.00 outside US.

Reviewed by AN Sherbourne (Dept Civil Eng, Univ of Waterloo, Waterloo, ON, N2L 3G1, Canada).

A structural frame is an assembly of beam-column elements, and its stability analysis requires an investigation of overall as well as individual member behavior. Accurate methods for the stability analysis of beam-columns and frames are readily available; however, analytical and computational complexities do not permit easy implementation in day to day design practice. This has led to the development of numerous and simple approximate methods for stability analysis. This book is written with the objective of reviewing these analytical procedures and presenting a number of useful approximate design methods, which were mainly developed by the authors over the years. The authors suggest that the major issues of practical relevance in stability design are inelastic effects, moment-gradient, second order P-delta effects, and joint flexibility. The subject matter is thus centred around these topics

The book is divided into seven chapters. In the first chapter, the inelastic analysis of beam-columns is presented in detail, using the Newmark method and its more refined extension, the Cranston method. In the second chapter, design issues related to P-delta effects, moment-gradient, effective length factors, and interaction equations are addressed, and various design rules are summarized. In chapter 3, standard methods of elastic, nonlinear analysis, eg, finite element and beam-column approaches, are outlined. A method proposed by Lui, referred to as the pseudo-load method, is an interesting way of accommodating nonlinear effects in the load vector thus avoiding the need for updating the stiffness matrix in each cycle of computation.

For approximate second order inelastic analysis, gradual stiffness loss with progressive yielding is modeled by rotational springs attached to the member ends as discussed in chapter 4. In chapter 5, the characteristics of the more common types of beam-column connections are described and various empirical moment-rotation equations are reviewed. Chapter 6 describes the elastic and inelastic analysis of frames, including the effects of joint flexibility. The design of semi-rigid frames is intrinsically more complex than rigid frames because of the difficulty of predicting the moment-rotation behavior of connections. In chapter 7, however, a simple design approach, based on empirical moment-rotation curves, is developed.

A major feature of the book is to summarize a number of approximate methods for simplified stability analysis of frames, mainly derived from the authors research work. In some ways this limits the scope of the monograph. These approximate methods are essentially systematic attempts to amplify loads or deliberately weaken the structure to take into account second-order and inelastic effects. In this respect, *Stability Design of Steel Frames* should prove more useful to structural designers than university research workers.

9N13. Adhesive Bonding of Aluminum Alloys. - Edited by Edward W Thrall *(Aeronaut Struct Consult, Point Arena CA)* and Raymond W Shannon *(Aeronaut Struct Consult, Ray Shannon & Assoc, Santa Ana CA)*. Marcel Dekker, New York. 1993. 520 pp. ISBN 0-8247-7405-1. $140.00.

Contents of the book include: chromic acid anodize process as used in Europe; sealed chromic acid anodize; phosphoric acid anodize; surface analysis; adhesive selection from the user's viewpoint; epoxy adhesives; elevated-temperature-resistant adhesives; mechanical properties of adhesives; environmental-durability testing; chemical analysis for control; coatings; structural analysis of adhesive-bonded joints; basic principles for tooling design and inspection; nondestructive inspection; and adhesive-bonded aluminum structure repair.

9N14. Atlas of Fatigue Curves. - Edited by Howard E Boyer. ASM Int, Materials Park OH. 1986. 518 pp. ISBN 087170-214-2. $172.00.

This book contains more than 500 fatigue curves for industrial ferrous and nonferrous alloys. It also includes a thorough explanation of fatigue testing and interpretation of test results. Each curve is presented independently and includes an explanation of its particular importance. The curves are titled by standard industrial designations (AISI, CDA, AA, etc.) of the metals, and a complete reference is given to the original source to facilitate further research. The correction includes standard S-N curves, curves showing effect of surface hardening on fatigue strength, crack growth-rate curves, curves comparing the fatigue strengths of various alloys, effect of variables (ie temperature, humidity, frequency, aging, environment, etc.), and much more. This one volume consolidates important and hard-to-find fatigue data in a single comprehensive source.

9N15. Atlas of Stress-Strain Curves. - Edited by HE Boyer. ASM Int, Materials Park OH. 1986. 640 pp. ISBN 087170-240-1. $172.00.

This book contains more than 600 stress-strain curves for ferrous and nonferrous alloys. Curves show monotonic versus cyclic behavior, effect of strain rate, alloying elements, product forms, deformation mode, grain size, work hardening, temperature, and much more. Each curve is titled by standard industrial designations (AISA, CDA, AA, etc.) and thoroughly referenced to the original source to facilitate further research. Compiled from an exhaustive survey of the published literature and consolidated into this single comprehensive source.

9N16. Handbook of Aluminum Bonding Technology and Data. - J Dean Minford *(Consultant, Hilton Head SC)*. Marcel Dekker, New York. 1993. 744 pp. ISBN 0-8247-8817-6. $195.00.

This reference offers comprehensive discussions on important aspects of aluminum bonding for each level of manufacturing--from mill finished to deoxidized, conversion coated, anodized, and painted surfaces--and provides an extensive up-to-date review of adhesion science, covering all significant developments of the past century. It features a chronologically arranged numbering system for more than 4600 literature citations and more than 200 tables of data.

Contents include: factors affecting adhesion; surface characteristics of aluminum; surface treatment of aluminum adherends; selection of an adhesive; design of aluminum-bonded joints; mechanisms of bond joint failure; water in the service environment; test evaluation standards; durability of permanence of aluminum-bonded joints; and applications of adhesives in bonding aluminum structures.

9N17. Hardness Testing. - ASM Int, Materials Park OH. 1987. 188 pp. ISBN 087170-244-4. $87.00.

This technical manual is a practical handbook dealing with all aspects of hardness testing. Coverage includes specific hardness testing methods; Brinell, Rockwell, Vickers, and microhardness testing, and other hardness testing methods, such as scleroscope ultrasonic, scratch and file testing, and hardness evaluation by eddy current testing. One chapter examines how to select the correct hardness testing method. Another chapter deals with hardness testing applications. Use of hardness testing to measure case depth and evaluate hardenability is also examined. The last chapter looks at the factors that determine the optimum hardness testing method for a specific application. A directory of manufacturers, distributors and suppliers of hardness testing equipment and supplies in the United States and Canada is also included.

9N18. STP 1156 Composite Materials: Fatigue and Fracture, 4th vol. - Edited by Wayne W Stinchcomb *(VPI)*. ASTM. 1993. 664 pp. ISBN 0-8031-1498-2. $134.00.

Fatigue and fracture are topics of primary importance to the development of damage-tolerant composite materials, to the design of high-performance composite components and structures, and to the certification of composite products. STP 1156 addresses current issues related to fatigue and fracture of composites.

The technical results contained in this STP provide practical insights on new developments in areas of continuing interest, such as damage and failure analysis and test methods. They also provide new directions for emerging technology areas, such as micromechanics and interfacial analysis, which are applicable to fatigue and fracture of composites. The materials addressed are thermosetting and thermoplastic polymer matrix composites, metal matrix composites, and ceramic matrix composites, as well as specialty laminates. Results were obtained for several configurations of composites ranging from laboratory specimens to subcomponents to structural elements.

In all, 34 peer-reviewed papers are presented in sections on: Strength and failure modes; Damage: Measurement, analysis and modeling; Intralaminar and interlaminar fracture; Micromechanics and interfaces; Fatigue of polymer matrix composites; Fatigue of ceramic matrix, metal matrix, and specialty composites.

9N19. STP 1174 High Temperature and Environmental Effects on Polymeric Composites. - Edited by Charles E Harris and Thomas S Gates *(NASA Langley Res Center)*. ASTM. 1993. 222 pp. ISBN 0-8031-1491-5. $67.00.

Contents of the publication include: Part 1 Damage Mechanisms and Failure: measurement of stress corrosion crack growth in sheet molding compounds; mode I delamination of carbon fiber reinforced thermoplastic polymer under static and cyclic creep at elevated temperatures; delamination onset and accumulation in polymeric composite laminates under thermal and mechanical loads; high temperature behaviors of an innovtive polymeric matrix composite; Part 2 Materials Behavior Under Combined Effects: the effect of seawater environment on the galvanic corrosion behavior of graphite-epoxy composites coupled to metals; the simulation and detection of electrochemical damage in BMI-graphite fiber composites using electrochemical impedance spectroscopy; the effect of the interphase-interface region on creep and creep rupture of thermoplastic composites; determination of a load, heat, time-to failure surface of polymeric composites; property improvements of polymer composites after loading at high temperatures; Part 3 Constitutive Models: the effects of physical aging on the creep response of a thermoplastic composite; the effects of moisture sorption on the creep behavior of fibers; and the effects of elevated temperature on the viscoplastic modeling of graphite\polymeric composites.

9N20. STP 1210 Slow Strain Rate Testing for the Evaluation of Environmentally Induced Cracking: Research and Engineering Applications. - Edited by Russell D Kane *(Cortest Labs)*. ASTM. 1993. 304 pp. ISBN 0-8031-1870-8. $73.00.

Due to concerns for environmentally induced cracking, corrosion and material specialists have worked consistently for the development of better and more predictive laboratory tests for this phenomenon. STP 1210 highlights some of the new directions in testing for environmentally induced cracking using a variety of slow strain rate techniques.

Nineteen papers written by researchers from industry, government agencies, and universities from the United States, England, Germany, Spain and Japan, address: Development and application of slow strain rate testing techniques; Uses of slow strain rate SCC testing to control or monitor industrial processes: Applications in nuclear power; Research applications and developments in slow strain rate testing techniques; Industrial applications of slow strain rate testing to evaluate environmentally induced cracking; and Use of slow strain rate testing for qualification of SCC resistance of corrosion resistant alloys: Case histories in petroleum production.

Papers describe both fundamental research studies and more practical engineering applications.

Electrodeposition. The Materials Science of Coatings and Substrates. - JW Dini *(LLNL)*. Noyes, Park Ridge NJ. 1993. 367 pp. ISBN 0-8155-1320-8. $78.00. (Under review)

Soldering Processes and Equipment. - Michael G Pecht *(CALCE Electron Packaging Res Center, Univ of Maryland, College Park MD)*. Wiley, New York. 1993. 304 pp. ISBN 0-471-59167-X. $64.95. (Under review)

Statics and Mechanics of Materials. - RC Hibbeler. Macmillan, New York. 1993. 810 pp. Disk incl. ISBN 0-02-354091-5. (Under review)

V. MECHANICS OF FLUIDS

9R21. Hydrostatic Lubrication, Theory and Practice. Tribology Series, 22. - R Bassani *(Eng, Univ di Pisa, Pisa, Italy)* and B Piccigallo *(Gruppo Construzioni e Tecnologie, Accad Navale, Livorno, Italy)*. Elsevier, New York. 1992. 542 pp. ISBN 0-444-88498-X. $180.00. Dfl 315.00.

Reviewed by William E VanArsdale (Mech Eng Dept, Univ of Houston, 4800 Calhoun Rd, Houston TX 77204-4792).

Hydrostatic lubrication uses an external pressurization system to maintain a fluid film between bearing surfaces. This type of lubrication provides low friction and negligible wear, but requires a more complex supply system than other techniques. Hydrostatic bearings have been in use since the middle of the last century. They have found application in everything from large telescopes down to smaller equipment, such as vibration attenuators and dynamometers. These applications involve a wide variety of thrust and radial bearing configurations subject to both static and dynamic loading as well as thermal effects.

Bassani and Piccigallo summarize progress in this field during the past 25 years. The authors approach is: "...the study of externally pressurized lubrication, both from the theoretical and the technical point of view." They provide useful background material on compensating devices and lubricants. Their review of basic equations suffers from minor inconsistencies, though, such as an unusual notation for divergence and confusing tensors with their components. However, the authors provide a thorough analysis of various pad and rotational bearings, as well as sections describing dynamics, optimization, and temperature effects. They conclude with chapters on experimental tests and applications. Throughout the book, the authors also provide "...design suggestions for the most common types of hydrostatic bearing..." to their intended audience of researchers, students, and technical designers.

Hydrostatic Lubrication is a technical reference for graduate students and specialists in bearing design. This book includes a useful listing of cited authors as well as a subject index. Illustrations are consistently good, with many drawings of different bearing designs. There are 46 examples used to illustrate applications in various chapters. The authors also cite a substantial number of references, but very few within five years of the copyright date (1992). The high list price and lack of exercises are a deterrent to classroom use. However, I recommend purchase by libraries and individuals with an interest in the design and analysis of hydrostatic bearings and lubrication systems.

9N22. Engineering Turbulence Modelling and Experiments -2. - Edited by W Rodi *(Karlsruhe, Germany)* and Martelli *(Florence, Italy)*. Elsevier, UK. 1993. 994 pp. ISBN 0-444-89802-6. $371.50.

The 89 papers, including 5 invited papers, in this volume present and discuss new developments in the area of turbulence modelling and measurements, with particular emphasis on engineering-related problems. Contents include: turbulence modelling; applications of turbulence models; direct and large-eddy simulations; experimental techniques; experimental studies; transition; turbulence control; aerodynamic flows; turbomachinery flows; combustion systems; and two-phase flows.

9N23. Fluid Transients in Pipe Networks. Computational Engineering Series. - Edited by AB de Almeida *(Dept of Civil Eng, Lisbon, Portugal)* and E Koelle *(Dept of Mech Eng, Sao Paulo, Brazil)*. Comput Mech, Billerica MA. 1992. 590 pp. ISBN 1-56252-096-2. $216.00.

This book presents modeling and computational techniques for fluid transients in pipe networks, including open channel flow.

Contents include: Pressure transient modeling and analysis network operational control; Pipe network systems and mathematical modeling; Pipe element modeling: Basic assumptions; Unified basic equations; Special dynamic effects; Global computer model and operational control: Network safety assessment; Control of pressure surges and case studies: Accident causes and pressure control tactics; Rapid flow disturbances; Surge control or protection; Flow control and valve maneuvers; Free surface transient flow: Basic equations; Uniform channels; Non-uniform channels; Free surface pipe elements; Dry bed; Node equation; Non-channel elements: Upstream Reservoir; Fast transients modeling: Secondary waves; and Open channel network simulation.

9N24. Plant Engineering's Fluid Power Handbooks, Vols 1 and 2. - Anton H Hehn *(Hehn & Assoc)*. Gulf Publ, Houston. 1993. 608 pp. ISBN 0-88415-089-5; 0-88415-072-0. $98.00. Info is for 2-vol set.

Fluid power equipment is used in nearly every branch of industry, including plastics processing, packaging, pharmaceuticals, petrochemicals, and others. This ever-increasing use of fluid power has resulted in a growing need for engineers, managers, technicians, and mechanics who are familiar with the operation, use, and care of this equipment. This two-volume set provides operating personnel with a ready resource in this field. Focusing on the design, application, maintenance, and troubleshooting aspects of fluid power systems, these guides--from the pages of *Plant Engineering* magazine--show how to avoid extended repairs and costly downtime.

Volume 1: *System Design, Maintenance, and Troubleshooting* provides an overview of the basic principles of hydraulic and pneumatic systems. This volume explains how the components are used, how they function, and how to maintain and troubleshoot fluid power systems. Volume 2: *System Applications and Components* deals with the design and application aspects of these same systems. Chapters cover component sizing and selection procedures, hydraulic circuit design, and applications of hydraulic and pneumatic systems. In each volume, the emphasis is on the cause-effect-cure relationships of systems, helping to readily identify faulty components.

9N25. Tribology in Metalworking: Friction, Lubrication and Wear. - John A Schey. ASM Int, Materials Park OH. 1983. 736 pp. ISBN 087170-155-3. $144.00.

This book acquaints you with plastic deformation and cutting; friction, wear and lubrication, lubricant classes, formulations, application, treatment and removal; measurement and evaluation techniques; and individual processes such as: rolling, drawing, extrusion, forging, sheet metalworking, and metal removal.

9N26. Vortex Flows and Related Numerical Methods. Proceedings of the NATO Advanced Research Workshop, Grenoble, France, June 15-19, 1992. - Edited by JT Beale *(Math, Duke Univ, Durham NC)*, GH Cottet *(Lab de Modelisation et Calcul, Univ Joseph Fourier, Grenoble, France)*, S Huberson *(Lab de Modelisation et Calcul, Univ du Havre, Grenoble, France)*. Kluwer, Norwell MA. 1993. 396 pp. ISBN 0-7923-2250-9. $165.00. £109.

Many important phenomena in fluid motion are evident in vortex flows, eg, flows in which vortical structures are significant in determining the whole flow. This book, which consists of lectures given at a NATO ARW held in Grenoble, France in June, 1992, provides an up-to-date account of current research in the study of these phenomena by means of numerical methods and mathematical modeling.

Such methods include Eulerian methods (finite difference, spectral and wavelet methods) as well as Lagrangian methods (contour dynamics, vortex methods) and are used to study such topics as 2- or 3D turbulence, vorticity generation by solid bodies, shear layers and vortex sheets, and vortex reconnection.

Intended for researchers and graduate students in computational fluid dynamics, numerical analysis, and applied mathematics.

VI. HEAT TRANSFER

9R27. Applied Thermodynamics for Engineering Technologists. - TD Eastop *(Univ of Exeter)* and A McConkey *(Mech and Indus Eng, Dundee Col of Tech)*. Wiley, New York. 1993. 695 pp. ISBN 0-582-09193-4.

Reviewed by John Rumierz (Chemistry, SKF Bearing Indust, 1100 First Ave, King of Prussia PA 19406).

The fifth edition of this standard text is aimed at undergraduate engineering students involved in programs which cover thermodynamics or design of thermal plants and equipment. This is a softcover book with an attractive format and many useful figures and diagrams. The topics are presented in a uncluttered fashion which provides easy access to the subject matter. A good subject index is provided.

The text follows the usual exposition of the material, with Chapters 1-4 covering the First and Second Law with parallel development of the necessary working fluid and process definitions. Specifically, the First Law is discussed and the concepts of reversibility and conservation of energy explained. Equations for the non-flow and the steady flow cases are derived. The concept of the working fluid leads to an introduction to the use of steam tables. Derivation of the perfect gas law is followed by a detailed discussion of reversible and irreversible processes. The development of the notion of the Second Law includes the concept of entropy and the consequences of irreversibility. The notion of exergy is introduced. All concepts covered are supported with examples of computations and problems for the student to solve.

Chapters 5, 6, and 7 start with the heat engine cycle and develop the necessary concepts and definitions to lead the student to practical combustion computations. Discussion of heat engine cycles is followed by absolute temperature scale and perfect gas cycles. The Carnot, Otto, and Diesel are among the cycles covered in detail. Dalton's Law and the Gibbs-Dalton Law for perfect gases and their mixtures are explained. Air and water vapor mixtures are discussed and appropriate definitions covered. The final chapter of this group extensively analyzes combustion processes from a practical perspective. Basic chemistry, combustion equations, and product analysis are discussed. Enthalpy of formation, enthalpy of reaction, and related quantities are defined. Finally, the calorific values of fuels and power plant efficiency are covered. Again, all topic discussions are supported by diagrams, examples, and problems.

Gas turbines, nozzles, and propulsion are covered in chapters 8-10. Steam cycles are again taken up, focusing on the Rankine cycle. Enthalpy-entropy charts are developed and used to discuss the reheat and regenitive cycles with practical topics, such as plant efficiencies and process steam considerations.

Nozzle and jet propulsion topics are developed in detail with critical discussions on pressure ratio, nozzle efficiency, and stagnation conditions following.

Chapters 11 and 12 discuss rotodynamic and positive displacement machines. Steam and gas turbine units are detailed, specifically impulse steam, radial flow, and axial flow turbines. Efficiency and reheat factors are discussed. Thermodynamic treatment of reciprocating compressors, vacuum pumps, and air motors are included in the units modelled.

Chapter 13 is devoted to reciprocating internal-combustion engines. A standard discussion of two-stroke and four-stroke cycle engines is followed by a treatment of new developments and alternate forms in this area.

Chapter 14 discusses refrigeration and heat pumps with an emphasis on the heat pump and the vapor-absorption plant. A section on refrigerants discusses the loss of atmospheric ozone and ozone-depleting substances. Analysis of exhaust gases, emission control of internal combustion engines, and the greenhouse effect are also included.

Chapter 15 covers psychrometry and air conditioning. The water vapor air mixture is now developed for the specific case of moist ambient air. The concepts of humidity, enthalpy, and specific heat capacity are defined and used in practical examples relevent to this area.

Chapter 16 is a long (102 pages) exposition of heat transfer. Aspects of Fourier's Law and Newton's Law buttress the discussion. Topics include: heat flow through ideal solids, steady and transient conduction, forced and natural convection, heat exchangers, black-body radiation, and the Stefan-Boltzmann Law. Extensive study problems and further topics for study are included.

Finally, chapter 17 addresses energy sources and related use and management. Included are sections on cogeneration, nuclear power and alternate energy sources. There are also discussions on combined heat and power, energy recovery, and a mention of pinch technology.

Applied Thermodynamics for Engineering Technologists approaches the topic of thermodynamics in a straightforward manner suitable for the freshman or sophomore engineering student. The mathematics involved are minimal, and the treatment of the subjects is readily comprehensible to all with a good background in high school mathematics. The English origin of the text will have little impact on the topical relevence or material accessibility to the American student. A two semester course may be needed to cover all the topics presented, although certain programs, such as chemical engineering, may allow only one for the subject at this level.

9R28. Benard Cells and Taylor Vortices. - E L Koschmieder *(Univ of Texas at Austin).* Cambridge UP, New York. 1993. 288 pp. ISBN 0-521-40204-2. $64.95.

Reviewed by Turgut Sarpkaya (Mech Eng Dept, Naval Postgraduate Sch, Code ME-SL, Monterey CA 93943-5000).

I do not know any teacher or researcher in fluid dynamics and heat transfer that would not want to have his name associated with an instability! Aside from being instruments of immortality to man (in name only), instabilities are windows to the soul of nature and temples of our knowledge. Thus, a book dealing with one or two of them that updates contributions (as well as papers) of a new generation of theoreticians and experimentalists (without demanding two PhDs in applied mathematics), presents critical accounts of historical facts, difficulties and continuing efforts, sorts out the essential facts, demands verification, and holds the interest of the reader from the beginning to the end with intriguing hints is indeed a welcome contribution. One cannot help but be impressed by the effort, sophistication and ingenuity that Koschmieder has exercised in writing this book. He deserves our congratulations.

The book may be used either as a reference or as a text for an advanced course. However, it should not be read because of a need, it should be read by all workers in heat transfer and fluid mechanics because it is there. About 340 pages long with an index and a large number of references (even after intentionally leaving out some papers), the book has two parts, as the title suggests. The first part, "Benard Convection and Rayleigh-Benard Convection," describes, in eight sections, all that is known and some of what "remains to be done in the future." I, for one, having taught fluid mechanics for nearly 40 years without ever contributing anything to either the Benard cells or Taylor vortices, enjoyed the clarity of the explanations and gained new insights. The second part, "Taylor Vortex Flow," is just as exciting and covers practically everything from the humble beginnings of the circular Couette flow, to Rayleigh's stability criterion, to GI Taylor's incomparable and immortal contribution in 1923 (as Koschmieder noted, "This paper is unique among the nearly 500 papers discussed in this book, in that it is the only one in which the basic theoretical and experimental results are combined in the same paper"), and the tremendous progress that has been made since then. The author raises the question: "One may ask whether it is worth the effort to pursue these obviously very difficult nonlinear aspects of the Taylor vortex problem:" *(irregular or chaotic flow, turbulent Taylor vortices)*, and notes that, "The answer to this question seems to be yes, because in the case of Taylor vortex flow we can pursue the formation of turbulence from laminar flow to full turbulence with great precision in all detail through a number of very characteristic stages." We certainly agree. What better place to look for the Holy Grail of turbulence?

I would enthusiastically recommend *Benard Cells and Taylor Vortices* to all researchers and graduate students interested in fluid dynamics, heat transfer, and scientific research. Cambridge University Press should be complimented for a superb production and publication.

9R29. HVAC Controls and Systems. - John I Levenhagen *(Johnson Controls)* and Donald Spethmann *(Honeywell Commercial Build Group)*. McGraw-Hill, New York. 1993. 334 pp. ISBN 0-07-037509-7.

Reviewed by Harry J Sauer Jr (Mech and Aerospace Eng, Univ of Missouri, Rolla MO 65401).

The authors have written an excellent introductory text on the basics of automatic control systems as related to air-conditioning [alias HVAC (heating, ventilating, and air-conditioning)] systems. For engineers entering the HVAC field, the book should provide a good background on how commerical HVAC systems are intended to function and the role that control systems play toward obtaining proper operation. However, the book does not get into the "technical" details of control theory, nor the design of such HVAC control systems.

The first few chapters of the book present the operation of some of the HVAC system components necessary for the control function: thermostats, dampers, and valves. Chapters 5 through 9 provide descriptive material on the controls, and direct digital control systems are covered. Chapters 10 through 14 delve deeper into the various types of air-conditioning systems and the means for providing the desired heating and cooling. Chapter 14 also integrates the typical control techniques with descriptions of the equipment used for providing hot and cold fluids.

Supervisory control, the total system monitoring and overall control of all subsystems, (also referred to as the building automation system), is the topic of chapter 15. In this significant chapter, the authors discuss such topics as system configurations and communications, proprietary versus open systems, energy management functions, and operator interface functions. Chapter 16 goes into the operations and maintenance of all types of HVAC systems, including the system as well as the associated controls. Chapter 17 provides a brief coverage of control selection, examined from the perspective of the type of organization that will be occupying and running the facility.

The book often presents a historical perspective and helps the reader to develop an appreciation for the improvements which have occurred with time and experience. The text does an excellent job of bringing the reader up-to-date on current practices in the HVAC field.

In summary *HVAC Controls and Systems* will be worthwhile reading for all system design engineers entering the HVAC field.

9N30. Combustion Efficiency Tables. - Harry Taplin, PE. ASM Int, Materials Park OH. 1992. 228 pp. ISBN 0-88173-143-9. $44.00.

Ninety-three combustion efficiency tables are contained in this reference. The tables are based on the ASME-ANSI Power Test Code 4.1, and are designed to systematically illustrate how different variables impact the combustion process.

9N31. Innovative Energy Design for the '90s. - Milton Meckler, PE. ASM Int, Materials Park OH. 1993. 403 pp. ISBN 0-88173-123-4. $64.00.

Contents include: Building HVAC system optimization; Multi-source hydronic heat pump systems; Advanced thermoelectric heat pumps; Cost-effective evaporative chilling; Integrated fire sprinkler and thermal energy storage systems; Geothermal power development; Introduction to daylighting; Evaluating daylight availability; Use of daylighting sky model; Use of light shelves; Use of geometric daylighting models; Applying daylighting computer models; Hybrid daylighting and space heating systems; Integrated desiccant cold air distribution system; New developments in desiccant cooling; Hybrid solar thermal systems; Hybrid photovoltaic systems for space power generation; and Hybrid heat pipe applications.

9N32. Manual on the Use of Thermocouples in Temperature Measurement, 4th ed. - ASTM. 1993. 311 pp. ISBN 0-8031-1466-4. $49.00. ASTM members, $44.

This new edition from ASTM (formerly STP 470B) includes principles, circuits, standard electromotive force (EMF) tables, stability and compatibility data, installation techniques, and other information that will aid users of thermocouples.

Completely revised in accordance with the International Temperature Scale of 1990 (ITS-90), the contents include: principles of thermoelectric thermometry; thermocouple materials; typical thermocouple designs; sheathed, compacted, ceramic-insulated thermocouples; thermocouple output measurements; reference junctions; calibration of thermocouples; application considerations; reference tables for thermocouples; cryogenics; temperature measurement uncertainty; terminology; list of ASTM standards pertaining to thermocouples; and the international temperature scale of 1990 (ITS-90).

Chemical Change in Deforming Materials. - Brian Bayly *(Dept of Geol, RPI)*. Oxford UP, New York. 1993. 225 pp. ISBN 0-19-506764-9. $75.00. (Under review)

Heat Exchange Engineering, vols 1 and 2. vol 1; design of heat exchangers; vol 2; compact heat exchangers; techniques of size reduction. - EA Foumeny *(Chem Eng, Univ of Leeds, UK)* and PJ Heggs *(Chem Eng, Bradford Univ, UK)*. Ellis Horwood, Chichester UK. 1991. 600 pp. ISBN 0-13-382409-8; 0-13-382391-1. (Under review)

Numerical Modeling in Combustion. - TJ Chung *(Univ of Alabama, Huntsville AL)*. Taylor & Francis, Washington DC. 1993. 632 pp. ISBN 0-89116-822-2. $199.50. (Under review)

Reduced Kinetic Systems for Application in Combustion Systems. - N Peters *(Inst fur Tech Mech, Templergraben, Germany)* and B Rogg *(Univ of Cambridge, Templergraben, UK)*. Springer, New York. 1993. 360 pp. ISBN 0-387-56372-5. $55.00. (Under review)

VIII. ENERGY & ENVIRONMENT

9N33. Alternative Energy Handbook. - Paul Rosenberg. ASM Int, Materials Park OH. 1993. 259 pp. ISBN 0-88173-140-4. $74.00.

This book is a guide to cost-effective alternative energy applications. A full range of alternative methods for generating power are examined, including innovative solar electric power systems, hydropower technologies, wind power, cogeneration, and independent electric power generators using a variety of fuel types. The latest developments in biomass and wood fuels are also examined. You'll get the facts on cost-effective heating strategies using solar, geothermal, and wood-burning technologies. An update on the latest developments in storage batteries for electric vehicles is also included.

IX. BIOENGINEERING

9N34. STP 1178 Composite Materials for Implant Applications in the Human Body: Characterization and Testing. - Edited by Russel D Jamison *(Smith and Nephew Richards)* and Leslie N Gilbertson *(Zimmer)*. ASTM. 1993. ISBN 0-8031-1852-X. $45.00.

Contents include: comparative study of carbon polymer composite and titanium femoral stems in dogs using computed tomography by EJ Char, AE Grierson, DT Reilly, CB Sledge and M Spector; environmental effect on a thermoplastic elastometer (TPE) for use in a composite intervertebral disc spacer by M Vuono Hawkins, MC Zimmerman, JR Parsons, NA Langrana and CK Lee; fatigue testing of femoral hip prostheses with a two-beam simulated femoral bone support fixture by SM Humphrey and LN Gilbertson; in vitro studies on the electrochemical behavior of carbon fiber composites by P Kovacs; the effect of interfacial bonding upon compressive strength and fracture energy of carbon fiber reinforced polymer (CFRP) composite: a theoretical investigation by RA Latour and G Zhang; a life prediction model for fatigue loaded composite femoral prosthesis by K Liao and KL Reifsnider; creep testing of a composite material human hip prosthesis by GR Maharaj and RD Jamison; intraoperative impact: characterization and laboratory simulation on composite hip prostheses by GR Maharaj and RD Jamison; stability of polysulfone composite materials in a lipid environment by RA Salzstein and JM Moran; characterization and optimization of small particle dental composites by TK Vaidyanathan, J Vaidyanathan and S Waknine; and a mechanical and historical analysis of the bonding of bone to hydroxylapatite-polymer composite coatings by MC Zimmerman, PS Boone, H Scalzo and JR Parsons.

Biomechanics. Mechanical Properties of Living Tissues. - YC Fung *(UCSD)*. Springer, New York. 1990. 433 pp. ISBN 0-387-90472-7. $49.50. (Under review)

REVIEW OF THE JOURNAL LITERATURE

for core list of journals scanned see Index Issue, published as Part 2 of the Dec issue of last year

I. FOUNDATIONS & BASIC METHODS

100. Continuum mechanics

9A1. Study of constitutive relations for pseudo-elasticity and shape memory behavior. - Zhigang Wang and Keh-chih Hwang *(Dept of Eng Mech, Tsinghua Univ, Beijing 100084, China).* Acta Mech Sinica 9(1) 44-52 (1993).

Constitutive relations are given for the description of the deformation behavior of shape memory materials. The deformation is the superposition of the elastic, the thermal, and the phase transformation deformation caused by the transformation from one to the other among the high temperature phase, the low temperature phase, and the stress induced phase. The phase transformation is controlled by the driving force, ie, the Gibbs energy difference between the phases.

See also the following:

9T985. Mathematical 3D solid modeling of biventricular geometry

102. Finite element methods

102C. STRUCTURAL APPLICATIONS

9A2. FE analysis of vibration and damping of laminated composites. - R Rikards *(Riga Tech Univ, Kalku str 1, Riga 226047, Latvia).* Composite Struct 24(3) 193-204 (1993).

A sandwich composite beam and plate finite superelements with viscoelastic layers for vibration and damping analysis are presented. Each layer is considered as simple Timoshenko's beam or Mindlin-Reissner plate FE. The energy dissipation in the viscoelastic layers is taken into account with complex modulus of elasticity theory. Two methods for damping analysis of laminated composite beams or plates is considered: the method of complex eigenvalues and the energy method. The first one is an "exact method", in which the modal loss factors of structure for each frequency are determined as the ratio of imaginary and real parts of complex eigenvalues. The second method is approximate, in which the modal loss factors of structure for each frequency are calculated as the ratio of dissipated and elastic strain energy for one cycle of steady state-vibrations. For sandwich beams and plates with a viscoelastic middle layer, the vibration and damping analysis for a wide range of materials and geometric parameters was carried out. Comparison of the results obtained by the two methods gives good agreement with the results of other authors.

See also the following:

9A48. Vibration and damping analysis of conical shells with constrained damping treatment

9A248. Upper bound on the collapse load of plate bending by using a quasi-conforming element and the Monte-Carlo method

9A257. Generalized conforming quadrilateral plate element by using semi-loof constraints

9A258. New discrete Kirchhoff-Mindlin element based on Mindlin-Reissner plate theory and assumed shear strain fields Part 1. An extended DKT element for thick-plate bending analysis

9A259. New discrete Kirchhoff-Mindlin element based on Mindlin-Reissner plate theory and assumed shear strain fields Part II. An extended DKQ element for thick-plate bending analysis

9A260. Performance of a reformulated four-node plate bending element in moderately thick to very thin plate applications

9A415. A *Global-Local* approach to lengthwise cracked beams: Dynamic analysis

9A450. Shape optimization of axisymmetric structures with adaptive FE procedures

9A463. Stress resultant FE analysis of reinforced concrete plates

9A479. Simplified FE representation of fuselage frames with flexible castellations

9A849. Piecewise hierarchical p-version axisymmetric shell element for nonlinear heat conduction in laminated composites

102E. OTHER SOLID MECHANICS APPLICATIONS

9A3. Deforming FEM for analysis of alloy solidification problems. - Yimin Ruan, Joshua C Liu, O Richmond *(Alcoa Tech Center, Aluminum Co of Amer, 100 Technical Dr, Alcoa Center PA 15069).* Finite Elements Anal Des 13(1) 49-63 (Apr 1993).

A better understanding of the heat transfer associated with any alloy solidification process may lead to precise control of the solidification process and improvement of the quality of castings. This requires accurate modeling of heat flux discontinuities and the multiple phases (solid, liquid, and mush) inside solidifying bodies. To deal with the complexity of the problem and improve the accuracy of numerical results, a deforming FEM for alloy solidification is developed in this paper. In this method, the velocities of the solid-mush and mush-liquid interfaces are primary variables. In the example problems of solidification of binary alloys, Scheil's equation and the lever rule are used to calculate the solid fraction in the mushy region. This method is accurate and can be easily implemented.

See also the following:

9A175. FE analysis of viscoelastic fracture

9A210. FE simulation of the micromechanics of interlayered polymer-fiber composites: A study of the interactions between the reinforcing phases

9A278. Effects of cap thickness and pile inclination on the response of a pile group foundation by a 3D nonlinear FE analysis

9A427. Incompatible numerical simulation of the axisymmetric cracked body made of ideally elastic-plastic material

102G. FLUID MECHANICS APPLICATIONS

See the following:

9A586. Perturbation solution to 3D nonlinear supercavitating flow problems

9A597. Least squares Petrov-Galerkin FEM for the stationary Navier-Stokes equations

9A600. Stream function vorticity solution using high-p element-by-element techniques

102J. OTHER APPLICATIONS

9A4. Local force calculation in 3D FEM with edge elements. - Akihisa Kameari *(Mitsubishi Atomic Power Industries, 4-1 Shibakouen 2-chome, Minato-ku Tokyo 105, Japan).* Int J Appl Electromagnetics Mat 3(4) 231-240 (Apr 1993).

A nodal force method has been proposed to calculate the local magnetic force in conductors and magnetic materials using the 3D FEM. It is formulated by volume integrations of the Maxwell's magnetic stress tensor with the virtual nodal displacement. The method can be easily implemented into the FEM programs. Numerical test calculations show that the calculated results agree well with analytic solutions and an experiment.

See also the following:

9A571. Finite element analysis of synchronous belt tooth failure

102L. SOLUTION ALGORITHMS

9A5. Analysis of element-by-element preconditioners for nonsymmetric problems. - MB van Gijzen *(Delft Univ of Tech, Delft, Netherlands).* Comput Methods Appl Mech Eng 105(1) 23-40 (May 1993).

A group of preconditioners for systems of linear equations arising from FE discretization, which is of increasing interest, is the class of element-by-element preconditioners. These preconditioners allow the solution of a system without the need to assemble the global stiffness matrix. The success of a preconditioner depends on how much it reduces the condition number of the global stiffness matrix. In this paper a bound on the condition number of the preconditioned stiffness matrix is derived in terms of norms of the element stiffness matrices, the element preconditioning matrices and the flexibility matrix.

9A6. Construction of stiffness matrices to maintain the convergence rate of distorted FEs. - MS Ingber and HL Schreyer *(Dept of Mech Eng, Univ of New Mexico, Albuquerque NM 87131).* Int J Numer Methods Eng 36(11) 1927-1944 (15 Jun 1993).

High-order elements are an option for providing an enhanced rate of convergence. However, it is not widely known that if a high-order element based on a mapping from a master-element space is distorted by displacing one of the side nodes slightly from the traditional midside position then the rate of convergence drops one order. The proof for a three-node element in 1D has been given previously. Here, a numerical demonstration is presented to show how quickly the rate is lost as the second node is moved from the midpoint. The numerical investigation shows that convergence appears to be retained but that the error associated with the incompatibility is greater than the error obtained with the use of distorted isoparametric elements. The results of this study are particularly appropriate for domains with curved boundaries and for nonlinear problems in which node positions are updated according to the deformation history.

9A7. Development of FE analysis post processing program. - R Karpurapu and RJ Bathurst *(Dept of Civil Eng, R Military Col of Canada, Kingston, ON, K7K 5L0, Canada).* Adv Eng Software 16(1) 15-22 (1993).

FE analyses may produce large amounts of response output that can obscure an understanding of model behavior by simply looking at the numbers produced by the numerical simulation. It is desirable to utilize a post processing program that can display selected aspects of model response in graphical form in order to properly interpret the results produced by FE analyses. This paper discusses some methods for efficient data management and principles for the development of post processing programs to analyse the response data produced by FE programs.

9A8. Virtual bubbles and Galerkin-least-squares type methods: GaLS. - C Baiocchi, F Brezzi *(Dipartimento Matematica dell'Univ Pavia, IAN-CNR, Corso Carlo Alberto 5, 27100 Pavia, Italy),* LP Franca *(Lab Nacional Computacao Cientifica, LNCC-CNPq, Rua Lauro Muller 455, 22290 Rio de Janeiro, Brazil).* Comput Methods Appl Mech Eng 105(1) 125-141 (May 1993).

The equivalence between stabilized FEMs (or Galerkin-least-squares type methods, GaLs) and the standard Galerkin method with bubble functions is established in an abstract framework. The results are applicable to various FE spaces, including high order elements, and applications to the advective diffusive model and to the Stokes problem are presented, illustrating the potential of the abstract theory introduced here.

102N. ELEMENT DEVELOPMENT

9A9. Consistent FE formulation of nonlinear membrane shell theory with particular reference to elastic rubberlike material. - A Ibrahimbegovic *(Ecole Polytech Fed Lausanne DGC LSC, CH-1015 Lausanne, Switzerland)* and F Gruttmann *(Inst Baumech, Numer Mech, Appelstr 9A, D-3000 Hannover 1, Germany).* Finite Elements Anal Des 13(1) 75-86 (Apr 1993).

In this paper we present a nonlinear membrane theory for rubberlike shells accounting for large elastic strains. We discuss the material model given as a general coaxial form of stress and strain measures. It includes, as a special case, the hypereleastic model in terms of principal stretches which is often used to characterize rubberlike materials. The displacement-based FEs are used. Cartesian coordinate systems are constructed locally at each numerical integration point in order to simplify computations.

9A10. Diagonal mass and associated stiffness matrices for isoparametric 5-node quadrilateral and 9-node hexahedron elements. - G Sauer *(Technischer Uberwachungsverein, Bayern, Munchen, Germany).* Finite Elements Anal Des 13(1) 37-47 (Apr 1993).

Expanded displacement interpolation functions that generate diagonal mass matrices are presented for the isoparametric 5-node quadrilateral and 9-node hexahedron. By applying 2×2 or $2 \times 2 \times 2$ Gauss integration, respectively, the modified interpolation functions contract the mass in the central node. The corner nodes are freed from masses. It is shown that the elements defined by the modified interpolation functions and the corresponding integration order are suited to satisfactorily reflect the dynamic structural properties.

9A11. Parallel FEM algorithms based on recursive spatial decomposition II. Automatic analysis via hierarchical substructuring. - M Saxena *(Solid Mech Lab, GE Corporate R&D, Schenectady NY 12301)* and R Perucchio *(Dept of Mech Eng, Univ of Rochester, Rochester NY 14267).* Comput Struct 47(1) 143-154 (3 Apr 1993).

In the companion paper, we discussed the applicability of a recursive spatial decomposition (RSD) based automatic meshing procedure for concurrent implementation. This paper describes an automatic substructuring scheme based on RSD of the domain, that can be closely integrated with the RSD-based automatic meshing procedure. The hierarchical data structures used to represent RSD-based automatically derived meshes also provide a one-to-one mapping between spatially decomposed subdomains and analytical substructures. Such a hierarchical organization of the substructures and the inherent parallelism of RSD are exploited to design the substructuring scheme suitable for parallel processing.

9A12. Verification of a general-purpose laminated composite shell implementation: Comparisons with analytical and experimental results. - YD Murray *(APTEK, San Jose CA 95129)* and LE Schwer *(SE&CS, 1070 Leslie Dr, San Jose CA 95117).* Finite Elements Anal Des 13(1) 1-16 (Apr 1993).

The constitutive behavior of a laminated shell element, implemented in a nonlinear FE code, is verified by analyzing a series of analytical and experimental results. Comparisons between the laminated shell model and analytical results available in the literature verify the implementation of the model for the membrane response, bending response with and without transverse shear, and the coupled response between the membrane and bending modes. The theoretical basis of the laminated shell model is verified by analyzing an impulsively loaded ring test.

9A13. An *a priori* geometry check for a single isoparametric FE. - DG Roddeman and LF Jansen *(TNO Build and Construct Res, PO Box 49, 2600 AA Delft, Netherlands).* Comput Struct 47(1) 69-72 (3 Apr 1993).

In order to check initial element geometry, the error in the displacement field is *a priori* bounded. The distorted element displacement field is determined by requiring a least squares difference with respect to a non-distorted (ie, reference) element solution. The least squares residual qualifies the element's approximation capabilities. An extra check on high aspect ratio is proposed. Several examples of geometry checks are included.

See also the following:

9A366. Comparison of two quarter-point element extrapolation equations for 3D mixed-mode problems

104. Finite difference methods

9A14. Evaluation of various high-order-accuracy schemes with and without flux limiters. - P Tamamidis and DN Assanis *(Dept of Mech and Indust Eng, Univ of Illinois, 1206 W Green St, Urbana IL 61801).* Int J Numer Methods Fluids 16(10) 931-948 (30 May 1993).

Conventional high-order schemes with reduced levels of numerical diffusion produce results with spurious oscillations in areas where steep velocity gradients exist. To prevent the development of non-physical oscillations in the solution, several monotonic schemes have been proposed. In this work, three monotonic schemes, namely Van Leer's scheme, Roe's flux limiter and the third-order SHARP scheme, are compared and evaluated against schemes without flux limiters. The latter schemes include the standard first-order upwind scheme, the second-order upwind scheme and the QUICK scheme. All the above schemes are applied to four 2D problems: (i) rotation of a scalar "cone" field, (ii) transport of a scalar "square" field, (iii) mixing of a cold with a hot front and (iv) deformation of a scalar "cone" field. These problems test the ability of the selected schemes to produce oscillation-free and accurate results in critical convective situations. The evaluation of the schemes is based on several aspects, such as accuracy, economy and complexity. The tests performed in this work reveal the merits and demerits of each scheme. It is concluded that high-order schemes with flux limiters can significantly improve the accuracy of the results.

9A15. Completed Richardson extrapolation. - PJ Roache and PM Knupp *(Ecodyn Res Assoc, PO Box 8172, Albuquerque NM 87198).* Commun Numer Methods Eng 9(5) 365-374 (May 1993).

The Richardson extrapolation method, which produces a 4th-order-accurate solution on a subgrid by combining 2nd-order solutions on the fine grid and the subgrid, is "completed" – in the sense that a higher-order-accurate solution is produced on all the fine grid points.

9A16. Fourier analysis of multigrid methods for general systems of PDEs. - P Lotstedt and B Gustafsson *(Dept of Sci Comput, Uppsala Univ, Uppsala, Sweden).* Math Comput 60(202) 473-493 (Apr 1993).

Most iteration methods for solving boundary value problems can be viewed as approximations of a time-dependent differential equation. In this paper we show that the multigrid method has the effect of increasing the time-step for the smooth part of the solution leading back to an increase of the convergence rate. For the nonsmooth part the convergence is an effect of damping. Fourier analysis is used to find the relation between the convergence rate for multigrid methods and singlegrid methods. The theoretical results are confirmed in simple numerical experiments.

9A17. Generation of unstructured tetrahedral meshes by advancing front technique. - H Jin *(Orbital Engine, 1 Whipple St, Balcatta WA 6021, Australia)* and RI Tanner *(Dept of Mech Eng, Univ of Sydney, NSW 2006, Australia).* Int J Numer Methods Eng 36(11) 1805-1823 (15 Jun 1993).

An algorithm for generating unstructured tetrahedral meshes by the advancing front technique is presented. Emphasis is placed on the construction of tetrahedral elements. Several measures are employed to prevent difficult situations. A control line-surface scheme is used to specify element size. Numerical examples are provided to show the performance of the algorithm.

9A18. New estimates for multilevel algorithms including the V-cycle. - JH Bramble *(Dept of Math, Cornell)* and JE Pasciak *(Dept of Appl Sci, BNL).* Math Comput 60(202) 447-471 (Apr 1993).

The purpose of this paper is to provide new estimates for certain multilevel algorithms. In particular, we are concerned with the simple additive multilevel algorithm discussed recently together with J Xu and the standard V-cycle algorithm with one smoothing step per grid. We shall prove that these algorithms have a uniform reduction per iteration independent of the mesh sizes and number of levels, even on nonconvex domains which do not provide full elliptic regularity. We also prove uniform convergence rates for the multigrid V-cycle for problems with nonuniformly refined meshes.

9A19. Runge-Kutta methods and local uniform grid refinement. - RA Trompert and JG Verwer *(Center for Math and Comput Sci, PO Box 4079, 1009 AB Amsterdam, Netherlands).* Math Comput 60(202) 591-616 (Apr 1993).

Local uniform grid refinement (LUGR) is an adaptive grid technique for computing solutions of partial differential equations possessing sharp spatial transitions. Using nested, finer-and-finer uniform subgrids, the LUGR technique refines the space grid locally around these transitions, so as to avoid discretization on a very fine grid covering the entire physical domain. This paper examines the LUGR technique for time-dependent problems when combined with static regridding. The present paper considers the general class of Runge-Kutta methods for the numerical time integration.

9A20. Some necessary conditions for convergence of the GBDF methods. - M Bin Suleiman *(Dept of Math Fac of Sci and Env Stud, Univ Pertanian Malaysia, 43400 UPM, Serdang)*. Math Comput 60(202) 635-649 (Apr 1993).

The Generalized Backward Differentiation methods for solving stiff higher-order ordinary differential equations are described. The convergence, zero stability and consistency of these methods are defined. Next, the zero stability and consistency conditions necessary for convergence are proven. The order for which the methods are zero stable is also determined.

106. Other methods in computational mechanics

9A21. Boundary element analysis of thermal stress intensity factors for cusp crack in transient state. - Kang Yong Lee *(Dept of Mech Eng, Yonsei Univ, Seoul 120-749, Korea)* and Jeong Kyun Hong *(Dept of Welding Eng, Ohio State Univ, Columbus OH 43210)*. Eng Fracture Mech 45(3) 309-320 (Jun 1993).

The BEM is applied to determine thermal stress intensity factors for a cusp crack in a transient state. In the steady temperature field, numerical values of thermal stress intensity factors for a Griffith crack and a symmetric lip cusp crack in a finite body are in good agreement within ±5% when compared with the previous solutions. In a transient state, the numerical values of thermal stress intensity factors for the Griffith crack are also in good agreement when compared with the previous solutions. In both steady and transient states, those for the symmetric lip cusp crack with the crack surface insulated or fixed to a constant temperature are calculated with various effective crack lengths, configuration parameters and uniform heat flow angles. The variations of the thermal boundary conditions of the crack surface have a great effect on stress intensity factors. The signs on the values of thermal stress intensity factors can be changed with time variation.

9A22. Simulating the non-isothermal mixing of polymer blends using the BEM. - PJ Gramann, JC Matzig, TA Osswald *(Dept of Mech Eng, Polymer Processing Res Group, Univ of Wisconsin, Madison WI 53706-1572)*. J Reinforced Plastics Composites 12(7) 787-799 (Jul 1993).

In most polymer processes the quality of the final part stems back in great part to the mixing of the compound and the viscous heating that occurs during the process. To date, these processes have been simulated using the finite difference or FEMs which rely on cumbersome remeshing techniques, restricting the analysis to simple geometries. However, mathematical manipulations of the governing equations results in boundary integrals, allowing the solution of complicated moving boundary problems without domain meshing. The resulting BEM and simulation results of the flow and heat transfer effects during mixing of polymer blends is presented in this article.

9A23. Orthogonal spline collocation Laplace-modified and alternating-direction methods for parabolic problems on rectangles. - B Bialecki and RI Fernandes *(Dept of Math, Univ of Kentucky, Lexington KY 40506)*. Math Comput 60(202) 545-573 (Apr 1993).

A complete stability ad convergence analysis is given for two- and three-level, piecewise Hermite bicubic orthogonal spline collocation, Laplace-modified and alternating-direction schemes for the approximate solution of linear parabolic problems of rectangles. It is shown that the schemes are unconditionally stable and of optimal-order accuracy in space and time.

9A24. Polynomial collocation using a domain decomposition solution to parabolic PDE's via the penalty method and explicit-implicit time marching. - K Black *(Center for Res in Sci Computation, N Carolina State Univ, Box 8205, Raleigh NC 27695-8205)*. J Sci Comput 7(4) 313-338 (Dec 1992).

A domain decomposition method is examined to solve a time-dependent parabolic equation. The method employs an orthogonal polynomial collocation technique on multiple subdomains. The subdomain interfaces are approximated with the aid of a penalty method. The time discretization is implemented in an explicit-implicit finite difference method. The subdomain interface is approximated using an explicit Dufort-Frankel method, while the interior of each subdomain is approximated using an implicit backwards Euler's method. The principal advantage to the method is the direct implementation on a distributed computing system with a minimum of interprocessor communication. Theoretical results are given for Legendre polynomials, while computational results are given for Chebyshev polynomials. Results are given for both a single processor computer and a distributed computing system.

9A25. Rate of convergence of the nonlinear Galerkin methods. - C DeVulder, M Marion *(Dept Math-Info-Syst, Ecole Centrale de Lyon, BP 163, 69131 Ecully, France)*, ES Titi *(Dept of Math, UC, Irvine CA 92717)*. Math Comput 60(202) 495-514 (Apr 1993).

In this paper we provide estimates to the rate of convergence of the nonlinear Galerkin approximation method. In particular, and by means of an illustrative example, we show that the nonlinear Galerkin method converges faster than the usual Galerkin method.

9A26. Neural networks in material processing and manufacturing: A Review. - JP Coulter *(Dept of Mech Eng and Mech, Lehigh Univ, Bethlehem PA 18015)*, LI Burke *(Dept of Indust Eng, Lehigh Univ, Bethlehem PA 18015)*, HH Demirci *(Dept of Mech Eng and Mech, Lehigh Univ, Bethlehem PA 18015)*. J Mat Processing Manuf Sci 1(4) 431-443 (Apr 1993).

Artificial neural systems have been proposed as advanced generic computer based tools that can lead to a wide variety of scientific, technological, and business improvements if properly utilized. In this article, a brief discussion of the background related to neural networks is provided, along with a summary of the application areas for which these biological intelligence based tools have been traditionally considered. Following this, a review of material processing and manufacturing studies during which artificial neural system technology has been investigated is presented. Processes such as welding, material removal, and tool wear monitoring, which served as the focus of a number of studies, are covered in detail. Additional manufacturing processes, such as injection molding and thermoplastic composite material tape consolidation, are also discussed. It is concluded that in all instances the proper implementation of neural networks in material processing and manufacturing applications has led to beneficial results, and that artificial neural system technology should be considered for an increased variety of manufacturing related applications in the years to come.

9A27. Comparison of coarse and fine grain parallelization strategies for the simple pressure correction algorithm. - AJ Lewis and AD Brent *(Newcastle Lab, BHP Res, PO Box 188, Wallsend NSW 2287, Australia)*. Int J Numer Methods Fluids 16(10) 891-914 (30 May 1993).

The primary aim of this work was to determine the simplest and most effective parallelization strategy for control-volume-based codes solving industrial problems. It has been found that for certain classes of problems, the coarse-grain functional decomposition strategy, largely ignored due to its limiting scaling capability, offers the potential for significant execution speed-ups while maintaining the inherent structure of traditional serial algorithms. Functional decomposition requires only minor modification of the existing serial code to implement and, hence, code portability across both concurrent and serial computers is maintained. Fine-grain parallelization strategies at the "DO loop" level are also easy to implement and largely preserve code portability. Both coarse-grain functional decomposition and fine-grain loop-level parallelization strategies for the SIMPLE pressure correction algorithm are demonstrated on a Silicon Graphics 4D280S eight CPU shared memory computer system for a highly coupled, transient 2D simulation involving melting of a metal in the presence for thermal-buoyancy-driven laminar convection. Problems requiring the solution of a larger number of transport equations were simulated by including further scalar variables in the calculation. While resulting in slight degradation of the convergence rate, the functional decomposition strategy exhibited higher parallel efficiencies and yielded greater speed-ups relative to the original serial code.

See also the following:

9A49. Steady-state analysis of a rotor mounted on nonlinear bearings by the transfer matrix method
9A87. Resonance frequencies and structures of sound fields in the enclosures of acoustical systems
9A165. Completed double layer BEM in elasticity
9A193. Bounds and estimates of overall moduli of composites with periodic microstructure
9A365. Boundary element crack closure calculation of 3D stress intensity factors
9A420. Analysis of surface cracks using the line-spring BEM and the virtual crack extension technique
9A586. Perturbation solution to 3D nonlinear supercavitating flow problems
9A900. Stochastic approach for groundwater flow in a semiconfined aquifer subject to random boundary conditions

II. DYNAMICS & VIBRATION

150. Kinematics and dynamics

9A28. Bounds on the friction-dominated motion of a pushed object. - JC Alexander and JH Maddocks *(Dept of Math and Inst for Phys Sci and Tech, Univ of Maryland, College Park MD 20742)*. Int J Robotics Res 12(3) 231-248 (Jun 1993).

We consider the friction-dominated, or quasistatic, motion of a rigid body being pushed over a horizontal plane in situations where the precise frictional interaction cannot be determined. Consequently, the complete set of motions corresponding to all possible friction distributions must be found. We demonstrate that if the contact region between the body and the supporting plane has one or two components, the set of all possible motions coincides with the set of motions arising for friction distributions restricted to two-point contact in the boundary in the contact region. Various examples are presented, and an effective numerical scheme based on a dissipation function is implemented.

9A29. Rotation angles. - WC Hassenpflug *(Dept of Mech Eng, Univ of Stellenbosch, Stellenbosch, S Africa)*. Comput Methods Appl Mech Eng 105(1) 111-124 (May 1993).

Problems of rigid body motion can be classified into three different types. For each one, different parameters may be the most suitable or natural coordinates to describe rotational position in space. As a common basis for comparison of different methods, we assume that the equations of motion are integrated numerically. For hinged bodies the three hinge angles are the most suitable, which for orthogonal hinges in different coordinates become the familiar different versions of the Euler angles. In this paper, we show that for free body motion, it may be preferable to use the nine elements of the rotation tensor directly. For elastically attached bodies, the most natural are the three elements of the rotation angle vector, for which we propose the name *Argyris* angles.

9A30. Stability of Ziegler's pendulum with eccentric load and load-dependent stiffness. - A Guran *(Dept of Civil and Env Eng, RPI)* and RH Plaut *(Dept of Civil Eng, VPI)*. Arch Appl Mech 63(3) 170-175 (Apr 1993).

The stability of Ziegler's pendulum with eccentric load and load-dependent stiffens is considered. It is shown that the flutter load is affected by a support that stiffness as it is compressed, and by eccentricity of the tangential load.

9A31. Study of stick-slip motion and its influence on the cutting process. - Jih-Hua Chin and Chun-Chien Chen *(Dept of Mech Eng, Natl Chiao Tung Univ, Hsinchu, Taiwan, ROC)*. Int J Mech Sci 35(5) 353-370 (May 1993).

The stick-slip motion of a machine tool has been investigated on the basis of a complete kinematic and kinetic model. The model is a generalized description of stick-slip motion of the machine tool which governs the whole cyclic process of this phenomenon and not just its slipping mode. Using this method some dynamic characteristics of this motion have been clarified. Further, an extended theory for chip-formation dynamics has been suggested to include the variation of feed.

9A32. Dynamic coupling between the joint and elastic coordinates in flexible mechanism systems. - AA Shabana and YL Hwang *(Dept of Mech Eng, Univ of Illinois, Chicago IL 60680)*. Int J Robotics Res 12(3) 299-306 (Jun 1993).

The aim of this investigation is to develop an efficient procedure for decoupling the joint and elastic accelerations while maintaining the nonlinear inertia coupling between the rigid body motion and the elastic deformation. The inertia projection schemes used in most existing *recursive methods* for the dynamic analysis of flexible robotics and mechanism systems lead to dense coefficient matrices in the acceleration equations, and consequently there is a strong dynamic coupling between the joint and elastic coordinates. This investigation discusses the problems associated with the inertia projection schemes used in the existing recursive methods, and it is shown that decoupling the joint and elastic accelerations using these methods requires the factorization of nonlinear matrices whose dimensions depend on the number of elastic dof of the system. The use of the procedure developed in this article is demonstrated using a four-bar flexible mechanism.

9A33. Analysis of a civil aircraft main gear shimmey failure. - R Van der Valk *(Fokker Aircraft BV, EDBS-BOO, 1117 ZJ Schiphol, Netherlands)* and HB Pacejka *(Vehicle Res Lab, Delft Univ of Tech, 2628 CD Delft, Netherlands)*. Vehicle Syst Dyn 21(2) 99-121 (1993).

A dynamic model is presented to analyze the stability of motion of the two-wheeled "Fokker F28-like" landing gear including tyres. The model is equally applicable to similar landing gears. The influence of the introduction of a specially designed torsional damper on the dynamical behavior of the landing gear-tyre combination is investigated. Results of the stability calculations are supported by test results.

9A34. Studies in spatial motion of a gyro on an elastic foundation. - A Guran *(Dept of Civil Eng, RPI)*, V Schlegel *(Arbeitsbereich Meerestechnik II Strukturmech, Tech Univ Hamburg-Harburg, Hamburg, Germany)*, K Ossia, FPJ Rimrott *(Atomic Energy of Canada, Sheridan Park Res Community, Mississauga, ON, Canada)*. Mech Struct Machines 21(2) 185-199 (1993).

To investigate the spatial motion of an axisymmetric gyro on an elastic foundation, a simplified model is proposed. The model is as simple as possible, yet designed to have all characteristics required to study its nonlinear behavior. Using Euler's law, the full nonlinear equations of motion are derived and then written in nondimensional form. Following analysis, numerical examples are investigated, and the evolution of nutation, precession, and spin angles is plotted.

9A35. Chaotic motion of a Kelvin type gyrostat in a circular orbit. - A Guran *(Dept of Civil and Env Eng, RPI)*. Acta Mech 98(1-4) 51-61 (1993).

The present paper deals with the following question: How does the inclusion of a symmetrical rotor affect the stability of an orbiting rigid axisymmetric body? To answer this question, the full nonlinear equations of motion of a rigid gyrostat in a gravitational field are obtained in a Hamiltonian formalism. Various dynamic behaviors of the spinning gyrostat satellite, eg, periodic, quasiperiodic, and chaotic, are studied via the Poincare map technique. The results show that some beneficial effects can be produced easily, eg, by increasing the rotor speed, chaotic motion of the satellite will become regular.

9A36. Fast recursive algorithm for molecular dynamics simulation. - A Jain *(JPL)*, N Vaidehi *(AA Noyes Lab of Chem Phys, CA IT, Pasadena CA 91125)*, G Rodriguez *(JPL)*. J Comput Phys 106(2) 258-268 (Jun 1993).

In this paper, we develop a recursive algorithm for solving the dynamical equations of motion for molecular systems. We make use of internal variable models which have been shown to reduce the computation times of molecular dynamic simulations by an order of magnitude when compared with Cartesian models. The O(N) algorithm described in this paper for solving the equations of motion provides additional significant improvements in computational speed. We make extensive use of the spatial operator methods which have been developed recently for the analysis and simulation of the dynamics of multibody systems. An alternative square factorization of the mass matrix leads to a closed form expression for its inverse. From this follows the recursive algorithm for computing the generalized accelerations. The computational cost of this algorithm grows only linearly with the number of dof.

See also the following:

9A132. Dynamic analysis and control of a Stewart platform manipulator
9A133. Efficient method for inverse dynamics of manipulators based on the virtual work principle
9A134. Exact methods for determining the kinematics of a Stewart platform using additional displacement sensors
9A136. Inverse kinematics and inverse dynamics for control of a biped walking machine
9A137. Kinematic decoupling in mechanisms and application to a passive hand controller design
9A139. Kinematics and control of a fully parallel force-reflecting hand controller for manipulator teleoperation
9A478. Analysis of the multi-link independent suspension system

152. Vibrations of solids (basic)

9A37. General stochastic oscillatory systems. - EF Abdel Gawad and MA El Tawil *(Eng Math Dept, Fac of Eng, Cairo Univ, Giza, Egypt)*. Appl Math Model 17(6) 329-335 (Jun 1993).

We present a general stochastic nonlinear oscillatory system with a single dof. Square and cubic nonlinearities are considered. The excitation function is a nonstationary Gaussian process with zero mean. The solution moments are obtained using the small-parameter perturbation method with the Wiener-Hermite expansion approach. Computer results along with graphs are presented.

9A38. Response amplitude probability functions of a hardening Duffing oscillator subjected to filtered white noise. - PK Koliopulos, SR Bishop *(Dept of Civil Eng, Univ Col London, Gower St, London WC1E 6BT, UK)*, GD Stefanou *(Dept of Civil Eng, Univ of Patras, GR-26110 Patras, Greece)*. Comput Methods Appl Mech Eng 105(1) 143-150 (May 1993).

The problem of estimating the probability distribution of the response amplitude of a hardening Duffing oscillator subjected to narrow band excitation is addressed. A method is presented which is based on a quasi-static approximation of system behavior and is capable of reproducing the resulting concave shape of probability functions when a jump phenomenon occurs. Predictions are compared with those obtained via stochastic averaging techniques and with digital simulations.

9A39. Comparison of Mandelshtam's conditions with convergence conditions for iterative procedures in the analysis of complex dynamic systems by means of partial models. - TL Stanczyk *(Tech Univ, Kielce, Poland)*. Eng Trans 40(4) 457-467 (1992).

The convergence conditions for iterative procedures in the analysis of dynamic systems with the use of partial models are compared with Mandelshtam's conditions (uncoupling of vibrations of partial models). Both basic iteration procedures are discussed. The conditions for iterative procedures are found to be much weaker than those formulated by Mandelshtam. A simplified criterion for the selection of the type of procedure (a manner in which a system is to be decomposed) is presented.

9A40. Sturm sequence recurrence formula for eigensolution of locally modified systems. - M Kashiwagi *(Fac of Eng, Kyushu Tokai Univ, 9-1-1 Toroku, Kumamoto-shi 862, Japan)*, I Hirai *(Fac Eng, Kumamoto Univ, 2-39-1 Kurokami, Kumamoto-shi 862, Japan)*, T Katayama *(Sasebo Heavy Indust Co, 1 Tategami, Sasebo-shi 857, Japan)*, WD Pilkey *(Dept of Mech and Aerospace Eng, Univ of Virginia, Charlottesville VA 22901)*. Finite Elements Anal Des 13(1) 31-36 (Apr 1993).

This paper proposes a recurrence formula for the fundamental equation derived on the basis of the Sturm sequence property for the eigensolution of locally modified systems. The fundamental equation expressed using a condensed matrix, of order equal to the order of the modified part of the system, requires the multiple calculation of a determinant. The number of calculations is equal to the order of the original system. The recurrence formula set forth in this paper avoids multiple evaluations of the determinant.

See also the following:

9A274. A few properties of the resonant frequencies of a piezoelectric body

154. Vibrations (structural elements)

154B. BEAMS, COLUMNS, RODS, AND BARS

9A41. Nonlinear vibrations of spatial viscoelastic beams. - S Wojciech *(Tech Univ, ul Majakowskiego 11/12, 80-952 Gdansk-Wrzeszcz, Poland)* and I Adamiec-Wojcik *(Branch of Lodz Tech Univ, ul Willowa 2, 43-309 Bielsko-Biala, Poland)*. Acta Mech **98**(1-4) 15-25 (1993).

This paper describes the solution of high amplitude cantilever spatial beam vibration problems. The standard linear damping model has been taken into consideration. In order to allow the large displacement analysis the rigid FEM has been introduced to discretize the beam. Denavit-Hartenberg's matrices and Lagrange's equations have been used to formulate the equations of motion. Both, numerical calculations and conclusions on the accuracy of the above mentioned method are shown.

9A42. Stability of a column with a follower load and a load-dependent elastic support. - A Guran *(Dept of Mech Eng, Univ of Toronto, 5 King's College Rd, Toronto, ON, M5S 1A4, Canada)* and RH Plaut *(Charles E Via, Jr Dept of Civil Eng, VPI)*. Acta Mech **97**(3-4) 205-214 (1993).

The influence of an elastic support on the stability of an elastic column under a follower load is investigated. The support is pinned and has a rotational spring whose stiffness is either constant or increases as the load is applied. Linear and quadratic stiffening functions are treated. An adjoint variational principle and a generalized Rayleigh-Ritz method are developed for this system. Characteristic curves are examined and the critical load, which is associated with flutter instability, is determined. The effects of the initial spring stiffness and the stiffening rate on the critical load are studied. It is found that an increase in either one of these parameters may lower the critical load, which is unexpected, and that support stiffening may have a significant influence on the vibrations and stability of a nonconservative system.

9A43. Torsional vibration of pretwisted thin-walled cantilevered I-beams. - OG McGee *(Sch of Civil Eng, Georgia Tech)*, MI Owings *(Am Precast Concrete, 3400 Jackson Pike, Grove City OH 43235)*, JW Harris *(Marathon Oil, 439 S Main St, Findlay OH 45840)*. Comput Struct **47**(1) 47-56 (3 Apr 1993).

Analytical natural frequencies and mode shapes are derived for the torsional vibration of pretwisted thin-walled cantilever I-beams. A multifilament model of a pretwisted thin-walled I-beam undergoing warp deformation and a moderately large twist about the axis of shear centers is used to derive the nonlinear boundary-value equations. Exact torsional vibration solutions are derived from the linear terms of the nonlinear boundary-value equations.

9A44. Vibration of bent tubes and rods in fluid flow. - S Devnin *(Krylov Res Inst, Russia)*. Heat Transfer Res **24**(5) 663-669 (1992).

Methods for prediction vibrations of bent pipes and rods in flowing fluids are derived. It is shown that the calculations involved in these predictions can be simplified by making use of the experimentally established fact of synchronicity of vortex shedding from bent rods in flows whose velocity changes along the tube axis. More experiments are needed to prove our computational technique.

See also the following:

9A911. Modeling of dynamic networks of thin thermoelastic beams

154G. PLATES

9A45. Elastodynamics of thin plates with internal dissipative processes Part II. Computational aspects. - PA Fotiu *(Dept of Appl Mech and Eng Sci, UCSD)*. Acta Mech **98**(1-4) 187-212 (1993).

In part one of this paper an integral solution of the dynamic behavior of viscoplastic isotropic thin plates with ductile damage is derived. The main topic of the second part is the numerical solution of these integral equations. Green's functions due to external and internal excitation are split into quasistatic part and a purely dynamic part. Often the quasistatic part can be computed in a more convenient way than the complete dynamic fundamental solution. This paper develops an implicit time integration algorithm where the resulting system of equations is solved by an accelerated Newton-Raphson method.

9A46. Inhomogeneous annular plates with exactly beam-like radial spectra. - HPW Gottlieb *(Div of Sci and Tech, Griffith Univ, Nathan Brisbane, Queensland 4111, Australia)*. IMA J Appl Math **50**(2) 107-112 (1993).

There are seven classes of inhomogeneous beams which are isospectral with each other and with the homogeneous beams in the clamped-clamped configuration. By a logarithmic coordinate transformation, eight classes of inhomogeneous clamped annular plates may thereby be obtained which have different radial distributions for densities and flexural rigidities but which all have the same radial vibration spectrum characteristics of a clamped homogeneous beam.

9A47. Large amplitude vibration of antisymmetric imperfect cross-ply laminated plates. - Jenq-Yiing Yang and Lien-Wen Chen *(Dept of Mech Eng, Natl Cheng Kung Univ, Tainan, Taiwan, ROC)*. Composite Struct **24**(2) 149-159 (1993).

In this paper the large amplitude vibration of an initially stressed, imperfect, cross-ply plate is studied. The nonlinear equations of motion for an imperfect cross-ply plate in a general state of non-uniform initial stress are derived. The effects of both the transverse shear deformation and rotatory inertia are included. A multi-mode solution is formulated for a simply supported imperfect cross-ply plate. The modal equations are obtained by performing the Galerkin procedure and then solved by the Runge-Kutta method. It is found that the existence of geometric imperfections may result in a drastic change on the large amplitude vibration behavior. The effects of various parameters on the nonlinear vibration frequencies are investigated.

154H. SHELLS

9A48. Vibration and damping analysis of conical shells with constrained damping treatment. - TC Ramesh and N Ganesan *(Machine Dyn Lab, Dept of Appl Mech, Indian IT, Madras 600 036, India)*. Finite Elements Anal Des **13**(1) 17-29 (Apr 1993).

This paper presents an analysis of conical shells with a constrained viscoelastic damping treatment. A FE based on a discrete layer theory is developed for the purpose. The effects of core-to-facing thickness ratio, slant length and semi vertex angle of the cone on the frequencies and loss factors of conical shells with isotropic facings are investigated for three boundary conditions: clamped at both ends, simply supported at both ends and clamped at the small end.

See also the following:

9A453. Structural shape optimization of vibrating shells and folded plates using two-noded finite strips

154K. ROTATING SHAFTS (CRITICAL SPEED, BALANCING)

9A49. Steady-state analysis of a rotor mounted on nonlinear bearings by the transfer matrix method. - An-Chen Lee *(Dept of Mech Eng, Natl Chiao Tung Univ, Hsinchu 30049, Taiwan, ROC)*, Yuan Kang *(Dept of Mech Eng, Chung Yuan Christian Univ, Chung Li 32023, Taiwan, ROC)*, Shin-Li Lu *(Dept of Mech Eng, Natl Chiao Tung Univ, Hsinchu 30049, Taiwan, ROC)*. Int J Mech Sci **35**(6) 479-490 (Jun 1993).

The steady-state response of subharmonic, superharmonic and synchronous vibrations of a flexible rotor supported by bearings of power nonlinearity (ie, the bearing force satisfies a power law of the deflection) are studied. The transfer matrix method is applied to formulate the transfer matrices of nonlinear rotor-bearing systems with MDOF (multi dof) and in conjunction with the harmonic balance method to obtain the steady-state responses. Two examples of rotor-bearing systems with cubic nonlinearity spring characteristics are given to investigate the effects of nonlinearity on frequency response and the whirling orbits.

154L. FRAMES, TRUSSES, AND ARCHES

9A50. Dynamic reliability of large frames. - S Mahadevan and S Mehta *(Vanderbilt Univ, Nashville TN 37235)*. Comput Struct **47**(1) 57-67 (3 Apr 1993).

This paper presents a stochastic FEM (SFEM) for the reliability analysis of dynamically loaded large frames. This is facilitated by the computation of the sensitivity of dynamic response of the randomness in the dynamic excitation as well as in structural properties, by applying the chain rule of differentiation to the deterministic analysis. Since such computation requires large amounts of memory and computational time, matrix condensation is incorporated in SFEM for structures with a large number of dof. The computation of response sensitivity and variability is formulated in the context of stiffness and mass matrix condensation. A numerical example with a six-story frame is used to illustrate the proposed model.

See also the following:

9A445. Optimality criterion for maximum fundamental frequency of free vibrations of frames including axial and bending effects

154N. COMPOSITE MATERIALS

See the following:

9A2. FE analysis of vibration and damping of laminated composites

154O. STRUCTURAL ELEMENTS ON FOUNDATIONS

9A51. General solution to vibrations of beams on variable Winkler elastic foundation. - Zhou Ding *(Dept of Mech Eng, E China IT,* *Nanjing, Jiangsu 210014, Peoples Rep of China).* Comput Struct 47(1) 83-90 (3 Apr 1993).

A general solution to vibrations of beams on variable Winkler elastic foundation is presented. The exact solution of the dynamic response of the beam is obtained by considering the reaction force of the foundation on the beam as the external force acting on the beam, which is an integral equation including the displacement of the beam. The four unknown constants in the solution are decided by the boundary conditions of the beam. The integrals in the solution are approximately and numerically calculated by means of the trapezoidal rules. The analysis and programming are very simple. It is possible to find the natural frequencies and mode shapes of vibrations by using a small number of the discrete nodes in the trapezoidal quadrature and it is concluded that the use of the method yields better convergence at lower computation costs.

9A52. **Hammer foundation analysis by the wave equation.** - YK Chow and DM Yong *(Dept of Civil Eng, Natl Univ of Singapore, 10 Kent Ridge Crescent, Singapore 0511).* Comput Struct 47(1) 107-110 (3 Apr 1993).

The vibration amplitudes of hammer foundations must be kept within acceptable limits during operation. A 1D wave equation model based on the FEM is proposed for the analysis of these foundations. The results of the wave equation model are shown to compare favorably with some reported solutions and with experimental measurements. The versatility of the model allows the various components of the hammer-foundation system to be readily simulated.

154P. COMPLEX SYSTEMS

9A53. **Dynamics of fluidelastic vibrations of tube bundles in heat exchangers.** - S Kaplunov and N Makhutov *(Blagonravov Mech Eng Inst, Russian Acad of Sci, Russia).* Heat Transfer Res 24(5) 641-662 (1992).

The principal relationships governing the flow-induced vibrations of heat exchanges tube bundles, the knowledge of which is needed in the design stage in order to prevent destructive vibrations with runaway amplitudes, are derived by the general dynamic analysis of the fluidelastic behavior of the bundle, as well as its mechanical. The method employs probabilistic estimates of the possibility of actual attainment of the necessary frequency detuning to prevent resonance and generalized data on damping of the characteristic tube vibrations.

154Y. COMPUTATIONAL TECHNIQUES

9A54. **Adaptive time integration of nonlinear structural dynamic problems.** - BP Jacob and NFF Ebecken *(Civil Eng Dept, COPPE-Fed Univ Rio de Janeiro, PO Box 68506, 21945 Rio de Janeiro RJ, Brasil).* Eur J Mech A 12(2) 277-298 (1993).

This work presents the development of an adaptive computational strategy for the efficient nonlinear dynamic analysis of large-scale structural systems, particularly oriented towards the analysis of compliant structures for deepwater oil exploration and production. This strategy is devised having in mind the following requirements: (a) Superior computational efficiency when compared with conventional nonlinear dynamic analysis tools; (b) User-friendliness, reflected in savings in the time spent by the engineer for the preparation and submis[illegible] the computer jobs necessary to obtain [illegible]ponse; and (c) Improved charact[illegible] and robustness, reflected b[illegible]sults and the ability to complete an analysis without abnormal terminations. Applications on the nonlinear dynamic analysis of deepwater compliant structures are presented, to evaluate the aforementioned characteristics of the computational system.

9A55. **Perturbation analysis of vibration modes with close frequencies.** - Su-Huan Chen, Ahong-Sheng Liu, Chun-Sheng Shao, You-Qun Zhao *(Dept of Mech, Jilin Univ of Tech, Changchun 130022, Peoples Rep of China).* Commun Numer Methods Eng 9(5) 427-438 (May 1993).

This paper focuses on how parameter changes in a vibration system expressed by a discrete eigenvalue problem affect vibration modes in the special case of closely spaced eigenvalues, ie "eigenvalue clusters". For this class of problems, a perturbation analysis is developed that can be used to compute changes in eigenvalues and eigenvectors in response to small parameter changes. The analysis is applied to a 6-dof spring-mass system containing a single pair of closely spaced eigenvalues.

156. Vibrations (structures)

9A56. **Prediction of gear dynamics using fast Fourier transform of static transmission error.** - Hsiang Hsi Lin *(Dept of Mech Eng, Memphis State Univ, Memphis TN),* DP Townsend, FP Oswald *(Mech Syst Tech Branch, NASA Lewis Res Center, Cleveland OH).* Mech Struct Machines 21(2) 237-260 (1993).

An analytical computer simulation procedure for dynamic modeling of low-contact-ratio spur gear systems is presented. The procedure computes the gear static transmission error and uses a Fast Fourier Transform to generate its frequency spectrum at various tooth profile modifications. The dynamic loading response of an unmodified (perfect involute) gear pair is compared with that of gears with profile modifications. Correlations are found between several profile modifications and the resulting dynamic loads. Optimum profile modifications can be determined from the design curves, to yield a minimum dynamic effect for a gear system. This provides an essential tool for improved gear design.

9A57. **Statistical analysis of the dynamic cutting coefficients and machine tool stability.** - MA El Baradie *(Sch of Mech and Manuf Eng, Dublin City Univ, Dublin 9, Ireland).* J Eng Indust 115(2) 205-215 (May 1993).

Machine tool chatter is a statistical phenomenon since it is dependent on the interaction of two statistical quantities, these being the dynamic characteristics of the machine tool structure and the transfer function of the cutting process. In this paper, a generalized statistical theory of machine tool chatter has been developed. This takes into consideration the scatter of the dynamic data of the machine structure and/or that of the cutting process. The dynamics of the cutting process have been represented by a mathematical model which derives the cutting coefficients from steady state cutting data, based on a nondimensional analysis of the cutting process. The dynamics of the machine tool structure and the cutting process, being the input data to the theory, were determined experimentally. The predicted stability charts were plotted to take into consideration the scatter in the machine structure dynamics and/or the cutting process.

9A58. **Unified transfer function (UTF) approach for the modeling and stability analysis of long slender bars in 3D turning operations.** - IN Tansel *(Dept of Mech Eng, Florida Int Univ, Miami FL 33199).* J Eng Indust 115(2) 193-204 (May 1993).

A new approach is introduced to model 3D turning operations that are used for the stability analysis of long slender bars. This approach utilizes the unique relationship between externally created feed direction tool displacements (input) and the resultant thrust direction workpiece vibrations (output) to estimate stability limits in 3D turning operations from the data of a single dynamic cutting test. In this paper, this unique relationship is referred to as the "Unified Transfer Function" and its expressions are derived from conventional cutting and structural dynamics transfer functions. The proposed approach considers in-process structural and cutting dynamics and can be automatically implemented without any input from the operator for the traverse turning of a long slender bar.

9A59. **Semi-active damping with an electromagnetic force generator.** - D Ryba *(Fac of Mech Eng and Marine Tech, Univ of Tech, Delft, Netherlands).* Vehicle Syst Dyn 21(2) 79-95 (1993).

The main shortcoming of vehicle suspension systems is the amplification of input vibrations at the resonant frequency. A non-amplifying suspension system with a semi-active damping is being developed. The use of an electronically controlled rotational damper has been studied theoretically. A new spring seat is being designed for the improvement of the working conditions for drivers of road and terrain vehicles.

9A60. **Six-dof active vibration isolation using a Stewart platform mechanism.** - Z Geng and LS Haynes *(Intelligent Autom, 1370 Piccard Dr, Rockville MD 20850).* J Robotic Syst 10(5) 725-744 (Jul 1993).

Intelligent Automation has performed a study of a six-dof active vibration isolation system based on a Stewart platform mechanism to be used for precision control of a wide range of space-based structures as well as earth-based systems. This article presents part of the study results, which includes a new Terfenol-D actuator design and analysis, a design of a Stewart platform as a vibration isolation device and robust adaptive filter algorithms for active vibration control. Prototype hardware of a six-dof active vibration isolation system has been implemented and tested. About 30 dB of vibration attenuation is achieved in real-time experiments.

See also the following:

9A33. Analysis of a civil aircraft main gear shimmey failure
9A85. Liquid-structure-foundation interaction of slender water towers

158. Wave motions in solids

158A. GENERAL THEORY

See the following:

9A969. Comparison of mass-loading and elastic plate models of an ice field

158B. RODS AND BEAMS, ELASTIC

9A61. **Discrete modelling of wave propagation in bars with piecewise-linear characteristics.** - Z Szczesniak *(Military Tech Acad, Warszawa, Poland).* Eng Trans 40(4) 483-500 (1992).

A method is proposed to model 1D wave propagation problems in a discrete manner as applied to the material with piecewise-linear stress-strain relationship in loading and rigid-elastic behavior in unloading. The method consists in a simple combination of basic models, ie, an elastic model and a plastic model with rigid unloading to obtain a combined model. It turns out to be accurate and effective. Numerical algorithm is described. Errors are discussed and an example of unloading stress wave is given.

9A62. Torsional mode coupling and filtering in a composite waveguide with multiperiodic interface corrugations. - OR Asfar *(Dept of Elec Eng, Univ of Sci and Tech, Irbid, Jordan)* and MA Hawwa *(Dept of Eng Sci and Mech, VPI)*. J Acoust Soc Am 93(5) 2468-2473 (May 1993).

This study is concerned with the interaction of six torsional modes in a composite axisymmetric waveguide whose interfaces are sinusoidally corrugated in the axial direction. The modes are interacting when two resonant conditions on the codirectional modes and a Bragg condition occur simultaneously. In light of the weakness of the interface corrugations, the perturbation method of multiple scales is used to derive the mode coupling equations. A novel numerical scheme for two-point boundary-value problems is used to solve the coupled amplitude equations. The power reflection coefficient of a filter section is then calculated for the cases of uniform, tapered, and chirped corrugations. An optimal filter is realized by combining both taper and chirp thus producing a nearly ideal characteristics.

9A63. Traveling waves on a wire. - DS Jones *(Dept of Math and Comput Sci, The University, Dundee DD1 4HN, UK)*. Arab J Sci Eng 17(4B) 541-563 (Oct 1992).

The problem of the initiation and reflection of traveling waves on a long thin wire of finite length when it is simulated by a plane wave is investigated. By modeling the wire as a narrow tube it is shown that all the traveling waves, except the one supported by a longitudinal symmetrical current, decay exponentially at a rapid rate. The form of the longitudinal current is determined as well as its launching coefficient. The reflection coefficient when such a traveling wave encounters an end is also found. Expressions for the field scattering by the wire and the back scattering are derived in addition.

See also the following:

9A76. Cylindrical wave solutions to the Korteweg-de Vries equation

158C. PLATES AND SHELLS, ELASTIC

See the following:

9A969. Comparison of mass-loading and elastic plate models of an ice field

158D. INFINITE AND SEMI-INFINITE MEDIA, ELASTIC

9A64. Point force excitation of an elastic infinite circular cylinder with an embedded spherical cavity. - S Olsson *(Div of Mech, Chalmers Univ of Tech, S-41296 Goteborg, Sweden)*. J Acoust Soc Am 93(5) 2479-2488 (May 1993).

In this paper the scattering of elastic waves in an infinite circular cylinder is considered. The elastic medium of the cylinder is assumed to be homogeneous, isotropic, and linear except for a finite inhomogeneity which, for simplicity, is chosen as a spherical cavity. By applying the null field approach (or T matrix method), the scattered field is obtained as a complicated expression containing the transition matrix of the cavity, the reflection matrix of the cylinder, and the transformation function between the spherical and cylindrical vector wave functions. Numerical results, both in the frequency and time domain, are presented.

158F. SURFACE WAVES

9A65. Surface stress waves in a transversely isotropic nonhomogeneous elastic semispace Part I. Equations of motion and equations of a Rayleigh-type surface wave. - T Roznowski *(Dept of Civil Eng and Operations Res, Princeton)*. Arch Mech 44(4) 417-435 (1992).

Plane state of strain of a transversely isotropic medium, nonhomogeneous in the plane of isotropy is considered; equations of motion expressed in terms of stresses are used to formulate the problem of propagation of Rayleigh-type surface stress waves. It is proved that in the case of a harmonic wave, the problem may be reduced to a solution of a fourth-order, ordinarily differential equation, with variable coefficients, for the "stress function" $\beta(z)$, ie, the normal stress σ_{zz} amplitude distribution in the semispace along the vertical direction; the remaining amplitudes are expressed in terms of $\beta(z)$. The form makes it possible to formulate and discuss several particular cases of the media under consideration. Equations are proved to be identical with those derived by J Ignaczak. The methods of solution of the equations of motion are presented. Conclusions are drawn.

9A66. Surface stress waves in a transversely isotropic nonhomogeneous elastic semispace Part II. Surface stress wave in a "weakly anisotropic" semi-space with "small nonhomogeneity". - T Roznowski *(Inst of Fund Tech Res, Polish Acad of Sci, Warszawa, Poland)*. Arch Mech 44(4) 437-451 (1992).

A Rayleigh-type surface stress propagation is considered in a "weakly anisotropic" semispace of "small nonhomogeneity"; two elastic shear moduli are assumed to be monotone functions of depth, the ratio of Young's moduli is limited to the first two terms of a power series expansion. Waves of such type are described by the solution of an ordinary, fourth order differential equation with variable coefficients satisfying the corresponding boundary conditions. In this particular case of variability of the elastic moduli, the problem has a closed-form solution expressed in terms of Bessel functions. Analysis of the dispersion equation proves the Rayleigh wave speed C_R to depend on the wave-length and on the anisotropy and nonhomogeneity parameters. Using the asymptotic expansions of Bessel functions, the dispersion equation is written in an approximate form enabling a numerical analysis of the influence of the anisotropy and nonhomogeneity parameters upon the surface wave speed.

158H. PLASTIC, VISCOPLASTIC WAVES

9A67. Riemann solver and a second-order Godunov method for elastic-plastic wave propagation in solids. - X Lin and J Ballmann *(Lehr und Forschungsgebiet Mechanik, RWTH Aachen, Templergraben 64, 5100 Aachen, Germany)*. Int J Impact Eng 13(3) 463-478 (Aug 1993).

By use of three basic paths of elastic-plastic loading, a Riemann solver is established for the 1D combined longitudinal and torsional stress wave problem of the thin-walled elastic-plastic tube. Based on this, a second-order Godunov method is developed for the numerical computation of elastic-plastic waves. Finally, the numerical method is applied to some basic problems with known exact solutions and the comparison of results is made.

158I. VISCOELASTIC WAVES

9A68. Theory and computation of the steady state harmonic response of viscoelastic rubber parts. - AB Zdunek *(Dept of Struct, Aeronaut Res Inst of Sweden, Box 11021, S-161 11 Bromma, Sweden)*. Comput Methods Appl Mech Eng 105(1) 63-92 (May 1993).

A robust FEM for the determination of the static response due to small harmonic excitations superposed on a prestrained equilibrium state presented for rubber engineering applications. The method presented here is based on a Key-type variational formulation, for a nearly incompressible rubber-elasticity problem. The problems originating from the difficulty in approximating the accumulated pressure, common to several popular nonlinear single field strain projection methods, are removed. Use of a local elementwise pressure approximation allows elimination of pressure increments at the element level. Incrementally, the method is therefore reduced to a single field but distinct from pure displacement based formulations. Applications are provided as a verification of the computer implementation and as a support of the approach.

158J. ULTRASONIC PROPAGATION

See the following:

9A107. Inverse problem of the scattering of ultrasound by a boundary inhomogeneity in an isotropic solid

158K. ANISOTROPIC MEDIA

9A69. Self-consistent analysis of waves in a polycrystalline medium. - FJ Sabina *(Inst Investigaciones Matematicas Appl Sistemas, Univ Nacional Autonoma, Apdo PO Box 20-726 Admon No 20, Delegacion Alvaro Obregon 01000 Mexico DF, Mexico)* and JR Willis *(Sch of Math Sci, Univ of Bath, Claverton, Down BA2 7AY, UK)*. Eur J Mech A 12(2) 265-275 (1993).

A simple method, of self-consistent type, which was developed recently for a matrix-inclusion composite, is placed in a form suitable for application to composites in which no clearly-defined matrix phase exists, as in a polycrystal. Information on grain size and shape is incorporated through the solution of relevant single scattering problems; approximate account of multiple scattering is taken through "self-consistent" choice of a background, "effective", medium. Finding the properties to assign to the effective medium is facilitated by the adoption of simple approximate solutions of the single scattering problems; when the scatterers can be modelled as spheres, this approximation becomes exact in the static limit.

158Q. REFLECTION, REFRACTION, DIFFRACTION, AND SCATTERING

See the following:

9A105. Acoustic and elastic wave scattering from elliptic cylindrical shells

9A413. High frequency scattering of plane horizontal shear waves by a Griffith crack propagating along the bimaterial interface

158Y. COMPUTATIONAL TECHNIQUES

9A70. Boundary integral equation approach to elastodynamic inequality problems and applications. - E Mitsopoulou-Papasoglou *(Dept of Civil Eng, Aristotle Univ, GR-54006 Thessaloniki, Greece)*, PD Panagiotopoulos *(Inst for Tech Mech, RWTH, D-5100 Aachen, Germany)*, PA Zervas *(Dept of Civil Eng, Aristotle Univ, GR-54006 Thessaloniki, Greece)*. Eng Anal Boundary Elements 11(2) 145-155 (1993).

In the present paper the method of boundary integral equations (BIE) is extended to dynamic inequality problems involving convex energy superpotentials, ie, to problems involving monotone, possibly multivalued, relations between reactions and displacements, stress and strains, etc. Using semidiscretization with respect to time the authors obtain, within each time step, a minimum potential energy formulation, the equivalent variational inequality formulation and some equivalent saddle point formulations using appropriate Lagrangian functions. An elimination technique gives rise to minimum principles, on the boundary with respect to the unknown displacements or stresses of the time step under consideration; parameters are the velocities, etc, of the previous time step.

9A71. Choice of interpolation schemes for the BEM in elastodynamics. - TW Wu and L Lee *(Dept of Mech Eng, Univ Kentucky, Lexington KY 40506)*. Commun Numer Methods Eng 9(5) 375-385 (May 1993).

It is known that the BE coefficient matrices in steady-state elastodynamics are frequency-dependent. For a multifrequency run, the coefficient matrices have to be reformed at each different frequency. This procedure usually involves heavy numerical integration, and hence is very time consuming. In this paper, two interpolation schemes are initially introduced to accelerate the process of matrix reformation without sacrificing the solution accuracy. In the first scheme, the coefficient matrices are first slightly transformed and then interpolated in the frequency domain. In the second scheme, the Green function is interpolated in the spatial domain. Comparison between these two schemes both in terms of accuracy and efficiency is presented. Finally, a hybrid scheme that takes advantage of the best of both interpolation schemes is proposed. Numerical examples are given to demonstrate the three different interpolation schemes.

160. Impact on solids

9A72. Local loading of simply-supported steel-grout sandwich plates. - GG Corbett *(Dept of Eng, Kings College, Aberdeen Univ, Fraser Noble Build, Aberdeen AB9 2UE, UK)* and SR Reid *(Dept of Mech Eng, UMIST, PO Box 88 Sackville St, Manchester M60 1QD, UK)*. Int J Impact Eng 13(3) 443-461 (Aug 1993).

The results of tests are described in which simply-supported plates having steel skins and a grout filler were subjected to local penetration under both quasi-static and dynamic conditions. The influence of the grout thickness was examined in detail and the dominant deformation and failure mechanisms were identified. The results show that, in contrast to tubes of a similar construction, the energy absorbing performance of these plates is inferior to that of monolithic steel plates. The reasons for this are discussed. It is shown that despite this, the behavior of the sandwich plates is noticeably less sensitive to projectile nose shape than monolithic steel plates, and therefore this type of plate construction may be useful, in a modified form, in situations where monolithic steel plates are vulnerable to unfavorable impact conditions. Under impact loading conditions the lower skin of the sandwich plate is shown to behave similarly to a free standing quasi-statically loaded skin and to be the dominant energy absorbing component. The grout filler under impact loading absorbs energy in proportion to its thickness.

9A73. Quasi-static and dynamic local loading of monolithic simply-supported steel plate. - GG Corbett *(Dept of Eng, Kings Col, Aberdeen Univ, Fraser Noble Bldg, Aberdeen AB9 2UE, UK)* and SR Reid *(Dept of Mech Eng, UMIST, PO Box 88 Sackville St, Manchester M60 1QD, UK)*. Int J Impact Eng 13(3) 423-441 (Aug 1993).

The results of a series of experimental tests on the local loading of circular plates resting on a ring support are presented. Both quasi-static and impact loading tests were performed using hemispherically-tipped and flat-ended cylindrical indenters. The contrasts between the quasi-static and dynamic responses are examined as are the differences produced by the different indenters. The maximum energy absorbing capacity of the plates when subjected to impact from hemispherically-tipped and flat-faced projectiles are determined experimentally and compared with the available empirical formula. Two empirical formulae for the prediction of the energy required to perforate a steel plate with a hemispherically-tipped projectile, adapted from the well-known SRI and Neilson formulae for flat-faced projectiles, are proposed.

9A74. Numerical computation of 2D unsteady detonation waves in high energy solids. - JK Clarke *(Col of Aeronaut, Cranfield IT, Bedford MK43 0AL, UK)*, S Karni *(Dept of Math, Univ of Michigan, Ann Arbor MI 48109)*, JJ Quirk *(Inst for Comput Appl in Sci and Eng, NASA Langley Res Center, Hampton VA 23665)*, PL Roe *(Dept of Aerospace Eng, Univ of Michigan, Ann Arbor MI 48109)*, LG Simmonds, EF Toro *(Col of Aeronaut, Cranfield IT, Bedford MK32 0AL, UK)*. J Comput Phys 106(2) 215-233 (Jun 1993).

We are concerned with theoretical modelling of unsteady, 2D detonation waves in high energy solids. A mathematical model and a numerical model to solve the associated hyperbolic system of equations are presented. The model consists of the Euler equations augmented by extra conservation laws and source terms to account for chemical reaction and tracking of materials. Both the thermodynamics and the chemistry are treated in a simple way. The numerical method selected for the full model is an extension of the conservative, shock capturing technique of Roe, together with an adaptive mesh refinement procedure that allows the resolution of the fine features such as reaction zones. Results for some typical tests problems are presented.

9A75. Experimental investigation of the scaling laws for metal plates struck by large masses. - He Ming Wen and N Jones *(Impact Res Centre, Dept of Mech Eng, Univ of Liverpool, PO Box 147, Liverpool L69 3BX, UK)*. Int J Impact Eng 13(3) 485-505 (Aug 1993).

An experimental investigation is presented into the geometrically similar scaling laws for circular plates impacted by cylindrical strikers with blunt ends travelling at velocities up to 5 m s^{-1} which produce permanent transverse displacements and perforation in some cases. The experimental results obey the geometrically similar scaling laws within the accuracy expected for such tests. It is observed that the impossibility of geometrically similar scaling of the material strain rate sensitive effects appears not to influence the plate perforation energies, at least within the range of experimental parameters studied in the present investigation.

See also the following:

9A228. Impact characterization of graphite fiber reinforced thermoplastic laminates

9A403. Prediction of delamination in composite laminates subjected to low velocity impact

162. Waves in incompressible fluids

9A76. Cylindrical wave solutions to the Korteweg-de Vries equation. - Yunkai Chen *(Dept of Math and Comput Sci, Fayetteville State Univ, Fayetteville NC)* and Shih-Liang Wen *(Dept of Math, Ohio Univ, Athens OH)*. Arch Mech 44(4) 479-483 (1992).

Cylindrical wave solutions for the Korteweg-de Vries equation are obtained within a reasonable approximation. They are shown to be representable as infinite sums of cylindrical solitons.

9A77. Experimental and numerical study of nonlinear internal waves. - DP Renouard *(IMG-LEGI, (UJF-CNRS-INPG), BP 53 X, 38041 Grenoble Cedex, France)*, GG Tomasson *(RMS, Parsons Lab, MIT)*, WK Melville *(Scripps Insts of Oceanog, USCD)*. Phys Fluids A 5(5) 1401-1411 (Jun 1993).

Nonlinear internal waves were measured on the large rotating platform at the Inst de Mecanique de Grenoble. The experimental data complement the results presented in Renouard *et al* and support the assumption that the solitary Kelvin wave is accompanied by Poincare waves. Based on the assumption of weak nonlinear, dispersive, and rotational effects, governing equations of the Boussinesq type are derived to model the evolution of an initial disturbance in a two-layer rotating fluid. The numerical study is based on these equations which are analogous to the Boussinesq equations of shallow-water theory and are not constrained to almost unidirectional propagation. Comparison of numerical solutions of the equations and experimental results are very good for moderately nonlinear conditions. These results provide supporting evidence for the resonant interaction of nonlinear Kelvin waves and linear Poincare waves, as described by Melville *et al.*

9A78. Nonlinear, dispersive, shallow-water waves developed by a moving bed. - M Villeneuve *(LaSalle Consult Group, Montreal, PQ Canada)* and SB Savage *(Dept of Civil Eng and Appl Mech, McGill Univ, Montreal, PQ Canada)*. J Hydraul Res 31(2) 249-266 (1993).

Landslides and avalanches plunging into lakes or reservoirs located in mountainous regions can generate large waves which can result in loss of life and significant property damage. As in the case with tsunamis generated in the ocean by underwater seismic activity, landslide induced water waves result from the motion of a solid boundary of the fluid. The present study deals with the mathematical modeling of water waves developed in a channel by a moving bed. A set of depth-averaged governing equations is derived to predict the evolution of the free surface resulting from a predetermined bed motion. These equations, which constitute a generalization of the Boussinesq system for waves over a flat bed, include both nonlinear and dispersive effects. Numerical solutions are obtained by using the finite difference method coupled with a Flux Corrected Transport (FCT) algorithm. The resulting model is used to predict the waves resulting from simple bed motions.

9A79. Transmission of an obliquely incident surface wave train through a submerged horizontal slot in a vertical wall. - PK Kundu *(Dept of Appl Math, Vidyasagar Univ, Midnapore 721 102, India)*. Acta Mech 98(1-4) 177-186 (1993).

Linear water wave theory is used for surface waves obliquely incident on a thin vertical wall in which there is an infinitely long submerged horizontal slot in deep water. The problem is reduced to an integral equation (IE) of the first kind over the slot. Assuming that the depth of submergence of the midsection of the slot is large compared to its breadth, a simple approximate solution to the IE is found, leading to an approximation for the transmission coefficient. A particular limiting case for the transmission coefficient is shown to produce the known result.

9A80. BEM for diffraction of oblique waves by an infinite cylinder. - M Rahman and M Chen *(Dept of Appl Math, Tech Univ of Nova Scotia, Halifax, NS, B3J 2X4, Canada).* Eng Anal Boundary Elements 11(1) 17-24 (1993).

This paper presents the solutions of the BEM for the potential flow problem associated with the diffraction of oblique waves by a horizontal cylinder of infinite length on a free surface. This physical model usually has its direct applications in engineering, such as in strip theory. The mathematical model for this problem is a 2D Helmholtz equation, whose BEM formulation involves kernels in the form of modified Bessel function. The application to this problem is among the first for this method. The diffraction forces and moment for a fixed rectangular cylinder have been calculated and compared with the existing results of KJ Bai, as an illustration of the effectiveness of the developed BEM code. The paper also compares results obtained using constant and linear elements.

9A81. Overhauser BE solution for periodic water waves in the physical plane. - JC Ortiz and SL Douglass *(Univ of S Alabama, Mobile AL 36688).* Eng Anal Boundary Elements 11(1) 47-54 (1993).

An Overhauser BEM for the modeling of nonlinear periodic waves in the physical plane is described. The Overhauser element, used to eliminate dicontinuities of the slope on the free surface of the wave, is described in detail. Examples for nonlinear steady and breaking waves are shown. The Overhauser element is compared to Lagrangian linear and cubic elements. It is noted that the Overhauser element system is very stable. Neither "smoothing" nor any other manipulation of the BEM results are necessary within the time-stepping algorithm to achieve a stable solution.

164. Waves in compressible fluids

9A82. Calculating the effects of variations in composition on wave propagation in gases. - RJ Pearson and DE Winterbone *(Dept of Mech Eng, UMIST, PO Box 88, Sackville St, Manchester M60 1QD, UK).* Int J Mech Sci 35(6) 517-537 (Jun 1993).

The equations of gas dynamics in one space dimension are solved whilst considering variations in gas composition and properties. A species continuity equation is derived and coupled in a single vector equation with the three usual conservation equations; the resulting system is solved directly in conservation law form using the two-step Lax-Wendroff technique. The effects of variable gas properties and composition on wave propagation are illustrated via the shock tube, or Riemann, problem. Significant errors are introduced, in the cases investigated, by assuming that the fluid is a perfect gas of constant composition. Flux-corrected transport (FCT) and nonupwind total variation diminishing (TVD) approaches are evaluated as a means of mitigating the spurious oscillations produced at discontinuities by the classical Lax-Wendroff scheme; these oscillations can give rise to mass fraction values from the species equation which are greater than unity or less than zero. It is found that the FCT algorithm does not suppress completely the oscillations at discontinuities and this corrupts the species transport calculations. The TVD algorithm eliminates the oscillations at shock waves and contact surfaces in the cases tested, thus maintaining the integrity of the species calculations. This is achieved at the expense of a 65% increase in computational effort over the constant gas property, constant composition case. The resolution of both the shock wave and contact surface can be improved significantly by the use of the artificial compression technique, but at an additional computational cost.

9A83. Shock wave reflection close to the leading edge of a wedge. - B Schmidt and J Fuchs *(Inst Stromungslehre und Stromungsmaschinen, Univ Karlsruhe, Karlsruhe, Germany).* Arch Mech 44(4) 453-462 (1992).

The aim of the present investigation is to show the development of the shock reflection process as soon as a shock wave hits a wedge. To resolve the structure of the shock waves, the experiments were performed under rarefied gas conditions. Because no field method is sufficiently sensitive, a laser differential interferometer was used. Varying the wedge angle, the development of the different types of reflection (regular reflection, Mach reflection) could be observed.

9A84. Variation of the specific heat ratio and the speed of sound in air with temperature, pressure, humidity, and CO_2 concentration. - O Cramer *(11588 Waresley St, Maple Ridge BC, V2X 9Z2, Canada).* J Acoust Soc Am 93(5) 2510-2516 (May 1993).

This paper describes a precise numerical calculation of the specific heat ratio and speed of sound in air as a function of temperature, presure, humidity, and Co_2 concentration. The above parameters are calculated using classical thermodynamic relationships and a real gas equation of state over the temperature range 0°C - 30°C. The shortcomings of previous determinations are also discussed. For both parameters, the coefficients of an interpolating equation are given, which are suitable for use in applications requiring high precision. The overall uncertainty in the specific heat ratio is estimated to be less than 320 ppm and the uncertainty in the speed of sound is similarly estimated to be less than 300 ppm.

166. Solid fluid interactions

9A85. Liquid-structure-foundation interaction of slender water towers. - HA Dieterman *(Fac of Civil Eng, Tech Univ, Stevinweg 1, 2628 CN Delft, Netherlands).* Arch Appl Mech 63(3) 176-188 (Apr 1993).

The dynamic behavior of a slender water tower based on a (deep) foundation is studied by a lumped model in which the parameters have been derived analytically from continuous models. The effects of the liquid and foundation on the structural dynamics can be studied analytically using this model, sensitivity analyses are easily performed. Ring baffles in the liquid tank and the local yielding of the pile-soil interaction along the shaft of the foundation piles may reduce the dynamic response.

See also the following:

9A80. BEM for diffraction of oblique waves by an infinite cylinder

172. Acoustics

172A. GENERAL THEORY

9A86. Finite amplitude standing waves in harmonic and anharmonic tubes. - DF Gaitan and AA Atchley *(Physics Dept, Naval Postgrad Sch, Monterey CA 93943).* J Acoust Soc Am 93(5) 2489-2495 (May 1993).

Finite amplitude standing waves have been studied in closed tubes filled with air and driven by a piston at frequencies near 200 Hz. The tubes were driven at resonance generating standing waves with amplitudes of up to 160dB re: 20 \mPa. The main objective was to measure the dissipation of the energy by the fundamental frequency and the higher harmonics, as well as by other nonacoustic mechanisms. A formulation developed by Coppens and Sanders using a single nonlinear equation to describe standing waves in cavities of arbitrary resonance frequencies and quality factors was used successfully to predict the higher harmonics. In addition, the effect of detuning the tubes on the energy dissipation was measured in tubes with variable cross sections. It was found that the detuned tubes effectively suppress the energy transfer into (and energy dissipation by) the higher harmonics. It was also found that expanding rather than contracting the cross section of the tubes minimized the dissipation of energy through nonacoustic mechanisms.

9A87. Resonance frequencies and structures of sound fields in the enclosures of acoustical systems. - IA Aldoshina and MV Olyushin *(AS Popov, All-Union Sci Res Inst, Russia).* Sov Phys Acoust 38(6) 529-534 (Nov-Dec 1992).

Methods based on perturbation theory are proposed for calculating resonance frequencies in the enclosures of acoustical systems having a complex geometry. Computational methods using the BE approach and eigenfunction expansions of the structure of the internal sound fields are investigated.

172B. SOUND GENERATION BY MOVING SURFACES

See the following:

9A621. Particle force and heat transfer in a dusty gas sustaining an acoustic wave

172D. SOUND WAVES IN GASES

9A88. Analysis of ultrasonic velocities in hydrocarbon mixtures. - JG Berryman *(LLNL).* J Acoust Soc Am 93(5) 2666-2668 (May 1993).

Ultrasonic velocity data on hydrocarbon mixtures were shown by Wang and Nur to agree quite well with the predictions of a simple mixing rule. The same data were reanalyzed using Wood's formula and the time-average approximation. Wood's formula for acoustic velocity is shown to be always less than the time-average formula, which is itself always less than the simple mixing rule result. Although the volume average rule agrees best with the data on binary mixtures of 1-decene and 1-octadecene, all these formulas agree with the data to within 1% and, therefore, it is not possible to distinguish among the formulas using this data set. Similar results are also found for six multicomponent hydrocarbon mixtures.

172E. SOUND WAVES IN LIQUIDS (UNDERWATER ACOUSTICS)

9A89. Application of ray theory with beam displacement to 3D sound propagation in a wedge shaped ocean. - KV Avudainayagam and GV Anand *(Dept of Elec Commun Eng, Indian Inst of Sci, Bangalore, 560 012, India)*. J Acoust Soc Am 93(5) 2581-2591 (May 1993).

Ray theory with beam displacement (RTBD) has been developed to evaluate the acoustic field in 3D in a wedge-shaped ocean with a lossy fluid bottom. An algorithm for tracing eigenrays in 3D is described. A procedure for determining the location of caustics in 3D is also presented. It is shown that the density of caustics reduces with increasing bottom attenuation. Sharp spurious peaks appear in the acoustic field in the vicinity of caustics. These caustic-related peaks can be readily identified and smoothed out, and no further corrections would be necessary in most situations of practical interest. Agreement between the smoothed RTBD solution and the "exact" two-way coupled mode solution is quite good for the 2D problem of up-slope propagation in the ASA benchmark wedge with a penetrable lossy bottom. Numerical results for the 3D problem are presented for several bottom slopes and directions of propagation.

9A90. Correlation of deep ocean noise (0.4 - 30 Hz) with wind, and the Holu Spectrum: A worldwide constant. - CS McCreery, FK Duennebier *(Sch of Ocean and Earth Sci and Tech, Univ of Hawaii, 2525 Correa Rd, Honolulu HI 96822)*, GH Sutton *(Woods Hole Oceanog Inst, RD2 Box 167C, Stone Ridge NY 12484)*. J Acoust Soc Am 93(5) 2639-2648 (May 1993).

One year of ambient ocean noise data, 0.4 to 30 Hz, from the Wake Island hydrophone array in the NW Pacific are compared to surface wind speeds, 0-14 m-s (0 - 28 kn). Between 0.4 and 6 Hz, noise levels increase with wind speed at rates of up to 2dB per m/s until a saturation is reached having a slope of about -23 dB-octave and a level of 75 dB relative to $1\mu Pa/\sqrt{Hz}$ at 4 Hz. This noise saturation, called the "Holu Spectrum", likely corresponds to saturation of short-wavelength ocean wind waves. It is probably a worldwide constant. Between 4 and 30 Hz, noise also increases with wind speed at rates of up to 2 dB per m-s, but no saturation level is observed and the slope increases to about 4 dB-octave. This may be acoustic noise from whitecaps. On a hydrophone less than 3 km from Wake, noise between 0.5 and 10 Hz increases with wind speed at a rate up to 2 dB per m-s, but absolute noise levels are significantly higher than levels on the other hydrophones more distant from Wake, and no saturation is apparent. Surf breaking against the shore of the island is the probable source of this noise.

9A91. Evolution of local spectra in smoothly varying nonhomogeneous environments: Local canonization and marching algorithms. - BZ Steinberg *(Dept of Interdisciplinary Stud, Fac of Eng, Tel-Aviv Univ, Tel Aviv 69978, Israel)*. J Acoust Soc Am 93(5) 2566-2580 (May 1993).

By applying the windowed Fourier transform directly to the Helmholtz wave equation a new formulation that governs the evolution of the local spectra of wave fields in a general nonhomogeneous environment is derived. By further invoking the so-called locally homogeneous approximation, a simplified evolution equation, termed as the locally homogeneous wave equation is developed, together with an upper bound on the error associated with the approximation. It is shown how simple analytical solutions of the new wave equation in a general smoothly varying nonhomogeneous environment can be obtained using well-known analytical techniques, and how the marching methodology connects these new solutions to the original problem described by the Helmholtz equation.

9A92. Experimental demonstration of sound-speed inversion with matched-field processing. - CC Karangelen *(Dept of Mech Eng, Catholic Univ of Am, Washington DC 22064)* and O Diachok *(Acoust Div, Code 5120, Naval Res Lab, Washington DC 20375-5000)*. J Acoust Soc Am 93(5) 2649-2655 (May 1993).

Matched-field processing is shown to be effective for estimating sound speed in a deep, range-independent ocean environment. The amplitude and phase of signals from a distant source measured on a large aperture vertical array are sensitive to changes in sound speed. This measured on a large aperture vertical array are sensitive to changes in sound speed. This sensitivity is exploited to infer the environment's sound-speed profile by matching predicted and measured amplitude and phase. Simulations and an initial experimental demonstration of the power of the technique are based on a modified version of Munk's canonical sound field model. This model is used in a simulated environment with a 15 Hz source where source and receiver locations are known. The simulation demonstrates that changes in the depth and strength of the modeled sound channel axis directly result in trackable errors in range and depth as well as in reduction of the received power level. The same model is used to determine sound-speed profile using a 15 Hz signal from a 244-m explosive source detected on a 675-m vertical array at a range of 53 km in a deep water Pacific environment, characterized by a classical range-independent sound channel at 700-m. The search for the best estimated profile is conducted by varying the sound channel axis strength and depth in the modified Munk equation, while maintaining a constant sound-speed profile at great depths. For the single test case, resultant differences between the matched-field estimated and measured profiles are less than ±2 m-s; the sound channel axis depth is determined within 20 m of the measured axis depth.

9A93. Form factor of a cylinder sonic source and application in borehole acoustics. - Shoumian Yu *(Dept of Phys, Shandong Univ, Jinan, Shandong 250100, Peoples Rep of China)* and Yinbin Liu *(Inst of Geophys, Chinese Acad of Sci, Beiging 100101, Peoples Rep of China)*. J Acoust Soc Am 93(5) 2592-2598 (May 1993).

By introducing the concept of a form factor for a cylindrical sonic source, a new method is constructed for solving boundary value problems of the wave field produced by such sources when the solutions for a simple source is known, provided the boundary conditions are axisymmetrical and are linear and homogeneous in the potentials. The form factor is defined in cylindrical coordinates as a function F(k) of the wave number k. The analytic properties of F(k) are described. It is proved that F(k) can be obtained from the farfield approximation and is related to the directional factor through a simple transformation. The form factors of several simple-shaped sources are derived. The theory is applied to the case of a borehole to shoe that the effect of the form factor on the profile of the full wavetrain is prominent in certain cases.

9A94. High frequency bistatic reverberation from a smooth ocean bottom. - S Stanic, E Kennedy, RI Ray *(Naval Ocean and Atmos Res Lab, Ocean Acoust Div, Stennis Space Center MS 39529-5004)*. J Acoust Soc Am 93(5) 2633-2638 (May 1993).

High-frequency bistatic reverberation was measured from a smooth, sandy featureless bottom located 19 miles south of Panama City, FL. Bistatic scattering variability is presented as a function of frequency (20 - 180 kHz), grazing angles (9.5° - 30°), and small horizontal and vertical bistatic scattering angles. Results show that bistatic variabilities tend to decrease with decreasing grazing angles and decreasing source beamwidths. Possible explanations for these decreasing variations are also presented.

9A95. Low frequency Arctic reverberation Part II. Modeling of long- range reverberation and comparison with data. - TC Yang and TJ Hayward *(Naval Res Lab, Washington DC 20375-5350)*. J Acoust Soc Am 93(5) 2524-2534 (May 1993).

In this paper a normal-mode model of scattering from surface and bottom protuberances is applied to model long-range reverberation data collected during the CEAREX 89 experiment in the Norwegian-Greenland Seas. Modeled reverberation spectrum levels at 23 Hz are compared with data to investigate the relative contributions of the ice and bottom to the measured reverberation. The normal-mode model of boundary scattering is based on a generalization of recent work of Ingenito treating scattering from a rigid sphere in a stratified waveguide. Adiabatic normal mode theory is used to model the propagation to and back from the scatterer in a range-dependent waveguide. Using the small ka approximation for the scattering functions, where k is the wave number and a is the dimension of the boundary protuberance, the normal-mode calculations of the long range reverberation levels are found to agree rather well with the CEAREX data for four different measurements involving different bottom bathymetries and source depths. For a source at 91 m depth in the 3000 m deep basin, it is found that the reverberation level for a receiver at 60 m is dominated by scattering from the ice except for reverberation associated with certain identifiable bottom features. For the same environment but a deeper source (244-m), reverberation levels from the ice and bottom are more comparable. For a strongly range dependent environment, returns from bottom features are clearly identifiable in the data.

9A96. Low frequency volume reverberation measurements. - T Akal *(SACLANT Undersea Res Center, La Spezia, Italy)*, RK Dullea *(Naval Underwater Syst Center, New London CT 06320)*, G Guido *(SACLANT Undersea Res Center, La Spezia, Italy)*, JH Stockhausen *(Defence Res Est Atlantic, Dartmouth, NS, Canada)*. J Acoust Soc Am 93(5) 2535-2548 (May 1993).

An experimental technique has been developed to measure broadband low-frequency volume reverberation. Experiments were performed in the North Atlantic with broadband explosive sources in conjunction with the end-fire beam of a vertical line array to provide scattering strength contours from measurements sampled in both frequency (~ 12 Hz) and depth (~ 4 m). The experimental and analysis techniques are described along with representative examples that compare high and low scattering levels observed during the experiment.

9A97. Low-frequency Arctic reverberation I. Measurement of under ice backscattering strengths from short-range direct-path returns. - TJ Hayward and TC Yang *(Naval Res Lab, Washington DC 20375-5350)*. J Acoust Soc Am 93(5) 2517-2523 (May 1993).

Under ice scattering strengths in the backward direction were measured in April 1989 during the CEAREX 89 field experiment in the Norwegian-Greenland Sea using a large-aperture vertical hydrophone array and 1.8 lb SUS explosive sources. Scattering strength estimates for frequencies of 24-105 Hz are presented as a function of scattering angle (2.5° - 40° grazing), averaged over incident angles in the range 10° - 15° grazing. The corresponding (monostatic) backscattering strength is found to be approximately 10dB below that reported by Milne for data collected at approximately the same time of year in 1962 near the Canadian Archipelago. The results are compared with scattering functions derived by Burke-Twesky model, which represents the ice ridges as rigid elliptical half-cylinders. The variations of the measured scattering strength with both scattering angle and frequency are well fitted by this model for scattering angles below 20° grazing.

9A98. Measurements of bottom-lined ocean impulse responses and comparisons with the time-domain parabolic equation. - RL Field and JH Leclere *(Naval Res Lab Detachment, Stennis Space Center MS 39529-5004)*. J Acoust Soc Am 93(5) 2599-2616 (May 1993).

Ocean impulse response functions computed with the time-domain parabolic equation model are shown to be consistent with response functions measured in a bottom-limited ocean located off the east coast of the US. The geoacoustics used in the model are developed from Deep Sea Drilling Project sites near the experimental area. Measured impulse responses are obtained by correlating the measured source signature of a 25 to 150 Hz linear, frequency-modulated signal with the signals received on a 15-element vertical line array. Correlation coefficients computed as a function of depth are used as a measure of comparison between measured and modeled responses. The capability of the time-domain parabolic equation to model wide-angle (68° - 75\edg) multipaths and subbottom layers with high impedance contrasts is shown. Correlation loss between response functions measured from different transmissions at the same range is shown to be attributable to the degree to which spatial invariance of the ocean can be assumed.

9A99. Modeling 3D propagation in an oceanic wedge using parabolic equation methods. - JA Fawcett *(Defence Res Est Pacific, FMO Victoria BC, V0S 1B0, Canada)*. J Acoust Soc Am 93(5) 2627-2632 (May 1993).

In this paper the predictions of aximuthally uncoupled and azimuthally coupled parabolic equation (PE) methods for 3D acoustic propagation in a penetrable oceanic wedge are compared. The individual modes of the waveguide at the source position are used as the initial field for the PE methods and the resulting PE fields are compared to the ray diagrams of 3D adiabatic mode theory.

9A100. Monostatic and bistatic reverberation results using linear frequency-modulated pulses. - JR Preston *(SACLANTCEN, CMR 426, APO, AE 09613)* and WA Kinney *(NRL, Stennis Space Center MS 39529)*. J Acoust Soc Am 93(5) 2549-2565 (May 1993).

Estimates of reverberant scattering strength are presented as a function of range and bearing for selected monostatic and bistatic geometries of a reverberation experiment. Diffuse scattering strengths were found to be comparable (within ~ 3 dB) for both monostatic and bistatic geometries. This experiment was performed off the west coast of Sardinia in approximately 2800 m of water during February of 1990. The receiver was a horizontal array of approximately 20 wavelengths. Source and receiver depths ranged from 50 to 120 m. The signals used consisted of linear frequency-modulated pulses centered near 1 kHz with durations ranging from 8 to 16 s and bandwidths ranging from 32 to 64 Hz. Monostatic and bistatic scattering strength values are estimated using uncorrelated (ie, not matched-filtered) pulses. The scattering strengths presented vary from -29 to -48 dB for ranges up to 40 km (but not data near fathometer returns). A method is described that shows different correlator gains against noise and reverberation. Comparisons of measured and modeled reverberation are presented using the generic sonar model (GSM) and curve fits with the decay in monostatic diffuse backscatter show good agreement with Lambert's rule using a -32 dB constant. Finally, GSM is used to estimate grazing angles from which plots of measured scattering strength versus grazing angle in the 10° - 26° interval are presented. Using this method, a Lambert's rule constant of ~ 30 dB was a better fit to the data.

9A101. Neural network feature vectors for sonar targets classifications. - A Svardstrom *(Circuits and Syst Group, Dept of Tech, Uppsala Univ, Box 534, S-751 21 Uppsala, Sweden)*. J Acoust Soc Am 93(5) 2656-2665 (May 1993).

This paper deals with classification of objects using active sonar and neural network classifiers. Various methods of feature extraction, ie, transformations of the recorded data to a form better suited as inputs to the classifier, have been applied to recorded active sonar data. The well-known multilayer perceptron architecture has been used. To reduce the computational effort and the number of parameters to estimate, the number of input nodes were limited, and it has been shown that feature vectors using Walsh transform coefficients are superior to feature vectors using Fourier transform coefficients under this constraint. Particularly with low SNR, the feature vectors based on Walsh transform coefficients outperform the Fourier based vectors. Some minor effort has been expended on optimizing the neural network implementation.

9A102. Performance stability of high-resolution matched-field processors to sound-speed mismatch in a shallow-water environment. - GB Smith, HA Chandler, C Feuillade *(Naval Res Lab, Stennis Space Center MS 39529-5004)*. J Acoust Soc Am 93(5) 2617-2626 (May 1993).

The effects of variations in water sound-speed parameters on the performance of four matched-field processing algorithms (Bartlett, maximum-likelihood, sector-focusing, and multiple constraint) have been investigated. The SNAP propagation model was used to generated the replica acoustic pressure field for a shallow water channel with a depth variable sound-speed profile typical of a midlatitude summer environment. It was also used to simulate a "detected" field due to an acoustic source. These were then correlated using the four algorithms for selected degrees of mismatch of the water sound-speed profile. The maximum likelihood and multiple constraint estimators achieved good peak resolution and high accuracy for small degrees of mismatch. The maximum likelihood estimator deteriorated quickly as the mismatch increased. The multiple constraint estimator performed significantly better, but both failed to give correct location estimates at the higher mismatch values. In contrast, the sector focusing estimator continued to give accurate location estimates over the whole range of sound-speed mismatch, with slightly less peak resolution at small mismatch values. It also performed significantly better overall than the Bartlett estimator, which was found to give accurate location estimates over the whole range of mismatch values used, but with poor peak resolution against a background containing many high sidelobes.

See also the following:

9A109. Sound scattering by thin-walled elastic cylinders of finite length

172G. SOUND WAVES IN NONHOMOGENEOUS, POROUS AND RANDOM MEDIA

9A103. Microstructural characteristics of wave propagation in a saturated porous medium. - VP Bandov and VS Khalilov *(Bashkir State Univ, Russia)*. Sov Phys Acoust 38(6) 534-538 (Nov-Dec 1992).

The mechanisms of dynamic interaction of the phases in a model of a saturated porous medium is investigated. An idealized matrix deformation model in the form of close-packed identical spheres immersed in a compressible liquid is used to establish several deformation characteristics of the investigated medium, in particular, the influence of the geometrical structure of the phase interface and the elastic properties of the interstitial liquid on the compressibility of the medium. A hydrodynamic model in the form of a planar pore channel filled with a viscous liquid and bounded by movable walls is used to calculate the structure of the interstitial flows associated with wave propagation. The dependence of the filtration return flows on the properties of the medium and the wave parameters is determined. It is shown that these flows influence the wave propagation velocity and attenuation.

9A104. Propagation in an anisotropic periodically multilayered medium. - C Potel and JF de Belleval *(LG2MS, URA CNRS 1505, Univ de Tech, BP 649, 60206 Compiegne Cedex, France)*. J Acoust Soc Am 93(5) 2669-2677 (May 1993).

An anisotropic multilayered medium is studied using the method of transfer matrices, developed by Thomson and Haskell. The propagation equations in each layer of the multilayered medium use the form developed by Rokhlin et al. Physical explanations are given, notably when a layer is made up of a monoclinic crystal system medium. The displacement amplitudes of the waves in one layer may be expressed as a function of those in another layer using a propagation matrix form, which is equivalent to relating the displacement stresses of a layer to those in another layer. An anisotropic periodically multilayered medium is then studied by using a propagation matrix that has particular properties: a determinant equal to one and eigenvalues corresponding to the propagation of the Floquet waves. An example of such a medium with the axis of symmetry of each layer perpendicular to the interfaces is then presented together with the associated reflection coefficients as a function of the frequency or of the incident angle.

172H. REFLECTION, REFRACTION, DIFFRACTION, AND SCATTERING

9A105. Acoustic and elastic wave scattering from elliptic cylindrical shells. - RP Radlinski *(Naval Undersea Warfare Center Detachment, New London CT 06320)* and MM Simon *(Alliant Telesyst, Everett WA 98204)*. J Acoust Soc Am 93(5) 2443-2453 (May 1993).

An acoustic scattering formulation has been derived from a modification of the extended boundary integral method (null-field approach) developed for elastic wave scattering from infinite cylindrical shells of arbitrary shape. Thin shell theory is assumed to describe the motion of the scatterer. Acoustic and elastic p-p wave scattering calculations are presented for elliptic-cylindrical shells of different materials and eccentricities. At low frequencies, the scattering by an elliptical shell in a fluid is dominated by the bending resonances. At higher frequencies, the acoustic scattering is strongly dependent on the angle of incidence, material characteristics, and the predominately extensional structural resonances. In an elastic material, resonant modal responses of the shell were found to increase mode conversion of dilatational waves into shear waves. By comparison with elasticity theory for shells and by extrapolations from thick and thin plate theories, the limitations of the thin shell theory are shown to be material dependent. The present method is used to re-examine examples of backscatter from elliptic-cylindrical shells reported in other studies.

9A106. Backscattering of chirped bursts by a thin spherical shell near the coincidence frequency. - G Kaduchak and PL Marston *(Dept of Phys, Washington State Univ, Pullman WA*

99164-2814). J Acoust Soc Am 93(5) 2700-2706 (May 1993).

Previous ray calculations and observations have shown that tone bursts with a carrier frequency ka close to the coincidence frequency of a thin spherical shell in water exhibit a backscattering enhancement. A distinct feature associated with the a_{0-} guided wave was enhanced relative to the specular reflection by a factor close to 3.1. In the present research, a Fourier synthesis from the partial wave series is used to investigate how chirping the frequency of the incident burst influences the enhancement. An enhancement is still evident even when the incident burst is swept through the entire ka range of interest sufficiently rapidly for the specular and guided wave echoes to remain distinct. The enhancement is larger when ka is swept from high-to-low than from low-to-high. This is a consequence of a decrease in the group velocity with ka resulting in a localization of the echo for the high-to-low sweep. The enhancement can now exceed the aforementioned value of 3.1 and should increase the signal-to-noise ratio. Experimental records confirm the effect on a real shell.

9A107. Inverse problem of the scattering of ultrasound by a boundary inhomogeneity in an isotropic solid. - VA Burov, IP Prudnikova, NS Sirotkina *(MV Lomonosov State Univ, Moscow, Russia).* Sov Phys Acoust 38(6) 555-558 (Nov-Dec 1992).

The 2D problem of the scattering of ultrasound by an unknown void in a solid is investigated. A nonlinear functional is formulated, and the minimum conditions for it are used to derive a system of nonlinear equations for determining the characteristic function of the object. The number of positions from which to irradiate the object in order to guarantee a unique solution of the problem is discussed.

9A108. Quantitative reconstruction of internal density distributions from laser ultrasonic data. - Yichi Lu, JA Goldman, HNG Wadley *(Intelligent Processing of Mat Lab, Sch of Eng and Appl Sci, Univ of Virginia, Charlottesville VA 22903).* J Acoust Soc Am 93(5) 2678-2687 (May 1993).

An ultrasonic method has been investigated for the quantitative recovery of density distributions of porous bodies similar to those produced by pressure-assisted sintering of powders. It relies upon the strong relationship between the ultrasonic velocity and the density of a porous body. Noncontact laser generated -nterferometrically detected ultrasound has been propagated along ray paths in a planar cross section of model samples and ultrasonic time-of-flight projections obtained. Two approaches have been explored for reconstructing the internal velocity (and thus density) distribution from the projection data. The first approach was a standard convolution backprojection algorithm used frequently in computerized tomographic reconstruction. A combination of ray bending (due to refraction by the velocity gradient within the sample), noise in the projections, and practical limits upon the number of projections that can be obtained have all adversely affected the reconstruction quality of this method. The second approach explored a (nontomographic) nonlinear least-squares approach. It utilized *a priori* information about the general functional form of the velocity (density) distribution (which is available from predictive models of the densification process) and gave significantly better results for samples with simple geometry even when projection data were sparse.

9A109. Sound scattering by thin-walled elastic cylinders of finite length. - AV Lebedev and AI Khil'ko *(Inst of Appl Phys, Russian Acad of Sci, Russia).* Sov Phys Acoust 38(6) 578-582 (Nov-Dec 1992).

The scattering of acoustic fields by thin-walled elastic cylinders of finite length is investigated. An approximate scattering model based on the method of successive reflections is used for the calculations and estimations. The range of geometrical parameters of the shell for the observation of clearly pronounced forward scattering is determined.

9A110. Ultrasonic nondestructive evaluation of thin (sub-wavelength) coatings. - VK Kinra and C Zhu *(Center for Mech of Composites, Dept of Aerospace Eng, Texas A&M Univ, College Station TX 77843).* J Acoust Soc Am 93(5) 2454-2467 (May 1993).

This paper describes a technique for ultrasonic nondestructive evaluation (NDE) of a thin coating on a thick substrate; here thin means the thickness of the coating is less than the wavelength of the ultrasonic wave used to interrogate it. A plane longitudinal wave that is normally incident upon the coating is considered. Transfer functions have been derived for both the coating-side and the substrate-side insonification. A systematic analysis of the sensitivity of the transfer functions to the thickness and wave speed has been carried out. An inverse algorithm, which utilizes the well-known Newton-Raphson method, has been developed to reconstruct the thickness and the phase velocity through a comparison of the theoretical and the measured transfer functions; fortunately, this algorithm is independent of substrate thickness. Using this technique both the thickness and the wave speed of the coating can be extracted from the same measurement without knowing either. The technique is fully automated and computer-controlled and can be easily used for in-situ NDE applications. The technique was used to measure the thickness and wave speed of epoxy and Plexiglas coatings (50-100 \umm) on an aluminum substrate using low-frequency (10- and 20-MHz) transducers; the ratio of thickness-wavelength was about 1/3. The precision in the measurement of the thickness and the wave speed was found to be $\pm\mu m$ and $\pm 3\%$, respectively.

172I. ACOUSTIC PROPERTIES OF MATERIALS

9A111. Characteristic dimensions and prediction at high frequencies of the surface impedance of porous layers. - D Lafarge, JF Allard, B Brouard *(Lab d'Acoustique, CNRS URA No 1101, Fac de Sci du Mans, BP 535, Ave Olivier Messiaen, F-72017 Le Mans Cedex, France),* C Verhaegen, W Lauriks *(Lab voor Akoestiek, Katholieke Univ Leuven, Celestijnenlaan 200 D, B-3001 Heverlee, Belgium).* J Acoust Soc Am 93(5) 2474-2478 (May 1993).

The surface acoustic impedance of a glass wool and a reticulated foam is measured in a free field up to 20 000 Hz. The characteristic dimensions Λ and Λ` can be calculated for the glass wool, and the surface impedance can be predicted with no adjustable parameters. The motion of the frame is not taken into account. The agreement between measurement and prediction is good. For the foam, the characteristic dimensions cannot be calculated, because the geometry of the frame is not simple. A correct choice of Λ and Λ` allows a precise prediction of the surface impedance for a large range of frequencies and different thicknesses.

172J. NOISE CONTROL AND REDUCTION (INCL ACTIVE CONTROL)

9A112. Acoustic control by wave field synthesis. - AJ Berkhout, D de Vries, P Vogel *(Lab of Seismics and Acoust, Delft Univ of Tech, PO Box 5046, 2600 GA Delft, Netherlands).* J Acoust Soc Am 93(5) 2764-2778 (May 1993).

The acoustics in auditoria are determined by the properties of both the direct sound and the later arriving reflections. If electroacoustics means are used to repair disturbing deficiencies in the acoustics, one has to cope with unfavorable side effects such as localization problems and artificial impressions of the reverberant field (electronic flavor). To avoid those side effects, the concept of electroacoustic wave front synthesis is introduced. The underlying theory is based on the Kirchhoff-Helmholtz integral. In this new concept the wave fields of the sound sources on stage are measured by directive microphones; next they are electronically extrapolated away from the stage, and finally they are re-emitted in the hall by one or more loudspeaker arrays. The proposed system aims at emitting wave fronts that are as close as possible to the real wave fields. Theoretically, there need not be any differences between the electronically generated wave fields and the real wave fields. By using the image source concept, reflections can be generated in the same way as direct sound.

9A113. Active control of point acoustic sources in a half-space. - KA Cunefare and S Shepard *(George W Woodruff Sch of Mech Eng, Georgia Tech).* J Acoust Soc Am 93(5) 2732-2739 (May 1993).

Analysis of active noise control applications generally neglect the presence of nearby reflective surfaces, such as a ground plane. The research presented in this paper examines the impact of the presence of a nearby reflective plane on the active control of sound radiated by a number of point sources. It is shown that when the sources to be controlled are within one wavelength of the reflective plane, be it rigid or pressure release, that the plane can significantly impact the control versus control under free-field conditions with the same source separations. The orientation of the noise sources and the control sources with respect to each other and to the plane also significantly influences the control. For sources more than one wavelength away from the reflective plane, the use of the simpler free-space analysis yields acceptable results as compared to using the more complex half-space analysis.

9A114. Active control of sound power using acoustic basis functions as surface velocity filters. - K Naghshineh *(Acoust and Radar Tech Lab, SRI Int, 333 Ravenswood Ave, Menlo Park CA 94025)* and GH Koopmann *(Center for Acoust and Vib, 157 Hammond Build, Penn State).* J Acoust Soc Am 93(5) 2740-2752 (May 1993).

An improved method of active structural acoustics control is presented that is based on the minimizations of the total power radiated from any structure expressed in terms of a truncated series sum. Each term of this sum is related to the coupling between the orthogonal eigenvectors of the radiation impedance matrix (referred to as "basis functions" in this paper) and the structural surface velocity vector. The basis functions act as surface velocity filters. These acoustic basis functions are found to be weak functions of frequency but their corresponding weighting coefficients increase monotonically with frequency. The minimization of the radiated power is shown to result in a structural surface velocity vector that couples poorly to those acoustic basis functions that account for high-efficiency sound radiation. This strategy is demonstrated numerically for a clamped-clamped baffled beam in air. Point force primary and control actuators (shakers) are used to explore the control mechanisms. As expected, the minimization of the radiated power results in a controlled beam response that contains much lower supersonic wave-number content than that of the uncontrolled beam response. Finally, an unexpected benefit of the control strategy described is that it provides a rational procedure for selecting the number and placement of actuators and sensors on a structure for effective control. This development is significant since this procedure does not require *a priori* knowledge of the dynamics of the structure.

9A115. Active control of sound radiation from a simply supported beam: Influence of bending near field waves. - C Guigou and CR Fuller *(Vib and Acoust Labs, Mech Eng Dept, VPI)*. J Acoust Soc Am 93(5) 2716-2725 (May 1993).

Active control of sound radiation from a baffled simply supported finite beam is analytically studied. The beam is subjected to a harmonic input force and the resulting acoustic field is minimized by applying a control point force. For a single frequency, the flexural response of the beam subject to the input and control forces is expressed in terms of flexural waves of both propagating and near-field types. The optimal control force complex amplitude is derived by minimizing the acoustic radiated pressure at one point located in the far-field. The far-field radiated pressure, the displacement of the vibrating beam, and the 1D wave-number spectrum of the beam velocity are extensively studied. In order to further understand control mechanisms, the radiated pressure due to the flexural propagating wave and the flexural near-field wave, respectively, is investigated at the minimization point before and after the control is involved. The analysis shows that, when the control is applied, the combination of the radiated pressure due to the two different types of waves (as their associated radiation is out-of-phase) at the minimization point causes the large pressure attenuation. These results demonstrate that structural near-fields are important in terms of predicting performance in active control of structurally radiated sound.

9A116. In situ estimation of an acoustic source in an enclosure and prediction of interior noise by using the principle of vibroacoustic reciprocity. - Bong-Ki Kim and Jeong-Guon Ih *(Dept of Mech Eng, Korea Adv Inst of Sci and Tech, 373-1 Kusung-dong, Yusung-ku Taejon 305-701, Korea)*. J Acoust Soc Am 93(5) 2726-2731 (May 1993).

The volume velocity of an acoustic source can be widely used in determining the vibroacoustic transfer functions, in measuring the acoustic transfer impedances, and in finding the generated power of an acoustic source. Several techniques utilizing special experimental devices have been proposed for this purpose, including the laser velocimetry, the internal pressure measurement, and the face-to-face electroacoustic measurement. However, for a source in an enclosure with flexible walls the vibroacoustic coupling should be considered, especially in the case of a loudspeaker source that has low internal mechanical impedance. The present method, which uses the principle of vibroacoustic reciprocity, can give a reasonable estimation of the transfer functions and can be used in determining the volume velocity of a source *in situ*. Because the present method does not require a special facility or the information of the source surface vibration, the method can be applied to any irregularly shaped source in a flexible enclosure. With the obtained vibroacoustic transfer functions, the interior noise field in an enclosure can be predicted by vectorial summation when the boundary points are excited by uncorrelated dynamic forces. The predicted internal pressure in an enclosure is in good agreement with the measured internal pressure, even in the presence of sound absorbers inside the enclosure.

9A117. Numerical method for noise optimization of engine structures. - MG Milsted *(nCode Int, Sheffield, UK)*, T Zhang *(MG Bennett and Assoc, Rotherham, UK)*, RA Hall *(Ricardo Consult Eng, Shoreham-by-Sea, UK)*. Proc Inst Mech Eng D 207(D2) 135-143 (1993).

A numerical procedure is described for optimizing FE models of engine structures for minimum noise radiation. A statistical technique is used to select sample points in a multi-dimensional design variable space from which an approximating response surface is derived. Optimization of this analytic model is then carried out interactively with variable bounds and constraints are required to meet design objectives. The underlying noise analysis calculation uses a modal analysis algorithm to determine the surface vibration velocity and hence the radiated sound power.

9A118. Optimization of location and amount of viscous damping to minimize random vibration. - VH Neubert *(Dept of Eng Sci and Mech, Penn State)*. J Acoust Soc Am 93(5) 2707-2715 (May 1993).

A novel procedure is presented for minimizing random vibrations of a linear, elastic structure by optimizing the size and location of viscous damping devices, with a constraint on the total amount of damping available. Viscous damping, represented symbolically by dashpots between structural nodes, can be achieved practically by using fluid devices or magnetic eddy-current devices. The problem is developed as a nonlinear optimization problem. Nonproportional damping is considered. Since the mean-square response depends on the modal damping ratios, first, the sensitivities, or partial derivatives, of the modal damping ratios with respect to the system damping parameters are discussed. The sensitivities are sometimes negative, which means that simply increasing the size of some dashpots could increase response. Second, the sensitivities of the mean-square amplitudes to the system damping parameters are determined and used to minimize the response. A two-parameter example is presented for a ten-bar truss for which the optimum parameters are found by a modification of the method of steepest descent. The problem was solved using the program TPSENS, developed as part of this study. A ten-parameter optimization is also described, which was accomplished by coupling TPSENS with CONMIN, an available NASA FORTRAN program for constrained function minimization.

9A119. Simulating transfer functions in a reverberant room including source directivity and head-shadow effects. - M Kompis and N Dillier *(ENT Dept, Univ Hospital, CH-8091 Zurich, Switzerland)*. J Acoust Soc Am 93(5) 2779-2787 (May 1993).

A new procedure for simulating the acoustical response of a receiver to a source in a reverberant room is proposed. Convolving such an impulse response with an input signal, eg, speech, is useful in applications where an acoustical environment must be highly reproducible, easily controllable, or is unavailable for an actual recording. The proposed procedure is an extension of the image method by Allen and Berkley. The new features include the possibility to simulate simple source and microphone directivity, as well as head-shadow effects, which can be considerable for subjects with microphones mounted close to the head. A rigid sphere diffracting a plane wave provides a good approximation for the effects of speaker as well as listener head shadow and allows simple yet realistic simulations of many relevant situations. Implementational issues are discussed and the method is verified by comparing simulation results with recordings in actual rooms. It was found that by including source directivity and head shadow, transfer functions become significantly more realistic.

172Y. COMPUTATIONAL TECHNIQUES

9A120. Influence of frequency and width of an ultrasonic bounded beam in the investigation of materials: Study in terms of heterogeneous plane waves. - K Van Den Abeele *(Belgian Natl Found for Sci Res)* and O Leroy *(Interdisciplinary Res Center, KUL Campus Kortrijk, B-8500 Kortrijk, Belgium)*. J Acoust Soc Am 93(5) 2688-2699 (May 1993).

Theoretically obtained 3D plots showing the behavior of the reflection coefficient for heterogeneous plane waves upon arbitrary layered media as function of incidence angle and heterogeneity, supply valuable information for the investigation of the reflector when using bounded ultrasonic beams. The presence of leaky interface modes and their angular positions for a specific sample are determined by the fd products (frequency times thickness) of the constituent layers. Deformations of the reflected and transmitted bounded beam profiles and the contribution of surface wave radiation at vibrational mode angles are governed by the fW product (frequency times beamwidth). For a given layered medium, optimum conditions for observing particular mode vibrations and large deformations of reflected ultrasonic profiles can be predicted theoretically.

9A121. Recovery of perturbations in an acoustic medium with attenuation from several plane wave responses. - BJ Chaderjian *(Dept of Math, California State Univ, Long Beach CA 90840)* and KP Bube *(Dept of Math, Univ of Washington, GN-50, Seattle WA 98195)*. SIAM J Appl Math 53(3) 829-846 (Jun 1993).

A linearized inverse problem is studied for recovering a stratified acoustic medium with attenuation from reflection data known at the medium's surface. The inverse problem is based on a plane wave decomposition of the medium's response to a point-source input. This paper shows that the inverse problem for recovering perturbation in density, wave speed, and the coefficient of attenuation from known perturbations in three plane wave responses is well posed in the appropriate function spaces. The question of whether the medium itself can be recovered from the point-source response is discussed.

9A122. Strong localized perturbations of eigenvalue problems. - MJ Ward *(Dept of Math, Stanford)* and JB Keller *(Dept of Math and Mech Eng, Stanford)*. SIAM J Appl Math 53(3) 770-798 (Jun 1993).

This paper considers the effect of three types of perturbations of large magnitude but small extent on a class of linear eigenvalue problems for elliptic partial differential equations in bounded or unbounded domains. The perturbations are the addition of a function of small support and large magnitude to the differential operator, the removal of a small subdomain from the domain of a problem with the imposition of a boundary condition on the boundary of the resulting hole, and a large alteration of the boundary condition on a small region of the boundary of the domain. For each of these perturbations, the eigenvalues and eigenfunctions for the perturbed problem are constructed by the method of matched asymptotic expansions for $\in$ small, where $\in$ is a measure of the extent of the perturbation.

172Z. EXPERIMENTAL TECHNIQUES

9A123. Determination of the acoustic far field of a radiating body in an acoustic fluid from boundary measurements. - GV Borgiotti *(Dept of Elec Eng and Comput Sci, George*

Washington Univ, Washington DC 20052) and KE Jones *(David Taylor Res Center, Bethesda MD 20084)*. J Acoust Soc Am 93(5) 2788-2797 (May 1993).

The far field (FF) of a radiating or scattering object immersed in an acoustic fluid can be represented in the frequency domain as a finite dimension linear combination of basis functions, which are determined by the shape and the size of the object in acoustic wavelengths. The coefficients of the linear combination are obtained as the outputs of a bank of spatial filters whose inputs are either the boundary normal velocity – or the radiation problem – or the boundary pressure and the normal velocity – for the scattering problem – measured by a dense set of sensors. The filter outputs provide the information sufficient to reconstruct the radiated or scattered far field, amplitude and phase. The structure of the filters is identified from the singular valve decomposition of the appropriate radiation or scattering operator, mapping the boundary normal velocity, or the combination of normal velocity and pressure, into the FF. Also, from the filter outputs, the efficiently radiating component of the boundary field can be extracted. For example the boundary total normal velocity may have a localized high peak, which however may be completely or almost completely absent in the radiating component. Selected results of an extensive simulation are presented illustrating the accuracy of the reconstruction of the FF from the spatial filtering of the boundary field.

III. AUTOMATIC CONTROL

200. Systems theory and design

9A124. Sensitivity analysis of multiple eigenvalues. - AP Seyranian *(Inst of Problems in Mech, Acad of Sci, Moscow, Russia)*. Mech Struct Machines 21(2) 261-284 (1993).

This paper is devoted to sensitivity analysis of eigenvalues of nonsymmetric operators that depend on parameters. Special attention is given to the case of multiple eigenvalues. Due to the non-differentiability (in the common sense) of multiple roots, directional derivatives of eigenvalues and eigenvectors in parametric space are obtained. Sensitivity analysis is based on the perturbation method of eigenvalues and eigenvectors. The generalized eigenvalue problem and vibrational systems are also investigated. The results obtained are important for qualitative and quantitative study of mechanical systems subjected to static and dynamic instability phenomena.

9A125. Space structures and the crossing number of their graphs. - A Kaveh *(Inst Allgemeine Mech, Tech Univ, Vienna, Austria)*. Mech Struct Machines 21(2) 151-166 (1993).

In this paper, theorems are proved that relate the degree of statical indeterminancy of space structures to their planar topological properties. An algorithm is developed for suboptimal layout of an arbitrary space structure in a plane, and a lower bound is established to the crossing number of its graph model.

202. Control systems

9A126. Numeri[illegible] of H^∞ optimal performar[illegible] [illegible] *(Appl and Comput Math, Princeton)* and JM Orszag *(Dept of Economics, Univ of Michigan, Ann Arbor MI 48109)*. J Sci Comput 7(4) 289-311 (Dec 1992).

We present new algorithms for computing the H^∞ optimal performance for a class of single-input and single-output infinite-dimensional systems. The algorithms here only require use of one or two fast Fourier transforms and Cholesky decompositions; hence the algorithms are particularly simple and easy to implement. Numerical examples show that the algorithms are stable and efficient and converge rapidly. The method has wide applications including to the H^∞ optimal control of distributed parameter systems. We illustrate the technique with applications to some delay problems and a partial differential equation model. The algorithms we present are also an attractive approach to the solution of high-order finite-dimensional models for which use of state space methods would present computational difficulties.

See also the following:

9A978. Optimization of the structure and movement of the legs of animals

204. Systems and control applications

9A127. New tool for solving industrial continuous optimization problems. - R Ouellet and RT Bui *(Dept Sci Appl, Univ Quebec, Chicoutimi, PQ, Canada)*. Appl Math Model 17(6) 298-310 (Jun 1993).

A numerical method is proposed to tackle the continuous optimal control problems involving industrial thermal processes. The latter are characterized by their complex mathematical models. Formulated through various calculus using the Pontryagin maximum principle, the resulting two-point boundary value problem is discretized with a Euler central differentiation scheme. Solution is obtained by the Newton-Raphson method, and Richardson extrapolation is used to increase accuracy and refine the grid automatically as needed. The Jacobian matrix is evaluated numerically. This new method promises to open new possibilities for applications in an important class of engineering problems.

9A128. Engineering functional analysis. Part I. - MR von Spakovsky. *(Dept Mec, Lab Energetique Indust, Ecole Polytech Fed, Lausanne, Switzerland)* and RB Evans *(Woodruff Sch of Mech Eng, Georgia Tech)*. J Energy Resources Tech 115(2) 86-92 (Jun 1993).

In this paper, a new formalism called *Engineering Functional Analysis* is presented. This formalism results in higher degrees of decentralization for engineering systems optimization than is otherwise possible. By *decentralization*, it is meant that the improvement or optimization of individual components by *themselves* (ie, components which are *isolated economically* from the rest of the overall system), serves to improve or optimize the system as a whole (with some degree of error, which defines the *degree of decentralization*).

9A129. Engineering functional analysis. Part II. - RB Evans *(Woodruff Sch of Mech Eng, Georgia Tech)* and MR von Spakovsky *(Dept Mec, Lab Energetique Indust, Ecole Polytech Fed, Lausanne, Switzerland)*. J Energy Resources Tech 115(2) 93-99 (Jun 1993).

In this paper, a new formalism called *Engineering Functional Analysis* is presented. This formalism results in higher degrees of decentralization for engineering system optimization than is otherwise possible. By *decentralization*, it is meant that the improvement or optimization of individual components by *themselves* (ie, components which are *isolated economically* from the rest of the overall system) serves to improve or optimize the system as a whole (with some degree of error, which defines the *degree of decentralization*). Higher degrees of decentralization are important in that they provide a more stable economic environment for individual components, thus permitting more rapid synthesis and greater system improvement than could otherwise be obtained.

206. Robotics

206B. END EFFECTORS

9A130. Computing two-finger force-closure grasps of curved 2D objects. - J Ponce, D Stam *(Beckman Inst, Dept of Comput Sci, Univ of Illinois, Urbana IL 61801)*, B Faverjon *(ALEPH Tech, Batiment Heliopolis, 38400 Saint Martin d'Heres, France)*. Int J Robotics Res 12(3) 263-273 (Jun 1993).

This article presents an algorithm for computing force-closure grasps of piecewise-smooth, curved, 2D objects. We consider the case of a gripper equipped with two hard fingers and assume point contact with friction. Object boundaries are represented by collections of polynomial parametric curves, and force-closure grasps are characterized by systems of polynomial constraints in the parameters of these curves. The algorithm has been implemented on a distributed architecture, and experiments using a PUMA robot equipped with pneumatic two-finger gripper and a vision system are presented.

9A131. Family of Stewart platforms with optimal dexterity. - KH Pittens and RP Podhorodeski *(Adaptive Robotic Telesyst Lab (ARTLAB), Dept of Mech Eng, Univ of Victoria, Victoria, BC, V8W 3PG, Canada)*. J Robotic Syst 10(4) 463-479 (Jun 1993).

Stewart platform configurations (architectures and poses) optimizing local dexterity are investigated. The condition number of the Jacobian matrix is used to quantify the dexterity of the manipulator. For a platform-centered Jacobian reference location and a given characteristic length for scaling purposes, a two-parameter family of optimal configurations is shown to exist. Two suitable architectural parameters defining the family are identified and properties of the optimal configurations are discussed. The optimization results are shown to be easily extended for other Jacobian reference locations and for other singular value-based local dexterity measures.

206E. KINEMATICS, DYNAMICS

9A132. Dynamic analysis and control of a Stewart platform manipulator. - G Lebret, K Liu, FL Lewis *(Autom and Robotics Res Inst, Univ of Texas, 7300 Jack Newell Blvd, S Ft Worth TX 76118)*. J Robotic Syst 10(5) 629-655 (Jul 1993).

In this article, we study the dynamic equations of the Stewart platform manipulator. Our derivation is closed to that of Nguyen and Pooran because the dynamics are not explicitly given but are in a step-by-step algorithm. However, we give some insight into the structure and properties of these equations. We obtain compact expressions of some coefficients. These expressions should be interesting from a control point of view. A stiffness control scheme is designed for milling application. Some path-planning notions are discussed that take into account singularity positions and the required task. The objective is to make the milling station into a semiautonomous robotic tool needing some operator interaction but having some intelligence of its own. It should interface naturally with part delivery and other higher level tasks.

9A133. Efficient method for inverse dynamics of manipulators based on the virtual work principle. - Chang-De Zhang and Shin-Min Song *(Dept of Mech Eng, Univ of Illinois, PO Box 4348, Chicago IL 60680)*. J Robotic Syst 10(5) 605-627 (Jul 1993).

The computational efficiency of inverse dynamics of a manipulator is important to the real-time control of the system. For serial manipulators, the recursive Newton-Euler method has been proven to be the most efficient. However, for more general manipulators, such as serial manipulators with closed kinematic loops or parallel manipulators, it must be modified accordingly and the resultant computational efficiency is degraded. This article presents a computationally efficient scheme based on the virtual work principle for inverse dynamics of general manipulators. The present method uses a forward recursive scheme to compute velocities and accelerations, the Newton-Euler equation to calculate inertia forces-torque, and the virtual work principal to formulate the dynamic equations of motion. This method is equally effective for serial and parallel manipulators. For serial manipulators, its computational efficiency is comparable to the recursive Newton-Euler method. For parallel manipulators or serial manipulators with closed kinematic loops, it is more efficient than the existing methods. As an example, the computations of inverse dynamics (including inverse kinematics) of a general Stewart platform require only 842 multiplications, 511 additions, and 12 square roots.

9A134. Exact methods for determining the kinematics of a Stewart platform using additional displacement sensors. - KC Cheok, JL Overholt, RR Beck *(Syst Simulation and Tech Div, US Army Tank-Automotive Command, Warren MI 48397-5000)*. J Robotic Syst 10(5) 689-707 (Jul 1993).

This article describes two new direct and exact methods for computing the translational and rotational displacements of an Stewart platform (SP) by employing extra translational displacement sensors (TDSs), in addition to the existing TDSs for the six links of the SP. The key for the approach lies in knowing where to employ the TDSs for determining positional vectors of strategic platform locations. By taking advantage of a tetrahedral geometry, *closed form* solutions for the forward kinematic transformation can then be derived and directly evaluated. The new methods produce accurate solutions with only minimal computation necessary. The advantages and disadvantages of the proposed methods are discussed and compared to an existing method. The exact methods are being investigated for an on-line implementation of a nonlinear adaptive control system and redundancy scheme for a 25-ton Stewart platform based Crew Station-Turret Motion Base Simulator at the US Army Tank Automotive Command.

9A135. Geometric analysis of antagonistic stiffness in redundantly actuated parallel mechanisms. - Byung-Ju Yi *(Dept of Mech Eng, Korea IT and Educ, 37-1 San, Gajeon Ri, Byungcheon Myun Cheonan Kun Chungnam, Korea)* and RA Freeman *(Dept of Mech Eng, Univ of Texas, Austin TX 78712)*. J Robotic Syst 10(5) 581-603 (Jul 1993).

Parallel closed-chain mechanical architectures allow for redundant actuation in the force domain. Antagonistic actuation, afforded by this input force redundancy, in conjunction with nonlinear linkage geometry creates an effective stiffness directly analogous to that of a wound metal spring. A general stiffness model for such systems is derived and it is shown that the constitutive relationship between actuation effort and active stiffness is the second-order kinematic constraint set relating the actuation sites. The extent of stiffness modulation possible is then evaluated and necessary conditions for full stiffness modulation are obtained. Configuration-dependent, second-order, geometric singularities affecting stiffness generation are illustrated in terms of a 3-dof parallel spherical mechanism example and discussed in relation to their more commonly investigated-first order counterparts that affect force and velocity transmission. Finally, a load distribution methodology for simultaneous motion and stiffness generation is introduced, and it is shown that with hyperredundant actuation the internal load state of the mechanism can be controlled independent of its motion and effective stiffness.

9A136. Inverse kinematics and inverse dynamics for control of a biped walking machine. - Ching-Long Shih *(Dept of Elec Eng, Natl Taiwan IT, Taipei, Taiwan, ROC)*, WA Gruver *(Sch of Eng Sci, Simon Fraser Univ, Burnaby, BC, V5A 1S6, Canada)*, Tsu-Tian Lee *(Dept of Elec Eng, Natl Taiwan IT, Taipei, Taiwan, ROC)*. J Robotic Syst 10(4) 530-555 (Jun 1993).

Analytical techniques are presented for the motion planning and control of a 12 dof biped walking machine. From the Newton-Euler equations, joint torques are obtained in terms of joint trajectories, and the inverse dynamics are developed for both the single-support and double-support cases. Physical admissibility of the biped trajectory is characterized in terms of the equivalent force-moment and zero-moment point. A simulation example illustrates the application of the techniques to plan the forward-walking trajectory of the biped robot. The implementation of a prototype mechanism and controller is also described.

9A137. Kinematic decoupling in mechanisms and application to a passive hand controller design. - V Hayward, C Nemri, Xianze Chen, B Duplat *(Res Center for Intelligent Machines, McGill Univ, 3480 University St, Montreal, PQ H3A 2A7, Canada)*. J Robotic Syst 10(5) 767-790 (Jul 1993).

Observations regarding the kinematics of mechanisms are applied to the synthesis of a passive hand controller. It is argued that stiffness (and damping) properties are central to the effectiveness of such devices and in particular that the simplicity of these properties is crucial. What simple means is analyzed and it is shown that only certain types of manipulators can appropriately be used. In effect, decoupling is shown to be architecture and configuration dependent. The properties of parallel mechanisms are reviewed and found appropriate for restricted-workspace hand controllers. A particular kinematic design is then derived and a practical implementation described.

9A138. Kinematic design of serial link manipulators from task specifications. - CJJ Paredis and PK Khosla *(Dept of Elec and Comput Eng, Robotics Inst, Carngie Mellon Univ, Pittsburgh PA 15213-3890)*. Int J Robotics Res 12(3) 274-287 (Jun 1993).

The Reconfigurable Modular Manipulator System (RMMS) consists of modular links and joints that can be assembled into many manipulator configurations. This capability allows the RMMS to be rapidly reconfigured to custom tailor it to specific tasks. An important issue related to the RMMS is the determination of the optimal manipulator configuration for a specific task. This article addresses the problem of mapping *kinematic* task specifications into a *kinematic* manipulator configuration. For the design of 2-dof planar manipulators, an *analytical* solution is derived. The numerical procedure determines the Denavit-Hartenberg parameters of a nonredundant manipulator with joint limits that can reach a set of specified positions-orientations in an environment that may include parallelepiped-shaped obstacles.

9A139. Kinematics and control of a fully parallel force-reflecting hand controller for manipulator teleoperation. - MD Bryfogle *(Sci Appl Intl, McLean VA 22102)*, CC Nguyen, SS Antrazi, PC Chiou *(Robotics and Control Lab, Dept Elec Eng, Catholic Univ of Am, Washington DC 20064)*. J Robotic Syst 10(5) 745-766 (Jul 1993).

Force feedback can enhance the efficiency of a teleoperation system by providing the operator with a sense of *feel* forces and torques arising from the interaction of the slave manipulator with the remote environment. This article addresses the kinematic analysis and control of a Parallel Force-Reflecting Hand Controller (PFORHC) whose design and implementation are based on a fully parallel mechanism. Kinematic analysis on the PFORHC is performed and results in a closed-form solution for the inverse kinematics. The forward kinematics is solved by Newton-Raphson's method. A fixed-gain PD control scheme is developed for force feedback control. Experiments are conducted to study the performance of the force-reflecting capability of the PFORHC. Experimental results show that the force control scheme utilizing a handgrip force sensor provides smaller steady-state errors as compared to the case utilizing no handgrip force sensor.

9A140. Kinematics of an infinitely flexible robot arm. - PJ Choi, JA Rice, JC Cesarone *(Dept of Mech Eng, Univ of Mech Eng, Chicago IL 60680)*. J Robotic Syst 10(4) 407-425 (Jun 1993).

This article describes a research effort to develop a command and control algorithm for a proposed flexible arm. This robot arm, unlike previous arms, is assumed to be extremely flexible, possessing a large number of dof and functioning as a "tentacle". Algorithms for commanding smooth motion of this arm in the presence of obstacles are developed, including both forward and inverse kinematics. This approach is based on the use of Catmull-Rom splines and local radius of curvature commands to discrete actuators along the arm's length. Several example trajectories are presented and explained.

9A141. Periodic motions of a hopping robot with vertical and forward motion. - RT M'Closkey and JW Burdick *(Dept of Mech Eng, California IT, Pasadena CA 91125)*. Int J Robotics Res 12(3) 197-218 (Jun 1993).

This article analyzes the global dynamic behavior of simplified hopping robot models that are analogous to Raibert's experimental machines. We first review a 1D vertical hopping model that captures both the vertical hopping dynamics and nonlinear control algorithm. Second, we present a more complicated 2D model that includes both forward and vertical hopping dynamics and a foot placement algorithm. These systems are analyzed using a Poincare return map. The approximate return map is shown to closely predict the behavior of the exact map for small forward running velocities. In addition, the approximate return map can be used to quantitatively explore the coupling of vertical and lateral dynamics and to determine the effect of the foot placement algorithm on dynamical behavior.

9A142. Synthesis and analysis of a new class of six-dof parallel minimanipulators. - Lung-Wen Tsai *(Mech Eng Dept and Syst Res Center, Univ of Maryland, College Park MD 20742)* and F Tahmasebi *(Robotics Branch, NASA, Goddard Space Flight Center, Greenbelt MD 20771)*. J Robotic Syst 10(5) 561-580 (Jul 1993).

A new class of 6-dof parallel minimanipulators is introduced. The minimanipulators are designed to provide high resolution and high stiffness for fine position and force control in a hybrid serial-parallel manipulator system. 2-dof planar linkages and inextensible limbs are used to improve positional resolution and stiffness of the minimanipulators. The 2-dof linkages serve as drivers for the minimanipulators. The minimanipulators require only three inextensible limbs and, unlike most of the six-limbed parallel manipulators, their direct kinematics can be reduced to solving a polynomial in a single variable. In addition, by using three limbs instead of six other benefits such as lower possibility of mechanical interference between limbs can be realized. All of the minimanipulators actuators are base-mounted. As a result, higher payload capacity, smaller actuator sizes, and lower power dissipation can be obtained. In addition to the design discussion, kinematic analysis of the minimanipulators is also presented.

See also the following:

9A28. Bounds on the friction-dominated motion of a pushed object

9A32. Dynamic coupling between the joint and elastic coordinates in flexible mechanism systems

9A60. Six-dof active vibration isolation using a Stewart platform mechanism

206F. SENSORS AND CONTROLS

9A143. **Adaptive control of a Stewart platform-based manipulator.** - CC Nguyen, SS Antrazi, Zhen-Lei Zhou *(Robotics and Control Lab, Dept of Elec Eng, Catholic Univ of Am, Washington DC 20064)*, CE Campbell Jr *(NASA, Goddard Space Flight Center, Greenbelt MD 20771)*. J Robotic Syst 10(5) 657-687 (Jul 1993).

This article presents the implementation of a joint-space adaptive control scheme used to control noncompliant motion of a Stewart platform-based manipulator (SPBM) that is used in a facility called the Hardware Real-Time Emulator developed at Goddard to emulate space operations. The SPBM is comprised of two platforms and six linear actuators driven by dc motors, and possesses 6 dof. The article briefly reviews the development of the adaptive control scheme, which is composed of proportional-derivative controllers whose gains are adjusted by an adaptation law driven by the errors between the desired and actual trajectories of the SPBM actuator lengths. The derivation of the adaptation law is based on the concept of model reference adaptive control and Lyapunov direct method under the assumption that SPBM motion is slow as compared to the controller adaptation rate. An experimental study is conducted to evaluate the performance of the adaptive control scheme implemented to control the SPBM to track a vertical and circular path under step changes in payload. Experimental results show that the adaptive control scheme provides superior tracking capability as compared to fixed-gain controllers.

9A144. **Analysis and design of a robotic distance sensor.** - O Partaatmadja, B Benhabib, AA Goldenberg *(Comput Integrated Manuf Lab, Dept of Mech Eng, Univ of Toronto, Toronto, ON, M5S 1A4, Canada)*. J Robotic Syst 10(4) 427-445 (Jun 1993).

Analysis and design of a robotic electrooptical distance sensor, based on the phase-shift measurement of a modulated light intensity, is addressed in this article. The transducer of this sensor employs two light sources (light-emitting diodes), whose intensities are modulated by different-phase sine-wave signals, and one photodiode receiver. The distance of an object's surface with respect to the sensor is measured by investigating the received phase shift. Experiments undertaken show that these parameters indeed affect the performance of the sensor. The exemplary optimization analysis carried out considered only two performance aspects of the sensor, namely, sensitivity and operational range, and yielded corresponding optimal design parameters.

9A145. **Contact sensing from force measurements.** - A Bicchi *(Dept of Elec Syst and Autom DSEA Centro "E Piaggio", Univ Pisa, via Diotisalvi 2, 56125 Pisa, Italia)*, JK Salisbury, DL Brock *(Artificial Intelligence Lab, MIT)*. Int J Robotics Res 12(3) 249-262 (Jun 1993).

This article addresses contact sensing (ie, the problem of resolving the location of a contact, the force at the interface, and the moment about the contact normals). Called "intrinsic" contact sensing for the use of internal force and torque measurements, this method allows for practical devices that provide simple, relevant contact information in practical robotic applications. Such sensors have been used in conjunction with robot hands to identify objects, determine surface friction, detect slip, augment grasp stability, measure object mass, probe surfaces, and control collision and for a variety of other useful tasks. This article describes the theoretical basis for their operation and provides a framework for future device design.

9A146. **Coordinated dynamic hybrid position-force control for multiple robot manipulators handling one constrained object.** - Tsuneo Yoshikawa and Xin-Zhi Zheng *(Dept of Mech Eng, Kyoto Univ, Kyoto 606, Japan)*. Int J Robotics Res 12(3) 219-230 (Jun 1993).

In coordinated manipulation of a single object using multiple robot arms or a multifingered robot hand, simultaneous control of the object motion and of the internal force exerted by arms or fingers on the object is required. Furthermore, in the case where the motion of the object is constrained in some directions because of contact with its environment, control of the constraint force also becomes necessary. In this article, we propose a coordinated dynamic hybrid control method for multiple robotic mechanisms. Several experimental results that show the validity of the proposed approach are presented. The results of this article will be useful for the fine manipulation tasks using multiple robotic mechanisms, where the individual specifications of the object motion, the interaction force between the object and its environment, and the grasping force of the object are given.

9A147. **Design of robust PD-type control laws for robotic manipulators with parametric uncertainties.** - SM Shahruz *(Berkeley Eng Res Inst, Berkeley CA 94709)*, G Langari *(Dept of Mech Eng, Texas A&M Univ, College Sta TX 77843)*, M Tomizuka *(Dept of Mech Eng, UCB)*. J Robotic Syst 10(4) 447-462 (Jun 1993).

In this article, design of a simple robust control law that achieves desired positions and orientations for robotic manipulators with parametric uncertainties is studied. A discontinuous control law is proposed, which consists of a high-gain linear proportional plus derivative (PD) term and additional terms that compensate for the effect of gravitation. The stability of the robotic system under the proposed control law is proved by LaSalle's stability theorem. Furthermore, by the theory of singularly perturbed systems, it is shown that if the proportional and derivative gain matrices are diagonal with large positive elements then the system is decoupled into a set of first-order linear systems. Simulation results are presented to illustrate the application of the proposed control law to a two-link robotic manipulator.

9A148. **Nonlinear control with end-point acceleration feedback for a two-link flexible manipulator: Experimental Results.** - F Khorrami and S Jain *(Control-Robotics Res Lab, Sch of Elec Eng and Comput Sci, Polytech Univ, Brooklyn NY 11201)*. J Robotic Syst 10(4) 505-530 (Jun 1993).

Experimental results for end-point positioning of multi-link flexible manipulators through end-point acceleration feedback are presented in this article. The advanced controllers are implemented on a two-link flexible arm developed at the Control-Robotics Research Laboratory at Polytechnic University. The advocated approach in this article is based on a two-stage control design. The first stage is a nonlinear O(1) feedback linearizing controller corresponding to the rigid body motion of the manipulator. Because this scheme does not utilize any feedback from the end-point motion, significant vibrations are induced at the end effector. Experimental and simulation results validate the fact that the end-effector performance is significantly better with the proposed O(1) feedback linearizing control as compared with the linear independent joint PD control. In addition, the nonlinear control offers other advantages in terms of smaller and smoother actuator torques and reducing the effects of nonlinearities.

9A149. **Review and unification of reduced-order force control methods.** - MT Grabbe *(BDM Eng Services, Huntsville AL 35806)*, JJ Carroll, DM Dawson *(Dept of Elec and Comput Eng, Clemson Univ, Clemson SC 29634-0915)*, Z Qu *(Dept of Elec Eng, Univ of Central Florida, Orlando FL 32816-0450)*. J Robotic Syst 10(4) 481-504 (Jun 1993).

In this article, we compare some of the recent methods developed for simultaneous position and force control of a single n-link constrained robot manipulator. Mathematical models of the constrained manipulator are introduced and the advantages and disadvantages of the associated control formulations are discussed. The similarities between each of the proposed formulations are also highlighted.

206I. MISCELLANEOUS APPLICATIONS

9A150. **The NIST Robocrane.** - J Albus, R Bostelman, N Dagalakis *(Robot Syst Div, NIST)*. J Robotic Syst 10(5) 709-724 (Jul 1993).

The Robot Systems Division of the National Institute of Standards and Technology (NIST) has been experimenting for several years with new concepts for robot cranes. These concepts utilize the basic idea of the Stewart platform parallel link manipulator. The unique feature of the NIST approach is to use cables as the parallel links and to use winches as the actuators. As long as the cables are all in tension, the load is kinematically constrained and the cables resist perturbing forces and moments with equal stiffness to both positive and negative loads. The result is that the suspended load is constrained with a mechanical stiffness determined by the elasticity of the cables, the suspended weight, and the geometry of the mechanism. Based on these concepts, a revolutionary new type of robot crane, NIST ROBOCRANE, has been developed that can control the position, velocity, and force of tools and heavy machinery in all 6 dof (x, y, z, roll, pitch, and yaw). Depending on what is suspended from its work platform, the ROBOCRANE can perform a variety of tasks. Examples are: cutting, excavating, and grading, shaping and finishing, lifting, and positioning. A 6-m version of the ROBOCRANE has been built and critical performance characteristics analyzed.

206Y. COMPUTATIONAL TECHNIQUES

9A151. **Identification of position-independent robot parameter errors using special Jacobian matrices.** - CR Mirman *(Eng Dept, Wilkes Univ, Wilkes-Barre PA 18766)* and KC Gupta *(Dept of Mech Eng, Univ of Illinois, Chicago IL 60680)*. Int J Robotics Res 12(3) 288-298 (Jun 1993).

Common production manipulators are designed to be controlled through the use of a closed-form kinematic solution algorithm. This closed-form solution uses manufacturer-specified nominal parameter values to model the given manipulator. These position-independent parameters, link lengths, twists, and offsets are geometrical and do not change as the manipulator is driven. However, manufacturing tolerances or usage may cause the actual parameters to deviate from the nominal robot parameters. The iterative regression algorithm for parameter identification uses the end-effector information at several arbitrary manipulator positions, as well as nominal parameter and joint variable information to compute the parameter error values. The use of the special Jacobian matrices allows for easy determination of mathematical singularity conditions. Through several examples, it will be shown that the use of this parameter identification algorithm produces accurate results. This article will discuss the possibilities of deterministic as well as probabilistic parameter errors.

208. Manufacturing

9A152. **Knowledge-based expert system for ballscrew grinding.** - SS Billatos *(Dept of Mech Eng, Univ of Connecticut, Storrs CT 06269-3139)* and JA Webster *(Grinding Center, Univ of Connecticut, Storrs CT 06269-3237)*. J Eng Indust 115(2) 230-235 (May 1993).

This paper discusses the ballscrew grinding process and provides a newly structured knowledge-based expert system (KBES) developed to automate the process based on fuzzy pattern recognition techniques for shape control with recommendations for further optimization considering practical machining constraints. The KBES offers several advantages including the use of semiskilled operators who can monitor several machines simultaneously, the consistent production of high quality parts, and the significant reduction in cycle time due to automatic adjustment of steadies.

IV. MECHANICS OF SOLIDS

250. Elasticity

250A. GENERAL THEORY

9A153. **Application of the Green and the Rayleigh-Green reciprocal identities to path-independent integrals in 2D and 3D elasticity.** - NI Ioakimidis *(Div of Appl Math and Mech, Sch of Eng, Univ of Patras, PO Box 1120, GR-261 10 Patras, Greece)* and EG Anastasselou *(Div of Mech, Natl Tech Univ, PO Box 61-28, GR-151 10, Greece)*. Acta Mech 98(1-4) 99-106 (1993).

An elementary but quite general method for the construction of path-independent integrals in plane and 3D elasticity is suggested. This approach consists simply in using the classical Green formula in its reciprocal form for harmonic functions and, further, the more general Rayleigh-Green formula also in its reciprocal form, but for biharmonic functions. A large number of harmonic and biharmonic functions appears in a natural way in the theory of elasticity. An application to the determination of stress intensity factors at crack tips is considered in detail and only the sum of the principal stress components is used in the path-independent integral.

9A154. **Elastic analysis of the half plane inhomogeneity problem.** - DA Kouris and JP Nuxoll *(Dept of Mech and Aerospace Eng, Arizona State Univ, Tempe AZ 85287-6106)*. Acta Mech 97(3-4) 169-184 (1993).

The paper presents an analytical solution for the elastic field in the vicinity of a semi-circular inhomogeneity, embedded at the free surface of an elastic half-plane. This bi-material system is loaded by uniform remote tension or a constant eigenstrain sustained by the inhomogeneity.

250C. NONLINEAR AND FINITE DEFORMATION PROBLEMS

9A155. **Bifurcation of a solid circular elastic cylinder under finite extension and torsion.** - ED Duka *(Phys and Mech Div, Sch of Tech, Aristotle Univ, 54006 Thessaloniki, Greece)*, AH England *(Dept of Theor Mech, The University, University Park, Nottingham N97 2RD, UK)*, AJM Spencer *(Dept of Theor Math, The University, University Park, Nottingham N97 2RD, UK)*. Acta Mech 98(1-4) 107-121 (1993).

The problem of bifurcation of a solid circular cylinder subjected to finite extension and torsion is investigated using the theory of small deformations superposed on large elastic deformations. The material of the cylinder is assumed to be isotropic, elastic, homogeneous and incompressible. A numerical scheme is adopted to solve the system of partial differential equations and the associated boundary conditions governing the problem for a class of strain-energy functions. The numerical results obtained determined the critical twist corresponding to a given extension of the cylinder.

9A156. **Cylindrical and spherical inflation in compressible finite elasticity.** - JM Hill *(Dept of Math, Univ of Wollongong, NSW 2500, Australia)*. IMA J Appl Math 50(2) 195-201 (1993).

Murphy (1992) examined cylindrical and spherical inflation of compressible perfectly elastic materials having three spherical forms of the strain-energy function. In this paper a general procedure for handling such problems for any strain-energy function is proposed. This procedure is used to confirm some of the results by Murphy as well as to deduce new solutions. One solution obtained by that author for cylindrical infiltration is found to be incorrect.

9A157. **Expansion of a cavity in a rubber block under unequal stresses.** - Y-W Chang, AN Gent, JP Padovan *(Inst of Polymer Eng, Univ of Akron, Akron OH 44325-0301)*. Int J Fracture 60(3) 283-291 (1 Apr 1993).

Elastic expansion of a small spherical void in the interior of a rubber block has been investigated by FE analysis (FEA). The block was subjected to a far-field tensile or compressive stress while an internal pressure was applied to the cavity. The rubber was assumed to be virtually incompressible in volume and neo-Hookean in elastic behavior. Critical stress states were determined at which the void would become indefinitely large - a form of elastic instability. An applied tensile stress was found to lower the critical inflation pressure for instability, in agreement with experimental observations whereas a compressive stress increased it. The critical mean stress was lowest for an isotropic stress system (when the applied tension was zero). It was higher when either compressive or tensile stresses were applied, ie, under non-isotropic stresses, in agreement with the analysis of Hou and Abeyaratne. However, the present results show a considerably smaller effect of tensile stress than predicted by Hou and Abeyaratne.

9A158. **Stress rate measure for finite elastic plastic deformations.** - Z Xia and F Ellyin *(Dept of Mech Eng, Univ of Alberta, Edmonton T6G 2G8, Canada)*. Acta Mech 98(1-4) 1-14 (1993).

A new stress rate, based on the spin of a material triad that coincides momentarily with the principal axes, is applied to the analysis of constrained and unconstrained shear with and without superposed normal stresses of hypoelastic and rigid plastic, kinematically hardening solids. A comparative study of various alternative stress rates that have been proposed, including the Jaumann rate, favors the new formulation from the viewpoint of qualitative behavior, general applicability and ease of implementation.

See also the following:

9A1. Study of constitutive relations for pseudo-elasticity and shape memory behavior

250E. STRESS CONCENTRATIONS AND SINGULARITIES

9A159. **Stress concentration around holes in composite laminates with variable fiber spacing.** - Le Chung Shiau and GC Lee *(Inst of Aeronaut and Astronaut, Natl Cheng Kung Univ, Tainan, Taiwan, ROC)*. Composite Struct 24(2) 107-115 (1993).

An 18 dof higher-order triangular plane stress element is developed to investigate the effect of variable fiber spacing on the stress concentration around a hole in a composite laminated plate subjected to in-plane boundary loading. This element accounts for the irregular in-plane elastic properties across the element domain, thus, the nonuniformly spaced fibers in the laminate can be easily incorporated into the element stiffness matrix through the fiber content calculated at each Gaussian integration point. Results show that reducing the fiber volume ratio near the hole edges can significantly reduce the stress concentration in that region.

9A160. **Stress concentration in the bending of sandwich beams with transversely flexible core.** - Y Frostig *(Fac Civil Eng, Technion Israel IT, Haifa 32000, Israel)*. Composite Struct 24(2) 161-169 (1993).

Stress concentrations in sandwich beams with a soft core subjected to bending loading are investigated and the level of stresses is analytically determined. The cases discussed include stress concentration effects (i) in the vicinity of concentrated loads and supporting zones; (ii) at the edges of debonding regions edge and inner delamination types at the interface layer between the skins and the core; and in the vicinity of vertical cut-off connections; and (iii) at the location of diaphragms that are bonded and unbonded with adjacent core and embedded in it. The results are determined with the aid of a variational rigorous analytical systematic elastic high-order theory that uses closed form solutions. This theory is applicable to any type of sandwich construction with and without discrete diaphragms (i) to any type of loading, concentrated or distributed; and (ii) to any type of boundary conditions including cases in which at the same section the conditions at the upper skin are different from those at the lower skin. The stress concentration effects are presented in terms of deflections, internal forces, and normal stresses (peeling) in the interface layers between the skin and core. A parametric study is conducted and investigates the level of stresses as a result of (i) the vertical modulus of elasticity of the core; (ii) the delamination length; (iii) the reinforcing diaphragm in a typical connection; and (iv) the presence of diaphragms, either bonded or unbonded with the adjacent core, at specific locations.

See also the following:

9A309. Three coplanar moving Griffith cracks in an infinite elastic strip

250F. ELASTIC IMPERFECTIONS (DISLOCATIONS, ETC)

See the following:

9A416. Effective elastic properties of a solid with crazes

250H. CONTACT PROBLEMS AND INCLUSIONS

9A161. **About multi-Hertzian-contact hypothesis and equivalent conicity in the case of S1002 and UIC60 analytical wheel-rail profiles.** - J-P Pascal *(Lab Tech Nouvelles, Inst Rech sur les Transports leur Securite, BP 34, 94114 Arcueil, France).* Vehicle Syst Dyn 21(2) 57-78 (1993).

In a previous paper, a new method using "multi-Hertzian" elasticity for identifying equivalent parameters of railway wheelsets rolling on defined tracks was presented. Another method also using Hertzian elasticity has produced different results. Without knowing the origin of these discrepancies, the question was asked, whether any of these methods could adequately describe actual non-Hertzian contacts. This paper, using as a basis Kalker's "Contact" software which solves the non-Hertzian case for normal and tangential forces, answers this question, demonstrating that the assumption of summing Hertzian contacts is realistic provided that enough ellipses are considered.

9A162. **Almost constant contact stress distributions by shape optimization.** - A Klarbring *(Dept of Mech Eng, Linkoping IT, S-581 83 Linkoping, Sweden)* and J Haslinger *(KFK MFF UK, Charles Univ, Ke Karlovu 5, 120 00 Praha, Czechoslovakia).* Struct Optim 5(4) 213-216 (Apr 1993).

This paper addresses the problem of finding shapes of contacting bodies avoiding undesirable stress concentrations. It has previously been shown that designing the shape of a rigid body in contact with a fixed linear elastic body by minimizing the equilibrium potential energy under an isoparametric constraint results in a uniform contact pressure distribution. As an extension of this result, it is shown here that when the shape of an elastic body in contact with a flat rigid foundation is chosen on the same premises, the uniform pressure distribution is found only if displacement gradients can be considered small. From the point of view of applications, an important conclusion is that this smallness holds in a case when linear elasticity is physically valid.

9A163. **Numerical treatment of the nonmonotone (zig-zag) friction and adhesive contact problems with debonding.** Approximation by monotone subproblems. - ES Mistakidis *(Dept of Civil Eng, Aristotle Univ, GR-54006 Thessaloniki, Greece)* and PD Panagiotopoulos *(Fac of Math and Phys, RWTH, D-5100 Aachen, Germany).* Comput Struct 47(1) 33-46 (3 Apr 1993).

Nonmonotone friction problems or adhesive contact friction problems introduce zig-zag-type laws which cannot be effectively treated by the classical numerical methods for nonlinear stress-strain laws. In order to calculate accuracy the arising free boundaries we propose a new approximation method of the nonmonotone problem by monotone ones. The proposed method finds its justification in the approximation of a hemivariational inequality by a sequence of variational inequalities.

See also the following:

9A409. Stress analysis around a partially bonded rigid cylinder in an elastic medium with process zones

250I. ANISOTROPIC MEDIA

See the following:

9A406. Analysis of finite anisotropic media containing multiple cracks using superposition

250K. RESIDUAL STRESSES

9A164. **Residual stresses in welded jumbo box columns.** - Sheng-Jin Chen and SC Chang *(Dept of Construct Eng, Natl Taiwan IT, Taipei, Taiwan).* J Construct Steel Res 25(3) 201-209 (1993).

Eight full-scale welded jumbo box columns fabricated with different details are selected to examine the distribution and magnitude of residual stresses. It is found that the maximum tensile residual stresses can be as high as 1.1 F_y and the maximum compressive residual stress is 0.43 F_y, where F_y, is the yield stress.

250Y. COMPUTATIONAL TECHNIQUES

9A165. **Completed double layer BEM in elasticity.** - N Phan-Thien and D Tullock *(Dept of Mech Eng, Univ of Sydney, NSW 2006, Australia).* J Mech Phys Solids 41(6) 1067-1086 (Jun 1993).

This paper reports on indirect BEM in elasticity that is most suitable to deal with particular solids. The method involves a distribution of a double layer potential and, after a suitable completion and deflation, is amenable to iterative solution techniques. It can therefore accommodate a large number of particles with complex geometries. Convergence of the method is significantly improved by the introduction of a simple domain decomposition to solve the system of equations. The method is illustrated by the translating sphere problem, the load transfer problem between two spheres at near contact, and the shear deformation of a cluster of 125 spheres initially in a simple cubic array.

9A166. **Complex method for the elliptical hole in an unsymmetric laminate.** - W Becker *(Dornier GmbH Deutsche Aerospace, Abteilung RST 111, Postfach 1420, W-7990 Friedrichshafen 1, Germany).* Arch Appl Mech 63(3) 159-169 (Apr 1993).

Within the framework of linear-elastic classical laminated plate theory, the problem of an elliptical hole in an infinitely extended unsymmetric laminate is treated. For the underlying non-symmetric layup arbitrary bending extension coupling is admitted and is taken into account by means of a new complex potential approach. The derived solution describes all essential plate quantities in any vicinity of the elliptical hole and it reveals interesting features of the considered bending extension coupling.

9A167. **Convex multilevel decomposition algorithms for non-monotone problems.** - GE Stavroulakis and PD Panagiotopoulos *(Sch of Tech, Aristotle Univ, GR-54006 Thessaloniki, Greece).* Int J Numer Methods Eng 36(11) 1945-1966 (15 Jun 1993).

A convex, multilevel decomposition algorithm is proposed in this paper for the solution of static analysis problems involving non-monotone, possibly multivalued laws. The theory is developed here for a model structure with non-monotone interface or boundary conditions. First the nonmonotone laws are written in the form of a difference of two monotone functions. Under this decomposition, the nonlinear elastostatic analysis problem is equivalent to a system of convex variational inequalities and to non-convex minmin problems for appropriately defined Lagrangian functions. Numerical results concerning the calculation of elastic and rigid stamp problems and of material inclusion problems with delamination and non-monotone stick-slip frictional effects illustrate the theory.

9A168. **Fast algorithm to solve the Beltrami equation with applications to quasiconformal mappings.** - P Daripa *(Dept of Math, Texas A&M Univ, College Station TX 77843).* J Comput Phys 106(2) 355-365 (Jun 1993).

Two algorithms are provided for the fast and accurate computation of the solution of Beltrami equations in the complex plane in the interior of a unit disk. There are two integral operators which are fundamental in the construction of this solution. A fast algorithm to evaluate one of these integrals is given by Daripa. An algorithm for fast evaluation of the second integral is provided here. These algorithms are based on representation of the solution in terms of a double integral, some recursive relations in Fourier space, and fast Fourier transforms. A numerical method is provided and explored numerically for the construction of quasiconformal mappings using the Beltrami equation.

9A169. **Fundamental solutions of the I-st plane problem of micropolar elasticity with a harmonically varying distortion field.** - J Dyszlewicz and J Wytrazek *(Inst of Math, Wroclaw Univ of Tech, Wroclaw, Poland).* Eng Trans 40(4) 419-434 (1992).

The paper deals with the I-st plane problem of microelasticity in the case of a distortion field varying harmonically in time. Differential equations of the problem, expressed in terms of displacements and rotations, are solved by direct integration with the help of the Fourier integral transforms. Fundamental solutions are obtained for the displacements and rotations induced by concentrated distortions acting in an infinite plane. All limit cases of the fundamental solutions are given which are relevant to derived theories.

9A170. **New description of the tensors of elasticity based upon irreducible representations.** - Y Surrel *(Dept of Mech and Mat Eng, Ecole Nationale Superieure Mines de Saint-Etienne, 158 Cours Fauriel, 42023 Saint-Etienne Cedex 2, France).* Eur J Mech A 12(2) 219-235 (1993).

This paper gives the irreducible decomposition of the representations of the spatial group of rotations realized by the tensors of elasticity. From the tensor components are defined some complex quantities spanning the irreducible subspaces. The law of transformation of those quantities under spatial rotations is explicitly given, as well as the law of elasticity with this formalism, in the most important material symmetry cases.

9A171. **Three dimensional anisotropic elasticity with BEM using the isotropic fundamental solution.** - NA Schclar and PW Partridge *(Wessex IT, Univ of Portsmouth, Ashurst Lodge, Southampton SO4 2AA, UK).* Eng Anal Boundary Elements 11(2) 137-144 (1993).

The anisotropic fundamental solution for BEM analysis of elasticity problems cannot be expressed in a closed form in such a way that numerical integration and interpolation must usually be employed in its evaluation with a resulting increase in computer run times. An alternative is to express the anisotropic constants as a sum of average isotropic values and residuals, thus permitting the use of an isotropic fundamental solution. In this paper the dual reciprocity method is used to approximate the residuals and take the relevant domain integral to the boundary.

252. Viscoelasticity

9A172. Effects of stress rates on the strength and deformation of concrete at ambient and elevated temperatures. - GD Stefanou *(Sch of Eng, Univ of Patras, GR-261 10 Patras, Greece)*, P Koliopoulos *(Sch of Eng, Univ College, Gower St, London WC1, UK)*, E Nichol *(Sch of Eng, Univ College London, Gower St, London WC1, UK)*. Eng Fracture Mech 45(2) 265-276 (May 1993).

Experimental data relating to standard rates of loading are studied on concrete control specimens 28 days after casting. Normal concrete with an oven-dry density in the range of 2000 - 2800 kg/m^3 is used for the specimens. The rates of compression are about 0.3 $N/mm^2/sec$, or a strain rate of about $30 \times 30^{-6}/sec$ and the corresponding rates of tension are 0.03 N/mm^2 sec or $3 \times 10^{-6}/sec$. Examples of stress-strain relationships are given. The effects of stress and strain rates are discussed.

9A173. Interpretation of impression creep data using a reference stress approach. - TH Hyde, KA Yehia, AA Becker *(Dept of Mech Eng, Univ of Nottingham, University Park, Nottingham NG7 2RD, UK)*. Int J Mech Sci 35(6) 451-462 (Jun 1993).

A sound, mechanics-based approach has been developed to allow conventional creep data to be obtained from impression creep test data; the reference stress method was used, to analyze the results of axisymmetric finite calculations, for this purpose. The equivalent stress was found to be 0.296 times the mean indenter pressure and the effective gauge length was found to be about 0.755 times the indenter diameter. These values correspond closely with those which have been obtained by fitting indenter creep data to conventional uniaxial creep data.

9A174. Viscoelastic effects on intralaminar fracture toughness of epoxy-carbon-fibre laminates. - R Frassine, M Rink, A Pavan *(Dept Chimica Industriale Ingegneria Chimica, Politec Milano, P Leonardo da Vinci, 32-20133 Milano, Italy)*. J Composite Mat 27(9) 921-933 (1993).

The Double Torsion technique has been applied to characterize the fracture resistance of a unidirectional and a woven epoxy and carbon-fibre composite material. The crack speed has been varied by about four orders of magnitude for testing temperatures ranging from below the glass transition of the rubber modifier of the epoxy matrix to the glass transition of the matrix itself. A noteworthy variation was found in the fracture toughness and surface morphology of the unidirectional composite. Decreasing fracture toughness values were observed by increasing crack speed at 23°C, which is somewhat unusual for viscoelastic materials. Results have been discussed in the framework of viscoelastic fracture mechanics, and the fracture behavior at different rates and temperatures has been shown to be related to different viscoelastic mechanisms.

9A175. FE analysis of viscoelastic fracture. - JR Masuero and GJ Creus *(Dept of Civil Eng, Univ Federal Rio Grande do Sul, 90210 Porto Alegre RS, Brazil)*. Int J Fracture 60(3) 267-282 (1 Apr 1993).

A numerical procedure based on the FEM and Schapery's formulation is proposed to determine the critical condition of cracks in viscoelastic structures. Some initial results trying to couple fracture mechanics with continuum damage mechanics also are presented.

9A176. Analysis of identification methods for the viscoelastic properties of materials. - L Dietrich and K Turski *(Inst of Fund Tech Res, Polish Acad of Sci, Warszawa, Poland)*. Eng Trans 40(4) 501-523 (1992).

A complete solution of the constitutive equations for the viscoelastic material described by Burgers model is presented under various initial conditions. Possibilities to determine the viscoelastic properties of materials for various loading patterns of a specimen are pointed out. Test results on asphalt mixture obtained under various loads and strain rates are discussed. Creep, cyclic deformations and constant strain rate loading are found to enable the viscoelastic properties to be determined in different ranges of strain rates. The obtained results of these types of tests provide a consistent spectrum of these properties as functions of the initial strain rates.

See also the following:

9A913. Effects of viscoelasticity on seismic wave propagation in fault zones, near-surface sediments, and inclusions

254. Plasticity and viscoplasticity

See the following:

9A354. Ductile fracture by the growth and coalescence of microvoids of nonuniform size and spacing

254A. GENERAL THEORY

9A177. Plasticity model for punching shear of laterally restrained slabs with compressive membrane action. - JS Kuang and CT Morley *(Dept of Eng, Univ of Cambridge, Trumpington St, Cambridge CB2 1PZ, UK)*. Int J Mech Sci 35(5) 371-385 (May 1993).

A plastic theoretical model is presented for the punching shear failure of laterally restrained concrete slabs, in which a parabolic Mohr failure criterion for concrete is adopted. The proposed method allows for the effect of compressive membrane action and a membrane-modified flexural theory of elasto-plasticity is used to calculate the compressive membrane forces. The predictions by the proposed analysis shows good agreement with a wide range of experimental test results.

254C. NONLINEAR AND FINITE DEFORMATION PROBLEMS

9A178. Effect of frictional force on the steady state axisymmetric deformations of a viscoplastic target. - X Chen and RC Batra *(Dept of Mech and Aerospace Eng and Eng Mech, Univ of Missouri, Rolla MO 65401-0249)*. Acta Mech 97(3-4) 153-168 (1993).

We study steady state axisymmetric deformations of a thick viscoplastic target being penetrated by a fast-moving long rigid cylindrical rod with a hemispherical nose. The deformations of the target appear steady to an observer situated on the penetrator nose tip and moving with it. The objective of this work is to investigate the effect of the frictional force acting on the target-penetrator interface upon the deformations of the target. It is postulated that the frictional force at a point on the target-penetrator interface is proportional to the normal traction there and depends upon the speed of the target particle relative to the penetrator. It is found that the frictional force affects significantly the variation of the tangential speed and the second invariant of the strain-rate tensor on the penetrator nose surface, but minimally the distribution of the normal stress there, since the dominant component of the normal stress is the hydrostatic pressure which is affected little by the consideration of friction forces.

9A179. Loss of hyperbolicity in elastic-plastic material at finite strains. - Lianjun An *(Dept of Math and Stat, McMaster Univ, Hamilton L8S 4K1, ON, Canada)*. SIAM J Appl Math 53(3) 621-654 (Jun 1993).

In this paper, a linear analysis is carried out for partial differential equations (PDEs) describing granular flow. Regarding constitutive effects, elasticity and shear hardening with a nonassociative flow rule are included. The paper shows that flutter illposedness is an essential feature of many such constitutive models. In the paper, a readily applicable criterion for the occurrence of flutter illposedness is developed. The paper demonstrates this material with a deviatorically associative flow rule at small strains; although flutter illposedness does not occur, a generic small perturbation will cause flutter illposedness.

9A180. Model of internal stress superplasticity based on continuum micromechanics. - E Sato and K Kuribayashi *(Inst of Space and Astron Sci, 3-1-1 Yoshinodai Sagamihara, Kanagawa 229, Japan)*. Acta Metall Mat 41(6) 1759-1767 (Jun 1993).

A new theoretical model is proposed to explain internal stress superplasticity under a simultaneous applied stress during thermal cycling. The analyzed material is an elastically uniform body containing an elastic spherical inclusion, surrounded by a plastic matrix obeying a power law creep. It is assumed that only relaxation by interface diffusion is significant. At first it is shown that an inclusion dilatation can be counterbalanced by a certain matrix plastic flow. Assuming a certain stress distribution for this condition, a stationary flow on heating or cooling results. Typical behavior of this stationary flow is analyzed for the specific cases of high or low applied stresses.

See also the following:

9A158. Stress rate measure for finite elastic plastic deformations

9A377. Computational procedure for the simulation of ductile fracture with large plastic deformation

254E. CONTACT PROBLEMS AND INCLUSIONS

9A181. Elasto-plasticity of slackened systems. - A Gawecki *(Poznan Univ of Tech, Poznan, Poland)*. Arch Mech 44(4) 363-390 (1992).

The paper concerns the so-called "slackened" systems, ie, systems with gaps (clearances) at the joints between FEs. Fundamental theoretical problems of mechanics of such systems made of the elastic-plastic materials have been presented. Only quasi-static processes, within the framework of the geometrically linear theory, are considered, and all friction effects are neglected. Several theorems concerning the problems of analysis and synthesis have been derived. Particular attention has been paid to the problems of uniqueness of solutions. A mathematical problem proposed in the work can describe the behavior of locking elastic-plastic systems. This model covers a considerably wide class of time-independent materials. The theory allows us to describe the frictionless cases of unilateral constraints in the frame of small deformations. Results obtained in the paper can be applied in structural and solid mechanics.

254G. WORK HARDENING

See the following:

9A239. Effect of axial restraints on the deflection of strain hardening beams

9A381. Higher order asymptotic crack fields in a power-law hardening material

254I. VISCO- AND ELASTO-PLASTIC MEDIA

9A182. Identification and validation of viscoplastic and damage constitutive equations. - G Amar and J Dufailly *(Lab Mec Tech ENS Cachan-CNRS, Univ Paris-VI, 61 Ave President Wilson, 94235 Cachan Cedex, France)*. Eur J Mech A 12(2) 197-218 (1993).

This paper is devoted to the lifetime prediction of structures to very severe thermomechanical loadings leading to very small numbers of cycles to rupture (10 to 100). An isothermal elasto-viscoplastic model coupled to the damage constitutive relation is considered. Its complete identification under isothermal conditions is developed and the corresponding experimental program is described.

9A183. Inadaptation analysis with hardening and damage. - A Siemaszko *(Inst of Fund Tech Res, Swietokrzyska 21, PL-00 049 Warsaw, Poland)*. Eur J Mech A 12(2) 237-248 (1993).

The paper presents a method of inadaptation (non-shakedown) analysis of elastic-plastic discrete structures subjected to variable repeated loading. The method accounts for nonlinear geometrical effects, nonlinear isotropic or kinematic hardening and progressive damage of the material. The problem is formulated as a sequence of linear programming tasks and is solved by a step-by-step procedure. The method provides the most stringent plastic deformation path of the structure (so called inadaptation curve) constituting an envelope of all the possible inadaptation processes. The inadaptation analysis method, presented here, is applied to the example of elastic-plastic frame structures subjected to variable loads.

9A184. Pareto solution of an inverse problem in elastoplasticity. - LMC Simoes *(Dept Eng Civil, Fac Ciencias Tec, Univ Coimbra, 3049 Coimbra, Portugal)*. Adv Eng Software 16(2) 103-110 (1993).

An elastic-perfectly plastic discretized structure subjected to given proportional loads, undergoes displacements, some of which are measured. On the basis of this experimental data the yield limits and the hardening coefficients are sought, whereas the elastic properties are known. A number of possible ways of tackling this inverse problem are outlined and discussed. The present paper contains results on the sensitivity analysis for elastoplastic problems in the case of discrete structures modeled by the FEs.

9A185. Ratchetting behavior in viscoplasticity, a technical note. - AD Freed *(NASA Lewis Res Center, Cleveland OH 44135)* and KP Walker *(Eng Sci Software, Smithfield RI 02917)*. Eur J Mech A 12(2) 191-196 (1993).

Viscoplastic models that use the [Armstrong & Frederick, 1966] kinematic hardening relationship are known to generally overpredict the observed accumulation of ratchet strains [Inoue *et al*, 1991]. The reason for this behavior is a consequence of the mathematics used to describe Hooke's law and the evolution equations for plastic strain and back stress. Conditions for ratchetting exist whenever there is a cycle-averaged mean stress present over a cyclic loading path. Overcoming the possible adverse trends in predicted ratchetting behavior is a difficult task, and how one ought to go about doing this is not yet completely clear. We therefore choose to discuss the mathematical cause of ratchetting and how it has been dealt with to date in the literature, but we make no attempt to correct this flaw.

254K. ANISOTROPIC AND NONHOMOGENEOUS MEDIA

See the following:

9A380. Failure analysis of a cracked plate based on endochronic plastic theory coupled with damage

254Y. COMPUTATIONAL TECHNIQUES

9A186. Fundamental issues in FE analyses of localization of deformation. - R DeBorst *(Dept of Civil Eng, TNO Build and Construct Res, Univ of Tech, PO Box 5048, Delft, Netherlands)*, LJ Sluys *(Dept of Civil Eng,Univ of Tech, PO Box 5048, Delft, Netherlands)*, H-B Muhlhaus *(Div of Geomech, CSIRO, PO Box 54 Mt Waverley, Vic, Australia)*, J Pamin *(Dept of Civil Eng, Univ of Tech, PO Box 5048, Delft, Netherlands)*. Eng Comput 10(2) 99-121 (Apr 1993).

Classical continuum models, ie, continuum models that do not incorporate an internal length scale, suffer from excessive mesh dependence when strain-softening models are used in numerical analyses and cannot reproduce the size effect commonly observed in quasi-brittle failure. In this contribution three different approaches will be scrutinized which may be used to remedy these two intimately related deficiencies of the classical theory, namely (i) the addition of higher-order deformation gradients, (ii) the use of micropolar continuum models, and (iii) the addition of rate dependence. By means of a number of numerical simulations it will be investigated under which conditions these enriched continuum theories permit localization of deformation without losing ellipticity for static problems and hyperbolicity for dynamic problems.

9A187. HyperQ/Plastics: An intelligent design aid for plastic material selection. - K Beiter, S Krizan, K Ishii *(Dept of Mech Eng, Ohio State Univ, Columbus OH)*, L Hornberger *(Apple Computer)*. Adv Eng Software 16(1) 53-60 (1993).

The selection of material and processing techniques for plastic parts is a challenging task for design engineers. This paper describes the development of an intelligent program that helps engineers perform this task. An extensive survey of practicing engineers, product designers and material specialists revealed that these experts used both qualitative and quantitative selection methodologies. The program described, HyperQ/Plastics, is a HyperCard program that uses PROLOG to combine these two types of selection methodologies. The current version of this program is undergoing tests at several industrial sites.

9A188. Non-unique numerical solutions in visco-plasticity. - HJ Antunez *(Inst of Fund Tech Res, Polish Acad of Sci, Warszawa, Poland)*. Eng Trans 40(4) 525-536 (1992).

We present the numerical analysis of a series of cutting problems for a visco-plastic material. The model is implemented in a FE program written in the flow formulation framework. Almost ideal plasticity is achieved as the limit case of a visco-plastic material. Solution dependence on the chosen initial configuration (the final one being not known) suggests non-uniqueness inherent to the visco-plastic material with free surfaces, since a residual rate dependence is conserved in the model.

9A189. Strength analysis of axially symmetric elements with a series of rectangular notches. - L Dietrich, J Miastkowski, R Szczebiot *(Inst of Fund Tech Res, Polish Acad of Sci, Warszawa, Poland)*. Eng Trans 40(4) 435-456 (1992).

Complete solutions for axially-symmetric tensile rods with rectangular notches of arbitrary spacing are presented. On the basis of the obtained solutions both limit values of a diameter of the rod outside notch and appropriate spacings of a series of notches have been determined. Strength analysis of such elements within entire range of their geometrical parameters has also been made. The obtained results are compared with experimental tests on specimens made of aluminium alloy.

See also the following:

9A383. J-integral computations in the incremental and deformation plasticity analysis of small-scale yielding

254Z. EXPERIMENTAL TECHNIQUES

9A190. On the yield surface behavior in the case of proportional cyclic loading histories. - W Trampczynski and E Sender *(Inst of Fund Tech Res, Polish Acad of Sci, Warszawa, Poland)*. Arch Mech 44(4) 391-408 (1992).

Experimental results concerning the yield surface evolution in the case of proportional cyclic loading histories are reported. They were obtained for 18G2A steel, at room temperature, using one specimen technique, where the "offset" yield definition was assumed to be n = 0.0005. The experiments were carried out on thin-walled tubes under cyclic tension-compression and opposite torsion with constant strain rate $\dot{\varepsilon}_e$ = 3.4×10^{-4} s^{-1}. The influence of former plastic strain history on the yield surface shape and magnitude in steady cyclic state is shown. It was found that yield surface in the σ_x, $\sqrt{3}\tau_{xy}$ space can be described by an ellipse, + 8%; - 6% accuracy, independently on the former plastic strain history.

256. Composite material mechanics

See the following:

9A297. Effect of mandrel material on the processing-induced residual stresses in thick filament wound composite cylinders

256A. GENERAL THEORY

9A191. Antiplane shear problems of perfect and partially damaged matrix-inclusion systems. - Xiangzhou Zhang *(Dept of Aircraft Eng, NW Polytech Univ, Xian 710072, China)* and Norio Hasebe *(Dept of Civil Eng, Nagoya IT, Nagoya 466, Japan)*. Arch Appl Mech 63(3) 195-209 (Apr 1993).

Antiplane shear problem of an infinite medium containing a circular inclusion of different material is investigated in this article. Perfectly bonding between the matrix and the inclusion, as well as partial debonding in the form of a circumferential crack occurring at the interface of these two constituents, are considered. Using the complex variable method in conjunction with a semi-inversed technique, exact expressions for the stress, displacement and stress intensity factor in the problem are obtained for various external loading conditions, including that brought about by stress singularities.

9A192. **Beneficial influence of matrix anisotropy in fiber composites.** - PS Theocaris *(Acad of Athens, PO Box 77230, 17510 Athens, Greece)*. Acta Mech 97(3-4) 127-139 (1993).

It has recently been shown that the stress concentrations in anisotropic materials with distinct complex or imaginary roots of the respective characteristic function are much higher than in materials with equal roots. It was further shown that anisotropic materials with equal roots behave like quasi-isotropic materials. Modern carbon-carbon and metal-ceramic composites are intuitively using these facts to create much stronger materials by reinforcing the matrix properties. A theory is presented in this paper where the coupling of strongly anisotropic fibers along their axis with strongly anisotropic matrices along either the fiber direction or the transverse plane to the direction of the fibers, either deteriorates, or improves perceptibly the mechanical behavior of the composites. It was shown that anisotropy of the matrix, increasing its mechanical properties on the transverse isotropic plane of the composite, increased the transverse Poisson's ratio, whereas decreased the longitudinal shear modulus G_{LC}. This resulted in values of the eigenangle ω_c receding from the corresponding value ω_{ic} for the respective isotropic case. This resulted in deterioration of the mechanical performance for the composite since the material now has the tendency to develop higher stress concentrations for equivalent loadings. On the contrary, a strong anisotropic matrix along the direction of the fibers yielded the inverse results for the various moduli of the anisotropic composite. The most important results is the increase of the longitudinal shear modulus G_L, so that ratio $E_L/2G_L$ is consistently decreasing, thus yielding values of the eigenangle ω_c tending to approach the critical value ω_i for the isotropic material. This decrease of ω_c indicates the improvement of the quality of the composite, which develops relatively lower stress concentration factors approaching their respective isotropic values. This fact makes the anisotropic composite material to approach an equivalent state of quasi-isotropy and thus to improve the strength of the material by reducing considerably the eventual anisotropic stress concentration factors of the respective structural elements. Examples with T300-N5208 Graphite-Epoxy composites and Borsic-1100 Aluminum metal-metal composites indicate clearly the beneficial effect of the anisotropy of their matrices.

9A193. **Bounds and estimates of overall moduli of composites with periodic microstructure.** - S Nemat-Nasser *(Center for Excellence for Adv Mat, Dept of Appl Mech and Eng Sci, UCSD)*, N Yu *(Dept of Eng Sci and Mech, Univ of Tennessee, Knoxville TN 37996)*, M Hori *(Dept of Civil Eng, Univ of Tokyo, Bunkyo-ku, Tokyo 113, Japan)*. Mech Mat 15(3) 163-181 (May 1993).

Bounds on the overall moduli of a broad class of composites with periodic microstructure are obtained by generalized Hashin-Shtrikman variational principles. Piecewise constant eigenstrains and eigenstresses are used, and exact, computable bounds are developed. The formulation is valid for composites comprised of an anisotropic (or isotropic) matrix with an arbitrary number of periodically distributed anisotropic (or isotropic) inhomogeneities. Examples of two-phase particulate whisker, and fiber-reinforced composites are considered for illustration. Finally, an estimate of the overall moduli, based on the selection of the effective medium as the reference material, is proposed for periodic microstructure.

256B. PARTICULATE MEDIA, INCL CEMENTS

9A194. **Behavior of high-strength concrete under confined stresses.** - K Lahlou, P-C Aitcin, O Chaallal *(Dept of Civil Eng, Fac of Appl Sci, Univ de Sherbrooke, Sherbrooke, PQ J1K 2R1, Canada)*. Cement & Concrete Composites 14(3) 185-193 (1992).

This paper presents the preliminary results of an experimental investigation on confined high-strength concrete, which is ongoing in the Civil Engineering Department of the University of Sherbrooke. The results of the present preliminary study limited to concentrically loaded short circular columns show that confining high strength concrete in a steel tube greatly increases its strength and results in outstanding new ultrahigh-strength concrete; confining high-strength concrete in a steel tube improves its ductility; and the confinement efficiency slightly increases with concrete compressive strength.

9A195. **Computational modeling of impact tests on steel fiber reinforced concrete beams.** - LJ Sluys and R De Borst *(Dept of Civil Eng, TNO Build and Construct Res, Univ of Tech, Delft, Netherlands)*. Heron 37(4) 3-69 (1992).

Concrete fracture under impact loading is modeled using rate-independent and rate dependent smeared crack representations. Both models have been used to simulate the behavior of concrete beams with both conventional and steel-fiber reinforcement. The rate-dependent crack model turns out to be superior in the sense that it properly captures the experimentally observed distributed crack pattern, but the differences in the prediction of the global structural response are hardly noticeable.

9A196. **Effect of field and lab curing on the durability characteristics of plain and Pozzolan concretes.** - H Saricimen, M Maslehuddin, AI Al-Mana, O Eid *(Res Inst, King Fahd Univ of Pet and Minerals, PO Box 1686, Dhahran 31261, Saudi Arabia)*. Cement & Concrete Composites 14(3) 169-177 (1992).

The environmental conditions in the Arabian Gulf countries are classified as aggressive and severely corrosive. Field and lab studies have shown that concrete in this region should be designed not only for strength but also for durability. Utmost emphasis should be given to produce dense and impermeable concrete, to extend the service life of structures. In this study, concrete samples were prepared using various types of cements and fly ashes at various mix designs. The samples were cured in the field and in lab conditions. The permeability was determined by volume of permeable voids and absorption tests. The results showed that continuous water curing is necessary to obtain the least permeable concrete for both plain and pozzolan concretes. Irrespective of curing procedure followed, the fly ash concrete exhibited lower permeability than plain concrete for an initial test period of 7 days during curing. The fly ash concrete samples cured in the lab exhibited lower initial surface absorption than control concretes after 90 days of curing for all fly ash additions (10-40%) and cement factors (275-450 kg-m^3) used.

9A197. **Energy principle of the indentation-induced inelastic surface deformation and hardness of brittle materials.** - M Sakai *(Dept of Mat Sci, Toyohashi Univ of Tech, Tempaku-cho, Toyohashi 441, Japan)*. Acta Metall Mat 41(6) 1751-1758 (Jun 1993).

Energy-based considerations on the inelastic surface deformation of brittle materials are conducted. The hysteresis loop energy U_r which is dissipated during the indentation loading-unloading cycle is related to the true hardness H, apparent hardness H, and the work-of-indentation Γ_I. The true hardness has its energy-derived meaning of the irreversible energy consumption to create a unit volume of the indentation impression of ideally plastic materials. The relationships between U_r and the three-half power of indentation load $P^{3/2}$, and between U_r and the volume of the indentation impression V_I are used to separate the plastic contribution from the complicated plastic-elastic surface deformation processes in indentation hardness tests. The mechanical and physical meanings of the conventional Vickers indentation hardness of brittle materials are also addressed in relation to H, H and Γ_I.

9A198. **Influence of curing methods on the strength and permeability of GGBFS concrete in a simulated arid climate.** - SA Austin, PJ Robins, A Issaad *(Struct Mat Res Group, Dept of Civil Eng, Univ of Tech, Loughborough LE11 3TU, Leics, UK)*. Cement & Concrete Composites 14(3) 157-167 (1992).

Problems are frequently encountered in producing good-quality concrete in hot climates. Inadequate curing results in early cracking or porous and permeable concrete, or both; these effects, in turn, make structures prone to reinforcement corrosion and other processes of degradation. This research compares the development of strength and permeability of ordinary Portland cement (OPC) and ground granulated blast furnace slag (GGBFS)-modified concretes which were cured in a simulated arid climate. This was achieved with an environmental room in which temperature and humidity were cycled to imitate a typical Algerian Sahara climate. Four curing regimes were investigated to encompass the range of practical methods encountered on site. Specimens were placed in the hot environment immediately after casting and conditioned for up to 28 days. The strength of the GGBFS concretes was higher than that of the OPC control concrete at all test ages (7, 14, and 28 days) when good curing was provided. Partial cement replacement with GGBFS therefore offers the potential to produce stronger and more durable concrete in hot climates. The disadvantage of GGBFS concretes is that they proved to be more sensitive to poor curing than OPC concrete. In this case, both their strength and permeability, and hence their durability, were seriously impaired. Therefore, special care must be taken when using this type of concrete, especially on site, where the working conditions and the application of curing are not as easy to control as in the lab.

9A199. **Microstructure of the interfacial zone around aggregate particles in concrete.** - JA Larbi *(TNO Build and Construct Res, Dept of Build Tech, Rijswijk, Netherlands)*. Heron 38(1) 3-69 (1993).

The study is aimed at examining the microstructural characteristics of the interfacial region around aggregate particles in concrete and exploring the influence of this interfacial zone on some of the properties of concrete such as, the compressive strength, the water transport capacity, and the diffusion of ions into concretes prepared with and without mineral additives.

9A200. **Mutual compatibility of mortar and concrete in composite members.** - N Ignatiev *(Dept of Civil Eng, Univ of Architect and Civil Eng, Sofia, Bulgaria)* and S Chatterji *(Danish Tech Inst, Copenhagen, Denmark)*. Cement & Concrete Composites 14(3) 179-183 (1992).

In many countries, a layer of cement-sand mortar is applied to concrete structures, either for decoration or protective purposes. Often this mortar layer develops a crack pattern soon after it application. Reasons for this crack formation have been investigated. A physicochemical and a mathematical analysis show that this is due to an incompatibility between the properties of the mortar layer and the underlying concrete, and that this crack formation will occur even when both the components are individually made with the best materials. This crack formation could be avoided only by adjusting the properties of the mortar layer. A few typical examples have been worked out to show the effect of this incompatibility on the age of crack formation.

See also the following:

9A327. Chloride corrosion of steel rebars in mortars with fly ash admixtures
9A390. Delamination, fiber bridging and toughness of ceramic matrix composites
9A407. Correlation between crack tortuosity and fracture toughness in cementitious material

256D. CARBON FIBER REINFORCED MEDIA

9A201. **Effect of fiber concentration on the thermal conductivity of a polycarbonate-pitch-based carbon fiber composite.** - A Demain and J-P Issi *(Unite Physico-Chimie Phys Mat, Univ Catholique Louvain, Place Croix du Sud 1, B-1348 Louvain-la-Neuve, Belgium)*. J Composite Mat 27(7) 668-683 (1993).

Results of measurements of the thermal and electrical conductivities of polycarbonate samples as a function of chopped pitch-based carbon fiber concentration are reported. The fibers, roughly 500 μm long, were found to be strongly oriented in the composite leading to a highly anisotropic thermal conductivity. We proposed a new model which is a derivation of equations used for continuous fibers composites. This model is quite well in accordance with the linear dependence of the longitudinal thermal conductivity on the fiber concentration of our data.

9A202. **Increasing the limit of usability of CFRP tubes by built in stresses.** - RG Cuntze *(MAN Tech AG, Bauschingerstr 20, D 8000 Munchen 50, Germany)* and R Heibel *(URENCO, Oxford Rd, Marlow SL7 2NL, UK)*. Composite Struct 24(3) 251-264 (1993).

The limit of usability of a CFRP structure is often determined by first ply failure (FPF) indicated by interfiber-matrix cracking. It will be shown how for certain types of CFRP structures this crack initiation threshold can be delayed. The process used here is prestraining in analogy to that of prestressed concrete. It is so-called thermo-mechanical after treatment, inducing advantageous compression built-in stresses, ie, negative strains transverse to the fibers. Cylindrical tube specimens were wound, prestrained and submitted to hydraulic pressurization or spin load testing. Acoustic emission monitoring and crack counting following sectioning confirmed and an increase in crack threshold level for this specimen type from $\epsilon_{hoop} \approx 0.8\%$ to 1.3%, which is higher than the operational strain, normally defined as tensile failure strain $e^{\parallel}$ of the fiber divided by the usual design factor $j_u = 1.5$. Theoretical investigations were done in support of the design of the prestraining device and of the tube specimen, as well as an evaluation of experimental data.

See also the following:

9A174. Viscoelastic effects on intralaminar fracture toughness of epoxy-carbon-fibre laminates
9A387. Combined experimental and FE study to predict the failure mechanisms in SiC coated carbon-carbon composites at room and elevated temperatures under flexural loading
9A395. Fracture surface of hybrid fibre composites
9A845. Low-temperature flexural dynamic measurements on PEEK, HTA and some of their carbon fibre composites
9A848. Thermal degradation of an end-capped bismaleimide resin matrix (PMR-15) composite reinforced with pan-based carbon fibres

256F. OTHER FIBER REINFORCED MEDIA

9A203. **Anelastic deformation of a thermoplastic-matrix fiber composite at elevated temperature Part I.** Neat resin structure characterization. - AW-L Chen *(Eastman Kodak, Rochester NY)*, A Miyase *(Univ of Houston, Houston TX 77204)*, PH Geil *(Natl Center for Composite Mat Res, Col of Eng, Univ of Houston, 1304 W Green St, Urbana IL 61801)*, SS Wang *(Univ of Houston, Houston TX 77204)*. J Composite Mat 27(9) 862-885 (1993).

This is part of a series of articles on the properties of thermoplastic polyamide matrix [PACM-12, DuPont, poly(bis-4-4'-dicyclohexylmethane) n-dodecane-diamide]/graphite fiber (AS4, Hercules) composite. The structural characterization of the neat resin by differential scanning calorimetry (DSC) and X-ray diffraction as a function of processing history is described here. PACM-12, considered a representative thermoplastic matrix polymer for advanced composites, as well as an engineering plastic, is partially crystalline (ca 20%) under normal composite processing conditions, but can be quenched to a completely amorphous state. The complex DSC results are shown to result, at least in part, from the presence of a different crystal structure in slow cooled PACM-12 than in quenched, annealed or fiber samples, to a melting-re-crystallization-melting process during heating and to the effect of heating rate.

9A204. **Anelastic deformation of a thermoplastic-matrix fiber composite at elevated temperature Part II.** Time-temperature dependent matrix behavior. - A Miyase *(Dept of Mech Eng, Univ of Houston, Houston TX 77204)*, AW-L Chen *(Eastman Kodak, Rochester NY)*, PH Geil *(Natl Center for Composite Mat Res, Col of Eng, Univ of Illinois, Urbana IL 61801)*, SS Wang *(Dept of Mech Eng, Univ of Houston, Houston TX 77204)*. J Composite Mat 27(9) 886-907 (1993).

The tensile deformation and failure behavior, dynamic mechanical properties and creep behavior of PACM-12 (DuPont, poly(bis 4-4' dicyclohexylmethane n-dodecanediamide), a representative thermoplastic polymer for use as a matrix in advanced composites and as an engineering plastic, as a function of processing history are described. Although injection molded PACM-12 fails in a brittle fashion at room temperature, completely amorphous PACM-12 is ductile; the difference is attributed to variations in cooling in the interior of the samples due to sample thickness effects. Partially crystalline samples are brittle at room temperature, with all samples being ductile near and above T_g. A master creep curve for the partially crystalline samples can be obtained by horizontal shift alone.

9A205. **Anelastic deformation of a thermoplastic-matrix fiber composite at elevated temperature Part III.** Structure and thermomechanical properties of AS4-PACM-12 composite. - A Miyase, SS Wang *(Dept of Mech Eng, Univ of Houston, Houston TX 77204)*, AW-L Chen *(Eastman Kodak, Build 35 Kodak Park, Rochester NY 14650)*, PH Geil *(Dept of Mat Sci and Eng, Univ of Illinois, Urbana IL 61801)*. J Composite Mat 27(9) 908-920 (1993).

Structural characterization of AS4-graphite fiber-PACM-12 matrix composites was conducted using Differential Scanning Calorimetry (DSC) and Wide-Angle X-Ray Diffraction (WAXD) analyses. The DSC results indicate the significant effect of processing variables on the morphology, microstructure and crystallinity of the fiber reinforced semicrystalline thermoplastic matrix prepreg and unidirectional laminates. From WAXD results the crystallinity was determined. Time-temperature dependent thermomechanical properties of the laminates were evaluated using dynamic mechanical spectroscopy and creep compliance measurements. Dynamic mechanical spectra revealed the matrix-dominated time-temperature dependent behavior of the laminate under torsional loading. Elevated temperature creep compliance in the longitudinal direction showed time-temperature independent behavior whereas transverse creep deformation was found to be significantly time-temperature-stress dependent.

9A206. **Application of the statistical strength model of fiber-reinforced composites.** - YT Zhu and Guisheng Zong *(Center for Mat Sci and Eng, Univ of Texas, Austin TX 78712-1063)*. J Composite Mat 27(9) 944-959 (1993).

Further research was done on the previously reported unidirectional fiber-reinforced composite tensile strength model so as to overcome the mathematical difficulties in its applications. A computer program was developed to calculate the composite strength based on the composite strength model. With this computer program, the composite tensile strength can be directly calculated once certain basic fiber and matrix properties are known. Comparisons with several other composite strength models showed that this model has the best agreement with experimental data and is relatively easy to use. Applications of this model to the composite strength design were also discussed.

9A207. **Cavity formation during tensile straining of particulate and short fibre metal matrix composites.** - AF Whitehouse and TW Clyne *(Dept of Mat Sci and Metall, Univ of Cambridge, Pembroke St, Cambridge CB2 3QZ, UK)*. Acta Metall Mat 41(6) 1701-1711 (Jun 1993).

The formation of cavities in commercially pure aluminium composites, made by both powder and casting routes and reinforced with alumina (short fibres, angular particles and spherical particles), has been monitored using periodic density measurements during tensile testing and microstructural examinations. Stable cavities always form well before final failure, usually adjacent to the reinforcement, particularly when it is elongated in the loading direction and has a relatively flat surface normal to the stress axis. A simple geometrical model is proposed, allowing prediction of the failure strain as a function of the reinforcement content, aspect ratio and strain to failure of the unreinforced matrix. The data presented are in good agreement with predictions from this model.

9A208. **Dimensioning and numerical modeling of metal fiber reinforced concrete (MFRC) structures.** - P Rossi and X Wu *(Lab Central des Ponts et Chaussees, 58 Blvd Lefebvre, 75732 Paris Cedex 15, France)*. Cement & Concrete Composites 14(3) 195-198 (1992).

This paper discusses points related to the inclusion of MFRCs in French design rules and to numerical modeling (FEM) of these fibrous composite materials. It is shown that as the use of these design rules for dimensioning of fiber reinforced concrete structures leads to an inoperative result, it is necessary to develop numerical modeling to justify, mechanically, the interest in this type of application. In this framework, a numerical modeling method is proposed.

9A209. **Effects of material properties and crush conditions on the crush energy absorption of fiber composite rods.** - WH Tao, RE Robertson *(Dept of Mat Sci and Eng, Univ of Michigan, Ann Arbor MI 48109-2136)*, PH Thornton *(Ford Motor, Dearborn MI 48121-2053)*. Composites Sci Tech 47(4) 405-418 (1993).

Crushing along the fiber axis of unidirectional E-glass fiber composite rods was examined to determine the effects of fiber volume fraction, fiber diameter, matrix compressive yield strength, crush rate, fiber surface treatment, and crush plate geometry. The volume specific energy absorption was found to increase with fiber content, fiber diameter, matrix yield strength, and crush rate. The crush load stability was found to be independent of fiber content and fiber diameter but not of matrix yield strength. The crush load became less stable as the yield strength increased. The crush behavior of specimens containing clean fibers was about the same as with sized fibers, but specimens with a release agent on the fiber surface crushed with less energy absorption that decreased even as the fiber content increased, but the crush load was more stable than with sized or clean fibers. The volume specific energy absorption was greater when the rod specimens were crushed against concave surfaces than against a flat plate. A relatively simple model was able to account for the dependence of the energy absorption on fiber volume fraction and matrix yield strength.

9A210. **FE simulation of the micromechanics of interlayered polymer-fiber composites: A study of the interactions between the reinforcing phases.** - V Nassehi, J Dhillon, L Mascia *(Loughborough Univ of Tech, Loughborough, Leicestershire LE11 3TU, UK)*. Composites Sci Tech 47(4) 349-358 (1993).

FE analysis has been applied to study the mechanical behavior of composites with ductile thermoplastic and rubbery interlayers between fibers and matrix. The stress distribution in the transverse direction and the interactions between fibers was investigated with particular emphasis on the effect of varying the modulus and thickness of the interlayers. The results of the analysis show that the use of interlayers is more beneficial at higher fiber volume fractions in enhancing the energy absorbing capabilities of a polymer-fiber composite. In particular, ductile interlayers are clearly shown to have a less detrimental effect than rubbery interlayers on the modulus of coated fiber composites.

9A211. **Interlaminar shear test for fibre-reinforced plastics.** - E Sideridis *(Eng Sci Dept, Tech Univ, Athens, Greece)*, JN Ashton, R Kitching *(Dept of Mech Eng, Univ of Manchester, Inst of Sci and Tech, Manchester, UK)*. Proc Inst Mech Eng E 207(E1) 61-74 (1993).

The measurement of the interlaminar shear strength of glass-reinforced plastic laminates is proposed using an offset four-point bend test on a beam where two (P) of the four forces differ from the other two (Q) and the ratio $\lambda = P/Q$ depends upon the relative positions along the beam. The paper describes the development of this test which appears simpler, more economic and more realistic in many aspects than other test methods. It is demonstrated theoretically and experimentally that the span length (L), thickness (t) and the ratio λ are important test parameters in determining whether the failure is by shear or by flexure.

9A212. **Plastic strain distribution and texture development in fiber composites.** - RE Bolmaro, FM Guerra, UF Kocks, RV Browning *(Center for Mat Sci, LLNL)*, PR Dawson *(Dept of Mech and Aerospace Eng, Cornell)*, JD Embury, WJ Poole *(McMaster Univ, Hamilton, ON, Canada)*. Acta Metall Mat 41(6) 1893-1905 (Jun 1993).

A model situation – plane-strain deformation of a composite with many infinitely long, regularly arranged, undeformable fibers perpendicular to the plane of straining – has been analyzed by FE simulation of an isotropic continuum and subsequent polycrystal simulation of texture development for the strain and rotation paths of some characteristic material points. The principal effect of the inclusions is a change in flow pattern in the area far away from them; by comparison, "dead-zone" or "cluster" effects in the immediate vicinity of the inclusions are quite small in extent. The changed flow pattern in about half the matrix material consists of shears and rotations that change both with progressing deformation and with location.

9A213. **Prediction of the overall moduli of a cylindrical short-fiber reinforced composite.** - Shanyi Du and Linzhi Wu *(Harbin IT, Harbin 150006, China)*. Acta Mech Sinica 9(1) 53-60 (1993).

With respect to the effective elastic moduli of the composite, the present theory differs from both Eshelby's equivalent inclusion method and Hill's self-consistent one, both of which only consider the mechanical properties of the matrix and the inclusion (fibers). In fact, the inclusion-inclusion interaction is more pronounced when the volume fraction of inclusions of the composite increases. Hence, in this paper the effective elastic moduli of the composite are derived by taking into account the shapes, sizes, and distribution of inclusions, and the interactions between inclusions.

9A214. **Temperature resistant glass fiber-epoxy composites.** - W Eichberger *(Isovolta, Osterreichische Isolierstaffwerke AG, A-2355 Wiener Neudorf, Austria)*. Composite Struct 24(3) 205-212 (1993).

This paper deals with a new group of epoxy-resin based composites developed by Isovolta which exhibit properties close to those of expensive advanced composites but with price levels closer to those of conventional thermosetting composites. Efforts in the field of epoxy resin chemistry led to the development of a special resin-hardener system, the so-called Isoval system, which is used to produce laminates that have served the electrical industry for many years. Continuing improvements of this resin system and in-depth studies of the properties of those laminates showed that they possess vastly superior temperature and chemical resistance in comparison to standard epoxy resin composites. Laminates and prepregs based on this resin system (Isoval and Isopreg) offer composites which are economical, have long-term temperature endurance between 180 and 200°C and can be heated to temperatures up to 300°C for short periods of time.

9A215. **Unit cell geometry of 3D braided structures.** - Guang-Wu Du and Frank K Ko *(Fibrous Mat Res Lab, Drexel Univ, Philadelphia PA 19104)*. J Reinforced Plastics Composites 12(7) 752-768 (Jul 1993).

The traditional approach used in modeling of composites reinforced by 3D braids is to assume a simple unit cell geometry of a 3D braided structure with known fiber volume fraction and orientation. In this article, we first examine 3D braiding methods in the light of braid structures, followed by the development of geometric models for 3D braids using a unit cell approach. The limiting geometry has been computed by establishing the point at which yarns jam against each other. Using this factor makes it possible to identify the complete range of allowable geometric arrangements for 3D braided preforms.

See also the following:

9A251. Pseudo-transient large-deflection elastic analysis of fibre reinforced composite plates
9A296. Direct processing of continuous fibers onto injection molding machines
9A298. Simultaneous process of filament winding and curing for polymer composites
9A317. Mode I fatigue cracking in a fiber reinforced metal matrix composite
9A347. Creep and creep damage of glass fiber reinforced polypropylene
9A351. Physical aging in the creep behavior of thermosetting and thermoplastic composites
9A386. Actual contribution of crack deflection in toughening platelet-reinforced brittle-matrix composites
9A388. Damage development in a short fiber reinforced composite
9A394. Fracture strength testing of δ-alumina fibers with variable diameters and lengths
9A396. Matrix cracking and modulus reduction during the fatigue of an injection-moulded glass-nylon composite
9A397. Micromechanical elastic cracktip stresses in a fibrous composite
9A398. Mixed-mode delamination of fibre composite materials
9A404. Pull-out of fibres with a branched structure and the interference of strength and fracture toughness of composites
9A405. Role of coatings in axial tensile strength of long fiber reinforced metal-matrix composites
9A843. Aspects of residual thermal stresses in continuous-fiber-reinforced ceramic matrix composites
9A844. Effects of thermal residual stresses and fiber packing on deformation of metal-matrix composites

256H. LAYERED MEDIA

9A216. **Compression of laminated composite beams with initial damage.** - NL Breivik, Z Gurdal, OH Griffin JR *(Dept of Eng Sci and Mech, VPI)*. J Reinforced Plastics Composites 12(7) 813-824 (Jul 1993).

Compression testing is conducted for specimens with well-documented initial damage states obtained from three-point bending testing. Strengths and failure modes are determined for specimens with four quasi-isotropic stacking sequences and two thicknesses. Initial damage prior to compression testings is divided into three classifications based on the extent and location of the damage. It was found that specimens with short multiple delaminations experienced the greatest reduction in compression strength compared to the undamaged specimens. All of the sublaminates formed by the delamination failed at the same time with no indication of sublaminate buckling.

9A217. **Design of composite laminates by a Monte Carlo method.** - Chin Fang and GS Springer *(Dept of Aeronaut and Astronaut, Stanford)*. J Composite Mat 27(7) 721-753 (1993).

A Monte Carlo procedure was developed for optimizing symmetric fiber reinforced composite laminates such that the weight is minimum and the Tsai-Wu strength failure criterion is satisfied in each ply. The laminate may consist of several materials including an idealized core, and may be subjected to several sets of combined in-plane and bending loads. The procedure yields the number of plies, the fiber orientation, and the material of each ply and the material and thickness of the core. A user friendly computer code was written for performing the numerical calculations. Laminates optimized by the code were compared to laminates resulting from existing optimization methods.

9A218. **Finite-rotation theories for composite laminates.** - Y Basar *(Inst Konstruktiven Ingenieurbau, Ruhr-Univ Bochum, Lehrstuhl Statik und Dynamik, D-W 9630 Bochum, Germany)*. Acta Mech 98(1-4) 159-176 (1993).

For the FE analysis of arbitrary composite laminates various finite-rotation theories are presented in a single formulation. First a refined theory is derived which allows a quadratic shear deformation distribution across the thickness. The so-called difference vector appearing in the kinematic relations is expressed in terms of rotational dof permitting a clear determination of the deformed normal vector in every nonlinear range. The constitutive relations derived are applicable to orthotropic material properties varying arbitrarily across the thickness and to curvilinear laminate coordinates as well. This refined theory is then transformed into simplified theories of Kirchhoff-Love and Mindlin-Reissner types.

9A219. Mechanical properties for CFRP-damping-material laminates. - Jun Fujimoto, Tetsuya Tamura *(Resources and Env Protection Res Lab, NEC, 1-1 Miyazaki 4-chome Miyamae-ku Kawasaki, Kanagawa 216, Japan)*, Kazuhide Todome *(Space Dev Div, NEC, 4035 Ikebe-cho Midori-ku Yokohama, Kanagawa 227, Japan)*, Toshio Tanimoto *(Dept of Mat Sci and Ceramic Tech, Shonan IT, 1-1-25 Tsujido-nishikaigan Fujisawa, Kanagawa 251, Japan)*. J Reinforced Plastics Composites 12(7) 738-751 (Jul 1993).

New materials that possess high damping capabilities and have high strength properties have been studied in carbon fiber reinforced plastics (CRFP). These materials are referred to in this article as CFRP-damping-material laminates. The CFRP-damping-material laminates investigated here are composed of a unidirectional carbon-epoxy prepreg sheet and a polyethylene-based damping material sheet used as an interleaf. Cantilever beam tests revealed the high damping properties of these laminates. Tensile test results for quasi-isotropic laminated based composites indicated that the damping material interleaf is effective for suppressing delamination and multiple splitting in the 0° angle layer.

9A220. Probabilistic methods for the calculation of laminate properties. - HL McManus *(Rm 33-311, MIT)*. J Reinforced Plastics Composites 12(6) 712-722 (Jun 1993).

A method for calculating the properties of advanced composite laminates, including their variations due to known variations in the properties of the individual plies and the laminate geometry, is presented. The method is useful for understanding scatter in the measured properties of composite laminates. The scatter is particularly important in the design of ultra-low coefficient of thermal expansion (CTE) laminates. Such laminates are designed with a theoretically zero CTE, but in practice have a distribution of non-zero CTEs. Information useful for designing ultra-low expansion laminates is discussed.

See also the following:

9A2. FE analysis of vibration and damping of laminated composites
9A47. Large amplitude vibration of antisymmetric imperfect cross-ply laminated plates
9A159. Stress concentration around holes in composite laminates with variable fiber spacing
9A160. Stress concentration in the bending of sandwich beams with transversely flexible core
9A241. Detachment of an elastic beam from a viscoelastic support: A variational approach
9A242. Mechanics of thin-walled laminated composite beams
9A250. Bending analysis of laminated plates using a refined shear deformation theory
9A265. Effect of varying the support conditions on the buckling of laminated composite plates
9A389. Delamination growth in composite plates subjected to transverse loads
9A391. Effects of fabric weave and surface texture on the interlaminar fracture toughness of aramid-epoxy laminates
9A399. Modeling of anisotropic damage at a crack tip in composite laminates
9A400. Modelling of 90° ply cracking in crossply laminates, including 3D effects
9A402. Phenomenon of curved microcracks in $[(S)/90_n]_s$ laminates: Their shapes, initiation angles and locations
9A403. Prediction of delamination in composite laminates subjected to low velocity impact
9A455. Active control of composite plates using piezoelectric stiffeners
9T578. Stress analysis and testing of parallel and tapered adhesive butt joints

256J. MICROMECHANICS

9A221. From micro to macroproperties of polymer based composite systems by integration of the characteristics of the interphase regions. - AH Cardon *(Composite Syst and Adhesion Res Group of the Free Univ Brussels, VUB TW-KB, Pleinlaan 2, B-1050 Brussels, Belgium)*. Composite Struct 24(3) 213-217 (1993).

After an overview and discussion about the amount of information on the interphase region given by classical "single number" characterization methods such as ILST, pull-out and fragmentation tests, different models of the interphase region considered as classical continuum are analyzed. A model is proposed, based on an interphase region with varying properties. By integration of those varying properties over the thickness of the interphase region, from the bulk properties of one phase to those of the other phase, assuming the transverse dimensions as very small, the control parameters, or integrated moduli, of the interphase region are obtained. This model indicates the importance of the gradients of the properties of the interphase region on the stress transfers between the original phases. The application of this model under specific stress states used for the classical mechanical "single number" tests can give insight in the physical meaning of the results of those tests and can give a rational way to compare the scales for the results of those tests.

9A222. Micromechanical behavior of Kevlar-149 and S-glass hybrid seven-fiber microcomposites I. Tensile strength of the hybrid composite. - Yiping Qiu *(Dept of Mech Eng, MIT)* and P Schwartz *(Fiber Sci Program, Cornell)*. Composites Sci Tech 47(3) 289-301 (1993).

To understand the mechanism of the hybrid effect on the tensile properties of "hybrid" composites, single fiber type and hybrid microcomposites were fabricated by using Kevlar-149 as the low elongation fiber and S glass fibers as the high elongation fiber, in a DER 331-DER 732 epoxy mixture (70/30, w/w). Kevlar-149 fiber showed a significantly higher tensile strength in the microcomposite than as a single filament. For the hybrid, Kevlar-149 fibers usually broke one by one. A positive hybrid effect for the failure strain but a negative hybrid effect for the strength of the hybrid were observed. Tensil strength of the microcomposites predicted by Monte Carlo simulation agreed with the experimental results reasonably well. The tensile modulus of the hybrid followed the rule of mixtures.

9A223. Micromechanical behavior of Kevlar-149 and S-glass hybrid seven-fiber microcomposites II. Stochastic modeling of stress-rupture of hybrid composites. - Yiping Qiu *(Dept of Mech Eng, MIT)* and P Schwartz *(Fiber Sci Program, Cornell)*. Composites Sci Tech 47(3) 303-315 (1993).

To understand the stress-rupture behavior of hybrid composites, single-fiber type (SFT) and hybrid microcomposites were fabricated with Kevlar 149 as the low-elongation fiber and S-glass as the high-elongation fiber in a DER 331-DER 732 epoxy mixture (70/30, w/w). The microcomposites were stress-rupture tested at 80, 85, and 90% of their Weibull scale parameters for tensile strength. Both the model and the stress-rupture tests of the hybrid and Kevlar 149 SFT microcomposites indicated that there is a negative hybrid effect for lifetime at high stress ratio while a positive hybrid effect exists at low stress ratio. The higher fraction of the total load for each LE fiber was responsible for the negative hybrid effect at high stress ratio, while smaller static and dynamic overstress was beneficial to the positive hybrid effect at low stress ratio.

9A224. Microstructure and mechanical properties of mullite-zirconia reaction-sintered composites. - R Torrecillas *(Inst Tec Mat, 33428 Llanera, Asturias, Spain)*, JS Moya, S De Aza *(Inst Ceramica, Vidrio CSIC, Arganda del Rey, 28500 Madrid, Spain)*, H Gros, G Fantozzi *(GEMPPM INSA de Lyon, 69621 Villeurbanne, Cedex, France)*. Acta Metall Mat 41(6) 1647-1652 (Jun 1993).

The flexural strength, fracture toughness (K_{IC}), creep behavior and thermal shock of mullite-zirconia and mullite-zirconia-alumina composites obtained by reaction-sintering of zircon + alumina mixtures have been studied in the temperature interval ranging from room temperature to 1400° C. The results are discussed in terms of the microstructural features of the reaction-sintered composites.

See also the following:

9A213. Prediction of the overall moduli of a cylindrical short-fiber reinforced composite
9A847. Residual thermal stresses in filamentary polymer-matrix composites containing an elastomeric interphase

256L. MACROSCOPIC CHARACTERIZATION

9A225. Young's modulus of a composite: Reinforced with (n - 1) different inclusions. - S Rajesh *(Sharma Inst, Shimla View Cottage, Chakkar Shimla 171 005, India)* and S Anupam *(Dept of Civil Eng, Rec - Rourkela, Orissa 769 008, India)*. J Reinforced Plastics Composites 12(6) 670-676 (Jun 1993).

A mathematical result is obtained for estimating the overall longitudinal Young's modulus of a unidirectional composite reinforced with (n - 1) different inclusions, so as to have an in-depth study of the work, which was restricted to two phase composite body. The distribution of stresses and strains are discussed in accordance with the corresponding elastic energies and the mixture is assumed to possess the properties described.

See also the following:

9A193. Bounds and estimates of overall moduli of composites with periodic microstructure
9A213. Prediction of the overall moduli of a cylindrical short-fiber reinforced composite
9A273. Effective properties of piezoelectric composites with spheroidal inclusions

256N. DYNAMIC BEHAVIOR

9A226. Aspects of dynamic mechanical analysis in polymeric composites. - M Akay *(Dept of Mech and Indust Eng, Univ of Ulster, Newtownabbey Co Antrim, N Ireland BT37 0QB, UK)*. Composites Sci Tech 47(4) 419-423 (1993).

Patterns of behavior of dynamic and mechanical properties in the glass transition region have been considered and it is shown that the tan δ peak always occurs at a higher temperature than the E" peak. The temperature interval between the peaks varies significantly in unidirectional carbon-fiber-epoxy laminates, depending on the fiber orientation with respect to the applied load. The E" peak is shown to be a more consistent indicator of the behavior of the composites. Fiber incorporation reduces viscoelastic damping beyond that possible by matrix volume reduction alone. This was observed in various fiber reinforced polymers and is explained in terms of fiber matrix interactions.

9A227. Experimental study on the use of static effective modulus theories in dynamic problems. - JJ Ditri and JL Rose *(Dept of Eng*

Sci and Mech, 114 Hallowell Bldg, Penn State). J Composite Mat 27(9) 934-943 (1993).

In a recent paper the effective elastic constants of a $[0, \pm45, 0]_{34}$ graphite epoxy laminated composite were determined by ultrasonic wave velocity information, and the Young's moduli calculated from these constants were compared to those obtained using a quasi-static loading technique for six different directions. In this article, the previously obtained results are compared to those predicted using a 3D static effective modulus theory. It is shown that, if low frequency ultrasonic waves are used, the calculated Young's moduli compare favorably with both the static measurements and those predicted by the effective modulus theory. Comments on the applicability of the various measurement techniques for different purposes are also discussed.

9A228. **Impact characterization of graphite fiber reinforced thermoplastic laminates.** - J Chaudhuri, GH Choe *(Dept of Mech Eng, Natl Inst for Aviation Res, Wichita State Univ, Wichita KS 67208)*, JR Vinson *(Dept of Mech Eng, Univ of Delaware, Newark DE 19716)*. J Reinforced Plastics Composites 12(6) 677-685 (Jun 1993).

Instrumented drop-weight impact testings were conducted in conjunction with the ultrasonic C-scan and scanning electron microscopy to characterize the impact response at low velocities. Thermoplastic composite materials in the simply supported case showed dramatic improvements in impact damage resistance compared to the thermoset composite materials as reported. Scanning electron microscopy examination of the fracture surface revealed fiber-matrix-debonding, fiber pull-out, and few delaminations. Matrix behavior can be characterized by a hackly appearance.

See also the following:

9A315. Evaluation of composites under dynamic load
9A392. Evaluation of the stress intensity factor of brittle polymers based on the crack arrest concept

256Q. STRUCTURAL APPLICATIONS

9A229. **Composites with multiple cutouts.** - TJ Walsh and OO Ochoa *(Center for Mech of Composites, Dept of Mech Eng, Texas A&M Univ, College Station TX 77843-3123)*. Composite Struct 24(2) 117-124 (1993).

An experimental and analytical study of composite coupons and panels with multiple cutouts are presented. Coupons with circular and rectangular cutouts with aligned and staggered hole configurations were examined under tensile loads. 2D and 3D FE analysis is utilized to predict in-plane and interlaminar stress response, respectively. A stiffened hat panel is selected as the structural component to illustrate the effects of cutouts in actual composite parts. Throughout testing, C-scans and X-ray photographs were utilized to document the damage formation. Both numerical and experimental results highlighted the presence of reduced stress fields in the vicinity of the rectangular cutout versus the circular.

9A230. **Construction and analysis of high performance composites.** - B Knauer *(Inst fur Luftfahrttechnik und Leichtbau EV, Elsasser str 7/204, 0-8019, Dresden, Germany)*. Composite Struct 24(3) 181-191 (1993).

High performance composites are defined here, and they are classified in a general survey of polymer composites. The memory and computer aided design will be promoted and generalized. For calculations, refer to norm-standards and software. The proof of reliability has been calculated by the method of marginal maintains. The designing of, and the designing with high performance composites will be based on the static, dynamic, and tribologic load.

9A231. **Experimental and analytical investigation of composite drive shafts with noncircular end cross-sections.** - RS Gross *(Aerospace Eng Dept, Auburn Univ, 211 AE Bld, Auburn AL 36849)* and JG Goree *(Dept of Mech Eng, Clemson Univ, Clemson SC 29634)*. J Composite Mat 27(7) 702-720 (1993).

An optimization methodology is presented for the selection of the end cross-sectional shape of composite torque tubes (drive shafts) with noncircular end geometries. In a typical application, metal inserts are adhesively bonded in the ends of the tubes to allow for torque transmission. The worst case scenario of bond failure with subsequent torque transmission via insert-tube contact is considered. Optimization of the tube end cross-sectional shape under this worst case situation is the goal of this study. This methodology is verified through comparison with experimental data. Results obtained from the analytical and experimental studies indicate a spline-like cross-sectional shape as the optimal design.

See also the following:

9A393. Fracture analysis of dental composites
9T578. Stress analysis and testing of parallel and tapered adhesive butt joints
9A846. Recent developments of thermosetting polymers for advanced composites

256V. PLASTICS, ELASTOMERS, RUBBERS

See the following:

9A22. Simulating the non-isothermal mixing of polymer blends using the BEM

256Y. COMPUTATIONAL TECHNIQUES

9A232. **Analysis of thin-walled composite beams by energy method.** - KB Subrahmanyam *(Dept of Mech Eng, NBKR Inst of Sci and Tech, Vidyanagar 524 413 Nellore District, Andhra Pradesh, India)*. J Reinforced Plastics Composites 12(6) 642-669 (Jun 1993).

Utilization of fiber reinforced plastics in the aerospace structures has become commonplace recently. However, considerable amount of research work is needed to understand the various coupling phenomena that arise from the use of the FRP materials, and in efficiently modeling the coupling behavior in analytical formulations. The present effort describes the formulation and solution of FRP box beam type of structures through the use of the total potential energy functional in conjunction with the Ritz method. Results obtained from the present effort are compared to those obtained from a FE formulation and also to those from experimental results available in the literature.

9A233. **Overall potentials and extremal surfaces of power law or ideally plastic composites.** - PM Suquet *(Lab Mec Acoustique, CNRS, 31 Chemin Joseph Aiguier, 13402 Marseille Cedex, 20, France)*. J Mech Phys Solids 41(6) 981-1002 (Jun 1993).

A method is proposed for bounding the overall properties of a class of composite materials in terms of the properties of the individual phases and of their arrangements. It applies to power law materials and, as a special case, to rigid ideally plastic materials. A link between the overall potential of a nonlinear composite and the overall energy of a fictitious linear composite is presented with no assumptions on the arrangement of the phases. With this method, any upper bound available for linear materials can easily be transposed to nonlinear materials. A new characterizing of the extremal surface of ideally plastic composites is given.

See also the following:

9A12. Verification of a general-purpose laminated composite shell implementation: Comparisons with analytical and experimental results
9A243. Linear and geometrically nonlinear analysis of composite beams under transverse loading
9A262. Euler buckling of pultruted composite columns

256Z. EXPERIMENTAL TECHNIQUES

9A234. **Analysis of a mini-sandwich compression test specimen.** - Seng C Tan *(Wright Mat Res, PO Box 31667, Dayton OH 45431)*. Composites Sci Tech 47(4) 369-382 (1993).

Mini-sandwich compression specimens have been analyzed by using a rule-of-mixtures approach and a FEM which takes into account the mechanical and nonmechanical loadings. The results of stress analysis are illustrated for an $[(AS4/3501\text{-}6)/3501\text{-}6]_s$ specimen and an $[(AS4/APC\text{-}2)/APC\text{-}2]_s$ specimen as examples. Both specimen configurations contain face sheets consisting of two plies of 0° orientation. The compressive strengths of these two unidirectional composites were computed from the experimentally measured strengths of the minisandwich specimen and the stress state predicted by the present analysis. The present result shows that a rule-of-mixtures approach can cause considerable error in the interpretation of the compressive strength of unidirectional face sheets. Procedures for the accurate determination of the compressive strength of the face sheets for mini-sandwich specimens are presented. A simplified nonlinear approach reveals that it is important to consider the final tangent or secant material properties rather than the initial material properties to obtain accurate stress distributions of the specimen prior to failure.

9A235. **Four-point bending tests on off-axis composites.** - M Grediac *(Dept Mec and Mat, Ecole Natl Superieure des Mines de Saint-Etienne, 158, cours Fauriel, 42023 Saint-Etienne Cedex 2, France)*. Composite Struct 24(2) 89-98 (1993).

This paper deals with the accurate measurement of longitudinal off-axis bending compliances of composites using four-point bending tests. The effect of supports that induce additional twisting moments is examined analytically, numerically, and experimentally. A new testing device allowing the rotation of the tested sample about its principal axis is described and used to assess longitudinal bending compliances of several specimens. It is shown that usual four-point bending devices provide apparent compliances that are lower than actual ones.

9A236. **Measurement of residual stresses in sapphire fiber composites using optical fluorescence.** - Qing Ma and DR Clarke *(Mat Dept, UC, Santa Barbara CA 93106)*. Acta Metall Mat 41(6) 1817-1823 (Jun 1993).

The residual stresses in c-axis sapphire fibers in a γ-TiAl matrix and in a polycrystalline Al_2O_3 matrix as a function of distance below a surface are determined. They are obtained from the shift in frequency of the characteristic R_2 fluorescence line of chromium in sapphire obtained by focusing an optical probe at different depths in a sapphire fiber intersecting the surface of the composite. The method is described together with its calibration. Both the axial and radial components of the residual stress in the fiber are observed to vary over a depth of approximately the fiber diameter and are then almost independent of depth.

9A237. Whole-field strain analysis of the Iosipescu specimen and evaluation of experimental errors. - YM Xing, CY Poon, C Ruiz *(Dept of Eng Sci, Univ of Oxford, OX1 3PJ, UK)*. Composites Sci Tech 47(3) 251-259 (1993).

A whole-field strain analysis is performed on the Iosipescu specimen by both moire interferometry and the FEM. The strain distribution outside and within the test section is examined for a graphite-epoxy woven (0°, 90°) laminate specimen. The effect of factors such as twist, bending moment and loading points, which cause the experimental errors, is studied.

258. Cables, ropes, beams, etc

9A238. Strength and stiffness of a flexible high-pressure spiral hose. - PC Bregman *(Trelleborg BV, PO Box 33, NL-9600 AA Hoogezand, Netherlands)*, M Kuipers *(Fac of Math and Phys Sci, Dept of Math, Univ of Groningen, PO Box 800, NL-9700 AV Groningen, Netherlands)*, HLJ Teerling *(Trelleborg BV, PO Box 33, NL-9600 AA Hoogezand, Netherlands)*, WA van der Veen *(Fac of Math and Phys Sci, Dept of Math, Univ of Groningen, PO Box 800, NL-9700 AV Groningen, Netherlands)*. Acta Mech 97(3-4) 185-204 (1993).

We consider a flexible high-pressure rubber hose with separate reinforcing cylinders which each consist of one family of spiralized fibres. The straight tube is radially and axially loaded by an internal pressure. This paper gives an approximate analysis of the stresses and strains occurring in the rubber and the filaments. Some numerical values could be compared with experimental findings obtained by Trelleborg BV, Hoogezand. It appeared possible to estimate some unknown parameters, introduced in the approximate calculation model beforehand, so that a reasonable agreement between the theoretical and empirical findings could be attained.

9A239. Effect of axial restraints on the deflection of strain hardening beams. - AN Sherbourne and F Lu *(Dept of Civil Eng, Univ of Waterloo, ON, N2L 3G1, Canada)*. Int J Mech Sci 35(5) 397-423 (May 1993).

Centrally loaded, rigid-linear strain hardening rectangular beams with variable axial restraints are investigated. Load-deflection solutions are presented for beams with four common types of end conditions. It was found that the effect of strain hardening cannot be neglected, especially for beams of larger depth to length ratios. By considering strain hardening, the influence of such beam depth to length ratio on the load-deflection curve can be quantified and the length of the plastic zone estimated.

9A240. Minimizing deflection and bending moment in a beam with end supports. - SV Amiouny, JJ Bartholdi III, JH Vande Vate *(Sch of Indust and Syst Eng, Georgia Tech)*. Mech Struct Machines 21(2) 167-184 (1993).

In this paper, heuristics are given to sequence blocks on a beam, like books on a bookshelf, to simultaneously minimize the maximum deflection and maximum bending moment of the beam. For a beam with simple supports at the ends, one heuristic places the blocks so that the maximum deflection is no more than $16/9\sqrt{3} \approx 1.027$ times the theoretical minimum and the maximum bending moment is within four times the minimum. Similar results hold for beams with fixed supports at the ends.

9A241. Detachment of an elastic beam from a viscoelastic support: A variational approach. - A Drozdov and I Gertsbakh *(Dept of Math and Comput Sci, Ben Gurion Univ of the Negev, Beer-Sheva, Israel)*. Int J Mech Sci 35(6) 463-478 (Jun 1993).

The paper is devoted to the analysis of failure in multi-layer composite materials. For the experimental study of the failure mechanisms, the peel tests are used. The peel test is modeled as the detachment of an elastic beam attached to a rigid adherend by a viscoelastic adhesive layer. For solving this problem, we use the principle of minimum free energy and derive a new energy criterion for the detachment. We propose a model of aging viscoelastic material describing the viscoelastic behavior in terms of elastic objects. Using this model we propose an expression for the specific potential energy of an aging viscoelastic medium and derive a new formulation of the principle of minimum free energy for a viscoelastic system. A numerical method for solving nonlinear integro-differential equations describing the detachment process is developed, and its convergence is established. We analyze numerically the dependence of the detachment on the construction and material parameters, and on the loading history. We demonstrate the existence of a limited training effect, which allows considerable reduction of the detachment zone by a special preliminary loading program ("training").

9A242. Mechanics of thin-walled laminated composite beams. - EJ Barbero *(Dept of Mech and Aerospace Eng, W Virginia Univ, Morgantown WV 26506-6101)*, R Lopez-Anido, JF Davalos *(Dept of Civil Eng, W Virginia Univ, Morgantown WV 26506-6101)*. J Composite Mat 27(8) 806-829 (1993).

A formal engineering approach of the mechanics of thin-walled laminated beams based on kinematic assumptions consistent with Timoshenko beam theory is presented. Thin-walled composite beams with open or closed cross sections subjected to bending and axial load are considered. A variational formulation is employed to obtain a comprehensive description of the structural response. An explicit expression for the static shear correction factor of thin-walled composite beams is derived from energy equivalence. A numerical example involving a laminated I-beam is used to demonstrate the capability of the model for predicting displacements and ply stresses.

9A243. Linear and geometrically nonlinear analysis of composite beams under transverse loading. - K Chandrashekhara *(Dept of Mech and Aerospace Eng and Eng Mech, Univ of Missouri, Rolla MO 65401)* and KM Bangera *(EGS Inc, Oak Park MI 48237)*. Composites Sci Tech 47(4) 339-347 (1993).

The flexural analysis of fiber-reinforced composite beams based on a higher-order shear deformation theory is studied. The geometric nonlinearity is incorporated in the formulation by considering the von Karman strains. The FEM is used to solve the nonlinear governing equations by direct iteration. Unlike conventional beam models, the present beam model accounts for y direction strains. It is observed that the solution obtained from the two approaches differ slightly in the case of cross-ply laminates, but there exists a considerable difference in the case of angle-ply laminates. The influence of boundary conditions, beam geometries, and ply orientations on the deflections and stresses of laminated beams is shown both in tabular and graphical form.

9A244. NDT and structural condition monitoring of mechanical cables. - PAA Laura *(Inst of Appl Mech (CONICET-SENID-ACCE) and Dept of Eng, Univ Nacional del Sur, 8000 Bahia Blanca, Argentina)*. Appl Mech Rev 46(4) 133-138 (Apr 1993).

This article concerns the problem of evaluating the structural health of cables or ropes by means of non-destructive testing methods. Special emphasis is placed upon electromagnetic techniques and the acoustic emission method.

See also the following:

9A61. **Discrete modelling of wave propagation in bars with piecewise-linear characteristics**
9A189. **Strength analysis of axially symmetric elements with a series of rectangular notches**

260. Plates, shells, membranes, etc

260B. NONLINEAR AND FINITE DEFORMATION THEORY

See the following:

9A73. **Quasi-static and dynamic local loading of monolithic simply-supported steel plate**
9A75. **Experimental investigation of the scaling laws for metal plates struck by large masses**
9A988. **Mechanics of axially symmetric liposomes**

260C. PLATES (FLEXURE AND TORSION)

9A245. Cracked plates subjected to out-of-plane tearing loads. - MJ Young and CT Sun *(Sch of Aeronaut and Astronaut, Purdue)*. Int J Fracture 60(1) 1-18 (1 Mar 1993).

Cracked plates subjected to out-of-plane tearing loads were investigated using both classical plate theory and Reissner-Mindlin plate theory. It was shown that the total strain energy release rate according to Reissner-Mindlin plate theory converges to that of classical plate theory as the thickness to crack length ratio approaches zero. It was demonstrated that it is not meaningful to separate mode II and mode III strain energy release rates using classical plate theory.

9A246. Family of shear deformation theories for shallow shells. - Z Rychter *(Dept of Arhictec, Tech Univ of Bialystok, Krakowska 9, 15-875 Bialystok, Poland)*. Acta Mech 98(1-4) 221-232 (1993).

Two-dimensional shear deformation type theories for shallow elastic shells are presented as a one-parameter family embedded in a family of 3D displacement and stress fields of uniform order of accuracy throughout the range of the parameter. Families of admissible physical interpretations for the generalized displacement of shell theory are provided, allowing diverse models of geometric boundary conditions to choose from. The relationship between the parameter (shear factor) and the generalized displacements is established. As a special, degenerate case, results for Kirchhoff-Love type shell theories are derived.

9A247. Suitable microcomputer method for the bending analysis of arbitrary quadrilateral plates with general boundary conditions. - Chen Jun *(Changsha Eng Military Acad, Peoples Rep of China)*, Lanfen Li, Sjiuap Long *(Hunan Univ, Peoples Rep of China)*, Y Zhan *(Central South Univ Tech, Peoples Rep of China)*. Adv Eng Software 16(1) 7-13 (1993).

In this paper, a spline Kantorovich method on a cubic B-spline function is presented to obtain an approximate solution for the bending problem of quadrilateral plates with various boundary conditions by the variational principle and bilinear coordinate transformation. The spline Kantorovich method is a typical numerical Kantorovich method, which can, not only, transform 2D problems into 1D problems, but also has the advantages of the spline method, such as high precision and rapid convergence. A computational scheme is derived which is well suited to microcomputers. The numerical values of the deflection for arbitrary quadrilateral plates are compared with those from other investigators' methods and the FEM. The solutions to bending problems of trapezoidal, parallelogram and rectangular plates are given as particular examples.

9A248. Upper bound on the collapse load of plate bending by using a quasi-conforming element and the Monte-Carlo method. - Hexiang Lu, Limin Tang, Xiaoling Wang *(Dept of Mech, Dalian Univ of Tech, Dalian 116024, China).* Finite Elements Anal Des 13(1) 65-73 (Apr 1993).

A new method to obtain the upper bound of collapse loads for plates is given by a quasi-conforming element technique and the Monte-Carlo method in this paper. A universal velocity pattern of the collapse for arbitrarily shaped plates is given without need of experimental reference. The advantage of this method is that whenever the collapse load of the plate is calculated, the collapse velocity pattern is obtained as well.

See also the following:

9A45. Elastodynamics of thin plates with internal dissipative processes Part II. Computational aspects

9A361. Strain energy release rate for a cracked plate subjected to out-of-plane bending moment

9A463. Stress resultant FE analysis of reinforced concrete plates

260D. SHELLS (MEMBRANE THEORY)

See the following:

9A9. Consistent FE formulation of nonlinear membrane shell theory with particular reference to elastic rubberlike material

260E. SHELLS (BENDING THEORY)

9A249. Dynamic carrying capacity of elasto-visco-plastic cylindrical shells. - A Baltov, O Minchev, J Ivanova *(Dept of Solid Mech, Inst of Mech and Biomech, "Acad G Bonchev", Str Block 4, 1113 Sofia, Bulgaria).* Arch Appl Mech 63(3) 189-194 (Apr 1993).

We consider axially-compressed thin cylindrical shells, which deform elasto-visco-plastically under high intensity external impulsive loading and in which volume damage can occur. The shell carrying capacity is determined in accordance with deformation, stability and strength criteria. Our propose is, introducing special dimensionless parameters, to obtain the relation between the geometrical sizes and the material characteristics of the shell – on one hand and the dynamic impulse parameters (amplitude and duration) on the other, when the shells lose their carrying capacity.

See also the following:

9A988. Mechanics of axially symmetric liposomes

260G. STIFFENED AND SANDWICH PLATES AND SHELLS

9A250. Bending analysis of laminated plates using a refined shear deformation theory. - Ji-Fan He, Mon Chou, Xiang Zhang *(Dept of Eng Mech, Tsinghua Univ, Beijing, Peoples Rep of China).* Composite Struct 24(2) 125-138 (1993).

In this paper the refinement of a previously published discrete-layer shear deformation laminated plate theory by the assumption that the transverse shear strains across any two layers are linearly dependent on each other is briefly described. The theory contains the same dependent variables as first-order shear deformation theory, but the set of governing differential equations is of the twelfth order. No shear correction factors are required. Solutions for simply-supported symmetric and antisymmetric cross-ply plates are discussed. The numerical results are compared with 3D elasticity solutions and first-order shear deformation theory solutions. The present theory gives a better estimate of the deflections and stresses even for fairly thick laminates. For laminates of the same thickness, it is shown that the solution accuracy improves as the number of layers increases.

9A251. Pseudo-transient large-deflection elastic analysis of fibre reinforced composite plates. - T Kant and JR Kommineni *(Dept of Civil Eng, Indian IT, Powai, Bombay 400 076, India).* Eng Comput 10(2) 159-173 (Apr 1993).

A unified approach is presented for the pseudo-transient (static) linear and geometrically nonlinear analysis of composite laminates. A FE idealization with a four-noded linear and a nine-noded quadrilateral isoparametric elements, both belonging to the Lagrangian family are used in space discretization. An explicit time marching scheme is employed for time integration of the resulting discrete ordinary differential equations with the special forms of diagonal fictitious mass and/or damping matrices. The usefulness and effectiveness of this approach is established by comparing computational time required by this approach and Newton-Raphson's approach.

See also the following:

9A72. Local loading of simply-supported steel-grout sandwich plates

260H. PLATES AND SHELLS ON FOUNDATIONS

9A252. Semi-infinite plate on a Winkler base, free along the edge, and subjected to a vertical force. - AD Kerr *(Dept of Civil Eng, Univ of Delaware, Dupont Hall, Newark DE 19716)* and Soon Seop Kwak *(Dept of Architec Eng, Chung Buk Natl Univ, Cheong Ju, Chung-Buk 360-763, Korea).* Arch Appl Mech 63(3) 210-218 (Apr 1993).

At first, a brief review of published data analyzed for related problems is presented. Then a new solution is derived for the case when plate is subjected to a concentrated force at any point on the plate. As in the reviewed papers, the analysis is based on the linear bending theory of thin plates. The solution procedure utilizes the closed-form Green's function for the infinite plate, in conjunction with the Fourier integral method. The advantage of the present approach is that the characteristic response of the plate near the load is represented by the closed-form Green's function which contains the proper singularity, whereas the other terms represent the correction due to the free edge.

260I. THICK PLATES AND SHELLS

9A253. Elastic and inelastic analysis of variable thickness plates, using equivalent systems. - DG Fertis and Chin T Lee *(Univ of Akron, Akron OH).* Mech Struct Machines 21(2) 201-236 (1993).

This paper develops a closed-form solution that can be used for both elastic and inelastic analysis of thin rectangular and circular plates with variable thickness in 1D. The solution is given in the form of an equivalent system of flat plates that replaces the original variable thickness plate. At a given point, the sum of the deflections, rotations, bending moments, or bending stresses of the flat plates is equal to that of the corresponding elements of the original variable thickness plates. A simplified equivalent system of constant rigidity is also obtained, in order to reduce the mathematical complexity of the variable thickness problem. Conclusions are derived by observing the changes in the load-deflection curves and the rigidity variation along one or two dimensions of the plate.

260Y. COMPUTATIONAL TECHNIQUES

9A254. BE for plate bending analysis. - WS Venturini and JB de Paiva *(Sao Carlos Sch of Eng, Univ of Sao Paulo, Av Dr Carlos Botelho 1465, Sao Carlos, SP 13 560, Brazil).* Eng Anal Boundary Elements 11(1) 1-8 (1993).

This paper is related to the applications of BEM to practical plate bending problems in engineering. Some aspects of the boundary formulations are shown, describing particular characteristics that can be considered to improve numerical solutions. Several different ways of defining the BE system of equations are proposed. Comparisons among them are also shown emphasizing some interesting behaviors.

9A255. BE analysis of the paradox circle-polygon in plate bending. - JB de Paiva *(Eng Sch of Sao Carlos, Univ Sao Paulo, 13 560 Sao Carlos, SP, Brazil).* Eng Anal Boundary Elements 11(2) 157-163 (1993).

A BE analysis of the so-called circle polygon paradox is presented and the results show that a polygon simply-supported plate does not converge to a circular supported plate, as the number of sides increase to infinity due to the boundary condition at the corners of the polygon plate. It shows too that a polygonal plate supported only at its corners does converge to a circular supported one as the number of sides increase to infinity.

9A256. General quadrilateral multilayered plate element with continuous interlaminar stresses. - M Di Sciuva *(Dept of Aerospace Eng, Politec Torino, Corso Duca delgi Abruzzi 24, 10129 Turin, Italy).* Comput Struct 47(1) 91-105 (3 Apr 1993).

The purpose of this work is the formulation of a general quadrilateral multilayered anisotropic plate element. The plate element is formulated on the basis of a refined third-order shear deformation plate theory recently proposed by the author. The plate model makes use of a displacement field that fulfills *a priori* the geometric and stress continuity conditions at the interfaces between the layers, and requires only five generalized displacements to describe the kinematics of the laminate deformation. To test the performance of the developed plate element, both closed-form and FE-based solutions are given and compared with results from 3D elasticity and other approximate 2D plate models.

9A257. Generalized conforming quadrilateral plate element by using semi-loof constraints. - Long Zhifei *(Dept of Civil Eng, N Jiaotong Univ, Beijing 100044, China).* Commun Numer Methods Eng 9(5) 417-426 (May 1993).

A 12-DOF quadrilateral element for plate bending is formulated based on the concept of generalized compatibility and semi-Loof constraints. The element DOFs are defined with the conventional displacements at corner nodes and the semi-Loof constraints are used in the formulation. This element is a generalized conforming one which passes Irons' patch test and can be used to solve problems with complicated boundaries. When overall considerations of simplicity, accuracy and reliability are taken into account, this new element is one of the best 12-DOF quadrilateral plate-bending elements currently available.

9A258. New discrete Kirchhoff-Mindlin element based on Mindlin-Reissner plate theory and assumed shear strain fields Part I. An extended DKT element for thick-plate bending analysis. - I Katili *(Dept of Civil Eng, Univ Indonesia, Kampus UI, Depok 16 424, Indonesia)*. Int J Numer Methods Eng 36(11) 1859-1883 (15 Jun 1993).

This is the first of a two-part paper on plate bending elements with shear effects included. This paper presents a new three-node, nine-dof triangular plate bending element valid for the analysis of thick to thin plates. The element, called DKMT, has a proper rank (contains no spurious zero-energy modes), passes the patch test for thin and thick plates in an arbitrary mesh and is free of shear locking. Very good results have been obtained for thin and thick plates by the element. An extended DKQ element for thick-plate bending analysis is evaluated in Part II.

9A259. New discrete Kirchhoff-Mindlin element based on Mindlin-Reissner plate theory and assumed shear strain fields Part II. An extended DKQ element for thick-plate bending analysis. - I Katili *(Dept of Civil Eng, Univ Indonesia, Kampus UI, Depok 16 424, Indonesia)*. Int J Numer Methods Eng 36(11) 1885-1908 (15 Jun 1993).

This is the second of a two-part paper on plate bending elements with shear effects included. This paper presents a new four-node, 12-dof quadrilateral plate bending element valid for the analysis of thick to thin plates. The element called DKMQ, has a proper rank (contains no spurious zero-energy modes), passes the patch test for thin and thick plates in an arbitrary mesh and is free of shear locking. Very good results have been obtained for thin and thick plates by the element. An extended DKT element for thick-plate bending analysis is evaluated in Part I.

9A260. Performance of a reformulated four-node plate bending element in moderately thick to very thin plate applications. - D Briassoulis *(Dept of Agri Eng, Agri Univ, Athens, Greece)*. Comput Struct 47(1) 125-141 (3 Apr 1993).

This paper analyzes the behavior of a reformulated four-node Mindlin plate bending element in thin to very thin and in moderately thick element applications. The shear locking mechanism is rejected with the proposed formulation whereas machine-related locking remains the only problem potentially developed in thin element applications of the reformulated element. The solution to the machine locking problem may be achieved with the implementation of a simple technique rendering the element completely locking-free. In moderately thick element applications, the reformulated four-node plate bending element is shown to exhibit an excellent performance in accordance with Mindlin-Reissner theory.

See also the following:

9A12. Verification of a general-purpose laminated composite shell implementation: Comparisons with analytical and experimental results

9A849. Piecewise hierarchical p-version axisymmetric shell element for nonlinear heat conduction in laminated composites

262. Structural stability (buckling, postbuckling)

9A261. Design of transversely stiffened webs of I-beams. - MA Bradford *(Dept of Struct Eng, Sch of Civil Eng, Univ of New S Wales, Kensington, NSW 2033, Australia)*. J Construct Steel Res 25(3) 229-240 (1993).

The design rules for webs in shear given in the limit states British and Australian steel standards are reviewed. The semi-analytical complex finite strip method of buckling analysis is then used to obtain the elastic local buckling coefficients of the webs of I-beams subjected to shear when the restraint provided by the flanges is included. It is shown quantitatively how the flange restraint increases the local buckling coefficient above the value for a web with simply supported edges, the latter forming the basis of the strength rules in the present standards.

9A262. Euler buckling of pultruted composite columns. - EJ Barbero and IG Raftoyiannis *(Mech and Aerospace Eng, W Virginia Univ WV 26506-6101)*. Composite Struct 24(2) 139-147 (1993).

Pultruted composite structural members with open or closed thin-walled sections are being used as columns for structural applications where buckling is the main consideration in the design. An analytical model for Euler buckling is developed herein. Failure envelopes for some commercially available structural shapes are presented. The analytical model presented can be used to predict the behavior of any new material.

9A263. Large plane dynamic postcritical deformations of elastic beam. - Z Wesolowski and J Widlaszewski *(Inst of Fund Tech Res, Polish Acad of Sci, Warszawa, Poland)*. Eng Trans 40(4) 469-481 (1992).

Large elastic deformations of a prismatic beam with inextensible axis are analysed. The beam at rest is an elastic arch formed by buckling from an initially straight beam and fixing its ends. The beam is modelled as a system of rigid elements connected by means of elastic hinges. The resulting equations are integrated numerically. The initial-boundary problem is solved with the use of Lagrange multipliers at each time step. Static characteristics are obtained with the use of the dynamic relaxation method.

9A264. Lateral post-buckling analysis of beams. - G Ioannidis *(Struct Anal and Steel Bridges, Natl Tech Univ, 42 Patission St, Athens 147, Greece)*, O Mahrenholtz *(Arbeitsbereich Meerestech II, Tech Univ Hamburg-Harburg, Postfach 90 10 52, W-2100 Hamburg 90, Germany)*, AN Kounadis *(Struct Anal and Steel Bridges, Natl Tech Univ, 42 Patission St, Athens 147, Greece)*. Arch Appl Mech 63(3) 151-158 (Apr 1993).

The nonlinear lateral buckling response of prefect stocky beams in the vicinitiy of the critical bifurcational state is discussed. Attention is focused on the initial post-buckling response. This depends on the nature of the critical branching point which is explored by using a nonlinear (lateral) bending-curvature relationship. It is found that the plane of loading (associated with the major moment of inertia) looses its stability through a stable symmetric bifurcation point. Hence, the above beams are not sensitive to imperfections, exhibiting post-buckling strength.

9A265. Effect of varying the support conditions on the buckling of laminated composite plates. - Gin Boay Chai and Poh Wah Khong *(Nanyang Tech Univ, Nanyang Ave, Singapore 2263, Singapore)*. Composite Struct 24(2) 99-106 (1993).

The buckling analysis of laminated composite plates using a semi-numerical approach called the finite strip method is presented. The composite plates are subjected to in-plane compression and their boundary conditions on the unloaded edges are simulated to vary from the free condition to clamp condition using a quintic polynomial function. Along the loaded edges three different support conditions are simulated using single term trigonometric functions. The coupling influence in these laminated plates on the buckling behavior is accounted for in the analysis through the use of the reduced bending stiffness concept. The validity of the results obtained are verified by comparison with published results and experimental results. Some parametric studies towards the end of this paper give an interesting insight into the effect of changing the support conditions on the buckling behavior of laminated composite plates. The limitations using the finite strip method found in the present study are also discussed.

9A266. Thermal post buckling behavior of rectangular antisymmetric cross-ply composite plates. - G Singh, G Venkateswara Rao *(Struct Des and Anal Div, Struct Eng Group, Vikram Sarabhai Space Centre, Trivandrum 695 022, India)*, NGR Iyengar *(Dept of Aerospace Eng, Indian IT, Kanpur 108 016, India)*. Acta Mech 98(1-4) 39-50 (1993).

The thermal post buckling behavior of simply-supported, antisymmetric cross-ply plates with immovable edges is investigated in this paper. For this purpose, a one term approximation for the in-plane and transverse displacements is assumed and Rayleigh-Ritz method is used to obtain the equations of equilibrium. It is shown that nonlinear bending stiffness for such plates is direction dependent, because of an extra quadratic nonlinear term in addition to the usual cubic nonlinear term in the governing equilibrium equation. Results are presented for various plate configurations.

9A267. Shear capacity of large fabricated steel cylinders: A truss model. - KH Obaia *(Syncrude Canada, Ft MacMurray, AB, Canada)*, AE Elwi, GL Kulak *(Dept of Civil Eng, Univ of Alberta, Edmonton, AB, T6G 2G7, Canada)*. J Construct Steel Res 25(3) 211-227 (1993).

Failure of large diameter steel cylinders fabricated from hot rolled sheet steel plates and subjected to transverse beam shear occurs when large diagonal buckles develop in the panels formed by the circumferential stiffeners. The load-carrying capacity then drops to a slightly lower level than the ultimate strength level. Whereas the ultimate strength has been shown to be significantly reduced in the presence of fabrication residual stresses, the postbuckling load level is not affected. Further, this load level is stable. It is advocated, therefore, that the postbuckling load can be used as a conservative design base for calculation of shear capacity.

9A268. Elastic stability of skew laminated composite plates subjected to biaxial follower forces. - C-L Liao and Z-Y Lee *(Dept of Mech Eng, Natl Taiwan IT, Taipei, Taiwan, ROC)*. Int J Numer Methods Eng 36(11) 1825-1847 (15 Jun 1993).

The present study investigates the elastic stability of skew laminated composite plates subjected to biaxial inplane follower forces by the FEM. The plate is assumed to follow first-order shear deformation plate theory. The kinetic and strain energies of skew laminated composite plate and the work done by the biaxial inplane follower forces are derived by using tensor theory. Then, by Hamilton's principle, the dynamic mathematical model to describe the free vibration of this problem is formed. Numerical results are presented to demonstrate the effects of those parameters, such as various inplane force combinations, skew angle and lamination scheme, on the elastic stability of skew laminated composite plates subjected to biaxial inplane follower force.

9A269. Dynamic contact instability of spherical caps. - Long-Yuan Li and TCK Molyneaux *(Dept of Civil Eng, Univ of Liverpool, Liverpool L69 3BX, UK)*. Int J Impact Eng 13(3) 479-484 (Aug 1993).

This paper presents a numerical study of the dynamic contact instability of shallow spherical shells. The problem considered is that of a spherical shell loaded through a massless rigid circular plate by a sudden step load acting in the direction normal to the loading plate and along the axis of symmetry of the shell. The numerical analysis demonstrates that the system may be dynamically stable even if local snap-through buckling occurs in the central area of the spherical shell. Dynamic instability occurs only in the case where the spherical shell exhibits an overall snap-through buckling.

264. Electromagneto solid mechanics

9A270. A new method for magnetic field computation on anisotropic permanent magnets. - Fumihito Mohri *(Electron Mat Res Lab, Kaneka, 1-1 2-chome Hieitsuji Ohtsu, Shiga 520-01, Japan)*. Int J Appl Electromagnetics Mat 3(4) 241-248 (Apr 1993).

A new magnetic field computation method has been developed for simulation of magnetizing anisotropic permanent magnets. The absolute value of the magnetization and its rotational angle are chosen as the unknown variables. All material data are obtained from only two curves; the curve for the axis for easy magnetization and the curve for the axis for hard magnetization. To treat the imperfection of particle orientation simply, a new quantity, "the residual angle", and a new model, "the representative particle model" have been introduced. Two-dimensional magnetization measurement has been used to examine the method.

9A271. Large strain ferroelectrics for micromechatronics. - KR Udayakumar *(Mat Res Lab, Penn State)*, AM Flynn *(MIT Artificial Intelligence Lab, Cambridge MA 02139)*, J Chen, LE Cross *(Mat Res Lab, Penn State)*. Int J Appl Electromagnetics Mat 3(4) 307-311 (Apr 1993).

The overall intent of this work has been done to develop batch-fabricatable micromotors that can couple power to a load. Ferroelectric thin films of lead zirconate titanate (PZT) fabricated for application as flexure-wave piezoelectric micromotors are generally characterized by low speed and high torque, eliminating complex gearing. In this paper, alternate thin film material systems that engender higher strain levels through new mechanisms as active elements of an actuator are examined.

9A272. Phase change of electromagnetic wave induced by static strain. - Chau-Shioung Yeh and Chun-Bo Lin *(Inst of Appl Mech, Natl Taiwan Univ, Taipei, Taiwan, ROC)*. Int J Appl Electromagnetics Mat 3(4) 269-288 (Apr 1993).

The electromagnetic wave in a deformable body such as optical fibers will be affected by applying mechanical disturbance. Some previous investigators have focused on the phase change of the electromagnetic wave caused by strain and then applied the photoelastic theory to explain the experimental results. In this paper, we develop another approach based on coupled electromagnetic and mechanical equations for deformable electrodynamics to study the same phenomena. Constitutive equations which are derived from rational mechanics rather than measured by experiments are used to fit the coupled equations mentioned above. The relationships between electrostriction constants and elasto-optical coefficients, which are very important and valuable to make the result derived from deformable electrodynamics comparable to that from the photoelastic theory, are developed and discussed.

9A273. Effective properties of piezoelectric composites with spheroidal inclusions. - Biao Wang and Shanyi Du *(Sch of Astronaut, Harbin IT, Harbin 150006, China)*. Int J Appl Electromagnetics Mat 3(4) 289-295 (Apr 1993).

In this paper, general relations between the overall properties of piezoelectric composites and the properties of their constituents are derived. Based on the solution for an ellipsoidal inclusion in a piezoelectric material developed by Wang, it is found that the coupled elastic and electric field inside a spheroid inclusion in a transversely isotropic, piezoelectric matrix can be expressed in terms of a system of the linear algebraic equations which contains only some simple integrals. These internal fields are then used to obtain the effective constants of a piezoelectric composite.

9A274. A few properties of the resonant frequencies of a piezoelectric body. - JS Yang *(Dept of Math and Comput Sci, Fayetteville State Univ, Fayetteville NC)*. Arch Mech 44(4) 475-477 (1992).

This paper presents a constraint variational formulation for the resonant frequencies of a piezoelectric body. The formulation is in a nonnegative form which is then used to prove a few properties of the lowest resonant frequency.

9A275. Preliminary determination of measurement device position in biomagnetic research. Using a reference source. - MA Primin *(Inst of Cybernetics, Ukrainian Acad of Sci, Akademik Glushkov St 40, 252207 Kiev, Ukraine)*. Int J Appl Electromagnetics Mat 3(4) 263-268 (Apr 1993).

Analytical methods of data processing and algorithms of measurement of a reference magnetic source field are proposed and allow one to determine the measurement device position in a coordinate system associated with this source in biomagnetic investigations. Possible effects of magnetic noise, reference source dimensions, etc, to the accuracy of the inverse problem are numerically simulated.

See also the following:

9A437. Inverse problems in electromagnetic nondestructive evaluation

266. Soil mechanics (basic)

9A276. Reevaluation of the adhesive relationship between the tire and the soil. - G Komandi *(Univ of Agri Sci, Godollo, Hungary)*. J Terramech 30(2) 77-83 (Mar 1993).

The author proved in an earlier article that the shear diagram is not in accord with its mechanical definition. The shear stress cannot be zero at the beginning of the initial rising portion of the curve. Shearing is not an increasing loading process, rather it is a limiting case to which a finite shear stress belongs. On the other hand the sheared surface varies under the tire. There are kinematic reasons for this. Points on the tire surface describe a looped cycloid and they slip in a backward direction (opposite to the direction of travel) while contacting the soil. Thus the driving force, which points in the direction of travel, is the product of the shear stress of finite magnitude and the sheared area. The latter increases proportionally with slip. The author describes his equation which is based on the principles discussed above. He supports his theory with a numerical example.

9T277. Experimental characterization of dynamic soil-track interaction on dry sand. - K Watanabe *(Dept of Mech Eng, Natl Defense Acad, Hashirimizu, Yokosuka 239, Japan)*, H Murakami *(Dept of Appl Mech and Eng Sci, UCSD)*, M Kitano, T Katahira *(Dept of Mech Eng, Natl Defense Acad, Hashirimizu, Yokosuka 239, Japan)*. J Terramech 30(2) 111-131 (Mar 1993).

See also the following:

9A179. Loss of hyperbolicity in elastic-plastic material at finite strains

9A276. Reevaluation of the adhesive relationship between the tire and the soil

9T277. Experimental characterization of dynamic soil-track interaction on dry sand

268. Soil mechanics (applied)

9A278. Effects of cap thickness and pile inclination on the response of a pile group foundation by a 3D nonlinear FE analysis. - MM Zaman *(Sch of Civil Eng and Env Sci, Univ of Oklahoma, Norman OK 73019)*, YM Najjar *(Dept of Civl Mech and Env Eng, George Washington Univ, Washington DC 20052)*, A Muqtadir *(Dept of Civil Eng, Univ of Eng and Tech, Dhaka, Bangladesh)*. Comput Geotech 15(2) 65-86 (1993).

Effects of pile-cap and pile inclination on the distribution of displacements, stresses, axial forces, shear forces and bending moments in different piles in a group are investigated using a nonlinear 3D FE technique. An algorithm based on the interpolation of nodal displacements and finite difference approximation of the displacement field is developed to evaluate the bending moments and the shear forces in the piles and pile cap. Emphasis is given to identify the manner in which loads are shared by individual piles in the group.

9T279. Internal waves in a large offshore storage tank. - SK Chakrabarti *(Chicago Bridge and Iron Tech Services, Plainfield IL 60544-8929)*. J Energy Resources Tech 115(2) 133-141 (Jun 1993).

9A280. Long-term allowable tensile stresses for polyethylene geomembranes. - RR Berg *(2190 Leyland Alcove, Woodbury MN 55125)* and R Bonaparte *(GeoSyntec Consult, 5775 Peachtree Dunwood Rd, Ste 200F, Atlanta GA 30342)*. Geotextiles Geomembranes 12(4) 287-306 (1993).

The objective of this paper is to present a rational methodology for establishing long-term allowable tensile stresses for polyethylene geomembranes used in waste-containment applications. Procedures currently used in the USA do not account for all of the factors that may significantly affect this parameter. The proposed procedure is intended to address this limitation by providing a framework to account for time, temperature, exposure environment, seam response, and boundary-stress and deformation conditions. The proposed procedure is conceptually similar to procedures used to establish the long-term allowable tension for geosynthetic reinforcement.

9A281. Study of soil-geotextile interaction by an X-ray method. - M Kharchafi and M Dysli *(Inst of Soils, Rocks and Found, Fed IT, Lausanne, Switzerland)*. Geotextiles Geomembranes 12(4) 307-325 (1993).

The study presented in this paper consists of an aspect of geotextile utilization in the reinforcement of embankments and retaining walls. Emphasis was placed on the behavior of the anchorage zone. For this purpose, several pullout tests were carried out with a nonwoven geotextile and two kinds of soil: a dry sand and a damp silt. The effects of several parameters, such as the stiffness of geotextile, its anchorage length, the normal stress applied, the type of soil, and their consequences on the entire reinforced mass, such as deformability and the tension in the geotextile were studied. Some recommendations for practical design were established concerning the friction angle to take into account for the soil-inclusion, the tensile distribution in the geotextile, and the size of the soil zone influenced by the movement of the reinforcement.

270. Rock mechanics

9A282. **Deformation of brittle rocks under compression - with particular reference to microcracks.** - Chunlin Li and E Nordlund *(Div of Rock Mech, Lulea Univ, S-951 87 Lulea, Sweden)*. Mech Mat 15(3) 223-239 (May 1993).

A constitutive model for brittle rocks has been developed based on the analysis of microcracks. The macroscopic deformation of a rock is decomposed into three components: response of the rock matrix, closure of open cracks and deformation due to the fracture of microcracks. The main contribution of this approach is the prediction of macroscopic deformation induced by microcracking. The basic model units are sliding cracks. Wing cracks are initiated at tips of sliding cracks and propagated in the major loading direction. The relationships between the compressive stress, the length of the growing crack and deformation due to the fracture of cracks are established. A deformation solution to an elliptic crack is employed to describe the closure effect of an open crack under compression. The total deformation caused by the closure and fracture of cracks is obtained by the sum of the components of individual cracks. In this model, the nonlinear behavior of deformation results either from the closure of open cracks at low stress levels, or from the fracture of microcracks at high stress levels. Hysteresis is captured under cyclic loading. Comparisons of the model simulations with experimental data are presented and show good agreement in the prefailure stage.

9A283. **Fracture of rock: Effect of loading rate.** - ZP Bazant, Shang-Ping Bai, R Gettu *(Center for Adv Cement-Based Mat, NWU)*. Eng Fracture Mech 45(3) 393-398 (Jun 1993).

Fracture parameters of limestone at loading rates ranging over four orders of magnitude in the static regime are determined using the size effect method. Three sizes of three-point bend notched specimens were tested under crack-mouth opening displacement control. The fracture toughness and nominal strength decrease slightly with a decrease in rate, but the fracture process zone length and the brittleness of failure are practically unaffected. The effect of material creep on the fracture of limestone is negligible in the time range studied here. However, the methodology developed for characterizing rate effects in static fracture can be easily applied to other brittle-heterogeneous materials. The decrease of fracture toughness as a function of the crack propagation velocity is described with a power law. A formula for the size- and rate-dependence of the nominal strength is also presented.

9A284. **Factors related to propellant-driven anchoring in rock.** - Ghang Zhou *(Dept of Aeronaut, Imperial Col, London SW7 2BY, UK)* and W Goldsmith *(Dept of Mech Eng, UCB)*. Int J Impact Eng 13(3) 403-421 (Aug 1993).

The penetration into rocks comprising the ocean floor by propellant-driven model projectiles and their resistance to extraction at oblique angles were investigated both experimentally and numerically. The required static and dynamic friction coefficients between steel and rock were also measured. Targets were examined subsequent to impact by sectioning and by means of X-rays. The projectile penetration into soft sandstone target was simulated using DYNA2D. The scaling law for the oblique pull-out case has been established by using a similarity analysis.

9A285. **Thermal aspect in design of rotary drill bit supports.** - AK Dzhanakhmedov, TG Faradzhev, RA Rasulov *(M Azizbekov Azerbaigan Indus Inst, Baku, Russia)*. Sov J Friction Wear 13(6) 41-46 (1992).

Main causes of decreasing rotary bit wear resistance are considered. The rotary bit is taken as a hollow sphere with an internal source of heat. The sphere is cooled by a circulating drilling fluid from outside. While solving heat equation for the given case the temperature and thermal stress distributions are determined. With decreasing rotation velocity thermal stresses in support are shown to decrease under other conditions being equal. Thus, with the rotation velocity decreases from 400 to 25 rpm radial thermal stresses decrease more than 18 times and the tangential stresses - more than 20 times. The stress increases with duration of continuous drilling. A cooling (drilling fluid) affects significantly the heating depth of the surface layers.

272. Materials processing

272B. APPLICATIONS OF PLASTICITY THEORY

9A286. **Analysis of 3D deep drawing by the energy method.** - HS Lee *(Dept of Precision Eng and Mechatronics, Korea Adv Inst of Sci and Tech, Taejon, Korea)* and DY Yang *(R&D Dept, Prod Eng, Kia Motors, Kwang-Myung, Korea)*. Int J Mech Sci 35(6) 491-516 (Jun 1993).

A systematic approach of the energy method is proposed for analysis of 3D sheet metal forming of noncircular cups with complicated shape. In the proposed method, the whole deforming region is divided into several zones by considering the geometric characteristics and contact boundary condition. The geometric shape is expressed by sweeping the section curves defined on the boundary of each zone. Velocity fields are expressed in a similar manner by sweeping the boundary velocity functions. The solution is found through optimization of the total energy dissipation with respect to some parameters assumed in the kinematically admissible velocity field defined over each zone. In order to check the effectiveness of the present method, 3D deep drawing by the elliptic punch and the clover-type punch are analyzed and compared with the corresponding experiments. In analyzing the deep drawing process by the elliptic and clover-type punches, the total deforming region has been divided into five zones. The computed results are shown to be in good agreement with the experiment in punch load, deformed edge contour and distribution of thickness strain.

See also the following:

9A3. Deforming FEM for analysis of alloy solidification problems

272D. EXTRUSION

9A287. **Model for predicting slip velocity during extrusion with fluoropolymer processing additives.** - CW Stewart, RS McMinn, KM Stika *(EI du Pont de Nemours, Exp Sta, PO Box 80323, Wilmington DE 19880-0323)*. J Reinforced Plastics Composites 12(6) 633-641 (Jun 1993).

A molecular model, based on the concept of the activation rate theory, is developed for slip of a polymer as it flows through a die. The model correctly predicts the dependence of the apparent slip velocity of high molecular weight, linear polyethylene resins on wall shear stress, up to the onset of gross melt fracture.

272E. ROLLING

9A288. **Comparison of asymptotic and numerical rolling models for quasi-3D problems.** - ME Karabin *(Alcoa Tech Center, Pittsburgh PA 15069)* and RE Johnson *(Univ of Illinois, Urbana IL 61801)*. Int J Mech Sci 35(5) 425-439 (May 1993).

This study compares two quasi-3D steady-state rolling models. The validity of both models assumes that the ratio of strip half-thickness to contact length is small. Thickness to length ratios less than 0.3 are acceptable, and sometimes the models work well beyond this limit. One model is a FE calculation which uses one layer of elements through the strip half-thickness. The other is an asymptotic approach which includes both first- and second-order terms. An important feature of the solution is that it is very sensitive to the spread. Small changes in spread often lead to significant changes in stresses. The predicted spreads are always found small and their magnitudes are typical of those found in practice.

272F. DRAWING

9A289. **Production of tapered cups by sequential deep drawing of sheet metals using drawn cups as a part of punch.** - K Yamaguchi *(Dept of Mech and Syst Eng, Kyoto IT, Matsugasaki Sakyo-ku, Kyoto 606, Japan)*, K Kanayama *(Government Indust Res, Inst of Nagoya, Hirate-machi Kita-ku, Nagoya 462, Japan)*, MH Parsa, N Takakura *(Dept of Mech and Syst Eng, Kyoto IT, Matsugasaki Sakyo-ku, Kyoto 606, Japan)*. J Eng Indust 115(2) 224-229 (May 1993).

A new deep drawing process of sheet metals is developed to facilitate small-lot production of deep cups with large drawing ratio. In this process, unlike the conventional deep drawing method, a few drawn cups are always stacked on the punch and used as a part of punch for the subsequent deep drawing of a given blank. Before drawing a new blank, a drawn cup which is in contact with the punch is stripped off. In this paper, this new deep drawing process is applied to the production of tapered cups and the main feature of the process is shown.

272G. SHEET METAL FORMING AND STAMPING

9A290. **Rigid plastic implicit scheme for non and 3D analysis of metal forming by FEM.** - G De Saxce *(Lab de Mec des Mat et des Struct, Faculte Polytech de Mons, 9 rue de Houdain, B-7000 Mons, Belgium)*, ZQ Feng *(Dept de Genie Mech, Univ de Tech de Compiegne, BP 649, F-60206 Compiegne, France)*, G Touzot *(Dept Genie Mech, Univ Tech de Compiegne, BP 649, F-60206 Compiegne, France)*. Eng Comput 10(1) 49-60 (Feb 1993).

This paper is devoted to the analysis of metal forming with assumption of rigid-plastic behavior with strain hardening. As opposed to the classical rate problem formulation based on Markov's principle and the explicit scheme, a more satisfactory incremental approach is deduced from Moreau's catching up algorithm. This implicit scheme, although more complicated, gives better results concerning convergence and numerical stability. Using an internal variable representing the strain hardening, an incremental strain energy density is defined which leads to a principle of minimum of the total incremental strain energy. In the numerical approximation using FE, the nonlinear equilibrium equations are solved by classical Newton's method. An approximation of Coulomb's criterion is used in order to represent friction with a rigid foundation. The simple compression test is simulated and shows that the implicit scheme is faster than the explicit one.

272H. MACHINING (INCL NM)

9A291. Computer simulation and experimental analysis of chip monitoring for deep hole drilling. - Jih-Hua Chin, Jang-Shyong Wu, Rouh-Song Young *(Dept of Mech Eng, Natl Chiao Tung Univ, Hsinchu, Taiwan, ROC)*. J Eng Indust 115(2) 184-192 (May 1993).

Chip congestion is a long time bottleneck in deep hole drilling. This paper addresses the problem of chip state monitoring in single-edge deep hole drilling by computer simulation and experimental analysis. Two phenomenological models were proposed to interpret the physics of chip discharging in normal and congested states, respectively. Length and diameter of the chip are chosen to represent the geometric features of the chip, and the formation of a chip signal is discussed. Computer simulation shows that the normal chip discharging in a real drilling process can be interpreted by the proposed slug flow model.

9A292. Modeling complex force systems Part 2. A decomposition of the pad forces in deep drilling. - BJ Griffiths and RJ Grieve *(Dept of Manuf and Eng Syst, Brunel Univ, UK)*. J Eng Indust 115(2) 177-183 (May 1993).

This paper is a continuation of the earlier Part I paper in which it was shown that the force system existing during a deep hole drilling operation was complex and indeterminate using a single dynamometer approach. However, by using complementary dynamometers in conjunction with a force relationship to model the radial and tangential pad forces the system could be analyzed.

9A293. Modeling complex force systems, Part I. The cutting and pad forces in deep drilling. - BJ Griffiths *(Dept of Manuf and Eng Syst, Brunel Univ, UK)*. J Eng Indust 115(2) 169-176 (May 1993).

This paper is the first part of a two-part series which analyzes the complex force system existing within a deep hole drilling operation where cutting forces exist at a single cutting edge and burnishing and friction forces exist at two pads. In this first paper the forces at the pads and cutting edges are determined by (1) assuming that the pad forces are related by coefficients and (2) by the use of complimentary dynamometers.

9A294. Monitoring and control of electrochemical machining (ECM). - KP Rajurkar, B Wei *(Indust and Man Syst, Eng Dept, Univ of Nebraska, Lincoln NE 68588-0518)*, CL Schnacker *(Hewlett Packard, Cupertino CA 95014)*. J Eng Indust 115(2) 216-223 (May 1993).

The main advantages of the electrochemical machining (ECM) process, such as high material removal rates and smooth, damage-free machined surface, are often offset by the poor dimensional control and process stability resulting from the complex and stochastic nature of the interelectrode gap (IEG) states. Full economic utilization of ECM will be realized only when reliable dimensional and process control systems are developed. This paper presents an ECM control model based on the basic ECM dynamics that accounts for the dynamic nature of the ECM process. The signals are digitized and analyzed with an IBM PC. The frequency analysis of the signal leads to a better insight of the physical mechanism of the ECM process. A comprehensive review of the state-of-the-art ECM research and development efforts in the areas of spark and short circuit detection and IEG control is also included in the paper.

See also the following:

9A31. Study of stick-slip motion and its influence on the cutting process
9A57. Statistical analysis of the dynamic cutting coefficients and machine tool stability
9A58. Unified transfer function (UTF) approach for the modeling and stability analysis of long slender bars in 3D turning operations

272I. GRINDING

See the following:

9A152. Knowledge-based expert system for ballscrew grinding

272J. CASTING

9A295. Numerical simulation of continuous casting solidification by BEM. - E Majchrzak *(Inst of Mech Theory, Silesian Tech Univ, Ul Pstrowskiego 16, 44-100 Gliwice, Poland)*. Eng Anal Boundary Elements 11(2) 95-99 (1993).

The problem of casting solidification modelling on the basis of the BEM is a rather difficult one. Yet, essential advantages of the BEM suggests that the use of this method for numerical simulation of Stefan's problem should be the subject of numerous scientific investigations in the range of effective algorithms construction. This paper presents a different algorithm. The BEM and the alternating phase truncation method APTM are used in order to identify the solidification front and temperature field in the volume of rectangular copper continuous casting.

272M. WRAPPING AND LAYING-UP (COMPOSITE MATERIALS)

9A296. Direct processing of continuous fibers onto injection molding machines. - FM Truckenmuller *(Inst Kunststofftech, Univ Stuttgart, Boblingerstr 70, 7000 Stuttgart 1, Germany)*. J Reinforced Plastics Composites 12(6) 624-632 (Jun 1993).

A new injection molding process "DIF" (Direct Incorporation of Continuous Fibers) is proposed whereby roving strands are directly incorporated into the polymer melt by using a reciprocating-screw-plasticating unit. The DIF-technology offers the possibility to substitute the relatively expensive pultrusion process which is used to produce long fiber pellets. Furthermore it can be used as a fast and flexible R&D tool. The results of fundamental mechanical and physical property investigations are presented including dispersion of fiber clusters and bundles, fiber length distribution, and fiber orientation.

9A297. Effect of mandrel material on the processing-induced residual stresses in thick filament wound composite cylinders. - SR White and Z Zhang *(Dept of Aeronaut and Astronaut Eng and Dept of Theor and Appl Mech, Univ of Illinois, Urbana IL 61801)*. J Reinforced Plastics Composites 12(6) 698-711 (Jun 1993).

Residual stresses are known to be detrimental to a number of mechanical properties in composite materials. The mechanisms by which they develop in the filament winding of composite cylinders and tubes is not fully understood. In this work a process model is presented to predict the residual stresses induced during the processing of two-layer composite cylinders. Chemical shrinkage, thermal expansion-contraction, and cure-dependent properties are accounted for in the model. The influence of mandrel stiffness and thermal expansion coefficient is examined and a case study of an aluminum and a steel mandrel is compared.

9A298. Simultaneous process of filament winding and curing for polymer composites. - VN Korotkov, YA Chekanov, BA Rozenberg *(Dept of Polymer and Composite Mat, Inst of Chem Phys, Russian Acad of Sci, Chernogolovka Moscow Region 142432, Russia)*. Composites Sci Tech 47(4) 383-388 (1993).

The simultaneous process of filament winding and curing a composite cylindrical shell is considered. From the macrokinetic point of view it is characterized by the small thickness of the relative effective reaction zone. The thermochemical conditions in manufacturing are governed by the following process variables: speed of winding, initial conversion and temperature of the filament bundle wound, and the heating applied. A thermochemical model is developed for simulation of the temperature and conversion distributions during the process. An approximate solution of the thermochemical model in the form of the constant traveling wave is derived for constant values of process variables and a thermally isolated mandrel. A non-uniform cure stress model of the process is developed for the case of using elastic orthotropic constitutive relations for a composite material. It is found that the thickness of the relative effective reaction zone drastically influences the cure stresses. The dependence of the stress level on the process variables is analyzed.

See also the following:

9A215. Unit cell geometry of 3D braided structures

272P. RAPID SOLIDIFICATION

9A299. Variational algorithms and pattern formation in dendritic solidification. - R Almgren *(Dept of Math, Univ of Chicago, Chicago IL 60637)*. J Comput Phys 106(2) 337-354 (Jun 1993).

We present a completely new variational algorithm for computing dendritic solidification. This algorithm reproduces the Gibbs-Thomson relation as a balance between bulk and surface energy and is able to operate in the infinity-mobility limit with no unphysical time-step restriction. It may be used with arbitrary non-smooth surface energy functions and may include finite kinetic mobility. We perform computations with isotropic and anisotropic surface energy; from a small irregular seed we generate radial tip-splitting structures for isotropic energy and parabolic dendrites with side-branching for anisotropic energy.

272R. MICROPROCESSING (EG BY LASER AND ION BEAMS)

9A300. Microwave heating of dispersive media. - GA Kriegsmann *(Dept of Math, Center for Appl Math and Stat, NJIT, University Heights, Newark NJ 07102)*. SIAM J Appl Math 53(3) 655-669 (Jun 1993).

The heating of a compact dispersive target by a pulsed, plane microwave is modeled and studied herein. The dispersive character of the medium is described by a Debye model, and the conductive nature is modeled by an ionic conductivity. The electrical and thermal parameters are allowed to depend upon temperature, which gives rise to a highly nonlinear initial boundary value problem. A two-step algorithm is proposed for the numerical solution of these equations. When convection is weak, the algorithm converges very slowly. Specifically, the temperature is spatially uniform in the target and evolves in time according to a first-order ordinary differential equation. The nonlinearity in this equation is a functional of the electric field within the target. The equation is solved for a number of specific examples, and physical conclusions are drawn about certain heating processes.

272T. CERAMICS, REFRACTORIES, GLASSES

9A301. Role of rheology in colloidal processing of ZrO_2. - YK Leong, N Katiforis, DBO'C Harding, TW Healy, DV Boger *(Adv Mineral Prod Res Center, Univ of Melbourne, Parkville 3052, Australia)*. J Mat Processing Manuf Sci 1(4) 445-453 (Apr 1993).

Wet colloidal processing techniques such as milling, spray drying, slip casting, pressure filtration and centrifuge casting are employed to produce ceramics of improved reliability. Each of these processes requires a specific rheological behavior or type of particle interaction which can be achieved by surface chemistry control. Results showing the effects of pH, ionic strength and the addition of adsorbing anionic polyacrylate and cationic polyallylamine hydrochloride on the rheological properties of ZrO_2 suspensions are presented. ZrO_2 suspensions exhibit a maximum in viscosity or yield stress at the isoelectric point (IEP) of pH 7.0. The suspensions deflocculate at a pH of about 5.0 and 10.0. The pH of maximum yield stress and the deflocculation pH were lowered significantly by the adsorbed polyacrylate, while these same pHs were increased by the addition of polyallylamine hydrochloride. More significantly, at relatively high additive concentrations (0.5% dwb or g/100 g ZrO_2), the maximum yield stress at the isoelectric point is greatly reduced. This reduction can be explained by the adsorbed polymer keeping the interacting particles further apart as a result of steric mechanisms and possibly the reduction of the effective Hamaker constant, as the polymer Hamaker constant is 2.5 times less than that of ZrO_2. At low concentrations of polyallylamine hydrochloride, a slight increase in the maximum yield stress was observed. This increase may be due to bridging flocculation and hydrophobic interaction of the adsorbed polymer. Surface property measurements showed excellent agreement between the isoelectric point and the pH of maximum yield stress for a wide range of polymer additive concentrations.

See also the following:

9A362. Fracture criterion for the axisymmetric disking process

9A371. Stress intensity factors for a crack in planar disking

272V. PLASTICS, ELASTOMERS, RUBBERS

9A302. Crystallization and its effect on the processing of polypropylene. - Tay-Yuan Chen, VW Wang *(AC Tech, 31 Dutch Mill Rd, Ithaca NY 14850)*, MJ Bozarth *(Himont USA, 800 Greenbank Rd, Wilmington DE 19808)*. J Reinforced Plastics Composites 12(6) 686-697 (Jun 1993).

In this article, the kinetics of crystallization for semi-crystalline polymers has been successfully incorporated into a cavity flow simulation. The flow resistance, in terms of filling pressure, can be significantly underestimated if crystallization is neglected during the calculation. In addition, the filling behavior for nucleated semi-crystalline materials is quite different from that of its virgin counterpart.

9A303. Shrinkage and warpage prediction for injection molded components. - SF Walsh *(Moldflow Pty, 259-261 Colchester Rd, Kilsyth, Vic 3137, Australia)*. J Reinforced Plastics Composites 12(7) 769-777 (Jul 1993).

Shrinkage and warpage analysis is now and important part of Computer Aided Engineering for injection molded components. The theory behind this analysis (including effects of crystallinity, orientation and cooling stress relaxation) is presented, along with a number of case studies showing the successful application of this technology.

274. Fracture and damage processes

274B. CRACK INITIATION

9A304. New approach to the determination of the macrocrack nucleation period near a stress concentrator. - VV Panasyuk, GS Ivanitska, OP Ostash *(GV Karpenko Physico-Mech Inst, Ukrainian Acad of Sci, 5 Naukova St, Lviv, Ukraine)*. Fatigue Fracture Eng Mat Struct 16(4) 453-464 (Apr 1993).

The stress-strain state of a rectangular plate with a central circular hole and a disc with an edge notch is analyzed both for elastic and elastic-plastic behavior when cracks emanate from the contours of these concentrators. Stress intensity factors are determined as well as the value of the inelastic deformation at stress concentration zones. The parameters describing the process of crack nucleation are established.

274C. SUBCRITICAL CRACK PROPAGATION

9A305. Experimental and FE study on stable crack growth in three point bending. - SK Maiti and AS Keshbat *(Dept of Mech Eng, Indian IT, Bombay 400 076, India)*. Int J Fracture 60(2) 179-194 (15 Mar 1993).

Experimental and FE results are presented on mode I and mixed mode (involving I and II only) stable crack growth under static loading through an aircraft grade aluminium alloy (D16AT) in three point bending. The results include load-displacement diagrams, J-integrals, plastic zones, tunneling (or crack front curving), etc. During experiment a substantial amount of tunneling is observed, the extent of which increases as the extension progresses in both mode I and mixed mode. The tunneling reduces as a_0/w increases. The crack extends initially almost along a straight line at an angle with the initial crack in a mixed mode. The maximum load is observed to be as high as 1.6 times the initiation load in the whole range examined. From the FE study it is seen that, in a mixed mode, the J-integral at the onset of extension is the lowest compared with the values at the later stages. The plastic zone size grows as the stable extension progresses; the growth is approximately the maximum along the crack extension line. The direction of initial crack extension in a mixed mode can be predicted through an elastic FE analysis and using the criterion of maximum tangential principal stress. The study also indicates that the load-displacement diagram associated with a mixed mode stable crack growth can be predicted reasonably accurately using the criterion of crack opening angle.

9A306. Fatigue crack growth under biaxial loading. - YC Lam *(Dept of Mech Eng, Monash Univ, Clayton, Vic 3168, Australia)*. Fatigue Fracture Eng Mat Struct 16(4) 429-440 (Apr 1993).

Fatigue crack growth under biaxial loading for long cracks subjected to low cyclic stress levels was investigated. The biaxial stress ratio λ ranging from - 0.5 to + 1.0 was considered. The strain energy density factor range was used as the criterion for predicting the crack growth rates and crack path. The agreement between prediction and experimental results was reasonable for crack growth rates and marginal for crack paths.

9A307. Influence of strength and stress ratio on short-crack thresholds and non-propagating fatigue cracks. - DN Lal *(Dept of Metall Eng, IT, Banaras Hindu Univ, Varanasi 221 005, India)*. Fatigue Fracture Eng Mat Struct 16(4) 419-428 (Apr 1993).

Quantitative predictions of the influence of yield strength and stress ratio, R, on the physically small crack fatigue threshold stress intensity, $\Delta K_{0(S)}$, are presented. It is shown that at R = 0 to - 1, although the threshold stress $\Delta\sigma_0$ increases, the threshold stress intensity, $\Delta K_{0(s)}$, decreases with increasing yield strength. Moreover, a lower bound value, $\Delta K_{0(s)(min)}$, is shown to have a constant value, irrespective of the strength and stress ratio. The formation and length of non-propagating fatigue cracks, a_{np}, are also discussed. The methods suggested for estimating $\Delta K_{0(s)}$ and a_{np} may be found useful in design procedures.

9A308. Mechanisms and behavior of overload retardation in AISI 304 stainless steel. - CS Shin and SH Hsu *(Dept of Mech Eng, Natl Taiwan Univ, Taipei, ROC)*. Int J Fatigue 15(3) 181-192 (May 1993).

The overload retardation phenomenon has been investigated in AISI 304 stainless steel under different baseline ΔKs, overload ratio and R ratios. Both the crack growth and crack closure behavior were carefully monitored. It was found that the extent and degree of retardation increase with overload ratio, decrease with R ratio, but are not correlated in a simple manner with the baseline ΔK. For R $\leq$ 0.6, momentary acceleration followed by well-defined delayed retardation were observed. The crack growth behavior before maximum retardation can be correctly predicted by Paris' law taking into account the experimentally measured crack closure value. Such a correlation failed beyond the maximum retardation point because of the occurrence of a discontinuous closure mechanism. Artificial introduction of crack closure by vacuum-infiltrating epoxy resin into the crack flanks also produced a similar retardation phenomenon. On the other hand, for R ratio $\geq$ 0.65, immediate retardation was observed. Mechanisms that have been proposed to explain the overload retardation phenomenon are reviewed and examined against the current experimental observations. It is concluded that the major mechanism causing overload retardation is plasticity-induced crack closure. Secondary mechanisms, such as crack-tip blunting and residual compressive stress ahead of the crack tip are significant only at high R ratios when crack closure is suppressed.

See also the following:

9A378. Dependence of acoustic emission for low strength steels upon the embrittlement and the plastic zone reduction at the crack tip during corrosion fatigue crack propagation

274D. DYNAMIC PROCESSES

9A309. Three coplanar moving Griffith cracks in an infinite elastic strip. - AN Das *(Dept of Math, N Bengal Univ, W Bengal, Darjeeling, India)*. Arch Mech 44(4) 463-474 (1992).

The dynamic anti-plane problem of determining stress and displacement due to three coplanar Griffith cracks moving steadily at a subsonic speed in an infinite elastic strip has been considered. Employing Fourier integral transform, the problem when the lateral boundaries are subjected to shearing stress, has been reduced to solving a set of four integral equations. These integral equations have been solved using finite Hilbert transform technique and Cook's result to obtain the exact form of crack opening displacement and stress intensity factors. Numerical results for stress intensity factors have been presented in the form of graphs.

274E. FATIGUE CHARACTERISTICS OF MATERIALS

9A310. Creep-fatigue interaction behavior of type 308 stainless steel weld metal and type 304 stainless steel base metal. - K Bhanu, S Rao, R Sandhya, SL Mannan *(Mat Dev Div, Indira Ghandhi Centre for Atomic Res, Kalpakkam 603 102, India)*. Int J Fatigue **15**(3) 221-229 (May 1993).

The effects of hold condition (tension-only, compression-only and tension-plus-compression holds of 1 min duration) and hold time (up to 10 min in tension) on the low-cycle fatigue behavior of type 304 stainless steel base metal and type 308 stainless steel all-weld metal were investigated at 923 K. All the tests were performed in total axis strain control in air, employing a strain range of 1.0%. The welds were prepared by a submerged metal arc welding process. The microstructure of the base metal and the weld consisted of gamma phase and duplex gamma-delta ferrite respectively. The results clearly indicated a reduction in continuous cycling as well as creep-fatigue interaction life of type 308 SS weld metal compared with type 304 SS base metal under identical testing conditions. Hold times displayed an effect on life that was dependent not only on material condition but also on the position of the hold in cycle. Fatigue lives recorded for type 308 SS weld in the 1 min hold-time tests were in the order: compression hold → continuous cycling → tension-plus-compression hold → tension hold. Fatigue lives of 304 SS were in the order: continuous cycling → compression hold → tension-plus-compression hold → tension hold. A significant reduction in the life of the weld metal was noted on increasing the duration of tension hold time to 10 min. 308 SS weld metal exhibited cyclic softening whereas 304 SS base metal showed rapid initial hardening followed by a saturation stage. The observed variations in life are explained on the basis of crack initiation and propagation modes and microstructural changes that occurred during low-cycle fatigue and creep-fatigue interaction testing.

9A311. Cyclic deformation and fatigue behavior of the low carbon steel SAE 1045 in the temperature regime of dynamic strain aging. - M Weisse, CK Wamukwamba, H-J Christ, H Mughrabi *(Inst fur Werkstoffwissenschaften, Lehrstuhl 1, Friedrich-Alexander-Univ Erlangen Nurnberg, Martenstr 5 DW-8520 Erlangen, Germany)*. Acta Metall Mat **41**(7) 2227-2233 (Jul 1993).

The cyclic deformation behavior of normalized SAE 1045 steel (german steel grade Ck 45) has been investigated over a range of temperatures between 20 and 375°C. Special attention has been paid to the effects of dynamic strain aging, which are most pronounced around 300°C. Different types of deformation tests (tension tests, incremental step tests, and constant amplitude cyclic deformation tests under stress control with a stress amplitude of 400 MPa as well as under plastic strain control with a plastic strain amplitude of 0.5%) were carried out to observe the influence of temperature on the macroscopic mechanical behavior. These tests were followed by TEM studies on microstructural features. In the temperature range of maximum dynamic strain aging, the material was found to show maximum strength in unidirectional as well as in cyclic deformation tests. While the fatigue life is maximum at the temperature of maximum dynamic strain aging in stress controlled tests, it is minimum in plastic strain controlled tests. At the temperature of maximum dynamic strain aging around 300°C, the dislocations are arranged in dense dislocation tangles and parallel dislocation walls, whereas at room and at higher temperatures (375°C) mainly dislocation cell structures are observed.

9A312. Cyclic strain resistance and cyclic fracture behavior of 2124 aluminium alloy. - TS Srivatsan *(Dept of Mech Eng, Univ of Akron, Akron OH)*, D Lanning Jr *(Dept of Aerospace Eng, Ohio State Univ, Columbus OH 43201)*, KK Soni *(Dept of Mat Sci and Eng, Lehigh Univ, Bethlehem PA)*. Int J Fatigue **15**(3) 231-242 (May 1993).

In this paper, the cyclic strain resistance and cyclic fracture behavior of aluminium alloy 2124 are examined. Test specimens of the alloy were cycled using tension-compression loading, under total strain control, over a range of plastic strains giving less than 10^4 cycles to failure. The alloy displayed hardening in both the longitudinal and transverse directions of the wrought plate. The observed hardening behavior is ascribed to contributions from synergistic influences of dislocation multiplication and dislocation-disclocation interactions. The alloy followed the Coffin-Manson relation and exhibited a single slope for the variation of cyclic plastic strain amplitude with reversals to failure. Fracture of the alloy samples was predominantly transgranular for both orientations, with microscopic crack propagation along the grain boundaries. The low-cycle fatigue characteristics and fracture behavior of the alloy are discussed in terms of competing and synergistic influences of cyclic plastic strain amplitude, response stress, intrinsic microstructural effects and dislocation-microstructure interactions during cyclic straining.

9A313. Effect of surface texture on fatigue life in a squeeze-cast 6082 aluminium alloy. - S Gungor and L Edwards *(Fracture Res Group, Mat Discipline, Fac of Tech, Open Univ, Milton, Keynes MK7 6AA, UK)*. Fatigue Fracture Eng Mat Struct **16**(4) 391-403 (Apr 1993).

The effect of surface texture on fatigue life in a squeeze-cast Al-Mg-Si alloy has been investigated in terms of initiation and subsequent propagation of small fatigue cracks. Small cracks nucleated from defects on both as-cast and polished surfaces. However, the large (~90 μm in diameter) surface defects found on as-cast surfaces caused an approximate 20% reduction in fatigue life when compared to polished surfaces where cracks initiated from smaller (~12 μm in diameter) microporosity. Integration of averaged and small fatigue crack growth data enables the fatigue lives of both types of specimen to be predicted at stresses above the fatigue limit, showing that the difference in fatigue behavior is principally due to the extra period of crack growth in the polished surfaces.

9A314. Effects of temperature and frequency on fatigue crack growth in 18% Cr ferritic stainless steel. - K Makhlouf and JW Jones *(Dept of Mat Sci and Eng, Univ of Michigan, Ann Arbor MI 48109)*. Int J Fatigue **15**(3) 163-171 (May 1993).

The fatigue crack growth behavior of a ferritic stainless steel has been investigated as a function of test temperature, thermal exposure and frequency at intermediate growth rates. In general, fatigue crack growth rates increased with increasing temperature and in the temperature range 500-700 °C growth rates were described by a kinetic process with an activation energy of 48 kJ/mole. Higher than normal growth rates at 475 °C were observed and attributed to an embrittlement process which is known to occur in this temperature regime in high-chromium ferritic stainless steels. The influence of frequency on fatigue crack growth rates was examined at 500 and 655 °C for a load ratio of 0.1 and over four decades of frequency. A transition from time-independent to time-dependent behavior was observed at each temperature as frequency was lowered. The frequency at which this transition occurred was dependent on temperature. For all temperatures investigated, near threshold crack propagation occurred by a crystallographic or faceted propagation mechanism. At high crack growth rates, crack-tip plasticity was significant and propagation proceeded by a ductile striation formation process. At intermediate growth rates a mixed-mode fatigue crack growth mechanism was observed where some intergranular fracture occurred.

9A315. Evaluation of composites under dynamic load. - F Orth, L Hoffmann, H Zilch-Bremer, GW Ehrenstein *(Lehrstuhl fur Kunststofftech der Friedrich-Alexander-Univ Erlangen-Nurnberg, Demonstrationszentrum fur Faserverbundwerkstoffe, D-8520 Erlangen-Tennenlohe, Am Weichselgarten 9, Germany)*. Composite Struct **24**(3) 265-272 (1993).

During the dynamic fatigue test it is desirable not only to determine the fatigue strength, but also to characterize the damage in the material. The observation of characteristic quantities provides information on the dynamic fatigue performance. Hysteresis measurements allow measurement of four kinds of quantities: stresses, extensions, stiffnesses and mechanical energies. By means of the stored energy and the energy loss the damping factor is calculated. It is also possible to distinguish between the material behavior in the tensile loading phase and the compression loading phase. The experimental equipment and procedure for hysteresis measurements are presented here. The application of this test method is demonstrated by two investigations. The first one deals with the dynamic fatigue behavior of glass fiber reinforced laminates for rotor blades of wind turbines and the second one is the evaluation of a valve spring retainer of carbon fiber reinforced plastic.

9A316. Fatigue behavior of a commercial aluminium alloy in sea water at different temperatures. - MR Bayoumi *(Dept of Prod Eng and Mech Syst Des, King Abdulaziz Univ, PO Box 9027, Jeddah 21413, Saudi Arabia)*. Eng Fracture Mech **45**(3) 297-307 (Jun 1993).

Fatigue tests of a commercial aluminium alloy are conducted in sea water at different temperatures using a specially designed experimental environmental chamber installed on a standard rotating bending fatigue testing machine. The tests are carried out in air at 20°C to establish the σ-N curve for this alloy as a reference curve, while tests in sea water are at 20, 30, 50 and 80°C to investigate the role of temperature on the fatigue behavior. Changing the medium from air to sea water during fatigue results in a significant decrease in the fatigue endurance limit. Increasing the temperature from 20 to 80°C reduces the endurance limit from 0.58 to 0.3 σ_y. In a generalized empirical estimation formula, the present study suggests an incorporation of an environmental factor (C_E) which depends on both the working medium and the temperature. Fracture surface examination on the scanning electron microscope indicates a great dependence of the pitting and/or intergranular corrosion fatigue cracks on the testing temperature and the applied cyclic stress levels.

9A317. Mode I fatigue cracking in a fiber reinforced metal matrix composite. - DP Walls *(United Tech, Pratt and Whitney, W Palm Beach FL 33410-9600)*, G Bao *(Dept of Mech Eng,* *Johns Hopkins Univ, Baltimore MD 21218)*, FW Zok *(Mat Dept, UC, Santa Barbara CA 93106-5050)*. Acta Metall Mat 41(7) 2061-2071 (Jul 1993).

The mode I fatigue crack growth behavior of a fiber reinforced metal matrix composite with weak interfaces is examined. In the longitudinal orientation, matrix cracks initially grow with minimal fiber failure. The tractions exerted by the intact fibers shield the crack tip from the applied stress and reduce the rate of crack growth relative to that in the unreinforced matrix alloy. In some instances, further growth is accompanied by fiber failure and a concomitant loss in crack tip shielding. The measurements are compared with model predictions, incorporating the intrinsic fatigue properties of the matrix and the shielding contributions derived from the intact fibers. The magnitude of the interface sliding stress inferred from the comparisons between experiment and theory is found to be in broad agreement with values measured using alternate techniques. The results also indicate that the interface sliding stress degrades with cyclic sliding, an effect yet to be incorporated in the model. In contrast, the transverse fatigue properties are found to be inferior to those of the monolithic matrix alloy, a consequence of the poor fatigue resistance of the fiber-matrix interface.

274F. STRESS OR STRAIN LIFE ANALYSIS OF FATIGUE

9A318. Analytical master curve for Goodman diagram data. - A Berkovits and D Fang *(Fac of Aerospace Eng, Technion Israel IT, Haifa 32000, Israel)*. Int J Fatigue 15(3) 173-180 (May 1993).

Estimation of the remaining safe life of structural parts which are not easily inspectable continues to be a problem. Even when load histories are available, laborious interpolation of Goodman diagram data is required in order to determine the remaining fatigue life of such parts. An analytical formulation of Goodman diagram data would expedite the life check. It is shown in this paper that, for many engineering materials at room temperature, the entire range of Goodman diagram data collapses on to a single master curve when presented as the ratio of lifetime with mean stress to lifetime at R = -1 for a given stress amplitude, as a function of a non-dimensional load parameter consisting of stress amplitude, mean stress, and material strength. The master curve is conveniently expressed in terms of two easily determined Weibull constants. Stress-concentration factor influences the value of the constants, as does the strain-rate sensitivity of some materials. By use of the master curve formula in an algorithm together with the Manson-Coffin life relation and Miner cumulative damage rule, computed fatigue lives lay within a factor of 2 of results obtained in tests under aircraft spectrum loads.

9A319. Improved technique for the prediction of axial fatigue life from tensile data. - JH Ong *(Nanyang Tech Univ, Nanyang Ave, Singapore 2263)*. Int J Fatigue 15(3) 213-219 (May 1993).

This paper introduces an improved technique over existing methods for the prediction of axial fatigue life from uniaxial tensile data. The method uses multilinear regression analysis for initial prediction of the elastic and plastic strain amplitudes at 10^6 and 10^4 reversals to failure respectively from uniaxial tensile data. The fatigue strength coefficient is assumed to be equal to the true fracture stress of the material. The fatigue ductility coefficient is approximated to be equal to the logarithmic ductility of the material. The fatigue strength exponent and fatigue ductility exponent are then located on the strain-life curve by making use of the estimated elastic-plastic strain amplitudes, logarithmic ductility and the true fracture stress of the material. The validity of the method was investigated by examining 49 steels whose material properties cover a wide range of variables that might affect fatigue behavior.

9A320. Stress field intensity approach for predicting fatigue life. - Weixing Yao *(Dept of Aircraft, Nanjing Aeronaut Inst, Nanjing 210016, Peoples Rep of China)*. Int J Fatigue 15(3) 243-245 (May 1993).

In this paper a new design approach for predicting fatigue life – the stress field intensity approach – is presented from the point of view of macromechanics on the basis of the mechanism of fatigue damage of metals. In this new approach the stress field intensity over the local region of damage, instead of the stress peak values as in the local stress-strain approach, was taken as the parameter with which to measure the fatigue strength of structures. Many fatigue phenomena, which the nominal stress approach and the local stress-strain approach could not explain, can be explained reasonably in this new approach.

9A321. Textures induced by tension and deep drawing in low carbon and extra low carbon steel sheets. - D Daniel *(Pechiney - Centre Rech Voreppe, BP 27, 38340 Voreppe, France)*, J Savoie, JJ Jonas *(Dept of Metall Eng, McGill Univ, 3450 Univ St, Montreal, H3A 2A7, PQ Canada)*. Acta Metall Mat 41(6) 1907-1920 (Jun 1993).

The texture evolution induced by tensile deformation and by deep drawing was investigated. For this purpose, the textures of 3 types of steel (rimmed, Al-killed drawing quality, and interstitial free) were measured and analyzed using the series expansion method. The results indicate that the initial texture changes drastically after a few percent of plastic strain and evolves towards a single orientation for which the <110> direction is aligned with the tensile or drawing axis.

274G. OTHER ASPECTS OF FATIGUE

9A322. Anisotropic damage mechanics model for fatigue failure. - June Wang *(Dept of Mech, Huazhong Univ of Sci and Tech, Wuhan, Hubei 430074, Peoples Rep of China)*. Eng Fracture Mech 45(3) 349-355 (Jun 1993).

The development of an anisotropic theory of continuum damage mechanics for fatigue failure is described. The fatigue damage evolution model is based on earlier publications of the author on the anisotropic ductile damage and uniaxial fatigue damage theories. A more general damage characteristic tensor capable of characterizing micro-crack growth on the maximum shear plane as well as on the plane normal to the maximum tensile stress is formulated. The validity of the damage model proposed is verified by comparing the predicted and measured number of cycles to failure for RS50 steel and excellent agreement has been achieved.

9A323. Durability evaluation for components by simulating fatigue test and extreme value analysis. - Chuan-Yao Chen and Da-Xing Gao *(Dept of Mech Eng, Huazhong Univ of Sci and Tech, Wuhan 430074, Peoples Rep of China)*. Eng Fracture Mech 45(1) 25-29 (May 1993).

A simulating fatigue testing method and requirements are explored to evaluate quantitatively the durability of components which cannot be conveniently and economically tested. Three requirements for analogies are necessary, ie, the geometry and manufacturing quality of critical detail, stress and stress gradient at the expected cracking plane, and the crack initiation position and crack propagation path. The initial fatigue quality of components may be described by using the simulation test results and the extreme value theory. The distribution of time to reach any given crack size and the probability of crack exceedance, which is the measurement of component damage in service, are then obtained.

9A324. Effect of stress ratio on the fatigue threshold condition of physically small cracks. - DN Lal *(Dept of Metall Eng, IT, Banaras Hindu Univ, Varanasi 221 005, India)*. Fatigue Fracture Eng Mat Struct 16(4) 405-418 (Apr 1993).

An approach is proposed to predict the intrinsic threshold of physically small cracks without invoking crack closure considerations. The basic assumption invoked is that a ΔK representation is valid for short cracks, hence the lower-bound threshold value, $\Delta K_{0(s)(min)}$ for short cracks can be numerically equated with the lower-bound threshold value of long cracks, $\Delta K_{x0(1)(min),s}$ of the same material. Several experimental observations provide a basis for this rationalization.

9A325. Formation of slip bands in aluminium foil subject to variable stress loading and the application of this technique to stress measurement. - Y Nagase, Y Sawaki, H Yoshida *(Dept of Mech Eng, Shizuoka Univ, 3-5-1 Johoku, Hamamatu 432, Japan)*. Int J Fatigue 15(3) 205-211 (May 1993).

In this paper, the fundamental characteristics of fatigue slip bands formed in an aluminium foil are investigated under both constant and variable stresses, and this phenomenon is utilized to monitor the stress amplitude with the use of the foil. It is found that variation of stress amplitude hardly affects the increase of slip bands, and the fraction of slip bands under variable stress is correlated with the equivalent stress defined by $(\Sigma\sigma^{\alpha}_i N_i/\Sigma N_i)^{1/\alpha}$, where σ_i, N_i and α are stress amplitude, the number of cycles and the material factor which is peculiar to the foil used, respectively. It is concluded that the fraction of slip bands can be a measure of stress evaluation for both constant and variable stresses.

9A326. Possible effects of magnetic fields in fatigue. - IK Bhat *(Dept of Mech Eng, Inst of Eng Tech, Lucknow, India)*, MK Muju *(Dept of Mech Eng, Indian IT, Kanpur, India)*, PK Mazumdar *(General Eng Dept, Univ of Puerto Rico, Mayaguez 00680, Puerto Rico)*. Int J Fatigue 15(3) 193-197 (May 1993).

The fatigue life of mild steel (a ferromagnetic metal) in a magnetic field seems interesting: at a given stress level, after decreasing initially with increasing applied magnetic field (ie, current), the life approaches a limiting value as magnetic inductance (or magnetization) of the metal assumes its saturated (maximum limiting) value, which occurs when the applied magnetic field exceeds a critical value. This possibility is examined here through a life model that includes the effects of an applied field on dislocation flow as well as the strain which domains experience along their magnetization direction (called magnetostriction). The magnetic field apparently reduces life by affecting strain to a greater extent. Other possibilities that could contribute to life reduction by affecting both crack nucleation and propagation are also indicated. These include large-scale crack-tip plasticity due to easier dislocation flow, reduced crack closure during stage II cracking, and the stress concentration effects arising from possible diffusion of carbon atoms to the surface as impurities.

274H. CORROSION AND EMBRITTLEMENT

9A327. Chloride corrosion of steel rebars in mortars with fly ash admixtures. - N Kouloumbi and G Batis *(Section of Mat Sci and Eng, Natl Tech Univ, Heroon Polytechniou 9, Zografou 15773, Athens, Greece)*. Cement & Concrete Composites 14(3) 199-207 (1992).

This paper presents the results of an experimental investigation of the corrosion of steel rebars in different types of mortars immersed in 3.5% sodium chloride solution. The corrosion rate of the steel bars was determined in relation to the curing time and to the addition of Greek fly ash at 15 wt% and 30 wt%. The corrosion activity was evaluated by measuring (a) the gravimetric weight loss of the reinforcing steel bars; (b) their corrosion rate using the linear polarization resistance technique; and (c) the total and free chloride content of the various mortars used, by a selective chloride electrode. Additionally some X-ray diffraction measurements were made in order to identify the complex substances formed. The results indicate that the addition of Greek fly ash, at both percentages, improves the corrosion behavior of the reinforcing steel bars by lowering the free chloride content. Also, the 28-days of curing time increases the corrosion resistance of the specimens, especially those without additive. In all cases the 28 days cured specimens show a lower content of total and free chloride and a reduced corrosion rate with respect to the 1- and 7-days cured specimens.

9A328. Influence of additives in a H_2SO_4 environment on the stress corrosion cracking of type 304 stainless steel. - M Asawa *(Col of Educ, Shinshu Univ, Nishi-nagano, Nagano 380, Japan)*. Arab J Sci Eng **17**(4A) 445-452 (Oct 1992).

This study evaluates the resistance of type 304 stainless steel to stress corrosion cracking in sulfuric acid solutions with after addition of potassium cyanate, potassium selenocyanate, decomposition products of cyanate (NH_4OH, $NaHCO_3$, or $(NH_4)_2CO_3$), and NaOH. Cracking or localized attacks occurred at sulfate ion concentrations of 1.5-4 M and at pH values less than 0.35. The results show that addition of KOCN, NH_4OH, $NaHCO_3$ and $(NH_4)_2CO_3$ cause cracking to predominate by inhibiting general corrosion both by neutralization of some of the aggressive H^+ ions and, by adsorption of these species on the metal surface. KSeCN induces localized attack but inhibits general corrosion, through adsorption. NaOH induces SCC by its inhibitive effect decreasing the H^+ ion concentration.

9A329. Influence of loading profile and superimposed flutter load frequency on the fracture behavior of a submarine hull steel in seawater. - MZ Shah Khan *(Mat Res Lab, Ship Struct and Mat Div, Defence Sci and Tech Org, PO Box 50, Ascot Vale, Vic 3032, Australia)*. Int J Fatigue **15**(3) 199-203 (May 1993).

Fracture surface examination is a useful approach in gaining an understanding of the fracture behavior of materials. In this study, the fracture surfaces of submarine hull steel specimens, which failed by corrosion fatigue in seawater, were examined in order to determine the micromechanics of the fracture process. Results show that the early stage of crack advance, corresponding to an approximate zone of 0.5 mm from crack initiation, was environment-controlled and independent of the loading profile and superimposed flutter load frequencies. Beyond this zone the influence of loading profile and superimposed flutter frequency on the fracture morphology was clearly in evidence. The changes in the fracture morphology are described. The combinations of loading profile and superimposed flutter load frequency which influenced the cracking behavior are identified. The influence of cracking modes on the overall fatigue life is also discussed.

9A330. Investigation of corrosion prevention method for determination of steel structure condition. - LD Dukic *(Fac of Civil Eng, Univ of Zagreb, Rakuse 1 PO Box 165, Zagreb 41001, Croatia)* and I Stern *(Fac of Chem Eng and Tech, Univ of Zagreb, Pierottijeva 6 PO Box 177, Zagreb 41001, Croatia)*. J Construct Steel Res **25**(3) 167-183 (1993).

Corrosion influences the service life of building materials and accordingly the service life of whole structures. In order to avoid corrosion activity, it is necessary to separate the structures from the aggressive environment. The investigation has been made to develop a comprehensive expert system corrosion prevention method (ESCPM), to establish the condition of corrosion protection on structures during their service life. New types of assessment have been proposed to create a uniform assessment of corrosion protection on structures, and an optimum procedure has been developed for its maintenance.

See also the following:

9A338. Performance of aluminium alloys and particulate reinforced aluminium metal matrix composites in erosive-corrosive slurry environments

9A936. Radiation embrittlement mechanistic modelling

274I. FRETTING, WEAR, AND EROSION

9A331. The differential effect of the hardness of metallic materials on their erosion and abrasion resistance. - G Sundararajan *(Defence Metall Res Lab, Kanchanbagh, Hyderabad 500258, India)*. Wear **162-164**(PART B) 773-781 (13 Apr 1993).

The resistances of annealed pure metals to solid particle erosion and two-body abrasion increases linearly with increasing hardness and thus are similar. However, alloyed metal shows a contrasting behavior. For example, a substantial increase in the hardness of steels achieved by quenching and tempering does not alter the erosion resistance. The abrasion resistance, however, does increase, although not as dramatically as in the case of pure metals. The objective of this paper is to understand the reasons behind such contrasting erosion and abrasion in conjunctions with the estimates of the average strain rates at which the plastic deformation occurs within the plastic zone, leads to the conclusion that deformation occurs under fully adiabatic conditions only during erosion and not under abrasion conditions. This conclusion, when incorporated in the localization models for erosion and abrasion proposed earlier by the present author, results in theoretical expressions for erosion and abrasion resistance which have different dependences on hardness. Thus the differential effects of hardness on erosion and abrasion are explained.

9A332. Effect of fretting on electroplated Pd-Ni contacts. - Hideaki Murata *(Yazaki, 1500 Misyuku Susono, Shizuoka 410-11, Japan)*, Yasuo Imada, Fumihiro Honda, Koichi Nakajima *(Toyota Tech Inst, 2 Hisakata Tempaku, Nagoya 468, Japan)*. Wear **162-164**(PART A) 339-346 (13 Apr 1993).

Surface observations of the composition and chemical state were carried out to understand the fretting behavior of an electroplated of Pd-20wt%Ni contact compared with that of an electroplated Pd contact. The experiments were conducted in ambient room air and in the relevant organic vapor. By fretting in ambient room air, the Pd-Ni contact acquired a high contact resistance because of oxidation, but with an Au-flash plating 0.1 μm thick on it, it remained stable and with a low contact resistance. This is attributed to the solid lubricant effect because of the soft, thin layer of gold on the much harder Pd-Ni. By fretting in the environmental containing toluene vapor, organic deposits (frictional polymers) were found on the Pd-Ni contact surface as well as on the Pd contact. Investigation of a possible correlation between the quantities of C and O on the contact surface detected by electron probe microanalysis revealed the existence of a small amount of organic deposits. At a low toluene concentration, some metal oxides were produced during the formation of organic products, and the correlation coefficient of C and O were reduced. By Fourier transform IR spectroscopy, the organic products were observed to include aryl or unsaturated esters. Organic deposits on the Pd-Ni contact functioned as a lubricant and inhibited the oxidation of the metal surface. This inhibitory effect was confirmed by characterizing X-ray spectrum analysis. In contrast, the deposits on the Pd contact did not act sufficiently as a lubricant, resulting in an increased contact resistance. Therefore, the Pd-Ni contact has some advantages over the Pd contact in the environment containing toluene vapor.

9A333. Effects of erodent recycling in solid particle erosion testing. - AJ Sparks and IM Hutchings *(Dept of Mat Sci and Metall, Univ of Cambridge, Pembroke St, Cambridge CB2 3QZ, UK)*. Wear **162-164**(PART A) 139-147 (13 Apr 1993).

In solid particle erosion tests, recycling of the erodent can lead to rounding, or in some cases significant fracture, of the particles, and thus to a progressive change in the test conditions. This work examines changes in particle size and shape resulting from impact, for a typical silica sand and for glass spheres. The target material was a glass-ceramic, and experiments were performed with an air-blast erosion rig. Erodent particles classified by sieving contained a significant proportion outside the nominal size range. Particle size distributions determined by sieving and optical methods showed disparities, due to particle shape effects. Both types of particles showed extensive fragmentation on striking glass-ceramic targets at 89 - 98 m s^{-1} at normal incidence. Repeated impact led to further fragmentation and a progressive reduction in the average particle size in the erodent sample, although some particles remained unbroken after more than ten impacts. The fragmentation of the particles led to changes in the measured erosion rate as they were recycled. At least three factors were responsible: the intrinsic size effect, aerodynamic effects in the gas-blast erosion rig, and changes in particle angularity due to fracture.

9A334. Erosive wear behavior of chemical vapor deposited multilayer tungsten carbide coating. - D Garg and PN Dyer *(Air Prod and Chem, 7201 Hamilton Blvd, Allentown PA 18195)*. Wear **162-164**(PART A) 552-557 (13 Apr 1993).

Erosive wear of components by solid particle impingement is a problem faced by many industries. A variety of protective coatings deposited by thermal spray, physical vapor deposition, and chemical vapor deposition techniques have been developed over the years to reduce erosive wear of components and increase their useful life. These coatings generally provide adequate protection in a mild, low-impingement angle environment, but they fare poorly in a harsh, high-impingement angle environment. This paper describes a new multilayer tungsten carbide-based coating, which has been developed to protect components both in low and high impingement angle environments. The multilayer coating is deposited by the chemical vapor deposition technique and consists of an outer tungsten carbide layer with a fine-grained, layered morphology at the top of a columnar tungsten inner layer. It can be deposited on several metals and alloys used by the aerospace industry at low temperatures without degrading their mechanical properties. The erosive wear behavior of the multilayer coating is compared with titanium nitride coatings deposited by the physical vapor deposition technique.

9A335. Gross slip criteria in fretting. - O Vingsbo and J Schon *(Dept of Mech Eng, Univ of Houston, Houston TX)*. Wear **162-164**(PART A) 347-356 (13 Apr 1993).

One of the most important characteristics in fretting is the transition from mixed stick-slip conditions to gross slip, as given by the corresponding regime boundary in fretting maps. The regime boundary is determined by the critical values of frequency, normal force, tangential force amplitude and displacement amplitude. Three sets of criteria for incipient gross slip have been studied in the present investigation: fretting scar morphology tangential force and displacement amplitude interrelations, and fretting energy dissipation. A fully computerized fretting tester has been used, in which the relative displacement between the specimens can be very accurately controlled and measured. Tangential force and relative displacement measurements can be made with resolutions of 2 nm and 5 mN respectively. Pure copper (UNS C11) specimens were studied. Post-test studies of fretting scars were performed by SEM. With some practice, it is possible to identify scar morphologies characteristics of the different regimes. The last two criteria were compared by plotting tangential force amplitude and energy dissipation together as functions of displacement amplitude in so-called FED (force energy displacement) diagrams. Some FED diagrams display force curves without a well-defined critical force amplitude, rendering the force criterion difficult to apply. The energy curves, however, always have a sharp bend, corresponding to a change in energy dissipation characteristics at the gross slip transition. The energy criterion occurs for a lower critical displacement amplitude than the force criterion (when applicable). A possible explanation of this observation is discussed.

9A336. **Influence of nozzle roughness on conditions in a gas-blast erosion rig.** - PH Shipway and IM Hutchings *(Dept of Mat Sci and Metall, Univ of Cambridge, Pembroke St, Cambridge CB2 3QZ, UK)*. Wear **162-164**(PART A) 148-158 (13 Apr 1993).

Although the gas-blast method of erosion testing is widely used, little is known about the distribution of particle velocities and trajectories in the plume of erodent particles leaving the nozzle. In this work, experimental methods have been developed to study and describe these, and in particular the influence of the internal roughness of the nozzle has been examined. An analytical function has been derived which describes the angular distribution of particle trajectories in the plume; this distribution is uniquely described by a single dimensionless "focus coefficient", β, which depends, among other factors, on the nozzle bore roughness and on the nature of the erodent particles. The nozzle roughness also significantly affects the velocity of the erodent particles; a rough nozzle bore is associated with lower erodent velocity, a greater spread of velocities and a more widely spread plume. The results are relevant to erosion testing by the gas-blast method, and suggestions are made for improvements in the control and standardization of the erosion conditions in such tests.

9A337. **Modeling of abrasive particle trajectories during erosion by a slurry jet.** - S Turenne *(Indust Mat Inst, NRC, Boucherville, Canada)* and M Fiset *(Dept of Mines and Metall, Laval Univ, PQ, Canada)*. Wear **162-164**(PART B) 679-687 (13 Apr 1993).

The aim of this study was to investigate the effect of fluid flow on the trajectories of abrasive particles near a specimen surface subjected to slurry erosion. In order to identify the different erosion mechanisms, it is necessary to know the impact parameters, such as the impact angle and the local velocity of the abrasive particles. An analysis based on potential and stream functions led to the determination of the velocity components of the fluid in the axisymmetrical jet (normal incidence). The boundary conditions corresponding to the free surface of the jet were included in the numerical resolution of the differential equations given by the inverse formulation of the fluid flow. From the velocity components of the fluid, it was possible to evaluate the viscous drag force on a particle and consequently the particle trajectories. The theoretical predictions show that the particle trajectories are, in some conditions, strongly deviated near the test surface. The observation of the eroded surfaces of the aluminum specimens was useful to verify the predictions that could be made from these particle trajectories. The observation pointed out the influence on particle trajectories of the abrasive particle size and the abrasive concentration in the slurry.

9A338. **Performance of aluminium alloys and particulate reinforced aluminium metal matrix composites in erosive-corrosive slurry environments.** - JA Bester and A Ball *(Dept of Mat Eng, Univ of Cape Town, Private Bag, Rondebosch 7700, S Africa)*. Wear **162-164**(PART A) 57-63 (13 Apr 1993).

A range of aluminium alloys and particulate reinforced aluminium metal matrix composites has been tested in an apparatus which simulates the erosive-corrosive action of a slurry. The slurry used in the investigation is composed of synthetic mine water and silica sand. The corrosion component of the mass loss was found to be an important synergistic factor. The addition of ceramic reinforcement particles to the matrix alloys has a detrimental effect on the slurry erosion resistance.

9A339. **Relationship between surface hardness and erosion damage caused by solid particle impact.** - YI Oka, M Matsumura, T Kawabata *(Dept of Chem Eng, Fac of Eng, Hiroshima Univ, Higashi-Hiroshima 724, Japan)*. Wear **162-164**(PART B) 688-695 (13 Apr 1993).

A model for erosion caused by solid particles was studied and an equation based upon the relationship between dynamic indentation and the hardness of the material was proposed. This equation was established by the relationship between the surface hardness and the erosion damage to the materials. Erosion tests using a gas gun unit were conducted on five materials over a wide range of hardness values (Hv number 9 - 1100) up to an impact velocity of 150 m s^{-1}. An increase in the hardness was seen on the fully eroded surfaces obtained in the case of iron and aluminium, but a decrease was seen in the case of quenched carbon tool steel. No change in the hardness was seen in the cases of the acrylic resin and nylon. The hardness of the eroded surfaces, as opposed to that of the non-eroded surfaces, slightly improved the correlation with erosion damage, but it was not necessarily sound. The softening observed on the eroded surface of the quenched carbon tool specimen suggested that heat was generated during the impact of the particles and also that the surface hardness during the course of erosion was different from that both before and after erosion. The temperature increase of an iron leaf sample owing to the impact of a 3.18 mm steel ball or silica sand particles pointed to a transiently high temperature on the impacted surfaces and the possibility of softening during the course of the erosion process. As a result, the surface hardness of each material estimated with respect to work hardening and softening reasonably correlated with the erosion damage. Also, numerical formulation and the soundness of this equation were discussed through many erosion tests under various conditions.

9A340. **SEM studies of material damage in alumina ceramics by angular single and multiple particle impacts.** - Jianren Zhou *(Dept of Mech Eng, Prairie View A&M Univ, Prairie View TX 77446)* and S Bahadur *(Dept of Mech Eng, Iowa State Univ, Ames IA 50011)*. Wear **162-164**(PART A) 285-295 (13 Apr 1993).

The mechanisms of erosion in alumina ceramics have been investigated by scanning electron microscopy. The five commercial aluminas tested ranged from pure alumina to those containing different proportions of silicate glassy phase and zirconia. In single particle impact tests, the targets were impacted with 1035 μm angular SiC particles and in multiple particle tests with 151 μm SiC particles. The particles were always impacted under normal impact condition with an impingement velocity of 50 m s^{-1}. It was found that whereas brittle failure was the basic erosion mechanism, the morphological features of eroded surfaces were quite different for different materials and depended upon their compositions. The presence of secondary phases improved the bonding between alumina grains and also increased toughness by absorbing part of the impact energy. Therefore, the erosion resistance was enhanced by the presence of secondary phases in alumina. The erosion rates of these materials are analyzed briefly in terms of the erosion mechanisms. It was found that the classical lateral cracks which are typical of brittle indentation fracture was not present on the eroded surfaces of aluminas.

9A341. **Solid-particle erosion of *in situ* reinforced Si_3N_4.** - M Marrero, J Routbort *(Mat Sci Div, ANL)*, P Whalen, Chien-Wei Li *(Allied-Signal, Morristown NJ 07962-1021)*, KR Karasek *(Allied-Signal, Des Plaines IL 60017-5016)*. Wear **162-164**(PART A) 280-284 (13 Apr 1993).

Steady-state solid-particle erosion has been investigated on *in situ* reinforced Si_3N_4 and the "equivalent" fine-grained hot-isostatically-pressed Si_3N_4 whose R-curve beahviors are quite different, having K_{IC} values in the long-crack limit of 8.3 and 5.6 MPa $m^{1/2}$ respectively. Experiments were carried out at 20 °C, using SiC abrasives, whose diameters ranged from 42 to 1035 μm, varying the angle of impact from 15 to 90° and the velocity from 50 to 100 to 150 m s^{-1}. The erosion rates of the two materials were, within a factor of two, the same, indicating that the long-crack-length-limit toughness is not an indication of erosion resistance, for the range of particle size and velocities studied.

9A342. **Specimen diameter, impact velocity, erosion rate and particle density in a slurry pot erosion tester.** - HM Clark *(Dept of Mech Eng, Univ of Kansas, Lawrence KS 66045-2234)*. Wear **162-164**(PART B) 669-678 (13 Apr 1993).

Using the technique of measuring impact crater size, stagnation line impact velocities of glass spheres (mean diameter 666 μm) suspended in diesel oil at 40° C on cylindrical copper erosion test specimens ranging in diameter from 3.2 mm to 9.5 mm tested at normal speed of 18.7 m s^{-1} in a slurry pot tester have been measured. Similarly, the variation in normal impact velocity of the same glass spheres as a function of angular location about the specimen has been measured for a 4.7 mm diameter specimen. Erosion rates for 1020HR steel specimens in the diameter range 3.2 mm to 9.1 mm were determined using a 1.2 wt% suspension in diesel oil of silicon carbide particles, mean size 136 μm. Stagnation line impact velocities have been measured for spherical particles ranging in density between 2420 kg m^{-3} and 7830 kg m^{-3} suspended in diesel oil. The changes in impact conditions and erosion rates were analyzed using a model of suspension flow about, and particle impact on, a cylindrical target. It is shown that changes in erosion rate can be well accounted for by the changes in mean kinetic energy dissipated in collision and the frequency of particle impact, themselves controlled by the conditions of two-phase flow. It was also found that while the dispersion of solid particles in a slurry pot tester is very fast, the test method is subject to uncertainty in the value of the free-stream velocity. This effect is thought to be caused by rotation of the suspension in the test apparatus. A method of estimating its magnitude is given.

9A343. **A study of the fundamental mechanisms of erosion using Hertzian fracture tests.**

- Jyh-Woei Lu *(Supertech Consult, Chandler AZ 85224)*, GA Sargent *(Univ of Dayton, Dayton OH 45469)*, H Conrad *(N Carolina State Univ, Raleigh NC 27695)*. Wear 162-164(PART B) 856-863 (13 Apr 1993).

Hertzian fracture tests were conducted at room temperature on Pyrex glass under static and dynamic loading conditions to study the fundamental mechanisms of erosion. The effects of specimen surface roughness, a grease coating, loading rate and indenter materials, size and roughness on the fracture load and ring crack radius were considered. It was found that the ratio of the ring crack radius to contact radius decreased with increasing load, indenter size and loading rate. Also, the above ratio and fracture load increased with increase in elastic modulus mismatch between indenter and specimen and with abrasion of the indenter and/or specimen. The effects of abrasion and indenter material on Hertzian fracture behavior were in quantitative accord with predictions of friction and roughness effects proposed by Johnson *et al.* The increase in critical load to fracture observed in the dynamic tests compared with the static tests, and the increase in critical load due to the grease coating were concluded to be due to kinetic effects associated with the presence of water vapor at the crack tip.

9A344. Study on mechanism of combined action of abrasion and cavitation erosion on some engineering steels. - Zhao Kang, Gu Chenqing, Shen Fusan, Lou Bingzhe *(Dept of Mat Sci, Shaanxi Mech Eng Inst, Xi'an, Shaanxi 710048, China)*. Wear 162-164(PART B) 811-819 (13 Apr 1993).

The abrasion and cavitation erosion properties as well as the relevant failure mechanisms of several steels to be used for hydraulic turbine parts were investigated. The tests were carried out using rotating disc equipment under simulated working conditions, instead of the conventionally used venturi tube or vibration apparatus. Different weight loss curves were obtained. The experimental results obtained from our scanning electron microscopy, transmission electron microscopy, light microscopic observations, X-ray analysis and other test methods proved that it is more reasonable to consider the cavitation erosion as a failure of low cycle (plastic strain) fatigue. Hence, it was derived from the Manson-Coffin relation that the resistance to cavitation erosion depends on the square of the product of the hardness and that the true fracture strain ε_f of the steel. Sand-water abrasion is actually a microcutting of the surface layer of the steels and, here, the hardness of the steels is proved to be the main resistance factor. The failure of steels in muddy and sand-carrying water is due to the combined action of abrasion and cavitation erosion, and the consequent weight loss rate is the weighted sum of the individual rates of abrasion and cavitation erosion. Equations that relate the weight loss rate of abrasion and also of cavitation erosion to the mechanical properties of the steels were developed. The calculated values and the experimental data agree well. Conclusions drawn give useful reference principles for the microstructural design of steels to be selected and also for the improvement of their heat treatment.

9A345. Surface temperatures and fretting corrosion of steel under conditions of fretting contact. - HM Ghasemi, MJ Furey, C Kajdas *(Dept of Mech Eng, VPI)*. Wear 162-164(PART A) 357-369 (13 Apr 1993).

One of the fundamental questions in tribology is the magnitude of surface temperatures generated in the fretting of steel and if this is a factor in the formation of metallic oxides. An infrared microscope was used as a means of direct measurement of surface temperatures generated under low frictional heat rates (lower than 1.5 J s^{-1}) encountered in fretting experiments. A photo-video technique was developed to view the fretting contact interface in "real time" and to observe the process of oxide formation. In addition, wear scars on the steel were examined using both photomacrography and scanning electron microscopy. Spherical 52100 steel specimens, 1.25 cm in diameter, were studied under various loads (4 N-20 N), amplitudes (20 μm and 100 μm), and at a constant frequency of 150 Hz. Studies in air showed that even with surface temperatures as low as 25-30 °C, significant quantities of oxides quickly formed on the steel ball in contact with sapphire during fretting. The observed formation of iron oxides in low surface temperature tribological experiments is explained in terms of exoelectron emission is suggested by Kajdas. The measured surface temperature rises were also compared with Archard's theoretical model. The wear rates of steel under these fretting conditions depended on load, vibration amplitude, and environment - the latter two effects being greatest. For example, in air, increasing the amplitude from 20 to 100 μm resulted in a 20 fold increase in wear for a given sliding distance. Fretting experiments in nitrogen, under high load and high amplitude conditions, resulted in a 100 fold decrease in wear compared with that observed in air. However, the magnitudes of surface temperature rise in air and in nitrogen were not significantly different.

See also the following:

9A526. Wear-corrosion-resistant materials for mechanical components in harsh environments

274J. CREEP

9A346. Application of double cantilever beam model to the analysis of creep crack growth under neutron irradiation. - S Murakami, K Hayakawa *(Dept of Mech Eng, Nagoya Univ, Furo-cho Chikusa-ku, Nagoya 464-01, Japan)*, M Mizuno *(Dept of Mech Eng, Kyoto Univ, Yoshida-honmachi Sakyo-ku, Kyoto 606-01, Japan)*. Eur J Mech A 12(2) 249-263 (1993).

The effect of neutron irradiation on creep crack growth in an infinite plate is analyzed by use of a double cantilever shear beam model. The model is assumed to consist of a stripe of creep damage zone which includes the crack plane and is in a state of uniaxial tension perpendicular to the crack plane, combined with the shear dominant elastic zone outside the creep damage zone. The creep crack growth in the creep damage zone is modeled by the constitutive equations of irradiation creep and irradiation creep damage proposed by the present authors.

9A347. Creep and creep damage of glass fiber reinforced polypropylene. - J Hugo, M Sova, J Cizinsky *(Natl Res Inst for Mat, Opletalova 25, 113 12 Prague 1, Czech Republic)*. Composite Struct 24(3) 233-244 (1993).

Composites based on isotactic polypropylene matrix and short glass fibers were tested for creep, creep damage and creep rupture at different temperatures and stress levels. Four composites of 5-30 wt% of glass fiber content having standard fiber-matrix adhesion were used, while two materials with 20 and 30 wt% of fibers were prepared as elevated adhesion composites. Unreinforced polypropylene was tested as a reference material. The rate of steady-state creep (which was determined by an arbitrary method) was used as a criterion for the examination of glass fiber content and fiber-matrix adhesion effects on creep. Secondary criteria, type and extent of damage and time to rupture were applied. Up to 40°C the steady state creep and creep damage of all tested polypropylene composites are retarded by glass fibers according to the fiber content. At 60°C and above, there is a distinct difference between composites of standard and elevated fiber-matrix adhesion. At higher temperatures the creep and creep damage are more or less accelerated by higher content of standard adhesion fibers; these fibers induce crazing (as a typical creep damage) at relatively low stress. Fibers of elevated adhesion shift the processes of nonrecoverable creep and crazing to the higher stress range, even if their craze inducing activity remains. It was found that the creep, creep damage and creep rupture are controlled by the steady state creep mechanism of polypropylene, a conclusion which was deduced from the stress and temperature dependence of the creep rate, as well as from the morphological analysis of damaged and ruptured specimens.

9A348. Effects of grain boundary diffusion and power law creep on cylindrical cavity deformation. - YS Lee *(Dept of Mech Eng, Chung BUK Natl Univ, Cheong JU, Chung-BUK 360-763, S Korea)*, TA Kozlosky, TJ Batt *(Westinghouse Elec, PO Box 2728, Pittsburgh PA 15230-2728)*. Acta Metall Mat 41(6) 1841-1854 (Jun 1993).

Volume growth rate, rupture time and the phenomenological creep damage parameter are investigated using both grain boundary diffusion and power law creep. Voids are assumed to be cylindrically shaped with a dihedral angle of $\pi/2$, and are arrayed in the grain boundary at constant spacing and radius. The grain boundary separation velocity is obtained from a modification of the stress analysis result obtained from a previous analysis. The results obtained in the analysis are compared with the results obtained using the spherical cap (dihedral angle, $\psi = 70°$) of Needleman and Rice. The results show that if L/a is large, cavity deformation is controlled by the grain boundary diffusion mechanism while power law creep controls the deformation in the range of small L/a. These results are consistent with the results obtained by Needleman and Rice.

9A349. Experimental study of behavior of low alloy steels in the initial growth stage of creep cracks. - Akio Fuji, Masaki Kitagawa *(Res Inst, Ishikawajima-Harima Heavy Indust, Toyosu Kotu-ku, Tokyo 135, Japan)*, A Toshimitsu Yokobori *(Dept of Mechatronics and Precision Eng, Tohoku Univ, Aoba, Sendai 980, Japan)*. Eng Fracture Mech 45(1) 39-50 (May 1993).

In the early stage of creep crack growth, low alloy steels exhibit a transitory behavior of which the expression for the crack growth rate (da/dt or a) as a function of the Cx integral or of the load line displacement rate (δ) becomes anomalous: the data deviate from the linearity describing a nose, thereby forming a part called the tail. In empirically analyzing the phenomenon, which has been taken to indicate the extent of degradation of the material, the following observations are made for its formation mechanism and chronological progress for 1CrMoV steel and 2.25 Cr-1Mo steel. The electrical potential method overestimates the crack length while it is small.

9T350. Life extension of high temperature components. - BF Dyson *(Div of Mat Appl, Natl Phys Lab, Teddington, Middlesex TW11 0LW, UK)* and FA Leckie *(Dept of Mech and Env Eng, UC, Santa Barbara CA 93106)*. Appl Mech Rev 46(5) 229-231 (May 1993).

9A351. Physical aging in the creep behavior of thermosetting and thermoplastic composites. - JL Sullivan, EJ Blais, D Houston *(Ford Motor, PO Box 2053, Dearborn MI 48121)*. Composites Sci Tech 47(4) 389-403 (1993).

The creep behavior of a series of fiber-reinforced plastics (FRP) and corresponding resins has been studied, with emphasis on elucidating the role of physical aging effects on FRP viscoelastic behavior. Thermosetting and thermoplastic composites were studied, representing semicrystalline, amorphous, adn highly filled amorphous polymer matrix FRPs. It was found that physical aging effects are operative for all FRPs including the semicrystalline systems. Time-aging-time and time-temperature superposition are found to be valid procedures for short-term creep behavior; they cannot be applied to long-term creep behavior. However, long-term creep can be satisfactorily predicted from momentary creep by using an effective time theory. Evidence of a universal, temperature shift factor temperature dependence is presented.

274K. ABLATION, SPALLATION, DELAMINATION

9A352. **Description of 2D spallation in pure copper.** - Ze Ping Wang *(Inst of Appl Mech, SW Jiaotong Univ, Chengdu, Sichuan 610031, Peoples Rep of China)*, Feng Lei Huang, Min Hou, Shou Rong Yun, Jing Ding *(Mech Eng Dept, Beijing IT, PO Box 327, Beijing 100081, Peoples Rep of China)*. Int J Fracture 60(3) 195-208 (1 Apr 1993).

A new ductile dynamic failure model, based on a porous element consisting of a single spherical void of radius a in a sphere of radius b subject to internal pressure P_g and external stress $\sigma_r = -\alpha P + (\alpha - 1)P_g$, is developed in the present work. Work-hardening behavior, rate-dependent contribution and inertial effects are taken into account in the model. Stress controlling mechanism is adopted while considering the contribution of void nucleation to rate of porosity Φ. The mathematical model presented here is incorporated in a hydrodynamic 2D finite-difference computer code, to simulate 2D spallation of pure copper. Comparison of numerical calculation with experimental results show that the model described the process of spall experiment successfully. The future improvements of the model are discussed.

9A353. **Role of indentation fracture in free abrasive machining of ceramics.** - R Chauhan, Y Ahn, S Chandrasekar, TN Farris *(Sch of Indust Eng and Aeronaut and Astronaut, Purdue)*. Wear 162-164(PART A) 246-257 (13 Apr 1993).

Free abrasive machining (FAM) is widely used for stock removal and surface finishing of ceramics. In FAM, material removal results from mechanical action between the abrasive slurry, which is trapped between the workpiece and a rotating lapping block, and the workpiece. Microscopic observations of the machined surface show that lateral cracking due to indentation by the abrasive particles contributes substantially to material removal. A simple model of FAM is developed which is based on indentation fracture and takes into account the abrasive particle distribution in the slurry. The model is used to predict the number of particles actually involved in the machining process, the distribution of load among these particles, and the depth of the plastically deformed layer on the workpiece surface. Many of the predictions of the model are well supported by experimental observations from the FAM of aluminum oxide, Ni-Zn ferrite, and glass using a silicon carbide slurry.

274M. MICROMECHANISMS

9A354. **Ductile fracture by the growth and coalescence of microvoids of nonuniform size and spacing.** - PF Thomason *(Dept of Aeronaut and Mech Eng, Univ of Salford, Salford M5 4WT, UK)*. Acta Metall Mat 41(7) 2127-2134 (Jul 1993).

A 2D plane strain model of void growth and coalescence in a rigid-plastic solid, containing void sizes and spacings which can be highly non-uniform, is developed to investigate the effects of non-uniform distributions of void-nucleating particles on the ductility of a metal. The theoretical void-growth strains to ductile fracture for a wide variation in void diameters and spacings show that, for a given volume fraction of voids, the minimum ductile fracture strain occurs when the voids are of uniform size and spacing. For the same volume fraction voids, greatly increased ductility is likely to be achieved when the void sizes and spacings are highly non-uniform and the sub-cell volume fractions are also non-uniform.

274X. STOCHASTIC ASPECTS

9A355. **Comparison of analytical counting methods for Gaussian processes.** - V Bouyssy *(Tech Univ, Munchen, Germany)*, SM Naboishikov *(Tech Univ, Vinniza, Ukraine)*, R Rackwitz *(Tech Univ, Lehrstuhl Massivbau, Arcisstr 21, D-8000 Munchen 2, Germany)*. Struct Safety 12(1) 35-57 (Apr 1993).

For structural components under random loading, realistic fatigue life predictions require a damage accumulation law together with a cycle counting method. If the classical, linear and memory-less summation rule according to Palmgren-Miner is adopted and the underlying stress process is ergodic substantial simplifications can be reached. From experiments and certain theoretical considerations, so-called rainflow range or local range counting appears most appropriate. Even if the underlying is a Gaussian process, easy analytical solutions are at most available for special types of processes. Therefore, counting usually must be done numerically at observed or artificial stress histories which is extremely time consuming.

9A356. **Mechanistically based approach to probability modeling for corrosion fatigue crack growth.** - DG Harlow and RP Wei *(Dept of Mech Eng and Mech, Lehigh Univ, Bethlehem PA 18015)*. Eng Fracture Mech 45(1) 79-88 (May 1993).

An approach and methodology for developing a probability model for life prediction and its utility are demonstrated. The goal of this probabilistic approach is to make stochastically tight estimates of life for conditions that are beyond the range used in typical supporting data. Probability models, versus statistically based modes, are used to describe the influences of fundamental variables through mechanistically based models of the failure processes. The approach and methodology is illustrated through the use of a simplified model for reaction controlled corrosion fatigue and crack growth for ferrous alloys in aqueous environments.

9A357. **Note on cycle counts in irregular loads.** - I Rychlik *(Dept of Math, Univ of Lund, Box 118, S-22100 Lund, Sweden)*. Fatigue Fracture Eng Mat Struct 16(4) 377-390 (Apr 1993).

In this paper we discuss cycle counting methods, such as rainflow-, crest-to-trough-, positive peak-count and different damage accumulation rules, for irregular random loads, which have an infinite number of local extremes in finite intervals, eg, the fourth spectral moment is infinite. We present conservative bounds for the expected damage for such loads from the upcrossing intensity. These results are illustrated by examples of Gaussian x^2-, and Morison-loads.

9A358. **Statistical analysis of material damage with changing internal structure.** - CW Woo and DL Li *(Dept of Mech Eng, Univ of Hong Kong, Hong Kong)*. Eng Fracture Mech 45(2) 245-254 (May 1993).

An investigation on the mechanical properties of material with changing internal structure or damage induced by large deformation is carried out. A new experimental procedure has been established for the ductile damage test with a large number of specimens for the purpose of the statistical analysis. The experimental results show that the macroscopic mechanical properties of material both prior to and during the process of the mechanical damage vary in a random manner. The statistical analysis reveals that the scatter of the material properties during the process of damage evolution is larger then that of the original material properties. When the original material properties are treated separately as deterministic and random ones, the obvious statistical discrepancy during the process of the damage evolution is exposed. The results obtained provide much useful information for the prediction of material damage based on the probabilistic formulation.

276. Fracture and damage mechanics

276A. GENERAL THEORY

9A359. **Fracture mechanics-based failure analysis.** - AR Rosenfield and CW Marschall *(Battelle, Columbus OH 43210)*. Eng Fracture Mech 45(3) 333-338 (Jun 1993).

Twenty case studies, involving the application of fracture mechanics to structural integrity, have been reviewed and compared to a similar report published in 1978. Sixteen of the new cases discussed failures, while four were fitness-for-purpose analysis (ie, evaluation of safe operating conditions of defect-containing structures). In reviewing the case studies, it was found that the calculated value of stress intensity at failure was usually only approximately equal to the reported value of fracture toughness. Furthermore, in a number of cases, the calculated stress intensity was significantly less than the reported fracture toughness, thereby indicating a non-conservative fracture mechanics analysis. The probable cause for this relatively poor correlation was that the inputs into the analyses, particularly fracture toughness were often approximations. Both reviews suggest that the likelihood of failure is particularly large when there is a defect greater than 25 mm (1.0 in) in size and when the fracture toughness: yield strength ratio is less than $0.16\sqrt{m}$ ($1.0\sqrt{in}$). No significant improvement in accuracy of failure analysis was detected compared to the earlier paper.

9A360. **Screw dislocation dipoles near an internal crack.** - KM Lin *(Dept of Mat Sci, Feng Chia Univ, Taichung, Taiwan, ROC)*, CT Hu, Sanboh Lee *(Dept of Mat Sci and Eng, Natl Tsing Hua Univ, Hsinchu, Taiwan, ROC)*. Eng Fracture Mech 45(3) 321-331 (Jun 1993).

Based upon the results of previous work the system of the screw dislocation dipole interacting with an internal crack is studied. The analytic formulae of the physical variables, such as stress field, strain energy and flipping energy, image force and image torque, and stress intensity factor, are obtained. Both dipole emission from the crack and the effect of the dipole on crack shielding are discussed in detail. If a dipole near an internal crack is originated from the crack, it must be at an orientation angle α_{max} corresponding to a state of maximum energy when emission occurs, and then rotates to lower its strain energy to an orientation angle α_{min} in the range of $(90° + \lambda/2)$ and $(270° + \lambda/2)$ due to the image torque, where λ denotes the angle between emission and crack planes. A dipole orienting at an angle α_{min} shields both crack tips simultaneously. In addition, the behavior of a dipole coplanar with the crack is also investigated. It is found that (1) under the action of a mode III applied stress, a zero-force point exists in front of the crack tip when the dipole orients at $\alpha = 180°$; and (2) a maximum shielding (for $\alpha = 180°$) or antishielding (for $\alpha = 0°$) on the left-hand crack tip occurs when the ratio of the half crack length to the distance from the right-hand tip to the dipole center (l/p) is equal to 0.25.

9A361. Strain energy release rate for a cracked plate subjected to out-of-plane bending moment. - MJ Young and CT Sun *(Sch of Aeronaut and Astronaut, Purdue)*. Int J Fracture 60(3) 227-247 (1 Apr 1993).

For a through-the-thickness crack in an infinite plate subjected to out-of-plane uniform bending moment, the strain energy release rate is determined using the virtual crack extension and the variation of potential energy. It is shown that the strain energy release rate for the Reissner's plate approaches the classical plate solution as the ratio of plate thickness to crack size becomes infinitesimally small. By using this result, the limiting expression of the stress intensity factor can be explicitly obtained. For general problems, the modified crack closure method is shown to be an efficient tool for evaluating the strain energy release rates from which the stress intensity factor can be calculated. Both the classical plate element and the Mindlin plate element are investigated, and the applicability of the classical plate element is evaluated. Because the stress-free conditions along the crack face lead to inter-penetration of the plate, a line contact model is assumed to investigate the closure effect using Reissner plate theory. Closure at the compressive side is shown to reduce crack opening displacement and consequently the stress intensity factors. When closure is considered, the strain energy rate based on the Reissner plate theory converges to the classical plate solution. This is similar to the nonclosure case.

276B. LINEAR ELASTIC FRACTURE MECHANICS

9A362. Fracture criterion for the axisymmetric disking process. - S Santhanam *(Dept of Mech Eng, Villanova Univ, Villanova PA 19085)*. Int J Fracture 60(1) 65-77 (1 Mar 1993).

Disking is a process designed to cut brittle plates and rods. In axisymmetric disking, a pre-cracked cylindrical rod is placed in an elastic, annular sheath and the composite is subjected to biaxial fluid pressure. At a critical pressure the crack runs across the circular section of the rod producing a clean cut. A linear elastic fracture mechanics analysis is used to develop a fracture criterion for the process. The problem is formulated as a singular integral equation of the first kind with a Cauchy type kernel. The stress intensity factors are determined as a function of crack size and shear moduli.

9A363. Stress intensity factors and interaction of three cracks on both edges of finite width sheet. - MJ Shu *(Dept of Mech Eng, Univ of Pet, Shandong, Dongying 257062, Peoples Rep of China)*, J Petit, ZD Jiang, G Bezine *(Lab Mec Phys Mat, URA CNRS 863, ENSMA 86034 Poitiers, Cedex, France)*. Eng Fracture Mech 45(3) 407-414 (Jun 1993).

Two equal parallel cracks on one edge and one unequal parallel crack on the other edge of a finite width sheet are studied. Formulae for calculating the stress intensity factors (SIF) of this crack configuration are obtained from the results of FE analysis. The differences between the formula and the FE results is less than 3%. On this basis, the influence of crack interactions on SIF is discussed.

See also the following:

9A245. Cracked plates subjected to out-of-plane tearing loads
9A324. Effect of stress ratio on the fatigue threshold condition of physically small cracks
9A842. Three-dimensional analysis of thermally loaded cracks

276D. STRESS INTENSITY FACTOR CALCULATIONS

9A364. Applications of the weight function method. - TPJ Mikkola *(Tech Res Centr, VTT, Ship Lab, Vuorimiehentie 5, SF-02150 Espoo, Finland)*. Eng Fracture Mech 45(2) 209-231 (May 1993).

New solutions were developed for the stress intensity factor and the crack opening displacement at the crack center for the semi-elliptical surface crack in a wide plate under remote tension and bending loads. The solutions were based on results of FE analyses made by an automated program system and the accuracy of the results were carefully studied. The new solutions were used for developing weight functions for the structure. The accuracy of the present weight function method is sufficient for practical applications.

9A365. Boundary element crack closure calculation of 3D stress intensity factors. - TN Farris and M Liu *(Sch of Aeronaut and Astronaut, Purdue)*. Int J Fracture 60(1) 33-47 (1 Mar 1993).

A general method for BE-crack closure integral calculation of 3D stress intensity factors is presented. An equation for the strain energy release rate in terms of products of nodal values of tractions and displacements is obtained. Embedded and surface cracks of modes I, II, and III are analyzed using the proposed methods. The multidomain BE technique is introduced so that the crack surface geometry is correctly modeled and the unsymmetrical boundary conditions for mode's II and III crack analysis are handled conveniently. For all the examples demonstrated in this paper, 54 BEs are used, and the most suitable ratio of the width of crack front elements to the crack depth is 1/10 and the calculation error is kept within ± 1.5%.

9A366. Comparison of two quarter-point element extrapolation equations for 3D mixed-mode problems. - Li Sen Chen and Jao Hwa Kuang *(Dept of Mech Eng, Natl Sun Yat-Sen Univ, Kaohsiung 80424, Taiwan, ROC)*. Eng Fracture Mech 45(1) 21-23 (May 1993).

Two quarter-point extrapolation equations for the stress intensity factors in 3D mixed-mode problems are compared, one set of equations proposed by Rhee and the other derived from the Tracey-Barsoum equations. The nodal displacements of the collapsed quarter-point elements around the crack tip are employed by both methods to extrapolate the stress intensity factors. The analytical derivations indicate good agreement between the methods.

9A367. Generalized WF solution for mode I 2D part-elliptical cracks. - GS Wang *(Struct Div, Aeronaut Res Inst, S-161 11 Bromma, Sweden)*. Eng Fracture Mech 45(2) 177-208 (May 1993).

A generalized approximate weight function solution is achieved for the 2D mode I part-elliptical crack subjected to arbitrary crack surface pressure. This solution can be used to solve the general crack problem according to the superposition principle. The weight functions are derived from one or several stress intensity factor results and the corresponding crack surface pressures. A newly developed generalized approximate crack surface displacement solution for the arbitrary crack type and crack surface pressure, along with a criterion, is used in the solution so that good accuracy can be achieved for various problems. Examples are given to demonstrate this procedure.

9A368. Influence of crack closure on SIF for plates under bending: A mixed mode case. - KN Ramachandran Nambissan *(Dept of Civil Eng, REC, Calicut 673 601, India)* and M Sreekumar *(Dept of Civil Eng, MIT, Manipal 576 119, India)*. Eng Fracture Mech 45(2) 149-158 (May 1993).

Solutions to mixed mode problems for plates under bending, with inclined through-the-thickness cracks, are obtained taking the closure phenomenon on the compression zone into account. A 3D FEM using singular and transition elements to model the crack tip region is employed for the analysis. The closure region on the crack faces is determined by a trail and error procedure.

9A369. Mixed-mode stress intensity factors for interacting semi-elliptical surface cracks in a plate. - RB Stonesifer *(Comput Mech, Julian PA 16844)*, FW Brust and BN Leis *(Dept of Eng Mech, Battelle, Columbus OH 43201)*. Eng Fracture Mech 45(3) 357-380 (Jun 1993).

Mixed-mode stress intensity factor solutions are presented for two parallel, but not necessarily coplanar, interacting surface cracks in a plate. The plate is subjected to a remote uniaxial stress acting normal to the crack planes. The crack separation distances, measured normal and parallel to the crack planes, are varied to provide 24 crack geometries. The smallest separation distances is equal to a quarter of the plate thickness. The equal sized interacting cracks have fixed depth-to-thickness ratio of 0.5 and fixed half-width-to-depth ratio of 3. The FE alternating method is used to develop the solutions. The tendency for the cracks to grow apart or to coalesce is discussed.

9A370. Simple estimates of stress intensity factors by crack path approximation with application to fatigue reliability. - HH Harkness *(Dept of Theor and Appl Mech, NWU)* and T Belytschko *(Dept of Civil Eng, NWU)*. Eng Fracture Mech 45(2) 255-264 (May 1993).

Simple methods for estimating stress intensity factors are developed for non-rectilinear edge cracks in 2D. These methods are based on observations that the stress intensity factors depend primarily on only a few crack geometry characteristics; for edge cracks in a uniaxial stress field, the location of and tangent to the crack tip are critical. Examples demonstrate that the stress intensity factor estimates obtained by approximating the shape of edge cracks are highly accurate.

9A371. Stress intensity factors for a crack in planar disking. - S Santhanam *(Dept of Mech Eng, Villanova Univ, Villanova PA 19085)*. Int J Fracture 60(1) 19-32 (1 Mar 1993).

Disking is a relatively new manufacturing process for cutting-slicing brittle plates and rods. In the planar disking configuration, a pre-cracked plate is placed against plate and the two are squeezed together by fluid pressure. At a critical pressure the crack runs across the thickness of the brittle plate producing a clean cut. In this paper a fracture criterion is developed for the process using linear elastic fracture mechanics. The problem is formulated in terms of a singular integral equation with the derivative of the crack surface displacement (dislocation density) as the unknown function. Numerical quadrature is used to determine the stress intensity factors as a function of the parameters of the problem.

9A372. Weight functions for interface cracks. - L Banks-Sills *(Eda and Jaime David Dreszer Fracture Mech Lab, Dept of Solid Mech Mat and Struct, Fac of Eng, Tel-Aviv Univ, 69978 Ramat Aviv, Israel)*. Int J Fracture 60(1) 89-95 (1 Mar 1993).

Weight functions are developed for determining stress intensity factors of cracks along an interface between two linear, elastic materials. As a result of the interface, both mode I and II components will be present for all but very special loading cases. The weight functions are employed to produce exactly the known stress intensity factors of a crack along an interface loaded by tensile and shear point forces.

See also the following:

9A21. Boundary element analysis of thermal stress intensity factors for cusp crack in transient state

276E. VISCOELASTIC PROBLEMS

9A373. **Effect of grain-size on the stress and velocity fields ahead of a crack in a material which deforms by Coble creep.** - J Pan and ACF Cocks *(Dept of Eng, Cambridge Univ, Trumpington St, Cambridge CB2 1PZ, UK)*. Int J Fracture 60(2) 121-134 (15 Mar 1993).

The stress and velocity fields ahead of a grain-boundary crack in a material which deforms by Coble creep are investigated for a series of grain sizes using the numerical analysis technique established by Cocks. The numerical results are compared with the linear viscous fields obtained by the BEM and the FEM. It is demonstrated that a detailed knowledge of the micromechanical processes of material transport and deformation are required to determine the stress and displacement fields for the grains which immediately surround the crack tip. But the response of the surrounding material can be adequately described from a conventional linear viscous analysis of the problem.

9A374. **Void growth ahead of a dominant crack in a material which deforms by coble creep.** - ACF Cocks and J Pan *(Dept of Eng, Cambridge Univ, Trumpington St, Cambridge CB2 1PZ, UK)*. Int J Fracture 60(3) 249-265 (1 Apr 1993).

This paper examines the process of void growth ahead of a dominant crack in a material which deforms by grain-boundary diffusion. A numerical technique recently developed by the authors is used to analyze the full interaction between void growth and deformation ahead of the crack tip. For the situation where voids only grow within a narrow zone directly ahead of the crack tip, it is possible to develop a range of simple analytical models. It is demonstrated that for this class of problem of suitable utilization of the dislocation model suggested by Thouless provides a good estimation of the void growth rate.

See also the following:

9A175. FE analysis of viscoelastic fracture

276F. CRACK TIP PLASTICITY PROBLEMS

9A375. **Best fit curve through crack growth fracture resistance data.** - BK Neale *(Nucl Elec, Berkeley Tech Centre, Berkeley, Glos GL13 9PB, UK)*. Fatigue Fracture Eng Mat Struct 16(4) 465-472 (Apr 1993).

The ESIS recommendations for determining the fracture resistance of ductile materials make use of an offset power law to evaluate the best fit curve to crack growth fracture resistance data. Evaluation of the offset power requires the use of nonlinear regression analysis, although an iterative linear regression analysis can be used if the data are transformed by taking logarithms. The two analyses are compared with a proposed alternative formulation for the offset power law which can be evaluated using an iterative linear regression analysis without the need to transform the data.

9A376. **Complete theoretical analysis for higher order asymptotic terms and the HRR zone at a crack tip for mode I and mode II loading of a hardening material.** - S Yang, YJ Chao, MA Sutton *(Dept of Mech Eng, Univ of S Carolina, Columbia SC 29208)*. Acta Mech 98(1-4) 79-98 (1993).

A complete development for the first two terms of the crack tip fields for both Mode I and Mode II loading of a hardening material in either plane stress or plane strain is performed, including the elastic deformation in the analysis. It is shown that the determination of the order of the second term depends on both n and whether plane stress or plane strain is considered. In addition, regions of HRR dominance at a crack tip for the field variables are estimated.

9A377. **Computational procedure for the simulation of ductile fracture with large plastic deformation.** - S Roy, RJ Dexter, AF Fossum *(Eng and Mat Sci Div, SWRI)*. Eng Fracture Mech 45(2) 277-293 (May 1993).

It is now well-known that the applicability of the single-parameter J-approach is restricted only to high constraint crack geometries and materials of low ductility. Consequently, there is a need to develop a ductile fracture criterion that does not suffer from the geometry dependence exhibited by the J-integral. The purpose of this paper is to describe the formulation and implementation of an efficient finite deformation algorithm that can be used for the prediction of elasto-plastic fracture in ductile materials where J-dominance is violated. The application of continuum damage models as potential ductile fracture criteria is discussed. The overall efficiency of the code is enhanced by means of the BFGS (Broyden, Fletcher, Goldfarb and Shanno) solution algorithm. The effectiveness of including material damage in the constitutive behavior to predict ductile failure in a notched tensile specimen is addressed.

9A378. **Dependence of acoustic emission for low strength steels upon the embrittlement and the plastic zone reduction at the crack tip during corrosion fatigue crack propagation.** - ZF Wang, J Li, W Ke *(Corrosion Sci Lab, Inst of Corrosion and Protection of Metals, Acad Sinica, Shenyang, China)*, Z Zhu *(State Key Lab for Fatigue and Fracture of Mat, Inst of Metal Res, Acad Sinica, Shenyang, China)*. Fatigue Fracture Eng Mat Struct 16(4) 441-451 (Apr 1993).

Acoustic emission signals were continuously monitored during fatigue crack propagation for two kinds of low strength steel placed in either laboratory air or 3.5% NaCl solution. The plastic deformation of the materials at the crack tips were compared by determining the changes in specimen geometry at the fracture surface in the thickness direction while the hydrogen distribution from the crack tip material was analyzed by SIMS. The results showed that acoustic emission was less active in an aqueous solution than in air and that the plastic zone size was reduced in a corrosive medium.

9A379. **Determination of the asymptotic fields for steady crack growth through the application of path independent integrals.** - FJ Barth *(Lehrstuhl Tech Mech, Univ Kaiserslautern, Erwin Schrodinger Str, 6750 Kaiserslautern, Germany)*. Int J Fracture 60(1) 79-87 (1 Mar 1993).

An asymptotic analysis of the near tip fields is given for a steadily propagating crack. The power hardening material is characterized by J_2 flow theory as well as deformation theory. A further condition for steady state crack growth is obtained. By using a new path independent integral, explicit results are given for the order of the crack tip singularity. It was found that the singularities calculated by using the different material models are not the same.

9A380. **Failure analysis of a cracked plate based on endochronic plastic theory coupled with damage.** - CL Chow *(Dept of Mech Eng, Univ of Michigan, Dearborn MI 48128-1491)* and XF Chen *(Dept of Mech Eng, Univ of Hong Kong, Pokfulam Rd, Hong Kong)*. Int J Fracture 60(1) 49-63 (1 Mar 1993).

An anisotropic model of damage mechanics for ductile fracture incorporating the endochronic theory of plasticity is presented in order to take into account material deterioration during plastic deformation. An alternative form of endochronic (internal time) theory which is actually an elasto-plastic damage theory with isotropic-nonlinear kinematic hardening is developed for ease of numerical computation. Based on this new damage model, a FE algorithm is formulated and then employed to characterize the fracture of thin aluminum plate containing a center crack. A new criterion termed as Y_R-Criterion is proposed to define both the crack initiation angle and load.

9A381. **Higher order asymptotic crack fields in a power-law hardening material.** - S Yang, YJ Chao, MA Sutton *(Dept of Mech Eng, Univ of S Carolina, Columbia SC 29208)*. Eng Fracture Mech 45(1) 1-20 (May 1993).

The asymptotic stress and deformation fields for plane problems are developed for a crack tip embedded in a power-law elastic-power material. Using an asymptotic expansion and separation of variables for the stress function, a series solution is obtained for the stress and deformation at a crack tip. The most singular term in the series solution is the HRR solution, after Hutchinson and Rice and Rosengren. Good agreement with the FE results confirm the analytical findings. It is further demonstrated that in the plane strain, Mode I case the first three terms, controlled by two parameters, can be used to characterize the crack tip stress fields for a variety of specimen geometries and materials with various hardening exponents.

9A382. **Influence of plasticity on mixed mode interface toughness.** - V Tvergaard *(Solid Mech Dept, Tech Univ, Lyngby, Denmark)* and JW Hutchinson *(Div of Appl Sci, Harvard Univ, Cambridge MA)*. J Mech Phys Solids 41(6) 1119-1135 (Jun 1993).

Calculation are reported for the mixed mode toughness of an interface joining an elastic-plastic solid to a solid which does not yield plastically. A potential function of the components of the crack face displacements is used to generate the tractions along the interface where the fracture processes causing separation occur. The two main parameters characterizing this potential are the work of separation per unit area and a peak normal stress. This description of the interface process is embedded within the continuum description as a boundary condition on the interface linking the adjoining solids. Particular emphasis is placed on the ratio of the steady-state interface toughness to the "intrinsic" work of separation as it depends on plastic yielding and on the combinations of modes 1 and 2. Plasticity enhances the interface toughness for all modes of loading, but substantially more so in the presence of a significant mode 2 component of loading than in near-mode 1 conditions.

9A383. **J-integral computations in the incremental and deformation plasticity analysis of small-scale yielding.** - DM Stump *(Idaho Natl Eng Lab, PO Box 1625 MS 2218, Idaho Falls ID 83415-2218)* and E Zywicz *(UC PO Box 808 L-122, LLNL)*. Eng Fracture Mech 45(1) 61-77 (May 1993).

Detailed numerical studies of small-scale yielding in elastic power-law plastic materials under Mode I loading reveal a path dependence of the J-integral in small-strain incremental-theory plasticity calculations, while corresponding studies employing deformation-theory plasticity show no such behavior. The path dependence of the incremental-theory calculations is sensitive to the pressure of T-stresses and deviates substantially from the remote elastic J-value at radial distances, r, on the order r ≤ CTOD (crack-tip opening displacement). A comparison of the fields predicted by the two different plasticity implementations reveals that deep within the plastic zones, stresses are in reasonable agreement over the angular interval 10° < θ < 160° with moderate disagreement in the regions near the crack faces.

9A384. On a mixed-mode Dugdale model. - DW Nicholson *(Mech and Aerospace Eng, Univ of Central Florida, Orlando FL 32816)*. Acta Mech 98(1-4) 213-219 (1993).

A model attributed to Dugdale provides a correction for plasticity effects at crack tips in Mode I, under the assumption of small-scale yielding. Similar models have been proposed for Modes II and III, the former fairly recently. In the present study, the Dugdale model is extended to cases combining Modes I, II, and III, based on the von Mises yield criterion. The combined model provides an a posteriori estimate for plasticity effects, based only on the stress intensity factors from the elasticity solution.

9A385. Two-dimensional model for numerical investigations of stable crack growth in thick smooth fracture mechanics specimens. - GX Shan, O Kolednik *(Erich-Schmid-Inst Festkorperphys, Osterreichischen Akad, Wissenschaften 8700, Leoben, Austria)*, FD Fischer *(Inst Mech, Montanuniv Leoben, Christian-Doppler-Lab Mikromech Werkstoffe 8700, Leoben, Austria)*, HP Stuwe *(Erich-Schmid-Inst Festkorperphys, Osterreichischen Akad, Wissenschaften 8700, Leoben, Austria)*. Eng Fracture Mech 45(1) 99-106 (May 1993).

A numerical simulation for the stable crack growth in a thick smooth compact tension specimen with 2D elastic-plastic FE analyses is presented. The different fracture behaviors in the center and near the side surfaces of the specimen were accounted for by using plane strain analysis for the center part and plane stress analysis for the surface part. The input data to control the fracture initiation and crack growth, ie, $CTOD_i$ and $CTOA_c$, were directly measured from the center and the side surfaces of specimens. The calculated results were compared with the experimental ones.

See also the following:

9A308. Mechanisms and behavior of overload retardation in AISI 304 stainless steel

276J. COMPOSITES

9A386. Actual contribution of crack deflection in toughening platelet-reinforced brittle-matrix composites. - G Pezzotti *(Inst of Sci and Indust Res, ISIR Osaka Univ, Ibaraki 567, Osaka, Japan)*. Acta Metall Mat 41(6) 1825-1839 (Jun 1993).

The effectiveness of crack deflection as a single toughening mechanism is evaluated in the case of brittle-matrix reinforced by high aspect-ratio platelets. Microstructural parameters characterizing size, morphology, orientation and distribution of the second phase including aspect ratio, volume fraction and interparticle distance, were experimentally obtained by means of image analysis techniques on a model composite. It is concluded that crack deflection processes may play an important role only as precursors for other operative mechanisms, being, in the general case, the deflection of the crack path only phenomenologically related to toughening.

9A387. Combined experimental and FE study to predict the failure mechanisms in SiC coated carbon-carbon composites at room and elevated temperatures under flexural loading. - H Mahfuz, PS Das, Dongwei Xue, J Krishnagopalan, S Jeelani *(Mat Res Lab, Tsukegee Univ, Tsukegee AL 36088)*. J Reinforced Plastics Composites 12(7) 825-842 (Jul 1993).

Response of quasi-isotropic laminates of SiC coated Carbon-Carbon (C-C) composites have been investigated under flexural loading at various temperatures. Variation of load-deflection behavior with temperatures are studied. Increase in flexural strength and stiffness are observed with the rise in temperature. Extensive analyses through Optical Microscope and Non-Destructive Evaluation have been performed to understand the failure mechanisms. Data generated using FE analysis are presented to corroborate the experimental findings, and a comparison in respect of displacement and stress-strain behavior are given to check the accuracy of the FE analysis. Reasonable correlation between the experimental and FE results have been established.

9A388. Damage development in a short fiber reinforced composite. - Kai-Youarn Hour *(B&W Nucl Env Services, Lynchburg Tech Center, PO Box 11165, Lynchburg VA 24506)* and Huseyin Sehitoglu *(Dept Mech and Mat, Natl Sci Found, 1800 G St NW, Washington DC 20550)*. J Composite Mat 27(8) 782-805 (1993).

The important issue of finding a relationship between a macroscopic damage variable and the process of damage accumulation within a material is addressed in this article. Monotonic and cyclic deformation behavior has been studied in a randomly distributed glass reinforced polyester matrix composite. The composite material is called sheet molding compound, abbreviated as SMC, with a short glass fiber weight of 30%. Based on these measurements, the damage volumetric strain was calculated that increased continuously with cycles in load-controlled experiments. Microscopic observations revealed that cracks grew along the matrix-fiber interfaces as well as the matrix-filler interfaces. Many of these cracks are normal to the specimen thickness direction.

9A389. Delamination growth in composite plates subjected to transverse loads. - LE Doxsee, P Rubbrecht, L Li, I Verpoest *(Dept of Metall and Mat Eng, Katholieke Univ, Leuven, Belgium)*, M Scholle *(DSM-Res, Geleen, Netherlands)*. J Composite Mat 27(8) 764-781 (1993).

Experiments were performed to study the growth of damage in fiber reinforced cross-ply carbon-epoxy composite plates subjected to transverse loads. The plates were repeatedly loaded and unloaded, with the maximum displacements of each loading cycle greater than or equal to the previous cycle. After certain loading cycles, the extent of damage was measured by a combination of C-scanning, optical microscopy, and radiography. The critical strain energy release rate for delamination growth was determined by relating the delamination area to the amount of energy dissipated by the formation of that delamination.

9A390. Delamination, fiber bridging and toughness of ceramic matrix composites. - DAW Kaute, HR Shercliff, MF Ashby *(Eng Dept, Cambridge Univ, Mat Group Trumpington St, Cambridge CB2 1PZ, UK)*. Acta Metall Mat 41(7) 1959-1970 (Jul 1993).

Delamination cracks in long-fiber reinforced ceramic matrix composites are found to be bridged by fibers which span the crack wake at a shallow angle. The *in situ* observation of bridging fibers reveals that these are subject to considerable tensile forces, giving rise to a substantial crack closure force. The overall crack closure force is determined by the number of bridging fibers, steadily reduced by fiber failure caused by high bending moments at the root of each fiber. This leads to a model for crack closing forces combining simple mechanics and Weibull statistics. The model relates these forces to the properties of fibers, matrix and their interface.

9A391. Effects of fabric weave and surface texture on the interlaminar fracture toughness of aramid-epoxy laminates. - BJ Briscoe, RS Court, DR Williams *(Dept of Chem Eng and Chem Tech, Imperial Col of Sci Tech and Med, Kensington, London SW7 2BY, UK)*. Composites Sci Tech 47(3) 261-270 (1993).

The mode I interlaminar fracture toughness of woven aramid-fibre and epoxy resin laminates has been investigated as a function of the fabric weave and the fabric surface texture used in the construction of the laminates. The experimental values of G_{IC} were found to increase significantly with increasing crack length for all the materials investigated. This behavior is ascribed to the presence of fibre bridging during crack propagation. The presence of fibre bridging in the cracks has been observed directly. The maximum values of G_{IC} determined were in the range of 0.5 - 3.0 kJ/m^2, depending upon both the fabric weave and the surface texture. An optical comparison of sections of these laminates confirmed an enhanced concentration of fibre ends in the resin-rich interply zones for the fabrics with the most obvious concentration of fibre ends in their surface. This type of fabric surface texture provided a more homogeneous fibre distribution in the composite which resulted in enhanced levels of fibre bridging and, as a consequence, enhanced fracture toughness.

9A392. Evaluation of the stress intensity factor of brittle polymers based on the crack arrest concept. - K Idonije, M Motuku, I Shehata, H Aglan *(Dept of Mech Eng, Tuskegee Univ, Tuskegee AL 36088)*. J Reinforced Plastics Composites 12(7) 778-786 (Jul 1993).

One of the commonly used criteria for characterizing the fracture resistance of brittle glassy polymers or their composites is the critical stress intensity factor or crack resistance. Specimen geometries such as single edge notch, compact tension, and three-point bend etc, are conventionally used for this purpose. On this basis, the critical stress intensity factor is evaluated at the onset of crack propagation by using the length of the initial notch. Plastics in general experience a slow crack growth regime before the avalanche-like fracture, which is not taken into consideration in the calculation of the critical stress intensity factor. Hence, serious errors are encountered in the evaluation of the resistance of plastics to crack propagation based on the critical stress intensity factor concept, when standard test geometries are employed. In the present work, a crack arrest experiment employing a double cleavage drilled compression specimen is proposed to evaluate the resistance of brittle polymers to fracture.

9A393. Fracture analysis of dental composites. - RMV Pidaparti, WA Boehmer *(Dept of Mech Eng, Purdue Univ, Indianapolis IN 46402)*, MW Beatty *(Section of Dental Mat, Dept of Adult Restorative Dentistry, Univ of Nebraska, Lincoln NE 68583)*. Eng Fracture Mech 45(1) 51-59 (May 1993).

Three dental composite materials were tested in three-point bending to determine fracture toughness using the stress intensity factor approach. Finite element analysis was used to model the specimens and the fracture toughness was calculated using the J integral and crack closure methods. The effects of tension, compression, and tension-compression moduli on the fracture toughness are presented and discussed. The results from J integral and crack closure methods were in good agreement with experimental data for the three dental composites considered.

9A394. Fracture strength testing of δ-alumina fibers with variable diameters and lengths. - AS Kim *(Div of Eng, Brown Univ, Providence RI 02912)*, S Bengtsson *(Studsvik AB, Hot Cell Lab, S-611 82 Nykoping, Sweden)*, R Warren *(Dept of Mat Sci and Prod Tech, Lulea*

Univ, S-951 87 Lulea, Sweden). Composites Sci Tech 47(4) 331-337 (1993).

Tensile tests were performed on individual δ-alumina fibers (Safil, RF grade). The results revealed a large scatter in strengths and a clear dependence of the fracture strength on the specimen volume. The tests were evaluated on the basis of the Weibull probability function, a special modification of the Weibull analysis being developed that successfully copes with the problem of testing fibers with various diameters and test lengths. For the sample studied the Weibull modulus, m, was found to be 2.2, with a scaling constant σ_0=6.0MPa (units of volume mm^3; ie, $V_0=1mm^3$).

9A395. Fracture surface of hybrid fibre composites. - MA French *(British Aerospace, Stevenage, UK)* and G Pritchard *(Sch of Appl Chem, Kingston Univ, Penrhyn Rd, Kingston upon Thames Surrey KT1 2EE, UK)*. Composites Sci Tech 47(3) 217-223 (1993).

A study has been made of the fracture surfaces of unidirectional hybrid glass-carbon-epoxy laminates after environmental stress corrosion (ESC) by dilute sulphuric acid. Labelled isotope studies showed that the acid does not diffuse through the uncracked epoxy resin matrix, and must therefore travel through microcracks. Photomicrographs show how the carbon fibre plies can act as primary crack stoppers. Secondary cracks continue into the glass plies, often at a short distance along the carbon fibres from the primary crack. The sequence of events by which ESC cracks fracture the glass fibres and propagate through glass plies is discussed. It is proposed that some of the damage observed in glass fibres occurs after fibre fracture rather than before.

9A396. Matrix cracking and modulus reduction during the fatigue of an injection-moulded glass-nylon composite. - SA Hitchen and SL Ogin *(Dept of Mat Sci and Eng, Univ of Surrey, Guildford, Surrey GU2 5XH, UK)*. Composites Sci Tech 47(3) 239-244 (1993).

Damage accumulation in the core layer of a 50% by weight discontinuous glass fibre reinforced Nylon composite has been studied. Damage in the core, in the form of transverse cracks, has been quantified by means of a dye penetrant-sectioning technique and related to a modulus reduction measured during fatigue cycling. The experimental data are compared with the predictions of a shear lag model developed for continuous fibre cross-ply laminates relating modulus reduction to the average crack spacing.

9A397. Micromechanical elastic cracktip stresses in a fibrous composite. - J Fish *(Dept of Civil Eng and Sci Comput Res, RPI)*, N Fares *(Dept of Civil Eng, Polytech Univ, Brooklyn NY 11201)*, A Nath *(Dept of Civil and Sci Comput Res Center, RPI)*. Int J Fracture 60(2) 135-146 (15 Mar 1993).

This paper presents elastic stress distributions near a cracktip in a continuous fiber composite. The material heterogeneity is explicitly accounted for by using the FEM and a new Mesh Superposition Technique. This new technique superposes a fine mesh with heterogeneous material properties over a coarse mesh with homogeneous ones. The results indicate that the load transferred by fibers near a cracktip may be well described by the homogeneous orthotropic elastic K_I field. A technique to postprocess the K_I field to accurately obtain the detailed stress distributions within the fiber and matrix is also presented.

9A398. Mixed-mode delamination of fibre composite materials. - AJ Kinloch, Y Wang, JG Williams, P Yayla *(Dept of Mech Eng, Imperial Col of Sci Tech and Med, Exhibition Rd, London SW7 2BX, UK)*. Composites Sci Tech 47(3) 225-237 (1993).

The present paper is concerned with an investigation of the mixed-mode delamination of polymeric fibre composite materials. Various test geometries have been used to measure the interlaminar fracture energy, G_c, of both thermoplastic and thermosetting carbon fibre composites when subjected to various ratios of mode I to mode II loadings. In particular, the mixed-mode bending delamination test has been studied in detail and the results from this test method compared to those obtained from the fixed-ratio mixed-mode (FRMM) test method. Further, for the FRMM results, two methods of partitioning the measured interlaminar fracture energy G_c, have been employed; namely, by way of a local single-field approach and by a global method based on a consideration of the applied energy release rates.

9A399. Modeling of anisotropic damage at a crack tip in composite laminates. - WF Li and SY Du *(Sch of Astronaut, Harbin IT, Harbin 150006, Peoples Rep of China)*. Eng Fracture Mech 45(3) 381-385 (Jun 1993).

Anisotropic continuum damage mechanics was applied to analyze the damage at a crack tip in composite laminates. An initial attempt was made to connect continuum damage mechanics with fracture mechanics. Some quantitative relations such as those between stress, energy release rate and damage variables were established by means of the model described in this paper. It was shown that the formula $G_I = K^2_I/E$ is not applicable when the damage at a crack tip is taken into account. Also, the relation between the critical crack length and the critical damage variables was estimated and it was proved that damage variables can describe the fracture condition of composite laminates.

9A400. Modelling of 90° ply cracking in crossply laminates, including 3D effects. - FJ Guild, SL Ogin, PA Smith *(Dept of Mat Sci and Eng, Univ of Surrey, Guildford GU2 5XH, Surrey, UK)*. J Composite Mat 27(7) 646-667 (1993).

The mechanics of transverse ply cracking in crossply composite laminates is examined in detail. A 3D FE model has been developed. This has been used to calculate fracture mechanics parameters associated with transverse ply crack growth across the width of a glass fiber reinforced epoxy laminate. The predictions of the model are shown to be in good agreement with existing shear-lag analyses and experimental results from the literature.

9A401. Near-tip fields for a crack along an interface between an elastic-ideally plastic crystal and a rigid substrate. - V Gupta *(Thayer Sch of Eng, Dartmouth Col, Hanover NH 03755)*. J Mech Phys Solids 41(6) 1035-1066 (Jun 1993).

Asymptotic, plane strain stress and deformation fields are derived near the tip of stationary and a quasi-statically growing crack at an interface idealized as being rigid on one side, and single crystal on the other side. The crystalline substrate is assumed to have a limited set of possible slip systems and to have a critical resolved shear stress for plastic flow to occur on each. Two crack orientations with some previous experimental background are considered. One orientation considered is such that the interface crack is parallel to the (001) plane with its tip along [110] and growing along the perpendicular face direction, [110]. The second orientation considers the crack parallel to the prism plane (0110) of an hcp crystal, with its tip along [2110] and growing in the [0001] direction. For both these orientations, the near-tip stress state is shown to be locally constant within the angular sectors that are stressed to yield levels at a stationary crack tip, and to change discontinuously from sector to sector. Families of solutions with both compressive and tensile normal stresses in the wake region are also found. For both the growing and the stationary crack cases, solutions are obtained for a very limited range of the possible crack line near-tip shear-normal stress ratios.

9A402. Phenomenon of curved microcracks in $[(S)/90_n]_s$ laminates: Their shapes, initiation angles and locations. - Shoufeng Hu, JS Bark, JA Nairn *(Mat Sci and Eng, Univ of Utah, Salt Lake City UT 84112)*. Composites Sci Tech 47(4) 321-329 (1993).

A variational analysis of the stress state in microcracked cross ply laminates has been used to investigate the phenomenon of curved microcracking in $[(S)/90_n]_s$ laminates. Previous investigators proposed that the initiation and orientation of curved microcracks are controlled by local maxima and stress trajectories of the principal stresses. We have implemented a principal stress model using a variational mechanics stress analysis and were able to make predictions about curved microcracks. The predictions agree well with experimental observations and therefore support the assertion that the variational analysis gives an accurate stress state that is useful for modeling the microcracking properties of cross ply-laminates. An important prediction about curved microcracks is that they are a late stage of microcracking damage. They occur only when the crack density of straight microcracks exceeds some critical value-the critical crack density for curved microcracking. The predicted critical crack density for curved microcracking agrees well with experimental observations.

9A403. Prediction of delamination in composite laminates subjected to low velocity impact. - CJ Jih and CT Sun *(Sch of Aeronaut and Astronaut, 1282 Grissom Hall, Purdue)*. J Composite Mat 27(7) 684-701 (1993).

A method for predicting impact-induced delamination in composite laminates was proposed. This method is suitable for low velocity impact with heavy impactors. Static delamination fracture toughness was used to predict delamination crack growth under impact conditions. Curing stresses were also considered and found to play a significant role in evaluating the fracture toughness of some laminates such as $[90_5/0_5/90_5]$. The prediction of delamination size using static fracture toughness was found to agree very well with the experimental results.

9A404. Pull-out of fibres with a branched structure and the interference of strength and fracture toughness of composites. - Shaoyun Fu, Benlian Zhou, Chiwei Lung *(Inst of Metal Res, Acad Sinica, Shenyang 110015, Peoples Rep of China)*. Composites Sci Tech 47(3) 245-250 (1993).

In an experimental investigation of the pull-out of synthetic fibres with a branched structure, it was generally observed that the force and energy of fibre pull-out are greater than those for plain fibres, and increase with the branching angle. An approximate theory of pull-out of fibres with branched structure from a matrix is developed with the aim of quantifying the effects of the branched structure of the fibre. This theory agrees well with the experimental results by adjusting the snubbing friction coefficient between fibre and matrix and neglecting the bending of the fibre at the fibre branching point.

9A405. Role of coatings in axial tensile strength of long fiber reinforced metal-matrix composites. - Zhenhai Xia *(Dept of Metallic Mat Sci and Eng, Hebei IT, Tianjin 300130, Peoples Rep of China)*. Acta Metall Mat 41(7) 2097-2104 (Jul 1993).

A model that includes effects of coatings, interfacial behavior, plastic deformation of matrix and reaction zone has been developed for analysis of the behavior of metal-matrix composites reinforced by coated fibers. The stress concentration caused by the cracks in the reaction zone was calculated from the model and the results show that it can be relaxed by choosing coatings of low modulus and controlling interfacial strength to a relatively low value. The predictions of the model in composite strength are consistent with that from the Griffith relationship with strong interfacial bonding and the experimental results for SiC-coated C/Al composites. Both the theory and the experiment show that high strength of the composites can be maintained by SiC coating even when there is a serious reaction at the coating-matrix interface.

See also the following:

9A195. Computational modeling of impact tests on steel fiber reinforced concrete beams

276L. OTHER ANISOTROPIC AND NONHOMOGENEOUS MEDIA

9A406. Analysis of finite anisotropic media containing multiple cracks using superposition. - MS Wu *(Dept of Eng Mech, Univ of Nebraska, 212 Bancroft Hall, Lincoln NE 68588-0347)*. Eng Fracture Mech 45(2) 159-175 (May 1993).

A method is presented for estimating the stress intensity factors of interacting cracks in a finite anisotropic medium. The method is based on the simultaneous application of two superposition schemes. In the first scheme, concentrated forces and couples acting at various locations along an imaginary curve within an infinite medium are superposed using the framework of the boundary force method. In the second scheme, approximating tractions acting on crack lines are superposed to compute the stress fields required for determining stress intensity factors. It is shown that the computed stress intensity factors of a single crack or several cracks in rectangular specimens agree closely with published data for isotropic specimens.

9A407. Correlation between crack tortuosity and fracture toughness in cementitious material. - MA Issa, AM Hammad, A Chudnovsky *(Dept of Civil Eng, Mech and Metall, Univ of Illinois, Chicago IL 60680)*. Int J Fracture 60(2) 97-105 (15 Mar 1993).

This paper proposes a new technique for the evaluation of fractal dimension (D) of fracture surface and a quantitative correlation between D and fracture toughness of cementitious materials. The experimental program has been performed on compact tension (CT) specimens (600 × 525 × 125 mm) with three different aggregate sizes (d_{max} = 4.7mm, 18.8mm and 37.5mm). The fractal geometry concept is utilized in the evaluation of fracture surface roughness. To avoid indirect or destructive experimental procedures that are prohibitively laborious and time consuming, a new non-destructive technique is presented. Results of the analysis indicate that the concept of fractal geometry provides a useful tool in the fracture surface characterization. The results also suggest that the fracture toughness can be correlated with the fractal dimension of fracture surface.

9A408. Fracture parameters for the orthotropic bimaterial interface cracks. - Chyanbin Hwu *(Inst of Aeronaut and Astronaut, Natl Cheng Kung Univ, Tainan 70101, Taiwan, ROC)*. Eng Fracture Mech 45(1) 89-97 (May 1993).

In order to define a proper bimaterial stress intensity factor, a general solution for the collinear interface cracks between dissimilar anisotropic media is applied to the near tip of an interface crack. Through the operation of normalization, scaling, nondimensionalization and transformation, a comparable definition which can be reduced to the classical stress intensity factors for a crack tip in homogeneous media has been obtained.

9A409. Stress analysis around a partially bonded rigid cylinder in an elastic medium with process zones. - K Fujii, Y Kato *(Dept of Civil Eng, Gifu Univ, Yanagido, Gifu 501 11, Japan)*, S Duan *(Dept of Civil Eng, N China Inst of Water Conservancy and Hydroelec Power, Handan, Hebei 05621, Peoples Rep of China)*, K Nakagawa *(Dept of Civil Eng, Gifu Univ, Yanagido, Gifu 501 11, Japan)*. Eng Fracture Mech 45(1) 31-38 (May 1993).

The stress and displacement field around a circular-arc interface crack between a rigid cylinder and an infinite elastic medium is analyzed. Two process zones at the crack tips along the interface are formed, and a concentrated force P is applied at the center of the cylinder along the x-axis. The solution is given by the Fourier series. It is shown that both tensile and shear stresses exist along the interface but no oscillation appears.

9A410. Stresses near the edge of bonded dissimilar materials described by two stress intensity factors. - D Munz and YY Yang *(Univ of Karlsruhe and Nucl Res Center, Karlsruhe, Germany)*. Int J Fracture 60(2) 169-177 (15 Mar 1993).

Stresses near the free edges of the interface of bonded dissimilar materials can be described by the sum of a regular stress term and one or two stress singularity terms. A method for the calculation of the corresponding stress intensity factors from FE results is presented which is useful to determine two stress intensity factors together. Results for some geometries show that all three terms may contribute significantly to the stress distribution near the free edge of the interface for thermal stress.

See also the following:

9A322. Anisotropic damage mechanics model for fatigue failure

276Q. IMPULSIVE LOADING AND IMPACT

9A411. Smeared crack analysis for reinforced concrete structures under blast-type loading. - FBA Beshara *(Dept of Civil Eng, Fac of Eng, Zagazig Univ, Shoubra, Egypt)*. Eng Fracture Mech 45(1) 119-140 (May 1993).

A smeared crack analysis is presented for the nonlinear FE analysis of plane and axisymmetric reinforced concrete structures under blast and impulsive loading conditions. Based on the fixed crack approach, a rate dependent strain criterion is proposed to serve as a crack initiation condition. The crack propagation is governed by nonlinear reversible formulations to model concrete tension softening as a function of concrete fracture energy, tensile strength, cracking strain and crack characteristic length. Shear transfer due to aggregate interlock and dowel bars is simulated by a nonlinear model dependent on the strain across the crack. A new crack monitoring algorithm, as part of a comprehensive computer program FEABRS, is developed which follows the cracking behavior with the time stepping scheme. The results of some dynamic applications are presented and compared with those from other numerical and experimental sources.

See also the following:

9A283. Fracture of rock: Effect of loading rate

276S. DYNAMIC CRACK PROPAGATION

9A412. Crack-interfaces of fractal type with friction. - PS Theocaris *(Natl Acad, PO Box 77230, GR-17510 Athens, Greece)* and PD Panagiotopoulos *(Dept of Civil Eng, Aristotle Univ, GR-54006 Thessaloniki, Greece)*. Acta Mech 98(1-4) 63-78 (1993).

Here a theory is presented for the study of frictional effects on crack interfaces which have given geometry of fractal type. The arising problems are of non-classical nature, not only due to the fact that the interface conditions are expressed in terms of the non-differentiable friction superpotential, but also because of the fractal interface geometry and the singularities introduced by the crack. The fractal interface is analyzed by means of a sequence of classical-geometry interface problems. They result from the mathematical description of the fractal interface: it is the "fixed point" or the "deterministic attractor" of a given transformation. The theory is illustrated by a numerical application.

9A413. High frequency scattering of plane horizontal shear waves by a Griffith crack propagating along the bimaterial interface. - SC Pal *(Comput Centre, Univ of N Bengal, Darjeeling District, W Bengal 734 430, India)* and ML Ghosh *(Dept of Math, Univ of N Bengal, Darjeeling District, W Bengal 734 430, India)*. Eng Fracture Mech 45(1) 107-118 (May 1993).

The problem of diffraction of horizontally polarized shear waves by a finite crack moving on a bimaterial interface is studied. In order to obtain a high frequency solution, the problem is formulated as an extended Wiener-Hopf problem. The expressions for the dynamic stress intensity factor at the crack tip and the crack opening displacement are derived for the case of wave lengths which are short compared to the length of the crack.

9A414. Principle of maximum energy dissipation rate in crack dynamics. - LI Slepyan *(Fac of Eng, Tel-Aviv Univ, POB 39040 Ramat Aviv, 69978 Tel Aviv, Israel)*. J Mech Phys Solids 41(6) 1019-1033 (Jun 1993).

The principle of maximum energy dissipation rate is introduced as an energy criterion for crack dynamics. That allows us to explain observed limiting crack speeds in brittle materials, and to complete the crack dynamics formulation. The upper limits of the crack speed is perfectly elastic and elastic-plastic bodies are obtained. It is found that the theoretical maximum crack speed in an isotropic elastic body (in the first mode of crack propagation) is approximately equal to half the shear wave speed. The self-similar problem for the fracture mode III is solved (assuming the plastic zone to be narrow) and the crack speed limit is found as a function of the ratio of loading to yield limit: the plasticity decreases the crack speed limit and the latter tends to zero with the yield limit.

9A415. *Global-Local* approach to lengthwise cracked beams: Dynamic analysis. - TN Farris and JF Doyle *(Sch of Aeronaut and Astronaut, Purdue)*. Int J Fracture 60(2) 147-156 (15 Mar 1993).

A simple model is developed for the calculation of dynamic stress intensity factors for lengthwise cracked beams subjected to impact or transient loading. The model is based on a *Global-Local* approach that separates the *Global* structural dynamics from the *Local* crack tip zone dominated by singular stresses. The *Global* model is that of connected waveguides while the *Local* model is based on a novel application of the J-integral that converts dynamic structural resultants directly into strain energy release rate. The accuracy of this approach is assessed by comparing it to a fully 2D FE analysis in which the modified crack closure integral is used to calculate the dynamic strain energy release rate. Both mode I and mode II examples are given, and situations with multiple wave reflections are emphasized.

See also the following:

9A352. Description of 2D spallation in pure copper

276W. MICROMECHANISMS

9A416. Effective elastic properties of a solid with crazes. - S Wu and A Chudnovsky *(Dept of Civil Eng Mech and Metall, Univ of Illinois, Chicago IL 60680)*. Eng Fracture Mech 45(2) 233-243 (May 1993).

The effective elastic properties of an elastic solid with a craze array are discussed. The effective elastic properties of a crazed material with a low density craze array are obtained by nonlinear analysis of a craze. For the high density craze array case, the effective elastic properties are obtained by a simple beam model. Results of effective elastic properties for all cases depend on a dimensionless parameter which represents the rigidity of fibrils inside the craze.

9A417. Near-tip field of anti-plane crack in a micro-cracked power-law solid. - Ch Zhang and D Gross *(Inst of Mech, TH Darmstadt, W-6100 Darmstadt, Germany)*. Int J Fracture 60(2) 107-120 (15 Mar 1993).

Asymptotic near-tip field is investigated for an anti-plane (mode III) crack in a power-law solid permeated by a distribution of micro-cracks. The micro-crack location is assumed to be random, while the micro-crack orientation is taken to be non-random. The anisotropic nature of this kind of damage gives rise to anistropic constitutive equations for the overall macroscopic strains and stresses. The structure of the asymptotic field at a macro-crack tip is analyzed by solving a nonlinear eigenvalue problem. It is shown that under the assumptions made in this analysis the asymptotic crack tip field of the damaged solid has the same structure as the mode III HRR-field of the undamaged solid. Numerical results are presented for the angular functions, the contours of constant effective shear stress, the normalization constant arising in the near-tip field, and the crack opening displacement. By means of these results, the effects of the micro-crack density and orientation on the crack-tip field will be explored.

9A418. Significance and role of deformation micromechanisms in life-predictive modeling of aging structures. - KL Murty *(Dept of Nucl Energy, N Carolina State Univ, Raleigh NC 27695-7909)*. Appl Mech Rev 46(5) 194-200 (May 1993).

Transitional creep mechanisms are exhibited by materials used in power systems and a thorough knowledge of these is a prerequisite in reliable extrapolations of short-term data to service conditions mainly due to the dominance of viscous creep mechanisms such as Nabarro-Herring, Coble and more importantly Harper-Dorn creep at low stresses. The paper summarizes the deformation mechanisms pertinent to various classes of materials.

9A419. Stable damage evolution in a brittle continuous medium. - GA Francfort *(Lab Central des Ponts Chaussees, 58 Blvd Lefebvre, 75732 Paris Cedex 15, France)* and J-J Marigo *(Lab Proprietes Mec Thermodyn Mat, Inst Galilee Univ Paris XIII, Ave JB Clement, 93430 Villetaneuse, France)*. Eur J Mech A 12(2) 149-189 (1993).

A model of partial brutal damage is investigated for a class of brittle solids. A global stability criterion is proposed. It is shown to prohibit the existence of a undamaged-damaged type solution and to promote fine mixtures of the undamaged and damaged phases. Thus microstructures appear as a byproduct of the criterion and not as the constitutive element of the model, in striking contrast with the micromechanical approach to damage. The resulting model is studied, especially in the 2D problems and for the problem of cylindrical torsion.

276Y. COMPUTATIONAL TECHNIQUES

9A420. Analysis of surface cracks using the line-spring BEM and the virtual crack extension technique. - Zhao-Jing Zeng, Shu-Ho Dai, Yi-Min Yang *(Dept of Mech Eng, Nanjing Inst of Chem Tech, 5 New Model Rd, Nanjing 210009, Peoples Rep of China)*. Int J Fracture 60(2) 157-167 (15 Mar 1993).

The authors have developed a new line-spring BEM which couples the line-spring model with the BEM to deal with the problem of a surface cracked plate. However, the drawback of the line-spring model is that a reliable stress intensity factor could not be directly obtained near the free surface intersection. Therefore, the virtual crack extension technique is employed in a post-processor of the line-spring BEM to obtain the stress intensity factor at the crack front-free surface intersection. Theoretical analysis is described. Stress intensity factors for surface cracks are calculated to verify the proposed method. The interaction of two surface cracks is also investigated. The solutions obtained by the line-spring BEM show that the method proposed is efficient and reasonably accurate.

9A421. Analytical stress intensity solution for the stable Poisson loaded specimen. - LJ Ghosn *(Sverdrup Tech, Lewis Res Center Group, Brook Park OH 44142)*, AM Calomino *(NASA, Lewis Res Center, Cleveland OH 44135)*, DN Brewer *(US Army Res Lab, Lewis Res Center, Cleveland OH 44135)*. Int J Fracture 60(3) 209-220 (1 Apr 1993).

An analytical calibration of the Stable Poisson Loaded (SPL) specimen is presented. The specimen configuration is similar to the ASTM E-561 compact-tension specimen with displacement controlled wedge loading used for R-curve determination. The crack mouth opening displacement (CMOD) are produced by the diametral expansion of an axially compressed cylindrical pin located in the wake of a machined notch. Due to the unusual loading configuration, a 3D FE analysis was performed with gap elements simulating the contact between the pin and specimen. In this report, stress intensity factors, CMOD's and crack displacement profiles, are reported for different crack lengths and different contracting conditions. It was concluded that the computed stress intensity factor decreases sharply with increasing crack length thus making the SPL specimen configuration attractive for fracture testing of brittle, high modulus materials.

9A422. Applications of the BE and dislocation density methods in plane crack problems. - A Sturt, D Nowell, DA Hills *(Dept of Eng Sci, Univ of Oxford, Parks Rd, Oxford OX1 3PJ, UK)*. Eng Anal Boundary Elements 11(2) 129-135 (1993).

Crack modeling using the dislocation density method has become an increasingly popular technique for plane crack problems and allows the fast, efficient determination of stress intensity factors. The range of geometries which may be solved by the basic technique is, however, somewhat limited and this paper outlines a hybrid formulation combining the dislocation density technique with constant displacement discontinuity BEs to satisfy a range of far boundary conditions. The method described can analyze configurations with an arbitrary number of buried or surface breaking cracks and can be implemented on a personal computer to provide an efficient tool for crack analysis.

9A423. Comparison of accurate with approximate expressions of stresses for the interface crack problem. - CP Spyropoulos *(Sec of Mech, Dept of Eng Sci, Natl Tech Univ, Athens GR-157 73, Greece)*. Eng Fracture Mech 45(3) 339-348 (Jun 1993).

The plane problem of two bonded dissimilar materials with a central crack along the common interface and subjected to biaxial load at infinity is examined by comparing the accurate expression for stresses, equally valid everywhere, both near and far from the crack tip regions, with the approximate expressions for the stresses used up to now which have a limited accuracy and area of validity. To illustrate the advantages of the closed form expressions for the stresses over the approximate ones based on the singular solution, improved by taking into account the non-singular term due to the biaxial loading parameter, selective stress distributions for both expressions are presented. On these charts, for reasons of better comparison, the relative errors between the closed form expressions and the best approximate expressions for each of the stress components are presented. The existing significant differences urge one to make use of the proposed expressions in any problem related to the subject of this article.

9A424. Damage simulation in heterogeneous materials from geodesic propagations. - D Jeulin *(Center de Geostat, Ecole des Mines de Paris, 77305 Fontainebleau, France)*. Eng Comput 10(1) 81-91 (Feb 1993).

We propose a simplified method to simulate damage evolution in hetergeneous media from geodesi propagation calculations. The method introduced for the case of porous media (polycrystalline graphite), was generalized to multiphase media, and then to a continuous variation of local fracture energy. It is based on a minimization of the fracture energy criterion, ignoring the local variations of the stored strain energy. Our approach is illustrated from 2D simulations corresponding to various types of microstructure involving the following microgeometrical distributions of the local fracture energy: isotropic and anisotropic two-phase media, polycrystal with cleavage and intergranular fracture, material with a continuous distribution of surface energy.

9A425. Eigenstrain methods in 3D crack problems: An alternative integration procedure. - DN Dai, D Nowell, DA Hills *(Dept of Eng Sci, Univ of Oxford, Parks Rd, Oxford OX1 3PJ, UK)*. J Mech Phys Solids 41(6) 1003-1017 (Jun 1993).

In this paper 3D crack problems are analyzed using the eigenstrain method (body force method). The formulation leads to set of hypersingular integral equations which is solved numerically using a discretization technique. An analytical expression is derived for the evaluation of the singular integrals, ie, the 2D singular integrals are reduced to regular integrals along the contour of the domain, thus avoiding the direct calculation of cumbersome singular integrals and minimizing the numerical effort. The analytical expression is independent of the size and shape of the domain, allowing the use of high order elements in numerical solutions.

9A426. Hypersingular-boundary integral equation method for the solution of an elastic multiple interacting crack problem. - WT Ang *(R&D Section, Hong Leong Eng Pte, 117 Jalan Tun HS Lee 50000, Kuala Lumpur, Malaysia)* and G Noone *(Electron Res Lab, PO Box 1600, Salisbury, S Australia)*. Eng Anal Boundary Elements 11(1) 33-37 (1993).

The authors formulate the antiplane problem concerning a finite elastic body with an arbitrary number of coplanar cracks in its interior in terms of a system of boundary integral equations coupled with Hadamard finite-part singular integral equations. These integral equations are readily amenable to numerical treatment and, for the purpose of illustrations, they are employed to obtain numerical values of the stress intensity factors for certain specific problems.

9A427. Incompatible numerical simulation of the axisymmetric cracked body made of ideally elastic-plastic material. - YK Cheung *(Dept of Civil and Struct Eng, Univ of Hong Kong, Hong Kong)* and Chang-Chun Wu *(Dept of Modern Mech, Univ of Sci and Tech, Hefei, China)*. Eng Fracture Mech **45**(3) 399-405 (Jun 1993).

It is well known that isoparametric axisymmetric elements always encounter various numerical difficulties in computational plasticity. An incompatible axisymmetric element which can avoid the above-mentioned difficulties is presented and then used to solve axisymmetric ductile fracture problems. As an example a stretched cylinder with a circumferential crack is investigated, and elastic, elastic-plastic solutions, and plastic limit loads of the cracked cylinders are given and examined. In addition, the path-independence of the J integral is inspected, and the limits for use of the axisymmetric J integral are suggested.

9A428. Using a symbolic manipulator to solve fracture problems in composite materials. - AK Kaw, KS Gadi, D Jadhav *(Dept of Mech Eng, Univ of S Florida, Eng 118, Tampa FL 33620-5350)*. Adv Eng Software **16**(1) 31-36 (1993).

A symbolic manipulator is used to understand the mechanics of a crack problem in fiber reinforced composite materials. Stress intensity factors in the front of crack tips are found directly in terms of the stiffness properties of the constituents, for constant crack lengths. The results are compared with the numerical solutions available in the literature.

276Z. EXPERIMENTAL TECHNIQUES

9A429. New method for measurement of fracture toughness K_{IC} by three point bend specimen. - Zhe-ming Zhu *(Dept of Basic Sci, Fuxin Mining Inst, Fuxin 123000, Peoples Rep of China)*. Eng Fracture Mech **45**(2) 141-147 (May 1993).

The relationship between the three-point bend (TPB) specimen size and the measured fracture toughness K_{IC} value is analyzed by the theory of crack opening displacement. According to the concept of plane strain fracture toughness K_{IC}, a new formula for K_{IC} is presented. For small-scale or large-scale TPB specimens, the K_{IC} values of material can all be obtained for the new formula and the corresponding curve of load versus crack mouth opening displacement. For large-scale specimens, the new formula is compatible with the ASTM standard.

280. Materials testing and stress analysis

9A430. Investigation of the nonlinear elastic properties of metals by a vibration method. - LA Rozenblyum *(Inst of Appl Phys, Russian Acad of Sci, Russia)*. Sov Phys Acoust **38**(6) 587-591 (Nov-Dec 1992).

A method is proposed for determining the nonlinearity parameters of the stress-strain curve of metals in the microplasticity region, based on the dependence of the resonance shift, the variation of the reciprocal quality factor Q^{-1}, and the second- and third-harmonic amplitudes on the vibration amplitude of the mechanical oscillatory circuit formed by a metal rod sample loaded with weights at both ends. A phenomenological model of the stress-strain curve of a metal is proposed for interpreting the observed nonlinear effects.

9A431. Two-function method for the prediction of concrete creep under decreasing stress. - LL Yue and L Taerwe *(Magnel Lab for Reinforced Concrete, Univ of Ghent, Technologiepark Zwijnaarde 9, B9052 Ghent, Belgium)*. Mat Struct **26**(159) 268-273 (Jun 1993).

It is well known that the application of the principle of superposition in the service stress range yields an inaccurate prediction of concrete creep when unloading takes place. It appears that after a period of compression creep, the experimental creep recovery is significantly less than predicted by the principle of superposition. In the present study, this nonlinear behavior, attributed to the sustained compressive preload, is modeled by a two-function method. In this approach, a creep function is used for modeling the time-dependent deformations due to increasing stress and a separate creep recovery function represents the behavior under decreasing stress. Good agreement with test data is achieved.

9A432. Abrasive wear study of selected white cast irons as liner materials for the mining industry. - Xu Liqun, C Vose, D StJohn *(CRA, Adv Tech Dev, Perth PO Box 347, Cannington WA 6107, Australia)*. Wear **162-164**(PART B) 820-832 (13 Apr 1993).

The abrasive wear behavior of three white cast irons, designed as 10Cr-3.5Ni, 15Cr-3Mo and 16.5Cr-1.5Mo irons (where the compositions are in weight per cent), was studied in a field test as liners installed in a transfer of an iron ore operation and in three laboratory wear tests (pin-on-drum, dry-sand-rubber-wheel (DSRW) and paddle testers) to determine the relevance of the laboratory wear tests to the field liner test. The results from the wear tests and wear mechanism study showed that under the test conditions, the DSRW test most closely predicts the relative wear rate of the white irons in the field liner test. However, a perfect match of both the wear mechanism and the rank of the wear rate for the iron from the laboratory wear test to the field liner test was not achieved, owing to the complexity of the field liner wear condition. The wear mechanisms were elucidated by microscopic examination of the worn surfaces for both field-tested liners and laboratory-tested specimens, and by subsurface examination of paddle-tested specimens, together with the microstructural study of the irons. The predominant wear mechanisms depend upon both the wear conditions and the microstructural properties of the irons. It was found that the wear resistance of the white irons for the low stress abrasion is controlled by the matrix, and that for the high stress abrasion and impact abrasion is mainly determined by the bulk hardness of the irons.

9A433. Repeated impact-abrasion testing of alloy white cast irons. - IR Sare, BK Arnold *(CSIRO Div of Manuf Tech, Adelaide Lab, PO Box 4, Woodville SA 5011, Australia)*, GA Dunlop *(AMDEL, PO Box 338, Torrensville SA 5031, Australia)*, PG Lloyd *(CSIRO Div of Manuf Tech, Adelaide Lab, PO Box 4, Woodville SA 5011, Australia)*. Wear **162-164**(PART B) 790-801 (13 Apr 1993).

A small Hazemag rotary impact crusher has been adapted for the assessment of the repeated impact-abrasion properties of alloy white cast irons. The test specimens were cast as blow bars for use in the crusher, and each test involved the comminution of 2000 kg of quarry stone. A series of six alloy white cast irons has been tested in the crusher in order to assess the influences of chemical composition, hardness, eutectic carbide volume fraction and retained austenite content on combined repeated impact-abrasion performance. The results showed that hardening by heat treatment, and hence variations in retained austenite content, has no influence on weight loss, but that weight loss increased significantly with increasing eutectic carbide volume fraction. Post-wear examination of worn blow bars revealed significant gouging and impact damage on the surface, and on a finer scale, extensive fracture of eutectic fracture of eutectic carbides, decohesion at carbide-matrix interfaces, matrix fracture, and microscope spall formation.

9A434. Current trends in obtaining deformation data from grids. - PJ Sevenhuijsen *(Struct and Mat Div, Natl Aerospace Lab, Amsterdam, Netherlands)*, JS Sirkis *(Dept of Mech Eng, Univ of Maryland, College Park MD)*, F Bremand *(Lab Mech des Solides, Univ Poitiers, Cedex, France)*. Exp Tech 17(3) 22-26 (May-Jun 1993).

Grid methods offer a means of measuring the deformation of structural components. Grids are made to conform to structures so that grid motion monitored through a loading history is indicative of structural deformation. Grid characteristics such as location of points, pitches of points, pitches of lines, and the directions of lines can all be measured and compared to a prescribed state for different load conditions. These comparisons provide such useful quantities as displacement, curvatures and strains. Current trends in extracting useful information from these comparisons is presented here. Emphasis is on using digital-image processing and digital-pattern recognition as a tool in the extraction of data from structural in-plane grid methods. The term, structured grid, refers to some regular array of lines or dots. The purpose of this paper is to familiarize the reader with some of the current trends in the grid methods and to provide the basis for comparison to the more traditional grid methods.

9A435. Impact-echo response of concrete plates containing delaminations: Numerical, experimental, and field studies. - C Cheng and M Sansalone *(Dept of Struct Eng, Cornell)*. Mat Struct **26**(159) 274-285 (Jun 1993).

This paper describes the use of the impact-echo technique - a non-destructive testing technique based on the use of transient stress waves - for detecting delaminations in concrete plate-like structures such as bridge decks, slabs, and walls. Results obtained from numerical (FE) analysis and controlled-flaw laboratory studies are presented and used to explain the elastic impact response of delaminated plates. Current impact-echo instrumentation is described, and results obtained from concrete bridge decks containing delaminations caused by corrosion of reinforcing steel are presented. These results provide a better understanding of the impact response of delaminated plates.

9A436. Basic study for predicting the disaster in rock engineering with an acoustic emission technique. - Yin Fei *(Res Div, Reconnaissance Planning and Des Inst, Yellow River Conservance, Zhengzhou, Peoples Rep of China)*. Eng Fracture Mech **45**(3) 387-391 (Jun 1993).

This paper deals with the prediction of disaster in rock engineering with an acoustic emission technique. Variations of acoustic emission signals have been detected on the specimens from two dam areas in the process of rock fracture, and the relationship between these variations has been investigated. The results show that it is possible to detect and predict the unstable tendency of surrounding rocks, slide and collapse on the bases of their roles of acoustic emission in the process of rock deformation and damage. Though there are some difficulties in using this method *in situ*, no doubt, this method is one of hopeful means to predict the occurrence of disaster, and is worth researching further.

9A437. Inverse problems in electromagnetic nondestructive evaluation. - HA Sabbagh *(Sabbagh Assoc, 4639 Morningside Dr, Bloomington IN 47407)* and RG Lautzenheiser *(Rose-Hulman IT, Terre Haute IN 47803)*. Int J

Appl Electromagnetics Mat 3(4) 253-261 (Apr 1993).

We present a rigorous model for electromagnetic (eddy-current) nondestructive evaluation. It consists of a pair of coupled integral equations, in which the unknowns, the electric field and conductivity of the flaw, appear multiplied together. This nonlinear (bilinear) inverse problem is solved using gradient techniques. Conclusions concerning the use of alternative algorithms, such as simulated annealing and statistical decision theory, to start and finish the inversion process are made.

282. Structures (basic)

282A. GENERAL THEORY

9A438. **Concepts of models to a theory.** - K Moser *(Dept for Struct Anal and Reinforced Plastics, Fac of Struct Eng and Architect, Univ of Innsbruck, Innsbruck, Austria).* Composite Struct 24(3) 173-179 (1993).

Besides being real structures, models can also be theoretical constructions. They are presented here as a common link used by both theoretically oriented natural scientists and practically oriented engineers. Often-used idealized models and a proven model for fiber polymer composites are demonstrated.

See also the following:

9A970. Ice pressures on vertical and sloping structures through dimensional analysis and similarity theory

282C. STRUCTURAL OPTIMIZATION

9A439. **Exposition of the material derivative approach for structural shape sensitivity analysis.** - JS Arora *(Optimal Des Lab, Col of Eng, Dept of Civil and Env Eng and Mech Eng, Univ of Iowa, Iowa City IA 52242).* Comput Methods Appl Mech Eng 105(1) 41-62 (May 1993).

The material derivative approach for structural shape design sensitivity analysis is described in a unified manner using the continuum formulation. Both the direct differentiation and adjoint methods are derived and computer implementation aspects are discussed. The basic purpose of the paper is to present the shape design sensitivity analysis as an application of the material derivative concept of continuum mechanics, and the calculus of variation procedures for taking variations of integrals over the variable domains. It is also shown that the use of a recently developed variational principle for design sensitivity analysis greatly simplifies derivation of the adjoint method.

9A440. **Finding the optimal distribution of material properties.** - UT Ringertz *(Dept of Lightweight Struct, Royal IT, S-100 44 Stockholm, Sweden).* Struct Optim 5(4) 265-267 (Apr 1993).

The compliance of 2D structures is minimized using the elements of the costitutive matrix as design variables. The amount of materials to be used is required to be less than a prescribed amount and further constraints on the constitutive matrix are imposed as matrix inequalities. The apparent nonsmoothness of the matrix inequalities is removed by use of a barrier transformation.

9A441. **General related variational approach to shape optimum design.** - A Longo, J Unzueta, E Schaeidt, A Alvarez, JJ Anza *(Anal and Des Dept, LABEIN Cuesta de Olabeaga 16, 48013 Bilbao, Spain).* Adv Eng Software 16(2) 135-142 (1993).

A general variational approach to shape optimum design is presented. The paper is concerned mainly with two fundamental subjects involved within shape optimization methodologies: the Geometric Representation or Design Model definition and the evaluation of shape sensitivities. Within this context, the term variational is related, on one hand, to the use of variational geometry concepts at the level of Design Model and, on the other hand, to the evaluation of sensitivities by means of the material derivative concept of generalized calculus of variations. At the end of the paper, an industrial application, called SIDOMAT, is described.

9A442. **Method for structural optimization which combines second-order approximations and dual techniques.** - T Larsson and M Ronnqvist *(Dept of Math, Linkoping IT, S-581 83 Linkoping, Sweden).* Struct Optim 5(4) 225-232 (Apr 1993).

A structural optimization problem is usually solved iteratively as a sequence of approximate design problems. Traditionally, a variety of approximation concepts are used, but lately second-order approximation strategies have received most interest since high quality approximations can be obtained in this way. Furthermore, difficulties in choosing tuning parameters such as step-size restrictions may be avoided in these approaches. Methods that utilize second-order approximations can be divided into two groups; the first, a Quadratic Programming (QP) subproblem including all available second-order information is stated, after which it is solved with a standard QP method, whereas the second approach uses only an approximate QP subproblem whose underlying structure can be efficiently exploited. The numerical results show that the proposed solution is a valid approach to solve the QP subproblems arising in second-order approximation schemes.

9A443. **Optimal topology of trusses or perforated deep beams with rotational restraints at both ends.** - GIN Rozvany, T Lewinski, O Sigmund, D Gerdes, T Birker *(FB 10, Essen Univ, Postfach 103764, D-4300 Essen, Germany).* Struct Optim 5(4) 268-270 (Apr 1993).

This note discusses the least-weight layout of a truss having support conditions similar to those for a clamped deep beam. Numerical solutions are presented and confirmed by analytical considerations based on Michell's optimality criteria.

9A444. **Optimality criteria design method for tall steel buildings.** - DE Gierson and C-M Chan *(Dept of Civil Eng, Univ of Waterloo, N2L 3E5 ON, Canada).* Adv Eng Software 16(2) 119-125 (1993).

An efficient computer-based method is developed for the optimum design of tall steel building frameworks. Specifically, an optimality criteria method is applied to minimize the weight of a lateral load-resisting structural system of fixed topology subject to constraints on overall and interstorey drift. By exploiting the fact for building frameworks that member forces are relatively insensitive to changes in member sizes, rigorously-derived optimality criteria are shown to be readily satisfied through an iterative redesign procedure that converges in but a few cycles.

9A445. **Optimality criterion for maximum fundamental frequency of free vibrations of frames including axial and bending effects.** - W Szyszkowski and JM King *(Dept of Mech Eng, Univ of Saskatchewan, Saskatoon, SK, S7N 0W0, Canada).* Struct Optim 5(4) 250-255 (Apr 1993).

An optimality criterion for maximum multiple fundamental frequency of free vibrations for structures of prescribed weights is presented. The criterion includes both axial and bending effects and can be used for analysis of truss, beam and frame structures. The error norm based on the criterion is proposed and used to verify trial designs against the optimum. The accompanying iterative procedure reduces this error norm to zero and drives a trial design to the optimum. The modality of the design at the optimum and the corresponding set of Lagrange multipliers are determined automatically.

9A446. **Optimization applications for aircraft engine design and manufacture.** - TK Pratt, LH Seitelman, RR Zampano, CE Murphy *(Man Info Syst, Pratt & Whitney, United Tech, E Hartford CT 06108),* F Landis *(Dept of Mech Eng, Univ of Wisconsin, Milwaukee WI 53201).* Adv Eng Software 16(2) 111-117 (1993).

Numerical optimization is an important tool in many aspects of jet engine design, development, and test. Early optimization work centered on structural optimization projects, while more recent applications are multidisciplinary in nature. A variety of constrained and unconstrained minimization techniques have been applied to the solution of these problems. Some projects have resulted in substantial cost savings relative to previously used methods; others have provided automated solutions not previously attainable when an engineer was part of the iteration process. An interesting hybrid solution process combines the penalty function and constrained optimization techniques. An acoustic data reduction project has provided an automated procedure to match analytical models to engine data.

9A447. **Optimum design of rectangular panels with a hole.** - CS Han *(Dept of Mech and Mat Eng, Wright State Univ, Dayton OH 45435)* and BP Wang *(Dept of Mech Eng, Univ of Texas, Arlington TX 76019).* Adv Eng Software 16(2) 127-134 (1993).

The optimum design of composite panels with a circular or an elliptical hole is considered in this paper. The objective is to find the best hole location, size and orientation so as to minimize the maximum tangential strain along the circumference of the hole. The problem is treated as a shape optimization problem, and the hole boundary parameterization method is developed in order to maintain the required hole shape. The parameterized relation is further utilized to transform the sensitivity data. The optimization problem is solved iteratively using p-method FE analysis and linear programming.

9A448. **Optimum design of thin wall structures under variable amplitude fatigue loading.** - MEM El-Sayed and EH Lund *(Dept of Mech Eng, Florida Int Univ, Miami FL 33199).* Adv Eng Software 16(2) 97-101 (1993).

This paper presents a method for considering fatigue life requirements in the optimal design of thin wall structures under variable amplitude load histories. The basic concept is to use the load histories combined with the stresses of the structure and the material fatigue properties to calculate the fatigue life during the optimization process. The life requirement is considered as a side constraint and the structure weight as the objective function.

9A449. **Shape optimal design of an engine exhaust manifold.** - RJ Yang and SC Poe *(Ford Motor, Village Plaza, Ste 1100, 23400 Michigan Ave, Dearborn MI 48124).* Struct Optim 5(4) 233-239 (Apr 1993).

An engine exhaust manifold made of cast iron cracks during thermal shock testing. The test process is simulated by FE analysis. The manifold is formulated as a linear heat transfer and thermo-elasticity problem in a variational form. Analytical expressions for shape design sensitivities of general 3D problems are presented, using the material derivative approach. A hybrid approach is described and used during the optimization process. This approach takes advantage of the direct and the adjoint variable methods and is the most efficient in calculating the sensitivity of the structural responses. After the FE model is verified by comparing the results with those from testing, the engine exhaust manifold is optimized with respect to its geometry.

9A450. Shape optimization of axisymmetric structures with adaptive FE procedures. - M Ozakca, E Hinton, NVR Rao *(Dept of Civil Eng, Univ Col, Singleton Park, Swansea SA2 8PP, UK)*. Struct Optim 5(4) 256-264 (Apr 1993).

A robust and versatile algorithm for shape optimization with adaptive FE procedures is developed for the design of axisymmetric structures. The algorithm is based on the use of boundary parameterization with cubic splines for describing shape changes and takes advantage of the utilities available in an advancing front type mesh generator. Six-noded triangular elements are adopted. Shape optimization examples involving solid axisymmetric structures are presented to illustrate the various features of the integrated approach.

9A451. Structural optimization based on relaxed compatability and overlapping decomposition. - G Thierauf and F Spengemann *(Univ of Essen, Essen, Germany)*. Adv Eng Software 16(2) 89-95 (1993).

A two stage sequential technique for the solution of a wide class of structural optimization problems is proposed. It is based on an overlapping decomposition of the structural domain, which is assumed to be discretized by FEs. The optimal overlapping decomposition is derived from the nullspace of the equilibrium equations which is computed by a turn-back LU-decomposition minimizing the overlap of the subdomains. The iterative solution of the structural optimization problem is performed by a two level approach where the nodal displacements are the coordination variables.

9A452. Structural optimization of multiple attributes. - DL Thurston and R Sun *(Decision Syst Lab, Dept of General Eng, Univ of Illinois, Urbana IL 61801)*. Struct Optim 5(4) 240-249 (Apr 1993).

This paper presents a methodology for structural design optimization of multiple objectives, or attributes. The method represents an improvement over Pareto optimization-based methods by quantitatively representing trade-offs between conflicting objectives in a single multi-attribute objective function. Classical utility analysis is first used to determine a multi-attribute evaluation function for a particular structure from the designer's viewpoint. A one-bay, three storey steel frame building example demonstrates the methodology for determining the design configuration with the best combination of cost and drift index.

9A453. Structural shape optimization of vibrating shells and folded plates using two-noded finite strips. - E Hinton, M Ozakca, NVR Rao *(Dept of Civil Eng, Univ Col, Swansea SA2 8PP, UK)*. Eng Comput 10(2) 139-157 (Apr 1993).

This paper deals with the structural shape optimization of vibrating prismatic shells and folded plates. The finite strip method is used to determine the natural frequencies and modal shapes based on Mindlin-Reissner shell theory which allows for transverse shear deformation and rotatory inertia effects. An automated optimization procedure is adopted which integrates finite strip analysis, parametric cubic spline geometry definition, automatic mesh generation, sensitivity analysis and mathematical programming methods. The objective is to maximize the fundamental frequency by changing thickness and shape design variables defining the cross-section of the structure, with a constraint that the total volume of the structure remains constant.

9A454. Thirty years of modern structural optimization. - GN Vanderplaats *(VMA Eng, 5960 Mandarin Ave, Ste F, Goleta CA 93117)*. Adv Eng Software 16(2) 81-88 (1993).

Modern structural optimization began in earnest in 1960 when Schmidt first combined FE analysis with nonlinear numerical optimization methods to created what he called "Structural Synthesis". Since that time, the methods have been continually developed and improved, so that today we can say that this technology has matured to become a practical design tool. The purpose here is to review the history of structural optimization and to identify the present state of the art.

See also the following:

9A125. Space structures and the crossing number of their graphs

9A162. Almost constant contact stress distributions by shape optimization

282D. ACTIVE CONTROL, SMART STRUCTURES

9A455. Active control of composite plates using piezoelectric stiffeners. - V Birman *(Eng Educ Center, Univ of Missouri-Rolla, 8001 Natural Bridge Rd, St Louis MO 63121)*. Int J Mech Sci 35(5) 387-396 (May 1993).

The governing equations for geometrically nonlinear, arbitrarily laminated rectangular plates reinforced by stiffeners which include piezoelectric and composite layers are presented. General equations obtained in the paper are reduced to a single equation of motion for piezoelectrically reinforced, geometrically linear, specially orthotropic plates. A criterion for an effective control of forced vibrations of such plates using piezoelectric stiffeners and a static electric field is illustrated. Numerous active control problems can be addressed using the theory outlined in the paper.

282E. PROBABILISTIC DESIGN

See the following:

9A217. Design of composite laminates by a Monte Carlo method

9A220. Probabilistic methods for the calculation of laminate properties

9T925. Treatment of parameter uncertainty and variability for a single seismic hazard map

282G. RELIABILITY DESIGN

9T456. Risk management for existing energy facilities: A global approach to numerical safety goals. - ME Pate-Cornell *(Dept Indust Eng and Eng Man, Stanford)*. Appl Mech Rev 46(5) 242-245 (May 1993).

9T457. Robust inspection and interpretation techniques. - DL Marriott *(Stress Eng Services, 415 Glensprings Dr, Ste 200, Cincinnati OH 45246)*. Appl Mech Rev 46(5) 232-239 (May 1993).

9T458. Session VI Summary: Structures. - RG Bea *(Dept of Civil Eng and Dept of Naval Architec and Offshore Eng, UCB)*. Appl Mech Rev 46(5) 227-228 (May 1993).

9T459. Session VII Summary. Inspection and monitoring. - MF Kanninen *(Eng Mech and Mat Sci, PO Drawer 28510, SWRI)*. Appl Mech Rev 46(5) 240-241 (May 1993).

9A460. Time-dependent system reliability analysis by adaptive importance sampling. - Yasuhiro Mori and BR Ellingwood *(Dept of Civil Eng, Johns Hopkins Univ, Baltimore MD 21218)*. Struct Safety 12(1) 59-73 (Apr 1993).

A method for evaluating time-dependent reliability of a structural system subjected to stochastic loads is presented. Structural deterioration due to environmental stressors is also taken into account. An adaptive Monte Carlo simulation procedure combined with conditional expectation is proposed. The optimum common ratio of the standard deviation of an importance sampling variables to that of the corresponding valuables is estimated iteratively as well as their mean values. Unlike systems evaluated by simple Monte Carlo simulations, the accuracy of the failure probability evaluated by adaptive importance sampling is relatively insensitive to the magnitude of the probability.

See also the following:

9A418. Significance and role of deformation micromechanisms in life-predictive modeling of aging structures

9T928. Materials considerations in service life prediction

282H. CONCRETE (REINFORCED)

9A461. Effect of hot weather on strength of reinforced concrete beams. - A-GF Abbasi, A-HJ Al-Tayyib, MB Al-Ali *(Dept of Civil Eng, King Fahd Univ of Pet and Minerals, Dhahran 31261, Saudi Arabia)*. Cement & Concrete Composites 14(3) 209-221 (1992).

Many development projects being executed in hot-climate countries involve construction of reinforced concrete structures in hot weather. Three basic concepts for which these structures are designed are moment, shear, and bond-development length. This paper presents results of tests conducted on 52 reinforced concrete beams of various dimensions containing reinforcing bars of various sizes and yield strengths. The beams were prepared and cured in hot-weather environments at various concrete mix temperatures. The results of the tests show that, even if proper precautions are taken to obtain the required compressive strength of the concrete, the strength of the reinforced concrete beams prepared and cured in hot weather could be reduced by as much as 25% when the concrete mix temperature reaches 45 °C (126.00°C).

9A462. Sensitivity study of criteria governing collapse of centrally loaded R-C slabs. - MSA Abbasi, MH Baluch, AK Azad *(Dept of Civil Eng, King Fahd Univ of Pet and Minerals, Dhahran 31261, Saudi Arabia)*, HH Abdel-Rahman *(Dept of Civil Eng, King Abdulaziz Univ, Jeddah 21413, Saudi Arabia)*. Eng Comput 10(2) 175-187 (Apr 1993).

This paper presents the full range sensitivity study of various components of material model on the response of reinforced concrete slabs subjected to central patch loads using nonlinear FE analysis. A layered degenerate quadratic plate element with five dof was employed. Smeared crack model was used with orthogonal cracking. The components considered in this work are: perfectly plastic models *versus* hardening models, role of crushing condition on collapse load, influence of dowel effect on punching capacity, parametric variation of tension stiffening parameter, parametric variation of degraded shear modulus and the role of yield criterion.

9A463. Stress resultant FE analysis of reinforced concrete plates. - A Ibrahimbegovic and F Frey *(Dept of Civil Eng, Swiss Fed IT, EPFL, GC, LSC, CH-1015, Lausanne, Switzerland)*. Eng Comput 10(1) 15-30 (Feb 1993).

An efficient implementation of a constitutive model for reinforced concrete plates is discussed in this work. The constitutive model is set directly in terms of stress resultants and their energy conjugate strain measures, relating their total values. The latter simplification is justified by our primary goal being an evaluation of the limit load of a reinforced concrete plate. A concept of the "rotating crack model" is utilized in proposing the constitutive model to relate the principal values of bending moments and the corresponding values of curvatures. Efficient implementation is provided by a very robust, but inexpensive plate element. The element is based on an assumed shear strain field and a set of incompatible bending modes, which provides that the nonlinear computations, pertinent to constitutive model, can be carried out locally, ie, independently at each numerical integration point. Set of numerical examples is presented to demonstrate a very satisfying performance of the proposed model.

See also the following:

9A177. Plasticity model for punching shear of laterally restrained slabs with compressive membrane action
9A411. Smeared crack analysis for reinforced concrete structures under blast-type loading
9A431. Two-function method for the prediction of concrete creep under decreasing stress
9A435. Impact-echo response of concrete plates containing delaminations: Numerical, experimental, and field studies

282L. DYNAMIC AND RANDOM LOADING

9T464. **Dynamic characteristics of deteriorating engineering structures.** - LN Virgin *(Dept of Mech Eng and Mat Sci, Duke Univ, Durham NC 27708-0300)*. Appl Mech Rev 46(5) 220-226 (May 1993).

9A465. **Effect of aging on the seismic performance of petrochemical facilities.** - GS Johnson *(EQE Int, 44 Montgomery St, Ste 3200, San Francisco CA 94104)*. Appl Mech Rev 46(5) 217-219 (May 1993).

This paper discusses the effects of aging of petrochemical facilities with regard to the impact on seismic performance. Examples of typical construction and serious concerns are presented. Requirements in evaluation and retrofits are discussed. A comparison is made with the current state-of-practice in offshore platforms and nuclear power plants.

282P. DESIGN CODES

9T466. **Current progress toward natural phenomena hazards mitigation for aging DOE structures, systems, and components.** - RC Murray *(LLNL)*. Appl Mech Rev 46(5) 250-255 (May 1993).

9A467. **Structures and geriatrics from a failure analysis experience viewpoint.** - DH Hopper *(Hopper & Assoc Eng, 300 Vista Del Mar, Redondo Beach CA 90277)*. Appl Mech Rev 46(5) 213-216 (May 1993).

In a failure analysis consulting engineering practice one sees a variety of structural failures from which observations may be made concerning geriatric structures. Representative experience with power plants, refineries, offshore structures, and forensic investigations is summarized and generic observations are made regarding the maintenance of fitness for purpose of structures.

282Y. COMPUTATIONAL TECHNIQUES

9A468. **Matroids in structural mechanics.** - A Kaveh *(Inst Allgemeine Mech, TU-Wien, A-1040 Vienna, Austria)*. Comput Struct 47(1) 169-174 (3 Apr 1993).

Matroids encountered in various branches of structural mechanics are presented. It is shown that minimal bases for matroids involved in the force method of structural analysis can theoretically be obtained using the Greedy algorithm for the combinatorial optimization. The problems encountered in the practical use of this algorithm are discussed and methods are suggested for their solution.

9A469. **Nth-order stiffness sensitivities in structural analysis.** - MB Fuchs *(Dept of Solid Mech Mat and Struct, Fac of Eng, Tel Aviv Univ, 69978 Ramat Aviv, Israel)*. Struct Optim 5(4) 207-212 (Apr 1993).

This paper presents a general expression for the Nth-order stiffness sensitivities in linear elastic frames. It is based on modeling the structure as being composed of unimodal elements. It is shown that the sensitivity of the structural response to the variation of the stiffness of an arbitrary component depends only on the corresponding elemental displacements. These are the nodal displacements due to nodal element loads applied to the structure at the end nodes of the considered element. Partial derivatives with respect to several element stiffnesses are obtained from the elemental displacements of the considered elements. The method is equally applicable to more general FE models. It requires, however, the preliminary decomposition of the FE into their unimodal components.

284. Structures (ground)

9A470. **Initial shape of cable-stayed bridges.** - PH Wang, TC Tseng, CG Yang *(Dept of Civil Eng, Chung-Yuan Christian Univ, Chung-Li, Taiwan, ROC)*. Comput Struct 47(1) 111-123 (3 Apr 1993).

A FE computation procedure for determining the initial shape of cable-stayed bridges under the action of dead load of girders and pretension in inclined cables is presented. The system equation of cable-stayed bridges including the nonlinearities due to large displacement, beam-column, and cable sag effects is first set up and then solved using the Newton-Raphson method on increment-iterationwise. Based on a reference configuration and an assumed cable pretension force, the equilibrium configuration under dead load is found. Further, by adjusting cable forces, a shape iteration is carried out and a new equilibrium configuration, ie, a more reasonable initial shape, can be determined.

9T471. **Methods for assessing the safety of dams which may have applicability to energy facilities.** - MG Schaefer *(Washington State Dept of Ecology, Dam Safety Section, Water Resources Program, PO Box 47600, Olympia WA 98504-7600)*. Appl Mech Rev 46(5) 246-249 (May 1993).

9A472. **Minimizing distortion in truss structures: A comparison of simulated annealing and tabu search.** - RK Kincaid *(Dept of Math, Col of William and Mary, Williamsburg VA 23185)*. Struct Optim 5(4) 217-224 (Apr 1993).

Inaccuracies in the length of members and the diameters of joints of large space structures may produce unacceptable levels of surface distortion. Based on the influence matrices generated by a small deformation linear analysis, we formulate a combinatorial optimization problem to maximize surface distortion (DRMS). A deterministic heuristic, tabu search, is presented for DRMS. A comparison of the computational performance of tabu search is made with a randomized heuristic, simulated annealing.

9A473. **Modified elastic-plastic analysis including graphical processing of plane framed structures.** - SC Patodi and JS Patel *(Appl Mech Dept, Fac of Tech and Eng MS, Univ of Baroda, Baroda-390 001, India)*. Comput Struct 47(1) 155-161 (3 Apr 1993).

A stiffness-based modified approach is developed for the elastic-plastic analysis of rigid jointed plane frames by tracing the response of the frame under increasing loads from the beginning to collapse by a stepwise electric analysis. An important feature of the suggested approach is that it involves treating each span, which may or may not have plastic hinges and which may be subjected to concentrated and or uniform loads, as an undivided member with six dof. Each aspect of the analysis is translated into a C language instruction with emphasis on the development of graphics processors.

See also the following:

9A443. Optimal topology of trusses or perforated deep beams with rotational restraints at both ends
9A469. Nth-order stiffness sensitivities in structural analysis
9A574. New semi-rigid joint elements for nonlinear analysis of flexibly connected frames

286. Structures (ocean and coastal)

9T474. **Industry approach to aging offshore platforms.** - DJ Wisch *(Central Offshore Eng, Texaco, PO Box 430, Bellaire TX 77402-0430)*. Appl Mech Rev 46(5) 172-175 (May 1993).

9T475. **Platform removal.** - JB Weidler *(Brown & Root, PO Box 3, Houston TX 77001-0003)*. Appl Mech Rev 46(5) 176-177 (May 1993).

9T476. **Reassessment of offshore platforms.** - VVD Nair and JM Kuhn *(Dallas E&P Eng, Mobil Res and Dev, PO Box 819047, Dallas TX 75381-9047)*. Appl Mech Rev 46(5) 256-261 (May 1993).

9T477. **Session III Summary: Offshore platforms.** - JB Weidler *(Brown & Root, PO Box 3, Houston TX 77001-0003)*. Appl Mech Rev 46(5) 178 (May 1993).

See also the following:

9A970. Ice pressures on vertical and sloping structures through dimensional analysis and similarity theory

288. Structures (mobile)

9A478. **Analysis of the multi-link independent suspension system.** - DMA Lee *(Dept of Mech Eng, Univ of W Ontario, London N6J 4A4, ON, Canada)*, DM Pascoe *(Universe Eng, Markham L3R 8E4, ON, Canada)*, WH ElMaraghy *(Dept of Mech Eng, Univ of W Ontario, London N6J 4A4, ON, Canada)*. Int J Vehicle Des 14(1) 44-58 (1993).

The most prevalent type of suspension found in most high performance vehicles has been the double wishbone suspension. Expanding upon the idea of the wishbone types, this paper deals with the analysis of the multi-link (five-link) independent suspension system which is adopted by the automotive industry in some high performance vehicles. The multi-link suspension is similar in construction to the double wishbone; however, the upper (and lower) control arms are divided into four distinct links. This allows variations to be made in the suspension parameters so that certain stability criteria can be satisfied. A brief introduction to the multi-link suspension is provided and a discussion of the effectiveness of the suspension design is presented at the conclusion. The theoretical development presented has been implemented as a PC-based CAD software package.

9A479. Simplified FE representation of fuselage frames with flexible castellations. - ME Heerschap *(Fac of Aerospace Eng, Univ of Tech, PO Box 5058, 2600 GB Delft, Netherlands).* Comput Struct 47(1) 19-32 (3 Apr 1993).

The frames in an aircraft fuselage are commonly attached to the skin by flexible castellations to reduce the stresses in the frames when the fuselage is pressurized. This results in a complex deformation of the frames and castellations. Nevertheless it is impractical to model these in detail in a FE model of the fuselage as a whole, because of the number of frames and castellations present in the fuselage and the many elements which would be needed to model a single frame and castellation. A suitable, highly simplified representation of the frame with castellations is developed here. It is shown that the errors, with regard to stresses in the skin, can be reduced to an acceptable level.

290. Structures (containment)

9A480. Identification of support conditions of buried pipes using a vibrating pig. - UG Kopke *(Vipac Engs and Scientists, Woodville, Australia)* and HEM Hunt *(Dept of Eng, Univ of Cambridge, UK).* Proc Inst Mech Eng E 207(E1) 29-40 (1993).

This paper describes a method for monitoring the variation in support condition of pipelines using a vibration technique. The method is useful for detecting poor support of buried pipelines and for detecting spanning and depth of cover in subsea lines. Variation in the pipe support condition leads to increased likelihood of pipe damage. A vibrating "pig" has been developed and tested on buried pipelines. Certain features of pipe support, such as voids and hard spots, display characteristic responses to vibration, and these are measured by the vibrating pig. Post-processing of the measured vibration data is used to produce a graphical representation of the pipeline support and certain "feature characteristics" are identified.

9A481. Transverse vibration of buried pipelines due to internal excitation at a point. - UG Kopke *(Vipac Engs and Scientists, Woodville, Australia).* Proc Inst Mech Eng E 207(E1) 41-59 (1993).

This paper is concerned with the dynamic response of buried pipelines due to excitation located inside the pipe. This work is important for application to techniques that employ vibration to investigate pipeline support conditions using a vibrating pipe inspection device. Three different theoretical models are developed and investigated. Good agreement between these modes is demonstrated. The beam-on-elastic Pasternak foundation model is successfully used to predict "signatures" of the pipe-soil response that characterize soil support features, such as hard and soft supports.

9A482. Stress evaluation along the sidewalls of a box-shaped spillway structure. - EC Kalkani *(Dept of Civil Eng, Natl Tech Univ, Patission 42, Athens 10682, Greece).* Comput Struct 47(1) 163-167 (3 Apr 1993).

The stress distribution along the walls of a box-shaped spillway-chute is investigated to locate the destressed areas on the structure. The deformed shape of the structure is also examined. The analysis is performed considering gravity loads, hydrostatic loads, equipment loads and uplift pressures. The distribution of maximum principal stresses indicate that the box-shaped structure is subject mainly to compression due to the cumulative effect of all external forces. The maximum principal stresses developed are checked against the allowable stresses in the concrete.

292. Friction and wear

292A. GENERAL THEORY

9A483. Modelization of damage by abrasion. - A Magnee *(Dept of Appl Sci, Metall and Mat Sci, Centre Rech Metal and Univ of Liege, rue E Solvay, 11-B-4000 Liege, Belgium).* Wear 162-164(PART B) 848-855 (13 Apr 1993).

This paper takes step to determine the non-negligible parameters governing the wear process. Modelization leads to the generalization of the Archard law. A new nondimensional law is proposed in which the sharpness of the abrasive, its mineralogical hardness and the microstructural characteristics (elasto-plasticity and toughness) of the abraded material are taken into account. The mathematical expression constituents the theoretical formulation of numerical experimental results, including those achieved several years ago by a well-known worker in the field, MM Khrushchov.

9A484. Self-organization and concepts of wear resistance of tribosystems. - LI Bershadskii *(Inst of Prob in Mat Sci, Ukrainian Acad of Sci, Kiev).* Sov J Friction Wear 13(6) 101-114 (1992).

A number of experimental facts of basic cognitive significance in tribology are discussed in terms of systematized features of self-organization (synergetics). Some ideas and models related to self-organization of tribosystems are analyzed, mainly those published in the Soviet Journal of Friction and Wear. Concepts of wear resistance of tribosystems and materials and some unsolved problems of tribosynergetics are discussed.

292B. FRICTION

9A485. Effects of surfactants on the tribological properties of a Cr_2O_3 coating. - Jianjun Wei and Qunji Xue *(Lab of Solid Lubrication, Lanzhou Inst of Chem Phys, Chinese Acad of Sci, Lanzhou, China).* Wear 162-164(PART A) 229-233 (13 Apr 1993).

A block-on-ring tester was used to investigate the effects of surfactants on the tribological properties of a Cr_2O_3 coating at ambient conditions. The results show that the critical micelle concentration (CMC) of surfactants have significant effects on the friction and wear properties of Cr_2O_3 coating. The friction and wear decrease rapidly up to the CMC but become stable above the CMC. Compared with water, the surfactants (above the CMC) can markedly reduce the friction; sodium dodecyl benzyl sulphanate and sorbitan monooleate have effective wear-reducing functions. X-ray photoelectron spectroscopy analyzes show that the lubricity of surfactants is due to their physical adsorption on rubbing surfaces.

9A486. Friction and wear of self-lubricating composites at temperatures to 450 °C in vacuum. - Mineo Suzuki *(Natl Aerospace Lab, Chofu, Tokyo, Japan)*, Minoru Moriyama *(Pure Mat Lab, Kokubunji, Tokyo, Japan)*, Makoto Nishimura *(Natl Aerospace Lab, Chofu, Tokyo, Japan)*, Masaji Hasegawa *(Pure Mat Lab, Kokubunji, Tokyo, Japan).* Wear 162-164(PART A) 471-479 (13 Apr 1993).

The tribological characteristics of hot-pressed self-lubricating composites, consisting of molybdenum disulfide, refractory metal oxides and refractory metals, were evaluated at temperatures up to 450 °C in vacuum. Sliding bearings made from the composites were run against 304 stainless steel shafts at a rotational speed of 120 rev min^{-1} under an applied load of 1.7 N for (6-10) × 10^6 revolutions. Wear was negligible at temperatures under 100 °C. However, wear of the composite bearings, at a specific wear rate of (2-5) × 10^{-8} mm^3 N^{-1} mm^{-1}, occurred at 300 °C. At 450 °C, a weight loss of about 10-30 mg of the shaft and a weight gain of almost the same amount of the bearings were observed. X-ray photoelectron spectroscopy analysis revealed iron and traces of iron sulfide on the bearing surface, indicating that a chemical reaction had occurred between the composite bearing and the steel shaft. To examine the effect of counterpart materials, pin-on-disk friction tests using a composite pin and an Si_3N_4 disk were performed at temperatures up to 450 °C. In contrast to the 304 steel counterpart, an excellent tribological response was found with the Si_3N_4 disk. The specific wear rate of the composite pin at 450 °C was 2.2 × 10^{-10} mm^3 N^{-1} mm^{-1} and the wear of the Si_3N_4 disk was negligible. An attempt was made to improve the strength of the composite. By adding 304 stainless steel in a fraction of 5% to the composition, an improvement in strength of the composite of about 30% was obtained. Furthermore, this had a good effect on the tribological performance of the composite at high temperature.

9A487. Friction behavior of ceramic fiber-reinforced aluminum metal-matrix composites against a 440C steel counterface. - SV Prasad and KR Mecklenburg *(Mat Directorate, Wright Lab, WL/MLBT, WPAFB).* Wear 162-164(PART A) 47-56 (13 Apr 1993).

This paper describes the friction behavior of kaowool (Al_2O_3•SiO_2) and saffil (Al_2O_3) fiber-reinforced aluminum metal-matrix composites (MMCs) prepared by the squeeze infiltration technique. A hypoeutectic Al-Si alloy was used as the matrix. Friction measurements were made using a ball-on-disc configuration, in which a 440C stainless steel ball was held against a rotating MMC disc. Wear tracks on MMC discs and material transfer to the steel counterface were examined using a scanning electron microscope equipped with an energy dispersive X-ray spectroscope. There were also no significant differences in the friction behavior of the three MMCs and the unreinforced alloy when metallographically polished samples were used as test specimens. In all four cases, the friction trace was rough with large fluctuations in friction force; the coefficients of friction varied between 0.4 and 0.6. When the surface of the MMC was etched, the friction coefficient dropped to a low value of 0.18 and the stick-slip type behavior disappeared. With increase in normal load (and sliding distance), the stick-slip behavior type, characteristic of polished surfaces, reappeared. The transition from smooth to stick-slip behavior is correlated to the microstructure and surface topography of the MMC. Factors influencing the transfer of aluminum (from the MMC disc) to steel are discussed.

9A488. Friction microprobe investigation of particle layer effects on sliding friction. - PJ Blau *(Metals and Ceramics Div, ORNL).* Wear 162-164(PART A) 102-109 (13 Apr 1993).

Interfacial particles (third bodies), resulting from wear or external contamination, can alter and even dominate the frictional behavior of solid-solid sliding in the absence of effective particle removal processes (eg, lubricant flow). A unique friction microprobe, developed at ORNL, was used to conduct fine-scale friction studies using 1.0 mm diameter stainless steel spheres sliding on several sizes of loose layers of fine aluminum oxide powders on both aluminum and alumina surfaces. Conventional, pin-on-disk experiments were conducted to compare behavior with the friction microprobe results. The behavior of the relatively thick particle layers was found to be independent of the nature of the underlying substrate, substantiating previous work by other investigators. The time-dependent behavior of friction, for a spherical macrocontact starting from rest, could generally be represented by a series of five rather distinct phases involving static compression, slider breakaway, transition to steady state, and dynamic layer instability. A friction model for the steady state condition, which incorporates lamellar powder layer behavior, is described.

9A489. Frictional behavior of extremely smooth and hard solids. - DE Kim *(Ohio State Univ, 206 W 18th Ave, Columbus OH 43210)* and NP Suh *(Dept of Mech Eng, MIT)*. Wear **162-164**(PART B) 873-879 (13 Apr 1993).

Frictional behavior of extremely smooth (average roughness ~ 1 nm) and hard (approximately 800 - 2200 kg mm^{-2}) solids in air has been investigated. The present study was conducted to obtain the minimum friction under dry sliding conditions by eliminating the friction components due to mechanical interactions such as plowing and asperity deformation. By using extremely smooth and hard materials (silicon, sapphire, SiC, quartz and glass), static friction coefficients as low as 0.06 and steady state friction coefficients between 0.09 and 0.17 could be obtained with an undetectable amount of wear. The low friction and wear behavior of smooth and hard solids in air has attributed to the low probability of asperity interaction wear particle generation as well as to surface films. Even for such low frictional interaction, plastic deformation is still the major cause of friction in crystalline systems, as suggested by the existence of dislocation etch pits on silicon surfaces along the sliding track.

9A490. Further investigation on the tribological behavior of Cu-20% Nb *in situ* composite. - P Liu *(Sch of Tech, E Illinois Univ, Charleston IL 61920)*, S Bahadur *(Dept of Mech Eng, Iowa State Univ, Ames IA 50011)*, JD Verhoeven *(Ames Lab, USDOE, Dept of Mat Sci and Eng, Iowa State Univ, Ames IA 50011)*. Wear **162-164**(PART A) 211-219 (13 Apr 1993).

Sliding friction and wear behavior of Cu-20 vol% Nb *in situ* composite sliding against a tool steel disk was studied under dry ambient conditions. Studies were directed towards the understanding of the roles of the filament and the matrix materials during sliding. It was found that Nb filaments underwent reorientation, shearing and refinement. Irrespective of their prior orientation, Nb filaments close to the contact surface were oriented along the sliding direction. These processes resulted from the friction-induced surface deformation and led to the strengthening of the subsurface layer of the composite. There was no separation of Nb filaments from Cu matrix observed in the sliding process. The effects of annealing, sliding speed and filament orientation on the friction and wear behavior of the composite were also investigated. The micromechanisms of wear were studied by scanning electron microscopy. Surface deformation, filament reorientation and refinement, and oxidation seemed to play important roles in the friction and wear processes.

9A491. Hardness, friction and wear of multiplated electrical contacts. - PA Engel *(Mech and Indust Eng Dept, Binghamton Univ, Binghamton NY 13902-6000)*, EY Hsue *(IBM Dev Lab, Endicott NY 13760)*, RG Bayer *(Consult, Vestal NY 13850)*. Wear **162-164**(PART A) 538-551 (13 Apr 1993).

Full interpretation of the composite (eg, Vickers) microhardness is given for typical multilayer platings used for electrical contacts. For relatively thick layers plated on a Cu substrate, an effective highly stressed region (delimited by the "plastic boundary") is identified, which introduces a significant modification in the prior interpretive theory of thin platings. An approximate computation for the internal plastic work is devised. The work done on the underlying substrate is shown to correlate well with findings of the subsurface deformation theory of multiplated contacts. In particular, wear and friction are shown to be, respectively, proportional and inversely proportional, to the plastic work done on the substrate during multiple passes of a slider.

9A492. Role of dielectric properties in the tribological behavior of insulators. - S Fayeulle, H Berroug, B Hamzaoui, D Treheux *(Lab Mat-Mec Phys, URA CNRS 447, Ecole Centrale de Lyon, 69131 Ecully, France)*, CL Gressus *(CEA-DAM, Bruyeres, Le Chatel, France)*. Wear **162-164**(PART B) 906-912 (13 Apr 1993).

The friction properties of single-crystal alumina were investigated under dry conditions. The relative humidity was kept to less than 1% and the contact pressure was chosen to be very small to prevent the formation of wear debris at the interface. The tangential force and acoustic emission were recorded continuously during tests. The dielectric properties of samples were characterized before and after tribological tests using scanning electron microscopy. The effect of X-ray irradiation on the dielectric and friction properties was investigated. Sapphire samples annealed at 1500° C did not charge, but after X-ray irradiation the charging capacity was highly increased, as was the friction coefficient (by a factor of 4). After the friction tests, the charging capacity of sapphire was observed both inside and outside the wear track. X-ray irradiation of the samples outside the wear track also modified the friction behavior. Based on the results, others from the literature and on the increasingly understood correlation between the mechanical and electrical properties of dielectrics, an energetic explanation of the friction and wear behavior of insulator materials is proposed. Friction and wear are shown to be related to the mechanisms of storage and dissipation of energy. Because of the dielectric properties of insulators, this energy results from electrostatic interactions: polarization of the material and displacements of electrical charges. Polarizaton is quickly achieved and increases during friction because of the build-up of a space charge in the material owing to the trapping of charge carriers. This trapping of defects already present in materials before testing or created during friction allows the storage in the lattice of very high amounts of energy (5 eV or more per charge) which, when dissipated, can lead to catastrophic failure.

9A493. Sliding friction and wear of ceramics in neutral, acid, and basic aqueous solutions. - B Loffelbein, M Woydt, K-H Habig *(Fed Inst for Mat Res and Testing, BAM, Unter den Eichen 87, W-1000 Berlin 45, Germany)*. Wear **162-164**(PART A) 220-228 (13 Apr 1993).

Self-mated sliding couples of SSi_3N_4, $HIP-RBSi_3N_4$ SSiC, SiSiC, $MgO-ZrO_2$ and Al_2O_3 were tested in different aqueous solutions (H_2O, NaOH, KOH, NH_4OH, HNO_3, H_2SO_4, H_3PO_4, CH_3COOH, HCI, $HClO_4$) under conditions of boundary or mixed lubrication. The friction and wear behavior depended considerably on the composition of the ceramics, but the nature of the aqueous solutions was of minor importance. The best frictional behavior was observed with couples of SSiC, with steady state friction coefficients of 0.05. The lowest wear coefficients were measured for couples of the two types of Si_3N_4, SSiC and Al_2O_3 with values of approximately 10^{-7} mm^3 Nm^{-1}. If low friction and low wear are required, couples of SSiC seem to be the best choice in most aqueous solutions.

9A494. Sliding friction and wear up to 600° C of high speed steels and silicon nitrides for gas turbine bearings. - THC Childs *(Dept of Mech Eng, Univ of Leeds, Leeds LS2 9JT, UK)* and A Mimaroglu *(Dept of Mech Eng, Univ of Bradford, Bradford, UK)*. Wear **162-164**(PART B) 890-896 (13 Apr 1993).

The sliding friction coefficients and specific wear rates of a range of differently processed (sintered and wrought) high speed steels and (hot isostatically pressed, hot pressed and sintered) silicon nitrides have been measured in both dry and boundary lubricated conditions at temperatures from 20 to 600° C (dry) or 200° C (lubricated). In dry conditions, the wear of high speed steels and silicon nitrides on themselves was similar up to 400° C, rising from 5×10^{-9} mm^3 mm^{-1} N^{-1} at 20° C to 5×10^{-8} mm^3 mm^{-1} N^{-1}. However, in the range 400 - 600° C, the wear rates of the silicon nitrides continued to rise, while those of the tungsten high speed steels stayed constant and those of the molybdenum steels decreased. There was no effect of processing route. The boundary lubricated testing was carried out under a synthetic ester with and without a zinc dithiophosphate (ZDDP) additive. For all the materials, the specific wear rates were in the range 10^{-11} - 10^{-10} mm^3 mm^{-1} N^{-1} but these rates were near the measurement limit and running-in waves was still progessing over the 1 to 2 km sliding distance of the tests. A small amount of dry testing has been performed with silicon nitride sliding on high speed steel and on alumina and these results also are reported. A characteristic of all the dry testing was the formation of surface films from which the wear debris was formed. This perhaps explains the lack of any processing route effect.

9A495. Study of friction feed paper separation. - KD Stack and RC Benson *(Mech of Flexible Struct Project, Dept of Mech Eng, Univ of Rochester, Rochester NY 14267)*. J Eng Indust **115**(2) 236-241 (May 1993).

An understanding of the mechanics of paper separation is very important to the design of reliable photocopiers, and in this paper a model is developed to simulate friction feed paper separation. The importance of such system parameters as roller acceleration and compressive load is demonstrated. The variability of friction coefficients is shown to have a significant effect on feeding reliability. Experimental data are shown to be in good agreement with predicted results. Recommendations are made for the design of reliable friction feed paper separators.

9A496. Tribological behavior of a titanium-nickel alloy. - P Clayton *(Dept of Mat Sci and Eng, Oregon Graduate Inst of Sci and Tech, 19600 NW Von Neumann Dr, Beaverton OR 97006-1999)*. Wear **162-164**(PART A) 202-210 (13 Apr 1993).

Titanium-nickel alloys based on the unusual intermetallic compounds TiNi exhibit a ductility comparable with metallic alloys. The primary interest in these materials has focused on their shape memory alloy effects. The mechanical behavior of a titanium-nickel alloy in sliding and rolling-sliding contacts has been investigated. The purpose was to examine the potential of the material as a rim for a locomotive wheel. The possible benefits include an enhancement of the coefficient of friction between wheel and rail under the typical conditions of mild contamination. Wear tests were carried out under non-lubricated conditions to compare the material with conventional pearlitic steel. The titanium-nickel alloy exhibits a high resistance to wear under severe contact conditions. It also gives excellent resistance to water lubricated rolling contact fatigue when run against itself. In tests of titanium-nickel alloy on steel, some steel rollers failed at very short lives and others wore and did not experience fatigue. The wear and rolling contact fatigue results are discussed in the context of monotonic and cyclic stress-strain properties. The capacity of TiNi for cyclic strain hardening is considered to be very significant.

See also the following:

9A501. Combined effect of speed and humidity on the wear and friction of silicon nitride

9A519. Tribological behavior of blends in polyether ether ketone and polyether imide

9A556. Dry sliding wear of TiN based ternary PVD coatings

292D. WEAR (UNINTENTIONAL)

9A497. **Accelerated wear testing using the grit size effect.** - D Forrest *(Trib Res Program, Dept of Mech Eng, MIT)*, Kaoru Matsuoka *(Matsushita Elect Indust, Osaka, Japan)*, Ming-Kai Tse, E Rabinowicz *(Trib Res Program, Dept of Mech Eng, MIT)*. Wear 162-164(PART A) 126-131 (13 Apr 1993).

This paper describes a technique for wear prediction. It has been empirically established that the wear rate of an abraded workpiece is directly related to the grit size of the abrasive. Using this relationship, the wear rate of material subjected to very mild abrasion can be predicted from the measured wear rates of the same material under more severe conditions. This technique has been successfully applied to estimate the wear of magnetic recording head materials in a video tape system. Our results demonstrate that the wear rate of the head can be accelerated by as much as four orders of magnitude using abrasive lapping tapes of large grit size. The results also indicate that the wear rate of the recording head material decreases significantly with the magnetic or abrasive tape wear, which typically occurs during the first five to ten tape passes. Microscopic examination using scanning electron microscopy indicates that this reduction in wear rate is not due to clogging of the abrasive tape but rather to changes in abrasive particle shape. This means a recording head subjected to continuous sliding with fresh tape will wear considerably faster than a head which slides repeatedly against a loop of tape. Accordingly, in reporting the wear rates of head materials, it is important to describe the corresponding tape condition of usage history explicitly.

9A498. **Ball-on-flat reciprocating sliding wear of single-crystal, semiconductor silicon at room temperature.** - E Zanoria and S Danyluk *(Dept of Civil Eng, Mech and Metall, Univ of Illinois, PO Box 4348, Mail Code 246, Chicago IL 60680)*. Wear 162-164(PART A) 322-338 (13 Apr 1993).

This paper describes the reciprocating linear sliding fiction and wear experiments of a polycrystalline silicon ball in a single-crystal, silicon flat at room temperature in an argon environment. The normal loads used were 2.65, 3.59, 4.73, and 5.80 N, and the sliding velocity was 1.3 cm s^{-1}. The coefficient of friction at a normal load of 2.65 N initially decreased from 0.45 and stabilized at 0.23 after 400 cycles. At higher normal loads, the coefficients of friction were initially 0.45 but later fluctuated between 0.2 and 0.4. The degree of frictional fluctuation as well as the wear volume increased with load. The fluctuation of the coefficient of friction is related to the geometry of the wear debris which form into a cylindrical shape ("rolls"). A mechanism for roll formation is described.

9A499. **Ceramic tool wear when machining austempered ductile iron.** - IR Pashby, J Wallbank, F Boud *(Warwick Manuf Group, Dept of Eng, Univ of Warwick, Coventry CV4 7AL, UK)*. Wear 162-164(PART A) 22-33 (13 Apr 1993).

Four different types of commercially available ceramic tools - Al_2O_3, Al_2O_3:TiC, Al_2O_3:SiC_w and a sialon - have been used to turn heat treated SG iron at speeds between 150 and 450 m min^{-1}. The irons were either hardened by an austempering treatment giving a hardness of ~350 Hv, or softened to a hardness of ~180 Hv by an annealing treatment. Wear on the flank of the tools was the most common cause of tool rejection although tool fracture occurred when machining the austempered iron at the highest speed. Sialon tools suffered rapid wear and the Al_2O_3:SiC_w significantly underperformed the other alumina based tools under most conditions. Fracture damage on the tools' cutting edge and chemical interaction between tool and workpiece have been identified as important wear mechanisms in controlling tool life.

9A500. **Characterization of wear behavior of steel and ceramics in the VAMAS round robin tests.** - Yuji Enomoto and Kazuyuki Mizuhara *(Mech Eng Lab, Namiki 1-2, Tsukuba Ibaraki 305, Japan)*. Wear 162-164(PART A) 119-125 (13 Apr 1993).

The first and the second wear round robin tests within the framework of the Versailles Project on Advanced Materials and Standards (VAMAS) have been performed with materials combinations of α-Al_2O_3, Si_3N_4 and AISI 52100 steel under given sliding conditions of the ball-on-disk test system. The results, as reported elsewhere, showed a characteristic wear behavior depending on the material pairing. To obtain a deeper understanding of the wear behaviors of these materials, some additional observations and analyzes of the worn surfaces were conducted by means of various observations and analytical tools, such as topographic scanning electron microcopy, micro-Fourier transform IR, and so on. It was shown that the wear of the steel and Si_3N_4 was not a simple process, but had a complex manner in that both tribo-oxidation action and abrasive action of the steel and Si_3N_4 wear particles contributed to the higher wear of these materials.

9A501. **Combined effect of speed and humidity on the wear and friction of silicon nitride.** - MG Gee and D Butterfield *(Div of Mat Metrology, Natl Phys Lab, Queens Rd, Teddington, Middlesex TW11 0LW, UK)*. Wear 162-164(PART A) 234-245 (13 Apr 1993).

A series of ball-on-ring wear tests was performed on sintered silicon nitride. The experiments were carried out to investigate a discrepancy in the literature on the effect of humidity on the wear of silicon nitride. In the experiments reported here, a range of different testing speeds was used and the humidity of the tests held at less than 5% relative humidity (RH), 50% (RH), or 90% (RH). It was found that at the lowest speed that was used, the wear rate at low humidity was higher than that for higher humidity. As the speed increased there was a maximum in the wear rate for the high humidity tests, and a minimum for the low humidity tests, with wear rates for the low humidity tests much lower than those for the high humidity tests. At high speeds, the wear rate for the low humidity tests was much lower than that for the high humidity tests. The main mechanism of wear was the tribochemical oxidation of the silicon nitride to form silicon oxide.

9A502. **Effect of grain size on friction and sliding wear of oxide ceramics.** - K-H Zum Gahr, W Bundschuh, B Zimmerlin *(Inst of Mat Sci, Univ of Karlsruhe and Nucl Res Center of Karlsruhe Inst of Mat Res, PO Box 3640, W-7500 Karlsruhe, Germany)*. Wear 162-164(PART A) 269-279 (13 Apr 1993).

Microstructures of Al_2O_3 and 3mol%Y_2O_3-ZrO_2 (TZP) with symmetrically varying average grain sizes were produced by sintering. The hardness and fracture toughness of the ceramics as well as the amount of tetragonal, cubic and monoclinic phases of TZP-ZrO_2 were measured. Wear tests were carried out on the different self-mated microstructures in dry unidirectional and reciprocating sliding contact respectively, using block-on-ring geometries in air at ambient temperatures. The microstructures and worn surfaces were systematically analyzed using scanning electron microscopy and X-ray diffraction techniques. Experimental results showed that plastic deformation, intercrystalline microfracture, grain fragmentation, surface layers and delamination fracture contributed to the friction and wear processes. The theoretical analysis of wear as a function of time or length of wear path revealed a sharp transition from a high to a low level of wear intensity with decreasing apparent surface pressure for both oxide ceramics. A transition in the wear intensity occurred also as a function of the average grain sizes. These effects were attributed to a change in wear mechanisms.

9A503. **Effect of microstructure on the wear transition of zirconia-toughened alumina.** - C He, YS Wang, JS Wallace, SM Hsu *(Ceramics Div, NIST)*. Wear 162-164(PART A) 314-321 (13 Apr 1993).

The mechanical properties of alumina ceramics can be improved by the addition of pure or partially stabilized zirconia particles. In the present study, the wear characteristics of zirconia-toughened alumina (ZTA) composites under a non-reactive fluid (paraffin oil) lubricated condition were investigated. The wear transition load (ie, the load at which a rapid increase in wear occurs) increased with increasing zirconia content up to 20 vol%. The transition from mild to fracture-controlled wear of ZTA depends on the material properties (eg, hardness, elastic modules), the contact conditions (eg, Hertzian stress, coefficients of friction) and the microstructure of the material. The effect of the microstructure on wear was demonstrated and a Hall-Petch-type relationship between the microfracture stresses and the grain size was found. The effect of the grain size distribution on the wear transition load was also shown.

9A504. **Effect of sliding velocity on the wear-effect of time-temperature equivalence.** - J Song and GW Ehrenstein *(Dept of Polymer Eng, Univ of Erlangen-Nuremberg, Am Weichselgarten 9, DW-8520 Erlangen-Tennenlohe, Germany)*. Wear 162-164(PART B) 662-668 (13 Apr 1993).

The product from sliding velocity and normal load is usually used to calculate the working life of sliding elements. The fundamentals for this calculation and a wear factor which is independent of normal load and one which is independent of sliding velocity. Nevertheless, both increasing and decreasing wear factors with increasing sliding velocity were observed in tribological tests on polymeric materials. The reasons for this behavior seem to be two compensating effects of sliding velocity on the viscoelastic properties of polymeric materials, namely time-temperature equivalence and temperature dependence of the mechanical properties. The principle of time-temperature equivalence tells us that the change in the rate of strain (sliding velocity for tribology) has an effect equivalent to that of the change in the temperature. A high rate of strain leads to a high Young's modulus. In contrast, a high sliding velocity leads to a high temperature rise. The Young's modulus and strength of polymeric materials decrease with increasing temperature. The wear factor decreases with decreasing modulus. The effect of the sliding velocity is the sum of both effects. Therefore, a strongly marked dependence of the mechanical properties of polymeric materials on rate of strain leads to decreasing wear factor with increasing sliding velocity. In the case of a weaker time-temperature effect, the temperature dependence of the mechanical properties is dominant. Therefore, a slightly increasing wear factor with increasing sliding velocity can be observed.

9A505. **An evaluation of the penetration of ceramic femoral heads into polyethylene acetabular cups.** - D Dowson, B Jobbins, A Seyed-Harraf *(Dept of Mech Eng, Univ of Leeds, Leeds LS2 9JT, UK)*. Wear 162-164(PART B) 880-889 (13 Apr 1993).

It is desirable to evaluate the performance of new designs of total replacement hip joints and new materials in joint simulators prior to clinical trials, yet few satisfactory hip joint simulators are available. In a previous paper we have reported on the design and development of a versatile hip joint simulator and recorded an initial study of the performance of a standard 22 mm diameter Charnley prosthesis. There is now considerable interest in the use of ceramic femoral heads in total replacement hip joints and in the present paper we report the performance of larger diameters (32 mm) femoral heads made from high purity, fine grain alumina. A new procedure for the evaluation of penetration and wear volumes based upon the use of coordinate and roundness measuring machines is described. The results show a relatively rapid initial penetration of the femoral heads into the ultra-high molecular weight acetabular cups during the first 1.5×10^6 cycles of loading, followed by a very low penetration rate of about 27 μm per million cycles. This is shown to compare favorably with the previous findings for smaller, metallic Charnley prosthesis femoral heads of 22 mm diameter.

9A506. **Increasing wear resistance in polymer-based composites using radiation-modified polymeric additives.** - YM Pleskachevskii, VV Smirnov, VN Aderikha *(Metal-Polymer Res Inst, Belarus Acad of Sci, Gomel 246652, Belarus)*. Wear 162-164(PART A) 426-431 (13 Apr 1993).

The effect of radiation treatment of polymers and polymeric compositions on their structure and service properties is examined. The treatment of commercial dispersed polymers and their compositions is shown to be an efficient method for preparing friction modifiers that ensure increased wear resistance of plastics.

9A507. **Influence of carbon content of martensitic matrix and retained austenite on wear of martensitic ductile iron.** - Chuan-Gui Li, Qing-De Zhou *(Dept of Mech Eng, Xian Jiaotong Univ, Xian 710049, China)*, Guang-Shun Song, Zhen-Shu Fang *(Steel Foundry Shop, Hubei Plant of Cement Machinery, Huangshi, Hubei 435000, China)*. Wear 162-164(PART A) 75-82 (13 Apr 1993).

The influence of the carbon content of the martensitic matrix (at different austenizing temperatures) and the amount of retained austenite (AR) on the two-body abrasion and impact abrasion wear of martensitic ductile iron was studied. The results showed that: (1) the wear of martensitic ductile iron in two-body abrasion is a process of plastic deformation fatigue in the case of a soft abrasive, but a process of cutting in the case of a hard abrasive; (2) the carbon content in the martensitic matrix has an optimal value in impact wear testing; (3) the effect of AR on wear resistance depends on the loading condition. When the load is without impact such as in two-body abrasion, the retained austenite contributes to the wear resistance if the process is controlled by a fatigue mechanism; however, it has no significant effect on wear resistance if the process is controlled by the cutting mechanism. However, under impact load, retained austenite is harmful to the wear resistance.

9A508. **Influence of retained austenite on the wear resistance of high chromium cast iron under various impact loads.** - Jun-Tong Xi, Qing-De Zhou *(Dept of Mech Eng, Xian Jiaotong Univ, Xian 710049, China)*, Shi-Hui Liu, Guang-Shun Song *(Steel Foundry Shop, Hubei Plant of Cement Machinery, Huangshi, Hubei 435000, China)*. Wear 162-164(PART A) 83-88 (13 Apr 1993).

A high chromium cast iron was heated and maintained at 980 °C, and then cooled in five media of different temperatures to obtain various amounts of austenite (designated Ar). The specimens were subjected to impact wear tests under impact loads ranging from 1 to 6.2 J. The number of impacts was 6000 for each test. The results showed that (1) the influence of Ar on the impact wear resistance of high chromium cast iron depended on the magnitude of the impact load and wear mechanism. (2) Under a small impact load the mechanism was mainly cutting wear and Ar has no significant effect on impact wear resistance. (3) Under heavy impact load the mechanism was mainly impact fatigue wear and Ar exhibited a harmful effect on the impact wear resistance of the iron.

9A509. **Lubricated sliding and rolling wear of austempered ductile iron.** - Wu-Sheng Zhou, Qing-De Zhou *(Dept of Mech Eng, Xian Jiatong Univ, Xian 710049, Peoples Rep of China)*, Shou-Kang Meng *(Dept of Mech Eng, Yunnan IT, Kunming, Yunnan 650051, Peoples Rep of China)*. Wear 162-164(PART B) 696-702 (13 Apr 1993).

A series of austempered ductile iron samples were prepared by varying the austenizing temperature and austempering temperature. The lubricated sliding and rolling wear were studied and the wear mechanisms discussed. The results showed that in the case of lubricated sliding wear the wear resistance decreased with increasing austenizing temperature (850 - 950° C) and austempering temperature (300 - 400° C), and the mechanism was fatigue wear and in the case of lubricated rolling wear the wear resistance decreased initially with increasing austempering temperature (300 - 400° C) to a minimum and then increased considerably, and the mechanism was mainly fatigue spalling. It was supposed that a structure composed of lower bainite and low carbon content retained austenite is always beneficial to wear resistance. Hardness was an important property influencing the wear resistance. The hardening due to the phase transformation of retained austenite contributed to the rolling wear resistance.

9A510. **Macroscopic and microscopic wear mechanisms in ultra-high molecular weight polyethylene.** - JR Cooper, D Dowson, J Fisher *(Dept of Mech Eng, Univ of Leeds, Leeds LS2 9JT, UK)*. Wear 162-164(PART A) 378-384 (13 Apr 1993).

Studies of the wear of ultra-high molecular weight polyethylene sliding on relatively smooth metallic and ceramic counterfaces under a wide range of tribological conditions in pin-on-disc and pin-on-plate tests, hip joint simulators and components taken from patients, have demonstrated evidence for two separate types of wear processes. Microscopic wear processes were associated with the very small asperities or the smooth counterfaces (less than 0.2 μm). Macroscopic polymer asperity wear processes were associated with stress concentrations under the much larger peaks in the polymer surface (amplitude less than 10 μm). For constant load tests with rougher counterfaces, microscopic asperity wear dominated. However for smooth counterfaces ($R_a < 0.02$ μm) under constant load, the contribution of microscopic asperity wear was small, and incremental increase in wear rates were caused by removal of macroscopic polymer asperities due to high subsurface strains and failure. In artificial joints under dynamic loading, the macroscopic polymer asperity wear processes were accelerated by subsurface cracking and fracture producing high wear factors on smooth counterfaces.

9A511. **Mechanisms of hard alloy wear in frictional processes with polymers and composite materials.** - AL Zaitsev *(Metal-Polymer Res Inst, Acad of Sci, Gomel 246652, Belarus)*. Wear 162-164(PART A) 40-46 (13 Apr 1993).

Wear mechanisms have been analysed for a hard alloy prepared from cobalt and tungsten carbide when rubbed against polymers and their composites. The influence of the polymer chemical structure on hard alloy wear by the oxidation-fatigue mechanism was considered, as well as the effect of the hard alloy surface roughness and composite formulation on the running-in process. The relative area of layers transferred by friction onto the hard alloy surface during contact interaction was found to affect the mechanism by which the surface wears. The abrasive wear mechanism changes for the oxidation mechanism in the case of steady friction transfer layer formation owing to weaker friction hardening of the hard alloy surface layer, and to fatigue tear-out of carbide grains.

9A512. **Microstructure and wear resistance of pearlitic rail steels.** - AJ Perez-Unzueta and JH Beynon *(Dept of Eng, Univ of Leicester, University Rd, Leicester LE1 7RH, UK)*. Wear 162-164(PART A) 173-182 (13 Apr 1993).

Despite competition from bainitic and martensitic steels, pearlitic microstrctures remain dominant for railway track. Techniques developed over recent years have progressively refined the interlamellar spacing to produce harder, more wear-resistant pearlitic steels. This study aims to explain the mechanisms for the wear performance by observing how the microstructure adapts to the wear loading. Four pearlitic rail steels, with similar chemical compositions but with different interlamellar spacings, have been examined. Wear tests have been performed under both pure sliding and rolling-sliding conditions, the latter designed to simulate track conditions. The worn surfaces and the plastically deformed subsurface regions have been examined by optical metallography and scanning electron microscopy. It was observed that the plastic deformation produced considerable fracturing and realignment of the hard cementite lamellae. The softer ferrite matrix was severely deformed, allowing a reduction in the interlamellar spacing on approaching the worn surface. The effect of these realignments on the surface was to present an increased area fraction of hard cementite lamellae on planes parallel to the surface. Thinner cementite lamellae, associated with low interlamellar spacings, were easier to bend before fracturing. It is believed that shear ductility plays an important role in the period of time that any particular volume of material remains at the surface before becoming a loose particle.

9A513. **Movement patterns of abrasive particles in three-body abrasion.** - L Fang, XL Kong, JY Su, QD Zhou *(Dept of Mech Eng, Xian Jiaotong Univ, 710049 Xian, China)*. Wear 162-164(PART B) 782-7789 (13 Apr 1993).

The movement patterns of abrasive particles in three-body abrasion are very important to the wear of materials. In the present paper, the movement of a single abrasive particle could be observed in detail through new wear apparatus for three-body abrasion. The new apparatus was used to carry out short-travel wear testing for a single particle sandwiched between two metal surfaces and to measure the frictional force at the same time. A number of experiments showed that there were mainly two kinds of movement patterns of the particles, ie, sliding and rolling. Based on the experimental results, a criterion was proposed for the movement patterns of abrasive particles. The criterion matched with the experiments quite well.

9A514. **Reactions during preparation and sliding of sintered Fe-Mo-S wear-resistant materials.** - Zhang Guowei, Ouyang Jinlin, Meng Xiukun, Ma Li, Qi Shangkui, Zhang Fu *(Lab of Solid Lubrication, Lanzhou Inst of Chem Phys, Chinese Acad of Sci, Gansu, 730 000 Lanzhou, China)*. Wear 162-164(PART A) 450-457 (13 Apr 1993).

Using quick hot-press sintering, Fe-Mo-S materials were prepared with the properties of low wear rates (eg, as an 8S28Mo64Fe pin sliding against a 45 steel disk in air, the specific wear of the pin is 8.6×10^{-14} M^3 N^{-1} M^{-1}, while that of the disk is 1.21×10^{-14} M^3 N^{-1} M^{-1}). Using X-ray diffraction, X-ray photoelectron spectroscopy, Auger electron spectroscopy, and differential thermal analysis, the reactions related to Fe-Mo-S mateials were studied. Thermodynamic analysis of the reactions to form sulphides was performed. It was found that a non-stoichiometric Mo-S compared with a crystal structure similar to hexagonal MoS_2 and $Fe_{1.3}Mo_6S_8$ formed in the materials during preparation. Grey-black films formed on the wear tracks of the steel disks during sliding against Fe-Mo-S pins in air. Oxides are the major constituents and sulphides the minor constituents of the films. Comapring Fe-Mo-S materials and the alloys without sulphur (eg, 45 steel or Fe-Mo alloy) indicates that the low wear rates of the materials are attributed to the formation of the films, and a catalytic effect of sulphides of the oxidation is a necessary condition in forming the films. The mechanism of improving the tribological properties by catalytic reaction films has been used successfully to develop Ni-Mo-S high temperature, self-lubricating materials.

9A515. Selected thermoplastic bearing materials for use at elevated temperatures. - AM Hager, K Friedrich *(Inst Verbundwerkstoffe, Univ Kaiserslautern, 6750 Kaiserslautern, Germany)*, R Junghans *(Wissenschaftsbereich Tribstech, Tech Univ, O-9010 Chemnitz, Germany)*. Wear **162-164**(PART B) 649-655 (13 Apr 1993).

Various polyaryletherketone-based composites were investigated with regard to their high temperature dry-sliding behavior. In the range between room temperature and 220° C, all grade with a polytetrafluoroethylene (PTFE) content of 10 - 15 wt% exhibited a friction behavior that is very similar to that of neat PTFE. Studies of the wear-pv relationship of some of the grades showed that fibre content of 30 wt% are found to stabilize the specific wear, up to pv products of 16 MPa m s^{-1}.

9A516. Study of some active wear mechanisms in a titanium-based cermet when machining steels. - H Thoors, H Chandrasekaran, P Olund *(Swedish Inst for Metals Res, Drottning Kristinas Vag 48, S-11428 Stockholm, Sweden)*. Wear **162-164**(PART A) 1-11 (13 Apr 1993).

This paper discusses the results from a study devoted to the understanding of the wear behavior of a Ti(CN)-based cermet tool material. Variation in the qualitative and quantitative nature of wear of this tool material in longitudinal and turning was effected by the choice of a steel type and cutting conditions. The three work materials (two quenched and tempered steels and one ball-bearing steel) have different microstructures and inclusion contents. The study revealed that the presence of conventional flank wear, varying degrees of crater wear and negligible notch wear, while plastic deformation of the cutting edge appears to be the life-limiting factor. Detailed investigation of the active surfaces of the tool revealed abrasion from hard phases and adhesion (micro and macro) to be dominant in the case of the quenched and tempered steel machining, while with ball-bearing steel microchipping, plastic deformation and cracking ply play an important role. Metallurgical interaction was also observed between the constituents of the tool material and the chip material or reaction products of inclusions, resulting in the embrittlement of the tool material and facilitating rapid wear. The observerd differences in the micromechanisms of wear were also in conformity with the variations in the evaluated tool-chip contact stress.

9A517. Study on reduction in wear due to magnetization. - K Kumagai *(Akita Univ, 1-1 Tegata Gakuen-machi, Akita 010, Japan)*, Koshi Suzuki *(Tohoku Elec Power, 3-7-1 Ichiban-cho Aoba-ku, Sendai 980, Japan)*, Osamu Kamiya *(Akita Univ, 1-1 Tegata Gakuen-machi, Akita 010, Japan)*. Wear **162-164**(PART A) 196-201 (13 Apr 1993).

Operating the pin-rotor type wear test using the ferromagnetic materials, an Ni pin and steel rotor combination, even a weak magnetization of the pin decreased the wear. In order to probe that phenomenon, the grain size distributions of wear particles have been analyzed by means of the computer-aided image analyzer. The experimental results indicate the relationship that wear rate reduces with the fining down of the wear particles. It is concluded that magnetization accelerated the oxidation at rubbing surfaces and wear particles. Oxidation prevents the rubbing surfaces from mutual material transfer and the consequent pile up to form larger particles, therefore the wear particles remain fine. The cause of wear reduction was the fining down of wear particles by accelerated oxidation in magnetic effect, and those oxidized as fine-wear-particles existed between rubbing surfaces and were attracted by a magnetic force, which acted as a lubricant and reduced the wear. The observation that the magnetization accelerated oxidiation was verified by the fact that the oxidation reaction of a magnetized steel piece was more severe than one without magnetization. Moreover, the oxygen density at the surface of ferromagnetic materials in air was a little increased by magnetization, which also contributed to the acceleration of oxidation at a rubbing surface.

9A518. Transmission electron microscopy study of wear of magnesia partially stabilized zirconia. - WM Rainforth *(Dept of Eng Mat, Univ of Sheffield, PO Box 600 Sir Robert Hadfield Build, Mappin St, Sheffield S1 4DU, UK)* and R Stevens *(Sch of Mat, Univ of Leeds, Leeds LS2 9JT, UK)*. Wear **162-164**(PART A) 322-331 (13 Apr 1993).

The role which the stress assisted transformations of the tetragonal to monoclinic phase plays in the wear of zirconia ceramics remains unclear. This paper discusses the use of detailed transmission electron microscopy of the worn surface to assess the role of transformation in the sliding wear of magnesia partially stabilized zirconia against a steel counterface. Three mechanisms were identified for the wear of the ceramic. Firstly, transformation occurred cooperatively in bands along the [100] directions which led to extensive microcrack formation. Coalescence of the microcracks promoted preferential wear from the bands. Thus, transformation of the tetragonal to the monoclinic phase has led to an increased wear rate. Secondly, clear experimental evidence was found of a tribochemical wear mechanism of the zirconia. In such areas, the transformation of the tetragonal to monoclinic phase played a minor role and was only found to a depth of 200 nm. Finally, abrasive grooving was shown to cause extensive plastic deformation. Interestingly, no evidence of fracture or transformation was found at the abrasive grooves. Thus, this work has demonstrated that under these particular sliding conditions, transformation toughening can have a detrimental as well as a beneficial effect on the tribological properties of zirconia.

9A519. Tribological behavior of blends in polyether ether ketone and polyether imide. - Jong Hyun Yoo and NS Eiss Jr *(VPI)*. Wear **162-164**(PART A) 418-425 (13 Apr 1993).

In this study polyether ether ketone (PEEK) and polyether imide (PEI) were blended to raise the glass transition temperature (T_g) above that of PEEK while retaining the low-wear characteristics of PEEK. The friction and wear of injection-molded blends were measured in dry sliding by a stainless steel ball sliding on a polymer blend disk. The test variables were normal load, sliding speed and the percentage of crystallinity of the PEEK component of the blend. The wear mechanism of the pure PEEK was plowing with no net loss of material. This mechanism persisted for blends up to 70% PEEK-30% PEI (70/30) for which the T_g was raised to 15 °C above that of PEEK. For 50/50 and pure PEI the wear mechanism was changed to that of fatigue, as evidenced by the generation of small particles after a period of sliding with no wear. The wear rates were higher for the PEI-dominated blends: as much as 40 times larger at the highest load and sliding speed. As the percentage of PEEK in the blends was reduced, the crystallinity of the PEEK component was also reduced; for the 50/50 blend the crystallinity was zero. Annealing the injection-molded samples raised the crystallinity of the PEEK in the blends to that of the pure PEEK injection-molded sample. In general, the increase in crystallinity caused by annealing reduced the wear rate of the blends. The coefficient of friction for the blends with low wear was below 0.15, while it was 0.2 to 0.3 for the blends which had the higher wear rates. For these latter blends, the friction coefficient was low until the wear track formed, at which time it increased to the higher level.

9A520. Tribological stability of metallic materials at elevated temperatures. - H Berns *(Inst Werkstoffe, Lehrstuhl Werkstofftech, Ruhr Univ, Postfach 102148, Bochum 1, Germany)* and A Fischer *(NU-TECH, Ilsahl 5, 2350 Neumunster, Germany)*. Wear **162-164**(PART A) 441-449 (13 Apr 1993).

The sliding abrasion wear rates of metallic materials against flint, measured between 25 and 1050 °C under an argon atmosphere, are shown and discussed. Above 550 °C, wear is governed mainly by the properties of the metal matrix and can be correlated with its resistance to plastic deformation. Thus, the hot hardness and work hardening capability affect the wear rate under stationary conditions. Instabilities occur when dynamic recrystallization appears within the metal matrix, bringing about a total loss of its work hardening capability. Hard phases have only a small effect on the tribological behavior under stationary and non-stationary conditions.

9A521. Wear and film formation in the presence of methanol and formic acid. - L Mattsson, B Olsson *(Dept of Phys, Chalmers Univ of Tech, S-412 96 Goteborg, Sweden)*, PH Nilsson, G Wirmark *(Tech Dev, Dept 06170, AB Volvo, S-412 88 Goteborg, Sweden)*. Wear **165**(1) 75-83 (May 1993).

Increased wear in methanol fuelled engines has been observed, especially at low operating temperatures. Combustion intermediates, for instance, formic acid, are believed to promote wear in the piston ring-cylinder liner assembly. In this study, tribological effects of methanol and formic acid were investigated in a model system. The study was focused on the running-in process under normal conditions and how the running-in was affected by the presence of methanol and formic acid in oils with different lubricant additives. The study showed that a tribosystem with the anti-wear additive ZDDP (zinc dialkyldithiophosphate) had the ability to redistribute the surface layer. After an initial phase of large wear, this redistribution process resulted in a surface film with excellent wear resistance. Adding methanol and formic acid contaminants to this lubricant disturbed the film formation process and a higher steady state wear was observed. A more fully formulated lubricant, with detergent and dispersant, could better withstand these contaminants even though a rise in the steady state wear rate was found in experiments performed at room temperature.

9A522. Wear and scratch hardness of 304 stainless steel investigated with a single scratch test. - TA Adler and RP Walters *(US Dept of the Interior, Bureau of Mines, 1450 Queen Ave SW, Albany OR 97321-2198)*. Wear **162-164**(PART B) 713-720 (13 Apr 1993).

The wear and scratch hardness of 304 stainless steel was investigated with a scratch test developed by the US Bureau of Mines. The scratch was produced by a diamond indenter with a 0.2-mm spherical tip in air and in a corrosive environment. Scratch hardness was calculated from the width of the scratch and was correlated with Vickers hardness. Wear was measured by integrating the area between the profile of the scratch and the original surface. At low loads wear occurs in a rubbing mode. At higher loads wear debris was formed. The transition from rubbing wear to wear with a continuous formation of debris occurred at a critical value of the attack angle. A relationship between the attack angle, the radius of the tip of the scratcher, and the load on the scratcher, and the hardness of the material is presented. Stainless steel was scratched at an anodic potential (with a passive film on the surface) and at a cathodic potential (with no passive film on the surface). The presence or absence of the passive film had no effect on the scratch hardness or wear for either the rubbing mode or the mode of wear with debris. The interface shear strength was not affected by the change in potential.

9A523. **Wear deformation of ordered Fe-Al intermetallic alloys.** - HE Maupin, RD Wilson *(US Bureau of Mines, Albany Res Center, Albany OR 97321-2198)*, JA Hawk *(US Bureau of Mines, Albany Res Center, Albany OR 97321-2198)*. Wear 162-164(PART A) 432-440 (13 Apr 1993).

The Bureau of Mines conducted abrasive wear research in DO_3 ordered and disordered Fe_3Al intermetallics. The effect of abrasion on these alloys were studied through microscopy, X-ray diffraction and hardness measurements. The region near the wear surface undergoes dynamic recrystallization, ie, the original microstructural morphology of micron-size grains is replaced by one with nanosize grains. Abrasions of the Fe_3Al alloys also results in a loss of the DO_3 ordering in the wear surface region. The bulk temperature rise of the specimen during abrasion was approximately 28 °C which is insufficient to cause recrystallization in these alloys. Therefore, the flash temperature due to interface frictional heating is considered more important than the bulk temperature when considering dynamic recrystallization as the transformation mechanism in the near wear surface region.

9A524. **Wear mechanisms of ultrahard, nonmetallic cutting materials.** - W Konig and A Neises *(Lehrstuhl Tech Fertigungsverfahren, WZL RWTH, Steinbachstr 53 B, W-5100 Aachen, Germany)*. Wear 162-164(PART A) 12-21 (13 Apr 1993).

Basic wear mechanisms of polycrystalline diamond (PCD) and polycrystalline cubic boron nitride (PCBN) composite cutting materials were examined. The investigation included the planning and realization of model wear test systems closely connected to and including the main tribological parameters of the real cutting process during turning of metals. Considerable attention has been given to the chemical composition and the microstructure of the cutting tool materials. A series of diffusion and abrasion model tests were carried out to reveal the effect of the diffusion mechanism on the abrasion resistance of PCD and PCBN during cutting processes. The forms of wear which occurred during the model tests were compared with the wear state produced by means of real turning tests and found to be useful in explaining the wear behavior of PCB and PCBN during cutting operations. The diminution of the abrasion resistance of the cutting material owing to graphitization seems to be the dominant wear mechanism when turning a titanium alloy at elevated cutting speed with PCD composites. However, the wear rate obviously is dependent on the grain size of the diamond crystals. In the case of PCBN, the chemical composition of the binder and its percentage in the composite is important for thermal stability, as it is required for cutting tools. PCBN samples, exposed to the diffusion tests with steel as the workpiece material at elevated temperatures up to 950° C suffered significant changes in the structure of the binder. This seems to result in a reduction of the bulk material resistance to abrasive wear. Scanning electron microcopy and energy-dispersive spectroscopy investigation of inserts used in real cutting tests turning a bearing steel helped to ascertain the practical relevance of the results achieved with the model test series.

9A525. **Wear reduction systems for coal-fueled diesel engines I. The basics of powder lubrication.** - H Heshmat *(Mech Tech, 968 Albany-Shaker Rd, Latham NY 12110)*. Wear 162-164(PART A) 508-517 (13 Apr 1993).

The objective of this investigation is to resolve the problem of severe wear occurring in systems using coal-water particulates as fuels or as a process material. The approach discussed herein consists of replacing conventional oil lubrication with a powder lubrication system that uses the process particles, either alone or in combination with another powder. Unlike previous work in this field, this approach is based on the postulate of the quasi-hydrodynamic nature of powder lubrication. This postulate is deduced from past observation and present verification that there are a number of basic features of powder flow in narrow interfaces that have the characteristic behavior of fluid film lubrication. In addition to corroborating the basic mechanism of powder lubrication, the conceptual and experimental work performed in this investigation provide guidelines for selection of the proper geometries, materials, and powders suitable for this tribological process. The present investigation describes the fundamentals of quasi-hydrodynamic powder lubrication and defines the rationale underlying the design of the test facility. A follow-up paper dealing with the performance and the results of the experimental investigation presents conclusions reached regarding design requirements as well as the formulation of a proper model of quasi-hydrodynamic powder lubrication.

9A526. **Wear-corrosion-resistant materials for mechanical components in harsh environments.** - PL Ko *(Trib and Mech Lab, NRC, 3650 Wesbrook Mall, Vancouver BC, V6S 2L2, Canada)*, A Wozniewski *(Project and Tech Services, Esso Resources Canada, 237 4th Ave SW, Calgary Alta, T2P 0A6, Canada)*, PA Zhou *(Wear Res Group, CAAMS, 1 Beishatan Deshengmen Wai, Beijing, China)*. Wear 162-164(PART B) 721-732 (13 Apr 1993).

In pumping the deviated and slant oil wells, many commonly used materials are readily attacked by the combined effect of mechanical wear and the harsh environment at the bottom hole. Three groups of new materials that include ceramics, alloys and hard coatings were evaluated for the downhole application. Two sets of tests, which involved scaling and corrosion for the first, and wear for the second, were carried out in parallel. The wear tests were further divided into reciprocating sliding and impact-fretting, in dry and in 2% sand slurry conditions. The investigation identified the wear mechanism involved. The test results showed that a steel alloy with a titanium carbide composite in a martensitic matrix, and both nitrided and chrome-plated carbon steels could provide good wear resistance for both dry and slurry conditions.

See also the following:

9A285. Thermal aspect in design of rotary drill bit supports
9A432. Abrasive wear study of selected white cast irons as linear materials for the mining industry
9A484. Self-organization and concepts of wear resistance of tribosystems
9A486. Friction and wear of self-lubricating composites at temperatures to 450 °C in vacuum
9A490. Further investigation on the tribological behavior of Cu-20% Nb *in situ* composite
9A491. Hardness, friction and wear of multiplated electrical contacts
9A493. Sliding friction and wear of ceramics in neutral, acid, and basic aqueous solutions
9A496. Tribological behavior of a titanium-nickel alloy
9A674. Development of fracture resistant, multilayer films for precision ball bearings
9A677. Wear reduction systems for coal-fueled diesel engines II. Experimental results and hydrodynamic model of powder lubrication

292E. CONTACT FATIGUE

9A527. **Load ratings of spherical plain bearings.** - Yang Xian Qi and Jiang Shao Feng *(Luoyang Bearing Res Inst, Jiling Rd, Luoyang 471039 Henan, China)*. Wear 165(1) 35-39 (May 1993).

Up to now, the load ratings of spherical plain bearings have been calculated using a nominal contact pressure and a projected bearing surface area. This type of method does not show real capacity of the bearings. In this paper, the steel-steel spherical plan bearings under load were studied by the FEM. The contact stress distribution in the bearing was determined. A relationship between maximum contact pressure and deformation was found. Based on these results, new definitions for the bearing load ratings are recommended, and general formulae to calculate the ratings are determined.

9A528. **Rolling-contact-fatigue wear characteristics of diamond-like hydrocarbon coatings on steels.** - Ronghua Wei, PJ Wilbur *(Colorado State Univ, Ft Collins CO 80523)*, MJ Liston *(NTN Tech Center, Ann Arbor MI 48108)*, G Lux *(Charles Evans and Assoc, Redwood City CA 94063)*. Wear 162-164(PART A) 558-568 (13 Apr 1993).

Adherent diamond-like hydrocarbon (DLHC) coatings were applied on AISI M-50, 52100, 4118 and 440C steel rods by using an approximately 0.2 μm amorphous-silicon-hydrocarbon (a-SiHC) bonding layer between the DLHC and the steel. Both the a-SiHC and DLHC coatings were applied using a single, broad-beam ion source. The rods were subjected to rolling-contact-fatigue (RCF) testing under high cyclic Hertzian stress (5.5 GPa), low lubricant-film-thickness parameter (lambda = 0.7) conditions. Order of magnitude increase in the fatigue lives of all four rod materials were observed. Systematic RCF tests coupled with microscopic examination after various test intervals show that micro-polishing by hard DLHC coating fragments may play an important role in prolonging fatigue lives. Raman spectroscopic measurements suggest that cyclic stressing of the DLHC layer causes it to transform from what was initially amorphous carbon into the more lubricous and stable graphite phase.

See also the following:

9A531. Calculation of flat surface wearing by spherical indenter under random contact

292F. THERMOMECHANICAL EFFECTS

9A529. **Effect of temperature on the wear of unfilled and filled liquid crystal polymers.** - Yoshitaka Uchiyama, Yutaka Uezi *(Fac of Tech, Kanazawa Univ, Ishikawa 920, Japan)*, Atsushi Kudo, Takeshi Kimura *(Starlite, Tsurumi-ku, Osaka 538, Japan)*. Wear 162-164(PART B) 656-661 (13 Apr 1993).

The friction and wear properties of unfilled and filled liquid crystal polymers (LCPs) (polyester derived from terephthalic acid, P-hydroxybenzoic acid and P,P-biphenol) were examined in the longitudinal (L), transverse (T) and normal (N) directions of the polymer molecules. When rubbed against an abrasive paper, the wear rate of the unfilled LCP depended on the sliding direction. The maximum wear rates were observed in the T direction, the minimum wear rates in the N direction and medium wear rates in the L direction. The wear rates steeply increased above 100° C. In the LCPs filled with graphite only, or graphite in combination with polytetrafluoroethylene (PTFE), the orientation was minimized but there was no minimizing effect of the wear rates. When rubbed against a chromium-plated disk at room temperature, the wear rates of the unfilled LCP were of the order of 10^{-7} mm^3 N^{-1} m^{-1}. The wear rates steeply increased, above room temperature and reached a figure of the order of 10^{-4} mm^3 N^{-1} at 100° C. The filled LCPs in the N direction showed very low rates of the order of 10^{-8} mm^3 N^{-1} m^{-1} at room temperature. However, the wear rates in the L and T directions were of the order of 10^{-7} mm^3 N^{-1} at room temperature. The wear rates for the graphite-filled LCP steeply increase beyond room temperature and maximum wear rates of the order of 10^{-5} mm^3 N^{-1} at room temperature. However, the wear rates in the L and T directions were of the order of 10^{-7} mm^3 N^{-1} m^{-1} occurred at 120° C in the temperature range examined. At 160° C, the wear rates were much lower than those at 120° C. The wear rates for the LCP filled with graphite in combination with PTFE also steeply increased above room temperature. However, the wear rates at temperatures from 60 to 160° C were lower than those of the graphite-filled LCP. The friction coefficients for the filled LCPs were relatively high at room temperature but tended to decrease above 60° C. The filled graphite with PTFE had obvious reducing effects on the wear rates at elevated temperaures.

See also the following:

9A285. Thermal aspect in design of rotary drill bit supports

292H. SURFACE EFFECTS, TOPOGRAPHY, COATINGS

9A530. **Abrasion, erosion and scuffing resistance of carbide and oxide ceramic thermal sprayed coatings for different applications.** - G Barbezat, AR Nicoll *(Plasma-Tech, Rigackerstr 16, 5610 Wohlen, Switzerland)*, A Sickinger *(Electro-Plasma, Irvine CA)*. Wear 162-164(PART A) 529-537 (13 Apr 1993).

In the area of antiwear coatings, carbide-containing coatings (Cr_3C_2-NiCr, WC-Co, WC-Ni etc). and oxide ceramic coatings (Al_2O_3, Cr_2O_3 etc) are applied using different thermal spray processes in the form of individual layers. In many industries these coatings have become technically significant on components where wear and friction can cause critical damage in the form of abrasion, erosion and scuffing together with corrosion. Carbide-containing and ceramic coatings have been produced with different thermal spray processes (atmospheric plasma spraying, vacuum plasma spraying, high velocity flame spraying and detonation gun spraying) for the determination of abrasive, adhesive and erosive wear resistance. Two types of abrasion tests, namely an adhesion wear test and an erosion test in water at a high velcoity (up to 170 m s^{-1}), were used for the characterization of wear resistance under different conditions. The coatings were also characterized with regard to microstrucutre, composition and fracture toughness. The influence of the thermal spraying process parameters on the microstructure is presented together with the influence of the microstructure on the behavior of the coatings under simulated service conditions.

9A531. **Calculation of flat surface wearing by spherical indenter under random contact.** - IA Soldatenkov *(Inst for Prob, Russian Acad of Sci, Moscow, Russia)*. Sov J Friction Wear 13(6) 8-14 (1992).

The analysis is presented for a flat surface wearing by a sliding spherical indenter. The indenter moves along the surface with random deviations of its center from the given trajectory. Load is varied randomly. A joint probability density of the center deviations from the trajectory and the load are assumed to to be given. Averaging the dependence of wear rate on the contact pressure by its parameters we derive an equation of wear kinetics in terms of averages. The case of low wear is considered and a solution of wear kinetics equation is obtained in explicit form. In general case, the equation is solved numerically.

9A532. **Experimental study of self-welding of materials in high temperature liquid sodium.** - S Chander, C Meikandamurthy, RD Kale *(Dept of Atomic Energy, Indira Gandhi Centre for Atomic Res, Kalpakkam, Tamil Nadu 603 102, India)*, R Krishnamurthy *(Indian IT, Madras, India)*. Wear 162-164(PART A) 458-465 (13 Apr 1993).

The study self-welding of materials in high temperature liquid sodium, an experimental set-up consisting of a sodium-circulating loop, a test vessel, a loading mechanism for material specimens and instrumentation were designed, installed, and operated at IGCAR, Kalpakkam. Combinations of austenitic stainless steel, hard chrome plating and Stellite-6 with the surface finish of the contact surfaces typical of that of components in fast breeder reactors were exposed to liquid sodium at 530 °C under load intensities of 10 and 40 MPa for 500 and 1000 h. The paper discusses the experimental set-up installed and the results of self-welding of these material combinations. The role of surface finish on self-welding tendency is also briefly discussed.

9A533. **Failure of poly (ether ether ketone) in high speed contacts.** - BJ Briscoe, BH Stuart, S Sebastian *(Dept of Chem Eng and Chem Tech, Imperial Col, London SW7 2BY, UK)*, PJ Tweedale *(Natl Centre for Trib, AEA Tech, Risley, Warrington WA3 6AT, UK)*. Wear 162-164(PART A) 407-417 (13 Apr 1993).

The paper describes an experimental study, with an associated analysis incorporating supplementary data, of the anti-boundary lubricating action of an alkane-aliphatic carboxylic acid lubricant system in a poly (ether ether ketone)-mild steel contact. The experiments involve progressively increasing the load in a contact formed between a polymer plate and a rotating steel shaft and estimating the frictional work dissipated. Scuffing is identified when a rapid increase in frictional work is noted at a characteristic normal load. It is shown that the additive induces premature scuffing. Subsidiary data is provided using Raman spectroscopy and hardness probes, and confirms that certain additives such as decanoic acid and dodecylamine will induce surface plasticization in poly (ether ether ketone). The trends in the frictional data have been interpreted using the adhesive model of friction in conjunction with temperature-dependent interfacial rheology and bulk mechanical property data. It is proposed that the scuffing is induced prematurely as a consequence of excessive additive-induced subsurface plasticization. Restricted surface plasticization in this system provides an enhanced self-lubricating capacity.

9A534. **Friction and wear of heterogeneous coating under boundary lubrication Part 2. Sliding parts with hard coatings.** - YP Serdobintsev and SI Sharavin *(Machine-Tool Inst, Moscow, Russia)*. Sov J Friction Wear 13(6) 25-30 (1992).

A mathematical model is developed which takes into account a nature of boundary lubrication of rough surfaces and physicochemical adsorption in tribocontact. A portion of load supported by a lubricant film adsorbed on asperities is determined. Analytical relationships for friction coefficient depending on roughness parameters and lubricant molecule size are derived, provided that low friction occurs in the situation of inadequate or irregular lubrication. The relationships may be used to develop technological principles of surface formation.

9A535. **A general model for sliding wear in electrical contacts.** - RG Bayer *(4609 Marshall Dr W, Vestal NY 13850)*. Wear 162-164(PART B) 913-918 (13 Apr 1993).

A variety of models, generally either based on abrasive, adhesive or surface fatigue wear concepts, have been used with some success in describing the sliding wear of electrical contacts. There are also empirical observations which support the individual or simultaneous occurrence of these various mechanisms in wear of such contacts. In addition to these mechanisms, which may be referred to as surface wear mechanisms, a subsurface mechanism has also been identified in recent studies of the wear of a card-edged connector system. This mechanism is associated with the plastic deformation of the substrate and can coexist with all, or any, of the surface mechanisms. In this paper, a model is developed for this subsurface mechanism and combined with models for the surface mechanism to provide a general model for the sliding wear of contact systems. The relationships, which result from these models, are shown to agree with observed behavior in the case of a card-edge contact system. It is suggested that the method of combining the effects of several simultaneous wear mechanisms may be applicable to more general wear situations.

9A536. **The generation of worn surfaces by the repeated interaction of parallel grooves.** - Y Xie and JA Williams *(Eng Dept, Cambridge Univ, Trumpington St, Cambridge CB2 1PZ, UK)*. Wear 162-164(PART B) 864-872 (13 Apr 1993).

Whenever loaded surfaces are in relative tangential motion, hard asperities on one of them, or perhaps hard particles entrained between them, may be dragged across the surface and give rise to the surface degradation and wear. Damage caused by individual asperity or particle interactions builds up and the profiles of the worn surface are the result of many superimposed wear events. The practical, quantitative prediction of wear rates, and thus of component lives, depends on having both a satisfactory understanding of individual interactions and a suitable procedure for combining these under circumstances when subsequent contacts are made on a surface whose topography and material properties may have been much changed from their initial states. Experiments have been carried out on a novel rig which provides very precise control over the position of a representative asperity and the worn surface it generates, and in this paper we describe a number of tests in which the wear arising from the repeated interaction of parallel wear tracks has been investigated. Three different regimes of wear debris production have been identified, namely micromachining, surface ductile fracture and subsurface fatigue, and the wear rates associated with each measured. An analytical model is being developed to produce a wear map appropriate to the abrasion of a metal surface. On the basis of such a map it is possible to identify the predominant wear mechanisms and predict the wear rates of real wearing surfaces.

9A537. **Grain size effect on abrasive wear mechanisms in alumina ceramics.** - AK Mukhopadhyay and Yiu-Wing Mai *(Center for Adv Mat Tech, Dept of Mech Eng, Univ of Sydney, Sydney, NSW 2006, Australia)*. Wear 162-164(PART A) 258-268 (13 Apr 1993).

Despite the wealth of literature on the friction and wear behavior of ceramics, their wear mechanisms are far from well understood. The need to develop a precise understanding of the wear mechanisms is imperative for the development of better wear-resistant ceramics. Particularly in alumina ceramics, grain coarsening has been found to improve the crack growth resistance characteristics. However, if the same would be beneficial for wear resistant applications has not been systematically investigated. To evaluate if there exists a strong grain size effect on abrasive wear mechanisms in ceramics, a series of tests were conducted under severe sliding contact conditions in an alumina ceramic. Unlubricated sliding wear tests were performed on alumina of three different grain sizes, 0.7, 5, and 25 μm, using a blunt conical diamond indenter of about 100-μm tip radius as the slider at room temperature under normal loads of 8-40 N and sliding distances up to 120 mm. The abrasive wear behavior was characterized by measuring the wear volume and wear rate as a function of normal load and sliding distance. In addition, the friction behavior was also studied simultaneously as a function of these two variables. The wear damage mechanisms were examined using both optical and electron microscopy as well as energy dispersive X-ray spectroscopy. For a given grain size and sliding distance, the width and depth of the worn track (hence wear volume) and the frictional force all increased with normal load. These observations were more markedly displayed in the coarse-grained than in the fine-grained alumina. In the 0.7-μm fine-grained alumina, the wear process appeared to be mainly controlled by plastic deformation especially at low loads (eg, < 10 N). At higher loads, however, both plastic deformation and grain boundary fracture processes seemed to be involved. In the 5-μm and 25-μm coarse-grained aluminas, the predominant material removal process was controlled by both intergranular and transgranular fractures.

9A538. High speed sliding of Al_2O_3 pins against an En-24 steel disc. - A Ravikiran and BN Pramila Bai *(Dept of Mech Eng, Indian Inst of Sci, Bangalore 560 012, India)*. Wear **162-164**(PART A) 296-304 (13 Apr 1993).

During the high speed sliding of an 87% Al_2O_3 pin against steel, surface chemical interactions lead to the formation of a surface layer. The coefficient of friction is affected by the surface layer and under certain conditions starts to oscillate between two levels, while under other conditions it has a steady single value. The factors which decide the nature of the friction appear to be not only the speed and pressure, but also the relative contact area (the ratio of the pin surface area to the disc track area). The following empirical relation has been suggested to identify the occurrence of oscillating friction: $N = S^2 P^{0.75} A^{0.5}$ where S is the speed (m s^{-1}), P the pressure (MPa) and A on the ratio of the contact area of the pin to the disc track area. For N < 19 the expected behavior is that of R3, for 19 < N < 21 the response can be of either regions and for N > 21 R4 behavior occurs.

9A539. In situ wear experiments in the scanning Auger spectrometer. - WA Glaeser *(Battelle Columbus Lab, 505 King Ave, Columbus OH 43201)*, D Baer, M Engelhardk *(Battelle Pacific NW Lab, Richard WA)*. Wear **162-164**(PART A) 132-138 (13 Apr 1993).

Sliding contact experiments have been conducted in the chamber of a high resolution Auger spectrometer. A pin-on-disk wear tester has been used. The Auger surface analysis capability has been used to characterize the disk surface before and after sliding in the chamber. The effect of surface chemistry on metal transfer during sliding contact and on boundary lubrication of zinc dialkyldithiophosphate (ZDDP) has been investigated. Hydrocarbon "contamination" from fabrication of the steel disk caused an induction period during sliding in which friction was low and no transfer occurred. The contaminant was eventually worn off but transfer did not take place until the native oxide film was substantially removed also. The oxide film on the steel surface plays an essential role in the boundary lubrication process of ZDDP. A resulting iron sulfide film effectively inhibits adhesive wear. This film was found only in the wear tracks, showing that the contact stress conditions trigger the boundary film reactions.

9A540. Material response to 2D scratching by wedges. - SV Kailas and SK Biswas *(Dept of Mech Eng, Indian Inst of Sci, Bangalore 560 012, India)*. Wear **162-164**(PART A) 110-118 (13 Apr 1993).

Flats of lead, aluminium copper and titanium were scratched by normally loaded wedges of attack angles varying from 15° to 45° under dry and lubricated conditions and sliding speeds of 1.66×10^{-5} m s^{-1} to 1.66×10^{-3} m s^{-1}. Scratching of lead showed a cutting mode at attack angles of more than 15°. As the scratched material was changed from lead to aluminium, copper and titanium, in that order, the propensity of cutting at these attack angles and the coefficient of friction decreased while the surface damage increased. On the basis of uniaxial compression data obtained at the strain rates which are of the same order as those experienced in scratching, it is inferred that the observed trends in scratching can be related qualitatively to the microstructural stability of these materials at these strains and strain rates.

9A541. Microscopic deformations in KCl single crystals by indentation and scratching with steel ball and pyramidal indenters. - S Kobayashi, T Okui *(Dept of Mech Eng, Doshisha Univ, Kyoto, Japan)*, S Miura *(Dept of Eng Sci, Kyoto Univ, Kyoto, Japan)*. Wear **162-164**(PART A) 92-101 (13 Apr 1993).

The subject of sliding friction is of great technological importance and has been studied extensively on an engineering basis. However, many of the underlying microscopic factors that control friction and wear remain obscure. The present study is part of an effort to relate sliding deformation to the crystal structures of the contacting surfaces. The methods used are to indent a steel ball or a diamond quadrangular pyramid and to scratch these indenters on the accurately finished {100} crystal face of KCl single crystals. Two scratch directions, <100> and <110>, were chosen in the scratch tests. The study was made to examine the appearance of the dislocation structure and the mechanism of microscopic deformation and to elucidate the topographical deformations and strain hardening due to indentations and scratches. The width of the scratched track, the distribution pattern of etch pits and the dislocation density around the indent or track were examined in detail. The width of the scratched track is wider in the <100> scratch than in the <110> scratch, whereas the plastic deformation range is greater in the <110> scratch. The plastic deformation produced by scratching is formed with a continuous series of deformations due to indentation. Dislocation motions with the slip system of $\{110\}_{90}\langle 110\rangle$ are mainly observed on the scratched surface, while $\{110\}_{45}\langle 110\rangle$ dislocations are observed on the cross-section perpendicular to the scratched surface.

9A542. Microstructures and tribological characteristics of electron-beam co-deposited Ag-Mo thin film coating. - SC Tung and YT Cheng *(Res Dept, General Motors Tech Center, 30500 Mound Rd, Warren MI 48090-9055)*. Wear **162-164**(PART B) 763-772 (13 Apr 1993).

The tribological characteristics of surface coatings on a metal substrate are affected by several factors including the microstructure of the coatings, the iterations between the coatings and metal substrate, and the mechanical properties of the substrate. Techniques are available to fabricate different types of metastable film structure to aid in unraveling their influences on tribological behavior. In this study, we investigated the friction and wear properties of thin film coatings consisting of Ag and Mo which were co-deposited by electron-beam evaporation in an ultra high vacuum. Ag and Mo were chosen because the metastable structures, such as extended solid solutions or nano-crystalline microstructures, can be formed by co-deposition, although alloys of the two metals cannot exist in thermodynamic equilibrium. Using a Cameron-Plint high frequency pin-on-plate friction machine, test results show that a co-deposited film having an optimum composite ratio of Ag:MO = 69:31 (denoted by $Ag_{69}Mo_{31}$, and having a thickness of 150 nm, has the lowest friction (20% - 25% reduction) and improved anti-wear properties compared with coatings of other compositions. A bare steel plate after dry sliding of 30 h against a steel sphere shows substantial wear and plastic deformation. In contrast, the same plate with a thin film coating of $Ag_{69}Mo_{31}$ shows a much smoother surface. The improved tribological characteristics may be attributed to the greater wear-resistant and shearing capabilities of nano-crystalline binary mixtures on iron surfaces.

9A543. Microwear processes of polymer surfaces. - R Kaneko *(NTT Interdisciplinary Res Lab, Midori-cho Musashino-shi, Tokyo 180, Japan)* and E Hamada *(Dev Section, Operation Headquarters 1, 1 Taiyo Yuden Co, Yawatabara-machi, Takasaki-shi, Gunma 370, Japan)*. Wear **162-164**(PART A) 370-377 (13 Apr 1993).

At atomic force microscope was used to scan-scratch polycarbonate (PC), polymethyl-methacrylate (PMMA), and epoxy (EP) surfaces. A diamond tip with a radius of 0.1 μm was used for scratching and for profile measurements. The sample surfaces were scan-scratched with a load of 500 nN and three different feeds (50, 25, and 12.5 nm). The surfaces were also scan-scratched repeatedly with a load of 200 nN and a feed of 10 nm. The microwear process of PC, PMMA, and EP were clarified from these experiments. (1) The microwear process of PC has three steps: the scan-scratched surface forms a plateau-like upheaval and no wear particles are produced (first step); the surface distorts to make projections and again no wear particles are produced (second step); and the surface is worn down and wear particles are produced (final step). (2) The microwear process of PMMA also has three steps, which are almost the same as those for PC. However, the deformation proceeds rapidly to destruction. (3) The microwear process of EP only has the final step. Wear particles are produced from the start. (4) The order of deformation is EP < PMMA < PC. However, the order of wear is EP < PC < PMMA. This suggests that the deformation of a material with a high elongation rate is large, but that the deformation rate is not related to the wear rate.

9A544. Plastic deformation and damage accumulation below the worn surfaces. - AT Alpas, H Hu, J Zhang *(Eng Mat Group, Univ of Windsor, ON, N9B 3P4, Canada)*. Wear **162-164**(PART A) 188-195 (13 Apr 1993).

Delamination of material layers adjacent to the worn surfaces is a commonly observed form of wear in unlubricated or poorly lubricated surfaces. In ductile materials, the delamination process usually involves large plastic deformation and subsurface damage. In this study, metallographic techniques have been used to determine the extent of plastic deformation and strain localization events during the sliding wear of annealed OFHC copper samples. Tests were performed using a block-on-ring type wear machine under constant load and constant velocity conditions. Subsurface displacement and microhardness gradients were measured as a function of sliding distance. It was observed that both the magnitude of plastic strain (and stress) gradients and the depth of highly deformed layers increased with the sliding distance. The flow stress and strains at the subsurface regions are shown to obey a Voce type constitutive equation. Wear proceeded mainly by a mechanism of delamination via subsurface crack growth. It is proposed that the competition between the plastic strain which enhances void growth and the hydrostatic pressure which suppresses it is responsible for the generation of a damage gradient so that the delamination takes place at a certain depth where the damage accumulation rate is maximum. A model based on the Rice and Tracey analysis of ductile void growth is developed and used to determine the location of subsurface crack propagation.

9A545. Reciprocating sliding wear evaluation of a polymeric-coating tribological system. - JF Braza and RE Furst *(Adv Tech Center, Torrington Co, 59 Field St, Torrington CT 06790)*. Wear 162-164(PART B) 748-756 (13 Apr 1993).

In a reciprocating tribotester, five polymeric materials were evaluated against viscous hard coatings deposited on a stainless steel substrate. The polymeric-coating systems were compared with the wear of a baseline phenolic impregnated polytetrafluoroethylene (PTFE)-polyester woven fabric composite against an uncoated stainless steel substrate. Water was used as the lubricant, which contained alumina (Al_2O_3) particulates to simulate a contaminated environment. The polymeric composites used were two polyimides, a polyamide-imide, a polybenzimidazole and an injection-moldable polyether ether ketone (PEEK). The processing techniques and the amounts of PTFE, carbon fiber, graphite and other additives to reduce friction and improve wear were the significant differences. The hard coatings were deposited on a precipitation hardened PH 13-8 Mo stainless steel by different techniques, such as electrospark alloying, thermal spraying, electroless chemical conversion and physical vapor deposition. The wear scar generated on the fabric was larger than the alternative polymeric materials. The polymeric composites that contained PTFE additives exhibited greater wear resistance than the composites that did not contain this additive. In general, the harder the coating, the more resistant it was to damage by the Al_2O_3 particulate contaminants, subsequently producing a smaller wear scar on the polymer specimen.

9A546. Review of multicomponent and multilayer coatings for tribological applications. - C Subramanian and KN Strafford *(Surface Eng Res Group, Dept of Metall, Gartrell Sch Mining, Metall and Appl Geol, Univ of S Australia, The Levels, SA 5095, Australia)*. Wear 165(1) 85-95 (May 1993).

Improvement in performance of engineering components is achieved through the proper choice of materials, design, or both. Materials perform more efficiently even under severe working conditions when they are surface-engineered, ie coated and/or surface treated. Physical and chemical vapor deposition techniques have found increasingly wider use in such applications in recent years. The so-called *first generation* coatings (eg TiN) are widely used in industrial applications, whereas adoption and implementation of *second generation* coatings (egt Ti(CN), (TiAl)N) are currently under serious consideration. The *third generation* of coatings – multicomponent and multilayer coating variants – are at the research stage. In this paper, the development of multicomponent and multilayer coatings for tribological applications are reviewed and the rationale behind the improved performance – established and anticipated – of such coatings is discussed.

9A547. Rolling-sliding behavior of rail steels. - M Sato *(Yawata R&D Lab, Nippon Steel, 1-1 Tobihata Tobata, Kitakyushu 804, Japan)*, PM Anderson, DA Rigney *(Mat Sci and Eng, Ohio State Univ, 116 W 19th Ave, Columbus OH 43210-1179)*. Wear 162-164(PART A) 159-172 (13 Apr 1993).

A twin disk-rolling-sliding contact machine has been used to investigate the deformation, wear, and cracking that occur during rolling-sliding of high-carbon rail and wheel steels. A martensitic wheel steel with initial hardness of 360 HV contacted pearlitic or martensitic rail steels of different initial hardness, 280 - 360 HV. Other variables included test time, test environment and slip ratio (0%, 5%, 10% and 26%). Tests were run in air, but with different lubrication conditions, eg, dry, with water, water with inhibitor, silicone oil, and various combinations. Wear was measured by weight loss. Wear surfaces, sample cross-sections and wear debris were observed by optical and scanning electron microscopy. Principal conclusions are as follows. The thickness of the highly deformed layer was very small for pure rolling compared with cases involving slip. Wear debris was generated from near-surface material in which the cementite phase had broken into small particles. Cracks initiated at the surface and propagated along lines of earlier plastic flow, rather than normal to the local direction of maximum tensile stress. The results of rolling-sliding in water or other liquids, after dry rolling-sliding indicate that extensive deformation from sliding during the dry stage prepares the material for extensive cracking during subsequent operation with a lubricant.

9A548. Study of antiwear adhesive coating under different erosion conditions. - Xiang-Dong Ma, Fu-Yan Lin, He-Sheng Shao *(Beijing Graduate Sch, China Univ of Mining and Tech, 100083 Beijing, China)*. Wear 162-164(PART A) 569-573 (13 Apr 1993).

The characteristics of antiwear adhesive coating in solid particle erosion and slurry erosion were investigated. The influence of the angle of impingement, the size of antiwear filler and the size of abrasive was studied. It was discovered that the erosion mechanisms of the coating under the two erosion conditions were similar. It was indicated that the filler (aluminium oxide) exhibited typical erosion behavior of brittle material and the binder exhibited semiductile behavior. These experiments also showed that the erosion resistance of the coating in slurry erosion was better than that in solid particle erosion.

9A549. Study of the comet-shaped carbides in the uppermost surface layer of bearings. - Fanju Meng *(Dept of Mech Eng, Muroran IT, 27-1 Mizumoto-cho, Muroran 050, Japan)*, Rujun Tang *(Shanghai Res Inst of Mat, Shanghai, China)*, Kohsuke Tagashira *(Dept of Mech Eng, Muroran IT, 27-1 Mizumoto-cho, Muroran 050, Japan)*. Wear 162-164(PART A) 466-470 (13 Apr 1993).

The structure of the uppermost surface layer for commercial bearings with poor grinding procedures has been studied by means of transmission electron microscopy, electron probe X-ray microanalysis, and Auger electron spectroscopy methods. It was found that a new etching-resistant phase with a comet shape appeared, which was identified by structure analysis as being $(Cr, Fe)_7C_3$ carbides. We supposed the formation of the new etching-resistant phase was due to the grinding heat and grinding force.

9A550. Transfer and wear of nylon and CuS-nylon composites: Filler proportion and counterface characteristics. - S Bahadur and Deli Gong *(Dept of Mech Eng, Iowa State Univ, Ames IA 50011)*. Wear 162-164(PART A) 397-406 (13 Apr 1993).

This work was done as a follow-up of an earlier study which showed that CuS as the filler in nylon was very effective in reducing the wear of nylon. The aspects investigated were the variation of wear with the filler proportion in CuS-nylon composite and the wear of nylon and its composite with counterface surface roughness and materials. It was found that 35 vol% CuS as the filler was most effective in reducing the wear of nylon. The wear rate of unfilled nylon increased with an increase in surface roughness R_a from 0.04 to 0.3 μm but that of the composite did not change with the increase in R_a from 0.04 to 0.11 μm. The wear rates of both the unfilled and filled nylons were considerably higher for sliding against glass counterfaces than against tool steel disks. The differences in wear rates with the counterface roughness and materials were examined in terms of the transfer film characteristics. X-ray photoelectron spectroscopy (XPS) studies revealed the presence of Cu in the transfer film of CuS-nylon composite, thereby indicating the decomposition of CuS during sliding conditions. The decomposition played a role in bonding between the composite transfer film and counterface materials.

9A551. Tribological behavior of unidirectional graphite-epoxy and carbon-PEEK composites. - BS Tripathy and MJ Furey *(Dept of Mech Eng, VPI)*. Wear 162-164(PART A) 385-396 (13 Apr 1993).

An infrared microscope system developed at VPI was used to study the tribological behavior as unidirectional graphite-epoxy and carbon-PEEK (PEEK = poly(ether ether ketone)) composites in sliding contact with sapphire. Effects of fiber orientation and sliding velocity on friction, surface temperature and wear were examined. The surface temperatures measured were on the order of 100-160 °C even at relatively low rates of frictional heat generation (up to 14 W). Surface temperatures were found to increase with an increase in velocity, but levelled off as the glass transition temperatures of the matrix materials were reached. The coefficients of friction were generally found to decrease with an increase in sliding velocity and were significantly influenced by fiber orientation. The influence of sliding velocity on wear was quite different for the two polymer composite systems. With graphite-epoxy, wear was found to decrease with increasing velocity and later increase - resulting in minimum wear at an intermediate velocity. However, with carbon-PEEK, the effect was just the opposite, leading to maximum in wear. From the scanning electron micrographs of the wear scars, we believe that wear is primarily due to a combination of adhesion and fatigue and that the difference in the wear behavior between the two composites is due to the difference in response of the respective matrices to fatigue loading. The relationship between surface temperature and wear is rather complex. An attempt is made here to explain this relationship through a proposed "two-velocity-regime" wear model. Estimation of the real area of contact was done using photomacro-video techniques. Comparison of experimental surface temperatures with temperatures predicted by Archard's and a new theory developed by VPI and SU was also made.

9A552. Wear mechanisms of silicon nitride, partially stabilized zirconia and alumina in unlubricated sliding against steel. - P Gautier and K Kato *(Dept of Mech Eng, Tohoku Univ, Sendai, Japan)*. Wear 162-164(PART A) 305-313 (13 Apr 1993).

The dry-sliding wear mechanisms of Si_3N_4, partially stabilized zirconia (PSZ) where Al_2O_3 were studied using a ball-on-disc wear apparatus. A wide range of sliding velocities and normal loads were tested in order to draw experimental load-velocity friction and wear maps through careful examination of wear morphologies. The three pairings behave differently, even if some wear mechanisms were common to the three systems. The PSZ-steel pair showed the least wear in mild load-velocity conditions, followed by the Si_3N_4-steel pair in harder sliding conditions. It is suggested that the wear of ceramics is mainly related to transgranular or intergranular fracture. Steel discs presented much more intricate wear patterns, including abrasion, oxidation, and delamination. Also, the wear rate ($mm^3 s^{-1}$) of each component is shown to be related to the "frictional power" provided to the tribological system. This important result led us to propose an alternative approach of the classical wear rate concept.

9A553. Wear of selected materials and composites sliding against MoS_2 films. - AW Ruff and MB Peterson *(Ceramics Div, Tech Admin, US Dept of Commerce, NIST)*. Wear **162-164**(PART A) 492-497 (13 Apr 1993).

Improved vacuum deposition methods are now available to produce dense, suitably oriented, durable films of molybdenum disulfide on substrates appropriate for tribological applications. It is of interest to examine materials in sliding contact with such films in order to identify optimum combinations, and to improve further tribological performance of the system. Results of wear and friction measurements are presented on a number of materials including self-lubricating composites sliding against four different types of vacuum-deposited MoS_2 films. The testing program utilized a controlled environment, pin-on-ring tribometer, with load and speed conditions appropriate to a possible application. Differences in wear over four orders of magnitude, and friction up to a factor of seven times, were measured among the materials. One application area of interest for these material combinations would be as ball retainers in rolling element bearings for space satellite systems.

9A554. Wear reduction by pyrolytic carbon tribosurfaces. - JL Lauer, BL Vlcek, BL Sargent *(Dept of Mech Eng, Aeronaut Eng and Mech, RPI)*. Wear **162-164**(PART A) 498-507 (13 Apr 1993).

Sliding tests with pin-on-disc tribometer and both sliding and rolling tests with a modified four-ball tester at bulk temperatures of about 500 °C and initial contact pressures of about 2.2 GPa have demonstrated up to 80% reductions of friction and wear with silicon nitride surface when a system of ethylene is directed into the conjunction region. The effects are even more pronounced when the ethylene is prenucleated by flow over a coil of nichrome wire electrically heated to about 800 °C and located about 30 cm upstream of the exit nozzle. Steel and Ni-plated steel are lubricated by this method even more efficiently at lower temperatures. The underlying mechanism is probably analogous to that of hydrocarbon pyrolysis by flash photolysis, which was studied by Porter in the 1950s, with the rapid heating to the "flash temperatures" and subsequent cooling occurring naturally in friction contacts. The observation that pyrolysis of hydrocarbons to solid carbon occurs in two stages, nucleation and particle growth, has allowed their physical separation, the former taking place in the ethylene stream and the latter in the frictional contact some distance away.

9A555. The wear resistance of diffusion treated surfaces. - KG Budinski *(Metall Group, Eastman Kodak, Bldg 23, 5th Fl, Kodak Park, Rochester NY)*. Wear **162-164**(PART B) 757-762 (13 Apr 1993).

For many years there has been a controversy over the relative abrasion and metal-to-metal wear resistance of wear resistant platings and diffusion coatings. Does chromium plating wear better than nitrided or carburized steel? Because these surface treatments can be as thin a 3 μm and as thick as 500 μm it is difficult to assess their relative wear resistance using the same tests. In this study, we used a modification of the ASTM dry sand abrasion test (G65) that is under study by the ASTM G2 Committee for coating evaluation and a newly developed tape abrasion test to rank the relative abrasion resistance of common diffusion treatments (carburizing, nitriding, boronizing, et) and compare their abrasion resistance with that of chromium, and electroless nickel platings. These same surface treatments were compared in a block-on-ring wear test (G77) self-mated and against a carburized counterface. The test results are intended to be a selection aid for use of these surface treatments.

292I. WEAR MONITORING

9A556. Dry sliding wear of TiN based ternary PVD coatings. - E Vancoille, JP Celis, JR Roos *(Dept of Metall and Mat Eng, Katholieke Univ Leuven, de Croylaan 2, B 3001 Heverlee, Belgium)*. Wear **165**(1) 41-49 (May 1993).

In order to understand the tribological characteristics of TiN, (Ti, Al)N, (Ti, Nb)N and Ti(C, N) coatings, ball-on-disc experiments were performed under dry sliding ambient conditions. The coefficient of friction and the wear resistance against a corundum counterbody were determined as a function of coating composition and sliding speed. The wear of the (Ti, Nb)N coatings was found to be comparable to that of the TiN coatings and this was related to the formation of a similar type of oxide in the tribo-contact. In the case of the (Ti, Al)N coatings, the wear volume increased markedly as the aluminium in the coating increased, and the tribo-oxide formed was found to be Al_2TiO_5. Ti(C, N) coatings exhibited an extremely low wear against corundum because of the low coefficient of friction. A mild-oxidational wear model was found to give a qualitative fit to the experiments. Measuring the coating wear as a function of sliding speed opens the possibility of calculating the activation energy for tribo-oxidation processes of thin coatings.

9A557. Investigation of the wear behavior of tyre steel cords using electrochemical methods. - A Reisenbauer, A Grunberger, P Federspiel, GE Nauer *(Inst for Phys Chem, Univ of Vienna, Wahringerstr 42, A-1090 Vienna, Austria)*. Wear **165**(1) 57-62 (May 1993).

The goal of our investigations was to characterize tyre steel cords of different constructions according to their wear behavior by measuring some corrosion parameters in dilute K_2SO_4 as electrolyte. The wear tests were performed using Hunter-type machines, where the probes with a length of 29.6 cm are fixed at one end by a guide hole and the other end is placed in a drilling jig. This drilling jig rotates with a definite velocity for different times (from 1 to 24 h). The effect of the fatigue on the corrosion behavior of the steel cords was measured on single filaments of the same cords. During the rotation the cord filaments show characteristic wear damage, which can be measured using electrochemical techniques, such as the determination of the time dependence of the corrosion potential and of the corrosion current densities (using modified Butler-Volmer techniques). It was possible to show that the wear damage of steel cords depends strongly on the surrounding atmosphere during the Hunter treatment and on the construction of the steel cords. In an air or oxygen-containing atmosphere the cathodic reaction of the overall corrosion process is oxygen reduction. According to the large area of exposed surface, where oxygen reduction can proceed, the total corrosion reaction rate is high and, in relatively short times, visible corrosion products appear on some parts of the steel cord with wear damage of single filaments. We found highly negative corrosion potentials in relation to the untreated reference materials. In an argon atmosphere the corrosion reaction proceeds more slowly and we found more positive corrosion potentials, only small corrosion current densities and no significant wear damage.

9A558. Measurements of wear and acoustic emission from fuel-wetted surfaces. - RJ Boness *(R Military Col of Canada, Kingston, ON, K7K 5LO, Canada)*. Wear **162-164**(PART B) 703-705 (13 Apr 1993).

This paper is concerned with the measurement and subsequent analysis of acoustic emission (AE) signals obtained during the wear testing of steel surfaces lubricated by Jet A-1 fuel. The results show that AE rms signals can detect different wear processes occurring in air and nitrogen atmospheres. Further wear studies of commercially available Jet A-1 fuel and clay-treated Jet A-1 fuel, in nitrogen, indicate that AE rms signals can identify the critical load at which gross failure, or scuffing of the test surfaces, occurs. Consequently, AE measurements are able to detect the presence of wear-reducing additives.

9A559. New look at carbide tool life. - D Mari *(Dept of Mat Sci and Eng, MIT)* and DR Gonseth *(UFEC SA, 1297 Founex, Switzerland)*. Wear **165**(1) 9-17 (May 1993).

The mechanical behavior of WC-Co composites can be divided into three temperature domains. WC-Co is brittle below 500°C, tough between 500 and 800°C and shows plastic deformation above 800°C. Once the tool temperature has been related to the cutting speed, the life of WC-Co cutting tools can be predicted based on the mechanical behavior of WC-Co as a bulk material. As a result, the plot of the tool life as a function of speed also shows three domains of behavior associated with the wear of the tool, due to brittle fracture, ductile fracture and plastic deformation. A model is presented to explain the observed behavior of the tool life versus speed for continuous cutting (Taylor curve). This curve is generally nonlinear on a log-log plot. The overall tool wear rate is generated by the superposition of a non-thermally activated process and two thermally activated ones. The interpretation of tool wear, based on three domains of temperature, also holds for interrupted cutting, such as milling. In this case, a qualitative model explains the brittle rupture observed below 500°C, and the occurrence of comb cracks above 500°C.

9A560. Quantitative analysis of cam follower wear in relation to various material properties. - Makoto Kano *(Nissan Res Centre, Mat Res Lab, Nissan Motor, 1 Natsushima-cho Yokosuka-shi, Kanagawa 237, Japan)* and Yoshitsugu Kimura *(Inst of Indust Sci, Univ of Tokyo, Tokyo, Japan)*. Wear **162-164**(PART B) 897-905 (13 Apr 1993).

Results of wear simulation motoring experiments are presented for various wear-resistant materials used to make automotive engine cam followers. A multiple regression analysis is conducted to find the relation between follower wear and typical material properties. A linear regression formula is derived which provides a high multiple correlation coefficient for a series of ferro-based powder metals which adhere to the regression formula. Close observation of worn cam follower surfaces reveals that a common wear mechanism is at work, ie, fatigue cracks propagate in the matrix around carbides to detach wear particles. This mechanism coincides with the implications of the formula.

9A561. Structure and dose effects on improved wear properties of ion-implanted polymers. - GR Rao, EH Lee, LK Mansur *(Metals and Ceramics Div, ORNL)*. Wear **162-164**(PART B) 739-747 (13 Apr 1993).

Polyethylene, polypropylene, polystyrene and polyethursulfone, representing an increasing complexity in molecular structure were implanted with 200 keV boron to three doses of 1.7, 5 and 17×10^{18} ions m^{-2}. Polystyrene was also implanted with 100 keV boron to the same three doses. The polymers were investigated for near-surface micromechanical property changes using a nanoindentation technique. Wear properties for the polymers were studied using a reciprocal tribometer with a nylon ball as the counterface. Tests were conducted for 10 000 sliding cylces using a 1 N normal load, a stroke length of 3 mm and an oscillation frequency of 100 cycles min^{-1}. The ion implantation increased the near-surface hardness of the four polymers and the increase was proportional to the dose and beam energy. A clear structure dependence was observed for the hardness changes that were related to cross-linking of molecular chains caused by the ion irradiation. In general, the implantation also significantly improved the wear properties of the four polymers. For each polymer, an optimum dose was identified that yielded the best wear improvement. With increasing dose, the dominant wear mechanism shifted from adhesive and abrasive wear to no observable wear to surface fatigue. Remarkable wear improvements were observed for polystyrene and polyethersulfone for which, at the optimum dose, no wear damage was visible even after 10 000 sliding cycles.

9A562. Study of the relationship between wear rate and nitrogen concentration profile and application to plasma source ion implanted Ti-6Al-4V alloy. - A Chen, J Blanchard, JR Conrad, P Fetherston, X Qiu *(Eng Res Center of Plasma-Aided Manuf, Univ of Wisconsin, 1500 Johnson Dr, Madison WI 53706)*. Wear 165(1) 97-101 (May 1993).

Nitrogen implantation by plasma source ion implantation was conducted on Ti-6Al-4V alloy. The wear performance was characterized using a pin-on-disk wear tester and an alpha-step profilometer. Nitrogen concentration depth profiles of implanted samples were studied using a scanning Auger microprobe. It is found that the lowest wear rate in the implanted zone corresponds to the nitrogen concentration peak. By varying the target temperature, the nitrogen concentration profile was engineered to achieve a better wear behavior. The pin-on-disk wear data agree with the expected result.

9A563. Three-body abrasive wear of 0.98% carbon steel. - S Das, BK Prasad, AK Jha, OP Modi, AH Yegneswaran *(Region Res Lab, Council of Sci and Indust Res, Hoshangabad Rd near Habibganj Naka, Bhopal 462026 MP, India)*. Wear 162-164(PART B) 802-810 (13 Apr 1993).

Low stress abrasion studies of hypereutectoid steel have been carried out using a rubber wheel abrasion test apparatus. Hardness of the steel was changed by subjecting the specimens to different heat treatment cycles. Abrasion tests were conducted at various loads and wheel speeds using crushed silica sand as the abrasive medium. Wear rates of the steel in all test conditions decreased significantly during the running-in period prior to attaining steady state values, which was considered to be due to the abrasion-induced work hardening of the regions close to the abraded surface. Results showed that the increase in bulk hardness of the steel specimen caused a linear increase in wear resistance. Furthermore, up to a bulk hardness of about 400 HV, the rate of increase was higher than that above 400 HV. Increase in the applied load caused lower wear resistance, while speed did not show any definite trend. One of the material removal mechanisms, in particular, was found to be microcutting as indicated by continuous grooves on the wear surface and generation of machining chips in the debris. Micropitting was found to be another wear mechanism as evidenced by the formation of craters on the wear surface and flake-shaped particles in the wear debris.

9A564. Tribological behavior of aluminium alloy composites: A comparative study with a copper-based alloy. - S Das and BK Prasad *(Regional Res Lab, CSIR, Hoshangabad Rd, near Habibganj Naka, Bhopal 462 026 MP, India)*. Wear 162-164(PART A) 64-74 (13 Apr 1993).

This paper describes the results of dry sliding wear tests of LM13 alloy and graphite-particle-reinforced LM13 alloy composite in cast and heat-treated conditions, and their comparison with a conventionally used copper-based bearing alloy. Sliding wear tests were conducted on a pin-on-disc wear test apparatus against a rotating steel (EN25) counterface at a sliding velocity of 2.68 m s^{-1}. Results of the present investigation showed that the wear rate of the composite was considerably less than that of the copper-based alloy at an applied pressure of less than 4.0 MPa. Above 4.0 MPa the composite samples seized. However, the seizure pressure of the composite was less than that of the copper-based alloy. Detailed studies of wear surfaces, wear debris and subsurface deformation have been carried out. The overall results indicate that the heat-treated aluminium alloy-graphite composite could be considered as an excellent substitute for a conventional bearing alloy, such as Cu-Sn-Pb, at relatively low applied pressures (below 4.0 MPa), while the copper-based alloy can withstand higher pressures (up to 10 MPa).

9A565. Tribological behavior of austempered spheroidal graphite aluminum cast iron. - SMA Boutorabi, JM Young, V Kondic *(Sch of Metall and Mat, Univ of Birmingham, Birmingham B15 2TT, UK)*, Dept of Mat Eng Salehi *(Isfahan Univ of Tech, Isfahan, Iran)*. Wear 165(1) 19-24 (May 1993).

The effects of austempering time and temperature on the microstructure and tribological behavior of austempered SG Al(2.2%) cast iron have been studied. An austenitizing temperature of 900°C, austempering temperatures of 250-400°C and austempering time of 5-240 min were used: lower and upper bainitic structures were obtained by austempering within this temperature range. The results show that the influence of aluminium (Al) on bainitic reaction is similar to silicon (Si) in conventional SG case irons: aluminium is a strong graphitizer and produces a bainitic structure with a high wear resistance. The transformation kinetics were investigated using X-ray diffraction and microstructural studies were undertaken using optical and scanning electron microscopy. Dry sliding wear tests were conducted on a modified Amsler-type machine from which it was found that the austempering fo SG Al iron significantly increases the wear resistance. The relationship between volume fraction of retained austenite and wear (weight loss) revealed that optimum tribological behavior can be obtained by varying the austempering temperature and time. The results show that the hardness and wear resistance decrease with an increase in austempering time and temperature. The observed changes in tribological behavior can be correlated with the kinetics and austempered microstructure of the irons.

9A566. Wear in Zn-Al-Si alloys. - Li Jian, EE Laufer *(Dept of Mining and Metall Eng, Tech Univ of Nova Scotia, PO Box 1000, Halifax NS, B3J 2X4, Canada)*, J Masounave *(Ecole de Tech Superieur, Montreal PQ, Canada)*. Wear 165(1) 51-56 (May 1993).

The zinc-aluminum based casting alloy ZA-27 is useful in bearing applications. Its tribological properties may be improved by replacing its small copper content with silicon. These are further improved if the silicon particle size is controlled by suitable additions of strontium. This effect is related to the observation that wear properties of the alloy are governed by the development of a thin surface film of the Al-rich α phase. The integrity of this surface film during wear is controlled by the interplay between the lubricant film thickness and particle size. Wear performance is optimum when the silicon particles are larger in diameter than the lubricant film thickness, but small enough that they may embed in the bearing surface and be covered by the surface film. It is suspected that a similar conclusion may hold for particles such as grit from a dirty operating environment.

9A567. Wear resistance of an Ni-Cu-P brush plating layer on different substrates. - Yan-Sheng Ma, Jia-Jun Liu, Bao-Liang Zhu, Guang-Jie Zhai, Lin-Qing Zheng *(Trib Res Inst, Tsinghua Univ, 100084 Beijing, China)*. Wear 165(1) 63-68 (May 1993).

In order to increase the bonding strength between plating layer and substrate and promote the formation of a transfer film, a new type of Ni-Cu-P brush plating layer with excellent wear resistance was developed on the basis of an Ni-P amorphous plating layer, although it showed different behavior when the substrate was changed. This paper systematically investigated its tribological behavior on a "ball-on-disc" testing machine under lubrication with paraffin oil, and analyzed in depth the effect of substrates (conventionally heat treated 1045 steel and nitrided 1045 steel) on its microstructure, hardness, wear resistance, and wear mechanism. The results showed that the load bearing capacity of an Ni-Cu-P brush plating layer on a nitrided 1045 steel substrate can be more than ten times that of a 1045 steel without a plating layer, and more than twice that of a 1045 steel substrate without a nitriding layer. The composite coating process can usually offer an immeasurable effect through the interaction between composite layers.

9A568. Wear resistance of C^+-implanted silicon investigated by scanning probe microscopy. - T Miyamoto *(NTT Interdisciplinary Res Lab, 3-9-11 Midori-cho Musashino-shi, Tokyo 180, Japan)*, S Miyake *(Nippon IT, 4-1 Gakuendai Miayshiro-machi, Minamisaitama-gun Saitama 345, Japan)*, R Kaneko *(NTT Interdisciplinary Res Lab, 3-9-11 Midori-cho Musashino-shi, Tokyo 180, Japan)*. Wear 162-164(PART B) 733-738 (13 Apr 1993).

A scanning probe microscope with a very sharp tip was used to investigate the wear resistance of single-crystal silicon and C^+-implanted silicon. The C^+ implantation conditions were 100 keV and 2×10^{17} ions cm^{-2}. The C^+ concentration was analysed using secondary ion mass spectrometry, while the chemical structures of C^+-implanted silicon and solid SiC were analysed using X-ray photoelectron spectroscopy. (1) The C^+ concentration in C^+-implanted silicon reached a maximum of 1.5×10^{22} atoms cm^{-3} at a depth of 290 nm. (2) Around this 290 nm depth the wear durability of C^+-implanted silicon was higher than that of single-crystal silicon. (3) The structure of the region in which the C^+ concentration was high was similar to that of solid SiC. This structure increases the hardness of the C^+-implanted layer and protects against plastic deformation, resulting in a high wear durability for C^+-implanted silicon.

See also the following:

9A494. Sliding friction and wear up to 600° C of high speed steels and silicon nitrides for gas turbine bearings

292Y. COMPUTATIONAL TECHNIQUES

9A569. BEM frictional contact analysis: Modeling considerations. - KW Man, MH Aliabadi *(Wessex IT, Univ of Portsmouth, Ashurst Lodge, Ashurst SO4 2AA, UK)*, DP Rooke *(Defense Res Agency, RAE Farnborough, Hants GU14 7TU, UK)*. Eng Anal Boundary Elements 11(1) 77-85 (1993).

In this paper, the use of linear and quadratic element for modeling frictional contact problems is studied. It is found that while linear elements are capable of modeling the frictional aspect of the problem accurately, the use of quadratic elements results in oscillations in the tangential tractions under certain contact conditions. Numerical studies of particular interest to these problems have been presented. The case of the oscillations in the quadratic results has been identified and eliminated by using linear elements locally, so that only those node-pairs nearest to the edges of contact can be brought into contact at any one load step. Outside the potential contact region, standard quadratic BE were used.

9A570. **Formulation and implementation of conditions for frictional contact.** - K Runesson *(Dept of Struct Mech, Chalmers Univ of Tech, S-41296 Goteborg, Sweden)*, M Klisinski, R Larsson *(Dept Struct Mech, Chalmers Univ Tech, S-41296 Goteborg, Sweden)*. Eng Comput 10(1) 3-14 (Feb 1993).

FE implementations of the classical (stick-slip) and regularized (elastic-slip) friction laws are compared for a class of nonlinear slip criteria. The fully implicit method is used for integrating the friction law. A novel implementation of the stick slip law, that involved transformation to a nonorthogonal coordinate system at each contact point, is assessed. A numerical comparison is carried out for a simple problem, that has previously been analyzed in the literature. The convergence of the elastic-slip law for increasing stiffness is evaluated in addition to convergence behavior of the adopted Newton iterations for a given law.

294. Machine elements

9A571. **Finite element analysis of synchronous belt tooth failure.** - KW Dalgarno, AJ Day *(Dept of Mech and Manuf Eng, Univ of Bradford, UK)*, THC Childs *(Dept of Mech Eng, Univ of Leeds, UK)*. Proc Inst Mech Eng D 207(D2) 145-153 (1993).

This paper describes a FE analysis of a synchronous belt tooth under operational loads and conditions with the objective of obtaining a greater understanding of belt failure by tooth root cracking through an examination of the strains within the facing fabric in the belt. The analysis used the ABAQUS FE program, and was based on a 2D FE model incorporating a hyperelastic material model for the elastomer compound. It is concluded that the critical strains in the facing fabric of the belt, and therefore the belt life, are largely determined by the tangential loading condition on the belt teeth.

9A572. **Design and analysis of an antilock brake control system with electric brake actuators.** - WC Lin *(Vehicle Syst Res Dept, General Motors NAO R&D Center, Warren MI 48090-9055)*, DJ Dobner *(Elec and Electron Eng Dept, General Motors NAO R&D Center, Warren MI 48090-9055)*, RD Fruechte *(Vehicle Syst Res Dept, General Motors NAO R&D Center, Warren MI 48090-9055)*. Int J Vehicle Des 14(1) 13-42 (1993).

This paper analyzes the feasibility of an antilock brake control system using an electric brake actuator. The analysis is focused on the closed-loop control of wheel slip. Wheel and vehicle dynamics during longitudinal braking on uniform surfaces are first analyzed to provide a model for performance evaluation using a linear feedback controller design with ideal feedback information from the vehicle, wheel and actuator sensors. The robustness of the linear controller is then analyzed by a parametric study of the system's root locus. Since the linear controller was found to have difficulty solving the sensitivity problem, a nonlinear feedback control was then analyzed.

9A573. **EHD analysis of a misaligned journal bearing.** - HB Sharda, HN Chandrawat, RC Bahl *(Dept of Mech and Indust Eng, Thapar Inst of Eng and Tech, Patiala 147 001, India)*. Int J Mech Sci 35(5) 415-423 (May 1993).

Elastohydrodynamic performance characteristics of a misaligned journal bearing are reported. It is observed that bush flexibility in a misaligned bearing, unlike that in an aligned bearing improves the bearing load capacity owing to an increase in minimum film thickness at higher values of load. The misalignment is found to improve the stability of the bearing, whereas the flexibility of the bush tends to reduce this improvement.

296. Machine design

See the following:

9A138. Kinematic design of serial link manipulators from task specifications

9A142. Synthesis and analysis of a new class of six-dof parallel minimanipulators

298. Fastening and joining

9A574. **New semi-rigid joint elements for nonlinear analysis of flexibly connected frames.** - W Atamaz Sibai and F Frey *(LSC, Dept of Civil Eng, Swiss Fed IT, CH-1015 Lausanne, Switzerland)*. J Construct Steel Res 25(3) 185-199 (1993).

Several 3D numerical simulations of beam-to-column welded joints in steel skeletal structures have been earlier performed, leading to a deep understanding of the joint mechanical behavior up to failure. This in turn motivated the authors to develop a new concept of semi-rigid FEs. The new element family considers the real dimensions of the joint and incorporates its different flexibility characteristics. It can be implemented into any general FE code and assembled with any existing beam element.

9A575. **Thermomechanical generalization of pin joints in finite-plates.** - Ripudaman Singh and TS Ramamurthy *(Dept of Aerospace Eng, Indian Inst of Sci, Bangalore 560 012, India)*. Comput Struct 47(1) 73-81 (3 Apr 1993).

The understanding of thermoelastic behavior of joints is significant in order to ensure the integrity of large and complex structures exposed to a thermal environment, particularly in fields such as aerospace and nuclear engineering. Thermomechanical generalization of partial contact behavior of a pin joint under combined in-plane mechanical loading and on-axis unidirectional heat flow has already been established by the authors for the analytically simpler domains of large plates. This paper successfully extends the on-going investigation to a single pin in a finite rectangular isotropic plate as a 2D abstraction from a practical situation of a multipin fastener joint.

9A576. **Computation of GMAW welding heat transfer with BEM.** - M Hang *(Welding Inst, Gansu Univ of Tech, Lanzhou 730050, Peoples Rep of China)* and A Okada *(Natl Res Inst Metals, 2-3-12 Nakameguro, Meguro-ku, Tokyo 153, Japan)*. Adv Eng Software 16(1) 1-5 (1993).

Based on the computation model for quasi-steady heat transfer problems of welding with the BEM, a computer program is developed and used for the computation of thermal cycles at heat affected zones with gas shielded metal arc (GMAW), welding on medium thickness plates. The computed results are in good agreement with those from experiments, showing the capabilities and versatilities of the BEM to deal with the computerized simulation of welding thermal processes.

9A577. **Thermal analysis for resistance welding of large-scale thermoplastic composite joints.** - ST Holmes and JW Gillespie Jr *(Center for Composite Mat and Dept of Mech Eng, Univ of Delaware, Newark DE 19716)*. J Reinforced Plastics Composites 12(6) 723-736 (Jun 1993).

The need for effective and reliable joining methods continues to grow as the use of thermoplastic composites becomes widespread. It is now possible to join large-scale components with the development of an automated sequential resistance welding process. The thermal history generated by the heating element placed at the interface between adherends determines the quality and performance of the welded joint. This article presents a thermal analysis for the resistance welding of large-scale components that overcomes the limitations of previous models. Regions of localized overheating where potential current leakage may occur were identified as a function of process parameters. Insights on promoting more uniform heating for the resistance welding process are discussed.

9T578. **Stress analysis and testing of parallel and tapered adhesive butt joints.** - A Buchman, F Weinstein, I Honigsberg, Y Holdengraber, H Dodiuk *(RAFAEL, PO Box 2250, Haifa 31021, Israel)*. J Adhesion Sci Tech 7(4) 385-397 (1993).

See also the following:

9A164. Residual stresses in welded jumbo box columns

V. MECHANICS OF FLUIDS

350. Rheology

See the following:

9A301. Role of rheology in colloidal processing of ZrO_2

352. Hydraulics

352C. OPEN CHANNEL FLOW (INCL HYDRAULIC JUMPS)

9T579. **Comparison of numerical model experiments of free surface flow over topography with flume and field observations.** - B Johns *(Dept of Meteorol, Univ of Reading, UK)*, RL Soulsby *(Dept of Meteorol, Hydraul Res, Wallingford, Oxon, UK)*, Jiuxing Xing *(Proudman Oceanog Lab, Bidston Observatory, Birkenhead, UK)*. J Hydraul Res 31(2) 215-228 (1993).

9T580. **Dam-break solutions for a partial breach.** - S Gozali *(Dept of Civil Eng, Catholic Parahyangan Univ, Bandung, Indonesia)* and C Hunt *(Dept of Civil Eng, Univ of Canterbury, Christchurch, New Zealand)*. J Hydraul Res 31(2) 205-214 (1993).

9A581. **Dambreak flood waves computed by modified Godunov method.** - LJ Savic *(Energoproject, Bulevar Lenjina 12, 11070 Beograd, Yugoslavia)* and FM Holly Jr *(Dept of Civil and Env Eng and Res Eng, Iowa Inst of Hyd Res, Univ of Iowa, Iowa City IA 52242)*. J Hydraul Res 31(2) 187-204 (1993).

The Godunov method, is adapted to computation of dambreak flood waves. Review of commonly used methods for discontinuous flows (flows with shocks) has shown the need for a new type of algorithm to cope efficiently with mixed flow regimes and strong shocks in non-prismatic channels. The 1D open-channel flow equations are solved with two variants of the Godunov method: one based on linear, the other on piecewise parabolic interpolation (PPM). The proposed methods agree well with the analytical solution (where available), and perform significantly better than the other compared methods for all examined cases.

9A582. Kinematics of the moving hydraulic jump. - JP Martin Vide, J Dolz, J Del Estal *(Dept of Hydraul Eng, Civil Eng Sch, Tech Univ of Catalunya, Barcelona, Spain)*. J Hydraul Res 31(2) 171-186 (1993).

The moving hydraulic jump, considered as an example of rapidly varied unsteady flow, is theoretically revised. Experimental work is conducted to study the kinematic characteristics of the jump propagation. The position, velocity and conjugate depths of the jump during its propagation either upstream or downstream are investigated and some semi-empirical equations are derived. From this work, some differences are observed between the moving hydraulic jump propagation upstream and downstream. A phenomenon called extinction of the moving hydraulic jump is reported in the latter case. This phenomenon is explained on the grounds of previous theoretical analysis.

9T583. Mathematical model of unsteady transport and its experimental verification in a compound open channel flows. - S Djordjevic *(Inst of Hydraul Eng, Fac of Civil Eng, Univ of Belgrade, Belgrade, Yugoslavia)*. J Hydraul Res 31(2) 229-248 (1993).

9A584. Use of a neural net for the study of a flood wave propagation in an open channel. - D Dartus, JM Courivaud, L Dedecker *(Inst Mec des Fluides de Toulouse, Ave du Professeur Camille Soula, France)*. J Hydraul Res 31(2) 161-170 (1993).

A neural net was used to study the propagation of a flood wave in an open channel. The aim was to show that this kind of tool is accurate enough to be used in real time management of sewers systems. Ability of such a neural network to answer correctly was highlightened with an extensive learning base and with a reduced one.

352E. UNSTEADY FLOW

See the following:

9T583. Mathematical model of unsteady transport and its experimental verification in a compound open channel flows

352G. OBSTRUCTIONS

See the following:

9T579. Comparison of numerical model experiments of free surface flow over topography with flume and field observations

352H. ORIFICES, NOZZLES, VALVES, AND GATES

See the following:

9T585. Hyraulic ram analysis

352K. STILLING BASINS AND OTHER ENERGY DISSIPATORS

9T585. Hyraulic ram analysis. - C Verspuy and AS Tijsseling *(Dept of Civil Eng, Univ of Tech, Delft, Netherlands)*. J Hydraul Res 31(2) 267-278 (1993).

352L. CAVITATION

9A586. Perturbation solution to 3D nonlinear supercavitating flow problems. - Quyuan Ye, Yousheng He, Shiquan Zhu *(Shanghai Jiao Tong Univ, Shanghai 200030, China)*. Acta Mech Sinica 9(1) 13-21 (1993).

A 3D nonlinear problem of supercavitating flow past an axisymmetric body at a small angle of attack is investigated by means of the perturbation method and the Fourier-cosine-expansion method. The first three order perturbation equations are derived in detail and solved numerically using the boundary integral equation method and iterative techniques. Computational results of the hydrodynamic characteristics and cavity shapes of each order are presented for nonaxisymmetric flow past cones with various apex-angles at different cavitation numbers. The numerical results are found to be in good agreement with experimental data.

352N. WATERWAYS

See the following:

9A581. Dambreak flood waves computed by modified Godunov method
9A584. Use of a neural net for the study of a flood wave propagation in an open channel

352P. COASTS, BEACHES, HARBORS

See the following:

9T580. Dam-break solutions for a partial breach

352R. ICE TRANSPORT

9A587. Static anaysis of floating ice block stability. - BA Coutermarsh and WR McGilvary *(USA Cold Regions Res and Eng Lab, Hanover NH 03755)*. J Hydraul Res 31(2) 147-160 (1993).

A laboratory study was performed to measure the pressures caused by fluid acceleration beneath a floating parallel-piped block. Dynamic fluid pressure was measured at discrete points beneath the block for various fluid velocities, block angles of attack and block thickness-to-depth ratios. Some of these pressures tended to stabilize the block while others tended to underturn it. The measured pressures were used to calculate block underturning moments and a hydrostatic analysis was used to calculate a block righting moment. From this, a densimetric Froude underturning criteria is presented.

352Y. COMPUTATIONAL TECHNIQUES

9A588. Efficient numerical method for subcritical and supercritical open channel flows. - P Glaister *(Dept of Math, Univ of Reading, PO Box 220, Whiteknights, Reading RG6 2AX, UK)*. Appl Numer Math 11(6) 497-508 (Apr 1993).

An efficient numerical method is developed for the 1D open channel flow equations. The scheme incorporates upwind differencing applied to a numerical characteristic decomposition, and produces satisfactory results to a problem of flow in a river whose geometry can induce a region of supercritical flow.

9A589. Explicit time-domain transmitting boundary for dam-reservoir interaction analysis. - R Yang, CS Tsai, GC Lee *(Dept of Civil Eng, Sch of Eng and Appl Sci, SUNY, Buffalo NY 14260)*. Int J Numer Methods Eng 36(11) 1789-1804 (15 Jun 1993).

An explicit time-domain transmitting boundary for the analysis of dam-reservoir interactions is presented. This transmitting boundary is a semi-analytical solution of the governing wave equation of the far field of the reservoir. By using this transmitting boundary, the radiation condition and water compressibility can readily be incorporated in the time-domain analysis of dam-reservoir systems. Numerical results have excellent agreement with the available analytical solution. Results also show that the proposed explicit transmitting boundary is more efficient computationally than the implicit transmitting boundary presented by Tsai and Lee.

354. Incompressible flow

354A. GENERAL THEORY

9A590. Laminar flow in an annulus between two concentric rotating porous spheres. - SD Gulwadi, AF Elkouh, T-C Jan *(Dept of Mech and Indust Eng, Marquette Univ, Milwaukee WI 53233)*. Acta Mech 97(3-4) 215-228 (1993).

An analysis is presented for the steady laminar flow of an incompressible Newtonian fluid in an annulus between two concentric porous spheres with injection-suction at their boundaries. The inner sphere rotates with constant angular velocity about its own fixed axis, while the outer sphere is stationary. A solution of the Navier-Stokes equations is obtained by employing a regular perturbation technique. The solution obtained is in the form of a power series expansion in terms of the rotational Reynolds number Re, and an injection-suction Reynolds number Re_w, and is valid for small values of these parameters. Results for the velocity distributions, streamlines, and viscous torques for various values of the flow parameters Re, Re_w and radius ratios λ are presented. Viscous torques at the inner and outer spheres are compared with those obtained from the numerical solution of the Navier-Stokes equations, in order to find the range of Re and Re_w for which this solution is accurate.

354B. IRROTATIONAL FLOW

See the following:

9T593. Nonlinear transient free-surface flow and dip formation due to a point sink

354C. ROTATIONAL (NONVISCOUS) FLOW, VORTICES

9A591. Vortex drift I. Dynamic interpretation. - N Rott and B Cantwell *(Dept of Aeronaut and Astronaut, Stanford)*. Phys Fluids A 5(5) 1443-1450 (Jun 1993).

Vortical flow, restricted to a finite domain (in 3D) in an unbounded incompressible viscous fluid that is at rest at infinity, is investigated by the consideration of the dynamics in the potential flow region that surrounds the vortical domain. The evolution equations are considered for a flow that is given at an initial time t. The potential change in the far field is connected to the pressure, which in turn is expressed as the solution of a Poisson equation with sources distributed over the whole flow field. The leading term of the pressure at infinity is a quadrupole, which is caused by a drifting dipole field with a constant strength that is given by the impulse. This "dynamic" value of the drift is then identified with the classical "kinematic" definition as the speed of the impulse centroid. The main new result obtained by this method is the solution of the asymptotic drift problem in 3D, complementing the corresponding solution of Cantwell and Rott for plane flow. The connection to the solution of the classical drift problem for a vortex ring is also established.

9T592. Vortex drift II. The flow potential surrounding a drifting vortical region. - N Rott and B Cantwell *(Dept of Aeronaut and Astronaut, Stanford)*. Phys Fluids A 5(5) 1451-1455 (Jun 1993).

354I. THERMAL CONVECTION FLOW

See the following:

9A694. Developing laminar flow and heat transfer in a square duct with one-walled injection and suction
9A695. Effects of longitudinal vortex generators on heat transfer and flow loss in turbulent channel flows
9A696. Experimental investigations of heat transfer enhancement and flow losses in a channel with double rows of longitudinal vortex generators
9A697. Experimental study of laminar entrance flow and heat transfer in finned tub annuli
9A701. Periodically developed flow and heat transfer in a ribbed duct
9A705. Analytical solution for transient laminar fully developed free convection in vertical concentric annuli
9A706. FE analysis of natural convection in horizontal concentric annuli
9A707. Investigation of the temporal thermal performance of the wheel outboard of an aircraft
9A708. Natural convection heat transfer in a 3D duct
9A709. Natural-convection heat transfer in inclined rectangular enclosure
9A710. Resonance of natural convection in an enclosure heated periodically from the side
9A712. Transient cooling of petroleum by natural convection in cylindrical storage tanks I. Development and testing of a numerical simulator
9A713. Transient cooling of petroleum by natural convection in cylindrical storage tanks II. Effect of heat transfer coefficient, aspect ratio and temperature-dependent viscosity
9A718. Stability of plane Poiseuille flow with temperature dependent viscosity
9A722. Measurements of laminar mixed convection in boundary-layer flow over horizontal and inclined backward-facing steps
9A723. Numerical analysis of mixed convection at the entrance region of a rectangular duct heated from below
9A725. Effect of wall conduction in reactor wall on the heat and fluid flow in a rotating disk CVD reactor
9A729. Unsteady laminar natural-convection heat transfer in an enclosure with fins

354J. STRATIFIED FLOW AND FREE SURFACE FLOW

9T593. Nonlinear transient free-surface flow and dip formation due to a point sink. - T Miloh *(Dept of Fluid Mech and Heat Transfer, Tel Aviv Univ, Tel Aviv 69978, Israel)* and PA Tyvand *(Dept of Agri Eng, Agri Univ of Norway, PO Box 5065, 1432 Ås, Norway)*. Phys Fluids A 5(5) 1368-1375 (Jun 1993).

354O. FLOW AROUND BODIES

See the following:

9A620. Experimental investigations on two-phase flow past a sphere using digital particle-image-velocimetry

354P. SURFACE TENSION FLOW (EG IN LOW GRAVITY ENVIRONMENTS)

9A594. Levelling of paint films. - SK Wilson *(Dept of Math, Univ of Strathclyde, Livingstone Tower, 26 Richmond St, Glasgow G1 1XH, UK)*. IMA J Appl Math 50(2) 149-166 (1993).

Using a brush to apply paint to a flat surface almost inevitably means that the bristles of the brush level behind an uneven paint surface. As the paint dries out, these non-uniformities tend to flatten out to leave a protective and aesthetically pleasing even coating; however, experiments have shown that some solvent-based high-gloss alkyd paints can exhibit more unusual behavior as they dry. In this paper the author presents a mathematical model for the drying of a layer of solvent-based high-gloss alkyd paint and analyzes the linear stability of a uniform layer of paint subject to an initial perturbation representing the endks left by a paint brush. Investigating the model highlights the crucial role played by solvent evaporation and leads to a plausible physical explanation of the observed phenomena.

354Y. COMPUTATIONAL TECHNIQUES

9A595. Analytical approach to the Oseen drag on a sphere at infinite Reynolds number. - AJ Weisenborn and BIM Ten Bosch *(Koninklijke-Shell-Lab, Shell Res BV, Badhuisweg 3, 1031 CM Amsterdam, Netherlands)*. SIAM J Appl Math 53(3) 601-620 (Jun 1993).

This paper analytically evaluates the Oseen drag coefficient C_D of a sphere at infinite Reynolds number. For this purpose, the method of induced forces is used. This method enables the obtainment of a series of rationals converging to the desired values for C_D. The best value for C_D on the basis of this series truncated to its first 50 terms has only a three-decimal accuracy.

9A596. Convenient method to convert 2D CFD codes into axisymmetric ones. - Sheng-Tao Yu *(Aeromech Dept, Sverdrup Tech, NASA Lewis Res Center, Brook Park OH 44142)*. J Propulsion Power 9(3) 493-494 (May-Jun 1993).

Although 3D CFD calculations are commonplace, axisymmetric flow solvers are indispensible tools, especially for flowfields of propulsion systems. In axisymmetric solvers, one applies curvilinear grids in the axial and radial directions and no grid is used in the azimuthal direction. Thus, each control volume is a body of revolution with constant 2D cross-sectional areas in the azimuthal direction. For the time being, we will call these coordinates the axisymmetric coordinate system. In this note, we propose a convenient and systematic procedure to convert 2D CFD codes into axisymmetric ones. First, we organize the governing equations in a form suitable for CFD applications. Then we carefully examine the calculations of the volume and surface areas of the axisymmetric control-volume element. Through the conversion process, the procedures of modifying the 2D codes becomes self-evident. Although we concentrate on the finite-volume method in this note, similar procedure could be applied for finite difference codes.

9A597. Least squares Petrov-Galerkin FEM for the stationary Navier-Stokes equations. - Tian-Xiao Zhou *(Comput Tech Res Inst, Chinese Aeronaut Est, Xi'an 710068, China)* and Min-Fu Feng *(Dept of Math, Xi'an Jiaotong Univ, Xi'an, China)*. Math Comput 60(202) 531-543 (Apr 1993).

In this paper, a Galerkin and least-squares-type FEM is proposed and analyzed for the stationary Navier-Stokes equations. The method is consistent and stable for any combination of discrete velocity and pressure spaces (without requiring a Babuska-Brezzi stability condition). The existence, uniqueness and convergence (at optimal rate) of the discrete solution is proved in the case of sufficient viscosity (or small data).

9A598. Numerical algorithm for hydrodynamic free boundary problems. - WG Szymczak *(Info and Math Sci Branch-Code R44, Naval Surface Warfare Center, Silver Spring MD 20903-5000)*, JCW Rogers *(Dept of Math, Polytechnic Univ, Brooklyn NY 11201-2907)*, JM Solomon, AE Berger *(Info and Math Sci Branch-Code R44, Naval Surface Warfare Center, Silver Spring MD 20903-5000)*. J Comput Phys 106(2) 319-336 (Jun 1993).

A generalized formulation of inviscid incompressible hydrodynamics as a system of conservation laws subject to a one-sided density constraint is used as the basis of a numerical algorithm for a variety of hydrodynamic free surface problems. Benchmark calculations for colliding masses of fluid and for the motion of a spherically symmetric bubble are compared with theoretical predictions. Also shown are profiles calculated for an evolving underwater bubble near a wall. Energy dissipation is introduced as a measure of turbulence and is used in analyzing the numerical results. Convergence behavior of the numerical algorithm is discussed.

9A599. Solution of the 2D incompressible flow equations on unstructured triangular meshes. - M Williams *(Rocketdyne Div, Rockwell Int, PO Box 7922, 6633 Canoga Ave, MS IB31, Canoga Park CA 91309-7922)*. Numer Heat Transfer B 23(3) 309-325 (Apr-May 1993).

A numerical method for calculating 2D turbulent incompressible flow on unstructured triangular meshes is developed. A primitive variable formulation is used. The Helmholtz equation algorithm is used to enforce the velocity continuity relation for incompressible flow. A careful treatment of the pressure dissipation model is presented. A standard k - ε model with wall functions is used to provide closure for the governing equations. A backward-facing step turbulent flow is calculated using an unstructured triangular mesh and the results are compared to experimental and computational data.

9A600. Stream function vorticity solution using high-p element-by-element techniques. - E Barragy and GF Carey *(Univ of Texas, Austin TX 78712)*. Commun Numer Methods Eng 9(5) 387-395 (May 1993).

A p-type FE scheme is introduced for Navier-Stokes problems in a fully coupled stream function-vorticity formulation. The resulting coupled nonlinear system is solved using a Newton iteration with incremental continuation in the Reynold's number. A biconjugate gradient (BCG) scheme in an element-by-element setting is applied to solve the linearized system at each Newton iteration. Pseudo-element block preconditioners produce a practical PBCG method, even for ill-conditioned systems arising from high-p elements in the case of Stokes flow. The problem at higher Reynolds numbers further limits p.

9A601. Vorticity-velocity method for the numerical solution of 3D incompressible flows. - G Guj and F Stella *(Dept Mec Aeronaut, Via Eudossiana 18, 00184 Rome, Italy)*. J Comput Phys 106(2) 286-298 (Jun 1993).

A new method for the numerical solution of the 3D Navier-Stokes equations written in terms of vorticity-velocity is presented. The advantages of this formulation with respect to primitive variables and vorticity-vector-potential ones are discussed in view of physical as well as engineering applications. A suitable form of the continuum equations, the most appropriate discretization scheme, and variable location in order to guarantee the solenoidality of the velocity and vorticity fields are introduced and justified. A 3D lid driven cavity problem for $400 \leq Re \leq 3200$ is chosen as a test case for comparison and validation purposes.

See also the following:

9A745. Solution of Navier-Stokes equations on non-staggered grid

356. Compressible flow

356C. TRANSONIC FLOW

9A602. Study of integral equation methods for transonic flow calculations. - Hong Hu *(Dept of Math, Hampton Univ, Hampton VA 23668)*. Eng Anal Boundary Elements 11(2) 101-107 (1993).

An integral equation method based on the full-potential equation for transonic flow calculations is presented. The full-potential equation is written in the moving frame of reference, in the form of the Poisson's equation. The integral equation solution in terms of the velocity field is obtained by the Green's theorem. The numerical solutions are obtained by a time-marching (if unsteady flows), iterative procedure. Through studying the method and computational examples, the capabilities and limitations of the transonic integral equation method are discussed. Finally, the need for further research is addressed.

9A603. Variational principles and generalized variational principles for fully 3D transonic flow with shocks in a turbo-rotor Part II. Rotational flow. - G-L Liu *(Shanghai Univ of Tech and Shanghai Inst of Appl Math and Mech, 149 Yan-Chang Rd, Shanghai 200 072, People's Republic of China)*. Acta Mech 97(3-4) 229-238 (1993).

Two variational principle (VP) families for fully 3D transonic potential, Beltrami rotational flows with shocks in a rotor are put forth in terms of stream functions. By making use of functional variations with variable domain one succeeded in converting most of the boundary conditions and matching conditions across unknown discontinuities (such as shocks and free trailing vortex sheets), including the generalized Rankine-Hugoniot shock relations, into natural ones. This paper is intended to provide a rigorous theoretical foundation for constructing a novel computational method which incorporates a new FE with self-adapting embedded discontinuities (now under development) and the artificial density concept, could capture all unknown discontinuities automatically and clearly. The applicability of VPs for rotational flow, in contrast to those for Beltrami flow, is not limited to transonic flow with moderate Mach numbers.

356D. SUPERSONIC FLOW

9A604. Numerical study of wave propagation in a confined mixing layer by eigenfunction expansions. - Fang Q Hu *(Dept of Math and Stat, Old Dominion Univ, Norfolk VA 23529)*. Phys Fluids A 5(5) 1420-1426 (Jun 1993).

It is well known that the growth rate of instability waves of a 2D free shear layer is reduced greatly at supersonic convective Mach number. In previous works, it has been shown that new wave modes exist when the shear layers are bounded by a channel due to the coupling effect between the acoustic wave modes and the motion of the mixing layer. The present work studies the simultaneous propagation of multiple stability waves using numerical simulation.

356E. HYPERSONIC FLOW

9A605. Density measurements in an expanding flow using holographic interferometry. - SP Sharma, SM Ruffin *(NASA Ames Res Center, Moffett Field CA 94035)*, SA Meyer, WD Gillespie *(Stanford)*, LA Yates *(Eloret Inst, Palo Alto CA 94303)*. J Thermophys Heat Transfer 7(2) 261-268 (Apr-Jun 1993).

A nonequilibrium expansion of nitrogen through a 2D nozzle of a reflected shock tunnel is investigated with laser holography, time-resolved pressure measurements, and emission spectroscopy to characterize the flowfield for future vibrational relaxation measurements. A 2D computation is used to simulate the nozzle flowfield. Synthetic holograms are generated using the computed density profiles and are compared with the experimental holograms. Computational accuracy of both models is assessed against the experimental data.

9A606. Development of braided rope seals for hypersonic engine applications: Flow modeling. - R Mutharasan *(Chem Eng, Drexel Univ, Philadelphia PA 19104)*, BM Steinetz *(Struct Dyn Branch, NASA Lewis Res Center, Cleveland OH 44135)*, Xiaoming Tao, Guang-Wu Du *(Fibrous Mat Res Center, Drexel Univ, Philadelphia PA 19104)*, F Ko *(Mat Eng, Drexel Univ, Philadelphia PA 19104)*. J Propulsion Power 9(3) 456-461 (May-Jun 1993).

A new type of engine seal is being developed to meet the needs of advanced hypersonic engines. A seal braided of emerging high-temperature ceramic fibers comprised of a sheath-core construction has been selected for study based on its low leakage rates. Flexible, low-leakage, high-temperature seals are required to seal the movable engine panels of advanced ramjet-scramjet engines, either preventing potentially dangerous leakage into backside engine cavities or limiting the purge coolant flow rates through the seals. To predict the leakage through these flexible, porous seal structures, new analytical flow models are required. Two such models based on Kozeny-Carman equations are developed herein and are compared to experimental leakage measurements for simulated pressure and seal preload conditions, showing good agreement. The models developed allow prediction of the gas leakage rate as a function of fiber diameter, fiber packing density, gas properties, and pressure drop across the seal. The first model treats the seal as a homogeneous fiber bed. The second model divides the seal into two homogeneous fiber beds identified as the core and the sheath of the seal.

9A607. Hypersonic shock-tunnel testing at an equilibrium interface condition of 4100 K. - MAS Minucci *(Divisao Lasers, Inst Estudos Avancados-CTA, Sao Jose dos Campos, Sao Paulo 12231, Brazil)* and HT Nagamatsu *(Dept of Mech Eng, RPI)*. J Thermophys Heat Transfer 7(2) 251-260 (Apr-Jun 1993).

An investigation has been conducted on the operation of the RPI 0.61-m-diam hypersonic shock tunnel at an equilibrium interface condition of 5.8 MPa and 4100 K. The numerical analysis shows a strong dependence of the equilibrium interface pressure and temperature on the initial driver temperature and incident interface speed. A fairly good agreement was observed between the measured equilibrium pressure and the predicted value for the shock-tunnel conditions.

9A608. Monte Carlo simulation of entry in the Martian atmosphere. - DB Hash and HA Hassan *(Mech and Aerospace Eng, N Carolina State Univ, Raleigh NC 27695)*. J Thermophys Heat Transfer 7(2) 228-232 (Apr-Jun 1993).

The Direct Simulation Monte Carlo method of Bird is used to investigate the characteristics of low density hypersonic flowfields for typical aerobrakes during Martian atmosphieric entry. The method allows both thermal and chemical nonequilibrium. Results are presented for a 60-deg spherically blunt cone for various nose radii and altitudes.

9A609. Theory of radiation from low velocity shock heated air. - DA Levin, RT Loda *(Sci and Tech Div, Inst for Defense Anal, 1801 N Beaugregard St, Alexandria VA 22311)*, GV Candler *(Dept of Mech Aerospace Eng, N Carolina State Univ, Raleigh NC 27695)*, C Park *(NASA Ames Res Center, Moffett Field CA 94035)*. J Thermophys Heat Transfer 7(2) 269-276 (Apr-Jun 1993).

Application of hypersonic computational fluid dynamics models to low velocity vehicles is examined. Important modeling aspects such as chemical kinetics, electronics excitation and de-excitation mechanisms, and existence of equilibrium vs nonequilibrium conditions in the flow were examined. Flowfields properties and in-band radiances in the wavelength region of 0.25 μ in the vicinity of the stagnation streamline are given for a hemisphere with a radius of 0.0762 m. Comparison with recent shock tube data is also shown.

356K. NONEQUILIBRIUM AND CHEMICAL EFFECTS

9A610. Coupled implicit method for chemical non-equilibrium flows at all speeds. - Jian-Shun Shuen *(Sverdrup Tech, NASA Lewis Res Center, Cleveland OH 44135)*, Kuo-Huey Chen *(Univ of Toledo, NASA Lewis Res Center, Cleveland OH 44135)*, Yunho Choi *(Sverdrup Tech, NASA Lewis Res Center, Cleveland OH 44135)*. J Comput Phys 106(2) 306-318 (Jun 1993).

A time-accurate, coupled solution procedure is described for the chemical nonequilibrium Navier-Stokes equations over a wide range of Mach numbers. This method employs the strong conservation form of the governing equations, but uses primitive variables (p_g, u, v, h, Y_i) as unknowns. Real gas properties and nonequilibrium chemistry are considered. Numerical tests include steady convergent-divergent nozzle flows with air dissociation-recombination chemistry, dump combustor flows with n-pentane-air chemistry, and nonreacting unsteady driven cavity flows. Numerical results for both the steady and unsteady flows demonstrate the efficiency and robustness of the present algorithm for Mach numbers ranging from the incompressible limit to supersonic speeds.

356L. THERMAL EFFECTS

See the following:

9A609. Theory of radiation from low velocity shock heated air

356Y. COMPUTATIONAL TECHNIQUES

9A611. Application of the locally implicit method to upwind TVD schemes. - Yih Nen Jeng and Uon Jien Payne *(Inst of Aeronaut and Astronaut, Natl Cheng Kung Univ, Tainan,* *Taiwan, ROC).* J Sci Comput 7(4) 339-357 (Dec 1992).

The local implicit scheme of Reddy et al is extended to the minmod and third-order upwind TVD schemes. Numerical tests show that the proposed scheme is stable. In addition, it is found that if the flow field has a dominant direction, setting the iteration sweep to align with this direction can significantly improve the converging speed.

9A612. **Chebyshev collocation method and multi-domain decomposition for Navier-Stokes equations in complex curved geometries.** - CR Schneidesch and MO Deville *(Unite Mec Appl, Univ Catholique, Louvain-La-Neuve, Belgium).* J Comput Phys 106(2) 234-257 (Jun 1993).

A general multidomain decomposition is proposed for the numerical solution of the 2D incompressible stationary Navier-Stokes equations. The solution technique consists in a Chebyshev orthogonal collocation method preconditioned by a standard Galerkin FE technique. The preconditioned system is then solved through a Richardson procedure. The domain of interest is decomposed into quadrilaterals, curved when needed. A Gordon transfinite interpolation performs the curvilinear grid generation of the obtained simply-connected planar subdomains. The study of model Stokes problems demonstrates that the current method still behaves spectrally in distorted geometries. For curvilinear distortion, a loss of several orders of magnitude is observed in the solution accuracy even when the distortion is very limited.

9A613. **Multigrid technique for the compressible Euler and Navier-Stokes equations.** - AE Kanarachos and IP Vournas *(Dept of Mech Eng, Natl Tech Univ, PO Box 64078, 15710 Athens, Greece).* Eng Comput 10(2) 123-137 (Apr 1993).

An optimized multigrid method (NSFLEX-MG) for the NSFLEX-code (Navier-Stokes solver using characteristic flux extrapolation) of MBB (Messerschmitt Bolkow Blohm GmbH) is described. The method is based on a correction scheme and implicit relaxation procedures and is applied to 2D test cases. The principal feature of the flow solver is a Godunov-type averaging procedure based on the eigenvalues analysis of the Euler equations by means of the inviscid fluxes are evaluated at the finite volume faces. Viscous fluxes are centrally differenced at each cell face.

9A614. **Semi-implicit spectral method for the anelastic equations.** - SR Fulton *(Dept of Math and Comput Sci, Clarkson Univ, Potsdam NY 13699-5815).* J Comput Phys 106(2) 299-305 (Jun 1993).

This paper describes the efficient and accurate solution of the 2D anelastic equations by a Fourier-Chebyshev spectral method. A fourth-order Runge-Kutta method is used for the time integration, with the diffusion terms treated implicitly and all other terms (including the pressure gradient) treated explicitly. The model is free from aliasing and converges quickly once the solution is resolved. Numerical results are given for nonlinear flow generated by an atmospheric density current.

9A615. **Solution of the compressible Navier-Stokes equations using improved flux vector splitting methods.** - D Drikakis *(Dept of Fluid Mech, Univ of Erlangen-Nurnberg, Cauerstr 4 D-8520, Germany)* and S Tsangaris *(Dept of Mech Eng, Natl Tech Univ, Athens, Greece).* Appl Math Model 17(6) 282-297 (Jun 1993).

In this paper the accuracy of two flux vector splitting methods using upwind schemes up to the fourth order for the solution of the unsteady compressible Navier-Stokes equations is improved. Two of the most well-known methods for the solution of the inviscid gas dynamic equations, the flux vector splitting method by Steger an[illegible] Warming and the flux vector splitting method [illegible] van Leer are presented for the first time in combination with a five-point upwind scheme. Inaccuracies of flux vector splitting methods, which have been presented in the recent literature, can be eliminated using the present schemes in conjunction with proposed corrections for the flux splittings. The present techniques can be used in compressible viscous flows, predicting with accuracy viscous phenomena such as separation and shock boundary layer interaction.

9A616. **Three BEM schemes for the calculating of subsonic compressible plane cascade flow.** - AX Liao *(2nd Dept of Mech Eng, SW Jiaotong Univ, Chengdu, Sichuan 610031, Peoples Rep of China)* and CX Lin *(Dept of Thermal Eng, Chongqing Univ, Chongqing, Sichuan 630044, Peoples Rep of China).* Eng Anal Boundary Elements 11(1) 25-32 (1993).

This paper reports research work on the calculation of slightly perturbed 2D subsonic compressible potential flow through a cascade by direct BEMs. The work has been performed in three schemes: 1) orthotropic medium method; 2) equivalent cascade method; 3) compressibility correction method. Using the above three schemes, six slightly perturbed cases of 2D subsonic compressible potential flow through a cascade composed of K-7 compressor-blades has been calculated. The results obtained according to these three schemes are compared with each other, and with the results of experiments performed by the authors. Satisfactory coincidence has been obtained.

9A617. **Use of a rotated Riemann solver for the 2D Euler equations.** - DW Levy, KG Powell, Bram van Leer *(Dept of Aerospace Eng, Univ of Michigan, Ann Arbor MI 48109).* J Comput Phys 106(2) 201-214 (Jun 1993).

A scheme for the 2D Euler equations that uses flow parameters to determine the direction for upwind-differencing is described. The approach respects the multidimensional nature of the equations and reduces the grid-dependence of conventional schemes. Several angles are tested as the dominant upwinding direction, including the local flow and velocity-magnitude-gradient angles. Roe's approximate Riemann solver is used to calculate fluxes in the upwind direction, as well as for the flux components normal to the upwinding directions. Solutions of the Euler equations are calculated for a variety of test cases. Substantial improvement in the resolution of shock and shear waves is realized.

358. Rarefied flow

9T618. **Kinetic theory analysis of steady evaporating flows from a spherical condensed phase into a vacuum.** - Yoshio Sone and Hiroshi Sugimoto *(Dept of Aeronaut Eng, Kyoto Univ, Kyoto 606-01, Japan).* Phys Fluids A 5(5) 1491-1511 (Jun 1993).

9A619. **Monte Carlo code describing the neutral gas transport in pipe configurations with attenuating media.** - A Nicolai *(Inst Plasmaphys Forschungszentrum Julich GmbH, Assoziation, EURATOM-KFA, Postfach 1913, D-5170 Julich, Germany).* J Comput Phys 106(2) 377-390 (Jun 1993).

A 3D Monte Carlo description of the neutral gas transport in pipe configurations with almost arbitrary torsion and curvature is presented. To avoid quadratic or even transcendental expression describing the pipe surfaces confining and guiding the neutral gas, a decomposition into plane geometrical elements is chosen. Furthermore, a [illegible] of the pseudo collision, "pseudo-[illegible] of the standard tracklength es[illegible]ced. The pseudo collision estimator or - mainly for comparison - the pseudo tracklength estimator are used in the plasma domain. This estimator combination allows us to treat the throat plasma similarly to a homogeneous absorbing medium (speeding up the geometrical and atomic physics related calculations) and to use the standard tracklength estimator if the tracklength is to be calculated during particle tracing anyway. To reduce the variances, important sampling is applied leading to an exponential 1D-importance function.

See also the following:

9A83. Shock wave reflection close to the leading edge of a wedge

360. Multiphase flows

9A620. **Experimental investigations on two-phase flow past a sphere using digital particle-image-velocimetry.** - M Schmidt and F Loffler *(Inst Mech Vefahrenstech und Mech, Univ Karlsruhe (TH), D-7500 Karlsruhe, Germany).* Exp Fluids 14(5) 296-304 (Apr 1993).

Digital Particle-Image-Velocimetry was applied to investigate particle trajectories in a gas flow past a sphere. The particle displacement was determined by autocorrelation analysis of image sections. To enhance the signal-noise ratio a synthetic image with idealized particle pictures was generated from the real image. The autocorrelation function was calculated using the Fast Hartley Transformation. The desired secondary maximum of this function was detected by an algorithm with subpixel resolution. A data validation step testing the plausibility of the velocity vectors completes the image analysis. Particle trajectories are traced with help of the particles' velocity vectors. The particle deposition on a sphere can be deduced from the course of these trajectories.

9A621. **Particle force and heat transfer in a dusty gas sustaining an acoustic wave.** - S Temkin *(Dept of Mech and Aerospace Eng, Rutgers Univ, Piscataway NJ 08855-0909).* Phys Fluids A 5(5) 1296-1304 (Jun 1993).

This work considers the effects of finite mass concentrations on the force and the heat transfer rate for a small particle in a dusty gas. The particular flow studied is a plane, monochromatic sound wave, where the particle velocity and temperature slips are very small. Assuming that the fluid's temperature and velocity near a test particle are changed by amounts of which depend on the mass loading and on the respective slips, it is shown that the heat transfer rate to a sphere in the suspension changes from the pure condition limit q_{k0}), applicable to an isolated sphere to q_{k0($1 + C_m c_{pp}/c_{pf}$), where C_m is the mass loading, c_{pp} is the specific heat of the particle material, and c_{pf} is the constant pressure specific heat of the gas. Another but less significant effect is to change the corresponding viscous force from the Stokes values, F_{v0}, to $F_{v0}\gamma m/\gamma_f$, where γ_m and γ_f are the specific heat ratios for the suspension and for the dust-free gas, respectively.

9A622. **Numerical solutions for the deformation of a bubble rising in dilute polymeric fluids.** - DS Noh, IS Kang *(Dept of Chem Eng, Pohang Inst of Sci and Tech, PO Box 125, Pohang 790-600, Korea),* L Gary Leal *(Dept of Chem and Nucl Eng, UC, Santa Barbara CA 93106).* Phys Fluids A 5(5) 1315-1332 (Jun 1993).

The steady-state deformation of a bubble rising in polymeric liquid has been investigated using a general numerical technique for the solution of free-boundary problems in non-Newtonian fluid mechanics. The technique is based on a finite-difference solution of the governing equations on an orthogonal curvilinear coordinate system, which is constructed numerically and adjusted to fit the boundary shape exactly at any time. This problem was analyzed based on the constitutive equation proposed by Chilcott and Rallison, which models a dilute polymer solution as a suspension of dumbbells with finite extensibility. Computations were carried out to investigate the effect of conformation change of polymer chains on the bubble deformation for various values of the Deborah number, maximum chain extensibility, (ie, roughly proportional to molecular weight), capillary number, and the Reynolds number. Numerical results show good agreement with existing experimental findings reported elsewhere. Especially, the tendency of transition from a prolate shape to a cusped shape has been observed in the creeping flow limit.

See also the following:

9A649. Brownian particle deposition in a directly simulated turbulent channel flow

362. Wall layers (incl boundary layers)

9A623. Strong vortex-boundary layer interactions Part I. Vortices high. - AD Cutler *(George Washington Univ JIAFS, NASA Langley Res Center, Hampton VA 23681)* and P Bradshaw *(Dept of Mech Eng, Stanford)*. Exp Fluids 14(5) 321-332 (Apr 1993).

Detailed measurements with hot-wires and pressure probes are presented for the interaction between a turbulent longitudinal vortex pair with "common flow" down, and a turbulent boundary layer. The interaction has a larger value of the vortex circulation parameter, and therefore better represents many aircraft and vortex interactions, then those studied previously. The vortices move down towards the boundary layer, but only the outer parts of the vortices actually enter it. Beneath the vortices the boundary layer is thinned by lateral divergence to the extent that it almost ceases to grow. Outboard of the vortices the boundary layer is thickened by lateral convergence, The changes in turbulence structure parameters in the boundary layer appear to be due to the effects of "extra-rate-of-strain" produced by lateral divergence (or convergence) and by free-stream turbulence. The effect of interaction on the vortices (other than inviscid effect of the image vortices below the surface) is small. The flow constitutes a searching test case for prediction methods for 3D turbulent flows.

9A624. Effect of distributed roughness on laminar-turbulent transition in the boundary layer over a rotating cone. - T Watanabe *(Dept of Mech Eng, Iwate Univ, Morioka 020, Japan)*, HM Warui, N Fujisawa *(Dept of Mech Eng, Gunma Univ, Kiryu 376, Japan)*. Exp Fluids 14(5) 390-392 (Apr 1993).

Laminar-turbulent transition in the 3D boundary layer over a rotating body is of fundamental importance in fluid mechanics. This phenomenon has been investigated both experimentally and theoretically since the experiment by Smith (1947) for the flow over a rotating disk. The main feature of this transition process is the appearance of spiral vortices in the transition region, which are caused by the combined instability mechanism of Tollmien-Schlichting waves and 3D Taylor-Gortler vortices.

9A625. Computations and experiments for a multiple normal shock-boundary-layer interaction. - BF Carroll, PA Lopez-Fernandez *(Dept of Aerospace Eng Mech and Eng Sci, Univ Florida, Gainesville FL 32611)*, JC Dutton *(Dept of Mech and Indust Eng, Univ Illinois, Urbana IL 61801)*. J Propulsion Power 9(3) 405-411 (May-Jun 1993).

Results from a numerical investigation of a Mach 1.61 multiple normal shock wave-turbulent boundary-layer interaction are compared to wall static pressure and laser Doppler velocimeter measurements. The computations used the explicit, time-dependent, second-order accurate MacCormack scheme to solve the mass-averaged Navier-Stokes equations. Turbulence was modeled by means of the Baldwin-Lomax algebraic model and the Wilcox-Rubesin two-equation model. The computation with the Wilcox-Rubesin model was able to capture the major features of the normal shock train and accurately predicted the flow reacceleration mechanisms which occur between shocks. However, this computation failed to accurately predict the level of flow separation under the first shock. The Baldwin-Lomax computation displayed a more limited ability to capture the features of this shock train flow.

9A626. Unsteady 3D boundary layer flow due to a stretching surface. - V Rajeswari, M Kumari, G Nath *(Dept of Math, Indian IT, Bangalore 560 012, India)*. Acta Mech 98(1-4) 123-141 (1993).

In this numerical study, the unsteady laminar incompressible boundary-layer flow over a continuously stretching surface has been investigated when the velocity of the stretching surface varies arbitrarily with time. Both the nodal and the saddle point regions of flow have been considered for the analysis. Results have been obtained for the stretching velocities which are accelerating and decelerating with time. Results show that the skin friction, the heat transfer and the mass transfer parameters respond significantly to the time dependent stretching velocities. The Prandtl number and the Schmidt number strongly affect the heat and mass transfer of the diffusing species, respectively.

9A627. Boundary layer flow of power-law fluids past arbitrary profiles. - M Pakdemirli *(Dept of Eng Sci and Mech, VPI)*. IMA J Appl Math 50(2) 133-148 (1993).

Two-dimensional steady-state boundary layer equations of power-law fluids are derived using a special coordinate system which makes the equations independent of the body shape immersed in the flow. In deriving the boundary layer equations, the method of matched asymptotic expansions is used. It is shown that the similarity solutions for power-law fluids are much the same as those for Newtonian fluids.

9A628. Developments on an unsteady boundary-layer analysis: Internal and external flows. - TH Ramin and RH Pletcher *(Dept of Mech Eng and Comp Fluid Dyn Center, Iowa State Univ, Ames IA 50011)*. Numer Heat Transfer B 23(3) 289-307 (Apr-May 1993).

A boundary-layer solution for 2D, compressible unsteady flows has been developed for the non-Cartesian generalized grids consistent with first-order boundary-layer theory. The scheme is applicable to both internal and external unsteady flows. Example results demonstrate advantages of using a non-Cartesian grid for external flows. Boundary-layer solutions were reported for the first time for a number of flows that had been computed only by quite different approaches, including the numerical solutions to the Navier-Stokes equations. The results computed for several test cases were found to be in good agreement with data available in the literature.

364. Internal flow (pipe, channel, Couette)

9A629. Tracer dispersion in rough channels: A 2D numerical study. - J Koplik *(Benjamin Levich Inst and Dept of Phys, CCNY)*, I Ippolito *(Lab Phys Mec Milieux Heterogenes, ESPCI, 10 rue Vauquelin, 75321 Paris Cedex 05, France)*, JP Hulin *(Lab Phys Mec Milieux Heterogenes, ESPCI, 10 rue Vauquelin, 75321 Paris Cedex 05, France)*. Phys Fluids A 5(5) 1333-1343 (Jun 1993).

Numerical results are presented on the hydrodynamic dispersion of passive tracer in flow through a 2D channel boundary by parallel plates, one having substatial rugosities perpendicular to the flow. The simulation is based on the numerical solution of the microscopic Stokes and convention-diffusion equations, over a range of Peclet numbers and of degrees of rugosity of the channel. One observes a tenfold increase of the effective dispersion between the smooth plate case (classical Taylor dispersion) and the maximum rugosity case, attributable to the trapping of tracer inside deep rugosities. The results were analyzed in terms of tracer exchange models, involving a characteristic exchange time between the low- and high-velocity zones and their relative volume fractions, as a function of the Peclet number and the relative depth of the rugosities. The simulations were compared to "echo" dispersion experiments in which the tracer is first injected into the model and then, upon reversal of the fluid flow, drawn back through the inlet.

9A630. Drag of plane microslot ducts with rough walls. - YP Dyban, NM Zotov, AA Khoroshavin *(Eng Thermophys Inst, Ukrainian Acad of Sci, Volgograd Polytechnic Inst, Kiev, Ukrain)*. Heat Transfer Res 24(3) 398-407 (Apr 1992).

Experimental results on flow of air in plane microslot ducts are presented. The effect of the roughness of the duct walls on the drag coefficient in different flow modes is investigated. With increasing roughness, transition to turbulent flow occurs at even lower Reynolds number. A technique for determining the equivalent height of the roughness for purposes of analysis of laminar flows in such ducts is suggested.

9A631. Computer simulation of gradually varied flow profiles in circular sections. - NA Zaghloul and MM Shahin *(Dept of Civil Eng, Kuwait Univ, PO Box 5969, Kuwait)*. Adv Eng Software 16(1) 37-46 (1993).

Most wastewater flow and storm drainage transportation systems consist largely of circular pipes. Gradually varied flow (GVF) conditions predominate in such systems. This paper presents a software package based on Lotus 1-2-3 to solve for GVF problems in circular pipes using the direct step method. The results are presented in tabular form. In addition, the Lotus print graph capabilities are used to delineate the GVF profiles.

See also the following:

9A629. Tracer dispersion in rough channels: A 2D numerical study

9A646. Time-dependent instabilities in curved rotating channel flows

366. Internal flow (inlets, nozzles, diffusers, cascades)

9A632. Inlet turbulence distortion and viscous flow development in a controlled diffusion compressor cascade at very high incidence. - GV Hobson and RP Shreeve *(Turbopropulsion Lab, Naval Postgraduate Sch, Monterey CA 93943)*. J Propulsion Power 9(3) 397-404 (May-Jun 1993).

Detailed two-component laser Doppler velocimeter (LDV) measurements of the flow through a controlled diffusion compressor cascade at a Reynolds number of about 700,000 and at a low Mach number are reported in this article. A very high-incidence angle (8° above design) was considered throughout this investigation, which included the full experimental characterization of the turbulence field. The LDV measurements were fully automated and were all taken in coincidence mode, thus turbulent flow correlations could be determined. Most significant was the measurement of the distortion of the inlet freestream turbulence upstream of the blade leading edges. Such information is important in assessing viscous codes which incorporate transport equations to describe the turbulence within the flowfield. The laminar-leading edge separation bubble, which reattached turbulent, was enlarged on the suction surface of the blade. Consistent with measurements at lower incidence angles, the suction surface boundary layer remained attached over the rear part of the blade. The pressure side boundary layer initially showed little or no growth, however, it finally developed into a profile similar to a wall jet. The wake profiles showed significant asymmetry due to the high loading on the blades at the increased incidence angle.

9A633. Study on vortex generator flow control for the management of inlet distortion. - BH Anderson *(NASA Lewis Res Center, Cleveland OH 44135)* and J Gibb *(Defense Res Agency, Bedford, England, UK)*. J Propulsion Power 9(3) 422-430 (May-Jun 1993).

The present study demonstrates that the reduced Navier-Stokes RNS3D code can be used very effectively to develop a vortex generator installation to minimize the engine face circumferential distortion by controlling secondary flow. The computing times required are small enough that studies such as this are feasible within an analysis-design environment with all its constraints of time and costs. This research study also established the nature of the performance improvements that can be realized with vortex flow control, and suggests a set of aerodynamic properties (called observations) that can be used to arrive at a successful vortex generator installation design. This study also indicated that scaling between flight and typical wind-tunnel test conditions is possible only within a very narrow range of generator configurations close to an optimum installation. Lastly, this study indicated that vortex generator installation design for inlet ducts is more complex than simply satisfying the requirement of attached flow, it must satisfy the requirement of minimum engine face distortion.

9A634. Computational study of advanced exhaust system transition ducts with experimental validation. - C Wu *(United Tech, USBI, PO Box 1900, Huntsville AL 35807)*, S Farokhi *(Aerospace Eng and Flight Res Lab, Univ of Kansas, Lawrence KS 66045)*, R Taghavi *(Aerospace Eng, Univ of Kansas, Lawrence KS 66045)*. J Propulsion Power 9(3) 437-442 (May-Jun 1993).

A subsonic, 3D parabolized Navier-Stokes code is used to construct stall margin design charts for optimum length advanced exhaust systems' circular to rectangular transition ducts. Computer code validation has been conducted to examine the capability of wall static pressure predictions. The comparison of measured and computed wall static pressures indicates a reasonable accuracy of the PNS computer code results. Computations have also been conducted on 15 transition ducts, 3 area ratios, and 5 aspect ratios. The three area ratios investigated are constant area ratio of unity, moderate contracting area ratio of 0.8, and highly contracting area ratio of 0.5. The degree of mean flow acceleration – ie, the area ratio of the duct – is identified as a dominant parameter in establishing the minimum duct length requirements. The effect of increasing aspect ratio in the minimum length transition duct is due to increase the length requirement, as well as to increase the mass-averaged total pressure losses.

9A635. Nonreflecting boundary conditions of 3D Euler equations calculations for strut cascades. - K Imanari and H Kodama *(R&D Dept, Aeroengine and Space Operations, Ishikawajima-Harima Heavy Indust, Tokyo, Japan)*. J Propulsion Power 9(3) 443-448 (May-Jun 1993).

In this article, 3D nonreflecting boundary conditions regarding pressure waves and associated components in density and velocity waves have been formulated and applied to time-marching Euler equation calculations of steady flows around uncambered thick strut cascades. The linearized solutions including a Fourier-Bessel double expansion with an exponential variation in the axial direction have been developed for far-field perturbations from the uniform freestream with subsonic axial velocity in a cylindrical annular duct, and used to provide the information for the correction of boundary conditions. Numerical examples for the symmetric struts, and the nonuniform strut cascades comprising two types of vanes, have demonstrated the correctness and accuracy of the present method, allowing a considerable reduction of the computational domain.

368. Free shear layers (mixing layers, jets, wakes, cavities, plumes)

9A636. Flow regimes and frequency selection of a cylinder oscillating in an upstream cylinder wake. - J Sun *(LRC, Univ Provence, 13397 Marseille, Cedex 13, France)*, J Li, B Roux *(Inst de Mec des Fluides, 1 Rue Honnorat, 13003 Marseille, France)*. Int J Numer Methods Fluids 16(10) 915-929 (30 May 1993).

This paper describes flow around a pair of cylinders in tandem arrangement with a downstream cylinder being fixed or forced to oscillate transversely. A sinusoidal parietal velocity is applied to simulate cylinder oscillation. Time-dependent Navier-Stokes equations are solved using FEM. It is shown that there exist two distinct flow regimes: "vortex suppression regime" and "vortex formation regime". Averaged vortex lengths between the two cylinders, pressure variations at back and front stagnation points as well as circumferential pressure profiles of the downstream cylinder are found completely different in the two regimes and, thus, can be used to identify the flow regimes. It is shown that frequency selection in the wake of the oscillating cylinder is a result of nonlinear interaction among vortex wakes upstream and downstream of the second cylinder and its forced oscillation. Increasing cylinder spacing results in a stronger oscillatory incident flow upstream of the second cylinder and, thus, a smaller synchronization zone.

9A637. Numerical simulation of vortex shedding past triangular cylinders at high Reynolds number using a κ - ε turbulence model. - SH Johansson, L Davidson, E Olsson *(Dept of Thermo and Fluid Dyn, Chalmers Univ of Tech, S-412 96 Gothenburg, Sweden)*. Int J Numer Methods Fluids 16(10) 859-878 (30 May 1993).

Calculations of unsteady turbulent flow around and behind triangular-shaped flameholders using a finite volume code with a $\kappa - \varepsilon$ model of turbulence are presented. The flow behind the flameholders is found to be unsteady (a von Karman vortex street appears) with a well defined Strouhal frequency (predicted Sr = 0.27 compared with an experimental value of 0.25). The predicted profiles of velocity and fluctuating kinetic energy agree well with experiments. The periodic motions in the vortex street are shown to be far more important than the turbulent stochastic motions in exchanging momentum in the transversal direction. The pressure-velocity coupling is handled with the SIMPLEC pressure correction procedure. The discretization in time is fully implicit and 90 time steps are used to resolve one time cycle. It was found that to capture the vortex street it is very important that the grid spacing is sufficiently fine (180 × 100).

9A638. Plane wake of a cylinder: Measurements and inferences on turbulence modeling. - D Aronson and L Lofdahl *(Thermo and Fluid Dyn, Chalmers Univ of Tech, 412 96 Goteborg, Sweden)*. Phys Fluids A 5(5) 1433-1437 (Jun 1993).

Hot wire measurements in the far field region of the plane wake of a cylinder have been carried out. The data obtained indicated that transverse distributions of mean-velocity and Reynolds stresses were self-preserving for a downstream distance greater than 400 momentum thicknesses. Dissipation rate and triple velocity correlations were measured at a downstream position of 880 momentum thicknesses, these measured profiles were compared with the profiles obtained from closure models for the Reynolds stress equations. It was found that the dissipation rate anisotropy could essentially be accounted for by the employed model, larger deviations were observed between the measured and modeled profiles for the triple velocity correlations.

See also the following:

9A604. Numerical study of wave propagation in a confined mixing layer by eigenfunction expansions

9A636. Flow regimes and frequency selection of a cylinder oscillating in an upstream cylinder wake

370. Flow stability

9A639. Optimal excitation of 3D perturbations in viscous constant shear flow. - BF Farrell *(Dept of Earth and Planet Sci, Harvard Univ, Cambridge MA 02138)* and PJ Ioannou *(Center for Meteorol and Phys Oceanog, MIT)*. Phys Fluids A 5(5) 1390-1400 (Jun 1993).

The 3D perturbation to viscous constant shear flow that increase maximally in energy over a chosen time interval are obtained by optimizing the complete set of analytic solutions. These optimal perturbations are intrinsically 3D of restricted morphology, and exhibit large energy growth on the advective time scale, despite the absence of exponential normal modal instability in constant shear flow. The optimal structures can be interpreted as combinations of two fundamental types of motion associated with two distinguishable growth mechanisms: streamwise vortices growing by advection of mean streamwise velocity to form streamwise streaks, and upstream tilting waves growing by the down gradient Reynolds stress mechanism of 2D shear instability. The optimal excitation over a chosen interval of time comprises a combination of these two mechanisms, characteristically giving rise to tilted roll vortices with generally amplified perturbation energy. It is suggested that these disturbances provide the initial growth leading to transition of turbulence, in addition to providing an explanation for coherent structures in a wide variety of turbulent shear flows.

9A640. Problems in the weakly nonlinear theory of hydrodynamic stability and its improvements. - Zhou Heng and Xueyi You *(Dept of Mech, Tianjin Univ, Tianjin 300072, China)*. Acta Mech Sinica 9(1) 1-12 (1993).

There are three main problems in the weakly nonlinear theory of hydrodynamic stability: 1) The radius of convergence with respect to the perturbation parameter is too small and there is no concrete estimation for it. 2) The solution has a special structure, thus in general, it can not satisfy the initial condition posed by many practical problems. 3) When the linear part of its solution does not correspond to a neutral case, there are more than one way in determining the Landau constants, and practically no one knows which is the best way. In this paper, problems (1) and (2) are solved theoretically, and ways for its improvement have been proposed. By comparing the theoretical results with those obtained by numerical simulation, problem (3) has also been clarified.

9T641. Singularities of the Euler equation and hydrodynamic stability. - S Tanveer *(Dept of Math, Ohio State Univ, Columbus OH 43210)* and CG Speziale *(Dept of Aerospace and Mech Eng, Boston Univ, Boston MA 02215)*. Phys Fluids A 5(5) 1456-1465 (Jun 1993).

9A642. Three-dimensional stability analysis of the periodic flow around a circular cylinder. - BR Noack *(Max-Plank-Inst fur Stromungsforschung, Bunsenstr 10, 3400 Gottingen, Germany)*. Phys Fluids A 5(5) 1279-1281 (Jun 1993).

The onset of 3D in the von Karman vortex street behind a circular cylinder is investigated by carrying out the first global, nonparallel, 3D stability analysis of the periodic flow. This flow is found to become unstable at a Reynolds number of 170 by a critical, 3D Floquet mode with a spanwise wavelength of 1.8 diam. The spatial structure of this mode indicates that the onset of 3D is due to a near-wake instability and not caused by a stagnation-line or a boundary-layer instability.

9A643. Pattern selection for the oscillatory onset in thermosolutal convection. - Yuriko Yamamuro Renardy *(Dept of Math and Interdisciplinary Center for Appl Math, VPI)*. Phys Fluids A 5(5) 1376-1389 (Jun 1993).

A layer of fluid lies between two parallel horizontal walls and the solute concentration and temperature are higher at the bottom wall. The onset of time-periodic instability in this double diffusion problem in 3D is analyzed. Periodicity with respect to the hexagonal lattice is assumed. The no-slip condition is imposed at the top and bottom boundaries. There are 11 bifurcating solutions, and their stability is presented. For relatively low solutal and thermal Rayleigh numbers, the solutions are found to be unstable. For the heating of salty water, situations are presented where the standing rolls, the standing patchwork quilt, and either the standing hexagons or the standing regular triangles, may be stable.

9A644. Kelvin-Helmholtz instability of Couette flow between vertical walls with a free surface. - JS Walker *(Dept of Mech and Indust Eng, Univ of Illinois, Urbana IL 61801)*, G Talmage *(Dept of Mech Eng, Penn State)*, SH Brown, NA Sondergaard *(Carderock Div, Naval Surface Warfare Center, Annopolis MD 21402-5067)*. Phys Fluids A 5(5) 1466-1471 (Jun 1993).

A novel type of Kelvin-Helmholtz instability model is developed from hydrodynamic theory. The classical Kelvin-Helmholtz instability involves a horizontal interface between two fluids with different parallel, uniform, horizontal velocities. If the upper fluid is a gas with a much smaller density than the lower fluid which is a liquid, then the phase velocity of the critical disturbance equals the liquid's velocity, so that the liquid sees a standing interfacial wave. The inertial force driving the interfacial instability involves only the gas, no matter how small its density is. In a much more realistic flow model, the liquid velocity at the free surface is not uniform, but varies across the free surface. The disturbance phase velocity can only equal the liquid velocity at one point, while liquid on either side of the point moves faster or slower than the wave. The inertial forces in the liquid then dominate and the gas plays a negligible role. The concept is developed from a Couette flow hydrodynamic model where the fluid flows between two parallel vertical walls with a free surface. The importance of a nonuniform liquid velocity is demonstrated. This modified theory will be applied in future work to study the ejection instability at the interface of the liquid metal and inert cover gas in sliding electrical contacts.

9A645. Meausrements on transition to turbulence in a Taylor-Couette cell with oscillatory inner cylinder. - KJ Maloy *(Fysisk Inst, Univ Oslo, Postboks 1048, Blindern N-0316 Oslo, Norway)* and W Goldburg *(Dept of Phys and Astron, Univ of Pittsburgh, Pittsburgh PA 15260)*. Phys Fluids A 5(5) 1438-1442 (Jun 1993).

The transition line at onset of instability and the distance between the vortex rolls in a Taylor-Couette with an oscillatory inner cylinder having zero mean velocity are measured. When the amplitude of the velocity oscillations increases slightly above the critical value, a transition to a turbulent "mixing regime" takes place. In this regime, homodyne correlation spectroscopy have been used to measure the characteristic velocity fluctuations $<\delta v_q(l)>$ between points separated by a distance l. Scaling of the correlation function $G(\tau,q,l)$ was found, ie, $G(\tau,q,l) = G(x)$, where $x=q\tau<\delta v_q(l)>$, with $<\delta v_q(l)>\sim l^{0.76}$.

9A646. Time-dependent instabilities in curved rotating channel flows. - OJE Matsson *(Dept of Mech and Fluid Phys, RIT, S-100 44 Stockholm, Sweden)*. Phys Fluids A 5(5) 1514-1516 (Jun 1993).

The *principle of exchange of instabilities* is not valid for certain regions of the parameter space of curved rotating channel flow and it is shown that for this situation the most unstable model is inclined traveling roll cells and hence this instability determines the critical Reynolds number.

9A647. Stability of liquid bridges between equal disks in an axial gravity field. - LA Slobozhanin *(Inst for Low Temp Phys and Eng, Ukrainian Acad of Sci, 47 Lenin Ave, 310164 Kharkov, Ukraine)* and JM Perales *(LamfIETSIA Lab Aerodin ETSI Aeronaut, Univ Politec, 28040 Madrid, Spain)*. Phys Fluids A 5(5) 1305-1314 (Jun 1993).

The stability of axisymmetric liquid bridges spanning two equal-diameter solid disks subjected to an axial gravity field of arbitrary intensity is analyzed for all possible liquid volumes. The boundary of the stability region for axisymmetric shapes (considering both axisymmetric and nonaxisymmetric perturbations) have been calculated. It is found that, for sufficiently small Bond numbers, three different unstable modes can appear. If the volume of liquid is decreased from that of an initially stable axisymmetric configuration the bridge either develops an axisymmetric instability (breaking in two drops as already known) or detaches its interface from the disk edges (if the length is smaller than a critical value depending on contact angle), whereas if the volume is increased the unstable mode consists of a nonaxisymmetric deformation. This kind of nonaxisymmetric deformation can also appear by decreasing the volume if the Bond number is large enough. A comparison with other previous partial theoretical analyses is presented, as well as with available experimental results.

372. Turbulence

9A648. Vortex-induced disturbance field in a compressible shear layer. - D Papamoschou *(Dept of Mech and Aerospace Eng, UC, Irvine CA 92717)* and SK Lele *(Dept of Mech Eng and Dept of Aeronaut and Astronaut, Stanford)*. Phys Fluids A 5(5) 1412-1419 (Jun 1993).

The disturbance field induced by a small isolated vortex in a compressible shear layer is studied using direct simulation in a convected frame. The convective Mach number, M_c, is varied from 0.1 to 1.25. The vorticity perturbation is rapidly sheared by the mean velocity gradient. The resulting disturbance pressure field is observed to decrease both in magnitude and extent with increasing M_c, becoming a narrow transverse zone for $M_c > 0.8$. A similar trend is seen for the perturbation velocity magnitude and for the Reynolds shear stress. By varying the vortex size, it was verified that the decrease in perturbation levels is due to the mean-flow Mach number and not the Mach number across the vortex. At high M_c, the vortex still communicates with the edges of the shear layer, although communication in the near-flow direction is strongly inhibited. The growth rate of perturbation kinetic energy declines with M_c primarily due to the reduction in shear stress. For $M_c \geq 0.6$, the pressure dilatation also contributes to the decrease of growth rates. Calculation of the perturbation field induced by a vortex doublet revealed the same trends as in the single-vortex case, illustrating the insensitivity of the Mach-number effect to the specific form of initial conditions.

9A649. Brownian particle deposition in a directly simulated turbulent channel flow. - H Ounis, G Ahmadi, JB McLaughlin *(Clarkson Univ, Potsdam NY 13699)*. Phys Fluids A 5(5) 1427-1432 (Jun 1993).

Diffusion of submicron particles in a simulated turbulent channel flow field is studied. The turbulent flow velocity field is generated by a direct numerical integration of the Navier-Stokes equation with the pseudospectral method. The equation of motion of particles including the Brownian effects is used and ensembles of particle trajectories are numerically evaluated and statistically analyzed. A uniform initial concentration of particles is used in the analysis. Effects of size on particle dispersion and wall deposition processes are studied. The results are compared with the existing models for the submicron particle deposition rate.

9A650. Large-eddy simulation scheme for turbulent reacting flows. - Feng Gao *(Center for Turbulence Res, Stanford)* and EE O'Brien *(Dept of Mech Eng, SUNY, Stony Brook NY 11794-2300)*. Phys Fluids A 5(5) 1282-1284 (Jun 1993).

A general methodology is developed for simulating complicated reacting flow problems. This method combines the large-eddy simulation technique with the existing probability density function approach for turbulent reacting flows and provides a closed form representation for all terms that are involved in the simulations. Some other issues related to this problem are also discussed.

9A651. Shock polar analysis and analytical expressions for vorticity deposition in shock-accelerated density-stratified interfaces. - R Samtaney and NJ Zabusky *(Dept of Mech and Aerospace Eng and CAIP Center, Rutgers Univ, Piscataway NJ 08855)*. Phys Fluids A 5(5) 1285-1287 (Jun 1993).

Vorticity is deposited due to baroclinic effects on the surface of a density-stratified interface accelerated by a shock. An analytical expression is presented, derived from shock polar analysis, for circulation per unit length on a fast-slow planar density interface inclined at an angle to the incident shock. The analytical expression is integrated to yield total circulation on nonplanar interfaces (sinusoidal and semicircular interfaces) accelerated by shocks. The analytical results agree well with diagnostics from numerical experiments using a second-order Godunov code for the Euler equations.

9A652. High Reynolds number calculations using the dynamic subgrid-scale stress model. - U Piomelli *(Dept of Mech Eng, Univ of Maryland, College Park MD 20742)*. Phys Fluids A 5(5) 1484-1490 (Jun 1993).

The dynamic subgrid-scale eddy viscosity model has been used in the large-eddy simulation of the turbulent flow in a plane channel for Reynolds numbers based on friction velocity and channel half-width ranging between 200 and 2000, a range including values significantly higher than in previous simulations. The computed wall stress, mean velocity, and Reynolds stress profiles compare very well with experimental and direct simulation data. Comparison of higher moments is also satisfactory.

9A653. Small-scale turbulence model. - TS Lundgren *(Dept of Aerospace Eng and Mech, Univ of Minnesota, Minneapolis MN 55455)*. Phys Fluids A 5(5) 1472-1483 (Jun 1993).

A previously derived analytical model for the small-scale structure of turbulence is reformulated in such a way that the energy spectrum may be computed. The model is an ensemble of 2D vortices with spiral structure, each stretched by an axially symmetric strain flow. Stretching and differential rotation produce an energy cascade to smaller scales in which the stretching represents the effect of instabilities and the spiral structure is the source of dissipation at the end of the cascade. The energy spectrum of the resulting flow may be expressed as a time integration involving only the enstrophy spectrum of the time evolving 2D cross-section flow, which may be obtained numerically. Examples are given in which a $\kappa^{-5/3}$ spectrum is obtained by this method. The $\kappa^{-5/3}$ inertial range spectrum is shown to be related to the existence of a self-similar enstrophy preserving range in the 2D enstrophy spectrum. The results are found to be insensitive to time dependence of the strain rate, including even intermittent on-or-off strains.

9A654. Measurement of the diffusion coefficient in a heated plane airstream. - E Pemha *(Lab de Mec, Fac Sci, BP 812, Yaounde, Cameroun)*, B Gay, A Taillard *(Lab de Mec des Fluides, Ecole Centrale de Lyon, 36 Ave Guy des Collongues, 69131 Ecully, France)*. Phys Fluids A 5(5) 1289-1295 (Jun 1993).

In order to measure the diffusion coefficient of a heated plane airstream, a single laser beam is passed through the jet, perpendicularly to the flow direction. The thermic turbulence in the airstream causes random fluctuations of the refractive index. Consequently, the beam direction undergoes, in the flow, random perturbations. After having traversed the jet, the beam produces a luminous trace on a photoelectric cell placed outside the jet. An experimental setup for measuring the probabilities of the beam impact positions in the cell is described. From the Markovian process model, applied along the whole random path of the beam, it has been possible to compute these probabilities by solving the Einstein-Fokker-Kolmogorov equation. The diffusion coefficient can be determined by adjusting the numerical solution to agree with the experimental results. In addition, the calculation procedure gives the order of magnitude of an integral scale, characterizing the dimension of the turbulent structures in which the propagation of light can be considered rectilinear. A good agreement between the results and the published data obtained by means of the cold-wire anemometer technique proves the validity of the method.

See also the following:

9A623. Strong vortex-boundary layer interactions Part I. Vortices high

9A638. Plane wake of a cylinder: Measurements and inferences on turbulence modeling

9A648. Vortex-induced disturbance field in a compressible shear layer

9A690. Heat transfer and flow past a backstep with the nonlinear k-ε turbulence model and the modified k-ε turbulence model

9A691. Heat transfer in a turbulent boundary layer disturbed by means of a manipulator for breaking up large eddies

9A692. Heat-transfer augmentation in a turbulent boundary layer disturbed by means of a vortex generator

9A698. Heat and mass transfer analysis of developing turbulent flow in a square duct

9A724. Turbulence model of fire-induced air flow in a ventilated tunnel

374. Electromagneto-fluid and plasma dynamics

9A655. Plasma engineering aspects of large tokamak operation. - FC Schuller and AAM Oomens *(FOM-Inst voor Plasmafysica Rijnhuizen Assoc, EURATOM-FOM, PO Box 1207, 3430 BE Nieuwegein, Netherlands)*. Fusion Eng Des 22(1-2) 35-55 (Mar 1993).

In this paper the plasma engineering aspects involved with the reliable and safe operation of present-day large tokamaks are described. First a brief review of the underlying empirical and theoretical knowledge of equilibrium and stability of tokamak plasmas is given. Then some of the recent experiments with disruption preventive actions are discussed. Finally the state of the art in feedback control systems, real-time protection circuits, and the application of pulse scenarios is reviewed.

9A656. Analysis of a power plant with an experimental thermonuclear reactor. - YV Smolkin *(Inst of Heat and Mass Transfer, Minsk, Russia)*. Heat Transfer Res 24(3) 366-373 (Apr 1992).

The structure and the parameters of a thermal diagram of a power plant with an experimental thermonuclear reactor have been analyzed. Recommendations concerning the types and parameters of turbine plants are given.

9A657. MHD flow in complex-geometry tubes. - VV Yakovlev *(Inst of Heat and Mass Transfer, Minsk, Russia)*. Heat Transfer Res 24(3) 310-317 (Apr 1992).

The problem of simulating electroconducting liquid flow with an inhomogeneous electromagnetic force distribution in complex-geometry tubes is considered. The development of specific MHD effects in such tubes is discussed. Special attention is paid to problems classified as local magnetohydrodynamic resistances (LMHDR). New experimental data concerning the resistance to motion in a number of LMHDRs are presented.

9A658. MHD flow with a free surface on the Tokamak contact diverter device. - MY Lebedev, BS Fokin, VV Yakovlev *(Inst of Heat and Mass Transfer, Minsk, Russia)*. Heat Transfer Res 24(3) 318-332 (Apr 1992).

The paper presents the results of an experimental investigation into film MHD flows on models of liquid-metal contact devices (LMCD) with solid and porous sublayers. The effect of wettability and electroconductivity of the sublayer and side walls material as well as of the sublayer porosity and magnetic field direction on the film flow formation conditions is investigated. An estimation of the thermal characteristics of the LMCD with a porous sublayer and energy receiver channel is made.

9A659. Thermal instability of a nonlinear magnetic fluid under the influence of both non-vertical magnetic field and Coriolis forces. - AA Abdullah *(PO Box 6337, Makkah, Saudi Arabia)*. Arab J Sci Eng 17(4B) 625-633 (Oct 1992).

This work examines the convective instability of a horizontal layer of a magnetohydrodynamic fluid of variable permeability when subjected to both a non-vertical magnetic field and Coriolis forces. A model proposed by PH Roberts (1981) in the context of neutron stars is used. The results obtained are also relevant to ferromagnetic fluids. This nonlinear relationship has no effect on the development of instabilities through the mechanism of stationary convection which is the preferred process in terrestrial applications. However, in non-terrestrial applications the nonlinearity influences the onset of overstable convection and overstability is the preferred mechanism. In the context of ferromagnetic fluids, both stationary and overstable instability can be expected to be realizable possibilities.

9A660. Unsteady MHD flow of a dusty viscous liquid in a rotating channel with Hall currents. - HS Takhar *(Dept of Eng, Univ of Manchester, Manchester M13 9PL, UK)*, PC Ram, SS Singh *(Dept of Math, Kenyatta Univ, Nairobi, Kenya)*. Int J Energy Res 17(1) 69-74 (Jan 1993).

The unsteady magnetohydrodynamic flow of a dusty, viscous, incompressible liquid in a rotating channel, in the presence of a transverse magnetic field with Hall currents, is considered. Analytical expressions for the velocities of the liquid and the dust particles are obtained. The effects of Hall current m, and the rotation parameter K on the velocity are shown graphically, and are discussed.

9A661. Magnetic field effects on the computed flow over a Mars return aerobrake. - G Palmer *(Aerothermodyn Branch, NASA Ames Res Center, Moffett Field CA 94035)*. J Thermophys Heat Transfer 7(2) 294-301 (Apr-Jun 1993).

A numerical algorithm is developed to calculate the electromagnetic phenomena simultaneously with the fluid flow in the shock layer over an axisymmetric blunt body in a thermal equilibrium, chemical nonequilibrium environment. The flowfield is solved using an explicit time-marching, first-order spatially accurate scheme. The electromagnetic phenomena are coupled to the real-gas flow solver through an iterative procedure. The technique is applied in calculating the flow over a Mars return aerobrake vehicle entering the Earth's atmosphere. With the application of an external magnetic field of 0.05 to 0.1 T, the solution indicates an increase in stagnation line shock standoff distance, wall pressure, and radiative heat transfer and a decrease in convective heat transfer.

9A662. Multiconstrained variational problems in magnetohydrodynamics: Equilibrium and slow evolution. - B Turkington *(Dept of Math, Univ of Massachusetts, Amherst MA 01003)*, A Lifschitz *(Dept of Math, Univ of Illinois, Chicago IL 60680)*, A Eydeland, J Spruck *(Dept of Math, Univ of Massachusetts, Amherst*

MA 01003). J Comput Phys 106(2) 269-285 (Jun 1993).

A computational method is proposed for solving magnetohydrodynamical equilibrium problems with prescribed flux and mass within the magnetic surfaces that foliate the plasma. Such problems arise in tokamak modeling, for instance, where they determine either equilibria with given adiabatic profiles or slowly evolving quasi-equilibra governed by the Grad-Hogan equations. The classical variational principles of Kruskal and Kulsrud and Woltjer, which express these problems in terms of energy minimization subject to infinite families of nonlinear, nonlocal constraints, are taken as the basis for a direct method of solutions. A natural discretization of the classical constraint families is devised, and an iterative algorithm is developed to solve the resulting optimization problems.

See also the following:

9A655. Plasma engineering aspects of large tokamak operation

9A661. Magnetic field effects on the computed flow over a Mars return aerobrake

9A728. Thermogravitational effects on liquid metal heat transfer in a longitudinal magnetic field

378. Aerodynamics

9A663. Experimental study of a turbulent wing-body junction and wake flow. - JL Fleming, RL Simpson, JE Crowling, WJ Devenport *(Dept of Aerospace and Ocean Eng, VPI).* Exp Fluids 14(5) 366-378 (Apr 1993).

The primary goal of this research was to determine the effects of the approach boundary layer characteristics on the function flow. To accomplish this goal, the authors' results were compared to several other junction flow data sets obtained using the same body shape. The trailing vortex leg flow structure was found to scale on T. A parameter known as the momentum deficit factor (MDF = $(Re_T)^2(\theta/T)$) was found to correlate the observed trends in mean flow distortion magnitudes and vorticity distribution. Changes in δ/T were seen to affect the distribution of u', with lower ratios producing well defined local turbulence maxima. Increased thinning of the boundary layer near the appendage was also observed for small values of δ/T.

9A664. Three-dimensional vortex method for parachutes. - M Humi *(Dept of Math Sci, Worcester Polytech Inst, 100 Institute Rd, Worcester MA 01609-2280).* Int J Numer Methods Fluids 16(10) 879-889 (30 May 1993).

We describe the implementation of a new 3D vortex algorithm for the computation of the drag and flow field around parachutes. Among its novel features, the algorithm couples large eddy simulation methodology with the vortex method, away from the wall region. Furthermore, boundary conditions for a wall (no-slip) and compliant boundaries were implemented. The results of several simulations using this algorithm are analyzed and discussed. The spectral contents of the vortex method are also considered.

9A665. Simulation of range-resolved DIAL measurements on in-flight rocket plumes. - CT Christou, RT Loda, DA Levin *(Sci and Tech Div, Inst for Defense Anal, Alexandria VA 22311).* J Thermophys Heat Transfer 7(2) 233-240 (Apr-Jun 1993).

Feasibility studies were carried out for a ground-based experiment using the differential absorption LIDAR (DIAL) method, to measure spatially resolved rocket plume temperature profiles from solid-aluminized propellants. The core of this effort was a numerical simulation of the dynamics of the laser-plume interaction and the retrieval of average temperatures from the received signals using parameters appropriate to a low-altitude rocket plume. Signal-to-noise ratios were adequate for the assumed experimental conditions and for both a clear and moderately clear atmosphere, to ensure detectability of the returned signals over most of the plume.

380. Machinery fluid dynamics

9A666. Consequences of recent gas turbine developments for industrial CHP applications. - J Stromberg *(Dept of Heat and Power Tech, Chalmers Univ of Tech, S-412 95 Goteborg, Sweden)*, P-A Franck *(CIT Energy Tech Anal, Sweden)*, T Berntsson *(Dept of Heat and Power Tech, Chalmers Univ of Tech, S-412 96 Goteborg, Sweden).* Heat Recovery Syst CHP 13(3) 219-231 (May 1993).

Developments in gas turbine (GT) technology have been considerable during the last few yeas. In this paper, consequences regarding the technical performance for industrial combined heat and power applications are discussed and the most important design parameters are identified. Some GT types, which represent different stages of the developmental trend, are analysed in the simple and the combined cycle. Both the industrial and the aero-derivative GT classes are included. Conclusions are: (i) Generally, the developments have broadened the span of achievable power-to-heat ratios (α-values). (ii) The total efficiencies available depend strongly, and differently for different GT types, on the nature of the heat demands in industrial processes. (iii) When opportunities do not exist to cool the exhaust gases in an economizer, ie, when the stack temperature is directly given by process heat demands, the total efficiency is independent of the GT classes. (iv) When opportunities exist to cool the exhaust gases in an economizer (which is often the case for the simple cycle and always for the combined cycle), the industrial GT developments have given improved ability to reach a high total efficiency. (v) When supplementary firing is applied, however, the total efficiency is high and similar for all various units and conditions. The new aero-derivative units have, in that case, superior α-values - especially in the combined cycle.

9A667. Design of rotor blades of high-temperature gas turbines for a specified service life and minimum loss of output power on blade cooling. - GP Nagoga, VI Tseytlin, VP Balter *(Kuybyshev Aviation Inst, Trud Corp, Kiev).* Heat Transfer Res 24(4) 483-493 (Apr 1992).

The problems of minimizing fuel (and potential turbine output power) losses on air cooling of a gas-turbine rotor blade while providing for the desired blade service is stated. A solution for a turbine with two sets of operating modes is given. It is shown that fuel losses can be minimized by employing a turbine cooling system in which the cooling-air flowrates are controlled solely by the operating conditions.

9A668. Multipassage 3D Navier-Stokes simulation of turbine rotor-stator interaction. - NK Madavan *(NASA Ames Res Center, M-S 202A-2, Moffett Field CA 94035)*, MM Rai *(Fluid Dyn Div, NASA Ames Res Center, M-S 258-1, Moffett Field CA 94035)*, S Gavali *(Supercomput Group, Fujitsu Am, 3055 Orchard Dr, San Jose CA 95134).* J Propulsion Power 9(3) 389-396 (May-Jun 1993).

This article deals with the development and validation of a 3D multipasage, Navier-Stokes code for predicting the unsteady effects due to rotor-stator interaction in turbomachines. Prior work in 2D has demonstrated the necessity of including multiple rotor and stator passages in order to closely approximate the stator-to-rotor airfoil count ratio, and thus accurately predict the unsteady flowfield resulting from rotor-stator interaction. In this article, this multipassage capability is extended to 3D. Numerical results obtained from a multipassage calculation of an axial turbine stage are presented. The stator-to-rotor airfoil count ratio (3:4) used in the present calculations is a close approximation to that in the actual turbine configuration (22:28). The numerical results are compared with experimental data wherever possible and to earlier single-passage calculations. The present multipassage approach results in a more accurate computation of the unsteady flowfield than that possible from a single passage approach.

9A669. Results from a set of low speed blade-vortex interaction experiments. - MB Horner, E Saliveros, A Kokkalis, RA McD Galbraith *(Dept of Aerospace Eng, Univ of Glasgow, Glasgow G12 8QQ, UK).* Exp Fluids 14(5) 341-352 (Apr 1993).

The results of a Blade-Vortex Interaction (BVI) experiment are presented. The experiments were the second series to be carried out at Glasgow Univ (see Kokkalis and Galbraith 1986, 1987), and reflect improvement to the facility. These improvements have resulted in sufficient resolution to observe clear evidence of vortex passage and propagative disturbances caused by the BVI. Additionally the quality of the pressure data permitted a meaningful assessment of force and moment coefficients, and a clear correspondence between their detailed time histories was observed. The data obtained are also compared with the results of previous studies, and qualitative and quantitative similarities are discussed.

9A670. Efficient hybrid scheme for the analysis of counter-rotating propellers. - R Srivastava *(NASA Lewis Res Center, Cleveland OH 44135)* and LN Sankar *(Sch Aerospace Eng, Georgia Tech).* J Propulsion Power 9(3) 382-388 (May-Jun 1993).

An efficient solution procedure has been developed for analyzing inviscid unsteady flow past counter-rotation propellers. This scheme is first-order accurate in time and second-order accurate in space. The spatial accuracy can be extended to fourth-order in the axial direction. The solution procedure has been applied to a two-bladed SR-7 single-rotor propeller and to a GE F7-A7 counter-rotating propeller. The pressure coefficients and the global quantities, power, and thrust, show good correlation with experimental measurements.

9A671. Using a full potential solver for propulsion system exhaust simulation. - RG Melvin *(Appl Math and Stat, Boeing Comput Services, MS 7H-96 PO Box 3707, Seattle WA 98124)*, FT Johnson *(Aerodyn Res, Boeing Commercial Airplane Group, MS 7H-96 PO Box 3707, Seattle WA 98124)*, DP Young *(Appl Math and Stat, Boeing Comput Services, MS 7H-96 PO Box 3707, Seattle WA 98124)*, DW Foutch *(Propulsion Res, Boeing Commercial Airplane Group, MS 7H-96 PO Box 3707, Seattle WA 98124)*, JE Bussoletti *(Aerodyn Res, Boeing Commercial Airplane Group, MS 7H-96 PO Box 3707, Seattle WA 98124)*, MB Bieterman *(Appl Math and Stat, Boeing Comput Services, MS 7H-96 PO Box 3707, Seattle WA 98124).* J Propulsion Power 9(3) 412-421 (May-Jun 1993).

The need for accurate simulations of engine installations on modern commercial transport aircraft has led to consideration of several formulations capable of modeling engine exhausts. Since such exhausts often interact with wings, struts, and nacelles, a complex geometry computational fluid dynamics (CFD) capability is desirable. Engine exhausts often contain nonlinear effects such as weak shock waves. There are very few

CFD codes that can model these effects for complex geometries in a timely way. However, a full potential formulation has been implemented in the general geometry code TRANAIR. This model incorporates certain assumptions, the main one being that the flowfield can be divided into a finite number of regions in each of which the total pressure and total temperature are constant. The purposes of this article are to state the theoretical assumptions made by the full potential and Euler models and to validate the methods on an axisymmetric test case. In the situations considered (typical of modern turbofan engines) the full potential and Euler results agree very well.

See also the following:

9A632. Inlet turbulence distortion and viscous flow development in a controlled diffusion compressor cascade at very high incidence

382. Lubrication

9A672. Numerical solution of heavily loaded elastohydrodynamic contact. - EL Airapetov, II Kudish, MY Panovko *(AA Blagonravov Inst of Machines Sci, Russian Acad of Sci, Moscow, Russia)*. Sov J Friction Wear 13(6) 1-7 (1992).

A numerical method is presented for analysis of isothermal elastohydrodynamic (EHD) problem at heavy loads. The method is based on quasi-linearization of the equation system for EHD contact. Numerical scheme makes it possible to determine a lubricant film thickness, exit location and pressure distribution, as well as to regularize the solution procedure, and to provide for the constancy of lubricant flow through the clearance. A numerical solution for isothermal heavily loaded EHD line contact with Newtonian lubricant was performed by using the method. The pressure distribution, lubricant film thickness, slip and roll tractions on the contact were obtained. A comparison shows that the Grubin formula underestimates significantly the film thickness under high load. The method permits to solve the problem for conditions of light and moderate loading.

9A673. Lubrication of a cylindrical synovial joint considering rolling motion and elastic incompressible cartilage. - M Hlavacek and D Vokoun *(Inst of Theor and Appl Mech, Czechoslovak Acad of Sci, Vysehradska 49, 12849 Prague 2, Czech Republic)*. Wear 165(1) 1-7 (May 1993).

In the analysis of lubrication of rolling cylinders with low modulus coatings, attention is drawn to elastic incompressible layers. The constrained column model (a simplified model where layer compression is assumed proportional to fluid pressure) fails for the Poisson ratio v of the layers close to 0.5. An approximate lubrication model is proposed for v = 0.5 and highly deformed coatings, ie for the low ratio of elastic layer thickness to fluid film length. This model does not result in a rigid differential equation for high loading as is the case with the constrained column model. The model is applied to the rolling motion of the human ankle joint.

9A674. Development of fracture resistant, multilayer films for precision ball bearings. - GB Hopple *(Lockheed Missiles and Space, PO Box 3504, Sunnyvale CA 94089-3504)*, JE Keem *(Ovonics Synthetic Mat, 1788 Northwood Dr, Troy MI 48084)*, SH Loewenthal *(Lockheed Missiles and Space, O/77-30 B/551, PO Box 3504, Sunnyvale CA 94089-3504)*. Wear 162-164(PART B) 919-924 (13 Apr 1993).

High density, sputtered MoS_2 films are being investigated as lubricants for the next generation of spacecraft bearings. Low bearing torque signatures and long life are the primary requirements of these films. Although multilayer (alternating MoS_2 with metal interlayers) films have exhibited relatively low wear rates (long lives) during laboratory testing using pin on disc-type testers, similar results have not been duplicated in actual precision ball bearings. Moreover, examination of bearing ball wear tracks on a race indicates little film remains intact even after relatively short period of bearing testing. The reason for this early loss of film appears to be associated with substrate surface roughness. Although these films worked well when used with a polished substrate, the high hardness and poor fracture toughness typical of these wear resistant films resulted in film delamination when applied to ground bearing race surfaces. In order to develop films that resist fracture associated with film ductility and substrate roughness, a specialized test that involved cycling a ball on a flat substrate was developed. Using this test combined with a scanning electron microscopy examination, dramatic differences in film fracture and delamination were observed between lapped and ground surfaces. Moreover, film fracture and delamination could be virtually eliminated on the ground surface by increasing the thickness of the metal layer in the film.

9A675. Mechanistic study of the synergism between Sb_2O_3 and MoS_2 lubricant systems using Raman spectroscopy. - JS Zabinski, MS Donley *(WL/MLBT, Mat Directorate, Wright Lab, WPAFB)*, NT McDevitt *(RAMSPEC Res, 4399 East Mohave Dr, Dayton OH 45431)*. Wear 165(1) 103-108 (May 1993).

A number of materials have been added to MoS_2 to improve its lubricating properties. However, the mechanism underlying this improvement is not fully understood. Perhaps the most widely used and studied additive is Sb_2O_3. While not a lubricant itself, it acts synergistically with MoS_2 to improve friction and wear properties. This paper is directed towards developing a better fundamental understanding of the synergism between Sb_2O_3 and MoS_2 in adhesively bonded films. A commercial preparation was used to form the films and laser Raman spectroscopy was used to analyze them before and after rubbing. It is shown that films layer as a result of tribostress – MoS_2 preferentially coats film surfaces and Sb_2O_3 becomes enriched in the next deeper layer. The mechanism proposed to explain the synergistic behavior is that only the thin layer of MoS_2 residing on top is exposed to degradation from the environment. The Sb_2O_3 layer acts as thermal and oxygen diffusion barrier to retard oxidation deeper into the film. Sb_2O_3 also acts as a beneficial support for MoS_2 as was demonstrated earlier by Centers (*Tribol Trans*, 31/32 (1987)149). The proposed mechanism suggests that protection is provided against tribo-oxidation but not necessarily thermal oxidation. To validate this concept, wear oxidation is evaluated in situ using a Raman tribotester and the results are compared with thermal oxidation data. Films containing Sb_2O_3 are indeed more resistant to tribo-oxidation than MoS_2 films. It is also shown that the transfer film surface is enriched with MoS_2. This indicates that friction is primarily governed by MoS_2 rubbing against MoS_2 and that Sb_2O_3 plays a secondary role.

9A676. Micromechanics of MoS_2 lubrication. - Chao Gao, L Bredell, D Kuhlmann-Wilsdorf, DD Makel *(Dept of Mat Sci, Univ of Virginia, Charlottesville VA 22901)*. Wear 162-164(PART A) 480-491 (13 Apr 1993).

The micromechanical behavior of MoS_2 acting as a solid lubricant and the effects of humidity thereon have been studied in moist nitrogen through simultaneous measurements of momentary friction and electrical contact resistance in the so-called hoop apparatus. The sliding couple consisted of the gold-plated copper substrate (the circumferential track inside the hoop) lubricated with a burnished MoS_2 film, and a slider in the form of three bundles of 50 μm thick gold-plated copper fibers. This geometry permits indirect detailed studies of the film conditions at the contact spots, since both the friction and the contact resistance are exclusively determined by the film. All measurements were found to be reversible, with the friction coefficient and contact resistance depending in a somewhat complex manner on average sliding speed between 0.05 and 3.0 cm s^{-1}, load between 0.5 N and 8 N, and relative humidity between 20% and 90%. The data indicate that adsorbed moisture causes the MoS_2 film to mechanically soften and that the film is partly pushed ahead to the sides of moving contact spots. As a result, the film thickness between the contact spots, presumably with the basal plane preferentially parallel to the interface, decreases with humidity but increases slightly with sliding speed and contact spot size, ie, load. Accordingly, the major part of the coefficient friction, namely $\mu_o \approx 0.1$ through distributed shearing of the MoS_2 film parallel to the basal plane, is little affected by any of the variables, but the contribution due to film plowing rises with increasing humidity from zero up to $\mu_P \approx 0.1$. The contact resistance, by contrast, varies through almost two orders of magnitude. It increases much faster than proportional with the film thickness at the a-spots, due to a strong increase of the MoS_2 resistivity with film thickness, on account of a semiconductor effect.

9A677. Wear reduction systems for coal-fueled diesel engines II. Experimental results and hydrodynamic model of powder lubrication. - Hooshang Heshmat *(Mech Tech, 968 Albany-Shaker Rd, Latham NY 12110)*. Wear 162-164(PART A) 518-528 (13 Apr 1993).

This paper is the second part of an investigation of the mechanism and performance of powder lubrication. In the first part of the investigation, the basic features of the quasi-hydrodynamic nature of particulate lubricants were conceptualized and the experimental setup for testing was described. In the tests described herein, load capacity, friction levels, and, most importantly, rates of wear were recorded for a wide range of operating conditions and various surface geometries, materials, and powder lubricants. The test results demonstrate the viability of powder lubrication. The results also corroborate the postulated quasi-hydrodynamic nature of particulate films. In addition, features specific to powder lubrication were brought to light, such as the onset of starvation with time, and the phenomenon of film adhesion. Based on these findings, design requirements for the proper functioning of practical powder-lubricated systems are described. Finally, a hydrodynamic model consisting of a mating surface, intermediate films, and a particulate lubrication film is presented. With these tools developed, analytical or semi-empirical relations should become available for the design of full-scale powder-lubricated tribosystems.

9A678. Ferrofluid lubrication of cylindrical rollers with cavitation. - P Sinha, P Chandra *(Dept of Math, Indian IT, Kanpur 208 106, India)*, D Kumar *(Dept of Math, Narmada Col of Sci and Tech, Bharuch, Gujrat, India)*. Acta Mech 98(1-4) 27-38 (1993).

This paper analyzes the ferrofluid lubrication of cylindrical rolls under combined rolling and normal motion. The analysis, which takes into account the rotation of magnetic particles, has been made for general cases where the magnetization vectors need not be parallel to the applied magnetic field. A perturbation scheme in terms of non-dimensional Brownian time relaxation parameter has been used and the effects of various parameters on bearing characteristics have been studied.

See also the following:

9A525. Wear reduction systems for coal-fueled diesel engines I. The basics of powder lubrication

9A534. Friction and wear of heterogeneous coating under boundary lubrication Part 2. Sliding parts with hard coatings

384. Flow measurements and visualization

9A679. **Experimental approach to the calibration and use of triple hot-wire-probes.** - TJ Gieseke and YG Guezennec *(Dept of Mech Eng, Ohio State Univ, Columbus OH 43210).* Exp Fluids 14(5) 305-315 (Apr 1993).

A method of calibrating and extracting velocities from arbitrary geometry triple hot-wire probes has been developed and tested. The three-step procedure involves experimental determination of an accurate cooling law for each wire in the array, use of these models to develop a set of tables relating anemometer output to flow velocity input, and a table look-up procedure to extract the velocities. The functional form for the cooling law can be arbitrarily chosen and these equations are never directly inverted. Solutions are tabulated making use of special variable transformations that separate the dependence on flow angle and velocity magnitude. Errors in the table look-up procedure are commensurate with those in exact inversion techniques. Most of the error arises from accurate determination of the cooling laws. An application to turbulent boundary layer measurements is presented as an example of the use of the method.

9A680. **Development and application of a fast-response DC-coupled flame ionization current sensor.** - Z Hu, JR Laker, E Mastorakos, C Vafidis, HM Xu *(Dept of Mech Eng, Thermofluids Section, Imperial Col of Sci Tech and Med, Exhibition Rd, London SW7 2BX, UK).* Exp Fluids 14(5) 316-320 (Apr 1993).

The principles of the design of a fast-response DC-coupled ionization probe and associated electronic circuit are described for the measurement of the mean and fluctuating components of the ion concentration in the reaction zones of stationary and transient flames. The performance of the ionization probe is evaluated by bench tests and with measurements of ion current mean and fluctuating levels in laminar and turbulent premixed flames and in the combustion chamber of a spark ignition engine. The results demonstrate the wide frequency bandwidth, good spatial resolution and electronic noise immunity of the ionization probe, making it suitable for a host of combustion applications.

9A681. **Backscatter phase-Doppler anemometry for transparent non-absorbing spheres.** - Y Hardalupas and CH Liu *(Thermofluids Section, Mech Eng Dept, Imperial Col of Sci Tech and Med, London SW7 2BX, UK).* Exp Fluids 14(5) 379-390 (Apr 1993).

The application of phase-Doppler anemometer for scattering angles between the main rainbow and direct backscatter, was examined by calculating the spatial intensity distribution and the phase of the light scattered by a particle crossing the measuring volume. Geometrical optics was assumed and contributions to the scattered light due to reflection on the external surface of the particle and first internal reflection were considered. The response curve of the technique was calculated for different particle refractive indices, beam intersection angles, collection angles and spacings between the collection apertures. Linear response curves were obtained after integration of the intensity of the scattered light over sufficiently large rectangular collection apertures, but they become non-monotonic after a critical value of phase shift, which varied with the optical arrangement between around 220° and 360°, did not scale with common scaling parameters used for forward scatter light, and limited the possible size range of the instrument for one optical arrangement. The particle refractive index determined the collection angle and limited sizing to particles with little uncertainty in refractive index, since 5% change in refractive index led to uncertainties in size of the order of 100%. An alternative sizing technique is suggested for the backscatter region.

VI. HEAT TRANSFER

400. Thermodynamics

9A682. **Analysis of regenerative gas-turbine cycles.** - VY Tikhoplav, II Kirillov, TS Tikhoplav *(Energomash TurboMachinery Works, Leningrad).* Heat Transfer Res 24(3) 424-432 (Apr 1992).

The results of an analysis designed to define the optimum cycle of a gas turbine with regeneration are presented. The independent variables that define the dof of the various thermodynamic cycles are identified. The theoretical possibilities for optimizing the cycle parameters and layouts of gas turbines are defined. It is shown that the gas-turbine efficiency can be greatly improved over a wide range of pressure gains in the compressor.

9A683. **Availability accumulation and destruction in a DI diesel engine with special reference to the limited cooled case.** - CD Rakopoulos, EC Andritsakis *(Thermal Eng Section, Mech Eng Dept, Natl Tech Univ, 42 Patission St, Athens 10682, Greece),* DK Kyritsis *(Princeton).* Heat Recovery Syst CHP 13(3) 261-276 (May 1993).

This work develops a method for the calculation of both the irreversibility produced during combustion and the work medium availability at the end of the expansion process in a high speed, direct injection (DI), naturally aspirated, four-stroke diesel engine, on which experiments were conducted at the author's laboratory. The experimental data were processed for the determination of fuel reaction rates; the combustion irreversibility production rate was then computed from the fuel reaction rates via an analytical mathematical expression which was developed by the present research groups, based on the combined resolution of the first and second laws of thermodynamics. These calculations are applied for a wide range of measured loads, injection timings and engine rotational speeds; they are also expanded in the direction of intensity of the rate of heat transfer loss (to the engine cooling medium) for every combination of the experimentally determined engine variables. Therefore, apart from investigating the effect of various operating parameters on the availability balance, it is possible to evaluate the effect of the engine heat transfer reduction (limited cooled engine), from the second law analysis point of view, on the potential for efficiency improvements made by using the increased exhaust in heat recovery devices (eg, the exhaust turbine or Rankine bottoming cycle compounding).

9A684. **Derived thermodynamic design data for refrigeration and heat pump systems operating on HCFC-123.** - S Devotta and S Gopichand *(Chem Eng Div, Natl Chem Lab, Pune 411 008, India).* Heat Recovery Syst CHP 13(3) 213-218 (May 1993).

The current status of HCFC-123 as the alternative to CFC-11 in air-conditioning refrigeration and heat pump systems is reviewed. The theoretical Rankine coefficient of performance (COP) and the present ratios have been presented for heat pumps operating on HCFC-123. Composite plots between pressure ratio, theoretical Rankine coefficient for performance and (T_{CO} - T_{EW}) for the appropriate temperature ranges of T_{EV} and T_{CO} are presented for HCFC-123 for refrigeration and heat pump systems, respectively.

9T685. **Power and refrigeration plants for minimum heat exchanger inventory.** - A Bejan *(Dept of Mech Eng and Mat Sci, Duke Univ, Durham NC 27706).* J Energy Resources Tech 115(2) 148 (Jun 1993).

9A686. **Sliding pressure analysis using the second law.** - GE Weber *(Fossil Tech Services, Commonwealth Edison, 125 S Clark St, Rm 227, Chicago IL 60603)* and WM Worek *(Dept of Mech Eng MC 251, Univ of Illinois, PO Box 4348, Chicago IL 60680).* Heat Recovery Syst CHP 13(3) 253-260 (May 1993).

Over the last 20 years many technical papers have been written by manufacturers on the concept of reducing or sliding the turbine inlet pressure at lower loads to reduce frictional losses. This paper takes a unique look at why sliding pressure is needed using both the first and second laws of thermodynamics. The derived equations are applied to the flow of steam across a single valve and then applied to a simplified turbine control valve system. The optimal control point at which to initiate sliding pressure is analyzed. It is also shown that the optimal operating point is not when the second-law efficiency is maximum, but when the first-law efficiency is maximized.

9A687. **Thermodynamic properties of molecular hydrogen plasma in thermal and chemical nonequilibrium.** - Kuan Chen *(Dept of Mech Eng, Univ of Utah, Salt Lake City UT 84112)* and TL Eddy *(Natl Eng Lab, EG&G Idaho, Idaho Falls ID 83415).* J Thermophys Heat Transfer 7(2) 277-284 (Apr-Jun 1993).

A nonequilibrium plasma model is developed for computing the thermodynamic properties of partially ionized molecular hydrogen in both non-local thermal equilibrium (non-LThE) and non-local chemical equilibrium (non-LChE). The model uses multitemperatures for thermal non-equilibrium. Nonzero chemical affinities are used as a measure of the deviation from chemical equilibrium. It is found that a positive affinity of the recombination reaction or a decrease in plasma pressure will cause ionization to occur at lower temperatures, resulting in higher plasma enthalpy, internal energy, and entropy. Increase of the temperature of a particular energy mode also increases the total energy and entropy of the plasma, but the translational temperature play a dominant role in the temperature range considered.

See also the following:

9A776. Engineering assessment to the relaxation time in thermal wave propagation

9A951. Optimal coupling and feasibility of a solar-powered year-round ejector air conditioner

402. One phase convection

402B. FORCED CONVECTION (EXTERNAL)

9A688. Conjugate problem of unsteady heat transfer in laminar flow over a plate, assuming temperature-dependent physical properties of the fluid. - YI Shvets, OI Didenko, OD Lipovetskaya *(Eng Thermophys Inst, Ukrainian Acad of Sci, Kiev)*. Heat Transfer Res 24(4) 433-439 (Apr 1992).

An iterationless method for the numerical solution of the unsteady conjugate problem of heat transfer with correction for the temperature dependence of thermophysical properties of the fluid is presented. Transfer of heat in both the flow and in the body is described by a single generalized equation, whose numerical analog was obtained by the control-volume technique. It is shown that the effect of variability of the properties is significant. It depends on the type of fluid and on the ratio of the thermal conductivities of the fluid and the body.

9A689. Coupling of conduction and forced convection past an impulsively started infinite flat plate. - A Pozzi, E Bassano *(Fac Ing, Inst Gasdin, Univ Naples, Italy)*, L de Socio *(Dipartimento di Mec ed Aeronaut, Univ of Rome, Italy)*. Int J Heat Mass Transfer 36(7) 1799-1806 (May 1993).

In this paper the unsteady coupling of conduction and convection for a thin body in a high speed stream is considered. The body is modeled as a strip on one side of which the fluid is impulsively started in motion whereas on the other side two different thermal boundary conditions are given: constant temperature or vanishing heat flux. In the first part of the analysis an approximate solution of the energy equation in the solid enables us to obtain relations between the temperature and the heat flux at solid-fluid interface which are more accurate than those currently used in the literature. In the second part the exact solution of the two problems that arise from the coupling of the thermofluid-dynamic equations and the relations between the temperature and its derivatives at the interface are presented.

9A690. Heat transfer and flow past a backstep with the nonlinear k-ε turbulence model and the modified k-ε turbulence model. - S Dutta and S Acharya *(Dept of Mech Eng, Louisiana State Univ, Baton Rouge LA 70803)*. Numer Heat Transfer A 23(3) 281-301 (Apr-May 1993).

This paper presents a comparative study of the standard k - ε model, the nonlinear k - ε model, and the modified k - ε model utilizing the double-pass procedure. The three models are used to predict the flow and heat transfer past a backstep, and the predictions are compared with selected experimental data. The comparison indicates that the modified and nonlinear k - ε models agree better with measurements than the standard k - ε model predictions.

9A691. Heat transfer in a turbulent boundary layer disturbed by means of a manipulator for breaking up large eddies. - Kyoji Inaoka, Kenjiro Suzuki, Hiroshi Suzuki, Hiroshi Kigawa *(Dept of Mech Eng, Kyoto Univ, Kyoto 606, Japan)*. Heat Transfer Japan Res 21(7) 705-720 (1992).

An experimental study was performed on a turbulent boundary layer disturbed by insertion of a single large eddy breakup manipulator. The skin-friction coefficient, heat-transfer coefficient, and averaged and fluctuating components of streamwise and cross-stream velocities were measured. A quadrant analysis was applied to the measured fluctuating velocity signals. The dissimilarity between the momentum transfer and heat transfer in this boundary layer is discussed in comparison with that found previously in a turbulent boundary layer disturbed by a cylinder.

9A692. Heat-transfer augmentation in a turbulent boundary layer disturbed by means of a vortex generator. - Kyoji Inaoka, Kenjiro Suzuki, Yoshimichi Hagiwara, Kazuyuki Suzuki *(Dept of Mech Eng, Kyoto Univ, Kyoto, 606, Japan)*, Hiroshi Suzuki *(Dept of Mech Eng, Hiroshima Univ, Japan)*. Heat Transfer Japan Res 21(7) 721-735 (1992).

An experimental study was conducted to determine if the deterioration in heat transfer caused by an insertion of a large eddy breakup manipulator (LEBU plate) could be recovered by attaching a half-delta-wing type vortex generator to the LEBU plate. The vortex generator was found to work well to augment the wall heat transfer over a large streamwise distance, although the LEBU plate itself is expected to eliminate the large-scale eddy motion in the boundary layer. Some geometric parameters of the inserted LEBU plate with the vortex generator attached were varied in several steps.

402C. FORCED CONVECTION (INTERNAL)

9A693. Analytical-numerical prediction of the 3D temperature variation in tubes having streamwise internal fins. - A Campo *(Col of Eng, Idaho State Univ, Pocatello ID 83209)* and JC Morales *(Dept of Mech Eng, Univ of Texas, Austin TX 78712)*. Numer Heat Transfer A 23(3) 319-339 (Apr-May 1993).

An analytical-numerical analysis is made of the hydrodynamic and heat transfer characteristics of a fluid flow through internal, longitudinal finned tubes. Employing control volume discretization in the cross section of the tube only, the 2D momentum equation is solved numerically, whereas the 3D energy equation is solved analytically. The pressure gradients are numerically determined, and the heat transfer rates, in terms of the tube length, are expressed in analytical form. The computational results are presented for different configurations corresponding to selected combinations of relative fin heights and the number of equally spaced fins in the array.

9A694. Developing laminar flow and heat transfer in a square duct with one-walled injection and suction. - GJ Hwang, YC Cheng *(Dept of Power Mech Eng, Natl Tsing Hua Univ, Hsinchu 300, Taiwan, ROC)*, ML Ng *(Energy and Resources Lab, Indust Tech Res Inst, Hsinchu 310, Taiwan, ROC)*. Int J Heat Mass Transfer 36(9) 2429-2440 (Jun 1993).

A numerical study was made to investigate the forced laminar convection in the entrance region of a square duct with one wall subjected to uniform mass transpiration and constant heat flux. Using the concept of pressure deviation and the vorticity-velocity method, the 3D Navier-Stokes equations and the governing energy equations were solved simultaneously. Results show that flow reversal occurs in the flow with strong suction. Typical velocity, pressure and temperature distributions along the flow direction are reported.

9A695. Effects of longitudinal vortex generators on heat transfer and flow loss in turbulent channel flows. - JX Zhu, NK Mitra, M Fiebig *(Inst Thermo- und Fluiddyn, Ruhr-Univ, D-4630 Bochum 1, Germany)*. Int J Heat Mass Transfer 36(9) 2339-2347 (Jun 1993).

The influences of four types of longitudinal vortex generators (delta wing, rectangular wing, delta wing pair and rectangular winglet pair) on heat transfer and flow loss in turbulent channel flows are investigated in the present work. A numerical solver of the Navier-Stokes equations, based on the MAC algorithm, has been extended with the k - ε turbulence model for this study. The results show that the longitudinal vortices produced by the vortex generators elevate significantly the level of turbulence kinetic energy in the flow and strongly disturb the thermal boundary layer.

9A696. Experimental investigations of heat transfer enhancement and flow losses in a channel with double rows of longitudinal vortex generators. - St Tiggelbeck, NK Mitra, M Fiebig *(Inst Thermo- und Fluiddyn, Ruhr-Univ, D-4630 Bochum, Germany)*. Int J Heat Mass Transfer 36(9) 2327-2337 (Jun 1993).

Flow structure, heat transfer, and drag by longitudinal vortices generated by double rows of delta wings in transient channel flow are investigated for the reduction of the gas side heat transfer resistance of compact heat exchangers. The experiments consist of flow visualization by laser light sheets, liquid crystal thermography for local heat transfer and balance measurements for drag. Angle of attack and channel Reynolds number have been varied. Aligned delta winglet double rows show higher heat transfer enhancement than staggered. The critical angle of attack for the formation of longitudinal vortices is smaller behind the second row than behind the first.

9A697. Experimental study of laminar entrance flow and heat transfer in finned tub annuli. - Shou-Shing Hsieh and Chang-Chun Lin *(Dept of Mech Eng, Natl Sun Yat-Sen Univ, Kaohsiung 80424, Taiwan, ROC)*. Int J Heat Mass Transfer 36(9) 2457-2471 (Jun 1993).

In this study, experiments were conducted to investigate the entrance effect of a double-pipe heat exchanger with isoflux inner finned tube. The geometry of the test section varied in fin pitch to height (p/e) ratios from 4 to 12, in fin width to height ratios (w/e) of 0.14 and 0.83, and with two inner diameter to outer diameter ratios (D_i/D_0) of 0.38 - 0.51. Reynolds number (Re) of the flow were 100 - 3000. Results are presented for a range of Reynolds number and for various values of the geometrical parameters. The experimental data were extracted and correlated in the form of Graetz number (Gz) to provide a thermal design basis for engineering application.

9A698. Heat and mass transfer analysis of developing turbulent flow in a square duct. - Hitoshi Sugiyama, Mitsunobu Akiyama *(Dept of Mech Syst Eng, Utsunomiya Univ, Japan)*, Katsuhiro Shibata *(Fuji Heavy Indust, Japan)*. Heat Transfer Japan Res 21(6) 601-614 (Apr 1992).

A numerical analysis has been performed on 3D developing turbulent flow in a square duct using a modified Reynolds stress model and a transport equation for the turbulent flux. Special attention was paid to the relation between the model constants and the Reynolds stress distribution and the developing process of the secondary flow of the second kind. Moreover, using a turbulent heat flux model, the mean Nusselt number was precisely predicted.

9A699. Hot spot locations and temperature distributions in a forced convection photochemical reactor. - Falin Chen *(Inst of Appl Mech, Natl Taiwan Univ, Taipei 10764, Taiwan, ROC)* and AJ Pearlstein *(Dept of Mech and Indust Eng, Univ of Illinois, 1206 W Green St, Urbana IL 61801)*. Int J Heat Mass Transfer 36(8) 2105-2114 (May 1993).

We have computed steady axisymmetric temperature distributions in a tubular photoreactor in which fluid in laminar flow absorbs light from an azimuthally uniform, radially incident light source. In addition to the primary on-axis temperature maximum, a second hot spot forms of the centerline as the optical density γ increases.

This results from a shift of light absorption toward the wall, which is held at a fixed temperature (eg, by forced convection cooling on the outside). At still larger γ the centerline hot spot disappears, leading to a decrease in the maximum temperature and accompanied by an increase in the temperature near the wall. The reduction in maximum centerline temperature may be advantageous for product selectivity and yield in the central core of the reactor, but may be disadvantageous with respect to the formation of light-absorbing deposits on the interior of the tube wall.

9A700. Numerical and experimental study of the forced convection inside a rotating disk-cylinder configuration. - X Ruiz, M Aguilo, J Massons, F Diaz *(Labs Fisica Aplicada Cristallografia Dept Quimica, Univ de Barcelona, 43005 Tarragona, Spain)*. Exp Fluids 14(5) 333-340 (Apr 1993).

In this paper, axisymmetric bulk flow patterns generated by moderate disk rotation and counter-rotation inside a coaxial disk-cylinder configuration with a fixed aspect ratio are obtained both experimentally and numerically. Experimental results are based on chronophotographic visualization and image processing techniques, while numerical results are computed using the full stationary Navier-Stokes equations assuming two different dynamic boundary conditions (no-slip and meridional free-slip) for all rigid walls. A comparative analysis between both numerical distributing and the patterns obtained experimentally is carried out in terms of streamfunction and vorticity meridional distributions.

9A701. Periodically developed flow and heat transfer in a ribbed duct. - S Acharya, S Dutta, TA Myrum, RS Baker *(Dept of Mech Eng, Louisiana State Univ, Baton Rouge LA 70803)*. Int J Heat Mass Transfer 36(8) 2069-2082 (May 1993).

Periodic fully developed flow and heat transfer results from a ribbed cut were obtained experimentally and numerically, using the nonlinear and standard k - ε turbulence model. Predicted recirculation lengths and maximum Nusselt number locations agreed well with the measured values. Both models performed poorly in the separated region just behind the ribs, where the Reynolds stresses were grossly underpredicted, the flow temperatures were overpredicted, and the mean velocity magnitudes were generally underpredicted. The local Nussel numbers were underpredicted by both models.

9A702. Transient conjugated forced convection heat transfer with fully developed laminar flow in pipes. - Kuan-Tzong Lee *(Dept of Mech Eng, Oriental IT, Pan-Chiao, Taipei 22064, Taiwan, ROC)* and Wei-Mon Yan *(Dept of Mech Eng, Hua Fan IT, Shih-Ting, Taipei 22305, Taiwan, ROC)*. Numer Heat Transfer A 23(3) 341-359 (Apr-May 1993).

This work deals with the problem of transient conjugated forced convection heat transfer with fully developed laminar flow in an infinitely long pipe, in which the external surface over a finite length of pipe is subject to a constant wall temperature. The effects are presented of Peclet number, ratios of pipe radii, wall-to-fluid diffusivity, and conductivity on the interfacial heat flux. The predicted results show that the unsteady heat transfer characteristics depend strongly on the ratios of outside and inside radii, wall-to-fluid conductivity, and thermal diffusivity.

402D. NATURAL CONVECTION (EXTERNAL)

9A703. Leading edge effect during transient buoyancy induced flow adjacent to a vertical cylinder. - K Velusamy *(Thermal Hydraul Section, Indira Gandhi Centre for Atomic Res, Kalpakkam 603 102, India)* and VK Garg *(NASA Lewis Res Center, MS 5-11, Cleveland OH 44135)*. Int J Heat Mass Transfer 36(7) 1853-1858 (May 1993).

The rate of propagation of the leading edge effect (LEE) during transient natural convection adjacent to a vertical solid cylinder is estimated from five differnt criteria. The cylinder has an appreciable thermal capacity and is subjected to a sudden heat generation. Numerical results are presented for a wide range of cylinder radii and heat flux values for two fluids, air and water. It is found that unlike the case of a flat plate, there is no unique criterion which would always estimate the fastest rate of propagation of LEE in water. Present results obtained by dropping the curvature terms in the governing equations match very well with previous analytical results for a flat plate.

9A704. Localized solutions of an equation governing Benard-Marangoni convection. - CI Christov *(Inst Nacional Meteorolgia, Ciudad Univ, Madrid, Spain)* and MG Velarde *(Fac Ciencias, Univ Nacional Educacion Distancia, Madrid, Spain)*. Appl Math Model 17(6) 311-320 (Jun 1993).

Provided here is numerical evidence of localized solutions, solitary waves, in a model equation for Benard convection driven by interfacial stresses (Marangoni effect).

402E. NATURAL CONVECTION (ENCLOSURES)

9A705. Analytical solution for transient laminar fully developed free convection in vertical concentric annuli. - MA Al-Nimr *(Dept of Mech Eng, Jordan Univ of Sci and Tech, Irbid, Jordan)*. Int J Heat Mass Transfer 36(9) 2385-2395 (Jun 1993).

Analytical solutions for transient fully developed natural convection in open-ended vertical concentric annuli are presented. Four fundamental boundary conditions have been investigated and the corresponding fundamental solutions are obtained. These four fundamental boundary conditions are obtained by combining each of the two conditions of having one boundary maintained at uniform heat flux or at uniform wall temperature with each of the conditions that the opposite boundary is kept isothermal at the inlet temperature or adiabatic. An expression for the transient Nusselt numbers is given for each case.

9A706. FE analysis of natural convection in horizontal concentric annuli. - Yasumasa Kato *(Res Lab of Asahi Glass Co Ltd, 1150 Matsubarg, Hazawa, Kanagawa-Ku, Yokohama 221, Japan)*, Takahiko Tanahashi *(Dept of Mech Eng, Keio Univ, Japan)*, Katsuya Ota *(Kajima Tech Res Inst, Japan)*. Heat Transfer Japan Res 21(7) 693-704 (1992).

In this paper, a simple FEM scheme is presented which simulates natural convection of incompressible viscous flow. The Navier-Stokes equations in rotational form with a buoyancy effect is simplified by the Boussinesq approximation. The main algorithm of the GSMAC method is employed to obtain time-dependent solutions. Natural convection in concentric horizontal annuli is investigated for various Rayleigh numbers in order to validate the present method. The temperature distributions obtained here are in good agreement with the experimental results.

9A707. Investigation of the temporal thermal performance of the wheel outboard of an aircraft. - CP Desai and K Vafai *(Dept of Mech Eng, Ohio State Univ, Columbus OH 43210)*. J Thermophys Heat Transfer 7(2) 377-384 (Apr-Jun 1993).

Three-dimensional transient natural convection flow and heat transfer around the wheel outboard portion of an aircraft brake housing was investigated. The wheel outboard is modeled as an annular cavity with one end open to the ambient surroundings. The temporal development of the flow and temperature fields and its effect on the thermal performance of the brake housing outboard is discussed. The transient results are presented here by means of the velocity and temperature fields and the average Nusselt numbers over the different surfaces of the geometry.

9A708. Natural convection heat transfer in a 3D duct. - A Moutsoglou and MR Park *(Dept of Mech Eng, S Dakota State Univ, Brookings SD 57007)*. J Thermophys Heat Transfer 7(2) 369-376 (Apr-Jun 1993).

A computational analysis is conducted to investigate the 3D heat transfer and flow characteristics of laminar natural convection in a vertical duct, open to the ambient at the top and bottom and enclosed on all four sides. Detailed data are presented for air (Pr = 0.7) in a square duct heated-cooled isothermally or uniformly on one side with the remaining three walls assumed adiabatic. Numerical data are also obtained and presented for comparisons by way of a 2D channel flow approximation. The channel flow model that neglects the slowing down of the streamwise velocities due to the friction of the lateral walls predicts considerably higher local and average Nusselt numbers than the 3D analysis for a square duct. The numerical data are in good agreement with the experimental data of Elenbaas, Wirtz and Stutzman, and Sobel *et al*, but significantly underpredict the experimental data of Sparrow and Bahrami.

9A709. Natural-convection heat transfer in inclined rectangular enclosure. - Teruo Kimura, Masanori Takeuchi *(Fac of Eng, Fukui Univ, Japan)*, Toshiharu Miyanaga *(Graduate Sch of Eng, Fukui Univ, Japan)*. Heat Transfer Japan Res 21(6) 615-630 (Apr 1992).

The effects of thermal conductivity of an inner body on heat-transfer phenomena in an inclined rectangular enclosure have been studied both numerically and experimentally. In the numerical analysis, the ratio of thermal conductivity of the inner body to that of the working fluid was varied parametrically. The flow and temperature fields are presented in detail and the heat-transfer coefficient is discussed from these results. It is clarified here that the inner body with a large thermal conductivity enhances the heat transfer of the enclosure at large inclinations but suppresses the heat transfer for small inclination angles of the enclosure.

9A710. Resonance of natural convection in an enclosure heated periodically from the side. - JL Lage *(Dept of Mech Eng, S Methodist Univ, Dallas TX 75275-0335)* and A Bejan *(Dept of Mech Eng and Mat Sci, Duke Univ, Box 90300, Durham NC 27708-0300)*. Int J Heat Mass Transfer 36(8) 2027 (May 1993).

This is a numerical and theoretical investigation of natural convection in a 2D square enclosure with one side cold and isothermal, and the other side heated with pulsating flux. It is shown numerically that the buoyancy induced circulation resonates to a certain (single) frequency of the pulsating heat input. The resonance is characterized by maximum fluctuations in the total heat transfer rate through the vertical midplane of the cavity. It is shown that the critical frequencies determined numerically can be anticipated based on theoretical grounds, by matching the period of the pulsating heat input to the period of the rotation (circulation) of the enclosed fluid.

9A711. Thermal buoyancy and Marangoni convection in a two fluid layered system. - N Ramachandran *(Univ Space Res Assoc, NASA Marshall Space Flight Center, Huntsville AL 35812)*. J Thermophys Heat Transfer 7(2) 352-360 (Apr-Jun 1993).

Thermal buoyancy and surface tension driven convection is numerically investigated in a system with two immiscible fluids. The geometry investigated has an open cavity configuration with the lighter fluid situated on top of the heavier fluid, forming a stable layered system. The upper fluid meniscus and the interface are assumed to be flat and undeformable in the calculations. The governing equations and boundary-interface conditions are solved by a control volume-based finite difference scheme for two pairs of immiscible fluids; the water-hexadecane system and a so-called generic system. The steady-state calculations predict dramatically different flows when interfacial tension effects are included or excluded from the system model. These differences are particularly appreciable in surface tension-dominated flows, that are typical of microgravity situations. Complex flow patterns, with induced secondary flows, are noticed in both the fluids.

9A712. **Transient cooling of petroleum by natural convection in cylindrical storage tanks I.** Development and testing of a numerical simulator. - MA Cotter *(Automotive Parts Manufs' Assoc, 195 W Mall, Suite 516, Toronto M9C 5K1, ON, Canada)* and ME Charles *(Dept of Chem Eng and Appl Chem, Univ of Toronto, Toronto M5S 1A4, ON, Canada)*. Int J Heat Mass Transfer 36(8) 2165-2174 (May 1993).

The transient natural convection of a warm crude oil contained in a large vertical cylindrical storage tank loaded in a cold environment is investigated. The governing mass, momentum and energy conservation equations, utilizing the Boussinesq approximation for density, are solved numerically in stream function-vorticity form by employing a control volume finite difference method. A temperature-dependent apparent viscosity is employed to model the change in non-Newtonian fluid rheology that occurs with cooling. Good agreement is found between experimental and simulated temperature vs time cooling profiles for discrete locations in the tank.

9A713. **Transient cooling of petroleum by natural convection in cylindrical storage tanks II.** Effect of heat transfer coefficient, aspect ratio and temperature-dependent viscosity. - MA Cotter *(Automotive Parts Manufs' Assoc, 195 W Mall, Suite 516, Toronto M9C 5K1, ON, Canada)* and ME Charles *(Dept of Chem Eng and Appl Chem, Univ of Toronto, Toronto M5S 1A4, ON, Canada)*. Int J Heat Mass Transfer 36(8) 2175-2182 (May 1993).

The transient natural convection of a warm crude oil contained in a large vertical cylindrical storage tank located in a cold environment is investigated numerically. The effect of the external heat transfer coefficient is examined by using four different values. Increasing this parameter is found to increase the rate of heat loss as expected, but only a minor effect on the resulting fluid flow is found. The effect of the tank aspect ratio (height to radius) on the natural convection process is investigated by using four different aspect ratios ranging from 0.25 to 2.0, and is found to affect the flow patterns that develop. The effect of the fluid viscosity is examined for a tank aspect ratio of 0.5 by using five different apparent viscosity-temperature relationships.

See also the following:

9A729. Unsteady laminar natural-convection heat transfer in an enclosure with fins

402F. THERMALLY UNSTABLE CONFIGURATIONS

9A714. **Buoyant-thermocapillary ... es in medium-Prandtl-number flui... to a horizontal temperature** ... Parmentier, VC Regnier, G L... *Liege Univ, B5 Sart-Tilm... Belgium)*. Int J Heat Mass Transfer 36(9) 2417-2427 (Jun 1993).

Coupled buoyant and thermocapillary instabilities in a fluid layer of infinite horizontal extent bounded below a rigid plane and above by a free flat surface and submitted to a temperature gradient are investigated. A general 3D mathematical formulation is used to determine the linearized perturbated equations of the steady state induced by the temperature gradient. Numerical results are obtained in the case of a horizontal temperature gradient, lower and upper surfaces are adiabatically isolated and the range of the Prandtl number is selected as $[10^{-2}, 10]$. The presence of travelling rolls is exhibited.

9A715. **Convective instability in saturated porous enclosures with a vertical insulating baffle.** - Falin Chen and CY Wang *(Inst of Appl Mech, Natl Taiwan Univ, Taipei 10764, Taiwan, ROC)*. Int J Heat Mass Transfer 36(7) 1897-1904 (May 1993).

The convective instability in 2D enclosures containing a fluid-saturated porous medium with an insulating baffle extending vertically from the bottom boundary is investigated. The baffle influences the stability through its height and its horizontal problem. It is found, in general, that a taller baffle does not necessarily result in a more stable state, the optimum height of the baffle changes as its position varies; a baffle located at the middle or at a position with $\lambda = \sqrt{(k(k+1))}$, $k = 1, 2, \dots$, where λ accounts for the normalized distance from the baffle to the left wall, corresponds to a relatively more stable state; while a baffle coincides with a dividing streamline has no influence on the stability.

9A716. **Finite-amplitude instability of mixed-convection in a heated vertical pipe.** - BB Rogers and LS Yao *(Dept of Mech and Aerospace Eng, Arizona State Univ, Tempe AZ 85287)*. Int J Heat Mass Transfer 36(9) 2305-2315 (Jun 1993).

The instability of flow in a heated vertical pipe is studied using weakly nonliner instability theory for both stably and unstably stratified cases. It is found that the dominant instability for stably stratified flow is a thermal-buoyant instability, while that of the unstably stratified case is a Rayleigh-Taylor instability. The results of the weakly nonlinear theory predicts supercritical instability for the stably stratified case, in agreement with experimental observations. In this case, it is found that a wide band of wave numbers are linearly unstable soon after the onset of the initial instability. The results of the weakly nonlinear calculations for unstably stratified flow indicate that the flow is potentially subcritically unstable, again in agreement with experimental observations. Analysis of energy transfer in the fundamental wave demonstrates that the thermal-buoyant instability is supercritical because increases in the viscous dissipation rate and the rate of transfer of energy from the fundamental wave back into the mean flow overcome the destabilizing effect of an increase in the rate of buoyant production.

9A717. **Stability of convective motion caused by inhomogeneous internal heat sources.** - AA Kolyshkin *(Dept of Appl Math, Riga Tech Univ, Riga 226010, Latvia)* and R Vaillancourt *(Dept of Math, Univ of Ottawa, Ottawa, ON, K1N 6N5, Canada)*. Arab J Sci Eng 17(4B) 655-662 (Oct 1992).

The stability of a convective fluid motion caused by inhomogeneous heat sources in a tall vertical annulus is investigated in this paper. Critical Grashof numbers are computed for different values of the ratio R of the internal to the external radii of the annulus, and Prandtl numbers for axisymmetric and asymmetric perturbations. Stability increases as the inhomogeneity of the heat sources increases. For strongly inhomogeneous heat sources, there is a transition from the axisymmetric to the asymmetric mode as the Prandtl number grows.

9A718. **Stability of plane Poiseuille flow with temperature dependent viscosity.** - P Schafer and H Herwig *(Inst Thermo- und Fluiddyn, Ruhr-Univ, 4630 Bochum, Germany)*. Int J Heat Mass Transfer 36(9) 2441-2448 (Jun 1993).

Classical linear stability theory is extended to include the effect of temperature dependent viscosity. This effect is studied asymptotically by using a Taylor series expansion of viscosity with respect to temperature. In its general form the asymptotic solution holds for all Newtonian fluids for which the temperature dependence of viscosity is the dominating variable property effect. A shooting technique with Gram-Schmidt orthonormalization for the zero-order equation (classical Orr-Sommerfeld problem) and a multiple shooting method for all other equations are applied to solve the stiff differential equations.

See also the following:

9A908. Boundary and inertia effects on vortex instability of a horizontal mixed convection flow in a porous medium

402G. COMBINED NATURAL AND FORCED CONVECTION

9A719. **Experimental studies of forced, combined and natural convection of water in vertical nine-rod bundles with a square lattice.** - MS El-Genk, Bingjing Su, Zhanxiong Guo *(Inst for Space Nucl Power Stud, Dept of Chem and Nucl Eng, Univ of New Mexico, Albuquerque NM 87131)*. Int J Heat Mass Transfer 36(9) 2359-2374 (Jun 1993).

Experiments of upflow- and downflow-forced turbulent and laminar convection natural convection and buoyancy-assisted combined convection of water are performed in uniformly heated, square arrayed, nine-rod bundles having P/D ratios of 1.25, 1.38 and 1.5. In the experiments, Re varies from 250 to 3×10^4, Pr from 3 to 9, Ra_q from 5×10^5 to 3×10^8 for natural convection and from 10^7 to 7×10^8 for combined convection, and Ri from 0.03 to 300. The heat transfer data are correlated in the respective convective regimes, where the heated equivalent diameter is used as the characteristic length in all dimensionless quantities and water properties are evaluated at the mean bulk temperature. A comparison with triangularly arrayed rob bundles shows that for the same flow area per rod, the rod arrangements negligibly affects Nu in both forced and natural convection regimes.

9A720. **Laminar mixed convection flow in a vertical tube.** - A Moutsoglou and YD Kwon *(Dept of Mech Eng, S Dakota State Univ, Brookings SD 57007)*. J Thermophys Heat Transfer 7(2) 361-368 (Apr-Jun 1993).

A computational study is conducted to quantify the buoyancy effects on laminar forced flow of air in a heated-cooled vertical tube. Buoyancy assisting and buoyancy opposing flow cases are considered for heating-cooling rates that provide either uniform wall temperature or uniform heat flux conditions. The nature of the observed effects of various heating-cooling rates and configurations on the velocity and temperature development, as well as on flow reversal, is explained. Critical buoyancy parameters that signal the onset of flow reversal, as well as axial locations where flow reversal first occurs, are determined in the study.

9A721. **Laminar mixed convection over horizontal flat plates with power-law variation in surface temperature.** - WR Risbeck, TS Chen, BF Armaly *(Dept of Mech and Aerospace Eng and Eng Mech, Univ of Missouri, Rolla MO)*. Int J Heat Mass Transfer 36(7) 1859-1866 (May 1993).

An analysis is performed to study the heat transfer characteristics of laminar mixed convective boundary-layer flow over a semi-infinite horizontal flat plate with non-uniform surface temperatures. The surface temperature is assumed to vary as a power of the axial coordinate measured from the leading edge of the plate. A nonsimilar mixed convection parameter X and a pseudo-similarity variable n are introduced to cast the governing boundary layer equations and their boundary conditions into a system of dimensionless equations which are solved numerically by a weighted finite-difference method. Numerical results are presented for Prandtl numbers of 0.1, 0.7, 7 and 100 and representative values of the exponent n for the power-law variation in wall temperature. It is found that an increase in the Prandtl number and exponent value n increases the local heat transfer rate.

9A722. **Measurements of laminar mixed convection in boundary-layer flow over horizontal and inclined backward-facing steps.** - HI Abu-Mulaweh, BF Armaly, TS Chen *(Dept of Mech and Aerospace Eng and Eng Mech, Univ of Missouri, Rolla MO 65401)*. Int J Heat Mass Transfer 36(7) 1883-1895 (May 1993).

Measurements and predictions of velocity and temperature distributions are presented for buoyancy-assisting mixed convection laminar boundary-layer flow over horizontal and inclined, 2D backward-facing steps. Laser-Doppler velocimeter and cold wire anemometer are used to measure simultaneously the velocity and the temperature distributions, respectively. The inclination angle, on the other hand, affects significantly the temperature and velocity distributions. As the inclination angle from the vertical increases, the local Nusselt number decreases, while the reattachment length and the location of the maximum Nusselt number behind the backward-facing step increase.

9A723. **Numerical analysis of mixed convection at the entrance region of a rectangular duct heated from below.** - U Narusawa *(Dept of Mech Eng, NE Univ, Boston MA 02115)*. Int J Heat Mass Transfer 36(9) 2375-2384 (Jun 1993).

An entrance region of a rectangular duct is examined numerically for a thermally-developing flow between a cooled top and heated bottom boundary. Based on the results, which agree well with previous experimental results, equations for the entrance lengths, L_1 for the onset and L_2 for the full development of mixed convection are proposed. Results on the effects of the sidewall thermal condition as well as the inlet gas temperature are also discussed in relation to thermal transport.

9A724. **Turbulence model of fire-induced air flow in a ventilated tunnel.** - H Xue *(Dept of Civil Eng, Natl Univ, 10 Kent Ridge Crescent, Singapore 0511)*, E Hihara *(Dept of Mech Eng, Univ of Tokyo, 7-3-1 Hongo Bunkyo-ku, Tokyo 113, Japan)*, T Saito *(Dept of Mech Eng, Univ of Tokyo, 70301 Hongo Bunkyo-ku, Tokyo 113, Japan)*. Int J Heat Mass Transfer 36(7) 1739-1748 (May 1993).

The fire-induced air flow in a ventilated tunnel with a local gas burner is investigated experimentally and numerically. To simulate the transient 3D turbulent buoyancy flow, calculations employ the turbulence k - ε model which is modified to take account of the effects of the mean streamline curvature. General curvilinear coordinates are generated for the computation. The prediction is compared with the experimental data and shown to be in reasonable agreement except the region close to the heat source. The present model can also be used to predict the location of the leading edge of the heated air flow.

402I. ROTATING FLUIDS OR SURFACES

9A725. **Effect of wall conduction in reactor wall on the heat and fluid flow in a rotating disk CVD reactor.** - FC Chou and SC Gong *(Dept of Mech Eng, Natl Central Univ, Chung-Li, Taiwan 32054, ROC)*. J Mat Processing Manuf Sci 1(4) 387-398 (Apr 1993).

The effect of conduction in the reactor wall on the steady, laminar, axisymmetric and circumferentially uniform flow and heat transfer in a rotating disk chemical vapor deposition reactor has been studied. The combined effects of buoyancy, rotating speed of the disk, reactor wall thickness and wall cooling rate have been considered. The primary parameters are the wall thickness parameter, the Biot number for convection cooling of the reactor wall, the disk Reynolds number and the Grashof number. It is found that whether the effect of wall conduction significantly affects the flow pattern in the reactor and heat transfer rate on the disk depends on the location of the recirculating vortex. When the vortex is above the disk, the effect of wall conduction is negligible, but if the vortex is near the reactor side wall, the effect of wall conduction cannot be neglected. Even under the frequently used "adiabatic" thermal boundary condition, the effect of wall conduction cannot be neglected in the cases of high rotating speed of the disk.

See also the following:

9A700. Numerical and experimental study of the forced convection inside a rotating disk-cylinder configuration

402K. HIGH SPEED FLOWS

9A726. **Study of a high-speed water jet in a jet-cutting mixing chamber.** - RS Amano, KF Neusen, T Gores *(Dept of Mech Eng, Univ Wisconsin, Milwaukee WI 53201)*. J Mat Processing Manuf Sci 1(4) 355-368 (Apr 1993).

A high-speed water jet is used in many industrial applications. This article presents a method for the computation of the flow in a water-air mixing chamber of a water jet cutting assembly by using a finite volume method. The turbulence model employed here is one based on the Reynolds-stress closure. In improving the computations of the Reynolds stresses, it was discovered that the closure models of the mean strain term of the pressure-strain correlation significantly affect the results in the separating flows. Thus, a tensor consisting of the products of the Reynolds stresses was set up in order to take non-isotropic turbulence into account. Computations have been performed using the above-mentioned method. Although the computations were performed for the present mixing chamber configuration, this method can be used for several different flow and geometric conditions to seek the optimum mixing chamber design of the water jet cutting technology. The results are compared with the experimental data obtained in this study. It was found that the present computational model successfully predicts the air suction rates in a water jet-abrasive mixing chamber.

402M. LIQUID METAL FLOWS

9A727. **Liquid-metal film protection of the reactor chamber first wall in a pulsed thermonuclear reactor.** - SA Berendeyev, VA Bernshtam, DN Kagan, SV Kozyrev, YV Poklonskiy *(Inst of Heat and Mass Transfer, Minsk, Russia)*. Heat Transfer Res 24(3) 333-339 (Apr 1992).

The possibility of using film flows of liquid metals to protect the reactor chamber first wall in a pulsed thermonuclear reactor are considered. To ensure a stable film flow, the use of a magnetic field is suggested. In order to estimate the instability development time, the governing relations obtained for flows without a field have been modified to account for the magnetic field. The magnetic field is shown to improve the characteristics of the film liquid-metal protection of the reactor chamber first wall.

9A728. **Thermogravitational effects on liquid metal heat transfer in a longitudinal magnetic field.** - SI Kovalyov and VG Sviridov *(Inst of Heat and Mass Transfer, Minsk, Russia)*. Heat Transfer Res 24(3) 354-365 (Apr 1992).

The heat transfer behavior of descending mercury flow in a heated tube in a gravity field and in the presence of a strong longitudinal magnetic field is investigated. The effect of thermogravitational convection on heat transfer under these conditions is revealed.

402O. UNSTEADY FLOWS

9A729. **Unsteady laminar natural-convection heat transfer in an enclosure with fins.** - Kengo Sasaguchi *(Dept of Mech Eng, Fac of Eng, Kumamoto Univ, 2-39-1 Kurokami, Kumamoto 860, Japan)*, Hiroyuki Takeo *(Hondo Co Ltd, Japan)*, Hiroyuki Kimura *(Nishinippon Railways Co Ltd, Japan)*. Heat Transfer Japan Res 21(7) 678-692 (1992).

The effects of aspect ratio, Prandtl number, and thermal conductivities of fins on 2D unsteady laminar natural convection in a rectangular cell surrounded by a vertical hot wall, a vertical insulated wall, and two horizontal conducting fins have been studied numerically using the SIMPLER algorithm. Transient velocity and temperature distribution, and timewise variation of the average Nusselt number on the hot wall are compared with those for a cell with nonconducting fins.

9A730. **Unsteady thermal processes accompanying transient flow.** - FI Kalbaliyev, ChM Verdiyev, FA Ragimov *(Russia)*. Heat Transfer Res 24(5) 625-640 (1992).

Experiment results on transient flow mixed convection heat transfer with $P > P_{cr}$, $t_i \le t_m \le t_w$ are given . Based on the heat flux and wall temperature, the oscillatory regime boundary has been determined depending on flow regime parameters and geometric dimensions of the tube. Computational formulae are presented. The presence of both normal and improved heat transfer regimes has been confirmed experimentally.

See also the following:

9A702. Transient conjugated forced convection heat transfer with fully developed laminar flow in pipes

402P. TRANSPORT MECHANISMS

9A731. **Investigation of multiple stability of forced-flow cooled cryogenic conductors.** - Toshiyuki Amano, Akinori Ohara *(Central Res Lab, Mitsubishi Elec, Japan)*, Atsushi Kamitani, Masakazu Katagiri *(Fac of Eng, Yamagata Univ, Japan)*. Heat Transfer Japan Res 21(6) 556-572 (Apr 1992).

Concerning the behavior of stability margins of forced-flow cooled conductors, it is known experimentally that the multiple-stability regions for certain combinations of operation current, magnetic field, ambient helium pressure, and externally imposed helium flow appear. This work is a study of the mechanism of multiple stability and of the influence of heat transfer on multiple-stability margins by means of our own numerical code. It is obvious that the multiple-stability margins of forced-flow cooled conductors are due to the interaction between enhancement of heat transfer by heating-induced flow and increase of temperatures of conductors and ambient helium.

9A732. Lateral velocity fluctuations and dissipation time scale ratios for prediction of mean and fluctuating temperature fields. - PJ Gehrke and K Bremhorst *(Dept of Mech Eng, Univ of Queensland, QLD 4072, Australia)*. Int J Heat Mass Transfer 36(7) 1943-1952 (May 1993).

Further testing of a previously developed diffusivity-based model for predicting mean and fluctuating temperatures in water and liquid sodium flows downstream of a multi-bore jet block in which one jet is heated is performed but using air as the working fluid. The apparatus used enabled geometric similitude with the previous studies. It was found that the lateral turbulence intensity was a more effective velocity scale to use and a length scale based on lateral velocity fluctuations was more apt. The Prandtl number effect on temperature dissipation rates found previously in water and sodium is extended by the results using air, leading to a simple algebraic relation between the Prandtl number and dissipation time scale ratio. The non-isotropic nature of the flow is identified and is seen to influence the results.

9A733. Mathematical model of glass flow and heat transfer in a platinum downspout. - R Ducharme, P Kapadia *(Dept of Phys, Univ of Essex, Colchester CO4 3SQ, UK)*, F Scarfe *(Electroglass Ltd, 4 Brunel Rd Benfleet, Essex SS7 4PS, UK)*, J Dowden *(Dept of Math, Univ of Essex, Colchester CO4 3SQ, UK)*. Int J Heat Mass Transfer 36(7) 1789-1797 (May 1993).

The possibility of using a heat exchanger system to control the flow of glass through a platinum downspout is investigated. Downspouts are used in place of refractory throats since they avoid some of the problems associated with throats. It is assumed that the flow is predominantly axial and an integral expression for the flow field is obtained. The temperature distribution in the glass is calculated using the finite difference method. The formulation of the heat transfer problem includes a detailed analysis of the anisotropic radiation field in the glass.

9A734. Modelling of the homogeneous turbulence dynamics of stably stratified media. - BA Kolovandin, VU Bondarchuk *(AV Luikov Heat and Mass Transfer Inst, 220072 Minsk, Belarus)*, C Meola, G de Felice *(Fac Eng, Univ Napoli, Napoli, Italy)*. Int J Heat Mass Transfer 36(7) 1953-1968 (May 1993).

Numerical simulation of the dynamics of homogeneous turbulence of a stable stratified fluid in the presence of a vertical constant-density gradient was carried out. The second-order model which is universal with respect to turbulent Reynolds and Peclet numbers and molecular Prandtl number is applied to the numerical simulation of the dynamics of the velocity and density field parameters up to the final stage of decay. At small evolution times Nτ, the results of simulation are compared with the familiar experimental data.

9A735. Solidification of an aqueous salt solution in the presence of thermosolutal convection. - S Chellaiah, RA Waters, MA Zampino *(Dept of Mech Eng, Florida Int Univ, Miami FL 33199)*. Warme Stoffubertragung 28(4) 205-216 (Mar 1993).

The freezing of water-salt (sodium chloride) solution on a vertical wall of a rectangular cavity has been studied experimentally. The influence of thermally and solutally driven [illegible] vection on the freezing process ha[illegible] The spatial and temporal vari[illegible] ure in the solid, mush and [illegible] en recorded. The thermosolutal convective flow strongly influence the rate of freezing. Due to the continuous rejection of salt, a solutally stratified stable region developed at the bottom of the test cell. The thickness of this region increased with the progress of freezing and it was separated from the remaining bulk liquid, when convective flow was present, by a thin interface.

9A736. Thermocapillary breakdown of falling liquid films at high Reynolds numbers. - MS Bohn *(Natl Renewable Energy Lab, 1617 Cole Blvd, Golden CO 80401)* and SH Davis *(Dept of Eng Sci and Appl Math, NWU)*. Int J Heat Mass Transfer 36(7) 1875-1881 (May 1993).

This paper presents a new correlation in which the heat flux required to break a falling liquid film can be determined from the film Reynolds number. The correlation is based on the balance of local forces in the substrate region for high-Reynolds number films. Validation of the correlation required experimental data for breakdown of wavy liquid films at a significantly higher Reynolds number and heat flux than have been presented in the past. These data are also presented in this paper. The results show that the correlation collapses the experimental data for three liquids with widely varying physical properties at film Reynolds numbers up to about 10^4.

402S. POROUS MEDIA

9A737. Free and forced convection boundary layer flow through a porous medium with large suction. - MD Abdus Sattar *(Dept of Math, Dhaka Univ, Dhaka 1000, Bangladesh)*. Int J Energy Res 17(1) 1-7 (Jan 1993).

An analytical study is made of the free and forced convection boundary layer flow past a porous medium bounded by a semi-infinite vertical porous plate. Locally similar solutions are then obtained by a perturbation method for large suction. Solutions for the velocity and temperature distributions are shown graphically for various suction velocities and values of the driving parameter G_r/R^2_e, where G_r is the Grashof number and R_e is the Reynolds number. The corresponding values of the skin friction coefficient and the Nusselt number are finally shown in tabular form.

9A738. Free convection effects on the oscillatory flow of a couple stress fluid through a porous medium. - PS Hiremath and Pm Patil *(Dept of Math, Karnatak Univ, Dharwad 580 003, India)*. Acta Mech 98(1-4) 143-158 (1993).

Effects of free convection currents on the oscillatory flow of a polar fluid through a porous medium, which is bounded by a vertical plane surface of constant temperature, have been studied. The surface absorbs the fluid with a constant suction and the free stream velocity oscillates about a constant mean value. Analytical expressions for the velocity of the angular velocity fields have been obtained, using the regular perturbation technique. The effects of cooling and heating of a polar fluid compared to a Newtonian fluid have also been discussed. The velocity of a polar fluid is found to decrease as compared to the Newtonian fluid.

9A739. Mixed convection along a nonisothermal vertical flat plate embedded in a porous medium: The entire regime. - JC Hsieh, TS Chen, BF Armaly *(Dept of Mech and Aerospace Eng and Eng Mech, Univ of Missouri, Rolla MO 65401)*. Int J Heat Mass Transfer 36(7) 1819-1825 (May 1993).

The problem of mixed convection about a vertical flat plate embedded in a porous medium is analyzed. Nonsimilarity solutions are obtained for the cases of variable wall temperature (VWT) in the form $T_w(x) = T_\infty + ax^n$ and variable surface heat flux (VHF) in the form $q_w(x) = bx^m$. The entire mixed convection regime is covered by two different nonsimilarity parameters $X = [1 + (Ra_x/Pe_x)^{1/2}]^{-1}$ and $Xx = [1 + (Rax_x/Pe^{3/2}{}_x)^{1/3}]^{-1}$, respectively, for VWT and VHF cases, from pure forced convection (X = 1 or Xx = 1) to pure free convection (X = 0 or Xx = 0). It is found that as X or Xx decreases from 1 to 0, the thermal boundary layer thickness increases first then decreases, but the local Nusselt number in the form $Nu_x(Pe^{1/2}{}_x + Ra^{1/2}{}_x)^{-1}$ or $Nu_x(Pe^{1/2}{}_x + Rax\{1/3\}_x)^{-1}$ decreases first and then increases.

9A740. Momentum and heat transfer over a continuous moving surface in a non-Darcian fluid. - A Nakayama *(Dept of Energy and Mech Eng, Shizuoka Univ, 3-5-1 Johoku, Hamamatsu 432, Japan)* and I Pop *(Fac of Math, Univ of Cluj, R-3400 Cluj Cp 253, Romania)*. Warme Stoffubertragung 28(4) 177-184 (Mar 1993).

The momentum and heat transfer characteristics associated with the boundary layer on a continuous moving flat surface in a non-Darcian fluid have been investigated exploiting a local similarity solution procedure. The full boundary layer equations, which describe the effects of convective inertia, solid boundary, and porous inertia in addition to the Darcy flow resistance, were solved using novel transformed variables, deduced from a scale analysis on the momentum and energy conservation equations. Details are provided for the effects of convective inertia and porous inertia on the velocity and temperature profiles. The resulting friction and heat transfer characteristics are found to be substantially different from those of forces convection over a stationary flat plate.

See also the following:

9A715. Convective instability in saturated porous enclosures with a vertical insulating baffle

402Y. COMPUTATIONAL TECHNIQUES

9A741. Arbitrary Lagrangian-Eulerian FE model for heat transfer analysis of solidification processes. - S Ghosh *(Dept of Eng Mech, Ohio State Univ, Columbus OH 43210)* and S Moorthy *(Dept of Mech Eng, Univ of Alabama, Tuscaloosa AL 35481)*. Numer Heat Transfer B 23(3) 327-350 (Apr-May 1993).

A heat transfer analysis for solidification problems has been conducted to evaluate the temperature field and the location of the phase-change interface. An arbitrary Lagrangian-Eulerian kinematic description has been utilized in the FE formulation to impart flexibility to the motion of the nodes. By detaching the nodal points from the underlying material, nodes can be monitored to follow the evolving front, while maintaining shapes of the elements. Special numerical techniques to smoothen the deforming front and to avoid continuous remeshing have been introduced. Numerical examples have been solved to establish the validity of the present model and its strength.

9T742. Current trends in heat transfer computations. - AF Emery, RJ Cochran *(Univ of Washington, Seattle WA 98195)*, DW Pepper *(Appl Res Projects, Moorpark CA 93021)*. J Thermophys Heat Transfer 7(2) 193-212 (Apr-Jun 1993).

9A743. Newton-based BEM for nonlinear convective diffusion problems. - BQ Li *(ALCOA Tech Center, 100 Tech DR, ALCOA Center PA 15069)*. Numer Heat Transfer B 23(3) 369-385 (Apr-May 1993).

A Newton-based BEM for the solution of nonlinear convective diffusion problems is presented. The problems are formulated through the use of the exponential transformation. The numerical procedures for the BE implementation of the formulation are discussed, and the treatment of nonlinear boundary conditions using the Newton-Raphson method is described in detail. Three numerical examples are provided. The results agree well with the analytical solutions whenever available. The method is free from numerical oscillations even for high Peclet numbers. The Newton-based iterative scheme, when integrated with the BEM, provides an efficient algorithm for the solution of nonlinear convective diffusion problems and is superior to the successive substitution approximation.

9A744. **Nonuniform grid accuracy test applied to the natural-convection flow within a porous medium cavity.** - DM Manole and JL Lage *(Dept of Mech Eng, S Methodist Univ, Dallas TX)*. Numer Heat Transfer B 23(3) 351-368 (Apr-May 1993).

The accuracy of numerical results obtained by using nonuniform grid distributions is strongly affected by the size of the grid spacing. The present work focuses on a detailed procedure for the accuracy tests of the numerical results obtained by using nonuniform grid distributions. It is shown that the degree of nonuniformity of a certain grid distribution with a fixed number of grid lines also has a strong effect on the numerical results.

9A745. **Solution of Navier-Stokes equations on non-staggered grid.** - AW Date *(Dept of Mech Eng, Indian IT, Powai, Bombay 400 076, India)*. Int J Heat Mass Transfer 36(7) 1913-1922 (May 1993).

When Navier-Stokes equations are solved on a non-staggered grid, the problem of checker board prediction of pressure is encountered. Over the last ten years, the problem has been cured by what is known as the momentum interpolation formula from which is applied for evaluation of the cell-face velocities. In this paper two contributions are made. Firstly it is shown that the momentum interpolation formula is a special case of a more general interpolation relationship that can be derived from a physical principle. In order to achieve unique interpolation practice, the second contribution of this paper relates to pressure-gradient interpolation. The results obtained from pressure-gradient interpolation compare extremely favorably with those obtained using staggered grid.

See also the following:

9A599. Solution of the 2D incompressible flow equations on unstructured triangular meshes

402Z. EXPERIMENTAL TECHNIQUES

9A746. **Modified method of three temperatures for hot-wire measurements of the temperature and velocity fluctuations and their correlations in the thermal boundary layer.** - EY Epik, TT Suprun, ML Pioro *(Eng Themophys Inst, Ukrainian Acad of Sci, Kiev, Ukraine)*. Heat Transfer Res 24(4) 501-508 (Apr 1992).

It is shown that the measurement error can be significantly reduced by appropriate selection of the pickup-wire temperature, coupled with the use of the appropriate smoothing functions. Specific recommendations for hot-wire measurements are presented and the pertinent equipment is described.

404. Two phase convection

404B. NUCLEATE POOL BOILING

9A747. **Influence of surface wear on boiling heat transfer.** - YV Bogdanov and SG Obukhov. Heat Transfer Res 24(4) 440-446 (Apr 1992).

Experimental results on boiling heat transfer on new worn surfaces are presented. Distilled water in a free state at saturation temperature was used as a coolant. Stainless steel tubes were used in the experiments. The test elements were heated by alternating electric current.

9A748. **Unified model for the prediction of bubble detachment diameters in boiling systems I. Pool boiling.** - LZ Zeng, JF Klausner *(Dept of Mech Eng, Univ of Florida, Gainesville FL 32611)*, R Mei *(Dept of Aerospace Eng Mech and Eng Sci, Univ of Florida, Gainesville FL 32611)*. Int J Heat Mass Transfer 36(9) 2261-2270 (Jun 1993).

A new model is proposed for the prediction of vapor bubble departure diameters in saturated pool boiling. The model utilizes a force balance which follows a similar form as that used by Klausner *et al* for flow boiling. The vapor bubble growth rate is a necessary input to the model, and its reliable estimation is required to predict accurately departure diameters. It is demonstrated that over the wide range of boiling data considered the departure diameter predicted using the present model is significantly improved over existing correlations.

404E. NUCLEATE FLOW BOILING (EXTERNAL)

9A749. **Film boiling on a horizontal surface.** - VS Granovskiy, AA Sulatskiy, VB Khabenskiy, SM Shmelev *(Russia)*. Heat Transfer Res 24(5) 577-593 (1992).

Saturated liquid film boiling on a face-up horizontal surface is considered. Based on the stability loss condition for phase interface, an expression is obtained for the group which determines the heat transfer intensity. The final form of the expression is refined after correlation of experimental data. Two different mechanisms of bubble generation on the vapor film surface are analyzed which explain the character of the relation obtained.

9A750. **Unified model for the prediction of bubble detachment diameters in boiling systems II. Flow boiling.** - LZ Zeng, JF Klausner, DM Bernhard *(Dept of Mech Eng, Univ of Florida, Gainesville FL 32611)*, R Mei *(Dept of Aerospace Eng and Mech and Eng Sci, Univ of Florida, Gainesville FL 32611)*. Int J Heat Mass Transfer 36(9) 2271-2279 (Jun 1993).

An improved model is proposed for the prediction of departure and lift-off diameters in saturated force convection boiling. The model utilizes a force balance similar to that proposed by Klausner *et al.* One significant improvement is that the inclination angle is determined on a dynamic basis and is not required as an input. Furthermore, it is hypothesized that the surface tension force is small compared to other forces acting on a vapor bubble at the points of departure and lift-off, and thus information on the bubble contact diameter and contact angles is not required. A new data set on mean vapor bubble lift-off diameters and probability density functions (pdfs) for flow boiling of refrigerant R113 on a nichrome heating strip has been obtained using the experimental facility described by Klausner *et al.*

404F. FLOW BOILING (INTERNAL)

9A751. **Concentrations of phases and spectral characteristics of a two-phase flow in bilaterally heated steam generating channels.** - SM Dmitriyev, AA Abramov, YuI Anoshkin, MV Dmitrousov, VYe Kulikov *(Russia)*. Heat Transfer Res 24(5) 594-602 (1992).

The distribution of local quality in the cross section of channels with inner spiral tubes is investigated. A dimensionless relation for the gas quality of a gas-liquid flow depending on the flow rate parameters is obtained. The dependence of the effective frequency and of the time macroscales of gas quality fluctuations on flow regime and geometric parameters are presented.

9A752. **Investigation of postcritical heat transfer for R-12 forced flow through a horizontal tube.** - PV Konstantinov and VV Yagov. Heat Transfer Res 24(4) 447-456 (Apr 1992).

The paper presents the results of experimental investigation into R-12 forced flow heat transfer in a horizontal tube at pressures of 0.5 - 2.6 MPa and mass velocities of 1500 - 2000 kg/(m^{2}s).

9A753. **Limited heat loads and burnout heat transfer in one-sided heated channels.** - VA Divavin, VN Tanchuk, AE Shrubok *(Russia)*. Heat Transfer Res 24(5) 612-624 (1992).

A procedure is described for predicting limiting heat loads in a channel with one side heated, with cooling provided by subcooling water flow. The concept of local and overall burnout heat transfer is introduced for such one-sided loading. The effect of flow regime and operational parameters is investigated.

9A754. **Low-quality dryout in horizontal helical coiled tubes.** - Osamu Watanabe, Naomichi Heya *(Dept of Mech Eng, Aichi IT, Yagusa-cho, Toyota, Japan)*, Yasumitsu Ohmi *(Nippon Denso, Japan)*, Hideomi Fujita *(Dept of Mech Eng, Nagoya Univ, Japan)*. Heat Transfer Japan Res 21(7) 736-746 (1992).

An experimental study was carried out to clarify the low-quality dryout phenomena in helical coiled tubes placed horizontally. The results obtained were as follows. (1) Low-quality dryout is caused by the separation of the liquid and vapor phases and it disappears at the transition from the separated flow to the slug flow regime. (2) Low-quality dryout generally takes place in the lower portion of a non-vertically placed helical coiled tube. (3) A criterion for the disappearance of low-quality dryout has been proposed based on the experiment.

9A755. **Mechanism of enhancement of heat and mass transfer in a vapor-generating channel with a transverse microfin roughness.** - YF Domashev, VF Godunov, GY Struchenko *(Eng Thermophys Inst, Ukrainian Acad of Sci, Kiev, Ukraine)*. Heat Transfer Res 24(4) 465-470 (Apr 1992).

The physics of the interaction of a micro-finned heated wall and the flow under different boiling conditions are explained, and the conditions for the break off of vapor bubbles in vortical flow zones are analyzed. It is shown that microfins that induce turbulence in only a thin layer are the most efficient in raising the critical heat flux density in emulsion and dispersed-annular flows.

9A756. **Pressure drop in steam-generating channels.** - VG Antipov *(Eng Thermophys Inst, Ukrainian Acad of Sci, Kiev, Ukraine)*. Heat Transfer Res 24(4) 457-464 (Apr 1992).

Experimental results on pressure drop in steam-water flows in heated channels ar presented. An expression for calculating irreversible pressure losses in a steam-generating pipe operating at pressures from 40 to 140 bar, mass velocities between 200 and 1250 kg/m^2-sec and average void fractions of 0 to 0.8 is suggested.

9A757. **Stability of stratified flow and its transition to other flow regimes.** - LN Persen *(Inst Mekanikk, Univ Trondheim, NTH 7034 Trondheim, Norway)*. Int J Heat Mass Transfer 36(7) 1969-1980 (May 1993).

Stratified two-phase flow in circular pipes has been tested extensively in the literature. The proposed presentation is based on the author's own paper which has the advantage of explicitly expressing the influence of the five parameters that govern the physical process. The investigation will show how the normal depth is determined, that it may be single-valued or double-valued, whereby the possibility of hydraulic jumps is present. It will be shown under what conditions the normal depth is stable or unstable. In particular it will be shown how pipeline geometry will affect the flow. Downward sloping pipelines in the direction of the flow will be discussed in detail. Upward sloping pipelines will also be discussed but in that case the stability of the flow may be overruled by geometrically induced slug flow.

9A758. **Subcooled convective boiling of binary mixtures over an array of heated elements.** - WR McGillis and VP Carey *(Dept of Mech Eng, UCB)*. J Thermophys Heat Transfer 7(2) 346-351 (Apr-Jun 1993).

Boiling data and the critical heat flux conditions are reported for both channel flow and jet impingement flow using varying concentrations of R-11 and R-113. An array of 10 flush-mounted heated elements on one wall of a vertical passage was cooled by subcooled boiling. Data indicate that for channel flow boiling, the addition of R-11 and R-113 does not produce a significant change in the critical heat flux condition. For channel flow boiling, the data indicate that addition of a small amount of a less volatile component slightly increased the critical heat flux, whereas, the addition of a small amount of a more volatile component decreased it. The critical heat flux data for channel flow were also found to agree well with critical heat flux correlations for pure fluids if the mole-weighted mean properties of the mixture were used to compute the critical heat flux from the pure fluid correlation. The significance of the findings of this study with regard to the use of the binary mixtures of dielectric fluids for immersion cooling of electronic components is discussed in this article.

404G. FLOW BOILING, PEAK HEAT FLUX (INTERNAL)

9A759. **Burnout heat transfer in steam generating channels under steady and unsteady conditions.** - II Gromova and VN Smolin *(Russia)*. Heat Transfer Res 24(5) 603-611 (1992).

The burnout heat transfer in curvilinear steam generating channels under steady and unsteady-state conditions and on exposure to a magnetic field is studied. Formulae are suggested for calculating the critical power of the channels.

9A760. **Critical heat flux measurements in a round tube for CFCs and CFC alternatives.** - RM Tain, SC Cheng *(Dept of Mech Eng, Univ of Ottawa, ON K1N 6N5, Canada)*, DC Groeneveld *(Chalk River Lab, Atomic Energy of Canada, Chalk River, ON K0J 1J0, Canada)*. Int J Heat Mass Transfer 36(8) 2039-2049 (May 1993).

Critical heat flux (CHF) measurements have been conducted for HFC-134a, HCFC-123, HCFC-22, CFC-12 and CFC-11 in a multi-fluid loop. The test pressures are up to 2 MPa (corresponding to water equivalent pressure of 7 - 10 MPa) and mass fluxes from 1000 to 4000 kg m^{-2} s^{-1}. The heated length is adjustable from 0.5 to 1 m, the ID of the tubular test section is 4.2 mm, and the critical quality varies from 0.07 to 0.6. The parametric trends of test results are examined and the test results show good agreement with existing CHF prediction methods.

9A761. **Dryout fluxes in annuli with nonuniformly heated inner pipes.** - AM Kichigin and AA Moskalenko *(Eng Thermophys Inst, Ukrainian Acad of Sci, Kiev, Ukraine)*. Heat Transfer Res 24(4) 471-478 (Apr 1992).

Experimental results on dryout flux densities in flow of water in an 14 mm-8mm annulus, in which the inner tube is heated are described. The heat flux distribution was made to increase or decrease toward the exit. The longitudinal heat release nonuniformity factor was 1.85 to 0.54, respectively, in these two cases. The pressure was 19.6 MPa and the mass velocities were 500 and 2000 kg/m^2-sec. A minimal effect of longitudinal variation of heat release on q_{cr} was found.

9A762. **Effect of turbulence generators on the critical dryout heat flux density in annuli.** - AM Kichigin, SG Povsten', AV Ostapenko *(Eng Thermophys Inst, Ukrainian Acad of Sci, Kiev, Ukraine)*. Heat Transfer Res 24(3) 408-414 (Apr 1992).

Experimental results on the effect of turbulence generators (promoters on the critical heat flux density q_{cr} are presented. The experiments were performed at 14.7 and 19.6 MPa and a mass velocity of 1000 kg/m^2-sec, the fluids being subcooled water and aqueous fluid with steam qualities x as high as 0.3. The semicircular, 0.5 mm high bumps used as turbulence generators were spaced 7 to 30 mm apart and were installed on the outer, non-heated side of the annulus. We found only minor enhancement of q_{cr} by the turbulence promoters.

404I. FILM BOILING (POOL)

9A763. **Numerical study of liquid film cooling along an inclined plate.** - WM Yan *(Dept of Mech Eng, Hua Fan IT, Shih Ting, Taipei 22305, Taiwan, ROC)* and CY Soong *(Dept of Aeronaut Eng, Chung Cheng IT, Tahsi, Taoyuan 33509, Taiwan, ROC)*. Warme Stoffubertragung 28(4) 233-241 (Mar 1993).

A numerical method of analyzing liquid film cooling along an inclined plate is presented. A marching procedure is employed for solution of the equations of mass, momentum, energy and concentration in the flow. Results for heat and mass transfer characteristics are presented for air-water system. The effect of the inclined angle ϕ, free-stream temperature T_∞, free-stream velocity u_∞, and inlet film thickness δ on the heat and mass transfer along the gas-liquid interface are examined in detail. Results show that an increase in free-stream temperature and velocity causes an increase in interfacial temperature while an increase in inclined angle and inlet film thickness causes a reduction in interfacial temperature.

404K. MIST FLOWS

9A764. **Study on transient characteristics of mist-cooling heat transfer from a horizontal upward-facing surface.** - Hidetoshi Ohkubo and Shigefumi Nishio *(Inst of Indust Sci, Univ of Tokyo, Japan)*. Heat Transfer Japan Res 21(6) 543-555 (Apr 1992).

The effects of cooling rate and thermal conductivity of a heat-transfer plate on mist-cooling heat transfer were investigated experimentally for the high-temperature regions. Experiments were conducted for horizontal upward-facing surfaces made of silver, stainless steel, and fused quartz. It was found that, in the case where the horizontal surfaces face upward, the thermal properties of surface material does not significantly affect the heat-transfer coefficient, but the cooling rate of the surface affects it if the heat capacity of the surface is less than a critical value.

404M. CONDENSATION (STATIC VAPOR)

9A765. **Microscope observations of the initial droplet formation mechanism in dropwise condensation.** - Tadao Haraguchi *(Fac of Eng, Ibaraki Univ, Japan)*, Ryohachi Shimada, Toshiro Takeyama *(Fac of Sci and Eng, Ishinomaki Senshu Univ, Japan)*. Heat Transfer Japan Res 21(6) 573-585 (Apr 1992).

Initial droplet formation in dropwise condensation is one of the important mechanisms for nucleation in phase-change phenomena. Film-fracture hypothesis has been proposed by other researchers and they have estimated the film thickness. But they could not observe the initial droplet formation. Here three experimental studies based on microscopic observations were performed. The authors observed that dropwise condensation nuclei were grown from a very thin film. Film thickness was from 0.1 μm to 0.3 μm and critical droplet size was from 0.8 μm to 1.3 μm. Critical droplet site densities of 1.4 - 2.8 • 10^7 sites/cm^2 were found.

404O. EVAPORATION

9A766. **Binary diffusion and heat transfer in mixed convection pipe flows with film evaporation.** - Wei-Mon Yan *(Dept of Mech Eng, Hua Fan IT, Shih Ting, Taipei 22305, Taiwan, ROC)*. Int J Heat Mass Transfer 36(8) 2115-2123 (May 1993).

A detailed numerical study has been performed to investigate the heat and mass transfer characteristics in laminar mixed convection pipe flows with film evaporation. Both the thermal conditions of constant wall temperature and uniform heat flux are considered. Results for interfacial Nusselt and Sherwood numbers are presented for air-water and air-ethanol systems for various conditions. Predicted results show that heat transfer along the gas-liquid interface is dominated by the transport of latent heat in association with the vaporization of the liquid film.

9A767. **Critical flow and heat transfer in field evaporator pipes.** - MK Bezrodnyy and YV Antoshkov *(Kiev Polytech Inst, Kiev)*. Heat Transfer Res 24(4) 543-548 (Apr 1992).

Relationships governing the flow and heat transfer in a steam-heated field evaporator pipe are derived on the basis of experimental data. Correlations for limits of operating stability of such a pipe are presented.

9A768. **Diffusion controlled evaporation of multicomponent droplet: Theoretical studies on the importance of variable liquid properties.** - R Kneer, M Schneider, B Noll, S Wittig *(Lehrstuhl Inst Thermische Stromungsmaschinen, Univ Karlsruhe (TH), Kaiserstr 12, W-7500 Karlsruhe, Germany)*. Int J Heat Mass Transfer 36(9) 2403-2415 (Jun 1993).

A well-known multicomponent droplet vaporization model, the Diffusion Limit Model, has been extended to account for property variations in the liquid phase. The model has been tested for typical conditions of modern gas turbine combustors. The results for a hexane-tetradecane droplet show that the temperature- and concentration-dependence of the liquid properties affect the vaporization process, especially with regard to a reduced diffusional resistance. Additionally, remarkable variations of the refractive index are observed yielding helpful information for the estimation of errors in optical particle sizing techniques.

9A769. **Heat transfer characteristics of a cranked, evaporative thermosyphon.** - GSH Lock and Jialin Fu *(Dept of Mech Eng, Univ of Alberta, Edmonton T6G 2G8, AB Canada).* Int J Heat Mass Transfer 36(7) 1827-1832 (May 1993).

The paper presents an exploratory study of an offset, evaporative thermosyphon. Laboratory experiments using a small bore rig were conducted for a cranked configuration with the evaporator and condenser aligned vertically. Heat transfer data revealed similarities with the equivalent linear system but also showed up some differences. The heat transfer rates were found to be much higher than those obtained under single-phase conditions. On the other hand, critical heat fluxes were much lower than in the equivalent linear system.

9A770. **Maximum heat-transferring capacity of two-phase thermosiphons with separate vapor and condensate streams.** - IL Pioro *(Eng Thermophys Inst, Ukrainian Acad of Sci, Kiev, Ukraine).* Heat Transfer Res 24(4) 535-542 (Apr 1992).

Experimental results on the effects of the geometry of the evaporator, the slope of the thermosiphon and the circulation velocity on the maximum heat flux in boiling of water in two phase straight-through thermosiphons, and also photographs of the boiling of water in a rectangular channel are presented.

9A771. **Molecular dynamics study of solid melting and vaporization by laser irradiation.** - Susumu Kotake and Masatugu Kuroki *(Dept of Mech Eng, Univ of Tokyo, Hongo, Tokyo 113, Japan).* Int J Heat Mass Transfer 36(8) 2061-2067 (May 1993).

The molecular processes of the phase change of melting and vaporization of solid materials by laser beam irradiation were studied numerically by using the molecular dynamics method. By absorbing the laser light energy, the solid atoms or molecules are excited in the interatomic or intermolecular potential energy to change their interacting forces. The resulting Hamiltonian equations of atomic or molecular motions are solved with the molecular dynamics method to understand the molecular behavior of the phase changing process. The excitation strength, that is, the laser energy of irradiation has the most predominant effect on the phase change of vaporization and melting.

See also the following:

9T618. Kinetic theory analysis of steady evaporating flows from a spherical condensed phase into a vacuum

404P. SURFACE TENSION EFFECTS

See the following:

9A704. Localized solutions of an equation governing Benard-Marangoni convection

404R. SOLID-FLUID FLOWS

9A772. **Modelling of the effect of turbulent two-phase flow friction decrease under the influence of dispersed phase elements.** - LV Zakharov, AA Ovchinnikov, NA Nikolayev *(Mech Fac, Kazan Inst of Chem Eng, Kazan 420015, Russia).* Int J Heat Mass Transfer 36(7) 1981-1991 (May 1993).

Consideration is given to the problem concerning the interaction of a continuous turbulent flow with a dispersed impurity uniformly distributed in it with the account of the involvement of particles into energy-intensive fluctuations of the continuous medium. Correlations are obtained relating the drag reduction in the turbulent two-phase flow to the size of particles and dispersed phase concentration. The limitations are established which should be imposed on the concentration size of particles to attain the regime of reduced drag in a two-phase turbulent flow.

9A773. **Numerical method for direct contact melting in transient process.** - Hiki Hong and Akio Saito *(Dept of Mech Eng, Tokyo IT, O-okayama 2-12-1 Meguro-ku, Tokyo 152, Japan).* Int J Heat Mass Transfer 36(8) 2093-2103 (May 1993).

Most of the research on direct contact melting has been carried out on the assumption of steady state or quasi-steady state. Such a methodology, however, is difficult to apply to problems in which the boundary conditions such as the temperature of heating plate or the external force exerted on the solid PCM change abruptly with time. In this study, we show an efficient algorithm to solve the transient behavior of direct contact melting, considering the solid movement by external forces exerted on a solid body as well as that by melting. The result shows good agreement with that by the previous steady state approach, and it is assured that the behavior during the transient process to steady state is very reasonable in a viewpoint of a physical phenomenon.

9A774. **Unsteady heat transfer to pulsatile flow of a dusty viscous incompressible fluid in a channel.** - N Datta, DC Dalal *(Dept of Math, Indian IT, Kharagpur 721 302, India),* SK Mishra *(Balimela Col of Sci and Tech, Balimela 764 051 Orissa, India).* Int J Heat Mass Transfer 36(7) 1783-1788 (May 1993).

The problem of unsteady heat transfer to pulsatile flow of a dusty fluid in a parallel plate channel has been studied. It is observed that the unsteady part of the fluid velocity as well as of the particle phase velocity has a phase lag which increases with increase of ϕ, ie, the volume fraction of the particles. The steady part of the heat transfer at the hotter plate decreases with increase of ϕ whereas it increases with increase of ϕ at the colder plate. The amplitude of the unsteady part of the heat transfer at both the plates decreases with increase of ϕ.

404Y. COMPUTATIONAL TECHNIQUES

See the following:

9T742. Current trends in heat transfer computations

404Z. EXPERIMENTAL TECHNIQUES

9A775. **Ultrasonic imaging and velocimetry in two-phase pipe flow.** - SL Morris and AD Hill *(Dept of Pet Eng, Univ of Texas, Austin TX 78712).* J Energy Resources Tech 115(2) 108-116 (Jun 1993).

This paper presents the first results of an experimental and theoretical investigation of the feasibility of using ultrasonic measurements in multiphase pipe flow. Extant downhole flow rate measurement technology used in the petroleum industry is not adequate in some multiphase flow regimes, particularly when the well is deviated from vertical. Ultrasonic offers Doppler velocity and imaging capabilities, both of which could be of great value in production logging. Some air-water measurements, both imaging and velocimetry, are presented, along with a discussion of pulsed Doppler theory.

406. Conduction

406A. GENERAL THEORY

9A776. **Engineering assessment to the relaxation time in thermal wave propagation.** - Da Yu Tzou *(Dept of Mech Eng, Univ of New Mexico, Albuquerque NM 87131).* Int J Heat Mass Transfer 36(7) 1845-1841 (May 1993).

The physical significance of the relaxation time in the wave theory of heat conduction is further studied in this work. Thermodynamically, it is confirmed that the relaxation time results from the rate-equation within the mainframe of the second law in the nonequilibrium, irreversible thermodynamics. Mechanically, on the other hand, the relaxation time results from the phase-lag between the heat flux vector and the temperature gradient in a high-rate response. In transition from a diffusion behavior to the wave propagation, lastly, the relaxation time is found to be the physical instant at which the intrinsic length scales merge with each other.

9A777. **Modified Fourier law. Comparison of two approaches.** - VA Cimmelli *(Dipartimento Matematica, Univ Degli Studi Della, Basilcata, Potenza, Italy),* W Kosinski *(Inst of Fund Tech Res, Polish Acad of Sci, Warszawa, Poland),* K Saxton *(Dept of Math Sci, Loyola Univ, New Orleans LA).* Arch Mech 44(4) 409-415 (1992).

The objective of this note is to compare two different models leading to modified Fourier laws. The first model uses the concept of semi-empirical temperature, the second one is built in the framework of extended thermodynamics. For both approaches three experimental curves, namely the specific heat, heat conduction coefficient and second sound speed, all given in terms of the absolute temperature, determine the models. Conditions under which both models lead to similar results are formulated.

406B. STEADY PROBLEMS

9A778. **Steady-state heat transfer from horizontally insulated slabs.** - M Krarti *(Joint Center for Energy Man, CEAE Dept, Univ of Colorado, Boulder CO 80309-0428).* Int J Heat Mass Transfer 36(8) 2135-2145 (May 1993).

A general solution for the steady-state heat conduction problem under a slab-on-grade floor with horizontal insulation is presented. The soil temperature field, the heat flux along the slab, and the total slab heat loss are obtained and analyzed using the Interzone Temperature Profile technique. The derived solution addresses all the common configurations for horizontal insulation of slab-on-grade floors. The effect of the outer inner edge insulation on heat flux variation along the slab floor surface and on total slab heat loss is discussed and analyzed.

9A779. **Steady-state heat transfer from slab-on-grade floors with vertical insulation.** - M Krarti *(Joint Center for Energy Man, CEAE Dept, Univ of Colorado, Boulder CO 80309-0428).* Int J Heat Mass Transfer 36(8) 2147-2155 (May 1993).

The steady-state temperature field distribution beneath a vertically insulated slab is derived using the Interzone Temperature Profile Estimation technique. A water table is considered at a finite depth below the soil surface. The heat flux variation along the slab is discussed as well as the effect of vertical insulation length and value on the total heat losses from the slab-on-grade floor. It is shown that when the depth and or the thermal resistance of the vertical insulation increases, slab heat loss decreases following the law of diminishing returns. The water table level was found to have a significant effect on total slab heat loss.

406C. TRANSIENT PROBLEMS

9A780. Some analytical solutions of time-dependent, continuously operating heat sources. - SM Zubair *(Dept of Mech Eng, King Fahd Univ of Pet and Minerals, Dhahran 31261, Saudi Arabia)* and MA Chaudhry *(Math Sci Dept, King Fahd Univ of Pet and Minerals, Dhahran 31261, Saudi Arabia)*. Warme Stoffubertragung **28**(4) 217-223 (Mar 1993).

The amount of heat released in a volume whose extent can be ignored as compared with the dimensions of the surroundings of interest, may be classified as (i) the point-heat source, (ii) the line-heat source, and (iii) the plane-heat source. The temperature solutions of these transient conduction problems in an extended, homogeneous, and isotropic medium, are discussed in closed form. It is found that the present analysis covers well known (classical) solutions as well as some new solutions.

9A781. Unsteady thermal analysis of an injection mold by the BEM. - Satoru Yamamoto, Takaaki Matsuoka, Yoshinori Inoue, Hideroh Takahashi *(Toyota Central R&D Labs, 41-1 Aza Yokomichi, Oaza Nagakute, Nagakute-cho, Aichi-gun, Aichi 480-11, Japan)*. Heat Transfer Japan Res **21**(7) 666-677 (1992).

An unsteady thermal analysis program has been developed to simulate transient heat transfer of molds in computer-aided engineering for injection molding of thermoplastics. The 3D unsteady thermal conduction equation is solved by using the BEM. Heat flux on the cavity and the runner during the cooling stage, which is calculated from 1D thermal analysis by using the finite-difference method, is taken into consideration as boundary conditions. Mold temperatures were calculated for the mold of a box-shaped part and were compared with experimental results. The calculated mold temperatures were in good agreement with the experimental ones during injection molding.

406E. CONTACT RESISTANCE

9A782. Inverse problem of estimating interface conductance between periodically contacting surfaces. - HRB Orlande *(N Carolina State Univ, Raleigh NC 27695)* and MN Ozisik *(Mech and Aerospace Eng Dept, N Carolina State Univ, Raleigh NC 27695)*. J Thermophys Heat Transfer 7(2) 319-325 (Apr-Jun 1993).

The conjugate gradient method of minimization with adjoint equation is used to solve the inverse problem of estimating the timewise variation of interface conductance between periodically contracting solids, under quasisteady-state conditions. It is assumed that no prior information is available on the functional form of the interface conductance, except the magnitude of the period. The accuracy of the inverse analysis is examined by using simulated inexact temperature measurements obtained at the interior of the region. Small periods are usually the most difficult on which to perform an inverse analysis. For such cases, the present method is found to be more accurate and stable then the B-Spline approach.

9A783. Thermal contact conductance of a phase-mixed coating layer by transitional buffering interface. - KC Chung, JW Sheffield, HJ Sauer Jr *(Dept of Mech and Aerospace Eng, Univ of Missouri, Rolla MO 65401)*, TJ O'Keefe *(Dept of Metal Eng, Univ of Missouri, Rolla MO 65401)*, A Williams *(Dept of Mech Eng, Monash Univ, Melbourne, Australia)*. J Thermophys Heat Transfer 7(2) 326-333 (Apr-Jun 1993).

The thermal contact conductances of metallic joints having phase-mixed coating layers applied by a novel transitional buffering interface technique was investigated. This study is restricted to relatively low contact pressure and to microhardness (P/H) ratios, $10^{-4} < P/H < 6 \times 10^{-4}$, where very little data exist. These results are extremely useful for some applications such as electrical contacts in spacecraft. The purposes of this work were 1) to conduct an experimental study to examine four different coating materials, two pure materials, and two phase-mixed materials; and 2) to develop a theoretical model for a phase-mixed coating layer to predict the thermal contact conductance under the first-load cycle. An extensive experimental program was carried out employing four different coating materials, as well as a broad range of surface roughness and microhardness.

406F. ANISOTROPIC MEDIA

9A784. Periodic heat transfer through inhomogeneous media Part 1. Slab. - A Sengupta, MS Sodha, MP Verma, RL Sawhney, M Asthana *(Sch of Energy Stud and Centre of Energy Stud and Res, Devi Ahilya Univ, Indore 452001, India)*. Int J Energy Res **16**(9) 787-802 (Dec 1992).

The paper presents exact analytical solutions of 1D periodic heat conduction through an inhomogeneous slab for a certain class of thermal conductivity profiles (including linear and exponential). The exact analytical solutions for some of these profiles have been compared with those obtained by considering the slab to be made up of a number of homogeneous layers with different thermal conductivities varying from layer to layer and using the layered structure (or matrix multiplication) method. The numerical results arrived at by the layered-structure method converge rapidly (with increasing number of layers considered) to the values obtained from the exact analytical solutions. This gives confidence in the application of the layered-structure method to periodic heat conduction through inhomogeneous slabs. The numerical results have been presented in the form of elements of a 2 x 2 matrix, relating the sinusoidal steady-state temperature and heat flux on the two sides of the slab.

9A785. Steady-state heat conduction problem of the interface crack between dissimilar anisotropic media. - CK Chao and RC Chang *(Dept of Mech Eng, Natl Taiwan IT, Taipei 106, Taiwan, ROC)*. Int J Heat Mass Transfer **36**(8) 2021-2026 (May 1993).

A solution is given for the steady-state heat conduction problem of the interface crack between dissimilar anisotropic media. Based on the Hilbert problem formulation and a special technique of analytical continuation, exact expressions are obtained for the temperature and temperature gradients for both the heat flux prescribed and temperature prescribed boundary conditions. It is found that the temperature gradients near the crack tip always possess the characteristic inverse square tool singularity in rectilinearly anisotropic bodies provided the heat conductivity coefficients are positive definite and symmetric. The strength of heat flux singularities related to the crack dimension is also discussed.

9A786. Two-port network formalism for 3D heat conduction analysis in multilayered media. - PH Leturcq, JM Dorkel, FE Ratolojanahary, S Tounsi *(Lab d'Automatique Anal Syst, CNRS 7, Ave Colonel Roche, 31077 Toulouse Cedex, France)*. Int J Heat Mass Transfer **36**(9) 2317-2326 (Jun 1993).

This paper demonstrates that the two-port network formalism, commonly used to treat 1D heat flow problems in composite slabs, is also applicable to 3D problems in the context of integral transform methods. This provides easy calculation means for temperature and heat flux distributions within multilayered systems. Both spectral and superposition methods are thus presented as examples in a variety of cases of interest to engineers.

406H. MULTIPHASE MEDIA

9A787. Analysis of the effect of the solid layer for the modified chemical vapor deposition process. - YT Lin *(Yvan-Ze IT, Chung-Li, Taiwan, ROC)*, M Choi *(Seoul Natl Univ, Seoul, S Korea)*, R Greif *(Dept of Mech Eng, UCB)*. Warme Stoffubertragung **28**(4) 169-176 (Mar 1993).

The heat transfer problem relative to the modified chemical vapor deposition process has been analyzed and the effects of solid layer thickness, torch speed and tube rotation are studied. The quasi-steady 3D energy equations have been solved for the temperature fields in the gas and the solid layer with a Gaussian heat flux boundary condition on the outer surface. Of particular interest is the effect of the solid layer thickness and the torch speed on inner surface temperature, gas temperature and thermophoretic velocity. The presence of the solid layer and tube rotation reduce the effects of nonuniform torch heating in the circumferential direction and the resulting surface temperatures are very uniform in this direction.

406I. PHASE CHANGE (FREEZING, MELTING)

9A788. Heat transfer in melt spinning of intermetallic materials. - JSJ Chen *(Dept of Mech Eng, Temple Univ, Philadelphia PA 19122)*, WE Frazier *(Adv Metallic and Ceramics Branch, Naval Air Warfare Center, Aircraft Div, Warminster PA 18974)*, AA Tseng *(Dept of Mech Eng, Drexel Univ, Philadelphia PA 19104)*. J Mat Processing Manuf Sci 1(4) 417-429 (Apr 1993).

Analyzes and experiments are performed to investigate heat transfer in melt spinning of intermetallic materials. Previous research efforts in the modeling, the analysis, and the measurement of melt spinning processes are reviewed. The importance of the process parameters, including melt temperature, melt pouring rate, wheel temperature, spinning speed, nozzle-to-wheel gap, and thermal properties of ribbon and wheel, is addressed. A 1D transient mathematical model is developed to predict thermal behavior of melt spinning. The solid-liquid interface velocity and the cooling rate for melt spun $TiAl_3$ are presented. The significance of solidification rate is demonstrated by comparing the macrostructures and microstructures of a rapidly solidified $TiAl_3$ ribbon with a conventionally solidified ingot of the same composition.

9A789. Interface tracking method applied to morphological evolution during phase change. - W Shyy, HS Udaykumar, S-J Liang *(Dept of Aerospace Eng Mech and Eng Sci, Univ of Florida, Gainesville FL 32611)*. Int J Heat Mass Transfer **36**(7) 1833-1844 (May 1993).

The focus of this work is the numerical simulation of interface motion during solidification of pure materials. First, we assess the applicability of the oft-used and quasi-stationary approximation for interface motion. Such an approximation results in poor accuracy for non-trivial Stefan numbers. Next, a generic interface tracking procedure is designed, which overcomes restrictions of single-valuedness of the interface imposed by commonly used mapping methods. The issue of appropriate scaling has been addressed. The Gibbs-Thomson effect for curved interfaces has been included. The evolution of the interface, with the competing mechanisms of undercooling and surface tension is found to culminate in tip-splitting, cusp formation and persistent cellular development.

9A790. Mixture continuum formulation of convection-conduction energy transport in multiconstituent solid-liquid phase change systems for BEM solution techniques. - B Sarler, B Mavko (*Reactor Eng Div, Jozef Stefan Inst, Univ of Ljubljana, Jamova 39, 6111 Ljubljana, Slovenia*), G Kuhn (*Appl Mech, Univ Erlangen-Nuremberg, Egerlandstr 5, D-8520 Erlangen, Germany*). Eng Anal Boundary Elements 11(2) 109-117 (1993).

This paper describes the two nonlinear boundary-domain integral equations for Fourier heat conduction and convection governed energy transport. The equations are compatible with the mixture continuum formulation of an incompressible multiconstituent solid-liquid phase change system. The equations assume the boundary conditions to be functions of thermal field, and thermal conductivity and specific heat to be functions of temperature and species concentrations. The constitutive enthalpy-temperature relation is assumed to be a function of the species concentrations. The presented equations, in connection with a similar integral description for mass, momentum and species conservation, will be used as a basis for the BEM computation of macroscopic transport phenomena characteristic for melting and solidification.

9A791. Numerical modeling of heat transfer in irregular solidification of a liquid. - NI Nikitenko and YN Kol'chik (*Eng Thermophys Inst, Ukrainian Acad of Sci, Kiev, Ukraine*). Heat Transfer Res 24(4) 519-528 (Apr 1992).

A mathematical model and a grid technique for predicting the continuous solidification of liquids in closed vessel, when the phase transition temperature becomes variable, are presented. Results of evaluation of the process of irregular freezing of water in a closed elastic pipe are given.

9A792. Numerical solution of the coupled heat and mass transfer problem of non-planar solidification and melting of aqueous solutions. - M Jochem (*L&C Steinmuller, D-5270 Gummersbach, Germany*) and Ch Korber (*European Patent Office, W-8000 Munchen, Germany*). Warme Stoffubertragung 28(4) 195-204 (Mar 1993).

During freezing of aqueous solutions containing solutes like sodium chloride or glycerol, pure ice is the first solid phase to form. A numerical model is presented for the case of non-planar (dendritic) freezing where local thermodynamic equilibrium can be assumed in the whole "mushy region", allowing a 1D treatment of the coupled heat and mass transfer in this region. Solute diffusion along the resulting interdendritic concentration gradient in the direction of freezing is taken into account by the model. Varying the geometric and thermodynamic boundary conditions, a parameter study was performed for obtaining more information on heat transfer during thawing of regular-shaped samples (plate, cylinder, sphere).

406Y. COMPUTATIONAL TECHNIQUES

9A793. Best approximation method applied to 3D steady-state heat transport. - TV Hromadka II (*Dept of Math, California State Univ, Fullerton CA 92634*) and RJ Whitley (*Dept of Math, UC, Urvine CA*). Adv Eng Software 16(1) 47-51 (1993).

The best approximation method is extended to the numerical solution of 3D steady-state heat transport problems. Two families of trial functions are used in the numerical solution; namely, harmonic polynomials and constant sources. Numerical approximation error is evaluated by means of approximate boundaries whereby error is visualized as a geometric displacement of the problem boundary. The problem considered is the determination of temperatures within a nuclear reactor.

9A794. Iterative CVBEM solution of nonlinear heat transfer problems. - AJ Kassab (*Dept Mech and Aerospace Eng, Univ of Central Florida, Orlando FL 32816-2450*) and S Chesla (*Pratt & Whitney Aircraft, Propulsion Syst Anal, W Palm Beach FL 33410*). Eng Anal Boundary Elements 11(1) 67-75 (1993).

An iterative technique is presented to extend the applicability of the CVBEM to the solution of heat transfer problems with nonlinear radiative boundary conditions. Additionally, nonlinearities arising from the variation of the thermal conductivity with temperature are addressed by means of the Kirchhoff transform. Simple substitution with underrelaxation leads to rapid convergence of the solution. Example problems are presented. The iterative approach is numerically validated and the CVBEM is shown to yield very accurate solutions in few iterations.

9A795. New implementation of the BE technique for time dependent pseudo stationary heat transfer. - JM Houghton (*Dept of Chem Eng, Univ of Bradford, UK*), DB Ingham (*Dept of Appl Math Stud, Univ of Leeds, Leeds LS2 9JT, UK*), PJ Heggs (*Dept Chem Eng, Univ of Bradford, Bradford, UK*). Eng Anal Boundary Elements 11(1) 55-65 (1993).

A new implementation of the BEM solution technique has been devised to investigate time-dependent heat transfer. This new approach has been applied to the problem of oscillatory heat transfer in an isolated fin. A comparison of the results with an existing analytical solution indicates that the BE technique developed in this paper is very efficient. Results are obtained for an aluminium fin over a wide range of heat transfer coefficients, fin dimensions, and amplitude and frequency of the base temperature oscillation of the fin.

See also the following:

9T742. Current trends in heat transfer computations

406Z. EXPERIMENTAL TECHNIQUES

9A796. Determination of the thermal conductivities of building and insulating materials by the probe method. - YH Hamid (*Fac of Eng, Univ of Khartoum, Khartoum, Sudan*) and OA Hamed (*Dept of Chem and Pet Eng, Fac of Eng, Univ of United Arab Emirates, PO Box 17555, Al-Ain, United Arab Emirates*). Int J Energy Res 16(9) 829-835 (Dec 1992).

A simple and inexpensive electrical circuit based on the transient probe method has been developed for the determination of thermal conductivities of building and insulating materials namely limebrick, gypsum, rockwool and polystyrene foam. The solution of the unsteady state heat conduction equation has been approximated by considering certain simplifying assumptions which have been justified by experimental observations. The overall accuracy of the thermal conductivity measurements is estimated to be within ± 3%.

408. Radiation and combined modes

408B. VIEW FACTORS

9A797. Accurate determination of diffuse view factors between planar surfaces. - A Ambirajan (*Dept of Mech Eng, Univ of Missouri, Rolla MO 65401*) and SP Venkateshan (*Dept of Mech Eng, Indian IT, Madras 600 036, India*). Int J Heat Mass Transfer 36(8) 2203-2208 (May 1993).

The contour double integral formula for the view factor between a pair of finite surfaces is a particularly simple formula to implement numerically. This paper suggests a method to improve the accuracy of the numerical results using this formula, both for non-intersecting surfaces, and for intersecting surfaces. In the latter case particularly, significant improvements in accuracy are achieved using the procedure outlined in the paper.

408C. THEORY OF RADIATIVE PROPERTIES

9A798. Effects of particle size distribution and refractive index on fly-ash radiative properties using a simplified approach. - Fengshan Liu (*Dept of Chem Eng, Queen's Univ, Kingston K7L 3N6, ON, Canada*) and J Swithenbank (*Dept of Mech and Process Eng, Univ of Sheffield, Sheffield S1 3JD, UK*). Int J Heat Mass Transfer 36(7) 1905-1912 (May 1993).

The radiative properties of a fly-ash polydispersion are calculated using a simplified approach based on Mie theory. The experimental data of fly-ash complex refractive index of Goodwin (Infrared optical constants of coal slags, Technical Report T-255, Stanford University, California) are employed in the calculation to take into account the wavelength-dependence of optical constants. The uncertainty in representing the particle size distribution is addressed explicitly. Due to this uncertainty, the uncertainty of the wavelength-integrated Planck mean absorption and scattering coefficients can be over 10%.

408D. INTERCHANGE AMONG SURFACES

See the following:

9A941. Calculation of the shape factor from a small rectangular plane to a triangular surface perpendicular to the rectangular plane without a common edge

408E. INVOLVEMENT OF PARTICIPATING MEDIA

9A799. Analysis of infrared radiation heating of plastics. - Toshiyuki Miyanaga and Yukio Nakano (*Central Res Inst of Elec Power Indust, Japan*). Heat Transfer Japan Res 21(6) 631-647 (Apr 1992).

In order to make more effective use of infrared radiation, we have developed a basic method of predicting the heating effect quantitatively. It presents a unidimensional heat-transfer analysis, taking spectral properties into account. We can estimate the distribution and the temporal variation of temperature inside the plastic plates which are to be heated. This method is applicable to heating systems without vaporization and enables us to predict what kind of emitter is most suitable to use with a particular plastic plate.

9A800. Calculation of heat transfer in a tank-type glassmaking furnace with correction for selectivity of the radiation of furnace gases. - Yel Semikin, AYe Yashin, VD Rumyantsev *(Dnepropetrovsk Metal Inst, Russia)*. Heat Transfer Res 24(5) 696-702 (1992).

Predictions of radiative heat transfer in a tank-type glassmaking furnace, with correction for selectivity of radiation of the furnace gases, are presented. It is shown that correction for the selectivity markedly improves the prediction. The predicted and experimental data for an opening furnace are also presented.

9A801. Discrete ordinates solutions for radiatively participating media in a cylindrical enclosure. - S Jendoubi *(Dept of Mech Eng, Univ of Minnesota, Minneapolis MN 55455)*, HaeOK Skarda Lee *(Propulsion Syst Div, NASA Lewis Res Center, Cleveland OH 44135)*, Tae-Kuk Kim *(Dept of Mech Eng, Chung-Ang Univ, Seoul 156-756, Korea)*. J Thermophys Heat Transfer 7(2) 213-219 (Apr-Jun 1993).

The radiative transfer equation is solved by the r-z discrete ordinates method in the 2D r-z coordinates system. The walls of the enclosure are diffuse, and the participating medium absorbs, emits, and anisotropically scatters the radiative energy. Diffuse wall incidence, isothermal medium emission, and collimated incidence problems are considered. Effects of the scattering phase functions on average incident radiation and net radiative heat fluxes are studied.

9A802. Experimental and theoretical study on the radiation of gases containing dust particles. - J Stasiek *(Tech Univ, Gdansk, Poland)* and MW Collins *(Thermo-Fluids Eng Res Centre, City Univ, Northampton Square, London EC1V 0HB, UK)*. Warme Stoffubertragung 28(4) 185-193 (Mar 1993).

The attenuation of thermal radiation within a dilute cloud of pulverized coal and ash is investigated experimentally and theoretically, for different ranges of particle size. An empirical expression is developed for obtaining the absorptivity and emissivity of a coal-ash cloud. A new nomogram is also presented on the basis of this expression.

9A803. Infrared continuum of pure water vapor: Calculations and high-temperature measurements. - JM Hartmann, MY Perrin *(Lab E M2 C CNRS (UPR288), Ecole Centrale Paris, Grande Voie des Vignes, 92295 Chatenay-Malabry Cedex, France)*, Q Ma *(Center for the Study of Global Habitability, Columbia Univ and Inst for Space Stud, Goddard Space Flight Center, New York NY 10025)*, RH Tipping *(Dept of Phys and Astron, Univ of Alabama, Tuscaloosa AL 35487)*. J Qantitative Spectroscopy Radiative Transfer 49(6) 675-691 (Jun 1993).

We present experimental and theoretical studies of medium infrared absorption by pure water vapor. Measurements have been made in the 1900-2600 cm^{-1} and 3900-4600 cm^{-1} regions, for temperature and pressures in the 500-900 K and 0-70 atm ranges, respectively. They are consistent with available data and enable the determination of continuum absorption parameters. It is shown that calculations with line shapes derived from the impact approximation are very inaccurate. Models accounting for the finite durations of collisions and line-mixing through wavenumber dependent effective broadening parameters are introduced. The latter have been determined using two different approaches, which are (i) empirical determinations from fits of experimental data and (ii) direct predictions from first principles using a statistical approach. Effective broadening parameters obtained using these two different approaches are in satisfactory agreement for both the temperature and wavenumber dependencies. These data are tested by calculation of continua in various spectral regions and the agreement with measured values is satisfactory. The remaining discrepancies probably result from the influence of the internal structures of the absorption bands considered and thus from the influence of line-mixing. Nevertheless, accurate predictions are obtained in wide temperature and spectral ranges when the total absorption at elevated density is considered. This agreement, which is due to the relatively weak continuum absorption and large contributions of nearby lines, makes the present models suitable for most practical applications involving elevated densities.

9A804. Infrared gas radiation from a homogeneously turbulent medium. - F Kritzstein and A Soufiani *(Lab Energetique Moleculaire Macroscopique Combustion, CNRS l'ECP Ecole Centrale Paris, Grande Voie des Vignes, 92295 Chatenay-Malabry, France)*. Int J Heat Mass Transfer 36(7) 1749-1762 (May 1993).

Mean infrared radiation from a turbulent, statistically uniform medium is studied theoretically. A stochastic approach is used in which instantaneous temperature and concentration fluctuations are generated by Fourier transforming various forms of the space-time correlation function. The effect of the shape of the spatial correlation function on the model results is found to be negligible. We discuss first the influence of the spectroscopic parameters of an isolated Lorentz line on mean radiative intensities. It is shown that the effects of turbulence depend strongly on the energy of the lower level of the transition. It is also found that the turbulence contribution to the radiative intensity, when integrated over the entire infrared spectrum, decreases quickly when the mean temperature increases in the range [800 - 2000 K].

9A805. Radiation transport around axisymmetric blunt body vehicles using a modified differential approximation. - Lin C Hartung *(Aerothermodyn Branch, Space Syst Div, NASA Langley Res Center, Hampton VA 23681)* and HA Hassan *(Dept of Mech and Aerospace Eng, N Carolina State Univ, Raleigh NC 27695)*. J Thermophys Heat Transfer 7(2) 220-227 (Apr-Jun 1993).

A moment method for computing 3D radiative transport is applied to axisymmetric flows in thermochemical nonequilibrium. Such flows are representative of proposed aerobrake missions. The method uses P-1 approximation to reduce the governing system of integro-differential equations to a coupled set of partial differential equations. A numerical solution for these equations given actual variations of the radiation properties in thermochemical nonequilibrium blunt body flows is devleoped. Initial results from the method are shown and compared to tangent slab calculations. The agreement between the transport methods is found to be about 10% in the stagnation region with the difference increasing along the flank of the vehicle.

9A806. Radiation trapping simulations using the propagator function method. - JE Lawler, GJ Parker *(Dept of Phys, Univ of Wisconsin, Madison WI 53706)*, WNG Hitchon *(Dept of Elec and Comput Eng, Univ of Wisconsin, Madison WI 53706)*. J Qantitative Spectroscopy Radiative Transfer 49(6) 627-638 (Jun 1993).

An integral method of solving the Holstein-Biberman equation based on a propagator function is described. This method is used to solve the equation with a Lorentz lineshape in an infinite plane parallel geometry and a hollow spherical geometry. The method is ideal for solving for both the time dependent and the steady state density of resonance atoms which results from an arbitrary production rate per unit volume. The propagator function method is 100 times faster than the Monte Carlo method. The greater speed of the propagator function method makes it well suited to fully self-consistent kinetic simulations of glow discharge plasmas.

9A807. Radiative transfer in 3D atmosphere-vegetation media. - RB Myneni *(USRA Assoc, NASA Goddard Space Flight Center, Code 923, Greenbelt MD 20771)* and G Asrar *(EOS Project, NASA Headquarters, Code SE, Washington DC 20546)*. J Qantitative Spectroscopy Radiative Transfer 49(6) 585-598 (Jun 1993).

The problem of radiation transfer in 3D atmosphere-vegetation media is formulated in this paper. The atmosphere is treated as a horizontally homogeneous medium but with spatially varying anisotropic lower boundsry. The boundary condition is defined in terms of vegetation canopy bidirectional reflectance factors to be evaluated from a numerical solution of the 3D canopy radiative transfer equation. Numerical results obtained with the discrete ordinates method are in good agreement with the Monte Carlo results of Pearce and field soybean reflectance data of Ranson et al.

9A808. Refractive index and scattering effects on radiative behavior of a semitransparent layer. - CM Spuckler *(Heat Transfer Branch, NASA Lewis Res Center, Cleveland OH 44135)* and R Siegel *(Lewis Res Acad, NASA Lewis Res Center, Cleveland OH 44135)*. J Thermophys Heat Transfer 7(2) 302-310 (Apr-Jun 1993).

Heat transfer characteristics are analyzed for a plane layer of semitransparent material with refractive index ≥ 1. Energy transfer in the material is by conduction, emission, absorption, and isotropic scattering. The layer surfaces are diffuse intending to model a ceramic layer in high temperature applications. Each side of the layer is heated by radiation and convection. Internal reflections at the boundary surfaces are included. For a refractive index larger than unity, there is internal reflection of some of the energy within the layer. The effect of scattering is examined by comparisons with results from an earlier paper for an absorbing layer. Results are given for a gray medium with a scattering albedo up to 0.999, and for a two-band spectral variation of the albedo with one band having low absorption.

406F. COMBINED RADIATION AND CONVECTION

9A809. Radiative-convective heat transfer in a system of two highly porous plates. - SA Zhdanok, SI Shabunya, VV Martynenko, VG Leytsina *(Inst of Heat and Mass Transfer, Minsk, Russia)*. Heat Transfer Res 24(3) 285-301 (Apr 1992).

An algorithm is suggested for a numerical solution of the problem of radiative-convective heat transfer in a system of highly porous plates. Numerical simulation is carried out over a range of problem parameters. The major parameters affecting the process of radiative-convective heat transfer are revealed.

406G. COMBINED RADIATION AND CONDUCTION

9A810. Analysis of the combined conductive - radiative heat transfer between a surface and a gas-fluidized bed at high temperature. - HM Shafey, AMA El-Ghany, AM Nassib *(Dept of Mech Eng, Assiut Univ, Assiut, Egypt)*. Int J Heat Mass Transfer 36(9) 2281-2292 (Jun 1993).

A theoretical investigation of the combined conductive-radiative wall-to-fluidized bed heat transfer is presented. The packet of emulsion is assumed to be an absorbing, emitting, and scattering nongray medium. Equations of energy and radiative transfer in the packet are solved simultaneously using an iterative numerical method. The bubble is modelled as a hemisphere of gas enclosed by the emulsion and the nongray heat transfer surface. Heat transfer coefficients were calculated for different bed systems in the temperature range 300 - 1000°C. The predictions by the present analysis were in good agreement with available experimental data.

9A811. Flowfield coupled excitation and radiation model for nonequilibrium reacting flows. - TA Gally, LA Carlson, D Green *(Texas A&M Univ, College Station TX 77843)*. J Thermophys Heat Transfer 7(2) 285-293 (Apr-Jun 1993).

A second-order method has been developed to correct a radiative transfer analysis for possible local thermodynamic nonequilibrium effects. This method uses a two-species excitation model for nitrogen with chemical reaction rates obtained from the detailed atomic transition method of Kunc and Soon. Results obtained from this new method show more atomic line radiation than the authors' previous first-order method. As improvements to the flowfield representation used in the computations, a full three-temperature energy model and a recently developed multi-component diffusional model have also been incorporated.

9A812. Thermal conductivities of quantum well structures. - G Chen and CL Tien *(Dept of Mech Eng, UCB)*. J Thermophys Heat Transfer 7(2) 311-318 (Apr-Jun 1993).

This work analyzes the size and the boundary effects of a gallium arsenide- (GaAs) based quantum well (QW) structure on the thermal conductivity of the well material. Calculations show that the order of phonon mean free path (MFP) is equal to or even longer than the typical dimensions of the well (~200 Å or less). Holland's model is applied to match the thermal conductivity data of bulk GaAs from 2 to above 600 K. The equation of phonon radiative transfer developed from Boltzmann transport equation is then introduced for the heat transport in the QW structure. Results show that the thermal conductivity at the quantum well can be of one order-of-magnitude lower than that of its corresponding bulk form at room temperature.

408H. COMBINED RADIATION, CONVECTION, AND CONDUCTION

9A813. Thermal processes in gas-powder laser cladding of metal materials. - VK Pustovalov and DS Bobuchenko *(Byelorussian State Polytech Acad, Minsk 220027, Belarus)*. Int J Heat Mass Transfer 36(9) 2449-2456 (Jun 1993).

Energy absorption, heating, melting and heat transfer in a gas-powder laser cladding of substrate metal powders are theoretically investigated. A system of equations is formulated which describes optical and thermal processes of the gas-powder laser cladding. Based on the numerical solution of the system of equations formulated, spatial temporal temperature distributions in 1D approximation and time dependence of the process parameters for continuous and pulse cladding modes are obtained. Some specific features of the pulse modes of the powdered material cladding are studied.

408Y. COMPUTATIONAL TECHNIQUES

9A814. Computation of radiant heat transfer on a nonorthogonal mesh using the finite-volume method. - EH Chui and GD Raithby *(Dept of Mech Eng, Univ of Waterloo, Waterloo N2L 3G1, Canada)*. Numer Heat Transfer B 23(3) 269-288 (Apr-May 1993).

The finite-volume method has been shown to effectively predict radiant exchange in geometrically simple enclosures where the medium is gray, absorbing, emitting, and scattering. Cartesian and circular cylindrical meshes have always been used. The present article shows that the method applies equally well to geometrically complex enclosures where nonorthogonal, boundary-fitted meshes are used. This development permits radiant heat transfer to be computed on the same mesh employed to solve the equations of fluid motion.

See also the following:

9T742. Current trends in heat transfer computations

410. Devices and systems

410B. HEAT EXCHANGERS (RECUPERATOR)

9A815. Field testing of a probe to measure fouling in an industrial flue gas stream. - MS Sohal *(Idaho Natl Eng Lab, EG&G Idaho Inc, Idaho Falls ID 83415)*. Heat Transfer Eng 14(2) 51-61 (Apr-Jun 1993).

In order to design an efficient heat exchanger accurately, a better understanding is needed regarding the foulants that are deposited on the heat transfer surfaces of heat exchangers to recover energy from hot flue gases in industrial furnaces. This article briefly describes the design and fabrication of a gas-side fouling measuring device, and its testing in an industrial environment. It describes probe fabrication, instrumentation used for recoding the data, field test location, tests performed, and data analysis.

9T816. Thermal design of three-fluid cross-flow heat exchangers. - VG Nosach and VYe Filipchuk *(Eng Thermophys Inst, Ukrainian Acad of Sci, Kiev, Ukraine)*. Heat Transfer Res 24(5) 690-695 (1992).

See also the following:

9A53. Dynamics of fluidelastic vibrations of tube bundles in heat exchangers

9A697. Experimental study of laminar entrance flow and heat transfer in finned tub annuli

9A719. Experimental studies of forced, combined and natural convection of water in vertical nine-rod bundles with a square lattice

410C. HEAT EXCHANGERS (REGENERATORS)

9A817. Shell-and-tube-side coefficients in a helium-helium regenerative heat exchanger. - NA Minaylenko, VI Usenko, YP Vorob'yev *(Eng Thermophys Inst, Ukrainian Acad of Sci, Kiev, Ukraine)*. Heat Transfer Res 24(4) 479-482 (Apr 1992).

Experimental data on heat transfer coefficients for a shell-and-tube regenerative heat exchanger are presented.

9A818. Some essential principles for adjustment of seal clearances in rotary regenerators. - T Skiepko *(Dept Eng Electromec, Univ Beira Interior, R Marques d'Avila e Bolama, 6200 Covilha, Portugal)*. Heat Transfer Eng 14(2) 27-43 (Apr-Jun 1993).

In the present study, attention is paid to some indispensable principles for making a useful adjustment of seal clearances in a rotary regenerator, illustrated by means of examples. First, the effect of leakages and their distribution within such a heat exchanger on the efficiency of a steam power plant is presented. Second, in order to show in which rotor state seal clearances should be adjusted, appropriate examples of experimental results concerning radial seal clearances in the hot and cold rotor state are compared. Next, on the basis of a leakage network and some experimental data before and after reduction in radial seal clearances, the effect of reduction in seal clearances on the total leakage and its distribution within a rotary regenerator is shown.

410D. EXTENDED SURFACES

9A819. Effects of internal heat generation, anisotropy, and base temperature nonuniformity on heat transfer from a 2D rectangular fin. - A Aziz *(Dept of Mech Eng, Gonzaga Univ, Spokane WA 99258)*. Heat Transfer Eng 14(2) 63-70 (Apr-Jun 1993).

A FE approach is used to study the 2D performance of a straight fin of rectangular profile operating in a convecting environment. The analysis includes the effects of internal heat generation, anisotropy of fin material, base temperature elevation (depression), and unequal heat transfer coefficients for tip and main convection surfaces. Numerical results are presented showing the impact of these effects on the heat removal capability of the fin.

410E. OTHER AUGUMENTATION TECHNIQUES

See the following:

9A695. Effects of longitudinal vortex generators on heat transfer and flow loss in turbulent channel flows

9A696. Experimental investigations of heat transfer enhancement and flow losses in a channel with double rows of longitudinal vortex generators

9A755. Mechanism of enhancement of heat and mass transfer in a vapor-generating channel with a transverse microfin roughness

9A770. Maximum heat-transferring capacity of two-phase thermosiphons with separate vapor and condensate streams

9A859. Theoretical investigation of acoustic enhancement of heat and mass transfer I. Pure oscillating flow

9A860. Theoretical investigation of acoustic enhancement of heat and mass transfer II. Oscillating flow with a steady velocity component

410F. HEAT PIPES

9A820. Analysis of capillary-induced rewetting in circular channels with internal grooves. - XF Peng, GP Peterson, XJ Lu *(Dept of Mech Eng, Texas A&M Univ, College Station TX 77843)*. J Thermophys Heat Transfer 7(2) 334-339 (Apr-Jun 1993).

A combined theoretical and experimental investigation was conducted to determine the rewetting characteristics of capillary-induced liquid flow in circular channels with microgrooves on the inside surface. This investigation provides a theoretical description of the mechanisms that govern the rewetting of these surfaces, and presents an experimentally verified method by which the location of the rewetting front in the evaporator section of high capacity heat pipes can be determined as a function of the applied heat flux. The rewetting velocity was found to be a function of the thermal properties of the liquid and the channel, the input heat flux, the radii of the groove and the channel, and the location of the liquid front.

9A821. Experimental investigation of an ion-drag pump-assisted capillary loop. - BR Babin, GP Peterson, J Seyed-Yagoobi *(Dept of Mech Eng, Texas A&M Univ, College Station TX 77843)*. J Thermophys Heat Transfer 7(2) 340-345 (Apr-Jun 1993).

A ion-drag pump was constructed and calibrated to determine the available pumping pressure as a function of input voltage for various working fluids. The experimental results were then compared with an analytical model and found to predict the ion-drag pump performance to within ± 15%. Using this information, an analytical model capable of predicting the performance enhancement of an ion-drag pump-assisted capillary loop was also developed and compared with the values obtained from experimental tests conducted on a thermal test loop. Although the analytical model slightly overpredicted the performance enhancement resulting from the ion-drag pump, the predicted trends were similar to those obtained from the experimental program.

9A822. Geothermal heat pipe stability: Solution selection by upstreaming and boundary conditions. - MJ McGuinness *(Math Dept, Victoria Univ of Wellington, New Zealand)*, M Blakeley *(DES, Univ of Auckland, New Zealand)*, K Pruess *(LBL)*, MJ O'Sullivan *(DES, Univ of Auckland, New Zealand)*. Transport Porous Media 11(1) 71-100 (Apr 1993).

In a geothermal reservoir, the heat pipe mechanism can transfer heat very efficiently, with vapor rising and liquid falling in comparable quantities, driven by gravity. For a given heat and mass flux that is not too large, there are two possible steady solutions with vapor-liquid counterflow, one liquid-dominated, and one vapor-dominated. Numerical solution of the equations for two-phase vertical counterflow displays intriguing stability behavior. If pressure and saturation are fixed at depth, and heat and mass flux specified at the top, the vapor-dominated solution is almost always obtained. That is, for a variety of boundary values, the solution settles to the vapor-dominated steady-state, and only for very special values is it possible to obtain the liquid-dominated case. Similarly the liquid-dominated solution is almost always obtained if the boundary conditions are reversed, with pressure and saturation fixed at the top and heat and mass flux specified at depth. This behavior is here explained in two complementary ways. It is shown to be a consequence of upstream differencing of the flow terms in the numerical method. It is also shown to be expected behavior for wavelike saturation solutions. Hence the observed behavior is not only a direct consequence of the numerical method used, but is fundamental to geothermal heat pipes.

9A823. Heat and fluid transport in an evaporative capillary pump. - HG Wulz *(Dept of Space Thermal Tech, Dornier GmbH, PO BOX 14 20, D-7990 Friedrichshafen, Germany)* and F Mayinger *(Dept of Thermodyn A, Tech Univ of Munich, Arcisstr 21, D-8000 Munchen 2, Germany)*. Int J Energy Res 16(9) 879-896 (Dec 1992).

The thermal and fluid mechanical properties of an evaporative capillary pump are described by means of characteristics that have been determined by tests. The capillary pump, which has been newly designed for an application in future space projects, serves a double function as the heat absorbing element in a closed loop as well as a pump circulating the working fluid. The working fluids used were CCl_3F (freon R11) and liquid anhydrous ammonia. The paper describes the associated heat and mass transport in the capillary pump, and the physical process of the capillary pumping is explained. Furthermore, a model is introduced which explains the boiling heat transfer in the porous structure of the capillary pump.

9A824. Mechanism of vaporization in reticulate wicks of low-temperature heat pipes. - GR Kudritskiy, YuN Ostrovskiy, VA Antonenko *(Eng Thermophys Inst, Ukrainian Acad of Sci, Kiev, Ukraine)*. Heat Transfer Res 24(4) 529-534 (Apr 1992).

We present the results of an experimental study of the mechanism of vaporization under conditions simulating heat transfer in a cell of a single-layer screen wick of a low-temperature heat pipe. The experiments involved still and motion-picture photography of the heated wall and photography of scale deposited on that wall under different vaporization conditions. It is shown that vaporization under capillary-suction feed of the wick is very different from nucleate boiling, particularly at high heat flux densities just below a boiling crisis.

9A825. Vapor flow analysis of an axially rotating heat pipe. - A Faghri, S Gogineni, S Thomas *(Dept of Mech Eng and Mat Eng, Wright State Univ, Dayton OH 45435)*. Int J Heat Mass Transfer 36(9) 2293-2303 (Jun 1993).

The vapor flow in an axially rotating heat pipe has been numerically analysed using a 2D axisymmetric model in cylindrical coordinates. A parametric study was conducted for radial Reynolds numbers of 0.01, 4.0, and 20.0, and rotational speeds ranging from 0 to 2800 rpm. The numerical results indicate that the pressure and the axial, radial, and tangential velocities are significantly affected by the rotational speed and the radial Reynolds number. In comparison to non-rotating heat pipes, the radial pressure distributions is no longer uniform. Also, above a certain rotational speed, flow reversal occurs near the centerline of the heat pipe.

See also the following:

9A767. Critical flow and heat transfer in field evaporator pipes

410G. DRYING AND FREEZING

9A826. Experimental verification of a heat pump assisted continuous dryer simulation model. - S Clements, Xiguo Jia, P Jolly *(Energy Lab, Univ of Queensland, Walcott St, 4072 Australia)*. Int J Energy Res 17(1) 19-28 (Jan 1993).

The experimental and predicted performance of a prototype heat pump assisted continuous dryer is reported. The dryer was shown to be capable of specific moisture extraction rates (SMERs) of between 1.5 and 2.5 kg/kWh using wetted foam rubber as the test material being dried. The results highlight the importance of maintaining conditions of high relative humidity within the air stream entering the evaporator; an increase in the relative humidity from 30 to 80% was shown to give a two-fold increase in the SMER. The predicted performance of the dryer using a simulation model developed previously by authors was in good agreement with the corresponding measured values.

9A827. Procedure for processing experimental data on drying. - MS Smirnov, AB Kurzayev, PP Lutsik *(Inst of the Food Indust, Moscow, Russia)*. Heat Transfer Res 24(4) 494-500 (Apr 1992).

Work up of experimental data on the drying of a mixture of quartz sand and silica powder is presented. The temperature distribution is approximated by polynomials, whereas the moisture-content distribution is given by an approximate expression for the drying curve.

410I. ENVIRONMENTAL CONDITIONING AND CONTROL

9A828. Change-point principal component analysis. (CP/PCA) Method for predicting energy usage in commerical buildings: The PCA model. - D Ruch, Lu Chen, JS Haberl, DE Claridge *(Dept of Mech Eng, Texas A&M Univ, College Station TX 77843)*. J Solar Energy Eng 115(2) 77-84 (May 1993).

A new method for predicting daily whole-building electricity usage in a commercial building has been developed. This method utilizes a Principal Component Analysis (PCA) of intercorrelated influencing parameters (eg, dry-bulb temperature, solar radiation and humidity) to predict electricity consumption in conjunction with a change-point method. This paper describes the PCA procedure and presents the results of its application in conjunction with a change-point regression, to predict whole-building electricity consumption for a commercial grocery store. Comparison of the results with a traditional Multiple Linear Regression (MLR) analysis indicates that a change-point, Principal Component Analysis (CP/PCA) appears to produce a more reliable and physically plausible model than an MLR analysis and offers more insight into the environmental and operational driving forces that influence energy consumption in a commercial building.

9A829. Chemical heat pump based on dehydrogenation and hydrogenation of i-propanol and acetone. - Gyung Kim Tae, Koo Yeo Yeong, Keun Song Hyung *(Chem Process Lab, Korea Inst of Sci and Tech, PO Box 131, Cheongryang Seoul 136-650, Korea)*. Int J Energy Res 16(9) 897-916 (Dec 1992).

A chemical heat pump, based on the reversible reaction couple of the i-propanol-acetone system, was investigated experimentally. The endothermic dehydrogenation of i-propanol occurred at 80°C with a Raney nickel catalyst suspended in the liquid phase. The unreacted i-propanol was separated from gaseous products in a condenser. The exothermic hydrogenation reaction of the acetone was performed at 200°C and 1 atm, in the presence of the Raney nickel catalyst. The positive value (ΔG) of the change of Gibbs free energy can make the dehydrogenation reaction of i-propanol rather difficult. This problem can, though, be overcome by the continuous removal of gaseous acetone and hydrogen products from the reaction medium. The dehydrogenation rate equation of i-propanol was obtained as $V = 0.1\ C_p/(1 + 7.0\ C_A)$. The gas phase hydrogenation reaction of acetone was performed in an exothermic tubular reactor. In order to estimate energy efficiency, a simulation of the separation stage was performed. Based on these experimental and simulation results, the optimal design specifications for the chemical heat pump were determined. The maximum hydrogenation of acetone was obtained when the mole ratio of acetone to hydrogen was 4.0. Energy efficiency was increased when the conversions of hydrogenation and dehydrogenation increased.

9A830. Influence of height above sea level on the COP of air-source heat pumps used for water heating. - JP Meyer and GP Greyvenstein *(Dept of Mech Eng, Potchefstroom Univ for CHE, Private Bag X6001, Potchefstroom 2520, S Africa)*. Heat Transfer Eng 14(2) 44-50 (Apr-Jun 1993).

In some countries (eg, S Africa), important market areas for air-source heat pumps are situated high above sea level, and it is therefore necessary to know what the influence of height is on the performance of heat pumps for water heating. Therefore, a study was conducted that predicts the influence of height on the coefficient of performance (COP) of air-source heat pumps. The results were verified by means of a simulation study. It was concluded that height has little influence on COP if the evaporator of the heat pump is wet on the air side. A more significant weakening in the performance occurs, however, when the air side of the evaporator is dry.

9A831. Infrared imaging results of an excited planar jet. - RB Farrington *(Natl Renewable Energy Lab, Golden CO 80401)*. J Solar Energy Eng 115(2) 85-92 (May 1993).

Planar jets are used for many applications including heating, cooling, and ventiliation. Generally, a planar jet provides good mixing within an enclosure. In building applications, the jet provides both thermal comfort and adequate indoor air quality. Increased mixing rates may reduce short circuiting of conditioned air, eliminate dead zones within the occupied zone, reduce energy costs, increase occupant comfort, and increase indoor air quality. This article discusses how an infrared imaging system was used to demonstrate how jet excitation affected the spread angle and the jet mixing efficiency. Digital data reduction and analysis shows changes in jet isotherms and quantify the increased mixing caused by excitation.

9A832. Measurement of ventilation and aerosol particles in buildings. - SB Riffat and KW Cheong *(Nottingham Sch of Architec, University Park, Nottingham NG7 2RD, UK)*. Int J Energy Res 17(1) 45-55 (Jan 1993).

The work described in this paper is concerned with the measurement of the flow of tracer gas and aerosol particles in rooms. Measurements were carried out in single- and two-zone systems using SF_6 tracer gas and oil-smoke particles. Initial tests were carried out in single-zone system using different arrangements of window opening. Results indicated that tracer-gas exchange rates were generally higher than particle exchange rates. This was due to the fact that the ventilation air entering the zone contained a significant concentration of particles but a neligible quantity of tracer gas.

9A833. Multi-unit heat pump and system. - E Bogdanova and A Grinberg *(Univ of Tech, bul kl Ohridsky 8, Sofia, Bulgaria)*. Int J Energy Res 16(9) 803-810 (Dec 1992).

In the paper, conditions for multi-unit heat pump (MUHP) stationary operation at the level of condenser and evaporator groups and in a system are considered. The matrices describing the equilibrium operation are defined, and the method of their determination are described.

9A834. Solid-gas chemical heat pumps: Field of application and performance of the internal heat of reaction recovery process. - P Neveu and J Castaing *(CNRS, Inst Sci Genie Materiaux Procedes, 52 Ave Villeneuve 66860 Perpignan, Cedex, France)*. Heat Recovery Syst CHP 13(3) 233-251 (May 1993).

With the four components of a chemical heat pump (two solid-gas reactors, an evaporator and a condenser) a cycle of the double-effect type can be applied to continuous refrigeration. The performance of this process is analyzed, allowing the infinite sink temperature and the couples of reactive salts to be used, which depend on the production temperature envisaged, to be selected. The results are presented in a diagram from which may be determined the required source temperature (as a function of the refrigeration temperature), the machine's coefficient of performance, its exergetic efficiency and the equilibrium drop, ie, the power level that can be reached. This process is compared to the double-effect cycle developed on solid adsorption machines.

9A835. Stationary operation of a unit in a multi-unit heat pump system. - E Bogdanova and A Grinberg *(Univ of Tech, bul kl Ohridsky 8, Sofia, Bulgaria)*. Int J Energy Res 16(9) 811-827 (Dec 1992).

In the paper, a method for the determination of the parameters of the units, stationary operating in a multi-unit heat pump system, is presented. This method is used for the consideration of six schemes of hydraulic connection of the heat exchangers in groups.

9A836. Use of simplified system models to measure retrofit energy savings. - S Katipamula and DE Claridge *(Energy Syst Lab, Dept of Mech Eng, Texas A&M Univ, College Station TX 77843)*. J Solar Energy Eng 115(2) 57-68 (May 1993).

The retrofit of dual-duct constant volume systems with energy-efficient variable air volume systems has become common in recent years. In general, the energy savings from such retrofits are estimated by developing a temperature-dependent regression model using whole building preretrofit energy consumption data. Model predictions are then compared with measured post retrofit consumption, to determine the savings. In cases where the preretrofit energy consumption is not available such a method cannot be implemented. This paper describes a method that can be used to calculate savings in such cases. The method is based on use of simplified calibrated system models. A VAV model was developed based on the ASHTRAE TC 4.7 Simplified Energy Analysis Procedure (SEAP) (Knebel, 1983) and calibrated with the postretrofit energy consumption of a large engineering center in Central Texas. The loads from the calibrated VAV model were then used with the DDCV model to estimate the preretrofit energy use, also based on TC 4.7 SEAP, and apparent savings were determined as the difference between the DDCV predicted consumption and measured energy consumption for the postretrofit VAV system.

See also the following:

9A850. Interzonal natural convective heat and mass flow through doorway-like apertures in buildings: Experimental results

410L. THERMAL ENERGY STORAGE SYSTEMS

9A837. Phase change thermal storage: Transient behavior analysis of a solar receiver-storage module using the enthalpy method. - C Bellecci *(Dept Fisica, Univ della Calabria, 87030 Rende, Italy)* and M Conti *(Dept Matematica Fisica, Univ Camerino, 62032 Camerino, Italy)*. Int J Heat Mass Transfer 36(8) 2157-2163 (May 1993).

The performance of a Solar Receiver Unit with a built-in thermal storage system is simulated by the enthalpy method. It is shown that accurate results can be obtained with a simplified modelling of the forced convection heat extraction. The results indicate some criteria to determine the optimal size of the storage system.

9A838. Study of the heat transfer behavior of a latent heat thermal energy storage unit with a finned tube. - M Lacroix *(Dept Genie Mec, Univ Sherbrooke, J1K 2R1, PQ, Canada)*. Int J Heat Mass Transfer 36(8) 2083-2092 (May 1993).

A theoretical model for predicting the transient behavior of a shell-and-tube storage unit with the PCM on the shell side and the HTF circulating inside the tubes is presented. The tubes are bare or finned. The multidimensional phase change problem is tackled with an enthalpy based method coupled to the convective heat transfer from the HTF. The numerical model is validated with experimental data. Results show that the annular fins are most effective for moderate mass flow rates and small inlet temperatures.

412. Thermomechanics of solids

412A. GENERAL THEORY

9A839. Compound effect of cutting depth and bit dull on cutters' temperature for polycrystalline diamond compact bits. - Ergun Kuru, Lsu Metu *(Pet Eng Dept, Middle E Tech Univ, Ankara, Turkey)*, AK Wojtanowicz, Lsu Conoco *(Pet Eng Dept, Louisiana State Univ, Baton Rouge LA 70893)*. J Energy Resources Tech 115(2) 124-132 (Jun 1993).

This paper presents a simulation study to evaluate the combined effect of cutting depth (drilling rate) and wear (bit dull) on the thermal response of polycrystalline diamond compact (PDC) cutters under downhole drilling conditions. A new understanding of frictionally generated heat between rock and PDC cutter is introduced from the analysis of forces active on the wearflat and the cutting (leading) surfaces of a cutter. This new concept is used to predict PDC bit performance with the controlled temperature of its cutters. Also demonstrated is the actual impact of these findings on field drilling practices. The example comparison is made by calculating the optimal-control surface. For practical applications, the study reveals that many field failures of PDC bits may have been caused by lack of understanding of operational limits imposed by heat considerations.

412B. THERMOELASTICITY (STEADY AND QUASI-STEADY)

See the following:

9A449. Shape optimal design of an engine exhaust manifold

412E. INELASTIC THERMOMECHANICS

See the following:

9A172. Effects of stress rates on the strength and deformation of concrete at ambient and elevated temperatures

412F. THERMOMAGNETIC AND THERMOELECTRIC EFFECTS

9A840. Thermo-elasto-viscoplasticity of isotropic porous metals. - A Zavaliangos and L Anand *(Dept of Mech Eng, MIT)*. J Mech Phys Solids 41(6) 1087-1118 (Jun 1993).

A rate and temperature dependent elastic-plastic model for isotropic, moderately porous metallic materials is formulated. This model is intended for material rate-sensitivities in the entire range spanning from highly rate-dependent behavior at high homologous temperatures to nearly rate-insensitive behavior at low homologous temperatures. The predictive capabilities of the constitutive models are verified by comparing results from FE calculations against results from physical experiments. Predictions from the computational procedures for both examples agree well with the experimental results. The new state variable rate and temperature dependent constitutive model for microporous materials and the associated computational procedures form a basis for the simulation and design of deformation processing operations. This new capability should be useful for the prediction of formation of defects during both cold-working when the material rate sensitivity is low, as well as hot-working when the material is highly rate sensitive.

412H. THERMAL FATIGUE AND STABILITY

9A841. Thermal cycling damage of metal matrix composites: Analytical study on dimensional change. - Minoru Taya *(Dept of Mech Eng, Univ of Washington, Seattle WA 98195)*, WD Armstrong *(Nagasaki R&D Center, Mitsubishi Heavy Indust LTD, Nagasaki 851-03, Japan)*, M Dunn *(Solid and Struct Mech 1562, Sandia)*. Appl Mech Rev 46(5) 201-210 (May 1993).

An analytical model to predict dimensional changes in thermal cycled metal matrix composites with and without constant stress is proposed. The present model assumes that the temperature-time relation to simulate thermal cycling is of a step-function type and the matrix metal deforms as elastic-plastic-creep material while the fiber remains elastic throughout thermal cycling. Another model is also constructed to simulate the later stage of thermal cycling damage where the debonding of the matrix-fiber interface would presumably take place progressively with number of cycles.

412J. THERMOFRACTURE MECHANICS

9A842. Three-dimensional analysis of thermally loaded cracks. - ST Raveendra, PK Banerjee, GF Dargush *(Dept of Civil Eng, SUNY, Buffalo NY 14260)*. Int J Numer Methods Eng 36(11) 1909-1926 (15 Jun 1993).

The stress intensity factors for cracks in 3D, thermally stressed structures are computed by using the BEM. While many boundary and volume-integral-based formulations are available for the treatment of thermoelastic problems in solids, the present analysis is based on a recently developed boundary-only formulation. The accuracy of the solutions in the present work is improved by using special elements at the crack front that accurately model the variation of displacement, temperature fields and singularity of traction, flux fields.

412L. COMPOSITE MATERIALS

9A843. Aspects of residual thermal stresses in continuous-fiber-reinforced ceramic matrix composites. - KL Powell, PA Smith, JA Yeomans *(Dept of Mat Sci and Eng, Univ of Surrey, Guildford, Surrey GU2 5XH, UK)*. Composites Sci Tech 47(4) 359-367 (1993).

An analytical model is presented that predicts the thermal stresses which arise from mismatch in coefficients of thermal expansion between a fiber and the surrounding matrix in a continuous fiber composite. The model consists of two coaxial isotropic cylinders. Stress transfer between the fiber and the matrix near an unstressed free surface has been modeled by means of a shear-lag analysis. Away from the free surface the theoretical approach satisfies exactly the conditions for equilibrium and continuity of stress at the fiber-matrix interface. Application of the model to a composite consisting of a glass-ceramic calcium aluminosilicate matrix containing unidirectional Nicalon fibers points to a strong dependence of stress on fiber volume fraction. Surface effects are significant for depths of the order of one fiber diameter. Near-surface shear stresses resulting from cooling from the stress-free temperature are sufficiently high to suggest that a portion of the fiber close to the surface is debonded at room temperature. Experimental results acquired with a scanning electron microscope equipped with a heating stage are consistent with this prediction. Consequently, the model has been modified in a simple way to incorporate frictional slip at the interface, according to the Coulomb friction law. Although detailed measurements are limited by the resolution of the technique, experimental evidence suggests that the transfer length is within an order of magnitude of the model prediction.

9A844. Effects of thermal residual stresses and fiber packing on deformation of metal-matrix composites. - T Nakamura *(Dept of Mech Eng, SUNY, Stony Brook NY 11794)* and S Suresh *(Div of Eng, Brown Univ, Providence RI 02912)*. Acta Metall Mat 41(6) 1665-1681 (Jun 1993).

The combined effects of thermal residual stresses and fiber spatial distribution on the deformation of a 6061 aluminum alloy containing a fixed concentration unidirectional boron fibers have been analyzed using detailed FE models. The geometrical structure includes perfectly periodic, uniformly spaced fiber arrangements in square and hexagonal cells, as well as different cells in which either 30 or 60 fibers are randomly placed in the ductile matrix. The results indicate that both fiber packing and thermal residual stresses can have a significant effect on the stress-strain characteristics of the composite. The thermal residual stresses cause pronounced matrix yielding which also influences the apparent overall stiffness of the composite during the initial stages of subsequent far-field loading along the axial and transverse direction.

9A845. Low-temperature flexural dynamic measurements on PEEK, HTA and some of their carbon fibre composites. - RD Adams *(Dept of Mech Eng, Univ of Bristol, Bristol BS8 1TR, UK)* and JM Gaitonde *(Dept of Aerospace Eng, Univ of Bristol, Bristol BS8 1TR, UK)*. Composites Sci Tech 47(3) 271-287 (1993).

Polymers and polymer matrix composites undergo mechanical relaxations which are dependent on the temperature and frequency. A major glass-rubber (α) transition occurs for most structural polymers above 100° C. The work reported here concerns the low-temperature β and γ transitions and their effect on the modulus and mechanical damping of some structural thermoplastic materials. To this end, the flexural moduli and specific damping capacities of unreinforced PEEK, HTA and some unidirectional PEEK-AS4 and HTA-AS4 specimens have been measured between - 196° C and room temperature in vacuo. Specimens containing PEEK show a linear decrease of modulus with temperature whereas those containing HTA show a decrease which incorporates a pronounced drop (as a result of a peak in the damping). Damping results are compared with theoretical predictions which were derived by the use of the viscoelastic correspondence principle. In particular, the derivation of a predictive formula for the transverse damping of a unidirectional composite is presented, and this is shown to produce good results in view of experimental scatter.

9A846. Recent developments of thermosetting polymers for advanced composites. - HD Stenzenberger *(Technochemie GmbH Verfahrenstechnik, D-6915, Dossenheim, Germany)*. Composite Struct 24(3) 219-231 (1993).

The aircraft-industry is the fastest growing market sector for advanced composites. To use fully the potential of advanced composites for demanding structural applications it requires improved properties of its constituents, the carbon fibers and polymer matrix resins. This article emphasizes new developments of thermosetting polymers such as epoxy resins and bismaleimides. The concepts to achieve improved thermosetting polymer matrix resins are new monomers (resins and curing agents), thermoplastic modification, liquid crystalline monomers and impact tolerant interleafed systems. The paper highlights thermoset resins and systems which provide improvements in the areas of moisture absorption, fracture toughness and high temperature stability.

9A847. Residual thermal stresses in filamentary polymer-matrix composites containing an elastomeric interphase. - SD Gardner, CU Pittman Jr *(Dept of Chem Eng, Mississippi State Univ, Mississippi State MS 39762)*, RM Hackett *(Dept of Civil Eng, Univ of Mississippi, University MS 38677)*. J Composite Mat 27(8) 830-860 (1993).

A three-phase micromechanical model based on the method of cells is formulated to characterize residual thermal stresses in filamentary composites containing an interphase between the fiber and the matrix. This is the first such study to incorporate a true three-phase version of the method of cells. The model's performance is critically evaluated using data generated from other micromechanical models. The data correlate the residual thermal stresses in the fiber, interphase and matrix as a function of the interphase thickness and fiber volume fraction within each model composite. The study makes a broad assessment of the stress-attenuating characteristics that each interphase imparts to the graphite-epoxy composites.

9A848. Thermal degradation of an end-capped bismaleimide resin matrix (PMR-15) composite reinforced with pan-based carbon fibres. - ZD Xiang and FR Jones *(Dept of Eng Mat, Univ of Sheffield, Sheffield S10 2TZ, UK)*. Composites Sci Tech 47(3) 209-215 (1993).

Kinetics of thermal degradation of carbon fibre composites based on the PMR-15 resin have been studied in the temperature range of 382 - 457° C both in air and in nitrogen. The decomposition temperature of the matrix occurs at approximately 420° C and is not affected by the surrounding atmosphere. Degradation of the laminates in air, which occurs at a significantly higher rate than in nitrogen, consists of three kinetically different stages. The activation energy of degradation in air has been found to be between 98 and 315 kJ mol^{-1} depending on temperature range. The activation energy for oxidation of the carbon fibres in air is estimated to be 100 kJ mol^{-1}.

See also the following:

- 9A201. Effect of fiber concentration on the thermal conductivity of a polycarbonate-pitch-based carbon fiber composite
- 9A203. Anelastic deformation of a thermoplastic-matrix fiber composite at elevated temperature Part I. Neat resin structure characterization
- 9A204. Anelastic deformation of a thermoplastic-matrix fiber composite at elevated temperature Part II. Time-temperature dependent matrix behavior
- 9A205. Anelastic deformation of a thermoplastic-matrix fiber composite at elevated temperature Part III. Structure and thermomechanical properties of AS4-PACM-12 composite
- 9A577. Thermal analysis for resistance welding of large-scale thermoplastic composite joints

412Y. COMPUTATIONAL TECHNIQUES

9A849. Piecewise hierarchical p-version axisymmetric shell element for nonlinear heat conduction in laminated composites. - A Bose and KS Surana *(Dept of Mech Eng, Univ of Kansas, 3013 Learned Hall, Lawrence KS 66045)*. Comput Struct 47(1) 1-18 (3 Apr 1993).

This paper presents a three-node axisymmetric shell FE formulation for nonlinear axisymmetric steady-state heat conduction in laminated composites where the temperature approximation for the laminate is piecewise hierarchical and is derived based on the p-version. The temperature approximation for the element is developed first by establishing a hierarchical temperature approximation for each lamina of the laminate and then by imposing inter-lamina continuity conditions of temperature at the interface between the laminas. Weak formulation of the Fourier heat conduction equation in the cylindrical coordinate system with temperature-dependent thermal conductivities, internal heat generation, film coefficients and radiation effects is constructed and the individual lamina matrices and equivalent nodal heat vectors are derived using this weak formulation and the hierarchical temperature approximation for the laminas. Due to the temperature dependence of thermal conductivities, internal heat generation, film coefficients and radiation parameters; the resulting discretized equations of equilibrium are nonlinear. These equations are solved using the modified Newton-Raphson method. The tangent matrix is derived using the nonlinear equations of equilibrium. Numerical examples are presented to demonstrate the accuracy, efficiency and overall superiority of the present formulation and the extremely good and fast convergence of the iteration process. Comparisons are made with the available results in the literature.

414. Mass transfer

414B. CONVECTION DOMINATED TRANSFER

9A850. Interzonal natural convective heat and mass flow through doorway-like apertures in buildings: Experimental results. - MNA Said, SA Barakat, EA Whidden *(Inst for Res in Construct, NRC, Ottawa K1A 0R6, ON, Canada)*. J Solar Energy Eng **115**(2) 69-76 (May 1993).

This paper presents the results of full-scale experiments in a realistic building to evaluate natural convective heat and mass transfer through doorway-like apertures under small temperature differentials. The zone-to-zone temperature differences were nominally between 1° C and 2.5° C. Heat transfer correlations, coefficient of discharge, and thermal stratification are reported for air (Pr = 0.71), an enclosure aspect ratio of 0.26, aperture height relative to the enclosure height in the range of 0.75 to 1, and aperture width relative to the enclosure width in the range of 0.29 to 0.79. In general, the results extend the validity of previous theoretical and experimental work in the literature to large doorway-like apertures and small temperature differentials across the aperture typical to residential building conditions.

414C. SUBLIMATION OR ABLATION

9A851. Current distribution in the cathode area of an arcjet. - P Durgapal *(NASA Ames Res Center, MS 229-4, Moffett Field CA 94034)*. J Thermophys Heat Transfer 7(2) 241-250 (Apr-Jun 1993).

A theoretical model of the electrode phenomena, leading to the computation of the current density distributions, are spot temperature, spot size, sheath voltage, ablation velocity, and ablation rates, is put forward. Computations for an atmospheric arc, at load currents ranging from 800 to 3000 A, in 1) one segment, and 2) four segment electrode configurations, are conducted. Spot size seems to vary linearly with load current, ranging from 1.82 to 3.22 mm for a rotating arcfoot, as the load current is varied from 800 to 3000 A. Computations for P = 50 atm and I = 6000 A reveal that arc rotation is even more essential in order to save the excessive material ablation. In order to achieve an acceptable level of material ablation at P = 50 atm and I = 6000 A, a rotational frequency of 300 - 400 Hz needs to be achieved.

9A852. Influence of the freezing process on vapor transport during sublimation in vacuum-freeze-drying of macroscopic samples. - M Kochs *(Pierburg GmbH, Alfred-Pierburg-Str 1, D-4040 Neuss 1, Germany)*, Ch Korber, I Heschel, B Nunner *(Helmholtz-Inst Biomed Technik, RWTH, Paulwelsstr 30, D-5100 Aachen, Germany)*. Int J Heat Mass Transfer **36**(7) 1727-1738 (May 1993).

The influence of freezing on mass transfer during subsequent sublimation was examined in macroscopic samples (cm scale). A matrix with regions of pure ice and regions of concentrated solution forms during freezing. In macroscopic samples, resulting from local differences in solidification conditions, this matrix is irregular, leading to local differences in mass transfer properties in the drying sample. Sample segments at positions where solidification started yield small diffusion coefficients, the value increasing with the distance from this position, reaching a maximum in a layer right below the sample surface. A covering layer forms a limiting barrier against vapor transport. In macroscopic samples, a decrease of the applied cooling rate leads to a significant shift of the profile of space dependent diffusion coefficients to higher values and therefore to reduced drying times.

414D. DIFFUSION

9A853. Use of random walk models with spatially variable diffusivity. - JR Hunter, PD Craig, HE Phillips *(Div of Oceanog, CSIRO, GPO Box 1538 Hobart, Tasmania, Australia)*. J Comput Phys **106**(2) 366-376 (Jun 1993).

The random walk technique is commonly used to model diffusion in the environment. For a constant diffusivity K and model time-step δt, the random step should be chosen from a distribution with variance $2K\delta t$. However, if K varies spatially, this choice of step leads to the accumulation of particles in regions of low diffusivity. This problem can be overcome either by the incorporation of an apparent advection velocity, or by transforming to a coordinate system in which the diffusivity is constant. The latter technique requires no immediate approximations, is applicable to any reasonable diffusivity field and is therefore the preferred approach. Three important aspects of model design are discussed: the selection of the random number generator, the time step and the total number of particles.

414E. CONVECTION WITH DIFFUSION

9A854. Comparison of the solidification of aqueous sodium chloride with augmenting and opposing thermosolutal buoyancy forces. - S Chellaiah, MA Zampino *(Dept of Mech Eng, Florida Int Univ, Miami FL 33199)*, RA Waters *(AB_2MT Consult, Miami FL 33156)*. J Mat Processing Manuf Sci 1(4) 399-415 (Apr 1993).

The results of an experimental study to compare and illustrate the effects of thermosolutal convection and augmenting and opposing buoyancy forces on the solidification of aqueous sodium chloride are reported. Three experiments were performed with initial solute concentrations in the hypoeutectic (5%), eutectic (23.3%), and hypereutectic (24.5%) range. For the hypoeutectic solution, solidification causes solute to be redistributed into the bulk melt and divides melt into two distinct regions separated by a double-diffusive interface. In each of these regions, the temperature and concentrations distributions were significantly different. At the eutectic composition, solidification occurs as for a pure substance and hence, only thermally induced natural convection was present. In the bulk melt, there was a stable vertical temperature stratification. During solidification of the hypereutectic solution, solute was not redistributed into the bulk melt, but instead, solid sodium dihydrate crystals were formed.

9A855. Diffusion-controlled mass transfer from a rotating cylinder. - HQ Yang *(CFD Res, 3325-D Triana Blvd, Huntsville AL 35805)*. Numer Heat Transfer A **23**(3) 303-318 (Apr-May 1993).

In the chemical vapor deposition process, the objective is to grow a crystal film as fast as possible, while at the same time ensuring its chemical uniformity and crystal graphic perfection. This paper studies the possible enhancement of diffusion-controlled mass transfer by rotating a cylindrical substrate, which is used in the manufacture of superconductor materials. The numerical inaccuracy associated with the use of the conventional weak conservation form of the Navier-Stokes equations in polar coordinates is shown to be around 15%. It is found that rotation has minor influences on the average mass transfer rate and it generally increases the uniformity of the transport process.

9A856. Effect of axial solid heat conduction and mass diffusion in a rotary heat and mass regenerator. - JY San and SC Hsiau *(Dept of Mech Eng, Natl Chung-Hsing Univ, 250 KuoKuang Rd, Taichung 400, Taiwan, ROC)*. Int J Heat Mass Transfer **36**(8) 2051-2059 (May 1993).

This research analyzes the effect of axial heat conduction and mass diffusion on the performance of a solid desiccant wheel. A 1D transient heat and mass transfer model which contains four nonlinear partial differential equations is developed. The equations are solved using a full-implicit finite-difference method. A limiting case with a zero solid diffusion resistance is considered. The parameter, (λ2/4Ntu/Bi) is found to be the most important factor governing the axial heat conduction and mass diffusion effect.

9A857. Local heat-mass transfer distribution in a square channel with full and v-shaped ribs. - RT Kukreja, SC Lau, RD McMillin *(Dept of Mech Eng, Texas A&M Univ, College Station TX 77843-3123)*. Int J Heat Mass Transfer **36**(8) 2013-2020 (May 1993).

Naphthalene sublimation experiments have been conducted to study the turbulent heat-mass transfer characteristics of airflow in a square channel, in which two opposite walls are roughened with aligned arrays of full ribs and V-shaped ribs. The detailed distributions of the local heat-mass transfer coefficient on the ribbed walls and on the smooth walls are obtained. Results show that there are significant spanwise as well as streamwise variations of the local heat-mass transfer coefficient of the exposed surfaces of the ribbed walls in the oblique full rib and V-shaped rib cases.

9A858. Study of the effects of chemical reaction on the modified chemical vapor deposition (MCVD) process. - S Joh, R Greif *(Dept of Mech Eng, UCB)*, YT Lin *(Yuan-Ze IT, Taoyuan, Taiwan)*. J Mat Processing Manuf Sci 1(4) 369-386 (Apr 1993).

A study has been made of the effects of chemical reaction on the heat transfer and the deposition of particles that occurs during the Modified Chemical Vapor Deposition process. The steady-state energy and species equations for the gas ($SiCl_4$) and the particles (SiO_2) have been solved numerically for flow in a tube. The first order reaction rate for $SiCl_4$ has been used to include the reaction energy source that results from exothermic oxidation. Of particular interest are the effects of the inlet gas ($SiCl_4$) concentration flow rate and maximum wall temperature on the temperature and deposition profiles. It is shown that a spike in the temperature profile may occur, which alters the deposition characteristics.

9A859. Theoretical investigation of acoustic enhancement of heat and mass transfer I. Pure oscillating flow. - Man Yeong Ha *(Dept of Mech and Prod Eng, Pusan Natl Univ, 30 Jangjeon-Don Kumjung-Ku, Pusan 609-735, Korea)* and S Yavuzkurt *(Dept of Mech Eng, Penn State)*. Int J Heat Mass Transfer 36(8) 2183-2192 (May 1993).

Effects of an oscillating flow induced by a high intensity acoustic field on heat and mass transfer to and from particles and droplets such as pulverized coal particles and coal-water slurry fuel droplets are investigated. Numerical solutions of 2D, unsteady, laminar conservation equations for mass, momentum and energy transport in the gas phase give the velocity and temperature fields around a particle for different oscillating flows without superposed steady component as a function of time. The local and space-averaged Nusselt numbers depend on the change of imposed oscillating velocity U due to body curvature and flow acceleration. The combined effects of curvature and flow acceleration result in the maximum difference of 9% in the space- and time-average Nusselt number for frequencies of 50, 1000 and 2000 Hz for the acoustic Reynolds number varying between 10 and 100. The present results show about 290% increase in the space- and time-averaged Nusselt number for an acoustic Reynolds number of about 100 compared to that without acoustic field.

9A860. Theoretical investigation of acoustic enhancement of heat and mass transfer II. Oscillating flow with a steady velocity component. - Man Yeong Ha *(Dept of Mech and Prod Eng, Pusan Natl Univ, 30 Jangjeon-Dong Kumjung-Ku, Pusan 609-735, Korea)* and S Yavuzkurt *(Dept of Mech Eng, Penn State)*. Int J Heat Mass Transfer 36(8) 2193-2202 (May 1993).

In order to study the effects of high intensity acoustic fields superposed on a steady flow on heat and mass transfer around spherical particles, a 2D, unsteady computer code which employs the 2D, unsteady conservation of mass, momentum and energy equations for laminar flow in spherical coordinates has been developed. Numerical solutions of these equations give the velocity and temperature fields around the particle for acoustically oscillating flow as a function of acoustic Reynolds number, Strouhal number, and the ratio of the acoustic velocity on the steady slip velocity between the particles and the main flow. The present results show about 85% increase in the space- and time-averaged quasi-steady Nusselt number normalized by its steady value when the ratio of the acoustic velocity to the steady slip velocity is about 5. The results demonstrate a definite enhancement of heat and mass transfer in the presence of high intensity acoustic fields particularly for the case of low steady slip velocity.

414F. DOUBLE DIFFUSION AND OTHER COMBINED EFFECTS

9A861. Double-diffusive convection during solidification of a binary system. - Tatsuo Nishimura *(Dept of Mech Eng, Yamaguchi Univ, Japan)*, Masaki Fujiwara, Hisashi Miyashita *(Dept of Mat Sci and Eng, Toyama Univ, Japan)*. Heat Transfer Japan Res 21(6) 586-600 (Apr 1992).

An experimental study of solidification is performed for a super-eutectic sodium carbonate solution (Na_2CO_3-H_2O) in a confined cavity with varying initial concentrations and temperatures. We show important features of transport processes of heat and species during horizontal solidification by quantitative measurements of temperature and concentration. Initial superheat is found to be responsible for the initiation of the double-diffusive cells. For a higher initial concentration, a larger initial superheat is required for the onset of the double-diffusive cells.

9A862. Experimental and numerical analyses of double diffusive natural convection heated and cooled from opposing vertical walls with an initial condition of a vertically linear concentration gradient. - Katsuyoshi Kamakura *(Toyama Natl Col of Tech, Toyama 939, Japan)* and Hiroyuki Ozoe *(Inst of Adv Mat Stud, Kyushu Univ, Kasuga 816, Japan)*. Int J Heat Mass Transfer 36(8) 2125-2134 (May 1993).

When a solution having a vertically linear concentration gradient is heated from a vertical wall and cooled from an opposing vertical wall, multi-layered roll cells separated by almost-horizontal sharp interfaces are observed. A Galerkin FEM was employed for the numerical analysis of this double diffusive convection. Multi-layered roll cells with sharp and almost-horizontal interfaces were formed in the numerical simulation and then the concentration in each layer became almost uniform. The experiment confirmed the numerical results.

9A863. Study of the effects of macrosegregation and buoyancy-driven flow in binary mixture solidification. - SK Sinha *(Dept of Mech Eng, Delhi IT, Kashmere Gate, Delhi 110 006, India)*, T Sundararajan *(Dept of Mech Eng, Delhi IT, Kanpur 208 016, India)*, VK Garg *(NASA Lewis Res Center, MS 5-11, 21000 Brookpark Rd, Cleveland OH 44135-3191)*. Int J Heat Mass Transfer 36(9) 2349-2358 (Jun 1993).

A generalized anisotropic porous medium approach is developed for modelling the flow, heat and mass transport process during binary mixture solidification. Transient predictions are obtained using FEM, coupled with an implicit time-marching scheme, for solidification inside a 2D rectangular enclosure. A parametric study focusing attention on the effects of solutal buoyancy and thermal buoyancy is presented.

See also the following:

9A643. Pattern selection for the oscillatory onset in thermosolutal convection

414I. POROUS MEDIA

9A864. Analytical approximation for nonlinear adsorbing solute transport and first-order degradation. - WJP Bosma and SEATM Van der Zee *(Dept Soil Sci and Plant Nutrition, Agri Univ, PO Box 8005, 6700 EC Wageningen, Netherlands)*. Transport Porous Media 11(1) 33-43 (Apr 1993).

Under some constraints, solutes undergoing nonlinear adsorption migrate according to a traveling wave. Analytical traveling wave solutions were used to obtain an approximation for the solute front shape, c(z,t), for the situation of equilibrium nonlinear adsorption and first-order degradation. This approximation describes numerically obtained fronts and breakthrough curves well. It is shown to describe fronts more accurately than a solution based on linearized adsorption. The latter solution accounts neither for the relatively steep downstream solute front nor for the deceleration in time of the nonlinear front.

9A865. Anisotropic thermoconvective effects on the onset of double diffusive convection in a porous medium. - MS Malashetty *(Dept of Math, Gulbarga Univ, 585 106 Karnataka, India)*. Int J Heat Mass Transfer 36(9) 2397-2401 (Jun 1993).

The linear stability of the thermodiffusive equilibrium of a binary mixture of two miscible fluids in a horizontal plane porous layer is investigated. The linear theory is based on the normal mode analysis under the small amplitude assumption. The effect of anisotropic thermo-convective currents on the stability is obtained. The effect of Prandtl number, ratio of diffusivities and separation parameter are presented graphically. It is found that the thermo-convective currents have a stabilizing effect as well as a destabilizing effect with respect to the case in which these currents are absent.

9A866. Diffusion of moisture in deformable porous media. Anisotropic fibrous materials. - J Cid *(Isover Saint-Gobain, CRIR Rantigny, France)*. Transport Porous Media 11(2) 117-138 (May 1993).

This paper presents a study on the deformation of anisotropic fibrous porous media subjected to moistening by water in the liquid phase. The deformation of the medium is studied by applying the concept of effective stress. Given the structure of the medium, the displacement of the solid matrix is not taken into account with respect to the displacement of the liquid phase. The transport equations are derived from the model proposed by Narasimhan. The transport coefficients and the relation between the variation in apparent density and effective stress are obtained by test measurements.

414Y. COMPUTATIONAL TECHNIQUES

9A867. Calculation of upstream concentrations from downstream data for a two-layer flow. - R Smith *(Dept of Math Sci, Univ of Tech, Loughborough LE11 3TU, UK)*. IMA J Appl Math 50(2) 91-105 (1993).

Is it possible to infer the time-dependent cross-sectionally uniform concentration as the entry to a sampling tube from concentration flux measurements at the exit? Alas, if the shear description within the sampling tube is modelled by a constant-coefficient diffusion equation, the answer is no: the inversion problem is ill-posed. However, the closely related and more accurate telegraph equation can be inverted. As the separation between entry and exit increases, the deconvolution formula grows exponentially and oscillates more rapidly.

9A868. Parabolic approximations of the convection-diffusion equation. - JP Loheac *(Dept Math, Info Syst, Ecole Centrale Lyon, BP 163 69131, Ecully Cedex, France)*, F Nataf *(Centre Math Appl, Ecole Polytech, 91128 Palaiseau Cedex, France)*, M Schatzman *(Lab D'Anal Numer, Univ de Lyon I, 43 Bd du 11 Novembre 1918, 69622 Villeurbanne Cedex, France)*. Math Comput 60(202) 515-530 (Apr 1993).

We propose an approximation of the convection-diffusion operator which consists in the product of two parabolic operators. This approximation is much easier to solve than the full convection-diffusion equation, which is elliptic in space. We prove that this approximation is of order three in the viscosity ad that the classical parabolic approximation is of order one in the viscosity.

See also the following:

9A743. Newton-based BEM for nonlinear convective diffusion problems

9A853. Use of random walk models with spatially variable diffusivity

414Z. EXPERIMENTAL TECHNIQUES

9A869. Determination of transfer coefficients by psychrometry. - A Kondjoyan and JD

Daudin *(Inst Natl Rech Agronomique, Sta Rech sur la Viande, Theix 63122, St-Genes-Champanelle, France)*. Int J Heat Mass Transfer 36(7) 1807-1818 (May 1993).

This paper presents a method based on psychrometry for measuring simultaneously heat and mass transfer coefficients in the case of forced convection exchanges between air and a body surface. This method is specially well adapted to bodies of complex shapes. The theoretical aspects are described. Errors linked to data treatments and to measurements are discussed.

416. Combustion

416B. FUNDAMENTALS

9A870. Recent developments in the theory of combustion of gases: A survey. - VN Kryzhanovskiy *(Polytech Inst, Kiev, Ukraine)*. Heat Transfer Res 24(4) 549-571 (Apr 1992).

A survey and analysis of the principal trends in the theory of premixed gas combustion are presented. The conformance of theories to experimental data is assessed critically, specifically in terms of the predicted structure of the laminar flame front and bulk combustion rate under different conditions. A kinetic theory that seems analytically sound, predicts the experimental findings well, and is adaptable to engineering design calculations is developed.

416E. TURBULENT FLAME PROPAGATION, FLAMMABILITY

9A871. Three-component LDV system for measurements of higher statistical moments in turbulent diffusion flames. - EP Hassel *(Fachgebiet Energie und Kraftwekstech, Tech Hochshule, Darmstadt, Germany)*. Forschung Ingenieur 59(4) 61-65 (Apr 1993).

A three-component LDV system was built with the following features: three colors, forward scattering, direction determination, avalanche photodiodes, transient recorder, fast Fourier transform. With this equipment measurements in a free air jet and a turbulent methane nitrogen diffusion flame were made. The following quantities were determined on the axis and on some levels: velocities u_i, spreading rate $r_{(0.5xuc)}/d$, centerline velocity decay u_0/u_c, Reynolds-stress tensor $u'_iu'_j$ and all third order moments $u'_iu'_ju'_k$. These quantities were normalized and compared with literature data and with Reynolds stress model calculations. One of the main objectives of these measurements was the supply of the exit velocity profiles because the predictions below the similarity region depend crucially on the boundary conditions. In this paper details of the equipment and of the data processing are explained and new results are shown.

416F. FLAME STABILITY AND STABILIZATION

9A872. Stabilization mechanism of the lifted jet diffusion flame in the hysteresis region. - Cheng-Kuang Lin *(Aeronaut Res Lab, Chun Shan Inst of Sci and Tech, Taichung, Taiwan, ROC)*, Ming-han Jeng, Yei-Chin Chao *(Inst of Aeronaut and Astronaut, Natl Cheng Kung Univ, Tainan, Taiwan, ROC)*. Exp Fluids 14(5) 353-365 (Apr 1993).

Recent experimental efforts focused on near-field coherent vortex dynamics, and their impact on stabilization of a lifted jet diffusion flame in the hysteresis region are reported. Simultaneous jet flow and flame visualizations are conducted first to obtain a global feature of flow-flame interaction. The statistical liftoff heights are calculated by a DIP (digital image processing) method. The gas concentration and velocity distributions induced by the vortex evolution as well as the corresponding flame from motion are deduced from phase-averaged measurements of planar Mie-scattering gas concentration images, LDV and ion-signals, respectively. The planar gas concentration technique employed here extends our previous work (Chao et al 1990, 1991a) to include phase-averaging. Results of the experiments show that the most probable flame base locations in the hysteresis region are at the coherent vortex roll-up and pairing locations. The deeply entrained air lump caused by large-scale vortices during roll-up and pairing is the main obstruction to flame propagation back to the nozzle exit and causes the hysteresis phenomenon.

416J. UNSTEADY COMBUSTION AND COMBUSTION ACOUSTICS

9A873. Issues associated with long-duration high-enthalpy scramjet combustor testing. - MW Thompson and MA Friedman *(Propulsion Group, Aeronaut Dept, Johns Hopkins Univ Appl Phys Lab, Laurel MD 20723)*. J Propulsion Power 9(3) 479-485 (May-Jun 1993).

Long-duration direct connect combustor tests are an essential element in the development of an effective supersonic combustion ramjet (scramjet). While test techniques and analysis methodology have been established for simulated flight Mach numbers at Mach 8 and below, phenomena associated with higher flight simulations require additional attention. In this article, technical issues associated with long-duration high-enthalpy direct-connect scramjet combustor tests are discussed. Since ground tests form the basis by which flight hardware is designed, it is important to quantify the differences between flight and ground test conditions. Analyses are presented herein which characterize the differences between ground test and flight combustor inlet properties. In particular, the effects of dynamic pressure and chemical nonequilibrium kinetics are investigated. Analytical results will also be presented which characterize aspects of the performance of a generic combustor operating at Mach 8, 11, and 12 flight simulations. One, two and three stream-mixing models are used to assess combustor performance and the predictions derived from the various models are contrasted.

416K. SUPERSONIC COMBUSTION

9A874. Experimental supersonic hydrogen combustion employing staged injection behind a rearward facing step. - JD Abbitt III, C Segal *(Dept Aerospace Eng Mech and Eng Sci, Univ of Florida, 231 Aerospace Build, Gainesville FL 32611)*, JC McDaniel, RH Krauss, RB Whitehurst *(Dept of Mech and Aerospace Eng, Univ of Virginia, Charlottesville VA 22903)*. J Propulsion Power 9(3) 472-478 (May-Jun 1993).

An experimental investigation of a Mach 2 combustor has been conducted in order to characterize flow properties in a supersonic reacting flowfield. Hydrogen was injected transversely as staged, underexpanded jets behind a rearward-facing step into a ducted Mach 2 air freestream. The effects of the chemical reaction on the supersonic flowfield was investigated using shadowgraphs, broadband flame emission photography, and planar laser induced fluorescence of OH. The shadowgraphs indicated that the wave pattern in the combustor along with flowfield unsteadiness was strongly affected by the heat release. The broadband flame emission photographs revealed large regions of no combustion in the vicinity of the fuel injectors where fuel-air mixing was insufficient to support combustion. These regions decreased in size as the freestream stagnation temperature was decreased for fixed hydrogen mass flow rate, consistent with an increase in the effective Q-ratio with combustion. The size of the zones containing OH in the planar fluorescence images also increased as the main flow stagnation temperature was decreased. Reaction zones were found in the planar fluorescence images away from regions containing injectant in a nonreacting study of the same geometry, indicating that the pressure rise associated with the reaction forced a large redistribution of the fuel.

9A875. High-temperature supersonic combustion testing with optical diagnostics. - TE Parker, MG Allen, WG Reinecke, HH Legner, RR Foutter, WT Rawlins *(Phys Sci, 20 New England Business Center, Andover MA 01810)*. J Propulsion Power 9(3) 486-492 (May-Jun 1993).

The development of supersonic combustion ramjet (SCRAMJET) engines requires testing using new, nonintrusive, instrumentation methods in high-speed high-enthalpy flow facilities. The stagnation temperatures for very high flight speeds (in excess of 3000 K) make the production of these flows impossible using conventional methods such as resistance heaters or vitiated flows. Similarly, measurements of properties in these flows is difficult since the measurement must be nonintrusive in nature. This article describes a test series using a shock tunnel to produce Mach 3.0 flows with stagnation temperatures in excess of 3000 K and an optical diagnostic set specifically tailored for measurements in supersonic high temperature systems. The test facility includes a hydrogen injection capability which makes combustion tests possible for these flows. This article describes the shock tunnel and its capabilities, provides an overview of the optical diagnostics used in the testing, and discusses the results of both combusting and noncombusting tests.

416O. COMBUSTORS AND AFTERBURNERS

9A876. Numerical simulation of turbine "hot spot" alleviation using film cooling. - DJ Dorney and RL Davis *(United Tech Res Center, Comput and Des Group, E Hartford CT 06108)*. J Propulsion Power 9(3) 329-336 (May-Jun 1993).

Experimental data have shown that combustor hot streaks can lead to pressure side "hot spots" on first-stage turbine rotor blades. In previous numerical studies, it has been shown that unsteady Navier-Stokes procedures can be used to predict the rotor pressure surface temperature increase associated with these combustor hot streaks. In the current investigation, similar 2D and 3D unsteady Navier-Stokes simulations have been performed to demonstrate the use of numerical tools in the optimization of film cooling configurations. In this study, the addition of prudently placed film cooling holes along the rotor pressure surface is shown to significantly diminish the adverse effects of the hot streak. Using a 2D Navier-Stokes procedure, a parametric study was performed to determine the impact of the location of the film cooling holes, fluid injection velocity, and fluid injection angle on the time-averaged rotor surface temperature. The experience gained from these 2D simulations was then applied to a series of 3D simulations in which the effects of the film cooling hole distribution on the rotor pressure surface temperature were studied. The results of these simulations indicate that computational procedures can be used to design feasible film cooling schemes which eliminate the adverse effects of combustor hot streaks.

416Q. LIQUID FUELS

9A877. Aspects of secondary atomization of aluminum-hydrocarbon slurry propellants. - DC Mueller *(Propulsion Eng Res Center, Penn State)* and SR Turns *(Dept of Mech Eng, 114 Res Build E, Penn State)*. J Propulsion Power 9(3) 345-352 (May-Jun 1993).

A theoretical and experimental investigation of the secondary atomization of Al-RP-1 slurry propellants was conducted. Theoretical efforts examined the effects of aluminum particle size in particle shell-crust formation on the surface of a burning slurry droplet. A model was developed for the pressure buildup and mechanical stresses in the shell for the time period after the shell becomes impermeable. Experimental efforts focused on the ignition and combustion of a dilute stream of slurry droplets. Measurements of individual particle diameters and velocities were made at various axial locations in the stream. Radiant emission from the particles was also monitored to determine whether aluminum was actively burning. Experimental aluminum agglomerate ignition times were found to be comparable to theoretical estimates. The experimentally measured minimum initial slurry droplet diameter for secondary atomization was 20-25μm, compared to a theoretical diameter of 35μm.

9A878. Improvement of combustion of gaseous and liquid fuels: A survey. - VN Kryzhanovskiy *(Kiev Polytech Inst, Ukraine)*. Heat Transfer Res 24(5) 703-730 (1992).

The principal trends in developing a theory of combustion and improving the technology of combustion of gaseous and liquid fuels are analyzed. Methods of describing the combustion process in terms of the flame length and of the volumetric rate of heat release, as well as the principal methods of combustion of these fuels are compared. It is shown that uniform distribution of fuel in the air stream prior to combustion is the most important way to improve combustion flames.

416S. FLAME AND FIRE (SPREAD AND EXTINCTION)

9A879. Experimental investigation of the blowout limits of a jet diffusion flame in co-flowing streams of different velocity and composition. - I Wierzba, K Kar, GA Karim *(Dept of Mech Eng, Univ of Calgary, AB, Canada)*. J Energy Resources Tech 115(2) 142-147 (Jun 1993).

The blowout limits of a methane diffusion flame in a co-flowing air-fuel or air-diluent stream were determined for a range of surrounding co-flow stream velocities, both laminar and turbulent, up to ~1.50 m/s. Methane, ethylene, propane and hydrogen were used as the fuels in the surrounding co-flow stream while nitrogen and carbon dioxide were used as diluents. The experimental results shown that velocity of the surrounding stream affects the blowout phenomena significantly. An increase in the stream velocity has a detrimental effect on the blowout limits at very low velocities up to 0.30 m/s (essentially laminar flow) and at velocities higher than 1.50 m/s (turbulent flow). The addition of a fuel to the air stream in most cases enhances the blowout limit of a methane diffusion flame.

9A880. The influence of external heat transfer on flame extinction of dilute sprays. - Shuhn-Shyurng Hou, Chi-Chang Liu, Ta-Hui Lin *(Dept of Mech Eng, Natl Cheng-Kung Univ, Tainan 701, Taiwan, ROC)*. Int J Heat Mass Transfer 36(7) 1867-1874 (May 1993).

The extinction of a dilute spray flame burning in a steady, 1D, low-speed, sufficiently off-stoichiometric, two-phase flow, and experiencing the external heat transfer from the spray to a tube wall upstream is further analyzed. The external heat transfer results in globally external heat loss, excess enthalpy burning and external heat gain, respectively, to the spray system with increasing the wall temperature. However, the droplet gasification provides the overall internal heat loss and heat gain for rich and lean sprays, respectively. Variations of the extinction curves under the influence of transition from overall external heat loss to heat gain, and the jump between the completely and partially prevaporized burnings on flame extinction, are reported and discussed for both lean and rich sprays.

416T. COMBUSTION, FLAME, AND FIRE MODELING

9A881. Control volume FE solution of a confined turbulent diffusion flame. - D Elkaim, M Reggio, R Camarero *(Dept of Mech Eng, Ecole Polytech Montreal, CP 6079 Succ A, Montreal H3C 3A7, PQ Canada)*. Numer Heat Transfer A 23(3) 259-279 (Apr-May 1993).

The control volume FEM in conjunction with the vorticity stream function formulation is used to produce a numerical solution of the confined turbulent diffusion flame. The turbulence is described by the k - ε model with wall functions near solid boundaries. The combustion kinetics are defined by a one-step infinte rate chemical reaction. The validity of the numerical method is assessed by a comparison between present numerical results and experimental data from the literature for a laboratory diffusion flame.

9A882. Modelling of unsteady combustion regimes for polydisperse fuels I. Instability and auto-oscillations. - YA Buyevich, NA Korolyova, IA Natalukha *(Dept of Math Phys, Urals State Univ, Ekaterinburg 620083, Russia)*. Int J Heat Mass Transfer 36(8) 2223-2231 (May 1993).

A general theory of instability and self-oscillating accompanying combustion of polydisperse assemblages of particles is elaborated on the basis of a model including heat and mass balance equations and the kinetic equation governing the particle size distribution. At arbitrary burning kinetics of particles and the particle influx rate they are reduced, under the condition of ideal mixing, to only two functional integrodifferential equations for the dimensionless temperature and oxidant concentration. Steady combustion processes are shown to be unstable in many important situations. The properties of possible slightly nonlinear auto-oscillations are studied in greater detail.

9A883. Modelling of unsteady combustion regimes for polydisperse fuels II. Parametrically controlled combustion. - YA Buyevich, NA Korolyova, IA Natalukha *(Dept of Math Phys, Urals State Univ, Ekaterinburg 620 083, Russia)*. Int J Heat Mass Transfer 36(8) 2233-2238 (May 1993).

Results of computer calculations of essentially nonlinear periodic combustion regimes originating far from the stability boundary are presented. The influence of the parametrical modulation of relevant processing parameters upon the neutral stability and upon the properties of oscillating combustion regimes is investigated. Modulation characteristics which cause either stabilization or destabilization of combustion are determined. Quasiperiodic combustion states forming outside the regions of frequency locking are studied.

418. Prime movers and propulsion

418B. FUNDAMENTALS

See the following:

9T685. Power and refrigeration plants for minimum heat exchanger inventory

418E. INTERNAL COMBUSTION, POSITIVE DISPLACEMENT ENGINES

9A884. Determination of the 3D temperature field on the spherical piston head in a high-speed internal-combustion engine. - MV Stradomskiy, VA Asmalovskiy, ON Vazhenin, VV Medyanovskiy, AK Gushchin *(Eng Thermophys Inst, Ukrainian Acad of Sci, Kiev, Ukraine)*. Heat Transfer Res 24(3) 415-423 (Apr 1992).

We present a technique for computer calculation of 3D temperature- and heat flux density distributions on the surface of the spherical head of a high-out-put internal combustion engine piston, based on temperatures measured in a limited number of points within the piston. The technique is useful in design of prevention of thermal overload on such pistons and similar devices.

9A885. Influence of nozzle sac volume on diesel spray droplet sizes. - JR Farrar-Khan, GE Andrews, PT Williams *(Dept of Fuel and Energy, Univ of Leeds)*. Proc Inst Mech Eng A 206(A4) 239-248 (1992).

The influence of nozzle sac volume and associated changes in the fuel hole upstream flow on the spray atomization velocity and penetration were studied. Four injectors, designed for applications in 1 liter per cylinder diesel engines, were investigated with the same 215 bar injector nozzle opening pressure and fuel flow quantity. A Malvern 2600c Series diesel spray laser diffraction spray analyzer was used. Significant differences in the spray characteristics were found which helped to explain some of the emission differences between the four injectors.

9A886. Stochastic-experimental investigation of the cyclic pressure variation in a DI single-cylinder diesel engine. - DA Kouremenos, CD Rakopoulos, KG Kotsos *(Thermal Eng Section, Mech Eng Dept, Natl Tech Univ, 42 Patission St, Athens 106 82, Greece)*. Int J Energy Res 16(9) 865-877 (Dec 1992).

This paper presents an analysis of the cycle-by-cycle combustion variation as reflected in the pressure indicator diagram of a single-cylinder, naturally aspirated, four-stroke, direct-injection, Lister LV1 diesel engine. A measuring set-up consisting of piezoelectric transducers with charge amplifiers, in the cylinder and the fuel injection pipeline, and a fast data-acquisition board installed on an IBM-compatible microcomputer was used to gather the data of 650 successive combustion cycles of the cylinder, under various combinations of injection timing and load conditions. The measured data were corrected for drift, and the top dead center of each cycle is determined thermodynamically. The data obtained by this technique were analyzed for the peak pressure, the peak rate of pressure rise, the crank angles at which these maximum values occur, and for the injection timing and ignition delay. The groups of parameters have been further statistically analyzed for averages, standard deviations, probability density functions, autocorrelation and power spectra. Crosscorrelation runs were also performed to observe any cause relationship between cyclic pressure variations and the fuel-injection-system operation. The results of the stochastic analysis technique have proved to be very useful for the investigation and interpretation of the existence of fluctuation phenomena in the diesel internal combustion engine and their cause relationships, thereby aiding the correct interpretation of the relevant experimental results and their associated errors.

9A887. Theoretical study of a variable compression ratio turbocharged diesel engine. - TJ Rychter, A Teodorczyk *(Warsaw Univ Tech, Poland)*, CR Stone, HJ Leonard, N Ladommatos *(Dept of Manuf and Eng Syst, Brunel Univ, Uxbridge, Middlesex, UK)*, SJ Charlton *(Sch of Mech Eng, Univ Bath, UK)*. Proc Inst Mech Eng A **206**(A4) 227-238 (1992).

A variable compression ratio concept that can give a different expansion ratio to the compression ratio has been evaluated by means of a simulation of a turbocharged diesel engine. The compression ratio is controlled by varying the ratio of the connecting rod length to the crank throw, hence the name variable crank radius-connecting rod length engine (VR-LE). The VR-LE mechanism kinematics have been defined and described, and the compression ratio and expansion ratio have been presented as a function of the eccentric phase angle (α_o. A zero dimensional engine simulation that has been the subject of comprehensive validation has been used as the basis of the VR-LE study. The effect of the compression ratio on the engine performance at fixed loads is presented. The principal benefits are a reduction in fuel consumption at part load of about 2% and a reduction in ignition delay that leads to an estimated 6 dB reduction in combustion noise. The study has been conducted within the assumption of a maximum cylinder pressure of 160 bar.

418G. GAS TURBINES

9A888. Optimizations for Brayton-Joule gas turbine cycles. - TH Frost, B Agnew, A Anderson *(Dept of Mech Mat and Manuf Eng, Univ of Newcastle upon Tyne, Newcastle upon Tyne, UK)*. Proc Inst Mech Eng A **206**(A4) 283-288 (1992).

Traditionally, the simple Brayton-Joule cycle has been optimized for maximum output and for minimum compressor and work with intercooling and maximum turbine work with reheat. To these Woods et al have added optimization for peak efficiency of the simple cycle with internal irreversibilities. The results now presented include both maximum output and peak efficiency for both regenerative and intercool-reheat cycles with internal irreversibilities. Two special cases, for a regenerative cycle and for a nonregenerative cycle with both reheat and intercooling, are identified where the conditions for maximum output and peak efficiency coincide.

418I. JET AND FANJET ENGINES

9A889. Approach to modeling continuous turbine engine operation from startup to shutdown. - MA Chappell *(Arnold Eng Dev Center, Sverdrup Tech, Arnold Air Force Base TN 37389)* and PW McLaughlin *(Simulation and Modeling Workshop, 176 Sunset Dr, Glastonbury CT 06033)*. J Propulsion Power **9**(3) 466-471 (May-Jun 1993).

A generalized turbine engine start simulation (mathematical model) has been developed and demonstrated. The model, designated as ATEST-V3, is capable of simulating engine operation continuously from near static (zero speed) conditions to maximum engine power including windmill starting, spooldown starting, and starter-assisted starting. The enhanced capability to simulate the engine starting process provides the means to characterize and understand engine system operational behavior during critical startup and shutdown operations. ATEST-V3 is based on an aerothermodynamic matching of the major components. The component-matching technique is widely used for steady-state and transient turbine engine simulations that typically exclude subidle and starting operations. The same approach is shown to be applicable to engine starting operations by modeling component behavior continuously from zero to maximum power. The combination of an existing transient engine simulation and a numerically stable component-matching algorithm provided a foundation for extending the simulation capability to subidle engine operation and engine starting. ATEST-V3 was applied to a modern flight-type turbofan engine which demonstrated the capability to simulate windmill, spooldown, and starter-assisted starts at various flight conditions. Finally, a comparison is made between model results and engine test data.

9A890. Commercial turbofan engine exhaust nozzle flow analyses. - KS Abdol-Hamid *(Anal Services and Mat, Hampton VA 23666)*, K Uenishi, BD Keith *(ATO-General Elec Aircraft Engines, Cincinnati OH 45201)*, JR Carlson *(Propulsion Aerodyn Branch, Appl Aerodyn Div, NASA Langley Res Center, Hampton VA 23681)*. J Propulsion Power **9**(3) 431-436 (May-Jun 1993).

The recently developed 3D code is able to perform a computational investigation of complex aircraft aerodynamic components. This code was developed for solving the simplified Reynolds-averaged Navier-Stokes equations in a 3D multiblock multizone structured mesh domain. The present analysis was applied to commercial turbofan exhaust flow systems. Solution sensitivity to grid density is presented. Laminar flow solutions were developed for all grids, and two-quation κ-ε solutions were developed for selected grids. Static pressure distribution, mass flow, and thrust quantities were calculated for on-design engine operating conditions. Good agreement between predicted surface static pressures and experimental data was observed at different locations. Mass flow was predicted within 0.2% of experimental data. Thrust forces were typically within 0.6% of experimental data.

418L. IONIC, ELECTRIC, AND PHOTONIC PROPULSION

9A891. Anode power deposition in magnetoplasmadynamic thrusters. - AD Gallimore *(Dept of Aerospace Eng, Univ of Michigan, Ann Arbor MI 41809)*, AJ Kelly, RG Jahn *(Elec Propulsion Lab, Princeton)*. J Propulsion Power **9**(3) 361-368 (May-Jun 1993).

Results of anode heat-flux and anode fall measurements from a multimegawatt self-field quasisteady magnetoplasmadynamic (MPD) thruster are presented. Measurements were obtained with argon and helium propellants for a variety of currents and mass flow rates. Anode heat flux was directly measured with thermocouples attached to the inner surface of a hollowed section. Anode falls were determined both from floating probes and through heat flux measurements. Comparison of data acquired through either method shows excellent agreement. Anode falls varied between 4-50 V with anode power fraction reaching 70% with helium at 150 kW, and 50% with argon at 1.9 MW. The anode fall was found to correlate well with electron Hall parameters calculated from triple Langmuir and magnetic probe data collected near the anode. Two possible explanations oro this result are proposed: 1) the establishment of large electric fields at the anode to maintain current conduction across the strong magnetic fields; and 2) anomalous resistivity resulting from the onset of microturbulence in the plasma. To investigate the latter hypothesis, electric field, magnetic field, and current density profiles measured in the vicinity of the anode were incorporated into Ohm's law to estimate the electrical conductivity. Results of this analysis show a substantial deviation of the measured conductivity from that calculated with classical formulas. These results imply that anomalous effects are present in the plasma near the anode.

9A892. Erosion rate diagnostics in ion thrusters using laser induced fluorescence. - CJ Gaeta *(Optical Phys Lab, Hughes Res Lab, Malibu CA 90265)*, JN Matossian *(Plasma Phys Lab, Hughes Res Lab, Malibu CA 90265)*, RS Turley *(Optical Phys Lab, Hughes Res Lab, Malibu CA 90265)*, JR Beattie, JD Williams, WS Williamson *(Plasma Phys Lab, Hughes Res Lab, Malibu CA 90265)*. J Propulsion Power **9**(3) 369-376 (May-Jun 1993).

We have used laser induced fluorescence (LIF) to monitor the charge-exchange ion erosion of the molybdenum accelerator electrode in ion thrusters. This real-time, nonintrusive method was implemented by operating a 30-cm-diam ring-cusp thruster using xenon propellant. With the thruster operating at a total power of 5 kW, laser radiation at a wavelength of 390 nm was directed through the extracted ion beam adjacent to the downstream surface of the molybdenum accelerator electrode. Molybdenum atoms, sputtered from this surface as a result of charge-exchange ion erosion, were excited by the laser radiation. The intensity of the laser-induced fluorescence radiation, which is proportional to the sputter rate of the molybdenum atoms, was measured and correlated with variations in thruster operating conditions such as accelerator electrode voltage, accelerator electrode current, and test facility background pressure. We also demonstrated that the LIF technique has sufficient sensitivity and spatial resolution to evaluate accelerator electrode lifetime in ground-based test facilities.

9A893. Simulating a 1-kW arcjet thruster using a nonlinear active load. - GP Altenburger *(Devilbiss-Ransburg Indust Liquid Syst, Toledo OH 43612)* and RJ King *(Dept of Elec Eng, Univ Toledo, Toledo OH 43606)*. J Propulsion Power **9**(3) 377-381 (May-Jun 1993).

Arcjet thrusters are known to have distinctly nonlinear electrical characteristics with negative incremental resistance throughout their normal operating region. The 1-kW arcjet simulator proposed here is an electronic load bank which accurately mimics these characteristics statically and dynamically up to 40 kHz. A power-processing unit (PPU) was tested using a resistive load bank, the simulator, and a 1-kW arcjet. The simulator was found to be an accurate stand-in for the arcjet during system transient testing, while the resistive load was not. The simulator uses resistors and insulated-gate bipolar transistors to dissipate the PPU output power; a nonlinear feedback is applied to produce the desired v-i characteristics. This feedback is analyzed dynamically. This arcjet simulator allows the development of a new PPU design to a higher level of confidence before beginning testing at an arcjet facility.

418N. OTHER DEVICES

9A894. Study on the application of nonazeotropic refrigerant mixture cycles to small-temperature-difference power-generation systems. - Akinobu Murata, Hiroyuki Takazawa, Takenobu Kajikawa *(Electrotech Lab, Japan)*. Heat Transfer Japan Res **21**(7) 649-665 (1992).

Conditions on which nonazeotropic refrigerant mixture cycle is efficient for small-temperature-difference power-generation systems are studied through numerical analysis using a pair of fluorocarbonic refrigerant mixture cycles.

VII. EARTH SCIENCES

452. Porous media

452B. FUNDAMENTALS OF FLUID FLOW

9A895. Diffusion in isotropic and anisotropic porous system. Three-dimensional calculations. - M Quintard *(LEPT-ENSAM, URA CNRS, Esplanade des Arts Metiers, 33405 Talence Cedex, France)*. Transport Porous Media 11(2) 187-199 (May 1993).

Effective diffusion coefficients were calculated numerically for 3D unit cells representative of different unconsolidated porous media. These numerical results were compared with the experimental results of Kim for packed beds of glass spheres, mica particles, and an artificial porous medium compound of mylar disks. These 3D numerical results confirm that the porosity is the essential parameter for the determination of the effective diffusion coefficient in the case of unconsolidated isotropic systems. In the case of anisotropic systems, better agreement is obtained between numerical predictions and actual data when the unit cell is 3D rather than 2D.

9A896. Interpretation of capillary pressure curves using invasion percolation theory. - Dengen Zhou *(Dept of Pet Eng, Stanford, Mitchell 360)* and EH Stenby *(Eng Res Centre, IVC-SEP, Inst for Kemitek, Bldg 229 DTH, DK-2800 Lyngby, Denmark)*. Transport Porous Media 11(1) 17-31 (Apr 1993).

Invasion percolation was studied on 3D regular lattices of various node numbers. A new model has been developed to obtain the pore-size distribution from capillary pressure measurements. The new model is superior to the conventional percolation model, since it takes into account the physical trapping of the wetting phase. The irreducible wetting phase saturation includes the film of the wall of the pores, the dead-end pore volume, and the main contribution by pores isolated from the outlet of the medium by the nonwetting phase. This has been related to the node number and the sample 3Ds. Over 100 capillary pressure curves of consolidated media have been collected. Good agreement was obtained between this data set out and our invasion percolation predictions using node numbers of 6-13, as reported by Mishra and Sharma. The pore-throat size distribution function estimated by our new model is broader than from the conventional percolation and the capillary tube models.

9A897. Network model evaluation of permeability and spatial correlation in a real random sphere packing. - SL Bryant *(BP Chem, Bo'ness Rd, Grangemouth Stirlingshire FK3 9XH, UK)*, PR King *(BP Res Centre, Chertsey Rd, Sunbury-on-Thames, Middlesex TW16 7LN, UK)*, DW Mellor *(Kerr-Mellor Assoc, 1 Woodside, Camberley, Surrey GU17 9JJ, UK)*. Transport Porous Media 11(1) 53-70 (Apr 1993).

In principle, network models can replicate exactly the microstructure of porous media. In practice, however, network models have been constructed using various assumptions concerning pore structure. This paper presents a network model of a real, disordered porous medium that invokes no assumptions regarding pore structure. The calculated permeability of the model agrees well with measured permeabilities, providing a new and more rigorous confirmation of the validity of the network approach. Several assumptions commonly used in constructing network models are found to be invalid for a random packing of equal spheres. In addition, the model permits quantification of the effect of pore-scale correlation (departure from randomness) upon permeability. The effect is comparable to reported discrepancies between measured permeabilities and predictions of other network models. The implications of this finding are twofold. First, a key assumption of several theories of transport in porous media, namely that pore dimensions are randomly distributed upon a network, may be invalid for real porous systems. Second, efforts both to model and to measure pore-scale correlations could yield more accurate predictions of permeability.

9A898. Percolation in layered media: A conductivity approach. - A Hansen *(GMCM, URA CNRS 804, Univ de Rennes 1, F-35042 Rennes, Cedex, France)*, EL Hinrichsen *(Center for Industriforskning, PO Box 124, N-0314 Oslo, Norway)*, D Stauffer *(Inst Theor Phys, Univ, D-5000 Cologne 41, Germany)*. Transport Porous Media 11(1) 45-52 (Apr 1993).

Long square-lattice and cubic-lattice samples consisting of many layers are simulated. Within each layer, the concentration of permeable bonds is constant whereas each layer has a different concentration chosen randomly from the interval between the percolation threshold and unit concentration. The conductivity of the random resistor network corresponding to this percolation model is calculated, both parallel and perpendicular to the layers, in both 2D and 3D. For the conductivity parallel to the layers, an effective medium calculation comes within 10% of the true conductivity. For the conductivity perpendicular to the layers, percolation theory is necessary.

9A899. Pore structures and transport properties of sandstone. - C David, M Darot *(EOPGS Lab Mat, 5 Rue Descartes, 67084 Strasbourg Cedex, France)*, D Jeannette *(CGS, 1 Rue Blessig, 67084 Strasbourg Cedex, France)*. Transport Porous Media 11(2) 161-177 (May 1993).

We report laboratory measurements of pore structure, capillarity, water permeability, and electrical conductivity on Fontainbleau sandstone specimens. Experimental, equipment and techniques are described. Water permeability measurements were performed on saturated cores with a 100 MPa permeameter. Various combinations of pore and confining pressures were used and an effective pressure law was determined. Differences between transport properties of the three types of sandstone are related to the microstructural characteristics of the pore network of each rock.

9A900. Stochastic approach for groundwater flow in a semiconfined aquifer subject to random boundary conditions. - MG Satish and Jianting Zhu *(Dept of Civil Eng, Tech Univ, PO Box 1000 Halifax, NS, B3J 2X4, Canada)*. Adv Water Resources 15(6) 329-339 (1992).

A methodology is presented for analyzing the groundwater flow through a shallow semiconfined aquifer with random parameters, governed by the Helmholtz equation and subject to stochastic boundary conditions. Stochasticity in an aquifer parameter is considered along with the stochasticity in the Dirichlet and Neumann boundary conditions. The BEM based on perturbation does not require specification of the probability density function of the parameters but only their expectations, variances and the covariance of the random quantities. The applicability of the method is demonstrated by presenting a groundwater flow example as well as by comparing the numerical results with analytical solutions for a special case without the Neumann boundary condition uncertainty.

452C. SEEPAGE (INCL POLLUTANTS)

See the following:

9A864. Analytical approximation for nonlinear adsorbing solute transport and first-order degradation

9T909. Shear stabilization of miscible displacement processes in porous media

9T910. Stability of miscible displacements in porous media with nonmonotonic viscosity profiles

452D. MULTIPHASE FLOW IN POROUS SOLIDS

9A901. A Lattice model of foam flow in porous media. A percolation approach. - WG Laidlaw, WG Wilson *(Chem Dept, Univ of Calgary, AB, T2N 1N4, Canada)*, DA Coombe *(Comput Model Group, 3512-33rd St NW Calgary, AB, T2L 2A6, Canada)*. Transport Porous Media 11(2) 139-159 (May 1993).

Because fluid flow in porous media is opaque to most observational techniques simulations of the processes occurring in porous media have become important. Typical reservoir simulations treat the flow as taking place in some averaged (Darcy-scale) medium but simulations can also be carried out at the level of the network of pores and throats of the porous medium. We report the results of a pore-scale investigation of mechanisms for the alteration of mobility by foam lamella blockage in a network of these spaces and channels of porous media. An explanation of the shift in breakthrough gas saturation and the deformation of the shape of permeability *vs* saturation curves upon introduction of foam is provided for a variety of blocking mechanisms.

9A902. Two-phase brine mixtures in the geothermal context and the polymer flood model. - R Young *(Appl Math, Indust Res, PO Box 31310, Lower Hutt, New Zealand)*. Transport Porous Media 11(2) 179-185 (May 1993).

Two-phase mixtures of hot brine and steam are important in geothermal reservoirs under exploitation. In a simple model, the flows are described by a parabolic equation for the pressure with a derivative coupling to a pair of wave equations for saturation and salt concentration. We show that the wave speed matrix for the hyperbolic part of the uncoupled system is formally identical to the corresponding matrix in the polymer flood model for oil recovery. For the class of *strongly diffusive* hot brine models the identification is more than formal, so that the wave phenomena predicted for the polymer flood model will also be observed in geothermal reservoirs.

452F. FLUIDIZED BEDS

9A903. Dynamics of burnup of coal in fluidized-bed combustion. - YuG Lekomtseva, VA Munts, YuN Fedorenko, AP Baskakov *(Ural Polytech Inst, Sverdlovsk, Russia)*. Heat Transfer Res 24(5) 670-676 (1992).

Experimental data on the burnup rates of brown coal in an electrically heated fluidized bed are presented. The concentrations of gas components in the flue gases were measured in the course of the fluidized-bed combustion by means of continuous analyzers and the coefficients of gas gas exchange induced by the reaction were calculated.

See also the following:

9A810. Analysis of the combined conductive - radiative heat transfer between a surface and a gas-fluidized bed at high temperature

452G. ELASTIC BEHAVIOR OF FLUID-FILLED SOLIDS

See the following:

9A103. Microstructural characteristics of wave propagation in a saturated porous medium
9A907. Study of massive water injection by thermoporomechanical coupling model

452I. THERMODYNAMICS, HEAT TRANSFER, AND COMBUSTION

9A904. **Bayesian estimation of heat transport parameters in fixed beds.** - DJ Gunn and MMA Misbah *(Dept of Chem Eng, Univ Col, Swansea SA2 8PP, UK)*. Int J Heat Mass Transfer 36(8) 2209-2221 (May 1993).

An approach based upon Bayes Theorem has been developed to resolve two major difficulties encountered in earlier experimental investigations concerned with the estimation of parameters for heat transfer in fixed beds. The first difficulty is in obtaining estimates of the Nusselt and Peclet groups with appropriate confidence intervals, and the second is the considerable variation found in the Peclet and Nusselt groups in the range of intermediate Reynolds number. In a new experimental investigation it has been found that estimates of the Peclet and Nusselt groups could be changed in a correlated way without changing the variance of experimental error about the theoretical values, an interaction that precluded the accurate estimation of either parameter. The Baysian approach identified a confidence region linking the Nusselt and Peclet groups from earlier work, and a confidence region for the two parameters obtained in the new investigation; the best estimates were obtained where the two confidence regions overlapped. In the final presentation the parameter values and independent estimates of parameter accuracy were found to be consistent with correlations established on the basis of earlier work, but with greatly improved confidence regions for the Nusselt and Peclet groups expressed as functions of Reynolds number.

See also the following:

9A715. Convective instability in saturated porous enclosures with a vertical insulating baffle
9A738. Free convection effects on the oscillatory flow of a couple stress fluid through a porous medium
9A739. Mixed convection along a nonisothermal vertical flat plate embedded in a porous medium: The entire regime
9A740. Momentum and heat transfer over a continuous moving surface in a non-Darcian fluid
9A863. Study of the effects of macrosegregation and buoyancy-driven flow in binary mixture solidification
9A865. Anisotropic thermoconvective effects on the onset of double diffusive convection in a porous medium

452K. RESERVOIR ENGINEERING

9A905. **Displacement of trapped oil from water-wet reservoir rock.** - Dengen Zhou *(Dept of Pet Eng, Stanford, Mitchel 360)* and EH Stenby *(Eng Res Center, IVC-SEP, Inst for Kemitek, Bldg 229 DTH, DK-2800 Lyngby, Denmark)*. Transport Porous Media 11(1) 1-16 (Apr 1993).

Displacement of oil trapped in water-wet reservoirs was analyzed using percolation theory. The critical capillary number of the CDC (Capillary Desaturation Curve) was be predicted based on the pore structure of the medium. The mobilization and stability theories proposed by Stegemeier were used to correlate oil cluster length to the capillary number needed to mobilize the trapped oil. Under the assumption that all pore chambers have the same size, a procedure was developed using the drainage capillary pressure curve and effective accessibility function to predict the CDC curve for a given medium. The prediction of critical capillary numbers was compared with the experimental data from 32 sandstone samples by Chatzis and Morrow. Also, the CDC curve of one sandstone sample was calculated using the procedure developed in this work and compared with the measured data. Very good agreements were obtained.

9A906. **Review of current trends in petroleum reservoir description and assessment of the impacts on oil recovery.** - FJ Fayers and TA Hewett *(Dept of Pet Eng, Stanford)*. Adv Water Resources 15(6) 341-365 (1992).

This paper gives a general review of the problems associated with realistic representation of reservoir heterogeneities and their impacts on current trends in reservoir simulation. The basic three-phase flow equations used in reservoir engineering are summarized and some of the uncertainties associated with the properties of two-phase relative permeabilities are reviewed. The approaches available for averaging both absolute and relative permeabilities in representative elements of volume are summarized, and examples are given of some of their attributes. For large reservoirs, a prediction procedure based on a synthesis from streamline solutions is sometimes attractive.

9A907. **Study of massive water injection by thermoporomechanical coupling model.** - JF Shao, JP Henry *(Lab of Mech of Lille, EUDIL, 59655 Villeneuve d'Ascq, France)*, F Skoczylaz, I Shahrour *(Lab of Mech of Lille, Ecole Centrale Lille, 59651 Villeneuve d'Ascq, France)*. Comput Geotech 15(2) 105-121 (1993).

In this paper, we present a numerical study of the massive water injection in petroleum reservoir. A FE model is developed using a complete coupling algorithm. The thermal convective effect is taken into account. This allows to deal with high fluid flow rate and high temperature variation during the injection time. Evolutions of pore pressure, temperature and rock compaction as function of injection time are studied. The obtained results show that it is possible to use a semi-decoupled model by eliminating some negligible coupling terms.

452L. FLOW STABILITY

9A908. **Boundary and inertia effects on vortex instability of a horizontal mixed convection flow in a porous medium.** - Kun-Nun Lie and Jiin-Yuh Jang *(Dept of Mech Eng, Natl Cheng-Kung Univ, Tainan 70101, Taiwan, ROC)*. Numer Heat Transfer A 23(3) 361-378 (Apr-May 1993).

Non-Darcian effects, including the effects of boundary and inertia, are examined on the flow and vortex instability of a horizontal mixed convective boundary layer flow in a high-porosity medium. In the base flow, the governing conservation equations are solved by using a suitable variable transformation and employing an implicit finite-difference scheme. The stability analysis is based on linear stability theory, and the resulting equations are solved on the basis of the local similarity approximations. The results show that the flow becomes more susceptible to the vortex mode of disturbances as buoyancy force is increased.

9T909. **Shear stabilization of miscible displacement processes in porous media.** - A Rogerson *(Center for Fluid Mech, Div of Appl Math, Brown Univ, Providence RI 02912)* and E Meiburg *(Dept of Aerospace Eng, Univ of S California, Los Angles CA 90089-1191)*. Phys Fluids A 5(5) 1344-1355 (Jun 1993).

9T910. **Stability of miscible displacements in porous media with nonmonotonic viscosity profiles.** - O Manickam *(Dept of Mech Eng, Stanford)* and GM Homsy *(Dept of Chem Eng, Stanford)*. Phys Fluids A 5(5) 1356-1367 (Jun 1993).

452Y. COMPUTATIONAL TECHNIQUES

9A911. **Modeling of dynamic networks of thin thermoelastic beams.** - JE Lagnese, G Leugering *(Dept of Math, Georgetown Univ, Washington DC 20057)*, EJPG Schmidt *(Dept of Math and Stat, McGill Univ, 805 Sherbrook St W, Montreal, PQ H3A 2K6, Canada)*. Math Methods Appl Sci 16(5) 327-358 (May 1993).

We derive a distributed-parameter model of a thin nonlinear thermoelastic beam in 3D. The beam can also be initially curved and twisted. Our main task is to formulate the nonhomogeneous initial, boundary and node value problem associated with the dynamics of a network of a finite number of such beams. The emphasis here is on a distributed-parameter modeling of the geometric and kinematic node conditions. The forces and couples appearing in the boundary and node conditions can then be viewed as control variables. The analysis of the resulting control systems and their controllability and stabilizability properties is the subject forthcoming papers.

See also the following:

9A744. Nonuniform grid accuracy test applied to the natural-convection flow within a porous medium cavity
9A900. Stochastic approach for groundwater flow in a semiconfined aquifer subject to random boundary conditions

452Z. EXPERIMENTAL TECHNIQUES

See the following:

9A827. Procedure for processing experimental data on drying

454. Geomechanics

454D. SEISMOLOGY

9A912. **3D primary zero-offset reflections.** - P Hubral, J Schleicher *(Geophys Inst, Univ Fridericiana Karlsruhe, Hertzstr 16 Bau 42, D-W7500 Karlsruhe 21, Germany)*, M Tygel *(Dept Mat Appl, Univ Est de Campinas, UNICAMP Caixa PO Box 6065, 13081 Campinas SP, Brazil)*. Geophys 58(5) 692-702 (May 1993).

Zero offset reflections resulting from point sources are often computed on a large scale in 3D laterally inhomogeneous isotropic media with the help of ray theory. The geometrical-spreading factor and the number of caustics that determine the shape of the reflected pulse are then generally obtained by integrating the so-called dynamic ray-tracing system down and up the two-way normal incidence ray. Assuming that this ray is already known, we show that one integration of the dynamic ray-tracing system in a downward direction with only the initial condition of a point source at the earth's surface is in fact sufficient to obtain both results. To establish the Fresnel zone of the zero-offset reflection upon th reflector requires the same single downward integration. By performing a second downward integration (using the initial conditions of a plane wave at the earth's surface) the complete Fresnel volume around the two-way normal ray can be found. This should be known to ascertain the validity of the computed zero-offset event. A careful analysis of the problem as performed here shows that round-trip integrations of the dynamic ray-tracing system following the actually propagating wave front along the two-way normal ray need never be considered. In fact some useful quantities related to the two-way normal ray (eg, the normal-moveout velocity) require only one single integration in one specific direction only. Finally, a two-point ray tracing for normal rays can be derived from one-way dynamic ray tracing.

9A913. **Effects of viscoelasticity on seismic wave propagation in fault zones, near-surface sediments, and inclusions.** - Ik Bum Kang and GA McMechan *(Center for Lithospheric Stud, Univ of Texas at Dallas, PO Box 830688, Richardson TX 75083-0688)*. Bull Seismol Soc Am 83(3) 890-906 (Jun 1993).

By defining anelastic effects through the superposition of relaxation mechanisms, and incorporating them into the wave equation in terms of memory variables, the time-domain computation of responses of viscoelastic media with arbitrary spatial variations is feasible. This approach is applied to simulation of the effects of realistic distribution of compressional and shear wave quality factors (Qp and Qs) in a sequence of viscoelastic models of increasing complexity from a homogeneous medium, to a fault zone, a near-surface attenuating zone, and inclusions with anomalous Qp and Qs values.

9A914. **Ground roll: A potential tool for constraining shallow shear wave structure.** - GI Al-Eqabi and RB Herrmann *(Dept of Earth and Atmos Sci, St Louis Univ, 3507 Laclede, St Louis MO 63103)*. Geophys 58(5) 713-719 (May 1993).

The objective of this study is to demonstrate that a laterally varying shallow S-wave structure, derived from the dispersion of the ground roll, can explain observed lateral variations in the direct S-wave arrival. The data set consists of multichannel seismic refraction data from a USGS-GSC survey in the state of Maine and the province of Quebec. These data exhibit significant lateral changes in the moveout of the ground-roll as well as the S-wave first arrivals. A sequence of surface-wave processing steps are used to obtain a final laterally varying S-wave velocity model. These steps include visual examination of the data, stacking, waveform inversion of selected traces, phase velocity adjustment by cross-correlation, and phase velocity inversion. These models are used to predict the S-wave first arrivals by using 2D ray tracing techniques. Observed and calculated S-wave arrivals match well over 30 km long data paths, where lateral variations in the S-wave velocity in the upper 1-2 km are as much as ± 8 percent. The modeled correlation between the lateral variations in the ground-roll and S-wave arrival demonstrates that a laterally varying structure can be constrained by using surface-wave data. The application of this technique to data from shorter spreads and shallower depths is discussed.

9T915. **Impact of broadband seismology on the understanding of strong motions.** - D Helmberger, D Dreger, R Stead, Hiroo Kanamori *(Seismol Lab, CA IT, Pasadena CA 91125)*. Bull Seismol Soc Am 83(3) 830-850 (Jun 1993).

9A916. **Longitudinal directions in media of arbitrary anisotropy.** - K Helbig *(Kiebitzrain 84, 3000 Honnover 51, Germany)*. Geophys 58(5) 680-691 (May 1993).

A longitudinal direction is one in which three pure modes can propagate. It is known that every medium has at least three longitudinal directions. Every axis of symmetry is such a "bound" longitudinal direction, but in most media there are additional "free" longitudinal directions which do not coincide with symmetry directions. In particular, there are longitudinal directions even in triclinic media that possess no symmetry except the point symmetry. The maximum number of distinct longitudinal directions is thirteen. Similarly, the polarization pattern in the vicinity of a longitudinal direction depends strongly on the type of the longitudinal direction and on the relative magnitude of some off-diagonal stiffnesses. Since the polarization pattern can be observed in suitable vertical seismic profiling surveys, it might be inverted to obtain information on elastic parameters that is difficult to obtain by other means. For orthorhombic symmetry, there are always the three bound longitudinal directions coinciding with the axes. In each plane of symmetry a pair of free longitudinal directions can exist, and there can be four symmetrically disposed free longitudinal directions outside the planes of symmetry. Existence and direction of these free directions follows from simple expressions in the elastic stiffnesses.

9A917. **Modeling teleseismic P-wave propagation in the upper mantle using a parabolic approximation.** - MG Bostock *(Dept of Theor Geophys, Utrecht Univ, PO Box 80 021, 3508 TA Utrecht, Netherlands)*, JC VanDecar *(Geophys Program, Univ of Washington, Seattle WA)*, RK Snieder *(Dept of Theor Geophys, Utrecht Univ, PO Box 80 021, 3508 TA Utrecht, Netherlands)*. Bull Seismol Soc Am 83(3) 756-779 (Jun 1993).

Teleseismic waves propagating in the upper mantle are subject to considerable distortion due to the effects of laterally heterogeneous structure. The magnitude and scale of velocity contrasts representative of features such as subducted slabs may be such that wave diffraction becomes an important process. In this case forward modeling methods based on high-frequency asymptotic approximations to the wave equation will not accurately describe the wavefield. A method is introduced to model the propagation of teleseismic P waves in a laterally heterogeneous upper mantle that accounts for distortion of the initial portion of the wavefield including the effects of multipathing and frequency-dependent diffraction. Numerical examples for a simple 2D subducting slab model demonstrates the application of the method and illustrates the effects of multipathing and diffraction which dominate waveform distortion at high and low frequencies, respectively.

9A918. **O'Doherty-Anstey formula and localization of seismic waves.** - SA Shapiro and H Zien *(Geophys Inst, Univ of Karlsruhe, Hertzstr 16, W-7500 Karlsruhe 21, Germany)*. Geophys 58(5) 736-740 (May 1993).

We have shown that the O'Doherty-Anstey result well known in the framework of multiple scattering in layered media, describes the localization effect, which is probably the main reason for seismic attenuation in sediments. In contrast to other statistical methods we eliminate the problem of ensemble averaging by considering only self-averaged quantities. This is the only way to describe the practical situation with an adequate theory such that measured results become predictable.

454Y. COMPUTATIONAL TECHNIQUES

9A919. **Efficient wave input procedure for infinite media.** - Chongbin Zhao and S Valliappan *(Sch of Civil Eng, Univ of New S Wales, PO Box 1, Kensington NSW 2033, Australia)*. Commun Numer Methods Eng 9(5) 407-415 (May 1993).

An efficient wave input procedure in the finite and infinite element coupled model is presented in this paper. Compared to the previous wave input method, the main advantage of the present wave input procedure lies in its computational efficiency because only a small region of the medium needs to be modeled by FEs. The equivalence between the present wave input procedure and the previous one has been theoretically proven when a harmonic wave propagates vertically in an isotropic homogeneous elastic half-space. In addition, the accuracy of the present wave input method has been evaluated based on the solutions obtained for SH-wave, SV-wave, and P-wave scattering problems in a semicircular canyon for which analytical solutions are already available.

9A920. **Eigenvalues and eigenvectors of linearized elastic inversion.** - Andrea de Nicolao, G Drufuca, F Rocca *(Politec di Milano, Piazza Leonardo Da Vinci 32, 20133 Milano, Italy)*. Geophys 58(5) 670-679 (May 1993).

Small contrasts in the parameters allow the linearization of elastic modeling and inversion. Although this assumption simplifies parameter estimation, it also impoverishes information: a linearized model, besides being an approximation, requires shrinking the data space to precritical angles. This work investigates the two basic questions regarding the type of information that can be retrieved and how to retrieve it. The method is the singular value decomposition of the transfer function between data and parameters. This tool allows a simple interpretation of the information contained in reflections, and it outlines a general estimation procedure. A medium characterized by a uniform background is considered; reflections are linearized according to the Born approximation. P-P reflections are analyzed. The simplicity of the model allows a theoretical study of the effects of velocity errors in the overburden. The analysis is performed for two different sets of elastic parameters. In both cases the conclusion is that only the estimate of one parameter can be accurate while the quality of the estimate of the second parameter critically depends upon the velocity uncertainty and the maximum incident angle; estimation of a third parameter is very difficult.

See also the following:

9A913. Effects of viscoelasticity on seismic wave propagation in fault zones, near-surface sediments, and inclusions
9A917. Modeling teleseismic P-wave propagation in the upper mantle using a parabolic approximation

454Z. EXPLORATIONS AND MEASUREMENTS

9A921. **Determination of Fresnel zones from traveltime measurements.** - P Hubral, J Schleicher *(Geophys Inst, Karlsruhe Univ, Hertzstr 16 Bau 42, 7500 Karlsruhe 21, Germany)*, M Tygel *(Dept Mat Appl, Univ Est de Campinas, UNICAMP Caixa PO Box 6065, 13081 Campinas, SP, Brazil)*, Ch Hanitzsch *(Geophys Inst, Karlsruhe Univ, Hertzstr 16 Bau 42, 7500 Karlsruhe 21, Germany)*. Geophys 58(5) 703-712 (May 1993).

For a horizontally stratified (isotropic) earth, the rms-velocity of a primary reflection is a key parameter for common-midpoint (CMP) stacking, interval-velocity computation (by the Dix formula) and true-amplitude processing (geometrical-spreading compensation). As shown here, it is also a very desirable parameter to determine the Fresnel zone on the reflector from which the primary zero-offset reflection results. Hence, the rms-velocity can contribute to evaluating the resolution of the primary reflection. The situation that applies to a horizontally stratified earth model can be generalized to 3D layered laterally inhomogeneous media. The theory by which Fresnel zones for zero-offset primary reflections can then be determined purely from a traveltime analysis – without knowing the overburden above the considered reflector – is presented. The concept of a projected Fresnel zone is introduced and a simple method of its construction for zero-offset primary reflections is described. The projected Fresnel zone provides the image on the earth's surface (or on the traveltime surface of primary zero-offset reflections) of that part of the subsurface reflector (ie, the actual Fresnel zone) that influences the considered reflection. This image is often required for a seismic stratigraphic analysis. Our main aim is therefore to show the seismic interpreter how easy it is to find the projected Fresnel zone of a zero-offset reflection using nothing more than a standard 3D CMP travel time analysis.

456. Earthquake mechanics

9A922. Ground motion model for the 1989 M 6.9 Loma Prieta earthquake including effects of source, path and site. - JF Schneider *(Elec Power Res Inst, PO Box 10412, Palo Alto CA 94025)*, WJ Silva, C Stark *(Pacific Eng and Anal, 311 Pomona Ave, El Cerrito CA 94530)*. Earthquake Spectra 9(2) 251-287 (May 1993).

The objective of this study is to assess the effects of source finiteness, crustal wave propagation, and site response upon recorded strong ground motions from the 1989 Loma Prieta earthquake. Our analysis uses band limited white noise with random vibration theory to produce site-specific estimates of peak acceleration and response spectral ordinates for both a point-source and finite-source model. Effects of nonlinear soil response are modeled through an equivalent-linear approach. The point-source model additionally accommodates crustal propagation effects in terms of direct-plus-postcritical reflections.

9A923. Earthquake microzoning from soil properties. - APW Hodder *(Dept of Earth Sci, Univ of Waikato, Hamilton, New Zealand)* and MZ Graham *(Dept Earth Sci, Univ of Waikato, Hamilton, New Zealand)*. Earthquake Spectra 9(2) 209-231 (May 1993).

The extent of damage caused by an earthquake in Wellington, New Zealand, in 1968 to buildings erected on a variety of regoliths and foundation materials is correlated with the thickness of the regolith, the depth to the water table and semi-quantitative parameters derived from soil profile descriptions, particularly related to soil type and soil structure. From linear regression correlations, the expected damage for a comparable earthquake elsewhere can be determined. The model was tested for soil data for the Edgecumbe area hit by a damaging earthquake in 1987. The predictions were sufficiently in accord with observations to suggest that soil properties that reflect the geotechnical properties of the upper parts of the regolith, particularly those that measure the shear strength, shear wave velocity, and viscous damping of that material, may be useful for earthquake microzoning purposes in areas where there is a considerable thickness of unconsolidated materials above bedrock.

9A924. Evaluation of seismic design criteria for highway bridges. - E Miranda *(Dept of Civil Eng, Swiss Fed IT, CH-1015 Lausanne, Switzerland)*. Earthquake Spectra 9(2) 233-250 (May 1993).

After an overview of the development of US seismic design specifications for highway bridges an evaluation of current Caltrans and AASHTO seismic criteria is presented. Linear and nonlinear response spectra of ground motions recorded on different soil conditions in the Loma Prieta earthquake and other recent earthquakes are compared with code recommendations. Special emphasis is placed on how present design procedures reduce elastic forces to take into account the energy absorption capacity of the structure, and on the estimation of maximum inelastic deformations. Results indicate that current design recommendations may underestimate strength and deformation demands, particularly for short-period bridges and for bridges on soft soils. Finally, recommendations are made on how seismic design specifications may be improved.

9T925. Treatment of parameter uncertainty and variability for a single seismic hazard map. - BK Bender *(2850 Kenwood Dr, Boulder CO 80303)* and DM Perkins *(US Geol Survey, MS 966 Federal Center, Box 25046 Denver CO 80225)*. Earthquake Spectra 9(2) 165-195 (May 1993).

See also the following:

9T915. Impact of broadband seismology on the understanding of strong motions
9A917. Modeling teleseismic P-wave propagation in the upper mantle using a parabolic approximation

458. Hydrology, oceanology, meteorology

9A926. Generation of a modified Lamb surface wave in the atmosphere by a underwater source. - LA Gasilova, IY Gordeeva, YV Petukhov *(Inst of Appl Phys, Russian Acad of Sci, Russia)*. Sov Phys Acoust 38(6) 567-570 (Nov-Dec 1992).

The dispersion properties of a modified Lamb surface wave propagating along the interface between an isothermal atmosphere and a "heavy" compressible fluid with a depth-invariant density and sound velocity (modeling the ocean) are investigated, and the frequency dependence of the wave excitation coefficients is determined for an underwater point mass source. It is shown that this wave, which exists only below a certain critical frequency, propagates with supersonic velocity above a certain resonance frequency and with subsonic velocity below the same frequency, which corresponds to the intersection of the frequency curves of the phase velocities of the modified Lamb wave and the hydrodynamic surface wave.

VIII. ENERGY & ENVIRONMENT

500. Fossil fuel systems

9T927. Aging of distribution and other lifeline systems due to corrosion. - J Isenberg *(Weidlinger Assoc, 4410 El Camino Real, Ste 110, Los Altos CA 94022-1049)*. Appl Mech Rev 46(5) 180-182 (May 1993).

9T928. Materials considerations in service life prediction. - RP Wei and DG Harlow *(Dept of Mech Eng and Mech, Lehigh Univ, Bethlehem PA 18015)*. Appl Mech Rev 46(5) 190-193 (May 1993).

9T929. Memphis light, gas and water division experience with aging of electric, gas, and water systems. - C Pickel *(Memphis Light, Gas and Water Div, PO Box 430, Memphis TX 38101)*. Appl Mech Rev 46(5) 183-186 (May 1993).

9T930. Operation and management of aging gas distribution systems. - JD McNorgan *(Pipeline Des, S California Gas, PO Box 3249, Los Angeles CA 90051)*. Appl Mech Rev 46(5) 179 (May 1993).

9T931. Session I Summary. Fossil fuel plants. - VL Hill *(Gas Res Inst, 8600 W Bryn Mawr Ave, Chicago IL 60631-3562)*. Appl Mech Rev 46(5) 151 (May 1993).

9T932. Session IV Summary: Distribution systems. - M Shinozuka *(Dept of Civil Eng and Operations, Princeton)*. Appl Mech Rev 46(5) 187-189 (May 1993).

See also the following:

9T474. Industry approach to aging offshore platforms
9T475. Platform removal
9A839. Compound effect of cutting depth and bit dull on cutters' temperature for polycrystalline diamond compact bits
9A907. Study of massive water injection by thermoporomechanical coupling model
9T965. Aging of energy production and distribution systems
9A966. Integrity assurance of natural gas transmission pipelines

502. Nuclear systems

9T933. Generic steam generator life cycle management from a utility perspective. - RL Baker *(Senior Consult Eng, Houston Lighting and Power, PO Box 289, Wadsworth TX 77483)*. Appl Mech Rev 46(5) 152-161 (May 1993).

9T934. Session II Summary: Nuclear power plants. - ME Lapides *(Elec Power Res Inst, 3412 Hillview Ave, PO Box 10412, Palo Alto CA 94303)*. Appl Mech Rev 46(5) 171 (May 1993).

9A935. Accident analysis and safety of future fusion devices. - H Loffler *(Gesellschaft Anlagen- und Reaktorsicherheit (GRS), mbH, Schwertnergasse 1, W-5000 Koln 1, Germany)*. Fusion Eng Des 22(1-2) 57-65 (Mar 1993).

In hypothetical beyond design accidents where all engineered safety systems are assumed to fail, fusion undoubtedly is less hazardous then fission. But for more frequent - though very still unlikely - events the sophisticated safety culture of fission is a challenge which must be taken seriously. A containment concept with three barriers is proposed. A scoping study of conceivable event progression shows that several physical phenomena charging the containment come into play in various order for different event progressions. The development of adequate tools for containment safety analysis is encouraged.

9A936. Radiation embrittlement mechanistic modelling. - WA Pavinich *(Groove Eng, 9040 Executive Park Dr, Ste 218, Knoxville TN 37923)*, WL Server *(ATI Consult, 2010 Crow Canyon Place, Ste 160, San Ramon CA 94583)*, T Griesbach *(Elec Power Res, 3412 Hillview Ave, Palo Alto CA 94303)*. Appl Mech Rev 46(5) 162-170 (May 1993).

The mechanistic models of radiation embrittlement for reactor vessel steels are reviewed and direction for improving these models is provided. Improvement in these mechanistic models will lead to predictive expressions for parameters of engineering interest. This paper provides the initial direction of modelling efforts that will improve existing or develop new predictive equations for damage attenuation, temperature effects, thermal annealing, the effect of post weld heat treatment, transition behavior and upper shelf behavior of reactor vessel steels.

506. Solar and other energy systems

506B. SOLAR COLLECTOR MECHANICS

9A937. Dynamic method for solar collector array testing and evaluation with standard database and simulation programs. - B Perers *(Vattenfall Utveckling AB, S-81070 Alvkarleby, Sweden).* Solar Energy 50(6) 517-526 (Jun 1993).

A measurement and evaluation method is described by which standard collector performance parameters can be derived directly from measured outdoor data. Standard programs with routines for multiple regression can be used for the parameter identification. A continuous flow is applied in the collector loop during the test. Data for the whole day can be used. The model is set up for thermal power output (and not efficiency). This forces the parameters to values that are suitable for prediction of long-term performance. The collector model and parameters correspond closely to those used in existing detailed simulation programs such as TRNSYS, WATSUN, or MINSUN.

9A938. Effect of pressure-induced stress on the design of shaped-glass evacuated solar collectors. - JD Garrison *(Phys Dept, San Diego State Univ, San Diego CA 92182-0325).* Solar Energy 50(6) 527-538 (Jun 1993).

Shaped-glass evacuated solar collectors have the lower portion of the turbulent glass vacuum envelope shaped and inside surface mirrored to concentrate sunlight onto an absorber tube in the vacuum. Upon evacuation, stresses are set up in the glass. The maximum surface tensile stress possible in glass, while keeping the probability of fracture small, is of the order of 7 MPa. This low maximum tensile stress places severe limitations on the amount the lower portion of the cross section of a cylindrical glass evacuated solar collector can deviate from circular to provide the concentration. Equations are developed for determining stress in the glass. Results of stress calculations leading to parameters for collector design are presented.

9A939. New design of nontracking seasonally adjusted plane mirror linear trough solar concentrator with a flat horizontal absorber. - RP Goswami, GD Sootha *(Solar Energy Centre, Dept of Non-conventional Energy Sources, Ministry of Power and Non-conventional Energy Sources, B-4, 9th Fl, CGO Complex, Lodi Rd, New Delhi 110 003, India)*, BS Negi *(Dept of Phys, Indian IT, Hauz Khas, New Delhi 110 016, India)*, ZH Zaidi *(Dept of Phys, Jamia Millia Islamic Univ, New Delhi 110 011, India).* Int J Energy Res 16(9) 837-849 (Dec 1992).

This paper presents an optical design based on a single-reflection criterion, and performance characteristics of an east-west aligned nontracking seasonally adjusted linear trough solar concentrator with a flat horizontal absorber, using plane mirror elements. The design procedure allows the use of any desired number of mirror elements to reflect solar energy onto the base absorber in one reflection. The angle of inclination of each mirror element with respect to the absorber surface, and the width of the mirror element, are determined so that a ray incident on the extreme upper edge of the mirror element at a specified angle to the normal to the concentrator aperture (acceptance half-angle), after reflection, strikes the extreme edge of the absorber on the opposite side of the mirror element. Other rays making angles less than the design acceptance half-angle are also reflected onto the base absorber in one reflection. Concentrator designs resulting from this approach appear to have the important characteristic of relatively smaller heights, and hence appear highly cost-effective in terms of the amount of material required for fabrication. Some numerical calculations have been carried out to illustrate the performance of concentrators for different acceptance half-angles. Results obtained are presented in graphic and tabular forms, and are discussed.

9A940. Thermal performance of a flat-plate heat-pipe collector array. - TY Bong, KC Ng, H Bao *(Dept of Mech and Prod Eng, Natl Univ, Singapore 0511).* Solar Energy 50(6) 491-498 (Jun 1993).

This article presents a theoretical model for the determination of the efficiency, the heat removal factor, and the outlet water temperature of a single collector and an array of flat-pipe heat-pipe collectors. The model is validated by on-site testing of 16 heat-pipe collectors under the typical weather conditions in Singapore. Within the operational range of interest of the hot water temperatures, the results show that the proposed model is sufficient to describe the steady-state performance of the collector array.

506D. SOLAR HEAT TRANSFER

9A941. Calculation of the shape factor from a small rectangular plane to a triangular surface perpendicular to the rectangular plane without a common edge. - HL Noboa, D O'Neal, WD Turner *(Dept of Mech Eng, Texas A&M Univ, College Station TX 77843).* J Solar Energy Eng 115(2) 117-120 (May 1993).

In developing an analytical model of radiative heat transfer inside attics, the necessity of calculating the shape factor from a small rectangle to a triangle plane may arise. This paper describes a methodology of calculation for such a shape factor from simple relations using shape-factor algebra. The shape factor is calculated using a mirror image of the triangular surface, in such a way that the small rectangular plane is positioned symmetrical between the two triangular surfaces. Numerical results are presented in graphical form.

9A942. Numerical analysis of greenhouse-type solar stills with high inclination. - A Palacio and JL Fernandez *(Inst of Eng UNAM, Ciudad Univ, Coyoacan 04510, Mexico).* Solar Energy 50(6) 469-476 (Jun 1993).

A numerical analysis has been carried out to evaluate the technical feasibility of single effect solar stills with a cover slop of up to 60°. The aim of the research is to establish the overall distillate productivity and the relative importance of the heat and mass transfer mechanisms when water diffusion is minimal and convection dominates. Experimental measurements of the distillate obtained from an already working unit are related to the number results by means of an "equivalent" Prandtl number that simplifies the analysis, allowing for the moist air in the inside of the cavity to be represented as a perfect gas.

9A943. Radiative cooling efficiency of white pigmented paints. - B Orel, M Klanjsek Gunde *(Natl Inst of Chem, PO Box 30, 61115 Ljubljana, Slovenia)*, A Krainer *(Dept of Civil and Architec Eng, Univ at Ljubljana, Slovenia).* Solar Energy 50(6) 477-482 (Jun 1993).

Nocturnal temperature measurements of various infrared selective radiators performing radiative cooling have been carried out. Measured temperature differences between the radiators and ambient temperature were about 10°C. Radiating surfaces have been prepared by applying different kinds of paints on aluminium substrates. It was shown that the addition of a $BaSO_4$ extender in the paint dispersion increased the cooling performance of the paint radiators.

9A944. Temperature distribution inside a solar collector storage tank of finite wall thickness. - MA Al-Nimr *(Dept of Mech Eng, Jordan Univ of Sci and Tech, Irbid, Jordan).* J Solar Energy Eng 115(2) 112-116 (May 1993).

A mathematical model for the transient conjugated behavior of a hot-water storage tank having finite wall thickness is presented. An analytical closed-form solution for the temperature field within the tank is obtained. This solution takes into consideration the axial conduction of heat in both fluid and solid wall and the heat capacity of the solid wall. Plots of the solution show that finite wall thickness tends, as expected, to decrease the thermal stratification within the tank.

506F. OTHER SOLAR ASPECTS

9A945. Comparison of experimental and simulated thermal ratings of drain-back solar water heaters. - JH Davidson, WT Carlson, WS Duff *(Solar Energy Appl Lab, Colorado State Univ, Ft Collins CO 80523)*, PJ Schaefer, WA Beckman, SA Klein *(Solar Energy Lab, Univ of Wisconsin, Madison WI).* J Solar Energy Eng 115(2) 101-105 (May 1993).

Short-term experimental tests of drain-back solar water heaters are compared to ratings obtained using TRNSYS to determine if computer simulations can effectively replace laboratory ratings of solar domestic hot water heating systems. The effectiveness of TRNSYS in predicting changes in ratings due to limited changes in collector area, collector flow rate, recirculation flow rate, storage tank volume, and storage tank design is validated to within ± 10%. Storage tank design is varied by using a stratification manifold in place of the standard drop tube.

9A946. Computerized numerical experimental study of average solar radiation penetration in plant stands. - SG Chen, BY Shao, I Impens *(Dept of Biology, Univ of Antwerpen, UIA B-2610 Wilrijk, Antwerpen, Belgium).* J Qantitative Spectroscopy Radiative Transfer 49(6) 651-658 (Jun 1993).

An important problem in radiation measurements is the averaging of radiant fluxes in horizontal directions. The use of downward cumulative foilage-areal index averaged over a horizontal surface for the calculation of the average penetration of solar radiation in a plant stand underestimates penetration unless the stand is horizontally uniform. Using a computerized numerical experimental method we show that the underestimation of penetration varies with the downward cumulative foilage-areal index, the extinction coefficient, as well as the foliage distribution pattern. The results show that the underestimation is strongly pronounced for some combinations of extinction coefficient and foliage-areal index. It is alwo shown that the use of a penetration value averaged over a horizontal surface (P_{AP}) to invert the stand foilage-areal index (LAI) by means of the logarithm formula LAI = $-\ln(P_{AP})/k$ can cause large underestimation of LAI, especially in the use of large LAI. Numerical results are presented in this paper to provide a basis for calibration.

9A947. Correlations for the yearly or seasonally optimum salt-gradient solar pond in Greece. - KA Antonopoulos and ED Rogdakis *(Dept of Mech Eng, Thermal Eng Section, Natl Tech Univ, 42 Patission St, Athens 106 82, Greece).* Solar Energy 50(5) 417-424 (May 1993).

Simple correlations and corresponding nomographs are presented, which express the maximum useful heat received from salt-gradient solar ponds throughout the year or during a specified season of the year, and the corresponding optimum depth of the nonconvective zone in terms of the thickness of the upper convective zone and the temperature under which the maximum useful heat is received. The correlations are valid for the Athens (Greece) area or for regions with a similar climate, because solar radiation and ambient temperature valid for Athens have been employed, obtained by a statistical process of hourly measurements over a period of about 20 years. Calculations of the useful heat are performed for a great number of values of the parameters of the problem, and the combinations of values that maximize useful heat are selected and used for developing correlations and corresponding nomographs. The correlations presented may be employed in the design of the optimum solar pond under the specific requirements of each application.

9A948. Mathematically integrable parameterization of clear-sky beam and global irradiances and its use in daily irradiation applications. - C Gueymard *(Florida Solar Energy Center, 300 State Rd 401, Cape Canaveral FL 32920)*. Solar Energy 50(5) 385-397 (May 1993).

A simple parameterized clear-sky short-wave irradiance model is derived from a detailed two-band physical model presented earlier. The inputs for the parameterized model (called PSIM) are the solar elevation, the amount of precipitable water (w), the Angstrom turbidity coefficient (β), the station's pressure (or its altitude), and the zonal surface albedo (for which a simple submodel is provided for N America). PSIM is intended to give accurate irradiance estimates in any atmosphere condition whenever $w < 5$ cm and $\beta < 0.45$. The parameterization uses a function of solar elevation that is integrable with time, so that a parameterized daily irradiation model (called DIM) is also obtained. It is also suggested that the original Angstrom's equation (to derive the average global irradiation from the fraction of possible sunshine) be used more extensively with DIM. Finally, it is demonstrated (using data from Albany, NY) that the monthly average beam irradiation may be obtained with a very simple equation from the fraction of possible sunshine and DIM, yielding more accurate estimates than the existing best-performance method.

9A949. Monolithic and mechanical multijunction space solar cells. - RK Jain and DJ Flood *(NASA Lewis Res Center, Cleveland OH 44135)*. J Solar Energy Eng 115(2) 106-111 (May 1993).

High-efficiency, lightweight, radiation-resistant solar cells are essential to meet the large power requirements of future space missions. Single-junction cells are limited in efficiency. Higher cell efficiencies could be realized by developing multijunction, multibandgap solar cells. Monolithic and mechanically stacked tandem solar cells surpassing single-junction cell efficiencies have been fabricated. This article surveys the current status of monolithic and mechanically stacked multi-bandgap space solar cells, and outlines problems yet to be resolved. More information is needed on the effect of temperature and radiation on the cell performance.

9A950. Numerical modeling of reflux solar receivers. - RE Hogan Jr *(Fluid and Thermal Sci Dept, Sandia)*. J Solar Energy Eng 115(2) 93-100 (May 1993).

Using reflux solar receivers to collect solar energy for dish-Stirling electric power generation systems is presently being investigated by several organizations, including Sandia. In support of this program, Sandia has developed two numerical models describing the thermal performance of pool-boiler and heat-pipe reflux receivers. Both models are applicable to axisymmetric geometries and they both consider the radiative and convective energy transfer within the receiver cavity, the conductive and convective energy transfer from the receiver housing, and the energy transfer to the receiver working fluid. The numerical modeling concepts presented are applicable to conventional tube-type solar receivers, as well as to reflux receivers. Good agreement between the two models is demonstrated by comparing the predicted and measured performance of a pool-boiler reflux receiver being tested at Sandia.

9A951. Optimal coupling and feasibility of a solar-powered year-round ejector air conditioner. - M Sokolov and D Hershgal *(Dept of Fluid Mech and Heat Transfer, Fac of Eng, Tel-Aviv Univ, Ramat-Aviv 69978, Israel)*. Solar Energy 50(6) 507-516 (Jun 1993).

An ejector refrigeration system that uses a conventional refrigerant (R-114) is introduced as a possible mechanism for providing solar-based air-conditioning. Optimal coupling conditions between the collector's energy output and energy requirements of the cooling system, are investigated. Operation at such optimal conditions assures maximized overall efficiency. Procedures leading to the evaluation of the performance of a real system are disclosed. Design curves for such a system with R-114 as refrigerant are provided.

9A952. Performance and testing of large-size solar water heater cum solar cooker. - NM Nahar *(Central Arid Zone Res Inst, Jodhpur 342-003, India)*. Int J Energy Res 17(1) 57-67 (Jan 1993).

The performance of a novel device has been tested. The device can be used as a collector cum storage type solar water heater using the winter, and, with minor adjustments, it can be used as a hot-box solar cooker. The device can provide hot water at 50 - 60° C in the evening, which can be maintained at 40 - 45° C until the following morning. It can also be used for cooking food for about 40 people. The efficiencies of the device as a solar water heater and as a solar cooker have been found to be 67•7% and 29•8% respectively. The payback period varies between 1•64 to 5•90 years depending on the fuel it replaces.

9A953. Role of buoyant thermals in salt gradient solar ponds and in convection more generally. - LB Mullett *(42 Grosvenor Ave, Bourne, Lincs PE10 9HU, UK)*. Int J Heat Mass Transfer 36(7) 1923-1941 (May 1993).

It is shown that the well accepted model of double-diffusive convection for strong heating from below a stable salinity gradient does not apply at the very modest level of solar radiation, more especially when part (or even all) of the heat is generated within the fluid. New models are developed in which buoyant thermals play casual roles (as indeed, they do in the case of strong heating). Thermals from all three kinds of boundaries are investigated, and it is found that although there is a limited quantity of fluid in a thermal, connection is retained with the source during its lifetime. Thermal ranges are found to be well defined and increase according to environmental (water) temperature, with a common form of range equation. The equation is calibrated experimentally for each type of thermal. Finally, it is shown that the onset of turbulence at Rayleigh numbers in the region of 5×10^4 to 10^5 marks the transition from laminar Benard-Rayleigh heat flow to quantised flow by thermals.

9A954. Solar position and right ascension. - HD Kambezidis and AE Tsangrassoulis *(Inst of Meteorol and Phys of the Atmos Env, Natl Observatory, PO Box 20048, Athens GR-118 10, Greece)*. Solar Energy 50(5) 415-416 (May 1993).

A new correction for right ascension, proposed by the authors, permits smooth SUNAE algorithm runs, minute by minute, for a period of a year.

9A955. Solar-assisted vapor compression-absorption cascaded air-conditioning systems. - JCV Chinnappa *(68 Mascar St, Upper Mount Gravatt Q 4122, Australia)*, MR Crees, S Srinivasa Murthy, K Srinivasan *(Dept of Civil and Syst Eng, James Cook Univ of N Queensland, Townsville 4811, Australia)*. Solar Energy 50(5) 453-458 (May 1993).

This article describes a hybrid airconditioning system consisting of a conventional R-22 vapor compression refrigeration svstem cascaded with a solar-operated, ammonia-water, vapour absorption system. The condenser of the R-22 system is cooled by the evaporator of the ammonia system. This facilitates operation of the R-22 system at a low condensing temperature and pressure. This is found to yield considerable savings in electrical energy consumption by the compression system.

9A956. Solar-pumped laser and its second harmonic generation. - H Arashi and Y Kaneda *(Res Inst for Sci Measurements, Tohoku Univ, 1-2, 2-Chome Katahira, Sendai, Japan)*. Solar Energy 50(5) 447-451 (May 1993).

Solar radiation concentrated by using a large solar collector was used to optically excite a Nd:YAG laser medium and was successfully converted into coherent laser light. The maximum laser output power attained 60W in multi-mode. This is the highest power so far reported on a solar-pumped laser. Q-switched pulse operation of the cw solar-pumped Nd:YAG laser light was performed by inserting an acousto-optic deflector into the laser cavity. Output pulses of peak power greater than 100 kW and FWHM of 100 ns were obtained at a repetition rate of 1 kHz. Using the pulsed solar-pumped Nd:YAG laser, second harmonics were generated at wavelength of 530 nm by a nonlinear KTP crystal.

9A957. Thermochromic gels for control of insolation. - A Beck, T Hoffmann, W Korner, J Fricke *(Physikalisches Inst, Univ Wurzburg, Am Hubland, D-8700 Wurzburg, Germany)*. Solar Energy 50(5) 407-414 (May 1993).

Thermochromic gels consist of a mixture of water, gelling agent, and a polyether reaction compound. They show a drastic increase of scattering when a characteristic switching temperature is surpassed. The hemispherical transmission consequently decreases from 90 to 50% for a 1-mm thick layer sandwiched between two glass panes. The increase in scattering is caused by a dramatic increase in number density and particle size of created scattering centers. Our measurements cover the directional-directional transmission, as well as the directional-hemispherical transmission and reflection, using a double-beam spectrophotometer with an integrating sphere. The thermochromic material is a low-cost, nontoxic product.

506H. GEOTHERMAL ENERGY

9A958. Drilling experience of K6-2, the high temperature and crooked geothermal well in Kakkonda, Japan. - Seiji Saito *(Japan Metals and Chem, Iwate-ken, Japan)*. J Energy Resources Tech 115(2) 117-123 (Jun 1993).

Well K6-2 was drilled for geothermal production for the Kakkonda No 2 Power Plant (to be built in 1995) at the Kokkanda geothermal field, northern Honshu Island, Japan from 1988 through 1989. The well was planned to be vertical and the target area was a 100 m radius at 2800 m. Mainly, because of the formation inclination, strong bit walk tendency was encountered below 1200 m. Because a pendulum BHA did not help to drop the inclination, downhole motors with bent subs were employed. Totals of six and seven downhole motors for 12 1/4 and 8 1/2 inch hole sections, respectively, were run. The estimated formation temperatures were over 350° C below 1900 m, so two mud cooling towers and 500 m^3 pit were used to cool the returned mud. These systems worked well, but at 2245 m the estimated mud circulation temperature on bottom went up to 150° C and the stator rubber of the downhole motors unbounded and broke up after a one hour run.

506L. OTHER ENERRGY SYSTEMS

9A959. Effect of the fuel-cell unit on the efficiency of a fuel-cell-topped Rankine power cycle. - WR Dunbar *(Dept of Mech Eng and Appl Mech, Univ of Penn, Philadelphia PA 19104-6315)* and RA Gaggioli *(Dept of Mech and Indust Eng, Marquette Univ, Milwaukee WI 53233-2886)*. J Energy Resources Tech 115(2) 105-107 (Jun 1993).

Dunbar, Lior and Gaggioli (1991) proposed a configuration of a fuel-cell-toped electrical Rankine power generating station and analyzed its performance. That study revealed that the fuel-cell topping improved plant efficiency to values up to 62 percent, versus the conventional plane efficiency of 41.5 percent. This work lays the foundation for a thermoeconomic analysis of such systems by relating exergy consumption to fuel-cell unit size, as follows: the relationship between system efficiency (and hence fuel consumption) and fuel-cell unit size is presented for a number of fuel-cell operating conditions; the relationship between fuel flow rate and fuel-cell unit size is shown; and the exergetic effects of the major plant components are discussed as a function of fuel-cell unit size.

9A960. Emf, Maximum power and efficiency of fuel cells. - RA Gaggioli and WR Dunbar *(Dept of Mech Eng, Marquette Univ, Milwaukee WI 53233-2286)*. J Energy Resources Tech 115(2) 100-104 (Jun 1993).

The ideal voltage of steady-flow fuel cells is usually expressed by Emf = $\Delta G°$- nf where $\Delta G°$ is the "Gibbs free energy of reaction" for the oxidation of the fuel at the supposed temperature of operation of the cell. Furthermore, the ideal power of the cell is expressed as the product of the fuel flow rate with this emf. Such viewpoints are flawed in several respects. Rather than with emf, the proper starting place is with power output. The ideal power is that which would be obtained if the fuel were oxidized without irreversible entropy generation. Among other factors, this ideal output depends upon the ratio of oxidant to fuel flow rate (eg, air-fuel ratio) and the percentage of fuel oxidation. Examples are presented which illustrate such affects and their importance for the evaluation of ideal power and of efficiency.

9A961. Integrated resource planning. - F Kreith *(Natl Conference of State Legislatures, Denver CO 80202)*. J Energy Resources Tech 115(2) 80-85 (Jun 1993).

This article presents the essential features of an integrated resource planning process designed to provide energy for societal and industrial needs at least cost. Use of renewable energy sources and energy conservation measures, as well as consideration of social costs, are described. Available data of social costs and estimates for energy costs of conservation measures and renewable energy systems are included.

9A962. Matching and work ratio in elementary thermal power plant theory. - IK Smith *(Dept of Mech Eng and Aeronaut, City Univ, London, UK)*. Proc Inst Mech Eng A 206(A4) 257-262 (1992).

For most thermal power plants, the Carnot cycle efficiency is not the true ideal. Matching the cycle to the source leads to alternative limits and improved perceptions of how practical power plant can be improved. A method of including the work ratio into an ideal cycle analysis is presented which simplifies the estimation of practical power plant efficiencies and highlights the historic course of thermal efficiency improvement.

9A963. Semiempirical model of a building with a passive evaporative cool tower. - B Givoni *(Graduate Sch of Architec and Urban Planning, UCLA)*. Solar Energy 50(5) 425-434 (May 1993).

An experimental mathematical model that calculates the performance of a passive evaporative cool tower (also known as downdraft evaporative chimney), has been developed by Cunningham and Thompson. The model calculates the tower's exit air temperature, flow rate and the speed of the air exiting from the tower, and the diurnal patterns of the indoor temperature of a lightweight building cooled by this system. Initial validation of the model, by comparing predictions with independent measurements of the indoor temperature of the test building, was done by Cunningham *et al.* In its present state the applicability of the model is limited to the use of evaporating pads of the type used in the Tucson study (CELdek) cooling a lightweight building (stud wall construction).

506N. ENERGY STORAGE

9A964. Lead acid battery storage model for hybrid energy systems. - JF Manwell and JG McGowan *(Renewable Energy Res Lab, Univ of Massachusetts, Amherst MA 01003)*. Solar Energy 50(5) 399-405 (May 1993).

This paper describes a new battery model developed for use in time series performance models of hybrid energy systems. The model is intended to overcome some of the difficulties associated with currently used methods. It is based on the approach of chemical kinetics. This model, which can be used for charging and discharging, is specifically concerned with the apparent changes in capacity as a function of charge and discharge rates. Examples of the deviation of the battery model constants and comparison of the new model with those used previously are given. Based on the success of the new model, it has been incorporated into the latest versions of the University of Massachusetts's wind-diesel simulation codes.

See also the following:

9T965. Aging of energy production and distribution systems
9A968. Session VIII Summary: Assessment

506Q. ENERGY DISTRIBUTION (INCL PIPELINES, TRANSMISSION LINES, ETC)

9T965. Aging of energy production and distribution systems. - MM Carroll and PD Spanos *(Dept of Energy Workshop, Rice Univ, Houston TX)*. Appl Mech Rev 46(5) 139-263 (May 1993).

9A966. Integrity assurance of natural gas transmission pipelines. - GJ Posakony *(J-TECH Consult, 1944 Pine St, Richland WA 99352)*. Appl Mech Rev 46(5) 146-150 (May 1993).

Natural gas transmission pipelines have proven to be a safe and efficient means for transporting the trillions of cubic feet of natural gas used annually in the US. Since the peak of construction of these pipelines occurred between 1950 and the mid-1960's, their average age is now over thirty years. However, replacement of these pipelines because of age would be prohibitively expensive and unnecessary. Preventive maintenance and rehabilitation programs put into practice by the pipeline industry provides the key to ensuring the continued integrity of the transmission pipeline system. This article reviews the preventive maintenance practices commonly used by the gas industry.

9T967. Session V Summary: Materials. - S Nemat-Nasser *(Center of Excellence for Adv Mat, Dept of Appl Mech and Eng Sci, UCSD)*. Appl Mech Rev 46(5) 211-212 (May 1993).

9A968. Session VIII Summary: Assessment. - CA Cornell *(Dept of Civil Eng, Stanford)*. Appl Mech Rev 46(5) 262-263 (May 1993).

The working group took its objective to be the formulation of a set of research and development recommendations for assessment of aging energy systems. The material discussed in every session at this workshop has relevance to the assessment of characteristics such as the current state of these facilities or their components. Indeed many of the items we cite will appear elsewhere as well. The focus we have maintained, however, is assessment for the direct purpose of decision making. The decisions may have to do with increasing inspection, monitoring or analysis, or with repair, or even with closure and replacement.

See also the following:

9T927. Aging of distribution and other lifeline systems due to corrosion
9T929. Memphis light, gas and water division experience with aging of electric, gas, and water systems
9T930. Operation and management of aging gas distribution systems
9T931. Session I Summary. Fossil fuel plants
9T932. Session IV Summary: Distribution systems

514. Environmental mechanics

9A969. Comparison of mass-loading and elastic plate models of an ice field. - VA Squire *(Dept of Math and Stat, Univ of Otago, PO Box 56, Dunedin, New Zealand)*. Cold Regions Sci Tech 21(3) 219-229 (May 1993).

A comparison is made between the two most common surface boundary conditions used to represent a marginal ice zone through which ocean waves are propagating. Although essentially the same – as the mass-loading model may be regarded as the limit of an elastic plate with no rigidity – the consequences of choosing one or the other boundary conditions are profound. With no rigidity, the wavelength in ice is less than that in the open sea; with the rigidity typical of an ice plate it is usually greater. The few data that exist indicate that a critical angle does occur which suggests that the full elastic plate theory may be necessary, although it is difficult to justify this as anything other than an effective parameterization for an ice field composed of discrete flows.

9A970. Ice pressures on vertical and sloping structures through dimensional analysis and similarity theory. - VM Arunachalam *(WISER Assoc, PO Box 13731 Station A St John's, NF A1B 4G3, Canada)* and DB Muggeridge *(Ocean Eng Res Centre, Memorial Univ of Newfoundland, St John's, NF A1B 3X5, Canada)*. Cold Regions Sci Tech 21(3) 231-245 (May 1993).

Experimental results from laboratory and field tests for ice pressures on vertical indentors and sloping structures have been compiled from original data and reanalyzed using dimensional analysis and similarity theory and equations for ice pressure have been separately derived. The data sets considered for the vertical indentors include most of the data sets contained in the derivation of Sanderson's pressure area curve (except the meso-scale model data), along with additional ones that have appeared in the public domain. The dimensionless pressure for a vertical structure decreased as a function of the product of aspect ratio and dimensionless strain rate. The effective pressure decreased with increasing value of aspect ratio defined in terms of the thickness of ice sheet, with decreasing values of velocity and of Young's modulus of ice.

IX. BIOENGINEERING

550. Biomechanics

550B. SKELETAL SYSTEMS, BONES, JOINTS, LIGAMENTS, ETC

9A971. **Bone and bones, architecture and stress, fossils and osteoporosis.** - CE Oxnard *(Centre for Human Biology, Univ of W Australia, Nedlands 6009, W Australia)*. J Biomech 26(SUPPL 1) 63-79 (1993).

The combined use of architectural and stress technologies in osteological studies is starting to provide the basic biomechanical underpinnings to both evolutionary and applied medical investigations of bone. The architectural investigations, though tested using invasive methods, are aimed at non-invasive ways of obtaining information from radiographs of bones, fossils and people. The stress studies, though initially involving older techniques such as photoelastic stress analysis, now employs FE analysis and, most recently, fast Lagrangian analysis of continua. Taken together, these methods are capable of providing more detailed knowledge of bone form and function that is important a) in revealing functional adaptation in evolutionary studies of fossils and b) for making early diagnosis and understanding pathological fractures in the late stages of osteoporosis.

9A972. **Design and development of an unconstrained dynamic knee simulator.** - CA McLean and AM Ahmed *(Dept of Mech Eng, McGill Univ, Montreal, Canada)*. J Biomech Eng 115(2) 144-148 (May 1993).

A dynamic knee simulation has been developed to allow in-vitro investigation of the mechanical response of the joint corresponding to dynamic functional activities, eg, walking. In the simulator, the controlled inputs are the time-histories of three parameters of a given dynamic activity: the flexion angle, and the flexion-extension moment and tibial axial force components of the foot-to-floor reaction. Satisfactory performance of the simulator has been established for walking gait conditions based on measurements on three fresh-frozen specimens.

9A973. **Improved dynamic model of the human knee joint and its response to impact loading on the lower leg.** - AE Engin *(Dept of Eng Mech, Ohio State Univ, Columbus OH 43210)* and ST Tumer *(Dept of Mech Eng, Middle E Tech Univ, Ankara 06531, Turkey)*. J Biomech Eng 115(2) 137-143 (May 1993).

Almost a decade ago, 3D formulation for the dynamic modeling of an articulating human joint was introduced. Two-dimensional version of this formulation was subsequently applied to the knee joint. However, because of the iterative nature of the solution technique, this model cannot handle impact conditions. In this paper, alternative solution methods are introduced which enable investigation of the response of the human knee to impact loading on the lower leg via an anatomatically based model.

See also the following:

9A393. Fracture analysis of dental composites
9T974. Biomechanical analysis of muscle strength as a limiting factor in standing posture
9T976. Human Morphology: Its role in the mechanics of movement
9A990. Sternal force-displacement relationship during cardiopulmonary resuscitation
9T996. Energetics of running and running shoes

550C. MUSCLE MECHANICS

9T974. **Biomechanical analysis of muscle strength as a limiting factor in standing posture.** - AD Kuo *(Des Div, Mech Eng Dept, Stanford)* and FE Zajac *(Mech Eng Dept, Stanford)*. J Biomech 26(SUPPL 1) 137-150 (1993).

9A975. **Neuromuscular adaptations during the acquisition of muscle strength, power and motor tasks.** - T Moritani *(Lab of Appl Physiology, Graduate Sch of Human and Env Stud, Kyoto Univ, Sakyo-ku, Kyoto 606, Japan)*. J Biomech 26(SUPPL 1) 95-107 (1993).

Neuromuscular performance is determined not only by the size of the involved muscles, but also by the ability of the nervous system to appropriately activate the muscles. Adaptive changes in the nervous system in response to training are referred to as neutral adaptation. This article briefly reviews current evidence regarding the neural adaptations during the acquisition of muscle strength, power and motor tasks and will be organized under four main topics; (i) muscle strength gain; neural factors versus hypertrophy, (ii) neural adaptation during power training, (iii) neuromuscular adaptations during the acquisition of a motor task, and (iv) neuromuscular adaptations during a ballistic movement.

See also the following:

9A971. Bone and bones, architecture and stress, fossils and osteoporosis
9T976. Human Morphology: Its role in the mechanics of movement
9T977. Muscle coordination of movement: A perspective
9A978. Optimization of the structure and movement of the legs of animals
9A994. Citius, altius, longius (faster, higher, longer): The biomechanics of jumping for distance
9T997. Sequential motions of the body segments in striking and throwing skills: Descriptions and explanations

550D. KINESIOLOGY

9T976. **Human Morphology: Its role in the mechanics of movement.** - RK Jensen *(Centre for Res in Human Dev and Sch of Human Movement, Laurentian Univ, Sudbury, ON, P3E 2C6, Canada)*. J Biomech 26(SUPPL 1) 81-94 (1993).

9T977. **Muscle coordination of movement: A perspective.** - FE Zajac *(Biomech Eng Program, Dept of Mech Eng, Stanford)*. J Biomech 26(SUPPL 1) 109-124 (1993).

9A978. **Optimization of the structure and movement of the legs of animals.** - R McNeill Alexander *(Dept of Pure and Appl Biology, Univ of Leeds, Leeds LS2 9JT, UK)*. J Biomech 26(SUPPL 1) 1-6 (1993).

The legs of animals, and their movements, have presumably been optimized by evolution and/or learning for the functions required of them in life. This paper presents a series of studies in which attempts have been made to formulate optimization problems, to which the legs and their movements may be solutions. These are studies of the ratio of radius to wall thickness in tubular bones; of the strengths of bones; of tendon thickness; of the gaits of turtles and of mammals; and of the technique of human high jumping. They illustrate some serious difficulties that may arise in inverse optimization studies but also show that the approach is helping to improve our understanding of legs and gaits.

See also the following:

9A971. Bone and bones, architecture and stress, fossils and osteoporosis
9A975. Neuromuscular adaptations during the acquisition of muscle strength, power and motor tasks
9A994. Citius, altius, longius (faster, higher, longer): The biomechanics of jumping for distance
9T997. Sequential motions of the body segments in striking and throwing skills: Descriptions and explanations

550E. MECHANICAL PROPERTIES OF TISSUES AND BLOOD

9T979. **Analysis of the time-dependent changes in intracellular calcium concentration in endothelial cells in culture induced by mechanical stimulation.** - FK Winston *(Children's Hospital of Philadelphia, Philadelphia PA 19104)*, LE Thibault *(Dept of Bioeng, Univ of Pennsylvania, Philadelphia PA 19104)*, EJ Macarak *(Connective Tissue Res Inst, Univ of Pennsylvania, Philadelphia PA 19104)*. J Biomech Eng 115(2) 160-168 (May 1993).

9T980. **Cellular response of mouse oocytes to freezing stress: Prediction of intracellular ice formation.** - M Toner *(Dept of Surgery, Massachusetts General Hospital, Harvard Med School, Charlestown MA 02129)*, EG Cravalho *(Harvard-IMT Div of Health Sci and Tech, MIT)*, M Karel *(Dept of Chem Eng, MIT)*. J Biomech Eng 115(2) 169-174 (May 1993).

9A981. **Characteristic recovery time of an erythrocyte from an extensional deformation.** - JC Lucero *(Graduate Sch of Electon Sci and Tech, Shizuoka Univ, Hamamatsu 432, Japan)*. J Biomech Eng 115(2) 206-207 (May 1993).

An analytical expression for the characteristic recovery time of an erythrocyte subject to an extensional deformation is derived using a previous nonlinear Kelvin-Voigt model. The recovery time thus obtained depends on the initial deformation in agreement with experimental observations, as a result of the nonlinearity of the model. The validity of the analytical results is confirmed using previous experimental data.

See also the following:

9A983. Biaxial mechanical properties of passive right ventricular free wall myocardium
9A990. Sternal force-displacement relationship during cardiopulmonary resuscitation

550F. ORGANS

9A982. **Aortic pressure estimation with electro-mechanical circulatory assist devices.** - JF Gardner, M Ignatoski, U Tasch, AJ Snyder, DB Geselowitz *(Penn State)*. J Biomech Eng 115(2) 187-194 (May 1993).

An adaptive technique for the estimation of the time history of aortic pressure (from applied voltage and position feedback) has been designed, implemented, and bench tested using the Penn State Electric Ventricular Assist Device (EVAD). This method, known in the field of automatic control as a dynamic observer, utilizes gains which were determined using experimental data collected while the EVAD was running on a mock circulatory system. An adaptive scheme provides the observer with a method of changing its initial conditions on a stroke-by-stroke basis which improves observer performance. In both determining the feedback gains and developing the adaptation scheme, a range of beat rates and pressure loads was taken into account to yield satisfactory observer performance over a range of operating conditions. The observer was implemented, its performance was verified in vitro and results are reported.

9A983. Biaxial mechanical properties of passive right ventricular free wall myocardium. - MS Sacks and CJ Chuong *(Joint Biomed Eng Program, Univ of Texas, Arlington TX 76019)*. J Biomech Eng 115(2) 202-204 (May 1993).

The biaxial mechanical properties of right ventricular free wall (RVFW) myocardium were studied. Tissue specimens were obtained from the sub-epicardium of potassium-arrested hearts and different stretch protocols were used to characterize the myocardium's mechanical response. To assess regional differences, we excised tissue specimens from the conus and sinus regions. The RVFW myocardium was found to be consistently anisotropic, with a greater stiffness along the preferred (or averaged) fiber direction.

9A984. Identification algorithm for systemic arterial parameters with application to total artificial heart control. - TL Ruchti, RH Brown *(Dept of Elec and Comput Eng, Marquette Univ, 1515 W Wisconsin Ave, Milwaukee WI 53233)*, DC Jeutter *(Dept of Biomed Eng, Marquette Univ, 1515 W Wisconsin Ave, Milwaukee WI 53233)*, Xin Feng *(Dept of Elec and Comput Eng, Marquette Univ, 1515 W Wisconsin Ave, Milwaukee WI 53233)*. Ann Biomed Eng 21(3) 221-236 (May-Jun 1993).

A new algorithm for estimating systemic arterial parameters from systolic pressure and flow measurements at the root of the aorta is developed and tested through a systems identification approach. The resulting procedure has direct application to a total artificial heart (TAH) control system currently under development. Identification models, representing the systemic arterial system, are developed from existing work in the area of cardiovascular modeling. Performance of the estimation algorithm was tested on data generated by a higher-order distributed model of the systemic arterial bed using normal canine parameters. Results from model-to-model experiments verify the consistency of the estimates and the ability of the estimator to converge quickly and track dynamically varying parameters.

9T985. Mathematical 3D solid modeling of biventricular geometry. - JS Pirolo *(Dept of Surgery, Div of Cardiothoracic Surgery, Washington Univ, St Louis MO)*, SJ Bresina *(Mallinckrodt Inst of Radiology, Washington Univ, St Louis MO)*, LL Creswell *(Dept of Surgery, Div of Cardiothoracic Surgery, Washington Univ, St Louis MO)*, KW Myers, BA Szabo *(Dept of Mech Eng, Center for Comput Mech, Washington Univ, St Louis MO)*, MW Vannier *(Mallinckrodt Inst of Radiology, Washington Univ, St Louis MO)*, MK Pasque *(Div of Cardiothoracic Surgery, Barnes Hospital, One Barnes Hospital Plaza, Suite 3108 Queeny Tower, St Louis MO 63110)*. Ann Biomed Eng 21(3) 199-219 (May-Jun 1993).

550G. MICROBIOMECHANICS

See the following:

9A989. Pressure propagation in pulsatile flow through random microvascular networks

550I. FLUID MECHANICS OF CIRCULATORY SYSTEMS AND OTHER BODY FLUIDS

9A986. Effects of the bifurcation angle on the steady flow structure in model saccular aneurysms. - Tong Miin Liou, TW Chang, WC Chang *(Dept of Power Mech Eng, Natl Tsing Hua Univ, Hsinchu, Taiwan 300, ROC)*. Exp Fluids 14(5) 289-295 (Apr 1993).

The effects of bifurcation angle on the steady flow structure in a straight terminal aneurysm model with asymmetric outflow through the branches have been characterized quantitatively in terms of laser-Doppler velocimetry (LDV)-measured mean velocity and fluctuating intensity distributions. The bifurcation angles investigated were 60°, 90°, and 140° and the Reynolds number based on the bulk average velocity and diameter of the afferent vessel was 500. It is found that the size of the recirculating zones in the afferent vessel, the flow activity (both mean and fluctuating motions) inside the aneurysm, and the shear stresses acting on the aneurysmal wall increase with increasing bifurcation angle. More importantly, both LDV-measured and flow-visualized results of the present study suggest the presence of a critical bifurcation angle below which the aneurysm is susceptible to thrombosis, whereas above this aneurysm is prone to progression or rupture.

9A987. Faster procedure for deriving regional blood flow by the noninvasive transient thermal clearance method. - M Nitzan *(Dept of Appl Phys and Electro-Optics, Jerusalem Col of Tech, PO Box 16031, Jerusalem 91160, Israel)*, Y Mahler, N Lifshitz *(Dept of Biomed Eng and Instrumentation, Hadassah Univ Hospital, Jerusalem, Israel)*. Ann Biomed Eng 21(3) 259-262 (May-Jun 1993).

The noninvasive transient clearance method provides absolute quantitative measurement of skin blood flow. It is based on thermally insulating the skin under investigation and measuring the time constant of the resultant experimental skin temperature increase. Conventional assessment of the time constant, by measuring the temperature increase until final equilibrium skin temperature is achieved, has the disadvantage of long time of measurement. The time constant of the exponential temperature increase is calculated without obtaining the final equilibrium temperature.

9A988. Mechanics of axially symmetric liposomes. - DC Pamplona *(Dept of Civil Eng, PUC-RJ, Rio de Janeiro CEP 22453, Brazil)* and CR Calladine *(Dept of Eng, Univ of Cambridge, Cambridge CB2 1PZ, UK)*. J Biomech Eng 115(2) 149-159 (May 1993).

Hotani has filmed morphological transformations in unilamellar liposomes, starting from a spherical shape, when the interior volume decreases steadily. Hotani's liposomes showed no evidence of general thermal fluctuations. We use a finite-deformation theory of axisymmetric, quasi-static thin shells to analyze theoretically bifurcations and changes of shape in liposomes under decreasing volume. The main structural action in a lipid bilayer is generally agreed to be its elastic resistance to bending, and it is usual to regard surface deformation as being like that of a 2D liquid.

9A989. Pressure propagation in pulsatile flow through random microvascular networks. - XS He *(Dept of Mech Eng and Mech, Drexel Univ, Philadelphia PA 19104)* and JG Georgiadis *(Dept of Mech and Indust Eng, Univ of Illinois, Urbana IL 61801)*. J Biomech Eng 115(2) 180-186 (May 1993).

A microvascular network with random dimensions of vessels is built on the basis of statistical analysis of conjunctival beds reported in the literature. Our objective is to develop a direct method of evaluating the statistics of the pulsatile hydrodynamic field starting from a priori statistics which mimic the large-scale heterogeneity of the network. The model consists of a symmetric diverging-converging dentritic network of ten levels of vessels, each level described by a truncated Gaussian distribution of vessel diameters and lengths. The results are presented in terms of the mean value and standard deviation of the pressure and flow rate waveforms at two positions along the network. It is shown that the assumed statistical variation of vessel lengths results in flow rate deviations as high as 50% of the mean, while the corresponding effect of vessel diameter variation is much smaller.

9A990. Sternal force-displacement relationship during cardiopulmonary resuscitation. - KG Gruben, AD Guerci, HR Halperin *(Peter Belfer Lab for Cardiac Mech, Cardiology Div of the Dept of Med, Johns Hopkins Univ and Med Inst, Baltimore MD)*, AS Popel *(Dept of Mech Eng, Johns Hopkins Univ and Med Inst, Baltimore MD)*, JE Tsitlik *(Peter Belfer Lab for Cardiac MechCH, Cardiology Div of the Dept of Med, Johns Hopkins Univ and Med Inst, Baltimore MD)*. J Biomech Eng 115(2) 195-201 (May 1993).

A viscoelastic model is presented to describe the dynamic response of the human chest to cyclic loading during manual cardiopulmonary resuscitation (CPR). Sternal force and displacement were measured during 16 clinical resuscitation attempts and during compressions on five CPR training manikins. The model was developed to describe the clinical data and consists of the parallel combination of a spring and dashpot. The manikins' elastic properties were stiffer and both elastic and damping properties were less dependent on displacement than the humans'.

9T991. Subclavian-carotid transposition for the subclavian steal syndrome: In vitro studies. - CM Rodkiewicz, J Centkowski *(Dept of Mech Eng, Univ of Alberta, Edmonton T6G 2G8, AB, Canada)*, S Zajac *(Polish Med Acad, Warsaw, Poland)*. J Biomech Eng 115(2) 205-206 (May 1993).

9A992. Theoretical analysis of the large blood vessel influence on the local tissue temperature decay after pulse heating. - LX Xu *(Dept of Appl Sci, College of State Island-CUNY, Staten Island NY 10301)*, MM Chen *(Dept of Mech and Indust Eng, and Bioeng Fac, Univ of Illinois, Urbana IL 61801)*, KR Holmes *(Dept of Veterinary Biosci and the Bioeng Fac, Univ of Illinois, Urbana IL 61801)*, H Arkin *(Natl Inst for Build Res, Technion, Haifa 32000, Israel)*. J Biomech Eng 115(2) 175-179 (May 1993).

The influence of a large blood vessel (larger than 500 μm in diameter) on the local tissue temperature decay following a point source heating pulse was determined numerically using a sink-source method. It was assumed that the vessel was large enough so that the temperature of blood flowing within it remained essentially constant and was unaffected by any local tissue temperature transients. Computations have been performed for a range of vessel sizes, probe-vessel spacings and local blood perfusion rates. It was found that the influence of a large vessel on the local tissue temperature decay is more sensitive to its size and location rather than to the local blood perfusion rate.

See also the following:

9T979. Analysis of the time-dependent changes in intracellular calcium concentration in endothelial cells in culture induced by mechanical stimulation

9A984. Identification algorithm for systemic arterial parameters with application to total artificial heart control

550J. BRAIN AND SPINAL TRAUMA

See the following:

9T991. Subclavian-carotid transposition for the subclavian steal syndrome: In vitro studies

550K. SHOCK AND VIBRATION EFFECTS

See the following:

9A973. Improved dynamic model of the human knee joint and its response to impact loading on the lower leg

550L. HEAT TRANSFER ASPECTS

See the following:

9T980. Cellular response of mouse oocytes to freezing stress: Prediction of intracellular ice formation

9A992. Theoretical analysis of the large blood vessel influence on the local tissue temperature decay after pulse heating

550Y. COMPUTATIONAL TECHNIQUES

See following:

9A981. Characteristic recovery time of an erythrocyte from an extensional deformation

9A995. Computer simulation in sport and industry

550Z. EXPERIMENTAL TECHNIQUES

See the following:

9A275. Preliminary determination of measurement device position in biomagnetic research. Using a reference source

9A972. Design and development of an unconstrained dynamic knee simulator

9A982. Aortic pressure estimation with electromechanical circulatory assist devices

9A986. Effects of the bifurcation angle on the steady flow structure in model saccular aneurysms

9A987. Faster procedure for deriving regional blood flow by the noninvasive transient thermal clearance method

552. Human factors, rehabilitation, sports

9T993. **Parametric design evaluation of lateral prophylatic knee braces.** - BJ Daley, JL Ralston, TD Brown, RA Brand *(Biomech Lab, Dept of Orthopaedic Surgery, Univ of Iowa, Iowa City IA 52242).* J Biomech Eng **115**(2) 131-136 (May 1993).

9A994. **Citius, altius, longius (faster, higher, longer): The biomechanics of jumping for distance.** - JG Hay *(Dept of Exercise Sci, Univ of Iowa, Iowa City IA 52242).* J Biomech **26**(SUPPL 1) 7-21 (1993).

The purpose of this paper is to review current knowledge concerning the long and triple jumps. Much has been learned over the past two decades about techniques in the long jump. Many myths have been dispelled and many training practices have been altered as a result. In all of this, the techniques employed during the takeoff have received little attention. The triple jump is an experimental task with potential for use in studies of human locomotion, of visual perception and control, of the strength of biological materials and of the mechanisms of soft tissue injury.

9A995. **Computer simulation in sport and industry.** - M Hubbard *(Dept of Mech, Aeronaut and Mat Eng, UC, Davis CA 95616).* J Biomech **26**(SUPPL 1) 53-61 (1993).

The last several decades have brought decreases in the specific cost of computer memory and increases in processor throughput. As a result simulation has become correspondingly more important as a component of industrial design and as a method for the study of general biomechanics and sports techniques. This paper illustrates, by way of examples, several of the more important aspects of the application of computer simulation to dynamic problems. Most industrial use of simulation is in the design process. A similar approach is equally valid in biomechanics and sport applications through the incorporation of design variables, which may be easily changed in the model experiment.

9T996. **Energetics of running and running shoes.** - MR Shorten *(2835 SE Tolman St, Portland OR 97202-8752).* J Biomech **26**(SUPPL 1) 41-51 (1993).

9T997. **Sequential motions of the body segments in striking and throwing skills: Descriptions and explanations.** - CA Putnam *(Sch of Phys Educ, Dalhousie Univ, Halifax, NS, B3H 3J5, Canada).* J Biomech **26**(SUPPL 1) 125-135 (1993).

See also the following:

9A972. Design and development of an unconstrained dynamic knee simulator

9T977. Muscle coordination of movement: A perspective

Author Index for September 1993

The codes after each name give the sequence numbers of the items in the Book Reviews section (R = Review, N = Note) or the Journal Literature section (A = Abstract, T = Title). Books listed by title only or as "under review" are not included in this index.

A

B

C

D

E

S

T

U

V

W

X

Y

Z

ABBREVIATIONS USED IN APPLIED MECHANICS REVIEWS

academy, academia, academic	acad
acoustical, acoustics	acoust
administration	admin
advanced, advances	adv
aerodynamics	aerodyn
aeronautical, aeronautics	aeronaut
agricultur-e, -al	agri
Am Inst of Aeronaut & Astronaut 1633 Broadway New York NY 10019	AIAA
Am Inst of Chem Eng 345 E 47 St, New York NY 10017	AIChE
Am Inst of Phys 345 E 45 St, New York NY 10017	AIP
America, American	Am
Am Soc for Testing and Mat 1916 Race St Philadelphia PA 19103	ASTM
Am Soc of Civil Eng 345 E 47 St, New York NY 10017	ASCE
Am Soc of Heating Refrigeration and Airconditioning Eng 1791 Tullie Circle NE Atlanta GA 30329	ASHRAE
Am Soc of Mech Eng 345 E 47th St New York NY 10017	ASME
Applied Mechanics Reviews	AMR
analysis, analytic, analytical	anal
angewandte	angew
applied, application	appl
Architecture, architectural	architec
Archive, Archivum, Archiwum	Arch
Argonne Natl Lab Argonne IL 60439	ANL
association, associates	assoc
astronomy, astronomical	astron
astronautical, astronautics	astronaut
atmosphere, atmospherical	atmos
Australian	Austral
automatic, automation	autom
biomedical	biomed
boîte postale	BP
Boundary Element	BE
Boundary Element Method	BEM
Brookhaven Natl Lab Upton NY 11973	BNL
building, builders	build
Bulletin	Bull
Canadian	Can
celestial	celest
Centre National de la Recherche Scientifique	CNRS
chemical, chemistry	chem
City College of the City Univ of NY, New York NY 10031	CCNY
College	Col
combustion	combust
Commonwealth Sci and Indust Res Org	CSIRO
communication	commun
Comptes Rendus	CR
computer, computational	comput
Computer-Aided Design	CAD
conference	conf
construction	construct
conversion	Conv
Cornell University, Ithaca NY 14853	Cornell
David Taylor Naval Ship Res and Dev Center	NSRDC
degree(s) of freedom	dof
department	dept
design	des
development, developmental	dev
Deutsche Forschungs- und Versuchsanstalt für Luft- und Raumfahrt	DFVLR
division	div
dynamics	dyn
east, eastern	E
edition, editor, edited (by)	ed
education, educational	educ
elastic, elasticity	elast
electrical, electricity	elec
electronic	electron
engineer, engineering	eng
environment, environmental	env
equilibrium	equil
Establishment	Est
evaluation	Eval
experimental	exp
explosion	explos
faculty	fac
Federal, Federation	Fed
Federal Republic of Germany	FRG
Finite Element	FE
Finite Element Method	FEM
Foundation	Found
Fundamental(s)	Fund
geology, geological	geol
Georgia Institute of Technology, Atlanta GA 30332	Georgia Tech
hydraulic	hydraul
identification	ident
Incorporated	Inc
industry, industrial	indust
information, informatique	info
institute, institution	inst
Inst Natl de Rech en Informatique et en Automatique	INRIA
Inst of Elec and Electron Eng 345 E 47 St, New York NY 10017	IEEE
Institute of Technology	IT
international	int
Int Union Theor Appl Mech	IUTAM
Jet Propulsion Lab California Inst of Tech Pasadena CA 91109	JPL
journal	J
laboratory	lab
Los Alamos National Lab, Los Alamos NM 87545	LANL
Lawrence Berkeley Lab Berkeley CA 94720	LBL
Lawrence Livermore Natl Lab Livermore CA 94550	LLNL
management	man
manufacture, manufacturing	manuf
Massachusetts Inst of Tech Cambridge MA 02139	MIT
materials	mat
mathematics, mathematical	math
measurement	meas
mécanique	mec
mecha-nics, -nical, -nism	mech
medicine, medical	med
metallurgy	metall
meteorology, meteorological	meteorol
modeling	model
molecular, molecules	mol
month	mo
national	natl
Natl Aeronaut & Space Admin	NASA
Natl Bureau of Standards Washington DC 20234	NBS(=NIST)
Natl Inst of Standards and Tech Gaithersburg MD 20899	NIST(=NBS)
Natl Res Council	NRC
Natl Sci Foundation	NSF
New Jersey Inst of Tech	NJIT
New South Wales, Australia	NSW
New York Univ, New York NY	NYU
Non-Destructive Evaluation	NDE
Non-Destructive Testing	NDT
north, northern	N
northeast	NE
northwest	NW
Northwestern Univ Evanston IL 60201	NWU
nuclear	nucl
number	n, no, Nr
numerical	numer
Oak Ridge Natl Lab Oak Ridge TN 37830	ORNL
oceanography	oceanog
ordinary differential equations	ODE
Office Natl d'Etudes et de Recherches Aerospatiales, BP 72, 92322 Chatillon, France	ONERA
Office of Naval Research	ONR
optimization, optimum	optim
organization	org
page	p
pages	pp
partial differential equations	PDE
Pennsylvania State Univ University Park PA 16802	Penn State
petroleum	pet
physics, physical	phys
planetary	planet
Post Office	PO
Princeton Univ Princeton NJ 08544	Princeton
problems	prob
probability	probab
proceedings	proc
product, production	prod
progress	prog
publication, publish-ing, -ers	publ
Purdue Univ W Lafayette IN 47907	Purdue
Quarterly	Quart
recherche	rech
rehabilitation	rehab
reliability	reliab
Rensselaer Polytechnic Inst Troy NY 12181	RPI
research	res
research and development	R&D
Review, Revue, revised	Rev
rheology, rheologic	rheol
Royal	R
Royal Inst of Tech	RIT
Sandia Natl Lab Albuquerque NM 87185	Sandia
Scandinavia, Scandinavica	Scand
science, scientific, scientifique	sci
seismology	seismol
school	sch
simulation	simul
society	soc
Soc for Indust and Appl Math 1400 Architects Bldg, 117 S 17 St, Philadelphia PA 19103-5052	SIAM
Solar Energy Res Inst, 1617 Cole Blvd, Golden CO 80401	SERI
south, southern	S
southeast	SE
southwest	SW
Southwest Res Inst, 6220 Culebra Rd, San Antonio TX 78284	SWRI
Soviet	Sov
Stanford University, Stanford CA 94305	Stanford
State University of New York	SUNY
Station	Sta
statistics, statistical	stat
structural, structure	struct
studies, studii	stud
Symposium	Symp
system	syst
technical, technology	tech
temperature	temp
Teoretyczna	Teor
theoretical, theorique	Theor
three-dimensional	3D
Transaction	Trans
translat-ed, -er, -ion	transl
tribology	trib
two-dimensional	2D
United Kingdom (England, Scotland, Wales)	UK
United States	US
United States of America	USA
University	Univ
Univ of California	UC
Univ of California at Berkeley Berkeley CA 94720	UCB
Univ of California at Los Angeles Los Angeles CA 90024	UCLA
Univ of California at San Diego La Jolla CA 92093	UCSD
University Press	UP
vibration	vib
Virginia Polytech Inst & State Univ, Blacksburg VA 24061	VPI
volume	v, vol
west, western	W
Wright-Patterson Air Force Base OH 45433	WPAFB
Zeitschrift	Z

(6/93)

APPLIED MECHANICS REVIEWS REPRINTS

Biomimetics: Advancing man-made materials through guidance from nature. AV Srinivasan, GK Haritos, and FL Hedberg. AMR 44(11) Part 1, 463-482 (Nov 1991) Reprint No AMR101 $18

Mechanics Pan-America 1991 (Proc PACAM-2, Valparaiso, Chile, Jan 1991). PA Kittl and DT Mook (eds). AMR 44(11) Part 2 (Nov 1991) Reprint No AMR106 $88 (members $44)

Structural and dynamic behavior of pretwisted rods and beams. A Rosen. AMR 44(12) Part 1, 483-516 (Dec 1991) Reprint No AMR102 $26

Hydroacoustics of transitional boundary-layer flow. GC Lauchle. AMR 44(12) Part 1, 517-531 (Dec 1991) Reprint No AMR103 $16

Index to Volume 44 (1991). Reprint No AMR108 $88 (members $44)

Stress minimum forms for elastic solids. LT Wheeler. AMR 45(1), 1-12 (Jan 1992) Reprint No AMR 107 $14

Micromechanics of composite materials. Special collection edited by AN Guz. AMR 45(2) 13-101 (February 1992) Reprint No AMR104 $54: (1) **Statics of laminated and fibrous composites with bent structures.** SD Akbarov and AN Guz. (2) **Dynamics of laminated and fibrous composites.** AN Guz and NA Shulga. (3) **Stability of fibrous composites.** IY Babich and AN Guz. (4) **Stability of laminated composites.** AN Guz and VN Chekhov.

Microbubble drag reduction in liquid turbulent boundary layers. C Merkle and S Deutsch. AMR 45(3) Part 1, 103-127 (March 1992) Reprint No AMR105 $22

Material Instabilities (22nd Midwestern Mechanics Conference, Rolla MO, Oct 1991) HM Zbib, TG Shawki, RC Batra (eds). AMR 45(3) Part 2 (March 1992) Reprint No AMR110 $66 (members $33)

Heat-transfer control: Principal focus on Japanese Research. T Aihara. AMR 45(4) 129-153 (April 1992) Reprint No AMR109 $16

Optimum dimensions of extended surfaces operating in a convective environment. A Aziz. AMR 45(5) 155-173 (May 1992) Reprint No AMR111 $18

Overview of micro heat pipe research and development. GP Peterson. AMR 45(5) 175-189 (May 1992) Reprint No AMR112 $16

Multiphase poroelastic finite element models for soft tissue structures. BR Simon. AMR 45(6) 191-218 (June 1992) Reprint No AMR114 $22

Dynamics and control of coherent structures in turbulent jets. RR Mankbadi. AMR 45(6) 219-248 (June 1992) Reprint No AMR113 $24

Addendum to: Bibliography of monographs and surveys on shells. W Pietraszkiewicz. AMR 45(6) 249-250 (June 1992) Reprint No AMR115 (free with AMR078 $14)

Romanian sources on applied mechanics. ME Popescu. AMR 45(6) 251-252 (June 1992) Reprint No AMR116 no charge.

Fluorescence thermometry. LJ Dowell. AMR 45(7) 253-260 (July 1992) Reprint No AMR117 $12.00

Micromechanical modelling of quasi-brittle materials behavior. VC Li (ed), 10 articles. AMR 45(8) 261-398 (Aug 1992) Reprint No AMR118 $60.

Recent developments in the force method of structural analysis. A Kaveh AMR45(9) 401-418 (Sep 1992) Reprint No AMR119 $18.

Computational models for high-temperature multi-layered composite plates and shells. AK Noor and WS Burton. AMR 45(10) 419-446 (Oct 1992) Reprint No AMR 120 $22.

Dynamics of periodic and near-periodic structures. Dong Li and H Benaroya. AMR 45(11) 447-460 (Nov 1992) Reprint No AMR121 $16.

Finite element analysis of aeroelasticity of plates and shells. MN Bismarck-Nasr. AMR 45(12) 461-482 (Dec 1992) Reprint No AMR122 $20.

Index to Volume 45 (1992). Reprint No AMR123 $88 (members $44)

Mathematical modeling of transport phenomena during alloy solidification. C Beckermann and R Viskanta. AMR 46(1) 1-28 (Jan 1993) Reprint No AMR124 $22.

Perturbation techniques in phase change heat transfer. A Aziz and VJ Lunardini. AMR 46(2) (Feb 1993) Reprint No AMR125 $28.

US machining and grinding research in the 20th century. R Komanduri, ME Merchant, MC Shaw. AMR 46(3) (Mar 1993) Reprint No AMR 126 $42

Nondestructive testing and structural condition monitoring of mechanical cables. PAA Laura. AMR 46(4) 133-138 (Apr 1993) Reprint No AMR127 $12.

Aging of energy production and distribution systems: DOE Workshop, Rice University, Houston TX, October 11-13, 1992. Edited by MM Carroll and PD Spanos. AMR 46(5) 139-263 (May 1993) Reprint No AMR128 $78.

Applied mechanics of a lunar base. Edited by H Benaroya. AMR 46(6) 265-358 (June 1993) Reprint No AMR129 $65.

Chaos and noise in dynamical systems. Edited by T Kapitaniak and J Brindley. AMR 46(7) 359-444 (July 1993) Reprint No AMR130 $59.

Boundary integral equations in aerodynamics. L Morino. AMR 46(8) 445-466 (August 1993) Reprint No AMR131 $20.

Vibrations of planar curved beams, rings, and arches. P Chidamparam and AW Leissa. AMR 46(9) 467-483 (Sep 1993) Reprint No AMR132 $20.

Subscription: ASME members (without Suppl.) $51 $____

ASME members (with Supplement) $84 $____

non-members (with Supplement) $534 $____

2nd library subscription $99 $____

Postage outside USA or Canada $102, airmail $156 $____

Reprint No:	*Reprint title:*	
________	________	$____
________	________	$____
________	________	$____
	TOTAL ORDER:	$____

ASME member prices for reprints (50% of list) apply to the purchase of 1 copy of any reprint for the member's personal use with shipment to his or her personal attention. *Bulk reprint prices:* $215 for 100 copies of an article of up to 8 pages, plus $85 for each additional 4 pages (add $25 and $5, respectively, for each additional 100 copies). *Ordering information:* Advance payment required if billed outside USA or Canada. Foreign and Canadian checks not accepted unless payable in US dollars through a US bank. CA, GA, IL, TX purchasers must add sales tax, Canadians 7% GST, or furnish tax exemption certificate.

Send order to: **ASME/AMR**
22 Law Drive, PO Box 2900
Fairfield NJ 07007-2900

or FAX form to: 1-201-882-5155

ASME members, to receive discount you must indicate your membership no.: ________

ASME Member Name: ________

Signature: ________

METHOD OF PAYMENT (check one):

[ ] Payment enclosed

[ ] Purchase Order No.: ________
(attach Purchase Order)

[ ] Charge card (circle one): Master Card VISA American Express Diners Club Discover

Account Number: ________

Mastercard Interbank No: ________

Expiration Date: ________

Signature: ________

BILL TO: Name: ________
Company: ________
Street address: ________
City, State, ZIP: ________
Country: ________

SHIP TO: Name: ________
Company: ________
Street address: ________
City, State, ZIP: ________
Country: ________

applied mechanics reviews

AIMS

The primary aim of *AMR* is to serve engineering scientists worldwide by assessing, reviewing, and reporting on advances in a broad range of mechanical engineering sciences. To this end *AMR* publishes (i) state-of-the-art review articles, bibliographic surveys, reviews with a special focus on emerging technology, tutorials, historical perspectives, periodic summaries of trends and advances; (ii) critical reviews of books, software, and databases; (iii) indexed compilations of carefully selected abstracts from high quality research journals; (iv) book-length monographs and symposium proceedings as special issues or supplements; and (v) editorials, announcements, and letters-to-the-editor.

A secondary aim of *AMR* is to serve technical and reference librarians, information specialists, professional engineers, and college professors through reliable, comprehensive, and timely information about all types of books within its subject scope. The annual cumulative index issue of *AMR* together with its monthly classified listings of abstracts is in effect a comprehensive bibliography of the mechanical engineering sciences, including essentially every article in some 50-60 core journals; this core includes all ASME Transaction journals.

SCOPE

The scope of *AMR* encompasses all the engineering sciences represented in the journals and symposia sponsored by the American Society of Mechanical Engineers and is outlined by *AMR*'s Subject Classification Scheme, which is reprinted on the back cover. It includes basic discipline-oriented areas such as dynamics, continuum mechanics, solid and fluid mechanics, structures, heat transfer, tribology, geomechanics, and biomechanics, as well as cross-disciplinary subjects and emerging critical technological areas such as new numerical and computational techniques, systems control technology, engineering design tools, manufacturing technology, materials and energy technology, and environmental engineering.

The American Society of Mechanical Engineers

INFORMATION FOR AUTHORS OF REVIEW ARTICLES

(1) Prospective authors are strongly urged to communicate with one of the Associate Editors or the Editor-in-Chief (TEL 201-882-1170, FAX 201-882-5155) before submitting an article, and to furnish a one-page outline of the proposed article and information as to its type, audience, and probable length. A form, *Prospectus for a Review Article,* is available for this purpose. Refer to the editorials in the January 1985 and March 1991 issues of *AMR* and the box at left for further discussion of *AMR*'s editorial criteria.

(2) *Submit four clean copies* of the manuscript to one of the Associate Editors or to the Editor-in-Chief. (Hold all separate original artwork until the article has been accepted.) All articles will be reviewed critically by at least two independent and anonymous referees chosen by the editor involved. This procedure will be followed even if the article is the result of solicitation or encouragement by the editors, or if the author is also an *AMR* editor. The final decision on publication is made by the Editor-in-Chief upon recommendation of an Associate Editor. If appropriate, the article will carry a footnote saying "Transmitted by Associate Editor . . ."

(3) Submission of a manuscript is a representation that it has not been published previously nor is currently being submitted for publication elsewhere. The authors will be asked to sign a statement *transferring copyright to ASME.* It is the author's responsibility to obtain permission to copy material from other sources, if needed.

(4) There are *no page charges* in *AMR* and no numerical length limitations. The length of the article should be appropriate to the subject and the audience. It is certainly one factor that will be evaluated by the editors and their referees, who may recommend changes (30-120 manuscript pages is typical). Each author of a review article will receive *a year's free subscription to AMR.* After publication the author will receive *100 free reprints* (to be shared if there are several authors). In addition, ASME will distribute reprints singly and in bulk.

(5) Along with the final *manuscript* send the *compuscript on diskette,* if available, (with format identified) incorporating all corrections and additions, and with the tables and figure captions *in place within the text.* If the figures are computer graphics, place them also within the compuscript where they belong. Also, send a head-and-shoulders *photograph and short biographical sketch* (100-200 words) of each author, including grades of ASME membership, if any; include the bio at the end of the compuscript.

(6) *Order of parts:* Title of article, authors' names, authors' institutional affiliations, abstract (200-300 words suitable for abstracting services), table of contents (only if the article is so long that it needs one), list of symbols and abbreviations (if necessary), main text incorporating tables (each starting with a caption) and figure captions (in place where you want them in the text), list of references, biographical sketch, and original figures (if computer graphics, place in text above captions).

(7) *Format (for details request Author Kit):* (a) Paper size: A4 or 8.5×11 inch (220×280 mm). (b) Word processor settings: One column of width 3.4 in (87 mm) leaving rest of page for referee and editorial comments; Type size 10 point (72 point = 6 pica = 1 inch = 25.4 mm) Times Roman or similar proportionally spaced style; Line spacing 12 points. These as-printed *AMR* specifications will help to insure that equations, tables, and figures are properly designed for the available space. (If a typewriter must be used, type double spaced with wide margins). (c) Use metric SI units; with other units in parentheses, if appropriate. (d) Cite references by last name and year; reference list at end alphabetical by author (in 7-point type). (e) Number figures with arabic numerals; design figures for column width (83 mm or 3.1 in), if possible; they should be professionally drawn or computer generated with lettering of consistent size (not smaller than the printed text after reduction); use your wordprocessor to place an empty box of the correct dimensions (or the figure itself, if a computer graphic) in the text above each figure caption. (f) Number tables with roman numerals. (g) Latin letters used as math symbols should be in italics both in text and in displayed equations. Subscripts and superscripts should be 20-30% smaller than letters on the main line. Fractional powers are preferred to root signs, exp(..) to $e^{\cdot\cdot}$, and a solidus (/) for fractions, if that will save vertical space.

(8) *Camera-ready copy:* Typeset (or near-typeset) quality pages or galleys generated by the author (after review and acceptance) would be very much appreciated, and could result in faster publication. Just reproduce the format of published *AMR* review articles (basically, two of the columns defined above per page). Templates and style sheets available for MS Word and Wordperfect.

SPECIAL ISSUES: From time to time Guest Editors are invited to produce Special Issues consisting of 3 or more articles grouped around a common theme. SUPPLEMENTS are booklength monographs or symposium proceedings published as part 2 of a regular issue. Proposals for Special Issues or Supplements are very welcome. GUEST EDITORIALS, LETTERS-TO-THE-EDITORS, ANNOUNCEMENTS: Contact the Editor-in-Chief.

2/93

MAIN HEADINGS FOR CLASSIFIED JOURNAL LITERATURE

(for full classification scheme and alphabetical index see December issue)

ISSN 0003-6900

JOURNAL CODE AMR

ISSUE CODE 9309

applied mechanics reviews

published by The American Society of Mechanical Engineers

Feature article:

Volume 46, Number 10, October 1993

applied mechanics reviews

AN ASSESSMENT OF THE WORLD LITERATURE IN ENGINEERING SCIENCES

Applied Mechanics Reviews (ISSN 0003-6900) is published monthly by the ASME, 345 E 47th St, New York NY 10017. 2nd class postage paid at New York NY and additional mailing offices. POSTMASTER: Send address changes to ASME/AMR, 22 Law Drive, Box 2300, Fairfield NJ 07007-2300. CHANGES OF ADDRESS must be received at ASME seven weeks before they are to be effective. Send old label and new address. SUBSCRIPTION PRICES: $534 (incl Annual Index and Suppl.), single copies $57 (Suppl. or Index $84). Countries outside USA and Canada add $102 for postage ($156 airmail). 2nd library subscription $99. Canadian goods and services tax registration #126 148 048.
Printed in the USA. (7/93)

The American Society of Mechanical Engineers

VOLUME 46, NUMBER 10, OCTOBER 1993

FEATURE ARTICLE

BOOK REVIEWS AND NOTES

REVIEW OF THE JOURNAL LITERATURE

APPLIED MECHANICS REVIEWS BOARD OF ASSOCIATE EDITORS

ABBREVIATIONS USED IN APPLIED MECHANICS REVIEWS

academy, academia, academic	acad
acoustical, acoustics	acoust
administration	admin
advanced, advances	adv
aerodynamics	aerodyn
aeronautical, aeronautics	aeronaut
agricultur-e, -al	agri
Am Inst of Aeronaut & Astronaut 1633 Broadway New York NY 10019	AIAA
Am Inst of Chem Eng 345 E 47 St, New York NY 10017	AIChE
Am Inst of Phys 345 E 45 St, New York NY 10017	AIP
America, American	Am
Am Soc for Testing and Mat 1916 Race St Philadelphia PA 19103	ASTM
Am Soc of Civil Eng 345 E 47 St, New York NY 10017	ASCE
Am Soc of Heating Refrigeration and Airconditioning Eng 1791 Tullie Circle NE Atlanta GA 30329	ASHRAE
Am Soc of Mech Eng 345 E 47th St New York NY 10017	ASME
Applied Mechanics Reviews	AMR
analysis, analytic, analytical	anal
angewandte	angew
applied, application	appl
Architecture, architectural	architec
Archive, Archivum, Archiwum	Arch
Argonne Natl Lab Argonne IL 60439	ANL
association, associates	assoc
astronomy, astronomical	astron
astronautical, astronautics	astronaut
atmosphere, atmospherical	atmos
Australian	Austral
automatic, automation	autom
biomedical	biomed
boîte postale	BP
Boundary Element	BE
Boundary Element Method	BEM
Brookhaven Natl Lab Upton NY 11973	BNL
building, builders	build
Bulletin	Bull
Canadian	Can
celestial	celest
Centre National de la Recherche Scientifique	CNRS
chemical, chemistry	chem
City College of the City Univ of NY, New York NY 10031	CCNY
College	Col
combustion	combust
Commonwealth Sci and Indust Res Org	CSIRO
communication	commun
Comptes Rendus	CR
computer, computational	comput
Computer-Aided Design	CAD
conference	conf
construction	construct
conversion	Conv
Cornell University, Ithaca NY 14853	Cornell
David Taylor Naval Ship Res and Dev Center	NSRDC
degree(s) of freedom	dof
department	dept
design	des
development, developmental	dev
Deutsche Forschungs- und Versuchsanstalt für Luft- und Raumfahrt	DFVLR
division	div
dynamics	dyn
east, eastern	E
edition, editor, edited (by)	ed
education, educational	
elastic, elasticity	
electrical, electricity	
electronic	
engineer, engineering	
environment, environmental	

equilibrium	equil
Establishment	Est
evaluation	Eval
experimental	exp
explosion	explos
faculty	fac
Federal, Federation	Fed
Federal Republic of Germany	FRG
Finite Element	FE
Finite Element Method	FEM
Foundation	Found
Fundamental(s)	Fund
geology, geological	geol
Georgia Institute of Technology, Atlanta GA 30332	Georgia Tech
hydraulic	hydraul
identification	ident
Incorporated	Inc
industry, industrial	indust
information, informatique	info
institute, institution	inst
Inst Natl de Rech en Informatique et en Automatique	INRIA
Inst of Elec and Electron Eng 345 E 47 St, New York NY 10017	IEEE
Institute of Technology	IT
international	int
Int Union Theor Appl Mech	IUTAM
Jet Propulsion Lab California Inst of Tech Pasadena CA 91109	JPL
journal	J
laboratory	lab
Los Alamos National Lab, Los Alamos NM 87545	LANL
Lawrence Berkeley Lab Berkeley CA 94720	LBL
Lawrence Livermore Natl Lab Livermore CA 94550	LLNL
management	man
manufacture, manufacturing	manuf
Massachusetts Inst of Tech Cambridge MA 02139	MIT
materials	mat
mathematics, mathematical	math
measurement	meas
mécanique	mec
mecha-nics, -nical, -nism	mech
medicine, medical	med
metallurgy	metall
meteorology, meteorological	meteorol
modeling	model
molecular, molecules	mol
month	mo
national	natl
Natl Aeronaut & Space Admin	NASA
Natl Bureau of Standards Washington DC 20234	NBS(=NIST)
Natl Inst of Standards and Tech Gaithersburg MD 20899	NIST(=NBS)
Natl Res Council	NRC
Natl Sci Foundation	NSF
New Jersey Inst of Tech	NJIT
New South Wales, Australia	NSW
New York Univ, New York NY	NYU
Non-Destructive Evaluation	NDE
Non-Destructive Testing	NDT
north, northern	N
northeast	NE
northwest	NW
Northwestern Univ Evanston IL 60201	NWU
nuclear	nucl
number	n, no, Nr
numerical	numer
Oak Ridge Natl Lab Oak Ridge TN 37830	ORNL
oceanography	oceanog
ordinary differential equations	ODE
Office Natl d'Etudes et de Recherches Aerospatiales, BP 72, 92322 Chatillon, France	ONERA
Office of Naval Research	ONR
optimization, optimum	optim
organization	org
page	p
pages	pp

partial differential equations	PDE
Pennsylvania State Univ University Park PA 16802	Penn State
petroleum	pet
physics, physical	phys
planetary	planet
Post Office	PO
Princeton Univ Princeton NJ 08544	Princeton
problems	prob
probability	probab
proceedings	proc
product, production	prod
progress	prog
publication, publish-ing, -ers	publ
Purdue Univ W Lafayette IN 47907	Purdue
Quarterly	Quart
recherche	rech
rehabilitation	rehab
reliability	reliab
Rensselaer Polytechnic Inst Troy NY 12181	RPI
research	res
research and development	R&D
Review, Revue, revised	Rev
rheology, rheologic	rheol
Royal	R
Royal Inst of Tech	RIT
Sandia Natl Lab Albuquerque NM 87185	Sandia
Scandinavia, Scandinavica	Scand
science, scientific, scientifique	sci
seismology	seismol
school	sch
simulation	simul
society	soc
Soc for Indust and Appl Math 1400 Architects Bldg, 117 S 17 St, Philadelphia PA 19103-5052	SIAM
Solar Energy Res Inst, 1617 Cole Blvd, Golden CO 80401	SERI
south, southern	S
southeast	SE
southwest	SW
Southwest Res Inst, 6220 Culebra Rd, San Antonio TX 78284	SWRI
Soviet	Sov
Stanford University, Stanford CA 94305	Stanford
State University of New York	SUNY
Station	Sta
statistics, statistical	stat
structural, structure	struct
studies, studii	stud
Symposium	Symp
system	syst
technical, technology	tech
temperature	temp
Teoretyczna	Teor
theoretical, theorique	Theor
three-dimensional	3D
Transaction	Trans
translat-ed, -er, -ion	transl
tribology	trib
two-dimensional	2D
United Kingdom (England, Scotland, Wales)	UK
United States	US
United States of America	USA
University	Univ
Univ of California	UC
Univ of California at Berkeley Berkeley CA 94720	UCB
Univ of California at Los Angeles Los Angeles CA 90024	UCLA
Univ of California at San Diego La Jolla CA 92093	UCSD
University Press	UP
vibration	vib
Virginia Polytech Inst & State Univ, Blacksburg VA 24061	VPI
volume	v, vol
west, western	W
Wright-Patterson Air Force Base OH 45433	WPAFB
Zeitschrift	Z

(6/93)

Thermal buckling of plates and shells

Earl A Thornton

Dept of Mech, Aerospace and Nuclear Engineering
University of Virginia, Charlottesville VA 22903-2442

This review discusses research on thermal buckling of plates and shells since the first work in the 1950s. Elastic thermal buckling of metallic as well as composite plates and shells is described. The role of material thermal properties on thickness and spatial temperature gradients is demonstrated first. Then thermal buckling and postbuckling research for plates, shallow shells and curved panels, cylindrical and conical shells is presented. Analytical, computational and experimental studies are described. Governing equations and formulas for critical buckling temperatures are presented for several practical applications. An assessment of past research is made, and future research needs are highlighted.

1. INTRODUCTION

In the fourth AIAA von Kármán lecture, Nicholas J Hoff, Hoff (1967), describes the evolution of thin-walled aircraft structures from the early days of aviation to the halcyon days of the Apollo program. A recurrent theme throughout his description of aerospace structures history is the engineer grappling with buckling problems of thin-walled structures. An early paper of Professor Hoff, Hoff (1946), traces aerospace buckling problems back to the wood-steel-fabric biplane era where the Euler buckling formula and beam-column theory were used to design struts of biplane wings and wing spars subjected to compressive loads. In the late 1920s solutions to buckling problems played an important role in the advancement of all-metal semi-monocoque construction. For several decades thereafter, engineers struggled with buckling problems of metallic thin-walled plates and shells under mechanical loads. The results of their work led to safe and reliable aircraft that made commercial aviation a worldwide economic success. Indeed, the basic construction ideas of riveted skin-stringer metallic structures made possible by the buckling analyses of the 1920s-1930s prevail today in modern commercial transports.

The importance of thermal effects on aircraft began after World War II with supersonic flight. Aerodynamic heating from supersonic flight induced elevated temperatures that affected material selection and significantly altered structural design practices. Thermal gradients and restrained thermal expansion introduced thermal buckling for the first time. A recent paper, (Thornton, 1992), describes development of thermal structures from the early days of supersonic flight to the more recent challenges presented by hypersonic flight. The development of the National Aerospace Plane (NASP) presents engineers with their greatest thermal structural challenges yet. New advanced metal matrix composites were developed for severe elevated temperature applications. Complex convectively-cooled thin-walled structures subjected to intense local heating provided unprecedented materials and structural modeling challenges. One example of such an extreme instance of a thin-walled structure subjected to intense local heating is the problem of shock-shock interactions.

As hypersonic vehicles accelerate at high speeds in the atmosphere, shocks sweep across the vehicle interacting with local shocks and boundary layers. These interactions expose structural surfaces to severe local pressures and heat fluxes. The first known instance of shock-shock interactions in high speed flight occurred on the X-15 in 1967. In that flight, the intense local heating induced severe local damage on a supporting pylon for a dummy ramjet engine, Thornton (1992). On the NASP these interactions occur on leading edges of integrated engine structures which experience intense, highly localized aerothermal loads. Dechaumphai *et al* (1989) studied issues relevant to the thermal-structure response of hydrogen cooled, super thermal-conducting leading edges subject to intense aerodynamic heating. A thermo-viscoplastic analysis of hypersonic engine structures, Thornton *et al* (1990), showed similar trends with thin-walled convectively cooled structures subjected to high internal pressures and intense local heating. Poleski *et al* (1992) describe a three-dimensional thermal structural analysis of a swept cowl leading edge subjected to skewed shock-shock interference heating. The analysis shows that due to the intense localized heating, the thin elastic leading edge experiences very large local compressive stresses. The high level of these compressive stresses suggests the possibility of localized inelastic behavior and/or local buckling. Clearly these

Transmitted by Associate Editor RB Hetnarski.

ASME Reprint No AMR133 $20

new, complex problems present structural analysts with new, unprecedented thermal-buckling challenges.

This article describes research on thermal buckling of plates and shells. Elastic thermal buckling is emphasized although recent experience on NASP problems has shown the importance of inelastic buckling. However, the literature available on elastic buckling is much more extensive than for inelastic buckling, and an assessment of these studies was given priority for this review. Thermal buckling of metallic as well as composite plates and shells is considered. Thermal buckling studies of composites are much more recent than for metallics, and recent progress with composites is described.

Temperature levels and their distributions have a major role in thermal buckling. The article begins with a brief description of temperature distributions in thin-walled structures. Then past literature on thermal buckling of plates and shells is described. In each instance, past research is assessed, and research needs are discussed. The article concludes with brief summarizing remarks.

2. TEMPERATURES IN THIN-WALLED STRUCTURES

The determination of temperatures in a thin-walled structure begins with conservation of energy. In the most general form with thermomechanical coupling, Allen (1991), the conservation of energy equation includes terms that represent the conversion of mechanical to thermal energy. In practical aerospace structural heat transfer, thermomechanical coupling is usually neglected. Then the conservation of energy equation involves temperature as the only dependent variable. It may be solved for the temperature distribution independently from the structural problem.

2.1 Structural Heat Transfer

Heat transfer in thin-walled structures is conduction dominated, and the classical heat conduction equation is used:

$$-\frac{\partial}{\partial x_i}\left(k_{ij}\frac{\partial T}{\partial x_j}\right)+\rho c\frac{\partial T}{\partial t}=Q \tag{1}$$

where $T(x_1, x_2, x_3, t)$ is temperature, k_{ij} are the components of the material's thermal conductivity tensor, ρ is the density, c is the specific heat, and Q is the internal heat generation rate per unit volume. The components of the thermal conductivity tensor and the specific heat are temperature dependent. The heat conduction equation is solved subject to an initial condition and boundary conditions on the structure's surface. The initial condition specifies the temperature distribution at time zero. The boundary conditions may consist of s[illegible] surface temperature, specified heat flow, con[illegible] exchange, and radiation heat exchange. T[illegible] written as

$$\begin{aligned}
T_s &= T_s(x_1,x_2,x_3,t) && \text{on } S_1\\
q_i n_i &= -q_s && \text{on } S_2\\
q_i n_i &= h(T_s - T_e) && \text{on } S_3\\
q_i n_i &= \sigma\varepsilon T^4 - \alpha q_r && \text{on } S_4
\end{aligned} \tag{2}$$

where q_i denotes components of heat flux, n_i denotes components of a unit outward normal vector, and S_i(i = 1,4) denotes portions of the surface. The specified surface temperature is T_s, and the specified heat flux (positive into the surface) is q_s. In the convective boundary condition on S_3, the convection coefficient is h, and the convective exchange temperature is T_e. In the radiation boundary condition on S_4, σ is the Stefan-Boltzmann constant, ε is the surface emissivity, α is the surface absorptivity, and q_r is the incident radiation flux. For structural heat transfer with surfaces at significantly different elevated temperatures, radiation exchanges can occur. The determination of radiation exchanges between surfaces is complicated because radiation emitted by a typical surface depends on its surface temperature which is unknown, and the geometrical relationship between surfaces affects the exchanges.

Thus the basic aerospace structural heat transfer problem is nonlinear because of temperature-dependent properties and radiation heat transfer. For practical structures, temperature is determined computationally, most often by finite difference methods (Schuh, 1965) but also by finite element methods (Huebner and Thornton, 1982).

2.2 Temperature Distributions

Complex thin-walled aerospace structures under service conditions rarely experience uniform temperatures. Often, the external heating is non-uniform. For example, leading edges of wings in high speed flight experience high local heating at stagnation points. Moreover, as the external flow traverses the airfoil, aerodynamic heating changes with surface curvature and increases significantly at a transition from laminar to turbulent flow. As mentioned in the Introduction, shock interactions cause intense local heating.

Even if the external heating is nearly uniform, spatial variations in skin temperatures occur due to internal reinforcements such as ribs, stiffeners and frames. At points or lines of attachment of local skin reinforcements, temperatures are lower than nearby skin temperatures because the reinforcement offers a greater material volume to absorb energy and a conduction path for heat transfer to the structure interior. Very early recognition of temperature variations in thin-walled structures was made for supersonic aircraft, Hoff (1951). Boley and Wiener (1960) describe research in the 1950s on temperature distributions and give additional references.

In orbiting space structures, temperatures are unsteady because of the variation of incident heat fluxes with

Table I
Thickness Temperature Gradients for Various Materials
q = 0.1 BTU/in²-s (16.4 W/cm²) h= 0.125" (0.318 cm)

	Material	Thermal conductivity k		Thermal Diffusivity κ		Temperature Gradient, ΔT	
		(BTU/in-s-°F)	(W/cm-°C)	(in²/s)	(cm²/s)	(°F)	(°C)
1	Graphite-Epoxy	2.2×10^{-5}	1.6×10^{-2}	1.5×10^{-4}	9.9×10^{-4}	280	160
2	Titanium (MIL-T-9047)	1.1×10^{-4}	8.3×10^{-2}	5.3×10^{-3}	3.4×10^{-2}	56	30
3	Carbon-Carbon	2.0×10^{-4}	1.5×10^{-1}	1.1×10^{-2}	7.2×10^{-2}	31	17
4	Stainless (17-8PH)	2.2×10^{-4}	1.7×10^{-1}	7.4×10^{-3}	4.8×10^{-2}	28	15
5	Hastelloy X	2.6×10^{-4}	1.9×10^{-1}	6.7×10^{-3}	4.3×10^{-2}	24	13
6	Copper (G3-Heat Treat)	5.6×10^{-4}	4.2×10^{-1}	2.1×10^{-2}	1.3×10^{-1}	11	6
7	Graphite-Magnesium	5.9×10^{-4}	4.4×10^{-1}	2.8×10^{-2}	1.8×10^{-1}	11	6
8	Magnesium (AZ80A-F)	1.0×10^{-3}	7.6×10^{-1}	6.3×10^{-2}	4.1×10^{-1}	6.1	3.4
9	Graphite-Aluminum	1.1×10^{-3}	8.3×10^{-1}	4.9×10^{-2}	3.1×10^{-1}	5.6	3.1
10	Aluminum (6061-T6)	2.2×10^{-3}	1.7	9.9×10^{-2}	6.4×10^{-1}	2.8	1.6

orbital position, Thornton and Paul (1985). Structural temperatures may experience extremes from +250°F to -250°F for an orbit where the spacecraft passes through the Earth's shadow. Temperatures vary spatially in orbiting structures because of nonuniform incident heat fluxes, structural conduction and radiation heat losses from surfaces. In the vacuum of space, radiation heat transfer is particularly significant. For example, thin cylindrical shells may have major circumferential temperature variations since typically one-half of the cylindrical surface experiences heating from the solar flux while the remaining portion of the surface is shaded. All surfaces of the cylinder, heated and unheated, experience thermal energy losses to space by radiation.

Finally, thermal properties of materials have a major effect on temperature distributions. Metallic and composite materials may have significant differences in thermal properties that yield substantially different temperature distributions.

To gain insight into how the properties of several common aerospace materials affect the temperature of a thin-walled structure, it is helpful to examine a simple heat conduction problem. Consider a thin plate of thickness h with the x,y,z coordinate system located at the middle surface. The initial temperature of the plate is zero. The surface $z = -h/2$ is perfectly insulated, and for time $t > 0$ the surface $z = h/2$ is uniformly heated by a constant heat flux q_s. To understand how material properties affect the temperature gradient through the plate thickness, consider the situation where there is no temperature variation with x and y, *ie* $T(z,t)$. Thermal properties are assumed constant. The solution to the initial/boundary value problem is given by Boley and Weiner (1960) as

$$T(z,t) = \frac{q_s h}{k}\left[\frac{\kappa t}{h^2} + \frac{1}{2}\left(\frac{z}{h}+\frac{1}{2}\right)^2 - \frac{1}{6} - \frac{2}{\pi^2}\sum_{n=1}^{\infty}(-1)^n \exp(-n^2\pi^2\kappa t/h)\cos n\pi\left(\frac{z}{h}+\frac{1}{2}\right)\right] \quad (3)$$

where the thermal diffusivity $\kappa = k/\rho c$. This solution predicts that after an initial transient, temperatures of the top and bottom surfaces of the plate increase linearly with time according to the first term in the square brackets. Thus, the infinite series contributes to the temperature distribution only during the initial transient, and after early time the series contribution becomes negligible. Neglecting the series permits the thickness temperature difference or gradient $\Delta T = T(h/2,t)-T(-h/2,t)$ to be expressed by the simple equation,

$$\Delta T = \frac{q_s h}{2k} \quad (4)$$

Equation 4 shows that the thickness temperature gradient varies linearly with the applied heat flux and plate thickness but inversely with the thermal conductivity. Table I gives thermal properties and thickness temperature gradients predicted for ten metallic and composite plates. Figures 1-2 show

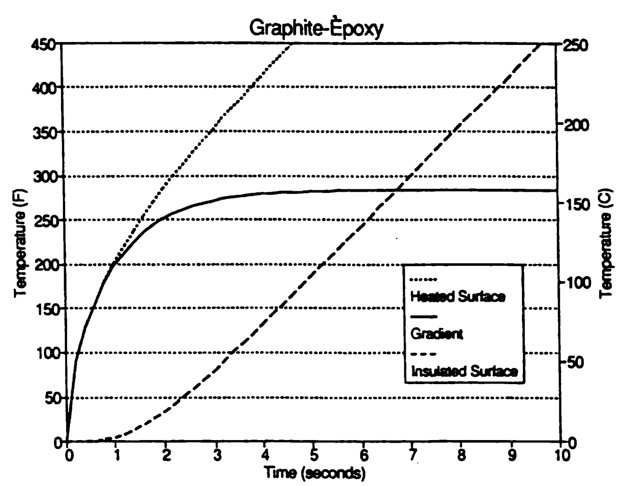

FIG 1 Thermal response of suddenly heated, thin graphite-epoxy plate, q_s = 0.1 BTU/in²-s (16 W/cm²) and h = 0.125 in (0.318 cm).

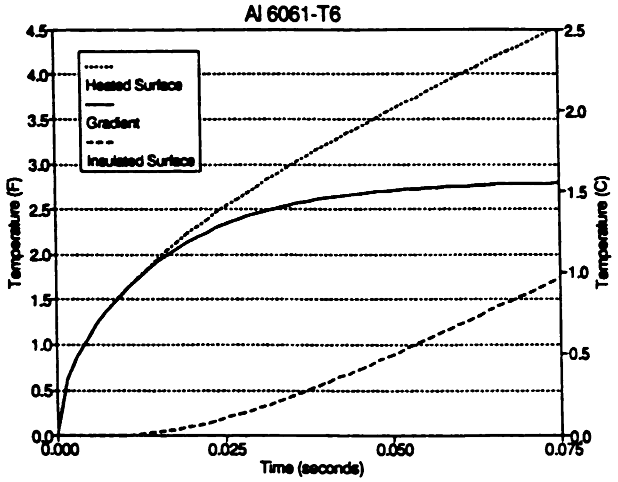

FIG 2 Thermal response of suddenly heated, thin aluminum alloy plate, $q_s = 0.1$ BTU/in^2-s (16 W/cm^2) and $h = 0.125$ in (0.318 cm).

transient temperatures for graphite-epoxy and aluminum plates. Graphite-epoxy and aluminum have the smallest and largest values of thermal conductivity, respectively, and produce extreme values for the temperature gradient. Graphite-epoxy has a very large thickness temperature gradient, and aluminum has a very small temperature gradient. Table I shows, in fact, that the graphite-epoxy composite is exceptional; its thermal conductivity is so low that an extraordinarily large thickness temperature gradient is predicted. Since the practical temperature range of this material is limited to less than 250°F (120°C), it is doubtful that such a large ΔT could ever occur in practice. The other metallics and metallic-based composites show relatively small thickness temperature gradients with titanium showing the largest and aluminum the smallest gradients, respectively. The thickness temperature gradients shown may be regarded

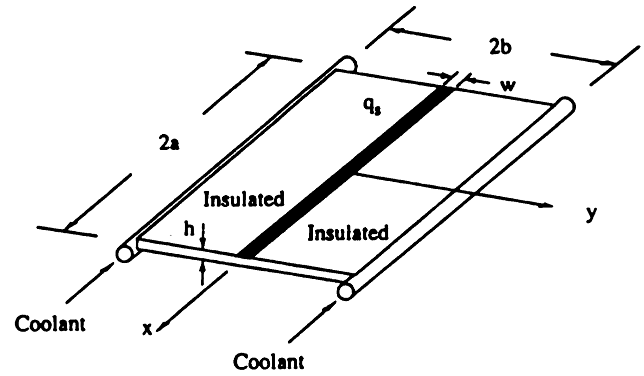

FIG 3 Centrally-heated, edge-cooled plate studied by Heldenfels and Roberts (1952).

as upper bounds since often thermal conductivity increases with increasing temperature, and the insulated boundary condition on the bottom surface will not be realized as energy losses will inevitably occur due to surface convection or radiation heat transfer. In addition, any heat conduction in the x-y plane due to plate supports or non-uniform heating will lessen the thickness temperature gradient. For thin-walled metallic structures, customary practice has been to neglect thickness temperature gradients.

Insight into the effect of thermal properties on the spatial variation of the thin plate temperature, $T(x,y)$, is provided by solution of the linear, unsteady initial/boundary value problem of a plate locally heated, Fig 3. The edges of the plate at $y = \pm b$ are maintained at constant temperature of zero by specified coolant flows. The bottom and top surfaces of the plate are perfectly insulated except along the centerline of the upper plate surface. For time $t > 0$, the plate experiences uniform heating q_s on a narrow strip along the x axis.

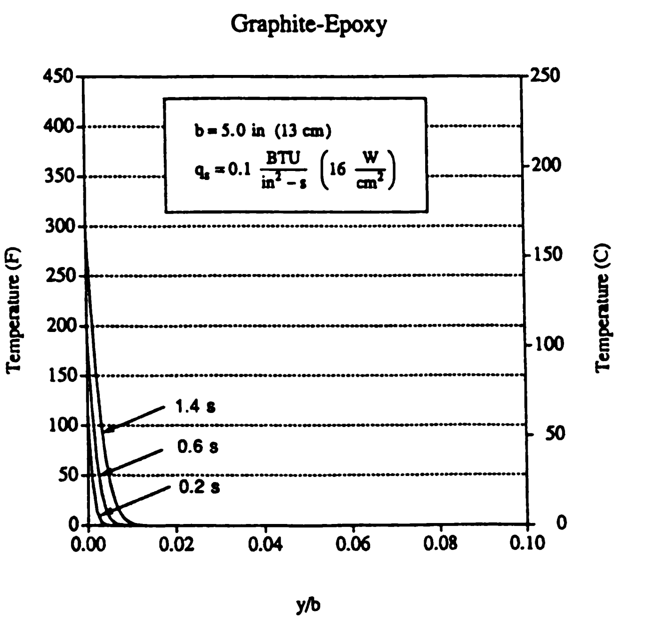

FIG 4 Temperature distribution for locall[illegible]e-epoxy plate, $q_s = 0.1$ BTU/in^2-s (16. W/cr[illegible]).

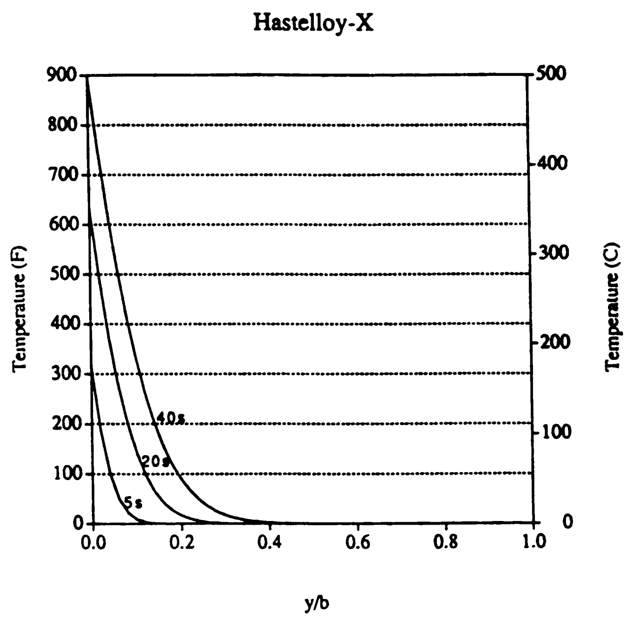

FIG 5 Temperature distribution for locally heated Hastelloy X plate, $q_s = 0.1$ BTU/in^2-s (16. W/cm^2), $b = 5.0$ in (13 cm).

Temperature is assumed uniform through the plate thickness. The solution to the symmetric, one-dimensional conduction problem is given by Carslaw and Jaeger (1980) as,

$$T(y,t) = \frac{q_o(b-y)}{2k} - \frac{8q_o b}{\pi^2 k}\sum_{n=0}^{\infty}\frac{(-1)^n}{(2n+1)}$$

$$\exp\left[-\pi^2(2n+1)^2\kappa t/4b^2\right]\sin\frac{\pi(2n+1)(b-y)}{2b} \tag{5}$$

where $q_o = q_s w/2h$ with w as the width of the heated strip, and as before, κ is the thermal diffusivity. For large time, plate temperatures approach steady-state with the peak temperature at the centerline and a linear decrease to the specified zero values on the plate edges. As with the previous solution, Eq 5 predicts plate transient temperature distributions that depend inversely on the material's thermal conductivity.

Using the thermal properties shown in Table I, transient thermal responses were computed for graphite-epoxy, Hastelloy X, and aluminum, (Figs 4-6). These results indicate the responses of low, medium and high thermal conductivity material plates to local heating. The results show for low thermal conductivity graphite-epoxy (Fig 4) that temperatures rise rapidly with very steep temperature gradients and a highly-localized heated region. On the other hand, for aluminum with high thermal conductivity (Fig 6) temperatures rise more slowly with lower gradients as thermal energy is conducted into the cooler boundaries. The response of the Hastelloy X, a high temperature nickel-based alloy, falls somewhere in between these two extremes, but the material demonstrates high local temperatures, steep gradients and a relatively small heated region. Thin walled structures of this alloy subjected to localized heating are likely to experience inelastic buckling behavior due to the high local temperatures.

These examples demonstrate two types of thermal gradient responses characteristic of thin-walled structures. For low thermal conductivity materials such as graphite-epoxy, high thickness temperature gradients will occur. However, for metals and metal matrix composites, thickness temperature gradients are negligible, and spatial temperature gradients are most likely to occur in applications.

3. THERMAL BUCKLING OF PLATES

This section reviews past research on thermal buckling of rectangular plates. The review is divided into three parts: (1) the plane stress problem, (2) the buckling problem, and (3) the postbuckling problem. Within each part papers are described in chronological order. A survey of thermally induced flexure, buckling and vibration of plates, Tauchert (1991), provided some of the references in this review. A recent review article by Noor and Burton (1992) describes computational models for high temperature multilayered composite plates and shells and lists 448 references.

3.1 The Plane Stress Problem

The classical plane stress problem consists of a thin, perfectly flat, isotropic rectangular plate heated so that the temperature is a function only of the spatial coordinates and time, *ie* $T(x, y, t)$. Since the temperature does not vary through the plate thickness the thermal moment is zero, and the plate remains flat as the temperature changes. A state of plane stress is assumed, and the non-zero stresses σ_x, σ_y, τ_{xy} are functions only of the spatial coordinates and time. Assuming elastic quasi-static behavior with constant properties, the elasticity problem may be formulated in terms of the two non-zero equilibrium equations, the strain-displacement relations and Hooke's law.

Some of the earliest thermal-stress analyses relevant to thermal buckling were concerned with solving the plane stress problem for a steady temperature distribution $T(x, y)$. A popular approach was to introduce an Airy stress function $F(x, y)$ such that

$$\sigma_x = \frac{\partial^2 F}{\partial y^2}$$
$$\sigma_y = \frac{\partial^2 F}{\partial x^2}$$
$$\tau_{xy} = -\frac{\partial^2 F}{\partial x \partial y} \tag{6}$$

Equilibrium is then satisfied, and by using the membrane strain compatibility equation F is a solution of the non-homogeneous biharmonic equation

$$\nabla^4 F = -E\alpha\nabla^2 T \tag{7}$$

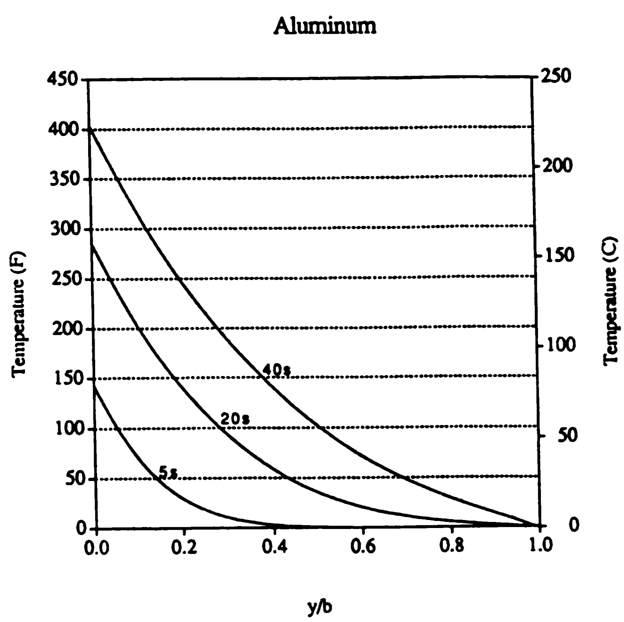

FIG 6 Temperature distribution for locally heated aluminum plate, q_s = 1 BTU/in^2-s (16. W/cm^2), b = 5.0 in (13 cm).

where E is the modulus of elasticity, and α is the coefficient of thermal expansion. The stress function F, of course, must satisfy appropriate boundary conditions on the plate edges.

Heldenfels and Roberts (1952) investigated the plane stress problem theoretically and experimentally. The theoretical studies produced an approximate complementary energy solution for the Airy stress function. In the experimental studies, simple "tentlike" steady-state temperature distributions were introduced by heating a rectangular plate along a centerline with a heating wire and maintaining constant temperature along parallel edges by water flow through coolant tubes (Fig 3). Top and bottom surfaces of the plate were insulated to produce uniform, one-dimensional, linear temperature variations between the heated centerline and cooled parallel edges. In the experimental study, in-plane plate displacements were permitted to occur freely, but out-of-plane displacements were prevented by restraints that forced the plate to remain flat. Thermocouples and strain gages were used to measure temperatures and strains, respectively. Experimental results were found to be in satisfactory agreement with the approximate theoretical results. The results showed important characteristics of the stress distribution. The tentlike temperature distribution (Fig 7) causes the central portion of the plate to be in compression. For example, the stress $\sigma_x(o,y)$ is compressive for $-b/2 < y < b/2$ where the transverse width of the plate is $2b$. For an unrestrained plate, these compressive stresses must be equilibrated by tensile stresses σ_x along the outer regions of the plate. The most important point, however, is that the unrestrained plate may experience thermal buckling due to compressive stresses induced by the spatial temperature gradients.

A few years later Przemieniecki (1959) used characteristic beam vibration modes to derive an approximate solution for the plane stress problem for arbitrary temperature distributions. Two years later, Rao and Johns (1961) compared various solutions for the

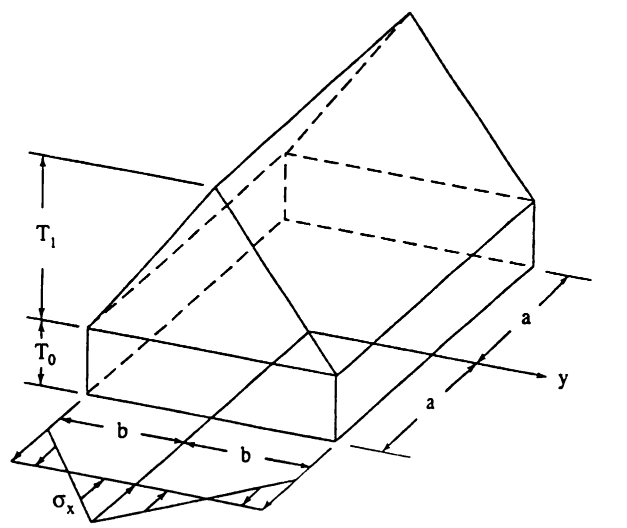

FIG 7 Tentlike tempera[illegible]d axial stresses in Heldenfels and Roberts

plane stress problem assuming a symmetrical temperature variation across the width of the plate. These investigations provided insight into the membrane thermal stress distributions that establish the possibility of thermal buckling due to the local compressive stresses. The plane-stress problem remains important today. In a study of the viscoplastic response of plates due to unsteady heating, Thornton and Kolenski (1991) investigated the plane stress problem using a finite element approach. Plate elastic and inelastic membrane stresses were investigated for prescribed transient temperature distributions. Local yielding significantly alters membrane stress distributions, and for rapid rises of temperature, the nickel-based alloy materials display initially higher yield stresses due to strain rate effects. As temperatures approach elevated values, yield stress and stiffness degrade rapidly and pronounced plastic deformation occurs.

3.2 Buckling

To determine the critical buckling temperature, small transverse bending displacements of the plate are assumed. The stresses obtained from the solution of the uncoupled plane stress problem is used to define the inplane stress resultants N_x, N_y, N_{xy} which are obtained by multiplying the stresses by the plate thickness h. The displacement $w(x,y)$ of the buckled plate is governed by the linear differential equation

$$D\nabla^4 w = N_x \frac{\partial^2 w}{\partial x^2} + 2N_{xy}\frac{\partial^2 w}{\partial x \partial y} + N_y \frac{\partial^2 w}{\partial y^2} \tag{8}$$

where D is the flexural rigidity of the plate, $D = Eh^3/12(1-\upsilon^2)$, and υ is Poisson's ratio. One of the basic thermal buckling solutions to Eq 8 is for a fully-restrained plate with a uniform temperature rise. For a rectangular plate with dimensions $(2a \times 2b)$ subjected to uniform compressive membrane forces N_x and N_y, Timoshenko and Gere (1961) give the critical condition as

$$N_x \frac{m^2\pi^2}{(2a)^2} + N_y \frac{n^2\pi^2}{(2b)^2} = D\left[\frac{m^2\pi^2}{(2a)^2} + \frac{n^2\pi^2}{(2b)^2}\right]^2$$

where m, n denote the number of half-waves in the x and y directions, respectively. Due to a uniform temperature rise ΔT, $N_x = N_y = hE\alpha\Delta T/(1-\upsilon)$ for the fully restrained plate. Thus the critical buckling temperature is determined by substituting for N_x and N_y and solving for ΔT_{cr}

$$\Delta T_{cr} = \frac{\pi^2 D(1-\upsilon)}{4E\alpha h}\left(\frac{m^2}{a^2} + \frac{n^2}{b^2}\right)$$

where the minimum value occurs for $m = n = 1$. Substituting for D yields,

$$\Delta T_{cr} = \frac{\pi^2 h^2}{48(1+\upsilon)\alpha}\left(\frac{1}{a^2}+\frac{1}{b^2}\right) \tag{9}$$

Equation 9 shows that the critical buckling temperature is independent of the material's modulus of elasticity. For thin plates fully-restrained against in-plane displacements, Eq 9 predicts quite small critical buckling temperatures. For example, an aluminum plate with a = 18 in, b = 12 in and h = 0.25 in buckles at a critical temperature $\Delta T_{cr} = 8.4°F$.

Shortly after the Heldenfels and Roberts paper on the plane stress problem was published at NASA Langley, a closely related paper by Gossard, Seide and Roberts (1952) described the buckling and post buckling behavior of the same plate. The paper made two important contributions. First, the critical buckling temperature for the unrestrained plate with the tentlike temperature distribution was determined analytically. Secondly, the post-buckling nonlinear, out-of-plane bending displacement $w(x,y)$ was studied analytically and experimentally.

The critical buckling temperature was obtained for simple supports by the principle of minimum potential energy using a series of trigonometric functions for the transverse displacement. The in-plane displacements are unrestrained. For a panel with aspect ratio of a/b = 1.57, the critical buckling temperature was determined to be

$$T_{1_{cr}} = \frac{5.39\pi^2}{12}\frac{1}{1-\upsilon^2}\frac{1}{\alpha}\frac{h^2}{b^2} \tag{10}$$

In Eq 10, T_{1cr} is the critical value of the temperature differential, the difference T_1 between the center and edge temperatures in a tentlike temperature distribution, Fig 7. The paper also studied the plate's postbuckling behavior which will be described in the next section.

After the Gossard, Seide and Roberts paper, other authors investigated bifurcation thermal buckling of rectangular plates. Hoff (1956) investigated thermal buckling of supersonic wing panels. Temperature and thermal stress distributions due to aerodynamic heating were analyzed for supersonic wing structures. An analytical approach for determining critical thermal buckling stresses for wing cover plates was developed. van der Neut (1957) investigated approximate analysis methods for determining critical buckling temperature for panels with assumed distributions of thermal stress. Klosner and Forray (1958) studied buckling of simply supported plates under an arbitrary symmetrical temperature distribution. In-plane displacements of the plate are assumed to be elastically restrained by supporting edge members. The critical buckling temperature was determined by a Rayleigh-Ritz procedure. Miura (1961) used a similar procedure to obtain the critical buckling temperature when in-plane displacements are completely restrained. Critical buckling temperatures were computed in these two papers for a plate of dimensions $(2a \times 2b)$ and the parabolic temperature distribution,

$$T = T_0 + T_1\left[1-\left(1-\frac{x}{a}\right)^2\right]\left[1-\left(1-\frac{y}{a}\right)^2\right] \tag{11}$$

The results of these two papers showed that the critical buckling temperature is given by Eq 10 in the general form

$$T_{1_{cr}} = \frac{k_T}{1-\upsilon^2}\frac{1}{\alpha}\frac{h^2}{b^2} \tag{12}$$

where $T_{1_{cr}}$ is the critical value of the temperature rise. The thermal buckling coefficient k_T depends on the plate aspect ratio and in-plane boundary restraints. Equation 12 assumes fully restrained simple supports, and that the plate buckles in a single half-wave in each direction. The variation of the critical buckling temperature with the aspect ratio a/b for the parabolic temperature distribution is shown in Fig 8.

Thermal buckling of a simply-supported rectangular panel unrestrained in the plane is considered by Boley and Weiner (1960). The edges $x = 0,2a$ and $y = 0,2b$ are assumed to remain straight. A temperature distribution T T_0-T_1 $\cos \pi y/b$ is assumed. An analytical solution is

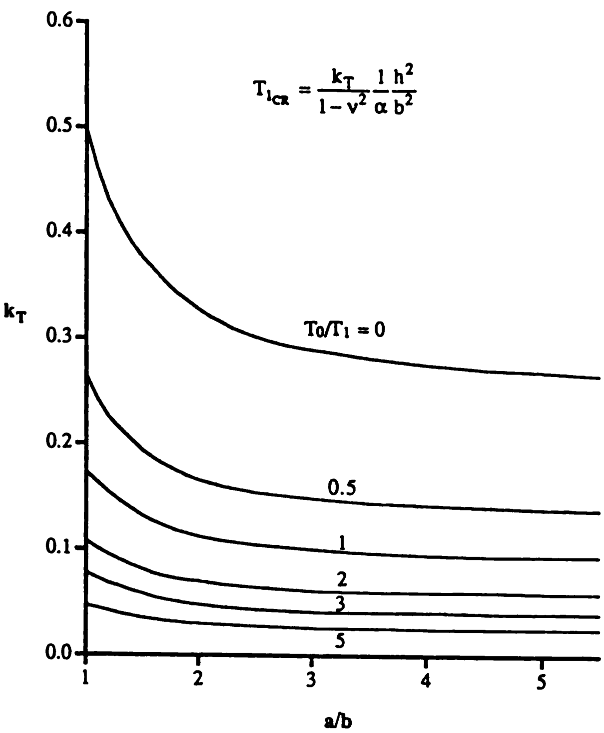

FIG 8 Buckling coefficient for simply-supported, fully-restrained plate with parabolic temperature distribution, Klosner and Forray (1952).

developed by first determining the stress function F that satisfies Eq 7. Then the transverse displacement $w(x,y)$ is expanded in an infinite series where a typical term has the form $A_{mn} \sin(m\pi x/2a) \sin(n\pi y/2b)$. Satisfaction of Eq 8 leads to an infinite determinant for computing the critical values of the buckling temperature T_1. (Note, as with the unrestrained plate of Gossard and Seide, that buckling does not depend on T_o.). The critical temperature has the form

$$\Delta T_{1_c} = \frac{k_1\pi^2}{24}\frac{1}{1-\nu^2}\frac{1}{\alpha}\frac{h^2}{b^2} \tag{13}$$

where k_1 is a function of m and the aspect ratio a/b; m is the number of half-waves in the x direction. A curve is given showing the variation of k_1 with aspect ratio. The minimum value of k_1 is 3.848. For an aspect ratio $a/b < 1.4$, the plate buckles in one half-wave, $m = 1$; for $1.4 < a/b < 2.5$, $m = 2$; for $2.5 < a/b < 3.5$, $m = 3$; etc. The Boley and Weiner text also includes the effect of an axial applied stress σ_X, and an interaction curve is given.

Thermal buckling of parallelogram (skewed) rectangular plates were investigated in the 1970s. For applications to aircraft wings Matsumoto (1973) analyzed parallelogram, shallow curved panels using Galerkin's method for clamped boundary conditions and an arbitrary temperature distribution. Using a measured temperature distribution, buckling temperatures were computed for parallelogram and rectangular panels. The critical buckling temperature for a parallelogram panel was higher than the corresponding rectangular panel. Shallow panel curvature increased buckling temperatures. Prabhu and Durvasula (1974a, b) analyzed skewed, flat plates using a Ritz method. Critical buckling temperatures are given as a function of the skew angle for restrained plates with simple and clamped transverse deflection boundary conditions.

More general analyses of thermal buckling of flat plates were presented in the 1980s. Thermal buckling of initially stressed thick plates was investigated by Chen et al. (1982). The paper shows that transverse shear effects can reduce the plate critical buckling temperature. Bednarczyk and Richter (1985) consider thermal buckling of unrestrained plates with self-equilibrated stresses. They study the influence of the spatial temperature distribution on critical buckling modes and seek the temperature distribution that yields the lowest critical buckling temperature. For square plates, the lowest eigenvalue occurs when the temperature distribution is piecewise constant. An example shows a central square patch of a plate having uniform temperature surrounded by a "picture frame" of zero temperature. The implication of the analyses is that minimum buckling temperatures occur under a condition of localized thermal st[illegible] Bargmann (1985) considers a rectangular flat [illegible] non-uniform temperature distribution and [illegible]d boundary conditions. In-plane forces [illegible] so that the plate edges remain straight during deformation. Stability conditions are derived for: (1) a uniaxial stress field, (2) biaxial combined compression and tension and (3) biaxial combined compression, tension and shear.

In a study of thermal buckling that occurs in the growth process for producing sheets of silicon, Ahmed and Dillon (1987) study thermal buckling of plates with reinforced edges. A prescribed temperature profile, $T(x)$, is assumed. The plane stress problem for the membrane stress is analyzed first, and then the industrial process is modeled as a cantilever plate. The role of the edge stiffeners is examined, and the authors conclude that edge stiffeners can either help or hinder thermal buckling as compared to a flat plate.

Studies of the effects of the environment on laminated composites in the 1970s led to the first thermal buckling analyses of composite plates. Whitney and Ashton (1971) used an energy formulation in conjunction with a Ritz method to determine critical buckling temperatures for restrained angle ply laminates. Flagg and Vinson (1978) used a similar approach to study the effects of moisture and temperature on critical buckling loads. It was shown that these hygrothermal effects reduce critical buckling loads.

Since the 1980s, much thermal buckling research has focused on buckling of composite laminated panels. The book by Whitney (1987) formulates the governing equations for expansional strain effects in laminated plates. Thermal buckling of rectangular plates with symmetric angle-ply laminates are analyzed using the Ritz method. Thermal buckling behavior has been studied also with approximate analytical methods by Tauchert (1987), Tauchert and Huang (1987), Chen and Chen (1987a), Chandrashekhara (1991a), Huang and Tauchert (1990), Sun and Hsu (1990) and Chang and Leu(1991) and computationally by the finite element method by Thangaratnam *et al* (1989), Chen and Chen (1989a,b), Chang and Shiao (1990) and Chang (1990). The effects of various laminated plate parameters have been investigated. A recent collection of papers on thermal effects on structures and materials edited by Birman and Hui (1990) includes additional references on thermally induced buckling of composites. Paley and Aboudi (1991) develop a method for determining critical buckling temperatures for metal matrix composite plates.

3.3 Postbuckling

The 1952 paper by Gossard, Seide and Roberts describes the first theoretical and experimental investigations of thermal postbuckling. When a plate's transverse displacements became large (*eg*, of the order of the plate thickness), stretching of the middle surface may occur. Because of this stretching, the membrane forces change as the plate deforms. The membrane stresses (or the stress function F) and the displacement $w(x, y)$ must be determined simultaneously. The postbuckling theoretical problem is described by von Kármán's equations,

$$h\nabla^4 F = Eh\left[\left(\frac{\partial^2 w}{\partial x \partial y}\right)^2 - \frac{\partial^2 w}{\partial x^2}\frac{\partial^2 w}{\partial y^2}\right] - \nabla^2 N_T$$

$$D\nabla^4 w = h\left[\frac{\partial^2 F}{\partial y^2}\frac{\partial^2 w}{\partial x^2} - 2\frac{\partial^2 F}{\partial x \partial y}\frac{\partial^2 w}{\partial x \partial y} + \frac{\partial^2 F}{\partial x^2}\frac{\partial^2 w}{\partial y^2}\right] - \frac{1}{1-\nu}\nabla^2 M_T \tag{14}$$

where the thermal force per unit length is

$$N_T = E\alpha\int_{-h/2}^{h/2} T(x,y,z)dz \tag{15}$$

and the thermal moment per unit length is

$$M_T = E\alpha\int_{-h/2}^{h/2} T(x,y,z)zdz \tag{16}$$

Equations (14) are solved subject to appropriate boundary conditions, see Boley and Weiner (1960). Gossard, Seide and Roberts (1952) obtain an approximate analytical solution based on the Galerkin method. Two cases are considered: (1) an initially perfectly flat plate, and (2) a plate with an initial deflection. Experimentally, the plate was tested with simple supports for bending displacements, and in-plane displacements were unrestrained. The plate was tested under steady conditions with the tentlike temperature distribution (Fig 7) used by Heldenfels and Roberts (1952). Temperature is assumed constant through the plate thickness, and the thermal moment is zero. The maximum temperature rise during the test was about 150°F, and the critical buckling temperature rise, Eq 10, was slightly less than 200°F. The experimental results showed that the effect of the initial plate deflection was appreciable. The maximum initial deflection was about 18% of the plate thickness. The test results show a strongly nonlinear variation of the plate deflection with the temperature rise even for deflections less than one-half the plate thickness. The largest plate deflection measured was less than a plate thickness. With initial deflections considered, good agreement was obtained between the experimental and theoretical results.

After the Gossard, Seide and Roberts paper, other authors in the 1950s and 1960s investigated thermal postbuckling of plates. Williams (1955,1958) performed a large deflection analysis to determine deflections and membrane stresses for an infinite strip (cylindrical bending) subjected to pressure and temperature variations. Forray and Newman (1962a,b) study the postbuckling behavior of flat simply supported rectangular plates with parabolic temperature variations in x and y. Wilcox and Clemmer (1964) analyzed the large deflections of a simply supported rectangular plate with elastic in-plane deflection restraints. Pressure and temperature changes were considered.

Subsequently, interest in thermal buckling of isotropic plates decreased with only a few papers over the next two decades. Prabhu and Durvasula (1976) investigated thermal post-buckling characteristics of clamped skew plates with restrained edges subjected to planar temperature distributions. Approximate solutions to the nonlinear partial differential equations are obtained by a perturbation method. The results showed that the plate nonlinearity tends to increase with skew angle for both uniform and nonuniform temperature distributions considered. HE Williams (1979) reconsidered the stability conditions for the cylindrical bending problem originally studied by ML Williams in the 1950s. Jones *et al* (1980) investigated thermal postbuckling of flat plates using Berger's approximation to plate bending theory. HE Williams (1982) studies buckling and postbuckling using the "Neale Plate" equations. The unique feature of this approach is the equations used are a generalization of von Kármán's equations in rate form. The approach is used to study thermal buckling of rectangular plates including plasticity.

The effect of temperature-dependent elastic modulus and coefficient of thermal expansion on the post-buckling behavior of heated square plates was investigated by Kamiya and Fukui (1982). Finite difference numerical solutions are obtained for constrained in-plane displacements and simply-supported and clamped edges. The temperature-dependent properties lowered critical buckling temperatures and reduced post-buckling stiffness for increasing temperature and deflection.

Paul (1982) developed a procedure for the prediction of the postbuckling behavior of clamped rectangular plates subjected to arbitrary planar temperature distributions. Design charts and tables are provided for several cases. The report concludes that thermally loaded plates possess considerable postbuckling load carrying capability which is not fully utilized in design practice.

Several recent papers study the thermal postbuckling for laminated composite plates. Huang and Tauchert (1988a, b) analytically study postbuckling behavior of flat angle-ply laminates for spatially symmetric parabolic variation of the plate temperature and uniform temperature. Ply angles are arranged antisymmetrically about the middle surface. The unsymmetric layup causes a coupling between the in-plane displacements u,v and the transverse displacement w. Thus as the temperature increases, out-of-plane displacements increase even for small deflections. Above the critical buckling temperature, transverse displacements increase rapidly as expected. Chen and Chen (1989b, 1991) study thermal postbuckling behavior of laminated composite plates by the finite element method. The influence of composite laminate characteristics on thermal postbuckling is studied first, and then the effects of temperature-dependent properties are considered. Temperature-dependent properties lower predictions of critical buckling temperatures. Librescu and Souza (1991) study the static postbuckling of simply supported, shear deformable composite flat panels exposed to a stationary temperature field and in-plane compressive edge loads.

An analytical approach using Galerkin's method is employed. Numerical results are presented for the postbuckling response of composite panels with an assumed sinusoidal temperature distribution. Meyers and Hyer (1991) analytically study the thermal buckling of flat, symmetrically laminated composite plates for a uniform temperature rise. For the symmetric layup, the plates demonstrate bifurcation buckling behavior similar to an isotropic plate. Effects of support conditions and material axis orientation are studied parametrically. Noor and Peters (1992a) study the postbuckling response of composite plates subjected to combined axial load and a uniform temperature distribution. The analysis is based on a first-order shear deformation, von Kármán nonlinear plate theory and used a mixed finite element formulation. Sensitivity derivatives are used to study the sensitivity of postbuckling to composite plate parameters. Noor and Peters (1992b) also study the thermal postbuckling of thin-walled composite stiffeners. Using the same approach employed in the previous paper, numerical studies are presented for anisotropic stiffeners with Zee and channel sections.

In one of the few recent experimental programs, a paper by Teare and Fields (1992) describes buckling analysis and test correlations of high temperature structural panels. A titanium, stiffened panel was simultaneously heated and subjected to axial compressive forces in a testing machine. Good correlation between test and analysis provided both a validation of the computational methods and verification of the structural concept. A postbuckling test indicated that the panel was capable of withstanding more than 200% of the initial buckling load without permanent deformation. The paper concludes that vehicle weight can be reduced by taking advantage of the postbuckled strength as exhibited in the test.

3.4 Assessment

Since the original investigations of Heldenfels and Roberts (1952) and Gossard, Seide, and Roberts (1952), numerous investigators have studied thermal buckling and thermal postbuckling of plates. Until the 1980s, most studies were performed for isotropic plates, but in the 1970s research was initiated for laminated composite plates. Figure 9 shows the relative number of papers on thermal buckling of metallic and composite plates over the last four decades. Almost all of the work has assumed: (1) perfectly flat initial configurations and (2) elastic behavior. There is a need for further study of buckling of plates with initial imperfections and inelastic behavior. Aerospace designers also need rapid postbuckling analysis methods for both mechanical and thermal loads. With the exception of the original (1952) papers and the recent paper by Teare and Fields, the investigations have been analytical or computational; there have been no further experimental studies. There is a need for further experimental studies of thermally induced buckling for both isotropic materials and laminated composites. Applications to aircraft structures strongly suggest that experimental programs be conducted for plates with spatial temperature variations.

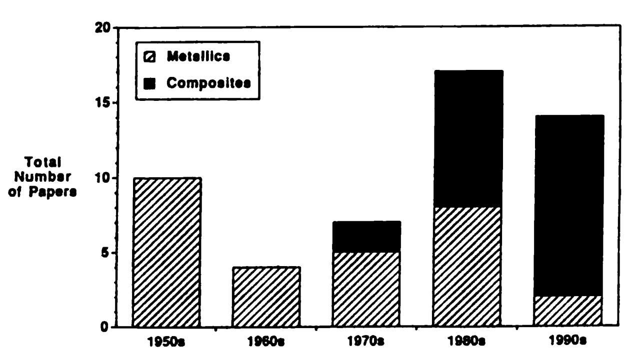

FIG 9 Relative number of papers on thermal buckling of metallic and composite plates.

4. THERMAL BUCKLING OF SHELLS

Buckling of shells has been the subject of extensive research in the aerospace industry because of the widespread use of shell structures in flight vehicles. Analytical, computational and experimental studies have investigated the behavior of shell structures subjected to mechanical loads. Much less research has occurred for buckling and postbuckling of shells in a thermal environment. And yet future designs of airframes for high speed flight and spacecraft structures will have to consider carefully the effect of the thermal environment on structural and material behavior.

There are several excellent textbooks on the theory and buckling of shells, but most classic books do not include temperature in the formulation of the equations nor address thermal buckling. Thus, with a few exceptions, solutions of shell thermal buckling problems appear in papers and reports rather than texts. Furthermore, in contrast to the study of shell buckling under mechanical loads, studies of thermal buckling are relatively more recent. For example, solutions for critical buckling loads of cylinders under axial loads were presented in the early 1900s, but studies of critical buckling temperatures for cylindrical shells were not undertaken until the 1950s. At that time, the design of lightweight structures for high speed flight of aircraft and missiles provided strong motivation for the first studies of thermal buckling. During the early days of supersonic flight, researchers learned that aerodynamic heating raised surface temperatures significantly and induced strong temperature gradients. Consideration of thermal effects on material and structural performance stimulated the first thermal buckling research for shells in the late 1950s and early 1960s. A paper on buckling at high temperatures by NJ Hoff (1957a) describes initial work on thermal buckling of thin circular cylindrical shells. Over thirty years later a survey article by Ziegler and Rammerstorfer (1989) summarizes thermoelastic stability research for elastic and viscoelastic structures including shallow and cylindrical shells. In the same volume, Lukasiewicz (1989) presents a comprehensive review of thermal stresses in shells and discusses thermal buckling. A book by Bushnell (1989) describes a computerized buckling analysis approach of shells for mechanical loads and presents thermal buckling examples. A comprehensive bibliography by Keene and Hetnarski (1990) lists 778 references to publications on thermal stresses in shells.

This section focuses on thermal buckling of shells with particular emphasis on aerospace applications. The review considers: (1) shallow shells, (2) cylindrical shells and (3) conical shells. Within each section papers are described in chronological order.

4.1 Shallow Shells and Curved Panels

The shallow shell idealization is used to consider the effects of curvature on the structural response of shell segments and panels. The idealization permits use of a simplified set of equations similar to the von Kármán equations for flat plates rather than the full shell equations. The classical shallow shell problem consists of a thin, doubly curved surface with curvatures k_x and k_y in the x and y directions, respectively. The temperature T may vary with the spatial coordinates x and y, through the thickness h of the shell, and with time. Typically quasistatic behavior with constant thermal properties is assumed, and published analyses have assumed steady temperature distributions. The non-zero stresses σ_x, σ_y, τ_{xy} are expressed in terms of an Airy stress function $F(x,y)$ by Eq 6 such that the in-plane equilibrium equations are satisfied. Satisfaction of membrane strain compatibility and the remaining transverse equilibrium equation produces for an isotropic material the nonlinear governing equations

$$h\nabla^4 F = Eh\left[\left(\frac{\partial^2 w}{\partial x \partial y}\right)^2 - \frac{\partial^2 w}{\partial x^2}\frac{\partial^2 w}{\partial y^2} - k_x\frac{\partial^2 w}{\partial y^2} - k_y\frac{\partial^2 w}{\partial x^2}\right] - \nabla^2 N_T \tag{17}$$

$$D\nabla^4 w = h\left[\frac{\partial^2 F}{\partial y^2}\frac{\partial^2 w}{\partial x^2} + \frac{\partial^2 F}{\partial x^2}\frac{\partial^2 w}{\partial y^2} - 2\frac{\partial^2 F}{\partial x \partial y}\frac{\partial^2 w}{\partial x \partial y} + k_x\frac{\partial^2 F}{\partial y^2} + k_y\frac{\partial^2 F}{\partial x^2}\right] - \frac{1}{1-\nu}\nabla^2 M_T \tag{18}$$

For a perfectly flat plate the curvatures k_x and k_y are zero, and Eqs 17-18 reduce to von Kármán's equations, Eq 14.

Among the earliest solutions of shallow shell equations of this type were studies of "snap-through" buckling of bimetallic spherical shells. Snap-through buckling is a dramatic form of elastic buckling of a shallow shell associated with large transverse deflections and a complete reversal of the curvature of the shell surface. Such shells have applications as temperature-sensitive components in automatic control instruments. Wittrick *et al* (1953) studied the stability of a closed-top bimetallic spherical shallow shell and analyzed the influence of the geometrical and physical parameters on such quantities as minimum arch height for buckling and the buckling temperature. Later, Tsu-tao *et al* (1966) developed a theory for an open bimetallic shallow shell. The critical buckling temperature is related to geometric and physical parameters including the extent of the shell opening. In a later paper Liu (1983) develops analytical solutions for thermal stability of a bimetallic shallow shell with a circular hole at the center and a bimetallic truncated shallow conical shell under a uniform temperature field.

Thermal buckling of isotropic shallow shells of rectangular planforms were studied in the 1960s by Mahayni (1966) and Haydl (1968). Mahayni considers a simply-supported panel with temperature that varies quadratically with x over the panel surface but is constant through the panel thickness. An approximate analytical solution of the nonlinear equations is obtained by Galerkin's method. Haydl considers similar problems by the same approach but with temperature varying sinusoidally with x and y and linearly through the shell thickness. The papers establish approximate analytical expressions for critical buckling temperatures and conditions for snap-through buckling. Haydl, for example, shows that shallow shells can have from one to three equilibrium positions. He demonstrates for an aluminum panel that relatively small temperature gradients (50° to 100°F) between the center and edge of a panel can result in snap-through.

Kamiya (1978) studied the nonlinear bending of shallow sandwich shells using Berger's plate approximation. Using Galerkin's method with sinusoidal spatial and linear thickness temperature variations, the nonlinear displacement response is derived and illustrated for two different panel aspect ratios.

In the last few years the design of lightweight structures from advanced composite materials has initiated thermal buckling studies of laminated curved panels and shells. In recent papers, Chen and Chen (1987b, 1990) have studied thermal buckling of laminated composite cylindrical panels. In the former, the Galerkin method is used to determine the critical temperatures of shallow laminated cylindrical panels subjected to a uniform temperature change. In the latter, thermal buckling behavior of cylindrical laminated plates subjected to a nonuniform temperature field is studied by the finite element method. In the finite element calculations, the temperature is assumed constant through the thickness, and a "tent-like" distribution with y is assumed. A matrix eigenvalue problem is solved to determine critical buckling temperatures. The effects of bending-extension coupling, lamination angle, modulus ratio, plate aspect ratio and radius of curvature on critical buckling temperature are studied.

Huang and Tauchert (1991) study thermally induced large deflections of laminated composite cylindrical and doubly-curved panels using the finite element method. First order shear deformation theory is used, and a uniform temperature rise is assumed. Post-critical equilibrium paths are traced and the strength limits of laminates are predicted using the Tsai-Wu criterion. For certain laminate configurations, the equilibrium path is characterized by the existence of limit-point and/or bifurcation instabilities. Some laminates are found to undergo two snap-throughs prior to failure. Kossira and Haupt (1991) study the buckling of laminated plates and cylindrical shells subjected to combined thermal and mechanical loads using the finite element method. The nonlinear pre- and post-buckling behavior of cylindrical composite shells is studied for three different temperature distributions. The effect of radius of curvature is studied, and computations show that the buckling temperature increases as the radius of curvature decreases. For large ply angles, snap-through behavior is predicted. Chandrashekhara (1991b) studies thermal buckling of anisotropic cylindrically curved panels using Sanders' shell theory extended to laminated shells. First order transverse shear deformation is included. Numerical results are presented using the finite element method, and the effect of various parameters on the critical buckling temperature of a curved graphite-epoxy panel with simple and clamped boundary conditions is demonstrated.

4.2 Cylindrical Shells

Early work on cylindrical shells was initiated to study potential thermal buckling of frame-reinforced fuselages for aircraft in high speed flight. Due to aerodynamic heating, the thin cylindrical shells experience higher temperatures than the heavier reinforcing frames. The hotter shell tends to expand radially more than the

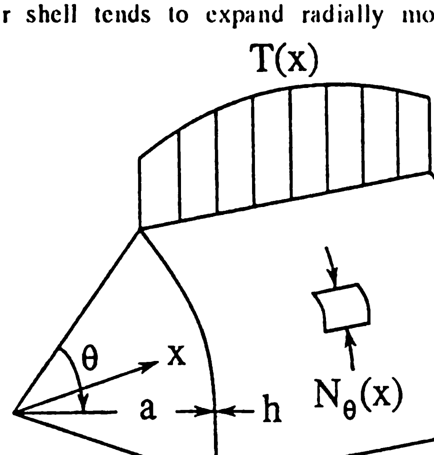

FIG 10 Circumferential membrane force induced by temperature distribution T(x) in cylindrical shell.

restraining frame inducing compressive circumferential membrane stresses $N_\theta(x)$, Fig 10. Initial research was aimed at determination of critical skin temperature levels for buckling due to the compressive membrane stresses. The first papers that studied thermal buckling of cylindrical shells solved the linear Donnell stability equations in uncoupled form:

$$\nabla^4 u = -\frac{\nu}{a}\frac{\partial^3 w}{\partial x^3} + \frac{1}{a^3}\frac{\partial^2 w}{\partial x \partial \theta^2} \tag{19a}$$

$$\nabla^4 v = -\frac{(2+\nu)}{a^2}\frac{\partial^4 w}{\partial x^2 \partial \theta^2} - \frac{1}{a^4}\frac{\partial^3 w}{\partial \theta^3} \tag{19b}$$

$$D\nabla^4 w + \frac{Eh}{a^2}\frac{\partial^4 w}{\partial x^4} - \nabla^4\left(N_x \frac{\partial^2 w}{\partial x^2} + \frac{2}{a}N_{x\theta}\frac{\partial^2 w}{\partial x \partial \theta} + \frac{1}{a^2}N_\theta \frac{\partial^2 w}{\partial \theta^2}\right) = 0 \tag{19c}$$

where a is the shell radius. The membrane forces, N_x, $N_{x\theta}$, and N_θ are obtained from a linear prebuckling analysis. Zuk (1957) described a solution procedure based on taking $N_x = N_{x\theta} = 0$ and assuming a form for N_θ proportional to $E\alpha\Delta T$. The temperature rise ΔT of the shell is assumed uniform. The N_θ membrane force was assumed to vary trigonometrically with x and to be compressive over the length of the shell. Assuming a shape for w that satisfied zero deflection and slope at each end of the shell, he used Galerkin's method to satisfy Eq 19 approximately. The result was an expression that permitted determination of the critical buckling temperature of a clamped cylindrical shell although no numerical results were presented. Later, Johns (1959, 1962) pointed out that circumferential stresses introduced at the junction of a frame and thin shell are localized and decrease rapidly away from the support. He proposed a function for the circumferential stress that decreased exponentially with x. Hoff (1957b) presented an analysis for the buckling of a simply-supported cylindrical shell where the circumferential stresses are determined from a prebuckling analysis. The displacement components u, v, w were assumed as infinite series of trigonometric functions that satisfied simply-supported boundary conditions. At the ends $x = 0, L$ of the shell, the radial and circumferential displacements as well as the axial membrane stress and the axial bending moment were assumed to vanish. The approach leads to an infinite determinant for the critical buckling stress. The prebuckling circumferential membrane force is obtained by first solving for the displacement w from the linear equilibrium equation,

$$\frac{d^4 w}{dx^4} + \frac{12(1-\upsilon^2)}{a^2h^2}w = \frac{12(1-\upsilon^2)}{ah^2}\alpha\Delta T \tag{20}$$

assuming a uniform rise ΔT in the shell temperature. For a steel cylinder with $a/h = 300$, a critical buckling temperature of over 2300°F was computed. The paper concluded that circumferential thermal stresses due to a uniform temperature rise are not likely to cause elastic buckling. In a closely related paper, Anderson (1962a) developed a similar theory to predict the buckling temperature of a uniformly heated, ring-stiffened shell and included axial compression. He used a shell theory by Batdorf and considers both simply supported and clamped shell end conditions. The paper concludes, consistent with Hoff, that buckling of a ring-stiffened cylinder due to uniform temperature alone will not occur for small values of the radius to thickness ratio, a/h. However, the paper notes that for large values of a/h (*eg*, a/h = 2000), such buckling can occur. Sunakawa (1962) also investigated the deformation and buckling of cylindrical shells due to aerodynamic heating. The book by Johns (1965) gives a simple formula for the critical temperature for buckling by circumferential membrane stresses,

$$T_{cr} = k\frac{h}{\alpha a} \tag{21}$$

where for a simple shell with simply supported ends k = 5.3, for a single or multibay shell with clamped ends k = 3.76, and for a multibay shell with simply supported ends k = 2.1.

This early work on cylinders with uniform temperatures was based on applications to fuselages with assumed axisymmetric heating. At about the same time, work began on cylinders nonuniformly heated around their circumference. Previous research on flat plates with spatial temperature gradients, *eg*, Gossard and Seide (1952), had established that thermal buckling could occur for relatively small spatial temperature gradients. Abir and Nardo (1959) investigated thermal buckling of circular cylindrical shells with circumferential temperature gradients. For a simply supported shell, they solved Eqs 19 following the approach employed previously by Hoff (1957b), but they investigated buckling due to the variation of the axial membrane force N_x around the shell circumference, Fig 11. The study concluded that the critical value of the axial thermal stress distribution occurs at a value equal to the critical stress in uniform axial compression. The critical stress for a cylinder in uniform axial compression is $\sigma_x = [3(1-\nu^2)]^{-1/2}\, Eh/a$, Timoshenko and Gere (1961). For a fully restrained cylinder the axial compression stress for a temperature increase ΔT is $\sigma_x = E\alpha\Delta T$. Thus the critical buckling temperature for uniform compression is

$$\Delta T_{cr} = \frac{1}{\left[3\left(1-\nu^2\right)\right]^{1/2}}\frac{h}{\alpha a} \tag{22}$$

Bijlaard and Gallagher (1960) also studied the elastic instability of a cylindrical shell under an arbitrary circumferential variation of axial stress. Their conclusions were consistent with Abir and Nardo.

In a closely related study, Hill (1959) analytically and experimentally studied buckling of circular cylindrical shells heated along an axial strip. In the analysis, the Donnell shell equations were used and were solved approximately using a Ritz method. A simplified axial thermal stress distribution was assumed where the stress is constant in x but varies around the circumference. In the experiments, aluminum and steel cylinders were locally heated by infrared lamps, and two types of cylinder end conditions were employed. Temperatures were measured with thermocouples, and displacements were measured with Linear Variable Differential Transformers (LVDTs). Cylinder buckling was demonstrated where the buckling deformations depended strongly on the experimental end conditions. For aluminum cylinders with a/h = 430, critical buckling temperatures were relatively low ranging from ΔT = 65°F to 100°F depending on end conditions. Experimental results for the critical buckling temperature were in reasonable agreement with the theoretical calculations. The study showed the difficulty of performing analytical predictions for the thermal buckling stresses due to localized temperature distributions and demonstrated the practical problems of creating experimental end conditions consistent with a mathematical model.

Anderson and Card (1962) described a study where several stainless steel ring-stiffened cylinders were subjected to a pure bending moment and heated rapidly until buckling occurred. For most of the cylinders the heating was non-uniform around the circumference. Temperature and deflections were measured at several locations, and in some tests strains were measured. Strains were successfully measured below 175°F, but data was unreliable for higher temperatures. An elementary thermal stress theory was found to be inadequate for the prediction of the thermal stresses. In a related paper, Anderson (1962b) reviews theoretical and experimental investigations on buckling of cylinders due to both circumferential and axial thermal stresses. The paper notes that the severity of the circumferential thermal stress is strongly dependent on the boundary conditions and suggested the need for additional experimental results. For cylinders that are heated non-

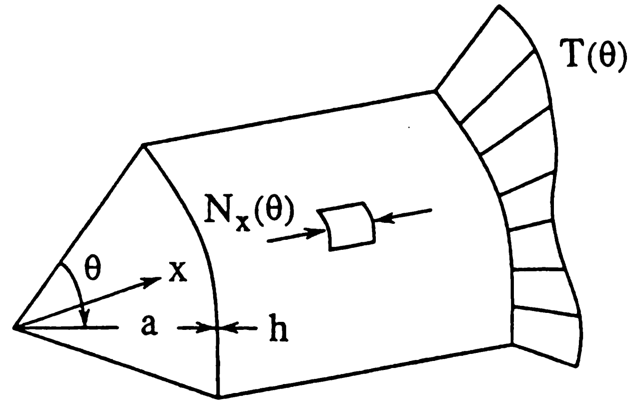

FIG 11 Longitudinal membrane force N_x induced by temperature distribution T(θ) in cylindrical shell.

uniformly, the paper discusses the difficulty of predicting axial thermal stresses and identified the need for research in thermal buckling of longitudinally stiffened cylindrical shells for launch vehicles.

In the mid-1960s, the Stanford University group of NJ Hoff continued to investigate thermal buckling of cylinders. Three papers describe further research on buckling of thin circular cylinders heated along an axial strip. Hoff, Chao and Madsen (1964) analytically study the problem assuming uniform compressive axial stress to occur in a narrow strip while the rest of the shell is stress free. The shell is assumed very long, and Donnell's equations are used. The results of the analysis support the earlier conclusion of Abir and Nardo (1959) that the critical stress of the heated strip is the same as the critical stress of a complete cylindrical shell subjected to uniform compression unless the heated strip is very small. With very narrow heated strips, the critical stress rises rapidly as the strip width decreases. Ross, Mayers and Jaworski (1965) continued and extended the experimental studies initiated by Hill. A series of stainless steel and cold-rolled steel cylinders (a/h = 334 and 291, respectively) were heated along an axial strip by infrared heat lamps. Ends supports were designed to simulate fully-fixed conditions. Instrumentation included thermocouples and a microphone to provide an audio signal at the instant of buckling. The heated width was varied from 1.5% to 18% of the total shell circumference. Tests were conducted by subjecting the cylinders instantaneously to maximum heating from the infrared lamps; axial and circumferential temperature distributions were then recorded until the shell buckled. For the stainless-steel cylinders, buckling temperatures were around 300°F; for the thicker, cold-rolled steel cylinders buckling occurred around 500°F. There was significant scatter in the data. For tests conducted on cylinders having narrow heated strip widths, buckling took place as a sudden localized "snap-through" accompanied by a distinctly audible sound. At larger values of the heated strip width, localized buckling patterns appeared simultaneously within the heated strip at several locations. For tests conducted on the thicker cold-rolled sheet steel cylinders with larger values of the strip width, a different failure mode occurred with a barrel-shaped deformation leading to yielding failure at the clamped support. Computations were performed with the Donnell theory using measured circumferential temperature distributions. Agreement of analysis with experiment was fair, but it was judged good enough for the authors to confirm previous conclusions of several investigators that the buckling temperature corresponding to uniform axial compression provides a lower limit of stability for thin cylindrical shells subjected to highly nonuniform circumferential heating. Hoff and Ross (1967) performed further analysis of the problem using the experimental temperature distributions and obtained reasonable agreement with the experimental data. The consistent trend demonstrated by these analyses was that experimental critical buckling temperatures were consistently *higher* than values predicted by analyses. This trend was in direct contradiction to the well-established trend that for mechanical loads experimental critical buckling values are consistently *lower* than predicted values.

Ross, Hoff, and Horton (1966) conducted additional experiments to address the thermal buckling anomaly. Six stainless-steel cylinders (a/h = 344) and five cold-rolled steel cylinders (a/h = 291) were heated axisymmetrically by an array of twelve infrared heat lamps. The cylinders' ends were longitudinally restrained and clamped. The test procedure was essentially the same as used by Ross *et al* (1965). Upon heating, a test cylinder experienced thermal expansion in the radial direction, and the thin cylindrical shell became barrel-shaped. Ultimately, the shell buckled near the clamped end supports. Comparison of experimental results with the predictions of available shell-buckling theories showed poor agreement. The authors concluded that because the cylinder "barrels out" during heating, the axial compressive stress is reduced resulting in higher critical temperatures than is predicted by linear buckling theory.

Hoff (1965) and Ross (1966) also investigated the use of simple models to explain thermal buckling of shells. Hoff uses a two bar mechanism with a nonlinear spring, and Ross uses a beam-column with a nonlinear spring.

Gellatly, Bijlaard, and Gallagher (1965) investigated thermal buckling of sandwich cylindrical shells for simply and clamped supports. Using the approach of Hoff (1957b), critical buckling temperatures were determined for circumferential stresses varying with x. Numerical results are presented for isotropic and sandwich cylinders.

By the late 1960s and early 1970s, digital computers had become widely used in engineering research, and numerical models were being developed to solve complex problems. Chang and Card (1970,1971) at NASA Langley developed programs for analyzing thermal buckling of orthotropic, multilayered, cylindrical shells stiffened by uniform, equally spaced rings and stringers. Thermal effects are accounted for by specifying axisymmetric temperature distributions in the shell and stiffeners. The theory was developed from strain energy expressions corresponding to nonlinear Donnell-von Kármán displacements, and equilibrium equations were derived by the principle of minimum potential energy. These equations were separated into equations governing axisymmetric prebuckling behavior and equations governing behavior at buckling. The ends of the stiffened cylinder were assumed to be free to expand longitudinally. In the analyses thermal buckling occurs as a consequence of circumferential compressive stresses (Fig 10) introduced by radial restraint at the boundaries (w = 0) and/or from restraints resulting from differences in expansion between the stiffeners and shell. The prebuckling and buckling solutions were based on finite difference discritizations of the shell equations. Thermal buckling behavior of unstiffened, ring-stiffened, stringer-stiffened and ring/stringer-stiffened shells were investigated. For unstiffened cylinders the numerical solutions were validated by comparisons with the analytical solutions of Hoff (1957b) and Sunakawa (1962). Recall that the Hoff analysis (1957b) of a simply supported cylinder under hoop stresses varying in the x direction predicted buckling at a very high temperature. Chang and Card's computer analysis of the same cylinder was unable to determine this critical buckling temperature; no buckling temperature could be found within a practical temperature range. The difference between the two analyses was determined to lie in the assumptions made in the linearized Donnell prebuckling equations employed by Hoff where rotations and derivatives of rotations are neglected. These prebuckling rotations were included in the Chang and Card formulation, but when these terms were suppressed the Chang and Card predictions were in agreement with Hoff. The conclusion was that the prebuckling rotations are required, and for simple supports the buckling temperature is beyond the elastic range. Chang and Card's predictions were in good agreement with Sunakawa's analysis for a clamped cylinder since Sunakawa's shell theory included prebuckling rotations. For ring-stiffened cylinders comparisons were made successfully with Anderson's analysis (1962b). Thermal buckling studies of an aluminum large diameter, longitudinally stiffened cylinder and a titanium ring- and stringer-stiffened cylinder were also conducted.

At about the same time, Bushnell of the Lockheed Palo Alto Research Laboratory was developing a computer program called BOSOR for the general analysis of shells of revolution. Applications of BOSOR to thermal buckling are described in a book (1989) and several papers (1971a, b, 1973). The BOSOR program is based on an energy formulation with the method of finite differences. Axisymmetric ring-stiffened shells are assumed. The program has been used to solve several of the thermal buckling problems discussed previously and other, more complex, thermal buckling problems. Bushnell (1971a) solves the Hoff (1957b) problem of the simply supported cylinder subjected to a uniform temperature rise. Buckling of a ring-stiffened aluminum cylinder subjected to axial compression, external pressure and various temperature distributions is also studied in detail. The effect of ring-out-of-plane bending stiffness on thermal buckling of ring-stiffened cylinders is discussed by Bushnell (1971b) and demonstrated to be important.

Bushnell and Smith (1971) describe calculations of thermal stresses and buckling of nonuniformly heated cylinders and cones. The BOSOR program was used to analyze several cylinder tests including the studies of Hill (1959), Anderson and Card (1962), Ross, Mayers and Jaworski (1965), as well as Ross, Hoff, and Horton (1966). These analyses are valuable because they represent the first systematic comparison of computational results with experimental data. In addition, the computational approach permitted issues to be addressed that previously had been intractable because of limitations of analytical methods. Particular attention was given to the effect of boundary conditions on predicted stress and critical temperatures. For example, the anomaly raised in the experimental study of Ross *et al* (1966) is attributed to undesired flexibility in the experimental boundary condition. The paper also concluded that for shells which are long compared to a "boundary layer $(ah)^{1/2}$", critical temperatures of uniformly heated monocoque cylinders and cones are as sensitive to initial imperfections as are critical axial loads.

In a later paper, Bushnell (1973) uses BOSOR to study thermal buckling of cylinders with axisymmetric thermal discontinuities. The first problem considered was buckling of a cylinder heated halfway along its length. The problem was considered because of questions raised by the Hoff (1957b) problem of thermal buckling due to circumferential stresses. Bushnell reaches the same conclusions that Chang and Card; prebuckling rotations should be included in the analysis, and elastic buckling will not occur for the simply supported cylinder with uniform temperature. The second problem considered was a clamped cylindrical shell (a/h = 2540) analyzed and tested by Johns (1962). A BOSOR analysis (with prebuckling rotations) of the Johns' cylinder predicted a critical temperature of 150°C whereas the experimental value was 324°C. Subsequent investigation showed that the large discrepancy between the computation and test could be explained by the presence of temperature gradients near the boundaries of the cylinder. The paper concludes that critical buckling temperature calculations are sensitive to the shape of the temperature distribution. To obtain good correlation between predictions and tests, temperature distributions have to be measured carefully and the spatial variations included in the analysis.

Two papers in the mid-1970s analyzed thermal buckling of orthotropic cylindrical shells. Gupta and Wang (1973) use a Rayleigh-Ritz approach to analyze a simply-supported orthotropic shell with uniform temperature. Prebuckling rotations are not considered. Parametric studies illustrate the effects of the axial and circumferential coefficients of thermal expansion. Radhamohan and Venkataramana (1975) analyze an orthotropic clamped cylindrical shell using an approach based on Sanders' nonlinear shell theory. Effects of prebuckling rotations, different forms of clamped boundary conditions and other parameters are studied.

A brief paper by Belov (1978) describes an experimental study of stability of cylindrical shells partially filled with liquid. The study was motivated by aerodynamic heating of fuel tanks. In the experimental program, cylindrical shells were subjected to heating and were loaded by axial compression and internal pressure.

Although good agreement between calculations and experiment data is stated, details of the analysis and tests are not given.

In the late 1970s, two test programs on buckling of cylinders with combined mechanical and thermal loads were conducted at the Technion in Israel. Frum and Baruch (1976) describe buckling of cylindrical shells heated along two opposite generators. A series of forty-six tests of aluminum cylinders with a/h = 301 were conducted. End supports were designed to be fully restrained. Axial loads were applied by a hydraulic jack. Two infrared line heaters were installed above and below the shell. The temperature distribution was measured with thermocouples, and displacements were measured with LVDTs. The instant of buckling was detected with a microphone. The effects of the u displacement boundary conditions were studied, and the authors conclude that previous investigators had not treated the condition with enough care. They conclude that the u displacement has a dominant influence on the buckling results. Comparisons of experimental data with computations are only fair. The experimental data was used to construct an axial load-temperature interaction curve. Ari-Gur, Baruch and Singer (1979) describe buckling of cylindrical shells under combined axial preload, nonuniform heating and torque. Similar test cylinders and the test rig employed in the previous study were used after modifications to allow torsion. A series of 35 tests were conducted. A temperature-torque interaction curve was developed from the experimental data.

Studies of thermal buckling of laminated composite circular cylinders began in the 1980s and continue to the present time. So far, the studies have been analytical; experimental studies have not yet been conducted. Wilcox and Ma (1989) use an energy approach to derive a set of equilibrium equations based on classical thin shell theory with Donnell's assumptions. Galerkin's method with an assumed trigonometric variation for w for a simply-supported cylinder leads to a matrix eigenvalue problem. Numerical results are presented for critical buckling temperatures for various composite parameters such as lamination angle. Thangaratnam *et al* (1990) uses the finite element method to conduct parameter studies of a simply supported cylinder with uniform temperature.

Birman (1991) studied the thermally induced dynamic response of reinforced composite cylinders. The study is based upon Donnell's theory of geometrically nonlinear shells and includes axial and ring stiffeners. Solutions are developed for a simply supported cylinder subjected to a uniform rise in temperature. The paper concludes that if a shell is subject to an instantaneous rise in temperature it exhibits stable steady-state oscillations but if the temperature exceeds a critical buckling level, the character of the response [illegible]es and the deflections can increase dramatically.

4.3 Conical Shells

Work on thermal buckling of conical shells began in the mid-1960s and was motivated by aerodynamic heating effects. The analyses typically were based on Donnell-type equations written in terms of a stress function F and the w displacement. A truncated cone with vertex angle 2α is considered. The non-zero stresses are defined in terms of the Airy stress function $F(s, \phi)$ where a point on the middle surface of the shell is defined by the longitudinal coordinate σ and an angular coordinate ϕ defined by

$$\phi = \theta \sin \alpha$$

where θ is the circumferential angular coordinate. The non-zero stresses are

$$\sigma_s = \frac{1}{s}\frac{\partial F}{\partial s} + \frac{1}{s^2}\frac{\partial^2 F}{\partial \phi^2} \qquad \sigma_\theta = \frac{\partial^2 F}{\partial s^2}$$

$$\sigma_{s\theta} = -\frac{1}{\partial s}\left(\frac{1}{s}\frac{\partial F}{\partial \phi}\right) \tag{23}$$

The nonlinear governing equations are

$$\nabla^4 F = E\left[-\frac{1}{s}\left(\cot\alpha + \frac{\partial w}{\partial s} + \frac{1}{s}\frac{\partial^2 w}{\partial \phi^2}\right)\frac{\partial^2 w}{\partial s^2} + \frac{1}{s^2}\left(\frac{\partial^2 w}{\partial s \partial \phi} - \frac{1}{s}\frac{\partial w}{\partial \phi}\right)^2\right] - E\alpha\nabla^2 T \tag{24}$$

$$D\nabla^4 w = h\left[\left(\frac{1}{s}\frac{\partial F}{\partial s} + \frac{1}{s^2}\frac{\partial^2 F}{\partial \phi^2}\right)\frac{\partial^2 w}{\partial s^2} + \frac{1}{s}\left(\cot\alpha + \frac{\partial w}{\partial s} + \frac{1}{s}\frac{\partial^2 w}{\partial \phi^2}\right)\frac{\partial^2 F}{\partial s^2} - 2\frac{\partial}{\partial s}\left(\frac{1}{s}\frac{\partial F}{\partial \phi}\right)\frac{\partial}{\partial s}\left(\frac{1}{s}\frac{\partial w}{\partial \phi}\right)\right] \tag{25}$$

where

$$\nabla^2 = \frac{\partial^2}{\partial s^2} + \frac{1}{s}\frac{\partial}{\partial s} + \frac{1}{s^2}\frac{\partial^2}{\partial \phi^2} \tag{26}$$

In the above, the temperature is assumed uniform through the thickness of the shell, and the thermal moment is zero. For $\alpha = 0$, Eqs 24 and 25 reduce to the von Kármán equations for a flat circular plate.

Some of the earliest analytical and experimental work on conical shells was done by Bendavid and Singer (1967) who studied buckling of truncated conical shells heated along a generator. The work is closely related to Hill's (1959) study of buckling of thin cylindrical shells heated along a strip. Critical buckling temperatures are investigated for axial compressive stresses induced by circumferential temperature distributions. A Rayleigh-Ritz analysis is employed, and numerical results are compared with an experimental study. In the experimental study a steel cone with vertex angle α = 12.4°, thickness h = 0.0155 in and a small opening radius of 6 in was heated along a generator with a quartz lamp.

The experimental temperature distribution varied both in the circumferential and axial directions. Boundary conditions are assumed simply supported, and the ends are assumed restrained in the direction of the generator. The experimental buckling temperature was 103°C and the calculated value was 137°C.

Lu and Chang (1967) calculated thermal stresses and bifurcation buckling temperatures of axisymmetrical and nonsymmetrically heated simply-supported cones. In the axisymmetric case, the temperature varies along the generator which is restrained at the ends. In the other case, the temperature varies circumferentially as well, but the shell is assumed free of axial forces at the ends. A formulation similar to Eqs 24-25 is used, but the nonlinear von Kármán strains are neglected. A Galerkin approach with assumed deflection shapes is used to obtain critical temperatures. The variation of critical temperatures with various shell parameters such as the average radius-thickness ratio, the average radius-height ratio and the cone's vertex angle are evaluated. The radius-thickness ratio has the most significant effect on the critical temperature. In further work, Chang and Lu (1968) included the nonlinear strain terms neglected in their previous paper. The analysis showed that the nonlinear theory predicted lower critical temperatures than the linear theory. A brief discussion is given of an experimental study of a brass cone heated uniformly by heat lamps. The experimental cone had vertex angle $\alpha = 10°$, an average radius to thickness ratio of 500 and a height to average radius ratio of 2. The ends of the cone were assumed simply-supported but restrained against axial expansion. The average experimental buckling temperature for three tests was 128°F, and the predicted value was 98°F.

Bushnell and Smith (1971) used the computer program BOSOR to analyze thermal buckling of conical shell experiments performed by Smith (1964) at Stanford University. Truncated steel conical shells with clamped ends restrained against axial displacement were heated along axial strips of various widths by quartz lamps. Test cones have a wall thickness of 0.0155 in, a small opening radius of 6 in, a large opening radius of 12 in and a slant length of 28 in. Circumferential and axial temperature variations were induced and measured with thermocouples. The instant of buckling was determined by a microphone; buckling occurred with a loud noise. Critical buckling temperatures for eight test specimens varied from about 55°C to over 100°C; the scatter in the data was attributed to initial imperfections in the test specimens. In the analyses, a test was modeled in three ways: as a fully clamped shell, as a simply supported shell, and as a portion of a larger structure which includes the test rig. Using measured critical temperature distributions, axial membrane stress distributions were computed for the three models. Treatment of the test rig as a structure of finite flexibility led to results that were with 5% of those obtained with the assumption that the test rig is rigid. In the stability analysis, the meridional prebuckling membrane stress distribution was assumed to be axisymmetric. Depending on the experimental temperature distribution used, the discrepancy between test and theory for critical temperatures was from 11% to 52%.

Tani (1978) studied the effect of axisymmetric initial deflections on the thermal buckling of shallow, truncated conical shells under uniform heating. The shell is analyzed for two cases where the supports are assumed clamped but may be either constrained or free in the axial direction. A uniform temperature distribution is assumed. Nonlinear buckling equations based on Eqs 17-18 are modified to include initial shell deformations. A central finite difference scheme is used to discritize the equations in the s direction with a cos nq expansion in the circumferential coordinate. Numerical results show that the buckling temperature and number n of circumferential buckling waves of shallow cones with axial constraint vary significantly with the amplitude of axisymmetric initial deflections. Without axial restraint, the initial imperfections have only small effects on the buckling mode. Initial deflection amplitudes equal to plus or minus the shell thickness were studied. In shallow shells, local buckling occurred near the cone edges due to hoop compression. In a further study Tani (1984) analyzed instability of truncated conical shells under combined uniform pressure and uniform temperature. Following the approach of the previous paper, the Donnell-type shell equations with nonlinear prebuckling deflections are solved using a finite difference method. Numerical results show that for shallow conical shells, the critical combination of buckling loads changes with the loading order; for deep conical shells, the critical combination of buckling loads does not change with loading order. Generally, the critical buckling temperature increases with internal pressure.

4.4 Assessment

In the 1950s and 1960s, there was significant research on thermal buckling of metallic shells as aerodynamic heating became important in the design of supersonic aircraft and missiles. Since then, research in thermal buckling of metallic shells has diminished. Beginning in the 1970s, there has been significant growth in the research efforts devoted to thermal buckling of composites. Figure 12 shows a bar graph illustrating the relative research efforts devoted to thermal buckling of metallics and composites as measured by published papers. In the 1990s thermal buckling research so far has been devoted exclusively to composites.

Table II

Experimental Studies of Thermal Buckling of Shells

Cylindrical Experiments	Year	Materials	Loading
1. Hill	1959	Aluminum and steel	Heating Along an Axial Strip
2. Johns	1962	Steel	Axisymmetric Heating
3. Anderson and Card	1962	Stainless steel	Bending Moment and Non-uniform Heating
4. Ross, Mayers and Jaworski	1965	Stainless and cold-rolled steel	Heating Along Axial Strip
5. Ross, Hoff and Horton	1966	Stainless and cold-rolled steel	Heating Along Axial Strip
6. Frum and Baruch	1976	Aluminum	Heated Along Two Opposite Generators and Axial Loads
7. Ari-Gur, Baruch and Singer	1979	Aluminum	Combined Axial Preload, Nonuniform Heating and Torque
Cone Experiments			
8. Smith	1964	Steel	Heating Along Axial Strip
9. Bendavid and Singer	1967	Steel	Heating Along Axial Strip

Since the original investigations of Hoff (1957), numerous investigators have studied thermal buckling of shells. Many of the studies have been analytical particularly through the 1950s-1960s, but since 1970 there has been increasing reliance on computational methods. Many of the computer programs such as BOSOR have used finite difference methods, but analyses of composite shells are using the finite element method. There was also an effort made through the 1950s-1970s to investigate thermal buckling of shells experimentally. Table II summarizes experimental studies for cylinders and cones. The vast majority of the experimental studies considered monocoque shells. With the exception of the study by Anderson and Card (1962), there have been no further investigations of stiffened shells. Experimental measurements were typically limited to a modest number of transducers. No data are available for initial imperfections, details of temperature distributions are lacking, and little documentation of post-buckling damage is available. Virtually no strain data was taken in the experiments because of strain gage limitations at elevated temperatures. Most experiments were conducted on steel or stainless steel. There is limited data available for aluminum, and no experiments have studied the buckling of titanium shells. Experimental studies of composite shells have not yet been published.

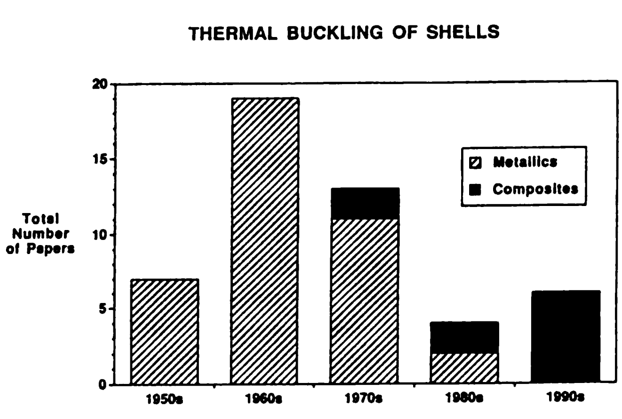

FIG 12 Relative number of papers on thermal buckling of metallic and composite shells.

Details of shell temperature distributions, particularly in stiffened shells, have an important role in the buckling response. The assumption of uniform temperature between stiffeners is usually not a good approximation. Since material properties such as thermal conductivity have significant effects upon the shape of temperature distributions, thermal buckling tests should be conducted using the materials that will be used in actual structures.

With one notable exception, there have been no validation studies of computer analyses of thermal buckling of shells. The exception is the very thorough analyses of several experiments by Bushnell using the computer code BOSOR. Generally, agreement between analytical solutions, computer solutions and experimental data has been only fair to good. A typical reason cited for discrepancies has been uncertainties in experimental boundary conditions. There have been relatively few tests with combined mechanical and thermal loads. For example, no tests of heated cylinders with internal pressures have been reported. There is a need for further experimental studies of thermally induced buckling of shells for both isotropic materials and laminated composites. Applications to aerospace structures strongly suggest the need for experimental programs for unstiffened and stiffened shells with thermal loads as well as combinations of thermal and mechanical loads.

5.0 CONCLUDING REMARKS

Thermal buckling research for plates and shells has been described. The role of material thermal parameters on thickness and spatial temperature gradients was demonstrated first. For metallic and metal matrix composites subjected to surface heating, thickness temperature gradients are small and may be neglected in applications. Indeed, this assumption has been made in most analytical and computational research studies, and it has been validated experimentally. Of the materials considered, only graphite-epoxy which has very low thermal conductivity exhibited an appreciable thickness temperature gradient. However, most materials, particularly in aerospace applications, will experience spatial (in-plane) temperature gradients. Due to localized heating, metals with relatively low thermal conductivity, *eg*, stainless steels, will exhibit high local temperature gradients and are likely to experience inelastic buckling. Metal panels with high thermal conductivity, *eg*, aluminum, tend to have much smaller temperature gradients as they conduct thermal energy to supporting structural members.

The review of research on thermal buckling of plates showed research in the 1950s-1960s was limited to metals. Composite plates were considered first in the 1970s, and since then the majority of research has been for composite plates. The majority of research in the last two decades has been analytical or computational with very few experimental studies. There is a need for further experimental studies of thermally induced buckling for both isotropic materials and laminated composites. Applications to aerospace structures strongly suggest that experimental programs be conducted for plates with spatial temperature variations.

The review of thermal buckling research for shells showed trends similar to thermal plate buckling. Research in the 1950s and 1960s considered only metallic shells. Research on composites began in the 1970s and has become the predominant effort since then. However, the current level of research on thermal buckling of composites is still relatively small compared to the efforts devoted to metallic shells in the 1960s. Many of the early shell thermal buckling studies were analytical, but since the 1970s there has been increasing reliance on computational methods. There was a significant early effort to study thermal shell buckling experimentally although there are deficiencies in the experiments, *eg*, the lack of strain data. Another deficiency has been uncertainties in experimental boundary conditions. So far, there have been no published experimental studies of thermal buckling of composite shells. There is a clear need for such studies for high temperature metallics such as titanium as well as for composite shells. There is also a need for experimental studies of heated cylinders (with and without stiffeners) subjected to mechanical loads including internal pressure. As with plates, the experimental programs should be conducted with spatial temperature distributions.

For both thermal buckling of plates and shells, renewed emphasis should be placed on validation of analytical/computational studies with experimental data. Computational analyses of several thermal-buckling experiments by Bushnell are described in the review. The lessons learned from these analyses include the uncertainties in boundary conditions previously mentioned as well as limitations and/or gaps in experimental data. On the other hand, such comparisons in the past have also identified deficiencies in computational models.

An interesting contrast between buckling due to mechanical and thermal loads is the respective roles of elastic material properties. Critical buckling forces for beams, plates and shells made from isotropic materials are directly proportional to the modulus of elasticity. Critical buckling temperatures for isotropic materials are typically independent of the modulus of elasticity and are inversely proportional to the coefficient of thermal expansion. Thus for optimum performance under combined mechanical and thermal loads, desirable material characteristics are high elastic modulus and low coefficient of thermal expansion. Of materials available, only advanced composites provide the potential for achieving such beneficial characteristics.

ACKNOWLEDGEMENTS

The research efforts of the author are supported in part by the Aerothermal loads Branch and the Aircraft Structures Branch at NASA Langley and the Light Thermal Structures Center at the University of Virginia. The author is most appreciative of the encouragement of his NASA technical monitors Drs Allan R Wieting and James H Starnes, Jr. The author is also grateful for very helpful discussions with Dr Michael P Nemeth of the Aircraft Structures Branch. Max L Blosser of the Aircraft Structures Branch provided important assistance in identifying and obtaining references and valuable discussion of past experimental studies.

REFERENCES

Abir, D, and Nardo, SV (1959). Thermal Buckling of Circular Cylindrical Shells Under Circumferential Temperature Gradients. *J Aero Sci*, 26, 803-808.

Ahmed, M, and Dillon, OW (1987). Thermal Stresses and Buckling of Elastic Plates with Reinforced Edges. *J Therm Stresses*. 10, 125-145.

Allen, DH (1991). Thermomechanical Coupling in Inelastic Solids. *Appl Mech Reviews*, 44(8), 361-373.

Anderson, MS (1962a). Combinations of Temperature and Axial Compression Required for Buckling of a Ring-Stiffened Cylinder. (NASA TN D-1224).

Anderson, MS (1962b). Thermal Buckling of Cylinders. *Collected Papers on Instability of Shell Structures-1962*. (NASA TN D-1510).

Anderson, MS, and Card, MF (1962). Buckling of Ring-Stiffened Cylinders Under a Pure Bending Moment and a Nonuniform Temperature Distribution. (NASA TN D-1513).

Ari-Gur, J, Baruch, M, and Singer, J (1979). Buckling of Cylindrical Shells Under Combined Axial Preload, Nonuniform Heating and Torque. *Exp Mech*, 19, 406-410.

Bargmann, HW (1985). Thermal Buckling of Elastic Plates. *J Therm Stresses*, 8, 71-98.

Bednarczyk, H, and Richter, M (1985). Buckling of Plates Due to Self-Equilibrated Thermal Stresses. *J Thermal Stresses*, 8, 139-152.

Belov, VK (1978). Experimental Study of Shell Stability Under Heating and Loading. *Soviet Aeronaut*, 21(1), 1-3.

Bendavid, D, and Singer, J (1967). Buckling of Conical Shells Heated along a Generator. *AIAA J* 5(9), 1710-1713.

Bijlaard, PP, and Gallagher, RH (1960). Elastic Instability of a Cylindrical Shell Under Arbitrary Circumferential Variation of Axial Stress. *J Aeronaut Sci*, 27(11), 854-859.

Birman, V (1990). Thermal Dynamic Problems of Reinforced Composite Cylinders. *J Appl Mech*, 57, 941-947.

Birman, V, and Hui, D (eds) (1990). *Thermal Effects on Structures and Materials*, AMD- 110. Papers presented at the Winter Annual Meeting of ASME, Dallas, TX, November 25-30, 1990.

Boley, BA, and Weiner, JH (1960). *Theory of Thermal Stresses*. : John Wiley. Currently available through Krieger Publishing, Malabar, Florida.

Bushnell, D (1971a). Analysis of Ring-Stiffened Shells of Revolution Under Combined Thermal and Mechanical Loading. *AIAA J* 9(3), 401-410.

Bushnell, D (1971b). Effect of Ring Out-of-Plane Bending Stiffness on Thermal Buckling Prediction for Ring-Stiffened Cylinders. *AIAA J*, 9(8), 1653-1654.

Bushnell, D (1973). Nonsymmetric Buckling of Cylinders with Axisymmetric Thermal Discontinuities. *AIAA J*, 11(9), 1292-1295.

Bushnell, D. (1989). Computerized Buckling Analysis of Shells. Kluwer Academic Publishers, 168-179.

Bushnell, D., and Smith, S. (1971). Stress and Buckling of Nonuniformly Heated Cylindrical and Conical Shells. *AIAA Journal*, 9(12), 2314-2321.

Carslaw, HS, and Jaeger, JC (1980). *Conduction of Heat in Solids*. (Second Edition),: Oxford at Clarendon.

Chandrashekhara, K (1991a). Buckling of Multilayered Composite Plates Under Uniform Temperature Field. V. Birman, and D. Hui (editors), *Thermal Effects on Structures and Materials*. New York: ASME, 29-33.

Chandrashekhara, K (1991b). Thermal Buckling of Anisotropic Laminated Cylindrically Curved Panels. *32nd AIAA/ASME/ASCE/AHS/ASC Structures, Structural Dynamics, and Materials Conference* Vol Paper No AIAA 91-0915-CP, 933-937.

Chang, J (1990). FEM Analysis of Buckling and Thermal Buckling of Antisymmetric Angle-Ply Laminates According to Transverse Shear and Normal Deformable High Order Displacement Theory. *Comput Struct*, 37(6), 925-946.

Chang, J, and Leu, S (1991). Thermal Buckling Analysis of Antisymmetric Angle-Ply Laminates Based on a Higher-Order Displacement Field. *Composites Sci and Tech*, 41, 109-128.

Chang, J, and Shiao, F (1990). Thermal Buckling Analysis of Isotropic and Composite Plates with a Hole. *J Thermal Stresses*, 13, 315-332.

Chang, LK, and Card, MF (1970). Thermal Buckling in Stiffened Cylindrical Shells. *AIAA/ASME 11th Structures, Structural Dynamics, and Materials Conference*. (pp 260-272). New York: AIAA.

Chang, LK., and Card, MF (1971). *Thermal Buckling Analysis for Stiffened Orthotropic Cylindrical Shells*. (NASA TN D-6332).

Chang, LK, and Lu, SY (1[illegible] [illegible]onlinear Thermal Elastic Buckling of Conical Shells. *Nu[illegible] [illegible]ng and Design* 7, (pp 159-169). Amsterdam: Nort[illegible]

Chen, L, Brunelle, EJ, and Chen, LY (1982). Thermal Buckling of Initially Stressed Thick Plates. *J Mech Des*, 104, 557-584.

Chen, LW, and Chen, LY (1987a). Thermal Buckling of Laminated Composite Plates. *J Thermal Stresses*, 10, 345-356.

Chen, LW, and Chen, LY (1987b). Thermal Buckling of Laminated Cylindrical Plates. *Composite Struct.*, 8, 189-206.

Chen, LW, and Chen, LY (1989a). Thermal Buckling Analysis of Composite Laminated Plates by the Finite-Element Method. *J Thermal Stresses*, 12, 41-56.

Chen, LW, and Chen, LY (1989b). Thermal Postbuckling Analysis of Laminated Composite Plates by the Finite Element Method. *Composite Structures*, 12, 257-270.

Chen, LW, and Chen, LY (1989c). Thermal Buckling Behavior of Laminated Composite Plates with Temperature-Dependent Properties. *Composite Structures*, 13, 275-287.

Chen, LW, and Chen, LY (1990). Thermal Buckling Analysis of Laminated Cylindrical Plates by the Finite Element Method. *Comput Struct*, 34(1), 71-78.

Chen, LW, and Chen, LY (1991). Thermal Postbuckling Behavior of Laminated Composite Plates with Temperature-Dependent Properties. *Composite Structures*, 19, 267-283.

Dechaumphai, P, Thornton, EA, and Wieting, AR (1989). Flow-Thermal-Structural Study of Aerodynamically Heated Leading Edges. *J Spacecraft and Rockets*, 26(4), 201-209.

Flagg, DI, and Vinson, JR (1978). Hygrothermal Effects on the Buckling of Laminated Composite Plates. *Fibre Sci and Tech*, 11, 353-365.

Forray, M, and Newman, M (1962a). On the Postbuckling Behavior of Rectangular Plates. *J Aerospace Sci*, 29, 754-755.

Forray, M, and Newman, M (1962b). The Postbuckling Analysis of Heated Rectangular Plates. *J Aerospace Sci*, 29, 1262.

Frum, Y, and Baruch, M (1976). Buckling of Cylindrical Shells Heated Along Two Opposite Generators Combined with Axial Compression. *Exp Mech*, 16(4), 133-139.

Gellatly, RA, Bijlaard, PP, and Gallagher, RH (1965). Thermal Stress and Instability of Sandwich Cylinders on Rigid Supports. *J Aircraft*, 2(1), 44-48.

Gossard, ML, Seide, P, and Roberts, WM (1952). *Thermal Buckling of Plates*. (NACA TN 2771).

Gupta, SD., and Wang, I (1973). Thermal Buckling of Orthotropic Cylindrical Shells. *Fibre Sci and Tech*, 6, 39-45.

Haydl, HM (1968). Elastic Buckling of Heated Doubly Curved Thin Shells. *Nucl Eng and Des* 7, (pp. 141-151). Amsterdam: North-Holland.

Heldenfels, RR, and Roberts, WM (1952). *Experimental and Theoretical Determination of Thermal Stresses in a Flat Plate*. (NACA TN 2769).

Hill, DW (1959). *Buckling of a Thin Circular Cylindrical Shell Heated Along an Axial Strip*. (AFOSR-TN-59-1250).

Hoff, NJ (1946). A Short History of the Development of Airplane Structures. *American Scientist*, 34(2 and 3), 212-225 and 370-388.

Hoff, NJ (1951). Structural Problems of Future Aircraft. *Proceedings of the Third Anglo-American Aeronautical Conference*, Brighton, England, 1951, September (pp 77-114). London: Royal Aeronautical Society.

Hoff, NJ (1956). Thermal Buckling of Supersonic Wing Panels. *J Aeronaut Sci*, 23(11), 1019-1028.

Hoff, NJ (1957a). Buckling at High Temperature. *J Royal Aeronaut Soc*, 61, 756-774.

Hoff, NJ (1957b). Buckling of Thin Cylindrical Shell Under Hoop Stresses Varying in Axial Direction. *J Appl Mech*, 24(3), 405-412.

Hoff, NJ (1965). A Nonlinear Model Study of the Thermal Buckling of Thin Elastic Shells. *J Appl Mech*, 32(1), 71-75.

Hoff, NJ (1967). Thin Shells in Aerospace Structures. *Astronaut and Aeronaut*, 5(2), 26-45.

Hoff, NJ, Chao, C, and Madsen, WA (1964). Buckling of a Thin-Walled Circular Cylindrical Shell Heated Along an Axial Strip. *J Appl Mech*, 31(2), 253-258.

Hoff, NJ, and Ross, B (1967). A New Solution of the Buckling Problem of Thin Circular Cylindrical Shells Heated Along an Axial Strip. B Broberg, J Hult, and F Niordson (eds.), *Recent Progress in Applied Mechanics: The Folke Odqvist Volume*, (pp. 251-271). New York: John Wiley and Sons.

Huang, NN, and Tauchert, TR (1988a). Large Deformation of Antisymmetric Angle-Ply Laminates Resulting from Nonuniform Temperature Loadings. *J Thermal Stresses*, 11, 187-197.

Huang, NN, and Tauchert, TR (1988b). Postbuckling Response of Antisymmetric Angle-Ply Laminates to Uniform Temperature Loading. *Acta Mech*, 72, 173-183.

Huang, NN, and Tauchert, TR (1990). Thermal Buckling of Clamped Symmetric Laminated Plates. *Impact and Buckling of Structures Vol* ASME AD-V20, AMD-V114, (53-59).

Huang, NN, and Tauchert, TR (1991). Large Deflections of Laminated Cylindrical and Doubly-Curved Panels Under Thermal Loading. *Comput Struct*, 41(2), 303-312.

Huebner, KH, and Thornton, EA (1982). *The Finite Element Method for Engineers* (Second Edition).: John Wiley.

Johns, DJ (1959). Comments on 'Thermal Buckling of Clamped Cylindrical Shells'. *J Aeronaut Sci* (Reader's Forum), 26(1), 59.

Johns, D. J. (1962). Local Circumferential Buckling of Thin Circular Cylindrical Shells. *Collected Papers on Instability of Shell Structures-1962*. (NASA TN D-1510).

Johns, DJ (1965). *Thermal Stress Analysis*. London: Pergamon.

Jones, R, Mazumdar, J, and Chung, YK (1980). Vibration and Buckling of Plates at Elevated Temperatures. *Int J Solids Struct*, 16, 61-70.

Kamiya, N (1978). An Approximate Approach to Nonlinear Thermal Bending of Shallow Sandwich Shells and Flat Plates. *J Thermal Stresses*, 1, 87-97.

Kamiya, N, and Fukui, A (1982). Finite Deflection and Postbuckling Behavior of Heated Rectangular Plates with Temperature-Dependent Properties. *Nucl Eng and Des*, 72, 415-420.

Keene, FW, and Hetnarski, RB (1990). Bibliography on Thermal Stresses in Shells. *J Thermal Stresses*, 13(4), 341-545.

Klosner, JM, and Forray, MJ (1958). Buckling of Simply Supported Plates Under Arbitrary Symmetrical Temperature Distributions. *J Aeronaut Sci*, 181-184.

Kossira, H, and Haupt, M (1991). Buckling of Laminated Plates and Cylindrical Shells Subjected to Combined Thermal and Mechanical Loads. JF Jullien (editor), *Buckling of Shell Structures, On Land, in the Sea and in the Air*. (pp 201-212). New York: Elsevier Applied Science.

Librescu, L, and Souza, MA (1991). Postbuckling Behavior of Shear Deformable Flat Panels under the Complex Action of Thermal and In-Plane Mechanical Loadings. *32nd AIAA/ASME/ASCE/AHS/ASC Structures, Structural Dynamics and Materials Conference*. Baltimore, MD (AIAA 91-0913).

Liu, RH (1983). Non-Linear Thermal Stability of Bimetallic Shallow Shells of Revolution. *Int J Non-Linear Mech*, 18(5), 409-429.

Lu, SY, and Chang, LK (1967). Thermal Buckling of Conical Shells. *AIAA Journal*, 5(10), 1877-1882.

Lukasiewicz, SA (1989). Thermal Stresses in Shells. R. Hetnarski (editor), *Thermal Stresses III*, (355-553). Elsevier Science Publishers.

Mahayni, MA (1966). Thermal Buckling of Shallow Shells. *Int J Solids Struct*, 2, 167-180.

Matsumoto, E (1973). Thermal Buckling Analysis of Parallelogram Panels Subjected to Heating. *Theoretical and Applied Mechanics: Proceedings of the 23rd Japan National Congress for Applied Mechanics*, (69-81).

Meyers, CA, and Hyer, MW (1991). Thermal Buckling and Postbuckling of Symmetrically Laminated Composite Plates. *J Thermal Stresses*, 14, 519-540.

Miura, K (1961). Thermal Buckling of Rectangular Plates. *J Aerospace Sci*, 28, 341-342. See also "Thermal Buckling of Rectangular Plates" by K Miura, Aeronautical Research Institute, University of Tokyo, Report No 53, Vol 26, No 4, May 1960, pp 51-75.

Noor, AK, and Burton, WS (1992). Computational Models for High Temperature Multilayered Composite Plates and Shells. *Appl Mech Reviews*, 45(10), 419-445.

Noor, AK, and Peters, JM (1992a). Postbuckling of Multilayered Composite Plates Subjected to Combined Axial and Thermal Loads. EA Thornton (editor), *Thermal Structures and Materials for High Speed Flight, Progress in Astronaut and Aeronaut*. AIAA, 183-203.

Noor, AK, and Peters, JM (1992b). Thermal Postbuckling of Thin-Walled Composite Stiffeners. *Comput Syst in Eng*, 2(1), 1-15.

Noor, AK, Starnes, JH, and Peters, JM (1992). Thermomechanical Buckling and Postbuckling of Multilayered Composite Panels. *33rd AIAA/ASME/ASCE/AHS/ASC Structures, Structural Dynamics and Materials Conference* Vol AIAA 92-2541, Dallas, TX, 1992, April 13.

Paley, M, and Aboudi, J (1991). Inelastic Thermal Buckling of Metal Matrix Laminated Plates. *J Thermal Stresses*, 14, 479-497.

Paul, DB (1982). *Large Deflections of Clamped Rectangular Plates with Arbitrary Temperature Distributions*. Flight Dynamics Lab, Air Force Wright Aeronautical Labs (AFWAL-TR-81-3003).

Poleski, SP, Dechaumphai, P, Glass, CE, and Pandey, AK (1992). Three-Dimensional Thermal-Structural Analysis of a Swept Cowl Leading Edge Subjected to Skewed Shock-Shock Interference Heating. *J Thermophys and Heat Transfer*, 6(1), 48-54.

Prabhu, MSS, and Durvasula, S (1974a). Elastic Stability of Thermally Stressed Clamped-Clamped Skew Plates. *J Appl. Mech*, 96, 820-821.

Prabhu, MSS, and Durvasula, S (1974b). Thermal Buckling of Restrained Skew Plates. *J Eng Mech Div*, Proc ASCE, 100, 1292-1295.

Prabhu, MSS, and Durvasula, S (1976). Thermal Post-Buckling Characteristics of Clamped Skew Plates. *Comput Struct*, 6, 177-185.

Przemieniecki, JS (1959). Thermal Stresses in Rectangular Plates. *Aeronaut Quart*, 65-78.

Radhamohan, SK, and Venkataramana, J (1975). Thermal Buckling of Orthotropic Cylindrical Shells. *AIAA J*, 13(3), 397-399.

Rao, KR, and Johns, DJ (1961). Some Thermal Stress Analyses for Rectangular Plates. *J Aeronaut Soc of India*, 13(4), 99-104.

Ross, B (1966). An Analog Study of the Thermal Buckling Behavior of Thin Cylindrical Shells. *AIAA J*, 4(8), 1437-1439.

Ross, B, Hoff, NJ, and Horton, WH (1966). The Buckling Behavior of Uniformly Heated Thin Circular Cylindrical Shells. *Exp Mech*, 6(11), 529-537.

Ross, B, Mayers, J, and Jaworski, A (1965). Buckling of Thin Cylindrical Shells Heated Along an Axial Strip. *Exp Mech*, 5(8), 247-256.

Schuh, H (1965). *Heat Transmission in Structures* Pergamon Press.

Smith, S (1964). *An Experimental Investigation of the Thermal Buckling of Conical Shells*. Unpublished doctoral dissertation, Stanford University,

Sun, LX, and Hsu, TR (1990). Thermal Buckling of Laminated Composite Plates with Transverse Shear Deformation. *Comput Struct*, 36(5), 883-889.

Sunakawa, M (1962). *Deformation and Buckling of Cylindrical Shells Subjected to Heating*. Univ. Tokyo: Aero. Res. Inst. (Rep. 370).

Tani, J (1978). Influence of Axisymmetric Initial Deflections on the Thermal Buckling of Truncated Conical Shells. *Nucl Eng and Des 48*, (pp. 393-403). Amsterdam, North-Holland.

Tani, J (1984). Buckling of Truncated Conical Shells Under Combined Pressure and Heating. *J Thermal Stresses*, 7, 307-316.

Tauchert, TR (1987). Thermal Buckling of Thick Antisymmetric Angle-Ply Laminates. *J Thermal Stresses*, 10, 113-124.

Tauchert, TR (1991). Thermally Induced Flexure, Buckling, and Vibration of Plates. *Appl Mech Rev*, 44(8), 347-360.

Tauchert, TR, and Huang, NN (1987). Thermal Buckling of Symmetric Angle-ply Laminated Plates. IH Marshall (editor), *Composite Structures 4 (4th ICCS)*, Paisley, Scotland. London: Elsevier, 1.424-1.435.

Teare, WP, and Fields, RA (1992). Buckling Analysis and Test Correlation of High Temperature Structural Panels. EA Thornton (editor), *Thermal Structures and Materials for High Speed Flight, Progress in Astronaut and Aeronaut* (pp 337-352).

Thangaratnam, KR, Palaninathan, and Ramachandran, J (1989). Thermal Buckling of Composite Laminated Plates. *Comput Struct*, 32(5), 1117-1124.

Thangaratnam, RK, Palaninathan, R, and Ramachandran, J (1990). Thermal Buckling of Laminated Composite Shells. *AIAA J*, 28(5), 859-860.

Thornton, EA, and Paul, DB (1985). Thermal-Structural Analysis of Large Space Structures: An Assessment of Recent Advances. *J Spacecraft and Rockets*, 22(4), 385-393.

Thornton, EA, Oden, JT, Tworzydlo, WW, and Youn, SK (1990). Thermo-Viscoplastic Analysis of Hypersonic Structures Subjected to Severe Aerodynamic Heating. *J Aircraft*, 27(9), 826-835.

Thornton, EA, and Kolenski, JD (1991). Viscoplastic Response of Structures with Intense Local Heating. *32nd AIAA/ASME/ASCE/AHS/ASC Structures, Structural Dynamics and Materials Conference*, Baltimore, MD, April 8, 1991, AIAA 91-1149.

Thornton, EA (1992). Thermal Structures: Four Decades of Progress. *J Aircraft*, 29(3), 485-498.

Thornton, EA, Kolenski, JD, and Marino, RP, Finite Element Study of Plate Buckling Induced by Spatial Temperature Gradients. (1993). *AIAA/ASME/ASCE/AHS/ASC 34th Structures, Structural Dynamics and Materials Conference*, April 19, 1993, AIAA Paper No 93-1572.

Timoshenko, S, and Gere, JS (1961). *Theory of Elastic Stability* (Second Edition).: McGraw-Hill.

Tsu-tao, L, De-yao, N, Han-dong, L, Wi-wen, L, and Jian-xun, S (1966). Thermal Snap-Through Buckling of a Bimetallic Shallow Spherical Shell. *Acta Mech Sinica*, 9(1), 1-14.

van der Neut, A (1957). Buckling Stresses Caused by Thermal Stresses. Nicholas J Hoff, *High Temperature Effects on Aircraft Structures*. New York: Pergamon, 215-247.

Whitney, JM (1987). *Structural Analysis of Laminated Anisotropic Plates*. Technomic Publishing, Lancaster, PA.

Whitney, JM, and Ashton, JE (1971). Effect of Environment on the Elastic Response of Layered Composite Plates. *AIAA J*, 9(9), 1708-1713.

Wilcox, MW, and Clemmer, LE (1964). Large Deflection Analysis of Heated Plates. *J Eng Mech Div: Proceedings of the American Society of Civil Engineers*, 165-189.
Wilcox, MW., and Ma, S (1989). Thermal Buckling of Antisymmetric Angle-Ply Composite Circular Cylindrical Shells. *30th AIAA/ASME/ASCE/AHS/ASC Structures, Structural Dynamics and Materials Conference Vol* AIAA Paper No 89-1172-CP,. 1989, April 3 (pp 113-120). Also Ma, S-F and Wilcox, MW, "Thermal Buckling of Antisymmetric Angle-Ply Laminated Cylindrical Shells." *Composite Eng*, Vol 1, No 3, 1991, pp 183-192.
Williams, HE (1979). On the Stability of the Postbuckling Behavior of Long Heated Rectangular Flat Plates. *J Thermal Stresses*, 2, 291-308.
Williams, HE (1982). 'Neale Plate' Equations and Applications to Buckling of Rectangular Plates. *J Thermal Stresses*, 5, 207-243.
Williams, ML (1955). Large Deflection Analysis for a Plate Strip Subjected to Normal Pressure and Heating. *Transactions of ASME*, 77, 458-464.
Williams, ML (1958). Further Large Deflection Analysis for a Plate Strip Subjected to Normal Pressure and Heating. *J Appl Mech*, 25, 251-258.
Wittrick, WH, Myers, DM, and Blunder, WR (1953). Stability of a Bimetallic Disk. *Quart J Mech and Appl Math*, 6(1), 15-31.
Ziegler, F, and Rammerstorfer, FG (1989). Thermoelastic Stability. R Hetnarski (editor), *Thermal Stresses III*, (pp 108-189). Elsevier Science Publishers.
Zuk, W (1957). Thermal Buckling of Clamped Cylindrical Shells. *J Aeronaut Sci*, 24(5), 389 (Reader's Forum).

Earl A Thornton is Professor of Aerospace Engineering and Director of the Center for Light Thermal Structures at the University of Virginia. He received his PhD in 1968 from Virginia Polytechnic Institute and State University. For over 20 years, he has conducted computational research for aerospace structures at elevated temperatures. He is co-author of the textbook The Finite Element Method for Engineers, *an Associate Fellow in the AIAA, and an Associate Editor of the* Journal of Spacecraft and Rockets.

BOOK REVIEWS

Items with a reviewer byline (coded R) are by AMR's corps of dedicated outside volunteer reviewers. AMR will attempt to get critical reviews of all relevant textbooks, professional books, reference works, and handbooks. Items without a reviewer byline (coded N) are prepared by AMR in-house staff and are largely based on material such as a book's table of contents and editor's preface or foreword. In the interest of timeliness most conference proceedings and multi-author contributed volumes will receive descriptive notes in this fashion. Books deemed to be somewhat peripheral to AMR's basic scope may simply be listed by title (no code; not included in annual index). Also listed by title when first received are books under review.

I. FOUNDATIONS & BASIC METHODS

10R1. Mechanics of Continuous Media. Mechanika osrodkow ciaglych. (Polish). - Czeslaw Rymarz *(Dept of Theory of Continuous Media, Polish Academy of Sci and WAT Military Academy of Tech, Warsaw, Poland)*. 1993. 514 pp. ISBN 83-01-11061-9.

Reviewed by R Wojnar (IPPT, Polish Acad of Sci, Swietokrzyska 21, 00-049 Warszawa, Poland).

Let me begin with some general remarks which arose in my mind after reading this excellent book.

It is well known that in describing a physical phenomenon one can use a number of mathematical models and each of the models only partially explains the phenomenon; eg, in quantum mechanics the nature of the light can be described either by an undulatory or a corpuscular model. Also, in classical continuum mechanics a wave equation describing sound propagation is patterned after the Newton equation of motion of a single particle, (see ch 3 of the reviewed book). These two examples indicate a degree to which one can describe a real phenomenon.

A description of matter was proposed a long time ago by the ancient philosophers Democritus (circa 460-370 BC) and Lucretius (circa 98-55)[1] from one point of view, and by Aristotle (384-322) from another standpoint. The first two thinkers believed that matter is composed of atoms and voids while the third one argued that nature abhors a vacuum. These philosophers stirred up a controversy in the subject that lasted until the beginning of this century. Nowadays we believe that matter is made of particles and fields, and the particles are regarded as some singularities associated with the fields.

The mechanics of continuous media that came into being in eighteenth century [2,3,4] is also based on the concept of a particle. Using contemporary language, this theory replaces a structure of particles (a granular structure) by a homogenized continuous constitution. One performs a smearing-out of material properties of microbodies to obtain the continuous distributions of mass, momentum, angular momentum, and energy of the continuous medium (cf Introduction of the reviewed book).

The book is based on lecture notes for classes taught at WAT (Technical Physics Dept) in Warsaw by Professor Rymarz, well known for his many contributions in the field of mechanics of continuous media. The book goes well beyond what can usually be covered in class and provides an in-depth introduction to several research topics.

There are 12 chapters, three appendices, references, and an index. Every chapter ends with problems and control exercises. The appendices cover tensor calculus, foundations of group theory, differential manifolds, and elements of measure theory.

Chapter 1 deals with dynamic processes in the material bodies. The mechanics of continuous media is treated as a theory describing a phenomenological model of reality. The concept of a material point (which should not be confused with that of atoms and molecules) is introduced, and the Euler and Lagrange descriptions of motion in terms of homeomorphisms are presented.

In chapter 2 a description of finite and infinitesimal deformations is given; also various types of derivatives of the displacement and velocity fields are defined; and a description of deformation in various reference frames is included. Moreover, the fundamental properties of a velocity field listed in the Helmholtz - Zorawski and Kelvin theorems are formulated. Schematic figures showing motion of a continuous medium in various descriptions are also included.

Chapter 3 introduces the laws of motion of a continuous medium, such as the laws of evolution and conservation laws; a variational formulation of these laws and principles is also given. Chapter 4 deals with the principles of classical thermodynamics, the theory of irreversible phenomena, and some modern theories of rational thermodynamics.

Chapter 5 considers classifications of constitutive equations and studies their properties. An apparatus of group theory is used and thermodynamical limitations are discussed. A principle on the principal strains and stresses in an isotropic medium due to Truesdall, Beaker, and Ericksen is also included. Chapter 6 deals with dimensional analysis and similitude theory. In such a theory, the problem of choice of a unit system is the most important one.

Chapter 7 covers fundamental and selected topics of classical fluid mechanics. Both ideal and viscous hydrostatics and hydrodynamics are discussed. Also, integrals of motion due to Bernoulli and Cauchy-Lagrange are given; and a curl theorem due to Helmholtz and a Bierknes theorem on the material derivative of circulation are obtained; the latter theorem is applied to investigate the whirl phenomena in an ocean or in the atmosphere.

In chapter 8 the elements of elasticity theory, both linear and nonlinear, local and non-local, are discussed. Emphasis is placed on wave problems; it is regretted that a stress formulation of linear elastodynamics is only mentioned, Eq (8.128) in the book and [5].

Chapter 9 takes up viscoelastic media; a comprehensive classification of non-Newtonian fluids and rheological materials is given. Also, the properties of polymers are at issue and non-classical effects in viscoelastic non-Newtonian fluids, such as the Poynting, Merrington, and Weissenberg effects are discussed.

Chapter 10 considers plastic bodies. Two groups of theories of an elastoplastic body are distinguished: flow theories and deformation theories. The postulates on stability and plasticity due to Drucker and Ilyushin, respectively, as well as hypotheses on the transformation of an elastic material into a plastic one are discussed. Also, the Levy - von Mises types of flow laws are discussed. Moreover, models of elasto-plastic and elasto-viscous plastic bodies, and associated limit problems are discussed.

Chapter 11 deals with the non-classical models of a continuous media. Special attention is paid to liquid crystals and to defects in solid bodies. The Kroener description (1960) of a dislocation in which the dislocation density represents a non-Euclidean character of space is discussed.

In chapter 12 the continuous media in which a process is produced by non-mechanical loads are dealt with. The effects of diffusion and heat transfer are discussed, and attention is paid to the influence of an electromagnetic field on continuous media. The Lorentz transformation is introduced, and materials with different kinds of susceptibility with regard to electric and magnetic fields (dielectrics, magnetics, ferromagnetics, conductors) are described. Emphasis is given to the interaction of electromagnetic fields with a condensed matter.

The bibliography contains 248 items; the American and European authors are quoted; the works of the Polish school of mechanics are emphasized (almost 1/3 of the items). The subject of thermoelasticity developed in well-known monographs by W Nowacki, cf [6], and of mechanics of stochastic media presented in several sources (eg K Sobczyk [7]).

The book under review is one complementary to other well-known books on continuum mechanics, [8], [9]. Polish students who have been studying from the book praise it as a useful reference in continuum mechanics theory.

Given the wealth of information and a systematic presentation of the subject, *Mechanics of Continuous Media* is highly recommended by this reviewer as a useful academic textbook and a reference book for an engineer and researcher. To make the book accessible to a wider range of students and researchers in the field, an English translation of the book would be beneficial.

References:

1) T Lucretius Carus, On the nature of things, i, 420, Bude series, Paris 1925;

2) L Euleri, Opera omnia, Lausannae 1911-1955;

3) C Truesdell, Essays in the history of mechanics, Springer, Berlin 1968;

4) S Timoshenko, History of strength of materials, Mc Graw-Hill, New York 1953;

5) J Ignaczak, A completeness problem for stress equations of motion in the linear elasticity theory, *Arch Mech Stos* 15, 225-234 (1963); also ME Gurtin, The linear theory of elasticity in S Fluegge's Handbuch der Physik Bd. VIa/2 Springer, Berlin 1972;

6) W Nowacki, Thermoelasticity, PWN;

7) Sobczyk K, Stochastic differential equations with applications to physics and engineering, Kluwer Acad Pub, Dortrecht 1991;

8) LD Landau and EM Lifshitz, Mechanics of continuous media (in Russ) Moskva 1954, *Fluid Mechanics* (in Engl transl);

9) W (A) Rubinowicz, Lectures in mechanics of continuous media (in Polish) PWN, Lodz - Warszawa 1959

10N2. Computational Mechanics-From Concepts to Computations, vol 1. Proceedings of the second Asian-Pacific conference on Computational Mechanics held in Sydney, New South Wales, from August 3-6, 1993.. - Edited by S Valliappan, VA Pulmano, F Tin-Loi *(Univ of New South Wales, Sydney, Australia)*. Balkema, Rotterdam, Netherlands. 1993. ISBN 90-5410-333-7.

Keynote papers include: Modeling in computational structural engineering: An overall view by ER de Arantes e Oliveira and J Bento; A FE analysis of shallow water flow with open boundary condition by T Kodama and M Kawahara; State vector method and symplectic eigensolutions of gyroscopic systems by W Zhong, J Zhu and J Lin; Evolutionary structural optimization with FEA by GP Steven and YM Xie.

Additional papers under the heading, Solid Mechanics, address the following: In elastic local buckling of plates using bubble functions; Harmonic by harmonic method for the postcritical computation of axisymmetric shells; A nonlinear fatigue strength assessment using FEM; Hybrid/mixed FEM for the analysis of metal forming processes; Application of time-domain BEM to elastodynamics analysis; Large deflections of a beam subjected to moment at one end; Analysis of circular cylindrical storage tanks resting on an elastic foundation; Spline finite point method for analysis of laminated composite plates and shells; Analysis of thick laminated composite plates; Transient analysis of plate bending problems by BEM; Shape analysis of unstable structures with constraint conditions; A simple FEM for free vibration of beams on elastic foundation; Stress analysis in a solid with rectangular holes; Estimation of maximum frequency for FE mesh; Computerized Rayleigh-Ritz method for elastic plate analyses; Numerical implementation of Lamb's solution to strip load on elastic half space; Numerical integration of nonlinear dynamic equations using the Newmark scheme; 3D flow with gross deformation of energy absorbing rubber; Local *a-posteriori* error estimates for incompatible elements; FE algorithm for 3D contact problems of turbomachinery blade attachments; A simple approach for cold rolling of foil; A four-node hybrid FE for the analysis of laminated plates; FE analysis of local buckling of a cracked and pin-loaded plate; Spline FE analysis of a butterfly shell roof; A FE algorithm for finite deformation contact problems; Viscoelastic finite strip analysis of folded plate structures; A study on problems of determining curved surface forms using geometrical stiffness; Multi-variable nonlinear quasi-conforming FEM; Fundamental study on nonlinear dynamics of elasto-plastic structures; Elastic contact FE analysis of spiral beval gear meshing; Diffracted acoustic field by rigid plane baffles using integral-equation method; Vibration analysis of a hot roughing mill during asymmetrical rolling; A general numerical method for some singular frictionless line contact problems; Simple analysis of axisymmetrically loaded shells by transfer matrix; Buckling characteristics of single-layer latticed domes; Development of new four node plate and eight node brick elements; A uniform approach to the calculation of eigenvectors; *Invited paper*: Lower and upper bounds for stability limits on geometrically nonlinear prebuckling paths; *Invited paper*: Nonlinear analysis of shells using flat facet FEs; Nonlinear dynamic analysis of flexible beams under large overall motions; FE analysis of orthotropic thick plates; A moderate thick shallow shell hybrid stress element with rational stress mode; An artificial compression method for contact discontinuities; Error estimates of h- and p-convergence in multi field FEs.

Papers under the heading Geomechanics include: Backward Euler and subincrementation schemes in computational plasticity; *Invited paper*: FE analysis for constitutive model with strain softening; Theoretical and numerical modeling of swelling phenomenon of rocks in tunnel excavations; FE analysis of steel grid reinforced embankment on soft Bangkok clay; A new model for nonlinear analysis of vibrating foundations on clays; Ground loss caused by tunnelling for Taipei mass rapid transit system; 3D areal analysis for land subsidence; Numerical analysis of deep excavation in Taipei; Application of spectral collocation method in geomechanics; *Invited paper*: Strain softening effects in the stability analysis of geotechnical problems; New technique of non-linear FE analysis for caisson foundation; *Invited paper*: Constitutive models in nonlinear computational procedures; Multi wedge stability analyses for layered soils; Mechanical behavior after excavation of undergournd space; 3D numerical simulation for dynamic soil-pile foundation-structure interaction; *Invited paper*: Homogenisation techniques for strain localization and interface analysis; Study on the group factor of pile groups; Numerical prediction of side resistance of axially loaded tapered piles; Generalized model for reinforced fill on soft clay; Simulation of stratified rock masses: The Cosserat laminated model; Screening effectiveness of soft in-filled trench using BEM; Bearing capacity of the reinforced soils by rigid plastic FE analysis; A modified Ramberg-Osgood power law; *Invited paper*: Back analysis of non-elastic behavior of soils and heavily-jointed rocks; Identification of coefficient of horizontal subgrade reaction by EK - WGI method; Shaft friction on piles in layered soil; Dynamic analysis of caissons under lateral loads; Discrete-mechanical formulation and simulation analysis of granular mateials; Splitting of rock medium with an explosive charge; Determination of maximum stress location under an arbitrary shaped foundation; A new prediction approach to geotechnical engineering problems; FE approach to lower and upper bound solutions of reinforced soils; and Numerical modeling of mining induced subsidence.

10N3. Computational Mechanics-From Concepts to Computations, vol 2. Proceedings of the second Asian-Pacific conference on Computational Mechanics, held in Sydney, Australia, August 3-6, 1993.. - Edited by S Valliappan, VA Pulmano, F Tin-Loi *(Univ of New South Wales, Sydney, Australia)*. Balkema, Rotterdam, Netherlands. 1993. ISBN 90-5410-333-7.

Topics of volume 2 include: Fracture and damage mechanics; Structural engineering; Optimization-parameter identification; Wave propagation; Earthquake engineering/vibrations; Mass transport/tidal current; Hydrodynamics; Biomechanics and Computational techniques.

Partial contents include: *Fracture and damage mechanics*--Computer experiment on defect accumulation for a llinear arrangement of 2D defects; Parametric variation of stress intensity factors for cracks in lugjoints; Fractal two level FEMs for 2D crack problems; *Invited paper*: 2D damage failure propagation model of jointed rock mass; Fractal analysis of crack distribution; Fraacture energy experiments of rock-concrete and its fractal analysis; *Invited paper*: A coupled seepage-damage analysis model for jointed rock masses; Detection of structual damage by vibration test and neural network techniques; Application of a post-yield crack algorithm; Thermorheological analysis of surface crack in semi-rigid pavements.

Partial structural engineering papers include: Modal coordinate analysis of reinforced concrete structures with local nonlinearity; Branching predictor in bifurcation of 2D elastic frames; Punching shear failure analysis of RC flat plates with spandrel beams by FEM; Developments in FE analysis of single bolted timber joints; FE modeling of horizontally nail-laminated wood beams; Crack analysis of RC structures including tension stiffening; Analysis of concrete structures by FEM-BEM superposition method; Evaluation of plastic deformability for steel beam-columns subjected to sidesway; Relationship between axial load and vibration frequency of plane trusses; Elasto-plastic behavior of reinforced concrete member under high temperature; Temperature distribution in a concrete box culvert using 3D FEM; Joint compatibility problems with the frame method; Optimum design of reinforced concrete shear walls; Ultimate analysis of cable-supported prestressed concrete frames; Knowledge-based approaches for concrete frame building structural design; Elastic lateral-torsional instability of thin-walled beams under the effect of shear; Buckling and post-buckling collapse analysis of space frame structures; Ultimate strength of RC columns of arbitrary cross-sections subjected to biaxial loading; Dynamic structural analysis with nonlinear material models based on internal variables; FE analysis of steel fiber concrete beams; and LCP formulation for large displacement elastoplastic analysis of semirigid frames.

10N4. Computational Methods and Experimental Measures VI, vol 1 (Heat and Fluid Flow) and vol 2 (Stress Analysis). - Edited by CA Brebbia *(Wessex IT, Southampton, UK)* and Carlomagno *(Univ of Naples, Italy)*. Comput Mech, Billerica MA. 1993. 1150 pp. ISBN 1-56252-152-7. $480.00. Info is for two-volume set.

These books contain the edited versions of the papers presented at the Sixth International Conference on Computational Methods and Experimental Measurements, which was held in Siena, Italy, May 3-5, 1993.

Computational methods and experimental measurements as tools applied to the solution of engineering problems share common aims and experiences, and their interaction should play an important and influential role in their respective paths of development. The need for a forum to bring the computational and experimental camps together prompted the establishment, more than 10 years ago, of the present series of conferences.

The books reflect the objectives of this series of conferences. State-of-the-art contributions by authors from many countries report innovative approaches in the fields of numerical methods and experimental studies with particular emphasis on their interaction and potential application to engineering problems.

Topics covered include: Experimental vs analytical or numerical models; Interaction of computer codes and experimental models; Material property characterization through numerical models and experimental prototypes.

10N5. Impact of Computational Mechanics on Engineering Problems. Proceedings of the Seminar on Impact of Computational Mechanics on Engineering Problems, held in Sydney, Australia, August 2, 1993.. - Edited by VA Pulmano and V Murti *(Univ of New South Wales, Australia)*. Balkema, Rotterdam, Netherlands. 1993. ISBN 90-5410-324-8.

Contents include: Solution difficulties in multi-wedge stability analyses; FE analysis of the artificial freezing of sand; A generalized material parameter identification procedure in geotechnical engineering; Fundamental study on in-situ fault traxial compression test of rock mass; Analogy between analysis of flow in pipe networks and slope-deflection in rigid frames; An efficient scheme for land subsidence and negative skin friction; Some applications of homogenization method in rock mechanics; Application of numerical modeling to consequence-of-sliding analysis; Recent advances on numerical analysis of interaction problems: The Australian scene; FEs in biomechanics: Some new developments; Development of a microscopic view traffic flow simulation model for expressway; An adaptive *hp*-FEM in frictional contact problems; FE analysis of steel fiber reinforced cement composites; Measures of fuzziness in FE geotechnical solutions; Computations of vertical soil stresses underneath foundations with curved boundary using parametric mapping technique; Field investigation of mechanical behavior of a shallow tunnel due to ground surface excavation; Complex number expression of 3D deviatoric tensor; Pollutant transport in deformable semi-saturated geomaterials; Design of rock bolts with numerical models; Hardening models: Some implications for elastoplastic analysis by mathematical programming; Fractal analysis on the fracture damage propagation of rock; Fatigue damage analysis of hammer foundation; and Numerical evaluation of bridge approach settlement.

Methods of Engineering Mathematics. - Edward Haug *(The Univ of Iowa IA)* and Kyung K Choi *(The Univ of Iowa)*. Prentice-Hall, Englewood Cliffs NJ. 1993. 575 pp. ISBN 0-13-579061-1. (Under review)

Optimal Control and the Calculus of Variations. - Enid R Pinch *(Math, Univ of Manchester, Manchester, UK)*. Oxford UP, New York. 1993. 232 pp. ISBN 0-19-853217-2. $49.95. (Under review)

II. DYNAMICS & VIBRATION

10N6. Civil Engineering Dynamics-Design, Analysis, Testing and Performance. Society for Earthquake and Civil Engineering Dynamics. - Telford, London. 1990. 506 pp. ISBN 0-86292-327-1. £65 UK and Europe.

This book deals with the design, analysis, testing and dynamic performance of existing or new structures, with special emphasis given to analysis design and test methods. Actual case histories illustrate the principles involved.

The structures considered include buildings, bridges, dams, nuclear power stations, chemical plants, and cable structures. Environmental loads provided by earthquakes and winds are covered, together with manmade vibration, explosion and impact loads. Dynamic testing at full and laboratory scale, and dynamic performance of real structures are given particular attention.

Impact and Explosion: Structural Analysis and Design. - MYH Bangash *(Middlesex Polytech, London, UK)*. CRC Press, Boca Raton FL. 1992. 880 pp. ISBN 0-8493-7742-0. $245.00. (Under review)

Modern Kinematics-Developments in the Last Forty Years. Wiley Series in Design Engineering. - Arthur G Erdman *(Univ of Minnesota MN)*. Wiley, New York. 1993. 604 pp. ISBN 0-471-55459-6. (Under review)

III. AUTOMATIC CONTROL

10R7. Controlled Markov Processes and Viscosity Solutions. - Wendell H Fleming *(Div of Appl Math, Brown Univ, Providence RI 02912)* and H Mete Soner *(Carnegie-Mellon Univ, Schenley Park, Pittsburgh PA 15213)*. Springer, New York. 1993. 428 pp. ISBN 0-387-97927-1.

Reviewed by Tamer Basar (Coordinated Sci Lab, Univ of Illinois, 1308 W Main St, Urbana IL 61801).

This book provides an introductory but exhaustive treatment of the optimal control of Markov processes with perfect state measurements and the viscosity solutions of the Hamilton-Jacobi-Bellman equations associated with the optimal value function.

The approach adopted in the book being that of dynamic programming, the authors first discuss (in chapter I) optimal control of deterministic processes, derivation of the dynamic programming equation for the associated optimal cost function, and its relationship with Pontryagin's maximum principle and the classical calculus of variations. What is emphasized in this chapter is that even though the value function can be shown to satisfy a first-order nonlinear partial differential equation (PDE) (the Hamilton-Jacobi-Bellman equation), it is generally not sufficiently smooth to be viewed as a classical solution of this PDE. What is shown, however -- and this is the topic of chapter II -- is that the value function can always be viewed as a weaker solution of the HJB PDE, interpreted in the viscosity sense. This weak solution (leading though to very strong results) is introduced in precise terms and in a general abstract framework in chapter II, and many of its appealing properties, such as existence, uniqueness, and smoothness are studied in detail for a large class of optimal control problems, including problems with state and control constraints, unbounded control sets, and finite and infinite horizons.

Following these two chapters, the rest of the book (seven chapters) has been devoted to stochastic control problems. Chapter III introduces Markov processes and their evolution operators. It discusses a formal derivation of dynamic programming (DP) equations, and a verification theorem (for the case when the DP equation admits a sufficiently smooth classical solution), in both finite and infinite horizons. These results are then strengthened in Chapter IV for the special case of controlled Markov diffusions in IR^n, in which case the DP equation is a parabolic HJB PDE. When this equation is uniformly parabolic, it admits a unique solution in the classical sense, but if it is not, one has to consider generalized solutions, which are studied carefully (by appropriate approximations and bounding techniques) in the second part of chapter IV. This naturally leads to the next chapter where the visocosity solutions of second-order nonlinear parabolic PDE's are studied and existence and uniqueness results are proven using some tools recently developed by R Jensen.

Chapters VI and VIII discuss extensions in different directions. The first of these deals with logarithmic transformations, which arise naturally when the backward evolution operator of a Markov process depends on some small parameter (say $\varepsilon > 0$), which shows structural change when $\varepsilon = 0$. One application is the "small noise" problem, which is studied in this chapter in some detail. Of particular importance is the derivation of asymptotic series for the solution of the perturbed ($\varepsilon > 0$) problem in terms of solutions and properties of the unperturbed ($\varepsilon = 0$) problem. The discussion of singularity is continued in chapter VII in the study of the convergence of a sequence of viscosity solutions of a perturbed PDE to the viscosity solution of the unperturbed (or equivalently, limiting) one. A recent approach due to Barles and Perthame that circumvents some mathematical difficulties associated with precompactness of the sequence in uniform topology is first presented, and then it is applied to the problem of vanishing viscosity and to a large deviations problem for exit probabilities, in which context an exponential convergence is established. The final chapter on singularities (Chapter VIII) deals with singular stochastic control problems, where the control is not necessarily continuous in time, but is generally of bounded variation. The authors first derive a DP equation for such problems, then prove a verification theorem and establish the viscosity property of the value function. The primary focus is on infinite-horizon problems with no absolutely continuous control, but also discussed is the "mixed" case, as it arises in an optimum portfolio selection problem with transaction costs.

The last chapter of the book (chapter IX) provides a brief introduction to numerical solutions of the HJB PDE. Here two approaches are covered: (1) a finite difference scheme due to H Kushner, applied to the value function of a controlled Markov diffusion on a finite horizon, and (2) approximations based on viscosity solutions. Chapter IX is followed by five appendices, giving some background results on optimization, stochastic processes and differential equations, and semiconvex functions.

As to be expected from the authors, *Controlled Markov Processes and Viscosity Solutions* has been written very competently, with deep mathematical results supported by intuitive explanations and supplemented by various simple but important applications. Because of recent interest in viscosity solutions in the field of nonlinear and robust control (as they arise in nonlinear "H^∞-optimal" control), the book should be of interest not only to researchers in stochastic control, but also those in nonlinear and robust control, and differential games.

10R8. Mechatronics: Electromechanics and Contromechanics. - Denny K Miu *(Dept of Mech, Aerospace and Nucl Eng, UCLA)*. Springer, New York. 1992. 232 pp. ISBN 0-387-97893-3.

Reviewed by Michael K Brown (Interactive Syst Res, Bell Labs, 600 Mountain Ave, Murray Hill NJ 07060).

In the preface, the author describes mechatronics as a field covering such diverse topics as mechanics, electronics, and information. This book, derived from class notes for a graduate course at UCLA, concentrates on the first two of these topics. A cursory examination of the table of contents reveals that the topics are developed from first principles of physics to an introductory level in continuum mechanics

The book contains 232 pages, a small index, and ten chapters. Most chapters have exercises and/or references, there are four appendices. Many of the figures appear to be hand drawn without the aid of a ruler but are clearly readable. After the introductory chapter 1, the remaining chapters are split into two parts entitled "Electromechanics" and "Contromechanics."

Part 1 begins chapter 2 which reviews Newton's second law and the basic physics of mechanical dynamics. Chapters 3 and 4 cover electrostatics, magnetostatics and electromagnetics. DC and stepper motors are introduced in chapter 5. The coverage in those first chapters is strictly at the undergraduate level. The depth of coverage is not great, but is sufficient for a basic introduction.

Chapter 6 breaks away from the classical topics and begins to explore newer territory in the area of piezoelastics. It starts with a description of an incremental linear motor called "inch-worm" motor, which can crawl along a cylindrical shaft by alternately expanding and contracting a set of piezoceramic elements. Other similar motors are described. Discussion continues with topics such as electrical and mechanical properties of piezomaterials, resonance, and electrical equivalent circuit models.

Part II starts with an introduction to linear time-invariant control theory in chapters 7 and 8. Chapter 8 also analyzes continuous and coupled dynamical systems. Chapter 9, "Residual Vibration," introduces principles of optimal control theory specifically aimed at minimization of vibration in point-to-point mechanical positioning. A technique called "Laplace domain synthesis" is described. The technique is applied with minimization of energy and jerk (temporal derivative of acceleration).

The topic returns to piezomaterials in the last chapter, which discusses active damping methods for controlling flexible structures. Active damping is achieved by laminating piezopolymer onto the controlled structures. Some discussions of the resulting kinematics and dynamics are given. This chapter is primarily an overview of the work of CK Lee.

Appendices A, B, and C cover physical units, vector calculus and tensors. Appendix D describes a real control system design for computer disk read-write head positioning. This is a detailed discussion including plots of system performance for a commercially designed system currently in use.

This textbook is probably best suited for teaching at the senior undergraduate or first-year graduate engineering level. Much of the book is written at a level suitable for review, but not sufficient for a first exposure to physics or control theory. Most of the chapters are devoted to this review of classical material. Only chapters 6 and 10, covering piezomaterials, introduce topics not usually found in other textbooks. Some uncommon material is also covered in chapters 8 and 9. *Mechatronics: Electromechanics and Contromechanics* is easy to read for someone familiar with the material covered, but is terse and perhaps difficult reading for a first introduction.

10R9. Rapid Automated Prototyping: An Introduction. - Lamont Wood *(San Antonio TX)*. Indust Press, New York. 1993. 140 pp. ISBN 0-8311-3047-4. $32.95.

Reviewed by Serope Kalpakjian (Mech & Aerospace Eng Dept, Illinois IT, 10 W 32nd St, Chicago IL 60616-3793).

Rapid prototyping, also known as desktop manufacturing or free-form fabrication, is a relatively new technology (since mid 1980s) by which a solid physical model of a part is made directly from a 3D CAD drawing. The time involved is far less than traditional prototyping methods. The process is coming into wide use particularly in the automotive, aerospace, and medical industries. Although equipment costs are substantial, ranging from about $100,000 to $500,000, the technology is particularly suitable for studying and analyzing the esthetic, technical, and functional (including assembly) aspects of product models prior to finalizing their design. In addition to numerous articles in trade magazines and papers in professional journals, books are now beginning to appear on this important subject. The stated purpose of this book by Wood is to provide the reader with full descriptions of each technique and the available hardware and software.

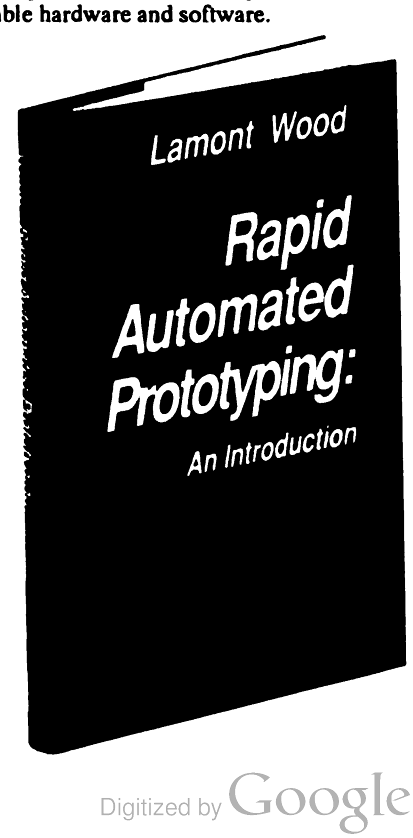

Rapid Automated Prototyping: An Introduction is a slim volume with little and uneven technical content. However, it is replete with data and brief specifications on machines and supplies and their prices, photographs of parts made and the equipment used, vendor addresses and phone numbers, and a great deal of commentary from customers on their experiences with making parts using various rapid prototyping equipment. It also includes a brief glossary.

The seven chapter titles are: Introduction, Stereolithography systems, Selective laser sintering, Fused deposition modeling, Lamination methods, Scanners, and Software. The author is a freelance writer in the high-technology field. His writing style is somewhat casual but straightforward, and more appropriate for technical and trade magazines.

While the book lacks technical depth and has no bibliography, it is nevertheless a good and brief introduction to the subject and useful to manufacturing personnel unfamiliar with the topic. It is successful in giving a brief perspective to help those who are considering rapid prototyping systems for reducing costs and production times. Those interested in this subject should also consider another book, *Automated Fabrication - Improving Productivity in Manufacturing* by Marshall Burns (PTR Prentice Hall, 1993). This 369-page book is much more detailed and comprehensive while addressing basically the same audience.

CAD for Control Systems. - Derek A Linkens *(Dean of Eng, Univ of Sheffield, UK)*. Marcel Dekker, New York. 1993. 600 pp. ISBN 0-8247-9060-X. $150.00. (Under review)

IV. MECHANICS OF SOLIDS

10R10. Elasticity: Theory and Applications, Second Edition. - Adel S Saada *(Civil Eng, Case Western Reserve Univ, Cleveland OH)*. Krieger, Melbourne FL. 1993. 796 pp. ISBN 0-89464-561-7. $119.50.

Reviewed by Oscar L Bowie (Star Route - Box 317, Phippsburg ME 04562).

This textbook on elasticity is a second edition of the author's work written several years ago. The primary addition to the original version of the subject involves the use of complex variable methods in several areas of problem-solving. A basic review of the subject is presented in a manner which will be of special interest to the applied mathematician. The design engineer's interests are not emphasized, although considerable care is given to provide the necessary background to the mathematical arguments. The book is divided into three segments, with deformation and stress occupying the first two parts, respectively. The third part addresses elasticity with its several models and approximations, along with mathematical methods of solutions.

Part I provides the mathematical descriptions of displacements, deformation and strain in a continuous media. The first three chapters are concerned with displacement and linear transformations of points. Matrix algebra is introduced and the corresponding operations and notation are reviewed. Chapter 4 identifies the portions of displacements which can be considered as strain. The components of strain in Cartesian coordinates are defined in both the linear and nonlinear ranges. Following this topic is a chapter on the formulation in terms of Cartesian tensors. Chapter 6 concludes this segment with a detailed treatment of the strain components in terms of orthogonal coordinates.

Part II consists of a single chapter dealing with the analysis of stress. The stress tensor is introduced and it is shown that its components must satisfy three partial differential equations for equilibrium. These requirements are modified by the simplifying assumptions of the two-dimensional theories. The arguments are carried out in both Cartesian and orthogonal curvilinear coordinate systems.

Part III consists of 12 chapters dealing explicitly with elasticity and problem-solving. In chapter 8, the elastic stress-strain relations according to the generalized Hooke's Law are introduced and systematically modified for isotropy, plane stress, plane strain, etc. The boundary-value problems of elasticity are discussed and the equations required for solution are described in terms of both stresses and displacements. In chapter 9, several classical approaches to problem-solving with the use of potentials are reviewed. Both displacement and stress functions are considered. Torsion of prismatic bars is the subject of chapter 10. Saint-Venant's semi-inverse method is applied to a variety of cross-sections. A relatively brief treatment of thick cylinders, disks, and spheres is presented in chapter 11. Several solutions are summarized for cases in which the boundary-value problems are simple. The following two chapters deal with straight and curved beams, respectively. Axial and shearing forces along with bending moments on the ends are considered using Airy's stress function. The results are compared with those of elementary beam theory.

In chapter 14, the stress analysis for semi-infinite solids and plates is presented for several load distributions. The contact problem corresponding to a rigid die in the form of a circular cylinder acting on a semi-infinite medium is analyzed. The stresses in 2D wedges and triangular rectangular retaining walls are derived. Energy principles and the corresponding variational methods are introduced in chapter 15. Such matters as the principle of virtual work, the reciprocal laws, energy theorems, etc are reviewed. Applications of the arguments are provided for wires and beams. The elastic stability of columns and beams under compression and bending is considered in chapter 16. The buckling loads are calculated for several end conditions. Flat plate theory, based on the Kirchhoff assumptions, is reviewed in chapter 17. Bending problems are addressed for several geometric configurations, loading conditions, and edge constraints. In chapter 18 the theory of thin shells is introduced, with emphasis on the role to which differential geometry should be considered. The appropriate mathematical descriptions are reviewed at some length. Stress resultants and couples are then defined along with the corresponding equations of equilibrium and boundary conditions. Applications of the theory are provided primarily for circular cylindrical shells.

The final chapter is concerned with the applications of complex variable theory to the 2D problems. The properties of analytic functions, Cauchy integrals, series representation, the calculus of residues, conformal mapping, etc are reviewed. Applications to the torsion of prismatic bars with several cross-sections are described. The plane problems of elasticity which reduce to the solutions of biharmonic equations are then addressed. The properties of the two analytic functions describing such solutions for simply and multiply-connected regions are reviewed. The arguments are illustrated by several examples, including circular and elliptical holes in large plates.

The author presents an organized review of the subject that introduces the reader to its status 50 years ago. The more recent developments, eg, the role of elasticity solutions in fracture mechanics, problem-solving with the use of FE, etc are not addressed in any detail. However, *Elasticity: Theory and Applications* is well-written and provides a good basic background to the fundamentals.

10R11. Mechanical Behavior of Materials. Engineering Methods for Deformation, Fracture, and Fatigue. - Norman E Dowling *(Col of Eng, VIP)*. Prentice-Hall, Englewood Cliffs NJ. 1993. 775 pp. ISBN 0-13-579046-8.

Reviewed by David W Nicholson (Dept of Mech and Aerospace Eng, Univ of Central Florida, PO Box 25000, Orlando FL 32816).

The text under review is intended for use in a junior course typically entitled *Mechanical Behavior of Materials*. It assumes "Strength of Materials" as a prerequisite. The text competes with several well known books, among which *Mechanical Metallurgy* by Meyers and Chawla comes to mind. It emphasizes the materials viewpoint, in contrast to some books with similar titles that emphasize stress analysis (eg, Fletcher).

The book is very well written and attractively presented, using graphical materials extensively. It incorporates a large number of exercises and a fair number of worked-out problems in the text. Problems are identified for solution using a personal computer, although no software is provided. The topics are presented at a consistent level of sophistication.

The main departure from competing texts seems to be the emphasis on fracture concepts, both for static fracture and fatigue. This makes the text quite attractive to the present reviewer. There is also some discussion of nonmetallic materials and composites.

Chapters 1 through 3 are largely descriptive and qualitative accounts of the microscopic basis for mechanical properties in different types of materials. Chapter 4 presents the basic concepts of stress and strain and of stress-strain relations for elasticity, plasticity, and creep, as well as for anisotropic materials. There is also a brief mention of thermal strains. Chapter 5 gives a very extensive account of the tests needed to evaluate the properties identified in chapter 4. Finally, chapter 6 extends the basic treatment of chapter 4 to complex states of stress.

Chapter 7 presents elementary notions and models for yielding and plasticity. The notion of residual stress is explained. The topic is revisited in chapters 12 and 13, which treat the analysis of plastic deformation in simple members. Chapter 8 gives a very comprehensive account of linear elastic fracture mechanics, including a discussion of testing. Chapter 9 likewise gives a very extensive account of fatigue crack growth. Chapters 9, 10 and 14 discuss fatigue using stress-based and strain-based models such as the Goodman diagram. There is some discussion of remaining life assessment. Finally, chapter 15 discusses creep and damping, starting with elementary viscoelastic models.

The length of the text and the large range of topics covered makes it necessary for the instructor to pick and choose in constructing a course. Some suggestions are given in the preface.

From a pedagogical viewpoint, the text is excellent. Its coverage of fracture is an especially welcome feature. Compared to many texts with similar titles, *Mechanical Behavior of Materials: Engineering Methods for Deformation Fracture and Fatigue* does not emphasize stress analysis or the design of components; instead, it is attractive to intructors wishing to emphasize the materials viewpoint.

10R12. Mechanism Analysis. Simplified Graphical And Analytical Techniques. - Lyndon O Barton *(E I du Pont de Nemours, Wilmington DE)*. Marcel Dekker, New York. 1993. 752 pp. ISBN 0-8247-8794-3. $150.00.

Reviewed by Pradip Sheth (Mech Eng, University of VA, AH Small Bldg for Computer-Aided Engineers, Charlottesvile VA 22901).

This is book on kinematic analysis of mechanisms, written primarily for mechanical design engineers and mechanical design engineering students. The material is presented in five distinct parts.

Part I contains introductory concepts including: definitions of kinematic terminology of higher-lower pairs, Gruebler's equation for degree of freedom, inversion, motion characteristics for planar rotations, and translations. Simple expressions involving graphical interpretations of displacements velocity and acceleration relationships are presented. Vectors and graphical treatment of vector manipulations are introduced.

Part II details graphical techniques for velocity and acceleration analysis of simple mechanisms. The concept of instant centers is introduced, including the relationship between instant centers and velocity analysis. Graphical treatment of coriolis acceleration component is explained. Graphical techniques for differentiation and integration are presented. The use of equivalent linkages to simplify analysis of the higher pair mechanisms by viewing them as equivalent lower pair mechanisms is explained. Graphical procedures for determining centers of curvature of path traced by points in a mechanism are presented.

Part III presents analytical techniques - based upon vectors and complex algebra - for a variety of planar mechanisms. These include variation on the slider crack, the four bar, the quick return mechanism, sliding coupler, and cam-follower systems.

Part IV introduces gears. Spur, helical, Herringbone, bevel, hypoid, rack worm, and annular types are covered, along with the gear terminology. The law of gearing and the involute tooth action are described in detail. Simple, compound, planetary, and epicyclic gear trains are treated. The bevel differential as in the automobile differential is presented.

Part V is devoted to cam systems, including the treatment of motion design of follower systems.

An extensive set of practice problems is provided for all of the chapters in the book. In the Appendix, Fortran programs for the four bar, the slier crank, and the quick return mechanisms and Basic Program for gear design for external gear pair for standard involute tooth profile are presented. Calculator programs for the HP-41C programmable calculator are also included.

An attractive feature of this book is the clear, physical intuitive methods of analyzing mechanisms, including graphical procedures. These graphical methods of mechanism analysis are rapidly disappearing from the undergraduate mechanical design engineering curricula, and perhaps a few examples from this book could indeed be utilized to reinforce the practical nature and the "back of the envelop" quick evaluations of mechanisms.

As a teacher of an undergraduate mechanical engineering course on mechanisms and theory of machines, this reviewer cannot recommend the book as a textbook for adoption in a mechanical engineering degree program because of what is *not* covered in the book. Despite the size (752 pages), the book is devoted primarily to velocity and acceleration analysis of simple mechanisms. Forces (static or dynamic) are not treated. the usefulness of the programmable calculator programs is questionable. The entire treatment offered by this book would cover approximately 35-40% of an undergraduate course on mechanisms. It should also be noted that the place of a course on mechanisms in mechanical engineering curriculum is itself in a state of flux, with increasingly more material on programmable motion control. Systems (stepper and servo motors) and the use of CAE software on PCs add workstations for mechanism design and analysis.

A mechanical engineering *technology* curriculum, on the other hand, may find this book of some merit, perhaps as a reference or as an adjunct to some other textbook. Similarly, this book should also be considered as a library reference in an engineering curriculum and also by the practicing design engineer.

10N13. Deep Foundations on Bored and Auger Piles BAP II. Proceedings of the 2nd International Geotechnical Seminar on Deep Foundations on Bored and Auger Piles held in Ghent, Belgium, June 1-4, 1993.. - Edited by WF Van Impe *(Ghent Univ and Leuven Catholic Univ, Belgium)*. Balkema, Rotterdam, Netherlands. 1993. ISBN 90-5410-313-2.

Keynote lectures address the following: Installation, monitoring and design of caissons by H Brandl; Design of auger displacement piles from in situ tests by M Bustamante and L Gianeselli; Updating realism on large-diameter bored piles by VFB de Mello and N Aoki; Design of bored piles, including negative skin friction and horizontal loading by E Franke; Interaction problems related to the installation of pile groups by S Hansbo; Base capacity of bored piles in sands from in situ tests by VN Ghionna, M Jamiolkowski, R Lancellotta and S Pedroni; Case studies on cast-in-place bored piles and some considerations for design by R Matsui; Settlement prediction for bored pile groups by HG Poulos; and Efficient design of piled rafts by MF Randolph and P Clancy.

Interaction problems related to pile groups. Papers under this heading include: Cap-pile interaction of pile groups; Field tests and analyses on ultimate behavior of lateral loading bored piles; Group action of laterally loaded piles; and Load distribution in bored pile groups.

Installation problems of bored and auguer piles-Monitoring of pile installation-Case studies. Papers include: Bored vs displacement piles in sand-experimental study; Pile foundation for the 'Pont de Normandie'-Special aspects; Influence of the concreting on the bearing capacity; Pile walling with the PCS method; Bored cast-in-situ piles in weathered rocks-Evaluation of design parameters; Instrumentation of pile installation as a management tool; Effect of dosage and exposure time of slurries on perimeter load transfer in bored piles; Case studies concerning installation of large diameter piles used in Romania; Evaluation of the influence of pile execution parameters on the soil condition around the pile shaft of a PCS-pile.

Pile testing, statically and dynamically - Integrity testing. Papers include: The behavior of bored piles subjected to load testing as compared to theoretical estimates; Large diameter bored piles in pyroclastic soils; Aspects of the bearing capacity of root piles in some Brazilian soils; A method of analysis of stress induced displacement in soils with respect to time; Analysis of loading tests of short large-diameter piles; Nonlinear load-settlement behavior of bored piles; Augered cast-in-place pile testing in Southern California; First experiences with statnamic load testing of foundation piles in Europe; Dynamic testing of an instrumented drilled shaft.

Design of bored piles, including negative skin friction and horizontal loading. Partial papers include: Shaft resistance of model pile in granular soil; Evaluation of bearing capacity and settlement of Wolfsholz piles bored into layered subsoil; Bored piles in clay-shale using expansive concrete; The Romanian code for large diameter bored piles; Punching effects for bored piles; Analysis and design of piles under lateral loads; Investigation of horizontal ground massive collapse deformations influence on piles; New promising concept for bored piles and tension piles; Laterally loaded pile analysis using a 3D BEM formulation; Large diameter bored piles for an office building 'Amstelhoek' in Amsterdam; Bearing mechanisms of nodal piles in sand; An hydraulic gradient study of pile's base enlargement.

Settlement behavior of groups of bored or auger piles-Piled rafts. Partial papers include: Tests of auger piles for design of pile-supported rafts; and Development of locked stresses and negative shaft resistance at the piled raft foundation Messeturm Frankfurt/Main.

10N14. Engineering Plastics and Composites, Second Edition. - Edited by WA Woishnis (*Plastics Design Library*). ASM Int, Materials Park OH. 1993. 700 pp. ISBN 0-87170-483-8. $139.00.

This updated version of the popular reference book follows the same format in section one as the first edition, allowing you to quickly look up plastics, reinforced plastics, and resin composites by trade name. This section includes descriptions of each material by class, family, chemical type, composition and supplier, and also includes information on processes (injection or compression molding), comments, features and uses. Property data has been greatly expanded from the first edition, with coverage of mechanical and physical property data for up to 18 properties. Section two provides an index by chemical type, and lists the supplier, trade name, composition, features and uses. Section three provides an alphabetic listing of suppliers and shows the trade names and chemical types they produce. Section four gives complete supplier contact information, including addresses, phone and fax numbers. Includes listings for more than 5000 trade name materials.

10N15. Metallizing of Plastics: A Handbook of Theory and Practice. - Edited by R Suchentrunk. ASM Int, Materials Park OH. 1993. 348 pp. ISBN 087170-306-8. $105.00.

This book describes the use of metallized plastics in the aerospace, automotive, and appliance industries, plus in electronics housing, EMI-RFI shielding and CDs. Also included is information on etching and pretreatment, matching the plastic to the process, the use of swelling agents, and a step-by-step guide to the metallizing processes themselves. Treatment of effluent arising from metallizing operations and methods for extending the life of processing solutions are also covered.

10N16. Nondestructive Evaluation of Concrete in the Infrastructure. - Soc Exp Mech, Bethel CT. 1993. 600 pp. Softbound. ISBN 0-912053-42-9. $110.00.

This conference, held June 9-11, 1993, consisted of presentations by experts in the field. A partial list of topics presented were: Bridge condition assessment by modal flexibility; Damage identification of reinforced concrete shear wall structures; Nondestructive testing of bridge, highway, and airport pavements; electromagnetic properties of concrete for nondestructive testing; Analysis of localization in concrete and rocks through stereophotogrammetry, spleckle laser and replica; Two-dimensional electronic speckle pattern interferometry and concrete fracture processes; Study of acoustic waveguides in reinforced concrete structures; Quantitative ultrasonic evaluation of concrete; Three-dimensional computer vision technique for evaluation of large structural surfaces; Nondestructive evaluation of concrete structures by digital shearography; Advanced NDT methods for concrete structures; A survey of existing and new approaches for the generation of stress waves in concrete; The NDT as a useful tool in the practical quality control of structures; Evaluation of fracture energy by means of in situ pull-off test; Energy dissipation mechanisms associated with rapid fracture of concrete; Comparison between optical microscopy and scanning acoustic microscopy for detecting flaws in concrete, and more.

10N17. Proceedings of the 1993 50th Anniversary Spring Conference of the Society for Experimental Mechanics. - Soc Exp Mech, Bethel CT. 1993. 1300 pp. Softbound. ISBN 0-912053-39-9. $145.00.

The June 1993 Spring Conference marked the 50th year of service by SEM to the experimental mechanics community. The technical program consists of 225 presentations.

Session topics included: Dynamic systems; Holo-interferometry; Strain gage research topics; Contact stress; Electronic packaging; Mechanics and material science of composites I and II; Application of numerical methods to residual stress analysis; Moire methods applied to composites; Application of experimental methods to determination of residual stresses; Fatigue, interface and dynamic fracature; Speckle, Moire interferometry I and II; Applied-industrial applications of photoelasticity I and II; Composites: Time dependence and durability issues; Thermographic measurement for structural assessment; Fracture mechanics I and II; Time dependent models I and II; Fifty years of structural test analysis; Embedded optical fibers in smart structures; Optical methods-Data reduction, transducers and sensors; Fracture in particulate composite materials I and II; Sensors in robotic applications; Sensors for smart structures; Photoelasticity; Analytical methods in mechanics and digital image processing; and Structural testing.

10N18. Processing, Fabrication and Application of Advanced Composites. Proceedings of ASM International's 1993 Conference. - Edited by K Upadhya. ASM Int, Materials Park OH. 1993. 570 pp. ISBN 087170-473-0. $95.00.

In this volume the papers describe real-world applications of putting composites to work. Once thought of as solutions in search of problems, many of these composites are being mainstreamed into commercial applications. Nearly one-third of the book deals with physical and mechanical properties of ceramic matrix composites; other areas covered in detail are processing and characterization of intermetallic matrix composites and metal matrix composites; processing, fabrication and application of polymer matrix composites; fabrications of functionally gradient materials; and processing applications of carbon-carbon composites. Contributing authors hail from university, government and defense research facilities, as well as from aerospace companies across the country.

10N19. Strength of Metals and Alloys. - Edited by DG Brandon, R Chaim, A Rosen. Freund, London. 1993. 1174 pp. $220.00. 2 vols.

10N20. Structural Testing Technology at High Temperature-II. - Soc Exp Mech, Bethel CT. 1993. 100 pp. Softbound. ISBN 0-912053-40-2. $27.00.

This conference is the follow-up to the 1991 (Dayton, Ohio) conference on the same topic.

The proceedings (which will take place in the fall) will contain approximately 28 papers on five topics. Sessions include: High-temperature structural testing I and II, Instrumentation I and II, and materials.

Basic Structural Behaviour. - Barry Hilson (*Civil Eng, Univ of Brighton, UK*). Telford, London. 1992. 112 pp. ISBN 0-7277-1907-6. £12.95 Europe and UK. (Under review)

Composite Materials in Maritime Structures, vol 1 (Fundamental Aspects) and vol 2 (Practical Considerations). Cambridge Ocean Technology Series 4 and 5. - Edited by R Ajit Shenoi and John F Wellicome (*Univ of Southampton, UK*). Cambridge UP, New York. 1993. 688 pp. ISBN 0-521-45153-1; 0-521-45154-X. $125.00. Info is for 2-vol set. (Under review)

Dual Boundary Element Analysis of Crack Growth. Topics in Engineering, Vol 14. - A Portela (*Wessex IT, UK*). Comput Mech, Billerica MA. 1993. 178 pp. ISBN 1-56252-116-0. $88.00. (Under review)

V. MECHANICS OF FLUIDS

10R21. Water and Wastewater Engineering Hydraulics. - TJ Casey (*Civil Eng, Centre for Water Resources Res, Univ Col, Dublin, Ireland*). Oxford UP, New York. 1992. 270 pp. ISBN 0-19-856360-4. $72.95. Paper $35.95.

Reviewed by John Tuzson (Indust Energy Syst, Gas Res Inst, 8600 W Bryn Mawr Ave, Chicago IL 60631).

This very well written book is very utilitarian without excessive verbiage. It contains all the essential information needed by the users of calculation methods without dwelling on the deeper mysteries of the science of fluid mechanics. Such a style, is difficult to keep up. No wonder then, in an effort to simplify the complexity of fluid mechanics fundamentals, a few mistakes slip in. These errors will not mislead readers with some familiarity of the subject, but might confuse some students. Such glitches, for example, include the statement that "flow is obviously rotational where the streamlines are curved," and omissions to state that conservation of momentum applied to a stream tube must be written independently in the three coordinate directions, and that the momentum equations and energy equation are not independent of each other. Switching from cartesian to streamline coordinates without explanation does not help comprehension.

The author's intent is to derive, explain, and computerize hydraulic calculation procedures frequently used in the design of water distribution and wastewater collection systems. Such subjects include steady and variable flow pattern in piping and open channel systems. While based on solid scientific fundamentals, the calculations are supplemented with empirical constants and correlations which assure that the results are realistic. References to data sources are given. Some uncertainties remain, such as the practical numerical value of the water hammer wave propagation velocity when air is admixed. The author has appended computer program listings for all calculation procedures and offers to send computer discs on demand. These could be very helpful.

Considering the large number of symbols used, it would have been helpful to include a list of symbols and their definitions. This would have helped to avoid coincidences such as alpha for sonic velocity and also for the kinetic energy factor. A conceptually confusing coincidence is the designation of y for the elevation of the free surface in channel flow and also for the independent vertical coordinate.

Clarification of "head" would have been desirable; an English word of many meanings and not particularly appropriate, albeit well entrenched, in hydraulics. We read about piezometric head, total head, differential represented by H or h with a profusion of subscripts which offer opportunities for confusion to a novice.

A three page index is adequate but does not contain such words as "phreatic surface."

The material in *Water and Wastewater Engineering Hydraulics* should be very useful to practicing engineers and could also be used as a text for students who plan to specialize in the practical aspects of water distribution and wastewater collection system design and operation.

10N22. Advances in Turbulence IV. Proceedings of the Fourth European Turbulence Conference, June 30-July 3, 1992. - Edited by FTM Nieuwstadt *(Lab for Aero and Hydromech, Delft Univ of Techn, Netherlands)*. Kluwer, Netherlands. 1993. 576 pp. ISBN 0-7923-2282-7. $198.00. £132.

This volume, reprinted from Applied Scientific Research, 50:3-4, contains contributions from the fourth European Turbulence Conference held in Delft on June 30-July 3, 1992. The papers are grouped into the following main topics of the meeting: Dynamical systems and transition; Statistical physics and turbulence; Experiments and novel experimental techniques; Particles and bubbles in turbulence; Simulation methods; Coherent structures, and Turbulence modeling and compressibility effects.

10N23. Computational Fluid Dynamics. von Karman Institute for Fluid Dynamics-Lecture Series Monographs. - VKI Fluid Dyn, Rhode-St-Genese, Belgium. 1993. ISBN VKI LS 1993-04. $211.00.

The aim of this annual lecture series was to provide in-depth presentations on well-established methods and on recent advances in the field of numerical flow simulation. The program was at a specialist level complementary to the Introduction to CFD. This year's program focussed on higher order space discretization methods for the compressible and incompressible flow equations, and related algorithms. The space discretizations studied were finite volume, FE and spectral methods. Applications were covered in the field of both incompressible flow and aerodynamics, including chemically reacting reentry flows.

The course started with an introduction to the theory of hyerbolic conservation laws, including a comparison of the currently used high-resolution TVD finite volume schemes with newly developed 4th order schemes, including application to unstructured grids.

Alternative discretizations which received equal attention were variational methods such as the FEM and spectral methods. Three lectures were devoted to an overview of variational approaches applied in incompressible and compressible fluid dynamics. Similarly, three lectures were devoted to a review of spectral methods and spectral element methods as an extension towards body-fitted domains. The recent progress in multidimensional upwind discretization was surveyed, including status reports of multidimensional scalar advection schemes and wave decompositions for the compressible Euler equations.

Next to the basic discretizations, attention was given to the time integration methods for unsteady flows and to the iterative solution methods for steady state computations. Acceleration techniques based on preconditioned conjugate gradients, GMRES and multigrid were discussed. Special attention was given to the exploitation of parallellism on distributed memory platforms such as the N-cube, the Intel ipsc or clusters of workstations using PVM.

Contents include: By R Sanders, U Houston, TX: High-order non-oscillatory schemes for the compressible Euler equations; A multigrid acceleration technique for computing steady solutions to the equation of compressible flow. By CP Li, NASA Johnson Space Center, USA: Computational techniques for high speed flows with viscous and chemical effects. By R Abgrail, INRIA, Sophia Antipolis, France: ENO schemes on unstructured meshes; By M Rudgyard, Cerfacs, Toulouse, France: Multidimensional wave decompositions for the Euler equations; Cell vertex methods for steady inviscid flow. By H Deconinck, R Strujis and G Bourgois, von Karman Institute, and PL Roe, U Michigan, USA: Compact advection schemes on unstructured grids. By M Hafez, U California, Davis, USA: Variational approaches to CFD: Applications to potential, Euler, and Navier-Stokes equations. By Y Maday, U Pierre and Marie Curie, Paris, France: Introduction to spectral methods, Application to the Stokes problem; and Introduction to spectral methods for hyperbolic system of conservation laws. By D Roose, KU Leuven, Belgium: Distributed memory parallel computers and computational fluid dynamics.

10N24. Computational Methods for Free and Moving Boundary Problems in Heat and Fluid Flow. - Edited by LC Wrobel and CA Brebbia. Comput Mech, Billerica MA. 1993. 412 pp. ISBN 1562521454. $198.00.

The mathematical modeling of free and moving boundary problems is characterized by the presence of one or more surfaces which are initially unknown or move throughout the analysis. The determination of the location of these surfaces is an important part of the solution procedure, generally involving the use of iterative or time-marching algorithms. Examples of practical engineering problems are numerous, eg. nonlinear wave motion, cavitating flows, solidification and melting, and metal casting, to name a few. The present volume concentrates on computational methods of the solution of such problems with emphasis on boundary and finite elements.

Chapter 1 discusses direct iteration and optimization techniques used in conjunction with the BEM for solution of gravity and pressure-driven free surface flow problems. Chapter 2 uses Baiocchi's integral transformation in a fixed domain method for free surface flow in porous media. Chapters 3 and 4 deal with nonlinear wave motion. The former describes a wave model based on the fully nonlinear potential flow equation to study wave motion in shallow water, including wave overturning induced by the ocean bottom or by coastal engineering structures.

The flow about submerged partially or supercavitating axisymmetric bodies both at zero and non-zero angle of attack is considered in chapter 5. Chapter 6 discusses two implementations of the BEM to solve the slow viscous flow of a fluid moving between parallel plates which are in relative motion. The situations in which petroleum reservoir models generate shocks are considered in chapter 7.

When rain runs down a window pane in a stream, it normally meanders instead of going straight. This interesting problem is analyzed in chapter 8, which presents the condition of stable meandering of water rivulets on an inclined smooth plate, derived by the bend theory including the effect of surface tension.

A series of heat flow problems are considered in chapters 9 to 13. Chapter 9, on solidification problems, presents a macroscopic model for the treatment of the macrosegregation process in a binary material, and a microscopic model of the microsegregation process in the secondary arms of a columnar dendritic mushy region. Chapter 10 presents a complete mathematical model for freezing processes in foodstuffs. Modeling of the thermoelectrical behavior of an aluminum electrolytic cell is presented in chapter 11. This model predicts and asseses fundamental variables in cell operation: form and thickness of the frozen bath, heat flows, position of isotherms, electric potentials, and more.

Chapter 12 presents a resume of work involving the isotherm Migration method. Applications include implicit moving boundaries (oxygen diffusion through absorbing tissues) and melting ranges (mushy problems). The modeling of the filling stage of casting processes is the subject of chapter 13, where a 2D FEM to treat non-steady flows of Newtonian fluids, coupled with heat transfer and turbulence, is described.

Chapter 14 discusses the steady, irrotational, ideal fluid flow produced by a submerged source, or sink, from a region containing three homogeneous layers of fluids at different densities with gravity as the restoring force. In chapter 15 the motion and deformation of viscous drops and gas bubbles, which occur in many industrial and biological systems, are studied through a complete double layer boundary integral equation method. Finally, chapter 16 reviews the historical development and state-of-the-art in Green's function structured discrete approximation methods for modeling microscopic and macroscopic transport phenomena in solid-liquid phase-change systems.

All of the contributors to this book are well-known in their respective fields, with many having research histories extending back over 10 to 20 years or longer. Such experience qualifies them to present these major topics of interest in this field.

10N25. Computational Modelling of Free and Moving Boundary Problems II. - Edited by LC

Wroebel and CA Brebbia (*Wessex IT, UK*). Comput Mech, Billerica MA. 1993. 504 pp. ISBN 1853122424. $139.00. £89.

Free and moving boundary problems are of importance in a large variety of physical situations. The common feature is the presence, in the mathematical modeling, of an initially unknown surface which moves throughout the analysis, the determination of which is an essential part of the solution procedure. These nonlinear problems are difficult to solve analytically but for the simplest cases; because of this, a numerical method of solution usually has to be resorted to. Whichever method is chosen, an efficient computational implementation will require advanced features such as grid adaptivity, moving meshes, particle tracking, or other algorithms.

Although the physical problems under consideration can be completely different in nature, there are several common features in their mathematical modeling and computer methods of solution. This book will therefore be of interest to scientists and engineers from a wide variety of fields working on the development of numerical models for free and moving boundary problems. It contains the edited proceedings of papers presented at the Moving Boundaries Conference held in June, 1993.

Parital contents include: Flow through porous media: Transient simulation of water table aquifers using a pressure dependent storage law; Wave propagation: Flow calculations for a ship traveling in the vicinity of a pycnocline; Stokes flow: A BEM solution for the simulation of axisymmetric viscous sintering; Cavitational flow: Potential flow past a bluff body with and without separation; Free surface flow: A porosity method to compute 3D turbulent free surface flows; FE simulation of free surface flows using arbitrary Lagrangian-Eulerian method; Sediment transport: Numerical simulation of coastal changes; Computational hydraulics: Numerical simulation of flooding and drying in a depth-averaged boundary-fitted tidal model; Solidification and melting: Fusion of PCM in finned plane cavities; Metal casting and welding: A coherence between a castings shape and its total solidification time; Inverse problems: The inverse Stefan design problem; Elasticity problems: Stability and bifurcation of plane cracks of arbitrary shapes; Mathematical formulations and computational techniques: Mass transfer in turbulent flow.

10N26. Introduction to the Modeling of Turbulence. von Karman Institute for Fluid Dynamics-Lecture Series Monographs. - VKI Fluid Dyn, Rhode-St-Genese, Belgium. 1993. ISBN VKI LS 1993-02. $211.00.

The purpose of this lecture series was to provide an introduction to the fundamental physical principles of turbulence and of its modeling, and to make a survey of the models currently available and of their domain of application.

Emphasis was given to those models which can be considered ready for application to a range of problems of practical interest and, in particular, to recent advances in second moment closures, but fields of advanced turbulence modeling, such as Large Eddy Simulation and compressible flow turbulence, were also discussed.

Because of its nature and content, the course was valuable to both researchers and practicing engineers interested in acquiring a fundamental knowledge of the problems and opinions in the domain of turbulence modeling in view of its application to their specific field of interest.

Contents include: By BE Launder, UMIST, Manchester, UK: Introduction; An introduction to second moment closure; Modeling force-field effects on turbulence; A new form of second-moment closure; An introduction to single-point closure methodology; Second moment closure: Present...and future?; and Contribution to the modeling of near-wall turbulence.

By MA Leschziner, UMIST, Manchester, UK: Two-equation models for high Reynolds flow number; Two-equation models for low Reynolds number variants; Inclusion of second-moment closures into finite volume solvers; Numerical implementation and performance of Reynolds stress closures in finite volume computations of recirculating and strongly swirling flows; Application to second-moment closure in complex flows; Modeling engineering flows with Reynolds stress turbulence closure; and Turbulence modeling challenges posed by complex flows.

By W Rodi, U Karlsruhe, Germany: Examples of turbulence model applications. By U Schumann, DLR Oberpffaffenhofen, Germany: Direct and LES of turbulence-summary of the state-of-the-art 1993; LES of turbulent diffusion in stably stratified shear flow; and Numerical simulation of turbulent convective flow over wavy terrain. By D Vandromme, U Rouen, France: Turbulence modeling for compressible flows and implementation in Navier-Stokes solvers.

10N27. Measurement Techniques. von Karman Institute for Fluid Dynamics-Lecture Series Monographs. - VKI Fluid Dyn, Rhode-St-Genese, Belgium. 1993. ISBN VKI LS 1993-05. $211.00.

The aim of this annual lecture series was to provide, on the one hand, general concepts widely applicable in experimental techniques; on the other hand, to select a few topics for in-depth discussions. Some of them are of wide use, others represent recent developments in a particular domain. This year's program focuses on general data acquisition principles and treatment as an example of widely used techniques for different kinds of measurements. The specialized topics retained for the present program were: Pressure measurements; Infrared thermography and Liquid crystal techniques; all of which can be categorized as non-intrusive.

The lectures on pressure measurements only dealt with special, recently developed techniques, such as pressure sensitive paints and laser-induced luminescence. The physical properties on which the techniques are based were explained, and possible applications were illustrated with test cases. The other two techniques were devoted to temperature and heat transfer measurements. The physics of each were discussed in an introductory lecture on Infrared Thermography (IT) and Liquid Crystals (LC). The emphasis was placed on IT. The application domain and limitations of IT and LC were discussed and illustrated. The advantages and disadvantages of one technique or detector with respect to another were covered, and methods for data handling and enhancement were proposed. The illustrations were selected to demonstrate the wide applicability in fluid dynamics of the methods presented. Finally, some perspectives for future developments were discussed, such as faster response instruments. It is expected that this lecture series will stimulate research in the development of these tools for flowfield investigations.

Contents include: By RW Ainsworth, Oxford U, UK: Data acquisition in aerodynamic research; Recent developments in fast response aerodynamic probe technology. By F Lemoine and B Leporcq, IMFL, Lille, France: Static pressure measurements for near isentropic flows using laser induced iodine fluorescence. By RC Crites, McDonnell Douglas Aerospace, St Louis, USA: Pressure sensitive paint technique. By D Balageas and A-M Bouchardy, ONERA Chatillon, France: Fundamentals of infrared thermography; Application of infrared thermography in fluid mechanics; Heat transfer quantitative characterization:Passive and active methods; Perspective and future possibilities. By GM Carlomagno, U Naples, Italy: Infrared thermography. By P Ireland, Oxford U, UK: Liquid crystal heat transfer measurements. By G Rau, J Vanhalst and T Arts, von Karman Institute, Belgium: The application of liquid crystal techniques to determine heat transfer rates.

10N28. Methodology of Hypersonic Testing. von Karman Institute for Fluid Dynamics-Lecture Series Monographs. - VKI Fluid Dyn, Rhode-St-Genese, Belgium. 1993. ISBN VKI LS 1993-03. $211.00.

The aim of this course was to present a comprehensive overview of the methods used in hypersonic testing and evaluation, and to explain the principles behind those test techniques. Lectures were presented by seven American scientists with considerable expertise in hypersonic ground testing. They are all directly or closely affillated with the USAF Arnold Engineering and Development Center; thus, a highly coherent and structured set of lectures was developed.

Topics covered include: an introduction to hypersonic aerodynamics with descriptions of chemical and gas dynamic phenomena associated with hypersonic flight; categories and application of various hypersonic ground test facilities; characterization of facility flowfields; measurement techniques (both intrusive and nonintrusive); hypersonic propulsion test principles and facilities; computational techniques and their integration into test programs; ground-test-to-flight data correlation methods, and test program planning.

Lecturers include: AH Boudreau-AEDC; RA Crawford-U Tennessee Space Institute; RK Matthews-Calspan Co/AEDC Operations; JR Maus-Calspan Co/AEDC Operations; VK Smith-Sverdrup Technology Inc/AEDC Group; BM Wettlaufer-Sverdrup Technology/AEDC Group; and WD Williams-Calspan Co/AEDC Operations.

Contents include: Hypersonic overview; Hypersonic flow phenomenology; Hypersonic propulsion characterization; Characterization of flowfields in hypersonic ground test facilities; Aerodynamic and aerothermal facilities; Aeropropulsion facilities; Computational techniques and capabilities; Test and evaluation methods; Materials-structures testing; Aeropropulsion test and evaluation methods; Hypersonic flowfield measurements-nonintrusive; Hypersonic flowfield measurements-intrusive; Hypersonic flight test; Extrapolation of ground test data to flight; Boundary layer transition; Shock-boundary layer-shock interactions; Electromagnetic wave test; Propulsion integration; and Generic test planning.

10N29. Non-Intrusive Measurement Techniques. von Karman Institute for Fluid Dynamics, Lecture Series Monographs. - VKI Fluid Dyn, Rhode-St-Genese, Belgium. 1993. ISBN VKI LS 1993-09. $211.00.

In recent years non-intrusive measurement techniques have been the object of a spectacular development. They are now used in all fields of fluid dynamics and they allow the measurement of many scalar flow parameters as well as velocity. It is the objective of this lecture series to present an up-to-date review of the available techniques and of their implementation in various types of measurement problems in fluid dynamics.

Optical interferometry is an old classic in fluid dynamics, but it recently received considerable attention. This is the reason why lectures present the state of the art of this technique. Lectures are also devoted to a presentation of infrared imaging techniques and their potential. The fast growing domains of laser induced fluorescence (LIF), electron beam fluorescence (EBF), and raman scattering (CARS) are the object of several lectures. Principles as well as applications of these techniques are presented and discussed. Velocity measurements are among the most important ones in fluid dynamics. This is the reason why several courses are devoted to them. The recent developments of laser doppler velocimetry and particle image velocimetry are presented in a series of lectures. Basic principles as well as practical aspects, such as seeding and signal processing, are discussed. This lecture series should allow an overall appraisal of the present potential of available non-intrusive measurement techniques applied to fluid dynamics.

Contents include: By A Deom, ONERA, France: Infrared imaging. By C Dankert, DLR, Germany: Laser induced interferometry; Electron beam fluorescence. By M Pealat, ONERA, France: Raman scattering techniques. By L Lourenco, FAMU-FSU, USA: Particle image velocimetry. By A Boutier, ONERA, France: Laser doppler velocimetry. By W Merzkirch, U of Essen, Germany: Interferometric methods.

10N30. Supercomputing in Fluid Flow. - Edited by TKS Murthy and CA Brebbia *(UK)*. Comput Mech, Billerica MA. 1992. 368 pp. ISBN 0945824599. $180.00. £100.

The speed and power of supercomputers is continually being improved, and new types of architecture and algorithms are simulataneously being developed so that supercomputing applications can take advantage of them. Among all the applications of supercomputing for numerically intensive problems, perhaps the most significant is in computational fluid dynamics (CFD), particularly in the graphic visualization of the fluid flow field. In the problems of the aerodynamics of aircraft, spacecraft and automobiles, mathematical modeling with supercomputing is now a viable alternative for obtaining speedy and less expensive results compared to model testing. This book contains the edited versions of the papers presented at the International Seminar on Supercomputing in Fluid Flow, held in Massachusetts, USA in 1989.

The international flavor of the contents of the book is evidenced by the contributions of authors from nine different countries. The volume presents and discusses advances in the application of supercomputing to numerically intensive problems in the simulation of fluid flow, mainly centered on the solution of the Navier-Stokes or the Euler equations for which several high-level algorithms and codes are now being developed. These new algorithms and codes are required in order to exploit the increasingly sophisticated types of architecture, such as parallel processing and vector processing, which are now available.

Contents include: FE algorithms for the Euler equations on the connection machine; Design of a 3D multidomain Euler code; 3D full Navier-Stokes solvers for incompressible flows past arbitrary geometrics using supercomputers; A unified parallelizable multigrid approach to solve steady Euler- and Navier-Stokes equations; Computation of incompressible fluid flows about bodies with appendages; Simulation of unsteady 3D flows around an automobile and its visualization; Applications of LES to complicated flow fields; Mathematical modeling, numerical solution and visualization of steady 3D swirling fluid flow with turbulence and solid particles; Turbulence modeling for transition studies; Navier-Stokes computations of turbulent transonic flow around aircraft wings; Numerical simulation of 3D viscous transonic flows with separation; Supercomputing in hypersonic flow with non-equilibrium effets; Restructuring CFD algorithms for vector and parallel computers; and Numerical simulation of internal flows in the automotive industry.

10N31. Ventilation. von Karman Institute for Fluid Dynamics, Lecture Series Monographs. - VKI Fluid Dyn, Rhode-St-Genese, Belgium. 1993. ISBN VKI LS 1993-07. $211.00.

Following a general introduction to the subject of ventilation, the lectures in this series dealt with the indoor air quality and the thermal environment in ventilated or air-conditioned spaces identifying the newest information for design rules.

The principles and citeria of ventilation systems are then discussed. Natural and mechanical ventilation and contaminent control methods are covered. Different empirical flow calculations for steady state and time-dependent contaminent generation and air flow rate situations are presented. Their application to sizing of air diffusers, ...al exhausts, filters and air curtains are illustrated in the cases of laboratory fume and biological safety hoods, grinding booths and spray painting rooms.

The theory of age distribution and N-zone models are described. The use of these tools are illustrated in distinguishing different principles, such as displacement or mixing ventilation. Their practical interest in evaulating the effectiveness of ventilation systems are underlined. Emphasis is then given to design methodology and innovative technology in the field of industrial ventilation. In particular are lectures given on dust and dust control systems, field testing, and monitoring aspects. Application of capital and operating cost databases are exemplified through case studies.

The last session of the course demonstrates the benefit of computational fluid dynamics in the scope of ventilation design. Several numerical models developed to simulate the thermo-aeraulic behavior of ventilating systems are presented. Simulations of displacement flow, contaminent transport and flow around obstacles are exemplified. New developments in this field focus on the international benchmark exercise Annexe 20.

Contents include: By G Aubertin, INRS, France: Introduction to the design of ventilation systems. By O Fanger, Technical U of Denmark: Human requirements to the indoor air quality and the thermal environment. By L Olander, National Board of Occupational Safety and Health, Sweden: Ventilation systems. By E Skaret, Norwegian Building Research Institute, Norway: Theory of age distribution; Ventilation models. By H Goodfellow, Environmental and Occupational Health, Canada: Industrial ventilation; Ventilation cost and air cleaning. By PV Nielsen, Aalborg U, Denmark: Computational fluid dynamics (CFD) in ventilation:Theory and 1D test case; CFD in ventilation: Theory and codes; CFD in ventilation: The IEA Annex and 20 Work; Commercial applications of CFD in ventilation; New developments in CFD with relevance to ventilation. By JR Fontaine, INRS, France: CFD in ventilation: A practical approach. By T Bidot, Simulog, France: CFD in ventilation: A practical approach.

Incompressible Computational Fluid Dynamics. Trends and Advances. - Edited by Max D Gunzburger *(VPI)* and Roy A Nicolaides *(Carnegie Mellon Univ)*. Cambridge UP, New York. 1993. 468 pp. ISBN 0-521-40407-X. (Under review)

Topics in Fluid Mechanics. - Rene Chevray *(Columbia Univ)* and Jean Mathieu *(Univ of Lyon I, France)*. Cambridge UP, New York. 1993. 384 pp. ISBN 41082-7. Paper ISBN 42272-8. $125.00. Paper $49.95. (Under review)

Wave Propagation in Gas-Liquid Media, 2nd ed. - VE Nakoryakov, BG Pokusaev, IR Shreiber *(Thermophys, Russian Acad of Sci, Novosibirsk, Russia)*. CRC Press, Boca Raton FL. 1993. 224 pp. ISBN 0-8493-9906-8. $129.00. Outside US, $155.00. (Under review)

VI. HEAT TRANSFER

10R32. Introduction to Thermal Sciences; Second Edition. Thermodynamics, Fluid Dynamics, Heat Transfer. - Frank W Schmidt, R E Henderson, C H Wolgemuth *(Penn State)*. Wiley, New York. 1992. 476 pp. ISBN 0-471-54939-8.

Reviewed by Franklin T Dodge (Div of Mech and Fluids Eng, SWRI, PO Drawer 28510, San Antonio TX 78228-0510).

As the preface states, this textbook is meant to give an overview of thermodynamics, fluid dynamics, and heat transfer to engineering undergraduates who are not mechanical engineering majors, for the purpose of introducing them to the important principles of energy and its use, transfer, and conversion. In order to cover the multitude of topics encompassed by this subject, the authors have generally adopted a scheme in which the principles or theory of a topic are described briefly and then further explained in the form of detailed work examples, including explanatory comments. This is satisfactory for the intended audience, but probably would not be optimal for mechanical engineering majors who are expected to be able to apply the principles to new problems.

The topical coverage of the book is thorough, and the chapters include: Thermodynamic concepts and definitions; Properties of pure substances; System analysis-first and second laws; Control volume analysis; External flow - fluid viscous and thermal effects; Internal flows - fluid viscous and thermal effects; Conduction heat transfer; and Thermal radiation heat transfer. Chapters 6 and 7 are about equally divided between fluid flow and convection heat transfer. These two chapters also include some of the more application-oriented topics, such as heat exchangers. The authors have included example problems throughout the book that should be of interest to civil and electrical engineers. However, the reviewer did not notice, except for one or two homework problems, any coverage of the increasingly important topic of electronic component cooling.

The book is attractively printed with clear, well drawn figures and many photographs. Good use is made of highlighting to emphasize important material. As might be expected of a book written by three authors, the writing style varies from chapter to chapter. For example, the chapters on thermodynamics are dominated by example problems, while the chapters on fluid flow contain a lot of theory and discussion as well as examples. The total amount of material covered appears to be considerably too much for a one semester course, although the authors state that is the book's intended use.

There is presently a wide selection of texts covering the combined "thermal sciences" from which teachers can select. *Introduction to Thermal Sciences* is one of the better ones, and I would not hesitate to recommend it.

Transport Processes and Unit Operations, Third Edition. - Christie J Geankoplis *(Univ of Minnesota MN)*. Prentice-Hall, Englewood Cliffs NJ. 1993. 915 pp. ISBN 0-13-930439-8. (Under review)

VII. EARTH SCIENCES

10R33. Statics and Kinematics of Granular Materials. - R M Nedderman

(Dept of Chem Eng, Univ of Cambridge, Cambridge MA). Cambridge UP, New York. 1992. 352 pp. ISBN 0-521-40435-5.

Reviewed by Anthony Rosato (Dept Mech & Indust Eng, NJIT, 200 Central Ave, Newark NJ 07102).

The widespread use of granular materials in diverse fields, such as agriculture, pharmaceuticals, coal and mineral handling, chemical processing, metal and ceramic composites, and in natural geophysical flows, has stimulated extensive research into understanding the behavior of these materials. Nedderman attempts to provide a resource, directed to a wide audience (from undergraduates to researchers in the field), in which "principles of granular materials are rigorously treated" from a continuum approach. As the title implies, the book is divided into two parts. Following a brief introduction and a presentation of the usual concepts of stress, strain, and Mohr's circle, chapters 3-7 discuss the statics of granular materials based on Couloumb's yield criterion and flow kinematics. The second part, chapters 8-10, is concerned with flow kinematics. Each chapter includes a succinct introductory summary of what follows. This feature is extremely useful to help the reader place the material within the larger framework of the book.

In chapter 3, the author provides a clear exposition of the ideal Coulomb material, Mohr-Coulomb failure, and active and passive states, concluding with the criterion for failure or slip along a wall. The derivations are presented well with good physical insight. The material flows easily to the next chapter, "Coulomb's Method of Wedges," which starts from an analysis of the force exerted by a cohesionless material on a vertical retaining wall and progresses to twin retaining walls. Assumptions are stated at the outset and reinforced in the explanations so that the reader does not lose sight of the applicability of the method.

Chapter 5 presents Jannsen's original analysis in short form, highlighting its inherent assumptions for the stress distribution in a cylindrical bunker filled with a cohesionless granular material. Included is an analysis of bunkers with arbitrary cross-sections. A discussion of Walker's improved analysis follows with application to conical and wedge-shaped hoppers. Failure of bunkers as a result of a stress jump near the wall at discharge initiation is then demonstrated using Walter's qualitative switch stress treatment. The chapter concludes with a discussion of Enstad's study in a conical hopper for which it is assumed that the minor or principal stress is constant on a spherical surface across the hopper.

Material properties and their influence on flow behavior is treated in chapter 6. After short description of the effects of pressure on densification, a few pages are devoted to particle size analysis which is concluded with a sample problem. The next section briefly touches on permeability related to fluid flow through a granular bed. This topic is oddly placed and does not fit in well with the theme of the chapter and the book in general - kinematic analysis of dry granular flows. Internal failure property measurement and interpretation of shear cell results is discussed; the chapter concludes with a brief note on wall frictional properties.

Chapter 7, "Exact Stress Analysis," examines the stress distributions in granular materials based on the Coulomb yield criterion in a more precise manner. After introducing the basic equations, particular solutions are presented for the asymptotic stress distributions between parallel planes and cylindrical bunkers. Problems associated with the solution technique for fully rough walls and procedures for cohesive materials conclude the section. This is followed by an analysis of the concical hopper in which numerical solutions of the governing equations are explained. In section 7.5, useful comparisons of the distribution factor in cylindrical bins and the radial stress field are made with the approximate results from chapter 5. The method of characteristics is carefully explained in section 7.6, and a variety of different applications are presented in the sections that follow (ie, single retaining walls with and without surcharges, inclined top surfaces and walls, and twin retaining walls). The remainder of the chapter discusses the stress discontinuity in the context of the method of characteristics; the chapter concludes with a more rigorous treatment of the switch stress which was briefly introduced in section 5.9.

Chapter 8 focuses on modeling the velocity field in flowing-discharging granular materials using concepts from plasticity theory. As background, the chapter begins with a brief discussion of kinematic modeling by citing the contributions of Mullins and Litwiniszyn and then detailing the work of Nedderman and Tuzun. The concepts of yield function, plastic potential, and flow rules are introduced and the principle of coaxiality is developed in algebraic form. Evaluation of the radial velocity field in constant cross-section bunkers as well as conical or wedge-shaped hoppers is followed by a prediction of the transition from core to mass flow in conical hoppers. The chapter concludes with a discussion of the method of characteristics and discontinuous velocity fields.

The topic of chapter 9 is the Conical Yield function, which is derived and compared with the Coulomb criterion. This is followed by a discussion of Levy's flow rule used to find the radial stress distribution and velocity fields for radial incompressible hopper flow. The material of this chapter is presented well and the connections made with the analyses in chapter 7 are very helpful.

The final chapter, concerned with the prediction of mass flow rates, begins with a discussion of various mass flow rate correlations and some early theories based on the existence of a "free-fall arch." A well-written discussion of the hour-glass theory as originally developed by Savage, is presented in 10.4, while the effects of rough walls on hopper discharge rates is developed in section 10.5. The remainder of the chapter addresses various related topics such as air-augmented flow, fine powder flows, arching, and flooding.

Statics and Kinematics of Granular Materials provides a very good treatment of this important subject. Concepts and ideas are clearly developed with an emphasis on connections between experiments and theories. The book could be enhanced by incorporating example problems in the chapter discussions to illustrate the theories, by including additional homework problems placed at the end of each chapter rather than the existing compilation of all problems at the end of the book, and by expanding the somewhat narrow list of references. Despite these shortcomings, it is suitable as a text for a graduate level course and the first six chapters could easily be adapted for an upper level undergraduate course. The author has presented a self-contained treatment of the statics and kinematic behavior of particulates and it should be an important resource in this field.

Nonlinear Dynamics of Reservoir Mixtures. - Vladimir S Mitlin *(Univ of Texas, Austin TX).* CRC Press, Boca Raton FL. 1993. 257 pp. ISBN 0-8493-4416-6. $79.95. (Under review)

Soil Dynamics and Earthquake Engineering VI. - Edited by AS Cakmak *(Princeton Univ NJ)* and CA Brebbia *(Wessex IT, Southampton, UK).* Comput Mech, Billerica MA. 1993. 944 pp. ISBN 1-56252-154-3. (Under review)

VIII. ENERGY & ENVIRONMENT

10R34. Planning of Geothermal District Heating Systems. - Alberto Piatti *(Techint, Italy),* Carlo Piemonte *(Polytech of Milan, Italy),* Edoardo Szego *(Techint, Italy).* Kluwer, Netherlands. 1992. 328 pp. ISBN 0-7923-1968-0. $129.00. £68.

Reviewed by Gladius Lewis (Dept of Mech Eng, Memphis State Univ, Memphis TN 38152).

The existence of geothermal energy resources in many parts of the world is well known. In recent years, the exploitation of these resources for a variety of end-use(s) has surged. These include: electricity generation in the Imperial Valley and the

Geysers, California, USA; greenhouse warming in Tuscany, Italy; district heating in Reykjavik, Iceland; and refrigeration in Rotorua, New Zealand. Nonetheless, little has appeared in the open literature on the details of the design of existing or planned geothermal energy-driven schemes. Perhaps because of this dearth of information, design of such schemes is usually perceived to be abstruse if not esoteric.

Thus, a simple litmus test of the success of any publication (especially a book, which has any hopes of attracting a wide readership) on the design of such schemes should be the extent to which it is simultaneously easy to read and accurate in its contents. It is against this background that this book has been evaluated by the present reviewer.

The book is arranged into six chapters and two appendices containing details of a computer program that is a necessary adjunct to the text.

The first two chapters set the tone for the style of the book. They contain a brief background to the events that led to and culminated in the writing of the book; a statement of its aims and objectives, which are precisely enunciated as being "to analyze the influence of the different parameters that may affect the energy balances and the economic feasibility of geothermal district heating systems"; and an enumeration of elements of the systems considered (namely, the heat exchanger, heat pump, and peak load boiler) and three research phases. Finally, an outline is presented of the methodology that is followed in the examination of the schemes studied.

There are eight sections in the third chapter, "District Heating Thermal Production Stations Fed by Geothermal Energy: Types of Flow Systems." The first section provides an introduction of the main features and definitions of the energy efficiency for the four "basic flow systems" considered. These are identified as: heat exchanger between the geothermal fluid and the district heating water; heat pump only, with direct connections between the evaporator of the pump and the geothermal fluid; heat pump assisted, with direct evaporation; and heat pump assisted, with indirect evaporation (referred to in the book by the acronyms HE, HPO, HPA-DE, and HPA-IE, respectively).

The next four sections contain details of each of the aforementioned systems, with the authors clearly identifying the conditions under which each may be used; addressing the issue of the relative investment and operating costs; and carefully deriving (making use of appropriate diagrams) expressions for the energy efficiency ratios [(thermal power extracted from the geothermal fluid)/(mechanical power input of heat pump compressor), $P_g/P_m c$; and (base load units total thermal power)/(electric power input of heat pump motor or thermal power of the fuel consumed by the heat pump engine), P_b/P_x] in the case of the HPO, HPA-DE, and HPA-IE systems.

The sixth section contains a comprehensive comparison of the aforemetioned energy efficiency ratios of the different flow systems that use heat umps. Here, the authors have encapsulated the relevant results in the form of suitable graphs. One example are graphs showing the variation of P_b/P_x with district heating water outlet temperature from the heat pump condenser for different combinations of geothermal fluid discharge and district heating water return temperatures in the case of engine- and electricity-driven HPA-DE systems (for a specified geothermal fluid well-head temperature). Based on the results presented in these sections, the authors go on to summarize the main conclusions regarding the relative utility of the HPO, HPA-DE, and HPA-IE systems. Thus, they report that the energy efficiency of a heat pump-only system is lower than that of a heat pump-assisted one, and that a HPA-IE system allows a greater design and operational flexibility, but has a lower efficiency compared to a HPA-DE one.

The seventh section in this chapter deals with the characteristics of the various formats for connecting heat pumps (such as series, parallel, and series-parallel). In the final section, the similarities and differences between the two "basic systems" selected for detailed study in the book (namely, the HPO and the engine- and electricity-driven HPA-DE ones) are presented.

In the first part of the fourth chapter, "Selection of the Application Cases to be Examined," six parameters that are perceived by the authors to exert the greatest influence on the performance (and, hence, the economic viability) of geothermal district heating systems are identified. These are: well-head characteristics [temperature, flow rate, depth, type of fluid, and distance between the well(s) and the heat production station]; supply and return temperatures of the heating network; characteristics of the use of the thermal energy (such as thermal density and peak load power); cost of fuels used by the thermal plants prior to the connection to the geothermal scheme; characteristics of the heat production station (such as type of flow system and type of heat pump prime mover); and cost of fuel and electrical energy used in the heat production system.

In the second part of this chapter, the role of each of these parameters is examined in a qualitative manner. In the third part, a detailed quantitative examination of three of these parameters (which are considered to define the "base cases" for study) is performed. These are: the well-head fluid temperature; district heating temperature; and the type of heat pump prime mover. Then, 21 such "basic cases" are selected, representing three combinations of well-head fluid temperature (and, hence, well-head depth) and maximum delivery and return temperatures of the network; and two types of heat pump prime mover. In addition, the authors selected other cases that allowed sensitivity analyses of six other relevant parameters (such as the type of the geothermal fluid and the number of heat pumps) [when well-head fluid temperature and maximum delivery-return temperatures of the network are held constant].

The final part of this chapter is dedicated to miscellaneous topics. These include: a consideration of the differences in design approach when the constraint is variable total thermal power required by the users and when it is constant total thermal power required by the users; geothermal fluid flow rate; and heat exchanger systems.

The fifth chapter, "Selection of the Input Data for the Examined Cases," presents all the data needed for the analysis of the cases studied. Thus, the chapter contains explanations and details of the technical data (such as well-head temperature of between 30°C and 90°C; a fixed head of 2bar for the pumping units; 85% efficiency for the peak load boilers; and 4320 h/y of heating required); the time schedule for the development of the system (for example, 50% of the user connections to the network during the year in which the network is installed); and expressions that are used to calculate the relevant economic variables (such as distribution network and geothermal well utilities costs) as well actual economic data (such as 0.38ECU/kg for the price of gasoil and 35,000 ECU/year for a clerk's salary).

In the sixth chapter, "Results and Comparisons," results (obtained with the aid of a computer program, GEOTERM, whose flow chart and example output are given in the appendices) are presented for the energy and economic analyses of 96 cases that represent the effect of 7 parameters (such as type of heat pump prime mover, district heating network temperatures, and well-head depth) on the performance of the case (as reflected in the magnitude of both engineering and economic characteristics, such as yearly energy savings, internal rate of return, and steady yearly cash flow). After each set of results, the authors have provided a narrative that contains the conclusions and implications drawn from the results.

The book has many attractive features, such as the conciseness of its presentation; the clearly-drawn, well-annotated, easy-to-read graphs; the sensible use of tables to present results; and the emphasis on the engineering performance-economic feasibility nexus. Its *piece de resistance*, undoubtedly, is the breadth and depth of the sensitivity analyses of the effect of a wide array of relevant parameters on the performance of geothermal district heating systems. The treatment here is certainly comprehensive and probably exhaustive.

My only reservation about this book is one that I offer *en passant*. This is the observation that nothing is included on the geothermal energy resource itself (aspects such as how it arises; methods of measuring the magnitude of the thermal gradient; the relative merits and drawbacks of the dry steam, hot water, and hot dry rock manifestation of the resource; and environmental issues) *vis a vis* its use for district heating. This material (either in a succinct manner in the main body of the text itself or in a more detailed fashion in an appendix) would have added some contexual weight to the book. The issue of environmental impact is particulary apposite.

All things considered, though, *Planning of Geothermal District Heating Systems* is a fine text on a subject which has not received much attention (as far as books are concerned) and which deals with an application that is very attractive in many parts of the world, from Iceland and Italy in the northern hemisphere to Australia and Indonesia in the southern. Thus, the reader for this book is potentially quite large, and this reviewer highly recommends it to thermal systems designer engineers and energy economists alike.

X. GENERAL & MISCELLANEOUS

The Life of Isaac Newton. - Richard S Westfall. Cambridge UP, New York. 1993. ISBN 43252-9. $24.95. (Under review)

REVIEW OF THE JOURNAL LITERATURE

for core list of journals scanned see Index Issue, published as Part 2 of the Dec issue of last year

I. FOUNDATIONS & BASIC METHODS

102. Finite element methods

102A. GENERAL THEORY

10A1. Adaptive FE analysis of large strain elastic response. - K Kato, NS Lee, KJ Bathe *(Dept of Mech Eng, MIT)*. Comput Struct 47(4-5) 829-855 (3 Jun 1993).

Some basic studies and developments for adaptive procedures in large strain FE analysis are presented: an evaluation of higher-order elements, two pointwise indicators for errors in stresses, a mesh generator for remeshing on the deformed configuration of the body, and a general mapping scheme for transferring solution variables across models. The methods discussed constitute the ingredients of a proposed adaptive process that is demonstrated in solutions of 2D stress analyses of rubber-like materials including contact conditions.

10A2. Inf-sup test. - D Chapelle and KJ Bathe *(MIT)*. Comput Struct 47(4-5) 537-545 (3 Jun 1993).

We briefly review the inf-sup condition for the FE solution of problems in incompressible elasticity, and then propose a numerical test on whether the inf-sup condition is passed. The evaluation of elements with this test is simple, and various results are presented. This inf-sup test will prove useful for many discretizations of constrained variational problems.

102C. STRUCTURAL APPLICATIONS

10A3. Variable node plate bending element for mat foundation analysis. - CK Choi and HS Kim *(Dept of Civil Eng, Korea Adv Inst of Sci and Tech, Taejon 305-701, Korea)*. Comput Struct 47(3) 371-381 (3 May 1993).

The variable node plate bending element, ie, an element with one or two additional mid-side nodes is used effectively in the analysis of a mat foundation. The variable node elements can generate a nearly ideal grid for mat foundation analysis in which more nodes are defined near the column location where the steep stress gradient is expected. The plate bending element used in this study is based on Mindlin-Reissner plate theory with substitute shear strain fields. The nodal stresses of that element are obtained by local smoothing. The interaction between the soil and the mat foundation is modeled with Winkler springs connected to nodal points in the mat model. The vertical stiffness of the soil material is represented in terms of a modulus of subgrade reaction and is computed in a similar way to the computation of consistent nodal force of uniform surface loading. Several mesh schemes were proposed and tested in order to find the most suitable scheme for mat foundation analysis.

See also the following:

10A64. Improved two-node Timoshenko beam FE
10A422. Indentation of laminated filament-wound composite tubes
10A479. Elimination of self-straining in four-noded plate elements for large deflection analysis
10A483. Two generalized conforming plate elements based on semiLoof constraints
10A719. Effects of eyebar shape and pin-hole tolerance on its ultimate strength

102E. OTHER SOLID MECHANICS APPLICATIONS

See the following:

10A385. Appropriate boundary conditions for FE-modeled elastic half-plane
10A387. FE procedure for axisymmetric elastomeric solids under general loading
10A429. 3D FE progressive failure analysis of composite laminates under axial extension
10A431. Analysis of delamination in cross-ply laminates initiating from impact induced matrix cracking
10A432. Analysis of matrix cracking and local delamination in $(0/\theta/-\theta)_s$ graphite epoxy laminates under tensile load
10A470. Axisymmetric deformation of varying thickness composite cylindrical shell with various end conditions
10A528. Analysis of 3D hexagonal closed-die heading by the FE flow formulation
10A532. Simplified 3D FE analysis of the non-axisymmetric extrusion processes

102G. FLUID MECHANICS APPLICATIONS

10A4. Computationally efficient modification of mixed FEMs for flow problems with full transmissivity tensors. - J Koebbe *(Dept of Math and Stat, Utah State Univ, Logan UT 84322-3900)*. Numer Methods PDE 9(4) 339-356 (Jul 1993).

The mixed FEM for approximatly solving flow equations in porous media has received a good deal of attention in the literature. The main idea is to solve for the head-pressure and fluid velocity (Darcy velocity) simultaneously to obtain a higher-order approximation of the fluid velocity. In the case of a diagonal transmissivity tensor the algebraic equations resulting from the discretization can be reduced to a system of algebraic equations for the head-pressure variable alone. This reduction results in a smaller number of unknowns to be solved for an iterative method such as a preconditioned conjugate gradient method. The fluid velocity is then obtained from an algebraic relationship. In the cases of full transmissivity tensor, the algebraic reduction is more difficult. This paper investigates some algorithms resulting from the modification of the mixed FE that take advantage of the mixed FEM for the diagonal tensor case. The resulting schemes are more efficient implementations that maintain the same order of accuracy as the original schemes.

10A5. Element diameter free stability parameters for stabilized methods applied to fluids. - LP Franca *(Lab Nacional Comput Cientifica, LNCC-CNPq, Rua Lauro Muller 455, 22290 Rio de Janeiro RJ, Brazil)* and AL Madureira *(Inst Politenico, Rua Alberto Rangel s/N, 28630 Nova Friburgo RJ, Brazil)*. Comput Methods Appl Mech Eng 105(3) 395-403 (June 1993).

Stability parameters for stabilized methods in fluids are suggested. The computation of the largest eigenvalue of a generalized eigenvalue problem replaces controversial definitions of element diameters and inverse estimate constants, used heretofore to compute these stability parameters. The design is employed in the advective-diffusive method, incompressible Navier-Stokes equations and the Stokes problem.

See also the following:

10A752. FE analysis of viscous incompressible flows using primitive variables
10A755. Progress on adaptive hp-FEMs for the incompressible Navier-Stokes equations
10A757. SUPG FE computation of viscous compressible flows based on the conservation and entropy variables formulations
10A758. Three-step FEM for unsteady incompressible flows
10T954. Numerical analysis of steady generalized Newtonian blood flow in a 2D model of the carotid artery bifurcation

102J. OTHER APPLICATIONS

10A6. FE analysis of heat transfer in anisotropic solids: Application to manufacturing problems. - P Newnham and S Abrate *(Dept of Mech and Aerospace Eng and Eng Mech, Univ of Missouri, Rolla MO 65401)*. J Reinforced Plastics Composites 12(8) 854-864 (Aug 1993).

A general formulation for the FE analysis of heat transfer problems in anisotropic laminated composite materials is presented. Two-dimensional analyses using quadrilateral isoparametric elements are performed for two classes of problems: laser cutting of laminates and non-destructive testing using thermography. Results show complex temperature distributions near the laser beam. The size of the heat affected zone fibers relative to the cutting direction. Temperature distributions in laminates with delaminations subjected to heat flow through the thickness, are shown to be strongly affected by the location of the delamination.

10A7. Studies of an interface relaxation domain decomposition technique using FEs on a parallel computer. - KP Wang and JC Bruch Jr *(Dept of Mech and Env Eng, UC, Santa Barbara CA 93106-5070)*. Numer Methods PDE 9(4) 373-394 (Jul 1993).

Studies are presented for an interface relaxation domain decomposition technique using FEs on an iPSC-2 D5 Hypercube Concurrent computer. The general type of problem to be solved is one governed by a partial differential equation. The application of the approach, however, will be extended to a free boundary value problem by appropriate modification of the numerical scheme. Using the domain decomposition technique, the computation domain is subdivided into several subdomains. In addition, on the interfaces between two adjacent subdomains are imposed a continuity condition on one side and an equilibrium condition on the other side. Successive over-relaxation processes are then carried out in all subdomains with a relaxation iterative process imposed on the interfaces. With this domain decomposition technique, the problem can be solved parallelly until convergence is reached both in the interiors and on the interfaces of all subdomains.

See also the following:

10A49. Random vibration of structures by the FEM

102L. SOLUTION ALGORITHMS

10A8. FE spaces with discontinuity capturing Part I. Transport problems with boundary layers. - EG Dutra do Carmo *(Programma Eng Nucl - COPPE-UFRJ CP 68 509 - CEP 21 945, Rio de Janeiro RJ, Brazil)*. Comput Methods Appl Mech Eng 105(3) 299-314 (June 1993).

New FE spaces are proposed for transport problems to accurately approximate the solution inside the boundary layers. To this end, discontinuity capturing functions are introduced with additional dof only in the elements that contain the boundary layers. Numerical results show the high accuracy of the approximate solution in the new spaces with usual meshes.

10A9. Galerkin FE technique for stochastic field problems. - SA Ramu *(Dept of Civil Eng, Indian Inst of Sci, Bangalore 560 012, India)* and R Ganesan *(Dept of Mech Eng, Concordia Univ, Montreal, H3G 1M8, Canada)*. Comput Methods Appl Mech Eng 105(3) 315-331 (June 1993).

A new FEM is developed to analyze the structures with more than one parameter behaving in a stochastic manner. The Galerkin weighted residual method is used. As a generalization, this paper treats the random eigenvalue problem arising when the material property values of the structural systems are having stochastic fluctuations, ie, the measurement errors can be accounted for when probabilistic modeling is used. The free vibration problem of a stochastic beam whose Young's modulus and mass density are distributed stochastically is considered. Using Galerkin's weighted residual procedure, a stochastic FEM is developed and implemented to arrive at a random algebraic eigenvalue problem. The stochastic characteristics of eigensolutions are derived in terms of the stochastic material property variations. Numerical examples are given. It is demonstrated that through this formulation the FE discretization need not be dependent on the characteristics of stochastic fields describing the fluctuations in the material property values. Further, calculation of covariances between stiffness elements, mass elements, etc, is carried out in a relatively simple manner and is more general in nature.

10A10. Implementation of FE nonlinear Galerkin methods using hierarchical bases. - J Laminie, F Pascal, R Temam *(Lab d'Analyse Numerique, Batiment 425, 91405 Orsay Cedex, France)*. Comput Mech 11(5-6) 384-407 (1993).

The nonliner Galerkin methods are investigated in the framework of FE discretization. We first describe the theoretical background in relation with multilevel and FE approximations of the attractors. Then on the computational side, we recall the definition of the hierarchical bases and analyze the structure associated to these bases. Finally we present the scheme and report on numerical experiments performed on 2D equations of the Burgers and Navier-Stokes type. Their consistency with the approximation that we make and with the structure of the algorithm is discussed.

10A11. Numerical solution of the Fokker-Planck equation for nonlinear stochastic systems. - BF Spencer Jr *(Dept of Civil Eng and Geol Sci, Univ of Notre Dame, Notre Dame IN 46556-0767)* and LA Bergman *(Dept of Aeronaut and Astronaut Eng, Univ of Illinois, Urbana IL 61801-0236)*. Nonlinear Dyn 4(4) 357-372 (Aug 1993).

The FEM is applied to the solution of the transient Fokker-Planck equation for several often cited nonlinear stochastic systems accurately giving, for the first time, the joint probability density function of the response for a given initial distribution. The method accommodates nonlinearity in both stiffness and damping as well as both additive and multiplicative excitation, although only the former is considered herein. In contrast to the usual approach of directly solving the backward Kolmogorov equation, when appropriate boundary conditions are prescribed, the probability density function associated with the first passage problem can be directly obtained. Standard numerical methods are employed, and results are shown to be highly accurate. Several systems are examined, including linear, Duffing, and Van der Pol oscillators.

10A12. Parallel FEM with a supercomputer network. - G Yagawa, A Yoshioka, S Yoshimura *(Dept of Nucl Eng, Univ of Tokyo, 7-3-1 Hongo Bunkyo, Tokyo 113, Japan)*, N Soneda *(Central Res Inst, Elec Power Indust, 2-11-1 Iwatokita Komae, Tokyo 201, Japan)*. Comput Struct 47(3) 407-418 (3 May 1993).

Computer simulations are about to replace experiments in various fields, and the scale of the models to be simulated tend to be extremely large. To perform large-scale FE analyses, the authors propose the parallel use of multiple supercomputers connected to one another through a high-speed network. In other words, a supercomputer network is regarded as a parallel computer. As a parallel numerical algorithm for the FE analysis, we adopt the domain decomposition method (DDM) combined with an iterative solver, ie, the conjugate gradient (CG) method, where a whole analysis domain is fictitiously divided into a number of subdomains without overlapping. FE analyses of the subdomains are performed under the constraint of both displacement continuity and force equivalence among subdomains. Such a constraint can be satisfied through iterative calculations such as the CG method. The present DDM-based parallel FE algorithm is combined with the server-client model for data and processor management to have the workload balanced dynamically between the processors, and is implemented first on an engineering workstation (EWS) network and then on a supercomputer network. The accuracy and parallel performance of the present system are tested using the network composed of various EWSs. Finally, it is demonstrated that the present system implemented on the supercomputer network can solve the 3D elasticity problem of over one million dof at an extremely high average speed of 1.74 GFLOPS.

10A13. Recent advances for practical FE analysis. - KJ Bathe *(MIT)*, J Walczak, H Zhang *(ADINA R&D, 71 Elton Ave, Watertown MA 02172)*. Comput Struct 47(4-5) 511-521 (3 Jun 1993).

This paper illustrates some recent advances in FE procedures that are important for practical engineering analysis. Capabilities to solve large FE systems using iterative methods, and some significant advances in FE procedures for the nonlinear analysis of structures and fluids are demonstrated. The emphasis is on presenting solution results that demonstrate the applicability of FE procedures rather than on theoretical developments (which are available in references).

10A14. Relationship between nodal schemes and mixed-hybrid FEs. - JP Hennart *(Dept Metodos Matematicos y Numericos, Inst Investigaciones en Matematicas Aplicadas Sist, Univ Nacional Autonoma, Apartado Postal 20-726, 01000 Mexico)* and E Del Valle *(Dept Ingenieria Nucl, Escuela Superior Fisica Matematicas Inst Politec Nacional, Unidad Profesional "Adolfo Lopez Mateos", 07738 Mexico)*. Numer Methods PDE 9(4) 411-430 (Jul 1993).

The relationships between a general family of nodal schemes and primal nonconforming as well as mixed-hybrid FE formulations are explored in this paper. It is shown in particular that the nodal schemes proposed are quite natural extensions in rectangular geometry of the Raviart-Thomas-Nedelec mixed-hybrid FEs. This paper is a revised and extended version with new numerical results of part of a previous research report.

102N. ELEMENT DEVELOPMENT

10A15. Assumed strain stabilization of the eight node hexahedral element. - T Belytschko and LP Bindeman *(McCormick Sch of Eng and Appl Sci, Dept of Civil Eng, Tech Inst, NWU)*. Comput Methods Appl Mech Eng 105(2) 225-260 (Jun 1993).

An accurate and robust stabilization based on the assumed strain method and an operator orthogonal to constant strain fields is presented for an eight-node hexahedral element with uniform reduced integration. The stabilization forces depend only on the element geometry and material properties. User specified parameters are not needed, yet the assumed strain stabilization is nearly as fast as perturbation type hourglass control in an explicit code. It has an excellent coarse mesh accuracy for linear elastic bending, and is easily incorporated into a nonlinear program. The assumed strain field is also used with four-point integration which does not require stabilization. In addition, two forms of the B-matrix are studied and it is shown that the mean form is more efficient since it passes the patch test in a simplified form.

10A16. Fast algorithm for generating constrained Delaunay triangulations. - SW Sloan *(Dept of Civil Eng and Surveying, Univ of Newcastle, Shortland NSW 2308, Australia)*. Comput Struct 47(3) 441-450 (3 May 1993).

A fast algorithm for generating constrained 2D Delaunay triangulations is described. The scheme permits certain edges to be specified in the final triangulation, such as those that correspond to domain boundaries or natural interfaces, and is suitable for mesh generation and contour plotting applications. Detailed timing statistics indicate that its CPU time requirement is roughly proportional to the number of points in the data set. Subject to the conditions imposed by the edge constraints, the Delaunay scheme automatically avoids the formation of long thin triangles and thus gives high quality grids. A major advantage of the method is that it does not require extra points to be added to the data set in order to ensure that the specified edges are present.

106. Other methods in computational mechanics

10A17. Anti-plane shear crack in a sandwich composite. - Jiun-Der Yu *(Princeton)* and Kuang-Chong Wu *(Inst of Appl Mech, Natl Taiwan Univ, Taipei, Taiwan 10764, ROC)*. Eng Fracture Mech 44(6) 875-885 (Apr 1993).

An analysis of an anti-plane shear crack in a sandwich composite is presented. The sandwich composite is formed by bonding one layer and two half spaces, each being anisotropic and dissimilar. The crack is assumed to be located in the middle layer and is inclined by an angle. The analysis is done by a complex-variable integral equation formulation based on the fundamental solution of a dislocation in the layer. The numerical results for vanishingly thin layers are shown to be consistent with those obtained by the J-integral.

10A18. Evaluation of fracture parameters of composites subjected to thermal shock using the BEM and sensitivity analysis techniques. -

R Chella, R Aithal, N Chandra *(Col of Eng, Florida A&M Univ - Florida State Univ, Tallahassee FL 32316-2175)*. Eng Fracture Mech 44(6) 949-961 (Apr 1993).

Quasi-static crack extension in fiber-reinforced composites subjected to thermal shock is analyzed using the boundary integral equation method, in combination with sensitivity analysis techniques. Buekner's formulation is employed to evaluate the stress intensity factor in a cracked body. This method eliminates the need for special element types to model the crack tip, as well as the use of a large number of elements near the cracked zone of interest. A numerical procedure involving sensitivity analysis techniques based on the adjoint structure approach has been developed to evaluate the energy integrals in the cracked body. Gradients of the functionals of response quantities with respect to variables such as the crack length, necessary for the evaluation of fracture parameters, are determined directly by this method. The numerical differentiation used in other numerical methods, such as the FEM, which requires the repeated solution of the equations for different crack sizes is avoided. Results for stress intensity factors as a function of crack length are presented for various composite systems. These results are in good agreement with analytical results and results from the FEM. The present approach results in significantly improved computational efficiency.

10A19. Standard eigenvalue analysis by BEM. - N Kamiya and E Andoh *(Dept of Mechano-Informatics and Syst Eng, Nagoya Univ, Nagoya 464-01, Japan)*. Commun Numer Methods Eng 9(6) 489-495 (Jun 1993).

A method for analyzing eigenvalues of the Helmholtz equation using a standard existing subroutine for eigenvalue determination is developed in this paper. It is based on the boundary integral equation formulation known as the multiple reciprocity method. The above-mentioned formulation, having polynomial matrices in terms of the eigenvalue as the coefficient matrices, is transformed into the standard-type eigenvalue problem. The resulting formulation makes it possible to determine the required eigenvalues only by boundary discretization without any initial rough estimation.

10A20. Numerical solution of partial differential equations on curved domains by collocation. - JJ van Blerk *(Atomic Energy, PO Box 582, Pretoria 0001, S Africa)* and JF Botha *(Inst for Ground-Water Stud, Univ of the Orange Free State, PO Box 339, Bloemfontein 9300, S Africa)*. Numer Methods PDE 9(4) 357-371 (Jul 1993).

The application of the FE collocation method to 2D and 3D partial differential equations is hampered by the fact that its accuracy depends largely on the position of the collocation points. The method has, in the past, thus mainly been applied to 2D differential equations defined on rectangular domains. In this case the method yields an optimal global convergence rate, when the Gauss-Legendre quadrature points are used as collocation points. It is shown in this paper that the same accuracy can also be achieved in the case of differential equations defined on nonrectangular domains. The only prerequisite for this is to solve the differential equation on a rectangular domain, mapped onto the nonrectangular domain of the differential equation by a bilinear blended map.

10A21. General hyperbolic solver: The CIP method applied to curvilinear coordinate. - Pei-Yuan Wang, Takashi Yabe *(Dept of Electron Eng, Gunma Univ, Tenjin-chou 1-5-1, Kiryu, Gunma 376, Japan)*, Takayuki Aoki *(Dept of Energy Sci, Tokyo IT, Nagatsuta, Midori-ku, Yokohama 227, Japan)*. J Phys Soc Japan 62(6) 1865-1871 (Jun 1993).

A general hyperbolic solver, the CIP method, is extended to curvilinear coordinate systems. Although the coordinate is curvilinear, the velocity components in the Cartesian coordinate are used as dependent variables. The scheme is applied to strong explosion and natural convection heat transfer. The code accurately describes a cylindrically symmetric explosion even with rectangular or distorted grids. The simulation result of heat transfer agrees well with an experimental result.

See also the following:

10T249. Globally convergent algorithm for solving nonlinear equations
10T268. Parallel asynchronous Newton algorithm for unconstrained optimization
10A386. Effective BE approach for higher order singularities
10A390. Application of BEM to geotechnical analysis
10A436. Interlaminar stresses around hole boundaries of composite laminates subjected to in-plane loading

II. DYNAMICS & VIBRATION

150. Kinematics and dynamics

150B. KINEMATICS OF RIGID BODIES AND PARTICLES

10A22. Development of a seven DOF crane with three wires: Inverse kinematics of the crane. - Hisashi Osumi, Tamio Arai, Hajime Asama.*(Japan)*. J Japan Soc Precision Eng 59(5) 767-772 (May 1993).

A 7 dof crane with three wires is proposed for automatic heavy parts assembly. The crane can control not only desired position but also orientation of a suspended object. The position and orientation control method of the crane is discussed under a static condition. By solving the simultaneous equations given by the geometrical constraints of the wire lengths and force contraints of gravity, the kinematics is calculated. Since the equations are nonlinear, Newton-Raphson method is used. The kinematic characteristics of the crane is analyzed and the relationship between the desired orientation and the shape of the object is obtained. Redundancy of the crane is used to minimize the maximum value among the three tensions of the wires. The algorithm of the inverse kinematics is proposed and experimental results using a prototype crane prove the verification of the algorithm.

10A23. Inverse problem of the kinematics of a positioner with linear actuators. - NT Monashko *(Odessa)*. J Machinery Manuf Reliab 6 27-29 (1992).

For a known motion of an object of manipulation explicit expressions allowing determination of linear displacements of inlet links of a positioner with linear actuators, are derived.

150D. DYNAMICS OF RIGID BODIES AND PARTICLES

10A24. Oscillations of a rigid body containing an elastic element with distributed parameters. - LD Akulenko *(Moscow, Russia)*. J Appl Math Mech 56(6) 911-919 (1992).

The motions of a hybrid (discrete-continual) system, consisting of a carrier rigid body and an elastic element with distributed parameters fastened to it are investigated. Two types of fastening are considered: 1) both ends are clamped, and 2) one of the ends is clamped while the other is free. A closed system of integro-differential equations is obtained which describes the state of the system under arbitrary initial conditions and forces applied to the rigid body. The perturbed motion of the rigid body in the case of a quasi-linear restoring force is investigated using asymptotic methods. The motions are studied both when there is internal resonance between the oscillations of the rigid body and the natural oscillations of the element, and when there are no such resonances. Qualitative effects are found.

150G. DEFORMABLE BODY DYNAMICS

10A25. Flexible multibody dynamics based on a fully Cartesian system of support coordinates. - N Vukasovic, JT Celigueta, J Garcia de Jalon *(Dept of Appl Mech, Univ of Navarra, Manuel de Lardizabal 15, 20009 San Sebastian, Spain)*, E Bayo *(Dept of Mech Eng, UC, Santa Barbara CA 93106)*. J Mech Des 115(2) 294-299 (Jun 1993).

In this paper we present an extension to flexible multibody systems of a system of fully cartesian coordinates previously used in rigid multibody dynamics. This method is fully compatible with the previous one, keeping most of its advantages in kinematics and dynamics. The deformation in each deformable body is expressed as a linear combination of Ritz vectors with respect to a local frame whose motion is defined by a series of points and vectors that move according to the rigid body motion. Joint constraint equations are formulated through the points and vectors that define each link. These are chosen so that a minimum use of local reference frames is done. The resulting equations of motion are integrated using the trapezoidal rule combined with fixed point iteration. An illustrative example that corresponds to a satellite deployment is presented.

See also the following:

10A128. Newton's and Poisson's rules of percussive dynamics
10A171. Pointing accuracy of a dual-spin satellite due to torsional appendage vibrations
10A340. Inverse dynamics of a flexible robot arm by optimal control
10A714. Modal analysis solution technique to the equations of motion for elastic mechanism systems including the rigid-body and elastic motion coupling terms

150H. STABILITY OF MOTION

10A26. Global feedback stabilization of the angular velocity of a symmetric rigid body. - V Andriano *(Dipartimento Matematica Politecnica, 10129 Torino, Italy)*. Syst Control Lett 20(5) 361-364 (May 1993).

In this paper we prove that the angular velocity equations of a symmetric rigid body can be globally stabilized by means of linear feedback when two control torques act on the body.

See also the following:

10A31. Nutational stability and core energy of a quasirigid gyrostat
10A235. Maneuver and vibration control of hybrid coordinate systems using Lyapunov stability theory

150I. GYRODYNAMICS

10A27. Analytical determination of time-dependent functions of drifts of a triaxial gyrostabilizer. - SV Sokolov *(Rostov-on-Don)*. J Appl Math Mech 56(6) 955-957 (1992).

Equations which describe the time-dependence of the vector of the instantaneous velocity of rotation of a triaxial gyrostabilizer (TGS) platform located on Earth, with respect to the gyroscopical system of coordinates, are obtained within the framework of the precession theory at an arbitrary polynomial dependence of the rate of the drift on overloads. Based on the properties of the TGS and the details of its use we discuss the approximation of these equations from which the analytical time-dependent function of the drift rate of a gyrostabilized platform is found. The results obtained significantly simplify the procedure of solving the problems of identification of the TGS's parameters and estimating its current orientation relative to the specified system of coordinates in inertial navigation systems.

10A28. Global stability of the steady rotations of a solid. - GA Leonov and AV Morozov *(St Petersburg)*. J Appl Math Mech 56(6) 897-901 (1992).

The dynamical Euler equations describing the motion of a non-symmetrical solid about the centre of mass in the field of a constant external moment and a dissipative one are considered. It is assumed that the external moment specified with respect to axes attached to the body acts about the intermediate central axis of inertia of the body. The conditions for global asymptotic stability as well as the stability in total of steady rotations of the solid are obtained.

10A29. Kinetic energy and complementary kinetic energy in gyrodynamics. - FPJ Rimrott *(Dept of Mech Eng, Univ of Toronto, Toronto, ON, M5S 1A4, Canada)*, WM Szczygielski *(Univ of Toronto, Toronto, ON, M5S 1A4, Canada)*, B Tabarrok *(Univ of Victoria, Toronto, BC, Canada)*. J Appl Mech 60(2) 398-405 (Jun 1993).

The concepts of kinetic energy and complementary kinetic energy permit to distinguish between two different formulations of what happens to be the same quantity in Newtonian mechanics. These formulations turn out to play a significant role in gyrodynamics in which they can be used very effectively to establish fundamental equations. It is relatively straightforward to establish a complementary kinetic energy expression. The establishment of the kinetic energy expression is, in spite of its unambiguous definition, more complicated, and a way is presented how to obtain it without too much difficulty. Equations are presented for the more common angle systems, ie, for Euler's angles of the first kind, Cardan angles of the first kind, both because of their fundamental importance, and Cardan angles of the fifth kind because of its prevalence in aeronautics.

10A30. Local boundedness of the perturbed motions of an imperfect gyroscope in gimbals with dissipative and accelerating forces. - SA Belikov *(St Petersburg)*. J Appl Math Mech 56(6) 903-910 (1992).

An unbalanced dynamically symmetrical gyroscope in gimbals with constructive imperfections is considered in a central Newtonian field of forces. It is assumed that there is a moment of forces of viscous friction acting on the axis of rotation of one of the rings of the suspension and an accelerating (electromagnetic) moment applied to the axis of rotation of another ring. The equations of motion have a partial solution for which the basic plane of the frame is perpendicular to the direction from the specified fixed point of the frame to the centre of gravitation, the basic plane of the mantle is parallel to this direction and the rotor rotates with an arbitrary constant angular velocity. The equations of perturbed motions of the reduced system with 2-dof are obtained to within third-order terms at the corresponding position of equilibrium. In the domain of admissible values of the parameters F_0 the characteristic equation of the system is considered and its coefficients are written down. A domain in F_0 is specified in which complex conjugate pairs of the eigenvalues have small moduli of the real parts but the absolute values of the second- to fourth-order off-resonance mistuning between the imaginary parts are not small. For an imperfect gyroscope in gimbals with dissipative and accelerating forces the sufficient conditions of the local uniform boundedness of motions perturbed with respect to the specified partial solution are obtained in this domain. The conditions found provide the local uniform boundedness of solutions irrespective of the forms of higher than the third order in the equations of perturbed motions. These conditions are obtained in the form of constraints for the coefficients of the normal form and, finally, for the original parameters of the system and the real imaginary parts of the eigenvalues. To provide a clear interpretation of the results, special cases when all but two parameters are fixed are analyzed. The domains of local uniform boundedness are constructed in the 2D domains F_0 using a personal computer.

10A31. Nutational stability and core energy of a quasirigid gyrostat. - IM Ross *(Dept of Aeronaut and Astronaut, Naval Postgraduate Sch, Mail Code AA-Ro, Monterey CA 93943)*. J Guidance Control Dyn 16(4) 641-647 (Jul-Aug 1993).

The asymptotic nutational stability of a quasirigid gyrostat is analyzed. The primary purpose of this analysis is to resolve a debate concerning the use of the energy-sink method of analysis for systems containing driven rotors. It is shown that when the work done by the motor torque is not taken into account, the analysis leads to a contradiction even when the total energy is dissipative. A proper application of Landon's original idea yields a relationship between the time rate of change of Hubert's "core energy" and the energy dissipation rate of the damping mechanisms in the spacecraft. The analysis shows that the core energy might increase during a rotor despin condition; hence, the minimality of core energy - a previous criterion - is not always guaranteed. A criterion for the design of the damper to insure dissipation of the core energy is presented; this condition is always satisfied for the case of a constant relative rotor spin speed that facilitates a "closed-form" solution to the nutation angle time history of an axisymmetric gyrostat. The stability condition resulting from this analysis is consistent with the Landon-Iorillo stability criterion.

10A32. Two-axis dry tuned-rotor gyroscopes: Design and technology. - WM Mansour *(McMaster Univ, Hamilton, ON, L8S 4L7, Canada)* and C Lacchini *(DIGICON SA, Gravatai 94000, Rio Grande de Sul, Brazil)*. J Guidance Control Dyn 16(3) 417-425 (May-Jun 1993).

The dry tuned-rotor gyro (DTG) is a 2-dof sensor of angular velocities about two mutually orthogonal axes. It is a relatively recent development in conventional sensor technology. The first tuned two-axis oscillatory gyro was developed in 1945 by the Royal Aircraft Establishment (RAE) in England and was reported in a technical note in 1948. The first oscillogyro was patented by Barnes. Other variations of the DTG were patented by Howe, Krupick et al and Erdley. This class of instrument has been adopted for the control of tracking radar systems; the perforation of petroleum wells; the navigation of ships, aircraft, helicopters, and terrestrial vehicles. Its major application is encountered in the guidance of unmanned space and underwater vehicles. The DTG has several advantages. It requires no fluid to support. It is small in size, can resist radiation, and is amenable to thermal modeling. It can be used in a gimballed or strapdown system. It is low in cost per axis and of reliable technology. There are a few suppliers in the world who dominate the technology of *inertial-quality* DTGs, ie, DTGs of low drifts and high dynamic range, Brown gave a list of such suppliers, together with the technical specifications for their products. DTGs that belong to this class are difficult to acquire and their price is high. This publication reports the latest advances in DTGs.

150K. NONLINEAR DYNAMICS (INCL CHAOS, BIFURCATION, FRACTALS)

10A33. Adjoining cell mapping and its recursive unraveling Part I. Description of adaptive and recursive algorithms. - PJ Zufiria *(Dept de Matematica Aplicada a las Tecnologias de la Info, GTI, DSSR, ETSI de Telecommunicacion, UPM, 28040 Madrid, Spain)* and RS Guttalu *(Dept of Mech Eng, USC, Los Angeles CA 90089-1453)*. Nonlinear Dyn 4(3) 207-226 (Jun 1993).

A new type of cell mapping, referred to as an adjoining cell mapping, is developed in this paper for autonomous dynamical systems employing the cellular state space. It is based on an adaptive time integration employed to compute an associated cell mapping for the system. This technique overcomes the problem of determining an appropriate duration of integration time for the simple cell mapping method. Employing the adjoining mapping principle, the first type of algorithm developed here is an *adaptive mapping unraveling algorithm* to determine equilibria and limit cycles of the dynamical system in a way similar to that of the simple cell mapping. The second type of algorithm developed in this paper is a *recursive unraveling algorithm* based on adaptive integration and recursive partitioning of state space into blocks of cells with a view toward its practical implementation. It can find equilibria of the system in the same manner as the simple cell mapping method but is more efficient in locating periodic solutions.

10T34. Adjoining cell mapping and its recursive unraveling, Part II. Application to selected problems. - RS Guttalu *(Dept of Mech Eng, Univ of S California, Los Angeles CA 90089-1453)* and PJ Zufiria *(Dept Matematica Aplicada Tecnologias Info, GTI DSSR ETSI de Telecommun UPM, 28040 Madrid, Spain)*. Nonlinear Dyn 4(4) 309-336 (Aug 1993).

10A35. Chaotic attitude motion of gyrostat satellites in a central force field. - X Tong and FPJ Rimrott *(Dept of Mech Eng, Univ of Toronto, ON, Canada)*. Nonlinear Dyn 4(3) 269-278 (Jun 1993).

The nonlinear attitude motion of gyrostat satellites in a central force field is investigated, with particular emphasis on their long-time dynamic behavior for a wide range of parameters. The numbers of equilibrium solutions, as well as their stability, vary with the rotor speed, and bifurcation diagrams have been obtained. Various dynamic behaviors of gyrostat satellites, eg, periodic, quasiperiodic, and chaotic, are studied via the Poincare map technique. It is shown that the rotor speed has a significant effect on the dynamic behavior of gyrostat satellites.

10T36. Constructing invariant tori for two weakly coupled van der Pol oscillators. - DE Gilsinn *(Manuf Eng Lab, Bldg 233 B106, NIST)*. Nonlinear Dyn 4(3) 289-308 (Jun 1993).

10A37. Quasi-harmonic analysis of the behavior of a hardening duffing oscillator subjected to filtered white noise. - PK Koliopulos and SR Bishop *(Dept of Civil Eng, Univ Col London, Gower St, London WC1E 6BT, UK)*. Nonlinear Dyn 4(3) 279-288 (Jun 1993).

The behavior of a hardening Duffing oscillator subjected to narrow band random excitation is examined. The influence of possible jumps, between competing states, on the probability distribution of the response amplitude is addressed. A quasi-harmonic approximation of system behavior is adopted which is capable of reproducing the observed concave shape of probability functions and compares well with predictions obtained via stochastic averaging techniques and with digital simulations.

10A38. Transition of flow-induced cylinder vibrations to chaos. - P Plaschko, E Berger

(Hermann-Fottinger-Inst fur Thermo- und Fluiddyn, Tech Univ Berlin, Germany), K Brod *(Inst fur Tech Akustik, Tech Univ, Berlin, Germany)*. Nonlinear Dyn 4(3) 251-268 (Jun 1993).

Flow-induced oscillations of rigid cylinders exposed to fully developed turbulent flow can be described by a fourth order autonomous system. Among the pertinent constants, the mass ratio is the control parameter governing the transition from limit cycle oscillations to chaotic vibrations. Particular attention is paid to the stability of the limit cycles: it has been found that they lose their stability at the point of appearance of quasi-periodic motion. The documentation of this transition is performed in terms of Lyapunov exponents, phase plots, Fourier spectra, bifurcation diagrams, and Poincare maps. As opposed to the calculation of the Lyapunov exponents where remarkable numerical difficulties were encountered, the investigation of the remaining quantities shows clearly the passage of cylinder motions from limit cycle oscillations to more and more irregular vibrations, leading finally to chaos.

See also the following:

10A11. Numerical solution of the Fokker-Planck equation for nonlinear stochastic systems
10A50. Control of nonlinear structural dynamic systems: Chaotic vibrations
10A68. Whirling of a forced cantilever beam with static deflection II. Superharmonic and subharmonic resonances
10A69. Whirling of a forced cantilevered beam with static deflection I. Primary resonance
10A507. Stability of the damped hill's equation with arbitrary, bounded parametric excitation
10A701. Routes to chaos in ball bearings

150Y. COMPUTATIONAL TECHNIQUES

10A39. Parametric excitation of computational mode of the leapfrog scheme applied to the Van der Pol equation. - DongSheng Cai *(Inst of Info Sci and Electron, Univ of Tsukuba, Ibaraki 305, Japan)*, Akira Aoyagi *(Fac of Eng, Kyushu Sangyo Univ, 3-1 Matsukadai 2-chome Higashi-ku, Fukuoka 813, Japan)*, Kanji Abe *(Col of Arts and Sci, Univ of Tokyo, Komaba 3-8-1 Meguro-ku, Tokyo 153, Japan)*. J Comput Phys **107**(1) 146-151 (Jul 1993).

The leapfrog scheme is applied to the Van der Pol equation. When the amplitude of oscillation of the physical mode exceeds a critical value, the computational mode is parametrically excited by the physical mode. The growth of the computational mode interrupts the integration based on the leapfrog scheme. The critical amplitude of the physical mode is determined by the linear stability analysis and the parametric excitation theory. The Runge-Kutta smoother eliminating the computational mode enables the longtime integration based on the leapfrog scheme.

10A40. Poisson integration of rigid body systems. - MA Austin *(Dept of Civil Eng and Inst for Syst Res, Univ of Maryland, College Park MD 20742)*, PS Krishnaprasad *(Dept of Elec Eng and Inst for Syst Res, Univ of Maryland, College Park MD 20742)*, Li-Sheng Wang *(Inst of Appl Mech, Natl Taiwan Univ, Taipei, Taiwan, ROC)*. J Comput Phys **107**(1) 105-117 (Jul 1993).

In this paper we discuss the numerical integration of Lie-Poisson systems using the mid-point rule. Since such systems result from the reduction of Hamiltonian systems with symmetry by Lie group actions, we also present examples of reconstruction rules for the full dynamics. A primary motivation is to preserve in the integration process, various conserved quantities of the original dynamics. A main result of this paper is an $O(h^3)$ error estimate for the Lie-Poisson structure, where h is the integration step-size. We note that Lie-Poisson systems appear naturally in many areas of physical science and engineering, including theoretical mechanics of fluids and plasmas, satellite dynamics, and polarization dynamics. In the present paper we consider a series of progressively complicated examples related to rigid body systems. We also consider a dissipative example associated to a Lie-Poisson system. The behavior of the mid-point rule and an associated reconstruction rule is numerically explored.

152. Vibrations of solids (basic)

152A. GENERAL THEORY

10A41. Dynamic behavior of discretized nonconservative systems. - Y Xiong *(Dept of Mech Eng, Univ of British Columbia, Vancouver, BC V6T 1W5, Canada)* and B Tabarrok *(Dept of Mech Eng, Univ of Victoria, Victoria, BC V8W 3P6, Canada)*. J Sound Vib **162**(3) 429-439 (22 Apr 1993).

The dynamic behavior of discretized nonconservative systems is investigated in the present study, and the conclusion drawn by the authors is verified for the problems of this kind. The necessary and sufficient condition for existence of solutions of symmetric and positive-definitive matrices to an inverse eigenvalue problem is obtained. Through analysis of examples, some observations of interest on the characteristic curves and the vibration modes of flutter-type nonconservative systems and the associated conservative ones are presented.

10A42. Modeling of material nonlinearities in steel structures subjected to transient dynamic loading. - AS Elnashai and BA Izzuddin *(Civil Eng Dept, Imperial Col of Sci, Tech, and Medicine, Imperial College Rd, London SW7 2BU, UK)*. Earthquake Eng Struct Dyn **22**(6) 509-532 (Jun 1993).

This paper is concerned with the modeling of the behavior of steel under cyclic and dynamic loading conditions. After a general discussion regarding the requirements for accurate and efficient modeling in dynamics, two models are described and implemented. The bilinear stress-strain constitutive relationship with kinematic hardening is widely used in many computer codes, hence is used for control purposes. The multisurface plasticity model is said to exhibit the important qualities of strain hardening, softening and relaxation to a mean stress. This model is described in detail and notes on model parameter evaluation are given. A number of validation examples are presented, due to the complexity of implementation of the multisurface formulation. This is followed by comparisons between the bilinear response predictions and those of the multisurface model for cyclic and dynamic tests on beam-columns. It is concluded that in the absence of material test data under cyclic loading, the bilinear model provides acceptable accurate response predictions. However, the multisurface model provides a significantly closer fit to experimental results, due to its ability to model a yield plateau and a nonlinear strain hardening regime as well as cyclic degradation. It can also be used for new types of steel where no distinct yield point is observed.

10A43. Multiple scales analysis of nonlinear, localized modes in a cyclic periodic system. - A Vakakis, T Nayfeh, M King *(Dept of Mech and Indust Eng, Univ of Illinois, Urbana IL 61801)*. J Appl Mech **60**(2) 388-397 (Jun 1993).

In this work the nonlinear localized modes of an n-dof nonlinear cyclic system are examined by the averaging method of multiple scales. The set of nonlinear algebraic equations describing the localized modes is derived and is subsequently solved for systems with various numbers of dof. It is shown that nonlinear localized modes exist only for small values of the ratio (k/μ), where k is the linear coupling stiffness and μ is the coefficient of the grounding stiffness nonlinearity. As (k/μ) increases the branches of localized modes become nonlocalized and either bifurcate from "extended" antisymmetric modes in inverse, "multiple" Hamiltonian pitchfork bifurcations (for systems with even-dof), or reach certain limiting values for large values of (k/μ) (for systems with odd-dof). Motion confinement due to nonlinear mode localization is demonstrated by examining the responses of weakly coupled, perfectly periodic cyclic systems caused by external impulses. Finally, the implications of nonlinear mode localization on the active or passive vibration isolation of such structures are discussed.

See also the following:

10A108. Vibration absorbers for a class of self-excited mechanical systems

152B. LINEAR THEORY

10A44. Relationship between fundamental natural frequency and maximum static deflection for various linear vibratory systems. - CW Bert *(Sch of Aerospace and Mech Eng, Univ of Oklahoma, Norman OK 73019)*. J Sound Vib **162**(3) 547-557 (22 Apr 1993).

It is shown that the fundamental natural frequency of a wide variety of discrete and continuous systems is inversely proportional to the gravitational acceleration divided by the maximum static deflection, raised to the 1/2 power. The value of the constant of proportionality is determined for multi dof discrete systems, axially vibrating prismatic and tapered rods, prismatic and tapered slender beams, membranes and thin plates of many planforms. Particular attention is paid to the effects of taper, axial preload, geometry and boundary conditions. The results of this investigation should be useful in predicting the approximate fundamental natural frequency from the static deflection, either calculated or determined experimentally.

10A45. Uncoupling and solving the equations of motion of vibrating linear discrete systems. - SF Felszeghy *(Dept of Mech Eng, California State Univ, Los Angeles CA 90032-8153)*. J Appl Mech **60**(2) 456-462 (Jun 1993).

The equations of motion governing the vibrations of a linear, viscously damped, discrete system are generally mutually coupled. This article examines the problem, when the viscous damping is nonclassical, of how best to uncouple and solve by approximation the governing second-order differential equations of motion. It is shown that when the equations of motion are expressed in normal coordinates, the equations can then be transformed by an orthogonal coordinate transformation to a new generalized coordinate system in which a bound on the relative error introduced in the response by discarding all the coupling terms is a minimum. This approach extends the applicability of undamped modal analysis to certain types of nonclassically damped systems. The analytical results and the effectiveness of the proposed method are illustrated with four examples taken from other previously published approaches to the stated problem.

152D. STOCHASTIC EFFECTS, INCL RANDOM EXCITATION

10A46. Dynamic response of continuous systems including model uncertainty. - WD Iwan *(Div of Eng and Appl Sci, California IT, Pasadena CA 91125)* and H Jensen *(Univ Tecnica Federico, Santa Maria, Valparaiso, Chile)*. J Appl Mech **60**(2) 484-490 (Jun 1993).

This paper presents a technique for obtaining the response of linear continuous systems with parameter uncertainties subjected to deterministic excitation. The parameter uncertainties are modeled as random fields and are assumed to be time independent. The general formulation of the method is developed for a particular class of partial differential equations with random coefficients. Random shape functions are introduced to approximate the solution in the spatial domain and in the random space. A system of linear ordinary differential equations for the unknowns of the problem is derived using the weighted residual method. The system of equations is integrated in time and the response variability is computed. Application of the new method is made to a continuum described by the 1D wave equation in which the stiffness properties exhibit a spatial random variation. Validation calculations show that the results from the method agree well with those obtained by direct numerical integration.

10A47. Equivalent linearization: A suitable tool for analyzing MDOF-systems. - HJ Pradlwarter and GI Schueller *(Inst of Eng Mech, Univ of Innsbruck, Innsbruck, Austria)*. Probab Eng Mech 8(2) 115-126 (1993).

A method for the evaluation of the stochastic response of MDOF-systems, based on the equivalent linearization (EQL) method, is presented. This paper focuses on the applicability and accuracy of EQL within design procedures of realistic structures. A numerical approach for evaluating the linearization coefficients is introduced for the benefit of high flexibility, simplicity, and most realistic modeling of restoring force laws. It is shown that the generally made assumption of a normally distributed response introduces some arbitrariness in the estimated stochastic response. The source and effect of this arbitrariness on the accuracy and convergence of the equivalent linearization procedure is studied and discussed. Finally, the procedure is applied to investigate the effect of damping devices assembled in an eight story building subjected to bi-directional stochastic, ie, earthquake excitation. The stationary solution obtained by Monte Carlo simulation, conventional EQL as well as the present approach are compared and discussed.

10A48. Power spectral density of nonlinear system response: The recursion method. - R Valery Roy *(Dept of Mech Eng, Univ of Delaware, Newark DE 19716)* and PD Spanos *(LB Ryon Chair in Eng, Rice Univ, Houston TX 77251)*. J Appl Mech 60(2) 358-365 (Jun 1993).

Spectral densities of the response of nonlinear systems to white noise excitation are considered. By using a formal solution of the associated Fokker-Planck-Kolmogorov equation, response spectral densities are represented by formal power series expansion for large frequencies. The coefficients of the series, known as the spectral moments are determined in terms of first-order response statistics. Alternatively, a J-fraction representation of spectral densities can be achieved by using a generalization of the Lanczos algorithm for matrix tridiagonalization, known as the "recursion method". Sequences of rational approximations of increasing order are obtained. They are used for numerical calculations regarding the single-well and double-well Duffing oscillators, and Van der Pol type oscillators. Digital simulations demonstrate that the proposed approach can be quite reliable over large variations of the system parameters. Further, it is quite versatile as it can be used for the determination of the spectrum of the response of a broad class of randomly excited nonlinear oscillators, with the sole prerequisite being the availability, in exact or approximate form, of the stationary probability density of the response.

10A49. Random vibration of structures by the FEM. - I Elishakoff and Liping Zhu *(Center for Appl Stochatics Res and Dept of Mech Eng, Flordia Atlantic Univ, Boca Raton FL 33431-0991)*. Comput Methods Appl Mech Eng 105(3) 359-373 (June 1993).

This paper is directed at two objectives: (1) to develop an improved FE formulation of beams subjected to random loading; (2) to provide a benchmark example which can also be solved exactly. Systematic formulation of element and global spectral matrices of both the excitation and response are presented. Two approximations for evaluation of the element spectral densities of excitation are compared with the result of direct numerical calculation. It is shown that, in the benchmark example, the FE and exact solutions are in perfect agreement.

See also the following:

10A11. Numerical solution of the Fokker-Planck equation for nonlinear stochastic systems
10A94. Stochastic FE for a beam on a random foundation with uncertain damping under a moving force
10T250. Stochastic averaging using elliptic functions to study nonlinear stochastic systems

152F. DAMPING, DECAY, AND CONTROL OF VIBRATIONS

10A50. Control of nonlinear structural dynamic systems: Chaotic vibrations. - EK Hall II *(Aerospace Corp, Los Angeles CA)* and SV Hanagud *(Sch of Aerospace Eng, Georgia Tech)*. J Guidance Control Dyn 16(3) 470-476 (May-Jun 1993).

In recent years, chaotic behavior has been observed in a large number of physical systems. The appearance of these unpredictable, broadband frequency responses in structural dynamic systems presents a possible threat to the integrity of aerospace structures because of their erratic time histories. Thus, the objective of this paper is to investigate the control of chaotic motions through the simple example of a buckled beam. As an initial attempt, a nonlinear control methodology termed feedback linearization was utilized. In this method, the nonlinearities causing chaos are eliminated from the closed-loop system through nonlinear feedback. Although effective in eliminating chaotic motions this scheme does have some disadvantages such as the demand for accurate models and, in general, full state measurements. As an alternative, the feasibility of using smart structural concepts to control chaotic vibrations was examined. This technique utilized the introduction of so-called electronic damping to move the system out of a chaotic parameter region. The method was shown to be feasible and holds promise for future applications. Thus, this work demonstrates that a controller capable of controlling a chaotic system can be developed. From this study, directions for further research in the area of controlling chaotic systems were obtained.

10A51. Control-structure interactions of space station solar dynamic modules. - RD Quinn *(Dept of Mech and Aerospace Eng, Case Western Reserve Univ, Cleveland OH 44106)* and IS Yunis *(Struct Syst Dyn Branch, NASA Lewis Res Center, Cleveland OH 44135)*. J Guidance Control Dyn 16(4) 623-629 (Jul-Aug 1993).

Potential control-structures interaction problems of large flexible multibody structures in the presence of pointing and tracking requirements are addressed. A control approach is introduced for the simultaneous tracking and vibration control of multibody space structures. The application that is discussed is the planned Space Station Freedom configured with solar dynamics modules. The solar dynamic fine-pointing and tracking requirements may necessitate controller frequencies above the structural natural frequencies of space station and the solar dynamic modules themselves. It is well known that this can give rise to control-structure interaction problems if the controller is designed without giving due consideration to the structural dynamics of the system. Possible control-structure interaction problems of Freedom's solar dynamic power systems are investigated. A FE model of Freedom is used to demonstrate these potential control-structure interaction problems and the proposed tracking and vibration control approach.

10A52. Decoupling vibration control of a flexible rotor system with symmetric mass and stiffness properties. - ST Chen and AC Lee *(Dept of Mech Eng, Natl Chiao Tung Univ, Taiwan, ROC)*. J Syst Control Eng 207(I1) 9-14 (1993).

The paper investigates the control problem for a flexible rotor system with symmetric mass and stiffness properties and proposes an internal and external decoupling control scheme to simplify the controller design for such a system, where the existence of gyroscopic effects during rotation is neglected. The whole flexible rotor system can eventually be separated into four flexible subsystems without knowledge of the system parameters, and the control algorithm for each subsystem can be designed and implemented independently. Simulation results demonstrate the effectiveness of using the proposed scheme in conjunction with the optimal modal space control scheme.

10A53. Passive damping for robust feedback control of flexible structures. - R Gueler *(Prod Eng Lab, Matsushita Elec Indust, Osaka 571, Japan)*, AH von Flotow, DW Vos *(Dept of Aeronaut and Astronaut, MIT)*. J Guidance Control Dyn 16(4) 662-667 (Jul-Aug 1993).

This paper investigates the benefits of passive damping in single-input single-output (SISO) and multi-input multi-output (MIMO) feedback controlled structures. Theoretical formulations are derived verifying improved stability robustness characteristics for simple controlled structures on phase margin, gain margin, and root locus properties of a SISO system. Control design techniques for closed-loop bandwidths beyond the first modal frequency require accurate knowledge of the structural dynamics, particularly at crossover. The use of passive damping in the structural design allows for a greater margin of error in pole-zero cancellation at crossover, thus improving the stability robustness. Minimum levels of required passive damping are derived for robust control of uncertain structures. The derivations are extended to suggest application to MIMO systems. Robustness improvements are quantified in case studies for an 8th-order SISO example and an 18th-order MIMO example and compared to the simple derivations.

10T54. Performance of higher harmonic control algorithms for helicopter vibration reduction. - SR Hall *(Dept of Aeronaut and Astronaut, MIT)* and NM Wereley *(BDM International, Arlington VA 22203)*. J Guidance Control Dyn 16(4) 793-797 (Jul-Aug 1993).

10A55. Sensitivity-based characterization and optimization of viscoelastically damped honeycomb structures. - S Kodiyalam *(Solid Mech Lab, Bldg K-1 Rm 2A25, General Electric R&D Center, PO Box 8, Schenectady NY 12301)* and J Molnar *(Mech Anal Group, General Electric Astro Space, Princeton NJ 08543)*. J Guidance Control Dyn 16(3) 484-489 (May-Jun 1993).

Control of dynamic vibrations is critical to the operational success of many aerospace systems. Large space structures, for practical reasons, are lightweight and hence highly flexible. This paper addresses the problem of vibration control of such structures through passive damping, using viscoelastic materials. A new sensitivity-based approach to characterize viscoelastic material property variation with frequency is outlined. It is demonstrated that, using structural optimization techniques, viscoelastically damped honeycomb structures can be tailored to provide weight-effective vibration damping. A spacecraft payload mounting platform is used as the demonstration structure.

10A56. Simulation of active vibroprotective systems. - VV Yablonskii and BO Marder *(Moscow, Russia)*. J Machinery Manuf Reliab 6 76-82 (1992).

A method for active vibration protection of a mechanism, based on decomposing the vector of vibration forces acting in the supports, into the natural forms of vibration of the mechanism viewed as a rigid bogy with elastic ties, is proposed. Also used are wide-band compensation and damping of singled-out components (modal control) with the help of electromechanical feedback. The calculated results show that the efficiency and noise immunity of a modal-control vibroprotective system may be increased as compared with the known results.

10A57. Simultaneous design of active vibration control and passive viscous damping. - MLD Gaudreault, BS Liebst, RL Bagley *(Dept of Aeronaut and Astronaut, Air Force IT, WPAFB)*. J Guidance Control Dyn 16(4) 654-661 (Jul-Aug 1993).

Structural engineers have found that passive damping can reduce the amount of active damping required to control structural vibration. Conversely, improperly designed passive damping can inadvertently increase system reaction times, reducing control effectiveness. This paper presents several techniques for blending active vibration control and passive viscous damping. A closed-form optimal solution for minimizing a quadratic cost functional is derived, but it is shown to be dependent on the initial conditions that produces time-varying damping coefficients. To eliminate the dependence on initial conditions, solution techniques for suboptimal, state independent solutions are developed. The suboptimal solutions require less computation effort, but still give good estimates of the optimal solution. The advantages and disadvantages of the different solution techniques are discussed with respect to computation requirements and robustness. Methods of comparing competing designs are also discussed. Several numerical examples illustrate the similarities and differences of the various techniques. More importantly, the examples demonstrate the significant improvements achievable by simultaneously designing passive and active damping.

See also the following:

10A283. Vibration and robust control of symmetric flexible systems

152Y. COMPUTATIONAL TECHNIQUES

10A58. Time integration algorithm for structural dynamics with improved numerical dissipation: The generalized-α method. - J Chung and GM Hulbert *(Dept of Mech Eng and Appl Mech, Univ of Michigan, Ann Arbor MI 48109-2125)*. J Appl Mech 60(2) 371-375 (Jun 1993).

A new family of time integration algorithms is presented for solving structural dynamics problems. The new method, denoted as the generalized-α method, possesses numerical dissipation that can be controlled by the user. In particular, it is shown that the generalized-α method achieves high-frequency dissipation while minimizing unwanted low-frequency dissipation. Comparisons are given of the generalized-α method with other numerically dissipative time integration methods; these results highlight the improved performance of a new algorithm. The new algorithm can be easily implemented into programs that already include the Newmark and Hilber-Hughes-Taylor-α time integration methods.

154. Vibrations (structural elements)

154B. BEAMS, COLUMNS, RODS, AND BARS

10A59. Analysis of vibration spectrum of a Timoshenko beam with boundary damping by the wave method. - MP Coleman *(Dept of Math and Comput Sci, Fairfield Univ, Fairfield CT 06430)* and H Wang *(Dept of Math and Stat, Wichita State Univ, Wichita KS 67208)*. Wave Motion 17(3) 223-239 (May 1993).

The Timoshenko beam is a model of a thick beam and is important in structural engineering. Recently, there has been considerable interest in the analysis and control of the vibration of the Timoshenko beam. The understanding of the spectrum of vibration is fundamental in order to accomplish such research. The classical separation of variables approach leads to complicated transcendental equations which are difficult to analyze. In this paper, we develop the wave propagation method to tackle this problem. Asymptotic estimates for the eigenfrequencies are obtained for a Timoshenko beam with dissipative conditions. Such estimates show that the Timoshenko beam has two branches in its spectrum corresponding to the propagation of waves with two velocities for the displacement and angular rotation variables. The asymptotic estimates are confirmed by numerical computations using a high accuracy Lengendre-tau spectral method.

10A60. Construction of an Euler-Bernoulli beam from spectral data. - BD Lowe *(Dept of Math, Texas A&M Univ, College Station TX 77843-3368)*. J Sound Vib 163(1) 165-171 (8 May 1993).

A numerical method for approximating coefficients in an Euler-Bernoulli beam equation from spectral data is proposed. The technique is based on a shooting method and constructs a beam that has the given spectral data. Numerical examples illustrate the performance of the method.

10A61. Dynamical analysis of a general mass-spring arrangement in beam systems. - I Kaljevic, S Saigal *(Dept of Civil Eng, Carnegie Mellon Univ, Pittsburgh PA 15213)*, CH Broome Jr *(Dept of Civil Eng, Howard Univ, Washington DC 20059)*. J Sound Vib 163(1) 67-81 (8 May 1993).

The free vibration analysis of general structural arrangements consisting of beams with discrete spring mass oscillators is presented. A detailed derivation of the governing differential equation of motion for such systems is presented. The self-adjoint property of the resulting differential operator is shown which assures that the eigenvalues of the dynamical system are both real and positive. The orthogonality conditions for the eigenfunctions are also derived. Two methods, namely, the Green's function method and the particular integral method, are developed to treat the resulting differential equation of motion. Detailed parametric studies are performed to study the vibrational characteristics of general dyanamical systems. A Galerkin method solution is also derived for comparison and for validation of the formulations presented.

10A62. Flexural-torsional behavior of a straight elastic beam subject to terminal moments. - Z Tan and JA Witz *(Dept of Mech Eng, Univ Col, London WC1E 7JE, UK)*. J Appl Mech 60(2) 498-505 (Jun 1993).

This paper discusses the large-displacement flexural-torsional behavior of a straight elastic beam with uniform circular cross-section subject to arbitrary terminal bending and twisting moments. The beam is assumed to be free from any kinematic constraints at both ends. The equilibrium equation is solved analytically with the full expression for curvature to obtain the deformed configuration in a 3D Cartesian coordinate system. The results show the influence of the terminal moments on the beam's deflected configuration.

10A63. Forced nonlinear oscillations of discretely-jointed thin-walled beams. - BA Antuf'ev. Russian Aeronaut 35(3) 72-78 (1992).

We present the approximate solution of the problem on the forced nonlinear transverse oscillations of the thin-walled structure, consisting of the several discretely-jointed shells. We consider the dynamic structural model that represents a number of the linear subsystems interconnected by the equivalent imponderable springs with nonlinear rigid characteristics that are specified by the local pliability of the shells in their attachment points.

10A64. Improved two-node Timoshenko beam FE. - Z Friedman and JB Kosmatka *(Dept of Appl Mech and Eng Sci, UCSD)*. Comput Struct 47(3) 473-481 (3 May 1993).

The stiffness, mass, and consistent force matrices for a simple two-node Timoshenko beam element are developed based upon Hamilton's principle. Cubic and quadratic Lagrangian polynomials are used for the traverse and rotational displacements, respectively, where the polynomials are made interdependent by requiring them to satisfy the two homogeneous differential equations associated with Timoshenko's beam theory. The resulting stiffness matrix, which can be exactly integrated and is free of "shear-locking", is in good agreement with the exact Timoshenko beam stiffness matrix. Numerical results are presented to show that the current element exactly predicts the displacements of a short beam subjected to complex distributed loadings using only one element, and the current element predicts shear and moment resultants and natural frequencies better than existing Timoshenko beam elements.

10A65. Statics, stability, and vibration of non-prismatic beams and columns. - JD Aristizabal-Ochoa *(Dept of Civil Eng and Eng Mech, California State Univ, Fullerton CA 92634)*. J Sound Vib 162(3) 441-455 (22 Apr 1993).

An algorithm that evaluates the static, stability and vibration response of nonprismatic beams and columns is presented. Matrix equations are derived that can be readily included in existing computer programs on the analyses of 2D and 3D framed structures with prismatic and nonprismatic members. It is shown in this paper that the analyses of framed structures with nonprismatic and prismatic members under any loading and support conditions can be carried out once the main stiffness coefficients are determined. Numerical examples on the statics, stability and dynamics of nonprismatic beams are included for easy verification and compared with available results from other anlaytical methods to show the power of the proposed algorithm.

10A66. Studies on dynamic behavior of a beam with symmetrically varying thickness. - PK Roy and N Ganesan *(Machine Dyn Lab, Dept of Appl Mech, Indian IT, Madras 600 036, India)*. Comput Struct 47(2) 265-274 (Apr 1993).

A detailed study has been conducted on the effect of different types of variation in profile and thickness on the amplitude and the dynamic bending stress of a beam under a point harmonic load. The end conditions considered are clamped or simply supported at both the ends. The response has been calculated for the first three modes of vibration. In each case the results obtained for different types of thickness variation are compared with those obtained for a uniform thickness beam. It is observed that a considerable reduction in amplitude and bending stress can be achieved by proper selection of thickness variation.

10A67. Vibroimpact interaction in systems of bars. - VV Klubovich and VN Sakevich *(Vitebsk)*. J Machinery Manuf Reliab 6 13-20 (1992).

The specifics of vibroimpact interaction of nonidentical waveguides are analyzed. It is shown, both theoretically and experimentally, that an increase in the force compressing a pair of interacting waveguides, results in the ratio of the amplitudes of interacting end faces tending to a certain limit. The limiting ratio of the amplitudes of interacting waveguides end faces is determined by the waveguides acoustic parameters and is independent of the ratio of amplitudes of disturbing forces acting on the corresponding waveguides. It is also shown that if the natural frequency of a waveguide-reflector is smaller than that of the waveguide-concentrator connected with an ultrasonic transformer, then the amplitude of relative vibration of interacting end faces is much higher than in the opposite case.

10A68. Whirling of a forced cantilever beam with static deflection II. Superharmonic and subharmonic resonances. - IMK Shyu, RH Plaut, DT Mook *(VPI)*. Nonlinear Dyn 4(4) 337-356 (Aug 1993).

Secondary resonances of a slender, elastic, cantilevered beam subjected to a transverse harmonic load are investigated. The effects of nonlinear curvature, nonlinear inertia, viscous damping and static load are included. Cubic terms in the governing equations lead to subharmonic and superharmonic resonances of order three. The static displacement produced by the weight of the beam introduces quadratic terms in the governing equations, which cause subharmonic and superharmonic resonances of order two. Out-of-plane motion is possible in all of these secondary resonances when the principal moments of inertia of the beam cross section are approximately equal.

10A69. Whirling of a forced cantilevered beam with static deflection I. Primary resonance. - I-MK Shyu, DT Mook, RH Plaut *(VPI)*. Nonlinear Dyn 4(3) 227-249 (Jun 1993).

The response of a slender, elastic, cantilevered beam to a transverse, vertical, harmonic excitation is investigated. The effects of nonlinear curvature, nonlinear inertia, viscous damping and static load are included. Previous work often has neglected the static deflection caused by the weight of the beam, which adds quadratic terms in the governing equations of motion. Galerkin's method is used with three modes and approximate solutions of the temporal equations are obtained by the method of multiple scales. Primary resonance is treated here, and out-of-plane motion is possible in the first and second modes when the principal moments of inertia of the beam cross-section are approximately equal. In Parts II and III, secondary resonances and nonstationary passages through various resonances are considered.

See also the following:

10A460. Axisymmetric problems of a partially embedded rod with radial deformation

154C. STRINGS, CABLES, CHAINS, AND ROPES

10A70. Lateral vibrations of steel cables including structural damping. - M Raoof and Yu Ping Huang *(Sch of Architec and Civil Eng, S Bank Univ, London, UK)*. Struct Build 99(2) 123-133 (May 1993).

The paper provides theoretical means of predicting structural damping of axially preloaded spiral strands undergoing lateral vibrations due, for example, to vortex-shedding. In line with the previously reported experimental observations and theoretical studies, it is assumed that frequency-independent cable damping arises from the frictional energy dissipation between the individual wires in contact. For pin-ended and axially preloaded spiral strands undergoing plane-section bending, it is now possible to show significant variations of the equivalent damping ratio with the type of strand construction details, length of the cable and mode of vibration. This is in contrast to the traditional approaches, which have invariably assumed a constant damping ratio based on rather limited (and sometimes even questionable) experimental observations.

154F. MEMBRANES

10A71. Modes of a circular membrane of nonuniform radial density. - TM Kalotas and AR Lee *(Dept of Phys, La Trobe Univ, Bundoora, Australia)*. Acustica 78(4) 220-225 (May 1993).

The normal modes of a circular symmetric clamped membrane of arbitrary nonuniform radial mass density are analyzed with the aid of the method of constant density radial segments. Using a 2×2 matrix formalism, a generic mode condition is derived from which the characteristic frequencies and standing wave patterns are directly computed. For the purpose of manipulating these mode frequencies through small changes in membrane density, an explicit first order perturbational connection between these quantities is established. Computed examples are given to demonstrate the results.

10A72. A superposition-Rayleigh-Ritz method for free vibration analysis of non-uniformly tensioned membranes. - MJ Gorman *(Univ of Ottawa, Ottawa, ON K1N 6N5, Canada)* and RK Singhal *(Directorate of Space Mech, Canadian Space Agency, Ottawa, ON K2H 8S2, Canada)*. J Sound Vib 162(3) 489-501 (22 Apr 1993).

An accurate analytical method is described for establishing initial stress distributions in corner tensioned rectangular membranes. With the stress distributions available it is shown how the Rayleigh-Ritz method is employed to obtain membrane free vibration frequencies and mode shapes. The initial stress distributions are obtained by the superposition of three judiciously chosen Airy stress functions. Verification tests are performed to demonstrate that this general computational method gives results in agreement with known classical problems where uniform edge loading is employed. The method described has immediate application in the static and dynamic analysis of large membranes proposed for space antennae.

154G. PLATES

10A73. Approximate 3D analysis of rectangular thick laminated plates: Bending, vibration, and buckling. - YK Cheung and J Kong *(Dept of Civil and Struct Eng, Univ of Hong Kong, Hong Kong, China)*. Comput Struct 47(2) 193-199 (Apr 1993).

A global-local approach is proposed to analyze thick laminated plates. This approach treats a thick laminated plate as a 3D inhomogeneous anisotropic elastic body. The cross-section of a laminated plate is first discretized into conventional eight-node elements. The interpolation function along the span of the plate is defined by the cubic B_3-spline function. The displacement functions can be expressed as the product of the usual isoparametric shape functions and the spline function. A set of global polynomials of an appropriate order is selected to transform the nodal variables of the cross-section to a much smaller set of generalized parameters associated with the polynomials. These parameters can be obtained by means of the standard Rayleigh-Ritz technique. The total number of unknowns involved is drastically reduced with a minor sacrifice of accuracy. The six components of stresses, the fundamental natural frequencies and the critical buckling loads can be determined with acceptable accuracy. Numerical examples are given to demonstrate the accuracy and effectiveness of the global-local procedures.

10A74. Effects of boundary constraints and thickness variations on the vibratory response of rectangular plates. - CW Lim and KM Liew *(Div of Appl Mech, Sch of Mech and Prod Eng, Nanyang Tech Univ, Nanyang Ave, Singapore 2263)*. Thin-Walled Struct 17(2) 133-159 (1993).

The present study concentrates on the first known free flexural vibration of doubly-tapered rectangular plates subject to a variety of boundary constraints ranging from a cantilevered plate to a fully clamped plate. The Rayleigh-Ritz minimum total energy approach complemented by the global pb-2 shape functions as the admissible plate displacement amplitude functions is employed. The shape functions are, in principle, the product of a set of mathematically complete 2D polynomials and a basic function. The basic function is formed from a product of the boundary piecewise geometric expressions of the plate each of which is raised to the power of 0, 1 or 2 corresponding to a free, simply supported or clamped edge, respectively. The shape functions satisfy the kinematic boundary conditions at the outset. This proposed computational model has a great advantage over the conventional FE and the finite strip methods in terms of computation cost, numerical preparation and implementation, application versatility, and, in certain aspects, numerical accuracy. Comprehensive numerical results for six classes of plates with selected mode shapes are presented. These results may serve as a benchmark for future reference since no literature can be found for symmetric doubly-tapered plates as considered in this study.

10A75. Exact analytical solutions for the vibrations of sectorial plates with simply-supported radial edges. - CS Huang *(Dept of Civil Eng, Ohio State Univ, Columbus OH 43210)*, AW Leissa *(Dept of Eng Mech, Ohio State Univ, Columbus OH 43210)*, OG McGee *(Dept of Civil Eng, Ohio State Univ, Columbus OH 43210)*. J Appl Mech 60(2) 478-483 (Jun 1993).

The first known exact analytical solutions are derived for the free vibrations of sectorial thin plates having their radial edges simply supported, with arbitrary conditions along their circular edges. This requires satisfying: (1) the differential equation of motion, (2) boundary conditions along the radial and circular edges, and (3) proper regularity conditions at the vertex of the radial edges. The solution to the differential equation involves ordinary and modified Bessel functions of the first and second kinds, of non-integer order, and four constants of integration. Utilizing a careful limiting process, the regularity conditions are invoked to develop two equations of constraint among the four constants for sector angles exceeding 180° (re-entrant corners). Moment singularities for re-entrant corners are shown to be the same as the ones determined by Williams (1952) for statically loaded sectorial plates. Frequency determinants and equations are generated for circular boundaries which are clamped, simply-supported, or free. Nondimensional frequency parameters are presented for all three types of configurations for sector angles of 195°, 210°, 270°, 330°, and 360° (ie, re-entrant corners).

10A76. Large amplitude vibrations of imperfect antisymmetric angle-ply laminated plates. - A Bhimaraddi *(Diversified Computer Eng and Development, Clawson MI 48017)*. J Sound Vib 162(3) 457-470 (22 Apr 1993).

This paper deals with the large amplitude vibrations of imperfect anitsymmetric angle ply and symmetric cross ply laminated plates using the von Karman type nonlinear plate model. The basic plate equations correspond to those of the parabolic shear deformation plate theory. Five governing differential equations of the plate are first reduced to a single nonlinear time differential equations, using the single mode approach to a simply supported plate. This equation involves the quadratic and cubic nonlinearities for imperfect plates. Nonlinear to linear frequency ratios have been obtained using the perturbations method and the exact method. Numerical results indicate that the perturbation methods are unreliable for certain plate problems and lead to wrong conclusions. It has been observed that whether the plate exhibits a hardening or softening type of nonlinearity depends on both the initial imperfection value and the amplitude of vibration.

10A77. Large-amplitude FE flexural vibration of plates-stiffened plates. - SR Rao, AH Sheikh, M Mukhopadhyay *(Dept of Naval Architec, Indian IT, Kharagpur 721 302, India)*. J Acoust Soc Am 93(6) 3250-3257 (Jun 1993).

Large-amplitude free flexural vibration of stiffened and unstiffened plates has been studied by using the FEM. An isoparametric quadratic plate-bending element has been used both for the plate and the stiffener. The dynamic version of von Karman's field equations has been adopted and the formulation has been done in the total Lagrangian coordinate system. The in-plane deformation and inertia have been taken into account. The resulting nonlinear equations have been solved by the direct iteration technique using a linear mode shape as the starting vector. The stiffener has been elegantly modeled so that it can be placed anywhere within the plate element and it need not follow the nodal lines. This has increased the flexibility of the mesh generation considerably. The arbitrary orientation and eccentricity of the stiffener have been incorporated in the formulation. The shear deformation has been incorporated according to Mindlin's hypothesis. Stiffened and unstiffened plates that have various boundary conditions have been analyzed and the results have been compared with those available in the literature.

10A78. Modeling of dynamic networks of thin elastic plates. - JE Lagnese and G Leugering *(Dept of Math, Georgetown Univ, Washington DC 20057)*. Math Methods Appl Sci 16(6) 379-407 (Jun 1993).

The purpose of this paper is to derive junction conditions for networks of thin elastic plates and to analyze the dynamic equations of such networks. Junction conditions for networks of Kirchhoff plates and networks of Reissner-Mindlin plates are derived based on geometric considerations of the deformation at a junction. It is proved that the dynamic system which describes the Reissner-Mindlin network is well-posed is an appropriate energy space. It is further established that the Kirchhoff network is obtained in the limit of the Reissner-Mindlin network as the shear moduli go to infinity.

10A79. Transverse vibration of annular circular and elliptic plates using the characteristic orthogonal polynomials in 2D. - B Singh *(Dept of Math, Univ of Roorkee, Roorkee UP 247 667, India)* and S Chakraverty *(Comput Center, Central Build Res Inst, Roorkee, India)*. J Sound Vib 162(3) 537-546 (22 Apr 1993).

Characteristic orthogonal polynomials in two variables have been generated over the annular region occupied by a circular or elliptic plate satisfying the essential boundary conditions. These are used ot express the displacement in the transverse vibration of the plate. The Rayleigh-Ritz method is then applied to study the fundamental mode of vibration. Comparison has been made with the known results for circular annular plates in some cases. The results for the elliptic annular plate are entirely new and are not available elsewhere. All the results are summarized in tables covering various combinations of the boundary conditions.

10A80. Vibration analysis of annular plates with concentric supports using a variant of Rayleigh-Ritz method. - CM Wang and V Thevendran *(Dept of Civil Eng, Natl Univ of Singapore, Kent Ridge 0511, Singapore)*. J Sound Vib 163(1) 137-149 (8 May 1993).

A variant of the Rayleigh-Ritz method is presented for solving the free vibration problem of annular plates with internal axisymmetric supports. The method is simple, accurate and may be readily programmed and run on a microcomputer. A comprehensive tabulation of the fundamental frequencies is presented for isotropic annular plates with an internal concentric support. Results for full circular plates with concentric supports are also obtained by making the inner radial edge free and permitting the inner radius to become very small.

10A81. Vibration analysis of orthotropic Mindlin plates with edges elastically restrained against rotation. - JH Chung, TY Chung *(Korea Res Inst of Ships and Ocean Eng, Daeduk Sci Town, Daejon, Korea)*, KC Kim *(Dept of Naval Architec, Seoul Natl Univ, Seoul, Korea)*. J Sound Vib 163(1) 151-163 (8 May 1993).

The free vibration analysis of the orthotropic Mindlin plates with edges elastically restrained against rotation has been accomplished using the Rayleigh-Ritz method. Polynomials with properties corresponding to those of the Timoshenko beam functions are introduced as trial functions in the spatial representation of the deflection and rotations of cross sections in two directions of the plates. The results obtained by using polynomials are nearly the same as the Timoshenko beam function results, but were obtained with considerably less numerical efforts.

10A82. Vibrations of multispan all-round clamped stiffened plates by modified dynamic edge effect method. - I Elishakoff *(Center for Appl Stochastic R&D and Dept of Mech Eng, Florida Atlantic Univ, Boca Raton FL 33431-0991)*, A Sternberg *(RAPHAEL, Kiriat Mozkin PO Box 2250, Haifa 31021, Israel)*, TJ Van Baten *(Dept of Aerospace Eng, Delft Univ of Tech, HS 2629 Delft, Netherlands)*. Comput Methods Appl Mech Eng 105(2) 211-223 (Jun 1993).

The modified dynamic edge effect method is applied to dynamic analysis of continuous skin-stringer panels. The number of spans is assumed finite; all panels and interior stringers are identical. The solution procedure involves formulation of two auxiliary problems of the Voigt-Levy type in conjunction with an eigenfrequency wave-number relationship. The treatment yields a pair of transcendental equations in terms of wave numbers. The method has advantages over other approximate approaches in the sense that the number of spans enters one of the transcendental equations explicitly, so that numerical complexity does not increase with it.

See also the following:

10A3. Variable node plate bending element for mat foundation analysis
10A185. Low-frequency vibrations and radiation of a circular plate
10A304. Integrated design and control of laminated hybrid plates with dynamic response and buckling objectives

154H. SHELLS

10A83. Thickness expansions for higher-order effects in vibrating cylindrical shells. - JG McDaniel *(BBN Syst and Tech, Cambridge MA 02138)* and JH Ginsberg *(Sch of Mech Eng, Georgia Tech)*. J Appl Mech 60(2) 463-469 (Jun 1993).

In the spirit of Mindlin and others who have used series expansions to express transverse dependence in thin bodies, the present work uses Ritz expansions in a variational formulation for cylindrical shell vibrations. By expanding displacements in spatial coordinates, integral expressions for strain and kinetic energy are converted to quadratic sums involving time-dependent generalized coordinates. Hamilton's principle provides ordinary differential equations for these coordinates. This viewpoint yields physical insight into the mechanisms of energy storage and avoids the geometrically thin assumption inherent to many formulations. A set of Legendre polynomials multiplied by a radial factor repesent the radial dependences of displacement components, while circumferential variations are represented by sinusoidal functions. Excellent agreement in natural frequencies is found between this approach and analytical solutions over the entire range of shell thicknesses, including the limiting case of a solid cylinder. Comparisons to several thin shell theories are given, leading to conclusions about the range of validity of these theories.

See also the following:

10A63. Forced nonlinear oscillations of discretely-jointed thin-walled beams
10A112. Axisymmetric response of nonlinearly elastic cylindrical shells to dynamic axial loads

154I. PLATES AND SHELLS (THICK)

10A84. Natural frequencies and modes of a circular plate welded to a circular cylindrical shell at arbitrary axial positions. - DT Huang and W Soedel *(Sch of Mech Eng, Purdue)*. J Sound Vib 162(3) 403-427 (22 Apr 1993).

The modal characteristics of a plate shell coupled structure consisting of a simply supported thin circular cylindrical shell and a circular plate which may be joined to the shell at any arbitrary axial position were studied using the receptance method. Line receptances were formulated from the responses of the plate and the shell to line force and line moment loadings distributed harmonically along the interface of the plate and the shell, utilizing natural modes and frequencies of the plate and shell, respectively. The system frequency equation was generated and solved numerically to obtain the natural frequencies and mode shapes of the combined structure under different joining configurations. The effects of length, thicknesses and joining positions on the modal characteristics of the combined structure were investigated. Certain results obtained from the receptance method and a FE program were compared for verification purposes and showed good agreement. The structural coupling behavior between the plate and the shell and the coupling relationship between the line force loading and the line moment loading were explored.

154J. DISCS AND BLADES

10A85. Natural frequencies and stability of a flexible spinning disk-stationary load system with rigid-body tilting. - Jen-San Chen *(Dept of Mech Eng, Natl Taiwan Univ, Taipei, Taiwan 107)* and DB Bogy *(Comput Mech Lab, Dept of Mech Eng, UCB)*. J Appl Mech 60(2) 470-477 (Jun 1993).

The effects of rigid-body tilting on the natural frequencies and stability of the head-disk interface of a flexible spinning disk are studied both by analysis and numerical computation. Another problem of a stationary flexible disk with rigid body tilting subject to a rotating load system is also studied. In the conventional case without rigid-body tilting, these two problems are mathematically identical except for the additional membrane stress terms arising from the centrifugal force. When the rigid-body tilting is included, however, these two problems differ not only by the centrifugal effect, but also by additional terms which arise from the gyrodynamic effect. After properly defining the inner product between two state vectors, the set of equations of motion is proven to fall into the category of gyroscopic systems. Then the derivatives of the eigenvalues of the coupled system are obtained to provide a better understanding of the numerical results.

10A86. Vibration and damping analysis of pre-twisted composite blades. - S Mohamed Nabi and N Ganesan *(Machine Dyn Lab, Dept of Appl Mech, Indian IT, Madras 600 036, India)*. Comput Struct 47(2) 275-280 (Apr 1993).

Vibration characteristics of pre-twisted composite blades are analyzed using a three-noded triangular cylindrical shell element. The specific example of glass fibre reinforced plastic material is analyzed with its material damping. The effect of different parameters such as pre-twist, fibre orientation, skew angle, taper ratio on natural frequency and system loss factor is investigated. It is found that the maximum fundamental frequency and maximum fundamental loss factor occur at different twist angles and at different fibre orientations. The influence of taper ratio and aspect ratio on 0° and 90° fibre orientations is reported. The effect of skew angle on natural frequency and on system loss factors is seen to be low.

154K. ROTATING SHAFTS (CRITICAL SPEED, BALANCING)

10A87. Vibration and stability of a rotating shaft containing a transverse crack. - SC Huang *(Dept of Mech Eng, Natl Taiwan IT, Taipei, Taiwan 10772, ROC)*, YM Huang *(Dept of Mech Eng, Natl Central Univ, Chung-Li, Taiwan, ROC)*, SH Shieh *(Dept of Mech Eng, Natl Taiwan IT, Taipei, Taiwan 10772, ROC)*. J Sound Vib 162(3) 387-401 (22 Apr 1993).

The dynamic response of a rotating shaft containing a transverse crack is investigated. The local flexibility due to the crack is first evaluated from the theory of fracture mechanics. The results show that an increase of crack depth magnifies the response amplitude as expected. It is discovered that the crack affects the dynamic response more significantly when it occurs near a place where the bending moment exhibits a larger value. From the FFT analysis of the displacement responses, it is seen that the 1Ω and 2Ω components are excited prominently due to crack. Hence, they provide possibly good indices for an online crack monitoring system. The stability of a cracked shaft is examined via the Floquet theory, and the results show that, for an integer multiple of the shaft bending frequency when the crack depth reaches half of the radius. However, a small amount of damping is found to raise effectively the unstable region.

See also the following:

10A52. Decoupling vibration control of a flexible rotor system with symmetric mass and stiffness properties

154L. FRAMES, TRUSSES, AND ARCHES

10A88. Lanczos-based technique for exact vibration analysis of skeletal structures. - HA Smith *(Dept of Civil Eng, Stanford)*, DC Sorensen *(Dept of Math Sci, Rice Univ, Houston TX 77251)*, RK Singh *(Dept of Civil Eng, Stanford)*. Int J Numer Methods Eng 36(12) 1987-2000 (30 Jun 1993).

This paper presents and discusses a Lanczos-based eigensolution technique for evaluating the natural frequencies and modes from frequency-dependent eigenproblems in structural dynamics. The new solution technique is used in conjunction with a mixed FE modeling procedure which utilizes both the polynomial and frequency-dependent displacement fields in formulating the system matrices. The method is well suited to the solution of large-scale problems. The new solution methodology presented here is based on the ability to evaluate a specific set of parameterized nonlinear eigenvalue curves at given values of the parameter through an implicitly restarted Lanczos technique. Numerical examples illustrate that the implicitly restarted Lanczos method with secant interpolation accurately evaluates the exact natural frequencies and modes of the nonlinear eigenproblem and verifies that the new eigensolution technique coupled with the mixed FE modeling procedure is more accurate than the conventional FE models. In addition, the eigenvalue technique presented here is shown to be far more computationally efficient on large-scale problems than the determinant search techniques traditionally employed for solving exact vibration problems.

10A89. Vibration of laminated composite arches with deep curvature and arbitrary boundaries. - MS Qatu *(Dept of Mech Eng, Franklin Univ, 201 S Grant Ave, Columbus OH 43215)* and AA Elsharkawy *(Dept of Mech Eng, Ohio State Univ, Columbus OH 43210)*. Comput Struct 47(2) 305-311 (Apr 1993).

Exact solutions for the title problem are presented for general boundary conditions. No numerical frequencies are presented using these solutions, instead natural frequencies are obtained using the Ritz method. This method has the important shortcoming that the assumed displacements have to be changed when various boundary conditions are treated. This shortcoming is overcome in this paper by assuming the displacement functions as polynomials having a general form. Accurate frequencies are obtained for arbitrary boundary conditions. The results can be useful for designers, engineers, and researchers who are interested in the problem. The method can also be generalized to plate- and shell-like structures.

See also the following:

10A42. Modeling of material nonlinearities in steel structures subjected to transient dynamic loading

10A65. Statics, stability, and vibration of nonprismatic beams and columns

154N. COMPOSITE MATERIALS

10A90. Dynamic analysis of laminates with elliptical cutouts using the hybrid-stress FE. - S Ramakrishna, KM Rao, NS Rao *(Dept of Mech Eng, Indian IT, Kharagpur 721 302, India)*. Comput Struct 47(2) 281-287 (Apr 1993).

An eight-noded hybrid-stress FE is used to analyze the dynamic behavior of laminated plates with elliptical cutouts. The first four natural frequencies are evaluated by varying a number of parameters, such as the fibre orientation, width-to-thickness ratio, hole size and major-to-minor axes ratio.

10A91. Effect of thermal stresses on the vibration of composite cantilevered plates. - JM Klosner and T-H Cheng *(Dept of Mech and Indust Eng, Polytech Univ, Farmingdale NY 11735)*. J Composite Tech Res 15(2) 123-135 (Sum 1993).

This study explores the effects of thermal stresses on the dynamic characteristics of composite cantilevered plates. The induced thermal stresses are determined by appealing to the principle of minimum strain energy, while the Raleigh-Ritz procedure is used to obtain the plate frequencies. Extensive numerical calculations have been carried out in order to gain quantitative understanding of how different choices of aspect ratios and temperature change intensities (T_0) influence the natural frequencies of composite cantilevered plates. It has been shown that the first bending mode frequencies are unaffected by the induced stresses, while the first torsional mode frequencies decrease quite significantly with increasing values of T_0, and therefore with increased magnitudes of the thermal stresses.

10A92. Vibration of clamped moderately thick general cross-ply plates using a generalized Navier approach. - RA Chaudhuri *(Dept of Civil Eng, Univ of Utah, Salt Lake City UT 84112)* and HRH Kabir *(Eng Mech Res Corp, Troy MI 48084)*. Composite Struct 24(4) 311-321 (1993).

A hitherto unavailable analytical solution to the free vibration problem of general cross-ply laminated rigidly clamped rectangular plates, incorporating first-order shear deformation, and rotatory and in-plane inertias into the formulation, is presented. A recently developed boundary continuous displacement based generalized Navier solution technique is used to solve the five highly coupled linear second-order partial differential equations with constant coefficients, and the associated geometric boundary conditions. The assumed solution functions are in the form of double Fourier series, which satisfy the rigidly clamped boundary conditions *a priori* in a manner similar to the conventional Navier method. Convergence characteristics of the natural frequencies of both symmetric and antisymmetric cross-ply plates are numerically established. Other numerical results presented herein include (i) comparison with the corresponding available first-order shear deformation theory-based Galerkin and classical lamination theory-based-boundary discontinuous analytical solutions, and (ii) study of the effects of thickness and aspect ratio on the natural frequencies.

154O. STRUCTURAL ELEMENTS ON FOUNDATIONS

10A93. Free vibrations of foundation beams on two-parameter elastic soil. - C Franciosi and A Masi *(Dept of Struct Eng and Soil Mech, Univ of Basilicata, Via della Tecnica 3, 85100 Potenza, Italy)*. Comput Struct 47(3) 419-426 (3 May 1993).

A FE free vibration analysis of beams on a two-parameter elastic foundation is performed using the exact shape functions. The stiffness matrix and the mass matrix are deduced in closed form for the whole parameter range. Numerical comparisons and examples allow us to check the performance of the proposed FE. A practical example ends the paper.

10A94. Stochastic FE for a beam on a random foundation with uncertain damping under a moving force. - L Fryba *(Inst of Theor and Appl Mech, Acad of Sci, Prague, Czech Republic)*, S Nakagiri, N Yoshikawa *(Dept of Appl Phys and Appl Mech, Inst of Indust Sci, Univ of Tokyo, Tokyo, Japan)*. J Sound Vib 163(1) 31-45 (8 May 1993).

It appears that a stochastic stationary process occurs, viewed by an observer moving together with the moving force. A stochastic FE analysis by means of the first order perturbation and first order second-moment method provides an evaluation of the variance of the deflection and of the bending moment of the beam. The effects of several parameters and of various types of correlation functions are investigated. It is shown that the randomness of the foundation is of greater importance than the uncertainty in the damping. The dynamic and stochastic effects increase with increasing speed of the movement of the force in the subcritical domain, but decrease in the supercritical domain. The coefficient of variation of the deflection of the beam is larger than that if the bending moment at the point of application of the moving force.

154Y. COMPUTATIONAL TECHNIQUES

10A95. Model reduction methods for dynamic analyses of large structures. - B Haggblad *(Dept of Solid Mech, RIT, S-100 44 Stockholm, Sweden)* and L Eriksson *(Corp Res, ASEA Brown Boveri, S-721 78 Vasteras, Sweden)*. Comput Struct 47(4-5) 735-749 (3 Jun 1993).

User-friendly FE pre-processors permit detailed modeling of engineering structures with complicated topologies, often resulting in a much larger number of dof than that motivated by the expected complexity of the structural response. Dynamic analyses of these large-scale models might require a prohibitive amount of CPU time. In particular, the uncoupling of the equations of motion for linear systems with non-proportional damping by means of a complex eigenvector basis is computationally very demanding. We present general model reduction procedures, applicable to whole structures or substructures, that produce a series of reduced models each spanning appropriate subspaces (general Krylov spaces) of the solution space. Crucial steps in such procedures are the selection of basis vectors for the (sub) structures and the control of reduction errors. The set of basis vectors is generated by using a simple physical approach for successively reducing the residual error in the governing equilibrium equations. A frequency window method (shifting) is used to capture the relevant frequency content. The residuals of the equilibrium equations, computed on fully expanded level, are used as reliable measures of the reduction errors. The efficiency of the techniques is demonstrated in some numerical experiments and on a large engineering problem, using a program based on SAP IV.

10A96. Post-processing technique and an a posteriori error estimate for the Newmark Method in dynamic analysis. - N-E Wiberg and XD Li *(Dept of Struct Mech, Chalmers Univ of Tech, S-412 96, Gothenburg, Sweden)*. Earthquake Eng Struct Dyn 22(6) 465-489 (Jun 1993).

In this paper, we present a post-processing technique and an *a posteriori* error estimate for the Newmark method in structural dynamic analysis. By post-processing the Newmark solutions, we derive a simple formulation for linearly varied third-order derivatives. By comparing the Newmark solutions with the exact solutions expanded in the Taylor series, we achieve the local post-processed solutions which are of fifth order accuracy for displacements and fourth-order accuracy for velocities in one step. Based on the post-processing technique, *a posteriori* local error estimates for displacements, velocities and, thus, also the total energy norm error estimate are obtained. If the Newmark solutions are corrected at each step, the post-processed solutions are of third-order accuracy in the global sense, ie, one-order improvement for the original Newmark solutions is achieved. We also discuss a method for estimating the global time integration error. We find that, when the total energy norm is used, the sum of the local error estimates will give a reasonable estimate for the global error. We present numerical studies on a SDOF and a 2 dof example in order to demonstrate the performance of the proposed technique.

10A97. Reciprocal relations in nonlinear vibrations. - VL Berdichevsky *(Sch of Aerospace Eng, Georgia Tech)*. Int J Eng Sci 31(8) 1215-1218 (Aug 1993).

General reciprocal relations between the response of a nonlinear system and the exciting force are derived. A variational principle for the amplitude characteristics of the response is formulated.

See also the following:

10A58. Time integration algorithm for structural dynamics with improved numerical dissipation: The generalized-α method

10A163. Supersonic flutter analysis of composite plates and shells

156. Vibrations (structures)

156B. BUILDINGS AND FOUNDATIONS

See the following:

10A936. Review of reference models for assessing inelastic seismic torsional effects in buildings

156D. BRIDGES

10A98. Analysis of continuous box girder bridges including the effects of distortion. - B Kermani *(Acer Consultants, Bristol, UK)* and P Waldron *(Dept of Civil and Struct Eng, Univ of Sheffield, PO Box 600 Mappin St, Sheffield S1 4DU, UK)*. Comput Struct 47(3) 427-440 (3 May 1993).

Torsional warping and distortion of the cross-section are important features of thin-walled beams and must be considered fully in the design of box girder bridges. A method of elastic analysis is developed based on the stiffness approach which includes the effects of warping torsion and distortion in addition to the more familiar actions of bending moment and torsion. The method, which is applicable to straight single cell box girders with at least one axis of symmetry, is demonstrated here in the analysis of three different box girder models for which experimental or analytical results were already available. The method is shown to be easy and economical to use and provides a physical insight into the structural response of thin-walled box girder bridges under general loading conditions.

10A99. Parametric study of cable-stayed bridge response due to traffic-induced vibration. - MA Khalifa *(Dept of Civil Eng, Univ of Nebraska, Lincoln NE 68588-0531)*. Comput Struct 47(2) 321-339 (Apr 1993).

The dynamic response of long-span cable-stayed bridges due to moving traffic loads is investigated utilizing 3D models. Modal analysis is conducted using the deformed dead-load tangent stiffness matrix. A new concept, presented by discretization of cable into several elements, is used to study the effect of cable vibration on bridge dynamics. A computer algorithm is developed to simulate the applied traffic loads for both directions of the bridge deck. The algorithm is flexible in terms of handling different loading capacities, speeds and configurations. Parametric studies are conducted to investigate the effect of cable vibration, damping, vehicle-structure interaction, random roughness of the bridge deck, as well as span length and vehicle-speed. Cases of asymmetric traffic loading clustered in one direction are also considered in order to study the torsional response of the bridge. Results are discussed, summarized and plotted.

156E. HYDRAULIC STRUCTURES

10A100. Investigation of the Mauvoisin concrete arch dam subjected to maximum credible earthquake. - K-V Kniffka *(Electrowatt Eng Services, Zurich, Switzerland)*. Comput Struct 47(4-5) 787-800 (3 Jun 1993).

The response of the 250 m high Mauvoisin arch dam, located in southern Switzerland was investigated with respect to the maximum credible earthquake and a peak ground acceleration of 0.33 g. The results of an artificially generated spectrum-compatible earthquake with three stochastically independent components of the ground motion were compared with those of the natural earthquake of Friuli. Significant system parameters were calibrated with the measured behavior and structure-foundation-fluid interaction was considered. Assuming massless foundation and a compressible reservoir, a linear dynamic analysis was carried out in the time domain.

156F. MARINE STRUCTURES

10A101. Response statistics of nonlinear, compliant offshore structures by the path integral solution method. - A Naess *(Fac of Civil Eng, Norwegian IT, Rich Birkelands vie IIa, N-7034 Trondheim, Norway)* and JM Johnsen *(Kvaerner Eng, PO Box 222, N-1234 Lysaker, Norway)*. Probab Eng Mech 8(2) 91-106 (1993).

The paper investigates the applicability of the path integral solution method for calculating the response statistics of nonlinear dynamic systems whose equations of motion can be modeled by use of the Ito stochastic differential equations. The state vector process associated with such a model is generally a diffusion process, and the probability density function of the process thus satisfies a Fokker-Planck-Kolmogorov equation. It is shown in the paper that the path integral solution technique combined with an appropriate numerical scheme constitutes a powerful method for solving the Fokker-Planck-Kolmogorov equation with natural boundary conditions. The method distinguishes itself by high accuracy and numerical robustness even at very low probability levels. These features are high-lighted by application to example studies of nonlinear, compliant offshore structures.

156G. VEHICLES (INCL LOCOMOTIVES)

See the following:

10A299. Applications of optimal control to advanced automotive suspension design

156I. AIRCRAFT

10A102. Vibration analysis of composite wing with tip mass using FEs. - In Lee and Jung-Jin Lee *(Dept of Aerospace Eng, Korea Adv Inst of Sci and Tech, Taejon, Korea)*. Comput Struct 47(3) 495-504 (3 May 1993).

The analysis of vibration characteristics, including the natural frequencies and modes for various shaped composite wings with a tip mass and an engine, has been performed using the FEM based on the shear deformable theory. The present analysis presents the effect of tip mass, engine, sweep angle, fiber orientation, and aspect ratio of a composite wing, which is composed of graphite-epoxy laminate with a symmetric stacking sequence, on vibration characteristics. At a specific fiber orientation, the natural frequencies of the two modes approach each other. The natural frequencies of the wing with the tip mass and the engine are lower than those of the wing without the tip mass and the engine. However, for the wing and the tip mass, the natural frequencies of the chordwise mode increase due to the increase of the bending stiffness of the tip mass. This present FEM, which uses eight-node quadrilateral elements, gives very accurate results.

See also the following:

10T54. Performance of higher harmonic control algorithms for helicopter vibration reduction

10A692. Use of brittle strain-sensitive coatings in strength tests of full-scale aircraft structures

156J. SPACECRAFT, SPACESTATIONS

10A103. Dynamic characteristics of liquid motion in partially filled tanks of a spinning spacecraft. - BN Agrawal *(Dept of Aeronaut and Astronaut, Naval Postgraduate Sch, Monterey CA 93943)*. J Guidance Control Dyn 16(4) 636-640 (Jul-Aug 1993).

This paper presents a boundary-layer model to predict dynamic characteristics of liquid motion in partially filled tanks of a spinning spacecraft. The solution is obtained by solving three boundary-value problems: an inviscid fluid problem, a boundary-layer problem, and a viscous correction problem. The boundary-layer solution is obtained analytically, and the solutions to inviscid and viscous correction problems are obtained by using FEMs. The model has been used to predict liquid natural frequencies, mode shapes, damping ratios, and nutation time constants for a spinning spacecraft. The results show that the liquid motion in general will contain significant circulatory motion due to Coriolis forces except in the first azimuth and first elevation modes. Therefore, only these two modes can be represented accurately by equivalent pendulum models. The analytical results predict a sharp drop in nutation time constants for certain spacecraft inertia ratios and tank fill fractions. This phenomenon was also present during on-orbit liquid slosh tests and ground air-bearing tests.

See also the following:

10A51. Control-structure interactions of space station solar dynamic modules

10A55. Sensitivity-based characterization and optimization of viscoelastically damped honeycomb structures

10A228. Multiple-input, multiple-output time-series models from short data records

156K. MACHINE ELEMENTS

10A104. Unsteady aerodynamic response of 2D subsonic and supersonic oscillating cascades with chordwise displacement and flexible deformation. - M Namba and K Toshimitsu *(Dept of Aeronaut and Astronaut, Kyushu Univ, Hakozaki, Higasi-ku Fukuoka 812, Japan)*. J Sound Vib 162(3) 503-527 (22 Apr 1993).

In this paper the double linearization theory applied to lightly loaded 2D subsonic and supersonic cascades undergoing oscillation with chordwise displacement or flexible deformation is presented. Numerical computation based on this theory have been conducted to demonstrate parametric dependence of the unsteady aerodynamic work on blades. The translational oscillation can be destabilized by chordwise displacement for both subsonic and supersonic cascades. The contribution of chordwise displacement to the unsteady aerodynamic work is strongly dependent upon the phase difference between the chordwise and normal components of the blade motion. The unsteady aerodynamic work for flexible blade motion also is substantially influenced by steady loading. For the supersonic cascades, the effect of displacement of Mach line reflection points due to the chordwise blade motion gives a significant contribution to the unsteady aerodynamic force.

See also the following:

10A718. Effect of slit nuts on durability of threaded connections manufactured of heat-resistant steels and subjected to cyclic loading

156L. MACHINE TOOLS

See the following:

10A371. Practical implications in the calibration of translational tables

156M. ROTATING MACHINES AND TURBOMACHINERY

See the following:

10A87. Vibration and stability of a rotating shaft containing a transverse crack

10A189. Sound generation by rotating stall in centrifugal turbomachines

156N. DAMPING

10A105. Active distributed damping of flexible structures using piezo-electric actuator-sensors. - F Pourki *(Dept of Mech Eng and Mech, Drexel Univ, Philadelphia PA 19103)*. Mech Res Commun 20(4) 279-285 (Jul-Aug 1993).

The concept of "space stations" and the growing number of space missions, during which, different manned or unmanned manoeuvres are exercised, has led to emergence of so called "adaptive" or "smart structures". In these structures, the principles of control engineering are used, to make the structure adapt to a set of required geometric or dynamic constraints during a manoeuvre. Examples of "adaptive" or "smart structures" are abundant in "organic and biological systems" in nature. For instance, the birds' wings and navigation or steering organs of sea animals are formed in such ways to make them adaptable to variations in their manoeuvres. These "biological structures", embody proper actuators and sensors to vary their performance according to changes in environment, while their bodies support structural integrity and maintain appropriate rigidity. Muscular system, which deploys variable shapes for different tasks is another sophisticated biological example of adaptive structure with biochemical actuation mechanisms.

10A106. Transfer function modeling of damping mechanisms in distributed parameter models. - JC Slater and DJ Inman *(Mech Syst Lab, Dept of Mech and Aerospace Eng, SUNY, Buffalo NY 14260)*. Mech Res Commun 20(4) 287-292 (Jul-Aug 1993).

This work formulates a method for modeling of material damping characteristics in distributed parameter models which may be easily applied to models such as rod, plate, and beam equations. The general linear boundary value vibration equation is modified to incorporate hysteresis effects represented by complex stiffness using the transfer function approach proposed by Golla and Hughes. The governing characteristic equations are decoupled through separation of variables yielding solutions similar to those of undamped classical theory, allowing solution of the steady state as well as transient response. An example problem and solution is provided demonstrating the similarity of the solution to that of the classical theory and the transient response of non-viscous systems.

156O. ISOLATION

10A107. Damped resonant appendages to increase inherent damping in buildings. - R Villaverde and LA Koyama *(Dept of Civil Eng, UC, Irvine CA 92717)*. Earthquake Eng Struct Dyn 22(6) 491-507 (Jun 1993).

It is demonstrated that the addition of a tuned mass-spring-dashpot system with a relatively small mass and a high damping ratio can be an effective way to increase the inherent damping characteristics of buildings and reduce, thus, their response to earthquake excitations. The demonstration is based on a theoretical formulation and on numerical and experimental studies that confirm this formulation. In the theoretical formulation, it is shown that, if certain conditions are satisfied, the damping ratios in two of the modes of the system that is formed by a building and an appendage in resonance are approximately equal to the average of the corresponding damping ratios of the building and the appendage. Based on this finding, it is then shown that an attached appendage with a high damping ratio and tuned to the fundamental frequency of a building may increase the damping ratio in the fundamental mode of the building to a value close to half the damping ratio of the appendage. In the numerical study, the response of a ten-storey shear building is analysed under two different earthquake ground motions with and without the proposed resonant appendages. Appendages with damping ratios of 20 and 30% are considered. In this study, it is found that under one of the ground motions the maximum displacement of the building's roof is reduced 30% with the appendage with 20% damping and 39% with the one with 30% damping. Similarly, with these two appendages the building's base shear is reduced 31 and 41%, respectively. In the experimental study, a wooden three-storey structural model is tested in a shaking table with and without an appendage designed and constructed to have a damping ratio of 52.5%. The test is conducted under random and sinusoidal base excitations. In the shaking table test under random excitation, the attached appendage reduces the response of the model 38.6%, while in that under sinusoidal vibration 45.2%.

10A108. Vibration absorbers for a class of self-excited mechanical systems. - S Natsiavas *(Dept of Mech and Aerospace Eng, Arizona State Univ, Tempe AZ 85287)*. J Appl Mech 60(2) 382-387 (Jun 1993).

An averaging methodology is employed in studying dynamics of a two-dof nonlinear oscillator. The main system is modeled as a van der Pol oscillator under harmonic forcing. The objective is to reduce its amplitude of oscillation near resonance, by attaching it to a damped vibration absorber with a Duffing spring. It is first shown that substantial reduction in the response amplitude can be achieved in this way. However, for some combinations of the parameters, the low-amplitude periodic motion of the system in the original resonance regime becomes unstable through a Hopf bifurcation of the averaged equations. Direct numerical integration shows that this gives rise to amplitude modulated or chaotic response of the oscillator, with much higher vibration amplitudes than the unstable periodic response, which coexists with these complex motions. Finally, it is shown that the present analysis can be employed in selecting the parameters in ways that exploit the significant practical advantages arising from the presence of the absorber, by predicting and avoiding these instabilities.

156Y. COMPUTATIONAL TECHNIQUES

10A109. Sensitivity based method for structural dynamic model improvement. - RM Lin, H Du, JH Ong *(Sch of Mech and Prod Eng, Nanyang Tech Univ, Nanyang Ave 2263, Singapore)*. Comput Struct 47(3) 349-369 (3 May 1993).

Sensitivity analysis, the study of how a structure's dynamic characteristics change with design variables, has been used to predict structural modification effects in design for many decades. In this paper, methods for calculating the eigensensitivity, frequency response function sensitivity and its modified new formulation are presented. The implementation of these sensitivity analyses to the practice of FE model improvement using vibration test data, which is one of the major applications of experimental modal testing, is discussed. Since it is very difficult in practice to measure all the coordinates which are specified in the FE model, sensitivity based methods become essential and are, in fact, the only appropriate methods of tackling the problem of FE model improvement. Comparisons of these methods are made in terms of the amount of measured data required, the speed of convergence and the magnitudes of modeling errors. Also, it is identified that the inverse iteration technique can be effectively used to minimize the computational costs involved. The FE model of a plane truss structure is used in numerical case studies to demonstrate the effectiveness of the applications of these sensitivity based methods to practical engineering structures.

See also the following:

10A96. Post-processing technique and an a posteriori error estimate for the Newmark Method in dynamic analysis

158. Wave motions in solids

158A. GENERAL THEORY

10A110. Morawetz's method for the decay of the solution of the exterior initial-boundary value problem for the linearized equation of dynamic elasticity. - A Charalambopoulos *(Dept of Math, Natl Tech Univ, Athens, Greece)*. J Elast 31(1) 47-69 (Apr 1993).

In this paper, the behavior of the solution of the time-dependent linearized equation of dynamic elasticity is examined. For the homogeneous problem, it is proved that in the exterior of a star-shaped body on the surface of which the displacement field is zero, the solution decays at the rate t^{1} as the time t tends to infinity. For the nonhomogeneous problem with a harmonic forcing term, it is proved that for large times, the elastic material in the exterior of the body, tends to a harmonic motion, with the period of the external force. The convergence to the steady harmonic state solution is at the rate $t^{1/2}$ as t tends to infinity, and is uniform on bounded sets.

158B. RODS AND BEAMS, ELASTIC

10A111. Numerical prediction of the propagation of elastic waves in longitudinally impacted rods: Applications to Hopkinson testing. - C Bacon *(Lab Mec Phys, Univ de Bordeaux I, 351, cours de la Liberation, 33 405 Talence, Cedex, France)*. Int J Impact Eng 13(4) 527-539 (Nov 1993).

Simple expressions, based on 1D elastic wave theory, are established which permit prediction of normal force and particle velocity at cross-sections of a non-uniform linearly-elastic rod. The initial normal force and particle velocity at each cross-section of that rod must be known. In order to assess the validity of the assumptions, an experimental test on a cone-shaped rod is performed. Numerical results are provided for two different configurations: a rod shaped at one end in order to perform the Hopkinson three-point bend test and a rod heated at one end for a high temperature dynamic test. The given expressions are so easy to program that a common spreadsheet program is sufficient to implement and perform the calculation. They enable the influence of an impedance variation to be quantified *a priori*. In the case of the Hopkinson three-point bend test, the wave distortion is not very important if the rise time is long and the length of the shaped end is short. For a heated rod, the conventional Hopkinson treatment is not available when the temperature is too high. Some effects of an idealized quasi-static specimen for both Hopkinson three-point bend and non-uniform temperature are included.

See also the following:

10A59. Analysis of vibration spectrum of a Timoshenko beam with boundary damping by the wave method

158C. PLATES AND SHELLS, ELASTIC

10A112. Axisymmetric response of nonlinearly elastic cylindrical shells to dynamic axial loads. - R Gilat, E Feldman, J Aboudi *(Dept of Solid Mech Mat and Struct, Fleishman Fac of Eng, Tel Aviv Univ, Ramat Aviv 69978, Israel)*. Int J Impact Eng 13(4) 545-554 (Nov 1993).

The axisymmetric response of nonlinearly elastic cylindrical shells subjected to dynamic axial loads is analyzed by using an incremental formulation. The material elastic nonlinearity is modeled by the generalized Ramberg-Osgood representation. The time-dependent displacements of the shell are assumed to be governed by nonlinear equations of motion based on the von Karman-Donnell kinematic relations; moreover, both in-surface and out-of-surface inertia terms are included. The finite difference method with respect to the spatial coordinate and the Runge-Kutta method with respect to time are employed to derive a solution. Numerical results demonstrate the effect of the material nonlinearity on the deflections, stiffness matrices and dynamic buckling behavior of cylindrical shells.

158F. SURFACE WAVES

10A113. Propagation of surface waves across a vertical layer with non-rigid contacts. - EN Its and JS Lee *(Dept of Civil and Env Eng, Clarkson Univ, Potsdam NY 13676)*. Int J Eng Sci 31(8) 1151-1163 (Aug 1993).

Propagation of surface waves across a vertical wave barrier inserted between two laterally homogeneous quarter-spaces is considered in this paper. Based on the Green's function technique, an analytical approach is developed to examine the reflection and transmission of Rayleigh surface waves across a composite barrier. The composite barrier consists of a high velocity layer sandwiched between two thin layers of low shear velocity materials. The high velocity layer is represented by differential matrix operators which relate the wave fields on each side of the layer. The low velocity layers are modeled by non-rigid or "unwelded" contact conditions which allow partial sliding at the interfaces. Screening ratios of barriers with various combinations of material, geometric, and non-rigidness parameters are compared and discussed in some detail.

158G. NONLINEAR MOTIONS

10A114. Existence of stationary nonlinear Rayleigh waves. - MF Hamilton, YA Il'insky, EA Zabolotskaya *(Dept of Mech Eng, Univ of Texas, Austin TX 78712-1063)*. J Acoust Soc Am 93(6) 3089-3095 (Jun 1993).

The existence of stationary nonlinear Rayleigh waves is investigated theoretically on the basis of new model equations for the propagation of finite amplitude Rayleigh waves in isotropic solids. The spectral components of the proposed stationary waveforms are governed by coupled quadratic algebraic equations that are similar in form to those used by Parker and Talbot. However, whereas the theoretical investigation of Parker and Talbot predicted the existence of stationary nonlinear Rayleigh waves, the present investigation does not, unless artificial constraints are imposed on the frequency spectrum. Differences between nonlinearity in Rayleigh wave propagation in isotropic solids and nonlinearity in sound wave propagation in fluids is briefly discussed.

158K. ANISOTROPIC MEDIA

10A115. Directional attenuation of SH waves in anisotropic poroelastic inhomogeneous media. - A Ben-Menahem *(Dept of Appl Math and Comput Sci, Weizmann Inst of Sci, Rehovot 76100, Israel)* and RL Gibson Jr *(LGIT-IRIGM, Univ Joseph Fourier, BP 53X, 38041 Grenoble, Cedex, France)*. J Acoust Soc Am 93(6) 3057-3065 (Jun 1993).

The equations of motion for anisotropic poroelastic inhomogeneous media admit separable SH wave motion for the case of azimuthal isotropy coupled with coaxial inhomogeneity and poroelasticity with a diagonal permeability tensor. In homogeneous examples of such media, the low-frequency waves exhibit differential attenuation that is more pronounced along the symmetry axis. If this differential attenuation can be observed, it may be used to determine the permeability of the medium. Media with a vertical gradient of both elastic and permeability properties show different effects. For low-frequency waves, the attenuation acts so as to reverse the effects of elastic parameter gradients on SH wave amplitudes.

10A116. Eigenfunction expansion of the elastic wave Green's function for anisotropic media. - DE Budreck *(Dept of Math, Dept of Aerospace Eng and Eng Mech, Iowa State Univ, Ames IA 50011)*. Quart J Mech Appl Math 46(1) 1-26 (Feb 1993).

We consider the propagation of aves in a 3D, homogeneous, general anisotropic elastic medium of infinite extent. A special representation of the corresponding Green's function is derived. This representation expresses the Green's function as a bilinear expansion in the eigenfunctions of the linear elastic Hookean operator. The expansion follows from a completeness property which these eigenfunctions possess. Since the eigenfunctions of this operator correspond physically to freely-propagating plane waves, the eigenfunction-expansion representation affords a very natural physical interpretation of the Green's function as a modal and angular superposition of these freely-propagating modes. From this representation two additional results are derived: (1) a generalized completeness relation involving the freely-propagating modes which is shown to generate functional transform pairs which use the wave modes as the underlying basis set, and (2) a far-field asymptotic representation of the Green's function as a superposition of products of the freely-propagating modes with geometrically decaying spherical waves. The Green's function representation and generalized completeness relation are valid for elastic media of general anisotropy. The asymptotic representation is here derived within the constraint that the elastic media be isotropic, for which a simple integration-by-parts procedure provides the full expansion.

158L. LAYERED AND NONHOMOGENEOUS MEDIA

10A117. Discontinuity waves cannot describe evanescent waves. - F Bampi *(Inst Matematico di Ing, Univ Genova, Piazzale Kennedy Pad D, 16129 Genova, Italy)* and C Zordan *(Dipt Ing Biofis Electtron, Univ Genova, Via all'Opera Pia 11a, 16145 Genova, Italy)*. Wave Motion 17(3) 213-222 (May 1993).

The problem of oblique incidence of plane waves on a boundary between two linear media is examined in detail especially in connection with generation of evanescent waves. It is shown that, unlike plane waves, evanescent waves are fully determined by two functions, which are to be chosen as the Hilbert transform of each other so as to guarantee an appropriate behavior of the solution at infinity. When such an approach is contrasted with the theory of discontinuity waves, it turns out that the usual information about discontinuities does not suffice for calculating evanescent waves. In conclusion, the oblique incidence problem does not admit a consistent answer within the sole framework of discontinuity waves.

10A118. New stacking layer elements for analyses of reflection and transmission of elastic waves to inhomogeneous layers. - T Ohyoshi *(Dept of Mech Eng, Mining Col, Akita Univ, 1-1 Tegata-Gakuen-Cho, Akita City 010, Japan).* Mech Res Commun 20(4) 353-359 (Jul-Aug 1993).

A new model of a layer element is presented for the analysis of a general inhomogeneous elastic layer. The element is inhomogeneous and its mechanical impedance varies linearly with layer thickness. Stacking of the elements simulates well a real inhomogeneous layer with small number of elements. The analytical formulation of the stacked multi-layer structure is made by the transfer matrix method. Benefits of such the new elements to the analysis are examined by comparison with conventional approximate method of piling up of many homogeneous layers. Studies on reflections and transmission of elastic waves due to inhomogeneous layer have been reported by many researchers. Modern problems related to functionally gradient materials are generally difficult ones to analyze without resorting to some numerical approach. Most analyses of papers relating to an inhomogeneous elastic layer may be classified into two kinds of approaches. One is the approximation by piling up a large number of homogeneous thin layers, which is likely to lead to a large amount of numerical calculations. The other approach is a theoretical analysis using a restricted function to describe the inhomogeneous property inside a material. The function should be chosen so that the governing equations have manageable solutions. To improve such the unsatisfied approaches, the new element is proposed here. Stacking of the elements may improve much the adaptability to various real inhomogeneous solids with small number of elements.

See also the following:

10A208. Time domain Green functions technique for a point source over a dissipative stratified half-space with a phase velocity mismatch at the surface

158M. GRANULAR AND POROUS MEDIA

See the following:

10A186. Nonlinear acoustoelastic properties of granular media

10A920. Elastic waves through a simulated fractured medium

158N. RANDOM WAVES OR MEDIA

10A119. Method for obtaining evolution equations for nonlinear waves in a random medium. - B Gurevich *(VNII Geosys, Varshavskoe Shosse 8, Moscow 113105, Russia),* A Jeffrey *(Dept of Eng Math, Univ of Newcastle upon Tyne, NE1 7RU, UK),* EN Pelinovsky *(Inst of Appl Phys, 48 Ul'anova St 603600 Nizhny, Novgorod, Russia).* Wave Motion 17(3) 287-295 (May 1993).

Most of the methods used to derive deterministic equations governing the evolution of linear waves in random media are based on the mean field approach. For a given linear system of equations with random coefficients this approach results in an approximate deterministic equation (or system) for the mean (averaged over the set of all realizations) field. The coefficients of such equations are associated with the statistical moments of the random coefficients of the initial system. Sometimes similar approaches are also applied to nonlinear problems. However, recently, in a number of examples, it was shown that the mean field approach in nonlinear problems may give the wrong results. The error is related to the infinite growth of the root-mean-square phase fluctuations due to fluctuations of the wave velocity in an inhomogeneous medium. To overcome this effect the idea of eliminating the unbounded growth of phase fluctuations by using an appropriate coordinate transformation was proposed resulting in a method called the "mean waveform method". In the present paper we extend the idea of the mean waveform method in order to develop a systematic approach which enables the construction of an approximate deterministic evolution equation for a given quasi-hyperbolic and quasi-linear system of equations with weak nonlinearity and stationary random coefficients. The applicability of the proposed approach is demonstrated by means of an example.

158Q. REFLECTION, REFRACTION, DIFFRACTION, AND SCATTERING

10A120. Diffraction of SV waves by underground, circular, cylindrical cavities. - VW Lee and J Karl *(Dept of Civil Eng, Univ of Southern California, Los Angeles CA 90089).* Soil Dyn Earthquake Eng 11(8) 445-456 (1992).

The scattering and diffraction of plane SV waves by underground, circular, cylindrical cavities at various depths in an elastic half space is studied in this paper. The cavities, studied here, are at depths of two to five cavity radii, measured from the surface to the center of the cavity. Fourier-Bessel series are used to satisfy the wave equation and the boundary conditions. When the angle of incidence of the plane SV wave exceeds the critical angle, surface waves are generated, which are expanded in terms of Fourier series, which also involve Bessel functions. The surface displacement amplitudes and phases that are presented show that the results depend on the following parameters: (1) The angle of incidence, θ_β; (2) the ratio of cavity depth to the cavity radius, h/a; (3) the dimensionless frequency of the incident SV wave, η; and (4) Poisson's ration, ν. The presence of the cavity in the half space results in significant deviation of both the displacement amplitudes and phases on the nearby half space surface from that of a uniform half space.

10A121. Scattering of ultrasonic wave by cracks in a plate. - SW Liu *(Dept of Mech Eng, Chinese Air Force Acad, Taiwan, ROC)* and SK Datta *(Dept of Mech Eng, CIRES and Center for Space Construct, Univ of Colorado, Boulder CO 80309-0427).* J Appl Mech 60(2) 352-357 (Jun 1993).

A hybrid numerical method combining FEs and the boundary integral representation is used to investigate the transient scattering of ultrasonic waves by a crack in a plate. The incident wave models the guided waves generated by a steel ball impact on the plate. Two surface-breaking cracks and one subsurface crack are studied here. The results show that the location and depth of cracks have measurable effects on the surface responses in time and frequency domains. Also, the scattered fields have distinct differences in three cases.

10A122. Strain localization and bifurcation in a nonlocal continuum. - G Pijaudier-Cabot and A Benallal *(Lab de Mec et Tech, ENS Cachan CNRS, Univ Paris 6, 61, ave du President Wilson, 94235 Cachan Cedex, France).* Int J Solids Struct 30(13) 1761-1775 (1993).

The conditions for localization and wave propagation in a strain softening material described by a nonlocal damage based constitutive relation are derived in closed form. Localization is understood as a bifurcation into a harmonic mode. The criterion for bifurcation is reduced to the classical form of singularity of a pseudo "acoustic tensor"; this tensor is not a material property as it involves the wavelength of the bifurcation mode through the Fourier transform of the weight function used in the definition of the nonlocal damage. A geometrical solution is provided to analyze localization. The conditions for the onset of bifurcation are found to coincide in the nonlocal and in the corresponding local cases. In the nonlocal continuum, the wavelength of the localization mode is constrained to remain below a threshold which is proportional to the characteristic length of the continuum. The analysis in dynamics exhibits the well known property of wave dispersion. In some instances, ie, for large wavelength modes, wave celerities become imaginary, but waves with a sufficiently short wavelength are found to propagate during softening in all the situations.

158Y. COMPUTATIONAL TECHNIQUES

10A123. Direct integration method of elastodynamics using FE time discretization. - Dae Ill Lee and Byung Man Kwak *(Dept of Mech Eng, Korea Adv Inst of Sci and Tech, 373-1 Kuseong-dong Yuseong-ku, Taejon 305-701, Korea).* Comput Struct 47(2) 201-211 (Apr 1993).

The FE time discretization is utilized to develop a new direct integration method. The derived recurrence formula is implicit and self-starting. There are no undetermined parameters which are often used to control stability and accuracy in the traditional direct time integration methods. The method is analytically shown to be unconditionally stable and second-order accurate. The test with a single dof linear model has supported the analysis of convergence and errors. It has been shown that the proposed method gives consistently better response history than the two well-known methods even with larger time steps. A 2-dof Hertzian impact model is solved to show its performance for a typical nonlinear problem. It is concluded that the proposed method works very well with useful properties as expected.

158Z. EXPERIMENTAL TECHNIQUES

10A124. New technique for measuring Rayleigh and Lamb wave speeds. - T Kundu *(Dept of Civil Eng and Eng Mech, Univ of Arizona, Tucson AZ 85721)* and B Maxfield *(Indust Sensors and Actuators, 400 Hester St, San Leandro CA 94577).* J Acoust Soc Am 93(6) 3066-3073 (Jun 1993).

A new technique is proposed in this paper to measure Rayleigh and Lamb wave speeds in solid half-spaces and plates. In this technique two transducers are positioned above the specimen in a pitch-catch orientation. The time of flight of the signal from the transmitter to the receiver is recorded. Then the rate of change of this time as the distance between the reflector and the transducer varies is experimentally determined. This rate remains constant when leaky Rayleigh of Lamb waves are generated but it varies when these waves are not generated. Thus surface waves are detected in an indirect manner. An expression is derived to relate the surface wave speed to the signal flight time change rate with the transducer specimen distance. Using this expression Rayleigh and Lamb wave speeds have been accurately determined in isotropic metals and anisotropic composites.

160. Impact on solids

160B. DYNAMIC CONTACT PROBLEMS

10A125. Bogie impact loads. - M Irvine *(Dept of Civil Eng, Univ of NSW, Sydney, Australia)*. Int J Impact Eng 13(4) 541-544 (Nov 1993).

Simple formulae are presented for the linear elastic and elasto-plastic response of a line of carriages or freight cars that are arrested suddenly. Starting with impact at the leading car, a wave of compression flows along the train during which, ideally, a quarter of a period passes until rest is momentarily achieved. Kinetic energy of the vehicles is changed into strain energy and heat in the couplers. The formulae are approximate but are, nonetheless, useful for design purposes, it being assumed that de-railing does not occur during this collision or buffer incident.

10A126. Dynamic response of a grillage under mass impact. - WQ Shen *(Sch of Syst Eng, Univ of Portsmouth, Porthsmouth PO1 3DJ, UK)* and N Jones *(Impact Res Center, Dept of Mech Eng, Univ of Liverpool, PO Box 147, Liverpool L69 3BX, UK)*. Int J Impact Eng 13(4) 555-565 (Nov 1993).

An approximate theoretical analysis is presented in this paper for the dynamic plastic response of a clamped beam grillage when struck transversely by a mass at the centre which produces large transverse displacements. The theoretical rigid-plastic predictions are compared with some recent experimental results on grillages struck by large masses and the predictions of a quasi-static method of analysis. The influence of inertia is explored for the behavior of a grillage when struck by a small striker travelling with a high velocity.

10A127. Dynamic response of dolos armor units to pendulum impact loads. - BT Rosson *(Dept of Civil Eng, Univ of Nebraska, Lincoln NE 68588)* and JW Tedesco *(Dept of Civil Eng, Auburn Univ, Auburn AL 36849)*. Comput Struct 47(4-5) 641-652 (3 Jun 1993).

Design methods for concrete armor units have come under scrutiny because of several recent breakwater failures. The catastrophic failure of the Sines breakwater in Portugal and other less spectacular failures such as the one at Cresent City, CA have kindled doubts as to the structural integrity of the large dolos concrete armor unit. A major difficulty encountered in rationally designing dolosse (or any other armor unit) is the specification of the loads. The complexity of the *in situ* loading conditions preclude an exact solution. Therefore, the pendulum test was developed to simulate the impact of broken units that are thrown around by the waves. This paper summarizes the results of a comprehensive numerical analysis to determine the states of stress in dolosse, with varying dimensions and concrete properties, subject to pendulum impact loads. A 3D FEM analysis of pendulum impact tests was conducted through implementation of the ADINA FE computer programs. The results of the FEM analyses are used to develop an analytical procedure which accurately predicts the peak tensile stresses in the shank and fluke of dolosse subject to pendulum impacts.

10A128. Newton's and Poisson's rules of percussive dynamics. - JA Batlle *(Dept of Mech Eng, Polytech Univ of Catalunya, 08028 Barcelona, Spain)*. J Appl Mech 60(2) 376-381 (Jun 1993).

Newton's and Poisson's rules are widely used in percursive dynamics because they lead to an "all linear" solution. However, they are in general energetically inconsistent in rough collisions. The equivalence between both rules and a broad condition for them to be energetically consistent is presented for single point collisions in multibody systems with perfect constraints. It is fulfilled in collisions described by equations of motion with constant coefficients - sliding in the same direction or no sliding - and in "balanced" collisions - sliding velocity would not change if friction were negligible - Coulomb's friction and infinite tangential stiffness are assumed at the collision point.

10A129. Predicting the enhanced punching strength of restrained slabs. - JS Kuang *(Dept of Civil and Struct Eng, Hong Kong Univ of Sci and Tech, Clear Water Bay, Kowloon, Hong Kong)*. Mech Res Commun 20(4) 361-366 (Jul-Aug 1993).

It is widely recognized that the punching load-carrying capacity of concrete slabs is significantly increased when the slab edges are restrained against lateral movement. This restraint induces large arching forces within the slab between the supports - a phenomenon of compressive membrane action. It is this arching effect which is responsible for the enhanced strength of the slab. The development of compressive membrane action is considered to be an important aspect of concrete slab behavior which has been ignored in the formulation of punching shear strength provisions in present design requirements. This may lead to a conservative prediction of the ultimate load capacity of a restrained slab as no direct account is taken of the enhancement due to the in-plane restraint in many types of reinforced concrete slab systems, such as bridge decks, flat slab construction, off-shore structures, marine platforms, protective shelters, and nuclear containment vessels. A need exists to develop a physically meaningful and consistent theoretical approach which can properly and clearly present the important structural characteristics of punching shear in concrete slabs with compressive membrane action. The purpose of this study is to present a plastic method of analysis for punching shear of laterally restrained concrete slabs. The proposed analysis allows for the effect of compressive membrane action, and the predictions show good agreement with a wide range of experimental test results.

10A130. Shear and torsional impact of cracked viscoelastic bodies: A numerical integral equation-transform approach. - HG Georgiadis *(Mech Div, Sch of Tech, Aristotle Univ, PO Box 422, 54006 Thessaloniki, Greece)*. Int J Solids Struct 30(14) 1891-1906 (1993).

The transient elastodynamic stress intensity factor was determined for a cracked linearly viscoelastic body under impact loading. Two separate geometries along with associated loading conditions were considered. In the first case, the body is in the form of an infinite strip containing a central finite-length crack and is subjected to antiplane shear tractions. Various strip heights are considered including the possibility of a body of nearly infinite extent. In the second case, the body is of infinite extent containing a finite-length penny-shaped crack and is subjected to radial shear and torsional (twisting) tractions. The analytical parts of the solutions are either given by a previous analysis of HG Georgiadis or are obtained from results by GC Sih through the use of the correspondence principle. The numerical procedure consists of solving integral equations and then inverting the Laplace transformed solution by the Dubner-Abate-Crump technique. Numerical results were given for the standard linear solid by considering several combinations of material constants.

10A131. Steady state axisymmetric penetration of a kinematically hardening thermoviscoplastic target. - RC Batra *(Dept of Mech and Aerospace Eng and Eng Mech, Univ of Missouri, Rolla MO 65401-0249)* and R Jayachandran *(Dept of Mech Eng, MIT)*. Int J Eng Sci 31(9) 1309-1323 (Sep 1993).

We study axisymmetric thermomechanical deformations of a thick target being penetrated by a fast-moving rigid cylindrical rod with a hemispherical nose, and presume that target deformations appear steady to an observer situated at the penetrator nose tip. Both isotropic and kinematic hardening of the target material are considered. It is found that kinematic hardening increases the normal stress acting on the penetrator nose surface and the temperature rise of target particles abutting the penetrator. However, the value of the hydrostatic pressure at a point in the deforming target region is affected very little by the consideration of kinematic hardening. For suitable values of material parameters appearing in the evolution equation of the back-stress, the computed values of the back-stress at target particles abutting the penetrator nose surface equal three times the yield stress of the target material in a quasistatic simple compression test.

See also the following:

10A67. Vibroimpact interaction in systems of bars

160F. SPALLATION AND FRACTURE

See the following:

10A435. Indentation-flexure and low-velocity impact damage in graphite epoxy laminates

160Y. COMPUTATIONAL TECHNIQUES

10A132. Calculation of impact loads for high energy drops of cylindrical containers. - GK Miller *(Idaho Natl Eng Lab, EG&G Idaho, Idaho Falls ID)*. Int J Impact Eng 13(4) 511-526 (Nov 1993).

The regulatory criteria for containers that are used to transport radioactive materials require that the container maintain structural integrity for an accidental drop of up to 30 ft onto a non-yielding surface. Storage containers for radioactive materials are also designed for accidental drops, usually of lesser heights. The design of these containers generally requires a determination of the peak magnitude of the impact force acting on the container. This paper presents an analytical solution that can be used to estimate the primary impact forces for cylindrical containers. Equations are derived for essentially all drop orientations.

10A133. FEM for dynamic contact-impact problems. - RL Taylor *(Dept of Civil Eng, UCB)* and P Papadopoulos *(Dept of Mech Eng, UCB)*. Int J Numer Methods Eng 36(12) 2123-2140 (30 Jun 1993).

This paper addresses the formulation and discrete approximation of dynamic contact-impact initial-value problems. The continuous problem is presented in the context of nonlinear kinematics. Standard semi-discrete time integrators are introduced and are shown to be unsuccessful in modeling the kinematic constraints imposed on the interacting bodies during persistent contact. A procedure that bypasses the aforementioned difficulty is proposed by means of a novel variational formulation. Numerical simulations are conducted and the results are reported and discussed.

10A134. Splitting pinball method for contact-impact problems. - T Belytschko and IS Yeh *(Dept of Civil Eng, McCormick Sch of Eng and Appl Sci, Tech Inst, NWU)*. Comput Methods Appl Mech Eng 105(3) 375-393 (June 1993).

In the pinball contact-impact algorithm, the interpenetration check is simplified by enforcing it only on a set of spheres emebedded within the elements. In the splitting pinball adaptation of this algorithm, the parent pinball is split into a hierarchy of descendent pinballs whenever interpenetration of the parent pinballs is detected. The interpenetration check is then applied to the descendent pinballs and contact forces are generated. This provides a better representation of the contact surface for thin shell elements. The implementation of the method with a penalty contact method is described and examples are given. It is also shown that the method easily and automatically handles edge-to-edge, edge-to-surface, and self-surface contact without any user specification.

162. Waves in Incompressible fluids

162A. GENERAL THEORY

10A135. Simplified model for wave height and set-up in the surf zone. - RH Swift *(Res Center, ABP Res and Consultancy, Maritime Way, Southampton SO1 1AE, UK)*. Coastal Eng 19(3-4) 189-206 (May 1993).

Based upon a simple extension of the analytical solution by Dally et al, a closed form expression has been developed for the variation of long-crested regular wave heights in the surf zone including the effect of set-up. The expression predicts wave height and set-up values which compare favorably with experimental data.

10A136. Theta functions and the dispersion relations of periodic waves. - Kwok W Chow *(Dept of Math, Univ of Arizona, Tucson AZ 85721)*. J Phys Soc Japan 62(6) 2007-2011 (Jun 1993).

The phase speeds or the dispersion relations for the periodic waves of certain nonlinear evolution equations can be expressed in remarkably compact forms by using theta functions.

See also the following:

10A137. Unified theory of nonlinear wave propagation in two-layer fluid systems

162C. NONLINEAR, FINITE AMPLITUDE, AND SOLITARY WAVES

10A137. Unified theory of nonlinear wave propagation in two-layer fluid systems. - Yoshimasa Matsuno *(Dept of Phys, Fac of Liberal Arts, Yamaguchi Univ, Yamaguchi 753)*. J Phys Soc Japan 62(6) 1902-1916 (Jun 1993).

A unified theory is presented which describes nonlinear wave propagation in two-layer inviscid and incompressible fluid of arbitrary depth. We consider the 2D systems, in which a layer of lighter fluid overlies a layer of heavier one resting on a flat bottom. The two cases of rigid and free upper boundaries are dealt with separately. We derive approximate nonlinear evolution equations (NEEs) for interfacial and free surface elevations on the basis of a systematic perturbation method with respect to the steepness parameter. We also discuss on NEEs arising from various limiting cases of fluid depth and compare them with existing NEEs. It is found that our theory includes almost all existing nonlinear theories as special cases.

See also the following:

10A136. Theta functions and the dispersion relations of periodic waves

10A144. Steady trapped solutions to forced long-short interaction equation

162D. GRAVITY WAVES (INCL BREAKING, ETC)

10A138. Wave scattering over uneven depth using the mild-slope equation. - PG Chamberlain *(Dept of Eng Sci, Univ of Oxford, Parks Rd, Oxford OX1 3PJ, UK)*. Wave Motion 17(3) 267-285 (May 1993).

This paper examines the scattering of a train of small-amplitude harmonic surface waves on water by 1D topography, using the multi-slope equation. The associated boundary value problem is converted into a pair of integral equations whose solutions are approximated by variational techniques, which also supply error bounds. Excellent approximations to the reflection and transmission coefficients and to the free surface shape are produced with only 2D or 3D trial spaces, by choosing these spaces to be problem dependent. The bed profiles considered include localized humps and taluds which join two horizontal planes at different depths.

162F. CAPILLARY WAVES AND WAVES IN THIN FILMS

10A139. Capillary-gravity solitary waves with damped oscillations. - F Dias and G Iooss *(Inst Non-Lineaire, UMR CNRS 129, Univ de Nice Sophia-Antipolis, 06108 Nice Cedex 2, France)*. Physica D 65(4) 399-423 (15 Jun 1993).

Capillary-gravity solitary waves with damped oscillations are studied analytically. The analysis follows the work of Iooss and Kirchgassner who proved that these waves exist for all values of the Froude number smaller than one. The water-wave problem is reduced to a system of ordinary differential equations by using the center manifold theorem. The normal form of this reduced system can be obtained and a good approximation to these waves for small amplitude is constructed. The limit as the water depth becomes infinite is considered as a special case. A comparison with existing numerical results is made for small-amplitude waves.

10A140. Construction of stationary waves on a falling film. - H-C Chang *(Dept of Chem Eng, Univ of Notre Dame, Notre Dame IL 46556)*, EA Demekhin, DI Kopelevich *(Dept of Appl Math, Krasnodar Polytech Inst, Krasnodar 350072, Russia)*. Comput Mech 11(5-6) 313-322 (1993).

Waves on a film falling down a vertical wall exhibit many distinct features. They tend to be locally stationary over several wavelengths, viz they travel with constant speeds and shapes over a long distance. In the limit of very long (solitary) waves, these stationary waves also exhibit two length scales with small and short capillary waves running ahead of a large tear-drop shaped hump. We present a spectral-element method for this difficult multi-scale free surface problem. A boundary layer approximation of the equation of motion allows a Fourier expansion in the streamwise direction in conjunction with a domain decomposition in the direction normal to the wall that eliminates numerical instability. This mixed method hence enjoys both the exponential convergence rate of a spectral technique and the numerical advantage provided by a compactly supported basis which yields sparse projected differential operators. All stationary wave families, parameterized by the wavelength, are then constructed using a Newton continuation scheme. The constructed waves are favorably compared to experimentally measured wave shapes.

10A141. Excitation of capillary waves by longer waves. - KM Watson *(Marine Phys Lab, Scripps Inst of Oceanog, UCSD)* and JB McBride *(Sci Appl Int, 10260 Campus Point Dr, San Diego CA 92121)*. J Fluid Mech 250 103-119 (May 1993).

At low wind speeds the shortest capillary waves appear to be generated hydrodynamically and not by the wind. This phenomenon is investigated using a Hamiltonian representation of the surface wave dynamics. A perturbation technique of Kolmogorov is used to transform away non-resonant, nonlinear interactions. Resonant interactions are treated by the Hasselmann transport equation, applied to the transformed variables. Calculated spectra show reasonable agreement with the observations of Jahne & Riemer (1990).

162H. REFLECTION, REFRACTION, DIFFRACTION, AND SCATTERING

10A142. Interaction of short-crested random waves and large-scale currents. - TS Hedges, RG Tickell, J Akrigg *(Dept of Civil Eng, Univ of Liverpool, PO Box 147, Liverpool, L69 3BX, UK)*. Coastal Eng 19(3-4) 207-221 (May 1993).

Methods are outlined for determining the transformations to directional wave spectra induced by large-scale currents. The problems considered are those where waves move from quiescent water on to a current, or from one current region to another. Situations involving wave generation on currents are not discussed. The principle of wave action conservation is used to relate the wave energy densities in the two regions, and an equilibrium range constraint is applied to the high frequency tail of the transformed spectrum in instances where wave action is not conserved and energy is dissipated by wave breaking. Examples are presented which highlight how current-induced wave refraction and energy dissipation may have important consequences for the transformed spectrum.

10A143. Two-dimensional wave-scattering problems involving parallel-walled ducts. - P McIver *(Dept of Math Sci, Loughborough Univ of Tech, Loughborough, LE11 3TU, UK)* and AD Rawlins *(Dept of Math and Stats, Brunel Univ, Uxbridge, Middlesex, UB8 3PH, UK)*. Quart J Mech Appl Math 46(1) 89-116 (Feb 1993).

A previously-published solution for the 2D scattering of long waves by a parallel-walled duct, obtained by an informal application of the method of matched asymptotic expansions, is known to be incorrect. Here a formal procedure is used to obtain the correct solution. The power of the method is further illustrated by obtaining solutions for two other related 2D problems which have no known exact solutions. The first is scattering by a rectangular inlet in an otherwise plane wall and the second is a variation on this problem with barriers projecting out from the inlet.

See also the following:

10T939. Bottom friction effects in the combined flow field of random waves and currents

162L. STRATIFIED FLOWS AND INTERNAL WAVES

10A144. Steady trapped solutions to forced long-short interaction equation. - Mitsuaki Funakoshi *(Res Inst for Appl Mech, Kyushu Univ, Kasuga, Fukuoka 816, Japan)*. J Phys Soc Japan 62(6) 1993-2006 (Jun 1993).

In a two-layer fluid system, both wave generation by bottom topography and resonant interaction between two wave modes are examined simultaneously. An evolution equation is derived which describes not only the resonant interaction between long internal mode and the wave packet of short surface mode, but also the generation of internal mode due to the resonant motion of the fluid relative to a bottom unevenness of large horizontal scale. According to this equation, steady coupled waves trapped by a localized symmetric bottom unevenness of sech-type are computed numerically both for positive and negative unevenness. Consequently, in addition to symmetric waves with one or two peaks in short-wave envelope, a variety of waves with many peaks, antisymmetric waves, and asymmetric waves are found.

See also the following:

10A137. Unified theory of nonlinear wave propagation in two-layer fluid systems

10A940. Energy flux and group velocity in currents of uniform vorticity

162Y. COMPUTATIONAL TECHNIQUES

10A145. Lagrangian FE analysis of time-dependent viscous free-surface flow using an automatic remeshing technique: Application to metal casting flow. - F Muttin, T Coupez, M Bellet, JL Chenot *(Ecole Natl Superieure des Mines de Paris, Centre de Mise en Forme des Mat CNRS UA1374, 06904 Sophia, Antipolis, France).* Int J Numer Methods Eng 36(12) 2001-2015 (30 Jun 1993).

The Navier-Stokes incompressible model is used to describe 2D metal casting flow. Such flows involve moving free boundaries. A new numerical algorithm has been developed using the Lagrangian FEM. It allows treatment of flows with moderate Reynolds number. The main feature is to avoid the calculation of the convective term, together with an automatic remeshing technique, to cure the mesh distortions. The problem of the free oscillation of a liquid is treated to verify the formulation. An application of this method to the computation of an industrial metal casting flow situation is presented.

10A146. Mathematical and numerical modeling of shallow water flow. - VI Agoshkov *(Inst of Numer Math, Russian Acad of Sci, Moskow, Russia)*, D Ambrosi *(Dept of Eng Aerospace, Polytech of Milano, Milan, Italy)*, V Pennati *(Central Ricerca Hydraul and Struct, ENEL, Milan, Italy)*, A Quarteroni *(Dept of Math, Polytech of Milano, Milan, Italy)*, F Saleri *(Central Ricerca, Cviluppo e Studi Superior in Sardegna, Calgliari, Italy).* Comput Mech 11(5-6) 280-299 (1993).

This paper deals with shallow water equations. We discuss the mathematical model, the admissible boundary conditions, some popular numerical methods in the specialized literature, as well as we propose new approaches based on fractional step and finite element methods.

See also the following:

10A136. Theta functions and the dispersion relations of periodic waves

164. Waves in compressible fluids

10A147. Approximate and numerical solutions of a gaseous flow with shocks. - RR Sharma *(Dept of Appl Math, IT, Banaras Hindu Univ, Varanasi-221 005, India)*, VD Sharma *(Dept of Math, IIT, Bombay 76, India)*, BD Pandey *(Dept of Math, Ohio State Univ, Marion Campus, Columbus OH)*, P Shukla *(Dept of Appl Math, IT, Banaras Hindu Univ, Marion Campus, Varanasi-221 005, India).* Quart J Mech Appl Math 46(1) 141-152 (Feb 1993).

A technique is provided to obtain a closed-form approximate solution and a fast-converging numerical solution to unsteady non-isentropic gas flow with two shock boundaries. The approximate treatment is found to be very close to the numerical solution.

10A148. Infinite system of compatibility conditions along a shock ray. - R Ravindran and P Prasad *(Dept of Math, Indian Inst of Sci, Bangalore 560 012, India).* Quart J Mech Appl Math 46(1) 131-140 (Feb 1993).

To study the position and strength of a shock discontinuity as it propagates into a medium at rest, an infinite system of compatibility conditions can be derived. Each of these involves derivatives of a single flow variable and is in the form of a transport equation along shock rays. For 2D shock propagation, the first two compatibility conditions are derived in detail.

10A149. Limitations of linear theory for sonic boom calculations. - CM Darden *(Vehicle Integration Branch, Adv Vehicles Div, NASA Langley Res Center, Hampton VA 23665).* J Aircraft 30(3) 309-314 (May-Jun 1993).

Current sonic boom minimization theories have been reviewed to emphasize the capabilities and flexibilities of the methods. Preliminary comparisons of sonic booms predicted for two Mach 3 concepts illustrate the benefits of shaping. Finally, for very simple bodies of revolution, sonic boom predictions were made using two methods: a modified linear theory method and a nonlinear method for both far-field N-waves and midfield signature shapes. Preliminary analysis on these simple bodies verified that current modified linear theory prediction methods become inadequate for predicting midfield signatures for Mach numbers above three. The importance of impulse in sonic boom response and the importance of 3D effects which could not be simulated with the bodies of revolution will determine the validity of current modified linear theory methods in predicting midfield signatures at lower Mach numbers.

10A150. Plane compression front steepening in nonlinear media forms both a shock and a reflected wave. - CL Morfey *(Inst of Sound and Vib Res, Univ of Southampton, Southampton SO9 5NH, UK)* and VW Sparrow *(Graduate Program in Acoust, 157 Hammond Bldg, Penn State).* J Acoust Soc Am 93(6) 3085-3088 (Jun 1993).

An exact solution is given for the reflected wave formed in a nonlinear medium when a plane compression front steepens into a shock. The solution predicts both a shock and a reflected wave. In the small-amplitude limit the reflected wave strength varies as $(\delta P)^3$, where δP is the strength of the initial wave front.

10A151. Electric discharge excited blast waves in a flat subsonic nozzle. - P Luchini *(Inst Gasdinamica Fac Ingegneria, Univ Naples, P le Tecchio 80, Naples 80125, Italy).* AIAA J 31(6) 1060-1067 (Jun 1993).

The persistence of pressure waves generated by an electric discharge in the throat of a subsonic nozzle is studied analytically and numerically with particular reference to the operation of the high-power EUREKA excimer laser under construction at the national Italian ENEA Frascati laboratories. The attention is focused on transverse waves traveling parallel to the discharge electrodes. After some analytical estimates, a quasi-2D numerical simulation is presented for the propagation of these waves in the anticipated geometry of the discharge chamber of the EUREKA laser. The possibility of reflection of pressure waves on the thermal slug left behind by the previous discharge is also considered.

10A152. Multidimensional upwind schemes based on fluctuation-splitting for systems of conservation laws. - H Deconinck, H Paillere, R Struijs *(CFD Group, von Karman Inst for Fluid Dyn)*, PL Roe *(Aerospace Dept, Univ of Michigan).* Comput Mech 11(5-6) 323-340 (1993).

A class of truly multidimensional upwind schemes for the computation of inviscid compressible flows is presented here, applicable to unstructured cell-vertex grids. These methods use very compact stencils and produce sharp resolution of discontinuities with no overshoots.

See also the following:

10A888. Autowave propagation for general reaction diffusion systems

166. Solid fluid interactions

166A. GENERAL THEORY

See the following:

10A156. Dynamical stability of cylinders placed in cross-flow

10A187. Optical theorem for a plate-stratified fluid system

166C. EXTERNAL FLOW

See the following:

10A157. Dynamics of a rotatable cylinder with splitter plate in uniform flow

166D. INTERNAL FLOW (INCL SLOSHING)

10A153. New outflow model for cylindrical shells conveying fluid. - VB Nguyen, MP Paidoussis, AK Misra *(Dept of Mech Eng, McGill Univ, Montreal, PQ, H3A 2K6, Canada).* J Fluids Struct 7(4) 417-419 (May 1993).

A new so-called outflow model is presented, which overcomes some numerical difficulties encountered with previous models in solving problems of cylindrical shells conveying fluid. Numerical results are given to illustrate convergence of the solution obtained with the new model.

10A154. Sloshing frequencies. - DV Evans and CM Linton *(Sch of Math, Univ of Bristol, University Walk, Bristol, BS8 1TW, UK).* Quart J Mech Appl Math 46(1) 71-87 (Feb 1993).

The normal frequencies of oscillation of fluid inside certain containers are calculated by expressing the velocity potential as a linear combination of harmonic functions each of which satisfies the free-surface boundary condition. The unknown coefficients are then determined by the application of the bottom boundary condition. This is done for three different geometries; a 2D cylinder with semicircular cross-section, a cylinder with semicircular cross-section of finite length and a hemisphere. The method is also used to solve the interior Dirichlet problem the solutions of which correspond to the "irregular frequencies' that occur when solving the exterior forcing problem using a source distribution to represent the velocity potential. The method provides accurate results for the lower frequencies by truncation of simple homogeneous infinite systems of equations.

10A155. Vortex-induced vibrations of a long flexible circular cylinder. - D Brika and A Laneville *(Dept de genie Mec, Univ de Sherbrooke, Sherbrooke, PQ, J1K 2R1, Canada).* J Fluid Mech 250 481-508 (May 1993).

In an experimental study of the vortex-induced oscillations of a long flexible circular cylinder, the observed stationary amplitudes describe an hysteresis loop partially different from earlier studies. Each branch of the loop is associated with a vortex shedding mode and, as a jump from one branch to the other occurs, the phase difference between the cylinder displacement and the vortex shedding undergoes an abrupt change. The critical flow velocities at which the jump occurs concur with the flow visualization observations of Williamson & Roshko (1988) on the vortex shedding modes near the fundamental synchronization region. Impulsive regimes, obtained at a given flow velocity with the cylinder initially at rest or pre-excited, and progressive regimes resulting from a variation of the flow velocity, are examined. The occurence of bifurcations is detected for a flow velocity range in the case of the impulsive regimes. The coordinates of the bifurcations define a boundary between two vortex shedding modes, a boundary that verifies the critical curve obtained by Williamson & Roshko (1988). The experimental set-up of this study simulates half the wavelength of a vibrating cable, eliminates the end effects present in oscillating rigid cylinder set-up and has one of the lowest damping ratios reported for the study of this phenomenon.

See also the following:

10A103. Dynamic characteristics of liquid motion in partially filled tanks of a spinning spacecraft

166E. VIBRATION OF STRUCTURES IN FLUIDS

10A156. Dynamical stability of cylinders placed in cross-flow. - J Planchard and B Thomas *(Electricite de France, Etudes et Rech, 1, Ave du General de Gaulle, 92141 Clamart, France)*. J Fluids Struct 7(4) 321-339 (May 1993).

The aim of this paper is to investigate the dynamical stability of an elastic tube bundle placed in a cross-flow which is governed by the Navier-Stokes equations. The stability of this coupled system is derived from the study of a quadratic eigenvalue problem arising in the linearized equations. The instability occurs when the real part of one of these eigenvalues becomes positive; the steady state is then replaced by a time-periodic state which is stable (Hopf bifurcation phenomenon).

10A157. Dynamics of a rotatable cylinder with splitter plate in uniform flow. - JC Xu, M Sen, M Gad-El-Hak *(Dept of Aerospace and Mech Eng, Univ of Notre Dame, Notre Dame IN 46556)*. J Fluids Struct 7(4) 401-416 (May 1993).

This is a numerical study of the dynamics of a rotatable cylinder-splitter-plate body sumerged in a uniform flow, with emphasis on fluid-structure interaction. The 2D, incompressible, unsteady Navier-Stokes equations expressed in terms of stream function and vorticity are solved by using a finite-difference method on a numerically generated, boundary-fitted, moving curvilinear coordinate system. The flow field is solved in conjunction with the rotational dynamics of the body. It is found that for subcritical Reynolds numbers, the splitter plate aligns itself in the flow direction. On increasing the Reynolds number, a symmetry-breaking bifurcation appears and the splitter plate migrates to a stable off-axis position. On further increasing the Reynolds number, there is a Hopf bifurcation after which the flow becomes unsteady and the body exhibits finite-amplitude oscillations. Various subharmonics become evident in the oscillation spectra at higher Reynolds numbers.

10T158. Flow-induced vibrations of prismatic bodies and grids of prisms. - E Naudascher and Y Wang *(Inst fur Hydromech, Univ Karlsruhe, 7500 Karlsruhe 1, Germany)*. J Fluids Struct 7(4) 341-373 (May 1993).

10T159. Fluid-induced loading of cantilevered circular cylinders in a low-turbulence uniform flow Part 3. Fluctuating loads with aspect ratios 4 to 25. - TA Fox and CJ Apelt *(Dept of Civil Eng, Univ of Queensland, Brisbane, Queensland 4072, Australia)*. J Fluids Struct 7(4) 375-386 (May 1993).

See also the following:

10A38. Transition of flow-indu[illegible] [illegible]inder vibrations to chaos

10A185. Low-frequency vibrations and radiation of a circular plate

10A192. Plane vibrations and radiation of an elastic layer lying on a liquid half-space

10A941. Generation of a Stoneley-Scholte-Lamb atmospheric surface wave by an acoustic source located in an ocean waveguide

166F. INTERACTIONS OF WAVES WITH FLEXIBLE STRUCTURES

10A160. Mean drift force and yaw moment on marine structures in waves and current. - J Grue and E Palm *(Dept of Math, Mech Div, Univ of Oslo, Norway)*. J Fluid Mech **250** 121-142 (May 1993).

The effect of the steady second-order velocities on the drift forces and moments acting on marine structures in waves and a (small) current is considered. The second-order velocities are found to arise due to first-order evanescent modes and linear body responses. Their contributions to the horizontal drift forces and yaw moment, obtained by pressure integration at the body, and to the yaw drift moment, obtained by integrating the angular momentum flux in the far field, are expressed entirely in terms of the linear first-order solution. The second-order velocities may considerably increase the forward speed part of the mean yaw moment on realistic marine structures, with the most important contribution occurring where the wave spectrum often has its maximal value. The contribution to the horizontal forces obtained by pressure integration is, however, always found to be small. The horizontal drift forces obtained by the linear momentum flux in the far field are independent of the second-order velocities, provided that there is no velocity circulation in the fluid.

166H. FLEXIBLE TANKS AND CONTAINERS

See the following:

10A155. Vortex-induced vibrations of a long flexible circular cylinder

166K. OCEAN STRUCTURES

See the following:

10A160. Mean drift force and yaw moment on marine structures in waves and current

166N. FLUTTER AND FLUTTER CONTROL

10A161. Evaluation and extension of the flutter-margin method for flight flutter prediction. - SJ Price *(Dept of Mech Eng, McGill Univ, Montreal, PQ, Canada)* and BHK Lee *(High Speed Aerodyn Lab, Inst for Aerospace Res, Ottawa, ON, Canada)*. J Aircraft 30(3) 395-402 (May-Jun 1993).

For a binary flutter the so called flutter-margin method is a good way of extrapolating from subcritical flight test data to estimate the flutter speed; the best estimates are obtained with a linear extrapolation. Good estimates of the flutter speed can be obtained from data at speeds as slow as 50% of the flutter speed. The flutter-margin is shown to be relatively insensitive to errors in the damping measurements, but is very sensitive to errors in frequency measurements. It does not give good predictions of the flutter speed when the instability is dominated by a single dof mechanism. A new for of flutter-margin has been developed for a trinary flutter, which also varies in a sensibly linear manner with dynamic pressure; it is also relatively insensitive to errors in damping, but is very sensitive to errors in frequency.

10A162. Large-amplitude FE flutter analysis of composite panels in hypersonic flow. - CE Gray Jr *(Fac Eng Div, NASA Langley Res Center, Hampton VA 23681)* and Chuh Mei *(Dept of Mech Eng and Mech, Old Dominion Univ, Norfolk VA 23529)*. AIAA J 31(6) 1090-1099 (Jun 1993).

A FE approach is presented for determining the nonlinear flutter characteristics of 3D thin laminated composite panels using the full third-order piston, transverse loading, aerodynamic theory. The unsteady, hypersonic, aerodynamic theory and the von Karman large-deflection plate theory are used to formulate the aeroelasticity problem. Nonlinear flutter analyses are performed to assess the influence of the higher order aerodynamic theory on the structure's limit-cycle amplitude and the dynamic pressure of the flow velocity. A solution procedure is presented to solve the nonlinear panel flutter FE equations. Nonlinear flutter analyses are performed for different boundary support conditions and for various system parameters: aspect ratio a/b; material orthotropic ratio, lamination angle θ, and number of layers; Mach number M; flow mass density to panel mass density ratio μ/M; dynamic pressure λ; and maximum deflection to thickness ratio c/h. The large-amplitude panel flutter results for the full third-order piston aerodynamic theory are presented to assess the influence of the nonlinear aerodynamic theory.

10A163. Supersonic flutter analysis of composite plates and shells. - RMV Pidaparti *(Dept of Mech Eng, Purdue)* and HTY Yang *(Dept of Aeronaut Astronaut and Eng, Purdue)*. AIAA J 31(6) 1109-1117 (Jun 1993).

A high-precision doubly curved quadrilateral thin shell FE is used for studying the supersonic flutter behavior of laminated composite plates and shells. The composite material property is included using classical lamination theory, and the supersonic aerodynamic effect is included using linearized piston theory. To reduce the number of dof of the FE aeroelastic system, the normal modes approach is adopted. Results are presented to illustrate the behavior of flutter characteristics for composite plates and curved panels, and composite cylindrical and conical shells. Parametric studies concerning the effects of boundary conditions, fiber orientation, degree of orthotropy, and flow angle on the flutter characteristics are presented for a series of selected examples. The accuracy, efficiency, and applicability of the present FEM are demonstrated by illustrative examples, and, whenever possible, the results are compared to alternative solutions available in the literature.

166T. AEROELASTICITY (INCL AEROTHERMOELASTICITY)

See the following:

10A907. Advanced pogo stability analysis for liquid rockets

166Y. COMPUTATIONAL TECHNIQUES

10A164. Arbitrary Lagrangian-Eulerian velocity potential formulation for fluid-structure interaction. - C Nitikitpaiboon and KJ Bathe *(MIT)*. Comput Struct 47(4-5) 871-891 (3 Jun 1993).

Finite-element formulations for fluid-structure interaction, assuming an inviscid fluid, can be classified into two major categories: displacement-based formulations and potential-based formulations. Although displacement-based formulations have been used widely, the methods suffer from the presence of spurious calculation modes and locking behavior. Potential-based formulations are inherently irrotatinal and do not have the difficulties of the displacement-based formulations. Nevertheless most of the applications of these methods are still limited to cases with relatively small motions. We introduce in this paper an arbitrary Lagrangian-Eulerian formulation using the velocity potential and the density as fluid variables. The formulation can be applied to problems in which the fluid undergoes very large boundary motions and can be used equally well for both compressible and incompressible fluids.

168. Astronautics (celestial and orbital mechanics)

158A. GENERAL THEORY

10A165. **Review of planetary and satellite theories.** - PK Seidelmann *(US Naval Observatory)*. Celest Mech **56**(1-2) 1-12 (1993).

Planetary and satellite theories have been historically and are presently intimately related to the available computing capabilities, the accuracy of observational data, and the requirements of the astronomical community. Thus, the development of computers made it possible to replace planetary and lunar general theories with numerical integrations, or special perturbation methods. In turn, the availability of inexpensive small computers and high-speed computers with inexpensive memory stimulated the requirement to change from numerical integration back to general theories, or representative ephemerides, where the ephemerides could be calculated for a given data rather than using a table look-up process. In parallel with this progression, the observational accuracy has improved such that general theories cannot presently achieve the accuracy of the observations, and, in turn, it appears that in some cases the models and methods of numerical integration also need to be improved for the accuracies of the observations.

168D. CELESTIAL MECHANICS

10A166. **Computer-aided analysis of the Sitnikov problem.** - J Hagel *(CERN, SL-AP, CH-1211 Geneva 23, Switzerland)* and T Trenkler *(Tech Univ, Petersgasse 16, A-8010 Graz, Austria)*. Celest Mech **56**(1-2) 81-98 (1993).

We deal with the problem of a zero mass body oscillating perpendicular to a plane in which two heavy bodies of equal mass orbit each other on Keplerian ellipses. The zero mass body intersects the primaries plane at the system barycenter. This problem is commonly known as the Sitnikov Problem. In this work we are looking for a first integral related to the oscillatory motion of the zero mass body. This is done by first expressing the equation of motion by a second order polynomial differential equation using a Chebyshev approximation techniques. Next we search for an autonomous mapping of the canonical variables over one period of the primaries. For that we discretize the time dependent coefficient functions in a certain number of Dirac Delta Functions and we concentrate the elementary mappings related to the single Delta Function Pulses. Finally for the so obtained polynomial mapping we look for an integral also in polynomial form. The invariant curves in the 2D phase space of the canonical variables are investigated as function of the primaries eccentricity and their initial phase.

10A167. **Numerical results to the Sitnikov-problem.** - R Dvorak *(Inst of Astron, Univ of Vienna, Turkenschanzstr 17, A-1180 Vienna)*. Celest Mech **56**(1-2) 71-80 (1993).

We present numerical results of the so-called Sitnikov-problem, a special case of the 3D elliptic restricted three-body problem. Here the two primaries have equal masses and the third body moves perpendicular to the plane of the primaries' orbit through their barycenter. The circular problem is integrable through elliptic integrals; the elliptic case offers a surprisingly great variety of motions which are until now not very well known. Very interesting work was done by J Moser in connection with the original Sitnikov-paper itself, but the results are only valid for special types of orbits. As the perturbation approach needs to have small parameters in the system we took in our experiments as initial conditions for the work moderate eccentricities for the primaries' orbit ($0.33 \le e_{primaries} \le 0.66$) and also a range of initial conditions for the distance of the 3rd body (= the planet) from very close to the primaries orbital plane of motion up to distance 2 times the semi-major axes of their orbit. To visualize the complexity of motions we present some special orbits and show also the development of Poincare surfaces of section with the eccentricity as a parameter. Finally, a table shows the structure of the phase space for these moderately chosen eccentricities.

168G. ORBITAL MECHANICS

10A168. **Stability of outer planetary orbits around binary stars: A comparison of Hill's and Laplace's stability criteria.** - A Kubala, D Black *(Lunar and Planetary Inst, Houston TX 77058)*, V Szebehely *(Univ of Texas, Austin TX 78712)*. Celest Mech **56**(1-2) 51-68 (1993).

A comparison is made between the stability criteria of Hill and that of Laplace to determine the stability of outer planetary orbits encircling binary stars. The restricted, analytically determined results of Hill's method by Szebehely and coworkers and the general, numerically integrated results of Laplace's method by Graziani and Black are compared for varying values of the mass parameter $\mu = m_2/(m_1 + m_2)$. For $0 \le \mu \le 0.15$, the closest orbit (lower limit of radius) an outer planet in a binary system can have and still remain stable is determined by Hill's stability criterion. For $\mu > 0.15$, the critical radius is determined by Laplace's stability criterion. It appears that the Graziani-Black stability criterion describes the critical orbit within a few percent for all values of μ.

10A169. **Stable orbits about the martian moons.** - WE Wiesel *(Air Force IT, WPAFB)*. J Guidance Control Dyn **16**(3) 434-440 (May-Jun 1993).

A dynamics of a satellite of Phobos or Deimos is developed that includes Mars' gravity and oblateness and the moon's orbital eccentricity and its nonspherical shape. Two special cases of the dynamics are studied. If the moon's eccentricity is zero, then we have an autonomous system and families of periodic orbits exist. If the eccentricity is not zero, we have a time-periodic dynamical system which still permits isolated periodic orbits. The zero eccentricity periodic orbits are constructed and found to be stable at any period. In addition, the most important nonzero eccentricity period orbits are given. Sensitivity to poorly known system parameters is explored, and accuracy requirements for spacecraft insertion maneuvers are established. Stable orbits exist about both moons and are well enough known to be used by unmanned spacecraft.

10A170. **Stable planetary orbits around one component in nearby binary stars II.** - D Benest *(OCA, Observatoire de Nice, BP 229 F-06304 NICE, Cedex 4, France)*. Celest Mech **56**(1-2) 45-50 (1993).

Numerical simulations are made within the framework of the plane restricted three-body problem in order to find out if stable orbits for planets around one of the two components in double stars can exist. For any given set of initial parameters (the mass ratio of the two stars and the eccentricity of their orbit around each other), the phase-space of initial positions and velocities is systematically explored. In previous works, systematic exploration of the circular model as well as studies of more realistic (elliptic) cases such as Sun-Jupiter and the nearby α Centauri and Sirius systems, large stable planetary orbits were found to exist around both components of the binary, up to distances from each star of the order or more than half the binary's periastron separation. The first results presented here for the η Coronae Borealis system confirm the previous studies.

168K. STABILITY AND CONTROL

10A171. **Pointing accuracy of a dual-spin satellite due to torsional appendage vibrations.** - MC Stabb and AL Schlack *(Dept of Eng Mech and Astronaut, Univ of Wisconsin, 1415 Johnson Dr, Madison WI 53706)*. J Guidance Control Dyn **16**(4) 630-635 (Jul-Aug 1993).

This paper deals with the attitude motion of a dual-spin satellite with a finite sized rigid body attached to the end of a flexible beam. The equations of motion are derived using Lagrange's equations and are solved using the perturbation technique known as the Krylov-Bogoliubov-Mitropolsky method. The special case of torsional flexibility is presented in its entirety. The relationships between the satellite, beam and tip mass parameters, and pointing accuracy of the satellite are examined.

10T172. **Rotational motion and guidance system approximations in optimizable operational launch vehicle simulations.** - RA Luke *(Aerospace Corp, Albuquerque NM 87119)*. J Guidance Control Dyn **16**(3) 477-483 (May-Jun 1993).

10T173. **Time-closed optimal transfer by two impulses between coplanar elliptical orbits.** - DF Lawden *(Univ of Aston, Alcester B49 6NU, UK)*. J Guidance Control Dyn **16**(3) 585-588 (May-Jun 1993).

See also the following:

- 10A31. Nutational stability and core energy of a quasirigid gyrostat
- 10A35. Chaotic attitude motion of gyrostat satellites in a central force field
- 10A55. Sensitivity-based characterization and optimization of viscoelastically damped honeycomb structures
- 10A103. Dynamic characteristics of liquid motion in partially filled tanks of a spinning spacecraft
- 10A169. Stable orbits about the martian moons
- 10A261. Inverse dynamics approach to trajectory optimization for an aerospace plane
- 10A269. Quasi-closed-form solution to the time-optimal rigid spacecraft reorientation problem
- 10A271. Saturating and time-optimal feedback controls
- 10A272. Singular control in minimum time spacecraft reorientation
- 10A274. Time-optimal three-axis reorientation of a rigid spacecraft
- 10A283. Vibration and robust control of symmetric flexible systems
- 10A295. Guidance for an aerocapture maneuver
- 10A296. Quaternion-based rate-amplitude tracking system with application to gimbal attitude control
- 10A308. Reaction wheel low-speed compensation using a dither signal

168P. OTHER TOPICS IN ASTRONAUTICS

See the following:

10A842. Refinements in determining satellite drag coefficients: Method for resolving density discrepancies

10T908. Development and flight history of the SERT II spacecraft

168Y. COMPUTATIONAL TECHNIQUES

10A174. Application of KAM theory to the planetary three body problem. - P Robutel *(Bureau des Longitudes, Equipe Astron et Syst Dyn, 77 Ave Denfert-Rochereau, 75014 Paris, France)*. Celest Mech 56(1-2) 197-199 (1993).

In 1963 Arnold proved a theorem of conservation of invariant tori, in degenerate quasi-integrable Hamiltonian systems (Arnold, 1963). Then, he applied this theorem to the planetary problem; he used Leverier's tables and asymptotic expansions of the perturbative function in the semi-major axes. He obtained a result of stability in the planar problems of two planets, in the asymptotic case, when the ratio of the semi-major axes goes to zero. In Arnold's paper, a statement is made about the general case, but the computation does not appear in the paper.

10A175. Fourth-order solution of the ideal resonance problem. - B Erdi *(Dept of Astron, Eotvos Univ, Budapest, Hungary)* and J Kovacs *(Gothard Observatory of the Eotvos Univ, Szombathely, Hungary)*. Celest Mech 56(1-2) 221-230 (1993).

The second-order solution of the Ideal Resonance Problem, obtained by Henrard and Wauthier (1988), is developed further to fourth order applying the same method. The solutions for the critical argument and the momentum are expressed in terms of elementary functions depending on the time variable of the pendulum as independent variable. This variable is related to the original time variable through a "Kepler-equation". An explicit solution is given for this equation in terms of elliptic integrals and functions. The fourth-order formal solution is compared with numerical solutions obtained from direct numerical integrations of the equations of motion for two specific Hamiltonians.

10A176. Frequency analysis of a dynamical system. - J Laskar *(Bureau des Longitudes, Equipe Astron et Syst Dyn, 77 Ave Denfert-Rochereau, F75014 Paris, France)*. Celest Mech 56(1-2) 191-196 (1993).

Frequency analysis is a new method for analyzing the stability of orbits in a conservative dynamical system. It was first devised in order to study the stability of the solar system. It is a powerful method for analyzing weakly chaotic motion in Hamiltonian systems or symplectic maps. For regular motions, it yields an analytical representation of the solutions. In cases of 2 dof system with monotonous torsion, precise numerical criterions for the destruction of KAM tori can be found. For a 4D symplectic map, plotting the frequency map in the frequency plane provides a clear representation of the global dynamics and describes the actual Arnold web of the system.

10A177. Generalized Lyapunov exponents indicators in Hamiltonian dynamics: An application to a double star system. - E Lohinger, C Froeschle *(Observatoire de la Cote d'Azur, BP 229, 06304 Nice Cedex 4, France)*, R Dvorak *(Inst of Astron, Univ of Vienna, Turkenschanzstr 17, 1180 Wien, Austria)*. Celest Mech 56(1-2) 315-322 (1993).

The Lyapunov characteristic numbers which are defined as the mean value of the distribution of the local variations of the tangent vectors to the flow ($=\ln\alpha^i_k$) (see Froeschle, 1984) have been found to be sensitive indicators of stochasticity. So we computed the distribution of these local variations and determined the moments of higher order for the integrable and stochastic regions in a binary star system with $\mu = 0.5$.

10A178. Generalized Lyapunov-characteristic indicators and corresponding Kolmogorov like entropy of the standard mapping. - C Froeschle, CH Froeschle, E Lohinger *(Observatoire, Cote d'Azur, BP 229, 06304 Nice Cedex 4, France)*. Celest Mech 56(1-2) 307-314 (1993).

Lyapunov characteristic indicators are currently defined as the mean, ie, the first moment, of the distribution of the local variations of the tangent vector to the flow. Higher moments of the distribution give further information about the fluctuations around the average.

10A179. Global solution of the N-body problem. - LK Babazanjanz *(Astron Obs, St Petersburg State Univ, Bibliotech Pl2 Petrodvorets, St Petersburg 198904, Russia)*. Celest Mech 56(3) 427-449 (1993).

In connection with the publication (Wang Qiu-Dong, 1991) the Poincare type methods of obtaining the maximal solution of different equations are discussed. In particular, it is shown that the Wang Qiu-Dong's *global solution of the N-body problem* has been obtained in Babadzanjanz (1979). First the more general results on differential equations have been published in Babadzanjanz (1978).

10A180. Introduction to Hamiltonian dynamical systems and practical perturbation methods: New insight by successive elimination of perturbation harmonics. - A Morbidelli *(Dept Math, FUNDP, 8 Rempart de la Vierge, B-5000 Namur, Belgique)*. Celest Mech 56(1-2) 177-190 (1993).

Among the studies on dynamical systems one can generally recognize two different approaches: a theoretical approach, where the general properties of such systems are investigated, along the lines opened by the KAM and the Nekhoroshev theorems, and a more applicative approach, where practical perturbation techniques are developed and applied in order to achieve a satisfactory description of some given specific systems of interest. This last approach is the most common one in Celestial Mechanics.

10A181. Local integrals and the plane motion of a point in rotating systems. - VA Antonov *(Inst of Theor Astron, 10 Kutuzov Quay, St Petersburg 191187, Russia)* and FT Shamshiev *(Astron Dept, Tashkent Univ, 700095 TashGU, Tashkent-95, Uzbekistan)*. Celest Mech 56(3) 451-469 (1993).

This paper deals with the plane motion of a star in the gravitational field of a system which is in a steady state and rotates with a constant angular velocity. For these systems a class of potentials permitting a local integral, linear with respect to the velocity components, has been found. The concept of the local integral itself was introduced by one of the authors of the present paper (Antonov, 1981). A detailed model has been constructed. The corresponding domain of the particle motion and the form of the trajectory coil have been determined. The result is compared with the motion in a more realistic potential.

10A182. Onset of chaotic motion in the restricted problem of three bodies. - RH Smith and V Szebehley *(Univ of Texas, Austin TX)*. Celest Mech 56(3) 409-425 (1993).

A full characterization of a nonintegrable dynamic system requires an investigation into the chaotic properties of that system. One such system, the restricted problem of three bodies, has been studied for over two centuries, yet few studies have examined the chaotic nature of some of its trajectories. This paper examines and classifies the onset of chaotic motion in the restricted three-body problem through the use of Poincare surfaces of section, Liapunov characteristic numbers, power spectral density analysis, and a newly developed technique called numerical irreversibility. The chaotic motion is found to be intermittent and becomes first evident when the Jacobian constant is slightly higher than C_2.

10A183. Recent progress in the theory and application of symplectic integrators. - Haruo Yoshida *(Natl Astronomical Observatory, Mitaka, Tokyo 181, Japan)*. Celest Mech 56(1-2) 27-43 (1993).

In this paper various aspect of symplectic integrators are reviewed. Symplectic integrators are numerical integration methods for Hamiltonian systems which are designed to conserve the symplectic structure exactly as the original flow. These are explicit symplectic schemes for systems of the form $H = T(p) + V(q)$, and implicit schemes for general Hamiltonian systems. As a general property, symplectic integrators conserve the energy quite well and therefore an artificial damping (excitation) caused by the accumulation of the local truncation error cannot occur. Symplectic integrators have been applied to the Kepler problem, the motion of minor bodies in the solar system and the long-term evolution of outer planets.

10A184. Resonant motion in the restricted three body problem. - JD Hadjidemetriou *(Dept of Theor Mech, Univ of Thessaloniki, GR-540 06 Thessaloniki, Greece)*. Celest Mech 56(1-2) 201-219 (1993).

The resonant structure of the restricted three body problem for the Sun-Jupiter asteroid system in the plane is studied, both for a circular and an elliptic orbit of Jupiter. Three typical resonances are studied, the 2:1, 3:1, and 4:1 mean motion resonance of the asteroid with Jupiter. The structure of the phase space is topologically different in these cases. These are typical for all other resonances in the asteroid problem. In each case we start with the unperturbed two-body system "Sun-asteroid" and we study the continuation of the periodic orbits when the perturbation due to a circular orbit of Jupiter is introduced. Families of periodic orbits of the first and of the second kind are presented. The structure of the phase space on a surface of section is also given. Next, we study the families of periodic orbits of the asteroid in the elliptic restricted problem with the eccentricity of Jupiter as a parameter. These orbits bifurcate from the families of the circular problem. Finally, we compare the above families of periodic orbits with the corresponding families of fixed points of the averaged problem. Different averaged Hamiltonians are considered in each resonance and the range of validity of each model is discussed.

170. Explosions and ballistics

See the following:

10A21. General hyperbolic solver: The CIP method applied to curvilinear coordinate

10A759. Aerodynamic computations for a transonic projectile at angle of attack by total variation diminishing schemes

172. Acoustics

172A. GENERAL THEORY

10A185. Low-frequency vibrations and radiation of a circular plate. - RI Veitsman and EV Zinov'ev *(AA Blagonravov Inst of Mech Eng,* *Russian Acad of Sci, Moscow, Russia).* Acoust Phys 39(1) 15-19 (Jan-Feb 1993).

The low-frequency vibrations of a circular elastic plate in an unbounded acoustic medium are calculated by expanding the unknown solution of the problem in normal modes of vibration of the plate in vacuum. The load exerted by the surrounding fluid is taken into account as an additional mass and is determined by the numerical solution of the Neumann problem for the Helmholtz equation. The velocity of the plate and the pressure and energy flux in the fluid are analyzed. Cases in which the fluid occupies all space or a half-space bounded by a baffle are discussed, along with the two types of edge conditions: a free edge and a rigidly built-in edge.

10A186. Nonlinear acoustoelastic properties of granular media. - IY Belyaeva, VY Zaitsev, LA Ostrovskii *(Inst of Appl Phys, Russian Acad of Sci, Moscow, Russia).* Acoust Phys 39(1) 11-15 (Jan-Feb 1993).

The nonlinear properties of a medium consisting of randomly packed spherical granules are investigated, where the interstitial pore space can be occupied by a fluid. The equation of state of the medium is derived, and the dependence of nonlinearity parameters on the properties of the granule material, the characteristics of the fluid, and the initial static strain is analyzed. It is shown that granular media have an anomalously high nonlinearity in comparison with homogeneous materials. Experimental data obtained for model samples of granular media are in good quantitative agreement with the theoretical conclusions. Published results of full-scale experiments to determine the nonlinear characteristics of loose rock are also in good agreement with the theoretical estimates.

10A187. Optical theorem for a plate-stratified fluid system. - IV Andronov *(State Univ, St Petersburg).* Acoust Phys 39(1) 5-7 (Jan-Feb 1993).

An analog of the optical theorem is formulated for a 3D system that contains an infinite plate in addition to a scattering obstacle, and in which additional scattering channels are created by stratification of the acoustic medium.

172B. SOUND GENERATION BY MOVING SURFACES

10A188. Propeller noise reduction by means of unsymmetrical blade-spacing. - W Dobrzynski *(Deutsche Forschungsanstalt fur Luft und Raumfahrt DLR, Inst fur Entwurfsaerodyn, Abteilung Technische Akustik Flughafen, 3300 Braunschweig, Germany).* J Sound Vib 163(1) 123-136 (8 May 1993).

The noise reduction potential of propellers with circumferentially unsymmetrical blade spacing is predicted on theoretical grounds and substantiated through both aerodynamic and aeroacoustic full scale wind tunnel experiments. To avoid potential balancing problems such propellers have two pairs of opposite blades, each such pair constituting a symmetric two-blade propeller. Spacing angles between these individual blade pairs are optimized towards achieving minimum A-weighted noise radiation in the plane of rotation. The result is then compared with the corresponding noise level from a symmetrical reference propeller with the same total number of geometrically identical blades. The study reveals that the value of the optimum spacing angle depends almost entirely on the operational helical blade tip Mach number assuming values of about 40° at a Mach number of 0.5 and decreasing to 15° at a Mach number of 0.8.

10A189. Sound generation by rotating stall in centrifugal turbomachines. - DE Thompson *(Appl Res Lab, University Park PA 16801),* L Mongeau *(Sch of Mech Eng, Purdue),* DK McLaughlin *(Penn State).* J Sound Vib 163(1) 1-30 (8 May 1993).

Experiments were conducted in order to investigate the relatively low frequency aerodynamic sound generating mechanism in centrifugal turbomachines. A facility consisting of a centrifugal water pump impeller with various discharge configurations and an inlet duct was designed and built for the experiments. Air was used as the fluid medium. The inlet duct provided a controlled, quiet inflow to the impeller. Measurements of the acoustic noise radiated in the pump surroundings were made in parallel with fluid dynamic measurements in order to establish correlations. The most significant conclusion reached is that a form of rotating stall dominated the low frequency noise production in various configurations with no outlet diffuser or casing.

172C. SOUND GENERATION BY FLOW

See the following:

10A809. Measurement of the nonsteady flow field in the opening of a resonating cavity excited by grazing flow
10A941. Generation of a Stoneley-Scholte-Lamb atmospheric surface wave by an acoustic source located in an ocean waveguide

172E. SOUND WAVES IN LIQUIDS (UNDERWATER ACOUSTICS)

10A190. Active and passive acoustic behavior of bubble clouds at the ocean's surface. - A Prosperetti *(Dept of Mech Eng, Johns Hopkins Univ, Baltimore MD 21218),* NQ Lu *(Appl Phys Lab, Submarine Tech, Hydrodyn Group, Johns Hopkins Rd, Laurel MD 20723-6099),* HS Kim *(Acoust Lab, Korea Res Inst of Ships and Ocean Eng, Daeduk Science Town, PO Box 1, Daejeon 305-606, Korea).* J Acoust Soc Am 93(6) 3117-3127 (Jun 1993).

The emission and scattering of sound from bubble clouds is studied theoretically. It is shown that clouds having a size and air content similar to what might be expected as a consequence of the breaking of ocean waves can oscillate at frequencies as low as 100 Hz and below. Thus cloud oscillations may furnish an explanation of the substantial amount of low-frequency wind-dependent oceanic ambient noise observed experimentally. Detailed results for the backscattering from bubble clouds – particularly at low grazing angles – are also presented and shown to be largely compatible with oceanic data. Although the cloud model used here is idealized (a uniform hemispherical cloud under a plane water free-surface), it is shown that the results are relatively robust in terms of bubble size, distribution, and total air content. A similar insensitivity to cloud shape is found in a companion paper.

10A191. Backscattering of underwater noise by bubble clouds. - K Sarkar and A Prosperetti *(Dept of Mech Eng, Johns Hopkins Univ, Baltimore MD 21218).* J Acoust Soc Am 93(6) 3128-3138 (Jun 1993).

This paper is a continuation of an earlier one in which the low-frequency backscattering of sound by hemispherical bubble clouds at the ocean's surface was studied. Here, clouds of various geometrical shapes (spheroids, spherical segments, cones, cylinders, ellipsoids) are considered and results in substantial agreement with the earlier ones and with the experiments of Chapman and Harris are found. The implication is that the backscattering levels are not strongly dependent on the shape of the clouds, which strengthens the earlier conclusion that bubble clouds produced by breaking waves can very well be responsible for the unexpectedly high backscattering levels observed experimentally. The accuracy of the Born approximation used by others for similar problems is also examined in the light of the exact results. Significant differences are found for gas concentrations by volume of the order of 0.01% or higher. Finally, shallow nonaxisymmetric plumes are briefly considered.

10A192. Plane vibrations and radiation of an elastic layer lying on a liquid half-space. - JD Kaplunov and DG Markushevich *(Inst for Problems in Mech, Russian Acad of Sci, pr Vernadskogo 101, 117526 Moscow, Russia).* Wave Motion 17(3) 199-211 (May 1993).

Forced vibrations and acoustic radiation of an elastic layer lying on a liquid half-space are investigated. The vibration frequency is assumed to be outside the range of applicability of the classical theory of plates. The case of plane strain is considered. The main results of the paper are concerned with the description of hydroelastic high-frequency long-wave vibrations arising in a neighborhood of the so-called "thickness stretch response frequencies". These frequencies are of particular interest since jumps of the radiation power are observed at such frequencies. Simple approximate formulas for the long-wave component of vibrations and for the radiation power jumps are obtained. It is shown that their height depends significantly on the Poisson ratio of the material of the layer. The efficiency of approximations based on the asymptotic method is tested by comparing the results of direct numerical computations.

10A193. Riemann invariant characteristic method for the solution of the nonlinear field in front of a partially reflecting boundary. - P Caine *(Dept of Math and Comput Sci, Univ of Salford, Manchester M5 4WT, UK)* and M West *(Dept of Appl Acout, Univ of Salford, Manchester M5 4WT, UK).* Appl Acoust 39(4) 277-289 (1993).

A nonlinear relationship between the pressure and the particle velocity at an air fluid interface is derived under the assumption that propagation in the fluid is exclusively outgoing. The derivation employs Riemann invariants. The relationship is then incorporated with the author's existing interior scheme for nonlinear propagation (NLPP method) to allow a solution for a large amplitude acoustic pulse incident at a fluid interface.

10A194. Underwater sound generated by heavy rainfall. - JA Nystuen, CC McGlothin, MS Cook *(Dept of Oceanog, Naval Postgraduate Sch, Monterey CA 93943).* J Acoust Soc Am 93(6) 3169-3177 (Jun 1993).

The underwater acoustic signature of heavy rainfall is very different from that of light rainfall. During heavy rainfall sound levels are observed to rise with increasing rainfall rate at all frequencies monitored (4 - 21 kHz) and the 15 - kHz spectral peak observed during light rainfall is absent. The sound levels are most highly correlated ($r \approx 0.8$) with heavy rainfall rate for frequencies less than 10 kHz. Lower correlations between sound levels and heavy rainfall rate were observed for frequencies above 10 kHz under several different conditions. When wind speed exceeds 10 m/s, wave breaking mixes bubbles downward and creates a layer of bubbles. This bubble layer attenuates subsequent surface-generated sound (from the raindrop splashes) for frequencies above 10 kHz. Extremely heavy rainfall (total rainfall above 150 mm/h) also generates a subsurface bubble layer. This rainfall-generated bubble layer is evidence of rainfall-induced turbulent mixing of the ocean surface layer and has implications for air-sea exchange processes (momentum, heat, and gas exchange). Finally, previous studies have shown that light rain generates acoustic energy above 10 kHz and that this sound is poorly correlated with total rainfall rate. A simple empirical acoustic rainfall rate algorithm for heavy rain is offered. This algorithm may be site specific. Furthermore, it overestimates rainfall rate early in the rain events examined here (convective rain events), and then underestimates rainfall rate later in the same events. This observation is shown to be consistent with likely changes in the drop size distribution during the lifetime of the rain event. The sound produced by large drops within heavy rain (drop diameter greater than 2.2 mm) is shown to dominate the underwater sound field. The empirical acoustic rainfall rate algorithm is therefore more correctly a measure of the rainfall rate from large raindrops. Fortunately, the rainfall rate from large raindrops is highly correlated with the total rainfall rate, making acoustic monitoring of underwater sound an effective measure of rainfall rate in oceanic regions.

See also the following:

10A221. Temperature fluctuations and gradients in a liquid sample as a source of errors in ultrasound velocity measurements

172F. SOUND WAVES IN SOLIDS

10A195. Application of the Wigner Distribution to the identification of structure-borne noise components. - TJ Wahl and JS Bolton *(Ray W Herrick Lab, Purdue)*. J Sound Vib 163(1) 101-122 (8 May 1993).

In this paper it is shown that time frequency analysis of a transient structural response may be used to identify the wave types carrying the significant energy through a structure. The identification of various wave types is possible since each is characterized by its own dispersion relation, with the result that each wave type may be associated with characteristic features in the time frequency domain representation of a structural response. In the work described here, the Wigner Distribution has been used to obtain time frequency representations of structural transient responses. Practical aspects of the Wigner Distribution are discussed briefly, and examples of its application to the analysis of transient structural responses are given. Additionally, time frequency filtering techniques are described that can be used both to detect the presence of and to quantify the energy carried by both nondispersive and dispersive waves.

10A196. Low frequency acoustic ground impedance measurement techniques. - MW Sprague, R Raspet, HE Bass *(Phys Acoust Res Group, Dept of Phys and Astron, Univ of Mississippi MS 38677)*, JM Sabatier *(Natl Center for Phys Acoust, Univ of Mississippi MS 38677)*. Appl Acoust 39(4) 307-325 (1993).

The low frequency (below 150 Hz) acoustic ground impedance was determined on a large uncultivated field using an impedance meter, the probe microphone method, a modified Biot-Stoll type calculation, and the phase gradient method. The impedance measured with the impedance meter has lower real and imaginary parts than the impedance determined from the probe microphone measurements. The modified Biot-Stoll type description of acoustic to seismic transfer based upon seismic and acoustic measurements gives an impedance which is consistent with probe microphone meaurements. The impedance measured by the phase gradient method is largely consistent with the other measurements, but shows much more structure. This structure is believed to be caused by unwanted reflections during the measurement procedure rather than by actual structure in the ground impedance undetected by the other methods.

10A197. Radiation of Lamb waves by a system of internal stress sources in an isotropic elastic layer. - KA Chishko *(Physicotech Inst of Low Temp, Ukrainian Acad of Sci)*. Acoust Phys 39(1) 80-84 (Jan-Feb 1993).

Expressions are obtained for the spectral composition and space-time profile of acoustic radiation formed by Lamb waves radiated from an arbitrary system of dynamic sources of internal stresses concentrated in a finite zone of an isotropic elastic layer. The example of Lamb waves radiated by a system of moving dislocation loops is discussed.

10A198. Transmission and dissipation of sound waves in tube bundles. - XY Huang and MA Heckl *(Dept of Math, Keele Univ, Keele, UK)*. Acustica 78(4) 191-200 (May 1993).

Analytical and numerical studies have been undertaken in this paper to examine the transmission and dissipation of sound waves in tube bundles. The tube bundles consist of parallel layers of tube rows submerged in a viscous fluid. The individual tube rows act like acoustic diffraction gratings; their scattering behavior is described by grating theory which has been extended in two ways: (i) the motions of the individual tubes are taken into account, (ii) the dissipation at the tube-fluid interfaces is included. A layered medium consisting of several spaced tube rows has been considered and results for the transmission and reflection coefficient are presented. The calculations are based on an iteration scheme where multiple backward and forward scattering at each row is taken into account. Despite the fact that only a finite number of tube rows was considered, the formation of passing and stopping bands, which are expected to be found in the transmission spectrum of a periodic medium, can be recognized. Stopping bands occur around frequencies where integral multiples of half a wavelength in the surrounding fluid coincide with the spacing of the tube rows.

See also the following:

10A943. Role of microstructure in the propagation of ultrasound in bainitic low-alloy steels

172G. SOUND WAVES IN NONHOMOGENEOUS, POROUS AND RANDOM MEDIA

10A199. Coherence of acoustic scattering from a dynamic rough surface. - DR Dowling *(Dept of Mech Eng and Appl Mech, Univ of Michigan, Ann Arbor MI 48109)* and DR Jackson *(Appl Phys Lab Col of Ocean and Fishery Sci, Univ of Washington, Seattle WA 98105)*. J Acoust Soc Am 93(6) 3149-3157 (Jun 1993).

Numerical studies of the angular and temporal coherence of rough-surface acoustic scattering are presented at kh = 12, 20, and 32, and where k is the acoustic wave number and h is the root-mean-square surface height fluctuation. The computations are based on point-source illumination of a 1D pressure-release Pierson-Moskowitz dynamic rough surface, and the Kirchhoff approximation. In the region near specular, for a source-location grazing angle of 20°, the angular variation of the scattered field coherence is found to predominantly depend on the product of k and a fixed length scale. The computed results show only a mild dependence on kh. For the same geometry, the temporal variation of the scattered field coherence is found to depend predominantly on ($g\delta t/U$)kh, where g is the acceleration of gravity, δt is the time shift, and U is the wind speed. A general method for scaling the scattered field coherence in terms of k, δt, U, and the angular separation of the field points is suggested based on the findings. The effects of wind direction and surface-wave frequency cutoff on acoustic scattering are also noted.

10A200. Slow wave propagation in air-filled permeable solids. - PB Nagy *(Dept of Welding Eng, Ohio State Univ, Columbus OH 43210)*. J Acoust Soc Am 93(6) 3224-3234 (Jun 1993).

The propagation of slow compressional waves in air-saturated permeable solids was studied by experimental means between 10 and 500 kHz. The velocity and attenuation coefficient were measured as functions of frequency from the insertion delay and loss of airborne ultrasonic waves transmitted through thin slabs of 1-5 mm in thickness. Porous ceramics of 2-70 Darcy and natural rocks of 200-700 mDarcy permeability were tested. In the low-frequency (diffuse) regime, the experimental results are consistent with theoretical predictions; the phase velocity and attenuation coefficient are essentially determined by the permeability of the specimen and both increase proportionally to the square root of frequency. In the high-frequency (propagating) regime, the experimental results are consistent with the theoretical predictions for the phase velocity but not for the attenuation coefficient. The phase velocity asymptotically approaches a maximum value determined by the tortuosity of the specimen while the attenuation coefficient becomes linearly proportional to frequency instead of the expected square-root relationship. It is suggested that the observed discrepancy is due to the irregular pore geometry that significantly reduces the high-frequency dynamic permeability of the specimens.

10A201. Sound attenuation in a coarse granular medium. - D Wu, ZW Qian, D Shao *(Inst of Acoustics, Acad Sinica, Beijing 100080, Peoples Rep of China)*. J Sound Vib 162(3) 529-535 (22 Apr 1993).

In order to investigate the deviation of the spherical particle model from practical granular media in nature, the sound attenuation in a kind of water saturated riverbed coarse sand was measured in the high frequency range 40-600 kHz. The results reveal that the rough surface and non-spherical shape factors of the sand particles have strong effects on the acoustic attenuation under experimental conditions in which βR is greater than 60 in the whole frequency range and in which kR is not far less than 1 when the frequency is higher than 300 or 400 kHz, where β is the viscous wavenumber, k is the compressional wavenumber and R is the average radius of the sand particles.

10A202. Ultrasonic propagation, scattering, and defocusing in suspensions. - J Adach, RC Chivers, LW Anson *(Dept of Phys, Univ of Surrey, Guilford, Surrey GU2 5XH, UK)*. J Acoust Soc Am 93(6) 3208-3219 (Jun 1993).

Fine resolution narrow-band pressure amplitude distribution measurements have been performed using a hydrophone in the field of a weakly focused bowl transducer radiating into castor oil and 1% and 2% by volume suspensions of 320-μm polystyrene beads in castor oil over the frequency range 1.0 to 2.5 MHz at 20° C. The axial distributions permitted determination of the excess attenuation due to scattering in the suspensions as a function of frequency. The frequency range included a resonance. The excess attenuation measured was compared with the theoretical predictions of Waterman and Truell and good agreement was obtained. The values of the excess attenuation obtained were used to predict axial pressure amplitude distributions in the suspension. Although the excess attenuation was determined from far-field measurements, the agreement between the predicted axial distributions and those measured experimentally extended well into the near field. Lateral distributions were measured at seven frequencies at the position of the geometrical center of curvature of the source and at the position of the true focus in the 1% suspension. Comparison with similar scans in castor oil alone revealed no detectable defocusing due to the presence of the scatterers.

172H. REFLECTION, REFRACTION, DIFFRACTION, AND SCATTERING

10A203. Acoustic scattering from a rough sphere. - P-A Jansson *(Div of Mech, Chalmers*

Univ of Tech, S-412 96 Goteborg, Sweden). J Acoust Soc Am 93(6) 3032-3042 (Jun 1993).

The scattering of a plane acoustic wave from a random rough sphere is studied using the null field approach. The starting point is an integral representation derived from the Helmholtz equation. The incident field, the scattered field, and the free-space Green's function are all expanded in terms of suitably chosen basis functions. In this way a relation between the incident and the scattered fields is obtained, which is expressed by the transition matrix (T matrix). The scattered field is expanded in a power series of a small parameter, namely the product of the wave number and the root-mean-square height of the irregularities. Analytical expressions for the leading terms of the series have been calculated. In particular, ensemble averages of the far-field amplitude and scattering cross section have been determined. As the analytical results are somewhat complicated, some numerical results are presented. Numerical computations of higher-order terms indicate that the convergence of the series is satisfactory as long as the root-mean-square height is small compared to a correlation length describing the average distance between the peaks of the surface.

10A204. Acoustical field in a space with obstacles part II: Propagation between buildings. - E Walerian and R Janczur *(Inst of Fund Tech Res, Polish Acad of Sci, Warsaw, Poland).* Acustica 78(4) 210-219 (May 1993).

The patterns of the computer simulation program, for calculating noise levels in an urban area are presented. Having the layout of the urban system geometry, the reflection and transmission coefficients of the objects, and the traffic parameters (flow density, typical noise spectrum) it is possible, by the use of this simulation program, to forecast the noise level on building facades.

10A205. Analysis of scattering from structures containing a variety of length scales using a source-model technique. - E Erez *(Kibbutz Ein Hashofet, Israel)* and Y Leviatan *(Dept of Elec Eng Tech, Israel IT, Haifa 32000, Israel).* J Acoust Soc Am 93(6) 3027-3031 (Jun 1993).

Fictitious source models have been applied extensively in recent years to a variety of electromagnetic and acoustic wave scattering problems. This paper is introducing an extension of the source-model technique that facilitates the solution to problems subsuming scatterers that contain a variety of length scales. This extension is in tune with the source-model technique philosophy of using simple sources the fields of which are analytically derivable. It amounts to letting the coordinates of some of the source centers assume complex values. Positioned in complex space, the simple sources radiate beam-type fields, which are more localized and are better approximations of the scattering from the smooth expanses of the structure. The coordinates of the other source centers retain their conventional real values. These latter sources are used, of course, to approximate the fields in the vicinity of the more rapidly varying expanses of the structure. The new approach is applied to analyze acoustic scattering from a structure comprising two adjacent pressure-release spheres of different size. It is found to render the solution computationally more effective at the expense of only a slight increase in its complexity.

10A206. Comparison of the Rayleigh and T-matrix theories of scattering of sound from an elastic shell. - L Kazandjian *(Commissariat a l'Energie Atomique, Centre d'Etudes de Vaujours-Moronvilliers, BP 7 77181, Courtry, France).* J Acoust Soc Am 93(6) 3139-3148 (Jun 1993).

The Rayleigh and T-matrix mathematical formalisms of scattering of sound from an elastic shell are established and compared. It is shown that the two formalisms have a unique solution and are theoretically equivalent when used to calculate the pressure field sufficiently far away from the obstacle. From a numerical point of view, the closeness of the results obtained with the two methods does not depend on the validity of the Rayleigh hypothesis. These results enable one to analyze the validity of the wave superposition and retracted boundary integral formalisms when the auxiliary retracted surface is located inside the inscribed sphere. Some comments are made about the numerical results expected from these methods.

10A207. Large membrane array scattering. - GA Kriegsmann *(Dept of Math Center for Appl Math and Stat, NJIT, Newark NJ 07102)* and CL Scandrett *(Dept of Math, Naval Postgraduate Sch, Monterey CA 93942).* J Acoust Soc Am 93(6) 3043-3048 (Jun 1993).

The scattering of a time harmonic acoustic wave by an array of N identical baffled membranes is considered in the limit as $N \to \infty$. The method of matched asymptotic expansions is used to construct an inner and outer expansion; the inner expansion contains the physics of the local periodic structure and the outer expansion has the proper behavior in the far field. The matching process is used to determine a set of unknown coefficients in the analysis and the result is a far-field pattern for the structure that blends the physics of both expansions. In particular, the far-field pattern is highly localized about the Bragg or mode angles of the inner representation. The maximum value of this function is directly proportional to the reflection coefficient determined numerically from the inner problem. Several numerical examples are presented illustrating these features. Moreover, it is observed that the asymptotic theory agrees quite well with the exact answer (obtained by using a finite scheme) when N = 3.

10A208. Time domain Green functions technique for a point source over a dissipative stratified half-space with a phase velocity mismatch at the surface. - Sailing He, Yidong Hu, S Strom *(Dept of Electromagnetic Theory, RIT, S-10044 Stockholm, Sweden).* Wave Motion 17(3) 241-254 (May 1993).

A point source over a dissipative stratified half-space with a discontinuity for both the phase velocity and the dissipation coefficient at the surface is considered. The axial symmetry of the problem is exploited in a spatial Hankel transform. The Green functions technique based on wave splitting is used to solve both the direct and inverse problems in the time domain. A Green tensor is introduced which directly maps the physical incident field outside the inhomogeneous half-space to the internal split fields. The PDEs for the Green functions are derived. In the direct problem, the internal fields are calculated as well as the reflected field. The phase velocity is reconstructed in the inverse problem. Simultaneous reconstruction of the phase velocity and dissipation coefficient using two different values of the Hankel transform parameter is analyzed. Two special cases, namely a point source over a homogeneous non-dissipative half-space and over a homogeneous dissipative half-space, are discussed and it is shown that the solution for the reflected fields is given by Volterra equations of the second kind.

10A209. Transient acoustic pressure radiated from a finite duct. - P Stepanishen and RA Tougas Jr *(Dept of Ocean Eng, Univ of Rhode Island, Kingston RI 02881).* J Acoust Soc Am 93(6) 3074-3084 (Jun 1993).

The time-dependent pressure radiated from a finite, rigid, circular duct of constant cross section is determined for the specified motion (velocity or acceleration) of a piston source at the inner end of the duct. The internal field is represented as an eigenfunction expansion over the duct cross section, and a time- and space-dependent Green's function is used to develop a generalized boundary condition which describes the effect of the external surroundings at the duct exit. Solution of this boundary value problem results in a duct transfer function which is then cascaded with the transfer function connecting the duct exit port and a selected external field point. In this paper, inversion to the time domain is accomplished via the FFT algorithm. Numerical examples demonstrating the external time-dependent pressure are presented based upon the specification of a gated sinewave piston acceleration over an assumed piston spatial profile. The numerical results show that the time-dependent pressure for the cross modes develops its peak value off-axis and is always zero on-axis, while the plane wave mode peaks on-axis.

See also the following:

10A187. Optical theorem for a plate-stratified fluid system

172I. ACOUSTIC PROPERTIES OF MATERIALS

10A210. Influence of lightweight partitions on the loss factor of concrete floors in multistorey buildings. - RA Novak *(Dept of Build Tech, RIT, S-100 44 Stockholm, Sweden).* Appl Acoust 39(4) 253-264 (1993).

It is shown that the presence of lightweight walls have an influence on the loss factor of concrete floors, especially at low frequencies. Measurement results and theoretical deliberations also show that the coupling loss factor depends on the design and construction of the walls. Furthermore, it is shown that the coupling loss factor increase is due mainly to the energy transmission through the partitions as longitudinal waves; the bending waves are less significant in this respect.

10A211. Multiple diffraction at edges and right angle wedges. - E Walerian *(Inst of Fund Tech Res, Polish Acad of Sci, Warsaw, Poland).* Acustica 78(4) 201-209 (May 1993).

The paper offers a procedure for the calculation of double and higher order diffraction at edges and right angle wedges, in the high frequency approximation. Such effects appear when double walled screens are erected along highways, and when waves are diffracted at the sides of buildings.

See also the following:

10A186. Nonlinear acoustoelastic properties of granular media

172J. NOISE CONTROL AND REDUCTION (INCL ACTIVE CONTROL)

10A212. Broadband active acoustic absorbing coating with an adaptive digital controller. - Zhen Wu, Xiao-Qi Bao, VK Varadan, VV Varadan *(Dept of Eng Sci and Mech, Center for the Eng of Elec and Acoust Mat, Penn State).* Smart Mat Struct 2(1) 40-46 (Mar 1993).

A modified active acoustic coating system using an adaptive digital controller has been developed for absorbing the sound incident on an underwater object. The redesigned control system, featuring a digital delay-line feedforward scheme, is predicted theoretically and verified experimentally to have a broader control bandwidth than the analog phase-shifter system which was developed previously. Another significant improvement to the system is the use of a multichannel delay-line network to achieve on-board monitoring of sound reflection from the coating, so that the system performance can be self-evaluated and then optimized by adjusting its control parameters. The adaptive adjustment function is realized through software on a personal computer interfaced with the digital delay-line network. This adaptive digital controller design enables the active absorbing coating to achieve a high echo reduction over a wide frequency band. The experimental implementation and testing of the active coating system was conducted in a water-filled pulse tube for normally incident plane waves. An echo reduction above 30dB was achieved in an operating frequency range from 4-11 kHz.

10A213. Experimental study implementing model reference active structural acoustic control. - RL Clark, GP Gibbs, CR Fuller *(Mech Eng Dept, VPI)*. J Acoust Soc Am 93(6) 3258-3264 (Jun 1993).

Model reference active structural acoustic control is experimentally investigated in this study for physical systems characterized by stationary, narrow-band disturbances in which the acoustic field remains relatively unchanged. The filtered-x version of the multichannel adaptive least-mean-square algorithm was implemented on a TMS320C25 digital signal processing board to achieve the desired control approach, and control inputs were generated with piezoelectric actuators. Model reference control provides the designer with a method of replacing acoustic error sensors such as microphones located in the far-field with error sensors such as accelerometers located on the surface of the structure. As opposed to driving the response of the structure to zero at the coordinates of the accelerometers, the response is driven to some predetermined "reference" value corresponding to the desired far-field acoustic directivity pattern. In essence, the uncontrolled structure is adaptively modified to behave like the reference structure under acoustic control conditions. Results from this study indicate that the same acoustic directivity pattern can be achieved with model reference control, and the only requirement is that the number of structural sensors used in the control approach is at least equal to the number of control actuators required to achieve the desired acoustic directivity pattern.

172Y. COMPUTATIONAL TECHNIQUES

10A214. Analysis of axisymmetric waves propagating along a hollow cylindrical ultrasonic transmission line. - Nobuhiro Kanbe, Yoshiro Tomikawa, Kazunari Adachi *(Dept of Elec and Info Eng, Yamagata Univ, Yonezawa, Yamagata 992, Japan)*, Takehiro Takano *(Dept of Commun Eng, Tohoku IT, Sendai, Miyagi 982, Japan)*. J Acoust Soc Am 93(6) 3235-3241 (Jun 1993).

A new ultrasonic device for feeding powder with the use of a hollow acrylic cylinder, on which an axisymmetric progressive elastic wave is excited, has previously been proposed. Its characteristics have also been reported. To find vibrational behaviors of the hollow cylinder for feeding powder, the elliptic particle movement on the inside surface was analyzed. The authors have found many forms of elliptic motion. Some of them can move objects inside the cylinder toward the vibration source, as expected, but, on the contrary, the others move in the wave propagation direction.

10A215. Application of the Gaussian beam approach to sound propagation in the atmosphere: Theory and experiments. - Y Gabillet, H Schroeder *(Centre Sci Tech du Batiment, 38400 St-Martin-d'Heres, France)*, GA Daigle, A L'Esperance *(Inst for Microstruct Sci, NRC, Ottawa, ON, K1A 0R6, Canada)*. J Acoust Soc Am 93(6) 3105-3116 (Jun 1993).

The Gaussian beam approach solves the wave equation in the neighborhood of the conventional rays using the parabolic approximation. The solution associates with each ray a beam having a Gaussian amplitude profile normal to the ray. The approximate overall solution for a given source is then constructed by a superposition of Gaussian beams along nearby rays. The solution removes ray-tracing artifacts such as perfect shadows and infinite energy at caustics without the computational difficulties of numerical solutions to the wave equation. In this paper, the Gaussian beam approach is applied to atmospheric sound propagation in the presence of refraction above a ground surface. A brief overview of the method is presented. Calculations obtained from Gaussian beam tracing are compared to those obtained from the fast field program and to experimental measurements. The experiments were made above a concave surface indoors that simulates propagation under downward refraction (inversion or downwind) in the cases of a hard and finite impedance surface. These experiments include measurements in the presence of a barrier. Measurements were also made in a wind tunnel in the presence of wind and temperature gradients. The results suggest that beam tracing can be applied to complex atmospheric sound propagation problems with advantages over conventional ray tracing and full-wave solutions.

10A216. Approximate evaluation of the spectral density integral for a large planar array of rectangular sensors excited by turbulent flow. - W Thompson Jr *(Dept of Eng Sci and Mech and Appl Res Lab, Penn State)* and RE Montgomery *(Underwater Sound Reference Detachment, Naval Research Lab, PO Box 568337, Orlando FL 32856-8337)*. J Acoust Soc Am 93(6) 3201-3207 (Jun 1993).

An approximate numerical procedure has been developed for rapidly evaluating the spectral density integral that predicts the output of a planar array of many sensors excited by turbulent boundary layer pressure fluctuations. This procedure is particularly useful in cases where the transfer function factor of the integrand is not a simple function of the wave numbers in the flow and transverse directions. The procedure exploits the facts that the entire integrand is a separable function of these two wave numbers and, when the number of sensors is large, the array function factor of the integrand is a rapidly varying function of wave number, characterized by many similar shaped lobes. In addition, a model for multilayered media is employed to provide the transfer function for boundary conditions that closely correspond to reality. Results generated by this procedure were compared to those from an exact evaluation of the integral which is possible if the transfer function is taken to be constant; there was agreement to within 0.2 dB or better over a broad frequency interval. Some results for a realistic transfer function are presented, such as the case of an elastomeric layer backed by an elastic plate with the sensors embedded at an arbitrary position within the layer.

10A217. Evaluation of the Kirchhoff approximation in predicting the axial impulse response of hard and soft disks. - GV Norton *(Naval Res Lab, Stennis Space Center, MS 39529-5004)*, JC Novarini *(Planning Systems, Inc, 115 Christian Lane, Slidell LA 70458-1350)*, RS Keiffer *(Naval Res Lab, Stennis Space Center, MS 39529-5004)*. J Acoust Soc Am 93(6) 3049-3056 (Jun 1993).

To test the ability of the Kirchhoff approximation for estimating the various components in the near-field impulse response of a circular disk, the predictions from a time domain formulation of the Helmholtz-Kirchhoff solution are benchmarked against results obtained via the Fourier synthesis of highly accurate frequency domain solutions. In these numerical experiments, a collocated point source and receiver lie on the symmetry axis of an acoustically hard (rigid) or soft (pressure release) disk. A time-domain analysis is carried out in order to unambiguously evaluate the Kirchhoff approximation for different components of the scattered field. It is found that, while Helmholtz-Kirchhoff predicts the correct reflected component, it fails to accurately predict the strength of the diffracted component. The magnitude of the error depends on whether the disk is soft or hard and on the source-receiver height above the disk. The error in the diffracted component exceeds, in some cases, 100%. Furthermore, it is observed that the Helmholtz-Kirchhoff approach does not include the secondary or multiply diffracted arrivals which are more pronounced for the hard disk.

10A218. Validity of the wedge assemblage method for pressure-release sinusoids. - RS Keiffer *(Naval Res Lab, Stennis Space Center MS 39529-5004)*. J Acoust Soc Am 93(6) 3158-3168 (Jun 1993).

In the past, the wedge assemblage (WA) method for calculating the acoustic scattering from rough, long-crested, or corrugated surfaces has been compared with both experimental data and exact theory with good results. Nevertheless, significant questions about what physics is included in the method and its realm of validity remain unanswered. In this paper, the WA method is applied to scattering from pressure-release sinusoidal surfaces in order to further explore these topics. Comparisons with accurate benchmark calculations are carried out over a broad range of kh and kΛ (k is the acoustic wave number; h and Λ are the amplitude and wavelength of the sinusoid, respectively) indicate that the primary limitation of the WA method stems from its current failure to include multiple scattering effects. It is also shown that quite good agreement with the benchmark can be achieved by a "diffraction-only" WA model even when $kh \ll 1$ and "reflectionlike" scattering patterns are observed.

172Z. EXPERIMENTAL TECHNIQUES

10A219. Error estimates for free-decay damping measurements. - F Orduna-Bustamante and RR Boullosa *(Seccion de Acust, Centro de Instrument, Univ Nacional Autonoma, Apdo Postal 70-186, Mexico DF, Mexico)*. J Acoust Soc Am 93(6) 3265-3270 (Jun 1993).

An estimate is presented of the errors introduced by digital sampling of an analog time signal when the logarithmic decrement method is used to measure damping. Some computer simulations were made in order to verify that the error estimate is adequate. Other factors that influence the error in the measured damping ratio, such as noise and the value of the damping ratio, are also studied by computer simulation. It is shown that, on average, the digital sampling error depends mainly on the total number of sampled points, but that it is affected also by the ratio between the sampling frequency and the frequency of the signal. Digital sampling errors combined with the errors introduced by different signal-to-noise ratios impose bounds to the values of the damping ratio that can be measured accurately. It is also shown that the optimum number of data points, when digital sampling error is combined with noise, varies according to the signal-to-noise ratios and the value of the damping ratio. A brief discussion of other decay methods compared to the logarithmic decrement method is also given.

10A220. Method of measuring the dynamic flow resistance and reactance of porous materials. - Mingzhang Ren *(Dept of Mech Eng, Xi'an Jiaotong Univ, Shaanxi, Peoples Rep of China)* and F Jacobsen *(Acoust Lab, Tech Univ, Bldg 352, DK-2800 Lyngby, Denmark)*. Appl Acoust 39(4) 265-276 (1993).

A method of measuring the frequency dependent flow resistance and reactance of porous materials in a duct is presented and examined. The method involves measuring the transfer function between the signals from two microphones placed on either side of a sample of the material. The validity of the method is tested by comparing measured values of the surface impedance of the material with values predicted from the measured flow resistance and reactance.

10A221. Temperature fluctuations and gradients in a liquid sample as a source of errors

in ultrasound velocity measurements. - S Ernst, W Marczak, R Manikowski *(Inst of Chem, Silesian Univ, Szkolna 9, 40-006 Katowice, Poland)*. Acoust Lett 16(8) 177-183 (Feb 1993).

Temperature gradients were measured at 283, 293 and 303K in the sample cell of an ultrasound velocimeter of sing-around type. They were found to be considerably higher than the measured short-time temperature fluctuations and quite close to the long-time ones. The velocity errors caused by temperature gradients are similar to the residual errors of the calibration line, and since the gradients are not reproducible they cannot be reduced by making appropriate corrections.

III. AUTOMATIC CONTROL

200. Systems theory and design

200B. CONTROLLABILITY, OBSERVABILITY, REALIZABILITY

10T222. Observers for discrete-time nonlinear systems. - G Ciccarella, M Dalla Mora, A Germani *(Dept of Elec Eng, Univ L'Aquila, Monteluco, 67100 L'Aquila, Italy)*. Syst Control Lett 20(5) 373-382 (May 1993).

200D. STABILITY, ROBUSTNESS

10T223. Overview of extremal properties for robust control of interval plants. - M Dahleh *(Dept of Mech and Env Eng, UC, Santa Barbara CA 93106)*, A Tesi *(Dept di Sist Info, Univ di Firenze, Via di Santa Marta, 3-50139, Firenze, Italy)*, A Vicino *(Dept of Ingegneria Elettrica, Univ di L'Aquila, 67040 Poggio di Roio, L'Aquila, Italy)*. Automatica 29(3) 707-721 (May 1993).

10A224. Robustness bounds for linear systems under uncertainty: Eigenvalues inside a wedge. - TR Alt *(Space Sta Div, McDonnell Douglas Aerospace, 5301 Bolsa Ave MS 15-1, Huntington Beach CA 92465)* and F Jabbari *(Dept of Mech and Aerospace Eng, UC, Irvine CA 92717)*. J Guidance Control Dyn 16(4) 695-701 (Jul-Aug 1993).

This paper deals with robustness bounds for linear systems with uncertainty, where both stability and a measure of performance robustness are desired. Here, performance robustness is defined by guaranteeing that the eigenvalues of the perturbed system remain in a specific region in the complex plane such as a wedge. Using standard Lyapunov techniques, for analysis, bounds on the uncertain parameters are obtained that guarantee that the system eigenvalues remain in the desired region, whereas for synthesis, bounds and state feedback gains can also be obtained that place the closed loop system eigenvalues in the desired region. An optimization algorithm is also presented that was successfully used in the examples.

10A225. Robustness evaluation of a flexible aircraft control system. - MR Anderson *(Dept of Aerospace and Ocean Eng, VPI)*. J Guidance Control Dyn 16(3) 564-571 (May-Jun 1993).

The structured singular value analysis technique is used to generate stability and performance robustness guidelines for multivariable, flexible aircraft flight control systems. A stability augmentation and structural mode control system, designed using the same classical technique as on the original production aircraft, is evaluated to produce the new guidelines. Stability margins are computed for simultaneous gain and phase uncertainty in each of the control system feedback loops. Performance weighing filters are chosen specifically from military flying qualities specifications. The results of this research define exactly how robust a control system of this type should be, such that any performance improvements achieved using more advanced design techniques can be compared directly.

See also the following:

10A26. Global feedback stabilization of the angular velocity of a symmetric rigid body
10A53. Passive damping for robust feedback control of flexible structures
10A235. Maneuver and vibration control of hybrid coordinate systems using Lyapunov stability theory
10T254. Closed-form solutions to discrete-time LQ optimal control and disturbance attenuation
10A287. Linear, multivariable robust control with a μ perspective
10A307. Quantitative feedback theory applied to the design of a rotorcraft flight control system

200E. IDENTIFICATION AND ESTIMATION

10T226. Design of a robust estimator for target tracking. - ET Kim *(Flight Control Dept, Korean Aerospace Res Inst, Teadok Science Town, Taejon, S Korea)* and D Andrisani II *(Sch of Aeronaut and Astronaut, Purdue)*. J Guidance Control Dyn 16(3) 595-597 (May-Jun 1993).

10A227. Maximizing the efficiency of wave-energy plant using complex-conjugate control. - P Nebel *(Dept of Mech Eng, Univ of Edinburgh)*. J Syst Control Eng 206(I4) 225-236 (1992).

A method of determining the hydrodynamic coefficients of a floating wave-energy absorber is outlined, and the coefficients of a Salter's duck are measured experimentally. A complex-conjugate synthesizer, derived from these coefficients, is used both theoretically and experimentally to predict and to measure the efficiency of a duck in unidirectional monochromatic waves. The synthesis produces a higher efficiency over a greater bandwidth than has been achieved before. The reason for the improvement in efficiency is explained, and conclusions are drawn about the implications of complex-conjugate control for predicting practical engineering constraints on the design of a full-sized wave-energy absorber.

10A228. Multiple-input, multiple-output time-series models from short data records. - JJ Hollkamp *(Wright Lab, WL-FIBGC, WPAFB)*. J Guidance Control Dyn 16(3) 549-556 (May-Jun 1993).

An algorithm to estimate multiple-input, multiple-output, time-series models for structural system identification using short time histories is presented. The method uses order overspecification to reduce estimation bias and automatically sorts identified system modes from computational modes. The system natural frequencies, damping factors, mode shapes, and modal participation factors are estimated and can be used to reconstruct single-input, single-output models for every input-output pair. Experimental data from a large cantilevered flexible truss are used to demonstrate the technique. Modal estimates are comparable to those obtained using accepted methods such as the eigensystem realization algorithm.

10A229. Wind identification along a flight trajectory, Part 3. Two-dimensional dynamic approach. - A Miele, T Wang, CY Tzeng *(Aero-Astronaut Group, Rice Univ, Houston TX)*, WW Melvin *(Delta Airlines, Atlanta GA)*. J Optim Theory Appl 77(1) 1-30 (Apr 1993).

This paper deals with the identification of the wind profile along a flight trajectory by means of a 2D dynamic approach. In this approach, the wind velocity components are computed as the difference between the inertial velocity components and the airspeed components. The airspeed profile as well as the nominal thrust, drag, and lift profiles are obtained from the available DFDR measurements. The actual values of the thrust, drag, and lift are assumed to be proportional to the respective nominal values via multiplicative parameters, called the thrust, drag, and lift factors. The thrust, drag, and lift factors plus the inertial velocity components at impact are determined by matching the flight trajectory computed from DFDR data with the flight trajectory available from ATCR data. This leads to a least-square problem which is solved analytically under the additional requirement of closeness of the multiplicative factors to unity.

See also the following:

10T237. Analytical development of an equivalent system mismatch function
10T240. Validation of engineering methods for predicting hypersonic vehicle control forces and moments
10A241. Composite adaptive control of flexible joint robots
10T245. Milito-Cruz adaptive control scheme for Markov chains

200F. SENSITIVITY

10A230. Comparison of methods for design sensitivity analysis for optimal control of thermal systems. - JM House *(Dept of Mech Eng, Univ of Iowa, Iowa City IA 52242)*, JS Arora *(Dept of Civil and Env Eng, Univ of Iowa, Iowa City IA 52242)*, TF Smith *(Dept of Mech Eng, Univ of Iowa, Iowa City IA 52242)*. Optimal Control Appl Methods 14(1) 17-37 (Jan-Mar 1993).

The objective of this study is to examine two analytical methods for the design sensitivity analysis of optimal control problems and to develop the analyses necessary for the application of the methods to thermal systems. The two methods are the direct differentiation method and the adjoint variable method. Results for these methods are compared with those obtained using central finite difference approximations for design sensitivity analysis. The adjoint variable method has the potential to reduce significantly computational times for design sensitivity analysis while sacrificing only a small amount of accuracy. As the number of functionals requiring design sensitivity analysis increases, however, the adjoint variable method becomes less attractive and the direct differentiation method becomes more attractive.

10A231. Simple discrete-time regulator minimizing sensitivity. - A Tarczynski *(Sch of Electron and Manuf Syst Eng, Univ of Westminister, 115 New Cavendish St, London W1M 8JS, UK)*. Automatica 29(3) 793-796 (May 1993).

A simple algorithm for minimizing sensitivity of SISO discrete-time control systems is presented. The method delivers an explicit solution for the controller. It allows the designer to maintain control over the order of the controller. Another advantage of the method is that it offers significant flexibility in weighting sensitivity and complementary sensitivity functions in the performance criterion as the weights do not have to be the magnitudes of some transfer functions.

See also the following:

10A291. Strong diagonal dominance by quantitative feedback theory

200H. DESIGN METHODS

10T232. Controller design with regional pole constraints: Hyperbolic and horizontal strip

regions. - Y William Wang and DS Bernstein *(Dept of Aerospace Eng, Univ of Michigan, Ann Arbor MI 48109)*. J Guidance Control Dyn 16(4) 784-787 (Jul-Aug 1993).

10A233. Frequency domain design for robust performance under parametric, unstructured, or mixed uncertainties. - S Jayasuriya *(Dept of Mech Eng, Texas A&M Univ, College Station TX 77843-3123)*. J Dyn Syst Meas Control 115(2B) 439-451 (Jun 1993).

This article looks at direct frequency domain design for satisfying robust performance objectives in uncertain, linear time invariant (LTI) plants embedded in a single feedback loop. The uncertain plants may be described by parametric, nonparametric (or unstructured), or mixed uncertain models. Quantitative Feedback Theory (QFT) is one frequency domain design methodology that is direct and is equally effective with any of these models. It can be separated from other frequency domain robust control methods such as H^∞ optimal control, μ synthesis, and LQG-LTR for at least (i) its emphasis on cost of feedback measured in terms of controller bandwidth, (ii) its ability to deal nonconservatively with parametric, nonparametric and mixed uncertainty models, and (iii) its utilization of both amplitude and phase of the loop transfer function, pointwise in frequency, for the quantification of robust performance. An exposition of these attributes, unique to QFT, and the basic design methodology, coupled with a recently developed mathematical framework and some existence results for the standard single-loop QFT problem are the salient features of this paper.

10A234. Lead-lag compensator design by the Hough transform. - Yen-Ting Hsu, Yau-Tarng Juang *(Dept of Elec Eng, Natl Central Univ, Chung-Li, Taiwan 32054, ROC)*, Te-Ping Tsai *(Chung Shan Inst of Sci and Tech, PO Box 90008-16-17 Lungtan, Taoyuan, Taiwan, ROC)*. Syst Control Lett 20(5) 365-372 (May 1993).

The frequency response of a compensator can be expressed as a curve in the complex plane. The Hough transform is very useful in finding a mathematical model which matches the curve in a plane very well. We combine these two concepts to generate a new method of compensator design. Two examples are illustrated to explain the design procedure and results.

10A235. Maneuver and vibration control of hybrid coordinate systems using Lyapunov stability theory. - JL Junkins *(Dept of Aerospace Eng, Texas A&M Univ, College Station TX 77843)* and Hyochoong Bang *(Dept of Aeronaut and Astronaut, Naval Postgraduate Sch, Monterey CA)*. J Guidance Control Dyn 16(4) 668-676 (Jul-Aug 1993).

In this study, we present a generalized control law design methodology that covers a large class of systems, especially flexible structures by hybrid discrete-distributed coordinate systems. The Lyapunov stability theory is used to develop globally stabilizing control laws. A hybrid version of Hamilton's canonical equations is introduced, which provides a direct path to designing stabilizing control laws for general nonlinear hybrid systems. The usual loss of robustness due to model reduction is overcome by this Lyapunov approach, which does not require truncation of the flexible systems into finite dimensional discrete systems.

10A236. Robust pole assignment in a specified region using output feedback. - Myungho Oh, Da-Wei Gu, SK Spurgeon *(Dept of Eng, Univ of Leicester, University Rd, Leicester LE1 7RH, UK)*. Optimal Control Appl Methods 14(1) 57-66 (Jan-Mar 1993).

An output feedback pole assignment method is presented which seeks to achieve a robust solution where the assigned poles are as insensitive as possible to perturbations in the closed-loop system. The freedom available to obtain a robust solution is realized by assigning poles not to exact locations but within specified regions of the complex plane. The problem is formulated as a nonlinear programming problem with a set of nonlinear constraints of matrix-valued functions as well as a set of linear constraints. A numerical algorithm is presented in two forms and the results obtained are compared with those generated from other algorithms for a series of test examples taken from the literature.

See also the following:

10T226. Design of a robust estimator for target tracking
10A230. Comparison of methods for design sensitivity analysis for optimal control of thermal systems
10A251. Quantitative feedback design of decentralized control systems
10A265. Optimal discrete-time dynamic output-feedback design: A w-domain approach
10A360. Dejavu: Case-based reasoning for mechanical design

200I. MODELLING AND SIMULATION

10T237. Analytical development of an equivalent system mismatch function. - MR Anderson *(Dept of Aerospace and Ocean Eng, 215 Randolph Hall, VPI)*. J Guidance Control Dyn 16(4) 712-716 (Jul-Aug 1993).

10A238. Inverse simulation of large-amplitude aircraft maneuvers. - C Gao *(Chung Shien Inst of Sci and Tech, Taiwan, ROC)* and RA Hess *(Dept of Mech, Aeronaut and Mat Eng, UC, Davis CA 95616)*. J Guidance Control Dyn 16(4) 733-737 (Jul-Aug 1993).

Inverse simulation techniques are computational methods that determine the control inputs to a dynamic system that will produce desired system outputs. Such techniques can be useful tools for the analysis and evaluation of problems associated with maneuvering flight. As opposed to current inverse simulation methods that require numerical time differentiation in their implementation, the proposed technique is essentially an integration algorithm. It is applicable to cases where the number of inputs equals or exceeds the number of constrained outputs. The algorithm is exercised in determining the trim condition and then the control inputs that force a nonlinear model of an F-16 fighter to complete large-amplitude maneuvers.

10A239. Reflections on engineering systems and bond graphs. - RC Rosenberg *(Dept of Mech Eng, Michigan State Univ, E Lansing MI 48824)*. J Dyn Syst Meas Control 115(2B) 242-251 (Jun 1993).

An important aspect of modern engineering systems is their great diversity. Often they include interactions among different physical domains, contain control sub-systems, and are large-scale and complex. The bond graph is a powerful and versatile tool that can help the engineer to design modern engineering systems. Three issues are explored from a bond graph perspective: modeling of engineering systems, simulation of their behavior, and teaching about engineering systems. It is the author's observation that bond graph methodology is one of the most useful engineering system techniques available and belongs in the problem-solving tool kit of every mechanical engineer. This paper develops a rationale for this viewpoint both for readers familiar with bond graph methods and for readers to whom they are new.

10T240. Validation of engineering methods for predicting hypersonic vehicle control forces and moments. - M Maughmer *(Aerospace Eng Dept, Penn State)*, L Ozoroski *(Aeronaut Eng, Lockheed Eng and Sci Co)*, D Straussfogel, L Long *(Aerospace Eng Dept, Penn State)*. J Guidance Control Dyn 16(4) 762-769 (Jul-Aug 1993).

See also the following:

10T267. Optimal open multistep discretization formulas for real-time simulation
10A317. Modeling and state estimator design issues for model-based monitoring systems
10A370. Modeling and control of manufacturing processes: Getting more involved

200J. ADAPTIVE AND LEARNING SYSTEMS

10A241. Composite adaptive control of flexible joint robots. - Jing Yuan and Y Stepanenko *(Dept of Mech Eng, Univ of Victoria, Victoria, BC, V8W 3P9, Canada)*. Automatica 29(3) 609-619 (May 1993).

A composite adaptive controller is developed for flexible joint robots with inertia parameter uncertainty. It does not require any restrictions on the joint stiffness, since a full-order dynamic model is used in the design and stability analysis. Previously published results based on the fourth-order model require at least joint jerk feedback and derivatives of the manipulator regressor (up to the second-order). In contrast, the proposed adaptive controller requires at most joint acceleration feedback. Its adaptive law is of the same complexity as the well-known Slotine and Li's algorithm for rigid-body robots. Asymptotic stability of the adaptive controller is established in the Lyapunov sense. Simulation results are included to demonstrate the tracking performance.

10A242. Evolution of adaptive control. - ID Landau *(Lab d'Automat de Grenoble, INPG-CNRS, Groupement de Rech Automat, ENSIEG-BP 46 38402, St-Martin d'Heres, France)*. J Dyn Syst Meas Control 115(2B) 381-391 (Jun 1993).

The evolution of the adaptive control algorithms driven by the results obtained in the application of the 1st generation of adaptive controllers (model reference adaptive control, self-tuning minimum variance) is examined. Research in the field of adaptive control has been directed, on the one hand, toward the development of a robust general purpose adaptive controller and, on the other, towards the extension of the model reference adaptive control approach to nonlinear systems. Research has also investigated the stability-passivity approach for developing dedicated adaptive control algorithms for particular classes of nonlinear plants (eg, rigid robots). The paper will review the results obtained in these directions both from the theoretical and the practial points of view. In the final part, current research directions will be included.

10A243. Learning control of robot manipulators. - R Horowitz *(Dept of Mech Eng, UCB)*. J Dyn Syst Meas Control 115(2B) 402-411 (Jun 1993).

Learning control encompasses a class of control algorithms for programmable machines such as robots which attain, through an iterative process, the motor dexterity that enables the machine to execute complex tasks. In this paper we discuss the use of function identification and adaptive control algorithms in learning controllers for robot manipulators. In particular, we discuss the similarities and differences between betterment learning schemes, repetitive controllers and adaptive learning schemes based on integral transforms. The stability and convergence properties of adaptive learning algorithms based on integral transforms are highlighted and experimental results illustrating some of these properties are presented.

10A244. Low velocity friction compensation and feedforward solution based on repetitive control. - ED Tung *(Dept of Mech Eng, UCB)*, G Anwar *(Integrated Motions, Berkeley CA)*, M

Tomizuka *(Dept of Mech Eng, UCB)*. J Dyn Syst Meas Control 115(2A) 279-284 (Jun 1993).

One of the most significant sources of tracking error for an X-Y table is static friction, a nonlinear disturbance at low velocity. In traversing a circular profile, an X-Y table encounters zero velocity crossings at 90° intervals around the circle, leaving relatively large tracking errors referred to as "quadrant glitches". To learn the control input which eliminates errors caused by stiction, repetitive control, a subclass of learning control, is employed. Experiments, conducted on the X-Y bed of a CNC milling machine, demonstrate that near-perfect tracking can be achieved in twelve cycles or less. Of particular interest is the velocity command input generated by repetitive control. The input containt feedforward information for developing perfect trajectories at low velocities.

10T245. Milito-Cruz adaptive control scheme for Markov chains. - VS Borkar *(Dept of Elec Eng, Indian Inst of Sci, Bangalore, India)*. J Optim Theory Appl 77(2) 387-397 (May 1993).

10A246. Robust adaptive control of revolute flexible-joint manipulators using sliding technique. - Chi-Man Kwan and KS Yeung *(Dept of Elec Eng, Univ of Texas, Box 19016, Arlington TX 76019)*. Syst Control Lett 20(4) 279-288 (Apr 1993).

In this paper, we present a 3-step procedure to robustly control the revolute flexible-joint manipulator in the presence of parameter variations and bounded input disturbances such as torque ripples. By treating the difference of motor angle and link angles as the input to the rigid link part of the manipulator dynamics, our first step is to design a smooth adaptive reference signal for this input to globally stabilize the rigid subsystem. The second step is to drive the difference of motor and link angles to this desired reference signal exponentially by using sliding control. In the third step we exploit the model reduction capability of sliding control to perform the stability analysis. It is well-known that sliding control can reduce the system order by n if the number of control inputs is n. The exploitation of this property of sliding control makes our stability analysis a lot simpler than other approaches. Global stability in the sense of Lyapunov can be guaranteed and errors in link position and velocity are driven to zero when the system is in sliding mode. No weak elasticity assumption is needed.

10A247. State space self-tuning controller with integral action. - P Desai *(Sch of Eng and Eng Tech, Penn State Univ, Erie PA 16523-0203)* and AK Mahalanabis *(Dept of Elec Eng, Penn State)*. Optimal Control Appl Methods 13(4) 301-319 (Oct-Dec 1992).

The paper is concerned with the problem of designing a state space self-tuning controller with integral action for a class of unknown linear stochastic systems. The observer form of the innovations model of the system is used along with a single-stage *quadratic-in-state-and-control* performance index which includes a cross-weighting between system states and inputs. This results in a *proportional estimated state plus integral output* $(P + I)$ controller in an incremental form. While it is analogous to the LQG-theory-based optimal adaptive controller in structure, computational simplification is achieved by the choice of a single-stage performance index and a direct estimation of the state estimator gain matrix. The new controller has the advantages of being applicable to both single-input and single-output and multi-input and multi-output minimum phase and non-minimum phase systems. The results are illustrated numerically through two simulation examples.

10A248. Suitable generalized predictive adaptive controller case study: Control of a flexible arm. - M M'Saad, L Dugard, SH Hammad *(Lab d'Automat de Grenoble, ENSIEG - INPG, BP 46, 38402, St-Martin-d'Heres, France)*. Automatica 29(3) 589-608 (May 1993).

This paper presents an adaptive control case study involving a flexible arm. The underlying control design consists in a judicious combination of the pole placement concept and the generalized predictive control design. The former allows one to incorporate a suitable tracking capability while the latter is more advisable from practical use point of view. A particular emphasis is put on the fundamental design features of the adaptive controller, namely the tracking capability, the adaptation alertness and the robustness with respect to reduced order modeling.

See also the following:

10A279. Torque regulation of induction motors
10A284. Decoupling control based on the modified root locus approach
10A324. Real-time expert system for fault-tolerant supervisory control
10A349. Design and performance studies of model-based variable-structure adaptive controllers for industrial manipulators
10A352. Variable-structure linear-model-following control of manipulators
10A360. Dejavu: Case-based reasoning for mechanical design
10A367. Integration of coordinate measuring machines within a design and manufacturing environment

200M. NONLINEAR SYSTEMS

10T249. Globally convergent algorithm for solving nonlinear equations. - J Abaffy and F Forgo *(Inst of Math and Comput Sci, Univ of Economics, Budapest, Hungary)*. J Optim Theory Appl 77(2) 291-304 (May 1993).

10T250. Stochastic averaging using elliptic functions to study nonlinear stochastic systems. - Win-Min Tien, N Sri Namachchivaya *(Aeronaut and Astronaut Eng Dept, Univ of Illinois, Urbana IL 61801)*, VT Coppola *(Dept of Aerospace Eng, Univ of Michigan, Ann Arbor MI 48109)*. Nonlinear Dyn 4(4) 373-387 (Aug 1993).

See also the following:

10A33. Adjoining cell mapping and its recursive unraveling Part I. Description of adaptive and recursive algorithms
10A37. Quasi-harmonic analysis of the behavior of a hardening duffing oscillator subjected to filtered white noise

200P. DECENTRALIZED SYSTEMS

10A251. Quantitative feedback design of decentralized control systems. - ODI Nwokah and Chin-Horng Yau *(Sch of Mech Eng, Purdue)*. J Dyn Syst Meas Control 115(2B) 452-464 (Jun 1993).

In the spirit of practical applicability, design transparency and quantitative specifications, this paper presents a new robust decentralized control design framework – model reference quantitative feedback design (MRQFD) – for multivariable control systems with large plant uncertainty and strong cross-coupling. The MRQFD method provides a connection between Rosenbrock's Nyquist array and Horowitz's quantitative feedback theory. There are two main stages in the MRQFD method. First, an internal model reference loop, based on non-negative matrix theory, is used to obtain robust generalized diagonal dominance and hence the reduction of uncertainty in the resultant compensated internal loop system. Then a single-loop quantitative feedback design scheme is applied to solve the resulting series of individual loops to guarantee the satisfaction of predefined MIMO quantitative specifications. The design procedure can be carried out either in the direct or in the inverse plant domains, as in Rosenbrock's Nyquist array. The conditons of robust diagonal stabilization are also given for the MRQFD framework. The effectiveness of the MRQFD method and its ease of application are demonstrated by a 3 × 3 uncertain multivariable example.

200Q. STOCHASTIC OR FUZZY SYSTEMS

See the following:

10T250. Stochastic averaging using elliptic functions to study nonlinear stochastic systems

200Y. COMPUTATIONAL TECHNIQUES

See the following:

10A238. Inverse simulation of large-amplitude aircraft maneuvers

202. Control systems

202A. GENERAL THEORY

10T252. Stabilizability of linear quadratic state feedback for uncertain systems. - Rong-Jyue Wang and Wen-June Wang *(Dept of Elec Eng, Natl Central Univ, Chung Li, 320, Taiwan, ROC)*. J Guidance Control Dyn 16(3) 597-600 (May-Jun 1993).

202B. OPTIMIZATION TECHNIQUES AND ALGORITHMS

10A253. Algorithm for optimal scheduling of a class of cascade water supply systems. - MA Brdys *(Sch of Electron and Elec Eng, Univ of Birmingham, PO Box 363, Birmingham B15 2TT, UK)*. Optimal Control Appl Methods 13(4) 265-287 (Oct-Dec 1992).

The problem of determining overall optimized control schedules for a class of cascade water supply systems containing only fixed speed pumps is examined. The system control is by nature an on-off type. The optimal scheduling problem can be formulated as dynamical optimal control problems with purely discrete symbols, discrete controls, and also with continuous intermediate variables interrelated in a highly nonlinear way. An efficient problem solver is proposed. Its high efficiency is achieved by exploiting, through a suitable decomposition, certain structural properties of the problem. Lagrange relaxation is applied in order to break down the time structure of discrete control variables. The decomposition also enables consideration of mixed integer optimization on purely static grounds. The dynamical optimization constitutes only that part of the solver which deals with entirely continuous variables. There is a duality gap in the problem. However, certain but not complete, information obtained through solving the dual problem (dual optimal information) is close to that which corresponds to the true (primal) optimal solution. This is an important property of the scheduling problem, which together with the problem structure creates a basis for the solver design.

10T254. Closed-form solutions to discrete-time LQ optimal control and disturbance attenuation. - Katsuhisa Furuta and Manop Wongsaisuwan *(Dept of Control Eng, Tokyo IT, 2-12-1 Oh-Okayama Meguro-ku, Tokyo 152, Japan)*. Syst Control Lett 20(6) 427-437 (Jun 1993).

10A255. Computation of the digital LQG regulator and tracker for time-varying sys-

tems. - LG Van Willigenburg *(Dept of Agri Eng and Phys Agrotechnion, Wageningen Univ, Bomenweg 4, 6703 HD Wageningen, Netherlands).* Optimal Control Appl Methods 13(4) 289-299 (Oct-Dec 1992).

Digital optimal control problems, ie, problems where a continuous-time system is controlled by a digital computer, are very often approximated by either discrete-time or continuous-time optimal control problems. A digital controller based on one of these approximations requires a *small sampling time* and constitutes only an *approximate solution.* The digital LQG regulator and tracker constitute solutions to real digital control problems which involve sampled-data, piecewise constant controls and integral criteria. Until now only the numerical computation of the digital LQG regulator in the case of time-invariant system and criterion matrices has been considered in the literature. The control of nonlinear stochastic systems about state trajectories is very often performed by an LQG regulator based on the linearized dynamics about the trajectory, which constitutes a *time-varying system.* We present a numerical procedure to compute the digital LQG regulator and a tracker in the case where the system and criterion matrices are time-varying. Finally we present a numerical example.

10A256. Control of motion of complex mechanical systems. Synthesis of algorithms on the basis of Euler equations. - PD Krut'ko *(Moscow, Russia).* J Machinery Manuf Reliab 6 83-90 (1992).

Adaptive algorithms for controlling motion of objects modeled by the Euler equations, are synthesized. The algorithms are of non-traditional structure and make the systems weakly sensitive to parameters variations and external disturbances. The structure of the algorithms is found by optimizing the systems in the minimum-acceleration-energy criterion. The algorithms may be used for automatic control of motion of mechanical and aeromechanical objects, as well as of stabilized and controlled platforms, with respect to their centers of masses.

10A257. Disturbance model for control-structure optimization with full state feedback. - GL Slater *(Dept of Aerospace Eng and Eng Mech, Univ of Cincinnati, ML No 70, Cincinnati OH 45221)* and MD McLaren *(Space Syst-LORAL, M-S G75, Palo Alto CA 94303).* J Guidance Control Dyn 16(3) 523-533 (May-Jun 1993).

This paper deals with a technique for the integrated optimization of structure and control in the design of flexible spacecraft and other flexible systems. This current approach uses the concept of response to dynamic constraints to establish tradeoffs between control energy and structural mass. This approach gives a concise variational methodology to total system optimization and eliminates the need to specify rather arbitrary trade-offs between control energy and structural mass. Results give an explicit dependency between structural stiffness (hence mass), disturbance magnitude, control energy available, and deflection constraints. For the special case of linear controls and quadratic constraints the problem reduces to a standard linear quadratic regulator problem plus a structure optimization. The method is general, however, and can be extended to more general problems such as output feedback, nonlinear controls, and slew optimization.

10A258. Feedback control of minimum-time optimal control problems using neural networks. - CJ Goh, J Edwards *(Dept of Math, Univ of W Australia, Nedlands, W Australia 6009, Australia),* AY Zomaya *(Dept of Elec and Electron Eng, Univ of W Australia, Nedlands, W Australia 6009, Australia).* Optimal Control Appl Methods 14(1) 1-16 (Jan-Mar 1993).

This paper presents an optimal feedback controller capable of driving a nonlinear control system from an arbitrary initial state to a fixed final state in minimum time. The controller is based on a feedforward multilayer neural network trained repeatedly using open-loop optimal control data which densely span the field of extremals of the nonlinear system. The effectiveness of the controller is clearly demonstrated by a simulation on a two-link robot manipulator. The effect of sensor-actuator noise and parameter variation is also included to confirm the robustness of the controller.

10T259. First-order models for satellite survivability optimization. - ML Howard *(Tracor Aerospace, Austin TX 78725).* J Guidance Control Dyn 16(3) 462-469 (May-Jun 1993).

10A260. General adaptive guidance using nonlinear programming constraint-solving methods. - L Skalecki *(Consult Eng, Boeing Defense & Space Group, 7264 Beresford Ave, Parma OH 44130)* and M Martin *(Space Transportation Syst, Boeing Defense & Space Group, PO Box 3999, MS 8C-09, Seattle WA 98124).* J Guidance Control Dyn 16(3) 517-522 (May-Jun 1993).

An adaptive, general-purpose, constraint-solving guidance algorithm has been developed by the authors in response to the requirements for the advanced launch system. The algorithm can be used for all mission phases for a wide range of space transportation vehicles without code modification because of the general formulation of the nonlinear programming problem, and the general trajectory simulation used to predict constraint values. The approach allows onboard retargeting for severe weather and changes in payload or mission parameters, increasing flight reliability and dependability, while reducing the amount of preflight analysis that must be performed. The algorithm is described in general in this paper. Three-dof closed-loop simulation results are presented for application of the algorithm to advanced launch system ascent, re-entry of a low lift-to-drag vehicle, and Mars aerobraking. Flight processor throughput requirement data are shown for each of these applications.

10A261. Inverse dynamics approach to trajectory optimization for an aerospace plane. - Ping Lu *(Dept of Aerospace Eng and Eng Mech, Iowa State Univ, Ames IA 50011).* J Guidance Control Dyn 16(4) 726-732 (Jul-Aug 1993).

An inverse dynamics approach for trajectory optimization is proposed. This technique can be useful in many difficult trajectory optimization and control problems. The application of the approach is exemplified by ascent trajectory optimization for an aerospace plane. Both minimum-fuel and minimax types of performance indices are considered. When rocket augmentation is available for ascent, it is shown that accurate orbital insertion can be achieved through the inverse control of the rocket in the presence of disturbances.

10A262. Linear quadratic Gaussian-loop transfer recovery design for a helicopter in low-speed flight. - JJ Gribble *(Dept of Electron and Elec Eng, Univ of Glasgow, G12 8QQ, UK).* J Guidance Control Dyn 16(4) 754-761 (Jul-Aug 1993).

A control law for a helicopter in low-speed flight is designed using the linear quadratic Gaussian-loop transfer recovery method. The specifications are adapted from a subset of the US Army helicopter handling qualities requirements. The design model consists of the rigid-body dynamics linearized about the 30 kt forward flight condition, together with a simplified, low-order representation of actuator and rotor dynamics. Evaluation is performed using higher-order models, obtained by linearization about several different points in the flight envelope, covering the speed range from 10 to 50 kt. These models contain more accurate representations of the high-frequency actuator and rotor modes. The final selection of the numerical values of the linear quadratic parameters is made by numerical optimization of the loop shape. It is found that the specifications considered can be satisfied for all of the evaluation models without gain scheduling.

10A263. Near-optimal observer-based control of discrete two-time-scale systems. - Ming-Shyan Wang, Tzuu-Hseng S. Li, York-Yih Sun *(Control System Lab, Dept of Elec Eng, Natl Cheng-Kung Univ, Tainan, Taiwan 70101, ROC).* J Franklin Inst 330(4) 651-663 (Jul 1993).

The design of near-optimal observer-based controllers for discrete two-time-scale systems with inaccesssible states is considered. The controller is established by the design of the controllers of slow and fast subsystems via the quasi-steady-state method. The stability bound of the singular perturbation parameter and the value of the minimum performance index for the actual closed-loop system are determined. A digital flight control system of a twin-engine aircraft is used to demonstrate the desired scheme.

10A264. Nonlinear optimal regulator problem. - CJ Goh *(Dept of Math, Univ of W Australia, Nedlands, W Australia 6009, Australia).* Automatica 29(3) 751-756 (May 1993).

The linear quadratic regulator is one of the most widely used tools for control systems design. Many real world systems, however, are inherently nonlinear and can only be optimally regulated using a nonlinear controller. This is, in general, much more difficult to achieve than the linear quadratic case. In this paper we show that a nonlinear feedback controller can be synthesized by appropriate training of a feedforward neural network to satisfy the corresponding nonlinear Hamilton-Jacobi-Bellman (HJB) partial differential equation in a restricted domain of the state space. Asymptotic stability of the closed-loop system is shown to be a natural consequence of the HJB equation.

10A265. Optimal discrete-time dynamic output-feedback design: A w-domain approach. - Cheolkeun Ha, Uy-Loi Ly *(Dept of Aeronaut and Astronaut, Univ of Washington, Seattle WA 98195),* MC Berg *(Dept of Mech Eng, Univ of Washington, Seattle WA 98195).* J Guidance Control Dyn 16(3) 534-540 (May-Jun 1993).

An alternative method for optimal digital control design is described in this paper. The method is based on the usage of the w-transform and has many attractive design features. One of these is its immediate connection with frequency loop-shaping techniques that are now popular and effective for multivariable control synthesis in the continuous-time domain. Furthermore, any design algorithms originally developed for continuous-time systems can now be immediately extended to the discrete-time domain. The main results presented in this paper are the exact problem formulation and solution of an optimal discrete-time dynamic output-feedback design in the w domain involving a quadratic performance index to random disturbances. In addition, necessary conditions for optimality are obtained for the numerical solution of the optimal output-feedback compensator design. A numerical example is presented illustrating its application to the design of a low-order dynamic compensator in a stability augmentation system of a commercial transport.

10A266. Optimal impulsive intercept with low-thrust rendezvous return. - CA Lembeck *(NASA Johnson Space Center, Houston TX 77058)* and JE Prussing *(Univ of Illinois, Urbana IL 61801).* J Guidance Control Dyn 16(3) 426-433 (May-Jun 1993).

Primer vector theory is used to investigate a specific class of minimum-fuel spacecraft trajectory problems in which high- and low-thrust propulsion systems are utilized sequentially. The problem considered assumes a spacecraft initially on-station is an established orbit about the earth. It is desired to intercept a predetermined position in space in a timely manner for collision avoidance or platform surveillance, using an optimal high-thrust program. The spacecraft then returns to the original orbit station using optimal low-thrust propulsion. Fixed-time minimum-fuel solutions are obtained using the Clohessy-Wiltshire linearized dynamic model. In the time-open case, the optimal final time is unbounded. For this case a composite performance index involving both fuel consumption and the final time is minimized to obtain optimal finite-time solutions.

10T267. Optimal open multistep discretization formulas for real-time simulation. - DD Moerder *(Spacecraft Control Branch, NASA Langley Res Center, Hampton VA 23665)*, AJ Calise *(Sch of Aerospace Eng, Georgia Tech)*, P Clemmons *(Sch of Aerospace Eng, Georgia Tech, Hampton)*. J Guidance Control Dyn 16(3) 557-563 (May-Jun 1993).

10T268. Parallel asynchronous Newton algorithm for unconstrained optimization. - D Conforti and R Musmanno *(Dept of Elettron Info e Sist, Univ della Calabria, Rende, Cosenza, Italy)*. J Optim Theory Appl 77(2) 305-322 (May 1993).

10A269. Quasi-closed-form solution to the time-optimal rigid spacecraft reorientation problem. - RM Byers *(Dept of Mech and Aerospace Eng, Univ of Central Florida, Orlando FL 32816)* and SR Vadali *(Dept of Aerospace Eng, Texas A&M Univ, College Station TX 77843)*. J Guidance Control Dyn 16(3) 453-461 (May-Jun 1993).

The problem of slewing a rigid body from an arbitrary initial orientation to a desired target orientation in minimum time is addressed. The nature of the time-optimal solution is observed via an open-loop solution using the switch time-optimization algorithm developed by Meier and Bryson. Conclusions as to the number and timing of control switches are drawn and substantiated analytically. The solution of the kinematic differential equations for Euler parameters is examined for systems in which the applied torque is much greater than the nonlinear terms in Euler's equations. An approximate solution to these equations is used to construct the state transition matrix as a function of a given control sequence and control intervals. This allows a rapid solution for the required switch times for all admissible control sequences. Uncoupled switching functions can be generated given the approximate switch times for the optimal sequence. The resulting feedforward-feedback control is suitable for online computation.

10T270. Riccati equation approach to the singular LQG problem. - Y Halevi *(Dept of Mech Eng, Ohio State Univ, 206 W 18th Ave, Columbus OH 43210-1107)*, WM Haddad *(Dept of Mech and Aerospace Eng, Florida IT, Melbourne FL 32902)*, DS Bernstein *(Dept of Aerospace Eng, Univ of Michigan, Ann Arbor MI 48109-2140)*. Automatica 29(3) 773-778 (May 1993).

10A271. Saturating and time-optimal feedback controls. - M Bikdash *(Bradley Dept of Elec Eng, VPI)*, EM Cliff *(Dept of Aerospace and Ocean Eng, VPI)*, AH Nayfeh *(Dept of Eng Sci and Mech, VPI)*. J Guidance Control Dyn 16(3) 541-548 (May-Jun 1993).

The open-loop solution of the soft-constrained time-optimal control problem can be efficiently computed in terms of the controllability Grammian matrix, but a closed-loop implementation was found to be cumbersome. This control was observed to have a saturation property strongly reminiscent of the hard-constrained time-optimal control problem. In this paper, we present a theoretical justification for the observed saturation and propose a modification of the problem statement that gives a suboptimal solution and results in a drastically simpler implementation of the feedback time-optimal soft-constrained control. Moreover, we generalize the proposed approach to generate a family of saturating control laws occupying a middle ground between linear state-feed-back and hard-constrained time-optimal controls. For illustration, we consider the simultaneous slewing and vibration suppression of an undamped flexible beam that is reducible to a marginally stable linear system. As an example, we design a simple and elegant feedback control law where the regulation time and control amplitude saturate like the square root of the norm of the state vector.

10A272. Singular control in minimum time spacecraft reorientation. - H Seywald and RR Kumar *(Spacecraft Control Branch, NASA Langley Res Center, 17 Research Dr, Hampton VA)*. J Guidance Control Dyn 16(4) 686-694 (Jul-Aug 1993).

Time-optimal solutions for the reorientation of an inertially symmetric rigid spacecraft with independent three-axes controls are investigated. All possible optimal control strategies are identified. These include bang-bang solutions, finite-order singular arcs and infinite-order singular arcs. Necessary conditions for optimality of finite-order singular arcs are presented. Nonoptimality of principal-axis rotation for rest-to-rest minimum time reorientation is proved. Numerical examples of time-optimal solutions with finite- and infinite-order singular arcs are presented. A simple example of "a car in a parking lot" is discussed. It clearly illustrates that infinite-order singular control may be the "unique" solution to an optimal control problem and cannot be ignored when choosing the optimal control strategies.

10A273. Terminal repeller unconstrained subenergy tunneling (TRUST) for fast global optimization. - BC Cetin *(Dept of Elec Eng, California IT, Pasadena CA)*, J Barhen *(Nonlinear Sci and Info Processing Group, JPL)*, JW Burdick *(Dept of Mech Eng, California IT, Pasadena CA)*. J Optim Theory Appl 77(1) 97-126 (Apr 1993).

A new method for unconstrained global function optimization, acronymed TRUST, is introduced. This method formulates optimization as the solution of a deterministic dynamical system incorporating terminal repellers and a novel subenergy tunneling function. Benchmark tests comparing this method to other global optimization procedures are presented, and the TRUST algorithm is shown to be substantially faster. The TRUST formulation leads to a simple stopping criterion. In addition, the structure of the equations enables an implementation of the algorithm in analog VLSI hardware, in the vein of artificial neural networks, for further substantial speed enhancement.

10A274. Time-optimal three-axis reorientation of a rigid spacecraft. - KD Bilimoria *(Aerospace Res Center, Arizona State Univ, Tempe AZ 85287)* and Bong Wie *(Dept of Mech and Aerospace Eng, Arizona State Univ, Tempe AZ 85287)*. J Guidance Control Dyn 16(3) 446-452 (May-Jun 1993).

New results are presented for the minimum-time rest-to-rest reorientation control problem of a rigid spacecraft with independent three-axis control. It is shown that in general the eigenaxis rotation maneuver is not time optimal. An inertially symmetric (eg, spherical or cubical) rigid body is examined to demonstrate that an eigenaxis rotation about a control axis of even such a simple body is not time optimal. The computed optimal solution is bang-bang in all three control components and has a significant nutational component of motion. The total number of switches is found to be a function of the specified reorientation angle.

See also the following:

10A224. Robustness bounds for linear systems under uncertainty: Eingevalues inside a wedge
10A230. Comparison of methods for design sensitivity analysis for optimal control of thermal systems
10A361. Dispelling the manufacturing myth
10A372. Decomposition approach to the public transport scheduling problem
10T843. Minimum-effort interception of multiple targets

202C. NONLINEAR SYSTEMS

10A275. Analysis and control of nonlinear systems. - JK Hedrick *(Dept of Mech Eng, UCB)*. J Dyn Syst Meas Control 115(2B) 351-361 (Jun 1993).

This paper describes my work on nonlinear analysis and control over the last twenty years. The first part of the paper concerns the development of nonlinear analysis tools for predicting stability and forced response characteristics of high speed ground vehicles. The principal motivation was to develop an alternative to "brute force" time domain simulation. The developed tools were extensions of "describing function" or "equivalent linearization" methods for both periodic and stochastic excitation. The "statistical linearization" analysis tools were then extended and applied to design control laws for nonlinear stochastic regulators. The second part of the paper was motivated by control system design for highly nonlinear, multivariable systems, such as automotive powertrain control and aircraft flight control. For these classes of systems, statistical linearization procedures are computationally cumbersome and also provide no stability or robustness guarantees. A method which has proven extremely powerful, both theoretically and experimentally, is "sliding control." This technique is a form of input-output linearization that directly incorporates model error information with stability and performance measures. My students and I found several difficulties in the direct application of this method to automotive and aircraft control. This paper describes our solutions to the problems of repeated model differentiation, differentiation of model error, undesirable "internal dynamics" and systems with saturating control inputs.

10A276. Control of uncertain nonlinear systems. - M Corless *(Sch of Aeronaut and Astronaut, Purdue)*. J Dyn Syst Meas Control 115(2B) 362-372 (Jun 1993).

This paper describes some of my research in the analysis and control of nonlinear uncertain systems in which the uncertainties are modeled deterministically rather than stochastically. The main applications are to mechanical-aerospace systems, such as robots and spacecraft; the underlying theoretical approach is based on Lyapunov theory.

10A277. Elaboration of a control law for switching nonlinear systems. - V Abadie and G Dauphin-Tanguy *(Ecole Central de Lille, LAIL, URA CNRS D 1440, BP 48 Cite Scientifique, 59651 Villeneuve d'Ascq, Cedex, France)*. J Franklin Inst 330(4) 685-693 (Jul 1993).

The purpose of this paper is to elaborate upon a control law for a class of nonlinear system with Boolean inputs. First the affine system is studied, and then the control law is calculated by an input-output feedback linearization, assuming the system is continuous. The final control law is then determined by a discretization of the input vector. The results are applied to an asynchronous machine and its power electronics control system.

10A278. One approach to the control of uncertain systems. - G Leitmann *(Col of Eng, UCB)*. J Dyn Syst Meas Control 115(2B) 373-380 (Jun 1993).

This paper is a personal history of one area of research with which I have been concerned over the past twenty years and which continues to attract my albeit waning attention, the control of dynamical systems based on uncertain models. Thus, it is a subjective account of various factors which I believe to have steered me to approach the problem via a constructive use of Lyapunov stability theory.

10A279. Torque regulation of induction motors. - R Ortega *(Univ de Tech, Heudiasyc URA CNRS 817, BP 233 60206 Compiegne, Cedex, France)* and G Espinosa *(Univ Nacional Autonoma, DEPFI, PO Box 70-256, DF, Mexico)*. Automatica 29(3) 621-633 (May 1993).

A controller design methodology to solve an output tracking problem for a class of systems described by its Euler-Lagrange equations with less control actions than dof was recently presented by Ortega and Espinosa. The procedure is based on the idea of "shaping" the total energy of the closed-loop system with the nice feature that it achieves the tracking objective without the need of cancelling dynamics but by associating a natural reference ("steady state") behavior for all state variables. In this paper we use the procedure to solve the problem of torque regulation of a nonlinear induction motor model which includes both electrical and mechanical dynamics. We derive a nonlinear state observer plus state feedback control that insures exponential stability provided the desired torque does not exceed a given value. The latter condition can be removed if the motor full state is measurable. An adaptive version of the scheme that does not require exact knowledge of the rotor resistance or load torque is also shown to be asymptotically convergent. Three key features of the proposed scheme are: first, it attains the field orientation objective of the highly successful "vector control" strategies. Second, using the energy balance equation of the induction motor, identifies the nonlinear terms that represent "workless forces" to avoid (intrinsically nonrobust) exact cancellation of model nonlinearities. Third, the control law calculation is extremely simple and globally defined, thus the strategy is applicable for all motor operation regimes including start-up. Some simulation results illustrate the controller performance.

See also the following:

10T222. Observers for discrete-time nonlinear systems
10A246. Robust adaptive control of revolute flexible-joint manipulators using sliding technique
10A264. Nonlinear optimal regulator problem
10A271. Saturating and time-optimal feedback controls
10A308. Reaction wheel low-speed compensation using a dither signal

202D. DISCRETE SYSTEMS

10A280. Design of digital tracking controllers. - Masayoshi Tomizuka *(Dept of Mech Eng, UCB)*. J Dyn Syst Meas Control 115(2B) 412-418 (Jun 1993).

This paper describes my work on the design of digital tracking controllers over the past two decades. In tracking control, the control object must be moved along a time varying desired output and the transient path error must be minimized. Tracking control is discussed for the following two typical situations: one is the situation where the desired output is known in advance and the other is where the desired output itself is not known but has a certain known property, eg, it is periodic with a known period. Control algorithms for dealing with these situations will be reviewed and applications to mechanical systems are discussed.

10A281. Precision tracking control of discrete time nonminimum-phase systems. - Chia-Hsiang Menq and Jin-jae Chen *(Dept of Mech Eng, Ohio State Univ, Columbus OH 43210)*. J Dyn Syst Meas Control 115(2A) 238-245 (Jun 1993).

In this paper, a precision tracking control scheme for linear discrete time nonminimum-phase systems is proposed. This control scheme consists of a preview filter, a tracking-performance filter, a command feedforward controller, and a feedback controller. A command feedforward controller, whose design is based on the minimal order inverse model of the plant being controlled, will result in a completely decoupled system. The preview filter is introduced to compensate the phase and gain errors induced by the nonminimum phase zeros or lightly damped zeros of the system. Using the command feedforward controller along with the proposed preview filter, the tracking performance of the proposed control scheme can be characterized by the frequency response of the tracking-performance filter. For the design of the preview filter, a generalized Nth order preview filter and its associated penalty function that quantifies the tracking error of a design are defined. It is shown that, given the desired bandwidth and the order of the preview filter, the optimal solution for the design of the preview filter can be obtained explicitly. The proposed control scheme together with the optimal preview filter is shown to be very effective in achieving precision tracking control of discrete time MIMO nonminimum phase systems. It is also shown that the tracking performance is improved as the order N of the preview filter is increased.

See also the following:

10T222. Observers for discrete-time nonlinear systems
10A231. Simple discrete-time regulator minimizing sensitivity
10A255. Computation of the digital LQG regulator and tracker for time-varying systems
10A265. Optimal discrete-time dynamic output-feedback design: A w-domain approach
10A285. Discrete-time repetitive control system design using the regeneration spectrum

202E. DISTRIBUTED PARAMETER AND DELAYED SYSTEMS

10A282. Controlled motion in an elastic world. - WJ Book *(George W Woodruff Sch of Mech Eng, Georgia Tech)*. J Dyn Syst Meas Control 115(2B) 252-261 (Jun 1993).

The flexibility of the drives and structures of controlled motion systems are presented as an obstacle to be overcome in the design of high performance motion systems, particularly manipulator arms. The task and the measure of performance to be applied determine the technology appropriate to overcome this obstacle. Included in the technologies proposed are control algorithms (feedback and feedforward), passive damping enhancement, operational strategies, and structural design. Modeling of the distributed, nonlinear system is difficult, and alternative approaches are discussed. The author presents personal perspectives on the history, status and future directions in this area.

10A283. Vibration and robust control of symmetric flexible systems. - Song-Tsuen Chen and An-Chen Lee *(Dept of Mech Eng, Natl Chiao Tung Univ, 1001 Ta Hsueh Rd, Hsinchu 30049, Taiwan, ROC)*. J Guidance Control Dyn 16(4) 677-685 (Jul-Aug 1993).

The use of symmetry in the vibration analysis and control of symmetric flexible systems is investigated. For a symmetric flexible system with actuators-sensors being systematically allocated, an internal and external decoupling control scheme is developed to simplify the controller design. The whole flexible system can be separated into two uncoupled subsystems under the decoupling scheme, and the control algorithm for each subsystem can be designed and implemented independently. Consider the case of a direct output feedback based controller design with actuators and sensors collocated. Two robustness properties of this controller, ie, full-order closed-loop stability and reliable control, are exploited. For demonstrative purposes, the optimal modal space approach is adopted for controller design of each subsystem and to illustrate the advantages of the decoupling control scheme. Simulation results of the control of a uniform simply supported beam are given to show the effectiveness of this proposed scheme.

See also the following:

10A225. Robustness evaluation of a flexible aircraft control system
10A248. Suitable generalized predictive adaptive controller case study: Control of a flexible arm
10A312. Lateral and longitudinal dynamic behavior and control of moving webs

202F. STOCHASTIC SYSTEMS

See the following:

10A247. State space self-tuning controller with integral action

202H. OTHER SYSTEMS AND TECHNIQUES

10A284. Decoupling control based on the modified root locus approach. - Feng-Sheng Wang *(Autom Res Center, Natl Chung Cheng Univ, Chiayi 621, Taiwan, ROC)*. Optimal Control Appl Methods 14(1) 39-55 (Jan-Mar 1993).

Two control strategies, unity-feedback, and modified Smith predictor configuations, are introduced to design non-square decoupling control systems. The complete decoupler has the same function structure for both systems. The root locus approach is extended to design the multiloop controllers for both configurations. Pole-zero cancellation is not included in the design procedures for the respective control strategies, so the control laws can handle minimum or non-minimum phase reachable decoupling processes. The tuning region of the appropriate decoupling control configuration is determined through internal stability analysis. From the analysis we observe that if the product of the tuning parameter and the pseudogain of the subsystem is much smaller than unity, the control effects for the two decoupling control systems are no different. Since both decoupling controllers are essentially based on the process model, the control strategies are implemented in adaptive control schemes in the simulation examples.

10A285. Discrete-time repetitive control system design using the regeneration spectrum. - FR Shaw and K Srinivasan *(Dept of Mech Eng, Ohio State Univ, Columbus OH 43210)*. J Dyn Syst Meas Control 115(2A) 228-237 (Jun 1993).

The stability, transient response, and stability robustness of discrete-time repetitive control systems characterized by large values of the time delay inherent in such systems are examined here using a function of frequency termed the regeneration spectrum. The ability to infer different aspects of controlled system performance from the regeneration spectrum, and its ease of computation, makes it a valuable tool for controller analysis and synthesis. A design procedure for discrete-time repetitive control systems, based on the regeneration spectrum, is outlined and a controller form suggested to effectively handle the trade-off between the different aspects of controlled system behavior. The controller design procedure is applied to an electrohydraulic material testing application characterized by strong nonlinearities, and shown experimentally to be effective in improving the controlled system performance.

10T286. Gain scheduling simplification by simultaneous control design. - FM Al-Sunni *(Dept of Syst Eng, King Fahd Univ of Pet and Minerals, Dhahran 31261, Saudia, Arabia)* and FL Lewis *(Autom and Robotics Res Inst, Univ of*

Texas, Ft Worth TX 76118). J Guidance Control Dyn 16(3) 602-603 (May-Jun 1993).

10A287. Linear, multivariable robust control with a μ perspective. - A Packard *(Mech Eng, UCB)*, J Doyle *(Elec Eng, Caltech, Pasadena, CA)*, G Balas *(Aerospace Eng, Univ of Minnesota, Minneapolis, MN)*. J Dyn Syst Meas Control 115(2B) 426-438 (Jun 1993).

The structured singular value is a linear algebra tool developed to study a particular class of matrix perturbation problems arising in robust feedback control of multi-variable systems. These perturbations are called linear fractional, and are a natural way to model many types of uncertainty in linear systems, including state-space parameter uncertainty, multiplicative and additive unmodeled dynamics uncertainty, and coprime factor and gap metric uncertainty. The structured singular value theory provides a natural extension of classical SISO robustness measures and concepts to MIMO systems. The structured singular value analysis, coupled with approximate synthesis methods, make it possible to study the tradeoff between performance and uncertainty that occurs in all feedback systems. In MIMO systems, the complexity of the spatial interactions in the loop gains make it difficult to heuristically quantify the tradeoffs that must occur. This paper will look at the role played by the structured singular value (and its computable bounds) in answering these questions, as well as its role in the general robust, multivariable control analysis and design problem.

10T288. Multi-step ahead prediction based on the principle of concatenation. - MO Koynak *(Bogazici Univ, Bebek, Istanbul, Turkey)*. J Syst Control Eng 207(I1) 57-62 (1993).

10A289. Robust internal model control. - YZ Tsypkin *(Inst of Control Sc, Moscow 117342, Russia)*. J Dyn Syst Meas Control 115(2B) 419-425 (Jun 1993).

This paper discusses the method of control systems design for dynamic plants under bounded uncertainty. The structure of these systems coincides with the structure of systems with an internal model. But the choice of an internal model and a controller depends on the demand of the bounded decrease of system sensitivity to the change of plant characteristics and external action and on the demand of modal control. The absorption principle is used for the synthesis of a controller of such robust modal control systems. The realization conditions of robust systems of modal control are stated.

10A290. Robust time-delay control. - T Singh and SR Vadali *(Aerospace Eng, Texas A&M Univ, College Station TX 77843-3141)*. J Dyn Syst Meas Control 115(2A) 303-306 (Jun 1993).

A method is presented to minimize residual vibration of structures or lightly damped servomechanisms. The method, referred to as the proportional plus multiple delay (PPMD) control, involves the use of multiple time delays in conjunction with a proportional part to cancel the dynamics of the system in a robust fashion. An interesting characteristic of the controller involves addition of a basic single time-delay control unit in cascade to the existing controller, for every additional requirement of robustness. It is shown that the proposed time-delay controller produces results that are exactly the same as those obtained by the shaped input technique. In addition, it is simpler to arrive at the relative amplitudes of the time-delayed signals for any number of delays even in a multi-input setting.

10A291. Strong diagonal dominance by quantitative feedback theory. - RA Perez *(Dept of Mech Eng, Univ of Wisconsin, Milwaukee WI 53201)*, ODI Nwokah, DF Thompson *(Sch of Mech Eng, Purdue)*. J Dyn Syst Meas Control 115(2A) 246-252 (Jun 1993).

This paper uses strong diagonal dominance theory to obtain a systematic solution of the MIMO-QFT problem by an n times solution of the SISO-QFT sensitivity constraint problem. This is analogous to the current MIMO-QFT formulation that requires an n times solution for the elements of the closed-loop transfer matrix. Of equal but independent interest is the establishment of the first early verifiable existence and uniqueness conditions for robust diagonal stabilizability.

10A292. Synthesis and evaluation of an H_2 control law for a hovering helicopter. - MC Takahashi *(Aeroflightdyn Directorate, US Army Aviation Syst Command, MS-211-2, NASA Ames Res Center, Moffett Field CA 94035)*. J Guidance Control Dyn 16(3) 579-584 (May-Jun 1993).

The design and simulator evaluation of a rate-command flight-control law for a UH-60 helicopter in near-hover flight conditions are described. The multivariable control law was synthesized using an H_2 method, which, through weighting functions, directly shapes the singular values of the sensitivity $(I + GK)^{-1}$, complementary sensitivity $GK(I + GK)^{-1}$, and control input $K(I + GK)^{-1}$ transfer-function matrices. The design was implemented on the vertical motion simulator, and four low-speed hover tasks were used to evaluate the control system characteristics. The pilot comments indicated good decoupling and quick response characteristics, but also revealed a mild pilot-induced oscillation tendency in the roll axis.

See also the following:

10A53. Passive damping for robust feedback control of flexible structures
10A57. Simultaneous design of active vibration control and passive viscous damping
10A227. Maximizing the efficiency of wave-energy plant using complex-conjugate control
10T232. Controller design with regional pole constraints: Hyperbolic and horizontal strip regions
10A233. Frequency domain design for robust performance under parametric, unstructured, or mixed uncertainties
10A234. Lead-lag compensator design by the Hough transform
10A235. Maneuver and vibration control of hybrid coordinate systems using Lyapunov stability theory
10A236. Robust pole assignment in a specified region using output feedback
10A244. Low velocity friction compensation and feedforward solution based on repetitive control
10A251. Quantitative feedback design of decentralized control systems
10T252. Stabilizability of linear quadratic state feedback for uncertain systems
10A272. Singular control in minimum time spacecraft reorientation
10A281. Precision tracking control of discrete time nonminimum-phase systems
10A283. Vibration and robust control of symmetric flexible systems
10A307. Quantitative feedback theory applied to the design of a rotorcraft flight control system
10A321. Intelligent control systems: Are they for real?
10A322. Neurocontrol design and analysis for a multivariable aircraft control problem
10T845. Zero-gravity atmospheric flight by robust nonlinear inverse dynamics

204. Systems and control applications

204B. GUIDANCE, NAVIGATION, MOTION CONTROL

10T293. Extremal vehicle reorientation maneuvers: Symmetries and group properties. - S Bocvarov, FH Lutze, EM Cliff *(Aerospace and Ocean Eng Dept, VPI)*. J Guidance Control Dyn 16(4) 648-653 (Jul-Aug 1993).

10A294. Generalized guidance law for collision courses. - Y Baba, M Yamaguchi *(Dept of Aerospace Eng, Natl Defense Acad, Yokosuka 239, Japan)*, RM Howe *(Dept of Aerospace Eng, Univ of Michigan, Ann Arbor MI 48109)*. J Guidance Control Dyn 16(3) 511-516 (May-Jun 1993).

A new generalized guidance law for collision courses is presented. When the missile and target axial accelerations or decelerations are constant, there exists a rectilinear collision course. The guidance law presented, which is called the true guidance law, gives theoretical lateral acceleration commands to guide the missile on a collision course. However, since it is very difficult to realize the true guidance law on most existing tactical missiles, this paper shows a method for simply implementing the guidance law, which is called the simplified guidance law. The small perturbation equation of the true guidance law shows that the definition of an effective navigation constant is the same expression as that in the case of conventional proportional navigation. The performance of the two guidance laws presented is compared with that of proportional navigation using simulation studies of a simple model of a short range air-to-air missile. The simulation results show that the guidance laws presented can intercept the target using far smaller lateral acceleration commands than prepared for proportional navigation. The inner launch envelope shows that the guidance laws presented provide an overall performance improvement over proportional navigation.

10A295. Guidance for an aerocapture maneuver. - JG Gurley *(Syst Lab Directorate, Space and Commun Group, Hughes Aircraft, 10901 Savona Rd, Los Angeles CA 90077)*. J Guidance Control Dyn 16(3) 505-510 (May-Jun 1993).

Aerocapture, which has been described as "essential for cost-effective space transportation," imposes severe guidance and control problems. A closed-loop control law is formulated that provides stable control in the presence of reasonable errors in approach guidance and in knowledge of the atmospheric density profile. Navigational accuracy requirements can be satisfied by a combination of approach tracking and onboard inertial measurements, supplemented, in the case of a Mars encounter, by a radar altimeter or its functional equivalent.

10A296. Quaternion-based rate-amplitude tracking system with application to gimbal attitude control. - H Weiss *(Rafael, PO Box 2250, Haifa 31021, Israel)*. J Guidance Control Dyn 16(4) 609-616 (Jul-Aug 1993).

The paper deals with rate and attitude control of a rigid body. The discussed control system contains an inner velocity loop that tracks the desired rate and an outer attitude loop that tracks the desired attitude command. The control algorithm uses quaternions as a measure of attitude errors to achieve tracking via instantaneous eigenaxis rotation. The paper discusses the stability of the new algorithm and presents its application to multiaxis gimbal attitude control.

See also the following:

10A171. Pointing accuracy of a dual-spin satellite due to torsional appendage vibrations
10T172. Rotational motion and guidance system approximations in optimizable operational launch vehicle simulations
10A238. Inverse simulation of large-amplitude aircraft maneuvers
10A256. Control of motion of complex mechanical systems. Synthesis of algorithms on the basis of Euler equations
10A260. General adaptive guidance using nonlinear programming constraint-solving methods
10A266. Optimal impulsive intercept with low-thrust rendezvous return

204C. CONTROL OF STRUCTURES AND VEHICLES

10A297. The active control of panel vibrations with piezoelectric actuators. - J D'Cruz *(Aeronaut Res Lab, Defence Sci and Tech Org, 506 Lorimer St, Fishermen's Bend, Vic 3207, Australia).* J Intelligent Mat Syst Struct **4**(3) 398-402 (Jul 1993).

The active control of vibration using point actuators has received much attention. Presented here is a means by which panel vibrations may be controlled through the action of a distributed actuator. The actuator consists of a single-sheet piezoceramic adhesively bonded to the surface of the panel. Control is achieved by a digital control law that artificially increases the damping of the modes which dominate the panel response, the sensing being provided by a single accelerometer mounted on the panel surface. Presented are the results that demonstrate the effectiveness of the control law-piezoceramic actuator combination. In order to show that a reduction in vibration levels is also achieved at points other than at the sensing accelerometer, acceleration levels are monitored at other points on the plate. The results show that the panel vibrations may indeed be successfully controlled through the action of the distributed piezoceramic actuator.

10A298. Alternative approximations for integrated control-structure aeroservoelastic synthesis. - E Livne *(Dept of Aeronaut and Astronaut, Univ of Washington, Seattle WA 98195).* AIAA J **31**(6) 1100-1108 (Jun 1993).

A discussion of alternative complex pole and gust response approximations is presented, motivated by the need to extend nonlinear programming-approximation concepts optimization methodology from structural synthesis for the integrated control-structure synthesis of aeroservoelastic systems. Two new approximations are presented for the high-order, weakly damped linear time-invariant systems representing actively controlled airplanes in high-speed flight. They are compared with Taylor series, differential equations, and Rayleigh quotient approximations. The accuracy and computational efficiency of the alternative approximations are discussed. Although the development has been motivated by aeroservoelasticity and the examples used are from that domain, the new approximations are general and applicable to a wide range of control problems.

10A299. Applications of optimal control to advanced automotive suspension design. - D Hrovat *(Res Staff, Ford Motor, Dearborn MI 48121).* J Dyn Syst Meas Control **115**(2B) 328-342 (Jun 1993).

The paper surveys applications of optimal control techniques to the design of active suspensions, starting from simple quarter-car, 1D models, which are followed by their half-car, 2D, and full-car, 3D, counterparts. The emphasis is on linear-quadratic optimal control and automotive vehicles.

10A300. Design approaches for shaping polyvinylidene fluoride sensors in active structural acoustic control. - RL Clark *(Dept of Mech Eng and Mat Sci, Duke Univ, Durham NC 27708-0300),* RA Burdisso, CR Fuller *(Dept of Mech Eng, VPI).* J Intelligent Mat Syst Struct **4**(3) 354-365 (Jul 1993).

A design methodology is presented for shaping structural polyvinylidene fluoride sensors for active structural acoustic control applications. A structural PVDF sensor yielding a controlled response equivalent to that obtained when implementing a microphone error sensor perpendicular to the surface of a simply supported beam was designed and tested. In addition, the equivalent PVDF sensor design approach for the simply supported plate is presented; however, practical limitations in achieving the desired 3D polarization profile prevent physical impelmentation. Results from tests conducted on the simply supported beam demonstrate that PVDF structural sensors can be designed to achieve directional acoustic control of structure-borne sound. While this design approach is currently limited to structures whose response can be described as a function of 1D, the potential for applications in more complex structures is readily achieved upon determining a practical method of varying the polarization profile of the material as a function of 2D.

10A301. Development of control laws for an orbiting tethered antenna-reflector system test scale model. - Zhong Li and PM Bainum *(Dept of Mech Eng, Howard Univ, Washington DC 20059).* J Intelligent Mat Syst Struct **4**(3) 343-353 (Jul 1993).

Tethered systems can be used to change the geometry and inertial characteristics of space structural systems to meet the gravity gradient stability requirements. The control law design for an orbiting shallow spherical shell (antenna and reflector) system connected by a massive and flexible tether to a subsatellite is investigated in this article. The subsatellite is nominally deployed below the antenna along the yaw axis at a sufficient distance to provide a favorable composite moment of inertia ratio for gravitational stabilization. It is assumed that the tether would be deployed through the end of a rigid boom attached to the shell apex. The tension control strategy is used for stationkeeping and deployment and the control gains are obtained based on the structural data for a future proposed real space antenna and reflector. In order to prove the feasibility of this concept, a test scale model for an in-orbit experiment is also studied. The scale model should be small enough so that it could be accommodated within the volume and size limitations of the space shuttle cargo bay. Since the orbital angular velocity (determined by the orbital altitude of the space shuttle), tether diameter, etc, may not be directly scaled, the control gains will be adjusted to fit the requirements for the scale model.

10A302. ER fluid applications to vibration control devices and an adaptive neural-net controller. - Shin Morishita *(Dept of Naval Architec and Ocean Eng, Yokohama Natl Univ, 156 Tokiwadai Hodogaya-ku, Yokohama 240, Japan)* and Tamaki Ura *(Inst of Indust Sci, Univ of Tokyo, 7-22-1 Roppongi, Minato-ku, Tokyo 106, Japan).* J Intelligent Mat Syst Struct **4**(3) 366-372 (Jul 1993).

This article describes several applications of electro-rheological (ER) fluid to vibration control actuators and an adaptive neural-net control system suitable for the controller of ER actuators. ER fluid a kind of colloidal suspension, and has a notable characteristic feature in that its apparent viscosity can be controlled in response to applied electric field strength. Viscosity can be varied in a wide range and the response time is very short, as short as several milliseconds. According to previous studies, one promising application is a controllable damper. In the present article, four applications are proposed: a shock absorber system for automobiles, a squeeze film damper bearing for rotational machines, a dynamic damper for multi-dof structures and a vibration isolator. Furthermore, an adaptive neural-net control system, composed of a forward model network for structural identification and a controller network, was introduced for the control system of these ER actuators.

10A303. Influence of a locally applied electro-rheological fluid layer on vibration of a simple cantilever beam. - Gong Haiqing, Lim Mong King, Tan Bee Cher *(Sch of Mech and Prod Eng, Nanyang Tech Univ, Nanyang Ave, Singapore 2263).* J Intelligent Mat Syst Struct **4**(3) 379-384 (Jul 1993).

This experimental work is concerned with the vibration characteristics of a cantilever beam locally linked by an electro-rheological fluid layer to ground. Such a novel vibration control strategy can drastically change the vibration characteristics of the beam system, owing to the mechanism that the locally applied ER fluid layer serves as a complex spring and thus change the stiffness matrix, or the structural configuration, of the original beam system under the electric field. It is found that the vibration characteristics of the cantilever beam with the locally applied ER fluid layer treatment is more sensitive to the electric field than a sandwich beam. The influence of the nonlinear deformation of the ER fluid due to the presence of the yield stress on the vibration of the cantilever beam is also investigated.

10A304. Integrated design and control of laminated hybrid plates with dynamic response and buckling objectives. - IS Sadek *(Dept of Math Sci, Univ of N Carolina, Wilmington NC 28403),* JM Sloss, S Adali *(Dept of Math, UC, Santa Barbara CA 93106),* JC Bruch Jr *(Dept of Mech and Env Eng, UC, Santa Barbara CA 93106).* J Sound Vib **163**(1) 57-66 (8 May 1993).

An integrated approach is given to determine to optimal level of hybridization and feedback control force for symmetric, cross-ply laminates. The optimization objectives are the maximization of the biaxial buckling load and the minimization of the vibrational energy subject to constraints on the thickness and control energy. The plate is constructed as a sandwich hybrid laminate with outer and inner layers being constructed from high stiffness and low stiffness materials, respectively. Comparative numerical results are given for hybrid and nonhybrid laminates, and the similarities and differences between them are discussed. It is observed that a low stiffness and inexpensive material such as glass fiber reinforced plastics can be used in inner layers with minimal effect on the performance of the plate and substantial material cost savings.

10A305. Integrated structure-control-aerodynamic synthesis of actively controlled composite wings. - E Livne *(Dept Aeronaut and Astronaut, Univ of Washington, Seattle WA 98195),* LA Schmit, PP Friedmann *(Mech Aerospace and Nucl Eng, UCLA).* J Aircraft **30**(3) 387-394 (May-Jun 1993).

A new multi-disciplinary optimization capability for integrated synthesis of actively controlled composite wings is reviewed. it is shown that the nonlinear programming approximation concepts approach to design optimization, combined with appropriate simplified analysis techniques for the different disciplines, make multidisciplinary wing synthesis both feasible and practical for the conceptual and preliminary design stages. The composite wing of a remotely piloted vehicle is used for numerical experimentation. Synthesis studies with design variables and constraints that span the disciplines of structures, control, and aerodynamics are presented. These studies provide new insight into the complex nature of multidisciplinary interactions in wing designs.

10A306. Optimal open-closed loop control of mechanical systems with structural damping. - RS Esfandiari *(Mech Eng Dept, California State Univ, Long Beach CA 90840),* IS Sadek *(Dept of Math Sci, Univ of N Carolina, Wilmington NC 28403),* JM Sloss *(Dept of Math, UC, Santa Barbara CA 93106).* J Sound Vib **163**(1) 47-56 (8 May 1993).

A technique is proposed to actively damp out the undesired vibrations via open and closed loop control A performance measure, involving energy at terminal time, as well as open and closed loop control efforts, is introduced. The closed loop control law is assumed to be of proportional type and the optimal open loop control relative to the performance measure is obtained by using the techniques of calculus of variations. Subsequently, the corresponding optimal closed loop control is found numerically. The proposed method is applied to a beam exhibiting structural damping, and the numerical results are presented in graphical form. The effectiveness of a feedback control in the presence of an open loop control is also discussed.

10A307. Quantitative feedback theory applied to the design of a rotorcraft flight control system. - RA Hess and PJ Gorder *(Dept of Mech, Aeronaut, and Mat Eng, UC, Davis CA 95616)*. J Guidance Control Dyn 16(4) 748-753 (Jul-Aug 1993).

Quantitative feedback theory describes a frequency-domain technique for the design of multiple-input multiple-output control systems that meet time- or frequency-domain performance criteria when specified uncertainty exists in the linear description of the vehicle dynamics. Quantitative feedback theory is applied to the design of the longitudinal flight control system for a linear model of the AH-64 rotorcraft incorporating uncertainty. In this model, the uncertainty is assigned and is assumed to be attributable to actual uncertainty in the dynamic model and to the changes in the vehicle aerodynamic characteristics that occur near hover. The model includes an approximation to the rotor and actuator dynamics. The design example indicates the manner in which handling qualities criteria may be incorporated into the design of realistic rotorcraft control systems in which significant uncertainty exists in the vehicle model.

10A308. Reaction wheel low-speed compensation using a dither signal. - JB Stetson Jr *(General Electric Astro Space Div, Princeton NJ 08543)*. J Guidance Control Dyn 16(4) 617-622 (Jul-Aug 1993).

A method for improving low-speed reaction wheel performance on a three-axis controlled spacecraft is presented. The method combines a constant amplitude offset with an unbiased, oscillating dither to harmonically linearize rolling solid friction dynamics. The complete, nonlinear rolling solid friction dynamics using an analytic modification to the experimentally verified Dahl solid friction model were analyzed using the dual-input describing function method to assess the benefits of dither compensation. The modified analytic solid friction model was experimentally verified with a small dc servomotor actuated reaction wheel assembly. Using dither compensation abrupt static friction disturbances are eliminated and near linear behavior through zero rate can be achieved. Simulated vehicle response to a wheel rate reversal shows that when the dither and offset compensation is used, elastic modes are not significantly excited, and the uncompensated attitude error reduces by 34:1.

10A309. Vibration control of a laminated plate with piezoelectric sensor-actuator: FE formulation and modal analysis. - Woo-Seok Hwang, Hyun Chul Park, Woonbong Hwang *(Dept of Mech Eng, Pohang Inst of Sci and Tech, PO Box 125, Pohang 790-600, Korea)*. J Intelligent Mat Syst Struct 4(3) 317-329 (Jul 1993).

The combined effects of passive and active control on the vibration control of a composite laminated plate with piezoelectric sensors and actuators are investigated. FE formulation modal and analysis are presented. Classical laminated plate theory with the induced strain actuation and Hamilton's principle are used to formulate the equation of motion of the system. The total charge developed on the sensor layer is calculated from the direct piezoelectric equation. The equations of motion and the total charge are discretized with 4-node, 12-dof quadrilateral plate bending elements. The stiffness and damping property changes of composite structures by varying the layer angles are used as a passive control method. Piezoelectric sensors and actuators with negative velocity feedback control are used as an active control method. By numerical simulation, the effects of stiffness and damping property changes of composite structures and the effects of sensor and actuator division on the response of the structure and the performance of the vibration control are investigated. Since active control and passive control affect each other, the active control and the passive control should be considered simultaneously in designing the efficient adaptive structures.

10A310. Vibration suppression for large scale adaptive truss structures using direct output feedback control. - Lyan-Ywan Lu *(Natl Center for Res on Earthquake Eng, Natl Taiwan Univ, Taipei, Taiwan, ROC)*, Senol Utku *(Dept of Civil and Env Eng, Duke Univ, Durham NC 27706)*, BK Wada *(Appl Tech Section, JPL)*. J Intelligent Mat Syst Struct 4(3) 385-397 (Jul 1993).

In this article, the vibration control of adaptive truss structures, where the control actuation is provided by length adjustable active members, is formulated as a direct output feedback control problem. A control method named Model Truncated Output Feedback (MTOF) is presented. The method allows the control feedback gain to be determined in a decoupled and truncated modal space in which only the critical vibration modes are retained. The on-board computation required by MTOF is minimal; thus, the method is favorable for the applications of vibration control of large scale structures. The truncation of the modal space inevitably introduces spillover effect during the control process. In this article, the effect is quantified in terms of active member locations, and it is shown that the optimal placement of active members, which minimizes the spillover effect (and thus, maximizes the control performance), can be sought. The problem of optimally selecting the locations of active members is also treated.

See also the following:

10A50. Control of nonlinear structural dynamic systems: Chaotic vibrations
10A51. Control-structure interactions of space station solar dynamic modules
10A52. Decoupling vibration control of a flexible rotor system with symmetric mass and stiffness properties
10A53. Passive damping for robust feedback control of flexible structures
10T54. Performance of higher harmonic control algorithms for helicopter vibration reduction
10A56. Simulation of active vibroprotective systems
10A57. Simultaneous design of active vibration control and passive viscous damping
10A225. Robustness evaluation of a flexible aircraft control system
10A228. Multiple-input, multiple-output time-series models from short data records
10A257. Disturbance model for control-structure optimization with full state feedback
10A262. Linear quadratic Gaussian-loop transfer recovery design for a helicopter in low-speed flight
10A282. Controlled motion in an elastic world
10A290. Robust time-delay control
10A292. Synthesis and evaluation of an H_2 control law for a hovering helicopter
10T293. Extremal vehicle reorientation maneuvers: Symmetries and group properties
10A313. Engine control using cylinder pressure: Past, present, and future
10A322. Neurocontrol design and analysis for a multivariable aircraft control problem
10A323. Predictive sliding control with fuzzy logic for fuel-injected automotive engines
10A372. Decomposition approach to the public transport scheduling problem

204D. PROCESS CONTROL

10A311. Control of machining processes. - AG Ulsoy and Y Koren *(Dept of Mech Eng and Appl Mech, Univ of Michigan, Ann Arbor MI 48109-2125)*. J Dyn Syst Meas Control 115(2B) 301-308 (Jun 1993).

This paper reviews the important recent research contributions for control of machining processes (eg, turning, milling, drilling, and grinding). The major research accomplishments are reviewed from the perspective of a hierarchical control system structure which considers servo, process, and supervisory control levels. The use and benefits of advanced control methods (eg, optimal control, adaptive control) are highlighted and illustrated with examples from research work conducted by the authors. Also included are observations on how significant the research to date has been in terms of industrial impact, and speculations on how this research area will develop in the coming decade.

10A312. Lateral and longitudinal dynamic behavior and control of moving webs. - GE Young and KN Reid *(Sch of Mech and Aerospace Eng, Oklahoma State Univ, Stillwater OK 74078)*. J Dyn Syst Meas Control 115(2B) 309-317 (Jun 1993).

A web refers to any material in continuous flexible strip form which is either endless or very long compared to its width, and very wide compared to its thickness. This paper discusses the dynamic analysis and control of the lateral and longitudinal motions of a moving web which correspond to fluctuations perpendicular and parallel, respectively, to the primary direction of web transport. Historical perspectives are provided, from the early work of Osborne Reynolds in the late 1800s to current research. An overview of the control of both lateral and longitudinal web motion, which includes the control of tension, is presented. Present limitations in understanding and controlling lateral and longitudinal web behavior are discussed. The Journal of Dynamic Systems, Measurement, and Control has played a pivotal role in the advancement of research in this area.

See also the following:

10A230. Comparison of methods for design sensitivity analysis for optimal control of thermal systems
10A284. Decoupling control based on the modified root locus approach
10A370. Modeling and control of manufacturing processes: Getting more involved
10A721. Closed-loop control of a weld penetration using front-face vision sensing

204E. POWER SYSTEMS

10A313. Engine control using cylinder pressure: Past, present, and future. - DJ Powell *(Mech Eng, Stanford)*. J Dyn Syst Meas Control 115(2B) 343-350 (Jun 1993).

Research into the use of cylinder pressure measurements from reciprocating internal combustion engines for real time automotive engine control has been investigated for the last 20 years. The measurement has been investigated for spark timing, fuel-air ratio control, charge temperature measurements, and misfire detection. The cost of the sensors has inhibited widespread use in production vehicles; however, it was introduced in domestic Japanese production for spark control five years ago. Its use for misfire detection is also being actively considered.

204F. FLUIDIC SYSTEMS, PNEUMATICS

10A314. Evaluation of an electrohydraulic forge valve behavior using a CAD package. - J Watton *(Sch of Eng, Univ of Wales, Col of Cardiff, PO Box 917, Cardiff CF2 1XH, UK)* and J Nelson *(Simtek Res, Banbury, Oxford, UK)*. Appl Math Model 17(7) 355-368 (Jul 1993).

An electrohydaulic system of the type used to control the position of a forging press cylinder is studied analytically and experimentally. The main control component is a flow bypass valve that controls flow rate into and out of the main hydraulic line and is of the poppet-following type. The steady-state pressure-flow characteristics of the bypass valve with an existing seated poppet is compared with a new vee notch poppet design intended to improve the steady-state characteristic and hence the closed-loop press cylinder position response characteristic. Dynamic modeling of the flow bypass valve is then considered and the transient performance is assessed for the two poppet designs and with the valve in an idealized circuit. The complete system dynamic model is then established and a recently developed CAD package is used to simulate the position response of the press cylinder. Both poppet designs are studied, and it is deduced that there is a negligible difference in transient performance, attributable to unique features of the control system. Good comparisons between simulation and experimental results were achieved.

See also the following:

10A227. Maximizing the efficiency of wave-energy plant using complex-conjugate control
10A253. Algorithm for optimal scheduling of a class of cascade water supply systems
10A316. Interaction between the actuators in loaded multi-channel electrohydraulic drives
10A330. Automated fault analysis for hydraulic systems Part I. Fundamentals
10A331. Automated fault analysis for hydraulic systems Part 2: Applications

204G. DIGITAL AND NUMERICAL CONTROL SYSTEMS

10A315. Advanced NC verification via massively parallel raycasting. - JP Menon *(TS Watson Res Center, IBM Res Div, Yorktown Heights NY 10598)* and DM Robinson *(Sibley Sch of Mech and Aerospace Eng, Cornell)*. Manuf Rev 6(2) 141-154 (Jun 1993).

Numerical control (NC) verifiers are computer programs that seek to determine automatically whether an NC machining program, when executed in a given machining environment, will produce a specified part from specified stock without undesirable side effects. NC verifiers that detect spatial errors, such as cutter collisions, have been under development for more than a decade, but they suffer from restricted geometric coverage, poor performance, and incomplete error-condition tests. This article describes a new method of NC verification using ray representations (ray-reps) in combination with the RayCasting Engine (RCE), a new, highly parallel computer for processing ray-reps. The ray-rep-RCE combination removes many of the current limitations in spatial verification, and extends the range of verifiable phenomena to include part tolerance assessment, machining dynamics, and spatial sensing (touch-sense probing). The publicly available P2NC verifier, which uses the PADL-2 solid modeling system as a geometry engine, has been modified to use the RCE as a geometric evaluator and accelerator.

See also the following:

10A244. Low velocity friction compensation and feedforward solution based on repetitive control
10A255. Computation of the digital LQG regulator and tracker for time-varying systems
10A265. Optimal discrete-time dynamic output-feedback design: A w-domain approach
10A280. Design of digital tracking controllers

204H. CONTROL COMPONENTS, SENSORS

10A316. Interaction between the actuators in loaded multi-channel electrohydraulic drives. - S Ramachandran *(Aircraft Controls Div, Moog, E Aurora NY 14052)* and P Dransfield *(Dept of Mech Eng, Monash Univ, Clayton, Vic 3168, Australia)*. J Dyn Syst Meas Control 115(2A) 291-302 (Jun 1993).

This paper describes some of the interaction effects arising between two electrohydraulic servoactuator systems operating to sustain predetermined and separate force programs on a cantilever beam load system. The work is intended to be relevant to the simultaneous multi-channel drive situations of structure fatigue testing rigs, flight simulators, industrial robots and some machine tools. Simulation and experimental responses of a single-actuator system for a few locations of the drive on the beam and of the two-actuator system for a number of location combustions are presented, compared and discussed. Combinations of step inputs of desired force were used to excite the system. Simulation and experimental responses show reasonable agreement. Interaction and its effects are quantified in terms of dynamic characteristics of the force responses of the actuators measured from the simulation and experimental results. The model for simulation was obtained via power bond graph modeling technique. The results show that the interaction modifies the responses of the actuators, and that the level of interaction, its magnitude and nature are functions of the relative positions of the actuators. Interactions and its effects are also examined using simulation for a three-actuator force control system. The results confirm the earlier observation.

10A317. Modeling and state estimator design issues for model-based monitoring systems. - JL Stein *(Dept of Mech Eng and Appl Mech, Univ of Michigan, Ann Arbor MI 48109-2125)*. J Dyn Syst Meas Control 115(2B) 318-327 (Jun 1993).

The Journal of Dynamic Systems, Measurement, and Control has a rich history in the areas of system modeling, control theory, and system design. In this paper, I demonstrate the primary importance of modeling to the design and performance of model-based (dynamic, observer-based) monitoring systems. The focus is on monitoring rather than diagnostics, but the results show, nevertheless, that good monitoring systems impact the design and performance of diagnostic systems. Modeling procedures, some based on results from the automated modeling literature, are developed to produce not only simple, accurate models to improve estimation accuracy, but also to utilize existing sensors to measure accessible signals, generate models for which estimation techniques exist, and finally to produce models that reduce the complexity of the diagnostic task, thus reducing the heavy reliance on empirical rule-based decision systems. In addition, for model-based monitors based on deterministic state estimators, a design procedure is described to control the shape of the transient error and the steady-state bias error of the estimates. This procedure utilizes a performance index, which accounts for many of the realistic problems encountered in implementing these systems, such as model uncertainty, round-off errors, and unknown initial conditions. Machine tool drive systems are used to motivate and illustrate the monitoring ideas and techniques. Model-based monitoring appears, despite its current limited use in machine monitoring, to hold great potential as the basis for high-performance, low-cost machine monitoring systems.

10A318. Robust control for servo-mechanisms under inexact friction compensation. - C Canudas de Wit *(Lab D'Automatique de Grenoble, BP 46, 38402 St-Martin d'Heres, France)*. Automatica 29(3) 757-761 (May 1993).

Uncertainties in the parameters but also in the structure of the friction model may lead to inexact friction compensation in servo-mechanisms. This will lead to differences between the predicted friction and the real friction forces, provoking, in certain cases (overcompensation) an oscillatory behavior. This paper proposes a new control scheme seeking to strengthen the closed-loop system properties in the eventuality of friction overcompensation. This control design has the advantage that, in the case of friction overcompensation, the oscillations can be reduced in amplitude and modified in frequency independently of the closed-loop system specifications.

See also the following:

10A32. Two-axis dry tuned-rotor gyroscopes: Design and technology
10A279. Torque regulation of induction motors
10A319. Computer as liberator: The rise of mechanical system control
10A334. Sensor failure detection and isolation in flexible structures using system realization redundancy
10A337. Miniature mobile robot using piezo vibration for mobility in a thin tube
10A353. Vision and touch sensors for dimensional inspection
10A695. New sensor for real-time milling tool condition monitoring

204I. INSTRUMENTATION, COMPUTER HARDWARE

10A319. Computer as liberator: The rise of mechanical system control. - DM Auslander *(Mech Eng, UCB)*. J Dyn Syst Meas Control 115(2B) 234-238 (Jun 1993).

In this essay, on the observance of the 50th anniversary of the founding of ASME's Dynamic Systems and Control Division, I try to connect the technology of control to the way in which control practitioners think. Despite some tension between the conclusions implied in the introductory paragraphs and conclusions drawn later in the essay, I have left them to stand in their original form to emphasize tensions in control thinking, for which the source might not be apparent. The opinions expressed here are strictly my own, but I must acknowledge the creative proddings of my colleagues in getting these thoughts recorded at all.

204K. SOFTWARE, EXPERT SYSTEMS, ARTIFICIAL INTELLIGENCE

10A320. Angular position control of objects using a transputer-based vision system and fuzzy logic techniques. - H Ekerol and DC Hodgson *(Sch of Manuf and Mech Eng, Univ of Birmingham)*. J Syst Control Eng 207(I1) 47-55 (1993).

A demonstrator system for closed-loop control of rectangular objects by non-contacting means is developed. The system consists of a transputer-based vision system and two power air jets actuated by piezoelectric translators. The first air jet is employed to give the initial angular displacement and the second for correcting any positional errors during the passage of the object in front of it. The overall control algorithm employs fuzzy logic techniques. The potential use of the system in industry for collating soft or brittle products moving on conveyer belts, before being fed into cartoning machinery, is also discussed.

10A321. Intelligent control systems: Are they for real?. - R Shoureshi *(Sch of Mech Eng, Purdue)*. J Dyn Syst Meas Control 115(2B) 392-401 (Jun 1993).

The fundamental concept of feedback to control dynamic systems has played a major role in many areas of engineering. Increases in complexity and more stringent requirements have introduced new challenges for control systems. This paper presents an introduction to and appreciation for intelligent control systems, their application areas, and justifies their need. Specific problem related to automated human comfort control is discussed. Some analytical derivations related to neural networks and fuzzy optimal control as elements of proposed intelligent control systems, along with experimental results, are presented. A brief glossary of common terminology used in this area is included.

10A322. Neurocontrol design and analysis for a multivariable aircraft control problem. - T Troudet *(Struct and Mat Dept, Sverdrup Tech, Brook Park OH 44142)*, S Garg, W Merrill *(Adv Controls Tech Branch, NASA Lewis Res Center, Cleveland OH 44135)*. J Guidance Control Dyn 16(4) 738-747 (Jul-Aug 1993).

The feasibility of using artificial neural networks as control systems for modern, complex aerospace vehicles is investigated via an aircraft control design study. The problem considered is that of designing a controller for an integrated airframe and propulsion longitudinal dynamics model of a modern fighter aircraft to provide independent control of pitch rate and airspeed responses to pilot command inputs. An explicit model-following controller using H_∞ control design techniques is first designed to gain insight into the control problem as well as to provide a baseline for evaluation of the neurocontroller. Using the model of the desired dynamics as a command generator, a multilayer feedforward neural network is trained to control the vehicle model within the physical limitations of the actuator dynamics. This is achieved by minimizing an objective function that is a weighted sum of tracking errors and control input commands and rates. To gain insight into the neurocontrol design, linearized representations of the neurocontroller are analyzed along a commanded trajectory. Linear robustness analysis tools are then applied to the linearized neurocontroller models and to the baseline H_∞ based controller. Robustness issues of the neurocontrol design are identified and addressed in the context of neural training. Future areas of research are identified to enhance the practical applicability of neural networks to flight control design.

10A323. Predictive sliding control with fuzzy logic for fuel-injected automotive engines. - S-K Nam *(Agency for Defence Dev of Korea, Taejon, Korea)*, M-H Lee, W-S Yoo *(Dept of Mech Eng, Pusan Natl Univ, Pusan, Korea)*. J Syst Control Eng 206(14) 237-244 (1992).

An alternative algorithm is proposed for a variable-structure control to design a closed-loop fuel-injection system. Sliding control using fuzzy logic is combined with current oxygen sensors to maintain the stoichiometric air-fuel ratio. Predictive control is also introduced to compensate for the time delay in the combustion process. This synthesis provides a practical and flexible design for an engine controller because its hybrid structure meets given robustness and performance requirements. The potential of the proposed algorithm is shown through real-time simulations utilizing both a typical engine-only model on an AD-100 computer and an implemented controller on an Intel 80C186 with an 80C187 processor.

10A324. Real-time expert system for fault-tolerant supervisory control. - K Ramamurthi *(Process Des and Control, Semiconductor Process and Des Center, Texas Instruments, Dallas TX 75265)* and AM Agogino *(Dept of Mech Eng, UCB)*. J Dyn Syst Meas Control 115(2A) 219-227 (Jun 1993).

Many mechanical systems are sufficiently complex that it is impractical to describe their dynamics by exact mathematical models. In the presence of such modeling uncertainties, advanced controllers like adaptive controllers perform better than linear feedback controllers since they actively reduce the uncertainty by online parameter estimation. Unfortunately, the advanced control strategies, due to their lack of robustness, can become unstable in the presence of unpredictable external disturbances, and hence, there exists a need for a fault-tolerant approach to preserve the overall system integrity even at the cost of design performance. This motivated the research, presented in this paper, to investigate the suitability of the IDES (Influence Diagram Based Expert System) as an expert supervisory controller to predict incipient instability, a significant failure mode, and take corrective action in real-time when closed loop stability appears to be in danger. The expert supervisory control scheme is demonstrated on a model-referenced adaptive controller as applied to robotic manipulator. The real-time expert system, with the information from sensors dynamically optimizes the cost of control and as a result chooses between a robust auxiliary controller and the nonrobust adaptive controller depending on inferences made from the observable variables. IDES, as a real-time expert supervisory controller, preserves the stability of the system even under potentially destabilizing unexpected disturbances, exhibiting on demand a fault-tolerant behavior by trading design performance for overall system integrity. The results indicate the potential for influence diagram expert systems in monitoring and controlling mechanical systems where exact mathematical modes are difficult or not practical to obtain.

10A325. Review of expert systems for process planning of cold forging. - Guobin Yang *(Nichidai Corp, Takigi, Tanabe-cho, Tuzuki-gun, Kyoto 610-03, Japan)* and Kozo Osakada *(Fac of Eng Sci, Osaka Univ, 1-1 Machikaneyama-cho, Toyonaka, Osaka 560, Japan)*. Manuf Rev 6(2) 101-113 (Jun 1993).

The authors present the state of the art in expert systems for cold forging process planning and discuss goals for future systems. First, they conduct an extensive historical review of research activities in computer-aided process planning of forging. They then present the current status of expert systems for cold forging process planning, using the system developed at Osaka University as an example. Finally, they discuss areas for continued and more in-depth research in this area.

See also the following:

10A258. Feedback control of minimum-time optimal control problems using neural networks
10A264. Nonlinear optimal regulator problem
10A273. Terminal repeller unconstrained subenergy tunneling (TRUST) for fast global optimization
10A330. Automated fault analysis for hydraulic systems Part I. Fundamentals
10A331. Automated fault analysis for hydraulic systems Part 2: Applications
10A368. Intelligent inspection planning and computer aided inspection
10T524. Expert system for the design of geotextiles
10A723. Estimation of weld pool sizes in GMA welding process using neural networks

204M. MECHATRONICS (COMPUTER-INTEGRATED ELECTROMECHANICAL SYSTEMS)

10A326. Electromechanical properties of smart materials. - RE Newnham and GR Ruschau *(Mat Res Lab, Penn State)*. J Intelligent Mat Syst Struct 4(3) 289-294 (Jul 1993).

A smart material is one that can perform both sensor and actuator functions. This definition allows for some flexibility in deciding how to qualify a material as "smart", since the fundamental mechanisms of operation may differ greatly between types of smart materials. From the point of view of an electroceramist, piezoelectric materials, which show reversible electromechanical coupling, may be thought of as "naturally" smart materials since the same piezoelectric material may act as a sensor and/or an actuator. Piezoelectric single crystals, polymers, and poled poly-crystalline ceramics all show good electromechanical coupling. In addition, they may be combined in a composite material that exaggerates their beneficial properties by eliminating their detrimental properties. Some common piezoelectric materials are reviewed, along with some examples of smart materials that incorporate piezoelectric ceramics.

10A327. Safety critical systems: so what ...?. - PA Bennett *(Centre for Software Eng, Flixborough, Scunthorpe)*. J Syst Control Eng 206(14) 197-205 (1992).

Safety critical systems contain advanced computer, microprocessor and software technologies to a degree of sophistication that is frequently beyond the understanding of many practicing engineers. Many of these systems control the safe operation of everyday things such as anti-lock braking on cars, personnel lifts and trains, as well as industrial process and fly-by-wire aircraft. This paper describes the nature, processes, standards and assessment methods currently being employed with safety critical systems, and addresses various questions that the practicing engineer may ask. It demonstrates that although the technology and methods may be novel, concerns surrounding the evaluation of safety critical systems are yet another instance of the age-old dilemma involved in exercising engineering judgement.

10A328. Self-service banking and mechatronics: The first twenty years. - J Dinsdale *(Dept of Appl Phys and Electron and Manuf Eng, Univ of Dundee)* and AJ Hutcheon *(NCR Manuf, Dundee)*. J Syst Control Eng 207(11) 1-8 (1993).

The past two decades have seen a remarkable increase in the automation of banking operations and financial transactions. A comparative examination of modern automated teller machines (ATMs) and electronic banking systems alongside the mechanical machines in use less than half a century ago illustrates how this rapid introduction of advanced technology has been made possible through the interaction of mechanical engineering (especially mechanisms), electronic actuators and sensors, and computer software, an activity which has become known as "mechatronics". The paper describes the evolution of the modern ATM, highlighting the interdisciplinary engineering skills that are necessary to achieve the performance goals of speed, reliability, security and user-friendliness.

See also the following:

10A320. Angular position control of objects using a transputer-based vision system and fuzzy logic techniques

204P. MICROELECTROMECHANICS, NANOTECHNOLOGY

10A329. Macroscopic phenomenological formulation for coupled electromechanical effects in piezoelectricity. - XD Zhang and CA Rogers *(Center for Intelligent Mat Syst and Struct, VPI)*. J Intelligent Mat Syst Struct 4(3) 307-316 (Jul 1993).

A phenomenological formulation of polarization reversal of piezoelectric materials is proposed based on the dynamics of domain switching. This formulation provides a method to describe the hysteresis in piezoelectricity as well as in electromagnetics. It is shown that a good approach to describe the nonlinear induced strain-field behavior and electromechanical hysteresis in piezoelectricity is by combining the macroscopic phenomenological aspects with the microscopic material properties. A 1D thermo-electro-mechanical constitutive model for piezo-ceramics which undergo polarization reversal is presented using a continuum mechanics approach. This model is based on thermodynamic principles and reflects the essence of the electromechanical behavior of piezoceramics in a simple form. It is illustrated that this theory can describe the electromechanical behavior of piezoceramics simply and reasonably well.

See also the following:

10A371. Practical implications in the calibration of translational tables

204R. FAULT DIAGNOSIS, FAILURE DETECTION, AND ISOLATION

10A330. Automated fault analysis for hydraulic systems Part 1. Fundamentals. - RM Atkinson, MR Montakhab, KDA Pillay, DJ Woollons *(Sch of Eng, Univ of Exeter)*, PA Hogan, CR Burrows, KA Edge *(Fluid Power Centre, Univ of Bath)*. J Syst Control Eng 206(14) 207-214 (1992).

Early expert systems for fault analysis tended to be based on shallow, heuristic knowledge. For success in engineering applications, it is argued that the complementary knowledge of the underlying principles (deep knowledge) should also be modeled. An object-oriented software library representing models of components of hydraulic circuits is being built using deep knowledge alone. The software modules within this library are reusable for the construction of model-based expert systems for the performance of failure mode and effects analysis and fault tree analysis on any arbitrary hydraulic circuit.

10A331. Automated fault analysis for hydraulic systems Part 2: Applications. - PA Hogan, CR Burrows, KA Edge *(Fluid Power Centre, Univ of Bath)*, RM Atkinson, MR Montakhab, DJ Woollons *(Sch of Eng, Univ of Exeter)*. J Syst Control Eng 206(14) 215-224 (1992).

The paper provides further details of the automated failure modes and effects analysis (FMEA) program outlined in Part 1. Some of the more difficult development problems are discussed, and solutions are presented. The functionality of the program was tested through application to two experimental rigs, namely a closed-loop hydrostatic transmission with a dynamometer and a regenerative pump test rig. Non-destructive faults, such as abnormally low relief valve settings and excessive loads, were manually inserted into these rigs, and the measured effects were compared with the predictions from the program to validate the software. The difference in complexity and configuration evident in the two examples considered serves to highlight the generality of the approach. The ease of reconfigurability of the software reflects the key aim of producing a program cable of analyzing a wide range of hydraulic circuits.

10A332. Prediction of the service life of pneumatic rubber-cord elastic elements subjected to complex loading. - VG Tsyss and VV Ustinov *(Omsk, Russia)*. J Machinery Manuf Reliab 6 97-101 (1992).

The problem of prediction of the service life of pneumatic rubber-cord elastic elements is considered. Methods for solving the problem are developed on the basis of the generalized fatigue curves and reduction of real operational modes to an equivalent one. An example is presented.

10A333. Safety of sophisticated technological systems. - AN Severtsev *(Moscow, Russia)*. J Machinery Manuf Reliab 6 30-36 (1992).

Qualitative problems of safety are considered from the methodological point of view. Safety criteria and indicators aiming the researcher at their formalization, are defined, and attested. The temporal affluence criterion determining safe operation of systems, is considered in detail.

10A334. Sensor failure detection and isolation in flexible structures using system realization redundancy. - DC Zimmerman *(Dept of Aerospace Eng, Mech and Eng Sci, Univ of Florida, Gainsville FL 32611)* and TL Lyde *(Subsyst Eng, Lockheed, Marietta GA)*. J Guidance Control Dyn 16(3) 490-497 (May-Jun 1993).

Sensor failure detection and isolation for flexible structures is approached from a system realization perspective. Instead of using hardware or analytical model redundancy, system realization is utilized to provide an experimental based model redundancy. The failure detection and isolation algorithm utilizes the eigensystem realization algorithm to determine a minimum-order state-space realization of the structure in the presence of noisy measurements. The failure detection and isolation algorithm utilizes statistical comparisons of successive realizations to detect and isolate the failed sensor component. Because of the nature in which the failure detection and isolation is formulated, it is also possible to classify the failure mode of the sensor. Results are presented using both numerically simulated and actual experimental data.

See also the following:

10A327. Safety critical systems: so what ...?
10A715. Asymptotic estimates of the probability of failure-free performance, obtained using "load-resistance" models

204T. OTHER APPLICATIONS

See the following:

10A721. Closed-loop control of a weld penetration using front-face vision sensing

206. Robotics

206C. ACTUATORS (PRIME MOVERS)

10A335. Design of actuators based on biased magnetostrictive rare earth-iron alloys. - N Lhermet, F Claeyssen *(Cedrat Rech, 10 ch du Pre-Carre, 38240 Meylan, France)*, P Wendling *(Magsoft, 1223 People's Ave, Troy NY 12180)*, G Grosso *(Eramer, ZI du Camp Laurent, 83500 La Seyne sur Mer, France)*. J Intelligent Mat Syst Struct 4(3) 337-342 (Jul 1993).

The objective of this article is to present the results of a comparative study, including modeling and prototypes, on the different means to generate a high bias field in Terfenol-D. The aim of the research was to get bias field higher or equal to 80 kA/m. Among all the possible types of bias, only three types appear able to produce a high enough field. This has led to three different prototypes. To design them, an extensive effort of modeling has been required, FLUX2D and FLUX3D softwares have been used for the bias design; ATILA code has been used for the electromechanical design. A first prototype has a bias done by DC current in the coil surrounding the rods. The second prototype has a 100 kA/m bias done by a permanent magnet configuration of the series type. The third prototype is equipped with a new magnet configuration, providing about 90 kA/m bias. Finally, it appears that all these solutions work as well as expected and have their own advantages.

10A336. Piezoelectric actuator models for active sound and vibration control of cylinders. - HC Lester *(Struct Acoust Branch, NASA Langley Res Center, Hampton VA 23681-0001)* and Sylvie Lefebvre *(MATRA, Guyancourt, BP n°235 F-78052, St-Quentin-en-Yvelines Cedex, France)*. J Intelligent Mat Syst Struct 4(3) 295-306 (Jul 1993).

Analytical models for piezoelectric actuators, adapted from flat plate concepts, are developed for noise and vibration control applications associated with vibrating circular cylinders. The loadings applied to the cylinder by the piezoelectric actuators for the bending and in-plane force models are approximated by line moment and line force distributions, respectively, acting on the perimeter of the actuator patch area. Coupling between the cylinder and interior acoustic cavity is examined by studying the modal spectra, particularly for the low-order cylinder modes that couple efficiently with the cavity at low frequencies. Within the scope of this study, the in-plane force model produced a more favorable distribution of low-order modes, necessary for efficient interior noise control, than did the bending model.

See also the following:

10A316. Interaction between the actuators in loaded multi-channel electrohydraulic drives
10A337. Miniature mobile robot using piezo vibration for mobility in a thin tube

206D. LOCOMOTION (MOBILITY)

10A337. Miniature mobile robot using piezo vibration for mobility in a thin tube. - Shin-ichi Aoshima, Takeshi Tsujimura, Tetsuro Yabuta *(NTT Transmission Syst Lab, Ibaraki-Ken 319-11, Japan)*. J Dyn Syst Meas Control 115(2A) 270-278 (Jun 1993).

This paper proposes a miniature mobile robot that uses piezo vibration to move within a thin tube. The robot consists of a piezo bimorph with elastic fins attached at an angle. Robot movement is driven by differences in the friction of the fin's against the tube wall between the forward and backward fin movements induced by piezo vibration. After analyzing the dynamics of the piezo elements, we analyzed the robot's mobile mechanism by extending Hamilton's principle using the dynamic results of the piezo vibration analysis. Measurements of both mobile velocity and tractive force of an experimental robot agree closely with theoretical results. This indicates that the proposed dynamic mobile mechanism accurately expresses robot motion within a thin tube.

206E. KINEMATICS, DYNAMICS

10A338. Comparative study in linearized robot models. - A Swarup and M Gopal *(Dept of Elec Eng, Indian IT, New Delhi 110 016, India)*. J Intelligent & Robotic Syst 7(3) 287-300 (June 1993).

For representing the input-output behavior of a robot manipulator by a linear time-invariant model, four direct linearization schemes are (i) state linearization, (ii) linearization based on an identification method, (iii) linearization based on neglecting velocity-dependent and gravity terms and (iv) linearization based on neglecting the velocity-dependent term only (rate linearization). In order to make an appropriate choice of linear model for the development of real-time control, these schemes are extensively studied in this paper. It is shown that the rate linearization method leads to a satisfactory tradeoff between computation, accuracy, and stability. In the case of high velocity motions, a combination of state linearization and rate linearization is proposed.

10A339. Determining the effects of Coulomb friction on the dynamics of bearings and transmissions in robot mechanisms. - A Gogoussis and M Donath *(Productivity Center, Dept of Mech Eng, 111 Church St SE, Univ of Minnesota, Minneapolis MN 55455)*. J Mech Des 115(2) 231-240 (Jun 1993).

The general guidelines for analyzing friction at the joints will be discussed. It will be shown that friction can be related to the joint coordinates and their first and second time derivatives. The resulting extended robot dynamics formulation will be investigated as it applies to the inverse and forward robot dynamics problems. The analytical dependency of Coulomb friction on joint interactions is explicitly examined. As an illustration of friction effects in transmissions, we elaborate on the friction in harmonic drives and develop a method for its evaluation. The effect of friction in the bearings on the dynamics is also considered and a quantitative characterization of several specific cases is provided. This study is significant to understanding the design and control issues as they relate to achieving high speed precision robot motion.

10A340. Inverse dynamics of a flexible robot arm by optimal control. - T Kokkinis and M Sahraian *(Dept of Mech and Env Eng, UC, Santa Barbara CA 93106)*. J Mech Des 115(2) 289-293 (Jun 1993).

The problem of end-point positioning of flexible arms is discussed. Because of the nonminimum phase nature of the problem, inversion fails to produce bounded joint torques. Bounded noncausal joint torques for achieving the task of end-point tracking for a multilink arm are found using optimal control theory. The torques obtained have no high-frequency content, and are suitable for practical applications. The method is illustrated by simulation of a single-link arm, for which stability and robustness considerations for design are given.

10A341. Kinematic and dynamic synthesis of geared robotic mechanisms. - Dar-Zen Chen and Lung-Wen Tsai *(Mech Eng Dept and Syst Res Center, Univ of Maryland, College Park MD 20742)*. J Mech Des 115(2) 241-246 (Jun 1993).

This paper describes a methodology for the design of geared robotic mechanisms. It is shown that certain gear-coupled manipulators can be designed to possess kinematic isotropy property at a given end-effector position. For these gear-coupled manipulators, the train values can be treated as a product of two-stage gear reductions. The second-stage reduction can be uniquely determined from the kinematic isotropic condition, while the first-stage reduction can be determined from dynamic consideration. This approach, through proper choice of gear ratios, can provide these gear-coupled manipulators with desired kinematic and dynamic characteristics.

10A342. Kinematic modules for singularity free movement with three Cartesian freedoms. - GL Long, JM McCarthy *(Mech and Aerospace Eng, UC, Irvine CA 92717)*, RP Paul *(Comput and Info Sci, Univ of Pennsylvania, Philadelphia PA 19104)*. J Mech Des 115(2) 207-213 (Jun 1993).

The singularity conditions of three-revolute-joint serial chain manipulators are investigated by considering the motion of an arbitrary point on a terminal link. A distinction is made between singular configurations and singular surfaces. Of particular interest is a class of 3R manipulators - each manipulator within this class forms a third-order screw system. We outline the structural requirements for this 3R class, and then determine the singularity conditions for several cases. For several manipulators within this 3R class, we describe a strategy to develop four-revolute-joint kinematic modules for singularity-free movement with three Cartesian freedoms. The algorithm to control the kinematic modules is simple and can be implemented in real-time.

10A343. Mapping of kinematic and dynamic parameters for coupled manipulators. - Zhiming Ji and Ming C Leu *(Dept of Mech and Indust Eng, NJIT, Newark NJ 07102)*. J Mech Des 115(2) 283-288 (Jun 1993).

The concept of the mapping matrix is used in this paper for establishing relationships of torque, speed, Jacobian, and compliance of these manipulators with those obtained with conventional methods. A method of constructing the mapping matrix systematically is discussed. Two examples show that the proposed method is easy to implement.

10A344. Optimal control of a flexible manipulator. - W Szyszkowski and D Youck *(Dept of Mech Eng, Univ of Saskatchewan, Saskatoon, S7N 0W0, Canada)*. Comput Struct 47(4-5) 801-813 (3 Jun 1993).

Manipulators handling payload masses several times larger than their own weight are considered. The optimal control rule, based on rigid body dynamics, is used to minimize the time of slewing maneuver of a single link. The performance of such control is simulated using ADINA. The influence of various flexibility parameters on the performance of the optimal control is discussed.

10A345. Stability of conventional controller design for flexible manipulators. - L Tang *(Mech Dyn, Ann Arbor MI 48187)* and SB Skaar *(Dept of Aerospace and Mech Eng, Univ of Notre Dame, Notre Dame IN 46556)*. J Appl Mech 60(2) 491-497 (Jun 1993).

The paper investigates the independent joint control of flexible manipulators which are acted upon by gravity. Both finite-dimensional coordinates, and infinite-dimensional, spatially varying, distributed coordinates are used to describe the deformation of of the flexible links. The effects of the flexibility on the closed-loop system behavior in the presence of both derivative and integral feedback control are studied both in the Laplace transform domain using the linearized model of the original nonlinear system and in the time domain using the original nonlinear model. The use of infinite-dimensional coordinates is shown to be especially effective in obtaining the frequency domain characteristics of the linearized model because the exact frequency content of the linearized system may be extracted without involving the difficult order reduction problem. The problem of convergence onto an incorrect solution which is associated with using the eigenvectors of a clamped-free beam as the comparison functions in approximating the motion of the flexible arm is demonstrated and various factors affecting the performance of the flexible manipulator, such as control gains and material damping, are studied.

10A346. State estimation in robotic manipulators: Some experimental results. - S Nicosia *(Dept Ing Electtron II, Univ Roma Tor Vergata, via O Raimondo 00173, Rome, Italy)*, A Tornambe *(Fondazione Ugo Bordoni, via Baldassarre Castiglione 59, 00142 Rome, Italy)*, P Valigi *(Dept Ing Elettron II, Univ Roma Tor Vergata, via O Raimondo 00173, Rome, Italy)*. J Intelligent & Robotic Syst 7(3) 321-351 (June 1993).

A simple asymptotic observer is proposed for the estimation of the generalized velocities of a robotic manipulator. The singular perturbation theory is used in the stability analysis of the error dynamics. High-gains are used in the attenuation of the nonlinearities characterizing the dynamic behavior of the robot. The accuracy of the proposed algorithm is illustrated in simulation runs and verified through some experimental tests.

10A347. Workspace of a general geometry planar 3-dof platform-type manipulator. - GR Pennock and DJ Kassner *(Sch of Mech Eng, Purdue)*. J Mech Des 115(2) 269-276 (Jun 1993).

This paper focuses on the direct workspace problems of a general geometry fully-parallel-actuated, planar 3-dof platform type manipulator. A set of equations are presented that determine the workspace as a function of the platform orientation. The reachable positions of the end-effector point, for a specified platform orientation, are analyzed. The paper includes a detailed discussion of the total primary workspaces of the manipulator. The approach adopted here is to regard the manipulator as a combination of three planar, three-revolute open chains. For the sake of completeness, the influence of special manipulator geometry on the workspace is also discussed. Finally, the paper includes the conditions that cause stationary configurations of the manipulator. Insight into these undesirable configurations is provided by a study of the location of the absolute instant center of the platform.

See also the following:

10A23. Inverse problem of the kinematics of a positioner with linear actuators
10A698. Redundant-drive backlash-free robotic mechanisms
10A713. Design of multi-dof mechanisms for optimal dynamic performance
10A959. Design guide of master arms considering operator dynamics

206F. SENSORS AND CONTROLS

10A348. Controls of servomotors for carry hospital robots. - Sangho Jin, Ichiro Kimura, Keigo Watanabe *(Dept of Mech Eng, Fac of Sci and Eng, Saga Univ, Honjomachi-1, Saga 840, Japan)*. J Intelligent & Robotic Syst 7(3) 353-369 (June 1993).

Two methods for controlling servomotors with pulse encoders are presented for improving the movement of a carry hospital robot (CHR) along a desired line. Some simulation studies have been executed for the design of a PI controller or optimal regulator for the control of the DC servomotor. By applying the simulation results, we actually design a PI controller in an analogue circuit and experimentally compare the results of the PI control with those of a PLL (Phase Locked Loop) control. It is then clarified that the latter approach is effective in improving the accuracy of the CHR.

10A349. Design and performance studies of model-based variable-structure adaptive controllers for industrial manipulators. - SK Tso and PL Law *(Dept of Elec and Electron Eng, Univ of Hong Kong)*. J Syst Control Eng 206(14) 245-262 (1992).

A model-based variable-structure adaptive control scheme recently proposed for the trajectory tracking of robot manipulators has shown significant promise. By actual implementation with a commercial manipulator, the practical means for improvement are examined, the design trade-offs are systematically explored, and the distinguishing features of the performance achievable in the improved version are brought out and compared with those of earlier schemes.

10A350. Experiments on the tracking control of a flexible one-link manipulator. - Chia-Hsiang Menq and Jack Zhijie Xia *(Dept of Mech Eng, Ohio State Univ, Columbus OH 43210)*. J

Dyn Syst Meas Control 115(2A) 306-308 (Jun 1993).

Experimental study on the tracking control of a flexible one-link manipulator is reported in this paper. A tracking control scheme is developed based on the system transfer function. In the proposed control scheme, the desired control input for a given end-point trajectory is obtained by using a command feedforward controller instead of solving the inverse dynamic equations of the system. The proposed control scheme requires small amount of computations and can be easily implemented for real time control. The experimental results are presented, which shows very good tracking performance.

10A351. Localization of hybrid controllers for manipulation on unknown constraints. - JS Bay *(Bradley Dept of Elec Eng, VPI)* and Hooshang Hemami *(Dept of Elec Eng, Ohio State Univ, Columbus OH 43210)*. J Intelligent & Robotic Syst 7(3) 301-320 (June 1993).

A robotic control problem is proposed in which a six dof manipulator is to explore the surface of an object which is *a priori* unknown to the controller. Choice of an exploration strategy is discussed. The exploration strategy developed uses the maximal freedom of choice allowed under the restrictions of the problem. In particular, it is shown that any admissible reference trajectory can be used, provided it lies in a 2D manifold which maps continuously into the surface. The inverse kinematic velocity problem is then solved using pseudo-inverses which fully exploit the redundancy of the system. The controller used as an example uses computed torque for linearization and compliant motion theory for movement along the desired path. The solution to the inverse kinematic problem together with the on-line generation of "selection-mappings" constitute a hybrid force-velocity controller. Successful exploration is shown to depend heavily on reliable force control, so PI force feedback is also proposed. Simulation and experimental results demonstrate the effectiveness of the overall design.

10A352. Variable-structure linear-model-following control of manipulators. - SK Tso, ML Lai, PL Law *(Dept of Elec and Electron Eng, Univ of Hong Kong, Hong Kong)*. J Syst Control Eng 207(I1) 35-45 (1993).

The paper describes the interaction between modeling, control, and adaptation of a variable-structure model-following method applied to highly nonlinear plants. The method is particularly appealing in the control of high-performance robot manipulators. The problems concerned with its application are discussed with reference to the use of a controller in a commercial manipulator as a case study.

10A353. Vision and touch sensors for dimensional inspection. - M Nashman *(Robot Syst Div, Bldg 220, Rm B124, NIST)*. Manuf Rev 6(2) 155-162 (Jun 1993).

In the manufacturing process, various sensors can be used for the dimensional inspection of part geometry. The sensors detect discrepancies between a machined part and its specified geometry as defined in a computer-aided design (CAD) model or other model data base. The part is then either accepted or rejected and sent to scrap or rework as part of the inspection process. Within this system, vision and touch sensors can be used in combination, which adds significantly to their effectiveness and the body of knowledge that can be obtained from them. However, the use of multiple sensors is relatively new and few commercially available coordinate measuring machines (CMMs) have multiple sensor capabilities. In light of these conditions, the author considers the current use of vision and touch sensors in dimensional inspection and suggests several strategies for developing CMMs with multiple sensor capabilities, using the system currently under development at the NIST as an example.

See also the following:

10A241. Composite adaptive control of flexible joint robots
10A243. Learning control of robot manipulators
10A246. Robust adaptive control of revolute flexible-joint manipulators using sliding technique
10A248. Suitable generalized predictive adaptive controller case study: Control of a flexible arm
10A258. Feedback control of minimum-time optimal control problems using neural networks
10T288. Multi-step ahead prediction based on the principle of concatenation

206G. POSITION APPLICATIONS

10A354. Geometry of interference with application to obstacle avoidance. - YJ Choi, CD Crane III, GK Matthew, J Duffy *(Center for Intelligent Machines and Robotics, Dept of Mech Eng, Univ of Florida, Gainesville FL)*. J Mech Des 115(2) 300-305 (Jun 1993).

A mapping which transforms the relative displacements of one object with respect to a reference object into image points has been developed by interpreting the relative displacement in terms of affine coordinates. The mapping provides a novel mathematical tool that solves interference problems of objects in 3D space. By use of this mapping, the geometrical condition of interference of objects is represented by simple inequalities. The inverse mapping provides the means of avoiding interference and can be utilized for articulation of robot arms so as to avoid collision with obstacles.

10A355. Solving the robotic "pick and place" findpath problem. - Wei Li and Bo Zhang *(Dept of Comput Sci, Natl Lab for Intelligent Tech and Syst, Tsinghua Univ, Beijing 100084, Peoples Rep of China)*. Manuf Rev 6(2) 114-128 (Jun 1993).

This article presents a practical approach for solving the findpath problem for industrial robots, and entails determining the path through space that a robot will follow in completing its tasks. The findpath problem consists of two phases, mapping and quick search. Mapping is based upon defining the fundamental obstacles in a workspace and their images in configuration space. The search phase consists of building a free subspace by slice configuration of these obstacles, in which a model of each obstacle is generated by evaluating slices of the area under consideration, and then planning a collision-free path. To achieve these objectives, the authors propose an analytical model for mapping fundamental obstacles. For more complex obstacles, they discuss several mapping algorithms and linear interpolation. The proposed approach, combining the analytical model with the algorithms and interpolation, can be used in real-time path planning for robot transfer movements, consisting of a robotic gripper and its playload, over a range of industrial applications.

10A356. Swing-up control of inverted pendulum using pseudo-state feedback. - K Furuta, M Yamakita *(Dept of Control Eng, Tokyo IT, Japan)*, S Kobayashi *(NSK Limited, Japan)*. J Syst Control Eng 206(I4) 263-269 (1992).

Swing-up control, that is the transfer of a pendulum from a pendant state to the inverted one, is a good laboratory experiment of optimal control theory for nonlinear control systems. The optimal control can be determined by the maximum principle and obtained as a function of time. Since the control is, however, determined in a feedforward fashion, the control is not robust to disturbances and uncertainties of the system, and the transfer of the state of the pendulum is not assured. In the paper, a robust swing-up control using a subspace projected from the whole state space is proposed. Based on the projected state space or pseudo-state, the control input is determined depending on the partitioning of the state as a bang-bang type control. The control algorithm is applied for a new type of pendulum (TITech pendulum), and the effectiveness and robustness of the proposed control are examined by experiments.

See also the following:

10A22. Development of a seven DOF crane with three wires: Inverse kinematics of the crane
10A318. Robust control for servo-mechanisms under inexact friction compensation

206H. ASSEMBLY APPLICATIONS

10A357. Qualitative template matching using dynamic process models for state transition recognition of robotic assembly. - BJ McCarragher *(Austral Natl Univ, Canberra, Australia)* and H Asada *(Center for Info-Driven Mech Syst, MIT)*. J Dyn Syst Meas Control 115(2A) 261-269 (Jun 1993).

This paper presents a model-based approach to the recognition of discrete state transitions for robotic assembly. Sensor signals, in particular, force and moment, are interpreted with reference to the physical model of an assembly process in order to recognize the state of assembly in real time. Assembly is a dynamic as well as a geometric process. Here, the model-based approach is applied to the unique problems of the dynamics generated by geometric interactions in an assembly process. First, a new method for the modeling of the assembly process is presented. In contrast to the traditional quasi-static treatment of assembly, the new method incorporates the dynamic nature of the process to highlight the discrete changes of state, eg, gain and loss of contact. Second, a qualitative recognition method is developed to understand a time series of force signals. The qualitative technique allows for quick identification of the change of state because dynamic modeling provides much richer and more copious information than the traditional quasi-static modeling. A network presentation is used to compactly present the modelling state transition information. Lastly, experimental results are given to demonstrate the recognition method. Successful transition recognition was accomplished in a very short period of time: 7-10 ms.

See also the following:

10A355. Solving the robotic "pick and place" findpath problem
10A366. From robots to design

206I. MISCELLANEOUS APPLICATIONS

See the following:

10A320. Angular position control of objects using a transputer-based vision system and fuzzy logic techniques
10A356. Swing-up control of inverted pendulum using pseudo-state feedback
10A960. Human centered control in robotics and consumer product design
10A961. Human extenders

206Y. COMPUTATIONAL TECHNIQUES

10A358. Model reference adaptive inverse control of a single link flexible robot. - S Wu and S Cetinkunt *(Dept of Mech Eng, Univ of Illinois, Chicago IL 60680)*. Comput Struct 47(2) 213-223 (Apr 1993).

A new model reference adaptive inverse control algorithm is proposed for the end point position control of flexible manipulators. This controller forms a series model reference adaptive system where an estimated system inverse is placed in the feed forward path to provide an inverse control through regulation of controller parameters. It differs from other model reference control strategies in that a signal synthesis loop is included to compensate for the estimation error of the inverse controller and the output tracking error, and to improve stability. The stability of the overall control system is shown to be guaranteed using hyperstability theory. The proposed control scheme is applied to control the tip position of a single link flexible robot. A non-dimensionalized model is developed. Its zero-order hold equivalence in discrete time domain is described by an auto-regressive and moving average form. A lattice filter is utilized as a deconvolution filter. The time-delay behavior from the driving torque to the robot tip position due to robot structural flexibility is investigated.

10A359. Use of linked lists in the simulation of controller-structure interaction. - R Quan *(Frank J Seiler Lab, US Air Force Acad, Colorado Springs CO 80840).* Comput Struct 47(2) 225-231 (Apr 1993).

An algorithm for the computer simulation of large space structures under active control is considered. Linked lists are used in a matrix data structure to implement the trapezoidal rule on system differential equations. The use of the trapezoidal rule ensures that the numerical stability is equivalent to the system stability, which is essential for this type of simulation. The sparsity of the system matrices is exploited by the linked lists, and the algorithm efficiently steps through the lists in an orderly fashion. Results of simulations on a NASA large space structure experiment are reported.

206Z. EXPERIMENTAL TECHNIQUES

See the following:

10A350. Experiments on the tracking control of a flexible one-link manipulator

208. Manufacturing

208B. PRODUCT AND PROCESS DESIGN

10A360. Dejavu: Case-based reasoning for mechanical design. - T Bardasz *(Computervision Corp, Bldg 14-13, 14 Crosby Dr, Bedford MA 01730)* and I Zeid *(Dept of Mech Eng, Northeastern Univ, Boston MA 02115).* AI Eng Des Anal Manuf 7(2) 111-124 (1993).

The architecture and implementation of a mechanical designer's assistant shell called DEJAVU is presented. The architecture is based on an integration of design and CAD with some of the more well known concepts in case-based reasoning (CBR). DEJAVU provides a flexible and cognitively intuitive approach for acquiring and utilizing design knowledge. It is a domain independent mechanical design shell that can incrementally acquire design knowledge in the domain of the user. DEJAVU provides a desigu environment that can learn from the designer until it can begin to perform design tasks autonomously or semi-autonomously. The main components of DEJAVU are a knowledge base of design plans, an evaluation module in the form of a design plan system, and a blackboard-based adaptation module. The existence of these components are derived from the utilization of a CBR architecture. DEJAVU is the first step in developing a robust designer's assistant shell for mechanical design problems. One of the major contributions of DEJAVU is the development of a clean architecture for the utilization of case-based reasoning in a mechanical designer's assistant shell. In addition, the components of the architecture have been developed, tailored or modified from a general CBR context into a more synergistic relationship with mechanical design.

10A361. Dispelling the manufacturing myth. - Chun Zhang and Hsu-Pin Wang *(Dept of Indust Eng, Univ of Iowa, 4106 Eng Bldg, Iowa City IA 52242).* Manuf Rev 6(1) 60-71 (Mar 1993).

Tolerance design and synthesis is a major task in product and process design now under extensive study because of the increasing demand for quality products and the growing requirements for automation in machining and assembly. Optimum tolerance design and synthesis ensures good quality products at low cost. This article provides an analysis of the tolerance optimization problem in three parts. First, the tolerance synthesis problem was formulated as a nonlinear discrete optimiztion model that had as its objective minimum manufacturing cost. Second, the discrete optimization model was treated as a continuous optimization model and was solved with the sequential quadratic programming (SQP) method. Optimality of the continuous model was examined to understand the characteristics of the problem. Third, a simulated annealing (SA) algorithm was coded to solve the discrete tolerance optimization model, and was compared with the SQP method on a range of problems. The SA algorithm appears to be effective choice, particularly for problems with a wide process capability range or nonoverlapping cost curves.

10A362. Efficient design for service considerations. - A Subramani and P Dewhurst *(Dept of Indust and Manuf Eng, Univ of Rhode Island, Gilbreth Hall, Kingston RI 02881).* Manuf Rev 6(1) 40-47 (Mar 1993).

Future serviceability is an important facet of product design that affects a manufacturer's profit, warranty costs, customer satisfaction, product life, and market share. In this article, the authors propose a generic scheme, based on the costs and labor involved in service work, to assess this important area early in the product concept and design stages. Several metrics are developed in the scheme to measure the effects of variables such as service time, parts cost and accessibility, and labor cost, for developing efficient design strategies. Two examples of commonly occurring automotive service tasks are evaluated using the metrics to assess the efficiency of design and service in automotive engineering and to test the suitability of the metrics.

10A363. Process planning and concurrent engineering system for PCBs. - Jong-Shin Liau and RE Young *(Group for Intelligent Syst in Design and Manuf, Dept of Indust Eng, N Carolina State Univ, Campus Box 7906, Raleigh NC 27695).* Manuf Rev 6(1) 25-39 (Mar 1993).

With continuous advancements in the development of electronics components and automatic assembly machines, the design and manufacture of printed circuit boards (PCBs) has become more versatile and complex. This increasing complexity, coupled with frequent enhancements in the PCB manufacturing environment [especially the success of surface mount devices (SMDs)], and continuing inefficiency in planning time, has led to the need for more sophisticated computer-aided process planning (CAPP) systems for PCB assembly. Most existing CAPP systems generate a process plan from design inputs, but do not provide feedback to the design process. In contrast, concurrent engineering is an approach to design and manufacturing that takes into account not only the functionality of a product but also its manufacturability. By applying concurrent engineering criteria to PCB design and production, the authors have developed a process planning and concurrent engineering system, called PACE, that uses PCB process planning knowledge formulated as constraints to build interactive process plans and to assess their manufacturability. PACE was constructed using the Spark constraint modeling language and environment, and not only generates process plans for PCB assembly from design attributes, but also detects inconsistencies between the PCB design and the production facility. Thus, concurrent engineering concepts are enforced in the design stage. An example is presented in the article to illustrate the application of the PACE system.

10A364. Tool for optimal manufacturing design decisions. - DL Thurston and SK Essington *(Dept of General Eng, Decision Syst Lab, Univ of Illinois, Urbana IL 61801).* Manuf Rev 6(1) 48-59 (Mar 1993).

Interest in concurrent engineering has arisen because design engineers have realized that they need to integrate manufacturing cost considerations directly into the engineering design process. When optimizing designs for manufacturing, engineers should develop a design that offers the best combination of mechanical performance and manufacturing costs. Weighted average methods, frequently used for optimizing designs, have the limitation of not accurately reflecting the nonlinear value imparted by various design attributes and the decision maker's sometime reluctance to make trade-offs between attributes. In this article, the authors present a computer-based aid for design decisions that accurately considers multiple design attributes simultaneously. A spreadsheet interface facilitates the analysis of design alternatives in a form that is readily used by design engineers. The authors do not present a new method for manufacturing cost estimation, but rather one for directly integrating cost estimation procedures into the design decision-making process. They demonstrate that this tool provides engineers with the means to formulate a multiattribute design optimization problem, compare the relative merits of alternative materials and designs, and determine the optimal material and component geometry. The sensitivity analysis capabilities of the spreadsheet for variations in production volume and the user's willingness to make trade-offs between attributes are also demonstrated.

See also the following:

10A22. Development of a seven DOF crane with three wires: Inverse kinematics of the crane

10A325. Review of expert systems for process planning of cold forging

10A327. Safety critical systems: so what ...?

10A357. Qualitative template matching using dynamic process models for state transition recognition of robotic assembly

10A365. Development of a flexible assembly center

10A367. Integration of coordinate measuring machines within a design and manufacturing environment

10A541. Fluid flow, heat transfer and inclusion behavior in continuous casting tundishes

208E. SYSTEMS DESIGN, INTEGRATION, AND CONTROL

10A365. Development of a flexible assembly center. - Masahito Uno, Ichiro Taniguchi, Koichi Sugimoto, Toru Mita, Siyuki Sakaue, Hisashi Onari. J Japan Soc Precision Eng 59(5) 737-742 (May 1993).

The authors created a flexible assembly center that can be organized to meet the needs of various assembly operations. For this, a precision autonomous robot that does not require a teaching process was developed. The flexible assembly center is composed of multiple table robots, arm robots, and part-tool feeders, and has the following characteristics: (1) complicated operations can be performed by using the flexible arm and table setup. (2) The positioning accuracy necessary for precision assembly can be maintained through the use of direct drive mechanisms and auto-calibration, without requiring a teaching process. (3) Precise operation can be accomplished autonomously by real-time control with visual and force sensor feedback. This system is particularly effective for production systems involving frequent setup changes.

10A366. From robots to design. - DE Whitney *(Charles Stark Draper Lab, Cambridge MA 02139)*. J Dyn Syst Meas Control 115(2B) 262-270 (Jun 1993).

This paper describes the evolution of the author's research focus from a single manufacturing technology, robots, to a broader and less technical focus on design processes. This evolution was not haphazard, but was prompted by technical and nontechnical lessons acquired while performing research and attempting to apply it in industrial settings. The inability of any one technology to solve a wide range of problems, and the inability of technology alone to impact the complexities of manufacturing are among the facts learned. What follows is a rather personal account of this evolution.

10A367. Integration of coordinate measuring machines within a design and manufacturing environment. - AJ Medland, G Mullineux, C Butler, BE Jones *(Dept of Manuf and Eng Syst, Brunel Univ, Uxbridge, Middlesex)*. Proc Inst Mech Eng B 207(B2) 91-98 (1993).

The role of the coordinate measuring machine within the inspection process has changed throughout its brief development. With its integration with industrial computer aided design (CAD) systems, its role is to change yet again. This paper presents the difficulties and limitations of current practice and identifies the inputs and decisions that need to be made within an integrated manufacturing environment. A research program was undertaken to investigate an approach based upon intelligent communications between systems. This led to the creation of a demonstration system that was employed in the measurement of industrial components. A case study, using a standard test block, is included to illustrate the processes undertaken. This includes feature identification, probe calibration and selection strategies and automatic re-routing to minimize changes in probes and orientations. It is proposed that the approach demonstrated can be incorporated within a concurrent engineering environment to provide feedback and information about machine adjustments through a constraint modeling process.

10A368. Intelligent inspection planning and computer aided inspection. - JDT Tannock, H Lee, DR Cox, JH Sims Williams *(Dept of Mech Eng, Univ of Bristol)*. Proc Inst Mech Eng B 207(B2) 99-104 (1993).

Quality inspection is the source of vital information for business control and improvement in manufacturing. This paper describes research at the University of Bristol, in collaboration with Rolls-Royce plc, to develop automated inspection planning and computer aided inspection applications. The inspection planning system involves the representation of inspection features and the manufacturing process model, together with an automated planning mechanism driven by rule-based plan reasoning. The shop-floor computer aided inspection workstation uses hand-held instruments interfaced to a computer, and provides flexible, interactive assistance for the dimensional inspection task. Batch and component traceability and control, together with a range of quality information storage and reporting functions, are provided.

10A369. Making circuits more than once: The manufacturing challenges of electronics intensive products. - DJ Williams, PP Conway, DC Whalley *(Dept of Manuf Eng, Loughborough Univ of Tech)*. Proc Inst Mech Eng B 207(B2) 83-90 (1993).

This paper is a review of some of the problems facing manufacturers of current and future generation electronic products. It presents a brief overview of work carried out by the Interconnection Group at Loughborough in the support of manufacturing industry, and in particular defines some of the limitations of the manufacturing processes. The paper closes by identifying research areas that can be addressed by the academic community to assist industry in its efforts to maintain competitiveness. Research areas focused on are conventional packaging, multi-chip modules and some aspects of the organization of international manufacture.

10A370. Modeling and control of manufacturing processes: Getting more involved. - DE Hardt *(Lab for Manuf and Productivity, MIT)*. J Dyn Syst Meas Control 115(2B) 291-300 (Jun 1993).

The discipline of control has had numerous yet sporadic contacts with the manufacturing world over the past few decades, almost always as an afterthought or addendum, and typically in the role of machine and not as process control. Much of this detachment comes from an absence of control techniques that can deal directly with the actual manufacturing process, ie, a material transformation process that produces a desired object both in terms of specific geometry and internal properties. Instead, most efforts have focused on using existing methods on process independent problems, such as position control and trajectory following, or on straightforward process parameter control, thereby only indirectly influencing the actual process output. This paper presents the reasons behind and the means to eliminate this estrangement, using the author's own research as an example of a more direct approach to process modeling and control.

10A371. Practical implications in the calibration of translational tables. - E Mainsah, PJ Sullivan, KJ Stout *(Sch of Manuf and Mech Eng, Univ of Birmingham, Edgbaston, Birmingham B15 2TT, UK)*. Manuf Rev 6(2) 129-140 (Jun 1993).

The accuracy and repeatability of translational tables, as ascertained through consistent and systematic calibration, are vital parameters that form the basis of the decision to choose any particular translational table for use in the 2D or 3D assessment of the topography of engineering surfaces. The absence of an international table calibration standard designed to cope with the specifics of surface topography analysis can lead to problems with the traceability of individual calibrations. This article assesses the procedures for determining the accuracy and repeatability of positioning translational tables in the x- and y-axes and shows how calibration errors can be analyzed and minimized. The authors review and quantify measurement errors that occur both as a result of the calibration system (which in this case is a laser interferometer) and the system operator. These include errors introduced by temperature, relative humidity, and pressure changes in ambient conditions, leading to a change in the refractive index of air. This affects the measurements taken, and may lead to the thermal expansion of the table resulting in virtual table translation. A simplified equation is derived that brings together earlier results by Edlen, Jones, and Birch and Downs, and that can be used in a laboratory for correcting errors introduced to the laser measurement system due to changes in temperature, pressure, relative humidity, and carbon dioxide concentration. Preliminary results show that the model is satisfactory, especially in situations where errors in the region of one ppm are acceptable.

See also the following:

10A363. Process planning and concurrent engineering system for PCBs
10A364. Tool for optimal manufacturing design decisions
10A373. Impact of manufacturing practices on the global bicycle industry
10T827. On the utility of tokamaks for engery

208H. MANAGEMENT AND ECONOMICS

10A372. Decomposition approach to the public transport scheduling problem. - W Grega *(Inst of Autom, Univ of Mining and Metall, 30-059 Krakow, Al Mickiewicza 30-BI, Poland)*. Automatica 29(3) 745-750 (May 1993).

This paper presents a new approach for solving timetable optimization problems. The original problem is decomposed into subproblems along the discrete time axis. For each subproblem the motion of vehicles is described by treating headways between them as the state variables. The layover times at the terminals are considered as the decision variables. This model allows the implementation of optimal control theory with quadratic criterion and technical constraints imposed on the state and control. The problem is to obtain after a fixed number of trips a desired configuration of headways and to "glue" partial timetables together creating the final timetable. A numerical example is given to illustrate the idea.

10A373. Impact of manufacturing practices on the global bicycle industry. - R Suri, JL Sanders, PC Rao *(Dept of Indust Eng, Univ of Wisconsin, 1513 University Ave, Madison WI 53706)*, A Mody *(World Bank, Room S 4141, 1818 H St NW, Washington DC 20433)*. Manuf Rev 6(1) 14-24 (Mar 1993).

This article presents the findings of a study on the impact of modern manufacturing technologies and managerial practices on global competitiveness in the bicycle industry. Three classes of countries were studied: developed countries (DCs), newly industrialized economies (NIEs), and less developed countries (LDCs). Based on extensive literature surveys and on-site interviews, analytical models were developed that enable prediction of manufacturing costs in the three types of countries. Some of the study findings include the following observations: NIEs are currently the most cost competitive countries; massive infusions of state-of-the-art technologies can have dysfunctional consequences for LDCs; and gains from automation for all three types of countries are greater when it is introduced after implementing total quality control (TQC) and just-in-time (JIT) manufacturing practices. Although a DC firm gains significantly TQC and JIT, product cost differences continue to be substantial, implying that DCs need to target additional criteria to remain competitive. It is also shown that by focusing on flexible manufacturing methods, firms can attain greater product flexibility and shorter lead times without prohibitive increases in costs. While some of these findings are not new, the study provides substantial quantitative evidence to back up these statements. In addition, the methodology presented here should be of interest to researchers, because it presents a systematic way to quantify many of the managerial practices essential to the competitiveness of modern firms.

See also the following:

10A368. Intelligent inspection planning and computer aided inspection
10A369. Making circuits more than once: The manufacturing challenges of electronics intensive products

IV. MECHANICS OF SOLIDS

250. Elasticity

250A. GENERAL THEORY

See the following:

10A380. Global extremum principle for the analysis of solids composed of softening material

10A438. Micromechanics as a basis of random elastic continuum approximations

250B. LINEAR THEORY

See the following:

10A678. Axisymmetric residual stresses in tubes with longitudinally nonuniform stress distribution

250C. NONLINEAR AND FINITE DEFORMATION PROBLEMS

10A374. Construction of two-phase equilibria in a non-elliptic hyperelastic material. - E Fried *(Dept of Eng Sci and Mech, Penn State)*. J Elast 31(2) 71-123 (May 1993).

This work focuses on the construction of equilibrated two-phase antiplane shear deformations of a non-elliptic isotropic and incompressible hyperelastic material. It is shown that this material can sustain metastable, two-phase equilibria which are neither piecewise homogeneous nor axisymmetric but, rather, involve nonplanar interfaces which completely segregate inhomogeneously deformed material in distinct elliptic phases. These results are obtained by studying a constrained boundary value problem involving an interface across which the deformation gradient jumps. The boundary value problem is recast as an integral equation and conditions on the interface sufficient to guarantee the existence of a solution to this equation are obtained. The constraints, which enforce the segregation of material in the two elliptic phases, are then studied. Sufficient conditions for their satisfaction are also secured. These involve additional restrictions on the interface across which the deformation gradient jumps – which, with all restrictions satisfied, constitutes a phase boundary. An uncountably infinite number of such phase boundaries are shown to exist. It is demonstrated that, for each of these, there exists a solution – unique up to an additive constant – for the constrained boundary value problem. As an illustration, approximate solutions which correspond to a particular class of phase boundaries are then constructed. Finally, the kinetics and stability of an arbitrary element within this class of phase boundaries are analyzed in the context of a quasistatic motion.

250E. STRESS CONCENTRATIONS AND SINGULARITIES

10A375. Analysis of stress singularities at the corner point of square hole and rigid square inclusion in elastic plates by conformal mapping. - H Ishikawa and Y Kohno *(Dept of Mech and Control Eng, Univ of Electro-Commun, 1-5-1 Chofugaoka Chofu, Tokyo 182, Japan)*. Int J Eng Sci 31(8) 1197-1213 (Aug 1993).

The plane elastostatic problem of a square hole and a rigid square inclusion in the infinite plate under tension loading are examined by the conformal mapping and Goursat stress functions. A new method is developed for the calculation of the orders of singularity and the stress intensity factors of a singular point, such as the corners of a square hole and square inclusion (non-rotation) in the elastic plates submitted to an overall tension at infinity. Coefficients of Goursat stress functions are determined, respectively, for the number m of terms of the finite series of the function for the conformal mapping. Then, the two types of the orders of stress singularities λ_I and λ_{II} which correspond to Mode I (opening mode) and Mode II (in-plane shear mode) deformations, respectively, are determined and their numerical results are in good agreement with the exact solutions by Williams. Also the stress intensity factors K_I and K_{II} are determined for arbitrary equivalent Poisson's ratio κ. Singular stress and displacement fields corresponding to Mode I and Mode II deformations around a corner point of a square hole and a rigid square inclusion are also obtained.

10A376. Westergaard stress functions for displacement-prescribed crack problems I. - H Tada *(Washington Univ, St Louis MO 63130)*, HA Ernst *(Sch of Mech Eng, Georgia Tech)*, PC Paris *(Washington Univ, St Louis MO 63130)*. Int J Fracture 61(1) 39-52 (1 May 1993).

The single stress function approach of Westergaard has been effective for a certain class of stress-prescribed crack problems. In the present study, the Westergaard approach was successfully extended to displacement-prescribed crack problems. The method presented, which requires no more than the evaluation of integrals, significantly simplifies the analysis. The method is easily extended to crack problems involving displacement-prescribed and stress-prescribed conditions. This initial study laid the ground work for the subsequent extension to the mixed problem.

250F. ELASTIC IMPERFECTIONS (DISLOCATIONS, ETC)

10A377. Green's function for the elastic field of an edge dislocation in a finite orthotropic medium. - A El-Azab and NM Ghoniem *(Mech Aerospace and Nucl Eng Dept 46-147G Eng IV, UCLA)*. Int J Fracture 61(1) 17-37 (1 May 1993).

A fundamental solution of plane elasticity in a finite domain is developed in this paper. A closed-form Green's function for the elastic field of an edge dislocation of arbitrary Burger's vector at an arbitrary point in an orthotropic finite elastic domain, that is free of traction, is presented. The method is based on the classical theory of potential fields, with an additional distribution of surface dislocations to satisfy the free traction boundary conditions. A solution is first developed for a dislocation in a semi-infinite half-plane. The resulting field is composed of two parts: a singular contribution from the original dislocation, and a regular component associated with the surface distribution. The Schwarz-Christoffel transformation is then utilized to map the field quantities to a finite, polygonal domain. A closed form solution containing Jacobi elliptic functions is developed for rectangular domains, and applications of the method to problems of fracture and plasticity are emphasized.

10A378. Overall elastic response of materials containing spherical inhomogeneities. - GJ Rodin *(Dept of Aerospace Eng and Eng Mech, Univ of Texas, Austin TX 78712)*. Int J Solids Struct 30(14) 1849-1863 (1993).

It is proposed to determine the overall response of linear elastic materials containing non-intersecting spherical inhomogeneities without altering the microscopic geometry of a given representative volume element. In the proposed method, a system of integral equations formulated for such an element is accurately approximated by a system of linear algebraic equations.

See also the following:

10A588. Locating a crack of arbitrary but known shape by the method of path-independent integrals

250G. VARIATIONAL AND ENERGY METHODS

10A379. Energy extremum principle for local action. - V Minutolo and L Nunziante *(Univ di Napoli "Frederico II", Dip di Scienza della Construzioni, Piazzale V Tecchio n80, 80125 Fuorigrotta Napoli, Italy)*. Int J Solids Struct 30(13) 1717-1723 (1993).

This work describes the solution in terms of the energy of the mixed boundary problem, formulated for the elastic body subjected to prescribed boundary displacements field. The extremum theorems herein proved are particular corollaries of the classical reciprocity theorems. Let us consider a part, δV_P, of the unconstrained boundary containing point P one which a displacement field u_P shall be prescribed. The displacement is produced by tractions acting a part, δV_P, of the unconstrained boundary containing a point Q and disjoined from δV_P. The strain energy of the body in this elastic state is greater than the strain energy produced by boundary forces acting on δV_P and creating the same displacement field u_P there. The lower bound theorem herein proved gives a quantification of Boussinesque's local perturbation principle and a measure of the stain energy related to local action. The theorem applies both for structures and solids.

10A380. Global extremum principle for the analysis of solids composed of softening material. - JE Taylor *(Dept of Aerospace Eng, Col of Eng, Univ of Michigan, Ann Arbor MI 48109)*. Int J Solids Struct 30(15) 2057-2069 (1993).

An extremum principle is presented covering problems in solid mechanics equilibrium analysis for piecewise linear softening materials. Problems formulated according to this principle are expressed on a mixed "stress and deformation" form. The mechanics interpretation is limited according to linear deformation kinematics. More specialized models, such as *an extremum principle in mixed form for linearly elastic materials*, an equivalent to the *minimum complementary energy principle*, and a statement of a *bound theorem of Limit Analysis* are identified as special cases within the general formulation. Numerical results are presented for two examples of 1D structures made of inhomogeneous, softening material. The evolution of material degradation is demonstrated via a set of solutions obtained for increasing load. Each solution of the set is produced from a single application of a general purpose computer program for constrained nonlinear programming problems, operating on a FE interpretation of the nonlinear continuum.

250H. CONTACT PROBLEMS AND INCLUSIONS

10A381. Dundurs correspondence between cavities and rigid inclusions. - X Markenscoff *(Dept of Appl Mech and Eng Sci, UCSD)*. J Appl Mech 60(2) 260-264 (Jun 1993).

In plane elasticity the solutions of the stress field of rigid inclusion problems yield the solutions of cavity problems loaded by uniform shear tractions $\sigma = 2\mu(\Omega - \omega_0)|_{\kappa = -1}$, where Ω is the rotation of the inclusion and ω_0 the rotation of the material (evaluated at $\kappa = -1$), k being the Kolosov constant). It is proved that *if the limit of the stress field for the inclusion problem exists at $\kappa = -1$, then it corresponds to a constant rotation field.*

10A382. Virtual contact loading method for elastic contact problems. - Hua Zhao, Zhong-Hua Li, Zhen-Bang Kuang *(Inst of Eng Mech, Xi'an Jiaotong Univ, Xi'an 710049, Peoples Rep of China)*. Commun Numer Methods Eng 9(6) 455-461 (Jun 1993).

The virtual contact loading method, a highly efficient numerical method to solve elastic contact problems, is proposed in this paper. Having applied virtual loads on the possible contact region (PCR) of a structure system, we carried out the usual FE calculations only once and made a local iteration analysis in PCR then the contact region (shape and size), contact state (stick, slide or mixed), contact normal and shear stress distributions, and the stress and displacement fields in contact bodies were all obtained simultaneously. This method is very simple and easy to use. The elastic problems for cylinder-cylinder are solved in this paper and the results agree well with those in previous work.

See also the following:

10A509. Rotation of a rigid ellipsoidal inclusion embedded in an anisotropic piezoelectric medium

10A611. Analysis of composite shear walls with interface separation, friction and slip using BEM

250I. ANISOTROPIC MEDIA

10A383. Eigenvalues for a self-equilibrated, semi-infinite, anisotropic elastic strip. - EC Crafter, RM Heise, CO Horgan, JG Simmonds *(Dept of Appl Math, Univ of Virginia, Charlottesville VA 22903)*. J Appl Mech 60(2) 276-281 (Jun 1993).

The linear theory of elasticity is used to study an homogeneous anisotropic semi-infinite strip, free of tractions on its long sides and subject to edge loads or displacements that produce stresses that decay in the axial direction. If one seeks solutions for the (dimensionless) Airy stress function of the form $\phi = e^{-\gamma x}F(y)$, γ constant, than one is led to a fourth-order eigenvalue problem for F(y) with complex eigenvalues γ. This problem, considered previously by Choi and Horgan (1977), is the anisotropic analog of the eigenvalue problem for the Fadle-Papkovich eigenfunctions arising in the isotropic case. The decay rate for Saint-Venant end effects is given by the eigenvalue with smallest positive real part. For an isotropic strip, where the material is described by two elastic constants (Young's modulus and Poisson's ratio), the associated eigencondition is *independent* of these constants. For transversely isotropic (or specially orthotropic) materials, described by *four* elastic constants, the eigencondition depends only on *one* elastic parameter. Here, we treat the fully anisotropic strip described by *six* elastic constants and show that the eigencondition depends on only *two* elastic parameters. Tables and graphs for a scaled complex-valued eigenvalue are presented. These data allow one to determine the Saint-Venant decay length for the *fully anisotropic* strip, as we illustrate by a numerical example for an end-loaded off-axis graphite-epoxy strip.

250K. RESIDUAL STRESSES

10A384. Residual stress in an elastic body: A theory for small strains and arbitrary rotations. - A Hoger *(Dept of Appl Mech and Eng Sci, UCSD)*. J Elast 31(1) 1-24 (Apr 1993).

Residual stress is the stress present in a body which is in mechanical equilibrium in the absence of external loading. Thus the residual stress is symmetric, satisfies the equilibrium equation with zero body force, and on the surface of the body the associated traction vanishes. This zero traction condition causes the residual stress to be dependent on body geometry. It is of interest to note that a nonzero residual stress field cannot be uniform. This follows from Signorini's mean stress theorem and the fact that the external forces vanish. In this paper a general theory for elastic materials is presented in which the strains are presumed to be small, but arbitrarily large rotations are allowed. No assumptions are made concerning the origin of the residual stress; in particular, it need not be the result of prior elastic behavior. In Section 2 standard results are gathered which will be used in the remainder of the paper. In Section 3 the derivation of a constitutive equation for a compressible elastic material with residual stress is presented for the case of small strains and arbitrary rotations. The response function for the Piola-Kirchhoff stress is expressed in terms of the right stretch tensor and linearized under the assumption that the right stretch is close to the identity tensor. It is shown that this constitutive equation reduces to that of the classical linearized theory with residual stress when the rotations are also assumed to be close to unity. The use of the right stretch for the linearization, rather than the Cauchy-Green deformation tensor, is briefly discussed. The section closes with the derivation of the linearized response function for Cauchy stress. In Section 4 incompressible elastic materials with residual stress are considered. As was done for compressible materials, a constitutive equation is derived for these materials under the assumption of small strains and arbitrary rotations. For incompressible materials the stress response function is defined only for those deformations that satisfy the constraint of incompressibility, ie, those deformations for which the determinant of the right stretch is one. This set of admissible deformations is not open, so the standard approach of linearizing the stress response cannot be used becase it involves differentiating the response function. An approach formulated by Marlow is employed to perform the linearization by use of the manifold structure of the set of right stretch tensors associated with admissible deformations. The basic field equations for small strain, arbitrary rotation elastostatics with residual stress are collected in Section 5.

250Y. COMPUTATIONAL TECHNIQUES

10A385. Appropriate boundary conditions for FE-modeled elastic half-plane. - HL Bjarnehed *(Div of Solid Mech, Chalmers Univ of Tech, S-412 96 Goteborg, Sweden)*. Commun Numer Methods Eng 9(6) 497-501 (Jun 1993).

The completely adhesive contact between an FE-modeled orthotropic half-plane and a vertically loaded rigid flat punch is studied. Interface normal and shear-stress distributions between the punch and half-plane are FE-calculated and compared for some sets of half-plane boundary conditions frequently used in the literature for contact problems with friction. These results are compared with analytical solutions, and appropriate half-plane boundary conditions are recommended for frictional contact problems.

10A386. Effective BE approach for higher order singularities. - Xiao-yan Lei, Xiuxi Wang, Mao-kuang Huang *(Dept of Mech, Univ of Sci and Tech of China, Anhui, Hefei 230026, Peoples Rep of China)*. Int J Solids Struct 30(15) 2109-2115 (1993).

The paper presents a new BE approach which introduces a "source line". It is very effective for higher order singularity. The scheme will be discussed in some detail with plane elasticity. Numerical results for meshes with unequal BEs are reported. Higher precision than the general BEM is obtained for both deflection and force.

10A387. FE procedure for axisymmetric elastomeric solids under general loading. - RE Marusak *(MicroFab Technologies, 1104 Summit Ave Suite 110, Plano TX 75074)* and EB Becker *(Dept of Aerospace Eng and Eng Mech, Univ of Texas, Austin TX 78712)*. Int J Numer Methods Eng 36(12) 2031-2084 (30 Jun 1993).

A FE procedure, which utilizes Fourier series, is developed to compute the large deformations and deflections in axisymmetric elastomeric solids subjected to non-axisymmetric loading. Nearly incompressible and incompressible, isotropic strain energy density functions describe the elastic properties. The nearly incompressible functions become compatible with an analytical integration scheme by using a novel variable to approximate the dilatation. A large spherical elastomeric bearing is analyzed with this procedure.

252. Viscoelasticity

10A388. Stress analysis for rolling contact between two viscoelastic cylinders. - Guangqiu Wang *(BMW & Rolls Royce Aero Engines GmbH, D-8044 Lohhof, Munchen, Germany)* and K Knothe *(Aerospace Inst, Tech Univ, D-1000 Berlin 10, Germany)*. J Appl Mech 60(2) 310-317 (Jun 1993).

The 2D viscoelastic rolling contact with Coulomb's dry friction is considered for steady-state rolling. A so-called standard linear solid (three parameter model) is used to characterize the viscoelastic material behavior. Rolling contact stresses between two rolling cylinders are investigated by a BEM, based on the half-space theory. Numerical results are presented including the stress distribution at the contact surfaces and in viscoelastic bodies as well as rolling resistance.

10A389. Self-consistent modeling of visco-elastic polycrystals: Application to irradiation creep and growth. - PA Turner and CN Tome *(Fac Sci Exactas, Eng y Agrimensura, Univ Natl, Pellegrini 250, 2000 Rosario, Argentina)*. J Mech Phys Solids 41(7) 1191-1211 (Jul 1993).

We present a model that permits the simulation of the transient response of polycrystalline aggregates to externally imposed loads and temperature gradients. The mechanical response of the constitutive grains includes elastic, Newtonian (linearly viscous), thermal and growth terms. The formulation explicitly accounts for the anisotropy in the elastic, creep, thermal and growth properties of both grains and polycrystals, and describes the time evolution of the overall visco-elastic moduli and of the internal stresses. It also provides, as limit cases, the correct overall elastic, thermal, creep and growth moduli of the polycrystal. The model is applied to analyse the characteristics of irradiation creep and growth in reactor tubes subjected to hydrostatic pressure. The influence of texture, grain anisotropy, grain shape, and thermal stresses over the predicted polycrystal response, and especially over the transient regime, is analysed in detail.

10A390. Application of BEM to geotechnical analysis. - T Shinokawa *(Eng Res Inst, Sato Kogyo, 47-3 Sanda, Atsugi, Kanagawa, Japan)* and Y Mitsui *(Dept of Architec and Civil Eng, Fac of Eng, Shinshu Univ, 500 Wakasato, Nagano, Japan)*. Comput Struct 47(2) 179-187 (Apr 1993).

A numerical method of viscoelastic boundary element analysis using the time marching method is presented and is combined with FEM. Some numerical examples in the viscoelastic analysis are presented to confirm the applicability of the BEM to geotechnical analysis. As an application of BEM to practical geotechnical engineering, the stability of a pillar (an area between two tunnels when they cross obliquely) is examined using the elastic BE analysis. It is concluded that BEM can be efficiently applied in practical geotechnical analysis.

10A391. Quasi-elastic computation of viscoelastic bodies under cyclic loading and its appli-

cation for polymers with ADINA. - Linan Qiao *(Iwan N Stranski Inst, Tech Univ, Berlin, Germany)*. Comput Struct 47(4-5) 757-765 (3 Jun 1993).

A method for quasi-elastic computation of viscoelastic bodies under cyclical loading is suggested. At first, a quasi-Young's modulus is put forward which depends on the loading frequency of the viscoelastic body. Then the method is applied to a polymer material with viscoelastic features using the ADINA program.

10A392. Simultaneous use of 4 × 4 and 2 × 2 bilinear stress elements for viscoelastic flows. - GC Georgiou *(Dept of Math, Univ of Cyprus, Kallipoleos 75, PO Box 537, Nicosia, Cyprus)* and MJ Crochet *(Unit of Appl Mech, Univ Catholique, 2 Place du Levant, B-1348 Louvain-la-Neuve, Belgium)*. Comput Mech 11(5-6) 341-354 (1993).

Mixed FEs for viscoelastic flows based on a 4 × 4 sub-linear interpolation for the extra stress components satisfy the Babuska-Brezzi condition and are highly stable. They have been proved to be quite satisfactory in solving problems with strong stress boundary layers. In this work, we examined the simultaneous use of 4 × 4 and 2 × 2 bilinear stress elements in an attempt to reduce the computational cost without sacrificing the accuracy. The 4 × 4 bilinear elements are employed in regions where the stress field is anticipated to be steep while the 2 × 2 elements carry the burden elsewhere with a much smaller number of stress nodes. Additional constraints along the sides shared by different elements are necessary in order to preserve conformity. The method is applied to the creeping flow of a Maxwell fluid around a sphere falling along the axis of a cylindrical tubes. Results are given for three mixed FE formulations: the Galerkin method, the consistent streamline-upwind-Petrov-Galerkin method and the non-consistent streamline-upwind method. Particular emphasis is given on the calculated drag correction factors. The effect of the sphere-cylinder diameter ratio is also examined.

See also the following:

10A577. Methodology for modeling tertiary creep behavior of engineering alloys under oxidizing conditions

254. Plasticity and viscoplasticity

See the following:

10A490. Ultimate strength design of biaxially loaded steel box beam-columns

254A. GENERAL THEORY

10A393. Computational modeling of single crystals. - AM Cuitino and M Ortiz *(Div of Eng, Brown Univ, Providence RI 02912)*. Model Simulation Mat Sci Eng 1(3) 225-263 (Apr 1993).

The physical basis of computationally tractable models of crystalline plasticity is reviewed. A statistical mechanical model of dislocation motion through forest dislocations is formulated. Following Franciosi and co-workers, the strength of the short-range obstacles introduced by the forest dislocations is allowed to depend on the mode of interaction. The kinetic equations governing dislocation motion are solved in closed form for monotonic loading, with transients in the density of forest dislocations accounted for. This solution, coupled with suitable equations of evolution for the dislocation densities, provides a complete description of the hardening of crystals under monotonic loading. Detailed comparisons with experiment demonstrate the predictive capabilities of the theory. An adaptive FE formulation for the analysis of ductile single crystals is also developed. Calculations of the near-tip fields in Cu single crystals illustrate the versatility of the method.

10A394. Internal variable theory of inelastic behavior derived from the uniaxial rigid-perfectly plastic law. - G Romano, L Rosati, F Marotti de Sciarra *(Dept Scienza Costruzioni Fac Ingegneria, Univ Napoli Federico II, 80125 Piazzale Tecchio, Napoli, Italy)*. Int J Eng Sci 31(8) 1105-1120 (Aug 1993).

In the general framework provided by the internal variable theories of associated inelastic behavior the formulation of constitutive relations is addressed in this paper. Attention is focused on the basic properties of the evolution relation involving rates of internal variables and dual thermodynamic forces. It is shown that a suitable generalization of the uniaxial rigid-perfectly plastic law can be performed by introducing the definition of step-shaped constitutive maps. This definition allows us to derive a general theory of associated inelastic behavior with its characteristic properties: convexity of the elastic locus, normality rule, existence of a sublinear dissipation functional and of a canonical yield functional. Finally the formulation of the constitutive relation in terms of yield functionals and related inelastic multipliers is discussed. The analysis is performed on the basis of a chain rule of subdifferential calculus, recently contributed by the authors, which provides an effective tool to develop the theory of Kuhn-Tucker vectors in optimization problems.

254C. NONLINEAR AND FINITE DEFORMATION PROBLEMS

10A395. Evolution of the anistropy of a polycrystalline aggregate. - Ying Zhang *(Army High Performance Comput Res Center, Univ of Minnesota, Minneapolis MN 55415)* and JT Jenkins *(Dept of Theor and Appl Mech, Cornell)*. J Mech Phys Solids 41(7) 1213-1243 (Jul 1993).

The macroscopic properties of a polycrystalline aggregate depend upon the orientational distribution of the single crystals. Here we determine how this distribution of orientations is established for a single crystal whose deformation is assumed to be identical to that of the aggregate. We first derive the equation of evolution for the orientation of a single crystal of arbitrary type that deforms through the mechanism of rate independent crystallographic slip. We then introduce an orientational distribution function to characterize how the orientations of the single crystals are distributed, and derive the equation of evolution for this function. We further consider an approximate representation of the orientational distribution function and derive the linear, first-order ordinary differential equations for the evolution of the coefficients associated with the anisotropic term of the representation. Solutions to these equations can be obtained numerically. These may be used, for example, to describe the development of anisotropy in numerical simulations of metal forming processes.

10A396. Ship bow response in high energy collisions. - H Kierkegaard *(Dept of Ocean Eng, Tech Univ, DK-2800 Lyngby, Denmark)*. Marine Struct 6(4) 359-376 (1993).

A mathematical method for calculating force-indentation relations has been derived for high energy collisions involving ship bow structures. The theory is based on axial crushing mechanisms for basic elements such as L-, T- and X-elements. The internal energy is determined for these elements under the assumption of a rigid plastic material. The energy is related to an external mean crushing force. Stiffened plates are included in the crushing mechanism by introducing an orthotropic plastic plate theory. In a numerical calculation, the bow structure is modelled as an assembly of basic axial elements. The total crushing force is calculated in a simple time simulation, where the strain effect on the flow stress is included. The structure is crushed from the front, and the simulation procedure is able to handle rigid body motions of crushed and non-crushed structure. The calculated collision forces are compared with results from model tests and good agreements are found. Furthermore, a calculation for a longitudinal stiffened bow is given and discussed.

10A397. Thermal expansion coefficient and specific heat at constant strain for finite plastic deformation. - CW Bert and S Huang *(Sch of Aerospace and Mech Eng, Univ of Oklahoma, Norman OK 73019-0601)*. J Appl Mech 60(2) 449-455 (Jun 1993).

General expressions for thermal expansion coefficient and specific heat at constant strain in the case of finite plastic deformation are derived from a general analysis of thermodynamics and finite plasticity theory. The present results show that these two thermal parameters are dependent, in a very complicated way, on the mechanical behavior of the material, such as the plastic yielding and flow, work-hardening and stress-strain relation. They are not constants but vary with the stress state, deformation state, and deformation history. It is shown that previously published experimental observations on thermal expansion coefficient can be described by the theory presented in this paper.

See also the following:

10A484. Finite strip method for the elastic-plastic large displacement analysis of thin-walled and cold-formed steel sections

10A529. Constitutive model for cold deformation of aluminium at large strains and high strain rates

10A662. Accurate and efficient method for large deflection inelastic analysis of frames with semi-rigid connections

254F. MATERIAL CHARACTERIZATION

10A398. Hardening rule between stress resultants and generalized plastic strains for thin plates of power-law hardening materials. - CH Chou, J Pan *(Mech Eng and Appl Mech, Univ of Michigan, Ann Arbor MI 48109)*, SC Tang *(Ford Motor, Dearborn MI 48121)*. J Appl Mech 60(2) 548-554 (Jun 1993).

For power-law hardening materials, a stress resultant constitutive law of incremental plasticity nature for thin plates is constructed. The yield function in the stress resultant space is approximated in quadratic form and an equivalent stress resultant is defined. One of two parameters in the yield function is analytically determined based on the concept of complementary potential surface. The other is determined by the least square method to fit the complementary potential surface of Chou et al, (1991). In analogy to the work of Hill (1979), the equivalent work-conjugate generalized plastic strain rate is derived. Finally, the hardening rule between the equivalent stress resultant and generalized plastic strain is obtained based on the results of Chou et al, (1991) for power-law materials under proportional straining conditions.

See also the following:

10A393. Computational modeling of single crystals

254G. WORK HARDENING

10A399. Anisotropic strain hardening in polycrystalline copper and aluminium. - F Hess *(Mat Sci Center, Dept of General Phys, Rijksuniversiteit Groningen, Nijenborgh 4, 9747*

AG Groningen, Netherlands). Int J Plasticity 9(4) 405-420 (May 1993).

A new viscoplastic model for the plastic stress-strain behavior of fcc metals is presented. In this model the strain hardening results from increasing dislocation densities. The observed stagnation of strain hardening after strain reversals is explained by a lowering of the increase in dislocations due to annihilation of dislocations with opposite polarity. The model is applied to Bauschinger and x-y tests on commerical copper and aluminium, and to cyclic tests on copper. The theoretical results are in good agreement with the measurements.

10A400. New approach to the Koiter's inequality for shakedown. - J Atkociunas *(Dept of Struct Mech, Vilnius Tech Univ, Vilnius, Lithuania).* Mech Res Commun 20(4) 301-308 (Jul-Aug 1993).

An elastic-perfectly plastic discrete structure subject to cyclic loading is considered, the physical parameters being prescribed. The loading defined by the limits of variation is assumed to cause shakedown of the structure. Residual displacements are related to the history of loading. The energy bounds of possible states of shakedown are usually included in the constraints of the mathematical models of problems for the estimation of displacements. The minimum value of the elastic potential of the residual forces and the maximum value of energy dissipation are within these bounds, only the variation limits of cyclic loading being prescribed. The reliability of the results obtained by solving mathematical optimization problems for determining the variation limits of residual displacements largely depends on the accuracy of these energy values. The well known Koiter's inequality that enables to approximately determine the upper bounds of energy dissipation is not valid when the values of safety coefficients at shakedown approach a unity. The minimum energy principle of residual forces of a fictitious structure obeying the holonomic law permits the upper bound of energy dissipation to be defined more accurately even within the scope of Koiter's inequality.

10A401. Temperature dependence of the residual strength and ductility of a type-316 LN austenitic stainless-steel after prior cold work by tension and swaging. - KG Samuel, SL Mannan *(Mat Dev Div, Indira Gandhi Centre for Atomic Res, Kalpakkam 603 102, India)*, VM Radhakrishnan *(Dept of Metall Eng, Indian IT, Madras 600 036, India).* J Mat Processing Tech 38(3) 517-526 (May 1993).

The influence of temperature and prior cold work on the residual tensile strength and ductility of a type-316 LN austenitic stainless-steel has been studied in the temperature range 300-1123 K after prior deformation at room temperature by tension and swaging. In general, it was observed that the effect of prior cold work by different modes of deformation on the mechanical response of the material has a qualitatively common trend of increasing the strength and reducing the ductility. A structure-sensitivity parameter (the ratio of the yield strength of the prior cold-worked material to that of the as-received material at a given temperature) is proposed and found to increase with temperature and the degree of prior cold work. The additional strengthening of the structure in the temperature range up to 823 K is considered to arise due to dislocation interaction with solutes or precipitates. The decrease of the structure-senstivity parameter above 823 K is attributed to dynamic recovery processes and/or the absence of dislocation solute interaction.

254H. CYCLIC AND VARIABLE LOADING

10A402. Effective stresses and microstructure in cyclically deformed 316L austenitic stainless steel: Effect of temperature and nitrogen content. - J-B Vogt, T Magnin, J Foct *(Lab de Metall, Univ de Lille I, URA CNRS 234, Bat C6, F-59655 Villeneuve d'Ascq, Cedex, France).* Fatigue Fracture Eng Mat Struct 16(5) 555-564 (May 1993).

This paper reports a study on the factors influencing dislocation slip during cyclic deformation of 316L austenitic stainless steel. TEM investigations show that low temperature and interstitial nitrogen content favor planar slip and lead to higher effective stress values. Measurements of effective and internal stresses with the Handfield-Dickson technique indicate that the contribution of nitrogen in the effective component is more important than that of temperature. It is deduced that nitrogen acts through a pinning effect, while low temperature exerts an effect on friction stress. The results also suggest that cyclic plasticity could modify the short range order leading to a redistribution of nitrogen.

254I. VISCO- AND ELASTO-PLASTIC MEDIA

10A403. Elastoplastic modeling for the ductile behavior of polycrystalline sodium chloride with SUVIC. - M Aubertin and DE Gill *(Dept of Mineral Eng, Ecole Polytech, CP 6079, Succ A, Montreal, PQ, H3C 3A7, Canada).* Int J Plasticity 9(4) 479-505 (May 1993).

A unified viscoplastic model with evolutionary state variables, called SUVIC, is reduced to its rate-independent counterpart, and is applied to the inelastic behavior of polycrystalline sodium chloride (salt) in the ductile regime. The proposed model includes a von Mises-type yield criterion, an associated flow rule, and three state variables, producing a mixed (kinematic and isotropic) hardening. The evolution laws are expressed through a particular formulation of the Voce law, which is mathematically similar to the Armstrong-Frederick formulation used in numerous mechanical models. This rate-independent version of SUVIC is a simple extension of the well-known two-surface models and can be reduced to various classical elastoplastic models.

10A404. Study on plastic shakedown of structures Part I. Basic properties. - C Polizzotto *(Dipartimento Ing Strutturale & Geotec, DISEG, Univ Palermo, I-90128 Palermo, Italy).* J Appl Mech 60(2) 318-323 (Jun 1993).

For a continuous elastic-perfectly plastic solid body subjected to a combination of cyclic (mechanical and/or kinematical) load and of a steady (mechanical) load such as to produce plastic shakedown (ie, alternating plasticity), a number of characterizing properties are established and discussed. The conditions for the body's transition from plastic shakedown to ratchetting are also addressed.

10A405. Study on plastic shakedown of structures Part II. Theorems. - C Polizzotto *(Dipartimento Ing Strutturale & Geotec, DISEG, Univ Palermo, I-90128 Palermo, Italy).* J Appl Mech 60(2) 324-330 (Jun 1993).

For a continuous elastic-perfectly plastic solid body subjected to a combination of cyclic (mechanical and/or kinematical) load and of a steady (mechanical) load, two theorems of plastic shakedown are presented, one stating a necessary condition, another stating a sufficient condition. The problem of the direct determination of the plastic shakedown boundary is also briefly adressed.

See also the following:

10A130. Shear and torsional impact of cracked viscoelastic bodies: A numerical integral equation-transform approach
10A420. Axisymmetric micromechanics of elastic-perfectly plastic fibrous composites under uniaxial tension loading
10A421. Elastoplastic constitutive relations for fiber-reinforced solids
10A461. Viscoelastic response of a strand
10A642. Optimization of elastoplastic systems under random loading

254M. PHYSICAL THEORY (DISLOCATIONS, ETC)

10A406. Collective micro shear processes and plastic instabilities in crystalline and amorphous structures. - H Neuhauser *(Inst fur Metallphys, und Nukleare Festkorperphys, Tech Univ, Mendelssohnstr 3, D-3300 Braunschweig, Germany).* Int J Plasticity 9(4) 421-435 (May 1993).

The mechanisms that may lead to plastic instabilities are reviewed briefly, and their intimate connection with localization of plastic shear is emphasized. The combination of macro and micro experiments, ie, analysis of stress fluctuations and serrations, and of slip and shear band evolution during deformation, for investigations of these mechanisms is demonstrated with examples of LUDERS and PORTEVIN-LeCHATELIER band propagation in single glide oriented crystals, and of shear band formation in predeformed mono- and polycrystals as well as amorphous materials. The problems connected with collective effects of the micro units of deformation (ie, dislocations in crystalline, local shear transformations in amorphous materials) are indicated, and the necessity to study the mechanism of transfer of slip (shear) to neighboring regions is stressed.

254Y. COMPUTATIONAL TECHNIQUES

10A407. Computational aspects of large elastoplastic deformations in the presence of anisotropy and plastic spin. - B Loret, F Hammoum *(Natl Polytechnic Inst, Inst of Mech, BP 53X, 38041 Grenoble Cedex, France)*, YF Dafalias *(Dept of Civil Eng, UC, Davis CA 95616).* Comput Methods Appl Mech Eng 105(2) 151-180 (Jun 1993).

A constitutive framework for large elastoplastic deformations is briefly presented, along the lines of Mandel's theory, in a form most appropriate for computational convenience. A general purpose stress-point algorithm is adapted to the present large deformation framework. An accuracy analysis is carried out and the performance of several variants are compared, particularly those related to the anisotropic intensity and plastic spin in reference to two specific anisotropic models. The effect of elastic deformations on the overall response is demonstrated for special loading paths.

10A408. Discontinuous displacement approximation for capturing plastic localization. - R Larsson, K Runesson *(Dept of Struct Mech, Chalmers Univ of Tech, S-41296 Goteborg, Sweden)*, NS Ottosen *(Dept of Solid Mech, Univ of Lund, Box 118, S-22100 Lund, Sweden).* Int J Numer Methods Eng 36(12) 2087-2105 (30 Jun 1993).

It is proposed to capture localized plastic deformation via the inclusion of regularized displacement discontinuities at element boundaries (interfaces) of the FE subdivision. The regularization is based on a kinematic assumption for an interface that resembles that which is pertinent to the classical shear band concept. As a by-product of the regularization, an intrinsic band width is introduced as a "constitutive" property rather than a geometric feature on the FE mesh. In this way the spurious mesh sensitivity, which is obtained when the displacement approximation is continuous, can be avoided. Another consequence is that the interfacial relation between the elements is derived directly from the conventional constitutive properties of the continuously deforming material. An interesting feature is that the acoustic tensor will not only play a role for diagnosing discontinuous bifurcation but will also serve as the tangent stiffness tensor of the interface (up to within a scalar factor). An analytical investigation of the behavior of the interface is carried out and it is shown that dilatation may indeed accompany slip within a "shear" band for a general plasticity model. The significance of proper mesh alignment is demonstrated for a simple problem in plane strain and plane stress. It is shown that a unique structural post-peak response (in accordance with nonlinear fracture mechanics) can be achieved when the plastic softening modulus is properly related to the bandwidth. The paper concludes with a numerical simulation of the gradual development of a shear band in a soil slope.

10A409. Numerical approach for nonclassical plasticity. - X Peng and J Fan *(Dept of Eng Mech, Chongqing Univ, Chongqing 630044, Peoples Rep of China)*. Comput Struct 47(2) 313-320 (Apr 1993).

A new incremental form of constitutive equation and the corresponding nonlinear FEM approach are developed based on an endochronic constitutive equation without using a yield surface; a kind of nonclassical theory of plasticity. Compared with the numerical method proposed elsewhere, the new algorithm greatly reduces the error induced in the numerical process, especially in the region of initial extremely small inelastic strain with its slope of stress-plastic strain curve being sufficiently large. The residual stress field of an autofrettaged thick-walled cylinder and the cyclic stress responses of a notched plate are then analyzed.

See also the following:

10A393. Computational modeling of single crystals

10A666. Computer-aided interactive plastic design of frames

254Z. EXPERIMENTAL TECHNIQUES

10A410. Numerical analysis of high strain rate splitting-tensile tests. - ML Hughes *(Air Force Civil Eng Support Agency, Tyndall AFB FL 32403)*, JW Tedesco *(Dept of Civil Eng, Auburn Univ, Auburn AL 36849)*, CA Ross *(Graduate Eng Center,Univ of Florida, PO Box 1918, Elgin AFB FL 32542-1918)*. Comput Struct 47(4-5) 653-671 (3 Jun 1993).

Experimental splitting-tension tests were conducted on 2-in diameter concrete specimens in a Split Hopkinson Pressure Bar at strain rates of 4.4, 10.6, and 14.7-sec. The specimens were instrumented with electrical resistance strain gages and break circuits to detect crack initiation crack growth. Experimental results indicate that there is a shift of crack initiation time relative to the peak stress. Also, experimental strength vs strain rate data reveal that the dynamic tensile strength of concrete is significantly higher than the static tensile strength. A comprehensive numerical analysis was conducted on the splitting-tensile experiments to investigate the effects of varying the uniaxial tensile strength of the concrete on the crack initiation time, stress state, crack growth characteristics, and failure mode in the concrete specimens. The results of the numerical analyses are used to enhance the understanding of concrete tensile strength strain rate sensitivity.

256. Composite material mechanics

See the following:

10A470. Axisymmetric deformation of varying thickness composite cylindrical shell with various end conditions

256A. GENERAL THEORY

10A411. Geometrical description of particle distributions in materials. - JB Parse and JA Wert *(Dept of Material Sci and Eng, Univ of Virginia, Charlottesville VA 22903-2442)*. Model Simulation Mat Sci Eng 1(3) 275-296 (Apr 1993).

This paper describes a geometrical technique, based on the Dirichlet tessellation, for quantitative characterization of inhomogeneities in the spatial distribution of second-phase particles. The Dirichlet tessellation representation allows a detailed, statistical description of particle distribution properties, including local particle density and vector nearest-neighbor distances. Extension of the tessellation technique by specifying a distance over which second-phase particles are assumed to interact mechanically (particle interaction distance) facilitates quantitative characterization of particle clustering by allowing evaluation of characteristics such as the fraction of particles clustered, and the number, size, and spatial distribution of clusters. The tessellation and clustering characteristics of several types of computer-generated particle arrays (random, clustered, and hexagonal cellular) are presented. The effects of plane-strain deformation on the tessellation and clustering characteristics of the particle arrays have been examined. Tessellation and clustering characteristics of the random particle arrays are insensitive to plane-strain deformation. Several tessellation and clustering characteristics of the clustered and hexagonal-cellular particle arrays exhibit varying behavior with increasing plane-strain deformation. These changes in tessellation and clustering characteristics may be understood by considering the effects of deformation on the various types of inhomogeneous particle distributions.

10A412. Symmetric model of stress-strain hysteresis loops in shape memory alloys. - Krzysztof Wilmanski *(Physikalische Ingenieurwissenschaft, Tech Univ, Strasse des 17 Juni 135, D-1000 Berlin 12, Germany)*. Int J Eng Sci 31(8) 1121-1138 (Aug 1993).

The paper contains the construction of phenomenological model of processes, appearing during the stress-induced isothermal martensitic phase transformations in shape memory materials. In contrast to earlier papers on this subject, the Gibbs free energy is assumed to contain the contribution of the energy of pattern formation. This contribution is constructed in such a way that changes of internal variables are identical in yield and recovery (symmetric model), as suggested by experimental results. It is shown that such a Gibbs free energy together with the principle of least work and an assumption on admissible classes of processes, yields a unique description of internal loops of force-elongation diagrams. It is also demonstrated that the present model reproduces qualitatively all paths appearing in tensile experiments carried on shape memory single crystals in hard loading devices.

See also the following:

10A510. Universal relations in piezoelectric composites with eigenstress and polarization fields Part I. Binary media: Local fields and effective behavior

10A511. Universal relations in piezoelectric composites with eigenstress and polarization fields Part II. Multiphase media: Effective behavior

256B. PARTICULATE MEDIA, INCL CEMENTS

10A413. Nonlinear elastic properties of particulate composites. - Yi-Chao Chen and Xiaohu Jiang *(Dept of Mech Eng, Univ of Houston, Houston TX 77204)*. J Mech Phys Solids 41(7) 1177-1190 (Jul 1993).

A method of computing effective elastic moduli of isotropic nonlinear composites is developed by using a perturbation scheme. It is demonstrated that only solutions from linear elasticity are needed in computing higher order moduli. As an application of the method, particulate composites of nonlinear elastic materials are analysed.

See also the following:

10A411. Geometrical description of particle distributions in materials

10A572. Analysis of damage in a ceramic matrix composite

256D. CARBON FIBER REINFORCED MEDIA

10A414. Carbon fibers from oriented polyethylene precursors. - Dong Zhang *(Textile Mat Res Lab, Univ of Tennessee, Knoxville TN 37996-1900)*. J Thermoplastic Composite Mat 6 38-48 (Jan 1993).

In this research, an effort is made to produce carbon fibers from a highly ordered and oriented polyethylene fiber. Sulfonation of the fiber is studied as a method of stabilizing this thermoplastic fiber for higher temperatures of carbonization. The effect of time, temperature, tension and medium of sulfonation is being studied systematically. The progress of reactions and the extent of stabilization is studied by thermal analyses (Differential Scanning Calorimetry and Thermogravimetric Analysis). Other techniques like Scanning Electron Microscopy and Instron Tension Testing are used to investigate the changes in morphology of the fibers with stabilization treatment. Also, the properties of the carbon fibers produced from these precursors are investigated.

10A415. Concrete reinforced with up to 0.2 vol% of short carbon fibres. - Pu-Woei Chen and DDL Chung *(Composite Mat Res Lab, SUNY, Furnas Hall, Buffalo NY 14260)*. Composites 24(1) 33-52 (1993).

The use of short pitch-based carbon fibres (0.5% by weight of cement, 0.189 volume % (vol%) of concrete), together with a dispersant, chemical agents and silica fume, in concrete with fine and coarse aggregates resulted in a flexural strength increase of 85%, a flexural toughness increase of 205%, a compressive strength increase of 22%, and a material price increase of 39%. The slump was 102 mm (4 in) at the optimum water-cement ratio of 0.50. The air content was 6%, so the freeze-thaw durability was increased, even in the absence of an air entrainer. The aggregate size had little effect on the above properties. The minimum carbon fibre content for flexural strength increase was 0.1 vol%, although the flexural toughness was still increased below this fibre volume fraction. The optimum fibre length was such that the mean fibre length decreased from 12 mm before mixing to 7 mm after mixing, which used a Hobart mixer. The drying shrinkage was decreased by up to 90%. The electrical resistivity was decreased by up to 83%.

10A416. Effect of carbon coating on mechanical strength of SiC whisker-reinforced alumina composites. - I Thompson and VD

Krstic *(Dept of Mat and Metall Eng, Queen's Univ, Kingston, ON, K7L 3N6, Canada)*. Theor Appl Fracture Mech 19(1) 61-67 (Jun 1993).

Microstructure and mechanical response of alumina matrix reinforced with carbon coated and uncoated SiC whiskers were examined. Carbon coating was used in order to modify the interface and possibly relax the residual thermal stresses developed on cooling from the hot-pressing temperature. Crack propagation behavior and interfacial properties of the composite were studied using scanning and transmission electron microscopy. Resistance to fracture were assessed by using four point bend test and failure load were determined using four point chevron notched beam and double cantilever beam specimens. The improvement in fracture resistance in carbon coated whisker composites was attributed to whisker pull out, crack bridging and crack deflection.

10A417. Effect of processing conditions on the properties of carbon fiber-LaRC TPI composites made by suspension prepregging. - TH Yu and RM Davis *(Dept of Chem Eng, VPI)*. J Thermoplastic Composite Mat 6 62-90 (Jan 1993).

Unidirectional carbon fiber-LaRC TPI composites were made by prepregging carbon fiber tow with particles of LaRC TPI suspended in aqueous solutions of the ammonium salt of the LaRC TPI polyamic acid. The prepregging was followed by drying and consolidation steps designed to facilitate water removal. The effects of processing conditions on composite properties were investigated. The processing conditions included the degree of overlap of the fiber bundle in the prepreg, the fiber tension during prepregging, and the use of vacuum during the consolidation step. It was found that volume % increased with increasing fiber tension and that consolidation under vacuum resulted in composites with void content as low as 0.14 volume %. Fourier transform infrared spectroscopy and thermogravimetric analysis coupled with mass spectroscopy established that most of the water was removed from the prepreg and most of the polyamic acid was converted to polyimide prior to consolidation. The properties of the resulting unidirectional laminates were quite reproducible. Shear moduli were comparable to those for graphite and fiber-epoxy and graphite-fiber and PEEK laminates.

10A418. Hybrid composites based on polyethylene and carbon fibres Part 6. Tensile and fatigue behavior. - AAJM Peijs and JMM de Kok *(Center for Polymers and Composites, Univ of Tech, PO Box 513, 5600 MB Eindhoven, Netherlands)*. Composites 24(1) 19-32 (1993).

The tensile and fatigue behavior of undirectional carbon-high-performance polyethylene-epoxy hybrid composites has been studied, including the effect of hybrid design and surface treatment of the high-performance polyethylene (HP-PE) fibres. Results indicated that the tensile behavior of carbon-HP-PE hybrids in both monotonic and fatigue testing can be interpreted, adopting the conventional "constant strain" model for hybrid composites. Deviations from this constant strain model, so-called hybrid effects, were observed in monotonic tensile testing for those hybrid systems with the highest degree of fibre dispersion, incorporating either untreated or treated HP-PE fibres, whereas only the latter displayed synergistic fatigue performance. Hybrid effects under tensile loading conditions were in reasonable agreement with calculations accounting for statistical effects and stress concentrations as determined by FE analyses.

10A419. Strength of carbon-epoxy laminates with countersunk hole. - C-G Aronsson *(Dept of Mech Eng, Linkoping IT, S-581 83 Linkoping, Sweden)*. Composite Struct 24(4) 283-289 (1993).

The aim of this study is to predict the static strength of carbon-epoxy laminates with countersunk hole. Also, three-point bend (TPB) specimens with the same lay-up were analyzed. For this purpose, the notched strength of the laminates was analyzed by a damage zone model (DZM), where damage around the notch is represented by an "equivalent crack" with cohesive forces acting between the crack surfaces. The DZM requiring only basic properties of the laminate such as unnotched tensile strength, σ_0, fracture energy, $G^x{}_c$, and stiffnesses of the laminate. However, the complex geometry around the countersunk hole implies that both σ_0 and $G^x{}_c$ will vary in this area, and in order to avoid this problem an approximate geometry of the countersunk hole is used in the DZM calculations. With this approximation, good agreement between experimental and calculated strength was observed for the laminates with countersunk hole. This was also the case for the TPB specimens.

See also the following:

10A615. Effect of molding parameters on the interfacial strength in PEEK-carbon composites

256F. OTHER FIBER REINFORCED MEDIA

10A420. Axisymmetric micromechanics of elastic-perfectly plastic fibrous composites under uniaxial tension loading. - Jong-Won Lee *(Korea Aerospace Res Inst, PO Box 15, Daeduck Science Town, Daejun 305-606, Korea)* and DH Allen *(Center for Mech of Composites, Texas A&M Univ, College Station TX 77843)*. Int J Plasticity 9(4) 437-460 (May 1993).

The uniaxial response of a continuous fiber elastic-perfectly plastic composite is modeled herein as a two-element composite cylinder. An axisymmetric analytical micromechanics solution is obtained for the rate-independent elastic-plastic response of the two-element composite cylinder subjected to tensile loading in the fiber direction for the case wherein the core fiber is assumed to be a transversely isotropic elastic-plastic material obeying Tsai-Hill's yield criterion, with yielding simulating fiber failure. The matrix is assumed to be an isotropic elastic-plastic material obeying Tresca's yield criterion. It is found that there are three different circumstances that depend on the fiber and matrix properties: (1) fiber yield, followed by matrix yielding; (2) complete matrix yield, followed by fiber yielding; and (3) partial matrix yield, followed by fiber yielding, followed by complete matrix yield. The order in which these phenomena occur is shown to have a pronounced effect on the predicted uniaxial effective composite response.

10A421. Elastoplastic constitutive relations for fiber-reinforced solids. - G deBotton and PP Castaneda *(Dept of Mech Eng and Appl Mech, Univ of Pennsylvania, 220 Towne Bldg, 220 S 33rd St, Philadelphia PA 19104)*. Int J Solids Struct 30(14) 1865-1890 (1993).

In this paper, we make use of a procedure for estimating the effective properties of nonlinear composite materials, proposed recently by Ponte Castaneda, to study the effective constitutive behavior of ductile, fiber-reinforced composites. Both estimates and rigorous bounds are obtained for the effective energy functions of multiple-phase, fiber composites with general ductile behaviors (in the context of deformation theory of plasticity) for the isotropic constituent phases. The resulting expressions for the energy functions may be differentiated in a straightforward manner to obtain corresponding estimates for the anisotropic effective stress-strain relations. Explicit calculations are carried out for the case of an aluminum-matrix composite reinforced with boron fibers. The results reveal some interesting features distinguishing the constitutive behavior of ductile-matrix, fiber-reinforced composites from that of linear-elastic, fiber-reinforced composites. One such feature is the strong coupling between the dilatational and distortional modes for the ductile fiber composites. Finally, comparisons are made with available experimental data.

10A422. Indentation of laminated filament-wound composite tubes. - S Li, PD Soden, SR Reid *(UMIST, UK)*, MJ Hinton *(DRA RARDE, UK)*. Composites 24(5) 407-421 (Jul 1993).

The FEM has been used to analyse the behavior of thin-walled, 100 mm diameter filament-wound GRP tubes supported on a flat plate and indented with a 50 mm diameter spherical indenter. The tube wall was treated as an angle-ply laminate and a half-tube model was employed with appropriate rotational symmetry conditions. The strain results were compared with those from a quarter-tube monolithic material model (homogeneous throughout and orthotropic with principal axes coincident with the axial and circumferential directions). The theoretical predictions were compared with experimental results. Local resin cracks occurred under the indenter. Two-cover (four-layer), 1 mm thick, ± 55° and ± 75° winding angle tubes finally failed at large indenter displacements by local shell buckling caused by the development of local axial compressive forces some distance away from the indenter. Four-cover (eight-layer), 2 mm thick, ± 55° tubes delaminated under the indenter and failed by shell fracture, again some distance away from the indenter.

10A423. Microstructural image analysis applied to fibre composite materials: A review. - FJ Guild *(Queen Mary & Westfield Col, UK)* and J Summerscales *(Univ of Plymouth, UK)*. Composites 24(5) 383-393 (Jul 1993).

Current definition of the microstructure of fibre-reinforced composite materials is usually limited to the definition of the materials used and the proportion and orientation of the fibres. Significant differences can be achieved within such a definition, particularly in respect of the spatial distribution of fibres within the material. The microstructure-mechanics relationship is gaining importance as the discipline of mesomechanics. Recent advances in computer hardware, and in software for image processing and analysis, have permitted the rapid definition of spatial microstructural parameters. This paper reviews the preparation of samples for optical microscopy and the use of image analysis for the definition of microstructure in fibre-reinforced composites.

10A424. Modeling damage in plain weave fabric-reinforced composite material. - DM Blackletter *(Univ of Idaho, Moscow ID 83843)*, DE Walrath, AC Hansen *(Univ of Wyoming, Laramie WY 82071)*. J Composite Tech Res 15(2) 136-142 (Sum 1993).

A method for describing damage propagation in a woven fabric-reinforced composite material subjected to tension or shear loading is presented. A 3D unit cell description of a plain weave graphite-epoxy fabric reinforced composite was constructed. From this description, FE models were generated. An incremental iterating FE algorithm was developed to analyze loading response. This FE program included capabilities to model nonlinear constitutive material behavior and a scheme to estimate the effects of damage propagation by stiffness reduction. Tension and shear loadings were modeled. Results from the FE analysis compared favorably with experimental data. Nonlinear shear stress-strain behavior of the fabric composite was shown to be principally caused by damage propagation rather than by plastic deformation of the matrix.

10A425. Review of recent research in the former Soviet Union on fibrous composites. - RP Dickenson *(Univ of Greenwich, UK)* and MR Hill *(Loughborough Univ of Tech, UK)*. Composites 24(5) 379-382 (Jul 1993).

Research into fibrous composites in the former Soviet Union is reviewed for the period 1982-1992. Carbon-carbon materials were used widely in the Soviet space program and had comparable properties to Western composites, although production methods were inferior. Metal-matrix materials also has properties up to Western levels; a significant amount of research was found on the fibre-matrix interface. Research on ceramic-ceramic composites was at a very early stage.

10A426. Simple material model for unidirectionally aligned fiber reinforced composites. - SFM Abd-El-Naby *(3 Iashac Yacoub St, Zamalek 11211, Cairo, Egypt)*, L Hollaway, M Gunn *(Dept of Civil Eng, Univ of Surrey, Guildford, Surrey GU2 5XH, UK)*. Composite Struct 24(4) 323-331 (1993).

A material model for the nonlinear behavior of composite materials is proposed. The model combines the linear elastic fiber properties with the nonlinear behavior of the matrix in order to obtain the average properties of the composite. The interaction between the fiber and the matrix is considered using stress partitioning factors, which are based on the experimental behavior of the material.

10A427. Some further considerations of the theory of fibre debonding and pull-out from an elastic matrix Part 1. Constant interfacial frictional shear stress. - SY Fu *(Inst of Metal Res, Acad Sinica, Shenyang 110015, Peoples Rep of China)*, BL Zhou *(Inst of Metal Res and Int Center for Mat Phys, Acad Sinica, Shenyang 110015, Peoples Rep of China)*, X Chen, CF Xu *(Inst of Metal Res, Acad Sinica, Shenyang 110015, Peoples Rep of China)*, GH He, CW Lung *(Inst of Metal Res and Int Center for Mat Phys, Acad Sinica, Shenyang 110015, Peoples Rep of China)*. Composites 24(1) 5-11 (1993).

In this paper, some further considerations of the theory of fibre debonding and pull-out from an elastic matrix are performed. The form of the fibre tensile stress and of the interfacial shear stress disbribution along the embedded fibre length is determined and its dependence on fibre and matrix elastic properties, fibre volume fraction and embedded fibre length is shown for each case. According to this theory, the fibre-matrix interface can start to debond from the loaded fibre end and/or the embedded fibre end. The maximum fibre pull-out stress necessary to cause complete debonding and eventual pull-out is determined and its dependence on fibre and matrix elastic properties, fibre volume fraction, embedded fibre length and the ratio between the frictional shear stress and the interfacial shear strength is described in detail. This theory can be used to determine easily the shear strength of the interfacial bond and the interfacial frictional shear stress.

10A428. Some further considerations of the theroy of fibre debonding and pull-out from an elastic matrix Part 2. Non-constant interfacial frictional shear stress. - SY Fu *(Inst of Metal Res, Acad Sinica, Shenyang 110015, Peoples Rep of China)*, BL Zhou *(Inst of Metal Res and Int Center for Mat Phys, Acad Sinica, Shenyang 110015, Peoples Rep of China)*, X Chen *(Inst of Metal Res, Acad Sinica, Shenyang 110015, Peoples Rep of China)*, GH He, CW Lung *(Inst of Metal Res and Int Center for Mat Phys, Acad Sinica, Shenyang 110015, Peoples Rep of China)*. Composites 24(1) 13-17 (1993).

Solutions for fibre debonding and pull-out from an elastic matrix have previously been obtained under the condition that the interfacial frictional shear stress is independent of the bond length. However, this condition is not strictly valid. In this paper, an analysis of fibre debonding and pull-out is carried out by considering the dependence of the interfacial frictional shear stress on bond length. The maximum fibre pull-out stress necessary to cause complete debonding and eventual pull-out is determined to be dependent on the fibre-to-matrix elastic modulus ratio, the interfacial shear strength, the interfacial frictional coefficient, the fibre volume fraction and the embedded fibre length. Excellent agreement between the present theoretical analyses and existing experimental results is obtained.

See also the following:

10A501. Influence of local fiber undulations on the global buckling behavior of filament-wound cylinders
10A555. Flexural fatigue characteristics of FRP sandwich beams
10A616. Matrix cracking in fiber reinforced ceramics

256H. LAYERED MEDIA

10A429. 3D FE progressive failure analysis of composite laminates under axial extension. - YS Reddy *(Dept of Eng Sci and Mech, VPI)* and JN Reddy *(Dept of Mech Eng, Texas A&M Univ, College Station TX 77843)*. J Composite Tech Res 15(2) 73-87 (Sum 1993).

A 3D progressive failure algorithm is developed where the Layerwise Laminate Theory of Reddy is used for kinematic description. The FE model based on the layerwise theory predicts both inplane and interlaminar stresses with the same accuracy as that of a conventional 3D FE model. Besides, it provides a convenient format for modeling the 3D stress fields in composite laminates. The progressive failure algorithm is based on the assumption that the material behaves like a stable progressively fracturing solid. The stiffness reduction is carried out at the reduced integration gauss points of the FE mesh depending on the mode of failure. A parametric study is conducted to investigate the effect of out-of-plane material properties, 3D stiffness reduction methods, and boundary conditions on the failure loads and strains of a composite laminate under axial extension. The results indicate that different parameters have a different degree of influence on the failure loads and strains. Finally, the predictive ability of various phenomenological failure criteria is evaluated in the light of experimental results available in the literature, and the predictions of the Layerwise Laminate Theory are compared with those of the First-Order Shear Deformation Theory. The study concludes that the 3D stress analysis is necessary to predict accurately the failure behavior of composite laminates.

10A430. Adhesion improvement in polypropylene-aluminum laminates. - W Chinsirikul, TC Chung, IR Harrison *(Polymer Sci Program, Dept of Mat Sci and Eng, Penn State)*. J Thermoplastic Composite Mat 6 18-28 (Jan 1993).

Laminates or laminar composites provide materials with useful mechanical properties. There are many possible combinations of materials, and desired laminate properties can often be achieved by choosing appropriate components. In this study, polymer-metal laminates were selected as potential materials of interest, since such laminates should combine the drawability of polymers and the high modulus of metal. The matrix chosen is polypropylene (PP), and the reinforcing element is aluminum (Al); this pair was selected as part of a search for materials with exceptional specific properties.

10A431. Analysis of delamination in cross-ply laminates initiating from impact induced matrix cracking. - SA Salpekar *(Anal Services and Mat, Hampton VA 23666)*. J Composite Tech Res 15(2) 88-94 (Sum 1993).

Several 2D FE analyses of $(0_2/90_8/0_2)$ glass-epoxy and graphite-epoxy composite laminates were performed to investigate some of the characteristics of damage development due to an impact load. A cross section through the thickness of the laminate with fixed ends, and carrying a transverse load in the center, was analyzed. Inclined matrix cracks, such as those produced by a low-velocity impact, were modeled in the 90° ply group. The introduction of the matrix cracks caused large interlaminar tensile and shear stresses in the vicinity of both crack tips in the 0/90 and 90/0 interfaces. The large interlaminar stresses at the ends of the matrix cracks indicate that matrix cracking may give rise to delamination. The ratio of Mode I to total strain energy release rate, G_I/G_{total}, at the beginning of delamination, calculated at the two (top and bottom) matrix crack tips was 60 and 28%, respectively, in the glass-epoxy laminate. The corresponding ratio was 97 and 77% in the graphite-epoxy laminate. Thus, a significant Mode I component of strain energy release rate may be present at the delamination initiation due to an impact load. The value of strain energy release rate at either crack tip increased due to an increase in the delamination length at the other crack tip and may give rise to an unstable delamination growth under constant load.

10A432. Analysis of matrix cracking and local delamination in $(0/\theta/-\theta)_s$ graphite epoxy laminates under tensile load. - SA Salpekar *(Anal Services and Mat, Hampton VA 23666-0001)* and TK O'Brien *(US Army Vehicle Struct Directorate, NASA Langley Res Center, Hampton VA 23665)*. J Composite Tech Res 15(2) 95-100 (Sum 1993).

Several 3D element analyses of $(0/\theta/-\theta)_s$ graphite epoxy laminates, where θ = 15, 20, 25, 30, and 45°, subjected to axial tensile load, were performed. The interlaminar stresses in the $\theta/-\theta$ interface were calculated with and without a matrix crack in the central $-\theta$ plies. The interlaminar normal stress changes from a small compressive stress when no matrix crack is present to a high tensile stress at the intersection of the matrix crack and the free edge. The analysis of the local delamination from the $-\theta$ matrix crack indicates a high strain energy release rate and a localized Mode I component near the free edge, within one-ply distance from the matrix crack. To examine the stress state causing the matrix cracking, the maximum principal normal stress in a plane perpendicular to the fiber direction in the $-\theta$ ply was calculated in an uncracked laminate. The corresponding shear stress parallel to the fiber was also calculated. The principal normal stress at the laminate edge increased through the ply thickness and reached a very high tensile value at the $\theta/-\theta$ interface indicating that the crack in the $-\theta$ ply may initiate at the $\theta/-\theta$ interface. Predicted crack profiles on the laminate edge in the $-\theta$ ply were constructed from the principal stress directions. The cracks were found to be more curved for layups with smaller θ angles, which is consistent with experimental observations in the literature.

10A433. Composite sandwich construction with syntactic foam core. A practical assessment of post-impact damage and residual strength. - C Hiel, D Dittman, O Ishai *(EEM Branch, NASA Ames Res Center, Moffet Field CA 94035)*. Composites 24(5) 447-450 (Jul 1993).

The purpose of this note is to report on a successful inspection method for sandwich panels with syntactic foam core and to summarize a procedure for the practical assessment of post-impact damage and residual strength.

10A434. First-ply failure of laminated composite plates. - D Bruno, G Spadea, R Zinno *(Dept of Struct Eng, Univ of Calabria, 87030 Arcavacata di Rende, Cosenza, Italy)*. Theor Appl Fracture Mech 19(1) 29-48 (Jun 1993).

Composite laminates offer superior carrying capacity. Reliable application of such structures requires a knowledge of their stress-strain and failure behavior. Past treatments involved assumptions in both the stress and failure analyses; they become increasingly more difficult when the failure of the microstructure constituents is to be included in the continuum analysis of the laminates. Recognizing the conventional failure criteria used for composite material analyses, this work adopts the first-ply failure criterion by application of a polynomial function and the FE procedure. The laminates are modeled by the Reissner-Mindlin plate theory that accounts for moderate rotation. This is because shear effects are more pronounced in composite laminates whose transverse shear modulus is low relative to the Young's modulus. Failure loads are obtained for different laminate thicknesses, stacking sequences and aspect ratios and different failure criteria. The results show that predictions made from the maximum stress criterion are nearly the same as the other, except for those obtained by the Hill criterion.

10A435. Indentation-flexure and low-velocity impact damage in graphite epoxy laminates. - YS Kwon and BV Sankar *(Dept of Aerospace Eng Mech and Eng Sci, Univ of Florida, Gainesville FL 32611-2031)*. J Composite Tech Res 15(2) 101-111 (Sum 1993).

Static indentation-flexure and low-velocity impact tests were performed on quasi-isotropic and cross-ply graphite-epoxy composite laminates. The load-deflection relations in static tests and impact force history in impact tests were recorded. The damage was assessed by using ultrasonic C-scanning and photo-micrographic techniques. Some features of the static behavior were explained by simple analytical models. A good correlation existed between the load-deflection curves for static and impact loading. It was found that results from a few static indentation-flexure tests can be used to predict the impact force history and delamination radius in composite laminates due to low-velocity impact.

10A436. Interlaminar stresses around hole boundaries of composite laminates subjected to in-plane loading. - WJ Yen and C Hwu *(Inst of Aeronaut and Astronaut, Natl Cheng Kung Univ, Tainan, Taiwan 70101 ROC)*. Composite Struct 24(4) 299-310 (1993).

Due to the complex stress state near the curvilinear edge of composite laminates, 3D FE analysis is usually applied even if it is time consuming. In this paper, in order to save computer time and storage, an asymptotic analysis is employed to separate the 3D problem into two plane problems. One is an interior problem, the other is a boundary layer problem. The former is treated by classical lamination theory and is solved by a special BE, the latter is then solved by the FE developed for the generalized plane deformation problems. When the ratio of laminate thickness to hole diameter is small, the solutions for the laminates containing a circular hole are in good agreement with those obtained by the 3D FEM.

10A437. Sublaminate analysis method for predicting disbond and delamination loads in composite structures. - G Flanagan *(Grumman Aircraft Syst Div, MS B44-35, Bethpage NY 11714)*. J Reinforced Plastics Composites 12(8) 876-887 (Aug 1993).

A novel analysis method has been developed with the goal of providing accurate assessments of the forces that can delaminate composite laminates and bonded structures. The method uses interconnecting high-order plates to represent the cross section of a structural element. The plates can be both stacked and connected end-to-end. When stacked, the interfacial tractions generated between the plates can be calculated, providing a measure of the delamination stresses. The plate equations are solved exactly, thus giving accurate numerical results even in cases where the stress gradients are steep. The plate theory used incorporates a linear distribution through the thickness for the u, v, and w displacements. This set of assumed displacements makes the plate shear deformable, and allows stretching in the thickness direction. Consequently, both shearing and normal tractions can be computed at the interfaces between stacked plates.

See also the following:

10A579. Analysis of inelasticity effect due to damage on stress distributions in composite laminates
10A610. A 3D analysis of symmetric composite laminates with damage
10A614. Damage evolution and thermoelastic properties of composite laminates
10A617. Study of the opening displacement of transverse cracks in cross-ply laminates
10A641. Optimal design of a composite structure
10A872. Heat conduction across a semi-infinite interface in a layered plate

256J. MICROMECHANICS

10A438. Micromechanics as a basis of random elastic continuum approximations. - M Ostoja-Starzewski *(Dept of Mat Sci and Mech, Michigan State Univ, E Lansing MI 48824-1226)*. Probab Eng Mech 8(2) 107-114 (1993).

The problem of the determination of stochastic constitutive laws for input to continuum-type boundary value problems is analyzed from the standpoint of the micromechanics of polycrystals and matrix-inclusion composites. Passage to a sought-for random continuum is based on a scale dependent window playing the role of a Representative Volume Element (RVE). It turns out that an elastic microstructure with piecewise continuous realization of random tensor fields of stiffness cannot be uniquely approximated by a random field of stiffness with continuous realizations. Rather, two random continuum fields may be introduced to bound the material response from above and from below. As the size of the RVE relative to the crystal size increases to infinity, both fields converge to a deterministic continuum with a progressively decreasing strength of fluctuations. Since the RVE corresponds to a single FE cell not infinitely larger than the crystal size, two random fields are to be used to bound the solution of a given boundary value problem at a given scale of resolution. The method applies to a number of other elastic microstructures, and provides the basis for stochastic finite differences and elements. The latter point is illustrated by an example of a stochastic boundary value problem of a heterogeneous membrane.

See also the following:

10A411. Geometrical description of particle distributions in materials
10A582. Micromechanics approach for constucting locally averaged damage dependent constitutive equations in inelastic composites

256L. MACROSCOPIC CHARACTERIZATION

10A439. Effective elastic moduli of microcracked composite materials. - Y Huang, KX Hu, A Chandra *(Dept of Aerospace and Mech Eng, Univ of Arizona, Tucson AZ 85721)*. Int J Solids Struct 30(14) 1907-1918 (1993).

The self-consistent mechanics method has been widely used to estimate the macroscopic elastic moduli of solids containing microvoids and inclusions. Another method based on the crack energy release and potential energy balance has also been used to estimate the overall elastic moduli of a microcracked solid. It is shown here that these two approaches are equivalent for microcracked solids, thus one can take advantage of both methods to estimate the elastic moduli of inclusion-crack-matrix composites, ie, microcracked composite material. A solid containing spherical inclusions and randomly distributed penny-shaped cracks is then studied. The effective elastic moduli of a solid with spherical inclusions and parallel-distributed penny-shaped cracks are also studied. It is established that the effects of inclusions and microcracks on overall moduli are approximately decoupled for stiff inclusions, which are in most metal matrix composites. This conclusion is particularly useful since one may then obtain the moduli of composites by a simple two-step estimation. For compliant inclusions, including the limiting cases of voids, the decoupling does not hold.

10A440. Mechanical properties of non-crimped fabric-based composites. - PJ Hogg, A Ahmadnia, FJ Guild *(Queen Mary & Westfield Col, UK)*. Composites 24(5) 423-432 (Jul 1993).

The mechanical properties of composites prepared from two types of non-crimped fabric (NCF), namely biaxial, ± 45° and quadriaxial with a 0°, ± 45°, 90°, - 45° ply sequence, are examined as a function of fabric weight and compared with those of alternative composite forms. In general, the properties of NCF laminates decrease slightly as the areal weight of the fabric increases. Laminates produced from biaxial fabrics exhibit superior properties for a given volume fraction of reinforcement than do laminates produced using woven rovings or continuous fibre prepregs, while quadriaxial NCF laminates have equivalent properties to woven roving laminates at certain orientations but, unlike woven roving laminates, retain their properties when rotated through 45°. Biaxial NCFs loaded at 45° to the fibre and quadriaxial fabrics produce composites with superior properties to those predicted using FE and laminate analysis for idealized laminates based on the same results.

10A441. Mechanical properties of squeeze-cast zinc alloy matrix composites containing α-alumina fibres. - HX Zhu and SK Liu *(SW Jiatong Univ, Peoples Rep of China)*. Composites 24(5) 437-442 (Jul 1993).

α-Alumina fibre-reinforced ZA12 alloy matrix composites, with fibre volume fractions ranging from 7.5 to 30% were manufactured by squeeze casting. The alumina fibres were homogeneously distributed in the matrix and had a planar-random orientation. Mechanical properties of the composites such as hardness, tensile strength, Young's modulus, elongation and wear resistance were measured and the effect of fibre volume fraction on these properties was investigated. At room temperature the hardness, Young's modulus and wear resistance increased with increasing volume fraction of alumina fibres, but the other properties were inferior. At elevated temperature (above 80° C) the tensile strengths of the composites were higher than that of the matrix alloy.

10A442. Mechanical properties of triaxially braided composites: Experimental and analytical results. - JE Masters *(Lockheed Eng and Sci, NASA Langley Res Center, Mail Stop 188E, Hampton VA 23681)*, RL Foye *(Dept of Mech Eng, N Carolina A&T State Univ, Greensboro NC 27411)*, CM Pastore *(Dept of Textile Eng Chem and Sci, N Carolina State Univ, NCSU Box 8301, Greensboro NC 27695-8301)*, YA Gowayed *(Dept of Textile Eng, Auburn Univ, NCSU Box 8301, Auburn AL 36849)*. J Composite Tech Res 15(2) 112-122 (Sum 1993).

This paper investigates the unnotched tensile properties of 2D triaxial braid-reinforced composites from both an experimental and an analytical viewpoint. The materials are graphite fibers in an epoxy matrix. The unit cell structure of the triaxial braid was discussed with the assistance of computer analysis of the microgeometry. Photomicrographs of braid geometry were used to improve upon the computer graphics representations of unit cells. These unit cells were used to predict the elastic moduli with various degrees of sophistication. The simple and the complex analyses were generally in agreement, but none adequately matched the experimental results for all the braids.

10A443. Sensitivities and optimal design of hexagonal array fiber composites with respect to interphase properties. - SN Gulrajani and S Mukherjee *(Dept of Theor and Appl Mech, Cornell)*. Int J Solids Struct 30(15) 2009-2026 (1993).

The focus of this paper is the calculation of sensitivities of stresses at an interphase between a fiber and matrix, in a hexagonal cell of a fiber-reinforced composite, with respect to interphase stiffnesses, and the use of these sensitivities to carry out optimal design of the interphase stiffnesses. The interphase is modeled here as a spring layer. Sensitivities are of interest in the design of composites since interphase properties can substantially affect the mechanical and thermal behavior of the composite. The sensitivity calculations are carried out here by using the direct differentiation approach of the corresponding BEM formulation of the problem. Optimization calculations are carried out by coupling the standard and sensitivity analyses to an optimizer. The optimizer chosen here uses sequential quadratic programming to obtain the desired optimal values of interphase stiffnesses that minimize the possibility of failure of a composite under prescribed loading. Numerical results for sensitivities and optimization, for some illustrative examples, are presented in this paper.

10A444. Volume resistivity and mechanical properties of electrically conductive long fiber composites. - ME Weber and MR Kamal *(Polymer McGill, Dept of Chem Eng, McGill Univ, 3480 Univ St, Montreal PQ, H3A 2A7, Canada)*. J Reinforced Plastics Composites 12(8) 844-853 (Aug 1993).

Long, electrically conductive nickel-coated graphite fibers were employed to produce thermoplastic composites by compounding and processing with polypropylene resin. The fibers were blended into the resin in a Brabender mixer and the resulting composite was compression molded into square plaques. The fiber loading was varied from 2 to 20 weight percent. The effects of fiber loading on electrical and impact properties were studied and related to the composite microstructure. A device was constructed to measure the volume resistivity of the samples in two planes, longitudinal and latitudinal. A large initial density in resistivity occurs as fibers are added to the insulating matrix. Beyond some critical loading, the resistivity reaches a minimum and begins to level off. The resistivity is identical in the two perpendicular planes. Examination of the microstructure reveals that the fiber orientation is fairly random in the composite, which results in a uniform resistivity in two planes. Fiber attrition is more significant at low loadings where the mixing shear is greater. Impact tests show that the addition of the fiber results in an increase in sample stiffness, thereby reducing the force and energy needed to break the samples.

See also the following:

10A611. Analysis of composite shear walls with interface separation, friction and slip using BEM

256N. DYNAMIC BEHAVIOR

See the following:

10A91. Effect of thermal stresses on the vibration of composite cantilevered plates

10A92. Vibration of clamped moderately thick general cross-ply plates using a generalized Navier approach

256Q. STRUCTURAL APPLICATIONS

10A445. Comparison of eight variations of a higher-order theory for cylindrical shells. - RA Smith *(Flight Vehicles Branch, Weapons Flight Mech Div, Wright Lab, Elgin Air Force Base FL 32542)* and AN Palazotto *(Aeronaut and Astronaut Dept, Air Force IT, WPAFB)*. AIAA J 31(6) 1125-1132 (Jun 1993).

Eight variations of a geometrically nonlinear higher-order transverse shear deformation (HTSD) theory were developed for composite shells. Three attributes were varied to produce the eight variations. These attributes included: 1) the order of the thickness expansions used to approximate the shell shape factors, 2) the order of the assumed linear displacement field, and 3) the nonlinearity of transverse shear strain. Several cylindrical shell problems were investigated using a FE code with a 36-dof cylindrical shell element. MACSYMA, a symbolic manipulation code, was used to formulate the element independent stiffness arrays for each variation of the theory. When all nonlinear strain displacement terms for transverse shear were included for thin shallow isotropic cylindrical shells, the theory predicted a more flexible response during collapse. Higher-order thickness expansions had negligible effect on results. For deep shells nonlinearity was limited to in-plane strain-displacement relations. This quasinonlinear HTSD theory produced a more flexible response during collapse when the order of approximation of shell shape factor terms was increased.

10A446. Interlaminar stresses around a hole in symmetric cross-ply laminates under bending-torsion. - Chu-Cheng Ko and Chien-Chang Lin *(Inst of Appl Math, Natl Chung-Hsing Univ, Taichung, Taiwan 40227, ROC)*. AIAA J 31(6) 1118-1124 (Jun 1993).

An efficient approximate solution for calculating the complete state of stress around a circular hole in symmetric cross-ply laminates under a set of far-field bending and torsion is presented. This approach is based on the boundary-layer theory in conjunction with Lekhnitskii's solutions for anisotropic plates and the principle of minimum complementary energy. All of the boundary conditions around the hole edge of each ply and traction continuity at the ply interface are exactly satisfied. Numerical examples are compared with the NASTRAN FE solutions to demonstrate the efficiency and accuracy of the current method.

10A447. Performance enhancement of concrete through the use of waste injection molding pellets: A preliminary study of viability. - B Lennon, VM Karbhari, H Allen *(Center for Composite Mat and Dept of Civil Eng, Univ of Delaware, Newark DE 19716)*. J Thermoplastic Composite Mat 6 49-61 (Jan 1993).

The recycling of advanced polymers and composites is a major problem facing the composites industry due not only to problems related to the actual process itself but also to liability issues associated with reuse. This article presents the initial results of an ongoing investigation aimed at the reuse of waste pellets as aggregate in concrete to increase the compression strength and ductility of the resulting concrete. A variety of glass-filled materials, including nylon, polycarbonate, and polypropylene - as well as unreinforced polymers such as PET and PEEK - were used. Materials were substituted for traditional stone aggregate at a range of levels including complete replacement. Results demonstrate the viability of such use, and the article discusses implications in terms of future applications, as well as advances needed, in order to make this approach a reality.

10A448. Use of piezoelectric films in detecting and monitoring damage in composites. - SC Galea, WK Chiu, JJ Paul *(Defense Sci and Tech Org, Aeronaut Res Lab, Aircraft Struct and Mat Div, 506 Lorimer St, Fishermens Bend 3207, Victoria, Australia)*. J Intelligent Mat Syst Struct 4(3) 330-336 (Jul 1993).

The increasing emphasis over the past few years on intelligent material systems and structures has resulted in a significant research effort in the areas of embedded and bonded sensors and actuators. Of the many sensing materials available, piezoelectric sensors offer a number of advantages. The sensor output, proportional to changes in surface displacement over a large area, can be used to interpret variations in structural and material properties, ie, the compliance of the material. This type of sensor has also been used as an ultrasonic transducer. It offers the advantage of having a low structural impedance, thus giving an accurate measurement of the change in area, and consequently can only be used as an actuator on flexible structural systems. The aim of this article is to demonstrate the use of piezoelectric film sensors such as a structural integrity monitoring device for composite materials.

See also the following:

10A613. Bulging of cracked panel in extension due to unbalanced patching

10A674. Studies on metal matrix composite railroad wheels

256T. CERAMICS, REFRACTORIES, GLASSES

10T449. Fatigue behavior of glass ceramics under multiaxial stress states: Examination by diametral compression. - Kiyohiko Ikeda *(Dept of Mech Syst Eng, Miyazaki Univ, Gakuen Kibanadai, Miyazaki 889-21)*, Minoru Tamiaki *(Univ of Osaka, Gakuen-cho, Sakai 593)*, Yoshinobu Tanigawa *(Dept of Mech Syst Eng, Univ of Osaka, Gakuen-cho, Sakai 593)*, Hisashi Igaki *(Dept of Mech Eng, Osaka Sangyo Univ, Nakagaito, Daito 574)*. J Soc Mat Sci Japan 42(476) 496-501 (May 1993).

10A450. Heat transmission on the thermal shock test of ceramics. - Tadahiro Nishikawa, Tie Gao, Manabu Takatsu *(Dept of Mat Sci and Eng, Nagoya IT, Showa-ku, Nagoya 466)*. J Soc Mat Sci Japan 42(476) 507-511 (May 1993).

In order to apply the maximum thermal stress equation to water-quenching thermal shock tests of ceramics in practice, a novel method for evaluating the heat transmission behavior and measuring the effective heat transfer coefficient was proposed. Zirconia ceramic, whose heat conductivity does not change over a wide temperature range, was used for the study. In this experiment, the change of temperature at two different positions in the specimen was measured after water quenching. The dependences of heat transmission behavior on time and surface temperature were discussed. The present method made it possible to obtain the effective heat transfer coefficient data which clarify the relationship between the intrinsic properties of ceramics and the critical quenching temperature difference.

10A451. Interactions among cracks and rigid lines near a free surface. - Kai Xiong Hu and Abhijit Chandra *(Dept of Aerospace and Mech Eng, Univ of Arizona, Aero Bldg 16, Tucson AZ 85721)*. Int J Solids Struct 30(14) 1919-1937 (1993).

Cracks and rigid-line inclusions, or anticracks, are commonly observed in many engineering materials, such as intermetallics and ceramic composites. Interactions among these cracks and rigid lines can significantly affect the strength of these materials. Strength degradation due to finishing operations, such as grinding, also depend to a large extent on these interactions near a free surface and their associated surface and subsurface damage evolutions. Accordingly, modeling of interactions among general systems of cracks and rigid lines in the vicinity of a free surface, subject to general loading conditions, is the main thrust of this paper. An integral equation approach based on the fundamental solutions due to point loads and point dislocations in an elastic half space is utilized for this purpose. The integral equations are reduced to a system of linear equations consisting of the distributions of Burger's dislocation vectors and forces on the cracks and the anticracks, respectively. The proposed solution procedure also allows direct determination of the rigid-body rotations for the rigid lines. The results obtained from the present analysis are first verified against existing results for a single crack or rigid line near a free surface. The amplification and shielding effects on stress intensity factors due to interactions among various distributions of cracks and rigid lines are then investigated. Such interactions near a free surface play crucial roles in surface and subsurface damage evolutions during high-speed machining of ceramic materials.

10A452. Length effect of rods under three-point bending for determining the Weibull parameters of brittle materials. - SL Fok and J Smart *(Dept of Eng, Univ of Manchester, Manchester M13 9PL, UK)*. Probab Eng Mech 8(2) 67-73 (1993).

Brittle materials, such as ceramics, are commonly characterized using two parameters: one is a measure of the strength, the other a measure of the scatter. To determine these parameters three-point bending tests of circular rods are often used and the parameters determined using simple bending theory. However, the simple bending theory can be a poor representation of the stresses near the loading point particularly for small length:diameter ratio. To overcome the shortcomings of the simple theory, FE analyses have been performed for rods of varying length:diameter ratio and correction factors for the simple theory have been determined. These factors depend on both the length:depth ratio and the material property defining the scatter.

10T453. Present and future technology for ceramics. - Yuji Enomoto *(Mech Eng Lab, 1-2 Namiki Tsukuba-shi, Ibaraki 305, Japan)*. Japan J Trib 37(9) 1091-1100 (1992).

256V. PLASTICS, ELASTOMERS, RUBBERS

10A454. Overview on polymer composites for friction and wear application. - K Friedrich, Z Lu, AM Hager *(Inst for Composite Mat, Univ of Kaiserslautern, D-6750 Kaiserlautern, Germany)*. Theor Appl Fracture Mech 19(1) 1-11 (Jun 1993).

Composite materials are used more frequently as structural components that are required to sustain friction and wear loadings in service. Many of these composites consist of short fibers embedded in a metallic, polymeric or ceramic matrix. Others have a continuous fiber reinforced structure, arranged in the form of multidirectional laminates or woven fabrics. This overview delves on polymer matrix composites and describes the principal microstructural details of short fiber and thermoplastic matrix composites in addition to their friction and wear properties as a function of both microstructural composition and external testing conditions. Special attention is focussed on the effects of different polymer matrices, fiber reinforcements, and additional internal lubricants on the coefficient of friction and the specific wear rate of these materials when sliding against hard steel counterparts.

10A455. Stiffness characteristics of twisted cords for cord-rubber composites. - RMV Pidaparti *(Dept of Mech Eng, Purdue Univ, Indianapolis IN 46202)*. Composite Struct 24(4) 291-298 (1993).

A FE model is presented to predict the stiffness characteristics of twisted cords by treating them as structures and considering the stiffness couplings due to extension-bending-torsional deformations. The axial, bending, and torsional stiffnesses are calculated for both the aramid-cord and steel-cord, and compared to an approximate expression with good agreement where applicable. To illustrate the stiffness behavior, all three stiffnesses are presented with variations in the number of twists per unit length, the surrounding rubber modulus and the thickness. The stiffness couplings among the extension, bending, and twisting deformations are presented for aramid-cords with varying number of twists per unit length and rubber thickness. The results illustrate that stiffness characteristics are strongly dependent upon the number of twists per unit length, type of cord, surrounding rubber layer thickness, and modulus. The stiffness couplings presented illustrate the mechanisms of load transfer, which are important for understanding failure mechanisms of cords, and cord-rubber composites.

10A456. Vibration welding of polyamide 66. - H Potente, M Uebbing, E Lewandowski *(FB 10-Kunststofftechnologie, Univ GH Paderborn, Pohlweg 47-49, 4749 Paderborn, Germany)*. J Thermoplastic Composite Mat 6 2-17 (Jan 1993).

Working on the basis of a parameter study of standard PA 66 material, comparative investigations were conducted into material modifications using heat stabilizers, glass fibers and minerals. The evaluation criterion applied for the weld quality was the short-time welding factor, this being the quotient of the weld strength and the strength of the base material. With standard material, a weld strength almost equivalent to the strength of the base material was attained. With heat-stabilized and mineral-filled material, the welding factor fell to fs = 0.9. Glass-fiber-reinforced PA achieved a maximum value of fs = 0.58, which, in terms of absolute value, corresponds approximately to the base material strength of standard polyamide. Microtome section investigations show how the different weld results come about.

See also the following:

10A332. Prediction of the service life of pneumatic rubber-cord elastic elements subjected to complex loading

256Y. COMPUTATIONAL TECHNIQUES

10A457. Analytical formulae for calculating stresses in unidirectional cross-ply unbalanced laminates. - Zhu Caisheng *(Dept of Mech Eng, Monash Univ, Clayton, Vic 3168, Australia)*, M Heller *(Aeronaut Res Labs, Dept of Defence, Fishermens Bend, Vic 3207, Australia)*, YC Lam *(Dept of Mech Eng, Monash Univ, Clayton, Vic 3168, Australia)*. Composite Struct 24(4) 333-343 (1993).

A multilayer theory has been developed for unidirectional-cross-ply unbalanced laminates subjected to surface shear tractions, using the assumption of plane strain. The analytical solution for the stress field in the laminate is obtained and it is shown that the stresses in each layer are in good agreement with the results of a 3D FE analysis. Approximate formulae for the analytical stresses are also derived for a laminate subjected to an offset distributed force at one end. The accuracy of this solution is shown by comparison with a 3D FE analysis.

10A458. CDI: Linking material property databases to analysis codes. - WJ Rasdorf, LK Spainhour *(Dept of Civil Eng, N Carolina State Univ, Raleigh NC 27695)*, EM Patton, BP Burns *(Mech and Struct Branch, Army Res Lab, Aberdeen Proving Grounds, Aberdeen MD 21005)*. Adv Eng Software 16(3) 145-152 (1993).

Integration among programs designed to solve complex engineering problems is often lacking, and this is particularly a problem in the area of thick composite material analysis, and design where a large volume of input must be provided. Another problem is the lack of an archival repository in which to store input information in a generic format. To address these problems, we have developed a prototype of a FE material property reprocessing system, called the composites database interface (CDI). In this computer-aided analysis system, a materials database is integrated with several software components, including commercially available FE analysis (FEA) programs and preprocessors, and tools for manipulating and using composite materials data, resulting in the transfer of 2D and 3D composite materials property data into an FEA program. This paper presents the capabilities of this system, discusses the overall system integration through R:BASE, and provides a civil engineering application involving the design of a large cylindrical tank to illustrate the execution of the CDI system's various components. The paper ends by discussing the current status of this computer-aided analysis system.

256Z. EXPERIMENTAL TECHNIQUES

10A459. Review of multiaxial-biaxial loading tests for composite materials. - AS Chen and FL Matthews *(Imperial Col, UK)*. Composites 24(5) 395-406 (Jul 1993).

Multiaxial-biaxial loading tests of fibre-reinforced polymer-matrix composite materials are reviewed, and results of these experimental investigations under both monotonic and cyclic loadings are discussed. It is noted that composite materials could exhibit complicated behavior in the biaxial loading conditions which often exist in engineering practice. The importance of biaxial loading tests of composites is indicated by this assessment.

See also the following:

10A450. Heat transmission on the thermal shock test of ceramics

10A635. Ultrasonic backscattering using digitized full-waveform scanning technique

258. Cables, ropes, beams, etc

10A460. Axisymmetric problems of a partially embedded rod with radial deformation. - RYS Pak and AT Gobert *(Dept of Civil, Env and Architec Eng, Univ of Colorado, Boulder CO 80309-0428)*. Int J Solids Struct 30(13) 1745-1759 (1993).

A new mathematical formulation is presented for the analysis of a partially embedded rod under torsionless axisymmetric loadings. With an account of both the axial and radial compatibilities between the rod and the embedding medium through the use of a higher-order rod theory, the 3D load-transfer problem is reduced to a pair of Fredholm integral equations of the second kind whose solutions are computed. By virtue of the present formulation, a variety of physical loading-boundary conditions which were inhibited in past treatments can be evaluated. A comprehensive set of numerical results appropriate to different axial loading conditions, material parameters, and geometric configurations for the problem are provided as illustrations.

10A461. Viscoelastic response of a strand. - TA Conway *(Dept of Mech Eng, Univ of Akron, Akron OH 44325-3903)* and GA Costello *(Dept of Theor and Appl Mech, Univ of Illinois, Urbana IL 61801)*. J Appl Mech 60(2) 534-540 (Jun 1993).

A method is presented in which the axial viscoelastic response of a multiple filament strand, constrained by a no-end rotation boundary condition, may be predicted. This method is an initial attempt to describe the time-dependent response of the multilayer strand by incorporating the stress relaxation data for a linearly viscoelastic construction material. Specifically, a strand consisting of a core filament, six filaments in the second layer, and twelve filaments in the outer layer is analyzed. This analysis could, however, include any number of layers of filaments where each layer has a concentric helix radius. The particular material used in this paper is polymethyl methacrylate (PMMA). The stress relaxation method for PMMA is modeled analytically using the Schapery collocation method which determines the constant coefficient values for the elements of a Wiechert response model. Since this is a first approximation model, the approach is limited to linear viscoelasticity.

10A462. Multiply loaded Timoshenko beam on a stressed orthotropic half-plane via a thin elastic layer. - H Bjarnehed *(Div of Solid Mech, Chalmers Univ of Tech, S-412 96 Goteborg, Sweden).* J Appl Mech 60(2) 541-547 (Jun 1993).

The problem of bonded contact between a uniform finite Timoshenko beam and an orthotropic half-plane via a thin elastic layer is considered in this paper. The beam is loaded by distributions of normal and tangential forces, and a uniaxial stress load is applied to the half-plane. The Timoshenko beam theory is extended in such a way that the tangential load is included when the shear contribution to the beam central line deflection is calculated. The layer is formulated as a generalized Winkler cushion including also shear stresses and strains. Governing singular integral equations are stated and numerically solved for the unknown interface stresses. A comparison with a corresponding FE-model is also performed.

10A463. Flexural behavior of fixed-ended channel section columns. - KJR Rasmussen and GJ Hancock *(Sch of Civil and Mining Eng, Univ of Sydney, Sydney, Australia).* Thin-Walled Struct 17(1) 45-63 (1993).

The paper presents a study of the behavior of thin-walled channel sections compressed between fixed ends. The paper emphasises the differences between the behavior of fixed-ended and pin-ended channel sections, arising mainly from the fact that the local buckling induces bending of pin-ended channel sections but not of fixed-ended channel sections. As a result of the different effects of local buckling, the strength of a fixed-ended channel section column exceeds that of a pin-ended column of the same effective length. The increase in strength is quantified for a particular channel section, and is studied through the transition from pinned to fixed-end support by analyzing columns which are elastically restrained against rotations at the ends. The paper also investigates the imperfection sensitivity and post-ultimate behavior of fixed-ended channel section columns. It is shown that fixed-ended columns are less sensitive to local imperfections and that they exhibit greater post-ultimate ductility than pin-ended columns. The study is confined to columns whose overall buckling mode is the flexural mode.

See also the following:

10A485. Prop-imperfection subsea pipeline buckling

10A489. Thin-walled cold-formed sections subjected to compressive loading

10A549. Stick-slip in the thin film peel test I. The 90° peel test

260. Plates, shells, membranes, etc

260A. GENERAL THEORY

See the following:

10A623. Crack propagation in cylindrical shells

260C. PLATES (FLEXURE AND TORSION)

10A464. Elastic wrinkling of a tensioned circular plate using von Karman plate theory. - GG Adams *(Dept of Mech Eng, NE Univ, Boston MA 02115).* J Appl Mech 60(2) 520-525 (Jun 1993).

A circular elastic plate, with a uniform tension field applied at its outer edge, is acted upon by a centrally applied transverse force. As the force is increased, the tension state as determined from von Karman plate theory, changes. In particular for sufficiently large values of the transverse force or displacement, the plate can develop a compressive circumferential membrane stress. When this compressive stress becomes sufficiently large, wrinkling can result. The corresponding value of the transverse displacement is determined by investigating an eigenvalue problem in which wrinkling is indicated by the vanishing of the lowest eigenvalue. The results are the values of the central transverse deflection which induces wrinkling for a range of in-plane tensions and are sensitive to the in-plane boundary support conditions at the outer edge.

10A465. Stress distribution in an elastic perfectly plastic plate subjected to corrosive environmental loads. - A Kadic-Galeb and RC Batra *(Dept of Mech and Aerospace Eng and Eng Mech, Univ of Missouri, Rolla MO 65401-0249).* Int J Eng Sci 31(9) 1301-1307 (Sep 1993).

We analyze deformations of an isotropic elastic-perfectly plastic plate subjected to environmental effects such as the corrosive forces exerted by the surrounding medium. It is found that for the bounding surfaces of the plate to deform plastically, the corrosion process must propagate to a point whose distance from the outer bounding surface exceeds one third the half-thickness of the plate, and for the central unaffected material to also deform plastically the half-thickness of the corroded layer must exceed five eighths the half-thickness of the plate.

See also the following:

10A398. Hardening rule between stress resultants and generalized plastic strains for thin plates of power-law hardening materials

10A884. Thermal effects in Mindlin-type plates

260D. SHELLS (MEMBRANE THEORY)

10A466. Instability of a biaxially stressed thin film on a substrate due to material diffusion over its free surface. - LB Freund and F Jonsdottir *(Div of Eng, Brown Univ, Providence RI 02912).* J Mech Phys Solids 41(7) 1245-1264 (Jul 1993).

The configuration of an elastically strained thin film bonded to a relatively thick elastic substrate over a plane interface is considered. The free energy of the system is taken to be the surface energy of the free surface, which is initially flat, and the elastic strain energy. It is assumed that the film material can change the shape of its free surface by means of mass diffusion along the surface, and that this mass transport occurs coherently. As a result of this diffusion process, the free energy of the system changes due to a change in surface shape and due to a change in the elastic energy. If the change in free energy as the surface shape departs from planar is positive, then this change will tend to occur spontaneously and the flat shape is unstable. The stability of a biaxially stressed thin film due to material diffusion over its surface is considered here under both 2- and 3D conditions. The stability condition is derived in the form of a difference between two positive definite quantities, one associated with surface energy and the other associated with strain energy, and the sign of this difference depends on the relative stiffnesses of the materials, the thickness of the film, the surface energy of the film material, and the initial elastic stress in the film. It is demonstrated that the configuration with a flat free surface is unstable under sinusoidal perturbations in the shape of the surface for any combination of parameters, provided that the wavelength of the perturbation is larger than some critical value. Numerical results are presented for the critical value as a function of film thickness for several values of the ratio of elastic stiffnesses of the mterials.

260E. SHELLS (BENDING THEORY)

10A467. Energy-minimizing deformations of elastic sheets with bending stiffness. - MG Hilgers and AC Pipkin *(Div of Appl Math, Brown Univ, Providence RI 02912).* J Elast 31(2) 125-139 (May 1993).

Necessary conditions for energy-minimizing deformations are derived for a theory of sheets in which the strain energy function depends on the second derivatives of the deformation as well as its first derivatives. All of these conditions are extensions of well-known necessary conditions in classical calculus of variations. The interpretation of some of these conditions as material stability conditions is explained.

10A468. FE analysis of multilayered shells of revolution. - MA Rao *(Dept of Mech Eng, Andhra Univ, Visakhapatnam, India),* RV Dukkipati *(NRC, Ottawa, Canada),* M Tummala *(Dept of Mech Eng, Concordia Univ, 1455 de Maisonneuve Blvd, W Montreal, PQ, Canada).* Comput Struct 47(2) 253-258 (Apr 1993).

A FE formulation for the static and dynamic analysis of multilayered shells of revolution is developed. The basis of this formulation is a superparametric curved element having four dof per node including normal rotation. Element stiffness, mass and load matrices are derived for axisymmetric analysis of laminated shells. Static analysis of a multilayered pressure vessel, which has 27 layers in its thickness and a hemispherical cover at one end, is carried out using the formulation and the program developed. Results obtained for the static analysis of the pressure vessel are compared with results obtained by the standard code practices. Natural frequencies of shells of revolution corresponding to axisymmetric modes of vibration are presented.

10A469. Thin shells with finite rotations formulated in biot stresses: Theory and FE formulation. - P Wriggers *(Inst Mech, Tech Hochsch Hochschulstr 1, 6100 Darmstadt, Germany)* and F Gruttmann *(Inst Baumech und Numer Mech, Univ Hannover, Germany).* Int J Numer Methods Eng 36(12) 2049-2071 (30 Jun 1993).

A bending theory for thin shells undergoing finite rotations is presented, and its associated FE model is described. The kinematic assumption is based on a shear elastic Reissner-Mindlin theory. The starting point for the derivation of the strain measures are the resultant equilibrium equations and the associated principle of virtual work. Within this formulation the polar decomposition of the shell material deformation gradient leads to symmetric strain measures. The associated work-conjugate stress resultants and stress couples are integrals of the Biot stress tensor. This tensor is invariant with respect to rigid body motions and, therefore, appropriate for the formulation of constitutive equations. Finite rotations are introduced via Eulerian angles.

See also the following:

10A445. Comparison of eight variations of a higher-order theory for cylindrical shells

260F. ANISOTROPIC MEMBRANES, PLATES, SHELLS

10A470. Axisymmetric deformation of varying thickness composite cylindrical shell with various end conditions. - BSK Sundarasivarao and N Ganesan *(Machine Dyn Lab, Dept of Appl Mech, Indian IT, Madras 600 036, India).* Composite Struct 24(4) 345-352 (1993).

A varying thickness composite cylindrical shell subjected to axisymmetric deformation has been analyzed by the FE displacement method. The end conditions considered are clamped-clamped, clamped-free, simply sup simply supported. It is shown that, by properly selecting the thickness variation of the shell wall, both stresses and deflections can be reduced considerably in most cases.

10A471. Differential quadrature for static and free vibration analyses of anisotropic plates. - CW Bert *(Sch of Aerospace and Mech Eng, Univ of Oklahoma, 865 Asp Ave Rm 212, Norman OK 73019)*, Xinwei Wang *(Aircraft Eng Dept, Nanjing Aeronaut Inst, Nanjing, Peoples Rep of China)*, AG Striz *(Sch of Aerospace and Mech Eng, Univ of Oklahoma, 865 Asp Ave Rm 212, Norman OK 73019)*. Int J Solids Struct 30(13) 1737-1744 (1993).

The differential quadrature method is used to analyze the deflection, buckling, and free vibration behavior of anisotropic rectangular plates under various boundary conditions. The roots of Chebyshev polynomials are used to obtain grid-point locations and a new approach is used to apply boundary conditions. Results compare very well with existing numerical data, and less computational effort is required for the problems considered.

10A472. Refined 2D theory of anisotropic plates. - ME Fares *(Math Dept, Fac of Sci, Mansoura Univ, Egypt)*. Mech Res Commun 20(4) 319-327 (Jul-Aug 1993).

The classical theory of plates, in which it is assumed that normals to the midsurface before deformation remain straight and normal to the surface after deformation, overestimates natural frequencies and underpredicts deflections. These errors in deflections, stresses, natural frequencies, and buckling loads are even higher for plates with large ratio of thickness to side, particularly at high frequencies. The plate theories due to Reissner and Mindlin are improvements of the classical plate theory in that they include the effect of transverse shear deformation. Many refined shear deformation theories, in which the assumed displacement field is expanded in powers of the thickness coordinate, are available in the literature. These higher-order theories are cumbersome and computationally more demanding, because, with each additional power of the thickness coordinate, an additional dependent unknown is introduced into the theory. Further, these theories require an arbitrary correction to the transverse shear stiffnesses, and the transverse shear stresses do not satisfy the conditions on the top and bottom surfaces of the plate. Reddy suggested a consistent higher-order plate theory which not only accounts for the transverse shear deformation but also satisfies the zero transverse shear stress conditions on the plate surface and does not require shear correction factors. Because of the simplifications made in Reddy formulation, it is inadequate for the analysis of anisotropic plates subjected to a surface traction field with non-zero tangential components, and for anisotropic plate problems which require the inclusion of the effects of transverse normal strain and stress. The present formulation deals with a generalization of the shear deformation theory. The theory includes the effects of transverse normal strain as well as the effect of transverse shear deformation. Hamilton's mixed variational principle is used to derive the equation of motion and constitutive equations of an anisotropic plate subjected to a surface traction field with tangential and normal components. Therefore, these equations are adequate for the analysis of anisotropic plate problems with general surface conditions for example contact problems involving anisotropic plates with surface constrained. The advantages of applying this theory to the free vibration problems of anisotropic rectangular plates is examined.

260G. STIFFENED AND SANDWICH PLATES AND SHELLS

10A473. Bending analysis of bimodular laminates using a higher-order plate theory with the FE technique. - Yi-Ping Tseng and Kung-Pyng Bai *(Dept of Civil Eng, Tamkang Univ, Taiwan 25137, ROC)*. Comput Struct 47(3) 487-494 (3 May 1993).

The higher-order plate theory is adopted in the FEM to analyze composite plates laminated of orthotropic bimodular materials. The transverse shear deformation can be effectively evaluated where the correction coefficient is not required. The maximum deflections and neutral surface locations of several benchmark problems are determined. The accuracy of the formulation is then established by comparing the numerical results with the analytical solutions.

10A474. FE study of the transverse shear in honeycomb cores. - M Grediac *(Dept Mec et Mat, Ecole Natl Superieure des Mines, 158, cours Fauriel, 42023 St-Etienne Cedex 2, France)*. Int J Solids Struct 30(13) 1777-1788 (1993).

Knowledge of the transverse mechanical properties of honeycomb cores is essential for the design of sandwich panels. This paper deals with the calculation fof the transverse shear moduli of a honeycomb sandwich panel by making a FE study of a representative unit cell. Stress contours inside the honeycomb are also provided. Three cell geometries are studied and the influence of the thickness on the shear modulus and on the homogeneity of the shear stress field is investigated.

10A475. Structural analysis and design of sandwich panels with cold-formed steel facings. - Ken P Chong *(1211 Forestwood Dr, McLean VA 22101)* and JA Hartsock *(619 Sater La, Edmonds WA 98020)*. Thin-Walled Struct 16(1-4) 199-218 (1993).

Superior structural efficiency, ease of erection, mass-production capabilities and thermal-insulation qualities are making sandwich panels with flat or thin-walled cold-formed steel facings and rigid foamed insulating core increasingly popular as enclosures for system buildings. In this paper, the structural behavior – including flexural stresses, deflections, vibration and thermal stresses – is presented, summarizing more than two decades of research. Methods used are analytical (boundary-value approaches), numerical (finite-strip, finite-layer, finite-prism approaches) and experimental (full-scale testing). Key equations are formulated and results by different methods are compared. Design guidelines are also suggested.

10A476. Tests on intermediately stiffened plate elements and beam compression elements. - KH Hoon *(Sch of Mech and Prod Eng, Nanyang Tech Univ, Nanyang Ave, Singapore 2263)*, J Rhodes *(Div of Mech of Mat, Univ of Strathclyde, UK)*, LK Seah *(Sch of Mech and Prod Eng, Nanyang Tech Univ, Nanyang Ave, Singapore 2263)*. Thin-Walled Struct 16(1-4) 111-143 (1993).

This paper describes an experimental investigation into the behavior of cold-formed steel intermediately stiffened plates which are subject to pure compression and cold-formed beams with intermediately stiffened compression elements which are subject to bending. Each plate or beam has a central intermediate stiffener. The investigation is concerned with the performance of the intermediately stiffened elements with different degrees of rigidity provided by the stiffener. The ultimate loads are compared with the predictions of BS 5950 Part 5 Code and the first Draft Eurocode 3.

See also the following:

10A672. Simplified method for ultimate load prediction of all-steel sandwich panels

260I. THICK PLATES AND SHELLS

10A477. Correct asymptotic theories for the axisymmetric deformation of thin and moderately thick cylindrical shells. - RD Gregory *(Dept of Math, Univ of Manchester, Manchester M13 9PL, UK)* and FYM Wan *(Dept of Appl Math, Univ of Washington, FS-20, Seattle WA 98195)*. Int J Solids Struct 30(14) 1957-1981 (1993).

A refined shell theory is formulated for the elastostatics of long, moderately thick cylindrical shells in axisymmetric deformation. This theory corresponds to a two-term outer asymptotic expansion of the exact solution for small values of the dimensionless shell thickness parameter. The complexity of the known exact solution for the 3D elasticity problem has stimulated an interest in thin and thick shell theories to provide accurate approximate solutions in the shell interior without any reference (or matching) to the inner asymptotic solution. The principal difficulty in developing a shell theory lies in the determination of an appropriate set of 2D boundary conditions for the shell solution from the prescribed edge data of the 3D theory. The derivations of boundary conditions for the thin shell theory and the refined shell theory constitute a main contribution of this paper. Correct boundary conditions obtained for the first time include (i) displacement edge conditions for thin shell theory, and (ii) stress and two types of mixed edge conditions for the refined shell theory. Several applications of the refined theory are given to show that corrections to the thin shell solution can be important.

260K. ROTATING DISCS, BLADES, AND SHELLS

See the following:

10A506. Stability of spinning shear-deformable laminated composite plates

260Y. COMPUTATIONAL TECHNIQUES

10A478. Analysis and shape optimization of variable thickness prismatic folded plates and curved shells Part 1. Finite strip formulation. - E Hinton and NVR Rao *(Dept of Civil Eng, Univ Col of Swansea, Singleton Park, Swansea SA2 8PP, UK)*. Thin-Walled Struct 17(2) 81-111 (1993).

This paper deals with the linear elastic analysis of prismatic folded plate and shell structures supported on diaphragms at two opposite edges with the other two edges arbitrarily restrained. The analysis is carried out using curved, variable thickness, Mindlin-Reissner finite strips. The theoretical formulation is presented for a family of C(O) strips and the accuracy and relative performance of the strips are examined for curved situations. Some variable thickness and elastically supported plates are considered and the interesting phenomenon of the occurence of boundary layers in the twisting moments and shear forces is highlighted for a common boundary condition. Other examples analyzed include box girders and cylindrical shells. In all cases transverse shear deformation effects are included and the contributions to the strain energy from membrane, bending and transverse shear behavior noted. In a companion paper these accurate and inexpensive finite strips are used for structural shape optimization.

10A479. Elimination of self-straining in four-noded plate elements for large deflection analysis. - AK Soh and CK Soh *(Nanyang Tech Univ, Nanyang Ave, Singapore 2263)*. Comput Struct 47(2) 341-342 (Apr 1993).

A method has been proposed to solve the self-straining problem of four-noded plate elements by analyzing large deflection problems. The results obtained by the proposed method for a test example are found to be in good agreement with those of the exact solution.

10A480. Error analysis of FE results on plates with nonuniform grids. - R Sistla *(Anal Services and Mat, Hampton VA 23666)*. AIAA J 31(6) 1075-1076 (Jun 1993).

Discrete Dirac delta functions in 2D and the governing plate differential equations are used to produce continuous approximations from discrete FE data on nonuniform grids. The continuous approximation can be differentiated to compute continuous stresses and moments at any point in the plate and, when substituted in the differential equations, provides a residual error. The paper presents application of examples of the procedure and studies the use of the "smoothed" solution in a Zienkiewicz-Zhu error estimator to assess the performance of the present analysis. In an example involving the linear response of a clamped square plate under uniform transverse load, the present procedure dramatically corrected and smoothed the discrete FE results.

10A481. Research developments in analyses of plates and shells. - KM Liew *(Div of Appl Mech, Sch of Mech and Prod Eng, Nanyang Tech Univ, Nanyang Ave, Singapore)*, S Kitipornchai *(Dept of Civil Eng, Univ of Queensland, St Lucia, Australia)*, CM Wang *(Dept of Civil Eng, Natl Univ, Kent Ridge 0511, Singapore)*. J Construct Steel Res 26(2-3) 231-248 (1993).

The results presented in this paper are based on research collaborations between the three institutions, namely: (1) Nanyang Technological University, (2) The University of Queensland and (3) National University of Singapore. A software code named SEPSA, an acronym for super element for plate and shell analysis, has been developed. The software is applied to solve bending, buckling and vibration problems. The formulations and methods of analysis are briefly discussed. Several advantages of the present method over other approximate discretization methods are also addressed. To demonstrate the capability of SEPSA, some plate and shell solutions are presented.

10A482. Single Fourier series solutions for rectangular plates under in-plane forces, with particular reference to the basic problem of colinear compression Part 2. Stress distribution. - N Tahan *(SLP Eng London, Boundary House, Cricketfield Rd, Uxbridge, Middlesex, UK)*, MN Pavlovic *(Dept of Civil Eng, Imperial Col of Sci Tech and Med, London SW7 2BU, UK)*, MD Kotsovos *(Fac of Civil Eng, Natl Tech Univ of Athens, 42 Patission St, Athens, Greece)*. Thin-Walled Struct 17(1) 1-26 (1993).

In this, the second paper of a two-part report on colinearly compressed rectangular plates, a study of the mechanical aspects of the problem is conducted in order to obtain a reasonably general picture of the stress distribution as the relevant geometric and load parameters are varied. Special emphasis is placed on the degree of error inherent in the approximate single Fourier series scheme, and on what constitutes a "long" plate for the sort of systems in question. Finally, a possible practical implication for estimating the tensile strength of brittle materials through compression testing is suggested.

10A483. Two generalized conforming plate elements based on semiLoof constraints. - Zhifei Long *(Dept of Civil Eng, N Jiaotong Univ, Beijing 100044, Peoples Rep of China)*. Comput Struct 47(2) 299-304 (Apr 1993).

In this paper, the merits of both the generalized conforming element and the semiLoof element are utilized to establish nine-DOF triangular and 12-DOF rectangular thin-plate bending elements. The element DOFs are defined with the conventional displacements at corner nodes and the semiLoof constraints are used in the formulation. By using the concept of a generalized conforming element, these elements can pass Irons' patch test and accurate results are obtained with a much lower computational effort.

262. Structural stability (buckling, postbuckling)

262B. NONLINEAR AND FINITE DEFORMATION THEORY

10A484. Finite strip method for the elastic-plastic large displacement analysis of thin-walled and cold-formed steel sections. - PW Key and GJ Hancock *(Centre for Adv Struct Eng, Sch of Civil and Mining Eng, Univ of Sydney, NSW 2006, Australia)*. Thin-Walled Struct 16(1-4) 3-29 (1993).

A large deflection elastic-plastic analysis has been developed using the finite strip method of structural analysis to determine the nonlinear local buckling behavior of thin walled and cold-formed sections in compression. The analysis accounts for plate geometric imperfections, the variation of yield stress around a section, the stress-strain characteristics of the material forming the section and complex patterns of residual stress produced by the cold-forming process. The analysis is verified against reliable solutions for the nonlinear buckling behavior of plates and plate assemblies in axial compression and nonlinear overall buckling behavior of a strut. The analysis is further compared with the results of plates with a rounded stress-strain curve typical of cold-formed steel and aluminium.

262D. IMPERFECTION SENSITIVITY

10A485. Prop-imperfection subsea pipeline buckling. - N Taylor and Vinh Tran *(Sch of Construct, Sheffield City Polytech, Pond St, Sheffield S1 1WB, UK)*. Marine Struct 6(4) 325-358 (1993).

In-service buckling of subsea pipelines can occur due to the introduction of axial compressive forces caused by the constrained expansions set up by thermal and internal pressure actions. Proposed herein is a mathematical model relating to a pipeline, the otherwise horizontal and straight idealized lie of which is interrupted by an encounter with an isolated prop or point irregularity. The overbend produced can serve, in the presence of enhanced topologies involving trenching, burial, discrete or continuous, and fixed anchor points, to trigger vertical or upheaval buckling of the pipeline under in-service conditions. The results of a series of case studies are contrasted with data appertaining to alternative models available in the literature: experimental support is additionally noted. By questioning the implicit stress-free-when-straight assumption present in these alternative models, it is considered that a consistent, imperfection-prone isolated prop formulation is hereby provided, suitable for design application.

262E. COLUMNS AND BEAMS

10A486. Research on elastic buckling of columns, beams and plates: Focussing on formulas and design charts. - CM Wang *(Dept of Civil Eng, Natl Univ, Kent Ridge, 0511 Singapore)*, S Kitipornchai *(Dept of Civil Eng, Univ of Queensland, Queensland 4072, Australia)*, KM Liew *(Div of Appl Mech, Sch of Mech and Prod Eng, Nanyang Tech Univ, Nanyang Ave, Singapore)*. J Construct Steel Res 26(2-3) 211-230 (1993).

Although there are many numerical methods which may be used to evaluate critical elastic design parameters accurately, designers still prefer to sacrifice accuracy for simplicity. Approximate formulas or design charts from handbooks and standard texts are used, or conservative assumptions are made to simplify the problems so as to justify their use. Until powerful, user-friendly and inexpensive software becomes readily available to designers, approximate formulas and design charts continue to be used. In recent years, collaborative work between the authors and their research associates has yielded a number of approximate buckling formulas and design charts for critical loads for columns, beams and plates. A review of these research investigations is presented herein, together with some of the newly developed buckling formulas and design charts.

10A487. Static solutions of the Leipholz problem. - W Dmitriyuk *(49a Moshe Sharet St, Kiryat Haim 26260, Israel)*. Int J Solids Struct 30(15) 1997-2008 (1993).

If the external loads on a bar remain in the original direction after buckling, the character of the problem is conservative. When these loads are tangentially-directed the problem is non-conservative and in this case the critical load must be calculated by the dynamic and by the static adjoint method. In this paper the critical buckling load of the strut which is built in at the bottom and compressed by a distributed tangential load is calculated by the static adjoint method.

10A488. Theoretical investigation of the column behavior of cold-formed square hollow sections. - PW Key and GJ Hancock *(Centre for Adv Struct Eng, Sch of Civil and Mining Eng, Univ of Sydney, NSW 2006, Australia)*. Thin-Walled Struct 16(1-4) 31-64 (1993).

An experimental program investigating the column behavior of four sizes of square hollow section was undertaken at the Univerity of Sydney using Australian produced cold-formed square hollow sections. Stub and pin-ended column tests were performed and detailed measurements of the yield stress and residual stress taken around the sections. A large deflection elastic-plastic finite strip analysis including the measured distributions of yield stress and residual stress is used to investigate the behavior of the stub and pin-ended columns. In particular, the influence of the measured through thickness residual stress components on the ultimate load and behavior of the square hollow section columns is demonstrated. The analysis accounts for plate geometric imperfections, the variation of yield stress around a section, the stress-strain characteristics of the material forming the section and the highly complex patterns of residual stress produced by the cold-forming process. Comparison of the analytical results with the test results is provided.

10A489. Thin-walled cold-formed sections subjected to compressive loading. - J Loughlan *(Col of Aeronaut, Cranfield IT, Bedfordshire, MK43 0AL, UK)*. Thin-Walled Struct 16(1-4) 65-109 (1993).

The weakening effects of local buckling on the compressive load carrying capability of thin-walled cold-formed sections is examined and discussed. Theoretical results are presented for the pin-ended support condition and a study is made of the local buckling and overall bending interaction behavior of compression members with different cross-sectional shapes. It is shown that singly symmetric plain channel sections exhibit considerably different interactive equilibrium characteristics to those of I-sections for which the shear centre and section centroid are coincident. The theoretical results given have been obtained through the solution of a differential equation which governs, approximately, the overall bending behavior of a locally buckled compression member. Both local and overall imperfections are considered in the theoretical approach and it is shown that the effect of these is to reduce the ultimate compressive carrying capacity of cold-formed sections. An experimental investigation of the behavior of concentrically loaded pin-ended I-section struts and columns is reported and the findings from this are compared with theoretical predictions. The theoretical predictions of load-deflection equilibrium behavior and stress variations with load are shown to be in good agreement with those obtained from test. The provisions made in the UK Code of Practice and the American Specification pertaining to the design of cold-formed compression members are briefly outlined and compared. It is shown that with regard to I-section struts and columns the American design procedure gives, in general, more conservative estimates of collapse.

10A490. Ultimate strength design of biaxially loaded steel box beam-columns. - NE Shanmugam, JY Richard Liew, SL Lee *(Dept of Civil Eng, Natl Univ, 10 Kent Ridge Crescent, Singapore 0511)*. J Construct Steel Res 26(2-3) 99-123 (1993).

This paper is concerned with the analysis and design of box beam-columns subjected to axial load applied at biaxial eccentricities. A spread-of-plasticity method to predict the ultimate strength of box beam-columns of compact cross-sections is proposed. The method is then extended to study the behavior of thin-walled beam-columns in which the effects of local buckling are taken into account in terms of the effective width of the component plates. The analytical results are compared with the corresponding results obtained from experiments carried out by the authors. Design formulae are proposed to predict the ultimate strength of beam-columns of non-compact cross-sections under biaxial loading. Finally, some optimization results for designing thin-walled beam-columns with minimum weights, satisfying the strength limit state and other design constraints relevant to typical conditions in practice, are provided.

262F. RINGS AND ARCHES

10A491. Buckling analysis of steel arch bridges. - AS Vlahinos *(Dept of Civil Eng, Univ of Colorado, 1200 Larimer St, Denver CO 80204)*, JC Ermopoulos *(Dept of Civil Eng, Natl Tech Univ, 42 Patission St, 10682 Athens, Greece)*, Yang-Cheng Wang *(Dept of Civil Eng, Univ of Colorado, 1200 Larimer St, Denver CO 80204)*. J Construct Steel Res 26(1) 59-71 (1993).

Steel arch bridges are analyzed. The shape and the height of the arch are variable and the arch's support are either pinned or fixed. A uniformly distributed load and a moving concentrated load are considered. The location and the magnitude of the minimum elastic critical loads are computed for various values of height to span ratios and load combinations. The influence of arch rib height on the critical loads is studied and the interaction curves between critical concentrated and critical uniform loads are given. Finally the accurate optimum arch heights for all cases are obtained. The results are presented in graphical and tabular form.

262G. FRAMED STRUCTURES

10A492. Design of frames against buckling using a Rayleigh quotient approximation. - RA Canfield *(Dept of Aeronaut and Astronaut, Air Force IT, WPAFB)*. AIAA J 31(6) 1143-1149 (Jun 1993).

A Rayleigh quotient approximation is applied to the design of structures while guarding against elastic instability. It approximates buckling eigenvalues by separately estimating the model strain energy due to the linear and geometric stiffness of the structure. Previously used during structural optimization for the fundamental natural eigenvalue, the Rayleigh quotient approximation is derived for the buckling design problem for the first time. The critical buckling load is found by solving the eigenvalue problem that arises by considering the geometric nonlinearity of the deforming structure. Rayleigh's principle is used to justify the choice of intermediate design variables for approximating terms in the Rayleigh quotient. A truss model illustrates the importance of the design space chosen for approximating the modal strain energy. A beam-column, two plane frames, and a space frame are used to verify the formulation. Special attention is paid to difficult bimodal optima.

10A493. Example of 3D frame buckling. - WR Spillers, A Saadeghvaziri, A Luke *(Dept of Civil and Env Eng, NJIT, Newark NJ 07102)*. Comput Struct 47(3) 483-486 (3 May 1993).

Physical test results are presented to resolve existing disagreements in the literature concerning the collapse load of an L-shaped frame which fails through torsional buckling. Available computer solutions for this problem are compared with particular attention given to the symmetry of the geometric stiffness matrix.

10A494. Modified solution for finding the optimal angle of spacecraft walls under orbital debris impacts. - CP Pantelides and S-R Tzan *(Dept of Civil Eng, Univ of Utah, Salt Lake City UT 84112)*. AIAA J 31(6) 1162-1164 (Jun 1993).

In recent studies it has been shown both analytically and experimentally that orbital debris impact is a hazard to long duration near-Earth space structures. In addition, it has been determined that most space debris impacts will occur at oblique angles to the surface of the space structure. Experimental studies of oblique hypervelocity impact of multisheet structures have shown that there exists a critical debris particle trajectory angle beyond which projectile impacts produce ricochet debris that can cause major damage to orbiting structures.

10A495. Recent research on buckling of framed structures and curved beams. - Yeong-Bin Yang *(Dept of Civil Eng, Natl Taiwan Univ, Taipei, Taiwan 10617 ROC)*. J Construct Steel Res 26(2-3) 193-210 (1993).

Both the buckling of framed structures and the buckling of curved beams have been the focus of intensive research in recent years. However, very few researchers have realized that the problems encountered in the two seemingly independent areas are in effect correlated and can be resolved by the same means. This paper intends to review some of the most relevant works, especially those conducted by the writer and co-workers, on the buckling of framed structures and curved beams, with particular emphasis placed on the implementation of rational procedures for analyzing problems involving 3D rotations. It is recommended that such procedures be adopted in a general computer program for calculating the buckling loads of 3D framed structures.

262H. PLATES

10A496. Influence of lips on thin-walled sections. - LK Seah *(Dept of Mech and Prod Eng, Nanyang Tech Inst, Singapore 2263)*, J Rhodes *(Dept of Mech Eng, Univ of Strathclyde, Glasgow, UK)*, BS Lim *(Process Software Pte, Science Centre Rd, Unity House, #05-02, Singapore 2260)*. Thin-Walled Struct 16(1-4) 145-177 (1993).

Turning the free edge of an unstiffened flange inwards or outwards to form a "lip", can substantially improve the local buckling resistance of a member. The lip is the most common type of edge stiffener used in cold-rolled, thin-walled sections. In this paper the behavior of plate elements of thin-walled sections stiffened by compound lips (ie, lips which are folded twice to form "lips on the lips") is examined both theoretically and experimentally. An outline of a series of tests on compound edge-stiffened thin-walled sections of various geometries is given and some load-end compression displacement paths are compared with the theoretical predictions. Reasonably good agreement is obtained between the experimental and theoretical results. Comparisons of the theoretical predictions with experimental results of other researchers are also presented in this paper.

10A497. Linear elastic stability analysis of shear-deformable plates using a modified spline finite strip method. - YK Cheung and J Kong *(Dept of Civil and Struct Eng, Univ of Hong Kong, Hong Kong)*. Comput Struct 47(2) 189-192 (Apr 1993).

The stability of shear-deformable plates under constant initial stresses is studied by the spline finite strip method. Third-order plate theory is used as the basis for developing the strip element. The classical B_3-spline function is modified in such a way that the resulting spline finite strip element incorporates the merits of spline interpolation and the versatility of the FEM. A set of demonstration analyses are presented to show the validity of the modified spline finite strip method.

See also the following:

10A73. Approximate 3D analysis of rectangular thick laminated plates: Bending, vibration, and buckling
10A471. Differential quadrature for static and free vibration analyses of anisotropic plates

262I. SHELLS

10A498. Antisymmetric bifurcations in a compressible pressure-sensitive circular cylinder under axisymmetric tension and compression. - KT Chau *(Dept of Civil and Struct Eng, Hong Kong Polytech, Hung Hom, Hong Kong)*. J Appl Mech 60(2) 282-289 (Jun 1993).

This paper examines antisymmetric bifurcations of geometric diffuse modes, including buckling and surface rumpling modes, for a compressible pressure-sensitive circular cylinder of finite length under axisymmetric loadings. The analysis includes the effects of nonnormality, transverse isotropy, and confining stress on the appearance of antisymmetric geometric diffuse modes and their relationship to the onset of localization. The long wavelength limit of the eigenvalue equation is found corresponding to the Euler's buckling load; the short wavelength limit corresponds to the eigenstress for the surface rumpling mode if the cylinder is incompressible and satisfies plastic normality. If the lateral stress is nonzero, a finite solution exists for the antisymmetric long wavelength limit; for the cases that the in-plane bulk modulus becomes unbounded, this finite eigenstress equals to the plane-strain results obtained by Chau and Rudnicki (1990). The lowest possible bifurcation stresses are plotted for various constitutive parameters by combining the results of the bifurcation analyses for both the axisymmetric (Chau, 1992) and the antisymmetric modes. This eigenvalue surface also provides a condition that determines whether bulging (antisymmetric) or building (axisymmetric) appears first for a fixed specimen geometry under compression.

10A499. Axisymmetric dynamic buckling of submerged cylindrical shells. - B Mustafa, STS Al-Hassani, SR Reid *(Dept of Mech Eng, UMIST, Sackville St, Manchester M60 1QD, UK)*. Comput Struct 47(3) 399-405 (3 May 1993).

Dynamic buckling response of tubes immersed in water and subjected to an axisymmetric external throughwater pressure pulse is investigated using the FEM. A loading routine describing the hydrodynamic net pressure, incorporating incident and reflected pressure pulses on the structure was developed. This is interfaced with the general-purpose FE code ABAQUS to solve for the structural response which has non-linearity in both material properties and displacements. Idealized geometric imperfections in the radius are used in the FE model to trigger the radial buckling mode. The same numerical procedure was employed to predict the dynamic buckling response of tubes subjected to impulsive loading in air. Comparisons are made with plastic flow buckling theory and experiments reported in literature.

10A500. Buckling and post-buckling characteristics of pressure-loaded cylinders. - Seishi Yamada *(Toyohashi Univ of Tech, Toyohashi 441, Japan)* and JGA Croll *(Dept of Civil and Env Eng, Univ Col, London WC1E 6BT, UK)*. J Appl Mech 60(2) 290-299 (Jun 1993).

Nonlinear Ritz analysis is used to investigate the elastic buckling behavior of pressure loaded cylinders. Careful analysis of the energy changes during the buckling process allows definition of a reduced stiffness theoretical model. This reduced stiffness model provides a convenient means for estimating lower bounds to the imperfection sensitive elastic buckling behavior.

10A501. Influence of local fiber undulations on the global buckling behavior of filament-wound cylinders. - DW Jensen and SP Pai *(Dept of Aerospace Eng, Penn State)*. J Reinforced Plastics Composites 12(8) 865-875 (Aug 1993).

The predicted compressive stiffness and buckling strength of filament-wound cylinders using classical lamination theory is significantly higher than those observed experimentally. This discrepancy is partially influenced by the variation of mechanical properties in the region of fiber undulations. These regions are localized geometric defects intrinsic to the filament-winding, weaving, and braiding processes. In the present work, the average mechanical properties of the fiber undulation region are quantified using the modified models of woven-fabric composites to account for the 3D effects. The mechanical properties thus determined can be incorporated as local element properties into global FE models. Preliminary results from large-displacment analyses of filament-wound cylinders are relatively more accurate when fiber undulations are accounted for.

10A502. Sensitivity analysis in post-buckling problems of shell structures. - H Noguchi and T Hisada *(Res Center for Adv Sci and Tech, Univ of Tokyo, 4-6-1 Komaba Meguro-ku, Tokyo 153, Japan)*. Comput Struct 47(4-5) 699-710 (3 Jun 1993).

In this study, a method to evaluate sensitivities in post-buckling analysis is developed. The gradients of load values obtained under several constraint conditions are discussed. Unlike other methods for sensitivity analysis, the present method can cope with both snap-through and bifurcation problems without eigenvalue analysis. In addition, the load sensitivity at arbitrary points on an equilibrium path can be calculated. Using the MITC4 shell element, several numerical examples, such as a bifurcation buckling and a snap-through analysis of shell structures, are solved to show the performance of this sensitivity analysis method.

10A503. Stability loss in thick transversely isotropic cylindrical shells under axial compression. - GA Kardomateas *(Sch of Aerospace Eng, Georgia Tech)*. J Appl Mech 60(2) 506-513 (Jun 1993).

The stability of equilibrium of a transversely isotropic thick cylindrical shell under axial compression is investigated. The problem is treated by making appropriate use of the 3D theory of elasticity. The results are compared with the critical loads furnished by classical shell theories. For the isotropic material cases considered, the elasticity approach predicts a lower critical load than the shell theories, the percentage reduction being larger than increasing thickness. However, both the Flugge and Danielson and Simmonds theories predict critical loads much closer to the elasticity value than the Donnell theory. Moreover, the values of n, m (number of circumferential waves and number of axial half-waves, respectively, at the critical point) for both the elasticity, and the Flugge and the Danielson and Simmonds theories, show perfect agreement, unlike the Donnell shell theory.

262K. STIFFENED AND ANISOTROPIC STRUCTURES

10A504. Sandwich panels. - JM Davies *(Univ of Salford, Salford, UK)*. Thin-Walled Struct 16(1-4) 179-198 (1993).

In recent years, there has been increasing interest in the use of structural sandwich panels as the cladding of buildings and a good deal of research and development has been carried out. This paper reviews the state of the art with regard to the structural design of elements consisting of two thin metal faces separated by a lightweight core. Various aspects are discussed but two are given particular attention, namely methods of global analysis and the local buckling of compressed face elements. The analysis of sandwich panels under all possible loading and boundary conditions no longer poses any problem. Classical solutions, approximate solutions and numerical methods such as FE all have their place and are reviewed in detail. Local buckling phenomena in sandwich elements are similar to those in other thin-walled metal elements with the added consideration that buckling is resisted by the core material. This leads to some quite complex analysis which requires simplification for practical design. The paper includes a useful bibliography of recent references.

10A505. Stability of continuous composite plate girders with U-frame action. - RP Johnson *(Dept of Civil Eng, Univ of Warwick)* and Shiming Chen *(Inst of Urban Construct, Peoples Rep of China)*. Struct Build 99(2) 187-197 (May 1993).

Tests are reported on two half-scale twin double-cantilever girders with class 4 webs. In one, lateral stability of the bottom flanges was provided by continuous U-frame action; and in the other, by discrete U-frames that included the shear connection and the concrete slab, which was reinforced as the deck of a highway bridge. Four distinct types of lateral buckling failure were observed. They are discussed in relation to three design methods, including that of Eurocode 4: Part 1.1.

See also the following:

10A476. Tests on intermediately stiffened plate elements and beam compression elements
10A580. Energy balance and the speed of crack growth in a compressed plate with delamination
10A643. Active buckling control of smart composite plates: FE analysis

262L. DYNAMIC STABILITY

10A506. Stability of spinning shear-deformable laminated composite plates. - R Bhumbla and JB Kosmatka *(Dept of Appl Mech and Eng Sci, UCSD)*. J Sound Vib 163(1) 83-99 (8 May 1993).

A first order, shear deformation plate theory is used to study the buckling speeds and the corresponding deformed shape of spinning, laminated composite plates offset from the axis of rotation. The thoery accounts for geometric nonlinearity in the form of von Karman strains and the effects of rotatory inertia. A displacement FE model is developed to obtain the numerical solutions to this class of problems. The buckling speeds are presented as functions of spin vector location and orientation, and composite ply lay up. The phenomenon of tensile buckling is examined. the buckling speed is seen to decrease with the spin vector offset from the plate clamped root, and increasing pitch orientation. It is shown that laminated plates can be designed to buckle in specific modes and at specific speeds. Nonlinear effects have been shown to be significant for cases where there is coupling between in plane and out of plane deflections of the plate. This coupling is a result of either material anisotropy or the application of forces out of plane of the plate.

10A507. Stability of the damped hill's equation with arbitrary, bounded parametric excitation. - CD Rahn *(Dept of Mech Eng, Clemson Univ, Clemson SC 29634)* and CD Mote Jr *(Dept of Mech Eng, UCB)*. J Appl Mech 60(2) 366-370 (Jun 1993).

The minimum damping for asymptotic stability is predicted for Hill's equation with any bounded parametric excitation. It is shown that the response of Hill's equation with bounded parametric excitation is exponentially bounded. The parametric excitation maximizing the bounding exponent is identified by time optimal control theory. This maximal bounding exponent is balanced by viscous damping to ensure asymptotic stability. The minimum damping ratio is calculated as a function of the excitation bound. A closed form, more conservative estimate of the minimum damping ratio is also predicted. Thus, if the general (eg, unknown, aperiodic, or random) parametric excitation of Hill's equation is bounded, a simple, conservative estimate of the damping required for asymptotic stability is given in this paper.

See also the following:

10A65. Statics, stability, and vibration of nonprismatic beams and columns

262Y. COMPUTATIONAL TECHNIQUES

10A508. Tight lower and upper bounds to first eigenvalues. - R Schmidt *(Col of Eng and Sci, Univ of Detroit, Detroit MI 48221)*. Indust Math 42(1) 1-8 (1992).

Procedures for enclosing the first eigenvalue (such as the bifurcational buckling load or fundamental frequency of free vibrations) by rather tight lower and upper bounds are described in this note. The essence of the approach is to employ the Krylov-Bogolyubov enclosure theorem for the determination of a lower bound to the second eigenvalue and then to use that value in Temple's inequality to obtain a lower bound to the first eigenvalue. Furthermore, an upper-bound formula, based on three successive Rayleigh-Schwarz quotients, is used to calculate a tight upper bound. The bifurcational buckling of a heavy, slender, elastic cone fixed at its base serves as an illustrative and didactic example.

264. Electromagneto solid mechanics

10A509. Rotation of a rigid ellipsoidal inclusion embedded in an anisotropic piezoelectric medium. - Tungyang Chen *(Dept of Civil Eng, Natl Cheng Kung Univ, Tainan, Taiwan 70101, ROC)*. Int J Solids Struct 30(15) 1983-1995 (1993).

A rigid ellipsoidal inclusion is embedded in a homogeneous piezoelectric matrix and is rotated infinitesimally, about an axis through its center, by an imposed couple. Without having to solve the governing equations of equilibrium, we find directly the relation between the couple and rotation vectors, together with the stress, strain, rotation tensor, and electric fields just outside the ellipsoidal surface. In addition, we establish boundary integral formulae for evaluation of the fields in the matrix. Gaussian quadrature formulae with variable station points are employed in the numerical computations. Results are presented for a piezoelectric PZT-6B to show the effect of the aspect ratio of the spheroid on the rotational stiffness. This work extends the results of Walpole to piezoelectric media.

10A510. Universal relations in piezoelectric composites with eigenstress and polarization fields Part I. Binary media: Local fields and effective behavior. - Y Benveniste *(Dept of Solid Mech Mat and Struct, Fac of Eng, Tel-Aviv Univ, Ramat Aviv 69978, Israel).* J Appl Mech 60(2) 265-269 (Jun 1993).

Binary composite media of arbitrary phase geometry are considered. The constituent phases have general anisotropic piezoelectric behavior and contain constant eigenstress and spontaneous polarization fields. An electromechanical loading of the composite aggregate is found which results in uniform strain and electric field intensity throughout the solid. The existence of these uniform fields is used to derive exact universal relations between the local fields as well as between the effective constants of the composite aggregate.

10A511. Universal relations in piezoelectric composites with eigenstress and polarization fields Part II. Multiphase media: Effective behavior. - Y Benveniste *(Dept of Solid Mech Mat and Struct Eng, Tel-Aviv Univ, Tel-Aviv Univ, Ramat Aviv 69978, Israel).* J Appl Mech 60(2) 270-275 (Jun 1993).

We consider heterogeneous piezoelectric media in general and multiphase piezoelectric composites in particular. A distribution of statistically homogeneous eigenstress and spontaneous polarization fields is admitted in the solid which is itself statistically homogeneous, and the effective eigenstress and spontaneous polarizaton is sought. The method here is based on the use of virtual work theorems in piezoelectric media and therefore differs from the approach used in the companion paper (Benveniste, 1993). We show that the effective eigenstress and polarization follow from a knowledge of the influence functions related to an electromechanical loading of the composite aggregate in which no eigenstress and polarizations are present. When applied to the special case of binary systems with constant eigenstress and polarization fields in the phases, the above result implies that the effective eigenstress and polarization can be determined in terms of the effective elastic, piezoelectric dielectric tensors of the medium, the constituent properties, and the individual eigenstresses and polarizations.

10A512. Safety analysis of the superconducting magnet system of a next generation tokamak. - N Mitchell, L Bottura, S Chiocchio *(NET team, Max-Planck-Inst fur Plasmaphys, Boltzmannstr 2, W-8046 Garching bei Munchen, Germany).* Fusion Eng Des 22(3) 193-216 (Apr 1993).

A preliminary safety analysis of the superconducting magnet system of a "next generation" tokamak is performed. Such tokamaks must satisfy nuclear class safety standards to permit their operation. Designs are not sufficiently advanced to permit the full safety case to be made. However scoping calculations of the form presented here enable potential problems to be identified or eliminated. With a number of constraints on the design it is shown that "passive" safety could be achieved in such a magnet system ie, the magnets can not cause failure in adjacent nuclear components.

266. Soil mechanics (basic)

10A513. Hydraulic fracturing of soil during laboratory experiments Part I. Methods and observations. - LC Murdoch *(Center Hill Res Facility, Univ of Cincinnati, Cincinnati OH).* Geotechnique 43(2) 255-265 (Jun 1993).

Hydraulic fracturing appears to have useful environmental and geotechnical applications, but the details of fracture morphology and propagation in soil are poorly known. To identify those details, more than 100 hydraulic fractures were created by dyed glycerine injected into rectangular blocks of silty clay confined within a triaxial loading cell. The traces of the fractures were observed directly through a transparent loading plate in the experimental apparatus, and the fracture surfaces were described after they had been exposed by the blocks being split open. Steps and ridges on fracture surfaces, and lobes near the leading edge of a fracture were ubiquitous in silty clay, as they are on the surfaces of hydraulic fractures in rock or other brittle materials. Details of the leading edge, however, depend on the water content of the soil, which is one difference between hydraulic fractures in soil and those in rock. Fluid injected to create a hydraulic fracture appears to penetrate to the leading edge of the fracture when the pressure of pore fluid is less than atmospheric while the sample is under load. At greater water contents when the pore pressure is positive, the injected fluid lags behind the leading edge. It is inferred that this phenomenon occurs because water infiltrates into the fracture tip and prevents penetration of the injected fluid.

10A514. Hydraulic fracturing of soil during laboratory experiments Part II. Propagation. - LC Murdoch *(Center Hill Res Facility, Univ of Cincinnati, Cincinnati OH).* Geotechnique 43(2) 267-276 (Jun 1993).

The propagation of hydraulic fractures in soil was studied in the lab by glycerine injected at a constant rate into rectangular samples of silty clay confined in a triaxial cell. During propagation, the trace of a hydraulic fracture appeared on the side of the cell as a nearly straight, narrow line that tapered from 0-05 mm to negligible aperture at the tip. Pressure of the glycerine was recorded as a function of time and is characterized by a period of nearly linear increase, a break in slope followed by a period of increasing pressure but decreasing slope, a maximum, and then a period of decreasing pressure. Tests terminated early in that sequence of events indicated that the break in slope marks the onset of hydraulic fracturing. The pressure at the onset of the fracturing was predicted from a determination of the fracture toughness of the silty clay. The forms of the pressure records were markedly affected by the water content of the soil: increasing water content decreased the pressure required to initiate a hydraulic fracture (and decreased fracture toughness) and flattened the pressure record during propagation.

10A515. Hydraulic fracturing of soil during laboratory experiments Part III. Theoretical analysis. - LC Murdoch *(Center Hill Res Facility, Univ of Cincinnati, Cincinnati OH).* Geotechnique 43(2) 277-287 (Jun 1993).

A theoretical analysis is developed to explain observations from lab experiments where hydraulic fractures were created in silty clay soil. The analysis is based on a critical stress intensity criterion for propagation. The fracture is assumed to be a 2D slit embedded in an elastic material of infinite extent. It is assumed to be filled with one fluid that is injected at the mid-line of the fracture and another that infiltrates the fracture tip. Other parameters included in the analysis are initial fracture length, elastic modulus, pressure in the fracture tip, growth of the infiltrated region at the tip, fracture toughness, and the rate of the leakoff. Results of the analysis are presented to highlight the effects of a slight change in each parameter. The model is validated by the use of curve-fitting methods to estimate parameters required to mimic pressure records from lab experiments, and then by comparison of the estimated parameters with quantities measured in the lab. The results suggest that pore fluid infiltrating into the tip of a propagating fracture can control many of the details of hydraulic fracture development in soil, confirming a conceptual model postulated earlier based only on lab observations.

10A516. RES: A numerical program for reinforced-soil slopes based on the rigid-plastic theoretical model. - D Lesniewska *(Inst of Hydroeng, IBW PAN, Gdansk, Poland).* Geotextiles Geomembranes 12(5) 435-439 (1993).

A brief description of a rigid-plastic model of reinforced soil is presented with an account of its application – program RES, which may serve for numerical analysis of reinforced slopes. The program is able to solve the classical differential-boundary-value problem of slope-bearing capacity for reinforced and unreinforced soil in a wide range of soil and reinforcement parameters. The solution is obtained with a method of characteristics and contains the slope's bearing capacity (the value of the failure load), a definition of slip line, responsible for construction damage, and the total stresses in the plastic region of the slope.

10T517. Evaluation of a constitutive model for overconsolidated clays. - AJ Whittle *(Dept of Civil and Env Eng, MIT).* Geotechnique 43(2) 289-313 (Jun 1993).

10A518. Analytical interpretation of dilatometer penetration through saturated cohesive soils. - RJ Finno *(Dept of Civil Eng, NWU).* Geotechnique 43(2) 241-254 (Jun 1993).

A 3D numerical solution to the problem of penetration of a flat plate dilatometer through saturated cohesive soil is presented. Axisymmetric stream functions are used with those corresponding to a uniform velocity field to approximate the geometry of the stream lines during penetration. After the source strengths have been determined, velocities and strains are computed. The computed strain fields are compared with those for axisymmetric and plane strain penetrations to show the need to use a 3D analysis. Effective stresses are computed from the strains based on assumed constitutive response (in this case an anisotropic bounding surface model) and total stresses are computed based on equilibrium considerations. The method provides computed horizontal stress indices that compare favorably with field data. The effect of penetration on the horizontal stress index measured by the dilatometer is evaluated. This index is shown to be most sensitive to changes in overconsolidation ratio and at-rest earth pressure coefficient, which reflect the initial in situ stresses.

10A519. Dynamic effects in a saturated layered soil deposit: Centrifuge modeling. - I Krstelj and JH Prevost *(Dept of Civil Eng and Operations Res, Princeton).* Soil Dyn Earthquake Eng 11(8) 485-496 (1992).

The dynamic response of a saturated layer soil deposit was modeled on the Princeton Univ geotechnical centrifuge using various centrifugal acceleration levels. The layered soil deposit consists of a saturated Nevada sand layer overlaid by a slit layer of low permeability. Measured acceleration and pore-water pressure time histories are used to validate the scaling laws used in interpreting dynamic centrifugal modeling test results. Careful measurements of the settlements at the silt surface are performed using a non-contact displacement transducer, and comparisons are made with measurements obtained with standard linear voltage displacement transducer. Finally, the experimental results are used to verify the validity of the numerical procedures encompassed in the computer code DYNAFLOW.

10A520. Rigid-plastic boundary in statically indeterminate problems in the mechanics of granular materials. - D Harris *(Univ of Manchester Inst of Sci and Tech, PO Box 88, Manchester, M60 1QD, UK)*. Quart J Mech Appl Math 46(1) 41-69 (Feb 1993).

A complete formulation for general statically indeterminate boundsry-value problems is presented for a continuum, rigid-plastic, model of granular materials satisfying the stress-equilibrium conditions, the Coulomb yield criterion and the double-shearing kinematic equations. Equations for the velocity field in the neighborhood of a finite stress discontinuity are derived. The calculus of variations is used to formulate a method for obtaining the characteristic curves which separate the rigid and deforming regions and which are subject to a mixed boundary condition containing both stress and velocity variables. The criterion is applied to the region in the vicinity of the exit of a wedge-shaped channel under conditions of converging flow. On the assumptions of radial flow sufficiently far inside the channel, rigid flow on exit and a transitional region which includes a curvilinear fan of characteristic curves it turns out that velocity and stress fields can be found satisfying all the required boundary conditions but that the necessary condition that the work-rate be everywhere non-negative fails to be satisfied.

10A521. Molecular dynamical study of granular fluids I. The unforced granular gas in 2D. - I Goldhirsch *(Dept of Fluid Mech and Heat Transfer, Fac of Eng, Tel-Aviv Univ, Ramat Aviv, Tel-Aviv 69978, Israel)*, M-L Tan, G Zanetti *(CRS4, PO Box 488, I-09124, Cagliari, Italy)*. J Sci Comput 8(1) 1-40 (Mar 1993).

Results of a numerical study of the dynamics of a collection of disks colliding inelastically in a periodic 2D enclosure are presented. The properties of this system, which is perhaps the simplest model for rapidly flowing granular materials, are markedly different from those known for atomic or molecular gases, in which collisions are of elastic nature. The most prominent feature characterizing granular systems, even in the idealized situation in which no external forcing exists and the initial condition is statistically homogeneous, is their inherent instability to inhomogeneous fluctuations. Granular "gases" are thus generically nonuniform, a fact that suggests extreme caution in pursuing direct analogies with molecular gases. We find that once an inhomogeneous state sets in, the velocity distribution functions differ from the classical Maxwell-Boltzmann distribution. Other characteristics of the system are different from their counterparts in molecular systems as well. For a given value of the coefficient of restitution, e, a granular system forms clusters of typical separation $L_0 \approx l(1 - e^2)^{1/2}$, where l is the mean free path in the corresponding homogeneous system. Most of the fluctuating kinetic energy then resides in the relatively dilute regions that surround the clusters. Systems whose lienar dimensions are less than L_0 do not give rise to clusters, still they are inhomogeneous, the scale of the corresponding inhomogeneity being the longest wavelength allowed by the system's size. The present article is devoted to a detailed numerical study of the above-mentioned clustering phenomenon in 2D and in the absence of external forcing. A theoretical framework explaining this phenomenon is outlined. Some general implications as well as practical ramifications are discussed.

268. Soil mechanics (applied)

10A522. Creep response of laterally loaded piles in ice and permafrost. - UGA Puswewala, RKND Rajapakse, L Domaschuk, H Shields *(Univ of Manitoba)*. Geotechnique 43(2) 223-240 (Jun 1993).

A computationally efficient pile element and a time-incremental FE code are developed to model laterally loaded piles in ice-permafrost, by modeling the pile as a beam supported on a spring-dashpot system. A numerical method involving plane strain FE analyses of laterally loaded rigid cores in frozen media is proposed to derive the appropriate spring and dashpot relationships for the pile element. Results of analyses using the pile element agree satisfactorily with experimental findings on laterally loaded rods in ice. Creep response of laterally loaded piles in icy permafrost is analyzed using the code. The deformation behavior of laterally loaded floating piles in ice predicted by the simple pile element is confirmed by rigorous analysis of the identical problem using 3D continuum elements. The computer code incorporating this simple pile element is a valuable predictive tool for practising engineers.

10A523. Two computer programs for the design and analysis of geosynthetic-reinforced soil-retaining walls. - RJ Bathurst *(Dept of Civil Eng, R Military Col, Kingston, ON, K7K 5L0, Canada)* and MR Simac *(Earth Improvement Tech, 100 Mayflower Court, Cramerton NC 28032)*. Geotextiles Geomembranes 12(5) 381-396 (1993).

The paper describes two commercially available programs that can be used to design and analyze soil-retaining walls that are constructed with horizontal sheets of geosynthetic reinforcement. The programs differ in their scope, program interface, and flexibility to optimize design during a user session. Both programs have been written for micro-computers operating under MS-DOS 3.0 or greater and have a graphical interface that allows the user to view the probelm cross-section at any stage in the design process. The analyses that are implemented in the programs are based on current recommended practice in North America. External stability is examined by using a "gravity wall structure" analog, and "tie-back wedge" approach is used for internal stability.

10T524. Expert system for the design of geotextiles. - G Mannsbart and S Resl *(Polyfelt Ges mbH, St Peterstr, 21, A-4021, Linz, Austria)*. Geotextiles Geomembranes 12(5) 441-450 (1993).

10A525. Stability analysis of reinforced slopes. - JR Greenwood *(Travers Morgan, Euribon House, Shortwood Close, Nottingham, NG1 7JF, UK)* and M Zytynski *(MZ Assoc, Llwynhaf, Llanddarog Rd, Carmarthen, Dyfed, SA32 8AR, UK)*. Geotextiles Geomembranes 12(5) 413-424 (1993).

The application of routine stability analysis to reinforced slopes is described. Problems are encountered in introducing reinforcement forces into certain established analytical methods. It is shown that the simple (or simplified) method of analysis lends itself to the inclusion of reinforcement forces. Two computer programs are described (i) SLIP4, a development of a hand calculation for determining the factor of safety of a single slip surface by four different methods and calculating the benefits of reinforcement, and (ii) STABLE, a sophisticated search program for analysis of non-circular or circular slips, including the effects of geotextile or geogrid reinforcement or other anchor forces.

10A526. End restraint in triaxial testing of soils. - J Feda, J Bohac, I Herle *(Inst of Theor and Appl Mech, Acad of Sci, Vysehradska 49, 128 49 Praha 2, Czech Republic)*. Acta Tech CSAV 38(2) 197-220 (1993).

The effect of end restraint of specimens of sand and reconstituted loess on their deformation was investigated. Triaxial CID tests with specimens' diameter 3.8 cm and height-dia ratio 2:1 and 1:1 were carried out to explore the effectiveness of different arrangement of lubrication layers and of quality of lubrication agent. Correlations of the peak angle of internal friction φ'_f, volumetric strain gradient at failure $(d\varepsilon_v/d\varepsilon_a)_f$ and of axial and volumetric strain at failure ε_{af} and ε_{vf} vs the initial porosity and consolidation pressure $\sigma'_r c$ were found and analyzed for effectively lubricated and unlubricated specimens with slenderness 2:1 and 1:1. The effect of lubrication with (dilatant) sand, though unimportant for strength and strain gradient with 2:1 (and lubricated 1:1) specimens, increases strains at failure, especially for 1:1 lubricated specimens. In this case, the stress field is uniform and strains equal about twice the standard value. The respective ratio depends on the initial porosity and can be used to transform the results of standard tests to the tests with uniform stress-strain fields. Loess specimens (contractant) did not show any considerable effect of end restraint. Some abnormities in the behavior were ascribed to the effect of aging.

See also the following:

10A516. RES: A numerical program for reinforced-soil slopes based on the rigid-plastic theoretical model

10A518. Analytical interpretation of dilatometer penetration through saturated cohesive soils

10A522. Creep response of laterally loaded piles in ice and permafrost

10A525. Stability analysis of reinforced slopes

272. Materials processing

10A527. State-space representation and optimal control of nonlinear material deformation using the FEM. - RV Grandhi, A Kumar *(Dept of Mech and Mat Eng, Wright State Univ, Dayton OH 45435)*, A Chaudhary *(UES Inc, Dayton OH)*, JC Malas *(Mat Eng, WPAFB)*. Int J Numer Methods Eng 36(12) 1967-1986 (30 Jun 1993).

A state-space model for representing the nonlinear material deformation and an optimal control scheme for obtaining desired process conditions in the deforming material are presented in this paper. The formulation is general for various metal-forming processes including forging and extrusion operations. The state variables selected in the formulation are the die-billet contact nodal velocities and the nodal velocities of the critical FEs of the billet. The control input is the ram velocity, which is determined by using the linear quadratic regulator theory to maintain desired strain rates within the selected FEs. The influence of an optimally designed ram velocity on the deforming material is studied using performance measures. This paper includes the development of the state-space model from nonlinear FE formulation, optimal control strategy and numerical example cases with discussions.

See also the following:

10A615. Effect of molding parameters on the interfacial strength in PEEK-carbon composites

10A722. Computer-aided design of explosive welding systems

272B. APPLICATIONS OF PLASTICITY THEORY

10A528. Analysis of 3D hexagonal closed-die heading by the FE flow formulation. - PAF

Martins and MJM Barata Marques *(Seccao Tecnologia Mecanica, Inst Superior Tecnico, Avenida Rovisco Pais, 1096 Lisboa, Portugal).* J Mat Processing Tech 38(3) 553-566 (May 1993).

Modeling 3D metal-forming processes with the FE flow formulation based on the Doraivelu et al, constitutive equations is considered. The basic theory is reviewed. Special emphasis is placed on the numerical implementation of such formulation. The authors discuss the substitution of the Gauss by the Irons numerical integration rule for the evaluation of the deviatoric component of the generalized stiffness matrix, and present two criteria for analyzing mesh degeneracy and mesh-die interference. Three-dimensional contact problems are discussed briefly. Three-dimensional closed-die hexagonal heading, starting from a cylindrical aluminium-alloy billet, is reported. Theoretical and experimental results for the punch load-punch displacement evolution are analyzed, good agreement between them being found.

10A529. Constitutive model for cold deformation of aluminium at large strains and high strain rates. - S Tjotta and A Mo *(Senter for Industriforskning, PO Box 124 Blindern, 0314 Oslo 3, Norway).* Int J Plasticity 9(4) 461-478 (May 1993).

A temperature-dependent constitutive model for viscoplastic deformation of aluminium based on a single, scalar internal variable is presented. The model is designed particularly for the strains, strain rates, and temperatures important for cold forging. Special attention is paid to the underlying physical processes that determine the flow stress in the metal. The kinetic constitutive equation is based on thermal activation of dislocations over an average potential barrier from various kinds of obstacles. Strain hardening is modeled through the internal variable which represents the increasing height of these barriers. The model is generalized to three dimensions, and it has been implemented in the FE code ABAQUS. Simulations of simple forging operations are presented.

10A530. Free surface ductility in upsetting. - Hitoshi Moritoki *(Mining Col, Akita Univ, 1-1 Gakuen-cho, Tegata Akita 010, Japan).* Int J Plasticity 9(4) 507-523 (May 1993).

Cold upsetting of a circular cylinder is often used to evaluate the cold forgeability of forming materials. The index of the forgeability is the critical strain at which a crack occurs on the expanding free surface of the upsetting cylinder. The forming limit due to the cracking is analyzed by a method based on the sufficient condition for the collapse of the unique solution. The modes of cracking are determined by comparing the stabilities of deformation from the forming limit to the two modes able to permit strain rate discontinuity on the plane of localized necking. Numerous experiments published in the literature have shown a linear relationship with the slope of -0.5 in circumferential strain vs axial strain at the forming limit. The forming limit and the mode predicted are in very good agreement with the experimental results.

272C. FORGING

10A531. Validation of FE codes for prediction of machining distortions in forgings. - U Chandra *(Concurrent Tech, 1450 Scalp Ave, Johnstown PA 15904).* Commun Numer Methods Eng 9(6) 463-473 (Jun 1993).

When a forging is machined to its net shape, unacceptably large distortions can occur if the final part shape is complex. Such distortions can be predicted with the application of the FEM. However, numerical errors associated with the FE technique can render such predictions unreliable. This paper presents benchmark problems for verifying the accuracy of machining distortions predicted by any prospective FE code. Also, a comparison between two industry-standard general-purpose codes, ANSYS and ABAQUS, is presented.

See also the following:

10A325. Review of expert systems for process planning of cold forging

272D. EXTRUSION

10A532. Simplified 3D FE analysis of the non-axisymmetric extrusion processes. - Hyun-Woo Shin *(Inst of Adv Machinery and Des, Seoul Natl Univ, 56-1 Shinrim-Dong Kwanak-Gu, Seoul 151-742, S Korea),* Dong-Won Kim *(Dept of Mech Des and Prod Eng, Seoul Natl Univ, Seoul, S Korea),* Naksoo Kim *(Dept of Mech Eng, Hong-Ik Univ, Seoul, S Korea).* J Mat Processing Tech 38(3) 567-587 (May 1993).

In this study a new simplified 3D numerical method and the associated computer program have been developed to simulate non-axisymmetric extrusion processes. To define the die geometry for non-axisymmetric extrusion, the area mapping technique has been used. A stream-lined die surface was used to minimize the total extrusion pressure. The extrusion of square, hexagonal, and "T" sections from round billet has been both simulated and explored experimentally using a model material. The computed results for the cross-sectional grid distortion have been found to be in good agreement with the experimental results. Computational results will thus be valuable for the designing of tool geometries and the corresponding processes.

10A533. Urethane clamp as a metal-forming tool. - S Thiruvarudchelvan *(Sch of Mech and Prod Eng, Nanyang Tech Univ, Nanyang Ave, Singapore 2263).* J Mat Processing Tech 38(3) 491-500 (May 1993).

A clamp making use of a tubular urethane rod was constructed recently and used in the semi-continuous extrusion of aluminium rod of 19.3 mm diameter. Using axial clamping pressures of up to 75 MPa on the urethane, axial compressive forces of up to 45 kN were generated on the aluminium feedstock. Clamps of this type may be designed and used with several other metal-forming processes with beneficial effects, some of these processes being identified in this paper. The advantages and limitations of the use of this clamp in these processes are discussed.

272F. DRAWING

10A534. Stressed-strained state of a blank at the initial stage of hydrodynamical drawing. - VM Popkov and SV Lapin *(Kaluga).* J Machinery Manuf Reliab 6 68-75 (1992).

A mathematical model of the stressed-strained state of a blank at the initial stage of hydrodynamical drawing is proposed. Some results computed using the model, are presented. The theoretical results are compared with experimental data.

272G. SHEET METAL FORMING AND STAMPING

10A535. Analysis of the hydrostatic bulging of an elliptic diaphragm by the energy method. - HS Lee *(Prod Eng, R&D Dept, Kia Motors, Kwang-Myung, S Korea)* and DY Yang *(Dept of Precision Eng and Mechatronics, Korea Adv Inst of Sci and Tech, Taejon, S Korea).* J Mat Processing Tech 38(3) 539-552 (May 1993).

An approach using the energy method is proposed for the analysis of 3D sheet-metal forming. There are some limitations in analysis by the energy method, eg, the analytical expression of the geometric configuration and the construction of a proper kinematically-admissible velocity field are very difficult and the estimation of strain rate at a point on the surface is very complicated. In the method suggested, the principal components of strain increment are calculated directly from the change of geometric profile for an arbitrary triangular element. The corresponding solution is found through optimization of the total energy consumption with respect to some parameters assumed in the kinematically-admissible velocity field and the geometric profile. In order to check the validity of the method proposed, the hydrostatic bulging of an elliptic diaphragm has been analyzed. In comparison of the computed results with existing experimental results, good agreement has been obtained for the pressure curve, the polar membrane strains and the strain distributions and it has thus been shown that the approach is applicable to the analysis of 3D sheet-metal forming.

10A536. Cold-formed thin-walled framework with flexible joint. - Tan Soon Huat *(Sch of Mech and Prod Eng, Nanyang Tech Univ, Nanyang Ave, Singapore 2263, Singapore)* and J Rhodes *(Dept of Mech Eng, Univ of Strathclyde, UK).* Comput Struct 47(3) 451-458 (3 May 1993).

The behavior of symmetrical double storey frameworks of cold-formed thin-walled plain channel members and semi-rigid connections is investigated analytically. A method of analysis, which is based on the matrix stiffness method, is developed and written into a computer program. Generalized relationships between forces and displacements at the ends of an element with semi-rigid connections are presented in a matrix form. The analysis takes account of member local buckling, connection strength and full moment-rotation behavior, axial load effects and shortening due to flexure. Using the theoretical analysis, the elastic critical load of the framework can be established.

10A537. Simulation, control and optimization of the gas-pressure forming of aluminium alloy sheet at elevated temperature. - PS Bate, DC Price, DJ Barrett, WT Roberts *(IRC in Mat for High Performance Appl, Univ of Birmingham, Birmingham B15 2TT, UK).* J Mat Processing Tech 38(3) 589-612 (May 1993).

The superplastic forming of Al-4.5% Mg alloy sheet, using gas pressure at elevated temperatures, has been studied. By using suitable models of material behavior and friction, it was possible to simulate this process with FEM. A rigid-plastic model was used, with the assumption that the material behaved as a membrane, to model axisymmetric forms. Such simulations could then be used to optimize the process, in terms of minimizing the forming time required whilst minimizing the amount of cavitation damage or retaining acceptable material thickness. To apply the optimization in practice, and for the generation of experimental data, a high degree of process control was required. Control of forming pressure is not sufficient for this purpose and volume-rate control was used. Good correlation was found between the predictions of the simulation and results from formed parts, and friction was found to be a very important factor in the process. It was possible to reduce the amount of cavitation significantly by applying an optimized volume-rate cycle.

272H. MACHINING (INCL NM)

10A538. Effects of carbon content and microstructure on the metal removal rate in electrochemical machining. - Ming-Chang Jeng, Ji-Liang Doong, Chih-Wen Yang *(Dept of Mech Eng, Natl Central Univ, Chung-Li, Taiwan 320, ROC).* J Mat Processing Tech 38(3) 527-538 (May 1993).

The present study investigates the effects of carbon content, microstructure and working pressure on the metal removal rate and current efficiency in the electrochemical machining of carbon steels. Four different carbon contents and various heat-treatment procedures (quenching, temperature and annealing) were performed. Some important experimental results are shown, as follows: (1) The removal rate and current efficiency increase with carbon content. (2) The quenched microstructures and tempered microstructures have a greater removal rate and current efficiency than those of the annealed microstructures. (3) The workpiece machined at the low working pressure of 3-4 kg/cm^2 has the greatest removal rate and current efficiency. (4) The machined surface roughness of all kinds of microstructure decreases with increase in the carbon content. (5) The roughness of the machined surface for annealed microstructures is greater than those of the quenched and tempered steels.

10A539. Remote sensing for on-line temperature estimation in machining: A basic framework. - S Raman *(Sch of Indust Eng, Univ of Oklahoma, Norman OK 73019)* and PH Cohen *(Penn State)*. J Mat Processing Tech 38(3) 613-632 (May 1993).

Remote thermocouple sensing (RTS) is a technique that utilizes analytical and experimental evidence to create models for temperature sensing, thus integrating the advantages of both approaches. The remote solution is an inverse problem of predicting the source based on some remote location temperatures. An accurate forward solution should be available that determines the relation between the source and sink, for estimation of the inverse relationship. Extensive simulation has been performed on the forward solution, thus establishing a need for fast and accurate computation.

See also the following:

10A311. Control of machining processes
10A315. Advanced NC verification via massively parallel raycasting
10A695. New sensor for real-time milling tool condition monitoring

272J. CASTING

10A540. Analysis of high-temperature behavior of solidified material within a continuous casting machine. - JR Boehmer, FN Fett, G Funk *(Inst of Energy Eng, Dept of Mech Eng, Univ of Siegen, Paul-Bonatz-Str 9-11, D-5900 Siegen, Germany)*. Comput Struct 47(4-5) 683-698 (3 Jun 1993).

The continuous casting of metals is determined by a multitude of dof, the combination of which conditions the quality of the products. To investigate in a theoretical way the principal possibilities that influence the process, an analysis is performed to simulate the high-temperature behavior of the solidified material within the continuous casting machine, ie, within the mould (with respect to contact and shrink gap formation) and the following secondary cooling zone (regarding support rolls and spray cooling). For the simulation of mass transport, solidification and/or remelting, and heat transfer, a finite difference method is applied; for the calculation of the thermomechanical stresses and strains the ADINA program is used as a FEM. Both thermal and stress analysis have been iteratively coupled to consider feedback. Emphasis is put on the highly nonlinear material behavior at temperatures near the solidification temperature as well as on the 3D and transient contact between strand and mould. To guarantee both accuracy and efficiency of computation, there is need for a problem-specific discretization, load history and stress-state formulation, material modeling, and coupling strategy.

10A541. Fluid flow, heat transfer and inclusion behavior in continuous casting tundishes. - Kouji Takatani, Yoshiyasu Shirota, Yoshihiko Higuchi, Yoshinori Tanizawa *(Iron and Steel Res Lab, Sumitomo Metal Indust, Oaza Sunayama 16, Hasaki-machi, Kashima-gun, Ibaraki-ken 314-02, Japan)*. Model Simulation Mat Sci Eng 1(3) 265-274 (Apr 1993).

A mathematical model to represent fluid flow, heat transfer and inclusion separation in continuous casting tundishes has been developed. The influence of tundish depth and length, flow rate, pouring method of molten steel and presence of a dam on the rate of inclusion separation is investigated for slab caster tundishes. A comparison of the present numerical results to simple analytical results has been made.

272P. RAPID SOLIDIFICATION

10T542. Review of the chemical vapor deposition (CVD) of the refractory compounds of titanium: A unique family of coatings. - HO Pierson *(Albuquerque NM 87120)*. Mat Manuf Processes 8(4-5) 519-534 (Jul-Sep 1993).

272T. CERAMICS, REFRACTORIES, GLASSES

See the following:

10T453. Present and future technology for ceramics
10A688. Development of plasma sprayed lubricant free slide plates with ceramic coat for railway use

274. Fracture and damage processes

See the following:

10A429. 3D FE progressive failure analysis of composite laminates under axial extension
10A431. Analysis of delamination in cross-ply laminates initiating from impact induced matrix cracking
10A432. Analysis of matrix cracking and local delamination in $(0/\theta/-\theta)_s$ graphite epoxy laminates under tensile load

274B. CRACK INITIATION

10A543. Assessment of data for dynamic crack initiation under shock pressure loading Part I. Experiment. - LH Hernandez-Gomez *(Inst Invetigaciones Electricas, Dept Ing Mec, Dante 36 6o Piso Apdo Postal 5-849, 11590 Mexico DF, Mexico)* and C Ruiz *(Dept of Eng Sci, Univ of Oxford, Oxford OX1 3PJ, UK)*. Theor Appl Fracture Mech 19(1) 75-83 (Jun 1993).

A technique for analyzing crack initiation and growth in polymeric materials is described. The specimen is a circular plate fixed at the edge and subjected to a pressure shock wave loading. The design of the test is shown to reflect the loading history. Static tests can also be performed with the same equipment. The results of both static and dynamic tests are compared in terms of the load intensity required for crack initiation. It is found that this is higher for the static tests than for the dynamic tests, as expected.

10A544. Assessment of data for dynamic crack initiation under shock pressure loading Part II. Analysis. - LH Hernandez-Gomez *(Inst Investigaciones Electricas, Dept Ing Mec, Danta 36 6o Piso Apdo Postal 5-849, 11590 Mexico DF, Mexico)* and C Ruiz *(Dept of Eng Sci, Univ of Oxford, Oxford OX1 3PJ, UK)*. Theor Appl Fracture Mech 19(1) 85-94 (Jun 1993).

Presented in Part I is a shock-tube testing device for assessing the dynamic crack initiation characteristics. Data were found to obtain the critical dynamic stress intensity factor. Part II of this work is considered with the FE dynamic stress analysis to assist the interpretation of the experimental data for a center cracked PMMA specimen. Results are compared with the corresponding static data and show that they are not comparable with the stress intensity factor interpretation because of the dynamic loading rate effect.

10A545. Two-dimensional cracks at an angle to an interface. - B Chen and TJ Lardner *(Dept of Civil Eng, Univ of Massachusetts, Marston Hall, Amherst MA 01003)*. Int J Solids Struct 30(13) 1725-1735 (1993).

In this paper, we provide additional numerical results for the energy release rate and the stress intensity factors at the tip of a straight 2D crack at an angle to an interface of a bimaterial system. Three cases are considered: a semi infinite crack under a pair of point loads, a finite crack under a pair of point loads, and a finite crack under uniform pressure. The formulations for each of these cases lead to a system of singular integral equations which can be solved numerically. The effects of the orientation of the crack, the distance between the crack and the interface, and the material properties, α, \Beta, are investigated. The results are compared to the corresponding asymptotic results of Hutchinson et al for the subinterface crack (crack parallel to the interface).

274C. SUBCRITICAL CRACK PROPAGATION

10A546. Elevated temperature fatigue crack growth in alloy 718 Part I. Effects of mechanical variables. - H Ghonem *(Mech of Solids Lab, Dept of Mech Eng and Appl Mech, Univ of Rhode Island, Kingston RI 02881)*, T Nicholas *(Wright Lab, Mat Directorate, WPAFB)*, A Pineau *(Centre des Materiaux, Ecole des Mines de Paris, 91000 Evry, France)*. Fatigue Fracture Eng Mat Struct 16(5) 565-576 (May 1993).

In this paper observations concerning the effects of mechanical variables on the crack growth process in alloy 718 are reviewed and analyzed on the basis of the related deformation characteristics in the crack tip region. The variables included temperature, frequency, wave shape, hold time, load ratio and load interaction. These analyses have suggested that the role of each parameter in the acceleration of crack tip damage is governed mainly by their relative influence on the nature of the corresponding plastic deformation and associated slip line density. On the basis of this view (which assumes crack growth damage covers the range from cyclic- to fully time-dependent processes), the interactive effects of loading parameters are discussed when considering the corresponding fracture mode. Conflicting experimental observations under different operating conditions are examined.

10A547. Mixed mode fatigue crack growth with a sudden change in loading direction. - YC Lam *(Dept of Mech Eng, Monash Univ, Clayton, Vic 3168, Australia)*. Theor Appl Fracture Mech 19(1) 69-74 (Jun 1993).

With a sudden change in the maximum load level, there will be a corresponding change in the crack driving force regardless of whether the load is applied monotonically or cyclically. The effective strain energy density factor range $\Delta S_{p,eff}$ has been used to correlate mixed mode fatigue crack propagation where the crack growth direction is not known as in a priori. Examined in this work is a sudden change of load direction on fatigue crack growth while the load level remains unchanged. Yielding is assumed to be localized near the crack tip such that the crack growth behavior can be described adequately by the elastic stress field. Under the conditions investigated, minimal change on crack growth rates is observed. No firm conclusion could be drawn on deviation of crack path for the case considered.

10A548. Review of crack propagation under unsteady loading. - HH Bryan and KK Ahuja *(Georgia Tech)*. AIAA J 31(6) 1077-1089 (Jun 1993).

This paper presents an overview of the theories and research currently available on crack propagation under unsteady loadings, especially those of acoustic origin. Although all efforts have been taken to provide a thorough review of the subject, inadvertent omissions of relevant material are unavoidable.

10A549. Stick-slip in the thin film peel test I. The 90° peel test. - K-H Tsai and K-S Kim *(Div of Eng, Brown Univ, Providence RI 02912)*. Int J Solids Struct 30(13) 1789-1806 (1993).

An analysis of the process of stick-slip in the 90° peel test is carried out using a slender elastic beam theory which considers both stretching and bending of the film. Using an energy based crack propagation criterion, it is shown that the intersection between the energy release rate curve and the interface toughness curve delineates the limit cycle on the interface toughness versus crack-growth rate plane for stick-slip 90° peeling. As a result of this analysis, it has been found that the effects of bending are significant and cannot be neglected in the general case. In addition, the stick-slip period and frequency have been found to depend on Young's modulus, and the thickness and length of the free film, and the dependence differs for the bending-dominant and stretching-dominant peel tests.

See also the following:

10A597. Shape of surface cracks in fatigue

274D. DYNAMIC PROCESSES

10A550. Vibration of elastic structures with cracks. - IY Shen *(Dept of Eng Mech, Univ of Nebraska, Lincoln NE 68588-0347)*. J Appl Mech 60(2) 414-421 (Jun 1993).

An analytical algorithm is proposed to represent eigensolutions $[\lambda^2{}_m, \psi_m(r)]^\infty{}_{m=1}$ of an imperfect structure C containing cracks in terms of crack configuration σ_c and eigensolutions $[\omega^2{}_n, \phi_n(r)]^\infty{}_{n=1}$ of a perfect structure P without the cracks. To illustrate this algorithm on mechanical systems governed by the 2D Helmholtz operator, the Green's identity and Green's function of P are used to represent $\psi_m(r)$ in terms of an infinite series of $\phi_n(r)$. Substitution of the $\psi_n(r)$ representation into the Kamke quotient of C and stationarity of the quotient result in a matrix Fredholm integral equation. The eigensolutions of the Fredholm integral equation then predict $\lambda^2{}_m$ and $\psi_m(r)$ of C. Finally, eigensolutions of two rectangular elastic solids under antiplane strain vibration, one with a boundary crack and the other with an oblique internal crack, are calculated numerically.

See also the following:

10A87. Vibration and stability of a rotating shaft containing a transverse crack

274E. FATIGUE CHARACTERISTICS OF MATERIALS

10A551. Effect of crack deflection and branching on the R-curve behavior of an Al-Li alloy 2090 sheet. - N Eswara Prasad, SV Kamat, G Malakondaiah *(Defence Metall Res Lab, PO Kanchanbagh, Hyderabad-500 258, India)*. Int J Fracture 61(1) 55-69 (1 May 1993).

The methodology to predict the increase in crack growth resistance due to crack deflection and branching is described. These procedures are discussed with respect to an Al-Li alloy 2090 sheet in T6 condition, the R-curve tests on which revealed that the crack path in L-T orientation was deflected and branched while it remained nominally straight in T-L orientation. The resistance to slow stable crack extension in L-T orientation was found to be significantly higher as compared to that in T-L orientation. Such behavior is rationalized in terms of crack deflection and branching. The observed variation in the crack path morphology and the resulting R-curves in L-T and T-L orientations can be understood in terms of the microstructural features of the alloy.

10A552. Effect of yield strength on the basic fatigue strength of welded joints. - A Ohta, Y Maeda, N Suzuki *(Natl Res Inst for Metals, 2-3-12 Nakameguro, Meguro-ku, Tokyo 153, Japan)*. Fatigue Fracture Eng Mat Struct 16(5) 473-479 (May 1993).

The basic fatigue strength of welded joints in four steels having different yield strengths has been obtained by tests in which the maximum applied stress was held constant and equal to the yield strength, to simulate the tensile residual stress in real large-scale structures. In the long-life region superior properties occurred with a decrease in the yield strength. It is therefore suggested that both low yield strength steel, which can be produced by a thermo-mechanical control process without affecting the tensile strength, and steels or welding consumables which show a low transformation temperature, may have a high fatigue strength.

10A553. Elevated temperature fatigue crack growth in Alloy 718 Part II. Effects of environmental and material variables. - H Ghonem *(Mech of Solids Lab, Dept of Mech Eng and Appl Mech, Univ of Rhode Island, Kingston RI 02881)*, T Nicholas *(Wright Lab, Mat Directorate, WPAFB)*, A Pineau *(Centre Mat, Ecole des Mines de Paris, 9100 Evry, France)*. Fatigue Fracture Eng Mat Struct 16(6) 577-590 (Jun 1993).

Observations concerning the effects of the environments and material variables on the crack growth process in alloy 718 are reviewed and analyzed on the basis of deformation characteristics in the crack tip region. The review of the role of material variables has focused on the effects of chemical composition and microstructure parameters including precipitate size and morphology as well as grain size and morphology. These analyses have suggested that the governing mechanism at the crack tip is the degree of homogeneity of plastic deformation and associated slip density. For conditions promoting homogeneous plastic deformation, with a high degree of slip density, the environmental damage contribution is shown to be limited, thus permitting the dominance of cyclic damage effects which are characterized by a transgranular crack growth mode and a lower crack growth rate. Under conditions leading to inhomogeneous plastic deformation and lower slip density the crack tip damage is described in terms of grain boundary oxidation and related intergranular fracture mode. Considering the crack growth damage mechanism in alloy 718 ranges from fully cyclic dependent to fully environmental dependent, conflicting experimental observations under different operating conditions are examined and a sensitizing approach is suggested to increase the alloy resistance to environmental effects.

10A554. Fatigue life assessment of aluminum alloys with casting defects. - B Skallerud *(SINTEF Struct Eng, N-7034 Trondheim, Norway)*, T Iveland, G Harkegard *(Div of Appl Mech, Norwegian IT, N-7034 Trondheim, Norway)*. Eng Fracture Mech 44(6) 857-874 (Apr 1993).

The fatigue lifetimes of cylindrical aluminum specimens containing shrinkage cavities were measured. The results were compared with those of specimens without macroscopic cavities (DC cast). Two different heat treatments were considered: T4 (naturally aged) and T6 (near peak aged). The pore shape and distribution in the specimens were complex. Pores with a maximum diameter larger than 0.2 mm resulted in a significant reduction of the lifetime. Numerical calculations were carried out to predict the fatigue life, and crack growth model taking crack closure effects into account was used. This model tended to give somewhat nonconservative results when compared with test results. Modification of the model, taking a short crack effect into account, gave conservative results.

10A555. Flexural fatigue characteristics of FRP sandwich beams. - RA Shenoi, S Aksu *(Dept of Ship Sci, Univ of Southampton, Southampton SO9 5NH, UK)*, HG Allen *(Dept of Civil Eng, Univ of Southampton, Southampton SO9 5NH, UK)*. Fatigue Fracture Eng Mat Struct 16(6) 649-662 (Jun 1993).

The flexural fatigue characteristics of FRP sandwich beams are investigated. The skins of the beams are made from hybrid glass-aramid fibres set in epoxy resin and the core material is made from linear PVC foam. The beams under investigation have practical application in marine operations. The applied load is uniformly distributed throughout the length of the beam which is simply supported. From both static and fatigue tests, it is revealed that the failure occurred in the core due to excessive shear, in turn, resulting in large deflections. An empirical expression is derived to postulate a failure criterion.

10A556. Fracture and fatigue of bonded rubber blocks under compression. - AN Gent, TYP Chang *(Univ of Akron, Akron OH 44325)*, MB Leung *(Exxon Prod Res, Houston TX 77252)*. Eng Fracture Mech 44(6) 843-855 (Apr 1993).

Fracture and fatigue failure of bonded rubber cylinders are discussed. Under large compressive forces, two modes of fracture are possible: splitting open of the free surface and tearing at or near the bonded edges; tearing energy T for the latter case is estimated. Under cyclic compression, the probably fracture mode of rubber is by crack propagation, leading to the bulged volume breaking away. The corresponding tearing energy is calculated. To predict the fatigue life, the rate of crack growth dc/dn is assumed to be proportional to T^2. A life prediction equation is thus obtained, of the form: load cycle $N = (K/g)^5$, where K is a constant, about 10 for a typical soft natural rubber compound, and g is the maximum shear strain set up at the edges of the bonded surfaces.

10A557. Modeling the long-life fatigue behavior of a cast aluminum alloy. - Jason C Ting *(Walsin Lihwa, 3F-1 No 286-8 Shih-Ya Rd Chein-Chen District, Kaohsiung, Taiwan, ROC)* and FV Lawrence Jr *(Dept of Civil Eng and Mat Sci and Eng, Univ of Illinois, 205 N Mathews, Urbana IL 61801)*. Fatigue Fracture Eng Mat Struct 16(6) 631-647 (Jun 1993).

As-cast specimens and smooth specimens of a AA 319 cast aluminium alloy containing casting porosity were fatigue tested with special attention given to the long-life region ($N \leq 1.25 \times 10^8$ cycles). Fatigue cracks were observed to initiate from the near-surface casting pores or from discontinuities resulting from the as-cast surface texture. The observed fatigue lives were strongly dependent on the size ($\sqrt{\text{area}}$) of these casting defects. The effect of casting defects on the fatigue life was modeled assuming the fatigue life to be the sum of the crack nucleation and the crack propagation life (including both the growth of short and long cracks). The crack growth behavior of (mechanically) short cracks was considered in detail by a developed crack-closure-at-a-notch (CCN) model. The CCN model predicted the fatigue lives for both as-cast and machined-notched specimens. Extension of the CCN model to reliability-based design was attempted using the measured size distribution of the fatigue-initiating casting pores.

10A558. Study of the effect of defects on the fatigue behavior and the fracture toughness for low carbon steel (API 5L grade B) gas transmission pipelines. - HAEA Atwa *(Egypt Gas, Egypt)*, NM Mawsouf, MYA Younan *(Dept of Mech Design and Prod, Fac of Eng, Cairo Univ,* *Giza, Egypt)*. Eng Fracture Mech 44(6) 921-935 (Apr 1993).

The use of low carbon steel pipes in gas transmission pipelines and network gas pipes has increased. API 5L grade B (American Petroleum Inst) pipes are welded and inspected according to the BGC/PS code (British Gas Standard). Since root undercut and lack of penetration are common defects, the acceptance and nonacceptance of these defects based on the BGC/PS/P2 code of butt welded pipes are evaluated. Pipes are welded with different degrees of root undercut and lack of penetration defects and are X-rayed. The defects are categorized based on both X-ray films and final crack area. Specimens are cut and fatigue precracked at different periods depending on the initial defect size. An equivalent crack length is calculated based on Paris' law for each defect size in the fatigue crack propagation. The crack opening displacement technique, J-integral method based on Begley and Landes and the residual strength method have been used to determine the fracture toughness. The results have been compared to the parent material and the initial defect size to evaluate the restrictions of the BGC/PS/P2 code. The equivalent crack length results showed that the depth of lack of penetration welding defect should be taken into consideration for both API and BGC codes since this depth has a significant effect on the equivalent crack length. The application of the Begley and Landes approach is shown to be suitable since it permits the use of specimens of different initial crack lengths. The technique is applied here for cracks of different shapes. The results are close and can be used as comparative results between different categories and the parent material since the conditions of specimen dimensions are not valid as restricted by Begley and Landes. Critical crack opening displacement is calculated which gives reliable results for different categories. Crack opening displacement technique based on the British Standard requires different specimens with the same initial crack length, which is not satisfied. The residual strength method based on ASTM gives reliable results for the different categories of defects. The depth of lack of penetration welding defect should be taken into consideration for both API and BGC codes. The BGC code should specify an allowable depth for the root undercut welding defects.

274F. STRESS OR STRAIN LIFE ANALYSIS OF FATIGUE

10A559. Cyclic notch tip strains in very high strain amplitude fatigue. - L'ubomir Gajdos *(Inst of Theor and Appl Mech, Acad of Sci, Vysehradska 49, 128 49 Prague 2, Czech Republic)*. Acta Tech CSAV 38(2) 167-174 (1993).

Measurements of cyclic notch tip strains variations in low alloy reactor steel 15 Kh2MFA have been carried out, to compare the experimental results with theoretical predictions via i) Neuber's method, ii) Hardrath-Ohman's method, and iii) equivalent energy method. The comparison shows considerable differences between experiment and prediction in all three methods. A modification of the Neuber method is suggested, to improve the reliability of prediction.

10A560. Damage tolerance assessment of the fighter aircraft 37 Viggen main wing attachment. - B Palmberg, M-O Olsson, P-O Boman, AF Blom *(Fatigue and Fracture, Struct Dept, FFA Aeronaut Res Inst of Sweden, PO Box 110 21, S-161 11 Bromma, Sweden)*. J Aircraft 30(3) 377-381 (May-Jun 1993).

This article deals with the reassessment of the newest wing attachment frame for the fighter version of the aircraft. The purpose of this article is to briefly show the extent and complexity of the assessment. Because of the original safe life design, resulting in rather high stresses, very extensive FE analyses were necessary in order to obtain accurate stress distributions and 3D stress intensity factors in critical sections. Also, high demands have been place on the accuracy of the crack growth predictions. Hence, extensive validation of the crack growth prediction technique was required. Structural testing, including artificial flaws, was carried out with the aim of obtaining crack growth data for correlation to the prediction technique. It is concluded that the state-of-the-art methodology used was successfully verified. Furthermore, damage tolerance of the considered parts were analytically proven and experimentally verified. Finally, extension of the original design life may be possible following further considerations.

10A561. Influence of load misalignment during uniaxial low-cycle fatigue testing I. Modelling. - FA Kandil and BF Dyson *(Div of Mat Metrology, Natl Phys Lab, Teddington, Middlesex TW11 0LW, UK)*. Fatigue Fracture Eng Mat Struct 16(5) 509-527 (May 1993).

A quantitative model has been proposed which predicts the extent of lifetime scatter in low-cycle fatigue due to the influence of bending caused by load misalignment. The main components of the model are the mechanism of bending, the type of extensometer used to control strain and the fatigue characteristics of the material being assessed. Three mechanisms of bending have been studied and it is argued that the most damaging one is a consequence of a lateral offset in the centre-lines of the load-train with respect to either a machine's frame or ram. Scatter in lifetime is a maximum when strain is controlled by a single extensometer (which is generally the case) and when fatigue behavior is dictated by crack initiation at the largest surface defect. Two types of scatter have been examined, (i) repeatability scatter due to testing practice within a single laboratory, and (ii) reproducibility scatter between laboratories. An example of the magnitude of reproducibility scatter due to bending has been given by using an equation based on the universal slopes method due to Manson.

10A562. Influence of load misalignment during uniaxial low-cycle fatigue testing II. Applications. - FA Kandil and BF Dyson *(Div Mat Metrology, Natl Phys Lab, Teddington, Middlesex TW11 0LW, UK)*. Fatigue Fracture Eng Mat Struct 16(5) 529-537 (May 1993).

Models for predicting scatter bands due to bending have been applied to four alloys, namely AISI 316L, Nimonic 101, 9 Cr-1 Mo, and IN 718. The alloys were tested extensively by 26 laboratories in an international round robin exercise sponsored by the Community Bureau of Reference (BCR) of the EC. After initially selecting data for analysis on the basis of their confirmed conformance to the ASTM bending criterion, it has been shown that in all four materials a major fraction of the data scatter could be attributed to bending. Furthermore, at the lowest strain range the predicted bending component represents the highest proportion of the experimental interlaboratory scatter. Many laboratories did not report any measure of bending and so could not be used in the inital analysis. However, a further interesting deduction from the models is that the entire BCR data-set can be encompassed within a scatter band based upon a bending criterion that is twice the allowable ASTM limit. Differences in the extent of scatter between materials at a given total strain range can be attributed to the gradient of the logarithmic plot of total strain range as a function of lifetime.

10A563. Numerical and experimental verification of a new model for fatigue life. - T Svensson and M Holmgren *(Dept of Mat and Mech, Swedish Natl Testing and Res Inst, PO Box 857, 501 15 Boras, Sweden)*. Fatigue Fracture Eng Mat Struct 16(5) 481-493 (May 1993).

A new model for fatigue life prediction has been presented. The model is based on Palmgren-Miner's rule in combination with a level crossing analysis. Here an effort is made to verify the model, numerically and experimentally. Data from the literature and experimental data generated by us have been compared with fatigue life predictions made with the new model. The data have also been compared with traditional fatigue life estimations based on the rain flow count method. The fatigue lives predicted by the new model often agree better with actual lives than predictions made with the RFC-method. This is especially pronounced when the loading sequence is very irregular, ie, when the sequence contains many small cycles superimposed on large cycles. The new method is both fast and simple to use.

10A564. Possibility of estimating stress and strain at the fatigue limit of steels from the results of low cycle fatigue tests. - J Kucera *(Vysoka skola banska, fakulta strojni, trida 17, listopadu 708 33, Ostrava, Czech Republic)*. Acta Tech CSAV 38(2) 175-195 (1993).

The calculation of the fatigue limit, together with relevant threshold plastic strain, based on an extrapolation of low-cycle fatigue results is described. In the study cyclic stress-strain curve parameters, K' and n', of 222 melts and/or heat-treated modifications of 104 unalloyed and low alloyed steel grades were utilized. Results of extrapolation-fatigue limit and threshold plastic strain-were correlated with the ultimate tensile strength of these steels and are in good agreement with experimental and theoretical results published in the literature.

274G. OTHER ASPECTS OF FATIGUE

10A565. Fatigue strength evaluation from surface yielding data. - J He, H Wang, J Nan *(Xi'an Jiaotong, Xi'an, China)*. Fatigue Fracture Eng Mat Struct 16(6) 591-596 (Jun 1993).

Surface yielding was detected by X-ray diffraction. The surface yield strength σ_{sy} was significantly less than the bulk yield strength, and depends on the physical state and roughness of the surface. However σ_{sy} does not change with changes in surface residual stress. Determination of surface yielding, measured under static loading, indicates that a remarkable number of grains have been plastically deformed at the σ_{sy} stress level, which will result in damage accumulation under cyclic loading. Crack initiation predominates at the level of the fatigue endurance life for smooth parts and experiments indicate that σ_{sy} equals the smooth specimen fatigue limit, particularly that associated with a high survival probability.

10A566. Geometry factors in corrosion fatigue crack propagation. - M Jakubowski *(Ship Res Inst, Tech Univ of Gdansk, Poland)*. Fatigue Fracture Eng Mat Struct 16(5) 495-507 (May 1993).

Fatigue crack growth rates for a steel in saltwater at different but constant stress intensity factor ranges have been evaluated as a function of the crack length (as measured from the notch root) for cracks longer than so-called "short" cracks. Equations describing the crack growth rate as a function of both the crack length and the stress intensity factor range have been obtained, and the effect of simulated infinite thickness of the specimens is discussed. The equations satisfactorily describe the numerous literature data for different steels, different specimens and different test conditions.

274H. CORROSION AND EMBRITTLEMENT

10A567. Influence of microstructure and non-metallic inclusions on sulphide stress corrosion cracking in low-alloy steels. - VI

Astafjev *(Samara State Univ, 1 Pavlov St, Samara 443011, Russia)*, SV Artamoshkin, TV Tetjueva *(Res Inst Vniitneft, 110 Aurora St, Samara 443086, Russia)*. Int J Pressure Vessels Piping 55(2) 243-250 (1993).

The resistance of some low-alloy tubular steels to sulphide stress corrosion cracking (SSCC) was assessed. The influence of microstructure and non-metallic inclusions on SSCC susceptibility was investigated. Three groups of differently heat-treated low-allow steels with various microstructure and shape of non-metallic inclusions were used. Threshold values σ_{th} and K_{ISSC} were determined. To analyze specific microstructural mechanisms of damage accumulation in SSCC processes the fractographic and metallographic methods were used.

10A568. Problems related to safety and reliability of materials in environments polluted by hydrogen sulphide. - G Casarini *(Instituto Ricerche Breda, 20126 Milan, Italy)*. Int J Pressure Vessels Piping 55(2) 313-322 (1993).

The results of hydrogen-induced cracking, hydrogen stress corrosion cracking (HSCC) and HSCC tests under cathodic protection obtained on the normalized medium-high strength steels for marine applications, ASA 56, ASA F56 and ASA F60, are reported. Fatigue precracked WOL specimens were loaded at room temperature and simultaneously exposed to synthetic seawater, saturated or not by hydrogen sulphide (H_2S) and at two initial pH values (pH = 1; pH = 3). Here indications are given on the types of mechanisms controlling the damaging, the comparison of the values of the crack propagation threshold stress intensity factor in air and in corrosive media, the influence of the presence of H_2S, the role of inclusions and of their plane's orientation, the relationship between the damaging phenomena, the effect of the cathodic protection.

10A569. Summary report of an ESIS working party on fracture control guidelines for environmentally assisted cracking of low alloy steels. - G Gabetta *(CISE, Tec Innovative, CP 12081, I-20134 Milano, Italy)* and I Cole *(CSIRO, Div of Build and Construct Eng, PO Box 56, Highett Vic 3190, Australia)*. Fatigue Fracture Eng Mat Struct 16(6) 603-618 (Jun 1993).

This paper provides guidelines for obtaining and using Environmentally Assisted Cracking (EAC) test data for low alloy steels, which are used in a wide range of industrial applications. Both fracture mechanics and non-fracture mechanics tests are considered, but the emphasis is on using fracture mechanics as a part of an overall strategy - a fracture control plan - to prevent or control EAC in service. Prevention is the usual strategy, but the control of crack growth is possible for thick-walled components. Fracture control planning can, for low and medium strength steel structures, be directed to both preventing and controlling EAC in service.

274I. FRETTING, WEAR, AND EROSION

10A570. Erosion resistance of diamond coatings. - MV Kral, JL Davidson, JJ Wert *(Dept of Mat Sci and Eng, Vanderbilt Univ, Nashville TN 37235)*. Wear 166(1) 7-16 (15 Jun 1993).

Preliminary solid particle erosion testing of 10 μm thick diamond films on silicon substrates showed excellent erosion resistance. The application of diamond coatings to materials that are commonly used in erosive environments should result in significant improvement over other erosion-resistant coatings. Diamond films were applied to silicon, tungsten Ti-6Al-4V using a high-pressure microwave-assisted plasma deposition system and were determined to have a high degree of sp^3 bonding using Raman spectroscopy. Erosion tests were performed on diamond-coated silicon, tungsten and Ti-6Al-4V, as well as on uncoated substrates and alternative coatings. The erosion resistances of the target materials were compared using volume loss *versus* erodent mass plots and steady-state erosion-rate data. Diamond-coated silicon showed the highest erosion resistance. Diamond-coated Ti-6Al-4V also showed high erosion resistance when compared with uncoated materials. Erosion mechanisms were identified by examination of eroded surfaces using scanning electron microscopy. Diamond coatings on Ti-6Al-4V substrates failed by delamination of the coating from the substrate. This is believed to be a result of high residual stresses and stress concentrations at the coating-substrate interface. Diamond coatings on silicon and tungsten substrates are gradually removed by a brittle erosion process.

10A571. Hydro-abrasive erosion characteristics of 30vol%SiC_p/6061-T6 Al composite at shallow impact angles. - M Ramulu, SP Raju *(Dept of Mech Eng, Univ of Washington, FU-10, Seattle WA 98195)*, H Inoue *(Dept of Mech Eng, Univ of Osaka Prefecture, Osaka 591, Japan)*, J Zeng *(Dept of Mech Eng, Univ of Rhode Island, Kingston RI 02881)*. Wear 166(1) 55-63 (15 Jun 1993).

Hydro-abrasive erosion characteristics were investigated for 30vol%SiC_p/6061-T6 Al composite material and 6061-T6 aluminium alloy at steady-state conditions using abrasive waterjets. The erosion rates were measured for shallow impact angles (<20°) and the influence of the abrasive size, flow rate and the impact angle on the erosion process was studied. Scanning electron microscopy were used to characterize the eroded surface and the results showed that erosion in the composite occurred due to microcutting of the aluminium matrix material, with the SiC particulates being removed subsequently by the shovelling action of the oncoming jet. The experiments also revealed that the erosive wear rates for the 30vol%SiC_p6061-T6 Al composite were less than the erosive wear rates of the 6061-T6 aluminium alloy by a factor of two.

274J. CREEP

10A572. Analysis of damage in a ceramic matrix composite. - BF Sorensen *(Mat Dept, Riso Natl Lab, DK-4000 Roskilde, Denmark)* and R Talreja *(Sch of Aerospace Eng, Georgia Tech)*. Int J Damage Mech 2(3) 246-271 (Jul 1993).

Mechanisms of damage and the associated mechanical response are studied for a unidirectionally fiber-reinforced ceramic matrix composite subjected to uniaxial tensile loading parallel to fibers. A multi-stage development of damage is identified, and for each stage the governing mechanisms are discussed. For distributed matrix microcracking a continuum damage model is used as the basis for describing the associated stress-strain behavior. A simplified analysis of frictional sliding at the fiber-matrix interface is made to elucidate its effect on the stress-strain response.

10A573. Comparisons of fracture parameter evaluations for power law hardening creep. - TK Hellen *(Oakfield House, Lower Morton, Thornbury, Bristol BS12 1LD, UK)* and J Joch *(Nuclear Res Inst, 25068 Rez u Prahy, Czech Republic)*. Eng Fracture Mech 44(6) 831-841 (Apr 1993).

Convergence properties of various FE based methods for the evaluation of the crack-tip field amplitude in creep C are examined on ome representative examples. In particular, the case of non-steady-state creep, when C is contour-dependent with significant interior convergence properties, is studied. It is demonstrated that the virtual crack extension (VCE) implementation exhibits significantly better convergence properties than the conventional domain and contour integral method. The VCE method also exhibits very good convergence for J evaluation, which does not have any direct physical interpretation for dominating creep but can be useful for C estimates. The background for these estimates is summarised.

10A574. Creep damage and creep crack growth in low-alloyed heat-resisting steels. - D Regener *(Technische Univ Otto von Guericke Magdeburg, Inst fur Werkstofftech und Werkstoffprufung, O-3010 Magdeburg, PSF 4120, Germany)*. Int J Pressure Vessels Piping 55(2) 323-332 (1993).

Development of damage in components exposed to, and loaded at, high temperatures is mainly the result of creep processes as a function of time. The damage accompanying the creep crack was studied and quantified in conjunction with crack growth investigations conducted on low-alloyed heat resisting steels. The relationship between failure behavior, load, and structure is discussed.

10A575. Creep-fatigue crack growth and fractography of metallic materials in air and vacuum at elevated temperatures. - R Koterazawa *(Inst of Eng Mech, Univ of Tsukuba, Tsukuba, Japan)*. Fatigue Fracture Eng Mat Struct 16(6) 619-630 (Jun 1993).

Creep-fatigue crack growth behavior of a Type 304 stainless steel, a quenched 2-1/4Cr-1Mo steel, Hastelloy X, a Ti-6242 alloy, and a low carbon steel under different reversed loading patterns (P-P, C-P, and C-C) were investigated in air and a vacuum environment. The results are discussed in the light of fracture mechanics and fractography. Crack growth rates for all of the materials tested were successfully correlated in terms of the cyclic J integral range (ΔJ) irrespective of the loading patterns. In the low growth rate region, where fatigue fracture was predominant, crack growth rates of all the materials were about the same for the same value of ΔJ. On the other hand, growth rates were somewhat different, depending on the creep ductility of the material in the region of high growth rate, where creep fracture was predominant. Materials with lower ductility exhibited higher growth rates for the same ΔJ values. Differences were insignificant between the crack growth rates in air and vacuum and were consistent with the small differences observed in the fracture surface morphology in the two environments.

10A576. Effect of cyclic overload on the crack growth behavior during hold period at elevated temperature. - Kee Bong Yoon, A Saxena, DL McDowell *(Mech Properties Res Lab, Georgia Tech)*. Int J Fracture 59(3) 199-211 (1 Feb 1993).

Effect of tensile overload on elevated temperature crack growth behavior during the subsequent load hold period has been studied by numerical and experimental methods. FE analysis of compact specimens shows that when the tensile overload precedes the load hold period, C_t during the hold period is significantly smaller (ie, retarded) compared to the case without the overload. This is due to crack tip stress relaxation associated with large crack tip plasticity generated by the overload. A modified C_t estimation scheme is proposed by introducing a new equation for t_{pl}. Using this scheme, the retardation behavior of C_t due to the overload is successfully modeled. Creep-fatigue crack growth data for an ex-service 1.25Cr-0.5Mo steel at 538°C (1000°F) were generated in air. The hold times are 10 seconds, 98 seconds and 10 minutes. Time-dependent crack growth rate during the load hold period $(da/dt)_{avg}$ is correlated with $(C_t)_{avg}$ estimated by the new estimation scheme. $(da/dt)_{avg}$ data from all the tests with overload are higher than those from the tests without overload. The peak stress associated with the overload seems to have enhanced void nucleation and to increase the time-dependent crack growth rate due to creep. This argument is supported by microscopic observations.

10A577. Methodology for modeling tertiary creep behavior of engineering alloys under oxidizing conditions. - S Osgerby and BF Dyson *(Div of Mat Metrology, Natl Phys Lab, Teddington, Middlesex TW11 0LW, UK)*. Int J Pressure Vessels Piping 55(2) 333-341 (1993).

Several mechanisms of creep-oxidation interaction have been discussed and placed within the framework of a creep-corrosion interaction diagram by modeling the individual mechanisms, using continuum creep damage mechanics. Although validation of the models is difficult because experimental data are rare, some agreement with model predictions has been achieved where appropriate data are available.

10A578. Power law creep of a composite material containing discontinuous rigid aligned fibers. - RM McMeeking *(Dept of Mat and Dept of Mech Eng, UC, Santa Barbara CA 93106)*. Int J Solids Struct 30(13) 1807-1823 (1993).

An asymptotic analysis is presented for the power law creep of a matrix containing discontinuous rigid aligned fibers. The fibers analyzed have a high aspect ratio. As a result, the fiber length is much greater than both the fiber diameter and the spacing between neighboring fibers. For this situation, flow around the fiber ends can be neglected when the creep strength is being calculated. When the matrix is not slipping on the fiber surface or is nearly stuck, shearing flow dominates the behavior. The radial gradient of shear stress is balanced by the axial gradient of hydrostatic stress. Longitudinal, radial and circumferential deviatoric stresses are negligible. The resulting power law creep rate of the composite material is inversely proportional to the fiber aspect ratio raised to the power $1 + 1/n$ where n is the creep index. The fiber volume fraction also influences the creep rate. When the matrix slips freely on the fiber surface, or nearly so, stretching dominates the matrix flow. In this situation, the composite creep strength is not much better than the unreinforced matrix.

274K. ABLATION, SPALLATION, DELAMINATION

10A579. Analysis of inelasticity effect due to damage on stress distributions in composite laminates. - CL Chow *(Dept of Mech Eng, Univ of Michigan, Dearborn MI 48128-1491)*, F Yang, A Asundi *(Dept of Mech Eng, Univ of Hong Kong, Hong Kong)*. J Reinforced Plastics Composites 12(8) 888-915 (Aug 1993).

A damage mechanics model characterizing damage behavior of composite materials proposed earlier by the authors is employed to analyze the damage effects on stress field near the free edge in symmetrically laminated graphite-epoxy composites of finite dimensions under uniaxial tension. A quasi 3D FE analysis is developed for the present investigation. The results from the damaged and undamaged stress distributions of $[0/90°]_s$, $[90/0°]_s$ and $[\pm 45°]_s$ laminates are compared and examined. The processes of initiation and development of damage zone in these composite laminates are also discussed.

10A580. Energy balance and the speed of crack growth in a compressed plate with delamination. - W-L Yin *(Sch of Civil Eng, Georgia Tech)*. Int J Solids Struct 30(15) 2041-2055 (1993).

The evolution of the crack growth speed in a buckled 1D delamination model is studied and two approximate solutions are presented. In the quasi-dynamic analysis one assumes that the time-dependent deflection of the delaminated layer may be approximated by the static post-buckling solution for the current delamination length. In a refined analysis one introduces an indeterminate amplitude function. The local growth condition at the crack tip is not enforced but a global energy-balance condition is used. The crack growth speeds are found to be comparable to the speeds of flexural waves. For slow and moderate rates of crack growth, the present results are in close agreement with the finite-difference solutions of the dynamic problem.

See also the following:

10A434. First-ply failure of laminated composite plates
10A437. Sublaminate analysis method for predicting disbond and delamination loads in composite structures

274M. MICROMECHANISMS

10A581. Influence of microstructure on micromechanisms of failure in HSLA steels. - L Parilak and J Dojcak *(Inst of Mat Res, Slovak Acad of Sci, Watsonova 47, 043 53 Kosice, Slovak Republic)*. Int J Pressure Vessels Piping 55(2) 353-360 (1993).

In the present work the strength properties and fracture resistance of weldable high-strength steels are described. After the fracture toughness testing in the temperature range from -196°C to +20°C the basic stretch and process zone parameters were determined with the aid of microfractographic methods. The microstructural and temperature factors of forming of stretch and process zone were described in the above mentioned steels. Original transition temperatures T_{xo} and T{xoD} were defined.

10A582. Micromechanics approach for constucting locally averaged damage dependent constitutive equations in inelastic composites. - JG Boyd, F Costanzo, DH Allen *(Center for Mech of Composites, Texas A&M Univ, College Station TX 77843-3141)*. Int J Damage Mech 2(3) 209-228 (Jul 1993).

Homogenization techniques are utilized herein to construct locally averaged mechanical constitutive equations for composites. Techniques are first reviewed for elastic composites, followed by a review of elastic composites with cracks and inelastic composites without cracks. These reviews are followed by a development of homogenized equations for inelastic composites with cracks. All equations are constructed for the case wherein a representative volume element is subjected to spatially uniform boundary strains. Several examples are presented for a representative SiC/Ti continuous fiber composite subjected to tensile deformations transverse to the fiber direction. It is demonstrated that as the damage and matrix material model are increased in complexity, the computational requirements needed to obtain homogenized properties increase to the point where homogenization techniques may not be computationally tenable when applied recursively in macroscale structural analysis.

10A583. Numerical simulation with experimental verification of the fracture behavior in granite under confining pressures based on the tension-softening model. - T Hashida, H Oghikubo, H Takahashi, T Shoji *(Res Inst for Fracture Tech, Fac of Eng, Tohoku Univ, Sendai 980, Japan)*. Int J Fracture 59(3) 227-244 (1 Feb 1993).

The use of the tension-softening model for analyzing fracture processes of rock is examined with special reference to the effect of confining pressure on the fracture extension. Tension-softening curves are measured by means of the J-based technique from unconfined tests performed on compact tension (CT) specimens of granite. On the basis of the determined tension-softening relation, numerical analyses are executed using a BEM to simulate fracture of the granite under confining pressures. Numerical results are compared to the experimental results of two series of tests for which CT specimens and thick-walled cylindrical specimens were loaded to failure under confining pressures ranging from 0 to 26.5 MPa. It is shown that the BEM analyses can predict the observed fracture behavior. Based on the results, it is demonstrated that the tension-softening relation provides a suitable model to analyze the fracture process in the rock. The source mechanism for the pressure sensitive fracture is discussed by examining the growth of the fracture process zone.

10A584. Thermal and mechanical load induced damage behavior of a low allow steel: Mechanisms and modeling. - Tie-Jun Wang *(Dept of Eng Mech, Xi'an Jiaotong Univ, Xi'an 710049, Shaanxi, Peoples Rep of China)*. Eng Fracture Mech 44(6) 971-980 (Apr 1993).

A series of experiments, including macroscopic damage measurement and *in situ* microscopic observation at room temperature and tensile tests at eight different temperatures ranging from 20 to 900°C, is carried out. Mechanical load induced ductile damage evolution law and micromechanisms are presented, where damage evolution law is measured through a new ac potential system and the micromechanisms of damage and fracture are observed through an *in situ* technique in conjunction with a scanning electron microscope (SEM) equipped with a tensile platform. A continuum damage mechanics (CDM) model for ductile fracture proposed by Wang is employed to model and to analyse the evolution law of damage in the steel. Comparison of experimental and modelling results is presented and good agreement is found. The effect of stress triaxiality on damage evolution is also discussed in the framework of CDM. The effect of temperature rise on tensile properties including Young's modulus, yield and ultimate tensile strength and ductility (elongation and reduction in area), is also reported.

See also the following:

10A424. Modeling damage in plain weave fabric-reinforced composite material
10A590. Universal physically consistent definition of material damage

274X. STOCHASTIC ASPECTS

10A585. Probabilistic fracture mechanics analysis based on 3D J-integral database. - G-W Ye, G Yagawa, S Yoshimura *(Dept of Nucl Eng, Univ of Tokyo, 7-3-1 Hongo, Bunkyo-ku, Tokyo 113, Japan)*. Eng Fracture Mech 44(6) 887-893 (Apr 1993).

The development is described of a novel Probabilistic Fracture Mechanics (PFM) code based on the 3D J-integral database, giving so-called fully plastic solutions. An efficient technique for the evaluation of leak and break probabilities is also utilized, based on the Stratified sampling Monte Carlo simulation (SMC). The outline of the present PFM code is described, and the J-integral database and the numerical technique are presented. Nonlinear effects of materials on failure probabilities are discussed through the analysis of a surface cracked structure subjected to cyclic tension.

See also the following:

10A647. Effect of reliability of crack propagation measurement on the assessment of life-times for structural elements having flaws

274Y. COMPUTATIONAL TECHNIQUES

See the following:

10A593. Interaction of penny-shaped cracks with a half-plane crack

274Z. EXPERIMENTAL TECHNIQUES

10A586. Determination of stress intensity factors and J-integrals using the method of caustics. - Ouk Sub Lee and Seong Kyeong Hong *(Dept of Mech Eng, Inha Univ, 253 Yong-Hyun Dong, Nam-Ku, Inchon 402-751, Korea).* Eng Fracture Mech 44(6) 981-989 (Apr 1993).

Applications of the optical shadow method of reflective caustics to the measurement of the stress intensity factor and J-integral in various specimens are investigated. The necessary experimental requirements to help in determining an accurate stress intensity factor and J-integral are described. The ratios of r_0 (radius of initial curve)/r_p (plastic zone size) and r_0/t (thickness of specimen) are found to be very important experimental parameters with which to obtain meaningful stress and/or strain intensities surrounding crack tips. The appropriate ranges to determine accurate values of stress intensity factor and J-integral for polycarbonate (compact tension) and aluminum (c-shaped tension) specimens are presented.

10A587. Load separation and η_{pl} development in precracked specimen test records. - MH Sharobeam *(Stockton State Col, Pomona NJ 08240-9988)* and JD Landes *(Univ of Tennessee, Knoxville TN 37996-2030).* Int J Fracture 59(3) 213-226 (1 Feb 1993).

Load separation is the theoretical basis for the single specimen J form and the incremental calculation of J-R and J_M-R curves. It is based on the assumption that the load can be represented as a multiplication of two separate functions; a crack geometry function and a material deformation function. Until recently, the main experimental basis for such an assumption was the approximate agreement between the experimental results of the single specimen J form and the energy rate interpretation of J in blunt notched bending geometries. The load separation assumption has been also implied in the growing crack records in order to develop the R-curve analysis. Both the crack geometry and material deformation functions were assumed to maintain their forms as the crack grows. Recently, an experimental study investigated the load separation in the test records of stationary crack specimens of different geometry, material, and constraint. The study showed that the load can be represented by a separable form for the entire plastic region except for a limited region at the early region of plastic behavior. Also, it was found that the load separation is not limited to a certain geometry, material, or constraint, but it is a dominant property in the ductile fracture behavior of stationary crack specimens. The study also showed that the crack geometry function is a power law function. Hence η_{pl} is a constant equal to the power law exponent of the geometry function. The objective of this study is to investigate the extension of load separation to growing crack records. Sets of test records from three different materials are used in this study. For each material three or four precracked specimen test records and one blunt notched record are analyzed for the compact specimen geometry. The study will discuss the main condition to have a separable behavior in a growing crack test record. It will also construct the geometry and deformation functions for the materials studied, these functions are compared with those obtained from stationary crack records.

See also the following:

10A583. Numerical simulation with experimental verification of the fracture behavior in granite under confining pressures based on the tension-softening model

276. Fracture and damage mechanics

276A. GENERAL THEORY

10A588. Locating a crack of arbitrary but known shape by the method of path-independent integrals. - NI Ioakimidis *(Div of Appl Math and Mech, Sch of Eng, Univ of Patras, PO Box 1120, GR-261 10 Patras, Greece).* Int J Solids Struct 30(14) 1939-1956 (1993).

The solution of a crack problem of an arbitrary, but known, shape inside an infinite plane isotropic elastic medium can be achieved in general by the method of complex singular integral equations and their numerical solution by using the Gauss- or the Lobatto-Chebyshev methods. In a few special cases, like straight or circular-arc-shaped cracks, this solution is available in closed form. In this paper we will not contribute to the above methods of solution of crack problems, but we will propose a method for the determination of the exact position of such a crack inside a closed contour in the elastic medium by gathering and using information along this contour only (by experimental techniques) and applying the method of complex path-independent integrals for the location of the crack. This paper constitutes a nontrivial generalization of relevant previous results by the author and it is of quite general applicability in fracture mechanics for nondestructive testing. Numerical results for the particular case of a straight crack are displayed for the illustration of the efficiency of the method. The generalization of the present results to the determination of additional geometric and loading parameters of the crack is also suggested very briefly and related numerical results, concerning the length of the crack and the pressure distribution on it, in the aforementioned numerical application are also presented.

10A589. $r^{-1/2}$ (ln r) singularities at interface cracks in monoclinic and isotropic bimaterials due to heat flow. - G Yan and TCT Ting *(Dept of Civil Eng Mech and Metall, Univ of Illinois, Chicago IL 60680).* J Appl Mech 60(2) 432-437 (Jun 1993).

It is known that the stress singularities at an interface crack tip of bimaterials with the effects of heat flow may have the form $r^{-1/2}$(ln r). The existence conditions of the higher order singularity $r^{-1/2}$(ln r) are studied for monoclinic bimaterials whose plane of symmetry is at $x_3 = 0$. It is shown that the higher order singularity does not exist if the bimaterial is mismatched. If the bimaterial is non-mismatched, the higher order singularity does not exist when a certain condition is satisfied. This condition is given explicitly for monoclinic bimaterials with the plane of symmetry of $x_3 = 0$ and in a simple form for isotropic bimaterials.

10A590. Universal physically consistent definition of material damage. - CW Woo and DL Li *(Dept of Mech Eng, Univ of Hong Kong, Pokfulam Rd, Hong Kong).* Int J Solids Struct 30(15) 2097-2108 (1993).

This paper proposes a physically consistent definition of material damage. The definition is based on the physical concepts of inter-atomic energy and the breaking and re-establishing of the atomic bonds. The states of material damage are physically determined in a broad sense by the configuration of the atomic bonds. The meso characteristics, such as vacancies, dislocations, pores, slips, microcavities, microcracks and so on, could be quantified through the use of subsystems each corresponding to a special configuration. The constitutive equations, referring to the material damage represented by the definition, could be developed by following both nonlocal and local theories.

See also the following:

10A451. Interactions among cracks and rigid lines near a free surface
10A545. Two-dimensional cracks at an angle to an interface
10A548. Review of crack propagation under unsteady loading
10A604. Domain integrals for axisymmetric interface crack problems

276B. LINEAR ELASTIC FRACTURE MECHANICS

10A591. Analogies between crack tip and rigid line tip stresses and displacements. - D Radaj and S Zhang *(Diamler-Benz AG, D-7000 Stuttgart 80, Germany).* Eng Fracture Mech 44(6) 913-919 (Apr 1993).

The analogies between crack tip and rigid line tip stresses and displacements are stated in respect of loading modes with singular stresses, loading modes with non-singular stresses, distribution of singular stresses, ligament related limit value formulae for stress intensity factors, notch stress related limit value formulae for stress intensity factors and elementary explicit formulae for stress intensity factors.

10A592. Axisymmetric crack problem in a nonhomogeneous medium. - M Ozturk and F Erdogan *(Dept of Mech Eng and Mech, Lehigh Univ, Bethlehem PA 18015).* J Appl Mech 60(2) 406-413 (Jun 1993).

In this paper, the axisymmetric crack problem for a nonhomogeneous medium is considered. It is assumed that the shear modulus is a function of z approximated by $\mu = \mu_0 e^{\alpha z}$. This is a simple simulation of materials and interfacial zones with intentionally or naturally graded properties. The problem is a mixed-mode problem and is formulated in terms of a pair of singular integral equations. With fracture mechanics applications in mind, the main results given are the stress intensity factors as a function of the nonhomogeneity parameter α for various loading conditions. Also given are some sample results showing the crack opening displacements.

10A593. Interaction of penny-shaped cracks with a half-plane crack. - X Huang *(Sch of Civil and Mining Eng, Univ of Sydney, NSW 2006, Australia)* and BL Karihaloo *(Inst of Mech, Aalborg Univ, Pontoppidanstraede 101, DK 9220 Aalborg E, Denmark).* Int J Solids Struct 30(15) 2117-2139 (1993).

Three-dimensional interactions between a half-plane crack and penny-shaped cracks which are not necessarily located in the same plane are analyzed using the "weight function" method of 3D crack analysis. Analytical expressions are given for the interaction kernels in the integral equations with the opening displacements of penny-shaped cracks as unknown functions. By using the Rayleigh-Ritz method the singularities of the kernels are weakened to make them suitable for FE calculations. The weak form equations are solved by a simple method after approximating the opening displacement over each crack by a constant times a square root function of the distance from its edge. This simple method of solution is shown to give results which are in excellent agreement with those of Laures and Kachanov (1991).

10A594. Interfacial fracture mechanics for anisotropic bimaterials. - J Qu *(Sch of Mech Eng, Georgia Tech)* and JL Bassani *(Dept of Mech Eng and Appl Mech, Univ of Pennsylvania, Philadelphia PA 19104-6315).* J Appl Mech 60(2) 422-431 (Jun 1993).

This paper focuses on aspects of fracture mechanics of interface cracks in anisotropic bimaterials. In this case there is a coupling of all three crack-tip fracture modes in the natural interface-crack coordinate system, whereas in the isotropic case, mode 3 is decoupled from modes 1 and 2.

This paper intends to shed light on how to interpret the crack-tip fields which are given explicitly along the interface in terms of two (real 3 × 3) bimaterial matrices W and D. A matric function Y is defined in terms of W and D which determines the coupling and oscillations in the crack-tip fields. Explicit expressions for the crack-tip fields and the associated stress intensity factors are given as well as for the energy release rate. The finite (Griffith) interface crack is considered in detail.

10A595. Perturbation eigensolutions of elastic structures with cracks. - IY Shen *(Dept of Eng Mech, Univ of Nebraska, Lincoln NE 68588-0347)*. J Appl Mech 60(2) 438-442 (Jun 1993).

The purpose of this paper is to determine approximate eigensolutions of a class of cracked mechanical systems governed by the 2D Helmholtz equation through a perturbation approach. Shen (1993) shows that exact eigenvalues λ^2_m and their corresponding crack-opening shapes $\Delta\Psi_m$ of such mechanical systems satisfy a Fredholm integral equation $A(\lambda^2_m)\Delta\Psi_m = 0$. Following the integral equation approach, the approximation in this paper consists of formulating the Rayleigh quotient of the Fredholm operator A (λ^2) and estimating eigenvalues $\mu(\lambda^2)$ of the operator A (λ^2) through perturbation and stationarity of the Rayleigh quotient. The zeros of $\mu(\lambda^2)$ then approximate eigenvalues λ^2_m of the cracked systems. Finally, approximate λ^2_m are calculated for 2D elastic solids under antiplane-strain vibration with an oblique internal crack and a boundary crack.

10A596. Relation between the magnitudes of J_D and J_M for test specimen geometrical configurations. - E Smith *(UMIST Mat Sci Centre, Manchester Univ, Grosvenor St, Manchester M1 7HS, UK)*. Int J Eng Sci 31(9) 1259-1268 (Sep 1993).

The paper investigates the difference between the magnitudes of the modified J and integral J_M and the deformation J integral J_D, with consideration being focused on those test configurations where the remaining ligament width is small. The results provide underpinning for the view that with a bend configuration, the J_M resistance curve lies above the J_D resistance curve, whereas the reverse is true with a tensile loading configuration. With a material having a high crack growth resistance, and provided yield is contained, the J_D and J_M resistance behaviors are essentially the same, for both bend and tensile loading. However, when the deformation is extensive, there can be a significant difference between the J_D and J_M resistance behaviors, this difference being greater with the bend configuration than with the tensile configuration.

10A597. Shape of surface cracks in fatigue. - JC Radon *(Dept of Mech Eng, Imperial Col, Exhibition Rd, London SW7 2BX, UK)*. Int J Pressure Vessels Piping 55(2) 275-285 (1993).

The shape development of surface cracks under pure bending fatigue is basically independent of the load type. Crack shape variations are initially influenced by the geometry of the starter notch, but specimen dimensions predominate in later stages of fatigue life. Also, residual stresses may significantly affect the initial crack geometry variations; however, their influence diminishes as the crack growth progresses. This paper describes the shape changes observed under constant amplitude fatigue in bending. Slight differences noted in the random loading fatigue will not be considered here and are the subject of a separate study.

10A598. Solids with periodically distributed cracks. - S Nemat-Nasser *(Center for Excellence for Adv Mat, Dept of Appl Mech and Eng Sci 0411, UCSD)*, N Yu *(Dept of Eng Sci and Mech, Univ of Tennessee, Knoxville TN 37996)*, M Hori *(Dept of Civil Eng, Univ of Tokyo, Bunkyo-ku, Tokyo 113, Japan)*. Int J Solids Struct 30(15) 2071-2095 (1993).

A systematic method is presented for estimating the overall properties of solids with periodically distributed cracks. In view of the periodicity, the displacement, strain, and stress fields of the cracked solid can be expressed in Fourier series. Elastic solids with periodically distributed flat voids are considered first. The results for cracks are then obtained by letting the thickness aspect ratio of the void approach zero. This limiting process is performed with care. The only approximation involved is the distribution of the homogenization eigenstrains, which is assumed to be piecewise constant. The estimate of overall elastic moduli, crack opening displacements and stress intensity factors eventually reduces to the calculation of several infinite series. The formulation is valid for elliptic as well as 2D line (slit-like) cracks, and cracks with arbitrary shapes. It fully includes the interaction effects.

276C. NONLINEAR ELASTIC FRACTURE PROBLEMS

10A599. Deformable bodies with cracks in nonlinear elasticity. - J Vala *(Inst of Phys Metall, Acad of Sci, 616 62 Brno, Zizkova 22, Czech Republic)*. Acta Tech CSAV 38(2) 125-144 (1993).

This paper generalizes the existence result for the problem of deformation, caused by surface and body forces, of a partially supported hyperelastic body occupying an open set with sufficiently smooth boundary in the 3D Euclidean space to the larger class of open sets, useful for modeling incipient defects in materials.

See also the following:

10A549. Stick-slip in the thin film peel test I. The 90° peel test

276D. STRESS INTENSITY FACTOR CALCULATIONS

10A600. Part-circular surface cracks in round bars under tension, bending and twisting. - A Levan and J Royer *(Lab Mec Struct, Ecole Centrale Nantes, 1 rue de la Noe, Nantes 44072 Cedex 03, France)*. Int J Fracture 61(1) 71-99 (1 May 1993).

Circular-formed cracks in round bars subject to tension, bending and twisting are considered. Numerical expressions are given allowing the calculation of stress intensity factors K_I, K_{II}, K_{III} at every point on the crack front for a wide range of crack geometries. Comparisons are made with analytical, experimental and numerical results available in the literature. Crack shapes satisfying the iso-K_I criterion are also determined, making it possible to investigate the problem of crack growth behavior under tensile or bending fatigue loads.

276E. VISCOELASTIC PROBLEMS

10A601. Self-similar and transient void growth in viscoelastic media at low concentration. - YM Wang and GJ Weng *(Dept of Mech and Aerospace Eng, Rutgers Univ, New Brunswick NJ 08903)*. Int J Fracture 61(1) 1-16 (1 May 1993).

An incremental scheme governing the self-similar and the transient void growth of aligned spheroidal voids is developed for a class of linear viscoelastic materials at low concentration and moderate strain. The theory is based upon Eshelby-Mori-Tanaka's concept in elasticity, but extended to the viscoelastic media by the Laplace transform and developed in a way suitable for the calculation of void growth. The condition of self-similar void growth is established, and it is found that the result of Budiansky, Hutchinson and Slutsky originally derived for the growth of a single void in an incompressible Maxwell solid with no elastic response continues to hold here. This incremental scheme further allows one to calculate the evolution of semi-axes of the voids, and of the void shape and concentration. It also permits one to predict the asymptotic shape of the voids towards which the voids will evolve under a given combination of axisymmetric loadings. Specific results are displayed for the transient void growth of initially spherical voids, and for the self-similar void growth of several selected oblate and prolate shapes at an initial concentration of $c_1 = 5\%$.

276F. CRACK TIP PLASTICITY PROBLEMS

10A602. Cohesive zone modeling of damage at the tip of cracks in slender beam structures. - S Ostlund and F Nilsson *(Dept of Solid Mech, RIT, 100 44 Stockholm, Sweden)*. Fatigue Fracture Eng Mat Struct 16(6) 663-676 (Jun 1993).

The use of simple beam theory for cohesive zone modelling of the damage response at the crack tip in linear elastic isotropic double cantilever beam (DCB) specimens has been investigated. Damage resistance curves (DR-curves) relating the applied stress intensity factor to the growth of the cohesive zones for beam theory modelling has been compared with 2D elasticity calculations for different material parameters and specimen dimensions. A substantial difference is observed between DR-curves for the two types of models. As expected this difference vanishes for decreasing beam heights. For large beam heights the DR-curves calculated by 2D elasticity are approaching small-scale yielding DR-curves, ie, DR-curves for an edge crack in an infinite plate. The beam height for which beam theory is applicable could be up to 10^{-3} times the height for which small scale bridging DR-curves are applicable.

10A603. Comparison of the J_D and J_M crack growth resistance curves for small-scale yielding conditions and the relevance to the integrity assessment of a cracked engineering structure. - E Smith *(UMIST Mat Sci Centre, Manchester Univ, Grosvenor St, Manchester M1 7HS, UK)*. Int J Eng Sci 31(9) 1269-1278 (Sep 1993).

A theoretical analysis, for small-scale yielding conditions, suggests that for ductile materials used in engineering structures, the deformation J integral (J_D) material crack growth resistance curve for a cracked engineering structure is essentially the same as the modified J integral (J_M) resistance curve. This means that provided small-scale yielding conditions are operative and provided J_M is preferred to J_D as a crack growth characterizing parameter, then assessment of the integrity of a cracked engineering structure can be performed by matching the J_D crack driving force curve for the structure with the material's J_M crack growth resistance curve, as obtained from a small specimen where the crack tip region is subjected to high constraint, eg, a compact tension specimen. This gives more realistic predictions than if the corresponding small specimen J_D material resistance curve is used.

10A604. Domain integrals for axisymmetric interface crack problems. - R Nahta and B Moran *(Dept of Civil Eng, NWU)*. Int J Solids Struct 30(15) 2027-2040 (1993).

New domain integrals for axisymmetric interface crack problems are derived. Special attention is given to the specification and subsequent treatment of auxiliary fields for the extraction of mixed-mode stress intensity factors using interaction energy integrals. The effect of crack front curvature is shown to play an important role in the derivation of the integrals. Numerical examples include an interphase penny-shaped crack and a longitudinal interface crack (fiber pull-out problem), and yield very accurate and consistent results, when compared with analytical solutions from the literature. The method is particularly suited for the analysis of fiber pull-out experiments and the accurate determination of fracture-parameters such as energy release rate G, mixed-mode stress-intensity factors K_I and K_{II} and phase angle ψ.

10A605. FE solutions of crack growth in incompressible elastic-plastic solids with various yielding extents and loadings: Detailed comparisons with analytical solutions. - N Liu and WJ Drugan *(Dept of Eng Mech, Univ of Wisconsin, Madison WI 53706)*. Int J Fracture 59(3) 265-289 (1 Feb 1993).

We have conducted numerical FE studies of plane strain quasistatic crack growth in elastic-plastic material for a wide range of applied loading conditions and yielding extents, especially general yielding. To facilitate precise comparisons with previous *analytical* results, we have employed a fully incompressible, nonhardening material model. A reduced-selected integration procedure is successfully used to enforce material incompressibility. For crack growth under bending-dominant conditions, we employ an experimentally-measured applied load versus crack length history for a compact tension specimen that experiences crack growth from small-scale yielding through general yielding conditions. A constant crack tip opening angle crack growth criterion is employed to investigate crack growth under tension-dormant loadings in the same geometry. We have also conducted a small-scale yielding crack growth simulation employing a highly refined mesh, and several additional general yielding stationary crack solutions to further explore the effects of different far-field loading combinations. Detailed comparisons of the FE results with Drugan and Chen's 'm-family' of asumptotic analytical solutions are made in an effort to assess the latter's accuracy and range of applicability, and to identify their asumptotically indeterminate parameters m and R as functions of crack growth history. Among several interesting results, we find that Drugan and Chen's near-tip characterizing parameter has a nearly constant value of m ≈ 1.23 for the entire crack growth process from small-scale yielding through general yielding conditions under *bending-dominant* loading when specimens have traction-free sides. However, we find m to vary significantly from that value as general yielding conditions are approached in *tension-dominant* loading situations, and whenever specimen sides are subjected to uniform applied loading. The numerical solutions confirm that Chen and Drugan's global approximate analytical solutions for general yielding crack growth are remarkably accurate to substantial distances from the crack tip under a wide variety of loading conditions. The fully incompressible material model employed also facilitates great physical insight into the global stress and deformation fields accompanying general yielding crack growth: numerous figures display the slip lines (which are characteristics for both the stress and velocity fields) throughout the plastically deforming regions.

10A606. Fractal characteristics of J-R resistance curves of Ti-6Al-4V alloys. - Bo Gong and Zu Han Lai *(State Key Lab for Fatigue and Fracture of Mats, Inst Metal Res, Acad Sinica PRC, Dept of Phys, Northeast Univ of Tech, Shenyang 110006, Peoples Rep of China)*. Eng Fracture Mech 44(6) 991-995 (Apr 1993).

J-R resistance curves of slow crack growth in Ti-6Al-4V alloys can be expressed in terms of fractal dimensions. The lineal fractal dimension D_f of crack growth profile obtained by the J-R technique correlates well with SEM observation of the crack surface.

10A607. J-R curve dependence on specimen geometry and microstructure in two austenitic: Ferritic stainless steels. - R Roberti, W Nicodemi *(Dept of Mec, Politec di Milano, 20123 Milano, Italy)*, GM La Vecchia *(Dept of Mec, Univ di Brescia, 25060 Brescia, Italy)*, S Basha *(Lab i Studimit te Materialeve, ISP6, Tirana, Albania)*. Int J Pressure Vessels Piping 55(2) 343-352 (1993).

The geometry dependence of J-R curves is a still-debated matter as it is of relevance for their transferability from laboratory test pieces to structural components. In the present research work J-R curves have been obtained for SENT and SENB specimens machined in the longitudinal and transverse direction from two duplex stainless-steel plates. The role of crack tip constraint, contained or uncontained yield, and microstructural directionality, has been considered to explain the observed geometry dependence of the J-R curves.

10A608. Quasi-static extension of cohesive crack described by the energy partition technique. - B Amini and MP Wnuk *(Univ of Wisconsin, PO Box 784, Milwaukee WI 53201)*. Int J Fracture 59(3) 245-264 (1 Feb 1993).

Nonlinear differential equation governing mode I fracture under small scale yielding condition has been derived on the basis of the energy partition concept. This technique is associated with a cohesive crack model. The nonlinear zone which precedes a propagating crack has been assumed to have a structured nature. In addition to this microstructural assumption, it has been postulated that the energy dissipated within the process zone (Δ), embedded in a larger nonlinear zone (R), remains invariant to the extent of crack growth. Upper and lower bounds of the tearing modulus have been related to the material ductility via closed form expressions. It has been demonstrated that the energy screening, measured by the ratio of the true fracture energy (W) to the total work expended in the cohesive zone during the process of irreversible deformation, is a monotonic function of the crack growth increment, resembling a reciprocal of the apparent material resistance to cracking described by an R-curve.

10A609. Stress structure and deformation behavior of mode I 3D crack in elastic-plastic state. - XM Chen and HG Hahn *(Lehrstuhl for Tech Mech, Univ Kaiserslautern, Postfach 3049, Geb 44, 6750 Kaiserslautern, Germany)*. Eng Fracture Mech 44(6) 895-912 (Apr 1993).

The effects of load and geometry on the stress structure of a Mode I 3D crack are investigated by means of FEM. The functions of plastic deformation and stress triaxiality constraint, during the failure process, are then analyzed. It is found that three regions, namely the plane strain similar zone ZI, the plane stress similar zone ZIII and the transition layer between them ZII, exist in front of the crack tip; 3D deformation behavior is different from that in 2D states even in the ZI and ZIII zones. It is also revealed that the failure form and position of a Mode I 3D crack will be determined by both plastic strain and stress triaxiality.

See also the following:

10A530. Free surface ductility in upsetting

276J. COMPOSITES

10A610. A 3D analysis of symmetric composite laminates with damage. - CL Chow *(Dept of Mech Eng, Univ of Michigan, Dearborn MI 48128-1491)*, F Yang, A Asundi *(Dept of Mech Eng, Univ of Hong Kong, Hong Kong)*. Int J Damage Mech 2(3) 229-245 (Jul 1993).

Damage behavior of a symmetric composite laminate without an initial imperfection or macro-crack is analyzed based on a 3D lamination theory under multi-axial loading. The global response of the laminate during the damaging process is determined from the individual response of its constituent plies and their mutual relations. Some specific results are presented to illustrate the damage characteristics of several typical composite laminates when they are subjected to proportional loading. The application of the method to characterize damage initiation and growth in more complex structures is also discussed.

10A611. Analysis of composite shear walls with interface separation, friction and slip using BEM. - JT Katsikadelis and FT Kokkinos *(Dept of Civil Eng, Natl Tech Univ, Inst of Struct Anal Zografou Campus, GR 157 73 Athens, Greece)*. Int J Solids Struct 30(13) 1825-1848 (1993).

In the present investigation a simple, efficient, versatile, and easily adaptable, iterative BE technique is presented for solving frictional contact problems with tensionless bonding arising in the analysis of composite shear walls and infilled frames. The method is developed using the total deformation formulation and is based on logical steps to establish the contact geometry and regions of slip, interface separation and adhesion. Numerical results are presented to illustrate the method and demonstrate its effectiveness.

10A612. Annular crack surrounding an elastic fibre in transversely isotropic elasticity. - HS Saxena and RS Dhaliwal *(Dept of Math and Stat, Univ of Calgary, Calgary AB, T2N 1N4, Canada)*. Eng Fracture Mech 44(6) 963-969 (Apr 1993).

The axisymmetric problem of an infinitely long transversely isotropic elastic fibre perfectly bonded to a dissimilar transversely isotropic elastic matrix containing an annular crack is considered. The annular crack, surrounding the fibre, is subjected to prescribed longitudinal tension. A potential function approach is used to find the solution of the basic equations. The mixed boundary value problem is reduced to the solution of a singular integral equation, which is further reduced, by using Chebyshev polynomials, to a system of algebraic equations.

10A613. Bulging of cracked panel in extension due to unbalanced patching. - RC Chu *(Aviation and Space Indust Dev Admin, 333 Keelung Rd, Section 1, Taipei, Taiwan, ROC)* and YS Lin *(Inst of Appl Math, Natl Chung-Hsing Univ, Taichung, Taiwan, ROC)*. Theor Appl Fracture Mech 19(1) 13-27 (Jun 1993).

When a cracked panel is patched only on one side, there is a tendency for the reinforced panel to bulge even if the load is applied in the plane. The Mindlin plate theory is applied to examine such an effect. Considered are variations of transverse shear across the adhesive and transverse normal stresses through the sheet and patch. The formulation makes use of the variational principle for determining the constitutive relations. FE is employed to discretize the system of equations and to solve for the displacements of cracked panels with unbalanced patching. Stress intensity factor solutions and stresses are obtained and compared well with available numerical results and experimental data.

10A614. Damage evolution and thermoelastic properties of composite laminates. - Weilin Zang *(Swedish Inst of Composites, Box 271, S-941 26 Pitea, Sweden)* and P Gudmundson *(Dept of Solid Mech, RIT, S-100 44 Stockholm, Sweden)*. Int J Damage Mech 2(3) 290-308 (Jul 1993).

An analytic model for the prediction of the thermoelastic properties of micro cracked composite laminates is presented. The expression for the calculations of energy release rates due to growth of micro cracks is also provided. Numerical results are presented that show that the present method, to a very good accuracy, can predict thermoelastic properties of micro cracked laminates at varying crack densities and layup configurations. In addition, a resistance curve behavior of the energy release rate is observed for both carbon-epoxy and glass-epoxy composite laminates. The reasons for this R-curve behavior are discussed. Criterion that govern the initiation and growth or micro cracks in composite laminates are discussed and compared to experimental data.

10A615. Effect of molding parameters on the interfacial strength in PEEK-carbon composites. - T Vu-Khanh and J Denault *(Indust Mat Inst, NRC, 75 De Mortagne Boucherville, PQ, J4B 6Y4, Canada).* J Reinforced Plastics Composites 12(8) 916-931 (Aug 1993).

The objective of this work was to investigate the effects of molding conditions (molding temperature, residence time at melt temperature and cooling rate) on the interfacial performance in PEEK-carbon composites made from both prepreg and commingled forms. The results show that a minimum molding temperature and residence time are essential requirements to produce efficient fiber-matrix adhesion in the commingled fabric system. Moreover, a transition between cohesive and adhesive fractures is observed when the cooling rate increases from 30°C/min to 63°C/min for the composite made from the commingled fabric. While good fabric-matrix bonding is always present in the PEEK-carbon prepreg form, the interfacial strength of the APC-2 laminates is also significantly affected by the cooling rate.

10A616. Matrix cracking in fiber reinforced ceramics. - Yih-Cheng Chiang *(Center for Composite Mats, Dept of Mech Eng, Univ of Delaware, Newark DE 19716)*, ASD Wang *(Dept of Mech Eng, Drexel Univ, Philadelphia PA 19104)*, Tsu-Wei Chou *(Center for Composite Mats, Dept of Mech Eng, Univ of Delaware, Newark DE 19716).* J Mech Phys Solids 41(7) 1137-1154 (Jul 1993).

This paper addresses critical stress at the propagation of a fiber-bridged matrix crack of arbitrary length in fiber-reinforced brittle matrix composites. The formulation of the problem follows the approach adopted earlier by Marshall, Cox and Evans, but a new shear-lag model that accounts for the matrix shear deformation above the slipping region is used here to derive the relationship between the crack opening displacement and the crack surface closure traction. The inclusion of the matrix shear deformation above the slipping region significantly affects the calculated crack tip stress intensity factor and the prediction of the critical stress at the propagation of the crack. Illustrative examples are cited using three available composite systems of SiC-borosilicate, C-borosilicate, and Nicalon-lithium-aluminosilicate (LAS).

10A617. Study of the opening displacement of transverse cracks in cross-ply laminates. - J Varna, LA Berglund *(Dept of Mat and Prod Eng, Lulea Univ of Tech, 95187 Lulea, Sweden)*, R Talerja *(Sch of Aerospace Eng, Georgia Tech)*, A Jakovics *(Dept of Phys and Math, Latvia Univ, LV 1098 Riga, Latvia).* Int J Damage Mech 2(3) 272-289 (Jul 1993).

Transverse cracks in cross-ply laminates are investigated experimentally to reveal the essential characteristics of their opening displacement under tensile loads. The average crack growth displacement is studied as a function of the longitudinal overall strain and effects of matrix toughness and transverse ply thickness on this parameter are examined. The interactive effects between closely spaced transverse cracks are also examined and found to be significant. Implications of the experimentally observed features on the micromechanics and continuum damage type models are discussed.

See also the following:

10A17. Anti-plane shear crack in a sandwich composite
10A18. Evaluation of fracture parameters of composites subjected to thermal shock using the BEM and sensitivity analysis techniques
10A419. Strength of carbon-epoxy laminates with countersunk hole
10A578. Power law creep of a composite material containing discontinuous rigid aligned fibers
10A687. Determination of probabilistic characteristics of the microgeometry of composite surfaces

276L. OTHER ANISOTROPIC AND NONHOMOGENEOUS MEDIA

10A618. Experimental and numerical analysis of fracture processes in concrete. - E Schlangen *(Fac of Civil Eng, Delft Univ of Tech, Delft, Netherlands).* Heron 38(2) 1-117 (1993).

A combined experimental and numerical approach is adopted to investigate fracture processes in concrete. The experimental programme focuses on the failure of concrete subjected to mixed model I and II laoding. The influence of shear load on the nucleation and propagation of cracks in concrete is studied by means of four-point-shear tests on single and double edge notched beams. A numerical model for simulating fracture is developed in which the heterogeneous microstructure of concrete is implemented. The model is used to carry out simulations of different fracture experiments. The main conclusion derived from the experimental part of this investigation is that fracture in concrete is a mode I mechanism, even if the external loading on a specimen is a combination of tensile and shear. The numerical model developed has proved able to predict fracture in concrete quite accurately. Simulations with the model increase insight into the fracture mechanism.

10A619. R-curve model of certain ceramic composites. - M Olsson and AE Giannakopoulos *(Dept of Solid Mech, RIT, S-100 44 Stockholm, Sweden).* Fatigue Fracture Eng Mat Struct 16(5) 539-554 (May 1993).

The influence of crack-bridging on the R-curve for certain types of ceramic composites is modeled. Small scale bridging conditions are assumed. A recurrence procedure is used to solve the governing coupled integral equations, resulting in R-curves (stress intensity factor versus crack growth) that depend on well defined microstructural parameters. In addition, the bridging stresses and the crack opening diplacements were computed for all stages of the R-curve development. The numerical scheme is quite general and can be used for a variety of bridging laws. The convergence of the solution method is uniform, and the accuracy is a priori controlled. The results are normalized so that they can be applied for a large variety of composites with different micromechanical parameters. R-curves were computed for different bridging laws, and were found to be sensitive to the specific bridging law used each time. Some strength-toughness relations are also discussed. The results are particularly suitable for slow crack growth analysis.

10A620. Regularization in 3D for anisotropic elastodynamic crack and obstacle problems. - E Becache, J-C Nedelec *(CMAP, Ecole Polytech, 91128 Palaiseau Cedex, France)*, Naoshi Nishimura *(Dept of Civil Eng, Kyoto Univ, Kyoto 606, Japan).* J Elast 31(1) 25-46 (Apr 1993).

We propose, in this paper, a unified method of generating a regularized integral equation in the double layer potential approach for 3D anisotropic elastodynamics. Our regularization preserves the causality in the time-domain. The method is based on a special decomposition of the hypersingular kernel which appears in the integral represenation of the stress tensor.

276N. CRACK STABILITY AND BRANCHING

See the following:

10A513. Hydraulic fracturing of soil during laboratory experiments Part I. Methods and observations

276Q. IMPULSIVE LOADING AND IMPACT

See the following:

10A952. Fracture mechanics in modeling of icebreaking capability of ships

276S. DYNAMIC CRACK PROPAGATION

10A621. Analysis of dynamic mixed mode stress fields in bimaterials by the method of caustics. - KP Herrmann and A Noe *(Lab Tech Mech, Paderborn Univ, Pohlweg 47-49, W-4790 Paderborn, Germany).* Theor Appl Fracture Mech 19(1) 49-59 (Jun 1993).

The equations of caustics for dynamically extending curvilinear interface cracks are derived where optical isotropy and anisotropy of the material have been considered, respectively. The equations have been obtained by applying the methods of generalized complex potentials. Moreover, an algorithm for the determination of stress intensity factors from experimentally obtained caustics is presented for the case of dynamic crack extension.

10A622. Assessment of dynamic fracture characteristics of weld metal. - Q Liu *(Tech Versuchs- und Forschungsanstalt, Univ of Tech, Vienna, Austria)* and T Varga *(Tech Versuchs- und Forschungsanstalt, Inst of Mat Sci and Mat Testing, Univ of Tech, Vienna, Austria).* Int J Pressure Vessels Piping 55(2) 223-232 (1993).

The dynamic fracture toughness of weld metals was tested by using the dynamic specific energy, Y_{pj}, as a measure. The results show that this approach can be used to estimate the dynamic fracture toughness of different microstructural areas of weld metal. Depending on the microstructure, different values of Y_{pj} were observed. The dynamic fracture toughness J_{Id} measured and calculated by using Y_{pj} within ±15%.

10A623. Crack propagation in cylindrical shells. - M Farshad and P Flueler *(Swiss Fed Lab for Mats Testing and Res (EMPA), Uberlandstr 129, CH-8600 Dubendorf, Switzerland).* Eng Fracture Mech 44(6) 937-947 (Apr 1993).

Results of a theoretical study of dynamic steady crack propagation in a circular cylindrical shell are presented. Equations of thin circular cylindrical shells are utilized for theoretical investigation. The semi-analytic crack tip stress solutions to shell equations are obtained by the perturbation method as well as an iterative method. Plots of internal stresses in the shell with a stationary as well as a steadily running crack are presented. These results are compared with those related to flat plates. It is concluded that the shell curvature has a pronounced effect on increasing the values of crack tip stresses. It would also qualitatively affect the variation of stress field around the crack tip. In some cases, the curvature action is shown to be even more pronounced than the inertia effects.

See also the following:

10A514. Hydraulic fracturing of soil during laboratory experiments Part II. Propagation

276Y. COMPUTATIONAL TECHNIQUES

10A624. Application of the strain energy density concept to the determination of a crack propagation direction initiated at a sharp notch tip. - Z Knesl *(Inst of Phys Metall, Acad of Sci, Zizkova 22, 616 62 Brno, Czech Republic).* Acta Tech CSAV 38(2) 221-234 (1993).

The strain energy density distribution in the vicinity of a V-notch and the generalized strain energy density factor are used as the criteria determining directions of propagation of cracks initiated at the V-notch. It is shown that the direction of propagation depends on the ratio of notch stress intensity factors corresponding to the shear and normal modes of loading. The method for estimation of the ratio, based on FE calculation, is suggested.

10A625. Applications of ADINA to evaluate analysis methodologies for predicting cleavage arrest and reinitiation of a deep crack in an RPV. - J Keeney-Walker and BR Bass *(Marin Marietta Energy Syst, ORNL)*. Comput Struct 47(4-5) 553-564 (3 Jun 1993).

Several calculational procedures are compared for predicting cleavage arrest of a deep crack in the wall of a prototypical reactor pressure vessel (RPV) subjected to pressurized-thermal-shock (PTS) types of loading conditions. The three procedures examined in this study used the following models: (1) a static FE model (full bending); (2) a radially constrained static model; and (3) a thermoelastic dynamic FE model. A PTS transient loading condition was selected that produced a deep arrest of an axially oriented, initially shallow crack according to calculational results obtained from the static (full-bending) model. Results from the two static models were compared with those generated from the detailed thermoelastic dynamic FE analysis using ADINA. The dynamic analyses modeled cleavage-crack propagation using a node-release technique and application-mode methodologies. Comparisons presented here indicate that the degree to which dynamic solutions can be approximated by static models is highly dependent on several factors, including the material dynamic fracture curves and the propensity for cleavage reinitiation of the arrested crack under PTS loading conditions. Additional work is required to develop and validate a satisfactory dynamic fracture toughness model applicable to postcleavage arrest conditions in an RPV.

10A626. Numerical analysis of cyclic deformations and crack growth of pre-cracked steel components using the ADINA program system. - D Azodi and P Bachmann *(Gesellschaft fur Anlagen- und Reaktorsicherheit, GRS mbH, Schwertnergasse 1, 5000 Kolhn 1, Germany)*. Comput Struct 47(4-5) 565-589 (3 Jun 1993).

Our aim was to achieve a basic understanding of the vessel investigations under cyclic deformations and to validate ductile fracture mechanics concepts concerned with the cyclic J-integral. Several 3D FE analyses have been performed for components subjected to cyclic plastic deformations. Based on the slightly modified virtual crack extension method, cyclic J-integral values were computed and have been discussed. As long as the material plasticity around the crack tip is confined, the J-integral method is applicable and appears to be a suitable parameter for handling low-cycle fatigue problems.

10A627. Numerical evaluation of interface fracture parameters using ADINA. - KM Lee, O Buyukozturk, CKY Leung *(Dept of Civil and Env Eng, MIT)*. Comput Struct 47(4-5) 547-552 (3 Jun 1993).

The problem of cracking at interfaces is pertinent not only to composite materials but also to structures with adhesive joints, thin films and coatings. Criteria are needed for the study of the crack growth scenarios in the interfacial region where relative magnitudes of the fracture energy for the constitutent materials and that of the interface play an important role in cracking behavior. Interface fracture occurs when the interfacial energy release rate G is equal to the interfacial fracture energy Γ_i, that is characterized as a function of the loading phase ψ. Therefore, for the analysis of interfacial fracture both the energy release rate (G) and the loading phase angle (ψ) must be evaluated. In this paper, a numerical method is presented to obtain the values of these two parameters at the tip of an existing interface crack. Numerical analyzes of three models containing interface cracks are performed using the ADINA FE program. In general, good agreement between the results from the numerical calculation and the analytical solutions is obtained.

See also the following:

10A376. Westergaard stress functions for displacement-prescribed crack problems I

276Z. EXPERIMENTAL TECHNIQUES

10A628. Closer look at estimation of fracture toughness from Charpy v-notch tests. - HJ Schindler and U Morf *(Swiss Fed Lab of Mat Testing and Res, Ueberlandstr 129, CH-8600 Dubendorf, Switzerland)*. Int J Pressure Vessels Piping 55(2) 203-212 (1993).

Although it is well known that the adequate parameters to characterise the toughness of materials are those according to the theory of fracture mechanics, the classical Charpy fracture energy is still often used in testing practice. Many efforts have been made to correlate these two types of toughness parameters with each other. In many cases these correlations give no satisfying results. In this paper it is investigated under what circumstances such correlation can exist and what type they are of. It is shown – from a theoretical point of view – that correlations are restricted to certain families of materials, ie, that there are no general applicable correlation formulas. For those purposes the standard Charpy tests have to be replaced by instrumented tests on sharp notched or pre-cracked specimens.

10A629. Evaluation method of dynamic fracture toughness by the computer-aided instrumented Charpy Impact Testing System. - I Yamamoto and T Kobayashi *(Toyhashi Univ of Tech, Tempaku-cho, Toyohashi 441, Japan)*. Int J Pressure Vessels Piping 55(2) 295-312 (1993).

The instrumented Charpy impact test has been widely used as a simple method semi-empirically evaluating the material impact toughness. The authors have developed a new dynamic fracture toughness evaluation system using a instrumented Charpy impact testing machine aided with a personal computer, which has been called "CAI (Computer-Aided instrumented Charpy Impact testing)" system. Using the CAI system, dynamic fracture toughness such as K_d, J_d, T_{mat} and various energies can be obtained from the load-deflection curve of a single pre-cracked specimen. In this paper, in addition to the detail of the CAI system, the elastic deformation behavior of the Charpy testing machine and its correspondence in the CAI system are described.

10A630. Evaluation of J_{1c} for weldment constituents by multispecimen test method. - I Glavardanov *(Fac of Tech Sci, 21 000 Novi Sad, V Perica Valtera 2, Yugoslavia)* and S Sedmak *(Fac of Tech and Metall, 11 000 Belgrade, Karnegijeva 4, Yugoslavia)*. Int J Pressure Vessels Piping 55(2) 213-221 (1993).

Crack-resistance properties of weldment constituents are required in a safety analysis of highly stressed penstock produced from 700 MPa nominal yield strength high-strength low alloy steel. Small size specimens (10 x 10 x 55 mm) with fatigue pre-crack in base metal (BM), weld metal (WM) and heat-affected zone (HAZ) were used in multi-specimens test method for J_1c evaluation. Tests were performed at room and low temperatures down to -98°C. A low-temperature cabinet for these tests has been designed based on flow of nitrogen gas, developed by heating liquid nitrogen. Fracture toughness of BM is found to be high at room temperatures (800 kN-m), but "pop-in" effect reduced it at temperatures below -40°C (650 kN-m at -40°C, 300 kN-m at -80°). Similar behavior was found for WM and HAZ, but with lower fracture toughness values compared to BM and significant scatter of results.

10A631. Measurement of dynamic elastic-plastic fracture toughness parameters using various methods. - H-W Viehrig *(Res Centre Rossendorf Inc, D-O-8051 Dresden, PF 19, Germany)*, K Popp *(Radioecology Group, Eng Ltd IAF, D-O-8054 Dresden, Karpatenstr 20, Germany)*, R Rintamaa *(Metals Lab, Tech Res Centre of Finland, SF-02151 Espoo 15, Kemistintie 3, Finland)*. Int J Pressure Vessels Piping 55(2) 233-241 (1993).

Two improved impact testing facilities are used for the dynamic fracture toughness evaluation of precracked Charpy v-notch specimens. The methods of single specimen acoustic emission and crack mouth opening displacement testing are assumed to indicate the initiation points of stable crack growth. Thus, the dynamic ductile initiation J integral J_{Id} can be derived. It was shown that the toughness J_{Id} of the heat-resistant steel 10CrMo9.10 cannot be approximated by the J value at the maximum of the load deflection curve.

10A632. Practical use of virtual reflection caustics. - RA Kitchin and EA Patterson *(Dept of Mech and Process Eng, Univ of Sheffield, Mappin St, Sheffield S1 3JD, UK)*. Fatigue Fracture Eng Mat Struct 16(6) 597-602 (Jun 1993).

The method of reflected caustics has in recent years become a widely used technique for the study of stress and strain distributions at singularities. Despite the increasing use of this technique, simple and practical descriptions of the production of caustics are limited. A particular area of ambiguity is the production and recording of the virtual caustic. The term "virtual" classically implies that the image may only be seen through a lens and cannot be focused on a screen, however a virtual caustic may be viewed on a screen, which contravenes this classical definition. Despite this contradiction much of the published literature assumes that the reader has knowledge of how the virtual caustic is produced, thus making the technique less accessible to would-be practitioners. This paper aims to clarify the definition, formation and use of the virtual caustic.

10A633. Reproducibility of measuring the crack propagation with a clip gauge. - G Nagy and J Lukacs *(Univ of Miskolc, Miskolc-Egyetemvaros H-3515, Hungary)*. Int J Pressure Vessels Piping 55(2) 269-274 (1993).

This paper describes that during measuring the fatigue crack propagation the optical and compliance methods result in approximately the same crack length. The difference is so small, that the resulted difference among the exponents of Paris-Erdogen law cannot be statistically quantified.

See also the following:

10A513. Hydraulic fracturing of soil during laboratory experiments Part I. Methods and observations

280. Materials testing and stress analysis

10A634. Acoustic emission monitoring of pressure vessels. - P Pellionisz *(Central Res Inst for Phys, KFKI, PO Box 49, Budapest 1525, Hungary)* and P Szucs *(Central Testing Lab of Power Plants, EROKAR, PO Box 67, Budapest 1602, Hungary)*. Int J Pressure Vessels Piping 55(2) 287-294 (1993).

This paper summarizes the main features of the acoustic emission testing method. A short overview is given of how common failures can be detected at pressure vessel testing and how measurement results are evaluated. Acoustic emission monitoring of pressure vessels for the power plant industry has been introduced also in Hungary: an overview is given and some of the measurement results are presented.

10A635. Ultrasonic backscattering using digitized full-waveform scanning technique. - J Schuster *(Dipl Ing, Inst fur Verbundwerkstoffe, Univ Kaiserslautern, 6750 Kaiserslautern, Germany)* and KV Steiner *(Center for Composite Mat, Univ of Delaware, Newark DE 19716-3144)*. J Composite Tech Res 15(2) 143-148 (Sum 1993).

This paper presents the results of backscattering tests based on full-waveform scans performed on composite specimens. Five samples were manufactured with varying fiber directions and different numbers of laminae per direction. Ultrasonic backscattering tests of these samples were performed using digitized full-waveform scans. An algorithm was developed to determine the fiber direction with a tolerance of 2 to 3° and the number of laminae within a range of ±0.5 lamina for sections close to the front surface.

10A636. Through-transmission equations for remote-field eddy current inspection of small-bore ferromagnetic tubes. - DD Mackintosh, DL Atherton, PA Puhach *(Dept of Phys, Queen's Univ, Kingston, ON, K7L 3N6, Canada)*. Mat Eval 51(6) 744-748 (June 1993).

The remote-field eddy current (RFEC) method is widely used for nondestructive testing of ferromagnetic tubes such as those found in heat exchangers. An exciter coil generates an electromagnetic field that diffuses through the pipe wall, axially along the outside of the pipe, and back through the pipe wall to a detector coil. Phase and amplitude readings can be interpreted to characterize pipe defects. Skin depth theory is commonly used to calculate through-transmission effects and to predict the effects of corrosion in RFEC signals. Experimentally measured deviations from skin depth theory are described. A theoretical investigation is made of through-transmission for a cylindrical wave impinging on a conducting tube. The cylindrical through-transmission equations agree well with RFEC data. The application of the new equations to RFEC defect signal analysis is discussed. A case study of an RFEC scan of a metal loss defect is described. The through-transmission equations were found to hold at the defect. However, the RFEC scan data deviated slightly from the value predicted by the through-transmission equations. The deviation was attributed to a perturbation of the field on the outside of the pipe caused by the defect, an effect not considered in a through-transmission analysis.

10A637. Radar inspection of structures. - JH Bungey and SG Millard *(Dept of Civil Eng, Univ of Liverpool, UK)*. Struct Build 99(2) 173-186 (May 1993).

During the past few years, surface scanning impulse radar systems have begun to achieve popularity in the UK for a wide range of civil engineering applications. Investigation of the structural details and of the integrity of both concrete and masonry structures has proved to be a particularly fruitful field of application. The fundamental background is outlined briefly and a wide range of reported usage on a worldwide basis is reviewed. Features of currently available equipment are described, with particular emphasis on the factors that influence reproducibility and interpretation of results, including the use of color displays and computerized signal enhancement procedures. Advantages and limitations of the technique are examined critically, and areas for future study and development are identified.

See also the following:

10A121. Scattering of ultrasonic wave by cracks in a plate

10A197. Radiation of Lamb waves by a system of internal stress sources in an isotropic elastic layer

10A448. Use of piezoelectric films in detecting and monitoring damage in composites

10T449. Fatigue behavior of glass ceramics under multiaxial stress states: Examination by diametral compression

10A450. Heat transmission on the thermal shock test of ceramics

10A649. Carbon fiber reinforced concrete for smart structures capable of nondestructive flaw detection

10A724. Behavior of bolted joints tightened in plastic region: Analysis based on rigid-plastic model

282. Structures (basic)

282B. LIMIT DESIGN (SHAKEDOWN)

10A638. Limit states design of semi-rigid frames using advanced analysis Part 1. Connection modeling and classification. - JYR Liew *(Dept of Civil Eng, Natl Univ, 10 Kent Ridge Crescent, Singapore 0511)*, DW White, WF Chen *(Sch of Civil Eng, Purdue)*. J Construct Steel Res 26(1) 1-27 (1993).

This paper presents a method for modeling connection moment-rotation curves which are essential for proportioning 2D semi-rigid steel frame structures analyzed based on a second-order inelastic analysis. Procedures for calculating the key parameters used to describe the moment-rotation curves of various types of angle connections are presented. Design aids are generated in which salient size parameters that affect the moment-rotation behavior of the connection can be identified. Two schemes by which connections can be classified in terms of strength, stiffness and rotation capacity are presented, and their design implications are discussed. Analysis and design methodologies are provided in Part 2, a companion paper in which the ultimate strength and serviceability limit state behavior of a semi-rigid frame example are studied using an advanced analysis. The aim of these two-part papers is to advance the use of second-order plastic hinge based analysis for proportioning 2D semi-rigid frames without the need of separate specification equation checks.

10A639. Limit states design of semi-rigid frames using advanced analysis Part 2. Analysis and design. - JYR Liew *(Dept of Civil Eng, Natl Univ, 10 Kent Ridge Crescent, Singapore 0511)*, DW White *(Sch of Civil Eng, Purdue)*, WF Chen *(Dept of Civil Eng, Purdue)*. J Construct Steel Res 26(1) 29-57 (1993).

This paper presents an integrated advanced inelastic analysis method for proportioning semi-rigid steel frame structures in which the beam-to-column connections are composed of angles. The modeling of connection moment-rotation curves and their classifications have been presented and discussed in a companion paper. An approach called the second-order refined plastic hinge analysis is introduced. The method is validated by comparing the results with those obtained based on a more exact plastic zone analysis. It is shown that the refined plastic hinge analysis provides a good representation of inelastic behavior, and that it enables the full assessment of system and member inelastic behavior up to the limit state of strength. This analysis method is used to assess the adequacy of a 2D semi-rigid frame, and its members and connections in resisting the factored load effects. The design is evaluated with respect to the system's strength and serviceability limit states, including conformance with the code requirements for strength and stability of individual members, and rotation capacity of connections. The inclusions of connection nonlinear effects in advanced inelastic analysis provide a straightforward task for proportioning of frame members and connections, thus avoiding the complexity of having to perform specification member capacity checks for individual frame members.

282C. STRUCTURAL OPTIMIZATION

10A640. New approach to 2D eigenvalue shape design. - YA Melnikov *(Dept of Math and Stat, Middle Tennessee State Univ, PO Box 34, Murfreesboro TN 37132)* and SA Titarenko *(Baltic Mechanical Plant, St Petersburg, Russia)*. Int J Numer Methods Eng 36(12) 2017-2030 (30 Jun 1993).

A new approach to solve problems in the optimal shape design of eigenvalues is presented. The idea behind the approach is based on a combination of the known material derivative method and a specially adapted Green's functions formulation. In the current study, numerical testing has been limited to 2D shape optimization. The two test cases involve the first eigenvalues of boundary value problems which model (i) free vibrations of a fixed membrane and (ii) natural frequencies of clamped thin plates. The basic algorithm can easily be adapted to serve other types of boundary value problems dealing with the highest eigenvalues that occur in applied mechanics. Computational aspects of the proposed approach, such as accuracy of the obtained sensitivities, cost of computation and so on are discussed.

10A641. Optimal design of a composite structure. - DL Graesser *(Dept of Mech Eng, Univ of Washington, Seattle WA 98195)*, ZB Zabinsky *(Indust Eng Program, Univ of Washington, Seattle WA 98195)*, ME Tuttle, GI Kim *(Dept of Mech Eng, Univ of Washington, Seattle WA 98195)*. Composite Struct 24(4) 273-281 (1993).

This paper presents a design methodology for a laminated composite stiffened panel, subjected to multiple in-plane loads and bending moments. Design variables include the skin and stiffener ply orientation angles and stiffener geometry variables. Optimum designs are sought which minimize structural weight and satisfy mechanical performance requirements. Two types of mechanical performance requirements are placed on the panel, maximum strain and minimum strength. Minimum weight designs are presented which document that the choice of mechanical performance requirements cause changes in the optimum design. The effects of lay-up constraints which limit the ply angles to user specified values, such as symmetric or quasi-isotropic laminates, are also investigated.

10A642. Optimization of elastoplastic systems under random loading. - A Cyras and A Norkus *(Dept of Struct Mech, Vilnius Tech Univ, Sauletekio aleja 11, 2054 Vilnius, Lithuania)*. Mech Res Commun 20(4) 293-299 (Jul-Aug 1993).

One of the first investigations of the optimization problem of elastoplastic systems under random loading was that of (1) on the reference list. The shakedown theorem (2) to derive the mathematical model of the problem and the random process crossing theory for determination of extreme elastic stresses were used in the investigation. The Turkstra rule in determining the extreme elastic stresses was applied in this paper.

282D. ACTIVE CONTROL, SMART STRUCTURES

10A643. Active buckling control of smart composite plates: FE analysis. - K Chandrashekhara *(Dept of Mech and Aerospace Eng and Eng Mech, Univ of Missouri, Rolla MO 65401)* and K Bhatia *(Hartwick Prof, Troy MI)*. Smart Mat Struct 2(1) 31-39 (Mar 1993).

A FE model is developed for the active buckling control of laminated composite plates using piezoelectric materials. The FE model is based on the first order shear deformation plate theory in conjunction with linear piezoelectric theory. The piezoelectric sensors and actuators can be surface bonded or embedded and can be either continuous or segmented. The model does not introduce voltage as an additional dof and takes into account the mass and stiffness of the piezoelectric patches. The dynamic buckling behavior of the laminated plate subjected to a linearly increasing uniaxial compressive load is investigated. The sensor output is used to determine the input to the actuator using a proportional control algorithm. The forces induced by the piezoelectric actuators under the applied voltage fields enhance the critical buckling load. FE solutions are presented for composite plates with clamped and simply supported boundary conditions and the effectiveness of piezoelectric materials in enhancing the buckling loads is demonstrated.

10A644. Bending bilayer strips built from polyaniline for artificial electrochemical muscles. - Qibing Pei, O Inganas, I Lundstrom *(Lab of Appl Phys, Dept of Phys, IFM Linkoping Univ, S-581 83 Linkoping, Sweden)*. Smart Mat Struct 2(1) 1-6 (Mar 1993).

Electrically conducting conjugated polymers such as polyaniline (PANi) usually show gel properties with volume changes in the range 1-100% in response to some external stimuli. The bending beam method provides an effective and sensitive way to detect and make use of these volume changes. Bipolymer laminate strips (2.5 × 0.2 cm^2), made of PANi layer (10 μm thick) and a substrate polyimide layer (45 μm thick) bound together, were prepared. These strips bend, corresponding to volume changes in the PANi layer, during electrochemical redox of the PANi in aqueous solutions. The extension (≤ 1.0 cm) and velocity (≤ 48 cm min^{-1}) of the movement of the strips can be controlled by applying appropriate potentials and currents. We are able to obtain significant and reversible movement back and forth in seconds. The bending force of the strip is estimated to be more than 20 times the total self-weight of the strip, with an energy efficiency of around 1%. The volume change of PANi associated with the redox is ≤1%.

10A645. Neural network for feedforward controlled smart structures. - SD Synder and Nobuo Tanaka *(Vib Eng Div, Mech Eng Lab, Ministry of Int Trade and Indust, 1-2 Namiki Tsukuba Sci City, Ibaraki 305, Japan)*. J Intelligent Mat Syst Struct 4(3) 373-378 (Jul 1993).

A neural network and adaptive algorithm suitable for driving nonlinear feedforward control systems used with "smart" structures to actively control sound and vibration is presented. The neural network-algorithm combination can be viewed as an extension to the commonly used transversal filter-filtered-x LMS algorithm combination, in that the neural network is essentially a transversal filler with a nonlinear hidden layer placed between the input delay chain and output accumulator. The algorithm accommodates the transfer function and time delay between the control signal output and error signal input. The arrangement is shown in simulation to be capable of suppressing a primary disturbance, which is a nonlinear function of the reference signal fed to the control filter, and of suppressing harmonics introduced into a system by a control actuator exhibiting nonlinear performance characteristics. The results are compared to those similarly obtained using a linear adaptive control arrangement, which is incapable of providing attenuation in either case.

10A646. Systematic formulation of model uncertainties for smart structures. - R Kashani and O Fluder *(Mech Eng-Eng Mech Dept, Michigan Tech Univ MI 49931-1295)*. Smart Mat Struct 2(1) 47-54 (Mar 1993).

In this work a systematic approach is presented to formulate the structured uncertainties due to variations in the values of natural frequencies and the modal damping ratios, ie, the parameters of the A matrix of the structure's state-space model, as well as the unstructured uncertainty resulting from the fact that only a limited number of modes are included in the model of the smart structure. A computer program has been developed that takes the percentage of the variation on the parameters, as well as the desired number of modes to be included in the model and provides the user with the appropriate formulation of the uncertainty.

See also the following:

10A326. Electromechanical properties of smart materials

282G. RELIABILITY DESIGN

10A647. Effect of reliability of crack propagation measurement on the assessment of lifetimes for structural elements having flaws. - J Lukacs *(Univ of Miskolc, H-3515 Miskolc-Egyetemvaros, Hungary)*. Int J Pressure Vessels Piping 55(2) 261-268 (1993).

The assessment of the life-time for structural elements having crack-like defects as well the judgement of the effects of material features on it are becoming more and more important. An effective solution for these problems is inconceivable without computer-aided systems. This paper outlines the structure of such a computer-aided system and an example illustrates some of its possible applications.

282H. CONCRETE (REINFORCED)

10A648. Behavior of concrete beams with exposed reinforcement. - J Cairns and Z Zhao *(Dept of Civil and Offshore Eng, Heriot-Watt Univ, Edinburgh)*. Struct Build 99(2) 141-154 (May 1993).

Reinforcement corrosion is the principal cause of deterioration of reinforced concrete. It has been estimated that around £500 million is spent annually in the UK on concrete repairs. Of the alternative techniques available to extend the useful life of concrete structures, removal of concrete around affected reinforcement and subsequent reinstatement with a concrete or mortar remains the most commonly used. A detailed description of the changes in structural behavior that arise when reinforcement is exposed is provided, based on principles of equilibrium of forces and compatibility of deformations. The numerical model is shown to predict strain behavior and failure loads with good accuracy. The model is applied to specific examples to estimate loss of strength on exposure of reinforcement and to evaluate the length of bar which may be exposed without loss of ultimate strength.

10A649. Carbon fiber reinforced concrete for smart structures capable of nondestructive flaw detection. - Pu-Woei Chen and DDL Chung *(Dept of Mech and Aerospace Eng, SUNY, Box 604400, Buffalo NY 14260-4400)*. Smart Mat Struct 2(1) 22-30 (Mar 1993).

Electrically conducting concrete, as provided by the addition of short carbon fibers (0.2-0.4 vol. %) to concrete, can function as a smart structure material that allows nondestructive electrical probing for the monitoring of flaws. The electrical signal is related to an increase in the concrete's volume resistivity during crack generation or propagation and a decrease in the resistivity during crack closure. The linearity between the volume resistivity change and the compressive stress was good for mortar containing carbon fibers together with either methylcellulose or latex as dispersants. However, the linearity was poor for mortar containing carbon fibers together with both methylcellulose and silica fume, as this mortar required a minimum compressive stress for crack closure, whereas the other two mortars did not. When the compressive stress was increased in the first cycle up to the fracture stress, the volume resistivity increased by 1040% for the mortar containing carbon fibers and methylcellulose, but only 385% for that containing fibers and latex. In contrast, mortars without carbon fibers showed no variation of the resistivity upon compression up to fracture.

10A650. Effect of vertical contraction joints in concrete arch dams. - JR Mays *(Dept of Civil Eng, Univ of Colorado, Denver CO)* and LH Roehm *(US Bureau of Reclamation, PO Box 25007, Denver CO 80225)*. Comput Struct 47(4-5) 615-627 (3 Jun 1993).

The vertical joints between the blocks of concrete in arch dams allow for contraction as the concrete cools during construction. Linear analyses, which ignore the presence of these joints, indicate large horizontal tensile stresses near the joints particularly when seismic loading is included. The US Bureau of Reclamation is studying the nonlinear behavior of these vertical joints by making comparisons between parallel linear and nonlinear analyses of East Canyon Dam. This paper reports on the use of ADINA's gap element to model the contraction joints. The nonlinear analysis shows decreased values of the horizontal tensile stress at the expense of larger compressive stresses and increasing values of vertical tensile stress.

10A651. Interface effects on box-type reinforced concrete structures I. Theory. - Y Chen *(Dept of Civil Eng, Penn State Univ, Middletown PA 17057-4898)*. Comput Struct 47(3) 383-390 (3 May 1993).

A simplified interface model for studying the overall behavior of a soil-concrete interface, and the effects of the interface model on system responses are discussed. Theoretical aspects for this subject are presented in part I, and then followed by implementation and applications in part II. The paper concludes with a number of realistic examples with comparisons of the results with the others.

10A652. Interface effects on box-type reinforced concrete structures II. Implementation. - Y Chen *(Dept of Civil Eng, Penn State, Middletown PA 17057-4898)*. Comput Struct 47(3) 391-398 (3 May 1993).

Implementation, modeling, and verification of the interface model described in part I of this paper are discussed in this part. A number of realistic examples are studied by using a combined finite difference-FE approach with substructuring. The behavior of interface and the effects of interface on box-type reinforced concrete structures are also discussed. The results obtained from the study are compared with the others and those adopted by the current design code.

10A653. Nonlinear FE analysis of concrete structures. - Yuan-Gao Zhang, Ming-Wan Lu, Keh-Chih Hwang *(Dept of Eng Mech, Tsinghua Univ, Beijing 100084, Peoples Rep of China)*. Z Angew Math Phys 44(3) 537-555 (May 1993).

This paper deals with 3D nonlinear FE analysis of concrete structures. A new three-parameter failure criterion, formulated in terms of three stress invariants, is suggested for plain concrete. The criterion can accurately describe available experimental data throughout the stress range from tensile stresses to high compressive stresses. The constitutive matrix of a cracked concrete element is deduced by coupling the normal and tangential effects of crack bands. The modeling of reinforcement and its interaction with concrete are also discussed. Numerical examples of plain and reinforced concrete are presented. The computational results compare satisfactorily with experimental data.

10A654. Optimal design of reinforced concrete frames based on inelastic analysis. - KS Dinno and BB Mekha *(Dept of Civil Eng, Col of Eng, Univ of Baghdad, Iraq)*. Comput Struct 47(2) 245-252 (Apr 1993).

A new algorithm is presented for use in conjunction with the imposed rotation method as reformulated by Kaneko as a (n × 2n) linear complementarity problem. The inelastic trilinear moment rotation law, which is modelled to reflect behavior at critical sections, is adjusted during the incremental analysis in order to adhere the nonholonomic behavior of reinforced concrete (RC) when stress unloading occurs. The algorithm is utilized in performing inelastic analysis for the optimal design of RC frames. Optimum concrete dimensions and reinforcement are evaluated for minimum cost. Optimization, following the multilevel approach, is carried out on typical frames using SUMT and Rosenbrock minimization methods.

10A655. Static and dynamic refined analysis of reinforced concrete bridges. - Y Chen *(Dept of Civil Eng, Penn State Univ, Middletown PA 17057-4898)*. Comput Struct 47(4-5) 601-613 (3 Jun 1993).

A refined method for analyzing a bridge structure and system is discussed. An effective and efficient combined numerical integration scheme is proposed for dynamic analyses. Modeling techniques, distribution of vehicle live loads, seismic analysis methods, and ground motion and soil-structure interaction effects on structural responses are discussed in detail. The results obtained from the present study are compared with those from the current bridge design code. The paper concludes with a number of real examples.

10A656. Steel deck institute method for designing composite slabs. - RB Heagler *(Nicholas J Bouras and United Steel Deck, Summit NJ 07902-0662)*. Thin-Walled Struct 16(1-4) 319-326 (1993).

The Steel Deck Institute (SDI) of the US has synthesized the research and testing done on composite slabs and is ready to present a design rationale based on customary reinforced concrete methods. Two design procedures are shown: one for when there are no shear studs on the beams and the other for when there are studs. A partial composite factor is introduced for cases when shear studs may be sparsely applied.

See also the following:

10A415. Concrete reinforced with up to 0.2 vol% of short carbon fibres
10A934. One and 2D maximum softening damage indicators for reinforced concrete structures under seismic excitation
10A937. Seismic energy demands on reinforced concrete moment-resisting frames

282I. CONCRETE (PRESTRESSED)

10A657. Alternative crack width computation for prestressed members. - H Scholz *(Dept of Civil Engineering, Univ of Witwatersrand, Johannesburg)*. Struct Build 99(2) 135-140 (May 1993).

This paper describes a new method to compute the crack width attributable to the loading of prestressed flexural members. Use is made of the similarities that exist between the deflection theory and the crack theory of prestressed sections and elements. A comparison with test measurements has confirmed that the suggested alternative method is acceptable for engineering purposes. The benefits of the approach are enumerated and a numerical example is presented to illustrate the method. It is argued that for the first time a consistent interrelated method is proposed that covers cracking and deflection of prestressed members.

10A658. User-supplied concrete material model for ADINA. - M Ala Saadeghvaziri *(Dept of Civil Eng, NJIT, Newark NJ 07102)*. Comput Struct 47(4-5) 591-600 (3 Jun 1993).

ADINA's capability in providing the user with the option to construct his or her own material model is employed to add a simple concrete material model. The simplicity of the model arises from the assumption of a uniaxial state of stress and it can be used for nonlinear analysis of members under primarily flexural and/or axial load. The effectiveness of the model under monotonic, as well as cyclic loading, is shown through analyses of three test problems.

See also the following:

10A129. Predicting the enhanced punching strength of restrained slabs

282M. THERMAL LOADING

See the following:

10A677. Stress analysis method of U-shaped bellows and its experimental verification

282Z. EXPERIMENTAL TECHNIQUES

See the following:

10A671. Load testing of beam and block concrete floors

284. Structures (ground)

284B. BRIDGES

10A659. Behavior of concrete box girder bridges of deformable cross-section. - B Kermani *(Acer Consult, Bristol)* and P Waldron *(Dept of Civil and Struct Eng, Univ of Sheffield)*. Struct Build 99(2) 109-122 (May 1993).

Distortion of the cross-section, which commonly occurs in thin-walled box girder bridges that contain few intermediate diaphragms, may modify the distribution of stress throughout the structure to a significant degree. A method of analysis is presented which allows for the effects of cross-sectional distortion in addition to those of torsional warping. The approach is a rational extension of thin-walled beam theory and may be applied to continuous or simply-supported box girders of either straight or curved configuration in plan. As few test data of continuous girders were available against which the accuracy of the method could be verified, two scaled models - one straight, the other curved in plan - were fabricated for this purpose. The construction and testing of these models under a variety of concentrated and distributed torsional loads are briefly described. Results from these tests show excellent general agreement with those from the proposed analytical method.

10A660. Nonlinear modelling of cable-stayed bridges. - W Kanok-Nukulchai and Guan Hong *(Div of Struct Eng and Construct, Asian IT, GPO Box 2754, Bangkok 10501, Thailand)*. J Construct Steel Res 26(2-3) 249-266 (1993).

This paper presents an application of a powerful thin-walled element and a special cable element for 3D modelling of steel cable-stayed bridges. Both linear and nonlinear effects are considered, as geometric nonlinearity may arise from the finite displacement of the bridge deck as well as the cables. As cable-stayed bridge decks are normally built-up thin-walled cross-sections, the effects of flexural-torsion coupling as well as warping restraint are included. Finally, several examples of cable-stayed bridges serve to demonstrate the effectiveness of this most comprehensive model.

10A661. Strength and stiffness of discrete U-frames in composite plate girders. - RP Johnson *(Dept of Civil Eng, Univ of Warwick)* and Shiming Chen *(Inst of Urban Construct, Peoples Rep of China)*. Struct Build 99(2) 199-209 (May 1993).

Tests are reported elsewhere on a structure of inverted U-section consisting of twin double-cantilever composite plate girders, restrained laterally by discrete U-frames, each with the reinforced concrete slab acting as the horizontal member. Results are given here of the tests of the connections between this member and the steelwork. These and earlier tests provide the basis for tentative design rules, relating to stiffness, diagonal tension cracking of the slab, and local yielding of the steel top flange.

See also the following:

10A491. Buckling analysis of steel arch bridges
10A505. Stability of continuous composite plate girders with U-frame action

284E. FRAMES, TRUSSES, AND ARCHES

10A662. Accurate and efficient method for large deflection inelastic analysis of frames with semi-rigid connections. - Goman Wai-Ming Ho *(Ove Arup and Partners)* and Siu-Lai Chan *(Dept of Civil and Struct Eng, Hong Kong Polytech, Hong Kong)*. J Construct Steel Res 26(2-3) 171-191 (1993).

In the conventional analysis and design of steel frames, a pinned or rigid jointed assumption is normally made. However, all practical joints are neither frictionless pinned nor fully rigid. This characteristic has an important influence on the behavior of the structure. The bending moment determined according to these extreme joint conditions is also erroneous. In this paper, a displacement-based FE technique using the incremental secant stiffness approach and considering the effects of joint flexibility for the nonlinear analysis of 2 and 3D frames is presented. The suggested method has the advantage over the currently available methods in its accuracy in handling large deflection analysis in 3D space and fast rate of convergence.

10A663. Analysis of frame-cable structures. - W Shan, C Yamamoto, K Oda *(Centre for Space Struct Res, Taiyo Kogyo, 3-20 Syodai-Tajika Hirakata-shi, Osaka 573, Japan)*. Comput Struct 47(4-5) 673-682 (3 Jun 1993).

An approach for the analysis of frame-cable structures which are prestressed cable nets incorporating space frames is presented. The interaction between the frame members and the cables is considered and the application of ADINA in shape finding and loading analysis is discussed. A technique is described for integrated loading analysis of frame-cable structures containing beam elements. The numerical examples demonstrate the practical importance of accounting for the effects of the frame deformations.

10A664. Cold-formed steel design and research in Germany. - R Baehre *(Versuchsanstalt fur Stahl, Holz und Steine, Univ Karlsruhe, Kaiserstr 12, 7500 Karlsruhe, Germany)*. Thin-Walled Struct 16(1-4) 293-305 (1993).

The availability of authorized design rules confirms a general approval of scientific-based knowledge and provides confidence for the designer. In the field of light-gauge structures, rules for the design of sheeting and members are approved in Germany since the second part of the 1980s. They have been worked out parallel to the appropriate ECCS recommendations and to Eurocode 3, Annex A, and are considerably harmonized documents. An overall view about the contents of the German design rules is given as well as some examples for special design models. Ongoing research activities in Germany demonstrate the unbroken expansion of light-weight building techniques.

10A665. Cold-formed steel members: Design aproaches in the US. - RL Brockenbrough *(RL Brockenbrough & Assoc, Pittsburgh PA)*. Thin-Walled Struct 16(1-4) 307-317 (1993).

In the US, design specifications for cold-formed steel structural members have been developed and refined over a period of 50 years or so by a consensus group managed by the American Iron and Steel Institute (AISI). Recently the scope of these specifications has broadened significantly. The traditional allowable stress design (ASD) specification for carbon and high-strength steel sheets was extensively revised in 1986 to reflect an allowable member moment or load approach. Referred to as the unified approach, the revised specification treats all types of compression elements with a consistent effective width approach and treats all types of compression members in a consistent manner. The specification was further modified by a 1989 addendum to reflect the results of continuing research. In 1991, the ASD specification was supplemented by a separate load and resistance factor design specification (LRFD), intended to provide a more consistent index of structural reliability. The ASD and LRFD specifications of the AISI have been organized on a parallel basis to facilitate consolidation at an appropriate date. Also, as discussed in a separate paper, a new specification for the design of cold-formed stainless steel members has been recently developed by a consensus group under the auspices of the American Society of Civil Engineers (ASCE). This ASCE document, which replaces an AISI ASD specification that had not been updated for many years, is an LRFD specification that includes an appendix with the ASD approach. Thus, specification development for the design of cold-formed members in the USA has been very active. This made possible not only by the efforts of the supporting groups, but by the extensive volunteer efforts of the many engineers who participate.

10A666. Computer-aided interactive plastic design of frames. - WAM Alwis *(Dept of Civil Eng, Natl Univ, 10 Kent Ridge Crescent, Singapore 0511)*. J Construct Steel Res 26(2-3) 141-151 (1993).

A computer method for analysis and design of plane frames is presented. The method is meant primarily for plastic collapse analysis. Optimal design and elastic-plastic deformation analysis capabilities are provided as options on the same computational platform such that all activities share common internal data structures. A specific feature is the interfacing of user input with analysis calculations, resulting in an interactive design system. Four sequential levels of input data are considered: frame topology, geometry, member sections and loading. Separate calculation modules are activated at each level of input, permitting interactive data modifications, computational work that needs to be repeated to obtain the new solution is that of the modification level and the following levels if any.

10A667. Design approaches for cold-formed steel structures in the People's Republic of China. - Zhong-Quan Zhang *(Zhongnan Build Design Inst, Wuhan, Hubei 430071, Peoples Rep of China)*. Thin-Walled Struct 16(1-4) 327-341 (1993).

This paper briefly describes the limit state design method for cold-formed steel structures in China. Some basic factors affecting the structural safety, such as the reliability index, partial coefficients for loads and resistances etc. and design general expression are systemically discussed and presented. Besides, the design method for various cold-formed steel structural members and connections adopted by current Chinese Specification (GBJ 18-87) are also given in the text.

10A668. European design methods for cold-formed steel. - A Toma *(TNO Build and Construct Res, Delft, Netherlands)*. Thin-Walled Struct 16(1-4) 275-291 (1993).

A survey has been given of the framework of the Eurocodes. These codes should be regarded as the structural design codes for Europe starting in the 1990s. The safety concept of the codes is in the form of load and resistance factor design (LRFD). As far as it concerns the material steel (hot-rolled and cold-formed) the codes are largely based on ECCS documents. The hot-rolled steel has been treated in Eurocode 3, Part 1.1 and the Annexes to Part 1.1 and the cold-formed steel in the Eurocode 3, Part 1.3. In this paper the design rules for cold-formed steel and their eventual difference with the rules for hot-rolled steel are envisaged. Also the background document for the rules of cold-formed steel is reported.

10A669. Local stresses at the intersection of cross-beam flange with box girder web. - Ichiro Okura and Yuhshi Fukumoto *(Dept of Civil Eng, Osaka Univ, 2-1 Yamadaoka, Suita, Osaka 565, Japan)*. Thin-Walled Struct 17(2) 113-131 (1993).

Local stresses at the intersection of a top flange of a cross beam with a box-girder web are investigated analytically and experimentally. FE analyses of a T-shaped welded joint and a loading test of a cantilever beam of acrylic material reveal that a local stress which is different from the one caused by the stress concentration at a weld toe is developed at the intersection. FE analyses of an I-section beam show that the restraint of the vertical deformation of the cross beam at the box-girder web induces the local stress. It is pointed out that the local stress must be considered in fatigue design. A method of determining the local stress is proposed.

10A670. Use of external T-stiffeners in box-column to I-beam connections. - SL Lee, LC Ting, NE Shanmugam *(Dept of Civil Eng, Natl Univ, Kent Ridge, Singapore 0511)*. J Construct Steel Res 26(2-3) 77-98 (1993).

The effects of various types of stiffeners on the connection behavior between box-column to I-beams has been studied both experimentally and analytically using the FEM. The external T-stiffener has been found to provide the most suitable form of stiffening in terms of stiffness, strength, ductility and ease in fabrication which are the basic criteria for a good moment connection. A simple design method to determine the dimensions of the external T-stiffener for both the two-way and four-way connections has been proposed. A method for predicting the moment-rotation characteristic of the connection using a least-square curve-fitting procedure is also described. Finally, two four-way full-scale specimens designed in accordance with the design guidelines were tested to failure. The experimental results as well as results from FE analysis show the validity of both the design guidelines and the proposed moment-rotation functions.

See also the following:

10A492. Design of frames against buckling using a Rayleigh quotient approximation

10A638. Limit states design of semi-rigid frames using advanced analysis Part 1. Connection modeling and classification

10A639. Limit states design of semi-rigid frames using advanced analysis Part 2. Analysis and design

284J. OTHER GROUND STRUCTURES

10A671. Load testing of beam and block concrete floors. - RM Moss *(Struct Performance Div, Build Res Est)*. Struct Build 99(2) 211-223 (May 1993).

A study is made of the structural behavior of beam and block concrete floors under static and thermal loads. Particular issues addressed include the need to estimate the transverse load distribution in a floor during a load test, and the ability to compensate measured deflections for the effects of environmental temperatute changes. The research described focuses on these aspects and leads to specific recommendations for the load testing of beam and block floors. The work is limited to a study of a particular arrangement of beam and block floor which was tested at different stages of construction so that the behavior of the separate components (an ungrouted floor, a grouted floor and a floor with different screed types) could be established. Apart from a final test to failure on the floor with a bonded screed, the load levels were restricted so that repeatability could be achieved at each stage and the degree of structural interaction determined. It is noted that the additional stiffness provided by different screed types, particularly bonded screeds, could be substantial, and that a sand-cement grout simply brushed over the surface of the floor, and only partially filling the joints between components, still provides an increase in stiffness. Approximate methods using linear theory and heat conduction analysis, leading to assessment of load distribution, thermal deflections and load corrections, are developed for use in the load testing of structures. The results of these analyses compare satisfactorily with results of tests on the floor assemblies.

10A672. Simplified method for ultimate load prediction of all-steel sandwich panels. - KH Tan, TS Lok, SP Chiew *(Sch of Civil and Struct Eng, Nanyang Tech Univ, Nanyang Ave, Singapore 2263)*. Thin-Walled Struct 17(1) 27-44 (1993).

This paper is concerned with the ultimate load prediction of a sandwich panel manufactured from a steel plate assembly. The panel essentially consists of two facing plates, spot welded onto a corrugated steel core. All the plates of a panel have identical thicknesses. Three groups of panels with varying plate thicknesses were examined. The typical panel considered in this study had plan dimensions of 2.1 m × 1.0 m with a core consisting of top-hat stiffeners of depth 60 mm, placed side by side. The panel was simply supported across its y-direction boundaries and subjected to uniform lateral loading over its entire surface. The plastic hinge theory is used to evaluate the ultimate collapse load of the panel. In this respect, two approaches are compared: one based on full-section properties and the other based on the effective width concept. It is shown that the effective section gives more reliable collapse-load predictions than the full section. Theoretical collapse-load predictions agree very well with the experimental collapse load for a series of 13 panels. To accentuate the salient features of the technique, a numerical example is presented.

See also the following:

10A680. Dynamic analysis of a reinforced retaining wall using finite and infinite elements coupled method

286. Structures (ocean and coastal)

10A673. Hot spot stresses of K tubular joints subjected to combined loadings. - Ai-Kah Soh and Chee-Kiong Soh *(Nanyang Tech Univ, Nanyang Ave, Singapore 2263, Republic of Singapore)*. J Construct Steel Res 26(2-3) 125-140 (1993).

An approach has been proposed to verify, and modify if necessary, the conventional method for determining the peak hot spot stresses of various configurations of tubular joints subjected to combined loadings. A typical K tubular joint, which was subjected to various loading conditions, was employed to illustrate the proposed approach. It is found that the accuracy of the peak hot spot stresses estimated by the conventional method for combined loadings are closely related to the types of loading condition involved. This is due to the possible change in peak stress locations and directions when various basic load types are combined. The peak hot spot stresses of some combined loadings are significantly over estimated by the conventional method and, thus, can be reduced in order to provide accurate data for fatigue analysis.

See also the following:

10A142. Interaction of short-crested random waves and large-scale currents

288. Structures (mobile)

10A674. Studies on metal matrix composite railroad wheels. - TC Ramesh and N Ganesan *(Machine Dyn Lab, Dept of Appl Mech, Indian IT, Madras 600 036, India)*. Comput Struct **47**(2) 259-263 (Apr 1993).

The use of metal matrix composites in railway wheel applications is explored in this paper. Static and dynamic analysis of railroad wheels made of metal matrix composites are made using the FEM. The deflections, stresses, factor of safety, and natural frequencies of these wheels are compared with those in steel as well as graphite-epoxy wheels.

10A675. Fundamentals of low radar cross-sectional aircraft design. - AC Brown *(Dept of Eng, Lockheed, 4500 Park Granada Blvd, Calabasas CA 91399)*. J Aircraft **30**(3) 289-290 (May-Jun 1993).

There are two basic approaches to passive radar cross-sectional reduction, shaping to minimize backscatter, and coating for energy absorption and cancellation. Both of these approaches have to be used coherently to achieve required levels over the appropriate frequency range. Design details are extremely important.

See also the following:

10A51. Control-structure interactions of space station solar dynamic modules
10A55. Sensitivity-based characterization and optimization of viscoelastically damped honeycomb structures
10A257. Disturbance model for control-structure optimization with full state feedback
10T259. First-order models for satellite survivability optimization
10A262. Linear quadratic Gaussian-loop transfer recovery design for a helicopter in low-speed flight
10A292. Synthesis and evaluation of an H_2 control law for a hovering helicopter
10A396. Ship bow response in high energy collisions
10A560. Damage tolerance assessment of the fighter aircraft 37 Viggen main wing attachment
10A692. Use of brittle strain-sensitive coatings in strength tests of full-scale aircraft structures
10T908. Development and flight history of the SERT II spacecraft

290. Structures (containment)

10A676. Fracture mechanical analysis of a reactor pressure vessel under thermal shock loading. - P Reimers *(IwiS GmbH, Pariser Str 3, D-1000 Berlin 15, Germany)*. Comput Struct **47**(4-5) 815-827 (3 Jun 1993).

Improved knowledge of cooling conditions in nuclear power plants in the case of potential emergencies and increasing irradiation embrittlement of reactor pressure vessel materials are two reasons for the fact that the safety of plant components is under permanent observation. In a loss-of-coolant accident it is possible that the injected cooling water runs in stripes down the vessel wall. This causes high thermal stresses and high stress gradients in the wall combined with a decrease of fracture toughness of the ferritic material. Assuming a circumferential crack in this region the temperature and loadtime-dependent stress intensity factors along the crack front are to be determined and compared with the temperature and life-time-dependent material toughness for the evaluation of pressure vessel safety against unstable crack propagation. Considering a reactor pressure vessel in operation the necessary ADINA FE analysis of (i) transient heat transfer through the wall of the vessel and (ii) the stress and strain fields for thermoelastic-plastic material behaviors are presented. The virtual crack extension method was used for the calculation of J-integral values along the crackfront, which were converted into the stress intensity factors being compared with the material toughness.

10A677. Stress analysis method of U-shaped bellows and its experimental verification. - H Takatsu, M Yamamoto, M Shimizu, M Ohta *(Japan Atomic Energy Res Inst, Naka-machi, Naga-gun, Ibaraki-ken, Japan)*. Fusion Eng Des **22**(3) 239-250 (Apr 1993).

A new FEM modeling technique was developed for the stress analysis of the U-shaped bellows, which is more convenient for the stress analysis of such a complicated structure as the JT-60 vacuum vessel. In the present modeling method, the bellows are replaced by an orthotropic plate having the same rigidity as the bellows. The real stress of the bellows is obtained by transformation equations, which express a physical correspondence between the membrane stresses and bending moments of the orthotropic plate and those of the bellows. The applicability of the present modeling technique was verified using four kinds of test models. The experimental results agreed well with the computed ones, and the present stress analysis method of the U-shaped bellows was found to be sufficiently applicable to the stress analysis of the JT-60 vacuum vessel.

10A678. Axisymmetric residual stresses in tubes with longitudinally nonuniform stress distribution. - T Nishimura *(Dept of Mech Eng, Tokyo Metropolitan Col, Higashiohi 1-10-40 Shinagawa-ku, Tokyo 140, Japan)*. J Appl Mech **60**(2) 300-309 (Jun 1993).

New equations for calculating residual stress distribution are derived from the theory of elasticity for tubes. The initial distribution of the stresses including the shearing stress is computed from longitudinal distributions of residual stresses measured by the X-ray methods at the surface after removal of successive concentric layers of material. For example, the residual stresses of a steel tube quenched in water were measured by the X-ray diffraction method. The new method was also applied to a short tube with hypothetical residual stress distribution. An alternative FE analysis was made for a verification. The residual stresses computed by FE modeling agreed well with the hypothetical residual stresses measured. This shows that good results can be expected from the new method. The equations can also be used for bars by simple modification.

10A679. Stress analyses of wrinkle bends in pipelines. - NW Murray *(Dept of Struct Eng, Monash Univ, Clayton, Vic 3168, Australia)*. Thin-Walled Struct 17(1) 65-80 (1993).

Wrinkle bends are made by developing local outwards-directed folds at the intrados. The stresses can arise from any combination of internal pressure and change of angle, the latter often arising from thermal effects. Although wrinkle bends are not commonly used in large pipelines nowadays, there are many in existing pipelines built years ago. The paper shows that the stresses are mainly due to local bending of the pipe wall and have peak values which can be quite large especially on the inside surface of the highest point of the wrinkle. Graphs which enable these stresses to be evaluated separately for internal pressure and for longitudinal displacement (or thermal loading) are provided.

10A680. Dynamic analysis of a reinforced retaining wall using finite and infinite elements coupled method. - Chongbin Zhoa and S Valliappan *(Sch of Civil Eng, Univ of New S Wales, PO Box 1, Kensington, NSW 2033, Australia)*. Comput Struct **47**(2) 239-244 (Apr 1993).

A simplified method for the dynamic analysis of reinforced retaining walls during earthquakes is presented, based on the plane strain assumption and the concept of the equivalent material behind the wall. The dynamic soil-retaining wall interaction is included in this method and the system is divided into several subregions. The greatest merit of this simplified method lies in that it includes all the important factors which may affect the response of the reinforced retaining wall. Since this simplified method is based on the finite and infinite elements coupled method, not only can the natural soil and the reinforced retaining wall be simulated rigorously but also the wave propagation mechanism in the system can be modelled more realistically. Some numerical results from the analysis of a reinforced retaining wall under SV- and P-wave incidences demonstrate that the backfill soil behind the retaining wall has considerable effects on the dynamic response of the wall during higher frequency wave incidences and thus the change of material properties of the backfill should be considered in the seismic design of retaining projects.

See also the following:

10A634. Acoustic emission monitoring of pressure vessels

292. Friction and wear

292B. FRICTION

10A681. Analysis of the friction behavior of bolted joints. - MB Karamis *(Eng Fac, Dept of Mech Eng, Erciyes Univ, 38090 Kayseri, Turkey)* and B Sulcuk *(Eng Fac, Dept of Mech Eng, Cumhuriyet Univ, Sivas, Turkey)*. Wear **166**(1) 73-83 (15 Jun 1993).

In this study, the effect of surface roughness of bolted joint members on the friction behavior of the joint was investigated by considering theoretical studies carried out previously. For this purpose, AISI 366 structural steel sheet was used as the sample material. After the contact areas of the samples were defined and polished to different surface qualities, the surface asperities were recorded and the samples were bolted under different compressional moments and then subjected to a torsional moment on a torsion machine. The effects of surface roughness, compressional moment and torsional angle on the torsional moment were determined. It was observed that the surface roughness plays a major role in the joint reliability. High R_a values of the interfaces lead to easy loosening of the joint. Therefore, improvement of the surface quality of mechanical joints is very useful for tightening the joints.

10A682. Mechanics of friction in self-lubricating composite materials I. Mechanics of second-phase deformation and motion. - N Alexeyev *(Inst for Problems in Mech, Moscow, Russia)* and S Jahanmir *(NIST)*. Wear **166**(1) 41-48 (15 Jun 1993).

This paper is devoted to the analysis of plastic deformation of self-lubricating composite materials that contain soft second-phase particles and are subjected to sliding friction. Slip-line field analysis of plastic deformation is used to analyze the processes of deformation and flow of the soft phase toward the sliding surface. As a result of this analysis, a general relationship for the deformation and flow of the soft phase is obtained. It is shown that the properties of both the hard matrix and the soft second-phase particles, as well as the shape and size of the particles, control the processes of deformation and flow of the soft phase. The results may be used to optimize the microstructure of self-lubricating composites to obtain the best tribological performance.

10A683. Mechanics of friction in self-lubricating composite materials II. Deformation of the interfacial film. - N Alexeyev *(Inst for Problems in Mech, Moscow, Russia)* and S Jahanmir *(NIST)*. Wear **166**(1) 49-54 (15 Jun 1993).

The process of film formation in self-lubricating composites and deformation of the film are analyzed by the slip-line field method. The results show that the size of the second-phase particles in the composite, the relative shear yield limit of the matrix and the soft phase, and the thickness of the film control the tribological performance of these composites. In a given contact condition, it is possible to modify the composite's microstructure to achieve an optimum performance, ie, the lowest possible coefficient of friction.

See also the following:

10A339. Determining the effects of Coulomb friction on the dynamics of bearings and transmissions in robot mechanisms

292D. WEAR (UNINTENTIONAL)

10A684. Unlubricated sliding wear of steels: The role of the hardness of the friction pair. - Singhai Bian, Sophie Maj, DW Borland *(Mat Group, Dept of Mech and Manuf Eng, Univ of Melbourne, Parkville, Vic 3052, Australia)*. Wear **166**(1) 1-5 (15 Jun 1993).

The influence of the hardness of the sliding elements on the unlubricated wear of steels has been investigated using a pin-on-ring configuration. Pins of quenched-and-tempered steel with varying hardness have been tested against countersurfaces that are also in the quenched and tempered condition and with a similar range of hardness. A change in the predominating wear process of the pin, from oxidative to metallic wear, occurs as the hardness of the countersurface decreases, for constant hardness of the pin.

10A685. Wear behavior of acetal gear pairs. - AR Breeds, SN Kukureka *(Sch of Metall and Mat, Univ of Birmingham, Edgbaston, Birmingham, B15 2TT, UK)*, K Mao, D Walton, CJ Hooke *(Sch of Manuf and Mech Eng, Univ of Birmingham, Edgbaston, Birmingham, B15 2TT, UK)*. Wear **166**(1) 85-91 (15 Jun 1993).

The wear behavior of polymer gear pairs has been little studied. Most wear studies have used pin-on-disc or polymer against steel tests. The non-conformal contact and high transient temperatures in polymer gear pairs make it essential to study wear under actual running conditions. This paper describes the design and operation of a novel test rig for measuring the wear behavior of polymer gears continuously. Preliminary results are presented and comparisons made between failures in acetal and nylon. Wear of acetal gears is studied in more detail. It is shown that wear of acetal gears is a complex process. Optical and scanning electron microscopy show the driving and driven gears to have different features on the worn flanks, with a ridge forming at the pitch line on the driven gear and a valley on the driving gear. The wear surfaces over the addendum and dedendum are also strikingly different. This is related to the direction of rolling and friction forces on each gear face. The limits to the use of acetal as a gear material are considered. At low torques, life is limited by wear and at high loads the maximum permissible surface temperature is a limiting factor.

See also the following:

10A454. Overview on polymer composites for friction and wear application

10A953. Role of liquid crystals in the lubrication of living joints

292E. CONTACT FATIGUE

10A686. Effect of ferrite contents on the contact fatigue property of medium carbon alloy steels. - JL Huang, YM Zhu, EY Shao *(Dept of Mat Eng, Luoyang IT, 471039 Henan, China)*. Wear **166**(1) 101-105 (15 Jun 1993).

The subcritical quenching technique was used in large size gear steels 45CrMnMo and 42CrMo to obtain ferrite and martensite compound structures with different ferrite contents. The effects of ferrite content on the contact fatigue properties of the two gear steels were investigated in systematic contact fatigue tests. The results show an obvious influence of ferrite content on the pitting lives of the tested steels. The pitting lives increase continuously with increasing ferrite content in the structures until they reach peak values with corresponding ferrite contents of 12% and 10% for 45CrMnMo steel and 42CrMo steel respectively.

292H. SURFACE EFFECTS, TOPOGRAPHY, COATINGS

10A687. Determination of probabilistic characteristics of the microgeometry of composite surfaces. - VS Luk'yanov, VR Soloveichik, AM Bykov *(Moscow, Russia)*. J Machinery Manuf Reliab **6** 46-51 (1992).

The probabilistic characteristics (the distribution and correlation functions) of a surface formed by superposition of roughnesses of different technologies origin are characterized by specific functional behavior, are obtained. The surfaces under study include those obtained by plateau honing and mechanical working of porous and sintered materials.

10A688. Development of plasma sprayed lubricant free slide plates with ceramic coat for railway use. - H Ono, T Teramoto *(R&D Dept, Nippon Sharyo, Nagoya, Atsuta, Japan)*, T Shinoda *(Dept of Mat Processing, Nagoya Univ, Furo-cho, Chikusa-ku, Nagoya, Japan)*. Mat Manuf Processes **8**(4-5) 451-463 (Jul-Sep 1993).

Ceramic coated slide plates were developed in order to ensure smooth sliding of the tongue rail and tight contact with stock rail. The 0.5 mm thickness thin metallic bonded layer was synthesized by spraying ceramic powders using conventional plasma spraying technique. Coated materials were mostly Al_2O_3 ceramic including metallic materials. It is concluded field tests that coated plates satisfied endurance specifications, corrosion, wear and load specifications without any maintenance of ceramic coated plates. Since field tests have been successfully performed, more than 10 000 slide plates are being used in Japan by Shin-kansen Rail Way and private railway companies.

10A689. Effect of atmospheric humidity on the dynamic fracture strength of SiC abrasives. - J Larsen-Basse *(NSF, 1800 G St NW 1108, Washington DC 20550)*. Wear **166**(1) 93-100 (15 Jun 1993).

Silicon carbide abrasive grits were fractured dynamically in a roller crusher at ambient temperature and under controlled levels of atmospheric humidity, covering the full range from 10 to 100% relative humidity. The fracture stress depends strongly both on the grit size below a certain value and on the partial pressure of the water vapor. The size effect causes an increase in fracture stress as the grit diameter is decreased below a certain size. This is thought to be due to scaling of the size of pre-existing surface defects with grit diameter. The moisture effect causes a drop in fracture stress at any moisture level above 0% relative humidity (rh) for sufficiently small specimens, while the number of fragments created in the crushing process increases. This effect is thought to be due to moisture-assisted sharpening of the tips of surface defects, which serve as crack initiation sites, during the early stages of loading. The tip sharpening facilitates initiation of brittle fracture. It lowers the measured fracture stress and enables smaller defects to initiate secondary fractures when the stored elastic energy suddenly is released during the primary fracture; therefore, more fragments form. The results explain the previously observed moisture-assisted self-sharpening of abrasives which may result in increased abrasive wear rates for metals as the levels of atmospheric moisture increase. The results may also have implications for the interpretation of certain types of ceramic wear.

10A690. Friction and wear behavior of a number of ceramic-coated steels matched as sliding pairs to various surface-treated steels. - YL Su and JS Lin *(Dept of Mech Eng, Natl Cheng Kung Univ, Tainan 70101, Taiwan, ROC)*. Wear **166**(1) 27-35 (15 Jun 1993).

Ceramic-coated steels (WC + 12%Co and Cr_3C_2 + 25%NiCr applied by continuous detonation spraying, and Cr_2O_3 applied by plasma spraying) were mated as sliding pairs to surface-treated steels (case hardened, tufftrided) under both dry wear and lubricated conditions in order to assess their tribological potential. Under dry wear conditions, WC-Co demonstrates the lowest coefficient of friction but surface-treated steels paired with Cr_3C_2-NiCr possess the best wear resistance under both dry wear and lubricated conditions. Five different types of generalized friction behavior were identified among the pairs studied. Under dry wear conditions, the worn surface of Cr_3C_2-NiCr is covered with continuous and "island"-transferred layers, while that of Cr_2O_3 exhibits numerous cracks. The worn surface of WC-Co can be divided into four distinct regions, each possessing a major wear characteristic in addition to that of surface polishing. Wear mechanisms for TF1 surface-treated steels include surface polishing, strain fatigue and fracture of the work-hardened layer, while those for carburized steel include surface polishing, plastic deformation, material transfer and pile-up of back-transferred material. Under lubricated conditions, the amount of material transferred is reduced.

10A691. Role of oxidation in the wear of plasma nitrided and PVD TiN coated steel. - Y Sun and T Bell *(Sch of Metall and Mat, Univ of Birmingham, Birmingham B15 2TT, UK)*. Wear **166**(1) 119-125 (15 Jun 1993).

The wear behavior of plasma nitrided En40B steel has been investigated under dry rolling contact with applied sliding traction. Particular attention has been paid to the examination of the tribochemical reaction, ie, oxidation, of the nitrided surface during the wear process. X-ray diffraction, optical and scanning electron microscopes have been employed to study the wear debris, worn surfaces and subsurfaces. Experiments revealed that, as a result of the hardening effect induced by plasma nitriding, wear of nitrided steel occurred in a mild mode via oxidation of the contact surfaces and the subsequent removal of the oxide products, and the overall wear rate was dominated by the rate of oxidation of the contact surfaces. However, the unnitrided steel was worn via surface and subsurface shear deformation, leading to severe wear. In order to further improve the wear resistance of the steel, a thin, hard titanium nitride (TiN) coating was deposited on top of the nitrided steel by ion plating. Such duplex treated steel possessed superior resistance to both subsurface shear deformation and tribo-oxidation, thus ensuring minimization of the wear rate.

10A692. Use of brittle strain-sensitive coatings in strength tests of full-scale aircraft structures. - AN Salin, BN Ushakov, AI Kosenko, NA Stepanov *(Moscow, Russia)*. J Machinery Manuf Reliab 6 91-96 (1992).

Some results of using the method of brittle strain-sensitive coatings for analyzing strain and stress fields in elements of aircraft structures, are presented. The research has been carried out jointly by the Institute of Machines Science at the Russian Acad of Sciences, Tupolev Special Design Bureau, and some other organizations.

10T693. Use of thin solid films at head-magnetic media interfaces. - N Ohmae *(Osaka Univ, 2-1 Yamadaoka, Suita, Osaka 565, Japan)*, H Hara, H Seki, I Endo *(Kubota Corp, 5-10 Okuhata, Itami, Hyogo 664, Japan)*. Mat Manuf Processes 8(4-5) 419-428 (Jul-Sep 1993).

See also the following:

10T542. Review of the chemical vapor deposition (CVD) of the refractory compounds of titanium: A unique family of coatings

292I. WEAR MONITORING

10A694. Antiwear mechanism of zinc dialkyl dithiophosphates added to a paraffinic oil in the boundary lubrication condition. - H So, YC Lin *(Dept of Mech Eng, Natl Taiwan Univ, Taipei 10617, Taiwan, ROC)*, Gibbs GS Huang, Terny ST Chang *(Refining and Manuf Res Centre, Chinese Pet, Chia-Yi 60036, Taiwan, ROC)*. Wear 166(1) 17-26 (15 Jun 1993).

The antiwear mechanism and performance of various zinc dialkyl dithiophosphates (ZDDPs) used in paraffin oil under the boundary lubrication condition are studied extensively. The condition of boundary lubrication is achieved with a flat-on-flat reciprocating sliding contact which can simulate the contacting condition near the top and bottom dead ends of a piston ring with the cylinder wall in an automotive engine. Three types of ZDDP, namely primary, secondary and commercial ZDDPs, are used as the antiwear additive. the antiwear performance of each ZDDP is evaluated with the contact (electrical) resistance and the worn scars on the contact surfaces. Then it is confirmed by electron spectroscopy for chemical analysis or energy-dispersive X-ray analyses on the worn surfaces. The results confirm that the antiwear mechanism depends upon the ratio of the rate of film formation to the rate of scraping the existing film. The compositions of the film formed on the contact zone affect this ratio but depend on the oil temperature and the condition of surface finish of the specimens. In general, the primary ZDDPs yield poor antiwear performance in a wide range of testing temperatures. The mixture of two secondary ZDDPs or the commercial ZDDPs provide much better antiwear performance. The formation of paste-like materials on the contact area at temperatures over 120°C also yields antiwear performance, but the paste formed with the lubricant added with ZDDPs provides a better antiwear performance.

10A695. New sensor for real-time milling tool condition monitoring. - C James Li *(Dept of Mech Eng, Columbia Univ, New York NY 10027-6699)* and SY Li *(Dept of Precision Machinery and Instruments, Changsha IT, Peoples Rep of China)*. J Dyn Syst Meas Control 115(2A) 285-290 (Jun 1993).

A new sensor has been developed to automatically detect face-milling insert fracture chipping, and wear. With a befitting PVDF (polyvinylidene fluoride) sensor, and an optical transmitter based on frequency modulation technique, a miniature sensor, with little influence on the cutting process, was positioned very close to the cutting site. Due to this closeness, the state of the insert can be reliably recognized with extremely simple and fast algorithms. A tool wear index which is sensitive to wear but insensitive to cutting conditions, a tool fracture index, and a chipping recognition scheme based on a linear pattern classifier have been developed and proven to be effective by experimental data.

10A696. Wear resistance of Ni-hard 4 and high-chromium cast iron re-evaluated. - Jinzhu Liu, Shizhuo Li, Yongfa Man *(Inst of Metal Res, Acad Sinica, Shenyang 110015, China)*. Wear 166(1) 37-40 (15 Jun 1993).

A comparison of the wear resistances of Ni-hard 4 and high-chromium (15-3) cast irons has been made under different testing conditions. Several kinds of wear tester were employed (reciprocating grooving tester, dry sand rubber wheel tester, single-pass pendulum impact grooving tester, and blasting erosion tester). The results show that whereas Ni-hard 4 seems to be more suitable to resist blasting erosion, high-chromium cast iron is better at resisting grooving wear, the ranking of materials changing with testing conditions. The measured wear resistance of the irons has been explained in terms of microstructure and hardness. Material removal occurred as a result of different mechanisms. For grooving wear, a harder metal surface is preferable, under blasting erosion conditions, material removal is mainly determined by the matrix.

294. Machine elements

10A697. Necessary and sufficient conditions for homokinetic transmission in chains of Cardan joints. - DA Johnson and PY Willems *(Dept of Mech Eng, Univ Catholique, Louvain-la-Neuve, Belgium)*. J Mech Des 115(2) 255-261 (Jun 1993).

The classical double universal joint for constant velocity ratio transmission is subject to strict geometrical requirements as regards configuration, and it is generally accepted that similar constraints also prevail for longer chains of joints. This paper examines the constant velocity conditions from a necessary point of view and establishes new configuration possibilities for chains of 3 or more joints, which allow to envisage more flexible design in some applications.

10A698. Redundant-drive backlash-free robotic mechanisms. - Sun-Lai Chang and Lung-Wen Tsai *(Mech Eng Dept and Syst Res Center, Univ of Maryland, College Park MD 20742)*. J Mech Des 115(2) 247-254 (Jun 1993).

In this paper, we introduce a new and innovative concept for the control of backlash in gear-coupled robotic mechanisms. Based on this concept, a methodology for the enumeration of admissible redundant-drive backlash-free robotic mechanisms has been established. Some typical 2 and 3 dof mechanisms have been sketched. Furthermore, actuator torques have been derived as functions of either joint torques or end-effector dynamic performance requirements.

10A699. Refined concept of the contact strength of gearings and the prospects for increasing their reliability. - RM Ignatishchev *(Mogilev, Russia)*. J Machinery Manuf Reliab 6 59-61 (1992).

In the process of normal operation of a gearing the teeth radii of curvature may suffer substantial changes. The recognition of this fact opens new vistas on the way to improving design calculations, allows developing an unprecedented industrial method for predicting the onset of pitting and increasing longevity of gears whose module exceeds 5 mm, by a factor of 2 to 5.

10A700. Load characteristics of radial cylindrical aerostatic supports with discrete sources. - VS Balasan'yan *(Moscow, Russia)*. J Machinery Manuf Reliab 6 52-58 (1992).

A method for calculating load characteristics and optimal parameters of radial cylindrical aerostatic supports with discrete sources is discussed. The method is based on introduction of discreteness, nonlinearity, and double-throttling coefficients into formulae obtained by solving analytically the gas-lubrication problem for small eccentricities and taking into account circumferential flow.

10A701. Routes to chaos in ball bearings. - B Mevel *(SNR Roulements, 1 rue des usines BP 17, F74010 Annecy, France)* and JL Guyader *(Lab Vibrations Acoustique Bt303, INSA de Lyon, 20 ave A Einstein, F69621 Villeurbanne Cedex, France)*. J Sound Vib 162(3) 471-487 (22 Apr 1993).

The dynamic motion of a lightly loaded ball bearing is studied in order to show and to gain understanding of the different mechanisms involved in transitions to chaotic behaviors. By varying a control parameter, different routes to chaos are described. The most widely known is the subharmoic route, which is characterized by an increasing number of subharmonics of the driving frequency. Alternance of period doubling and tripling has been noticed, as the ball pass frequency is around the first resonance of the bearing. The second route is a quasi periodic route. It is characterized by competition between the second resonance of the bearing and the ball pass frequency. It results in an increasing number of combinations of two incommensurate frequencies. During the quasi periodic sequence, mode locking occurs each time the two frequencies are locally commensurate. The last type of chaos that is observed is involved by the quasi periodic breakdown of an attractor. It looks like intermittency and, in the present case, it is obtained by introduction of some over sized balls. Finally, the occurrence of loss of contact between balls and raceways is studied and related to the existence of chaos.

10T702. Present and future technology for seals. - Shoji Shiomi *(R&D No 2 Dept, Eagle Indust, 1500 Katayanagi Sakado-shi, Saitama 350-02, Japan)*, Hiroo Tanoue *(Product Planning Dept, Eagle Indust, 1500 Katayanagi Sakado-shi, Saitama 350-02, Japan)*, Hidekazu Takahashi *(Seal Equip No 1 Dept, Eagle Indust, 1500 Katayanagi Sakado-shi, Saitama 350-02, Japan)*. Japan J Trib 37(9) 1139-1147 (1992).

10A703. Dimensional synthesis of closed-loop linkages to match force and position specifications. - C Huang and B Roth *(Dept of Mech Eng, Stanford)*. J Mech Des 115(2) 194-198 (Jun 1993).

By combining classical kinematic synthesis and static synthesis, we consider force conditions as well as motions in the dimensional synthesis of linkages. We are concerned with determining the dimensions of linkages that guide a rigid body through several positions and support a specified external load at each position. Three types of planar linkages are studied in detail: four-bar, slider-crank, and double-slider linkages. Incompletely specified problems and spring element synthesis are also discussed.

296. Machine design

296B. SYNTHESIS AND DESIGN

See the following:

10A364. Tool for optimal manufacturing design decisions

296C. BALANCING

10A704. Balancing of multithrow double-shaft separating mechanisms. - AB Roitman, SL Ryagin, AD Shamrovskii *(Zaporozh'e)*. J Machinery Manuf Reliab 6 21-26 (1992).

Balance of forces and moments of inertia acting on multithrow double-shaft separating mechanisms is analyzed by considering a five-section strawwalker of a harvester. Balanced shaft configurations differing only in the relative positions of cranks, are obtained. By varying cranks radii and section masses, balanced configurations with minimum stresses in the critical cross-sections, are found.

296E. OPTIMIZED DESIGN

10A705. Determination of optimal dimensions of the units of a rotor flow-modulation apparatus. - AM Balabyshko and AI Zimin *(Tula)*. J Machinery Manuf Reliab **6** 62-67 (1992).

The rotor flow-modulation apparatus considered in this paper, has been designed for generating fine stable emulsions and is the best of its kind. It was awarded the Golden Medal of the USSR Exhibition of the Achievements of People's Economy and surpasses the best domestic and foreign analogues in many technological and economic indicators.

296F. KINEMATICS OF MECHANISMS

10A706. Analytical method for the identification of redundant constraints in multiple-loop spatial mechanisms. - R Srivatsan, DA Hoeltzel, A Das *(Lab for Intelligent Des, Dept of Mech Eng, Columbia Univ, New York NY 10027)*. J Mech Des **115**(2) 324-331 (Jun 1993).

An analytical method for the explicit identification of redundant constraints in multiple-loop spatial mechanisms is presented. The kinematic constraint equations for each independent loop of multiple-loop mechanisms are developed. The independence of these equations is established and used to detect the presence of redundant constraints. The nature of the redundant constraints present is indicated by the type of redundant kinematic constraint equations present. Interaction of the constraints of adjacent loops in a multiple-loop mechanism also has to be taken into account. An example which illustrates the identification of redundant constraints in a cardan joint has been included to demonstrate the utility of this approach for real-world mechanism design problems. General guidelines for the elimination of redundant constraints, following their identification, are also provided.

10A707. Circuit analysis of Watt chain six-bar mechanisms. - JA Mirth *(Dept of Eng, Univ of Denver, Denver CO 80208)* and TR Chase *(Productivity Center, Mech Eng Dept, Univ of Minnesota, Minneapolis MN 55455)*. J Mech Des **115**(2) 214-222 (Jun 1993).

The number of circuits and the extent of each circuit are shown to be determinable from the circuit attributes of the two component four-bars and by the limits of motion that these two four-bars place on each other. The circuit composition of all pin jointed Watt mechanisms is summarized in chart form. The chart enables detecting a change of circuit between any two trial positions of the same mechanism. The chart is suitable for both automated and manual analysis. Examples of circuit analysis of both Watt I and Watt II mechanisms are provided.

10A708. Circuits and branches of single-dof planar linkages. - TR Chase *(Mech Eng Dept, Productivity Center, Univ of Minnesota, Minneapolis MN 55455)* and JA Mirth *(Dept of Eng, Univ of Denver, Denver CO 80208)*. J Mech Des **115**(2) 223-230 (Jun 1993).

Improved definitions for circuits and branches of mechanisms are proposed and discussed in application to planar linkages. The difficulty of circuit and branch identification of multi-loop planar linkages is introduced. The nomenclature used by various authors is correlated with the definitions proposed here. The danger of confusing circuits with branches is illustrated by demonstrating that mechanisms satisfying published "branch" criteria may actually require disassembly to reach all desired positions, rendering them useless in practice. Furthermore, a change of branch within a circuit is shown to be irrelevant to some applications.

10A709. Five position triad synthesis with applications to four and six-bar mechanisms. - T Subbian and DR Flugrad Jr *(Mech Eng Dept, Iowa State Univ, Ames IA 50011)*. J Mech Des **115**(2) 262-268 (Jun 1993).

The displacement equations for triads with motion generation and prescribed timing capabilities are developed and cast in polynomial forms. These equations are solved for five precision points using a continuation method. A detailed description of the method used to generate the solution curves is provided in the paper. Two infinities of solutions can be obtained for the problem under consideration as we are solving four equations in six unknowns. The solution procedure discussed is applied to synthesize a four-bar function generating mechanisms and a six-bar mechanism.

10A710. Opposite pole quadrilateral as a compatibility linkage for parameterizing the center point curve. - JM McCarthy *(Dept of Mech Eng, UC, Irvine CA 92717)*. J Mech Des **115**(2) 332-336 (Jun 1993).

In planar four-position kinematics, the centers of circles containing four positions of a point in a moving rigid body form the center point curve. This curve can be parameterized by analyzing a "compatibility linkage" obtained from a complex number formulation of the four-position problem. In this paper, we present another derivation of the center point curve using a special form of dual quaternions and the fact that it is identical to the pole curve. The defining properties of the pole curve lead to a parameterization by kinematic analysis of the opposite pole quadrilateral as a four-bar linkage. Thus the opposite pole quadrilateral becomes the compatibility linkage. This derivation generalizes to provide parameterizations for the center point cone of spherical kinematics and the central axis congruence of spatial kinematic theory.

10A711. Optimum tolerancing of planar mechanisms based on an error sensitivity analysis. - WL Cleghorn, RG Fenton, Jing-fan Fu *(Dept of Mech Eng, Univ of Toronto, Toronto, ON M5S 1A4, Canada)*. J Mech Des **115**(2) 306-313 (Jun 1993).

This paper presents an analytical procedure to determine the optimum set of tolerance bands of the dimensions of a planar mechanism. The analysis technique presented permits identification of the most sensitive link dimension, the most sensitive combination of input errors, and the most sensitive period within the entire cycle, which make the largest contribution to the output error. The optimum tolerancing procedure is then presented. Examples applied to single and multiple loop mechanisms are included.

10A712. Stewart platform of general geometry has 40 configurations. - M Raghavan *(Power Syst Res Dept, General Motors Res Labs, 30500 Mound Rd, Warren MI 48090-9055)*. J Mech Des **115**(2) 277-282 (Jun 1993).

The forward kinematics problem for the Stewart platform may be stated as follows: given the values of the six prismatic joint displacement inputs to the linkage, compute the position and orientation of the coupler link. This problem may be set up as a system of nonlinear multivariate polynomial equations. We solve this problem using a numerical technique known as polynomial continuation. We show that for Stewart platforms of general geometry (ie, platforms in which the linkage parameters are arbitrary complex numbers) this problem has 40 distinct solutions.

See also the following:

10A341. Kinematic and dynamic synthesis of geared robotic mechanisms

10A342. Kinematic modules for singularity free movement with three Cartesian freedoms

10A347. Workspace of a general geometry planar 3-dof platform-type manipulator

10A697. Necessary and sufficient conditions for homokinetic transmission in chains of Cardan joints

296G. DYNAMICS OF MECHANISMS

10A713. Design of multi-dof mechanisms for optimal dynamic performance. - Z Shiller and S Sundar *(Mech Aerospace and Nucl Eng Dept, UCLA)*. J Mech Des **115**(2) 199-206 (Jun 1993).

Design methods for selecting the actuator sizes and the link lengths of multi-dof mechanisms for minimum time motions along specified paths and between given end points are presented. The design problem is first formulated as a parameter optimization, using the actuator sizes and the link lengths as the design variables, and motion time along the path as the cost function. A more efficient method for obtaining near-optimal designs is then presented, based on the acceleration lines which have been shown to approximate the geometric shapes of time optimal paths. Near-optimal designs are simply obtained by curve fitting the acceleration lines to the desired path, or to the end points. Examples of the design of two and five-bar mechanisms demonstrate significant reductions in motion times for the optimal and the near-optimal designs, and significant savings in computation time for the approximate method.

10A714. Modal analysis solution technique to the equations of motion for elastic mechanism systems including the rigid-body and elastic motion coupling terms. - AG Jablokow *(Dept of Mech Eng, Penn State)*, S Nagarajan *(IBM Corp, Rochester MN 55901)*, DA Turcic *(Dept of Mech Eng, Univ of Wisconsin, Madison WI 53706)*. J Mech Des **115**(2) 314-323 (Jun 1993).

This paper presents a modal analysis solution technique for the matrix equations of motion of elastic mechanism systems including the rigid-body elastic motion coupling terms and general damping. The results obtained using the techniques developed within show this is true for some, but not all mechanisms. The solution technique adds the rigid-body elastic motion coupling terms to the system mass, damping, and stiffness matrices thus allowing them to affect the system response appropriately. The resulting nonsymmetric matrices are then rewritten in first order form allowing general damping to be included in the analysis. Modal analysis techniques are utilized to solve for the steady-state response of the elastic mechanism system. A number of examples are presented that establish the validity of this approach to the solution of the matrix equations of motion for elastic mechanism systems. The results show that the rigid-body elastic motion coupling terms can become significant at higher operating speeds.

See also the following:

10A704. Balancing of multithrow double-shaft separating mechanisms

296I. RELIABILITY ANALYSIS AND DESIGN

10A715. Asymptotic estimates of the probability of failure-free performance, obtained using "load-resistance" models. - VV Bolotin and VP Chirkov *(Moscow, Russia)*. J Machinery Manuf Reliab **6** 1-7 (1992).

Estimates of the probability of failure-free performance, obtained using "load-resistance" models, are proposed. The estimates are based on asymptotic distributions of extreme values of random quantities and approximation of integrands by asymptotic expansions and are the more accurate the smaller the failure probability. The estimates may be used for numerical prediction of safety indicators of technological objects with the help of structural integrity criteria.

298. Fastening and joining

298B. MECHANICAL JOINTS

10A716. Connections in cold-formed steel. - A Toma *(TNO Build and Construct Res, Delft, Netherlands)*, G Sedlacek, K Weynand *(Inst of Steel Construct, RWTH Aachen, Germany)*. Thin-Walled Struct **16**(1-4) 219-237 (1993).

A survey has been given of the fastening possibilities in cold-formed steel, being mechanical fasteners, welding and adhesive bonding. The selection of a fastening type should not be based only on structural requirements but also on non-structural requirements. For the mechanical properties of the connections has been referred to Eurocode 3 part 1.3. Furthermore, background studies has been presented for the rules for the mechanical fasteners. These studies are based on statistical evaluations and have led to improved versions of existing design rules and a uniform partial safety factor for resistance.

10A717. Design of bolted joints in cold-formed steel sections. - ER Bryan *(Univ of Salford, Manchester, UK)*. Thin-Walled Struct **16**(1-4) 239-262 (1993).

This paper gives background information on the behavior of bolted joints and the parameters that affect strength and flexibility. Design expressions for the bearing strength of bolted joints and for the joint movement under load are also given. Moment connections are considered and design expressions for moment capacity and moment-rotation relationships for various bolt groups under practical conditions are given. Computer analysis of cold-formed steel assemblies is outlined and two worked examples of manual analysis, incorporating the above design expressions, are given. It is shown how economical design may be achieved by selecting the correct semi-rigid joint in such assemblies.

10A718. Effect of slit nuts on durability of threaded connections manufactured of heat-resistant steels and subjected to cyclic loading. - RV Kagan and VA Kagan *(Vilnius)*. J Machinery Manuf Reliab 6 37-42 (1992).

A technique for estimating the coil-by-coil stressed state in threaded connections with longitudinally slit nuts, is discussed. Recommendations on disassembly and optimal design, substantiated by the results of service-life tests, are given. Cyclic durability was increased by a factor of 1.5 to 2.0.

10A719. Effects of eyebar shape and pin-hole tolerance on its ultimate strength. - YS Choo, KC Choi, KH Lee *(Natl Univ, 10 Kent Ridge Crescent, Singapore 0511)*. J Construct Steel Res **26**(2-3) 153-169 (1993).

The present paper addresses the problem of the nonlinear elasto-plastic behavior of an eyebar or pin-connection under increasing quasi-static load with reference to the effects of shape and pin-hole tolerance on the ultimate strength. The study uses ABAQUS to model the geometric and material nonlinearities of the eyebar and the boundary nonlinearity due to the increasing contact between the pin and plate-around the hole. The results are compared with those of other investigators and are found to be accurate. The effect of shape on ultimate strength is found to be limited. For an eyebar with given hole and plate dimensions, there appears to be an approximately linear reduction in strength due to an increase in pin-hole tolerance within the range of parameters investigated.

See also the following:

10A670. Use of external T-stiffeners in box-column to I-bean connections

298C. WELDING, BRAZING, AND SOLDERING

10A720. Analysis of welding-induced residual stresses with the ADINA system. - WW Wilkening and JL Snow *(Knolls Atomic Power Lab, General Electric, Schenectady NY 12301)*. Comput Struct **47**(4-5) 767-786 (3 Jun 1993).

The welding-induced residual stresses analysis procedure (WIRSAP), based on the ADINA system of nonlinear FE software, is described and the results of several WIRSAP analyses are discussed. Several 2D axisymmetric WIRSAP analyses have been performed for pipe girth welds and for several multi-pass girth-like welds attaching small nozzles to large, thick-walled pressure vessels. The analytical methodology follows closely the basic techniques outlined by Rybicki *et al*, enhanced by the use of several specialized modeling techniques available in the ADINA system. For example, the element birth option is used to simulate the addition of weld metal, and the mixed pressure-displacement element formulation is used, in conjunction with the temperature-dependent bilinear plasticity material model. Some of the welds analyzed involve backing rings, which were subsequently "machined off" via use of the element death option. The auto-time-stepping algorithm and the matrix update iteration scheme are used in the structural solutions. WIRSAP involves, in general, a pass-by-pass analysis of the uncoupled thermal and structural problems, but some analyses have been performed with an "enveloping" technique for grouping several weld passes together to study the feasibility of modeling multi-pass welds on a layer-by-layer basis.

10A721. Closed-loop control of a weld penetration using front-face vision sensing. - YM Zhang, R Kovacevic *(Center for Robotics and Manuf Syst and Dept of Mech Eng, Univ of Kentucky, Lexington KY)*, L Wu *(Natl Lab for Welding, Harbin IT, Harbin, China)*. J Syst Control Eng **207**(I1) 27-34 (1993).

Feedback control of weld penetration based on a front-face sensor is a challenging problem in the field of welding. A novel vision-based approach is proposed in this paper for full penetration control of the gas tungsten arc welding (GTAW). Owing to the relationship between the front-face weld geometry and the back-face weld width (representation of the full penetration state), which has been reported earlier by the present authors, it is possible to use the front-face geometry as feedback of full penetration. Based on the dynamic modeling and the analysis of accepted adaptive control algorithms, an adaptive predictive decoupling controller is developed. Simulations and experiments under a variety of welding conditions have been conducted to verify the effectiveness of the proposed approach and controller.

10A722. Computer-aided design of explosive welding systems. - PV Vaidyanathan and AR Ramanathan *(Fac of Eng and Tech, Annamalai Univ, Annamalainagar 608 002, India)*. J Mat Processing Tech **38**(3) 501-516 (May 1993).

Whilst explosive welding has reached the stage of commercial application in some parts of the globe, it remains at laboratory and research level in other parts. The techniques, the development of the right explosives, parameter optimization and know-how are kept secret. Despite a thorough understanding of the process through theoretical and experimental studies, optimization attempts had been, by and large, through trial-and-error means. The authors propose a procedure for the optimum fool-proof design of explosive welding systems. The procedure is based on the basic requirements of explosive bonding and conditions favorable for producing acceptable strong welds. A computer program has been developed for determining the optimum values of parameters of practical importance. The program is useable for clad plates of different metal combinations and thicknesses. The results obtained through the CAD not only suggest the correct explosive, its optimum loading and best suited geometry for acceptable strong welds, but also predicts the nature of the resulting interface. The authors believe that the CAD procedure proposed will be useful for both researchers and industry, as a means of avoiding trial-and-error.

10A723. Estimation of weld pool sizes in GMA welding process using neural networks. - TG Lim and HS Cho *(Dept of Autom and Des Tech Eng, Korea Adv Inst of Sci and Tech, Seoul, Korea)*. J Syst Control Eng **207**(I1) 15-26 (1993).

In gas metal arc (GMA) welding processes, the geometrical shape and size of the weld pool are utilized to assess the integrity of the weld quality. Monitoring of these geometrical parameters for on-line process control as well as for on-line quality evaluation, however, is an extremely difficult problem. The paper describes the design of a neural network estimator to estimate weld pool sizes for on-line use in quality monitoring and control. The neural network estimator is designed to estimate the weld pool sizes from surface temperatures measured at various points on the top surface of the weldment. The main task of the neural network is to realize the mapping characteristics from the point temperatures to the weld pool sizes through training. The chosen design parameters of the neural network estimator, such as the number of hidden layers and the number of nodes in a layer, are based on an estimation error analysis. A series of bead-on-plate welding experiments were performed to assess the performance of the neural network estimator. The experimental results shows that the proposed neural network estimator can estimate the weld pool sizes with satisfactory accuracy.

See also the following:

10A456. Vibration welding of polyamide 66
10A552. Effect of yield strength on the basic fatigue strength of welded joints
10A622. Assessment of dynamic fracture characteristics of weld metal
10A630. Evaluation of J_{Ic} for weldment constituents by multispecimen test method

298D. INTERFACIAL BONDING

10A724. Behavior of bolted joints tightened in plastic region: Analysis based on rigid-plastic model. - Hirokazu Tsuji and Kazuo Maruyama. J Japan Soc Precision Eng **59**(4) 589-594 (Apr 1993).

The axial tension of the bolt in the plastic region tightening method depends on the yield point load of the threaded portion under the combined loads of the axial tension and the thread torque induced by the tightening. A new estimation method for the yield point load of the threaded portion is proposed taking account of the general yield criterion based on the rigid-plastic solution for combined loads. Considering the coefficient of friction at the flank of the thread and the residual thread torque after tightening, simple formulas are derived for the yield clamping force and the maximum additional axial tension under externally loading. It is confirmed from the experimental results obtained by a combined loading test that the proposed estimation method is superior to the conventional one taking into account only the local yield criterion. Upon applying the local or general yield criterion, the range of the initial clamping force is bounded between the elastic region tightening, the yield point tightening and the plastic region tightening.

10A725. Dependence of contact durability on the hardened layer thickness. - ON Chermenskii *(Moscow, Russia)*. J Machinery Manuf Reliab **6** 43-45 (1992).

It is shown that the thickness of a hardened surface layer of a rolling part operating for a long time under load, should be no less than $b/2$. Experimental data on contact durability of specimens with a carburized surface layer of variable thickness, are presented. For thicknesses less than $b/2$ durability is shown to decrease drastically.

V. MECHANICS OF FLUIDS

350. Rheology

10A726. Applicability of simplified expressions for design with electro-rheological fluids. - D Brooks *(Adv Fluid Syst, 10-14 Pensbury Indust Estate, Pensbury St, London SW8 4TJ, UK)*. J Intelligent Mat Syst Struct **4**(3) 409-414 (Jul 1993).

There are three key factors that enable electrorheological (ER) fluids to be related to engineering hardware: *off-state*, which is characterized by the suspension viscosity; *on-state*, which is characterized by the excess shear stress; and *power requirement*, which is characterized by the current density. This article discusses the potential benefits of using ER fluids and outlines some of the basic design problems. Some simplified expressions are derived that permit parametric design of ER fluid-based systems.

10A727. Axial laminar channel flow of a Williamson liquid: Convergence of approximate solutions. - M Fortova *(Inst of Hydrodyn, Acad of Sci, Podbabska 13, 166 12 Prague 6, Czech Republic)*. Acta Tech CSAV **38**(2) 153-166 (1993).

To solve the equations of flow for a Bingham liquid, it is usually necessary to use a numerical method, even when the model is parametrized or replaced by a similar model. Proof is given in the paper for the existence and the uniqueness of the close solution for the Williamson model and for the convergence of approximate solutions. The problem is nonlinear and it is, therefore, convenient to solve it by minimization of the functional, whose characteristics were also studied.

10A728. Electrorheological material under oscillatory shear. - JH Spurk *(Tech Hochshule, Petersenstr 30, 6200 Darmstadt, Germany)* and Zhen Huang *(August Bilstein, Postfach 1151, 5828 Ennepetal, Germany)*. J Intelligent Mat Syst Struct **4**(3) 403-408 (Jul 1993).

Two typical electrorheological materials, which are anhydrous dispersions of silica particles in silicone oil with surface active additives are sheared in oscillatory motion in a gap, formed by an outer fixed cylinder and an inner, axially movable cylinder. The rheometer is operated at tuneable resonance frequencies, such that only the reaction of the material is measured. Long time oscillatory shear measurements show that the electroviscous stress deteriorates under dc electric field, while electroviscous stress is stable when ac fields are used. Electroviscous stress is found to depend on field frequency through the dependence of the dielectric constant of the disperse phase on field frequency. A dim[illegible]ss quantity, which relates the electr[illegible]tress to the electric field strength[illegible] all the experimental data for [illegible]li-tudes and shear frequencies for each fluid. The phenomenological theory of Huang and Spurk predicts this efficiency with satisfactory accuracy.

10A729. Energy considerations in the flow enhancement of viscoelastic liquids. - A Siginer and A Valenzuela-Rendon *(Dept of Mech Eng, Auburn Univ, Auburn AL 36849)*. J Appl Mech **60**(2) 344-351 (Jun 1993).

Flow enhancement effects due to different waveforms in the tube flow of rheologically complex fluids driven by a pulsating pressure gradient are investigated. It is found that the squarer the waveform the larger the enhancement. In each case the enhancement is strongly dependent on the viscosity function, but the elastic properties also play an important role. We determine that considerable energy savings may be obtained in the transport of viscoelastic liquids if an oscillatory gradient is superposed on a mean gradient. The closer the oscillation to the square wave the larger the energy savings.

10A730. Die swell in semi-rigid polymer solutions. - C Allain, M Cloitre *(Lab Fluides, Automatique et Syst thermiques, Bat 502, Campus Univ, 91405 Orsay, Cedex, France)*, P Perrot, D Quemada *(Lab de Biorheologie et d'Hydrodyn physicochimique, Tour 33-34, 2 place Jussieu, 75230, Paris, Cedex 05, France)*. Eur J Mech B **12**(2) 175-186 (1993).

This paper reports on an experimental study of jets of xanthan solutions. Die swell of this semi-rigid polymer is similar to that which is observed with flexible polymer solutions or fiber suspensions. At low shear rates, we relate the variation of the swell ratio to the shear thinning properties of the solutions. At high shear, stable delayed die swell is observed above a critical shear rate. Using the jet shape and the dependence on the shear rate of the distance from the nozzle to the station where the swelling is maximum, we show that delayed die swell can be either smooth or discontinuous depending on the polymer concentration.

352. Hydraulics

10A731. Solvability of water distribution networks with unknown pipe characteristics. - PF Boulos *(Dept of Comput Aided Eng, Montgomery Watson, 301 N Lake Ave, Suite 900, Pasadena CA 91101)*, T Altman *(Dept of Comput Sci and Eng, Univ of Colorado, Denver CO)*, JCP Liou *(Dept of Civil Eng, Univ of Idaho, Moscow ID)*. Appl Math Model **17**(7) 380-387 (Jul 1993).

Necessary and sufficient conditions for the solvability of water distribution networks with unknown pipe characteristics are developed. They are predicted on the interdependence between the unknown pipe characteristics and the network hydraulic performance. These characteristics are determined to exactly satisfy defined values of nonlinear boundary equality constraints. The constraint set consists of the stated supply pressure or energy grade requirements to be maintained at critical locations throughout the distribution network. The determination of such conditions is important for a comprehensive and effective modeling and optimization of water networks.

10A732. Vortex particle methods for periodic channel flow. - JJ Monaghan and RJ Humble *(Dept of Math, Monash Univ, Clayton, Vic 3168, Australia)*. J Comput Phys **107**(1) 152-159 (Jul 1993).

The boundary conditions for vortex particles in 2D channel flow with periodic boundary conditions require infinitely many image vortices. By using the Poisson summation formula with Ewald's trick the effect of image vortices can be calculated efficiently. When combined with a tree code and appropriate smoothing, a fast robust algorithm can be designed. Applications to Kirchhoff and Kida vortices are described.

See also the following:

10A135. Simplified model for wave height and set-up in the surf zone
10A142. Interaction of short-crested random waves and large-scale currents
10A740. Propagation of intrusion fronts of high density ratios
10A782. Particle-driven gravity currents

354. Incompressible flow

354C. ROTATIONAL (NONVISCOUS) FLOW, VORTICES

10A733. Hairpin removal in vortex interactions II. - AJ Chorin *(Dept of Math, UCB)*. J Comput Phys **107**(1) 1-9 (Jul 1993).

A vortex method in 3D is simplified through the removal of small folds ("hairpins"). The procedure is justified as a real-space renormalization, within a framework provided by recent results on the statistical equilibria of vortex filaments. An application to a vortex ring is carried out. Applications to other numerical methods as well as open questions are discussed.

10A734. Note on leapfrogging vortex rings. - N Riley and DP Stevens *(Sch of Math, Univ of E Anglia, Norwich NR4 7TJ, UK)*. Fluid Dyn Res **11**(5) 235-244 (May 1993).

In this paper we provide examples, by numerical simulation using the Navier-Stokes equations for axisymmetric laminar flow, of the "leapfrogging" motion of two, initially identical, vortex rings which share a common axis of symmetry. We show that the number of clear passes that each ring makes through the other increases with Reynolds number, and that as long as the configuration remains stable the two rings ultimately merge to form a single vortex ring.

10A735. Stratified Sadovskii flow in a channel. - S Chernyshenko *(Inst of Mech, Moscow Univ, 117192 Moscow, Russia)*. J Fluid Mech **250** 423-431 (May 1993).

Stably stratified and non-stratified flows past a touching pair of vortices with continuous velocity are considered. An asymptotic solution for the very long eddies is determined. Numerical results cover the whole range of subcritical stratification and eddy length.

354D. VISCOUS FLOW

10A736. Stokes flow past a sphere with mixed slip: Stick boundary conditions. - BS Padmavathi, T Amaranath, SD Nigam *(Sch of Math and Comput-Info Sci, Univ of Hyderabad, PO Central University, Hyderabad 500 134, India)*. Fluid Dyn Res **11**(5) 229-234 (May 1993).

We give a general solution of Stokes equations for an incompressible, viscous flow past a sphere with mixed slip-stick boundary conditions. The Faxen's law for drag and torque on the sphere is also given and illustrated with an example.

See also the following:

10A801. Eddy structure in Stokes flow in a cavity

354F. LOW REYNOLDS NUMBER (INCL CREEPING FLOW)

10A737. Arbitrary Stokes flow past a porous sphere. - D Palaniappan *(Dept of Math, Indian*

Int of Sci, Bangalore 560 012, India). Mech Res Commun 20(4) 309-317 (Jul-Aug 1993).

The motion of a fluid through porous particles is of great practical interest and has been extensively studied. A comprehensive review on this subject is given in Jones. The empirical boundary condition proposed by Beavers and Joseph proved to be an efficient one in dealing with Stokes flow problems involving permeable (ie, porous region where Darcy law holds) plane boundaries. Theoretical results of Beavers and Joseph were confirmed experimentally by Beavers et al, whereas Saffman provided a theoretical justification of the empirical condition using statistical approach. Jones subsequently generalized the Beavers-Joseph condition for cuved permeable surfaces. Using the generalized Beavers-Joseph condition together with continuity of normal velocity and pressure across the permeable surface, Jones solved the problem of uniform flow past a spherical shell. Nir exploited the same conditions as Jones and presented solutions for an isolated porous sphere either rotating in quiescent fluid or at rest in a linear shear-flow. He also gave an expression for effective viscosity of dilute suspension of porous spherical particles. However, these analyses of the flow field around a porous sphere in an unbounded fluid have been limited to the case when a particular velocity field is postulated at a large distance from the porous sphere. In this note, the flow fields interior to a porous sphere (where Darcy law holds) and exterior to it (Stokes flow region) are solved for the case when the velocity profile at a large distance is quite arbitrary. This has been made possible using the velocity representation of Stokes equations which is due to Palaniappan et al together with the boundary conditions of Jones. The expressions for velocity fields (both interior and exterior) are given explicitly. The Faxen's laws for a porous sphere are derived and the limiting cases of rigid and shear-free (bubble) spheres are then deduced. Some illustrative examples are given.

10A738. Flow past a spinning sphere in a slowly rotating fluid at small Reynolds numbers: A numerical study. - CV Raghava Rao and TVS Sekhar *(Dept of Math, Indian IT, Madras-600 036, India).* Int J Eng Sci 31(9) 1219-1231 (Sep 1993).

The axisymmetric flow due to a uniform stream at infinity past a slowly rotating sphere in a viscous, incompressible, rotating fluid is studied by numerical method and the results are presented mostly in the form of graphs of the streamlines and vorticity lines. The governing equations are the nonlinear Navier-Stokes equations. They are written as three coupled, nonlinear, elliptic partial differential equations for the stream function Ψ, vorticity ζ, rotational velocity component Ω. Finite difference method is used for solving the governing equations. Second order derivatives are approximated by central differences of order h^2 or k^2 and nonlinear terms are approximated by upwind differences of order h or k. A region of reversed flow and vortex formation is found to occur near the front or rear stagnation point or both under certain conditions depending upon the speed of the uniform stream at infinity, the radius of the sphere and the angular velocity of the sphere and fluid. The fluid may rotate in the same or opposite directions of the sphere rotation.

10A739. Oscillatory line singularities of Stokes' flows. - A Avudainayagam and J Geetha *(Dept of Math, Indian IT, Madras-600 036, India).* Int J Eng Sci 31(9) 1295-1299 (Sep 1993).

The fundamental singular velocity and pressure fields generated by the presence of an isolated force and a couple acting at a point in a 2D unbounded viscous incompressible medium executing oscillatory motions are obtained. These line singularities, the stokeslet and the rotlet, are used to construct new solutions for certain oscillatory plane viscous flow problems in the region exterior to a circular cylinder.

354I. THERMAL CONVECTION FLOW

See the following:

10A859. Laminar mixed convection heat transfer in 3D horizontal channel with a heated bottom
10A860. Mixed convection from a localized heat source in a cavity with conducting walls: A numerical study

354J. STRATIFIED FLOW AND FREE SURFACE FLOW

10A740. Propagation of intrusion fronts of high density ratios. - HP Grobelbauer, TK Fannelop *(Inst of Fluid Dyn, Swiss Fed IT, Zurich, Switzerland),* RE Britter *(Dept of Eng, Univ of Cambridge, Cambridge CB2 1P2, UK).* J Fluid Mech 250 669-687 (May 1993).

The propagation of gravity fronts of high density ratios has been studied experimentally (exchange flow) and by computer simulation. Non-Boussinesq fronts are known to occur in certain safety problems (chemical spills and fires), and we have investigated seven gas combinations giving density ratios from near unity to well over 20. The results are presented in terms of a density parameter ρx which remains finite both in the weak (ρx = 0) and the strong (ρx = 1) limit. The front velocities, measured by means of hot wires, are found to fall on two distinct curves, one for the slower light-gas fronts and one for the faster heavy-gas fronts. Two fractional depths, $\Phi = 1/2$ (lock exchange) and $\Phi = 1/6$, have been investigated in detail and results for the interesting case $\Phi \to 0$ have been obtained by extrapolation. To aid in the extrapolation and for comparison, all experimental (and some intermediate) cases have been simulated by means of a general purpose CFD-code (PHOENICS). Good agreement is found for cases without convergence problems, ie, for heavy-gas fronts of density ratio less than 5. Further information on frontal shape etc. has been obtained from visualization. The extrapolations to infinite depth indicate a limiting speed for both the heavy- and light-gas fronts close to the values predicted from shallow-layer theory for the analogous dam-break problem.

See also the following:

10A144. Steady trapped solutions to forced long-short interaction equation
10A735. Stratified Sadovskii flow in a channel

354K. ROTATING FLOW OR SURFACES

10A741. Barotropic flow over finite isolated topography: Steady solutions on the beta-plane and the initial value problem. - L Thompson *(Sch of Oceanog WB-10, Univ of Washington, Seattle WA 98195)* and GR Flierl *(54-1426, MIT).* J Fluid Mech 250 553-586 (May 1993).

Solutions for inviscid rotating flow over a right circular cylinder of finite height are studied, and comparisons are made to quasi-geostrophic solutions. To study the combined effects of finite topography and the variation of the Coriolis parameter with latitude a steady inviscid model is used. The analytical solution consists of one part which is similar to the quasi-geostrophic solution that is driven by the potential vorticity anomaly over the topography, and another, similar to the solution of potential flow around a cylinder, that is driven by the matching conditions on the edge of the topography. When the characteristic Rossby wave speed is much larger than the background flow velocity, the transport over the topography is enhanced as the streamlines follow lines of constant background potential vorticity. For eastward flow, the Rossby wave drag can be very much larger than that predicted by quasi-geostrophic theory. The combined effects of finite height topography and time-dependence are studied in the inviscid initial value problem on the f-plane using the method of contour dynamics. The method is modified to handle finite topography. When the topography takes up most of the layer depth, a stable oscillation exists with all of the fluid which originates over the topography rotating around the topography. When the Rossby number is order one, a steady trapped vortex solution similar to the one described by Johnson (1978) may be reached.

10A742. Slow axisymmetric rotation of a sphere in a transversely-isotropic fluid. - G Iosilevskii *(Fac of Aerospace Eng, Technion-Israel IT, Technion City, Haifa 32000, Israel),* AE Mendoza-Blanco *(Dept of Phys, Univ Natl Autonoma de Mexico, Ciudad Univ, 04510 Mexico DF),* H Brenner *(Dept of Chem Eng, MIT).* Quart J Mech Appl Math 46(1) 153-161 (Feb 1993).

The creeping flow engendered by the steady axisymmetric rotation of a sphere in a transversely-isotropic Newtonian fluid is investigated in the limiting case when the material properties of the fluid are unaffected by the fluid motion. By introducing an appropriate coordinate transformation, the problem is reduced to that of a spheroid rotating about its axis of symmetry in an isotropic fluid. Closed-form results are obtained for both the velocity field and the couple required to maintain the rotation.

See also the following:

10A768. Swirling free surface flow in cylindrical containers

354O. FLOW AROUND BODIES

10A743. Numerical simulation of flows past periodic arrays of cylinders. - AA Johnson, TE Tezduyar *(Dept of Aerospace Eng and Mech, Army High Performance Comput Res Center,, Minnesota Supercomput Inst, Univ of Minnesota, 1200 Washington Ave S, Minneapolis MN 55415),* J Liou *(Tulsa Res Center, Amoco Prod, Tulsa OK 74102).* Comput Mech 11(5-6) 371-383 (1993).

We present a detailed numerical investigation of three unsteady incompressible flow problems involving periodic arrays of staggered cylinders. The first problem is an uniperiodic flow with two cylinders in each cell of periodicity. The second problem is a biperiodic flow with two cylinders in each cell, and the last problem is a uniperiodic flow with ten cylinders. Both uniperiodic flows are periodic in the direction perpendicular to the main flow direction. In all three cases, the Reynolds number based on the cylinder diameter is 100, and initially the flow field has local symmetries with respect to the axes of the cylinders parallel to the main flow direction. Later on, these symmetries break, vortex shedding is initiated, and gradually the scale of the shedding increases until a temporally periodic flow field is reached. We furnish extensive data, including the vorticity and stream function fields at various instants during the temporal evolution of the flow field, time histories of the drag and lift coefficients, Strouhal number, initial and mean drag coefficients, amplitude of the drag and lift coefficient oscillations, and the phase relationships between the drag and lift oscillations associated with each cylinder. Our data confirms that, at this Reynolds number, there are no stable steady-state solutions with local cylinders parallel to the main flow direction and taking half of the computational domain needed normally. In such cases, the "steady-state" flow fields obtained would be identical to the flow fields observed at the initial stages of our computations. However, we show that such flow fields do not represent the temporally periodic flow fields even in a time-averaged sense, because, in all three cases, the initial drag coefficients are different from the mean drag coefficients. Therefore, we conclude that stability studies involving periodic arrays of cylinders should be carried out, as it is done in this work, with the true implementation of the spatial periodicity.

10A744. Numerical solution of steady viscous flow past a streamlined cylinder in von Mises coordinates. - I Husain and OP Chandna *(Dept of Math and Stat and Fluid Dyn Res Inst, Univ of Windsor, Windsor, ON, N9B 3P4, Canada)*. Mech Res Commun **20**(4) 343-352 (Jul-Aug 1993).

The numerical solution of steady viscous incompressible flow past a cylinder of streamlined cross-section have been obtained using the von Mises coordinates, (x, ψ), where ψ is the streamfunction of the flow. The governing equations are reduced to a system of two equations in two unknowns $y(x,\psi)$ and $\omega(x,\psi)$. This system is solved subject to the appropriate boundary conditions in the von Mises computational domain at Reynolds numbers up to 40 for two specific cross-sections.

See also the following:

10A736. Stokes flow past a sphere with mixed slip: Stick boundary conditions

354P. SURFACE TENSION FLOW (EG IN LOW GRAVITY ENVIRONMENTS)

See the following:

10A863. Surface motion induced by the interaction of pulsed laser radiation with highly absorbing dielectric fluids

354Y. COMPUTATIONAL TECHNIQUES

10A745. Application of the small-parameter method to the problem of the spatial flow of a viscous gas past bodies. - GA Tirskii, SV Utyuzhnikov, NK Yamaleyev *(Moscow, Russia)*. J Appl Math Mech **56**(6) 929-938 (1992).

The solution of the problem of the spatial hypersonic flow of a viscous gas past spherically blunted bodies is considered using the system of equations of a complete viscous shock layer (CVSL). The use of the small-parameter method (SPM) in conjunction with the method of global iterations enables one to reduce the computer time required by a factor of approximately 100 compared with the time needed to calculate similar problems in a strictly spatial formulation by establishment methods. The flow past blunt cones and bicones of long length at low angles of attack is considered as well as the flow past a body, which differs slightly from an axisymmetric one, at zero angle of attack. The applicability of the SPM is confirmed by comparison with experimental and computed data.

10A746. Behavior of a three-torus in truncated Navier-Stokes equations. - C Giberti and R Zansai *(Dipartimento Matematica Pura Appl, Univ Modena, via Campi 213 B, 41100 Modena, Italy)*. Physica D **65**(3) 300-312 (30 May 1993).

The presence of a three-torus in a seven-mode truncation of the 3D Navier-Stokes equations is investigated numerically by means of cross-section and power spectra. Furthermore, by taking advantage of particular features of the model, rotation vectors, circle maps and torus maps can be computed with high accuracy and used to study the dynamics. In particular, some interesting phenomena of partial phase-locking are described in deep detail. The three-torus, which arises via a Hopf bifurcation and persists in a wide parameter range, is found to break and originate a strange attractors. The onset of chaos and the associated bifurcation point can be defined quite precisely.

10A747. Biorthogonal series method for Oseen type flows. - HC Kuhlmann *(Center of Appl Sci Tech and Microgravity, Univ of Bremen, Hochschulring-Am Fallturm, 2800 Bremen 33, Germany)* and RR Adabala *(Dept of Math, Indian Inst of Sci, Bangalore-560 012, India)*. Int J Eng Sci **31**(9) 1243-1258 (Sep 1993).

A biorthogonal series method is developed to solve Oseen type flow problems. The theory leads to a new set of eigenfunctions for a specific class of linear non-self-adjoint operators containing the biharmonic one. These eigenfunctions differ from those given earlier in the literature for the biharmonic operator. The method is applied to the problem of thermocapillary flow in a cylindrical liquid bridge of the finite length with axial through flow. Flow and temperature distributions are obtained at leading order of an expansion for small surface tension Reynolds number and Prandtl number. Another related problem considered is that of cylindrical cavity flow. Solutions for both cases are presented in terms of biorthogonal series. The effect of axial through flow on velocity and temperature fields is discussed by numerical evaluation of the truncated analytical series. The presence of axial through flow not only convectively shifts the vortices induced by surface forces in the direction of the through flow, but also moves their centers toward the outer cylindrical boundary. This process can lead to significantly asymmetric flow structures.

10A748. Comparison of GMRES and CGSTAB accelerations for incompressible Navier-Stokes problems. - P Chin *(Dept of Elect and Comput Eng, Univ Waterloo ON, Canada)* and PA Forsyth *(Dept of Comput Sci, Fac of Math, Univ of Waterloo ON, Canada)*. J Comput Appl Math **46**(3) 415-426 (Jun 1993).

Recently, incomplete LU preconditioned conjugate-gradient-type matrix solvers have been used in conjunction with Newton or Newton-like methods to solve the fully-coupled incompressible Navier-Stokes equations. A number of acceleration methods can be used for the large sparse nonsymmetric linear systems that arise from such situations. In this work, we compare GMRES and CGSTAB, a "stabilized" variant of CGS. By observing the effect of various factors (eg, grid size, preconditioning), we attempt to determine the classes of problems to which each acceleration method is best suited. Numerical results obtained with several 2D geometries are provided.

10A749. Convergence analyses of Galerkin least-squares methods for symmetric advective-diffusive forms of the Stokes and incompressible Navier-Stokes equations. - LP Franca *(Lab Nacional Computacao Cientifica, LNCC-CNPq, Rua Lauro Muller 455, 22290 Rio de Janeiro RJ, Brazil)* and TJR Hughes *(Div of Appl Mech, Durand Bldg, Stanford)*. Comput Methods Appl Mech Eng **105**(2) 285-298 (Jun 1993).

Symmetric advective-diffusive forms of the Stokes and incompressible Navier-Stokes equations are presented. The Galerkin least-squares method for advective-diffusive equations is used for both systems and is related to other stabilized methods previously studied. The presentation reveals that the convergence analysis for advective-diffusive equations, as applied before to a linearized form of the compressible Navier-Stokes equations, carries over in a straightforward manner to the Stokes problem and to a linearized form of the compressible Navier-Stokes equations.

10A750. Convergence of Fourier methods for the Navier-Stokes equations. - E Weinan *(Sch of Math, Inst for Adv Study, Princeton NJ 08540)*. SIAM J Numer Anal **30**(3) 650-674 (Jun 1993).

Optimal orders of convergence for the Fourier-Galerkin method for 2D Navier-Stokes equations in various energy norms and in LP-norms of the velocity field are proved. Optimal orders of convergence for the Fourier-collocation method are also proved. Extensions of these results to 3D Navier-Stokes equations in the original form and the rotational form are presented. Semigroup formulations and the variation of constants formula are the essential tools in the analysis.

10A751. Efficient 3D calculation procedure for incompressible flows in complex geometries. - SK Choi, HY Nam, YB Lee, M Cho *(Fast Breeder Reactor Coolant Dept, Korea Atomic Energy Res Inst, PO Box 7 Daeduk-Danji, Daejon 305-606, Korea)*. Numer Heat Transfer B **23**(4) 387-400 (Jun 1993).

A 3D finite-volume calculation procedure for incompressible flows in complex geometries is presented. The scheme is based on the modified Rhie and Chow momentum interpolation method, in which the original scheme has been modified to employ the curvilinear covariant velocity components as cell face velocities to provide always a simple and diagonal dominant pressure or pressure correction equation. The coupling between the continuity equation and the momentum equations is effected using the SIMPLE algorithm. The present scheme is applied to test problems, and the results are compared with available experimental data and other numerical results.

10A752. FE analysis of viscous incompressible flows using primitive variables. - JN Reddy *(Dept of Mech Eng, Texas A&M Univ, College Station TX 77843-3123)*. Comput Struct **47**(4-5) 857-869 (3 Jun 1993).

This paper contains an overview of the primitive variable FE models of viscous, incompressible fluids in 3D enclosures, with emphasis on penalty FE models. The mixed and penalty FE models are described and their computational aspects are discussed. Methods for the solution of large systems of equations associated with the FE analysis of 3D problems are also discussed. Numerical results are included to illustrate the applicability of the penalty FE model and solution methods described here.

10A753. FE solution of the 3D compressible Navier-Stokes equations by a velocity-vorticity method. - G Guevremont, PL Kotiuga, WG Habashi *(Concordia Univ, Montreal, PQ, H3G 1M8, Canada)*, MM Hafez *(UC, Davis CA 95616)*. J Comput Phys **107**(1) 176-187 (Jul 1993).

This paper presents an alternative formulation to the primitive variable form of the Navier-Stokes equations. The approach is based on the use of the velocity and vorticity variables as a logical extension of the stream function-vorticity method which is quite effective for 2D flows. Second-order equations are obtained for the variables and discretization is through a weak-Galerkin FEM, followed by a Newton linearization. The velocity and vorticity components are solved simultaneously by a direct solver. The scheme is demonstrated for 2D and 3D incompressible and subsonic internal enclosed flow problems.

10A754. Iterative method of integral relations scheme for wake flows. - R-J Yang *(Dept of Eng Sci, Natl Cheng-Kung Univ, Taiwan, ROC)* and W-S Yeung *(Dept of Mech Eng, Univ of Lowell, Lowell MA)*. Commun Numer Methods Eng **9**(6) 525-531 (Jun 1993).

The orthonormal method of integral relations is extended to calculate wake flow problems. Two previous difficulties are overcome: (1) the non-constant integral domain is eliminated by introducing a linear transformation in the formulation; (2) the difficulty associated with determining unique orthonormal weighting functions is overcome by an iterative scheme. The new formulation is applied to calculate a wake flow. A high-order solution for N up to 4 is obtained with relative ease.

10A755. Progress on adaptive hp-FEMs for the incompressible Navier-Stokes equations. - JT Oden *(Tex Inst for Computational Mech, Univ of Texas, Austin TX)*, SR Kennon, WW Tworzydlo, JM Bass, C Berry *(Computational Mech, Austin TX)*. Comput Mech **11**(5-6) 421-432 (1993).

This paper outlines recent results obtained in the development and application of hp-adaptive

FEMs to 3D problems in incompressible viscous flow simulation.

10A756. Second-order convergence of a projection scheme for the incompressible Navier-Stokes equations with boundaries. - TY Hou *(Courant Inst of Math Sci, 251 Mercer St, New York NY 10012)* and BTR Wetton *(Dept of Math, Univ of British Columbia, Vancouver, BC, V6T 1Y4, Canada)*. SIAM J Numer Anal 30(3) 609-629 (Jun 1993).

A rigorous convergence result is given for a projection scheme for the Navier-Stokes equations in the presence of boundaries. The numerical scheme is based on a finite-difference approximation, and the pressure is chosen so that the computed velocity satisfies a discrete divergence-free condtion. This choice for the pressure and the particular way that the discrete divergence is calculated near the boundary permit the error in the pressure to be controlled and the second-order convergence in the velocity and the pressure to the exact solution to be shown. Some simplifications in the calculation of the pressure in the case without boundaries are also discussed.

10A757. SUPG FE computation of viscous compressible flows based on the conservation and entropy variables formulations. - SK Aliabadi, SE Ray, TE Tezduyar *(Dept Aerospace Eng and Mech, Army High Performance Comput Res Center, Minnesota Supercomput Inst, Univ of Minnesota, 1200 Washington Ave S, Minneapolis MN 55415)*. Comput Mech 11(5-6) 300-312 (1993).

In this article, we present our investigation and comparison of the SUPG-stabilized FE formulations for computation of viscous compressible flows based on the conservation and entropy variables. This article is a sequel to the one on inviscid compressible flows by Le Beau et al (1992). For the conservation variables formulation, we use the SUPG stabilization technique introduced in Aliabadi and Tezduyar (1992), which is a modified version of the one described in Le Beau et al (1992). The formulation based on the entropy variables is same as the one introduced in Hughes et al (1986). The two formulations are tested on three different problems: adiabatic flat plate at Mach 2.5, Reynolds number 20 000; Mach 3 compressions corner at Reynolds number 16 800; and Mach 6 NACA 0012 airfoil at Reynolds number 10 000. In all cases, we show that the results obtained with the two formulations are very close. This observation is the same as the one we had in Le Beau et al (1992) for inviscid flows.

10A758. Three-step FEM for unsteady incompressible flows. - Chun Bo Jiang and Mutsuto Kawahara *(Dept of Civil Eng, Chuo Univ, Kasuga 1-13-27, Bunkyo-ku Tokyo 112, Japan)*. Comput Mech 11(5-6) 355-370 (1993).

This paper describes a three-step FEM and its application to unsteady incompressible fluid flows. The stability analysis of the 1D purely convection equation shows that this method has third-order accuracy and an extended numerical stability domain in comparison with the Lax-Wendroff FEM. The method is cost effective for incompressible flows, because it permits less frequent updates of the pressure field with good accuracy. In contrast with the Tayler-Galerkin method, the present three-step FEM does not contain any new higher-order derivatives, and is suitable for solving non-linear multi-dimensional problems and flows with complicated outlet boundary conditions. The three-step FEM has been used to simulate unsteady incompressible flows, such as the vortex pairing in mixing layer. The properties of the flow fields are displayed by the marker and cell technique. The obtained numerical results are in good agreement with the literature.

See also the following:

10A21. General hyperbolic solver: The CIP method applied to curvilinear coordinate

10A867. Solution of nonlinear elliptic convection-diffusion problems through the integral transform method

356. Compressible flow

356B. SUBSONIC FLOW

See the following:

10A836. Indicial lift approximations for 2D subsonic flow as obtained from oscillatory measurements

356C. TRANSONIC FLOW

10A759. Aerodynamic computations for a transonic projectile at angle of attack by total variation diminishing schemes. - Herng Lin and Ching-Chang Chieng *(Natl Tsing Hua Univ, Hsinchu, Taiwan, ROC)*. J Spacecraft Rockets 30(3) 304-315 (May-Jun 1993).

Several total variation diminishing (TVD) schemes and the Beam-Warming solution algorithm have been incorporated in a computer code for solving 3D time-dependent, Reynold's averaged Navier-Stokes equations in generalized coordinates. A finite-volume fully implicit, approximately factored scheme is employed with a time-step convergence acceleration. Transonic turbulent flows past a scant ogive cylinder boat tail projectile at Mach numbers 0.94 and 0.97 including base flow region were studied. Conditions at 0- and 2-deg angle of attack were computed. Results of zero angle of attack showed that third-order TVD schemes gave little improvements over the second-order TVD schemes. Van Leer's third-order MUSCL-type TVD scheme yields somewhat better results and faster convergence than Chakravarthy's upwind-biased TVD scheme. The convergence rate of the Beam-Warming scheme is similar to that of the second-order TVD schemes. The Beam-Warming scheme gives comparative results over most of the projectile except regions of coarse grids because the scheme is very sensitive to grid resolution. For angle-of-attack computations, Van Leer's third-order MUSCL-type TVD scheme still gives better agreement with measurement.

10A760. On boundary-layer transition in transonic flow. - RI Bowles and FT Smith *(Dept of Math, Univ Col, Gower St, London WC1E 6BT, UK)*. J Eng Math 27(3) 309-342 (Aug 1993).

Boundary-layer transition in transonic external flow is addressed theoretically. The transonic area is rich in different flow structures, and transition paths, and the work has wide potential application in transonic aerodynamics, including special reference to the example of flow transition over an engine nacelle. The investigation is intended partly to aid, compare with, and detect any limitations of, a quasi-parallel empirical methodology for design use in the area, especially with respect to the transonic range, and partly to develop an understanding and possible control of the nonlinear natural or by-pass properties of the compressible transition present. The mechanisms behind three major factors, (a) substantial external-flow deceleration, (b) rapid boundary-layer thickening, (c) 3D nonlinear interactions, are identified; these three are involved in the specific application above and in more general configurations, depending on the disturbance background present. It is found also that some similarities exist with the phenomenon of buffeting on transonic airfoils, and the relevant physics and governing equations throughout are identified. Sensitive nonlinear effects are important in all the factors (a)-(c), especially a resonance linkage between shock buffeting and boundary-layer thickening, and nonlinearly enhanced 3D growth triggered by slight 3D warping for instance, peculiar to the transonic range. The latter enhanced growth is perhaps the most significant finding. The implications, in the general setting as well as for the nacelle-flow context in particular, are also presented.

356D. SUPERSONIC FLOW

10A761. Lifting line theory for supersonic flow applications. - I Jadic *(Dept of Numer Simul in Fluid Mech, Inst of Appl Math, Bd Pacii 220 Section 6, Bucharest, Romania)* and VN Constantinescu *(Aeronaut Eng Fac, Polytech Inst, Bucharest, Romania)*. AIAA J 31(6) 987-994 (Jun 1993).

The paper is devoted to the study of a supersonic lifting line theory intended to provide both a means of aerodynamic calculation and a benchmark for the validation of the control point position for the related constant pressure panel methods. The model is based on the small perturbations assumption. A constant distribution of bound vortices is assumed along the chord whereas the spanwise load distribution is calculated by means of trigonometrical series, formally similar to the subsonic methods. The calculated aerodynamic coefficients are in good agreement with the reference data, the precision being compatible with the small perturbations assumption. The control point position obtained is shown to vary as a function of aspect ratio from 100 to 88% of the local chord.

356E. HYPERSONIC FLOW

10A762. Comparison of gas-dynamic models for hypersonic flow past bodies. - SV Zhluktov, SV Utyuzhnikov, VS Shchelin, VG Shcherbak *(Moscow, Russia)*. J Appl Math Mech 56(6) 939-944 (1992).

Various gas-dynamic models for describing chemically non-equilibrium flows are compared using the example of the steady flow past the blunt nose of the "Buran" and "Space Shuttle" vehicles during their descent from orbit. Models of locally self-similar approximations of the Navier-Stokes equations, of a chemically equilibrium and non-equilibrium complete viscous shock layer (CVSL) and a model of a thin viscous shock layer (TVSL) are considered. In all the models the occurrence of physicochemical processes was taken into account in the same way using fixed values of the constants for the gas-phase chemical reactions. Good agreement between the results of calculations of the heat flux at the critical point is found. Chemically non-equilibrium flows have been considered earlier using the approximate Navier-Stokes equations, within the framework of a TVSL and a CVSL. The TVSL and CVSL models were compared in the case of flows of a uniform gas.

10A763. Extension of unsteady embedded Newtonian theory. - LE Ericsson *(Lockheed Missiles & Space, Sunnyvale CA 94086)* and HHC King *(ETAK, Menlo Park CA)*. J Spacecraft Rockets 30(3) 316-322 (May-Jun 1993).

A previously developed unsteady embedded Newtonian theory has been extended to be able to predict the hypersonic unsteady aerodynamics of axisymmetric bodies of general shape with the accuracy needed for preliminary design. The static aerodynamics determined by a 3D finite difference method are used together with unsteady embedded Newtonian flow concepts to provide the vehicle dynamics without significantly adding computational time to the static computer program.

10A764. Numerical solution of the kinetic model equations for hypersonic flows. - Nobuyuki Satofuka, Koji Morinishi, Tsutomu Oishi *(Kyoto IT, Matsugasaki, Sakyo-ku, Kyoto*

606, Japan). Comput Mech 11(5-6) 452-464 (1993).

A numerical method for solving the model kinetic equations for hypersonic flows has been developed. The model equations for the distribution function are discretized in phase space using a second order upwind finite difference scheme for the spatial derivatives. The resulting system of ordinary differential equations in time is integrated by using a rational Runge-Kutta scheme. Calculations were carried out for hypersonic flow around a double ellipse under various free stream conditions. Calculated results are compared with the Navier-Stokes solutions and the Direct Simulation Monte Carlo (DSMC) method for the corresponding case. The agreement is quite excellent in general.

10A765. Stabilization of the Burnett equations and application to hypersonic flows. - X Zhong, RW MacCormack, DR Chapman *(Dept of Aeronaut and Astronaut, Stanford)*. AIAA J 31(6) 1036-1043 (Jun 1993).

Numerical solutions of the Burnett equations for hypersonic flow at high altitudes in the continuum transitional regime were not possible except for some 1D flows. It is shown from both analytical investigation and numerical computations that the Burnett equations are unstable to disturbances of small wavelengths. This fundamental instability arises in numerical computations when the grid spacing is less than the order of a mean free path and precludes Burnett flowfield computations above a certain maximum altitude for any given aerospace vehicle. A new set of equations termed the "augmented Burnett equations" has been developed and shown to be stable both by a linearized stability analysis and by direct numerical computations for 1D and plane 2D flows. The latter represents the first known Burnett solutions for 2D hypersonic flow over blunt leading edges. The comparison of these solutions with the conventional Navier-Stokes solutions reveals that the difference is small in low-altitude low-speed flows but significant in high-altitude hypersonic flows.

See also the following:

10A162. Large-amplitude FE flutter analysis of composite panels in hypersonic flow

356F. UNSTEADY EFFECTS, VORTICES

See the following:

10A733. Hairpin removal in vortex interactions II

356I. FLOW AROUND BODIES

See the following:

10A760. On boundary-layer transition in transonic flow

356K. NONEQUILIBRIUM AND CHEMICAL EFFECTS

10A766. Hydrodynamics, gravitational sensitivity, and transport phenomena in continuous flow electrophoresis. - MS Bello *(Inst of Macromol Compounds, Russian Acad of Sci, 199004 Bolshoi pr 31, St Petersburg, Russia)* and VI Polezhaev *(Inst for Prob in Mech, Russian Acad of Sci, 117527 pr Vernadskogo 101, Moscow, Russia)*. AIAA J 31(6) 997-998 (Jun 1993).

A multizone mathematical model for hydrodynamics, heat and mass transfer in continuous flow electrophoresis (CFE) is reported. The model divides the electrophoretic cell into three zones: the entrance region, the zone of the mixture injection, and the zone of the parallel fluid flow. Three-dimensional transport equations, including Navier-Stokes equations, and equations of heat and mass balance are significantly simplified in each zone. The length of the cell entrance region and recirculation flows in the CFE cell are found to be affected by thermal convection caused by internal heating of the fluid. The influences of convective diffusion and electro-osmosis on concentration profiles of separated fractions are studied numerically for a wide range of the Peclet number.

356M. ROTATING FLUIDS OR SURFACES

10A767. Geometrical and numerical considerations in computing advanced propellar noise. - VL Wells *(Dept Mech and Aerospace Eng, Arizona State Univ, Tempe AZ 85287)* and A Han *(Dept Mech and Aerospace Eng, VPI)*. J Aircraft 30(3) 365-371 (May-Jun 1993).

A previously developed technique for numerically solving the acoustic analogy equation for rotating surfaces with supersonic regions results in smooth pressure time waveforms. The method appears to provide results superior to those of other schemes because it eliminates erratic noise in the computed waveforms and deals only with nonsingular integrals. This article discusses the application of the method to propellar type rotor blades. Several different sweep geometries are considered, and presented results show the effect of blade shape on the noise produced and on the numerical procedure for computing that noise. Computed waveforms exhibit expected behavior, deduced from analysis of the retarded blade shapes and the critical points along the blade edges where the Mach number in the direction of the observer equals one.

10A768. Swirling free surface flow in cylindrical containers. - A Siginer and R Knight *(Dept of Mech Eng, Auburn Univ, Auburn AL 36849)*. J Eng Math 27(3) 245-264 (Aug 1993).

Free surface flow in a cylindrical container with steadily rotating bottom cap is investigated. A regular domain perturbation in terms of the angular velocity of the bottom is used. The flow field is made up of the superposition of azimuthal and meridional fields. The meridional field is solved both by biorthogonal series and a numerical algorithm. The free surface on the liquid is determined at the lowest significant order. The aspect ratio of the cylinder may generate a multiple cell structure in the meridional plane which in turn shapes the free surface.

10A769. Unsteady blade pressure on a propfan at takeoff: Euler analysis and flight data. - M Nallasamy *(Aeromech Dept, NASA Lewis Res Center Group, Sverdrup Tech, Brook Park OH 44142)*. J Aircraft 30(3) 372-376 (May-Jun 1993).

The unsteady blade pressures due to the operation of the propfan at an angle to the direction of the mean flow are obtained by solving the unsteady 3D Euler equations. The configuration considered is the eight-bladed SR7L propfan operating at takeoff conditions, and the inflow angles considered are 6.3, 8.3, and 11.3 deg. The predicted blade pressure waveforms are compared with in flight measurements. At the inboard radial station ($r/R = 0.68$) the phase of the predicted waveforms show reasonable agreement with measurements, whereas, the amplitudes are overpredicted in the leading edge region of the blade. At the outboard radial station ($r/R = 0.95$), the predicted amplitudes of the waveforms on the pressure surface are in good agreement with flight data for all inflow angles. The measured waveforms show a relative phase lag compared to the computed waveforms. The phase lag depends on the axial location of the transducer and the surface of the blade. On the suction surface, in addition to the relative phase lag, the measurements show distortion of the waveforms. The extent of the distortion increases with increase in the inflow angle. This distortion seems to be due to viscous separation effects which depends on the azimuthal location of the blade and the location of the transducer.

356Y. COMPUTATIONAL TECHNIQUES

10A770. Comparison of two Navier-Stokes codes for simulating high-incidence vortical flow. - NM Chaderjian *(Appl Computation Fluids Branch, NASA Ames Res Center, Moffett Field CA 94035)*. J Aircraft 30(3) 357-364 (May-Jun 1993).

Computations from two Navier-Stokes, NSS and F3D, are presented for a tangent-ogive cylinder body at high angle of attack. Features of this steady flow include a pair of primary vortices on the leeward side of the body, as well as secondary vortices. The topological and physical plausibility of this vortical structure is discussed. The accuracy of these codes are assessed by comparison of the numerical solutions with experimental data. The effects of turbulence model, numerical dissipation, and grid refinement are presented. The overall efficiency of these codes are also assessed by examining their convergence rates, computational time per time step, and maximum allowable time step for time accurate computations. Overall, the numerical results from both codes compared equally well with experimental data, however, the NSS code was found to be significantly more efficient than the F3D code.

10A771. Energy-bounded flow approximation on a Cartesian-product grid over rough terrain. - DK Purnell and MJ Revell *(Atmos Div, Natl Inst of Water & Atmos Res, Wellington, New Zealand)*. J Comput Phys 107(1) 51-65 (Jul 1993).

We construct a method for modeling the 3D, time dependent, compressible fluid flow in a gravitational field on a rotating Cartesian-product grid with a spatially rough metric that bounds solutions by the total initial physical energy. Specifically: (1) the total physical energy is an l_2 norm on the model state and (2) this total energy cannot increase provided the timestep does not exceed CFL limits. In particular, the first property means that our measure of the energy is always positive unless the mass, momentum, and internal energy are all everywhere zero. These conditions guarantee that no error can grow unchecked. This is thought to be a desirable property, although only in the case of linear systems is it sufficient for convergence of a consistent approximation to the true solution.

10A772. Global coefficient adjustment method for Neumann condition in explicit Chebyshev collocation method and its application to compressible Navier-Stokes equations. - Jian-ping Wang, Yoshiaki Nakamura *(Dept of Aeronaut Eng, Nagoya Univ, Nagoya 464-01, Japan)*, Michiru Yasuhara *(Aichi IT, Toyoda 470-03, Japan)*. J Comput Phys 107(1) 160-175 (Jul 1993).

The present paper consists of two parts. In part 1, a new technique of treating Neumann boundary conditions with an explicit Chebyshev collocation method is developed. Any Neumann boundary condition can be satisfied by adjusting all the Chebyshev coefficients of a solution, which results in a small influence on the solution and its derivatives except at the boundary. Comparisons between the new technique and several traditional ones are made for a 1D advection-diffusion problem, which confirms the superiority of the new technique. The spectral accuracy of the new technique is also demonstrated. In part 2, a Chebyshev collocation code for the compressible Navier-Stokes equations is developed to solve the high-speed flows around a sphere. Good resolutions are obtained in the boundary layer by using the new technique, and comparison between the calculation and the experiment shows good agreement.

10A773. New flux splitting scheme. - Meng-Sing Liou and CJ Steffen Jr *(Internal Fluid Mech Div, NASA Lewis Res Center, Cleveland OH 44135)*. J Comput Phys **107**(1) 23-39 (Jul 1993).

A new flux splitting scheme is proposed. The scheme is remarkably simple and yet its accuracy rivals, and in some cases surpasses, that of Roe's solver in the Euler and Navier-Stokes solutions carried out in this study. The scheme is robust and converges as fast as the Roe splitting. We propose an appropriately defined cell-face advection Mach number using values from the two straddling cells via associated characteristic speeds. This interface Mach number is then used to determine the upwind extrapolation for the convective quantities. Accordingly, the name of the scheme is coined as the advection upstream splitting method (AUSM). We also introduce a new pressure splitting which is shown to behave successfully, yielding much smoother results than other existing pressure splittings. Of particular interest is the supersonic blunt body problem in which the Roe scheme gives anomalous solutions. The AUSM produces correct solutions without difficulty for a wide range of flow conditions as well as grids.

10A774. Non-oscillatory spectral element Chebyshev method for shock wave calculations. - D Sidilkover and GE Karniadakis *(Dept of Mech and Aerospace Eng, Program in Appl and Comput Math, Princeton)*. J Comput Phys **107**(1) 10-22 (Jul 1993).

A new algorithm based on spectral element discretization and non-oscillatory ideas is developed for the solution of hyperbolic partial differential equations. A conservative formulation is proposed based on cell averaging and reconstruction procedures, that employs a staggered grid of Gauss-Chebyshev and Gauss-Lobatto-Chebyshev discretizations. The non-oscillatory reconstruction procedure is based on ideals similar to those proposed by Cai *et al* but employs a modified technique which is more robust and simpler in terms of determining the location and strength of a discontinuity. It is demonstrated through model problems of linear advection, inviscid Burgers equation, and 1D Euler system that the proposed algorithm leads to stable, non-oscillatory accurate results. Exponential accuracy away from the discontinuity is realized for the inviscid Burgers equation example.

10A775. Numerical aspects of a block structured compressible flow solver. - BJ Geurts and H Kuerten *(Dept of Appl Math, Univ of Twente, PO Box 217, 7500 AE Enschede, Netherlands)*. J Eng Math **27**(3) 293-307 (Aug 1993).

A block structured compressible flow solver based on a finite volume approach with central spatial differencing is described and its performance in 2D on flow around an airfoil is studied. Variations in the number and dimensions of the blocks do not influence the convergence behavior nor the solution, irrespective of the relative positions of a possible shock and the block-interfaces. Mixed calculations, in which the governing equations, either Euler or Reynolds averaged Navier-Stokes, differ per block, give accurate results provided that Euler blocks are defined outside the boundary layer and or in the far field wake regions. Likewise, extensive grid distortions near block interfaces can be allowed for outside the boundary layer. Finally, an unbalanced advancement in time, in which each block is advanced independently over several time steps gives no serious decrease in convergence rate.

10A776. Posteriori error bounds for numerical solutions of regularized compressible flow problems. - Koichi Niijima *(Dept of Civil Eng and Sci, Kyushu IT, Iizuka 820, Japan)*. Commun Numer Methods Eng **9**(6) 511-523 (Jun 1993).

We give *a posteriori* error bounds for numerical solutions of regularized compressible flow problems. To verify the efficiency of our method, numerical experiments are performed.

See also the following:

10A759. Aerodynamic computations for a transonic projectile at angle of attack by total variation diminishing schemes

10A763. Extension of unsteady embedded Newtonian theory

358. Rarefied flow

10A777. Theoretical estimates of vibrational relaxation in nitrogen up to 40,000 K. - CF Hansen *(Chem Phys Inst, Univ of Oregon, Eugene OR 97403)*. AIAA J **31**(6) 1044-1050 (Jun 1993).

Vibrational relaxation of N_2 molecules is considered at temperatures up to 40,000 K in gas mixtures that contain electrons as well as heavy collision partners. The theory of vibrational excitation due to N_2-N_2 collisions is fit to experimental data to 10,000 K by choice of the shape of the intermolecular potential and size of the collision cross section. These values are then used to extrapolate the theory to 40,000 K. Electron collisions promote vibrational transitions much more readily than the heavy particle collisions; and equilibration of vibrational temperature with the electron temperature occurs almost instantaneously for many practical purposes. Subsequently, vibrational relaxation depends on heavy particle collisions; the electrons merely drain off some of the vibrational energy changes and delay the approach to full equilibrium. As temperature increases beyond 10,000 K, multiple quantum jumps become increasingly important and small perturbation assumptions become invalid. However, these effects compensate such that small perturbation results provide a fair approximation at somewhat higher temperatures than might be expected. Anharmonic effects do not appear to be highly important to the total relaxation rate at temperatures up to 40,000 K, though they distort the transition rates in the uppermost levels.

360. Multiphase flows

360A. GENERAL THEORY

See the following:

10A781. Microstructure suspended in 3D flows

360B. MIXTURES OF LIQUID OR GAS WITH SOLID PARTICLES (EG SLURRIES)

10A778. Character of two-phase gas-particulate flow equations. - AD Fitt *(Fac of Math, Univ of Southampton, Southampton SO9 5NH, UK)*. Appl Math Model **17**(7) 338-354 (Jul 1993).

Complex characteristics arise as a result of multiphase flow averaging, and the consequent omission of important physical terms. With care, however, these effects may be reintroduced into the equations. Using such as approach, the specific case of gas-particular two-phase flow is considered. The aim is not to propose a definitive, demonstrably "correct" system of equations for unsteady two-phase gas-particulate flow; the assumptions made are too general and specific cases must be treated on their individual merit. Rather a methodology of analysis is illustrated and qualitative results concerning the nature of added terms in the equations are obtained. The effect of each term and also of combinations of terms is studied, and general conclusions are drawn concerning the hyperbolicity of the equations.

10A779. Experimental studies of the deformation of a synthetic capsule in extensional flow. - KS Chang and WL Olbricht *(Sch of Chem Eng, Cornell)*. J Fluid Mech **250** 587-608 (May 1993).

Experiments are described to study the motion and deformation of a synthetic, liquid-filled capsule that is freely suspended in hyperbolic extensional flow. The capsule is a composite particle consisting of a viscous liquid drop surrounded by a thin polymeric membrane. The method used to fabricate capsules suitable for macroscopic flow experiments is described. The deformation of the capsule is measured as a function of strain rate for an extensional flow generated in a four-roll mill. The data agree well with results from small-deformation theory developed by Barthes-Biesel and co-workers, provided the deformation of the capsule is not too large. Using the theory to correlate the experimental data produces an estimate for the elastic modulus of the membrane that agrees reasonably well with the elastic modulus obtained by an independent technique. However, for sufficiently large strain rates, the membrane exhibits strain hardening and a permanent change in its structure, both of which are reflected in the shape of the capsule.

10A780. Experimental studies of the deformation and breakup of a synthetic capsule in steady and unsteady simple shear flow. - KS Chang *(Kimberly-Clark, 2100 Winchester Rd, Neenah WI 54957-0999)* and WL Olbricht *(Sch of Chem Eng, Cornell)*. J Fluid Mech **250** 609-633 (May 1993).

An experimental study is reported of the motion, deformation, and breakup of a synthetic capsule that is freely suspended in Couette flow. The capsule is a liquid drop surrounded by a thin polymeric membrane. The shape and orientation of the capusle are measured in steady flow and following the start-up of Couette flow. Results are compared with predictions of the small-deformation theory of Barthes-Biesel and co-workers. The data suggest that the capsule membrane is viscoelastic, and comparisons with theory yield values of the membrane elastic modulus and the membrane viscosity. The values of the elastic modulus of the capsule membrane deduced from the flow data are compared with independent measurements for the same capsule. When the flow-induced deformation becomes sufficiently large, the capsules break. Breakup begins at points on the membrane surface near the principal strain axis of the undisturbed flow. By examining the local deformation within the membrane, it is shown that breakup is correlated with local thinning of the membrane and is initiated at points where the thickness is a minimum.

10A781. Microstructure suspended in 3D flows. - AJ Szeri *(Dept of Mech and Aerospace Eng, UC, Irvine CA 92717-3975)* and LG Leal *(Dept of Chem and Nucl Eng, UC, Santa Barbara CA 93106)*. J Fluid Mech **250** 143-167 (May 1993).

The dynamical behavior of stretchable, orientable microstructure suspended in a general 3D fluid flow is investigated. Model equations given by Olbricht, Rallison & Leal (1982) are examined in the case of microstructure traveling through arbitrarily complicated flows of the carrier fluid. As in the 2D analysis of Szeri, Wiggins & Leal (1991), one must first treat the orientation dynamics problem; only then can the equation for stretch of the microstructure be analyzed rationally. In 3D flows that are steady in the Lagrangian frame, attractors for the orientation dynamics are shown to be equilibria or limit cycles; this asymptotic behavior was first deduced by Bretherton (1962). In 3D flows that are time periodic in the Lagrangian frame (eg, recirculating flows), the orientation dynamics may be characterized by periodic or quasi-periodic attractors. Thus, robust (generic) behavior in these cases is always characterized by a single global attractor; there is no asymptotic dependence of orientation dynamics on the initial orientation. The type of asymptotic orientation dynamics – steady, periodic, or quasi-periodic – is signified by a simple criterion. Details of the relevant bifurcations, as well as history-dependent strong flow criteria are developed. Examples which illustrate the various types of behavior are given.

10A782. Particle-driven gravity currents. - RT Bonnecaze *(Dept of Chem Eng, Univ of Texas, Austin TX 78712-1062)*, HE Huppert, JR Lister *(Inst of Theor Geophys, Dept of Appl Math and Theor Phys, Univ of Cambridge, Silver St, Cambridge CB3 9EW, UK)*. J Fluid Mech **250** 339-369 (May 1993).

Gravity currents created by the release of a fixed volume of a suspension into a lighter ambient fluid are studied theoretically and experimentally. The greater density of the current and the buoyancy force driving its motion arise primarily from dense particles suspended in the interstitial fluid of the current. The dynamics of the current are assumed to be dominated by a balance between inertial and buoyancy forces; viscous forces are assumed negligible. The currents considered are 2D and flow over a rigid horizontal surface. The flow is modeled by either the single- or the two-layer shallow-water equations, the two-layer equations being necessary to include the effects of the overlying fluid, which are important when the depth of the current is comparable to the depth of the overlying fluid. Because the local density of the gravity current depends on the concentration of particles, the buoyancy contribution to the momentum balance depends on the variation of the particle concentration. A transport equation for the particle concentration is derived by assuming that the particles are vertically well-mixed by the turbulence in the current, are advected by the mean flow and settle out through the viscous sublayer at the bottom of the current. The boundary condition at the moving front of the current relates the velocity and the pressure head at that point. The resulting equations are solved numerically, which reveals that two types of shock can occur in the current.

360C. LIQUID-GAS MIXTURE

10A783. Optical measurement of slope, thickness, and velocity in liquid film flow. - CF Than, KC Tee, KS Low *(Univ of Malaya, 59100 Kuala Lumpur, Malaysia)*, CP Tso *(Nanyang Tech Univ, Singapore 2263, Singapore)*. Smart Mat Struct **2**(1) 13-21 (Mar 1993).

A new optical system for measuring the slope, thickness and wave velocity of a liquid film flow is presented. The theory of the system is discussed and the equations derived are employed in simulations involving film flow with low- and high-amplitude waves. The results, which show that it is possible to determine the three parameters for a low-amplitude wave, while only the wave velocity may be found for a high-amplitude wave, may have potential applications in multiphase flow systems.

360E. LIQUID DROP FORMATION

10A784. Breakup of latex doublets by impaction. - W John *(Air and Indust Hygiene Lab, CA Dept of Health Services, 2151 Berkeley Way, Berkeley CA 94704)* and V Sethi *(Dept of Civil and Env Eng, Univ of Cincinnati, Cincinnati OH 45221)*. Aerosol Sci Tech **19**(1) 57-68 (Jul 1993).

The breakup by impaction of a simple agglomerate consisting of two identical spherical particles has been studied. The agglomerates were doublets produced by nebulizing suspensions of latex particles. The doublet concentrations before and after impaction were determined from the particle size spectra obtained with an optical particle counter. Preliminary experiments showed that the latex doublets did not break up in the acceleration nozzle of the impactor. The doublet fraction (DF) is defined as the doublet-singlet concentration ratio after impaction to that before impaction. The DF of 299-μm Dow latex measured at $\sqrt{Stk} = 1.62$ decreased by a factor of 2 as the relative humidity (RH) was varied from 8% to 85%. The remaining experiments were made at low RH with seven different surfactant-free suspensions of polystyrene latex stabilized by the addition of charged surface functional groups. All the data, for particle sizes ranging from 1.62 to 4.07 μm and impact velocities from 10 to 80 m-s, could be fitted by the expressions, $DF = 18.2\ v^{0.58}D^{-1.60}$, where the impact velocity v is in m-s and the particle diameter D is in μm. The van der Waals adhesion energy is calculated to be less than 1/3000 of the kinetic energy needed to break up half of the doublets. The repulsive electrostatic energy of the surface functional groups is estimated to be about 1.25 times larger than the van der Waals adhesion energy. It is concluded that the doublets are probably bound by bridges of residue left after droplet evaporation.

10A785. Threshold for resuspension by particle impaction. - W John *(Air and Indust Hygeine Lab, CA Dept of Health Services, 2151 Berkeley Way, Berkeley CA 94704)* and V Sethi *(Dept of Civil and Env Eng, Univ of Cincinnati, Cincinnati OH 45221)*. Aerosol Sci Tech **19**(1) 69-79 (Jul 1993).

The threshold velocity for the resuspension of 8.6-μm, diameter ammonium fluorescein particles from a Tedlar surface by impaction of 3-μm ammonium fluorescein particles has been measured to be 9.3 ± 4.3 m-s. The resuspension rate, observed with an optical particle counter, has a wide variability. Image analysis of the particle patterns on the surface suggests that particle resuspension takes place at a radius somewhat smaller then that of the nozzle of the impactor used in the experiments. Exposure of some test surfaces to laboratory air for several days prior to the measurements did not change the results significantly. A theoretical model has been shown to predict a threshold velocity within a factor of 2 of the experiment. The major uncertainty involves the value of the surface energy parameter, a difficulty encountered previously in a study of particle bounce. The model is based on the transfer of vertical momentum to the struck particle which is subsequently compressed against the surface. Elastic rebound then supplies the lift-off force to overcome the surface adhesion force. An alternative calculation based on inceptive rotational motion induced by off-center impacts predicts a threshold almost two orders of magnitude lower than observed.

360F. BUBBLE DYNAMICS

10A786. Deformation and location of an acoustically levitated liquid drop. - Yuren Tian, RG Holt, RE Apfel *(Dept of Mech Eng, Yale Univ, New Haven CT 06520)*. J Acoust Soc Am **93**(6) 3096-3104 (Jun 1993).

A theoretical method to determine the location and static deformation of an acoustically levitated liquid drop in air is presented. The interacation between drop and sound field, involving nonspherical acoustic scattering and drop volume variation, is the crux of this analysis, which is valid for drops with aspect ratio as large as 2. Numerical calculations are presented of drop shape and location as functions of sound pressure, surface tension, and drop volume in both gravity (1g) and gravity-free (0g) environments. The numerical results agree well with our experimental measurements and those of other researchers.

10A787. Dynamic simulations of flows of bubbly liquids at large Reynolds numbers. - AS Sangani *(Dept of Chem Eng and Mat Sci, Syracuse Univ, Syracuse NY 13244)* and AK Didwania *(Dept of Appl Mech and Eng Sci, UCSD)*. J Fluid Mech **250** 307-337 (May 1993).

Results of dynamic simulations of bubbles rising through a liquid are presented. The Reynolds number of the flow based on the radius and the terminal speed of bubbles is large compared to unity, and the Weber number, which is the ratio of inertial to surface tension forces, is small. It is assumed that the bubbles do not coalesce when they approach each other but rather bounce instantaneously, conserving the momentum and the kinetic energy of the system. The flow of the liquid is assumed to be irrotational and is determined by solving the many-bubble interaction problem exactly. The viscous force on the bubbles is estimated from the rate of viscous energy dissipation. It is known that the random state of bubbly liquids under these conditions is unstable and that the bubbles form aggregates in planes transverse to gravity. These aggregates form even when the size distribution of the bubbles is nonuniform. While the instability results primarily from the nature of inertial interaction among pairs of bubbles, which causes them to be attracted toward each other when they are aligned in the plane perpendicular to gravity, it is shown that the presence of viscous forces facilitates the process.

360Y. COMPUTATIONAL TECHNIQUES

10A788. Aerosol bolus transport through a hollow airway cast by steady flow in different gases. - JK Briant *(Pacific NW Lab, 902 Battelle Blvd, Richland WA 99352)* and M Lippmann *(Nelson Inst of Env Med, NYU Med Center, 350 First Ave, New York NY 10016)*. Aerosol Sci Tech **19**(1) 27-39 (Jul 1993).

Transport of aerosol through the airways of a hollow cast of a canine tracheobronchial tree was measured for steady flow in different gas mixtures. A small bolus of 0.5-μm aerosol particles was inserted as a tracer of convective motion in the flow at the entrance of the trachea, and particles were collected and counted as they arrived at a flow-balanced sampling bag at a peripheral segment of the cast. Transport was fastest in the gas of highest kinematic viscosity (helium), and slowest in the gas of lowest kinematic viscosity (sulfur hexafluoride). This is consistent with the lubrication theory that describes an axial core in the divergent flow field of the bronchial tree. The finer core in helium transports the particles at a greater velocity to distal airways. Transport of gases through the in vivo respiratory tract should also be influenced by these fluid mechanics of convection resembling Poiseuille flow that is substantially modified according to lubrication theory. As predicted by some other investigators, gas and aerosol particles penetrate much deeper into the lungs than the volumetric depth of inhalation.

See also the following:

10A787. Dynamic simulations of flows of bubbly liquids at large Reynolds numbers

360Z. EXPERIMENTAL TECHNIQUES

10A789. Determination of particle vapor pressures using the tandem differential mobility analyzer. - Shou-Hua Zhang, JH Seinfeld, RC Flagan *(Dept of Chem Eng, California IT, Pasadena CA 91125)*. Aerosol Sci Tech **19**(1) 3-14 (Jul 1993).

The application of the tandem differential mobility analyzer (TDMA) as a means of measuring vapor pressures of aerosol species is extended to include vapor saturation effects in the particle evaporator. To verify the analysis experiments were conducted with the controlled evaporation of dioctyl phthalate (DOP) particles with initial sizes ranging from 60 to 95 nm in diameter in a laminar flow evaporator. Vapor pressures of DOP determined with the TDMA were found to agree within 14% of those available in the literature. The results presented enable the use of the TDMA as a means to determine particle vapor pressure for substantially higher particle number concentrations than previously reported.

10A790. Respirator leak detection by ultrafine aerosols: A predictive model and experimental study. - Benjamin YH Liu *(Particle Tech Lab, Mech Eng Lab, Univ of Minnesota, Minneapolis MN 55455)*, Jae-Keun Lee *(Dept of Mech and Precision Eng, Pusan Natl Univ, Pusan 609-735, Korea)*, H Mullins, SG Danisch *(Occupational Health & Env Saftey Products Div, 3M, St Paul MN 55144)*. Aerosol Sci Tech 19(1) 15-26 (Jul 1993).

The leak performance of half-mask, maintenance-free respirators was studied theoretically and experimentally. A predictive model for the theoretical protection factor and leakage flow has been developed that uses the equation of particle conservation inside and outside the respirator. An experimental study was conducted using NaCl particles of 10 nm in diameter and a condensation nucleus counter as the particle detector. A respirator fitted with controlled leak holes of 20-3000 μm in diameter was tested at steady flow rates of 10, 32, and 100 L-min. Results showed that the aerosol penetration into a respirator was strongly influenced by the filter efficiency, leak hole size, and flow rate through the respirator. The results are in good agreement with theory, but some discrepancy has been noted at lower flow rates and smaller leak hole sizes. For the dust-mist respirators, the experimental protection factor for ultrafine 0.01-μm NaCl particles ranged from 3145 to as low as 3. For the high efficiency dust-mist-fume-radionuclide respirator, a protection factor as high as 4.1×10^9 was measured on the ultrafine aerosol. For all respirators, the protection factors decreased rapidly with increasing leak hole size and increased as flow rate decreased.

See also the following:

10A779. Experimental studies of the deformation of a synthetic capsule in extensional flow

362. Wall layers (inci boundary layers)

10A791. Buoyancy effects in stably stratified horizontal boundary-layer flow. - PG Daniels and RJ Gargaro *(Dept of Math, City Univ, Northampton Square, London, EC1V 0HB, UK)*. J Fluid Mech 250 233-251 (May 1993).

This paper describes numerical and asymptotic solutions of the steady 2D boundary-layer equations governing buoyant flow on a horizontal, thermally insulated surface. The class of flows considered is one for which there is a uniform external stream at constant temperature but for which conditions upstream lead to a statically stable temperature field within the boundary layer. This has the effect of generating an adverse pressure gradient which, if sufficiently strong, causes the boundary-layer solution to terminate in a singularity. Results are obtained for a range of Prandtl numbers.

10A792. Temperature dissipation in a turbulent round jet. - RA Antonia and J Mi *(Dept of Mech, Univ of Newcastle, NSW, 2308, Australia)*. J Fluid Mech 250 531-551 (May 1993).

Parallel cold wires used to measure the temperature derivative, in each of the three spatial directions, in the self-preserving region of a turbulent round jet. The temperature derivative variances were inferred from the correlation method and from the temperature derivative spectra after correcting these for the effect of wire separation. Both methods yielded fully consistent results for the components of the average temperature dissipation: the radial and azimuthal values are nearly equal and only slightly larger than the axial component. The resulting departure from isotropy of the temperature dissipation is small, especially when compared with results in other free shear flows. The high-wavenumber behavior of the corrected temperature derivative spectra conforms closely with isotropy on the jet axis but small departures occur away from the axis. Conditional averages, based on spatially coherent temperature jumps, indicate that, while the organized motion makes a significant contribution to the temperature variance, its contribution to the temperature-derivative variances is small.

10A793. Mechanism for bypass transition from localized disturbances in wall-bounded shear flows. - DS Henningson *(Dept of Math, MIT)*, A Lundbladh, AV Johansson *(Dept of Mech, RIT, S-10044 Stockholm, Sweden)*. J Fluid Mech 250 169-207 (May 1993).

The linear, nonlinear and breakdown stages in the transition of localized disturbances in plane Poiseuille flow is studied by direct numerical simulations and analysis of the linearized Navier-Stokes equations. Three dimensionality plays a key role and allows for algebraic growth of the normal vorticity through the linear *lift-up* mechanism. This growth primarily generates elongated structures in the streamwise direction since it is largest at low streamwise wavenumbers. For finite-amplitude disturbances such structures will be generated essentially independent of the details of the initial disturbance, since the preferred nonlinear interactions transfer energy to low streamwise wavenumbers. The nonlinear interactions also give a decrease in the span-wise scales. For the stronger initial disturbances the streamwise vorticity associated with the slightly inclined streaks was found to roll up into distinct streamwise vortices in the vicinity of which breakdown occurred. The breakdown starts with a local rapid growth of the normal velocity bringing low-speed fluid out from the wall. This phenomenon is similar to the low-velocity spikes previously observed in transition experiments. Soon thereafter a small turbulent spot is formed. This scenario represents a *bypass* of the regular Tollmien-Schlichting, secondary instability process. The simulations have been carried out with a sufficient spatial resolution to ensure an accurate description of all stages of the breakdown and spot formation processes. The generality of the observed processes is substantiated by use of different types of initial disturbances and by Blasius boundary-layer simulations. The present results point in the direction of universality of the observed transition mechanisms for localized disturbances in wall-bounded shear flows.

10A794. Subharmonic transition spectra generation and transition prediction in boundary layers. - MB Zelman and II Maslennikova *(Inst of Theor and Appl Mech, Russian Acad of Sci, Novosibirsk, Russia)*. Eur J Mech B 12(2) 161-174 (1993).

The nonlinear resonant interaction of Tollmien-Schlichting waves is investigated within the first-order weakly nonlinear approximation to explain and model the broadening of the frequency and wave-number spectra of disturbances in subharmonic (S –) type laminar-turbulent transition in boundary layers. The transition process is concluded to be initiated by a cascade of energy towards 3D low frequency waves, whose "explosive" growth can be restricted only by transition. The results we obtain are applied to explain experimental measurements and to design a new approach to the determination of transition Reynolds number Re_{tr} in the case of low initial disturbance amplitudes. A physically based interpretation of the semiempirical e^N-method used to compute Re_{tr} is suggested.

10A795. Rational extension of the Clauser Eddy viscosity model to compressible boundary-layer flow. - T Kiss and JA Schetz *(Aerospace and Ocean Eng Dept, VPI)*. AIAA J 31(6) 1007-1013 (Jun 1993).

An extension of the Clauser eddy viscosity model for the outer part of a compressible, turbulent boundary layer is proposed. This extension, unlike all of the previous ones, is based on a derivation, and not on ad hoc assumptions. The logic of the derivation of the original model is followed, except that the Crocco integral and the Howarth-Dorodnitsyn transformation are used for the purpose of the comparison with the velocity defect law. Predictions with the new model and two earlier ad hoc extensions of the Clauser model are compared to the measured data. Improved predictions are obtained with the new model for both the outer part of the layer and the skin friction coefficient.

See also the following:

10A799. Calculation of heat exchange and friction in convergent divergent nozzles with the aid of transport turbulence equations

364. Internal flow (pipe, channel, Couette)

10A796. Investigation of a contoured wall injector for hypervelocity mixing augmentation. - IA Waitz *(Dept of Aeronaut and Astronaut, MIT)*, FE Marble, EE Zukoski *(Dept of Mech Eng, California IT, Pasadena CA 91125)*. AIAA J 31(6) 1014-1021 (Jun 1993).

An experimental and computational investigation of a contoured wall fuel injector is presented. The injector was aimed at establishing shock-enhanced mixing for the supersonic combustion ramjet engines currently envisioned for applications on hypersonic vehicles. Three-dimensional flowfield surveys and temporally resolved, planar Rayleigh scattering measurements are presented for Mach 1.7 helium injection into Mach 6 air. These experimental data are compared directly with a 3D Navier-Stokes simulation to provide a detailed characterization of the flow about the injector array. Time-mean mixing rate data and preliminary conclusions concerning various sources for axial velocity are presented.

10A797. Corrective technique for numerical prediction of liquid flow rate in annular flow study. - CP Tso *(Sch of Mech and Prod Eng, Nanyang Tech Univ, Nanyang Ave, Singapore 2263)* and S Sugawara *(O-arai Eng Center, Power Reactor and Nucl Fuel Dev, Japan)*. Commun Numer Methods Eng 9(6) 533-542 (Jun 1993).

The computer code FIDAS-3DT, developed by Power Reactor & Nuclear Fuel Development Corporation of Japan, has been used to solve by the finite-difference method an air-water horizontal annular flow problem based on two-phase, three-fluid and two-component velocity modeling. In an attempt to improve the water flow rate results, as compared with those of a reported experiment, several corrections applied to the code are investigated, and the recommended technique is presented.

10A798. Shear layer flow in a channel: Estimate on the dimension of the attractor. - A Miranville *(Lab d'Anal Numer, Univ Paris-Sud, Batiment 425, 91405 Orsay, France)*. Physica D 65(1-2) 135-153 (May 1993).

Our aim in this article is to derive an upper bound on the dimension of the attractor for the shear-layer channel flow in space dimension two. In that case we improve the result obtained in R. Temam, Infinite Dimensional Dynamical Systems in Mechanics and Physics for a fluid driven by its boundary passing from a bound which is exponential with respect to the Reynolds number to a physically more realistic bound of the form cRe^3.

366. Internal flow (inlets, nozzles, diffusers, cascades)

10A799. Calculation of heat exchange and friction in convergent divergent nozzles with the aid of transport turbulence equations. - GP Kalmykov, AV Dmitrenko, LD Gutkin. Russian Aeronaut 35(3) 15-19 (1992).

We present the results of boundary-layer calculations for the divergent-convergent nozzles with the use of the original model of turbulence. We compare the obtained, relations with the experimental data on nozzles, and with the relations obtained using integral equations.

10A800. Flow development in entrance region of ducts. - TMB Carvalho, RM Cotta *(Programma Eng Mec, EE-COPPE-UFRJ Univ Fed Rio de Janeiro, Brazil)*, MD Mikhailov *(Inst for Appl Math and Infor, PO Box 384, Sofia 1000, Bulgaria)*. Commun Numer Methods Eng 9(6) 503-509 (Jun 1993).

The integral transform method is used to compute numerically the development of the velocity profile in the hydrodynamic entrance region for laminar flow inside a parallel plate channel. The results have user-prescribed accuracy and can be used to test other numerical methods.

See also the following:

10A151. Electric discharge excited blast waves in a flat subsonic nozzle

368. Free shear layers (mixing layers, jets, wakes, cavities, plumes)

368B. LAMINAR INCOMPRESSIBLE

10A801. Eddy structure in Stokes flow in a cavity. - PN Shankar *(Comput and Theor Fluid Dyn Div, Natl Aeronaut Lab, Bangalore 560 017, India)*. J Fluid Mech 250 371-383 (May 1993).

Stokes flow in a 2D cavity of rectangular section, induced by the motion of one of the walls, is considered. A direct, efficient calculational procedure, based on an eigenfunction expansion, is used to study the eddy structure in the cavity. It is shown that some of the results of earlier studies are quantitatively in error. More importantly, two interesting questions, namely the extent of the symmetry of the corner eddies and their relationship to the large-eddy structure are settled. By carefully examining the rather sudden change in the main eddy structure for cavities of depth around 1.629, it is shown that the main eddies are formed by the merger of the primary corner eddies; the secondary corner eddies then become the primary corner eddies and so on. Thus, in the evolution of the large-eddy structure the corner eddies, in some sense, play the role of progenitors. This explicit prediction should be experimentally verifiable.

368C. LAMINAR COMPRESSIBLE

10A802. Zones of influence in the compressible shear layer. - Dimitri Papamoschou *(Dept Mech and Aerospace Eng, UC, Irvine CA 92717)*. Fluid Dyn Res 11(5) 217-228 (May 1993).

The effect of Mach number on communication between regions of a shear layer is analyzed in the limit of geometric acoustics. Communication is quantified in terms of the acoustic intensity emitted by a point source and received by an observer moving with the flow. The generalized Snell's law is used to trace the sound rays which are shown to be highly distorted because of the Mach-number gradient. Sound-intensity calculations reveal that the influence of the source on the surrounding medium becomes confined to a smaller and smaller area as the Mach number increases. The zones of influence on the Lagrangian observer are funnel-shaped and become narrower with increasing Mach number. Communication is inhibited primarily in the axial direction, both upstream and downstream, and to a lesser extent in the transverse direction. Hindrance of communication may be the fundamental reason for enhanced stability of high Mach numbers.

368D. TURBULENT INCOMPRESSIBLE

10A803. Control of circular cylinder flow by end plates. - S Szepessy *(Dept SKSS, Alfa Laval Separation AB, S-147 80 Tumba, Stockholm, Sweden)*. Eur J Mech B 12(2) 217-244 (1993).

The present work involves an experimental study of the effect of end plate boundaries on the flow around a circular cylinder for Reynolds numbers 4×10^3-4.8×10^4 and cylinder aspect ratios $0.25 < L/d < 27.6$. The deviation from uniformly distributed flow along the body span is measured and discussed. End plate design is found to have a strong influence on the spanwise variation of the base pressure. A sufficiently long trailing edge distance is of vital importance in obtaining as uniform a pressure distribution along the span as possible, but the leading edge distance is also found to influence the flow. Within the measured Reynolds number range it is possible to define an optimized end plate design that, as far as possible, reduces spanwise flow nonuniformities. The end plate performance is markedly better at $Re = 4 \times 10^4$ than at 1×10^4. The influence of the end plate horse shoe vortex layer is found to be weak. Details of its formation are analyzed and discussed. Varying the cylinder aspect ratio showed a strong Reynolds number dependence and extreme flow patterns were found at an aspect ratio around 1. Keeping the aspect ratio about 1, in combination with the use of a short leading edge distance, was found to inhibit the onset of vortex shedding, resulting in a steady wake for Re $< 1 \times 10^4$. At $Re = 4 \times 10^4$, in contrast, a peak in base suction indicating the strongest vortex shedding was observed with $L/d=1$.

368E. TURBULENT COMPRESSIBLE

See the following:

10A819. Momentum and heat transport in the turbulent intermediate wake of a circular cylinder

368F. STRATIFICATION

10A804. Buoyancy induced heat and mass transfer from a concentrated point source. - R Ganapathy *(Dept of Math, Natl Col, Tiruchirapalli 620 001, India)*. Fluid Dyn Res 11(5) 187-196 (May 1993).

This paper reports an analytical study of an unsteady heat and mass transfer flow induced by an instantaneous concentrated point source in an unbounded fluid. Assuming the thermal Rayleigh number to be small, analytical solutions are obtained for the flow field, temperature, and species concentration in the form of series expansions of the dependent variables in terms of the Rayleigh number. The impact of species diffusion on the buoyancy induced heat and fluid flow has been highlighted. Streamlines are drawn to demonstrate the evolution of the flow field at different times. Even though heat was specified to be one of the two diffusion mechanisms, the results apply as well to the case where the source generates simultaneously two different chemical components.

10A805. Mixing by a turbulent plume in a confined stratified region. - SSS Cardoso and AW Woods *(Inst of Theor Geophys, Dept of Appl Math and Theor Phys, Univ of Cambridge, Silver St, Cambridge CB3 9EW, UK)*. J Fluid Mech 250 277-305 (May 1993).

An experimental and theoretical study of the mixing produced by a plume rising in a confined stratified environment is presented. As a result of the pre-existing stable stratification, the plume penetrates only part way into the region; at an intermediate level it intrudes laterally forming a horizontal layer. As time evolves, this layer of mixed fluid is observed to increase in thickness. The bottom front advects downward in a way analogous to the first front in the filling box of Baines & Turner (1969), while the lateral spreading of the plume occurs at an ever-increasing level and an ascending top front results. We develop a model of this *stratified filling box*; the model predicts the rate at which the two fronts advance into the environment.

368I. JET-SOLID SURFACE INTERACTION

10A806. Flapping motion of a planar jet impinging on a V-shaped plate. - Cheng-Kuang Lin *(Aeronaut Res Lab, Chung Shan Inst of Sci and Tech, Taichung Taiwan, ROC)*, Fei-Bin Hsiao, Shyh-Shiun Sheu *(Inst of Aeronaut and Astronaut, Natl Cheng Kung Univ, Tainan, Taiwan, ROC)*. J Aircraft 30(3) 320-325 (May-Jun 1993).

The behavior of a planar jet impinging on a V-shaped plate is studied experimentally by means of pressure and velocity measurements and flow visualization. The plate with a symmetrically variable opening angle is located downstream at distance L from the jet exit. Data indicate that, for the presence of the plate, not only the large-scaled coherent structures in the shear layers exist in the jet, but also the whole jet column exhibits a prominent periodic flapping motion with a preferred frequency f_F in the flowfield. Results also show an unstable regime occurring for the flapping motion, in which criteria to determine the boundary of the regime are governed by the location and the opening angle of the plate. Moreover, the nondimensional Strouhal number $f_F L/U_j$ is found to maintain a constant value of 0.11, and this value is nearly insensitive to the opening angle of the plate in the operating Reynolds number range.

10A807. Onset of stochastic pulsations at the early nonlinear stage of the development of perturbations in the jet of an incompressible fluid propagating along a wall. - AA Burov and OS Ryzhov *(Moscow, Russia)*. J Appl Math Mech 56(6) 921-927 (1992).

The Korteweg-De Vries equation, which describes the nonlinear propagation of perturbations in a jet of incompressible fluid emanating from a slit in a planar screen and propagating along a wall is considered. When account is taken of the natural vibrations of the wall, the equation becomes inhomogeneous. If an external action is specified in the form of a running wave, the particular solution of the inhomogeneous equation may be sought in an analogous form. As a result, the simplest problem in the theory of dynamical systems in the Hamiltonian formulation arises. As usual, the existence of a homoclinic structure in the neighborhood of the separatrices is deduced from an analysis of a Poincare transformation. Among the trajectories belonging to the homoclinic structure in the secant plane, there are some with properties which are formulated in terms of determinate chaos. A fundamentally important conclusion concerning the dual role of solitons at the nonlinear stage of the wave motion of the fluid follows: on the one hand, they serve as the nuclei of large-scale coherent structures and, on the other hand, they are responsible for the onset of stochastic pulsations.

368J. JET-FLOW INTERACTION

10A808. Flip-flop jet nozzle extended to supersonic flows. - G Raman *(NASA Lewis Res Center Group, Sverdrup Tech, Brook Park OH 44142)*, M Hailye *(Univ of Michigan, Ann Arbor MI 48103)*, EJ Rice *(NASA Lewis Res Center, Cleveland OH 44135)*. AIAA J 31(6) 1028-1035 (Jun 1993).

An experiment studying a fluidically oscillated rectangular jet flow was conducted. The Mach number was varied over a range from low subsonic to supersonic. Unsteady velocity and pressure measurements were made using hot wires, piezoresistive pressure transducers, and pitot probes. In addition, smoke flow visualization using high-speed photography was used to document the oscillation of the jet. For the subsonic flip-flop jet, it was found that the apparent time-mean widening of the jet was not accompanied by an increase in the mass flux. Fluidically oscillated jets up to a Mach number of about 0.5 have been reported before, but to our knowledge there is no information on fluidically oscillated supersonic jets. It was found that it is possible to extend the operation of these devices to supersonic flows. The streamwise velocity perturbation levels produced by this device were much higher than the perturbation levels that could be produced using conventional excitation sources such as acoustic drivers. In view of this ability to produce high amplitudes, the potential for using a small-scale fluidically oscillated jet as an unsteady excitation source for the control of shear flows in full-scale practical applications seems promising.

10A809. Measurement of the nonsteady flow field in the opening of a resonating cavity excited by grazing flow. - HR Graf *(Lab for Vib and Acoust, Sulzer Brothers, CH-8401 Winterthur, Switzerland)* and WW Durgin *(Dept of Mech Eng, Worchester Polytech Univ, Worcester MA 01609)*. J Fluids Struct 7(4) 387-400 (May 1993).

Flow past the opening of a cavity can excite acoustic resonsance. The periodic velocity field in the region of the cavity opening has been measured for various flow conditions and the vorticity distribution has been computed from the measured data using numerical differentiation. The results indicate that the shear layer rolls up into discrete vortices, which travel across the cavity opening. Two resonances were found. The first is characterized by a single vortex being present and results in the greatest amplitude. The second is characterized by the presence of two vortices which excite a distinct but lesser amplitude resonance. As the flow velocity changes, the position of these vortices shifts relative to the phase of the acoustic cycle. The timing of the interaction between the moving vortices and the acoustic particle velocity determines, to a large extent, the intensity of the excitation, and therefore also the oscillation amplitude. The measurements also indicate that the boundary layer upstream of the leading edge pulsates considerably.

10A810. Numerical simulation of nonswirling and swirling annular liquid jets. - SG Chuech *(Taiwan Aerospace, Taipei, Taiwan, ROC)*. AIAA J 31(6) 1022-1027 (Jun 1993).

A numerical simulation method is described for analyzing the fluid dynamics of nonswirling and swirling annular liquid jets. In the present theoretical study, a general mathematics model for simulating these two types of annular film jets has been established using a curvilinear coordinate system conforming to the film boundaries. The study involves the derivation of governing equations, numerical solutions for annular film flow structure of both nonswirling and swirling cases, and model validation with available measurements. The solutions of flow structure consist of jet velocity, film thickness, and jet trajectory. The present model can predict the "transition" phenomenon of jet-shape formation from nonswirling "bell" to swirling "hollow cone". In verification studies, first the model is validated against other measurements and analyses of non-swirling bell-like jets. The second case includes a validation study on spray angle of swirling conical sprays and a comparison of fuel spray configuration of a pressure atomizer. The assessment results are encouraging and indicate a good capability of the current model.

See also the following:

10A796. Investigation of a contoured wall injector for hypervelocity mixing augmentation

368L. NONEQUILIBRIUM AND CHEMICAL EFFECTS

See the following:

10A914. Penetration of jets into fluidized beds

370. Flow stability

10A811. Spatial stability of the Daniels and Eagles profiles. - ME Muwezwa *(Math Dept, Univ of Botswana, Gaborone, Botswana, Africa)*. J Eng Math 27(3) 233-244 (Aug 1993).

Daniels and Eagles obtained velocity profiles for exponential slender tubes. The spatial stability of these profiles is examined using a quasi-parallel approach. Contrary to expectation the profiles turn out to be stable.

10A812. Dynamics of liquid jets revisited. - RMSM Schulkes *(Dept of Appl Math and Theor Phys, Univ of Cambridge, Silver St, Cambridge CB3 9EW, UK)*. J Fluid Mech 250 635-650 (May 1993).

In this paper we investigate the long-wavelength approximations of the equations governing the motion of an inviscid liquid jet. Using a formal perturbation expansion it will be shown that the 1D equations presented by Lee (1974) are inconsistent. The inconsistency arises from the fact that terms which have been retained in the boundary conditions should have been rejected in view of the approximations made in the momentum equations. With the correct equations a number of anomalies between Lee's model and other models are eliminated. An explicit periodic solution to the nonlinear evolution equations we have derived is presented. However, it turns out that the wavenumbers for which this solution is valid lie outside the range in which the long-wavelength approximations are applicable. In addition we present numerical solutions to the nonlinear equations we have derived. In the unstable regime we find that, as disturbances grow, the characteristic axial lengthscales of the major features are typically of the order of the radius of the jet. This casts some doubt on the validity of the long-wavelength approximations in the study of nonlinear liquid jet dynamics.

10T813. Monotonicity and boundedness in the Boussinesq-equations. - BJ Schmitt and W von Wahl *(Lehrstuhl fur Angewandte Math, Univ Bayreuth, PO Box 101251, W-8580 Bayreuth, Germany)*. Eur J Mech B 12(2) 245-270 (1993).

10A814. Numerical investigations from compressible to isobaric Rayleigh-Benard convection in 2D. - J Frohlich *(Fachbereich Math, Univ Kaiserslautern, 6750 Kaiserslautern, Germany)* and S Gauthier *(Centre d'Etudes de Limeil-Valenton, 94195 Villeneuve-St-Georges, Cedex, France)*. Eur J Mech B 12(2) 141-159 (1993).

In studies of non-constant density flows several different sets of continuum equations are used in the literature, depending on the physical situation that is being considered. The present paper is concerned with the so-called Low Mach Number equations that allow, in contrast of the classical Boussinesq equations, large variations in the density. In particular the transition between regimes covered by these equations and those requiring the complete Navier-Stokes equations is studied. The discussion of the different regimes shows some essential features of the modeling of convection. Numerical results obtained by spectral methods for the 2D Rayleigh-Benard problem quantify the effect of compressibility on the flow field and furnish some indication on when to use one or the other set of equations.

10A815. Oscillatory instabilities produced by heat from a temperature-controlled hot wire below an interface. - C Roze, G Gouesbet, R Darrigo *(Lab d'Energetique des Syst et Procedes, URA CNRS no 230, INSA de Rouen, BP 08-76131, Mont St Aignan Cedex, France)*. J Fluid Mech 250 253-276 (May 1993).

New experimental results are reported for the motion of a liquid surface caused by the heat released from a hot wire below the surface. Starting from a base state with steady convection and steady deformation of the free surface caused by variations in surface tension and heat transport to the surface, the system loses its stability through a supercritical Hopf bifurcation occurring on a curve $f(\delta T_x, d) = 0$ in which d is the distance between hot wire and surface and δT_x a critical temperature difference. These experiments are a model for more complex laser heating experiments in which chaotic motions may occur. Some emphasis is placed on the characterization of propagating waves produced on the surface after the occurrence of the bifurcation.

10A816. Convection in a rotating spherical fluid shell with an inhomogeneous temperature boundary condition at infinite Prandtl number. - K Zhang and D Gubbins *(Dept of Earth Sci, Univ of Leeds, Leeds, LS2 9JT, UK)*. J Fluid Mech 250 209-232 (May 1993).

We examine thermal convection in a rotating spherical shell with a spatially nonuniformly heated outer surface, concentrating on three distinct heating modes: first, with wavelength and symmetry corresponding to the most unstable mode of the uniformly heated problem; secondly, with the critical wavelength but opposite equatorial symmetry; and thirdly, with wavelength much larger than that of the most unstable mode. Analysis is focused on boundary-locked convection, the associated spatial resonance phenomena, the stability properties of the resonance solution, and time-dependent secondary convection. A number of new forms of instability and convection are found: the most interesting is perhaps the saddle-node bifurcation, which is the first to be found for realistic fluid systems governed by partial differential equations. An analogous Landau amplitude equation is also analyzed, providing an important mathematical framework for understanding the complicated numerical solutions.

10A817. Measurements of the primary instabilities of film flows. - Jun Liu, JD Paul, JP Gollub *(Dept of Phys, Haverford Col, Haverford PA 19041)*. J Fluid Mech 250 69-101 (May 1993).

We present novel measurements of the primary instabilities of thin liquid films flowing down an incline. A fluorescence imaging method allows accurate measurements of film thickness h(x,y,t) in real time with a sensitivity of several microns, and laser beam deflection yields local measurements with a sensitivity of less than one micron. We locate the instability with good accuracy despite the fact that it occurs (asymptotically) at zero wavenumber, and determine the critical Reynolds number R_c for the onset of waves as a function of angle β. The measurements of $R_c(\beta)$ are found to be in good agreement with calculations, as are the growth rates and wave velocities. We show experimentally that the initial instability is convective and that the waves are noise-sustained. This means that the waveform and its amplitude are strongly affected by external noise at the source. We investigate the role of noise by varying the level of periodic external forcing. The nonlinear evolution of the waves depends strongly on the initial wavenumber (or frequency f). A new phase boundary $f^x_s(R)$ is measured, which separates the regimes of saturated finite amplitude waves (at high f) from multipeaked solitary waves (at low f). This boundary probably corresponds approximately to the sign reversal of the third Landau coefficient in weakly nonlinear theory. Finally, we show that periodic waves are unstable over a wide frequency band with respect to a convective subharmonic instability. This instability leads to disordered 2D waves.

10A818. Nonlinear evolution of waves on a vertically falling film. - H-C Chang *(Dept of Chem Eng, Univ of Notre Dame, Notre Dame IN 46556)*, EA Demekhin, DI Kopelevich *(Dept of Appl Math, Krasnodar Polytech Inst, Krasnodar 350072, Russia)*. J Fluid Mech 250 433-480 (May 1993).

Wave formation on a falling film is an intriguing hydrodynamic phenomenon involving transitions among a rich variety of spatial and temporal structures. Immediately beyond an inception region, short, near-sinusoidal capillary waves are observed. Further downstream, long, near-solitary waves with large-tear-drop humps preceded by short, front-running capillary waves appear. Both kinds of waves evolve slowly downstream such that over about ten wavelengths, they resemble stationary waves which propagate at constant speeds and shapes. We exploit this quasi-steady property here to study wave evolution and selection on a vertically falling film. All finite-amplitude stationary waves with the same average thickness as the Nusselt flat film are constructed numerically from a boundary-layer approximation of the equations of motion.

372. Turbulence

10A819. Momentum and heat transport in the turbulent intermediate wake of a circular cylinder. - M Matsumura *(Dept of Appl Mech Eng, Kitami IT, Kitami, Hokkaido, 090, Japan)* and RA Antonia *(Dept of Mech Eng, Univ of Newcastle, NSW, 2308, Australia)*. J Fluid Mech 250 651-668 (May 1993).

Hot-wire anemometry has been used in the intermediate wake (x/d = 10 to 40) of a slightly heated circular cylinder in order to quantify the contribution from the coherent motion to various conventionally averaged quantities, in particular the average momentum and heat fluxes. The overall contribution to the lateral heat flux is always greater than that to the Reynolds shear stress, indicating that the turbulent Karman vortex street transports heat more effectively than momentum. The difference in these contributions is reflected in the topologies of the velocity and temperature fields. There is significant streamwise evolution of these topologies througout the intermediate wake. At x/d = 10, the net heat transport associated with the vortical motion occurs in the downstream region of each vortex. At other downstream stations, the net heat transport is equally distributed between the upstream and downstream regions of individual vortices.

10A820. Direct numerical simulation of laminar and turbulent flow over riblet-mounted surfaces. - DC Chu and GE Karniadakis *(Dept of Mech and Aerospace Eng, Program in Appl and Comput Math, Princeton)*. J Fluid Mech 250 1-42 (May 1993).

The flow in a channel with its lower wall mounted with streamwise riblets is simulated using a highly efficient spectral element-Fourier method. The range of Reynolds numbers investigated is 500 to 3500, which corresponds to laminar, transitional, and turbulent flow states. A complete study is presented for V-groove riblets; the effect of rounded riblets is also investigated. Our results suggest that in the laminar regime there is no drag reduction, while in the transitional and turbulent regimes drag reduction exists (approximately 6% at Reynolds number 3500) for the riblet-mounted wall in comparison with the smooth wall of the channel. For the first time, we present detailed turbulent statistics (turbulence intensities, Reynolds shear stresses, skewness and flatness) as well as a temporal analysis using a numerical analog of the VITA technique. The flow structure over the riblet-mounted wall is also analyzed in some detail and compared with the corresponding flow over the smooth wall in an attempt to identify the physical mechanisms that cause drag reduction. The accuracy of the computation is established by comparing flow quantities corresponding to the smooth wall with previous direct numerical simulation results as well as with experimental results; on the riblet-mounted wall comparison is made with available experimental results. The agreement is very good for both cases. The current computation is the first direct numerical simulation of turbulence in a complex geometry domain.

10A821. Structure of a 3D turbulent boundary layer. - AT Degani *(Dept of Mech Eng and Mech, Lehigh Univ, Bethlehem PA 18015)*, FT Smith *(Math Dept, Univ Col London, London WC1E 6BT, UK)*, JDA Walker *(Dept of Mech Eng and Mech, Lehigh Univ, Bethlehem PA 18015)*. J Fluid Mech 250 43-68 (May 1993).

The 3D turbulent boundary layer is shown to have a self-consistent two-layer asymptotic structure in the limit of large Reynolds number. In a streamline coordinate system, the streamwise velocity distribution is similar to that in 2D flows, having a defect-function form in the outer layer which is adjusted to zero at the wall through an inner wall layer. An asymptotic expansion accurate to two orders is required for the cross-stream velocity which is shown to exhibit a logarithmic form in the overlap region. The inner wall-layer flow is collateral to leading order but the influence of the pressure gradient, at large but finite Reynolds numbers, is not negligible and can cause substantial skewing of the velocity profile near the wall. Conditions under which the boundary layer achieves self-similarity and the governing set of ordinary differential equations for the outer layer are derived. The calculated solution of these equations is matched asymptotically to an inner wall-layer solution and the composite profiles so formed describe the flow throughout the entire boundary layer. The effects of Reynolds number and cross-stream pressure gradient on the cross-stream velocity profile are discussed and it is shown that the location of the maximum cross-stream velocity is within the overlap region.

10A822. Systematic comparison of mathematically simple turbulence models for 3D boundary layers. - MSG Bettelini and TK Fannelop *(Dept of Fluid Dyn, Swiss Fed IT, Zurich 8092, Switzerland)*. AIAA J 31(6) 999-1006 (Jun 1993).

The paper presents a systematic comparison of some widely used turbulence models with one another and with experiments. The mathematically simplest models applicable to 3D steady, incompressible boundary layers are of primary interest. Besides the more widely used algebraic formulations, models using simplified transport equations for turbulence quantities, such as the Johnson-King model, are considered. These models are applied to a variety of well-established 2D and 3D test cases, for which accurate and reliable experimental data are available. To avoid differences associated with different numerical integration procedures, all models have been used with the same finite difference method especially developed for this purpose. This method solves the first-order boundary-layer equations written in terms of streamline coordinates. One broad conclusion of this study is that all models considered give reasonable predictions for the gross boundary-layer parameters, but important differences become apparent for certain local values. Specific recommendations for the choice of turbulence model in practical applications are included.

10A823. Numerical computation of convective dispersion in turbulent buoyant jets. - JCF Pereira and JMP Rocha *(Dept of Mech Eng, Inst Superior Tecnico-Tech Univ of Lisbon, l'Av Rovisco Pais, 1096 Lisboa Codex, Portugal)*. Numer Heat Transfer A 23(4) 399-414 (Jun 1993).

Numerical predictions of mean and turbulent characteristics of the axisymmetric vertical jet and plume are reported. An algebraic stress and flux model is used to close the time-averaged Navier-Stokes and energy equations. Special attention was given to the numerical model, which is based on a finite-volume discretization of the elliptic form of flow equations. A special procedure is used to treat free boundaries and to compute the flow up to the similarity regime. The model was applied to the prediction of the flow for the momentum-dominated (jet) and buoyancy-dominated (plume) regime. The results show that the essential characteristics of the flows, especially for the plume, are correctly reproduced. However, some discrepancies arise from the comparison of predicted and experimental levels.

10A824. Intermittency in a cascade model for turbulence. - R Benzi, L Biferale, G Parisi *(Dipartimento di Fisica, Univ "Tor Vergata", Via della Ricerca Scientifica, I-00133 Rome, Italy)*. Physica D 65(1-2) 163-171 (May 1993).

In this note we study the possibility of performing analytic computations of the exponents characterizing the multifractal behavior of turbulence. A simple analytic computation is presented in the framework of the cascade model (or shell model).

10A825. Implementation of a one-equation turbulence model within a stabilized FE formulation of a symmetric advective-diffusive system. - K Jansen, Z Johan, TJR Hughes *(Div of Appl Mech, Durand Bldg, Stanford)*. Comput Methods Appl Mech Eng 105(3) 405-433 (June 1993).

The success of stabilized FEMs for symmetric advective-diffusive formulations of the laminar Navier-Stokes equations has motivated extension of these concepts to turbulent flows. A one-equation model which preserves the symmetry of the system's advective and diffusive matrices has been developed. This model is based on the work of Norris and Reynolds and utilizes a transport equation for the turbulent velocity scale q and an algebraic relation for the turbulent length scale l. From these two quantities, an eddy viscosity can be calculated. This model has been implemented by way of a Galerkin-least-squares FEM. Solutions are presented which verify the good behavior of the formulation.

10A826. Low Reynolds number κ-ε modeling with the aid of direct simulation data. - W Rodi *(Inst fur Hydromech, Univ Karlsruhe, Kaiserstr 12, Karlsruhe, Germany)* and NN Mansour *(NASA Ames Res Center, Moffett Field CA 94035)*. J Fluid Mech 250 509-529 (May 1993).

The constant $C\mu$ and the near-wall damping function $f\mu$ in the eddy-viscosity relation of the κ-ϵ model are evaluated from direct numerical simulation (DNS) data for developed channel and boundary-layer flow, each at two Reynolds numbers. Various existing f_μ model functions are compared with the DNS data, and a new function is fitted to the high-Reynolds-number channel flow data. The ε-budget is computed for the fully developed channel flow. The relative magnitude of the terms in the ε-equation is analyzed with the aid of scaling arguments, and the parameter governing this magnitude is established. Models for the sum of all source and sink terms in the ε-equation are tested against the DNS data, and an improved model is proposed.

See also the following:

10A792. Temperature dissipation in a turbulent round jet

10A793. Mechanism for bypass transition from localized disturbances in wall-bounded shear flows

10A805. Mixing by a turbulent plume in a confined stratified region

374. Electromagneto-fluid and plasma dynamics

10T827. On the utility of tokamaks for energy. - BG Logan *(LLNL)*. Fusion Eng Des 22(3) 145-149 (Apr 1993).

10T828. Comparison of exact solutions and the phase mixing approximation for dissipative Alfven waves. - LMBC Campos *(Max-Planck Inst fur Aeronomie, 3411 Katlenburg-Lindau, Germany)*. Eur J Mech B 12(2) 187-216 (1993).

10A829. Collisional effects in plasmas modeled by a simplified Fokker-Planck equation. - LRT Gardner, GA Gardner *(Sch of Math, Univ of Wales UCNW, Bangor, Gwynedd LL57 1UT, UK)*, SI Zaki *(Dept of Math, Suez Canal Univ, Ismailia, Egypt)*. J Comput Phys 107(1) 40-50 (Jul 1993).

A computer code has been developed to simulate collisional effects in plasmas for the regime where plasma instabilities are dominant but are modified by weak collisions. The numerical method developed for the code is composed of a Galerkin method embedded within a locally 1D approach. This algorithm is used to solve, over the (x,v) phase plane, a simplified Fokker-Planck equation with a 1D Fokker-Planck operator, including a velocity dependent collision frequency. A stability analysis for the numerical scheme is given. The effects of small angle collisions on the Landau damping of plasma waves and the two-stream instability are examined. Results confirm and extend earlier numerical observations.

10A830. Explicit symplectic integration scheme for plasma simulations. - JR Cary and I Doxas *(Astrophys Planet and Atmos Sci Dept, Univ of Colorado, Boulder CO 80309-0391)*. J Comput Phys 107(1) 98-104 (Jul 1993).

An explicit symplectic integration scheme which describes the self-consistent wave particle interaction is developed. The integrator does not split the Hamiltonian trivially into a kinetic and potential part. The integrator yields accurate growth rates for the gentle-bump instability even when the timestep is of the order of the inverse plasma frequency. This represents up to a tenfold reduction in computation compared to conventional schemes. The integrator is generalizable to arbitrary order without increase in storage requirements, but tests show that when the accuracy requirements are of the order of a few percent, the second-order method is the most efficient.

10A831. Particle loading for a plasma shear layer in a magnetic field. - D Cai *(Inst of Info Sci and Electron, Univ of Tsukuba, Ibaraki 305, Japan)*, LRO Storey, T Neubert *(STAR Lab, Stanford)*. J Comput Phys 107(1) 84-97 (Jul 1993).

Some new particle loading methods have been developed for use in simulating a plasma shear layer with nonuniform density and temperature in the presence of a magnetic field, especially with a large effective ion gyroradius. The numerical approach to the shear instability with strong velocity shear consists of starting a simulation from a state of equilibrium, perturbing this equilibrium in some way, then observing the linear growth of the perturbation and its ultimate saturation. With the usual particle loading method, it is difficult to reproduce the equilbrium state if the ion gyroradius is not small on the scale of the shear. The reason is that, with nonuniform velocity shear, ie, with the nonuniform E-field, a particle may have more than one guiding-center, the particle distribution cannot be obtained analytically, and it may need to be evaluated numerically. If an equilibrium state is not achieved in the particle loading, the shear may relax by means of an "artificial instability" in the course of the simulation, obscuring the physics' of interest. With the particle loading method here presented, we simulate a shear layer in a state close to equilibrium without having to solve the Vlasov-Boltzmann equation.

10A832. Simulation of low-frequency electromagnetic phenomena in kinetic plasmas of 3D. - Motohiko Tanaka *(Natl Inst for Fusion Sci, Nagoya 464-01, Japan)*. J Comput Phys 107(1) 124-145 (Jul 1993).

An advanced kinetic simulation method has been developed and implemented in the HIDENEK code to study large space-scale, low-frequency electromagnetic phenomena occurring in inhomogeneous plasmas. The present method is specially designed for high magnetic field ($\omega_{ce} \geq \omega_{pe}$), inhomogeneous plasma simulations. The guiding-center approximation with magnetic drifts is adopted to the perpendicular motion of the electrons, whereas the inertia effect is retained in their parallel motion. Also, a slightly backward time-decentered scheme is introduced to the equations of motion and the Maxwell equations. These equations are combined to yield the full-implicit coupled, field-particle equations which allow us to determine the future electromagnetic field in a large time step compared to the electron time scales with the diamagnetic drift and magnetization currents being included.

376. Naval hydromechanics

See the following:

10A952. Fracture mechanics in modeling of ice-breaking capability of ships

378. Aerodynamics

378B. WINGS AND AIRFOILS

10A833. Aerodynamics of maneuvering slender wings with leading-edge separation. - TS Tavares *(Aeromech Div, Comput Fluid Dyn Branch, US Air Force Wright Lab, WPAFB)* and JE McCune *(Dept of Aeronaut and Astronaut, MIT)*. AIAA J 31(6) 977-986 (Jun 1993).

A nonlinear theoretical technique is presented for treating the unsteady aerodynamics of low-aspect-ratio wings with leading-edge separation in incompressible flow. Cases are treated for wings in steady flight and for those undergoing severe unsteady maneuver. The treatment extends classical slender wing theory to allow for large-scale motion along with possibly asymmetric wake development. Calcualted results are presented for a variety of cases and are compared with related analyses and experiments. Examples studied include wings of delta and clipped-delta planform. Flight conditions and maneuvers treated include sideslip, sudden plunge, and rapid constant-rate roll at zero angle of attack. New results are interpreted in the light of wake history effects, a framework which provides a simplified means of interpreting the aerodynamic response in the severe maneuver case. The ability of the calculations to reproduce observed phenomena under a wide variety of conditions supports the practical usefulness of the extended slender wing treatment as a tool for gaining increased insight into the unsteady interaction between low-aspect-ratio wings and their wakes.

10A834. Contruction and calculation of optimal nonlifting critical airfoils. - DW Schwendeman, MCA Kropinski, JD Cole *(Dept of Math Sci, RPI)*. Z Angew Math Phys 44(3) 556-571 (May 1993).

Numerical calculations are carried out in the hodograph plane to construct optimal critical airfoil shapes and the flow about them. These optimal airfoil shapes give the highest free-stream Mach number M_∞ for a given thickness ratio δ and tail angle θ_T (nonlifting) for which the flow is nowhere supersonic. A relationship between M_∞ and δ for various θ_T is given. Analytical and numerical solutions to the same problem are found on the basis of transonic small-disturbance theory. These results provide a limiting case as $M_\infty \to 1$, $\delta \to 0$ and agree well with the calculations of the full problem. Using a numerical method to calculate the flow about general (subsonic) airfoils, a comparison is made between the critical free-stream Mach numbers for some standard airfoil shapes and the optimal free stream Mach number of the corresponding δ and θ_T. A significant increase in the critical free-stream Mach number is found for the optimal airfoils.

10A835. Effects of blowing on delta wing vortices during dynamic pitching. - LS Miller *(Dept Aerospace Eng, Wichita State Univ, Wichita KS 67208)* and BE Gile *(Appl Aerodyn Div, Subsonic Aerodyn Branch, NASA Langley Res Center MS 286, Hampton VA 23665)*. J Aircraft 30(3) 334-339 (May-Jun 1993).

An experimental investigation was conducted in a water tunnel to identify the effects of apex blowing on two delta wing models undergoing constant pitch-rate motion. One wing was of 60° sweep and the other was of 76° sweep. Flow visualization methods were utilized to determine vortex burst locations for a range of pitch up and pitch down rates, apex jet strengths, and blowing directions. Results indicate, individually, that blowing direction on the 60° wing and blowing rate on the 76° wing have the greatest effect on vortex behavior under both static and dynamic pitch-up conditions. Vortex improvements, for any blowing direction or rate examined, are most dramatic during dynamic pitch-down conditions. In this case, the use of blowing resulted in the reformation of unburst vortices with significant length.

10A836. Indicial lift approximations for 2D subsonic flow as obtained from oscillatory measurements. - JG Leishman *(Dept Aerospace Eng, Univ of Maryland, College Park MD 20742)*. J Aircraft 30(3) 340-351 (May-Jun 1993).

An approach is described to obtain generalized approximations to the indicial lift response due to angle of attack and pitch rate in 2D subsonic flow. Starting from an assumed representation, the approximations are accomplished by means of a nongradient optimization algorithm in which the coefficients of the approximation are free parameters. The optimization is subject to prescribed constraints in terms of the known initial and asymptotic behavior of the indicial response, and by requiring the response duplicate the known exact solutions at earlier values of time. The approach is applied to extract the intermediate forms of the indicial lift response, generalized in terms of Mach number and pitch axis location, from experimental measurements of the unsteady lift in the frequency domain.

10A837. Nonequilibrium turbulence modeling study on light dynamic stall of a NACA0012 airfoil. - M Dindar, U Kaynak *(TUSAS Aerospace Insdust, PO Box 18, Ankara, Turkey)*, K Fujii *(Inst of Space and Aeronaut Sci, Kanagawa, Japan)*. J Aircraft 30(3) 304-308 (May-Jun 1993).

A computational study on the nonequilibrium turbulence modeling effects for the prediction of the light stall phenomenon has been done for the NACA0012 airfoil. For this, an unsteady thin-layer Navier-Stokes solver was developed that is capable of solving the flowfield around an airfoil undergoing unsteady harmonic motion. In the program, the Baldwin-Lomax and Cebeci-Smith turbulence models were used as baseline models, and the Johnson-King turbulence model was used to study the nonequilibrium effects. It was found that the nonequilibrium effects are important for the prediction of the light stall, and only the Johnson-King model yields light stall hysteresis loop that is similar to the experiment. It was also found that the wind tunnel wall effects are important, and a mean angle of attack increase in the computation was necessary to yield a better agreement with the experiment.

10A838. Slender wing rock revisited. - LE Ericsson *(Lockheed Missiles and Space, Sunnyvale CA 94088)*. J Aircraft 30(3) 352-356 (May-Jun 1993).

Analysis of experimental results for slender delta wings reveals that asymmetric liftoff of the leading-edge vortices on slender delta wings does not start the wing rock, although it is responsible for the large limit cycle amplitude observed in experiments. As a consequence, the interaction of slender wing rock does not depend upon the interaction between the two leading-edge vortices, but can be generated by one wing half by itself, making slender wing rock more likely to occur on high agility aircraft than previously thought.

10A839. Velocity and vorticity distributions over an oscillating airfoil under compressible dynamic stall. - MS Chandrasekhara *(Dept of Aeronaut and Astronaut, NASA Ames Res Center, MS 260-1, Moffett Field CA 94035-1000)* and S Ahmed *(MCAT Inst, San Jose CA 95127)*. AIAA J 31(6) 995-996 (Jun 1993).

The velocity and vorticity fields around an oscillating airfoil in compressible dynamic stall are reported. Phase averaged, two component laser velocimetry data were obtained at a freestream Mach number of 0.3 and a reduced frequency of 0.05. This is the first set of velocity data available at a high Reynolds number (540,000) under compressible flow conditions and it serves as a good database for development and validation of computer codes. Of particular interest is the formation of a separation bubble, which bursts coincidentally with the formation of the dynamic stall vortex, adding an extra degree of physical complexity to the problem.

10A840. Vortex generators used to control laminar separation bubbles. - M Kerho *(Aerospace Eng, Univ Illinois, Urbana IL)*, S Hutcherson, RF Blackwelder, RH Liebeck *(Aerospace Eng, USC, Los Angeles CA 90089)*. J Aircraft 30(3) 315-319 (May-Jun 1993).

This study examines the effect of various forms of vortex generators on the laminar separation bubble of a 2D low Reynolds number Liebeck LA2573A airfoil. The objective of this research was to determine the effects that different generator sizes and spacings have upon the separation bubble and the drag. Windtunnel measurements were made on several generator configurations at Reynolds numbers ranging from 200 000 to 600 000 at angles of attack less than the stall angle where the separation bubble can provide a significant contribution to the airfoil drag. The vortex generators used were constructed small enough to be contained completely within the laminar boundary layer. Wind tunnel data included airfoil drag and mean and fluctuating velocity measurements in the laminar and turbulent boundary layers. Results have shown that the use of vortex generators provides a measurable decrease in airfoil drag at the lower range of Reynolds number tested. At the airfoil's design condition and Reynolds number of 235 000, the submerged vortex generators were shown to decrease the airfoil drag by a maximum of 38% at $C_l = 0.572$.

See also the following:

10A104. Unsteady aerodynamic response of 2D subsonic and supersonic oscillating cascades with chordwise displacement and flexible deformation

10A305. Integrated structure-control-aerodynamic synthesis of actively controlled composite wings

378D. WING BODY COMBINATIONS

10A841. FE multigrid solution of Euler flows past installed aero-engines. - J Peraire, J Peiro *(Dept of Aeronaut, Imperial Col, London SW7 2BY, UK)*, K Morgan *(Dept of Civil Eng, Univ Col, Swansea SA2 8PP, UK)*. Comput Mech 11(5-6) 433-451 (1993).

A FE based procedure for the solution of the compressible Euler equations on unstructured tetrahedral grids is described. The spatial discretization is accomplished by means of an approximate variational formulation, with the explicit addition of a matrix form of artificial viscosity. The solution is advanced in time by means of an explicit multi-stage time stepping procedure. The method is implemented in terms of an edge based representation for the tetrahedral grid. The solution procedure is accelerated by use of a fully unstructured multigrid algorithm. The approach is applied to the simulation of the flow past an installed aero-engine nacelle, at three different free stream conditions. Comparison is made between the numerical predictions and experimental pressure observations.

378G. LIFT, DRAG, STALL

10A842. Refinements in determining satellite drag coefficients: Method for resolving density discrepancies. - MM Moe *(Dept of Physics, Sch of Phys Sci, UC, Irvine CA 92717)*, SD Wallace *(Dept of Elec and Comput Eng, Sch of Eng, UC, Irvine CA 92717)*, K Moe *(Acquisition Meteorol Office, Space and Missile Syst Center, Los Angeles AFB CA 90009)*. J Guidance Control Dyn 16(3) 441-445 (May-Jun 1993).

The discrepancies in atmospheric densities deduced from satellites of compact and long cylindrical shapes can be used to improve our knowledge of drag coefficients. Constraints on the accommodation coefficient imposed by experiments in space and in the laboratory make it possible to resolve the discrepancies and gain information on the angular distribution of molecules reemitted from satellite surfaces. We present a sample calculation based on some limited published data. If the published nominal length-to-diameter ratio of the cylindrical satellites is the actual ratio, then we can conclude that the assumption of a diffuse angular distribution of reemitted molecules is adequate (at least near 200-km altitude), even for the long cylindrical sides where most of the molecules strike at grazing incidence. The method can be used with detailed orbital data and precise satellite shapes to infer reflection characteristics and drag coefficients for a range of altitudes and perigee velocities.

378I. PERFORMANCE

See the following:

10A229. Wind identification along a flight trajectory, Part 3. Two-dimensional dynamic approach

378J. FLIGHT PATH AND TRAJECTORIES

10T843. Minimum-effort interception of multiple targets. - JZ Ben-Asher *(Dept of Electron Syst, Tel-Aviv Univ, Tel-Aviv 69978, Israel)*. J Guidance Control Dyn 16(3) 600-601 (May-Jun 1993).

10T844. New analytical solutions for proportional navigation. - MN Rao *(Defence R&D Lab, Hyderabad, 500 258, India)*. J Guidance Control Dyn 16(3) 591-594 (May-Jun 1993).

10T845. Zero-gravity atmospheric flight by robust nonlinear inverse dynamics. - F Mora-Camino *(Air Transportation Dept, ENAC, 7 Av Edouard Belin, Toulouse 31055, France)* and AK Achaibou *(LAAS, Centre Natl de la Rech Sci, 7 Av Colonel Roche, Toulouse 31077, France)*. J Guidance Control Dyn 16(3) 604-607 (May-Jun 1993).

See also the following:

10A229. Wind identification along a flight trajectory, Part 3. Two-dimensional dynamic approach

10A294. Generalized guidance law for collision courses

378K. STABILITY AND CONTROL

10A846. Computational investigation of a pneumatic forebody flow control concept. - K Gee *(MCAT Inst, MS 258-1, Moffett Field CA 94035)*, D Tavella *(CSC Corp, Ames Res Center, Moffett Field CA 94035)*, LB Schiff *(High Alpha Tech, Fluid Dyn Div, NASA Ames Res Center, MS 258-1, Moffett Field CA 94035)*. J Aircraft 30(3) 326-333 (May-Jun 1993).

The effectiveness of a tangential slot blowing concept for generating lateral control forces on an aircraft forebody is analyzed using computational fluid dynamics (CFD). The flow about a fighter forebody is computed using a multiple-zone, thin-layer Navier-Stokes code. Tangential slot blowing is modeled by the use of an actuator plane. The effects of slot location and slot length on the efficiency of the system are analyzed. Results of the study indicate that placement of the slot near the nose of the aircraft greatly enhances the efficiency of the system, whereas, the length and circumferential location of the slot are of secondary importance. Efficiency is defined by the amount of side force or yawing moment obtained per unit blowing coefficient. The effect of sideslip on the system is also analyzed. The system is able to generate incremental changes in forces and moments in flow with a sideslip angle of 10 deg comparable to those obtained at zero sideslip. These results are used to determine a baseline configuration for an experimental study of the tangential slot blowing concept.

See also the following:

10A225. Robustness evaluation of a flexible aircraft control system

10A907. Advanced pogo stability analysis for liquid rockets

378L. UNSTEADY EFFECTS

10A847. Unsteady transonic 2D Euler solutions using FE. - GA Davis and OO Bendiksen

(Mech Aerospace and Nucl Eng Dept, UCLA). AIAA J 31(6) 1051-1059 (Jun 1993).

A FE solution of the unsteady Euler equations is presented, and demonstrated for 2D airfoil configurations oscillating in transonic flows. Computations are performed by spatially discretizing the conservation equations using the Galerkin weighted residual method and then employing a multistage Runge-Kutta scheme to march forward in time. Triangular FEs are employed in an unstructured O-mesh computational grid surrounding the airfoil. Grid points are fixed in space at the far-field boundary and are constrained to move with the airfoil surface to form the near-field boundary. A mesh deformation scheme has been developed to efficiently move interior points in a smooth fashion as the airfoil undergoes rigid-body pitch and plunge motion. Both steady and unsteady results are presented, and a comparison is made with solutions obtained using finite volume techniques. The effects of using either a lumped or consistent mass matrix were studied and are presented. Results show that the FEM provides an accurate solution for unsteady transonic flows about isolated airfoils.

378M. AERODYNAMIC LOADS

10A848. Millisecond aerodynamic force measurement with side-jet model in the ISL shock tunnel. - KW Naumann, H Ende, G Mathieu, A George *(Dept of Gas Dyn, French-German Res Inst, 68301 St Louis, France)*. AIAA J 31(6) 1068-1074 (Jun 1993).

This paper presents a description of a novel millisecond aerodynamic force meausurement technique and the first experiments in hypervelocity flow with a model, which is equipped with laterally blowing jets and a set of accelerometers. A fast-acting mounting support releases the model and grips it again after a free flight duration of some milliseconds. Using measured acceleration and Pitot pressure histories allows direct straightforward time-dependent evaluation of the aerodynamic coefficients. This procedure is insensitive against nonlinearities or disturbances in the starting phase of the flow and compensates flow variations, if the flow is quasistationary and maintains a roughly uniform Mach number. The results quantify the time necessary to establish quasistationary flow for the actual test conditions. Quantitaitve results are also obtained for the force, which is produced by interaction of side jets and ambient flow and acts on the surface of the model. At the troposheric hypervelociy conditions of our test, the interaction force on a flat plate substantially increases jet thrust.

378O. FLIGHT TESTS AND INSTRUMENTATION

See the following:

10T845. Zero-gravity atmospheric flight by robust nonlinear inverse dynamics

378Y. COMPUTATIONAL TECHNIQUES

10A849. Implicit finite volume methods and application to a delta wing problem. - CP Li. Comput Mech 11(5-6) 408-420 (1993).

Numerical performance of three schemes has been assessed by focusing on the formulations of convective flux for inviscid and viscous supersonic flows. The central scheme stabilized by flux limiters and Lax-Friedrichs' viscosity has significantly improved the solution obtained by the conventional scheme blended with artificial damping. Themodified scheme produces nearly as nonoscillatory results for solution discontinuities as the upwind-biased TVD schemes and as accurate viscous layer as the centered scheme for supersonic flow past a delta wing. Its attractive attributes include generality, simplicity and independence of tuning parameters.

10A850. Multiblock Navier-Stokes solutions about the F/A-18 wing-LEX-fuselage configuration. - F Ghaffari, JM Luckring *(Transonic Aerodyn Branch, Appl Aerodyn Div, NASA Langley Res Center, Hampton VA 23665)*, JL Thomas *(Comput Aerodyn Branch, Fluid Mech Div, NASA Langley Res Center, Hampton VA 23665)*, RT Biedron *(Anal Services and Mat, Hampton VA 23666)*. J Aircraft 30(3) 293-303 (May-Jun 1993).

3D thin layer Navier Stokes computations are presented for the F/A 18 configuration. The modeled configuration includes an accurate surface representation of the fuselage, leading-edge extension (LEX), and wing, both with and without leading-edge flap deflection. A multiblock structured grid strategy is employed to decompose the computational flowfield domain around the subject configuration. Steady-state solutions are obtained from an algorithm that solves the compressible Navier-Stokes equations with an upwind biased, flux difference splitting approach. The results presented are based on a fully turbulent flow assumption, simulating the high Reynolds number flow conditions that correspond to a recent F/A-18 flight experiment. Good agreements between the computations and the flight test results are obtained for both surface flow patterns as well as surface pressure distributions. Furthermore, a correlation between the computed LEX vortex-core and the flight test results, observed by the way of smoke visualization, is also presented.

378Z. EXPERIMENTAL TECHNIQUES

See the following:

10A848. Millisecond aerodynamic force measurement with side-jet model in the ISL shock tunnel

380. Machinery fluid dynamics

10A851. Experimental and theoretical study for nonlinear aeroelastic behavior of a flexible rotor blade. - DM Tang *(Dept of Mech Eng and Mat Sci, Duke Univ, Durham NC 27706)* and EH Dowell *(Sch of Eng, Duke Univ, Durham NC 27706)*. AIAA J 31(6) 1133-1142 (Jun 1993).

The purpose of this paper is to study the flutter instability and forced response of a nonrotating flexible rotor blade model with a geometrical structural nonlinearity and a freeplay structural nonlinearity. The ONERA stall aerodynamic model is used. External excitations are provided by base harmonic excitations in the pitch angle and the chordwise direction, respectively. Two cases are considered in this paper. Case A is for a nonlinear blade structure with an unstalled unsteady aerodynamic model. Case B is for the nonlinear blade structure with a large effective mean angle of attack. The effects of the structural and aerodynamic nonlinearities and initial disturbance on instability and forced response behavior are discussed. A wind-tunnel test has also been carried out in the Duke University low-speed wind-tunnel. The wind-tunnel tests show generally good agreement between theory and experiment for both static and dynamic behavior. Although the mathematical and experimental model of the nonrotating blade is different from the operational rotating hingeless rotor blade, the results from the experimental-theoretical correlation study provide fundamental understanding of the nonlinear aeroelastic behavior for a flexural-flexural-torsional hingeless rotor blade.

382. Lubrication

10A852. Fast method for the analysis of thermal-elastohydrodynamic lubrication of rolling-sliding line contacts. - Rong-Tsong Lee and Chao-Ho Hsu *(Dept of Mech Eng, Natl Sun Yat-Sen Univ, 80424 Kaohsiung, Taiwan)*. Wear 166(1) 107-117 (15 Jun 1993).

A fast method for the analysis of thermal-elastohydrodynamic lubrication between two deformable cylinders was developed at high loads and high slip ratios with low computing time in a personal computer. The coupled Reynolds, elasticity, rheology, and energy equations are solved simultaneously by combining the advanced multilevel method and the Newton-Raphson method based on a mean viscosity across the film. Standard second-order central differences are used to approximate the Reynolds and energy equations to reduce the error in the mass flow-continuity. The new approach is in very good agreement with exact solutions and predicts closer values than Cheng's to the traction measurement. Results show that the maximum mean temperature rise, the minimum film thickness, the coefficient of friction, and the pressure spike are significantly influenced by the slide-roll ratio. The thermal effect must be included in the EHL analysis to predict the reliable lubrication performance. The algorithm can also be extended to treat the complete problem of the thermal-elastohydrodynamic lubrication of point contacts with high computational and storage efficiency.

10A853. Present and future technology for lubricants. - Yuji Ikemoto *(Nippon Oil, 8 Chidori-cho Naka-ku Yokohama-shi, Kanagawa 231, Japan)*. Japan J Trib 37(9) 1057-1066 (1992).

In this report, lubricating oil which is presently used for the mechanical elements of general industrial machines, aircraft, and automobiles under severe environmental and operating conditions is described. Also, the future perspective for lubricating oil is stated.

10T854. Present and future technology for gas-lubricated bearings. - Hiroshi Yabe *(Dept of Precision Mech, Fac of Eng, Kyoto Univ, Yoshida-honmachi Sayko-ku Kyoto-shi, Kyoto 606, Japan)*. Japan J Trib 37(9) 1129-1138 (1992).

10A855. Present and future technology for lubricating grease. - Toshiaki Endo *(Kyodo Yushi, 4-1 Kandai 1-chome Tsujido Fujisawa-shi, Kanagawa 251, Japan)*. Japan J Trib 37(9) 1067-1077 (1992).

In this report, among value-added greases, urea grease and fluorinated grease which have recently been focused upon are described. Also, as extreme environments, high temperature, low temperature, vacuum and radioactive environment are mentioned. The application examples of grease are discussed.

10A856. Tribological technology in particular fluid environment. - Shintaro Watanabe and Yoshimi Kagimoto *(Trib Lab, Nagasaki R&D Center, Tech Headquarters, Mitsubishi Heavy Indust, 1-1 Akunoura-machi Nagasaki-shi, Nagasaki 850-91, Japan)*. Japan J Trib 37(9) 1149-1160 (1992).

Here, as special environments, a fused resin environment at a high temperature and high pressure, a new coolant environment for refrigerating compressors, which meets the CFCs (chlorofluorocarbon) control for protecting the global environment, and a foreign matter environment in the case where the entrapment of foreign matter in the operating fluid is inevitable are mentioned, and countermeasures by the authors are introduced.

384. Flow measurements and visualization

10A857. Effective use of transonic stabilization law in calibration of pressure probes. - S Santhakumar *(Dept of Aerospace Eng, Indian IT, Madras-600 036, India).* Mech Res Commun 20(4) 329-333 (Jul-Aug 1993).

Experimental studies play an important role in the study of fluid flows and of turbo-machinery cascade flows in particular. In experimental studies, the most important task is in the calibration of measuring instruments since the accuracy of the obtained results depends on it. It should also be worthwhile to establish the accuracy of the calibration charts if such a facility can be made available. This paper deals with the calibration of five-hole pressure probe used in turbomachinery cascade flow measurements. The calibration had to be carried out for a wide velocity range which included transonic speeds. It is well known that getting accurate experimental results in the transonic regime is very difficult owing to blockage and wall interference. In order to check the accuracy of the results obtained experimentally, the transonic stabilization law was made use of. Stabilization law is traditionally applied to pressure data in the form of a pressure coefficient as a function of free stream Mach number. It can be seen from this paper that this form is cumbersome to use. Two other non-dimensional presentations of pressure data are found to be more convenient from the view point of ease of application of the law.

See also the following:

10A815. Oscillatory instabilities produced by heat from a temperature-controlled hot wire below an interface

VI. HEAT TRANSFER

402. One phase convection

402D. NATURAL CONVECTION (EXTERNAL)

See the following:

10A804. Buoyancy induced heat and mass transfer from a concentrated point source

402E. NATURAL CONVECTION (ENCLOSURES)

See the following:

10A814. Numerical investigations from compressible to isobaric Rayleigh-Benard convection in 2D

402G. COMBINED NATURAL AND FORCED CONVECTION

10A858. Effects of blowing and suction on free convection boundary layers on vertical surfaces with prescribed heat flux. - MA Chaudhary and JH Merkin *(Dept of Appl Math, Univ of Leeds, Leeds LS2 9JT, UK).* J Eng Math 27(3) 265-292 (Aug 1993).

The effects that blowing and suction have on the free convection boundary layer on a vertical surface with a given surface heat flux are considered. Similarity equations are derived first, their solutions being dependent on the wall flux exponent n and a dimensionless transpiration parameter γ, (as well as on the Prandtl number). The range of existence of solutions is considered, with it being shown that solutions exist only for $n > -1$ for blowing, whereas they exist for all $n > n_0$ for suction, where $n_0 < -1$ depends on γ. The solutions for strong suction and blowing are derived. In the latter case the asymptotic structure is found to be different for n in the three ranges $-1 < n < -1/4$, $-1/4 < n < 7/2$, $n > 7/2$. Results are then obtained for the non-similarity problem of constant heat flux with a constant transpiration velocity. Solutions valid for large distances from the leading edge for both suction and blowing are derived.

10A859. Laminar mixed convection heat transfer in 3D horizontal channel with a heated bottom. - Heiu-Jou Shaw *(Dept of Naval Architec and Marine Eng, Natl Cheng Kung Univ, Tainan, Taiwan 70101, ROC).* Numer Heat Transfer A 23(4) 445-461 (Jun 1993).

Mixed convection heat transfer phenomena are studied in a 3D channel with a cavity heated from below. A general purpose computer program is developed to analyze the flow field and temperature distribution in the channel. Numerical computation is performed by using the alternating direction implicit method based on the SIMPLER algorithm. The influences of Reynolds number and Grashof number on the Nusselt number of the cavity are discussed. As a convenience to the reader, 3D streaklines and 3D isothermal surfaces are presented.

10A860. Mixed convection from a localized heat source in a cavity with conducting walls: A numerical study. - E Papanicolaou *(Adv Thermal Eng Lab, IBM, Endicott NY 13760)* and Y Jaluria *(Dept of Mech and Aerospace Eng, Rutgers Univ, New Brunswick NJ 08903).* Numer Heat Transfer A 23(4) 463-484 (Jun 1993).

Mixed convection is studied numerically in the case of an isolated, constant source of heat input within a rectangular enclosure. An external flow enters the enclosure through an opening in the left vertical wall and exits from another opening in the right vertical wall. This configuration leads to a conjugate heat transfer problem and simulates the air cooling of electronic components. Various parameters arise in this problem, particularly the Reynolds number, the buoyancy parameter Gr-Re^2, the ratio of thermal conductivity of the wall material to that of the fluid taken as air, and several geometric parameters. The time-dependent continuity and Navier-Stokes equations are transformed into a system of equations with the stream function and the vorticity as the dependent variables. The energy equation is solved over the entire domain, using the corresponding properties for the solid and fluid regions. The control volume approach is employed in order to discretize the governing equations for their numerical solution. A time marching procedure is followed, until steady state is reached. Results are presented for different values of the buoyancy parameter in the laminar regime, and the critical value of Gr-Re^2, ie, the highest value that leads to a convergent steady solution, is determined. Oscillatory results characterized by a single frequency were observed as this value was exceeded, up to a point where the oscillations showed irregular patterns, indicating that the flow was approaching the turbulent regime. Of particular interest here is the heat transfer, from the heat source to the fluid and from all the inner walls (solid-fluid interfaces) to the fluid, expressed in terms of the corresponding Nusselt numbers.

402I. ROTATING FLUIDS OR SURFACES

See the following:

10A816. Convection in a rotating spherical fluid shell with an inhomogeneous temperature boundary condition at infinite Prandtl number

402M. LIQUID METAL FLOWS

10A861. Study of the transport process of buoyancy-induced and thermocapillary flow of molten alloy. - Wei Shyy and Ming-Hsiung Chen *(Dept of Aerospace Eng Mech and Eng Sci, Univ of Florida, 231 Aerospace Bldg, Gainesville FL 32611).* Comput Methods Appl Mech Eng 105(3) 333-358 (June 1993).

Two-dimensional numerical computations have been conducted to investigate the steady-state convection and scalar transport characteristics of buoyancy-induced and thermocapillary flow of molten alloys. The cases considered are for temperature-induced convection counteracting either solute-induced convection or surface tension-induced convection. A finite volume approach utilizing the non-orthogonal curvilinear coordinates is employed. Various combinations of the dimensionless parameters, including the Marangoni number, thermal and solutal Grashof numbers, Prandtl number, Schmidt number, and aspect ratio have been studied. A wide variety of transport characteristics evolve in a qualitatively orderly manner with respect to changes in these parameters, resulting in different numbers, sizes, and directions of the convection eddies. The strong effects of the fluid properties on the transport processes are particularly noticeable. For flow domain with non-unity aspect ratio, issues of multiple steady-state solutions have also been explored.

402P. TRANSPORT MECHANISMS

10A862. Numerical model for dendritic solidification of binary alloys. - SD Felicelli, JC Heinrich *(Dept of Aerospace and Mech Eng, Univ of Arizona, Tucson AZ 85721),* DR Poirier *(Dept of Mat Sci and Eng, Univ of Arizona, Tucson AZ 85721).* Numer Heat Transfer B 23(4) 461-481 (Jun 1993).

A FE model capable of simulating solidification of binary alloys and the formation of freckles is presented. It uses a single system of equations to deal with the all-liquid region, the dendritic region, and the all-solid region. The dendritic region is treated as an anisotropic porous medium. The algorithm uses the bilinear isoparametric element, with a penalty function approximation and a Petrov-Galerkin formulation. Numerical simulations are shown in which an NH_4Cl-H_2O mixture and a Pb-Sn alloy melt are cooled. The solidification process is followed in time. Instabilities in the process can be clearly observed and the final compositions obtained.

10A863. Surface motion induced by the interaction of pulsed laser radiation with highly absorbing dielectric fluids. - KA Naugol'nykh, OV Puchenkov, VV Zosimov, AE Pashin *(NN Andreev Acoust Inst, 117036 Moscow, Russia).* J Fluid Mech 250 385-421 (May 1993).

The disturbances on the free surface of dielectric fluids resulting from intense laser heating of their boundary layer are studied theoretically and experimentally. The heating is accompanied by pronounced evaporation from the surface and thereby leads to a recoil pressure momentum applied to the surface. For small values of total momentum transferred to the fluid, the low-amplitude initially hollow-like displacement of the surface in the impact zone decays to produce linear gravity-capillary waves (GCW) spreading out on the surface. This regime is treated analytically and the results obtained are compared with experiments involving weakly viscous (water, ehtanol) and highly viscous (glycerol) liquids. An experimental arrangement for remote generation and subsequent detection of probe GCW-packets is given. The evolution of broadband GCW-disturbances on clean and surfactant-contaminated water surfaces are described. Results of GCW-attenuation spectrum measurements on clean water surfaces and on film-covered surfaces are presented.

See also the following:

10A823. Numerical computation of convective dispersion in turbulent buoyant jets

402S. POROUS MEDIA

10A864. Non-Darcy free convection from vertical surfaces in thermally stratified porous media. - P Singh and K Tewari *(Dept of Math, Indian IT, Kanpur, India)*. Int J Eng Sci 31(9) 1233-1242 (Sep 1993).

In this paper, non-Darcy free convection boundary layer flow along an isothermal vertical plate embedded in a thermally stratified fluid saturated porous medium has been described. The main aim in the analysis is to study the effect of stratification on non-Darcian free convection flow and heat transfer. The solutions are obtained by perturbation technique and the resulting ordinary differential equations are solved numerically. It is found that the heat transfer is significantly affected by the modified Grashof number and the stratification parameter.

402Y. COMPUTATIONAL TECHNIQUES

10A865. Hybrid relaxation: A technique to enhance the rate of convergence of iterative algorithms. - R Marek and J Straub *(Inst A for Thermodyn, Tech Univ, Arcisstr 21, W-8000 Munich 2, Germany)*. Numer Heat Transfer B 23(4) 483-497 (Jun 1993).

In solving multidimensional transient fluid flow and heat transfer problems, the strongly coupled conservation laws of mass, momentum, and energy require segregated iterative procedures. Derived from the SIMPLE algorithm, the fully explicit iteration scheme MAPLE (Modified Algorithm for Pressure-Linked Equations) for the pressure-velocity coupling is introduced here. A substantial speedup is gained in the iteration by utilizing hybrid relaxation, a combination of under- and overrelaxation, instead of the usual underrelaxation. Moreover, hybrid relaxation is not restricted to pressure-velocity algorithms only, but can be applied in more general iterations.

10A866. Multidimensional single-step vector upwind schemes for highly convective transport problems. - G de Felice, FM Denaro, C Meola *(Dept Energetica Termofluidodinamica e Condizionamenti Ambientali, Univ delgi Stude di Napoli Federico II, 80125 Napoli, Italy)*. Numer Heat Transfer B 23(4) 425-460 (Jun 1993).

After a synthesis of existing numerical approaches, a family of single-step time-marching upwind schemes is proposed for the convective-diffusive balance of a scalar in multidimensional incompressible laminar flows. A functional description of the new approach is given too. The schemes are adequate to the simulation of purely or highly convective transport phenomena. The proposed schemes were applied to a scalar test problem (rotating hill) and the results evaluated after an analysis of the intrinsic limitations of test itself. A third-order, fully upwind-biased scheme of the family is applied to the lid-driven and thermally driven square cavity problems. In the lid-driven case a steady-state solution is not achieved at Re = 10^4.

10A867. Solution of nonlinear elliptic convection-diffusion problems through the integral transform method. - AJK Leiroz and RM Cotta *(Mech Eng Dept EE-COPPE-UFRJ, Univ Fed Rio de Janeiro, Cidade Univ, Cx PO Box 68503, Rio de Janeiro-RJ 21945, Brazil)*. Numer Heat Transfer B 23(4) 401-411 (Jun 1993).

The hybrid numerical-analytical solution of nonlinear elliptic convection-diffusion problems is investigated through extension of the ideas in the generalized integral transform technique. An application is selected to illustrate the convergence characteristics of the proposed eigenfunction expansion approach, for different values of the parameters that govern the relative importance of convection and diffusion effects.

See also the following:

10A751. Efficient 3D calculation procedure for incompressible flows in complex geometries

404. Two phase convection

10A868. Hysteresis phenomena in subcooled flow boiling of well-wetting fluids. - GP Celata, M Cumo, T Setaro *(ENEA Casaccia, ENE-IMPRE-IPROT, Via Anguillarese, 301 00060 Rome, Italy)*. Exp Heat Transfer 5(4) 253-275 (Oct-Dec 1992).

Detailed knowledge of the physical phenomena involved in subcooled boiling is of great interest for the design of liquid-cooled heat-generating systems with high heat fluxes. An electrically heated stainless steel tube, 2.3 m long, with a 7.57-mm inner diameter, was used to study the incipience of flow boiling in subcooled, well-wetting fluids (R-12 and R-114) over a wide range of pressure, mass flux, and heat flux. Hysteresis in boiling observed by increasing and decreasing heat flux seems to be ascribed to the small contact angle of refrigerants on surfaces such as stainless steel, allowing the larger cavities in the wall to be flooded. A higher temperature excess may be reached in the wall before boiling sets in than the temperature achieved when boiling has been developed. Some existing correlations were tested, revealing the general inadequacy in predicting the higher superheating required in well-wetting fluids for the onset of nuclear boiling. Classic theory on bubble growth, heat transfer relationships, and the force balance equation at the bubble-liquid interface, coupled with an empirical correlation for the determination of the boiling incipience conditions, accomplish a very successful prediction of the experimental data.

10A869. Behavior of bubbles and heat transfer in transition boiling. - Kinichi Torikai, Kohichi Suzuki, Masatoku Yamaguchi, Syuichi Kobayashi *(Dept of Mech Eng, Sci Univ of Tokyo, 2641 Yamazaki, Noda-shi, Japan)*. Exp Heat Transfer 5(4) 277-292 (Oct-Dec 1992).

The behavior of boiling bubbles on a heating surface made of transparent quartz glass is observed directly from its back side. The surface is heated by a fused salt that is transparent at high temperature. Freon R-11 and R-113 are used as the boiling liquids. In transition boiling, dry parts of bubbles contacting the heating surface develop into larger vapor films with increasing superheat of the surface. Vapor film patches appear repeatedly in a short period. The behavior of bubbles and vapor films is different from that in nucleate boiling and in film boiling.

10A870. Evaporation of a circular meniscus of NH_3 flowing parallel to a gaseous NH_3-H_2 stream. - DA Kouremenos, KA Antonopoulos, A Stegou-Sagia *(Dept of Mech Eng, Thermal Section, Natl Tech Univ, 42 Patission St, Athens 106 82, Greece)*. Numer Heat Transfer A 23(4) 415-431 (Jun 1993).

A solution is presented for the 3D heat and mass transfer during evaporation of a circular meniscus of liquid NH_3, flowing parallel to a gaseous NH_3-H_2 stream, as encountered in the evaporator of small neutral gas absorption refrigerators. The procedure developed is based on a finite difference solution of a set of differential equations expressing the 3D transport of momentum, heat, and mass. Expressions are also provided for the thermodynamic and transport properties of the real NH_3-H_2 mixture. The results of the numerical solution include the fields of velocity, temperature, NH_3 mass fraction, enthalpy, and entropy.

10A871. Liquid film thickness and topography determination using fresnel diffraction and holography. - J Yang, LC Chow, MR Pais *(Dept of Mech Eng, Univ of Kentucky, Lexington KY 40506)*, A Ito *(Dept of Prod Syst Eng, Oita Univ, Oita 870-11, Japan)*. Exp Heat Transfer 5(4) 239-252 (Oct-Dec 1992).

A noninvasive experimental method to measure time-averaged maximum film thickness and surface topography is developed. The film thickness is measured by the change in the line of sight using a laser beam. The surface topography is measured using a holographic technique. In the holographic method, interference patterns created by the substrate and the superajacent film surface are used to determine the topography. Measurements of liquid film thickness and topography under conditions of droplet impingement on a surface were taken, and the results are presented. Applicability and limitations of the techniques are discussed.

See also the following:

10A865. Hybrid relaxation: A technique to enhance the rate of convergence of iterative algorithms

406. Conduction

10A872. Heat conduction across a semi-infinite interface in a layered plate. - FD Zaman *(Dept of Math Sci, King Fahd Univ of Pet and Minerals, Dhahran 31261, Saudi Arabia)*. Utilitas Math 43 89-96 (May 1993).

We consider the problem of heat flow across a semi-infinite plane contact in a two-layered plate in which the contact between the layers takes place in one part of the interface while the other part is perfectly insulated. The Wiener-Hopf technique has been employed to obtain the solution in a closed form.

10A873. Measurements of thermal conductivity and optical properties of porous partially stabilized zirconia. - Pei-feng Hsu and JR Howell *(Dept of Mech Eng, Univ of Texas, Austin TX 78712)*. Exp Heat Transfer 5(4) 293-313 (Oct-Dec 1992).

Experimental measurements of the high-temperature ($300 < T < 800$ K) thermal conductivity of highly porous (porosity greater than 80%), partially stabilized zirconia (PSZ) were performed. A method of simultaneously inverting conductivity and extinction coefficient from the experimental data is presented. The effect of natural convection within the porous plates with heating from below was found to be negligible. The thermal conductivity integral method was incorporated into the version of conductivity and radiative properties from the diffusion approximation of the combined radiation and conduction heat flux measurement. The measured conductivity decreased slightly as the pore size of the PSZ increased. The extinction coefficient decreased with increased pore size, and for pore size greater than 0.6 mm the trend had good agreement with the geometric optics limit prediction.

10A874. Analysis of transient heat transfer in straight fins of various shapes with its base subjected to a decayed exponential function of time in heat flux. - Jung-Kuei Tseng *(Dept of Mech Eng, Chinese Military Acad, Feng-Shang, PO Box 90602-6 Kao-Hsiung, Taiwan, ROC)*, Chia-Lin Shih *(Tahan Junior Col of Eng and Business, Hua-Lien, Taiwan, ROC)*, Wen-Jyi Wu *(Dept of Mech Eng, Chinese Military Acad, Feng-Shang, PO Box 90602-6, Kao-Hsiung, Taiwan, ROC)*. Comput Struct 47(2) 289-297 (Apr 1993).

The theoretical study of heat flow within finned heat exchangers is of considerable practical importance because of the extensive utilization of finned surfaces for heat transfer enhancement in applications varying from air-cooled heat exchangers in the process industries to heat rejection equipment in space vehicles. This paper investigates the transient heat transfer in 2D straight fins of various shapes with its base subjected to a decayed exponential function of time in a heat flux. In order to obtain the solutions of the governing equation, which is a partial differential equation, the following procedures of analysis should be performed: 1) normalize the governing partial differential equation subjected to the appropriate initial and boundary conditions, 2) take a Laplacian transform with respect to time, 3) utilize the integral method to solve the transformed system and 4) achieve and inverse Laplace transform by the Fourier series technique.

10A875. Semianalytic approach to general transient problems and its applications to heat transfer. - JY Zhang *(Col of Machine and Elec, Tianjin Univ, Tianjin 300380, China)*, RW Lewis *(Dept of Civil Eng, Univ of Wales, Swansea SA2 8PP, UK)*, JS Peng *(Dept of Phys, Normal Univ of Sichuan, Nanchong 637002, China)*. Numer Heat Transfer B 23(4) 413-424 (Jun 1993).

In this article a new method of solving the transient problems is developed that is based on convolution-type variational principles, where FE discretization in the space domain and series representation in the time domain are considered. This approach can overcome the shortcomings of existing methods and combine the advantages of those methods for solving transient problems. The examples show that the new method is a most effective method of obtaining solutions for transient problems.

See also the following:

10A6. FE analysis of heat transfer in anisotropic solids: Application to manufacturing problems

408. Radiation and combined modes

10A876. Formulation of model equations for heating by microwave radiation. - JM Hill *(Dept of Math, Univ of Wollongong, NSW 2522, Australia)* and MJ Jennings *(Dept of Appl Math and Theor Phys, Univ of Cambridge, Silver St, Cambridge CB3 9EW, UK)*. Appl Math Model 17(7) 369-379 (Jul 1993).

In general, heating by microwave radiation involves simultaneously solving Maxwell's equations of electromagnetism coupled with the heat equation and for which all electrical, magnetic, and thermal parameters are nonlinearly dependent upon the temperature T. The solution of this coupled nonlinear system, either analytically or numerically, is formidable even if sufficient data existed to properly specify the various electrical and magnetic parameters. Accordingly, the proposition of reducing the problem to studying the heat equation alone with a certain nonlinear body heating Q(T) is an extremely attractive one. In order to identify the body heating term Q(T) as accurately as possible, an exhaustive examination is made of existing experimental results of von Hippel, which have been available for almost 40 years. We show that for the higher frequencies the experimental data are very accurately approximated by both parabolic and linear fits for the body heating Q(T). At the lower frequencies one of two types of exponential curves provides an adequate fit of the experimental data. At intermediate frequencies in the experimental data exhibit both parabolic and exponential behavior, and we propose a body heating term Q(T), consisting of a linear combination of the previously used exponential curves, which very accurately fits the data over the full range for which it is available. Finally, we demonstrate the changes in variation of Q(T) with changing frequency but for which insufficient data exist to properly quantify. The principal objective of this investigation is to obtain simple analytical forms for Q(T) rather than an application of elaborate curve-fitting procedures, and the mathematical consequences of the specific forms established here will be the subject of future work.

10A877. Numerical model for combined conductive and radiative heat transfer in annular packed beds. - K Kamiuto, S Saito, K Ito *(Dept of Prod Syst Eng, Oita Univ, Dannoharu 700, Oita 870-11, Japan)*. Numer Heat Transfer A 23(4) 433-443 (Jun 1993).

A numerical model is developed for quantitatively analyzing combined conductive and radiative heat transfer in concentric annular packed beds. A packed bed is considered to be a continuous medium for heat transfer, but the porosity distribution within a packed bed is taken into account. To examine the validity of the proposed model, combined conductive and radiative heat transfer through annular packed beds of cordierite or porcelain beads is analyzed numerically using finite differences under conditions corresponding to heat transfer experiments of these packed beds. The resultant temperature profiles and heat transfer characteristics are compared with the experimental results.

412. Thermomechanics of solids

10A878. State space approach to thermoelasticity with two relaxation times. - HH Sherief *(Dept of Math, Fac of Sci, Univ of Alexandria, Alexandria, Egypt)*. Int J Eng Sci 31(8) 1177-1189 (Aug 1993).

In this work the state space formulation of thermoelasticity with two relaxation times is introduced. The formulation is valid for problems with or without heat sources. The resulting formulation together with the Laplace transform technique are applied to a variety of problems. The solution to a thermal shock problem and to a problem of a layer media both without heat sources are obtained. Also a problem with a distribution of heat sources is considered. A numerical method is employed for the inversion of the Laplace transforms. Numerical results are given and illustrated graphically for the problems considered. Comparisons are made with the results predicted by the coupled theory and with the theory of generalized thermoelasticity with one relaxation time.

10A879. Temperature changes due to elastic deformations, and Poisson's equation in thermodynamics of metals. - V Pekarek *(Inst of Elec Eng, Acad of Sci, Dolejskova 5, 182 02 Prague 8, Czech Republic)*. Acta Tech CSAV 38(2) 145-152 (1993).

The internal pressure in the interior of a metal, is modified through external mechanical load acting upon the system (adiabatic process). Elastic changes in volume, aroused in this way, are interrelated with the changes in internal pressure through the same equation as that derived by Poisson for adiabatic processes in gases. The validity of the equation in thermodynamics of metals is investigated in the present paper and proved in terms of the theory of elasticity. Poisson's equation along with the First Law allow temperature changes due to elastic deformations in metals to be evaluated.

10A880. Buckling and post-buckling of composite plates and shells subjected to elevated temperature. - V Birman *(Eng Educ Center, Univ of Missouri, St Louis MO 63121)* and CW Bert *(Sch of Aerospace and Mech Eng, Univ of Oklahoma, Norman OK 73019)*. J Appl Mech 60(2) 514-519 (Jun 1993).

Effects of temperature on buckling and post-buckling behavior of reinforced and unstiffened composite plates or cylindrical shells are considered. First, equilibrium equations are formulated for a shell subjected to the simultaneous action of a thermal field and an axial loading. These equations are used to predict a general form of the algebraic equations describing the post-buckling response of a shell. Conditions for the snap-through of a shell subjected to thermomechanical loading are formulated. As an example, the theory is applied to prediction of post-buckling response of flat large-aspect-ratio panels reinforced in the direction of their short edges.

10A881. Post-buckling of geometrically imperfect shear-deformable flat panels under combined thermal and compressive edge loadings. - L Librescu *(Dept of Eng Sci and Mech, VPI)* and MA Souza *(Dept of Civil Eng, Pontificia Univ Catholica, Rio de Janeiro, Brazil)*. J Appl Mech 60(2) 526-533 (Jun 1993).

The static post-buckling of simply-supported flat panels exposed to a stationary nonuniform temperature field and subjected to a system of subcritical in-plane compressive edge loads is investigated. The study is performed within a refined theory of composite laminated plates incorporating the effect of transverse shear and the geometric nonlinearities. The influence played by a number of effects, among them transverse shear deformation, initial geometric imperfections, the character of the in-plane boundary conditions and thickness ratio are studied and a series of conclusions are outlined. The influence played by the complete temperature field (ie, the uniform through thickness and thickness-wise gradient) as compared to the one induced by only the uniform one, is discussed and the peculiarities of the resulting post-buckling behaviors are enlightened.

10A882. Separation of strain components in composite materials from thermoelastic temperature measurements. - SA Dunn *(Dept of Mech and Manuf Eng, Univ of Melbourne, Parkville, Vic, Australia)*. J Appl Mech 60(2) 443-448 (Jun 1993).

In this paper experimental data is used to demonstrate how point-to-point strain components can be determined from thermoelastic temperature data. This is done by making use of the very obvious effects of thermal conduction on the cyclic surface temperature changes which can occur as a composite material undergoes an oscillating stress. By observing the cyclic surface temperature changes for different loading frequencies, the adiabatic heat generated in the different plies may be determined. With this knowledge, the strain components experienced by a composite laminate may be found.

10A883. Thermo-stress analysis of a plated-through-hole in a composite printed wiring board. - JM Whitney *(Graduate Mat Eng, Univ of Dayton, Dayton OH 45469-0240)*, IU Haq, SR Soni *(AdTech Syst Res, Dayton OH 45432)*. J Thermoplastic Composite Mat 6 29-37 (Jan 1993).

A stress analysis model for determining the thermal stresses in the vicinity of a plated-through-hole in a printed wiring board is presented. The model is based on an axisymmetric deformation and the superposition of an exact elasticity solution for far field stresses (away from the outer free surfaces) and an approximate near field solution (near the outer free surfaces). The approximate solution exactly satisfies point-by-point equilibrium, but violates compatibility.

10A884. Thermal effects in Mindlin-type plates. - P Schiavone *(Dept of Elec Eng and Appl Math Inst, Univ of Alberta, Edmonton AB, T6G 2G1, Canada)* and RJ Tait *(Dept of Math, Univ of Alberta, Edmonton AB, T6G 2G1, Canada)*. Quart J Mech Appl Math **46**(1) 27-39 (Feb 1993).

We derive a linear thermoelastic plate model based on a Mindlin-type assumption on the displacements. Initial-boundary-value problems of the Dirichlet, Neumann, and mixed type are formulated and appropriate uniqueness results are obtained. The exterior problems are solved in special classes of finite-energy functions having a specific 'far-field pattern' which allow some divergence at infinity. These are larger than the class of admissible functions used in classical elasticity. We also indicate how results on existence and uniqueness are obtained in problems of static equilibrium and steady thermoelastic oscillations. The latter are governed by systems of elliptic equations and can be solved numerically using a generalized Fourier-series technique developed earlier for thin micropolar plates. Finally, we mention the generalization to a theory of thermoelastic micropolar plates.

10A885. Thermoelastic frictional contact problems: Modeling, FE approximation and numerical realization. - L Johansson and A Klarbring *(Dept of Mech Eng, Div of Solid Mech and Strength of Mat, Linkoping Univ and IT, Linkoping, Sweden)*. Comput Methods Appl Mech Eng **105**(2) 181-210 (Jun 1993).

In this paper frictional contact including frictional heat generation and heat transfer across the contact interface is studied. A model for the behavior of the contact interface is proposed and combined with the conventional equations of linear thermoelasticity for the bulk material of the contacting bodies. A FE discretization in space and a finite difference discretization in time are introduced, and an iterative algorithm is proposed to deal with the coupled thermal-mechanical nature of the problem. Finally, several numerical examples are given.

See also the following:

10A541. Fluid flow, heat transfer and inclusion behavior in continuous casting tundishes

10A546. Elevated temperature fatigue crack growth in alloy 718 Part I. Effects of mechanical variables

414. Mass transfer

10A886. Application of the BE technique to periodic heat transfer in a fin assembly. - JM Houghton, DB Ingham *(Dept of Appl Math Stud, Univ of Leeds, Leeds LS2 9JT, UK)*, PJ Heggs *(Dept of Chem Eng, Univ of Bradford, Bradford BD7 1DP, UK)*. Numer Heat Transfer A **23**(4) 379-398 (Jun 1993).

Time dependent heat transfer has been investigated in a fin assembly comprising an array of fins attached to a supporting wall. Convective heat exchange from the supporting wall and thermal interactions between the wall and fins are considered. A new implementation of the BEM solution technique has been devised to investigate oscillatory heat transfer in a fin assembly and is extended to investigate fin assembly heat transfer that is of a general periodic nature.

10A887. Thermosolutal convection heat and mass transfer in a vertical annular enclosure. - LW Wang and CY Wei *(Dept of Mech Eng, Yuan-Ze IT, Taoyuan, Taiwan, ROC)*. Exp Heat Transfer **5**(4) 315-328 (Oct-Dec 1992).

The purpose of the present study is to investigate flows resulting from buoyancy forces due to a combination of temperature and species concentration effects in a vertical annular enclosure. An electrochemical system is described that enables opposing temperature and concentration gradients to be imposed. Complex flow patterns are observed as the parameters are varied.

10A888. Autowave propagation for general reaction diffusion systems. - IA Molotkov and SA Vakulenko *(Inst of the Terrestrial Magnetism Ionosphere and Radio Wave Propagation, ISMIR AN, Troitsk, Moscow 142092, Russia)*. Wave Motion **17**(3) 255-266 (May 1993).

We discuss autowave propagation for general reaction-diffusion systems. It is shown that when the front curvature is small, the wave behavior depends on two constants and does not depend on a nonlinearity form in detail. The formulae for the normal velocity of the front is found to contain the mean curvature and the two constants. We give an energetic interpretation for the equations describing wave propagation even when the original system has no clear energetic interpretation. New effects are found for multistable systems.

10A889. BEM for convective heat transfer. - Y Shi and PK Banerjee *(Dept of Civil Eng, SUNY, Buffalo NY 14260)*. Comput Methods Appl Mech Eng **105**(2) 261-284 (Jun 1993).

A BEM is developed for the linearized convective heat transfer problem using a newly derived integral formulation based on a convective fundamental solution. Details of the numerical implementation are provided for this linearized problem, which can be solved with only surface discretization. Significant attention is given to the algorithm so that the method could be applied to problems involving heat transfer at high Peclet numbers. Several numerical examples of steady state flows in 2D are included to demonstrate the accuracy of the present methodology, and to highlight its practical utility and limitations.

10A890. Eulerian-Lagrangian localized adjoint method: The theoretical framework. - I Herrera *(Inst Geofisica, UNAM, Apdo Postal 22-582, 14000 Mexico)*, RE Ewing *(Col of Sci, Texas A&M Univ, College Station TX 77843-3257)*, MA Celia *(Water Resources Program, Dept of Civil Eng and Operations Res, Princeton)*, TF Russell *(Dept of Math, Univ of Colorado, Denver CO 80204-5300)*. Numer Methods PDE **9**(4) 431-457 (Jul 1993).

This is the second of a sequence of papers devoted to applying the localized adjoint method, in space-time, to problems of advective-diffusive transport. We refer to the resulting methodology as the Eulerian-Lagrangian localized adjoint method (ELLAM). The ELLAM approach yields a general formulation that subsumes may specific methods based on combined Lagrangian and Eulerian approaches, so-called characteristic methods. In the first paper of this series the emphasis was placed in the numerical implementation and a careful treatment of implementation of boundary conditions was presented for 1D problems. The final ELLAM approximation was shown to possess the conservation of mass property, unlike typical characteristic methods. The emphasis of the present paper is on the theoretical aspects of the method. The theory, based on Herrera's algebraic theory of boundary value problems, is presented for advection-diffusion equations in both 1D and multidimensional systems. This provides a generalized ELLAM formulation. The generality of the method is also demonstrated by a treatment of systems of equations as well as a derivation of mixed methods.

10A891. Multi-grid methods for steady state diffusion in random media. - D Braess, M Biebighauser *(Inst for Math, Ruhr-Univ, D-4630 Bochum, Germany)*, P Grassberger, R Leuverink *(Dept of Phys, Univ of Wuppertal, D-5600 Wuppertal 1, Germany)*. J Comput Phys **107**(1) 118-123 (Jul 1993).

We apply multi-grid methods to study steady state densities for hopping diffusion in 2D random media. We show that these methods are very efficient. For our fastest algorithm, which also uses overrelaxation, CPU times increase as $L^{2.2}$ in order to reach equilibrium on square lattices of size $L \times L$ with a prescribed accuracy. Compared to standard Gauss-Seidel methods, this is at least an improvement by a factor $\propto L$. For $L = 128$, the improvement is about a factor of 10 and even more than 80 if overrelaxation is added.

416. Combustion

416C. IGNITION (THERMAL AND HETEROGENEOUS)

10A892. Self-ignition of small-ring hydrocarbons behind reflected shock waves. - VG Slutsky, OD Kazakov, ES Severin, EV Bespalov, SA Tsyganov *(Semenov Inst of Chem Phys and Russian Acad of Sci, Moscow 117977, Russia)*. Combust Flame **94**(1-2) 108-112 (Jul 1993).

Self-ignition of stoichiometric airlike argon mixtures of monocyclic and bicycle small-ring hydrocarbons was investigated behind reflected shock waves at 1200-1600 K and 0.6 ± 0.1 MPa. The reactivity of small-ring hydrocarbons has been found to be determined by the properties of their thermal decomposition products. New high-temperature decomposition channels for spiropentane, methylenecylobutane, and methylencyclopropane have been discovered.

416D. LAMINAR FLAME PROPAGATION

10A893. Experimental investigation of stretched premixed flames burning mixtures of methane and methyl chloride in air and comparison with numerical simulations. - MH Yang and IK Puri *(Dept of Mech Eng (M/C 251), Univ of Illinois, Chicago IL 60680-4348)*. Combust Flame **94**(1-2) 25-34 (Jul 1993).

Experimental measurements of the laminar burning velocities of flames burning methane-methyl chloride mixtures, and methyl chloride in air, are made in a counterflow burner. The flame speeds are observed to decrease with increasing chlorine loading, from 40 cm s^{-1} for a stoichiometric methane-air flame to 4.9 cm s^{-1} for a stoichiometric methyl chloride-air flame. Good agreement is found between flame speeds deduced from experiments and those predicted by numerical simulations at the periphery of the domain, ie, for methane-air and methyl chloride-air flames. The agreement between experiments and calculations at intermediate regions, that is, for varying methane-methyl chloride-air mixtures is at best reasonable. Sources for the discrepancies in the kinetic mechanism are identified. The critical extinction stretch rate for flames burning methyl chloride in air is measured, as is the stretched flame speed close to extinction.

10A894. Local response and surface properties of premixed flames during interactions with Karman vortex streets. - T-W Lee, JG Lee, DA Nye, DA Santavicca *(Turbulent Combust Lab, Dept of Mech Eng, Penn State)*. Combust Flame **94**(1-2) 146-160 (Jul 1993).

Premixed flames interacting with Karman vortex streets have been experimentally investigated, in which local flame responses consistent with the results of stretched laminar flame theories are observed in that the OH LIF intensity increases when the local flame curvature becomes positive (negative) for thermodiffusively unstable (stable) flames. Departure of the peak OH LIF intensity for hydrogen flames ranges from 20% to 150% of the value at zero flame curvature for flame curvature ranging from -1.5 to 0.7 mm^{-1}, while for propane-air flames the variation is within ±20% of the value at zero curvature. Variation in the averaged peak OH LIF intensity is nearly linear with respect to the variation in flame curvature from -1.2 to 0.8 mm^{-1}. The flame area during interactions with Karman vortex streets increases as a relatively weak function of the vortex velocity, while the vortex size affects the flame area increase in the smaller vortices are found to be less effective in generating flame area. The effect of Lewis number on the flame front is to enhance (suppress) the amplitude of the wrinkles generated by vortices for thermodiffusively unstable (stable) flames, thus resulting in larger (smaller) flame area. The flame curvature pdfs for flames interacting with Karman vortex streets exhibit a bias toward positive flame curvature due to the large area of positively-curved flame elements that develop downstream along the V-flame. A decrease in vortex size tends to increase the flame curvature and thus broadens the pdfs, while the vortex velocity, and Lewis number have relatively small effects on the flame curvature pdfs. The flame orientation distribution is peaked near the normal direction of flame propagation for small vortex velocity, while an increase in vortex velocity results in broadening of the flame orientation distribution and a shift toward large flame angle due to the increased distortions in the flame front and increases in the effective flame propagation speed, respectively.

416E. TURBULENT FLAME PROPAGATION, FLAMMABILITY

10A895. Direct simulations of premixed turbulent flames with nonunity Lewis numbers. - CJ Rutland *(Dept of Mech Eng, Univ of Wisconsin, 1513 University Ave, Madison WI 53760)* and A Trouve *(Center for Turbulence Res, Stanford)*. Combust Flame 94(1-2) 41-57 (Jul 1993).

A principal effect of turbulence on premixed flames in the flamelet regime is to wrinkle the flame fronts. For nonunity Lewis numbers, Le ≠ 1, the local flame structure is altered in curved regions. This effect is examined using direct numerical simulations of 3D isotropic turbulence with constant density, single-step Arrhenius kinetics chemistry. Simulations of Lewis numbers 0.8, 1.0, and 1.2 are compared. At the local level, curvature effects dominated changes to the flame structure while strain effects were insignificant. A strong Lewis-number-dependent correlation was found between surface curvature and the local flame speed. The correlation was positive for Le < 1 and negative for Le > 1. At the global level, strain-related effects were more significant than curvature effects. The turbulent flame speed changed significantly with Lewis number, increasing as Le decreased. This was found to be due to strain effects that have a nonzero mean over the flame surface, rather than to curvature effects that have a nearly zero mean. The mean product temperature was also found to vary with Lewis number, being higher for Le > 1 and lower for Le < 1.

10A896. Images of the quenching of a flame by a vortex: To quantify regimes of turbulent combustion. - WL Roberts, JF Driscoll *(Dept of Aerospace Eng, Univ of Michigan, Ann Arbor MI 48109)*, MC Drake *(General Motors Res Lab, Warren MI 48090)*, LP Gross *(Syst Res Lab, Dayton OH 45440)*. Combust Flame 94(1-2) 58-69 (Jul 1993).

A laminar toroidal vortex i[illegible]ted with a laminar premixed flame in [illegible] and to visualize some of the fur[illegible] of turbulent combustion. Lo[illegible] f the flame was observed [illegible]uced fluorescence imagin[illegible] OH molecules in the counterflow flamefront region near the vortex leading edge. A quenching limit curve was measured as a function of vortex size and strength. In the second part of the study, the measurements are combined with concepts proposed by Poinsot, Veynante, and Candel in order to infer the thin flame limit, namely, the onset of distributed reactions, on a classical premixed turbulent combustion regime diagram. The measured thin flame limit indicates when laminar flamelet theories become invalid, since quenching allows hot products and reactants to coexist. Results are compared with Klimov-Williams criterion. Vortex core diameters were as small as the flame thickness in some cases. The main conclusion is that small vortices are less effective at quenching a flame than was previously believed; therefore the inferred regime within which thin flame theories are valid extends to a turbulence intensity that is more than an order of magnitude larger than that which was previously predicted. Results also indicate that micromixing models, which assume that the smallest eddies exert the largest strain on a flame are not realistic. Measured trends are in agreement with the direct numerical simulations of Poinsot, et al, but absolute values differ.

416I. KINETICS AND MECHANISMS

10A897. Reduced kinetic mechanism for premixed CH_3Cl/CH_4/air flames. - KY Lee and IK Puri *(Dept of Mech Eng, Univ of Illinois, M/C 251, Chicago IL 60680-4348)*. Combust Flame 94(1-2) 191-204 (Jul 1993).

A reduced kinetic consisting of nine-global steps is derived to describe freely propagating flames burning mixtures of methyl chloride and methane in air. The fuel blend contains two fuels with distinct (methyl chloride and methane) thermochemical properties, whose contribution to the radical pool in the flame is different. Our objective is to (1) obtain predictions of flame speeds, particularly for rich flames, and (2) describe the gross chemistry by predicting the concentration profiles of the (a) fuels, (b) oxidizer, (c) products, in particular the C_2-containing species (since halogenated flames are generally sooting), and (d) the significant atomic-radical species in the flame. Chlorine atoms available from methyl chloride inhibit the flames, resulting in lower flame speeds. The mechanism is able to predict flame speeds for flames burning rich mixtures of equal molar amounts of methyl chloride and methane in air, and for stoichiometric flames burning methyl chloride and air in the range of 30%-67% methyl chloride in the methane-methyl chloride mixture. These predictions are in good agreement with simulations and measurements made in our laboratory though large discrepancies exist in the measured flame speeds when data due to other investigators is included. The species concentration profiles obtained by using the reduced mechanism are in agreement with those predicted by the detailed mechanism from which it is derived.

416L. HETEROGENEOUS AND MULTIPHASE COMBUSTION

10A898. Spray structure in counterflowing streams with and without a flame. - SC Li, PA Libby, FA Williams *(Dept of Appl Mech and Eng Sci, UCSD)*. Combust Flame 94(1-2) 161-177 (Jul 1993).

An experimental and theoretical study is performed on two-phase counterflowing streams with and without flames in which methanol sprays, transported in nitrogen from a lower circular duct, flow upward to meet a pure oxygen stream that flows downward from the upper circular duct. The spray structure and entire flowfield are measured by a two-component phase doppler particle analyzer. The relative motion of droplets as a function of droplet diameter and the effect of the flame on the counterflow field are determined. The influences of the flowfield and the flame sheet on spray structure are measured. A theoretical analysis of droplet behavior in counterflowing streams is also performed on the basis of the spray equation applied away from the stagnation plane. Comparisons between measured and predicted number density as a function of axial position are made. These experimental and theoretical results help in understanding the fundamental mechanisms of spray combustion.

10A899. Upper explosive limit of dusts: Experimental evidence for its existence under certain circumstances. - KJ Mintz *(Mining Res Lab, CANMET Energy Mines and Resources, Ottawa, ON, K1A 0G1, Canada)*. Combust Flame 94(1-2) 125-130 (Jul 1993).

An experimental study of the explosibility of cornstarch using the 20-L vessel shows that, for a narrow size fraction near its limiting particle size for explosibility, an upper explosion limit exists. Upper explosive limits were also observed with both cornstarch and Pittsburgh Standard coal dust at low oxygen concentrations. These upper limits occur at accessible dust concentrations. A simple mechanism, "the oxygen depletion" phenomenological concept, is described. The optimum dust concentration, calculated using this mechanism, gives reasonable agreement with the experimental values, as well as explaining the variation of optimum concentration with particle size and oxygen concentration.

416P. SOLID FUELS

10A900. Continuum limits of interacting particle systems. - JM Greenberg and R Peszek *(Dept of Math and Stat, UMBC, Baltimore MD 21228)*. Physica D 65(1-2) 172-190 (May 1993).

We study the continuum limits of discrete particle systems with short range repulsive forces. We establish the existence of a class of short range interparticle force laws with the property that the asymptotic trajectories of two sufficiently energetic particles of equal mass entering and leaving the region of a binary interaction are the same as the asymptotic trajectories of particles which undergo a simple point-mass elastic collision. Using such force laws, we consider the evolution of an N particle gas, each particle having mass 1-N, for initial data which are guaranteed to generate only binary collisions. We show that such problems are exactly solvable and we characterize the continuum limit ($N \to \infty$) of such solutions. These limit flows are independent of the details of the repulsive forces and are the same as obtained if one replaces the interparticle force law by the elastic collision rule which simply interchanges particle velocities during a collision.

416Q. LIQUID FUELS

10A901. Analytical and numerical modeling of flame-balls in hydrogen-air mixtures. - J Buckmaster *(Dept of Aeronaut and Astronaut Eng, Univ of Illinois, Urbana IL)*, M Smooke *(Dept of Mech Eng, Yale Univ, New Haven CT)*, V Giovangigli *(Centre Math Appl and CNRS, Ecole Polytech, Palaiseau, France)*. Combust Flame 94(1-2) 113-124 (Jul 1993).

Flame-balls are stationary spherical premixed flames observed in certain near-limit mixtures. It is believed that radiative heat losses are an important stabilizing influence. Numerical solutions of flame balls are constructed for hydrogen-air mixtures using an accurate description of the chemical kinetics, diffusive transport, and radiation losses. A lean limit equivalence ratio of 0.0866 is predicted and a rich limit of 2.828. For any equivalence ratio between the two limits there are two solutions. One is characterized by a small flame, incomplete reactant consumption, and negligible radiation losses. The other by a large flame, complete consumption of one of the reactants, and significant radiation losses. The maximum temperature varies between 1200 and 900 K as the two solution branches are traversed. Much of our discussion is a reprise and modification of previously published analytical results, for these provide physical insight into the nature of the solutions, and suggest that a portion of the large flame branch near the lean limit is stable and so corresponds to observable flames.

10A902. **Asymptotic analysis of monopropellant droplet burning for the reaction nA → B.** - AV Orlov *(Tashkentskaya St 10-2 39, Moscow 109444, Russia)*. Combust Flame 94(1-2) 35-40 (Jul 1993).

The transport phenomena of convection, diffusion, and thermal conduction are analyzed for large-activation-energy burning of a spherical monopropellant droplet. The reaction is assumed to be nA → B with arbitrary n. The reciprocal value of the activation energy is the small parameter. The two lowest-order terms of the mass flow rate, the flame position and the flame structure are obtained.

416Y. COMPUTATIONAL TECHNIQUES

10A903. **Numerical model for temperature gradient and particle effects on Rijke bruner oscillations.** - RL Raun *(Hercules Inc, Bacchus Works, Magna UT 84044)* and MW Beckstead *(Dept of Civil Eng, Brigham Young Univ, Provo UT 84602)*. Combust Flame 94(1-2) 1-24 (Jul 1993).

Equations that describe acoustic oscillations in a Rijke burner have been developed. Eigenvalues giving frequencies and growth rates of acoustic modes can be calculated from these equations. In their most general form, these acoustic equations include the effects of nonuniform gas temperature and entrained, burning particles. In general, analytical solution of the equations is not possible. A computer program has been developed that uses numerical methods to calculate eigenvalues from the general equations. For some limiting cases, analytical solution of the equations is possible. Analytical solutions are presented for three such cases. Eigenvalues predicted by the numerical model compare well to the analytical solutions. The Bailey and McIntosh flame-acoustic interaction models were tested with the computer program. Predicted frequencies and growth rates agreed well with experimental data when heat loss was taken into account. The program matched one experimental frequency and growth rate exactly when a time lag was added to the Bailey model. The McIntosh model did nearly as well as without any adjustments. A particle combustion-acoustic interaction model for burning aluminium particles has been developed. This model was also tested in the Rijke burner model. The predictions show qualitative but not quantitative agreement with experimental measurements of particle combustion effects. A mechanism is suggested that may explain the discrepancy.

416Z. EXPERIMENTAL TECHNIQUES

10A904. **Coherent anti-Stokes Raman spectroscopy (CARS) and laser-induced fluorescence (LIF) measurements in a rocket engine plume.** - DR Williams, D McKeown, FM Porter *(Combust Dept, Harwell Lab, Oxfordshire OX11 0RA, UK)*, CA Baker *(Epsilon Res, Buckinghamshire HP10 9BZ, UK)*, AG Astill *(Combust Dept, Harwell Lab, Oxfordshire OX11 0RA, UK)*, KM Rawley *(Defence Res Agency, Ft Halstead, Kent, UK)*. Combust Flame 94(1-2) 77-90 (Jul 1993).

Coherent anti-Stokes Raman spectroscopy (CARS) and laser-induced fluorescence (LIF) measurements in the plume of a liquid-fueled rocket engine are compared with the results predicted by a mathematical model of the plume. Single-shot CARS nitrogen thermometry extensively mapped the temperature profile of the plume. At most positions, high signal success rates were obtained. Success rates were lower during initial runs, while the system was optimized for operation in the rocket environment, and on axis close to the nozzle where the probing laser beams were severely deflected by the plume. For each position studied, the spectra taken were fitted for temperature and a mean temperature and standard deviation calculated from the results. The mean temperatures were compared with predicted temperature values obtained from a marching procedure parabolic computer program. CARS spectra from water vapor in the plume were also recorded and fitted for temperature and concentration. Excellent agreement between theory and experiment was obtained. Results showed a strong positive correlation between water vapor concentration and temperature at each measurement position - some contributions to this may arise from similarities of the effects of temperature and concentration on spectral shape. However, shear layer mixing and entrainment of cold gas into the plume may significantly affect the composition and temperature of the plume gases. LIF was used to visualize the plume structure. Imaging of the flow field was performed by detecting sodium fluorescence, after the oxidant was seeded with sodium. Images were obtained without excessively high background levels and large fluctuations in the plume structure were observed. This is consistent with the observations from the CARS experiments.

10A905. **Dynamic burning rate measurements of metalized composite propellants using the laser-recoil technique.** - MQ Brewster, MH Hites, SF Son *(Dept of Mech and Indust Eng, Univ of Illinois, Urbana IL 61801)*. Combust Flame 94(1-2) 178-190 (Jul 1993).

The combustion mechanism of metalized AP-HTPB-Al composite propellants have been investigated using a newly developed pulsed laser-recoil technique to measure dynamic propellant burning rate. The results demonstrate that aluminum has a stronger influence on the combustion of AP-HTPB propellants than is indicated by the small changes observed in macroscopically steady burning rate or the mean burning rate during macroscopically unsteady burning. The addition of 18% Al in AP-HTPB propellant causes only a 10% increase in the mean burning rate at 1 atm pressure but a 300% increase in the amplitude of the laser-perturbed fluctuating component of the burning rate at 40Hz. The prominent resonance observed at 40 Hz does not correspond to the classical thermal conduction-relaxation mechanism but appears to be related to the processes of unsteady accumulation, agglomeration, ignition, and departure of aluminum at the burning surface of the propellant. It was also found that a small quantity (1%) of chopped Kevlar fibers effectively damped the 40 Hz resonance and increased the steady burning rate at pressures below 5.4 MPa (800 psia). These observations are attributed to a flame-holding effect of the Kevlar fibers which protrude through the surface of the propellant and anchor the partially premixed, leading edge flame near the propellant surface.

418. Prime movers and propulsion

10A906. **Radial-piston gas engine for transformation of low-potential thermal energy.** - VI Ivlev and GV Kreinin *(Moscow, Russia)*. J Machinery Manuf Reliab 6 8-12 (1992).

The problem of transformation of low-potential thermal energy into mechanical work with the help of a radial-piston gas engine working on $LaNi_5$-H_2 heated and cooled by warm and cold water flows respectively, is considered. Experimental data on the dynamic characteristics of a thermosorption source are used for deriving relationships describing the pressure and temperature variations within the engine's working chambers. The mechanical and power characteristics and exergetic efficiency of the engine are estimated and compared with those of a nitinol thermal engine designed for analogous purposes.

10A907. **Advanced pogo stability analysis for liquid rockets.** - BW Oppenheim and S Rubin *(Vehicle and Control Syst Div, Aerospace Corp, El Segundo CA 90245)*. J Spacecraft Rockets 30(3) 360-373 (May-Jun 1993).

An advanced modeling method for determining engine-coupled Pogo oscillation modes, with general applicability to any liquid rocket vehicle, is presented. The modes result from interaction of structural vibrations with pressure and flow oscillations in the liquid propulsion system. A time-invariant linearized mathematical model of the system is developed for a selected flight time. Perturbations of the propulsion system are modeled using FE representations for its physical elements (such as flow duct, pump, accumulator, and thrust chamber), each of which undergoes structural motion described in terms of the vibration modes of the overall vehicle. The structural modes, developed in a separate analysis, are determined with the fluids frozen in place in the feedlines and engines and involve motions of the propulsion elements. The system equations are written in a homogeneous second-order matrix form in the Laplace domain, yielding coefficient matrices that are all complex, unsymmetric, and singular. The major advances are 1) rigorous treatment of arbitrary translational motions of the vessels through which the fluids flow, including all forces (pressure area, inertial, and momentum) that react on the structural system, and 2) a powerful numerical eigensolver that yields eigenvalues and eigenvectors directly, without requiring elimination of dependent fluid state variables (pressure and flows).

10T908. **Development and flight history of the SERT II spacecraft.** - WR Kerslake and LR Ignaczak *(NASA Lewis Res Center, Cleveland OH 44135)*. J Spacecraft Rockets 30(3) 258-290 (May-Jun 1993).

VII. EARTH SCIENCES

452. Porous media

10A909. **Flow over a highly porous inclined bed under surface traction: Boundary layer in the porous region.** - HS Guha *(Dept of Math, Taki Government Col, India)* and TK Chaudhury *(Dept of Math, Univ of Burdwan, Burdwan 713 104, India)*. Int J Eng Sci 31(8) 1191-1196 (Aug 1993).

The flow of viscous incompressible fluid over an inclined highly porous bed due to a uniform surface traction acting for a finite interval of time is investigated where the flow within the porous bed is taken to be governed by the Brinkman's equation. The growth of boundary layer thickness within the porous region due to surface traction is studied for different permeabilities. Equivalence of Darcy's law with slip-flow hypothesis (B-J condition) and Brinkman's equation with rigorous (physically realistic) boundary condition for the flow in the free-fluid region is established and the justification for using Darcy's law for flow in the porous region with small permeability is found from the boundary layer growth curves.

10A910. Mechanical model of lung parenchyma as a two-phase porous medium. - P Kowalczyk *(Inst of Fund Tech Res, Polish Acad of Sci, ul Swietokrzyska 21, 00-049 Warsaw, Poland)*. Transport Porous Media 11(3) 281-295 (Jun 1993).

The anatomy and geometry of the lung at the micro- and macroscopic level have been described briefly. A notion of lung parenchyma - a macroscopically continuous medium whose mechanical properties result from those of microstructural components - has been adapted. Simplifying assumptions propounded in the constitutive model have been discussed. Two phases have been distinguished in the medium: the solid phase - a highly deformable, nonlinearly elastic skeleton in the form of a thin-walled tissue structure on the micro-scale - and the fluid phase - perfect gas (air) filtrating through the structure. General constitutive relations for both phases and their mechanical interactions have been formulated. Further, the fundamental set of differential equations of the quasi-static coupled problem has been developed. Large deformations, material nonlinearities, and dependence of permeability on skeleton deformation have been included. Matrix formulation of the problem has been presented from the point of view of the FEM. An implicit time integration scheme has been proposed. The algorithm has been illustrated with results of simple numerical tests.

10A911. Use of conventional cocurrent and countercurrent effective permeabilities to estimate the four generalized permeability coefficients which arise in coupled, two-phase flow. - RG Bentsen *(Dept of Mining, Metall and Pet Eng, Univ of Alberta, Edmonton, AB, T6G 2G6, Canada)* and AA Manai *(Apex Energy Consult, Calgary, AB, T2P 3P2, Canada)*. Transport Porous Media 11(3) 243-262 (Jun 1993).

In the case of coupled, two-phase flow of fluids in porous media, the governing equations show that there are four independent generalized permeability coefficients which have to be measured separately. In order to specify these four coefficients at a specific saturation, it is necessary to conduct two types of flow experiments. The two types of flow experiments used in this study are cocurrent and countercurrent, steady-state permeability experiments. It is shown that, by taking this approach, it is possible to define the four generalized permeability coefficients in terms of the conventional cocurrent and countercurrent effective permeabilities for each phase. It is demonstrated that a given generalized phase permeability falls about midway between the conventional, cocurrent effective permeability for that phase, and that for the countercurrent flow of the same phase. Moreover, it is suggested that the conventional effective permeability for a given phase can be interpreted as arising out of the effects of two types of viscous drag: that due to the flow of a given phase over the solid surfaces in the porous medium and that due to momentum transfer across the phase 1-phase 2 interfaces in the porous medium. The magnitude of the viscous coupling is significant, contributing at least 15% to the total conventional cocurrent effective -ability for both phases. Finally, it is the nontraditional generalized which arise out of viscous couplin equal one another, even when t' is unity and the surface tension

10A912. Viscous coupling in two-phase flow in porous media and its effect on relative permeabilities. - R Ehrlich *(Chevron Oil Field Res, PO Box 446, La Habra CA 90633)*. Transport Porous Media 11(3) 201-218 (Jun 1993).

An idealized model of a porous rock consisting of a bundle of capillary tubes whose cross-sections are regular polygons is used to assess the importance of viscous coupling or lubrication during simultaneous oil-water flow. Fluids are nonuniformly distributed over tubes of different characteristic dimension because of the requirements of capillary equilibrium and the effect of interfacial viscosity at oil-water interfaces is considered. With these assumptions, we find that the importance of viscous coupling depends on the rheology of the oil-water interface. Where the interfacial shear viscosity is zero, viscous coupling leading to a dependence of oil relative permeability on oil-water viscosity ratio for viscosity ratios greater than one is important for a range of pore cross-section shapes and pore size distributions. For nonzero interfacial shear viscosity, viscous coupling is reduced. Using values reported in the literature for crude oil-brine systems, we find no viscous coupling.

10A913. Bifurcation of plane voidage waves in fluidized beds. - MF Goz *(Kernforschungszentrum Karlsruhe, Inst for Neutronenphys and Reaktortech, Pf 3640, W-7500 Karlsruhe 1, Germany)*. Physica D 65(4) 319-351 (15 Jun 1993).

A 2D fluidized bed model is investigated from a bifurcation point of view. It is shown that bifurcation to periodic travelling waves occurs when the basic state of uniform fluidization becomes unstable. The nature of these waves may be 1- or 2D. Here the main focus is on the bifurcation of oblique travelling waves, ie, plane voidage waves propagating into various directions in space. These waves can be described by a 2D dynamical system, which can be analysed extensively using phase plane methods. Several stationary and periodic solutions as well as homoclinic and heteroclinic orbits are shown to exist in the model studied.

10A914. Penetration of jets into fluidized beds. - PE Roach *(Inst of Fluid Dyn and Heat Transfer, Tech Univ, A-1040 Vienna, Austria)*. Fluid Dyn Res 11(5) 197-216 (May 1993).

The present paper is concerned with the penetration of jets into fluidized beds. Simple models are developed and compared with data from the author's experiments and those from the literature. Differentiation is made between three jet flow regimes: jetting, bubbling, and the transition between these two. Jet penetration length is found to increase as the orifice gas velocity increases, and the rate of increase is a function of the particular flow regime. This appears to be one of the main reasons for the large disagreement between the various correlations available in the literature. It is also found that the bed gas velocity has a first-order effect on the jet penetration length, something which is overlooked by most correlations in the literature. A simple analysis has been used successfully to define the extent of the transition zone.

10A915. Results on the nonlinear theory of dipolar porous elastic solids. - M Ciarletta *(Dept dell'Ingegneria dell'Informazione e Matematica Applicata, Univ Salerno, 84100 Salerno, Italy)* and A Scalia *(Dept Matematica, Univ Catania, Viale A Doria n-6-I, 95125 Catania, Italy)*. Int J Eng Sci 31(8) 1165-1172 (Aug 1993).

In this paper we establish some uniqueness and existence results in the framework of the nonlinear theory of porous elastic solids with microstructure.

10A916. Pressure transient response of stochastically heterogeneous fractured reservoirs. C Braester *(Dept of Civil Eng, Technion, Haifa 2000, Israel)* and DG Zeitoun *(Dept of Mech and Civil Eng, Univ of Vermont)*. Transport Porous Media 11(3) 263-280 (Jun 1993).

A stochastic model for flow through inhomogeneous fractured reservoirs of double porosity, based on Barenbiatt *et al's* continuum approach, is presented. The fractured formation is conceptualized as an interconnected fracture network surrounding porous blocks, and amenable to the continuum approach. The block permeability is negligible in comparison to that of the fractures, and therefore the reservoir permeability is represented by the permeability of the fracture network. The fractured reservoir inhomogeneity is attributed to the fracture network, while the blocks are considered homogeneous. The mathematical model is represented by a coupled system of partial differential random equations, and a general solution for the average and for the correlation moments of the fracture pressure are obtained by the Neumann expansion (or Adomian decomposition). The solution for pressure is represented by an infinite series and an approximate solution for radial flow, is obtained by retaining the first two terms of the series. The purpose of this investigation is to get an insight on the pressure behavior in inhomogeneous fractured reservoirs and not to obtain type curves for determination of reservoir properties, which owing to the nonuniqueness of the solution, is impossible. For the present analysis it is assumed an ideal reservoir with cylindrical symmetric inhomogeneity around the well. Fractured rock reservoirs being practically inhomogeneous, it is of interest to compare the pressure behavior of such reservoirs, with Warren and Roots's solution for (ideal) homogeneous reservoirs, used as a routine for determining the fractured reservoir characteristic parameters λ and ω, using the results of well tests. The comparison of the results show that inhomogeneous and homogeneous reservoirs exhibit a similar pressure behavior.

10A917. Darcy-Forchheimer natural, forced and mixed convection heat transfer in non-Newtonian power-law fluid-saturated porous media. - AV Shenoy *(Dept of Energy and Mech Eng, Shizuoka Univ, 3-5-1 Johoku, Hamamatsu 432, Japan)*. Transport Porous Media 11(3) 219-241 (Jun 1993).

The governing equation for Darcy-Forchheimer flow of non-Newtonian inelastic power-law fluid through porous media has been derived from first principles. Using this equation, the problem of Darcy-Forchheimer natural, forced, and mixed convection within the porous media saturated with a power-law fluid has been solved using the approximate integral method. It is observed that a similarity solution exists specifically for only the case of an isothermal vertical flat plate embedded in the porous media. The results based on the approximate method, when compared with existing exact solutions show an agreement of within a maximum error bound of 2.5%.

See also the following:

10A115. Directional attenuation of SH waves in anisotropic poroelastic inhomogeneous media

454. Geomechanics

454D. SEISMOLOGY

10A918. "Pull up and "push down" effects is seismic reflection:. A useful constraint. - J Dyment *(Inst Physique du Globe CNRS URA 323, Univ Louis Pasteur, 5 rue R Descartes, 67084 Strasbourg Cedex, France)* and M Bano *(Ndermarrja Gjeofizike, Qendra e Perpuimit Sizmik, Fier, Albania)*. Geophys Trans 37(4) 279-295 (Mar 1993).

"Pull up" and "push down" effects are commonly observed in seismic sections. These fictitious deformations of seismic reflections under local velocity anomalies can, if they are not identified, lead to misinterpretation of seismic sections. However, in some cases and using simplifying assumptions, these effects can provide a useful constraint in the estimation of the seismic velocities and therefore help interpretation in complex areas. Two examples are presented: the first displays a distinct "pull up" effect related to the high seismic velocities associated with a salt diapir, the second shows a significant "push down" effect related to the low velocity of sedimentary basins.

10A919. Effects of transverse isotropy on P-wave AVO for gas sands. - Ki Young Kim *(Marine Tectonics Lab, Korea Ocean R&D Inst, Ansan PO Box 29, Seoul 425-600, Korea)*, KH Wrolstad, F Aminzadeh *(Seismic Res and Appl Div, Unocal, 376 S Valencia Ave, Brea CA 92621)*. Geophys 58(6) 883-888 (Jun 1993).

Velocity anisotropy should be taken into account when analyzing the amplitude variation with offset (AVO) response of gas sands encased in shales. The anisotropic effect on the AVO of gas sands in transversely isotropic (TI) media are reviewed. Reflection coefficients in TI media are computed using a plane-wave formula based on ray theory. We present results of modeling special cases of exploration interest having positive reflectivity, near-zero reflectivity, and negative reflectivity.

10A920. Elastic waves through a simulated fractured medium. - Chaur-Jian Hsu *(Schlumberger-Doll Res, Old Quarry Rd, Ridgefield CT 06877-4108)* and M Schoenberg *(Schlumberger Cambridge Res, Madingley Rd, Cambridge CB3 0EL, UK)*. Geophys 58(7) 964-977 (Jul 1993).

Ultrasonic velocities were measured on a block composed of lucite plates with roughened surfaces pressed together with a static normal stress to simulate a fractured medium. The measurements, normal, parallel, and oblique to the fractures, show that for wavelengths much larger than the thickness of an individual plate, the block can be modeled as a particular type of transversely isotropic (TI) medium that depends on four parameters. This TI medium behavior is the same as that of an isotropic solid in which are embedded a set of parallel linear slip interfaces, specified by (1) the excess compliance tangential to the interfaces and (2) the excess compliance normal to the interfaces. At all static stress levels, we inverted the data for the background isotropic medium parameters and the excess compliances. The background parameters obtained were basically independent of stress level and agreed well with the bulk properties of the lucite. The excess compliances decreased with increasing static closing stress, implying that increasing static stress forces asperities on either side of a fracture into greater contact, gradually eliminating the excess compliance that gives rise to the anisotropy. A medium with such planes of excess compliance has been shown, theoretically, to describe the behavior of a medium with long parallel joints, as well as a medium with embedded parallel microcracks.

10A921. Propagation of a nonlinear seismic pulse in an anelastic homogeneous medium. - DW Kosik *(Butler Univ, 4600 Sunset Ave, Indianapolis IN 46208)*. Geophys 58(7) 949-963 (Jul 1993).

Seismic surveys are often conducted using dynamite charges buried near the surface in unconsolidated material. In such material a large zone near the source should exist wherein nonlinear anelastic wave propagation, can be expected to take place, and have a significant impact on the way in which a seismic pulse forms and how its energy gets distributed into the surrounding medium. To obtain a solution for a propagating pulse in this zone, the equations of motion for nonlinear anelastic wave propagation, good to second order in the displacements, are solved numerically for the problem of a Gaussian pressure pulse acting on the interior cavity of a cylindrically symmetric hole in the medium. An implicit finite-difference algorithm is used for the solution to the equations of motion for this problem. The anelastic medium is characterized by multivalued stress-strain relations that exhibit hysteresis, and therefore a loss of energy per cycle, corresponding to a medium with a constant Q factor. Several numerical examples are calculated contrasting the nonlinear anelastic, linear anelastic, and linear elastic propagating pulses to one another. The nonlinear anelastic propagating pulse is found to have an amplitude that is several times larger than would be expected for a pulse in a linear medium and has a peak propagation velocity that is slightly less than that for a linear pulse. Dispersive effects are also evident for the nonlinear pulse.

10A922. Vertical open fractures and shear-wave velocities derived from VSPs, full waveform acoustic logs, and televiewer data. - F Lefeuvre *(TOTAL, 24 Cours Michelet Cedex 47 La Defense 10, 92069 Paris La Defense, France)*, R Turpening, C Caravana, A Born *(Earth Res Lab, MIT)*, L Nicoletis *(Inst Francais du Petrole, BP 311, 92506 Rueil-Malmaison Cedex, France)*. Geophys 58(6) 818-834 (Jun 1993).

Fracture or stress-related shear-wave birefringence (or azimuthal anisotropy) from vertical seismic profiles (VSPs) is commonly observed today, but no attempt is made to fit the observations with observed in-situ fractures and velocities. With data from a hard rock (limestones, dolomites, and anhydrites) region of Michigan, fast and slow shear-wave velocities have been derived from a nine-component zero offset VSP and compared to shear-wave velocities from two full waveform acoustic logs. To represent the shear-wave birefringence that affects the shear wave's vertical propagation, a propagator matrix technique is used allowing a local measurement independent of the over-burden layers. The picked times obtained by using a correlation technique have been corrected in the birefringent regions before we compute the fast and slow velocities. Although there are some differences between the three velocity sets, there is a good fit between the velocities from the shear-wave VSP and those from the two logs. We suspect the formations showing birefringence to be vertically fractured. To support this, we examine the behavior of the Stoneley wave on the full waveform acoustic logs in the formation. In addition, we analyze the borehole televiewer data from a nearby well. There is a good fit between the fractures seen from the VSP data and those seen from the borehole.

454Y. COMPUTATIONAL TECHNIQUES

10A923. Mixed-phase wavelet estimation using fourth-order cumulants. - GD Lazear *(Conoco, 4494 RW PO Box 1267, Ponca City OK 74602-1267)*. Geophys 58(7) 1042-1051 (Jul 1993).

In recent years methods have been developed in the field of high-order statistics that can reliably estimate a mixed-phase wavelet from the noisy output of a convolutional process. These methods use high-order covariance functions of the data called cumulants, which retain phase information and allow recovery of the wavelets. The assumption is that the reflection coefficient series is a non-Gaussian, stationary, and statistically independent random process. The method described in this paper uses the fourth-order cumulant of the data, and a moving-average, noncasual parametric model for the wavelet. The fourth-order moment function of this wavelet matches the fourth-order cumulant of data in the minimum mean-squared error sense. Numerical simulations demonstrate that the method can accurately estimate mixed-phase wavelets, even when the reflectivity has a distribution close to Gaussian. Three seismic data examples demonstrate possible uses of the method. In the first two, an average source wavelet is estimated from marine shot records acquired with air gun and water gun sources, respectively. These wavelets compare favorably with recorded far-field signatures modified for receiver ghosting. In the third example, a wavelet estimate from marine stacked data is used to correct the phase of the stacked section, resulting in zero-phase water bottom and salt top reflections.

10A924. Reasonable choices for material constants in seismic modeling. - JH Rosenbaum *(Bellaire Res Center, Shell Dev, PO Box 481, Houston TX 77001)*. Geophys 58(7) 978-986 (Jul 1993).

In exploration geophysics, the seismic response is often modeled with the assumption that the earth consists of homogeneous formulations that may exhibit transverse isotropy and moderate, "constant Q" attenuation. The geophysicist usually has only incomplete knowledge of the formation characteristics and must make educated guesses at the unknown elastic and absorption parameters. An extension of the long-wavelength-equivalent-medium theory to the anelastic case has been used to derive default options and stability criteria, which require minimal information from the geophysicist, appear reasonable for many earth materials and reduce to a proper description in the case of isotropy. A very simple earth model is used to demonstrate that parasitic modes are excited and the computations can become unstable when the assumed anelastic model parameters violate some stability condition or are inconsistent.

10A925. Sensitivity of prestack depth migration to the velocity model. - R Jan Versteeg *(Dept of Comput and Appl Math, Rice Univ, PO Box 1892, Houston TX 77251-1892)*. Geophys 58(6) 873-882 (Jun 1993).

To get a correct earth image from seismic data acquired over complex structures it is essential to use prestack depth migration. A necessary condition for obtaining a correct image is that the prestack depth migration is done with an accurate velocity model. In cases where we need to use prestack depth migration determination of such a model using conventional methods does not give satisfactory results. Thus, new iterative methods for velocity model determination have been developed. The convergence of these methods can be accelerated by defining constraints on the model in such a way that the method only looks for those components of the true earth velocity field that influence the migrated image. In order to determine these components, the sensitivity of the prestack depth migration result to the velocity model is examined using a complex synthetic data set (the Marmousi data set) for which the exact model is known. The images obtained with increasingly smoothed versions of the true model are compared, and it is shown that the minimal spatial wavelength that needs to be in the model to obtain an accurate depth image from the data set is of the order of 200 m. The model space that has to be examined to find an accurate velocity model from complex seismic data can thus be constrained. This will increase the speed and probability of convergence of iterative velocity model determination methods.

10A926. Shortest path ray tracing with sparse graphs. - R Fischer and JM Lees *(Dept of Geol and Geophys, Yale Univ, Kline Geol Lab, 210 Whitney Ave, New Haven CT 06511-8130)*. Geophys 58(7) 987-996 (Jul 1993).

A technique for improving the efficiency of shortest path ray tracing (SPR) is presented. We analyze situations where SPR fails and provides quantitative measures to assess the performance of SPR ray tracing with varying numbers of nodes. Our improvements include perturbing the ray at interfaces according to Snell's Law, and a method to find correct rays efficiently in regions of low velocity contrast. This approach allows the investigator to use fewer nodes in the calculation, thereby increasing the computational efficiency. In 2D cross-borehole experiments we find that with our improvements, we need only use 2/3 as many nodes, saving up to 60% in time. Savings should be even greater in 3D. These improvements make SPR more attractive for tomographic applications in 3D.

10A927. Three dimensional time-variant dip moveout by the f-k method. - HA Meinardus and KL Schleicher *(Halliburton Geophys Services, PO Box 5019, Sugar Land TX 77487-5019)*. Geophys 58(7) 1030-1041 (Jul 1993).

The standard seismic imaging sequence consists of normal moveout (NMO), dip moveout (DMO), stack, and zero-offset migration. Conventional NMO and DMO processes remove much of the effect of offset from prestack data, but the constant velocity assumption in most DMO algorithms can compromise the ultimate results. Time-variant DMO avoids the constant velocity assumption to create better stacks, especially for steeply dipping events. Time-variant DMO can be implemented as a 3D f-k domain process using the dip decomposition method. Prestack data are moved out with a set of NMO velocities corresponding to discrete values of inline and crossline dips. The dip-dependent NMO velocity is computed to remove the trace offset and azimuth dependence of event times for an arbitrary velocity function of depth. After stacking the moved out CMP gathers, a 3D dip filter is applied to select the particular in-line and crossline dip. The final zero-offset image is obtained by summing all the dip-filtered sections. This process generates a saddle-shaped 3D impulse response for a constant velocity gradient. The impulse response is more complicated for a general depth-variable velocity function, where the response exhibits secondary branches, or triplications, at steeper dips. These complicated impulse responses, including amplitude and phase effects, are implicitly produced by the f-k process. The dip-decomposition method of 3D time-variant DMO is an efficient and accurate process to correct for the effect of offset in the presence of an arbitrary velocity variation with depth. The impulse response of this process implicitly contains complex features like a 3D saddle shape, triplications, amplitude, and phase. Field data from the Gulf of Mexico shows significant improvement on a steep salt flank event.

10A928. Two dimensional velocity inversion-imaging of large offset seismic data via the tau-p domain. - EC Reiter *(Aware, One Memorial Dr, Cambridge MA 02142-1301)*, GM Purdy *(Dept of Geol and Geophys, Woods Hole Oceanog Inst, Woods Hole MA 02543)*, MN Toksoz *(Earth Res Lab, Dept of Earth Atmos and Planet Sci, MIT)*. Geophys 58(7) 1002-1016 (Jul 1993).

We describe a method for determining a 2D velocity field from refraction data that has been decomposed into some function of slowness. The most common decomposition, intercept time-slowness or τ - p, is used as an intermediate step in an iterative wavefield continuation procedure previously applied to 1D velocity inversions. We extend the 1D approach to 2D by performing the downward continuation along numerically computed raypaths. This allows a correction to be made for the change in ray parameter induced by 2D velocity fields. A best fitting velocity model is chosen as a surface defined by critically reflected and refracted energy that has been downward continued in a 3D space of velocity, offset, and depth. Synthetic data are used to demonstrate how this approach can compensate for the effects of known lateral inhomogeneities while determining an underlying 1D velocity field. We also use synthetic data to show how multiple refraction lines may be used to determine a general 2D velocity model. Large offset field data collected with an Ocean Bottom Hydrophone are used to illustrate this technique in an area of significant lateral heterogeneity caused by a sloping seafloor.

10A929. Two-layer stacking procedure to enhance converted waves. - BLN Kennett *(Res Sch of Earth Sci, Austral Natl Univ, Canberra, ACT 0200, Australia)*. Geophys 58(7) 997-1001 (Jul 1993).

For marine seismic sources quite efficient conversion of P-waves to S-waves can occur at hard seafloors, eg, carbonate horizons in tropical waters. The S-waves are reflected back from structures at depth and are reconverted to P-waves in the water before detection by the receiver array. Such PSSP reflections can carry useful information on the structure beneath the sea bed but are most significant at large offsets and so are not easily stacked with a conventional normal moveout (NMO) procedure based on hyperbolic time trajectory. A two-layer stacking procedure that separates the water layer from the region below the seafloor provides a very effective means of extracting the PSSP arrivals, but also works well for P-waves. There is no direct analytic form for the stacking trajectories but they can be calculated quite efficiently numerically. A further advantage is that the stacking velocity for S-waves in the lower layer can be interpreted directly in terms of S-wave propagation, so that S-wave interval velocities can be found. Stacking procedures based on such simple physical models are likely to be useful in other cases where attention needs to be focused on a particular aspect of the wavefield.

10A930. Wave processes in vertically-inhomogeneous media. A new strategy for a velocity inversion. - AS Alekseev, AV Avdeev, AG Fatianov, VA Cheverda *(Comput Center, Siberian Div, Russian Acad of Sci, Novosibirsk 630090, Russia)*. Inverse Prob 9(3) 367-390 (Jun 1993).

This paper describes a closed cycle of mathematical modelling of wave propagation processes. The half-space $z > 0$ is assumed to be filled with a vertically-inhomogeneous medium with the wave propagation velocity $c(z)$. A source located on the free surface $z = 0$ causes the wave process $U(x,y,z,t)$, described by the initial boundary value problem for the wave equation. We consider two main problems: (1) assuming $c(z)$ is known for all z, we wish to calculate the wave field $U(x,y,z,t)$; (2) if $c(z)$ is unknown, we find it using the additional information $U(x,y,t) = U(x,y,0,t)$. In order to solve problem (2) the optimization approach is proposed and verified. Uniqueness and stability of the minimum point of the data misfit functional are proved and convergence if iterative methods for its search is investigated. The search for the minimum point in the domain of space-time frequencies can essentially increase the efficiency of the whole process of finding the velocity $c(z)$.

454Z. EXPLORATIONS AND MEASUREMENTS

10A931. Estimation of near-surface elastic parameters using multicomponent seismic data. - EZ Ata *(INTEVEP, SA Res and Dev Center, Apdo 76343, Caracas 1070A, Venezuela)*, D Corrigan *(ARCO Exploration and Prod Tech, 2300 W Plano Pkwy, Plano TX 75075)*, GA McMechan *(Center for Lithospheric Stud, Univ of Texas at Dallas, PO Box 830688, Richardson TX 75083-0688)*, JE Gaiser *(W Geophys, 7229 S Alton Way, Englewood CO 80112)*. Geophys 58(7) 1017-1029 (Jul 1993).

In multicomponent seismic reflection surveys, surface and near-surface effects can severely deteriorate the quality of reflection data. Such effects are more pronounced on shear-wave than on compressional-wave profiles. Amplitude anomalies, statics, and strong coherent source-generated noise (ie, surface waves) are often associated with inhomogeneous, poorly compacted near-surface sediments of the weathering layer. The magnitude of such effects increases when sources and receivers are deployed or near the surface in proximity to such inhomogeneities. Near-surface effects can be investigated with respect to their depth of occurrence by burying seismic sources and/or receivers at various depths below the inhomogeneous weathering layer. In this context, an experiment was conducted to collect multicomponent seismic field data on a borehole-controlled test site in E Texas. Data were recorded on three-component surface and buried receivers using a full-vector wave-field surface source. Although the geology appears simple, results of modeling one or two components of the field data with synthetics yields nonunique estimates of elastic parameters. Effects of anisotropy and heterogeneities are better identified and estimated with full-wavefield surface and buried receiver observations. Single fold data from buried receivers yield reflection events with higher signal-to-noise ratio than 30-fold CDP surface data previously acquired in the same area.

456. Earthquake mechanics

10A932. Note on attenuation of earthquake intensity in Macedonia. - LS Timiovska *(IZIIS, 9100 Skopje, Macedonia)*. Soil Dyn Earthquake Eng 11(8) 457-463 (1992).

The attenuation of strong shaking is related to the dissipation of earthquake energy. It varies with distance from the epicenter, and depends on the local geological conditions. The 1437 data points have been collected from the Atlas of Isoseismal Maps (Catalogue of Earthquakes) in the UNDP-UNESCO *Survey of the Seismicity of the Balkan Region* (1974) and from unpublished data on seismic intensities in the Balkan region up to 1989. A regression analysis has been performed to describe the attenuation of earthquake intensity in Macedonia in terms of epicentral intensity, I_0, epicentral distance, R, and local geological conditions at the recording site, s (s = 0, 1, or 2 for soft, medium and hard geological site conditions).

10A933. Nonlinear seismic response of antenna-supporting structures. - E Guevara and G McClure *(Dept of Civil Eng and Appl Mech, McGill Univ, Montreal, PQ, Canada)*. Comput Struct 47(4-5) 711-724 (3 Jun 1993).

In the event of a severe seismic excitation, preservation of essential infrastructures, such as telecommunication facilities, is of high priority. The objective of this paper is to investigate the geometrically nonlinear response of anetnna-supporting guyed towers under earthquake loading. Two guyed towers are analyzed: a 350 ft (107 m) tower with six stay levels and an 80 ft (24 m) mast with only two stay levels. Two horizontal accelerograms are used, El Centro and Parkfield, with each record being scaled to match the elastic design spectra of the 1990 National Building Code of Canada. Elements of response analyzed are: guy tensions, horizontal shears, and displacements and rotations at the tip of the mast. Results indicate that although the absolute values of the dynamic amplifications are well below the limit strength and serviceability criteria for such towers, dynamic interactions between the guy-wires and the mast are important, especially in the vertical direction. Multiple support excitation of the tallest tower also causes additional dynamic effects that are not present when only synchronous ground motion is studied.

10A934. One and 2D maximum softening damage indicators for reinforced concrete structures under seismic excitation. - SRK Nielsen *(Dept of Build Tech and Struct Eng, Univ of Aalborg, DK-9000 Aalborg, Denmark)*, HU Koyluoglu, AS Cakmak *(Dept of Civil Eng and Operations Res, Princeton)*. Soil Dyn Earthquake Eng 11(8) 435-443 (1992).

The maximum softening concept is based on the variation of the vibrational periods of a structure during a seismic event. Maximum softening damage indicators, which measure the maximum relative stiffness reduction caused by stiffness and strength deterioration of the actual structure, are calculated for an equivalent linear structure with slowly varying stiffness characteristics. In the paper, a 1D scalar-valued and a 2D vector-valued maximum softening damage indicator are defined. The 1D damage indicator, defined considering the variation in the first period of the structure, analogous to a SDOF system, is a genuine global damage index representing the average damage throughout the whole structure. The 2D damage indicator is defined considering the variations in the first and second periods, and thus is analogous to an equivalent linear two-dof system. The components of the damage vector can be interpreted as damage indicators for the lower half and the upper half of the structure, hence representing a simple local description of the damage state of the structure. Since statements on the post earthquake reliability should be obtained solely from knowledge of the latest recorded values of the damage indicators above defined, these are required to possess a Markov property. This problem has been investigated based on numerical Monte-Carlo simulations, and it is observed that the Markov assumption of the 1D damage indicator is justified for the mean value of the transition probability function, whereas some deviations are observed for the variance and higher order statistical moments.

10A935. Probabilistic seismic analysis of a steel frame structure. - Hitoshi Seya *(Tech Res Lab, Takenaka, Tokyo, Japan)*, ME Talbott *(Dept of Civil and Operations Res, Princeton)*, HHM Hwang *(Center for Earthquake Res and Info, Memphis State Univ, Memphis TN 38152)*. Probab Eng Mech 8(2) 127-136 (1993).

In this study we present a probabilistic seismic analysis of a steel frame structure to generate fragility curves and to investigate the correlation between the response modification factor and the system ductility factor. As an example, we use a five-story hypothetical steel frame structure located in New York City and designed according to the provisions specified in the ANSI standard A58.1-1982 and the AISC ASD specification. We quantify uncertainties in seismic and structure parameters that define the earthquake-structure system by choosing several representative values for each parameter. Then, by using the Latin hypercube sampling technique, we combine these representative values to establish 18 samples of the earthquake-structure system for probabilistic seismic response analysis. The nonlinear seismic analysis is performed by using the DRAIN-2D computer program.

10A936. Review of reference models for assessing inelastic seismic torsional effects in buildings. - JC Correnza, GL Hutchinson *(Dept of Civil and Env Eng, Univ of Melbourne, Parkville, Vic 3052, Australia)*, AM Chandler *(Dept of Civil and Env Eng, Univ Col, Gower St, London WC1E 6BT, UK)*. Soil Dyn Earthquake Eng 11(8) 465-484 (1992).

This paper reviews the various forms of reference model adopted for studies that evaluate inelastic seismic torsional effects and assess their implications for building design. Both qualitative and quantitative comparisons are presented. The importance of selecting an appropriate reference model in accordance with the above aims is emphasized. It is found that variations in the reference models adopted in analyses of inelastic seismic torsional effects may lead to significant differences in the results obtained and, hence, to the conclusions drawn from such studies. It is demonstrated that accidental torsional effects, as incorporated in code design provisions, result in significant changes to the distribution of element strengths and the inelastic response behavior of symmetric and generalized torsionally balanced reference models. Such changes should be considered when employing such models to evaluate the inelastic response of torsionally unbalanced building systems.

10A937. Seismic energy demands on reinforced concrete moment-resisting frames. - WK Tso *(Dept of Civil Eng and Eng Mech, McMaster Univ, 1280 Main St W, Hamilton, ON, Canada)*, TJ Zhu *(Buckland and Taylor, N Vancouver, BC, Canada)*, AC Heidebrecht *(Dept of Civil Eng and Eng Mech, McMaster Univ, 1280 Main St W, Hamilton, ON, Canada)*. Earthquake Eng Struct Dyn 22(6) 533-545 (Jun 1993).

This paper examines the seismic energy demands on reinforced concrete ductile moment-resisting frames. Three frames having 4, 10 and 18 storeys, representing low, medium and tall frames, were designed to the current Canadian seismic provisions and structural design requirements. Three groups of earthquake records having different frequency contents were selected as input ground motions. The input, hysteretic and damping energies were evaluated for these three frames and correlation was established with other response parameters. The use of equivalent single dof systems to estimate the energy demands on these frames was examined in order to simplify the computational effort. It is shown that the energy demand concept together with the equivalent single dof system is a viable design approach for low-rise frames. Additional research to allow for the higher modal effect is required before the same concept can be extended to medium and tall frames.

See also the following:

10A107. Damped resonant appendages to increase inherent damping in buildings

10A519. Dynamic effects in a saturated layered soil deposit: Centrifuge modeling

458. Hydrology, oceanology, meteorology

10T938. Empirical orthogonal function (EOF) analysis of spatial random fields: Theory, accuracy of the numerical approximations and sampling effects. - I Braud, C Obled *(Inst Mec, LTHE, Grenoble, France)*, A Phamdinhtuan *(Lab LMB-IMAG, Grenoble, France)*. Stochastic Hydrology Hydraul 7(2) 146-160 (1993).

10T939. Bottom friction effects in the combined flow field of random waves and currents. - Y Zhao *(Aeronaut Dept, Imperial Col of Sci Tech and Med, London SW7 2BU, UK)* and K Anastasiou *(Civil Eng Dept, Imperial Col of Sci Tech and Med, London SW7 2BU, UK)*. Coastal Eng 19(3-4) 223-243 (May 1993).

10A940. Energy flux and group velocity in currents of uniform vorticity. - I Brevik *(Div of Appl Mech, Univ of Trondheim, N-7034 Trondheim-NTH, Norway)* and R Sollie *(IKU, SINTEF Group, N-7034 Trondheim, Norway)*. Quart J Mech Appl Math 46(1) 117-130 (Feb 1993).

Linear water waves superimposed on an opposing current varying linearly down to a depth h are investigated. Fluxes of mass, momentum, and energy are calculated. Of main interest is the expression for the energy flux and its possible decomposition into terms in such as way that the contribution from wave energy is clearly shown. Such a decomposition would link the kinematic group-velocity concept to the dynamic concept of velocity of propagation of wave energy. We write the energy flux in a form that generalizes the simple expression found by Brink-Kjaer for the case of a linear current extending down to the bottom. In this expression the term corresponding to the group velocity appears quite naturally, as the energy flux of 'pure wave energy.'

10A941. Generation of a Stoneley-Scholte-Lamb atmospheric surface wave by an acoustic source located in an ocean waveguide. - LA Gasilova, IY Gordeeva, YV Petukhov *(Inst of Appl Phys, Russian Acad of Sci)*. Acoust Phys 39(1) 19-23 (Jan-Feb 1993).

The dispersion properties of a modified Stoneley-Scholte-Lamb surface wave propagating along the interface between an isothermal atmosphere and an ocean wave guide are investigated. The interface is modeled by a homogeneous compressible fluid layer on top of a homogeneous elastic half-space. The frequency dependence of the excitation coefficients of the wave is determined for perturbations of the pressure and particle velocity of the medium in the atmosphere for an underwater point mass source. It is shown that this wave exists only at frequencies below a certain critical frequency, which decreases with increasing depth of the water layer, and that it propagates with supersonic (for air) velocity above another critical frequency and with subsonic velocity below this frequency, which also decreases with increasing depth of the water layer.

See also the following:

10A741. Barotropic flow over finite isolated topography: Steady solutions on the beta-plane and the initial value problem

VIII. ENERGY & ENVIRONMENT

502. Nuclear systems

10A942. Material testing and evaluation from the point of view of the nuclear power plant safety. - P Trampus *(Paks Nucl Power Plant, PO Box 71, Paks H-7031, Hungary)*. Int J Pressure Vessels Piping 55(2) 187-202 (1993).

This paper describes the material testing and evaluation of the nuclear power plant's main components by aging of structural material during normal operation and accidents which affect the material structure. Specific feature of the Hungarian regulation are reported. Some examples of the in-service inspection and reactor pressure vessel surveillance activity at Paks NPP and the documentation system are also reported.

10A943. Role of microstructure in the propagation of ultrasound in bainitic low-alloy steels. - F Bergner, B Kohler, K Popp *(Central Inst for Nucl Res Rossendorf, Dresden O-8051, Germany)*. Int J Pressure Vessels Piping 55(2) 251-260 (1993).

The propagation characteristics of ultrasound in two types of bainitic Cr-Mo-V steels including the Soviet type reactor pressure vessel steel 15Kh2MFA have been examined. In order to find out the factors affecting the sound velocity the steels have been exposed to different heat treatments and to neutron irradiation. It turned out that the sound velocity is considerably changed by tempering but only slightly by neutron irradiation. The effect of tempering can be explained on the basis of the decomposition of retained austenite and carbide precipitation. The main mechanisms of ultrasonic attenuation are Rayleigh scattering at prior austenite grains and thermoelastic absorption in the vicinity of packet boundaries. Both effects have been shown to depend on the orientation relationship between bainitic ferrite and parent austenite.

See also the following:

10A512. Safety analysis of the superconducting magnet system of a next generation tokamak

506. Solar and other energy systems

10A944. CAD of transmission lines. - AH Peyrot *(Univ of Wisconsin, Madison WI 53706)*, EM Peyrot *(Power Line Syst, Madison WI 53705)*, T Carton *(Electricite de France, Paris, France)*. Eng Struct 15(4) 229-237 (Jul 1993).

This paper gives an overview of structural and geometric design concepts for electrical power lines. It presents a new integrated computerized environment for generating new designs or evaluating existing ones. In that environment, productivity can be radically improved and the risk of errors is reduced. New design concepts that achieve greater economy can be implemented. The manner in which such diverse utility groups as surveyors, planners, engineers and CAD technicans interact with each other can be improved. Electrical parameters or power lines are only discussed insofar as they affect the line geometry.

10A945. Guyed structures for transmission lines. - HB White *(PO Box 939 Hudson, PQ, Canada)*. Eng Struct 15(4) 289-302 (Jul 1993).

Guyed structures have become the dominant type for use on transmission lines remote from urban areas or where land use restrictions are prohibitive. All other attributes, including cost of materials, erections and performance are positive and the continuing pace of innovations of types and techniques is adding to their attractions. This review of old and new types and practices illustrates adaptability and some of the many new ideas produced in response to frequently changing demands and conditions.

10A946. Nonlinear FE analysis of latticed transmission towers. - FGA Al-Bermani and S Kitipornchai *(Center for Transmission Line Struct, Dept of Civil Eng, Univ of Queensland, St Lucia, Queensland 4072, Australia)*. Eng Struct 15(4) 259-269 (Jul 1993).

Current design practices for transmission tower structures are based on 3D linear elastic truss analyses and on full-scale testing experience. This paper reviews current practices and presents a nonlinear analytical technique for accurate simulation and prediction of the ultimate strength and behavior of transmission towers under static load conditions. Both geometric and material nonlinearities are accounted for in the analysis. A formex formulation is used for the automatic generation of data that is necessary for the analysis. The behavior of four different full-scale towers is described and the predicted results are compared with tests.

10A947. Optimization methods for transmission line design. - AH Peyrot *(Univ of Wisconsin, Madison WI 53706)*, EM Peyrot *(Power Line Syst, Madison WI 53705)*, A Senouci *(Univ of Wisconsin, Madison WI 53705)*. Eng Struct 15(4) 239-246 (Jul 1993).

The companion paper to this one "CAD of transmission lines" discussed the general parameters considered in the overall design of a line, and presented an integrated and interactive computerized environment for complete engineering of a line. This paper discusses the roles that standardization and optimization can play in the selection of some of the design parameters. It also presents new developments in the two areas where optimization has been used successfully: firstly, a primary optimization of the combination of conductor type, conductor tension, and structure family; and secondly, a secondary optimization for structure spotting.

10A948. Review of dynamic aspects of transmission line design. - BW Smith *(Flint & Neill Partnership, 14 Hobart Pl, London SW1W 0HH, UK)*. Eng Struct 15(4) 271-275 (Jul 1993).

A review of current practice in the UK is pro- ' regarding the dynamic problems associated with conductors, including galloping, wake induced vibrations and vortex excitation. The response of transmission line towers is discussed and the parameters which are of most importance highlighted. The background to the treatment adopted in the UK Code of Practice is described, including the development of the parameter to assess the dynamic sensitivity of towers. This parameter is used to judge whether simplified static procedures may be safely used in design.

10A949. Structural optimization of transmission line conductors. - HB White *(PO Box 939 Hudson, PQ, Canada)*. Eng Struct 15(4) 247-249 (Jul 1993).

Structural optimization of a transmission line requires careful attention to the structural properties of the conductor. In turn, the selection of the most efficient conductor will be governed by the controls or limits of use that are specified. The % rated tensile strength concepts that have guided the industry for the past many decades are slowly being replaced by limits on H/w or the catenary constant, which is itself a good measure of the stress in the outer aluminum wires as well as being an important parameter.

10A950. System reliability analysis of transmission lines. - HJ Dagher and Q Lu *(Dept of Civil Eng, Univ of Maine, Orono ME 04469)*. Eng Struct 15(4) 251-258 (Jul 1993).

Structural system reliability analysis of transmission lines is a useful tool in designing new lines and in evaluating or uprating existing lines. This paper describes a practical approach to estimate the system reliability of existing lines. The problem is divided into two components: firstly, obtaining the reliability of typical supporting structures; and secondly obtaining the reliability of the complete line. The first step may be carried out using standard structural system reliability analysis methods. A number of computer programs are currently available for structural system reliability analysis; those programs which are specifically designed for the reliability analysis of transmission structures are briefly described. It is shown that the reliability of every supporting structure in the line need not be obtained. Only the reliabilities of typical structures are needed. Once this is accomplished, the second step is to estimate the reliability of the entire line. This can be carried out using a simple approximate relationship between the reliability of a fully-utilized supporting structure and the reliability of the complete line. Two numerical examples are used to illustrate how the reliability of a complete line may be estimated.

10A951. Transmission tower development in the UK. - C Lomas *(Natl Grid, Woodbridge Rd, Guildford, Surrey GU1 1EJ, UK)*. Eng Struct 15(4) 277-288 (Jul 1993).

This paper looks back on the development of the lattice steel tower and the use of lattice towers on overhead transmission lines in the UK over the past sixty years. It reviews the current regulations and the National Grid Company's approach to alternative tower types.

514. Environmental mechanics

10A952. Fracture mechanics in modeling of icebreaking capability of ships. - RV Goldstein and NM Osipenko *(Lab on Mech of Strength and Fracture, Mat and Struct, Inst for Prob in Mech, Russian Acad of Sci, Prospect Vernadskogo 101, Moscow 117526, Russia)*. J Cold Regions Eng 7(2) 33-43 (Jun 1993).

The basis of the present paper is the approach suggested previously by the writers. By matching inner and outer solutions, a separate modeling of the deformation and fracture processes in stressed ice covers, taking into account the difference in relevant characteristic geometric and force parameters, is accomplished. In the outer problem, the scale is determined by the channel length; in the inner, by the size of the active fracture zone near the channel tip. A similarity criterion is introduced having the form of a characteristic length that incorporates the fracture toughness. Using this parameter, it is possible to formulate relations for critical loads or dimensions of fracture pieces that are formed in the process of icebreaker-ice-cover interaction. These relations may be derived separately for the inner problem, taking into account matching conditions with the outer problem. The characteristic form of the relation is shown for the case of fracture near an icebreaker hull due to cylindrical bending, taking into account the velocity effect of icebreaker motion. This paper presents a system for choosing modeling parameters for ice fracture using fracture toughness and strength dependencies, salinity, and temperature data for model ice. The data were collected from the ice basin of the Russian Artic and Antarctic Scientific Research Institute.

See also the following:

10A522. Creep response of laterally loaded piles in ice and permafrost

IX. BIOENGINEERING

550. Biomechanics

10A953. Role of liquid crystals in the lubrication of living joints. - BI Kupchinov, SF Ermakov, VG Rodnenkov, SN Bobrysheva, ED Beloenko, VN Kestelman *(Metal-Polymer Res Inst, Belarus Acad of Sci, Gomel 246652, Belarus)*. Smart Mat Struct 2(1) 7-12 (Mar 1993).

This investigation was devoted to the study of a natural phenomenon, low friction in living joints, and development of synthetic lubricants. The experiments conducted allowed us to establish that the known property of synovia to ensure the high antifrictional ability of joint cartilages is provided by the realization of a liquid-crystalline state of the lubricant in the friction zone that was unknown before. An idea was advanced that molecules of liquid-crystalline cholesterol compounds found in synovia are arranged with their longer axis aligned with prevailing microgroove locomotions on cartilage surfaces to make a liquid-crystalline nematic phase, thus reducing energy dissipation during relative motion of contacting cartilages and leading to the medicative effect revealed by experimentation.

10T954. Numerical analysis of steady generalized Newtonian blood flow in a 2D model of the carotid artery bifurcation. - JPW Baaijens, AA Van Steenhoven, JD Janssen *(Dept of Mech Eng, Univ of Tech, Eindhoven, Netherlands)*. Biorheol 30(1) 63-74 (Jan-Feb 1993).

10A955. Planar model for mucociliary transport: Effect of mucus viscoelasticity. - M King, M Agarwal, JB Shukla *(Pulmonary Defense Group, Univ of Alberta, 519 Newton Res Bldg, Edmonton, AB, T6G 2C2, Canada)*. Biorheol 30(1) 49-61 (Jan-Feb 1993).

A planar two-layer fluid model is proposed to study the transport of mucus in the respiratory tracts due to cilia beating and air motion by considering mucus as a viscoelastic fluid. The effect of air motion due to forced expiration and other processes is considered by prescribing shear stress at the mucus-air interface. It is shown that the transport of mucus increases as the pressure drop, shear stress due to air motion and the velocity generated by cilia tips and the serous sublayer increase. Mucus transport also increases as the shear modulus of elasticity decreases. This property is effective only in the presence of pressure drop or air motion. It is noted that the effect of gravity is similar to pressure drop. It is observed that mucus transport decreases as the viscosity of serous layer fluid increases, but any increase at high values of mucus viscosity does not seem to affect the mucus transport. It is also found that for a given total depth of serous and mucus layers, there exists a serous fluid layer thickness for which the mucus transport is maximum. The functional dependence of mucus transport predicted by the model is discussed in relation to experimental observations.

10A956. Study of numerical fluid analysis around a prosthetic heart valve using the finite difference method under steady flow conditions. - Yukiaki Kikuta, Toshio Yuhta, Satoru Igarashi *(Fac of Eng, Hokkaido Univ, N-13 W8 Kita-ku, Sapporo 060)*, Yoshinori Mitamura *(Fac of Eng, Hokkaido Tokai Univ, 5-1 Minaminosawa, Minami-ku Sapporo 005)*, Bu gil Kim *(Med Sch and Hospital, Chonbuk Natl Univ, 2-20 Keum-am Dong, Chonju 560-180, Korea)*. Int J Japan Soc Precision Eng 27(1) 54-60 (Mar 1993).

A simulation would be a very effective method for analysis associated with a prosthetic heart valve. In this paper we developed a simulation program with the finite difference method for fluid analysis under steady flow condition. The numerical fluid analysis that obtained by this analysis program was consistent with the results of flow visualization experiment. By combining the Euler method and the Lagrange method simulated flow visualization of imaged particles is possible. This is effective for an understanding of flow dynamics around prosthetic heart valves.

10A957. Dynamics of bipedal gait Part I. Objective functions and the contact event of a planar five-link biped. - Y Hurmuzlu *(Dept of Mech Eng, S Methodist Univ, Dallas TX 75275)*. J Appl Mech 60(2) 331-336 (Jun 1993).

Previous approaches to the problem of prescribing the motion of bipedal machines do not completely characterize the desired walking patterns in terms of coherent parameters. A well-structured parametric formulation that ties the objective functions to the resulting gait patterns has never been established. This article presents an approach that can be followed to formulate objective functions which can be used to prescribe the gait of a planer, five-element, bipedal automaton during single support phase. The motion of the biped is completely characterized in terms of progression speed, step length, maximum step height, and stance knee bias. Kinematic relations have been derived and the inverse problem has been solved to perform a parametric study that correlates the regions of the 4D parameter space with the respective gait patterns. Major limitations include the assumptions of rigid elements and point contact between the lower limbs and the walking surface. Most importantly, the motion of the biped is assumed to perfectly conform with the objective functions at the instant of contact. The control and stability issues are presented in Part II of this paper.

10A958. Dynamics of bipedal gait Part II. Stability analysis of a planar five-link biped. - Y Hurmuzlu *(Dept of Mech Eng, S Methodist Univ, Dallas TX 75275)*. J Appl Mech 60(2) 337-343 (Jun 1993).

A general approach based on discrete mapping techniques is presented to study stability of bipedal locomotion. The approach overcomes difficulties encountered by others on the treatment of discontinuities and nonlinearities associated with bipedal gait. A five-element bipedal locomotion model with proper parametric formulation is considered to demonstrate the utility of the proposed approach. Changes in the stability of the biped as a result of bifurcations in the 4D parameter space are investigated. The structural stability analysis uncovered stable gait patterns that conform to the prescribed motion. Stable nonsymmetric locomotion with multiple periodicity was also observed, a phenomenon that has never been considered before. Graphical representation of the bifurcations are presented for direct correlation of the parameter space with the resulting walking patterns. The bipedal model includes some idealizations such as neglecting the dynamics of the feet and assuming rigid bodies. Some additional simplifications were performed in the development of the controller that regulates the biped.

552. Human factors, rehabilitation, sports

10A959. Design guide of master arms considering operator dynamics. - Y Yokokohji and T Yoshikawa *(Dept of Mech Eng, Fac of Eng, Kyoto Univ, Kyoto 606, Japan)*. J Dyn Syst Meas Control 115(2A) 253-260 (Jun 1993).

In this paper, a design guide of master arms for teleoperation is discussed. The quality of the master arm design has a considerable influence on the maneuverability of master-slave systems. A quantitative measure of the manipulative ability of master arms is proposed, and is obtained by extending the concept of the dynamic manipulability. It is pointed out that the directional property of the manipulability ellipsoid in the work space is an important factor. A second quantitative measure is proposed which evaluates the similarity of the manipulability ellipsoids produced by two situations – when the operator maneuvers the master arm and when he has no payload. Numerical examples and several guidelines for master arm design are shown.

10A960. Human centered control in robotics and consumer product design. - H Asada *(Center for Info-Driven Mech Syst, Dept of Mech Eng, MIT)*, CC Federspiel *(Johnson Controls, Milwaukee WI)*, Sheng Liu *(Center for Info-Driven Mech Syst, Dept of Mech Eng, MIT)*. J Dyn Syst Meas Control 115(2B) 271-280 (Jun 1993).

Human factors in the control and programming of robots and electric appliances are addressed in this paper. Systems and control techniques for the enhancement of human-machine communication as well as learning and adaptation to human needs are described with exemplary case studies. First, fundamental issues and methodologies, as well as historical perspective of relevant fields, are summarized, and two case studies are then discussed. One is user-adaptable control of air conditioners, a new type of adaptive control that allows an air conditioner to learn the thermal preference of the user. The other is a user-friendly programming method for advanced robot control. A task-level adaptive control system is developed by acquiring control skills by direct communication with human experts. The importance of human-machine communication and its impact on product development are addressed from the systems and control point of view.

10A961. Human extenders. - H Kazerooni *(Mech Eng Dept, UCB)* and J Guo *(Inst of Naval Architec and Ocean Eng, Natl Taiwan Univ, Taipei, Taiwan, ROC)*. J Dyn Syst Meas Control 115(2B) 281-290 (Jun 1993).

A human's ability to perform physical tasks is limited by physical strength, not by intelligence. We coined the word "extenders" as a class of robot manipulators worn by humans to augment human mechanical strength, while the wearer's intellect remains the central control system for manipulating the extender. Our research objective is to determine the ground rules for the control of robotic systems worn by humans through the design, construction, and control of several prototype experimental direct-drive and non-direct-drive multi-dof hydraulic-electric extenders. The design of extenders is different from the design of conventional robots because the extender interfaces with the human on a physical level. The work discussed in this article involves the dynamics and control of a prototype hydraulic 6-dof extender. This extender's architecture is a direct drive system with all revolute joints. Its linkage consists of two identical subsystems, the arm and the hand, each having 3-dof. Two sets of force sensors measure the forces imposed on the extender by the human and by the environment (ie, the load). The extender's compliances in response to such contact forces were designed by selecting appropriate force compensators. The stability of the system of human, extender, and object being manipulated was analyzed. A mathematical expression for the extender performance was determined to quantify the force augmentation. Experimental studies on the control and performance of the experimental extender were conducted to verify the theoretical predictions.

Author Index for October 1993

The codes after each name give the sequence numbers of the items in the Book Reviews section (R = Review, N = Note) or the Journal Literature section (A = Abstract, T = Title). Books listed by title only or as "under review" are not included in this index.

N

O

P

Q

R

S

T

U

V

W

X

Y

Z

Statement of Ownership, Management and Circulation

APPLIED MECHANICS REVIEW

MONTHLY

TWELVE

345 East 47th Street, New York, NY 10017

The American Society of Mechanical Engineers, 345 East 47th Street, New York, NY 10017

Donna Thompson, ASME, 345 East 47th Street, New York, NY 10017

The American Society of Mechanical Engineers

Circulation Manager

APPLIED MECHANICS REVIEWS REPRINTS

Mechanics Pan-America 1991 (Proc PACAM-2, Valparaiso, Chile, Jan 1991). PA Kittl and DT Mook (eds). AMR 44(11) Part 2 (Nov 1991) Reprint No AMR106 $88

Structural and dynamic behavior of pretwisted rods and beams. A Rosen. AMR 44(12) Part 1, 483-516 (Dec 1991) Reprint No AMR102 $26

Hydroacoustics of transitional boundary-layer flow. GC Lauchle. AMR 44(12) Part 1, 517-531 (Dec 1991) Reprint No AMR103 $16

Index to Volume 44 (1991). Reprint No AMR108 $88

Stress minimum forms for elastic solids. LT Wheeler. AMR 45(1), 1-12 (Jan 1992) Reprint No AMR 107 $14

Micromechanics of composite materials. Special collection edited by AN Guz. AMR 45(2) 13-101 (February 1992) Reprint No AMR104 $54: (1) **Statics of laminated and fibrous composites with bent structures.** SD Akbarov and AN Guz. (2) **Dynamics of laminated and fibrous composites.** AN Guz and NA Shulga. (3) **Stability of fibrous composites.** IY Babich and AN Guz. (4) **Stability of laminated composites.** AN Guz and VN Chekhov.

Microbubble drag reduction in liquid turbulent boundary layers. C Merkle and S Deutsch. AMR 45(3) Part 1, 103-127 (March 1992) Reprint No AMR105 $22

Material Instabilities (22nd Midwestern Mechanics Conference, Rolla MO, Oct 1991) HM Zbib, TG Shawki, RC Batra (eds). AMR 45(3) Part 2 (March 1992) Reprint No AMR110 $66

Heat-transfer control: Principal focus on Japanese Research. T Aihara. AMR 45(4) 129-153 (April 1992) Reprint No AMR109 $16

Optimum dimensions of extended surfaces operating in a convective environment. A Aziz. AMR 45(5) 155-173 (May 1992) Reprint No AMR111 $18

Overview of micro heat pipe research and development. GP Peterson. AMR 45(5) 175-189 (May 1992) Reprint No AMR112 $16

Multiphase poroelastic finite element models for soft tissue structures. BR Simon. AMR 45(6) 191-218 (June 1992) Reprint No AMR114 $22

Dynamics and control of coherent structures in turbulent jets. RR Mankbadi. AMR 45(6) 219-248 (June 1992) Reprint No AMR113 $24

Addendum to: Bibliography of monographs and surveys on shells. W Pietraszkiewicz. AMR 45(6) 249-250 (June 1992) Reprint No AMR115 (free with AMR078 $14)

Romanian sources on applied mechanics. ME Popescu. AMR 45(6) 251-252 (June 1992) Reprint No AMR116 no charge.

Fluorescence thermometry. LJ Dowell. AMR 45(7) 253-260 (July 1992) Reprint No AMR117 $12.00

Micromechanical modelling of quasi-brittle materials behavior. VC Li (ed), 10 articles. AMR 45(8) 261-398 (Aug 1992) Reprint No AMR118 $60.

Recent developments in the force method of structural analysis. A Kaveh AMR45(9) 401-418 (Sep 1992) Reprint No AMR119 $18.

Computational models for high-temperature multi-layered composite plates and shells. AK Noor and WS Burton. AMR 45(10) 419-446 (Oct 1992) Reprint No AMR 120 $22.

Dynamics of periodic and near-periodic structures. Dong Li and H Benaroya. AMR 45(11) 447-460 (Nov 1992) Reprint No AMR121 $16.

Finite element analysis of aeroelasticity of plates and shells. MN Bismarck-Nasr. AMR 45(12) 461-482 (Dec 1992) Reprint No AMR122 $20.

Index to Volume 45 (1992). Reprint No AMR123 $88

Mathematical modeling of transport phenomena during alloy solidification. C Beckermann and R Viskanta. AMR 46(1) 1-28 (Jan 1993) Reprint No AMR124 $22.

Perturbation techniques in phase change heat transfer. A Aziz and VJ Lunardini. AMR 46(2) (Feb 1993) Reprint No AMR125 $28.

US machining and grinding research in the 20th century. R Komanduri, ME Merchant, MC Shaw. AMR 46(3) (Mar 1993) Reprint No AMR 126 $42

Nondestructive testing and structural condition monitoring of mechanical cables. PAA Laura. AMR 46(4) 133-138 (Apr 1993) Reprint No AMR127 $12.

Aging of energy production and distribution systems: DOE Workshop, Rice University, Houston TX, October 11-13, 1992. Edited by MM Carroll and PD Spanos. AMR 46(5) 139-263 (May 1993) Reprint No AMR128 $78.

Applied mechanics of a lunar base. Edited by H Benaroya. AMR 46(6) 265-358 (June 1993) Reprint No AMR129 $65.

Chaos and noise in dynamical systems. Edited by T Kapitaniak and J Brindley. AMR 46(7) 359-444 (July 1993) Reprint No AMR130 $59.

Boundary integral equations in aerodynamics. L Morino. AMR 46(8) 445-466 (August 1993) Reprint No AMR131 $20.

Vibrations of planar curved beams, rings, and arches. P Chidamparam and AW Leissa. AMR 46(9) 467-483 (Sep 1993) Reprint No AMR132 $20.

Thermal buckling of plates and shells. ER Thornton. AMR 46(10) 485-506 (Oct 1993) Reprint No AMR 133 $20.

Subscription: ASME members (without Suppl.) $51 $_____

ASME members (with Supplement) $84 $_____

non-members (with Supplement) $534 $_____

2nd library subscription $99 $_____

Postage outside USA or Canada $102, airmail $156 $_____

Reprint No:	*Reprint title:*	
________	________	$_____
________	________	$_____
________	________	$_____
	TOTAL ORDER:	$_____

ASME member prices for reprints (50% of list) apply to the purchase of 1 copy of any reprint for the member's personal use with shipment to his or her personal attention. *Bulk reprint prices:* $215 for 100 copies of an article of up to 8 pages, plus $85 for each additional 4 pages (add $25 and $5, respectively, for each additional 100 copies). *Ordering information:* Advance payment required if billed outside USA or Canada. Foreign and Canadian checks not accepted unless payable in US dollars through a US bank. CA, GA, IL, TX purchasers must add sales tax, Canadians 7% GST, or furnish tax exemption certificate.

Send order to: **ASME/AMR**
22 Law Drive, PO Box 2900
Fairfield NJ 07007-2900

or FAX form to: 1-201-882-5155

ASME members, to receive discount you must indicate your membership no.: ________

ASME Member Name: ________

Signature: ________

METHOD OF PAYMENT (check one):

[ ] Payment enclosed

[ ] Purchase Order No.: ________
(attach Purchase Order)

[ ] Charge card (circle one): Master Card VISA American Express Diners Club Discover

Account Number: ________

Mastercard Interbank No: ________

Expiration Date: ________

Signature: ________

BILL TO: Name: ________
Company: ________
Street address: ________
City, State, ZIP: ________
Country: ________

SHIP TO: Name: ________
Company: ________
Street address: ________
City, State, ZIP: ________
Country: ________

applied mechanics reviews

AIMS

The primary aim of *AMR* is to serve engineering scientists worldwide by assessing, reviewing, and reporting on advances in a broad range of mechanical engineering sciences. To this end *AMR* publishes (i) state-of-the-art review articles, bibliographic surveys, reviews with a special focus on emerging technology, tutorials, historical perspectives, periodic summaries of trends and advances; (ii) critical reviews of books, software, and databases; (iii) indexed compilations of carefully selected abstracts from high quality research journals; (iv) book-length monographs and symposium proceedings as special issues or supplements; and (v) editorials, announcements, and letters-to-the-editor.

A secondary aim of *AMR* is to serve technical and reference librarians, information specialists, professional engineers, and college professors through reliable, comprehensive, and timely information about all types of books within its subject scope. The annual cumulative index issue of *AMR* together with its monthly classified listings of abstracts is in effect a comprehensive bibliography of the mechanical engineering sciences, including essentially every article in some 50-60 core journals; this core includes all ASME Transaction journals.

SCOPE

The scope of *AMR* encompasses all the engineering sciences represented in the journals and symposia sponsored by the American Society of Mechanical Engineers and is outlined by *AMR*'s Subject Classification Scheme, which is reprinted on the back cover. It includes basic discipline-oriented areas such as dynamics, continuum mechanics, solid and fluid mechanics, structures, heat transfer, tribology, geomechanics, and biomechanics, as well as cross-disciplinary subjects and emerging critical technological areas such as new numerical and computational techniques, systems control technology, engineering design tools, manufacturing technology, materials and energy technology, and environmental engineering.

The American Society of Mechanical Engineers

INFORMATION FOR AUTHORS OF REVIEW ARTICLES

(1) Prospective authors are strongly urged to communicate with one of the Associate Editors or the Editor-in-Chief, Professor Arthur W Leissa, Department of Engineering Mechanics, Ohio State University, 155 W Woodruff Ave, Columbus, Ohio 43210 (TEL 614-457-4337 or 614-292-2680) before submitting an article, and to furnish a one-page outline of the proposed article and information as to its type, audience, and probable length. A form, *Prospectus for a Review Article*, is available for this purpose. Refer to the editorials in the January 1985 and March 1991 issues of *AMR* and the box at left for further discussion of *AMR*'s editorial criteria.

(2) *Submit four clean copies* of the manuscript to one of the Associate Editors or to the Editor-in-Chief. (Hold all separate original artwork until the article has been accepted.) All articles will be reviewed critically by at least two independent and anonymous referees chosen by the editor involved. This procedure will be followed even if the article is the result of solicitation or encouragement by the editors, or if the author is also an *AMR* editor. The final decision on publication is made by the Editor-in-Chief upon recommendation of an Associate Editor. If appropriate, the article will carry a footnote saying "Transmitted by Associate Editor . . ."

(3) Submission of a manuscript is a representation that it has not been published previously nor is currently being submitted for publication elsewhere. The authors will be asked to sign a statement *transferring copyright to ASME*. It is the author's responsibility to obtain permission to copy material from other sources, if needed.

(4) There are *no page charges* in *AMR* and no numerical length limitations. The length of the article should be appropriate to the subject and the audience. It is certainly one factor that will be evaluated by the editors and their referees, who may recommend changes (30-120 manuscript pages is typical). Each author of a review article will receive *a year's free subscription to AMR*. After publication the author will receive *100 free reprints* (to be shared if there are more than one author). In addition, ASME will distribute reprints singly and in bulk.

(5) Along with the final *manuscript* send the *compuscript on diskette*, if available, (with format identified) incorporating all corrections and additions, and with the tables and figure captions *in place within the text*. If the figures are computer graphics, place them also within the compuscript where they belong. Also, send a head-and-shoulders *photograph and short biographical sketch* (100-200 words) of each author, including grades of ASME membership, if any; include the bio at the end of the compuscript.

(6) *Order of parts:* Title of article, authors' names, authors' institutional affiliations, abstract (200-300 words suitable for abstracting services), table of contents (only if the article is so long that it needs one), list of symbols and abbreviations (if necessary), main text incorporating tables (each starting with a caption) and figure captions (in place where you want them in the text), list of references, biographical sketch, and original figures (if computer graphics, place in text above captions).

(7) *Format (for details, request Author Kit):* (a) Paper size: A4 or 8.5×11 inch (220×280 mm). (b) Word processor settings: One column of width 3.4 in (87 mm) leaving rest of page for referee and editorial comments; Type size 10 point (72 point = 6 pica = 1 inch = 25.4 mm) Times Roman or similar proportionally spaced style; Line spacing 12 points. These as-printed *AMR* specifications will help to insure that equations, tables, and figures are properly designed for the available space. (c) Use metric SI units; with other units in parentheses, if appropriate. (d) Cite references by last name and year; reference list at end alphabetical by author (in 7-point type). (e) Number figures with arabic numerals; design figures for column width (83 mm or 3.1 in), if possible; they should be professionally drawn or computer generated with lettering of consistent size (not smaller than the printed text after reduction); use your wordprocessor to place an empty box of the correct dimensions (or the figure itself, if a computer graphic) in the text above each figure caption. (f) Number tables with roman numerals. (g) Latin letters used as math symbols should be in italics both in text and in displayed equations. Subscripts and superscripts should be 7 point type. Fractional powers are preferred to root signs, exp(..) to $e^{\cdot\cdot}$, and a solidus (/) for fractions, if that will save vertical space.

(8) *Camera-ready copy:* Typeset (or near-typeset) quality pages or galleys generated by the author (after review and acceptance) are preferred, and could result in faster publication. Reproduce the format of published *AMR* review articles (basically, two of the columns defined above per page). Camera-ready pages along with a diskette (for DOS) is requested. Microsoft Word is suggested. Questions on this should be directed to the Production Editor at 201-882-1170, ext 232.

SPECIAL ISSUES: From time to time Guest Editors are invited to produce Special Issues consisting of three or more articles grouped around a common theme. SUPPLEMENTS are booklength monographs or symposium proceedings published as part 2 of a regular issue. Proposals for Special Issues or Supplements are very welcome. Guest Editorials, Letters-to-the-Editor, Announcements: Contact the Editor-in-Chief.

9/93

MAIN HEADINGS FOR CLASSIFIED JOURNAL LITERATURE

(for full classification scheme and alphabetical index see December issue)

ISSN 0003-6900

JOURNAL CODE AMR

ISSUE CODE 9310

applied mechanics reviews

published by The American Society of Mechanical Engineers

Volume 46, Number 11, Part 1, November 1993

applied mechanics reviews

AN ASSESSMENT OF THE WORLD LITERATURE IN ENGINEERING SCIENCES

Applied Mechanics Reviews (ISSN 0003-6900) is published monthly by the ASME, 345 E 47th St, New York NY 10017. 2nd class postage paid at New York NY and additional mailing offices. **POSTMASTER:** Send address changes to ASME/AMR, 22 Law Drive, Box 2300, Fairfield NJ 07007-2300. **CHANGES OF ADDRESS** must be received at ASME seven weeks before they are to be effective. Send old label and new address. **SUBSCRIPTION PRICES:** $534 (incl Annual Index and Suppl.), single copies $57 (Suppl. or Index $84). Countries outside USA and Canada add $102 for postage ($156 airmail). 2nd library subscription $99. **DISCLAIMER:** "The Society shall not be responsible for statements or opinions ...printed in its publications" (ASME Bylaws B7.1.3).

Printed in the USA. (7/93)

The American Society of Mechanical Engineers

VOLUME 46, NUMBER 11, PART 1, NOVEMBER 1993

BOOK REVIEWS AND NOTES

REVIEW OF THE JOURNAL LITERATURE

EDITORIAL

This is Part I of a two-part issue of *Applied Mechanics Reviews* for November, 1993. Part II is the Annual Supplement which is sent to libraries and other non-member subscribers throughout the world. It is entitled *Mechanics Pan America 1993.*

This year the Annual Supplement consists of 37 technical papers chosen from nearly 200 that were presented at the third Pan American Congress of Applied Mechanics (PACAM III) which took place in São Paulo, Brazil in early January of this year. They were selected by a committee as being among the best of those presented. Authors were invited to extend their short (4 page minimum) papers into full-length ones.

PACAM is an international congress devoted to the full range of areas in mechanics, open to participants from throughout the world. It takes place in the Western Hemisphere every odd-numbered year, in early January, sponsored by the American Academy of Mechanics. PACAM I was held in Rio de Janeiro, Brazil in 1989, and PACAM II in Viña del Mar, Chile in 1991. Annual Supplements of selected and extended papers from those congresses were also published by *Applied Mechanics Reviews.* PACAM IV will take place in Buenos Aires, Argentina, during January 3-6, 1995.

Arthur W Leissa
Editor-in-Chief

TECHNICAL EDITORS WANTED

Applied Mechanics Reviews is seeking qualified applicants for the position of Technical Editor. It is expected to fill one or more new positions during the next six months.

Technical Editors scan journals in their fields of expertise in mechanics and the mechanical engineering sciences and perform two essential functions:

1. Determine which articles are suitable to have their abstracts included in the *Review of the Journal Literature*, which is the primary section in *AMR* each month.

2. Classify each selected abstract in the *AMR* subject classification scheme (main headings are shown on the back cover of each issue; complete classification scheme is listed annually in the December issue).

The work is part-time, typically requiring 3 to 5 hours per week, with pay on an hourly basis. This is an excellent way for a researcher, who can spare the time, to keep up with most of the technical literature in his or her field. It is also an opportunity to be a member of the team which produces *AMR* each month --- Technical Editors, Associate Editors, and Production Staff.

Technical Editors should have at least 10 years of significant research experience beyond the PhD degree. Interested applicants should send a copy of their complete professional résumé and a statement elaborating upon their particular qualifications to:

Professor Arthur W Leissa
Editor-in-Chief
Department of Engineering Mechanics
Ohio State University
155 W Woodruff Ave
Columbus, Ohio 43210

APPLIED MECHANICS REVIEWS BOARD OF ASSOCIATE EDITORS

BOOK REVIEWS

Items with a reviewer byline (coded R) are by AMR's corps of dedicated outside volunteer reviewers. AMR will attempt to get critical reviews of all relevant textbooks, professional books, reference works, and handbooks. Items without a reviewer byline (coded N) are prepared by AMR in-house staff and are largely based on material such as a book's table of contents and editor's preface or foreword. In the interest of timeliness most conference proceedings and multi-author contributed volumes will receive descriptive notes in this fashion. Books deemed to be somewhat peripheral to AMR's basic scope may simply be listed by title (no code; not included in annual index). Also listed by title when first received are books under review.

I. FOUNDATIONS & BASIC METHODS

11N1. **Theoretical and Applied Mechanics 1992.** Proceedings of the 18th International Congress, Haifa, Israel, Aug 22-28, 1992. - Edited by SR Bodner, J Singer, A Solan, Z Hashin. Elsevier, UK. 1993. 492 pp. ISBN 0-444-88889-6. $185.75.

Contained in this volume are the full texts of the invited general and sectional lectures presented at this conference concerning mechanics and its development. The entire field of mechanics is covered, including analytical, solid and fluid mechanics and their applications. A survey of work in the fields of fluid and solid mechanics is also given. The papers are written by leading experts, which is reflected in the quality and diversity of the lectures and posters presented. They will provide a valuable key to the latest and most important developments in the various subfields of mechanics.

Contents include: Preface; Sponsoring organizations and companies; Congress committees; List of participants; Report on the Congress. Opening and Closing Lectures: Instability and turbulence in shear flows by A Roshko; Micromechanics of fracture by GI Barenblatt. Introductory lectures of minisymposia. Instabilities in solid and structural mechanics: Material instabilities and phase transitions in thermoelasticity by R Abeyaratne; Propagating instabilities in structures by S Kyriakides; Computational approaches to plastic instability in solid mechancis by Y Tomita. Sea surface mechanics and air-sea interaction: The role of wave breaking in air-sea interaction by WK Melville; Extreme waves and breaking wavelets by OM Phillips; Effect of wind and water shear on wave instabilities by PG Saffman. Biomechanics: Nature's structural engineering of bone on a daily basis by SC Cowin; Liquid layer dynamics in pulmonary airways by RD Kamm; Energy-saving mechanisms in animal movement by R McN Alexander. Sectional Lectures: Controlling chaotic convection by HH Bau; Application of structural mechanics to biological systems by CR Calladine; Viscous fingering as a pattern forming system by Y Couder; Mechanics in sport by G Grimvall; Aerodynamic sound associated with vortex motions; observation and computation by T Kambe; Nonlinear membrane theory by A Libai; On the role of wave propagation and wave breaking in atmosphere-ocean dynamics by ME McIntyre; Computational aspects of integration along the path of loading in elastic-plastic problems by JB Martin; Constitutive modeling and analysis of creep, damage, and creep crack growth under neutron irridation by S Murakami; Stability and bifurcation in dissipative media by QS Nguyen; Bubble mechanics: luminescence, noise, and two-phase flow by A Prosperetti; Wave propagation in non-isotropic structures by MB Sayir; Self-similar multiplier distributions and multiplicative models for energy dissipation in high Reynolds number turbulence by KR Sreenivasan and G Stolovitzsky; Cardiovascular fluid mechanics by AA van Steenhoven *et al*; Trends in transonic research by J Zierep.

Advanced Formulations in Boundary Element Methods. - Edited by MH Aliabadi and CA Brebbia. Comput Mech, Billerica MA. 1992. 300 pp. ISBN 1-56252-111-X. ASME Book No 08. $144.00. (Under review)

II. DYNAMICS & VIBRATION

11R2. **Turbomachinery Rotordynamics--Phenomena, Modeling & Analysis.** - Dara Childs *(Mech Eng, Texas A&M Univ, College Station TX)*. Wiley, New York. 1993. 476 pp. ISBN 0-471-53840-X. $89.95.

Reviewed by Joseph Motherway (555 Park Shore Dr #213, Naples FL 33940).

This is a professional book which presents analytical techniques and results useful in computer modeling and dynamic design of rotating machines. The author is well known for his extensive research in the dynamic behavior of fluid film bearings, liquid and gas seals, and fluid-structure interaction of rotors.

Curiously, the author divides the book rather unevenly into three parts. The first and third contain only one chapter each; page length is 85 and 26, respectively. The second part consists of six chapters. However, most of its materials, 262 out of 345 pages, is contained in chapters 3-6, covering the author's specialty. This emphasis also makes for uneven coverage of the field described by the title.

Part 1 deals with fundamental rotordynamic phenomena. These are illustrated by examining analytical results for some simple idealized models. This is the sort of material for which the designer must have a qualitative understanding before beginning a development of a simple rotating machine, eg, a single stage horizontal centrifugal pump for commercial application. It would also be useful to an engineer who is beginning to become involved in rotating machine failure analysis.

The second part constitutes the major portion of the book. Chapter 2 is a 45-page review of matrix structural analysis methods, and chapter 7 devotes an additional 36 pages to more advanced aspects of this topic. Together they compromise a rudimentary introduction to the mathematics associated with the most common eigenanalysis methods. However, no detail is given on the numerical and computer methods used to implement these analyses.

The middle four chapters of this part are devoted to developing the dynamic coefficients for stiffness and damping used in the modeling of bearings, seals, and rotors. Clearly, this is the meat of the book, containing 60% of its pages and listing 230 references. Chapter 3 is a very extensive treatment of hydrodynamic bearings and squeeze film dampers. Although full journal bearings are principally treated, there is also some discussion of multilobe, step, and tilting-pad bearings. Squeeze-film dampers are also included. The fourth chapter considers liquid annular seals. Equations and solutions for flow and pressure are presented. Force coefficients are developed, and moment coefficients resulting from rotor tilt are considered. Chapter 5 is devoted to annular gas seals. In these two seal chapters, there are several comparisons of theoretical and experimental results. Also, they both end with an interesting section which poses some practical questions and supplies their answers. Chapter 6 is a somewhat brief (40 pages) treatment of the modeling of forces induced by the interaction of turbines and pump impellers with their structural surroundings. Space limitations have restricted coverage of fluid dynamical computational methods in these four chapters, but the material presented is of considerable use to rotor dynamic analysts.

The eighth chapter is a somewhat brief description of the rotordynamic analysis of a high pressure fuel turbopump used in the Space Shuttle's main engine. It applies some of the material discussed earlier in the book. Although interesting, a more detailed treatment would have improved the utility of the book for engineers who are not expert in the field.

Unfortunately, several very important rotordynamics topics are not addressed. These include balancing, torsional and coupled lateral-torsional vibrations, and active control of bearings and dampers. Given the emphasis on bearings and dampers, active control is a particularly significant omission.

This author contends that this book could serve as a text for a rotordynamics course, or as a supplementary reference for machine design courses, as well as a source for practicing engineers involved in design, analysis and operation of turbomachines. This is much too broad a statement. Coverage of rotordyanmics is not sufficiently broad in scope or (except for chapters 3-6) detailed in presentation to warrant use as a text. The large majority of users of *Turbomachinery Rotordynamics: Phenomena, Modeling and Analysis* will be researchers in the field of dynamic behavior of bearings and seals.

11N3. Multibody Computer Codes in Vehicle System Dynamics. Supplement to Vehicle System Dynamics, vol 22. - Edited by W Kortum *(Deutsche Forschungsanstalt fur Luft and Raumfahrt, Germany)* and RS Sharp *(Cranfield IT, England)*. Swets N America, Berwyn. 1993. 265 pp. ISBN 90-265-1365-8.

Vehicle Dynamics is one of the prime areas for the application of multibody methods. Systems of great commercial interest typically require representation as many interconnected rigid or flexible bodies, making them difficult or prohibitive to analyze by hand. Several computer codes have been written to automate model building and solving, some of them having special affinity to vehicle dynamics problems.

In this volume, such computer codes are reviewed against a background of explanation of the technologies built into them and surrounding them. Much information supplied by the code developers has been organized and presented. Representative problems, two from rail vehicle dynamics and two from road vehicle dynamics, have been specified and they have then been solved by a number of contributors. Precise problem statements are made and "good" solutions to the problems established through agreement of independent solvers. The benchmarking problems are used to further characterize the codes reviewed and they are expected to provide a useful resource for code evaluations in the future.

Contents include: Introductions: Review of multibody computer codes for vehicle system dynamics by W Kortum; Testing and demonstrating the capabilities of multibody software systems in a vehicle dynamics context by RS Sharp. Section 2: Description of Programs: The A'GEM multibody dynamics package by RJ Anderson; Autodyn and Robotran by P Fisette, P Maes, J-C Samin and PY Willems; Autosim by MW Sayers; Bond graph based modeling using macros, an introduction to the progam Bamms by CH Verheul and HB Pacejka; CMSP-Multibody systems analysis and optimization program package by Dao Trong Lien; A brief description of COMPAMM; FASIM-a modular program for simulation of nonlinear vehicle dynamics by M Hiller, K-P Schnelle and A van Zanten; Program LMS by J Auzinsh and P Sliede; MADYMO (MAthematical DYnamical MOdel); Description of the general 3D computer program 3D-MCADA by C Orlandea and NV Orleanda; MECANO: A FE software for flexible multibody analysis by M Geradin, DB Doan and I Klapka; The multibody program MEDYNA by W Schwartz; The software NEWEUL by G Leister, E Kreuzer and W Schiehlen; NUBEMM: a special multibody system as a part of a modern simulation concept in the automotive industry by E Pankiewicz.

Also: Multibody program NUSTAR; OKAM2-General kinematic analysis and ODAM-General dynamic analysis by V Stejskal and M Valasek; An integrated MBS modeling environment for vehicle motion control studies by AS Cherry, AN Costa and RP Jones; Dynamic vehicle simulation "SIDIVE Program" by JG Gimemez, LM Martin and H Sobejano; SIMPACK-An [illegible]sis and design tool for mechanical syst[illegible]ka and A Eichberger; Multibody [illegible]are-VAMPIRE by GA Scott; [illegible]am-ics analysis software b[illegible]way dynamic codes-VOCO [illegible] for computation of multibody systems dynamics by J Cervinka and F Hofmann; ADAMS-Mechanical systems simulation software by RR Ryan; The program system alaska; An introduction to DADS in vehicle system dynamics by RR Kading and J Yen; MESA VERDE-Generation and application of complete simulation models for multibody systems by A Schmidt; NUCARS-New and untried car analytic regime simulation. Section 3: Description of Benchmarks: Benchmark to test wheel/rail contact forces; Railway benchmark model #2: Bogie vehicle; Simulation of the IAVSD railway vehicle benchmark #2 with MEDYNA, SIDIVE and VOCO; Simulation of the IAVSD road vehicle benchmark bombardier Iltis with FASIM, MEDYNA, NEWEUL and SIMPACK; Road vehicle benchmark 2- 5 link suspension; names and addresses of developers and distributors.

III. AUTOMATIC CONTROL

11R4. Measurement Errors: Theory and Practice. - Semyon Rabinovich. AIP. 1993. 270 pp. ISBN 0-88318-866-X. $100.00.

Reviewed by Eugene E Covert (Aeronaut and Astronaut Dept, MIT, Rm 33-215, Cambridge MA 02139-4307).

Encyclopedic in its discussion of the material described by the title, the book is made up of 10 chapters: General information about measurements; Measuring instruments and their properties; Prerequisites for the analysis of the inaccuracy of measurements and for synthesis of their components; Statistical methods for analysis of multiple measurements in the absence of systematic errors; Direct measurements; Indirect measurements; Simultaneous and combined measurements; Combining results of measurements; Calculation of the errors of measuring instruments and problems in the theory of calibration. Chapters 1 and 2 are largely definitional. Chapter 3 deals primarily with the difficulties and false leads that can arise in defining standards and procedures. Chapters 4, 5, 6, and 7 are standard material not usually located in a single source. The material in chapters 8, 9, and 10 are well described by their title.

This book is completely different from Kurt Lion's book, *Instrumentation in Scientific Research, Electrical Input Transducers* and HKP Neubert's book, *Instrument Transducers, An Introduction to their Performance and Design*. The former is a compendium of transducers. The latter is less complete in that regard, but very complete in its discussion of the role of instrument dynamics in treating unsteady data. RW Hamming's book, *Digital Filters* treats problems associated by sampling and is appropriate to the digital age. *A Practical Guide to Data Analysis for Physical Science Students* by Louis Lyons, treats elementary statistics as an adjunct to experimentation. (There are many other books that I could have listed and apologize to those authors in advance, but to keep this review short I had to make choices.) Rabinovich's book, *Physical Measurements and Analysis*, complements all those listed above. He discusses most of the topics in the books cited, but not in great depth.

Except for Lion's and Neubert's discussion of transducers, the book under review synthesizes the most material contained in the books cited above, as well as treating topics not usually discussed. To quote from the back cover of the book, "Building from the fundamentals of the theory of measurement, the author offers a wealth of practical recommendations and procedure." This is true.

I suggest that every technical library should own a copy of *Measurement Errors: Theory and Practice*. Serious experimentalists whose interests are broad will surely want to examine the book with the intent of buying it.

As for the more general audience, they ought to be sure their referencing system will remind them of this book when it is needed. At $100 per copy, it is not for everyone.

An Introduction to Fuzzy Control. - Dimiter Driankov, Hans Hellendoorn, Michael Reinfrank. Springer, New York. 1993. 315 pp. ISBN 0-387-56362-8. $59.00. (Under review)

Linear Control Systems Vol 2, Synthesis of Multivariable and Multidimensional Systems. - T Kaczorek *(Warsaw Univ of Tech, Poland)*. Wiley, New York. 1993. 392 pp. ISBN 0-471-93434-8. $125.00. (Under review)

Loop Transfer Recovery: Analysis and Design. - Ali Saberi, Ben M Chen, Peddapullaiah Sannuti. Springer, New York. 1993. ISBN 0-387-19831-8. $89.00. (Under review)

Parallel Algorithms for Optimal Control of Large Scale Linear Systems. - Z Gajic *(Rutgers Univ NJ)* and X Shen *(Univ of Alberta, Edmonton, Canada)*. Springer, New York. 1993. 455 pp. ISBN 0-387-19825-3. $79.00. (Under review)

Robotics and Remote Systems for Hazardous Environments. - Edited by Mohammad Jamshidi and Patrick J Eicker *(Albuquerque NM)*. Prentice-Hall, Englewood Cliffs NJ. 1993. 230 pp. ISBN 0-13-782590-0. (Under review)

Sensors for Industrial Inspection. - C Loughlin. Kluwer, Netherlands. 1993. 456 pp. ISBN 0-7923-2046-8. £125.50. (Under review)

IV. MECHANICS OF SOLIDS

11R5. Mechanics of Composite Structures. - Valery V Vasiliev *(Comp Struct, Moscow Aviation Tech Inst, Moscow, Russia)*. Taylor & Francis, Washington DC. 1993. 506 pp. ISBN 1-56032-034-6.

Reviewed by Charles Parr (Eng and Mat Sci Div, Southwest Res Inst, PO Box 28510, San Antonio TX 78284).

This is a book for engineers written in the Timoshenko tradition. The equations are written out in full; tensor notation is not used. Of the 48 references, half are to works published in the USSR (or Russia?). About one quarter are to Vasiliev's work. Most of the rest are English, which makes an interesting contrast with the number of Soviet works one would find referenced in an English language book.

The book is divided into seven chapters; the first two chapters cover constituent properties and the equations of elasticity of composite materials. The second chapter discusses simplification of the elasticity equations for thin-walled structures, hygrothermal effects, and several types of nonlinearity. Included are elastic-plastic behavior, nonlinear elasticity, structural nonlinearity, nonlinearity due to resin crazing, viscoelasticity, geometric nonlinearity, buckling, and dynamic response. This chapter takes 120 of the book's 500 pages.

The remaining chapters are devoted to standard structural forms: Composite beams, columns, and rings; Thin walled beams; Composite panels and plates; Circular cylindrical shells; and Axisymmetric deformation of shells of revolution. In these chapters, the equations are developed to the point that an engineer can easily apply them to a particular structure. Only brief mention is made of FEMs of solution.

This is the first English edition of the first Russian edition. It is edited by Robert Jones of VPI & SU who wrote one of the first books on mechanics of composites, the well known *Mechanics of Composite Materials* almost 20 years ago. The text is lucid, a tribute to Jones and the translator, Lucia Man of the Institute of Crystallography, Academy of Sciences, Moscow.

Mechanics of Composite Structures would be a very readable and useable text with only a first course in elasticity. No problems are given, however. It is also recommended for the practicing engineer who designs composite structures, but has a minimum amount of training in advanced mechanics.

11R6. The Science and Practice of Welding, 10th Edition, Vols 1 and 2. Vol 1: Welding science and technology; Vol 2: The practice of welding. - A C Davies *(Welding Inst, UK)*. Cambridge UP, New York. 1993. 500 pp. ISBN 0-521-43404-1. Paper ISBN 43566-8. $75.00. Paper $27.95.

Reviewed by Carl E Cross (Metallurgy, Colorado Sch of Mines, Hill Hall, Golden CO 80401).

This two volume text on welding science, technology, and practice serves as a general introduction to a very broad and encompassing subject. It is presented at a level that technicians can easily comprehend, requiring little more than a high school background. As such, no topic is treated in great depth, making this text of limited value to engineers or veteran welding technicians.

References are made to British Standards where appropriate and sample questions are presented from examinations of the City and Guilds of London Institute. Craftsmen working to such standards would find this information most useful, which undoubtedly accounts for its popularity. (There have been nine previous editions and ten reprintings since the book was first published in 1941.)

A serious effort is made to incorporate both English and metric (SI) units as well as British and American welding symbols and alloy designations. This duality permits the text to be used across continents and may be particularly useful to those having to work with both systems. On the other hand, this duality may also serve to confuse the beginning student.

The first volume, *Welding Science and Technology*, deals with some of the basic fundamentals of welding metallurgy, electrical power, inspection, testing, and design drawings. It suffers from poor organization of topics and inclusion of superfluous information. For example, details are given of atomic structure and extractive metallurgy processes that some might consider impertinent information for shop welders. Regarding structure (in the chapter on metallurgy), the discussion of alloys is found to oscillate between wrought cast, ferrous and non-ferrous topics in a disorganized, confusing manner. The chapter following the discussion of metallurgical principles is devoted to phase diagrams, inserted as if by accident or afterthought.

The breadth of subjects covered is comprehensive, including a discussion of modern-day issues such as duplex stainless steel and inverter-type power supplies. Also, a brief discussion is given to the crack-opening-displacement test, although the basic fundamentals of fracture mechanics are never addressed. Missing is an explanation of the important relationship between welding input, cooling rate, and microstructure using time-temperature transformation curves. Also missing is a good review of the many types of welding defects, although bits of information are scattered throughout the text. Also missing (in both volumes) is the use of references and a bibliography; suggestions for further reading are not given.

The second volume, *The Practice of Welding* consists of a comprehensive survey of welding methods, tools, equipment, and techniques. A wide spectrum of methods are addressed, but no one method is treated in depth. Concerns unique to certain alloys are identified, as are safety issues. A special chapter on the welding of plastics is included. Missing is information regarding the use of variable polarity welding, a relatively new innovation for welding aluminum.

In summary, Davies' two volume, comprehensive text on welding is designed primarily for the entry level technologist with guild (or union) certification in mind. It is particularly well suited for those who work to British Standards. Almost every pertinent welding subject is covered to a small extent, at a level that is easily comprehended. However, its organizational structure leaves much more to be desired. From the standpoint of nomenclature, other comparable texts may prove to be more suitable for use in North America, (eg, *Modern Welding Technology*, Prentice Hall Pub, 1989).

***Correction:** The second paragraph of review 6R23 on page B88 of AMR Vol 46, no 6, June 1993, appeared incorrectly. Our apologies to Professor Popescu. The corrected paragraph follows:*

This reviewer, who in 1987 was in charge of reviewing the first edition of the above mentioned successful book for *Engineering Geology* (Elsevier) is most pleased to review this new edition.

11N7. Advanced Materials and Coatings for Combustion Turbines. Proceedings from Materials Week '93. - Edited by V Swaminathan. ASM Int, Materials Park OH. 1993. 265 pp. ISBN 0-87170-487-0. $83.00.

This collection of papers provides critical information about developments and applications of advanced gas turbine materials, with emphasis on hot gas path components. These include superalloys used in transition ducts, nozzles, and blades. Application and service experience of newly developed alloys and coatings, as well as conventional alloys and coatings to both land-based gas turbine and aircraft engine components, are covered. Metallurgical and mechanical property degradation of alloys and coatings during service is also included.

Other areas covered include applications of aero-engine technology to land-based gas turbines; materials and coating in electric utility applications; chemistry and microstructural modifications on mechanical properties, corrosion, and oxidation resistance; effects of service exposure on properties and degradation of components; and directionally solidified and single crystal blade technology.

11N8. Computational Methods in Contact Mechanics. - Edited by MH Aliabadi and CA Brebbia. Comput Mech, Billerica MA. 1993. 360 pp. ISBN 1562521136. $160.00.

Modern engineering design leads to the realization of the importance of contact problems in many technological fields. Contact problems are complex and inherently nonlinear due to their moving boundaries and the existence of friction along contact surfaces. Until a few years ago, researchers were engaged only in the fundamental concepts of contact problems. Today, due to the great improvement in computer technolgy and computational methods, it is possible to solve many complex practical contact problems accurately and efficiently.

This book presents a comprehensive review of the current state of theory of contact mechanics with particular emphasis on computational methods. Much attention is devoted to the physical interpretation of the contact properties as well as to the numerical methodologies necessary to solve complex engineering problems. As such, the book covers formulations based on load incremental and mathematical programming approaches using both FE and BEMs. The mathematical modeling techniques described include the constraint method, the flexibility approach, the penalty method and the Lagrange multiplier technique. In chapter one, the applications of BEM to frictional contact problems are presented using a fully load incremental technique together with a constraint approach. Its application to fracture mechanics is also described. Chapter two deals with the BE flexibility formulation for the analysis of frictionless and frictional contact problems. The formulation is described in detail and several examples are presented to demonstrate the accuracy of the method.

In chapter three, the Lagrange multiplier formulation for the FEM is presented. General algorithms are described for the detection of overlapping meshes and the evaluation of contact forces. An example problem of contact stress analysis in an orthopedic knee is presented.

Chapters four and five concentrate on the application of the penalty method in contact problems using the FE and BEMs respectively. Particular attention is paid to the numerical implementation of the method, and several examples are presented to demonstrate the accuracy of the methods.

In chapter six, the application of the BEM to 3D contact problems is described. The authors present a detailed formulation of the problem before proceeding to solve some classical problems.

The remaining three chapters of the book deal with mathematical programming approaches. Chapter seven presents a formulation to deal with both small and large displacement contact problems. In chapter eight, a general solution method for 3D quasistatic frictional contact problems is presented. The formulation is based on the BEM and mathematical programming approaches. Finally, in chapter nine, the application of the FEM to elastic-plastic contact problems is presented employing a parametric quadratic programming approach.

11N9. Contact Mechanics. - Edited by MH Aliabadi and CA Brebbia *(Wessex Inst of Tech, UK)*. Comput Mech, Billerica MA. 1993. 536 pp. ISBN 1562521632. $157.00.

Modern engineering design leads to the realization of the importance of contact problems in many technological fields. Today, due to the great improvement in computer technology and computational methods, it is possible to solve many complex practical contact problems accurately and efficiently.

This book consists of the edited version of the papers presented at the First International Conference on Contact Mechanics, which took place July 13-15, 1993 in Southampton, UK. The conference attracted papers on mechanical models such as rolling, impact and shock, unilateral contact etc; numerical models such as FEM, BEM, mathematical programming etc; mathematical models such as penalty method, Lagrange multiplier, constraint methods, etc; and engineering applications such as fracture mechanics, composite materials, forming process, etc.

Contents: Analysis of 2D and axisymmetric contact and friction problems using BE software; Transitional contact and wrinkling in sheet metal forming; Computer modeling of layered conformal contact; FE modeling with contact and friction for plane strain sheet forming process; A nonlinear mathematical model for finite periodic rail corrugations; Influence of local slip in hertzian contacts on the subsurface elastic material stresses of rolling element components; A revisitation of the infinite element method for water wave diffraction problems; Numerical evaluation of Bessel functions with complex arguments, with application to plates resting on elastic foundations; Fast solver for 3D normal and tangential contact mechanics in the half-space; Numerical methods for 3D dynamical frictional contact problems; FE modeling of pavement joints for dynamic analysis; Unilateral contact and friction in fractal interfaces; Numerical applications; Numerical resolution of the contact vibrations under harmonic loads; Mechanical analysis of a flat, deformable layer underlain by a rigid foundation and indented by a paraboloidal punch; Thermomechanical contact elements for healing in polymers; Numerical modeling of contact for low velocity impact in compact laminates; FE analysis of indentation experiments; Perturbation method used for static and dynamic contacts in nonlinear materials; Contact analysis in clamping roller free wheel clutches; Complete 3D elasticity solutions in the half-space for constant and linearly varying pressure loads; Stress analysis model for contact problems involving rolling and sliding; Differential quadrature solution of uniformly loaded circular plate resting on an elastic half-space; Numerical study on interface between sand and steel; Contact and loading conditions in soil-structure interaction; and Frictional contact analysis using BEM.

11N10. The Effect of Temperature and Other Factors on Plastic. - ASM Int, Materials Park OH. 1993. ISBN #6336F. $285.00. 2-vol set.

This book is the first data-bank compiled with extensive and specific plastics design information which allows you to evaluate plastics properties as they are exposed to environments other than room temperature and standard humidity conditions. More than 600 uniform and easy to read graphs are provided for more than 45 generic types of plastics. Mechanical, electrical and physical properties are graphed as functions of temperature, humidity level, filler content and/or specimen thickness. Electrical properties are also provided vs frequency. Stress vs strain curves are provided at different temperatures, strain rates and humidity levels. Data for multiple grades of material within each generic family is provided, and specific grades and unique test methods are always shown.

11N11. Friction, Lubrication and Wear Technology for Advanced Composite Materials. - Edited by P Rohatgi. ASM Int, Materials Park OH. 1993. 200 pp. ISBN 0-87170-490-0. $88.00.

This volume, consisting of more than 20 contributed papers, covers many facets of the tribology of composite materials. Among the areas covered are wear behavior of aluminum alloy-based ceramic particulate composites, tribological properties of nonferrous and polymer based composites, plus papers on mechanics of friction in self-lubricating composite materials, tribological behavior of undirectional fiber-reinforced graphite-epoxy composites, ceramic composites for bearings, wear behavior of silicon nitride, and tribological characteristics of aluminum-matrix composites.

11N12. Joining and Adhesion of Advanced Inorganic Materials. Proceedings from the 1993 Spring MRS Symposium Proceedings held in San Francisco, California.. - Edited by AH Carim *(Penn St Univ)*, DS Schwartz *(McDonnell Douglas)*, RS Silberglitt *(FM Tech)*. Mat Res Soc, Pittsburgh PA. 1993. 249 pp. Available in microfiche. ISBN 1-55899-212-X. $63.00.

This book covers many aspects of materials joining and adhesion, from fundamental theoretical aspects of adhesion, to joining techniques being applied in the commercial world. Adhesion of thin films and coatings is discussed at the atomic-electronic level, as well as on the practical level of coatings for wear resistance. Joining of a broad range of materials is covered, including ceramics and ceramic matrix composites, metals and metal matrix composites, and semiconductors. Also discussed are a variety of novel joining techniques.

In 29 papers, the book covers the topics of: fundamentals and overviews of adhesion and bonding; interfacial thermodynamics, microstructure, and mechanical properties; microwave, laser, and infrared joining; advanced and novel joining techniques: capacitor discharge welding and SHS, other approaches; and joining and adhesion in electronic materials.

11N13. Machining Technology for Composite Materials. Proceedings from ASM's Materials Week '93. - Edited by TS Srivatsan, DM Bowden, CT Lane. ASM Int, Materials Park OH. 1993. 240 pp. ISBN 0-87170-489-7. $88.00.

A follow-up to the 1992 publication *Machining of Composite Materials*, this book offers the latest advances in the technology developed for machining all types of composite materials, from polymers and ceramics to metal-matrix composites, plus updates on machine tools, waterjet cutting systems, laser cutting, welding and processing, and drilling.

11N14. Materials Properties Handbook: Titanium Alloys. - Edited by R Boyer, EW Collings, G Welsch. ASM Int, Materials Park OH. 1993. 800 pp. ISBN 0-87170-481-1. $245.00.

This book provides a data base for information on titanium and its alloys, and the selection of specific alloys for specific applications. The most comprehensive titanium data package ever assembled provides extensive information on applications, physical properties, corrosion, mechanical properties (including design allowables where available), fatigue, fracture properties, and elevated temperature properties. The appropriate specifications for each alloy are included. This international effort has provided a broad information base that has been compiled and reviewed by leading experts within the titanium industry, from several countries, encompassing numerous technology areas. Inputs have been obtained from the titanium industry, fabricators, users, government and academia. This up-to-date package covers information from almost the inception of the titanium industry, in the 1950s, to mid-1992. The information, organized by alloy, makes this exhaustive collection an easy-to-use data base.

The 60-plus data sheets supply not only extensive graphical and tabular information on properties, but the datasheets also describe or illustrate important factors which would aid in the selection of the proper alloy or heat treatment. The datasheets are further supplemented with background information on the metallurgy and fabrication characteristics of titanium alloys. An especially extensive coverage of properties, processing and metallurgy is provided in the datasheet for the workhorse of the titanium industry, Ti-6A1-4V.

This compendium includes the newest alloys made public, even those still under development. In many cases, key references are included for further information on a given subject.

Comprehensive datasheets provide extensive information on: applications, specifications, corrosion, mechanical design properties, fatigue and fracture properties, fabrication characteristics, and effects of processing on properties.

11N15. Mechanisms and Mechanics of Composite Fracture. - Edited by R Bhagat, R Arsenault, S Fishman. ASM Int, Materials Park OH. 1993. 490 pp. ISBN 0-87170-488-9. $90.00.

From a veritable who's who in metal-and ceramic-matrix composites research, this volume delivers the state of the art on this constantly advancing topic.

Areas covered in this volume include deformation and damage in particulate composites; crack initiation and propagation; micromechanical modeling; interface debond analysis and creep; fracture and fatigue; and microstructural tailoring. The majority of papers deal with metal-matrix and ceramic-matrix composites, with submissions from government, industry and university research facilities. Contributed papers hail from all over the world: Canada, China, India, Japan, the

Netherlands, the Ukraine, as well as the United States.

11N16. Micromechanics of Concrete and Cementitious Composites. Proceedings of the International Conference JMX 13, EPFL, Lausanne, March 9-10, 1993.. - Edited by Christian Huet. Presses Polytech Romandes, Lausanne. 1993. $56.00.

Micromechanics of concrete and cementitious composites has stimulated immense worldwide activity during the past 20 years in close relationship to the distinctive microstructural characteristics of this material. In fact, cement-based materials are deformable and breakable heterogeneous media whose behavior also involves complex, interrelated chemical, thermal, and hygral phenomena. The problems which this posed at the outset have since opened up whole new areas in the development of science and mechanics of materials.

This book is devoted to the proceedings of the international conference held in Lausanne on this subject March 9 and 10, 1993, which gathered some 100 participants from Europe and other continents.

It comprises the full texts and discussions of the lectures given by 15 invited speakers. It provides a valuable overview of the work being carried out in this field around the world, as well as an outline of the Swiss contribution to this activity.

Contents include: Basic methods and current trends; The materials science approach for advanced studies in cement-based materials; Damage process and fracture mechanism of uniaxially loaded concrete; Optimization of high-performance concrete; Experimental and numerical study of effective properties of composite materials; Characterization and quantification of microcracking by electron microscopy; Ultrasound propagation in nonlinear microcracked medium; An integrated approach of concrete micromechanics; 3D simulation of microstructural development of cement paste during hydration; Analysis of fracture mechanisms in particle composites; Multilevel numerical microscopy and tri-dimensional reconstruction of concrete microstructure; Numerical and experimental study of size and boundary conditions effects on the apparent properties of specimens not having the representative volume; Interface fracture and crack propagation in concrete composites; Numerical simulation of thermo-mechanical behavior of concrete through a 3D granular cohesive model; A numerical model for studying the influences of pre-existing microcracks and granular character on the fracture of concrete materials and structures.

Advances in Boundary Element Methods in Fracture Mechanics. - Edited by MH Aliabadi and CA Brebbia. Comput Mech, Billerica MA. 1992. 300 pp. ISBN 0-9458-2485-8. $144.00. (Under review)

Flexural-Torsional Buckling of Structures. New Directions in Civil Engineering Series. - NS Trahair *(Univ of Sydney, Australia)*. CRC Press, Boca Raton FL. 1993. 384 pp. ISBN 0-8493-7763-3. $70.00. Outside US, $84.00. (Under review)

Handbook of the Moire Fringe Technique. - K Patorski and M Kujawinska. Elsevier, New York. 1992. 432 pp. ISBN 0-444-88823-3. $172.00. (Under review)

Micromechanics: Overall Properties of Heterogeneous Materials. North-Holland Series in Applied Mathematics and Mechanics. - S Nemat-Nasser *(Appl Mech and Eng Sci, UCSD)* and M Hori *(Civil Eng, Univ of Tokyo, Japan)*. Elsevier, UK. 1993. 708 pp. ISBN 0-444-89881-6. $120.00. (Under review)

Structural Analysis of Printed Circuit Board Systems. Mechanical Engineering Series. - Peter A Engel *(SUNY, Binghampton NY)*. Springer, New York. 1993. 290 pp. ISBN 0-387-97939-5. $79.00. (Under review)

Technological Mechanics of Porous Bodies. - B Druyanov *(Hebrew Univ of Jerusalem, Israel)*. Oxford UP, New York. 1993. 184 pp. ISBN 0-19-856364-7. $57.00. (Under review)

Vibrations of Shells and Plates. - Werner Soedel *(Purdue)*. Marcel Dekker, New York. 1993. 496 pp. ISBN 0-8247-9035-9. $135.00. (Under review)

V. MECHANICS OF FLUIDS

11R17. The Avoidance of Cavitation Damage. - Wolfgang Tillner, Horst Fritsch, Rudolf Kruft, Wilfried Lehmann, Hartmut Louis, Gunther Masendorf. ASME, New York. 1993. 268 pp. ISBN 0-85298-807-9. $134.00.

Reviewed by Clayton Purdy (30 Meadowbrook Rd, Syosset NY 11791).

This is a reference book for design and installation engineers specializing in centrifugal and axial pumps, positive displacement pumps, hydraulic turbines, and pump turbines. They also describe how cavitation occurs, how to avoid damage from cavitation, and also how to limit damage whenever it occurs. The authors describe how to detect cavitation directly by viewing and inspection, and indirectly by changes in performance. The types of pumps and their installations are treated in detail. The book includes an extensive discussion of requirements for selecting materials for components exposed to cavitation. There is a good subject index, good quality figures, and many relevant references.

The authors' aim, to transmit an extensive knowledge of cavitation to other engineers, has been achieved. The book is recommended for purchase by individual engineering companies specializing in design and installation of centrifugal and axial flow pumps, hydraulic turbines, and pump turbines as well as technical libraries.

This book, translated from German is well written. The following comments are considered minor and should not detract from the overall recommendation. No attempt was made to coordinate quantities, symbols, and dimensions where different chapters were written by different authors. The words "impeller" and "runner" are used interchangeably even though the rotating element of a pump is an impeller and that of a hydraulic turbine is a runner. Double suction pumps are called twin flow. A contradictory statement includes: "pumps should be mounted low down to avoid or minimize cavitation damage," and then, "pumps so mounted can be smaller and higher speed" (which leads to more cavitation). There is an error in Figure 4.7: "low section number" should be "low suction number." The titles of German references were not translated into English.

The Avoidance of Cavitation Damage would have been enhanced if a summary of recommendations and guidelines had been included. Although centrifugal pumps, hydraulic turbines, and pump turbines are similar machines with similar cavitation damage problems, there are no references in this book to cavitation damage avoidance produced by the hydraulic turbine industry. One such book that does address this topic is the two volume set, *Cavitation Pitting Mitigation in Hydraulic Turbines*, by the Electric Power Research Institute, August 1986.

11N18. Groundwater Modeling Utilities. - William C Walton *(Consultant, Mahomet IL)*. Lewis Publishers, Chelsea MI. 1993. ISBN CAT NO L679. $114.00.

This book is a handy reference guide designed to help groundwater industry professionals learn to use a variety of microcomputer software applications for groundwater modeling and numerical modeling in flow and contaminent migration studies.

The book provides the following: handy operation and logic reference supplements to selected groundwater model, pre-processor, post-processor, geostatics, graphics, CAD, and word processing software supporting documentation; selected model operation practice exercises with extensive step by step input-option prompt and response documentation; and six convenient model database manipulation utility programs stored on two 5-1/4" diskettes included with this book. The disks can be used with all IBM and IBM-compatible computers. The utility programs allow you to convert values from one system of units to another; interpolate between control data points on a curve or surface; calculate heads and partial penetration effects in production wells; create, edit, and covert grid, triplet, listed, and unformatted model data files; and view tabular and category displays of model data files.

This book covers some of the most popular and thoroughly tested public domain finite-difference numerical microcomputer model software; commercial model software; public domain geostatistics software; and commerical graphics, CAD, and word processing software. Using actual groundwater modeling-specific examples, learn to work with software such as MODFLOW, MOD PATH, MOC, INTERTRANS, INTERSAT, GEOPACK, GRAPHER, SURFER, CADD 5.0, and WordPerfect 5.1.

Encyclopedia of Fluid Mechanics. Supplement 1; Applied Mathematics in Fluid Dynamics. - Edited by Nicholas P Cheremisinoff *(Elastomers, Exxon Chem, Linden NJ)*. Gulf Publ, Houston. 1993. 672 pp. ISBN 0-87201-547-5. $139.00. (Under review)

Liquid Atomization. Combustion, An International Series. - L Bayvel *(Kings Col; Univ of London, UK)* and Z Orzechowski *(Tech Univ of Lodz, UK)*. Taylor & Francis, Washington DC. 1993. 462 pp. ISBN 0-89116-959-8. (Under review)

Rotating Fluids in Engineering and Science. - James P Vanyo *(Mech and Env Eng; Geol Sci, UC, Santa Barbara)*. Butterworth, Stoneham MA. 1993. 425 pp. ISBN 0-7506-9261-8. $89.95. (Under review)

VI. HEAT TRANSFER

11R19. Applied Combustion. - Eugene L Keating *(Env Branch, US Navy, Naval Surface Warfare Center, Annapolis MD)*.

Marcel Dekker, New York. 1993. 568 pp. ISBN 0-8247-8127-9. $150.00.

Reviewed by Tanvir Ahmad (Thermosci Dept - 254 REB, General Motors Res Labs, 30500 Mound Rd, Warren MI 48090-9055).

The author's stated intention is for this book to serve as a textbook as well as a technical reference. The objective seems to be to provide a broad engineering treatment of combustion theory and practical applications of the theory.

The book consists of 12 chapters. The first chapter sets the theme of the book by providing a perspective on the relationship between combustion-fuels and engines. Also discussed in this chapter is a general conceptual model of various stages in technology development. This chapter is expected to put the reader in a practical as opposed to a theoretical frame of mind. This theme recurs throughout the book in that after providing a minimal and often insufficient theoretical treatment of a concept, the focus is switched to example problems on practical applications. The compromise in covering theoretical details can be viewed as a necessary tradeoff in a book of this size (501 pages, excluding tables, etc)

Chapters 2 and 3 cover applications of the first and second laws of thermodynamics to reactive systems. A few useful example problems are presented to demonstrate calculations of flame temperature and specific heat, etc. Unfortunately, the energy-entropy charts, Figures 3.4 and 3.5, are reduced versions of the usual fold-in type illustrations and are illegible.

Chapters 4, 5, and 6 deal with solid, liquid, and gaseous fuels and their combustion, respectively. In the solid-fuels chapter, several practical combustion systems, including coal-combustion systems, solid-waste incinerators, and fluidized-bed systems, are described. However, no related theory is presented. In the liquid-fuels chapter, the physical and chemical properties of various fuel families are briefly discussed and simple stoichiometric-combustion calculations are presented. Similarly, in the gaseous-fuels chapter, the emphasis is on fuel properties and their stoichiometric equilibrium combustion. It is unusual for a combustion book to devote almost half of its pages to a largely descriptive discussion of fuel properties without discussing their combustion and aero-thermochemical behavior. For instance, in chapter 4, a treatment of surface-combustion processes, as encountered in coal-burning and fires, would have been highly desirable. Similarly, chapter 5 seems incomplete without even a mention of spray combustion and a wide variety of related practical problems. In this reviewer's opinion, most of the material on fuel properties and preparation is available in fuels handbooks and should have been left out. In its place, a thorough treatment of coal combustion, sprays, and gas-jet combustion would have been more consistent with the scope of the book.

Chapter 7, Fuel Mechanics, provides the student with only a bare minimum background in classical fluid mechanics of combustion. The chapter does contain a brief treatment of the conservation equations for compressible flows. However, important phenomena like turbulent combustion, which are of great significance to almost all practical combustion systems, are not covered at all. It appears that for even an undergraduate-level combustion course, this material would have to be supplemented by consulting another book providing a more detailed treatment of these areas. Chapter 8, on chemical kinetics, provides some background in this facet of combustion. Again, the basic flame theory and the subject of premixed and diffusion combustion are covered in a nonmathematical manner over a few pages.

Chapter 9, on combustion-engine testing, covers the nomenclature related to internal-combustion engines and discusses methods and examples of performance and emissions testing. In the next chapter, on spark-ignition engine combustion, simple thermodynamic calculations for fixed and variable specific heats are presented. The chapter lacks a discussion on flame propagation and the effect of engine-design parameters on flame speed and combustion efficiency. Also lacking is a treatment of mechancisms of NO_x and HC formation, which is an area of intense activity worldwide. Chapter 11 covers similar material on compression-ignition engines and has similar limitations except that diesel emissions are briefly discussed. The material covered in the last chapter, Gas Turbine Engine Combustion, closely resembles that in chapters 10 and 11 in terms of its deficiencies: details of combustion and emissions aspects of the turbine engine are not discussed.

In this reviewer's opinion, the book falls short of its stated objective of serving as a textbook. Its lack of detailed treatment of several important combustion, topics such as spray combustion, flame propagation, turbulent combustion, emissions, and fires, limits its ability to serve as a comprehensive textbook even for an undergraduate combustion course. The book provides a great deal of descriptive material on fuel properties that would better benefit a fuels handbook. On the positive side, the selection of the example problems does cover a broad spectrum of practical combustion systems. Each example problem is followed by useful tutorial comments about the significance of the problem. Additionally, the problems employ both the English and SI units and provide useful linkage between various prevalent dimensioning practices used by the practicing engineer.

Overall, *Applied Combustion* would have to be supplemented by at least another book on classical combustion theory in order to serve as a useful textbook.

11N20. Phase Transformations in Thin Films--Thermodynamics and Kinetics. Volume 311 in the MRS Symposium Proceedings Series. - Edited by M Atzmon *(Univ of Michigan, USA)*, AL Greer *(Cambridge Univ, USA)*, JME Harper *(IBM TJ Watson Res Center, USA)*, MR Libera *(Stevens IT, USA)*. Mat Res Soc, Pittsburgh PA. 1993. 399 pp. Microfiche. ISBN 1-55899-207-3. $72.00.

This book contains 61 papers and covers both basic and applied aspects of phase formation and atomic transport, including experimental, numerical, and theoretical studies. Based on a symposium held at the 1993 MRS Spring meeting in San Francisco, California, the book discusses interfacial reactions; solid-state amorphization, crystallization; stress effects on phase transformations; radiation effects on phase transformations; silicides; and film growth and fundamentals, microstructure.

Convective Heat Transfer, Second Edition. - Louis Burmeister *(Univ of Kansas)*. Wiley, New York. 1993. 576 pp. ISBN 0-471-57709-X. $79.95. (Under review)

Numerical Methods for Problems with Moving Fronts. - Bruce A Finlayson *(chem eng, Univ of Washington WA)*. RP, Seattle. 1993. 605 pp. Mackintosh diskette incl. ISBN 0-9631765-0-1. $60.00. (Under review)

VII. EARTH SCIENCES

11R21. Geotextiles in Filtration and Drainage. - Edited by Stephen Corbet *(G Maunsell and Partners, UK)* and John King *(Geotextiles, Don and Low Ltd, UK)*. Telford, London. 1993. 142 pp. ISBN 0-7277-1924-6. £35 UK and Europe.

Reviewed by Thomas Edgar (Dept of Civil and Architec Eng, Univ of Wyoming, PO Box 3295, Laramie WY 82071).

The use of geotextiles in construction has increased dramatically in the past twenty years. Typical applications of geotextiles include providing tensile strength in sands and gravels, support and separation of different soil types and (the subject of this volume) filtration and drainage of fluids in soil. This book contains the proceedings from the Geofad '92 Conference on Geotextiles in Filtration and Drainage, organized by the United Kingdom chapter of the International Geotextile Society and held in September, 1992. The book has 142 pages divided into eleven chapters.

The direction of fluid flow in filtration is typically perpendicular to the fabric. Drainage usually implies that flow is in the plane of the fabric or, in the case of geocomposites, is parallel to the fabric in open void spaces provided by a deformed core material. This volume deals with both the selection and specification of appropriate fabrics and applicable design methods for a variety of situations. Fabric selection and design procedures in filtration and drainage applications are made more complex because fluid flow can also cause the soil being filtered to enter the fabric structure and clog the pore spaces.

Topics of the papers include geotexties use in road construction and drainage, filtration of hazardous wastes and landfills, shoreline and dike protection, consolidation of soil augmented by wick drains, and testing procedures to determine long terms stability of the fabric. The papers are practice oriented, having results of field testing in almost every paper. Where appropriate, current research and design procedures in England, Europe, and the United states are discussed and compared. Several of the papers have printed discussions that provide a balanced view between the researchers, industry, and practice. The last four chapters are concerned with future uses of and required research in geotextiles from the viewpoint of consultants, manufacturers, clients and cooperative efforts in the European Economic community.

Unlike many conference proceedings, these papers are tightly integrated to present a clear picture of the state of knowledge in this area of geotextile use. People with little previous knowledge of geotextiles can easily read this book. I believe *Geotextiles in Filtration and Drainage* would be a valuable addition to the library of an engineer who works with specific geotextiles.

Developments in Dynamic Soil-Structure Interaction. Proceedings of the NATO Advanced Study Inst, Kemer, Antalya, Turkey, July 8-16, 1992. - Edited by Polat Gulkan *(Civ Eng and Earthquake Eng Res Center, Middle East Tech Univ, Ankara, Turkey)* and Ray W Clough *(Civil Eng, UCB, Ankara, Turkey)*. Kluwer, Norwell MA. 1993. 456 pp. ISBN 0-7923-2144-8. $196.00. £160.00. (Under review)

IX. BIOENGINEERING

11R22. Biomechanics. A Practical Approach. - Edited by Julian F V Vincent *(Center for Biomimetics, The University, Reading)*. Oxford UP, New York. 1992. 247 pp. Paperback. ISBN 0-19-963222-7. Cloth ISBN 0-19-963222-5. $50.00. Cloth $70.00.

Reviewed by V A Pollak (Dept of Elec Eng, Division of Biomed Eng, Univ of Saskatchewan, Saskatoon, SK S7N OWO, Canada).

Examination of a living organism or of its parts has two principal aspects: one is concerned with the material substrates of which the organism is composed, and one is the functionality of its systems. Of course the border between the two is fluent. Functionality dictates more often than not the necessary properties of the material which implements it and, reversely, these properties impose limits upon functional performance. That dichotomy applies equally to technological systems and to products of nature.

In technology the interdependence between material, form, and function has been recognized and has been the subject of extensive studies. In the life sciences emphasis has, for a long time, been on function. The properties of the material an organism uses to implement these functions have only recently become the focus of attention. In many respects these "biomaterials" differ dramatically from those used in technology. The techniques used for the examination of their properties are also, in many respects, significantly different from those used in standard engineering practice. Discussion of practical approaches to these tasks is the principal subject of this book. The study of biomaterials is a typical example of modern interdisciplinary work. To be successful in that field one has to have adequate expertise not only in the physical and engineering facets of the problem, but also in those which belong to the realm of biology and of the life sciences in general. There are not too many people around who have adequate knowledge in both of these two heterogeneous disciplines.

Presently, most of the work in this area is carried out by life science specialists with only limited expertise in the complementary discipline. It is mainly to members of this circle that the book addresses itself. As the title implies, little theory is offered. Emphasis is placed on practical and down-to-earth rules and advices to follow when examining and measuring the mechanical parameters of biomaterials, and how to avoid the most common mistakes. The effort to reduce theory to a minimum may have in some places been taken too far, which makes the underlying rationale to some recommendations for the non-specialist difficult to comprehend.

The discussion centers in general on established techniques for the measurement of the principal mechanical parameters of biomaterials and on the pitfalls likely to be encountered. The range of topics covered is very wide. The humorously styled introduction summarizes the intent of the book. This is accompanied by a list of mistakes, where lack of understanding of the complementary discipline has made laboriously obtained results practically worthless. The first chapter of the main text presents a lucid discussion of the mechanical properties of some biological liquids. It is followed by a sequence of six well-written chapters on different kinds of solid biomaterials of animal origin and their mechanical characteristics. The presentation is rounded off by an analogous, but less detailed, chapter on plant material. The book is terminated by an informative discussion on bio-adhesives, preceded by a treatise on fractures and on the mechanisms involved in the fracture failing of biomaterials.

Overall, the text is well organized and is accompanied by a multitude of largely schematic but nonetheless clear and informative illustrations. Attached to most chapters is a list of some pertinent publications and of reference material for further reading. A useful appendix contains the names and addresses of specialized material and equipment suppliers, which may prove helpful in some of the unconventional approaches.

The book should be of value to graduate students involved in the material aspects of biomechanics, and to practitioners in that vast field, especially to those with a life science background. But it might also be a helpful guide for those with an engineering or physics background when dealing with the hands-on design of specific tests and experiments on biological specimens. The index is well worked out and sufficiently detailed so that any specific topic treated in the book can be easily located.

In summary, the book is a useful addition to the existing rich literature on biomechanics and biomaterials. Its main value is in its practical orientation, which is quite underrepresented in present publications.

A future edition might profit from the inclusion of some reference to modern hybrid measurement methods, eg, of the mechano-optical or mechano-electrical type. Their discussion, if only brief, might be helpful for special applications of the science of biomaterials in human and veterinary medicine, and biology. They may also be of value for tests on materials of biological origin intended for technological applications.

11N23. Biomechanics. Clinical Aspects of Biomedicine Vol 2. - Edited by J Valenta *(Tech Univ of Prague, Czech)*. Elsevier, UK. 1993. 616 pp. ISBN 0-444-98764-9. $282.75.

Biomechanics is one of the branches of science contributing significantly not only to increasing our knowledge of the development of living systems but also to our understanding of the relevant laws of mechanics and their mechanical functions. Important anatomical and biomechanical data as related to the individual functions of the organism and their biomechanical significance are focussed on in this publication. The locomotor and circulatory apparatus and the identification of the mechanical properties of living tissue and materials used in osteosynthesis and alloarthroplasty are among the fields covered. The phenomena observed in the cardiovascular system are described using the basic equation of motion of viscous fluids. Suitable hydraulic models are proposed for investigation and testing of vascular grafts, artificial cardiac valves and artificial heart. Important research data are presented about biomechanical structures of the locomotoric apparatus, and joint rheology. A section is included presenting the fundamentals of biomechanical analysis in criminology and in bioballistics.

Contents include: Some phenomenological models of the mechanical response of biomaterials: Introduction by J Valenta; Identification of mechanical properties of living tissues; Application of the theory of catastrophes to the evolution of biosystems by J Valenta; On some aspects of the structure of bone tissue and its re-modelling; Biomechanical heterogeneity by V Kafka; Piezoelectric response of bone tissue to mechanical loading by J Valenta; Cyclic deformation and its constitutive model by M Satra; Basic mechanical properties of tissues of the locomotion system by P Komarek; Mechanical properties of tissues of the cardio-vascular system; Mechanical properties of some other tissues of the human body.

Materials used in osteosynthesis and alloartboplasty: Introduction; A list of metallic materials used in the manufacture of implants; Nonmetallic materials, and Plastics by K Lobl and S Beznoska.

Rheology of biological fluids and biomechanics of the cardio-vascular system: Introduction; Rheological properties of human blood; Rheometry of visco-elastic fluids; Mathematical modeling of flow curves; The effect of the physical and biological properties of blood on its viscosity; The limits of validity of continuum models of blood; Rheological properties of synovial fluids; Some aspects of the current state of knowledge and new trends in research into the hydrodynamics of the cardio-vascular system by F Klimes; The basic equations of motion and viscous fluids; Physical-mathematical models of the pulsating flow of blood in blood vessels; Fundamental theoretical analysis of oscillating and pulsatile flows of fluids in tubes; Harmonic analysis of some hydrodynamical variables of blood circulation in the vascular system; Hydrodynamic aspects of the formation of arteriosclerosis; Experimental research and testing of artificial heart valves and complete heart replacements; Hydrodynamics of the artificial heart; Some basic problems of microcirculation.

The locomotive apparatus of man by V Karas and S Otahal: Composition of the locomotive apparatus; Elements and bonds of the locomotive apparatus; System of skeletal muscles; Skeleton: the basic of the segmentary structure of the body; General problems of occupational and sports biomechanics.

Criminalistic biomechanics by V Porada: Introduction; Biomechanical analysis of tracks of human locomotion; Distribution of forces in human locomotion and their measurement; Some theoretical aspects of the identification of a criminal by his tracks in a dispersive environment; Method of measuring the geometric features with biomechanical content for the analysis of tracks of bare feet; Biobalistics; Subject index.

11N24. Biomolecular Materials. - Edited by C Viney *(Univ of Washington)*, ST Case *(Univ of Mississippi Medical Center)*, JH Waite *(Univ of Delaware)*. Mat Res Soc, Pittsburgh PA. 1993. 287 pp. Microfiche available. ISBN 1-55899-187-5. $69.00.

Biomolecular materials are partial, complete, or modified replicas of biological materials whose synthesis and utilization may be unrelated to their original biological source. This new book explores the goal of attaining biomolecular materials that have industrial, medical, or agricultural applications--whether the objective is to replicate the properties of a biological material, or to produce derivatives with novel properties.

Documenting proceedings from a symposium held at the 1992 MRS Fall meeting in Boston, this volume covers lessons from nature, cellular synthesis, non-cellular synthesis, structural and mechanical properties, and applications.

X. GENERAL & MISCELLANEOUS

11R25. Technobabble. - John A Barry. MIT Press, Cambridge MA. 1993. 268 pp. ISBN 0-262-52182-2. $12.50.

Reviewed by Everett E McEwen (Civ and Env Eng, Univ of Rhode Island, Bliss Hall, Kingston RI 02281).

Technobabble is an extremely well-written, easily read book. The author is a computer expert and linguist, and he probably has linguists in mind as his intended audience. The intent of the book is to present the history of computer and computer science development in terms of the words and phrases coined to describe this new technology. The author describes how the language of the computer user has found its way into more general language usage where, in many instances, it has no relation to technology.

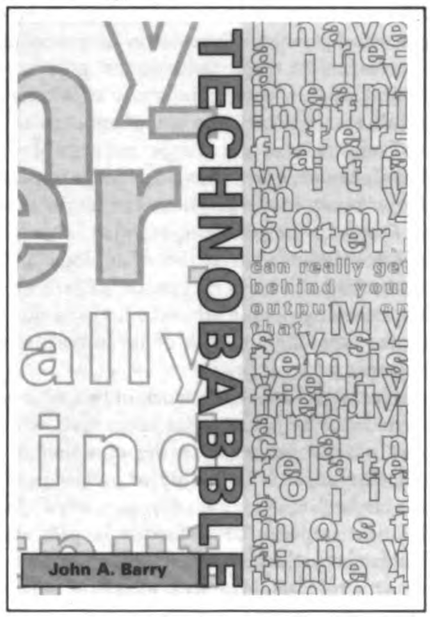

The author is obviously well versed in computerese and knowledgable in computer history. This is reflected in his ability to trace the development of hundreds of computer related words and expressions.

It appears that the chapters are almost independent of each other. It is possible to read the introduction to a chapter, and then to skip over that chapter without significant loss of continuity.

The subject index is very complete. The bibliography is not extensive, but the footnotes are very detailed, providing both informative and interesting reading. The glossary is excellent but somewhat limited in that it includes only terms generally not described elsewhere in the text. The format, appearance, and particularly the front section add to the readability of the text. The nature of the book precludes the use of figures.

Barry's book can perhaps best be classified as both general interest and reference. Although it is somewhat difficult to anticipate its potential audience, it could be of interest to: 1) computer scientists and engineers who are knowledgeable in computerese and who are interested in the linguistic development of the terminology; and 2) Linguists who perhaps have little knowledge or interest in computers but for whom the tracing of the history of hundreds of computer terms is of professional interest.

For anyone who has been a long time user of computers and who has never found the time to give much thought to the language that he has come to use on a daily basis, *Technobabble* is most enjoyable reading.

11N26. Complex Variables: An Introduction. Pure and Applied Mathematics: A Series of Monographs and Textbooks/176. - Watson Fulks *(Univ of Colorado, Boulder)*. Marcel Dekker, New York. 1993. 416 pp. ISBN 0-8247-9079-0. $49.75.

Contents include: Complex numbers and complex functions; Analyticity; Cauchy's theorem; Mappings; Residues; Potential theory; Bibliography; and Solutions and hints for selected problems.

11N27. Concise Encyclopedia of Building & Construction Materials. - Edited by Fred Moavenzadeh *(MIT)*. Pergamon, Tarrytown, NY. 1990. 698 pp. ISBN 0-08-034728-2. $200.00.

This book presents, in a single volume, the work of numerous specialists in the field. There are articles covering general building materials, their mechanical properties and economic and historical aspects, as well as those dealing specifically with the use of materials such as clays, ceramics, cement, sand, gravels, glass, metals, wood, polymers, plastics and composites. Intended primarily for all those interested in having a useful reference source in building and construction materials at hand, this work would also be a course reference for students in architecture, civil and structural engineering and related disciplines.

A selection of articles: Acoustic properties of wood; Architectural design and materials; Binders; clay minerals; Building materials: an introduction; Carbon-fiber-reinforced plastics; Ceramics as construction materials; Composites: an overview; Construction materials: industrial minerals; Corrosion of iron and steel; Design with polymers; Design with wood; Economics of materials, energy and growth; Electrogalvanized steel; Epoxy resins; Failure analysis; Fatigue: engineering aspects; Fracture and fatigue of glass; Glazing; Glued joints in wood; Glued laminated timber; International trade in materials; Iron production; Materials availability; Offshore structure materials; Paints, varnishes and lacquers; Particulate composites; Portland cements, blended cements and mortars; Recycling of demolition wastes; Roofing materials; Sand and gravel; Structural clay products; Structure of materials; Welding: an overview; Welding of bridges; Wood as a building material; Index.

11N28. Concise Encyclopedia of Composite Materials. - Edited by Anthony Kelly FRS *(Univ of Surrey, UK)*. Pergamon, Tarrytown, NY. 1989. 317 pp. ISBN 0-08-034718-5. $160.00.

The 55 articles in this encyclopedia provide a full and up-to-date account of all aspects of composite materials, including fiber composites, particulate composites, and naturally-occurring composite materials and their properties. Current coverage is also given to metal matrix composites and thermoplastic resins reinforced with fibers. This book will be of interest to materials scientists, mechanical and materials engineers and all other interested and informed parties seeking the most comprehensive and up-to-date account of composite materials available in a single volume.

A selection of articles: An introduction to composites; Aircraft and aerospace applications of composites; Artificial bone; Asbestos fibers; Automobile tires; Boron fibers; Carbon fibers; Carbon-carbon composites; Creep of composites;

Dental composites; Fiber-reinforced cements; Fiber-reinforced ceramics; Fibrous composites: Thermomechanical properties; Glass-reinforced plastics: thermoplastic resins; Laminates: elastic properties; Metal-matrix composites; Natural composites; Natural-fiber-based composites; Oxide inorganic fibers; Paper and paperboard; Plywood; Polymer-polymer composites; Silicon carbide fibers; Strength of composites; Toughness of fibrous composites; Whiskers; Wood-polymer composites; Woven fabric composites: properties; Index.

11N29. Concise Encyclopedia of Magnetic & Superconducting Materials. - Edited by J Evetts *(Univ of Cambridge, UK)*. Pergamon, Tarrytown, NY. 1992. 726 pp. ISBN 0-08-034722-3. $250.00.

This encyclopedia draws together, for the first time in a single volume, the remarkable advances seen in recent years in the discovery of new materials and improvements of existing materials, in the elucidation of a new and deeper understanding of their phenomenology, and in the expansion and diversification of their application in technology. Magnetic and superconducting materials have much in common: they both have experienced, over the past decade, a revolution that has revitalized and galvanized their respective fields. In each case, the impetus has come from the discovery of new materials; this, in turn, has stimulated a reevaluation of a wide range of basic mechanisms and phenomena. Details of all important materials systems and their properties are included, and key areas such as thin films are covered. The volume contains 110 articles, alphabetically organized and written by more than 120 acknowledged experts within the field of magnetic and superconducting materials.

Selected articles: AC applications of superconducting materials; AC losses in superconducting materials; Amorphous superconductors; Anisotropy in magnetic materials; Anisotropy in superconducting materials; Biomagnetic measurements; Chevrel phases; Coercivity and domain wall pinning; Coherence length, proximity effect and fluctuations; Design with magnetic materials; Design with magnetic materials: computer simulation; Domains and domain walls; Ferrites, hard; Fluids, magnetic; Flux creep phenomena; Flux pinning and the summation of pinning forces; Granular superconductors; High-frequency impedance of superconducting materials; High-frequency properties of magnetic materials.

Also: Josephson effects in weak links; Magnetic energy storage; Magnetic properties of superconductors; Magnetic separation; Magnetic storage media; Magnetic units and material specification; Magnetization imaging; Magnetocaloric effect; Magnetoelastic phenomena; Magnetooptic materials; Magnetooptic storage media; Millimeter-wave detection; Multifilamentary superconducting composites; Nanocrystalline soft magnetic materials; Niobium-titanium alloys; Nonequilibrium superconductivity; Nuclear magnetic resonance imaging; Optical properties of superconductors; Organic and molecular ferromagnets; Oxide glasses as magnetic materials; Oxide superconductors: ceramic processing; Oxide superconductors: physical properties; Oxide superconductors: thin-film deposition; Power loss in magnetic materials; Radiation effects on magnetic materials; Radiation effects on superconducting materials; Superconducting magnets; Superconducting materials: BCS and phenomenological theories; Thin films and multilayers, magnetic.

11N30. Concise Encyclopedia of Medical & Dental Materials. - Edited by David Williams *(Univ of Liverpool, UK)*. Pergamon, Tarrytown, NY. 1990. 432 pp. ISBN 0-08-036194-3. $180.00.

Containing more than 60 articles, this book presents the work of nearly 70 world experts on the current techniques and applications of materials which have been specially developed to staisfy the increasing needs of medical and dental science. Alphabetically arranged, articles cover the basic materials used including prostheses, implants, sutures and wound dressings. The biocompatibility, wear, corrosion, and surface properties of the materials are also covered, as well as the mechancis of their implantation, adhesion and repair. Widely illustrated and complemented by a comprehensive three-level subject index, this is an up-to-date survey of dental and medical materials available in a single volume.

Selected articles: Acoustic measurements of bone and bone-implant systems; Acrylic dental polymers; Acrylics for implantation; Adhesives in medicine; Aluminum oxide; Arteries, synthetic; Biocompatibility of dental materials; Biocompatibility: an overview; Biodegradation of medical polymers; Biomaterial-blood interactions; Carbons; Chemical adhesion in dental restoratives; Cobalt-based alloys; Collagen; Corrosion of dental materials; Dental amalgams; Dental implants; Dental materials: clinical evaluation; Dental plaster and stone; Dental porcelain; Denture base resins; Drugs: attachment to polymers; Endodontic materials; Elastomers for dental use; Fracture toughness; Glasses: agricultural and veterninary applications; Glasses: medical applications; Gold alloys for dental use; Heart-valve replacement materials, Hemodialysis membranes; Heparinized materials; Hydrogels; Invasive sensors; Iron-based alloys; Maxillofacial prostheses; Metals for medical electrodes; Ormosils: organically modified silicates; Polyesters and polyamides; Polymers for controlled drug delivery; Polysiloxanes; Polyurethanes; Porcelain-metal bonding in dentistry; Porous biomaterials; Silver in medical applications; Soluble polymers in drug delivery systems; Sterilization using ethylene oxide; Surface structure and properties; Suture materials; Tantalum and niobium; Titanium and titanium alloys; Wrought dental wires; Zirconia-toughened ceramics.

11N31. Differential Equations. Proceedings of the 1987 EQUADIFF Conference. - Edited by CM Dafermos *(Brown Univ, Providence RI)*, G Ladas *(Univ of Rhode Island, Kingston)*, G Papanicolaou *(NYU)*. Marcel Dekker, New York. 1993. 808 pp. ISBN 0-8247-8077-9. $160.00.

Partial contents include: The Jabotinsky equations by J Aczel and D Gronau; Global decoupling of coupled symmetric oscillators by JC Alexander and B Fiedler; Void formation in solidification by V Alexiades; Forced oscillations for Hamiltonian systems by O Arino and A Cherif; Eigenvalues, bifurcation, and center manifolds in the presence of noise by L Arnold and P Boxler; An unusual wave equation arising in water-wave theory by GA Athanassoulis; Controllability and approximate controllability for linear integral Volterra-Stieltjes equations by L Barbanti; Determinants for formally hyperbolic differential equations by P Berglez; Two new applications of Gurtin's coordinate transformation by M Bertsch and D Hilhorst; The thermal stability of a chemically reacting gas in a porous sphere by AR Bestman; Higher regularity of solutions of semilinear evolution equations and applications by MA Boudourides and AC Nikoudes; Maximal attractor of the scalar reaction diffusion equation by P Brunovsky.

Also: Stability of bifurcating solutions of reaction-diffusion equations in cylindrical domains by A Calsina; Numerical evaluation of the solutions to the equations of elastostatics for a stratified sphere by L Carlomusto and A Pianese; Existence of positive exponentially decreasing solutions for nonlinear differential equations in IR with an unbounded coefficient by A Chaljub-Simon; Shadowing lemma for maps in infinite dimensions by Shui-Nee Chow, Xiao-Biao Lin; and KJ Palmer; Asymptotic method for invariant solutions of IR_m maps by RL Clerc and C Hartmann; Orthogonal polynomials in symmetrical domains of R_m by J Cnops; Hyperbolic conservation laws with memory by CM Dafermos; Fully nonlinear equations in banach spaces by G Da Prato; The number of solutions of some semilinear boundary value problems by M d'Aujourd'Hui; Some nonlinear Sturmian theory for (Iu'IP-2) + c(t)IuIP-2u = 0 by M Del Pino and R Manasevich; Short survey of non standard analysis contribution to the theory of ordinary differential equations by F Diener and M Diener; New approach to inverse problems in linear kinetic theory by K Dressler; Bounded entire solutions of higher order semilinear equations by AL Edelson and R Vakilan.

Minors of the Wronskian of the differential equation $L_n y + p(x)y = 0$ and their applications by U Elias; Explicit solutions of the Fokker-Planck equation by MJ Englefield; Full and half-range eigenfunction expansions for an elliptic boundary value problem involving an indefinite weight by M Faierman and GF Roach; The general similarity solution of Laplace's equation with applications to boundary-value problems by Chao-Kang Feng; Uniform asymptotic stability in functional differential equations by T Furumochi; Removability of blowup points for semilinear heat equations by Y Giga and RV Kohn; and Behavior of the nonoscillatory solutions of first order neutral delay differential equations by JR Graef, MK Grammatikopoulos and PW Spikes.

11N32. Differential Equations in Banach Spaces. Lecture Notes in Pure and Applied Mathematics Series/148. - Edited by Giovanni Dore, Angelo Favini, Enrico Obrecht, Alberto Venni *(Univ of Bologna, Italy)*. Marcel Dekker, New York. 1993. 288 pp. ISBN 0-8247-9067-7. $115.00.

Contents include: Abstract linear non-autonomous parabolic equations: A survey, by P Acquistapace; On some classes of singular variational inequalities by ML Bernardi and F Luterotti; Non-uniqueness in L∞: An example by JE Bouillet; Some results on abstract evolution equations of hyperbolic type by P Cannarsa and G Da Prato; Interpolation and extrapolation spaces and parabolic equations by G Di Blasio; On the diagonalization of certain operator matrices related to volterra equations by KJ Engel; Second order abstract equations with nonlinear boundary conditions-applications to von Karman system with boundary damping by A Favini and I Lasiecka; Linear parabolic differential equations of higher order in time by A Favini and H Tanabe; Analytic and gevry class semigroups generated by -A +iB, and applications by A Favini and R Triggiani; The Kompaneets equation by JA Goldstein; and Multiplicative perturbation of resolvent positive operators by A Holderrieth.

Also: Uniform decay rates for semilinear wave equations with nonlinear and nonmonotone boundary feedback-without geometric conditions by I Lasiecka and D Tataru; Sharp trace estimates of solutions to Kirchhoff and Euler-Bernoulli equations by I Lasiecka and R Triggiani; Boundary values of holomorphic semigroups, H∞ functional calculi and the inhomogeneous abstract Cauchy problem by R deLaubenfels; Stability of linear evolutionary systems with applications to viscoelasticity by J Pruss; Generation of analytic semigroups by variational operators with L∞ coefficients by V Vespri; Asynchronous exponential growth in differential equations with homogeneous nonlinearities by GF Webb; The inversion of the vector-valued Laplace transform in Lp(X)-spaces by L Weis; Some quasilinear parabolic problems in applied mathematics by A Yagi.

11N33. Encyclopedia of Materials Science and Engineering, 11 vol set. - Edited by MB Bever *(MIT)*. Pergamon, Tarrytown, NY. 1986. 6200 pp. ISBN 0-08-042298-5. $3900.00.

A major eight-volume reference work providing the first complete coverage of the materials science and engineering field. Over 1550 authoratative articles, averaging 3000 words in length and complete with detailed bibliographies, make the encyclopedia indispensible for researchers, instructors and students in materials science and engineering who wish to gain access to specialist knowledge and modern interpretations across the entire field. The encyclopedia is extensively cross-referenced, carefully indexed and illustrated, and, in addition to its uniquely comprehensive scientific and technological coverage, contains many articles on the policy and social aspects of materials.

Selected articles include: Production, processing and properties of all the basic classes of materials such as metals, ceramics, and polymers; materials for specific applications including electronic, nuclear, biomedical and building materials; materials-related phenomena and methods such as investigative and analytical techniques, nondestructive evaluation, materials degradation, failure analysis, and surfaces and interfaces. Overview articles provide guidance in more than 40 specific areas of materials science and engineering. General subjects include materials science, materials engineering, materials resources, materials policy and economics.

11N34. Encyclopedia of Materials Science and Engineering, Supplementary volume 2. - Edited by Robert W Cahn *(Univ of Cambridge, UK)*. Pergamon, Tarrytown, NY. 1990. 831 pp. ISBN 0-08-036196-X. $380.00.

The continuing rapid development of materials science and engineering is graphically reflected in the 130 articles in this second supplementary volume to the highly acclaimed *Encyclopedia of Materials Science and Engineering*. More than 160 authorities worldwide provide new articles in the expanding areas of composite materials, advanced and traditional ceramics, electronic and superconducting materials, elastomers and polymer applications, wood and paper, industrial minerals, materials characterization, surfaces and interfaces, fundamental physical metallurgy and metals processing, production and fabrication. All articles are extensively cross-referenced, subject-indexed and provided with select bibliographies for further reading.

Selected articles include: Adhesive for wood: an update; Aluminum-based glassy alloys; Aluminum nitride; Armor, ceramic; Armor, composite; Automotive composite components: fabrication; Biomaterials: surface structure and properties; Ceramic powders: chemical preparation; Ceramics: construction applications; Coal: world resources; Colloidal crystals; Composite materials: aerospace applications; Composite materials: fatigue; Composite materials: structure-performance maps; Dental elastomers: an overview; Diamondlike and diamond thin films; Diffusion in silicon; Fiber-reinforced ceramics; Fumigation of wood; Gas sensors, solid state; Health hazards in wood processing; High-level radioactive waste disposal: safety; High-resolution electron microscopy; Lignin-based polymers; Lime; Microengineering of materials: laser fusion targets; Natural fiber based composites; Nitrogen in steels; Polyethylene processing to produce ultimate properties; Portland cement raw materials; Quasicrystals; Scanning tunnelling microscopy and spectroscopy; Silicon: preparation for semiconductors; Superconductors, ceramic; Superconductors, magnetic structure; Thin films: x-ray characterization; Titanium aluminides; Welding of thermoplastics; Wood: surface chemistry.

11N35. Encyclopedia of Materials Science and Engineering, Supplementary Vol 3. - Edited by Robert W Cahn FRS *(Univ of Cambridge, UK)*. Pergamon, Tarrytown, NY. 1993. 704 pp. ISBN 0-08-040590-8. $500.00.

The third and last supplementary volume to the *Encyclopedia of Materials Science and Engineering* continues the process of updating the 8-volume set by including further important developments made in the field since its publication in 1986.

Particular attention is paid to extractive metallurgy, polymer science and the characterization of materials; coverage is included in the areas of superconductivity and electronic materials where major advances have been made in recent years.

As with all the volumes of this exhaustive major work, Supplementary volume 3 provides detailed cross-references and bibliographies for all the articles, plus a cumulative analytical contents list and subject index for all the supplementary volumes, allowing efficient use in conjunction with the other volumes of the encyclopedia.

Selected articles include: A15 compound superconductors; Anodization spectroscopy; Arsenic production; Biocompatibility of biomedical materials; Biosynthetic and biomimetic materials; Bonding of elastomers and metals: processes; Brazing, reactive; Ceramics: cathodoluminescence analysis; Ceramics: mechanical performance and lifetime prediction; Crystal surfaces:melting and roughening; Diamond films: tribological properties; Diamond properties as a function of composition; Economics of the semiconductor industry; Elastomer processing hazards; Embedded atom method and related techniques; Fibers, superabsorbent; Grain boundary motion, diffusion-induced; Injection metallurgy; Lamp envelopes; Laser coating of surfaces; Magnetic alloys: rare earth intermetallics; Metal ores: bacterial leaching; Microtextural analysis; Microwave processing; Nonlinear optical effect: new crystals; Optical microscopy, confocal; Organic superconductors: anisotropic molecular metals; Organic superconductors: doped C_60 (Fullerene); Oxide superconductors: solid-state chemistry; Pitting corrosion; Polymer blends: phase separation; Polymer electrolytes; Prices of metals: history and current problems; Quantum wells; Radiation-induced segregation and diffusion; Recording head technology; Self-propagating high-temperature synthesis; Semiconductors: grain boundaries; Semiconductors: liquid phase epitaxy; Silicon nitride fibers; Silver: medical applications; SQUIDs: design, fabrication and application; Superconductors: magnetic properties; System design of materials; Thermal wave imaging; Thin films and multilayers, magnetic; Titanium alloys: surface treatment; Turbine materials for motor vehicles; Vulcanization, continuous; Welding in space; X-ray diffraction, time-resolved; X-ray emission, particle-induced.

REVIEW OF THE JOURNAL LITERATURE

for core list of journals scanned see Index Issue, published as Part 2 of the Dec issue of last year

I. FOUNDATIONS & BASIC METHODS

100. Continuum mechanics

11A1. **Geometric structure of the stress and strain tensors, dual variables and objective rates in continuum mechanics.** - C Sansour *(Inst Mechanik (Bauwesen), Univ Stuttgart, Stuttgart, Germany)*. Arch Mech 44(5-6) 527-556 (1992).

The geometric structure of the stress and strain tensors arising in continuum mechanics is investigated. All tensors are classified into two families, each consists of two subgroups regarded as physically equivalent since they are isometric. Special attention is focused on the Cauchy stress tensor and it is proved that, corresponding to it, no dual strain measure exists. Some new stress tensors are formulated and the physical meaning of the stress tensor dual to the Almansi strain tensor is made apparent by employing a new decomposition of the Cauchy stress tensor with respect to a Lagrangian basis. It is shown that push-forward and pull-back under the deformation gradient applied to the work conjugate stress and strain tensors do not result in further dual tensors.

11A2. **Axiomatic basis of space-time theory Part II. Construction of a C^0-manifold.** - J Schroter and U Schelb *(Dept of Phys, Univ of Paderborn, D-4790 Paderborn, Germany)*. Reports Math Phys 31(1) 5-27 (Feb 1992).

In this paper the investigations are continued. A physical theory ϕ_4 was formulated in the sense of Ludwig. In this paper ϕ_4 is extended by adding four axioms thus arriving at a theory ϕ_{T4}. These axioms are nonstructural ones so that the basic domain and the correspondence rules of ϕ_4 are the same. Within ϕ_{T4} a C^0-space-time-manifold is constructed which is also a full casual space.

11A3. **Relativistic Kepler problem in the Lobachevsky space.** - NA Chernikov *(Joint Inst for Nucl Res, Lab of Theor Phys, 141980 Dubna, Russia)*. Acta Phys Polonica B B24(5) 927-950 (May 1993).

Equations of gravitation in the Lobachevsky space are formulated. The problem of the gravitational field of point mass in the Lobachevsky space is solved. In the Newtonian (nonrelativistic) case, this problem was posed and solved by Lobachevsky himself. In the relativistic case, one should first find adequate equations for the metric describing the gravitational field and then find their solutions. These equations are found by the author on the basis of the theory, developed by him, with two affine connections; one called Christoffel and the other, background. The latter is given by the equations of motion of free material particle in the Lobachevsky space. It is independent of the light velocity c. The static spherically symmetric metric found here depends on the ratio of the gravitational radius γMc^{-2} of mass M to the Lobachevsky constant k for the visible world. In the limit $k \to \infty$ it turns into the well known Schwarzschild metric. The world line of a planet is geodesic with respect to this metric. The relativistic Kepler problem in the Lobachevsky space is reduced to a nonlinear differential equation.

11A4. **Stochastic motion of a particle in a model fluctuating medium.** - M Moreau *(Lab Phys Thorique Liquides, Univ P et M Curie CNRS-URA 765, Boite 121, 75252 Paris, France)*, B Gaveau *(UFR Math, Univ P et M Curie, Paris, France)*, M Frankowicz *(Fac of Chem, Jagellonian Univ, Ingardena 3, 30-060 Krakow, Poland)*, A Perera *(Lab Phys Thoriques Liquides, Univ P et M Curie CNRS-URA 765, Boite 121, 75252 Paris, France)*. Acta Phys Polonica B B24(4) 891-908 (Apr 1993).

We present several models of time fluctuating media with finite memory, consisting in 1 and 2D lattices, the nodes of which fluctuate between two internal states according to a Poisson process. A particle moves on the lattice, the diffusion by the nodes depending on their internal state. Such models can be used for the microscopic theory of reaction constants in a dense phase, or for the study of diffusion or reactivity in a complex medium. In a number of cases, the transmission probability of the medium is computed exactly; it is shown that stochastic resonances can occur, an optimal transmission being obtained for a convenient choice of parameters. In more general situations, approximate solutions are given in the case of short and moderate memory of the obstacles. The diffusion in an infinite 2D lattice is studied, and the memory is shown to affect the distribution of the particles rather than the diffusion law.

11A5. **The string model of dislocation damping revisited.** - F Marchesoni and D Segoloni *(Inst Nazionale Fisica Nucleare, Univ di Perugia, I-06100 Perugia, Italy)*. Acta Phys Polonica B B24(4) 865-890 (Apr 1993).

The classic Granato-Lucke model for dislocation damping is revisited by accounting for possible refinements to the basic vibration string mechanism. We argue that the perturbation approach, which consists in separating the (linear) dislocation dynamics from the equilibrium lattice environment, is not suitable, no matter how accurate the description of the coupling, to explain the finite decrement function observed experimentally in a variety of samples at vanishingly small frequencies. A few ideas for a more general theory are discussed in some detail.

11A6. **Tidal forces in vertical spaces of Finslerian space-time.** - PC Stavrinos *(Dept of Math, Univ of Athens, 15571, Greece)*. Reports Math Phys 31(1) 1-4 (Feb 1992).

The classical equation of geodesic deviation is extended in the case of vertical geodesics associated with a Finslerian space-time. It is shown that the deviations can appear only if the vertical component of the energy-momentum tensor differs from zero.

102. Finite element methods

102A. GENERAL THEORY

11A7. **Automation of the FEM: A personal historical view.** - EL Wilson *(Dept of Eng, Emeritus, UCB)*. Finite Elements Anal Des 13(2-3) 91-104 (Jun 1993).

A summary of the evolution of computational and numerical methods for the static and dynamic analysis of FE systems will be presented. The majority of the material discussed will reflect the personal experience of the author during the past 35 years. It is the opinion of the author, that at the present time, the FEM is far from being completely automated for complex structures.

11T8. **FE structural analysis and complementary energy.** - RH Gallagher *(Clarkson Univ, Potsdam NY 13676)*. Finite Elements Anal Des 13(2-3) 115-126 (Jun 1993).

11A9. **Field theory: A 2D case for not using FEs or BEs.** - WD Pilkey and Yongquan Liu *(Dept of Mech and Aerospace Eng, Univ of Virginia, Charlottesville VA 22903)*. Finite Elements Anal Des 13(2-3) 127-136 (Jun 1993).

A numerical solution methodology for 2D field theory problems is addressed. It is the contention of this paper that if the governing differential equation, eg, a Poisson's equation, of a 2D field theory problem can be transformed into an integral equation, the FEM may not be needed to solve the problem. Instead, such boundary solution methods as the BEM and the method of direct integration of the integral equation can be utilized, leading to better solutions than the FEM. The direct integration appears to give the most accurate and efficient solutions.

11T10. **Identifying the characteristics of FE analysis convergence curves.** - RJ Melosh *(Dept of Civil and Env Eng, Duke Univ, Durham NC 27706)*. Finite Elements Anal Des 13(2-3) 105-113 (Jun 1993).

102C. STRUCTURAL APPLICATIONS

11A11. **Applications of a super element model for nonlinear analysis of stiffened box structures.** - J Jiang and MD Olson *(Dept of Civil Eng, Univ of British Columbia, Vancouver, BC, V6T 1Z4, Canada)*. Int J Numer Methods Eng 36(13) 2219-2243 (15 Jul 1993).

Numerical investigations are carried out to verify the new super element model developed for nonlinear analysis of stiffened box girders. The results presented here are obtained from a variety of examples which are chosen to illustrate the accuracy and convergence of the model in various applications. Good agreement is obtained for most of the problems considered and the present formulation is found to be accurate and economical for preliminary engineering design.

11A12. **FE analysis of composite plates using a weak form of the Kirchhoff constraints.** - RS Rao and HK Stolarski *(Civil and Mineral Eng Dept, Univ of Minnesota, Minneapolis MN 55455)*. Finite Elements Anal Des 13(2-3) 191-208 (Jun 1993).

A six-node triangular C° plate element is developed using the assumed strain method. A weak form of the Kirchhoff constraints is used to define the assumed shear strain field. The element so developed is free of shear locking and performs well even when the element boundaries are curved. It is demonstrated that the element provides satisfactory results in the analysis of various composite plates.

11A13. **FE Analysis of flange connections.** - E Zahavi *(Pearlstone Center for Aeronaut Eng Stud, Mech Eng Dept, Ben-Gurion Univ of the*

Negev, Beersheva, Israel). J Pressure Vessel Tech 115(3) 327-329 (Aug 1993).

The present work pertains to nonlinear analysis of forces and deformation in pressurized flange connections, taking into consideration changes of geometry and friction. This allows greater accuracy in computing bolt forces and in predicting the leakage point.

11A14. FE Modeling of tillage tool design. - RL Kushwaha *(Dept of Agri and Bioresource Eng, Univ of Saskatchewan, Saskatoon, SK, S7N 0W0, Canada)*. Trans Can Soc Mech Eng 17(2) 257-269 (1993).

A nonlinear FE model was developed for 3D soil cutting by tillage tools. A hyperbolic constitutive relation for soil was used in the model. Analysis was carried out to simulate soil cutting with rectangular flat and triangular tillage blades at different rake angles and with curved blades. Interface elements were used to model the adhesion and the friction between soil and blade surface. Soil forces obtained from the FE model for the straight blades were verified with the results from laboratory tillage tests in the soil bin. The FE model predicted draft force accurately for both tillage tools. Results indicated that the draft was a function of rake angle, tool shape, and the curvature.

11A15. Super element model for nonlinear analysis of stiffened box structures. - J Jiang and MD Olson *(Dept of Civil Eng, Univ of British Columbia, Vancouver, BC, V6T 1Z4, Canada)*. Int J Numer Methods Eng 36(13) 2203-2217 (15 Jul 1993).

A numerical model for nonlinear static and dynamic analysis of stiffened box structures is presented. The model is based on a new super element formulation which provides complete C^1 continuity for both plate and beam elements. Geometric and material nonlinearities are included and the temporal equations are solved by the implicit Newmark-β method with Newton-Raphson subiteration. The new formulation has been applied to the static, vibration and transient analysis of various structures such as flat plates, folded plates and rectangular boxes. Both isotropic and beam stiffened structures are considered and the results obtained are compared with other available solutions. It is observed that the new super element formulation can provide reasonable solutions in both linear and nonlinear problem of stiffened box structures. The mathematical formulation of the model is presented in this paper, while the numerical verifications are given in the companion paper.

See also the following:

11A109. FE analysis of natural vibrations of an aeroplane with asymmetric variable wing geometry
11A118. Superelement method for transient dynamic analysis of structural systems
11A281. Hierarchic models for bidirectional composites
11A284. Static and dynamic analysis of sandwich plates with unidirectional variation of thickness
11A295. FE large displacement analysis of stiffened plates
11A551. Comparison of 2 and 3D FE analyses of adhesive joints

102E. OTHER SOLID MECHANICS APPLICATIONS

11A16. FE analysis of progressive failure for laminated FRP plates with inplane loading. - Li-Ren Tsau *(Dept of Mech Eng, Chung Cheng IT, Ta-Shi, Taiwan 33509 ROC)* and R Plunkett *(Dept of Aerospace Eng and Mech, Univ of Minnesota, Minneapolis MN 55455)*. Eng Fracture Mech 45(4) 529-546 (Jul 1993).

Composite materials can sustain a much higher load in inplane tension after the onset of local damage. The ultimate strength of composite laminates can be accurately predicted with FE analysis if the proper increment is used in each step. An analysis of the appropriate nodal spacing both in the plane of the specimen and in the thickness direction has been made with particular attention to the problem of stress concentration at the free edges. The load for final catastrophic failure and the failure pattern in progressive failure both agree well with experimental results.

11A17. FE simulation of elastic wave propagation in orthotropic composite materials. - KMA Jaleel *(Dept of Mech Eng, Univ of Toronto, ON, Canada)*, NN Kishore, V Sundararahan *(Dept of Mech Eng, Indian IT, Kanpur 208016, India)*. Mat Eval 51(7) 830-838 (Jul 1993).

Defects such as cracks and inclusions act as sources of wave scattering when illuminated by an incident ultrasonic pulse through reflection, diffraction, and mode conversion. Interaction of elastic waves with cracks provides all the necessary information regarding the inverse characterization of the defects which has not yet been thoroughly solved. In the present work, a plane strain FE model has been developed to study the elastic wave propagation and scattering in general anisotropic media. The interaction of pulsed compression waves and Rayleigh waves with cracks in isotropic material has been studied. The wave interaction with an interface crack in a layered graphite-epoxy composite structure has been investigated. It predicts the mode-conversion and diffraction of waves by cracks. It is found that for quasi-longitudinal waves the displacement along the fiber is prominent whereas for quasi-transverse, that displacement perdendicular to the fiber is prominent.

11A18. Improved preconditioned conjugate gradient method and its application in FEA for engineering. - Hong Zheng and Xiu-run Ge *(Inst of Rock and Soil Mech, Acad Sinica, Wuhan, China)*. Appl Math Mech 14(4) 371-380 (Apr 1993).

In this paper two theorems with theoretical and practical significance are given in respect to the preconditioned conjugate gradient method (PCCG). The theorems discuss respectively the qualitative property of the iterative solution and the construction principle of the iterative matrix. The authors put forward a new incompletely LU factorizing technique for the non-M-matrix and the method of constructing the iterative matrix. This improved PCCG is used to calculate the ill-conditioned problems and large-scale 3D FE problems, and simultaneously contrasted with other methods. The abnormal phenomenon is analyzed when PCCG is used to solve the system of ill-conditioned equations. It is shown that the method proposed in this paper is quite effective in solving the system of large-scale FE equations and the system of ill-conditioned equations.

11A19. Numerical analysis of IPIRG cracked pipe experiments subjected to dynamic and cyclic loading. - B Brickstad *(Swedish Plant Inspection, PO Box 49306, S-100 29 Stockholm, Sweden)*. Int J Pressure Vessels Piping 55(3) 395-422 (1993).

This report contains results of a FE study aiming to identify the influence of loading history and geometry for cracked pipes subjected to complex loading. The experiments have been performed within the International Piping Integrity Research Group Program. The majority of the numerically analyzed experiments were conducted on straight pipes with an outside diameter of 168 mm and containing a large circumferential through-wall crack. The considered pipes were loaded in four-point bending under displacement control and at a temperature of 288°C. The types of loading were combinations of either quasi-static or dynamic and also monotonic or cyclic loading with different loading ratios R. Some analyses were also performed on surface-cracked pipes subjected to slow, monotonic loading. In the FE study, 20-node solid elements were used for the through-wall cracked pipes and a combination of shell and nonlinear line spring elements for the surface-cracked pipes. Stable crack growth was simulated by gradual node relaxation and crack closure is accounted for by using simple contact elements. The J-integral for a remote contour is calculated and used as a characterizing fracture parameter although the cyclic loading violates the theoretical basis for this procedure. The near-tip J can not be used for growing cracks because of the weak energy singularity. The results of the numerical study confirm the trends from the experiments in that a high loading rate has a negative influence on the fracture properties of the studied carbon steel and that large cyclic loading, especially at R = -1, lowers the apparent J^R-curve for both carbon and stainless steels. To some extent geometry effects appear to be present when comparing the results from pipes containing surface cracks and through-wall cracks with results from CT specimens. These effects are more pronounced for large amounts of stable crack growth than at initiation.

See also the following:

11A259. Computational limit analysis of rigid-plastic bodies in plane strain
11A267. FE simulations of fiber pull-out
11A308. Postbuckling analysis of plates under combined loads by a mixed FEM and BEM
11A394. FEM modeling of stress intensity factors for fatigue crack growth at ultrasonic frequencies
11A396. Shearing effects on a shaft with circular surface crack under rotary bending
11A425. FE analysis of plane strain dynamic crack growth in materials displaying the Bauschinger effect
11A436. Strain energy release rates for internal cracks in rubber blocks

102G. FLUID MECHANICS APPLICATIONS

11A20. Behavior of several stress-velocity-pressure mixed FEs for Newtonian flows. - GC Buscaglia *(Div Mec Comput, DIA Centro Atomico Bariloche, CNEA, 8400-SC de Bariloche, Argentina)*. Int J Numer Methods Fluids 17(2) 99-113 (30 Jul 1993).

The Q_2/P_1, $P^+{}_2/P_1$, P_2/P_0 and Q_1/P_0 velocity-pressure mixed elements are extended to the stress-velocity-pressure formulation, using the same interpolants for stress and velocity, and tested in the 4-to-1 contraction problem for Stokes flow. The comparison shows significant differences among them, which are not present when the velocity-pressure formulation is used. To provide a better understanding of the phenomenon, several variants, of the previous elements are introduced, obtained by either changing the pressure space or by enriching the stress space with bubble functions. The formulation exhibits a strong sensitivity to the first alternative, while the second produces only a minor effect. These observations are confirmed by a convergence test effected on a regular problem with the explicit analytical solution. Also, as a result of the whole comparison, the $P^+{}_2/P^+{}_2/P_1$ element looks promising for three-field calculations.

11A21. Perturbation technique that works even when the nonlinearity is not small. - M Senator *(Davidson Lab, Stevens IT, Hoboken NJ 07030)* and CN Bapat *(Dept of Mech Eng, CCNY)*. J Sound Vib 164(1) 1-27 (8 Jun 1993).

We extend the Lindstedt-Poincare small nonlinearity based perturbation scheme to strongly nonlinear systems. The extended technique starts from a physically non-existent neighboring linear system. This system is created by adding an optimal linear spring term to the system side of each linear differential equation, starting at the zeroth level, and balancing that term by adding an equal one to the forcing side one level down. Unlike the Ritz method, which also works for strongly nonlinear systems, results can be obtained beyond the first level without resorting to numerical techniques. Thus, the extended method keeps the intuition-guiding straightforwardness to the perturbation method, while giving accurate, beyond first level, hand-derivable numerical results. Examples are presented for free vibrations with cubic and antisymmetric quadratic nonlinearities and for harmonic solutions of the undamped Duffing equation. The forms of the solution allow the regions of validity of the expansion to be estimated. An internal method of estimating accuracy of the perturbation solutions is developed and checked with the free vibration examples, the exact solution of which are available. The internal method is then used to estimate the accuracy of the new solutions to the Duffing equation. These new Duffing equation solutions give accurate results in all regions where stable harmonic solutions are known to exist. In particular, they give accurate results at and near the vertical tangent to the resonance curve, a region where Hayashi's amplitude expansion based perturbation solution necessarily breaks down.

11A22. Streamline upwind control volume FEM for modeling fluid flow and heat transfer problems. - CR Swaminathan *(Dept of Mech Eng, Univ of Minnesota, Minneapolis MN 55455)*, VR Voller *(Dept of Civil and Mineral Eng, Univ of Minnesota, Minneapolis MN 55455)*, SV Patankar *(Dept of Mech Eng, Univ of Minnesota, Minneapolis MN 55455)*. Finite Elements Anal Des 13(2-3) 169-184 (Jun 1993).

Galerkin and control volume FE approximations are compared and contrasted. Streamline upwinding and pressure stabilizing Petrov-Galerkin formulations for the numerical modeling of fluid flow problems are discussed. These formulations are then adapted to a control volume FE discretization. The resulting control volume FE scheme permits an equal order interpolation for velocity and pressure, is readily implemented and retains the property of local conservation, normally associated with control volume schemes.

See also the following:

11A155. Dynamic FE analysis for interaction between two phase saturated soil foundation and platform
11A236. Calculation of viscoelastic flow using molecular models: The CONNFFESSIT approach
11A590. Flow past a needle in a cylindrical tube

102J. OTHER APPLICATIONS

11A23. FE analysis of the 3D transient temperature field in steam turbine casings. - P Dhananjaya Rao, A Sarkar, VMK Sastri *(Dept of Mech Eng, Indian IT, Madras 600 036, India)*. Int J Mech Sci 35(7) 587-595 (Jul 1993).

One of the important considerations going into the process of optimization of start-up schedules for steam turbines is the estimation of thermal stresses during the transients. This in turn requires prediction of the transient temperature fields. In the case of the turbine casing, the procedures are complex in view of the irregular geometrical shape. FE analysis offers better scope in this regard and has been employed in the present work to compute the 3D transient temperature distribution in the casing metal. The metal results obtained by a code developed for a specific type of turbine casing have been compared with the values measured by experiment and have been found to validate the code. Time-temperature histories for two typical locations inside the casing metals are presented. Isotherm surfaces across the metal at a given instant are shown.

See also the following:

11A327. Numerical modeling of 2D magnetic properties for the FEM
11A430. Collapsed isoparametric element as a singular element for a crack normal to the bimaterial interface
11A458. Finite element simulation of eddy-current flaw detection systems
11A933. Determination of drying induced stresses in a prismatic bar

102L. SOLUTION ALGORITHMS

11A24. Closed-form error estimators for the linear strain and quadratic strain tetrahedron FEs. - PS Shiakolas, KL Lawrence, RV Nambiar *(Dept of Mech Eng, Univ of Texas, Arlington TX)*. Comput Struct 47(6) 907-915 (17 Jun 1993).

Closed-form representations of the Zienkiewicz-Zhu error estimators for straight edge linear and quadratic strain tetrahedral elements are presented. The closed-form representation of the element error estimators was developed using symbolic algebra. Dramatic computational time savings result in the element error estimator evaluation phase of the FEM process when the closed-form representation is used as compared with the use of Gaussian cubature.

11A25. Mesh stability study of FEM explicit algorithms for structural large-scale deformation impact responses. - Ming-Cheng Zhu *(Dept of Civil Eng, Tsinghua Univ, Beijing 100084, Peoples Rep of China)*, Lie-Quan Liu *(Dept of Mech, Huazhong Univ of Sci and Tech, Wuhan 430074, Peoples Rep of China)*, Sou-Yi Zheng *(Mech Teaching Group, Changsha Eng Inst, Changsha 410072, Peoples Rep of China)*. Acta Mech Solida Sinica 6(3) 302-308 (Jul 1993).

To FEM explicit algorithms for structural large-scale deformation impact responses, algorithm stability is discussed in the present paper. Algorithm stability is thought to include two aspects: one is called difference pattern stability and the other is called mesh stability. A self-adaptive adjusting method is proposed to ensure mesh stability with little amount of computation increased.

11A26. Optismoothing: An optimization-driven approach to mesh smoothing. - SA Canann, MB Stephenson *(Brigham Young Univ, Provo UT)*, T Blacker *(Sandia)*. Finite Elements Anal Des 13(2-3) 185-190 (Jun 1993).

This paper presents a mesh smoothing technique that uses optimization principles to minimize a distortion metric throughout a mesh. A comparison is made with Laplacian and isoparametric smoothing techniques.

11A27. Power method for the generalized eigenvalue problem. - W Kozlowski *(Warszawa, Poland)*. Matematyka Stosowana 35 5-19 (1992).

In this paper the Power Method for the generalized eigenvalue problem for matrix pencil ($A - \lambda B$) $x = 0$ is considered. At any step of this iterative process the system of linear algebraic $By = Ax$ has to be approximately solved with respect to y. We try to answer the question: how accurately we have to solve this system on each step of iteration, in order to guarantee resolution of the eigenproblem with given precision.

See also the following:

11A472. Multiparameter structural optimization using FEM and multipoint explicit approximations
11A484. Error estimate and step size control method for nonlinear solution techniques

102N. ELEMENT DEVELOPMENT

11A28. Construction of an optimal weakly divergence-free macroelement. - Xiu Ye *(Dept of Math and Stat, Univ of Arkansas, Little Rock AR 72204)* and CA Hall *(Dept of Math and Stat, Univ of Pittsburgh, Pittsburgh PA 15260)*. Int J Numer Methods Eng 36(13) 2245-2262 (15 Jul 1993).

The divergence-free FEM (DFFEM) is a method to find an approximate solution of the Navier-Stokes equations in a divergence-free space. That is, the continuity equation is satisfied *a priori*. DFFEM eliminates the pressure from the calculations and reduces significantly the dimension of the system to be solved at each time step. For the standard 8-node velocity and 4-node pressure DFFEM an optimal basis for the weakly divergence-free subspace is constructed such that each basis function has non-zero support on at most nine contiguous elements. Given this basis, weakly divergence-free macroelements are constructed.

11A29. Explicit FE formulation for very large deformations based on updated material reference frame. - Young M Yun *(Sch of Civil Eng, Purdue)*. Finite Elements Anal Des 13(2-3) 209-224 (Jun 1993).

An explicit FE formulation which has the capability of handling very large geometrical changes is developed. The formulation is based on an updated material reference frame and hence a true stress-strain test can be directly applied to properly characterize properties of materials which are subjected to very large deformations. For the large deformations, a consistent formulation based on the continuum mechanics approach is derived. The kinematics is referred to an updated material frame. Body equilibrium is also established based on the updated geometry. The second Piola-Kirchhoff stress tensor and the updated Lagrangian strain tensor are used in the formulation. Numerical examples of frame structures are solved to validate the presented formulation and to demonstrate the importance of imposing material properties properly.

11A30. Six-noded element for analyzing power-type singularities under thermal loads. - BK Dutta *(Reactor Eng Div, Bhabha Atomic Res Centre, Trombay, Bombay-400085, India)*. Int J Numer Methods Eng 36(13) 2287-2303 (15 Jul 1993).

The shape functions of a 6-noded triangular element have been derived to model power-type singularities under thermal loads. A number of case studies have been presented, which involve variable-order singularities under mechanical and thermal loads. The results show the usefulness of the element.

11A31. Symmetric Galerkin boundary formulations employing curved elements. - JH Kane and C Balakrishna *(Mech and Aeronaut Eng Dept, Clarkson Univ, Potsdam NY 13699)*. Int J Numer Methods Eng 36(13) 2157-2187 (15 Jul 1993).

Accounts of the symmetric Galerkin approach in BE analysis have recently been published. This paper attempts to add to the understanding of this method by addressing a series of fundamental issues associated with its potential computational efficiency. A new symmetric Galerkin theoretical formulation for both the (harmonic) heat conduction and the (biharmonic) elasticity problem that employs regularized singular and hypersingular boundary integral equations (BIEs) is presented. The novel use of regularized BIEs in the Galerkin context is shown to allow straightforward incorporation of curved, isoparametric elements. A symmetric reusable intrinsic sample point (RISP) numerical integration algorithm is shown to produce a Galerkin (ie, double) integration strategy that is competitive with its counterpart (ie, singular) integration procedure in the collocation BEA approach when the time saved in the symmetric equation solution phase is also taken into account. This new formulation is shown to be capable of employing hypersingular BIEs while obviating the requirement of C^1 continuity, a fact that allows the employment of the popular continuous element technology. The behavior of the symmetric Galerkin BEA method with regard to both direct and iterative equation solution operations is also addressed. A series of example problems are presented to quantify the performance of this symmetric approach, relative to the more conventional unsymmetric BEA, in terms of both accuracy and efficiency. It is concluded that appropriate implementations of the symmetric Galerkin approach to BEA indeed have the potential to be competititve with, if not superior to, collocation-based BEA, for large-scale problems.

104. Finite difference methods

11A32. Improved approximation technique to obtain numerical solution of a class of two-point boundary value similarity problems in fluid mechanics. - NG Kafoussias *(Dept of Math, Univ of Patras, 261 10 Patras, Greece)* and EW Williams *(Dept of Appl Math and Theor Phys, University, Liverpool L69 3BX, UK)*. Int J Numer Methods Fluids 17(2) 145-162 (30 Jul 1993).

A simple and efficient approximate numerical technique is presented to obtain solutions to a wide class of two-point boundary value similarity problems in fluid mechanics. This technique is based on the common finite difference method with central differencing, a tridiagonal matrix manipulation and an iterative procedure. The technique described in this paper has been successfully applied to three different representative similarity problems of fluid mechanics. Each one of these problems is described by a coupled, nonlinear system of three ordinary differential equations and has already been solved elsewhere using a different numerical method. So, the obtained numerical results, by our efficient numerical technique, permit a comparative study and show the accuracy and the effectiveness of this technique.

11A33. Finite difference method at arbitrary meshes for the bending of plates with variable thickness. - Guang-yao Li *(Dept of Comput Sci, Guizhou Univ, Guiyang, China)* and Han-bin Zhou *(Dept of Eng Mech, Tongji Univ, Shanghai, China)*. Appl Math Mech 14(3) 299-304 (Mar 1993).

A finite difference method at arbitrary meshes for the bending of plates with variable thickness is presented in this paper. The method is completely general with respect to various boundary conditions, load cases and shapes of plates. This difference scheme is simple and the numerical results agree well with those obtained by other methods.

11A34. Local uniform grid refinement and systems of coupled partial differential equations. - R Trompert *(CWI, PO Box 4079, 1009 AB Amsterdam, Netherlands)*. Appl Numer Math 12(4) 331-335 (Jun 1993).

In this paper we consider an adaptive grid method based on local uniform grid refinement to applied systems of coupled time-dependent PDEs. Local uniform grid refinement means that the PDEs are solved on a series of nested, uniform, increasingly finer subgrids which cover only a part of the domain. These subgrids are created up to a level of refinement where sufficient spatial accuracy is obtained and their location and shape is adjusted after each time step in order to follow the moving steep fronts. When a system of coupled PDEs is solved, the behavior of the local and global error associated with each separate PDE can be very different from one PDE to another. A refinement strategy based on a global error analysis has been developed which takes these differences into account. This refinement strategy aims at the domination of the global space error by the space discretization error at the finest subgrid.

11A35. The numerical solution of functional differential equations. A survey. - Z Jackiewicz *(State Univ, Tempe AZ)* and M Kwapisz *(Gdansk, Poland)*. Matematyka Stosowana 33 57-78 (1992).

Significant progress has been made in the last few years in the numerical solution of functional differential equations. It is the purpose of this paper to review the results in this area. Special attention is given to implementation on one-step methods and predictor corrector methods for functional differential equations including equations of neutral type and to the stability theory of numerical methods of these equations.

11A36. Surface grid generation with a linkage to geometric generation. - M Suzuki *(Inst of Comput Fluid Dyn, 1-16-5 Haramachi, Meguro-ku, Tokyo 152, Japan)*. Int J Numer Methods Fluids 17(2) 163-176 (30 Jul 1993).

This paper describes a new method to generate surface grids over complex configurations defined by a geometric generation system. The scheme is designed for direct utilization of the surface definition provided by a geometric modeller based on a boundary representation (the so-called B-rep modeller). Thus, the conversion of the geometric representation for the surface grid generator is not required. Consequently, this technique eliminates not only laborious tedium in the conversion of data, but also errors in the representation of the surface induced in the process of the conversion. The proposed method is accomplished over several stages. First, the triangulation is performed on the surface of the geometry, on which the area to be grided is laid. Then linear partial differential equations are mapped and solved on these triangular elements. Finally, the surface grid is constructed by searching for the contours inside the solution domain. After the co-ordinate values of the grid points are obtained by a linear interpolation within each triangular element, these values are mapped onto the surface of the geometry through surface parametric functions provided by the B-rep modeller. An example of generating surface grid over a car configuration is given to illustrate the capability of the method.

See also the following:

11A490. Affecting reliability of rail traffic vehicles in the phase of design and manufacturing

106. Other methods in computational mechanics

106A. BOUNDARY ELEMENT METHODS: GENERAL

See the following:

11A9. Field theory: A 2D case for not using finite or BEs

106B. BOUNDARY ELEMENT METHODS: APPLICATIONS

11A37. Adaptive BE for multiple subregions. - N Kamiya and M Koide *(Dept of Mech-Info and Syst, Nagoya Univ, Nagoya 464-01, Japan)*. Comput Mech 12(1-2) 69-80 (Jun 1993).

The sample point error analysis and related adaptive BE refinement, proposed by one of the present authors, is extended to the problem with subregion partition which is often required for maintaining higher accuracy and for treatment of composite dissimilar materials. The present study is devoted to regularization of the requirement that the interface between neighboring subregions should be discretized by the unified criterion for the both, while, in general, the error influences on the point on the interface from one region differs from that from the other. Two examples concerning the 2D Laplace equation are tested to verify the availability of the proposed method.

11A38. Compatible BEM for plane elasticity and fracture mechanics. - Lei Gu *(Dept of Civil Eng, Robert R McCormick Sch of Eng and Appl Sci, Tech Inst, NWU)*. Appl Math Model 17(8) 394-405 (Aug 1993).

A new compatible BE technique for solving biharmonic boundary value problems, based on Muskhelishvili's theory, is presented. The general solution of this kind of problem involves two independent analytic functions. These functions are represented by Vekua's integral formula where the path of the integral is taken around the external boundary of the solid. In this way, we derive a new type of boundary integral equation for plane elasticity problems as well as thin plate problems. In particular, the edge crack and central crack problems of plane elasticity have been investigated. The real density functions appearing in the boundary integral equations are determined by the BEM. The numerical results obtained show good agreement with the theoretical results.

11A39. Elastoplastic analysis of 2D problems with hole by BEM using complex variables. - S Tang *(Dept of Eng Mech, Tongji Univ, Shanghai 200092, Peoples Rep of China)* and R Kitching *(Dept of Mech Eng, Appl Mech Div, UMIST, Manchester, UK)*. Int J Mech Sci 35(7) 577-586 (Jul 1993).

A direct formulation of the BEM using complex variable functions for 2D elastoplastic analysis has been developed. Based on the initial stress approach and complex potential fundamental solutions, the method simplified the computer program and reduced the input data and the order of the equation system greatly; the function of the computer program has been improved and the singular solution behavior in the yield region near the boundary is eliminated. Two numerical examples have shown that the method can be used in practical applications of elastoplastic analysis in engineering.

See also the following:

11A376. BE model of cathodic well casing protection

11A433. Finite-part integral and BEM to solve embedded planar crack problems

106C. COLLOCATION, LEAST-SQUARE, GALERKIN, AND RELATED METHODS

See the following:

11A237. Spectral methods for the viscoelastic time-dependent flow equations with applications to Taylor-Couette flow

106E. HYBRID AND OTHER METHODS (INVERSE SCATTERING TRANSFORMS, PADE ETC)

11A40. Pole condition for singular problems: The pseudospectral approximation. - Weizhang Huang and DM Sloan *(Dept of Math, Univ of Strathclyde, Glasgow G1 1XH, UK)*. J Comput Phys 107(2) 254-261 (Aug 1993).

This paper deals with the pseudospectral solution of differential equations with coordinate singularities such as those which describe situations in spherical or cylindrical geometries. We use the differential equation, together with a smoothness assumption on the solution, to construct "pole conditions." The pole conditions, which are straightforward and easily implemented, serve as numerical boundary conditions at the coordinate singularity. Standard pseudospectral methods, including fast transformation techniques, can then be applied to the singular problem. The method is illustrated using the eigenvalue probelm of Bessel's equation and a Poisson equation on the unit disk. Numerical results show that spectral convergence is achieved.

106F. STOCHASTIC ANALYSIS

11A41. **Langevin equations with multiplicative noise. Application to domain growth.** - JM Sancho, A Hernandez-Machado *(Dept Estructura Constituents Materia, Univ Barcelona, Av Diagonal 647, E-08028 Barcelona, Spain)*, L Ramirez-Piscina, AM Lacasta *(Dept Fisica Aplicada, Univ Politec Catalunya, Jordi Girona Salgado 31, E-08034 Barcelona, Spain)*. Acta Phys Polonica B B24(4) 733-750 (Apr 1993).

Langevin Equations of Ginzburg-Landau form, with multiplicative noise, are proposed to study the effects of fluctuations in domain growth. These equations are derived from a coarse-grained methodology. The Cahn-Hilliard-Cook linear stability analysis predicts some effects in the transitory regime. We also derive numerical algorithms for the computer simulation of these equations. The numerical results corroborate the analytical predictions of the linear analysis. We also present simulation results for spinodal decomposition at large times.

11A42. **On randomly interrupted diffusion.** - J Luczka *(Dept of Theor Phys, Silesian Univ, Bankowa 14, 40-007 Katowice, Poland)*. Acta Phys Polonica B B24(4) 717-724 (Apr 1993).

Processes driven by randomly interrupted Gaussian white noise are considered. An evolution equation for single-event probability distributions are presented. Stationary states are considered as a solution of a second-order differential equation with two imposed conditions. A linear model is analyzed and its stationary distributions are explicitly given.

See also the following:

11A4. Stochastic motion of a particle in a model fluctuating medium

11A70. Non-conservatively loaded stochastic columns

11A385. Fatigue reliability in uniaxial state of stress produced by synchronous loads

11A876. Convection-driven growth in fluctuating velocity field

106G. ASYMPTOTIC AND PERTURBATION METHODS

11A43. **Solution for an irregular perturbation problem of viscoplastic spherical container under internal pressure.** - W Wojno *(Inst of Fund Tech Res, Polish Acad of Sci, Warszawa, Poland)*. Eng Trans 41(2) 209-235 (1993).

An irregular perturbation problem around a quasi-static solution for a motion of a thick-walled spherical container made from viscoplastic material and subjected to a time-dependent internal pressure is dealt with. Only the first perturbations are taken into account. A practically important case of a power excess stress function above the static yield stress is considered.

106I. ALGORITHMS AND SOFTWARE DEVELOPMENT

11A44. **Frontal approach for internal node generation in Delaunay triangulations.** - J-D Muller, PL Roe *(Dept of Aerospace Eng, Univ of Michigan, Ann Arbor MI 48109-2140)*, H Deconinck *(Von Karman Inst for Fluid Dyn, 72, Chaussee de Waterloo, B-1640 Rhode-Saint-Genese, Belgium)*. Int J Numer Methods Fluids 17(3) 241-255 (Aug 1993).

The past decade has known an increasing interest in the solution of the Euler equations on unstructured grids due to the simplicity with which an unstructured grid can be tailored around very complex geometries and be adapted to the solution. It is desirable that the mesh can be generated with minimum input from the user, ideally, just specifying the boundary geometry and, perhaps, a function to prescribe some desired mesh size. The internal nodes should then be found automatically by the grid generation code. The approach we propose here combines the Delaunay triangulation with ideas from the advancing front method of Peraire *et al* and Lohner *et al* Both methods are briefly reviewed in Section 1. Our method uses a background grid to interpolate local mesh size parameters that is taken from the triangulation of the given boundary nodes. Geometric criteria are used to find a set of nodes in a frontal manner. This set is subsequently introduced into the existing mesh, thus providing an updated Delaunay triangulation. The procedure is repeated until no more improvement of the grid can be achieved by inserting new nodes.

11A45. **Global approach to error estimation and physical diagnostics in multi-dimensional computational fluid dynamics.** - DC Haworth, SH El Tahry, MS Huebler *(Thermosci Dept, General Motors Res, 30500 Mound Rd, Warren MI 48090-9055)*. Int J Numer Methods Fluids 17(1) 75-97 (Jul 1993).

An approach for simultaneously assessing numerical accuracy and extracting physical information from multidimensional calculations of complex (engineering) flows is proposed and demonstrated. The method is based on global balance equations, ie, volume-integrated partial differential equations for primary or derived physical quantities of interest. Balances can be applied to the full computational domain or to any subdomain down to the single-cell level. Applications to in-cylinder flows in reciprocating engines are used for illustration. It is demonstrated that comparison of the relative magnitude of the terms in the balances provides insight into the physics of the flow being computed. Moreover, for quantities that are not conserved at the cell or control volume level in the construction of the numerical scheme, the imbalance allows a direct assessment of numerical accuracy in a single run using a single mesh. The mean kinetic energy imbalance is shown to be a particularly sensitive indicator of numerical accuracy. This simple and powerful diagnostic approach can be implemented for finite-difference, finite-volume or FEMs.

106K. COMPUTER ARCHITECTURES, SYSTEMS, HARDWARE

11A46. **Use of recursive stochastic algorithm for neural networks synthesis.** - AS Poznyak *(Inst of Control Sci, USSR Acad of Sci, Profsoyuznaya 65, Moscow, Russia)*, K Najim *(Dept of Chem Eng, Univ of Laval, PQ, G1K 7P4, Canada)*, M Chtourou *(CNRS URA 192, GRECO SARTA, ENSIGC, Chemin de la Loge 31078 Toulouse, Cedex, France)*. Appl Math Model 17(8) 444-448 (Aug 1993).

A new method based on a recursive stochastic algorithm is presented for neural networks synthesis. The cost function of the difference between the output of the net and the output of the process to be modeled by the net has nonunique stationary points. The common optimization techniques lead to local optima. It is shown that the solution of this optimization problem is connected with the construction of a convex envelope, characterized by local extrema of the intial problem. Then a recursive stochastic random search algorithm is derived for finding the optimum using realizations of a random variable associated with the function to be minimized. The application of this method is illustrated by an experimental example concerning neural networks synthesis for an industrial calcinator.

II. DYNAMICS & VIBRATION

150. Kinematics and dynamics

150A. GENERAL THEORY

11A47. **Formulation and solution for inverse problem of non-holonomic dynamics.** - Feng-li Liu *(Liaoning Univ, Shenyang, China)* and Feng-xiang Mei *(Peking IT, Beijing, China)*. Appl Math Mech 14(4) 327-332 (Apr 1993).

This paper presents a formulation and solution for the inverse problem of nonholonomic dynamics: to find the form of nonholonomic constraints when some integrals are given and to find the generalized reactive forces of constraint acting on the system when the expressions of the kinetic energy is given. An example is given to illustrate the application of the result.

11A48. **Principle of equal effects of general relativity and invariance of classical mechanics equations.** - Tian-lin Liang and Ling-yun Zhou *(Kunming IT, Kunming, China)*. Appl Math Mech 14(4) 361-366 (Apr 1993).

This paper gives the proof that the "inertial forces" in a noninertial system are not fabricated forces, but potential forces which actually act on the objects in motion in the acceleration field, according to the equivalent principle between gravitation and inertial forces in the theory general relativity. Further, the invariance of kinetical equation is illuminated.

150B. KINEMATICS OF RIGID BODIES AND PARTICLES

See the following:

11A200. Active systems in the vibration control of vehicles

150D. DYNAMICS OF RIGID BODIES AND PARTICLES

11A49. **Dynamical systems with impulses: Stroboscopic maps approach.** - A Kleczkowski *(Inst of Phys, Jagellonian Univ, Reymonta 4, PL-30-059 Krakow, Poland)*. Acta Phys Polonica B B24(6) 1061-1071 (Jun 1993).

A stroboscopic maps approach for continuous dynamic systems has been elaborated and generalized. For an impulse perturbation, the map equivalent to a given equation can be found analytically for a large class of systems, in the limit of the impulse width going to 0. This technique can be used for analyzing dynamical systems in which the perturbation has an impulse form, or can be joined with the Generalized Modulated Kicks Approximation to model a system with continuous or noisy perturbation. The validity of a "naive" method of finding the map is discussed.

150F. MULTIBODY AND VARIABLE MASS SYSTEMS

11A50. **Routh's equations for general non-holonomic mechanical systems of variable mass.** - Yao-huang Luo *(Yunnan Univ, Kunming, China)* and Yong-da Zhao *(Yunnan Inst of Educ,* *Kunming, China)*. Appl Math Mech 14(3) 285-298 (Mar 1993).

In this paper, Routh's equations for the mechanical systems of the variable mass with nonlinear nonholonomic constraints of arbitrary orders in a noninertial reference system have been deduced not from any variational principles, but from the dynamical equations of Newtonian mechanics. And then again the other forms of equations for nonholonomic systems of variable mass are obtained from Routh's equations.

150G. DEFORMABLE BODY DYNAMICS

11A51. Nonlinear dynamics of a flexible beam in a central gravitational field I. Equations of motion. - MRM Crespo da Silva and CL Zaretzky *(Dept of Mech Eng, Aeronaut Eng and Mech, RPI)*. Int J Solids Struct 30(17) 2287-2299 (1993).

The complete nonlinear differential equations governing the nonlinear motions of a beam able to undergo bending and pitching in space, are formulated in this paper. The formulation is based on a variational principle and accounts for all the nonlinearities due to deformation and gravity gradient effects. The nonlinearities due to deformation arise due to geometric effects, which consist of nonlinear curvature and nonlinear inertia terms. Expanded equations governing the nonlinear perturbed motion about an equilibrium are also developed for the case when the beam is in circular orbit. Such equations are suited for a perturbation analysis of the motion, and nonlinearities up to cubic order in a bookkeeping parameter are retained in them. Nonlinear motions involving interactions between bending and pitching of the beam are investigated in Part II of this work using the equations developed here.

11A52. Nonlinear dynamics of a flexible beam in a central gravitational field II. Nonlinear motions in circular orbit. - MRM Crespo da Silva and CL Zaretzky *(Dept of Mech Eng, Aeronaut Eng and Mech, RPI)*. Int J Solids Struct 30(17) 2301-2316 (1993).

The coupled nonlinear pitch-bending response of a free-free beam in a circular orbit, when the beam is subjected to a periodic external excitation, is analyzed. The nonlinearities present in the differential equations of motion are due to deformation of the beam (ie, curvature and inertia nonlinearities) and to the gravity-gradient moments. Perturbation methods are used to analyze the motion. Several resonant motions exhibited by the system are analyzed in detail, namely, harmonic resonances when the frequency of the external excitation, Ω, is either near the natural frequency of the flexural or the pitch motion, and a superharmonic resonance when Ω is near one half of the natural frequency for the pitch motion. The latter two resonances are associated with very low excitation frequencies.

150K. NONLINEAR DYNAMICS (INCL CHAOS, BIFURCATION, FRACTALS)

11A53. Bifurcations and chaos in voice signals. - H Herzel *(Inst of Theor Phys, Humboldt Univ, Invalidenstr 42, 0-1040 Berlin, Germany)*. Appl Mech Rev 46(7) 399-413 (Jul 1993).

The basic physical mechanisms of speech production is described. A rich variety of bifurcations and episodes of irregular behavior are observed. Poincare sections and the analysis of the underlying attractor suggest that these noise-like episodes are low-dimensional determ[illegible] chaos. Possible implications for the [illegible] diagnosis of brain disorder are discuss[illegible]

11A54. Chaos and noise in dynamical systems. - T Kapitaniak *(Div of Control and Dyn, Tech Univ of Lodz, Poland)* and J Brindley *(Sch of Math, Univ of Leeds, Leeds LS2 9JT, UK)*. Appl Mech Rev 46(7) 359-444 (Jul 1993).

This collection of papers is concerned with chaos and noise in a range of dynamical systems, mostly within a context of mechanics.

11A55. Controlling chaos in mechanical systems. - B Blazejczyk, T Kapitaniak, J Wojewoda *(Div of Control and Dyn, Tech Univ, Stefanowskiego 1-15, 90-924 Lodz, Poland)*, J Brindley *(Dept of Appl Math Stud and Centre for Nonlinear Stud, Univ of Leeds, Leeds LS2 9JT, UK)*. Appl Mech Rev 46(7) 385-391 (Jul 1993).

The problem of controlling chaos, that is to convert the chaotic behavior to a periodic time dependence is discussed. We described a number of effective controlling methods in the context of mechanical systems.

11A56. Destruction of quasiperiodic oscillations in weakly nonlinear systems. - AB Belogortsev *(Dept of Phys and Astron, Univ of Maine, Orono ME 04469)*, DM Vavriv *(Radio Astron Inst, Acad of Sci of Ukraine, Kharkov 310002, Ukraine)*, OA Tretyakov *(Dept of Radio Phys, Kharkov State Univ, Kharkov 310077, Ukraine)*. Appl Mech Rev 46(7) 372-384 (Jul 1993).

We consider the main regularities of the arising of the dynamical chaos in weakly nonlinear oscillatory systems. We show that the chaotic oscillations in such systems can occur due to the destruction of quasiperiodic oscillations. Various analytical approaches are applied to study the properties of the quasiperiodically forced passive and active single-mode oscillators as well as the conditions for the appearance of chaos. The results of numerical and experimental investigations are also discussed.

11A57. Dynamics of a rolling wheelset. - Hans True *(Tech Univ of Denmark and ES-Consult, DK-2800 Lyngby, Denmark)*. Appl Mech Rev 46(7) 438-444 (Jul 1993).

We discuss the kinematics and dynamics of a wheelset rolling on a railway track. The mathematical model of a suspended wheelset rolling with constant speed on a straight track is set up and its dynamics is investigated numerically. The results are presented mainly on bifurcation diagrams. Several kinds of dynamical behavior is identified within the investigated speed range. We find a stationary equilibrium point at low speeds and at higher speeds symmetric and asymmetric oscillations are found and ranges with chaotic motion are identified. The bifurcations are described.

11A58. Homoclinics in the reconstruction of dynamic systems from experimental data. - VS Anishchenko and MA Safonova *(Phys Dept, Saratov State Univ, Astrachanskaja B3, Saratov 410071, Russia)*. Appl Mech Rev 46(7) 361-371 (Jul 1993).

The role of homoclinic effects in solution of a reconstruction problem of system attractors and model equations from experimental observable in the presence of external noise is investigated numerically. It is shown that the possibility of reconstruction essentially depends on character of origin system homoclinic trajectories and noise intensity. If the homoclinic structure belongs to the attractor, then the reconstruction results in restoration origin system attractors. A small noise influence causes in this case a small perturbation of attractors probability measure and practically disappears due to filtering properties of the reconstruction algorithm. The homoclinic structure does not belong to the attractor, then in the absence of noise the probability measure concentrates at the attractor, the structure of which is not [illegible]ined by the homoclinics. The noise perturba[illegible] induces new regimes. Then the attractor [illegible]ure essentially depends on the homoclinics [illegible]ure and noise level. In this case the model system attractor of which reproduces "invisible" homoclinic structure, is obtained as a result of reconstruction.

11A59. Hopf bifurcation in gas journal bearings. - K Czolczynski *(Div of Control and Dyn, Tech Univ, Stefanowskiego 1-15, 90-924 Lodz, Poland)*. Appl Mech Rev 46(7) 392-398 (Jul 1993).

This paper reviews a numerical investigation of the problem of small self-excited vibrations in gas journal bearings. The method of analysis is based on the Hopf bifurcation theory, in which the approximate periodic solutions of nonlinear equations of motion are computed using the Fredholm alternative. This theory enables us to construct the bifurcating periodic solutions and to determine their stability. The equations of motion of the investigated gas journal bearing have been formulated after estimating the damping and stiffness coefficients of a gas film. For this purpose, a new method of identification has been proposed.

11A60. Sectional curvature and chaos in dynamical problems: Toward the invariant measure of chaos in Hamiltonian systems. - M Szydlowski *(Astron Observatory, Jagiellonian Univ, Orla 171, 30-244 Krakow, Poland)* and A Krawiec *(Dept of Economics, Jagiellonian Univ, Wislna 2, 31-007 Krakow, Poland)*. Appl Mech Rev 46(7) 427-437 (Jul 1993).

Chaotic phenomena in general relativity are investigated. In relativistic astrophysical problems no space-time coordinate system is privileged in any way as far as the physical description of phenomena is concerned. Effects which depend on the choice of the particular coordinate system should be treated as an artifact of the incorrect methods. To avoid such difficulties the gauge invariant theory of chaos is proposed.

11A61. Spatio-temporal versus temporal chaos in a spatially extended magnetic dynamical system. - JJ Zebrowski and A Sukiennicki *(Inst of Phys, Warsaw Univ of Tech, Koszykowa 75, 00-662 Warszawa, Poland)*. Acta Phys Polonica B B24(4) 785-800 (Apr 1993).

Nonlinear dynamical states of a spatially extended micromagnetic system - the Bloch wall - were analyzed by means of spatio-temporal diagrams and power spectral analysis in the spatial frequency domain. The system studied exhibits dynamics with propagating coherent spatial structures - Bloch lines - which have soliton properties. Although it is spatially extended only temporal chaos occurs. The symptoms of this type of chaos (spatially complex patterns changing violently with the time) in such a spatially extended system should not be confused with chaos in the space and time simultaneously. The system is not spatially chaotic due to the existence in it of coherent spatial structures with a fixed length scale (kink solitons).

11A62. Synchronization and chaotization of oscillations in coupled self-oscillating systems. - PS Landa *(Dept of Phys, Lomonosov Moscow State Univ, 119899 Moscow, Russia)* and MG Rosenblum *(Mech Eng Res Inst, Russian Acad of Sci, 101830 Moscow, Russia)*. Appl Mech Rev 46(7) 414-426 (Jul 1993).

The effects of synchronization of chaotic and periodic self-oscillation systems are discussed. Two mechanisms of synchronization of periodic systems which manifest themselves at synchronization of chaotic systems are determined. Examples of synchronization of chaotic systems by harmonic external force, mutual synchronization of periodic and chaotic systems, as well as of mutual synchronization of two and more chaotic systems are discussed.

See also the following:

11A49. Dynamical systems with impulses: Stroboscopic maps approach
11A113. Study and performance evaluation of some nonlinear diagnostic methods for large rotating machinery

150Y. COMPUTATIONAL TECHNIQUES

11A63. Accelerated iterative method for the dynamics of constrained multibody systems. - Kisu Lee *(Dept of Mech Eng, Chon Buk Natl Univ, Chon Ju, Chon Buk 560-756, Korea).* Comput Mech 12(1-2) 27-38 (Jun 1993).

An accelerated iterative method is suggested for the dynamic analysis of multibody systems consisting of interconnected rigid bodies. The Lagrange multipliers associated with the kinematic constraints are iteratively computed by the monotone reduction of the constraint error vector, and the resulting equations of motion are easily time-integrated by a well established ODE technique. The velocity and acceleration constraints as well as the position constraints are made to be satisfied at the joints at each time step. Exact solution is obtained without the time demanding procedures such as selection of the independent coordinates, decomposition of the constraint Jacobian matrix, and Newton Raphson iterations. An acceleration technique is employed for the faster convergence of the iterative scheme and the convergence analysis of the proposed iterative method is presented. Numerical solutions for the verification problems are presented to demonstrate the efficiency and accuracy of the suggested technique.

11A64. Sufficient conditions for penalty formulation methods in analytical dynamics. - AJ Kurdila *(Dept of Aerospace Eng, Texas A&M Univ, College Station TX 77843-3141)* and FJ Narcowich *(Dept of Math, Texas A&M Univ, College Station TX 77843-3368).* Comput Mech 12(1-2) 81-96 (Jun 1993).

This paper derives sufficient conditions for the convergence of a class of penalty methods by extending the Rubin-Ungar theorem. One advantage of the approach taken in this paper is that considerable simplification of the original Rubin-Ungar derivation is achieved for the convergence of transverse constraint velocities. This paper also emphasizes the importance of maintaining a rank condition on the Jacobian of the constraint matrix. This is of particular importance in that one claimed benefit of certain penalty methods is that they are effective in cases in which the constraint Jacobian loses rank. For the class of penalty methods considered in this paper, if the Jacobian does not meet the specified rank conditions, a diverse collection of spurious, pathological responses can be obtained using this method. In one sense, this type of pathological response is worse then encountering a "configuration-singular" generalized mass matrix and having a simulation diverge; indeed, the *regularized* solution procedure can proceed along some incorrect trajectory with little to no indication that something is amiss.

150Z. EXPERIMENTAL TECHNIQUES

11A65. Geometric methods in determining rigid-body dynamics. - GS Nusholtz *(Chrysler, 800 Chrysler Dr E, CIMS 483-05-10, Auburn Hills MI 48326-2757).* Exp Mech 33(2) 153-158 (Jun 1993).

This research develops a measurement system using linear accelerometers to determine the 3D, 6-dof, impact response of an anthropomorphic test device (dummy). A procedure using spherical geometric analysis (SGA) was developed. It uses three triaxial accelerometer clusters for determining angular velocity, angular acceleration, and linear acceleration. SGA differs in its calculation of angular velocity from other procedures which determine rigid-body motion. Unlike procedures which use linear accelerometers to determine angular velocity by integration of angular acceleration, SGA uses the topology of the sphere to obtain both angular acceleration and angular velocity through algebraic manipulation of the output from the linear accelerations. The validation of SGA is accomplished by the use of hypothetical as well as experimental data.

152. Vibrations of solids (basic)

152A. GENERAL THEORY

11A66. Forced harmonic response analysis of nonlinear structures using describing functions. - O Tanrikulu *(Tubitak-Sage, PK 119 Bahcelievler, Ankara, Turkey),* B Kuran, HN Ozguven *(Dept of Mech Eng, Middle E Tech Univ, Ankara 06531, Turkey),* M Imregun *(Dept of Mech Eng, Imperial Col of Sci Tech and Med, London SW7 2BX, UK).* AIAA J 31(7) 1313-1320 (Jul 1993).

The dynamic response of multiple-dof nonlinear structures is usually determined by numerical integration of the equations of motion, an approach which is computationally very expensive for steady-state response analysis of large structures. In this paper, an alternative semianalytical quasilinear method based on the describing function formulation is proposed for the harmonic response analysis of structures with symmetrical nonlinearities. The equations of motion are converted to a set of nonlinear algebraic equations and the solution is obtained iteratively. The linear and nonlinear parts of the structure are dealt with separately, the former being represented by the constant linear receptance matrix [α], and the latter by the generalized quasilinear matrix [Δ] which is updated at each iteration. A special technique that reduces the computation time significantly when the nonlinearities are localized is used with success to analyze large structures. The proposed method is fully compatible with standard modal analysis procedures. Several examples dealing with cubic stiffness, piecewise linear stiffness, and coulomb friction type of nonlinearities are presented in the case of a ten-dof structure.

11A67. Normal modes for nonlinear vibratory systems. - SW Shaw and C Pierre *(Dept of Mech Eng and Appl Mech, Univ of Michigan, Ann Arbor MI 48109).* J Sound Vib 164(1) 85-124 (8 Jun 1993).

A methodology is presented which extends to nonlinear systems the concept of normal modes of motion which is well developed for linear systems. The method is constructive for weakly nonlinear systems and provides the physical nature of the normal modes along with the nonlinear differential equations which govern their dynamics. It also provides the nonlinear co-ordinate transformation which relates the original system co-ordinates to the modal co-ordinates. Using this transformation, we demonstrate how an approximate nonlinear version of the superposition can be employed to reconstruct the overall motion from the individual nonlinear modal dynamics. The results presented herein for nonlinear systems reduce to modal analysis for the linearized system when nonlinearities are neglected, even though the approach is entirely different from the traditional one. The tools employed are from the theory of invariant manifolds for dynamical systems and were inspired by the center manifold reduction technique. In this paper the basic ideas are outlined, a few examples are presented and some natural extensions and applications of the method are briefly described in the conclusions.

See also the following:

11A21. Perturbation technique that works even when the nonlinearity is not small

152B. LINEAR THEORY

11A68. Note on modal summations and averaging methods as applied to statistical energy analysis. - AJ Keane *(Dept of Eng Sci, Univ of Oxford, Parks Rd, Oxford OX1 3PJ, UK).* J Sound Vib 164(1) 143-156 (8 Jun 1993).

In this note the power transmission between two, point spring coupled, axially vibrating rods under various conditions is examined. The effects of using a modal description for the rods, are examined, with particular attention being paid to the number of modes used when assessing energy flows. Also considered are the various methods commonly used to calculate the average energy flows for this system. These studies have been carried out as part of a larger study on variability in SEA predictions for more complex models. The differences between the averaging methods used are shown to be significant and demonstrate the inherent dangers of assuming that frequency and ensemble averages are equivalent, a common assumption of traditional SEA. The adoption of a modal description for the system being studied is seen to be sustainable provided that the correct number of modes is used within the calculations. This number rises with coupling strength and also if the point of coupling shows model coherence (such as occurs at the ends of the free-free rod). These results lend credence to the adoption of modal methods when studying SEA but indicate that frequency averaging should be handled with care.

152D. STOCHASTIC EFFECTS, INCL RANDOM EXCITATION

11A69. Chaotic behavior of a nonlinear oscillator. - Qin-Yuan Pei *(Changsha Railway Univ, Changsha, China)* and Li Li *(Peking Polytech Univ, Beijing, China).* Appl Math Mech 14(5) 395-405 (May 1993).

Behavior of bifurcation and chaos in a forces oscillator $x1 + \delta x1 + \omega^2{}_0 x1 - \beta x^2{}_0 = f\cos\omega\tau$ containing a square nonlinear term is investigated by using Mel'nikov method and digital computer simulations.

11A70. Non-conservatively loaded stochastic columns. - R Ganesan, TS Sankar *(Concordia Univ, Montreal, H3G 1M8, Canada),* SA Ramu *(Indian Inst of Sci, Bangalore, India).* Int J Solids Struct 30(17) 2407-2424 (1993).

A new FEM is developed to analyze non-conservative structures with more than one parameter behaving in a stochastic manner. As a generalization, this paper treats the subsequent non-self-adjoint random eigenvalue problem that arises when the material property values of the non-conservative structural system have stochastic fluctuations resulting from manufacturing and measurement errors. The free vibration problems of stochastic Beck's column and stochastic Leipholz column whose Young's modulus and mass density are distributed stochastically are considered. The stochastic FEM that is developed, is implemented to arrive at a random non-self-adjoint algebraic eigenvalue problem. The stochastic characteristics of eigensolutions are derived in terms of the stochastic material property variations. Numerical examples are given. It is demonstrated that, through this formulation, the FE discretization need not be dependent on the characteristics of stochastic processes of the fluctuations in material property value.

11A71. Spectral response of a bilinear oscillator. - RN Miles *(Dept of Mech and Indust Eng, SUNY, Binghamton NY 13902-6000).* J Sound Vib 163(2) 319-326 (May 1993).

An approximate analytical procedure is presented to estimate the response power spectral density of a randomly excited spring-mass-damper system having a bilinear spring. The approximate expression for the response spectrum is developed by representing the nonlinear oscillator as a linear system having a natural frequency that depends on the envelope of the random response. This approximate representation of the system leads to estimates of the response spectrum that agree extremely well with those obtained by direct numerical simulation of the governing equation.

See also the following:

11A133. Estimation of clearances and impact forces using vibroimpact response: Random excitation

11A134. Extension of clearance and impact force estimation approaches to a beam-stop system

152F. DAMPING, DECAY, AND CONTROL OF VIBRATIONS

11A72. Beam-like damper for attenuating transient vibrations of light structures. - LA Chen and SE Semercigil *(Dept of Mech Eng, McMaster Univ, Hamilton, ON, L8S 4L7, Canada)*. J Sound Vib **164**(1) 53-65 (8 Jun 1993).

When a flexible robot arm, a cantilevered beam type of structure, moves with a fast speed between workstations and is suddenly stopped after a new positioning is completed, excessive transient vibrations are produced as a result of the flexibility. An impact damping technique may be used to control these excessive transient vibrations. Effect of the orientation of the robot arm relative to the gravitational acceleration is investigated for the conventional impact damper. A new impactor, in the form of another cantilevered beam, is suggested here as an impact damper the performance of which is independent of the orientation of the arm. Design charts, produced from numerical simulations, are presented to demonstrate the vibration attenuation capability of the conventional and the proposed impact damper. Experiments are described briefly to confirm the validity of the numerical model.

152Y. COMPUTATIONAL TECHNIQUES

11A73. Community response to aircraft noise around six Spanish airports. - A Garcia, LJ Faus *(Lab of Acoust, Appl Phys Dept, Univ of Valencia, Spain)*, AM Garcia *(Preventive Med and Public Health Dept, Univ of Valencia, Spain)*. J Sound Vib **164**(1) 45-52 (8 Jun 1993).

The community response to aircraft noise has been studied through a social survey. A total of 1800 persons living in the vicinity of six major Spanish airports have been interviewed at their homes concerning the environmental quality of the area, dissatisfaction with road traffic noise and aircraft noise, activities interfered with by noise, most disturbing aircraft types, and subjective evaluation of airport impact. All the responses obtained in this survey have been compared with aircraft noise levels corresponding to the residence locations of the people interviewed (values of NEF levels were calculated with the INM model). The results obtained in this work allow one to evaluate the impact of aircraft noise under a wide range of different situations.

11A74. Computing eigenvector derivatives in structural dynamics. - Zhong-Sheng Liu, Su-Huan Chen, You-Qun Zhao, Chun-Sheng Shao *(Center for Comput Mech, Jilin Univ of Tech, Changchun 130022, Peoples Rep of China)*. Acta Mech Solida Sinica **6**(3) 291-299 (Jul 1993).

This paper presents an improved modal superposition method for computing eigenvector derivatives in which the contribution due to the unavailable higher modes to the eigenvector derivatives is considered. The proposed approach not only improves the accuracy previously published method, but also provides error estimates for the computed results.

11A75. FEM for computation of structural intensity by the normal mode approach. - L Gavric and G Pavic *(Dept Acoustique, CETIM, BP 67, 60304 Senlis, France)*. J Sound Vib **164**(1) 29-43 (8 Jun 1993).

A method for numerical computation of structural intensity in thin-walled structures is presented. The method is based on structural FEs (beam, plate and shell type) enabling computation of real eigenvalues and eigenvectors of undamped structure which then serve in evaluation of complex response. The distributed structural damping is taken into account by using the modal damping concept, while any localized damping is treated as an external loading, determined by use of impedance matching conditions and eigenproperties of the structure. Emphasis is given to aspects of accuracy of the results and efficiency of the numerical procedures used. High requirements on accuracy of the structural response (displacements and stresses) needed in intensity applications are satisfied by employing the "swept static solution", which effectively takes into account the influence of higher modes otherwise inaccessible to numerical computation. A comparison is made between the results obtained by using analytical methods and the proposed numerical procedure to demonstrate the validity of the method presented.

11A76. Rayleigh quotient method for computing eigenvalue bounds of vibrational systems with interval parameters. - Zi-Ping Qiu, Su-Huan Chen, Jing-Xin Na *(Center for Comput Mech, Jilin Univ of Tech, Changchun 130022, Peoples Rep of China)*. Acta Mech Solida Sinica **6**(3) 309-318 (Jul 1993).

In this paper, an effective method, the Rayleigh quotient iteration, for computing the bounds of structures with interval parameters is presented. When the uncertainty of the structural parameters is described by using the interval, ie, an unknown-but-bounded version, the structural vibration eigenvalues will become the interval. It is desirable to give these interval eigenvalues. An application of this method is illustrated by a numerical example. The results show that the Rayleigh quotient iteration method is very effective for constructing the upper and lower bounds on the eigenvalues of structures with interval parameters.

154. Vibrations (structural elements)

154B. BEAMS, COLUMNS, RODS, AND BARS

11A77. Application of the harmonic balance principle to the nonlinear free vibration of beams. - MI Qaisi *(Dept of Mech Eng, Jordan Univ, Amman, Jordan)*. Appl Acoust **40**(2) 141-151 (1993).

This paper presents an analytical method for determining the vibration modes of geometrically nonlinear beams under various edge conditions. The method assumes a continuum periodic solution which allows the harmonic balance principle to be employed to derive modal components that satisfy the equation of motion exactly. Nonlinear normal modes are constructed from four such components and used to compute the natural frequencies for beams with restrained ends and for cantilevered beams. Numerical results for beams with restrained ends show good agreement with those available from other techniques.

11A78. Small vibrations of flexible bars by using the FEM with equivalent uniform stiffness and mass methodology. - DG Fertis and AO Afonta *(Dept of Civil Eng, Univ of Akron, Akron OH 44325-3905)*. J Sound Vib **163**(2) 343-358 (May 1993).

The object of this research is to calculate natural frequencies and mode shapes of a small oscillation vibration, superimposed on large static displacement, by using the FEM in conjunction with the equivalent uniform stiffness and mass method. The equivalent uniform stiffness and mass matrices are determined from the differential equation by using Galerkin's method. The analysis herein is three-fold. First, the large static equilibrium configuration of the deformed flexible beam is established. This is achieved by using the Euler-Bernoulli equation in conjunction with equivalent pseudo-linear and/or equivalent nonlinear systems of constant stiffness. This concept and methodology were used quite extensively by the authors to study large deformation characteristics of various flexible beam problems of uniform and variable stiffness and of arbitrary loading conditions (see, for example, the work of Fertis and Afonta, and Fertis and Lee). Secondly, the differential equation of motion for small amplitude vibrations from the large static equilibrium configuration is derived. Galerkin's technique is used to approximate the differential equation of motion. Finally, the natural frequencies of vibration and the associated mode shapes are determined by solving the resulting eigenvalue problem. A canned eigensolver from the University of Akron IMSL is used to extract the eigenvalues and eigenvectors. The concept of equivalent pseudo-linear systems of constant stiffness is used extensively in this research, in order to simplify the solution of these complex nonlinear problems.

See also the following:

11A92. Influence of external damping on the stability and response of a horizontal rotor with anisotropic bending stiffness

11A309. Stabilization of beam parametric vibrations

154G. PLATES

11A79. Accurate free vibration analysis of clamped Mindlin plates using the method of superposition. - SD Yu and WL Cleghorn *(Dept of Mech Eng, Univ of Toronto, Toronto, ON, M5S 1A4, Canada)*. Trans Can Soc Mech Eng **17**(2) 243-255 (1993).

The method of superposition is further developed to analyze free flexural vibration of clamped rectangular Mindlin plates. Comparison of results given by Mindlin's theory of plates with those previously obtained by Reissner's theory has shown that the rotatory inertia does not significantly affect plate flexural vibration. Accurate eigenvalues are presented for a number of values of plate aspect ratio along with two representative values of thickness ratio.

11A80. Finite strip-elements for the dynamic analysis of orthotropic plate structures. - BW Golley and J Petrolito *(Dept of Civil Eng, Univ Col, Austral Defence Force Acad, Campbell ACT 2600, Australia)*. J Sound Vib **163**(3) 479-491 (22 May 1993).

A finite strip-element method is presented for the dynamic analysis of orthotropic plate structures. In the strip-element a hierarchical interpolation is used that is a combination of FE shape functions and trigonometric shape functions. A transformation of variables is used to calculate the strip-element stiffness and mass matrices. This enables continuous plates and plates with point and line supports to be analyzed. Convergence is rapid, with few hierarchical terms being required for engineering accuracy.

11A81. Generic free vibration of orthotropic rectangular plates with clamped and simply supported edges. - SD Yu and WL Cleghorn *(Dept of Mech Eng, Univ of Toronto, ON, M5S*

1A4, Canada). J Sound Vib 163(3) 439-450 (22 May 1993).

The generic free vibration of specially orthotropic rectangular plates with combinations of clamped and simply supported edges is investigated by the superposition technique. The introduction of affine transformation reduces the two rigidity parameters required for the free vibration analysis to one, making complete tabulation of computed eigenvalues much easier. Numerical calculations are performed on clamped plates, plates with one edge simply supported, and plates with two adjacent edges simply supported, along with a number of representative values of the generalized rigidity parameter and the affine aspect ratio.

11A82. Modeling the vibration restraints of wedge lock card guides. - DB Barker and YS Chen *(CALCE Electron Packaging Res Center, Univ of Maryland, College Park MD 20742).* J Electron Packaging 115(2) 189-194 (Jun 1993).

One of the most dominate parameters that influence the calculation of PWB's natural frequency is the boundary conditions along the edges of the board. A series of experiments was conducted with Calmark three and five-part wedge locks to determine the boundary condition restraint offered by these commonly used card guides. The wedge locks are modeled as simple supports preventing transverse deflection of the plate edge and as linear elastic springs restraining the rotation of the plate edge. The rotational spring constant for the wedge lock was then calculated in a semi-inverse manner by measuring the natural frequency response of a well-characterized plate.

11A83. Roles of domain decomposition method in plate vibrations: Treatment of mixed discontinuous periphery boundaries. - KM Liew, KC Hung, MK Lim *(Div of Appl Mech, Sch of Mech and Prod Eng, Nanyang Tech Univ, Nanyang Ave, Singapore 2263).* Int J Mech Sci 35(7) 615-632 (Jul 1993).

The detailed development of a domain decomposition method (DDM) for the vibrational modelling of rectangular plates with mixed-edge boundary conditions is presented. In the DDM, the complex plate domain is decomposed into small simple subdomains and the appropriate shape function of each subdomain is represented by sets of admissible orthogonal polynomials generated using the Gram-Schmidt recurrence process. The continuity matrices that couple the eigenvectors of adjacent subdomains are derived based on the satisfaction of continuity conditions along the interconnecting boundaries. The stiffness and mass matrices of each subdomain after pre- and post-multiplication by the respective continuity matrices are assembled to form the global stiffness and mass matrices. To demonstrate the effectiveness and accuracy of the DDM, a vibration study of several partially mixed edge plates have been carried out. Convergence tests for example problems are presented in which the accuracy of the results is established. The frequency parameters and mode shapes obtained, where possible, are verified by comparison with data published in the open literature.

11A84. Studies on dynamic behavior of a cantilever square plate with varying thickness. - PK Roy and N Ganesan *(Machine Dyn Lab, Dept of Appl Mech, Indian IT, Madras-600 036, India).* Comput Struct 47(6) 995-1003 (17 Jun 1993).

The effects of different types of variations in profile and thickness on the amplitude and the dynamic bending stresses of a square cantilever plate excited by a point harmonic load resonance has been investigated. A four-noded plate bending element has been used for the analysis. The response has been determined for the first three modes of vibration. In each case the results obtained for different thickness variations are compared with those of the uniform thickness plate. It is observed that considerable reductions in amplitude and/or bending stresses can be achieved by the proper selection of thickness variation.

11A85. Theoretical basis for the experimental realization of boundary conditions in the vibration analysis of plates. - AV Bapat *(Laser and Plasma Tech Div, PRIP Shed, Bhabha Atom Res Centre, Bombay 400 085, India)* and S Suryanarayan *(Dept of Aeronaut Eng, Indian IT, Bombay 400 076, India).* J Sound Vib 163(3) 463-478 (22 May 1993).

In the experimental analysis of beams and plates the realization of classical boundary conditions is one of the crucial prerequisites which governs the accuracy and reliability of the results obtained. The support structure used in the experimental set-up invariably has a small amount of flexibility when one wants it to be zero, and a large but finite flexibility when one wants it to be infinite. Hence one needs to evolve a criterion to be met by the design of the support structure to ensure that the edge conditions are simulated correctly. This paper is a study in this direction. A typical case of a rectangular plate with two opposite edges simply supported and uniform elastic restraint on the other two has been studied extensively. The numerical results presented clearly bring out the range of values and the interdependence of the translational and rotational flexibilities of the edge support for a good realization of classical boundary conditions. The application of the numerical results to a typical design of a simply supported edge is also presented.

11A86. Use of the substructure method for vibration analysis of rectangular plates with discontinuous boundary conditions. - KM Liew, KC Hung *(Div of Appl Mech, Sch of Mech and Prod Eng, Nanyang Tech Univ, Nanyang Ave, Singapore 2263),* KY Lam *(Dept of Mech and Prod Eng, Natl Univ, Kent Ridge Crescent, Singapore 0511).* J Sound Vib 163(3) 451-462 (22 May 1993).

A substructure method is presented for analysis of the free vibration of a rectangular plate with mixed edge boundary conditions. The method involves the partitioning of the entire plate domain into appropriate elements to approximate the deflection function of each element by a set of admissible orthogonal polynomials. The continuity conditions along the interconnecting boundaries provide the coupling between the coefficients of each element. Summing the strain and kinetic energies of each element, and minimizing the resulting Rayleigh quotient with respect to the unknown coefficients, leads to the governing eigenvalue equation for the entire plate. Several plate problems are solved to demonstrate the applicability and accuracy of the present method. Where possible, the results obtained are verified by comparisons with existing published values from the literature.

11A87. Vibration analysis of continuous plate structures using boundary integrals. - O Weiss and A Moshaiov *(Dept of Solid Mech Mat and Struct, Tel Aviv Univ, Tel Aviv 69978, Israel).* Comput Struct 47(6) 971-976 (17 Jun 1993).

The natural frequencies of thin continuous plates, including the influence of in-plane forces, are calculated using boundary integrals. This study deals in particular with continuous plate structures consisting of several fields of different thickness and possibly with the inclusion of internal supports. The concepts of compatibility and equilibrium conditions along the common boundaries have been imposed in conjunction with a BE formulation for each panel. Several examples are presented and the results are compared with analytical as well as FE solutions demonstrating the effectiveness of the formulation. Some numerical issues are discussed as well.

11A88. Vibration of rectangular Mindlin plates by the spline strip method. - T Mizusawa *(Dept of Construct and Civil Eng, Daido IT, Hakusuicho-40, Minami-ku, Nagoya 457, Japan).* J Sound Vib 163(2) 193-205 (May 1993).

This paper presents an analysis of the vibrations of rectangular Mindlin plates by the spline strip method. To demonstrate the convergence and accuracy of the method, several examples are solved, and results are compared with those obtained by analytical and other numerical methods. Stable convergence and excellent accuracy are obtained by using high order spline strip models. Frequencies of rectangular thick plates with several boundary conditions have been obtained and the results are presented in tabular form.

See also the following:

11A326. New numerical analysis method of dynamic behavior of a thin plate under magnetic field considering magnetic viscous damping effect

11A395. Frequency domain stress intensity calibration of damped cracked panels

154H. SHELLS

11A89. Magnetic damping effects on vibration of conductive shells. - Y Yoshida *(Nucl Eng Res Lab, Univ of Tokyo, 2-22 Shirakata-shirane, Tokai-mura, Ibaraki-ken 319-11, Japan),* K Miya, K Demachi, M Kurokawa *(Nucl Eng Res Lab, Univ of Tokyo, Tokai-mura Naka-gun Ibaraki, Japan).* Int J Appl Electromagnetics Mat 4(1) 1-11 (Jun 1993).

In conductors moving in magnetic field eddy current is induced by the electromotive force (given by v × B) that leads to the generation of Lorentz force acting against the original motion. Such kind of interaction between a moving conductor and a magnetic field is called magnetic damping. For thin structures of fusion reactors the damping effect is significant because the components are placed in a very strong magnetic field. In this paper two benchmark problems of the TEAM workshop were analyzed for vertifying the numerical code developed here. A simplified model of an ITER (International Thermonuclear Experimental Reactor) first wall was also analyzed to see the magnetic damping effect on the coupled vibration of the first wall under the magnetic environment of the ITER-CDA design. A verification of the code was done by the comparison between calculated and experimental results. The effect of wall thickness on the vibration was clarified.

See also the following:

11A153. Forced vibrations of a liquid filled shells of revolution. Bibliographical review

154J. DISCS AND BLADES

11A90. Dynamic response of a rotating blade with time-dependent rotating speed. - TH Young and GT Liou *(Dept of Mech Eng, Natl Taiwan IT, Taipei, Taiwan, ROC).* J Sound Vib 164(1) 157-171 (8 Jun 1993).

The general vibration of a rotating blade with time-dependent angular speed is investigated in this paper. A simple plate model is used to represent the blade, and its angular speed is characterized as a small periodic perturbation superimposed on a constant speed. Due to this non-constant rotational speed, terms with time-dependent coefficients appear in the equations of motion, which results in parametric instability. The method of multiple scales is used to derive approximate solutions and expressions for the boundaries of the unstable regions. All cases of possible resonant combinations up to the second order are studied, and the effects of system parameters, such as the damping coefficient, aspect ratio, rotating speed and setting angle, on the boundaries of the unstable regions are also investigated.

11A91. Point-load solution and simulation of a flexible spinning disk using various disk-to-

baseplate air-flow models. - GG Adams *(Dept of Mech Eng, Northeastern Univ, Boston MA 02115).* Trib Trans 36(3) 470-476 (Jul 1993).

In magnetic and/or optical recording on flexible media, an elastic disk rotates at a constant angular velocity in close proximity to a stationary baseplate. Such a configuration can be used to stabilize the transverse motion of the flexible disk, whose natural frequencies and critical speeds would otherwise be too low for stability of the flexible-disk-to-head interface. In this investigation, the air-flow between the disk and the baseplate is accounted for by two foundation parameters, stiffness and damping, for each Fourier mode. The effect of using this new model and three other models on the pointload solution and on the simulation of the disk-to-head interface is investigated. Steady-state solutions are obtained by using an exponential Fourier series expansion in the circumferential direction and a finite difference approximation radially. The simulation solution also accounts for the effect of disk-to-head contact in an approximate manner. It is further shown that the use of a Fejer sum for the Fourier series can accelerate the convergence of the simulation solution.

See also the following:

11A541. Three-dimensional computations of rotordynamic force distributions in a labyrinth seal

154K. ROTATING SHAFTS (CRITICAL SPEED, BALANCING)

11A92. Influence of external damping on the stability and response of a horizontal rotor with anisotropic bending stiffness. - C Rajalingham, RB Bhat, GD Xistris *(Dept of Mech Eng, Concordia Univ, Montreal, PQ, Canada).* Trib Trans 36(3) 393-398 (Jul 1993).

Design features, such as keyways of blind holes, produce noncircular cross-sections which introduce anisotropies in the bending stiffness characteristics of rotor shafts. Rotors with appreciable stiffness anisotropy have been found to exhibit vibrations at one-half the synchronous frequency. In horizontal single-disk rotors with anisotropic bending stiffness characteristics, gravity induces vibrations at one-half the synchronous frequency. Previous studies have neglected the damping effect of the surrounding medium and have predicted the operation of the rotor in between the two critical speeds to be unstable. This investigation examines the influence of external damping on rotor response to imbalance of gravity excitations and shows that sufficient amount of damping can suppress the reported instability caused by anisotropic bending stiffness characteristics.

See also the following:

11A319. Dynamic stability of a spinning beam carrying an axial dead load

11A537. Rotordynamic characteristics of flexure-pivot tilting-pad journal bearings

154L. FRAMES, TRUSSES, AND ARCHES

11A93. Application of the classical Rayleigh-Ritz method in dynamics of circular arches. - B Olszowski *(Krakow Univ of Tech, Krakow, Poland).* Eng Trans 41(1) 3-20 (1993).

The paper deals with Rayleigh-Timoshenko and Bernoulli-Euler models of circular arches with extensible or inextensible axes clamped with free radial sliding at both ends. The general algebraic equation defining the eigenproblem has been derived from Hamilton's principle. Spectra properties of the models were analysed by means of the classical Rayleigh-Ritz approximation method. Eigenfrequencies as functions of the subtending angle of the arch are plotted and tabulated.

11A94. Design of steel frames for specified seismic member ductility via inverse eigenmode formulation. - Tsuneyoshi Nakamura, M Tsuji, I Takewaki *(Dept of Architec, Kyoto Univ, Sakyo-ku, Kyoto 606, Japan).* Comput Struct 47(6) 1017-1030 (17 Jun 1993).

A new direct method of ductility design is presented for planar moment-resisting steel frames such that a set of member stiffnesses and the corresponding member strengths of a frame with realistic cross-sectional proportions are found for a specified distribution of member ductility factors under design major earthquakes. An inverse method of stiffness design is developed such that every predominant member-end strain in a frame under design earthquakes estimated on the basis of lowest eigenvibration would coincide with the specified value. A concept called "a set of similar cross-sections" is introduced to make it possible to obtain a set of members with realistic cross-sectional proportions. It is then shown that this inverse formulation for specified predominant member-end strains is quite useful for developing a direct stiffness design method for specified mean maximum member-end strains under design earthquakes.

11A95. Kinematic model for dynamic analysis of space frames. - R Karpurapu *(Dept of Civil Eng, Royal Military Col, Kingston, ON, K7K 5L0, Canada)* and M Yogendrakumar *(Golder Assoc, 224 W 8th Ave, Vancouver BC, V5Y 1N5, Canada).* Comput Struct 47(6) 945-955 (17 Jun 1993).

This paper presents a kinematic model for dynamic analysis of framed structures. The accuracy of the proposed method is demonstrated by analyzing the dynamic responses of two space frames of varying stiffness properties.

See also the following:

11A197. Multiobjective optimization of large-scale structures

11A243. Dynamic large deformation response of rigid plastic arches under impact

154M. SANDWICH MATERIALS

11A96. Dynamic response of sandwich beams with an adhesive damping layer (generalized Maxwell model for a viscoelastic adhesive layer). - T Fujii *(Dept of Mech Eng, Doshisha Univ, Kyoto 602, Japan).* Int J Adhesion Adhesives 13(3) 201-209 (Jul 1993).

A simple numerical method using a 1D approximation is presented for analyzing the dynamic response of adhesively bonded sandwich beams. The viscoelastic characteristics of the adhesive damping layer are represented by a generalized Maxwell model. Combining an incremental constitutive equation for a generalized Maxwell model solid between time t and $t + \Delta t$ with the FE discretization gives incremental equations of motion with respect to time for each element. A new method is proposed to obtain the frequency response function numerically. An impact test was carried out on a cantilever sandwich beam having an adhesive damping layer. Good agreement between the experimental and calculated results confirms the validity of the present method.

11A97. Vibration and damping analysis of multi-span sandwich beams with arbitrary boundary conditions. - S He *(Associated Spring, 10 Main St, Bristol CT 06010)* and MD Rao *(Dept of Mech Eng and Eng Mech, Michigan Tech Univ, Houghton MI 49931).* J Sound Vib 164(1) 125-142 (8 Jun 1993).

This paper presents an analytical model for the study of the coupled transverse and longitudinal vibration of multi-span sandwich beam systems with arbitrary boundary conditions. The energy method and Hamilton's principle approach is used to derive the governing equations of motion and the natural and forced boundary condition equations for each span. The shear, longitudinal and transverse strain energy of the adhesive layer are included in the analysis, together with the transverse and the longitudinal inertia of the composite beam system. A matrix equation to obtain the system natural frequencies and loss factors is developed based on the governing equations of motion for individual spans and system boundary and continuity conditions. Possible boundary conditions that can be programmed to obtain numerical solutions are discussed. Numerical results are generated for an example case of a two-span sandwich beam. The effects of the adhesive thickness, location of the intermediate support, operating temperature and the damping material properties on the system resonance frequency and modal loss factor are studied for the example case.

154N. COMPOSITE MATERIALS

11A98. Active vibration control of 1D piezoelectric laminates. - M Pietrzakowski *(Inst of Machine Des Fund, Warsaw Univ of Tech, Poland).* J Theor Appl Mech 31(3) 637-655 (1993).

In this paper a theoretical model of a simply supported three-layer 1D plate with a distributed actuator-sensor pair has been examined. A velocity feedback control is used to achieve active damping of structure. The transfer functions relating the out-of-plane deformation to the actuator voltage input for the system without control loop and for the system with velocity feedback as well as the open-loop transfer function are obtained. The numerical results show the influence of the actuator-sensor location and controller parameters on the modal system response.

11A99. FE analysis of damping the vibrations of laminated composites. - R Rikards, A Chate, E Barkanov *(Riga Tech Univ, Kalku St 1, Riga LV 1047, Latvia).* Comput Struct 47(6) 1005-1015 (17 Jun 1993).

There are several ways of decreasing the vibration energy of structures, such as diminishing the source energy, designing structures with desired eigen-frequencies and excitation frequencies, using materials that have damping properties, etc. Special damping layers made of various viscoelastic materials are widely applied in structures subjected to dynamic loading, especially those used in ship building and aerospace technology. A typical structure is that whose basic layer is covered with a damping layer and a thin constraining layer. Such classical sandwich structures have been widely investigated, especially with reference to the analysis of elastic vibrations.

154Y. COMPUTATIONAL TECHNIQUES

11A100. Analytical and numerical study of nonlinear behavior of the electromechanical system. - J Awrejcewicz *(Univ of Tech, Lodz, Poland).* J Tech Phys 34(1) 57-68 (1993).

The nonlinear behavior of a generator with an amplifier (modeled by a simple oscillator) supplying a current to the string embedded in the electromagnetic field is analyzed. The dynamics of this system is governed by a set of ordinary and partial differential equations and integral equations with a time delay. The method of averaging proposed and the symbolic computations applied lead to the set of four averaged amplitude ordinary differential equations. The numerical analysis reveals interesting nonlinear phenomena.

11A101. Application of the harmonic acceleration method for nonlinear dynamic analysis. - I Senjanovic *(Fac of Mech Eng and Naval Architec, Univ of Zagreb, Zagreb, Croatia)* and Z

Lozina *(Fac of Elec and Mech Eng and Naval Architec, Univ of Split, Split, Croatia)*. Comput Struct 47(6) 927-937 (17 Jun 1993).

The application of the harmonic acceleration method, which shows some advantages in linear transient vibration analysis compared to the other commonly used methods, is extended to nonlinear problems employing the mode superposition technique and an iteration procedure. Stability analysis shows that the method is unconditionally stable. A higher degree of accuracy is achieved. The efficiency of the method is illustrated by some numerical examples.

11A102. Eigensolutions sensitivity for nonsymmetric matrices with repeated eigenvalues. - A Luongo *(Dept of Struct Eng, Univ of L'Aquila, Monteluco Roio, 67040 L'Aquila, Italy)*. AIAA J 31(7) 1321-1328 (Jul 1993).

A perturbation algorithm is developed for evaluating eigenvalue and eigenvector directional derivatives of nonsymmetric defective matrices. Some properties of these matrices are recalled; in particular, chains of generalized right and left eigenvectors and their orthogonal properties are defined. Small perturbations of the matrix are then considered. An asymptotic expansion of the eigensolutions of the perturbed problem is obtained in terms of noninteger powers of the perturbation parameter. Marked sensitivity of the eigensolutions is highlighted. Particular attention is devoted to the eigenvectors of the perturbed system and to the strong coupling that occurs between the chains. An example is developed to illustrate the algorithm and compare perturbative and numerical solutions.

11A103. Linear system response by DFT: Analysis of a recent modified method. - JF Hall and JL Beck *(Div of Eng and Appl Sci, 104-44 Dept of Civil Eng, California IT, Pasadena CA 91125)*. Earthquake Eng Struct Dyn 22(7) 599-615 (Jul 1993).

An analysis of a recent modified frequency-domain procedure for computing the response of linear systems using the fast Fourier transform algorithm is described. This modified procedure eliminates the appended free-vibration interval that is used in the standard approach. The duration of the period of computation still needs to be longer than that of the response interval of interest, but only slightly. Reducing the period of computation lowers the number of frequencies at which the transfer function needs to be defined. The major drawback of the method is a high sensitivity to errors in the computed values of the transfer function, which reduces the role of interpolation in the transfer function definition. The modified method is related to the discrete Laplace transform.

See also the following:

11A80. Finite strip-elements for the dynamic analysis of orthotropic plate structures

11A86. Use of the substructure method for vibration analysis of rectangular plates with discontinuous boundary conditions

154Z. EXPERIMENTAL TECHNIQUES

See the following:

11A85. Theoretical basis for the experimental realization of boundary conditions in the vibration analysis of plates

156. Vibrations (structures)

See the following:

11A947. Influence of time-domain dam-reservoir interaction on cracking of concrete gravity dams

156F. MARINE STRUCTURES

11A104. Equivalent element representing local flexibility of tubular joints in structural analysis of offshore platforms. - Yuren Hu, Bozhen Chen, Jianping Ma *(Dept of Naval Architec and Ocean Eng, Shanghai Jiao Tong Univ, Shanghai 200030, Peoples Rep of China)*. Comput Struct 47(6) 957-969 (17 Jun 1993).

An equivalent element representing the local flexibility of tubular joints for structural analysis of offshore platforms is developed in this paper.

156G. VEHICLES (INCL LOCOMOTIVES)

See the following:

11A200. Active systems in the vibration control of vehicles

156H. SHIPS

11A105. Hovercraft overwater heave stability. - MJ Hinchey *(Ocean Eng Group, Memorial Univ of Newfoundland, St John's, NF, A1B 3X5, Canada)* and PA Sullivan *(Inst for Aerospace Stud, Univ of Toronto, Downsview, ON, M3H 5T6, Canada)*. J Sound Vib 163(2) 261-273 (May 1993).

The dynamic heave stability of an air cushion vehicle or hovercraft hovering over deep water without forward motion is investigated here analytically. The principal feature of the analysis is the modeling of the motion of the water surface beneath the cushion caused by fluctuations in the pressure of the cushion or cavity air. This surface motion interacts with the vehicle dynamics by modulating both the volume and exit flow area of the cushion. For analytical simplicity, the geometry chosen for study is a 2D section of a rigid wall plenum chamber; this enables exploitation of classical linear wave formulas developed by Lamb for the surface motion generated by a spatially uniform surface pressure oscillating sinusoidally in time. To assess stability characteristics, the Nyquist criterion is applied to the linearized equations. Results are presented for two cases: one is representative of a small test vehicle, and the other of a large ice-breaking platform. They show that the water surface motion significantly affects stability through both of the proposed mechanisms, with cushion exit flow area modulation usually being more important. A feature of the results is that as the weight of a vehicle decreases many stability transitions occur. This suggests that simple guidelines for avoiding instability may not exist, so that stability augmentation devices may be required for vehicles designed to hover for extended periods over water.

11A106. Kevin-Helmholtz wave generation beneath hovercraft skirts. - PA Sullivan, C Walsh *(Inst for Aerospace Stud, Univ of Toronto, Downsview, ON, M3H 5T6, Canada)*, MJ Hinchey *(Ocean Eng Group, Memorial Univ of Newfoundland, St John's, NF, A1B 3X5, Canada)*. J Sound Vib 163(2) 275-282 (May 1993).

When a hovercraft is hovering over water, the air flow beneath its skirts can interact with the water surface and generate waves. These, in turn, can cause the hovercraft to undergo violent self-excited heave motions. This note shows that the wave generation is due to the classical Kelvin-Helmholtz mechanism where, beyond a certain air flow rate, small waves at the air-water interface extract energy from the air stream and grow.

156I. AIRCRAFT

11A107. Analysis of helicopter spatial motion dynamics for different models of induced velocity field. - Z Dzygadlo and G Kowaleczko *(Warszawa, Poland)*. Biuletyn Wojskowej Akademii Technicznej 42(1) 3-31 (1993).

A spatial motion dynamics of a helicopter is discussed for three known from literature models of velocity field induced in the lifting rotor zone. There are the constant distribution of velocity and the Glauert and Mangler-Squire models, in which the velocity distribution depends on the azimuth and radius. A helicopter own motions were studied without and with consideration the coupling between the longitudinal and lateral motion for three mentioned above the induced velocity models.

11A108. Analysis of spatial motion dynamics of a helicopter for various models of the induced velocity field. - Z Dzygadlo and G Kowaleczko *(Military Univ of Tech, Warszawa, Poland)*. J Tech Phys 34(2) 119-143 (1993).

Problems of dynamics of spatial motion of a helicopter are considered making use of the three models of induced velocity field over the region of the main rotor, which are known from the literature. They are: the uniform velocity distribution and the Glauert and Mangle-Squire models, in which the velocity depends on the azimuth and the radius. The natural motions of the helicopter have been studied for the three models of induced velocity mentioned above, the couplings between the longitudinal and lateral motions being and not being taken into consideration.

11A109. FE analysis of natural vibrations of an aeroplane with asymmetric variable wing geometry. - J Blaszczyk *(Military Tech Acad, Warszawa, Poland)*. J Tech Phys 34(1) 79-100 (1993).

A dynamic model of an aeroplane with an aerofoil which can rotate in its plane about a cylindrical joint located on the fuselage. In the general case the aeroplane under consideration is an asymmetric structure, which means the existence of a coupling between the longitudinal and lateral motions. Equations of dynamic equilibrium of deformable assemblies are established by means of the FE technique and multistage synthesis of a structure. The vibration spectrum of an aeroplane are calculated of such configuration has been calculated assuming uniform distribution of the mass and the elastic parameters of assemblies, if the rotation angle of the wing varies within a range $x_s = 0$ to 70°.

11A110. Numerical analysis of aircraft free vibrations with unsymmetrical geometry of airfoil. - J Blaszczyk and W Krason *(Warszawa, Poland)*. Biuletyn Wojskowej Akademii Technicznej 42(1) 33-45 (1993).

The results are presented of numerical analysis of an aircraft with unsymmetrical alteration of the airfoil geometry, the dynamic model of which has been proposed earlier. The variation in oscillation spectrum for hypothetical aircraft of constant mass and geometrical parameters have been studied within the range of 0 - 70° for the rotation angle of airfoil. The conclusions are presented connected with accepted for the aircraft the aerodynamic constructional configuration, resulting from the studied spectrum.

156M. ROTATING MACHINES AND TURBOMACHINERY

11A111. Add-on suspension for controlling the vibrations of shafts accelerating to supercritical speeds. - TP Turkstra and SE Semercigil *(Dept of Mech Eng, McMaster Univ, Hamilton, ON, L8S 4L7, Canada).* J Sound Vib 163(2) 327-341 (May 1993).

An add-on switching support is proposed to limit the transient vibrations of a flexible beam by continuously varying its displacement response. A FE technique has been utilized to simulate the dynamic response of a flexible shaft operating at supercritical speeds. During acceleration, amplitude reductions of 66% are obtained with the actuation of the add-on support. Experimental verification is also described, achieving comparable amplitude reductions.

11A112. Development of an electrical controllable detuner for shaftings of combustion engines. - H Brunk *(Germanischer Lloyd, Vorsetzen 3203 65 Elbchaussee 277, 2000 Hamburg 11, Germany).* Ship Tech Res 40(2) 95-106 (May 1993).

For power packages with internal combustion engines the electrical, controllable vibration detuner in a novel, interesting alternative to traditional torsional vibration dampers. It combines simple structures with high efficiency and controllability and needs no maintenance. For laboratory tests a detuner for translational vibrations was built and tested. Experimental results were confirmed by FE-computations of the magnetic field. A rotational vibration detuner for a marine propulsion system was designed and simulated on a computer for examining its efficiency and for testing different control concepts.

11A113. Study and performance evaluation of some nonlinear diagnostic methods for large rotating machinery. - Liangsheng Qu, Ailin Xie, Xiao Li *(Res Lab of Machinery Surveillance and Diagnostics, Xian Jiaotong Univ, Xian 710049, ROC).* Mech Machine Theory 28(5) 699-713 (Sep 1993).

In this paper, some nonlinear diagnostic methods for large rotating machinery are introduced and evaluated from the practitioners' points of view, ie, their sensitivity to nonlinear phenomena, their applicability in machinery diagnostic practice, their effectiveness in computer execution and finally, their acceptability in the enterprises. The evaluated methods are pseudo-phase diagrams or limit cycle detection, singular spectrum analysis, the Wigner distribution and the Kullback index of the complexity based on information theory. Examples show the pseudo-phase diagrams are the most convenient for on-line diagnostics. It can be directly applied in the productional practice, while all the other methods can be used as supplementary diagnostic measures.

See also the following:

11A90. Dynamic response of a rotating blade with time-dependent rotating speed

156O. ISOLATION

11A114. Optimum damping in linear isolation systems. - JA Inaudi and JM Kelly *(Dept of Civil Eng, UCB EERC, Richmond Field Sta, 1301 S 46th St, Richmond CA 94804).* Earthquake Eng Struct Dyn 22(7) 583-598 (Jul 1993).

Optimum isolation damping for minimum acceleration response of base-isolated structures subjected to stationary random excitation is investigated. Three linear models are considered to account for the energy dissipation mechanism of the isolation system: a Kelvin element, a linear hysteretic element and a standard solid linear element, commonly used viscoelastic models for isolation systems comprising natural rubber bearings and viscous dampers. The criterion selected for optimality is the minimization of the mean-square floor acceleration response. The effects of the frequency content of the excitation and superstructure properties on the optimum damping and on the mean-square acceleration response are addressed. The study basically shows that the attainable reduction in the floor acceleration largely depends on the energy dissipation mechanism assumed for the isolation system as well as on the frequency content of the ground acceleration process. Special care should be taken in accurately modeling the mechanical behavior of the energy dissipation devices.

See also the following:

11A948. Seismic response of heavily damped base isolation systems

156P. ABSORPTION

11A115. Passive vibration control scheme using circular viscoelastic waveguide absorbers. - YS Shin, SJ Watson, KS Kim *(Dept of Mech Eng, Naval Postgraduate Sch, Monterey CA 60439).* J Pressure Vessel Tech 115(3) 256-261 (Aug 1993).

A waveguide absorber is a device mounted on a vibrating structure at the selected points to transfer energy from the structure to the device which dampens the energy. The waveguide absorbers reported here are made of viscoelastic material which absorbs vibration energy and dissipates it in the form of heat. The novelty of this approach to damping is the simplicity of application and the effectiveness in the braodband frequency range with relatively less material. In this study, the impedances of the circular viscoelastic waveguide absorbers were evaluated experimentally at different temperatures and the results were compared with those of prediction. The application of the waveguide absorbers in the most effective manner to maximize damping of the structure is also studied. The impedance matching techniques were studied to minimize the vibration amplitude of the structure.

156Y. COMPUTATIONAL TECHNIQUES

11A116. Identification and control of flexible civil structures with time delays. - M Abdel-Rohman *(Dept of Civil and Comp Eng, Kuwait Univ, PO Box 5969, Kuwait)*, OA Sebakhy *(Dept of Elec and Comput Eng, Kuwait Univ, PO Box 5969, Kuwait)*, M Al-Halabi *(Dept of Civil and Comp Eng, Kuwait Univ, PO Box 5969, Kuwait).* Comput Struct 47(6) 977-986 (17 Jun 1993).

The identification of flexible civil structures as discrete-time mathematical models in a ready form for computer control is shown by using a simple identification technique and neglecting the noise problem. The use of a control mechanism for the purpose of modeling and also for the control of the flexible structure justifies the noise-free consideration. The effect of time delay during a control process on the dynamics and stability of the structural systems is shown in illustrative examples. The design of a feedback control law to compensate for the detrimental effect of time delay is given with an application to control the response of a flexible frame structure using a tendon control mechanism.

11A117. Neural networks for computing in structural analysis: Methods and prospects of applications. - S Kortesis and PD Panagiotopoulos *(Dept of Comput Sci, Sch of Tech, Aristotle Univ, GR-54006 Thessaloniki, Greece).* Int J Numer Methods Eng 36(13) 2305-2318 (15 Jul 1993).

A neural network model is proposed and studied for the treatment of structural analysis problems. Both the cases of bilateral and unilateral constraints are considered and Hopfield-like neural models are proposed. Moreover, new results, generlizing the results of Hopfield and Tank, are obtained. Numerical applications illustrate the theory and show clearly the advantages of the neural network approach. Finally, the parameter identification problem is formulated and solved as a learning problem for a neural network.

11A118. Superelement method for transient dynamic analysis of structural systems. - MV Belyi *(Dept of Appl Math, Moscow Civil Eng Inst, 129337 Yaroslavskoe Shosse 26, Russia).* Int J Numer Methods Eng 36(13) 2263-2286 (15 Jul 1993).

A superelement algorithm for the transient dynamic analysis of structural systems is presented. The method represents a generalization of existing static and dynamic superelement (substructure) algorithms. Natural frequencies and modal spaces of a fixed boundary substructure are used to obtain equations of motion of a superelement. An implicit time-stepping algorithm is presented for the numerical solution of a resulting superelement system of equations of motion. Numerical examples are given to illustrate the presented approach. The method is believed to be effective for large-scale problems of structural analysis.

See also the following:

11A102. Eigensolutions sensitivity for nonsymmetric matrices with repeated eigenvalues
11A103. Linear system response by DFT: Analysis of a recent modified method
11A487. Fundamental of dynamical analysis of the blast-resistant underground structures

156Z. EXPERIMENTAL TECHNIQUES

11A119. Analysis of caterpillar strain influence on dynamic loading of tank crew. - L Prochowski and P Rybak *(Warszawa, Poland).* Biuletyn Wojskowej Akademii Technicznej 41(11) 55-74 (1992).

The results of studies on the dynamic loading of a tank subjected to the action of deterministic and random forcing are presented. The influence of initial strain of caterpillar on the dynamic loading of vehicle crew is evaluated and analysis of the structure and level of the loading is carried out.

158. Wave motions in solids

158B. RODS AND BEAMS, ELASTIC

11A120. Discrete model of wave propagation in a nonprismatic bar with rigid unloading characteristics. - Z Szczesniak *(Military Tech Acad, Warszawa, Poland).* Eng Trans 41(1) 77-96 (1993).

A discrete model is proposed for the propagation of waves in a nonprismatic bar made from a material whose unloading characteristic is rigid. Arbitrary time-dependent applied load is considered. In such a situation the modelling of wave propagation must allow in each cross-section for multiple effects of its alternating rigid and activated behavior. These effects are nonlinear and thus it is very difficult to approach them analytically. An algorithm for numerical solutions is proposed and errors of the results are discussed. Effectiveness and applicability of the model are illustrated by means of numerical examples.

See also the following:

11A201. Adaptive control of flexural waves propagating in a beam

158G. NONLINEAR MOTIONS

11A121. Nonlinear thermoelastic solid with uniaxial wave propagation. - MC Singh *(Dept of Mech Eng, Univ of Calgary, Calgary, AB, T2N 1N4, Canada)* and DVD Tran *(Combustion Dyn, Medicine Hat, AB, Canada)*. Trans Can Soc Mech Eng 17(2) 229-242 (1993).

This study is devoted to an examination of wave motion in nonlinear thermoelastic solids. For this purpose, a new materially nonlinear constitutive relation for thermoelastic solids has been developed. The development makes use of the principles of continuum thermomechanics and takes into account Gibb's free energy. On the basis of the nonlinear constitutive relations so developed the fundamental equations of wave propagation for a nonlinear thermoelastic uniaxial solid have been constructed. These are further simplified for a nonconducting nonlinear uniaxial material. The initial conditions and boundary conditions are stated. The jump conditions for simple waves and shock waves in such a material are derived. Shock amplitude relation has been obtained on the basis of kinematic compatibility relations. Solution of the system of basic equations, with boundary conditions, initial conditions and jump and shock conditions at the wave front has been obtained by the method of characteristics and a combination of finite difference and FEM. Numerical results are presented in graphical form for uniaxial waves.

158H. PLASTIC, VISCOPLASTIC WAVES

11A122. Isothermal and adiabatic flow laws of metallic elastic-plastic solids at finite strains and propagation of acceleration waves. - Nguyen Huu Viem *(Inst of Fund Tech Res, Polish Acad of Sci, Warszawa, Poland)*. Arch Mech 44(5-6) 595-602 (1992).

From the earlier proposed constitutive equations for metallic elastoplastic materials at finite strains with induced anisotropy, the flow laws for isothermal and adiabatic processes are derived and examined. If certain minor coupling effects are disregarded, the difference between them consists only in the hardening functions. It is shown that deviation from plastic normality may arise from the plastic spin. On the basis of these equations, we consider the propagation of acceleration waves and give the expressions for the eigenvalues. They reduce in the case of small deformations.

11A123. Propagation pressure of long cylindrical shells under external pressure. - JY Dyau and S Kyriakides *(Eng Mech Res Lab, Dept of Aerospace Eng and Eng Mech, Univ of Texas, Austin TX 78712-1085)*. Int J Mech Sci 35(8) 675-713 (Aug 1993).

Local imperfections induced in long tubes subjected to high external pressures can lead to local collapse, from which a propagating buckle can be initiated. This can result in catastrophic collapse of large sections of the structure. The *propagation pressure* is the lowest pressures at which such a buckle will propagate. For common structural metal tubes with diameter-to-thickness ratios of less than 100, the propagation pressure is typically half an order of magnitude lower than the collapse pressure of the intact tubes. As a result, the design of several tubular structures with external pressure loading requires that the collapse and propagation pressures be accurately known. This paper deals with the experimental and analytical challenges of establishing the propagation pressure. A special purpose 3D analysis, in combination with experimental observations and results, is used to demonstrate a mechanism of initiation of propagating buckles in long tubes, to study the parametric dependence of the propagation pressure and to illustrate the effect of axial tension on the propagation pressure. Propagation pressures predicted with this analysis are used to evaluate the strengths and weaknesses of simpler models developed in the past.

158I. VISCOELASTIC WAVES

11A124. Couple-stress effect on the propagation of waves in a thermo-visco-elastic layer. - TK Das, A Mukherjee *(Indian Inst of Mech of Continua, 201 Manicktala Main Rd, Suite 42, Calcutta 70054 W Bengal, India)*, RP Sengupta *(Dept of Math, Univ of Kalyani, W Bengal, India)*. Acta Geophys Polonica 40(3-4) 235-246 (1992).

The aim of this paper is to study the effects of couple-stress on the 2D thermo-visco-elastic wave propagation in an elastic solid layer of finite thickness. Considering the linearized theory of couple-stress visco-elasticity and using the influence of thermal field of thermo-visco-elasticty, firstly the field equations of motion have been derived. The displacement equations of motion have been solved by introducing two displacement potential functions. Making use of the boundary conditions for stresses, couple-stresses, viscosity and radiative conditions for temperature the wave velocity equation for propagation of 2D waves has been derived. It is then discussed for certain interesting particular cases of wave propagation in layer and semi-space with particular emphasis on surface waves. This wave velocity equation tallies with the corresponding classical wave propagation problem when the couple-stress, thermal effect and viscosity effect are vanishing small.

11A125. Mechanical energy dissipation in small deformation elasticity and the simple analytic expression for the viscous kink-shaped solitary wave. - A Blinowski *(Inst of Fund Tech Res, Polish Acad of Sci, Warszawa, Poland)*. Arch Mech 44(5-6) 615-620 (1992).

Wave propagation in the material abruptly changing its elastic moduli with the change of the deformation sign is considered. According to Cz Eimer, such a material models the behavior of a cracked linear elastic medium under 1D deformation. The solution obtained earlier for the shock propagation is compared now with the, proposed by the present author, simple analytic expression for diffuse shock propagation in Eimer's material endowed with the Voigt viscosity. It is shown that neither the propagation velocity, nor the total mechanic dissipation powers depends on the viscosity coefficient. These quantities retain, for arbitrary viscosity, the same values as in the case of discontinuity propagation in a purely elastic material. The slope of stress (strain) wave-profile changes with the viscosity change, tending to infinity if the latter tends to zero. The results obtained prove that an apparent paradox of a well-defined dissipation power, which can be calculated in the framework of purely elastic model within the small deformation approach in spite of the fact, that even the dissipation mechanism had not been defined earlier, can be explained on the basis of the limit transition for the viscoelastic solution.

158N. RANDOM WAVES OR MEDIA

See the following:

11A42. On randomly interrupted diffusion

158Q. REFLECTION, REFRACTION, DIFFRACTION, AND SCATTERING

11A126. Diffraction by a half-plane in a chiral medium (normal incidence). - S Przezdziecki *(Inst of Fand Tech Res, Polish Acad of Sci, Swietokrzyska 21, Warszawa, Poland)*. Acta Phys Polonica A 83(6) 739-750 (Jun 1993).

An exact, closed form solution is presented for a diffraction problem by a half-plane embedded in a chiral medium. The incidence direction of an electromagnetic plane wave is assumed to be normal to the edge of the half-plane. The problem has been reduced to a boundary value problem for two modal potentials satisfying distinct Helmholtz equations and coupled by the boundary conditions at the half-plane. A solution is constructed with the aid of the Wiener-Hopf technique. A basic feature of the problem is its two-mode character excited by: two families of diffracted rays, reflection coupling of the modes, excitation of lateral waves.

11A127. Diffraction of torsional elastic waves by a rigid annular disc at a bimaterial interface. - SC Mandal and ML Ghosh *(Dept of Math, N Bengal Univ, Darjeeling, India)*. Eng Trans 41(1) 97-116 (1993).

The problem of diffraction and normally incident torsional wave by an annular rigid disc lying at the interface of two bonded dissimilar semi-infinite elastic media is analysed. The three-part mixed boundary value problem is reduced to the solution of a set of integral equations which are solved by using iterative technique for low frequency, assuming that the ratio of the inner and outer radii is small. The stress distribution on the disc, the torque and far-field amplitudes of the displacement in both the media are evaluated. The variation of dynamic stress intensity factors with normalized frequency for various values of the material parameters, and also the variation in far-field amplitude with the polar angles for a fixed radial distance have been shown by means of graphs.

11A128. Extended X-ray bremsstrahlung isochromat fine structure. - E Sobczak *(Inst of Phys, Polish Acad of Sci, Al Lotnikow 32-46, 02-668 Warszawa, Poland)*. Acta Phys Polonica A 83(2) 135-156 (Feb 1993).

Main aspects concerning a new method of extended X-ray bremsstrahlung isochromat fine structures (EXBIFS) are specified and discussed. The EXBIFS effect is studied here by application of a single-scattering theory, which explains well the experimental phenomenon that EXBIFS of Cu and Pd is strikingly similar to the p partial density of states, although the s- and d-symmetry contributions are not negligible. The single-scattering model of EXBIFS has been successfully applied for explanation of temperature effects resulting in a smearing of oscillations for big k values. It is established here that interatomic distances can be evaluated from EXBIFS by means of the single-scattering theory and the Fourier analysis.

11A129. Fast algorithm to compute the wave-scattering solution of a large strip. - WC Chew and CC Lu *(Electromagnetics Lab, Dept of Elec and Comput Eng, Univ of Illinois, Urbana IL 61801)*. J Comput Phys 107(2) 378-387 (Aug 1993).

A truncated, nonuniform, finite array of strips does not have a closed form solution. Using translational symmetry, a recursive algorithm that calculates the scattering solution with $N\log^2 N$ computational complexity is described. First, the algorithm is validated with the method of moments for both the TM-to-z and TE-to-z polarizations. Then the scattering solution from a large strip is calculated for both TE and TM polarizations. The current distribution for the TE polarization shows small-length-scale oscillations not present in the TM polarization.

11A130. Scattering of compressional waves in an inhomogeneous medium. - BK Rajhans and SK Samal *(Dept of Appl Math, Indian Sch of Mines, Dhanbad 826004, India)*. Acta Geophys Polonica 40(3-4) 219-234 (1992).

Scattering of compressional waves by a rigid cylinder embedded in a inhomogeneous medium is considered. It is assumed that the velocity of compressional and shear waves are functions of the distance from the centre of the cylinder and are given by $\alpha = \alpha_0 r^q$, $\beta = \beta_0 r^q$, $q < 1$. The problem is investigated by the method of integral transformation developed by Friedlander. The resulting integrals are evaluated asymptotically to obtain the short-time estimate of the motion near the wave front in the illuminated zone. Numerical computations are done to investigate the behavior of reflected P and S waves, respectively. The results show that the expectations for a homogeneous earth are also valid in the heterogeneous case.

11A131. Transmission properties of single-mode W-type optical fibers. - J Tyl *(Military Tech Acad, Warszawa, Poland)*. J Tech Phys 34(1) 15-28 (1993).

A theoretical model for analysis of the phenomenon of propagation of electromagnetic waves based on an approximation (by means of Chebyshev series) to the profile of the refracting index and the distribution of the fields in the waveguide has been presented. Numerical analysis was performed for the transmission problem of a signal through a cylindrical waveguide with inner cladding (type W). The dependence of the transmission parameters on the type of distribution of the refracting index in the core and the inner cladding has been investigated.

158Y. COMPUTATIONAL TECHNIQUES

See the following:

11A120. Discrete model of wave propagation in a nonprismatic bar with rigid unloading characteristics

158Z. EXPERIMENTAL TECHNIQUES

See the following:

11A128. Extended X-ray bremsstrahlung isochromat fine structure

160. Impact on solids

11A132. Analytical modeling of hammer impact for pile driving. - AJ Deeks and MF Randolph *(Dept of Civil Eng, Univ of W Australia, Nedlands 6009, W Australia)*. Int J Numer Anal Methods Geomech 17(5) 279-302 (May 1993).

Estimation of the drivability of piles requires modelling of the hammer impact in order to provide the input force wave at the pile head. Historically, this has been achieved through a numerical model of the hammer components (ram, cushion and anvil), which is then linked with that of the pile in order to effect the drivability analysis. This paper presents an analytical model of hammer impact, based on lumped ram and anvil masses separated by a cushion with internal damping, and connected to the pile which is modelled as a dashpot. Force-time responses derived from the analytical model are compared with actual field data, and also with results from commercially available numerical models of hammer impact. The analytical model is then used to explore the characteristics of hammer impact, with particular attention to combinations of parameters that lead to hammer bounce and, hence, significant loss of energy transferred to the pile.

11A133. Estimation of clearances and impact forces using vibroimpact response: Random excitation. - SQ Lin and CN Bapat *(Dept of Mech Eng, CCNY)*. J Sound Vib 163(3) 407-421 (22 May 1993).

A novel clearance estimation approach has been developed for a randomly excited vibroimpact system. The clearance estimates based on this approach were obtained using data from the mechanical analogue of an impact oscillator and simulation using a digital computer, and they reasonably agree with the actual clearances.

11A134. Extension of clearance and impact force estimation approaches to a beam-stop system. - SQ Lin and CN Bapat *(Dept of Mech Eng, CCNY)*. J Sound Vib 163(3) 423-438 (22 May 1993).

Three novel approaches to estimate clearances and impact forces, developed for a one-dof impact oscillator, have been extended to a simple undamped beam-stop system to demonstrate the applicability of the previously proposed methods. The case considered here is more practical, as the impact location is remote from the sensing location. The predictions of estimations of impact forces and clearances obtained using data from the mechanical experiments were compared with measured impact forces and actual clearances respectively, and indicated a good agreement.

See also the following:

11A25. Mesh stability study of FEM explicit algorithms for structural large-scale deformation impact responses

11A397. Stress intensity factor of a subsurface inclined crack subjected to dynamic impact loading

162. Waves in incompressible fluids

11A135. High-order formulation of the water-wave problem. - M Glozman, Y Agnon, M Stiassnie *(Coastal and Marine Eng Res Inst, Fac of Civil Eng, Israel IT, Haifa 32000, Israel)*. Physica D 66(3-4) 347-367 (Jul 1993).

The water-wave problem has a Hamiltonian formulation as derived by Zakharov. This leads to coupled nonlinear evolution equations for discrete wave modes. Discrete spectra occur naturally for standing waves in a basin. For high enough order, high enough energy and a sufficient number of dof, chaos may emerge. We have derived the Hamiltonian and evolution equations to arbitrary order. The conditions for the convergence of the expansion of the Hamiltonian are discussed. We performed numerical studies of the interaction of two standing wave modes for various cases and for increasing order. Using Poincare sections, the onset of local chaos in resonance and near-resonance conditions is manifested. Chaos appears at low order models but vanishes with increasng order. The significance of the newly derived high-order formulation for water waves is clearly demonstrated.

11A136. Coastal amplification of a tsunami wave train. - B Hunt *(Dept of Civil Eng, Univ of Canterbury, Christchurch, New Zealand)*. J Hydraul Res 31(3) 415-423 (1993).

Steady-state wave solutions are obtained in closed form for two simple coastal geometries. The first model consists of two regions of constant depth separated by a step, and the second model consists of a constant-depth region joined by a step to a region in which the mean depth decreases linearly to a value of zero at the shore line. The step, which is used to model a continental shelf, can create resonance and large wave amplifications in both cases, but amplifications are found to be much greater for the second model. Furthermore, peak amplifications at resonance are found to not change with incident wave frequency for the first model but to increase with wave frequency for the second model. Finally, since wave amplifications in the second model depend very strongly on incident wave frequencies, periods are calculated for waves near the leading edge of a tsunami wave train moving through water of constant depth.

11T137. Interaction between two nonpropagating hydrodynamic solitons. - JR Yan, XH Yan, JQ You, JX Zhong *(China Center of Adv Sci and Tech (World Lab), PO Box 8730, Beijing 100080, Peoples Rep of China)*. Phys Fluids A 5(7) 1651-1656 (Jul 1993).

11A138. Singular behavior in the vicinity of intersection between the body and free surface. - Lin-sheng Zhu *(Huazhong Univ of Sci and Tech, Wuhan, China)* and Yi-shan Dai *(Shipbuild Eng Inst, Haerbin, China)*. Appl Math Mech 14(5) 459-468 (May 1993).

The singular behavior in the vicinity of intersection between the body and free surface is presented. It is shown that in the linear regime the singularity of velocity potential for transient problems is in $d^2 \ln d$. The singular behavior for harmonic problem is the same as the result for the transient problem. In particular, the singularity for the harmonic problem with infinite frequency is in $d^2 \ln d$ for velocity potential (d is the distance between field point and intersection).

11T139. Water wave refraction and diffraction over frictional topography. - Qihua Zuo, Guoquan Yao, Bingcan Ding *(Nanjing Hydraul Res Inst, Nanjing 210024)*. China Ocean Eng 7(1) 73-84 (1993).

11A140. Solitary waves in a two-layer fluid with surface tension. - SM Sun *(VPI)* and MC Shen *(Dept of Math, Univ of Wisconsin, Madison WI 53706)*. SIAM J Math Anal 24(4) 866-891 (Jul 1993).

This paper deals with permanent gravity-capillary waves on the interface with surface tension in a two-layer, inviscid, and incompressible fluid between two horizontal, rigid boundaries. It is shown that, if the Bond number τ, a nondimensional surface tension coefficient, is greater than some critical value τ_0, and the Froude number F is less than, but near some critical value F_0, there exists a solitary wave solution which decays to zero at infinity. When τ is less than τ_0, solitary waves plus a small oscillation at infinity will appear, and the existence of such type of solutions will be investigated in a subsequent paper. Discussions about several critical cases, such as τ and τ_0 or a density ratio near some critical value, are also given.

11T141. Energy of Rossby waves as a part of global atmospheric oscillations. - H Elbern and P Speth *(Inst for Geophys and Meteorol, Univ zu Koln, D-5000 Cologne, Germany)*. Tellus 45A(3) 168-192 (May 1993).

11T142. Evolution of Rossby waves, generated by wind stress in a closed basin, incorporating total mass conservation. - VM Kamenkovich *(Dept of Earth, Atmos and Planet Sci Rm 54-515, MIT)* and IV Kamenkovich *(Moscow Inst of Phys and Tech, Dolgoprudniy, Russia)*. Dyn Atmos Oceans 18(1-2) 67-103 (Jun 1993).

See also the following:

11A129. Fast algorithm to compute the wave-scattering solution of a large strip

164. Waves in compressible fluids

11T143. DSMC approach to nonstationary Mach reflection of strong incoming shock waves using a smoothing technique. - DQ Xu *(Asian Tech Center, General Motors Japan, Akishima, Tokyo, Japan)*, H Honma *(Dept of Mech Eng, Chiba Univ, Chiba, Japan)*, T Abe *(Inst of Space and Astronaut Sci, Sagamihara, Japan)*. Shock Waves 3(1) 67-72 (1993).

11T144. Focusing of weak shock waves on a target in a parabolic chamber. - N Apazidis *(Dept of Mech, RIT, S-100 44 Stockholm, Sweden)*. Shock Waves 3(1) 1-10 (1993).

11A145. Shock wave tracking for hyperbolic systems exhibiting local linear degeneracy. - Yuanping He and TB Moodie *(Appl Math Inst, Dept of Math, Univ of Alberta, Edmonton, AB, T6G 2G1, Canada)*. Stud Appl Math 89(3) 195-232 (Aug 1993).

Extending the results of our previous study, we now investigate the propagation of interior shocks corresponding to the signaling problem of small-amplitude, high-frequency type. We derive a formula for the shock front and show that the previously constructed asymptotic solution is valid on both sides of this front. This solution is further distinguished to a higher order in which the effects of material inhomogeneity are accounted for. Moreover, if $\lambda = \lambda(u,x)$ represents the eigenvalue under consideration, we show that the single-wave-mode boundary disturbance can lead only to a λ-shock. We also derive an entropy condition for the shock wave. As an application for our theory, the fluid-filled hyperelastic tube problem is further examined and an example calculation made in which we show that a compressive shock wave is generated at the shock-initiation point. This demonstration is effected as a particular example of the solution to a general bifurcation problem.

11A146. Stability of shock waves. - AA Barmin and SA Egorushkin *(Res Inst of Mech, Moscow State Univ, Michurin prosp 1, 119 899 Moscow V-192, Russia)*. Adv Mech 15(1-2) 3-37 (1992).

The article presents summary of papers dealing with the stability of shock waves in the gas. The following problems are being considered: linear theory of stability, connection of stability with correct formulation of a certain mathematical problem, influence of shock wave structure on its stability, nonlinear theory of shock wave stability, stability of flow with shock waves. The article discusses some urgent problems to be solved.

11A147. Weak shock structure on the basis of modified hydrodynamical equations. - AD Khonkin and AV Orlov *(Tashkentskaya St 10-2-39, Moscow 109444, Russia)*. Phys Fluids A 5(7) 1810-1813 (Jul 1993).

The structures of a normal shock wave is calculated on the basis of the hydrodynamics of fast processes to investigate the validity of the theory for this classical problem. The analysis shows that the theory predicts the continuous shock profile to exist only for $M < 1.27$. The shock thickness and the asymmetry factors resulting from the Mott-Smith method, the Navier-Stokes and the Burnett equations, and also from the experiments and simulations are compared to the present results for a gas of Maxwell molecules.

11A148. Wave motion of a compressible viscous fluid contained in a cylindrical shell. - JH Terhune and K Karim-Panahi *(GE Nucl Energy, General Elec, San Jose CA 95125)*. J Pressure Vessel Tech 115(3) 302-312 (Aug 1993).

The free vibration of cylindrical shells filled with a compressible viscous fluid has been studied by numerous workers using the linearized Navier-Stokes equations, the fluid continuity equation, and Fiugge's equations of motion for thin shells. It happens that solutions can be obtained for which the interface conditions at the shell surface are satisfied. Formally, a characteristic equation for the system eigenvalues can be written down, and solutions are usually obtained numerically providing some insight into the physical mechanisms. In this paper, we modify the usual approach to this problem, use a more rigorous mathematical solution and limit the discussion to a single thin shell of infinite length and finite radius, totally filled with a viscous compressible fluid. It is shown that separable solutions are obtained only in a particular gage, defined by the divergence of the fluid velocity vector potential, and the solutions are unique to that gage. The complex frequency dependence for the transverse component of the fluid velocity field is shown to be a result of surface interaction between the compressional and vortex motions in the fluid and that this motion is confined to the boundary layer near the surface. Numerical results are obtained for the first few wave modes of a large shell, which illustrate the general approach to the solution. The axial wave number is complex for wave propagation, the imaginary part being the spatial attentuation coefficient. The frequency is also complex, the imaginary part of which is the temporal damping coefficient. The wave phase velocity is related to the real part of the axial wave number and turns out to be independent of frequency, with numerical value lying between the sonic velocities in the fluid and the shell. The frequency dependencies of these parameters and fluid velocity field modes shapes are computed for a typical case and displayed in nondimensional graphs.

See also the following:

11T143. DSMC approach to nonstationary Mach reflection of strong incoming shock waves using a smoothing technique
11A147. Weak shock structure on the basis of modified hydrodynamical equations
11A166. Approximate analytical solution of the cylindrical detonation wave generated by the linear explosion
11A659. Steady, inviscid shock waves at continuously curved, convex surfaces

166. Solid fluid interactions

11A149. Hydraulic forces acting on a circular cylinder with surface source of minute air bubbles and its cavitation characteristics. - A Ihara, H Watanabe, Hiroyuki Hashimoto *(Inst of Fluid Sci, Tohoku Univ, Sendai, Japan)*. J Fluids Eng 115(2) 275-282 (Jun 1993).

Experiments are performed by using two circular cylinders made of porous filter material, that is, bronze sintered compact, with a different filter size, respectively, in a water tunnel. The effects of minute air bubbles injected from the surface of the circular cylinder into its boundary layer on its hydraulic force characteristics are investigated over the Reynolds number $(1.2 \sim 4.2) \times 10^5$, changing the airflow rate of bubble injection. The pressure distributions on the porous cylinders are also measured. Their cavitation characteristics are studied, too. Compared with a smooth surface cylinder, the critical Reynolds numbers of the porous cylinders decrease owing to the increase in the surface roughness caused by the bronze particles which compose the sintered compact. The effects of the bubble injection on the hydraulic force characteristics are different according to the size of the bronze particles. Though a little difference is recognized, the hydraulic force characteristics show a similar tendency in both cases of bubble injection and cavitation occurrence.

11A150. FE analysis of lateral sloshing response in axisymmetric tanks with triangular elements. - F Ru-De *(Dept of Comput Sci and Info Math, Univ of Electro-Commun, Chofu-shi, Tokyo, Japan)*. Comput Mech 12(1-2) 51-58 (Jun 1993).

A FE analysis is presented for the sloshing motion of liquid-filled axisymmetric tanks during lateral excitation, for a circumferential mode number, m = 1, antisymmetric. The system of FE equations concerned is derived by means of variational principle. Linear basis functions associated with the regular triangulation of Friedrichs-Keller type was used. The analytical expressions of the mass and stiffness matrices for a FE were obtained. Numerical results of the free vibration for cases of annular and cylindrical tanks were obtained, and compared with existing experiments and other predicted results, showing a good agreement between the experiment and numerical results.

11A151. Effects of layer thickness on the vibration response of a plate-fluid layer system. - T Onsay *(Dept of Mech Eng, Michigan State Univ, E Lansing MI 48824-1226)*. J Sound Vib 163(2) 231-259 (May 1993).

Dynamic interaction between the bending vibrations of a plate and a fluid layer is investigated by using analytical and experimental methods. The frequency response behavior of the coupled plate-fluid layer system is studied, with emphasis on the influence of the layer thickness. The effects of compressibility, viscosity and inertia of the fluid are included in the analytical model. A critical layer thickness is introduced and utilized in the illustration of linear dynamic regimes of a fluid layer. A detailed analysis is carried out for the wave modes of the system, the free wave number of the fluid layer and for the mode shapes of the plate. The use of a powerful transfer matrix method is demonstrated in the formulation of the coupled plate-fluid layer system response. The drive-point mobility, the power flow and the resonance behavior of a physical system are analyzed at different layer thicknesses. Detailed experiments are conducted to confirm the predicted frequency response behavior of a particular plate-air layer system. The attenuation and frequency shift of the plate's resonances are demonstrated with experimental results. Air layer attenuation is found to be very effective in damping the low frequency flexural vibrations of the plate.

11A152. Method for suppressing the irregular frequencies from integral equations in water wave-structure interaction problems. - S Liapis *(Aerospace and Ocean Eng, VPI)*. Comput Mech 12(1-2) 59-68 (Jun 1993).

It is well known that at certain frequencies the boundary integral equation describing water wave-structure interactions does not have a unique solution. Large numerical errors occur in a frequency band width close to each "irregular" frequency and the fact that these frequencies are not a priori known for a given body adds to the severity of the problem. The present work describes a new method to suppress the influence of the irregular frequencies. The boundary integral equation is supplemented with a set of moment equations - the null-field equations. The resulting overdetermined system is then solved by a least squares procedure. It is shown that this procedure will produce a unique solution. Numerical results for a circular cylinder and a box barge demonstrate the effectiveness of the method.

11A153. Forced vibrations of a liquid filled shells of revolution. Bibliographical review. (Polish). - B Blocka *(Poland)*. Marine Tech Trans 3 5-24 (1992).

Two basic approaches to dynamic problems of shells of revolution filled with liquid is considered. The first one is a semi-analytical approach in which the governing equations of motion of the liquid are solved analytically and the governing equations of the shell motion are solved by means of numerical methods. The second approach is to make use of numerical methods for the liquid and the shell field. The later allows to solve wider class of interaction problems, but the former one leads, generally, to the systems of differential equations of a smaller size.

11A154. Influence of stator-rotor gap on axial-turbine unsteady forcing functions. - T Korakianitis *(Dept of Mech Eng, Washington Univ, Campus Box 1185, One Brookings Dr, St Louis MO 63130)*. AIAA J 31(7) 1256-1264 (Jul 1993).

This paper investigates the effects of stator-to-rotor axial gap on the 2D propagation of pressure disturbances due to potential-flow interaction between the blade rows and viscous-wake effects from upstream blade rows in axial-turbine-blade rotor cascades. Results are obtained by modeling the effects of the upstream stator viscous wake and potential-flowfield on the downstream rotor flowfield, and computing the unsteady flowfields in the rotor frame. The amplitudes of the two types of disturbances for typical turbines are based on a review of available experimental and computational data. The potential-flowfield is modeled as a sinusoidal pressure disturbance of amplitude 4% of the local pressure across the stator trailing edges that decays downstream. This potential-flow disturbance from upstream is affected by the potential-flowfield of the downstream cascade. The velocity wake is modeled as a Gaussian velocity defect of varying amplitude and width, depending on the stator-rotor gap between the blade rows. The wake amplitudes and widths are based on conservation of loss of incoming momentum to the rotor due to the wake. The axial gap between rotor and stator is varied to show how the two disturbances propagating in different directions reinforce or counteract each other at different stator-rotor gaps. The corresponding forces on rotor blades are computed for typical values of reduced frequency. Analyses of this type will enable turbomachinery designers to predict (and with geometric design modifications to reduce) the unsteady stresses acting on turbomachinery blades.

11A155. Dynamic FE analysis for interaction between two phase saturated soil foundation and platform. - Lingxi Qian, Wanxie Zhong, Hongwu Zhang *(Dalian Univ of Tech, Dalian 116023)*. China Ocean Eng 7(1) 21-29 (1993).

In this paper, the foundation soil of offshore structure is simulated as a two phase saturated porous medium. The dynamic equations of porous medium and FE formulation are given. For structural analysis, the technique of multilevel substructure is used, and the saturated soil analysis is set in the highest level substructure model. Based on these theories a dynamic FE analysis program DIASS for the analysis of interaction between the two phase ocean soil foundation and platform structures has been developed. A numerical example is given here to illustrate the influence of the pore water in soil on the structural response of an ocean platform.

11A156. Investigation of the solid-liquid phase transition for SnIn alloys by the positron annihilation method. - S Chabik, W Rudzinska *(Inst of Phys, Pedagogical Univ, Oleska 48, 45-052 Opole, Poland)*, M Szuszkiewicz *(Inst of Exp Phys, Univ of Wroclaw, pl Maxa Borna 9, 50-204 Wroclaw, Poland)*, C Szymanski *(Inst of Phys, Pedagogical Univ, Oleska 48, 45-052 Opole, Poland)*. Acta Phys Polonica A 83(3) 261-266 (Mar 1993).

The monovacancy formation energy in Sn-17 wt% In and Sn-32 wt% In was determined on the basis of the temperature dependence of the peak counting rate for these alloys. A sudden increase in the counting rate was observed between solidus and liquidus temperatures. This phenomena is connected with the formation of large defects acting as positron traps.

170. Explosions and ballistics

170C. EXPLOSION, DETONATION, DEFLAGRATION

11A157. Analysis of jet and slug parameters in process of jet formation by charges with lined wedge cavities Part I. The hydrodynamic steady-state theory. - E Wlodarczyk *(Warszawa, Poland)*. Biuletyn Wojskowej Akademii Technicznej 41(12) 13-42 (1992).

This paper considers stationary model of cumulation theory. It is presented extensive analysis of parameters of jet and slug. Direction of detonation wave-front propagation and its influence on the jet and slug are discussed. It is presented a method describing explosively formed penetrators employing stationary cumulation model.

11A158. Computer simulation of cumulation flux creation process and its influence on armour. - K Jach, R Swierczynski, E Wlodarczyk *(Warszawa, Poland)*. Biuletyn Wojskowej Akademii Technicznej 41(12) 43-60 (1992).

This paper presents complex, spatial 2D numerical model enabling computer simulation of shaped charge jet formation and estimation of the penetration depth, surface temperature of the crater etc. The model describing schaped charge includes elastovisco-plasticity equations describing process of deformation of conical liner and metal casing. The model is complemented by semi-empirical relations describing metal behavior under dynamic loading (EOS state equation, Steinberg-Guinan model and cracks formation model). The detonation products behavior was described by hydrodynamics equations considering the JWL state equations. Received solution enables description of time-spatial distribution of mass velocity and jet density. The hollowed crater depth was calculated with help of hydrodynamics theory. It was evaluated, that the surface layers temperature of the crater hollowed by active part of the jet, exceeds melting temperature of penetrated material and can achieve its evaporation point.

11A159. Geometric singular perturbation analysis of detonation and deflagration waves. - I Gasser and P Szmolyan *(Inst Angewandte Numer Math, Tech Univ Wien, Wiedner, Hauptstr 8-10, Austria)*. SIAM J Math Anal 24(4) 968-986 (Jul 1993).

The existence of steady plane wave solutions of the Navier-Stokes equations for a reacting gas is analyzed. Under the assumption of an ignition temperature the existence of detonation and deflagration wave close to the corresponding waves of the ZND-model is proved in the limit of small viscosity, heat conductivity, and diffusion. The method is constructive, since the classical solutions of the ZND-model serve as singular solutions in the context of geometric singular perturbation theory. The singular solutions consists of orbits on which the dynamics are slow-driven by chemical reaction and of orbits on which the dynamics are fast-driven by gasdynamic shocks. The approach is geometric and leads to a clear, complete picture of the existence, structure, and asymptotic behavior of detonation and deflagration waves.

11A160. Modification of JWL equation of state - W equation of state. - E Wlodarczyk *(Warszawa, Poland)*. Biuletyn Wojskowej Akademii Technicznej 41(10) 3-24 (1992).

In the paper modification of the JWL isentrope and equation of state for detonation products of condensed explosives is proposed. The modified state equation has been called briefly the W state equation. The JWL isentrope was replaced by the Poisson isentrope with so called effective exponent γw. Besides it the two-term isentrope with discrete variable exponent (γw, $\gamma k1$) was constructed, which covers the entire range of variation of the state parameters of detonation products of condensed explosives during the process of gas expansion. For a variety of detonation products of these materials the γw and $\gamma k1$ exponents enable reduction of 1D gas-dynamic equations to the Euler-Darboux equation having known general solution. It simplifies remarkable solution of the boundary problems of 1D gas dynamics with participation of detonation products of condensed explosives.

170P. OTHER TOPICS IN EXPLOSIONS AND BALLISTICS

11A161. Analysis of explosive compaction conditions of a cermet copper-aluminium oxide. - R Trebinski and E Wlodarczyk *(Military Tech Acad, Warszawa, Poland)*. J Tech Phys 34(1) 3-13 (1993).

In the work the compaction process of a cermet copper-aluminium oxide in an explosion fixture with a shock adsorbing water layer has been analyzed. On the base of the mathematical modeling results of the wave processes, taking place in a multilayer cylindrical fixture loaded by a grazing detonation, pressure and temperature values have been appraised. Making use of the results of the theoretical estimations and the results of experiments, the conditions of explosion compaction have been estimated.

11A162. An analysis of the propellant gas outflow through the gap between the missile and the barrel surface. - A Paplinski and E Wlodarczyk *(Warszawa, Poland)*. Biuletyn Wojskowej Akademii Technicznej 41(10) 95-103 (1992).

Propellant gas pressure rise and the outflow of the gases through the interface between the missile and the gun tube face in the process of missile engraving into the barrel grooves is investigated. It was stated, that modification of missile barrel driving band characteristics enables to lower the propellant gases outflow and to restrain the erosive action of the gases upon the barrel surface.

11A163. Dynamical problems of aerial bomb motion processes family. - J Niczyporuk *(Warszawa, Poland)*. Biuletyn Wojskowej Akademii Technicznej 42(1) 47-62 (1993).

Description of a system of aerial bomb motion processes is proposed in the aiming consideration, in the form of performing the dependence between the regions of acceptable initial and aiming conditions, which is determined by kinetic operator L. A set of logically systematized problems explaining the fundamental concepts of the proposed theory are formulated. The method for investigation of solution set structure and the properties of evolution with respect to the initial conditions and parameters is presented. The methodology studies follows the need for the result suitability for solution of the superordinate problem of "unacceptable variance of bombarded processes".

11A164. Study of basic characteristics of aerial bomb fall processes system. - J Niczyporuk *(Warszawa, Poland)*. Biuletyn Wojskowej Akademii Technicznej 42(1) 63-88 (1993).

A method is applied for modeling the dynamic properties of the bomb fall processes in a complex and aiming treatment in the form of the base variety: initial for release and aiming for fall. The problem has been solved for case of an object drop from the horizontal and diving flight in the range of small and medium angles of diving. The characteristics present the basic structures acceptable of description for bombardment process systems.

11A165. Transformations of graphite and boron nitrite in shock waves. - R Trebinski and E Wlodarczyk *(Warszawa, Poland)*. Biuletyn

Wojskowej Akademii Technicznej 41(10) 25-62 (1992).

In the present work the accessible information concerning polymorphous transformations of graphite and graphitic boron nitride is analysed. The peculiarities of dynamic compressibility curves of graphite and αBN are interpreted, basing on the data concerning the atomic mechanism of the transformation. It has been known that these peculiarities correspond to the formation of the wurtzitic modifications, ie, lonsdaleite and γBN. A survey of data concerning the mechanism of the new phase crystallization and the kinetics of the polymorphous transformation is preformed.

170Y. COMPUTATIONAL TECHNIQUES

11A166. Approximate analytical solution of the cylindrical detonation wave generated by the linear explosion. - Yi-wu Yuan *(Central S Univ of Tech, Changsha, China)*. Appl Math Mech 14(5) 437-441 (May 1993).

The solution of the cylindrical detonation wave generated by the linear explosion was obtained by numerical methods. In this paper, when the ratio of specific heat $\gamma >> 1$ by using the enlargement coordinate method, the first-order analytical solutions are obtained. The perturbation parameter is $\varepsilon = 1/\gamma_2$. The correction of these solutions is checked at the end of this paper.

172. Acoustics

172A. GENERAL THEORY

See the following:

11A53. Bifurcations and chaos in voice signals

172B. SOUND GENERATION BY MOVING SURFACES

See the following:

11A167. Low frequency aeroacoustics of buried nozzle systems

172C. SOUND GENERATION BY FLOW

11A167. Low frequency aeroacoustics of buried nozzle systems. - MV Taylor *(Int Comput, Lovelace Rd, Bracknell, Berkshire RG12 4SN, UK)*, DG Crighton *(Dept of Appl Math and Theor Phys, Univ of Cambridge, Silver St, Cambridge CB3 9EW, UK)*, AM Cargill *(Rolls-Royce, Moor La, Derby DE2 8BJ, UK)*. J Sound Vib 163(3) 493-526 (22 May 1993).

A simplified model of a "buried nozzle" aeroengine system is considered. The primary flow issues into a co-annular flow within a mixing chamber, and then the co-annular flow issues into the ambient medium from a secondary nozzle. Within the mixing chamber only fine scale mixing takes place, and shear layers within the mixing chamber and downstream of the secondary nozzle are assumed to sustain large scale instability waves. Excitation of this system is provided by low frequency plane waves, incident from upstream on the primary nozzle (and emanating from combustion processes in the hot core of an aeroengine). The response of this system, in the acoustic far field and in the mixing chamber, is obtained analytically from the asymptotic solution, at low frequency, of model sub-problems the solutions of which determine the wave reflection and transmission processes at the primary and secondary nozzles. In these sub-problems the shear layers are represented by vortex sheets and the nozzle walls by semi-infinite circular ducts, with Kutta conditions imposed on the unsteady flow at the primary and secondary nozzle lips. Analytical descriptions are given of the various wave modes (quasi-plane acoustic waves, and instability waves localized on the primary and secondary shear layers), of the acoustic field strength and directivity (essentially monopole, dipole, and quadrupole fields), and of the conditions under which near-resonant response may occur, with large amplitudes of the perturbations in the mixing chamber and in the acoustic field.

172D. SOUND WAVES IN GASES

11A168. Method for the prediction of peak sound pressure level related to opencast blasting. - M Clerico and M Patrucco *(Dept Georisorse e Territorio, Politec di Torino, Corsa Duca degli Abruzzi 24, 10129 Torino, Italy)*. Appl Acoust 40(1) 47-56 (1993).

The sudden noise caused by blasting can give rise to substantial complaints from people living in the proximity of opencast mines, quarries or construction sites. A measurement technique and simple prediction method are proposed which can be effectively applied for community exposure planning and reduction. The prediction method is based on measurements of the peak sound pressure level generated by small unconfined explosive charges; the sound propagation characteristics in the area can then be defined, as typical coefficients, and critical propagation directions can be taken into account. By means of a numerical relationship, in which also the main round parameters are considered, the peak sound pressure level in each position in the surrounding areas can be predicted.

172E. SOUND WAVES IN LIQUIDS (UNDERWATER ACOUSTICS)

11A169. Evaluation of ship radiated noise level from near-field measurements. - Takaaki Musha *(Acoust Dept, Ono Sokki, 1-16-1, Hakusan, Midori-ku, Yokohama, Japan)* and Akira Shinohara *(Fac of Textile Sci and Tech, Shinshu Univ, Ueda, Nagano-ken, Japan)*. Appl Acoust 40(1) 69-78 (1993).

Recently it has become necessary to determine far-field characteristics of marine vehicle noise from near-field measurements. It is possible to compute far-field characteristics from near-field measurements by using the Helmholtz integral equation. But this method is not practical because a great number of points are required to obtain them. This paper presents a simple equation to obtain the source levels of marine vehicles, which is used to evaluate far-field characteristics from near-field data. Good agreement with experimental results from ships is obtained.

11A170. Time-averages for plane traveling waves: The effect of attenuation I. Adiabatic approach. - SN Makarov *(Inst of Math and Mech, State Sankt-Petersburg Univ, Sankt-Petersburg-Petrodvoretz 198904, Russia)*. J Sound Vib 163(2) 311-317 (May 1993).

The analysis of the effect of attenuation on the time-averages for a plane traveling wave is presented. The barotropic equation of state is considered: ie, acoustic heating is assumed to be negligible. The problem statement consists of calculating means in a finite region bounded by a transducer surface as well as by a perfectly absorbing surface, respectively. Although the simple wave approximation cannot be used throughout the field it is still valid near the perfect absorber. The result for radiation pressure is different from the conclusions given previously by Beyer and Livett, Emery and Leeman.

172F. SOUND WAVES IN SOLIDS

See the following:

11A68. Note on modal summations and averaging methods as applied to statistical energy analysis

11A330. Fourier series with Legendre polynomials as solving functions of mixed multi-periodic boundary value problems

172H. REFLECTION, REFRACTION, DIFFRACTION, AND SCATTERING

11A171. Acoustic wave scattering from axisymmetric bodies. - HS Kim, JS Kim, HJ Kang *(Acoust Lab, Korea Res Inst of Ships and Ocean Eng, PO Box 1 Daeduk Science Town, Daejeon 305-606, Korea)*. J Sound Vib 163(3) 385-396 (22 May 1993).

Scattering from axisymmetric bodies subject to a non-axisymmetric incident wave is studied by means of the Helmholtz integral equation method. By expansion of circumferential components of the pressure and normal velocity as well as the incident wave into Fourier series, decoupled integral equations for each Fourier component are obtained. The fact that only discretization of the generator is needed offers a significant savings of computational efforts compared to that for surface discretization. The number of Fourier expansion terms needed to achieve convergence becomes larger as frequency increases, but it is still smaller than that or at least comparable to the number of nodes along the generator, which makes the present formulation attractive for acoustic wave scattering or radiation problems of axisymmetric bodies.

11A172. Analysis of 3D muffler with BEM. - Chao-Nan Wang, Chuan-Cheung Tse, Yih-Nan Chen *(Dept of Naval Architec, Natl Taiwan Univ, Taipei, Taiwan ROC)*. Appl Acoust 40(2) 91-106 (1993).

A numerical scheme for solving the 3D interior acoustic problem governed by the Helmholtz equation has been developed. The main feature of this formulation is that the singularity can be removed analytically. The boundary integral equation is solved for a specific geometry by using second-order quadrilateral surface elements and does not have the difficulty of non-uniqueness associated with the boundary integral equation formulation in an exterior problem. The transmission loss of a muffler is computed by using the derived four-pole parameters. The effects of higher-order modes due to the area discontinuity as well as the various inlet-outlet alignment on the acoustic performance of a muffler are also studied. The case of a muffler with elliptic cross-section, which is troublesome in analytical solution, can be treated easily by the present scheme. Finally, the transmission loss characteristics of a muffler with extended inlet-outlet are investigated. All the numerical results are compared with experimental measurement and agreement is good.

11A173. Axisymmetric integral equation formulation for free space non-axisymmetric radiation and scattering of a known incident wave. - P Juhl *(Acoust Lab, Tech Univ, Bldg 352, DK-2800 Lyngby, Denmark)*. J Sound Vib 163(3) 397-406 (22 May 1993).

This paper gives a brief account of the formulation of the Helmholtz integral equation specialized to the case of an axisymmetric body in free space. In this case of the surface integral of the Helmholtz integral equation may be reduced to a combination of a line integral and an integral over the angle of revolution; only the former integral needs to be discretized, and thus the dimension of the problem is reduced to one. In order to allow for non-axisymmetric boundary conditions the sound field is expanded in a cosine series over the angle of revolution. This expansion is as general as a full Fourier expansion but more efficient. The singularities in the Green function and its normal derivative are integrated analytically over the angle of revolution and expressed as sums of elliptic integrals. The formulation is tested for scattering and radiation problems.

11A174. Evaluation of methods for predicting the scattering from simple rigid panels. - TJ Cox and YM Lam *(Dept of Appl Acoust, Univ of Salford, Salford M5 4WT, UK)*. Appl Acoust 40(2) 123-140 (1993).

The accuracies and computational times of theoretical methods used to predict the scattering from rigid plane and curved reflectors have been evaluated. These methods were based on different solutions of the Helmholtz-Kirchhoff integral equation. The prediction results were compared to measurements. It was found that a boundary integral method provided accurate predictions for both panel types. For the more approximate prediction methods their limitations were defined in terms of the accuracy achieved and the range over which the methods were applicable. These methods were also used to investigate the use of cut-off frequency to describe the limit above which specular type reflections dominate the scattering. It was found to be applicable only close to the geometric scattering angle.

11A175. Theoretical and experimental analysis of the drift problem of cellouse fibres in an acoustic field. - H Czyz and J Smela *(Inst of Phys, Pedagogical Univ, Pl-00-000 Rzeszow, Rejtana 16A, Poland)*. Bull Polish Acad Sci Tech Sci 41(2) 153-156 (1993).

In the paper there was considered the problem of diffraction of a plane acoustic wave on a rigid cylinder in case of an arbitrary angle of incidence. The obtained formula was used to calculate the force and torque on a thin cylinder of a finite length. Some predictions were made concerning the acoustic radiation force on such particles and results of adequate experiments were reported.

11A176. Use of the diffraction phenomenon of a light wave on acoustic phase grating as a means of precision measurement of distance. - H Kowalski, A Klewski, M Figurski *(Military Tech Acad, Warszawa, Poland)*. J Tech Phys 34(1) 29-35 (1993).

The subject matter of the present paper are the principles of a new method for measuring distances, based on the phenomenon of light diffraction on acoustic waves. An information block diagram of a range-finder system has been presented in which a distance is measured by the frequency measurement of the angle between two diffraction orders. The advantages of the method are discussed.

11A177. Wave propagation and scattering in elastic plate with periodically grooved surface. - E Danicki and D Bogucki *(Inst of Fund Tech Res, Polish Acad of Sci, Swietokrzyska 21, 00-049 Warszawa, Poland)*. Arch Acoust 18(1) 113-130 (1993).

Bragg reflection of plate waves in isotropic elastic plate with a periodically grooved surface is analyzed. Mode-coupling effect is also taken into account. The analyzed problem may be applied in the construction of piezoelectric resonators and RAC filters.

172J. NOISE CONTROL AND REDUCTION (INCL ACTIVE CONTROL)

11A178. Design verification of ground run-up noise suppressors for afterburning engines. - SA Fisher, AM Abdel-Fattah *(DSTO Aeronaut Res Lab, 506 Lorimer St, Fishermens Bend, Victoria Melbourne, Australia)*, LA Challis *(Challis and Associates Pty, PO Box 199 Kings Cross, NSW 2011 Sydney, Australia)*. J Propulsion Power 9(4) 628-635 (Jul-Aug 1993).

New facilities for ground running of engines in Royal Australian Air Force F-A-18 aircraft feature air-cooled exhaust augmentors for noise suppression. Aerothermodynamic aspects of the augmentor designs were appraised in some detail, making use of isothermal scale model tests, ejector theory, and available empirical data. Quantitative assessments were made of cooling flow pumping performance, and geometric features were identified which are important to the symmetry of the flow in the augmentor ducts. The final designs displayed satisfactory aerodynamic behavior, tolerant to both inlet asymmetries and reasonable levels of engine jet misalignment. The estimated pumping performance exceeded the design requirements.

11A179. Investigations into hygienic attenuators. - KO Ballagh *(Marshall Day, PO Box 5811 Wellesley St, Auckland, New Zealand)*. Appl Acoust 40(2) 107-122 (1993).

Investigations have been made into the feasibility of using reactive elements in hygienic or cleanable duct mounted attenuators. Worthwhile attenuations can be achieved and plane wave theory can be used to provide initial estimates of performance. Flow of up to 15 m-s has little effect on the attenuation achieved. Further development is required to optimize designs for cleanability to improve the accuracy of prediction techniques and to achieve higher and more broadband attenuation.

172Y. COMPUTATIONAL TECHNIQUES

11A180. Acoustic wave propagation in mercury in constant external magnetic field. - A Skumiel *(Inst of Acoust, Adam Mickiewicz Univ, Matejki 48-49, 60-769 Poznan, Poland)*. Acta Phys Polonica A 83(2) 173-186 (Feb 1993).

This paper gives a theoretical analysis of the effect of an external constant magnetic field on the propagation of ultrasonic waves in electrically conducting liquids as well as the results of measurements carried out in mercury. The theoretical part is based on Euler's equation, the equation of continuity, the thermodynamical equation, and Maxwell's equations. In the experimental part we propose and apply two methods for the measurement of the ultrasonic propagation velocity and its variations, as well as a pulse method perfected by the use of analog memory for the determination of the amplitude absorption coefficient. The correctness of the theoretical basis underlying the calculation of the small changes in propagation velocity induced by the magnetic field is confirmed by the experiment.

11A181. Analysis and implementation of hydroacoustic methods for estimation of high densities of fish in sea pens. - A Stepnowski *(Dept of Electron, Tech Univ, 80-952 Gdansk, Poland)*. Arch Acoust 18(1) 67-82 (1993).

The paper presents the feasibility of different acoustic methods with reference to system design, capable of estimating high density of fish, eg, in aquaculture facilities. The velocity, attenuation and backscattering measurement methods are critically examined. The new, recursive echo integration method is introduced, which accounts for attenuation loss by dense collections of fish. The proposed implementation of this estimation technique employs the modified design of a dual-beam sonar-system ECOLOG II. The system provides the real-time absolute estimates of fish density in sea pens.

11A182. Dispersion-relation-preserving finite difference schemes for computational acoustics. - CKW Tam and JC Webb *(Dept of Math, Florida State Univ, Tallahassee FL 32306-3027)*. J Comput Phys 107(2) 262-281 (Aug 1993).

Acoustics problems are governed by the linearized Euler equations. According to wave propagation theory, the number of wave modes and their wave propagation characteristics are all encoded in the dispersion relations of the governing equations. Thus one is assured that the numerical solutions of a high order finite difference scheme will have the same number of wave modes (namely, the acoustic, vorticity, and entropy waves), the same wave propagation characteristics (namely, nondispersive, nondissipative, and isotropic) and the same wave speeds as those of the solutions of the Euler equations if both systems of equations have the same dispersion relations. Finite difference schemes which have the same dispersion relations as the original partial differential equations are referred to as dispersion-relation-preserving (DRP) schemes. A way to construct time marching DRP schemes by optimizing the finite difference approximations of the space and time derivatives in the wave number and frequency space is proposed. The stability of these schemes is analyzed and a sufficient condition for numerical stability is established. A set of radiation and outflow boundary conditions compatible with the DRP schemes is constructed. These conditions are derived from the asymptotic solutions of the governing equations. The asymptotic solutions are found by the use of Fourier-Laplace transforms and the method of stationary phase. A sequence of numerical simulations has been carried out. These simulations are designed to test the effectiveness of the DRP schemes and the radiation and outflow boundary conditions. The computed solutions agree very favorably with the exact solutions. The radiation boundary conditions perform satisfactorily causing little acoustic reflections. The outflow boundary conditions are found to be quite transparent to outgoing disturbances even when the disturbances are made up of a combination of acoustic, vorticity, and entropy waves.

11A183. Dynamic stiffness-BEM for the prediction of interior noise levels. - RS Langley *(Dept of Aeronaut and Astronaut, Univ of Southampton, Highfield, Southampton S09 5NH, UK)*. J Sound Vib 163(2) 207-230 (May 1993).

A method is presented for the prediction of the noise transmission into structures which have a constant cross-sectional geometry. The structural vibrations are analyzed by using the dynamic stiffness method, while the BEM is used to calculate the interior noise levels. The analysis procedure is a direct one, which means that there is no need to calculate the modes of vibration of either the structure or the interior airspace. Furthermore, a method is presented for the suppression of numerical damping in the BEM analysis, which allows the use of much fewer BE than would otherwise be needed. Particular attention is paid to the case of airborne noise transmission into an aircraft fuselage structure, and comparisons are made with previous experimental and theoretical results for a circular cylindrical test article.

11A184. Spectrum analysis of acoustic emission signals. - I Malecki *(Asfaltowa 11 M 12, Pl-02-527 Warszawa, Poland)*. Bull Polish Acad Sci Tech Sci 41(2) 111-117 (1993).

The processing channel influences the form of the received acoustic emission (AE) signals. There are compared various methods of analysis of the amplitude distribution and spectrum of a priori assumed group of AE sources. Each source is treated as the evaluating system with own relaxation time. The spectral distribution depends on the activation energy. In the model of randomly oscillating defects there is considered the dependence of the spectrum on the correlation degree. The amplitude distribution for continuous and burst AE signals is compared. The cases of amplitude distribution of the primary AE signal are: Rayleigh, rectangular and triangular.

11A185. Ultrasonic attenuation in alloys. - SK Kor and RK Singh *(Dept of Phys, Univ of*

Allahabad, Allahabad-211 002, India). Acta Phys Polonica A 83(6) 751-758 (Jun 1993).

Ultrasonic attenuation was evaluated in metallic alloys, Ni_xCu_{1-x} (x = 1.00, 0.70, 0.60, 0.45, and 0) due to phonon-phonon (p-p) interaction and thermoelastic loss in a wide temperature region along <110> crystallographic direction for longitudinal and shear waves. Ultrasonic Gruneisen parameters, nonlinearity constants and ultrasonic attenuation due to p-p interaction and thermoelastic loss were determined from 50 K to 500 K using the Born-Mayer and electrostatic potentials. The results were compared with available results.

11A186. Wide-band dispersive lines with an acoustic surface wave. - A Kawalec and J Filipiak *(Military Tech Acad, Warszawa, Poland)*. J Tech Phys 34(1) 69-78 (1993).

The subject matter of the present considerations are the results of numerical and experimental investigations into problems of dispersive delay lines with an acoustic surface wave with a 50% relative passband. The set of dispersive lines had a carrier frequency f_0 = 80 MHz, a passband B = 40 MHz and a slope μ = 4 MHz/μs and was composed of a transmitting and receiving dispersive lines. The transmitting dispersive line (TDL) had a flat amplitude characteristic in the passband while the characteristic of the receiving dispersive line (RDL) was described by the Hamming function. Width of the signal after compression was 35 ns and the sidelobe level was -32 dB. The dispersive lines were constructed with a crystal of quartz (Y,X). The insertion loss was minimum to amounting 50 dB.

See also the following:

11A75. FEM for computation of structural intensity by the normal mode approach

172Z. EXPERIMENTAL TECHNIQUES

11A187. Acoustic emission during nonhomogeneous tensile deformation of ARMCO-iron. - A Pawelek *(Aleksander Krupowski Inst of Metal Res, Polish Acad of Sci, ul Reymonta 25, 30-059 Krakow, Poland)* and S Pilecki *(Inst of Fund Tech Res, Polish Acad of Sci, ul Swietokrzyska 21, 00-049 Warszawa, Poland)*. Arch Acoust 18(1) 163-170 (1993).

Measurements of acoustic emission count rates and RMS value in the ARMCO-iron have been carried out in tensile loading. Specimens of the ARMCO-iron have been used in two stands: annealed or pre-rolled and cut in parallel or perpendicular direction. Experimental results have been discussed in the light of possibility proliferation and annihilation as well as their accelerated and decelerated movement.

11A188. Experimental investigation of discrete sound production in deep cavity exposed to airflow. - M Meissner *(Inst of Fund Tech Res, Polish Acad of Sci, ul Swietokrzyska 21, 00-049 Warszawa, Poland)*. Arch Acoust 18(1) 131-156 (1993).

The results are presented of the experimental investigation of the discrete sound generation in the process of airflow over the deep cavity. During the increase of the airflow velocity, three discrete components, referred to as A, B and C, are excited successively, which, as indicated by an analysis of results, are the f_{13}, f_{12} and f_{11} modes, respectively. In the process of sound generation two stages have been distinguished: stage 1, characterized by strong dependence of the frequencies of the discrete components A, B and C on the velocity of the airflow and stage 2, where the frequency, of the discrete component C, as the function of the velocity, varies approximately ten times less as compared with stage 1. In stage 1, the "leading edge - trailing edge interaction" is of fundamental significance in the production of the discrete components, whereas the stage 2 is dominated by the feedback involving the effect of cavity-resonance modes on the disturbances of the shear layer.

11A189. Influence of vapors of some organic compounds and water on acoustic properties of selected polymer layers. - W Jakubik and M Urbanczyk *(Inst of Phys, Silesian Tech Univ, 44-100 Gliwice, Poland)*. Arch Acoust 18(1) 157-161 (1993).

The paper deals with an investigation of the interaction of thin polymer layers with an ambient atmosphere in view to using them to design gas sensors. The changes in physical properties of a polymer layer were recorded as a change in a differential frequency of dual acoustic delay line with a surface wave. The preliminary results demonstrate a selective sensitivity of polymer layers to gases in the ambient atmosphere.

11A190. Intensity assessment employing probe reversal. - RW Guy *(Centre for Build Stud, Concordia Univ, Montreal, PQ, H3G 1M8, Canada)*. Appl Acoust 40(1) 57-68 (1993).

Pressure-pressure (P-P) intensity measurements with probe reversal are made within highly reactive standing wave fields. A formulation is developed to correct both channel phase mismatch and finite difference error when applied to reversal measurement in discrete frequency planar fields, and greatly improved accuracy is shown in estimating the true intensity both in magnitude and direction; the prospect of extending low-frequency limits for given probe spacing in these fields is also demonstrated. In addition, a probe reversal formulation for a corrected intensity in arbitrary field conditions is formalized and a general comparison made with an alternative mean square pressure based correction.

11A191. Measurement of reverberation time using time delay spectrometry (TDS). - G Papanikolaou, V Psaroudakis, M Nistikakis *(Dept of Elec Eng, Univ of Thessaloniki, Greece)*. Arch Acoust 18(1) 33-45 (1993).

The present authors, basing on their experience collected during TDS system applications, especially to reverberation measurements, present below a practical approach, facilitating the appropriate use of TDS measuring systems in various applications.

11A192. Microstructure of sound. Formants in the dynamical spectra of violin sounds. - H Harajda *(Lab of Acoust, Pedagogical Univ, 65-069 Zielona Gora Pl, Slowianski 6, Poland)*, W Mikiel *(Speech Acoust Lab Inst of Fund Tech Res, Polish Acad of Sci, Swietokrzyska 21, 00-049 Warszawa, Poland)*, P Gabryelczyk, P Fedyniuk *(Lab of Acoust, Pedagogical Univ, 65-069 Zielona Gora Pl, Slowianski 6, Poland)*. Arch Acoust 18(1) 17-32 (1993).

The aim of the present study was to obtain the picture of the structural changes occurring in the spectra of the violin sound, with the four bowing techniques: detache, staccato, legato and martele. FFT analysis has been carried out using the system Volyzer and Split on IBM XT personal computer. Experimental material selected for this investigation consisted of the isolated sounds g (196 Hz), d^1 (293.7 Hz), a^1 (440 Hz), e^2 (659.3 Hz) and d^3 (1175 Hz) obtained with five instruments. Total number of randomly selected dynamical spectra, was 35. The tone structures have been analyzed with 0-220 ms timescales, in 20 ms segments. In this time span the spectrum continually undergoes the changes comprising the range of the spectrum, the number of the format maxima and their amplitude levels. Three types of formats exist: continuous, non-continuous, and fragmentary. The changes of the position of the format maxima on the frequency scale, the forms in which the amplitude levels of these maxima vary, the durations of the specific format creation and the stabilization of the full format set in the spectrum of sound have been analyzed.

11A193. Modeling auditorium acoustics with light. - RJ Pinnington and CB Nathanail *(Inst of Sound and Vib Res, Univ of Southampton, Highfield, Southampton SO9 5NH, UK)*. Appl Acoust 40(1) 21-46 (1993).

An optical method is presented for estimating the loudness, subjective spaciousness or clarity index within a proposed auditorium. A mirrored small scale model is constructed which contains a finite size light source. The intensity and size of the multiple reflected images are related to the magnitudes and time delays of individual echos. Various wall surfaces giving combinations of specular reflection, diffuse reflection and absorption are investigated. A photographic method for measuring the size and intensity of the image is assessed.

11A194. Structure of cyclohexane + t-butanol mixtures from positron annihilation and ultrasonic velocity measurements. - K Jerie, A Baranowski *(Inst of Exp Phys, Univ of Wroclaw, pl Maxa Borna 9, 50-204 Wroclaw, Poland)*, J Glinski *(Inst of Chem, Univ of Wroclaw, F Joliot-Curie 14, 50-383 Wroclaw, Poland)*. Acta Phys Polonica A 83(3) 321-326 (Mar 1993).

The densities of and sound velocities in t-butyl alcohol solutions in cyclohexane were determined in the temperature range 25 to 45° C. From these data adiabatic compressibility coefficients of the solutions were calculated, as well as excess densities and compressibilities. The positron annihilation spectra of the solutions were measured at room temperature. The results plotted against alcohol concentration show structural processes, which can be attributed to dimerization of the solute molecules.

11A195. Ultrasonic and thermodynamic effects of self-association of aliphatic alcohols in c-C_6H_{12} II. Preliminary and tertiary pentanols. - K Bebek, R Manikowski, S Ernst *(Inst of Chem, Silesian Univ, 40-006 Katowice ul, Szkolna 9, Poland)*. Arch Acoust 18(1) 105-111 (1993).

The ultrasound velocities in and densities of mixtures of cyclohexane with n-pentanol [x_1n-$C_5H_{11}OH$ + $(1-x_1)C_6H_{12}$] and with 2-methylbutan-2-ol [$x_1$tert-$C_5H_{11}OH$ + $(1-x_1)C_6H_{12}$] have been measured at 293.15 K. Using this measurement results in connection with the literature data, the following quantities have been determined: isothermal and adiabatic compressibility coefficients, $\beta_T = -1/V(\partial V/\partial p)_T$ and $\beta_s = -1/V(\partial V/\partial p)_s$, respectively, the adiabatic compressibility, $x_s = -(\partial V/\partial p)_s$, the free intermolecular length, L, and the excess values of the molar volume, V^E, of the adiabatic compressibility coefficient, $\beta^E{}_s$, and of the adiabatic compressibility, $x^E{}_s$. The dependence of those excess functions on the mixture composition, expressed in mole fractions, were represented by Redlich-Kister equations.

See also the following:

11A175. Theoretical and experimental analysis of the drift problem of cellouse fibres in an acoustic field

11A180. Acoustic wave propagation in mercury in constant external magnetic field

11A186. Wide-band dispersive lines with an acoustic surface wave

11A535. Vibroacoustic monitoring of bearing points failures in the driving system of the mining main ventilation fans

III. AUTOMATIC CONTROL

200. Systems theory and design

11A196. Semi-analytical static nonlinear structural sensitivity analysis. - RT Haftka *(Dept of Aerospace and Ocean Eng, VPI)*. AIAA J 31(7) 1307-1312 (Jul 1993).

The paper discusses two uses of the semi-analytical method for nonlinear sensitivity analysis. First, the application to noncritical response is analyzed. It is shown that the semi-analytical method is equivalent to a particular form of the overall finite difference approach. It is concluded that the difference between overall finite differences and the semi-analytical approach is blurred for the case of nonlinear static response. Next, the application of the semi-analytical method to calculating sensitivities of limit loads is discussed. A formulation that is easy to implement in general purpose FE programs is derived. Three examples are used to demonstrate the application of the formulation and to explore its accuracy.

See also the following:

11A204. Analysis of distributed thermopiezoelectric sensors and actuators in advanced intelligent structures

202. Control systems

11A197. Multiobjective optimization of large-scale structures. - RV Grandhi, G Bharatram *(Dept of Mech and Mat Eng, Wright State Univ, Dayton OH 45435)*, VB Venkayya *(Anal and Optim Branch, Flight Dyn Directorate, WPAFB)*. AIAA J 31(7) 1329-1337 (Jul 1993).

This paper presents a multiobjective optimization algorithm based on generalized compound scaling techniques. The algorithm handles any number of objective functions, similar to handling behavior constraints. This technique generates a partial Pareto set while solving the optimization problem. A reliability-based decision criterion is used for selecting the best compromise design. The example cases considered in this work include various disciplines in airframe structures, such as stress, displacement, and frequency with hundreds of design variables and constraints. This paper also discusses the concept of Pareto-optimal solutions in the context of a multiobjective structural optimization problem and the commonly used methods of generating Pareto-optimal solutions.

11A198. Optimal location of actuators for active damping of vibration. - J Holnicki-Szulc *(Dept of Electromech, Univ da Beira Interior, 6200 Covilhai, Portugal)*, F Lopez-Almansa *(Dept of Architec and Struct Diagonal 649, Tech Univ of Catalonia, Barcelona 08028, Spain)*, J Rodellar *(Dept of Appl Math III, Gran Capitan, Tech Univ of Catalonia, Barcelona 08028, Spain)*. AIAA J 31(7) 1274-1279 (Jul 1993).

A computationally efficient procedure for selection of placement of actuators is described in this paper. This method is formulated in modal coordinates and is based on the so-called progressive collapse analogy of an adjoint structure made of a hypothetical elastic-brittle material and having the same shape as the eigenmodes of the structure to be controlled. The computer simulation of progressive collapse for the adjoint structure provides us (as a side effect) with the location of the most sensitive spots, the best for placement of actuators. The presented methodology can be applied to damping of free vibration as well as to quasistatic shape control problems.

11A199. Optimization algorithm based on Legendre polynomial method for the linear quadratic optimal control problem with disturbances. - J Pelczewski *(Inst of Math, Univ of Lodz, Ul Stefana Banacha 22, 90-238 Lodz, Poland)*. Bull Polish Acad Sci Tech Sci 40(4) 377-386 (1992).

The shifted Legendre polynomials method is employed in order to obtain the approximate algorithm for the linear quadratic optimal control problem with given deterministic disturbances. According to the properties of these polynomials the optimization procedure was reduced to the constrained minimization of an algebraic function with respect to elements of an unknown matrix. The numerical procedure is based on the obtained results.

11A200. Active systems in the vibration control of vehicles. - S Michalowski *(Dept of Mech Eng, Cracow Univ of Tech, Poland)*. J Theor Appl Mech 31(3) 513-523 (1993).

The optimization procedure for the vibrocontrol system of a vehicle is presented. The vehicle is represented by a two dof model with discrete parameters. Input random kinematic excitation is assumed to be stationary and ergodic. The elektrohydraulic compensator is working parallely with the convectional suspension system. The structure and parameters of the active part, respectively, were obtained for the optimum criterion taken as a quadratic form. The relationships between values of the system parameters and the coefficients that describe fair comfort and fair safety are discussed.

See also the following:

11A716. Major linear control problem

204. Systems and control applications

11A201. Adaptive control of flexural waves propagating in a beam. - SJ Elliott *(Inst of Sound and Vib Res, Univ of Southampton, Southampton SO9 5NH, UK)* and L Billet *(Dept of Acoust Mec Vib, Electricite France, Clamart, France)*. J Sound Vib 163(2) 295-310 (May 1993).

Broadband active control of flexural (bending) waves propagating along a beam is investigated theoretically and experimentally. In particular, a simple practical arrangement is studied in which the output of a single detection sensor (an accelerometer) is used to drive a single secondary force via a feedforward controller. The feedforward controller is implemented as an adaptive digital filter, the coefficients of which are adjusted to minimize the mean square output from a single downstream error sensor (another accelerometer). Fundamental limits on the performance of such an active control system are found at low and high frequencies. The low frequency limit is caused by the near field of the secondary source corrupting the output of the error sensor. The increasing group velocity of bending waves in the beam with frequency imposes a high frequency limit on the performance, because of the electrical delay in the controller. The bandwidth of useful operation imposed by these low and high frequency limits is found to increase as the thickness of the beam is reduced. Experimental results on a 6 mm steel beam confirm the predicted high frequency limit, although in practice the low frequency limit of control was found to be determined by a lack of coherence between the detection and error sensor due to background noise. Attenuation in the bending wave amplitude of between 10 and 30 dB were measured in the experiments over a frequency range from 100 to 600 Hz.

11A202. Enhancing induced strain actuator authority through discrete attachment to structural elements. - Z Chaudhry and CA Rogers *(Center for Intelligent Mat Syst and Struct, VPI)*. AIAA J 31(7) 1287-1292 (Jul 1993).

In structural control, induced strain actuators are used by bonding them or embedding them in a structure. With bonded or embedded actuators used for inducing flexure, the developed in-plane force contributes indirectly through a locally generated moment. Control authority in this configuration is thus limited by actuator offset distance. In this paper, a new concept of flexural or shape control is presented, whereby induced strain actuators such as piezoelectric ceramic patches or shape memory alloys are attached to a structure at discrete points (as opposed to being bonded). This paper specifically addresses discretely attached induced strain actuators like piezoceramic and electrostrictive actuators which are available in the form of plates or patches, and includes actuator flexural stiffness considerations. This configuration is different from the bonded actuator configuration in two ways. One, because the actuator and the structure are free to deform independently, the in-plane force of the actuator can result in an additional moment on the structure and enhanced control. Second, the actuator can be offset from the structure without an increase in the flexural stiffness of the basic structure. This allows for the optimization of the offset distance to maximize control. Enhanced control is demonstrated by comparing the static response of a discretely attached actuator beam system with its bonded counterpart system. The advantage of this configuration over the bonded configuration is also verified experimentally.

11A203. Some results of the APC-1p digital autopilot flight tests. - A Tomczyk and T Dziedzic *(Tech Univ of Rzeszow, Poland)*. J Theor Appl Mech 31(3) 601-619 (1993).

This paper presents methodology and results of the digital autopilot flight tests. The structure of autopilot, methods of experiment applied in tests on four prototypes with PZL M20 Mewa are shown. Ways of data analysis and some obtained results are discussed.

11A204. Analysis of distributed thermopiezoelectric sensors and actuators in advanced intelligent structures. - SS Rao and M Sunar *(Sch of Mech Eng, Purdue)*. AIAA J 31(7) 1280-1286 (Jul 1993).

The quasistatic equations of piezoelectricity and thermopiezoelectricity are used to develop a FE formulation of distributed piezoelectric and thermopiezoelectric media. The formulation is then integrated with the distributed sensing and control of advanced intelligent structure design. The procedure is illustrated with the help of two example problems. The purpose of the first example, which consists of two piezoelectric layers used as a bimorph robotic finger, is to check the accuracy of the FE solution with the analytical one. As a second example, an aluminum beam is utilized along with two polyvinylidene fluoride layers acting as distributed actuator and sensor to study the distributed control of the beam when thermal effects are present. It is concluded that the thermal effects are important in the precision distributed control of intelligent structures.

11A205. Back-propagation learning using the trust region algorithm and application to nondestructive testing in applied electromagnetics. - Fumio Kojima *(Mech Eng Dept, Osaka IT, 5-16-1, Ohmiya, Asahi-ku, Osaka 535, Japan)*. Int J Appl Electromagnetics Mat 4(1) 27-33 (Jun 1993).

An artificial neural network is applied by nondestructive inspections in aerospace materials. The use of an artificial neural network is presented for classifying testing data as corresponding to sample materials with defect and without defect. The back-propagation learning for a multilayer feed-forward neural network is applied to this classification. The trust region method is adopted to the back-propagation learning problem. Results of numerical tests are summarized.

11A206. Intelligent control of the gear-shaving process. - JS Zhong *(Dept of Mech Eng, Wuyi Univ, Jiangmen, Guangdong, Peoples Rep of China)* and LS Qu *(Dept of Mech Eng, Xi'an Jiaotong Univ, Xi'an, Peoples Rep of China)*. Proc Inst Mech Eng B 207(B3) 159-165 (1993).

The objective of this paper is to describe how AI (artificial intelligence) and fuzzy logic techniques can be combined to implement an on-line computer control of an axial gear-shaving process in order to improve the quality of workpiece gears. The basic principle of correcting the geometric errors of workpiece gears is introduced. The final knowledge base is obtained by the iterative procedure of trying the expert controller, observing the results and then modifying the control rules accordingly. Inference is provided by a fuzzy logic engine. Experimental results showed that accuracy of the shaved gears was greatly enhanced. The total cumulative pitch error and the individual pitch error was reduced by approximately two times. In particular, the flank grooves, which commonly occur in the middle of tooth profiles, were removed.

11A207. Trajectory planning using artificial intelligence. - M Eroglu and KF Gill *(Dept of Mech Eng, Univ of Leeds, UK)*. Proc Inst Mech Eng B 207(B3) 193-198 (1993).

In this paper, the aim is to introduce artificial intelligence techniques into trajectory planning and obstacle avoidance, to achieve the minimum time trajectory. The method presented has many areas of application including NC-CNC (numerically controlled and computer numerically controlled) machining operations, precision assembly and transportation problems.

See also the following:

11A98. Active vibration control of 1D piezoelectric laminates
11A111. Add-on suspension for controlling the vibrations of shafts accelerating to supercritical speeds
11A198. Optimal location of actuators for active damping of vibration
11A209. Walking machines
11A715. Control of vortices on a delta wing by leading-edge injection

206. Robotics

11A208. Certain methods of determining the ellipses and ellipsoids of the positioning accuracy of robot manipulators. - W Szczepinski and Z Wesolowski *(Inst of Fund Tech Res, Polish Acad of Sci, Warsaw, Poland)*. J Theor Appl Mech 31(3) 465-482 (1993).

When analyzing the problem of positioning accuracy of robot manipulators it is important to know how large many random deviations of the hand be from the desired position if the joint positioning errors possess a normal distribution. Two simple methods of determining the ellipses and ellipsoids of probability concentration are proposed. One of them consists in finding at first the polygon or polyhedron of the positioning accuracy, and then in finding the ellipse or ellipsoid of the principal axes and second order moments coinciding with those of the polygon or polyhedron, respectively. In the second of the proposed methods a computer generates random Gaussian deviations from the desired joint positions. The calculated numerous positioning errors are forming an elliptical or ellipsoidal pattern demonstrating good agreement with theoretically obtained ellipses or ellipsoids of probability concentration.

11A209. Walking machines. - DE Okhotsimsky, AK Platonov, AA Kiril'chenko, VV Lapshin, VG Tolstuosova *(Keldysh Inst of Appl Math, Russian Acad of Sci, Miusskaya sq 4, 125047 Moscow, Russia)*. Adv Mech 15(1-2) 39-70 (1992).

Problems arising in the development of walking machines with higher passability as compared with usual transport vehicles are discussed. Possible applications are described. Different control methods and motion control systems are considered along with information, mechanics power and structure problem. Statically and dynamically stable motion modes are studied. Examples of implemented designs of the legged machines are presented.

11A210. Approach for ensuring manipulator tip accuracy near singularities. - RP Podhorodeski *(Adaptive Robotic Telesyst Lab, Dept of Mech Eng, Univ of Victoria, PO Box 3055, Vic, BC, V8W 3P6, Canada)*. Mech Machine Theory 28(5) 641-649 (Sep 1993).

An approach for ensuring both manipulator tip accuracy and feasible joint rates near singularities is presented for serial-chain manipulators. The approach is based upon joint rate truncation and on-line planning of a suitable alternative end effector velocity. Screw quantities reciprocal to the nontruncated joint axes are used to define feasible alternative motions. Optimization, subject to these reciprocity-based motion feasibility constraints, is used to find an alternative velocity satisfying priority objectives of the original desired motion. In this work, alternative velocity components satisfying end tip translational accuracy at the sacrifice of minimal angular error are derived. Furthermore, a method for resolving the reciprocal screw quantities required to enforce alternative motion feasibility is presented. The method is suitable for manipulators having at least one pair of interesting revolute axes. Analytical and numerical results are presented to illustrate the alternative velocity planning approach.

11A211. Dynamic simulation and choice of generalized coordinates for a free-floating closed-chain planar manipulator. - SK Agrawal and MP Shelly *(Dept of Mech Eng, Ohio Univ, Athens OH 45701)*. Mech Machine Theory 28(5) 615-624 (Sep 1993).

Free-floating manipulators are inherently different from fixed-base planar manipulators due to conservation of linear and angular momentum. In this paper, we present simulation studies of a free-floating closed-chain planar manipulator. A fundamental question which an analyst is faced with during dynamic simulation of closed-chain mechanisms is how to choose the generalized coordinates during simulation. The independence of coordinates is dependent on the instantaneous properties of the governing constraints. For free-floating manipulators, this question becomes even more difficult due to the presence of constraints of momentum conservation. The objectives of this paper are to: (a) present a modular algorithm to build a rigid-body dynamic model of a free-floating closed-chain planar manipulator such that the instantaneous properties of the constraints can be easily studied; and (b) examine the momentum and closure constraints to build an algorithm for selection and switching of the generalized coordinates during simulation. In this algorithm, the free-floating manipulator is broken into component subsystems and the equations of constraint on these subsystems. This algorithm clearly describes the instantaneous properties of the constraints during the motion of the mechanism and helps in the selection of the generalized coordinates. The simulation results with this dynamic model and the algorithm for switching of coordinates are presented.

11A212. Feasibility study of manipulator inverse kinematics problems with applications of optimization principles. - Shinobu Sasaki *(Japan Atomic Energy Res Inst, Tokai-mura Naka-gun, Ibaraki-ken 319-11, Japan)*. Mech Machine Theory 28(5) 685-697 (Sep 1993).

This paper studies three different methods for solving inverse kinematics problems relevant to a six-link robot manipulator. In a problem formulation, governing kinematic equations are transformed into an unconstrained optimization problem with an objective function defined by a sum of squares of the errors, and then the two nonlinear models - ie, the variable metric method and the least squares method - are applied to derive stable joint solutions together with a practical linearized model. The results of computer simulation show that these numerical solutions are highly reliable over a much wider application range as compared with a traditional method.

11A213. Improvement of a robot performance due to elimination of both dynamic interactions and joint limits in the manipulator arm. - K Nazarczuk *(Inst of Aviation Eng and Appl Mech, Warsaw Univ of Tech, Poland)*. J Theor Appl Mech 31(3) 621-636 (1993).

The possibility of improvement of robot capabilities due to the elimination of both dynamic interactions and joint limits in its arm has not been fully exploited till now. Two different dynamic schemes of such an arm driven directly have been presented. A manipulator 1:5 model revealing the complete dynamic interactions elimination due to the suitable mass distribution in terms of a proper driving motors arrangement has been shown. Based on the presented dynamic analysis one can state that the designs being proposed ensures a considerable simplification of the robot control system as well as a great shortening of time taken in some motions.

11A214. Indirect discrete-time adaptive algorithm for manipulator control. - MS Mahmoud *(Dept of Elec and Comput Eng, Kuwait Univ, PO Box 5969, Safat 13060, Kuwait)* and AA Bahnasawi *(Dept of Electron and Commun Eng, Cairo Univ, Giza, Egypt)*. Appl Math Model 17(8) 423-429 (Aug 1993).

An adaptive controller design is proposed for discrete-time robotic control. The position of the robot arm is shown to converge to a desired point through two control loops. The first loop is an indirect adaptive perturbation controller based on the decoupled dynamics approach and using a perturbation model for the torque generation. The second loop generates the nominal torque component through a nonlinear controller representing the inverse manipulator dynamics. Simulation results on a typical three-link manipulator have indicated the potential and applicability of the developed design.

See also the following:

11A543. Kinematic-kinetic performance analysis and synthesis measures of multi-dof mechanisms

208. Manufacturing

11A215. From the islands of automation to the knowledge archipelago: The challenge for manufacturing strategy in the 1990s. - JA Brandon *(Sch of Eng, Univ of Wales Col of Cardiff, UK)*. Proc Inst Mech Eng B 207(B3) 141-146 (1993).

The paper examines the complementary issues of the availability of novel technological ideas and the receptiveness of managerial infrastructure. It suggests that the apparently conflicting philosophies of the technological minimalists, who seek to restore manufacturing effectiveness by empowerment of work groups, and those who advocate large-scale automation of manufacturing systems in cellular form can be reconciled using ideas from object-oriented programming system.

See also the following:

11A165. Transformations of graphite and boron nitrite in shock waves
11A207. Trajectory planning using artificial intelligence

IV. MECHANICS OF SOLIDS

250. Elasticity

250B. LINEAR THEORY

11A216. More general displacement solutions for the plane elasticity problems. - Yi-wu Yuan *(Central S Univ of Tech, Changsha, China)*. Appl Math Mech 14(3) 247-252 (Mar 1993).

In this paper, the author obtains the more general displacement solutions for the isotropic plane elasticity problems. The general solution obtained is merely the particular case of this paper. In comparison, the general solutions of this paper contain more arbitrary constants. Thus they may satisfy more boundary conditions.

250C. NONLINEAR AND FINITE DEFORMATION PROBLEMS

11A217. An approach to approximate analysis of deformation and strain. - Hui-Er Xiong *(Hunan Univ, Changsha 410082, Peoples Rep of China)* and Quan-Shui Zheng *(Jiangxi Polytech, Nanchang 330092, Peoples Rep of China)*. Acta Mech Solida Sinica 6(3) 261-273 (Jul 1993).

An approach to approximate analysis of deformation and strain is developed from recent work on Cauchy mean rotation. The approximate expressions of Green strain usually employed in solving problems of nonlinear mechanics and their errors are discussed. The estimation of error is strictly based on the definition of small strain and medium or large rotation.

11A218. FE analysis of rubber coextrusion using a power-law model. - GC Buscaglia *(Div Mecanica Computational DIA, Centro Atomico Bariloche CNEA, 8400-SC de Bariloche, Argentina)*. Int J Numer Methods Eng 36(13) 2143-2156 (15 Jul 1993).

A FEM to simulate coupled thermal viscous coextrusion is presented, with a power-law viscosity function obtained from viscometric data on rubber composites. It combines, by successive substitution iterations, various well-known schemes, such as streamline integration for updating interfaces and Lagrange-Galerkin treatment of the energy equation. Some details of the implementation are discussed. The method is then applied to a comparison of two pre-forming plates for the dual tuber head extruder of Farrel Corp. Both the normal stress and the temperature at the interface suggest that the presence of a deflector deteriorates the adherence properties. This prediction is in agreement with operational experience.

11A219. Finite deformations of polar elastic media. - PH Dluzewski *(Inst of Fund Tech Res, Swietokrzyska 21, 00-049 Warsaw, Poland)*. Int J Solids Struct 30(16) 2277-2285 (1993).

In many papers on oriented continua some orthonormal angular coordinates were proposed. With respect to the curvature of the orientation space, it is obvious that such coordinates could not be applied in practice. Therefore, instead of these coordinates a tensor field of rotations had to be used to define the wryness tensor. In this paper the curvilinear coordinates in orientation space are considered. The Euler angles are an example of such coordinates. The inertia conservation law is replaced here by a constitutive relation. From the physical point of view this relation is more general and seems to be better justified than the mentioned law. Within the framework of the polar continuum theory a micromorphic structure is discussed. Some remarks on the principle of a material frame-indifference are also presented.

11A220. Initial problem for elastodynamic equations of compressible bodies. - A Szymaniec *(Warszawa, Poland)*. Biuletyn Wojskowej Akademii Technicznej 41(12) 89-104 (1992).

The solvability of the solutions to the Cauchy problem for incompressible strongly elliptic hyperelastic materials was proved using the method of Sobolev spaces. In particular, the existence, uniqueness and continuous dependence on given data above mentioned solution has been proved for the nonlinear equations for elastodynamics of incompressible bodies.

11A221. Static and dynamic precursors of displacive transformations near crystalline defects. - PC Clapp *(Center for Mat Simul, Inst of Mat Sci, Univ of Connecticut, Storrs CT 06269-3136)*. Physica D 66(1-2) 26-34 (Jun 1993).

An exact nucleation energy formula has been derived for the fluctuation energy necessary to initiate a coherent martensitic transformation in the strain field of a defect of arbitrary potency within the framework of a standard Ginzburg-Landau strain free energy model of the form: $f(n) = g(n) + K_1(\nabla n)^2$. The formula is limited to planar defects and planar interface propagation geometries, and precursor metastable strain profiles are calculated exactly. The defect induced strain field expands as the driving force is increased until the athermal instability limit is reached. This limit can be simply expressed in terms of the defect potency, or alternatively in terms of the strain spinodal, but the latter condition proves to be the weaker of the two in most cases tested. Once the nucleation condition is achieved, the equations of growth become identical to those previously tested by Chan.

250D. THREE-DIMENSIONAL PROBLEMS

See the following:

11A462. Accurate measurement of 3D deformations in deformable and rigid bodies using computer vision

250E. STRESS CONCENTRATIONS AND SINGULARITIES

11A222. Problems of stress concentration in the neighborhood of a spherical defect. - GY Popov *(Russia)*. Adv Mech 15(1-2) 71-110 (1992).

A defect is understood as a surface, which if crossed leads to discontinuity of displacements and stresses. A review of publications in considering the problem of stress concentration in the neighborhood of a spherical defect, made in the paper, testifies that the problem in the non-axially-symmetric approach have not been previously investigated, neither have been examined the problems in the axially-symmetric approach for defects of more general nature than the cracks and thin inclusions. Here an exact solution of non-axially-symmetric problems of stress concentration in the neighborhood of a spherical defect has been obtained, it relates to such defects as a crack or a thin inclusion: the way to find the solution of the defect problem of more general nature has been pointed out, as for instance for an exfauliated rigid inclusion. The main difference between the proposed method of finding the exact solution and the earlier ones consists in that both the problem of the crack and that of the thin inclusion are reduced to three identical separately solved, 1D integral equations.

250F. ELASTIC IMPERFECTIONS (DISLOCATIONS, ETC)

11A223. Heterogeneous nucleation of dislocation loops under epitaxial strain. - Wei Yang and Hong Zhang *(Dept of Eng Mech, Tsinghua Univ, Beijing 100084, Peoples Rep of China)*. Acta Mech Solida Sinica 6(3) 243-259 (Jul 1993).

Heterogeneous nucleation of dislocation loops driven by high epitaxial strain describes a possible failure mode of multi-layer superlattice structures. The present paper furnishes a close form solution for the 2D mechanics analysis. A 3D BEM calculation facilitated by a singularity exclusion scheme is conducted for circular dislocation loops nucleated from a sperical void. The results show that the critical epitaxial strain necessary to nucleate a dislocation loop minimizes at an intermediate range of defect sizes.

11A224. Nonlinearities in the static energetics and in the kinematics of dislocations. - JP Hirth and RG Hoagland *(Mech and Mat Eng Dept, Washington State Univ, Pullman WA 99164-2920)*. Physica D 66(1-2) 71-77 (Jun 1993).

Methods for the atomistic simulation of dislocation core regions are discussed. Simulations of this type are shown to lead to a variety of core configurations and energies that are of nonlinear origin. The motion of dislocations by double kink formation is considered as an example of nonlinear dynamic effects.

250H. CONTACT PROBLEMS AND INCLUSIONS

11A225. Axial loading of a rigid circular anchor plate embedded in an elastic half-space. - APS Selvadurai *(Dept of Civil Eng and Appl Mech, McGill Univ, Montreal, PQ, H3A 2K6, Canada)*. Int J Numer Anal Methods Geomech 17(5) 343-353 (May 1993).

The present paper examines the axisymmetric problem related to the loading of a rigid circular anchor plate which is embedded in bonded contact with an isotropic elastic half-space. A Hankel transform development of the governing equations is used to reduce the associated mixed boundary value problem to a set of coupled Fredholm integral equations of the second kind. These equations are solved in a numerical fashion to generate results of engineering interest. In particular, the results indicate the influence of the depth of embedment of the axial stiffness of the rigid anchor plate.

11A226. BEM frictional contact analysis: Load incremental technique. - KW Man, MH Aliabadi *(Wessex IT, Ashurst, Southampton SO4 2AA, UK)*, DP Rooke *(Defense Res Agency, RAE Farnborough, Hants GU14 7TU, UK)*. Comput Struct 47(6) 893-905 (17 Jun 1993).

A BE formulation for solving structural problems associated with frictional contact is presented; it uses an efficient, iterative and fully load-incremental technique. Problems with any number of 2D bodies in contact can be analyzed using this technique; the bodies may be conforming or non-conforming, of similar or dissimilar materials. The interface may be frictionless or frictional and undergo slip or partial slip. Numerical solutions for both normal and tangential traction distributions can be obtained automatically for successive load increments. The technique utilizes automatic updating procedures in order to model the continuously changing boundary conditions occurring inside the contact region. Results obtained show that an accurate account of the nonlinear behavior, caused by the frictional effects, can be obtained only by following the loading history as well as the contact history.

11A227. General approach to axial deformation of bonded elastic mounts of various cross-sectional shapes. - MHBM Shariff *(Sch of Comput and Math, Univ of Teesside, Middlesbrough TS1 3BA, UK)*. Appl Math Model 17(8) 430-436 (Aug 1993).

Bonded elastic mounts of various cross-sections (3D) are widely used in engineering. Previous approximate explicit analyses have mainly been restricted to 2D analysis. None of the previous approximate analyses are based solely on the formal general equations of elasticity but involve mixed assumptions not necessarily related to each other. In this paper an approximate explicit 3D solution is obtained that is reasonable, easy to use, and compares well with experimental data. The method developed makes use of a variational principle that is equivalent to the general equations of elasticity expressed in terms of the displacement and a scalar function associated with the mean pressure. The analysis developed here unifies previous analyses and allows scope for better approximations. Upper and lower bounds on the axial nominal stress, energy, and apparent Young's modulus are given.

11A228. Simulation of the vertical split head failure in rails. - CH Kuo, LM Keer *(Dept of Civil Eng, NWU)*, RK Steele *(Tech Center, Assoc of American Railroads, 3140 S Federal St, Chicago IL 60616)*. Int J Solids Struct 30(16) 2177-2197 (1993).

A 2D analysis is presented to assess a possible mechanism to account for the axial cracking behavior in rails which is usually called a vertical split head failure. This failure is potentially damaging and may eventually lead to derailment. The vertical split head is simulated in the present analysis as a vertical crack in an eccentrically loaded infinite strip, representing the head, loaded on its upper surface and constrained on its lower surface, approximating the web constraint. The vertical crack is modeled as distributed dislocations. By using Fourier transforms, the interior stress field and stress intensity factors at the crack tip are determined from the derived coupled integral equations. The calculated stress field indicates that the initiation of a vertical defect is more likely to be caused by the influence of residual stresses upon an existing rail defect, such as an inclusion. Moreover, the growth of the crack is constrained to within the rail head by the high magnitudes of compressive stresses that occur beneath the contact loading and the head-web juncture.

See also the following:

11A432. Cracks of fractal geometry with unilateral contact and friction interface conditions

11A471. Mixed variational formulation for shape optimization of solids with contact conditions

250I. ANISOTROPIC MEDIA

11A229. On-line determination of texture-dependent materials properties. - HJ Bunge *(Dept of Phys Metall, TU Clausthal, Germany)*. J Nondestruct Eval 12(1) 3-11 (Mar 1993).

Macroscopic properties of polycrystalline materials may strongly depend on crystal orientation distribution, ie, the texture of the material. This applies to all kinds of crystallographically anisotropic volume and boundary properties. The necessary texture parameters can be determined from a low number of intensity values measured with a fixed-angle, X-ray texture analyzer which is particularly suited for on-line determination. Alternatively, the texture-property relationship can be used to calculate the texture parameters from property measurement in different sample direction. On-line measurement of the texture can also be used as an indicator for other material properties such as recrystallization or fatigue.

See also the following:

11A449. Application of nondestructive techniques for the prediction of elastic anisotropy of a textured polycrystalline material

250Y. COMPUTATIONAL TECHNIQUES

11A230. Evaluation of the stress tensor in 3D elastostatics by direct solving of hypersingular integrals. - O Huber, G Lang, G Kuhn *(Lehrstuhl Tech Mech, Friedrich-Alexander-Univ Erlangen-Nurnberg, Egerlandstr 5, 8520 Erlangen, Germany)*. Comput Mech 12(1-2) 39-50 (Jun 1993).

A new method of direct numerical evaluation of hypersingular boundary integrals has been applied to the differentiated form of the Somigliana-identity (hypersingular identity) in 3D elastostatics. Through this method it is possible to evaluate the stress tensor on the boundary of a complex 3D structure in a very accurate manner by employing the direct BEM. The geometry of the elements and their arrangements over the boundary of the structure are not subjected to any restrictions. Numerical examples illustrate the accuracy of the proposed method.

See also the following:

11A127. Diffraction of torsional elastic waves by a rigid annular disc at a bimaterial interface

252. Viscoelasticity

11A231. Hadamard-type stability of single integral constitutive equations for viscoelastic liquids. - Y Kwon and AI Leonov *(Dept of Polymer Eng, Univ of Akron, Akron OH 44325-0301)*. J Non-Newtonian Fluid Mech 47 77-91 (Jun 1993).

This paper studies the Hadamard type stability of viscoelastic constitutive equations (VECEs) of single-integral type by the analysis of local linear stability against extremely short and fast disturbances. The analysis is quite similar to that previously considered for Maxwell-like VECEs of differential type. The necessary and sufficient conditions for the global stability (ie, stability for any type of flow and any value of velocity gradient) are obtained in algebraic form for the time-strain separable single-integral VECEs with instantaneous elasticity. These conditions are then applied to the analysis of the stability for some single-integral VECEs proposed in the literature: Oldroyd-Lodge model, some specifications of the Kaye-BKZ model and two modifications of the VECEs proposed by Wagner. It is shown that apart from very particular cases, both Wagner's VECEs are unstable in the Hadamard-type sense, seemingly due to poor (or the absence of any) relations to thermodynamic description.

11A232. "Necking" in high-speed spinning revisited. - A Ziabicki *(Inst of Fund Tech Res, Polish Acad of Sci, 21 Swietokrzyska St, 00-049 Warsaw, Poland)* and Jianjun Tian *(Man-Made Fibers Res Inst, China Textile Univ, 1882 W Yan-An Rd, Shanghai 200051, China)*. J Non-Newtonian Fluid Mech 47 57-75 (Jun 1993).

The conditions required for "necking" in melt-spinning are discussed. The adopted criterion defines necking as a filament-radius profile R(x) exhibiting two inflexion points (R" = 0), one characterized by a negative, the other one by a positive, third gradient R"'. Analysis of the dynamics of spinning of a nonisothermal corotational Maxwell fluid leads to the conclusion that the conditions of necking require either long relaxation times (Deborah number > 1/2), or a large, positive tension gradient F' possibly controlled by inertia. In inertialess Newtonian filaments, the necking condition can also be satisfied by local reduction of viscosity. The above three mechanisms of necking, viscoelastic, inertial, and viscous, are analyzed and discussed.

11A233. Study of stress distribution in contraction flows of an LLDPE melt. - DG Kiriakidis, HJ Park, E Mitsoulis *(Dept of Chemical Eng, Univ of Ottawa, Ottawa, ON K1N 6N5, Canada)*, B Vergnes, J-F Agassant *(Center de Mise en Forme des Materiaux, Ecole des Mines de Paris, URA CNRS 1374 BP 207, 06904 Sophia Antipolis, France)*. J Non-Newtonian Fluid Mech 47 339-356 (Jun 1993).

Numerical simulations are carried out for a linear low-density polyethylene (LLDPE) flowing through an 8:1 planar contraction equipped with slit dies of different length (L/2H = 2 and 8) at two different temperatures (145 and 205° C). The emphasis is on determining the stress distribution and comparing it with birefringence experimental results that have previously appeared in the literature. The working constitutive equation is a realistic integral model of a K-BKZ type with a spectrum of relaxation times. The material parameters have been obtained by fitting experimental viscosity and normal stress data as measured in shear, and by using elongational viscosity data available in the literature. The numerical simulations are performed for a wide range of apparent shear rates ($10s^{-1} < \gamma_a < 140s^{-1}$) with good and fast convergence of the iterative scheme. The results show that as the apparent shear rate increases, viscoelastic effects dominate, exhibiting a delayed relaxation of stresses along the slit and stress overshoots at the die exit. This behavior is in close agreement with the experimental birefringence patterns. Elastic recovery is also captured in an enhanced extrudate swell which is always higher for the short die at the same temperature.

11A234. Modeling creep in thermoplastic composites. - Ilsup Chung, CT Sun *(Sch of Aeronaut and Astronaut, Purdue)*, IY Chang *(Composite Div, EI du Pont de Nemours, Wilmington DE 19880-0702)*. J Composite Mat 27(10) 1009-1029 (1993).

A creep model for unidirectionally reinforced fiber composites was developed on a one-parameter potential function. The same potential function was used to describe plastic flow and time-dependent creep deformation. The material constants in the model were terminated by using the uniaxial tension test of off-axis coupon specimens. In terms of effective stress and effective creep strain, the anisotropic creep behavior can be given by a stress-dependent master creep curve irrespective of loading direction relative to fiber orientation. DuPont's AS4/PEKK thermoplastic composites were used in the creep experiment. Results for both unidirectional and laminated composites were presented.

11A235. Viscoelastic analysis of bonded tubular joints under torsion. - Haiming Zhou and MD Rao *(Mech Eng, Eng Mech Dept, Michigan Tech Univ, Houghton MI 49931)*. Int J Solids Struct 30(16) 2199-2211 (1993).

In this paper, a theoretical analysis to evaluate the stress field in the adhesive layers of tubular bonded joints subjected to torsional loading is presented. The formulation is suitable to study the static behavior of the joint under general loading conditions as well as steady-state behavior under cyclic loading conditions. The adhesive material is modeled using linear viscoelasticity and numerical results for the shear stresses in the adhesives, joint compliance and joint loss factor are presented for various cases that provide some insights and guidelines in the design of the joint.

11A236. Calculation of viscoelastic flow using molecular models: The CONNFFESSIT approach. - M Laso and HC Ottinger *(Inst fur Polymere, Eidgenossische Tech Hochschule, ETH-Zentrum, CH-8092 Zurich, Switzerland)*. J Non-Newtonian Fluid Mech 47 1-20 (Jun 1993).

A new method for numerical calculation of viscoelastic flow based on simulation of molecular models of polymers is presented. The CONNFFESSIT (Calculation of Non-Newtonian Flow: FE and Stochastic Simulation Technique) approach directly combines standard FEM as currently used in the calculation of viscoelastic flow with stochastic simulations of polymer dynamics and thus obviates the need for a rheological constitutive equation to describe the fluid. The stresses are obtained from the molecular configurations rather than from constitutive equations. As an illustration of the method, the time development of plane Couette flow is studied for the upper-convected Maxwell, Oldroyd-BFENE-P and FENE fluids. For the upper-convected Maxwell, Oldroyd-B and FENE-P models comparisons with analytical and existing numerical solutions are presented. Significant deviations between the behavior of the FENE-P and FENE models for the start-up of plane Couette flow are found.

11A237. Spectral methods for the viscoelastic time-dependent flow equations with applications to Taylor-Couette flow. - M Avgousti *(Polymer Processing Inst and Dept of Chem Eng, Stevens IT, Hoboken NJ 07030)*, B Liu *(Dept of Chem Eng, UCLA)*, AN Beris *(Dept of Chem Eng, Univ of Delaware, Newark DE 19716)*. Int J Numer Methods Fluids 17(1) 49-74 (Jul 1993).

The time evolution of finite amplitude axisymmetric perturbations (Taylor cells) to the purely azimuthal, viscoelastic, cylindrical Couette flow was numerically simulated. Two time integration numerical methods were developed, both based on a pseudospectral spatial approximation of the variables, efficiently implemented using fast Poisson solvers and optimal filtering routines. The first method, applicable for finite Re numbers, is based on a time-splitting integration with the divergence-free condition enforced through an influence matrix technique. The second one, is based on a semi-implicit time integration of the constitutive equation with both the continuity and the momentum equations enforced as constraints. Stability results for an upper convected Maxwell fluid were obtained for the supercritical bifurcations, either steady or time-periodic, developed after the onset of instabilities in the primary flow. At small elasticity values, ε = De/Re, the time integration of finite amplitude disturbances confirms the stability of the single branch of steady Taylor cells. At intermediate ε values the rotating wave family of time-periodic solutions developed at the onset of instability is stable, whereas the standing wave is found to be unstable. At high ε values, and in particular for the limit of creeping flow ($\varepsilon = \infty$), the present study shows that the rotating wave family is unstable and the standing (radial) wave is stable, in agreement with previous FE investigations. It is thus shown that spectral techniques provide a robust and computationally efficient method for the simulation of complex, nonlinear, time-dependent viscoelastic flows.

See also the following:

11A443. Photovisco-elastoplastic behavior of polycarbonate material under creep and tension tests

254. Plasticity and viscoplasticity

254A. GENERAL THEORY

11A238. Application of the twelve-angled polygonal yield criterion to pressure vessel problems. - Xiaoying Zeng, Jinxiang Li, Jinwei Li, Gangling Li *(S China Univ of Tech, Bldg 26 Apt 101, S Living Quarters No 1, Guangzhou 510641, Peoples Rep of China)*, Zhichao Yang *(Petrochem Works, Guangzhou 510726, Peoples Rep of China)*, Jinyu Li *(Bai-Yun-Shan Med Works, Guangzhou 510515, Peoples Rep of China)*. Int J Pressure Vessels Piping 55(3) 385-393 (1993).

This paper deduces and expounds the general equations of a twelve-angled polygonal yield criterion, and it application to pressure vessels. We consider an open-ended cylinder made of ideal plastic material and deduce two practical integral formulas using the MN yield line and the MN plus MH yield lines. Thus far the calculation of an open-ended cylinder autofrettage is solved overall.

11A239. Deformation behavior of alloys comprising two ductile phases I. Deformation theory. - Z Fan and AP Miodownik *(Dept of Mat Sci and Eng, Univ of Surrey, Guildford, Surrey GU2 5XH, UK)*. Acta Metall Mat 41(8) 2403-2413 (Aug 1993).

A topological transformation has been proposed, which allows a two-phase microstructure with any combination of grain-size, grain-shape, and phase distribution, to be translated into a body consisting of three well-defined microstructural elements aligned along a particular direction of interest. The resultant three-element body is shown to be mechanically equivalent to the original body along this direction. The concept of contiguity and allied topological parameters have been combined with Eshelby's continuum transformation theory to determine the internal stresses and strains, the true stress strain curve, and the *in situ* stress and the *in situ* plastic strain distribution in the three microstructural elements and thus derive the mechanical properties of the aggregate. This approach incorporates the interaction between particles of the same phase and the effect of phase distribution as well as the effect of volume fraction. Applications of the theory are given in a companion paper.

11A240. Deformation behavior of alloys comprising two ductile phases II. Applications of the theory. - Z Fan and AP Miodownik *(Dept of Mat Sci and Eng, Univ of Surrey, Guilford, Surrey, GU2 5XH, UK)*. Acta Metall Mat 41(8) 2415-2423 (Aug 1993).

True stress-true strain curves, the mean internal stresses and the *in situ* stress and plastic strain distribution have been calculated for α-β titanium alloys, ferrite-martensite dual-phase steels and α-γ stainless steels, using the theory developed in Part I. It is shown that the theoretical predictions are in very good agreement with the experimental results drawn from the literature. The effects of microstructural parameters and the effect of differences in the mechanical properties of the constituent phases on the deformation behavior of these two-ductile-phase alloys are discussed in detail. In contrast to existing deformation theories, the present approach predicts that there are four deformation stages in the total deformation process of two-ductile-phase alloys, and that there should always be a drop in the flow stress after the onset of the plastic deformation in microstructural element III. This phenomenon has been explained in terms of internal stress changes and the balance of the elastic strain energy associated with prior plastic deformation in the three microstructural elements used to describe the overall deformation process.

11A241. Extremal properties of endochronic plasticity Part I. Extremal path of the constitutive equation without a yield surface. - Xianghe Peng *(Chongqing Univ, China)* and ARS Ponter *(Univ of Leicester, University Rd, Leicester LE 17 RH, UK)*. Int J Plasticity 9(5) 551-566 (1993).

Based on the general extremal properties of time-independent inelastic materials proposed by Ponter and Martin, some extremal properties of endochronic theory of plasticity are investigated. The extremal path of an endochronic constitutive equation without using a yield surface is found, which makes plastic work act as a potential such that the deviatoric stress can be derived from its derivative with respect to plastic strain. These properties are important because they provide the possibility for the irreversible thermodynamically based constitutive equations, which is strongly history-dependent, to be applied to simplified analysis in engineering problems. Using the derived extremal properties, the principal of minimum potential energy is extended to endochronic theory of plasticity. As an example, the stress and strain fields of a hinge-joint three-bar truss are analyzed.

11A242. Extremal properties of endochronic plasticity Part II. Extremal path of the constitutive equation with a yield surface and application. - Xianghe Peng *(Chongqing Univ, China)* and ARS Ponter *(Univ of Leicester, University Rd, Leicester LE 17RH, UK)*. Int J Plasticity 9(5) 567-581 (1993).

Extremal paths for endochronic constitutive equations without using a yield surface and the corresponding principle of minimum potential work were obtained in Part I of this article. In this paper, the extremal properties of endochronic constitutive equation with a yield surface and the corresponding method for deformation bound analysis are proposed. An example is presented that demonstrates that the application of endochronic constitutive models to simplified analysis is not significantly different from classical models due to the derived extremal properties. The adopted constitutive model involves both linear isotropic and kinematic hardening, which may provide more accurate results in simplified and bounding analysis.

254C. NONLINEAR AND FINITE DEFORMATION PROBLEMS

11A243. Dynamic large deformation response of rigid plastic arches under impact. - De-Min Wei and Gui-Tong Yang *(Taiyuan Univ of Tech, Taiyuan, Shanxi 030024, Peoples Rep of China)*. Acta Mech Solida Sinica 6(3) 275-289 (Jul 1993).

This paper presents a theoretical analysis of the dynamic large deformation response of highly circular arches under impact. By the Instantaneous Configuration Method, the solutions of the entire large deformation response process of the problem are obtained. The influences of the mass ratio, the energy ratio and the supported condition on the final deformation, the response time and the occurrence of plastic deformation are discussed in detail. The necessary conditon for occurrence of the "local reverse bending" phenomenon has been found. An approximate method is provided to describe the phenomenon. The numerical results are in good agreement with experimental data.

11A244. Effect of annealing, size and cut-outs on axial collapse behavior of circular tubes. - NK Gupta *(Dept of Appl Mech, Indian IT, Hauz Khas, New Delhi 110016, India)* and SK Gupta *(Centre for Mat Sci and Tech, Indian IT, Hauz Khas, New Delhi 110016, India)*. Int J Mech Sci 35(7) 597-613 (Jul 1993).

Axial compression tests were performed on round tubes of different sizes and made of aluminium and mild steel, both in as-received and annealed conditions. Length to diameter and diameter to thickness ratios of these tubes were varied in different tests, and cut outs in the form of circular holes, varying in diameter, number and position, were laterally drilled in them. Typical histories of their deformation and load-compression curves are presented and the influence thereon of the annealing process, the tube size, or the cut-outs is discussed. Relations are presented to describe these influences and to express the first peak and mean collapse loads in terms of the Vickers hardness number. It is seen that the presence of holes in the tubes alters their mode of collapse and, as a consequence, affords the possibility of avoiding Euler buckling even when relatively much longer tubes are employed.

11A245. Modeling of large plastic deformations based on the mechanism of micro-shear banding. Physical foundations and theoretical description in plane strain. - RB Pecherski *(Inst of Fund Tech Res, Polish Acad of Sci, Warszawa, Poland)*. Arch Mech 44(5-6) 563-584 (1992).

Shear banding is related to large plastic deformations produced by mechanisms of crystallographic slip and/or twinning and micro-shear. Physical foundations and motivations to formulate simplified phenomenological model are considered. Plane deformations of elastoplastic material accounting for micro-shear bands are studied. The derived relations show that the micro-shear bands produce the non-coaxiality between the principal directions of stress and rate of plastic deformations. It transpires that, depending on the contribution of the mechanisms involved in plastic flow, a fully active range, separated from the elastic range by a truly nonlinear zone called the partially active range, may exist. In case of continued plastic flow with the deviations from proportional loading contained within the fully active range the incremental plastic response is linear, whereas the constitutive relations derived for the partially active range appear thoroughly nonlinear. Relations to known nonlinear flow laws in rates of deformation and stress are discussed.

11A246. Theoretical and computational aspects in the shakedown analysis of finite elastoplasticity. - H Stumpf *(Lehrstuhl fur Allgemeine Mech, Ruhr-Univ Bochum, Postfach 10 21 48, W-4630 Bochum, Germany)*. Int J Plasticity 9(5) 583-602 (1993).

A fully nonlinear shakedown analysis is considered for structures undergoing large elastic-plastic strain. The underlying kinematics of finite elastoplasticity are based on the multiplicative decomposition of the deformation gradient into elastic and plastic parts. It is shown that the notion of a fictitious, self-equilibrated residual stress field of Melan's linear shakedown theorem has be replaced by the notion of real, self-equilibrated residual state. Path-dependent and path-independent shakedown theorems are presented that can be realized in an incremental step-by-step procedure using FE codes. The numerical implementation is considered for highly nonlinear truss structures undergoing large cyclic deformations with ideal-plastic, isotropic and kinematic hardening material behavior. Path-dependency of the residual states in the case of non-adaptation and path-independency in the case of shakedown are shown, and the shakedown domain is determined taking into account also the stability boundaries of the structure.

254F. MATERIAL CHARACTERIZATION

See the following:

11A351. Plain strain rigid plastic FE formulation for sheet metal forming process

254G. WORK HARDENING

11A247. Elastic-plastic response of thin-walled tubes under combined axial and torsional loads Part I. Monotonic loading. - W Jiang *(Mech Eng Dept, Florida Int Univ, Miami FL 33199)*. J Pressure Vessel Tech 115(3) 283-290 (Aug 1993).

This paper investigates the elastic-plastic response of thin-walled tubes subjected to combined axial and torsional loads. The kinematic hardening model is used and exact closed-form solutions are obtained for linear loading paths. The characteristics of the stress-strain relationships are discussed and the corresponding movements of the yield center are illustrated. The response of the material under nonproportional loading is proved to be path-dependent, and the hardening behavior is shown to be different from that under proportional loading. The investigation then shows that such a difference will finally disappear when the stresses tend to infinity.

11A248. Elastic-plastic response of thin-walled tubes under combined axial and torsional loads Part II. Variable loading. - W Jiang *(Mech Eng Dept, Florida Int Univ, Miami FL 33199)*. J Pressure Vessel Tech 115(3) 291-296 (Aug 1993).

This paper continues the investigation of the elastic-plastic response of thin-walled tubes subjected to combined axial and torsional loads. The stress-strain loop under arbitrary variable loading is first discussed. It is then shown that due to the kinematic hardening, a steady state, either one of the reversed plasticity or one of the elastic shakedown, can always be reached under cyclic loadings, with a hysteresis loop in the form of a parallelogram or a straight line. As a result, the difference in response between nonproportional and proportional loading will finally disappear. The investigation indicates that the simple kinematic hardening rule is able to describe, at least qualitatively, certain basic characteristics of the maerial behavior observed in nonproportional tests.

254H. CYCLIC AND VARIABLE LOADING

11A249. Extension of the static shakedown theorem to a certain class of inelastic materials with damage. - A Hachemi and D Weichert *(Ecole des Mines Douai and Lab Mec, Univ de Lille, Villeneuve, D'Ascq, France)*. Arch Mech 44(5-6) 491-498 (1992).

In this paper, an extension of the static shakedown theorem (Melan's Theorem) to elastic-plastic damaging material behavior is presented. Damage is taken into account by using the Ju-model, and the generalized standard material model with plastic hardening.

11A250. Macroscopic observations and related microscopic phenomena of the mechanical behavior of metallic materials. - B Wack and A Tourabi *(Lab des Sols Solides, Struct, Grenoble, France)*. Arch Mech 44(5-6) 621-662 (1992).

On the basis of some experimental macroscopic results a qualitative correspondence may be established between the macroscopic hysteresis behavior and the microstructural phenomena which are responsible for the deformation.

See also the following:

11A248. Elastic-plastic response of thin-walled tubes under combined axial and torsional loads Part II. Variable loading

254I. VISCO- AND ELASTO-PLASTIC MEDIA

11A251. Antiplane shearing motions of a visco-plastic solid. - JM Greenberg *(Dept of Math and Stat, Univ of Maryland, Baltimore County, Baltimore MD 21228)* and Anne Nouri *(Univ de Nice, Parc Valrose, 06034 Nice Cedex, France)*. SIAM J Math Anal 24(4) 943-967 (Jul 1993).

The authors consider antiplane shearing motions of an incompressible isotropic visco-plastic solid. The flow rule employed is a properly invariant generalization of Coulomb sliding friction and assumes a constant yield stress or threshold above which plastic flow occurs. In this model stresses above yield are possible; but when this condition obtains, the plastic flow rule forces the plastic strain to change so as to lower the stress levels in the material and dissipate energy. On the yield surface, the flow rule looks like the classical one for a rate independent elastic-perfectly plastic material when the velocity gradients are small enough but differs from the classical model for large gradients.

11A252. Elasto-plastic response of orthotropic pipes under bending, pressure, and axial force. - CJ Tay, KH Lee, ED David *(Dept of Mech and Prod Eng, Natl Univ, Singapore 0511)*. Thin-Walled Struct 17(3) 203-221 (1993).

An elasto-plastic analysis of circular thin-walled pipes in the non-buckled configuration subjected to bending moment, pressure, and axial loads is presented. Plastic stress-strain relationships based on Drucker's postulates, Hill's yield criterion,and the deformation theory are utilized. The analysis includes orthotropic behavior with the assumption of a linear strain-hardening material. Results are presented for both isotropic and orthotropic materials.

11A253. Fundamental requirements and formulation of elastoplastic constitutive equations with tangential plasticity. - K Hashiguchi *(Dept of Agri Eng, Kyushu Univ, Fukuoka 812, Japan)*. Int J Plasticity 9(5) 525-549 (1993).

In order to extend an elastoplastic constitutive equation to describe the dependency of a plastic stretching on a stress rate component tangential to the yield surface, two fundamental requirements are first formulated, which have to be fulfilled in elastoplastic constitutive equations. One of them is the *work rate* or *stiffness relaxation*. The other is the *continuity condition* of stress rate. The elastoplastic constitutive equation with a "single, smooth" yield surface is formulated to fulfill these requirements, in which a plastic stretching (its magnitude and direction) depends on a stress rate component tangential to the yield surface; thus it is called a *tangential plasticity*. Based on this, a concrete constitutive equation of metals with isotropic-kinematic hardening and tangential plasticity is formulated, which, among existing concrete constitutive equations with a tangential plasticity, is capable of describing the general loading behavior including nonproportional, reverse loading, and reloading. Its mechanical response is shown in comparison with the traditional J_2 flow theory with the associated flow rule.

11A254. Nonlocal versus local elastoplastic behavior of heterogeneous materials. - M Berveiller, D Muller *(Lab de Phys et Mec des Mat URA CNRS 1215, Univ of Metz, ISGMP Ile du Saulcy, 57045 Metz, France)*, J Kratochvil *(Czechoslovak Acad of Sci, Na Slovance 2, 18040 Prague 8, Czechoslovakia)*. Int J Plasticity 9(5) 633-652 (1993).

The scale transition methods have been developed for many years in order to obtain the overall behavior of polycrystalline materials from their microscopic behavior and their microstructure. Nevertheless, some basic aspects are absent from such formalisms. The most significant one seems to be the heterogenization by plastic straining which involves nonlocality of hardening. In this article, a nonlocal theory based upon crystalline plasticity is developed from which a nonlocal constitutive equation at the grain level is derived. With regard to the polycrystal, in order to deduce the behavior of a local equivalent homogeneous medium, an integral equation is proposed and solved for nonlocal inhomogeneous materials by the self-consistent approximation. This scheme is developed in case of a two-phase nonlocal material representing the dislocation cell structure induced during plastic straining. Numerical simulations based on a simplified model show significant effects on the intragranular heterogeneization.

11A255. Variational theory for finite-step elasto-plastic problems. - G Romano, L Rosati, F Marotti de Sciarra *(Dipartimento di Sci delle Construzioni, Fac Ing, Uinv Napoli Federico II, 80125 Piazzale Tecchio, 80-Napoli, Italy)*. Int J Solids Struct 30(17) 2317-2334 (1993).

An extended version of *generalized standard* elasto-plastic material is considered in the framework of an internal variable theory of associated plasticity. According to a backward difference scheme for time integration of the flow rule, a finite-step structural problem is formulated in a geometrically linear range. Convex analysis and a brand new potential theory for monotone multi-valued operators are shown to provide the natural mathematical setting for the derivation of the related variational formulation. A general stationarity principle is obtained and then specialized to obtain a minimum principle in terms of displacements, plastic strains and internal variables. A critical comparison with an analogous minimum principle recently proposed in literature is performed, showing the inadequacy of classical procedures in deriving non-smooth variational formulations.

254K. ANISOTROPIC AND NONHOMOGENEOUS MEDIA

11A256. Constitutive equations for finite deformations of elastic-plastic metallic solids with induced anisotropy. - Nguyen Huu Viem *(Inst of Fund Tech Res, Polish Acad of Sci, Warszawa, Poland).* Arch Mech **44**(5-6) 585-594 (1992).

The object of this paper is to formulate the constitutive relations for elastic-plastic metallic solids at finite strain, making some plausible physical assumptions and employing Mandel's formalism. Thermodynamic terms are included. The equations are further simplified which should make them more useful for solving problems.

11A257. Crystallography-based prediction of plastic anisotropy of polycrystalline materials. - KJ Kozaczek, CO Ruud *(Penn State)*, J Hirsch *(VAW Aluminum, Bonn, Germany)*, JC Conway Jr *(Penn State)*, CJ Yu *(Concurrent Technologies, Johnstown PA 15909).* J Nondestruct Eval **12**(1) 97-107 (Mar 1993).

Several models of plasticity of a polycrystalline material were reviewed, and their applicability to the prediction of plastic anisotropy of face-centered cubic (FCC) metals were evaluated. A tailored set of cold-rolled copper alloy samples was designed and manufactured, representing the wide spectrum of textures and cold work levels typical for the sheet metal industry. The texture was quantitatively described in the form of the orientation distribution functions derived by the inversion of four incomplete pole figures. The Taylor-Bishop-Hill model was applied in order to calculate the planar variation of the plastic strain ratio. The continuum mechanics of textured polycrystals approach was also used for the prediction of the plastic strain-rate ratio for the same set of deformed materials. The theoretical predictions were compared with the plastic strain ratios measured in tensile tests using strain gauges. The applicability of the models for prediction of the plastic anisotropy of FCC metals was discussed in view of the operating deformation mechanism and other factors such as strain hardening sensitivity and grain size-shape effects.

11A258. Deformation-induced plastic anisotropy of sheet metals. - W Szczepinski *(Inst of Fund Tech Res, Polish Acad of Sci, Warszawa, Poland).* Arch Mech **44**(5-6) 663-698 (1992).

Problems connected with the theoretical description of plastic flow of polycrystalline sheet metals are discussed and commented. Sheet metals display distinct anisotropic properties in the plastic range of deformation. It is observed that these properties may be different depending on the plastic deformation histories in the course of the manufacturing process. Much attention has been devoted to the experimental tests of plastic anisotropy of sheet metals and to the comparison of test results with various descriptions.

254L. RESIDUAL STRESS

See the following:

11A444. Effect of residual stresses on hardness measurements

254Y. COMPUTATIONAL TECHNIQUES

11A259. Computational limit analysis of rigid-plastic bodies in plane strain. - Yuan-Gao Zhang, Pi-Xin Zhang, Ming-Wan Lu *(Dept of Eng Mech, Tsinghua Univ, Beijing 100084, Peoples Rep of China).* Acta Mech Solida Sinica **6**(3) 341-348 (Jul 1993).

This paper deals with the computational methods for limit analysis of plane strain problems. The FE mathematical programming formula (FE-MPF) for determining the upper bound load multiplier established by the authors earlier is adopted and modified for plane strain problems. The penalty method is used to impose the incompressibility constraint. The FE-MPF is solved by a direct iteration procedure without the need of a searching process. This algorithm is not sensitive to the volumetric locking effect. And it can be easily extended to the limit analysis of 3D problems. The results of numerical examples are satisfactory and show the stable convergency of the present algorithm.

11A260. Symmetric formulation of tangential stiffnesses for non-associated visco-plasticity with an implicit time integration scheme. - Wen-lin Xiong *(Wuhan Univ of Hydraul and Elec Eng, Wuhan, China).* Appl Math Mech **14**(3) 269-276 (Mar 1993).

A numerical scheme is presented which enables the use of symmetric equation solvers in tangential stiffness programs for non-associated viscoplastic materials.

See also the following:

11A39. Elastoplastic analysis of 2D problems with hole by BEM using complex variables
11A43. Solution for an irregular perturbation problem of viscoplastic spherical container under internal pressure
11A486. Limit loads of framed structures and arches using the gloss r-node method

254Z. EXPERIMENTAL TECHNIQUES

11A261. Elastic-plastic strain analysis by photoelastic coating method. - J Kapkowski and B Kozlowska *(Fac of Fine Mech, Warsaw Univ of Tech, Poland).* J Theor Appl Mech **31**(3) 483-512 (1993).

In the paper the method of determining the strain and stress distribution in plastified zones of the construction by using isochromatic patterns obtained in testing by the method of photoelastic coating is presented. Calculation of the strain components (strain separation) requires introduction of both the schematization of the material characteristics and the physical relations valid in regions, where the yield point was exceeded. The introduced relations were applied to the strain separation along the axis of symmetry. The process of calculations was illustrated by an example.

See also the following:

11A250. Macroscopic observations and related microscopic phenomena of the mechanical behavior of metallic materials
11A447. New trends in optical methods for experimental mechanics Part II. High sensitivity grating interferometry for in-plane displacement measurement

256. Composite material mechanics

See the following:

11A417. Thermally-induced interlaminar crack-tip singularities in laminated anisotropic composites

256A. GENERAL THEORY

11A262. Prediction of electrical properties of plain-weave fabric composites for printed wiring board design. - RK Agarwal and A Dasgupta *(CALCE Electron Packaging Res Center, Univ of Maryland, College Park MD 20742).* J Electron Packaging **115**(2) 219-224 (Jun 1993).

A mechanistic model is presented for predicting the effective dielectric constant and loss tangent of woven-fabric reinforced composites with low-loss constituents. A two-scale asymptotic homogenization scheme is used to predict the orthotropic effective properties. A 3D unit-cell enclosing the characteristic periodic repeat patterns in the fabric weave is isolated and modeled mathematically. Electrostatic boundary value problems are formulated in the unit-cell and are solved analytically to predict effective dielectric constant of the composite, using 3D series-parallel reactance nets. Results are also verified numerically, using FEMs. The effective dielectric constant and the effective loss tangent are then obtained, analogous to mechanical viscoelastic problems for low-loss materials. The predicted dielectric constant and loss tangent are compared with experimental results for E-glass and epoxy laminates. Frequency dependence of the effective dielectric constant and loss tangent is obtained from the corresponding behavior of the constituent materials. Trade-off studies are conducted to investigate the effect of the constituent material properties on orthotropic effective dielectric permittivity.

256B. PARTICULATE MEDIA, INCL CEMENTS

11A263. Computer simulation of anisotropic grain growth in ceramics. - U Kunaver and D Kolar *(Inst Jozef Stefan, Univ of Ljubljana, Ljubljana, Slovenia).* Acta Metall Mat **41**(8) 2255-2263 (Aug 1993).

Anisotropic grain growth in ceramics has been simulated by a Monte Carlo computer model. Microstructures, similar to experimental ones, were obtained and the influence of the energy anisotropy and the number of anisotropical grains on microstructure development were studied. It was shown that a single grain with higher energy in one direction, embedded in a matrix of grains with the isotropic boundary energy, grows anisotropically with a nearly constant rate. The growth rate is linearly proportional to the energy anisotropy of the grain. The aspect ratio increases with the cube root of time. Faceted grain boundaries were simulated. Microstructures with less than 50% of anisotropic grains develop, after a short time, a bimodal grain size distribution. At this point, the mean aspect ratio of anisotropic grains reaches a maximum. The heights of the maxima are proportional to the energy anisotropy and inversely proportional to the fraction of anisotropic grains. Weighted aspect ratio distributions and their mean values agree well with experimental data.

11A264. Deformational resistance of fresh concrete through bent and tapered pipes. - Anura SM Nanayakkara *(Dept of Civil Eng, Univ of Moratuwa, Sri Lanka, Japan)*, K Ozawa *(Dept* *of Civil Eng, Univ of Tokyo, 7-3-1 Hongo Bunkyo-ku, Tokyo 113, Japan)*, K Maekawa *(Eng Res Inst, Univ of Tokyo, 7-3-1 Hongo Bunkyo-ku, Tokyo 113, Japan)*. Proc JSCE 466(V-19) 97-107 (May 1993).

This is to report on the resistance of deformation of fresh concrete when the rearrangement of constituent particles of fresh concrete, ie, gravel, sand, and cement, is introduced. For realizing the simple deformation field in shear, bent, and tapered pipe units were adopted in test and stable flow of fresh concrete through them was produced. Herein, the pressure at the inlet of deformed pipes was measured as an indicator of deformability of fresh concrete, which is regarded as the particulate assembly with different sizes. The effect of volume fraction of gravel, sand, and cementitious powder on the resistance to deformation was mainly focused in the series of test based upon the multiphase concept of hydrodynamics. The sensitivity of volume fractions to the total deformation resistance of concrete was of experimental interest to the authors.

11A265. **Interdependence of microstructure and strength of structural lightweight aggregate concrete.** - SL Sarkar *(Fac des Sci Appl, Univ de Sherbrooke, Sherbrooke, PQ, J1K 2R1, Canada)*, S Chandra, L Berntsson *(Div of Build Mat, Chalmers Univ of Tech, S-412 96 Gothenburg, Sweden)*. Cement & Concrete Composites 14(4) 239-248 (1992).

The demand for lightweight concrete is steadily increasing because of economic and practical considerations. Hence, the inherent internal and external features of lightweight aggregates have been a subject of intense research in recent years. This study provides new insight into the microstructural and chemical factors which influence the strength properties of structural lightweight aggregate concrete. These are described with respect to four expanded clay lightweight aggregates used in nine concrete compositions containing various types and proportions of dispersing dispersing agents such as water-reducing admixtures and superplasticizers, with silica fume and ground granulated blast-furnace slag as optional mineral admixtures. The microstructural characteristics of the paste-aggregrate interface and the paste porosity of these concretes are discussed. The methods used include scanning electron microscopy-energy-dispersive X-ray analysis, X-ray diffraction analysis, optical microscopy and compressive strength testing.

See also the following:

- 11A358. Stable crack growth in ceramics at ambient and elevated temperatures
- 11A360. High strain rate deformation and damage in ceramic materials
- 11A362. Cyclic fatigue-crack growth in grain bridging ceramics
- 11A412. Influence of grain size on the toughness of monolithic ceramics
- 11A413. Notch ductile-to-brittle transition due to localized inelastic band
- 11A418. Toughening mechanisms in quasi-brittle materials
- 11A455. Ultrasonic assessment of interfacial oxidation damage in ceramic matrix composites

256D. CARBON FIBER REINFORCED MEDIA

See the following:

- 11A364. Effect of mission cycling on the fatigue performance of SiC-coated carbon-carbon composites

256F. OTHER FIBER REINFORCED MEDIA

11A266. **Anisotropic permeability of fiber preforms: Constant flow rate measurement.** - AW Chan, DE Larive, RJ Morgan *(Michigan Molecular Inst, 1910 W St Andrews Blvd, Midland MI 48640)*. J Composite Mat 27(10) 996-1008 (1993).

Fiber preform permeability has a strong influence on the resin impregnation behavior during polymer composites fabrication. A straightforward procedure has been developed for determining the general anisotropic in-plane permeability character of fiber preforms from constant flow rate mold filling experiments. The procedure is based on the application of Darcy's law to a 2D in-plane flow situation. From experimental data changes in flow front position and inlet pressure with model filling time, the components of the in-plane permeability tensor can be calculated directly using parameters obtained from two linear plots. Experimental data for a commercial fabric confirms the applicability of the procedure. The required equipment setup and the analytical procedure are both uncomplicated in nature. The proposed method provides a simple solution to the measurement of permeability and comparison of different preforms for polymer composites application.

11A267. **FE simulations of fiber pull-out.** - GL Povirk and A Needleman *(Div of Eng, Brown Univ, Providence RI 02912)*. J Eng Mat Tech 115(3) 286-291 (Jul 1993).

Fiber pull-out is simulated through a quasi-static analysis of a circular elastic cylinder with a rigid cylindrical fiber embedded in its center. The interface between the fiber and the matrix is characterized in terms of a rate dependent internal variable friction constitutive relation. The analysis is carried out in two steps; one simulating the residual stresses that develop while cooling the cylinder from its processing temperature and the other simulating the mechanical response during fiber pull-out. Depending on parameter values, fiber pull-out can occur smoothly or a stick-slip instability can occur. Numerical simulations of fiber pull-out are presented that explore the effects of loading device stiffness, loading rate, and friction law parameters on the predicted behavior. For example, the amplitude of the load fluctuations during stick-slip was found to decrease as the rate of pull-out increased.

11A268. **Influence of cool-down temperature histories on the residual stresses in fibrous metal-matrix composites.** - Nan-Ming Yeh *(Marketing Dept Manager, Fu Chun Shin Machinery Manuf, Bay-Tow Village Kwang-Meow Hsiang, Tainan County, Taiwan, ROC)* and E Krempl *(Mech of Mat Lab, RPI)*. J Composite Mat 27(10) 973-995 (1993).

The vanishing fiber diameter model together with the thermoviscoplasticity theory based on overstress including a recovery of state formulation is introduced. They are employed to analyze the effects of temperature rate and of annealing at constant temperature on the residual stresses at room temperature when unidirectional fibrous metal-matrix composites are cooled down from 1000°C during the manufacturing process. For the present analysis the fibers are assumed to be transversely isotropic thermoelastic and the matrix constitutive equation is isotropic thermoviscoplastic including recovery of state. All material functions and constants can depend on current temperature. Yield surfaces and loading-unloading conditions are not used in the theory in which the inelastic strain rate is solely a function of the overstress, the difference between stress and the equilibrium stress, a state variable of the theory. Assumed but realistic material elastic and viscoplastic properties as a function of temperature which are close to W/9Cr-1Mo steel composite permit the computation of residual stresses. Due to the viscoplasticity of the matrix time-dependent effects such as creep and change of residual stresses with time are found. It is found that the residual stress, upon reaching room temperature, is highest for the fastest cooling rate, but after 30 days rest the influence of cooling rate is hardly noticeable since relaxation takes place. Annealing periods can reduce the residual stresses compared to continuous cooling.

11A269. **Modeling the densification of metal matrix composite monotape.** - DM Elzey and HNG Wadley *(Dept of Mat Sci and Eng, Univ of Virginia, Charlottesville VA 22903)*. Acta Metall Mat 41(8) 2297-2316 (Aug 1993).

The consolidation of monotapes consisting of a layer of continuous aligned ceramic fibers embedded in a plasma sprayed metal or intermetallic matrix is becoming a preferred approach for the processing of high performance composite systems. We present a first model that enables prediction of the density (and its time evolution) of a monotape lay-up subjected to a hot isostatic or vacuum hot pressing consolidation cycle. Our approach has been to break down the complicated (and probabilistic) consolidation problem into simple, analyzable parts and to combine them in a way that correctly represents the statistical aspects of the problem, the change in the problems interior geometry and the evolving contributions of the different deformation mechanisms. The model gives two types of output. One is in the form of maps showing the relative density dependence upon pressure, temperature, and time for step function temperature and pressure cycles. They are useful for quickly determining the best place to begin developing an optimized process. The second gives the evolution of density over time for any (arbitrary) applied temperature and pressure cycle. This has promise for refining process cycles and possibly for process control. Examples of the models application are given for Ti_3Al+Nb,γ TiAl, Ti6Al4V and pure aluminum.

11A270. **Silica particle-glass fiber-reinforced polyester resin.** - Y Zhang and J Cameron *(Mat and Metall Eng Dept, Queen's Univ, Nicol Hall, Kingston, ON, K7L 3N6, Canada)*. J Composite Mat 27(11) 1114-1127 (1993).

In this work, a method of producing silica particle-modified glass fibre-reinforced polyester composite is introduced. Silica particles, which are of low density, high hardness and good chemical compatibility with the polymer matrix, are coated on the glass fibre by a thin film of polyester resin which is also subsequently incorporated into the composite as the matrix phase. After initial coating of the fibre by the silica particles, the fibre plus polyester plus silica is passed through carefully spaced pressure rollers to produce a uniform coating on the continuous fibre. The effect of the particles on the viscosity of the bulk-phase polyester matrix and the shear strength of the composites made from the modified fibre were investigated. Also, the mechanism of reinforcement of the modified fibre is discussed. The modified fibres have higher shear strength, a larger surface area and show better bonding with the polyester matrix than conventional fibres.

11A271. **Treatments of polyproplylene fibres to optimize their reinforcing efficiency in cement composites.** - A Peled, H Guttman *(Sch of Appl Sci and Tech, Hebrew Univ, Israel Fibre Inst, Jersualem, Israel)*, A Bentur *(Natl Build Res Inst, Fac of Civil Eng, Technion IT, Haifa, Israel)*. Cement & Concrete Composites 14(4) 277-285 (1992).

The effect of the geometry of polypropylene fibres and their surface treatment by chemical and physical means was studied to obtain cementitious composites with optimal flexural properties. Monofilaments of polypropylene were more efficient than split film or bundled multifilament strands. Acid, detergent and rubbing treatments of monofilaments were found to be particularly effective in enhancing the first crack stress and post-cracking behavior of the composite. The influence of the various treatments was discussed in terms of the bonding nature as deduced by scanning electron microscope observations of the fibre-matrix interface.

See also the following:

11A234. Modeling creep in thermoplastic composites
11A318. Static and dynamic buckling of a fiber embedded in a matrix with interface debonding
11A381. Compressive failure of fiber composites: The roles of multiaxial loading and creep
11A389. Stochastic aspects of matrix cracking in brittle matrix composites
11A407. Criterion for splitting crack initiation in unidirectional fiber-reinforced composites
11A408. Fracture Mech of Ti/Al_2O_3 interfaces
11A414. Role of crack wake toughening on elevated temperature crack growth in a fiber reinforced ceramic composite
11A416. Thermally induced interfacial microcracking in polymer matrix composites
11A419. Transverse cracking in fiber-reinforced brittle matrix, cross-ply laminates
11A873. Predicting high temperature ultimate strength of continuous fiber metal matrix composites

256H. LAYERED MEDIA

11A272. Experimental investigation on impact response of laminated composite beams. - NC Pal and AK Ghosh *(Dept of Civil Eng, IIT Kharagpur, Kharagpur 721302, India)*. Exp Mech 33(2) 159-164 (Jun 1993).

Experiments based on a new technique were carried out to study the response of glass-epoxy laminated composite beams subjected to impact loading. A number of glass-epoxy composite beams with different fiber orientations, spans, thicknesses, and support conditions were impacted with an instrumented impact hammer and the responses were picked up using an accelerometer in conjunction with a spectrum analyzer. Free vibration test for some sample beams were also carried out to determine their fundamental frequencies.

11A273. Laminates and microstructures. - P Pedregal *(Dept Matematica Aplicada, Univ Complutense, 28040 Madrid, Spain)*. European J Appl Math 4(2) 121-149 (Jun 1993).

This paper deals with the mathematical characterization of microstructure in elastic solids. We formulate our ideas in terms of rank-one convexity and identify the set of probability measures for which Jensen's inequality for this type of function holds. This is the set of laminates. We also introduce generalized convex hulls of sets of matrices and investigate their structure.

11A274. Study on the application of work factor approach to composite laminates. - KY Rhee *(Dept of Mech and Aerospace Eng, Rutgers Univ, Piscataway NJ 08855-0909)* and HA Ernst *(Sch of Mech Eng, Georgia Tech)*. J Composite Mat 27(10) 962-972 (1993).

Static fracture tests using the cracked lap shear (CLS) specimens made of thermoplastic composite APC-2 were conducted to verify if the elastic work factor developed previously is a valid parameter to calculate energy release rate from a single specimen. Also, the elastic work factor was derived theoretically based on a beam analysis. The experimentally determined elastic work factor, $(\eta_{el})_{exp}$ was compared with those calculated from a beam analysis and a FE analysis. The results showed that the elastic work factors determined from these three ways are comparable to each other. In addition, the elastic work factor was applied to determine a critical energy release rate, and it was found that the elastic work factor approach can be used to determine energy release rate from a single specimen.

See also the following:

11A279. Can the curvature of an optical glass fiber be different from the curvature of its coating?
11A305. Analytical solutions for thick closed laminated cylindrical shells
11A315. Effects of multiple delaminations on compressive buckling behaviors of composite panels
11A316. Postbuckling behaviors of composite panels with multiple delaminations

256J. MICROMECHANICS

11A275. Modeling of non-uniform composite microstructures. - RK Everett and JH Chu *(Composites and Ceramics Branch, Code 6371, Naval Res Lab, Washington DC 20375-5343)*. J Composite Mat 27(11) 1128-1144 (1993).

The microstructural effects of non-uniform composite microstructures are modeled. Relationships are observed between the degree of nonuniformity and fiber spatial information which may be measured via image analysis or derived from Dirichlet cell tessellations. For artificial patterns containing chain-like clustering which simulate composite microstructures: (a) the nearest-neighbor distances of random and clustered patterns are smaller than those normally estimated by a square or hexagonal arrays, (b) increased clustering may be associated with increased mean cell volume fraction, cell volume fraction distribution standard deviation, number of cell sides, distribution standard deviation, nearest-neighbor distance distribution skewness, and decreased nearest-neighbor distances and (c) accounting for non-uniform fiber diameters is generally unnecessary, except possibly at low fiber volume fraction or with patterns exhibiting a high degree of chaining. For Nicalon SiC-zirconia titanate composite samples with microstructures which exhibit clustering, the maximum value of skewness, determined from sub-regions of the sample, correlates with the flexure strength of that sample.

11A276. Models of moisture transport and moisture-induced stresses in epoxy composites. - Myung Cheon Lee *(Dept of Chem Eng, Dongguk Univ, Chung-gu Pildong, Seoul, Korea)* and NA Peppas *(Sch of Chem Eng, Purdue)*. J Composite Mat 27(12) 1146-1171 (1993).

Mathematical models are presented to describe moisture transport in epoxy composites using concentration and stress dependent diffusion coefficients. These models take into consideration the stresses induced due to moisture and their influence on the transport mechanism. All governing differential equations are solved with appropriate boundary conditions to obtain concentration and stress profiles. It is concluded that non-Fickian and anomalous transport of moisture in epoxy composites can occur under certain conditions, leading to stress accumulation close to the fibers of the composite.

256L. MACROSCOPIC CHARACTERIZATION

11A277. Indentability of conventional and negative Poisson's ratio foams. - RS Lakes *(Dept of Theor and Appl Mech, Cornell)* and K Elms *(Dept of Mech Eng, Univ of Iowa, Iowa City IA 52242)*. J Composite Mat 27(12) 1193-1202 (1993).

The indentation resistance of foams, both of conventional structure and of a novel re-entrant giving rise to negative Poisson's ratio, was studied using holographic interferometry. In holographic indentation tests, re-entrant foams had higher yield strengths σ_y and lower stiffness E than conventional foams of the same original relative density. Damage in both kinds of foam occurred primarily directly under the indenter. Calculated energy absorption for dynamic impact is considerably higher for re-entrant foam than conventional foam.

256N. DYNAMIC BEHAVIOR

11A278. Dynamic deformation behavior of Al-Zn-Mg-Cu alloy matrix composites reinforced with 20 vol % SiC. - SI Hong, GT Gray III *(Mat Sci and Tech Div, LANL)*, JJ Lewandowski *(Dept of Mat Sci and Eng, Case W Reserve Univ, Cleveland OH 44106)*. Acta Metall Mat 41(8) 2337-2351 (Aug 1993).

The dynamic mechanical response and substructure evolution of underaged and overaged Al-Zn-Mg-Cu alloys with and without 20 vol% SiC particles were investigated and compared to those following quasi-static compression. The hardening rates of the overaged composites and control alloys were found to be smaller than those of their underaged counterparts. Overaged composites and the control alloys showed more strain rate sensitive behavior than the underaged composites and alloys. The flow stress of the composites was found to decrease at total strains larger than 0.15 in the high-rate Hopkinson pressure bar tests. A more rapid decrease in stress in the underaged composites suggests that microstructural damage in the underaged condition is greater than that in the overaged condition tested at high strain rates. Cracks near the SiC-matrix interfaces were observed more frequently in the underaged Hopkinson pressure bar samples. The more frequent interface cracks in the underaged composites are thought to result from much slower relaxation of the stresses and strains built up at the interface due to much more difficult thermally activated deformation.

See also the following:

11A17. FE simulation of elastic wave propagation in orthotropic composite materials

256Q. STRUCTURAL APPLICATIONS

See the following:

11A300. Efficient higher order composite plate theory for general lamination configurations
11A505. Behavior of GRP smooth pipe bends with tangent pipes under flexure or pressure loads: A comparison of analyses by conventional and FE techniques

256T. CERAMICS, REFRACTORIES, GLASSES

11A279. Can the curvature of an optical glass fiber be different from the curvature of its coating?. - E Suhir *(AT&T Bell Lab, 600 Mountain Ave, Rm 7D-326, Murray Hill NJ 07974)*. Int J Solids Struct 30(17) 2425-2435 (1993).

The study is aimed at the elevation of the relationship between the measured (or imposed) constant curvature of the coating of an optical glass fiber and the elastic curve of the fiber itself. It is shown that the buffering effect of the coating is different for different points along the curved area and depends on the length of this area, and the compliance of the coating. In the case of a very short curved area and/or a very compliant coating, the curvature of the glass fiber is smaller than the curvature of the coating and increases with an increase in the length of the curved area and the coating stiffness. In the case of a long curved area and/or a stiff coating, both curvatures are practically the same for almost the entire curved area. Only when approaching the ends of this area, the ratio of the curvature of the glass fiber to the coating curvature somewhat increases (by a factor of 1.043) and then rapidly drops to unity at the ends. There are, however, some "intermediate" unfavorable combinations of the lengths of the curved area and coating compliances that result in curvature ratios exceeding (by up to a factor of 1.086) the coating curvature in the midportion of the curved area. It is shown that such a paradoxical situation is due to the redistribution of the interfacial radial load at certain combinations of the lengths of the curved areas and spring constant of the coating. For a current AT&T dual-coated fiber design with 30 μm thick silicone primary coating, the curvature ratio is greater than unity when the lengths of the curved area fall within the range between 1.84 and 4.27 mm, and reaches the 1.086 value when the length of curved area is about 2.44 mm.

256V. PLASTICS, ELASTOMERS, RUBBERS

11A280. Physical discretization approach to evaluation of elastic moduli of highly filled granular composites. - VV Moshev and OC Garishin *(Ural Dept, Russian Acad of Sci, Inst of Continuous Media Mech, Academic Korolev St 1, Perm 614061, Russia).* Int J Solids Struct 30(17) 2347-2355 (1993).

A structural model for highly filled granular composites is suggested. Composites investigated represent rather dense random assemblies of hard spherical particles embedded in softer elastic matrices. The concept forming the foundation of the model approach is the so-called physical discretization principle which comes from the fact that the really complicated field interactions in the system considered here can be substituted by simpler linear elastic ones. The indispensable stages of model development are the generation of random composite architecture and the solution of some special boundary problems. The model reveals clearly the infuence of structural parameters of macroscale behavior. The predicted properties proved to be in reasonable agreement with experimental observations. Of particular concern is the insight into the internal pattern of structural forces that makes it possible to obtain new information about the peculiarities of composite internal elastic resistance.

See also the following:

11A552. Extended Maxwell Garnett formalism for composite adhesives for microwave-assisted adhesion of polymer surfaces

256Y. COMPUTATIONAL TECHNIQUES

11A281. Hierarchic models for bidirectional composites. - RL Actis and BA Szabo *(Center for Comput Mech, Washington Univ, St Louis MO 63130).* Finite Elements Anal Des 13(2-3) 149-168 (Jun 1993).

The formulation of a hierarchic sequence of models for bidirectional composites in cylindrical bending is presented and their performance is demonstrated on the basis of the degree to which the equilibrium equations of 2D elasticity are satisfied. A numerical example is presented.

11A282. Influence of concentrated body force on an interface crack in periodic two-layered elastic space. - A Kaczynski *(Inst of Math, Warsaw Univ of Tech, Plac Politech NIKI PL-00-661, Warszawa, Poland)* and SJ Matysiak *(Fac of Geol, Univ of Warsaw, Al Zwirki I Wigury 93 Pl-02-089, Warszawa, Poland).* Bull Polish Acad Sci Tech Sci 41(2) 67-78 (1993).

This paper deals with the plane problem of displacement and stress distributions in a periodic two-layer elastic space weakened by an interface crack. The body is subjected to an isolated force acting at the interior point. Within the framework of the homogenized model with microlocal parameters the exact solution of the considered problem is obtained. The stress singularities at the crack tips are discussed.

See also the following:

11A280. Physical discretization approach to evaluation of elastic moduli of highly filled granular composites

11A474. Optimum design of a composite structure with manufacturing constraints

256Z. EXPERIMENTAL TECHNIQUES

11A283. Optimal orientation of flakes in oriented strand board (OSB). - V Sharma *(Dept of Mech Eng, Rm E53-384, MIT)* and A Sharon *(Lab for Manuf and Productivity Room 35-237, MIT).* Exp Mech 33(2) 91-98 (Jun 1993).

Panelized housing can reduce both the cost and construction time of residential housing. The panels, generally comprised of rib-reinforced OSB sheets, are assembled into floor, wall, and roof structures. Irrespective of application, commerically available OSB sheets incorporate flakes oriented generally in the longitudinal direction along the faces and in the cross direction in the core. This often results in directional material properties that are not ideally suited for the specific application, requiring excessive sheet thickness and flake density in order to provide the necessary strength. It is proposed that through proper orientation of flakes, material properties of OSB can be tailored to a specific application, resulting in appreciable improvement in load-bearing capacity over commercially available OSB of equal density. In this paper we present a method for determining the near-optimal orientation of flakes in OSB sheets under specific loading. Using three-point bending and rupture tests, we experimentally verify that OSB with optimally oriented flakes is significantly superior to commerically available OSB of equal density.

11A284. Static and dynamic analysis of sandwich plates with unidirectional variation of thickness. - B Mrozek and I Nowotarski *(Military Univ of Tech, Warszawa, Poland).* J Tech Phys 34(2) 199-213 (1993).

General relationships for the static and dynamic calculations of sandwich plates with variable thickness of their cores are determined with the use of the FEM. The honey-comb-type core is treated as inextensible in the direction of its thickness and transmitting shearing stress only. In the thin faces a membrane stress state is assumed: its influence on the transverse shear action is taken into account. The computational results are compared with the results of authors tests.

See also the following:

11A447. New trends in optical methods for experimental mechanics Part II. High sensitivity grating interferometry for in-plane displacement measurement

258. Cables, ropes, beams, etc

11T285. Bounds for bearing capacity of steel rod structures. Examples of conclusions. - J Murzewski *(Tech Univ, Cracow, Poland).* Inzynieria Budownictwo 50(1) 18-21 (1993).

11A286. New higher order engineering beam theory. - GEO Widera *(Marquette Univ, Milwaukee WI 53233)* and WC Zheng *(Univ of Illinois, Chicago IL 60680).* J Pressure Vessel Tech 115(3) 325-326 (Aug 1993).

A refined engineering theory for beams is presented. It contains higher order effects not present in such refined theories as the one by Timoshenko. A comparison with the latter theory is carried out.

11A287. Calculations of the constraints in a thin film deposited on the substrate. - G Bertholon *(ENISE, 58 rue Jean Parot St-Etienne, 42023 Cedex, France),* C Dupuy *(Univ Claude Bernard-Lyon 1, Villeurbanne, 69622 Cedex, France),* C Surry *(ENISE, 58 Rue Jean Parot St-Etienne, 42023 Cedex, France),* R Redon *(Univ Claude Bernard-Lyon 1, Villeurbanne, 69622 Cedex, France),* H Zahouani *(ENISE, 58 rue Jean Parot St-Etienne, 42023 Cedex, France).* Acta Phys Polonica A 83(5) 581-586 (May 1993).

The aim of the present paper is to give simple calculations of the constraints in a thin film deposited on the substrate. The thin film can be obtained by recrystallization of the surface. It is considered in relation to its substrate, where the force is linearly proportional to the surface area of the film. On the other hand, it is considered to be under the action of a force related to the thermic and compressional constraints. The initial and final boundary conditions in the linearized model play an essential role in the model adopted.

11A288. Free vibrations of Timoshenko beams on rigid blocks. - NM Auciello *(Dept of Struct Eng and Soil Mech, Univ of Basilicata, Potenza, Italy).* Eng Trans 41(2) 177-186 (1993).

The aim of the paper is to analyze the vibration of Timoshenko beam resting on the most arbitrary elastically flexible supports. The boundary conditions are defined by means of a 2×2 flexibility matrix, and the structure is discretized according to the so-called cell procedure. The Lagrangian coordinates are selected to be the vertical displacement of the end points of the rigid bars, plus the four possible displacements of the external constraints. A numerical example is worked out in which the obtained results are compared with some known results.

11A289. Thin-walled beams with open and closed cross-sections. - A Prokic *(Koce Kapetana, 11000 Belgrade, Serbia, Yugoslavia).* Comput Struct 47(6) 1065-1070 (17 Jun 1993).

A new warping function for 3D thin-walled beams is proposed that enables the analysis of structures made up of members with arbitrary open and closed cross-sections. An updated Lagrangian formulation is used to give the stiffness matrix. The method is illustrated by examples.

11A290. Variationally correct assumed strain field for the simple curved beam element. - G Prathap and BR Shashirekha *(Struct Div, Natl Aeronaut Lab, Bangalore-560 017, India).* Comput Struct 47(6) 1071-1073 (17 Jun 1993).

The classical curved beam element (the cubic-linear element) has been discredited for a long time because of poor performance. In a previous paper, the first author showed that the poor performance could be attributed to the inconsistency in the membrane strain field interpolations and that this could be improved by designing a new membrane strain field which met the consistency requirements. This paper shows that this formulation can be improved by re-constituting the "assumed" strain field in a variationally correct manner.

See also the following:

11A93. Application of the classical Rayleigh-Ritz method in dynamics of circular arches

11A467. Compressive bars with bounded displacement at the task of optimal control

260. Plates, shells, membranes, etc

260A. GENERAL THEORY

11A291. Recent developments in the homogenization theory of elastic plates and their application to optimal design Part I. - T Lewinski *(Inst of Struct Mech, Civil Eng Fac, Warsaw Univ of Tech, Armii Ludowej 16, PL-00-637 Warsaw, Poland).* Struct Optim 6(1) 59-64 (Jun 1993).

The paper presents an upt-to-date review of results concerning the evaluation of the stiffnesses of elastic plates with periodic structure. The homogenization formulae of Kohn and Vogelius (1984) (model a = 1) are viewed as the formulae of reference. The paper discusses the range of applicability of the homogenization formulae for the 2D plate models of Kirchhoff and Reissner-Hencky. Transversely symmetric as well as asymmetric plates are considered. Particular attention is paid to plates stiffened asymmetrically with ribs in one direction. For this case, the closed formulae for effective membrane, reciprocal and bending stiffnesses are derived. The homogenization results overviewed are a prerequisite for the discussion of the methods of regularization of optimum design plate problems presented in Part II of the paper.

260B. NONLINEAR AND FINITE DEFORMATION THEORY

11A292. Problems of u-shaped bellows with nonlinear deformation of large axisymmetrical deflection I. Counting nonlinear deformations of ring shells and compressed angle of bellows. - Liang Hu *(Shanghai Inst of Appl Math and Mech, Shanghai Univ of Tech, Shanghai, China).* Appl Math Mech 14(3) 253-267 (Mar 1993).

This paper follows the work of [1,2]. There are some progress in dealing with moderately small rotations (the squares of rotation angles are the order of magnitude of strains) of middle surface normals of inside and outside ring shells and compressed angle of bellows. Calculation results agree with experiments well. To bellow design, the method given in this paper is of practical value and the discussion of the influence of compressed angle on characteristic relation is helpful.

11A293. Unified approach for the linear and nonlinear analysis of plates and shallow shells. - Jianqiao Ye *(Dept of Theor Mech, Univ of Nottingham, Nottingham NG7 2RD, UK).* Thin-Walled Struct 17(3) 223-236 (1993).

The geometric nonlinear behavior of thin plates and shells is studied in this paper by using a boundary integral equation approach. Two types of plates and shells are considered. One of them is rectangular with moveable edges and the other is axisymmetric with various boundary conditions. A plate analog procedure is suggested to simplify the solution. With such simplification, only a knowledge of the boundary integral equation of plates is required in the present study. A number of numerical examples are given in the paper to show the effectiveness of the proposed method.

260C. PLATES (FLEXURE AND TORSION)

11A294. Approximate solution with high accuracy of transverse bending of thin rectangular plates under arbitrarily distributed loads. - Ding Zhou *(E China IT, Nanjing, China).* Appl Math Mech 14(3) 241-246 (Mar 1993).

Ritz method is an effective way widely used to analyze the transverse bending of thin rectangular plates. Its accuracy depends completely on the basis functions selected. This paper selects the superposition of sine series with polynomials as the basis functions of thin rectangular plates. The calculating formulae are not only simple and easily programmed, but also have high accuracy. Finally, two numerical results are given and compared with those obtained by the classical method.

11A295. FE large displacement analysis of stiffened plates. - D Venugopal Rao, AH Sheikh, M Mukhopadhyay *(Dept of Naval Architec, Indian IT, Kharagpur-721 302, India).* Comput Struct 47(6) 987-993 (17 Jun 1993).

A FE analysis of the large deflection behavior of stiffened plates using the isoparametric quadratic stiffened plate bending element is presented. The evaluation of fundamental equations of the stiffened plates is based on Mindlin's hypothesis. The large deflection equations are based on von Karman's theory. The solution algorithm for the assembled nonlinear equilibrium equations is based on the Newton-Raphson iteration technique. Numerical solutions are presented for rectangular plates and skew stiffened plates.

11A296. Study of elastic behavior of plates containing cracks by FE analysis. - JM Minguez *(Dept Fisica Aplicade II, Fac Ciencias, Univ del Pais Vasco, Aptdo 644, 48080 Bilbao, Spain).* Comput Struct 47(6) 917-925 (17 Jun 1993).

This work applies FE analysis very simply to cracked plates. An infinite plate and a finite plate, both with a central crack, are considered to study their elastic behavior and some fracture mechanics concepts, such as the geometry factor and the fracture toughness. These magnitudes are calculated by means of FEMs and the results are in very good agreement with the established theory, which proves that the FE approach is very appropriate. The fracture toughness fraction is defined and calculated for a finite plate to predict its failure.

See also the following:

11A390. FE alternating approach to the bending of thin plates containing mixed mode cracks

260E. SHELLS (BENDING THEORY)

11A297. Bending analysis of orthotropic conical shells. - Liyong Tong *(Co-operative Res Center for Aerospace Struct, Unit 3 276-278 Abercrombie St, Chippendale, NSW 2008, Australia),* B Tabarrok *(Dept of Mech Eng, Univ of Victoria, Victoria, BC, V8W 3P6, Canada),* Tsun Kuei Wang *(Dept of Appl Mech, Beijing Univ of Aeronaut and Astronaut, Beijing, China).* Trans Can Soc Mech Eng 17(2) 215-227 (1993).

Using Donnell type shell theory a simple and exact procedure is presented for bending analysis of orthotropic conical shells under various loads. The solution is in the form of a power series in terms of a particularly convenient coordinate system, and its convergence radius is obtained.

11A298. Numerical stress analysis of intersecting cylindrical shells. - VN Skopinsky *(Mat Strength Chair Head, Motor-Car Construct Inst, Moscow 109280, Russia).* J Pressure Vessel Tech 115(3) 275-282 (Aug 1993).

This paper presents the numerical approach for the stress analysis of the intersecting shells. For a systematic study of this problem, the classification of the model joints is introduced. Stress analysis has been made with the application of the FEM based on the modified mixed formulation. The developed special-purpose computer program SAIS is used for elastic stress analysis of the model joints of the intersecting shells. Comparison of the calculated and experimental results for ORNL-1 model are presented for internal pressure and moment loadings. The parametric study of the model joints of the intersecting cylindrical shells under internal pressure loading was performed. The presented results show the effects of changing various geometric and angular parameters on the maximum effective stresses in the shells.

11A299. Thickness changes in pressurized shells. - LA Godoy and FG Flores *(Dept de Estructuras, FCEFyN, Univ Nacional de Cordoba, Casilla de Correo 916, Cordoba 5000, Argentina).* Int J Pressure Vessels Piping 55(3) 451-459 (1993).

A pressurized thin spherical shell with reductions in thickness is analyzed using a geometrically linear and a nonlinear version of a FE formulation. The change in thickness is assumed to have a circular shape and is symmetric about the middle surface of the shell. The influence of two parameters is considered on the nonlinear behavior: the change in thickness and the extent of the zone affected. The results show that the most critical stresses arise from the hoop membrane action at the edges of the zone affected. It is also shown that a linear analysis can be highly conservative in terms of bending action.

260G. STIFFENED AND SANDWICH PLATES AND SHELLS

11A300. Efficient higher order composite plate theory for general lamination configurations. - Maenghyo Cho and RR Parmerter *(Dept of Aeronaut and Astronaut FS-10, Univ of Washington, Seattle WA 98195).* AIAA J 31(7) 1299-1306 (Jul 1993).

An efficient higher order plate theory for laminated composites is developed. A composite plate theory for general lamination configurations is obtained by superimposing a cubic varying displacement field on a zig-zag linearly varying displacement. The theory has the same number of dependent unknowns as first-order shear deformation theory, and the number of unknowns is independent of the number of layers. The displacement satisfies transverse shear stress continuity conditions at the interface between layers as well as shear free surface conditions. Thus, an artificial shear correction factor is not needed. To demonstrate and compare with other theories, the analytical solution for cylindrical bending is obtained. The present theory gives deflections and stresses that compare well with other known theories.

11A301. Large deflections of rectangular Hoff sandwich plates. - Zhen-Qiang Cheng, Xiu-xi Wang, Mao-guang Huang *(Dept of Modern Mech, Univ of Sci and Tech, Hefei, Anhui 230026, Peoples Rep of China).* Int J Solids Struct 30(17) 2335-2346 (1993).

The nonlinear theory of Hoff type sandwich plates underlying geometrically nonlinear dynamic response is derived from Hamilton's principle. It is shown how the fundamental equations and boundary conditions of dimensionless form can be simplified to the Reissner-Mindlin type theory of moderately thick plates, the Reissner's theory of sandwich plates, and the Kirchhoff theory of thin plates. Nonlinear bending of rectangular sandwich plates is investigated under lateral pressure with some symmetric boundary conditions. Exact solutions of series form are obtained by developing a new technique of mixed Fourier series in nonlinear analysis. The nonlinear partial differential equations are reduced to an infinite set of simultaneous nonlinear algebraic equations, which are truncated and solved by iteration in numerical computations. The present solutions are satisfactory in comparison with other available results.

11A302. Nonlinear bending of simply supported rectangular sandwich plates. - Ren-huai Liu *(Shanghai Univ of Tech, Shanghai Inst of*

Appl Math and Mech, Shanghai, China) and Zhen-qiang Cheng *(Dept of Modern Mech, Univ of Sci and Tech, Hefei, China)*. Appl Math Mech 14(3) 217-234 (Mar 1993).

In this paper, fundamental equations and boundary conditions of the nonlinear bending theory for a rectangular sandwich plate with a soft core are derived by means of the method of calculus of variations. Then the nonlinear bending for a simply supported rectangular sandwich plate under the uniform lateral load is investigated by use of the perturbation method and a quite accurate solution is obtained.

See also the following:

11A409. Fracture mechanics of orthotropic laminated plates I. The through crack problem
11A410. Fracture mechanics of orthotropic laminated plates II. The plane strain crack problem for two bonded orthotropic layers
11A411. Fracture mechanics of orthotropic laminated plates III. The surface crack problem

260H. PLATES AND SHELLS ON FOUNDATIONS

11A303. Design of a circular plate on an elastic halfspace for minimum differential settlement. - M Zmerli and RH Plaut *(Charles E Via Jr, Dept of Civil Eng, VPI)*. Struct Optim 6(1) 52-58 (Jun 1993).

A circular plate resting on an elastic halfspace is considered. The plate is deflected downward by a uniform load and sometimes additional edge loads and moments. Translational and rotational supports at the edge are included in some cases. The interface between the plate and the halfspace is assumed to be frictionless. The plate has piecewise-constant thickness, and the segment thicknesses and radii are allowed to vary. For given total volume of the plate, the difference between the maximum deflection (which occurs at the centre) and minimum deflection (which occurs at the edge) is minimized. Optimal solutions depend on the relative stiffness between the plate and the halfspace. The results can be applied to the bottom plate of a ground-supported liquid storage tank.

11A304. Nonlinear static behavior of shallow spherical shell on a Kerr foundation. - DN Paliwal *(Inst-Indust Interaction Cell, Motilal Nehru Regional Eng Col, Allahabad 211004, India)* and R Srivastava *(Dept of Appl Mech, Motilal Nehru Regional Eng Col, Allahabad 211004, India)*. Int J Pressure Vessels Piping 55(3) 481-494 (1993).

A large deflection analysis of a shallow spherical shell on a Kerr foundation is carried out for a uniformly distributed load and for different edge conditions, using the Sinharay and Banerjee approach. Detailed parametric studies involving variations in geometric, material and foundation properties are made; load-deflection curves for shells on a Kerr foundation are compared with those for shells on an equivalent Pasternak foundation. This study shows that the deflection reduces if the curvature, the Poisson's ratio or the foundation parameters of the shear and lower spring layer are increased. Shells with immovable edges are found to be more prone and vulnerable to changes in various parameters than those with movable edges.

260I. THICK PLATES AND SHELLS

11A305. Analytical solutions for thick closed laminated cylindrical shells. - Jiarang Fan *(Dept of Appl Math and Mech, Hefei Univ of Tech, Hefei, Anhui, Peoples Rep of China)* and Kewei Ding *(Dept of Civil Eng, Anhui Architec Indust Col, Hefei, Peoples Rep of China)*. Int J Mech Sci 35(8) 657-668 (Aug 1993).

Discarding any assumption about displacement models and stress distributions, the state equation for orthotropy is established in full in a cylindrical coordinate system. The analytical solutions are presented for the statics, dynamics, and buckling of thick closed laminated cylindrical shells by means of dividing any layer into several thin plates. No matter how many layers are considered, the calculation always leads to the solution of a set of linear algebraic equations in three unknowns. Every equation of elasticity can be satisfied and all the elastic constants can be taken into account. Arbitrary precision of a desired order can be obtained.

11A306. Solution of cosine pressures on a hollow cylinder and the limit when k → 0. - Zhu-hai Liu *(NE Heavy Machinery Inst, Qiqihaer, China)* and Zuo-yu Qi *(Shanghai Heavy Machinery Plant, Shanghai, China)*. Appl Math Mech 14(5) 443-448 (May 1993).

A new stress function is found in this paper and then the problems of cosine pressures on a hollow cylinder are solved with the new stress function, which provides the basis for the solution of the problems of space symmetrical deformation of a hollow cylinder. When the pressures do not vary in the axial direction, that is, when k→0, the lame formulae can be deduced.

260K. ROTATING DISCS, BLADES, AND SHELLS

11A307. Accuracy of turbine blade thermal analysis by elementary balance method. - VA Trushin, AM Smyslov, OV Trushin *(Izvestiya VUZ, Aviatsionnaya Tekhnika, Russia)*. Russian Aeronaut 35(4) 39-43 (1992).

We show the agreement between the finite-difference thermal analyses and the theoretical calculations in nonlinear heat transfer problem formulation. We found that small channels beneath the shell in shell-type blades act as a thermal thicket.

260Y. COMPUTATIONAL TECHNIQUES

See the following:

11A12. FE analysis of composite plates using a weak form of the Kirchhoff constraints
11A33. Finite difference method at arbitrary meshes for the bending of plates with variable thickness
11T312. Interaction stability extreme for metal plates and shells in complex stress states
11A469. Improved approximation for stress contraints in plate structures

260Z. EXPERIMENTAL TECHNIQUES

See the following:

11A284. Static and dynamic analysis of sandwich plates with unidirectional variation of thickness

262. Structural stability (buckling, postbuckling)

262C. POSTBUCKLING THEORY

11A308. Postbuckling analysis of plates under combined loads by a mixed FEM and BEM. - Jianqiao Ye *(Dept of Theor Mech, Univ of Nottingham, University Park, Nottingham NG7 2RD, UK)*. J Pressure Vessel Tech 115(3) 262-267 (Aug 1993).

The postbuckling behavior of thin plates under combined loads is studied in this paper by using a mixed BEM and FEM. The transverse and the in-plane deformation of the plates are analyzed by the BEM and the FEM, respectively. Spline functions were used as the interpolation functions and shape functions in the solution of both methods. A quadratic rectangular spline element is adopted in the FE procedure. Numerical results are given for typical problems to show the effectiveness of the proposed approach. The possibilities to extend the method developed in this paper to more complicated postbuckling problems are discussed in the concluding section.

262E. COLUMNS AND BEAMS

11A309. Stabilization of beam parametric vibrations. - A Tylikowski *(Inst of Machine Des Fund, Warsaw Univ of Tech, Poland)*. J Theor Appl Mech 31(3) 657-670 (1993).

A theoretical investigation of dynamic stability for linear elastic beams due to time dependent harmonic axial forces is presented. The concept of intelligent structure is used to insure the active damping. In the present paper the applicability of active vibration control is extended to linear continuous system with parametric harmonic excitations. The study is based on the application of distributed sensors, actuators, and an appropriate feedback and is adopted for stability problems of system consisting of beam with control part governed by uniform partial differential equations with time dependent coefficients. To estimate deviations of solutions from the equilibrium state (the distance between a solution with nontrivial initial conditions and the trivial solution) a scalar measure of distance equal to the square root of the functional is introduced. The Lyapunov method is used to derive a velocity feedback implying nonincreasing of the functional along an arbitrary beam motion and in consequence to balance the supplied energy by the parametric excitation and the dissipated energy by the inner and control damping. In order to calculate the energetic norm of disturbed solution as a function of time the partial differential equation is solved numerically. The numerical tests performed for the simply supported beam with surface bounded actuators and sensors show the influence of the feedback constant on the vibration decrease.

262F. RINGS AND ARCHES

11A310. New phenomena in the buckling of arches described by refined theories. - SS Antman and RS Marlow *(Dept of Math and Inst for Phys Sci and Tech, Univ of Maryland, College Park MD 20742)*. Int J Solids Struct 30(16) 2213-2241 (1993).

In this paper we study the local and global behavior of buckled states of nonlinearly elastic circular arches under the action of hydrostatic pressure, concentrating on new effects exhibited by the solution branches. We employ very general (geometrically exact) models for arches that can suffer flexure, extension and shear. The constitutive equations used are intimately related to those of the 3D theory of nonlinear elasticity. These new effects are caused by the interaction of the nonlinearity of material response, the nature of boundary conditions, the cross-sectional geometry, the thickness and the location of the material curve on which the pressure is applied.

262G. FRAMED STRUCTURES

11A311. Worst shapes of imperfections for space trusses with multiple global and local

buckling modes. - Ralf Peek *(Dept of Civil Eng, Univ of Michigan, 2340 GG Brown Lab, Ann Arbor MI 48109).* Int J Solids Struct 30(16) 2243-2260 (1993).

The initial postbuckling behavior and imperfection sensitivity of truss-type structures in which the joints do not transmit moments is determined by means of the Lyapunov-Schmidt-Koiter approach. Such structures possess local buckling modes involving the buckling of individual members, and global modes involving axial deformations of all members but no member buckling. Of particular interest is the case in which thorough optimization (or otherwise) a number of local and global modes are coincident. The worst shape of imperfection for this case is determined from the bifurcated equilibrium branch on which the load drops most rapidly. It is shown that this critical bifurcated branch initially involves the buckling of one member only. The general theory is illustrated by a number of examples involving 2D and 3D lattice columns. The leading order asymptotic results for these examples are compared to exact results obtained by tracking the appropriate equilibrium branch numerically.

262H. PLATES

11T312. Interaction stability extreme for metal plates and shells in complex stress states. - ZK Mendera *(Tech Univ, Crakow, Poland).* Inzynieria Budownictwo 50(2) 50-52 (1993).

See also the following:

11A123. Propagation pressure of long cylindrical shells under external pressure

11A317. Postbuckling failure of composite plates with holes

262I. SHELLS

11A313. Compound strip analysis of ring-stiffened cylindrical shells under hydrostatic pressure. - Wen Chen, Huey-Ju Yang, Wei Zhang *(Eng Mech Dept, Tsinghua Univ, Beijing 100084, China).* Acta Mech Solida Sinica 6(3) 319-339 (Jul 1993).

The efficient compound strip method is used to analyze the buckling of ring-stiffened cylindrical shells under hydrostatic pressure. The eccentricity of stiffeners is taken into account. Numerical examples are given to illustrate the efficiency and accuracy of this method.

11A314. Simple formula for critical tension of truncated structurally orthotropic shells of revolution. - IV Andrianov *(Dnepropetrovsk Civil Build Inst, Dnepropertrovsk).* Eng Trans 41(1) 119-120 (1993).

A structurally orthotropic shell of revolution is loaded by tensile forces applied to the ends of the shell. Stability of the structure is analyzed by means of the asymptotic method and the Galerkin procedure.

262K. STIFFENED AND ANISOTROPIC STRUCTURES

11A315. Effects of multiple delaminations on compressive buckling behaviors of composite panels. - Hiroshi Suemasu *(Inst for Composite Mat, Univ of Kaiserslautern, Erwin-Schrodinger Str 6750, Kaiserslautern, Germany).* J Composite Mat 27(12) 1172-1192 (1993).

Compressive buckling stability of composite panels with through-width equally spaced multiple delaminations are investigated analytically and experimentally. An analytical method is formulated on the basis of Rayleigh-Ritz approximation technique. Timoshenko type shear effects are included. An experiment and a FE analysis are also conducted on the present model. The analytical results agree very well with the experimental and FE results. The buckling load, which is the compressive strength of the panel in the case of the present model, reduces significantly due to the existence of multiple delaminations. The mechanism causing the significant loss of the compressive buckling load due to the delaminations is well explained.

11A316. Postbuckling behaviors of composite panels with multiple delaminations. - Hiroshi Suemasu *(Inst for Composite Mat, Univ of Kaiserlautern, Erwin-Schrodinger Str, 6750 Kaiserlautern, Germany).* J Composite Mat 27(11) 1077-1096 (1993).

Compressive behaviors of composite panels with through-width, equal-size, equally-spaced multiple delaminations are investigated analytically. An analytical method is formulated on the basis of the Rayleigh-Ritz approximation technique. Contact problem on the delaminated surfaces is considered by the introduction of a constraint, which restricts a relative out-of-plane displacement and a relative slope between the upper and lower portions at a contact point. The postbuckling paths of delaminated panels are solved numerically and the results are compared with the experimental results. If appropriate initial imperfections are assumed, the analytical results can explain well the behaviors of the delaminated panels which are observed in the compressive experiment. The results of the postbuckling analysis indicate that the simplified buckling analysis, where the opening of the delamination is not considered, is sufficient to estimate the buckling load. A method to estimate a total energy release rate is also proposed.

11A317. Postbuckling failure of composite plates with holes. - HH Lee *(Agency for Defense Dev, Yuseong, Taejon, 305-600, S Korea)* and MW Hyer *(Dept of Eng Sci and Mech, VPI).* AIAA J 31(7) 1293-1298 (Jul 1993).

This paper summarizes a study focused on understanding the failure mechanisms present in a plate with a centrally located circular hole loaded in-plane into the postbuckling range of deflections. The study was numerical and experimental in nature and had as a goal the a priori prediction of failure using existing failure data and a stress analysis. The maximum stress failure criterion was used to predict failure and both intralaminar and interlaminar stresses were considered. Four laminates were studied. The phenomenon of modal interaction, or the jumping from one deformed configuration, is discussed. The study concludes that the failure of the $(\pm 45/0/90)_{2S}$ and $(\pm 45/0_2)_{2S}$ laminates is due to fiber compression failure and is predictable. The failure load is, for the most part, independent of response configuration. The $(\pm 45/0_6)_S$ laminate fails due to interlaminar shear along the simple support, while the response and failure of the $(\pm 45)_{4S}$ laminate is governed to a large degree by material nonlinearities and progressive failure.

11A318. Static and dynamic buckling of a fiber embedded in a matrix with interface debonding. - YW Kwon and M Serttunc *(Dept of Mech Eng, Naval Postgraduate Sch, Monterey CA 93943).* J Pressure Vessel Tech 115(3) 297-301 (Aug 1993).

Analyses were performed for static and dynamic buckling of a continuous fiber embedded in a matrix in order to determine effects of interfacial debonding on the critical buckling load and the domain of instability. A beam on elastic foundation model was used for the study. The study showed that a local interfacial debonding between a fiber and a surrounding matrix resulted in an increase of the wavelength of the buckling mode. An increase of the wavelength yielded a decrease of the static buckling load and lowered the dynamic instability domain. In general, the effect of a partial or complete interfacial debonding on the domain of dynamic instability was more significant than its effect on the static buckling load. For dynamic buckling of a fiber, a local debonding of size 10 to 20 percent of the fiber length had the most important influence on the domains of dynamic instability regardless of the location of debonding and the boundary conditions of the fiber. For static buckling, the location of a local debonding was critical to a free, simply supported fiber, but not to a fiber with both ends simply supported.

262L. DYNAMIC STABILITY

11A319. Dynamic stability of a spinning beam carrying an axial dead load. - MB Rosales *(Dept of Eng, Univ Nacional del Sur, 8000 Bahia Blanca, Argentina)* and CP Filipich *(Mech Syst Anal Group, Univ Tecnologica Nacional FRBB, 8000 Bahia Blanca, Argentina).* J Sound Vib 163(2) 283-294 (May 1993).

The linear dynamic behavior of a uniform beam with its cross-section having at least two symmetry axes (the shear centre is coincident with the centroid), rotating with constant velocity about its longitudinal axis and carrying an axial dead load is analyzed. Internal damping is also considered by means of the viscoelastic behavior of the beam material described by the Voigt-Kelvin model. The stability of the solution is investigated by characterizing the eigenvalues under the action of the two external control parameters (spin velocity and axial load). In this way instability and stability regions are distinguished in a map as the control parameters vary. Both (linear) divergence and flutter instabilities arise for certain ranges of compressive axial load. The inclusion of internal damping results in qualitative changes in the stability of the motion if compared with the undamped case. The particular case of a beam with $J_x = J_y$ is also included.

11A320. Nonlinear dynamic buckling and stability of autonomous structural systems. - AN Kounadis *(Dept of Struct Anal and Steel Bridges, Natl Tech Univ, 42 Patission St, Athens 106 82, Greece).* Int J Mech Sci 35(8) 643-656 (Aug 1993).

A general approach for the nonlinear dynamic buckling and stability of dissipative or nondissipative structural systems governed by the autonomous ordinary differential equations is presented. Geometrically imperfect systems with or without symmetric imperfections, as well as statically stable systems, which, in addition to a monotonically rising (stable) equilibrium path exhibit an unstable complementary path, are considered. The role of the dynamic buckling mechanism of the basin of attraction of a stable equilibrium point (on the prebuckling path), as well as the inset (stable) and outset (unstable) manifolds of a saddle (on a physical or complementary unstable path), are comprehensively explained. A static energy criterion for determining dynamic buckling loads for vanishing (but nonzero) damping and lower bound estimates of exact dynamic buckling loads are presented. Metastability, loading discontinuity and chaos-like phenomena are also revealed. The analysis is supplemented by two illustrative models of practical engineering importance.

262M. VISCOELASTIC AND CREEP BUCKLING

11A321. Bifurcation buckling of circular cylindrical shells subjected to axial compression during creep deformation. - N Miyazaki *(Dept of Chem Eng, Kyushu Univ, Higashi-ku, Fukuoka 812, Japan)* and S Hagihara *(Dept of Mech Syst Eng, Kyushu IT, Iizuka-shi, Fukuoka-ken 820, Japan).* J Pressure Vessel Tech 115(3) 268-274 (Aug 1993).

In the present work, analytical and experimental investigations were performed on creep buckling. Special attention was focussed on bifurcation behavior during creep deformation. The FEM was used to analyze creep buckling of circular cylindrical shells without initial imperfection. The number of circumferential waves obtained from the analyses agrees well with those of the experiments. The present experimental investigation shows that the circumferential waves are suddenly caused near a bulge. It is also found that there is no correlation between the wavelength of the circumferential waves observed at creep buckling and that of the circumferential initial imperfection. Deformation patterns at the bifurcation creep buckling obtained from the analyses are analogous to those of the experiments. It is concluded from the analyses and the experiments that the circumferential waves observed in creep buckling experiments are due to bifurcation buckling during creep deformation.

11A322. Creep buckling of cross-ply symmetric laminated cylindrical panels. - Ying-jian Wang *(Dept of Mech, Peking Univ, Beijing, China)* and Zhen-ming Wang *(Inst of Mech, Acad Sinica, Beijing, China)*. Appl Math Mech 14(4) 313-318 (Apr 1993).

A creep buckling analysis of cross-ply symmetric laminated cylindrical panels is given in this paper. By means of theoretical analysis, a method to determine the critical load of creep buckling of the panels with simply supported boundary conditions is obtained.

262N. PLASTIC AND ELASTOPLASTIC BUCKLING

11A323. Dynamic buckling and plastic collapse of rectangular strips under axial slamming impact. - Shi-Qi Ji and Ji-Jia Zheng *(Dept of Naval Architec and Ocean Eng, Huazhong Univ of Sci and Tech, 430074 Wuhan, Peoples Rep of China)*. Acta Mech Solida Sinica 6(3) 349-356 (Jul 1993).

The dynamic buckling and plastic collapse of elastic-plastic rectangular strips under axial slamming impact are investigated experimentally. The dynamic response of the specimens is measured by several back-to-back paris of strain gages located at different positions. According to the experimental records, the compressive and bending motions of the rectangular strips are analyzed. The strips exhibit three different critical dynamic conditions: buckling, plastic incipience, and plastic collapse. Based on the response characters, three criteria are proposed which completely define the elastic-plastic dynamic behavior of rectangular strips under axial slamming impact with loading durations ranging from 14 to 18 milliseconds. These conditions are estimated by introducing three critical axial compressive strains. Moreover, the effect of geometric imperfection on the dynamic behavior of the strips is discussed.

262Y. COMPUTATIONAL TECHNIQUES

See the following:

11A27. Power method for the generalized eigenvalue problem
11A869. Perturbation solution for thermal expansion buckling of no expansion joint slope pavement plate

264. Electromagneto solid mechanics

264C. MAGNETOELASTICITY

11A324. Influence of annealing time at 395-400°C on the ΔE effect, magnetostriction and magnetic anisotropy in $Fe_{78}Si_8B_{14}$ metallic glasses. - Luciano Lanotte *(Dept of Phys Sci, GNSM-CIFM Group, Univ of Naples, Piazzale V Tecchio 80, 80 125 Naples, Italy)*, Zbigniew Kaczkowski *(Polish Acad of Sci, Inst of Phys, Al Lotnikow 32-46, PL-02-668 Warsaw, Poland)*, Carlo Luponio *(Dept of Phys Sci, GNSM-CIFM Group, Univ of Naples, Piazzale V Tecchio 80, 80 125 Naples, Italy)*. Int J Appl Electromagnetics Mat 4(1) 59-64 (Jun 1993).

The Young's modulus (E), magnetostriction (λ) and magnetic anistropy (K_u) in rapid quenching $Fe_{78}Si_8B_{14}$ alloy were investigated. Effects of subsequent annealing at 395-400°C are reported. Connections between ΔE effect and magnetic anisotropy confirm the role of structural relaxations. A relation between E and minimum and maximum changes of magnetostriction is theoretically and experimentally pointed out.

11A325. Magnetic forces in high T_c superconductors. - CS Chou and JL Liang *(Inst of Appl Mech, Natl Taiwan Univ, Taipei, Taiwan, ROC)*. Int J Appl Electromagnetics Mat 4(1) 43-48 (Jun 1993).

Magnetic forces between a permanent magnet and bulk YBCO high T_c, superconducting specimens prepared in different processes are investigated in this paper. The magnetic forces in specimens prepared by melting growth are larger than those of the sintered specimens. Repulsion forces between magnet and specimens were measured when the superconducting specimens raised toward the magnet. The repulsion force decreased and became an attraction force in some specimens when the specimen was lowered away from the magnet. This attraction force is closely related to the pinning of the specimen. The levitation of a magnet on specimens having attraction force was stable in a continuous range of positions and orientations. The magnetic forces are closely related to the microstructures of the specimens which are discussed in this paper.

11A326. New numerical analysis method of dynamic behavior of a thin plate under magnetic field considering magnetic viscous damping effect. - T Takagi and J Tani *(Inst of Fluid Sci, Tohoku Univ, Katahira 2-1-1, Aoba-ku, Sendai 980, Japan)*. Int J Appl Electromagnetics Mat 4(1) 35-42 (Jun 1993).

A new numerical method, the so-called MMD method, for electromagnetomechanical coupling analysis was proposed and applied to a thin plate dynamic behavior analysis for its verification test. It becomes important to evaluate the dynamic behavior of electrically conducting structure under strong magnetic field. The coupling effect between eddy current and deformation of structure plays an important role in the dynamic behavior in the field. The method developed here considering the coupling effect is based on a modal analysis method and FEM. Magnetic viscous damping coefficient for each natural vibrational mode can be obtained. Using this coefficient eddy current and plate bending can be calculated separately but considering the coupling effect. Numerical results of the verification test show good agreement between the proposed method and the conventional one.

11A327. Numerical modeling of 2D magnetic properties for the FEM. - M Enokizono and K Yuki *(Dept of Elec Eng Fac of Eng, Oita Univ, 700 Dannoharu, Oita 870-11, Japan)*. Int J Appl Electromagnetics Mat 4(1) 49-58 (Jun 1993).

In the past, the magnetic properties of a material were estimated by measured scalar quantities in a measurement direction under the condition of an alternating magnetic field excitation. Also, in the conventional magnetic field analysis which is applied to such things as rotating machines, the magnetic properties of the arbitrary direction has been modeled by using the magnetic properties of the easy axis and its perpendicular direction. Such kind of numerical modeling cannot exactly show the phase difference between the magnetic flux density B and the magnetic field strength H in the case of a rotating magnetic field excitation. In this paper, we measure the B and H values as vector quantities in the case of the rotating magnetic field excitation. The magnetic properties of the material are expressed by the magnetic reluctivity tensor. This new expression can be applied to the rotting magnetic field analysis. As a result, it is shown that our new method is applicable to the problem in the case of the rotating magnetic field excitation.

11A328. Surface magnetostriction. - H Szymczak and R Zuberek *(Inst of Phys, Polish Acad of Sci, Al Lotnikow 32-46, 02-668 Warszawa, Poland)*. Acta Phys Polonica A 83(5) 651-660 (May 1993).

Experimental and theoretical research on magnetostriction of nanoscale magnetic multilayers is reviewed. The importance of interfaces and the occurrence of the surface magnetostriction is emphasized. It is shown that the dependence of magnetostriction on the magnetic layer thickness is due to the magnetostriction strain localized at the interface.

See also the following:

11A89. Magnetic damping effects on vibration of conductive shells

264D. ELECTROELASTICITY

11A329. Beltrami fields, within continuous source regions, volume integral equations, scattering algorithms and the extended Maxwell-Garnett model. - A Lakhtakia and B Shanker *(Dept of Eng Sci and Mech, Penn State)*. Int J Appl Electromagnetics Mat 4(1) 65-82 (Jun 1993).

Singularities of 3D and quasi-2D frequency-domain Green's dyadics are used to derive expressions for a Beltrami field in its source region. The mathematical developments are utilized to set up 3D volume integral equations and scattering algorithms for scattering by inhomogeneous bianisotropic scatterers embedded in a homogeneous biisotropic ambient medium. Application is also made towards the effective medium properties of a particulate composite formed by randomly dispersing bianisotropic particles in a biisotropic host medium.

11A330. Fourier series with Legendre polynomials as solving functions of mixed multi-periodic boundary value problems. - D Gafka *(Inst of Fund Tech Res, Polish Acad of Sci, Warszawa, Poland)*. J Tech Phys 34(2) 173-183 (1993).

A complementary pair of functions filling the multi-periodic conditions have been constructed. The Fourier series expansions of these functions have also been given. The coefficients of series are related to Legendre polynomials. The pair of functions presented can be used to obtain a numerical solution of any boundary value problem with mixed multi-periodic boundary conditions. It was used in electro-elasticity especially in surface acoustic wave propagation problems.

See also the following:

11A219. Finite deformations of polar elastic media

264E. PIEZOELECTRICITY

See the following:

11A98. Active vibration control of 1D piezoelectric laminates

11A177. Wave propagation and scattering in elastic plate with periodically grooved surface

264G. MECHANICS OF SUPERCONDUCTING MATERIALS

11A331. **Experimental and numerical analysis of 3D high-T_c superconducting levitation systems.** - M Uesaka, Y Yoshida, N Takeda, K Miya *(Nucl Eng Res Lab, Fac of Tokyo, Ibaraki-prefecture 319-11, Japan)*. Int J Appl Electromagnetics Mat 4(1) 13-25 (Jun 1993).

Magnetic levitation properties of MPMC-YBaCuO in 3D geometries of practical interests were investigated experimentally. Especially, it was confirmed that the vertical and horizontal magnetic forces are strongly dependent on grain structure, cracks and applied magnetic field configuration. Furthermore, a 3D computer code based on the current vector potential (T) method was upgraded. The dependence of critical current density (J_c) on applied magnetic field can be taken into account. Magnetic force behavior in several configurations was numerically analyzed by using this code and the results were compared with the experimental ones. It is concluded that the discrepancy between the experimental and numerical results is mainly due to material imperfections such as grain boundary, cracks and deterioration of J_c of large MPMG-YBaCuO samples.

11A332. **Influence of nanometer-scale copper filaments in niobium on mechanical and superconducting properties.** - R Zhou, S Hong *(Superconducting Tech, Oxford Instruments, 600 Milik St, Carteret NJ 07008)*, BH Kear *(Dept of Mech and Mat Sci, Rutgers Univ, New Brunswick NJ 08903)*, PJ Lee *(Appl Superconductivity Center, Univ of Wisconsin, Madison WI 53706-1687)*. Nanostruct Mat 2(1) 73-80 (Jan-Feb 1993).

Nanometer-scale copper filaments are introduced into niobium as artificial flux pinning centers (APC's) by multiple extrusion. A ribbon-like structure is observed in both niobium and copper at the final wire size. The composite experiences extensive work hardening during mechanical reduction. The pinning force of niobium with APC's is significantly enhanced relative to that of cold worked bulk niobium.

264Y. COMPUTATIONAL TECHNIQUES

11A333. **Exact solution for static analysis of an intelligent structure under cylindrical bending.** - MC Ray, KM Rao, B Samanta *(Dept of Mech Eng, Indian IT, Kharagpur-721 302, India)*. Comput Struct 47(6) 1031-1042 (17 Jun 1993).

An exact static analysis of a simply supported intelligent structure under cylindrical bending is presented. The performance of the actuator layer of the intelligent structure to cause induced axial and transverse stresses in the substrate layer is investigated. The capability of the sensor layer to sense the deformations of the structure is shown in terms of induced electric potential on its surface. The distribution of electric potential across the thickness of the piezoelectric sensor and actuator implies that the linear variation can be adopted for choosing the electric potential function to model the laminated intelligent structure for complicated geometry and boundary conditions with refined approximate tehcnique. The results presented here will be helpful to obtain correlation between theoretical and experimental results and to numerical analysis to verify their results.

264Z. EXPERIMENTAL TECHNIQUES

11A334. **Acoustoelectrical relaxation in GaAs by the formation and the recovery of metastable EL2x.** - J Ertel, HG Brion, P Haasen *(Inst Metallphys, Univ Gottingen, Hospitalstr 3-7, W-3400 Gottingen, Germany)*. Acta Phys Polonica A 83(1) 11-24 (Jan 1993).

The transformations between the normal and metastable state of EL2 in GaAs are investigated. We apply the internal friction technique as a probe for very small conductivities and discuss the changes in conductivity by the formation and recovery of EL2x. At 40 K both shallow acceptors and EL2 are photoquenched into neutral metastable states. The acceptors are likely to be associated with EL2x forming an electrically inactive state. We identify two damping peaks at 60 and 95 K with the regeneration of the acceptors and EL2 respectively. The latter indicates a regeneration via the charged deflect $(EL2)^+$.

11A335. **Dielectric properties of isatomalononitrile.** - SM Khalil *(Dept of Physics, Alexandria Univ, Egypt)* and AMA Hassaan *(Dept of Chem, El-Minia Univ, Egypt)*. Acta Phys Polonica A 83(4) 477-480 (Apr 1993).

The paper reports dielectric measurements carried out for isatomalononitrile at different temperatures (346 to 383 K) and various frequencies (50 to 5×10^5 Hz). Kramers-Kronig relations are used to ascertain the magnitude of the dc conductivity and to enhance the reliability of dielectric measurements. The analysis of the results shows that there exists certain very slow dielectric phenomena in isatomalononitrile. The frequency dependent conductivity of isatomalononitrile increases approximately linear with frequency. The frequency exponent has the value of 0.5, independent of temperature.

11A336. **Investigation of the dependence of dielectric properties of D-serine admixtured TGS crystals of the distance from the seed of the crystal growth.** - J Stankowska, A Czarnecka, B Dongo Gemi *(Inst of Phys, A Mickiewicz Univ, Grunwaldzka 6, 60-780 Poznan, Poland)*. Acta Phys Polonica A 83(4) 485-494 (Apr 1993).

Dielectric properties of a D-serine admixtured triglycine sulphate (TGS) crystal were studied on samples cut from different sites in the crystal. The value of spontaneous polarization P_S measured on b-cuts was found to be independent of the site. Whereas the coercive field E_c values were higher for the samples cut closer to the seed than for those cut at the ends of the crystals along b axis. After rejuvenation of the values of the bias field E_b increased in contrary to the effect observed in the pure TGS crystals. An exponentially decreasing dependence on the maximum permittivity ε_{max} on the site of samples (b-plates) cut along b axis from - b to + b positions, was obtained.

266. Soil mechanics (basic)

11A337. **Derivation of material variability from settlement measurements.** - DG Zeitoun *(Hydrological Service, POB 6381, 91063 Jersualem, Israel)* and J Uzan *(Dept of Civil Eng, Israel IT, 32000 Technion City, Israel)*. Int J Numer Anal Methods Geomech 17(5) 303-322 (May 1993).

In pavement evaluation using non-destructive testing (NDT), a large amount of deflection bowls are analysed in terms of the elastic moduli of the layers. The results are used to evaluate the material variability which could serve in an overlay design procedure based on the concept of reliability. The model currently used for interpreting deflection bowls is based on the random variable theory which neglects the spatial distributions of the elastic modulus of the material. Since the subgrade and pavement materials have a spatial distribution, the analysis of NDT could lead to an underestimate of the material variability. The random field theory, which is more adequate than the random variable theory, is presented and used to correct the NDT analysis. The pavement is modelled as a multilayer random elastic medium with, for each layer, a constant Poisson's ratio and a random shear modulus characterized by three statistical moments: average value, standard deviation and autocorrelation function. The stochastic integral formulation presented in the previous publication is generalized here for a multilayer system. The multilayer system is analysed with the random field theory and the covariance matrix of the deflection bowl is obtained and used to generate deflection bowls corresponding to the properties of the random field. These bowls are then interpreted with the current procedure and elastic modulus variabilities are computed. It is found that the current procedure for interpreting deflection bowls underestimates the variability of the subgrade, by a factor of 0.4-1.0.

11T338. **Settlement analysis. The deformation method.** - J Pieczyrak *(Silesian Tech Univ, Gliwice, Poland)*. Inzynieria Budownictwo 50(2) 70-73 (1993).

11A339. **Influence of surface active additives on the properties of asphalt and mineral-asphalt mixtures.** - B Stefanczyk *(Inst of Civil Eng, Szczecin Univ of Tech, Poland)*. Arch Civil Eng 38(4) 353-374 (1992).

The use of inferior quality aggregates such as gravel, sand-gravel mix and quartzite in the laying of bituminous pavements requires a modernization of the production process. In particular, inadequate bond of asphalt to those materials must be enhanced. The best results in this respect have been obtained by using certain surface active agents (SAA) that, depending on their chemical structure, can be aniono-active or cationo-active. In the described investigations two additives were used: aniono-active Pakwat Fe and cationo-active Kaminoaks D. Their effect on the asphalts of various Compositions (D70, D50, Dex70) were examined in a broad range of temperatures. Penetration and viscosity were tested above freezing point and higher temperatures, whereas their mechanical properties were measured below freezing point. The behavior of asphalts with and without the additives was investigated by means of thin films of binder on the surfaces of two different mineral materials (limestone, granite). In each particular test two different characteristics of the binder were examined: adhesion and cohesion. Effectiveness of the surface active additives were also tested in a medium-grained mineral-asphalt mixture on the basis of both Polish and American Codes. The investigation have led to the conclusion that the effectiveness of surface active additives depends on the chemical and mineralogical type or rock, chemical-group composition of asphalt as well as a type and amount of additives in the asphalt and in the mineral-asphalt mixture.

268. Soil mechanics (applied)

See the following:

11A228. Simulation of the vertical split head failure in rails

11A339. Influence of surface active additives on the properties of asphalt and mineral-asphalt mixtures

272. Materials processing

See the following:

11A501. Integral hydro-bulge forming of single and multi-layered spherical pressure vessels

272B. APPLICATIONS OF PLASTICITY THEORY

11A340. Limit strain predictions for out-of-plane stretching of sheet metals. - A Zeghloul and G Ferron *(Lab de Phys et Mec des Mat URA CNRS 1215 ISGMP, Univ of Metz, Ile du Saulcy, 57045 Metz Cedex 1, France).* Int J Plasticity 9(5) 603-618 (1993).

An investigation is performed to predict the limits of sheet metals stretchability in different out-of-plane experiments. Based on the time-independent flow theory, the analysis includes the effects of strain hardening and normal anisotropy and utilizes different yield functions with the assumption of isotropic hardening. The limit strains, determined either from the condition of bifurcation at maximum pressure for hydrostatic bulging, or from the analysis of flow localization in hemispherical punch stretching, depend on the type of the test. For a given test, however, the plot of the limit strains in the usual ε_1-ε_2 diagram does not exhibit a marked sensitivity to the yield function utilized. This behavior contrasts with the predictions of instability models assuming in-plane stretching.

272D. EXTRUSION

11A341. Development and application of aluminum extrusion for automotive parts, mainly bumper reinforcement. - Mitsuyuki Isogai and Satoshi Murakami *(Aisin Keikinzoku, Nagonoe 12-3, Shinminato-shi, Toyama, Japan).* J Mat Processing Tech 38(4) 635-654 (Jul 1993).

Whilst there is an advancing tendency toward lighter vehicles, the application of aluminum extrusion to the production of automotive parts has been quite rare due to cost, strength and corrosion problems. In this report, it is explained how new materials, product design, and processing have been developed to match the automotive parts to which is aimed the adoption of the aluminum extrusion technique. Also activity to solve the problems in applying this technique, and the endeavor to widen the application of aluminum extrusion are reported.

11A342. Hyperbolicity and change of type in steady co-extrusion flow of upper-convected Maxwell fluids. - KangPing Chen *(Dept of Mech and Aerospace Eng, Arizona State Univ, Tempe AZ 85287-6106).* J Non-Newtonian Fluid Mech 47 157-167 (Jun 1993).

The linearized equations governing the steady axisymmetric co-extrusion flow of two upper convected Maxwell fluids through a circular die are studied and conditions are found under which the vorticity equation can change its type from elliptic to hyperbolic in the core and the annulus regions.

11A343. Numerical prediction of extrudate swell of a high-density polyethylene: Further results. - A Goublomme *(Polyflow sa, 16 Place de L'Universitat, 1348 Louvain-la-Neuve, Belgium)* and MJ Crochet *(Unite de Mec Appl, Univ Catholique de Louvain, 2 Place du Levant, 1348 Louvain-la-Neuve, Belgium).* J Non-Newtonian Fluid Mech 47 281-287 (Jun 1993).

We investigate the effect of temperature and of the second normal stress difference on the extrudate swell of a high-density polyethylene at high shear rates with the use of a Wagner model. We find that the flow is indeed non-isothermal but that temperature has little effect upon the swelling ratio. However, the second normal stress difference produces major effects on the swelling ratio. We conclude that any realistic prediction of extrudate swelling requires an accurate measurement of the second normal stress difference.

11A344. Peripheral-recrystallized structures formed in Al-Zn-Mg-Cu-Zr alloy materials during extrusion and their quenching sensitivity. - S Kikuchi, H Yamazaki, T Otsuka *(Showa Aluminum, 480 Inuzuka, Oyama, Tochigi, Japan).* J Mat Processing Tech 38(4) 689-701 (Jul 1993).

A study was done on the peripheral-recrystallized structures formed in Al-Zn-Mg-Cu-Zr alloy materials during extrusion and on their quenching sensitivity. It was found that the peripheral-recrystallized structures were thicker at the head and tail sections of the extrusion than at the other sections. The further downwards towards the tail, the greater the thickness of the structures became. The peripheral-recrystallized structures had a remarkable quenching sensitivity and under some heat treatment conditions, attained only half of the hardness of the fiber structure. Even with the same fiber structure, the extrusion (material) tail had a higher quenching sensitivity than that of the head portion. It is thought that the drop in strength that is encountered frequently in the proximity of the tail portion of the extrusion during actual production of this type of alloy may occur under the same mechanism as controls the above-described phenomenon, and that the phenomenon of the sharpening of sensitivity to quenching is caused by the change of Al_3Zr from a precipitate coherent with the matrix to a precipitate incoherent with the matrix, resulting from the strain during extrusion. The incoherent Al_3Zr precipitate is thought to become an η-phase precipitation site. This zone of sharp quenching sensitivity responds to the surface or to the tail, which latter undergoes a large plastic strain during extrusion. In the section undergoing plastic strain, the quenching sensitivity is especially acute, and if an adequate quench rate cannot be achieved during solution treatment, such a high quenching sensitivity can be a cause of an insufficient increase in hardness after ageing. Most billet homogenizing treatments on this alloy are done at temperatures of about 450°C-480°C. However, it is shown that when a lower temperature of 400°C is selected as a homogenizing treatment parameter, the sharp sensitivity to quenching can be restrained.

See also the following:

11A218. FE analysis of rubber coextrusion using a power-law model

272F. DRAWING

11A345. Numerical and failure analysis on the drawing of a circular cylindrical cup. - CK Chao, CH Liu, HJ Wu *(Dept of Mech Eng, Natl Taiwan IT, Taipei, Taiwan 106, ROC).* Eng Fracture Mech 45(4) 439-450 (Jul 1993).

The incremental theory of plasticity is applied in conjunction with FEs for modeling of the circular cylinder cup. A punch-die system is prescribed such that a circular blank is displaced at constant increments of 0.005 mm until a cup of 16 mm deep is formed. Based on the strain energy density failure criterion, failure initiation accompanied by large dilation is located by the maximum of the minimum local strain energy density function, $(dW/dV)^{max}{}_{min}$, while yielding initiation accompanied by large distortion is located by the maximum strain energy density function, $(dW/dV)^{max}{}_{min}$. For a punch displacement of 16 mm, $(dW/dV)^{max}{}_{max}$ is near the critical value $(dW/dV)_c$ of the metal sheet which suggests the possibility of fracture initiation. The influence of material drawability and punch movement on the rate of cup formation could be evaluated from analytical simulation of the deep drawing process. Computer software developed in the present study can also be applied to evaluate the drawing characteristics of non-axisymmetric cups.

11A346. Square shell drawing characteristics of aluminum alloy sheet A5182-O. - T Kuwabara, K Akiyama, Y Nakayama *(Mech Syst Eng, Fac of Eng, Tokyo Univ of Agri and Tech, 2-24-16, Naka-cho, Koganei-shi, Tokyo 184, Japan).* J Mat Processing Tech 38(4) 737-749 (Jul 1993).

Deep-drawing experiments on aluminum alloy sheet A5182-O of 0.48 mm thickness have been conducted using square punches with the geometrical ratios r_c/l = 0.1, 0.15, 0.238, 0.25, and 0.5 (l is the side length of the punch, r_c is the corner radius of the horizontal section of the punch). Two types of fracture, punch-profile fracture and wall breakage, were found to limit the drawable heights, and the map which clarifies the relationship between blank shapes and the types of fracture was generated for all the punches. The optimum blank shape to give the deepest shell was determined also for each punch shape. The deep-drawing conditions which affect the wall breakage were discussed. The wall breakage was found to be restrained by preventing the blank-holding force from concentrating on the corner portions in the flange; in this case by sticking strips of stainless-steel tape onto the blank-holding plate, in front of the sides of the die cavity.

11A347. Tensile ductility and deep drawability of rate dependent sheet materials. - H Ohsawa *(Dept of Mech Eng, Col of Eng, Hosei Univ, Kajino chiyo, Koganei City, Tokyo, Japan)* and M Ikeda *(Olympus Optical, Kuboyama chiyo, hachioji City, Tokyo, Japan).* J Mat Processing Tech 38(4) 703-722 (Jul 1993).

The aim of this work is to clarify the role of appreciable rate dependency of the flow stress in practical sheet metal stamping operated at room temperature. The uniaxial ductility of rate-dependent sheet materials which have the ability of strain hardening as well as strain-rate sensitivity is examined. An analytical description combined with conventional instability theories predicts the significance of the rate of change of strain rate during uniaxial deformation in estimating the ductility. In accordance with the prediction, an Instron test machine is improved so as to be able to accelerate and decelerate the strain rate. Computational mechanics is introduced also to simulate the test. The precise examination on the influence of the rate dependency on the total elongation clarifies the nature of the rate of change of strain rate but results in a somewhat diverse conclusion. In deep drawing where the ductility of sheet metals is of little concern, the effect of continuous change of punch speed on the limiting drawing ratio (LDR) is investigated experimentally also. Sheet metals of pure aluminum and zinc are used in the test and the LDR is determined for each tool geometry. Measured LDRs show distinct differences, depending upon the punch-speed conditions, but systematic explanation of the trends displayed has not yet been accomplished.

See also the following:

11A456. Ultrasonic predictions of R-value in deep drawing steels

272G. SHEET METAL FORMING AND STAMPING

11A348. Development of an all-aluminum automotive body. - Y Muraoka *(Honda R&D, 321-33, 4630 Shimotakanezawa Haga-machi,* *Haga-gun Tochigi Pref, Japan)* and H Miyaoka *(Honda Eng, 350-13, 1-10-1, Shinsayama Sayama-shi, Saitama Pref, Japan)*. J Mat Processing Tech 38(4) 655-674 (Jul 1993).

To develop Honda's all-aluminum automotive body, many technical problems have had to be overcome, amongst which, the establishing of a press-forming technology was one of the most difficult. The aim was to give aluminum plate the same level of formed quality as that of steel plate, even though aluminum plate has a poorer formability than that of steel plate. For this purpose, it was required to develop and advance suitable technologies concerning the material, the die and the forming plan, with each of these items being closely related. This paper describes the detailed development and the various technical problems overcome, both up to the start of mass production of the all-aluminum body, and in the development concept.

11A349. Forming limit curves of aluminum and aluminum alloy sheets and effects of strain path on the curves. - S Kohara *(Dept of Mat Sci and Tech, Sci Univ of Tokyo, Noda, Chiuba 278, Japan)*. J Mat Processing Tech 38(4) 723-735 (Jul 1993).

For the applications of aluminum to automobile bodies, sheet forming is an essential process. The formability of sheet materials can be assessed by the forming-limit curve. However, little has been reported on the forming-limit curves of aluminum alloys. In this study, the forming-limit curves of aluminum and non-heat treatable aluminum alloy sheets were determined and the effects of the strain path on the curves were investigated. It was shown that larger limit strains without failure can be achieved by selecting a proper strain path.

11A350. Numerical simulation technology for lightweight aluminum can. - H Takeuchi *(Aluminum Res Dept, Aluminum and Copper Div, Kobe Steel, 15, Kinugaoka Moka-city, Tochigi 321-43, Japan)*. J Mat Processing Tech 38(4) 675-687 (Jul 1993).

About twenty years have passed since aluminum D&I cans were firstly produced in Japan. In this period, as the thickness of aluminum sheets for can bodies and can ends has become thinner, the weight of cans has become correspondingly lighter. In this paper, several recent technologies to lighten cans are described. In the material field, the new aluminum can stock 3004-H191, with high strength, has been developed. Numerical simulation by computer has been applied to optimize both the can profile and the can-manufacturing condition. Can bottom profiles resisting high internal pressure are clarified for one example of optimizing the can profile. Two numerical simulations in the can manufacturing process are also demonstrated. In the necked-in process, an optimum die profile to reduce the necking load and prevent the occurrence of buckling of the thin sidewall is obtained. In the scoring process on the can end, a desirable scoring-punch profile and punch-surface condition are investigated for the attainment of a good scoring performance.

11A351. Plain strain rigid plastic FE formulation for sheet metal forming process. - PAF Martins *(Dept de Eng Mec, Inst Superior Tec, Lisboa, Portugal)* and MJM Barata Marques *(Inst Nacional de Eng Tec Indust, Lisboa, Portugal)*. Proc Inst Mech Eng B 207(B3) 167-171 (1993).

A rigid plastic FE model for analyzing 2D plane strain sheet metal forming processes is described. The model is based on the large strain formulation using membrane theory, and the material is assumed to be rigid plastic, work hardening and conforms to Hill's anisotropic yield criterion and associated flow rules. The theoretical development follows the work of Kobayashi and Kim on the axisymmetric modeling of sheet metal forming. An application of the model for plane strain cylindrical punch stretching is presented. The results obtained are compared with those provided through an analytical membrane solution described in this work. The agreement found between both solutions is excellent.

272P. RAPID SOLIDIFICATION

11A352. Molecular-dynamics simulation of rapid solidification of aluminum. - J Lu and JA Szpunar *(Dept of Mining and Metall Eng, McGill Univ, 3450 University St, Montreal, PQ, H3A 2A7 Canada)*. Acta Metall Mat 41(8) 2291-2295 (Aug 1993).

A constant pressure molecular-dynamics simulation is used to examine changes in the structural characteristics of aluminum during rapid solidification. The glass formation and the crystallization from the liquid are predicted. The structure transformations which occur during solidification are described using the mean atomic volume, the internal energy, the radial distribution function and the surface tension. Changes in these parameters calculated as function of temperature display anomalies associated with a change in the structural ordering and change in the phase transformation.

272V. PLASTICS, ELASTOMERS, RUBBERS

See the following:

11A266. Anisotropic permeability of fiber preforms: Constant flow rate measurement

274. Fracture and damage processes

274B. CRACK INITIATION

11A353. Calculations of crack widths under pure torsion. - T Ciezak *(Fac of Civl and Sanitary Eng, Lublin Univ of Tech, Poland)*. Arch Civil Eng 38(3) 239-248 (1992).

A method to calculate widths of skew cracks generated by the action of twisting moment in the conditions of pure torsion is presented. Slip of both longitudinal reinforcement and stirrups with respect to concrete is allowed for. At the first stage of loading the width of the first crack is determined. At the stage of working load an average width of cracks is assumed to be dependent upon the stress increments in primary bars and stirrups above the stresses causing first cracks and upon a bond parameter. Further research is discussed necessary to apply the method in the practice of dimensioning of elements under torsion.

274C. SUBCRITICAL CRACK PROPAGATION

11A354. Aspects of fatigue affecting the design and maintenance of modern military aircraft. - SA Barter, JQ Clayton, G Clark *(DSTO Aeronaut Res Lab, Melbourne, Australia)*. Int J Fatigue 15(4) 325-332 (Jul 1993).

Over recent years, Australian aircraft operators have gained substantial experience with the early detection and management of cracking in critically stressed aircraft components. In the military sphere, the RAAF have been able to operate high-performance aircraft with cracks in specific locations in the airframe, by recognizing that an appropriate safety-by-inspection approach to cracking in critical components could permit continued operation, life extension, and maintenance efficiences. This approach has worked well in older aircraft, where cracks tend to initiate in well-defined high-stress areas, such as at fastener holes or similar design features, and where crack growth is sufficiently localized to allow crack length monitoring using established non-destructive inspection (NDI) techniques. Extension of this approach to newer aircraft, however, presents certain problems; in particular, the use of a variety of life-enhancing treatments (such as shot peening or cold expansion of fastener holes) in combination with high levels of average component stress has led to greater uncertainty about the number of potential cracking sites, their exact location within the structure, and the crack growth rates at these sites once cracks develop. This paper reviews the changing trends in aircraft design with respect to fatigue and fracture resistance, and discusses the influence of factors such as design approach, surface treatment technique, material behavior and NDI capability on life extension and the management of cracking in a fleet of military aircraft.

11A355. Creep-fatigue properties of Mod 9Cr-1Mo steel under variable straining. - M Miyahara and K Tokimasa *(Iron and Steel Res Lab, Sumitomo Metal Indust, Amagasaki 660, Japan)*. J Pressure Vessel Tech 115(3) 235-241 (Aug 1993).

Two-step variable straining tests, which included CP- (slow-fast) type and PC- (fast-slow) type tests, were conducted at 600°C in air for Mod 9Cr-1Mo steel. In the tests, CP and PC-type strain range level varied from high to low for the high-low test and from low to high for the low-high test. The deviations of the experimental data from the linear damage rule prediction were observed. These experimental results and the effect of the strain waveform on the creep-fatigue properties under variable straining were explained by the life prediction model previously proposed by the authors in which the strain range partitioned crack growth rate equations were applied.

11A356. Fatigue crack growth and closure behavior of semicircular and semi-elliptical surface flaws. - RG Chermahini, B Palmberg, AF Blom *(Struct Dept, Aeronaut Res Inst of Sweden FFA, PO Box 1102, S-161 11 Bromma, Sweden)*. Int J Fatigue 15(4) 259-263 (Jul 1993).

The growth behavior of semi-elliptical and semicircular cracks subjected to crack extensions due to tensile constant amplitude loading ($R = 0.1$) was investigated using a 3D elastic-plastic FE analysis of fatigue crack growth and closure. Based on this analysis, for both semicircular and semi-elliptical meshes, the crack first closed on the exterior (free) surface ($\theta = 0°$) and then closed towards the interior region upon further unloading of the cyclic loading. The closure and opening behavior of crack surfaces for both semicircular and semi-elliptical geometries are investigated. An experimental investigation of semi-elliptical flaws under fin spectrum loading was conducted to simulate relastic growth rate behavior for the semi-ellipticl geometry.

11A357. Multiple crack model for fatigue in welded joints. - S To *(FMG Timberjack, Woodstock, ON, N4S 7X1, Canada)*, SB Lambert, DJ Burns *(Dept of Mech Eng, Univ of Waterloo, Waterloo, ON, N2L 3G1, Canada)*. Int J Fatigue 15(4) 333-340 (Jul 1993).

Several linear elastic fracture mechanics models have been developed to simulate the fatigue performance of welded joints, particularly for offshore structures. Such models are used to estimate residual life when cracks are discovered in service. These models are also used to interpret available experimental results and may eventually be used in design. A key element to the success of such models is the realistic modeling of fatigue crack shape development. In all fatigue testing of welded T-plate, pipe-plate, and tubular joints in the Canadian Offshore Research Programme, care was taken to monitor crack shape development using beach marks and potential-drop techniques. Crack shape development was significantly influenced by specimen thickness, stress distribution and environment. A fatigue model is proposed which explicitly models the growth and coalescence of multiple semi-elliptic fatigue cracks. Such a model has the potential of modeling geometry and environmental effects through their influence on crack shape development. The basics of this model, including coalescence and the calculation of stress intensity factors, are discussed. Verification studies involving both T-plate and pipe-plate specimen geometries are presented.

11A358. Stable crack growth in ceramics at ambient and elevated temperatures. - JY Pastor, J Llorca, J Planas, M Elices *(Dept of Mat Sci, Polytech Univ, 28040-Madrid, Spain)*. J Eng Mat Tech 115(3) 281-285 (Jul 1993).

Quasi-static, stable crack propagation tests in ceramics are presented. The tests are performed using a recently developed technique in which the crack mouth opening displacement is continuously monitored during the test by means of a laser extensometer, and this signal is employed to control a servo-hydraulic testing machine. The advantages of such tests to characterize the fracture behavior of ceramics at high temperature are described, and the technique is used to study the fracture behavior of an ytria-partially stabilized zirconia ceramic at ambient and elevated temperatures.

11A359. Studies of mixed mode crack propagation in D16AT aluminium alloy. - V Srinivas and P Vasudevan *(Dept of Mech Eng, Indian IT, Bombay 400 076, India)*. Eng Fracture Mech 45(4) 415-430 (Jul 1993).

Mixed mode crack behavior was studied. Experiments were conducted on Compact Tension Shear (CTS) specimens at different angles including both mode I and mode II test conditions, and in both static and fatigue conditions. In addition to these tests overload tests were carried out to study the effect of mode I, mixed mode and mode II overload on subsequent mode I fatigue crack propagation. The experiments were conducted on D16AT Al alloy. Fractured specimens were analyzed under a scanning electron microscope. The effect of frequency and load ratio was analyzed at the microscopic scale in terms of striation spacing.

See also the following:

11A437. Automated procedure for determining crack opening level from differential displacement signal data

274D. DYNAMIC PROCESSES

11A360. High strain rate deformation and damage in ceramic materials. - G Raiser and RJ Clifton *(Div of Eng, Brown Univ, Providence RI 02912)*. J Eng Mat Tech 115(3) 292-299 (Jul 1993).

The objective of this investigation is to use a plate impact recovery experiment to identify the dominant failure mechanisms in conventional α-Al_2O_3 ceramics and thereby gain insight into the most promising, failure-resistant microstructurers. A "soft-recovery" configuration is used where in a star-shaped flyer imnpacts a square specimen. The impedances, shapes, thicknesses and orientation of all plates are designed to ensure a known history of longitudinal, planar stress waves throughout a central octagonal region of the specimen. The plane waves generated from this experiment are monitored by a laser interferometer system that allows data to be collected at four separate locations. The validity of the approach is demonstrated by a shot in which all plates were stressed within their elastic range. Subsequently, several experiments were conducted at nearly the same stress level with commercially sintered aluminas having different grain size and different glass content. These experiments, taken as a whole, demonstrate that improvement in alumina's dynamic compressive properties is obtained by reducing the grain size. In compression, a reduction in grain size lowers average residual stresses at triple junctions and grain boundaries and makes the material less susceptible to inelastic deformation and sliding at triple junctions and grain boundaries. A reduction in the weight percent of pre-processing impurities (and therefore the amount of intergranular glassy phase) yields strong improvements in the dynamic tensile strength of the ceramic. A decrease in the amount of glassy phase tends to make tensile damage less likely by improving grain boundary strength. These trends were tested by conducting recovery experiments on a high-purity, small-grain alumina, processed in-house through hot pressing. Both the compressive resistance and, especially, the tensile resistance were superior to those found for all other tested specimens. The overall results suggest that the best failure resistance will be obtained for new, high-purity, ultrafine-grain ceramics that are prepared by hot pressing of nanometer scale powders.

274E. FATIGUE CHARACTERISTICS OF MATERIALS

11A361. Application of a new model for fatigue threshold in a structural steel weldment. - L Bartosiewicz, AR Krause *(Ford Motor, PO Box 2053 MD-3083, Dearborn MI 48121)*, A Sengupta *(Dept of Mat Sci and Eng, Wayne State Univ, Detroit MI 48202)*, SK Putatunda *(Dept of Chem and Metall Eng, Wayne State Univ, Detroit MI 48202)*. Eng Fracture Mech 45(4) 463-477 (Jul 1993).

A new model for fatigue threshold has been proposed. The model takes into consideration the influence of material strength, grain size, and load ratio on fatigue threshold. Fatigue crack growth behavior of a structural steel weldment (ASTM Grade A 514) was investigated to examine the applicability of this model. The investigation also examined the influence of welding procedure [submerged arc welding (SMAW) versus metal inert gas welding (MID)] on the resultant microstructure and near the threshold fatigue crack growth behavior of the material in room temperature ambient atmosphere. The results of the present investigation demonstrated that the near threshold fatigue crack growth rates was lowest and fatigue threshold was highest when the crack propagated through the weldment. The fatigue threshold values predicted by the model were in good agreement with the experimentally determined values. The MIG welding process was found to be beneficial compared to the SMAW process as far as the fatigue threshold is concerned for weldment.

11A362. Cyclic fatigue-crack growth in grain bridging ceramics. - RH Dauskardt *(Center for Adv Mat, Mat Sci Div, LBL, UCB)*. J Eng Mat Tech 115(3) 244-251 (Jul 1993).

Cyclic fatigue degradation is contemplated in polycrystalline ceramics exhibiting grain bridging as the principle toughening mechanism. A frictional-wear-mechanism based on repetitive sliding wear degradation of frictional grain bridges is discussed. A micromechanical model is developed which provides an insight into the effects of salient mechanical and microstructural variables such as wear rate at the grain-matrix interface and initial residual stress of bridging grains, on fatigue-crack growth behavior. Results of the analysis are compared to experimentally observed fatigue-crack growth rates in coarse grained alumina and silicon nitride.

11A363. Cyclic near-tip fields for fatigue cracks along metal-metal and metal-ceramic interfaces. - C Woeltjen *(Des and Producibility Eng Div, Electron Syst Group, Westinghouse Elec, PO Box 746-MS336, Baltimore MD 21203)*, C.F. Shih, S Suresh *(Div of Eng, Brown Univ, Providence RI 02912)*. Acta Metall Mat 41(8) 2317-2335 (Aug 1993).

FE analyses were conducted with the objective of determining the cyclic near-tip fields ahead of a stationary tensile fatigue crack lying along the interface between two dissimilar solids. The model systems analyzed are (i) a metal-metal bimaterial whose components have the same elastic properties but different plastic deformation characteristics, and (ii) a metal-ceramic bimaterial. In both cases, monotonic loading to the peak tensile load results in a predominantly mode 1 field ahead of the crack. However, unloading in one or both components of the bimaterial with prior plastic deformation generates mixed-mode conditions at the crack tip. The mode mixity persists during a significant portion of the next loading phase and is gradually removed upon reloading to the peak stress. The cyclic plastic zone size directly ahead of the fatigue crack is approximately one-fifth the size of the monotonic plastic zone. The residual compressive stresses within the cyclic plastic zone are computed. The implications of reversed yielding and mixed-mode near-tip fields to constant-amplitude and variable-amplitude fatigue fracture are discussed.

11A364. Effect of mission cycling on the fatigue performance of SiC-coated carbon-carbon composites. - H Mahfuz, PS Das, S Jeelani *(Mat Res Lab, Tuskegee Univ, Tuskegee AL)*, DM Baker, SA Johnson *(General Dyn, Ft Worth TX)*. Int J Fatigue 15(4) 283-291 (Jul 1993).

The response of quasi-isotropic laminates of SiC-coated carbon-carbon (C-C) composites under flexural fatigue was investigated at room temperature. Virgin as well as mission-cycled specimens were tested to study the effects of thermal and pressure cycling on the fatigue performance of C-C. Tests were conducted in three-point bending with a stress ratio of 0.2 and frequency of 1 Hz. The fatigue strength of C-C has been found to be quite high: approximately above 90% of the ultimate flexural strength. The fatigue strength appears to be decreasing with the mission cycling of the specimens. This lower strength with the mission-cycled specimens is attributed to the increase in interfacial bond strength due to thermal and pressure cycling of the material. C-C is also found to be highly sensitive to the applied stress level during cyclic loading, and this sensitivity is observed to increase with the increase in the amount of mission cycling. Weibull characterization of the fatigue data has been performed, and a wide scatter in the Weibull distribution is discussed. Fractured as well as untested specimens were C-scanned, and the progressive damage growth during fatigue is presented. Optical microscopy including scanning electron microscopy for the failed specimens was also performed, to analyze the failure behavior. Degradation and separation of the porous matrix structure, localized damage and filament splitting within the yarns, complete failure of the fibre bundle, and delamination near the loading zone was observed.

11A365. Effect of temperature on the behavior of short fatigue cracks in Waspaloy using an *in situ* SEM fatigue apparatus. - RR Stephens *(Mech Eng Dept, Univ of Idaho, Moscow ID 83843)*, L Grabowski *(Rolls Royce, PO Box 31, DE2 8BJ, Derby)*, DW Hoeppner *(QIDEC, Univ of Utah, Salt Lake City UT 84112)*. Int J Fatigue 15(4) 273-282 (Jul 1993).

Short fatigue crack growth behavior was studied in Waspaloy at 25°C, 500°C, and 700°C under cyclic loading conditions at a stress ratio of 0.1. Specimens were tested within an elevated temperature fatigue apparatus coupled to a scanning electron microscope which allowed *in situ* observations to be made of the fatigue process. Crack formation was dominated by slip band cracking at 25°C and 500°C, while at 700°C cracks formed along slip bands and twin boundaries. Crack propagation proceeded by means of slip band cracking at 25°C and 500°C, while at 700°C crack growth was primarily stage II-mode

I type growth. Short fatigue crack growth rates were faster at 500°C than at 25°C for an equivalent stress intensity range, ΔK_1, owing to a change in slip character. Short crack growth rates tended to be lower at 700°C than at 500°C, owing to changes in the material leading to precipitate coarsening. As the temperature was increased, mircrostructural contributions to crack growth decreased, resulting in a reduced microstructural short crack effect.

11A366. Fatigue deformation of silver single crystals: STM evidence for crack nucleation, measurements of slip irreversibility and verification of a new scaling relationship for fatigue life. - TS Sriram *(Digital Equip, 77 Reed Rd, MS HL02-3 J12, Hudson MA 01769)*, Chih-Ming Ke, YW Chung *(Dept of Mat Sci and Eng, McCormick Sch of Eng and Appl Sci, NWU)*. Acta Metall Mat 41(8) 2515-2521 (Aug 1993).

Silver single crystals oriented in the single glide orientation were fatigued in air and in vacuum. The surface morphology was observed using a scanning tunneling microscope. A gold film deposited on the silver surface was used as a reference marker so that the same region can be observed upon repeated fatigue cycling. Pit-shaped features were observed to form within a narrow range of cycles and to eventually develop into micron-sized cracks, lending support to the notion that cracks are formed by a nucleation process. In addition, by measuring the slip band height and spacing as a function of cycling, we were able to determine the slip irreversibility and the Coffin-Manson exponents in both environments. With these two sets of data, we were able to verify a new scaling relationship for fatigue life based on our earlier theoretical work.

11A367. Fatigue process in short carbon-fiber reinforced polyamide 6.6 under rotating-bending and torsional fatigue. - H Nisitani, H Noguchi *(Fac of Eng, Kyushu Univ, Fukuoka 812, Japan)*, Y-H Kim *(Dept of Mat Eng, Korea Maritime Univ, Pusan 606-791, Korea)*. Eng Fracture Mech 45(4) 497-512 (Jul 1993).

Rotating-bending fatigue and torsional fatigue tests of the injection moulded short carbon-fiber reinforced polyamide 6.6 were carried out to investigate the fatigue characteristics. The fatigue mechanism in the composites was clarified through successive surface observations using the replica method. Moreover, the mechanism of the torsional fatigue was compared with that of the rotating-bending fatigue. The failure cracks in both fatigue tests are nucleated along the fibers aligued in the direction of the maximum principal stress. In the case of the rotating-bending fatigue test, the fatigue crack propagates at right angles to the direction of the principal stress. On the other hand, in the case of torsional fatigue, the cracks nucleated along the fibers cannot propagate under the low stress amplitude. However, the fatigue cracks nucleated from the fibers which are aligued in the direction of the principal shear stress can propagate, and lead to the final fracture.

11A368. In-service loading of AlSiII aluminium cast alloy in the very high cycle regime. - SE Stanzl-Tschegg, HR Mayer *(Inst for Met and Phys, Univ for Agri, Turkenschanzstr 1, A 1180 Vienna, Austria)*, EK Tschegg *(Inst for Appl and Tech Phys, Tech Univ, Karlsplatz 13, A 1040 Vienna, Austria)*, A Beste *(Audi AG, W 8070, Ingolstadt, Germany)*. Int J Fatigue 15(4) 311-316 (Jul 1993).

The fatigue properties of two AlSiII cast alloys as used for car wheels have been tested in the regime of 10^8-10^9 cycles. An AlSiII aluminium alloy with 0.12-0.20% Mn and one with 0.05% Mn and increased H_2 content during the pouring procedure are compared. It is shown that mainly cast voids determine the fatigue properties. These material inhomogeneities reduce the fatigue strength and lead to early fracturing. The number of cycles to failure decreases with increasing void cross-section. With a statistical analysis of the fatigue [illegible], it is shown that the mean number of cycles to failure is higher for the alloy with fewer large cast voids and a higher Mn content. This alloy is less susceptible to cast voids, and the threshold stress intensity value is approximately 10% higher.

11A369. Modeling of loading rate effect on fatigue crack growth. - KM Golos *(Warsaw Univ of Tech, Warszawa, Poland)*, HP Stuwe, R Pippan *(Erich Schmid Inst fur Festkorperphysik, Vienna, Austria)*. Eng Trans 41(2) 167-175 (1993).

A mechanical model of fatigue crack growth at low and intermediate ΔK values is presented. In the model the effect of the loading rate on the fatigue crack growth is considered. The local stress and strain are calculated based on the Hutchinson, Rice, and Rosengren solution. The required data for predicting fatigue crack growth rate can be found in standard material handbooks where cyclic and fatigue properties of the materials are presented.

11A370. Multiple-site damage in 2024-T3 alloy sheet. - O Partl and J Schijve *(Fac of Aerospace Eng, Univ of Tech, 2629 HS Delft, Netherlands)*. Int J Fatigue 15(4) 293-299 (Jul 1993).

A simple computational procedure, using the principles of fracture mechanics and a compounding K-solution method, was developed for predicting fatigue crack growth if multiple-site damage is present. The prediction method was verified using the results of a series of fatigue crack growth tests performed on 2024-T3 alloy sheet specimens with a row of collinear open holes and artificially introduced flaws at the three central holes. Three different geometrical configurations were adopted. A good agreement was found between the test results and the predictions. An obvious crack interaction effect was found, but it occurred mainly in the last part of the fatigue crack growth lives. The relative size of MSD cracks depends significantly on scatter of the size of the initial crack nuclei.

11A371. Study on threshold fatigue crack growth characteristics of electron beam welding in AISI 4130 steel. - Jiun-Ren Hwang and Hsiu-Hung Chang *(Dept of Mech Eng, Natl Central Univ, Chung-li, Taiwan 320, ROC)*. Eng Fracture Mech 45(4) 519-527 (Jul 1993).

Near-threshold fatigue crack growth of an electron beam weldment in AISI 4130 steel is studied. To increase the fatigue resistance ability, two different post-weld heat treatment processes are adopted to compare the near-threshold fatigue crack growth data with that of an as-welded specimen. The electron beam tempering in the vacuum chamber immediately after the welding and the traditional furnace tempering treatment are chosen for comparison. Strength of the welded joints is evaluated by a tensile test and near-threshold fatigue properties are investigated by K-decreasing method. The resistance to near-threshold fatigue crack growth is improved with post-weld heat treatment, due to the residual stress relief effect and existence of a toughened tempered structure. For electron beam post-weld heat treatment with 6 mm dot pattern width, the threshold stress intensity factor range increases by 14% compared to that of an as-welded specimen and the data of furnace post-weld heat treatment of 550°C can be improved by as much as 26%.

See also the following:

11A228. Simulation of the vertical split head failure in rails

11A538. Simplified method of bearing material fatigue strength investigation

274F. STRESS OR STRAIN LIFE ANALYSIS OF FATIGUE

11A372. Estimating the vibration fatigue life of quad leaded surface mount components. - DB Barker, YS Chen, A Dasgupta *(CALCE Electron Packaging Res Center, Univ of Maryland, College Park MD 20742)*. J Electron Packaging 115(2) 195-200 (Jun 1993).

This paper discusses the assumptions and details of the fatigue life calculations required to predict the fatigue life of a quad leaded surface mount components operating in a vibration environment. A simple approximate stress analysis is presented that does not require complex FE modeling, nor does it reduce the problem to a simple empirical equation or rule of thumb. The goal of the new method is to make PWB vibration solder joint reliability information available to the designer as early as possible and in an easily understood and implemented manner.

274G. OTHER ASPECTS OF FATIGUE

11A373. Constitutive behavior and low cycle thermal fatigue of 97Sn-3Cu solder joints. - Y-H Pao, S Badgley, E Jih, R Govila *(Res Lab, Ford Motor, Dearborn MI 48121-2053)*, J Browning *(RPI)*. J Electron Packaging 115(2) 147-152 (Jun 1993).

The thermal cyclic shear stress-strain hysteresis response and associated steady-state creep parameters of 97Sn-3Cu solder joints have been determined using a beam specimen previously developed by Pao et al, (1992a). The solder joint was subjected to a 40-minute thermal cycling from 40°C to 140°C. A constitutive equation based on elastic and steady-state creep deformation for the solder has been formulated and implemented in a FE program, ABAQUS, to model the experiment. The results show that the constitutive equation based on one single creep mechanism cannot fully account for the deformation during cooling, as opposed to the case of 90Pb-10Sn where the entire cyclic deformation can be well modeled by a similar constitutive equation (Pao et al, 1992c). This suggests that another creep mechanism is dominant for lower stresses and higher temperature. The thermal fatigue results show that the failure mechanism of 97Sn-3Cu joints is similar to that of 90Pb=10Sn joints, but the number of cycles to failure of 97Sn=Cu solder joints is at least 5 times longer than 90Pb-10Sn solder joints. This indicates the potential application of 97Sn-3Cu in place of 90Pb-10Sn solder.

11A374. Influence of the cycle frequency and wave shape on the fatigue life of leaded chip carrier printed wiring board interconnections. - HD Solomon *(GE Corp R&D Center, Schenectady NY 12301)*. J Electron Packaging 115(2) 173-179 (Jun 1993).

This study employed different cycle frequencies, to determine the influence of cycle frequency on the fatigue life of leaded chip carrier to printed wiring board (LCC-PWB) interconnections. Real LCC-PWB interconnections were mechanically cycled at 35° C or 125° C. The cycle frequency was varied by varying the ramp loading and unloading rates or by introducing hold times. Tests were run with equal hold times at the maximum and minimum displacements or only at the maximum displacement. The use of slower ramp cycling or the introduction in the hold times increased the plastic displacement and this decreased the fatigue life. The plastic displacement increase was corrected for, to unveil the underlying material response. The corrected data was similar to that observed in previous tests on simple, single, solder joints, where the plastic strain was kept constant while the cycle frequency was reduced. At 125° C there was a small influence of wave shape, with maximum displacement hold time tests showing the shortest fatigue lives and symmetric (maximum and minimum) hold time tests showing the longest fatigue lives. The fatigue lives of the tests run with ramp cycling were intermediate. This wave shape effect is relatively small, especially compared to the large overall influence of the cycle frequency.

11A375. Stress-based liftime prediction method for a general state of cyclic stress. - J Kolenda *(Poland)*. Marine Tech Trans 3 127-135 (1992).

Fatigue lifetime of constructional steels under multiaxial cyclic stress is considered. It is assumed that the design life consists of periods during which the stress components are synchronous, in-phase and have constant amplitudes. The case of combined load in cyclic bending and torsion is analyzed. The analysis is restricted to the failure subregion for elastic applications. It is concluded that the formulae for calculation of the safety factor in the safe region and in the failure subregion differ only in the definitions of partial safety factors. This permitted to use the known safety factor formula for a general state of cyclic stress in the safe region also for the considered failure subregion.

See also the following:

11A868. Computer simulation of thermo-mechanical fatigue of solder joints including microstructure coarsening

274H. CORROSION AND EMBRITTLEMENT

11A376. BE model of cathodic well casing protection. - SH Lee, DW Townley, KO Eshun *(Chevron Oil Field Res, PO Box 446, La Habra CA 90633-0446)*. J Comput Phys 107(2) 338-347 (Aug 1993).

An efficient BEM was developed to study cathodic protection of a well casing in a formation with layered conductivities. Even though the electrical potential in soil is governed by the linear Laplace equation, electrochemical reactions at the well casing introduce complex, nonlinear boundary conditons. Furthermore, the complexity of boundary geometries makes the numerical computation nontrivial. Use of Green's function allows a general solution of the Laplace equation to be expressed in the form of a Fredholm integral equation of the second kind. The present formula employs a fundamental solution that eliminates the discretization of the top ground surface. Because the potential distribution within the well casing metal greatly affects the current distribution, the model includes the potential change along the axial direction of the well casing. A Newton-Raphson method was employed to estimate iteratively the current distribution at the well casing, and then the integral equations of the BEM were numerically solved by a collocation technique. This BE model was used to investigate the effects of soil conductivities, well casing geometry, well casing resistivity, and the location of a current source on the current and potential distribution at the well casing.

11A377. Crack length effect on corrosion fatigue crack propagation. (Polish). - M Jakubowski *(Poland)*. Marine Tech Trans 3 97-108 (1992).

The crack length effect has been tested for a shipbuilding steel in saltwater at different, but constant for each specimen levels of the stress intensity factor range ΔK, at a loading frequency of 0.1 Hz, stress ratio R = 0.15. The ΔK values from the Paris Law range of the fatigue diagram, and the cracks longer than so-called "short cracks" have been chosen for testing. The crack growth rate and the coefficient of the relative corrosion effect β (ratio of the crack growth rate in saltwater to that in the air at the very same ΔK) has been evaluated as a function of the crack length a. Crack growth rates and coefficients β increased directly proportional to log a up to the maximum at a certain length. For cracks longer than 15-20 mm they approached a constant level, independent on the crack length, but lower than the maximum. In the shorter cracks range the corrosion effect was controlled mainly by crack length, not ΔK. According to British suggestion β = 6 can be used in conservative calculations of the corrosion fatigue life for offshore and ship structures. Mechanisms of the crack length effect have been discussed.

11A378. Effects of grain size and phosphorus on the corrosion of nanocrystalline Ni-P alloys. - R Rofagha, U Erb, D Ostrander *(Dept of Mat and Metall Eng, Queen's Univ, Kingston, K7L 3N6, Canada)*, G Palumbo *(Ontario Hydro Res Div, 800 Kipling Ave, Toronto, M8Z 5S4, Canada)*, KT Aust *(Dept of Metall and Mat Sci, Univ of Toronto, Toronto, M5S 1A4, Canada)*. Nanostruct Mat 2(1) 1-10 (Jan-Feb 1993).

The effects of grain size and phosphorous content on the corrosion characteristics of nanocrystalline Ni-P alloys tested in 0.1M H_2SO_4 by anodic polarization is evaluated and compared with the corrosion behavior of amorphous Ni-P and high purity conventional polycrystalline Ni. It is found that in contrast to conventional polycrystalline nickel neither nanocrystalline (grain sizes 22.6 and 8.4 nm) nor amorphous Ni-P passivate during potentiodynamic polarization. The electrochemical response and corrosion morphologies observed for the different materials are discussed in terms of their microstructural differences.

274I. FRETTING, WEAR, AND EROSION

11A379. Influence of the mass flux and impact angle of the abrasive on the erosion resistance of materials used in pulverized fuel bends and other components in thermal power stations. - PR Krishnamoorthy, S Seetharamu, P Sampathkumaran *(Mat Tech Div, Central Power Res Inst, Bangalore 560 094, India)*. Wear 165(2) 151-157 (1 Jun 1993).

This paper presents laboratory results and field data obtained on the erosion resistance of metallic and ceramic wear parts of low alloy steel, Nihard, high chromium cast iron, 85% alumina ceramic, and 91% alumina ceramic. The influence of the mass flux and impact angle is evaluated in the laboratory tests. The applicability of laboratory tests to predict wear life in the field is also discussed.

11A380. Machine for fretting wear testing of plasma surface modified materials. - PW Sandstrom, K Sridharan, JR Conrad *(Eng Res Center for Plasma Aided Manuf, Univ of Wisconsin, 1410 W Johnson Dr, Madison WI 53706)*. Wear 166(2) 163-168 (1 Jul 1993).

Microscopic damage caused by fretting wear is of significant concern in many engineering applications. We report the design and performance of a versatile fretting wear testing machine that uses an electromagnetic actuator under closed-loop control to provide a constant slip amplitude over a wide frequency range. The machine is equipped with a mechanism that allows for gradual sample contact and precise relocation of the stylus. An innovative method for monitoring frictional forces during the course of a test is incorporated. The machine has been successfully applied to materials by three types of plasma surface modification: nitrogen ion implantation, thin film alloy deposition and diamond-like carbon film deposition.

274J. CREEP

11A381. Compressive failure of fiber composites: The roles of multiaxial loading and creep. - WS Slaughter, NA Fleck *(Eng Dept, Cambridge Univ, Cambridge CB2 1PZ, UK)*, B Budiansky *(Div of Appl Sci, Harvard Univ, Cambridge MA 02138)*. J Eng Mat Tech 115(3) 308-313 (Jul 1993).

The roles of multiaxial loading and creep in compressive failure of aligned fiber composites are considered. Analytical models are developed based on the model given by Budiansky and Fleck (1992). The critical microbuckling stress in multiaxial loading is calculated for a rigid-perfectly plastic solid and an elastic-plastic strain hardening solid. The rigid-perfectly plastic results predict a plane compressive failure surface in stress space. The rigid-perfectly plastic results are sufficiently accurate, when compared to the strain hardening results, so long as the remote shear stress and stress normal to the fiber direction are not too large relative to the remote stress in the fiber direction. The model given for creep microbuckling is suitable for power-law viscous composite behavior. Deformation within a localized kink band is computed as a function of time. A creep life is predicted, based on a critical strain failure criterion.

11A382. Solder joint creep and stress relaxation dependence on construction and environmental-stress parameters. - RG Ross Jr, LC Wen, GR Mon *(JPL)*. J Electron Packaging 115(2) 165-172 (Jun 1993).

Creep strain is probably the most important time-dependent damage accrual factor affecting solder joint reliability. Under typical multi-hour loading conditions, creep-induced strain is a complex function of solder metallurgical structure, solder temperature, loading time per cycle, the applied stress, and the spring constant of the combined part-lead-board system. The complex system level creep-fatigue interactions involved in electronic part solder joints are shown to be a strong function of the relative stress ratio $_\kappa$, which is the ratio of the stiffness of the combined solder-lead system to the stiffness of the solder element by itself. For a leadless chip package, $_\kappa$ is close to unity. For a compliant leaded package, $_\kappa$ is typically in the 0.01 to 0.0001 range. Important environmental stress dependencies, including the effects of operating temperature, displacement amplitude due to thermal and mechanical cycling, and cyclic frequency of loading are investigated for different levels of $_\kappa$. Understanding the sensitivity of solder strain range to relative stiffness and these key environmental parameters is important to understanding the behavior of alternative packaging concepts and to achieving robust electronic packaging designs and testing approaches.

See also the following:

11A373. Constitutive behavior and low cycle thermal fatigue of 97Sn-3Cu solder joints

11A400. Stable crack growth in rate-dependent materials with damage

274K. ABLATION, SPALLATION, DELAMINATION

11A383. Delamination cracks originating from transverse cracking in cross-ply laminates under various loadings. - Yujun Kim and Seyoung Im *(Dept of Mech Eng, Korea Adv Inst of Sci and Tech, Sci Town, Taejon 305-701, Korea)*. Int J Solids Struct 30(16) 2143-2161 (1993).

Delamination cracks originating from transverse cracking in two types of cross-ply lamiantes $[90/0]_s$ and $[0/90]_s$ are analyzed for three types of loadings: plane strain extension, plane strain bending and antiplane shear. The asymptotic solution for stress and displacement field is constructed based upon the Stroh formalism for anisotropic elasticity and the method of eigenfunction expansion. Its structure is determined from appropriate near-field conditions leading to the eigenvalue equation, and then the singular hybrid FEM in conjunction with a quadratic programming procedure for treating the partial contact of crack faces is employed to complete the field solution. The stress intensity factor properly defined for anisotropic interfacial cracks and the energy release rate are computed from the complete solution. The stability of crack growth and the effect of the relative ply thickness upon the crack growth stability are examined in terms of the energy release rate and the phase angle.

274X. STOCHASTIC ASPECTS

11A384. Damage and fuzzy risk assessment in steam plants. - SKP Cheung-Mak and IL May *(Metall Consult Services, PO Box 5006, Saskatoon, SK, S7K 4E3, Canada)*. Trans Can Soc Mech Eng 17(2) 111-125 (1993).

The various methods of damage assessment in steam plants are reviewed. An example of estimating the remaining life of steam pipe welds containing cracks is discussed. Modeling techniques provide a quantitative evaluation of the risk of failure. However, damage assessment is not an exact science. Thus the fuzzy set method of risk assessment is introduced. Most material data for creep are obtained from accelerated tests, and the extrapolation of shorter time data to longer times at different stresses and temperatures is used in the prediction of remaining life. Inexact knowledge of load and temperature variations in the operation of actual steam plant further complicates overall risk assessment. Estimation of the overall risk of failure in the plant using the fuzzy set method requires identification of critical areas in different components at which damage may have accumulated, together with nondestructive testing, microstructural evaluation and other methods to define the extent of the damage. The importance of the particular component to the operation of the whole system must be assessed before a judgement can be made to provide a prediction of the plant's remaining life.

11A385. Fatigue reliability in uniaxial state of stress produced by synchronous loads. - J Kolenda *(Univ of Tech, Gdansk, Poland)*. Eng Trans 41(1) 21-30 (1993).

The paper deals with the stress-based fatigue analysis of structural members subjected to synchronous and in-phase loads. The uniaxial state of stress produced by combined bending and tension-compression is considered. Attention is focused on the failure subregion for high cycle fatigue where the linear logarithmic models for fatigue behavior are applicable. The relationships for calculation of fatigue reliability and number of cycles to failure are proposed. For the assessment of the probability of fatigue failure under the stress with normally distributed amplitudes of its components, the reliability index is determined.

11A386. Load-history sensitive cyclic curve concept in random load fatigue life predictions. - S Petinov and N Yermolaeva *(Div of Ship Struct, Marine Tech Univ, Lotsmanskaya str 3, St Petersburg 190008, Russia)*. Ship Tech Res 40(2) 107-111 (May 1993).

The results of two-level strain control tests of cyclic hardening aluminium alloy were used to derive the load-sensitive cyclic curve model (LHSCC). It incorporates effects of material cyclic strain hardening and of loading sequence. A computer algorithm for generating random load sequences is developed. It takes account of the statistical distribution of amplitudes and of autocorrelation properties of the process. A numerical example of a fatigue damage calculation based on the LHSCC concept is presented.

11A387. Rainflow analysis: Markov method. - M Frendahl and I Rychlik *(Dept of Math Stat, Univ of Lund, PO Box 118, S-22100 Lund, Sweden)*. Int J Fatigue 15(4) 265-272 (Jul 1993).

In this paper we discuss rainflow cycle counting methods and linear fatigue damage accumulation for stationary loads. The expected damage is computed by approximating the sequence of local extremes by a Markow chain. The algorithm is implemented as part of a "fatigue toolbox". Several examples illustrate the results.

11A388. Statistical theory of ceramic damage and fracture. - Xiaoxue Diao *(Dept of Mech Eng, Univ of Sydney, NSW 2006, Australia)* and Xiusan Xing *(Dept of Appl Phys, Beijing IT, PO Box 327, Beijing 100081, Peoples Rep of China)*. Eng Fracture Mech 45(4) 513-518 (Jul 1993).

The shortcomings of continuum damage mechanics are discussed. A new universal statistical definition of damage of ceramic materials is given from the viewpoint of stochastic evolution of microcracks. The kinetic equation and the accumulative rule of damage are derived. The connection between the micromechanisms of damage and macroscopic properties of ceramics is discovered.

11A389. Stochastic aspects of matrix cracking in brittle matrix composites. - SM Spearing *(BP Res Dept, BP America, Cleveland OH 44128-2837)* and FW Zok *(Mat Dept Col of Eng, UC, Santa Barbara CA 93106-5050)*. J Eng Mat Tech 115(3) 314-318 (Jul 1993).

A computer simulation of multiple cracking in fiber-reinforced brittle matrix composites has been conducted, with emphasis on the role of the matrix flaw distribution. The simulations incorporate the effect of bridging fibers on the stress required for cracking. Both short and long (steady-state) flaws are considered. Furthermore, the effects of crack interactions (through the overlap of interface slip lengths) are incorporated. The influence of the crack distribution on the tensile response of such composites is also examined.

See also the following:

11A415. Stochastic viscoelastic delamination onset failure analysis of composites

274Y. COMPUTATIONAL TECHNIQUES

11A390. FE alternating approach to the bending of thin plates containing mixed mode cracks. - Wen-Hwa Chen and Chih-Ming Shen *(Dept of Power Mech Eng, Col of Eng, Natl Tsing Hua Univ, Hsinchu, Taiwan 30043, ROC)*. Int J Solids Struct 30(16) 2261-2276 (1993).

A FE alternating procedure developed to deal with the cracked plate in symmetric bending is extended to analyze the more realistic case with single or multiple mixed mode cracks. This modified procedure involves the new derivation of the analytical solution for an infinite thin plate containing a crack subjected to arbitrary antisymmetric equivalent shear force on crack surfaces. Due to the natural limitation of Kirchhoff assumptions for a thin plate in bending, the appropriate treatment of constant twisting moments on the crack surfaces is devised. The interaction effect among cracks on the calculation of bending (symmetric) and shear (antisymmetric) stress intensity factors is also discussed. Several numerical examples are solved to demonstrate the validity and efficiency of the approach.

11A391. Integrity assessment of thick walled industrial furnace tubes. - RK Kizhatil and R Seshadri *(Indust Syst Eng, Univ of Regina, Regina, SK, S4S 0A2, Canada)*. Trans Can Soc Mech Eng 17(2) 127-143 (1993).

This paper examines various simplified methods proposed to analyze stresses and predict damage and remaining life in furnace tubes subjected to sustained primary pressure stresses and cyclic secondary thermal stresses resulting from a typical furnace operation. Operational effects such as tube fouling, firing rates, startup-shutdown cycles are considered. Component integrity assessments are carried out using some recently developed techniques. A numerical example of a furnace tube made of HK-40 material is presented, and results obtained using a nonlinear FE analysis are compared with predictions obtained using the elastic-core method.

See also the following:

11A249. Extension of the static shakedown theorem to a certain class of inelastic materials with damage

274Z. EXPERIMENTAL TECHNIQUES

See the following:

11A442. Micromechanical fatigue testing
11A455. Ultrasonic assessment of interfacial oxidation damage in ceramic matrix composites

276. Fracture and damage mechanics

See the following:

11A384. Damage and fuzzy risk assessment in steam plants
11A870. High temperature fracture toughness in silicon nitride and sialon

276A. GENERAL THEORY

11A392. Role of mechanics in plex: A technical perspective. - YS Garud *(S Levey Inc, 3425 S Bascom Ave, Campbell CA 95008)*. Trans Can Soc Mech Eng 17(2) 97-109 (1993).

The mechanics of materials and structures plays an important role in majority of life prediction and structural integrity evaluations. In many industrial systems this role gets integrated with effects of service environment and material aging; corrosion, oxidation, and irradiation are examples of such effects which require an interdisciplinary approach. Degradation mechanisms related to these effects have been identified as potentially significant to plant life extension (PLEX). In-service inspection and component monitoring are some of the cost effective steps emphasized in the life extension works; usefulness of the results of these steps can be enhanced through the methods needed for the component condition assessment. These methods, therefore, demand an ever increasing accuracy and improvements requiring a better appreciation and integration of the mechanics. The above aspects of PLEX are critically examined in this paper with a review of key degradation mechanisms elucidating the role of mechanics. Current design basis and recent developments in the life prediction techniques are discussed identifying areas of further work. Stress corrosion cracking, corrosion fatigue, pressurized thermal shock, and long term material stability under thermal and irradiation aging are some of the phenomena emphasized in this work. The significance of mechancis in treating the subcritical crack growth due to these phenomena is discussed. Also, from the point of view of final failure step, the role of impact energy and fracture toughness is examined with consideration of the time dependent changes in these properties. The additional objective of this presentation is to provide a perspective on the assessment of remaining life and safety margins with particular reference to the needs and challenges of the plant life extension.

276B. LINEAR ELASTIC FRACTURE MECHANICS

11A393. Equivalent elastic crack 1. Load-Y equivalences. - M Elices and J Planas *(Dept de Ciencia de Mat, Escuela de Ing de Caminos, Univ Politec, Ciudad Univ, 28040 Madrid, Spain)*. Int J Fracture 61(2) 159-172 (15 May 1993).

The use of crack growth resistance curves (R-δ a) to predict the behavior of cracked specimens is a well established practice for ceramic and cementitious materials. When the cohesive crack model can be applied to these materials it is shown that the use of R-δ a curves is equivalent to setting up an *elastic equivalence* that greatly simplifies the computations. This equivalence has its drawbacks and limitations. This paper analyzes a class of equivalences - the load (P) versus another variable - between cracked cohesive materials and linear elastic ones, ascertaining its applicability to the interpretations of fracture data.

See also the following:

11A222. Problems of stress concentration in the neighborhood of a spherical defect

11A357. Multiple crack model for fatigue in welded joints

276D. STRESS INTENSITY FACTOR CALCULATIONS

11A394. FEM modeling of stress intensity factors for fatigue crack growth at ultrasonic frequencies. - HR Mayer, SE Stanzl-Tschegg, DM Tan *(Inst for Meteorol and Phys, Univ of Agri, Turkenschanzstr 18, A-1180 Vienna, Austria)*. Eng Fracture Mech 45(4) 487-495 (Jul 1993).

The inverse iteration FEM is used to determine the stress intensity factor of a single edge notched specimen as used in ultrasonic resonance testing of fatigue crack growth. The stress intensity factor is determined as a function of velocity or amplitude at the specimen ends. Resonance frequency and tension-compression ratio R are calculated for different crack lengths. It is shown that the R-value increases from R = -1 to R = -0.90 when the relative crack length (a/W) increases from 0.067 to 0.4. The stress intensity factor for high frequency resonance loading is compared with the stress intensity amplitude for two static loading conditions. Significant differences are found in comparison with static concentric loading and similarities with static uniform displacement loading.

11A395. Frequency domain stress intensity calibration of damped cracked panels. - JF Doyle *(Sch of Aeronaut and Astronaut, Purdue)* and SA Rizzi *(Struct Acoust Branch, NASA Langley Res Center, Hampton VA 23665)*. Int J Fracture 61(2) 123-130 (15 May 1993).

This paper discusses two schemes for doing FE K calibration in the frequency domain. The baseline scheme uses the definition of K as a limit toward the crack tip. The limiting process requires using a very fine mesh around the crack tip making the scheme computationally very expensive. It is shown that the behavior of K as a function of frequency is very similar to a modal response. Taking advantage of this, a more efficient scheme involves a modal analysis of the cracked sheet and scaling the response to that of the static stress intensity. In this way, only a static K calibration need be performed. All the examples shown are for a frequency range spanning multiple resonances and with two levels of damping.

11A396. Shearing effects on a shaft with circular surface crack under rotary bending. - Ching-Hwei Chue, Ming-Long Wu, Chih-Hsiang Chang *(Dept of Mech Eng, Natl Cheng-Kung Univ, Tainan 701, Taiwan, ROC)*. Eng Fracture Mech 45(4) 479-486 (Jul 1993).

The shearing effects on the failure behavior of a rotating shaft with a cicular surface crack subjected to transverse concentrated load and torsion are investigated by employing FEM combined with strain energy density theory. Results of stress intensity factors and minimum strain energy density factor at an arbitrary point on the crack front are obtained for three different crack sizes. The plane strain condition has been assumed in order that the onset and direction of the mixed mode crack propagation can be determined. It is shown that the crack will distort and extend preferentially in a direction opposite to that of rotation and swing a small angle depending on the shearing stress effects.

11A397. Stress intensity factor of a subsurface inclined crack subjected to dynamic impact loading. - Chwan-Huei Tsai *(Dept of Mech Eng, Huafan IT, Taipei, Hsien, Taiwan 223, ROC)* and Chien-Ching Ma *(Dept of Mech Eng, Natl Taiwan Univ, No 1 Roosevelt Rd Section 4, Taipei, Taiwan 10764, ROC)*. Int J Solids Struct 30(16) 2163-2175 (1993).

To gain insight into the phenomena of the interaction of stress waves with a material defect, the transient problem of a half-space containing a subsurface inclined semi-infinite crack subjected to normal impact on the boundary of the half-space is studied. The solutions are determined by linear superposition of the fundamental solution in the Laplace transform domain. The fundamental solution is the exponentially distributed traction on crack faces proposed by Tsai and Ma. Due to the nature of the crack geometry, a combination of transient mixed mode I and II deformation fields in induced near the crack tip. The exact closed form solutions of stress intensity factor histories are obtained. These solutions are valid for the time interval from initial loading until the first wave scattered at the crack tip returns to the crack tip after being reflected by the free boundary. The probable crack propagation direction is predicted from different fracture criteria.

11A398. Stress intensity factors of the eccentric and edge cracked cylinders. - Wei-jiang Chen *(Lanzhou Univ, Lanzhou, China)*, Kai Wang *(Nantong Vocational Univ, Nantong, China)*, Ren-ji Tang *(Shanghai Jiaotong Univ, Shanghai, China)*. Appl Math Mech 14(4) 307-312 (Apr 1993).

Using the single crack solution and the regular solution of harmonic function, the torsion problem of a cracked cylinder is reduced to solving a set of mixed-type integral equations which can be solved by combining the numerical method of singular integral equation with the BEM. Several numerical examples are calculated and the stress intensity factors are obtained.

See also the following:

11A438. Comparison of standard measurement methods for critical stress intensity factor K_{Ic} for metals and rock

11A871. Thermally induced stress intensity factor of a semi-circular surface crack in a half-space

276E. VISCOELASTIC PROBLEMS

11A399. Failure of structures due to crack growth and damage. - LV Nikitin *(Geomech Div, Inst of Earth Phys, Russian Acad of Sci, 10 B Gruzinskaya 123810, Moscow, Russia)*. Struct Safety 12(2) 123-128 (Jun 1993).

Crack growth and damage in viscoelastic bodies are studied. Using the Sih criterion of fracture the safe and critical loads as well as delaytime of rupture for structure with a crack are determined. Damage is studied on the base of the energy approach. Evolution of damage, the threshold stress, delay time and limiting damage and strain in a rod under action of a constant load are found.

11A400. Stable crack growth in rate-dependent materials with damage. - L-O Fager *(Ericsson Network Eng AB, S-175 26 Jarfalla, Sweden)* and JL Bassani *(Dept of Mech Eng and Appl Mech, Univ of Pennsylvania, Philadelphia PA 19104)*. J Eng Mat Tech 115(3) 252-261 (Jul 1993).

A cohesive zone model of the Dugdale-Barenblatt type is used to investigate crack growth under small-scale-creep and damage conditions. The material inside the cohesive zone is described by a power-law viscous overstress relation modified by a one-parameter damage function of the Kachanov type. The stress and displacement profiles in the cohesive zone and the velocity dependence of the fracture toughness are investigated. It is seen that the fracture toughness increases rapidly with the velocity and asymptotically approaches the case that neglects damage.

See also the following:

11A355. Creep-fatigue properties of Mod 9Cr-1Mo steel under variable straining

276F. CRACK TIP PLASTICITY PROBLEMS

11A401. Applicability of local approaches for the determination of the failure behavior of ductile steels. - K Kussmaul, U Eisele, M Seidenfuss *(Staatiche Materialprufungsanstalt (MPA), Univ of Stuttgart, Stuttgart, Germany)*. J Pressure Vessel Tech 115(3) 214-220 (Aug 1993).

The strength and deformation behavior of specimens and components is, on the one hand, influenced by the local state of stress and strain, and on the other hand, by the chemical composition and the microstructure of the material used. Using two different steels, it was investigated in how far it is possible to predict the failure behavior of specimens and components equalitatively and quantitatively by means of local approaches. For this purpose, two methods differing considerably from the basic idea were chosen. For the description of the failure behavior, so-called damage models were used. These damage models try to describe numerically the process developing microscopically and finally leading to fracture by means of continuum mechanical approaches in order to calculate the macroscopical failure behavior. The results show that for ductile materials, the damage models allow a very accurate calculation of smooth and notched specimens and components. The efforts presently required for the calculation are, however, still very high. Analyses using fracture mechanics approaches (J-integral) in combination with the local stress states (multiaxiality) were performed to describe the failure behavior. With this approach, it was attempted to calculate crack initiation and maximum load of pre-cracked specimens and components. The fracture mechanics methods are to be preferred for cracked components if an engineering estimation of crack initiation and maximum load only is required since the calculation efforts of the fracture mechanics methods are much lower than those of the damage models.

11A402. Assessment of fully plastic J and Cx-integral solutions for application to elastic-plastic fracture and creep crack growth. - DR Lee and JM Bloom *(Struct Mech Section R&D Div, Babcock & Wilcox, Alliance OH 44601)*. J Pressure Vessel Tech 115(3) 228-234 (Aug 1993).

A critical part of the assessment of defects in power plant components, both fossil and nuclear, is the knowledge of the crack driving force (K_1, J, or Cx). While the determination of the crack driving force is possible using FE analyses, crack growth analyses using FEM can be expensive. Based on work by Il'yushin, it has been shown that for a power law hardening material, the fully plastic portion of the J-integral (or the Cx-integral) is directly related to an "h_1" calibration function. The value of h_1 is a function of the geometry and hardening exponent. The FE program ABAQUS was used to evaluate the fully plastic J-integral and determine the h_1 functions for various geometries. The Ramberg-Osgood deformation theory plasticity model, which may be used with the J-integral evaluation capability, allows the evaluation of fully plastic J solutions. Once it was established that the grid used to generate the h_1 functions was adequate (based on the more recent work of Shih and Goan), additional runs were made of other configurations given in the EPRI Elastic-Plastic Fracture Handbook. Differences as great as 55% were found when compared to results given in the Handbook (single edge crack plate under tension and plane stress with $a/b = 0.5$). Effects of errors in h_1 on predicted failure load and creep crack growth are discussed.

11A403. Precise and new analysis for a mode III growing crack in an elastic-perfectly plastic solid. - Zhi-jian Yi *(Bridge and Struct Eng, Chongqing Jiaotong Inst, Chongqing, China).* Appl Math Mech 14(4) 345-352 (Apr 1993).

The near crack line field analysis method has been used to investigate into Mode III quasistatically propagating crack in an elastic-perfectly plastic material. The significance of this paper is that the usual small scale yielding theory has been broken through. By obtaining the general solutions of the stresses and the displacement rate of the near crack line plastic region, and by matching the general solution with the precise elastic fields (not the usual elastic K-dominant fields) at the elastic-plastic boundary, the precise and new solutions of the stress and deformation fields, the size of the plastic region and the normal vector of the elastic-plastic boundary have been obtained near the crack line. The solutions of this paper are sufficiently precise near the crack line region because the roughly qualitative assumptions of the small scale yielding theory have not been used and no other roughly qualitative assumptions have been taken, either. The analysis of this paper shows that the assumingly "steady-state case" for stable crack growth, which has been discussed attentively in previous works, do not exist, and the plastic strains near the crack line do not have singularities. Two most important cases for stable crack growth have been discussed.

11A404. Rigid body rotation near mode I crack in infinite orthotropic plate. - A Bhattacharya *(Dept of Mech Eng, IT, Banaras Hindu Univ, Varanasi 221 005, India).* Eng Fracture Mech 45(4) 451-461 (Jul 1993).

Rigid body rotation is obtained at the points near the crack tip of a mode I crack in an infinite orthotropic plate. Using Lekhnitskii's complex analysis procedure the rotation is expressed in terms of complex potentials. A relation of rigid body rotation is presented by incorporating the stress intensity factor and material constants of orthotropic material. Crack opening displacement is obtained from the rotation of points lying on crack edges and the crack tip opening angle is shown to depend only on material parameters. The region of constant rotation around the crack tip plastic zone is described in the light of the difference between isotropic and orthotropic materials.

11A405. Supplementary study on anisotropic plastic stress fields at a stationary plane-stress crack-tip. - Bai-song Lin *(Central S Univ of Tech, Changsha, China).* Appl Math Mech 14(5) 429-436 (May 1993).

The results in Ref [1] are not suitable for the cases of $a \geq 2$. For this reason, we use the method in Ref [1] to derive the general expressions of the anisotropic plastic stress fields at a stationary plane-stress crack-tip for both the cases of $\alpha=2$ and $\alpha>2$. As an example, we give the analytical expressions of the anisotropic plastic stress fields as the stationary tips of mode I and mode II plane-stress cracks for the case of $\alpha=2$.

11A406. Time dependent fracture and cohesive zones. - WG Knauss *(Graduate Aeronaut Lab, California IT, Pasadena CA).* J Eng Mat Tech 115(3) 262-267 (Jul 1993).

This presentation is concerned with the fracture response of materials which develop cohesive or bridging zones at crack tips. Of special interest are concerns regarding crack stability as a function of the law which governs the interrelation between the displacement(s) or strain across these zones and the corresponding holding tractions. It is found that for some materials unstable crack growth can occur, even before the crack tip has experienced a critical COD or strain across the crack, while for others a critical COD will guarantee the onset of fracture. Also shown are results for a rate dependent nonlinear material model for the region inside of a craze for exploring time dependent crack propagation of rate sensitive materials.

See also the following:

11A369. Modeling of loading rate effect on fatigue crack growth

276J. COMPOSITES

11A407. Criterion for splitting crack initiation in unidirectional fiber-reinforced composites. - Keiichiro Tohgo *(Dept of Mech Eng, Shizuoka Univ, Hamamatsu 432, Japan),* Albert SD Wang *(Dept of Mech Eng and Mech, Drexel Univ, Philadelphia PA 19104),* Tsu-Wei Chou *(Center for Composite Mat and Dept of Mech Eng, Univ of Delaware, Newark DE 19716).* J Composite Mat 27(11) 1054-1076 (1993).

Unidirectional fiber-reinforced composites exhibit a high degree of anisotropy in strength. Crack initiation from a pre-existing crack almost always occurs along the fiber direction; it is known as the *splitting crack*. One criterion for the splitting crack initiation under mixed mode condition is proposed. In this criterion, the splitting crack initiation is characterized by a unique interaction curve on the K^f_σ-K^f_τ plane, where K^f_σ and K^f_τ are the tensile and shear stress intensity factors along the fiber direction. Fracture toughness tests under mixed mode loading are systematically carried out on two graphite-epoxy systems: AS4/3501-6 and IM7/8551-7. For both composites, the condition of the splitting crack initiation can be characterized by a vertical line of K^f_σ = constant on the K^f_σ-K^f_τ plane. This means that the tensile stress intensity factor along the fiber direction is responsible for the splitting crack initiation. Furthermore, it is found that under the conditions of $K^f_\sigma = 0$ or $K^f_\sigma < 0$, damage occurs at locations away from the tip of the preexisting crack initiation and that the fracture toughness under such conditions is high.

11A408. Fracture Mech of Ti/Al_2O_3 interfaces. - HF Wang, WW Gerberich *(Dept of Chem Eng and Mat Sci, Univ of Minnesota, Minneapolis MN 55455),* CJ Skowronek *(Metal Matrix Composites Program, 3M, St Paul MN 55144).* Acta Metall Mat 41(8) 2425-2432 (Aug 1993).

Measurement of mixed mode interfacial fracture toughness in Ti/Al_2O_3, bimaterial couples has been accomplished by four-point bending tests of sandwich specimens with symmetrical cracks for different processing temperatures and thickness of Ti interlayers. Fracture surfaces and sample cross sections were analyzed by SEM, XPS, EDAX, EPMA and AES. The interfacial fracture toughness measured with four-point bending tests increases with increasing applied bonding temperature up to 950°C. Above this temperature toughness decreases. The deterioration of toughness is found to be due to an intermetallic phase (Ti_3Al) produced by diffusion at high temperature. The interfacial fracture toughness also increases when the Ti interlayer is thicker. The measured critical strain energy release rate (or interfacial fracture energy) ranges from 10 to 45 J/m^2. This is much larger than the estimated true work of adhesion which is about 2 J/m^2. This is because of plastic energy dissipation in the Ti interlayer during the fracture process.

11A409. Fracture mechanics of orthotropic laminated plates I. The through crack problem. - Binghua Wu and F Erdogan *(Dept of Mech Eng, Lehigh Univ, Bldg No 19, Bethlehem PA 18015).* Int J Solids Struct 30(17) 2357-2378 (1993).

In this paper a laminated plate which consists of an arbitrary number of dissimilar orthotropic layers under membrane and bending loads is considered. The plate is assumed to have a through crack. The problem is formulated by using Mindlin's first order shear deformation theory and a higher order theory due to Reddy. The sample solutions obtained from these two theories, from the classical theory, and from Reissner's stress-based first order theory shows that the stress intensity factors given by the classical theory are highly inaccurate and the three transverse shear deformation theories give roughly the same results. Because of the nonhomogeneous nature of the medium under consideration, the simpler of the two displacement-based shear deformation theories was adopted to carry out the solution of the crack problem in the laminated plates. The main objective of the study is to investigate the influence of the material orthotropy, various stiffness ratios, and relative dimensions concerning the crack size and laminae thicknesses on the stress intensity factors. Only the mode I crack problem is considered. It is shown that if the laminate has a material symmetry with respect to the midplane of the plate, then the membrane and bending solutions of the problem are fully uncoupled.

11A410. Fracture mechanics of orthotropic laminated plates II. The plane strain crack problem for two bonded orthotropic layers. - Binghua Wu and F Erdogan *(Dept of Mech Eng, Lehigh Univ, Bldg No 19, Bethlehem PA 18015).* Int J Solids Struct 30(17) 2379-2391 (1993).

In this paper the plane strain problem for two bonded orthotropic layers containing a crack perpendicular to the laminate surfaces is considered. After deriving the integral equation for the general problem, the solution is obtained for three main crack geometries, namely an embedded crack, a surface crack and a crack terminating at the interface under a remotely applied membrane load or bending moment. For the crack terminating at the interface the necessary asymptotic analysis is carried out, the characteristic equation to determine the power of stress singularity β is obtained, and the influence of the material parameters on β is examined. The main results given in the paper consist of the stress intensity factors obtained for various crack geometries, material combinations and loading conditions.

11A411. Fracture mechanics of orthotropic laminated plates III. The surface crack problem. - Binghua Wu and F Erdogan *(Dept of Mech Eng, Lehigh Univ, Bldg No 19, Bethlehem PA 18015).* Int J Solids Struct 30(17) 2393-2406 (1993).

In this paper the line spring model originally developed to treat the surface crack problems in homogeneous plates is extended to laminates which may consist of bonded isotropic or orthotropic dissimilar elastic layers. By using the two fundamental solutions for a laminate with a through crack and the corresponding plane strain problem for an edge crack, the surface crack problem in laminates is reduced to a system of singular integral equations. Sample results showing the stress intensity factors are given for bonded orthotropic and isotropic layers which correspond to fiber-reinforced structural composites and ceramic-coated metal substrates, respectively.

11A412. Influence of grain size on the toughness of monolithic ceramics. - AF Bower and M Ortiz *(Div of Eng Solid Mech Program, Brown Univ, Providence RI 02917).* J Eng Mat Tech 115(3) 228-236 (Jul 1993).

Experiments have shown that there may be an optimal grain size which maximizes the toughness of polycrystalline ceramics. In this paper, we attempt to develop a theoretical model which can predict the effect of grain size on the toughness of ceramics. We assume that three principal mechanisms affect the toughness of the material: distributed microcracking; crack trapping by tough grains; and frictional energy dissipation as grains are pulled out in the wake of the crack. The grain size influences these mechanisms in several ways. The energy dissipated due to frictional crack bridging increases with the size of the bridging grains, tending to improve toughness. However, as the grain size increases, the density of microcracks in the solid also increases, which eventually weakens the material. In addition, the level of inter-granular residual stress is also reduced by microcracking, which as a detrimental effect on the toughening due to bridging. We have developed a simple model to quantify these effects. However, the model does not predict the dramatic loss of strength which has been observed to occur beyond a critical grain size. We have therefore proposed an alternative explanation for the apparent decrease in toughness in coarse grained ceramics. Calculations indicate that in a coarse grained material, the main contribution to toughness is due to frictional crack bridging. However, to produce this toughening, the bridging zone must be over 500 grains long. In practice, the length of the bridging zone in a coarse grained solid may be comparable to the dimensions of the specimen used to measure its toughness. Under these conditions, it is not appropriate to use the concept of a geometry independent toughness to characterize the strength of the specimen. We have therefore developed a simple model of a double cantilever beam fracture specimen, which accounts for the effects of large scale bridging. Using this model, we are able to prdict the apparent decrease in toughness measured in coarse grained specimens.

11A413. **Notch ductile-to-brittle transition due to localized inelastic band.** - Z Suo, S Ho, X Gong *(Mech and Env Eng Dept, UC, Santa Barbara CA 93106-5070)*. J Eng Mat Tech 115(3) 319-326 (Jul 1993).

Holes are often drilled in a panel for cooling or fastening. For a panel made of a monolithic ceramic, such a hole concentrates stress, reducing load-carrying capacity of the panel by a factor of 3. By contrast, for a ductile alloy panel, plastic flow relieves stress concentration so that the small hole does not reduce load-carrying capacity. A panel made of ceramic-matrix composite behaves in the middle: matrix cracks permit unbroken fibers to slide against friction, leading to inelastic deformation which partially relieves stress concentration. Load-carrying capacity is studied in this paper as an outcome of the competition between stress concentration due to the notch, and stress relaxation due to inelastic deformation. The inelastic deformation is assumed to be localized as a planar band normal to the applied load, extending like a bridged crack. The basic model is large-scale bridging. A material length, $\delta_0 E/\sigma_0$, scales the size of the inelastic band, where σ_0 is the unnotched strength, δ_0 the inelastic stretch at the onset of rupture, and E Young's modulus. Load-carrying capacity is shown to depend on notch size a, measured in units of $\delta_0 E/\delta_0$. Calculations presented here define the regime of notch ductile-to-brittle transition, where ceramic-matrix composites with typical notch sizes would lie. Both sharp notches and circular holes are considered. The shape of the bridging law, as well as matrix toughness, is shown to be unimportant to load-carrying capacity.

11A414. **Role of crack wake toughening on elevated temperature crack growth in a fiber reinforced ceramic composite.** - SV Nair and Tsung-Ju Gwo *(Dept of Mech Eng, Univ of Massachusetts, Amherst MA 01003)*. J Eng Mat Tech 115(3) 273-280 (Jul 1993).

Theoretical models were developed to predict the nature of the elevated temperature failure behavior in composites containing bridged cracks both for the case where crack front creep is absent (brittle regime) and for the case where a frontal creep process zone is present (ductile regime). The nature of the thermally activated time-dependent bridging of matrix cracks was first briefly reviewed from an earlier study and then applied to the case where crack front creep was present. Stable crack growth was predicted both in the presence and absence of crack front creep after an initial delay period, or initiation, which depends on crack size and wake parameters, such as, fiber diameter, volume fraction and interface properties. The dependence of the initiation time and crack growth rates on flaw size and wake parameters as well as on composite microstructure was derived both for the presence and absence of crack front creep. The implications of the results for elevated temperature composite component design are discussed.

11A415. **Stochastic viscoelastic delamination onset failure analysis of composites.** - HH Hilton *(Dept of Aeronaut and Astronaut Eng, Univ of Illinois, 18 Transportation Bldg, Urbana IL 61801-2997)* and Sung Yi *(Natl Center for Supercomput Appl, Univ of Illinois, 4113 Beckman Institute, Urbana IL 61801)*. J Composite Mat 27(11) 1097-1113 (1993).

The previously formulated deterministic viscoelastic quadratic time dependent delamination onset criterion is generalized to complete 3D stochastic environments. The analysis includes stochastic processes due to combined random loads and random delamination failure stresses as well as random anisotropic viscoelastic material properties including the influence of stochastic temperature fields, moisture contents and boundary conditions. It is shown that times for delamination onset occurrences in composites can be predicted probabilistically depending on any one or all of the above conditions. Illustrative examples are presented showing the relationship in terms of parametric variations between times to delamination and corresponding probabilities that such events will occur. Since uniaxial tension, compression, and shear viscoelastic delamination failure stresses decrease in time, the loading history is of significant importance. For cases where deterministic criteria predict no delamination failures, the present stochastic failure theory indicates high probabilities of failure at either early or long times depending on the load-time relations. The early time high probabilities of delamination onset predict short lifetimes and occur in conditions where the composite internal stresses relax at faster rates than the failure stresses are degrading. The effects of fiber orientation and of number of plies on delamination probabilities are also examined.

11A416. **Thermally induced interfacial microcracking in polymer matrix composites.** - DL Hiemstra *(Prince Corp, 1 Prince Center, Holland MI 49423)* and NR Sottos *(Dept of Theor and Appl Mech, Univ of Illinois, Urbana IL 61801)*. J Composite Mat 27(10) 1030-1051 (1993).

Novel experiments on a cluster of fibers combined with FE analysis was utilized to investigate the influence of both inter-fiber spacing and interphase properties on thermally induced microcracking. Local thermal stresses were predicted and microcracking observed as fiber spacing was systematically decreased and interphase properties were varied. Both the computational and experimental results demonstrated that interphase properties and fiber spacing alter the location of the maximum equivalent stress and the initiation of microcracks. Microcracks were predicted and observed to initiate first (at the lowest thermal load) in the case of a higher modulus interphase. The cracks initiated at the fiber-interphase interface at a lower thermal load than if no interphase were present. In contrast, computations for a low modulus interphase predicted the maximum equivalent stress to be lower than the case of no interphase and to occur in the matrix. Experimentally, microcracks were observed to initiate in the matrix at the interphase-matrix interface with higher thermal loads. The presence of the low modulus coating prevented cracks from reaching the fiber surface. Overall, the investigation demonstrated the ability of the interphase to enhance or hinder microcracking in a cluster of fibers. The interphase can be tailored to reduce the local stress state and reduce the initiation of microcracks in the composite.

11A417. **Thermally-induced interlaminar crack-tip singularities in laminated anisotropic composites.** - HJ Choi *(Korea Power Eng, Seoul, Korea)* and S Thangjitham *(Dept of Eng Sci and Mech, VPI)*. Int J Fracture 60(4) 327-347 (15 Apr 1993).

Thermally-induced stress singularities of an interlaminar crack in a fiber-reinforced composite laminate under a state of generalized plane deformation are examined within the framework of steady-state anisotropic thermoelasticity. The crack is assumed to be embedded within a matrix-rich interlaminar region of the composite. The Fourier integral transform technique and the flexibility-stiffness matrix method are introduced to formulate the current mixed boundary value problem. As a result, two sets of simultaneous Cauchy-type singular integral equations of the first kind are derived for the heat conduction and thermoelasticity. Within the context of linear elastic fracture mechanics, the mixed-mode thermal stress intensity factors are defined in terms of the solution of the corresponding integral equations. Numerical results are presented, addressing the effects of laminate stacking sequence, crack location and crack surface partial insulation on the values of thermal stress intensity factors.

11A418. **Toughening mechanisms in quasi-brittle materials.** - SP Shah and C Ouyang *(NSF Center for Sci and Tech of Adv Cement-Based Mat, NWU)*. J Eng Mat Tech 115(3) 300-307 (Jul 1993).

Fracture processes in cement-based materials are characterized by a large-scale fracture process zone, localization of deformation, and strain softening. Many studies have been conducted to understand the toughening mechanisms of such quasi-brittle materials and to theoretically model their nonlinear response. This paper summarizes two innovative experimental techniques which are being developed at the ACBM Center to better define the fracture process zone in cement-based materials. A brief summary is also given of two types of theoretical approaches which attempt to simulate some of the observed nonlinear fracture response of these materials.

11A419. **Transverse cracking in fiber-reinforced brittle matrix, cross-ply laminates.** - ZC Xia, RR Carr, JW Hutchinson *(Div of Appl Sci, Harvard Univ, Cambridge MA 02138)*. Acta Metall Mat 41(8) 2365-2376 (Aug 1993).

The topic addressed in this paper is transverse cracking in the matrix of the 90° layers of a cross-ply laminate loaded in tension. Several aspects of the problem are considered, including conditions for the onset of matrix cracking, the evolution of crack spacing, the compliance of the cracked laminate, and the overall strain contributed by release of residual stress when matrix cracking occurs. The heart of the analysis is the plane strain problem for a doubly periodic array of cracks in the 90° layers. A fairly complete solution to this problem is presented based on FE calculations. In addition, a useful, accurate closed form representation is also included. This solution permits the estimation of compliance change and strain due to release of residual stress. It can also be used to predict the energy release rate of cracks tunneling through the matrix. In turn, this energy release rate can be used to predict both the onset of matrix cracking and the evolution of crack spacing in the 90° layers as a function of applied stress. All these results are used to construct overall stress-strain behavior of a laminate undergoing matrix cracking in the presence of initial residual stress.

See also the following:

11A16. FE analysis of progressive failure for laminated FRP plates with inplane loading

11A274. Study on the application of work factor approach to composite laminates
11A363. Cyclic near-tip fields for fatigue cracks along metal-metal and metal-ceramic interfaces

276L. OTHER ANISOTROPIC AND NONHOMOGENEOUS MEDIA

11A420. Coplanar cracks in a finite rectangular anisotropic elastic slab under antiplane shear stresses: A hypersingular integral formulation. - WT Ang and G Noone *(Dept of Appl Math, Univ of Adelaide, Adelaide SA 5001, Australia)*. Eng Fracture Mech 45(4) 431-437 (Jul 1993).

An antiplane crack problem concerning an arbitrary number of pairs of coplanar cracks in a finite rectangular anisotropic elastic slab is considered. Using Fourier integral transforms and Fourier series, the problem is reduced to a system of Hadamard finite-part singular (hypersingular) integral equations which can be solved numerically by using a collocation technique. Once these integrals are solved, the relevant crack energy and stress intensity factors can be readily computed. Numerical results for a specific case of the problem are given.

11A421. Observation of deformation and damage at the tip of cracks in adhesive bonds loaded in shear and assessment of a criterion for fracture. - H Chai *(Dept of Mech Mat and Struct, Sch of Eng, Tel-Aviv Univ, Tel-Aviv, Israel)*. Int J Fracture 60(4) 311-326 (15 Apr 1993).

The evolution of damage at the tip of cracks in adhesive bonds deforming in shear was monitored in real time using a high-magnification video camera. Brittle and a ductile epoxy resins were evaluated, with the bond thickness t being an experimental variable. An extensive zone of plastic deformation developed ahead of the crack tip prior to fracture. In the case of the brittle adhesive, for relatively thick bonds tensile microcracks formed within that zone. Increased loading caused the microcracks to grow from the interlayer to the interface, which led to a complete bond separation after interface cracks emanating from adjacent microcracks linked. In contrast, for the ductile adhesive the crack always grew away from the tip. Strain gradients tended to develop there when the bond thickness was large. The adhesive shesr strain was determined from fine lines scratched on the specimen edge. For both adhesives, the average crack tip shear strain at crack propagation rapidly decreased with increasing t. This effect was attributed to the changing sensitivity of the bond to the presence of flaws; thicker bonds can accommodate large microcracks or mircovoids which cause greater stress concentration. For a given bond thickness, the critical crack tip shear strain agreed well with the ultimate shear strain of the unflawed adhesive γ_f previously determined using the napkin ring shear test. This suggests that the ultimate shear strain is a key material property controlling crack growth. The critical distortional strain energy-unit area of the unflawed adhesive W_s was determined from the area under the stress-strain curve in the napkin test ring. Good agreement between W_s and the adhesive mode II fracture energy was found for all joints tested except for relatively thick bonds. For the particular case of an elastic-perfectly plastic adhesive, the agreement above implies $G_{IIC} = W_s = t\tau_y\gamma_f$.

11A422. Rotation at the crack tip and COD of mode I crack in anisotropic plate. - A Bhattacharya *(Dept of Mech Eng, Inst of Tech, Banaras Hindu Univ, Varanasi 221 005, India)*. Int J Fracture 61(2) 131-138 (15 May 1993).

Rigid body rotation is obtained at the points near crack tip of mode I crack in infinite anisotropic plate. Using Lekhnitskii's complex analysis procedure the rotation is expressed in terms of complex potentials and complex parameters of the material. A relation of crack tip rotation is obtained by incorporating the stress intensity factor and complex parameters for the known crack configuration. An equation of crack opening displacement is derived. For the case of plates made of composite materials the features of crack tip rotation and crack edge profiles due to mode I loading are described.

See also the following:

11A388. Statistical theory of ceramic damage and fracture

276N. CRACK STABILITY AND BRANCHING

11A423. Fatigue crack growth rate in 63Sn37Pb solder joints. - Z Guo and H Conrad *(Mat Sci and Eng Dept, N Carolina State Univ, Raleigh NC 27695-7907)*. J Electron Packaging 115(2) 159-164 (Jun 1993).

Fatigue crack growth rate (FCGR) was determined in shear (Mode II) on notched 63Sn37Pb solder joints at room temperature. The FCGR data correlated reasonably well with the expression $da/dN = B(\Delta Y)^b$ where ΔY was either ΔK, ΔJ, or ΔW_p. The value of b for ΔJ and ΔW_p was similar to that generally obtained for metals in Mode I loading; however, it was 2-3 times larger in the case of ΔK. Although the fatigue cracks initiated at the centrally located notches, they soon wandered toward the solder-Cu interface and then propagated in the solder adjacent to the intermetallic compound. The fatigue crack mode was transgranular with no clear microstructure preference. The results obtained on the notched specimens are in accord with those reported previously on initially smooth specimens tested in shear.

276S. DYNAMIC CRACK PROPAGATION

11A424. Dynamic crack propagation: A literature study. - MM Banerjee *(Dept of Math, AC Col, Jalpaiguri-735 101, W Bengal, India)*, JN Das *(Dept of Phys, AC Col, Jalpaiguri-735 101, W Bengal, India)*, S Sikdar *(Belakoba HS Sch, Jalpaiguri, India)*. Int J Pressure Vessels Piping 55(3) 495-509 (1993).

Today, analysis in fracture mechanics has become so important that an international collaborative research programme in this field is being carried out. Its importance lies in the fact that the strength or the toughness of a material cannot be measured directly. Moreover, the present structures are often subjected to dynamic loading. Hence the determination of the dynamic fracture toughness values, in particular the crack arrest toughness and the initiation fracture toughness, at high loading rates has become an essential aspect of present investigations. The present work is primarily concerned with a literature survey on dynamic stress analysis, with specific attention to the determination of the stress analysis, with specific attention to the determination of the stress intensity factor K for three-point bending specimens. Future areas of investigation have been discussed.

11A425. FE analysis of plane strain dynamic crack growth in materials displaying the Bauschinger effect. - R Narasimhan *(Dept of Mech Eng, IISc, Bangalore 560012, India)* and CS Venkatesha *(Government Col of Eng, Davangere 577004, India)*. Int J Fracture 61(2) 139-157 (15 May 1993).

In this paper dynamic crack growth in an elastic-plastic material is analyzed under mode I plane strain small-scale yielding conditions using a FE procedure. The main objective of this paper is to investigate the influence of anisotropic strain hardening on the material resistance to rapid crack growth. To this end, materials that obey an incremental plasticity theory with linear isotropic or kinematic hardening are considered. A detailed study of the near-tip stress and deformation fields is conducted for various crack speeds. The results demonstrate that kinematic hardening does not oppose the role of inertia in decreasing the plastic strains and stresses near the crack tip with increase in crack speed to the same extent as isotropic strain hardening. A ductile crack growth criterion based on the attainment of a critical crack opening displacement at a small microstructural distance behind the tip is used to obtain the dependence of the theoretical dynamic fracture toughness with crack speed. It is found that for any given level of strain hardening, the dynamic fracture toughness displays a much more steep increase with crack speed over the quasistatic toughness for the kinematic hardening material as compared to the isotropic hardening case.

11A426. Process region influence on energy release rate and crack tip velocity during rapid crack propagation. - E Johnson *(Dept of Solid Mech, Lund IT, Lund Univ, Box 118, S-221 00 Lund, Sweden)*. Int J Fracture 61(2) 183-187 (15 May 1993).

A FE model of a plate with an edge crack is investigated. A cell mode of the material, with the cell size representing some characteristic intrinsic material length, is adopted. The size of the process region depends on the number of cells that have reached a state which is unstable at load control. The results show that the growth of the process region is a main factor responsible for the lack of a unique relation between the small scale yielding energy release rate and the crack tip velocity and also for the observed constant crack velocities that are significantly below the Rayleigh wave velocity. A rapidly propagating crack appears to meet an increase of the energy flow to the crack edge per unit of time by increasing the size of the process region rather than increasing its edge velocity.

276W. MICROMECHANISMS

11A427. Microcracking of an internally pressurized ceramic ring. - M Olsson and AE Giannakopoulos *(Dept of Solid Mech, RIT, S-100 44 Stockholm, Sweden)*. Acta Metall Mat 41(8) 2353-2364 (Aug 1993).

In the present work we investigated experimentally a thick ring configuration of Al_2O_3 ceramic subjected to internal pressure. Non-transforming ceramic of this type may exhibit stress induced microcracking. We model this possible microcracking process with an anisotropic damage constitutive equation. We solved the appropriate boundary value problem explicitly. Based on the experimental strain-load curve and the predictions of the model, we attemped to resolve the stress-strain behavior of a specific, coarse grained Al_2O_3 ceramic. The present results deal with the mechanics of the test. Some electron microscopy observation will follow. The proposed ring test can be very well used for analysis of transforming ceramics, as well as for biaxial creep.

11A428. Nanometer substructures and its effects on ductility and toughness at room temperature in nickel-rich NiAl. - Tianyi Cheng *(Metal Mat Section, Beijing IT, PO Box 327, Beijing 100081, Peoples Rep of China)*. Nanostruct Mat 2(1) 19-27 (Jan-Feb 1993).

A nanometer substructure in a rapidly solidified Ni-34.6 at% Al alloy with an average grain size of 2.2 μm was achieved and investigated. It was found that the nanometer substructures, in addition to fine grains, led to many interfaces with high density and homogeneous distribution, which played an effective role in improving the ductility and toughness of the NiAl at room temperature. The mechanism and a new definition of the nanostructured materials were discussed.

276Y. COMPUTATIONAL TECHNIQUES

11A429. BE formulation for the inverse elastostatics problem (IESP) of flaw detection. - LM Bezerra and S Saigal *(Dept of Civil Eng, Carnegie Mellon Univ, Pittsburgh PA 15213).* Int J Numer Methods Eng 36(13) 2189-2202 (15 Jul 1993).

A boundary integral formulation is presented for the detection of flaws in planar structural members from the displacement measurements at some boundary locations and the applied loadings. Such inverse problems usually start with an initial guess of the flaw location and size and proceed towards the final configuration of a sequence of iterative steps. A FE formulation will require a remeshing of the object corresponding to the revised flaw configuration in each iteration making the procedure computationally expensive and cumbersome. No such remeshing is required for the BE approach. The inverse problem is written as an optimization problem with the objective function being the sum of the squares of the differences between the measured displacements and the computed displacements for the assumed flaw configuration. The geometric condition that the flaw lies within the domain of the object is imposed using the internal penalty function approach in which the objective function is augmented by the constraint using a penalty parameter. A first-order regularization procedure is also implemented to modify the objective function in order to minimize the numerical fluctuations that may be caused in the numerical procedure due to errors in the experimental measurements for displacements. The flaw configuration is defined in terms of geometric parameters and the sensitivities with respect to these parameters are obtained in the BE framework using the implicit differentiation approach. A series of numerical examples involving the detection of circular and elliptic flaws of various sizes and orientations are solved using the present approach. Good predictions of the flaw shape and location are obtained.

11A430. Collapsed isoparametric element as a singular element for a crack normal to the bimaterial interface. - Yong-Li Wu *(Inst of Mech, Chinese Acad of Sci, Beijing 100080, Peoples Rep of China).* Comput Struct 47(6) 939-943 (17 Jun 1993).

It is shown that the variable power singularity of the strain field at the crack tip can be obtained by the simple technique of collapsing quadrilateral isoparametric elements into triangular elements around the crack tip and adequately shifting the side-nodes adjacent to this crack tip. The collapsed isoparametric elements have the desired singularity at crack tip along any ray. The strain expressions for a single element have been derived and in addition to the desired power singularity, additional singularities are revealed. Numerical examples have shown that triangular elements formed by collapsing one side lead to excellent results.

11A431. Compliance of three-point bend round beam specimens calculated with the slice synthesis method. - Wang Qizhi and Xian Xuefu *(Dept of Resources and Env Eng, Chongqing Univ, Sichuan 630044, Peoples Rep of China).* Eng Fracture Mech 45(4) 547-550 (Jul 1993).

The compliance of two kinds of three-point bend (3PB) round bend specimens is calculated with the slice synthesis method. In this method, the round beam is divided into a number of slices, and every slice is considered as a 3PB beam with a rectangular cross-section for which the compliance is known, then these slices are combined together to give the compliance of the round beam. The calculated results have shown good accuracy. It is postulated that the slice synthesis method can be used to obtain the compliance of bend specimens with a circular cross-section and various crack front shapes.

11A432. Cracks of fractal geometry with unilateral contact and friction interface conditions. - PS Theocaris *(Natl Acad of Athens, PO Box 77230, 17510 Athens, Greece)* and PD Panagiotopoulos *(Dept of Civil Eng, Aristotle Univ, 54006 Thessaloniki, Greece).* Int J Fracture 60(4) 293-310 (15 Apr 1993).

Structures involving cracks of fractal geometry are studied here, on the assumption that at the interface unilateral contact and friction boundary conditions hold. Approximating the fractal by a sequence of classical surfaces or curves and combining this procedure with a two-level contact-friction algorithm based on the optimization of the potential and of the complementary energy, we get the solution of the problem after some appropriate transformations relying on the SVD-decomposition of the equilibrium matrix. Numerical examples, using singular elements for the consideration of the crack singularity, illustrate the theory.

11A433. Finite-part integral and BEM to solve embedded planar crack problems. - TY Qin and RJ Tang *(Shanghai Jiao Tong Univ, Shanghai, Peoples Rep of China).* Int J Fracture 60(4) 373-381 (15 Apr 1993).

Using the Somigliana formula and concepts of the finite-part integral, a set of hypersingular integral equations to solve the arbitrary flat crack in 3D elasticity is derived, then its numerical method is proposed by combining the finite-part integral method with the BEM. In order to verify the method, several numerical examples are carried out. The results of the displacement discontinuities of the crack surface and the stress intensity factors at the crack front are in good agreement with the theoretical solutions.

11A434. Interface crack under combined loading: An eigenvalue problem for the gap. - AK Gautesen *(Ames Lab and Dept of Math, Iowa State Univ, Ames IA 50011).* Int J Fracture 60(4) 349-361 (15 Apr 1993).

To avoid the ductility of overlapping material near the crack tips, the tips of the crack are assumed to be closed (the Comninou model). The exact series solution to the problem of the interface crack under combined loading is complicated, and it is difficult to take advantage of the smallest of the left contact zone to obtain simple asymptotic approximations to the quantities of physical interest. Here, the gap is shown to satisfy an eigenvalue problem. The method of matched inner and outer expansions is used to obtain a simple uniform approximation to this quantity. Similar results are obtained for the tangential shift, which satisfies the same differential equation as the gap. The tractions at the interface also satisfy a second order differential equation and simple uniform approximations are obtained for these quantities.

11A435. Simple models of rapid fracture. - M Marder *(Center for Nonlinear Dyn and Dept of Phys, Univ of Texas, Austin TX 78712).* Physica D 66(1-2) 125-134 (Jun 1993).

The purpose of this article is to introduce the physics of fracture through simple scaling analysis and 1D models. Two 1D models are discussed. The first is a continuum model, for which it is simple to find the steady states and establish linear stability. The second model is a lattice version of the first, and its steady states can be found by the Wiener-Hopf technique. The lattice model steady states involves large quantities of radiation, and may help to explain dynamics observed in some recent unexplained experiments.

11A436. Strain energy release rates for internal cracks in rubber blocks. - Y-W Chang, AN Gent, J Padovan *(Inst of Polymer Eng, Univ of Akron, Akron OH 44325-0301).* Int J Fracture 60(4) 363-371 (15 Apr 1993).

Strain energy release rates have been calculated by FE analysis for growth of a small crack in a cylindrical rubber block under tension. The crack was assumed to lie in the center of the block in a plane perpendicular to the axis. The rubber was taken to be virtually incompressible in bulk and non-linearity elastic. Only small changes were found in the stress-concentrating effect of the crack for imposed tensile strains of up to 150%. Secondly, the rubber cylinder was assumed to be bonded between two parallel flat rigid plates. The stress-concentrating effect of the crack was found to increase markedly as the thickness of the bonded rubber block was reduced, but again it was only slightly dependent on the applied tensile strain.

See also the following:

11A19. Numerical analysis of IPIRG cracked pipe experiments subjected to dynamic and cyclic loading
11A296. Study of elastic behavior of plates containing cracks by FE analysis
11A390. FE alternating approach to the bending of thin plates containing mixed mode cracks

276Z. EXPERIMENTAL TECHNIQUES

11A437. Automated procedure for determining crack opening level from differential displacement signal data. - Chung-Youb Kim and Ji-Ho Song *(Dept of Autom and Design Eng, Korea Adv Inst of Sci and Tech, 207-43, Cheongryangridong, Dongdaemoongu, Seoul 130-012, Korea).* Int J Fatigue 15(4) 301-309 (Jul 1993).

The crack opening point is commonly measured from load-displacement records or load-differential displacement records. In this study, an automated method is developed to determine the crack opening point from differential displacement signal curves. To improve measurement precision, a noise reduction method using a digital low-pass filter was employed. In order to assess the measurement accuracy and precision of the proposed method, computer simulation was extensively performed, generating differential displacement signals of various S-N ratios. The measured results of crack opening points for these simulated signals show good accuracy and precision. The proposed method was applied in practice to constant-amplitude loading, and two kinds of random loading: narrow- and wide-band random loading. As a result, the method is found to be very effective even for random loadings.

11A438. Comparison of standard measurement methods for critical stress intensity factor K_{Ic} for metals and rock. - M Sklodowski *(Inst of Fund Tech Res, Polish Acad of Sci, Warszawa, Poland).* Arch Civil Eng 38(3) 223-238 (1992).

Methodology of measurements of critical stress intensity factors K_{Ic} as given in ASTM E399 for metals is compared with that suggested by the Commission on Testing Methods ISRM for rocks. Standard geometries of specimens are shown. Special attention is drawn to the differences in the methodology of measurements, important for the interpretation of experimental results and evaluation of their correctness.

11A439. Revisit to the determination of stress-intensity factors and J-integrals using the caustics method. - OS Lee, SK Hong, YS Kim *(Inha Univ, 253 Yong-Hyun Dong, Nam-Ku, Inchon 402-751, Korea).* Exp Mech 33(2) 133-138 (Jun 1993).

Applications of the optical (shadow) method of reflective caustics to measurement of the stress-intensity factor and J integral in various specimens are investigated. The necessary experimental requirements to help determine accurate stress-in-tensity factor and J integral are described. The ratios of r_0 (radius of initial curve)-r_p(plastic-zone size) and r_0-t(thickness of specimen) are found to be very important experimental parameters to obtain meaningful stress and/or strain intensities surrounding crack tips. The appropriate ranges to determine accurate values of stress-intensity factor and J integral for polycarbonate (compact tension) and aluminum (c-shaped tension) specimens are presented.

11A440. Test specimen with constant stress intensity factor for prescribed displacement. - HL Groth *(R&D, Avesta Sheffield AB, S-774 80 Avesta, Sweden)* and D Zenkert *(Dept of Aeronaut Struct and Mat, RIT, S-100 44 Stockholm, Sweden)*. Int J Fracture 61(2) 173-181 (15 May 1993).

A test specimen has been developed that gives a constant value of the stress intensity factor in mode I under fixed displacement loading conditions. The test specimen is a double contoured cantilever beam specimen whose shape is derived from engineering beam theory. A final shape for a range of crack extensions where stress intensity is constant was established using a FE analysis. It is believed that this specimen could be useful for many applications where a constant stress intensity factor is needed over a range of crack extension for constant displacment loading, eg, viscoelastic crack growth in an adhesive layer of stress corrosion cracking.

See also the following:

11A447. New trends in optical methods for experimental mechanics Part II. High sensitivity grating interferometry for in-plane displacement measurement

280. Materials testing and stress analysis

280B. SINGLE AND COMBINED LOADINGS

11A441. Filtering of the experimental data in plane stress and strain fields. - SA Lukasiewicz *(Univ of Calgary, 2500 University Dr, Calgary, AB, T2N 1N4, Canada)*, M Stanuszek *(Comput Center, Tech Univ, Cracow 21-155, Poland)*, JA Czyz *(NOWSCO Pipeline Surveys and Services, Calgary, AB, Canada)*. Exp Mech 33(2) 139-147 (Jun 1993).

The paper presents a filtering algorithm which corrects the results of measurements of strain and stress fields in order to satisfy the fundamental equations of the continuum. It is proved that the algorithm is very efficient and requires small computational time. The developed filter can be used to correct the measuring data from any experiments provided some additional information about the measured system is available.

280G. DETERMINATION OF ELASTIC CONSTANTS

See the following:

11A229. On-line determination of texture-dependent materials properties

280H. REPEATED LOADING (FATIGUE)

11A442. Micromechanical fatigue testing. - JA Connally *(Cummins Engine, 1900 McKinley Ave, Columbus IN 47202)* and SB Brown *(Rm 8-106, MIT)*. Exp Mech 33(2) 81-90 (Jun 1993).

This paper describes the design, modeling, and experimental test results of a single crystal silicon micromechanical device developed to evaluate fracture and fatigue of silicon based micromechanical devices. The structure is a cantilever beam, 300 microns long, with a large silicon plate and gold inertial mass at the free end. Torquing and sensing electrodes extend over the plate, and with associated electronics, drive the structure at resonance. Fatigue crack propagation is measured by detecting the shift in the natural frequency caused by the extension of a preexisting crack introduced near the fixed end of the cantilever. Experimental data are presented demonstrating time-dependent crack growth in silicon. Crack extensions of 10 to 300 nm have been measured with a resolution of approximately 2.5 nm, and crack tip velocities as low as 2.1×10^{-14} m-s. It is postulated that static fatigue of the native surface silica layer is the mechanism for crack growth. The methodology established here is generic in concept, permitting sensitive measurement of crack growth in larger fatigue specimens as well.

280I. DYNAMIC LOADING (IMPACT)

See the following:

11A554. Study of the cure of adhesives using dynamic mechanical analysis

280K. CREEP, RELAXATION AND PLASTIC FLOW TESTING

11A443. Photovisco-elastoplastic behavior of polycarbonate material under creep and tension tests. - MI Ait El Ferrane and A Lagarde *(Lab de Mec des Solides, 40 Ave du Recteur Pineau, 86022 Potiers Cedex, France)*. Exp Mech 33(2) 148-152 (Jun 1993).

Polymers are widely used as photomechanical models of a prototype material (often a metal). Photoplasticity is one of the methods used in order to show the behavior of plastic materials stressed beyond the linear elastic limit. To illustrate this process we have analyzed the photovisco-elastoplastic behavior of polycarbonate as a photoplastic material. In this paper a technique for local and simultaneous measurement of birefringence and principal strains is presented. The mechanical and optical properties, at room temperature, have been evaluated by means of uniaxial tension tests. A series of creep tests has been carried out in order to study the photovisco-elastoplastic behavior of polycarbonate. In two different experiments we analyzed nonlinear birefringence and the amplitude of the corresponding strains. We could thus evaluate the distribution of strains and the distribution of uniaxial stress for each birefringence state and vice versa.

See also the following:

11A261. Elastic-plastic strain analysis by photoelastic coating method

280N. HARDNESS, ABRASION, AND WEAR TESTING

11A444. Effect of residual stresses on hardness measurements. - J Frankel, A Abbate *(SMCAR-CCB-RA, Benet Labs, Watervliet Arsenal, Watervliet NY 12189-4050)*, W Scholz *(SUNY, Albany NY 12222)*. Exp Mech 33(2) 164-168 (Jun 1993).

The Rockwell C hardness, R_C, was measured as a function of position on steel rings with different residual-stress profiles through the thickness. An experimental correlation between residual stress and R_C was obtained. A relationship between the average pressure p of a spherical indenter, the yield strength Sy and the residual stress of the material was conceived and used in fitting the experimental data. In order to model the effects of residual stresses on the measured hardness, the von Mises-Hencky (power) yield criterion was utilized, together with an adaptation for residual stresses of the expression for the stress state under a spherical indenter, given in Shaw, Hoshi and Henry. A parameter α was introduced in our calculations to account for the effect of the nonperpendicularity of the residual stresses to the pressure p of the spherical indenter. The proposed model in large measure fits experimental hardness versus residual stress data, and results are consistent with different samples. This model can be used as a basis for the measurement of residual stresses in steel or other materials.

280R. OPTICAL NONDESTRUCTIVE TESTING (NDT)

11A445. Dual beam laser vibrometer for measurement of dynamic structural rotations and displacements. - MW Trethewey, HJ Sommer, JA Cafeo *(Dept of Mech Eng, Penn State)*. J Sound Vib 164(1) 67-84 (8 Jun 1993).

A novel non-contacting system for multiaxis vibration measurements (one translation and two angular deflections) is described. The system is based on monitoring the reflections of two laser beams from a planar reflective target. By utilizing the geometry of the beams and their respective reflections: range, pitch and roll of the target can be determined. The theory behind the system is discussed along with the development of a prototype device. Static and dynamic experiments are performed to determine the system's operational limits and utility. The prototype system demonstrated the capability of measuring motions up to 1 kHz with absolute accuracies of 0.04 mm for the translation variable and 0.03 degrees for the rotation variables. Measurement precision of 0.01 mm and 0.01 degrees approached the precision of the test stand and the theoretical resolution limits of the system over a usable workspace of ±2.5 mm and ±5 degrees.

11A446. New trends in optical methods for experimental mechanics Part I. Moire and grating projection techniques for shape and deformation measurement. - M Kujawinska and K Patorski *(Fac of Fine Mech, Warsaw Univ of Tech, Poland)*. J Theor Appl Mech 31(3) 539-561 (1993).

The influence of dynamic development in the field of personal computers and video techniques on optical methods used in the experimental mechanics is described. New methods of computer aided processing of the information encoded in the interferogram-moiregram patterns with special emphasis put on so-called phase methods are presented. The benefits of various modifications of the phase-stepping method are emphasized and illustrated by exemplary experimental results in the field of moire and grating projection topography used for the shape and deformation studies. The description of the equipment developed and sensitivity considerations are included.

11A447. New trends in optical methods for experimental mechanics Part II. High sensitivity grating interferometry for in-plane displacement measurement. - K Patorski and M Kujawinska *(Fac of Fine Mech, Warsaw Univ of Tech, Poland)*. J Theor Appl Mech 31(3) 563-582 (1993).

Recent developments in the high sensitivity grating interferometry for sub-micron in-plane displacement studies aiming at the automation of the data reduction process are presented. The implementation of phase methods of interferogram analysis using the polarized light approach together with the spatial carrier method are described. The versatility, speed, and accuracy of the methods and instrumentation developed are illustrated by the results of recent applications in plastic-elastic range of mechanics, fracture mechanics, and studies of composite materials.

11A448. Scanning Moire at high magnification using optical methods. - DT Read *(Mat Reliability Div, NIST, 325 Broadway, Boulder CO*

80303), JW Dally *(Mech Eng Dept, Univ of Maryland, College Park MD 20742)*, M Szanto *(Ben Gurion Univ, Beer Sheva, Israel)*. Exp Mech 33(2) 110-116 (Jun 1993).

Methods of employing scanning moire at high magnification are developed and demonstrated. Modern lithographic techniques for producing custom moire gratings with a frequency up to 250 l/mm are described. On a probing station equipped with a video system, pseudo-color moire fringes are produced using the scanning lines of the color charge-coupled-device camera. Fringe multiplication from 1 to 5 is possible with correct combinations of magnification and grating pitch. An analysis is given to show that strain sensitivity depends only on the number of scanning lines used to record the image. The grating pitch and the magnification are important because they reduce the gage length of strain measurement. The high-magnification scanning moire was used to study plastic- strain fields in an aluminum tensile specimen. Local disturbances in the strain field were observed at 2 to 2.5% applied strain. These discontinuities became more significant at high levels of applied strain.

See also the following:

11A439. Revisit to the determination of stress-intensity factors and J-integrals using the caustics method

11A874. Linear birefringence changes in betaine phosphite crystal

280S. ACOUSTIC NDT

11A449. Application of nondestructive techniques for the prediction of elastic anisotropy of a textured polycrystalline material. - CJ Yu *(Concurrent Technologies, PA 15904)*, JC Conway Jr *(Penn State)*, J Hirsch *(VAW Aluminum, Bonn, Germany)*, CO Ruud, KJ Kozaczek *(Penn State)*. J Nondestruct Eval 12(1) 79-95 (Mar 1993).

Effect of processing parameters including cold work and grain size on texture development in copper and 68:32 α-brass thin sheets is investigated. The preferred orientation of grains (texture) is represented quantitatively by the orientation distribution function (ODF) as derived either by X-ray diffraction or by ultrasonic velocity measurements. The texture-induced elastic moduli are derived in the sheet plane at various orientations to the rolling direction. The predicted values of elastic moduli are compared with the mechanically measured ones. An attempt is made to empirically correlate ODF coefficients to the mechanically measured elastic modulus and plastic strain ratio (r-value). The sources of discrepancies such as the limitations of the measuring techniques and the models applied are discussed.

11A450. Identification of partial plugging in a gas-transport pipeline by an acoustic method. - Hiroshi Koyama, Kajiro Watanabe *(Dept of Instrument and Control Eng, Col of Eng, Hosei Univ, 3-7-2 Kajinocho, Koganei, Tokyo 184, Japan)*, DM Himmelblau *(Dept of Chem Eng, Univ of Texas, Austin TX 78712)*. Appl Acoust 40(1) 1-19 (1993).

This paper describes how to locate and estimate accurately the degree of partial plugging in a gas-transport pipeline by acoustic methods. The acoustic method proposed is one of the indirect methods that identifies the inner structure of the pipeline from the acoustic standing waves introduced at one end of the pipeline by a source of noise. Both simulations and experiments have been carried out to validate the proposed technique. The method applies to straight sections of pipe without branches or leaks, and in the experiments we used pipe of length 4.113 m and uniform diameter of 16.0 mm (the cross-sectional area was 201 mm^2). Results of the experiments and simulations yielded very similar time responses, which showed clear pulses due to a partial plugging. From the shape of the pulse and the occurrence times of the pulse, the location and degree of the partial plugging could be calculated. A partial plug with an open diameter of 95% of the cross-sectional area of the pipeline was clearly located and estimated with reasonable accuracy.

11A451. Measurement of texture and formability parameters with a fully automated, ultrasonic instrument. - RB Thompson, EP Papadakis *(Center for NDE, Iowa State Univ, Ames IA 50011)*, DD Bluhm *(Ames Lab USDOE, Iowa State Univ, Ames IA 50011)*, GA Alers *(NIST)*, K Forouraghi *(Center for NDE, Iowa State Univ, Ames IA 50011)*, HD Skank *(Ames Lab, USDOE, Iowa State Univ, Ames IA 50011)*, SJ Wormley *(Center for NDE, Iowa State Univ, Ames IA 50011)*. J Nondestruct Eval 12(1) 45-62 (Mar 1993).

A fully automatic, ultrasonic instrument to measure texture and formability parameters on metal sheet is described. Arrays of EMAT transducers are used to transmit and receive S_0 Lamb waves propagating at 0°, 45°, and 90° with respect to the rolling direction. By analyzing the frequency dependence of this phase of the received signals, the long wavelength limit of the velocities is obtained. Included is a discussion of this algorithm, and subsequent processing steps to predict the ODC's W_{400}, W_{420}, and W_{440}. On steel, the prediction of drawability parameter r and Δ r based on a correlation developed previously by Mould and Johnson is also discussed. Results of blind field trials at facilities of three suppliers-users of steel sheet for automotive applications and one supplier of aluminium sheet for beverage can production are reported. The former confirmed the Mould-Johnson correlation for low r materials but indicated that refinement are needed for modern steels with high r. The aluminum data suggest a correlation between W_{440} and the degree of four-fold earing.

11A452. Methods to improve the accuracy of on-line ultrasonic measurement of steel sheet formability. - AV Clark *(Mat Reliab Div, NIST, 325 S Broadway, Boulder CO)*, Y Berlinsky *(NIST, 325 S Broadway, Boulder CO)*, N Izworski *(Ford Motor, Dearborn MI)*, Y Cohen, DV Mitrakovic *(NIST, 325 S Broadway, Boulder CO)*, SR Schaps *(Mat Res Div, NIST, 325 S Broadway, Boulder CO)*. J Nondestruct Eval 12(1) 33-43 (Mar 1993).

We report here on an ultrasonic system which quantifies factors which could degrade the resolution of the plastic strain ratio, or r-value, in sheet steel. We also present means to suppress these artifacts. We have developed a moving sheet device (MSD) to be used as a test bed to demonstrate the feasibility of on-line measurement of r-value in a steel mill. The device can move specimens at speeds comparable to those in industrial practice. An automated velocity measurement system has also been developed and integrated with the MSD. This allows ultrasonic measurements to be made with an array of transducers. Measurements were made in both static and dynamic mode. Artifacts due to sheet motion were small, and should not significantly degrade r-value resolution.

11A453. On-line measurement of plastic strain ratio of steel sheet using resonance mode EMAT. - K Kawashima, T Hyoguchi, T Akagi *(Appl Electron Lab, Electron Res Lab, Nippon Steel, 5-10-1 Fuchinobe Sagmihara, Kanagawa 229, Japan)*. J Nondestruct Eval 12(1) 71-77 (Mar 1993).

We have developed an on-line system for the measurement of plastic strain ratio of steel sheet using a thickness resonance EMAT that measures the thickness resonance frequencies of three different modes of bulk ultrasonic waves. The effective size of the EMAT is small, about 20 mm in diameter. A good correspondence was obtained between the in-plane average Young's modulus measured by this method and the in-plane average plastic strain ratio measured by tensile testing, with a standard deviation smaller than 0.04 in units of plastic strain ratio. The effects of temperature, lift-off, tensile stress, speed of the moving sheet and zinc coats were experimentally and theoretically analyzed. We show that none of them have a sizable effect on the measurement accuracy.

11A454. On-line measurement of steel sheet r-value using magnetostrictive-type EMAT. - M Hirao, H Fukuoka *(Fac of Eng Sci, Osaka Univ, Toyonaka, Osaka 560, Japan)*, K Fujisawa, R Murayama *(Syst Eng Div, Sumitomo Metal Industries, Amagasaki, Hyogo 660, Japan)*. J Nondestruct Eval 12(1) 27-32 (Mar 1993).

An ultrasonic on-line system to measure r values in cold rolled steel sheets has been developed with electromagnetic acoustic transducers (EMATs). These EMATs are composed of meanderline coils with electromagnets and operate with the magnetostrictive mechanism. The EMAT instrument measures the propagation times of the fundamental symmetrical Lamb (S_0) wave at a low frequency and relates them to the r values through a calibrated regression curve. Preliminary tests indicate that the on-line monitoring of r is quite feasible with a standard deviation of 0.07 for various low carbon steel sheets; the thicknesses range from 0.5 to 2.5 mm. The measuring time is 20 msec per data. The liftoff is allowed to 5 mm with 2 mm thick sheet. The r evaluation is independent of the line speed up to 325 m/min. These promising results promote installation of ultrasonic r-value measurement systems in steel production lines.

11A455. Ultrasonic assessment of interfacial oxidation damage in ceramic matrix composites. - YC Chu, SI Rokhlin *(Dept of Welding Eng, Ohio State Univ, Columbus OH 43210)*, GY Baaklini *(NASA Lewis Res Center, Cleveland OH 44135)*. J Eng Mat Tech 115(3) 237-243 (Jul 1993).

A new approach to characterizing oxidation damage in ceramic matrix composites using ultrasonic techniques is proposed. In this approach the elastic constants of the composite are determined nondestructively by measuring the angular dependence of both longitudinal and transverse wave velocities. A micromechanical model for composites with anisotropic constituents is used to find the anisotropic properties of an effective fiber which is a combination of the fiber and the interface. Interfacial properties are extracted from the properties of this effective fiber by analyzing the difference between effective and actual fiber properties. Unidirectional $[0]_{28}$ SiC/Si_3N_4 composites with 30% fiber volume fraction and 30% matrix porosity are used. The samples are exposed in a flowing oxygen environment at elevated temperatures, up to 1400°C, for 100 hours and then measured by ultrasonic methods at room temperature. The Young's modulus in the fiber direction of the sample oxidized at 600°C decreased significantly but it was unchanged for samples oxidized at temperatures above 1200°C. The transverse moduli obtained from ultrasonic measurements decrease continuously up to 1200°C. The shear stiffnesses show behavior similar to the transverse moduli. The effective elastic moduli of the interfacial carbon coating are determined from the experimental data and their change due to thermal oxidation is discussed.

11A456. Ultrasonic predictions of R-value in deep drawing steels. - J Savoie *(Dept of Metall Eng, McGill Univ, 3450 University St, Montreal H3A 2A7, Canada)*, D Daniel *(Centre de Rech de Voreppe SA, Pechiney, Voreppe, France)*, JJ Jonas *(Dept of Metall Eng, McGill Univ, 3450 Univ St, Montreal H3A 2A7, Canada)*. J Nondestruct Eval 12(1) 63-69 (Mar 1993).

The textures of five types of deep drawing steels were measured and analyzed using the series expansion method. Electromagnetic acoustic techniques were employed to determine the elastic anisotropy in terms of the angular variation of the ultrasonic variations. The series expansion formalism was employed for predicting the elastic and plastic anisotropies from texture data. Comparison with experimental measurements of Young's modulus indicates that the elastic energy method can accurately reproduce the elastic anisotropy if the single crystal elastic constants are appropriately chosen. The angular variation of the r-value in the rolling plane was calculated from the ODF coefficients by means of the pancake relaxed constraint model using an appropriate CRSS ratio for glide on the [112]<111> and [110]<111> slip systems. The fourth order and first sixth order ODF coefficients were calculated *nondestructively* from the anisotropy of the ultrasonic velocities. The calculated pole figures based on the ODF coefficients obtained in this way are similar to those derived from complex X-ray data. It is shown that the plastic properties of commercial deep drawing steels are predicted more accurately when the 4th- *and* 6th-order ODF coefficients are employed than when the 4th-order ones are used.

11A457. Ultrasonic technique for investigation of residual stresses in cylindrical forgings. - J Deputat, M Adamski *(Inst of Fund Tech Res, Polish Acad of Sci, Warszawa, Poland)*, J Goljasz, J Kalisiewicz *(Warszawa, Poland)*. Eng Trans 41(1) 61-76 (1993).

An ultrasonic method to examine statical stress fields in the subsurface layers of cylindrical steel forgings is described. The values of stresses are calculated from precise measurements of traveltimes of subsurface pulses of longitudinal and transverse waves propagating in the direction of generating line. Suitable apparatus is described and some results of investigation of a shipborne shaft forging with favorable and unfavorable distributions of residual stresses are shown. Longitudinal and hoop stresses in a steel mill roll are also examined.

See also the following:

11A187. Acoustic emission during nonhomogeneous tensile deformation of ARMCO-iron

280T. ELECTRICAL NDT

11A458. Finite element simulation of eddy-current flaw detection systems. - KM Gawrylczyk *(Szczecin Univ of Tech, Szczecin, Poland)*. J Tech Phys 34(2) 145-159 (1993).

A number of methods of computer simulation of eddy-current flaw detection systems have been described. As regards 2D cases, model of axial and plane-parallel symmetry have been discussed. Solutions were based on the Helmholtz equation for the magnetic vector potential A. The 3D model is based on the scalar potential ϕ. An essential novelty is the use of an impedance boundary condition for modeling eddy currents in the conducting plate and for modeling a flaw. The use of infinite elements for tetrahedrons, reduces considerably the error caused by cutting-off a part of the region. The examples shown prove the usefulness of numerical simulation of eddy-current flaw detection systems for the design and optimization of sensors. They are also applied in the domain of modern microcomputer-aided defectometers.

280U. OTHER NDT

11A459. Development of methods for on-line texture analysis. - P Blandford and JA Szpunar *(Dept of Mining and Metall Eng, McGill Univ, Montreal, PQ, Canada)*. J Nondestruct Eval 12(1) 21-26 (Mar 1993).

This work presents results obtained recently as part of the ongoing design of laboratory-scale equipment which will be used to develop and test methods for on-line texture analysis. The equipment is in the process of being built. A range of cold rolled and annealed IF deep-drawing steels were fully characterized using standard X-ray diffraction texture methods. They were then analyzed to obtain information which will be used to help optimize the measurement configuration of the laboratory-scale equipment for both a transmission and a reflection X-ray diffraction geometry. Texture measures in both geometries were then identified which are sensitive to texture changes produced by both cold rolling and annealing. The measures were then used to attempt some correlation between them and plastic properties calculated from the coefficients of the orientation distribution function. Satisfactory agreement between the texture measures and the average plasticity, R, were obtained for both the transmission and reflection geometries.

11A460. Industrial on-line texture determination in rolled steel strips. - H-J Kopineck *(Dortmund, Germany)*, R Loffel *(Loffel Verfahrenstechnik GmbH, Karlsruhe, Germany)*, H-B Otten *(Hoesch Stahl AG, Dortmund, Germany)*. J Nondestruct Eval 12(1) 13-19 (Mar 1993).

In the manufacture of sheet meal, it is of great importance that the quality should be homogeneous over the entire length of a strip. This can only be monitored using a continuous, on-line measuring method. A new X-ray transmission measuring technique has been developed for the nondestructive determination of texture-dependent technological data of rolled strip. It can be applied on-line for both hot and cold rolled metal strip, especially steel strip. The paper describes the measuring principle and gives information on the application for measuring the r_m-values and the earing-values of cold rolled steel strip. With the data from these values, the user can control the deep drawing characteristics of his strips. The extension of the basic measuring principle to a condition-free determination system will be demonstrated with its application for measuring textron dependent technological data of hot and cold rolled steel strip. Long term experience at Hoesch Stahl AG, typical results measured over the total strip length, integration in quality assurance systems, questions of maintenance etc, will be discussed.

11A461. Model for accelerated life testing. - H Strelec *(Dept of Stat, Univ of Tech Vienna, Wiedner Hauptstr 8-10, A-1040 Wien, Austria)*. Struct Safety 12(2) 129-136 (Jun 1993).

After a short motivation for the problem of extremely high reliability a nonparametric model for accelerated life testing is described. Besides well introduced classical models for high reliabilities are mentioned. Finally a stress-dependent model for crack growth based on fatigue accumulation is discussed.

See also the following:

11A205. Back-propagation learning using the trust region algorithm and application to nondestructive testing in applied electromagnetics

11A257. Crystallography-based prediction of plastic anisotropy of polycrystalline materials

11A553. Nondestructive evaluation of model adhesive joints by PVDF piezoelectric film sensors

280W. INSTRUMENTATION

11A462. Accurate measurement of 3D deformations in deformable and rigid bodies using computer vision. - PF Luo, YJ Chao, MA Sutton, WH Peters III *(Dept of Mech Eng, Univ of S Carolina, Columbia SC 29208)*. Exp Mech 33(2) 123-132 (Jun 1993).

Recently, digital-image-correlation techniques have been used to accurately determine 2D in-plane displacements and strains. An extension of the 2D method to the acquisition of accurate, 3D surface-displacement data from a stereo pair of CCD cameras is presented in this paper. A pin-hole camera model is used to express the transformation relating 3D world coordinates to 2D computer-image coordinates by the use of camera extrinsic and intrinsic parameters. Accurate camera model parameters are obtained for each camera independently by (a) using several points which have 3D world coordinates that are accurate within 0.001 mm and (b) using 2D image-correlation methods that are accurate to within 0.05 pixels to obtain the computer-image coordinates of various object positions. A nonlinear, least-squares method is used to select the optimal camera parameters such that the deviations between the measured and estimated image positions are minimized. Using multiple orientations of the cameras, the accuracy of the methodology is tested by performing translation tests. Using theoretical error estimates, error analyses are presented. To verify the methodology for actual tests both the displacement field for a cantilever beam and also the surface, 3D field displacement and strain fields for a 304L stainless-steel compact-tension specimen were experimentally obtained using stereo vision. Results indicate that the 3D measurement methodology, when combined with 2D digital correlation for subpixel accuracy, is a viable tool for the accurate measurement of surface displacements and strains.

See also the following:

11A445. Dual beam laser vibrometer for measurement of dynamic structural rotations and displacements

282. Structures (basic)

282A. GENERAL THEORY

11A463. Applications of generalized variational principles in nonlinear structural analysis. - Xiang-sheng Cheng *(Tonghi Univ, Shanghai, China)*. Appl Math Mech 14(5) 417-428 (May 1993).

This paper discusses the generalized variational principles founded by the technique of Lagrangian multipliers in structural mechanics and analyzes the nonlinear statically indeterminate structures. It is assumed that the stress-strain relationship of the materials of structures has the form of $\sigma = B\epsilon^{1/m}$ or $\tau = C\gamma^{1/m}$, namely, the physical equations of structures have the shape of exponential functions. Several examples are given to illustrate the statically indeterminate structures such as the trusses, beams, frames, and torsional bars.

11A464. FEM for predicting equilibrium shapes of solder joints. - NJ Nigro *(Dept of Mech Eng, Marquette Univ, Milwaukee WI 53233)*, SM Heinrich *(Dept of Civil and Env Eng, Marquette Univ, Milwaukee WI 53233)*, AF Elkoub, X Zou, R Fournelle *(Dept of Mech Eng, Marquette Univ, Milwaukee WI 53233)*, Ping S Lee *(Allen-Bradley Co, Rockwell Int, Milwaukee WI 53204)*. J Electron Packaging 115(2) 141-146 (Jun 1993).

This paper discusses the development and application of a FEM for determining the equilibrium shapes of solder joints which are formed during a surface mount reflow process. The potential energy governing the joint formation problem is developed in the form of integrals over the joint surface, which is discretized with the use of FEs. The spatial variables which define the shape of the surface are expressed in a parametric form involving products of interpolation (blending) functions and element nodal coordinates. The nodal coordinates are determined by employing the minimum potential energy theorem. The method described in this paper is very general and can be employed for those problems involving the formation of 3D joints with complex shapes. It is well suited for problems in which the boundary region is not known a priori (eg. "infinite tinning" problems). Moreover, it enables the user to determine the shape of the joint in parametric form which facilitates meshing for subsequent FE stress and thermal analyses.

282C. STRUCTURAL OPTIMIZATION

11A465. Accuracy tests for various sensitivity analysis methods with respect to shape variables in planar cantilever beams. - G-J Park *(Mech Des and Prod Eng, Col of Eng, Hanyang Univ, 17 Haengdang-Dong Seongdong-Ku, Seoul 133-791, Korea)*. Comput Struct 47(6) 1057-1063 (17 Jun 1993).

Sensitivity information is required in the optimal design process. In structural optimization, sensitivity calculation is a bottleneck due to its complexities. Various schemes have been proposed for the calculation. Analytic and finite difference methods are the most popular at the present time; however, they have their advantages and disadvantages. The semi-analytic method has been suggested to overcome these difficulties. In spite of its excellence, the semi-analytic method has been found to possess numerical errors with respect to shape variables. In this research, the errors from each method are evaluated and compared using a shape variable. A planar beam is selected as an example since it has a mathematical solution. An efficient method is suggested for the structural optimization which utilizes the FEM.

11A466. Analysis and shape optimization of variable thickness prismatic folded plates and curved shells Part 2. Shape optimization. - E Hinton and NVR Rao *(Dept of Civil Eng, Univ College, Singleton Park, Swansea SA2 8PP, UK)*. Thin-Walled Struct 17(3) 161-183 (1993).

This paper deals with the development of computational tools for structural shape optimization of shells and folded plates in which the strain energy or the weight of the structure is minimized subject to certain constraints. Both thickness and shape variables defining the cross-section of the structure are considered. The analysis is carried out using curved, variable thickness finite strips formulated and tested in Part I of this paper. Optimal shapes are presented for several shells and folded plates of variable thickness including plates on elastic foundation. The changes in the relative contributions of the bending, membrane and shear strain energies are monitored during the whole process of optimization. The tools developed in the present work can be used as an aid to structural engineers in designing novel forms for shells and folded plates and provide valuable insight into the structural behavior. It is concluded that the finite strip method offers an accurate and inexpensive tool for the optimization of a wide class of structures having regular prismatic-type geometry with diaphragm ends.

11A467. Compressive bars with bounded displacement at the task of optimal control. - L Mikulski *(Krakow Univ of Tech, Krakow, Poland)*. Eng Trans 41(2) 123-137 (1993).

The beam with bounded displacement compressed by the axial force is considered as an optimal control task. The constraints relative to displacement of the bar axis could be active pointwise or in some domain. To solve the task, maximum principle shall be used; necessary conditions reduce the problem of optimal control to a multipoint boundary value problem for ordinary differential equations. The boundary value problems with jump conditions are solved by multiple-shooting techniques.

11A468. Exact least-weight truss layouts for rectangular domains with various support conditions. - T Lewinski, M Zhou, GIN Rozvany *(FB 10, Essen Univ, D-4300 Essen 1, Germany)*. Struct Optim 6(1) 65-67 (Jun 1993).

A comprehensive review of both previously known and newly derived exact optimal layouts for rectangular domains with point loads and either line or point supports is given in this note.

11A469. Improved approximation for stress contraints in plate structures. - GN Vanderplaats and HL Thomas *(VMA Eng, 5960 Mandarin Ave Ste F, Goleta CA 93117)*. Struct Optim 6(1) 1-6 (Jun 1993).

An improved approximation for stresses (and strains) in plate structures is presented. This approximation is highly accurate because it is based on approximations of the element forces, which are more invariant than the element stresses and strains, and because it captures the nonlinearity in the stress recovery calculations. Both sizing and shape design problems are used as examples to show the increased accuracy and robustness of this approximation function.

11A470. Isoperimetric inequalities in optimal structural design. - VV Kobelev *(Muhr und Bender KG, W-5952 Attendorn, Germany)*. Struct Optim 6(1) 38-51 (Jun 1993).

Isoperimetric inequalities arising in exactly solvable structural optimization problems are discussed in this article. Most isoperimetric inequalities of mechanical problems have been proved using one of three known methods. The first tool is the variational method, which is a powerful way to prove inequalities for systems described by ordinary differential equations. For the systems described by equations with partial derivatives, the symmetrization method can be applied. Methods based on positivity properties of operators, for example, Hopf's maximum principle, are used to prove the inequalities for local functionals. Using these algorithms, the new isoperimetric inequalities for engineering problems were investigated. Classical examples, namely the St Venant-Polya inequality rigidity, the Faber-Krahn inequality for vibrating membranes, the Banichuk-Wheeler inequality for maximum stress in a perforated plane and the Keller-Ting inequality for static moments of a bar are treated. The inequalities for the maximum stress in twisted isotropic and orthotropic elastic bars are proved. For the perfectly-plastic solid, the inequalities for collapse load are considered. The other class of inequalities, associated with eigenvalue problems, arises in vibration, conservative, and non-conservative stability problems. The new inequalities for the bimodal critical axial compression load for bars with clamped ends, a generalized Pfluger column and a circular ring under hydrostatic pressure are stated.

11A471. Mixed variational formulation for shape optimization of solids with contact conditions. - HC Rodrigues *(CEMUL, Inst Superior Tecnico, Av Rovisco Pais, Lisbon, Portugal)*. Struct Optim 6(1) 19-28 (Jun 1993).

This paper is concerned with the development of a mixed variational formulation and computational procedure for the shape optimization problem of linear elastic solids in possible contact with a rigid foundation. The objective is to minimize the maximum value of the von Mises equivalent stress in a body (non-differentiable objective function), subject to a constraint on its volume and bound constraints on the design. For design purposes, the contact boundary is considered fixed. A FE model that is appropriate for the mixed formulation is utilized in the discretization of the state and adjoint state equations. An elliptical mesh generator was used to generate the FE mesh at each new design. The computational model is tested in several example problems.

11A472. Multiparameter structural optimization using FEM and multipoint explicit approximations. - VV Toropov *(Dept of Civil Eng, Univ of Bradford, Bradford, W Yorkshire BD7 1DP, UK)*, AA Filatov, AA Polynkin *(Dept of Solid Mech, Nizhny Novgorod Univ, 23 Gagarin Ave, 603600 Nizhny Novgorod, Russia)*. Struct Optim 6(1) 7-14 (Jun 1993).

A unified approach to various problems of structural optimization, based on approximation concepts, is presented. The approach is concerned with the development of the iterative technique, which uses in each iteration the information gained at several previous design points (*multipoint approximations*) in order to better fit constraints and/or objective functions and to reduce the total number of FE analyses needed to solve the optimization problem. In each iteration, the subregion of the initial region in the space of design variables, defined by move limits, is chosen. In this subregion, several points (designs) are selected, for which response analyses and design sensitivity analyses are carried out using FEM. The explicit expressions are formulated using the weighted least-squares method. The explicit expressions obtained then replace initial problem functions. They are used as functions of a particular mathematical programming problem. Several particular forms of the explicit expressions are considered. The basic features of the presented approximations are shown by means of classical test examples, and the method is compared with other optimization techniques.

11A473. Optimal design of rigid-plastic structures under dynamic loading. - U Lepik *(Dept of Theor Mech, Tartu State Univ, EE2400 Tartu, Estonia)*. Struct Optim 6(1) 15-18 (Jun 1993).

The optimal design of rigid-plastic beams with piecewise constant thickness under impulsive or dynamic pressure loading is considered. Such dimensions of the structure for which the beam of constant volume attains a minimum of local or mean residual deflection are sought. The equations of motion are integrated (i) exactly and (ii) approximately by making use of the method of mode form solutions. The method of solution is applied also to reinforced beams. The stiffness of the beam can be increased if we provide it with additional supports. The locations of such supports must be chosen so as to minimize the global compliance of the beam. Optimality conditions for this problem are discussed.

11A474. Optimum design of a composite structure with manufacturing constraints. - DP Costin and BP Wang *(Dept of Mech Eng, Univ of Texas, PO Box 19023, Arlington TX 76019)*. Thin-Walled Struct 17(3) 185-202 (1993).

Composite designs produced by multidisciplinary optimization computer programs are often expensive or impossible to produce. In this paper, constraints needed in the optimization process to reduce manufacturing cost or reduce the need for post-optimization design changes are presented. The interactions of the manufacturing constraints with other constraints and the design variable scheme are investigated. Additionally, a design case study is performed, comparing wings designed with a conventional method and the method described in this paper. The designs were built and tested to verify modeling assumptions and the effectiveness of the manufacturing constraints.

11A475. Structural modeling and sensitivity analysis of shape optimization. - Y Gu and G Cheng *(Res Inst of Eng Mech, Dalian Univ of Tech, Dalian 116024, Peoples Rep of China)*. Struct Optim 6(1) 29-37 (Jun 1993).

It is presented in this paper that the structural modeling of shape optimization is composed of, in general cases, four distinct processes on geometry, design, analysis, and perturbation models. The relationships between these models are discussed. An integrated modeling approach based on geometric shape parameterization and automatic mesh generation is proposed. In cooperation with this modeling approach, the semi-analytic sensitivity analysis has been effectively employed. These techniques join shape optimization with FEM and CAD packages and apply it versatilely to optimum designs of general structures. The implementation and applications of the integrated modeling approach and semi-analytic sensitivity analysis to shape optimization of structures with coupling of stress and temperature fields are illustrated.

See also the following:

11A291. Recent developments in the homogenization theory of elastic plates and their application to optimal design Part I

11A303. Design of a circular plate on an elastic halfspace for minimum differential settlement

282F. NONLINEAR THEORY

See the following:

11A29. Explicit FE formulation for very large deformations based on updated material reference frame

11A566. Motion resistance and pressure distribution in a delivery conduit during pumping of a concrete mixture

282G. RELIABILITY DESIGN

11A476. Crack initiation, propagation and arrest criteria for steel structure safety assessment. - T Varga *(Inst for Testing and Res in Mat Tech, Tech Univ, Vienna, Austria)*. Struct Safety 12(2) 93-98 (Jun 1993).

Linear Elastic Fracture Mechanics constitutes a numerical correlation between the acting tensile stress, the defect size and the fracture toughness. Usually initiation of material separation is considered to be the critical conditon. This, however, holds only for those cases, in which the weakest microstructural area can be located and tested. If this is not the case, a crack will be initiated somewhere else and the fact that it will grow from there onwards has to be considered. Crack propagation is possible in ductile or in cleavage manner. If ductile propagation is present, an R-curve approach may be adequate to be applied. However, if cleavage is triggered, timely arrest of the running crack becomes the only possibility to prevent the separation of the piece.

11A477. Generalized safety factor and reliability index in a multiaxial state of static stress. - J Kolenda *(Poland)*. Marine Tech Trans 3 111-118 (1992).

The problem of strength calculations in design of engineering components subjected to multiaxial static stress is considered. On the basis of the distortion-energy theory the formula for calculation of the generalized safety factor for aniostropic materials is derived. The dimensionless safety margins is defined, which is a function of safety factor. This permits calculations to be made of the failure probability when the stress components are random variables. Under assumption that the stress components are normally distributed and statistically independent the reliability index is determined.

11A478. Safety factor and reliability index in a general state of cyclic stress. - J Kolenda *(Poland)*. Marine Tech Trans 3 119-125 (1992).

Fatigue strength of constructional steels under multiaxial cyclic stress is considered. It is assumed that the stress components are synchronous and in-phase. The known result of fatigue tests at combined bending and torsion that the fatigue limits are correlated best by the distortion-energy theory is taken into account. Under assumption that this theory is applicable in a 3D state of cyclic stress, the generalized factor of safety and the reliability index at random fluctuations of amplitudes of the stress components are determined.

11A479. Solder joint reliability of surface mount connectors. - J Lau, T Marcotte, J Severine, A Lee, S Erasmus, T Baker, J Moldaschel, M Sporer, G Burward-Hoy *(Hewlett-Packard, Palo Alto CA 94304)*. J Electron Packaging 115(2) 180-188 (Jun 1993).

The solder joint reliability of five different surface mount connectors has been studied by eleven different experimental methods. A set of test methods and specifications for determining the reliability of the solder joints of surface mount connectors has been recommended.

282H. CONCRETE (REINFORCED)

11A480. Pullout tests of epoxy-coated reinforcement in concrete. - AR Cusens *(Dept of Civil Eng, Univ of Leeds, Leeds LS2 9JT, UK)* and Z Yu *(British Rail Res, PO Box 2, Derby DE24 8YB, UK)*. Cement & Concrete Composites 14(4) 269-276 (1992).

The bond strength and slip of epoxy-coated reinforcing bars in concrete have been evaluated by carrying out single pullout and double pullout tests. In extended single pullout tests, slip measurements were made while tensile force was applied to reinforcing bars embedded in concrete. In double pullout tests, 20 cycles of load were applied at levels of steel stress between zero and 0.5 times characteristic steel strength. Strains were measured by electrical resistance strain gauges glued inside the bars. Both epoxy-coated and uncoated bars were used in the investigation, to obtain comparative results. The strain gradient along the bar was found to be less for the coated reinforcement. In general, the epoxy coating was found to increase slip in bond and thereby reduce the bond performance of coated bars.

11A481. Ultimate moment capacity of ferrocement reinforced with weldmesh. - G Singh and GJ Xiong *(Dept of Civil Eng, Univ of Leeds, Leeds LS2 9JT, UK)*. Cement & Concrete Composites 14(4) 257-267 (1992).

An improved qualitative mechanical model which is thought to reflect more realistically the behavior of ferrocement in flexure is presented. In light of this model, three types of existing typical quantitative models of ultimate moment capacity based on yield strength of wire, nonlinear stress-strain function for cold-worked wire and ultimate wire strength have been evaluated. For singly weldmesh reinforced ferrocement the model based on ultimate wire strength is found to be simpler, more reliable and more economical than the other two types of models. For uniformly reinforced ferrocement a new model based on yield strength proposed by the authors appears to be more reliable and economical, and simpler than other models based on yield wire strength. A simpler and more economical model based on ultimate wire strength for uniformly weldmesh reinforced ferrocement is also put forward by the authors. This model shows a closer agreement with test results than the existing models based on yield wire strength or nonlinear stress-strain function of cold-worked wire.

See also the following:

11A264. Deformational resistance of fresh concrete through bent and tapered pipes

11A287. Calculations of the constraints in a thin film deposited on the substrate

282M. THERMAL LOADING

11A482. Analytical solutions of stresses in a cylindrical plate due to polynomial radial temperature distributions. - FFH Wu *(IBM TP, E Fishkill, Hopewell Junction NY)*. J Electron Packaging 115(2) 214-218 (Jun 1993).

Thermal stress is a significant contributor to a component's failure during manufacturing processes. In the electronic industry, for example, it is very common that components experience an extensive number of nonuniform, local heating cycles throughout its lifetime. In order to promote reliability, components are put through burn-in which creates a very nonuniform temperature distribution. In order to reduce cost, reworkability is considered to be a necessary option for the manufacturing processes to achieve high yield; these rework processes usually require localized heating. In addition, due to certain functionality requirements, materials with different coefficients of thermal expansion are cast together. The thermal mismatch caused by nonuniform temperature and/or different coefficients of thermal expansion will create thermal stress which could result in the cracking of the components. The fracture often initiates on the interface between the different materials or at the free edge of the surface. To make the problems mathematically tractable, the problems here are simplified as linear thermo-elastic and axisymmetric. It is concluded that the displacement distribution is one order higher than the temperature distribution if the temperature is a polynomial function of the radial distance from the center of a disk.

11A483. Effects of inclined free edges on the thermal stresses in a layered beam. - Wan-Lee Yin *(Georgia Tech)*. J Electron Packaging 115(2) 208-213 (Jun 1993).

A stress-function-based variational method is used to determine the thermal stresses in a layered beam with inclined free edges at the two ends. The stress functions are expressed in terms of oblique Cartesian coordinates, and polynomial expansions of the stress functions with respect to the thickness coordinate are used to obtain approximate solutions. Severe interlaminar stresses act across end segments of the layer interfaces. Local concentration of such stresses may be significantly affected by the inclination angle of the end planes. Variational solutions for a two-layer beam show generally beneficial effects of free-edge inclination in dispersing the concentration of interlaminar stresses. The significance of these effects is generally not indicated by the power of the stress singularity as compared from an elasticity analysis of a bimaterial wedge.

See also the following:

11A489. Static analysis of the influence of thermal load on hyperboloidal reinforced concrete cooling tower

282Y. COMPUTATIONAL TECHNIQUES

11A484. Error estimate and step size control method for nonlinear solution techniques. - MM Abdel-Ghaffar, DW White, Wai-Fah Chen *(Dept of Struct Eng, Sch of Civil Eng, Purdue)*. Finite Elements Anal Des 13(2-3) 137-148 (Jun 1993).

The condition number of the tangent stiffness matrix is shown to reflect the error encountered in the solution of nonlinear structural systems. Due to the linearization process in the incremental solution, two sources of error exist: (1) the error associated with the solution of the linearized set of equations; and (2) the error associated with the unbalanced force residual. While the condition number itself reflects the first error, its change from step to step represents the second error. Being an expensive quantity to compute, only an estimate of the condition number that is based on the L_1-norm of the tangent stiffness matrix has been effectively used in guiding the solution algorithm in adjusting the step size according to the degree of nonlinearity of the system. It is also used to identify the stable from the unstable paths of the response curve. Several examples are solved to show the applicability of the proposed step size control with different solution techniques.

282Z. EXPERIMENTAL TECHNIQUES

11A485. Development of a flexible, multiple-configuration structural test facility. - RA Shenoi, PJCL Read, CL Walters, SCM Thelu *(Dept of Ship Sci, Univ of Southampton, Southampton SO9 5NH, UK)*. Int J Fatigue 15(4) 317-323 (Jul 1993).

This paper deals with the development of a novel facility for testing relatively large structural specimens. It outlines the design process adopted in arriving at the final specification for the structural framework to hold the test specimens, the hydraulic power-pack with associated valves and pipework, and the data acquisition and control system based around a microcomputer. A brief mention is also made of the static and cyclic fatigue tests conducted to verify the workings of the facility.

284. Structures (ground)

11A486. Limit loads of framed structures and arches using the gloss r-node method. - CPD Fernando and R Seshadri *(Indust Syst Eng, Univ of Regina, Regina, SK, S4S 0A2, Canada)*. Trans Can Soc Mech Eng 17(2) 197-214 (1993).

An approximate method for determining limit loads of mechanical components and structures on the basis of two linear elastic FE analyses is described. The load-control nature of the redistribution nodes (r-nodes) leads to considerable simplifications. The combined r-node equivalent stress, which can be obtained by invoking an appropriate multibar mode, can be identified with the reference stress. The method is applied to beam, framed and arched structures, and the limit load estimates obtained are reasonably accurate.

11A487. Fundamental of dynamical analysis of the blast-resistant underground structures. - Yu-xiang Zhao, Xi-tai Song, Er-xuan Qian *(Luoyang Inst of Hydraul Eng, Luoyang, China)*. Appl Math Mech 14(5) 407-415 (May 1993).

In this paper, the generalized variational principle of dynamic analysis for the blast-resistant underground structures is established, and the corresponding generalized functionals of elastoplastic analysis for underground structures is derived, and the generalized variational principle of nonconservative system is given, thus the fundamental of dynamical analysis for underground structures to resist blast is proposed. Finally, for the underground cylindrical structure to resist blast, dynamical calculations are made, and compared with the test results.

11A488. Numerical calculations and structural analysis of a 150 m high cooling tower for various types of wind load. - J Dulinska and A Flaga *(Inst of Struct Mech, Krakow Univ of Tech, Poland)*. Arch Civil Eng 38(3) 205-222 (1992).

The paper presents quasistatic, deterministic approach to the wind load acting on a hyperboloidal cooling tower. Static component of the wind load is assumed with the allowance for the global gust wind load coefficient. Taking into account various aspects of geometry, structure and location of the cooling tower, various pressures of quasistatic wind loads were obtained. The investigations are limited to three cases of exposure factor depending on the types of the nearest buildings and the category of terrain roughness. Two cases of external wind pressure distribution along the circumference are assumed, one for a cooling tower with and the other without meridional ribs. Moreover, two values of internal wind pressure factor are adopted and two combinations of dead load and wind load are analysed concerning the characteristic loads and the design loads. Numerical calculations for wind and dead load acting on a cooling tower with the height H = 150 m were performed according to the author's program.

11A489. Static analysis of the influence of thermal load on hyperboloidal reinforced concrete cooling tower. - J Dulinska and A Flaga *(Inst of Struct Mech, Cracow Univ of Tech, Krakow, Poland)*. Arch Civil Eng 38(4) 301-322 (1992).

Thermal influences could be significant in the shell structures design. Polish Standards do not give guidelines to static calculations of hyperboloidal cooling towers under thermal load. The paper presents a short analysis of Polish Standard recommendations for adopting values of thermal load with regard to peculiar character of cooling tower structures. Obtained distributions of winter and summer temperatures were compared with distributions calculated or measured by other authors. The investigations were limited to two cases. 1. Working cooling tower in summer, nonsymmetric distribution of temperature along the circumference of the shell. 2. Working cooling tower in winter, axisymmetric distribution of temperature along the circumference of the shell. Numerical calculations of thermal load stresses for a representative cooling tower H = 150 m were performed according to the author's own program.

See also the following:

11A508. Behavior of a granular medium in a silo. Model tests in a plane silo with parallel walls. Part I

11A509. Behavior of a granular medium in a silo. Model tests in a plane silo with convergent walls. Part II

288. Structures (mobile)

288B. GROUND VEHICLES (INCL TIRES)

11A490. Affecting reliability of rail traffic vehicles in the phase of design and manufacturing. - J Marciniak *(Centrum Naukowo-Tech, Kolejnictwa ul Chlopickiego 50, 04-275 Warsaw, Poland)*. Zagadnienia Eksploatacji Maszyn 26(4) 487-498 (1991).

Demands for rail traffic vehicles in the range reliability and utility properties are presented. Different variants of operational properties of a vehicle (its strength) X_r and its loads X_0 are considered. Practical problems concerning reliability possible to solve in the design, were underlined. Methods of rail vehicles technical stand up prognosis were presented - the gradient method and the method of generalized parameter. Methods of increase of rail traffic vehicles reliability in the design phase were also considered with a vehicle service technological demands taken on account. In the final part of work conclusions are presented which should be fulfilled, to obtain high level of reliability of object in the phase of design, manufacture and exploitation.

288C. SHIPS, SUBMARINES

11A491. Aspects of interation between the hull and hatch covers of containerships. - AN Rodionov *(Tech Univ Hamburg-Harburg, Arbeitsbereigh Schiffstechnische Konstruktionen und Berechnungen, Lauenbruch Ost 1, 3100 HH90, Germany)*. Ship Tech Res 40(2) 59-70 (May 1993).

Damages caused by the interaction of hatch covers and hull in open-deck ships during torsional deformations are analyzed. Special emphasis is placed on the stopper system. Its traditional function is to keep covers with cargo on top from slipping during the ship's motion, and simultaneously to eliminate forces on covers due to hull deformations. However, stoppers may be used also to include the hatch covers, having large rigidity in their plane, into the hull rigidity and strength. Different versions of stopper systems are proposed, and the corresponding clearances are investigated. A special method of calculating joint deformations of hulls and covers is elaborated. Results are compared with experimental data. Some advantages of involving the hatch covers into the hull torsional resistance are shown.

288E. AIRPLANES

See the following:

11A354. Aspects of fatigue affecting the design and maintenance of modern military aircraft

288F. HELICOPTERS

See the following:

11A108. Analysis of spatial motion dynamics of a helicopter for various models of the induced velocity field

288I. SPACE VEHICLES AND SATELLITES

11A492. Applied mechanics of a lunar base. - H Benaroya *(Lab for Extraterrestrial Struct Res, Dept of Mech and Aerospace Eng, Rutgers Univ, New Brunswick NJ)*. Appl Mech Rev 46(6) 265-357 (Jun 1993).

This special issue of *Applied Mechanics Reviews* was created as a testimony, by the authors, to the importance of a continued presence in Space by representatives of this Nation. We have tried to examine some, but obviously not all, issues which are pertinent to the establishment of a permanent manned facility on the Moon. Hopefully, the interested reader will come away with enough information to permit a further, more advanced study. We have endeavored to provide broad perspectives rather than too narrow a focus. Structural concepts for the Moon are in flux. The first generation of bases will most likely be brought almost intact from Earth orbit, ready for habitation. More advanced bases, like those envisioned here by NASA artists, built of indigenous materials, will require many decades of research and development, analysis, design, and construction.

11A493. Applied mechanics of lunar exploration and development. - MB Duke *(NASA, Johnson Space Center, Houston TX 77058)* and H Benaroya *(Dept of Mech and Aerospace Eng, Rutgers Univ, Piscataway NJ 08855)*. Appl Mech Rev 46(6) 272-277 (Jun 1993).

An overview of current concepts for lunar outposts is provided, with emphasis on identifying design issues that are also prospective research problems in applied mechanics. The authors believe that the conjugation of new applications and the unique features of the lunar environment will provide many interesting problems whose solution will provide fundamental insights into problems in applied mechanics.

11A494. Engineering elements for transportation on the lunar surface. - BE Wallace and NS Rao *(Boeing Defense and Space Group, Huntsville AL)*. Appl Mech Rev 46(6) 301-312 (Jun 1993).

Major aspects of engineering planetary transportation vehicles are discussed. Emphasis is placed on the mechanics of mobility and mobility system design, including considerations for designing the wheels, drive, steering, and suspension systems. Because mobility performance of any vehicle is extremely sensitive to environmental (eg, soil properties) and design (eg, vehicle weight) parameters, the mechanics of mobility are addressed by parametric application as well as empirical (derived relationships and equations) form. Finally, and more philosophical in nature, discussions of the key considerations for designing and analyzing each of the components of mobility (locomotion, steering, suspension, and stability) are also included. These discussions include some general guidelines to assist in determining the values of key design parameters.

11A495. Indigenous materials for lunar construction. - JA Happel *(JR Harris, 1580 Lincoln, Denver CO 80203)*. Appl Mech Rev 46(6) 313-325 (Jun 1993).

An important step in the exploration and colonization of the solar system is to build a permanently inhabited base on the Moon. The lunar environment is stark and hostile to unprotected humans. Structures are needed that protect the inhabitants from vacuum, radiation, extreme temperatures, dust, and meteoroids. Transporting the necessary construction materials from Earth is extremely expensive. Fortunately, lunar structures can be built utilizing indigenous materials. The locally available materials include lunar regolith, cast regolith, glass and glass composites, metals and concrete. Their mechanical properties are summarized and their suitability for lunar construction is evaluated. The most promising materials are cast regolith and lunar glass. Several lunar bases concepts utilizing indigenous materials are described and evaluated. Precast modules and large cast in place structures can be fabricated from lunar concrete. Large cylindrical modules, curved and flat panels and arches cast from lunar regolith are also feasible. A tied arch system is considered very promising because of its structural efficiency.

11A496. Lunar environment. - LR Utreja *(Dynacs Eng, Huntsville AL 35806)*. Appl Mech Rev 46(6) 278-284 (Jun 1993).

As one of the key elements of the Space Exploration Initiative, the Moon provides a waypoint for scientific exploration and travel to Mars. The Moon's stable ground in the vacuum of space is an ideal platform for astronomical observatories. Conditions on the Moon are similar to what human beings will face on other planets, so it is a natural test bed to prepare for a manned mission to Mars. A knowledge of the lunar environment is therefore important before undertaking any missions of construction, operations, and habitation on the lunar surface. The purpose of this paper is to review and assemble information on the lunar environment so that engineers and scientists can refer to this as they begin lunar-based engineering studies. The lunar environment is categorized into three major elements: lunar physical constants, lunar atmosphere, and lunar surface. The description of lunar size, orientation, period of rotation, and lunar month are all treated as part of lunar physical constants. Lunar atmosphere includes gas composition, pressure and density, solar flux and radiation, micrometeorite flux, and lunar dust. The geophysical and geochemical properties are provided as lunar surface characteristics. The geophysical properties include terrain characteristics, topography and surface tremors; soil and rock characteristics; mechanical, thermal, electrical, magnetic, and optical properties. The chemical composition of the regolith and rocks are described in geochemical properties.

11A497. Mechanics of materials in lunar base design. - A Smith *(Eng and Mat Div, Eng Res Lab, US Army Construct, Champaign IL 61826-9005)*. Appl Mech Rev 46(6) 268-271 (Jun 1993).

The construction of a lunar base has been thought about for almost five decades. The earliest concepts dealt with size and shape concepts rather than actual design of structures and equipment. As the exploration of space has received emphasis in more recent times, the need to consider the factors of design and design approaches have received more attention. It still is not possible to completely rationalize the design of a habitat, for example, but we are now very aware of the need to include the fracture and fatigue properties of the materials of which the hardware of a lunar infrastructure is constructed. It is reasonably certain that the same techniques used for terrestrial designs can be used for lunar bases provided the space environment is taken into account. The extensive amount of research on fracture and fatigue that has been and is being conducted, along with the ease and speed of computation of their effects on alternative design features will be invaluable in providing a highly reliable, safe lunar base.

11A498. Properties and mechanics of the lunar regolith. - SW Johnson *(BDM Int, 1801 Randolph Rd, Albuquerque NM 87106)* and Koon Meng Chua *(Dept of Civil Eng, Univ of New Mexico, Albuquerque NM 87131)*. Appl Mech Rev 46(6) 285-300 (Jun 1993).

Knowledge of the lunar regolith is essential to success in lunar missions whether crewed or robotic. The regolith is the loose material overlying more intact strata on the Moon. It varies in thickness from several meters on the maria or lunar seas to many meters on the highlands of the Moon. The regolith is the material humans walked and drove on from 1969 to 1972. In the future, people will use it for radiation protection and as a resource for recovery of oxygen, silicon, iron, aluminum, and titanium. Implanted in the regolith by the solar wind are recoverable amounts of volatiles such as hydrogen and helium. Increasing our knowledge of the mechanical properties of the regolith will enable constructors of the 21st Century to build habitats, do mining, establish manufacturing, and erect telescopes on the Moon. We already know much of the regolith from robotic and astronaut missions to the Moon. There is much more to be learned.

11A499. Structural concepts for lunar-based astronomy. - Koon Meng Chua *(Dept of Civil Eng, Univ of New Mexico, Albuquerque NM 87131)*, SW Johnson *(Adv Basing Syst, BDM Int, 1801 Randolph Rd SE, Albuquerque NM 87106)*, ME Nein *(Program Dev, NASA Marshall Space Flight Center, Huntsville AL 35812)*. Appl Mech Rev 46(6) 336-357 (Jun 1993).

Lunar-based astronomy requires structures that provide the required stiffness, strength, and dimensional stability in the challenging lunar vacuum, thermal, radiation, micrometeorite, secondary ejecta, and dust environments. Materials used in the structures must be durable to provide extended service life. They must not outgas and thereby interfere with optics. Structures must function as part of an integrated system involving detectors, metrology, and optics. The thermal environment of the lunar surface is particularly taxing because the long-duration exposures to extremes of temperature. Designers must cope with transient thermal gradients associated with passing from sunlight to darkness and back to sunlight. Also, the shape of mirrors and other components at night-time low temperatures may differ from shape at day-time high temperatures because of material properties varying significantly over the range from about 70 K to nearly 400 K. Materials for structural components include several types of glass, metals and their alloys (eg, aluminum, beryllium, and titanium), graphite epoxy and the associated class of materials, and metal matrix composites (eg, graphite magnesium and graphite aluminum). Examples of material properties are presented. Structural design concepts for several possible observatories are presented. Structural configurations will be partially determined by the need to reduce direct human involvement in the construction process. Concepts discussed include the 16-meter optical-ultraviolet telescope and a small telescope with 0.8-m aperture intended to be landed on the Moon by a robotic spacecraft. For lunar-based astronomy, structures must rest on the lunar regolith with loads transferred to the regolith through a foundation. The overall response of the structure is dependent on the interaction of the foundation and the regolith.

11A500. Tensile-integrity structures for the moon. - H Benaroya *(Dept of Mech and Aerospace Eng, Rutgers Univ, PO Box 909, Piscataway NJ 08855)*. Appl Mech Rev 46(6) 326-335 (Jun 1993).

A brief review of lunar base structural concepts is presented followed by a discussion of tensile structural concepts. Specifically, tensile integrity (tensegrity) structures are suggested for study for possible use on the lunar surface due to their efficiencies and advantages. Such application could conceivably be for second generation structures. These structures, like pneumatic and truss structures, are self-sustaining and can be designed not to require any significant foundation structure. One exciting advantage of the class of structure discussed here is the possiblity of designing deployable versions.

290. Structures (containment)

11A501. Integral hydro-bulge forming of single and multi-layered spherical pressure vessels. - J Hashemi, J Rasty, S Li *(Dept of Mech Eng, Texas Tech Univ, Lubbock TX 79409)*, AA Tseng *(Dept of Mech Eng and Mech, Drexel Univ, Philadelphia PA 19104)*. J Pressure Vessel Tech 115(3) 249-255 (Aug 1993).

The recently developed integral hydro-bulge forming (IHBF) process was utilized in the manufacturing of single and multi-layered spherical pressure and storage vessels. Single-layered spherical vessels of 1.6-mm thickness and diameters of 316.5, 634.1, and 953.2 mm were manufactured. As an alternative means of manufacturing thick-walled spherical pressure vessels, the IHBF procedure was modified and used in forming double-layered composite pressure vessels with an effective thickness of 15 mm. The results showed that the modified IHBF process may successfully be applied in the manufacturing of multi-layered spherical vessels of various thicknesses and diameters. In this paper, the conventional and modified IHBF procedure will be outlined and the experimental results and analysis will be presented. Finally areas where further work is needed are identified.

11A502. Design procedure for flexibility factors of 90-deg curved pipe having various tangent lengths. - DJ Nordham *(Machinery R&D Directorate, Carderock Div, Naval Surface Warfare Center, Annapolis MD 21402-5067)* and LM Kaldor *(Arnold MD 21012)*. J Pressure Vessel Tech 115(3) 319-324 (Aug 1993).

A simple design procedure, based on 175 FE analyses, was derived to predict the flexibility factor due to an in-plane or out-of-plane moment for a 90° curved pipe with end constraints composed of tangents of any length terminated by rigid flanges and no internal pressure loads. The results of this design procedure were then compared to flexibility factors obtained from additional FE analyses and experimental work. Flexibility factors calculated using the design equations in the Power Piping Code were also compared to all FE and experimental work. It was found that this design procedure more accurately predicts the flexibility factors than the Power Piping Code.

11A503. Design procedure for stress intensification factors of 90-deg curved pipe having various tangent lengths. - DJ Nordham *(Machinery R&D Directorate, Carderock Div, Naval Surface Warfare Center, Annapolis MD 21402-5067)* and LM Kaldor *(Arnold MD 21012)*. J Pressure Vessel Tech 115(3) 313-318 (Aug 1993).

A simple design procedure, based on 114 FE analyses, was derived to predict the stress intensification factor for 90-deg curved pipe with end constraints composed of tangents of any length terminated by rigid flanges and no internal pressure loads. The results of this design procedure were then compared to stress intensification factors obtained from additional FE analyses and experimental work. Stress intensification factors calculated using the design equations in the Power Piping Code were also compared to all the FE and experimental work. It was found that this design procedure more accurately predicts the stress intensification factors than the Power Piping Code.

11A504. Elastic analysis of a circular flange joint subjected to axial force. - J Cao and AJ Bell *(Dept of Civil and Struct Eng, UMIST, PO Box 88, Manchester M60 1QD, UK)*. Int J Pressure Vessels Piping 55(3) 435-449 (1993).

In this paper the general use of a thin circular flange joint is analyzed and an exact elastic solution is derived. Formulae which enable the maximum stresses in the joint to be calculated easily are presented. Results obtained using the formulae are compared with those obtained from FE analyses and with results obtained using other common methods in regular use. The formulae presented are shown to be reliable, accurate and convenient for use in the design of various circular flange joints.

11A505. Behavior of GRP smooth pipe bends with tangent pipes under flexure or pressure loads: A comparison of analyses by conventional and FE techniques. - DR Hose *(Dept of Aeronaut and Mech Eng, Univ of Salford, UK)* and R Kitching *(Dept of Mech Eng, UMIST, PO Box 88 Sackville St, Manchester M60 1QD, UK)*. Int J Mech Sci 35(7) 549-575 (Jul 1993).

A detailed FE analysis has been carried out for a smooth pipe bend with straight pipe attachments made from glass reinforced polyester. The shell was modelled as a composite laminate made up of discrete isotropic laminae. The inside pipe diameter was 250 mm, the thickness was 9.52 mm and the bend radius was 250 mm. For in-plane flexural loading the deformation patterns were studied, especially in the vicinity of the smooth bend-straight pipe discontinuity. Warping of sections is reported, together with its influence on pipe bend flexibility for various bend angles. Comparisons of flexibilities and strain distributions are made with those calculated by making the frequently used assumption that the flattening sections along the entire pipe bend is uniform. The discontinuity effects for out-of-plane flexural and internal pressure loadings, treated separately, are also considered.

11A506. Pressure vessel manufacutring: Mechanical analysis of gas bottles with convex end-plates. - M Nicolich *(Istituto di Fisica Tecnica e di Tecnologie Indust, Univ di Udine, viale Ungheria 43, 33100 Udine, Italy)*. Int J Pressure Vessels Piping 55(3) 423-433 (1993).

The three-centre geometry design for the bottom end-plates of gas bottle cylinders is analyzed using an approximate method involving FE techniques. Shell elements are adopted to obtain the equivalent stress distribution along a generatrix of the bottle. The maximum stress profile in the bottom zone is plotted versus normalized geometrical parameters. The area which bounds acceptable solutions according to basic Standards Codes is outlined in the diagrams. Experimental measurements by means of electrical resistance strain gauges are compared with the numerical forecasts. The good correlation which was obtained confirms the validity of the proposed approach in dealing with industrial applications.

11A507. Stress analysis of a cylinder with a partition plate subjected to internal pressure. - Degui Fan *(Equipment Dept, Chengdu Chem Eng Corp of China, Chengdu, Peoples Rep of China)*. J Pressure Vessel Tech 115(3) 330-333 (Aug 1993).

This paper presents a method to calculate stresses of a cylinder with a partition plate, whose equations for determining bending stresses of a cylinder and its partition plate are different (less conservative) from those in ASME Boiler and Pressure Vessel Code, Section VIII, Division 1. The paper contains: 1) the derivation of equations for calculating bending stresses of a cylinder and its partition plate; 2) the comparisons between the method in ASME Code VIII-I and the author's method, and commentary on the equations for determining bending stresses of a cylinder and its partition plate in ASME Code VIII-I. Also, the recommendation to modify the equations for determining bending stresses of a cylinder and its partition plate in ASME Code VIII-I has been put forward.

11A508. Behavior of a granular medium in a silo. Model tests in a plane silo with parallel walls. Part I. - J Tejchman *(Fac of Civil Eng, Gdansk Univ of Tech, Poland)*. Arch Civil Eng 38(4) 375-394 (1992).

The paper deals with some phenomena occurring during flow of granular media out of a silo (shear zones formation, increase of lateral pressure on the silo wall, scale effect). Quasi-static problems during the onset of a mass flow in a plane strain model silo with parallel walls and a slowly moveable bottom are investigated. Experiments were carried out for different wall roughness (smooth, rough, very rough), sand density (from dense to loose) and silo width. The displacement of the upper surface of a silo fill were measured. The obtained results were compared with some silo formulae based on a slice equation by Janssen. It turns out that many available silo formulae are not realistic because they do not consider the real deformations in a silo fill during silo emptying. It is very important to consider the formation of wall shear zones with a definite thickness and the realistic boundary conditions along silo walls. That can be achieved with the FEM based on the elastoplastic Cosserat approach proposed by Muhlhaus in which grain rotations and couple stresses are considered using the mean grain diameter as a characteristic length.

11A509. Behavior of a granular medium in a silo. Model tests in a plane silo with convergent walls. Part II. - J Tejchman *(Fac of Civil Eng, Gdansk Univ of Tech, Poland)*. Arch Civil Eng 38(4) 395-414 (1992).

The paper deals with model tests carried out in a plane strain silo with convergent walls and a slowly moveable bottom. Quasi-static problems during the onset of a mass flow are investigated. Experiments are made for different wall roughness (smooth, rough, very rough) sand density (from dense to loose) and wall inclination. The resultant forces on the wall and on the bottom plate, the bottom displacements and the displacements of the upper surface of a silo fill are measured. The profiles of a moving sand are determined with the aid of horizontal colored sand layers. The experimental results are compared with the silo formulae by Drescher (based on a slice method), by Enstad (assuming the circular distribution of major principal stresses) and to the German Silo Code. The obtained test results show that an increase of wall stresses after bottom displacement is caused mainly by the deformations inside the moving material due to the wall inclination. For stress calculations it is important to take into account the formation of shear zones in the silo fill.

See also the following:

11A13. FE Analysis of flange connections
11A238. Application of the twelve-angled polygonal yield criterion to pressure vessel problems
11A252. Elasto-plastic response of orthotropic pipes under bending, pressure, and axial force
11A299. Thickness changes in pressurized shells
11A391. Integrity assessment of thick walled industrial furnace tubes
11A548. Improving toughness of electron beam welds of heavy Mn-Mo-Ni steel plates for pressure vessels
11A549. Materials data for high-temperature design of ferritic steel pressure vessel weldments

292. Friction and wear

292A. GENERAL THEORY

11A510. Quantitative investigation of displacement accommodations in third-body contact. - Y Sun *(CNRS CPPM, IN2P3, 163 Ave Luminy, 13228 Marseilles Cedex 9, France)*, Y Berthier, B Fantino, M Godet *(INSA Lab Mec Contacts, CNRS URA 856, Bat 113 20 Ave Albert Einstein, 69621 Villeurbanne Cedex, France)*. Wear 165(2) 123-131 (1 Jun 1993).

Recently, the "velocity accommodation" concept was introduced in tribology. In third-body contacts, velocity accommodation can occur in five sites and according to four modes, giving rise to 20 possible combinations, ie, 20 velocity accommodation mechanisms. The present paper addresses the role of third and first bodies in elastic and/or plastic deformations in velocity accommodation. For this, a simplified model is first proposed to represent third-body contacts separated by wear debris or solid lubricants. Then, by using the FEM, the relative movement between first bodies in contact under different types of loading is simulated and the deformation of the model as well as the stress and strain field in the third body is determined numerically. Results quantify the role of the third and first bodies in either elastic or plastic deformation. When only relative tangential displacement is imposed, a simple analytical formula based upon a model of two compliances in series is suggested in order to estimate the displacement accommodation of the third and first bodies.

292B. FRICTION

11A511. Elastic hysteresis in rolling elements which are loaded with normal force. - W Caban *(Politech Lodzka, Inst Maszyn, ul Stefanowskiego 1-15, 90-924 Lodz, Poland)*. Zagadnienia Eksploatacji Maszyn 26(4) 405-416 (1991).

Hysteresis losses in rolling friction have been written in this article. Author presents method of valuation rolling friction factor which depends of hysteresis losses. This method permits to use the characteristic of logarithmic amplitude decrement for construction materials. In this way we should get more true results, also that method helps to choose a material of rolling elements.

11A512. Mechanical and tribological behavior of Cu-Nb *in situ* composites. - P Liu *(Sch of Tech, E Illinois Univ, Charleston IL 61920)*, S Bahadur *(Dept of Mech Eng, Iowa State Univ, Ames IA 50011)*, JD Verhoeven *(Ames Lab USDOE, Dept of Mat Sci and Eng, Iowa State Univ, Ames IA 50011)*. Wear 166(2) 133-139 (1 Jul 1993).

The mechanical and tribological properties of Cu-Nb *in situ* composites were studied. The composites were prepared by consumable arc melting of Cn and Nb electrodes, by casting, and by successive deformation of the cast ingot. Dry sliding friction and wear tests were performed in a pin-on-disk set-up, with the composite pin rubbing under atmospheric conditions against a hardened tool steel disk surface. The effect of Nb proportion on the tribological behavior of Cu-Nb composites was studied. It was found that the coefficient of friction decreased with increasing Nb proportion in the composite and that Cu-20vol%Nb composite had the best wear resistance. The effect of prior deformation strain on the coefficient of friction and wear of Cu-15vol%Nb composites was also investigated. The micromechanisms of wear were studied by scanning electron microscopy. It was concluded that cracking in the severely work hardened regions led to the generation of wear particles.

11A513. Wear and friction properties of prosthetic joint materials evaluated on a reciprocating pin-on-flat apparatus. - V Saikko *(Lab of Machine Des, Helsinki Univ of Tech, SF-02150 Espoo, Finland)*. Wear 166(2) 169-178 (1 Jul 1993).

A three-station reciprocating pin-on-flat apparatus was constructed for tribological studies of materials for total replacement joints. Flat-ended cylindrical ultra-high molecular weight polyethylene (UHMWPE) pins were worn against Co-Cr-Mo, Al_2O_3, ZrO_2 and Si_3N_4 counterfaces in distilled, de-ionized water. The temperature of the test environment was 37 ± 1 °C. The nominal contact pressure was 4.8 MPa, sliding distance per cycle 50 mm, frequency 1 Hz and test length 7×10^6 cycles with ZrO_2 and 5×10^6 cycles with all other counterfaces. The wear of the pins were measured gravimetrically at intervals of 5×10^5 cycles. The frictional forces were recorded continuously. The average wear factors of UHMWPE against Co-Cr-Mo, Al_2O_3, ZrO_2 and Si_3N_4 were of the order of 10^{-7}, 10^{-9}, 10^{-9} and 10^{-8} mm^3 N^{-1} m^{-1}, and the average coefficients of static friction were 0.10, 0.11, 0.13 and 0.13, respectively. The results indicate that Al_2O_3 and ZrO_2 are distinctly superior to Co-Cr-Mo as counterfaces for UHMWPE in prosthetic joints. The difference between the wear of UHMWPE against Co-Cr-Mo and that against Al_2O_3 is consistent with clinical observations. The apparatus will be a useful tool in the screening of new materials, surface treatments with coatings for prosthetic joints.

292D. WEAR (UNINTENTIONAL)

11A514. Abrasion and abrasion-corrosion properties of a 9% chromium steel. - GE Gatzanis and A Ball *(Dept of Mat Eng, Univ of Cape Town, Library Rd, Univ Private Bag, Rondesbosch 7700, S Africa)*. Wear 165(2) 213-220 (1 Jun 1993).

A 9Cr2Ni0.7Mo steel was assessed for its dry abrasions and abrasion-corrosion performance using a laboratory test which simulates the conditions experienced by rock conveyors in S African gold mines. The alloy is found to exhibit abrasion and abrasion-corrosion properties comparable with most and better than several higher chromium containing alloys designed for mining applications. The good dry abrasion performance of the alloy is attributed to the good combination of high hardness, strength and toughness imparted to the alloy by its duplex microstructure of lath martensite and thin film of interlath retained austenite. The good abrasion-corrosion results are in a product of the good dry abrasion performance coupled with the excellent corrosion properties in the simulated mine water. The favorable corrosion properties are linked to the effect of the Ni and Mo additions on suppressing pitting tendencies thereby imparting corrosion resistance equivalent to higher chromium containing steels. Experimental evidence however shows that the alloy is operating at the limit of its passivity for the 46 h corrosion period employed in the corrision-abrasion test. Exposure for periods much in excess of this figure will lead to breakdown and poor corrosion-abrasion performance relative to higher chromium containing steels. The production variables of prior cold working and plate thickness are found to exert negligible influence on dry abrasion and abrasion-corrosion properties.

11A515. Effect of head wear and tape shear on the head-tape interface. - C Lacey and FE Talke *(UCSD)*. Trib Trans 36(3) 387-392 (Jul 1993).

The effects of transverse shear deformation in the tape and wear on the head profile are incorporated into a numerical simulation of the longitudinal head-tape interface. These effects can cause a significant change of the head-tape interface behavior for geometries that experience head-tape contact. The numerical implementation is described and results are compared to experimental measurements of head-tape spacing.

11A516. Sliding-wear behavior of ceramic particle-reinforced high-speed steel obtained by powder metallurgy. - M Vardavoulias, C Jouanny-Tresy, M Jeandin *(Ecole Mines de Paris, Centre des Mat PM Fourt, BP 87, 91003 Evry Cedex, France)*. Wear 165(2) 141-149 (1 Jun 1993).

The wear behavior of sintered high-speed steel-type particulate composites depends significantly on microstructural parameters, such as those of the metallic matrix and primary carbides, but also on some additional parameters related to the powder metallurgy processing. Pin-on-disc results, coupled with scanning electron microscopy observation of the wear tracks and microstructure image analysis, indicated the prominent role of the added ceramic particles. More precisely, the size, the mechanical resistance and the cohesion with the metallic matrix of TiC, uncoated Al_2O_3, and TiN-coated Al_2O_3 particles, largely determine the wear behavior of such materials. In addition, the roles of the residual porosity and of the presence of copper as a solid lubricant are pronounced in this investigation.

11A517. Study of abrasive wear resistance of transformation toughened ceramics. - Dongfang Wang, Jian Li, Zhiyuan Mao *(Dept of Math Sci and Eng, Zhejiang Univ, 310027 Hangzhou, China)*. Wear 165(2) 159-167 (1 Jun 1993).

The decreasing abrasive wear rate of tetragonal zirconia polycrystal ceramic (TZP) with increasing load under experimental conditions is believed to be caused by the martensitic transformation of t-ZrO_2 to m-ZrO_2 in the abraded surface. The transformation toughened ceramics (TZP) appeared to give the best abrasive wear resistance among the ceramics studied in this experimental work. The surface failure of these ceramics was mainly due to the microfractural dropping and powder-type polishing scratches resulting from the brittle microfracturing part of the grain(s). Raising the fracture toughness wherever possible, in conjunction with a suitable hardness, will be beneficial in improving the abrasive wear resistance of ceramics.

11A518. Wear transition diagram for silicon nitride. - X Dong *(Dept of Mech Eng, Univ of Maryland, College Park MD 20742)* and S Jahanmir *(Ceramics Div, NIST)*. Wear 165(2) 169-180 (1 Jun 1993).

In the present study, unlubricated wear tests were conducted on a hot isostatically-pressed silicon nitride under various test conditions in self-mated sliding tests in air. Following the tests, scanning electron microscopy was used to elucidate the wear mechanisms and particularly to delineate the effects of load and temperature on wear. The results of the tests and observations were used to construct a wear transition diagram, with load and temperature as the two axes. This diagram is divided into five regions plus one transition zone. The controlling mechanism and tribological data, ie, friction coefficient and wear coefficient, in each region are unique. At low loads and relatively low temperatures, the tribological behavior is controlled by tribochemical reactions between silicon nitride surface and water vapor in the environment. In the temperate range 400-700°C at low loads, selective oxidation of WC inclusions controls the wear behavior. Formation of crystalline precipitates from the amorphous magnesium silicate grain boundary phase controls the wear process from 700 to 900°C at low loads. At higher temperatures, oxidation of silicon nitride dominates the wear process.

See also the following:

11A512. Mechanical and tribological behavior of Cu-Nb *in situ* composites
11A513. Wear and friction properties of prosthetic joint materials evaluated on a reciprocating pin-on-flat apparatus

292E. CONTACT FATIGUE

11A519. Surface topography and fatigue life of rolling contact bearings. - RS Zhou *(Timken Co, Canton OH 44706-2798)*. Trib Trans 36(3) 329-320 (Jul 1993).

The contact stresses of bearings were analyzed by a micro-macrocontact model in which the macrocontact was elastic, and the microcontact was elastic-plastic. Subsurface stress maps were calculated for real contact surfaces, by including roughness, waviness, and profile. The predicted subsurface stress maps display the local stress levels for various elastohydrodynamic lubrication (EHL) film thicknesses and show why enhanced-finish bearings have longer lives than the standard-finish bearings. It is believed that the present approach provides an alternative to the empirical methods that are used for predicting life under thin-film EHL conditions.

292H. SURFACE EFFECTS, TOPOGRAPHY, COATINGS

11A520. Contribution of EXAFS-like techniques to the determination of local order. Application to tribology. - J Lopez, JC Le Bosse, G Hansali *(Lab Tribologie Dyn Syst CNRS URA 855, Ecole Natl Ing St Etienne, 58 rue Jean Parot, 42023 St Etienne, France)*, M Belin, JM Martin *(Lab Tribologie Dyn Syst CNRS URA 855, Ecole Centrale de Lyon, 36 ave Guy de Collongue BP 163, 69131 Ecully, France)*. Acta Phys Polonica A 83(5) 551-566 (May 1993).

The determination of local order of atomic scale becomes more and more fundamental for understanding superficial phenomena such as tribology and catalysis. Among a few techniques available in this field, we are only concerned with the EXAFS-like ones (EXAFS, SEXAFS, EXELFS, SEELFS, etc). The difficulties appearing all along the numerical treatment of such spectra are carefully analysed and a methodology is proposed in view to obtain reliable radial distribution functions. Some applications of these techniques are presented in two fields connected with tribology: friction induced amorphisation in high vacuum and characterization of interfacial solid bodies created during a wear process including an antiwear additive.

11A521. Determination of proper frequency bandwidth for 3D topography measurement using spectral analysis Part I. Isotropic surfaces. - TY Lin, L Blunt, KJ Stout *(Sch of Manuf and Mech Eng, Univ of Birmingham, Birmingham, Edgbaston B15 2TT, UK)*. Wear 166(2) 221-232 (1 Jul 1993).

Areal spectral analysis is applied to achieve proper frequency bandwidth for topography measurements from machined surfaces. The effect of aliasing on the spectrum of surface features due to a large sample spacing is evaluated. The characteristics of low-frequency components of a surface are also investigated. The low-frequency limit of measurement for obtaining the genuine features of a surface can be decided from the spectral analysis of low-frequency components of the surface. The guidelines for topography measurements are proposed for selecting an appropriate sampling bandwidth of surfaces with due consideration of limited computer memory. The guidelines developed are applied to study the general patterns of spectra from a range of isotropic engineering surfaces. An example is given to demonstrate the selection of a temporary sample spacing for a further measurement search for the low-frequency cut-off of a surface, which may be in turn used to determine the high-frequency limit with an estimate of aliasing influence. In spectral analysis, circular spectra and/or accumulation spectra have been shown to be suitable for the analysis of sample surfaces from isotropic machining processes.

11A522. Effects of real contact area and topographical features of wear surfaces on abrasive wear of metals. - T Hisakado, H Suda, H Ariyoshi, S Sakano *(Dept of Mech Eng, Fac of Eng, Gunma Univ, 1-5-1 Tenjincho Kiryu, Gunma 376, Japan)*. Wear 165(2) 181-191 (1 Jun 1993).

The aim of this study is to clarify various cross-sectional shapes and areas of wear grooves and ridges which are formed under multi-point contacts and to study the effect of the real contact area on the friction and wear properties in the two-body abrasive wear of metals. Two kinds of tests were performed: (1) the scratching test on an actual abrasive paper under two short sliding distances (less than 1 mm or 5mm), and (2) the friction and wear test under a long sliding distance (about 65 mm). The effects of the real contact area and surface topographical features of the wear surface of the pin on the friction and wear properties of abrasive wear are investigated systematically, and the friction and wear mechanisms are discussed. The following main results were obtained. (1) The mean area of the real contact point is affected by the existence of the embedded abrasive grains and the surface layer which is harder than the bulk material of the pin. (2) The mean cross-sectional area of the grooves on the worn surface of the pin, which is calculated from the profile curve measured perpendicular to the sliding direction, is a factor that has a direct effect upon the specific wear rate of a pin and that measured parallel to the sliding direction is the factor which affects the friction coefficient. (3) The specific wear rate for lead pins is approximately proportional to the real contact area for abrasive wear.

11T523. Experimental study of the parameters that determine take-off velocity and CSS performance of thin film disks. - S Suzuki, I Hayashi *(Asahi Glass America, Milpitas CA 95035)*, K Matsushita *(Asahi Glass, Yokohama 221, Japan)*. Trib Trans 36(3) 411-416 (Jul 1993).

11A524. Fast 2D-3D optical profilometer for wide range topographical measurement. - M Zahidi, M Assoul, J Mignot *(Lab Metrologie Interfaces Tech, Inst Univ Tech, 25009 Besancon, Cedex, France)*, B Bellaton *(Digital Surf SARL, Valparc Valentin, 29 route d'Epinal 25048, Besancon Cedex, France)*. Wear 165(2) 197-203 (1 Jun 1993).

An optical profilometer, based on a triangulation principle, has been designed to measure the topography of surfaces. It uses a laser diode source (λ = 0.788 μm) and position sensing detectors. Response is obtained with a minimum of error due to a double detection system. Sensitivity is about ±3 μm for a vertical range of 1 mm. Vertical range can attain 5 mm, and more than 10 mm with a wide range numerical arrangement. Non-contact with the surface means a scanning speed of about 4 mm s^{-1}, and a 512 × 512 matrix (with a 12 bit definition) can be created in 9 min.

11A525. Function: Hardness-load as surface layer characteristics. - F Rudol *(Politechnika Swietkrzyska, Zaklad Odlewnictwa, Kielce, Poland)*. Zagadnienia Eksploatacji Maszyn 26(4) 417-430 (1991).

A new method of estimation of surface layer depth and quality is presented with special regard to its tribological properties. This method is based on analysis of hardness as load function. The methods used here to hardness measurement were only those with geometrically similar indentations: mainly unified HU method and Vickers HV method. Tests with different loads bring hardness of particular zones of material surface layer and so called "essential hardness". The method worked out is a substitution of perpendicular and skew microsections and is complementation to existing layer ganges as those may be accurately calibrated. The tested detail is not destructed. Besides measurements of "zone hardness" it makes possible precise determination of finish treatment allowance. Examples given show advantages and usefulness of the method.

11A526. Influence of microgeometry of surfaces on the contact approach of elements with a surface layer. - A Polijaniuk and Z Handzel-Powierza *(Inst of Fund Tech Res, Polish Acad of Sci, Warszawa, Poland)*. Eng Trans 41(1) 51-60 (1993).

Effects of the microgeometry of surfaces on the contact approach of steel elements of joints at rest are investigated in the paper. A case of elements with nominally flat surfaces subjected to quasi-statical load is considered. The results of experiments are presented made with the use of an original device for studying contact phenomena, designed and constructed in the Inst of Fundamental Technologies Research of PAS (IPPT PAN). It is shown to what extent the contact approach depends on the microgeometry of a surface obtained in the machining process.

11A527. Interfacial mechanics of a tape wrapped around a flexible bumpy roll. - RC Benson *(Dept of Mech Eng, Univ of Rochester, Rochester NY 14627)*. Trib Trans 36(3) 375-380 (Jul 1993).

This paper presents a mathematical model and numerical solution for axisymmetic contact between an elastic tape and a flexible, bumpy roll. Regions of tape-roll contact and gap are identified. It is shown that slight imperfections in the roll's geometry can lead to extremely large deviations from the expected nominal values for interfacial pressure and hoop stress of the tape.

11A528. Physics of solids and morphology of surfaces. - J Rosseau *(Lab Tribologie Dyn Syst URA CNRS 855, Ecole Natl Ing, St Etienne, France)* and TG Mathia *(Lab Tribologie Dyn Syst URA CNRS 855, Ecole Centrale, Lyon, France)*. Acta Phys Polonica A 83(5) 535-550 (May 1993).

The morphology of surfaces is now an important field of research because of its direct connection with the industrial activity like manufacturing and optimizing of functional criteria through complicated interfacial phenomena. Presently, characterization of the surface morphology, via the profile metrology, is well modelled by a statistical description. The use of shape morphological parameters allows to identify features of the surface structures generated by the process techniques and the emergence of the different phases of the condensed matter. Starting from the solid state background knowledge, prediction of the surface morphology appears as a tedious way.

11A529. A simple model for the surface phenomena. - L Wojtczak *(Ecole Natl Ing St Etienne, St Etienne, France)*. Acta Phys Polonica A 83(5) 685-699 (May 1993).

The simplicity of the present model consists in the construction of the Hamiltonian based on the models of quasi-harmonic oscillators coupled to quasi-free electrons with the effective parameters which are estimated by means of the pseudoharmonic approach and coherent potential approximation, respectively. The geometry of the sample is determined by the topological disorder at the surface reflecting the surface roughness. The model is discussed in connection with the friction related to the melting and pre-melting phenomena. The backscattering of electrons seems to be a testing tool useful not only for decorated surfaces but also for quasi-liquid layers.

11A530. Some statistical properties of the rough surface. - T Balcerzak *(Solid State Phys Dept, Univ of Lodz, Pomorska 149-153, 90-236 Lodz, Poland)*. Acta Phys Polonica A 83(5) 597-610 (May 1993).

The temperature induced roughening of the solid surface is described by means of a discrete Gaussian model, using integral operator technique. On the basis of the exact statistical identities, the formulae for several local moments, ie, $\langle h_i \rangle$, $\langle (h_i)^2 \rangle$ and $\langle h_i h_j \rangle$ are derived. The results of computer calculations including surface specific heat, are presented for three lattices with z = 3,4, and 6. In discussion, some further applications of the presented method are suggested.

11A531. Three-body abrasion of brittle materials as studied by lapping. - M Buijs and K Korpel-van Houten *(Philips Res Lab, PO Box 80.000, 5600 JA Eindhoven, Netherlands)*. Wear 166(2) 237-245 (1 Jul 1993).

Lapping experiments on glass were performed to verify a model for three-body abrasion of brittle materials. The model is based on material removal by rolling abrasive particles. The particles indent the workpiece surface and remove material by lateral cracking. Median cracking introduces subsurface damage. The model leads to expressions for removal (or wear) rate, surface roughness, subsurface damage and load per particle as a function of particle shape, particle size, material parameters of workpiece and lapping plate, applied pressure and relative velocity between plate and workpiece. The model was found to give a good description of the experimental results, allowing among other things the calculation of removal rate, surface roughness or damage penetration from the measurement of either one of these parameters.

11A532. Tribochemical studies by XPS analysis of transfer films of Nylon 11 and its composites containing copper compounds. - S Bahadur, Deli Gong *(Dept of Mech Eng, Iowa State Univ, Ames IA 50011)*, JW Anderegg *(Ames Lab, Iowa State Univ, Ames IA 50011)*. Wear 165(2) 205-212 (1 Jun 1993).

The transfer films of Nylon 11 and its composites with CuS, CuAc and CuF_2 formed on the steel disk surfaces were studied by X-ray photoelectron spectroscopy. The study revealed that CuS and CuF_2 decomposed under the rubbing conditions and produced copper, FeF_6 group and $FeSO_4$. The analysis at different depths in the transfer films indicated higher concentrations of these species closer to the transfer film-counterface interface. There was no chemical change detected when unfilled Nylon 11 and CuAc-Nylon composite rubbed against the steel disk surfaces. These results have been used to hypothesize the mechanism by which the transfer films of these materials influence wear.

See also the following:

11A515. Effect of head wear and tape shear on the head-tape interface

292I. WEAR MONITORING

11A533. Effect of niobium on wear resistance of 15%Cr white cast iron. - He-Xing Chen, Zhe-Chuan Chang, Jin-Cai Lu, Huai-Tao Lin *(Wear Res Center, Guangzhou Inst of Nonferrous Metals, Wushan, Guangzhou 510651, China)*. Wear 166(2) 197-201 (1 Jul 1993).

Niobium addition to 15%Cr white cast iron can increase its wear resistance because (1) Nb forms extremely hard carbides (NbC) of hardness around HV 2400, (2) Nb can raise the matrix hardness of 15%Cr iron from HV 693 to HV 899, (3) Nb shifts the eutectic point to the right, therefore the iron can have a high carbon content without the danger of forming brittle hyper-eutectic carbides, and (4) the morphology of NbC is block-hook-like. The NbC particles can be kept firmly in the matrix during the wear process. The wear resistance was tested by wet rubber wheel abrasion tests. The optimum chemical composition of the iron found in these tests was used for making slurry pump components, which were field tested in a mineral mine. The field test confirmed the laboratory test results.

292Y. COMPUTATIONAL TECHNIQUES

11A534. Rudimentary considerations for adaptive gap-friction element based on the penalty method. - SH Lee *(MacNeal - Schwendler, 815 Colorado Blvd, Los Angeles CA 90041)*. Comput Struct 47(6) 1043-1056 (17 Jun 1993).

One of the major areas in nonlinear analysis that poses difficulties in convergence is known to be the application of penalty GAP elements, particularly with friction. The GAP element simulates a point-to-point contact, and is often used to simulate surface contact problems. Numerical difficulty is inherent in nature for the penalty method. Difficulties of the penalty GAP element are coped with by implementing an adaptive GAP element in MSC-NASTRAN. The adaptability comprises algorithms to subdivide the increment in the local process, to update the stiffness at an appropriate time, to bisect load or time step size when the increment is excessive, and to adjust penalty stiffnesses to the proper values in concert with the nonlinear and dynamic environment.

See also the following:

11A226. BEM frictional contact analysis: Load incremental technique

294. Machine elements

11A535. Vibroacoustic monitoring of bearing points failures in the driving system of the mining main ventilation fans. - T Zakrzewski *(Silesian Univ of Tech, 44-100 Gliwice, Poland)*. Arch Acoust 18(1) 47-66 (1993).

The purpose of the examinations carried out on separated bearing points was to evaluate the range of sensitivity of the introduced, relatively simple, estimates to the recorded vibratory signals, to changes of the degree of wear in the conditions of constant loading and increasing period of operation. The obtained results, and the analysis of these results, served as the basis for elaborating the criteria for the evaluation of the technical state of bearing points. Here, such diagnostic estimates were selected that their values determined at the moment of checking, allowed to draw conclusions on the functional characteristics of the bearing points.

11A536. High cycle fatigue strength of butt welded joints of small diameter pipes. - K Kishida, M Higuchi, M Fukuzawa *(Ishikawajima-Harima Heavy Indust, 1 Shin-nakahara-cho, Isogo-ku, Yokohama 235, Japan)*. Int J Pressure Vessels Piping 55(3) 375-383 (1993).

Fillet welds are usually used for joints of small pipelines with 2-inch nominal outer diameter or smaller. The fillet welded joints might not be strong enough to withstand the high cycle fatigue produced by steady-state vibrations, because they have inherent crack-like discontinuities in the root portion. The fatigue strength of butt welded joints is believed to be higher than that of fillet welded joints, so that it is desirable to use butt welded joints for small pipelines under steady-state vibrations. However, there are no available data on high cycle fatigue strength of small diameter piping butt welded joints. This paper presents new data on high cycle fatigue strength of butt welded joints in small diameter pipes and development of their fatigue strength reduction factors for design use.

11A537. Rotordynamic characteristics of flexure-pivot tilting-pad journal bearings. - RW Armentrout *(California Consultants, Danville CA)* and DJ Paquette *(KMC Div of Cookson America, Coventry RI)*. Trib Trans 36(3) 443-451 (Jul 1993).

Many of today's modern turbomachines, especially those running at high speeds and high power ratings, require the superior stability characteristics of tilting-pad journal bearings to prevent rotordynamic instabilities. Until now, the design complexity of tilting-pad bearings has precluded their use in many small, high-volume applications where cost and size are important. This paper introduces a new one-piece journal bearing design, the flexure-pivot bearing, that offers many of the beneficial rotordynamic advantages of tilting-pad bearings, without the complexities of a multi-piece design. Performance data for a flexure-pivot bearing is shown for an application requiring a highly stable design, illustrating the effectiveness of the flexure-pivot bearing in offering rotordynamic stability approaching that of a tilting-pad bearing.

11A538. Simplified method of bearing material fatigue strength investigation. - A Rigall and J Sikora *(Politech Gdanska, Wydzial Budowy Maszyn ul Majakowskiego 11-12, 80-952 Gdansk-Wrzeszcz, Poland)*. Zagadnienia Eksploatacji Maszyn 26(4) 387-404 (1991).

Fatigue strength investigation of slide bearing is extremely time-consuming and involves special difficulty in design, performing and analysis of the experiments. A new sequential procedure of the research, proposed in this article, is based on the principle of the two-point strategy and makes it possible to achieve effectively an assessment of important part of cumulative distribution function of bush sliding surface fatigue strength. A main statistical parameter which is estimated is a median of the distribution.

11A539. Tilting pad journal bearings: Measured and predicted stiffness coefficients. - DW Parkins *(Cranfield IT, Bedford, UK)* and D Horner *(Michell Bearings, Newcastle-upon-Tyne, UK)*. Trib Trans 36(3) 359-366 (Jul 1993).

This paper presents measured and calculated characteristics of a tilting pad journal bearing suitable for high speed machinery. Descriptions are given of the experimental techniques used with this variety of bearing and the theoretical model for predicting performance. Measured values of pad temperature, eccentricity, attitude angle, and the four stiffness coefficients are given for a range of loads and rotational speeds. Data are given for both load on pad and between pad configurations, the two principal loading arrangements. Comparisons are made between the measured and predicted bearing temperatures and stiffness coefficients over a wide range of values.

11T540. Importance of labyrinth seal through-flow deflection for enlarging clearance without increasing leakage. - DL Rhode and MJ Guidry *(Mech Eng Dept, Texas A&M Univ, College Station TX 77843)*. Trib Trans 36(3) 477-483 (Jul 1993).

11A541. Three-dimensional computations of rotordynamic force distributions in a labyrinth seal. - DL Rhode, SJ Hensel, MJ Guidry *(Turbomachinery Lab, Mech Eng Dept, Texas A&M Univ, College Station TX 77843)*. Trib Trans 36(3) 461-469 (Jul 1993).

A numerical method employing a finite volume approach for calculating the rotordynamic force on eccentric, whirling labyrinth seals has been presented. The SIMPLER algorithm is used to calculate the 3D flowfield within a seal. The modified bipolar coordinate system used accurately describes the geometry of an eccentric seal. The turbulent flow form of the fully elliptic Navier-Stokes equations was solved. A 3% eccentric, single labyrinth cavity rotating at 7000 cpm was investigated for three different inlet swirl conditions, each with and without a whirl orbit frequency of 3500 cpm. It was found that the circumferential pressure variation around the downstream tooth periphery is by far the most important contribution to both rotordynamic force components. Thus the flowfield details near each tooth throttling should be carefully considered. Further, a substantial increase of shaft whirl frequency was found to decrease and increase the effect of cavity inlet swirl on F_t and F_r, respectively.

See also the following:

11A206. Intelligent control of the gear-shaving process

11A519. Surface topography and fatigue life of rolling contact bearings

296. Machine design

11A542. Distribution of coupler curves for crank-rocker linkages. - De Lun Wang and Da Zhun Xiao *(Dept of Mech Eng, Dalian Univ of Tech, Dalian 116024, Peoples Rep of China)*. Mech Machine Theory 28(5) 671-684 (Sep 1993).

Based on a differential geometry approach, the basic equations for the coupler curve of the four-bar linkage are concisely derived. The geometric properties of coupler curves for the crank-rocker linkage are analyzed, and the distribution law of various shapes of coupler curves is revealed. The moving centrode, Ball's curve and the self-tangent curve divide the coupler plane into several areas. The points in each of these areas trace a specific shape of curves. Therefore, any shape of coupler curves with a cusp, inflection point, Ball's point, crunode, tacnode or oval shape, etc, for the first time, could be readily located.

11A543. Kinematic-kinetic performance analysis and synthesis measures of multi-dof mechanisms. - Ming-Yih Lee, AG Erdman, Y Gutman *(Productivity Center, Dept of Mech Eng, Univ of Minnesota, Minneapolis MN 55455)*. Mech Machine Theory 28(5) 651-670 (Sep 1993).

This paper discusses kinematic-kinetic performance characteristics of multi-dof mechanisms and proposes analytical and graphical representations for them. These performance characteristics are kinematic cross-coupling, directional motion mobility, force manipulability, and motion efficiency. Properties of the proposed analytical-graphical measures are elaborated on for the purpose of kinematic synthesis. Graphical performance distribution over the mechanism's reachable workspace enables the designer to view the performance as a whole. Critical performance points representing extreme conditions of these performance characteristics are identified and used for design. The proposed performance tools will be demonstrated for the performance analysis of various robotic mechanisms.

11A544. Synthesizing spatial 7R mechanism with 16-assembly configurations. - Qizheng Liao, Chonggao Liang *(Beijing Univ of Posts and Telecommun, Beijing 100088, Peoples Rep of China)*, Qixian Zhang *(Beijing Univ of Aeronaut and Astronaut, Beijing, Peoples Rep of China)*. Mech Machine Theory 28(5) 715-720 (Sep 1993).

Using complex numbers, a special case of a spatial 7R mechanism is discussed. The computer calculations show that the input-output equation of this mechanism is still 16 degree in tan-half-angle of the output angular displacement. By adjusting a group of dimensions of this mechanism, a general 7R mechanism with 16-assembly configurations is discovered.

11A545. Modeling of a torsion-bar cam mechanism. - KSH Sadek *(Sch of Mech and Manuf Eng, Sunderland Univ, Chester Rd, Sunderland SR1 3SD, UK)* and A Daadbin *(Dept of Mech Eng and Manuf Syst, Northumbria Univ, Ellison Build, Newcastle upon Tyne NE1 8ST,* *UK)*. Mech Machine Theory 28(5) 631-640 (Sep 1993).

In high-speed disc-cam mechanisms, vibration of the linkage is harmful in that the end motion deviates from the required schedule; but more importantly, the vibration may result in the loss of contact between the cam and the follower. This causes an increase in noise levels and excessive wear. A simplified mathematical model was developed to predict the dynamic behavior of a mechanism. Fed by the cam profile and the parameters of the mechanism, a computer program yields the output motion of the mechanism as well as the contact force between the cam and its follower. Since it has interactive features, the program can be used to help in the design of such systems.

11A546. Optium design of the RSS'R flexible space mechanism via multiplier techniques. - Yue-Qing Yu *(Section of the Theory of Machines and Mech, Beijing Polytech Univ, Beijing 100022, Peoples Rep of China)*. Mech Machine Theory 28(5) 625-630 (Sep 1993).

This paper presents a new procedure for the optimum design of a flexible space mechanism. An advanced optimization technique for the multiplier method is applied to design a completely elastic linkage having minimum mass while keeping stresses and deflection in the links under prescribed limits. Numerical solutions for the example of the RSS'R spatial mechanism, using the new procedure, are found to be more valid than those of the previously published works.

See also the following:

11A211. Dynamic simulation and choice of generalized coordinates for a free-floating closed-chain planar manipulator

298. Fastening and joining

11A547. Flanged joint analysis: A simplified method based on elastic interaction. - A Bouzid and A Chaaban *(Dept of Mech Eng, Ecole Polytech, Case postale 6079, Succ A, Montreal, PQ, H3C 3A7, Canada)*. Trans Can Soc Mech Eng 17(2) 181-196 (1993).

Structurally sound bolted joints often fail due to loss of tightness. This is because the clamping load is affected by the application of the internal fluid pressure. A good design technique should therefore encompass most aspects of joint behavior and produce efficient sealing performance within the clearly defined limits of the method used. This paper presents a simple analytical model based on an extension of the Taylor Forge approach taking into account flange rotation, flexibility of both the gasket and the bolts and, when applicable, the stiffness of the end closure. Examples will be discussed based on experimentally determined gasket properties.

11A548. Improving toughness of electron beam welds of heavy Mn-Mo-Ni steel plates for pressure vessels. - Y Tomita *(Nagoya R&D Lab, Nippon Steel, Tokai City, Aichi, Japan)*, K Tanabe, K Koyama *(Steel Res Lab, Nippon Steel, Futtsu City, Chiba, Japan)*. J Pressure Vessel Tech 115(3) 242-248 (Aug 1993).

Electron beam welding melts and solidifies steel plate without using any welding material, unlike the conventional welding. Therefore, the toughness at the weld metal can decrease, depending on the chemical composition of the steel plate. Toughness at the electron beam weld can be increased by turning the microstructure from upper bainite into lower bainite and making the effective grain size finer. The microstructure can be controlled by the addition of alloy elements and optimization of impurity elements. In case the chemical compositions cannot be varied, largely because of the specification for their ranges, and the weld metal microstructure remains as upper bainite even after the application of microstructure control, methods to improve the toughness of electron beam weld itself, regardless of steel grades, becomes necessary. Phenomena peculiar to the electron beam weld are segregation during solidification and intergranular segregation over the dendrite surface. The fracture initiation is accelerated by the microcracks caused by the segregations during solidification. The fracture propagation is promoted by intergranular cracking caused by the intergranular segregation. By reducing these segregations, the fracture initiation and propagation are restrained and toughness increases despite the upper bainite microstructure. This can be achieved by the higher purification of steel. Through the foregoing investigations, ASTM A533 Type B Class 2 steel plate of 100 mm in thickness for electron beam welds has been developed for pressure vessels. Various welding tests as pressure vessels have been conducted, and it becomes clear that the developed steel plate has excellent toughness at the weld superior to those obtainable by conventional welding. The use of this steel greatly reduces the welding period compared to the conventional welding method.

11A549. Materials data for high-temperature design of ferritic steel pressure vessel weldments. - ZP Wang and DR Hayhurst *(Dept of Mech and Process Eng, Univ of Sheffield, Mappin St, PO Box 600, Sheffield S1 4DU, UK)*. Int J Pressure Vessels Piping 55(3) 461-479 (1993).

To aid material selectors and engineering designers in the design of ferritic pressure vessel weldments, a data bank has been created of the creep deformation and rupture properties of weld materials and heat affected zone (HAZ) materials. The generated data are based on the properties of well-characterized typical materials and on information supplied by plant engineers. The presentation style allows the data to be used in materials selection at the earlier stages of design, or in Continuum Damage Mechanics based FE analysis at the detailed design stage.

11A550. Advances in bonding technology for electronic packaging. - Chin C Lee, Chen Y Wang, G Matijasevic *(Elec and Comput Eng, UC, Irvine CA 92717)*. J Electron Packaging 115(2) 201-207 (Jun 1993).

Recent progress in bonding materials is briefly reviewed with highlights of some of the advantages and disadvantages of the various attachment processes. The principle and experimental results of bonding with multilayer structures of Au-Sn and Au-In are presented. Using solid state as well as liquid phase diffusion of the multilayers, bonding temperatures less than the final melting point of the alloy can be used. This technique therefore allows reversal of the conventional soldering step hierarchy allowing a higher temperature process to follow the multilayer bonding step. Proper deposition of the multilayers inhibits oxidation of tin or indium. Die attachment experiments confirmed that high quality bonding can be obtained as seen in the void-free bonding layer image done by scanning acoustic microscopy. Cross-section examinations with SEM and EDX show near-eutectic alloy formation of good uniformity. Thermal shock tests confirmed the high strength of these solder alloys.

11A551. Comparison of 2 and 3D FE analyses of adhesive joints. - G Richardon, AD Crocombe *(Dept of Mech Eng, Univ of Surrey, Guildford GU2 5XH, UK)*, PA Smith *(Dept of Mat Sci and Eng, Univ of Surrey, Guildford GU2 5XH, UK)*. Int J Adhesion Adhesives 13(3) 193-200 (Jul 1993).

The validity of modeling adhesive joints as 2D problems has been assessed. Results are presented from a series of 3D adhesive joint analyses and, using these, modifications to 2D analyses are proposed which yield results that compare favorably with their 3D counterparts. This is achieved primarily by adjusting the 2D loading and is shown to be extremely effective. Comparison of both the adhesive stress distributions and the energy release rates associated with crack growth from the 2D and 3D analyses have been made.

11A552. Extended Maxwell Garnett formalism for composite adhesives for microwave-assisted adhesion of polymer surfaces. - B Shanker and A Lakhtakia *(Dept of Eng Sci and Mech, Penn State)*. J Composite Mat 27(12) 1203-1213 (1993).

Adhesives with dielectric loss are needed for microwave-assisted joining of polymeric substances. The dielectric loss in an otherwise suitable adhesive may be enhanced by doping it with fine metallic particles. Here we use a recently extended Maxwell Garnett formalism to estimate the complex dielectric constant of a metal-doped composite adhesive, with specific focus on the imaginary part of the dielectric constant of the composite adhesive.

11A553. Nondestructive evaluation of model adhesive joints by PVDF piezoelectric film sensors. - B Tang *(Wyle-Lab, Build 8252A Edwards AFB CA 93253-5000)*, J Mommaerts, RK Duncan, JC Duke Jr, DA Dillard *(Dept of Eng Sci and Mech, VPI)*. Exp Mech 33(2) 102-109 (Jun 1993).

Metallized poly(vinylidene fluoride) (PVDF) films can be etched into nondestructive evaluation (NDE) sensor devices. Since these sensors are relatively inexpensive, thin and lightweight, they can be attached permanently to adhesively bonded joints, laminated composites, and other structures to measure structural integrity. The present study has addressed techniques to design, attach, and utilize such sensors for adhesive joint and laminated composite applications. PVDF sensors have been successfully used as NDE transducers in pulse-echo, through-transmission, and acousto-ultrasonic techniques to monitor curing, and to detect porosity and crack propagation in different model joint geometries. Feasibility of several applications has been demonstrated, although several problems remain. The potential of using these techniques for practical bonded structures is also suggested.

11A554. Study of the cure of adhesives using dynamic mechanical analysis. - RW Cook and DA Tod *(Military Div, DRA, ET5 Ft Halstead, Sevenoaks Kent TN14 1BP, UK)*. Int J Adhesion Adhesives 13(3) 157-162 (Jul 1993).

Adhesives are being used extensively in fabrication as they offer many advantages over standard joining methods. As the adhesive forms an integral part of the structure, it is necessary to fully understand the initial mechanical properties of the material and how these change with ageing. Formal testing of materials often involves a considerable number of tensile tests. These are not only expensive but time consuming. One method of speeding up the process is to study the small strain mechanical properties of materials and therefore avoid the statistical uncertainty involved in fracture tests. The aim of this paper is to show how the technique of dynamic mechanical spectrometry can be applied to the study of adhesives and adhesive joints.

See also the following:

11A504. Elastic analysis of a circular flange joint subjected to axial force

V. MECHANICS OF FLUIDS

350. Rheology

11T555. Best fit for differential constitutive model parameters to nonlinear oscillation data.

- RS Jeyaseelan and AJ Giacomin *(Rheology Res Lab, Mech Eng Dept, Texas A&M Univ, College Station TX 77843-3123)*. J Non-Newtonian Fluid Mech 47 267-280 (Jun 1993).

11A556. Microscopic studies of static and dynamic contact angles. - PA Thompson *(Dept of Mech Eng and Mat Sci, Duke Univ, Durham NC 27708-0300)*, WB Brinckerhoff *(Dept of Phys, Ohio State Univ, 174 W 18th Ave, Columbus OH 43210)*, MO Robbins *(Dept of Phys and Astron, Johns Hopkins Univ, Baltimore OH 21218)*. J Adhesion Sci Tech 7(6) 535-554 (1993).

Molecular dynamics simulations are used to test macroscopic theories for static and dynamic contact angles. Young's equation is verified by comparing observed static contact angles to angles calculated from the independently measured surface tensions between phases. Laplace's relation between the interfacial curvature and pressure is also checked. Both equations agree with simulation results within statistical errors. Hydrodynamic theories of dynamic contact angles are less well defined because they produce diverging stresses at the contact line between the solid and fluid interfaces if the usual no-slip boundary condition is assumed. Our simulations show that slip occurs within about two molecular diameters of the contact line, and that local hydrodynamics breaks down in the slip region. The slip results from large tangential stresses along the solid wall. A surprising result is that changes in the boundary condition for single-fluid flow at molecular scales produce dramatic changes in the dynamic contact angle.

11A557. Brownian dynamics simulation of finitely extensible bead-spring chains. - BHAA van den Brule *(Shell Res BV, PO Box 60, 2280AB Rijswijk, Netherlands)*. J Non-Newtonian Fluid Mech 47 357-378 (Jun 1993).

The behavior of infinitely dilute solutions of finitely extensible nonlinear elastic (FENE) bead-spring chains in shear flow and uniaxial elongational flow is analyzed under both steady-state and transient conditions, using the method of Brownian dynamics. Three FENE chain models are considered: the original model using the Warner spring force law and models using the Peterlin approximation and the recently proposed PM approximation. It is shown that the two approximate models, which are based on pre-averaging of the spring constant, perform reasonably well in elongational flow but fail in describing shear flow.

11A558. Rheology of polydisperse polymers: Relationship between intermolecular interactions and molecular weight distribution. - P Cassagnau, JP Montfort, G Marin, P Monge *(Univ Pau et des Pays de l'Adour, Pau, France)*. Rheol Acta 32(2) 156-167 (Mar/Apr 1993).

An expression of the relaxation function of linear polydisperse polymers is proposed in terms of intermolecular couplings of reptative chains. The relaxation times of each molecular weight are assumed to be shifted according to a tube renewal mechanism accounting for the diffusion of the surrounding chains. The subsequent shift is applied to the relaxation function of each molecular weight obtained from an analytical expression of the complex compliance Jx(ω). Therefore the complex shear modulus Gx(ω) is derived from the overall relaxation function using the probability density accounting for the molecular weight distribution and four species-dependent parameters: a front factor A for zero-shear viscosity, plateau modulus G^0_N, activation energy E and characteristic temperature T_∞. All the main features of the rheology of polydisperse polymers are described by the proposed model.

11A559. Simultaneous solution for fiber orientation in axisymmetric radial flow. - S Ranganathan and *(Dept of Mech Eng, Center for C... Univ of Delaware, Newark DE 19716)*. J Non-Newtonian Fluid Mech 47 107-136 (Jun 1993).

The effect of the changing microstructure during the flow of fiber suspensions on the flow kinematics is studied. The suspension is assumed to consist of rigid cylindrical particles immersed in a highly viscous Newtonian fluid. Further, the suspension is modeled as an anisotropic fluid whose rheological properties are functions of the local microstructure. The effect of inertia is neglected during the flow of the suspension. The orientation of the particles is assumed to be governed by the flow field and the fiber-fiber interactions. The governing equations for the flow field and fiber orientation are coupled and are simultaneously solved in an axisymmetric radial-flow configuration. These solutions are compared to those obtained using the conventional decoupled approximation where the bulk flow field is assumed to be unaffected by the presence of the suspended particles.

11A560. Unsteady flow of a power-law dusty fluid with suction. - AJ Chamkha *(Fleetguard, Cookeville TN 38502)*. J Fluids Eng 115(2) 330-333 (Jun 1993).

Equations governing flow of a particulate suspension exhibiting finite volume fraction in non-Newtonian power-law fluids are developed and applied to the problem of unsteady flow past an infinite porous flat plate with suction. Numerical results for small volume fraction for the displacement thicknesses for both phases and the skin-friction coefficient for the fluid phase are obtained using an implicit finite difference scheme and presented graphically to elucidate interesting features of the solutions.

11A561. Electrorheological fluids applied to an automotive engine mount. - EW Williams, SG Rigby *(Dept of Appl Math and Theor Phys, Liverpool Univ, PO Box 147, Liverpool L69 3BX, UK)*, JL Sproston, R Stanway *(Dept of Mech Eng, Liverpool Univ, PO Box 147, Liverpool L69 3BX, UK)*. J Non-Newtonian Fluid Mech 47 221-238 (Jun 1993).

This paper is concerned with the mathematical modeling of electrorheological fluids when used in oscillating squeeze-flow mode; in a prototype automotive engine mount. A solution of the problem is found for the situation in which the non-Newtonian behavior of the fluid is represented by a Bi-Viscous characteristic. This permits the prediction of the vibration damping characteristics of the device. Finally these results are compared with recently published experimental values.

11A562. Prediction of viscosities using chemical graph theory. - EW Pitzer *(Aero Propulsion and Power Directorate, Wright Lab, WPAFB)*. Trib Trans 36(3) 417-420 (Jul 1993).

The viscosities of three groups of lubricant basestock molecules are predicted using chemical graph theory. Alkyl diphenylphosphates, trimethyloethane esters, and oligomers of chlorotrifluoroethylene are modeled. These compounds are similar for graph theoretical modeling purposes in that all are aliphatic in nature or vary only by aliphatic substituents. The graph theoretical approach for the modeling of these compounds uses summations of the shortest topological distances between atoms in the molecule. A new topological index is introduced that weights chlorine molecules in the chlorotrifluoroethylene oligomers. For each group modeled, the coefficient of determination γ^2 was in excess of 0.99 with a standard error of estimate well below five percent of the average value modeled.

11A563. Squeezing flow of a Bingham material. - SDR Wilson *(Dept of Math, Univ of Manchester, Manchester M13 9PL, UK)*. J Non-Newtonian Fluid Mech 47 211-219 (Jun 1993).

The "squeeze-flow paradox" for a Bingham material is investigated. The space between two parallel discs is filled with liquid material of the Bingham viscoplastic type and the discs are squeezed together; the paradox arises from the requirement that the material between the discs should move radially outwards, together with the observation that the shear stress on the midplane is zero so that the material should be solid. Here we argue that the Bingham model should be regarded as a limiting case of some other model (the biviscosity model, here) and that this limit clashes with the other limit process, in which normal stresses are neglected, giving rise to lubrication theory. A distinguished limit is demonstrated and a corrected theory is derived which contains the "paradoxical" theory as a special case.

See also the following:

11A343. Numerical prediction of extrudate swell of a high-density polyethylene: Further results
11T555. Best fit for differential constitutive model parameters to nonlinear oscillation data
11A560. Unsteady flow of a power-law dusty fluid with suction

352. Hydraulics

352A. GENERAL THEORY

11A564. Rheo-optical study of shear-thickening and structure formation in polymer solutions Part II. Light scattering analysis. - AJ Kishbaugh and AJ McHugh *(Dept of Chem Eng, Univ of Illinois, Urbana IL)*. Rheol Acta 32(2) 115-131 (Mar/Apr 1993).

Light scattering calculations based on Anomalous Diffraction Theory (AD), Rayleigh spheroids, and flexible macromolecules are used to propose a phenomenological explanation for the relationship between shear-thickening and structure formation in polymer solutions. Quantitative comparisons are made to experimental data for the rheo-optical behavior of fractionated polystyrene solutions presented in part I of this paper. Results from the ADA calculations suggest that the viscosity and dichroism behavior can be attributed to the production and growth of micron-size, optically isotropic structures during flow. The saturation dichroism behavior exhibited by the solutions which shear thin can be attributed to the formation of entanglement regions which achieve a fixed size and act as Rayleigh spheroids in their scattering behavior. The magnitude and shear rate dependence of the observed birefringence can be accounted for on the basis of the nonlinear, flexible macromolecule model, implying that birefringence is governed by the polymer chains remaining in solution which do not take part in the structure formation. The latter result is consistent with the experimental observation that the birefringence dependence on shear rate is the same whether the solution exhibits shear thickening or shear thinning in its viscosity behavior.

352B. CLOSED CONDUIT FLOW

11A565. Use of subdomains for inverse problems in branching flow passages. - AK Agrawal, S Krishnan, Tah-teh Yang *(Dept of Mech Eng, Clemson Univ, Clemson SC 29634-0921)*. J Fluids Eng 115(2) 227-232 (Jun 1993).

For inverse problems in complex flow passages, a calculation procedure based on a multizone Navier-Stokes method was developed. A heuristic approach was employed to derive wall shape corrections from the wall pressure error. Only two subdomains sharing a row of control volumes were used. The grid work in the common region was identical for both subdomains. The flow solver, inverse calculation procedure, multizone Navier-Stokes method and subdomain inverse calculation procedure were validated independently against experimental data or numerical predictions. Then, the subdomain inverse calculation method was used to determine the wall shape of the main duct of a branching flow passage. A slightly adverse pressure gradient was prescribed downstream of the sidebranch. Inverse calculations resulted in a curved wall diffuser for which the wall pressure distribution matched the design (prescribed) wall pressure distribution. The present method was illustrated for laminar, incompressible flows in branching passages. However, the method presented is flexible and can be extended for turbulent flows in multiply connected domains.

352C. OPEN CHANNEL FLOW (INCL HYDRAULIC JUMPS)

See the following:

11T656. Behavior of flow in a channel bend with a side overflow (flood relief) channel

352D. PIPE LOSSES (FRICTION AND GEOMETRY)

11A566. Motion resistance and pressure distribution in a delivery conduit during pumping of a concrete mixture. - A Halicka and M Krol *(Politechnika Lubelska, Poland)*. Inzynieria Budownictwo 50(7) 290-292 (1993).

The analytical description is proposed for a stationary motion of a concrete mixture in horizontal pipes. Resistances to such a motion are discussed.

352F. STRATIFIED FLOW

11A567. Diurnal stratification and its effects on wind-induced currents and water qualities in Lake Kasumigaura, Japan. - T Ishikawa *(Dept of Civil Eng, Tohoku Univ, Aoba, Aramaki, Sendai 980, Japan)* and M Tanaka *(Hydraul Eng Dept, Kajima Tech Res Inst, 19-1 Tobitakyu 2-Chome Chofu-shi, Tokyo 182, Japan)*. J Hydraul Res 31(3) 307-322 (1993).

Diurnal stratification and its effects on wind-induced current and water qualities in a shallow eutrophicated lake are discussed based on the field data obtained in Lake Kasumigaura. Diurnal stratification makes a weak thermocline with the temperature difference of about 1°C. Because a thermocline prevents the vertical momentum transport, it inevitably creates the two-layered flow pattern. The temperature profile has double-thermocline when the thermocline formed one day remains in the following morning. Then, the old thermocline tends to stay near the bottom for several days because the wind mixing works only on the new thermocline developed at upper elevation. DO concentration near the bottom markedly decreases under such condition, because the vertical DO transport is suppressed by the thermocline. PO_4-P is released at high rate from the bed sediments after DO concentration falls below 4 ppm. The entrainment rate is discussed with reference to the basic models which are the turbulent erosion model (TEM) and the dynamic instability model (DIM). It is concluded that DIM, rather than TEM, is suitable to explain the mixing of diurnal stratification observed in this study. The entrainment rate $E[U_m]$ is found to vary as $R_i[U_x]^{-1}$, where $E[U_m] = W_e/U_m$, W_e is the entrainment velocity, U_m is the vertically averaged velocity in the mixed layer, $R_i[U_x] = B/U^2_x$, B is the buoyancy of the mixed layer and U_x is the friction velocity at the water surface.

11A568. Numerical solutions of a nonlinear density current: A benchmark solution and comparisons. - JM Straka *(Sch of Meteor, Univ of Oklahoma, Energy Center Room 1310 100 E Boyd St, Norman OK 73019)*, RB Wilhelmson, LJ Wicker *(Univ of Illinois, Urbana IL 61801)*, JR Anderson *(Univ of Wisconsin, Madison WI 53706)*, KK Droegemeier *(Univ of Oklahoma, Norman OK 73019)*. Int J Numer Methods Fluids 17(1) 1-22 (Jul 1993).

A comparison between solutions from simulations of a nonlinear density current test problem was made in order to study the behavior of a variety of numerical methods. The test problem was diffusion-limited so that a grid-converged reference solution could be generated using high spatial resolution. Solutions of the test problem using several different resolutions were computed by the participants of the "Workshop on Numerical Methods for Solving Nonlinear Flow Problems", which was held on 11-13 September 1990 at the National Center for Supercomputing Applications. In general, it was found that when the flow was adequately resolved, all of the numerical schemes produced solutions that contained the basic physics as well as most of the flow detail of the reference solution. However, when the flow was marginally resolved, there were significant differences between the solutions produced by the various models. Finally, when the flow was poorly resolved, none of the models performed very well. While higher-order and spectral-type schemes performed best for adequately and marginally resolved flow, solutions made with these schemes were virtually unusable for poorly resolved flow. In contrast, the monotonic schemes provided the most coherent and smooth solutions for poorly resolved flow, however with noticeable amplitude and phase speed errors, even at finer resolutions.

11A569. Vertical distribution of particles in stratified lake. - X Casmitjana *(Phys Dept and Inst of Aquatic Ecology, Univ of Girona, P Hospital 6, 17071 Girona, Spain)* and G Schladow *(Center for Water Resources, Dept of Civil and Env Eng, Univ of W Australia, Nedlands 6009, Australia)*. J Env Eng 119(3) 443-462 (May-Jun 1993).

A model to account for the distribution of particulate matter in a lake is presented. This model represents the coupling of a stratified lake mixing model with a particle settling, coagulation, and diffusion model. Using parameterizations of the fundamental and mixing processes, the lake model simulates the response of the stratified water column to external forcing. At the same time, the particle model simulates the settling, aggregation, and diffusion of a given distribution of particles within this changing water column. Three different situations have been chosen in order to test the model. In the first, an input of mineral particles for different size classes has been attributed to an inflow. In the second, the evolution of a distribution of particles initially set up in equilibrium of a strongly stratified lake has been described and in the third, the same initial distribution of particles has been set up for a weakly stratified lake. These cases show the importance of the different mechanisms (settling, aggregation and diffusion) affecting the dynamics of the particles in natural waters.

352H. ORIFICES, NOZZLES, VALVES, AND GATES

11A570. Hydraulics-based-optimization methodology for gating design. - FJ Bradley, S Heinemann *(Dept of Mat Sci and Eng, Univ of Wisconsin, 1509 University Ave, Madison WI 53706)*, JA Hoopes *(Dept of Civil and Env Eng, Univ of Wisconsin, 1509 University Ave, Madison WI 53706)*. Appl Math Model 17(8) 406-414 (Aug 1993).

Advantages and disadvantages of the differential momentum balance and macroscopic control volume approaches to the analysis of flow during mold filling and the computer-aided design of gating systems are discussed. A gating design methodology based on a control volume hydraulics-based flow model and nonlinear optimization is described. Mathematical formulation of the model yields a system of equations that ensures mass continuity at nodes and conservation of energy along paths. In addition to computational efficiency, the hydraulics approach to flow analysis utilizes pipe-node-path representation of gating systems that facilitates the analysis of complex 3D configurations. Example simulations of flow distribution in water modeling systems and of flow distribution and mold filling in molten metal experiments are presented. It is concluded that good agreement between model-predicted and experimental results is obtainable if pertinent loss coefficient data are available. However, application of the hydraulics-based methodology to accurate analysis of flow in gating systems requires knowledge of loss coefficients that specifically relate to the flow conditions and types of runner-ingate geometric configurations encountered in industrial castings. An example formulation illustrating the application of nonlinear optimization to gating design is presented.

352K. STILLING BASINS AND OTHER ENERGY DISSIPATORS

11A571. Velocity measurements within high velocity air-water jets. - H Chanson *(Dept of Civil Eng, Univ of Queensland, St Lucia QLD 4072, Australia)*. J Hydraul Res 31(3) 365-382 (1993).

High velocity turbulent jets are often used in hydraulic structures to dissipate energy and to induce or enhance air entrainment. Examples include ski jumps and bottom aeration devices. This article presents new air concentration and velocity measurements performed in the flow development region of high velocity water jets. The measurements were obtained using a two-tips conductivity probe. The data are compared with analytical air concentration profiles derived from the diffusion equation, and theoretical velocity profiles of turbulent shear layers. The results highlight that the lower jet interface defined as C = 90% coincides with the streamline of maximum velocity gradient.

352L. CAVITATION

11A572. Scale effects for incipient cavitation under consideration of water quality. - G Eickmann *(Hydraul Res Lab Obernach, Munich Tech Univ, Munich, Germany)*. J Hydraul Res 31(3) 347-364 (1993).

By combined measurements of incipient cavitation and water quality, characterized by its tensile strength, the enormous influence of differences in water quality on cavitation data is demonstrated. After eliminating these water quality effects from the test results general similarity relations for velocity and size scale effects become clearly apparent. The knowledge of the effects of water quality and the application of these relations can help to predict cavitation performance more precisely.

See also the following:

11A149. Hydraulic forces acting on a circular cylinder with surface source of minute air bubbles and its cavitation characteristics

352M. EROSION, SCOURING, SEDIMENT TRANSPORT

11T573. Microbiological stabilization of sludge by aerobic digestion and storage. - RY Surampalli *(Dept of Env Eng, US EPA, Kansas City KS 66101)*, SK Banerji, JC Chen *(Dept of Civil Eng, Univ of Missouri, Columbia MO 65211)*. J Env Eng 119(3) 493-505 (May-Jun 1993).

11T574. Modeling contaminant dispersion in the River Severn using a random-walk model. - SE Heslop *(Dept for Continuing Educ, Univ of Bristol, Wills Memorial Bldg Queen's Rd, Bristol BS8 1HR, UK)* and CM Allen *(Deceased)*. J Hydraul Res 31(3) 323-331 (1993).

11A575. Seasonal cycle of a groundwater dominated lake. - X Casamitjana, E Roget *(Dept of Phys, Inst of Water Ecology, Univ of Girona, Spain)*, G Schladow *(Center for Water Res, Univ of W Australia, Perth, Australia 6009)*. J Hydraul Res 31(3) 293-306 (1993).

Lake Banyoles is a multibasin lake dominated by groundwater derived inflows. It is composed of three major basins, two of them being meromictic. The relatively warm and saline groundwater inflows, together with the basin morphometry, give rise to characteristic thermal structures in each basin, with different thermocline levels and temperature inversions distinguishing the basins. A 1D lake mixing model has been adapted to include the form of mixing associated with the groundwater inflows, and the results are compared with data collected from the lake.

See also the following:

11A569. Vertical distribution of particles in stratified lake

352N. WATERWAYS

11A576. Study on modeling the morphology of torrents on volcano slopes. - CJ Sloff *(Fac of Civil Eng, Delft Univ of Tech, Delft, The Netherlands)*. J Hydraul Res 31(3) 333-345 (1993).

An exploratory study is done to modeling of rivers on volcano slopes. Beside the occurrence of mud flows or lahars these rivers are characterized by unsteady supercritical flow and large suspended-sediment concentrations. A fully coupled 1D model is presented for the rivers, provided that lahars do not occur. It can simulate unsteady supercritical flow (Froude numbers between about 1 and 1.8) with volumetric sediment concentrations less than about 10%. The redistribution of the suspended-sediment concentration (ie, the lag between concentration and transport capacity due to sediment relaxation) causes instabilities of the bed conformable to antidunes. Calculations with a numerical model using Preissmann's implicit scheme, and applied to a river on the Kelud Volcano in Indonesia, show the rapidity of bed-level variations and the upstream propagation and growth of bed disturbances. These results offer a deeper understanding of the problems of the rivers on the Kelud. Furthermore, it yields a base for investigating the efficacy of sabo works.

352P. COASTS, BEACHES, HARBORS

11A577. Design method of armour Grate Plates for sloping breakwaters. - Guiqiu Wu *(First Inst of Oceanog, State Oceanic Admin, Qingdao 266003)*, Zaihua Ji, Xuexin Sun, Jiuzi Zhang *(Dept of Ocean Eng, Ocean Univ of Qingdao, Qingdao 266003)*. China Ocean Eng 7(1) 45-60 (1993).

Laboratory tests have been conducted on the basis of theoretical analysis of stability of armour Grate Plates with reference to 20 structures. Some empirical formulas of stability thickness of Grate Plates have been obtained in consideration of the effects of water depth in front of the structures and critical wave period. The test results have been compared with field data.

352Y. COMPUTATIONAL TECHNIQUES

11A578. Explicit approach for modeling closed pipes in water networks. - PF Boulos *(Dept of Computer-Aided Eng, Montgomery Watson, 301 N Lake Ave, Ste 900, Pasadena CA 91101)* and T Altman *(Dept of Comput Sci and Eng, Univ of Colorado, Denver CO)*. Appl Math Model 17(8) 437-443 (Aug 1993).

An explicit approach has been developed for use in modeling closed pipes in water distribution networks. The explicit approach is able to directly incorporate the zero-flow effect of closed pipes into the overall network modeling process. The resulting method is based on an analytical reformulation of the quasilinear set of flow continuity and energy equations governing the network hydraulics in terms of energy displacement for the individual closed pipes that exactly meet the corresponding zero-flow boundary constraint imposed. The proposed algorithm is shown to be robust and efficient, and is guaranteed to converge in an expeditious manner. The method compares favorably with others by eliminating numerical diffusion and computational instability or repetitive network topology alterations suffered by the previous procedures. An example application is presented. Enhancement of mathematical modeling of water distribution networks is a principal benefit of this methodology.

See also the following:

11A568. Numerical solutions of a nonlinear density current: A benchmark solution and comparisons

354. Incompressible flow

354A. GENERAL THEORY

11A579. Effect of mean flows on enhanced diffusivity in transport by incompressible periodic velocity fields. - AJ Majda and RM McLaughlin *(Dept of Math and Program in Appl and Comput Math, Princeton)*. Stud Appl Math 89(3) 245-279 (Aug 1993).

Avellaneda and one of the authors, have recently established that an upper bound for the enhanced diffusivity in the large scale, long time advection-diffusion with periodic steady incompressible velocity fields has the form CPe^2/κ where Pe is the Peclet number and κ is the reciprocal of the Prandtl number. In this paper, flow fields with maximal and minimal enhanced diffusion are studied. Maximal enhanced diffusion requires that in some directions, the enhanced diffusion tensor also has the lower bound CPe^2/κ. For minimal enhanced diffusion, the effect of the velocity field is to boost the enhanced diffusivity by a negligible amount that is bounded by a fixed constant times the bare diffusivity regardless of Peclet number. Stieltjes measure formulas are used to develop a simple, necessary, and sufficient condition for maximal enhanced diffusion and also to characterize minimal enhanced diffusion.

354B. IRROTATIONAL FLOW

11T580. Evidence for a singularity of the 3D incompressible Euler equations. - RM Kerr *(Geophys Turbulence Program, Natl Center for Atmos Res, PO Box 3000, Boulder CO 80307-3000)*. Phys Fluids A 5(7) 1725-1746 (Jul 1993).

11A581. Numerical solutions of Euler equations by using a new flux vector splitting scheme. - G-C Zha and E Bilgen *(Ecole Polytech, Univ of Montreal, PO Box 6079, St A Montreal, PQ, H3C 3A7, Canada)*. Int J Numer Methods Fluids 17(2) 115-144 (30 Jul 1993).

A new flux vector splitting scheme has been suggested in this paper. This scheme uses the velocity component normal to the volume interface as the characteristic speed and yields the vanishing individual mass flux at the stagnation. The numerical dissipation for the mass and momentum equations also vanishes with the Mach number approaching zero. One of the diffusive terms of the energy equation does not vanish. But the low numerical diffusion for viscous flows may be ensured by using higher-order differencing. The scheme is very simple and easy to be implemented. The scheme has been applied to solve the 1D and multidimensional Euler equations. The solutions are monotone and the normal shock wave profiles are crisp. For a 1D shock tube problem with the shock and the contact discontinuities, the present scheme and Roe scheme give very similar results, which are the best compared with those from Van Leer scheme and Liou-Steffen's advection upstream splitting method (AUSM) scheme. For the multidimensional transonic flows, the sharp monotone normal shock wave profiles with mostly one transition zone are obtained. The results are compared with those from Van Leer scheme, AUSM and also with the experiment.

354D. VISCOUS FLOW

11A582. Kinetic theory solution method for the Navier-Stokes equations. - MN Macrossan and RI Oliver *(Dept of Mech Eng, Univ of Queensland, St Lucia, Qld 4072, Australia)*. Int J Numer Methods Fluids 17(3) 177-193 (Aug 1993).

The kinetic-theory-based solution methods for the Euler equations proposed by Pullin and Reitz are here extended to provide new finite volume numerical methods for the solution of the unsteady Navier-Stokes equations. Two approaches have been taken. In the first, the equilibrium interface method (EIM), the forward- and backward-flowing molecular fluxes between two cells are assumed to come into kinetic equilibrium at the interface between the cells. Once the resulting equilibrium states at all cell interfaces are known, the evaluation of the Navier-Stokes fluxes is straightforward. In the second method, standard kinetic theory is used to evaluate the artificial dissipation terms which appear in Pullin's Euler solver. These terms are subtracted from the fluxes and the Navier-Stokes dissipative fluxes are added in. The new methods have been tested in a 1D steady flow to yield a solution for the interior structure of a shock wave and in a 2D unsteady boundary layer flow. The 1D solutions are shown to be remarkably accurate for cell sizes large compared to the length scale of the gradients in the flow and to converge to the exact solutions as the cell size is decreased. The steady-state solutions obtained with EIM agree with those of other methods, yet require a considerably reduced computational effort.

354G. UNSTEADY FLOW

11A583. Wavy mode of the streaked flow around an oscillating cylinder in a stratified fluid at rest. - M Tatsuno and T Karasudani *(Res Inst for Appl Mech, Kyushu Univ, Kasuga 816, Japan)*. Fluid Dyn Res 11(6) 313-318 (Jun 1993).

The structures of the flow induced by a vertical circular cylinder performing transverse oscillations in a linearly stratified fluid at rest are investigated. The density gradient inhibits the onset of the 3D instability. The instability appears as regularly spaced streaked flows along the cylinder axis. Each streaked flow follows a wavy path in the horizontal plane in a certain range of amplitude and frequency of the oscillations.

See also the following:

11A589. Added mass coefficient for rows and arrays of spheres oscillating along the axes of tubes

354I. THERMAL CONVECTION FLOW

See the following:

11A779. Convection heat transfer of closely-spaced spheres with surface blowing
11A781. Convective heat transfer in a curved annular-sector duct
11A783. Heat transfer and pressure drop of a transversely finned concentric annulus with longitudinal flow
11A785. Comparison of natural convection of water and air in a partitioned rectangular enclosure
11A787. Laminar free convection in a nonrectangular inclined cavity
11A788. Laminar natural convection in a horizontal rhombic annulus
11A789. Laminar natural convection in internally finned horizontal annuli
11A790. Numerical study of laminar and turbulent natural convection in an inclined square cavity
11A791. Scaling of the laminar natural-convection flow in a heated square cavity
11A792. Transition to time-periodicity of a natural-convection flow in a 3D differentially heated cavity
11A794. Thermally unstable convection with applications to chemical vapor deposition channel reactors
11A798. Laminar mixed convection in a duct with a backward-facing step: The effects of inclination angle and Prandtl number
11A801. Mixed convection in an inclined channel with a discrete heat source
11A805. Modeling of turbulent buoyant flow and heat transfer in liquid metals

354J. STRATIFIED FLOW AND FREE SURFACE FLOW

11T584. Calculation of interfacial flows and surfactant redistribution as a gas-liquid interface moves between two parallel plates. - F Wassmuth, WG Laidlaw *(Dept of Chem, Univ of Calgary, 2500 University Dr NW, Calgary, AB, T2N 1N4, Canada)*, DA Coombe *(Comput Model Group, Research Park, 3512-33 St NW Calgary, AB, T2L 2A6, Canada)*. Phys Fluids A 5(7) 1533-1548 (Jul 1993).

11T585. Computations of free surface flows Part 2: 2D unsteady bore diffraction. - JY Yang and CA Hsu *(Inst of Appl Mech, Natl Taiwan Univ, Taipei, Taiwan ROC)*. J Hydraul Res 31(3) 403-413 (1993).

11A586. Upstream stagnation points in stratified flow past obstacles. - PG Baines *(Div of Atmos Res, CSIRO, Aspendale Vic 3195, Australia)* and RB Smith *(Dept of Geol and Geophys, Yale Univ, New Haven CT 06511)*. Dyn Atmos Oceans 18(1-2) 105-113 (Jun 1993).

An experimental study has been made of stagnation points and flow splitting on the upstream side of obstacles in uniformly stratified flow. A range from small to large values of Nh/U (where N is the buoyancy frequency, h_m is the maximum obstacle height and U is the undisturbed fluid velocity) has been covered, for three obstacle shapes which are, respectively, axisymmetric, and elongated in the across-stream and in the downstream directions. Upstream stagnation for the first two of these models does not occur until $Nh_m/U>1.05$, where it occurs at $z \approx h_m/2$. On the central line below this point the flow descends and diverges, and we term this "flow splitting". For the third model (elongated in the downstream direction), upstream stagnation first occurs at $Nh_m/U \approx 1.43$, at $z \approx 0$. Results for this obstacle are not consistent with the "Sheppard criterion", and this upstream flow stagnation is not apparently related to lee wave overturning, in contrast to flow over 2D obstacles.

See also the following:

11A583. Wavy mode of the streaked flow around an oscillating cylinder in a stratified fluid at rest
11A588. Transient interface shape of a two-layer liquid in an abruptly rotating cylinder

354K. ROTATING FLOW OR SURFACES

11A587. Fluid flow and heat transfer between finite rotating disks. - VK Garg *(NASA Lewis Res Center, MS 5-11, Cleveland OH 44135)* and AZ Szeri *(Dept of Mech Eng, Univ of Pittsburgh, Pittsburgh PA)*. Int J Heat Fluid Flow 14(2) 155-163 (Jun 1993).

The laminar flow between finite rotating disks with a shroud has been analyzed using a velocity and a stream function formulation, employing Galerkin's method with B-spline basis. Though results from both formulations are in good agreement with the LDV data on velocity profiles, and with each other, we find the stream function formulation clearly superior computationally, and we employ it subsequently to study heat transfer between the disks. The calculations show strong boundary-layer character near the disks. The Nusselt number depends upon both geometry and the Reynolds number.

11A588. Transient interface shape of a two-layer liquid in an abruptly rotating cylinder. - Tae Gyu Lim, Sangmin Choi, Jae Min Hyun *(Dept of Mech Eng, Korea Adv Inst of Sci and Tech, Yusungku, Taejon 305-701, South Korea)*. J Fluids Eng 115(2) 324-329 (Jun 1993).

A description is made of the transient shape of interface of a two-layer liquid in an abruptly rotating circular cylinder. The density of the lower layer is higher than that of the upper layer, but the viscosities may assume arbitrary values. The overall Ekman number is much smaller than unity, and the cylinder aspect ratio is O(1). The classical Wedemeyer model, which deals with the spin-up from rest of a homogeneous fluid, is extended to tackle the two-layer liquid system. If the upper-layer fluid is of higher viscosity, the interface, at small and intermediate times, rises (sinks) in the center (periphery). After reaching a maximum height at the center, the interface tends to the parabolic shape characteristic of the final-state rigid-body rotation. If the lower-layer fluid is of higher viscosity, the interface, at small and intermediate times, sinks (rises) in the center (periphery). The deformation at the center reaches a minimum height, after which the interface approaches the final state parabola. The gross adjustment process is accomplished over the spin-up time scale, $E_n^{-1/2}\Omega^{-1}$, where E_n and Ω denote the lower value of the Ekman numbers of the two layers and the angular velocity of the cylindrical container, respectively. These depictions are consistent with the physical explanations offered earlier. A turntable experiment is performed to portray the transient interface shape. The model predictions of the interface form are in satisfactory agreement with the lab measurements.

See also the following:

11A237. Spectral methods for the viscoelastic time-dependent flow equations with applications to Taylor-Couette flow
11T595. Thermocapillary motion in a spinning vaporizing droplet

354O. FLOW AROUND BODIES

11A589. Added mass coefficient for rows and arrays of spheres oscillating along the axes of tubes. - Xiaolong Cai *(Fluid Flow Projects, Tulsa Univ, Tulsa OK 74104)* and GB Wallis *(Thayer Sch of Eng, Dartmouth Col, Hanover NH 03755)*. Phys Fluids A 5(7) 1614-1629 (Jul 1993).

Rows of single spheres were attached to springs and oscillated in water-filled tubes of several diameters and lengths with various boundary conditions at the ends of the tubes. Similar tests were performed using arrays of spheres in a closed-end tube. The added mass coefficient was deduced from the measured natural frequency. Results for finite systems were systematically extrapolated to predict the coefficient for an infinite system. The results are closely described by adapting the spheres-in-tube potential flow theory of Cai and Wallis and the image method applied to arrays by Wallis *et al.* The coefficient of added mass is shown to depend on the external impedance of a fluid circuit to which the system is connected. Wallis' and Zuber's coefficients are recovered as limiting cases.

11A590. Flow past a needle in a cylindrical tube. - Phan-Thien Nhan, Jin Hao, Zheng Rong *(Dept of Mech Eng, Univ of Sydney, NSW 2006, Australia)*. J Non-Newtonian Fluid Mech 47 137-155 (Jun 1993).

In this paper, the uniform flow past a needle place at the center-line of a tube is analyzed for a class of constitutive equations of the Maxwell type using a FE implementation of the explicitly elliptic momentum equation formulation. In the coupled FE approach, the Galerkin method is applied to the modified momentum equations and the continuity equation, while the treamline upwind Petrov-Galerkin method is applied to the constitutive equations of the viscoelastic fluids. For the power-law and the Phan-Thien-Tanner (PTT) fluids, an asymptotic analysis valid for slender needles is also given. The flow is of practical importance since it forms the basis of an existing commercial viscometer. The viscometer would provide the true shear stress-shear rate relationship if the nominal shear rate is given by KU/R, where U is the falling speed of the needle, R is the radius of the tube, and K is a constant. For the PPT model and the geometry used in this paper, this constant is approximately 4, which is also the value for power-law fluids with power-law index $n = 1/3$.

11A591. Point vortex model of the unsteady separated flow past a semi-infinite plate with transverse motion. - L Cortelezzi *(Dept of Math, UCLA)* and A Leonard *(Graduate Aeronaut Lab, California IT, Pasadena CA 91125)*. Fluid Dyn Res 11(6) 263-295 (Jun 1993).

Two-dimensional unsteady separated flow past a semi-infinite plate with transverse motion is considered. The rolling-up of the separated shear-layer is modeled by a point vortex whose time-dependent circulation is predicted by an unsteady Kutta condition. A power-law starting flow is assumed along with a power law for the transverse motion. The effects of the motion of the plate on the starting vortex circulation and trajectory are presented. A suitable vortex shedding mechanism is introduced and a class of flows involving several vortices is presented. Finally, some possibilities for actively controlling the production of circulation by moving the plate are discussed.

See also the following:

11A586. Upstream stagnation points in stratified flow past obstacles

354P. SURFACE TENSION FLOW (EG IN LOW GRAVITY ENVIRONMENTS)

11A592. Computer modeling of transient thermal flows on non-Newtonian fluids. - D Ding, P Townsend, MF Webster *(Dept of Comput Sci, Univ of Wales Inst of non-Newtonian Fluid Mech, Univ Col, Swansea SA2 8PP, UK)*. J Non-Newtonian Fluid Mech 47 239-265 (Jun 1993).

In this report two axisymmetric transient thermal non-Newtonian fluid problems are studied. The first is a capillary flow model problem for a thermal power-law fluid and Graetz number up to 60, governed by a derivative temperature boundary condition. The second is a glass oven flow problem for thermal, Newtonian and power-law fluids, flowing in a complex shaped domain driven by a gravitational body force for thermal Peclet numbers up to 100. The flow domain in this case is a straight pipe with a constriction formed from an axisymmetric angled obstruction on the wall. The results obtained for these problems provide good agreement with both experimental and numerical results supplied by industrial collaborators. Of particular concern here is the nature of the transient development of the flows involved under varying material properties. To this end the code has been validated under typical industrial conditions and found to be robust up to Peclet numbers of at least 100, and involving up to 1000 dof.

11A593. Thermocapillary convection in a multilayer system. - P Georis, M Hennenberg *(Univ Libre de Bruxelles, Brussels, Belgium)*, IB Simanovskii *(Perm State Pedagogical Inst, Perm, Russia)*, A Nepomniaschy *(Perm State Pedagogical Inst, Technion, Haifa, Israel)*, II Wertgeim *(Ural's Branch of Acad of Sci, Perm, Russia)*. Phys Fluids A 5(7) 1575-1582 (Jul 1993).

The Marangoni-Benard instability for a symmetrical three-layer system is examined theoretically. Linear stability analysis and nonlinear numerical simulations show that the ratio of the heat diffusivities determines the nature of the instability. Monotonic disturbances exist only when this parameter is far enough from one, the motion being driven by one interface. When the heat diffusivity ratio is close to one, oscillatory convection is observed. This is explained on a physical base: the oscillation rests on the coupling of both interfaces, which creates a flip-flop mechanism leading to a double inversion of the vortices rotation during one period of oscillation.

11A594. Thermocapillary migration of a small chain of bubbles. - Huailiang Wei and RS Subramanian *(Dept of Chem Eng, Clarkson Univ, Potsdam NY 13699-5705)*. Phys Fluids A 5(7) 1583-1595 (Jul 1993).

The quasistatic thermocapillary migration of a chain of two or three spherical bubbles in an unbounded fluid possessing a uniform temperature gradient is investigated in the limit of vanishing Reynolds and Peclet numbers. The line of bubble centers is permitted to be either parallel or perpendicular to the direction of the undisturbed temperature gradient. The governing equations are solved by a truncated-series, boundary-collocation technique. Results are presented which demonstrate the impact of the presence of other bubbles on a test bubble. In the three-bubble case, a simple pairwise-additive approximation is constructed from the reflections solution, and found to perform well except when the bubbles are close to each other. Also, features of the flow topology in the fluid are explored. Separated reverse flow wakes are found in the axisymmetric problem and other interesting structures are noted for case in which the line of centers is perpendic to the applied temperature gradient. The obs flow structure is shown to be the result of position of simpler basic flows.

11T595. Thermocapillary motion in a spinning vaporizing droplet. - D Lozinski and M Matalon *(Dept of Eng Sci and Appl Math, McCormick Sch of Eng and Appl Sci, NWU)*. Phys Fluids A 5(7) 1596-1601 (Jul 1993).

354R. NON-NEWTONIAN FLOW

11A596. Investigation of possible mechanisms of heterogeneous drag reduction in pipe and channel flows. - H-W Bewersdorff, A Gyr, K Hoyer *(Inst of Hydromech and Water Resources Man, Swiss Fed IT, Zurich, Switzerland)*, A Tsinober *(Fac of Eng, Tel-Aviv Univ, Israel)*. Rheol Acta 32(2) 140-149 (Mar/Apr 1993).

This study presents experimental results on the mechanism of this type of drag reduction. The experiments were carried out to find out whether this drag reduction is caused by small amounts of polymer removed from the thread and dissolved in the near-wall region of the flow or by an interaction of the polymer thread with the turbulence. The friction behavior of this type of drag reduction was measured for different concentrations in pipes of different cross-sections, but of identical hydraulic diameter. The parameters of the injection, ie, injector geometry as well as the ratio of the injection to the bulk velcoity, were varied. In one set of experiments the polymer thread was sucked out through an orifice and the friction behavior in the pipe was determined downstream of the orifice. In another experiment, near-wall fluid was led into a bypass in order to measure its drag reducing properties. Furthermore, the influence of a water injection into the near-wall region on the drag reduction was studied. The results provide a strong evidence that heterogeneous drag reduction is in part caused by small amount of dissolved polymer in the near-wall region as well as by an interaction of the polymer thread with the turbulence.

11A597. New approach to the pulsating and oscillating flows of viscoelastic liquids in channels. - R Steller *(Inst of Organic and Polymer Tech, Tech Univ, Wroclaw, Poland)*. Rheol Acta 32(2) 192-205 (Mar/Apr 1993).

An approximate method for mathematical description of unsteady flows of polymeric liquids in channels generated by pulsating pressure gradient or vibration channel wall is presented. The method is based on integration of the equation of motion and determination of the shear stresses and shear rates at channel walls, assuming the inertia effects to be suitably small. The approximate results have been compared with exact solutions using as examples the Newtonian fluid and a special form of a generalized Maxwell model. The applibility conditions of the proposed method have been extensively discussed.

11A598. Two-dimensional planar flow of a viscoelastic plastic medium. - A Isayev and YH Huang *(Inst of Polymer Eng, Univ of Akron OH)*. Rheol Acta 32(2) 181-191 (Mar/Apr 1993).

The present study is concerned with FE simulation of the planar entry flow of a viscoelastic plastic medium exhibiting yield stress. The numerical scheme is based on the Galerkin formulation. Flow experiments are carried out on a carbon black filled rubber compound. Steady-state pressure drops are measured on two sets of contraction or expansion dies having different lengths and a constant contraction or expansion ratio of 4:1 with entrance angles of 90°, 45°, and 15°. The predicted and measured pressure drops are compared. The predicted results indicate that expansion flow has always a higher pressure drop than ... ow. This prediction is in agreement ... al data only at low flow rates, but ... rates. The latter disagreement is ... ication that the assumption of ... low in the upstream and down... not realistic at high flow rates, ... length-to-thickness ratio channels employed. The evolution of the velocity, shear stress, and normal stress fields in the contraction or expansion flow and the location of pseudo-yield surfaces are also calculated.

See also the following:

11A342. Hyperbolicity and change of type in steady co-extrusion flow of upper-convected Maxwell fluids

11A590. Flow past a needle in a cylindrical tube

11A592. Computer modeling of transient thermal flows on non-Newtonian fluids

354Y. COMPUTATIONAL TECHNIQUES

11A599. Boundary integral equations for contact problems of plane quasi-steady viscous flows. - LK Antanovskii *(MARS Center, Via Diocleziano 328, 80125 Naples, Italy)*. European J Appl Math 4(2) 175-187 (Jun 1993).

Plane, quasi-steady, free-boundary flows of an incompressible viscous fluid with surface tension in a container are considered. The mathematical problem is decomposed into an auxiliary elliptic problem for the Stokes system in a fixed flow domain, whose solution leads to the Cauchy problem for the free boundary with the so-called normal velocity operator. By introducing the complex stress-stream function and applying time-dependent conformal mapping, the auxiliary problem is reduced to a boundary integral equation via consideration of two Hilbert problems for analytic functions in a unit disc. As an application, plane capillary flow with moving contact points is investigated asymptotically for small capillary numbers. We prove that in the case when a dynamic contact angle is equal to π, this problem is well-posed for a filling regime, and ill-posed for a drying one.

11A600. Determination of the stream function and pressure distribution in some plane discrete velocity fields. - WJ Prosnak and JM Elszkowski *(Lab of Numer Fluid Mech, Inst of Fluid Flow Machinery, Polish Acad of Sci, Fiszera 14 Pl-80-952, Gdansk, Poland)*. Bull Polish Acad Sci Tech Sci 41(2) 79-97 (1993).

The paper deals with the plane flow of viscous liquid. It contains a method for construction of a continuous stream function and a continuous pressure field. The both functions correspond to a plane, discrete, instantaneous velocity field, the rectangular velocity components u_{ij}, v_{ij} being given only in nodes i, j of a rectangular grid, introduced in the domain of the flow. The paper can be regarded as a complement.

11A601. Hele-Shaw flows with a free boundary produced by multipoles. - VM Entov *(Inst for Problems in Mech, Russian Acad of Sci, prosp Vernadskogo 101, Moscow, Russia)*, PI Etingof, DY Kleinbock *(Dept of Math, Yale Univ, 2155 Yale Sta, New Haven CT 06520)*. European J Appl Math 4(2) 97-120 (Jun 1993).

We study Hele-Shaw flows with a moving boundary and multipole singularities. We find that such flows can be defined only on a finite time interval. Using a complex variable approach we construct a family of explicit solutions for a single multipole. These solutions turn out to have the maximal possible lifetime in a certain class of solutions. We also discuss the generalized Hele-Shaw model in which surface tension at the moving boundary is considered, and develop a method of finding steady shapes. This method yields new one-parameter families of stationary solutions. In the Appendix we discuss a connection between these solutions and a variational problem of potential theory.

11A602. Improved implicit residual smoothing for steady state computations of first-order hyperbolic systems. - R Enander *(Dept of Sci Comput, Uppsala Univ, PO Box 120, Uppsala*

751 04, Sweden). J Comput Phys 107(2) 291-296 (Aug 1993).

In this paper we introduce a method to accelerate the computation of steady state solutions of first-order hyperbolic problems such as the Euler equations. The acceleration method is an improved version of the so-called *implicit residual smoother*. The new version, the *implicit explicit residual smoother* improves damping properties and numerical examples are presented showing considerably reduction in number of iterations needed to reach a steady state soluton.

11A603. Nonreflecting outlet boundary condition for incompressible unsteady Navier-Stokes calculations. - G Jin and M Braza *(Transferts en Ecoulements Laminaires et Turbulents, Inst de Mec des Fluides Toulouse, Lab Associe CNRS, URA D0005, Ave du Professeur Camille Soula, 31400 Toulouse Cedex, France).* J Comput Phys 107(2) 239-253 (Aug 1993).

The goal of this work is to adapt a nonreflecting outlet boundary condition, derived from a wave equation, to the numerical solution of the full incompressible Navier-Stokes equations, for an elliptic unsteady free shear flow. The numerical results show that a significant improvement is achieved with this nonreflecting boundary condition, in comparison with the results obtained by using free boundary layer type conditions. The physical phenomena studied concern the onset of the Kelvin-Helmholtz instability in the free (nonforced) shear layer and certain 2D characteristics of transition towards turbulence. These phenomena are simulated naturally, without imposing perturbations. The frequency of the organized vortices and the spread of the mixing layer are correctly predicted. The performances of the method are shown through comparison with the physical experiments. Owing to the nonreflecting boundary conditions, the feedback noises are inhibited effectively, so that the computation domain can be reduced and the dynamic characteristics of the flow are maintained up clearly to the outlet boundary.

11A604. Upwind finite-volume method with a triangular mesh for conservation laws. - San-Yih Lin, Tsuen-Muh Wu, Yan-Shin Chin *(Inst of Aeronaut and Astronaut, Natl Cheng Kung Univ, Tainan, Taiwan, ROC).* J Comput Phys 107(2) 324-337 (Aug 1993).

A new upwind scheme has been developed and analyzed for a finite-volume solution of the conservation laws on triangular meshes. The scheme is an upwind second-order extrapolation with simple local limiters, and it is weakly second-order accurate and satisfies maximum principles. In one dimension, the scheme reduces to a fully upwind second-order scheme with a simple local limiter. Preliminary numerical results demonstrating the performance of the scheme on a variety of initial-boundary value problems are presented. The order of convergence of the scheme is found to vary from 1.6 to 1.9 in L^1.

See also the following:

11A581. Numerical solutions of Euler equations by using a new flux vector splitting scheme
11A582. Kinetic theory solution method for the Navier-Stokes equations
11T585. Computations of free surface flows Part 2: 2D unsteady bore diffraction
11A591. Point vortex model of the unsteady separated flow past a semi-infinite plate with transverse motion
11A661. Streamwise computation of 3D flows using two stream functions

356. Compressible flow

356A. GENERAL THEORY

See the following:

11T144. Focusing of weak shock waves on a target in a parabolic chamber

356C. TRANSONIC FLOW

11A605. A functional approach to the solution of the Karman-Guderley equation. - M Pogu *(Service Math, ECN, 1 Rue La Noe, 44072 Nantes, France)* and G Tournemine *(Lab d'Anal Numer et Mec IRMAR, Univ De Rennes I, Campus Beaulieu, 35042 Rennes Cedex, France).* Bull Polish Acad Sci Tech Sci 40(4) 335-344 (1992).

The expansion procedure for transonic flows, in the first, leads to the Karman-Guderley equation (K-GE). The aim of the article is to propose a functional approach to the K-GE using the Sobolev spaces and an iterative algorithm. From the mathematical point of view there are two fundamental dilemmas. Firstly the equations become locally hyperbolic or elliptic which does not warrant the monotonicity of the associated operators. This lack of monotonicity has been already observed when solving exact equations (EE). Secondly, the expansion procedure implies that the nonlinear term is not so easy to be bounded as in the case of EE. The Kutta-Joukowski condition causes a new difficulty which is avoided here, since symmetrical flows are considered.

356D. SUPERSONIC FLOW

11T606. Normal shock wave oscillations in supersonic diffusers. - K Matsuo and H-D Kim *(Dept of Energy Conv Eng, Graduate Sch of Eng Sci, Kyushu Univ Kasuga, Fukuoka 816, Japan).* Shock Waves 3(1) 25-33 (1993).

See also the following:

11A685. Visual observations of supersonic transverse jets

356E. HYPERSONIC FLOW

11A607. Compression process in a free-piston shock-tunnel. - L Labracherie, MP Dumitrescu, Y Burtschell, L Houas *(Univ de Provence, Lab IUSTI, CNRS ura 1168 Dept MHEQ Fac Saint Jerome, 13397 Marseille Cedex 13, France).* Shock Waves 3(1) 19-23 (1993).

Preliminary results in the Marseille free-piston shock-tunnel facility are presented. The compression of the driver gas by the piston is studied experimentally for two different geometries of the end of the compression tube. Peak pressures obtained with the end of the compression tube closed, and with bursting of the diaphragm separating the high pressure from the low pressure chamber, are compared with calculated values in the cases of N_2 and He as driver gases. A phenomenon of accoustic resonance has been uncovered, generating strong pressure oscillations which, if not properly dealt with, could impair the quality of the useful flow in such a facility.

11A608. Damping of surface pressure fluctuations in hypersonic turbulent flow past expansion corners. - Kung-Ming Chung and Frank K Lu *(Aerodyn Res Center, Mech and Aerospace Eng Dept, Univ of Texas, Arlington TX 76019).* AIAA J 31(7) 1229-1234 (Jul 1993).

Surface pressure fluctuations of Mach 8 turbulent flow past a 2.5- and a 4.25-deg expansion corner maintained a Gaussian distribution but were severely attenuated by the expansion process. The pressure fluctuations did not recover to those of an equilibrium turbulent flow even though the mean pressures reached downstream inviscid values in four to six boundary-layer thicknesses. The fluctuations were convected with a velocity comparable to that on a flat plate, and they maintained their identities longer for the stronger expansion. The damping of pressure fluctuations at hypersonic Mach numbers, even by small corner angles, may be exploited in fatigue design.

11A609. Evaluation of thermochemical models for particle and continuum simulations of hypersonic flow. - ID Boyd and T Gokcen *(Eloret Inst, NASA Ames Res Center, MS 230-2, Palo Alto CA 94035).* J Thermophys Heat Transfer 7(3) 406-411 (Jul-Sep 1993).

Computations are presented for 1D, strong shock waves that are typical of those that form in front of a re-entering spacecraft. The fluid mechanics and thermochemistry are modeled using two different approaches. The first employs traditional continuum techniques in solving the Navier-Stokes equations. The second approach employs a particle simulation technique, the direct simulation Monte Carlo method. The thermochemical model employed in these two techniques are quite different. The present investigation presents an evaluation of thermochemical models for nitrogen under hypersonic flow conditions. Four separate cases are considered that are dominated in turn by vibrational relaxation, weak dissociation, strong dissociation, and weak ionization. In near-continuum, hypersonic flow, the nonequilibrium thermochemical model employed in continuum and particle simulations produce nearly identical solutions. Furthermore, the two approaches are evaluated successfully against available data for weakly and strongly dissociating flows.

See also the following:

11A668. Analysis of hypersonic nozzles including vibrational nonequilibrium and intermolecular force effects

356H. INTERNAL FLOW PROBLEMS

See the following:

11T144. Focusing of weak shock waves on a target in a parabolic chamber
11T606. Normal shock wave oscillations in supersonic diffusers

356L. THERMAL EFFECTS

See the following:

11A780. Computational study of coolant flow of liquid hydrogen through an externally heated duct

356Y. COMPUTATIONAL TECHNIQUES

11A610. Accuracy of flux-split algorithms in high-speed viscous flows. - D Gaitonde and JS Shang *(Flight Dyn Directorate, WL-FIMM, Wright Lab, WPAFB).* AIAA J 31(7) 1215-1221 (Jul 1993).

The flux-vector split methods of MacCormack and Candler (MC) and of van Leer (vL) and the flux-difference split method of Roe are investigated in problems representative of complex flows under laminar conditions: the blunt-body flow at Mach 16 and the flow past a 24-deg compression corner at Mach 14. Higher order accuracy is obtained with the monotonic upwind-centered scheme for conservation laws approach, viscous terms are centrally differenced, and an implicit relaxation method is employed for time integration. Emphasis is placed on evaluating the accuracy in prediction of surface quantities of engineering interest. The performance of the schemes is problem dependent. For the flow past the blunt body, the surface pressure is insensitive to the method as well as mesh resolution. Both the MC and Roe schemes predict accurate heat transfer rates whereas results with the vL method are dependent on the limiter employed. The overall distinction between the schemes is diminished for the compression corner especially on finer meshes. The extent of the separation region is notably influenced by the choice of the limiter. Several issues relating to the components of the calculation method are examined.

11A611. Central difference TVD schemes for time dependent and steady state problems. - P Jorgenson *(NASA Lewis Res Center, Cleveland OH 44135)* and E Turkel *(Sackler Fac of Exact Sci, Tel-Aviv Univ, Tel-Aviv 69978, Israel)*. J Comput Phys 107(2) 297-308 (Aug 1993).

We use central differences to solve the time dependent Euler equations. The schemes are all advanced using a Runge-Kutta formula in time. Near shocks a second difference is added as an artificial viscosity. This reduces the scheme to a first-order upwind scheme at shocks. The switch that is used guarantees that the scheme is TVD. For steady state problems it is usually advantageous to relax this condition. Then small oscillations do not activate the switches and the convergence to a steady state is improved. To sharpen the shocks different coefficients are needed for different equations, so a matrix-valued dissipation is introduced and compared with the scalar viscosity. The connection between this artificial viscosity and flux limiters is shown. Any flux limiter can be used as the basis of a shock detector for an artificial viscosity. We compare the use of the van Leer, van Albada, minmod, superbee, and the "average" flux limiters for this central difference scheme. For time dependent problems we need to use a small enough time step so that the CFL is less than one even though the scheme is linearly stable for larger time steps. Using a TVB Runge-Kutta scheme yields minor improvements in the accuracy.

11A612. Inviscid finite-volume lambda formulation. - F Casalini and A Dadone *(Inst Macchine Energetica, Politec di Bari, Via Re David 200, Bari 70125, Italy)*. J Propulsion Power 9(4) 597-604 (Jul-Aug 1993).

A finite-volume lambda formulation for solving Euler equations and able to handle compressible as well as transonic flow computations is presented. The easy extension of the methodology to the solution of Navier-Stokes equations is indicated. The integration scheme is in nonconservative form in smooth flow regions in order to take advantage of its superior accuracy and computational efficiency. It automatically switches to conservative form in shock regions, in order to capture them correctly. Computations of 2D and 3D shockless source flows prove the superior accuracy and computational efficiency of the proposed technique in comparison with a classical conservative upwind methodology. Moreover, computed results referring to some 2D and 3D test cases are compared with numerical or experimental published ones, thus showing the capabilities of the proposed formulation to deal with inviscid subsonic as well as transonic flow cases.

11A613. New artificial viscosity method for compressible viscous flow simulations by FEM. - S Boivin *(Dept Info Math, Univ du Quebec a Chicoutimi, G7H 2B1, Canada)* and M Fortin *(Dept of Math, Univ Laval, G1K 7P4, Canada)*. Int J Comput Fluid Dyn 1(1) 25-41 (1993).

A new artificial viscosity method is presented in the context of the resoltuion of the compressible Navier-Stokes equations. The method is used to solve the 2D time dependent equations by FEMs. The results of numerical experiments for the flow around a NACA0012 airfoil are presented and compared to results from a GAMM workshop in order to show the possibilities of the method.

11A614. Nonlinear relaxation Navier-Stokes solver for 3D, high-speed internal flows. - JR Edwards *(Dept of Mech Eng, N Carolina A&T State Univ, Greensboro NC 27411)* and DS McRae *(Dept of Mech and Aerospace Eng, N Carolina State Univ, PO Box 7910, Raleigh NC 27695)*. AIAA J 31(7) 1222-1228 (Jul 1993).

An efficient implicit Navier-Stokes method for computing steady, 3D flowfields characteristic of high-speed propulsion systems is presented. A nonlinear iteration strategy based on planar Gauss-Seidel sweeps is used to drive the solution toward a steady state, with approximate factorization errors within a crossflow plane reduced by the application of a quasi-Newton technique. A hybrid discretization approach is employed, with flux-vector splitting used in the streamwise direction and central differences with artificial dissipation used for the transverse fluxes. Convergence histories and comparisons with experimental data are presented for several 3D shock-boundary-layer interactions. Turbulent closure is provided by a modification of the Baldwin-Barth one-equation model. For the problems considered (206,000-335,000 mesh points), the algorithm provides steady-state convergence in 900-1700 CPU s on a single processor of a Cray Y-MP.

11A615. Pressure-based composite grid method for the Navier-Stokes equations. - JA Wright and W Shyy *(Dept of Aerospace Eng, Mech and Eng Sci, Univ of Florida, Gainesville FL 32611-2031)*. J Comput Phys 107(2) 225-238 (Aug 1993).

In this work, a pressure-based composite grid method is developed for solving the incompressible Navier-Stokes equations on domains composed of an arbitrary number of overlain grid blocks, where a conservative internal boundary scheme is devised to ensure that global conservation is maintained. Issues concerning the differences between the conservative internal boundary scheme developed for the pressure correction method with a staggered grid and that commonly used for density-based methods for compressible flow with nonstaggered grids are discussed. An organizational scheme is developed in order to provide a general and more flexible means for handling arbitrarily overlain grid blocks. Applications of the composite grid method to various model problems with complex geometry are used to illustrate the characteristics of the present procedure.

11A616. Spectral multigrid methods for the reformulated Stokes equations. - W Heinrichs *(Math Inst Heinrich-Heine, Univ Dusseldorf, Universitatsstr 1, D-4000 Dusseldorf 1, Germany)*. J Comput Phys 107(2) 213-224 (Aug 1993).

We present a spectral multigrid method for the reformulated Stokes equations. Here the continuity equation is replaced by a Poisson equation for the pressure. This system is discretized by a spectral collocation method without introducing a staggered grid. We observed no spurious modes except the physical one which is identical to a constant. Hence no filtering techniques are needed. We present an effective finite difference preconditioner which is employed for relaxation inside of the spectral multigrid method. Numercial results are presented which show the efficiency of our method.

11A617. Spectral solution of the viscous blunt-body problem. - DA Kopriva *(Dept of Math and Supercomput Comput Res Inst, Florida State Univ, Tallahassee FL 32306)*. AIAA J 31(7) 1235-1242 (Jul 1993).

The viscous blunt-body problem is solved with a shock-fitted Chebyshev spectral method. No explicit artificial viscosity or filtering is needed to obtain smooth, converged solutions. The method is applied to two problems. First, results for the flow over a right circular cylinder in the Mach number range of 5.5 - 6.0 are compared with experimental data. Second, a solution for a Mach 25 flow over a hyperbolic cone is compared with a viscous shock-layer calculation.

11A618. Vibrations of compressible fluid in a container closed by an elastic cover set in a baffle. - P Capodanno *(Lab Mec Theor UFR, Sci des Tech, F-25030 Besancon Cedex)*. Bull Polish Acad Sci Tech Sci 41(2) 99-110 (1993).

The author considers a 2D system formed by compressible fluid filling a container closed by an elastic cover set in an elastic finite baffle, regarded as a string. He gives a variational formulation of the vibration problem and proves the existence of the eigenfrequencies of the system by means of the functional analysis. He gives an analytical solution in the case of a symmetrical weightless system and a rectangular container.

See also the following:

11A602. Improved implicit residual smoothing for steady state computations of first-order hyperbolic systems
11A604. Upwind finite-volume method with a triangular mesh for conservation laws

356Z. EXPERIMENTAL TECHNIQUES

See the following:

11A607. Compression process in a free-piston shock-tunnel
11A720. Cryogenic wind tunnel
11A755. Investigation of factors influencing the calibration of five-hole probes for 3D flow measurements

358. Rarefied flow

11A619. Slip effects in a confined rarefied gas I. Temperature slip. - DC Wadsworth *(Dept of Aerospace Eng, Univ of S California, Los Angeles CA 90089-1191)*. Phys Fluids A 5(7) 1831-1839 (Jul 1993).

The model problem of a gas confined between stationary heated plates is analyzed numerically to quantify slip effects for gas densities ranging from near-continuum to highly rarefied conditions. Calculations are performed with the direct simulation Monte Carlo technique using two gas-surface interaction models and with a finite-difference Navier-Stokes method using slip boundary conditions. Comparisons are made with experimental density profiles and with previous discrete ordinate calculations using a model form of the Boltzmann equation. To the resolution of the experimental data, both direct simulation Monte Carlo and the Navier-Stokes equations with slip provide very good agreement for essentially all cases considered, while the discrete ordinate results are less accurate. The calculated pressure and temperature profiles show slightly larger differences. The details of the gas-surface interaction model have a relatively small effect on calculated density profiles. The direct simulation Monte Carlo and no-slip Navier-Stokes results are found to agree quantitatively for all properties at very small Knudsen number [$O(10^{-3})$]. Detailed direct simulation Monte Carlo quantities near the plates are used to quantify discrepancies in the continuum slip models and suggest possible improvements.

11A620. Models of thermal relaxation mechanics for particle simulation methods. - BL Haas *(NASA Ames Res Center, MS 230-2, Moffett Field CA 94035-1000)*, JD McDonald *(MasPar Comput, 749 N Mary Ave, Sunnyvale CA 94086)*, L Dagum *(Comput Sci, NASA Ames Res Center,* *MS T045-1, Moffett Field CA 94035-1000).* J Comput Phys 107(2) 348-358 (Aug 1993).

An improved phenomenological microscopic model is introduced in the present study and compared to existing models for simulating molecular vibrational relaxation in rarefied flows. These models are employed in statistical particle simulation methods such as the direct simulation Monte Carlo technique. In the traditional Borgnakke-Larsen model, collision energies are partitioned among contributing energy modes as dictated by fractions sampled from equilibrium distributions. Application of this method to fully excited continuous energy modes alone, such as in translation-rotation exchange, promotes the equilibrium state. However, application to translation-vibration exchange is afforded by unrealistically approximating the quantized distribution as continuous and partially excited, and employing individual collision "temperatures" in an attempt to capture the temperature-dependence of the necessary distributions. As proven in theoretical and numerical analyses, such an implementation of the Borgnakke-Larsen method may fail to promote the equilibrium relaxed state exactly and poses computational difficulties. The improved technique of the present work iterates between translation-rotation and rotation-vibration exchanges which does promote equilibrium exactly if the model for the latter process is compatible with quantized oscillators. This may be achieved by quantizing the total internal energy of a molecule and dividing the quanta randomly among the rotational and vibrational energy modes. This iteration-equipartition model retains computational simplicity and promotes thermal equilibrium even when applied to multi-species gas mixtures of non-degenerate anharmonic quantized oscillators.

11A621. Optimization of numerical algorithms for internal coordinate molecular dynamics. - VE Dorofeyev and AK Mazur *(Pacific Inst of Bioorganic Chem, Russian Acad of Sci, Vladivostok 690022, Russia).* J Comput Phys 107(2) 359-366 (Aug 1993).

Different computational procedures are compared for numerical solution of equations of motion for molecular dynamics of semi-rigid polymeric molecules with internal coordinates as general variables and an optimal method is proposed. The method uses forced conservation of momentum and angular momentum of the system and a predictor-corrector scheme with several iterations of correction for only generalized velocities at each time step. Variation of the accuracy of numerical solution with the time step and the order of the predictor-corrector algorithm is studied on three different partially fixed models of the oligopeptide $(Ala)_9$. The maximum possible time step gradually increases as fast dof are frozen. For dynamics in torsion angles the method provides a reasonable accuracy for the time step as large as 0.02 ps. The difference between the results obtained here and the earlier estimates made by using Newtonian molecular dynamics with constraints is discussed.

360. Multiphase flows

360B. MIXTURES OF LIQUID OR GAS WITH SOLID PARTICLES (EG SLURRIES)

11A622. Application of multi-phase model to the pipe flow of fresh concrete. - Kazumasa Ozawa *(Dept of Civil Eng, Univ of Tokyo, 7-3-1 Hongo, Bunkyo-ku, Tokyo 113, Japan),* Anura SM Nanayakkara *(Dept of Civil Eng, Univ of Moratuwa, Sri Lanka, Japan),* Koichi Maekawa *(Eng Res Inst, Univ of Tokyo, 7-3-1 Hongo, Bunkyo-ku, Tokyo 113, Japan).* Proc JSCE 466(V-19) 121-131 (May 1993).

This paper is to propose the mechanical modeling in terms of the collisional and frictional interaction of constituent particles for flowing fresh concrete through pipelines. The multi-phase formulation was adopted as the basis of computing the resistant force to the deformation arising in tapered and bent pipes. The effects of cement paste existing in fresh concrete on the particle interaction of sands and gravels was taken into account. Approximately 20 different mixtures of concrete were examined for verification of the numerical modeling. The analytical model was proved to be versatile to wider variety of fresh concrete having 3-27 cm by slump and any type of deformed pipe unit with different dimensions. It was emphasized that the pump pressure of concrete being driven through the deformed pipe units can be predicted well chiefly by the particle interaction model of aggregates and the multi-phase scheme.

11T623. Dynamics of small, heavy, rigid spherical particles in a periodic Stuart vortex flow. - Kek-Kiong Tio *(Dept of Appl Mech and Eng Sci, UCSD),* AM Ganan-Calvo *(Dept Ing Energetica Fluidomec, ETS Ing Indust Univ, 41012 Sevilla, Spain),* JC Lasheras *(Dept of Appl Mech and Eng Sci, UCSD).* Phys Fluids A 5(7) 1679-1693 (Jul 1993).

11A624. Multi-phase model for flow of liquid-solid assembly through pipelines. - Koichi Maekawa, Kazumasa Ozawa *(Eng Res Inst, Univ of Tokyo, 7-3-1 Hongo Bunkyo-ku, Tokyo 113, Japan),* Anura SM Nanayakkara *(Dept of Civil Eng, Univ of Moratuwa, Sri Lanka, Japan).* Proc JSCE 466(V-19) 109-120 (May 1993).

This paper is to propose the liquid-solid two phase modeling for simulating the flow and segregation of fresh concrete with the authors' intention of getting the mathematical background for mixture design concept serving super fluidized fresh concrete. The multi-component structure of solid phase was newly introduced into the frame of conventional liquid-solid two-phase model in fluid dynamics. The partial stresses carried by gravel, sand, and cement powder were implemented and the compatibility equations derived from experimental works were incorporated in the scheme of formulation for multi-component solid suspended by liquid. For verifying the capability of the physical model concerned, the trial model for particle-to-particle interaction was combined with the entire frame of formulation. It was examined that the model can follow the behaviors qualitatively in terms of the fluidity and segregation of particulate flow.

11T625. Particle size and chemical effects on contact filtration performance. - JE Tobiason *(Dept of Civil Eng, Univ of Massachusetts, Amherst MA 01003),* GS Johnson *(Wright-Pierce Engineers, Topsham ME 04086),* PK Westerhoff *(Dept of Civil Env and Architec Eng, Univ of Colorado, Boulder CO 80309),* B Vigneswaran *(Dept of Civil Eng, Univ of Massachusetts, Amherst MA 01003).* J Env Eng 119(3) 520-539 (May-Jun 1993).

See also the following:

11A703. Two-way interaction between homogeneous turbulence and dispersed solid particles I. Turbulence modification

360C. LIQUID-GAS MIXTURE

11T626. Correlation of adiabatic two-phase pressure drop data using the frictional law of corresponding states. - NT Obot, MW Wambsganss, DM France, JA Jendrzejczyk *(Mat and Components Tech Div, ANL).* J Fluids Eng 115(2) 317-323 (Jun 1993).

11A627. Extension and modification of Wohl equation of state. - A Hackel *(OMV Aktiengesellschaft, A-2214 Auersthal, Austria).* Arch Gornictwa 37(4) 447-490 (1992).

The Wohl fourth degree equation of state was modified in order to describe not only as in the past the gas-phase low density region but also and additionally the liquid and the liquid-gas two-phase region. The former negatively considered curvature downwards or the fourth degree Wohl function at high densities was interpreted positively in this work and utilized for the representation of the liquid volume along the two phase envelope. The modification was made in two steps: A-1: A general correlation parameter $t_cP_c(RT_c$ was introduced to correct the first constant b). A-2: The temperature dependent auxiliary functions for the second, ie, $f_a = f(T_r, w)$ and the third term, ie, $f_c = f(T_r, w)$ of the equation of state were newly defined on the bases of the Vetere-Pitzer-Curl correlation. A new definition of the third term is also capable to estimate the general third virial coefficient. The extension of the original Wohl functions was made in one step: B: Its symmetrical function was defined in a manner that the saturation pressure line in the two-phase region becomes the axis of symmetry of both functions in the two-phase region. The application of the Maxwell-Clausius criterion is outlined in detail for this case. The Wohl EQS describes now the liquid and the liquid-gas two-phase envelope besides the low density partition of the gas phase. For the not described rest of the high density gas phase region the modification steps (A 1-2) may be also applied to the constant (b) and the auxiliary temperature dependent function f_a of cubic equations of state especially the common widespread used Redlich-Kwong EQS or other socalled covolume equations of state - without a reflection of the worst of any equation. The limit of validity of the Wohl EQS between the low and high density region in the gas phase may be evenly described analytically by application of the principles of the proposed (A 1-2) to the Joffe-Dieterici EQS. A general application of the outlined modification is therefore possible. The verification of the solved problem was based on the examples of Argon and Nitrogen. For case of comparison all equations were presented in the reduced form.

See also the following:

11A628. Film-thickness, pressure-gradient, and turbulent velocity profiles in annular dispersed flows

360D. LIQUID-VAPOR MIXTURE

11A628. Film-thickness, pressure-gradient, and turbulent velocity profiles in annular dispersed flows. - AN Skouloudis and J Wurtz *(Process Eng Div, JRC, Ispra, Commission of the European Communities, 21020 Ispra, Italy).* J Fluids Eng 115(2) 264-269 (Jun 1993).

A regional model has been described for dispersed turbulent two-phase flow which accounts for the transverse variation of velocity. The two-phase turbulence parameters are introduced in direct analogy to well-known single-phase flow parameters which are then correlated to experimental data. The advantages of this approach are its simplicity and the absence of arbitrary parameters which need calibration at different experimental ranges. Its generality has been tested by comparisons at high and low operating pressures with air-water and steam-water mixtures. Comparisons between calculated and measured values have been carried out for the film thickness and the pressure gradient at different experimental setups.

360E. LIQUID DROP FORMATION

11T629. Collective effects of temperature gradients and gravity on droplet coalescence. - Xiaoguang Zhang, Hua Wang, RH Davis *(Dept of Chem Eng, Univ of Colorado, Boulder CO*

80309-0424). Phys Fluids A 5(7) 1602-1613 (Jul 1993).

360F. BUBBLE DYNAMICS

11A630. Discrete particle model for bubble-slug two-phase flows. - JA Trapp *(Colorado and Idaho Natl Eng Lab, Univ of Colorado, Idaho Falls ID 83415)* and GA Mortensen *(Idaho Natl Eng Lab, EG&G Idaho, Idaho Falls ID 83415)*. J Comput Phys 107(2) 367-377 (Aug 1993).

Most two-phase flow models are based on the fully averaged two-fluid concept. This paper describes a new discrete particle model that is intermediate between the numerically intractable local instant description and the fully averaged two-fluid model, thereby providing a more detailed but still tractable description of dynamical two-phase flow phenomena. The new model uses a Lagrangian description for a single dispersed bubble phase and a 1D Eulerian description for a single continuous liquid phase. In contrast to many other particle simulation models, the present model includes compressible phases and large bubbles whose size may be comparable to the computational cell size. The discrete Lagrangian description of the dispersed phase allows the particles to have a distribution of sizes, shapes, etc, thereby capturing the important statistical aspects of dispersed two-phase flow. In contrast to the two-fluid models, the discrete particle model allows the use of more mechanistic models for dispersed phase coalescence and breakup, wakes, etc, thereby allowing the dynamic prediction of flow regime evolution and transitions without the use of flow regime maps inherent in two-fluid models. Numerical simulations for two test problems are presented. Agreement with experimental data is generally satisfactory. Extensions of the model to heat transfer and to two discrete and two continuous phases will be described elsewhere.

11A631. Motion of long bubbles in tubes of square cross section. - WB Kolb and RL Cerro *(Dept of Civil Eng, Univ of Tulsa, Tulsa OK 74104-3189)*. Phys Fluids A 5(7) 1549-1557 (Jul 1993).

The flow of a long bubble in an otherwise liquid-filled tube is a hydrodynamics problem with interesting practical applications in enhanced oil recovery, the coating of monolithic structures, and more recently the design and operation of three-phase monolithic reactors. For intermediate to large capillary numbers the "bubble" is axisymmetric and the theoretical approach of Bretherton can be applied if the velocity profile of the fluid flowing between the bubble and the square tube wall is known. The velocity profile can be computed using an infinite series expansion of harmonic polynomials. A film evolution equation - which includes all the terms that are important throughout the entire bubble profile - is integrated using a parametric representation as a function of arclength and free-surface angle. The flow is analyzed and complete bubble profiles are generated. The results are shown to be in good agreement with experiment.

See also the following:

11T584. Calculation of interfacial flows and surfactant redistribution as a gas-liquid interface moves between two parallel plates

11A594. Thermocapillary migration of a small chain of bubbles

360G. FROTH FLOW AND SPRAY FLOW

11A632. Modeling of spray droplets deformation and breakup. - EA Ibrahim *(Dept of Mech Eng, Tuskegee Univ, Tuskegee AL 36088)*, HQ Yang, AJ Przekwas *(CFD Res, Huntsville AL 35805)*. J Propulsion Power 9(4) 651-654 (Jul-Aug 1993).

One of the most important processes that dominate spray combustion efficiency is spray drop deformation and breakup. Krzeckowski has conducted an experimental study of the deformation mechanisms of spray drops. These may be characterized as bag-type shear-type, with some transition in between. The present work is only concerned with the shear-type mechanism. Existing theoretical models for shear-type breakup may be categorized under two main categories. These are the 1) semianalytical and 2) the Taylor analogy models.

360Y. COMPUTATIONAL TECHNIQUES

11A633. Numericl study on the two-phase flow distribution in a T-junction. - LFM Moura *(Mech Eng Dept, Univ of Campinas, Campinas 13081, Brazil)* and KS Rezkallah *(Mech Eng Dept, Univ of Saskatchewan, Saskatoon, S7N 0WO, Canada)*. Int J Numer Methods Fluids 17(3) 257-270 (Aug 1993).

The main objective of this paper is to investigate the ability of a 2D two-fluid computer code to predict the phase separation in a T-junction. A new semi-implicit numerical scheme is developed for solving the two-fluid model equations. Special attention is directed to the modeling of the constitutive equations for the interfacial friction term. Detailed distribution of void fraction, pressure and velocities are obtained for an air-water mixture in a vertical tee. Good agreement was obtained between the computer code results and the experimental data for the phase separation in the T-junction.

360Z. EXPERIMENTAL TECHNIQUES

See the following:

11A194. Structure of cyclohexane + t-butanol mixtures from positron annihilation and ultrasonic velocity measurements

362. Wall layers (incl boundary layers)

11A634. Combined drag effects of riblets and polymers in pipe flow. - GW Anderson, JJ Rohr, SD Stanley *(Naval Ocean Syst Center, San Diego CA 92152)*. J Fluids Eng 115(2) 213-221 (Jun 1993).

The additional skin friction effect produced by a 3M riblet surface, used in conjunction with low concentration polymer solutions, is investigated in fully developed, turbulent pipe flow. Generally at the low concentrations of Polyox 301 and guar gum studied, the absolute drag reduction of the 3M riblets appears to be independent of the polymer presence, with a maximum between 5 and 7 percent occurring around $h^+ = 12$. Comparisons with previous polymer studies with 3M riblets, sand roughened and commercially rough surfaces are made.

See also the following:

11A975. Boundary layer development of pulsatile blood flow in a tapered vessel

362C. LAMINAR LAYERS

11A635. High-speed boundary-layer stability and transition. - VI Lysenko *(Siberian Branch, Russian Acad of Sci, Inst of Theor and Appl Mech, Novosibirsk, Russia)*. Eng Trans 41(1) 31-50 (1993).

In this paper peculiarities of the laminar hypersonic (Mach numbers 4 - 16) boundary layer stability and its transition to the turbulent one are studied experimentally and numerically at different facilities. The influence of various factors on the boundary-layer stability and the transition is considered.

362D. TURBULENT LAYERS

11A636. Frictional drag reduction by injecting high-viscosity fluid into turbulent boundary layer. - H Kato, Y Fujii, H Yamaguchi, M Miyanaga *(Dept of Naval Architec and Ocean Eng, Univ of Tokyo, Bunkyo, Tokyo 113, Japan)*. J Fluids Eng 115(2) 206-212 (Jun 1993).

This paper presents a new method to reduce turbulent frictional drag by injectiug high-viscosity fluid into the boundary layer. When the turbulent region of the boundary layer is filled with high-viscosity fluid, and the viscosity of the viscous sublayer is kept low, the Reynolds stress in the turbulent region is reduced and therefore requires a greater velocity gradient to transfer the momentum. The greater velocity gradient in the turbulent region results in a reduction of the velocity gradient at the viscous sublayer, which causes a drop in shear stress at the wall. Such a boundary-layer structure could be created by injecting two different fluids from double slits on a wall. Sugar syrup and water were used as the high-viscosity fluid and the low-viscosity fluid, respectively. The shear stress was directly measured by shear stress pick-ups mounted flush on the wall. The shearing stress was reduced by more than 50 percent at the optimum injection condition. A water-water injection experiment was also performed to show the effect of injection itself.

11A637. Strong vortex-boundary layer interactions Part II. Vortices low. - AD Cutler *(George Washington Univ, JIAFS NASA Langley Res Center, Hampton VA 23681)* and P Bradshaw *(Dept of Mech Eng, Stanford)*. Exp Fluids 14(6) 393-401 (May 1993).

This is the second of two papers on the interaction between a longitudinal vortex pair, produced by a delta-wing at angle of attack, and a turbulent boundary layer developing on a flat plate. In the first paper only the outer parts of the vortices entered the boundary layer whereas in this paper the vortices merge with it. In the resultant interaction, the boundary layer between the vortices is kept thin by lateral divergence and a 3D separation line is formed outboard of each vortex. Turbulent, momentum-deficient fluid containing longitudinal vorticity is entrained from the boundary layer along these lines and wrapped around the vortices. As a consequence, the turbulent region of the vortices increases in size and the circulation slowly decreases. It is shown that the flow near the separation line and in the vortices is complicated, and this interaction is expected to be more difficult to calculate than the first. Detailed mean flow and turbulence measurements are reported.

See also the following:

11A648. Comparison of numerical and experimental results for a turbulent flow field with a longitudinal vortex pair

362E. TRANSITION AND RELAMINARIZATION

11A638. Finite amplitude steady waves in the Blasius boundary layer. - JM Rotenberry *(Dept of Math, S Methodist Univ, Dallas TX 75275)*. Phys Fluids A 5(7) 1840-1842 (Jul 1993).

The stability of the flow over a flat plate to finite amplitude disturbances is studied using a model by Milinazzo and Saffman. The traveling wave solutions which bifurcate from the Orr-

Sommerfeld neutral stability curve to the Blasius profile are calculated numerically. The curve is the intersection of the zero energy plane with a neutral stability surface in energy, Reynolds number, and wave-number space. Although the bifurcation is supercritical at the "nose" of this curve, it is shown that it is subcritical elsewhere and that the minimum Reynolds number for the existence of traveling waves is less than the critical Reynolds number of the Orr-Sommerfeld neutral stability curve. This result suggests that finite amplitude disturbances can initiate transition.

11A639. Nonlinear evolution of secondary instabilities in boundary-layer transition. - JD Crouch *(Boeing Commercial Airplane Group, Seattle WA 98124)* and T Herbert *(Dept of Mech Eng, Ohio State Univ, Columbus OH 43210)*. Theor Comput Fluid Dyn 4(4) 151-175 (1993).

Methods of nonlinear stability theory are applied to analyze the evolution of disturbances in the 3D stage immediately preceding the breakdown of a laminar boundary layer. A perturbation scheme is used to solve the nonlinear equations and to develop a dynamical model for the interaction of primary and secondary instabilities. The first step solves for the 2D primary wave in the absence of secondary disturbances. Once this finite-amplitude wave is calculated, it is decomposed into a basic-flow component and an interaction component. The basic-flow component acts as a parametric excitation for the 3D secondary wave, while the interaction component captures the resonance between the secondary and primary waves. Results are presented in two principal forms: amplitude growth curves and velocity profiles. Our results agree with experimental data and the few available results of transition simulations, and moreover, reveal the origin of the observed phenomena. The method described establishes the basis for physical transition criteria in a given disturbance environment.

11A640. Optimization of multiple-panel compliant walls for delay of laminar-turbulent transition. - PW Carpenter *(Dept of Eng, Univ of Warwick, Coventry CV4 7AL, UK)*. AIAA J 31(7) 1187-1188 (Jul 1993).

Previous theoretical work has led to the development of methods for optimizing compliant-wall properties to achieve the greatest possible transition delay for flat-plate boundary-layer flows. It was found that the optimum wall properties for locally reducing the growth of disturbances depend quite strongly on the Reynolds number. This suggests that it would be advantageous to use multiple-panel walls with each compliant panel optimized for a particular Reynolds number range. Accordingly, the optimization procedure is extended to two-panel compliant walls, and the optimum wall properties are determined that correspond to the greatest transition delay. It is found that, based on a conservative value of n = 7, the e^n method predicts that the greatest transitional Reynolds number achievable using single- and two-panel compliant walls is respectively 4.6 and 6.05 times the rigid-wall value. The corresponding wall properties are readily realizable for operation in water, but are probably not feasible in air.

362F. COMPRESSIBLE AND HYPERSONIC LAYERS

11A641. New test cases in compressible thermo-fluid-dynamics. - A Pozzi *(Istituto di Gasdin, Univ di Napoli, Piazzale V Tecchio, Napoli 80-80125, Italy)*, A Bianchini *(Dept of Math, Univ di Ancona, Ancona, Italy)*, AR Teodori *(Dept of Math and Phys, Univ di Camerino, Camerino, Italy)*. Int J Heat Fluid Flow 14(2) 201-205 (Jun 1993).

This paper studies the thermo-fluid-dynamic field generated by a fast stream impinging on a plane. The Mach number is less than one, but not so small that compressibility effects can be neglected. The analysis requires first the nonviscous solution of the basic equation, obtained by assuming the velocity components as independent variables, and then the viscous solution in the boundary-layer approximation. The Dorodnitzin-Stewartson transformation is used to eliminate the dependence of the transport coefficients on the temperature. The values of 1 and 0.74 (air case) for the Prandtl number are considered. The viscous solution, obtained by means of a MacLaurin series of the Pade approximant technique, gives practically exact results.

362G. SHOCK WAVE BOUNDARY LAYER INTERACTION

11A642. High-speed turbulence modeling of shock-wave-boundary-layer interaction. - F Grasso and D Falconi *(Dept di Mec e Aeronaut, Univ di Roma La Sapienza, Via Eudossiana 18, Rome 00184, Italy)*. AIAA J 31(7) 1199-1206 (Jul 1993).

In the present paper some of the recent theoretical developments in compressible turbulence modeling are analyzed, and a model that accounts for compressibility and low Reynolds-number effects is developed. The leading compressibility terms have been identified in the dilatation-dissipation, pressure-dilatation, and the scalar product of the Favre velocity and mean pressure gradient. For the dilatation-dissipation a model similar to that of Zeman has been assumed; the pressure-dilatation is modeled according to Sarkar's model; and the "Favre" contribution has been modeled with a gradient law. The model also accounts for compressibility effects on the von Karman's constant and on the turbulence length scale, which affects the heating rates. A study of hypersonic boundary-layer flows and shock-wave and boundary-layer interactions shows that the effects of compressibility depend on the flow complexity.

11A643. Investigation of a hypersonic crossing shock wave-turbulent boundary layer interaction. - N Narayanswami, DD Knight *(Dept of Mech and Aerospace Eng, Rutgers Univ NJ)*, CC Horstman *(NASA Ames Res Center, Moffett Field CA)*. Shock Waves 3(1) 35-48 (1993).

A combined theoretical and experimental study is presented for the interaction between crossing shock waves generated by (10°, 10°) sharp fins and a flat plate turbulent boundary layer at Mach 8.3. The theoretical model is the full 3D mean compressible Reynolds-averaged Navier-Stokes equations incorporating the algebraic turbulent eddy viscosity model of Baldwin and Lomax. A grid refinement study indicated that adequate resolution of the flowfield has been achieved. Computed results agree well with experiment for surface pressure and surface flow patterns and for pitot pressure and yaw angle profiles in the flowfield. The computations however, significantly overpredict surface heat transfer. Analysis of the computed flowfield results indicates the formation of complex streamline and wave structures within the interaction region.

362M. SEPARATION AND REATTACHMENT

11A644. Investigation of turbulent separation-reattachment flow in a curved-wall diffuser. - Jun-Fei Yin *(Dept of Power Eng, Nanjing Aeronaut Inst, Nanjing 210016, Jiangsu Province, Peoples Rep of China)* and Shao-Zhi Yu *(Dept of Power Eng, Nanjing Aeronaut Inst, Nanjing, Jiangsu Province, Peoples Rep of China)*. Int J Heat Fluid Flow 14(2) 129-137 (Jun 1993).

A 2D laser velocimeter was employed to study the turbulent separation-reattachment flow field in a 2D diffuser, which is a lower curved wall and upper flat plate. There is a parallel channel connected with the exit of the diffuser. In the inlet of the diffuser, the Reynolds number is 5,000 based on the momentum thickness, and the inlet velocity is 25.2m-s. Mean velocity and Reynolds stresses were measured from upstream of the separation to downstream of the reattachment. The minimum distance from the surface is .3 mm. The significant features were that after transitory detachment, within the reversing flow, there exist the second extreme of u^2 and minus of -uv. Normal stresses and the cross-stream pressure gradient are important immediately in the separating flow and are associated with strong streamline curvature. The maximum of the displacement thickness curvature K^x_{max} corresponds to the intermittency transitory detachment. Several velocity profiles and Cebeci and Smith algebraic eddy-viscosity are compared with the experiment. A new approximate correction of the effect of normal stress is proposed and yields results in agreement with the experiment before the transitory detachment.

11T645. Vorticity dynamics and scalar transports in separated and reattached flow on a blunt plate. - D Tafti *(Natl Center for Supercomput Appl, Univ of Illinois, Urbana IL 61801)*. Phys Fluids A 5(7) 1661-1673 (Jul 1993).

See also the following:

11A634. Combined drag effects of riblets and polymers in pipe flow

362N. SUCTION AND INJECTION

See the following:

11A636. Frictional drag reduction by injecting high-viscosity fluid into turbulent boundary layer

362Q. HEAT ADDITION AND COOLING

See the following:

11A641. New test cases in compressible thermo-fluid-dynamics

362S. DRAG REDUCTION

11A646. Drag characteristics of extra-thin fin-riblets in an air flow conduit. - ZY Wang *(Dept of Power Machinery Eng, Xi'an Jiaotong Univ, Xi'an Shaanxi, Peoples Rep of China)* and J Jovanovic *(Lehrstuhl fur Stromungsmech, Univ Erlangen Nurnberg, D-8500, Erlangen, Germany)*. J Fluids Eng 115(2) 222-226 (Jun 1993).

An experimental study of riblets with extra thin fins (5μm thick) is presented. A drag reduction of 2-3 percent per quarter conduit wall is indicated when h^+ is around 3-15 in a square section of air flow conduit lined with the extra-thin-fin-riblets (ETFR) on one side wall. The pressure distributions along the conduit indicate the influence of the riblet front step on the drag reduction performance in the conduit flow. The measurement methods and the detailed structure of the ETFR are also discussed.

See also the following:

11A636. Frictional drag reduction by injecting high-viscosity fluid into turbulent boundary layer

364. Internal flow (pipe, channel, Couette)

364B. LAMINAR FLOW

11A647. Laminar, unidirectional flow of thixotropic fluid in a circular pipe. - J Billingham and JWJ Ferguson *(Schlumberger Cambridge Res, High Cross, Madingley Rd, Cambridge CB3 0EL, UK)*. J Non-Newtonian Fluid Mech 47 21-55 (Jun 1993).

In this paper we study the unidirectional, axisymmetric flow of a bentonite mud in a circular pipe. Bentonite mud is an inelastic, thixotropic, generalized-Newtonian fluid. We use a rheological model that characterizes this behavior in terms of a single parameter λ which is a measure of the amount of structure in the fluid. The behavior of λ is determined by a single rate equation which models the tendency of fluid structure to increase whilst being limited by the imposed shear rate. We find that, for certain parameter ranges, the model is not structurally stable, but that this problem can be eliminated by including diffusion of fluid structure. A graph of the equilibrium shear stress for a given shear rate (the rheogram) is not monotonic, yet no mechanical instability occurs in pipe flow. We contrast this with recent work on the pipe flow of a Johnson-Segalman-Oldroyd fluid which displays spurting and oscillatory behavior. The difference lies in the relative magnitude of normal stress effects in the two fluids. There appear to be no grounds for discarding the constitutive model studied here simply because of the nonmonotonicity of the equilibrium rheogram.

364C. TURBULENT FLOW

11A648. Comparison of numerical and experimental results for a turbulent flow field with a longitudinal vortex pair. - JX Zhu, M Fiebig, NK Mitra *(Inst fur Thermo und Fluiddyn, Ruhr-Univ Bochum, 4630 Bochum 1, Germany)*. J Fluids Eng 115(2) 270-274 (Jun 1993).

A numerical simulation of a 3D turbulent flow with longitudinal vortices embedded in the boundary layer on a channel wall is presented. The flow is described by the unsteady incompressible Reynolds averaged Navier-Stokes equations and the standard κ-ε turbulence model. A finite difference scheme based on the SOLA-algorithm is developed for the numerical solution of the governing equations. Comparison with the experimental data of Pauley and Eaton shows that the numerical computations predict the general characteristics of the flow correctly. Agreement to within 13 percent is obtained for the worst location in mean velocity fields. The average deviation of predicted mean streamwise velocity from the experimental data is 3.6 percent.

11T649. Generation of tripolar vortical structures on the beta plane. - JS Hesthaven, JP Lynov, JJ Rasmussen *(Optics and Fluids Dyn Dept, Assoc EURATOM, Riso Natl Lab, PO Box 49, DK-4000 Roskilde, Denmark)*, GG Sutyrin *(PP Shirshov Inst of Oceanog, Russian Acad of Sci, 23 Krasikova St, Moscow 117218, Russia)*. Phys Fluids A 5(7) 1674-1678 (Jul 1993).

11A650. Predicting equilibrium states with Reynolds stress closures in channel flow and homogeneous shear flow. - R Abid *(High Tech Corp, NASA Langley Res Center, Hamtpon VA 23681)* and CG Speziale *(Dept of Aerospace and Mech Eng, Boston Univ, Boston MA 02215)*. Phys Fluids A 5(7) 1776-1782 (Jul 1993).

Turbulent channel flow and homogeneous shear flow have served as basic building block flows for the testing and calibration of Reynolds stress models. In this paper, a direct theoretical connection is made between homogeneous shear flow in equilibrium and the log layer of fully developed turbulent channel flow. It is shown that if a second-order closure model of the standard type is calibrated to yield good equilibrium values for homogeneous shear flow, it will also yield good results for the log layer of channel flow provided that the Rotta coefficient is not too far removed from one. Most of the commonly used second-order closure models introduce an *ad hoc* wall reflection term in order to mask deficient predictions for the log layer of channel flow that arise either from an inaccurate calibration of homogeneous shear flow or from the use of a Rotta coefficient that is too large. Illustrative model calculations are presented to demonstrate this point which has important implications for turbulence modeling.

See also the following:

11A628. Film-thickness, pressure-gradient, and turbulent velocity profiles in annular dispersed flows

11A654. Experimental study of two flows through an axisymmetric sudden expansion

364E. UNSTEADY FLOW

11A651. Analytical solution of flow of second-order non-Newtonian fluids through annular pipes. - Wen-hui Zhu *(Natl Univ of Defence Tech, Changsha, China)* and Ci-qun Liu *(Inst of Porous Flow and Fluid Mech, Langfang, Hebei, China)*. Appl Math Mech 14(3) 209-215 (Mar 1993).

This paper presents an analytical solution to the unsteady flow of the second-order non-Newtonian fluids by the use of integral transformation method. Based on the numerical results, the effect of non-Newtonian coefficient Hc and other parameters on the flow are analyzed. It is shown that the annular flow has a shorter characteristic time than the general pipe flow while the correspondent velocity, average velocity have a smaller value for a given H_c. Else, when radii ratio keeps unchanged, the shear stress of inner wall of annular flow will change with the inner radius compared with the general pipe flow and is always smaller than that of the outer wall.

364K. ROTATING FLUIDS OR SURFACES

See the following:

11T649. Generation of tripolar vortical structures on the beta plane

364L. HEAT ADDITION

11A652. Cooling of a heat-generating board inside a parallel-plate channel. - A Bejan, AM Morega *(Dept of Mech Eng and Mat Sci, Duke Univ, Durham NC 27706)*, SW Lee *(Mech Tech Dept, IBM NS, Research Triangle Park NC)*, SJ Kim *(Thermal Eng Center, IBM ADSTAR, Tucson AZ)*. Int J Heat Fluid Flow 14(2) 170-176 (Jun 1993).

This paper addresses the fundamental question of how to position a heat-generating board inside a parallel-plate channel, where it is cooled by forced convection. It is shown that when the board substrate is a relatively good thermal conductor, the best board position is near one of the channel walls, and the worst position is in the middle of the channel. T[illegible] worst positions switch places w[illegible]rate is a relatively poor co[illegible]spacing between a heat-g[illegible]rm temperature, or un[illegible]nsulated wall [illegible]annel is [illegible]al conditions it is advantageous to divide a heat-generating board into two or more equidistant boards inside the same channel, when the total rate of heat generation of all the boards and the channel spacing are fixed.

See also the following:

11A657. Numerical study of fully developed laminar flow and heat transfer in a curved pipe with arbitrary curvature ratio

364M. NON-NEWTONIAN FLOW

See the following:

11A647. Laminar, unidirectional flow of thixotropic fluid in a circular pipe

364N. ROUGHNESS EFFECT

11A653. Evaluation of open channel flow with varying aspect ratio and roughness ratio. - Yongdi Yang and Atsuyuki Daido *(Dept of Civil Eng, Ritsumeikan Univ, 56-1 Kitamachi Tojin Kitaku, Kyoto 603, Japan)*. Proc JSCE 467(II-23) 103-113 (May 1993).

A flow pattern with varying aspect ratio (breadth-depth) and boundary roughness ratio (bed roughness-side wall roughness) in open channel is proposed in this paper. The distribution of boundary shear and the mean boundary shear are studied. On the basis of this, velocity distribution and flow resistance are further discussed. The evaluation formulate of boundary shear, velocity distribution, and flow resistance are derived systematically. The results are suitable for all aspect ratio and roughness ratio, and are better in agreement with a wide range of experimental data. These are much helpful to the study of sediment transport, flow diffusion, river engineering, etc.

364P. OBSTRUCTIONS

11A654. Experimental study of two flows through an axisymmetric sudden expansion. - WJ Devenport and EP Sutton *(Eng Dept, Cambridge Univ, Trumpington St, Cambridge, UK)*. Exp Fluids 14(6) 423-432 (May 1993).

Two turbulent separated and reattaching flows produced by a sudden expansion in a pipe have been studied. The first was produced by a simple axisymmetric sudden enlargement from a nozzle of diameter 80 mm to a pipe of diameter 150 mm. The second was the flow at the same enlargement with the addition of a center-body 90 mm downstream of the nozzle exit. Detailed measurements of velocity and skin friction (made primarily using pulsed wires) and of wall static pressure are presented. Without the centerbody the flow structure is similar to that observed in other sudden pipe expansions and over backward-facing steps. A turbulent free shear layer, bearing some similarity to that of a round jet, grows from separation and then reattaches to the pipe wall downstream. Reattachment is a comparatively gradual process, the shear layer approaching the wall at a glancing angle. The introduction of the centerbody causes the shear layer to curve towards the wall and reattach at a much steeper angle. Reattachment is much more rapid; gradients of skin friction and pressure along the wall are many times those without the centerbody. The high curvature of the shear layer strongly influences its turbulent structure, locally suppressing turbulence levels and reducing its growth rate.

11A655. Prediction of pressure drop for incompressible flow through screens. - E Brundrett *(Dept of Mech Eng, Univ of Waterloo, Waterloo, ON N2L 3G1, Canada)*. J Fluids Eng 115(2) 239-242 (Jun 1993).

A new pressure loss correlation predicts flow through screens for the wire Reynolds number range of 10^{-4} to 10^4 using the conventional orthogonal porosity and a function of wire Reynolds number. The correlation is extended by the conventional cosine law to include flow that is not perpendicular to the screen. The importance of careful specification of wire diameter for accurate predictions of porosity is examined. The effective porosity is influenced by the shape of the woven wires, by any local damage, and by screen tension.

See also the following:

11A652. Cooling of a heat-generating board inside a parallel-plate channel

364R. SECONDARY FLOW, EFFECTS OF CURVATURE

11T656. Behavior of flow in a channel bend with a side overflow (flood relief) channel. - YR Fares *(Dept of Civil Eng, Univ of Surrey, Guildford, UK)* and JG Herbertson *(Dept of Civil Eng, Univ of Glasgow, Glasgow, UK)*. J Hydraul Res 31(3) 383-402 (1993).

11A657. Numerical study of fully developed laminar flow and heat transfer in a curved pipe with arbitrary curvature ratio. - Ru Yang and Sung Fa Chang *(Inst of Mech Eng, Natl Sun Yat-Sen Univ, Kaohsiung, Taiwan, ROC)*. Int J Heat Fluid Flow 14(2) 138-145 (Jun 1993).

A finite-difference numerical method is applied to solve the full Navier-Stokes equations for the fully developed flow and heat transfer in an axially uniformly heated curved pipe with arbitrary curvature ratio (the ratio of the pipe radius to the pipe curvature). Previous studies were restricted to within a range of the curvature ratio less than 0.3. In this study, the ranges of the parameters are the curvature ratio varying from 0.01 to 0.9, the Reynolds number varying from 1 to 2,000, and the Prandtl number varying from 0.7 to 300. The results of the friction ratio and the Nusselt-number ratio are correlated with the parameters of the curvature ratio, the Dean number, and the Prandtl number.

11A658. Reconstruction of 3D particle trajectories in flows through curved circular tubes. - ML Lowe *(Phys Dept, Loyola Col, Baltimore MD 21210)*, PH Kutt *(Phys Dept, Univ of Pennsylvania, Philadelphia PA 19104)*, T York, LA Kazanov, B Leavy *(Phys Dept, Loyola Col, Baltimore MD 21210)*. Exp Fluids 14(6) 402-408 (May 1993).

An automated technique is described for reconstructing 3D trajectories of tracer particles in curved circular ducts. Individual particles are tracked in real time by a rotating camera under computer control. A digital imaging system enables the computer to locate the particle, adjust the speed of rotation, and store position and calibration data. By viewing the tube from approximately orthogonal directions, 3D information on the position of the particle is obtained. Its precise location is calculated by tracing rays from the camera to the interior of the tube. This technique yields detailed 3D position and velocity data along a trajectory.

11A659. Steady, inviscid shock waves at continuously curved, convex surfaces. - B Koren and E van der Maarel *(Center for Math and Comput Sci, PO Box 4079, 1009 AB Amsterdam, Netherlands)*. Theor Comput Fluid Dyn 4(4) 177-195 (1993).

An accurate and efficient numerical method for steady, 2D Euler equations is applied to study steady shock waves perpendicular to smooth, convex surfaces. The main subject of study is the flow near both ends of the hock wave: the shock-foot and shock-tip flow. A known analytical model of the inviscid shock-foot flow is critically investigated, analytically and numerically. The results obtained agree with those of the existing analytical model. For the inviscid shock-tip flow, two existing analytical solutions are reviewed. Numerical results are presented which agree with one of these two solutions. Good numerical accuracy is achieved through a monotone, second-order accurate, finite-volume discretization. Good computational efficiency is obtained through iterative defect correction iteration and a multigrid acceleration technique which employs local grid refinement.

11A660. Torsion effect on fully developed laminar flow in helical square ducts. - Wen-Hwa Chen and R Jan *(Dept of Power Mech Eng, Natl Tsing Hua Univ, Hsinchu 30043, Taiwan ROC)*. J Fluids Eng 115(2) 292-301 (Jun 1993).

The continuity equation and Navier-Stokes equations derived from a nonorthogonal helical coordinate system are solved by the Galerkin FEM in an attempt to study the torsion effect on the fully developed laminar flow in the helical square duct. Since high-order terms of curvature and torsion are considered, the approach is also applicable to the problems with finite curvature and torsion. The interaction effects of curvature, torsion, and the inclined angle of the cross section on the secondary flow, axial velocity, and friction factor in the helical square duct are presented. The results show that the torsion has more pronounced effect on the secondary flow rather than the axial flow. In addition, unlike the flow in the toroidal square duct, Dean's instability of the secondary flow, which occurs near the outer wall in the helical square duct, can be avoided due to the effects of torsion and/or inclined angle. In such cases, a decrease of the friction factor is observed. However, as the pressure gradient decreases to a small value, the friction factor for the toroidal square duct is also applicable to the helical square duct.

364Y. COMPUTATIONAL TECHNIQUES

11A661. Streamwise computation of 3D flows using two stream functions. - MS Greywall *(Dept of Mech Eng, Wichita State Univ, Wichita KS 67208)*. J Fluids Eng 115(2) 233-238 (Jun 1993).

An approach to compute 3D flows using two stream functions is presented. The independent variables used are χ, a spatial coordinate, and ξ and η, value of stream functions along two sets of suitably chosen intersecting stream surfaces. The dependent variables used are the streamwise velocity, and two functions that describe the stream surfaces. Since the value of a stream function is constant along the solid boundaries, this choice of variables makes it easy to satisfy the boundary conditions. To illustrate the approach, computations of incompressible potential flow through a circular-to-rectangular transition duct are also presented.

See also the following:

11A565. Use of subdomains for inverse problems in branching flow passages

364Z. EXPERIMENTAL TECHNIQUES

11T662. Computer operated traversing gear for 3D flow surveys in channels. - S Lau *(Inst fur Thermo und Fluiddyn, Ruhr Univ, D-4630 Bochum, Germany)*, V Schulz *(Betriebsforschungsinst, Sohnstr 10, D-4000 Dusseldorf)*, VI Vasanta Ram *(Inst fur Thermo und Fluiddyn, Ruhr Univ, D-4630 Bochum, Germany)*. Exp Fluids 14(6) 475-476 (May 1993).

366. Internal flow (inlets, nozzles, diffusers, cascades)

11A663. Bubbly flows through a converging-diverging nozzle. - R Ishii, Y Umeda, S Murata, N Shishido *(Dept of Aeronaut Eng, Kyoto Univ, Kyoto 606, Japan)*. Phys Fluids A 5(7) 1630-1643 (Jul 1993).

Characteristics of bubbly flow through a vertical, 2D, converging-diverging nozzle are investigated theoretically and experimentally. First, a new model equation of motion governing a dispersed bubble phase is proposed. This is compared in detail with those proposed previously by several researchers. Next, hyperbolicity of the resultant systems of governing equations for the bubbly flow is investigated in detail. Numerical simulations of bubbly flows through a converging-diverging nozzle are carried out by using the proposed system of model equations. In order to check the validity of the numerical results and then the proposed system, they are compared with the experiments which were performed previously in the authors' laboratory in a water-nitrogen blow-down facility. It will be shown that the numerical results obtained by using the proposed system of model equations agree well with the experiments.

11A664. Flow structures and their relevance to passive scalar transport in fume cupboards. - IB Ozdemir, JH Whitelaw *(Dept of Mech Eng, Imperial Col of Sci Tech and Med, London, UK)*, AF Bicen *(Invent UK Ltd, Imperial Col of Sci Tech and Med, London, UK)*. Proc Inst Mech Eng C 207(C2) 103-115 (1993).

This paper describes an experimental investigation of air flow patterns and related passive scalar transport inside an open-fronted containment facility, with emphasis on the interaction with the laboratory environment. Time-averaged and instantaneous structures of the turbulent flow were examined by visualization and local measurements inside the enclosure and at the front aperture of 1200mm × 500mm cross-section. The cabinet was scavenged at an extract flowrate of 0.310 m^3/s with 95% of the air passing through the front aperture at a spatially averaged air velocity of 0.5 m/s and 5% supplied through an auxiliary aperture of 1200mm × 15mm cross-section located at the front edge of the ceiling of the enclosure. Sulphur hexafluoride was used to mark the flow and the distributions of its time-averaged concentration over the front aperture and inside the cabinet were used to deduce the degree of mixing and passive scalar transport. The geometrical features of the cabinet provided a flow field with a spanwise vortex at the upper frontal part of the enclosure, whose cross-sectional dimension was larger close to the side walls where the velocity of the inflowing air was lower than in the central region. The spanwise vortex implemented to improve capture efficiency at low inflowing air velocities can be detrimental to the stability of the inflowing air stream along the sash handle, leading to severe leakage of the passive scalar encapsulated within the vortex itself.

11A665. Spatially resolved birefringence studies of planar entry flow. - SR Galante *(Calgon Water Man, Pittsburgh PA 15230)* and PL Frattini *(Eifle, 11465 Clayton Rd, San Jose CA 95127)*. J Non-Newtonian Fluid Mech 47 289-337 (Jun 1993).

Stress distributions near the re-entrant corners in 2D, 4:1 contraction flows of weakly elastic and more highly elastic poly(dimethylsiloxane) (PDMS) melts were investigated with a high-resolution, polarization modulated flow birefringence method. Measurements were taken at the limiting spatial resolution of 100 μm length scales, and

Weissenberg numbers We of the flows ranged from 0.12 to 0.91. For the weakly elastic liquid, measured profiles of the stress $\tau_{r\theta}$ were in general agreement with predictions of Second Order Fluid theory.

11A666. Flow in the Stirling regenerator characterized in terms of complex admittance Part 1: Theoretical development. - AJ Organ *(Dept of Eng, Univ of Cambridge, UK)*. Proc Inst Mech Eng C 207(C2) 117-125 (1993).

A wire mesh regenerator is studied, with one end closed and the other subject to a harmonic variation of flow. The methods of linear wave analysis are used to determine a *complex input admittance*, Y, for the system. Y is the ratio of the volume flow to pressure excess for a given frequency, and permits piston face pressure waveform to be determined directly in terms of prescribed velocity waveforms. A computational procedure is developed for finding the pressure waveform at the closed end. Computed waveforms are presented and discussed. Energy dissipated per cycle is calculated.

11A667. Flow in the Stirling regenerator characterized in terms of complex admittance Part 2: Experimental investigation. - AJ Organ *(Dept of Eng, Univ of Cambridge, UK)*. Proc Inst Mech Eng C 207(C2) 127-139 (1993).

Experiments are described that support the analysis of the practical Stirling cycle in terms of linear waves. All aspects of the theoretical approach are corroborated, including the incidence of amplitude attenuation and marked phase shift between pressure-time records on either side of the matrix, together with the overriding importance of the dimensionless groups N_{MA} and N_{SG} in characterizing these features.

11A668. Analysis of hypersonic nozzles including vibrational nonequilibrium and intermolecular force effects. - PW Canupp *(Dept of Mech and Aerospace Eng, N Carolina State Univ, Raleigh NC 27695)*, GV Candler *(Dept of Aerospace Eng and Mech, Univ of Minnesota, Minneapolis MN 55455)*, JN Perkins *(Dept of Mech and Aerospace Eng, N Carolina State Univ, Raleigh NC 27695)*, WD Erickson *(Hypersonic Tech Office, NASA Langley Res Center)*. AIAA J 31(7) 1243-1249 (Jul 1993).

A computational fluid dynamics technique is developed for the study of high-pressure, axisymmetric hypersonic nozzle flows. The effects of intermolecular forces and vibrational nonequilibrium are included in the analysis. The numerical simulation of gases with an arbitrary equation of state is discussed. Simulations for high-pressure nitrogen nozzles (p_0 = 138 MPa) demonstrate that both intermolecular forces and vibrational nonequilibrium affect the flow significantly. These nonideal effects tend to increase the Mach number at the nozzle exit plane. In addition, these effects may introduce weak expansion and compression waves in the nozzle that degrade test section flow quality. Thus, they must be included in the design and analysis of high-pressure hypersonic nozzles.

11A669. Multigrid calculation of 3D viscous cascade flows. - A Arnone *(Dept of Energy Eng, Univ of Florence, Via S Marta 3, Florence 50139, Italy)*, M-S Liou *(Internal Fluid Mech Div, NASA Lewis Res Center, Via S Marta 3, Cleveland OH 44135)*, LA Povinelli *(Internal Fluid Mech Div, NASA Lewis Res Center, Cleveland OH 44135)*. J Propulsion Power 9(4) 605-614 (Jul-Aug 1993).

A 3D code for viscous cascade flow prediction has been developed. The space discretization uses a cell-centered scheme with eigenvalue scaling to weigh the artificial dissipation terms. Computational efficiency of a four-stage Runge Kutta scheme is enhanced by using variable coefficients, implicit residual smoothing, and a full-multigrid method. The Baldwin-Lomax eddy-viscosity model is used for turbulence closure. A zonal, nonperiodic grid is used to minimize mesh distortion in and downstream of the throat region. Applications are presented for an annular vane with and without end wall contouring, and for a large-scale linear cascade. The calculation is validated by comparing with experiments and by studying grid dependency.

11A670. Turbulent flow through bifurcated nozzles. - DE Hershey, BG Thomas, FM Najjar *(Dept of Mech and Indust Eng, Univ of Illinois, 1206 W Green St, Urbana IL 61801)*. Int J Numer Methods Fluids 17(1) 23-47 (Jul 1993).

A FE model has been used to study steady-state turbulent flow through bifurcated submerged entry nozzles with oversized ports typical of those used in the continuous casting of steel. Both 2D and 3D simulations have been performed with the commercial code FIDAP, using the standard κ-ϵ turbulence model. Predicted velocities from 3D simulations compare reasonably with experimental measurements using a hot-wire anemometer conducted in a physical water model, where severe turbulent fluctuations are present. Results show that a 2D simulation can also capture the main flow characteristics of the jet existing the nozzle and requires two orders of magnitude less computer time than the 3D simulation. A model combining the nozzle and mould was set up to study the effect of the outlet boundary conditions of the nozzle on the jet characteristics. This modeling technique will assist in the design of submerged-entry nozzles, especially as applied to enhance steel quality in the continuous casting process. Further, the model will provide appropriate inlet boundary conditions for a separate numerical model of the mould.

368. Free shear layers (mixing layers, jets, wakes, cavities, plumes)

368B. LAMINAR INCOMPRESSIBLE

11A671. Experiments on the nonlinear stages of excited and natural planar jet shear layer transition. - FO Thomas and HC Chu *(Hessert Center for Aerospace Res, Dept of Aerospace and Mech Eng, Univ of Notre Dame, Notre Dame IN 46556)*. Exp Fluids 14(6) 451-467 (May 1993).

An experimental investigation focusing on the nonlinear stages of planar jet shear layer transition is presented. Experimental results for transition under both "natural" and low level artificial forcing conditions are presented and compared. The local spectral dynamics of the jet shear layer is modeled as a nonlinear system based upon a frequency domain, second-order Volterra functional series representation. The local linear and nonlinear wave coupling coefficients are estimated from time-series streamwise velocity fluctuation data. From the linear coupling coefficient, the mean dispersion characteristics and spatial growth rates may be obtained. With the estimation of the nonlinear power transfer function, the total, linear and quadratic nonlinear spectral energy transfer may be locally estimated. When these measures are used in conjunction with the local quadratic bicoherency and linear-quadratic coupling bicoherency, the local system output power may be completely characterized and the effect of nonlinearity on local mean flow distortion assessed.

11A672. Periodic flow in the near wake of straight circular cylinders. - P Plaschko *(Dept Fis, Univ Autonoma Metropolitana, Iztapalapa, CP 09340 Mexico DF)*, E Berger *(Hermann-Fottinger Inst, Tech Univ, D-1000 Berlin 12, Germany)*, R Peralta-Fabi *(Fac Ciencias, Dept Fisica, Univ Nacional Autonoma, CP 04510 Mexico DF)*. Phys Fluids A 5(7) 1718-1724 (Jul 1993).

The formation of periodic waves in the near wake of straight circular cylinders with arbitrary aspect ratios in crosswise flows at low Reynolds numbers (Re) is analyzed. Using a semiempirical model it is shown that raising of the Reynolds number beyond a critical value of about $Re^{(1)}$ = 22 yields a supercritical Hopf bifurcation preceding the known onset of the von Karman vortex flow at about $Re^{(2)}$ = 46.7. In agreement with experimental trends a stable periodic, secondary transversal motion arises in the previously steady crosswise flow.

11A673. Structure and flow patterns in turbulent wakes. - F Giralt and JA Ferre *(Escola Tecnica Superior Eng, Univ Rovira i Virgili, Crt de Salou S/n, 43006 Tarragona Catalunya, Spain)*. Phys Fluids A 5(7) 1783-1789 (Jul 1993).

A pattern recognition technique is used to detect and identify patterns and structures embedded in the velocity field of a turbulent wake behind a cylinder. Two component velocities u and v or u and w are measured with eight X-wire anemometers aligned with the vertical and spanwise directions in the wake at x/D = 420 and Re = 1600. The velocity patterns educed as averaged patterns or instantaneous structures are consistent with the presence of double-roller eddies, whose legs are continuously stretched by the rate of strain. Experimental u and v data suggest that the rollers are connected at the top, with vorticity parallel to the cylinder axis, forming a horseshoe vortex. The fine-scale activity, estimated by the envelope of the second derivatives, with respect to time of the velocity signals, confirms that this kind of structure can account for both the uv correlation and the continuous entrainment of potential flow into the wake.

11A674. Vortex shedding and lock-on in a perturbed flow. - MS Hall *(Sci Appl Intl, McLean VA 22102)* and OM Griffin *(Naval Res Lab, Washington DC 20375-5351)*. J Fluids Eng 115(2) 283-291 (Jun 1993).

Vortex shedding resonance or lock-on is observed when a bluff body is placed in an incident mean flow with a superimposed periodic component. Direct numerical simulations of this flow at a Reynolds number of 200 are compared here with experiments that have been conducted by several investigators. The bounds of the lock-on or resonance flow regimes for the computations and experiments are in good agreement. The computed and measured vortex street wavelengths also are in good agreement with experiments at Reynolds numbers from 100 to 2000. Comparison of these computations with experiments shows that both natural, or unforced, and forced vortex street wakes are nondispersive in their wave-like behavior. Recent active control experiments with rotational oscillations of a circular cylinder find this same nondispersive behavior over a three-fold range of frequencies at Reynolds numbers up to 15,000. The vortex shedding and lock-on resulting from the introduction of a periodic inflow component upon the mean flow exhibit a particularly strong resonance between the imposed perturbations and the vortices.

11A675. Wave interactions in the far wake of a body. - CHK Williamson and A Prasad *(Dept of Mech and Aerospace Eng, Upson Hall, Cornell)*. Phys Fluids A 5(7) 1854-1856 (Jul 1993).

There has been some question recently as to whether the far-wake structure of a bluff body is dependent on, or "connected" with, the precise details of the near-wake structure. Indeed, it has previously been assumed that there is no direct connection in scale or frequency. In the present work, observations are shown of a honeycomb-like 3D pattern in the far wake, which is caused by an interaction between the decaying oblique shedding waves from upstream, and large-scale 2D waves in the far wake. A clear "connection" between the 3D scales of the near and far wakes is thereby demonstrated. The symmetry and spanwise wavelength of Cimbala *et al's*, 3D pattern are precisely consistent with such wave interactions. In the presence of parallel shedding, the lack of a honeycomb pattern shows that the pattern is clearly dependent on oblique vortex shedding. It also follows that for oblique shedding, the far-wake 2D waves cannot possibly be the result of vortex pairing.

See also the following:

11A689. Oblique and parallel wave interaction in the near wake of a circular cylinder

368C. LAMINAR COMPRESSIBLE

11T676. Discrete shedding modes in the von Karman vortex street. - M Konig, BR Noack, H Eckelmann *(Max-Planck-Inst Stromungsforschung, Bunsenstr 10, 3400 Gottingen, Germany)*. Phys Fluids A 5(7) 1846-1848 (Jul 1993).

368D. TURBULENT INCOMPRESSIBLE

11A677. Adequacy of the the thin-shear-flow equations for computing turbulent jets in stagnant surroundings. - A el Baz, TJ Craft, NZ Ince *(Mech Eng Dept, UMIST, Manchester, M60 1QD, UK)*, BE Launder *(Mech Eng Dept, UMIST, PO Box 88, Manchester, M60 1QD, UK)*. Int J Heat Fluid Flow 14(2) 164-169 (Jun 1993).

This paper reports that the usual parabolic truncation of the Reynolds equations, used in conjunction with second-moment closure, leads to rates of growth in the self-similar region of the axisymmetric jet in stagnant surroundings that are some 12 percent greater than when the complete (elliptic) equation set is solved. The differences between the Reynolds stress profiles are relatively small, however. A term-by-term examination indicates that the omission of the normal-stress terms in the streamwise momentum equation and of the streamwise diffusion from the ε equation has the greatest effect on the spreading rate, the former raising the rate of spread by about 4.5 percent and the latter by 6 percent. The stress-generation terms associated with streamwise gradients have little effect on spreading rate but modify the stress profiles, particularly in the near-axis region. A comparable exploration for the plane jet shows qualitatively similar behavior, though the influence of the secondary terms arising from streamwise gradients is much less for this flow.

11A678. Flow structure and statistics of a passive mixing tab. - WJ Gretta *(Fluid Syst Eng, Morristown NJ 07960)* and CR Smith *(Dept of Mech Eng and Mech, Lehigh Univ, Bethlehem PA 18015)*. J Fluids Eng 115(2) 255-263 (Jun 1993).

Water channel flow visualization and anemometry studies were conducted to examine the flow structure and velocity statistics in the wake of a passive mixing tab designed for enhancement of cross-stream mixing by generation of flow structures characteristic of turbulent boundary layers. Flow visualization reveals that the mixing tab generates a wake comprising a combination of counterrotating, streamwise vortices enveloped by distinct hairpin vortex structures. The counterrotating streamwise vortices are observed to stimulate a strong ejection of fluid along the symmetry plane, which results in very rapid cross-stream mixing. The hairpin vortices are found to undergo successive amalgamation and coalescence downstream of the device, which aids in the streamwise mixing and outward penetration of ejected fluid. After an initially intense mixing process, the mixing tab wake rapidly develops mean velocity, turbulence intensity, and boundary layer integral properties characteristic of a significantly thickened turbulent boundary layer.

11A679. Observations of large-scale structures in wakes behind axisymmetric bodies. - S Cannon *(McDonnell Douglas Elec Syst, 1801 E St Andrew Pl, Santa Ana CA 92705)*, F Champagne *(Dept of Aerospace and Mech Eng, Univ of Arizona, Tucson AZ 85721)*, A Glezer *(Woodruff Sch of Mech Eng, Georgia Tech)*. Exp Fluids 14(6) 447-450 (May 1993).

Wakes behind disk-shaped axisymmetric bodies of varying solidity are studied using flow visualization and 2D Fourier decomposition of velocity measurements. Evidence of a reverse flow region behind some of the bodies is observed to coincide with the presence of large-scale structures in the near and far wake. Fourier analysis shows that these large-scale structures are predominantly helical ($m = \pm 1$) and occur at a characteristic frequency which corresponds to their wavelength as observed from flow visualization. Our measured value for this characteristic frequency agrees with vortex shedding frequencies observed for these types of wakes.

11A680. Partial cavities: Global behavior and mean pressure distribution. - Q Le *(Natl Polytech Inst, Hanoi, Vietnam)*, JP Franc, JM Michel *(Lab des Ecoulements, Geophys et Indust, Inst de Mec de Grenoble, 38041 Grenoble Cedex, France)*. J Fluids Eng 115(2) 243-248 (Jun 1993).

The results of an experimental work concerning the behavior of flows with partial cavities are presented. The tests were carried out using the plano-convex foil placed in the free surface channel of the IMG Hydrodynamic Tunnel. The experimental conditions concerning ambient pressure, water velocity, and body size were such that various and realistic kinds of flows could be realized. The main flow regimes are described and correlated to the values of foil incidence and cavitation parameter. Attention is paid to the shedding of large vapor pockets into the cavity wake and its possible periodic character. Aside from classical considerations to the cavity length and shedding frequency in the periodic regime, results concerning the wall pressure distribution in the rear part of the cavity are given. They lead to distinguish thin, stable, and closed cavities from the thick ones in which the reentrant jet plays a dominant role for the shedding of vortical structures and the flow unsteadiness.

11A681. Partial cavities: Pressure pulse distribution around cavity closure. - Q Le *(Natl Polytech Inst, Hanoi, Vietnam)*, JP Franc, JM Michel *(Inst de Mec de Grenoble, 38041 Grenoble Cedex, France)*. J Fluids Eng 115(2) 249-254 (Jun 1993).

Pressure pulse height spectra are measured in the case of partial cavitation attached to the leading edge of a hydrofoil. It is shown that the distributions of pressure pulses around cavity closure may significantly differ according to the type of cavity. In the case of a thin, well-closed and stable cavity, the pressure pulse distributions exhibit a strong maximum centered on the visible cavity termination. As the cavity becomes thicker and increasingly open and unsteady, the pressure pulse distribution widens. In the limit case of a cavity periodically shedding bubble clusters, no definite maximum in the pressure pulse distribution is observed. In addition, scaling of pressure pulse height spectra is approached from measurements at two different velocities. It is shown that the pressure pulse height spectra can be correctly transposed from a velocity to another one from two basic scaling rules concerning pulse heights and production rates of bubbles.

11A682. Steady laminar flow of liquid-liquid jets at high Reynolds numbers. - JR Richards, AN Beris, AM Lenhoff *(Dept of Chem Eng, Univ of Delaware, Newark DE 19716)*. Phys Fluids A 5(7) 1703-1717 (Jul 1993).

The axisymmetric steady-state laminar flow of a Newtonian liquid jet injected vertically into another immiscible Newtonian liquid is investigated for various Reynolds numbers. The steady-state solution was calculated by solving the axisymmetric transient equations of motion and continuity using a numerical scheme based on the volume of fluid method combined with the new continuum surface force algorithm. The analysis takes into account pressure, viscous, inertial, gravitational, and surface tension forces. Comparison with previous experimental measurements, performed on a xylene-water system, under conditions where all of these forces are important, shows good agreement over the entire range of conditions studied. Comparisons of the present numerical method with the numerical results of previous boundary-layer methods help establish their range of validity.

See also the following:

11A571. Velocity measurements within high velocity air-water jets

11A671. Experiments on the nonlinear stages of excited and natural planar jet shear layer transition

11A673. Structure and flow patterns in turbulent wakes

368E. TURBULENT COMPRESSIBLE

11A683. Prediction of turbulent coaxial streams of constant and variable density. - RW Johnson *(Idaho Natl Eng Lab, EG&G Idaho, Idaho Falls ID 83415)*. J Propulsion Power 9(4) 588-596 (Jul-Aug 1993).

The present study investigates the accuracy of well-known turbulence models in simulating the mean velocity, turbulence, and concentration fields for the cases of constant and variable density, turbulent, low Mach number, isothermal, confined coaxial streams of different bulk mean velocities, or axisymmetric mixing layers. The standard $\kappa \sim \varepsilon$ eddy viscosity model and an anisotropic thin shear algebraic stress model (ASM) are employed for the constant density care. Results for the $\kappa \sim \varepsilon$ model are determined to be qualitatively satisfactory and superior to those for the thin shear ASM, though both show excessive radial diffusion of axial momentum. Based on these conclusions, the $\kappa \sim \varepsilon$ model extended for variable density, is used for numerical simulations for a similar flow where the inner stream gas has a density four times that of the outer stream gas. Simulations for the velocity using the $\kappa \sim \varepsilon$ model are again found to be qualitatively accurate. Predictions for the concentration field, however, are in good agreement with the data. The flow fields studied are idealizations of a particular configuration once proposed for a gas core reactor nuclear propulsion engine. Nuclear propulsion for space travel, once considered in the 1960s and early 1970s, is being reconsidered, especially for manned interplanetary travel.

See also the following:

11A685. Visual observations of supersonic transverse jets

368J. JET-FLOW INTERACTION

11A684. Studies on the flowfield of multijet with square configuration. - GH Moustafa *(Dept of Mech Power Eng, Col of Eng and Tech, Menoufia Univ, Menoufia, Egypt)* and E Rathakrishnan *(Dept of Aerospace Eng, Indian IT, Kanpur 208 016, India)*. AIAA J 31(7) 1189-1190 (Jul 1993).

Measurements of mean velocity, spread rate, and merging point location were made to investigate the flowfield generated by four identical jets of air in a square configuration, issuing from axisymmetric nozzles in a common end wall and mixing with the ambient air. The effect of stagnation pressure ratios as well as the nozzle spacings on the flowfield behavior were investigated. The effect of nozzle configurations was also studied. The results show that the nature of the mean velocity profile as well as the mean velocity decay are unaffected by the pressure ratio. The nozzle spacing effect on the mean velocity decay is only marginal. The four jets interact with axis switching at the midpoint between them, which implies better mixing.

11A685. Visual observations of supersonic transverse jets. - D Papamoschou and DG Hubbard *(Dept of Mech and Aerospace Eng, UC, Irvine CA 92717)*. Exp Fluids 14(6) 468-471 (May 1993).

We present experimental results on penetration of round sonic and supersonic jets normal to a supersonic cross flow. It is found that penetration is strongly dependent on momentum ratio, weakly dependent on free-stream Mach number, and practically independent of jet Mach number, pressure ratio, and density ratio. The overall scaling of penetration is not very different from that established for subsonic jets. The flow is very unsteady, with propagating pressure waves seen emanating from the orifice of helium jets.

368K. HEAT OR MASS ADDITION

11A686. Computation of convective heat transfer in rotating cavities. - H Iacovides *(Mech Eng Dept, UMIST, PO Box 88, Manchester, M60 1QD, UK)* and JW Chew *(Design Sci Group, Rolls Royce, Derby, UK)*. Int J Heat Fluid Flow 14(2) 146-154 (Jun 1993).

In this paper, numerical solutions of the Reynolds-averaged Navier-Stokes equations are presented for convective heat transfer inside axisymmetric rotating disc cavities. The study involves the examination of three different disc-cavity configurations and the use of four different mathematical models of turbulence. The three configurations are a rotating cavity with flow entering axially at the center and leaving radially through the outer shroud, a rotating cavity with central axial throughflow, and a rotor-stator system with axial flow injection through the stator center and outflow through the annulus formed between the rotor disc and the outer shroud. Of the four turbulence models, three are based on the zonal modeling approach with the κ-ε model in the main flow region and alternative low-Reynolds number treatments across the near-wall regions. These near-wall alternatives consist of two versions of the mixing-length hypothesis and a one-equation κ-transport model. The fourth turbulence model is the mixing-length hypothesis applied over the entire cavity. Comparisons with available heat transfer measurements show that none of the models is successful in all cases examined. Considering overall performance, the κ-ε model with the one-equation near-wall treatment is preferred.

368Z. EXPERIMENTAL TECHNIQUES

11A687. Measurement and analysis of a small nozzle plume in vacuum. - PF Penko *(Aerospace Eng, NASA Lewis Res Center, Cleveland OH 44135)*, ID Boyd *(Aerospace Eng, Cornell)*, DL Meissner *(Owens Illinois, Toledo OH)*, KJ DeWitt *(Dept of Chem Eng, Univ of Toledo, Toledo OH 43606)*. J Propulsion Power 9(4) 646-648 (Jul-Aug 1993).

There is continuing development of small thrusters that operate on electrical power for both primary and auxiliary satellite propulsion. As a part of this development, a study is in progress to gain a better understanding of thruster-satellite interaction and design considerations in placing electric thrusters on satellites. Of particular interest is the prediction of thruster-plume expansion, especially in the off-axis region where the plume may impinge on spacecraft surfaces. The problem is being approached numerically, by modeling the nozzle flow and plume on both the continuum and molecular level, and experimentally by making plume flowfield measurements in a vacuum facility.

See also the following:

- 11A673. Structure and flow patterns in turbulent wakes
- 11A678. Flow structure and statistics of a passive mixing tab
- 11A773. Infrared imagery of an air-CO_2 axisymmetric jet

370. Flow stability

11A688. Mechanism of mode selection in Rayleigh-Benard convection with free-rigid boundaries. - Jiro Mizushima *(Dept of Mech Eng, Fac of Eng, Doshisha Univ, Imadegawa-Dori, Karasuma-Higashi-ru, Kamigyo-ku, Kyoto 602, Japan)*. Fluid Dyn Res 11(6) 297-311 (Jun 1993).

Higher harmonic resonances with wavenumber ratio of 1:2, 1:2:3 and so on are shown to take place in Rayleigh-Benard convection under free-rigid boundary condition. Bifurcation diagrams for 2D motion are obtained for the Prandtl number P = 7. The subharmonic instability is explained by a couple of amplitude equations obtained from weakly nonlinear stability theory. A straightforward extension of the coupled amplitude equations leads to a model which consists of n amplitude equations. The mechanism of mode selection is illustrated by numerical simulations of the model equations.

11A689. Oblique and parallel wave interaction in the near wake of a circular cylinder. - Pan-Mei Yang, Hussein Mansy, DR Williams *(Dept of Mech and Aerospace Eng, Illinois IT, Chicago IL 60616)*. Phys Fluids A 5(7) 1657-1660 (Jul 1993).

Detailed velocity measurements have been made to investigate the structure of the low-frequency vortex dislocations that appear in the indigenous wake of a circular cylinder. It is shown that one mechanism for the production of vortex dislocations is the *superposition* of two waves with slightly different frequencies, where the higher frequency wave is parallel to the cylinder axis and the lower frequency is an oblique wave. In contrast to the discrete vortex concept that implies discontinuous shedding frequencies, the measured amplitude and phase distribution of the interacting waves are shown to be continuous along the span of the cylinder. Both waves (parent modes) exist simultaneously and overlap in the wake. The difference mode associated with the vortex dislocations is produced by the nonlinear interaction of the parent modes, and its maximum amplitude is at the location where the parent modes have comparable magnitude. The spanwise phase and amplitude distributions of the difference modes are "predicted" by taking the product of the complex wave amplitudes of the parent modes.

11A690. Linear stability analysis of cone and plate flow of an Oldroyd-B fluid. - DO Olagunju and LP Cook *(Dept of Math Sci, Univ of Delaware, Newark DE 19716)*. J Non-Newtonian Fluid Mech 47 93-105 (Jun 1993).

A linear stability analysis of the cone and plate flow of an Oldroyd-B fluid is carried out. We show that the base flow is stable to a class of axisymmetric perturbations provided that the Deborah number is less than a critical value and that at the critical value there is exchange of stability. The value of the critical Deborah number for both creeping and non-creeping flow is obtained. The critical value of the Deborah number at which instability is predicted for non-creeping flows is shown to be less than the value for creeping flows, indicating that inertia is destabilizing.

11T691. Linearized approximation of the Benard convection problem. - JC Song *(Dept of Math, Hanyang Univ, Ansan, Kygunggido, 425-791, Seoul, Korea)*. Stability Appl Anal Continuous Media 2(1) 1-11 (Mar 1992).

11A692. Kelvin-Helmholtz instability for surface waves in currents of uniform vorticity. - I Brevik and H Sund *(Dept of Appl Mech, Univ of Trondheim NTH, N-7034 Trondheim, Norway)*. Phys Fluids A 5(7) 1644-1650 (Jul 1993).

The Kelvin-Helmholtz instability is investigated for the case when linear monochromatic water waves of wave number k are propagating in a current whose undisturbed horizontal velocity profile is linear down to some depth h, and zero beneath. The present paper generalizes the work of Esch to the case of finite water depth D. Surface tension is neglected. The result of the analysis is a quartic equation for the phase velocity. The presence of a finite water depth tends to stabilize the flow field. The interval in kh, for which complex roots of the dispersion equation occur, becomes narrower as the depth increases. Also, the growth rate of the flow decreases. The main results are illustrated graphically, and supplemented by analytic approximations in the limiting case when D/h lies close to unity.

See also the following:

- 11A231. Hadamard-type stability of single integral constitutive equations for viscoelastic liquids
- 11A593. Thermocapillary convection in a multilayer system
- 11A639. Nonlinear evolution of secondary instabilities in boundary-layer transition
- 11A671. Experiments on the nonlinear stages of excited and natural planar jet shear layer transition

372. Turbulence

372A. GENERAL THEORY

11A693. Investigation of the turbulent model for pressure fluctuations with spectral theory. - Sheng Jin and Han-gen Ni *(Dalian IT, Dalian, China)*. Appl Math Mech 14(4) 353-360 (Apr 1993).

The pressure fluctuations in turbulent shear flows are investigated with the theory of spectral analysis. An expression for pressure spectra is analytically derived in terms of velocity spectra. This deviation is based on a formal solution of the Navier-Stokes equation and the quasi-normal assumption to express the third and fourth order velocity correlations in terms of double velocity correlation. Then, a turbulent model for the computation of pressure fluctuation intensity with Reynolds stress and mean flow velocity gradients is established. The turbulent constants in the model are calculated from the assumptions that the general behavior of velocity spectra in high Reynolds number flows. Comparison with direct simulation of turbulent boundary-layer is made. It is found that the turbulent-turbulent, cross correlation, and turbulent-shear source terms for mean square value of pressure fluctuation are about the same magnitude.

11T694. Stationary probability density functions: An exact result. - SB Pope *(Sibley Sch of Mech and Aerospace Eng, Upson Hall, Cornell)* and ESC Ching *(Inst for Theor Phys, UC, Santa Barbara CA 93106)*. Phys Fluids A 5(7) 1529-1531 (Jul 1993).

372B. HOMOGENEOUS OR ISOTROPIC TURBULENCE

11A695. Analysis of subgrid-scale interactions in numerically simulated isotropic turbulence. - J Andrzej Domaradzki, Wei Liu *(Dept of Aerospace Eng, Univ of S California, Los Angeles CA 90089-1191)*, ME Brachet *(Lab Phys Stat, Ecole Normale Superieure, 75231 Paris, Los Angeles, Cedex 05, France)*. Phys Fluids A 5(7) 1747-1759 (Jul 1993).

Using a velocity field obtained in a direct numerical simulation of isotropic turbulence at moderate Reynolds number the subgrid-scale energy transfer in the spectral and the physical space representation is analyzed. The subgrid-scale transfer is found to be composed of a forward and an inverse transfer component, both being significant in dynamics of resolved scales. Energy exchanges between the resolved and unresolved scales from the vicinity of the cutoff wave number dominate the subgrid-scale processes and the energetics of the resolved scales are unaffected by the modes with wave numbers greater than twice the cutoff wave number. Correlations between the subgrid-scale transfer and the large-scale properties of the velocity field are investigated.

11A696. Study of multiscalar mixing. - SS Girimaji *(ASM, Hampton VA 23666)*. Phys Fluids A 5(7) 1802-1809 (Jul 1993).

A model for passive mixing of multiple scalars in homogeneous turbulence is developed. This model is based on the time-evolving mapping closure methodology. Calculations from the model are compared against heat conduction simulations (HCS) data. The agreement is excellent at the early stages of mixing and at the later stages it is fair.

11T697. Universal form of energy spectra in fully developed turbulence. - Zhen-Su She *(Dept of Math, Univ of Arizona, Tucson AZ 85721)* and E Jackson *(Program in Appl and Comput Math, Princeton)*. Phys Fluids A 5(7) 1526-1528 (Jul 1993).

372F. FREE SHEAR LAYERS

11A698. Behavior of streamwise rib vortices in 3D mixing layer. - JM Lopez *(Dept of Math, Penn State)* and CJ Bulbeck *(Defence Sci and Tech Org, Air Operations Div, Aeronaut Res Lab, Melbourne, Australia)*. Phys Fluids A 5(7) 1694-1702 (Jul 1993).

The structure and behavior of a streamwise rib vortex in a direct numerical simulation of a time-developing 3D incompressible plane mixing layer is examined. Where the rib vortex is being stretched, the vorticity vector is primarily directed in the vortex axial direction and the radial and azimuthal velocity distribution is similar to that of a Burgers vortex. In the region where the vortex stretching is negative, there is a change in the local topology of the vortex. The axial flow is decelerated and a negative azimuthal component of vorticity is induced. These features are characteristic of vortex breakdown. The temporal evolution of the rib vortex is similar to the evolution of an axisymmetric vortex in the early stages of vortex breakdown. The effect of vortex breakdown on the other parts of the flow is, however, not as significant as the interaction between the rib vortex and other vortical structures.

372G. BOUNDARY LAYERS

11A699. Kolmogorov behavior of near-wall turbulence and its application in turbulence modeling. - Tsan-Hsing Shih *(Center for Model of Turbulence and Transition, ICOMP, NASA Lewis Res Center)* and JL Lumley *(Cornell)*. Int J Comput Fluid Dyn 1(1) 43-56 (1993).

The near-wall behavior of turbulence is re-examined in a way different from that proposed by Hanjalic and Launder and followers. It is shown that at a certain distance from the wall, all energetic large eddies will reduce to Kolmogorov eddies (the smallest eddies in turbulence). All the important wall parameters, such as friction velocity, viscous length scale, and mean strain rate at the wall, are characterized by Kolmogorov microscales. According to this Kolmogorov behavior of near-wall turbulence, the turbulence quantities, such as turbulent kinetic energy, dissipation rate, etc at the location where the large eddies become "Kolmogorov" eddies, can be estimated by using both direct numerical simulation (DNS) data and asymptotic analysis of near-wall turbulence. This information will provide useful boundary conditions for the turbulent transport equations. As an example, the concept is incorporated in the standard κ-ε model which is then applied to channel and boundary layer flows. Using appropriate boundary conditions (based on Kolmogorov behavior of near-wall turbulence), there is no need for any wall-modification to the κ-ε equations (including model constants). Results compare very well with the DNS and experimental data.

11A700. Measurements in a pressure-driven 3D turbulent boundary layer during development and decay. - WR Schwarz *(Dept of Mech Eng, Stevens IT, Hoboken NJ 07030)* and P Bradshaw *(Dept of Mech Eng, Stanford)*. AIAA J 31(7) 1207-1214 (Jul 1993).

Measurements of the turbulence structure in the outer layer of a 3D turbulent boundary layer were made in an open-circuit low-speed blower tunnel. The 3D turbulent boundary layer on the floor of the tunnel was generated by a cross-stream pressure gradient using a 30-deg bend in the horizontal plane. Downstream of the bend, the 3D turbulent boundary layer gradually relaxed toward a 2D turbulent boundary layer as the crossflow decayed slowly after the cross-stream pressure gradient was removed. Mean velocities were measured with a three-hole pressure probe, and turbulence quantities, which included the Reynolds-stress tensor and the triple products, were measured with a cross-wire hot-wire anemometer. The experiment provides new data that isolate the effects of crossflow from the effects of an adverse streamwise pressure gradient that may have clouded the interpretations of previous 3D turbulent boundary-layer experiments. Another advance over previous work is that enough turbulence quantities were measured for all terms in the Reynolds-stress transport equations to be evaluated, allowing term-by-term tests of stress-transport turbulence models.

11A701. New time scale based κ-ε model for near-wall turbulence. - Z Yang and TH Shih *(Center for Model of Turbulence and Transition, Inst for Comput Mech in Propulsion, NASA Lewis Res Center, Cleveland OH 44135)*. AIAA J 31(7) 1191-1198 (Jul 1993).

A κ - ε is proposed for wall-bounded turbulent flows. In this model, the eddy viscosity is characterized by a turbulent velocity scale and a turbulent time scale. The time scale is bounded from below by the Kolmogorov time scale. The dissipation equation is reformulated using this time scale, and no singularity exists at the wall. The damping function used in the eddy viscosity is chosen to be a function of $R_y = (\kappa^{1/2}y/\nu)$ instead of y^+, as in the Lam and Bremhorst model. Hence, the model could be used for flows with separation. The model constants used are the same as in the high Reynolds number standard κ - ε model. Thus, the proposed model will also be suitable for flows far from the wall. Turbulent channel flows at different Reynolds numbers and turbulent boundary-layer flows with and without pressure gradient are calculated. Results show that the model predictions are in good agreement with direct numerical simulation and experimental data.

11A702. One-equation near wall turbulence modeling with the aid of direct simulation data. - W Rodi *(Univ of Karlsruhe, Karlsruhe, Germany)*, NN Mansour *(NASA Ames Res Center, Moffett Field CA 94035)*, V Michelassi *(Univ of Florence, Florence, Italy)*. J Fluids Eng 115(2) 196-205 (Jun 1993).

The length scales appearing in the relations for the eddy viscosity and dissipation rate in one-equation models were evaluated from direct numerical (DNS) simulation data for developed channel and boundary-layer flow at two Reynolds numbers each. To prepare the ground for the evaluation, the distribution of the most relevant mean-flow and turbulence quantities is presented and discussed, also with respect to Reynolds-number influence and to differences between channel and boundary-layer flow. An alternative model is examined in which $(v'^2)^{1/2}$ is used as velocity scale instead of $k^{1/2}$. With this velocity scale, the length scales now appearing in the model follow closely a linear relationship near the wall. The resulting length-scale relations together with a DNS based relation between v'^2/k and $y\times = k^{1/2}y/\nu$ form a new one-equation model for use in near-wall regions. The new model was tested as near wall component of a two-layer model by application to the developed-channel, boundary-layer and backward-facing-step flows.

See also the following:

11A637. Strong vortex-boundary layer interactions Part II. Vortices low

11A972. Probability distributions of concentration fluctuations of a weekly diffusive passive plume in a turbulent boundary layer

372I. STRATIFIED FLOWS

11A703. Two-way interaction between homogeneous turbulence and dispersed solid particles I. Turbulence modification. - S Elghobashi and GC Truesdell *(Dept of Mech and Aerospace Eng, UC, Irvine CA 92717)*. Phys Fluids A 5(7) 1790-1801 (Jul 1993).

The modification of decaying homogeneous turbulence due to its interaction with dispersed small solid particles ($d/\eta < 1$), at a volumetric loading ratio $\phi_u \leq 5 \times 10^{-4}$, is studied using direct numerical simulation. The results show that the particles increase the fluid turbulence energy at high wave numbers. This increase of energy is accompanied by an increase of the viscous dissipation rate, and, hence, an increase in the rate of energy transfer T(k) from the large-scale motion. Thus, depending on the conditions at particle injection, the fluid turbulence kinetic energy may increase initially. But, in the absence of external sources (shear or buoyancy), the turbulence energy eventually decays faster than in the particle-free turbulence. In gravitational environment, particles transfer their momentum to the small-scale motion but in an *anisotropic* manner. The pressure-strain correlation acts to remove this anisotropy by transferring energy from the direction of gravity to the other two directions, *but at the same wave number*, ie, to the small-scale motion in directions normal to gravity. This input of energy in the two directions with lowest energy content causes a *reverse cascade*. This reverse cascade tends to build up the energy level at lower wave numbers, thus reducing the decay rate of energy as compared to that of either the particle-free turbulence or the zero-gravity particle-laden flow.

372L. HEAT AND MASS TRANSFER (DIFFUSION, DISPERSION, ETC)

See the following:

11A777. Numerical modeling of turbulent flow and heat transfer in rotating cavities
11A806. Impinging jet studies for turbulence model assessment I. Flow-field experiments
11A807. Impinging jet studies for turbulence model assessment II. An examination of the performance of four turbulence models
11A902. Effects of momentum ratio on turbulent nonreacting and reacting flows in a ducted rocket combustor

372N. GEOPHYSICAL TURBULENCE

11T704. Energy and enstrophy transfer in numerical simulations of 2D turbulence. - ME Maltrud *(Fluid Dyn Group, MS B216, LANL)* and GK Vallis *(UC, Santa Cruz CA 95064)*. Phys Fluids A 5(7) 1760-1775 (Jul 1993).

372O. NONEQUILIBRIUM AND CHEMICAL EFFECTS

11A705. Calculation of turbulent combustion of propane in furnaces. - XS Bai and L Fuchs *(Dept of Mech-Appl CFD, RIT, S-100 44 Stockholm, Sweden)*. Int J Numer Methods Fluids 17(3) 221-239 (Aug 1993).

An evaluation of some numerical methods for turbulent reacting flows in furnace-like geometries is carried out. The Reynolds averaged Navier-Stokes equations and the two-equation κ - ε model together with either finite-rate or infinite-rate reaction models are solved numerically. Either single- or multiple-step reactions together with the "eddy dissipation concept" (EDC) are used to model reacting flows with finite reaction rates. The numerical scheme is finite difference based, together with a multi-grid method and a local grid refinement technique. These methods have been used to calculate the combustion of propane in a single- and multiple-burner configurations. In the former case, the sensitivity of the solution to variations in some model parameters (determining the reaction rate) and numerical parameters (mesh spacing) has been studied. It is noted that different dependent variables exhibit different levels of sensitivity to the variation in model parameters. Thus, calibration and validation of models for reacting flows require that one compares that most *sensitive* variables. For engineering purposes, on the other hand, one may calibrate and validate models with respect to the most *relevant* variables. Our conclusion is that since sensitivity of the temperature distribution is relatively mild, one can still use EDC-like methods in engineering applications where details of the temperature field are of minor importance.

372P. INTERMITTENCY AND OTHER FLOW STRUCTURE

11A706. Universality of geometrical invariants in turbulence: Experimental results. - A Bershadskii, E Kit, A Tsinober *(Dept of Fluid Mech, Fac of Eng, Tel Aviv Univ, Tel Aviv 69978, Israel)*. Phys Fluids A 5(7) 1523-1525 (Jul 1993).

Experimental results on probability distribution functions (pdfs) of full dissipation ε, enstrophy ω^2, and enstrophy generation $\omega_i\omega_j s_{ij}$ in two different turbulent flows: turbulent grid flow (Re_λ 74) and turbulent jet center ($Re_\lambda = 880$) demonstrate the possibility of universal behavior of the pdfs of these quantities.

See also the following:

11A678. Flow structure and statistics of a passive mixing tab
11A679. Observations of large-scale structures in wakes behind axisymmetric bodies
11A698. Behavior of streamwise rib vortices in 3D mixing layer
11A769. Reconstruction of a quasi-instantaneous image of coherent structures from hotwire signals obtained by a multi-point simultaneous measurement system

372Q. MODELING OF TURBULENCE

See the following:

11A650. Predicting equilibrium states with Reynolds stress closures in channel flow and homogeneous shear flow
11A670. Turbulent flow through bifurcated nozzles
11A677. Adequacy of the the thin-shear-flow equations for computing turbulent jets in stagnant surroundings
11A699. Kolmogorov behavior of near-wall turbulence and its application in turbulence modeling
11A702. One-equation near wall turbulence modeling with the aid of direct simulation data

372Y. COMPUTATIONAL TECHNIQUES

11A707. Three-dimensional mesh embedding for the Navier-Stokes equations using upwind control volumes. - BL Lapworth *(Rolls Royce, PO Box 31, Derby DE2 8BJ, UK)*. Int J Numer Methods Fluids 17(3) 195-220 (Aug 1993).

A numerical model for the compressible Navier-Stokes equations using local mesh embedding is presented. The model solves for 3D turbulent flow using an algebraic mixing length model of turbulence. The technique of control volume upwinding is used to produce a novel treatment, whereby the hanging nodes on the mesh interfaces are left with null control volumes. This yields an efficient discretization scheme which ensures second-order accuracy, flux conservation and stability at the mesh interfaces, whilst retaining a simple interpolative treatment for the hanging nodes. The discrete flow equations are solved using the semi-implicit pressure correction method. The accuracy of the embedded mesh solver is demonstrated by modeling the 3D flow through a cascade of turbine vanes at design and off-design conditions. Mesh embedding gives a saving of 48% in the number of nodes. The embedded mesh solutions compare well with fine structured mesh solutions and experimental measurements. The capability of the embedded mesh solver to perform solution adaptive calculations is demonstrated using a 2D mid-height section of the cascade at the off-design flow conditions.

See also the following:

11A705. Calculation of turbulent combustion of propane in furnaces

372Z. EXPERIMENTAL TECHNIQUES

11A708. Note on secondary flows in oscillating-mixing-box experiments. - HJS [illegible] IPD De Silva *(Dept of Mech and [illegible] Arizona State Univ, Tempe AZ)* [illegible]hys Fluids A 5(7) 1849-1851 (Jul 1993).

Oscillating-grid induced turbulence in confined geometries (tanks) is commonly used in the study of turbulence with zero-mean shear. It is demonstrated that the mean secondary circulation generated during such experiments can be reduced by selecting conditions that lessen the Reynolds-stress gradients within the fluid. A simple power law for the spatial decay of turbulent velocity fluctuations is realized only in the absence of such mean circulation.

374. Electromagneto-fluid and plasma dynamics

11A709. Modified theory of ferroelectric liquid crystals as micropolar medium on bundle space constitutive equations. - CZ Rymarz *(Military Univ of Tech, Warszawa, Poland)*. J Tech Phys 34(2) 185-197 (1993).

In this paper the verification and extension of the paper has been presented. The verification concerns the kinematics and, mostly, the conservation law and equations of evolution of the considered medium. The extension concerns the construction of the constitutive equations for nondissipative stresses and internal body force. The paper contains some necessary remarks on the kinematics of the considered medium, which supplement the results presented, derivation of the evolution equations from the conservation laws, both in the Euclidean space and in the fibre space, and the construction of the constitutive equations for the ferroelectric liquid crystalline medium. In the kinematics the components of directors d_k are presented as functions of the Euler angles ϕ, μ, ψ, which are microstructural dof. The simplified relations of the components of directors corresponding to the straight or slightly bent smectic layers have been presented. The generalized momentum conservation law in fibre space is introduced and the role of the angular momentum conservation law is discussed. The set of constitutive arguments is established, the integrity base and the set of invariants of the group of material symmetry are obtained. The constitutive relations for nondissipative stresses and internal body force are constructed.

11A710. Electromagnetic billards. - R Bolcato, J Etay, Y Fautrelle *(MADYLAM-ENSHMG-BP95-38402, St Martin D'Heres, Cedex, France)*, HK Moffatt *(DAMTP-Cambridge Univ, Silver St, Cambridge CB3 9EW, UK)*. Phys Fluids A 5(7) 1852-1853 (Jul 1993).

Moffatt has argued that it should be possible to control the motion of a metallic sphere immersed in a nonconducting fluid using the electromagnetic force and couple generated by means of a traveling and/or rotating magnetic field applied externally. Such a system has been realized experimentally: one or more aluminum spheres are placed in a vessel containing fluid (air, water, or silicone oil), the whole being placed in an inductor which provides an upward-traveling magnetic field. The spheres move in response to the induced electromagnetic forces, the motion being influenced by gravity, viscous drag, vessel boundary reaction, and collisions. A range of possible behaviors, stable, unstable, and chaotic, are identified and discussed. The term "electromagnetic billiards" seems appropriate to describe this phenomenon.

11A711. Bounded multi-scale plasma simulation: Application to sheath problems. - SE Parker *(Electron Res Lab, UCB)*, A Friedman, SL Ray *(LLNL)*, CK Birdsall *(Electron Res Lab, UCB)*. J Comput Phys 107(2) 388-402 (Aug 1993).

In our previous paper we introduced the *multi-scale* method, a self-consistent plasma simulation technique that allowed particles to have independent timesteps. Here we apply the method to 1D electrostatic bounded plasma problems and demonstrate a significant reduction in computing time. We describe a technique to allow for variable grid spacing and develop consistent boundary conditions for the direct implicit method. Also discussed are criteria for specifying timestep size as a function of position in phase space. Next, an analytically solvable sheath problem is presented, and a comparison to simulation results is made. Finally, we show results for an ion acoustic shock front propagating toward a conducting wall.

11A712. Implementation of a semi-implicit orbit-averaged gyrokinetic particle code. - BI Cohen and TJ Williams *(LLNL)*. J Comput Phys 107(2) 282-290 (Aug 1993).

A semi-implicit orbit-averaged time-integration algorithm has been successfully implemented in a gyrokinetic particle simulation code for the study of self-consistent phenomena in a strongly magnetized plasma. The semi-implicit aspect of the integration scheme relaxes the timestep constraints required to ensure numerical stability. The orbit averaging is useful in reducing statistical noise and relaxes the statistical constraints for kinetic simulation. For appropriate applications, the semi-implicit orbit-averaged algorithm should be more efficient than are traditional particle-in-cell plasma simulation algorithms with explicit time-integration schemes. Both a linear numerical dispersion analysis and illustrative simulation examples are presented.

11A713. Partially linearized algorithms in gyrokinetic particle simulation. - AM Dimits *(LLNL)* and WW Lee *(Plasma Phys Lab, Princeton)*. J Comput Phys 107(2) 309-323 (Aug 1993).

In this paper, particle simulation algorithms with time-varying weights for the gyrokinetic Vlasov-Poisson system have been developed. The primary purpose is to use them for the removal of the selected nonlinearities in the simulation of gradient-driven microturbulence so that the relative importance of the various nonlinear effects can be assessed. It is hoped that the use of these procedures will result in a better understanding of the transport mechanisms and scaling in tokamaks. Another application of these algorithms is for the improvement of the numerical properties of the simulation plasma. For instance implementations of such algorithms (1) enable us to suppress the intrinsic numerical noise in the simulation, and also (2) make it possible to regulate the weights of the fast-moving particles and, in turn, to eliminate the associated high frequency oscillations. Examples of their application to drift-type instabilities in slab geometry are given. We note that the work reported here represents the first successful use of the weighted algorithms in particle codes for the nonlinear simulation of plasmas.

376. Naval hydromechanics

11A714. SES Dynamics in the vertical plane. - AJ Sorensen, S Steen *(Div of Marine Hydrodyn, Norwegian IT, N7034 Trondheim, Norway)*, OM Faltinsen *(Postfach 52 03 65 Elbschaussee 277, 2000 Hamburg 52, Germany)*. Ship Tech Res 40(2) 71-94 (May 1993).

The dynamic response of Surface Effect Ships (SES) advancing at high speed in waves is studied. The results show dominating vertical accelerations in a frequency range of importance for passenger comfort and crew workability. These vibrations are analyzed using a mathematical model for the air cushion. It accounts for the motions and accelerations in heave and pitch induced by both the dynamic uniform and the spatially varying air cushion pressure. The latter is described by a modal representation. High ride quality can be achieved by compensating for these vibrations using a ride control system. Based on a mathematical model of such a system it is shown that optimal placement of the fan and the ride control system gives a significant improvement in ride quality.

378. Aerodynamics

11A715. Control of vortices on a delta wing by leading-edge injection. - W Gu, O Robinson *(Lehigh Univ, Bethlehem PA 18015)*, D Rockwell *(Dept of Mech Eng and Mech, Lehigh Univ, Bethlehem PA 18015)*. AIAA J 31(7) 1177-1186 (Jul 1993).

This experimental investigation addresses the control of flow past a half-delta wing at high angle of attack. Application of steady blowing, steady suction, or alternate suction-blowing in the tangential direction along the leading edge of the wing can retard substantially the onset of vortex breakdown and stall. The most effective period of the alternate suction-blowing is on the order of one convective time scale of the flow past the wing. As a result of this type of control, the vortex structure in the crossflow plane is modified from a fully stalled condition to a highly coherent leading-edge vortex. This transformation to a restabilized vortex is represented by instantaneous velocity fields, streamline patterns, and vorticity contours.

11A716. Major linear control problem. - AA Baloev and TK Sirazetdinov *(Izvestiya VUZ, Aviatsionnaya Tekhnika, Russia)*. Russian Aeronaut 35(4) 12-19 (1992).

We consider the stochastic alternate of solution of the major problem of control in the linear stationary formulation. We perform the numeric search method using as the base the method for constructing the linear differential equations.

11A717. Aerodynamic design and investigation of a high-loaded turbine. - J Guiming *(Marine Boiler and Turbine Res Inst, PO Box 77 Harbin, Heilongjiang Province 150036, Peoples Rep of China)*. Int J Turbo Jet Engines 10(1) 19-30 (1993).

This paper presents a design method with its specific features of a high-loaded turbine stage through a design practice to change a two-stage marine power turbine to a one-stage one. The design was conducted by using the meridional streamline curvature method based on a full radial equilibrium. In the design, a controlled vortex concept was adopted so as to attain a high-loaded stage. The advantages and disadvantages of the high-loaded turbine design are discussed through an analysis and comparison of both design results. In particular, some views and comments are made in this paper with respect to marine power turbine engine.

11A718. Complete thrust vectoring flight control for future civil jets, F-22 superiority fighter and cruise missiles Part I. Vectored F-22, F-16, and F-15. - B Gal-Or, V Sherbaum, M Lichtsinder, M Turgemann *(Jet Lab Technion, Israel IT, Haifa 32000, Israel)*. Int J Turbo Jet Engines 10(1) 1-17 (1993).

Tailless vectored F-22, F-16, F-15, stealth cruise missiles, stealth unmanned vehicles and civil-cargo designs are investigated. The fastest possible "Cobra" and Herbst-turn-back maneuvers are flight-demonstrated via new unique thrust-vectoring techniques. Maximized vectoring agility-controllability is flight-demonstrated by scaled F-22, F-16, F-15, and other prototypes. Introducing vectoring control laws and laboratory and flight-tests proves that new, fast-responding, roll-yaw-pitch nozzles, provide alternative flight-control for military and civil vehicles. Unaffected by flow on conventional fight control (CFC) surfaces, complete thrust-vectoring flight control (TVFC) dramatically enhances safety-agility-effectiveness during critical take-off, landing, spin, CFC-damage, and offensive-defensive, air-to-ground and air-to-air, post-stall combat maneuvers. Vulnerability, accuracy, terrain-following, range, payload, stealth limits, and final maneuverability of manned and unmanned vehicles, including cruise missiles, are expected to be significantly improved via proper CFC-TVFC.

11A719. Propulsion system flight test analysis using model techniques. - SJ Khalid *(Pratt & Whitney, PO Box 109600, W Palm Beach FL 33410-9600)* and MF Faherty *(General Dyn, Ft Worth TX)*. Int J Turbo Jet Engines 10(1) 31-43 (1993).

This paper presents the use of these analytical tools in emulating the in-flight performance and operation of a modern fighter engine designed to meet stringent operational requirements. The pre-flight predictions and accurate post-flight analyses contributed to the successful flight test evaluation of the F100-PW-229 (PW229) engine, which is an increased thrust derivative of the highly successful F100-PW-220 (PW220) engine. The use of simulation in the thorough pre-flight checkout of every logic path of the digital control is illustrated with the example of an enhanced failure mode accommodation of the PW229 Improved Digital Electronic Control. This increased capability control and its thorough verification, adds to the confidence in the safety and dependability of single engine installations. The suitability of the state-variable piece-wise linear model for the functional checkout of the control logic and for continuous engine performance synthesis over long periods of thermal non-equilibrium is explained. For applications requiring increased accuracy, use of test data driven nonlinear dynamic engine model is preferred and is illustrated by determining in-flight thrust response to small throttle movements. The significance of this analysis is that it helps identify small perturbation response requirements which greatly influence airplane handling during formation flying, refueling, approach, and landing. In addition, the paper includes calculation of quasi-steady net propulsive force and specific excess power which is substantiated by measured airplane acceleration.

11A720. Cryogenic wind tunnel. - MJ Goodyer *(Dept of Aeronaut and Astronaut, Univ of Southampton, Southampton, UK)*. Prog Aerospace Sci 29(3) 193-220 (1992).

Until recently engineers have been unable to reach full scale Reynolds number in most wind tunnel tests. The cryogenic wind tunnel has been introduced to provide the aerospace community with the means to test models at near-full-scale Reynolds numbers, satisfying a particular need at transonic speeds. The background to the need for high Reynolds number wind tunnels is outlined together with options. The main advantages of the cryogenic option are highlighted which led to this type being adopted for transonic testing. The novel technology is described together with brief descriptions of several of the more major tunnel projects.

See also the following:

11A146. Stability of shock waves

11A752. Aeroelastic response, loads, and stability of a composite rotor in forward flight

380. Machinery fluid dynamics

380B. FUNDAMENTALS

11A721. Conservation of rothalpy in turbomachines. - FA Lyman *(Dept of Mech and Aerospace Eng, Syracuse Univ, Syracuse NY 13244-1240)*. J Turbomachinery 115(3) 520-526 (Jul 1993).

The conditions under which rothalpy is conserved are investigated by means of the energy and moment-of-momentum equations for unsteady flow of a viscous, compressible fluid. Differential and integral equations are given for the total enthalpy and rothalpy in both stationary and rotating coordinates. From the equations in rotating coordinates it is shown that rothalpy may change due to: (1) pressure fluctuations caused by flow unsteadiness in the rotating frame; (2) angular acceleration of the rotor; (3) work done by viscous stresses on the relative flow in the rotating frame; (4) work done by body forces on the relative flow; (5) changes in entropy due to viscous dissipation and heat transfer. Conclusions of this investigation are compared with those of previous authors, some of whom have stated that rothalpy is conserved even in viscous flows. A modified Euler's turbomachine equation, which includes viscous effects, is derived and errors in previous derivations noted.

11A722. Discs and drums: The thermo-fluid dynamics of rotating surfaces. - FJ Bayley, CA Long, AB Turner *(Thermo-Fluid Mech Res Centre, Univ of Sussex, Brighton)*. Proc Inst Mech Eng C 207(C2) 73-81 (1993).

This paper reviews long-term experimental and theoretical research programs concerned with flow and heat transfer over the large rotating surfaces, commonly discs, often drums but sometimes conical, used to support the blades in turbomachinery. The account begins with a geometry found in turbomachinery from the oldest steam plant to the most modern gas turbine, in which a disc rotates near a stationary, usually coaxial member. The flow in the intervening "wheel-space" is well understood, but external conditions can affect the extent and nature of ingress from the surrounding fluid. In the gas turbine this fluid is the mainstream hot gas, an inflow of which could have serious consequences, so that the study of ingress has become the principal subject of research for rotor-stator systems and recent work is fully reported here.

See also the following:

11A539. Tilting pad journal bearings: Measured and predicted stiffness coefficients

11T738. Probabilistic simulation of fragment dynamics and their surface impacts in the SSME turbopump

380C. UNSTEADY FLOW AND SYSTEMS STABILITY

11A723. Rotordynamic coefficients of incompressible flow damping seals using Colebrook's formula. - JK Scharrer, N Rubin *(Rocketdyne Div, Rockwell Int, Canoga Park CA 91304)*, CC Nelson *(Texas A&M Univ, College Station TX 77843)*. Int J Mech Sci 35(8) 669-673 (Aug 1993).

The basic equations are derived for incompressible flow in an annular seal with large-scale roughness. The flow is assumed to be completely turbulent in the axial and circumferential directions with no separation, and is modeled using Colebrook's friction factor relationship. Linearized zeroth- and first-order perturbatio[n] equations are developed for small motion abo[ut] an arbitrary position by an expansion in the eccentricity ratio. The zeroth-order continuity and momentum equations are integrated, yielding the axial and circumferential velocity components and the pressure distribution. The first-order equations are integrated to satisfy the boundary conditions and yield the perturbation pressure distribution. This resultant pressure distribution is integrated along and around the seal to yield the force developed by the seal and the corresponding dynamic coefficients. Results of this analysis are compared with one using Moody's equation and with experimental data for leakage and rotordynamic coefficients.

380D. TURBINES (GAS AND VAPORS)

11A724. Aerodynamic design of turbomachinery blading in 3D flow: An application to radial inflow turbines. - YL Yang, CS Tan, WR Hawthorne *(Gas Turbine Lab, MIT)*. J Turbomachinery 115(3) 602-613 (Jul 1993).

A computational method based on a theory for turbomachinery blading design in 3D inviscid flow is applied to a parametric design study of a radial inflow turbine wheel. As the method requires the specification of swirl distribution, a technique for its smooth generation within the blade region is proposed. Excellent agreements have been obtained between the computed results from this design method and those from direct Euler computations, demonstrating the correspondence and consistency between the two. The computed results indicate the insensitivity of the pressure distribution to a lean in the stacking axis and a minor alteration in the hub-shroud profiles. Analysis based on a Navier-Stokes solver shows no breakdown of flow within the designed blade passage and agreement with that from a design calculation; thus the flow in the designed turbine rotor closely approximates that of an inviscid one. These calculations illustrate the cause of a design method coupled to an analysis tool for establishing guidelines and criteria for designing turbomachinery blading.

11A725. Aerodynamic performance of a transonic low aspect ratio turbine nozzle. - SH Moustapha *(Turbine Aerodyn, Pratt & Whitney, Montreal, PQ, Canada)*, WE Carscallen *(Combust and Fluid Eng Lab, NRC, Ottawa, ON, Canada)*, JD McGeachy *(Dept of Mech Eng, Queen's Univ, Kingston, ON, Canada)*. J Turbomachinery 115(3) 400-408 (Jul 1993).

This paper presents detailed information on the 3D flow field in a realistic turbine nozzle with an aspect ratio of 0.65 and a turning angle of 76°. The nozzle has been tested in a large-scale planar cascade over a range of exit Mach numbers from 0.3 to 1.3. The experimental results are presented in the form of nozzle passage Mach number distributions and spanwise distribution of losses and exit flow angles. Details of the flow field inside the nozzle passage are examined by means of surface flow visualization and Schlieren pictures. The performance of the nozzle is compared to the data obtained for the same nozzle tested in an annular cascade and a stage environment. Excellent agreement is found between the measured pressure distribution and the prediction of a 3D Euler flow solver.

11A726. Aeroloads and secondary flows in a transonic mixed-flow turbine stage. - KR Kirtley, TA Beach *(LeRc Group, Sverdrup Tech, Cleveland OH 44135)*, C Rogo *(Teledyne CAE, Toledo OH 43612)*. J Turbomachinery 115(3) 590-601 (Jul 1993).

A numerical simulation of a transonic mixed-flow turbine stage has been carried out using an average passage Navier-Stokes analysis. The n[...] turbine stage considered here consists [...]ozzle vane and a highly loaded [...]tion was run at the design pressure ratio and is assessed by comparing results with those of an established through flow design system. The 3D aerodynamic loads are studied as well as the development and migration of secondary flows and their contribution to the total pressure loss. The numerical results indicate that strong passage vortices develop in the nozzle vane, mix out quickly, and have little impact on the rotor flow. The rotor is highly loaded near the leading edge. Within the rotor passage, strong spanwise flows and other secondary flows exist along with the tip leakage vortex. The rotor exit loss distribution is similar in character to that found in radial inflow turbines. The secondary flows and nonuniform work extraction also tend to redistribute a nonuniform inlet total temperature profile significantly by the exit of the stage.

11A727. Incidence angle and pitch-chord effects on secondary flows downstream of a turbine cascade. - A Perdichizzi *(Dipt Meccanica, Univ Brescia, 25060 Brescia, Italy)* and V Dossena *(Dipt Energetica, Politec Milano, 20100 Milano, Italy)*. J Turbomachinery 115(3) 383-391 (Jul 1993).

This paper describes the results of an experimental investigation of the 3D flow downstream of a linear turbine cascade at off-design conditions. The tests have been carried out for five incidence angles from -60 to +35°, and for three pitch-chord ratios: s/c = 0.58, 0.73, 0.87. Data include blade pressure distributions, oil flow visualizations, and pressure probe measurements. The secondary flow field has been obtained by traversing a miniature five-hole probe in a plane located at 50% of an axial chord downstream of the trailing edge. The distributions of local energy loss coefficients, together with vorticity and secondary velocity plots, show in detail how much the secondary flow field is modified both by incidence and by cascade solidity variations. The level of secondary vorticity and the intensity of the crossflow at the endwall have been found to be strictly related to the blade loading occurring in the blade entrance region. Heavy changes occur in the spanwise distributions of the pitch-averaged loss and of the deviation angle when incidence or pitch-chord ratio is varied.

11A728. Investigation of rotor blade roughness effects on turbine performance. - JL Boynton, R Tabibzadeh *(Rocketdyne Div, Rockwell Int, Canoga Park CA 91303)*, ST Hudson *(NASA Marshall Space Flight Center, Huntsville AL 35812)*. J Turbomachinery 115(3) 614-620 (Jul 1993).

The cold air test program was completed on the SSME (Space Shuttle Main Engine) HPFTP (High-Pressure Fuel Turbopump) turbine with production nozzle vane rings and polished coated rotor blades with a smooth surface finish of 30 μin (0.76 μm) rms (root mean square). The smooth blades were polished by an abrasive flow machining process. The test results were compared with the air test results from production rough-coated rotor blades with a surface finish of up to 400 μin (10.16 μm) rms. Turbine efficiency was higher for the smooth blades over the entire range tested. Efficiency increased 2.1% points at the SSME 104% RPL (Rated Power Level) conditions. This efficiency improvement could reduce the SSME HPFTP turbine inlet temperature by 57 R (32 K), increasing turbine durability. The turbine flow parameter increased with the midspan outlet swirl angle became more axial with the smooth rotor blades.

11A729. Measurement and prediction of the tip clearance flow in linear turbine cascades. - FJG Heyes *(European Gas Turbines, Lincoln, UK)* and HP Hodson *(Whittle Lab, Cambridge Univ Eng Dept, Cambridge CB3 0DY, UK)*. J Turbomachinery 115(3) 376-382 (Jul 1993).

This paper describes a simple 2D model for the calculation of the leakage flow over the blade tips of axial turbines. The results obtained from calculations are compared with data obtained from experimental studies of two linear turbine cascades.

One of these cascades has been investigated by the authors and previously unpublished experimental data are provided for comparison with the model. In each of the test cases examined, excellent agreement is obtained between the experimental and predicted data. Although ignored in the past, the importance of pressure gradients along the blade chord is highlighted as a major factor influencing the tip leakage flow.

11A730. Progress towards understanding and predicting heat transfer in the turbine gas path. - RJ Simoneau and FF Simon *(NASA Lewis Res Center, Cleveland OH 44135)*. Int J Heat Fluid Flow 14(2) 106-128 (Jun 1993).

A new era is dawning in the ability to predict convection heat transfer in the turbine gas path. We feel that the technical community now has the capability to mount a major assault on this problem, which has eluded significant progress for a long time. In this paper we hope to make a case for this bold statement by reviewing the state of the art in three major and related areas, which we believe are indispensable to the understanding and accurate prediction of turbine gas path heat transfer: configuration-specific experiments, fundamental physics and model development, and code development. We begin our review with the configuration-specific experiments, whose data have provided the big picture and guided both the fundamental modeling research and the code development. Following that, we will examine key modeling efforts and comment on what will be needed to incorporate them into the codes. In this region we will concentrate on bypass transition, 3D endwalls, and film cooling. We will then review progress and directions in the development of computer codes to predict turbine gas path heat transfer. Finally, we will cite examples and make observations on the more recent efforts to do all this work in a simultaneous, interactive, and more synergistic manner. We will conclude with an assessment of progress, suggestions for how to use the current state of the art, and recommendations for the future.

11A731. Statistical approach to the experimental evaluation of transonic turbine airfoils in a linear cascade. - ML Shelton, BA Gregory *(Turbine Aero and Cooling Tech, General Elec Aircraft Engines, Cincinnati OH 45208)*, RL Doughty, T Kiss, HL Moses *(Dept of Mech Eng, VPI)*. J Turbomachinery 115(3) 366-375 (Jul 1993).

In aircraft engine design (and in other applications), small improvements in turbine efficiency may be significant. Since analytical tools for predicting transonic turbine losses are still being developed, experimental efforts are required to evaluate various designs, calibrate design methods, and validate CFD analysis tools. However, these experimental efforts must be very accurate to measure the performance differences to the levels required by the highly competitive aircraft engine market. Due to the sensitivity of transonic and supersonic flow fields, it is often difficult to obtain the desired level of accuracy. In this paper, a statistical approach is applied to the experimental evaluation of transonic turbine airfoils in the VPI and SU transonic cascade facility in order to quantify the differences between three different transonic turbine airfoils. This study determines whether the measured performance differences between the three different airfoils are statistically significant. This study also assesses the degree of confidence in the transonic cascade testing process at VPI and SU.

380H. CENTRIFUGAL FANS, PUMPS, COMPRESSORS

11A732. Aerodesign and performance analysis of a radial transonic impeller for a 9:1 pressure ratio compressor. - S Colantuoni *(Alfa Romeo Avio, Societa Aeromotoristica pA R&D, Napoli, Italy)* and A Colella *(Alta Romeo Avio, Societa Aeromotoristica pA R&D, Napoli, Italy)*. J Turbomachinery 115(3) 573-581 (Jul 1993).

The aerodynamic design of a centrifugal compressor for technologically advanced small aeroengines requires more and more the use of sophisticated computational tools in order to meet the goals successfully at minimum cost development. The objective of the present work is the description of the procedure adopted to design a transonic impeller having 1.31 relative Mach number at the inducer tip, 45° back-swept exit blade angle, and a tip speed of 636 m-s. The optimization of the blade shape has been done by analyzing the aerodynamic flowfield by extensive use of a quasi-3D code and a fully 3D Euler solver based on a time-marching approach and a finite volume discretization. Testing has been done on the impeller-only configuration, using a compressor rig that simulates real engine hardware, ie, having an S-shaped air-intake. The overall performance of the impeller is presented and discussed.

11A733. Experimental and computational investigation of the NASA low-speed centrifugal compressor flow field. - MD Hathaway *(US Army Res Lab, Vehicle Propulsion Directorate, Cleveland OH 44135)*, RM Chriss, JR Wood, AJ Strazisar *(NASA Lewis Res Center, Cleveland OH 44135)*. J Turbomachinery 115(3) 527-542 (Jul 1993).

An experimental and computational investigation of the NASA Low-Speed Centrifugal Compressor flow field has been conducted using laser anemometry and Dawes' 3D viscous code. The experimental configuration consists of a backswept impeller followed by a vaneless diffuser. Measurements of the 3D velocity field were acquired at several measurement planes through the compressor. The measurements describe both the throughflow and secondary velocity field along each measurement plane. In several cases the measurements provide details of the flow within the blade boundary layers. Insight into the complex flow physics within centrifugal compressors is provided by the computational analysis, and assessment of the CFD predictions is provided by comparison with the measurements. Five-hole probe and hot-wire surveys at the inlet and exit to the rotor as well as surface flow visualization along the impeller blade surfaces provide independent configuration of the laser measurement technique. The results clearly document the development of the throughflow velocity wake, which is characteristic of unshrouded centrifugal compressors.

11A734. Experimental and theoretical analysis of the flow in a centrifugal compressor volute. - E Ayder, R Van den Braembussche *(von Karman Inst for Fluid Dyn, Rhode St Genese, Belgium)*, JJ Brasz *(Carrier, Syracuse NY 13221)*. J Turbomachinery 115(3) 582-589 (Jul 1993).

Detailed measurements of the swirling flow in a centrifugal compressor volute with elliptical cross section are presented. They show important variations of the swirl and throughflow velocity, total and static pressure distribution at the different volute cross sections and at the diffuser exit. The basic mechanisms defining the complex 3D flow structure are clarified. The different sources of pressure loss have been investigated and used to improve the prediction capability of 1D mean streamline analysis correlations. The tangential flow loss model under decelerating flow conditions and the friction loss model are confirmed. New empirical loss coefficients are proposed for the exit cone loss model and the tangential flow loss model for the case of accelerating flow in the volute.

11A735. Investigation of compressor rotor wake structure at peak pressure rise coefficient and effects of loading. - J Prato and B Lakshminarayana *(Dept of Aerospace Eng, Penn State)*. J Turbomachinery 115(3) 487-500 (Jul 1993).

This paper reports an experimental study of the 3D characteristics of the mean velocity in the trailing-edge, near-wake, and far-wake regions of a highly loaded low-speed compressor rotor. The wake structure and decay characteristics are compared with the wake data in the same compressor with moderate loading. The experimental investigation was carried out using a rotating five-hole probe. The flow field was surveyed at various radial and axial locations downstream of the compressor rotor. Variations in the axial, tangential, and radial components of mean velocity at various axial and radial locations were derived from the data and compared with earlier data at lower loading to discern the effects of loading. It was found that the higher loading had the following effects: Higher total velocity defects were observed in the hub-wall region, increased wake growth rate in the tip region, faster decay of static pressure difference in the trailing-edge region, larger initial wake width in the trailing-edge region, increased rate of growth in the semi-wake width in the trailing-edge region, increased decay rate of radial velocity in the trailing-edge region, and decreased decay rate of radial velocity in the far wake region. Far wake properties were almost identical in both cases.

11A736. Investigations on a radial compressor tandem-rotor stage with adjustable geometry. - B Josuhn-Kadner *(Lehrstuhl Fluidenergemaschinen, Ruhr-Univ, Bochum, Germany)* and B Hoffmann *(Inst Antriebstech, DLR Koln, Germany)*. J Turbomachinery 115(3) 552-559 (Jul 1993).

A radial compressor stage has been investigated mainly experimentally for aerodynamic stage optimization. The rotor ($\pi_t = 3.9$) consists of a profiled axial inducer and a conventionally designed radial impeller. Inducer and impeller can be locked at different circumferential positions relative to each other, thus forming a tandem wheel with adjustable geometry. Conventional and Laser-2-Focus system measurements for the tandem rotor and the stage were performed at different operating points to study the influence of the circumferential clearance geometry between inducer and impeller with respect to compressor characteristics and performance. Furthermore, 3D Navier-Stokes calculations are being developed at design point condition to analyze the flow field. A small influence of the inducer adjustment on the rotor characteristics is observed. The maximum rotor efficiency of 93.5% varies in a range of less than 1% depending on the different inducer positions.

11A737. Numerical simulation of compressor endwall and casing treatment flow phenomena. - AJ Crook *(Allison Gas Turbine Div, Indianapolis IN 46206)*, EM Greitzer, CS Tan *(MIT)*, JJ Adamczyk *(NASA Lewis Res Center, Cleveland OH 44135)*. J Turbomachinery 115(3) 501-512 (Jul 1993).

A numerical study is presented of the flow in the endwall region of a compressor blade row, in conditions of operation with both smooth and grooved endwalls. The computations are first compared to velocity field measurements in a cantilevered stator-rotating hub configuration to confirm that the salient features are captured. Computations are then interrogated to examine the tip leakage flow structure since this is a dominant feature of the endwall region. In particular, the high blockage that can exist near the endwalls at the rear of a compressor blade passage appears to be directly linked to low total pressure fluid associated with the leakage flow. The fluid dynamic action of the grooved endwall, representative of the casing treatments that have been most successful in suppressing stall, is then simulated computationally and two principal effects are identified. One is suction of the low total pressure, high blockage fluid at the rear of the passage. The second is energizing of the tip leakage flow, most notably in the core of the leakage vortex, thereby suppressing the blockage at its source.

11T738. Probabilistic simulation of fragment dynamics and their surface impacts in the SSME turbopump. - A Hamed and H Moy *(Dept of Aerospace Eng and Eng Mech, Univ of Cincinnati, Cincinnati OH 45221)*. J Fluids Eng 115(2) 302-308 (Jun 1993).

11A739. Relative flow and turbulence measurements downstream of a backward centrifugal impeller. - M Ubaldi, P Zunino, A Cattanei *(Dipt Ing Energetica, Univ Genova, Genova, Italy)*. J Turbomachinery 115(3) 543-551 (Jul 1993).

The paper presents the results of an experimental investigation on the 3D relative flow at the exit of the backward bladed centrifugal impeller of the high-pressure stage of a two-stage biregulating pump-turbine model, operating at the pump nominal point. Mean velocity, Reynolds stress tensor, and total pressure of the relative flow have been measured with stationary hot-wire probes and fast response miniature pressure transducers, by means of a phase-locked ensemble-average technique. The results, shown in terms of secondary vector plots and contours of mean flow characteristics and Reynolds stress components, give a detailed picture of the flow kinematic structure and of the complex relative total pressure loss and turbulence distributions. In spite of strongly backswept blades, the flow leaving the impeller presents a jet and wake structure and an intense secondary flow activity. Large relative total pressure losses affect the wake and the region where secondary vortices interact. The turbulence data analysis provides information about the effects of the impeller rotation on the turbulence structure and about the mechanisms of the flow mixing process and of the secondary flow decay downstream of the impeller.

380I. AXIAL FANS, PUMPS, COMPRESSORS

11A740. Experimental study on the 3D flow within a compressor cascade with tip clearance Part I. Velocity and pressure fields. - S Kang and C Hirsch *(Dept of Fluid Mech, Vrije Univ, 1050 Brussel, Belgium)*. J Turbomachinery 115(3) 435-443 (Jul 1993).

Experimental results from a study of the 3D flow in a linear compressor cascade with stationary endwall at design conditions are presented for tip clearance levels of 1.0, 2.0, and 3.3% of chord, compared with the no-clearance case. In addition to five-hole probe measurements, extensive surface flow visualizations are conducted. It is observed that for the smaller clearance cases a weak horseshoe vortex forms in the front of the blade leading edge. At all the tip gap cases, a multiple tip vortex structure with three discrete vortices around the midchord is found. The tip leakage vortex core is well defined after the midchord but does not cover a significant area in transverse planes. The presence of the tip leakage vortex results in the passage vortex moving close to the endwall and the suction side.

11A741. Experimental study on the 3D flow within a compressor cascade with tip clearance Part II. Tip leakage vortex. - S Kang and C Hirsch *(Dept of Fluid Mech, Vrije Univ, 1050 Brussel, Belgium)*. J Turbomachinery 115(3) 444-452 (Jul 1993).

An analysis of the experimental data of a linear compressor cascade with tip clearance is presented with special attention to the development of the tip leakage vortex. A method for determining the tip vortex core size, center position, and vorticity or circulation from the measured data is proposed, based on the assumption of a circular tip vortex core. It is observed that the axial velocity profile passing through the tip vortex center is wakelike. The vorticity of the tip vortex increases rapidly near the leading edge and reaches its highest values at a short distance downstream, from which it gradually decreases. In the whole evolution, its size growing and its center is moving away from both the suction surface and the endwall, approximately in a linear way.

11A742. Investigation of tip clearance phenomena in an axial compressor cascade using Euler and Navier-Stokes procedures. - RF Kunz, B Lakshminarayana, AH Basson *(Dept of Aerospace Eng, Penn State)*. J Turbomachinery 115(3) 453-467 (Jul 1993).

Three-dimensional Euler and full Navier-Stokes computational procedures have been utilized to simulate the flow field in an axial compressor cascade with tip clearance. An embedded H-grid topology was utilized to resolve the flow physics in the tip gap region. The numerical procedures employed is a finite different Runge-Kutta scheme. Available measurements of blade static pressure distributions along the blade span, dynamic pressure and flow angle in the cascade outlet region, and spanwise distributions of blade normal force coefficient and circumferentially averaged flow angle are used for comparison. Several parameters that were varied in the experimental investigations were also varied in the computational studies. Specifically, measurements were taken and computations were performed on the configuration with and without: tip clearance, the presence of an endwall, inlet endwall total pressure profiles, and simulated relative casing rotation. Additionally, both Euler and Navier-Stokes computations were performed to investigate the relative performance of these approaches in reconciling the physical phenomena considered. Results indicate that the Navier-Stokes procedure, which utilizes a low Reynolds number κ-ε model, captures a variety of important physical phenomena associated with tip clearance flows with good accuracy. These include tip vortex strength and trajectory, blade loading near the tip, the interaction of the tip clearance flow with passage secondary flow, and the effects of relative endwall motion. The Euler computational provides good but somewhat diminished accuracy in resolution of some of these clearance phenomena. It is concluded that the level of modeling embodied in the present approach is sufficient to extract much of the tip region flow field information useful to designers of turbomachinery.

11A743. Measurement of the 3D tip region flow field in an axial compressor. - RC Stauter *(United Tech Res Center, E Hartford CT 06108)*. J Turbomachinery 115(3) 468-476 (Jul 1993).

A two-color, five-beam LDV system has been configured to make simultaneous three-component velocity measurements of the flow field in a two-stage axial compressor model. The system has been used to make time-resolved measurements both between compressor blade rows and within the rotating blade passages in an axial compressor. The data show the nature and behavior of the complex, 3D flow phenomena present in the tip region of a compressor as they convect downstream. In particular, the nature of the tip leakage vortex is apparent, being manifested by high blockages as well as the expected vortical motion. The data indicate that the radial flows associated with the tip leakage vortex begin to decrease while within the rotor passage, and that they temporarily increase aft of the passage.

11A744. Radial transport and momentum exchange in an axial compressor. - RP Dring *(United Tech Res Center, E Hartford CT 06108)*. J Turbomachinery 115(3) 477-486 (Jul 1993).

The objective of this work was to examine radial transport in axial compressors from two perspectives. The first was to compare the mixing coefficient based on a secondary flow model (using measured radial velocities) with that based on a turbulent diffusion model. The second was to use measured airfoil pressure forces and momentum changes to assess the validity of the assumption of diffusive radial transport, which is common to both models. These examinations were carried out at both design and off-design conditions as well as for two rotor tip clearances. In general it was seen that radial mixing was strongest near the hub and that it increased dramatically at near-stall conditions. It was also seen that radial transport could cause large differences ($\approx$ 100%) between the force on an airfoil and the change in momentum across the airfoil at the same spanwise location.

380L. ROTOR AND INDUCER BLADING

11A745. Blade loading and shock wave in a transonic circular cascade diffuser. - H Hayami *(Inst of Adv Mat Study, Kyushu Univ 86, Kasuga 816, Japan)*, M Sawae *(Nikko Kyodo, Chita 478, Japan)*, T Nakamura *(Toshiba, Yokohama 230, Japan)*, N Kawaguchi *(Inst of Adv Mat Stud, Kyushu Univ 86, Kasuga 816, Japan)*. J Turbomachinery 115(3) 560-564 (Jul 1993).

A low-solidity circular cascade, conformally transformed from a high-stagger linear cascade of double-circular-arc vanes with solidity 0.69, was tested as a part of diffuser systems of a transonic centrifugal compressor and the static pressures were measured around a vane of the cascade and on the side wall between cascade vanes in detail. The blade loading of cascade vane was discussed by integrating the pressure distribution around the vane. The experimental data for lift-coefficient of vane were almost on a single straight line with positive gradient against angle-of-attack over a wide range of inflow Mach number and inflow angle. The maximum lift coefficient reached about 1.5 and the vane worked well to the surge condition of the compressor. The structure of shock wave was also discussed by drawing a contour map of the flow Mach number between cascade vanes. The normal shock wave was observed on the suction surface of vane and it moved upstream along the suction surface with the decrease inflow angle. The vane did not fall in stall even though the Mach number upstream of the shock was over 1.4.

11A746. Design and rotor performance of a 5:1 mixed-flow supersonic compressor. - R Monig *(Siemens AG, KWU Group, Gas Turbine Tech, Mulheim, Ruhr, Germany)*, W Elmendorf, HE Gallus *(Inst Strahlantriebe and Turboarbeitsmaschinen Rheinisch Westfalische, Tech Hochsch, Aachen, Germany)*. J Turbomachinery 115(3) 565-572 (Jul 1993).

In consideration of further jet-engine developments required by applications for supersonic travel aircraft, airbreathing propulsion of space vehicles, or only the improvement of conventional high-performance turbo-engines, highly loaded supersonic compressors seem to meet the future demands. Particularly mixed-flow compressor stages with moderate supersonic rotor and stator inlet flow reveal the potential of high pressure rise and mass flow as well as favorable performance characteristics and efficiency. The first part of this paper presents analytical considerations for mixed-flow supersonic compressors with strong shock waves. This theoretical approach proves to be essential besides established design tools in order to ensure safe rotor and stage operation in accordance with the design objectives. In this context, the conditions for shock wave stabilization within a diagonal rotor passage are discussed in detail for design and off-design rotational speeds. The main part of this paper, however, presents the results and flow analysis obtained by extensive experimental investigations of the designed mixed-flow compressor rotor. The investigations were restricted to operation without stator in order to strictly separate rotor performance from rotor-stator interactions. The results reveal the design goals to be met in general. Mass flow, total pressure rise, and efficiency in particular show a good agreement with the design properties for near-surge operation at design and off-design conditions.

11A747. Off-design performance prediction for radial-flow impellers. - SC Lee *(Dept of Mech and Aerospace Eng, Univ of Missouri, Rolla MO)* and D Chen *(Univ of Missouri, Rolla MO)*. Int J Turbo Jet Engines 10(1) 45-60 (1993).

A numerical method was developed to consider the 2D flowfield between impeller blades of a given geometry. Solution of the laminar Navier-Stokes equations in geometry-oriented coordinates was obtained for stream functions and vorticities. Velocities and pressures were calculated to determine the output fluid-energy head. The circumferential components of the normal and shear stresses along the blade were evaluated to give the input mechanical-energy head. Performance predictions were obtained for different load conditions. Comparisons were made with the measured velocity vectors of the flowfield of an air-pump impeller and with the measured performance of a production water pump; good agreements were reached.

11A748. Separated flow in a low-speed 2D cascade Part I. Flow visualization and time-mean velocity measurements. - AM Yocum *(Appl Res Lab, Penn State Univ, State College PA 16804)* and WF O'Brien *(VPI)*. J Turbomachinery 115(3) 409-420 (Jul 1993).

This study was conducted for the purpose of providing a more fundamental understanding of separated flow in cascades and to provide performance data for fully stalled blade rows. Cascades of a single blade geometry and a solidity of unity were studied for three stagger angles and the full range of angle of attack, extending well into the stalled flow region. Results are presented from flow visualization and time-mean velocity measurements of stalled flow in the cascade. Surface and smoke flow visualization revealed that the blade stagger angle is a key parameter in determining the location of the separation line and the occurrence of propagating stall. Time-mean velocity measurements obtained with a dual hot split-film probe also showed that the separated velocity profiles within the blade passages and the profiles in the wake have distinctly different characteristics depending on the stagger angle.

11A749. Separated flow in a low-speed 2D cascade Part II. Cascade performance. - AM Yocum *(Appl Res Lab, Penn State)* and WF O'Brien *(VPI)*. J Turbomachinery 115(3) 421-434 (Jul 1993).

This study was conducted for the purpose of providing a more fundamental understanding of separated flow in cascades and to provide performance data for fully stalled blade rows. Cascades of a single blade geometry and a solidity of unity were studied for three stagger angles and the full range of angle of attack extending well into the stalled flow regime. The Reynolds number was also varied for a limited number of cases. Results from velocity and pressure measurements made in the cascade and the overall cascade performance evaluated from these measurements are presented. In addition, results from a numerical simulation of the flow through a cascade of flat plate airfoils are used to illustrate further the effects of blade stagger and to define the correct limits for the cascade performance. The results indicate that the slope of the total pressure loss versus angle of attack curve for the flow immediately downstream of the cascade is steeper for cascades with greater stagger. The normal force coefficient was found to increase to a peak value near the angle of attack where full leading edge stall first occurs. A further increase in angle of attack results in a decline in the normal force coefficient. The peak value of the normal force coefficient is greater and occurs at a higher angle of attack for the cascades with smaller stagger.

11A750. Shock formation in overexpanded tip leakage flow. - J Moore *(Dept of Mech Eng, VPI)* and KM Elward *(Gas Turbine Eng and Dev, General Elec, Schenectady NY 12345)*. J Turbomachinery 115(3) 392-399 (Jul 1993).

Shock formation due to overexpansion of supersonic flow at the inlet to the tip clearance gap of a turbomachine has been studied. The flow was modeled on a water table using a sharp-edge rectangular channel. The flow exhibited an oblique hydraulic jump starting on the channel sidewall near the channel entrance. This flow was analyzed using hydraulic theory. The results suggest a model for the formation of the jump. The hydraulic analogy between free surface water flows and compressible gas flows is used to predict the location and strength of oblique shocks in analogous tip leakage flows. Features of the flow development are found to be similar to those of compressible flow in sharp-edged orifices. Possible implications of the results for high-temperature gas turbine engine design are considered.

11A751. Supersonic turbomachine rotor flutter control by aerodynamic detuning. - KM Spara *(Tech Dept, Aerospace Corp, Los Angeles CA)* and S Fleeter *(Sch of Mech Eng, Thermal Sci and Propulsion Center, Purdue)*. J Propulsion Power 9(4) 561-568 (Jul-Aug 1993).

A mathematical model is developed to analyze the flutter stability characteristics of an aerodynamically detuned rotor operating in a supersonic inlet flowfield with a supersonic axial component. Alternate-blade aerodynamic detuning is considered, accomplished by alternating the circumferential spacing of adjacent rotor blades. The unsteady aerodynamics are determined by developing an influence coefficient technique which is appropriate for both aerodynamically tuned and detuned rotor configurations. The effects of this detuning on the flutter stability characteristics of supersonic axial flow rotors are then demonstrated by applying this model to baseline 12-bladed rotors. Results show that, dependent on the specific blade row and flowfield geometry, alternate blade aerodynamic detuning is a viable flutter control mechanism for supersonic through-flow rotors.

380R. PROPELLERS AND HELICOPTER ROTORS

11A752. Aeroelastic response, loads, and stability of a composite rotor in forward flight. - EC Smith *(Aerospace Eng Dept, Penn State)* and I Chopra *(Dept of Aerospace Eng, Center for Rotorcraft Educ and Res, Univ of Maryland, College Park MD 20742)*. AIAA J 31(7) 1265-1273 (Jul 1993).

The aeroelastic response, blade and hub loads, and shaft-fixed aeroelastic stability are investigated for a helicopter with elastically tailored composite rotor blades. A new FE-based structural analysis including nonclassical effects such as transverse shear, torsion related warping, and in-plane elasticity is integrated with the University of Maryland Advanced Rotorcraft Code. The structural dynamics analysis is correlated against both experimental data and detailed FE results. Correlation of rotating natural frequencies of coupled composite box-beams is generally within 5 - 10%. The analysis is applied to a soft-in-plane hingeless rotor helicopter in free flight propulsive trim. Changes in blade loads are relatively small; however, aeroelastic stability can be significantly improved by the use of elastic pitch-lag coupling. For example, lag mode damping can be increased 300% over a range of thrust conditions and forward speeds. The influence of attached flow unsteady aerodynamics on the blade response and vibratory hub loads is also investigated. The magnitude and phase of the flap response is substantially altered by the unsteady aerodynamic effects. Vibratory hub loads increase up to 30% due to unsteady aerodynamic effects.

380Y. COMPUTATIONAL TECHNIQUES

11A753. Practical application of solution-adaption to the numerical simulation of complex turbomachinery problems. - WN Dawes *(Whittle Lab, Cambridge Univ, Cambridge, UK)*. Prog Aerospace Sci 29(3) 221-269 (1992).

This paper describes some recent developments in the application of unstructured mesh, solution-adaptive methods to the solution of the 3D Navier-Stokes equations in turbomachinery flows. By adopting a simple, pragmatic but systematic approach to mesh generation, the variety of simulations which can be attempted ranges from simple turbomachinery blade-blade primary paths towards complex secondary gas paths and can include the interactions between the two paths. By adopting a hierarchical data structure, mesh refinement and derefinement can be preformed sufficiently economically that it becomes practical to perform unsteady flow simulations with zones of mesh refinement "following" unsteady flow features, like vortices and wakes, through a coarse background mesh. The combined benefits of the approach result in a powerful analytical ability. Solutions for a wide range of steady flows are presented including a transonic compressor rotor, a centrifugal impellor, the internal coolant passage of a radial inflow turbine and a turbine disc-cavity flow. Unsteady solutions are presented for a cylinder shedding vortices and for a turbine wake-rotor interaction.

See also the following:

11A707. Three-dimensional mesh embedding for the Navier-Stokes equations using upwind control volumes

380Z. EXPERIMENTAL TECHNIQUES

11A754. Blade row interaction effects on compressor measurements. - T Shang *(Gas Turbine Lab 31-256, MIT)*, AH Epstein *(Gas Turbine Lab 31-266, MIT)*, MB Giles *(Gas Turbine Lab 31-264, MIT)*, AK Sehra *(Compressor Aerodyn Dept LSD-10, Textron Lycoming, 550 Main St, Stratford CT 06497)*. J Propulsion Power 9(4) 569-578 (Jul-Aug 1993).

The influence of a downstream stator row on the measurement of compressor rotor performance has been examined using a 2D computational fluid dynamic code backed by laser anemometry data on a transonic fan stage. The upstream potential influence of the stator causes unsteady circulation about the rotor blades which is a function of the rotor circumferential position. This, in turn, results in a nonuniform circumferential pattern of time-averaged temperature and pressure in the stationary frame. A relatively fast calculational procedure using a linearized, potential flow approach coupled with an analytical theory relating the temperature and pressure variations to the circulation perturbation is developed and shown to give good agreement with the numerical calculations. The results of a parametric study show that the magnitude of this effect is a strong function of rotor-stator blade row spacing and relative blade counts. The effects range from negligible for large spacings typical of high bypass ratio fans, to several percent of the stage pressure and temperature rise for closely spaced blade rows typical of high compressors. Because the temperature and pressure perturbation are in spatial phase, the net effect on measured rotor efficiency is negligible so long as the pressure and temperature measurements are made in the same location relative to the stators. If they are not, errors of ±1.5% can result. The effects of axial position and stator loading are shown to be relatively small.

11A755. Investigation of factors influencing the calibration of five-hole probes for 3D flow measurements. - RG Dominy *(Sch of Eng and Comput Sci, Univ of Durham, Durham, UK)* and HP Hodson *(Whittle Lab, Cambridge Univ, Cambridge, UK)*. J Turbomachinery 115(3) 513-519 (Jul 1993).

The effects of Reynolds number, Mach number, and turbulence on the calibrations of commonly used types of five-hole probe are discussed. The majority of the probes were calibrated at the exit from a transonic nozzle over a range of Reynolds number ($7 \times 10^3 < Re < 80 \times 10^3$ based on probe tip diameter) at subsonic and transonic Mach numbers. Additional information relating to the flow structure were obtained from a large-scale, low-speed wind tunnel. The results confirmed the existence of two distinct Reynolds number effects. Flow separation around the probe head affects the calibrations at relatively low Reynolds numbers while changes in the detailed structure of the flow around the sensing holes affects the calibrations even when the probe is nulled. Compressibility is shown to have little influence upon the general behavior of these probes in terms of Reynolds number sensitivity but turbulence can affect the reliability of probe calibrations at typical test Reynolds numbers.

382. Lubrication

382A. GENERAL THEORY

11T756. Effect of fluid compressibility on journal bearing performance. - F Dimofte *(NASA Lewis Res Center, Cleveland OH 44135)*. Trib Trans 36(3) 341-350 (Jul 1993).

11A757. Effect of inertia forces on the performance of externally pressurized conical thrust bearings under turbulent flow conditions. - MF Khalil, SZ Kassab, AS Ismail *(Dept of Mech Eng, Fac of Eng, Alexandria Univ, Alexandria 21544, Egypt)*. Wear 166(2) 155-161 (1 Jul 1993).

The effects of convective and centrifugal inertia forces on the performance of externally pressurized conical thrust bearings, working under turbulent flow conditions, are studied. The study makes use of an algebraic Reynolds stress model proposed for turbulent lubrication. The governing equations are solved iteratively using the finite difference method. The study reveals that the effect of the convective inertia force on the conical bearing performance is opposite to the effect of the centrifugal force. Further, the effect of combined inertia forces is to decrease both the dimensionless pressure and the load of the bearing.

11A758. Lubrication in cold rolling: Elasto-plastic-hydrodynamic lubrication of smooth surfaces. - PM Lugt, AW Wemekamp, WE ten Napel *(Univ of Twente, PO Box 217, Enschede, Netherlands)*, P van Liempt, JB Otten *(Hoogovens Res Lab, PO Box 10000, IJmuiden, Netherlands)*. Wear 166(2) 203-214 (1 Jul 1993).

A model has been developed with respect to hydrodynamic lubrication in cold rolling. The basic model describes the configuration of a rigid, perfectly plastic sheet rolled by a rigid work roll. The governing equations have been solved throughout the complete contact area, ie, the inlet, the work zone and the outlet zone. Multi-level techniques have been applied to solve these equations together with boundary conditions, resulting in an algorithm solving the problem in O(n) operations. This means that the distribution of the pressure and the traction force in the lubricant film, and the shape of this film, as well as the plastic deformation of the sheet, can be accurately calculated for a large number of nodal points on a minicomputer. Subsequently elastic deformation, work hardening and dynamic behavior of the flow stress have been incorporated in the model. It will be shown that the influence of these effects on the film thickness or the pressure distribution is considerable.

11A759. Performance of externally pressurized conical thrust bearing under laminar and turbulent flow conditions. - MF Khalil, SZ Kassab, AS Ismail *(Dept of Mech Eng, Fac of Eng, Alexandria Univ, Alexandria 21544, Egypt)*. Wear 166(2) 147-154 (1 Jul 1993).

In the present theoretical investigation, the effect of turbulent lubrication, represented by Reynolds stresses, on the performance of externally pressurized circular and conical thrust bearings is studied. A recent algebraic Reynolds stress model is employed. The governing equations are solved iteratively using the finite difference method. Both the inertia forces and thermal effects are neglected in the present analysis. The effects of recess radius ratio, film thickness ratio and Poiseuille and Couette Reynolds numbers on the performance characteristics of the circular and conical bearinga are studied. The bearings' performances under laminar flow condition are also presented and compared with the turbulent condition. The present study reveals that the circular bearing has slightly higher dimensionless pressure, load and torque than the conical bearing. Further, the turbulent flow solution gives higher dimensionless pressure, load and torque than the laminar flow solution. Finally, increasing the film thickness ratio or the recess radius ratio has the effect of decreasing both the dimensionless load and torque.

382C. HYDRODYNAMIC AND HYDROSTATIC LUBRICATION

11A760. Dynamic characteristics of hydrostatic bearings. - Zhicheng Pang, Jingwu Sun, Wenjie Zhai, Qingming Liu, Wei Chi *(Dept of Mech Eng, Harbin IT, 802 Div, Harbin, China)*. Wear 166(2) 215-220 (1 Jul 1993).

The characteristics of hydrostatic bearings have been theoretically studied in terms of the compressibility of the air-contained oil. A formula for the stability criterion of a hydrostatic bearing system and a dynamic stiffness formula have been derived. The theory has been verified by experimental research, and provides a basis for hydrostatic bearing design.

11A761. Non-Newtonian effects on the coastdown phenomenon of hydrodynamic journal bearings. - D Sheeja and BS Prabhu *(Dept of Appl Mech, Indian IT, Madras 600 036, India)*. Trib Trans 36(3) 405-410 (Jul 1993).

The behavior of a rotating system after its power supply is cut off is called the coastdown phenomenon. An experimental investigation of the coastdown characteristics was carried out on a rotor rig, with different types of lubricants including a Newtonian oil, a blend of ISOVG 32 and hydrogenated styrene isoprene, multigrade oils, and aqueous polymer solutions in a hydrodynamic journal bearing. The characteristics were plotted in terms of deceleration vs speed, which resembled the Stribeck diagram of friction due to viscous drag. Thus, the apparent Stribeck diagrams of friction for the above oils were obtained by plotting the derived coefficient of friction against the reciprocal Sommerfeld number.

11T762. Nonlinear study of a misaligned hydrodynamic journal bearing. - FK Choy, MJ Braun, Y Hu *(Dept of Mech Eng, Univ of Akron, Akron OH 44325)*. Trib Trans 36(3) 421-431 (Jul 1993).

382D. ELASTOHYDRODYNAMIC LUBRICATION

11A763. Elastohydrodynamic lubrication of elliptical contacts with pure spin. - D Dowson, CM Taylor *(Dept of Mech Eng, Univ of Leeds, UK)*, H Xu *(T&N Tech, Cawston Rugby, Warwickshire, UK)*. Proc Inst Mech Eng C 207(C2) 83-92 (1993).

In a lubricated, non-conformal piezoviscous effects associated with the lubricant and elastic distortion of the bounding surfaces can have a significant influence upon the generation of the lubricant film and consequently upon the oil pressure distribution. In many widely studied cases which have been concerned with surface motions of rolling-sliding, it has been shown that these effects enhance the load-generating capability of the oil-film. However, some machine elements experience more complicated bearing surface motions. For example, spinning as well as entraining occurs in the elliptical contact regions of angular contact bearings and some forms of continuously variable speed drives. In this paper, results from a study on the elastohydrodynamic lubrication of elliptical contacts with pure spin are reported. In contrast to the former situation, an unfavorable influence of the surface deflection upon the generation of the fluid film has been observed. Comparison with experimental observation demonstrated encouraging agreement.

11A764. Experimental study on oil supply in a space bearing with an oil-impregnated retainer. - Jianhai Liu, Youwen Fan, Shizhu Wen *(Natl Trib Lab, Tsinghua Univ, Beijing 10084, Peoples Rep of China)*. Wear 165(2) 193-196 (1 Jun 1993).

Parched elastohydrodynamic lubrication (EHL) film thickness in a space ball bearing is measured by electrical capacitance and resistance, and parched transients of oil film and lubricant breakdown are observed. With different oil-impregnated polymer retainers, which are employed as oil supply resources, parched degradation is restricted to some degree, even lubricant breakdown disappears and a steady state of the oil film is produced. A long-term space ball bearing demands both the lowest driving torque and a steady state oil film, which depends on a strictly controlled oil supply from oil-impregnated retainers. The results of this experimental research describe the effects of oil supply by amounts of oil in retainers on parched EHL.

382E. LIQUID LUBRICANTS

See the following:

11A562. Prediction of viscosities using chemical graph theory

11T756. Effect of fluid compressibility on journal bearing performance

382F. GAS LUBRICANTS

11A765. Modeling supersonic inlet boundary-layer bleed roughness. - GC Paynter, DA Treiber, WD Kneeling *(Boeing, Seattle WA 98124)*. J Propulsion Power 9(4) 622-627 (Jul-Aug 1993).

Boundary-layer mass removal (bleed) through spanwise bands of holes on a surface is used to prevent or control separation in supersonic inlets. The rough wall algebraic turbulence model of Cebeci and Chang was added to both boundary-layer and Navier-Stokes analyses to simulate the overall effect of bleed on the growth of a boundary layer. Roughness values were determined for seven bleed configurations, a range of Mach numbers between 1.3-4, and bleed rates between zero and choked values. For the bleed experiments considered, the roughness was found to be a function of the fraction of the upstream boundary-layer mass flux removed. Choked bleed flow through holes at a low angle, with respect to the surface, minimized the roughness effect and gave the best improvement in the boundary-layer velocity distribution for separation control.

382H. OTHER LUBRICANTS

11A766. Laser chemical vapor deposition of fluorinated diamond thin films for solid lubrication. - PA Molian *(Dept of Mech Eng, Iowa State Univ, Ames IA 50011)*, B Janvrin, AM Molian *(Laser Sci, Ames IA 50010)*. Wear 165(2) 133-140 (1 Jun 1993).

A laser chemical vapor deposition process for growing fluorinated diamond thin films and the solid lubrication behavior of such films on two bearing materials (SiC and 440C stainless steel), were investigated. Raman spectroscopy analysis revealed that the films deposited on SiC consisted of a mixture of diamond and graphite, while the films deposited on 440C steel were composed of diamond-like carbon and graphite X-ray photoelectron spectroscopy analysis revealed the presence of significant amounts of C-F compounds, both in the surface and subsurface layers, in addition to carbon. Tribological tests (ball-on-disc and pin-on-disc) of laser-grown films under ambient environmental indicated a friction coefficient in the range of 0.1-0.3, depending on the wear couple, sliding speed and load, confirming the effectiveness of these films as solid lubricants for moving mechanical assemblies in space structures. Fluorination of carbon films has the following attributes: passivation of the surface of diamond-graphite films from absorption of water or oxygen, reduction of surface energy needed for shearing of the film during solid lubrication and protection from corrosive environments.

382Y. COMPUTATIONAL TECHNIQUES

11A767. Analysis of hydrodynamic journal bearings considering lubricant supply conditions. - JCP Claro and AAS Miranda *(Univ of Minho, Guimaraes, Portugal)*. Proc Inst Mech Eng C 207(C2) 93-101 (1993).

A method of analysis of steadily loaded hydrodynamic journal bearings with a single axial groove (either on the load line or at 90° to the load line) or two diametrically opposed axial grooves is described. The method is based on Elrod's cavitation algorithm (which ensures conservation of mass flow in both the full film and the cavitated regions) and is able to accommodate specified lubricant supply conditions, namely groove size and location and supply pressure. Special attention has been given to the determination of flowrate. The equation governing the distribution of pressure around the bearing has been solved numerically using a finite difference approximation and multi-grid techniques to accelerate the convergence of the solution. Performance predictions of the analysis are compared with published experimental data and with experimental measurements obtained in laboratory tests carried out by the authors. The data used cover all grooving arrangements studied.

382Z. EXPERIMENTAL TECHNIQUES

11A768. Possibilities of ultrasound cavitation application to estimation utility properties of power fluid Part II. Estimation of thermo-oxidation properties. - B Wislicki *(Inst Lotnictwa, Aleja Krakowska 110-114, 02-256 Warszawa, Poland)*. Zagadnienia Eksploatacji Maszyn 26(4) 431-440 (1991).

Examples of results of comparative tests of gear oil oxidation resistance acc FTM std No 791-5308 in toothed gear and by use of ultrasound cavitation are presented in the part II. Thirty percent higher effectiveness of cavitation methods has been stated. Similarity of oxidation processes by compared methods is confirmed by results of IR absorption spectrum tests. The possibility of development of effective method of laboratory estimation operational fluids oxidation resistance has been stated.

384. Flow measurements and visualization

11A769. Reconstruction of a quasi-instantaneous image of coherent structures from hotwire signals obtained by a multi-point simultaneous measurement system. - M Hino *(Katase-Yama 4-20-6, Fujisawa-Shi 251, Japan)* and Yan Meng *(Fluid Dyn Group, Env Eng Dept, IT, Shimizu Corp, Etchujima 3-chome, Koto-ku, Tokyo 135, Japan)*. Fluid Dyn Res 11(6) 245-261 (Jun 1993).

The turbulent velocity components (u,v) at 11 points in a reciprocating oscillatory turbulent flow have been measured simultaneously by a set of eleven X-type hotwire probes located in a plane perpendicular to the mean flow. Using a conditional sampling technique and a new method of data analysis for the inverse estimation of flow fields called "virtual plate-load and MASCON model", a quasi-instantaneous 3D image of coherent structures of turbulence was first reconstructed directly from the experimental velocity data. The quasi-instantaneous image was expressed in terms of the velocity components u, v, w and the vorticity components ω_x, ω_y, ω_z and we found that the large-scale coherent structure was composed of a pair of counter-rotating fluid motions with asymmetry which was quite different from that of the ensemble-averaged one. Flow patterns induced by the large-scale structure have been clarified by perspective representations visualized by computer simulations that produce timelines and streaklines of fluid particle traces. Results showed that the new experimental method was applicable for investigating the 3D feature of coherent structures including asymmetry.

11A770. Verification of the theoretical discharge coefficient of a subcritical airflow meter. - DJ Lahti *(Aerothermo Syst Integration, GE Aircraft Engines, Cincinnati OH 45215)* and A Hamed *(Dept of Aerospace and Eng and Appl Mech, Univ of Cincinnati, Cincinnati OH 45221)*. J Propulsion Power 9(4) 615-621 (Jul-Aug 1993).

Since many modern high bypass ratio turbofan engines have flow rates that exceed the capacity of most of the worlds airflow calibration facilities, their airflow metering bellmouth inlets cannot be calibrated, but rather their discharge coefficients must be determined theoretically. The objective of this program was to verify the theoretically derived discharged coefficient for a scale model of such a bellmouth which was small enough to allow its calibration in an existing laboratory facility. Extensive flowfield measurements were also made to further validate theoretical predictions. Thus, this program provides a "calibration" of the theoretical method used, and establishes a link between a traceable airflow metering standard and large engine bellmouth inlets that cannot be calibrated any other way.

11A771. Flow visualization in a circular-to-rectangular transition duct. - CK Lin *(Chung-Shan Inst of Sci and Tech, Taichung, Taiwan, ROC)*, JJ Miau, QS Chen *(Inst of Aeronaut and Astronaut, Natl Cheng-Kung Univ, Tainan, Taiwan, ROC)*, JH Chou *(Dept of Eng Sci, Natl Cheng-Kung Univ, Tainan, Taiwan, ROC)*, D Pan, SF Lin *(Inst of Aeronaut and Astronaut, Natl Cheng-Kung Univ, Tainan, Taiwan, ROC)*. Int J Turbo Jet Engines 10(1) 61-74 (1993).

This work reports on flow behaviors near the wall and secondary flow structures in a circular-to-rectangular transition duct at Reynolds number of 10^4. Flow visualization experiments were conducted under the conditions of uniform and swirling inlet flows. As found, flow structures observed at the rectangular exit under the swirling inlet condition appear very differently from those observed under the uniform inlet condition. In the former case the secondary flows are developed due to the detachments of the swirling flow from the contoured wall, while in the latter cases the secondary flows are known due to the mechanism of mean-flow straining in the corner regions.

11A772. Application of numerical and optical evaluation schemes for particle image velocimetry. - PV Farrell *(Dept of Mech Eng, Univ of Wisconsin, 1514 University Ave, Madison WI 53706)*. Exp Fluids 14(6) 433-446 (May 1993).

This paper will compare the performance of optical and numerical Fourier transform analysis of Young's fringes using speckle images. The repeatability and an estimate of the accuracy of the particle displacement will be shown for each method. A brief examination of the effects of small particle number density of PIV evaluation will also be presented. Finally, for a small part of an actual unsteady flow, the optical and numerical Fourier transform analysis methods will be compared.

11A773. Infrared imagery of an air-CO_2 axisymmetric jet. - DN Gordge *(SETD ACS SY73, Naval Air Warfare Center, Patuxent River MD 20670)* and RH Page *(Mech Eng Dept, Texas A&M Univ, College Station TX 77843-3123)*. Exp Fluids 14(6) 409-415 (May 1993).

This experiment uses an infrared imaging system to investigate a subsonic, non-isoenergetic, air-CO_2 axisymmetric jet. The classical limitations of using IR imagery with hot gases are presented and a novel approach to overcome these limitations is proposed. The results suggest that radial and axial irradiant profiles measured with the IR imager, when non-dimensionalized, collapse onto curves of similarity. This behavior could allow temperature, velocity, and concentration profiles to be deduced from the IR image.

11A774. Large-field high-brightness focusing schlieren system. - LM Weinstein *(Fluid Mech Div, Exp Methods Branch, NASA Langley Res Center, Hampton VA 23665)*. AIAA J 31(7) 1250-1255 (Jul 1993).

The analysis and performance of a large-field high-brightness focusing schlieren system is described. Techniques are described that allow the system to be used even through slightly distorting optical elements. The system can be used to examine complex 2D and 3D flows.

11T775. Absolute intensity measurements of impurity emissions in a shock tunnel and their consequences for laser-induced fluorescence experiments. - PC Palma, AFP Houwing, RJ Sandeman *(Dept of Phys and Theor Phys, Fac of Sci Austral Natl Univ, PO Box 4, Canberra 2601, Australia)*. Shock Waves 3(1) 49-53 (1993).

11A776. Indirect temperature determination of a hot gas stream. - A Kogan *(Technion, Haifa, Israel)* and I Hodara *(Solar Res Fac Unit, Weizmann Inst of Sci, Rehovot 76100, Israel)*. Exp Mech 33(2) 99-101 (Jun 1993).

The method for indirect temperature measurement of hot flowing gas presented in this paper evolved out of the need to determine experimentally the temperature of hot gas leaving a hydrogen production solar thermal water dissociation reactor. The method is based on Fanno line choked flow theory. It enables gas-temperature determination from gas flow rate and pressure measurement. The reliability of the method was tested by applying it to determine the temperature of a relatively cold gas stream and by comparing the result with gas temperature measured directly with a thermocouple.

See also the following:

11A655. Prediction of pressure drop for incompressible flow through screens

11A658. Reconstruction of 3D particle trajectories in flows through curved circular tubes

VI. HEAT TRANSFER

400. Thermodynamics

11A777. Numerical modeling of turbulent flow and heat transfer in rotating cavities. - R Schiestel, L Elena, T Rezoug *(Inst Mec des Fluides Marseille IM2, Unite Mixte CNRS 34, 1 Rue Honnorat, 13003 Marseille, France)*. Numer Heat Transfer A 24(1) 45-65 (Jul-Aug 1993).

The present work considers the numerical modeling of turbulent flow in rotating cavities with a radial imposed flux and a preliminary examination of heat transfer prediction. Two turbulence models are studied: the standard κ-ε low-Reynolds-number approach and a zonal approach using second-order algebraic stress model in the core region adapted to rotating flows. The computational procedure is based on a finite volume method. Predictions are compared with experimental data in the literature. The results bring to light the importance of a detailed near-wall treatment in order to properly capture the Ekman layer region. Second-order modeling seems to be necessary to attain a wider practical value, particularly in the presence of recirculation zones and 3D effects in strong rotation.

11A778. Geometrical aspect of symmetric conservative systems of partial differential equations. - S Piekarski *(Inst of Fund Tech Res, Polish Acad of Sci, Warszawa, Poland)*. Arch Mech 44(5-6) 603-614 (1992).

In mathematical physics, one often encounters systems of the first-order conservation laws which imply the additional conservation law and, as their special cases, symmetric conservative and symmetric hyperbolic systems. In particular, systems of the first-order conservation laws which imply the additional conservation are interesting from the point of view of phenomenological thermodynamics, where the additional conservation law is interpreted as the entropy law. In this paper the geometrical description of such systems, based on the geometrical approach proposed by Peradzynski and Piekarski is discussed. It should be stressed that this description is different from that usually applied in the theory of conservation laws (HH Johnson). The applications of the discussed formalism to the symmetric systems are also mentioned.

See also the following:

11A837. Optimal experimental design for estimating thermal properties of composite materials

402. One phase convection

402B. FORCED CONVECTION (EXTERNAL)

11A779. Convection heat transfer of closely-spaced spheres with surface blowing. - C Kleinstreuer *(Dept of Mech and Aerospace Eng, N Carolina State Univ, Raleigh NC 27695-7910)* and H Chiang *(Thermofluid Tech Div, Indust Tech Res Inst, Chutung, Taiwan, ROC)*. Warme Stoffubertragung 28(5) 285-293 (May 1993).

A validated computer simulation model has been developed for the analysis of colinear spheres in a heated gas stream. Using the Galerkin FEM, the steady-state Navier-Stokes and heat transfer equations have been solved describing laminar axisymmetric thermal flow past closely-spaced monodisperse spheres with fluid injection. Of interest are the coupled nonlinear interaction effects on the temperature fields and ultimately on the Nusselt number of each sphere for different free stream Reynolds numbers ($20 \leq Re \leq 200$) and intersphere distances ($1.5 \leq j \leq 6.0$) in the presence of surface blowing ($0 \leq v_b \leq 0.1$). Fluid injection (ie, blowing) and associated wake effects generate lower average heat transfer coefficients for each interacting sphere when the Reynolds number increases ($Re > 100$). Heat transfer is also reduced at small spacings especially for the second and third sphere. A Nusselt number correlation for each interacting (porous) sphere has been developed based on computer experiments.

402C. FORCED CONVECTION (INTERNAL)

11A780. Computational study of coolant flow of liquid hydrogen through an externally heated duct. - RG Carlisle and HG Wood III *(Dept of Mech and Aerospace Eng, Univ of Virginia, Charlottesville VA 22903)*. J Thermophys Heat Transfer 7(3) 418-425 (Jul-Sep 1993).

The computational modeling of the 2D flow of liquid hydrogen coolant within the leading edge of the National Aerospace Plane engine structure is described. The model includes consideration of the effects of the variable thermophysical properties of hydrogen, axial conduction within the leading-edge material, and the coupling of the energy and momentum equations in the flow. The reduced Navier-Stokes equations are solved by parabolic marching of the discretized finite difference equations down the coolant passage. The importance of the consideration of the above factors was demonstrated as the calculated temperatures agreed with those predicted by earlier empirical methods for moderate heat transfers, but differed for the heat transfer magnitude of interest. The form of the expression of the solid-fluid interface condition was found to be an important factor in determining the accuracy and speed of convergence of the algorithm. The ability of the hydrogen coolant system to cool the incident heat load was found to be marginal: moderately increased incident heat loads would exceed the capabilities of the modeled system. Parametric studies were done to show the relative importance of the temperature, pressure, and velocity of the coolant fluid on the cooling capabilities of the system.

11A781. Convective heat transfer in a curved annular-sector duct. - G Yang and MA Ebadian *(Dept of Mech Eng, Florida Int Univ, Miami FL 33199)*. J Thermophys Heat Transfer 7(3) 441-446 (Jul-Sep 1993).

A numerical analysis of heat transfer behavior in a curved annular-sector duct is presented in this article. A uniform axial heat flux and constant peripheral wall temperature boundary condition are applied in this study. The effects of three major parameters on the heat transfer process (the axial pressure gradient, the dimensionless radius ratio, and the dimensionless curvature) are systematically studied. The results indicate that completely different temperature distribution patterns are evident among the segmented duct in different locations relative to the symmetric centerline. The Nusselt number significantly increases as the pressure gradient increases. Furthermore, an increase of the dimensionless curvature will also enhance heat transfer because of strong secondary flow. Finally, the results indicate that heat transfer is improved dramatically as the duct radius ratio decreases, especially when the duct radius ratio is smaller than 0.6.

11A782. Flow of supercritical hydrogen in a uniformly heated circular tube. - B Youn and AF Mills *(Dept of Mech, Aerospace and Nucl Eng, UCLA)*. Numer Heat Transfer A 24(1) 1-24 (Jul-Aug 1993).

Turbulent flow of supercritical hydrogen through a uniformly heated circular tube has been investigated using numerical methods, for the range of $4 \times 10^5 \leq Re \leq 3 \times 10^6$, $5 \leq q_w \leq 10$ MW/m^2, $30 \leq T_{in} \leq 90$ K, and $5 \leq P_{in} \leq 15$ MPa. The purpose is to validate a turbulence model and calculation method for the design of active cooling systems of hydrogen-fueled hypersonic aircraft, where the hydrogen fuel is used as coolant. The PHOENICS software package was used for the computations, which required special provision for evaluation of the thermophysical properties of the supercritical hydrogen, and a low Reynolds number form of the κ-ε turbulence model. Pressure drop and heat transfer data were compared with experiment and existing correlations, and good agreement was demonstrated. For the pressure range considered here a "thermal spike" was observed and shown to be due to the secondary peak in specific heat, rather than the primary peak.

11A783. Heat transfer and pressure drop of a transversely finned concentric annulus with longitudinal flow. - Yuanyue Jin, Changming Ling, Zhongqi Chen, Ye Tian *(Dept of Power Machinery Eng, Xi'an Jiaotong Univ, Xi'an 710049, China)*. Warme Stoffubertragung 28(5) 243-249 (May 1993).

The characteristics of heat transfer and pressure drop have been experimentally studied for the fully developed concentric annular flow with transverse fins normal to the flow direction by the naphthalene sublimation technique. Correlations for calculating the heat transfer coefficient with different inner diameters D_o of the outer tube are presented. A "characteristic Reynolds number" has been proposed, by which the predominant role of the transverse fins can be evaluated. It has been indicated that the inner diameter D_o has much more effect on pressure drop than on heat transfer. The effect of D_o on the overall performance is also compared under the same flow velocity or flow rate. It has been found that the effect of developing flow on heat transfer is significant and should be taken into account during experiment.

402D. NATURAL CONVECTION (EXTERNAL)

11A784. Effect of blowing or suction on laminar free convective heat transfer on flat horizontal plates. - HJH Brouwers *(Dept of Civil Eng and Man, Univ of Twente, PO Box 217, 7500-AE Enschede, Netherlands)*. Warme Stoffubertragung 28(6) 341-344 (Jun 1993).

In the present paper laminar free convective heat transfer on flat permeable horizontal plates is investigated. To assess the effect of surface suction or injection on heat transfer a correction factor, provided by the film model (or "film theory"), is applied. Comparing the film model predictions with numerical results of previous boundary layer analysis yields good agreement for a wide range of dimensionless transpiration levels.

402E. NATURAL CONVECTION (ENCLOSURES)

11A785. Comparison of natural convection of water and air in a partitioned rectangular

enclosure. - Jamil A Khan and Guang-Fa Yao *(Dept of Mech Eng, Univ of S Carolina, Columbia SC 29208)*. Int J Heat Mass Transfer 36(12) 3107-3117 (Aug 1993).

A numerical solution comparing steady natural convection of water and air in a 2D, partially divided, rectangular enclosure is presented. Rayleigh numbers investigated range from 10^6 to 10^8, and the opening ratios studied are 0, 1/4, 1/6, and 1/8 respectively. To obtain a comparative study, Prandtl number of 7.0 (for water) and Prandtl number of 0.71 (for air) are used for the two working fluids. This study demonstrates that the conventional use of water to model air convection in partitioned enclosures gives reasonable heat transfer results. The average Nusselt number obtained for water is only 2 ~ 5% larger than that for air at the same conditions. The flow configuration and exchange flow rates for water and air are, however, different. The exchange flow rate for water is found to be 10 ~ 20% larger than that for air. It is observed that for the opened partition the average Nusselt number is 13 ~ 24% larger than that for unopened partition. On the other hand, an opening in the partition reduces the exchange volume flow rates by 5.68 ~ 15.2% for water and 1 ~ 11.4% for air, depending on the Rayleigh number and the opening ratio.

11A786. Conjugate natural-convection-conduction heat transfer in enclosures divided by horizontal fins. - CJ Ho and JY Chang *(Dept of Mech Eng, Natl Cheng Kung Univ, Tainan Taiwan ROC)*. Int J Heat Fluid Flow 14(2) 177-184 (Jun 1993).

This article presents a numerical study concerning conjugate heat transfer across a vertical rectangular water-filled enclosure divided by multiple horizontal fins. The objective of the study is mainly to explore the effects of the conducting horizontal fins on heat transfer due to conjugate natural convection-conduction in the finned enclosure. Numerical results via a finite-difference method for the governing differential equations of the problem considered have been obtained for two different conductive fins with Ra = 10^3 to 10^7, AR = 1, 5, 8, and 10, N = 1 to 4, and t = 0.00001 to 0.125. The results demonstrate that the feasibility and effectiveness of using horizontal fins to enhance heat transfer across a vertical rectangular enclosure depend strongly on the aspect ratio, the Rayleigh number, the thermal conductivity, and the number of fins in the enclosure.

11A787. Laminar free convection in a nonrectangular inclined cavity. - GN Facas *(Dept of Mech Eng, Trenton State Col, Trenton NJ 08650)*. J Thermophys Heat Transfer 7(3) 447-453 (Jul-Sep 1993).

Numerical calculations are presented for 2D natural convection flow in a nonrectangular inclined cavity. The governing equations in the stream function-vorticity formulation are solved using finite differences. Arakawa's differencing scheme is used to represent the convection terms. Flow characteristics are investigated for Grashof numbers and inclination angles in the range of 9.0 $\times 10^3$ to 1.25×10^5, and -30 to 30° (from the vertical), respectively. A multicellular flow structure is found to exist for all angles of inclination considered. Although steady-state solutions were achieved for all Grashof numbers and angles of inclination considered, the flow structure that was predicted (steady vs unsteady) was found to depend strongly on the initial condition and, in some cases, unsteady flows were predicted if the "wrong" initial condition was specified.

11A788. Laminar natural convection in a horizontal rhombic annulus. - F Moukalled, H Diab *(Fac of Eng and Architec, American Univ, Beirut, Lebanon)*, S Acharya *(Dept of Mech Eng, Louisiana State Univ, Baton Rouge LA 70803)*. Numer Heat Transfer A 24(1) 89-107 (Jul-Aug 1993).

This paper presents the simulation of heat transfer and flow patterns in an enclosure between two isothermal concentric cylinders of rhombic cross sections. Four different values of the enclosure gap (E_g = 0.875, 0.75, 0.5, and 0.25) and three different rhombic angles (Ω = 10°, 20°, and 30°) are considered. At low Rayleigh numbers (10^3-10^5) the flow is weak and conduction is the dominant mode of heat transfer. Convection plays a key role starting at higher Rayleigh numbers (10^6-10^7). For all cases studied, there is no tendency for flow separation at the horizontal corners. The flow strength is found to increase with increasing rhombic angle, increasing enclosure gap, and increasing Rayleigh number. The critical Rayleigh number at which the heat transfer is influenced by convection decreases with increasing gap values and increasing rhombic angle; it is as high as 10^6-10^7 for E_g = 0.25 and decreases to about 10^4, for E_g = 0.875.

11A789. Laminar natural convection in internally finned horizontal annuli. - JC Chai and SV Patankar *(Dept of Mech Eng, Univ of Minnesota, Minneapolis MN 55455)*. Numer Heat Transfer A 24(1) 67-87 (Jul-Aug 1993).

An analysis is made of laminar natural convection in two internally finned horizontal annuli. The governing equations were solved numerically by a control-volume-based finite difference method. Information about the flow patterns and temperature distributions is presented through velocity vectors, streamlines, and isotherm plots. The effects of Rayleigh number and fin height on the Nusselt numbers are presented for two selected fin orientations. Variations of the local Nusselt numbers along the inner cylinder are also presented. In the cases studied, orientations of the internal fins are found to have insignificant effects on the average Nusselt number.

11A790. Numerical study of laminar and turbulent natural convection in an inclined square cavity. - RA Kuyper, TH van der Meer, CJ Hoogendoorn, RAWM Henkes *(Fac of Appl Phys, Univ of Tech, Lorentzweg 1, 2628 CJ Delft, Netherlands)*. Int J Heat Mass Transfer 36(11) 2899-2911 (Jul 1993).

Two-dimensional numerical simulations of the natural convection flow of air in a differentially heated, inclined square cavity were performed for both laminar and turbulent flows. The angle of inclination of the cavity was varied from 0° (heated from below) to 180° (heated from above). For Rayleigh numbers between 10^4 and 10^{11} the natural convection flow has been calculated. A detailed analysis was made for Rayleigh numbers of 10^6 and 10^{10}. The standard κ - ε model for turbulence was used in the prediction of turbulent flows. Numerical predictions of the heat flux at the hot wall and the influence of the angle of inclination on the Nusselt number are presented. The Nusselt number shows strong dependence on the orientation of the cavity and the power law dependence on the Rayleigh number of the flow. Flow patterns and isotherms are shown to give greater understanding of the local heat transfer. For the high Rayleigh number calculations hysteresis of the solution was found at a transient of flow patterns.

11A791. Scaling of the laminar natural-convection flow in a heated square cavity. - RAWM Henkes and CJ Hoogendoorn *(JM Burgers Centre for Fluid Mech, Fac of Appl Phys, Delft Univ of Tech, PO Box 5046, 2600 GA Delft, Netherlands)*. Int J Heat Mass Transfer 36(11) 2913-2925 (Jul 1993).

The steady laminar natural-convection flow of air and water in a square heated cavity is calculated for increasingly large Rayleigh number. The flow is calculated by solving both the Navier-Stokes equations and the boundary-layer equations. The results are used to determine the proper scalings of the flow in the different asymptotic flow regions: vertical boundary layers, core region, corner region and horizontal boundary layers. In particular the scalings according to the Navier-Stokes equations agree with the asymptotic model for the core and vertical boundary layers as proposed by Gill.

11A792. Transition to time-periodicity of a natural-convection flow in a 3D differentially heated cavity. - RJA Janssen, RAWM Henkes, CJ Hoogendoorn *(JM Burgers Centre, Dept of Appl Phys, Univ of Tech, PO Box 5046, 2600 GA Delft, Netherlands)*. Int J Heat Mass Transfer 36(11) 2927-2940 (Jul 1993).

The steady and time-periodic flow of air in a differentially heated cubical cavity has been studied numerically, using the finite-volume method. In the steady flow regime, the scaling in the boundary layer along the wall has been investigated. In the periodic flow regime, the calculated frequency was almost the same as for the 2D square cavity, suggesting that the same instability mechanism is in both cases responsible for the bifurcation. There was, however, a strong 3D in the distribution of the amplitude of the oscillations.

402F. THERMALLY UNSTABLE CONFIGURATIONS

11A793. Instability of radiation-induced flow in an inclined slot. - Wen-Mei Yang and Mou-Chang Leu *(Dept of Mech Eng, Natl Chiao Tung Univ, Hsinchu, Taiwan 30049, ROC)*. Int J Heat Mass Transfer 36(12) 3089-3098 (Aug 1993).

The instability of radiation-induced flow of a participating fluid in an inclined slender slot irradiated from one boundary is studied numerically for the inclination from 0° to 90°. The Eddington approximation is employed for the equation of transfer, and the pseudospectral method is used to solve the linearized perturbed equations. At an angle smaller than the transition angle the instability sets in as stationary longitudinal rolls. At an angle greater than the transition angle the instability occurs in the form of traveling transverse waves. The transition angle for the fluid of Pr = 0.71 is found to be minimum at the optical thickness near unity. Increasing optical thickness decreases the penetration of radiant energy, consequently increases the stability. The critical Rayleigh number increases rapidly with increasing the optical thickness as the optical thickness is greater than one.

11A794. Thermally unstable convection with applications to chemical vapor deposition channel reactors. - G Evans *(Comput Mech Div, Sandia)* and R Greif *(Mech Eng Dept, UCB)*. Int J Heat Mass Transfer 36(11) 2769-2781 (Jul 1993).

The 3D, thermally unstable flow and heat transfer of a gas have been studied in a horizontal channel with applications to chemical vapor deposition. The cases examined include flows that exhibit a longitudinal roll instability and a combination of both transverse, traveling waves and longitudinal rolls. Detailed results are presented for two values of the temperature ratio $\varepsilon = (T_1 - T_0)/T_0$ = 0.01 and 2.33 (helium), Grashof number $Gr = g\varepsilon H^3/\nu^2_0$ = 125,000, Prandtl number $Pr = \nu_0/\alpha_0$ = 2/3, aspect ratios L/H = 10 and W/H = 2. For ε = 0.01 and Reynolds number $Re = uH/\nu_0$ = 250, longitudinal rolls result whereas for Re = 100 a combination of transverse waves and longitudinal rolls occurs. For ε = 2.33 and Re = 100 the longitudinal roll instability is present.

402G. COMBINED NATURAL AND FORCED CONVECTION

11A795. Cool-down of a vertical line with liquid nitrogen. - A Hedayatpour *(Adv Program Dev and Prod Support, McDonnell Douglas Space Syst, 689 Discovery Dr, Huntsville AL 35806)*, BN Antar *(Dept of Eng Sci and Mech, Univ of Tennessee Space Inst, Tullahoma TN 37388)*, M Kawaji *(Dept of Chem Eng and Appl Chem, Univ of Toronto, ON, Canada)*. J Thermophys Heat Transfer 7(3) 426-434 (Jul-Sep 1993).

Analytical and numerical modeling is presented for predicting the thermofluid parameters of the cool-down process of an open-to-air vertical tube carrying liquid nitrogen. A two-fluid mathematical model is employed to describe the flowfield. In this model, four distinct flow regions were analyzed: 1) fully liquid, 2) inverted annular film boiling, 3) dispersed flow, and 4) fully vapor. These flow regimes were observed in an experimental investigation constructed for validating the mathematical model, and also in previous experiments by other investigators. For the single-phase regions, the 1D form of mass, momentum, and energy equations were used. For the two phase regions, the volume-averaged, phasic 1D form of conservation equations were applied. The 1D energy equation was formulated to determine the tube wall temparature history. The numerical procedure is based on the semi-implicit, finite-difference technique. The calculations for the inverted annular film boiling were performed implicitly. The computations for the tube wall, fully liquid, and dispersed flow regions were performed implicitly. The computations for the tube wall, fully liquid, and dispersed flow regions were performed explicitly. In each region, the appropriate models for heat transfer and shear stress rates are used. Results and comparisons of the predicted numerical models with the experimental data for several constant inlet flow rates of liquid nitrogen into a vertical, insulated tube are presented.

11T796. Correlation formulas for mixed convection heat transfer in saturated porous media. - DA Nield *(Dept of Eng Sci, Univ of Auckland, Auckland, New Zealand)*. Int J Heat Fluid Flow 14(2) 206 (Jun 1993).

11A797. Investigation of transient mixed convection heat transfer of cold water in a tall vertical annulus with a heated rotating inner cylinder. - CJ Ho and FJ Tu *(Dept of Mech Eng, Natl Cheng Kung Univ, Tainan, Taiwan 701, ROC)*. Int J Heat Mass Transfer 36(11) 2847-2859 (Jul 1993).

The transient buoyant rotating convective flow and heat transfer in a tall vertical annulus containing cold water near the density inversion have been investigated via a finite difference procedure. Simulations are carried out by solving axisymmetric Navier-Stokes equations adhering to the Boussinesq approximation coupled to the energy equation for an aspect ratio A = 8 and radius ratio RR = 2, two density inversion parameters $\theta_m = 0.4$ and 0.5, three Reynolds numbers Re = 50, 100, and 150, and varying Rayleigh number (up to 10^6). Numerical results demonstrate that the transient mixed convective flow and heat transfer may evolve into sustained oscillation over a certain range of Rayleigh number at given θ_m and Re; outside such unstable Ra-range, the transient evolution converges to steady-state solution. The transition into oscillatory convection arises at higher Rayleigh number with higher Reynolds number. Within the unstable convection regimes, simple as well as complex periodic oscillation, and chaotic oscillations have been detected. Moreover, the unstable Ra-ranges under fixed Re for $\theta = 0.5$ are found to be wider than those for $\theta_m = 0.4$, clearly reflecting the effects of the density inversion on the transient buoyant rotating convective flow and heat transfer in the wall vertical annulus.

11A798. Laminar mixed convection in a duct with a backward-facing step: The effects of inclination angle and Prandtl number. - B Hong, BF Armaly, TS Chen *(Dept of Mech and Aerospace Eng and Eng Mech, Univ of Missouri, Rolla MO 65401)*. Int J Heat Mass Transfer 36(12) 3059-3067 (Aug 1993).

Mixed convective heat transfer results for 2D laminar flow in an inclined duct with a backward-facing step are presented for both the buoyancy assisting and the buoyancy opposing flow conditions. The wall downstream of the step is maintained at a uniform heat flux, while the straight wall that forms the other side of the duct is maintained at a constant temperature equivalent to the inlet fluid temperature. The wall upstream of the step and the backward-facing step are considered as adiabatic surfaces. The inlet flow is fully developed and is at a uniform temperature. The effects of the inclination angle and Prandtl number on the velocity and temperature distributions are reported.

11T799. Mixed convection flow in a curved annulus: Effect of radius ratio. - SO Park and HK Choi *(Korea Adv Inst of Sci and Tech, Kusong-Dong Yusung-Ku, Taejon, Korea)*. Phys Fluids A 5(7) 1843-1845 (Jul 1993).

11A800. Mixed convection heat transfer in open ended inclined channels with discrete isothermal heating. - C Yucel, M Hasnaoui, L Robillard, E Bilgen *(Ecole Polytech, Univ of Montreal, CP 6079 St A, Montreal, PQ, H3C 3A7, Canada)*. Numer Heat Transfer A 24(1) 109-126 (Jul-Aug 1993).

A numerical study is carried out on mixed convection heat transfer (laminar natural and forced convection) in inclined open ended channels. The isothermal discrete heating elements are equally distanced and placed on one side, while isothermal conditions are imposed on the other. The governing equations are solved using the finite difference method. Normalized average and local Nusselt numbers are calculated as functions of the Rayleigh number ($10^3 \le Ra \le 10^5$), Reynolds number ($10 \le Re \le 50$), inclination angle ($0 \le \theta \le 90$), various heat sources ($0.1 \le A \le 1$), and various aspect ratios ($5 \le B \le 20$). These include, as limiting cases, horizontal and vertical positions. Flow and temperature fields for various cases are also produced.

11A801. Mixed convection in an inclined channel with a discrete heat source. - CY Choi and A Ortega *(Dept of Aerospace and Mech Eng, Univ of Arizona, Tucson AZ 85721)*. Int J Heat Mass Transfer 36(12) 3119-3134 (Aug 1993).

The effects of laminar forced flow on buoyancy-induced natural convection cells throughout the regions of natural, mixed, and forced convection have been numerically investigated for a parallel planes channel with a discrete heat source. Emphasis is placed on the influence of the inlet flow velocity and the inclination angle of the channel, and the local buoyancy induced by the discrete source. The results indicate that the overall Nusselt number of the source strongly depends on the inclination angle (γ) in the natural and mixed convection regimes when $\gamma > 45°$. On the other hand, the changes in Nu and $\theta_{s,max}$ are negligible when the channel is from 0 to 45°, there is no significant penalty in heat transfer due to the inclination of the channel up to $\gamma = 45°$. As Gr increases at a fixed Re, the entrainment of the air from the downstream exit is observed for the case of aiding flow.

11A802. Mixed convective flow with mass transfer in a horizontal rectangular duct heated from below simulated by the conditional Fourier spectral analysis. - I Hosokawa, Y Tanaka *(Dept of Mech and Control Eng, Univ of Electro-Commun, Chofu, Tokyo 182, Japan)*, K Yamamoto *(Natl Aerospace Lab, Chofu, Tokyo 182, Japan)*. Int J Heat Mass Transfer 36(12) 3029-3042 (Aug 1993).

With application to a horizontal chemical vapor deposition apparatus in mind, mixed convection and mass transfer in a horizontal rectangular duct heated from below are numerically investigated. The computer simulation is carried out based on the conditional Fourier spectral method recently developed by the authors. Unsteady flo... occurring at rather high Grashof ... highlighted as good conditi... fo... spanwise uniformities of ...-a... ture distribution ... time-... number dis... bottom.

402I. ROTATING FLUIDS OR SURFACES

See the following:

11A587. Fluid flow and heat transfer between finite rotating disks

11A686. Computation of convective heat transfer in rotating cavities

402L. NON-NEWTONIAN FLOWS

11A803. Forced convection heat transfer to an elastic fluid of constant viscosity flowing through a channel filled with a Brinkman-Darcy porous medium. - AV Shenoy *(Dept of Energy and Mech Eng, Shizuoka Univ, 3-5-1 Johoku, Hamamatsu 432, Japan)*. Warme Stoffubertragung 28(5) 295-297 (May 1993).

An analysis is presented of fully developed flow and heat transfer in a channel confined by two parallel walls subjected to uniform heat flux in a highly porous medium saturated with an elastic fluid of constant viscosity. The Brinkman-extended Darcy model is used for studying the effect of the boundary viscous frictional drag on the heat transfer characteristics. The approximate integral method is employed to obtain a solution.

402M. LIQUID METAL FLOWS

11A804. Low Prandtl number convection in layers heated from below. - V Kek and U Muller *(Kernforschungszentrum Karlsruhe, Inst Angewandte Thermo- and Fluiddyna, Postfach 36 40, W-7500 Karlsruhe 1, Germany)*. Int J Heat Mass Transfer 36(11) 2795-2804 (Jul 1993).

Experimental results are presented for the heat transfer across a horizontal layer of liquid sodium heated from below. The experiments show that up to a Rayleigh number of Ra ~ 7000 heat is mainly transferred by conduction for this low Prandtl number fluid. Beyond this threshold value the heat transport by convection increases significantly. For higher values of the Rayleigh number the measured Nusselt numbers follow a power law $Nu \sim Ra^{0.2}$ which is slightly smaller than the one predicted for the so-called flywheel convection as suggested by Jones *et al.*

11A805. Modeling of turbulent buoyant flow and heat transfer in liquid metals. - AA Mohamad and R Viskanta *(Sch of Mech Eng, Purdue)*. Int J Heat Mass Transfer 36(11) 2815-2826 (Jul 1993).

Turbulent convection in a cavity filled with low Prandtl number fluids is investigated. The cavity is either heated from below and cooled from above or heated differentially and the other connecting walls are assumed to be thermally insulated. Direct numerical simulations, and 2D and 3D low Reynolds number κ-ε turbulence models are used. It is shown that the turbulent Prandtl number equal to one or slightly greater than one produces useful results, regardless of the value of molecular Prandtl number. A correlation is suggested for the Nusselt number as a function of Ra Pr (Boussinesq number) for natural convection in a differentially heated cavity. The flow becomes turbulent for $Ra\,Pr > 4.8 \times 10^3$.

402P. TRANSPORT MECHANISMS

...06. **Impinging jet studies for turbulence ...ssessment I. Flow-field experiments.** - ...per, DC Jackson, BE Launder, GX Liao *...Mech Eng, UMIST, Manchester, UK)*. Int ... Mass Transfer 36(10) 2675-2684 (Jul

The paper reports an extensive set of measurements of a turbulent jet impinging orthogonally onto a large plane surface. Two Reynolds numbers have been considered, 2.3×10^4 and 7×10^4, while the height of the jet discharge above the plate ranges from two to ten diameters, with particular attention focused on two and six diameters. The experiment has been designed so that it provides hydrodynamic data for conditions the same as those for which Baughn and Shimizu have recently reported Nusselt number data (at Re = 23,000). In both experiments, before discharge the air passed along a smooth pipe sufficiently long to give fully developed flow at the exit plane of the jet - a feature that is helpful in using the data for turbulence-model evaluation. Hot-wire measurements have been made with pipes of nominally one-inch (26 mm) and four inches (101.6 mm) diameter. Data are reported of the mean velocity profile in the vicinity of the plate surface and also of the three Reynolds-stress components lying in the x-r plane. Computational results reported in a companion paper indicate a good degree of internal consistency between the mean and turbulent field data in the models predicting the mean flow poorly (or well) also predict the turbulence data poorly (well).

11A807. Impinging jet studies for turbulence model assessment II. An examination of the performance of four turbulence models. - TJ Craft, LJW Graham, BE Launder *(Dept of Mech Eng, UMIST, Manchester, UK)*. Int J Heat Mass Transfer 36(10) 2685-2697 (Jul 1993).

Four turbulence models are applied to the numerical prediction of the turbulent impinging jets discharged from a circular pipe measured by Cooper *et al*, Baughn and Shimizu and Baughn *et al*. They comprise one κ-ε viscosity model and three second-moment closures. In the test cases selected, the jet discharge was two and six diameters above a plane surface orthogonal to the jet's axis. The Reynolds numbers were 2.3×10^4 and 7×10^4, the flow being fully developed at the discharge plane. The numerical predictions, obtained with an extended version of the finite-volume TEAM code, indicate that the κ-ε model and one of the Reynolds stress models lead to far too large levels of turbulence near the stagnation point. This excessive energy in turn induces much too high heat transfer coefficients and turbulent mixing with the ambient fluid. The other two second-moment closures, adopting new schemes for accounting for the wall's effect on pressure fluctuations, do much better though one of them is clearly superior in accounting for the effects of the height of the jet discharge above the plate. None of the schemes is entirely successful in predicting the effects of Reynolds number. It is our view, however, that the main cause of this failure is the two-equation eddy viscosity scheme adopted in all cases to span the near-wall sublayer rather than the outer layer models on which the present study has focused.

11A808. Multiple jet impingement cooling. - MR Pais, LC Chow *(Dept of Mech Eng, Univ of Kentucky, Lexington KY 40506)*, ET Mahefkey *(Aerospace Power Div, Aero Propulsion and Power Lab. Wright R&D Center, WPAFB)*. J Thermophys Heat Transfer 7(3) 435-440 (Jul-Sep 1993).

Experiments were performed to study the effect of nozzle rotation, flow rate, degrees of subcooling, number of jets, and velocity on the heat flux in jet impingement cooling using deionized distilled water. The heat flux is a strong function of the flow rate and degree of subcooling, attaining a maximum value of the order of 600 W/cm^2 at the highest flow rates. The heat flux shows no significant dependency on velocity and number of jets for fixed flow rates. The rate of rotation shows no significant effects on the heat flux within the forced convective and early nucleate boiling region. At temperatures close to the critical heat flux the rotation retards the heat flux (compared with a stationary jet) diminishing it by 20%. Comparisons with published results are presented.

11A809. Ohmic heating of complex fluids. - A Ould El Moctar, H Peerhossaini *(Lab de Thermocinetique URA de CNRS No 869, ISITEM, La Chantrerie, CP 3023, 44087 Nantes, France)*, P Le Peurian *(EDF-DER Dept ADE, Centre des Renardieres, BP No 1, 77250, Moret sur Loing, France)*, JP Bardon *(Lab de Thermocinetique URA de CNRS No 869, ISITEM, La Chantrerie, CP 3023, 44087 Nantes, France)*. Int J Heat Mass Transfer 36(12) 3143-3152 (Aug 1993).

This paper describes the basic principles and physical modeling of systems based on the ohmic heating of liquids by passage of mains frequency electric current through the liquid itself, in order to heat it on a continuous flow regime. Preliminary numerical results for non-Newtonian fluids of Herschel-Bulckley type (Carbopol 940) are presented and the effect of natural convection, and shear and temperature dependence are emphasized.

402S. POROUS MEDIA

11A810. Conduction and convection heat transfer in composite solar collector systems with porous absorber. - M Mbaye and E Bilgen *(Ecole Polytech, CP 6079 St A, Montreal, PQ, H3C 3A7, Canada)*. Warme Stoffubertragung 28(5) 267-274 (May 1993).

Steady natural convection and conduction heat transfer has been studied in composite solar collector systems. The system consists of a glazing, a porous layer and a massive wall installed in a room. The heat transfer in this system is studied by assuming the glazing and the vertical bounding wall isothermal at different temperatures, two horizontal bounding walls adiabatic and porous layer without vents. The aspect ratio A was from 0.1 to 1.0 but the detailed study was carried out with A = 1. The thickness of the porous wall F_p varied from 1/3 to 1, while the solid wall thickness was kept constant. The conductivity ratio of porous layer was from 10^{-2} to 10^{-2}, Ra from 10^3 to 10^7. The results are presented in terms of thermal parameters as function of Ra and non-dimensional geometrical parameters. The isotherms and stream lines within the system are produced.

11A811. Natural convection and heat transfer in a vertical cavity filled with an ice-water saturated porous medium. - Xiaoli Zhang *(Dept of Mech Eng, Ecole Polytech, Montreal, PQ, H3C 3A7, Canada)*. Int J Heat Mass Transfer 36(11) 2881-2890 (Jul 1993).

A numerical study is made of natural convection and heat transfer in a rectangular porous cavity filled with an ice-water saturated porous medium. The two vertical sides of the cavity are cooled and heated at temperatures below and above the fusion point. The remaining sides of the cavity are assumed perfectly insulated. Special attention is focused on the influence of the heating temperature on the steady solutions. The Landau-transformation is used to immobilize the ice-water interface and the Darcy-Boussinesq equations are solved by the finite-difference technique. It is found that local maximum and minimum average Nusselt numbers occur at heating temperatures of 5 and 8°C, respectively. The melt region is wider at the bottom if the heating temperature is less than 8°C while the inverse is true for heating temperatures higher than 8°C. The 4°C isotherm is the boundary between the two counter-rotating flows at a heating temperature of 8°C only, otherwise the dominant flow crosses the 4°C isotherm and penetrates into the other layer as the heating temperature is higher than 4°C.

11A812. Natural convection in vertical porous enclosures due to prescribed fluxes of heat and mass at the vertical boundaries. - F Alavyoon *(Vattenfall Utveckling AB, S 810-70 Alvkarleby, Sweden)*. Int J Heat Mass Transfer 36(10) 2479-2498 (Jul 1993).

Unsteady and steady convection in a fluid-saturated, vertical and homogeneous porous enclosure has been studied numerically on the basis of a 2D mathematical model. The buoyancy forces that induce the fluid motion are due to cooperative and constant fluxes of heat and mass on the vertical walls. For the steady state, an analytical solution, valid for stratified flow in slender enclosures, is presented. Scale analysis is applied to the two extreme cases of heat-driven and solute-driven natural convection. Comparisons between the fully numerical and analytical solutions are presented for $0.1 \le R_c \le 500$, $2 \le Le \le 10^2$, $10^{-2} \le N \le 10^4$ and $1 \le A \le 10$, where R_c, Le, N and A denote the solutal Rayleigh-Darcy number, Lewis number, inverse of buoyancy ratio and enclosure aspect ratio, respectively. The numerical results show that for any value of Le > 1, there exists a minimum A below which the concentration field in the core is rather uniform and above which it is linearly stratified in the vertical direction. For sufficiently high aspect ratios, the agreement between the numerical and analytical solutions is good. The results of the scale analysis agree well with approximations of the analytical solution in the heat-driven and solute-driven limits. The numerical results indicate that for Le > 1 the thermal layers at the top and the bottom of the enclosure are thinner than their solutal counterparts. In the boundary layer regime, and for sufficiently high A, the thickness of the vertical boundary layer of velocity, concentration and temperature are shown to be equal, regardless of the value of Le.

See also the following:

11T796. Correlation formulas for mixed convection heat transfer in saturated porous media

402Y. COMPUTATIONAL TECHNIQUES

11A813. Natural convection in a cylindrical cavity heated by an internally-located strong source. - J Slomczynska *(Inst of Fund Tech Res, Polish Acad of Sci, Warszawa, Poland)*. Eng Trans 41(2) 187-208 (1993).

Stationary natural convection caused by a strong source of heat centrally located in a cylindrical cavity is analyzed by a finite-difference method. Since gradients of pressure are much smaller than gradients of both the temperature and density, the axisymmetric flow is treated as incompressible while, for the same reason, variable density is fully accounted for. Viscosity and thermal conductivity are assumed to be functions of temperature. Coupled stationary equations of continuity, motion, and energy are formulated in the framework of primitive variables. Line integration of the equation of motion over a closed contour is used to eliminate pressure. The solution, ie, temperature (hence, density) and velocity distributions in the cavity, is found by a two-step iterative procedure based on line successive over-relaxation. Examples of computation showing the effects of change in the source heat-rate, mean value of pressure and the aspect ratio of the cavity are provided.

404. Two phase convection

404H. FLOW BOILING, PEAK HEAT FLUX (EXTERNAL)

11A814. CHF mechanism in flow boiling from a short heated wall I. Examination of near-wall conditions with the aid of photomicrography and high-speed video imaging. - JE Galloway

(Cummins Engine, Columbus IN 47202) and I Mudawar *(Boiling and Two-Phase Flow Lab, Sch of Mech Eng, Purdue)*. Int J Heat Mass Transfer 36(10) 2511-2526 (Jul 1993).

Results of flow visualization experiments are presented to clearly identify the trigger mechanism for critical heat flux (CHF) in flow boiling. It is shown that discrete bubbles which form following the onset of nucleation coalesce into a wavy vapor layer at fluxes well below CHF. Depressions in the layer interface were observed to touch the heater surface periodically, painting a thin liquid sub-film on the surface beneath the vapor layer. This sub-film was consumed by a combination of vigorous boiling and interfacial evaporation. As CHF was approached, boiling became more concentrated toward the leading edge of the heater surface and around regions where the vapor layer interface touched the surface, while the remaining parts of the surface were dry. CHF was exceeded when severe vapor effusion from the sub-film normal to the heater surface lifted the wavy interface away from the surface, precluding any sustained wetting and resulting in a global dry-out.

11A815. CHF mechanism in flow boiling from a short heated wall II. Theoretical CHF model. - JE Galloway *(Cummins Engine, Columbus IN 47202)* and I Mudawar *(Boiling and Two-Phase Flow Lab, Sch of Mech Eng, Purdue)*. Int J Heat Mass Transfer 36(10) 2527-2540 (Jul 1993).

A theoretical CHF model is presented which is based upon the flow visualization of the wavy liquid-vapor interface near the heated surface as reported in Part I of this study. At approximately 90% of CHF, bubbles coalesced into a continuous wavy vapor layer and vigorous boiling was observed in a liquid sub-film beneath the vapor layer. This efficient boiling mechanism was transformed to boiling at isolated regions, wetting fronts, at approximately 95% of CHF. Wetting fronts were established when minimum points in the wavy vapor interface made contact with the heater surface. Regions surrounding the wetting fronts remained dry as the supply of liquid was consumed. CHF was triggered by intense vapor production which lifted the upstream wetting front away from the heater surface, cutting the supply of liquid locally and causing the heat flux to become more concentrated at the remaining wetting fronts. Soon after, remaining wetting fronts were also lifted from the heater surface and the surface temperature increased more rapidly. The new mechanistic CHF model incorporates classical interfacial instability theory for a confined 2D wave, a separated two-phase flow model and a criterion for separation of the liquid-vapor interface from the heater surface. The model predictions show good agreement with the experimental data.

404J. FILM BOILING (FLOW)

11A816. Similarity solution for laminar film boiling over a moving isothermal surface. - J Filipovic, R Viskanta, FP Incropera *(Heat Transfer Lab, Sch of Mech Eng, Purdue)*. Int J Heat Mass Transfer 36(12) 2957-2963 (Aug 1993).

Forced film boiling arises when a liquid flows over a highly superheated surface or when the surface moves through a liquid which is stationary or is itself in motion. As a result of the vapor layer separating the surface and the liquid, there is a significant reduction in the drag force and heat transfer. In this study, a similarity solution of the boundary layer equations is obtained, and for a wide range of subcooling parameters and surface velocities, related numerical results are shown to be in excellent agreement with predictions based on an integral method.

11A817. Vapor-film-unit model and heat transfer correlation for natural-convection film boiling with wave motion under subcooled conditions. - Shigefumi Nishio and Hiroyasu Ohtake *(Inst of Indust Sci, Univ of Tokyo, 7-22-1 Roppongi Minato-ku, Tokyo 106, Japan)*. Int J Heat Mass Transfer 36(10) 2541-2552 (Jul 1993).

This report presents a heat transfer model and correlation of natural-convection film-boiling heat transfer with interfacial wave motion under subcooled conditions. First, the vapor-film-unit model developed for saturated film boiling in our previous report was extended to subcooled film boiling along inclined and vertical flat-plates and also around horizontal cylinders of large diameter. Next, based on the vapor-film-unit model, a general form of heat transfer correlation of film boiling with wave motion was developed. Comparisons with experimental data showed that the present heat transfer model and correlation can predict the effects of the fluid properties, liquid subcooling, wall superheat, the geometry, and the size of the heat transfer surface on film-boiling heat transfer with wave motion.

404L. TRANSITION BOILING

11A818. Second-order instability on an electrically heated temperature-controlled test section under forced convective boiling conditions. - XC Huang and G Bartsch *(Inst Energietech, TU Berlin, Marchstr 18, 1000 Berlin 10, Germany)*. Int J Heat Mass Transfer 36(10) 2601-2612 (Jul 1993).

During boiling experiments with electrically heated temperature-controlled test sections it was observed by many researchers that although stability conditions can be satisfied in the ordinary sense, wall temperature distribution may tilt over from one form to another quite different form near the CHF and the minimum film boiling conditions. The measured local boiling curves appeared to be discontinuous. By solving the heat conduction problem of the test section with a simplified continuous boiling topography as one of its boundary conditions it is shown that the discontinuous phenomena may be caused by the experimental construction rather than by boiling characteristics. Using an unsteady-state measurement system the two types of second-order instability are observed. Possible ways of getting a fully stable operation of the test section are proposed.

404M. CONDENSATION (STATIC VAPOR)

11A819. Condensation and evaporation of liquid droplets at arbitrary Knudsen number in the presence of an inert gas. - JB Young *(Whittle Lab, Univ of Cambridge, Madingley Rd, Cambridge CB3 0DY, UK)*. Int J Heat Mass Transfer 36(11) 2941-2956 (Jul 1993).

A new set of equations describing the growth and evaporation of stationary liquid droplets in a mixture of pure vapour and inert gas is presented. The equations, which model the heat and mass transfer between the droplet and its environment, are presented in a simple algebraic form and are suitable for practical calculations of droplet growth at any Knudsen number and at any concentration of inert gas. In particular, they are not restricted to the so-called \quasi-steady\rm regime of droplet growth when the droplet surface temperature has relaxed to its steady-state value. The physical model on which the theory is based is essentially that of Langmuir but some novel features are incorporated. Thus, the velocity distribution functions for vapour and inert gas molecules approaching the liquid surface are assumed to correspond to simplified Grad thirteen-moment distributions and this allows correct representation at a molecular level of the heat and mass fluxes at the outer edge of the Knudsen layer. In contrast to most simple models of condensation and evaporation, the theory predicts finite (as opposed to zero) temperature and vapour pressure jumps across the Knudsen layer in the continuum limit and shows that the former is directly proportional to the concentration of vapour present. The analysis also provides a physical interpretation for the origins of the *reversed temperature gradient phenomenon* in the Knudsen layer, an unusual feature predicted by more complex solutions of the Boltzmann equation itself. The transition from diffusion to kinetic control as the pure vapour limit is approached is also modeled by the theory which shows that the range of Knudsen numbers over which this occurs is of the same order as the mole fraction of inert gas present.

404O. EVAPORATION

11A820. Multicomponent droplet evaporation at intermediate Reynolds numbers. - M Renksizbulut and M Bussmann *(Dept of Mech Eng, Univ of Waterloo, ON, N2L 3G1, Canada)*. Int J Heat Mass Transfer 36(11) 2827-2835 (Jul 1993).

The convective evaporation of a binary hydrocarbon droplet (decane-hexadecane) in air at 1000 K and at a pressure of 10 atmospheres has been studied using numerical methods. All transient effects including droplet size and velocity variations, heat and mass transfer within the liquid phase, and thermophysical property variations with temperature and concentration in both phases are included in the analysis. As the rate controlling process, liquid phase mass transfer is examined in detail. It is demonstrated that the existing drag coefficient, Sherwood number, and Nusselt number correlations originally developed for single-component droplets can be used for multicomponent droplets as well.

11A821. Single droplet vaporization including thermal radiation absorption. - PLC Lage *(Dept of Chem Eng, COPPE-UFRJ, PO Box 68502, 21945 Rio de Janeiro, Brazil)* and RH Rangel *(Dept of Mech and Aerospace Eng, UC, Irvine CA 92717)*. J Thermophys Heat Transfer 7(3) 502-509 (Jul-Sep 1993).

Total hemispherical absorption distributions for n-decane and water droplets irradiated by a blackbody under spherically symmetric conditions are used in the calcualtion of transient droplet heating and vaporization. The gas model used is based on the extended film theory. Three liquid-phase models have been extended to include thermal radiation absorption. The results show that radiation absorption can be as important as, or more important than, the choice of liquid-phase model. Based on the effective-conductivity model, two dimensionless parameters expressing the ratios of radiation absorption and gas-liquid heat transfer to liquid conductive and convective heat transfer are defined. It is shown that the first parameter determines the droplet heating regime. Over 200 numerical calculations using the effective-conductivity model and various initial and ambient conditions have been performed for water and n-decane droplets. It is shown that the ratio of the 2D parameters evaluated at the initial time can be used to correlate and predict the radiation absorption influence on the droplet lifetime. All cases investigated correspond to the slow heating regime. Under the conditions analyzed, the nonuniformity of the radiation absorption has little effect on the overall droplet heating and vaporization process.

See also the following:

11A819. Condensation and evaporation of liquid droplets at arbitrary Knudsen number in the presence of an inert gas

404P. SURFACE TENSION EFFECTS

11A822. Role of surface tension and ellipticity in laminar film condensation on a horizontal elliptical tube. - Sheng-An Yang and Cha'o-Kuang Chen *(Dept of Mech Eng, Natl Cheng-Kung Univ, Tainan, Taiwan, ROC)*. Int J Heat Mass Transfer **36**(12) 3135-3141 (Aug 1993).

An analytical study is made into the process of heat transfer with the vapor condensation on a horizontal elliptical tube under the simultaneous effects of the forces of surface tension and gravity on the condensate film. Analytical expressions for both local condensate film thickness and heat transfer coefficient around the elliptical periphery have been derived under the effects of gravity and surface tension for various values of ellipticity, respectively. The dimensionless mean heat transfer coefficient - Nu for any ellipticity e and various Bond numbers Bo has been obtained; however, it is almost unaffected by surface tension force due to surface curvature changing. For special objects (vertical plate e = 1, circular tube e = O), the results are identical to some classical Nusselt-type solutions.

404R. SOLID-FLUID FLOWS

11A823. Interaction between liquid droplets and heated surface. - BI Nigmatulin, NI Vasiliev, VV Guguchkin *(Res Eng Centre, LWR Nucl Plants Safety, Bezymyannaya 6 142530 Elektrogorsk, Moscow Region, Russia)*. Warme Stoffubertragung **28**(6) 313-319 (Jun 1993).

In this paper, experimental methods and investigation results of interaction between droplets of different liquids and a heated surface are presented. Wetted area, contact time period and transition boundary from wetted to non-wetted interaction regimes are experimentally evaluated. A simple connection of the wetted area value and contact line period with the heat removal efficiency is shown.

11A824. Kinetic and heat transfer-controlled solidification of highly supercooled droplets. - M Epstein and HK Fauske *(Fauske & Assoc, 16W070 W 83rd St, Burr Ridge IL 60521)*. Int J Heat Mass Transfer **36**(12) 2987-2995 (Aug 1993).

An efficient integral profile computational method is used to solve the problem of the solidification of highly subcooled droplets. The effects of surface cooling by radiation and convection, interface crystallization kinetics and fully time-dependent heat conduction are included in the method. Particular attention is focused on the predicted drop surface temperature-time histories as these, together with available experimental luminosity-time traces for solidifying microspheres of Al_2O_3 and ZrO_2, are used to infer the coefficient of the kinetic law for Al_2O_3 crystallization - one of the crucial parameters in a recently proposed theory of underwater aluminum ignition.

404S. ELECTRIC FIELD EFFECTS

11A825. Magnetorheological control of heat transfer. - WI Kordonsky, SP Gorodkin, SA Demchuk *(AV Lukov Heat and Mass Transfer Inst, Acad of Sci, Minsk 220072, Belarus)*. Int J Heat Mass Transfer **36**(11) 2783-2788 (Jul 1993).

Results of experimental investigation of the effect of magnetic fields on thermal processes taking place in magnetorheological suspensions (MRS) are presented. It is shown that by varying the orientation and strength of the field it is possible to control heat transfer within a wide range. Anisotropy of the thermal conductivity of MRS is established. In the case of the field lines being co-directional with a heat flux, the thermal conductivity coefficient increases by about 70%, whereas with their normal relative orientation it decreases by about 50%. The effect of a rotating magnetic field on MRS shear flow in a gap causes an almost 15-fold enhancement of heat transfer. Heat transfer of a turbulent suspension flow in a channel is intensified by an order of magnitude on superposition of a homogeneous field, transversely to the channel axis, and is suppressed twice as much in the case of parallel orientation. Examples and recommendation for practical application of the regularities revealed are given.

404V. POROUS MEDIA

11A826. Two-phase mixture model of liquid-gas flow and heat transfer in capillary porous media I. Formulation. - Chao-Yang Wang and C Beckermann *(Dept of Mech Eng, Univ of Iowa, Iowa City IA 52242)*. Int J Heat Mass Transfer **36**(11) 2747-2758 (Jul 1993).

A model for two-phase transport in capillary porous media is presented, in which the two phases are viewed as constituents of a binary mixture. The conservation equations are derived from the classical separate flow model without invoking additional assumptions. The present formulation, owing to its analogy for conventional multicomponent mixture flow theories and to a considerable reduction in the number of the differential equations required for the primary variables, provides an alternative for the theoretical analysis and numerical simulation of two-phase transport phenomena in porous media. Several complicated problems such as boundary layer two-phase flows, conjugate two- and single-phase flows in multiple regions and transient flows are shown to become more tractable within the framework of this new formulation.

11A827. Two-phase mixture model of liquid-gas flow and heat transfer in capillary porous media II. Application to pressure-driven boiling flow adjacent to a vertical heated plate. - Chao-Yang Wang and C Beckermann *(Dept of Mech Eng, Univ of Iowa, Iowa City IA 52242)*. Int J Heat Mass Transfer **36**(11) 2759-2768 (Jul 1993).

The two-phase mixture model developed in Part I is applied to investigate a pressure-driven two-phase boiling flow along a heated surface embedded in a porous medium. The general governing equations in Part I for the transport of mass, momentum and liquid (constituent) mass for the two-phase mixture are simplified for the above system. The present formulation, owing to its strong analogy to the classical description of multicomponent convective flows, suggests that a thin capillary layer exists over the solid surface at high Peclet numbers and that the two-phase flow is confined only to this boundary layer. Using approximations analogous to the classical boundary layer theory, a set of boundary layer equations for two-phase flow is derived and solved by a similarity transformation. The resulting ordinary differential equations are numerically integrated using a combination of the Gear stiff method and a shooting procedure. Numerical results for the saturation field and the flow fields of the two-phase mixture and the individual phases are presented and discussed.

404Y. COMPUTATIONAL TECHNIQUES

11A828. Time-marching method for the prediction of 2D, unsteady flows of condensing steam. - AJ White and JB Young *(Dept of Eng, Whittle Lab, Univ of Cambridge, Madingley Rd, Cambridge CB3 0DY, UK)*. J Propulsion Power **9**(4) 579-587 (Jul-Aug 1993).

A time-accurate, 2D time-marching technique is presented which can predict unsteady phenomena in condensing steam flows. Conservation equations for the mixture are solved using a variation of a well-established Euler solver, while nucleation and droplet growth calculations are performed in a Lagrangian framework by tracking particle pathlines. A special averaging technique is used to retain a polydispersion of droplet sizes, necessary for the accurate modeling of the condensation processes, without consuming excessive storage or CPU time. The basic Euler solution technique has been validated by comparison with predictions from an independent source for the unsteady flow of air in a channel. The full scheme has been used to compute nucleating flows in convering-diverging nozzles for which agreement with experiment for both steady and unsteady cases is extremely good. All the results presented are for flows in nozzles for which experimental data are available, but the scheme may also be applied to turbine cascade geometries.

404Z. EXPERIMENTAL TECHNIQUES

11A829. Theory and measurement of local interfacial area using a four sensor probe in two-phase flow. - ST Revankar and M Ishii *(Sch of Nucl Eng, Purdue)*. Int J Heat Mass Transfer **36**(12) 2997-3007 (Aug 1993).

A theoretical foundation of the measurement method for the time averaged local interfacial area using a four sensor resistivity probe is presneted. Based on this theory, the four sensor resistivity probe was developed and employed to measure the interfacial velocity, local interfacial area concentration and void fraction in a vertical air-water cap bubbly flow. The four sensor probe measurements were checked against the global void measurement using a differential pressure. The results were very satisfactory. Theoretical profiles of the void fraction and interfacial area concentration were obtained using the pictures of cap bubbles. The theoretical predictions of the cap bubbles and the interfacial area concentration profiles compared very well with the four sensor data.

406. Conduction

406A. GENERAL THEORY

11A830. Transmittances and frequency characteristics of wave and diffusion heat transfer in the flat slab. - J Golebiowski and AJ Jordan *(Tech Univ, 15-893 Bialystok, Poland)*. Int J Heat Mass Transfer **36**(12) 3099-3105 (Aug 1993).

This paper on conduction heat transfer in a slab presents a frequency domain comparison between the usual diffusion model and a wave model which includes the effect of non-instantaneous heat propagation. This is accomplished using a transfer function approach. Additionally, transfer functions relating the temperature distribution to heat flux are presented for various cases. The limit frequency, f_{ij}, is developed as that frequency below which the difference between the diffusion model and the wave model is negligible. Above this frequency, the difference between the two models increases rapidly. The work of this paper is an essential generalization of various specific cases found in the previous literature. It also refers to previous papers written by the authors.

406C. TRANSIENT PROBLEMS

11A831. Heat conduction in a semi-infinite solid subject to time-dependent surface heat fluxes: An analytical study. - SM Zubair *(Mech*

Eng Dept, King Fahd Univ of Pet and Minerals, Dhahran 31261, Saudi Arabia) and MA Chaudhry *(Math Sci Dept, King Fahd Univ of Pet and Minerals, Dhahran 31261, Saudi Arabia)*. Warme Stoffubertragung **28**(6) 357-364 (Jun 1993).

A closed-form model for the computation of the transient temperature and heat flux distribution in the case of a semi-infinite solid of constant properties is investigated. The temperature and heat flux solutions are presented for time-dependent, surface-heat flux of the forms: (i) $Q_1(t) = Q_0(t/t\kappa)^{v-1}$, (ii) $Q_2(t) = Q_0\exp(-\lambda t)$, and (iii) $Q_3(t) = Q_0(t/t\kappa)\exp(-\lambda t)$, where λ is a real number and v is a positive real number. The dimensionless (or reduced) temperature and heat flux solutions are presented in terms of the Whittaker function, the generalized representation of an incomplete Gamma function $I_\alpha(b,x)$ which can also be expressed by the complementary error functions. It is also demonstrated that the present analysis covers some well known (classical) solutions as well as a family of new solutions for the heat transfer through a semi-infinite solid.

11A832. Transient heat conduction with uniform heat generation in a slab subjected to convection and radiation cooling. - N Onur and M Sivrioglu *(Dept of Mech Eng, Gazi Univ, 06570 Maltepe Ankara, Turkey)*. Warme Stoffubertragung **28**(6) 345-349 (Jun 1993).

A finite difference scheme with fourth-order Runge-Kutta method is employed to determine the unsteady state temperature distribution in a plane slab with uniform heat generation. The plane slab is insulated on one face and subjected to convective and radiative cooling at the other face. The plane slab has a uniform initial temperature and the ambient environment as well as the fluid temperatures are assumed to be constant. Heat conduction is considered to be 1D. Results are presented in dimensionless charts over a wide range of parameters.

11A833. Transient heat transfer from a solid sphere translating at low Reynolds number: Perturbation solution for low Peclet number. - SS Sadhal *(Dept of Mech Eng, Univ of S California, Los Angeles CA 90089-1453)*. Warme Stoffubertragung **28**(6) 365-370 (Jun 1993).

In this paper the heat transfer from a solid spherical particle translating at low Reynolds number is analytically examined for the limit of vanishing Peclet number. The temperature distribution within the solid sphere is treated as fully transient while the fluid phase is considered to be quasisteady. The temperature field in the dispersed phase is obtained by a singular perturbation expansion of the Acrivos-Taylor type. The time-dependence in the solid phase is handled by means of the Laplace transform. This approach allows the temperature and heat flux continuity conditions at the solid-liquid interface to be exactly satisfied. The solution in the time domain appears in the form of infinite series which have associated with them a set of eigenvalues for every order of the perturbation expansion. The Nusselt number to order Pe, however, depends only on the leading order eigenvalues. An analytical limit of the Nusselt number for large values of time is also obtained.

11A834. Two-dimensional linear transient inverse heat conduction problem: Boundary condition identification. - B Guerrier and C Benard *(URA 871 FAST, Natl Center for Sci Res, Batiment 502, Campus Univ, Orsay 91405, France)*. J Thermophys Heat Transfer 7(3) 472-478 (Jul-Sep 1993).

This article deals with the identification of unknown time- and space-dependent boundary conditions for systems driven by the heat equation. We first consider a 1D and single-input problem dealing with the identification of the time-dependent heat flux on one side of a 1D linear thermal wall, from temperature and heat flux measurements on the other side. We then focus on a quenching process; our interest is to identify the time- and space-dependent heat flux on the boundary of a metal piece from temperature measurements performed inside the material (2D geometry). Those inverse problems are solved by use of a regularization method, and the solution is obtained by minimization of a quadratic criterion. Because of the linearity of the input-output relationship, the solution of this minimization is derived from the linear quadratic optimal control theory (resolution of a nonstationary Riccati equation). The robustness of the method for very small signal-to-noise ratio is shown. In the 2D multi-input problem, the identification sensitivity to the localization of the measurement points is analyzed. In both cases, we consider input that are discontinuous in time, in order to show the method accuracy in the high-frequency domain.

See also the following:

11A23. FE analysis of the 3D transient temperature field in steam turbine casings

406F. ANISOTROPIC MEDIA

11A835. Discrete element method for composite media: 1D heat conduction. - S Hou, AC Cogley *(Dept of Mech Eng, Kansas State Univ, Manhattan KS 66506)*, A Sharma *(IBM Corp Res, Yorktown Heights NY 10598)*. Int J Heat Mass Transfer **36**(12) 3009-3016 (Aug 1993).

Green's functions for steady-state, 1D heat conduction for discretely inhomogeneous media are found by using an interactive principle. Exact solutions can therefore be expressed by Green's representation. An unsteady problem is solved numerically by treating the time derivative as a source term. The results demonstrate accuracy, stability, and efficiency.

11A836. Double conductivity media: A comparison between phenomenological and homogenization approaches. - JL Auriault and P Royer *(Lab Sols, Solides, Struct, Inst Mec, Lab Assoc CNRS, BP 53X, Grenoble Cedex, France)*. Int J Heat Mass Transfer **36**(10) 2613-2621 (Jul 1993).

The heat transfer model for the double conductivity medium is investigated. The medium is composed of two homogeneous materials which differ considerably in their conductivity characteristics. The aim of this paper is to compare the descriptions obtained by a phenomenological and a homogenization approach. The first one, which introduces two temperature fields, is shown to be inefficient for a large range of phenomena. The latter gives the rigorous description. The study enables us to improve the phenomenological description. It provides an approximation which is valid for the quasi-static conditions.

11A837. Optimal experimental design for estimating thermal properties of composite materials. - R Taktak, JV Beck *(Heat Transfer Group, Dept of Mech Eng, Composites and Struct Center, Michigan State Univ, E Lansing MI 48824-1226)*, EP Scott *(VPI)*. Int J Heat Mass Transfer **36**(12) 2977-2986 (Aug 1993).

Design of optimal transient experiments is needed for the efficient estimation of thermal conductivity and volumetric heat capacity of composite materials. One criterion for optimal experiments is minimization of the area (or volume) of the confidence region. The experimental designs are transient and involve both finite and semi-finite geometries with finite duration heating. Two cases are considered for the finite body: 1D heat conduction within cured composite materials and 1D heat conduction within composite materials undergoing curing. The optimal dimensionless heating and experimental times at the heated boundary and the optimal location of the temperatures sensors are determined.

11A838. Thermal diffusion in cyclic laminated composites: Spectral properties and application to the homogenization. - M Bouzidi and P Duhamel *(Lab Thermique, CNAM, 292 rue Saint-Martin 75141, Paris Cedex 03, France)*. Int J Heat Mass Transfer **36**(11) 2715-2723 (Jul 1993).

The eigenvalue problem associated with thermal diffusion studies in cyclic multilayered composites is considered. The transfer matrix of these walls can be made explicit with the help of Chebycheff's polynomials. This general property is exploited in a detailed study of the first group of eigenvalues in order to propose a homogenization process for these media. By this way it is possible to find a homogeneous medium which has approximately the same first eigenvalues as the actual multilayered composite. The application to a binary composite leads to an interpretation of the time scale of the homogenized medium. This example reveals a very good accuracy in the temperature calculations. A corrective term which takes into account the finite number of the pattern repetitions, when determining the physical characteristics of the homogenized wall, is at the origin of that remarkable accuracy.

406G. POROUS AND GRANULAR MATERIAL

11A839. Heat transfer in evacuated crinkled or embossed multilayer foil insulations. - K Georg Degen, S Rossetto, J Fricke *(Physikalisches Inst, Universitat, Am Hubland, D-8700 Wurzburg, Germany)*. J Thermal Insulation Build Envelopes 16 340-355 (Apr 1993).

Evacuated multilayer insulations with crinkled or embossed foils without spacers were investigated in a guarded hot plate apparatus. In order to quantify the heat transfer mechanisms as well a their interaction, temperature and dependent measurements of the total heat transfer coefficient were performed. The mean temperature was varied between 260 and 550 K. Important parameters were type, coating, and crinkling treatment of the foils as well as the number of foil layers at a given thickness. The radiative heat transfer contribution is characterized by an effective emissivity εx of the foils; εx is greater than the emissivity ε of the smooth foil depends on the ε as well as on the crinkling or embossing intensity. For 30 nm double-sided aluminized polyimide foils with $\varepsilon = 0.020$ at T = 300 K, effective emissivities of $\varepsilon x = 0.022$ to 0.040 were obtained. Foils with aluminum coating thickness $\delta < 30$ nm showed a much higher εx; for $\delta \approx 17$ nm and $\delta \leq 10$ nm, emissivities of $\varepsilon x \geq 0.05$ and $\varepsilon x \geq 0.18$, respectively, were determined.

11A840. Measured thermal resistance of frame walls with defects in the installation of mineral fibre insulation. - WC Brown, MT Bomberg, JM Ullett *(Build Performance Lab, Inst for Res in Construct, NRC (IRC-NRCC), Ottawa, ON, K1A 0R6, Canada)*, J Rasmussen *(Rockwool Int A-S, Hedehusene, Denmark)*. J Thermal Insulation Build Envelopes **16** 318-339 (Apr 1993).

Studies have shown that convective air flow can significantly reduce the thermal resistance of frame walls insulated with mineral fibre insulation (MFI). It has also been shown that convective air flow can be avoided if the MFI products are installed with at least one face against an air impermeable material. The evolution of MFI products has seen the introduction of products with small fibre diameters and lighter densities, and there is a dominance of the frame wall insulation market by friction fit products. The effect of these changes on the installed (field) performance of MFI products is unknown, as the effect of "minor" installation defects on the performance of frame wall insulation systems. This article examines, through a program of full scale laboratory measurements, the effect of corner installation defects and product density on the thermal resistance of frame walls insulated with MFI products.

406I. PHASE CHANGE (FREEZING, MELTING)

11A841. Freezing of aqueous sodium chloride solution saturated packed bed from a vertical wall of a rectangular cavity. - J Choi and R Viskanta *(Heat Transfer Lab, Sch of Mech Eng, Purdue)*. Int J Heat Mass Transfer 36(11) 2805-2813 (Jul 1993).

Freezing of an aqueous solid chloride (H_2O-NaCl) solution saturating a packed bed of glass spheres is investigated experimentally. Experiments are conducted on the hypoeutectic side, and the cold wall temperature is lower than the eutectic point. Spherical soda-lime glass beads 2.85 mm and 6 mm in average diameter constituted the packed bed. The effects of initial salt concentration, superheat and bead diameter are investigated. Three distinct regions came into existence during the freezing process. Supercooling was observed only at early times of the freezing process for an experiment with 5% initial salt concentration. However, small supercooling was observed throughout the freezing process for the 15% initial salt concentration experiment. Reheating of the mixture was intensified with an increase in the bead diameter, initial salt concentration, and near the vertical hot wall. At the end of the freezing process, remelting was observed only at the mush-liquid interface for the 10-15% initial salt concentration experiments. Flow visualization experiment and mush-liquid observations revealed natural convection in the upper part of the liquid region. An enriched and stratified fluid layer existed in the bottom of the liquid region. The intensity of natural convection was affected by both the Darcy and modified Rayleigh numbers.

11A842. Melting around a shaft rotating in a phase-change material. - AM Morega, AM Filip, A Bejan *(Dept of Mech Eng and Mat Sci, Duke Univ, Box 90300, Durham NC 27708-0300)*, PA Tyvand *(Dept of Agri Eng, Agri Univ, PO Box 5065, N-1432 As, Norway)*. Int J Heat Mass Transfer 36(10) 2499-2509 (Jul 1993).

In this paper we describe the thin-film melting of a block of solid phase-change material (the bearing) around a rotating cylinder (the shaft). We determine the relation between the force applied on the shaft and the speed with which the shaft migrates into the bearing, the relation between the applied force and the torque, and the angle between the applied force and the direction of migration into the bearing. The method is based on contact melting theory, which combines the Reynolds thin-film lubrication theory with an analysis of phase-change heat transfer in the melt. The paper addresses three limiting regimes of the contact melting phenomenon: (1) the long bearing with melting due to frictional heating in the melt layer; (2) the short bearing with melting due to frictional heating in the melt layer, and (3) the short bearing with melting due to a temperature difference imposed between the hot cylinder and the cold phase-change material.

11A843. Two-dimensional freezing of water filled between vertical concentric tubes involving density anomaly and volume expansion. - Charn-Jung Kim, Sung Tack Ro, Joon Sik Lee, Moo Geun Kim *(Dept of Mech Eng, Seoul Natl Univ, Seoul 151-742, Korea)*. Int J Heat Mass Transfer 36(10) 2647-2656 (Jul 1993).

Freezing of an initially superheated water filled with an axisymmetric enclosure is studied numerically. Simulation is carried out using a computational method recently developed by the authors to treat moving boundary problems in axisymmetric geometries. Emphasized is the influence of both volume expansion and density anomaly upon freezing via natural convection. Two distinctive types of thermal boundary conditions are identified and utilized to guide our efforts to investigate the freezing process. Due to the density anomaly of pure water, fluid flow direction reverses depending on the initial superheat of water and thereby the interface slope exhibits an inversion behavior. By assuming that the water does not flood over the ice surface, the volume-change-induced rise of ice formed results in a substantially curved surface. Effects of several parameters characterizing phase-change process of interest are investigated. Numerical results clearly reveal that freezing undergoes multiple stages and proceeds in a complicated manner especially when the water is superheated over the density-extremum temperature.

406Y. COMPUTATIONAL TECHNIQUES

11A844. Explicit vs implicit schemes for the spectral method for the heat equation. - GE Schneider and K Wittich *(Dept of Mech Eng, Univ of Waterloo, Waterloo, ON, Canada)*. J Thermophys Heat Transfer 7(3) 454-461 (Jul-Sep 1993).

Three different boundary condition enforcement and time-stepping formulations are detailed for the Chebyshev collocation spectral method. Application is made to the 1D heat equation with a saw-tooth initial condition and several boundary condition combinations. It is observed that for a small time step, the explicit time stepping-strong boundary condition implementation method and the implicit time-stepping method give essentially the same solutions for various numbers of collocation points. The explicit time-stepping and weak boundary condition enforcement scheme has significantly large error at low numbers of collocation points, and requires considerably more collocation points to achieve convergence. While implicit schemes can employ significantly larger time steps than can the explicit schemes, implicit schemes require some form of matrix inversion, and this can be costly. Conversely, the explicit schemes can exploit the use of fast transform techniques to economize each time-step solution, but stability considerations limit the size of the time step that can be employed. A series of parametric studies are conducted to assess the relative economies of explicit vs implicit time-stepping schemes. The 1D heat equation is used as the basis problem and Robin boundary conditions are considered. The maximum explicit time-step limit is determined and a correlation provided that includes the dependence on boundary condition parameter values.

11A845. Numerical analysis for hyperbolic heat conduction. - Han-Taw Chen and Jae-Yuh Lin *(Dept of Mech Eng, Natl Cheng Kung Univ, Tainan, Taiwan 701, ROC)*. Int J Heat Mass Transfer 36(11) 2891-2898 (Jul 1993).

A new numerical simulation of the hyperbolic heat conduction problem is investigated. The primary difficulty encountered in the numerical solution of such a problem is numerical oscillations in the vicinity of sharp discontinuities. In this work, it is shown that the hybrid technique based on the Laplace transform and control volume methods can successfully be applied to suppress these oscillations. The Laplace transform method is used to remove the time-dependent terms, and then the transformed equations are discretized by the control volume scheme. Various comparative examples involving a nonlinear problem with surface radiation and the hyperbolic heat conduction in a composite region are illustrated to verify the accuracy of the present method. Due to the application of the Laplace transform method, the present technique does not need to consider the effects of the Courant number on the numerical results.

11A846. Numerical solution of axisymmetric heat conduction problems using finite control volume technique. - BF Blackwell *(DMTS, Thermophys Dept 1553, Sandia)* and RE Hogan *(SMTS, Thermal and Fluid Eng Dept 1513, Sandia)*. J Thermophys Heat Transfer 7(3) 462-471 (Jul-Sep 1993).

A finite control volume technique is developed to solve 2D axisymmetric heat condition problems using an arbitrary quadrilateral mesh. In this technique, the integral form of the conservation of energy equation is applied to control volumes of finite size. The boundary conditions considered include specific flux, aerodynamic heating, convection, and radiation. Two example problems involving a specified heat flux boundary condition and a specified temperature in conjunction with a temperature-dependent source are presented to demonstrate quadratic convergence as the mesh is spatially refined. The temperature-dependent source problem is solved using both a rectangular and a skewed mesh; the method is capable of producing accurate results on both rectangular and skewed meshes. Numerical comparisons with a Galerkin FE code are also presented.

408. Radiation and combined modes

11A847. Improved thermal radiation extinction in metal coated polypropylen microfibers. - R Caps, MC Arduini-Schuster, H-P Ebert, J Fricke *(Univ Wurzburg, Am Hubland, 8700 Wurzburg, Germany)*. Int J Heat Mass Transfer 36(11) 2789-2794 (Jul 1993).

If polypropylen microfibers with 2-3 μm diameters are coated with aluminum the infrared extinction increases by a factor of 20 as compared to the non-coated fibers. This has been shown by Mie scattering calculations and infrared optical transmission and reflection measurements using an integrating sphere. Large infrared extinction is important for the reduction of thermal radiative heat transfer in low density insulations. Insulation systems with Al-coated polypropylen microfiber fleeces can be expected to provide the same excellent insulation performances as natural downs.

11A848. Optimum finned space radiators. - SS Kumar, V Nayak, SP Venkateshan *(Heat Transfer and Thermal Power Lab, Dept of Mech Eng, Indian IT, Madras 600036, India)*. Int J Heat Fluid Flow 14(2) 191-200 (Jun 1993).

The present study considers a space radiator with uniform area fins standing vertically on a nonisothermal parent surface to enhance heat transfer. The numerical study shows that the finned radiator exhibits an optimum number of fins for which the heat lost from the finned radiator is a maximum, for given values of N_{R-C}, N_{F-C}, ε, and r_{OPT}. The numerical data has been used to derive correlations, respectively, between the optimum heat loss ratio and the optimum fin number with the other influencing parameters. These formulas are useful to the designer for a quick calculation of the performance of the optimum configuration.

11A849. Inverse radiation problem in axisymmetric cylindrical scattering media. - MP Menguc and S Manickavasagam *(Dept of Mech Eng, Univ of Kentucky, Lexington KY 40506)*. J Thermophys Heat Transfer 7(3) 479-486 (Jul-Sep 1993).

A semianalytical technique has been developed to solve the inverse radiation problem in absorbing and scattering cylindrical media. The radiative properties in the medium are allowed to vary radially. Isotropic, linearly anisotropic, and Rayleigh scattering phase functions are considered, and both the first- and second-order scattering of radiation are accounted for in the analysis. The angular radiosity distribution obtained from the solution of the forward problem is employed as input to the inverse angle. A numerical inversion scheme is followed to determine the profiles of extinction coefficient in the single-scattering albedo. For an anisotropically scattering medium, the asymmetry factor is also recovered. It is shown that the method is simple and accurate, even though the inversion is limited to three- or four-layer media. This inversion procedure can easily be used in experiments to determine the effective radiative property distributions in cylindrical systems.

11A850. Monte-Carlo simulation of a radiative transfer problem in a random medium: Application to a binary mixture. - S Audic and H Frisch *(Lab DG Cassini, CNRS URA 1362 Observatoire de la Cote d'Azur, BP 229, 06304 Nice Cedex 4, France)*. J Quant Spectros Radiative Transfer 50(2) 127-147 (Aug 1993).

This paper considers monochromatic radiative transfer in a diffusive 3D random binary mixture. The absorption coefficient, along any line-of-sight is a homogeneous Markov process, which is described by a 3D Kubo-Anderson process. The transfer equation is solved numerically by Monte-Carlo simulations on a massively parallel computer (a Connection Machine) by attaching one or several photons to each processor. The implementation of the simulations on the machine is discussed in detail, in particular the association between photons and processors and the storage of the data concerning the photons and the realizations of the statistics. With a CM-2 having 8000 processors, it is possible, with an adequate strategy, to follow simultaneously millions of photons in hundreds of realizations and to reach optical thicknesses up to 100 with dispersions of order 10^{-2} for the reflection and transmission coefficients. The simulations are validated, in the case of the 1D rod geometry, by comparison with the exact analytical solution, constructed by averaging the solution of the non-stochastic problem (diffusion in a rod of given optical thickness) over the probability density of the optical thickness. The latter obeys a stochastic Liouville equation which is solved by a Green's function method. The influence of the dimension of the Kubo-Anderson process is studied for the case of a slab and it is shown that a slab consisting in a pile of layers (1D process) is more transparent than one which consists in a stack of lumps (3D process). A strategy for improving the efficiency of Monte-Carlo simulations, based on the distribution of the lengths of the individual steps of the photons, is presented and discussed.

11A851. Radiative transfer by the YIX method in nonhomogeneous, scattering, and nongray media. - Pei-feng Hsu *(Dept of Mech Eng, Univ of Texas, Austin TX 78712)*, Zhiqiang Tan *(Aerospace Eng and Eng Mech Dept, Univ of Texas, Austin TX 78712)*, JR Howell *(Dept of Mech Eng, Univ of Texas, Austin TX 78712)*. J Thermophys Heat Transfer 7(3) 487-495 (Jul-Sep 1993).

A numerical solution of the integral equation of radiative heat transfer using the YIX method involving a mixture of highly anisotropic scattering particles and a nongray absorbing gas is presented. To validate the 3D calculation, bench mark solutions are established on a model problem using a high-order accuracy method, the product integration method (PIM). Various effects, eg, the discrete ordinates sets, first integration point of the YIX quadrature, optical thickness of the medium, grid sizes, and spectral resolution on the accuracy of the 3D calculation are discussed. Results for 3D calculations are presented. For all cases, the pressure variation has less significant effect on the results than those by particle density or temperature variations. The 3D nonhomogeneous cases have different trends of variation in radiative flux and divergence due to their nonuniform particle density distribution and nonisothermal participating medium. The use of the YIX method with discrete ordinates for the multidimensional calculations of highly anisotropic scattering and spectrally-dependent medium is shown to be accurate and flexible.

11A852. Benchmark results for particle transport in binary non-Markovian mixtures. - Bingjing Su and GC Pomraning *(Sch of Eng and Appl Sci, 38-137 H Eng IV, UCLA)*. J Quant Spectros Radiative Transfer 50(2) 211-226 (Aug 1993).

Numerical benchmark results are reported for particle transport in a randomly mixed binary medium, with the stochastic mixing described by a variety of stationary and homogeneous renewal statistics. Such statistics are quantified by chord length distributions for the two immiscible components of the mixture. A simple Monte Carlo procedure is used to generate physical realizations of the statistics, and the transport equation is solved numerically for each realization. The ensemble-averaged solutions and certain variance results are obtained by appropriately averaging over a large number of such calculations. The geometry considered is the rod model of transport, in which particles are constrained to move along a single axis.

11A853. Combined conduction and correlated-radiation heat transfer in packed beds. - K Kamiuto, M Iwamoto, Y Nagumo *(Dept of Prod Syst Eng, Oita Univ, Dannoharu 700, Oita 870-11, Japan)*. J Thermophys Heat Transfer 7(3) 496-501 (Jul-Sep 1993).

A quasihomogeneous model for heat transfer in a plane-parallel packed bed of opaque spheres is presented. The proposed model takes into account the variable porosity distribution within a packed bed and the correlated radiative properties of packed spheres having gray diffuse surfaces. On the basis of the proposed model, combined conductive and radiative heat transfer through comparatively thin packed layers of cordierite spheres or oxidized steel spheres are analyzed numerically and the obtained results are compared with the experimental ones. Additionally, the adequacy of a simplified analytical formula for the total effective thermal conductivities of a packed bed is discussed. It is found that the detailed theoretical model accurately predicts the heat transfer characteristics and the temperature profiles of the plane-parallel packed beds, and the predictions derived from the approximate formula well-correlate with the present experimental data for the total effective thermal conductivities.

11A854. Measurement of local heat flow in flat evacuated glazing. - RE Collins, CA Davis, CJ Dey, SJ Robinson, J-Z Tang, GM Turner *(Sch of Phys, Univ of Sydney, Sydney 2006, Australia)*. Int J Heat Mass Transfer 36(10) 2553-2563 (Jul 1993).

A guarded hot-plate apparatus has been developed for measuring the local thermal conductance of flat evacuated glazing. Parasitic heat flows in the apparatus have been reduced to below an equivalent thermal conductance of 0.01 W $m^{-2} K^{-1}$. Techniques are described for determining the separate contributions to heat flow through the sample from pillar conduction, conduction through residual gas, and radiation. The accuracy of the measurement system is estimated to be better than ±2% and the reproducibility for sequential measurements is better than ±0.004 W $m^{-2} K^{-1}$ for a measurement area of approximately 1.7 cm^2.

See also the following:

11A793. Instability of radiation-induced flow in an inclined slot

11A821. Single droplet vaporization including thermal radiation absorption

11A832. Transient heat conduction with uniform heat generation in a slab subjected to convection and radiation cooling

11A839. Heat transfer in evacuated crinkled or embossed multilayer foil insulations

410. Devices and systems

410B. HEAT EXCHANGERS (RECUPERATOR)

11A855. Analytical solution for transient response of counter flow heat exchanger with finite wall capacitance. - DD Gvozdenac *(Inst of Thermal Energy and Process Eng, Univ of Novi Sad, 21000 Novi Sad, Yugoslavia)*. Warme Stoffubertragung 28(6) 351-356 (Jun 1993).

The Laplace Transform Method is applied to solve the transient response of the counter flow heat exchanger with finite wall capacitance problem. The mathematical model is based on three local energy balance equations which are solved assuming that only the fluid 1 inlet condition is perturbed (step change). As any counter flow problem could be reduced to an adequate integral equation, collocation method is used for solving such equation in the presented case. Results are given for the outlet temperatures of both fluids and temperature distributions for both fluids and the wall as an explicit analytical formula.

410D. EXTENDED SURFACES

11A856. Effect of dehumidification of air on the performance of eccentric circular fins. - H Kazeminejad, MA Yaghoubi, M Sepehri *(Dept of Mech Eng, Univ of Shiraz, Iran)*. Proc Inst Mech Eng C 207(C2) 141-146 (1993).

A theoretical analysis of the performance of cooling and dehumidifying an eccentric circular fin has been carried out. Numerical results for fin temperature distribution and fin efficiency were obtained for various ranges of physchometric conditions and compared with those of a dry fin. The effect of eccentricity on the fin efficiency was also investigated. It was found that the fin efficiency decreases as dehumidification or eccentricity is increased.

11A857. Performance analysis and optimization of convective annular fins with internal heat generation. - E Georgiou *(Dept of Mech Eng, Univ of Patras, Patras, Greece)* and P Razelos *(Dept of Appl Sci, College of Staten Island, CUNY, Staten Island NY 10301)*. Warme Stoffubertragung 28(5) 275-284 (May 1993).

An analysis of the thermal performance for convective annular fins, having a general trapezoidal profile and internal heat generation, is presented. The solution of the optimal problem is also given when either the heat dissipation rate or the volume of the fin is specified. The results are expressed in suitable nondimensional variables that are specified by the problem, and presented graphically. The effect of the fin's profile and thermal conductivity upon the optimum dimensions is discussed. It is shown that the presence of heat generation reduces the ability of the fin to convect heat. Furthermore, certain limiting values of the heat generation that may be imposed on the fin for a feasible optimization are also derived.

410E. OTHER AUGUMENTATION TECHNIQUES

11A858. Augmentative heat transfer in a vertical 2-pass tube through an air box by use of strip type inserts. - Shou-Shing Hsieh and Mao-Yu Wen *(Dept of Mech Eng, Natl Sun Yat-Sen Univ, Kaohsiung, Taiwan 80424, ROC)*. Int J Heat Mass Transfer 36(12) 3043-3057 (Aug 1993).

This work presents and discusses an experimental information of the augmentation of heat transfer in a vertical 2-pass tube through an air box by use of different inserts (strip type inserts-longitudinal strip, crossed-strip, and regularly interrupted strip in a crossflow heat exchanger. Flow visualization as well as the interferogram of the temperature field inside-outside the tube were made and analyzed. Correlations for Nusselt number and pressure drop factor are reported and comparisons of these results with those of smooth tubes are also discussed. In addition, the performance has been evaluated by two different criteria based on both constant pumping power and constant heat duty, which suggest the use of these inserts in certain ranges of the Reynolds numbers in the present crossflow heat exchanger.

11A859. Enhanced heat transfer in channels with staggered fins of different spacings. - MA Habib *(Mech Eng Dept, King Fahd Univ of Pet and Minerals, PO Box 1570, Dhahran 31261, Saudi Arabia)*, AM Mobarak, AM Attya, AZ Aly *(Mech Eng Dept, Faculty of Eng, Cairo Univ, Cairo, Egypt)*. Int J Heat Fluid Flow 14(2) 185-190 (Jun 1993).

The flow pattern and heat transfer across staggered fins inside a rectangular duct are presented. The influence of Reynolds number, fin spacing, fin material, and wall heat flux on local and average heat transfer coefficients are studied. Fin spacings ranged from 0.8 to 2.0 times the channel height. The fin height was 0.7 times the channel height. The investigated Reynolds number ranged from 8,000 to 18,000. The experimental results show that the flow must pass over three to six fins before it appears to be a thermally periodic, fully developed flow. The fins enhance the heat transfer significantly due to flow deflection and impingement upon the fins. Augmentation of heat transfer was obtained with increase in Reynolds number, thermal conductivity of fins, and decrease in fin spacing and wall heat flux.

11A860. Heat transfer enhancement in a serpentine channel. - B Snyder, KT Li, RA Wirtz *(Mech Eng Dept, Univ of Nevada, Reno NV 89557)*. Int J Heat Mass Transfer 36(12) 2965-2976 (Aug 1993).

Forced-convection heat transfer rates and pressure drops were measured in the thermally fully developed region of a serpentine channel over Reynolds numbers ranging from 250 to 10 000. The wall geometry was similar to #17.8-3/8W of Kays and London, but carefully designed to minimize the extent of flow separation. The spatially-periodic wall impingement currents and high shear stresses combined to make a more uniform streamwise variation in local heat flux compared with corrugated surfaces. On an equal-Re basis, the heated surface of the serpentine channel outperformed the baseline parallel-plate channel by about a factor of 9 in air and 14 in water. Thus wavy-walled channels may prove effective for enhancing heat transfer in laminar and transitional flow regimes.

11A861. Performance evaluation of a vortex generator heat transfer surface and comparison with different high performance surfaces. - U Brockmeier *(Inst Energeitech, Ruhr-Univ, Bochum, Germany)*, T Guentermann, M Fiebig *(Inst Thermo- and Fluiddyn, Ruhr-Univ, Bochum, Germany)*. Int J Heat Mass Transfer 36(10) 2575-2587 (Jul 1993).

A comparative assessment of five different heat transfer configurations for operation in compact heat exchangers is presented. The configurations under consideration are four standard heat exchanger surfaces - two plain fins, an offset strip and a louvered fin geometry - and one surface with so called vortex generators for heat transfer augmentation. In the case of the standard surfaces, the basic performance characteristics in the form of heat transfer and friction data versus the Reynolds number have been taken from published experimental results. In the case of the vortex generator surface, the performance characteristics have been derived from a numerical prediction of the flow and temperature field in a closely spaced parallel plate channel with vortex generators in the form of delta wings mounted on the channel walls. In comparison to the plain fin surface with a rectangular cross section, the vortex generator surface shows best performance characteristics allowing a reduction in heat transfer surface area of 76%, for fixed heat duty and for fixed pumping power.

410G. DRYING AND FREEZING

11A862. Advances in transport phenomena during convective drying with superheated steam and moist air. - P Perre *(ENGREF, 14 rue Girardet, 54042 Nancy, France)*, M Moser, M Martin *(LEMTA, URA CNRS n°875, av de la Foret de Haye 54516, Vandoeuvre, France)*. Int J Heat Mass Transfer 36(11) 2725-2746 (Jul 1993).

The latest developments in high temperature convective drying are presented. The process has been investigated experimentally and theoretically for two drying fluids; moist air and superheated steam, and for two materials: light concrete and softwood. The experimental investigation was made in an aerodynamic return flow wind-tunnel, using a new type of sensor which enables measurement of both temperature and pressure at the same point. The numerical model of heat and mass transfer developed over several years has been used to simulate the experimental test, in 1D for concrete and in 2D for softwood. Good agreement is obtained between the calculations and experiments. An analytical model taking into account the transfer mechanisms between the exchange surface and an assumed drying-front has also been developed, and enables the explanation of most of the phenomena observed, both in the experiments and the simulation. The main purpose of the present work was not only to determine the differences on the pressure and temperature fields, but also to give a good physical explanation for the moisture migration at temperatures when the wet bulb is other than the boiling point. Finally, it is shown that the process can be divided into three domains: (a) an initial drying period, where the medium is at the wet bulb temperature; (b) a second phase with stage more or less pronounced, at a temperature which depends on the air flow and on the material; and (c) a final stage, during which all the temperatures approach the dry bulb temperature.

410I. ENVIRONMENTAL CONDITIONING AND CONTROL

11A863. Comparative performance study of CFC502, HCFC22 and HCF125. - SM Sami, J Schnotale *(Mech Eng, Sch of Eng, Univ of Moncton, Moncton NB, E1A 3E9, Canada)*, JG Smale *(Du Pont Canada, Box 2200, Streetsville Mississauga, ON, L5M 2H3, Canada)*. Int J Energy Res 17(3) 143-151 (Apr 1993).

In the paper, the performance of HCF125 as an alternative to CFC502 and R22 is assessed under different operating conditions. Cycle characteristics, such as thermal capacity, coefficient of performance, pressure ratio, system pressures, temperatures, and compressor power are also discussed. Results obtained after extensive detailed experimental work indicate that the performance is degraded on using HCF125, relative to that obtained with HCFC22.

11A864. Residential space conditioning with solid sorption technology. - SV Shelton *(Sch of Mech Eng, Georgia Tech)*. Heat Recovery Syst CHP 13(4) 353-361 (July 1993).

Approximately 50% of residential energy use in the US is for space heating and cooling. The most popular type of system installed in US houses is a central air-circulating system combining a natural-gas-fired direct-air-heating furnace and an electric-driven vapor compression cooling system. Natural-gas-driven heat pump technology offers considerable benefits over these exciting technologies including a reduction in energy use, improved environmental impact, and reduced investment in electric power plant construction. However, over the past 30 years, more than 100 major natural-gas-driven heat pump development projects have been undertaken without a currently successful product. These past projects have focused on engine-driven vapor compression refrigeration cycles and liquid sorption refrigeration cycles. New solid sorption technology offers significant advantages over these engines and liquid sorption technologies. The fundamental advantages of solid sorption refrigeration technology in natural gas residential heat pumps are presented and the societal benefits over existing residential systems discussed.

11A865. Sorption refrigeration research at JPL-NASA. - JA Jones *(JPL)*. Heat Recovery Syst CHP 13(4) 363-371 (July 1993).

Since 1979, long-life, reliable heat-powered sorption refrigeration systems have been developed for spacecraft use at the JPL. JPL has successfully built and tested a series of cryogenic sorption refrigeration systems for spacecraft sensor cooling and is presently assembling a -263°C (10K) hydride sorption refrigerator, which will fly on the Space Shuttle in 1994. With the addition of novel regenerative heating techniques, this same technology has more recently been applied to design high efficiency, ground-based adsorption heat pumps. Using actual sorption isothermm data and detailed analytic thermal computer models, analysis has predicted that the cooling and heating COPs will be significantly better than for any other single stage, heat-powered heat pump. Specifically the cooling COP (COP_c) with the new regenerative system using ammonia is predicted to be as high as about 1.16. Recent tests on a signal carbon sorbent canister compressor have been performed with R22, R134a, and ammonia. Transient thermal response of the sorption compressor has compared well with computer predictions. With ammonia, the total amount of average cooling from the 0.51 kg bed of carbon has been measured to be about 1038 Btu h^{-1} (304 W) for a 6 min full cycle including both heating and cooling.

410L. THERMAL ENERGY STORAGE SYSTEMS

11A866. Thermal performance of roof evaporative cooling and floor coupled evaporatively cooled underground water storage tank systems. - MS Sodha, U Mahajan, RL Sawhney *(Sch of Energy Stud and Centre of Energy Stud and Res Dept, Devi Ahilya Univ, Indore-452 001, India)*. Int J Energy Res 17(2) 127-140 (Mar 1993).

The thermal performance of a room with two indirect evaporative cooling systems (operating independently and jointly) is analyzed. The two evaporative systems considered are a water-film roof evaporative cooling system, and an underground water storage tank beneath the floor of the room. The water in the tank is evaporatively cooled through a suitable aeration system. The performance of the room is analyzed in the hot-dry climate of Jodhpur and the composite climate of Delhi. It is found that the underground water storage system is marginally better than the roof evaporative cooling system for the Jodhpur and Delhi climates. A detailed parametric performance analysis of the room has also been carried out.

412. Thermomechanics of solids

11A867. One-dimensional quasi-static contact problem in linear thermoelasticity. - MIM Copetti and CM Elliott *(Sch of Math and Phys Sci, Univ of Sussex, Brighton BN1 9QH, UK)*. European J Appl Math 4(2) 151-174 (Jun 1993).

The existence, uniqueness and regularity of the solution to a 1D linear thermoelastic problem with unilateral contact of the Signorini type are established. A FE approximation is described, and an error bound is derived. It is shown that if the time step if $O(h^2)$, then the error in L^2 in the temperature and in L^∞ in the displacement is $O(h)$. Some numerical experiments are presented.

11A868. Computer simulation of thermo-mechanical fatigue of solder joints including microstructure coarsening. - P Hacke, AF Sprecher, H Conrad *(Mat Sci and Eng Dept, N Carolina State Dept, Raleigh NC 27695-7907)*. J Electron Packaging 115(2) 153-158 (Jun 1993).

Thermo-mechanical cycling (-30°/130°C) tests were performed on 63Sn37Pb solder joints with cycle periods of 12-48 min. The effect of phase (grain) size was incorporated into the integrated matrix creep damage concept to take into account the coarsening which occurred during the thermal cycling. It was thereby determined that failure (50% load drop) results at a total integrated matrix plastic strain (creep) of 1.39 and that the measured fatigue life is only 21% of that predicted assuming no coarsening. The coarsening during the thermo-mechanical cycling was in reasonable accord with the cubic coarsening law. However, it was more rapid than occurred during isothermal aging at zero stress.

11A869. Perturbation solution for thermal expansion buckling of no expansion joint slope pavement plate. - Jian-kang Chen *(Jiangsu Agri Col, Yangzhou, China)* and Ru-peng Wang *(Shanghai Col of Architec and Municipal Eng, Shanghai, China)*. Appl Math Mech 14(3) 277-284 (Mar 1993).

In this paper, the mechanical mechanism of thermal expansion buckling of no expansion joint slope pavement undergoing the action of a temperature field is analyzed. By using regular perturbation method, the formula of perturbation solution for this problem is derived, the relationship between critical laying temperature difference of slope pavement and of level straight pavement is studied, and the unified solution and its numerical results are also obtained. In terms of this research, rational laying temperature of no expansion joint slope pavement is given.

11A870. High temperature fracture toughness in silicon nitride and sialon. - Y Mutoh, N Miyahara, K Yamaishi *(Nagaoka Univ of Tech, Nagaoka-shi 940-21, Japan)*, T Oikawa *(NKK Corp, Kawasaki-ku, Kawasaki-shi 210, Japan)*. J Eng Mat Tech 115(3) 268-272 (Jul 1993).

Fracture Toughness of HIP-sintered silicon nitride decreased with increasing temperature up to 1200°C. The brittle-to-ductile transition was observed in the temperature range from 1200°C to 1275°C: the fracture toughness rapidly increased in the transition region. Above the transition temperature, the fracture toughness decreased with increasing temperature. Fracture toughness of sialon increased with increasing temperature. Transition of fracture mechanism was observed in sialon around 1300°C. The differences of temperature dependence of fracture toughness between two materials are interpreted in terms of the effects of grain-boundary glass phase on fracture.

11A871. Thermally induced stress intensity factor of a semi-circular surface crack in a half-space. - An-Yu Kuo, SS Tang *(Structural Integrity, 3150 Almaden Expressway, Ste 226, San Jose CA 95118)*, TP Yu *(Univ of Houston, Houston TX 77004)*. Int J Fracture 61(2) 101-122 (15 May 1993).

This paper presents thermal stress intensity factor solutions for a semicircular surface crack in a semi-infinite space, ie, a semicircular crack of radius a in a semi-infinite space $y \geq 0$. The cracked semi-infinite space is subjected to point heat sources with arbitrary time history $Q(t)$ at any points (x',y',z') in the region $y \geq 0$.

11A872. Formation of castings with complex geometry. Thermomechanical effects, growth and influence of the air gap. - JR Popov and IH Katzarov *(Inst for Metal Sci and Tech, Bulgarian Acad of Sci, Chapaev 53, 1574 Sofia, Bulgaria)*. Int J Heat Mass Transfer 36(11) 2861-2867 (Jul 1993).

In previous works we have proposed a method for mathematical modeling of the processes of heat and mass transfer in castings, which includes the construction of a boundary fitted coordinate system in a Riemannian coordinate space. Within this approach we obtain the deformations, stresses and strains in the casting-mould system within a linear thermoelastic model. The equations of stresses and deformations are derived from the corresponding laws of conservation in the coordinate space. Secondly, we consider the problem of heat transfer between the casting and the mould, while the boundary conditions change during the crystallization and formation of the crust due to the thermochemical interaction there. We describe the evolution of the air gap and consider its influence on the process of crystallization. Some consequences from this model, which may allow a more subtle description of the casting formation, like the segregation behavior in the two-phase region, are also discussed.

11A873. Predicting high temperature ultimate strength of continuous fiber metal matrix composites. - EJ Barbero *(Mech and Aerospace Eng Dept, W Virginia Univ, 315 Eng Bldg, Morgantown WV 26506-6101)* and KW Kelly *(Sci Appl Int, 1710 Goodridge Dr, McLean VA 22102)*. J Composite Mat 27(12) 1214-1235 (1993).

A model to predict the high temperature ultimate strength of a continuous fiber metal matrix composite (CFMMC) has been developed. The model extends the work of Rosen by including high temperature processes such as matrix creep, fiber-matrix debond, and the effects of randomly spaced fiber breaks which typically exist in the MMC prior to loading. A FE model (FEM), developed in the form of a representative volume element (RVE), is used to calculate the time-dependent stress field surrounding a fiber break. Variables included in the calculation are process-related parameters such as the fiber diameter, the fiber-matrix interface strength, and interface roughness. Statistical analysis is used to infer the strength of a large composite sample from the stress analysis of a single break provided by the FEM.

11A874. Linear birefringence changes in betaine phosphite crystal. - B Kosturek, J Przeslawski, Z Czapla *(Inst of Exp Phys, Univ of Wroclaw, Cybulskiego 36, 50-205 Wroclaw, Poland)*. Acta Phys Polonica A 83(6) 769-775 (Jun 1993).

Linear birefringence temperature changes are measured in the betaine phosphite crystal. The linear birefringence increments induced by antiferrodistortive, structural and ferroelectric phase transitions are analyzed. Temperature derivatives of the linear birefringences are shown for comparison. Critical exponents are determined for both transitions. The antiferrodistortive phase transition is close to a tricritical one.

See also the following:

11A121. Nonlinear thermoelastic solid with uniaxial wave propagation

11A268. Influence of cool-down temperature histories on the residual stresses in fibrous metal-matrix composites

11A307. Accuracy of turbine blade thermal analysis by elementary balance method

11A482. Analytical solutions of stresses in a cylindrical plate due to polynomial radial temperature distributions

414. Mass transfer

414D. DIFFUSION

11A875. Nonlinear functionals in existence theorems for reaction-diffusion systems. - B Kazmierczak *(Inst of Fund Tech Res, Polish Acad of Sci, Warszawa, Poland)*. Arch Mech 44(5-6) 557-562 (1992).

The notion of nonlinear functional is used to prove the existence of solutions for time-independent reaction-diffusion systems, in which nonlocal terms may occur and whose coefficients may depend on first derivatives.

See also the following:

11A42. On randomly interrupted diffusion

414E. CONVECTION WITH DIFFUSION

11A876. Convection-driven growth in fluctuating velocity field. - A Gadomski *(Dept of Polymer Phys, Silesian Univ, Sniezna 2, 41-200 Sosnowiec, Poland)* and J Luczka *(Dept of Theor Phys, Silesian Univ, Bankowa 14, 40-007 Katowice, Poland)*. Acta Phys Polonica B B24(4) 725-732 (Apr 1993).

The growth process of an initially ideal sphere in a convective fluctuation velocity field is considered. The influence of fluctuations of the velocity field on the growth process is examined.

11A877. Near-field solution for heat and mass transfer from buried nuclear waste canisters. - K Muralidhar *(Dept of Mech Eng, Indian IT, Kanpur-208 016, India)*. Int J Heat Mass Transfer 36(10) 2665-2674 (Jul 1993).

A numerical study of heat and mass transfer from cylindrical containers filled with nuclear waste and buried under the surface of the earth is reported here. For prescribed heat flux and leach rates the temperature and concentration distributions on the surface of the containers are determined under a variety of conditions. These conditions include the diffusion limit, the effect of superimposed flow, the multi-canister problem and radioactive decay of a parent-daughter chain. The equations governing unsteady transport are solved using a Galerkin FEM. Results using this method are compared with those obtained from boundary-layer analysis.

11A878. Spectral approximation to advection-diffusion problems by the fictitious interface method. - A Frati, F Pasquarelli *(Dept Matematica, Univ Cattolica, Brescia, Italy)*, A Quarteroni *(Dept Matematica, Politecnico di Milano, Milano, Italy)*. J Comput Phys 107(2) 201-212 (Aug 1993).

In this work we face the numerical approximation by spectral methods of advection-diffusion equations for convective dominated regimes. For either boundary and internal layer problems, it has been recently pointed out that effective methods can be based on dropping the viscous terms far from the thin layer. This yields a problem that couples two different model equations (one of hyperbolic type, the other one of parabolic type) through suitable matching conditions at subdomain interfaces. An extensive theory has been developed and effective algorithms have been derived. Here we apply this theory to spectral approximations to 2D steady problems. In particular, we investigate the issues of stability and convergence, and we propose effective algebraic solvers to face both the hyperbolic and elliptic problems.

See also the following:

11A802. Mixed convective flow with mass transfer in a horizontal rectangular duct heated from below simulated by the conditional Fourier spectral analysis

414F. DOUBLE DIFFUSION AND OTHER COMBINED EFFECTS

11A879. Inverse segregation for a unidirectional solidification of aluminum-copper alloys. - JH Chen and HL Tsai *(Dept of Mech and Aerospace Eng and Eng Mech, Univ of Missouri, Rolla MO 65401)*. Int J Heat Mass Transfer 36(12) 3069-3075 (Aug 1993).

A mathematical model has been developed to simulate the inverse segregation for a unidirectional solidification of Al-Cu alloys cooled from the bottom. It is found from the present study that the fluid flow of solute-rich liquid in the mushy zone caused by solidification shrinkage is the main driving force for the formation of inverse segregation. The predicted copper concentration in the solidified alloys is in good agreement with the published experimental data. Several interesting transient behaviors of solute redistribution in the mushy zone, which were not reported before, are also discussed.

11A880. Investigation of solutal convection during the dissolution of silicon in a sandwich system. - S Erbay, HA Erbay, N Djilali, S Dost *(Centre for Adv Mat and Related Tech and Dept of Mech Eng, Univ of Victoria, Victoria, BC, V8W 3P6, Canada)*. Int J Heat Mass Transfer 36(12) 3017-3027 (Aug 1993).

This paper considers natural convection due to solutal gradients during the dissolution of silicon in a substrate-solution-substrate "sandwich" system under isothermal conditions. This work is motivated by the need to understand the role of convection in liquid-phase epitaxial growth of semiconductor crystals. Unsteady 2D numerical simulations are presented for two dissolution experiments. Solutal convection is found to be predominant during the initial phase of the process and causes a rapid increase in the dissolution depths of both substrates. However, because convection is mostly confined to the lower half of the sandwich system, lower substrate dissolution depths are about twice as large. This result is in good agreement with available experimental data. Another interesting consequence of convection is the development of a wavy irregular surface along the lower substrate.

414I. POROUS MEDIA

11A881. Exact solution of coupled heat and mass transfer with double moving interfaces in a porous half-space Part 3. Effect of surface pressure and permeability on rates of sublimation and desorption. - S-W Peng *(Dept of Power Eng, Huazhong Univ of Sci and Tech, Wuhan, Hubei 430074, Peoples Rep of China)* and G-Q Chen *(Dept of Mech, Peking Univ, Beijing 100871, Peoples Rep of China)*. Int J Energy Res 17(3) 193-202 (Apr 1993).

Coupled heat and mass transfer with double moving interfaces, taking place in a porous half-space, is defined, and exact solutions for the temperature and moisture distributions, as well as the position of two moving fronts, are obtained. As in Part 2 of the paper, the interest is focused on the case of moderate vacuum environment pressure, where the moisture transfer is due to the result of the vapor concentration and pressure gradients. The temperature of sublimation is assumed to be unknown, whereas the temperature of desorption is still assumed to be known, and the pressure of desorption is determined by a linear assumption among pressures of sublimation, desorption and surface. The Clapeyron equation is incorporated on the sublimation front to close the equation system. The effects of the surface pressure and the permeability on the sublimation and desorption are analyzed. Conclusions are drawn on the basis of the results.

11A882. Heat and humidity transfer in non saturated porous media: Capillary hysteresis effects under cyclic thermal conditions. - CHA Molenda, P Crausse, D Lemarchand *(Inst de Mec des Fluides, Ave du Prof Camille Soula, 31400 Toulouse Cedex, France)*. Int J Heat Mass Transfer 36(12) 3077-3088 (Aug 1993).

An analysis of the influence of capillary hysteresis in the humidity migration in porous media is presented. Several situations have been considered: experimental and numerical study of transfer phenomena in porous media at impermeable boundaries, numerical simulation of the thermo-hydraulic behavior of the cellular concrete wall under cyclic thermal conditions. Effects of temperature on capillary properties and the relaxation time of the liquid flux by capillary effects, are also taken into account and studied.

11A883. Solidification of porous medium saturated with aqueous solution in a rectangular cell. - K Matsumoto, M Okada *(Dept of Mech Eng, Aoyamagakuin Univ, 6-16-1 Chitosedai Setagaya-ku, Tokyo 157, Japan)*, M Murakami *(Toshiba, 1-1-1 Shibaura Minato-ku, Tokyo 105-01, Japan)*, Y Yabushita *(Dept of Mech Eng, Aoyamagakuin Univ, 6-16-1 Chitosedai Setagaya-ku, Tokyo 157, Japan)*. Int J Heat Mass Transfer 36(11) 2869-2880 (Jul 1993).

Beads saturated with NaCl-solution used as porous medium were packed in a rectangular cell. The porous medium was solidified by cooling one of the vertical walls of the cell. The above solidification process was studied analytically and experimentally. The temperature and concentration distributions were measured for three kinds of beads and almost the same mean diameters. From both experimental and analytical results, the analysis, where permeability within the mushy region was expressed as the n-th power of the volume fraction of the liquid phase, was found to simulate approximately the solidification process. The characteristics of the solidification process were clarified herein.

414Y. COMPUTATIONAL TECHNIQUES

11A884. Eulerian-Lagrangian localized adjoint methods for linear advection or advection-reaction equations and their convergence analysis. - RE Ewing and H Wang *(Dept of Math, Univ of Wyoming, Laramie WY 82071)*. Comput Mech 12(1-2) 97-121 (Jun 1993).

In this paper, we develop Eulerian-Lagrangian localized adjoint methods (ELLAM) to solve the initial-boundary value problems for linear advection or advection-reaction equations. In contrast to many methods for advection-type problems, our ELLAM scheme naturally incorporates the inflow boundary conditions into its formulations and does not need an artificial outflow boundary condition. It does conserve mass. Moreover, optimal-order error estimates for ELLAM have been obtained. In contrast, many methods have only suboptimal-order estimates when applied to solve these problems. Furthermore, our ELLAM scheme provides a systematic approach to treat the interface problems of advection-type equations and can be naturally combined with domain decomposition and local refinement techniques to solve these problems. Numerical results in 1D and 2D are presented and discussed.

11A885. Spectrum enveloping technique for convection-diffusion computations. - VS Manoranjan and R Drake *(Dept of Pure and Appl Math, Washington State Univ, Pullman WA 99164-3113)*. IMA J Numer Anal 13(3) 431-443 (Jul 1993).

In a convection-diffusion equation, if the convection term is very dominant, the linear system of equations which result from either finite-differencing or finite elementing will not have a strictly diagonally dominant coefficient matrix. So, if one tries a standard iteration method (Jacobi or Gauss-Seidel) to solve the linear system of equations, the iteration matrix may not satisfy the spectral radius condition for convergence and hence no converging solution may be obtained. The problem can be overcome, under certain conditions, if one uses the two step iteration-spectrum enveloping procedure of de Pillis in the format of a Jacobi method. This paper extends the two step iteration-spectrum enveloping idea to a Gauss-Seidel format for a model convection-diffusion problem.

414Z. EXPERIMENTAL TECHNIQUES

11A886. Mass flow sensing with heat waves: The effect of gas pressure. - DK Lambert *(Phys Dept, General Motors Res and Env Staff, Warren MI 48090-9055)*. Int J Heat Mass Transfer 36(10) 2623-2634 (Jul 1993).

Two conceptual examples are given of mass flow sensors based on heat waves that have *exact* gas pressure self-compensation in uniform flow: one with a plane heat source through which the flow passes, and one with a line source. Both sensors ratio the heat wave amplitudes detected at equal distances upstream and downstream from the source. Heat wave fronts from either source expand symmetrically upstream and downstream. An automotive air flow sensor based on heat waves is also described and modeled. It is a microelectronic device on silicon. This sensor is approximately, but not exactly, self-compensated for pressure change.

416. Combustion

416B. FUNDAMENTALS

11T887. Coupled complex Ginzburg-Landau type equations in gaseous combustion. - DO Olagunju *(Dept of Math Sci, Univ of DE, Newark DE 19716)* and BJ Matkowsky *(Dept of Eng Sci & Appl Math, Tech Inst NWU)*. Stability Appl Anal Continuous Media 2(1) 32-58 (Mar 1992).

416C. IGNITION (THERMAL AND HETEROGENEOUS)

11A888. Computational and experimental study of a railplug igniter. - JL Ellzey, MJ Hall, X Zhao *(Dept of Mech Eng, Univ of Texas, Austin TX)*, H Tajima *(Dept of Mech Eng, Miyazaki Univ, Japan)*. Exp Fluids 14(6) 416-422 (May 1993).

The plasma plume generated by a new type of high energy igniter known as the railplug is examined. The railplug is a miniaturized railgun that has the potential for improving ignition characteristics of combustible mixtures in engines. The objective of the study is to gain an understanding of the characteristics of the plasma created by a transparent railplug and to validate a multidimensional computer simulation of the plasma and shock fronts. The nature of the plume emitted by the railplug was examined for three levels of electrical energy while firing into air at a pressure of 1 atm. The computer model is to be used to predict trends in railplug performance for various railplug designs, energies, and ambient conditions. The velocity of the plasma movement inside a transparent railplug was measured, as well as the velocity of the plume ejected from the cavity. A shock is produced at the initiation point of the arc and propagates down the cavity, eventually exiting the plug. The velocity of the shock was both measured experimentally and simulated by the model.

416D. LAMINAR FLAME PROPAGATION

11A889. Burning of a spherical fuel droplet in a uniform flowfield with exact property variation. - K Madooglu and AR Karagozian *(Dept of Mech Aerospace and Nucl Eng, UCLA)*. Combust Flame 94(3) 321-329 (Aug 1993).

An analytical and numerical model is developed for single droplet evaporation and burning in a convective flowfield. The model is based on the boundary-layer approach, and chemical reaction kinetics are represented by a one-step, finite-rate reaction mechanism, while variation of gas properties with temperature and gas composition is based on the kinetic theory of gases. Four droplet models differing in the degree of complexity concerning property variation and chemistry are compared. Comparisons are also provided with existing empirical correlations for convective droplet evaporation and burning.

11A890. Burning velocities of hydrogen-air mixtures. - GW Koroll, RK Kumar, EM Bowles *(AECL Res, Whiteshell Lab, Pinawa, MB, Canada)*. Combust Flame 94(3) 330-340 (Aug 1993).

Laminar and turbulent burning velocities of hydrogen-air mixtures have been determined in a 17-L vessel using the double-kernel technique for a range of hydrogen concentrations between 9% and 70% by volume. Over the range of mixtures investigated, simple empirical correlations yield laminar burning velocities that are in good agreement with those measured. A turbulent-burning-velocity correlation that includes the flame-generated turbulence produces burning velocities in good agreement with the values measured experimentally. The data and correlations for the hydrogen burning velocity are used in models to predict hydrogen combustion behaviour in enclosures containing hydrogen-air-diluent mixtures and in combustion systems that employ hydrogen as the fuel.

11A891. Compositional structure and the effects of exothermicity in a nonpremixed planar jet flame. - CJ Steinberger, TJ Vidoni, P Givi *(Dept of Mech and Aerospace Eng, SUNY, Buffalo NY 14260-4400)*. Combust Flame 94(3) 217-232 (Aug 1993).

Results are presented of direct numerical simulation (DNS) of a randomly perturbed compressible, spatially developing 2D planar jet under the influence of a finite rate chemical reaction of the type F + O → Product. The objectives of the simulations are to assess the compositional structure of the flame and to determine the influence of reaction exothermicity by means of statistical sampling of the DNS generated data. It is shown that even with this idalized kinetics model the simulated results exhibit features in accord with experimental data. These results indicate that the Damkohler number is an important parameter in determining the statistical composition of the reacting field and that the results are not very sensitive to the mechanism by which this parameter is varied. It is demonstrated that as the intensity of mixing is increased and the effect of finite rate chemistry is more pronounced, the magnitudes of the ensemble mean and variance of the product mass fraction decrease and those of the reactants' mass fractions increase. Also, at higher missing rates the joint probability density functions of the reactants' mass fractions shift towards higher values within the composition domain, indicating a lower reactedness. These trends are consistent with those observed experimentally and are useful in portraying the statistical structure of non-equilibrium diffusion flames. The DNS-generated data are also utilized to examine the applicability of the "laminar diffusion flamelet model" in predicting the rate of the reactant conversion with finite rate chemistry. This examination indicates that the performance of the model is improved as the value of the Damkohler number is increased. Finally, the simulated results suggest that in the setting of a "turbulent" flame, the effect of the heat liberated by the chemical reaction is to increase the rate of reactant conversion. This finding is different from those of earlier DNS results and laboratory investigations that indicate a suppressed chemical reaction with increasing heat release.

11A892. Liftoff characteristics of methane jet diffusion flames. - JP Seaba *(Dept of Mech Eng and Aerospace Eng, Univ of Missouri, Columbia MO 65211)*, L-D Chen *(Dept of Mech Eng, Univ of Iowa, Iowa City IA 52242)*, WM Roquemore *(Aero Propulsion and Power Directorate, Wright Lab, WPAFB)*. J Propulsion Power 9(4) 654-656 (Jul-Aug 1993).

The mechanisms responsible for the liftoff from the burner rim and stabilization of the jet flames are not clearly understood. Early works studied the stability of jet flames in open air and identified four different regimes concerning flame stability. Of the four stability regimes 1) liftoff, 2) blowoff, 3) lifted, and 4) blowout, only the liftoff process will be studied in this Note. The liftoff condition is referred to the instant when the flame detaches from the burner rim in a discontinuous manner. After the flame detaches from the burner rim, it may stabilize at a downstream location (ie, lifted flame) or it may result in flameoff conditions (or the blowoff condition).

416F. FLAME STABILITY AND STABILIZATION

11A893. Feedback control of an unstable ducted flame. - TP Parr, E Gutmark, DM Hanson-Parr, KC Schadow *(Res Dept, Code 3892, Naval Air Warfare Center Weapons Div, China Lake CA 93555)*. J Propulsion Power 9(4) 529-535 (Jul-Aug 1993).

Active control of a naturally unstable ducted flame was realized using acoustic forcing of either the shear layer of the flame jet or the duct itself. The feedback signal was derived from either the duct pressure signal or the CH intensity (related to the flame heat release rate), and delayed in time to produce cancellation of the natural resonant oscillations of the system. Direct driving of the shear layer using the duct pressure signal feedback produced the best control with the lowest power requirements. The controller was able to reduce the acoustic power in the duct at the resonant frequency from 19 Pa to about 0.7 Pa, or nearly 30 dB. When operating in the controlled mode, the driving speaker is producing a sound pressure level more than three orders of magnitude below the natural duct uncontrolled level (both measured in the duct), so the effect is clearly not just acoustic cancellation.

11A894. Review of active control of combustion instabilities. - KR McManus *(Phys Sci, 20 New England Bus Center, Andover MA 01810)*, T Poinsot, SM Candel *(Lab EM2C du CNRS, Ecole Centrale Paris, 92295 Chatenay-Malabry, France)*. Prog Energy Combust Sci 19(1) 1-29 (Aug 1993).

Combustion instabilities in modern high-perfomance propulsion systems are often manifested
as large amplitude pressure oscill[illegible] nd can
result in serious performance [illegible] se
pressure oscillations are of [illegible]
lations in heat release as [illegible]
the combustor throug[illegible]
tween vari[illegible] n
been trac[illegible] n
compone[illegible] ed
oscillations. Other phenomena which can lead to unstable oscillations have been identified as well, these include naturally occurring hydrodynamic instabilities and convectively coupled oscillations. Due to their potential harm to system performance, it is often necessary to find ways to reduce the magnitude of these oscillations in the course of developing a new combustion system. Historically, the control and suppression of combustion instabilities has been achieved through hardware design changes. These modifications have included changes in the fuel delivery system, including feedlines and pumps, changes in the fuel injection distribution pattern, and modifications to the combustor or the combustor liner geometry. In general, these design modifications have been made in an attempt to change the resonant behavior of the combustion system so as to avoid the resonantly coupled oscillations which lead to combustion instability. In recent years, much attention has been focused on the control and suppression of combustion instabilities by actively and continously perturbng certain combustion parameters in order to interrupt the growth and persistence of resonant oscillations. The strategies used in this field of active control vary greatly in nature, both with respect to the theoretical basis for the control system and the system hardware which is employed. The purpose of this paper is to present a discussin of different methods which can be used to suppress combustion instabilities using active control, as well as to give a review of the work which has recently been performed in this area of combustion research.

416I. KINETICS AND MECHANISMS

11A895. Reduced kinetic mechanisms and their numerical treatment I. Wet CO flames. - W Wang and B Rogg *(Dept of Eng, Univ of Cambridge, Trumpington St, Cambridge CB2 1PZ, UK)*. Combust Flame 94(3) 271-292 (Aug 1993).

In the present article we investigate laminar, premixed freely propagating wet CO flames, ie, flames whose initial mixture contains small amounts of hydrogen and water vapor. Attention is focused on the derivation and validation of reduced kinetic schemes that provide both more computational efficiency in the calculation and the basis for asymptotic analysis of such flames. Specifically, a short detailed mechanism and systematically reduced three-step, two-step, and one-step mechanisms are derived that allow realistic predictions of burning velocities and flame structures over a wide range of stoichiometries. *Inner iteration* is discussed in detail and its *black box* character is identified. Also presented and discussed are numerical tricks for efficient use of reduced kinetic mechanisms in flame calculations. In particular, the so-called *partially explicit* numerical schemes are identified.

11T896. Review of chemical-kinetic problems of future NASA missions I. Earth Entries. - C Park *(NASA Ames Res Center, Moffett Field CA 94035)*. J Thermophys Heat Transfer 7(3) 385-398 (Jul-Sep 1993).

416J. UNSTEADY COMBUSTION AND COMBUSTION ACOUSTICS

11A897. Low-frequency combustion oscillations in a model afterburner. - MA Macquisten *(Combustion Dept, Rolls Royce, Filton, Bristol BS12 7QE, UK)* and AP Dowling *(Eng Dept, Cambridge Univ, Trumpington St, Cambridge CB2 1PZ, UK)*. Combust Flame 94(3) 253-264 (Aug 1993).

Low-frequency combustion oscillations, involving the interaction between longitudinal acoustic waves and unsteady combustion, are investigated for a model afterburner. An experimental rig, in which a confined flame is stabilized in the wake of a conical gutter, is run with inlet conditions representative of an engine afterburner. Results are presented for inlet Mach numbers in the range of 0.15-0.27, with inlet temperatures up to 630 K. Comparison is made between theory and experiment. Although the theory was developed from low Mach number data, it is found to apply equally well at these faster flow rates. The theory is able to predict the frequency of the instability and the mode shape, accurately reproducing the changes due to variations in the inlet Mach number and temperature.The effect of altering the downstream boundary condition by replacing the open end by a choked nozzle is also investigated. Such a change is found to be highly destabilizing, both experimentally and theoretically. Again, predictions from the theory are in good agreement with the observations.

416K. SUPERSONIC COMBUSTION

11A898. Research on supersonic combustion. - FS Billig *(Johns Hopkins Univ, Laurel MD 20723)*. J Propulsion Power 9(4) 499-514 (Jul-Aug 1993).

This paper is not at all representative of the complete body of the research on supersonic combustion. Instead, what is presented is primarily based on material with which the writer has had either direct involvement or a first-hand knowledge. It does not do justice to the exemplary works of many other investigators. Hopefully, this is somewhat rectified by the extensive list of references. The reader is encouraged to. consult these manuscripts to obtain a more balanced perspective. This applied research must be viewed from the perspective of the engineer who is charged with expediting development and is in need of design tools. Exact physics have frequently been abandoned to produce functional models. Much of the experimental verification upon which the models are based has been obtained in facilities which have known imperfections with respect to duplication of flight conditions. Moreover, compromises have been made in the analysis and interpretation of the experimental data, in part due to imperfect or incomplete diagnostic instrumentation, and in part due to a limited understanding of the underlying physics. An example that embodies all of these deficiencies would be a design model that is based on the use of integral techniques to describe combustion in supersonic flow from experiments conducted in an arc-heated tunnel.

416L. HETEROGENEOUS AND MULTIPHASE COMBUSTION

11A899. New results in the theory of filtration combustion. - AP Aldushin *(Inst of Struct Macrokinetics, Russian Acad of Sci, Chernogolovka, Russia)*. Combust Flame 94(3) 308-320 (Aug 1993).

Approximative analytical as well as numerical techniques have been used to study the propagation of a heterogeneous chemical transformation autowave in a dissociating system with filtration of a gas mixture containing an active reaction component. The interaction of heat and reaction waves combined with dissociation results in a complex two-front combustion wave structure with two reaction zones. For simple situations, practically important wave characteristics are estimated analytically. It is shown that filtration combustion of dissociating systems can concentrate energy in the reaction zone by transport gases from the hot product region to the reaction zone. This is referred to as the superadiabatic effect. In contrast to nondissociating system, in which the superadiabatic effect causes a temperature rise in the reaction zone, in dissociating system it causes a decrease in the depth of conversion to product.

416M. FLAME RADIATION

11A900. Total radiative heat loss in jet flames from single point radiative flux measurements. - YR Sivathanu *(Thermal Sci and Propulsion Center, Sch of Mech Eng, 125 Chafee Hall, Purdue)* and JP Gore *(Sch of Mech Eng, Purdue)*. Combust Flame 94(3) 265-270 (Aug 1993).

A method for estimating total radiant output of turbulent jet flames based on the measurement of radiative heat flux at a single location is reported. The radiative flux from a variety of jet flames was measured and plotted in normalized coordinates to establish the feasibility of this approach. In addition, the radiative flux from acetylene-air diffusion flames to representative detector locations, for two different burner geometries and flow conditions, was calculated using the Planck-averaged equation of transfer coupled with a multiray technique. The local temperature and soot volume fractions for the calculations were obtained from emission and absorption measurements. The normalized calculated heat flux for the two flames also collapse with the experimental data. This result shows that scalar property distributions combined with the appropriate view factor for the single location are the basis for the single point technique.

416O. COMBUSTORS AND AFTERBURNERS

11A901. Demonstration of mode transition in a scramjet combustor. - GA Sullins *(Appl Phys Lab, Johns Hopkins Univ, Laurel MD 20723)*. J Propulsion Power 9(4) 515-520 (Jul-Aug 1993).

Direct-connect combustor hardware has been assembled at the Avery Propulsion Research Lab of the Johns Hopkins University Applied Physics Lab to investigate a hydrogen-fueled scramjet combustor. The test hardware was designed to perform tests at simulated Mach 5 to Mach 8 flight conditions. This is done using a combustion heater with H_2 fuel and makeup O_2. The air, H_2 and O_2 flow rates are all supplied through computer-controlled digital values. This system allows rapid changes in conditions and very steady flow rates can be maintained throughout the test. Recently, tests were performed in which the flow rates were systematically varied during the test to simulate an acceleration from $M = 5.9$ to 6.2. During this acceleration the fuel-air equivalence ratio was held constant and the combustor transitioned from a dual mode ramjet with a precombustion shock system creating subsonic flow at the injection plane, to a scramjet with no precombustion shock system. The results of these tests are presented along with descriptions of the hardware and control systems.

11A902. Effects of momentum ratio on turbulent nonreacting and reacting flows in a ducted rocket combustor. - TM Liou, L Chen, YY Wu *(Natl Tsing Hua Univ, Hsinchu, Taiwan 300, ROC)*. Int J Heat Mass Transfer 36(10) 2589-2599 (Jul 1993).

A numerical study of turbulent nonreacting and reacting flows in a ducted rocket combustor with an ASM turbulence model and a finite-rate combustion model is reported. In addition, detailed measurements of flow velocities and turbulence parameters have been conducted by use of a four-beam two-color LDV system. Three different values of the ratio of fuel momentum to air momentum were selected to investigate its effects on the turbulent flow structure, mixing and combustion characteristics. It is found that the momentum ratio has strong effects on the number, size, and rotational direction of dome region recirculation zones, reattachment length, axial fuel-jet spreading rate, and penetration ability, flame temperature distributions and total pressure loss in the ducted rocket combustor. A useful correlation between the reattachment length and momentum ratio is derived. Moreover, a moderate value of the momentum ratio is recommended for better combustion performance and lower total pressure loss. The reported data are believed to provide valuable guidelines for practical design of combustors.

11A903. Flow measurements in a model burner Part 2. - DFG Durao, MV Heitor, ALN Moreira *(Dept of Mech Eng, Inst Superior Tecnico, Tech Univ of Lisbon, 1096 Lisboa, Codex, Portugal)*. J Fluids Eng 115(2) 309-316 (Jun 1993).

The isothermal swirling flow in the vicinity of a model oxy-fuel industrial burner is analyzed with laser Doppler velocimetry together with laser-sheet visualization. The burner consists of a central axisymmetric swirling jet surrounded by sixteen circular jets, simulating the injection of oxygen in practical burners. The results extend those obtained for non-swirling flows, and presented in Part I of this paper, to the analysis of the dependence of the mixing efficiency of the burner assembly upon the swirl motion of the central jet and have the necessary detail to allow to assess the accuracy of calculation procedures of the flow in industrial burners. It is shown that swirl attenuates the 3D structure typical of multijet flows in such a way that turbulence production and transport in the near burner zone are dominated by swirl-induced processes.

416P. SOLID FUELS

11A904. Global rates of devolatilization for various coal types. - S Niksa *(Mol Phys Lab, SRI Int, 333 Ravenswood Ave, Menlo Park CA 94025)* and Chun-Wei Lau *(High Temp Gasdyn Lab, Stanford)*. Combust Flame 94(3) 293-307 (Aug 1993).

This modeling study reports global rate expressions for transient weight loss and yields of tar and gas for coals across the rank spectrum. A novel kinetic analysis demonstrates that the Distributed Activation Energy Model (DAEM) reliability correlates transient weight loss at various heating rates, and makes reasonably accurate extrapolations for pulverized coal (p.c.) firing conditions. This performance motivates solutions of the DAEM for arbitrary thermal histories, including approximate closed-form solutions for transient weight loss along linear temperature ramps and exponential temperature histories. Our analysis also rigorously defines the rate constants in single first order reactions that give the same devolatilization rate as the DAEM at every instant in any thermal history. For devolatilization during heatup at constant rates, frequency factors increase by a factor of 6 for every order-of-magnitude increase in heating rate, while activation energies remain constant. Throughout convective heating, however, both rate parameters decrease continuously, so that straight lines on Arrhenius diagrams do not represent rate constants for coal devolatilization. Rate variations for different coal ranks are modest by comparison. For ranks from lignite to high-volatile bituminous, rates decrease by up to a factor of 3. Low volatility coals are much more resistant to thermal decomposition; they devolatilize at rates up to 5 times slower than all other lower ranks Correlations for different coal types from FLASH2, a more detailed devolatilization model, describe separate gas and tar evolution rates, and replace hypothetical ultimate yield parameters by accurate predictions for ultimate tar and gas yields.

11A905. Slowly varying filtration combustion waves. - MR Booty *(Dept of Math, S Methodist Univ, Dallas TX 75275)* and BJ Matkowsky *(Dept of Eng Sci and Appl Math, NWU)*. European J Appl Math 4(2) 205-224 (Jun 1993).

We describe the slow evolution of the wave speed and reaction temperature in a model of filtration combustion. In the counterflow configuration of the process, a porous solid matrix is converted to a porous solid product by injecting an oxidizing gas at high pressure into one end of a fresh sample of the solid while igniting it at the other end. The solid and gas react exothermically at high activation energy and, under favorable conditions, a self-sustaining combustion travels along the sample, converting reactants to product. Since the reaction rate depends on the gas pressure p in the pores, small gradients p cause variations in the conditions of combustion, which, in turn, cause inhomogeneities in the physical properties of the product. We determine the slow evolution of the wave speed, the reaction temperature, and the mass flux of the gas downstream of the reaction zone. In the absence of a pressure gradient, there is a branch of steadily propagating solutions which has a fold. For planar disturbances on the slow time scale, we show that the middle part of the branch is unstable, with the change of stability occurring at the turning points of the branch. When the pressure gradient is nonzero, there are no steadily propagating solutions and the wave continually evolves. Conditions on the state of gas at the inlet are described such that the variation in the wave speed and reaction temperature throughout the process can be minimized.

416Q. LIQUID FUELS

11A906. Comparison of droplet combustion models in spray combustion. - TL Jiang and W Hsu *(Inst of Aeronaut and Astronaut, Natl Cheng Kung Univ, Tainan, Taiwan 70101, ROC)*. J Propulsion Power 9(4) 644-646 (Jul-Aug 1993).

For a spray-burning combustor, experimental observations reveal that different spray combustion modes are present under various atomization conditions. In a fine-droplet spray, fast evaporation of small droplets make gas-phase combustion much more significant than droplet combustion and a diffusion gas-phase flame, with a relatively short spray length with respect to the overall flame length results. As spray droplets become larger, both individual droplet burning of large droplets and group burning of small droplets are possible, and a mixed combustion mode consisting of diffusion gas-phase flame and droplet combustion occurs. Massive droplet combustion with either envelope or wake flames are observed when the spray droplet size is further increased.

11A907. Modeling and simulation of combustion processes of charring and non-charring solid fuels. - C Di Blasi *(Dept di Ing Chimica, Univ di Napoli, Piazzale V Tecchio, 80125 Napoli, Italy)*. Prog Energy Combust Sci 19(1) 71-104 (1993).

Some of the progress that, owing to modeling and numerical simulation, has been made to the understanding of chemical and physical processes, which occur during combustion of solid fuels, is presented. The first part of the review deals with thermal degradation processes of charring (wood and, in general, cellulosic materials) and non-charring (poly-methyl-methacrylate) materials. Gas-phase combustion processes (ignition, flame spread and extinction) are discussed in the second part of the review. Solid fuel degradation has been described by kinetic models of different complexity, varying from a simple one-step global reaction, to multi-step reaction mechanisms, accounting only for primary solid fuel degradation, and to semi-global reaction mechanisms, accounting for both primary solid degradation and secondary degradation of evolved primary pyrolysis products. Semi-global kinetic models have been coupled to models of transport phenomena to simulate thermal degradation of charring fuels under ablation regime conditions. The effects of bubble formation on the transport of volatiles during thermal degradation of non-charring fuels, described through a one-step global reaction, have also been modeled. On the contrary, very simplified treatments of solid phase processes have been used when gas phase combustion processes are also simulated. On the other hand, the latter have also always been described through one-step global reactions. Numerical modeling has allowed controllng mechanisms of ignition and flame spread to be determined and the understanding of the interaction between chemistry and physics during thermal degradation of solid fuels to be improved. However, the chemical processes are not well understood, the few kinetic data are in most cases empirical and variations of solid properties during degradation are very poorly known, so that even the most advanced models do not in general give quantitative predictions.

416S. FLAME AND FIRE (SPREAD AND EXTINCTION)

11A908. Extinction of pool flames by means of a DC electric field. - E Sher, G Pinhasi, A Pokryvailo, R Bar-On *(Dept of Mech Eng, Pearlstone Center for Aeronaut Stud, Ben-Gurion Univ of the Negev, Beer-Sheva, Israel)*. Combust Flame 94(3) 244-252 (Aug 1993).

The application of an electric field to a combustion system can produce large and potentially useful effects, such as reducing carbon formation, affecting flame velocity, extending flammability limits, increasing flame luminosity, and stabilizing and extinguishing flame. The present study is concerned primarily with the corona discharge interaction with pool fires. The fuel surface served as the blunt electrode and several specially designed sharp probes have been examined as the high-voltage electrode. The most effective sharp electrode appeared to be a simple thin wire parallel to the liquid surface situated above it at a distance of several millimeters. The flame was repelled from the probe, thus creating a possible pool flame extinction device. Similar results were achieved with a mechanical blower that reproduced the velocity profile of the electric wind. The gas composition in different locations was examined for both the corona and blower cases. No significant difference was found, and it was concluded that ion pumping has no influence on the extinction performance. It is suggested that extinction by corona discharge is caused solely by the aerodynamic action of the electric wind with its remarkably flat, sharp velocity profile. Fire extinctions under hot and aggressive environments are possible applications of the present device.

416T. COMBUSTION, FLAME, AND FIRE MODELING

11A909. Integral combustion simulation of a turbulent reacting flow in a channel with cross-stream injection. - SL Chang and SA Lottes *(Energy Syst Div, ANL)*. Numer Heat Transfer A 24(1) 25-43 (Jul-Aug 1993).

A new integral one-step reaction submodel has been developed for an Argonne combustion computer code to sir [illegible] ting flows of an advanced cor [illegible] etohydrodynamic power gen [illegible] ombustion code makes n [illegible] a reacting flow more eff [illegible] hile still preserving the major physical effects of the complex combustion processes. Results of the simulation indicate that (1) fluid mixing is mainly responsible for combustion performance and (2) counterflow injection with an injection angle in the range of 120° to 140° yields the best mixing and combustion performance.

11A910. Mixing of multiple jets with a confined subsonic crossflow. - JD Holdeman *(NASA Lewis Res Center, Cleveland OH 44135)*. Prog Energy Combust Sci 19(1) 31-70 (1993).

This paper summarizes experimental and computational results on the mixing of single, double, and opposed rows of jets with an isothermal or variable temperature mainstream in a confined subsonic crossflow. The studies from which these results came were performed to investigate flow and geometric variations typical of the complex 3D flowfield in the dilution zone of combustion chambers in gas turbine engines. The principal observations from the experiments were that the momentum-flux ratio was the most significant flow variable, and that temperature distributions were similar, independent of orifice diameter, when the orifice spacing and the square-root of the momentum-flux ratio were inversely proportional. The experiments and empirical model for the mixing of a single row of jets from round holes were extended to include several variations typical of gas turbine combustors, namely variable temperature mainstream, flow area convergence, noncircular orifices, and double and opposed rows of jets, both inline and staggered. All except the last of these were appropriately modeled with superposition or patches to the basic empirical model. Combinations of flow and geometry that gave optimum mixing were identified from the experimental and computational results. Based on the results of calculations made with a 3D numerical model, the empirical model was further extended to model the effects of curvature and convergence. The principal conclusions from this study were that the orifice spacing and momentum-flux relationships were the same as observed previously in a straight duct, but the jet structure was significantly different for jets injected from the inner wall of a turn than for those injected from the outer wall. Also, curvature in the axial direction caused a drift of the jet trajectories toward the inner wall, but the mixing in a turning and converging channel did not seem to be inhibited by the convergence, independent of whether the contraction was radial or circumferential. The calculated jet penetration and mixing in an annulus were similar to those in a rectangular duct when the orifice spacing was specified at the radius dividing the annulus into equal areas.

11A911. Prediction of the pulsation frequency of flames formed over a semi-infinite horizontal surface. - IK Puri *(Dept of Mech Eng, MC 251, Univ of Illinois, PO Box 4348, Chicago IL 60680)*. Int J Heat Mass Transfer 36(10) 2657-2663 (Jul 1993).

The pulsation frequency of horizontally situated semi-infinite reacting surfaces is studied using linear stability theory. The analysis considers the flow to consist of an initially laminar base flow and a periodic disturbance. The governing equations are cast into a self-similar form analogous to previous analyses of boundary layers. The base flow is analyzed in terms of a flame sheet approximation, the solution to which is required to solve the disturbed flow. Some boundary conditions pertaining to the disturbances are evident but some others are inferred herein. The governing equations are solved for a flame burning n-heptane, and the results of the analysis relate the disturbance frequency of the flame to a Grashof type number, which, in turn, is related to the length of the thermal boundary layer. It is determined that the frequency scales according to a power law expressed as $(\text{length})^{-0.8}$.

416Y. COMPUTATIONAL TECHNIQUES

See the following:

11A705. Calculation of turbulent combustion of propane in furnaces

416Z. EXPERIMENTAL TECHNIQUES

See the following:

11A888. Computational and experimental study of a railplug igniter

11A903. Flow measurements in a model burner Part 2

418. Prime movers and propulsion

11A912. Application of small deflection method in calculation of acceleration time of aircraft turbine engines. - M Orkisz *(Warszawa, Poland).* Biuletyn Wojskowej Akademii Technicznej 42(1) 99-110 (1993).

A method of small declinations was used for linearization the relations describing the turbine and compressor operation and then they were introduced into the equation for acceleration time of the turbine engine. The obtained relation enables the evaluation of influence the departure of turbine as well as the compressor parameters during the acceleration.

11A913. Ballistics of solid rocket motors with spatial burning rate variations. - SD Heister *(Sch of Aeronaut and Astronaut, Purdue).* J Propulsion Power 9(4) 649-651 (Jul-Aug 1993).

The solid rocket motor ballistician has the job of predicting the chamber pressure and thrust history for both new and existing motors utilizing propellant burning rate and grain geometry, ambient conditions, and nozzle geometry. For motors which do not have a test history, ballisticians introduce a constant "scale factor" to force predictions to match actual burn times of test units as well as time varying multiplier to improve "pointwise" matching of the pressure history. This pointwise burning anomaly rate factor, or BARF, is usually established as a function of web distance since it is generally acknowledged that the factor accounts for spatial burning rate variations within the grain. This ubiquitous quantity has gone by several names through the years: hump factor, surface burn rate error, and residual error to name a few.

11A914. Development of a dual-frequency microwave burn-rate measurement system for solid rocket propellant. - DT Foss *(Combust Turbine Eng, Westinghouse Elec, Orlando FL 32826),* RJ Roby, WF O'Brien *(Dept of Mech Eng, VPI).* J Propulsion Power 9(4) 497-498 (Jul-Aug 1993).

A dual-frequency microwave burn-rate measurement system for solid rocket motors has been developed. The system operates in the X-band (8.2-12.4 GHz) and uses two independent frequencies operating simultaneously to measure the instantaneous burn rate in a solid rocket motor. Computer simulation and limited laboratory testing of the system were performed to determine its ability to limit errors caused by secondary reflections and by uncertainties in material properties, particularly the microwave wavelength in the propellant. Simulations showed that the frequency ratio and the initial motor geometry determined the effectiveness of the system in reducing secondary reflections. Overall, the simulations showed that a dual frequency system can provide up to a 75% reduction in burn-rate error over that returned by a single-frequency system. The hardware and software for dual-frequency measurements was developed and tested; however, further instrumentation work is required to increase the data acquisition rate so its full potential can be realized.

11A915. Preliminary assessment of exhaust systems for high-Mach (4-6) fighter aircraft. - AP Kuchar *(Adv Tech Operation, Aircraft Eng Div, GE Aircraft Engines, 1 Neumann Way M-D A330, Cincinnati OH 45215)* and JP Wolf *(Adv Tech Operation, Aircraft Eng Div, GE Aircraft Engines, 1 Neumann Way, Cincinnati OH 45215).* J Propulsion Power 9(4) 636-643 (Jul-Aug 1993).

Exhaust systems designed for high-Mach fighter aircraft will operate at nozzle pressure ratios near 100 for a Mach 4 aircraft to possibly over 600, depending on inlet recovery, for a Mach 6 aircraft. Also, the nozzle pressure loading will be two to four times higher than current Mach 1.5-2.2 exhaust systems, and the exhaust gas temperatures will be significantly higher. These new operating conditions for high Mach nozzles will result in substantial increases in both nozzle size and weight relative to current exhaust systems. Analytical studies have been conducted to assess the internal performance of the conventional axisymmetric nozzle, the 2D, convergent-divergent (2DCD) nozzle, and the single expansion ramp nozzle (SERN) operating at high Mach conditions. Weight estimates have also been complete for the 2DCD nozzle matrix. As expected, results of the studies show that the 2DCD and SERN concepts can achieve desired levels of performance at the expense of size and weight. In general, the exhaust systems for Mach 4-6 aircraft will have to be three to four times as large and four to five times as heavy as those currently employed on Mach 1.5-2.2 aircraft. The axisymmetric nozzle has geometric constraints that limits its performance capability.

11A916. Scramjet nozzle experiment with hypersonic external flow. - S Watanabe *(Aerodyn Div, Natl Aerospace Lab, 7-44-1 Jindaiji-higashi-machi Chofu, Tokyo 182, Japan).* J Propulsion Power 9(4) 521-528 (Jul-Aug 1993).

An experimental study of a scramjet asymmetric nozzle flowfields is conducted to investigate the effects on nozzle performance of interactions between engine exhaust and hypersonic external flow. The test model consists of a flat-plate ramp and a short cowl. Tests are performed in a hypersonic wind tunnel ($M_\infty = 7.1$) whose freestream constitutes the external flow around an aerospace plane. Room temperature air is used to simulate engine exhaust flow. Model surface pressure and pitot pressure distributions in the flowfields are measured, from which nozzle performance is calculated. Flow visualizations are performed using several techniques. It is found that in underexpansion conditions, the external flow affects the model surface pressure only from the ramp sides because the intercepting shock (barrel shock) does not impinge upon the ramp surface. It is shown that the external flow produces an effect which suppresses boundary-layer separation on the ramp surface. When using a long side fence, spanwise expansion of the exhaust flow is restrained, thus, a slight gain of thrust can be obtained relative to that using a shorter side fence. The predicted nozzle performance by the 2D method of characteristics with boundary-layer correction agrees well with the long side fence experimental results.

11A917. Diagnostics and performance of a low-power MPD thruster with applied magnetic nozzle. - TM York, C Zakrzwski, G Soulas *(Aeronaut and Astronaut Eng Dept, Ohio State Univ, Columbus OH 43210).* J Propulsion Power 9(4) 553-560 (Jul-Aug 1993).

This study evaluates the performance of a 50-150-kW thruster which was 1/4-scale of a bench mark magnetoplasmadynamic (MPD) thruster; it was operated with and without applied magnetic nozzle fields. Capacitors (14 μF) and inductors (80 μH) in networks produced relatively constant currents for about 450 μs to generate the applied magnetic nozzle, and currents up to 2.3-kA constant for about 300 μs to drive the thruster. With the solid copper electrode, the applied magnetic field was excluded from the thrust chamber because of the short duration of the experiments. The 1/4-scale device was mass starved below m = 0.135 g/s; this was equivalent to 2 g/s for a full-scale MPD thruster with the same m/A. With m > 0.25 g/s, the device was found to operate smoothly and with little evident erosion. Current-voltage records were similar with and without applied magnetic nozzle fields, indicating little effect of the external nozzles on the power deposition. The current plume in the expansion region outside the thruster chamber was reduced in axial extent with the application of the magnetic nozzle in this transient experiment. Momentum flux in the exhaust flow was measured by the local pressure probes. For the same arc power, impact pressures with magnetic nozzles applied were 3-4 times larger than the self-field cases.

11A918. Thermal nonequilibrium in a low-power arcjet nozzle. - DM Zube *(Inst Raumfahrtsyst, Univ Stuttgart, 7000 Stuttgart 80, Germany)* and RM Myers *(NASA Lewis Res Group, Sverdrup Tech, Cleveland OH 44135).* J Propulsion Power 9(4) 545-552 (Jul-Aug 1993).

Emission spectroscopy measurements were made of the plasma flow inside the nozzle of a 1-kW-class arcjet thruster. The thruster propellant was a hydrogen-nitrogen mixture used to simulate fully decomposed hydrazine. Several 0.25-mm-diam holes were drilled into the 12-mm-long diverging section of the tungsten thruster nozzle to provide side-on optical access to the internal flow. Electron excitation for atomic species and molecular vibrational and rotational temperatures were determined for the expanding plasma using relative line ratio techniques. The atomic excitation temperature decreased from 18,000 K at a location 3-mm downstream of the constrictor to 9000 K at a location 9 mm from the constrictor, while the molecular vibrational and rotational temperatures decreased from 6500 to 3000 K and 8000 to 3000 K, respectively, between the same locations. The electron density, measured using H_β line Stark broadening, decreased from $\approx 10^{21} m^{-3}$ to $2 \times 10^{20} m^{-3}$ during the expansion in the nozzle. The results show that the plasma is in a nonequilibrium state throughout most of the nozzle, with relaxation times close to or larger than the particle residence time.

11A919. Temperature control of a liquid helium propulsion system. - P Wiktor *(Hansen Labs GP-B, Stanford).* J Propulsion Power 9(4) 536-544 (Jul-Aug 1993).

Two spacecraft, gravity probe B (GP-B) and the satellite test of the equivalence principle, incorporating onboard liquid helium cryogenic systems are scheduled to fly around the turn of the century. Effective propulsion systems can be implemented for these spacecraft by directing the helium gas which boils off from the cryogenic systems in specific directions through a set of thrusters. Due to extensive development and testing work, the ultra low flow rate helium thrusters for such a propulsion system are now considered proven technology. This article is concerned with implementing these thrusters into an effective overall propulsion system. A thermodynamic model relating the temperature, pressure, and flow rate of the propulsion system is derived. Based on this model a controller is developed which regulates the liquid helium supply temperature and pressure by varying the net helium mass flow rate through the thrusters. We show how the net mass flow rate can be controlled independently from the desired output thrust. The manifold pressure upstream of the thrusters is shown to remain remarkably stable even with fairly large flow rate variations. Using the GP-B spacecraft as an example we conclude that it is feasible to build a liquid helium based propulsion system with a very stable supply temperature and pressure.

See also the following:

11A730. Progress towards understanding and predicting heat transfer in the turbine gas path

VII. EARTH SCIENCES

452. Porous media

452B. FUNDAMENTALS OF FLUID FLOW

11A920. Modified percolation approach to simulating three-fluid capillary pressure-saturation relationships. - WE Soll *(LANL)* and MA Celia *(Dept of Civil Eng, Princeton)*. Adv Water Resources 16(2) 107-126 (1993).

A computational model was developed for simulating capillary pressure-saturation relationships for porous media systems containing two or three mobile fluids. The model is based on describing fluid displacement on a pore-by-pore basis over a large number of pores to produce bulk saturations in the medium. The computational approach utilizes percolation and network theories to describe fluid movement within the pore space. Percolation theory calls for a set of displacement rules to determine the movement of the fluids under capillary-driven transport. A comprehensive set of rules appropriate for either two-fluid or three-fluid systems is described. These rules account for a variety of processes affecting displacement, such as wetting films, hysteresis, trapping of fluids, and gravity. The model is shown to reproduce the basic characteristics of a two-fluid capillary pressure-saturation curve, and model predictions are shown to agree with both two- and three-fluid experimental data.

11A921. Simultaneous determination of dispersion and nonlinear adsorption parameters from displacement tests by using numerical models and optimization techniques. - CA Grattoni, RA Dawe *(Mineral Resources Eng, Imperial Col, London SW7 2AZ, UK)*, MS Bidner *(Lab de Ingenieria de Reservorios, Univ de Buenos Aires, Pabellon de Indust, Ciudad Universitaria, 1428 Buenos Aires, Argentina)*. Adv Water Resources 16(2) 127-135 (1993).

The determination of the dispersion and adsorption parameters (either for the Freundlich or Langmuir adsorption isothermal models) can be determined by optimizing the matching of the numerical solution of the adsorption-convection dispersion equation with the experimental effluent curves measured on displacement tests in core material using multivariable optimization techniques. The numerical solutions are obtained by solving the convection-disperion-nonlinear adsorption equation by finite differences using the Crank-Nicolson method with iterations to account for nonlinearities. The optimization routines are used to find the parameters that give the global minimum error between predicted and measured effluent curves. The results show that whenever the three parameters (the dispersion coefficient and two adsorption parameters) are simultaneously determined, the solution is not unique and depends on the adsorption model used. The nonuniqueness can be removed by performing an independent test such as a static adsorption test.

11A922. Travelling waves during the transport of reactive solute in porous media. Combination of Langmuir and Freundlich isotherms. - CJ van Duijn *(Fac of Tech Math and Info, Tech Univ, PO Box 356, 2600 AJ Delft, Netherlands)*, P Knabner *(Inst fur Angewandte Anal and Stochastik, Hausvogteiplatz 5-7, D 0-1086 Berlin, Germany)*, SEATM van der Zee *(Dept of Soil Sci and Plant Nutrition, Agri Univ, PO Box 8005, 6700 EC Wageningen, Netherlands)*. Adv Water Resources 16(2) 97-105 (1993).

Recently, it has been shown that in the case of nonlinear solute adsorption the displacement may be in the form of a travelling wave. In this paper, we investigate whether a travelling wave type of behavior can be expected when two different types of sorption sites can be distinguished with different isotherms and kinetics. Illustrations are given for cases where the overall isotherm comprises two contributions that follow the Langmuir and the Freundlich equations, respectively. Boundary conditions are chosen that ensure a decrease in concentration in the direction of flow. Depending on the value of the Freundlich power (p) the travelling wave may exist. For $p \leq 1$, the travelling wave always exists, where as for $1 < p \leq 2$ it depends on the values of the other adsorption parameters and whether a lower bound of the upstream concentration (at $x = -\infty$) is exceeded. For $p \geq 2$, the existence of the travelling wave requires that the upstream concentration does not exceed an (specified) upper bound. Besides illustrating some waves we show that two different rate functions have the Freundlich isotherm as their limit for an infinite rate parameter result in qualitatively different travelling waves.

See also the following:

11A931. Dispersion, permeability heterogeneity, and viscous fingering: Acoustic experimental observations and particle-tracking simulations

452C. SEEPAGE (INCL POLLUTANTS)

11A923. BE analysis of contaminant transport in fractured porous media. - CJ Leo and JR Booker *(Sch of Civil and Mining Eng, Univ of Sydney, Sydney 2006, Australia)*. Int J Numer Anal Methods Geomech 17(7) 471-492 (Jul 1993).

A 2D boundary integral method to analyze the flow of contaminant in fractured media having a 2D or 3D orthogonal fracture network is presented. The method assumes that the fractures provide the paths of least resistance for transport of contaminants while the matrix, because of its low permeability, acts as "storage blocks" into which the contaminant diffuses. Laplace transform is used to eliminate the time variable in the governing equation in order to facilitate the formulation of a boundary integral equation in the Laplace transform space. Conventional BE techniques are applied to solve for the contaminant concentrations at specified locations in the spatial domain. The concentration in the time domain is then obtained by using an efficient inversion technique developed by Talbot. The method is able to analyze the behaviour of waste repositories which have diminishing concentration due to the mass transport of the contaminant into the surrounding fractured media.

11A924. FE modelling of transport of organic chemicals through soils. - T Kuppasamy *(Dept of Civil Eng, VPI)*. Int J Numer Anal Methods Geomech 17(7) 457-469 (Jul 1993).

Aquifer contamination by organic chemicals in subsurface flow through soils due to leaking underground storage tanks filled with organic fluids is an important groundwater pollution problem. The problem involves transport of a chemical pollutant through soils via flow of three immiscible fluid phases: namely air, water, and an organic fluid. In this paper, assuming the air phase is under constant atmospheric pressure, the flow field is described by two coupled equations for the water and the organic fluid flow taking interphase mass transfer into account. The transport equations for the contaminant in all the three phases are derived and assuming partition equilibrium coefficients, a single convective-dispersive mass transport equation is obtained. A FE formulation corresponding to the coupled differential equations governing flow and mass transport in the three fluid phase porous medium system with constant air phase pressure is presented. Relevant constitutive relationships for fluid conductivities and saturations as function of fluid pressures lead to non-linear material coefficients in the formulation. A general time-integration scheme and iteration by a modified Picard method to handle the non-linear properties are used to solve the resulting FE equations. Laboratory tests were conducted on a soil column initially saturated with water and displaced by ρ-cyumene (a benzene-derivative hydrocarbon) under constant pressure. The same experimental procedure is simulated by the FE programme to observe the numerical model behaviour and compare the results with those obtained in the tests. The numerical data agreed well with the observed outflow data, and thus validating the formulation. A hypothetical field case involving leakage of organic fluid in a buried underground storage tank and the subsequent transport of an organic compound (benzene) is analyzed and the nature of the plume spread is discussed.

11A925. Modeling coupled heat and contaminant transport in groundwater. - PJ Hensley *(Dept of Civil and Env Eng, Univ of W Australia, Nedlands 2009, W Australia)* and C Savvidou *(Eng Dept, Cambridge Univ, Cambridge CB2 1PZ, UK)*. Int J Numer Anal Methods Geomech 17(7) 493-527 (Jul 1993).

This paper presents the results of a research program conducted on the geotechnical centrifuge at The Univeristy of Western Australia to investigate coupled heat and contaminant transport in the soil surrounding a buried waste source. The phenomena which govern heat and contaminant transport through porous media are discussed, the principles of geotechnical centrifuge modeling are outlines, and relevant scaling laws that govern the relationship between a centrifuge model and the prototype, with respect to the problem of coupled waste transport, are presented. A model test, simulating 2D migration from a buried heat and contaminant source, is described, and the results from four model tests are presented. The experimental data show that hydraulic instability is responsible for the transport of contaminant in the soil around the source and that the mode of instability is determined by the magnitude of the effective Rayleigh number.

11A926. Simulation of groundwater flow and containment transport at a landfill site using models. - TJ Franz *(Dames and Moore, 7560 Airport Rd, Mississauga, ON, Canada)* and RK Rowe *(Geotech Res Center, Fac of Eng Sci, Univ of W Ontario, London, ON, Canada)*. Int J Numer Anal Methods Geomech 17(7) 435-455 (Jul 1993).

Numerical and analytical modeling studies were conducted for the analysis of groundwater flow and contaminant transport at the Innisfil landfill site in the Town of Innisfil, County of Simcoe, in Ontario, Canada. Previously conducted field studies categorized the upper stratigraphy at the site into three units: upper sand unit, upper silt-clay unit, and Intermediate Sand unit. Essentially horizontal groundwater movement in the two sand units and vertical downward flow in the silt-clay unit were reported by the field hydrogeologists. In the following, application of three computer models (FLOWPATH, USGS MOC and POLLUTE) for the simulation of the groundwater flow and contaminant transport processes at the Innisfil landfill site is described. The paper focuses on the calibration of groundwater flow and contaminant transport systems, and demonstrates how the insight gained during the contaminant transport calibration was used to improve the initial groundwater flow characterization of the hydrogeological system.

11A927. Transient infinite elements for seepage problems in infinite media. - Chongbin Zhao and S Valliappan *(Sch of Civil Eng, Univ of New S Wales, PO Box 1 Kensington, NSW 2033, Australia)*. Int J Numer Anal Methods Geomech 17(5) 323-341 (May 1993).

In this paper, a time-dependent infinite element which can be used to simulate transient seepage problems in infinite media is presented. The hydraulic head distribution function of the element has been derived in detail and the property matrices of the element have been formulated. Since both space and time variables are used in the course of constructing the hydraulic head distribution function of the element, the present infinite element can be referred to as a transient one. Using the present infinite element to model the far field of a system, the mechanism of transient seepage problems in infinite media can be rigorously simulated because the property matrices of the element are evaluated at any time of interest in the analysis. Since explicit expressions can be written for the property matrices of the infinite element, they may be evaluated quite easily and this can be carried out by writing a simple subroutine in a computer program. In order to examine the accuracy and efficiency of the present infinite element, both a 1D transient seepage problem in a semi-infinite medium and a 2D transient seepage problem in a full plane have been solved using the finite and infinite element technique. It has been demonstrated that the present infinite element is very useful for the numerical solution of transient seepage problems in infinite media.

452D. MULTIPHASE FLOW IN POROUS SOLIDS

See the following:

11A826. Two-phase mixture model of liquid-gas flow and heat transfer in capillary porous media I. Formulation

11A827. Two-phase mixture model of liquid-gas flow and heat transfer in capillary porous media II. Application to pressure-driven boiling flow adjacent to a vertical heated plate

11A920. Modified percolation approach to simulating three-fluid capillary pressure-saturation relationships

452F. FLUIDIZED BEDS

11A928. Numerical modeling of circulating fluidized beds. - MK Patel, K Pericleous, M Cross *(Centre for Numer Model and Process Anal, Univ of Greenwich, London SE18 6PF, UK)*. Int J Comput Fluid Dyn 1(2) 161-176 (1993).

The development of the multi-phase flow algorithm MIPSA (Multi-InterPhase Slip-Algorithm) within a 2D Computational Fluid Dynamics (CFD) code called CASCADE is summarized with its application to the modeling of lean phase circulating fluidized beds. The well-known InterPhase Slip Algorithm (IPSA) technique for handling the presence of particles in an air stream is modified and extended, to handle explicitly a range of particle sizes simultaneously. The salient features of IPSA are retained; hence each size family is treated as a separate "phase" and its motion governed by its own momentum equations. The MIPSA algorithm is embedded within CASCADE, in a framework which ensures overall conservation of mass, momentum, and energy. In this paper, the MIPSA algorithm is used to model the hydrodynamic behavior of Circulating Fluidized Beds (CFB). CFB's are increasingly being employed by a wide range of process industries and their design for a specific application can be problematic. The objective of this paper is to show how CFB's can be analyzed to identify their mixing behavior and factors affecting their efficiency of operation. The present study considers hydrodynamic behavior in relation to single and multiple mixing cells in a columnar arrangement, with a range of recirculation rates together with the effect of different riser configurations. The results of the calculations are presented in the form of velocity vecotrs, pressure contours, temperature contours and solid particle distributions for mono- and multi-sized particle simulations. The relative efficiency of single and multiple units is compared, together with the effects of reentry.

452G. ELASTIC BEHAVIOR OF FLUID-FILLED SOLIDS

See the following:

11A276. Models of moisture transport and moisture-induced stresses in epoxy composites

452H. DYNAMICS OF FLUID-FILLED SOLIDS

11T929. Visualization of the effects of buoyancy on liquid-liquid displacements in vertically-aligned porous medium cells. - CA Page, HJ Brooks, GH Neale *(Dept of Chem Eng, Univ of Ottawa, Ottawa, ON K1N 6N5, Canada)*. Exp Fluids 14(6) 472-474 (May 1993).

See also the following:

11A922. Travelling waves during the transport of reactive solute in porous media. Combination of Langmuir and Freundlich isotherms

452I. THERMODYNAMICS, HEAT TRANSFER, AND COMBUSTION

11A930. Enhanced thermal performance of fibrous insulation containing nonhomogeneous fibers. - Siu-Chun Lee *(PO Box 90333, Industry CA 91715-0333)*. J Quant Spectros Radiative Transfer 50(2) 199-209 (Aug 1993).

This paper evaluates the applicability of nonhomogeneous fibers for improving the thermal insulation properties of the fiber matrix composites. Hollow silica fibers and silica fibers coated with alumina and silicon are considered for enhancing the surface reflectance and thermal radiative resistance of fibrous composites in which fibers are oriented parallel to planar boundaries. Analytical models are developed to determine the influence of coating material and thickness on these radiative characteristics. Numerical results reveal that silicon-coated silica fibers are most effective in increasing the insulation capacity of a fiber matrix. The results also show that the radiative resistance can be tailored to exhibit the desired spectral variation by combining an appropriate proportion of coated fibers with different coating thicknesses. The present results establish the feasibility of utilizing silicon-coated silica fibers to substantially enhance the thermal insulation capacity of fibrous composites.

See also the following:

11A810. Conduction and convection heat transfer in composite solar collector systems with porous absorber

11A811. Natural convection and heat transfer in a vertical cavity filled with an ice-water saturated porous medium

11A812. Natural convection in vertical porous enclosures due to prescribed fluxes of heat and mass at the vertical boundaries

11T929. Visualization of the effects of buoyancy on liquid-liquid displacements in vertically-aligned porous medium cells

452K. RESERVOIR ENGINEERING

See the following:

11A921. Simultaneous determination of dispersion and nonlinear adsorption parameters from displacement tests by using numerical models and optimization techniques

452L. FLOW STABILITY

11A931. Dispersion, permeability heterogeneity, and viscous fingering: Acoustic experimental observations and particle-tracking simulations. - HA Tchelepi, FM Orr Jr *(Dept of Pet Eng, Stanford)*, N Rakotomalala, D Salin, R Woumeni *(Lab Acoust Optique Matiere Condensee CNRS, Univ Pierre et Marie Curie, Tour 13 Boite 78, 4 pl Jussieu, 75252 Paris Cedex 05, France)*. Phys Fluids A 5(7) 1558-1574 (Jul 1993).

Stable and unstable displacement experiments were performed in millstone and limestone cores. Concentration histories at ten locations along the core samples were obtained by acoustic measurements. Particle-tracking simulations of the displacements were also made utilizing permeability distributions measured with a permeameter. The combination of experimental observations and simulations indicate that superstable ($M < 1$) displacements suppress the influence of heterogeneity; this suppression was reflected in smaller apparent dispersivities as the mobility ratio decreased below unity. In the millstone, which exhibited random heterogeneity, 2D particle-tracking simulations reproduce with reasonable accuracy the growth of the fingered region in unstable displacements. In homogeneous porous media, concentration histories obtained in 3D simulations did not differ significantly from their 2D counterparts. In the more heterogeneous limestone, unstable displacements accentuated the influence of heterogeneity leading to longer transition zones. Two distinct flow regimes were observed in unstable displacements: (1) an initial period of rapid transition zone growth and (2) a subsequent period in which leading and trailing edges of the transition zone travel at nearly constant velocities.

452M. NON-NEWTONIAN FLUIDS

11A932. Non-Newtonian flow in porous media: A laboratory study of polyacrylamide solutions. - S Flew *(11 Foxcombe Court Wyndyke Furlough, Abingdon OX14 1D2, UK)* and RHJ Sellin *(Dept of Civil Eng, Univ of Bristol, Bristol BS8 1TR, UK)*. J Non-Newtonian Fluid Mech 47 169-210 (Jun 1993).

Quantification of the rheological effects of polymer solutions flowing through a porous matrix must be achieved if high molecular weight polymers are to be used to the best effect in augmenting oil recovery. This investigation explores the extensional flow behavior of polyacrylamide solutions, at dilutions around those used in oilfield practice, in a variety of flow geometries including hexagonal-rod arrays and glass-bead packs.

See also the following:

11A803. Forced convection heat transfer to an elastic fluid of constant viscosity flowing through a channel filled with a Brinkman-Darcy porous medium

452Y. COMPUTATIONAL TECHNIQUES

11A933. Determination of drying induced stresses in a prismatic bar. - A Rybicki *(Inst of Fund Tech Res, Polish Acad of Sci, Poznan, Poland)*. Eng Trans 41(2) 139-156 (1993).

In the paper a solution of the 2D problem of convective drying of porous-capillary material is presented. The considered phenomenon is described by a system of coupled differential equations proposed by Kowalski. The problem is solved with the use of the FEM for spatial derivatives and of the three-point finite difference method for derivatives with respect to time. The obtained results with special emphasis on the stress distributions are shown diagrammatically.

11A934. Steady-state plane Lamb's problem for a fluid-saturated poro-elastic medium. - R Staroszczyk *(Inst of Hydroeng, Polish Acad of Sci, Szczecin, Poland)*. Arch Mech 44(5-6) 499-512 (1992).

In the paper the time harmonic plane Lamb's problem for a fluid-saturated porous elastic solid is investigated. The considerations are carried out on the basis of Biot's dynamical theory of consolidation. The problem is solved by means of the Fourier transformation technique. The solutions are derived in the form of improper integrals, which have been evaluated in a numerical way, described in the paper. In a limiting case of no pore fluid in the medium, the solutions obtained are shown to reduce to those known in the classical theory of elasticity. As an illustration, some results of numerical calculations performed for the material parameters corresponding to a water-filled coarse sand are presented.

See also the following:

11A920. Modified percolation approach to simulating three-fluid capillary pressure-saturation relationships
11A921. Simultaneous determination of dispersion and nonlinear adsorption parameters from displacement tests by using numerical models and optimization techniques
11A928. Numerical modeling of circulating fluidized beds

452Z. EXPERIMENTAL TECHNIQUES

11A935. Measurement technique and a new model for the wall heat transfer coefficient of a packed bed of (reactive) powder without gas flow. - M Pons *(CNRS-LIMSI, BP 133, 91403 Orsay Cedex, France)*, P Dantzer *(CNRS-URA 446 Bat 415, Univ Paris Sud, 91405 Orsay Cedex, France)*, JJ Guilleminot *(CNRS-LIMSI, BP 133, 91403 Orsay Cedex, France)*. Int J Heat Mass Transfer 36(10) 2635-2646 (Jul 1993).

An experimental technique, designed for investigating altogether the effective thermal conductivity and the wall heat transfer coefficient in a packed bed of hydride powder, and the coupling of heat transfer with the hydriding reaction, is presented. It consists of measuring transient temperature evolution in a reactor with only geometrical symmetry and of fitting to the experimental data the numerical solution of the heat equation in the 2D domain including the whole reactor. This method requires only a relatively small powder volume (30 cm^3). As a first step, results on non-reactive packed bed (500 μm glass beads with argon and 20 μm iron powder with hydrogen) validate the experimental technique. A new model for the wall heat transfer coefficient is developed for packed beds without gas flow. This model attempts to unify the current differing approaches of modeling this quantity. It predicts high values for small grain size and large variations in the Knudsen transition domain: this is qualitatively confirmed by experiments, with coefficients at around 3000 W m^{-2} K^{-1} being measured for 20 μm iron powder in hydrogen. Experimental results show that the pressure-dependent thermal resistances on wall and grain surfaces are not negligible.

11A936. Nonlinearity of flow in a porous medium and its origin. - R Skawinski *(Inst Mech Gorotworu, Polska Akad Nauk, 30-059 Krakow ul, Reymonta 27, Poland)*. Arch Gornictwa 37(4) 421-438 (1992).

The subject of the present paper is the consideration on the opinions and results of experiments concerning the flow of liquids in porous media, particularly the nonlinearity of this flow, ie, dependence of permeability on flow velocity. From all theoretical and experimental works it is evident that the assumption of fixed stream lines in flow in a pore space of porous medium is not in accordance with reality and that the deviations from Darcy's law originate in significant participation of the inertial forces in the formation of the velocity field in the pore space realized by changes in the stream lines with the occurrence of flow separation at microscopic points in the pore space where the flow diverges or is curved. For the study of phenomena in a packed bed a model which retains the converging-diverging character of the flow is needed. Such geometric formations as constrictions and expansions of the space embraced by the flow have been used in experimental investigations made in Strata Mechanics Research Institute of Polish Academy of Sciences in Cracow, as the main element in modelling the flow in porous media and in investigation of the velocity field and its changes in such flow. These investigations were performed by the visualization methods.

11A937. Transient method for measuring thermal properties of saturated porous media. - OV Trevisan *(Fac Eng Campinas, Univ Estadual, 13081 Campinas SP, Brazil)*, S Mohanty, MA Miller *(Dept of Pet Eng, Univ of Texas, Austin TX 78712)*. Int J Heat Mass Transfer 36(10) 2565-2573 (Jul 1993).

This paper describes the development of a transient technique to measure thermal diffusivity and conductivity of porous samples. The method uses the film heat sensor to probe heat flux. Temperature and heat flux are measured dynamically allowing conditions to vary in time at the point of measurement. The data are then treated by a deconvolution algorithm, rendering results proper to simpler models for the same geometry. The numerical treatment in the deconvolution procedure was verified for a hypothetical case. The method was finally tested in the laboratory, with experiments made on samples of natural rock.

454. Geomechanics

11A938. Model for nonlinear seismic waves in a medium with instability. - IA Beresnev *(Inst of Earth Sci, Acad Sinica, PO Box 1-55 Nankang, Taipei, Taiwan 11529, ROC)* and VN Nikolaevskiy *(Inst of Phys of the Earth, Bolshaya Gruzinskaya 10, Moscow 123 810, Russian Federation)*. Physica D 66(1-2) 1-6 (Jun 1993).

Experimental investigations show that the earth's crust is elastically nonlinear and contains the sources of accumulated elastic energy, so that it can be considered as a nonlinear active medium. The effects of simulation of narrow- and broad-band seismic emission and the existence of dominant frequencies for which the medium is transparent have been reported. A model evolutionary equation which takes into account nonlinearity, instability, dissipation of energy and dispersion is proposed and solved numerically. The temporal solution of chaotic signals results in the formation of quasi-sinusoidal steady-state wave trains. The dependence of their amplitude on the values of coefficients of nonlinearity and dispersion is found. The mathematical model proposed can be used to describe the observed seismic phenomena.

11A939. Evaluation of seismic hazard of large industrial objects. - Z Droste *(Inst of Geophys, Polish Acad of Sci, 01-452 Warsaw ul Ksiecia, Janusza 64, Poland)*. Acta Geophys Polonica 40(3-4) 247-270 (1992).

Methods for evaluation of seismic hazard in areas in which large industrial objects such as water power plants, nuclear power plants and the like are to be built have been discussed. The discussion is based on the reports prepared at the Institute of Geophysics for the planned nuclear power plant sites.

11A940. Heat flow from Okuniew-IG-1 borehole, Poland. - MAJ Slawomir *(Inst of Geophys, Polish Acad of Sci, 01-452 Warsaw ul, Ksiecia Janusza 64, Poland)*. Acta Geophys Polonica 40(3-4) 213-218 (1992).

The surface heat flow density from Okuniew-IG-1 borehole is estimated to be about 40-50 mW/m^2. Our indirect calculations are based, in general, on an empirical relation between the HF and seismic Pn wave velocity, and on the nonlinear HF-radiogenic heat production relationship for heat flow provinces. Statistical correlations between the thermal conductivities and some physical properties (such as mean velocity, density, and porosity) for sedimentary rocks are also used.

11A941. General relativity in geophysics. - AP Trofimenko *(Astron Section, Minsk Dept, Astron-Geodesical Society of CIS, Minsk-12 Abonent Box 7, 220012 Byelorussia)*. Acta Geophys Polonica 40(3-4) 303-322 (1992).

Geophysical manifestations of otons (objects of general relativity) are discussed. The values of energy and flow of neutrino from a microblack hole which can supply the energy of volcanos are specified. The energy of catastrophic volcano explosions coincides in the order of magnitude with the energy of exploding black holes. The question is put forward about the registration of high energy neutrino from exploding black holes by means of deep-water detectors. Short-time variations of gravitational potential derivatives (otonic gravi-impulses) are described, which are produced by fast moving otons in the Earth. The results of experimental registration of minute variations of the second and first derivatives of gravitational potential are presented.

11A942. Baroclinic instability of the atmosphere due to the nonhomogeneity of zonal flow. - R Brojewski *(Military Tech Acad, Warszawa, Poland)*. J Tech Phys 34(1) 37-43 (1993).

The subject matter of the present paper is the problem of stability of zonal flow of geophysical fluid using an example the two-layer model of baroclinic atmosphere. It has been shown that the occurrence of nonhomogeneity in zonal flow changes the wave range of cylogenesis in the model by moving it in the direction of long waves. Having sufficient degree of nonhomogeneity of flow it is unstable for any wavelength. In addition, the existence of the model is discussed of five parameters influencing its stability and the existence of three parameters having the character of bifurcation parameters has been pointed out.

11A943. Magnetotelluric response on a multilayered earth model with a layer having exponentially varying conductivity. - B Banerjee *(Central Geophys Div, Geol Survey of India, R&D Wing, P-49 CIT Rd, Beliaghata, Calcutta 70010, India)*. Acta Geophys Polonica 40(3-4) 293-302 (1992).

Magnetotelluric response of a horizontally stratified earth in which the conductivity or resistivity of any one of the layers varies exponentially with depth or with or without a discontinuity at the interfaces has been investigated. All previous works regarding this problem are particular cases of the present study.

11A944. Stability of zonal flow in the divergent-barotropic model of a geophysical fluid. - R Brojewski *(Military Tech Acad, Warszawa, Poland).* J Tech Phys 34(1) 45-56 (1993).

The stability of zonal flow in the divergent-barotropic model of the atmosphere is estimated making use of stability criteria connected with the method of disturbances as applied to locally linearized dynamics systems. The result obtained enables us to infer that any nonhomogeneous inviscid flow in the N-S direction is unstable under short-wave disturbances of sufficiently small wavelengths, of the type of Rossby waves. A numerical experiment that was presented shows that there exist, in the system, stable vibration states of a type of nonlinear vibration with modulated frequency.

See also the following:

11A94. Design of steel frames for specified seismic member ductility via inverse eigenmode formulation

11A782. Flow of supercritical hydrogen in a uniformly heated circular tube

456. Earthquake mechanics

11T945. Topographic eddies in multilayer flow. - MK Davey *(UK Meteorol Office, London Road, Bracknell RG12 2SY, UK)*, RGA Hurst *(Dept of Math, Univ Col, Gower St, London WC1E 6BT, UK)*, ER Johnson *(Dept of Math, Univ Col London, Gower St, London WC1E 6BT, UK).* Dyn Atmos Oceans 18(1-2) 1-27 (Jun 1993).

11A946. Hybrid modeling of soil-structure interaction problems for deeply embedded structures in a multilayered medium. - C Romanel *(Dept of Civil Eng, Catholic Univ, Rio de Janeiro, Brazil)* and T Kundu *(Dept of Civil Eng and Eng Mech, Univ of Arizona, Tucson AZ 85721).* Earthquake Eng Struct Dyn 22(7) 557-571 (Jul 1993).

Dynamic response of deeply embedded structures, such as underground tunnels and deep foundations, in multilayered elastic half-space are analyzed when the structure is excited by a plane P or SV wave propagating at some angle. The scattered field is represented by the sum of three Green's functions, corresponding to two oscillating forces and one oscillating moment at the centroid position of the buried structure. The amplitudes of these two forces and one moment are *a priori* unknown and are obtained by satisfying displacement and stress continuity conditions across the near-field and far-field boundary. The distinguishing feature of this technique from direct or indirect boundary integral techniques is that in these techniques a distribution of sources of unknown amplitude are considered at the near-field and far-field boundary, and a large number of sources are needed for different combinations of source-receiver arrangements. But in this technique the sources of unknown amplitude are placed at the location of the structure, not at the near-field and far-field boundary and, using the Saint Venant's principle, the scattered field is modeled. Thus, the number of sources required is reduced to only three. Two example problems are solved. The first one is for a deeply embedded footing in a three-layer soil mass and the second one is for a rectangular tunnel in a two-layer soil mass.

11A947. Influence of time-domain dam-reservoir interaction on cracking of concrete gravity dams. - DH Wepf *(WWI Wepf and Wepf Eng Services, 9230 Flawil, Switzerland)*, G Feltrin, H Bachmann *(Inst of Struct Eng, Swiss Fed IT, 8093 Zurich, Switzerland).* Earthquake Eng Struct Dyn 22(7) 573-582 (Jul 1993).

Based on a nonlinear dam-reservoir interaction model, a study investigating the earthquake response of concrete gravity dams is presented. For the propagation of cracks in unreinforced mass concrete, a discrete crack approach formulation based on the FEM is applied. A special crack element is used to follow a fictitious crack in order to account for a zone of microcracks developing at the crack tip. The reservoir is modeled using the BEM. At a fictitious boundary dividing the irregular finite part of the reservoir from the regular infinite part, the loss of energy due to pressure waves moving away towards infinity is taken into account rigorously. Analyses are performed on the tallest non-overflow monolith of the Pine Flat Dam located in Kern County, California. The interaction of a dam, which may exhibit cracks in mass concrete, with a reservoir domain of arbitrary geometry extending to infinity is studied. Some main parameters are investigated. The importance of tools capable of handling the non-linear dam-reservoir interaction is emphasized.

11A948. Seismic response of heavily damped base isolation systems. - Hsiang-Chuan Tsai *(Dept of Construct Eng, Natl Taiwan IT, Taipei, Taiwan, ROC)* and JM Kelly *(Dept of Civil Eng, UCB).* Earthquake Eng Struct Dyn 22(7) 633-645 (Jul 1993).

The development of an efficient energy-dissipating mechanism that works in conjunction with laminated elastomeric bearings in order to reduce the lateral deformation of the isolation system has always been a goal of base isolation research. Theoretically, this deformation will be reduced to the minimum if damping augmentation of the isolation system can reach a critical value. However, augmenting the isolation damping may cause some unwanted side effects. The purpose of this paper is to study the influence of isolation damping on the seismic response of heavily damped base-isolated buildings. The base isolation system is assumed to be linearly viscoelastic and is analyzed using the complex mode method. Solutions derived by using perturbation techniques for a 2-dof system and the computer simulation for a multiple-dof system reveal that augmenting the isolation damping can reduce efficiently the deformation of the isolation system, but at the price of increasing the high-frequency vibration in the superstructure. When the damping ratio of the isolation system is beyond some level, increasing the isolation damping will enlarge the extreme values of the base and superstructural accelerations. It is also found that approximate solutions derived from the use of classical damping and classical modes of vibration in the seismic analysis of heavily damped base isolation systems can be substantially in error.

11A949. Design study of an energy-dissipating cladding system. - JM Cohen *(Cladding Res Inst, 6 Commodore Dr, Suite 330, Emeryville CA 94608)* and GH Powell *(Dept of Civil Eng, UCB).* Earthquake Eng Struct Dyn 22(7) 617-632 (Jul 1993).

A design study has been conducted to explore the use of structural cladding panels with energy-dissipating cladding-to-frame connections for seismic-resistant design. The study identifies several issues involved in the modeling and analysis of frames with energy-dissipating cladding-to-frame connections, establishes concepts for design, and provides a preliminary assessment of the force and deformation demands that are likely to be placed on panels and connections. Nonlinear dynamic analyses indicate that the clad frames perform well, based on observations about maximum interstorey drifts, maximum plastic hinge rotations in the frames, and maximum ductility demands on the cladding-to-frame connections.

458. Hydrology, oceanology, meteorology

11T950. Comparison between direct and iterative methods to solve the linear systems arising from a time-dependent 2D groundwater flow model. - JG Blom, JG Verwer, RA Trompert *(CWI, PO Box 4079, 1009 AB Amsterdam, Netherlands).* Int J Comput Fluid Dyn 1(2) 95-113 (1993).

11T951. Eddy correlation measurement of CO_2 flux using a closed-path sensor: Theory and field tests against an open-path sensor. - AE Suyker and SB Verma *(Dept of Agri Meteorol, Univ of Nebraska, Lincoln NE 68583).* Boundary-Layer Meteorol 64(4) 391-407 (Jun 1993).

11T952. Linear unsteady mountain waves. - F Lott *(European Center for Medium Range Weather Forecast, Shinfield Park, Reading, Berkshire, RG29AX, UK)* and H Teitelbaum *(Lab Meteorol Dyn CNRS, Ecole Polytech, 91128 Palaiseau Cedex, France).* Tellus 45A(3) 201-220 (May 1993).

11T953. Regional shear stress of broken forest from radiosonde wind profiles in the unstable surface layer. - MB Parlange *(Hydrologic Sci, Dept of Land, Air, and Water Resources and Dept of Agri Eng, Veihmeyer Hall, UC, Davis CA 95616)* and W Brutsaert *(Sch of Civil and Env Eng, Hollister Hall, Cornell).* Boundary-Layer Meteorol 64(4) 355-368 (Jun 1993).

11T954. Simple parameterization of long-wave radiative cooling with application to the atmospheric boundary layer for clear sky conditions. - Junsei Kondo and Dai Matsushima *(Geophys Inst, Tohoku Univ, Sendai 980, Japan).* Boundary-Layer Meteorol 64(3) 209-229 (Apr 1993).

11A955. Stability analysis of the viscous geophysical fluid flow on a torus in a divergent-barotropic model, including rotation sources. - R Brojewski *(Military Univ of Tech, Warszawa, Poland).* J Tech Phys 34(2) 107-118 (1993).

The subject of the present considerations are some properties of the solution of a set of ordinary differential equations obtained as a result of application of Galerkin's method to the equation of divergent-barotropic model of viscous geophysical fluid on a torus, with sources of rotation. The stationarities of the system have been studied, the relevant stability criteria being found as well as the conditions of the system attractors existence in the form of closed orbits. The parameters of the latter have been determined. It has been demonstrated that there are no attractors of any other type, if the sources of rotation depend on a single variable which governs the Coriolis parameter, and are independent of time. In the case of pulsating sources of rotation it has been shown that resonances may occur in the system.

See also the following:

11A136. Coastal amplification of a tsunami wave train

11T141. Energy of Rossby waves as a part of global atmospheric oscillations

11T142. Evolution of Rossby waves, generated by wind stress in a closed basin, incorporating total mass conservation

11A567. Diurnal stratification and its effects on wind-induced currents and water qualities in Lake Kasumigaura, Japan

11A942. Baroclinic instability of the atmosphere due to the nonhomogeneity of zonal flow

11A944. Stability of zonal flow in the divergent-barotropic model of a geophysical fluid

VIII. ENERGY & ENVIRONMENT

500. Fossil fuel systems

11A956. The cooling power of mining air cooler. - J Waclawik *(Inst Gornictwa Podziemnego I Bezpieczenstwa Pracy, Akad Gorniczo-Hutnicza, 30-059 Krakow Al, Mickiewicza 30, Poland).* Arch Gornictwa 37(4) 393-408 (1992).

The paper presents a method of calculation of the air temperature and humidity in a working in the case when the air is cooled by air cooler. In the work is assumed, that the thermodynamic process of the humid air cooling is lying on the enthalpy-moisture content diagram on the straight line. The cooling powers of the air cooler is depending on the inlet valves of water temperature, air temperature and humidity, the area of cooled surface and on type of heat exchanger system.

11A957. An empirical study on the functioning of nonbranching air duct lines in mines in the context of airflows with mass and momentum exchange in accordance with the law of growth: The problem of air quantity. - H Bystron *(Glowny Inst Gornictwa, Kopalnia Doswiadczalna "Barbara", 40-951 Katowice Pl, Gwarkow 1, Poland).* Arch Gornictwa 37(4) 491-551 (1992).

The object of this present study, dealing with the problems of air quantity and air pressure, was to verify the hypothesis that the system of equations describing airflows with mass and momentum exchange should include the growth function, in which appears growth intensity expressed by equation. This equation refers to discriminant. Its integrals are not simple functions having corresponding simple antifunctions in the explicit form. For this reason a parameterized growth intensity was introduced and on this is based a family of theoretical growth functions. Making use of empirical data, empirical growth functions together with the corresponding families of theoretical functions are presented in tabular form. Starting from criterion based on standard deviations, appropriate theoretical growth functions were developed and also appropriate growth parameters and intensities.

11A958. Estimate changes of concentration of gases during stoping downcast ventilator in the area of liquidated ventilator gallery of longwall with caving. - H Kaletka *(Kopalina Wegla Kamiennego, Rymer, 44-270 Rybnik-Niedobczyce ul, Rymera 4, Poland).* Arch Gornictwa 37(4) 409-420 (1992).

In this article has been shown bloc scheme of diffusing gases in liquidated ventilation gallery of longwall with caving. The formula has been derived showing the course of concentration particular gases as a function of time during stoping downcast ventilator. Simplified flow of air and gas from cavings (or goaf gas) model, in the area longwall with caving, has been shown. This model allowed measure the influence of natural depression on velocity of changes concentration of gases in time period.

502. Nuclear systems

11A959. Creative design-by-analysis solutions applied to high-temperature components. - AK Dhalla *(Nucl Adv Tech Div, Westinghouse Elec, Pittsburgh PA 15230).* J Pressure Vessel Tech 115(3) 221-227 (Aug 1993).

Elevated temperature design has evolved over the last two decades from design-by-formula philosophy of the ASME Boiler and Pressure Vessel Code, Sections I and VIII (Division I), to the design-by-analysis philosophy of Section III, Code Case N-47. The benefits of design-by-analysis procedures, which were developed under a US-DOE-sponsored high-temperature structural design program, are illustrated in the paper through five design examples taken from two US liquid metal reactor (LMR) plants. Emphasis in the paper is placed upon the use of a detailed, nonlinear FE analysis method to understand the structural response and to suggest design optimization so as to comply with Code Case N-47 criteria. A detailed analysis is cost-effective, if selectively used, to qualify an LMR component for service when long-lead-time structural forgings, procured based upon simplified preliminary analysis, do not meet the design criteria, or the operational loads are increased after the components have been fabricated. In the future, the overall costs of a detailed analysis will be reduced even further with the availability of FE software used on workstations or PCs.

11A960. Combination of radiation and hydrogen damage of reactor pressure vessel materials. - K Splichal, M Ruscak, J Zd'arek *(Nucl Res Inst, 250 68 Rez, Czechoslovakia).* Int J Pressure Vessels Piping 55(3) 361-373 (1993).

The hydrogen embrittlement of low-alloyed base steel, austenitic cladding and heat affected zone (HAZ) of a reactor pressure vessel was measured for both unirradiated and irradiated materials. The fracture toughness decreased with both hydrogen charging and neutron irradiation; the shift of the fracture toughness-temperature transient curve is influenced by both damage processes. The plastic zone in hydrogen-charged material becomes smaller. The total elongation of both CrMoV and CrNiMoV HAZ decreases with increasing hydrogen content. This influence is pronounced in the HAZ after a weld process without subsequent annealing, a total loss of plasticity being observed in this case. The properties of the austenitic layer are not influenced at comparable hydrogen contents.

506. Solar and other energy systems

11A961. Heat and fluid flow in rectangular solar air heater ducts having transverse rib roughness on absorber plates. - D Gupta *(Dept of Mech Eng, Eng Col, Kota 324 009, India),* SC Solanki, JS Saini *(Dept of Mech and Indust Eng, Univ of Roorkee, Roorkee 247 667, India).* Solar Energy 51(1) 31-37 (Jul 1993).

An experimental investigation has been carried out to determine the effect of transverse wire roughness on heat and fluid flow characteristics in transitionally rough flow region ($5 < e+ < 70$) for rectangular solar air heater ducts with an absorber plate having transverse wire roughness on its underside. The investigation covered a Reynolds number range of 3000-18000 for a duct aspect ratio of 6.8-11.5, relative roughness height of 0.018-0.052 at a relative roughness pitch of 10 encompassing a range of roughness Reynolds number between 5-70. Simple correlations for a Nusselt number and friction factor have been developed in terms of geometrical parameters of roughness, duct cross section, and the flow Reynolds number.

11A962. Losses in a 3D compound parabolic concentrator as a second stage of a solar concentrator. - N Yehezkel, J Appelbaum *(Fac of Eng, Tel-Aviv Univ, Tel-Aviv 69978, Israel),* A Yogev *(Weizmann Inst of Sci, Rehovot, Israel),* M Oron *(Soreq Nucl Center, Yavne, Israel).* Solar Energy 51(1) 45-51 (Jul 1993).

In this article, the losses due to reflection properties in a 3D compound parabolic concentrator (3D CPC) are calculated and the effect of these losses on the concentration is analyzed. The 3D CPC is used as a second stage in two configurations of a two-stage concentrator: (a) a parabolic dish as a first stage, and (b) a Cassegrainian as a first stage. The nonplanar rays play an important role in 3D CPC losses. Thus, a ray-tracing procedure is needed to evaluate the losses. In this study, a rigorous 3D ray tracing program was specially developed. The reflection losses and their effect on the concentration were determined from the reflection distribution derived by the developed ray-tracing program. As a result, the reflection losses were approximated by a simple empirical linear model useful in practical ranges of the 3D CPC acceptance angles and reflectivities. This model facilitates design and system optimization by analytical methods without resorting to a ray-tracing procedure. The approach presented in this article may be used to compare the performance of the two-system configurations, taking into account the 3D CPC losses.

11A963. Experimental and numerical study of heat transfer in a simulated collector for a solar dryer. - PH Oosthuizen and A Sheriff *(Heat Transfer Lab, Dept of Mech Eng, Queen's Univ, Kingston, ON, K7L 3N6, Canada).* Trans Can Soc Mech Eng 17(2) 145-160 (1993).

Indirect passive solar crop dryers have the potential to considerably reduce the losses that presently occur during drying of some crops in many parts of the "developing" world. The performance so far achieved with such dryers has, however, not proved to be very satisfactory. If this performance is to be improved it is necessary to have an accurate computer model of such dryers to assist in their design. An important element is any dryer model is an accurate equation for the convective heat transfer in the collector. To assist in the development of such an equation, an experimental and numerical study of the collector heat transfer has been undertaken. In the experimental study, the collector was simulated by a 1m long by 1m wide channel with a gap of 4 cm between the upper and lower surfaces. The lower surface of the channel consisted of an aluminium plate with an electrical heating element, simulating the solar heating, bonded to its lower surface. Air was blown through this channel at a measured rate and the temperature profiles at various points along the channel were measured using a shielded thermocouple probe. Local heat transfer rates were then determined from these measured temperature profiles. In the numerical study, the parabolic forms of the governing equations were solved by a forward-marching finite difference procedure.

11A964. Anisotropic sky radiance model based on narrow field of view measurements of shortwave radiance. - AP Brunger *(Solar Thermal Res Lab, Dept of Mech Eng, Univ of Waterloo, Waterloo, N2L 3G1, Canada)* and FC Hooper *(Dept of Mech Eng, Univ of Toronto, Toronto, M5S 1A4, Canada).* Solar Energy 51(1) 53-64 (Jul 1993).

A model for the average anisotropic sky radiance (or intensity) as a function of the position of the sun, the diffuse fraction κ, and the atmospheric clearness index κ_t are presented in this article. The complete range of sky conditions from clear to turbid to overcast is covered. Analysis of the observed data indicates that the model can be used to estimate instantaneous sky radiance values with a mean bias error of -11% and a root mean square error of 65% of the mean. The model is shown to account for 83% of the deterministic part of the variance of the instantaneous sky radiance measurements.

11A965. Geostatistical properties and modeling of random cloud patterns for real skies. - R Perez, R Seals, J Michalsky *(Atmos Sci Res center, SUNY, 100 Fuller Rd, Albany NY 12205),* P Ineichen *(Groupe Phys Appl, Univ of Geneva, Switzerland).* Solar Energy 51(1) 7-18 (Jul 1993).

A new model that synthesizes sky luminance distribution from routine irradiance measurements for all insolation conditions was recently presented by the authors. The model produces continuous sky luminance distribution patterns representative by specific insolation conditions from overcast to clear through partly cloudy. In this article we address the discontinuous aspects of skylight, created by "one of a kind" cloud patterns. We show that these patterns, which are superimposed on the continuous luminance distributions, have predictable physical characteristics that can be parameterized as a function of insolation conditions. We present a method for incorporating these random but predictable luminance effects as an option in the continuous skylight distribution model.

11A966. Blade-pitch-angle-controllable windmill simulator. - T Toumiya *(Dept of Elec Eng, Anan Col of Tech, 265 Aoki Minobayashi Anan-City, Tokushima Prefecture 774, Japan)*, T Sakakibara *(Dept of Elec and Electron Eng, Fac of Eng, Toyahashi Univ of Tech, 1-1 Kumosuzumegaoka Tenpaku-cho Toyohashi-city, Aichi-prefecture 770, Japan)*, T Suzuki *(Dept of Elec and Electron Eng, Fac of Eng, Univ of Tokushima, 2-1 Minamijosanjima, Tokushima-city 770, Japan)*. Int J Energy Res 17(2) 89-104 (Mar 1993).

The paper describes the development of a windmill simulator, to simulate accurately the movement of a windmill. The simulator has a model to facilitate the change of windmill parameters, such as power coefficient or moment of inertia, by overcoming the weak points in the research and development environment for wind utilization, especially with the purpose of improving methods of windmill speed control or output. Also, to determine further the dynamic characteristics of the windmill speed with great accuracy, the simulator has a motor model to compensate for the slow response of the DC motor itself. The simulator is mainly composed of a separately-excited DC motor to directly simulate the movement of the windmill, a high-output DC amplifier to drive the motor, and a personal computer for control. It is ascertained that the developed simulator can fully reproduce the stationary and dynamic characteristics of a windmill from the experimental results. Also, a method is described to control the blade pitch angle to keep a windmill rotational speed constant. The results of the numerical simulation agree with the characteristics of the windmill simulator, and the effectiveness of the blade pitch angle control of the simulator is also affirmed.

11A967. Novel wind-diesel-battery hybrid energy system. - CV Nayar *(Power Electron Res Univ, Sch of Elec & Comput Eng, Curtin Univ of Tech, Perth, W Australia)*, SJ Phillips, WL James, TL Pryor, D Remmer *(Energy Res Inst, Murdoch Univ, S St, Murdoch, W Australia)*. Solar Energy **51**(1) 65-78 (Jul 1993).

In most of the remote areas of Australia and in many other parts of the world, diesel generators are used to provide electrical power. Such systems are often characterized by either poor efficiency and high maintenance costs because of prolonged operation at low load levels, or intermittent power because the unit is only run during period of significant load. The addition of a battery bank and a power conditioner to produce a diesel-battery-inverter hybrid system has been identified as producing a number of benefits. Such systems can be broadly classified according to their configuration as series, switched, or parallel hybrid systems. A new parallel hybrid energy system developed in W Australia is described in this article. The heart of the system is a high quality sinewave inverter which can also be operated in reverse as a battery charger. The system can cope with loads ranging from zero (inverter only operation) to approximately three times the generator capacity (inverter and diesel operating in parallel) with excellent efficiency. The system is fully automatic, provides continuous power, and can readily incorporate input from wind or photovoltaic systems. This article also includes a description of 5 kW wind generator charging a battery bank as part of the hybrid system, and an economic analysis indicates a favorable result for this hybrid system with payback period estimated to be the order of three years.

11A968. Analytical and experimental investigation of thermal stratification in storage tanks. - NM Al-Najem, AM AL-Marafie, KY Ezuddin *(Dept of Mech Eng, Kuwait Univ, PO Box 5969, SAFAT 13060, Kuwait)*. Int J Energy Res 17(2) 77-88 (Mar 1993).

An analytical and experimental investigation of transient turbulent 2D charging and discharging of a sensible heat storage tank has been conducted. Parametric studies showed that the turbulent mixing factor due to hydrodynamic disturbances at the inlet ports is the most significant item in the performance of thermal stratification storage tanks. Furthermore, the effect of the aspect ratio and convection at the walls in promoting stratification have been studied. Comparison with experimental data showed the capability of the present analytic approach to accommodate, with a satisfactory degree of accuracy, such problems.

11A969. Degradation of a stratified thermocline in a solar storage tank. - NM Al-Najem *(Dept of Mech Eng, Kuwait Univ, PO Box 5969, SAFAT 13060, Kuwait)*. Int J Energy Res 17(3) 183-191 (Apr 1993).

The thermal stratification behavior in a solar storage tank is simulated and analyzed using a theoretical model based on an integral transform technique. A comparison with available experimental and theoretical data is used to validate present theoretical results. The accuracy of the model in simulating the thermal behavior of stratification is reasonably good, especially when consideration is given to the complexity of the physical mechanisms involved, and the relative simplicity of the model. The effect of the heat loss parameter is investigated and it is found that initially it is strongly spatially and temporally dependent. Therefore, a functional form that accurately represents the heat loss parameter is needed for closer agreement with experimental results. However, after a relatively long time, the assumption of a constant heat loss parameter is adequate to produce acceptable predictions.

See also the following:

11A776. Indirect temperature determination of a hot gas stream

514. Environmental mechanics

11A970. Disagreements between gradient-diffusion and Lagrangian stochastic dispersion models, even for sources near the ground. - CJ Mooney and JD Wilson *(Univ of Alberta, Edmonton, AB, T6G 2H4, Canada)*. Boundary-Layer Meteorol **64**(3) 291-296 (Apr 1993).

It is well known that if turbulent mass convection is modeled as diffusion, errors result unless trajectories from the source (at h) to the point of observation (z_p) comprise many statistically-independent segments (Taylor, 1921). We show that this is not guaranteed merely by the Lagrangian timescale (τ) at the source being small (eg, source at ground), but that a better criterion is $t \gg \max[\tau(h), \tau(z_p)]$, where t is a typical travel time to z_p.

11A971. Mathematical model for the hydrodynamics and pollutants transport in long and narrow tidal rivers. - V Nassehi and JH Bikangaga *(Dept of Chem Eng, Univ of Tech, Loughborough, Leicestershire LE11 3TU, UK)*. Appl Math Model 17(8) 415-422 (Aug 1993).

This paper deals with the application of the Taylor-Galerkin FEM to the simulation of the tidal dynamics and transport of chemically reactive pollutants in a branching river-estuary system. The adopted mathematical technique is fully described and the derivation of the working equations of the scheme is outlined. To validate the model two case studies, namely, tidal dynamics and salt intrusion in Upper Milford Haven (Wales, UK) and heavy metal dispersion in the Fal estuary (Cornwall, UK) are reported. Results of the model simulation in both cases are in good agreement with the field observations.

11A972. Probability distributions of concentration fluctuations of a weakly diffusive passive plume in a turbulent boundary layer. - E Yee *(Defense Res Est Suffield, Box 4000, Medicine Hat,, AB, T1A 8K6, Canada)*, DJ Wilson, BW Zelt *(Dept of Mech Eng, Univ of Alberta, Edmonton, AB, T6G 2G8, Canada)*. Boundary-Layer Meteorol **64**(4) 321-354 (Jun 1993).

Results are presented from an experimental investigation of turbulent dispersion of a saline plume of large Schmidt number (Sc = 830) in a turbulent boundary-layer shear flow simulated in a laboratory water channel. The dispersion measurements are obtained in a neutrally buoyant plume from an elevated point source over a range of downstream distances where both plume meandering and fine-structure variations in the instantaneous plume are important. High-resolution measurements of the scalar fluctuations in the plume are made with a rake of conductivity probes from which probability distributions of concentration at various points throughout the plume are extracted from the time series.

11A973. Anisotropic, transversely isotropic nonlinear viscosity of rock ice and rheological parameters inferred from homogenization. - L Lliboutry *(Lab de Glaciologie et Geophys del l'Env, CNRS, BP 96, 38402 St-Martin d'Heres, France)*. Int J Plasticity 9(5) 619-632 (1993).

The stress-strain relations for an anisotropic, incompressible viscous body that is orthotropic, transversely isotropic, are drawn from symmetry considerations. This kind of material forms the largest part of polar ice sheets. The 10 parameters entering the rheological law would be extremely difficult to draw from torsion-compression tests, the only ones that are feasible on ice cores. Nevertheless, homogenization allows to infer them from the statistical distribution of the c-axes and only two parameters that are accessible by readily analyzed pure shear tests. Homogenization is done assuming for any crystal embedded in rock ice a rheology that differs from the onset of isolated monocrystals and microscopic stresses at the crystal level equal to the macroscopic stress. Both assumptions are argued, in the light of experimental evidence about a single system of active slip planes, very low dislocation velocities, pile-ups at the grain boundaries, and boundary migrations during strain. These migrations destroy the pile-ups, besides allowing the strains in neighbor crystals to be different.

See also the following:

11T573. Microbiological stabilization of sludge by aerobic digestion and storage
11A923. BE analysis of contaminant transport in fractured porous media
11A924. FE modeling of transport of organic chemicals through soils
11A925. Modeling coupled heat and contaminant transport in groundwater
11A926. Simulation of groundwater flow and containment transport at a landfill site using models

IX. BIOENGINEERING

550. Biomechanics

11A974. **Mineral-organic interfacial bonding and the mechanical properties of cortical bone tissue.** - WR Walsh *(Biomech Lab, Dept of Orthopaedics, Brown Univ Sch of Med, Providence RI 02912)* and N Guzelsu *(Univ of Med and Dentistry, SOM Biomech & Rutgers Univ, 675 Hoes La, Piscataway NJ 08854)*. Biomimetics 1(3) 199-218 (Sept 1992).

Interfacial bonding between the mineral fibers (a hydroxyapatite-like material) and the organic constituents of bone (collagen and noncollagenous proteins) plays an important role in determining strength and stiffness. This bonding arises, in part, through the strong adsorption affinity between the mineral and the organic phase of bone. Phosphate and fluoride ions can alter the mineral-organic interfacial bonding, causing a dramatic reduction in the mechanical properties. The present study reveals that the phosphate ion effect is reversible when phosphate ions are removed from the equilibrium buffer. The fluoride ion effect is irreversible and the mechanical properties are permanently altered. Mineral-organic interactions in bone may serve as a guide to develop man-made materials based on similar interactions.

11A975. **Boundary layer development of pulsatile blood flow in a tapered vessel.** - Ren-jing Cen and Chan Qin *(S China Univ of Tech, Guangzhou, China)*. Appl Math Mech 14(4) 319-326 (Apr 1993).

Assuming that the tapered angle is small, the problems of developing flow under unsteady oscillatory condition are studied in this paper. The formula of velocity distribution is obtained. The analyses for the results show that the blood flow in a converging tapered vessel remains a developing flow throughout the length, and the effects of tapered angle on the developing flow are increased with the increment of the tapered angle.

11A976. **Effects of body force on the pulsating blood flow in arteries.** - K Haldar *(Electron Univ, Indian Stat Inst, Calcutta, India)* and SN Ghosh *(Dept of Math, Manbhum Mahavidyalaya, Manbazar, India)*. Eng Trans 41(2) 157-166 (1993).

The present investigation deals with the study of pulsating blood flow in single arteries in the presence of body force which usually arises unintentionally during travel in a road vehicle, an aircraft or a spacecraft. A blood vessel considered here is assumed to be rigid. The resulting equation which governs the flow field in the tube is 1D and it is solved using the Fourier analysis. The results obtained in this analysis are the expressions for the local energy dissipation and the amplitude coefficients of mean velocity and wall shear stress. The numerical solutions of these results are shown graphically for better understanding of the problem.

ANNOUNCEMENT

Fifth Conference on Nonlinear Vibrations, Stability, and Dynamics of Structures

June 12-16, 1994

Virginia Polytechnic Institute and State University
Blacksburg, Virginia

GENERAL INFORMATION

The scope of the conference includes

1. Multibody dynamics,
2. Dynamics of composite structures,
3. Adaptive structures,
4. Fluid/structure interactions,
5. Parametric vibrations: single- and multi-frequency excitations of single- and multi-degree-of-freedom systems,
6. Computational techniques: efficient algorithms, use of symbolic manipulators, integration of symbolic manipulation and numerical methods, and use of parallel processors,
7. Experimental methods: benchmark experiments, measurements in hostile environments, and instrumentation techniques,
8. Influence of nonlinearities on control systems, and
9. Identification of nonlinear systems.

Authors will have the option of having their full-length papers considered for publication in *NONLINEAR DYNAMICS*.

The deadline for two-page abstracts is January 15, 1994
The deadline for full-length papers is April 1, 1994.

Professors Ali H. Nayfeh and Dean T. Mook
Department of Engineering Science and Mechanics
Virginia Polytechnic Institute and State University
Blacksburg, VA 24061-0219 USA
Telephone: 703-231-5453/FAX: 703-231-4574/BITNET: *Sally@vtvm1.cc.vt.edu*

Author Index for November 1993

The codes after each name give the sequence numbers of the items in the Book Reviews section (R = Review, N = Note) or the Journal Literature section (A = Abstract, T = Title). Books listed by title only or as "under review" are not included in this index.

A

B

C

D

E

F

M

N

O

P

Q

R

S

ABBREVIATIONS USED IN APPLIED MECHANICS REVIEWS

academy, academia, academic	acad
acoustical, acoustics	acoust
administration	admin
advanced, advances	adv
aerodynamics	aerodyn
aeronautical, aeronautics	aeronaut
agricultur-e, -al	agri
Am Inst of Aeronaut & Astronaut 1633 Broadway New York NY 10019	AIAA
Am Inst of Chem Eng 345 E 47 St, New York NY 10017	AIChE
Am Inst of Phys 345 E 45 St, New York NY 10017	AIP
America, American	Am
Am Soc for Testing and Mat 1916 Race St Philadelphia PA 19103	ASTM
Am Soc of Civil Eng 345 E 47 St, New York NY 10017	ASCE
Am Soc of Heating Refrigeration and Airconditioning Eng 1791 Tullie Circle NE Atlanta GA 30329	ASHRAE
Am Soc of Mech Eng 345 E 47th St New York NY 10017	ASME
Applied Mechanics Reviews	AMR
analysis, analytic, analytical	anal
angewandte	angew
applied, application	appl
Architecture, architectural	architec
Archive, Archivum, Archiwum	Arch
Argonne Natl Lab Argonne IL 60439	ANL
association, associates	assoc
astronomy, astronomical	astron
astronautical, astronautics	astronaut
atmosphere, atmospherical	atmos
Australian	Austral
automatic, automation	autom
biomedical	biomed
boîte postale	BP
Boundary Element	BE
Boundary Element Method	BEM
Brookhaven Natl Lab Upton NY 11973	BNL
building, builders	build
Bulletin	Bull
Canadian	Can
celestial	celest
Centre National de la Recherche Scientifique	CNRS
chemical, chemistry	chem
City College of the City Univ of NY, New York NY 10031	CCNY
College	Col
combustion	combust
Commonwealth Sci and Indust Res Org	CSIRO
communication	commun
Comptes Rendus	CR
computer, computational	comput
Computer-Aided Design	CAD
conference	conf
construction	construct
conversion	Conv
Cornell University, Ithaca NY 14853	Cornell
David Taylor Naval Ship Res and Dev Center	NSRDC
degree(s) of freedom	dof
department	dept
design	des
development, developmental	dev
Deutsche Forschungs- und Versuchsanstalt für Luft- und Raumfahrt	DFVLR
division	div
dynamics	dyn
east, eastern	E
edition, editor, edited (by)	ed
education, educational	educ
elastic, elasticity	elast
electrical, electricity	elec
electronic	electron
engineer, engineering	eng
environment, environmental	env
equilibrium	equil
Establishment	Est
evaluation	Eval
experimental	exp
explosion	explos
faculty	fac
Federal, Federation	Fed
Federal Republic of Germany	FRG
Finite Element	FE
Finite Element Method	FEM
Foundation	Found
Fundamental(s)	Fund
geology, geological	geol
Georgia Institute of Technology, Atlanta GA 30332	Georgia Tech
hydraulic	hydraul
identification	ident
Incorporated	Inc
industry, industrial	indust
information, informatique	info
institute, institution	inst
Inst Natl de Rech en Informatique et en Automatique	INRIA
Inst of Elec and Electron Eng 345 E 47 St, New York NY 10017	IEEE
Institute of Technology	IT
international	int
Int Union Theor Appl Mech	IUTAM
Jet Propulsion Lab California Inst of Tech Pasadena CA 91109	JPL
journal	J
laboratory	lab
Los Alamos National Lab, Los Alamos NM 87545	LANL
Lawrence Berkeley Lab Berkeley CA 94720	LBL
Lawrence Livermore Natl Lab Livermore CA 94550	LLNL
management	man
manufacture, manufacturing	manuf
Massachusetts Inst of Tech Cambridge MA 02139	MIT
materials	mat
mathematics, mathematical	math
measurement	meas
mécanique	mec
mecha-nics, -nical, -nism	mech
medicine, medical	med
metallurgy	metall
meteorology, meteorological	meteorol
modeling	model
molecular, molecules	mol
month	mo
national	natl
Natl Aeronaut & Space Admin	NASA
Natl Bureau of Standards Washington DC 20234	NBS(=NIST)
Natl Inst of Standards and Tech Gaithersburg MD 20899	NIST(=NBS)
Natl Res Council	NRC
Natl Sci Foundation	NSF
New Jersey Inst of Tech	NJIT
New South Wales, Australia	NSW
New York Univ, New York NY	NYU
Non-Destructive Evaluation	NDE
Non-Destructive Testing	NDT
north, northern	N
northeast	NE
northwest	NW
Northwestern Univ Evanston IL 60201	NWU
nuclear	nucl
number	n, no, Nr
numerical	numer
Oak Ridge Natl Lab Oak Ridge TN 37830	ORNL
oceanography	oceanog
ordinary differential equations	ODE
Office Natl d'Etudes et de Recherches Aerospatiales, BP 72, 92322 Chatillon, France	ONERA
Office of Naval Research	ONR
optimization, optimum	optim
organization	org
page	p
pages	pp
partial differential equations	PDE
Pennsylvania State Univ University Park PA 16802	Penn State
petroleum	pet
physics, physical	phys
planetary	planet
Post Office	PO
Princeton Univ Princeton NJ 08544	Princeton
problems	prob
probability	probab
proceedings	proc
product, production	prod
progress	prog
publication, publish-ing, -ers	publ
Purdue Univ W Lafayette IN 47907	Purdue
Quarterly	Quart
recherche	rech
rehabilitation	rehab
reliability	reliab
Rensselaer Polytechnic Inst Troy NY 12181	RPI
research	res
research and development	R&D
Review, Revue, revised	Rev
rheology, rheologic	rheol
Royal	R
Royal Inst of Tech	RIT
Sandia Natl Lab Albuquerque NM 87185	Sandia
Scandinavia, Scandinavica	Scand
science, scientific, scientifique	sci
seismology	seismol
school	sch
simulation	simul
society	soc
Soc for Indust and Appl Math 1400 Architects Bldg, 117 S 17 St, Philadelphia PA 19103-5052	SIAM
Solar Energy Res Inst, 1617 Cole Blvd, Golden CO 80401	SERI
south, southern	S
southeast	SE
southwest	SW
Southwest Res Inst, 6220 Culebra Rd, San Antonio TX 78284	SWRI
Soviet	Sov
Stanford University, Stanford CA 94305	Stanford
State University of New York	SUNY
Station	Sta
statistics, statistical	stat
structural, structure	struct
studies, studii	stud
Symposium	Symp
system	syst
technical, technology	tech
temperature	temp
Teoretyczna	Teor
theoretical, theorique	Theor
three-dimensional	3D
Transaction	Trans
translat-ed, -er, -ion	transl
tribology	trib
two-dimensional	2D
United Kingdom (England, Scotland, Wales)	UK
United States	US
United States of America	USA
University	Univ
Univ of California	UC
Univ of California at Berkeley Berkeley CA 94720	UCB
Univ of California at Los Angeles Los Angeles CA 90024	UCLA
Univ of California at San Diego La Jolla CA 92093	UCSD
University Press	UP
vibration	vib
Virginia Polytech Inst & State Univ, Blacksburg VA 24061	VPI
volume	v, vol
west, western	W
Wright-Patterson Air Force Base OH 45433	WPAFB
Zeitschrift	Z

(6/93)

APPLIED MECHANICS REVIEWS REPRINTS

Structural and dynamic behavior of pretwisted rods and beams. A Rosen. AMR 44(12) Part 1, 483-516 (Dec 1991) Reprint No AMR102 $26

Hydroacoustics of transitional boundary-layer flow. GC Lauchle. AMR 44(12) Part 1, 517-531 (Dec 1991) Reprint No AMR103 $16

Index to Volume 44 (1991). Reprint No AMR108 $88

Stress minimum forms for elastic solids. LT Wheeler. AMR 45(1), 1-12 (Jan 1992) Reprint No AMR 107 $14

Micromechanics of composite materials. Special collection edited by AN Guz. AMR 45(2) 13-101 (February 1992) Reprint No AMR104 $54: (1) **Statics of laminated and fibrous composites with bent structures.** SD Akbarov and AN Guz. (2) **Dynamics of laminated and fibrous composites.** AN Guz and NA Shulga. (3) **Stability of fibrous composites.** IY Babich and AN Guz. (4) **Stability of laminated composites.** AN Guz and VN Chekhov.

Microbubble drag reduction in liquid turbulent boundary layers. C Merkle and S Deutsch. AMR 45(3) Part 1, 103-127 (March 1992) Reprint No AMR105 $22

Material Instabilities (22nd Midwestern Mechanics Conference, Rolla MO, Oct 1991) HM Zbib, TG Shawki, RC Batra (eds). AMR 45(3) Part 2 (March 1992) Reprint No AMR110 $66

Heat-transfer control: Principal focus on Japanese Research. T Aihara. AMR 45(4) 129-153 (April 1992) Reprint No AMR109 $16

Optimum dimensions of extended surfaces operating in a convective environment. A Aziz. AMR 45(5) 155-173 (May 1992) Reprint No AMR111 $18

Overview of micro heat pipe research and development. GP Peterson. AMR 45(5) 175-189 (May 1992) Reprint No AMR112 $16

Multiphase poroelastic finite element models for soft tissue structures. BR Simon. AMR 45(6) 191-218 (June 1992) Reprint No AMR114 $22

Dynamics and control of coherent structures in turbulent jets. RR Mankbadi. AMR 45(6) 219-248 (June 1992) Reprint No AMR113 $24

Addendum to: Bibliography of monographs and surveys on shells. W Pietraszkiewicz. AMR 45(6) 249-250 (June 1992) Reprint No AMR115 (free with AMR078 $14)

Romanian sources on applied mechanics. ME Popescu. AMR 45(6) 251-252 (June 1992) Reprint No AMR116 no charge.

Fluorescence thermometry. LJ Dowell. AMR 45(7) 253-260 (July 1992) Reprint No AMR117 $12.00

Micromechanical modelling of quasi-brittle materials behavior. VC Li (ed), 10 articles. AMR 45(8) 261-398 (Aug 1992) Reprint No AMR118 $60.

Recent developments in the force method of structural analysis. A Kaveh AMR45(9) 401-418 (Sep 1992) Reprint No AMR119 $18.

Computational models for high-temperature multi-layered composite plates and shells. AK Noor and WS Burton. AMR 45(10) 419-446 (Oct 1992) Reprint No AMR 120 $22.

Dynamics of periodic and near-periodic structures. Dong Li and H Benaroya. AMR 45(11) 447-460 (Nov 1992) Reprint No AMR121 $16.

Finite element analysis of aeroelasticity of plates and shells. MN Bismarck-Nasr. AMR 45(12) 461-482 (Dec 1992) Reprint No AMR122 $20.

Index to Volume 45 (1992). Reprint No AMR123 $88

Mathematical modeling of transport phenomena during alloy solidification. C Beckermann and R Viskanta. AMR 46(1) 1-28 (Jan 1993) Reprint No AMR124 $22.

Perturbation techniques in phase change heat transfer. A Aziz and VJ Lunardini. AMR 46(2) (Feb 1993) Reprint No AMR125 $28.

US machining and grinding research in the 20th century. R Komanduri, ME Merchant, MC Shaw. AMR 46(3) (Mar 1993) Reprint No AMR 126 $42

Nondestructive testing and structural condition monitoring of mechanical cables. PAA Laura. AMR 46(4) 133-138 (Apr 1993) Reprint No AMR127 $12.

Aging of energy production and distribution systems: DOE Workshop, Rice University, Houston TX, October 11-13, 1992. Edited by MM Carroll and PD Spanos. AMR 46(5) 139-263 (May 1993) Reprint No AMR128 $78.

Applied mechanics of a lunar base. Edited by H Benaroya. AMR 46(6) 265-358 (June 1993) Reprint No AMR129 $65.

Chaos and noise in dynamical systems. Edited by T Kapitaniak and J Brindley. AMR 46(7) 359-444 (July 1993) Reprint No AMR130 $59.

Boundary integral equations in aerodynamics. L Morino. AMR 46(8) 445-466 (August 1993) Reprint No AMR131 $20.

Vibrations of planar curved beams, rings, and arches. P Chidamparam and AW Leissa. AMR 46(9) 467-483 (Sep 1993) Reprint No AMR132 $20.

Thermal buckling of plates and shells. ER Thornton. AMR 46(10) 485-506 (Oct 1993) Reprint No AMR 133 $20.

Mechanics Pan-America 1993 (Proc PACAM-3, São Paulo, Brazil, Jan 1993). MRM Crespo da Silva and CEN Mazzilli (eds). AMR 46(11) Part 2 (Nov 1993) Reprint No AMR134 $88

Subscription: ASME members (without Suppl.) $51 $_____
ASME members (with Supplement) $84 $_____
non-members (with Supplement) $534 $_____
2nd library subscription $99 $_____
Postage outside USA or Canada $102, airmail $156 $_____

Reprint No:	*Reprint title:*	
____________	____________	$_____
____________	____________	$_____
____________	____________	$_____
	TOTAL ORDER:	$_____

ASME member prices for reprints (50% of list) apply to the purchase of 1 copy of any reprint for the member's personal use with shipment to his or her personal attention. *Bulk reprint prices:* $215 for 100 copies of an article of up to 8 pages, plus $85 for each additional 4 pages (add $25 and $5, respectively, for each additional 100 copies). *Ordering information:* Advance payment required if billed outside USA or Canada. Foreign and Canadian checks not accepted unless payable in US dollars through a US bank. CA, GA, IL, TX purchasers must add sales tax, Canadians 7% GST, or furnish tax exemption certificate.

Send order to: **ASME/AMR**
22 Law Drive, PO Box 2900
Fairfield NJ 07007-2900

or FAX form to: 1-201-882-5155

ASME members, to receive discount you must indicate your membership no.: ____________

ASME Member Name: ____________

Signature: ____________ ____________

METHOD OF PAYMENT (check one):

[ ] Payment enclosed

[ ] Purchase Order No.: ____________
(attach Purchase Order)

[ ] Charge card (circle one): Master Card VISA American Express Diners Club Discover

Account Number: ____________
Mastercard Interbank No: ____________
Expiration Date: ____________

Signature: ____________

BILL TO: Name: ____________
Company: ____________
Street address: ____________
City, State, ZIP: ____________
Country: ____________

SHIP TO: Name: ____________
Company: ____________
Street address: ____________
City, State, ZIP: ____________
Country: ____________

applied mechanics reviews

AIMS

The primary aim of *AMR* is to serve engineering scientists worldwide by assessing, reviewing, and reporting on advances in a broad range of mechanical engineering sciences. To this end *AMR* publishes (i) state-of-the-art review articles, bibliographic surveys, reviews with a special focus on emerging technology, tutorials, historical perspectives, periodic summaries of trends and advances; (ii) critical reviews of books, software, and databases; (iii) indexed compilations of carefully selected abstracts from high quality research journals; (iv) book-length monographs and symposium proceedings as special issues or supplements; and (v) editorials, announcements, and letters-to-the-editor.

A secondary aim of *AMR* is to serve technical and reference librarians, information specialists, professional engineers, and college professors through reliable, comprehensive, and timely information about all types of books within its subject scope. The annual cumulative index issue of *AMR* together with its monthly classified listings of abstracts is in effect a comprehensive bibliography of the mechanical engineering sciences, including essentially every article in some 50-60 core journals; this core includes all ASME Transaction journals.

SCOPE

The scope of *AMR* encompasses all the engineering sciences represented in the journals and symposia sponsored by the American Society of Mechanical Engineers and is outlined by *AMR*'s Subject Classification Scheme, which is reprinted on the back cover. It includes basic discipline-oriented areas such as dynamics, continuum mechanics, solid and fluid mechanics, structures, heat transfer, tribology, geomechanics, and biomechanics, as well as cross-disciplinary subjects and emerging critical technological areas such as new numerical and computational techniques, systems control technology, engineering design tools, manufacturing technology, materials and energy technology, and environmental engineering.

The American Society of Mechanical Engineers

INFORMATION FOR AUTHORS OF REVIEW ARTICLES

(1) Prospective authors are strongly urged to communicate with one of the Associate Editors or the Editor-in-Chief, Professor Arthur W Leissa, Department of Engineering Mechanics, Ohio State University, 155 W Woodruff Ave, Columbus, Ohio 43210 (TEL 614-457-4337 or 614-292-2680) before submitting an article, and to furnish a one-page outline of the proposed article and information as to its type, audience, and probable length. A form, *Prospectus for a Review Article,* is available for this purpose. Refer to the editorials in the January 1985 and March 1991 issues of *AMR* and the box at left for further discussion of *AMR*'s editorial criteria.

(2) *Submit four clean copies* of the manuscript to one of the Associate Editors or to the Editor-in-Chief. (Hold all separate original artwork until the article has been accepted.) All articles will be reviewed critically by at least two independent and anonymous referees chosen by the editor involved. This procedure will be followed even if the article is the result of solicitation or encouragement by the editors, or if the author is also an *AMR* editor. The final decision on publication is made by the Editor-in-Chief upon recommendation of an Associate Editor. If appropriate, the article will carry a footnote saying "Transmitted by Associate Editor . . ."

(3) Submission of a manuscript is a representation that it has not been published previously nor is currently being submitted for publication elsewhere. The authors will be asked to sign a statement *transferring copyright to ASME.* It is the author's responsibility to obtain permission to copy material from other sources, if needed.

(4) There are *no page charges* in *AMR* and no numerical length limitations. The length of the article should be appropriate to the subject and the audience. It is certainly one factor that will be evaluated by the editors and their referees, who may recommend changes (30-120 manuscript pages is typical). Each author of a review article will receive *a year's free subscription to AMR.* After publication the author will receive *100 free reprints* (to be shared if there are more than one author). In addition, ASME will distribute reprints singly and in bulk.

(5) Along with the final *manuscript* send the *compuscript on diskette,* if available, (with format identified) incorporating all corrections and additions, and with the tables and figure captions *in place within the text.* If the figures are computer graphics, place them also within the compuscript where they belong. Also, send a head-and-shoulders *photograph and short biographical sketch* (100-200 words) of each author, including grades of ASME membership, if any; include the bio at the end of the compuscript.

(6) *Order of parts:* Title of article, authors' names, authors' institutional affiliations, abstract (200-300 words suitable for abstracting services), table of contents (only if the article is so long that it needs one), list of symbols and abbreviations (if necessary), main text incorporating tables (each starting with a caption) and figure captions (in place where you want them in the text), list of references, biographical sketch, and original figures (if computer graphics, place in text above captions).

(7) *Format:* (a) Paper size: A4 or 8.5×11 inch (220×280 mm). (b) Word processor settings: One column of width 3.4 in (87 mm) leaving rest of page for referee and editorial comments; Type size 10 point (72 point = 6 pica = 1 inch = 25.4 mm) Times Roman or similar proportionally spaced style; Line spacing 12 points. These as-printed *AMR* specifications will help to insure that equations, tables, and figures are properly designed for the available space. (c) Use metric SI units; with other units in parentheses, if appropriate. (d) Cite references by last name and year; reference list at end alphabetical by author (in 7-point type). (e) Number figures with arabic numerals; design figures for column width (83 mm or 3.1 in), if possible; they should be professionally drawn or computer generated with lettering of consistent size (not smaller than the printed text after reduction); use your wordprocessor to place an empty box of the correct dimensions (or the figure itself, if a computer graphic) in the text above each figure caption. (f) Number tables with roman numerals. (g) Latin letters used as math symbols should be in italics both in text and in displayed equations. Subscripts and superscripts should be 7 point type. Fractional powers are preferred to root signs, exp(..) to $e^{\cdot\cdot}$, and a solidus (/) for fractions, if that will save vertical space.

(8) *Camera-ready copy:* Typeset (or near-typeset) quality pages or galleys generated by the author (after review and acceptance) are preferred, and could result in faster publication. Reproduce the format of published *AMR* review articles (basically, two of the columns defined above per page). Camera-ready pages along with a diskette (for DOS) is requested. Microsoft Word is suggested. Questions on this should be directed to the Production Editor at 201-882-1170, ext 232.

SPECIAL ISSUES: From time to time Guest Editors are invited to produce Special Issues consisting of three or more articles grouped around a common theme. SUPPLEMENTS are booklength monographs or symposium proceedings published as part 2 of a regular issue. Proposals for Special Issues or Supplements are very welcome. Guest Editorials, Letters-to-the-Editor, Announcements: Contact the Editor-in-Chief.

9/93

MAIN HEADINGS FOR CLASSIFIED JOURNAL LITERATURE

(for full classification scheme and alphabetical index see December issue)

ISSN 0003-6900

JOURNAL CODE AMR

ISSUE CODE 9311

MECHANICS PAN-AMERICA 1993

Selected and Extended Papers from the
Third Pan-American
Congress of Applied Mechanics
January 1993, São Paulo, Brazil

edited by MRM Crespo da Silva and CEN Mazzilli

CONTENTS

MECHANICS PAN-AMERICA 1993

Selected and Extended Papers from the
Third Pan-American
Congress of Applied Mechanics
January 1993, São Paulo, Brazil

Editors:

by MRM Crespo da Silva and CEN Mazzilli

Applied Mechanics Reviews, Volume 46, Number 11, Part 2, November 1993

INTRODUCTION

The Third Pan American Congress of Applied Mechanics (PACAM III) was held at the *Escola Politécnica da Universidade de São Paulo*, in the city of São Paulo, Brazil, during January 4-8, 1993.

The PACAM congresses are sponsored by the American Academy of Mechanics (AAM) and are held every other year, during the first week of January, in one of the countries of the Americas. The objective of each congress is to promote technical interactions between research engineers, scientists, and graduate students.

The organizing and editorial committees of PACAM III accepted nearly 200 short papers from South America, North America, Europe, Africa, and Asia. These four-page papers appear in a 774-page proceedings of the congress, which was printed in Brazil.

This special supplement of *Applied Mechanics Reviews*, edited by the chairman of PACAM III and by the chairman of the local arrangements committee for the congress, contains the extended version of a number of the papers that were presented at PACAM III. These papers were selected by several reviewers who attended the congress.

We gratefully acknowledge the support received from the *Escola Politécnica da Universidade de São Paulo,* Rensselaer Polytechnic Institute, FAPESP (*Fundação de Amparo à Pesquisa do Estado de São Paulo)*, and the National Science Foundation.

The Fourth Pan American Congress of Applied Mechanics (PACAM IV) will be held in Buenos Aires, Argentina, in January 1995.

M R M Crespo da Silva
C E N Mazzilli
Co-Chairmen
Organizing and Editorial Committee

Theoretical and experimental study on nonlinear response of a rotor blade to a gust

DM Tang and EH Dowell

Department of Mechanical Engineering and Materials Science
Duke University, Durham NC 27706

A rotating slotted cylinder (RSC) gust generator installed in the Duke University low speed wind tunnel was used to generate a gust excitation field and the nonlinear response of a flexible rotor blade to gust excitations was studied theoretically and experimentally. The quantitative agreement between theory and experiment indicates that the assumption of an uniform chordwise gust angle of attack and an approximate solution procedure of the nonlinear equations proposed are allowable for the parameter range considered in this study. For a periodic gust flow field, the effects of geometric structural nonlinearity and aerodynamic nonlinearity on dynamic aeroelastic behavior are significant and lead to aperiodic or chaotic motion when stall occurs.

INTRODUCTION

From an earlier theoretical study of a linear rotor blade structure with a nonlinear aerodynamic model in forward flight, it was found that chaotic or aperiodic responses exist when the parameters of the rotor blade are near the flutter boundary or stall occurs, see Ref.[1]. Subsequent theoretical and experimental studies were conducted for a non-rotating rotor blade with a parabolic or a freeplay pitch stiffness nonlinear element, and using a linear or nonlinear aerodynamic model to determine limit cycle flutter, chaotic stall response and the influence of the initial conditions on response behavior. The experimental results from the wind tunnel test were compared to the theoretical prediction and the agreement was good, see Ref.[2] and [3] which considered a rigid, hinged (articulated) rotor blade. Ref.[4] extended the above studies to a flexible, hingeless (cantilevered) blade with geometric structural nonlinearity included in the analysis and experiment. The nonlinear static deflections, limit cycle flutter oscillation and stall chaotic responses were determined theoretically and experimentally.

The foregoing works considered an external excitation, such as a cyclic pitch control input from a swashplate of the helicopter, or a base harmonic excitation in the pitch and/or chordwise direction at the blade root, in addition to the self-induced aerodynamic forces. The purpose of the present paper is to study the forced response of a non-rotating flexible rotor blade due to an aerodynamic gust without any other external excitation sources. In order to evaluate the results obtained from the present analytical prediction, a gust response experiment with a rotating slotted cylinder (RSC) gust generator has been carried out in the Duke University low speed wind tunnel. The development of the experimental apparatus as well as the associated measurement technique for gust angle and flow field charecteristics are discussed in Ref.[5].

The study of helicopter gust response is important because of the normal conditions for helicopter operation and the successful application of advanced hub designs. Helicopters with hingeless and bearingless rotors are often more sensitive to gusts than articulated rotors. For a helicopter fitted with a wing (e.g. compound configurations), additional gust loads may be generated. These configurations require the accurate determination of rotor blade gust response for both handling qualities and structural loads design.

Linear theoretical gust response calculations and wind tunnel tests of helicopter rotors have been considered by several authors Ref.[6-10]. In this paper fundamental research on nonlinear response to a sinusoidal gust, or a periodic gust with two harmonic frequency components, or a linear frequency sweep gust excitation is described. In the present analysis, both the linear response below stall and nonlinear stall response through the stall angle of attack are described based on the Sears aerodynamic solution [11] and also the nonlinear ONERA aerodynamic model [12]. A comparison between the theoretical and experimental results has been made. The results may be helpful in understanding physically the nonlinear aeroelasticity phenomena.

In this paper, two major issues are discussed. One is the theoretical prediction of the unstalled and stalled gust response. An approximate solution procedure and numerical examples are included. Another issue is the comparison of theory and experiment for a cantilevered blade model with geometric structural nonlinearity. Results from the wind tunnel tests show generally good agreement with theory.

part of "MECHANICS PAN-AMERICA 1993" edited by MRM Crespo da Silva and CEN Mazzilli ASME Reprint No AMR134
Appl Mech Rev vol 46, no 11, part 2, November 1993

NUMERICAL ANALYSIS

Equations of motion

The present study is based upon a consistently derived system of equations of motion for an elastic hingeless blade model under a sinusoidal gust excition for a non-rotating blade which is cantilevered vertically as shown in Fig.1. v, w and ϕ are the chordwise, flapping bending deflections and twist about deformed elastic axis, respectively. According to the Hodges-Dowell equations [13], for a non-rotating uniform, untwisted elastic blade, neglecting cross-section warping, the equations of motion may be written as

$$EI_2 v'''' + \beta(\phi w'')'' + m\ddot{v} + v_{mg} = \frac{dF_v}{dx} \quad (1)$$

$$EI_1 w'''' + \beta(\phi v'')'' + m\ddot{w} + me\ddot{\phi} + w_{mg} = \frac{dF_w}{dx} \quad (2)$$

$$-GJ\phi'' + \beta w'' v'' + mK_m^2\ddot{\phi} + me\ddot{w} + M_k = \frac{dM_x}{dx} \quad (3)$$

where $\beta = E(I_2 - I_1)$. Note that in Eq.[1]-[3] only the most important geometric structural nonlinear terms, $(\phi w'')''$, $(\phi v'')''$ and $w''v''$ are retained from the Hodges-Dowell equations and the third and higher order geometrically nonlinear terms are neglected here. Also note that ϕ is measured with respect to the deformed elastic axis. For the blade structure with a pitch spring at the root, the torsional motion, ϕ, includes elastic torsional deformation along the blade span and pitch motion at the blade root.

The restoring stiffness terms v_{mg} , w_{mg} and M_k may be deduced by variational methods.

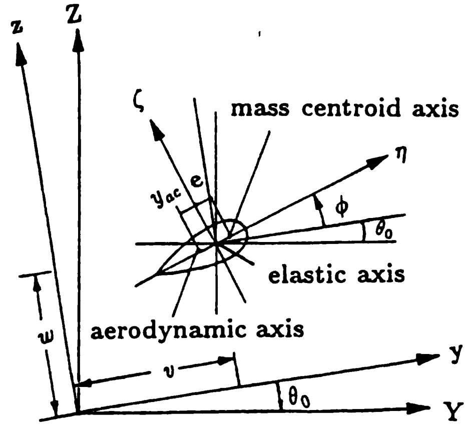

FIG 1. Deflection geometry of a flexible rotor blade

In Eq.(1)-(3), the components of the aerodynamic forces, dF_v, dF_w, and the aerodynamic moment about the elastic axis, dM_x, are obtained from the two-dimensional incompressible strip theory.

For determination of the aerodynamic lift, drag and pitching moment coefficients, C_l, C_d and C_m, in this theory, an ONERA aerodynamic stall model is used. The ONERA model is semi-empirically derived using measured wind tunnel data for an oscillating airfoil in conjunction with a parameter identification scheme as shown in Ref.[12].

For the ONERA aerodynamic stall model, the lift, drag and moment coefficients of each blade section in the differential equations are described in terms of a reduced time. This time scale is not convenient for the dynamic analysis of the blade, however. A more conventional differential operator relative to the real time, d/dt, is used in this paper for comparison with the experimental data.

The ONERA dynamic stall model is based on a blade airfoil element. Here, it is applied to a blade motion problem. A simple assumption is that the blade is divided into several spanwise aerodynamic sections, say NN, and the ONERA model is applied to each section.

When we use the ONERA model, a key consideration is how to express the gust angle of attack for an airfoil entering a sinusoial gust field. A general expression of the effective gust angle of attack, see Ref.[11], pp. 410, is

$$\alpha(t, \bar{y}) = \alpha_{G0}\sin(\omega t - k\bar{y}). \quad (4)$$

where $\bar{y}$ is the nondimensional streamwise coordinate fixed on the airfoil, with the origin $\bar{y} = 0$ located at the mid-chord point. k is the reduced frequency. Now recall that the lift acting on an airfoil at small angles of attack (linear regime) can be expressed as the Sears solution

$$L = \pi\rho c U^2 \alpha_{G0} e^{i\omega t}\phi_S(k), \quad (5)$$

where $\phi_S(k)$ is a Sears function.

In this paper, we assume that the chordwise distribution of the gust velocity may be regarded as constant at any instant of time and equal to the gust at the mid-chord point. The effective angle of attack is thus

$$\alpha(t) = \alpha_{G0}\sin\omega t \quad (6)$$

This assumption is valid for the conditions of the experiments described in this paper. For some helicopter applications, this assumption may need to be overcome by generalizing the present analysis.

The results of numerical simulations indicate that the assumption of an uniform chordwise gust effective angle of attack in the linear ONERA model is in good quantitative agreement with the Sears solution for a convecting gust field at small gust angles, ($\alpha_{G0} < 6^0$) and small reduced frequency k ($k < 0.3$). However, for the nonlinear (stall) ONERA model, the constant chordwise gust distribution assumption has not been verified independently, except through the subsequent comparison between theory and experiment for blade response.

Several periodic gust time histories are considered subsequently including the following:

(1) Continuous sinusoidal gust

$$w_G(t) = w_{G0}\sin\omega t \quad (7)$$

(2) Continuous periodic gust

$$w_G(t) = w_{G01}\sin\omega t + w_{G02}\sin(2\omega t + \epsilon) \quad (8)$$

(3) Continuous frequency sweep gust

$$w_G(t) = w_{G0}\sin(\omega_1 + \frac{\omega_2 - \omega_1}{2T}t)t \quad (9)$$

where ω_1, ω_2 and T are the minimum frequency, maximum frequency, and the sweep duration (in seconds).
An effective angle of attack component , α_G, due to the gust can be represented as

$$\alpha_G(t) = \frac{w_G(t)}{U}. \tag{10}$$

In Eq.(1)-(3), expansions in general mode shape functions are used to obtain ordinary differential equations in terms of generalized modal co-ordinates. They are expressed in series form as follows.

$$\bar{v} = \sum_{j=1}^{N} V_j(t)\psi_j(\bar{x}), \tag{11}$$

$$\bar{w} = \sum_{j=1}^{N} W_j(t)\psi_j(\bar{x}),$$

$$\phi = \sum_{j=1}^{N} \Phi_j(t)\Theta_j(\bar{x}),$$

where $(\bar{\ })$ indicates non-dimensionalization of the spanwise coordinate with respect to the blade span, R, and, ψ_j and Θ_j are the characteristic functions for cantilevered beam bending and torsional vibrations, respectively.
Substituting these expansions into Eq.(1)-(3), and using the Galerkin method one obtains a set of nonlinear modal equations of motion.

Solution procedure

Unstalled gust response solution

For the unstalled gust response problem, the aerodynamic drag and pitching moment coefficients are explicit algebraic functions of the effective angle of attack, but the lift coefficient is described as a first order differential equation which also depends upon the position of aerodynamic element. There are NN degrees of freedom for the aerodynamic model.

A linearized perturbation procedure was used to solve the nonlinear equations. The static equilibrium equations are 3N nonlinear algebraic equations in the static equlibrium values, V_{0j},W_{0j} and Φ_{0j} which are solved by iteration using the Newton-Raphson method. In addition, there is a set of 6N+NN first order linear non-homogeneous perturbation differential equations in the small time dependent structural perturbation variables, ΔV_j,ΔW_j $\Delta\Phi_j$ and the lift coefficient perturbation veriables, $\Delta C_{l\gamma l}$. It is expressed as a matrix equation of first order by:

$$\begin{bmatrix} M_{jj} & M_{jl} \\ M_{lj} & M_{ll} \end{bmatrix} \begin{Bmatrix} \Delta\dot{q}_{a1} \\ \Delta\dot{q}_{a2} \end{Bmatrix} = \begin{bmatrix} K_{jj} & K_{jl} \\ K_{lj} & K_{ll} \end{bmatrix} \begin{Bmatrix} \Delta q_{a1} \\ \Delta q_{a2} \end{Bmatrix} + \begin{Bmatrix} F_{jd} \\ F_{ld} \end{Bmatrix} \alpha_G + \begin{Bmatrix} F_{jv} \\ F_{lv} \end{Bmatrix} \dot{\alpha}_G \tag{12}$$

where

$$\{\Delta q_{a1}\}^T = \lfloor ....\Delta\dot{V}_j, \Delta V_j, \Delta\dot{W}_j, \Delta W_j, \Delta\dot{\Phi}_j, \Delta\Phi_j .... \rfloor$$

$$\{\Delta q_{a2}\}^T = \lfloor ....\Delta C_{l\gamma l} .... \rfloor$$

For the solution using the Sears aerodynamic model, the perturbation equations are expressed as a set of 6N first order linear non-homogeneous differential equations by:

$$[M_s]\{\Delta\dot{q}_{a1}\} = [K_s]\{\Delta q_{a1}\} + \{F_s\}\phi_s(k)\alpha_G + \{F_v\}\dot{\alpha}_G \tag{13}$$

Stalled gust response solution

Stalled gust response can be determined by the following procedure. The structural model are second order, nonlinear differential equations in the variables, V_j, W_j and Φ_j, respectively. Two state variables are required for each jth variable. Thus 2x3xN structural state variables are required. For the ONERA aerodynamic model, a third order system for the lift coefficient and a second order system for both drag and pitch moment coefficients are required. Hence, seven state variables are required per aerodynamic section. The total number of state variables for the aeroelastic system is thus 6N+7NN.

The resulting system of the state variable equations is given by:

$$\begin{bmatrix} \hat{M}_{jj} & \hat{M}_{jl} \\ \hat{M}_{lj} & \hat{M}_{ll} \end{bmatrix} \begin{Bmatrix} \dot{q}_{bj} \\ \dot{q}_{bl} \end{Bmatrix} = \begin{bmatrix} \hat{K}_{jj} & \hat{K}_{jl} \\ \hat{K}_{lj} & \hat{K}_{ll} \end{bmatrix} \begin{Bmatrix} q_{bj} \\ q_{bl} \end{Bmatrix} + \begin{Bmatrix} \hat{F}_j \\ \hat{F}_l \end{Bmatrix} \tag{14}$$

where

$$\{q_{bj}\}^T = \left\{....\dot{V}_j, V_j, \dot{W}_j, W_j, \dot{\Phi}_j, \Phi_j ....\right\}^T,$$

$$\{q_{bl}\}^T = \left\{....\dot{C}_{lbl}, C_{lbl}, C_{l\gamma l}, \dot{C}_{dbl}, C_{dbll}, \dot{C}_{mbl}, C_{mbl}, ...\right\}^T.$$

Eq.(14) is a set of nonlinear differential equations. The solution of the equations can be obtained by numerical time integration. The section angle of attack ,α_l, and section inflow angle ,$\phi_{\lambda l}$, involve the state variables V_j, W_j and Φ_j. The initial values of α_l and $\phi_{\lambda l}$ are determined by the initial values of the state variables that then change during the numerical integration in a time step fashion.

The following calculation results are for the blade divided into 4 equal length spanwise strips. The blade section is a NACA 0012 airfoil. The static lift, drag and pitch moment coefficients are identified from the experimental data using curve fitting.

EXPERIMENT

An experiment for a flexible rotor blade responding to a gust was performed in the Duke University low speed, closed circuit wind tunnel as shown in Fig.2. The gust was created by placing a rotating slotted cylinder (RSC) behind a rigid, fixed airfoil upstream of the flexible blade. The gust generator configuration in the wind tunnel had two airfoils or vanes and two rotating sl[illegible]ers.

The distance between these vanes was 12 inches. For details of the gust generator design, see Ref.[5]. The flexible blade model configuration (Model II), parameters and measurement sensors were described in Ref.[4], and also see Table 1.

Strain gages were used for measurement of flap and elastic torsional deflections. An axial gauge (flap) for bending modes and a 45^0 gauge for torsional modes were glued to the flexible rotor blade spar to measure the bending-torsional deflections of the blade tip. Signals from the strain gages were conditioned and amplified before their measurement through a low-pass filter. A micro-accelerometer was installed at the tip of the blade for measuring the chordwise response. The pitch angular displacement at the blade root was measured by a rotational velocity/displacement transducer, RVDT. The output signals from these strain gauges and transducers were amplified and directly recorded on a Macintosh IIci computer through a data acquisition package, NB-MIO-16, which consisted of a 16-channel analog to digital (A/D) plug-in interface board, a BNC termination box, and data acquisition and analysis software, LabVIEW. The digitized response data could be graphically displayed either on-line or off-line as a time history, phase plane plot, FFT, PSD, or Poincare map. In order to obtain a comparison of the theory with the test, a measurement system calibration was completed before the wind tunnel test. The dynamic calibration coefficients were determined by a ground vibration test. The dynamic calibration assumed that there was no significant coupling between the bending and torsional directions. This is a reasonable assumption for the present test configuration.

The longitudinal gust velocity and gust angle were measured with two differential presure probes mounted on a cylinder which is located at the blade chord position with the blade temporarily removed. The distance between the blade chord and airfoil/RSC system was 7 inches. The blade was placed in the symmetrical plane of the tunnel. The gust flow field measurements were described in Ref.[5].

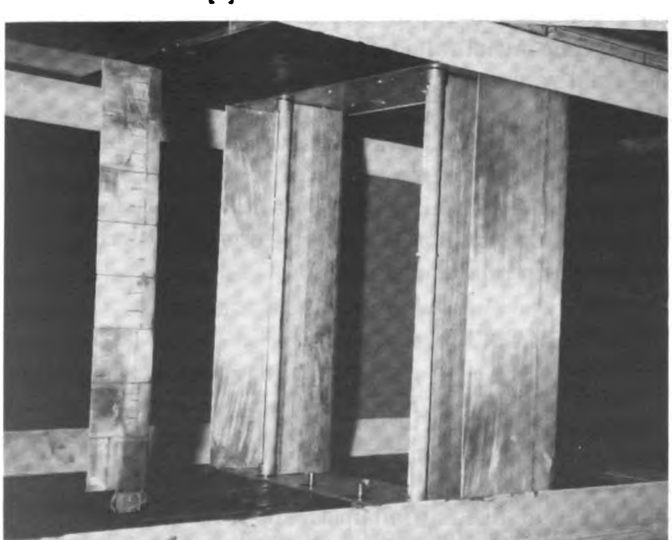

FIG 2. Photograph of experimental apparatus.

RESULTS AND DISCUSSIONS

In the next section, the response behavior of the blade to a single harmonic, a two harmonic or a continuous frequency sweep gust excitation is discussed. The ONERA stall aerodynamic model is used to calculate the gust response of this model for comparison with the experimental results. Two major issues are discussed here. One is the unstalled gust response, i.e. the initial pitch angle, θ_0, is 6^0. Another is the stalled gust response, i.e. $\theta_0 = 13^0$. The free stream velocity is U=15.6 m/s which is lower than the flutter critical speed ($U_{cr} = 24.4m/s$ for $\theta_0 = 13^0$) for the flexible blade model used here.

Single harmonic gust excitation

A typical measured gust angle (lateral gust wave) generated by the RSC gust generator is shown in Fig.3(a) for an airstream velocity of U=15.6 m/s, and cylinder rotation speed of $\omega_s = 5Hz$. The dominant gust frequency has been shown to be $2\omega_s$ [5]. A corresponding FFT plot is shown in Fig.3(b). The gust angle of the first harmonic frequency ($2\omega_s = 10Hz$) is 1.7^0, and the second harmonic ($4\omega_s = 20Hz$) is 0.16^0. A relatively pure tone lateral sinusoidal gust wave is obtained.

In the following, we will discuss unstalled and stalled response behavior for U=15.6m/s and $\alpha_G = 1.7^0$ as displayed in Fig.4-Fig.6. In those figures, (a) is for the theory and (b) for the test.

The theoretical calculations are based on Eq.(14). For unstalled gust response, the theoretical results indicate that the lift coefficient is linear vs the angle of attack. Flap, chord and pitch responses appear to be purely periodic with response primarily at the gust frequency. See Fig.4. The difference between the results for Type=0 (without geometric structural nonlinearity, i.e. $(\phi w'')''$, $(\phi v'')''$ and $w''v''$ in Eq.(1)-(3) are zero) and Type=1 (with geometric structural nonlinearity) is small except for the chordwise response. For Type=0 the chordwise response is much smaller than the one for Type=1. A typical theoretical flap response time history at the blade tip is shown in Fig.4(a) for $\theta_0 = 6^0$ and $\omega_s = 5Hz$. For a comparison, an experimental flap response is shown in Fig.4(b). The experimental results display a little more complex response for flap motion and more complex responses for chordwise and torsional motions than those of theory. This may be because the theoretical calculation did not include the longitudinal gust velocity. The quantitative agreement between theory and experiment is good for flap motion, and the agreement at the the fundamental frequency component ($2\omega_s = 10Hz$) is generally good for the chordwise and torsional motions. For brevity, the latter are not shown.

For stalled gust response, the theoretical results display aperiodic or chaotic behavior for $\theta_0 = 13^0$. This is because the aerodynamic forces are nonlinear functions of the angle of attack due to the airfoil motion arising from the gust. The phase plane plots of the lift, drag and pitch moment coefficients response vs α have substantial hys-

Table1

	model II
R	19.68 (in)
c	3.15 (in)
$\bar{c}$	0.16
ω_z	10 (Hz)
ω_y	23.5 (Hz)
ω_x	31.5 or 17.8 (Hz)
GJ	$.25*10^4(1bin^2)$
m	$.47*10^{-4}(1bs^2/in^2)$
K_m	1.149 (in)
$K_{\phi s}$	$18.62(1b.in/rad.)$
$\bar{y}_{am}$	-0.1
$\bar{y}_{ac}$	-.05

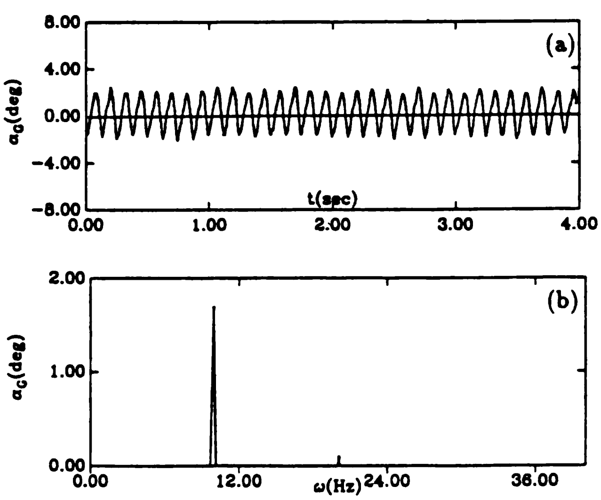

FIG 3(a)(b). Lateral gust of single harmonic gust excitation for $\omega_s = 5Hz$, U=15.6 m/s: (a) for time history, (b) for FFT.

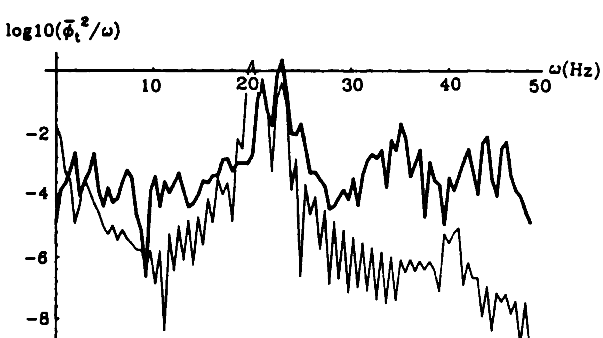

FIG 6. PSD plot of torsional response for single frequency gust excitation, —, for theory, ▬, for test.

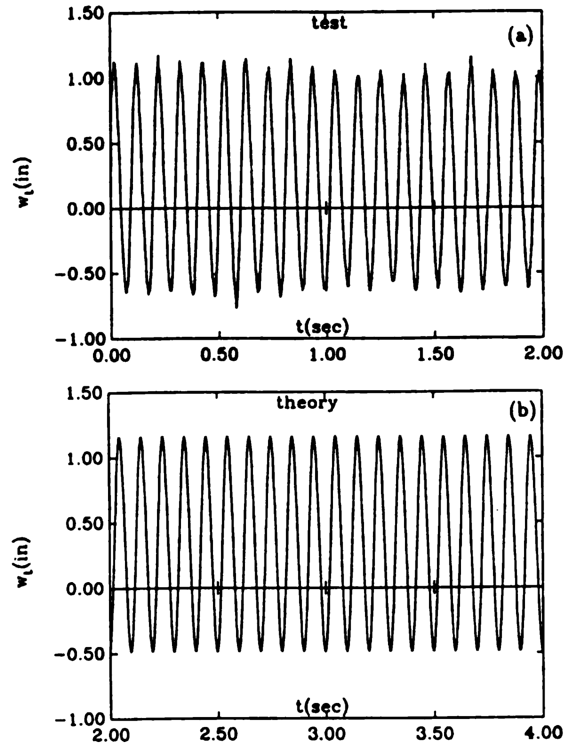

FIG 4(a)(b). Flap response time history for single frequency gust excitation, $\omega_s = 5Hz, \theta_0 = 6^0$, and U=15.6 m/s: (a) theory, (b) test.

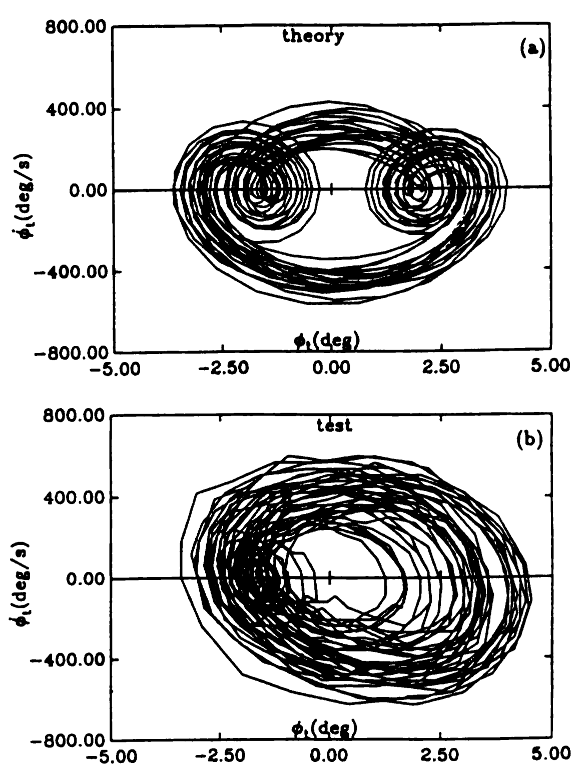

FIG 5(a)(b). Phase plane plot of torsional response for single frequency gust excitation, $\omega_s = 5Hz, \theta_0 = 13^0$ and U=15.6 m/s: (a) theory, (b) test.

teresis and the hysteresis loops are irregular. Also the effects of geometric structural nonlinearity on the response are significant for flap, lag and twist. The PSD plots of the responses with comparison of the results for Type=0, and Type=1 show that in addition to a dominant excitation frequency component, $2\omega_s = 10Hz$, more harmonic components and broader frequency bandwidth exist in the results for Type=1. A typical theoretical phase plane plot of torsional responses at the blade tip for $\theta_0 = 13^0$ is shown in Fig.5(a) and the experimental result is shown in Fig.5(b). The experimental results display somewhat more complex behavior than the theoretical ones. From the PSD plots (not shown), it is found that the peaks of the PSD are not exactly located at the natural frequencies ($\omega_{x1} = 31.5Hz, \omega_{y1} = 23.5Hz$ and $\omega_{z1} = 10Hz$). The PSD peak frequencies are lower than these natural frequencies. This is because the aerodynamic forces affect the aeroelastic modal behavior of the blade.

When we reduce or relax the constraint condition at the support of the pitch spring in the experimental model, a lower torsional natural frequency may be obtained. It is $\omega_{x1} = 22Hz$ which is near the chordwise natural frequency. Fig.6 shows the PSD plots of torsional response at the blade tip for $\theta_0 = 13^0$, $\omega_s = 10.18Hz$ and U=10.7m/s. An obvious beating oscillation is found. The agreement between theory and experiment for this beating phenomenon is generally good, but the frequency difference and oscillation frequency do not correspond precisely. Given the quite complex response due to the nonlinear aeroelastic effects, the agreement between calculation and test is encouraging.

Two harmonic gust excitation

In order to study how the flexible rotor blade will respond to a more general periodic gust excitation, a continuous periodic gust with two-frequency excitation is considered here. The emphasis is on the effect of the second harmonic component on the gust response. The theoretical calculations are based on Eq.(14) and Eq.(8). The gust response behavior can be described in terms of following parameters: $\kappa_w, \kappa_v, \kappa_\phi, \kappa_{\epsilon w}, \kappa_{\epsilon v}, \kappa_{\epsilon\phi}$ and μ. $\kappa_w(\kappa_v, \kappa_\phi)$ is the gust response ratio of *rms* flap (lag, twist) response amplitude undergoing two harmonic gust excitation to that under only a fundamental harmonic excitation when the phase angle, $\epsilon = 0$. $\kappa_{\epsilon w}(\kappa_{\epsilon v}, \kappa_{\epsilon\phi})$ is the *rms* flap (lag, twist) amplitude ratio for varying phase angle, ϵ, in Eq.(8) for a certain α_{G01} and α_{G02}. μ is the gust angle ratio given by $\alpha_{G02}/\alpha_{G01}$. Theoretical results are shown in Fig.7 for $\theta_0 = 6.5^0, \omega = 14Hz$, U=10m/s , $\omega_{x1} = 17.8Hz$ and Type=1. Fig.7 shows κ_w vs μ for $\epsilon = 0$ and a fundamental frequency gust angle of $\alpha_{G01} = 1^0, 2^0, 3^0$. It is seen that for unstalled gust response, ($\alpha_{G01} = 1^0$), κ_w is greater than 1 as μ increases. The effect of the second harmonic of the gust excitation is to increase the response compared to that for only a fundamental harmonic excitation. This effect is often observed for linear systems. However, for stalled gust response, ($\alpha_{G01} = 3^0$), the effect of the second harmonic gust excitation is to decrease the response amplitude. The above conclusions are also true for κ_v and κ_ϕ vs μ for unstalled and stalled gust responses. This "quenching" of the response by added harmonic excitation is known to be possible in nonlinear systems, see Ref.[16]. This offers possibilities for the control of nonlinear systems with strong harmonic content by imposing oscillations at higher frequencies.

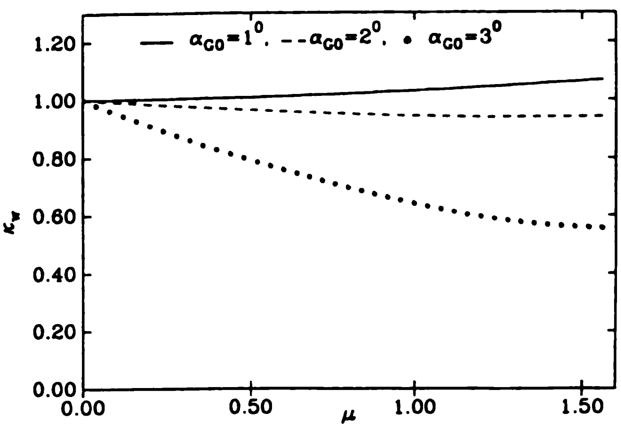

FIG 7. Gust response to two harmonic gust excitation for $\omega = 14Hz$, $\theta_0 = 6.5^0$, $\omega_{x1} = 17.8Hz$ and U=10 m/s: gust response ratio of *rms* flap response amplitude vs gust angle ratio.

More theoretical details are shown in Fig.8. Fig.8 displays the phase plane plots including a comparison with the results obtained from the single sinusoidal gust excitation (Fig.8(a)) for $\mu = 0.5, \epsilon = 0, \omega = 14Hz$ and $\alpha_{G01} = 3^0$, (stalled). The motion is aperiodic or chaotic as described above. In comparing Fig.8(a) and 8(b), it is seen that the effect of the second harmonic of the gust excitation is to decrease the response.

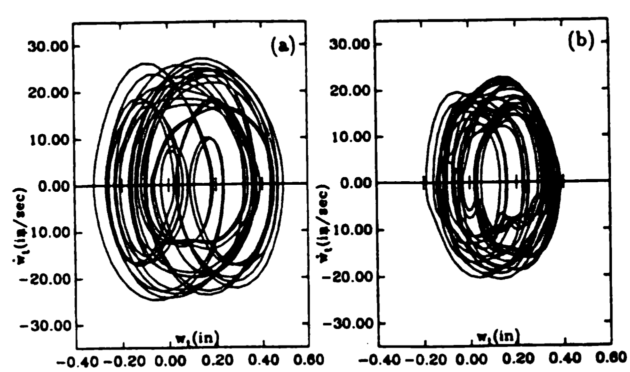

FIG 8(a)(b). Phase plane plot of flap response: (a) for single frequency gust excitation, (b) for two harmonic gust excitation.

In order to obtain experimentally a periodic gust with two harmonic frequency components (a fundamental frequency component plus a double frequency component) for a given motor speed, two distinct pulleys with different groove numbers (12 and 24) are fixed on the shaft end of the motor. A typical measured gust angle wave is shown in Fig.9(a) for an airstream velocity of U=15.6 m/s, and cylinder rotation speeds of $\omega_{s_1} = 3Hz$ and $\omega_{s_2} = 6Hz$. A corresponding FFT plot is shown in Fig.9(b). The gust angles of the first and second harmonic frequencies ($2\omega_{s_{1,2}} = 6Hz$ and $12Hz$) are .7^0 and 1.6^0, respectively . From this figure, the third frequency component ($\omega = 24Hz$) is also not small. Fig.10-11 show the phase plane plots and PSD plot of torsional responses at the blade tip for $\theta_0 = 13^0$. The response appears to be aperiodic or chaotic motion. For the w and v responses, the conclusion is the same. The quantitative agreement between theory and experiment at the dominant driving frequency, 12 Hz , is good as shown in the PSD plot of Fig.11. The experimental PSD has a broader frequency bandwidth. The experimental results are more complex than those of theory. This is because the experimental gust excitation includes more higher harmonic frequency components than the theoretical model as shown in Fig.9(b). In comparing Fig.10 and Fig.5, the response with two-frequency excitation is more chaotic than that with one-frequency excitation both for the theoretical and experimental results. The "quenching" phenomenon has not been found in the present tunnel test. This is because the required minimum first harmonic of the gust, α_{G0}, for generating "quenching" is 1.5^0 from theory, but the available experimental gust generator can only provide 0.7^0 as shown in Fig.9.

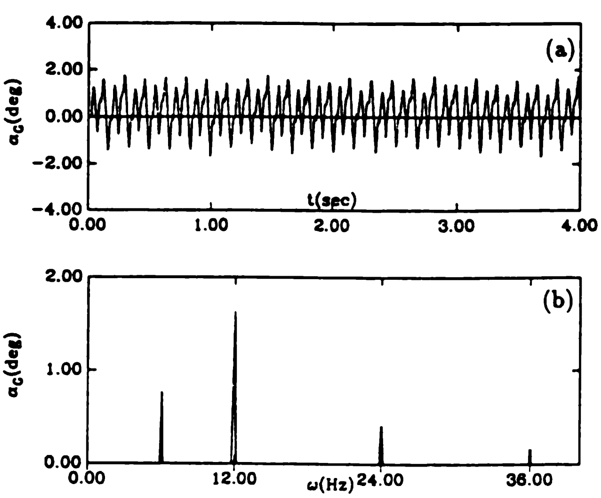

FIG 9(a)(b). Lateral gust of two harmonic gust excitation for $\omega_s = 3Hz$, U=15.6 m/s: (a) for time history, (b) for FFT.

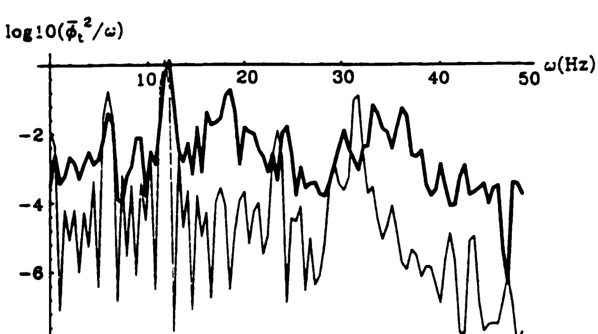

FIG 11. PSD plot of torsional response for two harmonic gust excitation, —, for theory, ▬, for test.

A continuous frequency sweep gust excitation

Theoretical calculations are based on Eq.(14) and (9). The gust excitation is continuous with a period T, i.e, the process is repeated using such a frequency sweep signal. The gust PSD is quite broad in the range of 0-50Hz. For unstalled gust response, the basic parameters of the frequency sweep are $\alpha_{G0} = .5^0, \omega_1 = 2Hz, \omega_2 = 50Hz$, $T = 4sec.$ and $\theta_0 = 6.5^0$, U=10m/sec. The motions are approximately periodic with period, T. A typical PSD plot of the theoretical flap response is shown in Fig.12. A comparison of the results for Type=0 (indicated by the thick solid line) and Type=1 (thin solid line) is also shown in this figure. For the response PSD, resonant behavior is very clear. As shown in Fig.12, there is no peak response at the chordwise natural frequency ($\omega_{y1} = 23.5Hz$) for Type=0, but there is for Type=1. For Type=0 we also find a large response at 5Hz which is equal to half the flap natural frequency. For the chordwise and torsional responses, the result is similar to Fig.12.

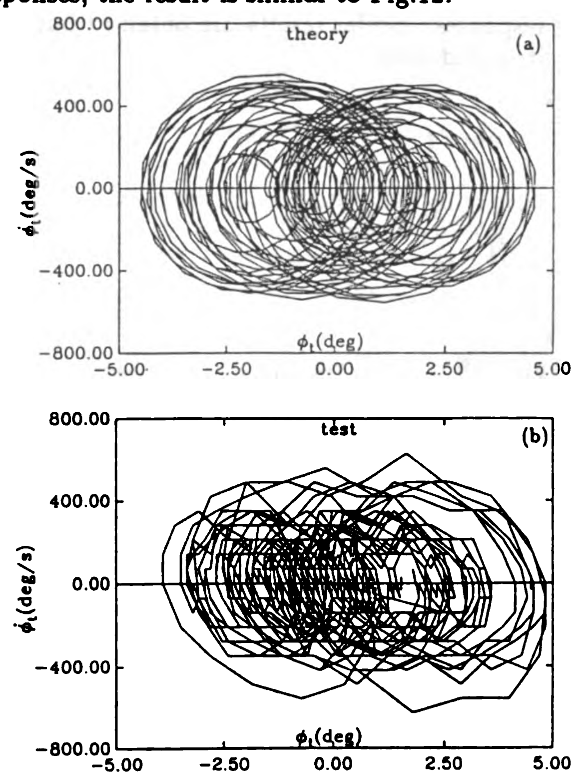

FIG 10(a)(b). Phase plane plot of torsional response for two harmonic gust excitation, $\omega_s = 3Hz$,$\theta_0 = 13^0$, and U=15.6 m/s: (a) theory, (b) test.

An experimental lateral gust wave generated by the linear frequency sweep RSC/airfoil system for an airstream velocity of $U = 10m/s$ and the cylinder rotation speed from 0 Hz to 20 Hz in 2.8 second is shown in Fig.15(a). A corresponding power spectra plot is shown in Fig.15(b) for an average over 200 sweep periods. It is noted that the measured lateral gust has about a 0.9 second time delay, i.e., the restarting time of the DC-motor for each repeated process. This is due to the rotational inertia of the DC-motor. The average angle of the linear frequency sweep gust is about 0.8^0.

Typical experimental results for the flap response of the blade model to this continuous frequency sweep gust excitation are shown in Fig.14-15 for $\theta_0 = 6.5^0$. The flap time history has two oscillation bursts in an approximate period for both the experiment and theory. This means that there are two dominant resonant frequency components, i.e., the flap and torsional components. These results are also found in the PSD plot as shown in Fig.15. In addition to the above components, there is a small peak at 23.5Hz which corresponds to the first lag natural frequency due to the structural nonlinearity. The theoretical results are also plotted in Fig.14(b) and Fig.15 for comparison. It is seen that the experimental PSD has a broader frequency bandwidth between the two peaks of the dominant frequency components. This is because the experimental background has random aerodynamic noise due to the shed vortex sheet behind the RSC/airfoil. The agreement between theory and experiment is reasonably good for the flap frequency component, but not as good for the torsional component (at 17.8Hz). For the torsional and lag responses, similar results are obtained but they are not presented here.

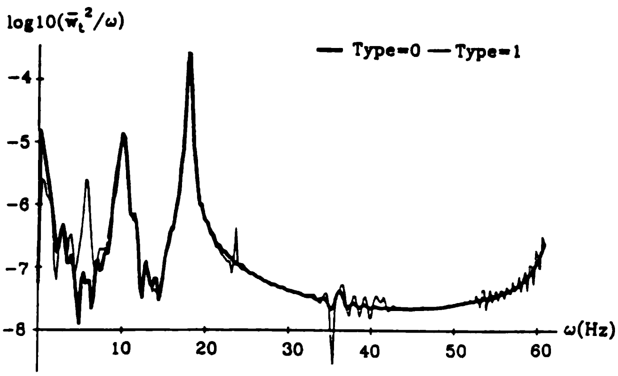

FIG 12. Theoretical PSD plot of flap response for frequency sweep gust excitation, $\theta_0 = 6.5^0$, $\omega_{x1} = 17.8Hz$, $\alpha_{G0} = .5^0$, T=4s and U=10 m/s.

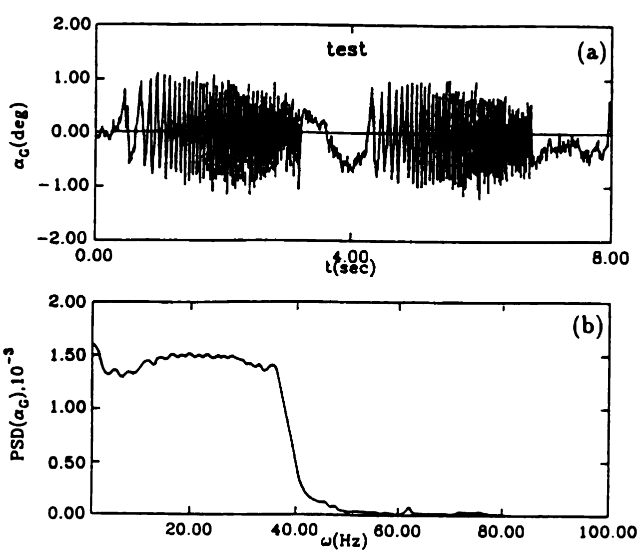

FIG 13(a)(b). Lateral gust of linear frequency sweep gust excitation for $\omega_s = 0 - 20Hz$, U=10 m/s: (a) for time history, (b) for PSD.

For stalled gust response, the basic parameters are $\alpha_{G0} = 1.5^0, \omega_1 = 2Hz, \omega_2 = 50Hz$, $T = 1sec.$ and $\theta_0 = 6.5^0$, U=10m/sec. The response is not repeated with a period, T, but appears chaotic over a long time history. This is because the angle of attack of the blade enters the stall range, and a more complex $C_z - \alpha$ hysteresis loops exists. Fig.16 shows the Poincare section map of the theoretical torsional response for an internal clock, i.e. at those times when $\dot{w}_t \equiv 0$. Over 3493 points for 100 seconds of time are shown. The diffuse nature of the Poincare points indicates the response is highly chaotic. For the chordwise and flap motions, similar maps are also found, see Ref.[15].

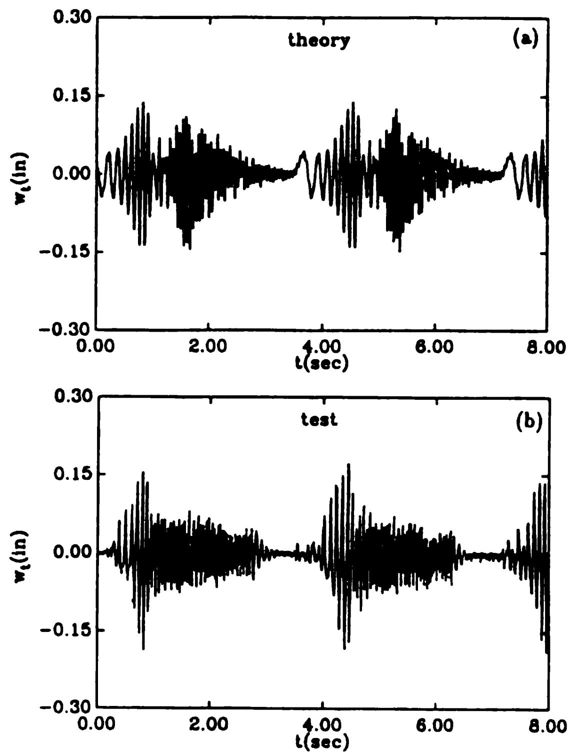

FIG 14(a)(b). Time history of flap response for linear frequency sweep gust excitation: (a) for theory, (b) for test.

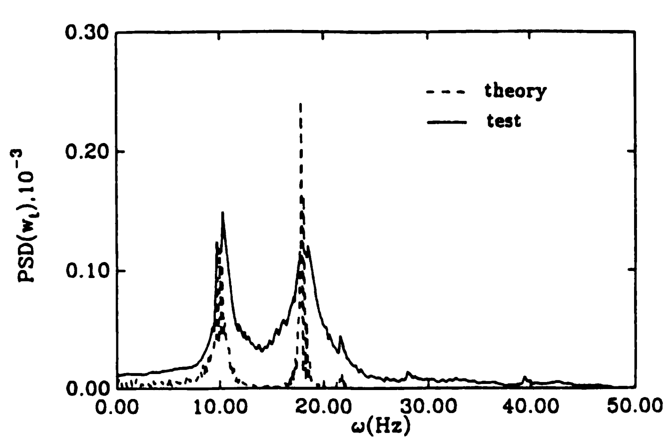

FIG 15. PSD plot of flap response for linear frequency sweep gust excitation, ––, for theory, —, for test.

CONCLUDING REMARKS

A theoretical and experimental study of the nonlinear response of a rotor blade to single and two harmonic, as well as a sweep frequency, gust excitation was made. The conclusions obtained are as follows:

1. The assumptions of a uniform chordwise gust angle of attack and a simple representation for lift forces in a gust flow field are allowable for the parameters of the present study.
2. The effects of geometric structural nonlinearity and aerodynamic nonlinearity on dynamic aeroelastic behavior are significant when stall occurs.
3. At a large pitch angle, the chordwise and twist responses display an aperiodic or possibly chaotic motion, and the flap response displays a more nearly periodic motion.
4. When this nonlinear system undergoes a two harmonic gust excitation, theory predicts a "quenching" phenomenon may occur for a certain combination of parameters. The effect of the second harmonic gust excitation is to decrease the response amplitude under these circumstances.
5. Generally good quantitative agreement between theory and experiment is obtained.

ACKNOWLEDGEMENTS

This work was supported by the Army Research Office under Grant DAAL03- 87-K-0023; Dr. Gary Anderson is the technical monitor. A much more extensive discussion of this topic will be published in the Journal of Fluids and Structures. See Ref.[5] and [15].

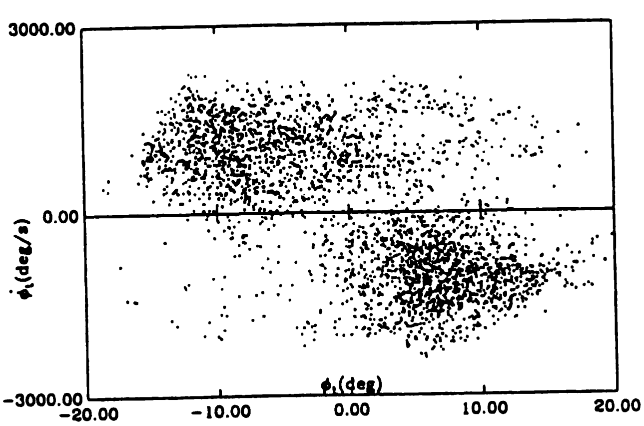

FIG 16. Theoretical Poincare section map of torsional response for frequency sweep gust excitation, $\theta_0 = 6.5^0$, $\omega_{z1} = 17.8Hz$, $\alpha_{G0} = 1.5^0$, T=1s and U=10 m/s.

REFERENCES

[1] Tang, D.M., and Dowell, E.H.," Chaotic Stall Response of a Helicopter in Forward Flight ," *Journal of Fluids and Structures*, (1992) 6, pp. 311-335.

[2] Tang, D.M., and Dowell, E.H.," Flutter and Stall Response of Helicopter Blade with Structural Nonlinearity," *Journal of Aircraft* , (1992), 29, pp. 953-960.

[3] Tang, D.M., and Dowell, E.H.," Comparison of Theory and Experiment for Nonlinear Flutter and Stall Response of a Helicopter Blade," *Journal of Sound and Vibration* , (1993), 162.

[4] Tang, D.M., and Dowell, E.H.," Experimental and Theoretical Study for Nonlinear Aeroelastic Behavior of a Flexible Rotor Blade," *AIAA Journal,* (1993), 31(6).

[5] Tang, D.M., A. Katz and Dowell, E.H.," An Experimental Investigation of A Rotating Slotted Cylinder Gust Generator in A Wind Tunnel", *Journal of Fluids and Structures,* (1993), (to be published).

[6] Drees, Jan M., and Harvey, Keith W.," Helicopter Gust Response at High Forward Speed," AIAA paper No.68-981, Oct. 1968.

[7] Arcidiacono, Peter J., Bergquist, Russell R., and Alexander, W. T., Jr, " Helicopter Gust Response Characteristics Including Unsteady Aerodynamic Stall Effects," *Rotorcraft Dynamics,* NASA SP-352, pp. 91-100, 1974.

[8] Jenkins, Julian L., Jr, and Yeager, William T., Jr, " An Analysis of the Gust-Induced Overspeed Trends of Helicopter Rotors," NASA TP-1213, AVRADCOM TR-78-24, 1978.

[9] Bir, Gunjit Singh, and Chopra, Inderjit," Gust Response of Hingeless Rotors," *J. American Helicopter Soc.*, (1986), 31, pp. 33-46.

[10] Mirick, Paul H., Hamouda, M-Nabil H., and Yeager, William T., Jr, "Wind-Tunnel Survey of an Oscillating Flow Field for Application to Model Helicopter Rotor Testing," NASA, TR 90-B-007, 1990.

[11] Fung, Y. C., *An Introduction to The Theory of Aeroelasticity,* John Wiley and Sons, Inc. 1955.

[12] Petot, D.,"Differential Equation Modeling of Dynamic Stall," Recherche Aerospatiale, No. 5, 1989.

[13] Hodges, D.H., and Dowell, E.H.," Nonlinear Equations of Motion for the Elastic Bending and Torsion of Twisted Nonuniform Rotor Blades," NASA TN D-7818, 1974.

[14] Dunn, Peter and Dugundji, John," Nonlinear Stall Flutter and Divergence Analysis of Cantilevered Graphite/Epoxy Wings," *AIAA Journal* , (1992), 30, pp. 153-161.

[15] Tang, D.M. and Dowell, E.H.," Nonlinear Response of a Rotor Blade to Gust: Theoretical and Experimental Study ", *Journal of Fluids and Structures,* (1993), (to be published).

[16] Pezeshki, C., Elgar, S. and Krishna, R. C., " An Examination of Multi-Frequency Excitation on the Buckled Beam," *Journal of Sound and Vibration,* (1991), 148, pp. 1-9.

Thermoelastoplastic analysis of a stainless steel plate considering phase transformations

TR Tauchert

Department of Engineering Mechanics
University of Kentucky
Lexington KY

GA Webster

Department of Mechanical Engineering
Imperial College of Science, Technology, and Medicine
London SW7 2BX
United Kingdom

RC Reed

Department of Materials
Imperial College of Science, Technology, and Medicine
London SW7 2BX
United Kingdom

A quasistatic thermoelastoplastic analysis is given for the response of a traction-free plate subject to surface heating. The formulation incorporates temperature-induced phase changes which model experimentally obtained data for X22 CrMoV 12 1 stainless steel. The plate is discretized into layers, with material properties considered homogeneous within each layer. An incremental, iterative approach based upon Kirchhoff bending theory is employed to obtain an approximate solution to the problem. Numerical results illustrate the effects of phase transformations and temperature sensitivity of the material properties upon the transient and residual stress distributions.

INTRODUCTION

The thermal stresses in a free plate of elastoplastic material subject to surface heating were investigated first by Weiner (1956). Landau and Weiner (1958) extended this analysis to the determination of transient and residual stresses due to a temperature distribution which is an arbitrary function of time and of the thickness coordinate. Yuksel (1958) considered the case of a free elastoplastic plate with periodically varying surface temperature. In each of these investigations, all material properties were taken to be independent of temperaure. Later, Landau *et al* (1960) (see also Boley and Weiner, 1960) examined the transient and residual stresses in a viscoelastic-plastic plate having a temperature-dependent yield stress.

In addition to residual stresses which occur as a result of plastic flow during heating followed by elastic response during cooling, residual stresses also may develop if the material experiences phase transformation. In this paper, an investigation is made of the thermoelastoplastic response of a traction-free stainless steel plate, characterized by both temperature-sensitive Young's modulus and yield strength, and temperature-induced phase transformations. Phase change behavior is modeled after experimental data presented in the following section. Temperature and stress fields are determined for a plate which undergoes surface heating followed by convective cooling.

part of "MECHANICS PAN-AMERICA 1993" edited by MRM Crespo da Silva and CEN Mazzilli ASME Reprint No AMR134
Appl Mech Rev vol 46, no 11, part 2, November 1993

MATERIAL BEHAVIOR

Whereas materials normally expand upon heating and contract during cooling, steel also undergoes phase transformations which alter its thermal expansion behavior over certain temperature ranges. An experimentally obtained plot (Reed, 1990) of longitudinal strain versus temperature for an unconstrained specimen of X22 stainless steel (X22 CrMoV 12 1) is shown in Fig. 1. The strain measurements were made using a quartz push-rod dilatometer.

Over a temperature range of approximately $813\ K<\theta<856\ K$, where θ denotes the rise in temperature from ambient (room) temperature, a phase change from martensite to austenite occurs. Temperature increases during this transformation period result in thermal contraction rather than expansion. Under subsequent cooling of the steel, a transformation from austenite back to martensite takes place. During this phase change, which begins at approximately $\theta = 262\ K$, the metal expands rather than contracts with decreasing temperature. The phase-transformation process is assumed here to be independent of time.

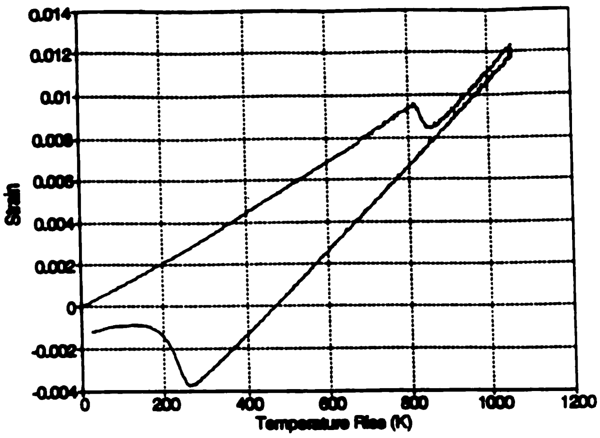

Fig. 1. Strain versus temperature curve for unconstrained specimen of X22 stainless steel.

For the purpose of the present analysis, the measured strain-temperature behavior described by Fig. 1 is represented by the piecewise linear approximation ABCDEF shown in Fig. 2. The slopes of the four line segments in this idealization represent the values of the coefficient of linear thermal expansion $\alpha(\theta)$ over the respective temperature ranges.

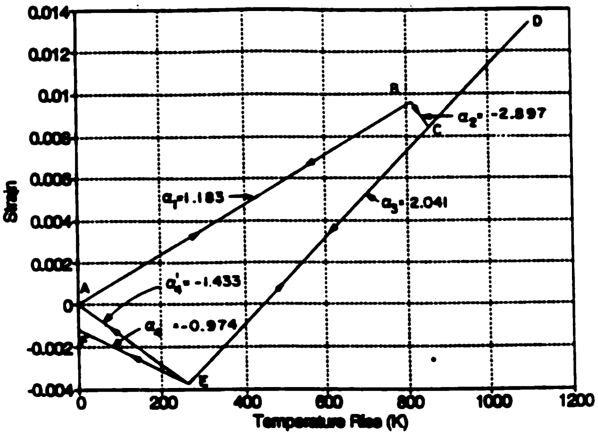

Fig. 2. Strain versus temperature curve used for the analysis (values of α given in 1/100K).

In addition to accounting for the influence of temperature on the thermal expansion coefficient, temperature-dependence of the material's elastic modulus and yield stress is included in this investigation. Other material properties are, however, assumed to be unaffected by temperature.

THEORETICAL ANALYSIS

Temperature Field

The plate under consideration (Fig. 3) is thermally insulated on its lower face (z=-h/2) and along its edges (x=0,a; y=0,b). During the time interval $0 < t < t_o$ there is uniform heat input q_o over the top face z=h/2, while thereafter this face is subject to convective cooling.

The temperature rise $\theta(z)$ in the plate is assumed to satisfy the Fourier heat conduction equation

$$\lambda \frac{\partial^2\theta}{\partial z^2} = \dot{\theta} \qquad (1)$$

in which $\theta = T - T_A$ is the temperature increase from an ambient, stress-free temperature T_A; $\lambda = k/\rho c$ is the thermal diffusivity, where k and ρc denote thermal conductivity and volumetric heat capacity, respectively.

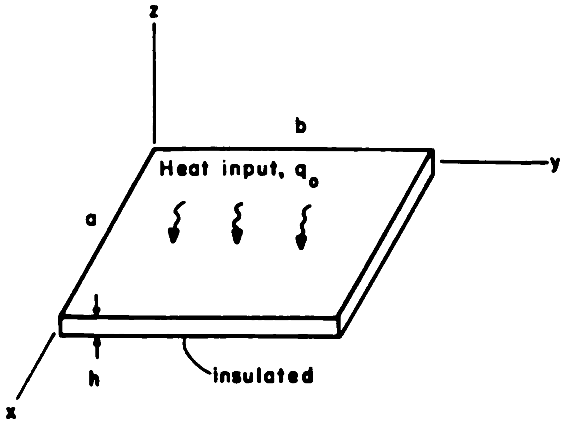

Fig. 3. Stainless steel plate.

The initial and boundary conditions for the problem are expressed mathematically as

$$\theta(z,0) = 0 \tag{2}$$

$$k\,\frac{\partial\theta(-h/2,t)}{\partial z} = 0 \qquad t>0 \tag{3}$$

$$k\,\frac{\partial\theta(h/2,t)}{\partial z} = -q_o \qquad 0<t<t_o \tag{4}$$

$$k\,\frac{\partial\theta(h/2,t)}{\partial z} = -H\,\theta(h/2,t) \qquad t>t_o \tag{5}$$

in which H is the boundary conductance at z=h/2.

The temperature distribution satisfying equations (1)-(5) is (Boley and Weiner, 1960)

$$t<t_o:\ \theta(z,t) = \frac{hq_o}{24k}\left[\frac{24\lambda t}{h^2} + 12\left(\frac{z}{h}\right)^2 + 12\left(\frac{z}{h}\right) - 1 - \frac{48}{\pi^2}\cdot \sum_{m=1}^{\infty}\frac{(-1)^m}{m^2}e^{\frac{-m^2\pi^2\lambda t}{h^2}}\cos m\pi\left(\frac{z}{h}+\frac{1}{2}\right)\right] \tag{6}$$

$$t>t_o:\ \theta(z,t) = \sum_{m=1}^{\infty} a_m e^{\frac{-\alpha_m^2\lambda(t-t_o)}{h^2}}\cdot \cos\alpha_m\left(\frac{z}{h}+\frac{1}{2}\right) \tag{7}$$

in which

$$a_m = \frac{1}{hb_m}\int_{-h/2}^{h/2}\theta(z,t_o)\cos\alpha_m\left(\frac{z}{h}+\frac{1}{2}\right)dz \tag{8}$$

$$b_m = \frac{1}{2}\left(\frac{\sin^2\alpha_m}{Hh/k}+1\right)$$

where α_m are the roots of the equation

$$\alpha\tan\alpha = Hh/k \tag{9}$$

Stress Field

In order to obtain an approximate solution for the stress field, the plate is idealized as a laminate having N layers. Within each layer the material's thermoelastoplastic properties are assumed to be uniform. For those properties which are presumed to vary with temperature, a value based upon the average temperature within the layer is used; i.e., a typical layer (k) occupying the region $z_{k-1} < z < z_k$ and having a mean temperature rise

$$\theta^{(k)} = [\theta(z_k) + \theta(z_{k-1})]/2 \tag{10}$$

has temperature-dependent properties

$$\alpha^{(k)} = \alpha(\theta^{(k)}),\quad E^{(k)} = E(\theta^{(k)}),\quad Y^{(k)} = Y(\theta^{(k)}) \tag{11}$$

The plate material is taken to be elastic-perfectly plastic, and to satisfy a temperature-sensitive von Mises yield criterion defined by the yield function

$$f = s_{ij}\,s_{ij} - \frac{2}{3}Y^2 \tag{12}$$

where s_{ij} denotes the component of the stress deviator. The behavior is assumed to be elastic if

$$f < 0, \text{ or if } f=0 \text{ and } \left(\frac{\partial f}{\partial s_{ij}}\dot{s}_{ij} + \frac{\partial f}{\partial \theta}\dot{\theta}\right) < 0 \tag{13}$$

whereas plastic flow is assumed to occur if

$$f = 0 \text{ and } \left(\frac{\partial f}{\partial s_{ij}}\dot{s}_{ij} + \frac{\partial f}{\partial \theta}\dot{\theta}\right) \geq 0 \tag{14}$$

Assuming that a state of plane stress exists for the traction-free plate under consideration, the stress components are taken to be

$$\sigma_{xx} = \sigma_{yy} = \sigma, \quad \text{all other } \sigma_{ij} = 0 \tag{15}$$

In this case equation (12) yields

$$f = \frac{2}{3}(\sigma^2 - Y^2) \tag{16}$$

and it follows that the stress state is elastic if

$$\sigma^2 < Y^2, \text{ or } \sigma^2 = Y^2 \text{ and } \sigma\dot{\sigma} - Y\dot{Y} < 0 \tag{17}$$

and plastic if

$$\sigma^2 = Y^2 \text{ and } \sigma\dot{\sigma} - Y\dot{Y} \geq 0 \tag{18}$$

The flow conditions (17) and (18) associated with the case $\sigma^2 = Y^2$ can be expressed in terms of incremental changes occurring during a small time interval Δt as follows. For elastic behavior

$$\sigma \ \Delta\sigma - Y \ \Delta Y < 0 \tag{19}$$

and for plastic flow

$$\sigma \ \Delta\sigma - Y \ \Delta Y \geq 0 \tag{20}$$

Considering thermoelastoplastic behavior, the constitutive relation is taken to be

$$\sigma = \frac{E(\theta)}{1-\nu} \cdot \left(e - e^P - \int_0^\theta \alpha(\tau)\, d\tau\right) \tag{21}$$

in which e^P denotes the plastic portion of the total strain component $e_{xx} = e_{yy} = e$. During thermoelastic response $(\Delta e^P = 0)$, the stress increment $\Delta\sigma = \Delta\sigma^E$ becomes

$$\begin{aligned}\Delta\sigma^E &= \frac{\partial\sigma}{\partial e}\Delta e + \frac{\partial\sigma}{\partial\theta}\Delta\theta \\ &= \frac{E(\theta)}{1-\nu}\Delta e + \frac{1}{1-\nu} \cdot \\ &\quad \left[\frac{dE(\theta)}{d\theta}\left(e - e^P - \int_0^\theta \alpha(\tau)\, d\tau\right) - \alpha(\theta)E(\theta)\right]\Delta\theta\end{aligned} \tag{22}$$

or introducing (21),

$$\Delta\sigma^E = \frac{E(\theta)}{1-\nu}(\Delta e - \alpha(\theta)\Delta\theta) + \frac{dE(\theta)}{d\theta}\frac{\sigma}{E(\theta)}\Delta\theta \tag{23}$$

If the usual assumptions of classical (Kirchhoff) theory of plates are employed, the strain component e is related to the middle-surface strain $e^o_{xx} = e^o_{yy} = e^o$ and curvature $(\kappa_x = \kappa_y = \kappa)$ by the expression

$$e = e^o + z\,\kappa \tag{24}$$

The strain increment Δe appearing in equation (23) thus becomes

$$\Delta e = \Delta e^o + z\,\Delta\kappa \tag{25}$$

For the layered idealization of the plate, it is convenient to define a function $g^{(k)}(t)$ (similar to that introduced by Boley and Weiner, 1960) which is equal to unity when layer k is in the elastic state, and zero when the layer is in the plastic state. Thus when $g^{(k)} = 1$:

$$\Delta\sigma^{E(k)} = \frac{E^{(k)}}{1-\nu}\cdot (\Delta\epsilon^{o}+z\Delta\kappa-\alpha^{(k)}\Delta\theta^{(k)}) + \frac{dE^{(k)}}{d\theta}\frac{\sigma^{(k)}}{E^{(k)}}\Delta\theta^{(k)} \tag{26}$$

and when $g^{(k)}=0$:

$$\Delta\sigma^{(k)} = \begin{cases} \Delta Y^{(k)} & \text{if } \sigma^{(k)}>0 \\ -\Delta Y^{(k)} & \text{if } \sigma^{(k)}<0 \end{cases} \tag{27}$$

in which $\Delta Y^{(k)}$ represents the change in magnitude of the yield stress for layer (k), resulting from the temperature change $\Delta\theta^{(k)}$.

Stress resultants are obtained through suitable integrations of the stress with respect to the thickness coordinate z. The resultant incremental in-plane force-per-unit-length ΔN and the incremental bending moment-per-unit-length ΔM are defined as

$$\begin{aligned}(\Delta N, \Delta M) &= \int_{-h/2}^{h/2}\Delta\sigma(1,z)\,dz \\ &= \sum_{k^E}\int_{z_{k-1}}^{z_k}\Delta\sigma^{(k)}(1,z)\,dz \\ &+ \sum_{k^P}\int_{z_{k-1}}^{z_k}\Delta\sigma^{(k)}(1,z)\,dz\end{aligned} \tag{28}$$

where $\sum_{k^E}$ designates a summation over all of the elastic layers, and $\sum_{k^P}$ designates a summation over the plastic layers. Substituting equation (26) into (28) and performing the indicated integration lead to

$$\begin{aligned}\Delta N &= A\Delta\epsilon^{o}+B\Delta\kappa-\Delta N^{\theta}+\Delta N^{P} \\ \Delta M &= B\Delta\epsilon^{o}+D\Delta\kappa-\Delta M^{\theta}+\Delta M^{P}\end{aligned} \tag{29}$$

in which A,B,D are extensional, coupling and bending stiffnesses defined by

$$(A,B,D) = \sum_{k^E}\frac{E^{(k)}}{1-\nu}\left(z_k-z_{k-1}, \frac{z_k^2-z_{k-1}^2}{2}, \frac{z_k^3-z_{k-1}^3}{3}\right) \tag{30}$$

Furthermore we have defined an incremental thermal force ΔN^{θ} and an incremental thermal moment ΔM^{θ} as

$$(\Delta N^{\theta}, \Delta M^{\theta}) = \sum_{k^E}\left[\frac{\alpha^{(k)}E^{(k)}}{1-\nu} - \frac{dE^{(k)}}{d\theta}\frac{\sigma^{(k)}}{E^{(k)}}\right]\left(z_k-z_{k-1}, \frac{z_k^2-z_{k-1}^2}{2}\right)\Delta\theta^{(k)} \tag{31}$$

Also appearing in equations (29) are the contributions to the total force and moment resultants offered by the plastic layers, namely

$$(\Delta N^{P}, \Delta M^{P}) = \sum_{k^P}\Delta\sigma^{(k)}\cdot\left(z_k-z_{k-1}, \frac{z_k^2-z_{k-1}^2}{2}\right) \tag{32}$$

with $\Delta\sigma^{(k)}$ given by equation (27).

In the case of a traction-free plate

$$\Delta N = \Delta M = 0 \tag{33}$$

in which case equations (29) yield

$$\begin{aligned}A\,\Delta\epsilon^{o} + B\,\Delta\kappa &= \Delta N^{\theta} - \Delta N^{P} \\ B\,\Delta\epsilon^{o} + D\,\Delta\kappa &= \Delta M^{\theta} - \Delta M^{P}\end{aligned} \tag{34}$$

The thermal stresses within each layer of the plate are calculated from the preceding equations by means of the iterative procedure described hereafter.

Computational Procedure

At each time increment Δt:

(i) Calculate layer temperature rises $\theta^{(k)}$ and $\Delta\theta^{(k)}$ according to (6) or (7).

(ii) Select appropriate values of $\alpha^{(k)}$, $E^{(k)}$ and $Y^{(k)}$ based upon $\theta^{(k)}$.

(iii) Assume that the quantities $g^{(k)}$ remain unchanged from their values at the preceding time. (Initially

$g^{(k)}=1$ for all k.)

(iv) Calculate incremental middle surface strain $\Delta\varepsilon^{o}$ and curvature $\Delta\kappa$ using (34).

(v) Calculate incremental strains $\Delta\varepsilon^{(k)}$ from (25).

(vi) Calculate incremental stresses according to either (26) or (27), depending upon values of $g^{(k)}$.

(vii) Calculate total stresses $\sigma^{(k)}$ by adding $\Delta\sigma^{(k)}$.

(viii) Calculate incremental elastic stresses $\Delta\sigma^{E(k)}$ from (26).

(xi) Apply yield criterion (19)-(20) to determine $g^{(k)}$.

(x) Compare each $g^{(k)}$ with its previous value. If any is different, repeat steps (iv) to (x); if all remain unchanged, continue.

(xi) Increment time, and repeat procedure.

NUMERICAL RESULTS AND DISCUSSION

As an illustrative example, consideration is given to an X22 steel plate of thickness h=0.1m, characterized by the temperature-induced phase changes described earlier (Fig. 1). The values of the thermal expansion coefficients α_1 employed to model the transformation behavior are those given in Fig. 2. Other material properties taken for this example, based upon data presented by Briggs and Parker (1962), Wegst (1983) and the ASME Boiler and Pressure Vessel Code (1989), are

$$
\begin{aligned}
k &= 26.0 \quad W/mK \\
\lambda &= 6.97 \times 10^{-6}\ m^2/s \\
\nu &= 0.3 \\
E(\theta) &= (216.8 - 0.9083\,\theta)\ GPa \\
Y(\theta) &= (896 + 0.1693\theta - 1.4015 \times 10^{-3}\theta^2)\ MPa
\end{aligned}
\qquad (35)
$$

Heat input over the top surface (z = h/2) of the plate is given by $q_o = 5.0 \times 10^5\ W/m^2$, while the convection coefficient for subsequent cooling is taken to be $H = 156\ W/m^2K$.

The plate is divided into a total of 12 layers. The top 4 layers (k = 9 to 12), which comprise the region where the gradients of temperature and stress are greatest, have thicknesses 0.005m; the remaining layers (k=1 to 8) are 0.01m thick.

Figure 4 shows the variations of stress in the thickness direction at nondimensionalized times $t^*=\lambda t/h^2 = 0.08, 0.4$ and 10.0 for the case of a heating duration $t_o^*=\lambda t_o/h^2=0.18$ and a strain-temperature response given by path ABCDEF (Fig. 2). These and later results were calculated using a time increment $\Delta t^*=0.001$.

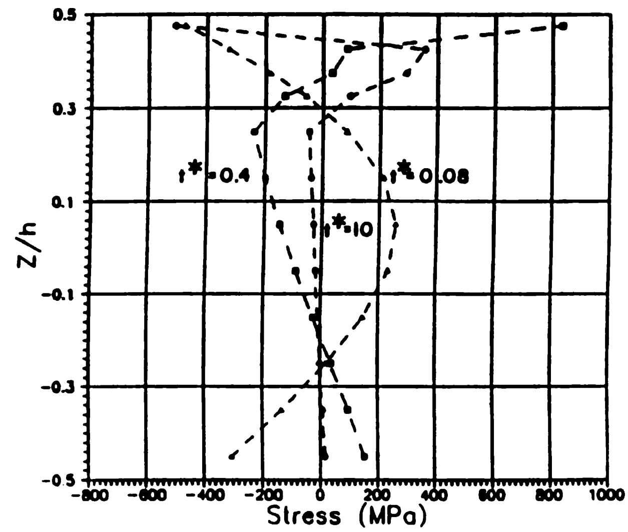

Fig. 4. Stress distributions for heating duration $t_o^*=0.18$.

At $t^*=0.08$ the computed maximum layer temperature rise $(\theta^{(12)}=568K)$ is below the temperature rise at which austenitic transformation begins $(\theta=813.3K)$. At this time no phase transformation or plastic flow has occurred. Observe (Fig. 4) that as a result of the large thermal expansion at the top of the plate, the upper four layers are in compression, the middle layers are in tension, and the bottom two layers are in compression. Force and moment equilibrium conditions are thereby satisfied.

When the applied surface heating ceases at $t^*=0.18$, the temperature rise in layer 12 exceeds the temperature at which full austenitic transformation has occurred $(\theta=856K)$. However the temperature rise in all other layers remains below $813K$. Consequently for this thermal loading condition, layer 12 alone undergoes phase transformation.

At $t^*=0.4$ layer 12 has cooled to a temperature $\theta^{(12)}=267K$, and is in a plastic state. Since the temperature in this layer is then lower than that in the central region of the plate, and since this layer alone has undergone contraction due to austenitizing, it experiences a large tensile stress (Fig. 4).

When $t^*=10.0$ all layer temperature increases $\theta^{(k)}$ are less than $3K$, indicating a near steady-state thermal condition has been reached. The plastic deformation which occurs in layer 12 during heating, followed by elastic response during cooling, results in residual compressive top surface stresses, tensile stresses immediately subsurface, and nearly zero stresses elsewhere.

Figure 5 shows a similar set of results for the stress distributions resulting from a larger heat input time, namely $t_o^* = 0.215$. In this case both layers 11 and 12 undergo phase transformations. Note that while the increased heating time results in a deeper zone of compression at the top of the plate, the magnitudes of the stresses within this zone are much reduced.

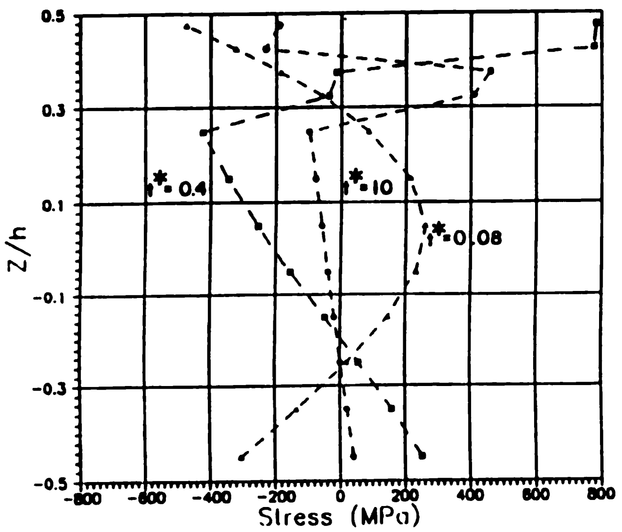

Fig. 5. Stress distributions for heating duration $t_o^*=0.215$.

The degree of martensite formation which takes place during cooling has a pronounced effect upon the residual stress magnitudes. To examine this effect, the calculated stress distributions are compared with those which would occur if the plate material were to return to its original microstructure following the phase transformations; i.e., if the martensitic transformation were represented by line EA rather than EF in Fig. 2. Note that curve ABCDEF characterizes a situation in which the contraction of the affected layers resulting from the austenite formation exceeds the expansion associated with the subsequent martensite formation, whereas for the "closed" curve ABCDEA the net deformation resulting from the two transformations is zero. The residual stress distributions for these two situations are plotted in Figs. 6 and 7, corresponding to heat input durations of $t_o^* = 0.18$ and 0.215, respectively. Since the expansion which occurs during martensitic transformation has the effect of increasing the compressive stresses in the affected layers, the magnitude of the compressive residual surface stresses are greater in the case of "complete" martensite formation (curves b) than in the case of incomplete martensitic transformation (curves a).

Also shown in Figs. 6 and 7, for the purpose of comparison, are residual stress distributions calculated assuming that no phase transformations occur (curves labelled c). In this case the upper region undergoes thermal expansion during heating which is large relative to expansion elsewhere in the plate, resulting in compressive surface stress and plastic flow. Following elastic unloading (cooling) the surface stresses become tensile, as indicated in the figures.

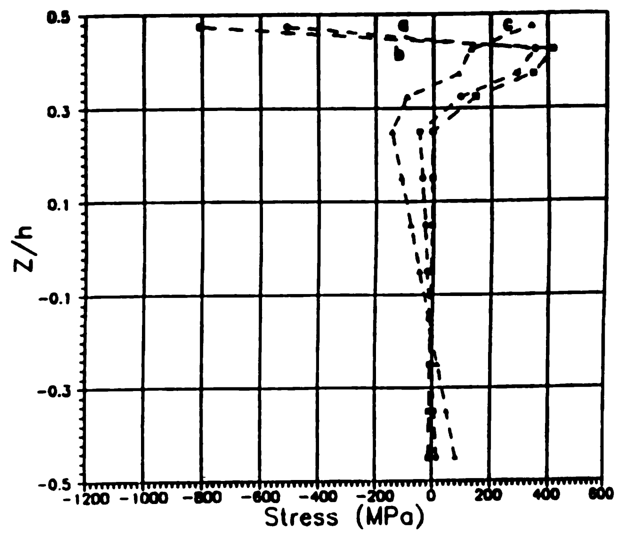

Fig. 6. Residual stress distributions for heating duration $t_o^*=0.18$. (a) incomplete martensitic formation;(b) complete martensitic formation; (c) no phase transformations.

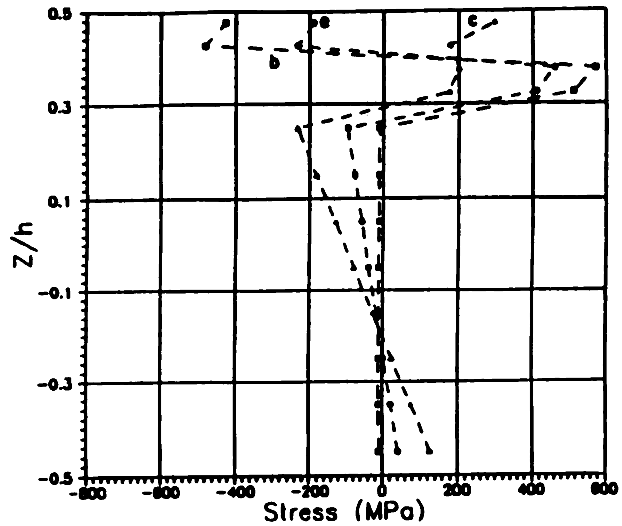

Fig. 7. Residual stress distributions for heating duration $t^*_o = 0.215$. (a) incomplete martensitic formation;(b) complete martensitic formation;(c) no phase transformations.

The effects of the temperature dependence of Young's modulus and yield stress upon residual stress also have been examined. Figures 8 and 9 show stress distributions calculated on the basis of the relations $E(\theta)$ and $Y(\theta)$ given in equation (36), as well as those based on constant modulus E(0) = 216.8 GPa and constant yield stress Y(0) = 896 MPa. For either of the elastic modulus expressions ($E(\theta)$ or $E(0)$), the predicted residual compressive stress at the heated surface is greater when the yield stress decreases with temperature than when it is considered constant (cf. curves a and c, or b and d in the figures). On the other hand, when either of the yield stress relations ($Y(\theta)$ or $Y(0)$) is employed, the compressive residual surface stress based upon a modulus which decreases with temperature is smaller than that based upon a constant value of modulus (cf. curves a and b, or c and d).

Also shown in Figs. 8 and 9 are residual stress distributions obtained from a purely elastic analysis ($Y=\infty$), assuming a temperature-dependent Young's modulus (see curves e). Nearly identical results (not shown) were found when a temperature-independent modulus E(0) was considered. In both cases residual tensile stresses develop at the heated surface as a consequence of overall contraction associated with the material's phase transformations.

CONCLUDING REMARKS

A procedure has been developed for predicting the transient stresses which develop when a steel plate is exposed to heat input over one surface. Plastic deformation which occurs in the higher temperature region of the plate, followed by elastic response during subsequent cooling, results in residual compressive surface stresses and tensile subsurface stresses. Such compressive surface stresses are beneficial from the point of view of reducing the likelihood of fracture due to surface cracking; however this advantage may be partially offset by the presence of tensile subsurface stresses. The numerical results presented indicate that the stress distributions are affected signficantly by the duration of applied heat input, the degree of phase transformation which occurs, and the temperature sensitivity of the thermomechanical properties of the material.

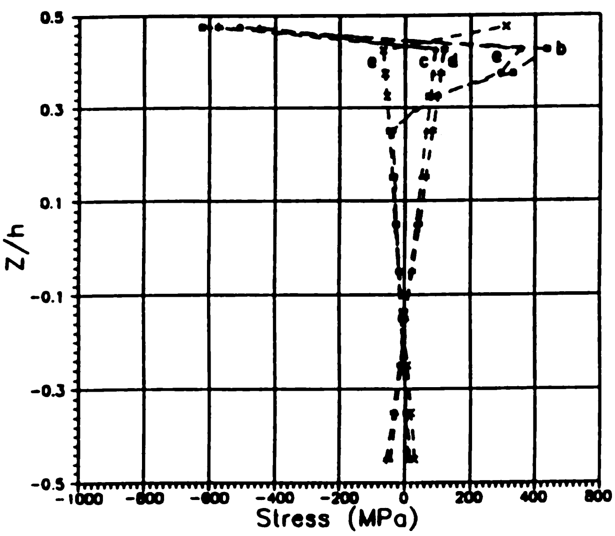

Fig. 8. Effect of temperature-dependent properties on residual stress distributions for $t^*_o = 0.18$.
(a) Y(θ),E(θ);(b) Y(θ),E(0);
(c) Y(0),E(θ);(d) Y(0),E(0);
(e)Y=∞,E(θ).

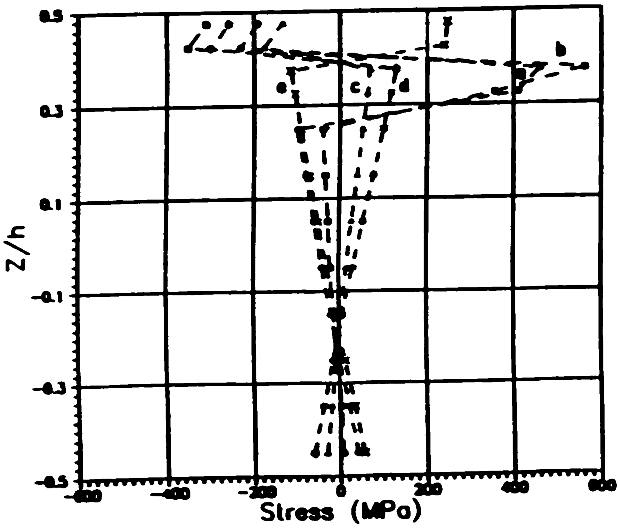

Fig. 9. Effect of temperature-dependent properties on residual stress distributions for $t_o^* = 0.215$.
(a) Y(θ),E(θ);(b) Y(θ),E(0);
(c) Y(0),E(θ);(d) Y(0),E(0);
(e) Y=∞,E(θ).

ACKNOWLEDGMENT

The helpful suggestions of Professor D. C. Leigh are gratefully acknowledged.

REFERENCES

ASME Boiler and Pressure Vessel Code (1989), Section VIII, Division 2 - Alternative Rules.

Boley, BA, and Weiner, JH (1960), *Theory of Thermal Stresses*, John Wiley and Sons, New York.

Briggs, JZ, and Parker, TD (1962), *The Super 12% Cr Steels*, Climax Molybdenum Co., New York.

Landau, HG, and Weiner, JH, (1958), Transient and Residual Stresses in Heat-Treated Plates, *ASME Journal of Applied Mechanics*, **25**, pp. 459-465.

Landau, HG, Weiner, JH, and Zwicky, Jr., EE (1960), Thermal Stresses in a Viscoelastic-Plastic Plate With Temperature-Dependent Yield Stress, *ASME Journal of Applied Mechanics*, **27**, pp. 297-302.

Reed, RC (1990), unpublished work, University of Cambridge.

Wegst, CW (1983), *Stahlschlussel*, Nachschlagewerk Stahlschlussel, Marbach, West Germany.

Weiner, J (1956), An Elastophastic Thermal-Stress Analysis of a Free Plate, *ASME Journal of Applied Mechanics*, **23**, pp. 395-402.

Yuksel, H (1958), Elastic, Plastic Stresses in Free Plate With Periodically Varying Surface Temperature, *ASME Journal of Applied Mechanics*, **25**, pp. 603-606.

Electroelastic analysis of piezoelectric laminated structures

Horacio Sosa and Marco Castro

Department of Mechanical Engineering and Mechanics
Drexel University, Philadelphia PA 19104

A two-dimensional electroelastic formulation is developed to study the response of piezoelectric laminated structures. The methodology is based on a state space formulation where a particular collection of elastic and electrical variables is used to determine the behavior of layered structures subjected to arbitrary loading conditions. The application of this methodology in the area of multilayer electromechanical devices and of adaptive or smart structures is discussed.

INTRODUCTION

This article is concerned with structures formed by assembling layers of various materials possessing very different elastic and electric characteristics. Of all the components present in the resulting layered system the most important in this study is a piezoelectric material which is placed in a continuous or discrete manner at different locations in the structure. The applications of such arrangements include electronic and electromechanical devices which are being used in spacecrafts, launch vehicles and military equipment. As a first example consider Fig 1 where we show a multilayer electromechanical device, such as a transducer, resonator or capacitor, where electrodes are embedded within a piezoelectric ceramic. If the thickness of the electrodes can not be neglected the structure is regarded as a multilayer system of conducting, rigid or deformable metal sheets and elastic piezoelectric ceramic. A second example is provided by Fig 2 where it is shown a schematic representation of a so-called smart structure. That is, a structure that responds in an autonomously or predetermined manner to external disturbances. This unique characteristic is achieved by embedding within the structure layers of piezoelectric material which are used as sensors and actuators to detect and react, respectively, to an external load.

The analysis of layered structures as the ones shown in Figs 1 and 2 is by no means trivial since phenomena such as material anisotropy and electromechanical coupling tend to introduce formidable mathematical difficulties. In addition, a mathematical method capable of describing the response of such a composite structure should furnish information on local as well as global behavior with equal ease. For example, in the case of the multilayer device of Fig 1 one may be interested on the local behavior of stresses induced in the neighborhood of the electrode's tip where high electric fields tend to occur. On the other hand, when dealing with smart or adaptive structures the main objective is to be able to predict the overall response of the structure to a given load.

In contrast to previous formulations which have been based on ad hoc, and some times unrealistic assumptions, we present a general, two-dimensional methodology to address problems where mechanical and electrical effects occur simultaneously. The method is based on the so-called state space formulation and can be regarded as a generalization of previous works developed within the framework of linear isotropic elasticity (Bahar, 1972 &1975, Sosa and Bahar, 1992). The formulation consists of casting the equations of electroelasticity in a mixed form, where a state vector is formed by collecting not only mechanical variables such as stress and

part of "MECHANICS PAN-AMERICA 1993" edited by MRM Crespo da Silva and CEN Mazzilli ASME Reprint No AMR134

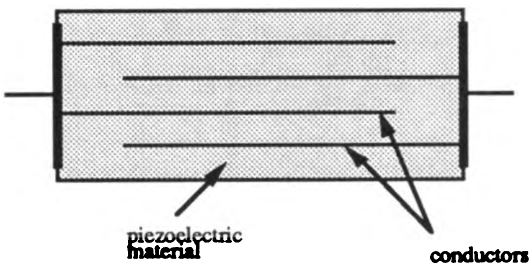

Figure 1: Multilayer electromechanical device

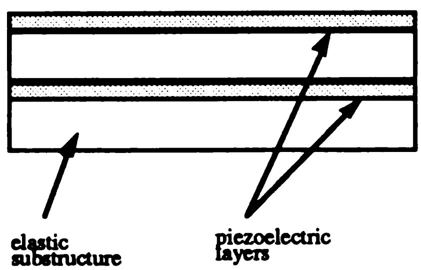

Figure 2: Smart structure

displacement but also electrical variables like induction (also known as the electric displacement) and electric potential. Furthermore, in view of the geometries under study use of the Fourier transform allows us to produce a system of ordinary differential equations which can be written in matrix form with the transform state vector and the depth within the medium playing the role of dependent and independent variables, respectively. The solution of the matrix differential equation is obtained in terms of a transfer matrix that allows us to find the transformed electroelastic variables anywhere in the medium once the state vector on the boundary (also referred to as the initial state vector) is known. Furthermore, the state vector in any layer can be obtained upon multiplication of the initial state vector by a chain of transfer matrices of the individual layers by the transfer matrix of the layer of interest. Finally, by Fourier inversion the electromechanical variables in the physical space are obtained.

The main objective of this article is to present the formalism behind the state space methodology in electroelasticity. Therefore, particular problems are not addressed although remarks are made with respect to the implementation of the method to attack some fundamental electromechanical boundary value problems. Finally, it is shown that despite the inherent complexities due to material anisotropy and coupling effects, the new electroelastic transfer matrix preserves the characteristics of the isotropic elastic transfer matrix found in the original works of Bahar (1972 & 1975).

THE PIEZOELECTRIC EFFECT AND PIEZOELECTRIC CERAMICS

As mentioned previously, within the realm of the present study the piezoelectric material is the most important component in the multilayer structures to be analyzed. Therefore, a brief description of the phenomenon of piezoelectricity is provided in this section as well as how this property can be induced in ceramics.

Piezoelectric materials are anisotropic dielectrics that deform under the effect of an electric field and conversely, they produce an electric voltage when subjected to mechanical loads. The now called direct piezoelectric effect (namely, the inducement of charge in response to applied pressure) was discovered in some crystals by J. and P. Curie in 1880 and its formal mathematical description was provided by Voigt in 1894 (Cady, 1964). Despite the importance of the piezoelectric phenomenon, the first applications did not occur until World War I, where crystal quartz was used for the emission of acoustic waves as a means to locate German submerged vessels.

The main property of a piezoelectric material is its electromechanical coupling parameter which gives an indication of how much mechanical energy can be transformed into electrical and vice versa. Pure crystals have small electromechanical coupling and, as a consequence, the range of their applications remained very limited. In the 1940's it was discovered that piezoelectricity could be induced in isotropic ceramics such as lead zirconate titanate (PZT) and barium titanate (Ba Ti O_3) by subjecting the ceramic to a high DC electric field, a process known as poling (Jaffe et al., 1971). The sequence of events involved in the inducement of piezoelectricity can be described as follows: A piezoelectric ceramic is first manufactured to its final shape and size by conventional methods. A microscopic look at the finished product will reveal a structure as the one shown in Fig 3 where dipoles

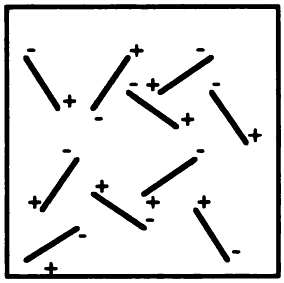

Figure 3: Ceramic before poling

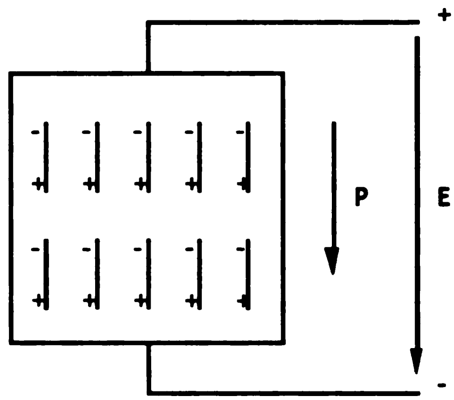

Figure 4: Ceramic after poling

(or molecules) are oriented in a random manner. From a macroscopic point of view, however, the material is regarded as isotropic with a net polarization vector equal to zero and, therefore, with no piezoelectric characteristics. The ceramic is next electroded and subjected to a DC electric field (the poling field) of the order of $10^6 - 10^7$ Volts/m at temperatures below $200^0 - 400^0$ C (known as the Curie temperature). The consequence of this procedure is an alignment of the dipoles in the direction of the applied field as shown in Fig 4. From a macroscopic point of view the ceramic is now transversely isotropic with the axis of transverse isotropy being parallel to the polarization vector **P**. Therefore, piezoelectricity can be manifested only on bulk materials lacking a center of symmetry. An important aspect of this procedure is that the polarization is permanent as long as in practical applications applied or induced fields do not exceed the poling field. Otherwise dielectric breakdown or depolarization may occur.

The popularity of piezoelectric ceramics as components of electromechanical and electronic devices stems from the following three characteristics: first, they have high piezoelectric constants; second, they can be given almost any shape and size with the direction of polarization freely chosen; and third, they are very stiff, therefore, they are capable of exerting and sustaining very large loads. An undesirable characteristic is their brittleness and therefore, low fracture resistance. Consequently, it is clear that studies of the induced stresses in these materials is an important subject to ensure reliable and more efficient structures.

MATHEMATICAL DESCRIPTION OF LINEAR PIEZOELECTRICITY

The mathematical representation of the piezoelectric effect makes use of two mechanical (stress and strain) and two electrical (field and polarization or electric displacement) variables. Depending on which two variables (one mechanical and one electrical) are regarded as independent one can obtain four different constitutive equations by making use of thermodynamic potentials (Cady, 1964). Denoting by $\boldsymbol{\sigma}$, $\boldsymbol{\varepsilon}$, $\mathbf{E}$, and $\mathbf{D}$ the stress tensor, the strain tensor, the electric field vector and the electric displacement vector, respectively, it can be shown that one possible set of constitutive relations is provided by

$$\boldsymbol{\sigma} = \mathbf{C}\,\boldsymbol{\varepsilon} - \mathbf{e}^T\,\mathbf{E}, \quad (1)$$

$$\mathbf{D} = \mathbf{e}\,\boldsymbol{\varepsilon} + \boldsymbol{\epsilon}\,\mathbf{E}, \quad (2)$$

where $\mathbf{C}$ is the fourth order elastic stiffness tensor (measured at constant electric field), $\mathbf{e}$ is third order piezoelectric tensor, $\boldsymbol{\epsilon}$ is the rank two dielectric tensor (measured at constant strain), and the superscript "T" in (1) denotes the transpose of the tensor. Alternate forms of constitutive equations can be obtained by considering different thermodynamic potentials. Numerical values for the material constants of different classes of piezoelectric ceramics can be found in Berlincourt et al. (1964).

In the most general case, Eqs (1) and (2) contain a total of 45 independent material constants (21 elastic, 18 piezoelectric and 6 dielectric). However, most piezoelectric materials used in electromechanical applications are transversely isotropic. As a consequence, only 5 elastic, 3 piezoelectric and 2 dielectric constants need to be considered. For example, if poling of the material occurs in the x_3-direction, the plane perpendicular to this axis remains isotropic. This condition becomes much easier to visualize by writing Eqs (1) and (2) in matrix form with respect to a Cartesian coordinate system (x_1, x_2, x_3). In such a case the electromechanical variables can be represented by column vectors

$$\begin{aligned}
\boldsymbol{\sigma} &= \{\sigma_{11}, \sigma_{22}, \sigma_{33}, \sigma_{32}, \sigma_{31}, \sigma_{12}\}^T, \\
\boldsymbol{\varepsilon} &= \{\varepsilon_{11}, \varepsilon_{22}, \varepsilon_{33}, 2\varepsilon_{32}, 2\varepsilon_{31}, 2\varepsilon_{12}\}^T, \\
\mathbf{D} &= \{D_1, D_2, D_3\}^T, \\
\mathbf{E} &= \{E_1, E_2, E_3\}^T,
\end{aligned}$$

while the material properties have the following matrix representations:

$$\mathbf{C} = \begin{Vmatrix} C_{11} & C_{12} & C_{13} & 0 & 0 & 0 \\ C_{12} & C_{11} & C_{13} & 0 & 0 & 0 \\ C_{13} & C_{13} & C_{33} & 0 & 0 & 0 \\ 0 & 0 & 0 & C_{44} & 0 & 0 \\ 0 & 0 & 0 & 0 & C_{44} & 0 \\ 0 & 0 & 0 & 0 & 0 & C_{66} \end{Vmatrix}$$

with

$$C_{66} = \frac{1}{2}(C_{11} - C_{22}),$$

$$\mathbf{e} = \begin{Vmatrix} 0 & 0 & 0 & 0 & e_{15} & 0 \\ 0 & 0 & 0 & e_{15} & 0 & 0 \\ e_{31} & e_{31} & e_{33} & 0 & 0 & 0 \end{Vmatrix}$$

and

$$\boldsymbol{\epsilon} = \begin{Vmatrix} \epsilon_{11} & 0 & 0 \\ 0 & \epsilon_{11} & 0 \\ 0 & 0 & \epsilon_{33} \end{Vmatrix}$$

With this representation it is immediate to recognize that a field E_3 induces only normal stresses through the piezoelectric constants e_{31} and e_{33}, while inplane deformations give rise to out-of-plane electric displacement. It is also important to note that if the material is anisotropic but does not possess piezoelectricity (or this effect is neglected) then e=0, leading to elastic and dielectric problems which can be solved independently of each other.

In addition to Eqs (1) and (2) the formulation of piezoelectric problems is based on field equations provided by the equations of motion and Gauss' law of electrostatics, namely

$$\begin{aligned}
\operatorname{div} \boldsymbol{\sigma} + \rho\, \mathbf{b} &= \rho\, \mathbf{a}, && (3) \\
\operatorname{div} \mathbf{D} &= q, && (4)
\end{aligned}$$

where ρ, $\mathbf{b}$, $\mathbf{a}$ and q denote the mass density, the body forces, the acceleration and the density of free charges, respectively. Finally it is convenient to introduce the elastic displacement $\mathbf{u}$ and electric potential ϕ which satisfy the equations

$$\begin{aligned}
\boldsymbol{\varepsilon} &= \frac{1}{2}\left(\nabla \mathbf{u} + \nabla \mathbf{u}^T\right), && (5) \\
\mathbf{E} &= -\nabla \phi. && (6)
\end{aligned}$$

We would like to note that despite the very different physical nature of the elastic and dielectric problems, these two phenomena are governed by equations with the same mathematical structure, that is, there is a one-to-one correspondence between the elastic and the electric variables as is illustrated below:

$$\begin{aligned}
\boldsymbol{\sigma} &\leftrightarrow \mathbf{D} \\
\boldsymbol{\varepsilon} &\leftrightarrow \mathbf{E} \\
\mathbf{u} &\leftrightarrow \phi.
\end{aligned}$$

Combining Eqs (1) through (6) yields a system of four partial differential equations coupling the three components of the displacement vector $\mathbf{u}$ with the electric potential ϕ, which must be solved subject to certain electrical and mechanical boundary conditions. Letting Ω be the piezoelectric solid bounded by $\partial\Omega$, and calling $\partial\Omega_t$, $\partial\Omega_u$, $\partial\Omega_D$ and $\partial\Omega_\phi$ the parts of the boundary where force, displacement, electric displacement, and electric potential can be prescribed, one can write in the most general case

$$\begin{aligned}
\boldsymbol{\sigma}\, \mathbf{n} &= \mathbf{t}_s \quad \text{on } \partial\Omega_t \\
\mathbf{u} &= \mathbf{u}_s \quad \text{on } \partial\Omega_u \\
[\mathbf{D}] \cdot \mathbf{n} &= \omega \quad \text{on } \partial\Omega_D \\
[\phi] &= 0 \quad \text{on } \partial\Omega_\phi
\end{aligned}$$

where $\mathbf{t}_s$ represents the traction (or stress vector), $\mathbf{n}$ is the outward unit normal to $\partial\Omega$, ω is a prescribed surface charge density and [.] indicates the jump of the enclosed quantity across the boundary.

STATE SPACE FORMULATION FOR ELECTROELASTICITY

The analysis of piezoelectric materials is mathematically highly involved because of electroelastic coupling and material anisotropy. A certain degree of simplification can be obtained if the analysis is reduced to two dimensions. However, to retain general coupling characteristics the plane of study can not be chosen arbitrarily. Indeed, as mentioned before if the material is poled in the x_3-direction, the plane (x_1, x_2) is isotropic and no electroelastic interactions take place. On the other hand, suitable planes to study coupling effects are (x_1, x_3) and (x_2, x_3). Choosing the former and renaming the coordinates as (x, z) the plane stress constitutive equation reduces to

$$\left\{\begin{array}{c}\sigma_{xx}\\ \sigma_{zz}\\ \sigma_{xz}\end{array}\right\} = \left\|\begin{array}{ccc}C_{11} & C_{13} & 0\\ C_{13} & C_{33} & 0\\ 0 & 0 & C_{44}\end{array}\right\| \left\{\begin{array}{c}u_{,x}\\ w_{,z}\\ u_{,z}+w_{,x}\end{array}\right\} + \left\|\begin{array}{cc}0 & e_{31}\\ 0 & e_{33}\\ e_{15} & 0\end{array}\right\| \left\{\begin{array}{c}\phi_{,x}\\ \phi_{,z}\end{array}\right\} \tag{7}$$

$$\left\{\begin{array}{c}D_x\\ D_z\end{array}\right\} = \left\|\begin{array}{ccc}0 & 0 & e_{15}\\ e_{31} & e_{33} & 0\end{array}\right\| \left\{\begin{array}{c}u_{,x}\\ w_{,z}\\ u_{,z}+w_{,x}\end{array}\right\} - \left\|\begin{array}{cc}\epsilon_{11} & 0\\ 0 & \epsilon_{33}\end{array}\right\| \left\{\begin{array}{c}\phi_{,x}\\ \phi_{,z}\end{array}\right\}. \tag{8}$$

where u and w are the components of displacement in the x- and z- directions, respectively, and a comma after a variable denotes partial differentiation. Moreover, assuming all physical variables to be independent of time, and neglecting body forces and electric charge density Eqs (3) and (4) become

$$\frac{\partial \sigma_{xx}}{\partial x} + \frac{\partial \sigma_{xz}}{\partial z} = 0 \tag{9}$$

$$\frac{\partial \sigma_{xz}}{\partial x} + \frac{\partial \sigma_{zz}}{\partial z} = 0 \tag{10}$$

$$\frac{\partial D_x}{\partial x} + \frac{\partial D_z}{\partial z} = 0 \tag{11}$$

The set of eight equations given by Eqs (7)-(11) constitutes eight coupled partial differential equations in eight unknowns (three components of stress, two components of electric displacement, two components of elastic displacement, and the electric potential). The state space formulation consists of describing physical phenomena in terms of the minimum possible number of variables. Towards this end, a first step is to reduce the variables involved in (7)-(11) by eliminating the components σ_{xx} and D_x, which renders

$$\begin{aligned}
\frac{\partial u}{\partial z} &= -\frac{\partial w}{\partial x} + \frac{1}{C_{44}}\sigma_{xz} - \frac{e_{15}}{C_{44}}\frac{\partial \phi}{\partial x}\\
\frac{\partial w}{\partial z} &= -\frac{\alpha}{\gamma}\frac{\partial u}{\partial x} + \frac{\epsilon_{33}}{\gamma}\sigma_{zz} + \frac{e_{33}}{\gamma}D_z\\
\frac{\partial \sigma_{zz}}{\partial z} &= -\frac{\partial \sigma_{xz}}{\partial x}\\
\frac{\partial \sigma_{xz}}{\partial z} &= \left(\frac{C_{13}^2}{C_{33}} - C_{11} - \frac{\beta^2}{\gamma C_{33}}\right)\frac{\partial^2 u}{\partial x^2}\\
&\quad + \left(\frac{e_{33}}{C_{33}}\frac{\beta}{\gamma} - \frac{C_{13}}{C_{33}}\right)\frac{\partial \sigma_{zz}}{\partial x} - \frac{\beta}{\gamma}\frac{\partial D_z}{\partial x}\\
\frac{\partial \phi}{\partial z} &= -\frac{\beta}{\gamma}\frac{\partial u}{\partial x} + \frac{e_{33}}{\gamma}\sigma_{zz} - \frac{C_{33}}{\gamma}D_z\\
\frac{\partial D_z}{\partial z} &= -\frac{e_{15}}{C_{44}}\frac{\partial \sigma_{xz}}{\partial x} + \frac{\kappa}{C_{44}}\frac{\partial^2 \phi}{\partial x^2}
\end{aligned} \tag{12}$$

where

$$\alpha = C_{13}\,\epsilon_{33} + e_{31}\,e_{33},\ \beta = C_{13}\,e_{33} - C_{33}\,e_{31},$$

$$\gamma = C_{33}\,\epsilon_{33} + e_{33}^2,\ \kappa = e_{15}^2 + \epsilon_{11}\,C_{44}.$$

Notice that in the process no mixed derivatives are involved in (12). The next step is to reduce this system of partial differential equations into a system of ordinary differential equations. This can be done by taking advantage of the particular geometrical configurations under study. That is, as shown in Figs 1 and 2 the laminated structures can be represented by the infinite strip: $-\infty < x < \infty$, $-h \le z \le h$. Thus, the Fourier transform, defined as

$$\hat{f}(\xi) = \int_{-\infty}^{\infty} f(x)\, e^{i\xi x}\, dx$$

can be used in (12) yielding

$$\frac{d\hat{\mathbf{S}}}{dz}(\xi, z) = \mathbf{A}(\xi)\ \hat{\mathbf{S}}(\xi, z) \tag{13}$$

where $\hat{\mathbf{S}}(\xi, z)$ is the Fourier transform of the state vector $\mathbf{S}(x, z) = \{u, w, \sigma_{zz}, \sigma_{xz}, \phi, D_z\}^T$, and it has been assumed that the quantities $u, u_{,x}, w, \sigma_{zz}, \sigma_{xz}, \phi, \phi_{,x}$ and D_z tend to zero as $x \to \infty$. Furthermore, $\mathbf{A}(\xi)$ is the 6×6 matrix given by

$$\mathbf{A} = \left\| \begin{array}{cccccc} 0 & i\xi & 0 & a_{14} & a_{15}i\xi & 0 \\ a_{21}i\xi & 0 & a_{23} & 0 & 0 & a_{26} \\ 0 & 0 & 0 & i\xi & 0 & 0 \\ a_{41}\xi^2 & 0 & a_{43}i\xi & 0 & 0 & a_{46}i\xi \\ a_{51}i\xi & 0 & a_{53} & 0 & 0 & a_{56} \\ 0 & 0 & 0 & a_{64}i\xi & a_{65}\xi^2 & 0 \end{array} \right\|$$

where the coefficients a_{jk} reflecting the material characteristics can be expressed as

$$\begin{aligned} a_{14} &= \frac{1}{C_{44}}, \; a_{15} = \frac{e_{15}}{C_{44}} \\ a_{21} &= \frac{\alpha}{\gamma}, \; a_{23} = \frac{\epsilon_{33}}{\gamma}, \; a_{26} = \frac{e_{33}}{\gamma} \\ a_{41} &= -\frac{C_{13}}{C_{33}} + C_{11} + \frac{\beta^2}{\gamma C_{33}}, \\ a_{43} &= -\frac{e_{33}}{\beta}\gamma C_{33} + \frac{C_{13}}{C_{33}}, \; a_{46} = \frac{\beta}{\gamma} \\ a_{51} &= \frac{\beta}{\gamma}, \; a_{53} = \frac{e_{33}}{\gamma}, \; a_{56} = -\frac{C_{33}}{\gamma} \\ a_{64} &= \frac{e_{15}}{C_{44}}, \; a_{65} = -\frac{\kappa}{C_{44}}. \end{aligned}$$

The solution to (13) is found to be (Ogata, 1967)

$$\hat{\mathbf{S}}(\xi, z) = \exp[z\mathbf{A}(\xi)]\; \hat{\mathbf{S}}(\xi, 0) \tag{14}$$

where the matrix exponential $\exp[z\mathbf{A}(\xi)]$ is the transfer matrix that propagates the "initial" transformed state vector $\hat{\mathbf{S}}(\xi, 0)$ into the field at any depth z, and whose explicit form can be determined by means of the following steps:

(i) The eigenvalues λ of $\mathbf{A}$ are found from the associated characteristic equation, that is

$$\lambda^6 + p\,\xi^2\lambda^4 + q\,\xi^4\lambda^2 + r\,\xi^6 = 0 \tag{15}$$

where the coefficients p, q and r are given by

$$p = \frac{1}{\gamma C_{44}}\Big[\alpha\, C_{33} + \beta\, e_{31}\,\frac{C_{33}}{C_{13}} - \gamma\, C_{11} + 2\,\beta\, e_{15} - \kappa\, C_{33}\Big],$$

$$\begin{aligned} q &= \frac{1}{\gamma^2 C_{44}}\Big[-(\alpha\, C_{33} + \beta\, e_{31}\,\frac{C_{33}}{C_{13}} - \gamma\, C_{11})(\epsilon_{33}\, C_{44} \\ &+ 2\, e_{15}\, e_{33} + \epsilon_{11}\, C_{33}) + \alpha\,(\gamma\, C_{44} + 2\,\beta\, e_{15} \\ &- \kappa\,(C_{33} + e_{33}) - 2\,\beta\,\kappa\, e_{33} - \beta^2\,\epsilon_{11})\Big], \end{aligned}$$

$$r = \frac{\kappa}{\gamma^2 C_{44}}\Big[\alpha\,(C_{33} - C_{13}) + \beta\, e_{31}\,(\frac{C_{33}}{C_{13}} - 1) - \gamma\, C_{11}\Big].$$

Since (15) is expressed in terms of even powers of λ its roots can be found in closed form. Moreover, it can be shown that for any physically admissible transversely isotropic piezoelectric material the roots can be expressed as

$$\lambda_{1,4} = \pm a|\xi|,\; \lambda_{2,5} = \pm(b + ic)|\xi|,\; \lambda_{3,6} = \pm(b - ic)|\xi|$$

where a, b, and c are real numbers which depend solely on the material constants.

(ii) The matrix exponential is expanded in a matrix polynomial, namely

$$\begin{aligned} \exp[z\mathbf{A}(\xi)] &= a_0\mathbf{1} + a_1\mathbf{A} + a_2\mathbf{A}^2 + a_3\mathbf{A}^3 \\ &+ a_4\mathbf{A}^4 + a_5\mathbf{A}^5 \end{aligned} \tag{16}$$

where no higher powers of $\mathbf{A}$ are needed on account of the Cayley-Hamilton theorem, which asserts that $\mathbf{A}$ satisfies its own characteristic equation, that is

$$\mathbf{A}^6 + p\,\xi^2\mathbf{A}^4 + q\,\xi^4\mathbf{A}^2 + r\,\xi^6\mathbf{1} = \mathbf{0}$$

(iii) The coefficients $a_0, \cdots, a_5$ appearing in (16) are determined in terms of the eigenvalues of $\mathbf{A}$ by noting that each λ satisfies also (16), therefore,

$$\exp[z\,\lambda] = a_0 + a_1\lambda + a_2\lambda^2 + a_3\lambda^3 + a_4\lambda^4 + a_5\lambda^5 \tag{17}$$

(iv) Use of (17) six times, one for each eigenvalue, yields a system of six equations in the unknowns $a_0, \cdots, a_5$, whose solution can be written compactly as

$$a_j = \frac{1}{2}\sum_{k=1}^{3}\Lambda_{jk}\left[e^{\lambda_k z} + (-1)^j e^{-\lambda_k z}\right], \quad j = 0, \cdots, 5 \tag{18}$$

where the coefficients Λ_{jk} are expressed in terms of the eigenvalues as follows:

$$\Lambda_{0k} = \prod_{j=k+1}^{k+2}\frac{\lambda_j^2}{d_k}; \quad \Lambda_{1k} = \prod_{j=k+1}^{k+2}\frac{\lambda_j^2}{\lambda_k d_k};$$

$$\Lambda_{2k} = \sum_{j=k+1}^{k+2}\frac{\lambda_j^2}{d_k}; \quad \Lambda_{3k} = \sum_{j=k+1}^{k+2}\frac{\lambda_j^2}{\lambda_k d_k};$$

$$\Lambda_{5k} = \frac{1}{d_k}; \quad \Lambda_{6k} = \frac{1}{\lambda_k d_k};$$

$$d_k = (\lambda_{k+1}^2 - \lambda_k^2)(\lambda_{k+2}^2 - \lambda_k^2), \quad k = 1, 2, 3$$

where the results $\lambda_1^2 = \lambda_4^2$, $\lambda_2^2 = \lambda_5^2$, and $\lambda_3^2 = \lambda_6^2$ must be used.

(v) Upon substitution of (18) together with the various powers of $\mathbf{A}$ into (16), the final expression for the matrix exponential is obtained, which henceforth will be denoted by $\mathbf{B}(M,\xi,z)$, where the argument M emphasizes the explicit dependence of the transfer matrix on the various material constants.

Finally, Eq (14) is rewritten as

$$\hat{\mathbf{S}}(\xi,z) = \mathbf{B}(M,\xi,z)\ \hat{\mathbf{S}}(\xi,0) \tag{19}$$

which gives the state vector consisting of the transformed stresses, displacements, electric potential and electric displacement at an arbitrary depth z in the field. It should be noted that while $\mathbf{B}$ is a unique matrix for a given material, $\hat{\mathbf{S}}(\xi,0)$ varies from problem to problem according to the prescribed boundary conditions.

To find the physical components of the state vector one must invert (19). This process may vary in difficulty according to the boundary value problem under consideration. In general, the inversion may have to be performed numerically, although some fundamental solutions can be obtained in an exact manner as we show in a forthcoming article. In closing this section we present important properties of the transfer matrix and an outline of the basic procedures to follow in the solution of actual boundary value problems.

Properties of the matrix B

As noted by Bahar (1975) the transfer matrix $\mathbf{B}$ has group properties that here we repeat for the sake of completeness.

(a) Identity property:

$$\text{Since}\ \ \mathbf{B}(\xi,z) = \exp[z\mathbf{A}(\xi)] \implies \mathbf{B}(\xi,0) = \mathbf{1}$$

That is, $\mathbf{B}(\xi,0)$ maps the initial state vector onto itself.

(b) Inversion property:

$$\mathbf{B}(\xi,-z) = \exp[-z\mathbf{A}(\xi)] = \mathbf{B}^{-1}(\xi,z)$$

Which means that the inverse of the transfer matrix carries the state vector in the field back into the initial state vector.

(c) Translation property:

$$\mathbf{B}(\xi,z_1+z_2) = \mathbf{B}(\xi,z_1)+\mathbf{B}(\xi,z_2) = \exp[(z_1+z_2)\mathbf{A}(\xi)]$$

Physically this means that the operation of carrying an input state vector first from 0 to z_1, then from z_1 to z_2 is equivalent to carrying the same vector from 0 directly to $z_1 + z_2$ in a single step. Consequently, the transfer matrix is independent of the choice of origin.

(d) Determinant property: A well established result of the theory of ordinary differential equations is (Coddington and Levinson, 1955)

$$\det\mathbf{B}(\xi,z) = \det\mathbf{B}(\xi,0)\ \exp\left[\int_0^z \mathrm{tr}\ \mathbf{A}(t)\ dt\right]$$

But $\det\mathbf{B}(\xi,0) = 1$, and $\mathrm{tr}\ \mathbf{A} = 0 \implies \det\mathbf{B} = 1$

That is, the transfer matrix is nonsingular.

Solution of Boundary Value Problems

Equation (19) represents the behavior in the transformed domain of a single piezoelectric layer provided the initial state vector is known in its entirety. In general, this is not the case and additional conditions must be imposed. For example, consider the case of a semi-infinite piezoelectric medium $z \geq 0$ subjected to a distributed mechanical or electrical load on the surface $z = 0$. In such a case only the values of the stresses and electric displacement on the surface of the medium will be known. The initial values of the displacement components and electric potential can be obtained by requiring that the state vector vanishes when $z \to \infty$. Once all the initial values are known the physical variables can be determined for all values of z.

When the problem under consideration consists of two or more layers as shown in Figs 1 and 2 it becomes necessary to generalize (19) in an appropriate manner. This is accomplished by using a continued matrix product in which the state vector approach is used to eliminate intermediate state vectors through the conditions existing among the divers variables at the various interfaces. That is, the relation (19) holds between successive interfaces. Letting N denote the number of a layer located at depth

$z = h_N$, (19) can be written as

$$\hat{\mathbf{S}}(\xi, h_N) = \mathbf{B}_N(M_N, \xi, h_N) \cdots \mathbf{B}_1(M_1, \xi, h_1)\ \hat{\mathbf{S}}(\xi, 0) \tag{20}$$

where $\mathbf{B}_1, \cdots, \mathbf{B}_N$ are the transfer matrices of the individual layers. Hence Eq (20) describes the overall response of the layered system in which all intermediate state vectors have been eliminated. Naturally, local information consisting of state vectors at arbitrary interfaces can also be obtained.

We notice at this point that the various layers composing the structure may have different electric and mechanical behavior. For example, one layer could be made of isotropic linear elastic material, in which case only elastic variables need to be used to describe its behavior. Thus, its transfer matrix will be only a 4×4 matrix, making impossible its product with the transfer matrix of a piezoelectric layer. To overcome this difficulty the purely elastic transfer matrix can be augmented and partitioned in a manner that makes explicit the elastic and electrical effects. Thus, it is convenient to write all the transfer matrices as

$$\left\{ \begin{matrix} \hat{\mathbf{S}}^m \\ \hat{\mathbf{S}}^e \end{matrix} \right\} = \left\| \begin{matrix} \mathbf{B}^m & \mathbf{B}^{me} \\ \mathbf{B}^{em} & \mathbf{B}^e \end{matrix} \right\| \left\{ \begin{matrix} \hat{\mathbf{S}}^m \\ \hat{\mathbf{S}}^e \end{matrix} \right\}_{z=0}$$

where $\mathbf{B}^m$, $\mathbf{B}^e$, $\mathbf{B}^{me}$, and $\mathbf{B}^{em}$ are 4×4, 2×2, 4×2 and 2×4 matrices reflecting the purely mechanical, purely electrical, mechanical-electrical and electrical-mechanical interactions, respectively. Furthermore $\hat{\mathbf{S}}^m = \{\hat{u}, \hat{w}, \hat{\sigma}_{zz}, \hat{\sigma}xz\}^T$ and $\hat{\mathbf{S}}^e = \{\hat{\phi}, \hat{D}_z\}^T$ are the transformed mechanical and electrical state vectors. Hence in the case of the isotropic elastic layer we have $\mathbf{B}^{me} = \mathbf{B}^{em} = \mathbf{0}$. An additional advantage of this representation stems from the fact that the matrices $\mathbf{B}^m$ and $\mathbf{B}^e$ are symmetric with respect to their secondary diagonals as a consequence of Maxwell's reciprocity theorem, introducing certain computational simplifications in the final calculations.

ACKNOWLEDGEMENTS

This work was partially funded by the National Science Foundation under Grant No. MSS-9215296. Mr. Castro was supported by the government of Brazil through a Capes scholarship. It is a pleasure to express our gratitude also to Professor Bahar for his comments and help.

REFERENCES

1. Bahar, L. Y., Transfer matrix approach to layered systems, *J. Eng. Mech. Div.*, **98**(EM5), 1159-1172 (1972).
2. Bahar, L. Y., A state space approach to elasticity, *J. Franklin Inst.*, **299**(1), 33-41 (1975).
3. Berlincourt, D. A., Curran, D. R. and Jaffe, H., Piezoelectric and piezoceramic materials and their function in transducers, in *Physical Acoustics*, Vol. I-A, W. Mason (ed), Academic Press, New York, 1964.
4. Cady, W. G., *Piezoelectricity*, revised edition, Dover Publications, Inc., New York, 1964.
5. Coddington, E. A. and Levinson, N., *Theory of Ordinary Differential Equations*, McGraw-Hill, New York, 1955.
6. Jaffe, B., Cook, W. R. and Jaffe, H., *Piezoelectric Ceramics*, Academic Press, New York, 1971.
7. Ogata, K., *State Space Analysis of Control Systems*, Prentice Hall, New Jersey, 1967.
8. Sosa, H. A. and Bahar, L. Y. Transition from Airy stress function to state space formulation of elasticity, *J. Franklin Inst.*, **329**(5), 817-828 (1992).

Experimental determination of stress intensity factor distributions in engineering problems

CW Smith

Department of Engineering Science and Mechanics
Virginia Polytechnic Institute and State University
Blacksburg VA 24061-0219

Following a brief introduction of the concept of stress intensity factor from fracture mechanics and the frozen stress method from photoelasticity, an algorithm is developed from fracture mechanics equations and the stress-optic law for converting stress fringe measurements into a form useful for determining the stress intensity factor. This algorithm covers all three local modes of deformation and is used to analyse frozen stress slices along the border of cracks to obtain distributions for stress intensity factors K_1, K_2 and K_3. The use of the method is illustrated by three examples from practical engineering problems and results are compared with the literature where possible.

I - INTRODUCTION

The present paper deals with the refinement and use of two old and established concepts for use in measuring the stress intensity factor (SIF) distribution in three dimensional cracked body problems.

A) Fracture Mechanics – Concept of SIF

The basic concepts of plane fracture mechanics were proposed in two papers (Griffith, 1921, 1925) and were prescribed on an energy basis using the solution of a narrow ellipse provided by Inglis (1913). Then Irwin (1948) and Orowan (1948) independently observed a concentration of plastic deformation in the surface layer of fractured steel specimens and extended Griffith's concept to include local plastic flow. Then Irwin (1957), utilizing a solution by Westergaard (1939), which treated the crack as a mathematical branch cut, developed the concept of the stress intensity factor (SIF) as the field strength of the crack tip stress singularity. The same result was obtained by Williams (1957). Irwin (1958) proposed a simple correction for local plasticity by extending the crack length in the computation. The result was known as Linear Elastic Fracture Mechanics (LEFM). Many subsequent developments have extended LEFM to include moderate to large scale plasticity as Elastic-Plastic Fracture Mechanics (EPFM) but these are not included in the present discussion.

In the sixties and seventies, rapid developments in both the hardware and software of digital computers opened the way for attacking three dimensional fracture problems through the use of numerical methods. However, validation of the computer codes was both expensive and difficult, lagging significantly developments in computational methods. Without code validation, some codes were called into question.

Around 1968, the author and his colleagues undertook an initial effort to develop a cost effective modelling technique for providing the needed validation at that time. The method of experimental verification selected for this purpose was known as frozen stress photoelasticity.

B) Photoelasticity – Concept of Frozen Stress

The photoelastic effect was discovered by Maxwell (1853) and current normal useage is described by Burger (1987). The frozen stress method of analysis was introduced by Oppel (1936). The method was subsequently widely used on three dimensional elastic problems for over a quarter of a century. The use of the method required construction of a scale model of a three dimensional body from a transparent photoelastic material of diphase characteristics. That is, at a certain temperature, the critical temperature, the material's elastic modulus dropped to about 0.2% of its room temperature modulus and became about 25 times more sensitive to stress fringes. When loaded above its critical temperature and then cooled slowly to room temperature, the stress fringes associated with the photoelastic effect above critical temperature are trapped permanently in the material along with accompanying deformations. When the load is later removed at room temperature, the recovery exhibited by the material which is 500 times stiffer than above critical temperature can be neglected. Moreover, thin slices can be removed from the "frozen" body without altering either stress fringes or deformations. In other words, no live stresses remain and it is the stress fringes and displacements obtained above critical temperature which remain.

After describing the refinements introduced in the two above concepts, several examples of the use of the resulting method of analysis will be described.

II – REFINEMENTS

A) The Algorithm for Converting Optical Data Into SIF Values

As a result of the analytical models described above for the plane problem, the local state of stress is usually described in terms of a single parameter, the SIF, for small scale yielding with Mode I loading. If all three local modes are present (Fig. 1) then three parameters K_1, K_2, K_3 are indicated. However, when making photoelastic measurements in the neighborhood of the crack tip, since the stress fringes are proportional to the maximum in plane shear stress, then, if the non-singular shear stress does not vanish near the crack tip, it must be included in the algorithms for converting stresses into K values. On the other hand, if one moves too far from the crack tip, then the contribution to the data from the non-singular stress field increases as the contribution from the singular field decreases. A number of algorithms have been proposed for converting data around the crack tip into K values. Smith and Olaosebikan (1984) have shown that all of these algorithms yield essentially the same results for near tip measurements in plane problems. In three dimensional problems, the singular zone is further constricted by nearby boundary effects. The following analysis has been used successfully in dealing with such problems.

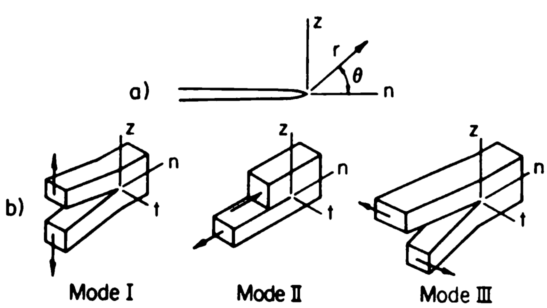

1. Local modes of deformation.

Consider a general mixed mode flaw geometry with notations as pict 2. It has been shown [Kassir and Sih (19 resses near the border of an elliptical ressed in terms of a set of local moving rectangular cartesian coordinates in a plane perpendicular to the flaw border, have the same form as the stresses in a plane perpendicular to the border of a straight front crack. Consider a half-space containing a surface flaw at an angle β to the boundary with remote uniform tension parallel to the z' direction (Figure 2). The local moving orthogonal coordinate system tnz is always oriented such that t is tangent to the flaw border and n is normal to the flaw border but both n and t are in the flaw plane. The z axis is normal to the flaw plane. In such a problem, all three local modes of near field deformation (i.e., Modes I, II and III) will be present as we move around the flaw border. We note that at $\alpha = 0$, however, Mode III will be absent.

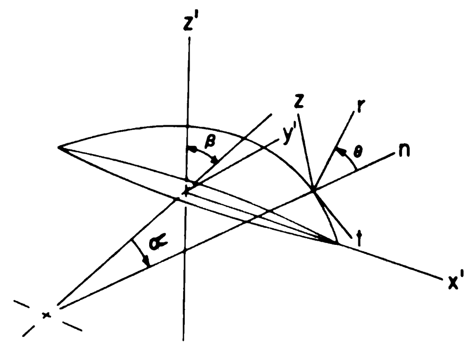

2. General problem geometry and notation.

The stress distribution near the part through crack in the data zone, corresponding to the opening mode of deformation can be taken as

$$\sigma_{nn} = \frac{K_1}{(2\pi r)^{1/2}}\cos\frac{\theta}{2}\left[1 - \sin\frac{\theta}{2}\ \sin\frac{3\theta}{2}\right] - \sigma^1_{nn} \quad (1)$$

$$\sigma_{zz} = \frac{K_1}{(2\pi r)^{1/2}}\cos\frac{\theta}{2}\left[1 + \sin\frac{\theta}{2}\ \sin\frac{3\theta}{2}\right] - \sigma^1_{zz} \quad (2)$$

$$\tau_{nz} = \frac{K_1}{(2\pi r)^{1/2}}\sin\frac{\theta}{2}\left[\cos\frac{\theta}{2}\ \cos\frac{3\theta}{2}\right] - \tau^1_{nz} \quad (3)$$

where K_1 is the Mode I SIF and the coordinates r and θ are shown in Figure 2. σ^1_{ij} represent the contribution of the Mode I regular stress field to the measurement zone which is taken far enough from the crack tip to avoid a non-linear zone very near the tip. While they may generally be regarded as expressible in Taylor Series Expansions, it turns out that only the leading terms of said series are normally necessary so that σ^1_{ij} are constants for a given point in the flaw border but vary from point to point. Stresses in the data zone corresponding to the Mode II can be taken as

$$\sigma_{nn} = \frac{K_2}{(2\pi r)^{1/2}}\sin\frac{\theta}{2}\left[2 + \cos\frac{\theta}{2}\ \cos\frac{3\theta}{2}\right] - \sigma^2_{nn} \quad (4)$$

$$\sigma_{zz} = \frac{K_2}{(2\pi r)^{1/2}} \sin\frac{\theta}{2} \cos\frac{\theta}{2} \cos\frac{3\theta}{2} - \sigma^2_{zz} \quad (5)$$

$$\tau_{nz} = \frac{K_2}{(2\pi r)^{1/2}} \cos\frac{\theta}{2} \left[1 - \sin\frac{\theta}{2} \sin\frac{3\theta}{2}\right] - \tau^2_{nz} \quad (6)$$

where K_2 and σ^2_{ij} are analogous to K_1 and σ^1_{ij}.

And finally the stresses in the data zone corresponding to the Mode III loading can be taken as

$$\tau_{nt} = -\frac{K_3}{(2\pi r)^{1/2}} \sin\frac{\theta}{2} - \tau^3_{nt} \quad (7)$$

$$\tau_{zt} = \frac{K_3}{(2\pi r)^{1/2}} \cos\frac{\theta}{2} - \tau^3_{zt} \quad (8)$$

with K_3 and τ^3_{ij} analogous to K_1 and σ^1_{ij}.

If the above modes of loading are superimposed, one gets the following stress distribution in a plane perpendicular to the crack front (the n-z plane)

$$\sigma_{nn} = \frac{K_1}{(2\pi r)^{1/2}} \cos\frac{\theta}{2} \left[1 - \sin\frac{\theta}{2} \sin\frac{3\theta}{2}\right] - \frac{K_2}{(2\pi r)^{1/2}} \sin\frac{\theta}{2} \left[2 + \cos\frac{\theta}{2} \cos\frac{3\theta}{2}\right] - \sigma^0_{nn} \quad (9)$$

$$\sigma_{zz} = \frac{K_1}{(2\pi r)^{1/2}} \cos\frac{\theta}{2} \left[1 + \sin\frac{\theta}{2} \sin\frac{3\theta}{2}\right] + \frac{K_2}{(2\pi r)^{1/2}} \sin\frac{\theta}{2} \cos\frac{\theta}{2} \cos\frac{3\theta}{2} - \sigma^0_{zz} \quad (10)$$

$$\tau_{nz} = -\frac{K_1}{(2\pi r)^{1/2}} \sin\frac{\theta}{2} \cos\frac{\theta}{2} \cos\frac{3\theta}{2} + \frac{K_2}{(2\pi r)^{1/2}} \cos\frac{\theta}{2} \left[1 - \sin\frac{\theta}{2} \sin\frac{3\theta}{2}\right] - \tau^0_{nz} \quad (11)$$

which are independent of equations (7) and (8); (i.e., the local field equations for Modes I and II are completely separate from those for Mode III).

While σ^0_{ij} has no influence upon the singular stress field itself, it does alter the isochromatic fringe pattern, which is proportional to the maximum in-plane shearing stress.

From the stress field given in equations (9)–(11), the maximum shearing stress in the plane perpendicular to the crack front, nz, can be obtained using

$$(\tau)^{nz}_{max} = \left[\left(\frac{\sigma_{zz} - \sigma_{nn}}{2}\right)^2 + \tau^2_{nz}\right]^{1/2} \quad (12)$$

and, truncating to the same order as equations (9)–(11), one gets

$$(\tau)^{nz}_{max} = \frac{A}{r^{1/2}} + B \quad (13)$$

for fringe loops approaching the shape of Fig. 3 where

$$A = \left\{\frac{1}{8\pi}\left[(K_1 \sin\theta + 2K_2 \cos\theta)^2 + (K_2 \sin\theta)^2\right]\right\}^{1/2} \quad (14)$$

and

$$B = B\left(\sigma^0_{ij}\right)$$

The maximum shearing stress in the nz plane, the left side of equations (12) and (13), is determined photoelastically.

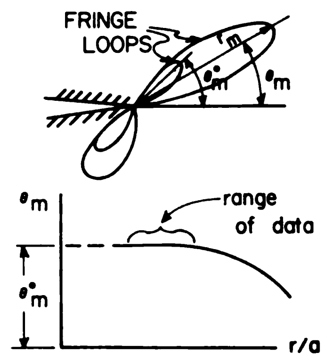

3. Determination of θ^0_m for mixed mode.

Now, in general, the effect of σ^0_{ij} involves both a folding and a change in eccentricity of the fringe loops (Figure 3). If folding occurs, θ_m, the angle along which the distance to a fringe from the crack tip is greatest, will vary with the fringe order n and one must plot θ_m vs r/a and extrapolate to the origin in order to obtain θ^0_m, the value of θ_m associated with K_1 and K_2. In the present problem θ_m was constant over the data range in the fashion indicated qualitatively by Figure 3. As noted in Fig. 3, data are always taken from forward leaning loops. In case $K_2 > K_1$, Eq. 13 and Fig. 3 may require modification. Upon computing

$$\lim_{\substack{r_m \to 0 \\ \theta_m \to \theta^0_m}} \left\{(8\pi r_m)^{1/2} \frac{\partial (\tau)^{nz}_{max}}{\partial \theta} \left(K_1, K_2, r_m, \theta_m, \sigma^0_{ij}\right)\right\} = 0 \quad (15)$$

one obtains

$$\left(\frac{K_2}{K_1}\right)^2 - \frac{4}{3}\left(\frac{K_2}{K_1}\right) \cot 2\theta^0_m - \frac{1}{3} = 0 \quad (16)$$

Since θ^0_m can be measured experimentally, (K_2/K_1) can be calculated from equation (16). Then by combining the Stress-Optic Law with a modified form of Equation (13)

$$(\tau)^{nz}_{max} = \frac{fn'}{2t'} = \quad (17)$$

where $K^*_{AP} = (\tau)^{nz}_{max}(8\pi r)^{1/2}$ is the "apparent" SIF, f is the material fringe value, n' is the fringe order, and t' is the slice thickness, hence

$$K^*_{AP} = \Big[(K_{1AP}\sin\theta_m + 2K_{2AP}\cos\theta_m)^2 + (K_{2AP}\sin\theta_m)^2\Big]^{1/2} \tag{18}$$

and one can solve for the individual values of K_1 and K_2.

In order to do this, one must obtain

$$K^* = \Big[(K_1 \sin\theta^0_m + 2K_2 \cos\theta^0_m)^2 + (K_2 \sin\theta^0_m)^2\Big]^{1/2} \tag{19}$$

from K^*_{AP} by plotting $K^*_{AP} = (\tau)^{nz}_{max}(8\pi r)^{1/2}$ vs $(r/a)^{1/2}$ identifying a linear zone, and extrapolating to the origin. This will yield K^*. A typical set of fringe data illustrating such a determination is given in Figure 4. Once K^*, K_2/K_1, and θ^0_m are known, K_1 and K_2 can be calculated which then can be normalized using proper quantities.

Note that the above approach utilizes a two parameter (A,B) model since the linear zone can be located experimentally (Figure 4). However, if one cannot locate such a zone experimentally then additional terms leading to an equation of the form

$$(\tau)^{nz}_{max} = \frac{A}{r^{1/2}} + \sum_{n=0}^{\infty} B_n r^{n/2} \tag{20}$$

with suitable truncation criteria must be considered.

Since such criteria are not yet established independent of experiment, this latter approach is avoided where possible and was not necessary in the studies described in the sequel.

The stress distribution (σ_{tt}), acting in a plane perpendicular to the crack surface and tangent to the crack front (zt plane) or in a plane parallel to the zt plane can be found from equations (9)–(10).

$$\sigma_{zz} = \frac{K_1}{(2\pi r)^{1/2}}\cos\frac{\theta}{2}\left[1+\sin\frac{\theta}{2}\sin\frac{3\theta}{2}\right] + \frac{K_2}{(2\pi r)^{1/2}}\sin\frac{\theta}{2}\left[\cos\frac{\theta}{2}\cos\frac{3\theta}{2}\right] - \sigma^0_{zz} \tag{21}$$

In order to arrive at a value of σ_{tt}, prior experiments by the authors indicate that the usual assumption of plane strain (for the plane problem) may not be valid here. However, if one assumes a state of nearly *generalized* plane strain such that the value of $\mathcal{E}_{tt}$ can be considered constant over a portion of the length of the flaw border, then the observed state of varying transverse contraint along the flaw border can apparently be approximated rather well. Thus, we assume

$$\mathcal{E}_{tt} = \frac{\sigma_{tt} - \nu(\sigma_{nn} + \sigma_{zz})}{E} \simeq \bar{\mathcal{E}} \tag{22}$$

whence $\sigma_{tt} \simeq E\bar{\mathcal{E}} + \nu(\sigma_{nn} + \sigma_{zz})$ where $\bar{\mathcal{E}}$ may be adjusted at intervals along the flaw border and where, again from equation (10),

$$\sigma_{nn} = \frac{K_1}{(2\pi r)^{1/2}}\cos\frac{\theta}{2}\left[1-\sin\frac{\theta}{2}\sin\frac{3\theta}{2}\right] - \frac{K_2}{(2\pi r)^{1/2}}\sin\frac{\theta}{2}\left[2+\cos\frac{\theta}{2}\cos\frac{3\theta}{2}\right] - \sigma^0_{nn} \tag{23}$$

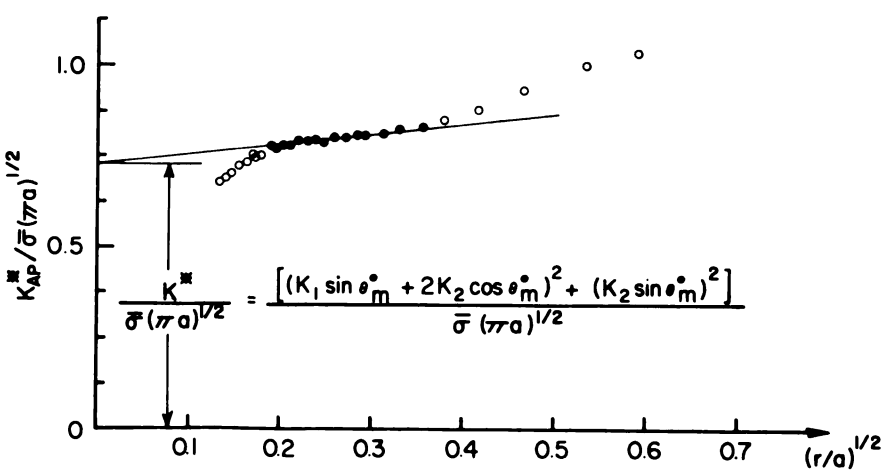

4. Det- -tion of K^* from test data. $\bar{\sigma}$ is the remote normal s' z' direction in Fig. 2.

For $\nu = (1/2)$ (as in the present experiments) we then have

$$\sigma_{tt} = \frac{K_1}{(2\pi r)^{1/2}}\cos\frac{\theta}{2} - \frac{K_2}{(2\pi r)^{1/2}}\sin\frac{\theta}{2} - \sigma_{tt}^0 + E\bar{\mathcal{E}} \quad (24)$$

Moreover, from Mode III, we have

$$\tau_{zt} = \frac{K_3}{(2\pi r)^{1/2}}\cos\frac{\theta}{2} - \tau_{zt}^0 \quad (25)$$

$$(\tau)_{max}^{zt} = \left[\left(\frac{\sigma_{zz} - \sigma_{tt}}{2}\right)^2 + \tau_{zt}^2\right]^{1/2} \quad (26)$$

Consider the line normal to the crack surface which passes through the crack tip in the zt plane. For this case $\theta = (\pi/2)$, and when substituted in equations (21), (24) and (25), there results

$$\sigma_{zz} = \frac{1}{4(\pi r)^{1/2}}[3K_1 - K_2] - \sigma_{zz}^0 \quad (27)$$

$$\sigma_{tt} = \frac{1}{2(\pi r)^{1/2}}[K_1 - K_2] - \sigma_{tt}^0 + E\bar{\mathcal{E}} \quad (28)$$

$$\tau_{zt} = \frac{K_3}{2(\pi r)^{1/2}} - \tau_{zt}^0 \quad (29)$$

then for a two parameter model as before,

$$(\tau)_{max}^{zt} = \frac{C}{r^{1/2}} + D \quad (30)$$

where

$$C = \frac{1}{(4\pi)^{1/2}}\left[\frac{1}{16}(K_1 + K_2)^2 + K_3^2\right]^{1/2} \quad (31)$$

and

$$D = D\left(E\bar{\mathcal{E}},\ \sigma_{ij}^0\right) \quad (32)$$

Now by combining the Stress-Optic Law with a modified form of equation (30)

$$(\tau)_{max}^{zt} = \frac{fn'}{2t'} = \frac{K_{AP}^{**}}{(8\pi r)^{1/2}} \quad (33)$$

where

$$K_{AP}^{**} = \left\{2\left[\frac{1}{16}(K_{1AP} + K_{2AP})^2 + K_{3AP}^2\right]\right\}^{1/2} \quad (34)$$

the value of K_3 can be obtained.

In order to do this, one must obtain

$$K^{**} = \left[2\left\{\frac{1}{16}(K_1 + K_2)^2 + K_3^2\right\}\right]^{1/2} \quad (35)$$

from K_{AP}^{**} by plotting a $K_{AP}^{**} = (\tau)_{max}^{zt}(8\pi r)^{1/2}$ vs $(r/a)^{1/2}$ curve, identifying a linear zone, and extrapolating to the origin. This will yield K^{**}.

At the points where the flaw border intersects the boundary of the plate, SIF values are uncertain and require a boundary layer analysis for an accurate evaluation.

(B) Methods for Increasing Fringe Sensitivity

Due to the lack of stiffness of the material above critical temperature, it is necessary to keep loads small in the frozen stress experiments in order to avoid finite deformations near the crack tip. Moreover, the slices which are removed from the stress frozen body which are oriented normal to the crack plane locally and the t direction will be quite thin ($t' < 0.5mm$). These limitations result in only a few stress fringes near the crack tip. In order to increase the number of fringes, two special techniques, the method of Tardy (1929) and the fringe multiplication method of Post (1966) are applied in tandem. In this way one fiftieth of a fringe is routinely measured, providing ample data near the crack tip.

Finally, as noted earlier, the value of Poisson's Ratio for stress freezing materials is nearly one half. No correction is made for this deviation from metals but it may slightly influence the results towards the locally plastic situation which actually exists in metals.

III - GENERAL APPROACH

Given a general cracked body problem with all three local modes of deformation, the general procedure for obtaining SIF distributions along the flaw border would be the following:

a) Construct transparent model from stress freezing material.

b) Insert crack of desired shape and size in desired location. Natural starter cracks can be made by striking a sharp blade held against the body surface with a hammer. Then the crack may be grown above critical temperature to desired size without knowing the crack shape a-priori. The shape is dictated by body shape and load orientation.

c) Reduce load required to grow the crack to stop growth and cool to room temperature.

d) Remove thin slices mutually orthogonal to flaw border and its surface at intervals along the flaw border and analyze photoelastically with polarized light directed along the t axis as in Fig. 3 for θ_m^0 and K_{AP}^*, and obtain K^* from Fig. 4. Then solve Eqs. 16 and 19 for K_1 and K_2.

e) Then remove a sub-slice from each main slice and analyze photoelastically with the polarized light directed along the n axis. Then using Eqs. (33)–(34) as described above determine K^{**} graphically and finally K_3 from Eq. (35).

Although the method can be applied to artificial cracks of pre-determined shape and size where a sharp (< 30°) vee notch is used to simulate the crack, it can also be used as described in (b) to generate the crack shape and size where neither are known a-priori.

IV - APPLICATION OF THE METHOD TO ENGINEERING PROBLEMS

When cracks grow in isotropic, homogeneous materials, the crack path follows the plane of the maximum principal tensile stress with only rare exceptions (Smith and Weirsma, 1986). Thus, once the crack begins to grow, it exhibits only Mode I locally. However, if a crack is loaded in a different way from that creating it, mixed modes may be present and cause the crack to change direction so as to recover Mode I during growth. In order to illustrate the application of the method to several different kinds of problems, three examples have been selected:

i) Surface crack growing in a rocket motor grain model (Mode I).

ii) Crack emanating from a hole filled with a rigid pin (Modes I and II).

iii) Circumferential crack in cylinder under pure torsion (Mode III).

Example 1

i) Crack in Rocket Motor Grain Model (Mode I)
Cracked test models as shown in Fig. 5 were loaded with internal pressure. This produced pure Mode I loading on the semi-elliptic crack surfaces. A typical Mode I stress fringe pattern for a slice prior to fringe multiplication or further enhancement is shown in

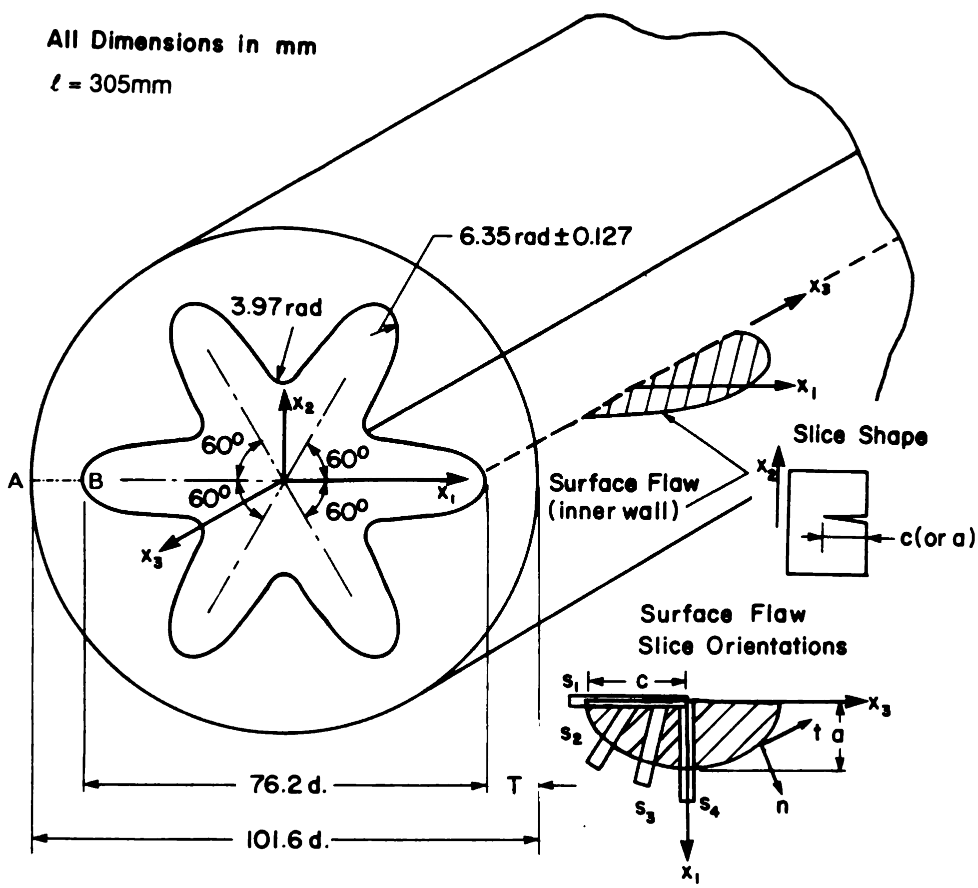

5. Cracked motor grain model and frozen slice orientation.

Fig. 6. Since the fringes spread approximately normal to the crack plane we can set $\theta = \pi/2$ in Eq. (14), and, if we replace σ_{ij}^0 with τ_0, the non-singular maximum shear stress resulting from σ_{ij}^0, Eq. 13 becomes:

$$(\tau)^{nz}_{max} = \frac{K_1}{(8\pi r)^{1/2}} + \tau_0 \quad \text{or} \tag{36}$$

$$(\tau)^{nz}_{max}(8\pi r)^{1/2} = K_1 + (8\pi)^{1/2}\tau_0 r^{1/2} \tag{37}$$

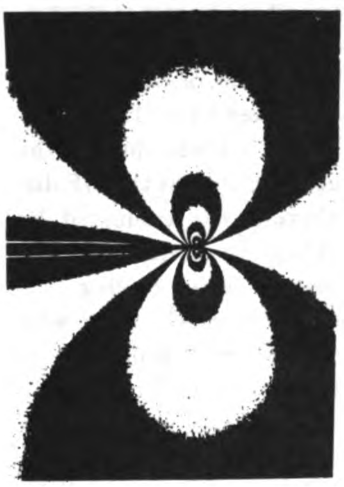

6. Mode I stress fringe pattern.

So if we define $K_{AP} = (\tau)^{nz}_{max}\,(8\pi r^{1/2})$, the apparent SIF, and normalize with respect to $\rho(\pi a)^{1/2}/_{\Phi}$ where ρ is the internal pressure, a the crack depth, and Φ is an elliptic integral defined in Fig. 7 which is known as the shape factor for a semi-elliptic crack, then

$$\frac{K_{AP}\Phi}{\rho(\pi a)^{1/2}} = \frac{K_1\Phi}{\rho(\pi a)^{1/2}} + \frac{(8)^{1/2}}{\rho}\tau_0\Phi\left(\frac{r}{a}\right)^{1/2} \tag{38}$$

Along $\theta = \pi/2$, we measure n' which determines τ^{nz}_{max} (Eq. 17) and corresponding values of r which allow computation of K_{AP}. Now, if one plots $\frac{K_{AP}\Phi}{\rho(\pi a)^{1/2}}$ vs $\left(\frac{r}{a}\right)^{1/2}$, a straight line results, the intercept of which is the normalized SIF, or K_1. Such a plot is shown in Fig. 7. In order to locate the appropriate linear zone in a three dimensional problem, such plots must be

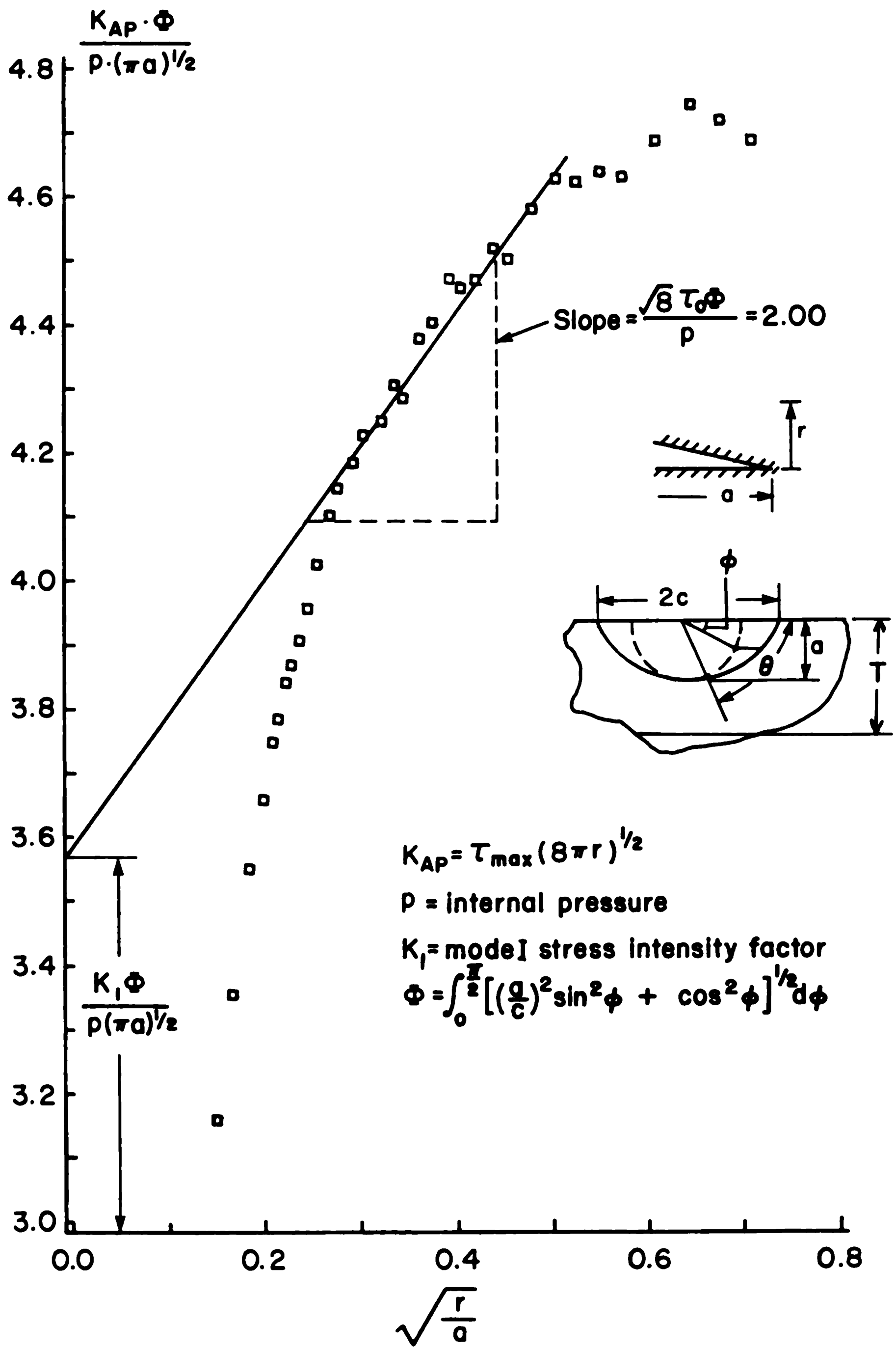

7. Determination of normalized SIF from test data.

obtained for several slices along the flaw border. The zone which is common to all slices usually lies between $\sqrt{r/a}$ of 0.2 and 0.4 (or greater). (Smith, et al, 1984.)

For cracks located on the axis of symmetry of the star finger, the crack remained planar as it grew but its aspect ratio, (a/c)(Fig. 7) changed somewhat and the data and resulting SIF distributions for several crack sizes are given in Fig. 8, suggesting that the cracks adjust their shapes during growth to maintain a nearly constant SIF along the flaw border. However, if cracks are initiated off of the axis of symmetry of the star finger, (Fig. 9) the surface orientation and SIF curves vary (Fig. 10). Crack E-2 broke through the outer surface but the SIF distribution was estimated by holding the internal pressure constant during cooling. When the crack paths were compared with principal planes obtained from uncracked frozen stress models at the crack midpoints, the paths were found to closely follow principal planes. Some details are found in Smith and Wang, (1992).

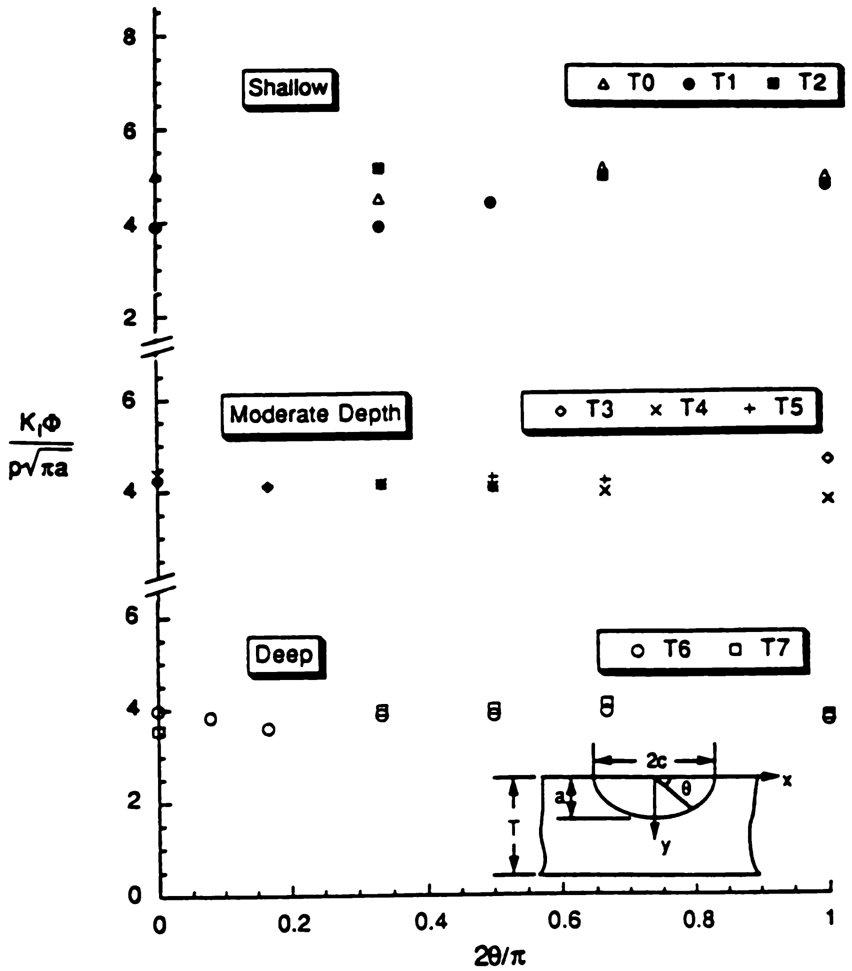

Test No.	a(mm)	a/c	a/T	Φ^1	p(KPa)^2
T0	3.6	.54	.28	1.23	26.9
T1	3.2	.52	.25	1.22	47.6
T2	4.1	.55	.32	1.24	47.6
T3	6.2	.46	.45	1.18	47.6
T4	6.6	.52	.52	1.22	42.1
T5	7.3	.43	.56	1.16	47.6
T6	8.4	.44	.66	1.17	47.6
T7	7.9	.45	.62	1.17	47.6

1. See figure 7.
2. Internal pressure.

8. T- ' data and SIF distributions for symmetric cracks.

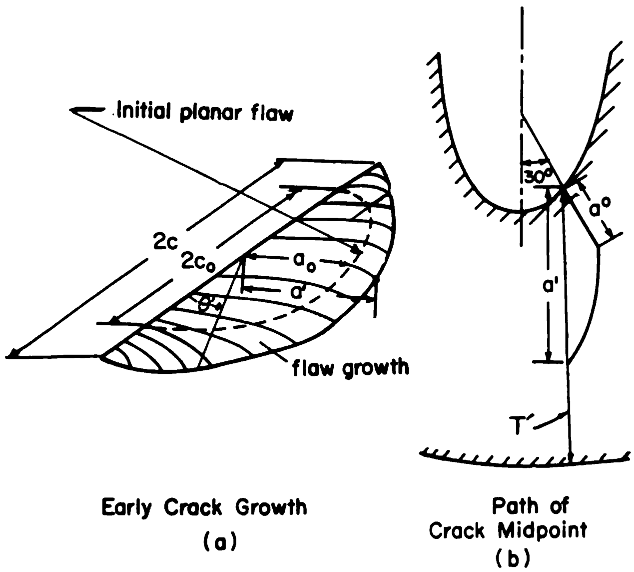

9. Crack shapes and notations for unsymmetric cracks.

Example 2

ii) Crack Emanating From Edge of Pin Loaded Hole (Modes I and II)

The test specimen and loading arrangement for this problem is pictured in Fig. 11. Only two slices [S] and [H] were removed and analyzed for the cracks which were planar as inserted and were not grown. The stress fringe patterns at H revealed a pure Mode I signature as shown in Fig. 6. However, at S, a mixed mode signature was obtained of the form sketched in Fig. 3. A typical set of results showing only the linear data is shown in Fig. 12 where $K_H^* = (K_1)_H$ since $(K_2)_H = 0$. K^* values were obtained as described earlier using Eqs. (17)–(19). Results, when compared with experiments on open holes showed that K_{1S} with the pin was two to four times that without the pin and K_{1H} with the pin was two to five times the value of K_{1H} without the pin. Details are given by Smith, Jolles and Peters, (1977).

Example 3

iii) Circumferential Crack Under Pure Torsional Load (Mode III)

A sharp circumferential notch (Fig. 13a) was cut into a 5.08 cm. diameter cylinder and stress frozen under a torsional load. Thin slices were removed oriented as shown in Fig. 13b. The polarized light field and observations of fringes were made along the n axis. A typical fringe pattern is shown in Fig. 14. Since K_1 and K_2 were zero, K_3 was obtained directly from a plot of Eq. (29) after normalizing with respect to the remote shear stress $\bar{\tau}$ times $(\pi a)^{1/2}$, that is:

$$\frac{K_{AP}}{\bar{\tau}(\pi a)^{1/2}} = \frac{K_3}{\bar{\tau}(\pi a)^{1/2}} - \frac{2\tau_{zt}^{o}}{\bar{\tau}}\left(\frac{r}{a}\right)^{1/2} \quad (39)$$

where $K_{AP} = \tau_{max}^{zt}(4\pi r)^{1/2}$. Again the fringe order n' (Eq. 17) and r are measured along $\theta = \pi/2$. Fig. 15 compares the results with other analyses. Details are furnished by Smith and Hardrath (1978).

Test No.	a'(mm)	a'/c	a'/T'[1]	Φ·2	p(Kpa)[3]
E1	11.4	0.62	0.88	1.29	41.4
E2	13.1	0.69	1.0	1.33	41.4
E3	7.95	0.65	0.61	1.30	41.4

1. T' is measured along a' to the outer boundary of the cylinder.
2. $\Phi' = \int_0^{\pi/2}\left[\left(\frac{a'}{c}\right)^2 \sin^2\phi' + \cos^2\phi'\right]^{1/2} d\phi'$.
3. p is the internal pressure.

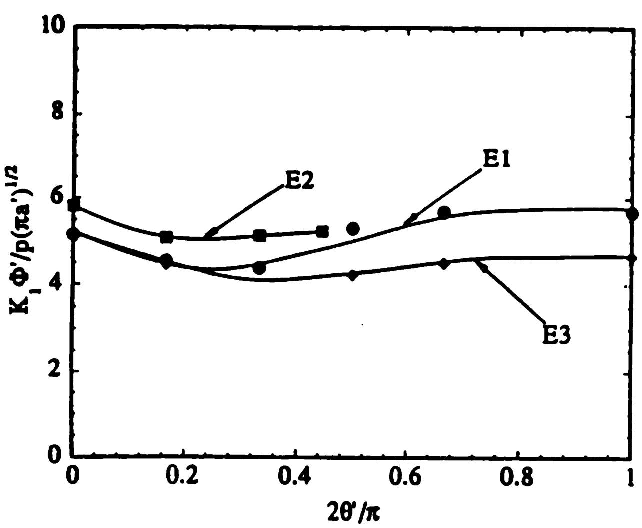

10. Data and SIF distributions for unsymmetric cracks.

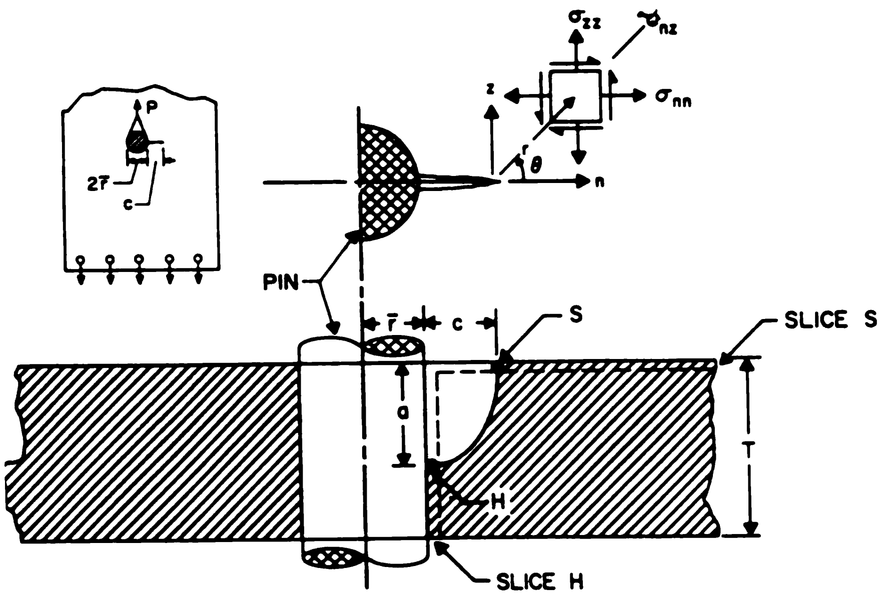

11. Loading and slice locations for pin loaded, cracked hole.

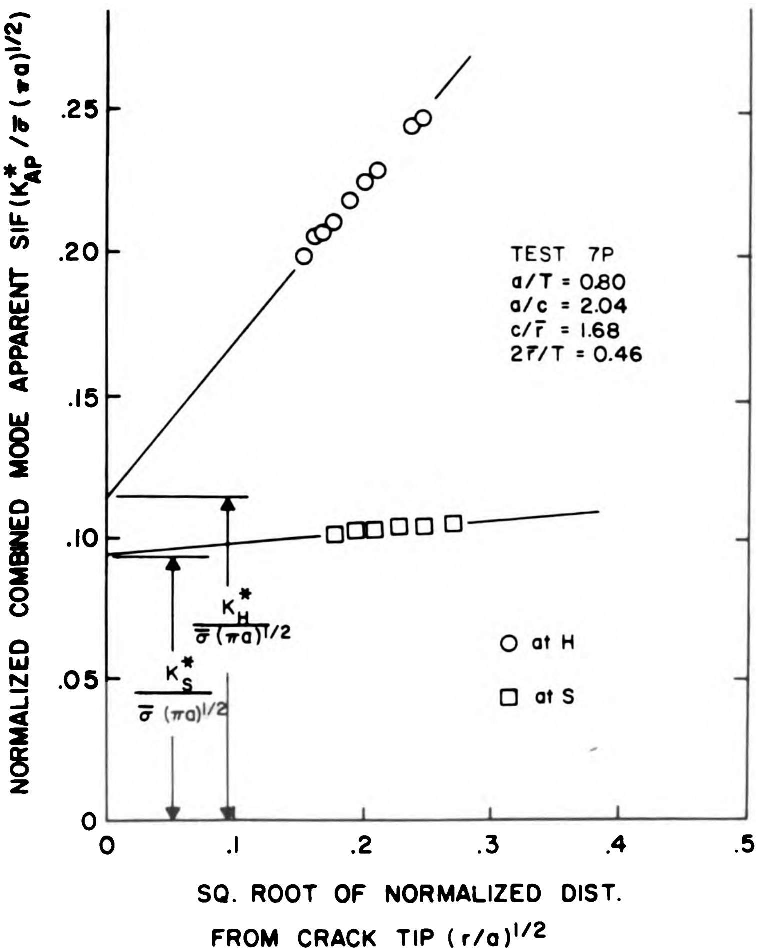

12. Normalized values for K^*_s and K^*_H for pin loaded cracked hole.

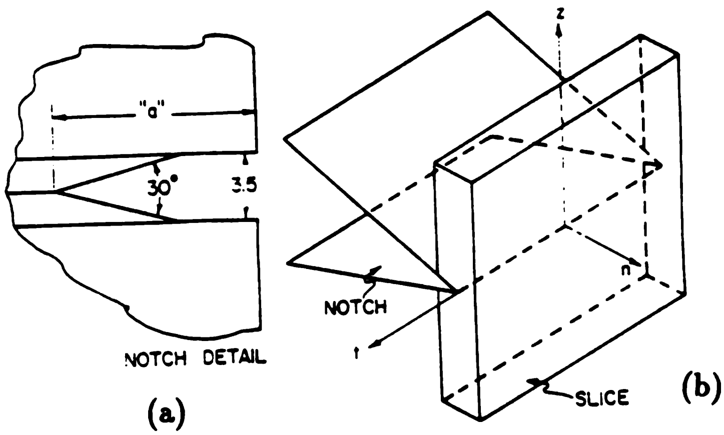

13. (a) Notch tip geometry
(b) Slice orientation for circumferentially cracked torsion bar.

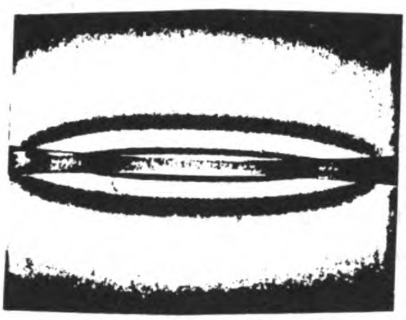

14. Mode III stress fringe pattern for slice from circumferentially cracked torsion bar.

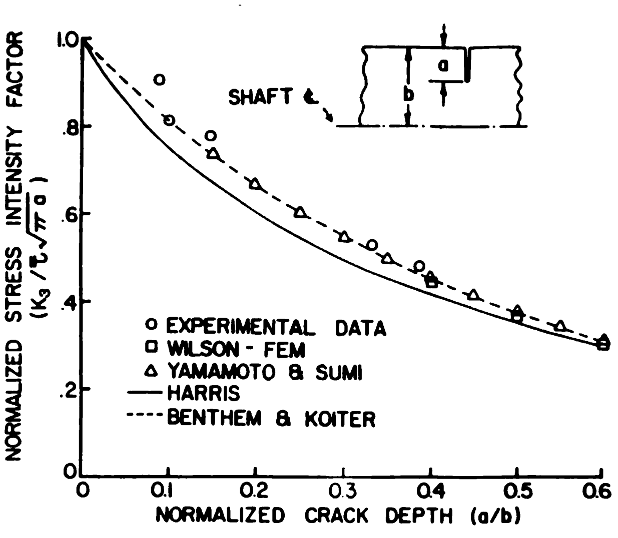

15. Comparisons of Mode III results.

SUMMARY

A modelling procedure based on frozen stress photoelasticity which has proven to be cost effective compared to full scale testing was described for estimating stress intensity factor distributions in a variety of three dimensional problems, even when the crack shape was not known a-priori. It is limited to LEFM and, while errors are normally less than 5% for Mode I problems, they may exceed 10% for shear mode results when all three modes are acting. Moreover the method does not accommodate significant amounts of plasticity. Nevertheless, it has found substantial use in supporting numerical analysis and improving the formulation of numerical solutions for a variety of three dimensional problems.

ACKNOWLEDGEMENTS

The author wishes to acknowledge the suggestions of Dr. C. T. Liu and the contributions of L. Wang, J. S. Epstein, W. T. Hardrath, J. C. Newman, Jr., C. C. Poe, W. H. Peters and M. Jolles, all fomer students, and the support of Phillips Laboratory, National Science Foundation and NASA Langley Research Center for parts of this work.

REFERENCES

Griffith, A. A., "The Phenomena of Flow and Rupture in Solids," *Philosophical Transactions of the Royal Society of London* A221, 1921, 163–198.

Griffith, A. A., "The Theory of Rupture," *Proceedings of the First International Congress of Applied Mechanics, DELFT*, 1925, 55–63.

Inglis, C. E., "Stresses in a Plate Due to the Presence of Cracks and Sharp Corners," *Transactions of the Institute of Naval Architecture* 55, 1913, 219–241.

Irwin, G. R., "Fracture Dynamics" *Fracturing of Metals*, American Society for Metals, Cleveland, 1948, 147–166.

Orowan, E., "Fracture and Strength of Solids," *Reports on Progress in Physics XII*, 1948, 185.

Irwin, G. R., "Analysis of Stresses and Strains Near the End of a Crack Traversing a Plate," *Journal of Applied Mechanics*, 24, 1957, 361–364.

Westergaard, H. M., "Bearing Pressures on Cracks," *Journal of Applied Mechanics*, G, 1939, 49–53.

Williams, M. L., "On the Stress Distribution at the Base of a Stationary Crack," *Journal of Applied Mechanics*, 24, 1957, 109–114.

Irwin, G. R., "Fracture," *Handbuch der Physik VI*, Springer, 1958, 551–590.

Maxwell, J. C., "On the Equilibrium of Elastic Solids," *Transactions of the Royal Society of Edinburgh*, XX-1, 1853, 87–120.

Burger, C. P., "Photoelasticity," *Handbook on Experimental Mechanics*, Chapter 5, 1987, 162–281.

Oppel, G., Polarisationsoptische "Untersuchung raumlicher Spannungs und Dehnungszustande," *Forsch. Geb. Ingenieurw*, 7, 1936, 240–248.

Smith, C. W. and Olaosebikan, "Use of Stress Intensity Factors from Photoelastic Data," *Journal of Experimental Mechanics*, 24, 4, 1984, 300–307.

Kassir, M. and Sih, G. C., "Three Dimensional Stress Distribution Around an Elliptical Crack Under Arbitrary Loadings," *Journal of Applied Mechanics*, 33, 3 Series E, 1966, 601–611.

Tardy, M. H. L., "Méthode Pratique D'examen de mesure de la biréfringence des verres d'optique," *Optics Reviews*, 8, 1929, 59–69.

Post, D., "Fringe Multiplication in Three Dimensional Photoelasticity," *Journal of Strain Analysis*, 1,5, 1966, 380–388.

Smith, C. W., Olasebikan, O. and Epstein, J. S., "An Analytical-Experiment Investigation of the Linear Elastic Zone for Photoelastic Mode I Extraction," *J. of Theoretical and Applied Fracture Mechanics*, 2, 1984, 157–169.

Smith, C. W. and Wiersma, S. J., "Stress Fringe Signatures for Propagating Cracks," *Journal of Engineering Fracture Mechanics*, 23, 1, 1986, 229–236.

Smith, C. W. and Wang, L., "Stress Intensity Factor Distribution and Crack Shapes in 3-D Problems Using Frozen Stress," *Advances in Local Fracture/Damage Models for the Analysis of Engineering Problems*, AMD 137, 1992, 109–120.

Smith, C. W., Jolles, M. and Peters, W. H., "Stress Intensities for Cracks Emanating from Pin Loaded Holes," ASTM Special Technical Publication No. 631, 1977, 190–201.

Harris, D. O., "Stress Intensity Factors for Hollow, Circumferentially Notched Round Bars," *Journal of Basic Engineering*, 89, 1, 1967, 49–54.

Benthem, J. P. and Koiter, W. T., "Asymptotic Approximations to Crack Problems," *Methods of Analysis and Solutions of Crack Problems*, Noordhoff, 1973, 131–178.

Wilson, W. K., "On Combined Mode Fracture Mechanics," Research Report No. 69-IE7-FMECH-R1, Westinghouse Research Laboratories, 1969.

Yamamoto, Y. and Sumi, Y., "Stress Intensity Factors for Three Dimensional Cracks," *Int. J. of Fracture*, 14, 1, 1978, 17–35.

Smith, C. W. and Hardrath, W. T., "Photoelastic Determination of Stress Intensities in Mode III," *Recent Advances in Engineering Science*, 15, 1978, 195–199.

Implementation of viscoelastic behavior in a time domain boundary element formulation

M Schanz and L Gaul

University of the Federal Armed Forces Hamburg
Postfach 70 08 22, D-22008 Hamburg, Federal Republic of Germany

The boundary element method (BEM) provides a powerful tool for the calculation of elastodynamic response in frequency and time domain. Field equations of motion and boundary conditions are cast into integral equations, which are discretized only at the boundary. The boundary data often are of primary interest because they govern the transfer dynamics of members and the energy radiation into a surrounding medium. Formulations of BEM currently include conventional viscoelastic constitutive equations in the frequency domain. In the present paper viscoelastic behaviour is implemented in a time domain approach as well. The constitutive equations are generalized by taking fractional order time derivatives into account.

INTRODUCTION

It is well known that the boundary element method (BEM) reduces the dimension of a boundary value problem by one. The variables in the domain of a 3–d problem are for example governed by the surface variables on the 2–d boundary via the boundary integral equation which includes the boundary conditions. The BEM provides a powerful tool for the 3–d calculation of elastodynamic response in frequency and time domain because in space only the boundary has to be discretized. The boundary data are CAD compatible and detailed constitutive properties can be modelled (Beskos D. E., 1987, Gaul L., 1990). Domain variables can be determined at arbitrary locations from the complete boundary data. If infinite (fullspace 3–d) or semi infinite (halfspace 3–d) domains are treated, no artificial boundaries with non reflecting boundary conditions need to be introduced. This is why the Sommerfeld radiation condition is fulfilled by the so called fundamental solution of the boundary integral equation. Formulations of BEM currently include conventional viscoelastic constitutive equations in the frequency domain. One aim of the present paper is to implement viscoelastic behaviour in a time domain approach as well. The elastic Stokes fundamental solution is converted to a viscoelastic one by adopting a correspondence principle. A novel viscoelastic fundamental solution is obtained analytically by inverse Laplace transformation. Viscoelastic constitutive equations are generalized by taking fractional order time derivatives into account (Gaul L., Schanz M., Fiedler C., 1992).

INTEGRAL EQUATION OF ELASTODYNAMICS

For consistency the boundary integral equation describing elastodynamics in time domain is recalled. The field equations of a homogeneous elastic domain Ω with boundary Γ are given by

$$\left(c_1^2 - c_2^2\right) u_{i,ij} + c_2^2\, u_{j,ii} + b_j = \ddot{u}_j \tag{1}$$

with displacement coordinates u_j and wave speeds

$$c_1^2 = \frac{K + \frac{4}{3}G}{\varrho}, \qquad c_2^2 = \frac{G}{\varrho} \tag{2}$$

with given boundary conditions

$$\begin{aligned} t_{(n)i}(\mathbf{x},t) = \sigma_{ik} n_k = p_i(\mathbf{x},t) \qquad & \mathbf{x} \in \Gamma_t, \\ u_i(\mathbf{x},t) = q_i(\mathbf{x},t) \qquad & \mathbf{x} \in \Gamma_u \end{aligned} \tag{3}$$

and initial conditions

$$\begin{aligned} u_i(\mathbf{x},0) &= u_{0i}(\mathbf{x}), \\ \dot{u}_i(\mathbf{x},0) &= v_{0i}(\mathbf{x}) \qquad \mathbf{x} \in \Omega. \end{aligned} \tag{4}$$

The 3-d Stokes fundamental solution of the Lamé equation (1) in an unbounded space, excited by $b_j(\mathbf{x},t) = \delta(t-\tau)\,\delta(\mathbf{x}-\boldsymbol{\xi})\,e_j$ is given by (e.g. (Eringen A. C., Suhubi E. S., 1975))

$$\begin{aligned} \tilde{u}_{ij}(\mathbf{x},\boldsymbol{\xi},t) = \; & \frac{1}{4\pi\varrho}\left\{\frac{t}{r^2}\left(\frac{3r_ir_j}{r^3} - \frac{\delta_{ij}}{r}\right)\cdot\right. \\ & \cdot \left[H\left(t-\frac{r}{c_1}\right) - H\left(t-\frac{r}{c_2}\right)\right] \\ & + \frac{r_ir_j}{r^3}\left[\frac{1}{c_1^2}\,\delta\left(t-\frac{r}{c_1}\right) - \frac{1}{c_2^2}\,\delta\left(t-\frac{r}{c_2}\right)\right] \\ & \left. + \frac{\delta_{ij}}{rc_2^2}\;\delta\left(t-\frac{r}{c_2}\right)\right\} \end{aligned} \tag{5}$$

where $r = \sqrt{r_ir_i}$, $r_i = x_i - \xi_i$. The corresponding fundamental traction vector components are obtained from

Eq. (3) after replacing the stresses by strains and displacements

$$\tilde{t}_{(n)ij} = \varrho\left(c_1^2 - 2c_2^2\right)\tilde{u}_{jm,m}\delta_{ik}n_k + \varrho c_2^2\left(\tilde{u}_{ji,k}n_k + \tilde{u}_{jk,i}n_k\right) \tag{6}$$

with the outward normal n_k.

The dynamic extension of Betti's reciprocal work theorem combining two states of displacements and tractions $(\tilde{u}_{ij}, \tilde{t}_{(\mathbf{n})ij})$ and $(u_{ij}, t_{(\mathbf{n})ij})$ leads to the integral equation

$$\varepsilon_{ij}(\xi)\, u_j(\xi, t) = \int_\Gamma \left[\tilde{u}_{ij} * t_{(n)j} - \tilde{t}_{(n)ij} * u_j\right] d\Gamma + \int_\Omega \varrho\left[\tilde{u}_{ij} * b_j + \tilde{u}_{ij} v_{0j} + \dot{\tilde{u}}_{ij} u_{0j}\right] d\Omega \tag{7}$$

where $*$ denotes the convolution with respect to time and $\varepsilon_{ij}(\xi) = \frac{\delta_{ij}}{2}$ for a smooth boundary. Initial conditions being zero and vanishing volume forces reduce (7) to a boundary integral equation. As a prerequisite for a later application of a correspondence principle, the Laplace transform of the fundamental solution (5) is given as

$$\begin{aligned} \tilde{u}_{ij}(\mathbf{x}, \xi, s) = \; & \frac{1}{4\pi\varrho}\left\{\frac{1}{r^2}\left(\frac{3r_i r_j}{r^3} - \frac{\delta_{ij}}{r}\right)\cdot\right. \\ & \cdot\left[\frac{s\frac{r}{c_1} + 1}{s^2} \quad e^{-\frac{r}{c_1}s} - \frac{s\frac{r}{c_2} + 1}{s^2} \quad e^{-\frac{r}{c_2}s}\right] \\ & + \frac{r_i r_j}{r^3}\left[\frac{1}{c_1^2} \quad e^{-\frac{r}{c_1}s} - \frac{1}{c_2^2} \quad e^{-\frac{r}{c_2}s}\right] \\ & \left. + \frac{\delta_{ij}}{r c_2^2} e^{-\frac{r}{c_2}s}\right\}. \end{aligned} \tag{8}$$

GENERALIZED VISCOELASTIC CONSTITUTIVE EQUATIONS

Linear constitutive equations are assumed to describe the propagation of small disturbances. Elastic–viscoelastic correspondence principles convert Hooke's law of elasticity

$$s_{ij} = 2Ge_{ij} \qquad \sigma_{ii} = 3K\varepsilon_{ii}, \tag{9}$$

with shear and bulk moduli G, K respectively to viscoelastic laws by adopting the differential operator concept or the hereditary integral concept (Flügge W., 1975). More flexibility in fitting measured data in a large frequency range with less parameters and lower order time derivatives is obtained by replacing integer order time derivatives in differential operator formulations by fractional order time derivatives.

The derivative of fractional order α

$$\frac{d^\alpha \varepsilon(t)}{dt^\alpha} = \frac{1}{\Gamma(1-\alpha)}\frac{d}{dt}\int_0^t \frac{\varepsilon(t-\tau)}{\tau^\alpha}d\tau \qquad 0 \le \alpha < 1 \tag{10}$$

defined with the gamma function

$$\Gamma(1-\alpha) = \int_0^\infty e^{-x} \tag{11}$$

is the inverse operation of fractional integration attributed to Riemann and Liouville (Ross B., 1977). It can be shown that the definition by Grünwald (Grünwald A. K., 1867)

$$\frac{d^\alpha \varepsilon(t)}{dt^\alpha} = \lim_{N\to\infty}\left\{\left(\frac{t}{N}\right)^{-\alpha}\sum_{j=0}^{N-1}\frac{\Gamma(j-\alpha)}{\Gamma(-\alpha)\Gamma(j+1)}\cdot \cdot\varepsilon\left[t\left(1-\frac{j}{N}\right)\right]\right\} \tag{12}$$

is equivalent and more convenient in constitutive equations treated by time–stepping algorithms. The generalized viscoelastic constitutive equations of differential operator type

$$\begin{aligned} \sum_{k=0}^{N} p_k' \frac{d^{\alpha_k}}{dt^{\alpha_k}} s_{ij} &= \sum_{k=0}^{M} q_k' \frac{d^{\alpha_k}}{dt^{\alpha_k}} e_{ij}, \\ \sum_{k=0}^{N} p_k'' \frac{d^{\alpha_k}}{dt^{\alpha_k}} \sigma_{ii} &= \sum_{k=0}^{M} q_k'' \frac{d^{\alpha_k}}{dt^{\alpha_k}} \varepsilon_{ii} \end{aligned} \tag{13}$$

correspond to Hooke's law (9).

As defined by Eq. (10) the fractional derivative appears complicated in time domain. However both Laplace and Fourier transforms reveal the useful results

$$\begin{aligned} \mathcal{L}\{\frac{d^\alpha}{dt^\alpha}\varepsilon(t)\} &= s^\alpha \mathcal{L}\{\varepsilon(t)\} = s^\alpha \bar{\varepsilon}(s), \\ \mathcal{F}\{\frac{d^\alpha}{dt^\alpha}\varepsilon(t)\} &= (i\omega)^\alpha \mathcal{F}\{\varepsilon(t)\}. \end{aligned} \tag{14}$$

Laplace transformation converts Eq. (13) to

$$\begin{aligned} \mathcal{P}'(s)\,\bar{s}_{ij} &= \mathcal{Q}'(s)\,\bar{e}_{ij}, \\ \mathcal{P}''(s)\,\bar{\sigma}_{ii} &= \mathcal{Q}''(s)\,\bar{\varepsilon}_{ii}, \end{aligned} \tag{15}$$

with e.g. $\mathcal{P}' = \sum_{k=0}^{N} p_k' s^{\alpha_k}$ and vanishing initial conditions.

NEW VISCOELASTIC FUNDAMENTAL SOLUTION IN TIME DOMAIN

The correspondence principle replaces the elastic moduli according to

$$3K \to \frac{\mathcal{Q}''(s)}{\mathcal{P}''(s)}, \qquad 2G \to \frac{\mathcal{Q}'(s)}{\mathcal{P}'(s)} \tag{16}$$

and leads to the transformed wave speeds

$$c_{1v}^2 = \frac{1}{\varrho}\left[\frac{1}{3}\frac{\mathcal{Q}''(s)}{\mathcal{P}''(s)} + \frac{2}{3}\frac{\mathcal{Q}'(s)}{\mathcal{P}'(s)}\right], \qquad c_{2v}^2 = \frac{1}{\varrho}\frac{1}{2}\frac{\mathcal{Q}'(s)}{\mathcal{P}'(s)}, \tag{17}$$

for a viscoelastic domain.

The rheological Maxwell model of a spring and dashpot in series (Fig. 1) with spring and damping coefficients $3K, F_K$ respectively corresponds to the constitutive equation (e.g. hydrostatic state)

$$\dot{\sigma}_{ii} + \gamma\sigma_{ii} = 3K\dot{\varepsilon}_{ii} \qquad \gamma = \frac{3K}{F_K}. \tag{18}$$

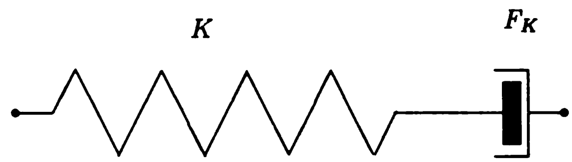

Figure 1: Maxwell model

The correspondence (16) leads to

$$3K \to \frac{3Ks}{s+\gamma}, \qquad 2G \to \frac{2Gs}{s+\gamma} \qquad \gamma = \frac{3K}{F_K} = \frac{2G}{F_G}, \tag{19}$$

if it is assumed for simplicity, that the same damping mechanism holds for the deviatoric and the hydrostatic state. This assumption relates the transformed viscoelastic wave speeds to the elastic ones according to

$$c_{1v}^2 = c_1^2 \frac{s}{s+\gamma}, \qquad c_{2v}^2 = c_2^2 \frac{s}{s+\gamma}. \tag{20}$$

The Laplace transformed viscoelastic fundamental solution is obtained by substituting the elastic wave speeds in (8) by the viscoelastic ones in (20).

A new fundamental solution has been calculated by inverse Laplace transformation. Details of the calculation, based on the theory of residues and integration along a modified Bromwich contour to assure a unique definition of complex roots, are omitted for the sake of brevity. The analytical solution is given by

$$\begin{aligned}\tilde{u}_{ij}(\mathbf{x},\boldsymbol{\xi},t) = \frac{1}{4\pi\varrho}\Bigg\{ & \frac{1}{r^2}\left(\frac{3r_ir_j}{r^3} - \frac{\delta_{ij}}{r}\right) \\ & \cdot\left[C_1(t) + \frac{r}{c_1}D_1(t) - \left(C_2(t) + \frac{r}{c_2}D_2(t)\right)\right] \\ & + \frac{r_ir_j}{r^3}\left[\frac{1}{c_1^2}A_1(t) + \frac{\gamma}{c_1^2}B_1(t) - \left(\frac{1}{c_2^2}A_2(t) + \frac{\gamma}{c_2^2}B_2(t)\right)\right] \\ & + \frac{\delta_{ij}}{rc_2^2}\left(A_2(t) + \gamma B_2(t)\right)\Bigg\}\end{aligned} \tag{21}$$

where the functions $A_\beta, B_\beta, C_\beta$ and D_β are given in the appendix. Inserting the new viscoelastic fundamental solution (21) in Eq. (6) leads to the viscoelastic fundamental solution of the traction vector components.

Different viscoelastic constitutive equations, including those with fractional time derivatives, can be treated as well. In general this requires numerical integration of the inverse Laplace integral.

VISCOELASTIC FORMULATIONS OF BEM IN TIME DOMAIN

The integral equation (7) reduces to a boundary integral equation for vanishing volume forces b_j and initial conditions. Discretization in space and time leads to the boundary element formulation. Only the time discretization by n equal steps Δt is discussed. For simple constitutive equations the aim is to integrate the convolution terms analytically. Linear shape functions for the displacements u_i and constant shape functions for the tractions t_i in time domain

$$\begin{aligned} u_i(\mathbf{x},\tau) &= \left(U_{il}^{m-1}\frac{t_m - \tau}{\Delta t} + U_{il}^m \frac{\tau - t_{m-1}}{\Delta t}\right)\eta_l(\mathbf{x}) \\ t_i(\mathbf{x},\tau) &= 1 \cdot T_{il}^m \cdot \mu_l(\mathbf{x}) \end{aligned} \tag{22}$$

are the simplest choice such that no terms drop out in the boundary integral equation. The actual time step is m; U_{il}^m, T_{il}^m are the nodal values at time $t_m = m\Delta t$ for the corresponding boundary element Γ_l. Inserting (22) reduces the boundary integrals in (7) to

$$\begin{aligned} & \int_0^t \int_\Gamma \Big[t_{(\mathbf{n})i}(\mathbf{x},\tau)\cdot\tilde{u}_{ij}(\mathbf{x},\boldsymbol{\xi},t-\tau) - \\ & \qquad \tilde{t}_{(\mathbf{n})ij}(\mathbf{x},\boldsymbol{\xi},t-\tau)\cdot u_i(\mathbf{x},\tau)\Big] d\Gamma d\tau = \\ & \sum_l \sum_{m=1}^n \int_{\Gamma_l} \int_{t_{m-1}}^{t_m} \Big[\tilde{u}_{ij}(\mathbf{x},\boldsymbol{\xi},t-\tau)\cdot 1 \cdot \mu_l(\mathbf{x})\cdot T_{il}^m - \\ & \qquad \tilde{t}_{(\mathbf{n})ij}(\mathbf{x},\boldsymbol{\xi},t-\tau)\cdot\eta_l(\mathbf{x})\cdot\left(\frac{\tau}{\Delta t}\left(U_{il}^m - U_{il}^{m-1}\right)\right. \\ & \qquad\qquad \left.+ U_{il}^{m-1}\frac{t_m}{\Delta t} - U_{il}^m\frac{t_{m-1}}{\Delta t}\right)\Big] d\tau d\Gamma. \end{aligned} \tag{23}$$

The associated time integrals

$$\begin{aligned} & \int_{t_{m-1}}^{t_m} \tilde{u}_{ij}(\mathbf{x},\boldsymbol{\xi},t-\tau)\,d\tau, \\ & \int_{t_{m-1}}^{t_m} \tilde{t}_{(\mathbf{n})ij}(\mathbf{x},\boldsymbol{\xi},t-\tau)\cdot\tau d\tau, \\ & \int_{t_{m-1}}^{t_m} \tilde{t}_{(\mathbf{n})ij}(\mathbf{x},\boldsymbol{\xi},t-\tau)\,d\tau \end{aligned} \tag{24}$$

can be integrated analytically for special constitutive equations (e. g. Maxwell model).

According to the arrival times of the shear wave front $\frac{r}{c_2}$ and the compression wave front $\frac{r}{c_1}$ the time integration of the fundamental solution has to be carried out in five intervals. With the abbreviations

$$\begin{aligned} f_0(r) &= \frac{3r_{,i}r_{,k} - \delta_{ik}}{r^3} \\ f_1(r) &= \frac{r_{,i}r_{,k}}{rc_1^2} \\ f_2(r) &= \frac{\delta_{ik} - r_{,i}r_{,k}}{rc_2^2} \end{aligned} \tag{25}$$

the first integral in (24) for example leads to

$$\int_{t_{m-1}}^{t_m} \tilde{u}_{ij}(\mathbf{x},\boldsymbol{\xi},t-\tau)\,d\tau =$$

$$\frac{1}{4\pi\varrho}\begin{cases} 0 & \textit{interval I} \\ \int_{t_{m-1}}^{t-\frac{r}{c_1}} G_1(r,t-\tau)\,d\tau & \textit{interval II} \\ \int_{t_{m-1}}^{t_m} G_1(r,t-\tau)\,d\tau & \textit{interval III} \\ \int_{t_{m-1}}^{t_m} G_1(r,t-\tau)\,d\tau & \\ -\int_{t_{m-1}}^{t-\frac{r}{c_2}} G_2(r,t-\tau)\,d\tau & \textit{interval IV} \\ \int_{t_{m-1}}^{t_m} \left[G_1(r,t-\tau)\right. & \\ \quad \left.-G_2(r,t-\tau)\right]d\tau & \textit{interval V} \end{cases} \tag{26}$$

with the abbreviations

$$G_1(r,t-\tau) = f_0(r)\left[C_1(t-\tau) + \frac{r}{c_1}D_1(t-\tau)\right] + f_1(r)\left[A_1(t-\tau) + \gamma B_1(t-\tau)\right]$$

$$G_2(r,t-\tau) = f_0(r)\left[C_2(t-\tau) + \frac{r}{c_2}D_2(t-\tau)\right] - f_2(r)\left[A_2(t-\tau) + \gamma B_2(t-\tau)\right] \tag{27}$$

and the time intervals

$$\begin{array}{ll} \textit{interval I} & t < t_{m-1} + \frac{r}{c_1} \\ \textit{interval II} & t_{m-1} + \frac{r}{c_1} < t < t_m + \frac{r}{c_1} \\ \textit{interval III} & t_m + \frac{r}{c_1} < t < t_{m-1} + \frac{r}{c_2} \\ \textit{interval IV} & t_{m-1} + \frac{r}{c_2} < t < t_m + \frac{r}{c_2} \\ \textit{interval V} & t_m + \frac{r}{c_2} < t. \end{array}$$

The time integration of the expressions A_β to D_β in (27)contain the integration of Dirac distribution, constant function or modified Bessel function only.

The modified Bessel functions are defined by

$$I_n(x) = \sum_{k=0}^{\infty} \frac{1}{k!\,(k+n)!}\left(\frac{x}{2}\right)^{2k+n}. \tag{28}$$

By inserting the argument $\frac{\gamma}{2}\sqrt{(t-\tau)^2 - \left(\frac{r}{c_\beta}\right)^2}$ in Eq. (28) the Bessel function becomes

$$I_n\left(\frac{\gamma}{2}\sqrt{(t-\tau)^2 - \left(\frac{r}{c_\beta}\right)^2}\right) =$$

$$\sum_{k=0}^{\infty}\left(\frac{\gamma}{2}\right)^{2k+n}\frac{1}{k!\,(k+ \quad \ldots \quad \frac{r}{c_\beta}\right)^2\Bigg)^{k+\frac{n}{2}} \tag{29}$$

After interchanging integration and summation the analytical time integration within a time step has to be carried out for expressions like

$$\int_{t_{m-1}}^{t_m}\left((t-\tau)^2 - \left(\frac{r}{c_\beta}\right)^2\right)^k e^{-\frac{\gamma}{2}(t-\tau)}d\tau. \tag{30}$$

Analytical integration becomes possible by decomposing the sum according to

$$\left((t-\tau)^2 - \left(\frac{r}{c_\beta}\right)^2\right)^k =$$

$$\sum_{\mu=0}^{k}(-1)^\mu \frac{k!}{\mu!\,(k-\mu)!}\left(\frac{r}{c_\beta}\right)^{2\mu}(t-\tau)^{2(k-\mu)} \tag{31}$$

where the binominal theorem (Bronstein I. N., Semendjajew K. A., 1984) has been used. Thus the integral reduces to

$$\int_{t_{m-1}}^{t_m}\left((t-\tau)^2 - \left(\frac{r}{c_\beta}\right)^2\right)^k e^{-\frac{\gamma}{2}(t-\tau)}d\tau =$$

$$= \sum_{\mu=0}^{k}(-1)^\mu \frac{k!}{\mu!\,(k-\mu)!}\left(\frac{r}{c_\beta}\right)^{2\mu} \int_{t_{m-1}}^{t_m}(t-\tau)^{2(k-\mu)}e^{-\frac{\gamma}{2}(t-\tau)}d\tau. \tag{32}$$

This integral is solved by partial integration n times

$$\int_{t-t_m}^{t-t_{m-1}} x^n e^{-\frac{\alpha}{2}x}dx =$$

$$\sum_{\nu=1}^{n}\left(\frac{2}{\alpha}\right)^\nu \frac{n!}{(n-\nu+1)!}\left[e^{-\frac{\alpha}{2}(t-t_m)}(t-t_m)^{(n-\nu+1)} - e^{-\frac{\alpha}{2}(t-t_{m-1})}(t-t_{m-1})^{(n-\nu+1)}\right]$$
$$+n!\left(\frac{2}{\alpha}\right)^{n+1}\left[e^{-\frac{\alpha}{2}(t-t_m)} - e^{-\frac{\alpha}{2}(t-t_{m-1})}\right]. \tag{33}$$

The above mentioned steps lead to the analytical time integration of Eq. (26).

After time and space integration the integral equation (23) reduces to a set of linear algebraic equations. The integrated fundamental solutions depend on the difference between the observation and impact time only. Because of this property it is possible to use the recursive equation (Steinfeld B., 1993)

$$\mathbf{C}^1\mathbf{y}^m = \mathbf{D}^1\bar{\mathbf{y}}^m + \mathbf{R}^m \tag{34}$$

of the associated elastic boundary integral equation. The algebraic equations in (34) are ordered such that $\mathbf{y}^m$

contains the unknown boundary values and $\bar{\mathbf{y}}^m$ contains the known values at time step m. The matrixes $\mathbf{C}^1$ and $\mathbf{D}^1$ contains the influence functions. The time history is stored in the vector

$$\mathbf{R}^m = \sum_{k=2}^{m} \left(\mathbf{U}^k \mathbf{t}^{m-k+1} - \mathbf{T}^k \mathbf{u}^{m-k+1} \right). \tag{35}$$

containing the influence functions of the integrated fundamental solutions of the displacements $\mathbf{U}^k$ and the tractions $\mathbf{T}^k$.

NUMERICAL EXAMPLE

The propagation of waves in a 3–d continuum has been calculated by a boundary element formulation in time domain. The problem geometry, with associated boundary discretization is shown in Fig. 3 with chosen viscoelastic material data. Linear shape functions have been used. The free end is excited by a pressure jump according to a unit step function $H(t)$. The opposite end is fixed in welded contact.

Fig. 2 shows the longitudinal displacement in the center of the free end cross section via time. An associated viscoelastic 3–d FE solution has been calculated by the FE–program MARC.

Both BEM and FEM solution are compared with the 1–d analytical elastic solution. Ongoing research analyzes the effect of time step and space discretization with respect to the errors of both discretization methods.

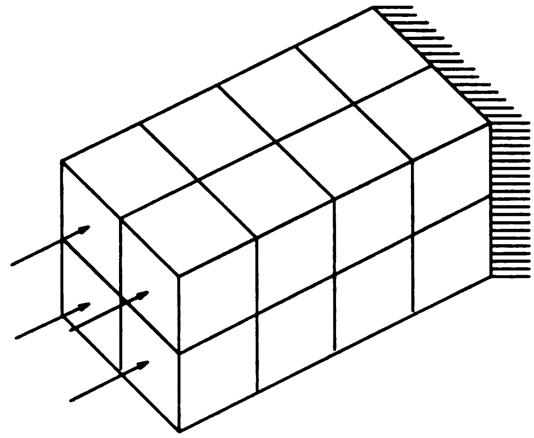

geometry data:

length l = 4 m
heigth = 2 m
width = 2 m

time step BEM:

$\Delta t = 0.002825$

viscoelastic material data:

$E = 100000 \frac{N}{m^2}$
$\nu = 0.25$
$\varrho = 1 \frac{kg}{m^3}$
$\gamma = 0.001$

Figure 3: Step function excitation of a free fixed bar

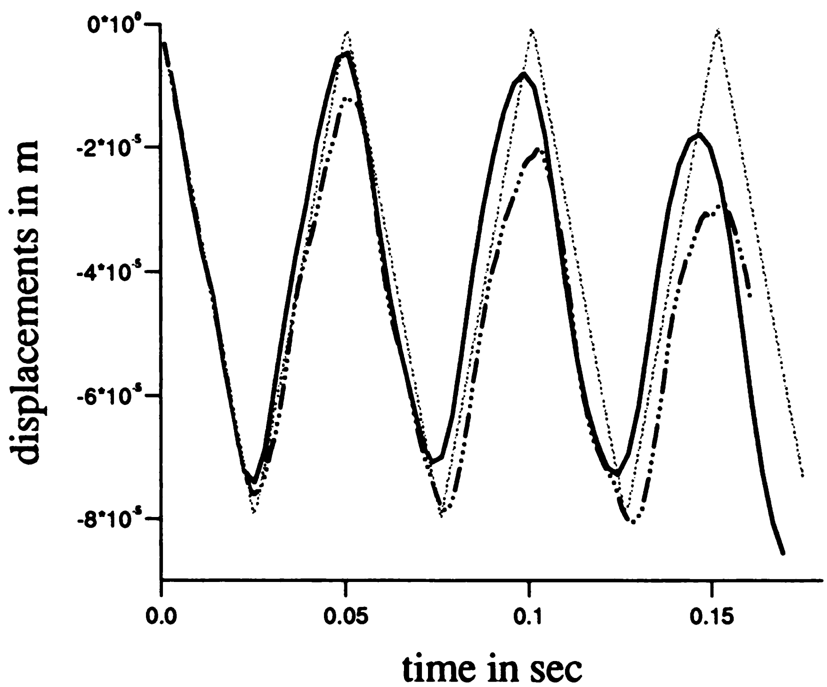

$$u(l,t)_{\text{analytic}} = -\frac{1}{\varrho c}\left(t + \sum_{n=1}^{\infty} (-1)^n \, 2\left(t - \frac{2nl}{c}\right) H\left(t - \frac{2nl}{c}\right)\right)$$

$$c = \sqrt{\frac{E}{\varrho}}$$

Figure 2: 3–d BEM and FEM solutions comparised with the analytic elastic 1–d solution

SUMMARY

An improved approach has been presented for calculating the elastodynamic response of solids in time domain by BEM. In addition to the so called geometrical damping by energy radiation the energy dissipation described by viscoelastic constitutive equations is taken into account. Conventional viscoelastic laws and those generalized by fractional time derivatives can be treated. An analytical fundamental solution has been derived in time domain for a viscoelastic Maxwell model.

ACKNOWLEDGEMENT

The subject of the paper is related to the authors project in a priority research program on BEM. Support by the German Research Council (DFG) is gratefully acknowledged.

REFERENCES

Beskos D. E., Boundary element methods in dynamic analysis, *Appl. Mech. Rev.* 40,1–23, 1987.

Bronstein I. N.,Semendjajew K. A., *Taschenbuch der Mathematik*, Harri Deutsch Verlag, Thun und Frankfurt/Main, 21. Edition, 1984.

Eringen A. C., Suhubi E. S., *Elastodynamics*, Volume II, Academic Press, New York, San Francisco, London, 1975.

Flügge W., *Viscoelasticity*, Springer–Verlag, New York, Heidelberg, Berlin, 1975.

Gaul L., Schanz M., Fiedler C., Viscoelastic Formulations of BEM in Time and Frequency Domain, *Engineering Analysis with Boundary Elements*, 10:137–141, 1992.

Gaul L., Calculation of Structurebourne Sound by Boundary Elements and Related Experiments, in *Proc. Int. Congress on Recent Developments in Air- and Structure Bourne Sound and Vibration*, Vol. I, 445–454, Auburn University, 1990.

Grünwald A. K., Ueber "begrenzte" Derivationen und deren Anwendung, *Zeitschrift f. Mathematik u. Physik*, 12:441–480, 1867.

Ross B., Fractional Calculus, *Mathematics Magazine*, 50:115–122, 1977.

Steinfeld B., *Numerische Berechnung dreidimensionaler Kontaktprobleme Bauwerk–Boden mittels zeitabhängiger Randintegralgleichungen der Elastodynamik*, Dissertation, Ruhr–Universität Bochum, 1993.

APPENDIX

The functions abbreviated in equation (21) are given by

$$A_\beta(t) = \begin{cases} 0 & t < \frac{r}{c_\beta} \\ e^{-\frac{\gamma}{2}\frac{r}{c_\beta}}\delta\left(t - \frac{r}{c_\beta}\right) + \frac{\gamma}{2}\frac{r}{c_\beta}e^{-\frac{\gamma}{2}t}\dfrac{I_1\left(\frac{\gamma}{2}\sqrt{t^2-\left(\frac{r}{c_\beta}\right)^2}\right)}{\sqrt{t^2-\left(\frac{r}{c_\beta}\right)^2}} & t > \frac{r}{c_\beta} \end{cases}$$

$$B_\beta(t) = \begin{cases} 0 & t < \frac{r}{c_\beta} \\ e^{-\frac{\gamma}{2}\frac{r}{c_\beta}} + \frac{\gamma}{2}\frac{r}{c_\beta}\int\limits_{\frac{r}{c_\beta}}^{t} e^{-\frac{\gamma}{2}\tau} \cdot \dfrac{I_1\left(\frac{\gamma}{2}\sqrt{\tau^2-\left(\frac{r}{c_\beta}\right)^2}\right)}{\sqrt{\tau^2-\left(\frac{r}{c_\beta}\right)^2}}\,d\tau & t > \frac{r}{c_\beta} \end{cases}$$

$$C_\beta(t) = \begin{cases} 0 & t < \frac{r}{c_\beta} \\ e^{-\frac{\gamma}{2}\frac{r}{c_\beta}}\left(t - \frac{r}{c_\beta}\right) + \frac{\gamma}{2}\frac{r}{c_\beta}\int\limits_{\frac{r}{c_\beta}}^{t} e^{-\frac{\gamma}{2}\tau} \cdot \dfrac{I_1\left(\frac{\gamma}{2}\sqrt{\tau^2-\left(\frac{r}{c_\beta}\right)^2}\right)}{\sqrt{\tau^2-\left(\frac{r}{c_\beta}\right)^2}}(t-\tau)\,d\tau & t > \frac{r}{c_\beta} \end{cases}$$

$$D_\beta(t) = \begin{cases} 0 & t < \frac{r}{c_\beta} \\ I_0\left(\frac{\gamma}{2}\sqrt{t^2-\left(\frac{r}{c_\beta}\right)^2}\right)e^{-\frac{\gamma}{2}t} + \gamma \cdot \int\limits_{\frac{r}{c_\beta}}^{t} e^{-\frac{\gamma}{2}\tau} I_0\left(\frac{\gamma}{2}\sqrt{\tau^2-\left(\frac{r}{c_\beta}\right)^2}\right)d\tau & t > \frac{r}{c_\beta} \end{cases}$$

where $\beta = 1, 2$ and I_n, $n = 0, 1$ denote the modified Bessel functions.

Transient and steady-state operational limits for ship roll

Steven R Bishop and Jesse Rebello de Souza

Centre for Nonlinear Dynamics and its Applications, University College London
Civil Engineering Building, Gower Street, London WC1E 6BT United Kingdom

This paper investigates the safe operational limits of roll for small vessels in regular waves through the use of an archetypal model of ship motion. The technique incorporates steady-state analysis with methods of quantifying the engineering integrity of transient motions. Both analytical and numerical methods are used and compared. The resonant response of the vessel is examined to reveal unacceptable solutions and superimposed on parameter space diagrams which include lower bounds for fractal erosion of basins of attraction.

CONTENTS

INTRODUCTION

The analysis of the motions of a small vessel in ocean waves poses the engineer or naval architect with challenging problems to determine stability and predict extreme excursions. Reports indicate that capsize remains a major problem for fishing boats and small vessels, including loss of life, Jons et al (1987). Studies conducted during the last two decades have identified several physical mechanisms of capsize, including pure resonant rolling, parametric excitation, broaching, and loss of static stability at a wave crest, Paulling et al (1975). This latter mechanism of capsize may be one of the most dangerous in some ways since it offers little or no information of the impending disaster prior to the event, Miller et al (1986). Broaching involves the loss of directional stability in waves, and it is mentioned in reports as a possible explanation for some disasters.

In this paper, however, we shall restrict our attention to resonant rolling motions of ships in regular beam seas. This problem is of particular relevance to vessels that have to keep fixed courses during operations such as towing arrays, digging trenches, or laying submarine pipelines. Those operations may require vessels to be exposed to beam waves that they would otherwise avoid by changing course. As we shall emphasize later in this paper, even a short train of regular waves can be very dangerous to the ship: this fact has been confirmed by experimental studies in wave tanks, Grochowalski (1989), and by reported descriptions of actual capsizings, USCG (1984).

We investigate here the dynamics of ships in waves through an archetypal model equation, Thompson et al (1990). This model represents in a simplified fashion the uncoupled rolling motion of a ship under harmonic forcing. Linear viscous-type damping is assumed, and a static bias due, for instance, to wind loading or cargo imbalance is implicit in the (asymmetric) shape of the restoring moment curve. In physical terms the model assumes the action of a constant lateral force such that capsize towards the direction of this force is very unlikely.

Firstly, we consider numerical methods to evaluate the operational wave conditions that lead to unacceptably large displacements in steady roll. We then introduce analytical and numerical methods to determine the engineering integrity of the vessel by examining its safe basin of attraction. This technique, which applies modern geometrical concepts of dynamical systems theory, is able to capture transient as well as long term behaviour. Bounds can then be placed on the system which ensure structural integrity and when these are coupled with steady-state analysis a guide to the safe operational limits for the vessel is produced.

LIMITS OF STEADY STATE RESONANT MOTION

A full dynamic analysis of the ship's motions is an extremely complicated task involving, at least, the solution of the ship as a rigid body with its full six degrees of freedom. Accurate calculation of ship-wave hydrodynamic interactions imposes yet further difficulties, leading invariably to highly complex mathematical models whose analyses can prove very demanding on computer time, Miller et al (1986). An alternative approach might be to use fundamental (or archetypal) mathematical models derived from first principles. These models have the advantages of being much simpler (thus allowing systematic parametrical studies and some analytical investigation) while, at the same time, being quite general in the sense that they depict fundamental aspects of the behaviour of a whole class of vessels, and indeed systems, Thompson and Stewart (1986). The simplest form of archetypal equation that has been used to study ship motions is a single degree of freedom oscillator which models the roll of a ship in beam seas, Virgin (1987).

A first approach is to consider the response of the vessel in regular waves represented here by a single frequency harmonic excitation. The restoring moment curve can be initially represented by a second order polynomial and the damping can be assumed linear. Normalizing time and the angle of roll to make the linear natural frequency and the angle of vanishing static stability equal to unity yields :

$$\ddot{x} + \beta\dot{x} + x - x^2 = F\sin(\omega t) \qquad (1)$$

In the equation above x is the non-dimensional angle of roll, β is the normalized damping coefficient, F and ω are the non-dimensional amplitude and frequency of the exciting moment, respectively; a dot denotes differentiation with respect to the normalized time t. Equation 1 captures many qualitative features of more complex descriptions, representing motions of a particle in a cubic potential well. It has been extensively studied and has been shown to display a variety of qualitatively distinct types of behaviour, including multiple steady state solutions, jumps to resonance, and period doubling cascades leading to chaos, Thompson (1989). Numerical integration for $\beta=0.1$ was performed and the resulting steady state nonlinear resonance curves for two values of the amplitude of excitation are shown in Fig 1. For the higher value of $F=0.050$ jumps to and from resonance as the system evolves with frequency, as well as the appearance of subharmonic resonances can be observed. From the analysis of such resonance curves it is possible to determine ranges of F and ω such that pre-specified limits of steady state response are exceeded. For pre-specified operational limits of 0.15, 0.40 and 0.70 times the angle of vanishing stability of the boat, Fig 2 shows curves on the (F,ω)-plane that separate acceptable from unacceptable conditions. Operational conditions defined by points lying within each region (i.e above the lines) correspond to unacceptable final amplitude of motion. These ranges of parameters impose a first set of restrictions which will be complemented by the consideration of transient behaviour and other phenomena as we shall discuss in the following section.

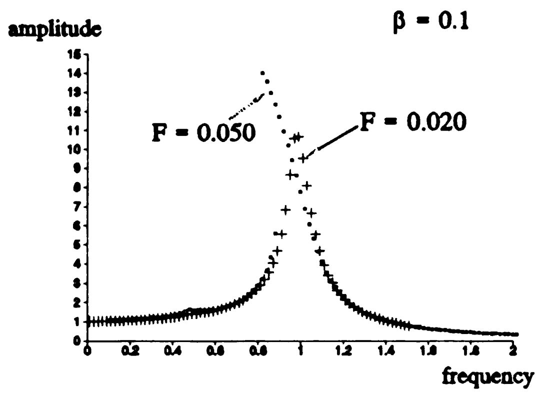

FIG 1. Steady-state resonance curves for Eq 1. The larger F value shows the influence of nonlinearities.

BOUNDS OF TRANSIENT STRUCTURAL INTEGRITY

A boat in a real marine environment will rarely be influenced by a long sequence of regular waves. Therefore the steady states shown in Fig 1, although revealing important dynamical features, are not likely to be reached. Nevertheless a short train of, say, up to 10 regular waves can indeed influence the boat under specific environmental conditions. Transient behaviour will then dominate motions and the analysis of the transient response is essential, Soliman and Thompson (1991). Furthermore, as we have already pointed out, dangerous large-amplitude motions can build up when the vessel is hit even by a short sequence of sufficiently steep waves. Capsize can occur after a small number of, say, less than eight waves have hit the vessel.

The existence of multiple solutions dependent solely on initial conditions requires additional care. In general, small-amplitude stable solution (or solutions) coexists with other solutions associated with unacceptably large -or even infinite- amplitudes. For a given configuration of parameters such as amplitude and frequency of excitation, the size and shape of the safe basin of attraction of the small-amplitude solution(s) is a fundamental measure of the safety of the system from an engineering point of view. Here we note that it has been shown that the local stability analysis traditionally performed in engineering may lead to grossly non-conservative results. This is due to the fact that, well before the small-amplitude solution loses its stability , its basin of attraction can be severely reduced, Thompson et al (1987). In such situations,

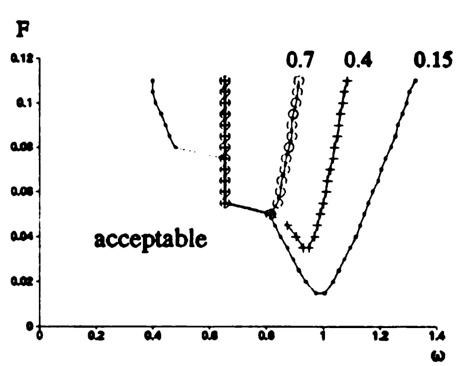

FIG 2. Boundaries of safe steady-state motion for Eq 1.

most trajectories will not be attracted to the safe solution, but to other, possibly unsafe, ones. We shall refer to this point again in the next section.

We identify the set of initial conditions $(x,\dot{x})$ that do not lead to escape as the *safe basin of attraction*, and the changes in shape and/or area experienced by this set as system parameters (amplitude and frequency of excitation, for instance) are varied provide valuable information about the systems structural integrity. Basins of attraction can be generated by various techniques including cell-to-cell mapping, Hsu (1987), and grids-of-starts.

A striking feature of the archetypal Eq 1 (and indeed of many other nonlinear models) is that the safe basin of attraction experiences a process of fractal erosion due to the homoclinic tangling of stable and unstable manifolds of the saddle-type fixed point, Thompson et al (1987). The incursion of fractal striations may cause a sharp decrease of safe area, well before the final loss of stability obtained by conventional steady state analysis, Thompson et al (1990). For relatively simple models the point of homoclinic tangency can be accurately predicted by a Melnikov analysis, Guckenheimer and Holmes (1983), giving rise to a lower bound for basin erosion. Similar boundaries can be generated for more complex systems by the use of numerical methods. In the next two sections we investigate these techniques in more detail.

ANALYTICAL PREDICTION OF BASIN EROSION

To better understand the relevance of basins of attraction in their connection with the steady-state and transient engineering integrity of the system, we adopt here a geometric point of view, proceeding from simpler to more realistic scenarios. We start with the Hamiltonian system associated with Eq 1:

$$\ddot{x} + x - x^2 = 0 \qquad (2)$$

This system has only two fixed points: a stable centre at $(x,\dot{x})=(0,0)$ and an unstable saddle-type point at $(x,\dot{x})=(1,0)$. The homoclinic orbit that connects the unstable fixed point to itself defines the boundary between trajectories that remain bounded for all time and those that escape to infinity. This special orbit is therefore the safe basin boundary for the unforced, undamped system, and it can be determined analytically, Thompson (1989).

Considering now small perturbations $\epsilon F\sin(\omega t)$ and $\epsilon\beta$ for excitation and damping, respectively, yields a different picture in which the fixed points of the unforced, undamped case are substituted by small-amplitude oscillations. The oscillation around the origin is stable, whereas the one around the hill-top saddle is unstable. Once again the inset (stable invariant manifold) of the hill-top saddle cycle is the separatrix between safe and unsafe starting conditions.

As we increase the magnitude of the excitation term, the next qualitative change takes place when the inset and outset (unstable invariant manifold) of the hill-top saddle cycle intersect in what is called a *homoclinic tangency*. Further increase in F generates a much more complex picture, in which an infinite tangling of the invariant sets of the hill-top saddle solution results in the creation of a Smale horseshoe, and the boundary of the safe basin of attraction becomes fractal. Perturbation schemes like the Melnikov method can be used to obtain good analytical approximations for the values at which such homoclinic tangency occurs. See chapter 10 of Barenblatt et al (1983) for an account of Melnikov method, and Thompson (1989) for an application of the method to Eq 1.

The importance of the homoclinic tangling phenomenon for the engineering integrity of the system given by Eq 1 is two-fold. First, the fractal nature of the safe basin boundary implies that there are regions of the phase plane in which an accurate prediction of escape is impossible. This fact alone does not seriously affect *practical* predictability if the fractal region is confined, for example, to the vicinity of the saddle-type fixed point. Studies have shown, however, that fractal areas quickly develop into the bulk of the safe basin, in what is called a *fractal erosion process*, Soliman and Thompson (1989). Moreover, such erosion takes place considerably before (i.e for smaller F values) the final loss of stability predicted by steady-state analysis. The rapid erosion of the safe basin of attraction is therefore the second reason for the interest in predicting the homoclinic tangency. This global phenomenon is a first signal of a complex chain of events, including a heteroclinic tangency, that will quickly result in loss of engineering integrity.

In view of the above it is of interest to compare, or rather combine, the results of steady-state limits of oscillation with a lower boundary for transient integrity as given by the Melnikov method prediction of safe basin erosion. Figure 3 combines steady state operational limits (as given by

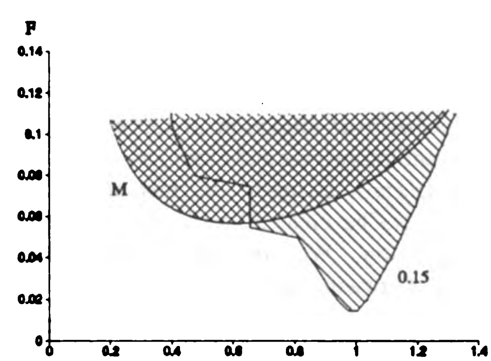

FIG 3. Combination of safe steady-state limits with a lower boundary for transient integrity for Eq 1.

acceptable amplitudes of response, e.g., 0.15 times the angle of vanishing static stability) and a lower bound for transient structural integrity signalled by the Melnikov curve M. The shaded areas above each one of those curves indicate unsafe operational conditions. As Fig 3 shows there are sizeable regions of the (F,ω)-plane that would be regarded as safe by steady state or transient analysis alone. In particular, the double-shaded area on the upper left corner (above Melnikov curve) would be considered safe even by quite stringent steady state criteria, but safe basins of attraction might be considerably eroded in these regions and actual engineering integrity may be reduced. Nonetheless, steady state analysis is able to detect conditions (denoted by the single-hatched area on the lower right corner in Fig 3) under which basins of attraction are smooth but lead to unacceptable final solutions.

NUMERICAL PREDICTION OF BASIN EROSION

Melnikov method is a perturbation technique, and therefore relies upon the knowledge of an exact solution for the unperturbed system. The possibility of obtaining closed-form solutions is limited to relatively simple systems; in the case of ship models, even when just one degree of freedom is considered, only very simplified expressions for the vessel's damping and restoring moments are allowed if analytical methods are to be used.

We propose here the use of a *coarse grid-of-starts* as a means of quickly and effectively detecting the erosion of the vessel's safe basin of attraction. The method is based on much the same geometrical ideas described in the previous section, as we briefly summarize here.

For a statically stable ship, the origin of the phase space (upright position, zero velocity) is clearly a stable fixed point of the unforced system. The basin of attraction for the unforced system is directly connected with the angle of vanishing static stability, beyond which the vessel capsizes from rest (i.e zero velocity initial condition).

A small excitation (sinusoidal forcing) will give rise to small-amplitude oscillations around the origin. The basin of attraction of this new solution can be expected to differ very little from the original, unforced case. For any given frequency of waves, as the amplitude of the excitation increases, the basin of attraction of the safe solution may experience quantitative (size and shape) as well as qualitative (smooth to fractal) changes or metamorphoses. New attractors can also be created, each of them with its own basin of attraction. We are particularly interested in distinguishing between safe and unsafe motions, and therefore we designate the *union* of all basins of attraction that do not lead to capsize as the safe basin of attraction of the system. Moreover, as we have already pointed out, short-term transient motions are more relevant within the context of periodically forced ship motions than their steady-state or long-term transient counterparts. We therefore concentrate here on transients of short duration. Accordingly, the safe basin of attraction is defined as the union of starting conditions that do not lead to capsize *within a given number of waves*.

By performing numerical simulations of trajectories from different starting points around the origin we are able to detect any significant change in the safe basin of attraction, be it in size/shape or nature (smooth to fractal). It should be mentioned that, although we know here, through previous analytical investigation, that the process that will determine safe limits for this specific system is indeed fractal basin erosion, a coarse grid-of-starts is capable of detecting the reduction of transient safe basin for any system that can be numerically integrated. This is important since it is reasonable to imagine that for different systems the sequence of events leading to reductions in safe basins will differ from the one observed for Eq 1. This method is envisaged as a practical means to detect those decreases in safe basin area of transient motions for a much broader class of mathematical models.

We discuss now in more detail the main points involved in the definition of a suitable grid-of-starts. Firstly, it should perhaps be emphasized that, whilst embedded in detailed

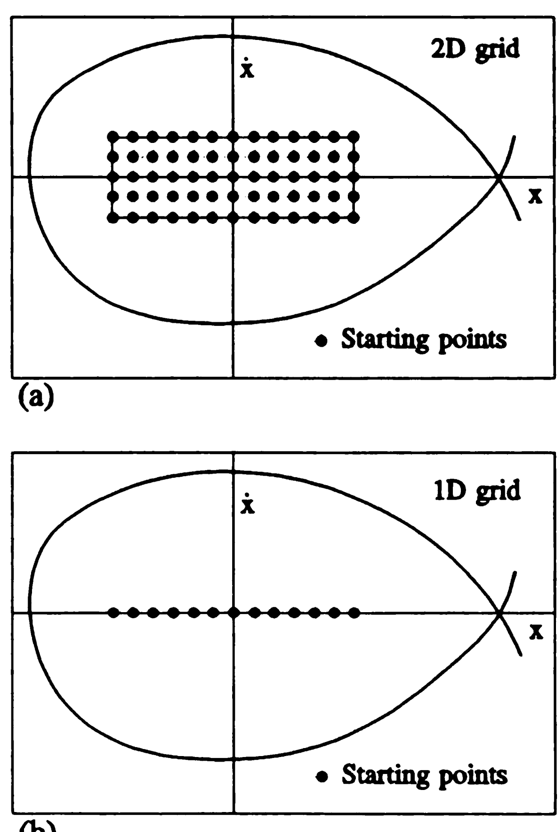

FIG 4. (a) Two-dimensional grid-of-starts in the phase plane of position and velocity. (b) One-dimensional grid-of-starts.

studies of the geometrical and bifurcational structures of the specific system illustrated here, this method is simple to apply, and does not require extensive computational resources. Furthermore, the method lends itself to direct experimental verification, and can be a valuable guide in selecting critical conditions for more detailed (and expensive) studies.

Figure 4a illustrates the idea of placing a coarse grid-of-starts in the phase plane of initial position (roll angle), x, and angular velocity, $\dot{x}$. We suggest here that the grid is placed *around the origin*, which has two basic advantages over placing the grid around fixed points of the associated Poincarè map. Firstly, the choice of a cross section for the definition of the Poincarè map can be a source of ambiguity, and furthermore the fixed point obviously moves in the phase plane as we wind up the amplitude of excitation. Secondly, it is very difficult to reproduce *both* initial angles and angular velocities in experiments with physical models, therefore jeopardizing the direct link of results between numerical and experimental studies. For this same reason, we favour the use of a *one-dimensional grid* (laid along the x axis), which of course has the additional benefit of speeding up computations considerably. For the sake of simplicity we restrict ourselves here to uniform grids, i.e grids formed by equally spaced starting points. Figure 4b shows a one-dimensional grid placed around the origin.

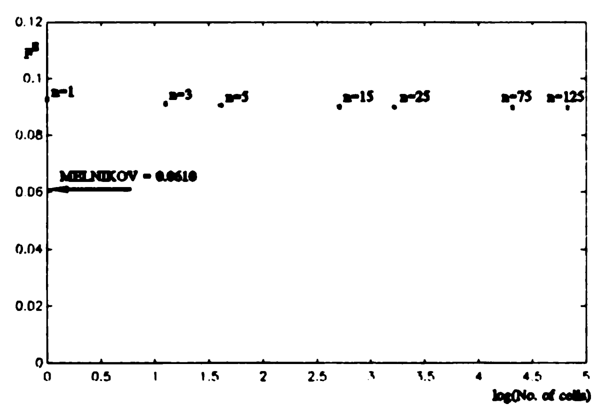

FIG 5. Basic grid parameters: effect of the number of starting points.

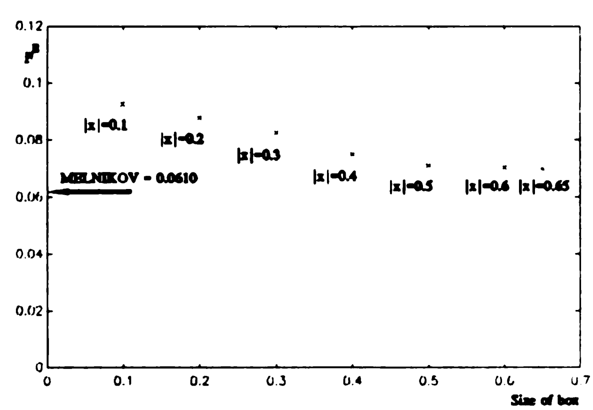

FIG 6. Basic grid parameters: effect of the size of grid in the phase plane.

The two basic parameters defining an uniform grid-of-starts are the number of starting points and the size of the grid in the phase plane. In the case of our one-dimensional grids we relate that second parameter to the *length* of the grid, which in physical terms is given by the difference between minimum and maximum starting roll angles. The first parameter bears direct relevance to the total computing time, and therefore it is of primary interest to keep it to a minimum.

We performed numerical sensitivity tests involving those two parameters. The tests consisted of determining, for a fixed excitation frequency of $\omega=0.80$, the minimum value of amplitude of excitation for escape (F^E) under transient conditions of up to 8 waves. The escape value F^E is defined as the smallest value of F for which escape occurs *for any starting point of the grid*. The idea is to place a sensible grid of starts and to simulate transient motions from each starting point of the grid. The process is repeated for increasingly higher F values until escape is detected for some point of the grid. The method is therefore capable of sensing reductions in safe basin area caused by both shrinkage and/or erosion.

Figure 5 shows the escape value F^E predicted using different number of points in the grid. Results show little sensitivity to the number of points of the grid: grids formed by 3 or 125 points give similar results, provided that they have equal lengths. In this case a range of $-0.1<x<0.1$ was used for all grids. In Fig 6 we show the influence of the length of the grid on the escape values predicted by the method. A fixed number of 3 starting points was used. In contrast with the first set of tests, results now display considerable sensitivity to the length of the grid: the longer the grid the smaller the escape value predicted. This can be readily understood for the specific system under study here if we recall the fractal erosion process that is responsible for early escape in Eq 1. Fractal striations develop from the tangling of invariant manifolds of the hill-top saddle-type cycle. The saddle-type fixed point itself sits near to the

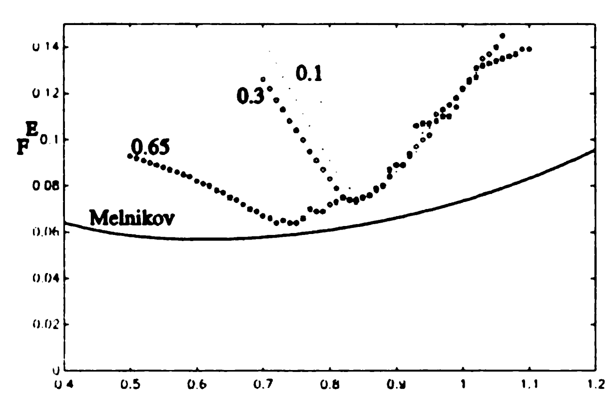

FIG 7. Numerical vs analytical prediction of basin erosion.

original unstable fixed point at $(x,\dot{x})=(0,1)$, and the fractal structures will emanate from that region of the phase space. Therefore, the nearer to saddle-type fixed point the starting point is located, the larger the chances of an early identification of one of the incursive areas of unsafe starting conditions. It can also be observed in Figs 5 and 6 that numerical prediction of escape gives less conservative estimates when compared with Melnikov method. Figure 6 indicates that Melnikov predictions tend to agree with numerical results for long grids.

From the results of the sensitivity study described above we selected three particular combinations of number of points and length of grid for further analysis and comparison with Melnikov method. We adopted grids of just 3 starting points and ranges covering $-0.10<x<0.10$, $-0.30<x<0.30$, and $-0.65<x<0.65$. Using these grids we established estimates for escape values for a range of frequencies, and compared the results with values predicted by Melnikov analysis. The shape and position of the numerically generated safe boundaries agree well with Melnikov curve. As we could expect, the longer grid gave escape values closer to Melnikov results, but always less conservative, as we can see from Fig 7.

With respect to the relation between numerically generated safe transient boundaries and steady-state limits of acceptable motion most of the comments already made in the context of the Melnikov method hold valid. Suitably defined grids reveal regions of the parameter plane in which steady-state limits may be acceptable but transient safe basins are already eroded.

CONCLUSIONS

The continuing loss of life due to the capsize of small vessels implies that attention must be paid to dynamic resonant effects. Transient as well as steady state phenomena play relevant roles in determining safe operational conditions and should both be constituent parts of a sound dynamic stability criterion that is still needed. We have proposed here the use of a *coarse grid-of-starts* as a means of detecting the erosion of the vessel's safe basin of attraction. The method is based on geometrical ideas of nonlinear dynamics, and although based upon detailed studies of the dynamic behaviour of the specific system illustrated here, this method is simple to apply, and does not require extensive computational resources. Furthermore, the method lends itself to direct experimental verification, and can be a valuable guide in selecting critical conditions for more detailed studies.

ACKNOWLEDGMENT

Steven Bishop is an Advanced Research Fellow of the Science and Engineering Research Council and he would like to acknowledge their support. Jesse Rebello de Souza is on leave from the Department of Naval and Ocean Engineering, Polytechnic School, University of São Paulo, and has been sponsored by the Brazilian Navy and FAPESP. Both authors would also like to thank their colleagues within the Centre for Nonlinear Dynamics for useful discussions.

REFERENCES

Barenblatt GI, Iooss G, and Joseph DD, (ed), *Nonlinear dynamics and turbulence*, Pitman Advanced Publishing Program, Boston, London, Melbourne, 1983.

Grochowalski S, Investigation into the physics of ship capsizing by combined captive and free-running model tests, *SNAME Transactions*, [illegible] 169-212 (1989).

Guckenheimer J and Holmes P, *Nonlinear oscillations, dynamical systems, and bifurcations of vector fields*, Springer-Verlag, New York, 1983.

Hsu CS, *Cell to cell mapping: a method of global analysis for nonlinear systems*, Springer-Verlag, New York, 1987.

Jons O, Fuller G, and Letorneau R, Fishing vessel stability: a case study for operator guidance and involvement, *SNAME Transactions*, (1987).

Miller DR, Tam G, Rainey RCT, and Ritch R, Investigation of the use of modern ship motions prediction models in identifying ships with a larger than acceptable risk of dynamic capsize, Arctec Canada Ltd.Report No. TP7407E for the Transportation Development Centre of the Canadian Government, 1986.

Paulling JR, Oakley OH, and Wood PD, Ship capsizing in heavy seas: the correlation of theory and experiments, in *Proceedings of the International Conference on Stability of Ships and Ocean Vehicles*, Dept. of Trade and Industry, London, 1975.

Soliman MS and Thompson JMT, Integrity measures quantifying the erosion of smooth and fractal basins of attraction, *Journal of Sound and Vibration*, 135(3), 453-475 (1989).

Soliman MS and Thompson JMT, Transient and steady state analysis of capsize phenomena, *Applied Ocean Research*, 13, 82-92 (1991).

Thompson JMT, Chaotic phenomena triggering the escape from a potential well, *Proceedings of The Royal Society London A*, 421, 195-225, (1989).

Thompson JMT and Stewart HB, *Nonlinear dynamics and chaos*, Wiley, Chichester, 1986.

Thompson JMT, Bishop SR, and Leung LM, Fractal basins and chaotic bifurcations prior to escape from a potential well, *Phys. Lett. A*, 121(3), 116-120, (1987).

Thompson JMT, Rainey RCT, and Soliman MS, Ship stability criteria based on chaotic transients from incursive fractals, *Phil. Trans. R. Soc. Lond. A*, 332, 149-167, (1990).

Virgin LN, The nonlinear rolling response of a vessel including chaotic motions leading to capsize in regular seas, *Applied Ocean Research*, 9(2), 89-95, (1987).

USCG - U.S. Coast Guard, Marine casualty report M/V Joan La Rie, 1984.

Passive vibration control: A probabilistic approach

Hector A Jensen

Department of Civil Engineering
Federico Santa Maria University
Valparaiso, Chile

Mehdi Setareh

College of Architecture and Design
Lawrence Technological University
Southfield MI 48075-1058

This paper is concerned with the behavior of vibration absorbers attached to systems with uncertain properties. The uncertainties of the main system properties are modeled in a probabilistic sense by means of a Bayesian probabilistic interpretation. The structural systems considered in this study are simple systems modeled as one-degree-of-freedom oscillators subjected to a white noise base excitation. Due to the uncertainty of the main system properties, the classical deterministic minimization problem becomes a stochastic optimization problem. An optimization technique is implemented to solve this non-classical problem, and the absorber parameters as well as the optimum response of the system are obtained. These results are then used to assess the performance of the vibration absorber. It is found that parameter uncertainties may have a significant effect on its effectiveness. Finally, an alternative approach that improves the absorber efficiency, when uncertainties in the main system properties are considered, is presented in this paper.

INTRODUCTION

For many years there has been considerable interest in the study of dynamic vibration absorbers that, when added to a structural system, will reduce significantly the vibration response. A number of publications have discussed the use of vibration absorbers to limit the response of single degree-of-freedom systems subjected to harmonic excitations. The well-known work of Den Hartog (1940) has been the first detailed study in this subject. Thompson (1965) and Anderson (1969) also discussed the use of tuned mass dampers to reduce the absolute motion of simple systems subjected to harmonic forces. Application of vibration absorbers to systems subjected to stochastic excitation has also been investigated by a number of researchers. Crandall and Mark (1963) presented an analysis of a single-degree-of-freedom absorber system subjected to a white noise base acceleration and they showed how to choose the proper absorber parameters. Curtis and Boykin (1961) presented some results concerning the relative displacement response to stochastic excitation and they considered its possible reduction using absorbers.

part of "MECHANICS PAN-AMERICA 1993" edited by MRM Crespo da Silva and CEN Mazzilli ASME Reprint No AMR134

The use of damped vibration absorbers to reduce the level of vibration of simple elastic systems such as rods in extension, beams in flexure, plates, and cylindrical shells has been discussed by several researchers, among them, Neubert (1964), Snowdon (1975) and Jacquot (1978). They represented the vibration of the elastic body by a single normal mode. Warburton and Ayorinde (1979) studied in what circumstances is it impossible, or at least inaccurate, to represent the vibration of such systems by a single mode. Recently, Setareh (1991) has developed a methodology that considers several normal modes explicitly into the analysis. He used the component mode synthesis method as the main tool for implementing such technique. The use of absorbers to limit the structural response to earthquake-like excitation has also been studied by a number of authors, among them, Wirsching and Campbell (1974). They have shown the effectiveness in reducing the structural response even with relatively small values of the absorber mass. In all these studies, the structural properties of the system were assumed to be described with a mathematical precision. Yet, uncertainty in the definition of many real systems does exist to some degree. In fact, to model the dynamic behavior of structural systems, model parameters such as frequencies, mass distributions and damping coefficients, need to be estimated. Different methods are employed in estimating these parameters, from empirical formulas to very detailed methods such as the finite element technique. All these methods lead to parameter values that have associated uncertainties or errors because of the numerous assumptions made when modeling the geometry, material properties and boundary conditions.

It is the objective of this paper to study the effects of uncertain system parameters on the performance of vibration absorbers, when the system is subjected to a white noise base excitation. The structural systems considered in this paper are simple oscillators or simple elastic systems, provided that their dynamic behavior can be represented by a single mode shape. The characterization of the system properties is based on a Bayesian probabilistic interpretation, and it depends on the relevant information available. The study reported in the present paper essentially generalizes the work done by Jensen et al to consider different probabilistic tuning procedures, which are then used to assess the efficiency of the vibration absorber. The performance of the absorber is evaluated and compared with the one obtained for the case of deterministic system properties.

The next section formulates the problem under study in a more formal fashion. The following section discusses the implementation of different optimization problems to be considered in this study. Then, a numerical example is presented to illustrate the effects of uncertainty on the absorber performance. Finally, a stochastic optimization approach is suggested for treating this type of problems.

STATEMENT OF THE PROBLEM

Consider a main system idealized as a single degree-of-freedom oscillator with mass m_m, stiffness k_m and viscous damper c_m. The absorber system, which is also modeled as a simple oscillator, has mass m_a, stiffness k_a and viscous damper c_a. It is easily shown that the stationary response variance for the displacement of the main system when subjected to a stochastic base excitation is

$$\sigma^2_{x_m} = \int_{-\infty}^{+\infty} \| H_{mm}(\omega) \|^2 \; S(\omega)\, dw \;, \quad (1)$$

where $S(\omega)$ is the power spectral density function of the random excitation and $H_{mm}(\omega)$ is the component of the frequency response matrix of the combined system corresponding to the displacement of the main system. For a white noise excitation, equation (1) can be computed analytically and it is given by (Crandall, 1963)

$$\sigma^2_{x_m} = \pi S_0 \frac{(\Gamma_0^2/\Delta_0)(\Delta_2\Delta_3 - \Delta_1\Delta_4)}{\Delta_1(\Delta_2\Delta_3 - \Delta_1\Delta_4) - \Delta_0\Delta_3^2} +$$

$$\pi S_0 \frac{\Delta_3(\Gamma_1^2 - 2\Gamma_0\Gamma_2) + \Delta_1\Gamma_2^2}{\Delta_1(\Delta_2\Delta_3 - \Delta_1\Delta_4) - \Delta_0\Delta_3^2}, \quad (2)$$

where S_0 is the power spectral density of the white noise excitation; $\Delta_0 = \omega_m^2\omega_a^2$; $\Delta_1 = 2\zeta_m\omega_m\omega_a^2 + 2\zeta_a\omega_a\omega_m^2$; $\Delta_2 = \omega_m^2 + (1+\mu)\omega_a^2 + 4\zeta_m\zeta_a\omega_m\omega_a$; $\Delta_3 = 2\zeta_m\omega_m + 2(1+\mu)\zeta_a\omega_a$; $\Delta_4 = 1$; $\Gamma_0 = -(1+\mu)\omega_a^2$; $\Gamma_1 = -2(1+\mu)\zeta_a\omega_a$; $\Gamma_2 = -1$; and where $\omega_m^2 = k_m/m_m$ = the natural frequency of the main system; $\zeta_m = c_m/(2m_m\omega_m)$ = damping ratio of the main system; $\omega_a^2 = k_a/m_a$ = the natural frequency of the absorber; $\zeta_a = c_a/(2m_a\omega_a)$ = damping ratio of the absorber; and $\mu = m_a/m_m$ = the mass ratio.

It is noted that a similar equation to Eq (2) can be obtained for the case of elastic bodies with attached vibration absorbers, provided that their vibration can be represented by a single normal mode. In those cases the parameters that described the main system can be defined by means of a modal analysis approach or by an energy balance approach (Wirsching and Campbell, 1974 ; Warburton and Ayorinde, 1980). In this study, the frequency and damping properties of the main system are assumed to be uncertain and they are described in a probabilistic sense. The mathematical characterization of the frequency parameter ω_m, and damping parameter ζ_m, is based on a Bayesian probabilistic interpretation together with the maximum entropy principle. Then, the probabilistic distributions for these parameters are chosen by the maximum entropy principle that produces the greatest uncertainty in the parameters consistent with the specified constraints. For example, if the set of plausible values for the parameters is a bounded region, then the principle produces uniform distributions. If additional information is available for the parameters, then other probabilistic characterizations can be used as well (Jaynes, 1968). Here, it is assumed that the only available information for the frequency and damping parameters of the main system is that they lie inside an interval. Therefore, the parameters ω_m and ζ_m are modeled as uniform random variables, with mean values $\bar{\omega}_m$ and $\bar{\zeta}_m$, and variances $\sigma_{\omega_m}^2$ and $\sigma_{\zeta_m}^2$, respectively. The mean values of ω_m and ζ_m represent their nominal values while the variances measure the variability of the parameters with respect to their nominal values.

In the classical analysis, the optimum absorber parameters are found by minimizing the response of the main system. Due to the uncertainties of the main system properties, the response of the system, measured by the variance of the displacement response, is itself uncertain. Therefore, the deterministic minimization problem becomes a stochastic optimization problem. The next section presents the optimization techniques that are considered in this study to assess the performance of the vibration absorber.

OPTIMIZATION PROBLEM

In the classical vibration control problem, the optimum absorber parameters, that is, the frequency and damping properties are found for a given value of the absorber mass by minimizing some response function of the main system. Then, the optimization problem can be stated as

$$Minimize_{(\omega_a,\zeta_a)}\,[Response\ \ Function] \quad (3)$$

for a given mass ratio μ.

The response function to be considered in this study is the standard deviation of the stationary displacement response of the main system. This response depends on the properties of the main system as well as the properties of the dynamic absorber. Since the frequency and damping parameters of the main system are assumed to be uncertain, then the response function is also uncertain and the classical minimization problem becomes a stochastic optimization problem. In order to determine the optimum absorber parameters, an equivalent deterministic optimization problem is defined by selecting a new objective function (Rao, 1984). It is defined as a linear combination of the expected value and the standard deviation of the response, that is

$$Response\ \ Function = \alpha_1\, E(\sigma_{x_m}) + \alpha_2\, \sqrt{Var(\sigma_{x_m})}, \tag{4}$$

where $E(\cdot)$ and $Var(\cdot)$ are the expectation and variance operations with respect to the uncertain parameters, respectively, α_1 and α_2 are nonnegative constants whose values indicate the relative importance of the expected value and standard deviation of the response function in the minimization problem. Thus, $\alpha_2 = 0$ indicates that the expected value of the response function is to be minimized without caring for the standard deviation of the response. On the other hand, if $\alpha_1 = 0$, it indicates that the interest is to minimize the variability of the response function about its mean value without considering about what happens to the mean value of the response. Similarly, if $\alpha_1 = 1$ and $\alpha_2 = 1$, it indicates that equal importance is given to the minimization of the mean value as well as the standard deviation of the response function. Therefore, the solution of the stochastic programming problem stated in Eq (3) can be obtained by solving the equivalent deterministic optimization problem

$$Minimize_{(\omega_a,\zeta_a)}\ \ \alpha_1 E(\sigma_{x_m}) + \alpha_2\sqrt{Var(\sigma_{x_m})} \tag{5}$$

for a given mass ratio μ.

The expected value and the standard deviation of the response function σ_{x_m}, which by definition are multiple integrals in the random space, are computed by numerical integration over the range of the uncertain parameters, evaluating the response function at every integration point from Eq (2). Since the uncertain parameters are modeled as uniform random variables, the number of integration points can be minimized by using a Gaussian quadrature in which the zeros of the Legendre polynomials are chosen as abscissas. The actual number of integration points needed in the quadrature depends on the level of uncertainty of the system parameters and on the degree of non-linearity of the response function as a function of the uncertain parameters.

In order to solve the equivalent deterministic optimization problem previously defined, an optimization technique was implemented to obtain the values of the absorber parameters that minimize the corresponding objective function. The response function evaluated at the optimum parameters will be referred as the optimum response.

EXAMPLE OF APPLICATION

Formulation

In this example problem, the nominal value of the stiffness parameter is selected in such a way that the nominal natural frequency of the main system is $1Hz$. The nominal damping coefficients of the main system considered here correspond to 1 and 5 percent of critical, and the mass ratio μ, varies between 0.005 and 0.2. Three levels of uncertainty of the frequency and damping parameters of the main system are considered, and they are given in terms of their coefficients of variation. The selected values are 10%, 20% and 30%, which represent low, moderate, and high variations on the main system properties, respectively. Recall that the coefficient of variation is the ratio between the standard deviation and the mean value of the parameter.

To quantify the effects of uncertain main system parameters on the performance of the vibration absorber, different performance parameters are considered in this study. When deterministic properties are assumed for the main system, the performance parameter is defined as

$$p_1 = \frac{\sigma_{x_m(optimum)}}{\sigma_0}, \tag{6}$$

where $\sigma_{x_m(optimum)}$ is the optimum standard deviation of the stationary displacement response of the main system with the vibration absorber attached to the system, and σ_0 is the standard deviation of the stationary displacement response of the main system without the absorber. The optimum standard deviation response $\sigma_{x_m(optimum)}$, corresponds to the standard deviation response evaluated at the optimum parameters of the vibration absorber. It is noted that if the performance parameter is less than one, the vibration absorber has decreased the level of response of the main system, and vice-versa. When uncertainties in the main system properties are taken into account, four performance parameters are considered in this study, and they are defined as

$$p_2 = \frac{E(\sigma_{x_m(optimum)})}{\sigma_0}, \tag{7}$$

where $E(\sigma_{x_m(optimum)})$ is the expected value of σ_{x_m} evaluated at the optimum parameters of the deterministic optimization problem defined in the previous section with $\alpha_1 = 1$ and $\alpha_2 = 0$, that is

$$Minimize_{(\omega_a,\zeta_a)}\,[E(\sigma_{x_m})]\ . \tag{8}$$

The next two performance parameters, p_3 and p_4, are defined as in Eq (7) but evaluating the expected value of σ_{x_m} at the optimum parameters of the optimization problems

$$Minimize_{(\omega_a,\zeta_a)}\left[\sqrt{Var(\sigma_{x_m})}\right] \tag{9}$$

and

$$Minimize_{(\omega_a,\zeta_a)}\quad E(\sigma_{x_m}) + \sqrt{Var(\sigma_{x_m})}\,, \tag{10}$$

respectively. These problems correspond to the general optimization problem defined in Eq (5) with $\alpha_1 = 0$ and $\alpha_2 = 1$, and $\alpha_1 = \alpha_2 = 1$, respectively. The last performance parameter p_5, is defined as

$$p_5 = \frac{E(\sigma_{x_m(optimum)})}{\sigma_0} + \frac{\sqrt{Var(\sigma_{x_m(optimum)})}}{\sigma_0}, \tag{11}$$

where $E(\sigma_{x_m(optimum)})$ is the expected value and $Var(\sigma_{x_m(optimum)})$ are is the variance of σ_{x_m}, respectively, evaluated at the optimum parameters of the optimization problem given by Eq (10).

Numerical Results

Figs 1,2 and 3 show the performance parameters as a function of mass ratio μ, for different levels of uncertainty of the main system properties. A nominal damping parameter of the main system corresponding to 1% of critical is considered in these figures. The comparison of the performance parameters p_2, p_3 and p_4 with p_1 shows that there is loss of effectiveness of the vibration absorber due to the uncertainty of the main system properties. This loss of effectiveness is particularly significant for high levels of uncertainty and for small mass ratios. That is, as the coefficient of variation of the main system parameters increases the efficiency of the vibration absorber decreases. For example, for a 30% coefficient of variation and for a mass ratio less than 5%, the optimum response of the main system is about twice its nominal response. Therefore, the loss of efficiency of the vibration absorber is quite severe.

The effects of uncertain main system properties on the performance of the vibration absorber are more dramatically illustrated by the performance parameter p_5. According to its definition, the main system response is taken as $E(\sigma_{x_m}) + \sqrt{Var(\sigma_{x_m})}$, evaluated at the optimum parameters of the optimization problem given by Eq (10). Then, the response function is defined as the expected value plus one standard deviation of the standard deviation of the main system stationary displacement response. So, if the response of the main system is measure in this form, the loss of efficiency of the absorber is quite significant, particularly for high levels of uncertainty and small mass ratios. On the other hand, these results indicate that once the level of uncertainty of the main system properties is high, the use of absorbers is not effective for vibration reduction if the system is subjected to a white noise base excitation.

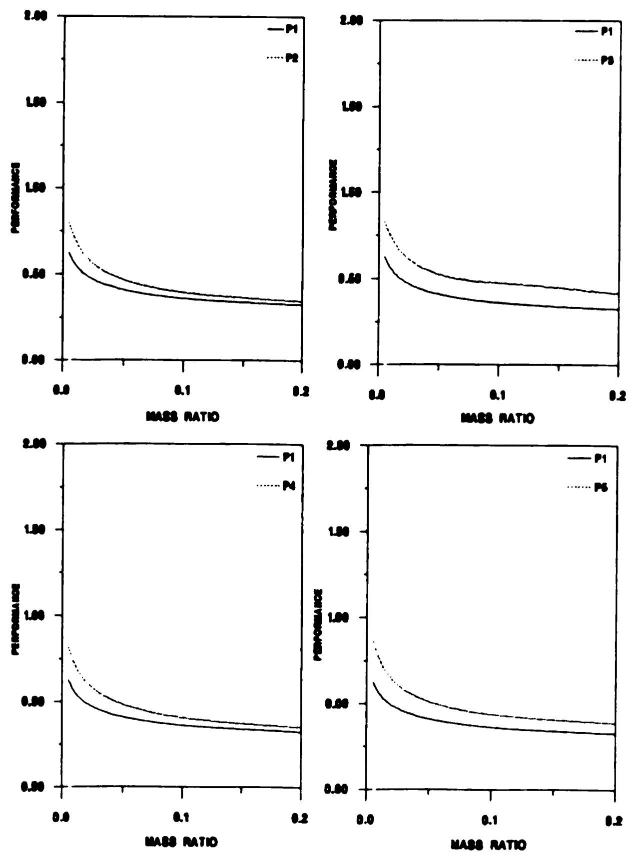

FIG 1. Comparison of performance parameters. Nominal main system damping parameter: 1% of critical. Level of uncertainty of the main system parameters: 10% coefficient of variation.

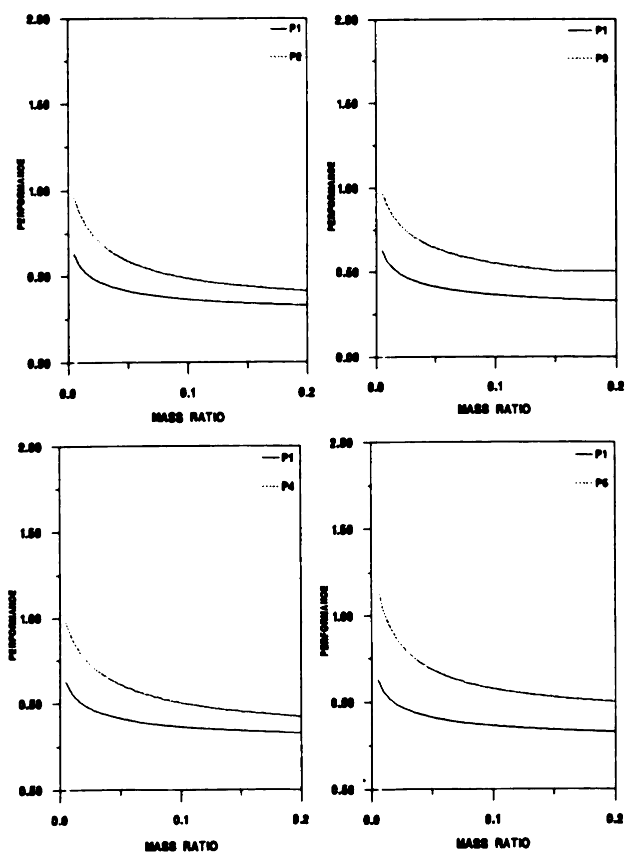

FIG 2. Comparison of performance parameters. Nominal main system damping parameter: 1% of critical. Level of uncertainty of the main system parameters: 20% coefficient of variation.

Figs 4,5 and 6 present the performance parameters when a nominal damping coefficient of the main system corresponding to 5% of critical is considered. The information given by these figures is qualitatively similar to that for the case of 1% of nominal critical damping. That is, uncertainty of the main system parameters produces a loss of efficiency in the performance of the vibration absorber. However, as can be observed, increasing the nominal damping parameter of the main system decreases the loss of efficiency, but for high levels of uncertainty and small mass ratios the effect on the absorber efficiency is still significant.

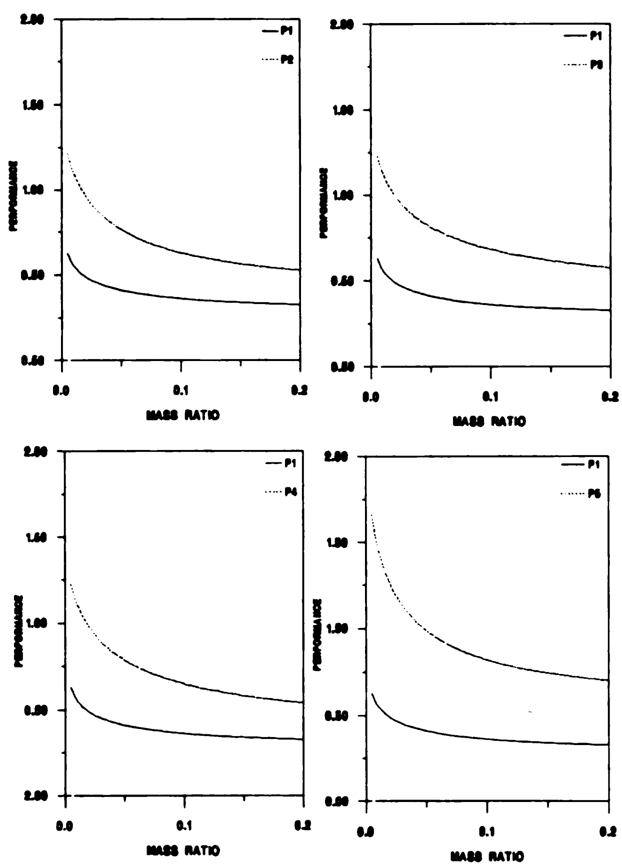

FIG 3. Comparison of performance parameters. Nominal main system damping parameter: 1% of critical. Level of uncertainty of the main system parameters: 30% coefficient of variation.

The results presented in Figs 1-6 show that the loss of effectiveness of the vibration absorber due to uncertain main system properties is invariant with respect to the performance parameter used to quantify the efficiency of the absorber. Thus, the effects of uncertainty on the efficiency of the absorber are qualitatively similar independently of the objective function used for minimization of the system response. The number of Gaussian integration points used throughout this example to compute the expected value and the standard deviation of the response function is the following. A second-order quadrature is used when a 10% coefficient of variation of the uncertain parameters is considered, a fourth-order quadrature is used for a 20% coefficient of variation, and a sixth-order quadrature is

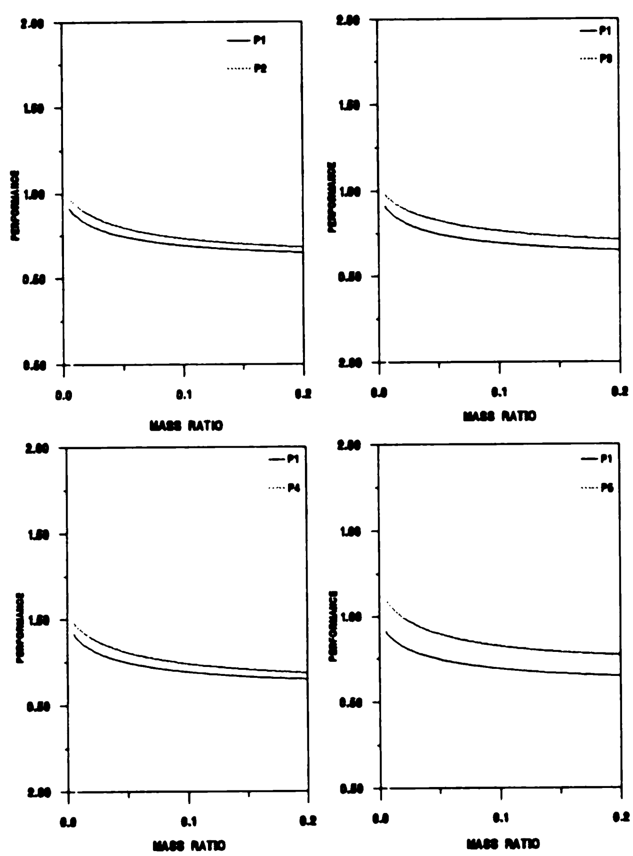

FIG 4. Comparison of performance parameters. Nominal main system damping parameter: 5% of critical. Level of uncertainty of the main system parameters: 10% coefficient of variation.

used for the case of a 30% coefficient of variation. It is found that these orders of integration are adequate for the present application since the use of higher-order quadratures produces essentially the same optimum parameters and therefore the same system response.

It is noted that as the uncertainty of the main system parameters increases, the optimum absorber frequencies, that are obtained from the optimization problems described in the previous section, decrease. Contrarily, the optimum damping parameters increase as the level of uncertainty increases. For low level of uncertainty the optimum absorber parameters are close to those obtained by assuming deterministic properties for the main system. However, for high level of uncertainty, such as 30% coefficient of variation, the difference is quite significant.

As stated before, the classical approach in passive vibration control is to find the optimum absorber parameters assuming nominal properties for the main system. Using this solution as the optimum solution, one can then include the effects of uncertain main system properties to compute different statistics of the solution. For example, the first statistical moment of the system response is given by $E(\sigma_{x_m(optimum)})$, where $\sigma_{x_m(optimum)}$ is the optimum standard deviation response obtained from the classical approach, and $E(\cdot)$ is the expected operation with respect to the uncertain parameters. In this manner, a new performance parameter can be defined as

$$p_6 = \frac{E(\sigma_{x_m(optimum)})}{\sigma_0} \,. \tag{12}$$

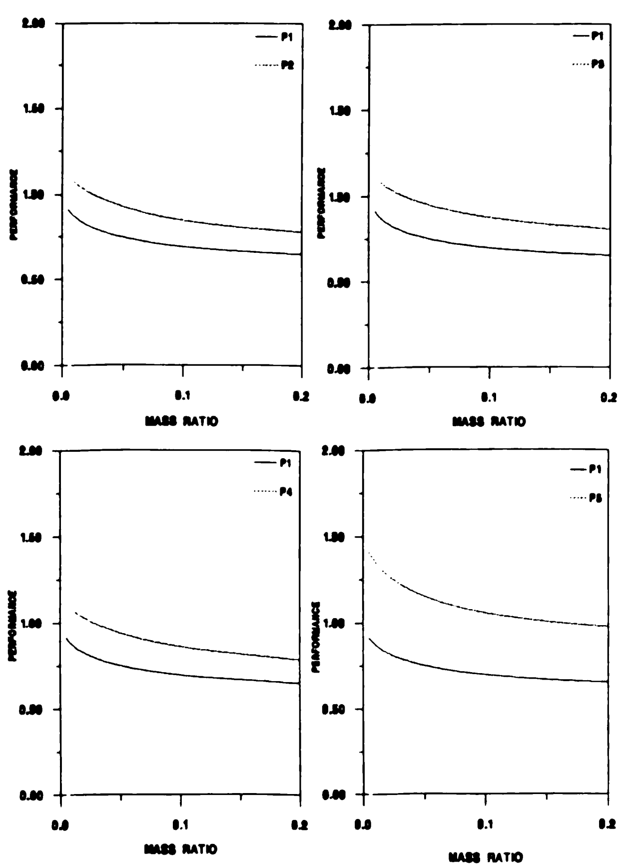

FIG 5. Comparison of perforr ... ters. Nominal main system damping parameter: ... Level of uncertainty of the main system ... % coefficient of variation.

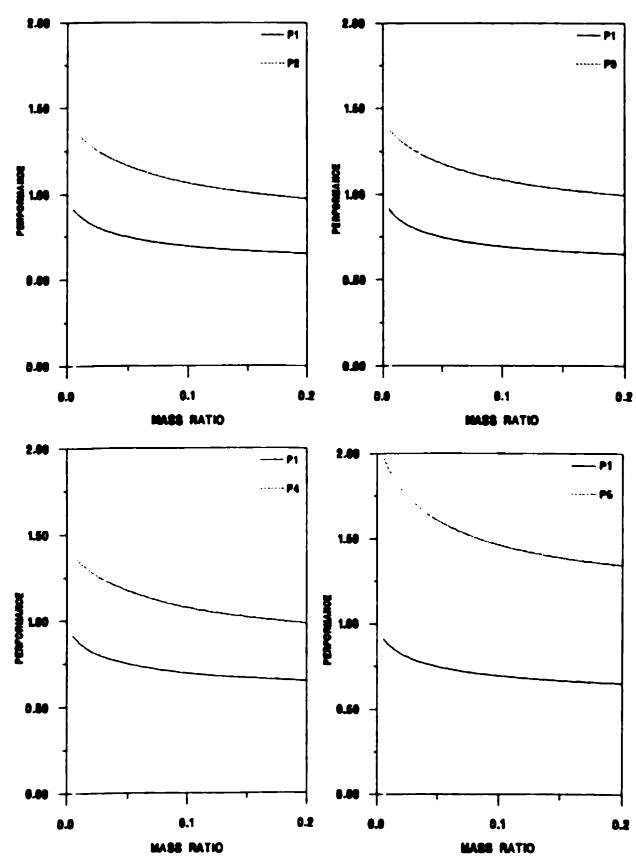

FIG 6. Comparison of performance parameters. Nominal main system damping parameter: 5% of critical. Level of uncertainty of the main system parameters: 30% coefficient of variation.

This performance parameter can be compared with the performance parameter p_2, defined in the previous section. Fig 7 shows a comparison of p_2 and p_6 for different levels of uncertainty of the main system properties. A nominal damping parameter of the main system corresponding to 1% of critical is considered in this case.

For low levels of uncertainty the two performance parameters are very similar. However, for high coefficient of variations, the difference is quite significant. These results show that the efficiency of the vibration absorber obtained from the stochastic approach is greater than the one from the classical approach. The same conclusions are obtained if other performance parameters are considered as well. Therefore, the stochastic approach considered in this study is suggested to be used instead of the deterministic approach if there is some level of uncertainty or error in the specification of the main system properties.

CONCLUDING REMARKS

The present study has shown the effects of uncertainty in the main system properties on the performance of vibration absorbers. Different response functions of the main system have been used to find the optimum absorber parameters and the optimum system response. It was found that the loss of efficiency is qualitatively similar, independently of the objective function used to minimize the system response. The numerical results have shown that uncertainty in the model parameters of the main system may cause significant changes on the response characteristics of the absorber. In these situations, the errors or uncertainties in the specification of the main system properties should be properly accounted for in the vibration control problem. If these uncertainties are not accounted for, then the performance of the vibration absorber can be affected significantly. On the other hand, the results obtained from this study suggest that for large levels of uncertainty, the use of vibration absorbers is not justified for the reduction of the main system response. This is specially true when the absorber mass is only a small fraction of the main system mass. Finally, when there is a moderate level of error in the specification of the main system properties, it is recommended to use the stochastic approach considered in this study instead of the classical deterministic approach. The new method may achieve a substantial improvement on the efficiency of the absorber compared with the one obtained by the classical tuning approach.

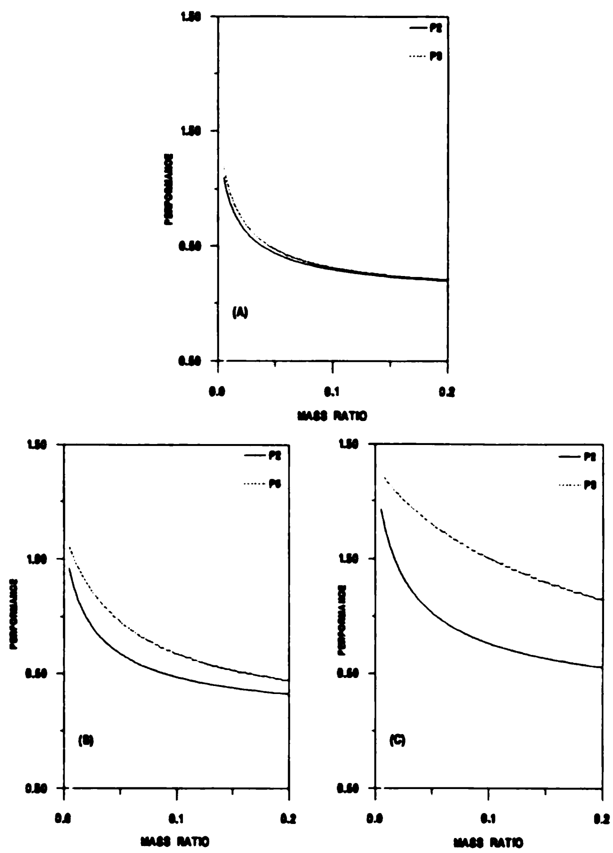

FIG 7. Comparison of performance parameters for different levels of undertain main system parameters: Stochastic versus Deterministic approach. (a) 10% coefficient of variation; (b) 20% coefficient of variation; (c) 30% coefficient of variation. Nominal main system damping parameter: 1% of critical.

ACKNOWLEDGEMENT

The research reported here was supported in part by CONICYT under Grant No. 1931112. The conclusions presented are those of the

writers and do not necessarily represent the views of the sponsor.

REFERENCES

Den Hartog JP (1940), *Mechanical Vibrations*. 2nd. Ed., McGraw-Hill Book Co., Inc., New York, N.Y.

Thompson WT (1965), *Vibration Theory and Applications*, Prentice-Hall, Englewood Cliffs, N.J.

Anderson RA (1969), *Fundamentals of Vibrations*, MacMillan, New York.

Crandall SH and Mark WD (1963), *Random Vibration in Mechanical Systems*, Academic Press, New York, N.Y.

Curtis JA and Boykin TR (1961), Response of two-degree-of-freedom systems to white noise base acceleration, *J. Acoust. Soc. Am.* 33, pp. 655-663.

Neubert VH (1964), Dynamic absorbers applied to a bar that has solid damping *J. Acoust. Soc. Am.*, 36, pp. 673-680.

Snowdon JC (1975), Vibration of simply supported rectangular and square plates to which lumped masses and dynamic vibration absorbers are attached , *J. Acoust. Soc. Am.*, 57, pp. 646-654.

Jacquot RG (1978), Optimal dynamic vibration absorbers for general beam systems, *J. Sound and Vibration*, 60, pp. 535-542.

Warburton GB and Ayorinde EO (1980), Optimum absorber parameters for simple systems, *Earthquake Engineering and Structural Dynamics*, Vol.8, pp. 197-217.

Setareh M (1990), Use of tuned mass dampers for the vibration control of floors subjected to human movements, Department of Civil Engineering, The University of Michigan, Research Report UMCE 90-10.

Wirsching PH and Campbell GW (1974), Minimal structural response under random excitation using vibration absorbers, *Earthquake Engineering and Structural Dynamics*, Vol. 2, pp. 303-312.

Jensen H, Setareh M, and Peek R (1991), TMDs for vibration control of systems with uncertain properties, *Journal of Structural Engineering*, Vol. 118, pp. 3285-3296.

Jaynes JM (1973), *A treatise on Probability*, The Royal Economic Society, Cambridge University Press, 2nd. Ed.

Rao SS (1984), *Optimization: Theory and Applications*, John Wiley & Sons, 2nd. Ed.

Flowing polymers through porous media: An experimental study of flow distribution, polymer degradation, and molecular weight effects

AJ Müller, LI Medina, O Pérez-Martin, S Rodriguez, C Romero, ML Sargenti, and AE Sáez

Grupo de Polimeros USB, Departamentos de Termodinámica y Ciencia de los Materiales, Universidad Simón Bolívar, PO Box 89000, Caracas 1080-A, Venezuela

The flow of aqueous poly(ethylene oxide) solutions through nonconsolidated porous media has been experimentally investigated. Three aspects of practical relevance have been addressed: the effect of polymer on flow distribution under nonuniform flow conditions, the mechanical degradation of the polymer in the porous media, and the effect of molecular weight on flow resistance. The nonuniform flow results indicate that, although the presence of polymer changes the distribution of the flow by affecting the region of the medium that is swept by the fluid, a significant increase in flow resistance is still observed above a critical Reynolds number, as it happens under uniform flow conditions. The degradation experiments show that the polymer is significantly degraded only in the region where a sizable increase in flow resistance is obtained with respect to the Newtonian behavior. The most significant effect of the molecular weight of the polymer is the fact that an increase in that parameter results in a substantial reduction of the Reynolds number at which the increased flow resistance is observed. Furthermore, the rate of change of this onset Reynolds number with polymer concentration appears to be independent of molecular weight. The results presented here indicate that the increase in flow resistance is not exclusively determined by the shear viscosity of the polymer solution.

CONTENTS

INTRODUCTION

In recent years there has been an increased interest in the characterization of the flow of polymer solutions through porous media. This has been motivated by the great importance of this phenomenon in practical applications such as enhanced oil recovery, filtration processes and gel permeation chromatography.

One of the most important hydrodynamic parameters used in the characterization of single phase flow through porous media is the pressure drop. In dimensionless form, the pressure drop through randomly packed, nonconsolidated porous media can be characterized by means of the resistance coefficient, defined by

$$\Lambda = \frac{\Delta P}{L}\,\frac{d^2\phi^3}{\eta_s u\,(1-\phi)^2} \qquad (1)$$

where $\Delta P/L$ is the pressure drop per unit length of porous medium, including gravitational potential contributions, d is the particle diameter, ϕ is the porosity of the medium, η_s is the viscosity of the fluid, and u is a characteristic superficial velocity.

For the case of uniform one-dimensional flow of a Newtonian fluid with superficial velocity u, the resistance coefficient is only a function of the Reynolds number, defined by

$$Re = \frac{\rho_s\, u\, d}{\eta_s\,(1-\phi)} \qquad (2)$$

where ρ_s is the fluid density. When polymer solution data are analyzed, it is customary to use the viscosity and density of the solvent in the calculation of resistance coefficient and Reynolds number. In this case, as it will be discussed, the resistance depends on Reynolds number, and polymer concentration and molecular weight.

For Newtonian fluids, the relation between Λ and Re is empirically expressed through the Ergun equation,

ASME Reprint No AMR134

$$\Lambda = A + B\,Re \qquad (3)$$

where A and B are constants.

At low Reynolds numbers, Eq (3) indicates that the resistance coefficient is a constant, which means that the pressure drop is directly proportional to the superficial velocity. This behavior is commonly known as the Darcian regime. At high Reynolds numbers, the pressure drop is proportional to u^2. In this regime, inertial effects in the pores dominate over viscous effects.

The constants A and B vary slightly from one packing to another, depending on shape and roughness of the particles, and packing procedure.

One of the most important aspects of the flow of solutions of high molecular weight polymers through porous media is the sizable increase in pressure drop with increasing flow rate that is commonly observed for polymers with flexible molecular conformations. This increase in pressure drop is much more pronounced than the one observed for Newtonian fluids, and it leads to a departure of the resistance coefficient from the Newtonian behavior.

Figure 1 shows a typical curve of resistance coefficient vs Reynolds number, comparing Newtonian with polymer solution behavior. The Newtonian fluid is in this case pure water and the polymer solution is a dilute solution of poly(ethylene oxide) (PEO) in water. The Newtonian fluid follows the behavior represented by Eq 3. Three characteristic regions can be distinguished in the polymer solution case. In region 1, the polymer solution behaves as a Newtonian fluid, yielding practically constant values of the resistance coefficient. In region 2, the departure from the Newtonian behavior occurs. This is characterized by a sudden increase in flow resistance. In region 3, the value of Λ reaches a plateau. Some investigators have reported the existence of a fourth region, at still higher values of the Reynolds number, in which the resistance coefficient drops from the plateau value (e.g. Kulicke and Haas, 1984). It has been argued that this fourth region is a consequence of the mechanical degradation of the polymer molecules in the medium.

The increase in flow resistance for polymer solutions was first analyzed by Marshall and Metzner (1967), and Dauben and Menzie (1967). These investigators quantified this effect in the flow of PEO and polyacrylamide (PAA) solutions through packed beds of spheres. They proposed that the thickening behavior was due to the elongational nature of the flow, caused by the frequent contractions and expansions experienced by the fluid as it passes through the pore space in the medium.

James and McLaren (1975) performed experimental studies of the flow of PEO through packed beds. They suggested that the increase in flow resistance with flow rate was a result of the increase in the ... nal viscosity of the solution due to the extension ... molecules in the pores. More recently, Hoag... mme (1989) have confirmed the stretch ... of flexible polymers in porous media t... he technique termed hydrodynamic chromatography, which is based upon the injection of a pulse of a dilute polymer solution into a porous medium conformed by small particle packing. This technique allows to measure the effective lateral size (in a direction perpendicular to the mean direction of flow) of the polymer molecules as they pass through the pores. Hoagland and Prud'homme found that this effective size decreases as the flow rate through the medium increases, indicating the existence of a stretched molecular conformation.

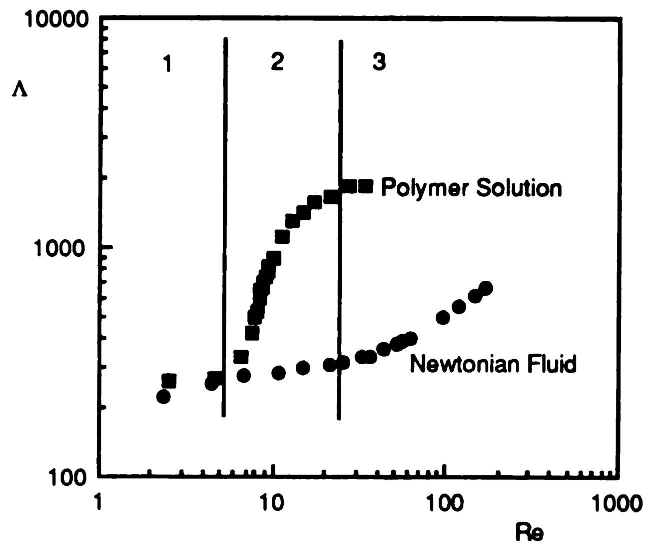

FIG 1. Typical behavior of flow resistance for Newtonian fluids and polymer solutions.

The hypothesis that molecular coil-stretch transition is the only mechanism responsible for the increase in flow resistance was challenged by Odell et al (1988) on the basis that the observed criticality of the phenomenon, in terms of the narrow range of Reynolds number through which it occurs, is not consistent with the wide molecular weight distributions of the polymers used. Odell et al proposed that the creation of transient networks of molecules was more consistent with the observations found in the literature. Recently, Rodríguez et al (1993) have provided more experimental evidence that suggests that in addition to coil-stretch transition, transient entanglement network formation seems to explain the sudden increase in flow resistance.

In the last two decades, a series of published works have assessed various aspects related to the flow of polymer solutions through porous media. Hill et al (1974) performed experiments with partially hydrolyzed PAA and xanthan polysaccharides, which are the polymers most commonly used in tertiary oil recovery. The PAA exhibited the increase in flow resistance discussed above, whereas the xanthan polymer showed shear thinning. They concluded that the xanthan polymers are less susceptible to mechanical degradation in the porous medium than the polyacrylamides. They also observed that degradation was evident only at flow rates that were higher than those corresponding to the onset of non-Newtonian behavior for PAA. Degradation of PAAs was also studied by Maerker (1976) and, more recently, by Farinato and Yen (1987). Maerker quantified the degradation in flow through consolidated and nonconsolidated porous media. Farinato and Yen analyzed the effect that polymer concentration has on molecular weight loss, defined as the ratio between the apparent molecular weight of the polymer after it passed through the medium and the original molecular weight. They concluded that the molecular weight loss is larger for solutions of lower concentrations.

James and McLaren (1975) reported that the non-Newtonian behavior and the mechanical degradation of the polymer were enhanced by a decrease in particle diameter. A lower particle diameter implies a locally higher stretching rate; i.e., a stronger elongational flow in the pores, which induces the changes in molecular conformation that produce the non-Newtonian effects and favor the break up of the polymer molecules. Since the increase in flow resistance is directly related to the elongational flow in the pores, one would expect the onset of this behavior to be controlled by the value of the average stretching rate (defined, for example, as the local fluid velocity divided by the particle diameter). Chauveteau (1986), through the analysis of experimental information, has confirmed that the onset stretching rate is independent of particle diameter.

The effect of solvent quality, solvent viscosity and solution temperature on the non-Newtonian effects was studied by Durst et al (1981), and Kulicke and Haas (1984). Invariably, any effect that leads to a decrease in the shear viscosity of the solution results in a decrease in the flow rate at which the onset of non-Newtonian effects is observed. In fact, this onset flow rate is inversely proportional to the shear viscosity of the solution, a fact that is consistent with the behavior observed in elongational flows through simple geometries, in which the relaxation time of the polymer molecules is known to be directly proportional to the viscosity of the solvent with which the molecules interact.

Kulicke and Haas (1984), Farinato and Yen (1987), and Rodríguez et al (1993) analyzed the effect of polymer concentration. Kulicke and Haas stated that the onset Reynolds number was independent of concentration in the dilute regime. However, Farinato and Yen, and Rodríguez et al found a definite decrease of onset Reynolds number with an increase in polymer concentration. The latter observation is consistent with the transient network hypothesis.

The parameter that has the greatest influence over the increase in flow resistance is the molecular weight of the polymer. Durst et al (1981) reported that an increase in molecular weight leads to a decrease in onset Reynolds number. The fact that the molecular weight can be considered the controlling factor of the non-Newtonian effects in flow through porous media has led several investigators to propose that a porous medium can be used as a rheometer in which resistance coefficient curves can be used for an approximate determination of the molecular weight of a polymer sample (Haas and Kulicke, 1984, Farinato and Yen, 1987).

To our knowledge, the increase in flow resistance with Reynolds numbers has not been reported in the literature for xanthan polysaccharides, which are polymers with semi-rigid (worm-like) molecular conformations. These polymers exhibit shear-thinning behavior in the porous medium. Sorbie and Huang (1991) have recently characterized this behavior. They observed the fact that the shear-thinning behavior was more drastic under shear flow conditions than in the porous medium. They attributed this observation to the existence, and change with the flow rate, of a layer close to the solid phase that exhibits lower concentration of polymer molecules due to topological restrictions caused by the worm-like structure of the xanthan.

In this work we address three aspects of the flow of polymer solutions through porous media. First, we study the nonuniform flow of such fluids, in order to establish the impact of the presence of polymer on the flow distribution, and the effect that the flow nonuniformities have on the macroscopic non-Newtonian pressure drops. Second, we analyze the degradation of the polymer in the porous medium, emphasizing the differences in degree of degradation encountered in the three different regions of behavior of the resistance coefficient (see Fig 1). Finally, we presents results regarding the effect of the molecular weight of the polymer of the non-Newtonian behavior.

EXPERIMENTAL

A detailed description of the experimental set up used can be found in a previous work (Rodríguez et al, 1993). The apparatus allows the fluid to pass through a bed packed with spheres of diameter 1 mm, and average porosity of 0.4. Two different beds were used. One of them was designed to ensure a one-dimensional (uniform) flow of the fluid through the packing. This bed was a cylinder with an internal diameter of 1.9 cm and a packing length of 30 cm. Nonuniform flow experiments were performed in a different bed, which was also cylindrical, but it had a diameter of 6 cm and a length of 27.5 cm. The flow pattern was completely three-dimensional since the entrance and exit of the fluid to the bed were located on the surface of the cylinder at a distance of 4.7 cm from the ends. Both entrance and exit were circular orifices with diameter equal to 3 mm.

The experiments were carried out at 20°C, and atmospheric pressure conditions at the exit of the set up. Pressure drops and fluid flow rates were measured at steady state. The fluids used were distilled water, and aqueous solutions of two polydisperse PEOs provided by Polysciences Inc. The viscometric average molecular weights of the polymers were 3E06 and 4E06. Measurements of shear viscosity of the solutions were performed by means of a Ubbelohde viscometer submerged in a temperature-controlled bath. These measurements were used to quantify polymer degradation by determining the viscometric molecular weight of the polymer.

RESULTS AND DISCUSSION

Flow distribution

The influence of the flow distribution on the resistance coefficient is presented in Fig 2, for PEO solutions with a viscometric molecular weight (M_v) equal to 4E06. For the uniform flow case, the water curve exhibits the expected behavior for Newtonian fluids, for which Λ is nearly constant at low Reynolds numbers, and increases for Re>10, a point at which inertial effects become important. When the PEO solutions flow through the uniform porous medium, they exhibit a sudden increase in Λ beyond a critical Reynolds number, which we denote as the onset Reynolds number (Re_0), where deviations from the Newtonian behavior occur. Notice that the onset Reynolds number undoubtedly decreases as the polymer concentration increases. It is also interesting to point out that the curves reach the expected plateau. The plateau value of the resistance coefficient increases with increasing concentration. Another aspect of interest is the fact that, for small Reynolds numbers, the results corresponding to high polymer concentrations (e.g. C=1000 ppm for the uniform flow case) do not reach the water value of Λ, but a higher value. This is due to the fact that the viscosity used in the calculation of the resistance coefficient is the viscosity of the solvent and not the shear viscosity of the solution. If this latter parameter were used, one would expect all the curves to reach the viscous limit of the water curves as the Reynolds number becomes small.

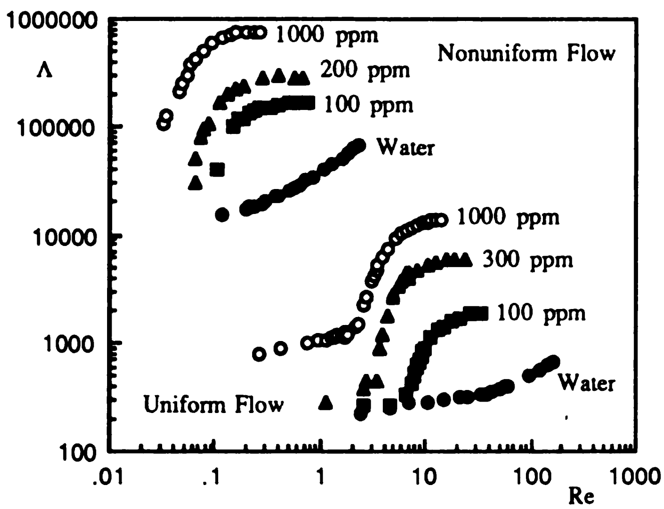

FIG 2. Effect of flow distribution on resistance coefficient, M_v = 4E06.

The behavior of the resistance coefficient in nonuniform flow is qualitatively similar to that observed for uniform flow (Fig 2). However, the Λ vs Re curves are shifted to much higher values of resistance coefficient, and to lower values of Reynolds number. This behavior is caused by the nonuniformity of the flow. The values of Λ represented in Fig 2 were calculated by considering a superficial velocity based on the total available cross-sectional area of the porous medium. Rodríguez et al (1993) have argued that, in the nonuniform flow case, the su---ficial velocity of the fluid is not constant over th... ...ow section, and therefore there are regions ... fluid velocity which contribute to increas... ...re drop and to decrease the Reynolds number for the onset of inertial and non-Newtonian effects. Rodríguez et al were able to show by means of a quantitative analysis of the data in Fig. 2 that the addition of polymer modifies the macroscopic flow field and that that flow modification effect is enhanced with increases in polymer concentration.

One of the most important aspects of the results shown in Fig 2 is the fact that, despite the flow modifications induced by the polymer in the nonuniform flow case, there is still a large increase in resistance coefficient with respect to the Newtonian value. We will now explore how the magnitude of this increase compares with the increase observed in uniform flow. For this purpose, we will quantify the increase corresponding to the plateau levels by normalizing the plateau resistance coefficient with respect to the Newtonian and water values.

Let Λ_p be the plateau value of the resistance coefficient. First we will express this value in terms of the shear viscosity of the solution. Consider the ratio of solution to solvent shear viscosities, defined by

$$x = \frac{\eta_{sln}}{\eta_s} \tag{4}$$

The parameter x should also be equal to the ratio between the resistance coefficients of solution and solvent as $Re \to 0$, since, in the viscous limit (Darcian regime), the pressure drop is proportional to the shear viscosity of the fluid.

The value of the plateau resistance coefficient that takes into account shear viscosity effects; i.e., the value of Λ_p calculated by using in Eq 1 the shear viscosity of the solution instead of that of the solvent, is given by

$$\Lambda_x = \frac{\Lambda_p}{x} \tag{5}$$

Let Λ_0 be the resistance coefficient of the solvent (water) at the Reynolds number at which the plateau is reached. Then, the ratio Λ_p/Λ_0 represents the maximum excess resistance coefficient caused by the presence of polymer, regardless of flow distribution effects. One might expect the curves Λ_p/Λ_0 vs C to be the same for uniform and nonuniform flow. These curves are presented in Fig 3. Notice that the maximum excess resistance coefficient is very close between uniform and nonuniform flow for low concentrations, but the nonuniform flow values are appreciably higher at high concentrations. This is caused by the fact that, in the nonuniform flow case, the solution is subjected to point velocities that are substantially higher than the superficial velocity. These high velocities lead to strong elongational flow fields in the pores, that yield a macroscopic pressure drop that exceeds that obtained in uniform flow. This analysis shows that the changes in rheological properties of the solution caused by the elongational flow field result in a higher friction at the pore level, instead of a drastic change in the flow distribution. These results have special relevance in the simulation of non-Newtonian flow in petroleum reservoirs, where the flow distribution is three dimensional.

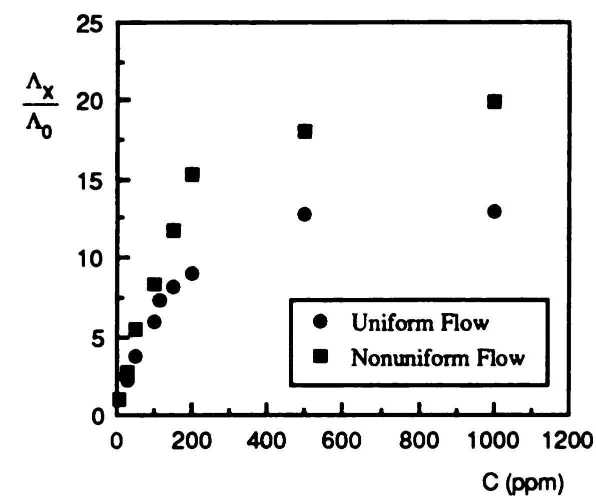

FIG 3. Effect of flow distribution on excess Λ values.

Flow-induced degradation

In order to investigate the mechanical degradation induced by the flow, two PEO (M_v=3E06) solutions (C=100 and 1000 ppm) were repeatedly passed through the uniform-flow porous medium at a constant flow rate while the pressure drop was being recorded.

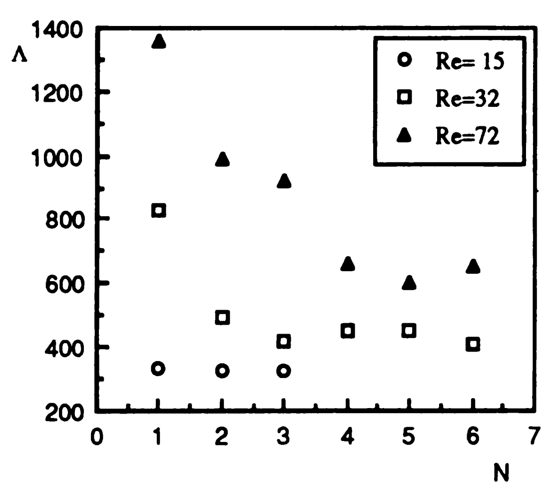

FIG 4. Decrease in resistance coefficient during mechanical degradation of the solution (C=100 ppm).

Figures 4 and 5 show the variation of the resistance coefficient with the number of passes (N) at constant Reynolds number. It can be seen that, at the lowest Reynolds number, there is no appreciable variation in the value of Λ with the number of passes (Fig 4). At higher Reynolds numbers the value of Λ rapidly decreases with N, achieving a nearly constant value after 3 to 4 passes. The decrease in the value of Λ at constant Reynolds number indicates that the solution is being degraded at a particular average strain rate, which is proportional to Reynolds number. Such strain rate for fracture is expected to be dependent on the polymer molecular weight (Odell et al, 1992). Hence when most of the molecules that can be broken at that particular strain rate have been degraded the resistance coefficient will become constant.

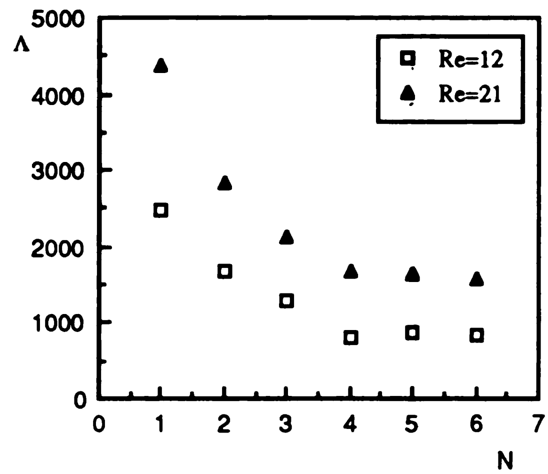

FIG 5. Decrease in resistance coefficient during mechanical degradation of the solution (C=1000 ppm).

The flow induced degradation can also be assessed by the relative displacement of the Λ versus Re curves measured after the solution was circulated at constant Reynolds number. Figures 6 and 7 show how the degradation of the polymer affects the Λ versus Re curves in the whole range of Reynolds number in which the polymer induces a non-Newtonian effect. The onset of non-Newtonian behavior of the solution is shifted to higher values of Reynolds number after degradation occurs. The increase in onset Reynolds number (Re_0) can be interpreted as an increase in the critical strain rate for chain extension or for the onset of transient entanglement network formation, depending on the theory used to explain the sudden increase in flow resistance (Müller et al, 1988). These theories predict that the onset strain rates are proportional to the longest relaxation time of the chain or to the disentanglement time of the molecule, respectively, and both quantities are proportional to the molecular length. Any increase in onset Reynolds number will therefore indicate a decrease in the average molecular weight of the polymer if the same porous medium is used and the solution concentration remains constant.

Figures 6 and 7 also show that the solution is significantly degraded only if the Reynolds number at which it is circulated through the porous medium is higher that the original Re_0 of the undegraded solution. In fact, the value of onset Reynolds number after degradation is close to the Reynolds number at which the solution was degraded. This result implies that most of the molecules break once they are in the stretched state either in isolation or as part of a transient entanglement network. A similar conclusion has been reported in idealized elongational flow experiments (Odell et al, 1990).

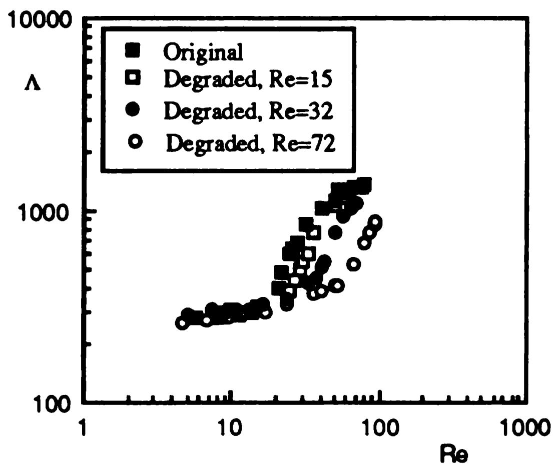

FIG 6. Resistance coefficients of original and degraded solutions, C=100 ppm.

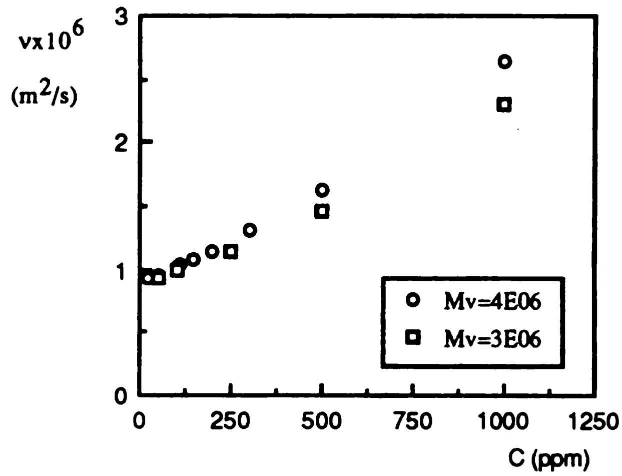

FIG 8. Kinematic viscosity as a function of polymer concentration.

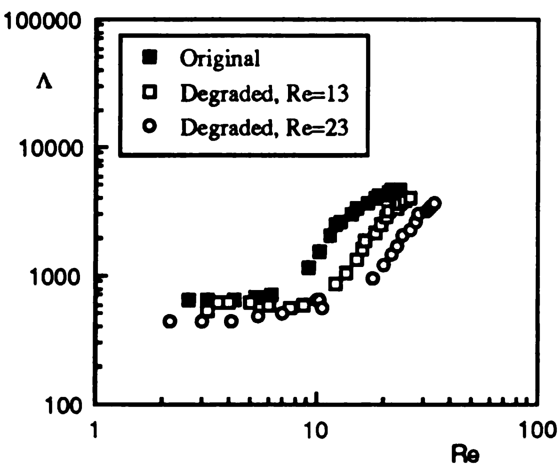

FIG 7. Resistance coefficients of original and degraded solutions, C=1000 ppm.

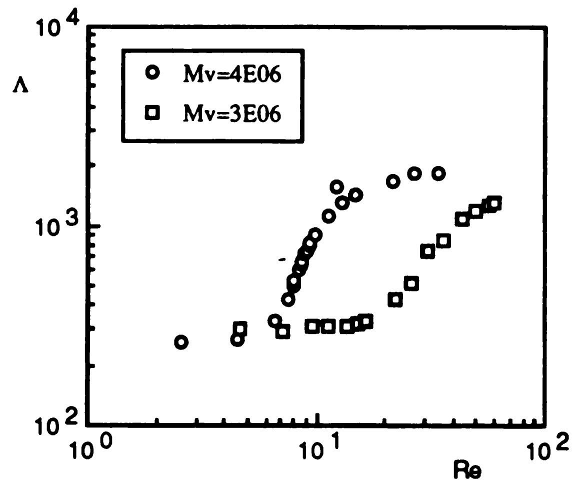

FIG 9. Resistance coefficient vs Reynolds number for 100 ppm PEO solutions.

Molecular weight effects

The effects of molecular weight on the resistance coefficient of polymer solutions in uniform flow were investigated by using two different PEOs (M_v=3E06 and 4E06). Figure 8 presents kinematic viscosity data (ν) as a function of concentration for solutions of both polymers. It can be seen that the shear viscosities do not differ much at low concentrations and it is only beyond 500 ppm where the lower molecular weight PEO exhibits lower viscosities than the higher molecular weight one. However, Figs 9 to 11 show that the porous media flow behavior of these polymer solutions is substantially different even at low concentrations.

Figures 9 to 11 show that the onset Reynolds number is higher for the lower molecular weight polymer. This trend is clearly seen in Fig 12, where the onset Reynolds number is plotted as a function of concentration for the solutions of both polymers. The fact that the drop in Re_0 with C observed is substantial has been used as an argument in favor of transient entanglement network formation as the most likely explanation of the non-Newtonian increases in flow resistance encountered in porous media flow (Rodríguez et al, 1993). Figure 12 also shows that the log-log representation of Re_0 vs C is nearly a straight line, whose slope is independent of molecular weight. Both curves are well fitted by the following relation

$$Re_0 = K\,C^{-0.6} \tag{6}$$

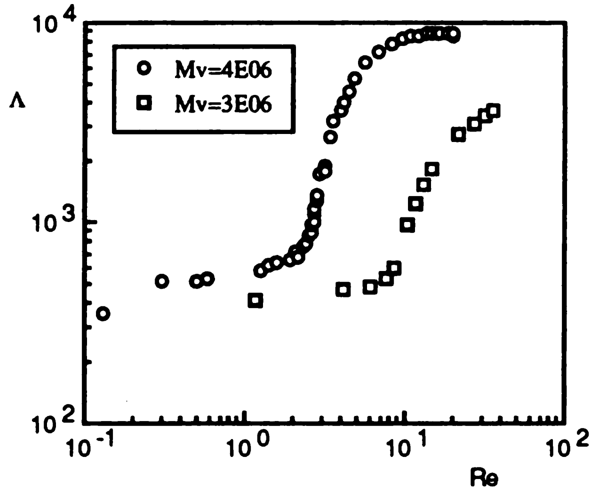

FIG 10. Resistance coefficient vs Reynolds number for 500 ppm PEO solutions.

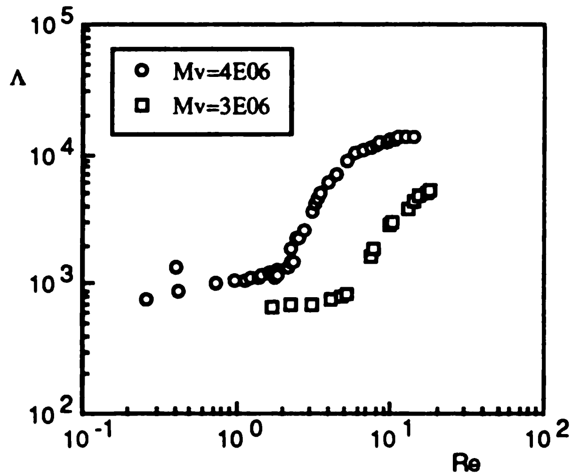

FIG 11. Resistance coefficient vs Reynolds number for 1000 ppm PEO solutions.

This is an interesting observation since it reflects a behavior that is independent of molecular weight. However, this result would have to be validated with the use of better characterized polymer samples such as closely monodisperse standards.

It should be noted that the two 100 ppm solutions used in Fig 9 have identical shear viscosities (see Fig 8); this is also indicated by the fact that the two values of resistance coefficients at very low Reynolds numbers are identical. When higher concentrations are used, the curves corresponding to the two polymers differ from the lowest Re numbers (see Figs 10 and 11). The difference in the saturation value of Λ (Λ_p) is evident from the lowest concentrations: the lower molecular weight polymer causes a lower increase in flow resistance as it is expected.

Due to the nature of the flow field in the porous medium the resistance coefficient should be proportional to the shear viscosities of the polymer solution, at low Reynolds numbers (both viscosities should be equal in this regime). Since no appreciable chain extension would be expected below the onset Reynolds number, the contribution of the elongational viscosity to the value of Λ at low Re would be constant with Reynolds number (Newtonian behavior). However, the value of Λ at high Re (after the sudden increase in Λ) should be influenced by two opposing effects: the shear viscosity of the solution might decrease with increasing shear rate (PEO/water solutions are known to be shear thinning, and this effect is more noticeable at moderate concentrations and it also depends on the molecular weight of the polymer, Dauben and Menzie, 1967) and the elongational viscosity increases with increasing strain rate. It is clear by the shape of the curves in Figs 9 to 11 that the increase in shear viscosity upon increasing solution concentration is responsible for the differences observed in the Λ values at low Reynolds number (Newtonian regime), while the elongational viscosity is dominating the behavior of the resistance coefficient at Reynolds numbers larger than the onset value.

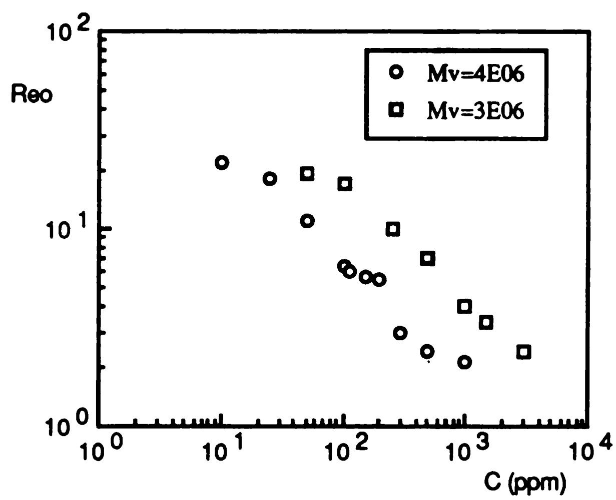

FIG 12. Concentration dependence of the onset Reynolds number for aqueous PEO solutions.

Other important aspects of comparing Λ versus Re curves of the two different molecular weight polymers used here can be appreciated in Figs 13 and 14. In Fig 13 two different concentrations have been deliberately chosen for which the two polymer solutions exhibit the same resistance coefficient plateau (which should be proportional to the elongational viscosity), approximately the same onset Reynolds number and different low Reynolds number resistance coefficients (which should be proportional to the shear viscosity). The case presented in Fig 13 illustrates that two solutions exhibiting very different shear viscosities might produce the same thickening action in porous media flow. Fig 14, on the other hand, depicts another possible case in which the shear viscosities of both polymer solutions are identical but their elongational response varies according to the molecular weight of the polymer. These results lead to conclude that the importance of the elongational viscosity should not be overlooked if polymers are to be selected for applications that involve complex flow situations like porous media flow (encountered, for instance, in enhanced oil recovery). Figs 13 and 14 clearly show that the selection should not be based exclusively on the shear flow behavior.

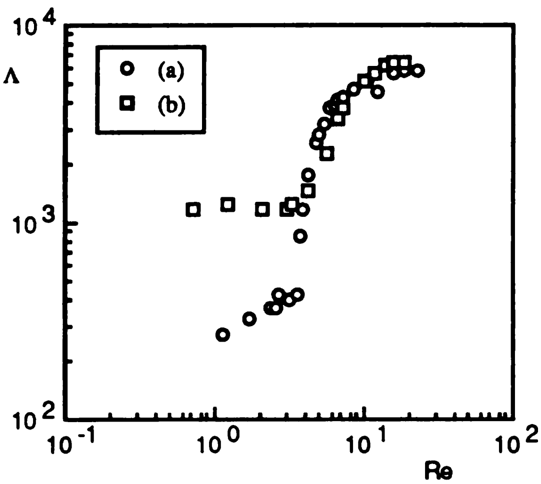

FIG 13. Comparison of resistance coefficient for: (a) M_V=4E06, C=300 ppm; (b) M_V=3E06, C=1500 ppm.

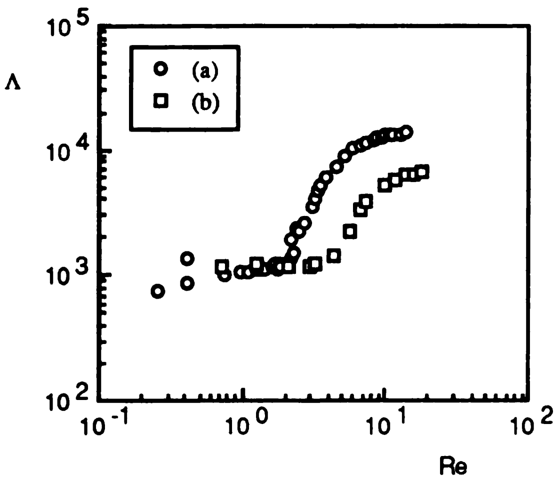

FIG 14. Comparison of resistance coefficient for: (a) M_V=4E06, C=1000 ppm; (b) M_V=3E06, C=1500 ppm.

CONCLUSIONS

We have investigated the effects of flow distribution, polymer degradation, and polymer molecular weight on the fluid dynamics of poly(ethylene oxide) aqueous solutions flowing through porous media. The addition of polymer induces a change in the macroscopic flow distribution within the porous medium. However, the characteristic non-Newtonian increases in flow resistance observed in uniform flow are also present in nonuniform flows. In uniform flows, the polymer molecules are significantly degraded only when non-Newtonian effects are present. An increase in polymer molecular weight results in a substantial reduction of the Reynolds number at which the non-Newtonian effects set in. An important conclusion is that the magnitude of increase in flow resistance caused by the polymer is not exclusively determined by the shear viscosity of the solution. The elongational viscosity plays a more important role at this respect.

ACKNOWLEDGMENTS

We wish to acknowledge the financial support of the European Community through the EC Cooperative Award No CI1-CT91-0887 (WNSN). We would also like to thank Dr JA Odell for helpful discussions.

REFERENCES

Chauveteau G, Fundamental criteria in polymer flow through porous media and their importance in the performance differences of mobility-control buffers, in *Water-Soluble Polymers*, JE Glass (ed), ACS, Washington, 1986, 227-267.

Dauben DL and Menzie DE, Flow of polymer solutions through porous media, *J of Petroleum Tech* **19**, 1065-1073 (1967).

Durst F, Haas R and Kaczmar BU, Flows of dilute hydrolyzed polyacrylamide solutions in porous media under various solvent conditions, *J Applied Polymer Sci* **26**, 3125-3149 (1981).

Farinato RS and Yen WS, Polymer degradation in porous media flow, *J Applied Polymer Sci* **33**, 2353-2368 (1987).

Haas R and Kulicke W-M, Flow behavior of dilute polyacrylamide solutions through porous media. 2. Indirect determination of extremely high molecular weights and some aspects of viscosity decrease over long time intervals, *Ind Eng Chem Fundam* **23**, 316-319 (1984).

Hill HJ, Brew JR, Claridge EL, Hite JR and Pope GA, The behavior of polymers in porous media, paper *SPE* 4748, 1974.

Hoagland DA and Prud'homme RK, Hydrodynamic chromatography as a probe of polymer dynamics during flow through porous media, *Macromolecules* **22**, 775-781 (1989).

James DF and McLaren DR, The laminar flow of dilute polymer solutions through porous media, *J Fluid Mech* **70**, 733-752 (1975).

Kulicke W-M and Haas R, Flow behavior of dilute polyacrylamide solutions through porous media. 1. Influence of chain length, concentration, and thermodynamic quality of the solvent, *Ind Eng Chem Fundam* **23**, 309-315 (1984).

Maerker JM, Mechanical degradation of partially hydrolyzed polyacrylamide solutions in unconsolidated porous media, *Society of Pet Eng J* 172-174, august (1976).

Marshall RJ and Metzner AB, Flow of viscoelastic fluids through porous media, *Ind Eng Chem Fundam* **6**, 393-400 (1967).

Müller AJ, Odell JA and Keller A, Elongational flow and rheology of monodisperse polymers in solution, *J Non-Newt Fluid Mech* **30**, 99-118 (1988).

Odell JA, Müller AJ and Keller A, Non-Newtonian behaviour of hydrolysed polyacrylamide in strong elongational flows: a transient network approach, *Polymer* **29**, 1179-1190 (1988).

Odell JA, Müller AJ, Narh KA and Keller A, Degradation of polymer solutions in extensional flows, *Macromolecules* **23**, 3092-3103 (1990).

Odell JA, Keller A and Müller AJ, Thermomechanical degradation of macromolecules, *Colloid & Polym Sci* **270**, 307-324 (1992).

Rodríguez S, Romero C, Sargenti ML, Müller AJ, Sáez AE and Odell JA, Flow of polymer solutions through porous media, *J Non-Newt Fluid Mech*, in press, 1993.

Sorbie KS and Huang Y, Rheological and transport effects in the flow of low-concentration xanthan solution through porous media, *J Colloid Interface Sci* **145**, 74-89 (1991).

Analysis of cylindrically curved panels based on a two field variable variational principle

Maher N Bismarck-Nasr

Divisão de Engenharia Aeronáutica, Instituto Tecnológico de Aeronáutica
Centro Técnico Aeroespacial, São José dos Campos, SP, 12228-900, Brazil

A variational formulation of thin cylindrically curved panels having transverse displacement and Airy stress function as field variable is presented. Euler-Lagrange equations and boundary conditions are obtained. A finite element based on this variational principle preserving $C^{(1)}$ continuity is formulated. Applications for free vibrations, buckling, and supersonic panel flutter analyses are given. Several numerical calculations are presented. The results obtained are discussed and are compared with previous analytical solutions, numerical calculations, and experimental findings.

INTRODUCTION

Structural analysis of plates and shells using two field variables, the transverse displacement w and the Airy stress function F, has been investigated by several authors. Donnell[9], Marguerre[17], and von Kármán[29] made the major contributions in obtaining the differential equations for static analysis. Reissner[23] introduced a variational principle with w and F being the field variables. Based on an order of magnitude analysis to justify the omission of the inplane inertias, Reissner[24] extended the application to dynamic analysis of shallow shells. In spite of the simplifications it introduces, Reissner's two filed variables principle is scarcely used in finite element applications. The main reason is attributed to the complications introduced for the application of the boundary conditions on Airy stress function[12-13].

In Ref 5, starting from Reissner's variational equation for free vibration of thin cylindrically curved panels, the Euler-Lagrange equations governing the problem and the boundary conditions were obtained. It was shown that the boundary conditions on F are as simple and direct to apply as on w. The variational principle was used to derive a C^1 continuity rectangular finite element and numerical results of free vibration for freely supported square curved panels were presented. In Ref 6, the formulation was extended to the buckling analysis of cylindrically curved panels and numerical results were presented for various classical end conditions and for different aspect ratios of the panel. In Ref 7, the formulation was applied to the supersonic flutter of cylindrically curved panels. Numerical results were presented for square panels with flow in the meridional direction for clamped, simply supported, and freely supported end conditions.

The present paper generalizes the formulation and amplifies the results of Refs 5-7. Several numerical results are presented and are compared with previous analytical solutions, numerical calculations, and experimental findings.

PROBLEM FORMULATION

The variational equation of thin cylindrically curved shallow shells, Fig 1, neglecting inplane inertias[24], considering the effect of the work done by an external non-stationary aerodynamic load[7], and the initial inplane prestress[6] can be expressed as,

$$\begin{aligned}\delta(\Pi^*) = \delta\Big\{ & \frac{1}{2}\int_A \rho\, h\, w_{,t}^2\, dA \\ & - \frac{D}{2}\int_A \left[w_{,xx}^2 + w_{,yy}^2 + 2\nu w_{,xx} w_{,yy} + 2(1-\nu) w_{,xy}^2\right] dA \\ & + \frac{1}{2Eh}\int_A \left[F_{,xx}^2 + F_{,yy}^2 - 2\nu F_{,xx} F_{,yy} + 2(1+\nu) F_{,xy}^2\right] dA \\ & - \int_A \frac{w}{R} F_{,xx}\, dA + \int_A w\,\Delta p\, dA \\ & - \frac{1}{2}\int_A \left[N_{xx} w_{,x}^2 + N_{yy} w_{,y}^2 + 2 N_{xy} w_{,x} w_{,y}\right] dA \Big\} = 0 \end{aligned} \tag{1}$$

The functions subjected to variation in Eq (1) are the transverse displacement w and the Airy stress function F. In Eq (1) ρ is the material mass density per unit of area, h is the shell thickness, $D = Eh^3/12(1-\nu^2)$ is the shell flexural rigidity, ν is Poisson's ratio, E is Young's modulus, R is the shell radius, Δp is the non-stationary aerodynamic pressure difference, and N_{xx}, N_{yy}, and N_{xy} are the initial prestresses. Using the quasi-static aerodynamic theory, the relationship between Δp and w can be written as[4]

$$\Delta p = -\frac{2Q}{\sqrt{M^2-1}}\left[\cos\Lambda \frac{\partial w}{\partial x} + \sin\Lambda \frac{\partial w}{\partial y}\right] \tag{2}$$

where $Q = \rho V^2/2$ is the dynamic pressure, M is the free stream Mach number, V is the velocity of the unperturbed external flow, and Λ is the angle between the free stream direction and the x-direction.

Performing the variational operation, grouping terms, and through application of Green's theorem, the variational equation (1) reads

$$
\begin{aligned}
&- \int_A \delta w \left[D\nabla^4 w + \frac{1}{R} F_{,xx} + \rho h w_{,tt} \right] dA \\
&+ \int_A \delta F \left[\frac{1}{Eh} \nabla^4 F - \frac{1}{R} w_{,xx} \right] dA \\
&- \int_C \delta w \left[M_{x,x} + 2 M_{xy,y} \right] dy + \int_C \delta w \left[M_{y,y} + 2 M_{xy,x} \right] dx \\
&+ \int_C \delta w_{,x} M_x \, dy - \int_C \delta w_{,y} M_y \, dx + \int_C \left[M_{xy} \delta w \right]_{,y} dy \\
&- \int_C \left[M_{xy} \delta w \right]_{,x} dx + \int_C \delta F u_{,yy} \, dy \\
&- \int_C \delta F v_{,xx} \, dx + \int_C \delta F_{,x} v_{,y} \, dy - \int_C \delta F_{,y} u_{,x} \, dx \\
&+ \frac{1+\nu}{Eh} \int_C \left[\delta F \cdot F_{,xy} \right]_{,y} dy - \frac{1+\nu}{Eh} \int_C \left[\delta F \cdot F_{,xy} \right]_{,x} dx \\
&+ \frac{2Q}{\sqrt{M^2-1}} \int_A \left[\cos\Lambda \, w_{,x} + \sin\Lambda \, w_{,y} \right] \delta w \, dA \\
&+ \int_A \left[N_{xx} w_{,xx} + N_{yy} w_{,yy} + 2 N_{xy} w_{,xy} \right] \delta w \, dA = 0 \quad (3)
\end{aligned}
$$

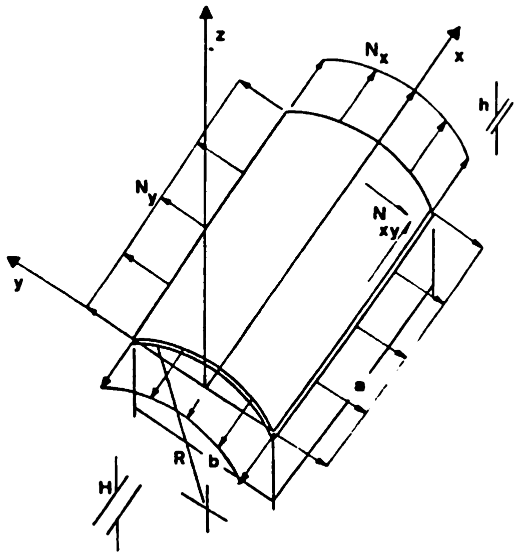

FIG 1. Shell geometry and notations.

Using Eq (3), the Euler-Lagrange equations governing the problem read,

$$
\begin{aligned}
&D\nabla^4 w + \frac{1}{R} F_{,xx} + \rho h w_{,tt} \\
&- \frac{2Q}{\sqrt{M^2-1}} \int_A \left[\cos\Lambda \, w_{,x} + \right.
\end{aligned}
$$

$$- N_{xx} w_{,xx} - N_{yy} w_{,yy} - 2 N_{xy} w_{,xy} = 0 \qquad (4)$$

$$\nabla^4 F - \frac{Eh}{R} w_{,xx} = 0 \qquad (5)$$

and the boundary conditions are given by

1. On $x =$ constant
   - w is prescribed or $M_{x,x} + 2 M_{xy,y} = 0$
   - $w_{,x}$ is prescribed or $M_x = 0$
   - F is prescribed or $u_{,yy} = 0$
   - $F_{,x}$ is prescribed or $v_{,y} = 0$
2. On $y =$ constant
   - w is prescribed or $M_{y,y} + 2 M_{xy,x} = 0$
   - $w_{,y}$ is prescribed or $M_y = 0$
   - F is prescribed or $v_{,xx} = 0$
   - $F_{,y}$ is prescribed or $u_{,x} = 0$
3. At a corner (discontinuity in C) $M_{xy} = 0$ (equivalent to $w_{,xy} = 0$) if w is not prescribed; and $F_{,xy} = 0$, if F is not prescribed.

The first conditions are the forced or geometrical conditions, and the second ones are the free or natural conditions. When using a variational formulation for a boundary value problem, the admissible functions should satisfy only the forced boundary conditions. Therefore, using the above conditions, we can write the classical boundary conditions on an edge say, $\nu =$ constant, as

1. Clamped edges $w = w_{,\nu} = 0$, and at the corner $F_{,\nu\eta} = 0$
2. Free edges $F = F_{,\nu} = 0$, and at the corner $M_{,\nu\eta} = 0$ ($i.e., w_{,\nu\eta} = 0$)
3. Simply supported edges $w = 0$ and at the corner $F_{,\nu\eta} = 0$
4. Freely supported edges $w = F = 0$

A finite element solution for the problem at hand can be performed using rectangular elements preserving C^1 continuity based on the functional given in Eq (1). Thus, we can write

$$
\begin{aligned}
z(x,y) = \sum_{i=1}^{2} \sum_{j=1}^{2} &\left[H_{0i}(x) H_{0j}(y) z_{ij} + H_{1i}(x) H_{0j}(y) z_{,x_{ij}} \right. \\
&\left. + H_{0i}(x) H_{1j}(y) z_{,y_{ij}} + H_{1i}(x) H_{1j}(y) z_{,xy_{ij}} \right] \qquad (6)
\end{aligned}
$$

where z stands for w or F, and H_{mn} are first order Hermitian polynomials; other notations are as given in Ref 3. Using the standard finite element technique we obtain for each element a set of two equations cast in the form below:

$$
\begin{aligned}
&[k_{ww}]\{w\} + [k_{wF}]\{F\} + [m]\{\ddot{w}\} + \lambda [a]\{w\} + \\
&\left[N_{xx}\left[k_{G_{N_{xx}}}\right] + N_{yy}\left[k_{G_{N_{yy}}}\right] + N_{xy}\left[k_{G_{N_{xy}}}\right] \right]\{w\} = \{0\} \qquad (7a) \\
&[k_{Fw}]\{w\} + [k_{FF}]\{F\} = \{0\} \qquad (7b)
\end{aligned}
$$

where $\lambda = 2Q/\sqrt{M^2-1}$ is the dynamic pressure parameter. The elements of the stiffness matrix $[k_{ww}]$, the compatibility matrix $[k_{FF}]$, the coupling matrix $[k_{wF}]$, the mass matrix $[m]$, the geometrical stiffness matrices $[k_G]$, and the aerodynamic matrix $[a]$ can be calculated as given in Refs 3, 4, and 5. Using the finite element standard assembly technique and applying the appropriate boundary conditions, the whole structure matrix equations read,

$$[K_{ww}]\{w\} + [K_{wF}]\{F\} + [M]\{\ddot{w}\} + \lambda[A]\{w\} + \left[N_{xx}\left[K_{G_{N_{xx}}}\right]\{w\} + N_{yy}\left[K_{G_{N_{yy}}}\right]\{w\} + N_{xy}\left[K_{G_{N_{xy}}}\right]\right]\{w\} = \{0\} \tag{8a}$$

$$[K_{Fw}]\{w\} + [K_{FF}]\{F\} = \{0\} \tag{8b}$$

The degrees of freedom $\{F\}$ can be eliminated using the compatibility equation (8*b*), reducing the problem to,

$$[K_{eq}]\{w\} + [M]\{\ddot{w}\} + \lambda[A]\{w\}$$
$$\left[N_{xx}\left[K_{G_{N_{xx}}}\right] + N_{yy}\left[K_{G_{N_{yy}}}\right] + N_{xy}\left[K_{G_{N_{xy}}}\right]\right]\{w\} = \{0\} \tag{9}$$

where

$$[K_{eq}] = [K_{ww}] - [K_{wF}][K_{FF}]^{-1}[k_{Fw}]$$

An examination of Eq (9) reveals that the computational effort required for the solution of the problem is equivalent to that of a flat plate problem when the present formulation is used. Further, the inplane boundary conditions are applied on F, $F_{,x}$, $F_{,y}$, and $F_{,xy}$, and are all nodal degrees of freedom.

APPLICATIONS

In this section three sets of applications are presented, namely, free vibration analysis, buckling analysis, and supersonic panel flutter analysis. Several numerical calculations are given and are discussed and compared with previous analytical solutions, numerical calculations, and experimental findings.

Free vibration analysis

The first series of calculations performed are for cylindrically curved panels freely supported on all edges. These calculations were made in order to compare the results obtained using the present formulation with the exact analytical solution of Reissner's equation[24]. It is anticipated that for the curved panels, with the increase of the curvature, higher modes will become the critical modes for buckling and supersonic flutter conditions. Therefore, the finite element model used must maintain a good precision for a wide range of the lower part of the frequency spectrum.

To study the convergence of the present method two meshes were used, namely, a 2x2 mesh and a 4x4 mesh. The numerical results showed that convergence to the exact solution was quite rapid and that the 4x4 mesh solution practically coincides with the exact solution. Fig 2 presents the results obtained for the first natural frequency parameter $\Omega = \omega(\rho h a^4/D\pi^4)^{1/2}$, where ω is the natural frequency, versus the shell rise parameter H/h,

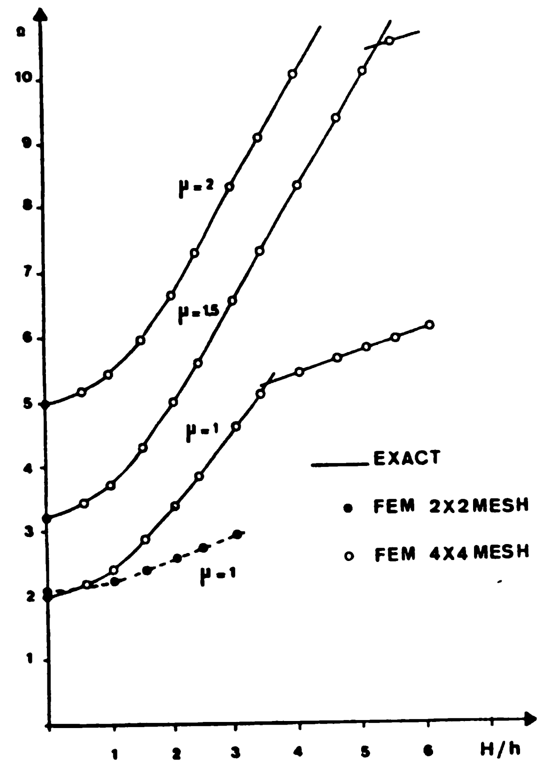

FIG 2. First natural frequency parameter versus curvature parameter.

for different aspect ratios $\mu = a/b$. The results are compared with Reissner's exact solution. Table I compares the results obtained using the present formulation and Reissner's solution for the first fifteen modes for $\mu = 1$ and $\alpha = 12(1-\nu^2)a^4/h^2R^2 = 734.64$ for a 4x4 mesh. The precision achieved using the present formulation was considered sufficient enough in order to proceed for further calculations where no exact solutions exist using a 4x4 mesh.

mode	m, n	Exact solution	Present analysis
1	1,1	2.426	2.426
2	1,2	5.030	5.043
3	2,1	5.461	5.471
4	2,2	8.117	8.134
5	1,3	10.004	10.155
6	3,1	10.301	10.441
7	2,3	13.027	13.155
8	3,2	13.138	13.263
9	1,4	17.001	18.241
10	4,1	17.195	18.677
11	3,3	18.053	18.828
12	2,4	20.008	21.482
13	4,2	20.120	21.576
14	3,4	25.020	26.321
15	4,3	25.062	26.359

Table I. Natural frequency parameter Ω for freely supported cylindrically curved panels of aspect ratio 1 and curvature parameter $\alpha = 734.64$.

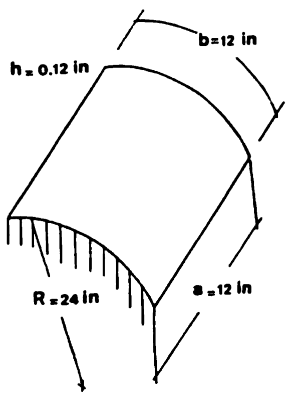

FIG 3. Cantilever thin cylindrically curved panel.

The second series of calculations were performed for the cantilever shallow shell depicted in Fig 3. The shell has dimensions $R = 24$ in, $h = 0.102$ in, and $a = b = 12$ in, and is of steel material.

This example has been chosen because it has a part of the boundary clamped whereas the rest of the boundary is free and, therefore, will present a good test for the application of the Airy function boundary conditions for these cases. This model has been extensively used in the literature for comparison purposes between various finite element models performance and analytical solutions. Further, experimental results for the model are available.

The results obtained are shown in Table II and are compared with previous solutions and experimental findings. Olson and Lindberg solution [22] is a finite element solution using a conforming, doubly curved shallow shell triangular element having 38 degrees of freedom. Walker solution[32] is also a finite element solution using a doubly curved quadrilateral helicoidal shell element with 40 degrees of freedom. Leissa solution[16] is a Rayleigh-Ritz solution using algebraic polynomials as trial functions. The experimental findings are due to Olson and Lindberg[22].

Theoretical analysis			Present analysis		Exp.
Olson 22	Walker 32	Leissa 16	$E=3.0$ Mpsi	$E=3.1$ Mpsi	Olson 22
86.6	86.6	85.9	83.6	85.0	85.6
139	140	138	137	139	135
251	249	249	249	253	259
349	351	343	329	334	351
393	399	387	374	380	395
533	535	532	534	543	531
746	749	736	697	709	751
752	761	738	705	716	743
790	806		769	782	790
814	820		807	820	809
1009	1012		1008	1025	997
1232	1241		1174	1194	1216
1246	1248		1175	1195	1252
1266	1273		1239	1259	1241
1286	1313		1259	1279	1281

Table II. Natural frequencies in Hz of the cantilever cylindrical shell panel.

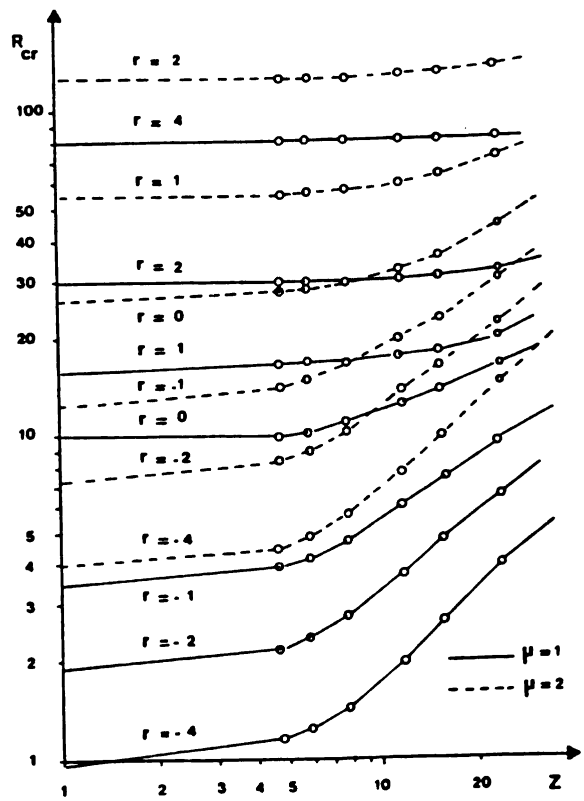

FIG 4. Combined shear and axial stress buckling parameter for all edges freely supported.

Table II presents two columns for the present formulation. In the first column was taken the value 3x10^6 psi for the Young's modulus E, as is commonly used in academic solutions and as was made in Refs 16, 22, and 32. In the second column was taken the value 3.1x10^6 psi for E in order to compare the results of the computations with the experimental results. Obviously, the two columns bear a constant ratio. The results show that good achievements have been obtained using the present formulation.

Buckling analysis

In Ref 6, buckling analysis of curved sheet panels under the action of pure shear and pure axial compression using the present formulation were presented for different aspect ratios and boundary conditions. In this section some of the results obtained for buckling of curved panels under the action of combined shear and axial loads are given.

The first series of calculations are performed for curved sheet panels with freely supported end conditions. The results of the computations are shown in Fig 4. The curves are plotted for the buckling stress resultant versus the curvature parameter z, $\left(z = b^2(1-\nu^2)^{1/2}/Rh\right)$ and is a length-curvature parameter commonly used in the buckling analysis of curved plates and axisymmetric shells[14]. In this figure, two sets of curves are given, one set for aspect ratio $\mu = 1$ and the other set for $\mu = 2$. For each aspect ratio set, the calculations have been done for ratios of axial stress to shear stress, $\sigma_{xx}/\sigma_{x\theta} = 0, 1, 2,$ and 4. The curves labelled with negative values are for compressive axial loads.

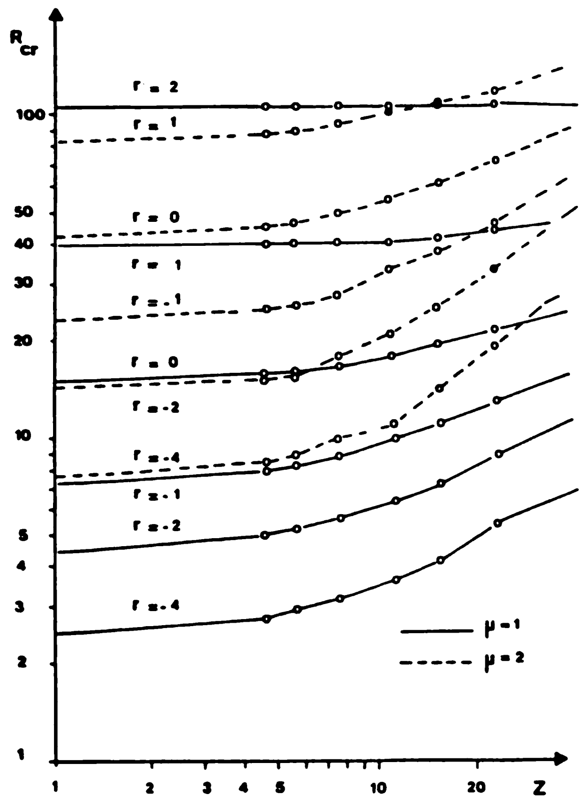

FIG 5. Combined shear and axial stress buckling parameter for all edges clamped.

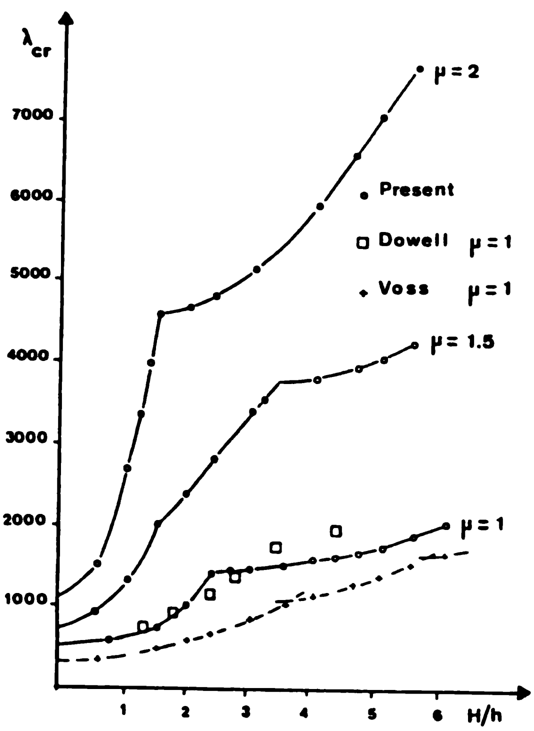

FIG 6. Flutter dynamic pressure parameter versus shell rise for flow in the x-direction and all edges freely supported.

The next set of computations was performed for curved panels with all edges clamped and for the same loading cases and aspect ratios as for the previous calculation set. The results are shown in Fig 5.

From the results of Figs 4 and 5, the following conclusions can be drawn:

- A curved panel under the action of inplane compression or shear is expected to buckle essentially as a flat plate when the curvature is small and to buckle in the same manner as a cylinder when the plate curvature is large. Between the two limits there is a transition region from one type of behavior to the other.

- The buckling loads depend not only on the geometry, but also on the boundary conditions. For the freely supported case the curves are smoother in the transition region if compared with the clamped end condition cases. Further, the buckling loads in the transition region are more affected for values of aspect ratio near unity.

- As the length-curvature parameter z increases, it is expected that the buckling load changes characterizing the flat plate behavior with buckling occurring with the first number of half waves to the cylinder behavior characterized by a large number of waves or a diamond-buckle-pattern deflection. In the transition region, it is, therefore, expected to find cups in the curves as the critical waves change by integer values.

Supersonic flutter analysis

Flutter characteristics determination of shallow shells is of prime importance in supersonic aircraft and launch vehicles designs. The first analytical research on supersonic flutter of thin cylindrically curved panels was made by Voss[30], who used Reissner's shallow shell equations, quasi-static aerodynamic theory, and the Galerkin method for the solution of freely supported ends boundary conditions. Nonlinear flutter analysis of two-dimensional[10] and three-dimensional[11] curved panels were performed by Dowell using a quasi-static aerodynamic theory. Dowell's investigations showed that the inplane edge restraints had a great influence on the flutter boundaries and this was attributed to the frequency spectrum of the shells analyzed. The effect of edge restraints was again investigated by Matsuzaki[18] using the Galerkin method for the solution of the problem.

Since the introduction of the aerodynamic matrix concept by Olson[20], many authors exploited the application of the finite element method in the field of supersonic panel flutter. The application of Olson's concept has been extended to three-dimensional plates[15,21,25], coupled plates[2], circular cylindrical shells[1], and conical shells[8,28]. Finite element flutter formulations with structural nonlinearities were studied by Mei[19], Rao and Rao[26] for flat plates and Ueda[27] for conical shells. Yang[31] introduced in the formulation of the aerodynamic matrix a numerical integration technique in order to obtain more accurate results tending to the exact linearized flow theory

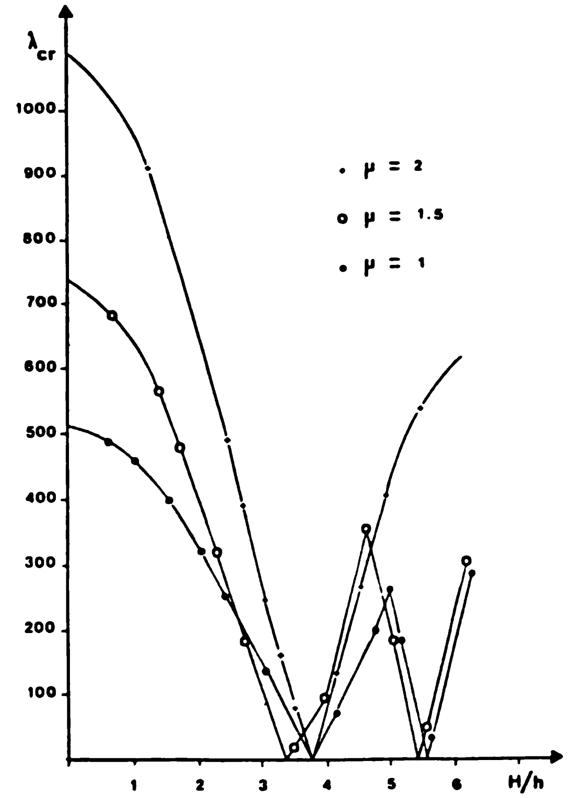

FIG 7. Flutter dynamic pressure parameter versus shell rise for flow in the y-direction and all edges freely supported.

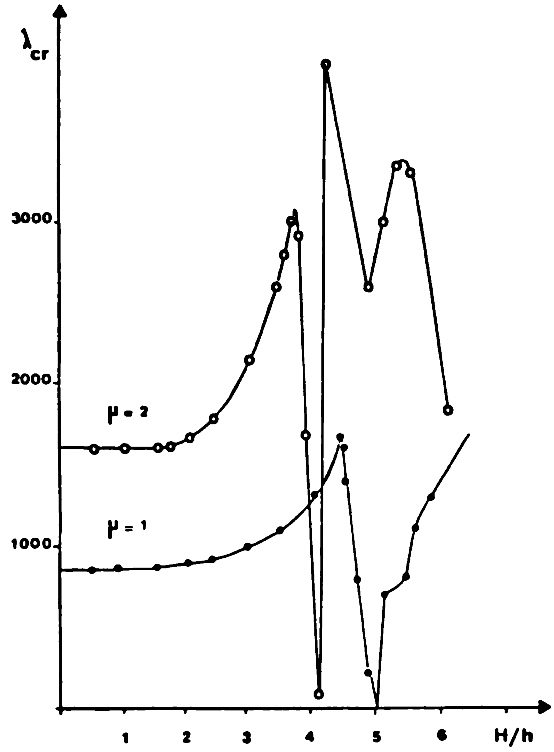

FIG 8. Flutter dynamic pressure parameter versus shell rise for flow in the x-direction and all edges clamped.

case of high order frequencies. Except for Ref 25, where the problem was formulated using a hybrid element coupled with the classical modal superposition technique for the solution of the flutter problem, all other formulations were performed based on the total potential energy principle with the displacements taken as field variables. In Ref 7 finite element analysis of the supersonic flutter of cylindrically curved panels based on Reissner's two field variable variational principle was presented and several numerical results were given. In this section further results not given in Ref 7 are presented, namely, the effect of aspect ratio is analyzed and the flow condition parallel to the y-axis is solved.

Figures 6 to 9 summarize the results obtained in the present investigation. Figure 6 presents the critical flutter parameter λ_{cr} versus the shell rise H/h, where H is the maximum shell height and h the shell thickness, for different values of the panel aspect ratio μ of rectangular freely supported panels. The results are compared with the two mode Galerkin's solution of Voss[30] and Dowell's solution[11].

Dowell's solution is a six chordwise mode Galerkin approximation with a half-sine wave in the cross-stream direction. Dowell's solution practically coincides with the present finite element solution for the part of the curve where $n = 1$ are the critical modes for instability. Voss' two mode solution, despite being conservative, shows the same trend as the present finite element solution with increasing values of n_{cr} as the [illegible] parameter H/h increases.

Figure 7 presents the results of freely supported panels with flow in the y-direction and for different aspect ratio of the panels. In Figs 8 and 9, the same cases analyzed in Figs 6 and 7 are repeated for panels clamped on all edges.

Observing the results of Figs 6 to 9, the following conclusions can be made:

- For flows parallel to the x-direction, the critical modes of flutter are for $n = 1$ and are for the first spanwise modes. In this region the curvature effect is stabilizing in the sense that the critical dynamic pressure increases with the increase of the curvature. With further increase of the curvature, the panel passes through a transition region characterized from a flat plate behavior to a deep shell behavior. This region is characterized by the dips, knees, and cups observed in the dynamic pressure parameter versus curvature effect, and is explained by the coalescence of successive higher modes to produce the first critical flutter condition. After this transition region, with further increase in the curvature, the panel behaves as a deep shell and the critical flutter modes are those with an elevated number of waves in the cross stream direction and the first spanwise modes. In this part the shallow shell theory is no longer adequate and deep shell theory must be used. The present shallow shell theory is, therefore, limited to the flat plate and the transition part behavior of the curved panels.

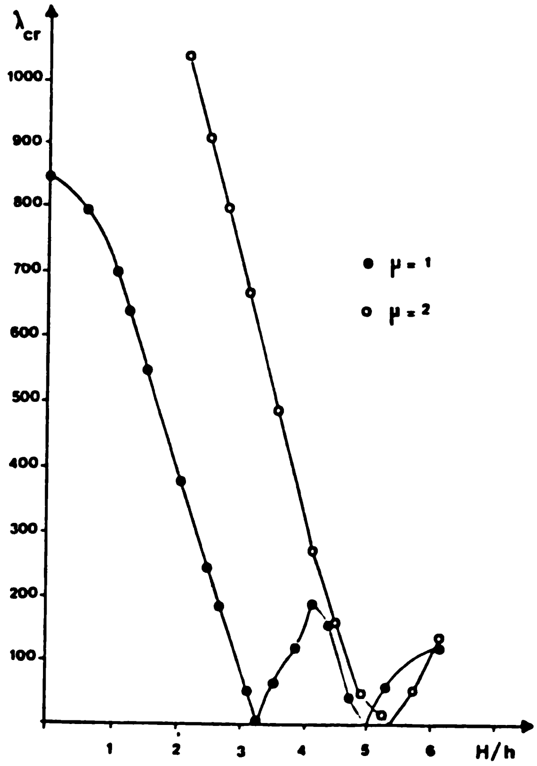

FIG 9. Flutter dynamic pressure parameter versus shell rise for flow in the y-direction and all edges clamped.

- For flow parallel to the y-direction, as can be seen from the results obtained in Figs 6 to 9, the curvature effect is destabilizing in the sense to decrease the flutter dynamic pressure with the increase of curvature. Again, this is explained by the frequency spectrum of the panel. In the transition region the panel is characterized by the same behavior demonstrated in the x-direction flow case and coalescence for successive values of n_{cr} occur.

- For clarity of the exposition, as was made in Ref 7, no damping effect, whether of structural or aerodynamic nature has been incorporated in the present formulation. If a constant viscous type structural damping and/or aerodynamic damping term pf the potential flow theory are used in the analysis, it can be shown that their effect is always stabilizing (see discussion of Ref 4) in the sense to increase the critical dynamic parameter. The effect of such dampings is small in the flat plate behavior and deep shell regions. In the transition region such dampings have a greater influence on the panel stability and remove the sharp minima or dips observed in the critical dynamic pressure parameter, which are due to coalescence of modes with nearly identical frequencies and small aerodynamic coupling.

CONCLUSIONS

Free vibration, buckling, and supersonic panel flutter analyses of cylindrically curved panels have been presented. The analyses are based on Reissner's two field variable variational principle. It is shown that the boundary conditions on Airy stress function are as simple and direct to apply as for the boundary conditions on the transverse displacement. The element used in the analyses is characterized by its high precision and direct application of the boundary conditions.

ACKNOWLEDGEMENT

Grant Number 300954/91-3 (NV) of CNPq (Conselho Nacional de Desenvolvimento Científico e Tecnológico - BRASIL) conceded to the author during the preparation of this work is gratefully acknowledged.

REFERENCES

1 - Bismarck-Nasr MN (1976), Finite element method applied to the supersonic flutter of circular cylindrical shells, *Int. J. Num. Meths. Engng.*, 10, 423-435.
2 - Bismarck-Nasr MN (1977), Finite element method applied to the flutter of two parallel elastically coupled flat plates, *Int. J. Num. Meths. Engng.*, 11, 1188-1193.
3 - Bismarck-Nasr MN (1991), On the sixteen degree of freedom rectangular plate element, *Int. J. Comp. Struct.*, 40, 1059-1060.
4 - Bismarck-Nasr MN (1992), Finite element analysis of aeroelasticity of plates and shells, *Appl. Mech. Rev.*, 45(12), Part 1, 461-482.
5 - Bismarck-Nasr MN (1993a), On vibration of thin cylindrically curved panels, *Proc. PACAM III*, São Paulo, 696-699.
6 - Bismarck-Nasr MN (1993b), Buckling analysis of cylindrically curved panels based on a two field variable variational principle, to appear in *Int. J. Compt. Struct.*
7 - Bismarck-Nasr MN (1993c), Supersonic panel flutter analysis of shallow shells, to appear in *AIAA J.*, 31.
8 - Bismarck-Nasr MN and Savio HRC (1979), Finite element solution of the supersonic flutter of conical shells, *AIAA J.*, 17, 1148-1150.
9 - Donnell LH (1934), A new theory for the buckling of thin cylinders under axial compression and bending, *ASME Trans.*, 56, 795-806.
10 - Dowell EH (1969), Nonlinear flutter of curved plates, *AIAA J.*, 7, 424-431.
11 - Dowell EH (1970), Nonlinear flutter of curved plates II, *AIAA J.*, 8, 259-261.
12 - Gallagher RH, Heinrich JC, and Sarigul N (1983), Complementary energy revisited, in *Hybrid and mixed finite element methods*, SN Atluri, RH Gallagher, and OC Zienkiewicz (eds), John Wiley, New York.
13 - Gass N and Tabarrok B (1976), Large deformation analysis of plates and cylindrical shells by a mixed finite element method, *Int. J. Num. Meths. Engng.*, 10(4), 731-746.
14 - Gerald G and Becker H (1957), Handbook of structural stability, Part III - Buckling of curved plates and shells, NACA TN-3783.
15 - Kari-Appa V and Somashekar BR (1969), Application of matrix displacement methods in the study of panel flutter, *AIAA J.*, 7, 50-53.
16 - Leissa AW, Lee JK, and Wang AJ (1981), Vibrations of cantilevered shallow cylindrical shells of rectangular planform, *J. Sound and Vibration*, 78(3), 311-328.
17 - Marguerre VK (1937), Die mittragende breite der gedrückten platte, *Luftfahrtforschung*, 14(3), 121-128.
18 - Matsuzaki V (1973), Natural vibration and flutter of cylindrically curved panels, *AIAA J.*, 11, 771-772.
19 - Mei C (1977), A finite element approach for nonlinear panel flutter, *AIAA J.*, 15, 1107-1110.
20 - Olson MD (1967), Finite elements applied to panel flutter, *AIAA J.*, 5, 2267-2270.
21 - Olson MD (1970), Some flutter solutions using finite elements, *AIAA J.*, 8, 747-751.
22 - Olson MD and Lindberg GM (1971), Dynamic analysis of shallow shells with doubly-curved triangular finite element, *J. Sound and Vibration*, 19(3), 229-318.
23 - Reissner E (1953-1954), On a variational theorem for finite elastic deformation, *J. Maths. and Physics*, 32(2-3), 129-135.
24 - Reissner E (1955), On transverse vibrations of thin shallow elastic shells, *Q. Appl. Maths.*, 13(2), 169-176.
25 - Rossetos JN and Tong P (1974), Finite element Analysis of vibration and flutter of cantilever anisotropic p' ' *Appl. Mech., Trans. ASME*, Ser E, 41, 1075-1080.

26 - Singa Rao K and Venkateswara Rao G (1983), Nonlinear supersonic flutter of panels considering shear deformation and rotary inertia, *Int. J. Compt. and Struct.*, 17, 361-364.
27 - Ueda T (1978), Nonlinear analysis of the supersonic flutter of a truncated conical shell using the finite element method, *Trans. Japan Aerospace Sci.*, 20, 225-240.
28 - Ueda T and Kobayashi S (1977), Supersonic flutter of truncated conical shells, *Trans. Japan Soc. Aerospace Sci.*, 20, 13-30.
29 - Von Kármán Th and Tsien HS (1941), The buckling of thin cylindrical shells under axial compression, *J. Aeron. Sci.*, 8(8), 303-312.
30 - Voss HM (1961), The effect of an external supersonic flow on the vibration characteristics of thin cylindrical shells, *J. of Aero/Space Sci.*, 28, 945-956, 961.
31 - Yang TY and Sung JH (1977), Finite element flutter in three dimensional supersonic unsteady potential flow, *AIAA J.*, 15, 1677-1683.
32 - Walker KP (1978), Vibrations of cambered helicoidal fan blades, *J. Sound and Vibration*, 59(1), 35-57.

New theoretical developments in aeroacoustics and aerodynamics

Mauricio Pazini Brandão

Aeronautical Engineering Division, Instituto Tecnológico de Aeronáutica
Centro Técnico Aeroespacial, 12228-900 São José dos Campos SP Brazil

The Acoustic Analogy is studied regarding its application to Aerodynamics. The concept of generalized derivatives is reviewed and extended. As consequences, new versions of the generalized continuity, momentum, energy, and energy momentum conservation equations are presented. These conservation laws form a basis for theoretical ideas regarding three-dimensional, linear and non-linear, potential and non-potential, steady and unsteady flows of incompressible and compressible, inviscid and viscous fluids. Extensions made in the definition of generalized derivatives relate fluid properties to new surface terms linked to tangential flow. In integral form, some of these relations recall the classical circulation and downwash integrals of Aerodynamics. An iterative solution technique of the resulting singular integral equations is proposed.

INTRODUCTION

In *On Sound Generated Aerodynamically, Part I – General Theory*, (1952) and *Part II – Turbulence as a source of sound*, (1954) Lighthill introduced a new theory in Acoustics. This theory, later summarized in Lighthill (1962), came to be known as *Acoustic Analogy*. Its main result may be represented by an inhomogeneous wave equation for the perturbation pressure generated by turbulence. This equation results from an exact algebraic fusion of the continuity and momentum equations. The forcing term, called quadrupole, translates into Mathematics the physical effect of fluid acting on itself as a mechanism of noise generation.

Since its introduction, the *Acoustic Analogy* has been useful not only in Aeroacoustics (see, for example, Ffowcs Williams (1984)), but also in determining the structural loading created by noise in rockets (see, for example, Ahuja (1973)). And many other applications have appeared in the pertinent literature.

The development of Lighthill was extended by Ffowcs Williams and Hawkings (1969) to include the effect of moving surfaces. Two new source terms, named in the literature monopole and dipole, appeared in this work on the right hand side of Lighthill's equation. The result allowed for the inclusion in the theory of physical mechanisms like those due to thickness displacement and pressure relaxation into the medium. Since its appearance, this analytical tool has been used to study the noise produced by the motion in the air of bodies of complicated geometry, like helicopters and prop-fans (see, for example, Farassat (1986)).

The result of Ffowcs Williams and Hawkings may be represented by an equation which combines in a single mathematical statement boundary conditions with the continuity and momentum equations. This result is in linear interpretation a wave equation for the perturbation pressure produced by bodies moving through fluids. Therefore, it has received wide acceptation among aeroacousticians.

Since aerodynamic noise is a pressure perturbation propagating through the air, with careful considerations the *Acoustic Analogy* can be applied to other contexts where pressure is the variable of interest. With this perception, Long (1983) and (1985) developed the first work in which this theory was applied to Aerodynamics. The objective was then to determine the pressure on the surface of moving bodies, something which should be realized as a limiting process in both Physics and Mathematics. This work opened a possibility of unification in the treatment of aeroacoustic and aerodynamic problems.

Long's formulation was simplified from the general context by considering the fluid inviscid and by neglecting the nonlinear quadrupole term. His results were not satisfactory, for the pressure distribution did not capture the full expansion on the surface of bodies of large thickness and some lifting effects appeared only after the adoption of *ad-hoc* computational schemes. These applications were restricted to small perturbation problems.

Brandão (1988*a*) tried in his thesis to improve on Long's results by incorporating in the interpretation of the fluid velocity vector the unknown components induced by thickness and lifting effects. The outcome of this attempt appeared in summarized form in Brandão (1989), showing that it was possible to obtain an increase in robustness of the associated computational schemes, as well as an improvement on the physical understanding of the role played by basic elements of the approach. However, this reference also showed a persistence of the above mentioned failures, indicating that the remedy for the problem was not then at hand.

Along the same line, Lee and Yang (1990) established a parallel between *Acoustic Analogy* and *Potential Aerodynamics*. With the clear admission that the equation of Ffowcs Williams and Hawkings lacked a lifting mechanism, they chose to work with a linear and inhomogeneous wave equation for the velocity potential ϕ. The results, though, continued to show the same traces of incompleteness in the description of the flow physics.

Brentner (1988) presented preliminary results of a research where lifting effects were captured with the inclusion in the formulation of the *non-linear* quadrupole term. A full account of this research can be found in his thesis (Brentner (1990)). However, his results were obtained only in the case of motion inside an incompressible fluid and need to be generalized. Furthermore, there are possibilities in which *linear* formulations may yield equivalent results. This feeling, still not proved, resulted from several recent attempts of the author (see, for example, Brandão (1991)) in investigating *non-linear* versions of the formulation, including the so-called quadrupole source term for compressible fluids. These attempts were developed in the quest for finding explanations for the previously described difficulties. Physical reasoning has led the author to the conclusion that something *basic, linear,* is missing in the formulation that might solve the problem. What has been missing should be linked to tangential flow and circulation around the body, elements which have been disregarded in previous works following this line of thought.

A more complete theory is necessary for applications to more general contexts and, perhaps, for explaining the previously mentioned failures. A wishful theory would possibly increase the number of linear sources in the Ffowcs Williams and Hawkings equation, so that linear versions of the mathematical model could still provide useful results regarding large perturbation and lifting problems. An extension to the existing theory is possible by reviewing the concept of generalized derivatives, an idea which constitutes an elegant tool for incorporating boundary conditions to differential equations. This revision appears to have reached the desired objectives.

In this paper we start by presenting new definitions on the concept of time and space generalized derivatives. From these definitions, inhomogeneous forms of the continuity, momentum, energy, and energy momentum equations are obtained. Connections between potential and non-potential theories of Aerodynamics and Aeroacoustics are then established. Finally, integral transformations of the new results are obtained and possibilities of applications are discussed.

This work intends to present recent theoretical results concerning the aeroacoustic approach to Aerodynamics. The approach may be regarded as an alternate analytical method in unsteady fluid dynamics, akin to a mixed boundary-volume element technique, which might prove useful for demanding applications in aeroelasticity.

A BRIEF REVIEW

Lighthill's acoustical equation can be obtained from an exact algebraic manipulation of the continuity and momentum equations. This equation appeared in Lighthill (1952) and reads

$$\Box^2\left[c^2(\rho-\rho_o)\right]=\frac{\partial^2\mathcal{T}_{ij}}{\partial x_i\partial x_j}$$

where

$$\Box^2=\frac{1}{c^2}\frac{\partial^2}{\partial t^2}-\frac{\partial^2}{\partial x_i\partial x_i}$$

is the D'Alembertian or wave operator,

$$\mathcal{T}_{ij}=\mathcal{P}_{ij}+\rho\, u_i u_j-\left[p_o+c^2(\rho-\rho_o)\right]\delta_{ij}$$

is the so-called Lighthill stress tensor, and c is the sound speed in the reference condition. The right hand side of this wave equation is the quadrupole term.

If the same derivation steps used to obtain Lighthill's equation are repeated, this time using the concept of generalized derivatives, the result is a more complete inhomogeneous wave equation for Lighthill's variable $c^2(\rho-\rho_o)$. This equation appeared in Ffowcs Williams and Hawkings (1969) and reads

$$\bar{\Box}^2\left[c^2(\rho-\rho_o)\right]=\frac{\bar{\partial}}{\partial t}\left[\rho_o v_n|\nabla f|\,\delta(f)\right]-\frac{\bar{\partial}}{\partial x_i}\left[\tilde{\mathcal{P}}_{ij}n_j|\nabla f|\,\delta(f)\right]+\frac{\bar{\partial}^2\mathcal{T}_{ij}}{\partial x_i\partial x_j}$$

where $\bar{\Box}^2$ stands for the generalized D'Alembertian operator. Comparing both wave equations, on the right hand side of the latter two new forcing terms appear. They are called monopole and dipole, respectively.

It can be shown (see, for example, Brandão (1991)) that in linear approximation Lighthill's variable is equivalent to the perturbation pressure p. Therefore, both equations can describe the propagation in the air of pressure waves generated by the physical mechanisms on their right hand sides.

It should be remarked that the equation of Ffowcs Williams and Hawkings, although considering information generated on the surface of a body moving in a fluid, is expressed in terms of a coordinate system fixed to the *immovable* fluid. This is not the common case in Aerodynamics, where variables of interest are usually described as viewed from a reference system fixed to the moving body. Finally, it can be observed that the surface terms are concerned only with mechanisms which act normally to the surface. Our interest here is to investigate the inclusion of tangential mechanisms of noise generation.

GENERALIZED DERIVATIVE - CONCEPT

Consider an infinite domain of quiescent fluid in standard conditions (pressure p_o, specific mass ρ_o, and temperature T_o), and an associated Cartesian coordinate system fixed to the fluid at rest. Consider inside this domain a body made out of fluid in the same standard conditions and delimited by a closed and impenetrable surface $f=0$. Therefore, except for a hypothetical surface of negligible thickness, the whole domain of interest in the problem is composed by fluid.

Note that the surface $f=0$ is in general represented by a mathematical function of space and time, and that this function can be defined uniquely, except for a multiplicative constant. This function is established so that inside the body $f<0$, and outside the body $f>0$. Thus, the gradient of f is normal to the surface and points towards the outer side of the surface, a fact which is used to construct vectors normal and tangent to the surface.

If this body moves with respect to the fixed fluid coordinate system and by hypothesis the internal fluid conditions are kept unchanged, fluid properties like pressure, density, velocity components, and temperature suffer finite jumps as we go through the surface, coming from inside. These property jumps have their greatest amplitudes close to the surface. Physical reasoning dictates that a gradual decrease in these amplitudes happens as increases the distance from the body and that disturbances should dye out completely far from the body.

Instead of considering two different domains of fluid separated by the surface $f = 0$, the idea of generalized derivative is to automatically handle these jumps by adding to the regular derivative terms valid only on the surface. Thus, a single mathematical formulation can be used to link information between the two distinct regions of fluid.

Let us consider a general fluid field property denoted by $\mathcal{F}(x_i, t)$, with $i = 1,2,3$. The generalized derivative of this function with respect to time has been defined previously (see, for example, Farassat (1977)) as

$$\frac{\bar{\partial}\mathcal{F}}{\partial t} = \frac{\partial \mathcal{F}}{\partial t} + \Delta\mathcal{F}\frac{\partial f}{\partial t}\delta(f) \tag{1}$$

where $\Delta\mathcal{F}$ represents the property jump through f, which is dictated by physical reasoning, and $\delta(f)$ stands for the Dirac delta function of the surface f. Note that the regular time derivative is recovered for all field points not on $f = 0$.

The difficulty here is that definition (1) is not unique, depending on a multiplicative constant contained implicitly inside the function f. This definition can be made unique as follows:

$$\frac{\bar{\partial}\mathcal{F}}{\partial t} = \frac{\partial \mathcal{F}}{\partial t} + \frac{\Delta\mathcal{F}}{|\nabla f|}\frac{\partial f}{\partial t}\delta(f) \tag{2}$$

because the gradient of f is defined in the whole domain and carries also the same multiplicative constant. Therefore, definition (2) is more rigorous than (1), and will be used whenever necessary in this paper.

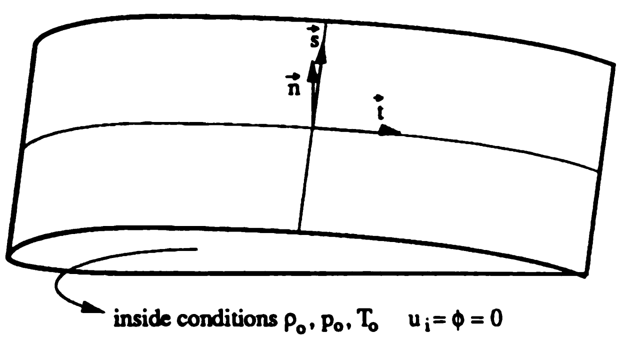

FIG 1. Definition of geometry and jump conditions.

Consider now a right-handed triad of unit vectors sitting on a point of the surface f, as depicted in Fig 1. This triad has a unit vector normal to the surface, here denoted by $\vec{n}$, and two mutually perpendicular tangential unit vectors, represented respectively by $\vec{t}$ and $\vec{s}$. Note that the directions of $\vec{t}$ and $\vec{s}$ are left free, being defined according to the problem at hand.

The generalized derivative of the fluid property $\mathcal{F}$ with respect to the spatial coordinate x_i, $i = 1,2,3$ has been defined previously (see, for example, Farassat (1977)) as

$$\frac{\bar{\partial}\mathcal{F}}{\partial x_i} = \frac{\partial \mathcal{F}}{\partial x_i} + \Delta\mathcal{F}\frac{\partial f}{\partial x_i}\delta(f) \tag{3}$$

Again, the first difficulty here is that this definition is not unique. Besides, the definition accounts only for property jumps normal to the surface.

It should be observed that a scalar property, like density, may present only normal jump across the surface. However, vector and tensor properties, like velocities and stresses, may present jumps in directions other than the normal to the surface.

To solve the problems pointed above, we propose the following alternative definition for this generalized derivative:

$$\frac{\bar{\partial}\mathcal{F}}{\partial x_i} = \frac{\partial \mathcal{F}}{\partial x_i} + \Delta\mathcal{F}\,(n_i + t_i + s_i)\,\delta(f) \tag{4}$$

Here, as before, $\Delta\mathcal{F}$ represents the fluid property jump across the surface. Furthermore,

$$n_i = \frac{1}{|\nabla f|}\frac{\partial f}{\partial x_i}$$

is the i-th component of the unit vector $\vec{n}$ normal to the surface at the point considered. The two remaining unit vectors can be obtained from the relations of orthonormality.

Note that if in this definition $\mathcal{F}$ is a vector or tensor property, from the Dirac delta term we obtain projections of these properties along the normal and tangential directions defined as shown in Fig 1.

The advantages of using definition (4) instead of (3) may be described as follows: first, the new proposition is established without ambiguity regarding surface definition; and second, it also accounts for property jumps occurring along the two tangential directions orthogonal to the normal defined at a point *on the body surface*. As we shall see, important effects may be introduced in the physics of the problem due to this extension on the concept of generalized derivatives.

CONSERVATION EQUATIONS

In Computational Fluid Dynamics it is common to work with homogeneous conservation equations, with later inclusion of forcing boundary conditions. The purpose of working with generalized derivatives is to include inhomogeneities at the very beginning of the mathematical fluid flow modeling, so that we do not have to worry about them later. Therefore, the goal of this section is to use definitions (2) and (4) to obtain generalized versions of first principles of Fluid Mechanics. Here, these principles will involve conservations of mass, momentum, energy, and energy momentum.

Continuity Equation

The equation of conservation of mass has its regular conservative form displayed as

$$\frac{\partial \rho}{\partial t} + \frac{\partial}{\partial x_i}(\rho u_i) = 0 \tag{5}$$

Here, ρ is the fluid particle specific mass (or density, according to the aerodynamicist usual parlance) in the perturbed state and u_i is the i-th component of the perturbed velocity vector related to the immovable reference system of coordinates. This is a single partial differential equation for four unknowns, namely, ρ and u_i, with $i = 1,2,3$.

If the time and space derivatives appearing in Eq (5) are generalized according to definitions (2) and (4) respectively, we obtain the following result, after collecting terms in suitable form:

$$\frac{\bar\partial \rho}{\partial t} + \frac{\bar\partial}{\partial x_i}(\rho u_i) = \left[\frac{\partial \rho}{\partial t} + \frac{\partial}{\partial x_i}(\rho u_i)\right] + \frac{\rho}{|\nabla f|}\left[\frac{\partial f}{\partial t} + u_i\frac{\partial f}{\partial x_i}\right]\delta(f) + \left[-\frac{\rho_o}{|\nabla f|}\frac{\partial f}{\partial t} + \rho\, u_i\,(t_i + s_i)\right]\delta(f) \qquad (6)$$

Above, the first square bracket on the right hand side is null because it is the regular continuity equation, which is equal to zero for all field points where it is valid. The second square bracket on the right hand side is also null due to Lamb's non-penetration condition (see Lamb (1945)). If this condition is applied again in the treatment of the third square bracket, there results

$$\frac{\bar\partial \rho}{\partial t} + \frac{\bar\partial}{\partial x_i}(\rho\, u_i) = [\rho_o\, v_n + \rho\,(v_t + v_s)]\,\delta(f) \qquad (7)$$

Here, v_n, v_t, and v_s are projections of the fluid particle velocity over the directions of the unit vectors normal and tangent to the body surface. If the body moves with velocity $\vec V$ with respect to the reference system of coordinates, due to the non-slip condition $\vec u$ is null and $\vec v = \vec V$ on the surface. However, for an inviscid fluid the projections appearing in Eq (7) are given by

$$v_n = V_i\, n_i = V_n \qquad v_t = (V_i + u_i)\, t_i = V_t + u_t$$

$$v_s = (V_i + u_i)\, s_i = V_s + u_s \qquad (8a-c)$$

because $u_n = u_i\, n_i = 0$. Thus, in any case, v_n is totally known from the motion alone, whereas in the inviscid case v_t and v_s include the unknown perturbation velocities generated by the motion.

Equation (7) is, in the present context, a generalized form of the continuity principle which presents new mechanisms of "mass generation" at the boundary $f = 0$.

Momentum Equation

The regular momentum equation in conservative form and in the absence of body forces is given by

$$\frac{\partial}{\partial t}(\rho\, u_i) + \frac{\partial}{\partial x_j}(\mathcal{P}_{ij} + \rho\, u_i\, u_j) = 0 \qquad (9)$$

Here,

$$\mathcal{P}_{ij} = p_s\, \delta_{ij} + \mathcal{E}_{ij}$$

is the compressive stress tensor which includes in its diagonal the static pressure p_s of a fluid element in the perturbed state, indicated by the Kronecker delta δ_{ij}, as well as the viscous stress tensor $\mathcal{E}_{ij}$. For a Newtonian fluid, (see Thompson (1972)) this tensor depends on the empirical viscosity coefficients μ and μ_v, called shear and bulk or volume coefficients, respectively, and on velocity gradients and divergent, as shown below:

$$\mathcal{E}_{ij} = -\mu\left(\frac{\partial u_i}{\partial x_j} + \frac{\partial u_j}{\partial x_i}\right) + \left(\frac{2}{3}\mu - \mu_v\right)\frac{\partial u_k}{\partial x_k}\,\delta_{ij}$$

Therefore, except for given viscosity coefficients, $\mathcal{E}_{ij}$ does not introduce in Eq (9) any new variables beyond those already used to describe the flow kinematics.

Equation (9) is a concise representation of three partial differential equations, each of them giving the equilibrium of momentum in the direction of one of the axes of the reference system. Together with Eq (5), Eqs (9) form a set of 4 equations with 5 unknowns, yielding a hint of the mathematical incompleteness which ultimately leads to the closure problem.

The generalization of the derivatives of Eq (9) according to Eqs (2) and (4) yields the following result after a proper algebraic arrangement:

$$\frac{\bar\partial}{\partial t}(\rho\, u_i) + \frac{\bar\partial}{\partial x_j}(\mathcal{P}_{ij} + \rho\, u_i\, u_j) = \left[\frac{\partial}{\partial t}(\rho\, u_i) + \frac{\partial}{\partial x_j}(\mathcal{P}_{ij} + \rho\, u_i\, u_j)\right] + \left[\frac{\rho\, u_i}{|\nabla f|}\left(\frac{\partial f}{\partial t} + u_j\frac{\partial f}{\partial x_j}\right)\right]\delta(f) + \left[\tilde{\mathcal{P}}_{ij}\, n_j + \left(\tilde{\mathcal{P}}_{ij} + \rho\, u_i\, u_j\right)(t_j + s_j)\right]\delta(f) \qquad (10)$$

where

$$\tilde{\mathcal{P}}_{ij} = \mathcal{P}_{ij} - p_o\delta_{ij}$$

is the perturbed compressive stress tensor, with the perturbation pressure $p = p_s - p_o$ in its diagonal.

On the right hand side of Eq (10), the first two square brackets contain the regular momentum equation and Lamb's non-penetration condition, respectively. Since both brackets vanish, we are left with

$$\frac{\bar\partial}{\partial t}(\rho\, u_i) + \frac{\bar\partial}{\partial x_j}(\mathcal{P}_{ij} + \rho\, u_i\, u_j) = \left[\tilde{\mathcal{P}}_{ij}\, n_j + \left(\tilde{\mathcal{P}}_{ij} + \rho\, v_i\, v_j\right)(t_j + s_j)\right]\delta(f) \qquad (11)$$

Equation (11) is the generalized version of the momentum equation obtained within the focus of the present work. Note that surface terms of tangential nature appear inside the equation as new "sources of momentum".

Energy Equation

In the absence of body forces, a hypothesis commonly adopted in Aerodynamics, the regular energy equation in conservative form reads

$$\frac{\partial e}{\partial t} + \frac{\partial}{\partial x_i}(e\, u_i + q_i + \mathcal{P}_{ij}\, u_j) = 0 \qquad (12)$$

Here,

$$e = \rho\, c_v\, T + \frac{1}{2}\rho\, u^2$$

is the total energy (internal plus kinetic) of a fluid element per unit of volume, c_v is the specific heat at constant volume, T is the absolute temperature of a fluid element in the perturbed state, and q_i is the i-th component of the heat flux vector.

Like the continuity equation (5), Eq (12) is another single partial differential equation involving several fluid properties. This equation introduces the temperature T

as a new variable in the set to be investigated. In addition, it accounts formally for heat transfer processes like conduction, convection, and radiation by means of the vector $\vec{q}$, which will be left undefined here because it is beyond the scope of the paper to discuss this specific subject further.

If we generalize the derivatives of Eq (12) according to the rules given by Eqs (2) and (4), we obtain

$$\frac{\bar{\partial} e}{\partial t} + \frac{\bar{\partial}}{\partial x_i}(e\,u_i + q_i + \mathcal{P}_{ij}\,u_j) =$$
$$\left[\frac{\partial e}{\partial t} + \frac{\partial}{\partial x_i}(e\,u_i + q_i + \mathcal{P}_{ij}\,u_j)\right]$$
$$+ \left[\frac{e}{|\nabla f|}\left(\frac{\partial f}{\partial t} + u_i\frac{\partial f}{\partial x_i}\right)\right]\delta(f)$$
$$+ (e_o\,v_n + q_n + \mathcal{P}_{ij}\,u_j\,n_i)\,\delta(f)$$
$$+ (e\,u_i + q_i + \mathcal{P}_{ij}\,u_j)(t_i + s_i)\,\delta(f)$$

Again, the two square brackets on the right hand side vanish. Therefore, we are left with

$$\frac{\bar{\partial} e}{\partial t} + \frac{\bar{\partial}}{\partial x_i}(e\,u_i + q_i + \mathcal{P}_{ij}\,u_j) =$$
$$[e_o\,v_n + e\,(v_t + v_s) + q_n + q_t + q_s]\,\delta(f)$$
$$+ \mathcal{P}_{ij}\,v_j\,(n_i + t_i + s_i)\,\delta(f) \qquad (13)$$

In this result, $e_o = \rho_o\,c_v\,T_o$ is the internal energy of the fluid in the reference state. This is also the *total* energy of reference, because the fluid does not move. Furthermore, $q_n = q_i\,n_i$ is the projection of the heat flux vector onto the direction normal to the body surface and similar projections are defined in the two tangential directions.

Note the similarity of structure between Eqs (7) and (13), which are two scalar equations with normal and tangential forcing terms. This similarity has sparked the question whether there would be other similarity to be established between the momentum equation, which is of vectorial nature, and other equation of interest to Fluid Mechanics. The answer to this question is discussed in the next subsection.

Energy Momentum Equation

The continuity equation can be understood as the conservation of a fluid physical property which is a moment of order zero of the fluid element mass with respect to its velocity. Thus, *mass* is a scalar property. Along this line of thought, the fluid physical property *momentum* can be regarded as a moment of first order of the fluid element mass with respect to its velocity. The momentum equation is, therefore, the mathematical statement of the physical relation between momentum and forces, being of vectorial nature. Similarly, *energy* can be considered as a second order moment of the fluid element mass with respect to its velocity. This scalar physical property has also a relation with other physical processes, involving heat and work, known as the energy equation. The question that naturally arises from this paragraph is whether there are moments of higher order which might be useful in establishing relationships among physical properties of interest in Fluid Mechanics.

The response to the question is not easily found in texts of Fluid Mechanics. In studies of turbulence (see, for example, Monin and Yaglom (1975)) we can find transport relationships of third or higher order. However, they relate fluid velocities in two or three different points, whereas here we are interested in these moments for a single fluid point. Moments of higher order of this type appear frequently in studies of Plasma Physics. See, for example, Shkanofsky and Johnston (1966) and Bernstein (1974). Here, we will limit the discussion to the third order moment, which will be denoted by eu_i and will be called *energy momentum*.

In the absence of other physical processes, which may not be of interest in problems of Fluid Mechanics, at least for low-speed flow regimes, we can state the conservation of this physical property as follows: *the rate of change of the material volume energy momentum is equal to the sum of the directional power of surface and body forces and the directional heat flux through the volume boundary.*

By directional power we should understand the power associated to a fluid element (a scalar property) animated by the corresponding fluid velocity vector. Therefore, directional power is a vectorial property. Similar understanding should be taken for the directional heat flux, by replacing the power by the normal component of the heat flux vector q_n. Mathematically, the statement of conservation, which can be viewed as a relation for the *energy acceleration*, can be written as follows:

$$\frac{d}{dt}\int_{\mathcal{V}} e\,u_i\,d\mathcal{V} = \int_{\mathcal{V}} \rho\,G_j\,u_j\,u_i\,d\mathcal{V}$$
$$+ \int_{\mathcal{S}} T_j\,u_j\,u_i\,d\mathcal{S} - \int_{\mathcal{S}} q_j\,n_j\,u_i\,d\mathcal{S} \qquad (14)$$

Here, $\rho\,G_j$ represents the j-th component of the body forces per unit of volume acting on any fluid element within the volume $\mathcal{V}$. Moreover, T_j denotes the j-th component of the surface forces per unit of area acting on the boundary $\mathcal{S}$ of the volume $\mathcal{V}$.

If we use the theorems of Reynolds and Gauss (see, for example, Thompson (1972)) together with the traditional expedient of the arbitrariness of size of the material volume, the integral conservation statement (14) can be transformed into the following differential one:

$$\frac{\partial}{\partial t}(eu_i) + \frac{\partial}{\partial x_j}(eu_iu_j) = \rho\,G_j\,u_j\,u_i$$
$$- \frac{\partial}{\partial x_j}(\mathcal{P}_{jk}\,u_k\,u_i) - \frac{\partial}{\partial x_j}(q_j\,u_i) \qquad (15)$$

In the absence of body forces, a simplification which is traditionally admitted as true in Aerodynamics, Eq (15) is reduced to

$$\frac{\partial}{\partial t}(eu_i) + \frac{\partial}{\partial x_j}(eu_iu_j + \mathcal{P}_{jk}\,u_k\,u_i + q_j\,u_i) = 0 \qquad (16)$$

This is the expression for the regular equation of energy momentum in conservative form. Rates of change of energy momentum are related to its transport, power of shear and normal forces, and heat transfer processes. Note the resemblance between the structure of Eqs (9) and (16), which are both of vectorial nature.

If we now transform the regular derivatives of Eq (16) into generalized ones, according to Eqs (2) and (4), we obtain

$$\frac{\bar{\partial}}{\partial t}(eu_i) + \frac{\bar{\partial}}{\partial x_j}(eu_iu_j + \mathcal{P}_{jk}\,u_k\,u_i + q_j\,u_i) =$$

$$\left[\frac{\partial}{\partial t}(eu_i) + \frac{\partial}{\partial x_j}(eu_iu_j + \mathcal{P}_{jk}\,u_k\,u_i + q_j\,u_i)\right]$$
$$+ \left[\frac{eu_i}{|\nabla f|}\left(\frac{\partial f}{\partial t} + u_j\,\frac{\partial f}{\partial x_j}\right)\right]\,\delta(f)$$
$$+ (q_n\,u_i + \mathcal{P}_{jk}\,u_k\,u_i\,n_j)\,\delta(f)$$
$$+ (eu_iu_j + q_ju_i + \mathcal{P}_{jk}u_ku_i)\,(t_j + s_j)\,\delta(f)$$

Deleting the two square brackets on the right hand side, based on the same arguments given before, there results

$$\frac{\bar{\partial}}{\partial t}(eu_i) + \frac{\bar{\partial}}{\partial x_j}(eu_iu_j + \mathcal{P}_{jk}\,u_k\,u_i + q_j\,u_i) =$$
$$[ev_i\,(v_t + v_s) + v_i\,(q_n + q_t + q_s)]\,\delta(f)$$
$$+ \mathcal{P}_{jk}\,v_k\,v_i\,(n_j + t_j + s_j)\,\delta(f) \qquad (17)$$

As expected, Eq (16) can be retrieved from Eq (17) if there are no surfaces of discontinuity in the flow. Equation (17) is the generalized form of the energy momentum equation derived within the present focus. This inhomogeneous partial differential equation states that changes of energy momentum are forced by boundary mechanisms which act normally and tangentially to the discontinuity surface. This idea, presented in preliminary form by Brandão (1988*b*), is here extended to a more general context.

A comparison between the generalized conservation equations here displayed with their previous counterparts shows that the inhomogeneous normal terms are now uniquely defined and that tangential terms are added as sources of mass, momentum, energy, and energy momentum. These results are consequences of the new definitions of the generalized derivatives with respect to time and space.

As a final remark, it may be observed that the conservation laws here presented are also valid for problems involving multiple bodies. In a wind tunnel, for example, the surface f may incorporate the body-fluid boundary of a testing model, as well as of the testing section walls. This possibility was successfully explored by Medeiros and Brandão (1991). For high-speed flows, shock surfaces may also be considered as additional sources of discontinuity, as described by Farassat (1987). Therefore, the generality of the present approach allows application of these results to both external and internal flows, ranging from the incompressible to the supersonic case.

POTENTIAL FLOW CONNECTIONS

A general approach should allow its reduction to simpler contexts. This approach is called *non-potential* because it makes no use of hypotheses of potentiality and also, because viscosity effects appear explicitly within the tensors $\mathcal{E}_{ij}$ and $\mathcal{P}_{ij}$. Here, we explore the [illegible] ally the simplification of the method to the w[illegible] ential theory framework, for the case of inc[illegible] d compressible fluids.

Incompressible fluids

Equation (5), when specialized for an incompressible fluid, reads simply

$$\frac{\partial u_i}{\partial x_i} = 0 \qquad (18)$$

If now we admit the existence of a potential function ϕ whose gradient yields the perturbation velocity vector, Eq (18) becomes the classical Laplacian equation

$$\frac{\partial^2\phi}{\partial x_i\partial x_i} = 0 \qquad (19)$$

The idea here is to generalized the derivatives of this equation.

If we consider that by hypothesis the velocity potential ϕ is equal to zero in the reference condition, as shown in Fig 1, according to definition (4), the first generalized derivative of the velocity potential with respect to the spatial coordinate x_i is given by

$$\frac{\bar{\partial}\phi}{\partial x_i} = \frac{\partial\phi}{\partial x_i} + \phi\,(n_i + t_i + s_i)\,\delta(f)$$

The second generalized derivative then yields

$$\frac{\bar{\partial}^2\phi}{\partial x_i\partial x_i} = \frac{\bar{\partial}}{\partial x_i}\left[\frac{\partial\phi}{\partial x_i} + \phi\,(n_i + t_i + s_i)\,\delta(f)\right]$$
$$= \frac{\partial^2\phi}{\partial x_i\partial x_i} + \left[\frac{\partial\phi}{\partial x_i}(n_i + t_i + s_i)\right]\delta(f)$$
$$+ \frac{\bar{\partial}}{\partial x_i}[\phi\,(n_i + t_i + s_i)\,\delta(f)]$$

If we now use Eq (19) and the velocity potential definition, the generalized Laplacian equation which governs the mass effects in incompressible fluids reads as follows:

$$\frac{\bar{\partial}^2\phi}{\partial x_i\partial x_i} = (v_n + v_t + v_s)\,\delta(f)$$
$$+ \frac{\bar{\partial}}{\partial x_i}[\phi\,(n_i + t_i + s_i)\,\delta(f)] \qquad (20)$$

This is a Poisson equation which incorporates normal and tangential boundary conditions. As it stands, the equation does not allow an immediate analytical or computational treatment due to the presence of Dirac delta terms of the surface function f on its right hand side. An integral transformation of the equation is required *a priori* to permit this objective to be achieved.

According to Morse and Feshbach (1953), the basic solution to the Poisson problem

$$\nabla^2\mathcal{G} = \frac{\partial^2\mathcal{G}}{\partial x_i\partial x_i} = \delta\left(\vec{X}(x_i,t) - \vec{Y}(x_i,t)\right)$$

reads

$$\mathcal{G}\left(\vec{X},\vec{Y},t\right) = -\frac{1}{4\pi r} \qquad (21)$$

where r is the distance between a source point at position $\vec{Y}(x_i,t)$ and the observer point at position $\vec{X}(x_i,t)$, that is, $r = |\vec{X}(x_i,t) - \vec{Y}(x_i,t)|$. This is the basic Green's function of Laplace's equation for the unbounded domain $\mathcal{V}$.

From here, a formal solution for Eq (20) can be constructed as follows:

$$\phi = -\frac{1}{4\pi}\int_{\mathcal{V}} \frac{v_n + v_t + v_s}{r}\,\delta(f)\,d\mathcal{V} - \frac{1}{4\pi}\frac{\bar{\partial}}{\partial x_i}\int_{\mathcal{V}} \frac{\phi\,(n_i + t_i + s_i)}{r}\,\delta(f)\,d\mathcal{V} \qquad (22)$$

The element of volume $d\mathcal{V}$ which appears in Eq (22) may be expressed in various forms. Among them, the most convenient to our purpose is the one which considers elements of distance conformed to the body surface and centered on the source point, as depicted in Fig 2, that is,

$$d\mathcal{V} = d\eta\, d\xi\, d\zeta = d\eta\, dS$$

Here, $d\eta$ is an element of distance along $\vec{n}$ from the surface source, whereas $d\xi$ and $d\zeta$ are elements of distance along the curvilinear coordinate axes locally tangent to $\vec{t}$ and $\vec{s}$ respectively, so that their product yields an element of area dS of the body surface.

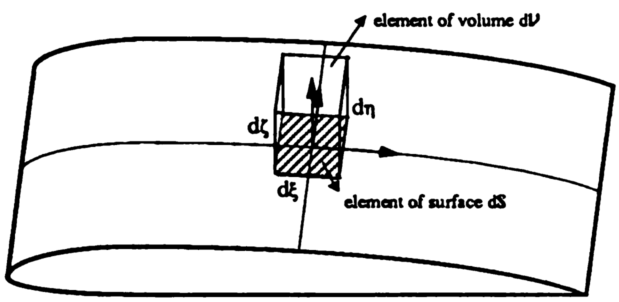

FIG 2. Body-fitted volume element.

With this geometrical set-up, Eq (22) assumes the following form:

$$\phi = -\frac{1}{4\pi}\int_{f=0}\int_0^{\infty} \frac{v_n + v_t + v_s}{r}\,\delta(f)\,dS\,d\eta - \frac{1}{4\pi}\frac{\bar{\partial}}{\partial x_i}\int_{f=0}\int_0^{\infty} \frac{\phi\,(n_i + t_i + s_i)}{r}\,\delta(f)\,dS\,d\eta \qquad (23)$$

Since the domain of integration on η contains the surface $f = 0$, which is equivalent to the lower bound $\eta = 0$, an operational property of the Dirac delta function of f allows us to reduce Eq (23) to

$$\phi = -\frac{1}{4\pi}\int_{f=0} \frac{v_n + v_t + v_s}{r}\,dS - \frac{1}{4\pi}\frac{\bar{\partial}}{\partial x_i}\int_{f=0} \frac{\phi\,(n_i + t_i + s_i)}{r}\,dS \qquad (24)$$

One could choose to solve this integro-differential equation for the velocity potential. The unknown variable ϕ appears independently and also inside both integrands on the right hand side. A numerical solution is possible by iteration, having as starting condition the known motion of the body with respect to the reference coordinate system, as well as a reasonable guess for the unknown velocity potential ϕ on the body surface. Note that Eq (24), although driven by surface information only, as it should, is valid for all field points.

One could also choose to differentiate Eq (24) to obtain a governing equation for the perturbation velocity component u_i. This choice may be motivated by the fact that is physically more appealing to work with velocities than with potentials. Then, if we take the gradient of ϕ in Eq (24), we obtain the following result:

$$u_i = -\frac{1}{4\pi}\frac{\partial}{\partial x_i}\int_{f=0} \frac{v_n + v_t + v_s}{r}\,dS - \frac{1}{4\pi}\frac{\partial\bar{\partial}}{\partial x_i \partial x_j}\int_{f=0} \frac{\phi\,(n_j + t_j + s_j)}{r}\,dS \qquad (25)$$

This equation relates a perturbed velocity component u_i to integrals on the surface of the moving body, having the motion kinematics as major information. If we replace v_n, v_t, and v_s by their expanded inviscid versions given by Eqs $(8a - c)$ and we keep on the left hand side what is unknown, the Eq (25) above can be expressed as the following integro-differential equation:

$$4\pi u_i + \frac{\partial}{\partial x_i}\int_{f=0} \frac{u_t + u_s}{r}\,dS + \frac{\partial\bar{\partial}}{\partial x_i \partial x_j}\int_{f=0} \frac{\phi\,(n_j + t_j + s_j)}{r}\,dS = -\frac{\partial}{\partial x_i}\int_{f=0} \frac{V_n + V_t + V_s}{r}\,dS \qquad (26)$$

where the meaning of the five velocity projections is now intuitive. Taking the velocity component u_i as reference, a result like this is known in the mathematical nomenclature as an integral equation of the Fredholm type, of the second kind, because the unknown u_i appears independently and inside one integrand on the left hand side. However, Eq (26) is a little bit more complicated than that, in the sense that it also includes another unknown, namely, the velocity potential ϕ.

If the body surface is smooth, we are allowed to replace the generalized derivatives of the surface integrals by regular ones and to commute the differential and integral operators. Then, we can rewrite Eq (26) symbolically as

$$4\pi u_i + \int_{f=0} \bar{\mathcal{K}}_{u_i}\,dS + \int_{f=0} \bar{\mathcal{K}}_{\phi_i}\,dS = -\int_{f=0} \bar{\mathcal{K}}_{V_i}\,dS \qquad (27)$$

where

$$\bar{\mathcal{K}}_{u_i} = \frac{\partial}{\partial x_i}\left[\frac{u_t + u_s}{r}\right]$$

$$\bar{\mathcal{K}}_{\phi_i} = \frac{\partial^2}{\partial x_i \partial x_j}\left[\frac{\phi\,(n_j + t_j + s_j)}{r}\right]$$

$$\bar{\mathcal{K}}_{V_i} = \frac{\partial}{\partial x_i}\left[\frac{V_n + V_t + V_s}{r}\right]$$

Note that Eq (27) represents a set of three linear equations for four unkonwns, namely, the three velocity components u_i and the velocity potential ϕ. Numerical solutions of this set can be obtained in an iterative fashion. To start the process, the unknown integrals on the left hand side can be ignored and the equations solved only for the known input on the right hand side. In the next iteration, the solution of the previous iteration can be plugged into the unknown integrals, and the process assessed with respect to convergence. To speed up the process, reasonable guesses for the perturbed velocity field and its potential can be prescribed in the first iteration in order to render known the integrands $\mathcal{K}_{u_i}$ and $\mathcal{K}_{\phi_i}$. Once a solution is achieved, the field pressure distribution can be obtained by means of a steady or unsteady version of Bernoulli's equation.

The success of these propositions are still to be evaluated with practical applications. However, since perturbation velocities are small compared to the velocity of reference, the greatest input in the process is already known and appears as the driving term on the right hand side of Eq (27). Perturbation techniques in Aerodynamics have long suffered when the starting point was a homogeneous equation. Here, the starting point is the solution of an inhomogeneous equation and, hopefully, closer to the final answer.

An important remark to be made here is that, for a two-dimensional problem, the surface integrals appearing in Eq (27) become closed line integrals along the cross section boundary. In this case, the integral with the tangential velocity term is linked to the classical circulation integral (see, for example, Karamchetti (1973)), whereas the other integral on ϕ may be connected to the classical downwash integral (see, for example, Mangler (1951)). Therefore, known lifting mechanisms have been introduced in the formulation and this inclusion is evident at its simplest framework. The validity of this statement wil be checked in future applications of this approach.

Compressible fluids

It is known in Compressible Aerodynamics that a sequence of derivation steps involving the regular continuity and momentum equations, with the help of a thermodynamic relation between pressure and density, leads to the so-called full-potential equation. Linearization of the complete, non-linear equation yields the convected wave equation for an observer on the body surface or the acoustical wave equation for an observer in the fixed fluid frame of reference. If exactly the same ingredients are used in the recipe, but now under generalized form, a new result can be obtained. However, in complete form the result is lengthy and cumbersome. In order to show connections between the present approach and already established theories, here we will choose to study the simplified framework of small perturbation problems.

The governing equation now is the wave equation

$$\Box^2\phi = \frac{1}{c^2}\frac{\partial^2\phi}{\partial t^2} - \frac{\partial^2\phi}{\partial x_i \partial x_i} = 0 \tag{28}$$

The generalized version of the Laplacian operator is given by Eq (20). According to Eq (2), the first generalized derivative of ϕ with respect to time is given by

$$\frac{\bar\partial\phi}{\partial t} = \frac{\partial\phi}{\partial t} + \frac{\phi}{|\nabla f|}\frac{\partial f}{\partial t}\,\delta(f)$$

Then, the second generalized derivative yields

$$\frac{\bar\partial^2\phi}{\partial t^2} = \frac{\bar\partial}{\partial t}\left[\frac{\partial\phi}{\partial t} + \right. \qquad =$$

$$\frac{\partial^2\phi}{\partial t^2} + \left[\frac{\partial\phi}{\partial t}\frac{1}{|\nabla f|}\frac{\partial f}{\partial t}\right]\delta(f) + \frac{\bar\partial}{\partial t}\left[\frac{\phi}{|\nabla f|}\frac{\partial f}{\partial t}\,\delta(f)\right]$$

$$= -\frac{\partial\phi}{\partial t}\,v_n\,\delta(f) - \frac{\bar\partial}{\partial t}\left[\phi\, v_n\,\delta(f)\right]$$

with the help of Eq (28) and Lamb's non-penetration condition. If we join this result accordingly with Eq (20), we obtain

$$\bar\Box^2\phi = -(v_n + v_t + v_s)\,\delta(f) - \frac{\bar\partial}{\partial x_i}\left[\phi\,(n_i + t_i + s_i)\,\delta(f)\right]$$

$$-\frac{1}{c^2}\left\{\frac{\partial\phi}{\partial t}\,v_n\,\delta(f) + \frac{\bar\partial}{\partial t}\left[\phi\,v_n\,\delta(f)\right]\right\} \tag{29}$$

Note that Eq (20), the incompressible limit of Eq (29), is recovered if we let the sound speed c go to infinity.

According to Morse and Feshbach (1953), the basic solution of the wave problem in unbounded domain

$$\Box^2\mathcal{G} = \frac{1}{c^2}\frac{\partial^2\mathcal{G}}{\partial t^2} - \frac{\partial^2\mathcal{G}}{\partial x_i x_i} = \delta(t-\tau)\,\delta\left(\vec{X}(x_i,t) - \vec{Y}(x_i,\tau)\right)$$

is given by

$$\mathcal{G}\left(\vec{X},\vec{Y},t,\tau\right) = \frac{\delta(g)}{4\pi r} \tag{30}$$

In this solution, $\delta(g)$ is the Dirac delta function of a sphere $g = t - \tau - r/c = 0$ of information triggered at a source position $\vec{Y}(x_i,\tau)$ at retarded time $\tau = t - r/c$ and received at an observer position $\vec{X}(x_i,t)$ at actual time t. In addition, $r = |\vec{X}(x_i,t) - \vec{Y}(x_i,\tau)|$ is the distance traveled by the information with constant speed c. As we can see, this model reproduces what happens in nature with propagation of perturbations in compressible fluids.

The application of the solution (30) to the governing equation (29) yields the following transformation:

$$4\pi\phi = -\int_{-\infty}^{t}\int_{\mathcal{V}}\frac{v_n + v_t + v_s}{r}\,\delta(f)\,\delta(g)\,d\mathcal{V}\,d\tau$$

$$-\frac{\bar\partial}{\partial x_i}\int_{-\infty}^{t}\int_{\mathcal{V}}\frac{\phi\,(n_i + t_i + s_i)}{r}\,\delta(f)\,\delta(g)\,d\mathcal{V}\,d\tau$$

$$-\frac{1}{c^2}\int_{-\infty}^{t}\int_{\mathcal{V}}\frac{\partial\phi}{\partial t}\frac{v_n}{r}\,\delta(f)\,\delta(g)\,d\mathcal{V}\,d\tau$$

$$-\frac{1}{c^2}\frac{\bar\partial}{\partial t}\int_{-\infty}^{t}\int_{\mathcal{V}}\frac{\phi\,v_n}{r}\,\delta(f)\,\delta(g)\,d\mathcal{V}\,d\tau$$

The integration on τ yields (see Brandão (1989))

$$4\pi\phi = -\int_{\mathcal{V}}\left[\frac{v_n + v_t + v_s}{r}(1 + M_r)\right]_{\text{ret}}\delta(f)\,d\mathcal{V}$$

$$-\frac{\bar\partial}{\partial x_i}\int_{\mathcal{V}}\left[\frac{\phi\,(n_i + t_i + s_i)}{r}(1 + M_r)\right]_{\text{ret}}\delta(f)\,d\mathcal{V}$$

$$-\frac{1}{c^2}\int_{\mathcal{V}}\left[\frac{\partial\phi}{\partial t}\frac{v_n}{r}(1 + M_r)\right]_{\text{ret}}\delta(f)\,d\mathcal{V}$$

$$-\frac{1}{c^2}\frac{\bar\partial}{\partial t}\int_{\mathcal{V}}\left[\frac{\phi\,v_n}{r}(1 + M_r)\right]_{\text{ret}}\delta(f)\,d\mathcal{V}$$

where $M_r = v_r/c = (v_i r_i)/(cr)$ is the source Mach vector projected onto the direction of propagating information (from source to observer). Here, for the purpose of demonstration only, it is admitted that the entire flowfield is subsonic. Moreover, the subscript "ret" means that during the convolution the information coming from a source and arriving at time t at the observer should be taken as having been emitted at the corresponding retarded time τ. If we now consider the volume integration as performed in the last subsection, we obtain

$$\begin{aligned}4\pi\phi = &-\int_{f=0}\left[\frac{v_n + v_t + v_s}{r}(1+M_r)\right]_{\text{ret}} dS \\ &-\frac{\bar{\partial}}{\partial x_i}\int_{f=0}\left[\frac{\phi(n_i+t_i+s_i)}{r}(1+M_r)\right]_{\text{ret}} dS \\ &-\frac{1}{c^2}\int_{f=0}\left[\frac{\partial\phi}{\partial t}\frac{v_n}{r}(1+M_r)\right]_{\text{ret}} dS \\ &-\frac{1}{c^2}\frac{\bar{\partial}}{\partial t}\int_{f=0}\left[\frac{\phi\, v_n}{r}(1+M_r)\right]_{\text{ret}} dS \qquad (31)\end{aligned}$$

One can choose to solve this integro-differential equation for the velocity potential ϕ or, as indicated for the incompressible case, to take its derivative and solve the result for the velocity component u_i. In the second case, if the body surface is smooth, we can rewrite Eq (31) in the following symbolic form:

$$\begin{aligned}4\pi u_i + \int_{f=0}\mathcal{K}_{u_i}\, dS + \int_{f=0}\mathcal{K}_{\phi_i}\, dS + \int_{f=0}\mathcal{K}_{\dot{\phi}M_i}\, dS \\ + \int_{f=0}\mathcal{K}_{\phi M_i}\, dS = -\int_{f=0}\mathcal{K}_{V_i}\, dS \qquad (32)\end{aligned}$$

where

$$\mathcal{K}_{u_i} = \frac{\partial}{\partial x_i}\left[\frac{u_t+u_s}{r}(1+M_r)\right]_{\text{ret}}$$

$$\mathcal{K}_{\phi_i} = \frac{\partial^2}{\partial x_i \partial x_j}\left[\frac{\phi(n_j+t_j+s_j)}{r}(1+M_r)\right]_{\text{ret}}$$

$$\mathcal{K}_{\dot{\phi}M_i} = \frac{\partial}{\partial x_i}\left[\frac{\partial\phi}{\partial t}\frac{M_n}{c\,r}(1+M_r)\right]_{\text{ret}}$$

$$\mathcal{K}_{\phi M_i} = \frac{\partial^2}{\partial x_i \partial t}\left[\frac{\phi\, M_n}{c\,r}(1+M_r)\right]_{\text{ret}}$$

$$\mathcal{K}_{V_i} = \frac{\partial}{\partial x_i}\left[\frac{V_n+V_t+V_s}{r}(1+M_r)\right]_{\text{ret}}$$

When comparing Eq (32) with its incompressible counterpart (Eq (27)), we observe that compressible effects appear in this mathematical model by means of

- the subsonic Doppler magnification factor $(1+M_r)$ shown inside all integrands;
- the consideration of the contents of all integrands at retarded time τ during integration; and
- the inclusion of the $\mathcal{K}_{\phi M_i}$ and $\mathcal{K}_{\dot{\phi}M_i}$ integrals in the equation.

As discussed for the incompressible model, the integro-differential equation (32) can be solved by iteration. To start the process, for a given motion the $\mathcal{K}_{V_i}$ integral is totally known and the $\mathcal{K}_{u_i}$, $\mathcal{K}_{\phi_i}$, $\mathcal{K}_{\phi M_i}$, and $\mathcal{K}_{\dot{\phi}M_i}$ can be estimated. Then, the velocity field can be computed and the answer compared to the estimate of the previous step. If convergence is not reached under a certain criterion, the process goes over another cycle and so on. From the velocity field we can proceed to compute pressure and temperature distributions.

Equation (29) and its integral solution (31) is more complete in terms of boundary sources than the one used by Lee and Yang (1990) to determine via a panel method the pressure distribution on the surface of rotating bodies and airfoils in the subsonic regime. Their governing equation can be obtained from Eq (29) if the v_t, v_s, t_i, and s_i terms are deleted.

The results obtained by Lee and Yang show a certain difficulty in capturing the full expansion on the surface of an ONERA rotor blade in the non-lifting case. The same difficulty is apparent for the pressure distribution on a NACA 0012 blade in a lifting condition. It is possible that they have experienced the same problems encountered by Long (1985) with large expansions and application of the Kutta condition to simulate viscosity effects. The new terms in Eq (29), linked to tangential information on the surface, may help in obtaining better correlation between theoretical and experimental results, thus, proving the adequacy of the approach for subsonic potential flows.

The incompressible model expressed by Eq (27), derived from the continuity equation, has no free-field contribution. The linear compressible model given by Eq (29), derived from the continuity and momentum equations, also has only surface contributions. Lee and Yang reported the adoption of dipoles in the wake to capture lift, a viable, though somewhat arbitrary measure. Had we considered the full potential equation as starting point, non-linear and well-defined volume and surface contributions would appear. Therefore, even better correlations can be obtained if the generalized version of the full potential equation is used. Besides, the applicability of the approach can then be extended into the transonic regime. An exploration of this issue is left for future studies regarding the present technique.

NON-POTENTIAL FLOW CONNECTIONS

The ultimate goal of the aerodynamicist is to solve the fluid mechanics about a body of given geometry in motion relative to the air, so that from this solution useful information can be extracted. Among what can be deemed useful certainly lies pressure and thermal loading, used to design the body shape and to analyze its performance in motion. When dealing with the concept of velocity potential, once a solution is obtained, we have to advance to velocity, then to pressure, and, finally, to temperature. In the last section we established connections of the present approach to the potential theory framework, so that a more direct formulation for velocity was obtained in the incompressible and compressible cases. The objective in this section is to proceed with these developments, now considering the complete physics given by the conservation laws. We will derive in this section two governing equations, one for pressure and another for energy propagation. There are no potential assumptions made in these derivations.

A governing equation for pressure

If exactly the same derivation steps leading to the equation of Ffowcs Williams and Hawkings are repeated, but, this time, using as major components the conservation laws (7) and (11), an even more complete governing equation can be obtained. The completeness here should be understood in the following senses:

- with respect to potential theory, the result includes fluid viscosity and should be regarded as a concise statement of the Navier-Stokes framework.
- with respect to the Ffowcs Williams and Hawkings equation, the result contains new source terms of tangential discontinuity and better definition of source terms of normal jump.

For the sake of completeness, the derivation of the governing equation occurs as described below:

1. Take the generalized time derivative of both sides of the continuity equation (7).
2. Take the generalized derivative of both sides of the momentum equation (11) with respect to x_i.
3. Subtract the result of the previous step from the result of step 1.
4. Subtract from both sides the term $c^2\,\bar{\nabla}^2\rho$.
5. Subtract from the result obtained in step 4 the following identity: $\bar{\Box}^2 c^2\rho_o = -\,c^2\,\bar{\nabla}^2\rho_o$.
6. Replace, where applicable, $\mathcal{P}_{ij}$ by $\tilde{\mathcal{P}}_{ij}$ in order to remove constants and work only with perturbations.

The result we are envisioning reads as follows:

$$\bar{\Box}^2\left[c^2(\rho-\rho_o)\right] = \frac{\bar{\partial}}{\partial t}\left[\rho_o v_n + \rho\,(v_t+v_c)\,\delta(f)\right] - \frac{\bar{\partial}}{\partial x_i}\left[\tilde{\mathcal{P}}_{ij}\,(n_j+t_j+s_j)\,\delta(f)\right] - \frac{\bar{\partial}}{\partial x_i}\left[\rho v_i\,(v_t+v_s)\,\delta(f)\right] + \frac{\bar{\partial}^2\mathcal{T}_{ij}}{\partial x_i\partial x_j} \tag{33}$$

With respect to the Ffowcs Williams and Hawkings equation, Eq (33) introduces two tangential mechanisms of perturbation generation which might be important in some problems of Fluid Mechanics. The new terms reinforce the monopole and dipole behaviors of sound directivity. Furthermore, the normal terms are now better defined, removing ambiguities created in the establishment of the surface function f.

The result represented by Eq (33) is quite general. It allows, among other possibilities, the limiting case where the fluid becomes incompressible. Letting c go to infinity, we obtain

$$\bar{\nabla}^2 p = -\frac{\bar{\partial}}{\partial t}\left[\rho_o\,(v_n+v_t+v_c)\,\delta(f)\right] - \frac{\bar{\partial}^2\bar{\mathcal{T}}_{ij}}{\partial x_i\partial x_j} + \frac{\bar{\partial}}{\partial x_i}\left\{\left[\tilde{\mathcal{P}}_{ij}\,(n_j+t_j+s_j)\qquad\right]\delta(f)\right\} \tag{34}$$

with

$$\bar{\mathcal{T}}_{ij} = \mathcal{E}_{ij} + \rho_o\,u_i\,u_j$$

This limit can find practical applications to low speed motions in air or to motions inside nearly incompressible fluids, like water.

Equations (33) and (34) involve boundary terms which can be handled more easily after integration processes. These mathematical operations are also useful to allow a practical interpretation of the $\delta(f)$ terms. If we make use of the Green's functions (30) and (21) for the wave and Laplace equations, respectively, and of other analytical tools applied in the last section, the integrated results are given by

$$\begin{aligned}4\pi c^2(\rho-\rho_o) + \frac{\bar{\partial}}{\partial x_i}\int_{f=0}\left[\frac{\tilde{\mathcal{P}}_{ij}(n_j+t_j+s_j)}{r}(1+M_r)\right]_{\text{ret}} d\mathcal{S} &= \frac{\bar{\partial}}{\partial t}\int_{f=0}\left[\frac{\rho_o v_n + \rho(v_t+v_s)}{r}(1+M_r)\right]_{\text{ret}} d\mathcal{S} \\ &\quad - \frac{\bar{\partial}}{\partial x_i}\int_{f=0}\left[\frac{\rho\,v_i(v_t+v_s)}{r}(1+M_r)\right]_{\text{ret}} d\mathcal{S} \\ &\quad + \frac{\bar{\partial}^2}{\partial x_i\partial x_j}\int_{\mathcal{V}}\left[\frac{\mathcal{T}_{ij}}{r}(1+M_r)\right]_{\text{ret}} d\mathcal{V}\end{aligned} \tag{35}$$

for the compressible case and

$$\begin{aligned}4\,\pi\,p + \frac{\bar{\partial}}{\partial x_i}\int_{f=0}\frac{\tilde{\mathcal{P}}_{ij}(n_j+t_j+s_j)}{r}\,d\mathcal{S} = {}& \frac{\bar{\partial}}{\partial t}\int_{f=0}\frac{\rho_o(v_n+v_t+v_s)}{r}\,d\mathcal{S} + \frac{\bar{\partial}^2}{\partial x_i\partial x_j}\int_{\mathcal{V}}\frac{\bar{\mathcal{T}}_{ij}}{r}\,d\mathcal{V} \\ &- \frac{\bar{\partial}}{\partial x_i}\int_{f=0}\frac{\rho_o v_i(v_t+v_s)}{r}\,d\mathcal{S}\end{aligned} \tag{36}$$

for the incompressible limit.

Now comes a critical issue. The Green's functions (21) and (30) are intrinsically singular. If derivatives of these solutions are taken, there result stronger singularities which cannot find interpretation in the ordinary sense, but can have meaning in the sense defined by Hadamard (1952). It is a matter of choice taking the derivatives before or after integration. Brandão (1987) and (1990) has shown that for better computing efficiency, which comprises both accuracy and time spent on numerical computations, it is always preferable to derive a singular integral and to handle its finite-part later than to compute the singular integral and to obtain later its numerical derivative.

With the singular integration issue in mind, Eq (35) can be written symbolically as

$$4\pi c^2(\rho-\rho_o) + \int_{f=0}\mathcal{K}^p_{\mathcal{S}}\,d\mathcal{S} = \int_{f=0}\mathcal{K}^v_{\mathcal{S}}\,d\mathcal{S} + \int_{\mathcal{V}}\mathcal{K}^v_{\mathcal{V}}\,d\mathcal{V} \tag{37}$$

This represents a *non-linear* integral equation for the perturbation pressure p, forced by velocity dependent boundary and volume integrals. Above, $\mathcal{K}^p_{\mathcal{S}}$ denotes a singular surface kernel for p, with a weak dependence on the velocity field. On the right hand side, $\mathcal{K}^v_{\mathcal{S}}$ symbolizes a singular surface kernel which depends on the velocity field only, whereas $\mathcal{K}^v_{\mathcal{V}}$ represents a singular volume kernel

INVISCID FLUIDS

The continuity equation (7) is valid for a compressible fluid and requires no specialization regarding viscosity. On the other hand, the momentum equation (11) for the inviscid case is reduced to

$$\frac{\bar{\partial}}{\partial t}(\rho u_i) + \frac{\bar{\partial}}{\partial x_j}(p\,\delta_{ij} + \rho\, u_i\, u_j) =$$

$$[p\,(n_i + t_i + s_i) + \rho\, v_i\,(v_t + v_s)]\,\delta(f) \tag{41}$$

From these four basic equations, a single wave equation can be obtained following the same steps described for the derivation of Eq (33). The result yields

$$\bar{\Box}^2\left[c^2(\rho - \rho_o)\right] = \frac{\bar{\partial}}{\partial t}\left[\rho_o v_n + \rho\,(v_t + v_c)\,\delta(f)\right]$$

$$-\frac{\bar{\partial}}{\partial x_i}\left[p\,(n_i + t_i + s_i)\,\delta(f)\right] + \frac{\bar{\partial}^2 t_{ij}}{\partial x_i \partial x_j}$$

$$-\frac{\bar{\partial}}{\partial x_i}\left[\rho v_i\,(v_t + v_s)\,\delta(f)\right] \tag{42}$$

where

$$t_{ij} = \rho\, u_i\, u_j + \left[p - c^2(\rho - \rho_o)\right]\delta_{ij} \tag{43}$$

is the inviscid version of Lighthill's stress tensor.

Equation (42) is a *non-linear* relation between the perturbation pressure p and several other fluid properties. The non-linearity is built inside Lighthill's variable $c^2(\rho - \rho_o)$ which also appears in the definition of t_{ij}, as given by Eq (43). For example, from a series expansion for Lighthill's variable given by Brandão (1991) we can rewrite this stress tensor as

$$t_{ij} \approx \rho\, u_i\, u_j + \frac{\gamma - 1}{2\,\rho_o\, c^2}\, p^2 \delta_{ij}$$

where $\gamma = c_p/c_v$ is the ratio between specific heat coefficients at constant pressure and volume. It is easily perceived that the non-linear pressure term is small in magnitude due to the squared perturbation pressure in its numerator and to the squared sound speed term in its denominator.

This non-linearity is equivalent, within compressible potential theory, to consider the sound speed c variable from point to point in the field, according to its thermodynamic state. This is *not* the case in the present approach, since here c is the speed of sound in the reference condition and, therefore, a constant. From this discussion, if the problem at hand excites only small perturbations, we are allowed to disregard this non-linearity and simplify Eq (42) to

$$\bar{\Box}^2 p = \frac{\bar{\partial}}{\partial t}\left[\rho_o v_n + \rho\,(v_t + v_c)\,\delta(f)\right] + \frac{\bar{\partial}^2 \rho u_i u_j}{\partial x_i \partial x_j}$$

$$-\frac{\bar{\partial}}{\partial x_i}\left\{\left[p\,(n_i + t_i + s_i) + \rho v_i\,(v_t + v_s)\right]\delta(f)\right\} \tag{44}$$

The addition of the hypothesis of incompressibility provides further reduction of Eq (44) to

$$\bar{\nabla}^2 p = -\frac{\bar{\partial}}{\partial t}\left[\rho_o\,(v_n + v_t + v_s)\,\delta(f)\right] - \frac{\bar{\partial}^2 \rho_o u_i u_j}{\partial x_i \partial x_j}$$

$$+\frac{\bar{\partial}}{\partial x_i}\left\{\left[p\,(n_i + t_i + s_i) + \rho_o v_i\,(v_t + v_s)\right]\delta(f)\right\} \tag{45}$$

Equation (42) should be considered as equivalent to the Euler equation in the Computational Fluid Dynamics parlance. The velocity potential ϕ does not appear there explicitly. During its derivation, the background is established in the sense that the fluid is inviscid, and nothing else in terms of hypotheses.

In integral form, Eq (42) assumes the same structure given by Eq (37), but with kernels given by

$$\mathcal{K}_S^p = \frac{\bar{\partial}}{\partial x_i}\left[\frac{p\,(n_i + t_i + s_i)}{r}(1 + M_r)\right]_{\text{ret}}$$

$$\mathcal{K}_S^v = \frac{\bar{\partial}}{\partial t}\left[\frac{\rho_o v_n + \rho\,(v_t + v_s)}{r}(1 + M_r)\right]_{\text{ret}}$$

$$-\frac{\bar{\partial}}{\partial x_i}\left[\frac{\rho\, v_i\,(v_t + v_s)}{r}(1 + M_r)\right]_{\text{ret}}$$

$$\mathcal{K}_\mathcal{V}^v = \frac{\bar{\partial}^2}{\partial x_i \partial x_j}\left[\frac{t_{ij}}{r}(1 + M_r)\right]_{\text{ret}}$$

Similarly, the incompressible limit (45) can be rewritten with the structure of Eq (38) but, this time, with the kernels simplified to

$$\bar{\mathcal{K}}_S^p = \frac{\bar{\partial}}{\partial x_i}\left[\frac{p\,(n_i + t_i + s_i)}{r}\right]$$

$$\bar{\mathcal{K}}_S^v = \frac{\bar{\partial}}{\partial t}\left[\frac{\rho_o\,(v_n + v_t + v_s)}{r}\right] - \frac{\bar{\partial}}{\partial x_i}\left[\frac{\rho_o\, v_i\,(v_t + v_s)}{r}\right]$$

$$\bar{\mathcal{K}}_\mathcal{V}^v = \frac{\bar{\partial}^2}{\partial x_i \partial x_j}\left[\frac{\rho_o u_i u_j}{r}\right]$$

As remarked previously, Eqs (42) and (45) are prototypes of general relations between pressure, density, and velocity for inviscid fluids. As such, these equations are single relations involving several variables. They cannot constitute solutions themselves, but can be used as mother-equations in iterative schemes already tested in simplified form (see Brandão (1989)) as well as others presently in development.

SUMMARY AND CONCLUSIONS

Results of theoretical nature have been presented concerning the application of an aeroacoustic approach to Aerodynamics. These results cover general issues, like non-linear, viscous, three-dimensional, unsteady, and compressible flows, as well as related simplifications. These simplifications have been discussed in order to construct parallels between the new governing equations and well-established mathematical models of Fluid Mechanics. Therefore, the discussion here has explored from the Navier-Stokes to the Laplacian context, passing through the Euler, full-potential, and linearized potential frameworks.

The inclusion of boundary conditions as source terms of partial differential equations is a characteristic of modern boundary element methods. This mathematical task can be accomplished with the help of the concept of generalized derivatives. In the approach, this trend of incorporating boundary conditions to the governing equations which depends heavily on the velocity field and weakly on the pressure field. For smooth surfaces, these kernels are given explicitly by

$$\mathcal{K}_S^p = \frac{\bar{\partial}}{\partial x_i}\left[\frac{\tilde{\mathcal{P}}_{ij}\,(n_j + t_j + s_j)}{r}\,(1 + M_r)\right]_{\text{ret}}$$

$$\mathcal{K}_S^v = \frac{\bar{\partial}}{\partial t}\left[\frac{\rho_o v_n + \rho\,(v_t + v_s)}{r}\,(1 + M_r)\right]_{\text{ret}} - \frac{\bar{\partial}}{\partial x_i}\left[\frac{\rho\, v_i\,(v_t + v_s)}{r}\,(1 + M_r)\right]_{\text{ret}}$$

$$\mathcal{K}_V^v = \frac{\bar{\partial}^2}{\partial x_i \partial x_j}\left[\frac{\mathcal{T}_{ij}}{r}\,(1 + M_r)\right]_{\text{ret}}$$

Similarly, Eq (36) can be represented concisely as

$$4\pi p + \int_{f=0} \bar{\mathcal{K}}_S^p\, d\mathcal{S} = \int_{f=0} \bar{\mathcal{K}}_S^v\, d\mathcal{S} + \int_{\mathcal{V}} \bar{\mathcal{K}}_V^v\, d\mathcal{V} \qquad (38)$$

with the following simplified kernels

$$\bar{\mathcal{K}}_S^p = \frac{\bar{\partial}}{\partial x_i}\left[\frac{\tilde{\mathcal{P}}_{ij}\,(n_j + t_j + s_j)}{r}\right]$$

$$\bar{\mathcal{K}}_S^v = \frac{\bar{\partial}}{\partial t}\left[\frac{\rho_o\,(v_n + v_t + v_s)}{r}\right] - \frac{\bar{\partial}}{\partial x_i}\left[\frac{\rho_o\, v_i\,(v_t + v_s)}{r}\right]$$

$$\bar{\mathcal{K}}_V^v = \frac{\bar{\partial}^2}{\partial x_i \partial x_j}\left[\frac{\bar{\mathcal{T}}_{ij}}{r}\right]$$

Equations (37) and (38) are single integral equations involving several unknowns. As before, an iterative solution technique is recommended to obtain the pressure field. This solution starts with a reasonable guess for the velocity field, which can be constructed taking as basis the known motion of the body with respect to the reference system at rest. This guess allows estimation of the $\mathcal{K}_S^v$ and $\mathcal{K}_V^v$ integrals, the driving input for pressure determination. Once one cycle is completed, the momentum equation can be used to yield a better distribution for the unknown perturbation velocity field. Then, the pressure can be recomputed and convergence evaluated. Further details on this solution algorithm have been provided by Brandão (1991). There are reasons to believe that convergence can be reached within a few cycles because iterations begin with an input very close to the converged solution. However, applications are necessary to demonstrate this point.

A governing equation for energy

It is known that for high speed air flows, the temperature of the fluid near or on the body surface becomes an important issue. Since Eq (33) is mostly concerned with pressure propagation generated by motion, no temperature information can be obtained from this equation. Therefore, studies regarding this objective are required. Here we explore a theoretical possibility, integrating into a single statement the physics of the energy and energy momentum equations, so that we can have access to temperature distributions in the field, as well as to mechanisms of energy propagation through the flow.

A new governing equation [illegible] tends the *Acoustic Analogy* into this issue, car[illegible] llowing the steps below, in complete simila[illegible] tion of Eq (33):

1. Take the generalized time derivative of both sides of the energy equation (13).
2. Take the generalized derivative of both sides of the energy momentum equation (17) with respect to x_i.
3. Subtract the result of the previous step from the result of step 1.
4. Divide the whole equation by c^2.
5. Subtract from both sides of the previous step the term $\bar{\nabla}^2 e$.

The result of this process yields

$$\bar{\Box}^2 e = \frac{1}{c^2}\left\{\frac{\bar{\partial}}{\partial t}\left[\mathcal{M}\;\delta(f)\right] - \frac{\bar{\partial}}{\partial x_i}\left[\mathcal{D}_i\;\delta(f)\right] - \frac{\bar{\partial}^2 \mathcal{Q}_{ij}}{\partial x_i \partial x_j} - \frac{\bar{\partial}^2}{\partial t \partial x_i}\left(q_i + \mathcal{P}_{ij} u_j\right)\right\} \qquad (39)$$

where we define

$$\mathcal{M} = e_o v_n + e\,(v_t + v_s) + (\mathcal{P}_{ij} v_j + q_i)\,(n_i + t_i + s_i)$$

$$\mathcal{D}_i = e v_i\,(v_t + v_s) + v_i\left(\tilde{\mathcal{P}}_{jk} v_k + q_j\right)(n_j + t_j + s_j)$$

and

$$\mathcal{Q}_{ij} = e u_i u_j + \mathcal{P}_{jk} u_k u_i + u_i q_j + c^2 e\,\delta_{ij}$$

as the energetic monopole scalar, dipole vector, and quadrupole tensor, respectively.

Equation (39) is a wave equation for the total fluid element energy e driven by two surface and two volume source terms of different natures. The surface terms, in the order given, have the behavior of the traditional monopole and dipole. The first volume term is a free-field quadrupole, like in Lighthill's equation. Finally, the second volume term is a free-field contributor of mixed nature, still to be interpreted.

If we now consider the incompressible limit of Eq (39), the following identity results:

$$\bar{\nabla}^2 e = \frac{\bar{\partial}^2 e}{\partial x_i \partial x_j}\,\delta_{ij} \qquad (40)$$

which gives no useful information. However, a result like this was expected because the energy equation introduces new effects in the flow physics only in the compressible case. The "locking phenomenon" is well-known in Computational Fluid Dynamics for low Mach number flows. The reduction of Eq (39) to identity (40) is just an equivalent manifestation of the same phenomenon.

Like the other governing equations before in this paper, Eq (39) can now the integrated and solved numerically by an iterative scheme. However, these details will be omitted here for reasons of brevity and to allow time for maturation of the concept.

Equations (33) and (39) are the most sophisticated results presented in this contribution. Together, they form a mathematical model within the Navier-Stokes environment of modern Computational Fluid Dynamics. For the sake of completeness, now we can simplify the context with the hypothesis of motion inside inviscid fluids, which places the mathematical model inside the Euler equations framework.

started with Ffowcs Williams and Hawkings (1969), as an outgrowth of Lighthill's *Acoustic Analogy*. Applications of the approach to Aerodynamics resulted in an incomplete description of the flow physics, which can be summarized by

- underevaluation of expansions;
- overevaluation of compressions; and
- difficulty in capturing circulation.

This incompleteness suggested to the author that what was missing in the earlier mathematical model could be related to its boundary conditions. The challenge then consisted not only on having a perception for the lacking information, but also on devising a logical mathematical device for its inclusion in the model.

With the objective of attempting corrections in these theoretical deficiencies, the concept of generalized derivatives has been revisited and extended, removing ambiguities of definition of surface functions and allowing for property jumps along tangential directions on the discontinuity surfaces. As results, new generalized versions of the continuity, momentum, energy, and energy momentum equations have been derived. Connections with potential flow theory have been presented for both incompressible and compressible fluids. In the second case, a new linear formulation has been derived which is more complete than the one used by Lee and Yang (1990). Integral transformations of the governing equations have been provided and possibilities of obtaining solutions via iteration have been presented.

By following the path which leads to the Ffowcs Williams and Hawkings equation, a new formulation relating pressure and velocity has been obtained for non-potential flows. This formulation presents new mechanisms of noise generation related to tangential flow, which may be important in aerodynamic applications. A similar relation between several fluid properties has been derived for the energy propagating from a moving body. The inviscid and incompressible limits of these relations have been made explicit to emphasize the generality of the approach. The corresponding integral transformations of these equations have been supplied and their solution algorithm given in very broad terms.

Although the association between circulation and vorticity is practically unavoidable in Aerodynamics, the word *vorticity* does not appear in this paper before this paragraph. The main issue raised by this contribution is the development of a mathematical model with correct and well-defined boundary conditions which, together with free-field effects, can reproduce experimental results in Fluid Mechanics. In discussing this issue, the author believes that the concept of vorticity, as established in the classical literature, is not necessary. However, this concept might be invoked to serve as reference or to correct the present model if it is proven incomplete.

The results shown here are based on logical assumptions. It is expected that studies based on the theory presented might help in the development of the aeroacoustic approach to Aerodynamics and in the clarification of the quoted unresolved issues. The theory is now established and ready to be checked in its validity. Future studies should include benchmark applications and comparisons of results with well-known experimental and/or theoretical data.

ACKNOWLEDGEMENTS

The Brazilian Ministry of Aeronautics, Fundação Casimiro Montenegro Filho, and Fundação de Amparo à Pesquisa do Estado de São Paulo provided support concerning the development and presentation of this research in technical meetings.

REFERENCES

Ahuja KK (1973), Correlation and prediction of jet noise, *J. Sound and Vibration*, 29(2), 155-168.
Bernstein IB (1974), Transport in axisymmetric plasmas, *The Physics of Fluids*, 17, 547-558.
Brandão MP (1987), Improper integrals in theoretical aerodynamics – the problem revisited, *AIAA Journal*, 25(9), 1258-1260.
Brandão, MP (1988a), On the aeroacoustics, aerodynamics, and aeroelasticity of lifting surfaces, PhD Thesis, Stanford University, SUDAAR-565.
Brandão MP (1988b), An acoustic-energetic analogy for external flows, *Proc. Second National Meeting of Thermal Sciences*, Águas de Lindóia, Brazil, 19-22.
Brandão MP (1989), Towards the unification of acoustics and fluid mechanics, *Appl. Mech. Rev.*, 42(11), Part 2, S20-S31.
Brandão MP (1990), Singular integrals in theoretical aerodynamics – their origin and computation, *Proc. Third National Meeting of Thermal Sciences*, Itapema, Brazil, 5-8.
Brandão, MP (1991), A mixed volume-boundary element approach for aerodynamics, *Appl. Mech. Rev.*, 44(11), Part 2, S36-S45.
Brentner KS (1988), The exact calculation of quadrupole sources for some incompressible flows, *Proc. Institute of Acoustics*, 10(2), 817-824.
Brentner KS (1990), The sound of moving bodies, PhD Thesis, Department of Engineering, University of Cambridge.
Farassat F (1977), Discontinuities in aerodynamics and aeroacoustics: the concept and applications of generalized derivatives, *J. Sound and Vibration*, 55(2), 165-193.
Farassat F (1986), The Ffowcs Williams-Hawkings equation – fifteen years of research, in *Aero- and Hydro-Acoustics*, G Comte-Bellot and JE Ffowcs Williams (eds), Springer-Verlag, New York, 175-180.
Farassat F (1987), Quadrupole source in prediction of the noise of rotating blades – a new source description, AIAA 11th Aeroacoustics Conference, Sunnyvale, Paper AIAA-87-2675.
Ffowcs Williams JE (1984), The acoustic analogy – thirty years on, *IMA J. Appl. Math.*, 32, 113-124.
Ffowcs Williams JE and Hawkings DL (1969), Sound generation by turbulence and surfaces in arbitrary motion, *Phil. Trans. Royal Society of London*, A264(1151), 321-342.
Hadamard JS (1952), *Lectures on Cauchy's problem in linear partial differential equations*, Dover, New York, 117-158.
Karamcheti K (1966), *Principles of ideal-fluid aerodynamics*, Robert E. Krieger, Malabar.
Lamb, H (1945), *Hydrodynamics*, Dover, New York, Article 9, 6-8.
Lee YJ and Yang JY (1990), A panel method for arbitrary moving boundaries problems, *AIAA Journal*, 28(3), 432-438.
Lighthill MJ (1952), On sound generated aerodynamically I. General theory, *Proc. Royal Society of London*, A211, 564-587.
Lighthill MJ (1954), On sound generated aerodynamically II. Turbulence as a source of sound, *Proc. Royal Society of London*, A222, 1-32.
Lighthill MJ (1962), Sound generated aerodynamically, *Proc. Royal Society of London*, A267, 147-182.
Long LN (1983), The compressible aerodynamics of rotating blades based on an acoustic formulation, NASA TP-2197.
Long LN (1985), An aerodynamic theory based on time-domain aeroacoustics, *AIAA Journal*, 23(6), 875-882.
Mangler KW (1951), Improper integrals in theoretical aerodynamics, Aeronautical Research Council, TR CP 94 (14,394).
Medeiros EF and Brandão MP (1991), Studies on wind tunnel wall interference following an aeroacoustic approach, *Proc. 11th Brazilian Congress of Mechanical Engineering*, São Paulo, Brazil, 209-212.
Monin AS and Yaglom AM (1975), Dynamic equations for the higher-order moments and the closure problem, in *Statistical fluid mechanics: mechanics of turbulence*, Vol 2, JL Lumley (ed), The MIT Press, Cambridge.
Morse PM and Feshbach H (1953), *Methods of theoretical physics*, McGraw-Hill, New York, 834-857 and 1252-1256.
Shkanofsky IP and Johnston TM (1966), *The particle kinetics of plasmas*, Addison-Wesley, Reading.
Thompson PA (1972), *Compressible-fluid dynamics*, McGraw-Hill, New York.

Nonlinear equations of the theories of elasticity and shells in terms of anholonomic components

Wolf Altman

Escola Politécnica da Universidade de São Paulo, Cidade Universitária, São Paulo, SP 05498-970 and Instituto Tecnológico de Aeronáutica, CTA, São José dos Campos, SP, 12228-900, Brazil

Antonio Marmo de Oliveira

Instituto Tecnológico de Aeronáutica, CTA, São José dos Campos, SP, 12228-900, Brazil

This paper is concerned with some new aspects of the theory of anholonomic components of tensors of single and double fields. Consistent definitions of these components are given. As applications, the geometrically nonlinear equations of elasticity and shells referred to general curvilinear coordinates are written in terms of anholonomic components of vectors and tensors involved.

INTRODUCTION

Historically, the notion of physical components of vectors was first introduced by Ricci and Levi-Civita in a memoir published in 1901. Thirring, as early as 1925, had noticed the connection existing between physical and tensorial components. Cissotti (1928) introduced the concept of physical components of covariant tensors of order n. An entirely satisfactory theory of physical components in orthogonal curvilinear coordinates was presented by McConnell (1931). For more details in early developments of the theory of physical components, see, for example, Truesdell (1953), Ericksen (1960), and Altman and Oliveira (1982).

With respect to non-orthogonal coordinate systems, different authors, e.g. Green and Zerna (1968), Sedov (1965), Synge and Schield (1949), and Truesdell (1953), produced distinct definitions of physical components of tensors. Usually, to avoid any ambiguity in these definitions, the tensor components are transformed to refer to an orthogonal coordinate system in order to allow the use of McConnell's concept of physical components. Truesdell (1953) dealt with mixed components and in (1954) pointed out the connection between his method and the theory of anholonomic coordinates (Schouten, 1951; Ericksen, 1960). A theory developed by Altman and Oliveira (1977, 1982) and Oliveira and Altman (1978), which includes all physical components (mixed, covariant, and contravariant), shows the compatibility and relationship among some of those definitions. In this context, each tensor is seen as a linear transformation between two vector spaces properly chosen. The concept of physical components depends fundamentally on this linear transformation and on the unit bases of the mentioned vector spaces. In the light of the work of Altman and Oliveira (1977), the connection between physical and anholonomic components, viewed as an isomorfism between vectorial spaces, is implicitly contained in the definition of physical components of tensors.

The purpose of this article is to present some new aspects of the theory of anholonomic components of tensors of single and double fields and to demonstrate their applications to representative problems in Solid Mechanics.

Convected coordinates were utilized by Altman and Bevilacqua (1991) in order to obtain the equations of motion in a Lagrangian description. The resulting equations, after being referred to a local orthogonal coordinate system, were written in terms of physical components of tensors. Here, in the description of the motion of a continuous body, the undeformed state is defined by curvilinear coordinates and the deformed state by either a new set of curvilinear coordinates or by its convected coordinates. The components of the first Piola-Kirchhoff stress tensor and of the deformation gradient, which enter into the equations of motion, are components of tensors of double field. A study of anholonomic components of second order tensors of single and double fields is provided in order to express the set of governing equations of a body in terms of these components.

As applications of the above mentioned theory, the geometrically nonlinear equations of elasticity and shells referred to general curvilinear coordiantes are written in terms of anholonomic components of the vectors and tensors involved.

Finally, in the last section of this paper, some comments about the suitability and generality of the theory of anholonomic components here presented are made.

PRELIMINARIES

Consider the body C, occupying in the undeformed state a region C that consists of the material volume $\mathcal{V}$ and its surface $\mathcal{S}$. The position of a point P in this region is denoted by a curvilinear coordinate system X^J $(J = \mathrm{I}, \mathrm{II}, \mathrm{III})$. In the deformed state, the material points of the region C go into a region c, consisting of a volume v and its surface s. A point in the deformed state may be represented by a new set of curvilinear coordinates x^j $(j = 1, 2, 3)$.

The covariant and contravariant base vectors at each point in $\mathcal{C}$ and at each one in c, are denoted by $\left(\left\{\vec{G}_J\right\},\left\{\vec{G}^J\right\}\right)$ and $(\{\vec{g}_j\},\{\vec{g}^j\})$, respectively. The base vectors and the corresponding metrics (G_{IJ},G^{IJ}) and (g_{ij},g^{ij}), are defined by

$$\vec{G}_J = \vec{R}_{,J} \quad , \quad (J = \mathrm{I},\mathrm{II},\mathrm{III}) \tag{1a}$$

$$G_{IJ} = \vec{G}_I \cdot \vec{G}_J \quad , \quad G_{IK}\, G^{JK} = \delta_I^J \quad ,$$
$$\vec{G}^I = G^{IJ}\,\vec{G}_J \tag{1b-d}$$

and

$$\vec{g}_j = \vec{r}_{,j} \quad , \quad (j = 1,2,3) \tag{2a}$$

$$g_{ij} = \vec{g}_i \cdot \vec{g}_j \quad , \quad g_{ik}\, g^{jk} = \delta_i^j \quad , \quad \vec{g}^i = g^{ij}\,\vec{g}_j \tag{2b-d}$$

where

$$\vec{R} = \vec{R}\left(X^{\mathrm{I}},X^{\mathrm{II}},X^{\mathrm{III}}\right) \quad , \quad \vec{r} = \vec{r}\left(x^1,x^2,x^3\right) \tag{3a,b}$$

are the position vectors of a point in $\mathcal{C}$ and of one in c, $\left(\delta_I^J,\delta_i^j\right)$ are the Kronecker symbols referred to the coordinates systems X^I and x^i, and the indices after a comma indicate derivatives with respect to X^J when they are majuscules and with respect to x^j when they are minuscules.

The displacement vector $\vec{u}$ is defined as the vector that extends from a material point in the undeformed body to the same material point in the deformed body. This vector will have components $\mathcal{U}^I$ referred to X^I and u^i referred to x^i, i.e.,

$$\vec{u} = \mathcal{U}^I\,\vec{G}_I = \mathrm{u}^i\,\vec{g}_i \tag{4a,b}$$

The displacement vector $\vec{u}$ may also be expressed in terms of its covariant components $\mathcal{U}_I$ and u_i as follows

$$\vec{u} = \mathcal{U}_I\,\vec{G}^I = \mathrm{u}_i\,\vec{g}^i \tag{4c,d}$$

Furthermore, the partial derivatives of $\vec{u}$ with respect to X^J and x^j, can be written as

$$\vec{u}_{,J} = \mathcal{U}^I_{;J}\,\vec{G}_I = \mathcal{U}_{I;J}\,\vec{G}^I \tag{4e,f}$$

$$\vec{u}_{,j} = \mathrm{u}^i_{;j}\,\vec{g}_i = \mathrm{u}_{i;j}\,\vec{g}^i \tag{4g,h}$$

where the symbols $(\ )_{;J}$ and $(\ )_{;j}$ denote the covariant derivatives with respect to X^J and x^j, respectively.

The motion of the body is expressed by

$$x^i = x^i\left(X^I,t\right) \quad \text{or} \quad X^I = X^I\left(x^i,t\right) \tag{5a,b}$$

Each point p in c at time t comes from a point P in $\mathcal{C}$ at time $t = 0$. It is assumed that the mappings $(5a,b)$ are single-valued and have continuous partial derivatives with respect to their arguments up to any order required. Each expression of $(5a,b)$ is the unique inverse of the other. Thus, since the transformations are reversible, the determinants (Jacobians)

$$\left|\frac{\partial x^i}{\partial X^I}\right| \quad \text{or} \quad \left|\frac{\partial X^I}{\partial x^i}\right|$$

are not zero.

ANHOLONOMIC COMPONENTS OF VECTORS

The physical dimensions of the covariant and contravariant components $\mathcal{V}_K$ and $\mathcal{V}^K$ of the same vector

$$\vec{V} = \mathcal{V}_K\,\vec{G}^K = \mathcal{V}^K\,\vec{G}_K \quad (K = \mathrm{I},\mathrm{II},\mathrm{III}) \tag{6a,b}$$

are different, since the vectors of their bases are not generally of unit length. The need of finding components of vectors, whose dimensions coincide with those of the vectors themselves, is accomplished by constructing the unit bases

$$\vec{U}_K = \frac{\vec{G}_K}{\sqrt{G_{KK}}} \quad \text{and} \quad \vec{U}^K = \frac{\vec{G}^K}{\sqrt{G^{KK}}} \tag{7a,b}$$

and their reciprocal bases

$$\underline{\vec{U}}^K = \sqrt{G_{KK}}\,\vec{G}^K \quad \text{and} \quad \underline{\vec{U}}_K = \sqrt{G^{KK}}\,\vec{G}_K \tag{7c,d}$$

respectively. Expanding the vector $\vec{V}$ with respect to these bases one obtains

$$\vec{V} = \left[\mathcal{V}^K\right]_U \vec{U}_K = [\mathcal{V}_K]_{U^*}\,\vec{U}^K =$$
$$[\mathcal{V}_K]_{\underline{U}}\,\underline{\vec{U}}^K = \left[\mathcal{V}^K\right]_{\underline{U}^*}\,\underline{\vec{U}}_K \tag{8a-d}$$

where $K = \mathrm{I},\mathrm{II},\mathrm{III}$ and

$$\left[\mathcal{V}^K\right]_U = \sqrt{G_{KK}}\,\mathcal{V}^K \quad , \quad [\mathcal{V}_K]_{U^*} = \sqrt{G^{KK}}\,\mathcal{V}_K \tag{8e,f}$$

$$[\mathcal{V}_K]_{\underline{U}} = \frac{\mathcal{V}_K}{\sqrt{G_{KK}}} \quad , \quad \left[\mathcal{V}^K\right]_{\underline{U}^*} = \frac{\mathcal{V}^K}{\sqrt{G^{KK}}} \tag{8g,h}$$

are called physical (Ericksen, 1960; Altman and Oliveira, 1982) or anholonomic components of $\vec{V}$ relative to the bases $U = \left\{\vec{U}_K\right\}$, $U^* = \left\{\vec{U}^K\right\}$, $\underline{U} = \left\{\underline{\vec{U}}^K\right\}$, and $\underline{U}^* = \left\{\underline{\vec{U}}_K\right\}$ respectively.

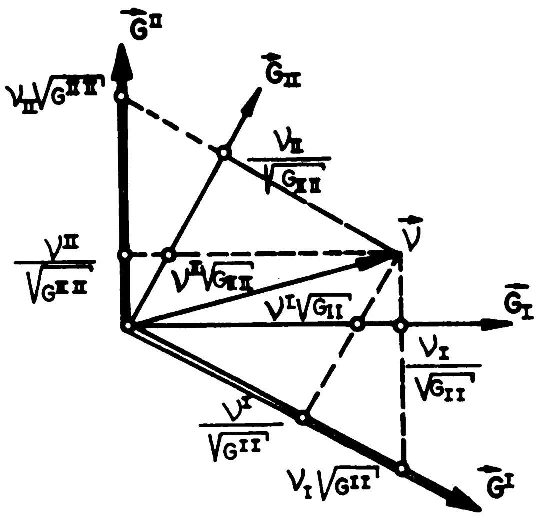

FIG 1. Physical or anholonomic components of a vector.

As it can be seen from Figure 1, the components defined by formulas $(8e,f)$ are the parallel projections of the vector $\vec{V}$ onto the directions $\vec{G}_K$ and $\vec{G}^K$, respectively, while the components $(8g, h)$ are the orthogonal projections over the same directions, respectively. Ricci and Levi-Civita (1901), had already introduced these four sets of components.

Observe that the double indices in the metric symbols do not contribute to the summation convention. For the deformed state, similar formulas as the preceding ones can be obtained by substituting the uppercase indices and letters which enter in the above expressions by lowercase ones.

ANHOLONOMIC COMPONENTS OF TENSORS OF DOUBLE FIELD

A second order tensor of double field $\mathcal{T}$ can be defined as linear combinations of tensor products of the type $\vec{\underset{\sim}{U}} \otimes \vec{\underset{\sim}{u}}$ (or $\vec{\underset{\sim}{u}} \otimes \vec{\underset{\sim}{U}}$), where $\vec{\underset{\sim}{U}}$ and $\vec{\underset{\sim}{u}}$ are elements that belong to one of the bases of the sets $\{U, \underline{U}, U^*, \underline{U}^*\}$ and $\{u, \underline{u}, u^*, \underline{u}^*\}$, respectively. For example, the expressions

$$\mathcal{T} = \sum_{M,m} [T^{Mm}]_{\mathcal{B}}\, \vec{\underline{U}}_M \otimes \vec{u}_m = \sum_{M,m} T^{Mm}\, \vec{G}_M \otimes \vec{g}_m \qquad (9a,b)$$

represent a covariant second order tensor of double field, where $\mathcal{B} = \underline{U}^* \otimes u$ is a basis of the considered tensorial space and the notation $[T^{Mm}]_{\mathcal{B}}$ denotes the anholonomic components of the tensor of double field referred to the basis $\mathcal{B}$. Taking into account the identity $(9a, b)$ and the expressions of $\vec{\underline{U}}_M$ and $\vec{u}_m$ as functions of $\vec{G}_M$ and $\vec{g}_m$, respectively, one obtains

$$[T^{Mm}]_{\mathcal{B}} = \frac{\sqrt{g_{mm}}}{\sqrt{G^{MM}}}\, T^{Mm} \qquad (9c)$$

where $M = \mathrm{I}, \mathrm{II}, \mathrm{III}$ and $m = 1, 2, 3$. Similarly, fifteen more anholonomic components of $\mathcal{T}$ can be obtained.

A third order tensor of double field can be defined as linear combinations of tensor products of anyone of the following types: $\vec{\underset{\sim}{U}}_1 \otimes \vec{\underset{\sim}{u}}_1 \otimes \vec{\underset{\sim}{u}}_2$, $\vec{\underset{\sim}{u}}_1 \otimes \vec{\underset{\sim}{U}}_1 \otimes \vec{\underset{\sim}{u}}_2$, $\vec{\underset{\sim}{u}}_1 \otimes \vec{\underset{\sim}{u}}_2 \otimes \vec{\underset{\sim}{U}}_1$, $\vec{\underset{\sim}{u}}_1 \otimes \vec{\underset{\sim}{U}}_1 \otimes \vec{\underset{\sim}{U}}_2$, $\vec{\underset{\sim}{U}}_1 \otimes \vec{\underset{\sim}{u}}_1 \otimes \vec{\underset{\sim}{U}}_2$, and $\vec{\underset{\sim}{U}}_1 \otimes \vec{\underset{\sim}{U}}_2 \otimes \vec{\underset{\sim}{u}}_1$, where $\vec{\underset{\sim}{U}}_i$ and $\vec{\underset{\sim}{u}}_i$ $(1 = 1, 2)$ are elements that belong to one of the bases of the sets $\{U, \underline{U}, U^*, \underline{U}^*\}$ and $\{u, \underline{u}, u^*, \underline{u}^*\}$, respectively. Similarly as above, the expressions

$$\mathcal{T} = \sum_{M,m,L} [T^{Mm}{}_L]_{\mathcal{B}}\, \vec{\underline{U}}_M \otimes \vec{u}_m \otimes \vec{U}^L = \sum_{M,m,L} T^{Mm}{}_L\, \vec{G}_M \otimes \vec{g}_m \otimes \vec{G}^L \qquad (10a,b)$$

represent a mixed third order tensor of double field, where $\mathcal{B} = \underline{U}^* \otimes u \otimes U^*$ is a basis of the considered tensorial space. The substitution of the vectors $\vec{\underline{U}}_M$, $\vec{u}_m$, and $\vec{U}^L$ as given by formulas (7) into expressions $(10a, b)$ leads to

$$[T^{Mm}{}_L]_{\mathcal{B}} = \frac{\sqrt{g_{mm}}}{\sqrt{G^{MM}}} \sqrt{G^{LL}}\, T^{Mm}{}_L \qquad (11)$$

which is the expression of the anholonomic components of a third order tensor of double field referred to the basis $\mathcal{B} = \underline{U}^* \otimes u \otimes U^*$.

It should be observed that since the covariant derivatives of the vectorial and tensorial components have also a tensorial character, the above theory can be utilized to obtain their anholonomic counterparts. For instance, utilizing formula (11) for the covariant derivative of the first Piola-Kirchhoff stress tensor with respect to X^L, denoted by $\hat{S}^{Kk}{}_{;L}$, one obtains

$$\left[\hat{S}^{Kk}{}_{;L}\right]_{\underline{U}^* \otimes u \otimes U^*} = \frac{\sqrt{g_{kk}}}{\sqrt{G^{KK}}} \sqrt{G^{LL}}\, \hat{S}^{Kk}{}_{;L} \qquad (12)$$

which is the expression of the anholonomic components of $\hat{S}^{Kk}{}_{;L}$, referred to the basis $\underline{U}^* \otimes u \otimes U^*$.

As a particular case, the anholonomic components of tensors of single field (Oliveira and Altman, 1981) can be obtained from the preceding theory by making $U = u$, $\underline{U} = \underline{u}$, $U^* = u^*$, and $\underline{U}^* = \underline{u}^*$. In this context the anholonomic components of the displacement gradient $\mathcal{U}^I_{;J}$ and $\mathcal{U}_{I;J}$ referred to the bases $U \otimes \underline{U}$ and $\underline{U} \otimes \underline{U}$, respectively, can be determined from the expressions

$$\sum_{I,J} [\mathcal{U}^I_{;J}]_{U \otimes \underline{U}}\, \vec{U}_I \otimes \vec{\underline{U}}^J = \sum_{I,J} \mathcal{U}^I_{;J}\, \vec{G}_I \otimes \vec{G}^J \qquad (13a)$$

and

$$\sum_{I,J} [\mathcal{U}_{I;J}]_{\underline{U} \otimes \underline{U}}\, \vec{\underline{U}}^I \otimes \vec{\underline{U}}^J = \sum_{I,J} \mathcal{U}_{I;J}\, \vec{G}^I \otimes \vec{G}^J \qquad (13b)$$

leading to

$$[\mathcal{U}^I_{;J}]_{U \otimes \underline{U}} = \frac{\sqrt{G_{II}}}{\sqrt{G_{JJ}}}\, \mathcal{U}^I_{;J} \qquad (13c)$$

and

$$[\mathcal{U}_{I;J}]_{\underline{U} \otimes \underline{U}} = \frac{1}{\sqrt{G_{II}}\sqrt{G_{JJ}}}\, \mathcal{U}_{I;J} \qquad (13d)$$

Furthermore, note that in the case of single field tensors, formula $(9c)$ coincides with Green and Zerna's physical components of the stress tensor.

Expressions (9) to (13) will be needed in the sequel.

DIMENSIONAL ANALYSIS OF ANHOLONOMIC COMPONENTS

In this section it will be proved the dimensional invariance of the anholonomic components of a second order tensor of double field, under transformation of coordinates.

Firstly, it should be observed that the dimension of $\sqrt{G_{II}}dX^I$ and of $\sqrt{g_{ii}}dx^i$ is L, where L denotes the dimension of length. This follows from the Riemannian metrics

$$dS^2 = G_{IJ}\, dX^I\, dX^J \quad , \quad ds^2 = g_{ij}\, dx^i\, dx^j \qquad (14a,b)$$

The dimensions of G^{II} and g^{ii} can be calculated as functions of G_{II} and g_{ii}, respectively, by observing that if $G_I = \dim(G_{II})$ and $g_i = \dim(g_{ii})$, then

$$\dim G = G_I\, G_J\, G_K \quad , \quad \dim g = g_i\, g_j\, g_k \qquad (15a,b)$$

where

$$G = \det[G_{IJ}] \quad , \quad g = \det[g_{ij}] \qquad (15c,d)$$

The substitution of expressions $(15a, b)$ into

$$G^I = \frac{\dim A_{II}}{\dim G} \quad , \quad g^i = \frac{\dim a_{ii}}{\dim g} \tag{15e, f}$$

where

$$\dim A_{II} = G_J\, G_K \quad , \quad \dim a_{ii} = g_j\, g_k \tag{15g, h}$$

lead to

$$G^I = \frac{1}{G_I} \quad , \quad g^i = \frac{1}{g_i} \tag{15i, j}$$

The dimension of a tensor of double field $\mathcal{T}$, which is denoted by dim $\mathcal{T}$, can be defined as being the dimension of its components in orthonormal cartesian systems (Y^M, y^m), $(M = \mathrm{I}, \mathrm{II}, \mathrm{III}\ ;\ m = 1,2,3)$. It can be proved that the dimension of the anholonomic components of $\mathcal{T}$ in any coordinate systems (X^K, x^k), where $K = \mathrm{I}, \mathrm{II}, \mathrm{III}$ and $k = 1,2,3$ is invariant and equal to dim $\mathcal{T}$. Let the contravariant components $\bar{T}^{Kk}$ be chosen to represent the double tensor field of second order in the coordinate systems (X^K, x^k) and T^{Mm} its components in the orthonormal cartesian systems (Y^M, y^m). From the formulas for changing coordinates

$$\bar{T}^{Kk}(X, x) = T^{Mm}(Y, y)\, \frac{\partial X^K}{\partial Y^M}\, \frac{\partial x^k}{\partial y^m} \tag{16}$$

one can write

$$\dim \bar{T}^{Kk} = \dim (X^K)\, L^{-1} \cdot \dim (x^k)\, L^{-1} \dim T^{Mm} \tag{17a}$$

or

$$\dim \bar{T}^{Kk} = \dim (X^K) \cdot \dim (x^k)\, L^{-2} \dim \mathcal{T} \tag{17b}$$

where

$$\dim T^{Mm} = \dim \mathcal{T} \tag{17c}$$

and dim (X^K) and dim (x^k) are the dimensions of the X^K and x^k coordinates, respectively. From formula $(9c)$, where $\mathcal{B} = \underline{U}^* \otimes u$, it can be written

$$\dim \left[\bar{T}^{Kk}\right]_{\mathcal{B}} = \dim \left(\sqrt{\frac{g_{kk}}{G^{KK}}}\right) \dim \bar{T}^{Kk} \tag{18a}$$

After substituting formula $(17b)$ into expression $(18a)$, one obtains

$$\dim \left[\bar{T}^{Kk}\right]_{\mathcal{B}} = \left[\sqrt{g_k}\, \dim(x^k)\right] \cdot \left[\sqrt{G_K}\, \dim(X^K)\right] L^{-2} \dim \mathcal{T} \tag{18b}$$

or

$$\dim \left[\bar{T}^{Kk}\right]_{\mathcal{B}} = \dim \mathcal{T} \tag{18c}$$

since

$$\sqrt{g_k} \dim (x^k) = \sqrt{G_K} \dim (X^K) = L \tag{18d}$$

By the same reasoning, it can be shown that the dimensions of the anholonomic counterparts of the covariant and mixed components of a double tensor field are also equal to dim $\mathcal{T}$. Furthermore, this theorem can be extended for higher order tensors of double field.

ELASTICITY EQUATIONS IN TERMS OF ANHOLONOMIC COMPONENTS

As an application of the preceding theory, the nonlinear elasticity equations of a continuous body will be written in terms of anholonomic components of vectors and tensors involved.

Equations of motion

Consider Cauchy's first law of motion expressed in terms of the reference state (Eringen, 1962)

$$\hat{S}^{Kk}{}_{:K} + P^k = \rho_o\, a^k \quad (k = 1,2,3) \tag{19a}$$

and the boundary conditions

$$\nu_K\, \hat{S}^{Kk} = F^k \quad (k = 1,2,3) \tag{19b}$$

where

$$\hat{S}^{Kk}{}_{:K} = \hat{S}^{Kk}{}_{,K} + \hat{S}^{Km}\, \Gamma^k_{ml}\, x^l_{,K} + \hat{S}^{Kk}\, \Gamma^L_{LK} \tag{19c}$$

In these expressions, $\hat{S}^{Kk}$ are the components of the first Piola-Kirchhoff stress tensor; Γ^R_{IS} and Γ^r_{is} are the Christoffel symbols in the reference state and in the deformed state, respectively; $x^l = x^l(X^K, t)$ express the motion of the body which carries various material points through various spatial positions; ρ_o is the mass density in the reference state; P^k and F^k are contravariant components in the directions $\vec{g}_k$ of the body force and prescribed surface traction referred to the unit volume and unit area before deformation, respectively; a^k are contravariant components of the acceleration in the directions $\vec{g}_k$; and finally, ν_K are the covariant components of the exterior normal in the directions $\vec{G}^K$, $(K = \mathrm{I}, \mathrm{II}, \mathrm{III})$.

Based on formula $(9c)$, the anholonomic components of $\hat{S}^{Kk}$ relative to the basis $\mathcal{B} = \underline{U}^* \otimes u$, denoted by $\hat{\sigma}^{Kk}$, reads

$$\hat{\sigma}^{Kk} = \left[\hat{S}^{Kk}\right]_{\mathcal{B}} = \frac{\sqrt{g_{kk}}}{\sqrt{G^{KK}}}\, \hat{S}^{Kk} \tag{20a}$$

Substituting expression $(20a)$ into equations $(19a, b)$ and taking the anholonomic components of P^k, F^k, a^k, ν_K as

$$p^k = \left[P^k\right]_u = \sqrt{g_{kk}}\, P^k \quad ,$$

$$f^k = \left[F^k\right]_u = \sqrt{g_{kk}}\, F^k \tag{21b-d}$$

$$\alpha^k = \left[a^k\right]_u = \sqrt{g_{kk}}\, a^k \quad ,$$

$$\eta_K = [\nu_K]_{U^*} = \sqrt{G^{KK}}\, \nu_K \tag{21e-h}$$

one obtains

$$\sqrt{g_{kk}} \left[\frac{\sqrt{G^{KK}}}{\sqrt{g_{kk}}}\, \hat{\sigma}^{Kk}\right]_{:K} + p^k = \rho_o\, \alpha^k \tag{22a}$$

and

$$\nu_K\, \hat{\sigma}^{Kk} = f^k \tag{22b}$$

which are the desired equations. Observe that if $L = K$, then formula (12) (where the symbol (;) was replaced by (:)) reduces to

$$\left[\hat{S}^{Kk}{}_{:K}\right]_u = \sqrt{g_{kk}}\, \hat{S}^{Kk}{}_{:K} \tag{23a}$$

or taking into account expression (20a)

$$\left[\hat{S}^{Kk}{}_{:K}\right]_u = \sqrt{g_{kk}}\left[\frac{\sqrt{G^{KK}}}{\sqrt{g_{kk}}}\,\hat{\sigma}^{Kk}\right]_{:K} \qquad (23b)$$

The latter expression gives the anholonomic components of the covariant derivative of the first Piola-Kirchhoff stress tensor directly in terms of the derivatives of its anholonomic components. The substitution of formulas (23b) and (21) into equations (22), yield

$$\left[\hat{S}^{Kk}{}_{:K}\right]_u + \left[P^k\right]_u = \rho_o\left[a^k\right]_u \qquad (24a)$$

$$[\nu_K]_{U^\bullet}\left[\hat{S}^{Kk}\right]_{\underline{U}^\bullet\otimes u} = \left[F^k\right]_u \qquad (24b)$$

which shows that the anholonomic components in equations (24a,b) are related just in the same way as their tensorial components in equations (19a,b).

Some authors prefer the use of convected coordinates which can be obtained from the foregoing coordinates by equating the numerical value of the coordinate x^k of a given point as to that of X^K. For these coordinates the following relation

$$\hat{S}^{KI} = (\delta^I_R + \mathcal{U}^I_{;R})\,S^{KR} \qquad (25a)$$

holds true, where the notations $\mathcal{U}^I_{;R}$, $\hat{S}^{KI}$, and S^{KR}, for $I, R, K = \mathrm{I}, \mathrm{II}, \mathrm{III}$, denote the displacement gradient tensor components, the first and second Piola-Kirchhoff stress tensors components, respectively. In this case equations (19) reduce to

$$\left[(\delta^I_R + \mathcal{U}^I_{;R})\,S^{KR}\right]_{;K} + P^I = \rho_o\,\ddot{\mathcal{U}}^I \qquad (25b)$$

$$\nu_K\,(\delta^I_R + \mathcal{U}^I_{;R})\,S^{KR} = F^I \qquad (25c)$$

where

$$\hat{S}^{KI}{}_{;K} = \hat{S}^{KI}{}_{,K} + \hat{S}^{KM}\,\Gamma^I_{KM} + \hat{S}^{KI}\,\Gamma^L_{LK} \qquad (25d)$$

In terms of anholonomic components equations (25b,c) can be written in the form

$$\sqrt{G_{II}}\left[\frac{\sqrt{G^{KK}}}{\sqrt{G_{II}}}\,(\sigma^{KI} + \mu^I_R\,\sigma^{KR})\right]_{;K} + p^I = \rho_o\,\ddot{u}^I \qquad (26a)$$

$$\eta_K\,(\sigma^{KI} + \mu^I_R\,\sigma^{KR}) = f^I \qquad (26b)$$

where the formulas

$$\ddot{\mu}^I = \left[\ddot{\mathcal{U}}^I\right]_U = \sqrt{G_{II}}\,\ddot{\mathcal{U}}^I\ ,$$

$$\mu^I_J = [\mathcal{U}^I_{;J}]_{U\otimes\underline{U}} = \frac{\sqrt{G_{II}}}{\sqrt{G_{JJ}}}\,\mathcal{U}^I_{;J}$$

$$\mu_{IJ} = [\mathcal{U}_{I;J}]_{\underline{U}\otimes\underline{U}} = \frac{\mathcal{U}_{I;J}}{\sqrt{G_{II}\,G_{JJ}}}\ ,$$

$$\sigma^{IJ} = [S^{IJ}]_{\underline{U}^\bullet\otimes U} = \frac{\sqrt{G_{JJ}}}{\sqrt{G\cdots}}\,S^{IJ}$$

$$p^I = [P^I]_U = \sqrt{G\cdots}$$

$$f^I = [F^I]_U = \sqrt{G_{II}}\,F^I \qquad (27a-l)$$

relate the vectorial and tensorial components which enter into equations (25b,c) to their anholonomic counterparts. The anholonomic components of $\mathcal{U}^I_{;J}$ and $\mathcal{U}_{I;J}$ can also be expressed as

$$\mu^I_J = \frac{\sqrt{G_{II}}}{\sqrt{G_{JJ}}}\left[\left(\frac{\mu^I}{\sqrt{G_{II}}}\right)_{,J} + \sum_{K=\mathrm{I}}^{\mathrm{III}}\frac{\mu^K}{\sqrt{G_{KK}}}\,\Gamma^I_{JK}\right] \qquad (28a)$$

$$\mu_{IJ} = \frac{1}{\sqrt{G_{II}}\sqrt{G_{JJ}}}\left[\left(\mu_I\sqrt{G_{II}}\right)_{,J} + \sum_{K=\mathrm{I}}^{\mathrm{III}}\sqrt{G_{KK}}\,\mu_K\,\Gamma^K_{IJ}\right] \qquad (28b)$$

by substituting into expressions (27d) and (27f) the following formulas

$$\mathcal{U}^I_{;J} = \left(\frac{\mu^I}{\sqrt{G_{II}}}\right)_{,J} + \sum_{K=\mathrm{I}}^{\mathrm{III}}\frac{\mu^K}{\sqrt{G_{KK}}}\,\Gamma^I_{JK} \qquad (28c)$$

$$\mathcal{U}_{I;J} = \left(\sqrt{G_{II}}\,\mu_I\right)_{,J} + \sum_{K=\mathrm{I}}^{\mathrm{III}}\mu_K\sqrt{G_{KK}}\,\Gamma^K_{IJ} \qquad (28d)$$

Kinematic and linear constitutive equations

The expression of Green strain tensor components

$$E_{IJ} = e_{IJ} + \frac{1}{2}\mathcal{U}_{M;I}\,\mathcal{U}^M_{;J} \qquad (29a)$$

when written in terms of anholonomic components, reads

$$\epsilon_{IJ} = \varepsilon_{IJ} + \frac{1}{2}\bar{\mu}_{MI}\,\mu^M_J \qquad (29b)$$

In these formulas

$$e_{IJ} = \frac{1}{2}(\mathcal{U}_{I;J} + \mathcal{U}_{J;I})$$

$$\epsilon_{IJ} = [E_{IJ}]_{U^\bullet\otimes\underline{U}} = \sqrt{\frac{G^{II}}{G_{JJ}}}\,E_{IJ}$$

$$\varepsilon_{IJ} = [e_{IJ}]_{U^\bullet\otimes\underline{U}} = \sqrt{\frac{G^{II}}{G_{JJ}}}e_{IJ} = \frac{1}{2}\sqrt{\frac{G^{II}}{G_{JJ}}}(\mathcal{U}_{I;J} + \mathcal{U}_{J;I})$$

$$\bar{\mu}_{MI} = [\mathcal{U}_{M;I}]_{\underline{U}\otimes U^\bullet} = \sqrt{\frac{G^{II}}{G_{MM}}}\,\mathcal{U}_{M;I}$$

$$\mu^M_J = [\mathcal{U}^M{}_{;J}]_{U\otimes\underline{U}} = \sqrt{\frac{G_{MM}}{G_{JJ}}}\,\mathcal{U}^M_{;J} \qquad (29c-l)$$

where $\mathcal{U}_{I;J}$ is given by Eq (28d) and

$$\mathcal{U}_{J;I} = \left(\sqrt{G_{JJ}}\,\mu_J\right)_{,I} + \sum_{K=\mathrm{I}}^{\mathrm{III}}\mu_K\sqrt{G_{KK}}\,\Gamma^K_{JI} \qquad (29m)$$

Furthermore, taking into account the last formula (and substituting J by M), the expression (29i) can be written as

$$\bar{\mu}_{MI} = \sqrt{\frac{G^{II}}{G_{MM}}}\left[\left(\sqrt{G_{MM}}\,\mu_M\right)_{,I} + \sum_{K=\mathrm{I}}^{\mathrm{III}} \sqrt{G_{KK}}\,\mu_K\,\Gamma^K_{MI}\right] \tag{30}$$

and the expression for μ^M_J is given by formula (28a) by making $M = I$.

In order to obtain the linear constitutive equations expressed in terms of anholonomic components, consider the following stress-strain relation

$$S^{IJ} = C^{IJKL}\,E_{KL} \tag{31}$$

where C^{IJKL} are the elastic coefficients. They depend on the metric of the undeformed body and on its physical properties. From the symmetries of the second Piola-Kirchhoff stress tensor S^{IJ} and Green's strain tensor E_{IJ}, it follows that $C^{IJKL} = C^{JIKL}$ and $C^{IJKL} = C^{IJLK}$. Furthermore, it should be pointed out that since the elastic potential is invariant under transformation of coordinates, the sets of anholonomic components of S^{IJ} and E_{IJ} are chosen so as to have reciprocal bases, that is, the bases $\underline{U}^* \otimes U$ and $U^* \otimes \underline{U}$, respectively. Thus, the anholonomic components of C^{IJKL} can be obtained from

$$\sum_{I,J,K,L} [C^{IJKL}]_B\,\vec{\underline{U}}_I \otimes \vec{U}_J \otimes \vec{\underline{U}}_K \otimes \vec{U}_L = \sum_{I,J,K,L} C^{IJKL}\,\vec{G}_I \otimes \vec{G}_J \otimes \vec{G}_K \otimes \vec{G}_L \tag{32a}$$

yielding

$$c^{IJKL} = \left[C^{IJKL}\right]_{\underline{U}^*\otimes U \otimes \underline{U}^* \otimes U} = \frac{\sqrt{G_{JJ}}\,\sqrt{G_{LL}}}{\sqrt{G^{II}}\sqrt{G^{KK}}} \tag{32b}$$

The substitution of formulas (27h), (29c), and (32b) into relation (31), leads to

$$\left[S^{IJ}\right]_{\underline{U}^*\otimes U} = \left[C^{IJKL}\right]_{\underline{U}^*\otimes U\otimes \underline{U}^*\otimes U}\,\left[E_{KL}\right]_{U^*\otimes \underline{U}} \tag{33a}$$

or

$$\sigma^{IJ} = c^{IJKL}\,\epsilon_{KL} \tag{33b}$$

As it can be seen from this discussion, the difference between equations (33b) and (31) lies only on their bases of reference.

SHELL EQUATIONS IN TERMS OF ANHOLONOMIC COMPONENTS

As another application, the geometrically nonlinear equations of the first order shear deformation shell theory (Pietraszkiewicz, 1979; Schmidt and Reddy, 1988; Altman and Palmerio, 1991 and 1992) will be expressed in terms of anholonomic components of vectors and tensors. In order to carry out this, the formulas for the anholonomic components of vectors and tensors on a surface will be determined and the derivation of the needed tensorial equations, based on the work of Altman and Palmerio (1991,1992), will be outlined in the next subsections.

Notation and geometry of a surface

Let $\mathcal{V}$ be the volume of the undeformed body bounded by the upper $\mathcal{S}^+$ and lower $\mathcal{S}^-$ surfaces, which are equidistant from the midsurface Ω, and by a lateral surface $\mathcal{A}$. The distance between $\mathcal{S}^+$ and $\mathcal{S}^-$, denoted by h, is the thickness of the shell. Let $\mathcal{A}_s$ and $\mathcal{A}_u$, be the two parts of the lateral boundary surface $\mathcal{A}$, where the stresses and displacements are prescribed, respectively. In addition, let Γ_s and Γ_u be the intersections of $\mathcal{A}_s$ and $\mathcal{A}_u$ with Ω, respectively. To each point of $\mathcal{V}$, it is associated a set of curvilinear coordinates $(\theta^{\mathrm{I}}, \theta^{\mathrm{II}}, \theta^{\mathrm{III}})$ where $(\theta^{\mathrm{I}}, \theta^{\mathrm{II}})$ denotes the curvilinear surface coordinates of a point in Ω and θ^{III} the normal coordinate to Ω. The position vector $\vec{R}$ at a point $(\theta^{\mathrm{I}}, \theta^{\mathrm{II}}, \theta^{\mathrm{III}})$ of $\mathcal{V}$ can be written as

$$\vec{R} = \vec{R}_0\,(\theta^{\mathrm{I}}, \theta^{\mathrm{II}}) + \theta^{\mathrm{III}}\,\vec{N}\,(\theta^{\mathrm{I}}, \theta^{\mathrm{II}}) \tag{34a}$$

where $\vec{R}_0$ is the position vector of a point $(\theta^{\mathrm{I}}, \theta^{\mathrm{II}})$ in Ω and $\vec{N}$ is the unit vector normal to Ω at point $(\theta^{\mathrm{I}}, \theta^{\mathrm{II}})$. In what follows, Greek indices will have range I, II, while Latin indices will have the values I, II, III. At each point in the undeformed shell space the covariant and contravariant base vectors $(\vec{G}_I, \vec{G}^I)$ and the corresponding components of metric tensor (G_{IJ}, G^{IJ}) are given by

$$\vec{G}_\Gamma = \vec{R}_{,\Gamma} = \vec{R}_{0,\Gamma} + \theta^{\mathrm{III}}\,\vec{N}_{,\Gamma} \quad , \quad \vec{G}_{\mathrm{III}} = \vec{N} \quad ,$$

$$G_{\Gamma\Lambda} = \vec{G}_\Gamma \cdot \vec{G}_\Lambda \quad , \quad \vec{G}^I = G^{IJ}\,\vec{G}_J \quad ,$$

$$G_{IK}\,G^{JK} = \delta^J_I \quad , \quad G^{\Gamma\mathrm{III}} = G_{\Gamma\mathrm{III}} = 0 \quad ,$$

$$G^{\mathrm{III}\,\mathrm{III}} = G_{\mathrm{III}\,\mathrm{III}} = 1 \tag{34b-k}$$

Similarly, at each point on the midsurface, the base vectors and their associated metrics read

$$\vec{A}_\Gamma = \vec{R}_{0,\Gamma} \quad , \quad A_{\Gamma\Lambda} = \vec{A}_\Gamma \cdot \vec{A}_\Lambda \quad ,$$

$$\vec{A}^\Gamma = A^{\Gamma\Lambda}\vec{A}_\Lambda \quad , \quad A^{\Gamma\Lambda}A_{\Omega\Lambda} = \delta^\Gamma_\Omega \tag{35a-d}$$

$$A^{\Gamma\mathrm{III}} = A_{\Gamma\mathrm{III}} = 0 \quad , \quad A^{\mathrm{III}\,\mathrm{III}} = A_{\mathrm{III}\,\mathrm{III}} = 1 \tag{35e-h}$$

The base vectors $\left(\vec{G}_I, \vec{G}^I\right)$ and their corresponding metrics (G_{IJ}, G^{IJ}) are related to those of the midsurface as follows:

$$\vec{G}_\Gamma = \lambda^\Lambda_\Gamma \vec{A}_\Lambda \quad , \quad \vec{G}^\Gamma = \left(\lambda^{-1}\right)^\Gamma_\Lambda \vec{A}^\Lambda \tag{36a,b}$$

$$G_{\Gamma\Lambda} = \lambda^\Omega_\Gamma \lambda^\Theta_\Lambda A_{\Omega\Theta} \quad , \tag{36c}$$

$$G^{\Gamma\Lambda} = \left(\lambda^{-1}\right)^\Gamma_\Omega \left(\lambda^{-1}\right)^\Lambda_\Theta A^{\Omega\Theta} \tag{36d}$$

where the components of the shifter tensor and its inverse are given by (Naghdi, 1963)

$$\lambda^\Lambda_\Gamma = \delta^\Lambda_\Gamma - \theta^{\mathrm{III}} B^\Lambda_\Gamma \quad , \quad \lambda^\Lambda_\Gamma \left(\lambda^{-1}\right)^\Omega_\Lambda = \delta^\Omega_\Gamma \tag{36e,f}$$

The components of the curvature tensor are defined by

$$B_{\Gamma\Lambda} = -\vec{A}_\Gamma \cdot \vec{N}_{,\Lambda} = \vec{N} \cdot \vec{A}_{\Gamma,\Lambda} \tag{36g,h}$$

The following definitions and relationships are needed in the sequel:

$$d\mathcal{V} = \mu\,d\theta^{\mathrm{III}}\,d\Omega \quad , \quad d\mathcal{S} = \mu\,d\Omega \quad , \tag{37a,b}$$

$$A = \det(A_{\Gamma\Lambda}) \quad , \quad G = \det(G_{IJ}) \quad , \qquad (37c,d)$$

$$\mu = \sqrt{G/A} \qquad (37e)$$

where dV is the volume element and $d\Omega$ and dS are the area elements of the midsurface and of a surface $\theta^{\mathrm{III}} \neq 0$, respectively.

The relative displacement vector $\vec{u}$ of any point in the shell space, referred to the undeformed configuration of the body, may be represented as

$$\vec{u} = \mathcal{U}^I \vec{G}_I = \mathcal{U}_I \vec{G}^I \qquad (38a,b)$$

or

$$\vec{u} = U^\Gamma \vec{A}_\Gamma + U^{\mathrm{III}} \vec{N} = U_\Gamma \vec{A}^\Gamma + U_{\mathrm{III}} \vec{N} \qquad (38c,d)$$

where $(\mathcal{U}_I, \mathcal{U}^I)$ and (U_Γ, U^Γ) are the covariant and contravariant components of the vector $\vec{u}$ in the shell space and on the midsurface, respectively. The derivative of $\vec{u}$ with respect to θ^J is given by

$$\vec{u}_{,J} = \mathcal{U}_{I;J} \vec{G}^I = \mathcal{U}^I_{;J} \vec{G}_I \qquad (38e,f)$$

where the symbol $(\ )_{;J}$ denotes the covariant derivative with respect to θ^J. The covariant derivative with respect to the surface metric is designated by a stroke, e.g., $(\ )_{|\Lambda}$. It should be noted that $\theta^J = \theta^j$ and $\theta^{\mathrm{III}} = \theta^3$, since the system of coordinates is supposed to be convective.

Anholonomic components of tensors on a surface

The vector $\vec{V}$ given by formulas $(6a,b)$ can also be expressed in terms of the base vectors $\vec{A}_\Gamma$ and $\vec{N}$ in Ω as

$$\vec{V} = V^\Gamma \vec{A}_\Gamma + V^{\mathrm{III}} \vec{N} = V_\Gamma \vec{A}^\Gamma + V_{\mathrm{III}} \vec{N} \qquad (39a,b)$$

with $\Gamma = \mathrm{I}, \mathrm{II}$, where (V^Γ, V_Γ) denote the contravariant and covariant components of $\vec{V}$ in Ω. Similarly, as it was done before, the unit base vectors read

$$\vec{N}_\Gamma = \frac{\vec{A}_\Gamma}{\sqrt{A_{\Gamma\Gamma}}} \quad , \quad \vec{N}^\Gamma = \frac{\vec{A}^\Gamma}{\sqrt{A^{\Gamma\Gamma}}} \quad ,$$

$$\vec{A}_{\mathrm{III}} = \vec{A}^{\mathrm{III}} = \vec{N} \qquad (39c-f)$$

and their reciprocal bases

$$\underline{\vec{N}}^\Gamma = \sqrt{A_{\Gamma\Gamma}} \vec{A}^\Gamma \quad , \quad \underline{\vec{N}}_\Gamma = \sqrt{A^{\Gamma\Gamma}} \vec{A}_\Gamma \quad ,$$

$$\underline{\vec{A}}^{\mathrm{III}} = \underline{\vec{A}}_{\mathrm{III}} = \vec{N} \quad , \quad \Gamma = \mathrm{I}, \mathrm{II} \qquad (39g-j)$$

Expanding the vector $\vec{V}$ with respect to these bases, one obtains

$$\vec{V} = [V^\Gamma]_N \vec{N}_\Gamma + V^{\mathrm{III}} \vec{N} = [V_\Gamma]_{N^*} \vec{N}^\Gamma + V_{\mathrm{III}} \vec{N} \qquad (40a,b)$$

$$= [V_\Gamma]_{\underline{N}} \underline{\vec{N}}^\Gamma + V_{\mathrm{III}} \vec{N} = [V^\Gamma]_{\underline{N}^*} \underline{\vec{N}}_\Gamma + V^{\mathrm{III}} \vec{N} \qquad (40c,d)$$

where

$$[V^\Gamma]_N = \sqrt{A_{\Gamma\Gamma}} V^\Gamma \quad , \quad [V_\Gamma]_{N^*} = \sqrt{A^{\Gamma\Gamma}} V_\Gamma \quad ,$$

$$[V^{\mathrm{III}}]_N = [V_{\mathrm{III}}]_{N^*} = V^{\mathrm{III}} = V_{\mathrm{III}} \qquad (40e-i)$$

$$[V_\Gamma]_{\underline{N}} = \frac{V_\Gamma}{\sqrt{A_{\Gamma\Gamma}}} \quad , \quad [V^\Gamma \quad ,$$

$$[V_{\mathrm{III}}]_{\underline{N}} = [V^{\mathrm{III}}]_{\underline{N}^*} = V_{\mathrm{III}} = V^{\mathrm{III}} \qquad (40j-n)$$

are the physical or anholonomic components of $\vec{V}$ on the surface Ω relative to the bases $N = \{\vec{N}_I\}$, $N^* = \{\vec{N}^I\}$, $\underline{N} = \{\underline{\vec{N}}^I\}$, and $\underline{N}^* = \{\underline{\vec{N}}_I\}$, $I = \Gamma, \mathrm{III}$.

A second order tensor of single field $\mathcal{T}$ on a surface Ω can be defined as linear combinations of tensor products of the type $\underset{\sim}{N}_1 \otimes \underset{\sim}{N}_2$, where $\underset{\sim}{N}_1$ and $\underset{\sim}{N}_2$ are elements that belong to one of the bases of the set $\{N, N^*, \underline{N}, \underline{N}^*\}$. For example, the expressions

$$\mathcal{T} = \sum_{I,J} [T^{IJ}]_{\mathcal{B}} \vec{N}_I \otimes \vec{N}_J = \sum_{I,J} T^{IJ} \vec{A}_I \otimes \vec{A}_J \qquad (41a,b)$$

represent a covariant second order tensor of single field on the surface Ω, where $I, J = \Gamma, \mathrm{III}$, $\mathcal{B} = N \otimes N$ is a basis of the considered tensorial space, and the notation $[T^{IJ}]_{\mathcal{B}}$ denote the anholonomic components of the tensor of single field referred to the basis $\mathcal{B}$. Taking into account the identity $(41a,b)$ and the expressions of $\vec{N}_I$ and $\vec{N}_J$ as functions of $\vec{A}_I$ and $\vec{A}_J$, respectively, one obtains

$$[T^{IJ}]_{N \otimes N} = \sqrt{A_{II}} \sqrt{A_{JJ}}\, T^{IJ} \quad I, J = \Gamma, \mathrm{III} \qquad (41c)$$

where $A_{\mathrm{III}} = A^{\mathrm{III}} = 1$. This formula will be utilized in the sequel to obtain the anholonomic components of the stress tensor and also as a starting point to construct a compatible set of anholonomic components for the shell equations.

Strain-displacement relations

The kinematic equations of a shell are derived here from the Green-Lagrange strain tensor which can be written in terms of the displacement gradient components in the shell space as

$$E_{IJ} = \frac{1}{2} (\mathcal{U}_{I;J} + \mathcal{U}_{J;I} + \mathcal{U}_{M;I}\, \mathcal{U}^M_{;J}) \qquad (42a)$$

This relation, along with

$$\mathcal{U}^{\mathrm{III}}_{;\Gamma} = \mathcal{U}_{\mathrm{III};\Gamma} = \Phi_{\Gamma\mathrm{III}} = U_{\mathrm{III},\Gamma} + B^\Lambda_\Gamma U_\Lambda \quad ,$$

$$\mathcal{U}^\Lambda_{;\Gamma} = G^{\Omega\Lambda}\, \mathcal{U}_{\Omega;\Gamma} \quad , \quad \mathcal{U}_{\Lambda;\Gamma} = \lambda^\Omega_\Lambda\, \Phi_{\Omega\Gamma} \quad ,$$

$$\mathcal{U}_{\Omega;\Gamma}\, \mathcal{U}^\Omega_{;\Lambda} = \Phi_{\Omega\Gamma}\, \Phi^\Omega_{.\Lambda} \quad , \quad \mathcal{U}^\Lambda_{;\mathrm{III}} = (\lambda^{-1})^\Lambda_\Omega\, U^\Omega_{,\mathrm{III}} \quad ,$$

$$\Phi_{\Lambda\Gamma} = U_{\Lambda|\Gamma} - B_{\Lambda\Gamma}\, U_{\mathrm{III}} \quad , \quad \Phi^\Lambda_{.\Gamma} = U^\Lambda_{|\Gamma} - B^\Lambda_{.\Gamma}\, U_{\mathrm{III}} \quad ,$$

$$\mathcal{U}_{\Gamma;\mathrm{III}} = \lambda^\Omega_\Gamma\, U_{\Omega,\mathrm{III}} = U_{\Gamma,\mathrm{III}} - \theta^{\mathrm{III}}\, B^\Omega_\Gamma\, U_{\Omega,\mathrm{III}} \quad ,$$

$$\mathcal{U}_{\mathrm{III};\mathrm{III}}\, \mathcal{U}^{\mathrm{III}}_{;\mathrm{III}} = (U_{\mathrm{III},\mathrm{III}})^2 \quad , \quad \mathcal{U}_{\Gamma;\mathrm{III}}\, \mathcal{U}^\Gamma_{;\mathrm{III}} = U_{\Gamma,\mathrm{III}}\, U^\Gamma_{,\mathrm{III}} \quad ,$$

$$\mathcal{U}_{\mathrm{III};\Gamma}\, \mathcal{U}^{\mathrm{III}}_{;\Lambda} = \Phi_{\Gamma\mathrm{III}}\, \Phi_{\Lambda\mathrm{III}} \quad , \quad \mathcal{U}_{\Lambda;\Gamma}\, \mathcal{U}^\Lambda_{;\mathrm{III}} = \Phi_{\Lambda\Gamma}\, U^\Lambda_{,\mathrm{III}} \quad ,$$

$$\mathcal{U}_{\mathrm{III};\Gamma}\, \mathcal{U}^{\mathrm{III}}_{;\mathrm{III}} = \Phi_{\Gamma\mathrm{III}}\, U_{\mathrm{III},\mathrm{III}} \qquad (42b-q)$$

yield the following expressions for the strain components:

$$E_{\Gamma\Lambda} = e_{\Gamma\Lambda} + \frac{1}{2} (\Phi_{\Gamma\mathrm{III}}\, \Phi_{\Lambda\mathrm{III}} + \Phi_{\Omega\Gamma}\, \Phi^\Omega_{\Lambda}) \quad ,$$

$$E_{\Gamma\mathrm{III}} = e_{\Gamma\mathrm{III}} + \frac{1}{2} U^\Omega_{,\mathrm{III}}\, \Phi_{\Omega\Gamma} + \frac{1}{2} \Phi_{\Gamma\mathrm{III}}\, U^{\mathrm{III}}_{,\mathrm{III}} \quad ,$$

$$E_{\mathrm{III}\mathrm{III}} = e_{\mathrm{III}\mathrm{III}} + \frac{1}{2} U^{\Omega}_{,\mathrm{III}}\, U_{\Omega,\mathrm{III}}$$

where

$$2\,e_{\Gamma\Lambda} = \Phi_{\Gamma\Lambda} + \Phi_{\Lambda\Gamma} - \theta^{\mathrm{III}} \left(B^{\Omega}_{\Gamma}\, \Phi_{\Omega\Lambda} + B^{\Omega}_{\Lambda}\, \Phi_{\Omega\Gamma}\right) \quad ,$$

$$2\,e_{\Gamma\mathrm{III}} = U_{\Gamma,\mathrm{III}} + \Phi_{\Gamma\,\mathrm{III}} - \theta^{\mathrm{III}}\, B^{\Omega}_{\Gamma}\, U_{\Omega,\mathrm{III}} \quad ,$$

$$e_{\mathrm{III}\mathrm{III}} = U_{\mathrm{III},\mathrm{III}} \qquad (43a-f)$$

Introducing the following representation of the displacement components across the shell thickness

$$U_I\left(\theta^{\Gamma},\theta^{\mathrm{III}},t\right) = \overset{(0)}{U}_I\left(\theta^{\Gamma},t\right) + \theta^{\mathrm{III}}\, \overset{(1)}{U}_I\left(\theta^{\Gamma},t\right) \qquad (44)$$

into relations $(43a-f)$, one obtains

$$E_{\Gamma\Lambda} = \overset{(0)}{E}_{\Gamma\Lambda} + \theta^{\mathrm{III}}\, \overset{(1)}{E}_{\Gamma\Lambda} + \left(\theta^{\mathrm{III}}\right)^2 \overset{(2)}{E}_{\Gamma\Lambda} \qquad (45a)$$

$$E_{\Gamma\mathrm{III}} = \overset{(0)}{E}_{\Gamma\mathrm{III}} + \theta^{\mathrm{III}}\, \overset{(1)}{E}_{\Gamma\mathrm{III}} \quad , \quad E_{\mathrm{III}\mathrm{III}} = \overset{(0)}{E}_{\mathrm{III}\mathrm{III}} \qquad (45b,c)$$

where

$$\overset{(0)}{E}_{\Gamma\Lambda} = \overset{(0)}{e}_{\Gamma\Lambda} + \frac{1}{2}\left(\overset{(0)}{\Phi}_{\Gamma\mathrm{III}}\, \overset{(0)}{\Phi}_{\Lambda\mathrm{III}} + \overset{(0)}{\Phi}_{\Omega\Gamma}\, \overset{(0)}{\Phi}{}^{\Omega}_{\Lambda}\right)$$

$$\overset{(1)}{E}_{\Gamma\Lambda} = \overset{(1)}{e}_{\Gamma\Lambda} + \frac{1}{2}\left(\overset{(0)}{\Phi}_{\Gamma\mathrm{III}}\, \overset{(1)}{\Phi}_{\Lambda\mathrm{III}} \right.$$

$$\left. + \overset{(1)}{\Phi}_{\Gamma\mathrm{III}}\, \overset{(0)}{\Phi}_{\Lambda\mathrm{III}} + \overset{(0)}{\Phi}_{\Omega\Gamma}\, \overset{(1)}{\Phi}{}^{\Omega}{}_{\Lambda} + \overset{(1)}{\Phi}_{\Omega\Gamma}\, \overset{(0)}{\Phi}{}^{\Omega}_{\Lambda}\right)$$

$$\overset{(2)}{E}_{\Gamma\Lambda} = \overset{(2)}{e}_{\Gamma\Lambda} + \frac{1}{2}\left(\overset{(1)}{\Phi}_{\Gamma\mathrm{III}}\, \overset{(1)}{\Phi}_{\Lambda\mathrm{III}} + \overset{(1)}{\Phi}_{\Omega\Gamma}\, \overset{(1)}{\Phi}{}^{\Omega}_{\Lambda}\right)$$

$$\overset{(0)}{E}_{\Gamma\mathrm{III}} = \overset{(0)}{e}_{\Gamma\mathrm{III}} + \frac{1}{2}\left(\overset{(1)}{U}{}^{\Omega}\, \overset{(0)}{\Phi}_{\Omega\Gamma} + \overset{(1)}{U}_{\mathrm{III}}\, \overset{(0)}{\Phi}_{\Gamma\mathrm{III}}\right)$$

$$\overset{(1)}{E}_{\Gamma\mathrm{III}} = \overset{(1)}{e}_{\Gamma\mathrm{III}} + \frac{1}{2}\left(\overset{(1)}{U}{}^{\Omega}\, \overset{(1)}{\Phi}_{\Omega\Gamma} + \overset{(1)}{U}_{\mathrm{III}}\, \overset{(1)}{\Phi}_{\Gamma\mathrm{III}}\right)$$

$$\overset{(0)}{E}_{\mathrm{III}\mathrm{III}} = \overset{(0)}{e}_{\mathrm{III}\mathrm{III}} + \frac{1}{2}\left(\overset{(1)}{U}{}^{\Omega}\, \overset{(1)}{U}_{\Omega} + \overset{(1)}{U}_{\mathrm{III}}\, \overset{(1)}{U}{}^{\mathrm{III}}\right) \qquad (46a-f)$$

and

$$\overset{(0)}{e}_{\Gamma\Lambda} = \frac{1}{2}\left(\overset{(0)}{\Phi}_{\Gamma\Lambda} + \overset{(0)}{\Phi}_{\Lambda\Gamma}\right) \quad ,$$

$$\overset{(1)}{e}_{\Gamma\Lambda} = \frac{1}{2}\left(\overset{(1)}{\Phi}_{\Gamma\Lambda} + \overset{(1)}{\Phi}_{\Lambda\Gamma} - B^{\Omega}_{\Gamma}\, \overset{(0)}{\Phi}_{\Omega\Lambda} - B^{\Omega}_{\Lambda}\, \overset{(0)}{\Phi}_{\Omega\Gamma}\right) \quad ,$$

$$\overset{(2)}{e}_{\Gamma\Lambda} = -\frac{1}{2}\left(B^{\Omega}_{\Gamma}\, \overset{(1)}{\Phi}_{\Omega\Lambda} + B^{\Omega}_{\Lambda}\, \overset{(1)}{\Phi}_{\Omega\Gamma}\right) \quad ,$$

$$\overset{(0)}{e}_{\Gamma\mathrm{III}} = \frac{1}{2}\left(\overset{(0)}{\Phi}_{\Gamma\mathrm{III}} + \overset{(1)}{U}_{\Gamma}\right) \quad , \quad \overset{(0)}{e}_{\mathrm{III}\mathrm{III}} = \overset{(0)}{U}_{\mathrm{III}} \quad ,$$

$$\overset{(1)}{e}_{\Gamma\mathrm{III}} = \frac{1}{2}\left(\overset{(1)}{\Phi}_{\Gamma\mathrm{III}} - B^{\Omega}_{\Gamma}\, \overset{(1)}{U}_{\Omega}\right) \quad ,$$

$$\overset{(0)}{\Phi}_{\Gamma\mathrm{III}} = \overset{(0)}{U}_{\mathrm{III},\Gamma} + B^{\Omega}_{\Gamma}\, \overset{(0)}{U}_{\Omega} \quad , \quad \overset{(1)}{\Phi}_{\Gamma\mathrm{III}} = \overset{(1)}{U}_{\mathrm{III},\Gamma} + B^{\Omega}_{\Gamma}\, \overset{(1)}{U}_{\Omega}$$

$$\overset{(0)}{\Phi}_{\Gamma\Lambda} = \overset{(0)}{U}_{\Gamma|\Lambda} - B_{\Gamma\Lambda}\, \overset{(0)}{U}_{\mathrm{III}} \quad , \quad \overset{(1)}{\Phi}_{\Gamma\Lambda} = \overset{(1)}{U}_{\Gamma|\Lambda} - B_{\Gamma\Lambda}\, \overset{(1)}{U}_{\mathrm{III}}$$

$$\overset{(0)}{\Phi}{}^{\Gamma}_{.\Lambda} = \overset{(0)}{U}{}^{\Gamma}_{|\Lambda} - B^{\Gamma}_{.\Lambda}\, \overset{(0)}{U}_{\mathrm{III}} \quad ,$$

$$\overset{(1)}{\Phi}{}^{\Gamma}_{.\Lambda} = \overset{(1)}{U}{}^{\Gamma}_{|\Lambda} - B^{\Gamma}_{.\Lambda}\, \overset{(1)}{U}_{\mathrm{III}} \qquad (47a-l)$$

Since the elastic potential is invariant under transformation of coordinates, the anholonomic components of the stresses and strains will be chosen so as to have the following reciprocal bases $N \otimes N$ and $\underline{N} \otimes \underline{N}$, respectively. Taking into account formulas (40), and the expressions which define the anholonomic components of second order tensors relative to the bases $\underline{N} \otimes \underline{N}$ and $N \otimes \underline{N}$, it can be written

$$\overset{(n)}{u}{}^{\Gamma} = \left[\overset{(n)}{U}{}^{\Gamma}\right]_{N} = \sqrt{A_{\Gamma\Gamma}}\, \overset{(n)}{U}{}^{\Gamma} \quad ,$$

$$\overset{(n)}{u}_{\Gamma} = \left[\overset{(n)}{U}_{\Gamma}\right]_{\underline{N}} = \frac{1}{\sqrt{A_{\Gamma\Gamma}}}\, \overset{(n)}{U}_{\Gamma} \quad ,$$

$$\overset{(n)}{u}{}^{\mathrm{III}} = \left[\overset{(n)}{U}{}^{\mathrm{III}}\right] = \overset{(n)}{U}{}^{\mathrm{III}} \quad , \quad \overset{(n)}{u}{}^{\mathrm{III}} = \overset{(n)}{u}_{\mathrm{III}} = \overset{(n)}{U}_{\mathrm{III}} \quad ,$$

$$b^{\Gamma}_{.\Lambda} = \left[B^{\Gamma}_{.\Lambda}\right]_{N\otimes\underline{N}} = \frac{\sqrt{A_{\Gamma\Gamma}}}{\sqrt{A_{\Lambda\Lambda}}}\, B^{\Gamma}_{.\Lambda} \quad ,$$

$$b_{\Gamma\Lambda} = \left[B_{\Gamma\Lambda}\right]_{\underline{N}\otimes\underline{N}} = \frac{B_{\Gamma\Lambda}}{\sqrt{A_{\Gamma\Gamma}}\sqrt{A_{\Lambda\Lambda}}} \quad ,$$

$$\overset{(n)}{u}_{\Gamma\Lambda} = \left[\overset{(n)}{U}_{\Gamma|\Lambda}\right]_{\underline{N}\otimes\underline{N}} = \frac{1}{\sqrt{A_{\Gamma\Gamma}}\sqrt{A_{\Lambda\Lambda}}}\, \overset{(n)}{U}_{\Gamma|\Lambda} \quad ,$$

$$\overset{(n)}{u}{}^{\Gamma}{}_{\Lambda} = \left[\overset{(n)}{U}{}^{\Gamma}{}_{|\Lambda}\right]_{N\otimes\underline{N}} = \frac{\sqrt{A_{\Gamma\Gamma}}}{\sqrt{A_{\Lambda\Lambda}}}\, \overset{(n)}{U}{}^{\Gamma}{}_{|\Lambda} \quad ,$$

$$\overset{(n)}{\varphi}_{\Gamma\Lambda} = \left[\overset{(n)}{\Phi}_{\Gamma\Lambda}\right]_{\underline{N}\otimes\underline{N}} = \frac{1}{\sqrt{A_{\Gamma\Gamma}}\sqrt{A_{\Lambda\Lambda}}}\, \overset{(n)}{\Phi}_{\Gamma\Lambda} \quad ,$$

$$\overset{(n)}{\varphi}{}^{\Gamma}{}_{.\Lambda} = \left[\overset{(n)}{\Phi}{}^{\Gamma}{}_{.\Lambda}\right]_{N\otimes\underline{N}} = \frac{\sqrt{A_{\Gamma\Gamma}}}{\sqrt{A_{\Lambda\Lambda}}}\, \overset{(n)}{\Phi}{}^{\Gamma}{}_{.\Lambda} \quad ,$$

$$\overset{(n)}{\varphi}_{\Gamma\mathrm{III}} = \overset{(n)}{\varphi}_{\mathrm{III}\Gamma} = \overset{(n)}{\varphi}{}^{\mathrm{III}}{}_{.\Gamma} = \left[\overset{(n)}{\Phi}_{\Gamma\mathrm{III}}\right]_{\underline{N}} = \frac{1}{\sqrt{A_{\Gamma\Gamma}}}\, \overset{(n)}{\Phi}_{\Gamma\mathrm{III}} \qquad (48a-z)$$

where $n = 0, 1$. After substituting in these formulas

$$\overset{(n)}{U}_{\Gamma|\Lambda} = \overset{(n)}{U}_{\Gamma,\Lambda} - \overset{(n)}{U}_{\Omega}\, \Gamma^{\Omega}_{\Gamma\Lambda} = \left(\sqrt{A_{\Gamma\Gamma}}\, \overset{(n)}{u}_{\Gamma}\right)_{,\Lambda}$$

$$- \sum_{\Omega=\mathrm{I}}^{\mathrm{II}} \left(\sqrt{A_{\Omega\Omega}}\, \overset{(n)}{u}_{\Omega}\right) \Gamma^{\Omega}_{\Gamma\Lambda} \qquad (49a,b)$$

$$\overset{(n)}{U}{}^{\Gamma}{}_{|\Lambda} = \overset{(n)}{U}{}^{\Gamma}{}_{,\Lambda} - \overset{(n)}{U}{}^{\Omega}\,\Gamma^{\Gamma}_{\Omega\Lambda} = \left(\frac{\overset{(n)}{u}{}^{\Gamma}}{\sqrt{A_{\Gamma\Gamma}}}\right)_{,\Lambda} - \sum_{\Omega=\mathrm{I}}^{\mathrm{II}} \frac{\overset{(n)}{u}{}^{\Omega}}{\sqrt{A_{\Omega\Omega}}}\Gamma^{\Gamma}_{\Omega\Lambda} \qquad (49c,d)$$

$$\overset{(n)}{\Phi}{}_{\Gamma\Lambda} = \overset{(n)}{U}{}_{\Gamma|\Lambda} - B_{\Gamma\Lambda}\,\overset{(n)}{U}{}_{\mathrm{III}} = \left(\sqrt{A_{\Gamma\Gamma}}\,\overset{(n)}{u}{}_{\Gamma}\right)_{|\Lambda} - \sqrt{A_{\Gamma\Gamma}}\sqrt{A_{\Lambda\Lambda}}\,b_{\Gamma\Lambda}\,\overset{(n)}{u}{}_{\mathrm{III}} \qquad (49e,f)$$

$$\overset{(n)}{\Phi}{}^{\Gamma}{}_{\Lambda} = \overset{(n)}{U}{}^{\Gamma}{}_{|\Lambda} - B^{\Gamma}_{\Lambda}\,\overset{(n)}{U}{}_{\mathrm{III}} = \left(\frac{\overset{(n)}{u}{}^{\Gamma}}{\sqrt{A_{\Gamma\Gamma}}}\right)_{|\Lambda} - \frac{\sqrt{A_{\Lambda\Lambda}}}{\sqrt{A_{\Gamma\Gamma}}}\,b^{\Gamma}_{\Lambda}\,\overset{(n)}{u}{}_{\mathrm{III}} \qquad (49g,h)$$

$$\overset{(n)}{\Phi}{}_{\Gamma\mathrm{III}} = \overset{(n)}{U}{}_{\mathrm{III},\Gamma} + B^{\Omega}_{.\Gamma}\,\overset{(n)}{U}{}_{\Omega} = \left(\overset{(n)}{u}{}_{\mathrm{III}}\right)_{,\Gamma} + \sqrt{A_{\Gamma\Gamma}}\,b^{\Omega}_{.\Gamma}\,\overset{(n)}{u}{}_{\Omega} \qquad (49i,j)$$

where

$$\Gamma^{\Omega}_{\Gamma\Lambda} = g^{\Omega\Theta}\,\Gamma_{\Gamma\Lambda\Theta} = \frac{1}{2}g^{\Omega\Theta}\left(A_{\Gamma\Theta,\Lambda} + A_{\Lambda\Theta,\Gamma} - A_{\Gamma\Lambda,\Theta}\right) \qquad (49k,l)$$

it is obtained

$$\overset{(n)}{u}{}_{\Gamma\Lambda} = \frac{1}{\sqrt{A_{\Gamma\Gamma}}\sqrt{A_{\Lambda\Lambda}}}\left[\left(\sqrt{A_{\Gamma\Gamma}}\,\overset{(n)}{u}{}_{\Gamma}\right)_{,\Lambda} - \sum_{\Omega=\mathrm{I}}^{\mathrm{II}}\sqrt{A_{\Omega\Omega}}\,\overset{(n)}{u}{}_{\Omega}\,\Gamma^{\Omega}_{\Gamma\Lambda}\right] \qquad (50a)$$

$$\overset{(n)}{u}{}^{\Gamma}_{\Lambda} = \frac{\sqrt{A_{\Gamma\Gamma}}}{\sqrt{A_{\Lambda\Lambda}}}\left[\left(\frac{\overset{(n)}{u}{}^{\Gamma}}{\sqrt{A_{\Gamma\Gamma}}}\right)_{,\Lambda} - \sum_{\Omega=\mathrm{I}}^{\mathrm{II}}\frac{\overset{(n)}{u}{}^{\Omega}}{\sqrt{A_{\Omega\Omega}}}\,\Gamma^{\Gamma}_{\Omega\Lambda}\right] \qquad (50b)$$

$$\overset{(n)}{\varphi}{}_{\Gamma\Lambda} = \frac{1}{\sqrt{A_{\Gamma\Gamma}}\sqrt{A_{\Lambda\Lambda}}}\left[\left(\sqrt{A_{\Gamma\Gamma}}\,\overset{(n)}{u}{}_{\Gamma}\right)_{|\Lambda} - \sqrt{A_{\Gamma\Gamma}}\,\sqrt{A_{\Lambda\Lambda}}\,b_{\Gamma\Lambda}\,\overset{(n)}{u}{}_{\mathrm{III}}\right] \qquad (50c)$$

$$\overset{(n)}{\varphi}{}^{\Gamma}_{\Lambda} = \frac{\sqrt{A_{\Gamma\Gamma}}}{\sqrt{A_{\Lambda\Lambda}}}\left[\left(\frac{\overset{(n)}{u}{}^{\Gamma}}{\sqrt{A_{\Gamma\Gamma}}}\right)_{|\Lambda} - \frac{\sqrt{A_{\Lambda\Lambda}}}{\sqrt{A_{\Gamma\Gamma}}}\,b^{\Gamma}_{\Lambda}\,\overset{(n)}{u}{}_{\mathrm{III}}\right] \qquad (50d)$$

$$\overset{(n)}{\varphi}{}_{\Gamma\mathrm{III}} = \frac{1}{\sqrt{A_{\Gamma\Gamma}}}\left[\left(\overset{(n)}{u}{}_{\mathrm{III}}\right) \qquad \overset{(n)}{u}{}_{\Omega}\right] \qquad (50e)$$

Furthermore, taking into account that the anholonomic components of $\overset{(m)}{E}{}_{\Gamma\Lambda}$, $\overset{(m)}{e}{}_{\Gamma\Lambda}$, $\overset{(n)}{E}{}_{\Gamma\mathrm{III}}$, $\overset{(n)}{e}{}_{\Gamma\mathrm{III}}$, $\overset{(o)}{E}{}_{\mathrm{III}\mathrm{III}}$, $\overset{(o)}{e}{}_{\mathrm{III}\mathrm{III}}$, for $m = 0, 1, 2$ and $n = 0, 1$, are given by

$$\overset{(m)}{\epsilon}{}_{\Gamma\Lambda} = \left[\overset{(m)}{E}{}_{\Gamma\Lambda}\right]_{\underline{N}\otimes\underline{N}} = \frac{1}{\sqrt{A_{\Gamma\Gamma}}\sqrt{A_{\Lambda\Lambda}}}\overset{(m)}{E}{}_{\Gamma\Lambda} \quad ,$$

$$\overset{(m)}{\varepsilon}{}_{\Gamma\Lambda} = \left[\overset{(m)}{e}{}_{\Gamma\Lambda}\right]_{\underline{N}\otimes\underline{N}} = \frac{1}{\sqrt{A_{\Gamma\Gamma}}\sqrt{A_{\Lambda\Lambda}}}\overset{(m)}{e}{}_{\Gamma\Lambda} \quad ,$$

$$\overset{(n)}{\epsilon}{}_{\Gamma\mathrm{III}} = \left[\overset{(n)}{E}{}_{\Gamma\mathrm{III}}\right]_{\underline{N}} = \frac{1}{\sqrt{A_{\Gamma\Gamma}}}\overset{(n)}{E}{}_{\Gamma\mathrm{III}} \quad ,$$

$$\overset{(n)}{\varepsilon}{}_{\Gamma\mathrm{III}} = \left[\overset{(n)}{e}{}_{\Gamma\mathrm{III}}\right]_{\underline{N}} = \frac{1}{\sqrt{A_{\Gamma\Gamma}}}\overset{(n)}{e}{}_{\Gamma\mathrm{III}} \quad ,$$

$$\overset{(0)}{\epsilon}{}_{\mathrm{III}\mathrm{III}} = \left[E_{\mathrm{III}\mathrm{III}}\right] = E_{\mathrm{III}\mathrm{III}} \quad ,$$

$$\overset{(0)}{\varepsilon}{}_{\mathrm{III}\mathrm{III}} = \left[\overset{(0)}{e}{}_{\mathrm{III}\mathrm{III}}\right] = \overset{(0)}{e}{}_{\mathrm{III}\mathrm{III}} \qquad (51a-l)$$

the substitution of the vector and tensor components of expressions (46) and (47) in terms of their anholonomic counterparts given by formulas (48) and (51), leads to

$$\overset{(0)}{\epsilon}{}_{\Gamma\Lambda} = \overset{(0)}{\varepsilon}{}_{\Gamma\Lambda} + \frac{1}{2}\left(\overset{(0)}{\varphi}{}_{\Gamma\mathrm{III}}\,\overset{(0)}{\varphi}{}_{\Lambda\mathrm{III}} + \overset{(0)}{\varphi}{}_{\Omega\Gamma}\,\overset{(0)}{\varphi}{}^{\Omega}_{.\Lambda}\right)$$

$$\overset{(1)}{\epsilon}{}_{\Gamma\Lambda} = \overset{(1)}{\varepsilon}{}_{\Gamma\Lambda} + \frac{1}{2}\left(\overset{(0)}{\varphi}{}_{\Gamma\mathrm{III}}\,\overset{(1)}{\varphi}{}_{\Lambda\mathrm{III}} + \overset{(1)}{\varphi}{}_{\Gamma\mathrm{III}}\,\overset{(0)}{\varphi}{}_{\Lambda\mathrm{III}} + \overset{(0)}{\varphi}{}_{\Omega\Gamma}\,\overset{(1)}{\varphi}{}^{\Omega}_{\Lambda} + \overset{(1)}{\varphi}{}_{\Omega\Gamma}\,\overset{(0)}{\varphi}{}^{\Omega}_{\Lambda}\right)$$

$$\overset{(2)}{\epsilon}{}_{\Gamma\Lambda} = \overset{(2)}{\varepsilon}{}_{\Gamma\Lambda} + \frac{1}{2}\left(\overset{(1)}{\varphi}{}_{\Gamma\mathrm{III}}\,\overset{(1)}{\varphi}{}_{\Lambda\mathrm{III}} + \overset{(1)}{\varphi}{}_{\Omega\Gamma}\,\overset{(1)}{\varphi}{}^{\Omega}_{.\Lambda}\right)$$

$$\overset{(0)}{\epsilon}{}_{\Gamma\mathrm{III}} = \overset{(0)}{\varepsilon}{}_{\Gamma\mathrm{III}} + \frac{1}{2}\left(\overset{(1)}{u}{}^{\Omega}\,\overset{(0)}{\varphi}{}_{\Omega\Gamma} + \overset{(1)}{u}{}_{\mathrm{III}}\,\overset{(0)}{\varphi}{}_{\Gamma\mathrm{III}}\right)$$

$$\overset{(1)}{\epsilon}{}_{\Gamma\mathrm{III}} = \overset{(1)}{\varepsilon}{}_{\Gamma\mathrm{III}} + \frac{1}{2}\left(\overset{(1)}{u}{}^{\Omega}\,\overset{(1)}{\varphi}{}_{\Omega\Gamma} + \overset{(1)}{u}{}_{\mathrm{III}}\,\overset{(1)}{\varphi}{}_{\Gamma\mathrm{III}}\right)$$

$$\overset{(0)}{\epsilon}{}_{\mathrm{III}\mathrm{III}} = \overset{(0)}{\varepsilon}{}_{\mathrm{III}\mathrm{III}} + \frac{1}{2}\left(\overset{(1)}{u}{}^{\Omega}\,\overset{(1)}{u}{}_{\Omega} + \overset{(1)}{u}{}_{\mathrm{III}}\,\overset{(1)}{u}{}^{\mathrm{III}}\right) \qquad (52a-f)$$

and

$$\overset{(0)}{\varepsilon}{}_{\Gamma\Lambda} = \frac{1}{2}\left(\overset{(0)}{\varphi}{}_{\Gamma\Lambda} + \overset{(0)}{\varphi}{}_{\Lambda\Gamma}\right) \quad ,$$

$$\overset{(1)}{\varepsilon}{}_{\Gamma\Lambda} = \frac{1}{2}\left(\overset{(1)}{\varphi}{}_{\Gamma\Lambda} + \overset{(1)}{\varphi}{}_{\Lambda\Gamma} - b^{\Omega}_{\Gamma}\,\overset{(0)}{\varphi}{}_{\Omega\Lambda} - b^{\Omega}_{\Lambda}\,\overset{(0)}{\varphi}{}_{\Omega\Gamma}\right)$$

$$\overset{(2)}{\varepsilon}{}_{\Gamma\Lambda} = -\frac{1}{2}\left(b^{\Omega}_{\Gamma}\,\overset{(1)}{\varphi}{}_{\Omega\Lambda} + b^{\Omega}_{\Lambda}\,\overset{(1)}{\varphi}{}_{\Omega\Gamma}\right) \quad ,$$

$$\overset{(0)}{\varepsilon}{}_{\Gamma\mathrm{III}} = \frac{1}{2}\left(\overset{(0)}{\varphi}{}_{\Gamma\mathrm{III}} + \overset{(1)}{u}{}_{\Gamma}\right) \quad , \quad \overset{(0)}{\varepsilon}{}_{\mathrm{III}\mathrm{III}} = \overset{(1)}{u}{}_{\mathrm{III}}$$

$$\overset{(1)}{\varepsilon}_{\Gamma\blacksquare} = \frac{1}{2}\left(\overset{(1)}{\varphi}_{\Gamma\blacksquare} - b_{\Gamma}^{\Omega}\,\overset{(1)}{u}_{\Omega}\right) \qquad (53a-f)$$

where $\overset{(n)}{\varphi}_{\Gamma\Lambda}$, $\overset{(n)}{\varphi}{}^{\Gamma}{}_{\Lambda}$, and $\overset{(n)}{\varphi}_{\Gamma\blacksquare}$ are defined by formulas $(50c-e)$, respectively.

Equations of motion and boundary conditions

The equations of motion and the boundary conditions will be obtained by a variational approach. Consider the dynamic version of the principle of virtual displacements written in the form

$$0 = \int_0^T \left(-\int_{\mathcal{V}} \rho\, \dot{U}^I\, \delta\dot{U}_I\, d\mathcal{V} + \int_{\mathcal{V}} \mathcal{S}^{IJ} \delta E_{IJ}\, d\mathcal{V}\right.$$
$$\left. - \int_{\mathcal{V}} f^I\, \delta U_i\, d\mathcal{V} - \int_{\mathcal{A}_\circ} \hat{S}^I\, \delta U_I\, d\mathcal{A} - \int_{\mathcal{S}} P^I\, \delta U_I\, d\mathcal{S}\right) dt \qquad (54)$$

where ρ is the mass density, $\dot{U}_I$ is the time derivative of the displacement components U_I, $\mathcal{S}^{IJ}$ are the components of the second Piola-Kirshhoff stress tensor, f^I are the body forces per unit volume of the undeformed body, $\hat{S}^I$ and P^I are the components of the specified stress vectors, for the undeformed body: $\hat{S}^I$ act on the lateral surface and P^I on the upper and lower surfaces, $\mathcal{S}^+$ and $\mathcal{S}^-$. In order to derive the equations of motion it will be made use of the linear displacement representation (44) and of the following definitions:

$$R_{(n)}^{IJ} = \int_{-h/2}^{h/2} \mu\, \mathcal{S}^{IJ}\, (\theta^{\blacksquare})^n\, d\theta^{\blacksquare} \quad ,$$

$$I_i = \int_{-h/2}^{h/2} \mu\, \rho\, (\theta^{\blacksquare})^{i-1}\, d\theta^{\blacksquare} \quad ,$$

$$\overset{(n)}{F}{}^{\Gamma} = \int_{-h/2}^{h/2} \mu\, f^{\Gamma}\, (\theta^{\blacksquare})^n\, d\theta^{\blacksquare} \quad ,$$

$$\overset{(n)}{F}{}^{\blacksquare} = \int_{-h/2}^{h/2} \mu\, f^{\blacksquare}\, (\theta^{\blacksquare})^n\, d\theta^{\blacksquare} \quad ,$$

$$\overset{(n)}{P}{}^{I} = \left[(\theta^{\blacksquare})^n\, \mu\, P^I\right]_{-h/2}^{h/2}$$

$$\int_{\mathcal{A}_\circ} \hat{S}^I\, \delta U_I\, d\mathcal{A} = \sum_{n=0}^{N} \int_{\Gamma_\circ} \left[\hat{S}_{(n)}^{\Gamma}\, \delta\overset{(n)}{U}_{\Gamma} + \hat{S}_{(n)}^{\blacksquare}\, \delta\overset{(n)}{U}_{\blacksquare}\right] d\Gamma$$

$$\hat{S}_{(n)}^{\Gamma} = \int_{-h/2}^{h/2} \mu\, \mu_{\Omega}^{\Gamma}\, \hat{\mathcal{S}}^{\Lambda\Omega}\, \nu_{\Lambda}\, (\theta^{\blacksquare})^n\, d\theta^{\blacksquare} \quad ,$$

$$\hat{S}_{(n)}^{\blacksquare} = \int_{-h/2}^{h/2} \mu\, \hat{\mathcal{S}}^{\Lambda\blacksquare}\, \nu_{\Lambda}\, (\theta^{\blacksquare})^n\, d\theta^{\blacksquare} \qquad (55a-h)$$

where $n = 0, 1$ and $\hat{\mathcal{S}}^{\Gamma I}$ are the first Piola-Kirchhoff stress tensor components which have been defined by formula $(25a)$. Thus, expression (54) takes the form

$$0 = \int_0^T \int_{\Omega} \left[\left(I_1\, \overset{(0)}{\ddot{U}}{}^I + I_2\, \overset{(1)}{\ddot{U}}{}^I\right) \delta\overset{(0)}{U}_I\right.$$
$$+ \left(I_2\, \overset{(0)}{\ddot{U}}{}^I + I_3\, \overset{(1)}{\ddot{U}}{}^I\right) \delta\overset{(1)}{U}_I$$
$$+ \left(B_{\Lambda}^{\Gamma}\, \overset{(0)}{T}{}^{\blacksquare\Lambda}\right) \delta\overset{(0)}{U}_{\Gamma} + \left(B_{\Lambda}^{\Gamma}\, \overset{(1)}{T}{}^{\blacksquare\Lambda} + \overset{(0)}{Q}{}^{\Gamma\blacksquare}\right) \delta\overset{(1)}{U}_{\Gamma}$$
$$- B_{\Gamma\Lambda}\, \overset{(0)}{T}{}^{\Gamma\Lambda}\, \delta\overset{(0)}{U}_{\blacksquare} + \left(-B_{\Gamma\Lambda}\, \overset{(1)}{T}{}^{\Gamma\Lambda} + \overset{(0)}{Q}{}^{\blacksquare\blacksquare}\right) \delta\overset{(1)}{U}_{\blacksquare}$$
$$+ \overset{(0)}{T}{}^{\Gamma\Lambda}\, \delta\overset{(0)}{U}_{\Gamma|\Lambda} + \overset{(1)}{T}{}^{\Gamma\Lambda}\, \delta\overset{(1)}{U}_{\Gamma|\Lambda}$$
$$+ \overset{(0)}{T}{}^{\blacksquare\Lambda}\, \delta\overset{(0)}{U}_{\blacksquare,\Lambda} + \overset{(1)}{T}{}^{\blacksquare\Lambda}\, \delta\overset{(1)}{U}_{\blacksquare,\Lambda}$$
$$\left. - \overset{(0)}{F}{}^{I}\, \delta\overset{(0)}{U}_I - \overset{(1)}{F}{}^{I}\, \delta\overset{(1)}{U}_I\right] d\Omega\, dt$$
$$- \int_0^T \int_{\Gamma_\circ} \left[\hat{S}_{(0)}^{I}\, \delta\overset{(0)}{U}_I + \hat{S}_{(1)}^{I}\, \delta\overset{(1)}{U}_I\right] d\Gamma\, dt$$
$$- \int_0^T \int_{\Omega} \left[\overset{(0)}{P}{}^{I}\, \delta\overset{(0)}{U}_I + \overset{(1)}{P}{}^{I}\, \delta\overset{(1)}{U}_I\right] d\Omega\, dt \qquad (56)$$

where

$$\overset{(0)}{T}{}^{\Gamma\Lambda} = \overset{(0)}{L}{}_{\Omega}^{\Gamma}\, R_{(0)}^{\Omega\Lambda} + \overset{(1)}{\Phi}{}^{\Gamma}_{.\Omega}\, R_{(1)}^{\Omega\Lambda} - B^{\Gamma}_{.\Omega}\, R_{(1)}^{\Omega\Lambda} + \overset{(1)}{U}{}^{\Gamma}\, R_{(0)}^{\blacksquare\Lambda}$$

$$\overset{(1)}{T}{}^{\Gamma\Lambda} = \overset{(0)}{L}{}_{\Omega}^{\Gamma}\, R_{(1)}^{\Omega\Lambda} + \overset{(1)}{\Phi}{}^{\Gamma}_{.\Omega}\, R_{(2)}^{\Omega\Lambda} - B^{\Gamma}_{.\Omega}\, R_{(2)}^{\Omega\Lambda} + \overset{(1)}{U}{}^{\Gamma}\, R_{(1)}^{\blacksquare\Lambda}$$

$$\overset{(0)}{T}{}^{\blacksquare\Lambda} = \overset{(0)}{\Phi}{}_{\Omega}^{\blacksquare}\, R_{(0)}^{\Omega\Lambda} + \overset{(1)}{\Phi}{}^{\blacksquare}_{.\Omega}\, R_{(1)}^{\Omega\Lambda} + \left(1 + \overset{(1)}{U}{}^{\blacksquare}\right) R_{(0)}^{\blacksquare\Lambda}$$

$$\overset{(1)}{T}{}^{\blacksquare\Lambda} = \overset{(0)}{\Phi}{}_{\Omega}^{\blacksquare}\, R_{(1)}^{\Omega\Lambda} + \overset{(1)}{\Phi}{}^{\blacksquare}_{.\Omega}\, R_{(2)}^{\Omega\Lambda} + \left(1 + \overset{(1)}{U}{}^{\blacksquare}\right) R_{(1)}^{\blacksquare\Lambda}$$

$$\overset{(0)}{Q}{}^{\Gamma\blacksquare} = \overset{(0)}{L}{}_{\Omega}^{\Gamma}\, R_{(0)}^{\Omega\blacksquare} + \overset{(1)}{\Phi}{}^{\Gamma}_{.\Omega}\, R_{(1)}^{\Omega\blacksquare} - B^{\Gamma}_{.\Omega}\, R_{(1)}^{\Omega\blacksquare} + \overset{(1)}{U}{}^{\Gamma}\, R_{(0)}^{\blacksquare\blacksquare}$$

$$\overset{(0)}{Q}{}^{\blacksquare\blacksquare} = \overset{(0)}{\Phi}{}_{\Omega}^{\blacksquare}\, R_{(0)}^{\Omega\blacksquare} + \overset{(1)}{\Phi}{}^{\blacksquare}_{.\Omega}\, R_{(1)}^{\Omega\blacksquare} + \left(1 + \overset{(1)}{U}{}^{\blacksquare}\right) R_{(0)}^{\blacksquare\blacksquare}$$

$$\overset{(0)}{L}{}^{\Gamma}{}_{.\Omega} = \delta_{\Omega}^{\Gamma} + \overset{(0)}{\Phi}{}^{\Gamma}{}_{.\Omega} \quad ,$$

$$\overset{(n)}{\phi}_{\Gamma\blacksquare} = \overset{(n)}{\phi}_{\blacksquare\Gamma} = \overset{(n)}{\phi}{}^{\blacksquare}{}_{.\Gamma} \quad , \quad n = 0, 1 \qquad (57a-i)$$

Finally, performing the classical operations, the equations of motion are obtained as follows:

$$\overset{(0)}{T}{}^{\Gamma\Lambda}{}_{|\Lambda} - B_{\Lambda}^{\Gamma}\, \overset{(0)}{T}{}^{\blacksquare\Lambda} = I_1\, \overset{(0)}{\ddot{U}}{}^{\Gamma} + I_2\, \overset{(1)}{\ddot{U}}{}^{\Gamma} - \overset{(0)}{F}{}^{\Gamma} - \overset{(0)}{P}{}^{\Gamma}$$

$$\overset{(0)}{T}{}^{\blacksquare\Lambda}{}_{|\Lambda} + B_{\Gamma\Lambda}\, \overset{(0)}{T}{}^{\Gamma\Lambda} = I_1\, \overset{(0)}{\ddot{U}}{}^{\blacksquare} + I_2\, \overset{(1)}{\ddot{U}}{}^{\blacksquare} - \overset{(0)}{F}{}^{\blacksquare} - \overset{(0)}{P}{}^{\blacksquare}$$

$$\overset{(1)}{T}{}^{\Gamma\Lambda}{}_{|\Lambda} - B_{\Lambda}^{\Gamma}\, \overset{(1)}{T}{}^{\blacksquare\Lambda} - \overset{(0)}{Q}{}^{\Gamma\blacksquare} = I_2\, \overset{(0)}{\ddot{U}}{}^{\Gamma} + I_3\, \overset{(1)}{\ddot{U}}{}^{\Gamma} - \overset{(1)}{F}{}^{\Gamma} - \overset{(1)}{P}{}^{\Gamma}$$

$$\overset{(1)}{T}{}^{\blacksquare\Lambda}{}_{|\Lambda} + B_{\Gamma\Lambda}\overset{(1)}{T}{}^{\Gamma\Lambda} - \overset{(0)}{Q}{}^{\blacksquare\blacksquare} = I_2\,\overset{(0)}{\ddot{U}}{}^{\blacksquare}$$

$$+ I_3\,\overset{(1)}{\ddot{U}}{}^{\blacksquare} - \overset{(1)}{F}{}^{\blacksquare} - \overset{(1)}{P}{}^{\blacksquare} \qquad (58a-d)$$

and the natural and essential boundary conditions as

$$\overset{(0)}{T}{}^{\Gamma\Lambda}\,\nu_\Lambda - B^{\Gamma}_{(0)} = 0 \quad , \quad \overset{(0)}{T}{}^{\blacksquare\Lambda}\,\nu_\Lambda - B^{\blacksquare}_{(0)} = 0$$

$$\overset{(1)}{T}{}^{\Gamma\Lambda}\,\nu_\Lambda - B^{\Gamma}_{(1)} = 0 \quad , \quad \overset{(1)}{T}{}^{\blacksquare\Lambda}\,\nu_\Lambda - B^{\blacksquare}_{(1)} = 0 \quad (59a-d)$$

and

$$\overset{(0)}{U}_I = \overset{(0)}{\bar{U}}_I \quad , \quad \overset{(1)}{U}_I = \overset{(1)}{\bar{U}}_I \qquad (59e,f)$$

respectively, where $\overset{(n)}{\bar{U}}_I$, with $n = 0, 1$, are the specified displacements.

Based again on the preceding theory, one can write

$$\overset{(n)}{t}{}^{\Gamma\Lambda} = \left[\overset{(n)}{T}{}^{\Gamma\Lambda}\right]_{N\otimes N} = \sqrt{A_{\Gamma\Gamma}}\sqrt{A_{\Lambda\Lambda}}\,\overset{(n)}{T}{}^{\Gamma\Lambda} \quad ,$$

$$\overset{(n)}{t}{}^{\blacksquare\Lambda} = \left[\overset{(n)}{T}{}^{\blacksquare\Lambda}\right]_{N} = \sqrt{A_{\Lambda\Lambda}}\,\overset{(n)}{T}{}^{\blacksquare\Lambda} \quad , \quad n = 0, 1$$

$$\overset{(0)}{q}{}^{\Gamma\blacksquare} = \left[\overset{(0)}{Q}{}^{\Gamma\blacksquare}\right]_{N} = \sqrt{A_{\Gamma\Gamma}}\,\overset{(0)}{Q}{}^{\Gamma\blacksquare} \quad ,$$

$$\overset{(0)}{q}{}^{\blacksquare\blacksquare} = \left[\overset{(0)}{Q}{}^{\blacksquare\blacksquare}\right] \qquad (60a-g)$$

where $\overset{(n)}{t}{}^{\Gamma\Lambda}$, $\overset{(n)}{t}{}^{\blacksquare\Gamma}$, $\overset{(0)}{q}{}^{\Gamma\blacksquare}$, and $\overset{(0)}{q}{}^{\blacksquare\blacksquare}$ denote the anholonomic components of $\overset{(n)}{T}{}^{\Gamma\Lambda}$, $\overset{(n)}{T}{}^{\blacksquare\Gamma}$, $\overset{(0)}{Q}{}^{\Gamma\blacksquare}$, and $\overset{(0)}{Q}{}^{\blacksquare\blacksquare}$ relative to the bases above indicated, respectively. Substituting formulas $(48a-l)$ and $(60a-g)$ into equations (58) and (59), and taking the anholonomic components of $\overset{(n)}{P}{}^{\Gamma}$, $\overset{(n)}{F}{}^{\Gamma}$, $B^{\Gamma}_{(n)}$, and ν_Γ as

$$\overset{(n)}{p}{}^{\Gamma} = \left[\overset{(n)}{P}{}^{\Gamma}\right]_{N} = \sqrt{A_{\Gamma\Gamma}}\,\overset{(n)}{P}{}^{\Gamma} \quad , \quad \overset{(n)}{f}{}^{\Gamma} = \left[\overset{(n)}{F}{}^{\Gamma}\right]_{N} = \sqrt{A_{\Gamma\Gamma}}\,\overset{(n)}{F}{}^{\Gamma}$$

$$\overset{(n)}{p}{}^{\blacksquare} = \left[\overset{(n)}{P}{}^{\blacksquare}\right] = \overset{(n)}{P}{}^{\blacksquare} \quad , \quad \overset{(n)}{f}{}^{\blacksquare} = \left[\overset{(n)}{F}{}^{\blacksquare}\right] = \overset{(n)}{F}{}^{\blacksquare}$$

$$b^{\Gamma}_{(n)} = \left[B^{\Gamma}_{(n)}\right]_{N} = \sqrt{A_{\Gamma\Gamma}}B^{\Gamma}_{(n)} \quad , \quad b^{\blacksquare}_{(n)} = \left[B^{\blacksquare}_{(n)}\right] = B^{\blacksquare}_{(n)}$$

$$\eta_\Lambda = [\nu_\Lambda]_{\underline{N}} = \frac{1}{\sqrt{A_{\Lambda\Lambda}}}\,\nu_\Lambda \qquad (61a-n)$$

one obtains the equations of motion

$$\sqrt{A_{\Gamma\Gamma}}\left[\frac{1}{\sqrt{A_{\Gamma\Gamma}}\sqrt{A_{\Lambda\Lambda}}}\overset{(0)}{t}{}^{\Gamma\Lambda}\right]_{|\Lambda} - b^{\Gamma}_{\Lambda}\,\overset{(0)}{t}{}^{\blacksquare\Lambda} =$$

$$I_1\,\overset{(0)}{\ddot{u}}{}^{\Gamma} + I_2\,\overset{(1)}{\ddot{u}}{}^{\Gamma} - \overset{(0)}{f}{}^{\Gamma} - \overset{(0)}{p}{}^{\Gamma} \qquad (62a)$$

$$\left[\frac{1}{\sqrt{A_{\Lambda\Lambda}}}\overset{(0)}{t}{}^{\blacksquare\Lambda}\right]_{|\Lambda} + b_{\Gamma\Lambda}\,\overset{(0)}{t}{}^{\Gamma\Lambda} =$$

$$I_1\,\overset{(0)}{\ddot{u}}{}^{\blacksquare} + I_2\,\overset{(1)}{\ddot{u}}{}^{\blacksquare} - \overset{(0)}{f}{}^{\blacksquare} - \overset{(0)}{p}{}^{\blacksquare} \qquad (62b)$$

$$\sqrt{A_{\Gamma\Gamma}}\left[\frac{1}{\sqrt{A_{\Gamma\Gamma}}\sqrt{A_{\Lambda\Lambda}}}\overset{(1)}{t}{}^{\Gamma\Lambda}\right]_{|\Lambda} - b^{\Gamma}_{\Lambda}\,\overset{(1)}{t}{}^{\blacksquare\Lambda} - \overset{(0)}{q}{}^{\Gamma\blacksquare} =$$

$$I_2\,\overset{(0)}{\ddot{u}}{}^{\Gamma} + I_3\,\overset{(1)}{\ddot{u}}{}^{\Gamma} - \overset{(1)}{f}{}^{\Gamma} - \overset{(1)}{p}{}^{\Gamma} \qquad (62c)$$

$$\left[\frac{1}{\sqrt{A_{\Lambda\Lambda}}}\overset{(1)}{t}{}^{\blacksquare\Lambda}\right]_{|\Lambda} + b_{\Gamma\Lambda}\,\overset{(1)}{t}{}^{\Gamma\Lambda} - \overset{(0)}{q}{}^{\blacksquare\blacksquare} =$$

$$I_2\,\overset{(0)}{\ddot{u}}{}^{\blacksquare} + I_3\,\overset{(1)}{\ddot{u}}{}^{\blacksquare} - \overset{(1)}{f}{}^{\blacksquare} - \overset{(1)}{p}{}^{\blacksquare} \qquad (62d)$$

and the boundary conditions

$$\overset{(0)}{t}{}^{\Gamma\Lambda}\,\eta_\Lambda - b^{\Gamma}_{(0)} = 0 \quad , \quad \overset{(0)}{t}{}^{\blacksquare\Lambda}\,\eta_\Lambda - b^{\blacksquare}_{(0)} = 0$$

$$\overset{(1)}{t}{}^{\Gamma\Lambda}\,\eta_\Lambda - b^{\Gamma}_{(1)} = 0 \quad , \quad \overset{(1)}{t}{}^{\blacksquare\Lambda}\,\eta_\Lambda - b^{\blacksquare}_{(1)} = 0 \quad (63a-d)$$

$$\overset{(0)}{u}_I = \overset{(0)}{\bar{u}}_I \quad , \quad \overset{(1)}{u}_I = \overset{(1)}{\bar{u}}_I \qquad (63e,f)$$

written in terms of anholonomic components. Furthermore, relations (57) are expressed as follows:

$$\overset{(0)}{t}{}^{\Gamma\Lambda} = \overset{(0)}{l}{}^{\Gamma}_{\Omega}\,r^{\Omega\Lambda}_{(0)} + \overset{(1)}{\varphi}{}^{\Gamma}_{.\Omega}\,r^{\Omega\Lambda}_{(1)} - b^{\Gamma}_{.\Omega}\,r^{\Omega\Lambda}_{(1)} + \overset{(1)}{u}{}^{\Gamma}\,r^{\blacksquare\Lambda}_{(0)}$$

$$\overset{(1)}{t}{}^{\Gamma\Lambda} = \overset{(0)}{l}{}^{\Gamma}_{\Omega}\,r^{\Omega\Lambda}_{(1)} + \overset{(1)}{\varphi}{}^{\Gamma}_{.\Omega}\,r^{\Omega\Lambda}_{(2)} - b^{\Gamma}_{.\Omega}\,r^{\Omega\Lambda}_{(2)} + \overset{(1)}{u}{}^{\Gamma}\,r^{\blacksquare\Lambda}_{(1)}$$

$$\overset{(0)}{t}{}^{\blacksquare\Lambda} = \overset{(0)}{\varphi}{}^{\blacksquare}_{\Omega}\,r^{\Omega\Lambda}_{(0)} + \overset{(1)}{\varphi}{}^{\blacksquare}_{.\Omega}\,r^{\Omega\Lambda}_{(1)} + \left(1 + \overset{(1)}{u}{}^{\blacksquare}\right) r^{\blacksquare\Lambda}_{(0)}$$

$$\overset{(1)}{t}{}^{\blacksquare\Lambda} = \overset{(0)}{\varphi}{}^{\blacksquare}_{\Omega}\,r^{\Omega\Lambda}_{(1)} + \overset{(1)}{\varphi}{}^{\blacksquare}_{.\Omega}\,r^{\Omega\Lambda}_{(2)} + \left(1 + \overset{(1)}{u}{}^{\blacksquare}\right) r^{\blacksquare\Lambda}_{(1)}$$

$$\overset{(0)}{q}{}^{\Gamma\blacksquare} = \overset{(0)}{l}{}^{\Gamma}_{\Omega}\,r^{\Omega\blacksquare}_{(0)} + \overset{(1)}{\varphi}{}^{\Gamma}_{.\Omega}\,r^{\Omega\blacksquare}_{(1)} - b^{\Gamma}_{.\Omega}\,r^{\Omega\blacksquare}_{(1)} + \overset{(1)}{u}{}^{\Gamma}\,r^{\blacksquare\blacksquare}_{(0)}$$

$$\overset{(0)}{q}{}^{\blacksquare\blacksquare} = \overset{(0)}{\varphi}{}^{\blacksquare}_{\Omega}\,r^{\Omega\blacksquare}_{(0)} + \overset{(1)}{\varphi}{}^{\blacksquare}_{.\Omega}\,r^{\Omega\blacksquare}_{(1)} + \left(1 + \overset{(1)}{u}{}^{\blacksquare}\right) r^{\blacksquare\blacksquare}_{(0)}$$

$$\overset{(0)}{l}{}^{\Gamma}{}_{.\Omega} = \hat{\delta}^{\Gamma}_{.\Omega} + \overset{(0)}{\varphi}{}^{\Gamma}{}_{.\Omega} \qquad (64a-g)$$

where

$$r^{\Omega\Lambda}_{(n)} = \left[R^{\Omega\Lambda}_{(n)}\right]_{N\otimes N} = \sqrt{A_{\Omega\Omega}}\sqrt{A_{\Lambda\Lambda}}R^{\Omega\Lambda}_{(n)} \quad ,$$

$$r^{\blacksquare\Lambda}_{(n)} = \left[R^{\blacksquare\Lambda}_{(n)}\right]_{N} = \sqrt{A_{\Lambda\Lambda}}R^{\blacksquare\Lambda}_{(n)} \quad , \quad n = 0, 1, 2$$

$$\overset{(0)}{l}{}^{\Gamma}{}_{.\Lambda} = \left[L^{\Gamma}_{.\Lambda}\right]_{N\otimes\underline{N}} = \frac{\sqrt{A_{\Gamma\Gamma}}}{\sqrt{A_{\Lambda\Lambda}}}\,L^{\Gamma}_{.\Lambda} \quad ,$$

$$\hat{\delta}^{\Gamma}_{.\Lambda} = \left[\delta^{\Gamma}_{.\Lambda}\right]_{N\otimes\underline{N}} = \frac{\sqrt{A_{\Gamma\Gamma}}}{\sqrt{A_{\Lambda\Lambda}}}\,\delta^{\Gamma}_{.\Lambda} \qquad (64h-o)$$

Constitutive equations

The linear constitutive equations of an anisotropic shell having elastic symmetry with respect to the surface $\theta^3 = 0$ read (Librescu, 1987)

$$R_{(0)}^{\Gamma\Lambda} = B_0^{\Gamma\Lambda\Omega\Theta} \overset{(0)}{E}_{\Omega\Theta} + B_1^{\Gamma\Lambda\Omega\Theta} \overset{(1)}{E}_{\Omega\Theta} + B_2^{\Gamma\Lambda\Omega\Theta} \overset{(2)}{E}_{\Omega\Theta} + B_2^{\Gamma\Lambda\blacksquare\blacksquare} \overset{(0)}{E}_{\blacksquare\blacksquare} \tag{65a}$$

$$R_{(1)}^{\Gamma\Lambda} = B_1^{\Gamma\Lambda\Omega\Theta} \overset{(0)}{E}_{\Omega\Theta} + B_2^{\Gamma\Lambda\Omega\Theta} \overset{(1)}{E}_{\Omega\Theta} + B_3^{\Gamma\Lambda\Omega\Theta} \overset{(2)}{E}_{\Omega\Theta} + B_3^{\Gamma\Lambda\blacksquare\blacksquare} \overset{(0)}{E}_{\blacksquare\blacksquare} \tag{65b}$$

$$R_{(2)}^{\Gamma\Lambda} = B_2^{\Gamma\Lambda\Omega\Theta} \overset{(0)}{E}_{\Omega\Theta} + B_3^{\Gamma\Lambda\Omega\Theta} \overset{(1)}{E}_{\Omega\Theta} + B_4^{\Gamma\Lambda\Omega\Theta} \overset{(2)}{E}_{\Omega\Theta} + B_4^{\Gamma\Lambda\blacksquare\blacksquare} \overset{(0)}{E}_{\blacksquare\blacksquare} \tag{65c}$$

$$R_{(0)}^{\Gamma\blacksquare} = 2\, B_0^{\Gamma\blacksquare\Omega\blacksquare} \overset{(0)}{E}_{\Omega\blacksquare} + 2\, B_1^{\Gamma\blacksquare\Omega\blacksquare} \overset{(1)}{E}_{\Omega\blacksquare} \tag{65d}$$

$$R_{(1)}^{\Gamma\blacksquare} = 2\, B_1^{\Gamma\blacksquare\Omega\blacksquare} \overset{(0)}{E}_{\Omega\blacksquare} + 2\, B_2^{\Gamma\blacksquare\Omega\blacksquare} \overset{(1)}{E}_{\Omega\blacksquare} \tag{65e}$$

$$R_{(0)}^{\blacksquare\blacksquare} = B_0^{\blacksquare\blacksquare\Omega\Theta} \overset{(0)}{E}_{\Omega\Theta} + B_1^{\blacksquare\blacksquare\Omega\Theta} \overset{(1)}{E}_{\Omega\Theta} + B_2^{\blacksquare\blacksquare\Omega\Theta} \overset{(2)}{E}_{\Omega\Theta} + B_2^{\blacksquare\blacksquare\blacksquare\blacksquare} \overset{(0)}{E}_{\blacksquare\blacksquare} \tag{65f}$$

where

$$B_n^{IJKL} = \int_{-h/2}^{h/2} \mu\, C^{IJKL} \left(\theta^{\blacksquare}\right)^n \, d\theta^{\blacksquare} \tag{65g}$$

and C^{IJKL} are the components of the spatial tensor of elasticity (elastic coefficients).

Adding to the above set of anholonomic components

$$b_{(n)}^{IJKL} = \left[B_{(n)}^{IJKL}\right]_{N\otimes N\otimes N\otimes N} = \sqrt{A_{II}}\sqrt{A_{JJ}}\sqrt{A_{KK}}\sqrt{A_{LL}}\; B_{(n)}^{IJKL} \tag{66}$$

equations $(65a-f)$ can be written as

$$r_{(0)}^{\Gamma\Lambda} = b_0^{\Gamma\Lambda\Omega\Theta} \overset{(0)}{\epsilon}_{\Omega\Theta} + b_1^{\Gamma\Lambda\Omega\Theta} \overset{(1)}{\epsilon}_{\Omega\Theta} + b_2^{\Gamma\Lambda\Omega\Theta} \overset{(2)}{\epsilon}_{\Omega\Theta} + b_2^{\Gamma\Lambda\blacksquare\blacksquare} \overset{(0)}{\epsilon}_{\blacksquare\blacksquare} \tag{67a}$$

$$r_{(1)}^{\Gamma\Lambda} = b_1^{\Gamma\Lambda\Omega\Theta} \overset{(0)}{\epsilon}_{\Omega\Theta} + b_2^{\Gamma\Lambda\Omega\Theta} \overset{(1)}{\epsilon}_{\Omega\Theta} + b_3^{\Gamma\Lambda\Omega\Theta} \overset{(2)}{\epsilon}_{\Omega\Theta} + b_3^{\Gamma\Lambda\blacksquare\blacksquare} \overset{(0)}{\epsilon}_{\blacksquare\blacksquare} \tag{67b}$$

$$r_{(2)}^{\Gamma\Lambda} = b_2^{\Gamma\Lambda\Omega\Theta} \overset{(0)}{\epsilon}_{\Omega\Theta} + b_3^{\Gamma\Lambda\Omega\Theta} \overset{(1)}{\epsilon}_{\Omega\Theta} + b_4^{\Gamma\Lambda\Omega\Theta} \overset{(2)}{\epsilon}_{\Omega\Theta} + b_4^{\Gamma\Lambda\blacksquare\blacksquare} \overset{(0)}{\epsilon}_{\blacksquare\blacksquare} \tag{67c}$$

$$r_{(0)}^{\Gamma\blacksquare} = 2\, b_0^{\Gamma\blacksquare\Omega\blacksquare} \overset{(0)}{\epsilon}_{\Omega\blacksquare} + 2\, b_1^{\Gamma\blacksquare\Omega\blacksquare} \overset{(1)}{\epsilon}_{\Omega\blacksquare} \tag{67d}$$

$$r_{(1)}^{\Gamma\blacksquare} = 2\, b_1^{\Gamma\blacksquare\Omega\blacksquare} \overset{(0)}{\epsilon}_{\Omega\blacksquare} + 2\, b_2^{\Gamma\blacksquare\Omega\blacksquare} \overset{(1)}{\epsilon}_{\Omega\blacksquare} \tag{67e}$$

$$r_{(0)}^{\blacksquare\blacksquare} = b_0^{\blacksquare\blacksquare\Omega\Theta} \overset{(0)}{\epsilon}_{\Omega\Theta} + b_1^{\blacksquare\blacksquare\Omega\Theta} \overset{(1)}{\epsilon}_{\Omega\Theta} + b_2^{\blacksquare\blacksquare\Omega\Theta} \overset{(2)}{\epsilon}_{\Omega\Theta} + b_2^{\blacksquare\blacksquare\blacksquare\blacksquare} \overset{(0)}{\epsilon}_{\blacksquare\blacksquare} \tag{67f}$$

which are the desired anholonomic equations.

COMMENTS

The following comments are pertinent:

1. The method of anholonomic components as developed by Truesdell (1954) and Ericksen (1960) does not include all cases as Ericksen (1960) himself says: *"Possible a method sufficiently general as to cover every proposal which might appeal on some or another intuitive grounds could be constructed. In this connection we mention only that the method of anholonomic components, which appears quite general does not include Green and Zerna's definition."* Truesdell and Ericksen dealt only with anholonomic components of single field referred to the bases U and $\underline{U}$ of the undeformed (or u and $\underline{u}$ of the deformed) configuration of the body and, therefore, omitting the bases U^* and $\underline{U}^*$ (or u^* and $\underline{u}^*$). Otherwise, it can easily be shown that the expression of Green and Zerna's (1968) physical components of Cauchy's stress tensor τ^{ij}
$$\sigma^{ij} = \sqrt{\frac{g_{jj}}{g^{ii}}}\, \tau^{ij} \tag{68}$$
is equal to the expression of the anholonomic components of τ^{ij} referred to the basis $\mathcal{B} = \underline{u}^* \otimes u$. Since Truesdell and Ericksen omitted the basis $\underline{u}^*$, they could not include the anholonomic counterpart of Green and Zerna's definition in their method. The theory here developed is more general; it deals with all the above mentioned bases.

2. Some authors refer the physical components of the stress and strain tensors at a point of the body to different bases which are not reciprocal. This procedure is in disagreement with the invariance of the elastic potential of a body under transformation of coordinates. Thus, in order to satisfy this requirement, the bases of the anholonomic counterparts of those components should be chosen as to be reciprocal.

3. There are several anholonomic components which are suitable for each stress tensor component since all of them have similar physical significance. In fact, the decompositions of the stress tensor in terms of anholonomic components generate stress vectors $\overset{i}{\vec{T}}$ which depend on the chosen bases. For instance, consider the following stress vectors:
$$\overset{i}{\vec{T}}_{(G)} = \left[\tau^{ij}\right]_{\underline{u}^*\otimes u} \vec{u}_j \tag{69a}$$
and
$$\overset{i}{\vec{T}}_{(S)} = \left[\tau^{ij}\right]_{u\otimes \underline{u}^*} \vec{\underline{u}}_j \tag{69b}$$
where $\overset{i}{\vec{T}}_{(G)}$ and $\overset{i}{\vec{T}}_{(S)}$ denote Green and Zerna's (1968) and Sedov's (1965) stress vectors, respectively. In these expressions
$$\left[\tau^{ij}\right]_{\underline{u}^*\otimes u} = \frac{\sqrt{g_{jj}}}{\sqrt{g^{ii}}}\, \tau^{ij} \tag{70a}$$

and

$$[\tau^{ij}]_{u \otimes \underline{u}^*} = \frac{\sqrt{g_{ii}}}{\sqrt{g^{jj}}} \tau^{ij} \qquad (70b)$$

Taking into account formulas (8a) and (8d), it can be seen that the coefficients (70a,b) of expressions (69a,b) are the anholonomic components of the stress vectors $\overset{i}{\vec{T}}_{(G)}$ and $\overset{i}{\vec{T}}_{(S)}$ in the directions $\vec{u}_j$ and $\underline{\vec{u}}_j$, respectively. These and the remaining anholonomic components of the stress tensor have analogous physical interpretations to the one given by Green and Zerna (1968) for the physical counterparts of formulas (69a) and (70a). Thus, the use of one or another anholonomic component of the stress tensor is a matter of choice or of further convenience.

4. Finally, the theory and results given here can be extended in order to be applicable to any tensorial system of equations referred to general curvilinear coordinates.

ACKNOWLEDGEMENTS

The authors would like to express their appreciation to Professors Dewey H. Hodges and Marcos A. Ortega for their interest and stimulating discussions during the preparation of this paper.

REFERENCES

Altman W and Bevilacqua L (1991), A small strain and moderate rotation theory in elasticity, *Proc II Pan-American Congress of Applied Mechanics*, Valparaiso, Chile, 302-305.
Altman W and Bevilacqua L (1991), Small strain and moderate rotation theory in elasticity and stability, *Appl Mech Rev*, 44(11), S3-S8.
Altman W and Oliveira AM (1977), Physical components of tensors, *Tensor*, NS, 31, 141-148.
Altman W and Oliveira AM (1982), A historical outline of physical components of tensors, *Tensor*, NS, 36, 195-199.
Altman W and Oliveira AM (1993), Nonlinear elasticity equations of motion expressed in terms of anholonomic components, *Proc III Pan-American Congress of Applied Mechanics*, São Paulo, Brazil, 137-140.
Altman W and Palmerio AF (1991), A refined theory for anisotropic shells in the presence of small strains and moderate rotations, *Int J Non-Linear Mech*, 26(5), 609-618.
Altman W and Palmerio AF (1992), Moderate rotations of shells under circulatory loading, to appear in *Proc First World Cong Nonlinear Analysts*, Tampa, Florida.
Cissotti U (1928), *Lezione di calcolo tensoriale*, Libreria Ed. Politecnica, Milano.
Ericksen, JL (1960), *Tensor fields*, Handbuch der Physik, Band III/1, Springer-Verlag, Berlin.
Eringen AC (1962), *Nonlinear theory of continuous media*, McGraw-Hill, New York.
Green AE and Zerna W (1968), *Theoretical elasticity*, 2nd Ed, Oxford University Press, Oxford.
Librescu L (1987), Refined geometrically nonlinear theories of anisotropic laminated shells, *Q Appl Math*,, XLV, 1-22.
McConnell AJ (1931), *Applications of absolute differential calculus*, Blackie, London.
Naghdi PM (1963), *Foundations of elastic shell theory*, *Progress Solid Mech*, Vol IV, North-Holland, Amsterdam.
Oliveira AM and Altman W (1978), Coordinate transformations of physical components of tensors, *Tensor*, NS, 32, 332-334.
Oliveira AM and Altman W (1981), Anholonomic components of vectors and tensors, *Tensor*, NS, 35, 283-286.
Pietraszkiewicz W (1979), *Finite rotations and Lagrangian description in the nonlinear theory of shells*, Polish Academy of Sciences, Institute of Fluid-Flow Machinery, Warszawa, Poland.
Ricci G and Levi-Civita T (1901), Méthodes du calcul différentiel absolu et leurs applications, *Math Annalen*, 54, 125-201.
Schmidt R and Reddy JN (1988), A refined small strain and moderate rotation theory of elastic anisotropic shells, *ASME J Appl Mech*, 55, 611-617.
Schouten JA (1951), *Tensor analysis for physicists*, Clarendon Press, Oxford.
Sedov LI (1965), *Introduction to the mechanics of continuous medium*, Addison-Wesley, London.
Synge JL and Schield A (1949), *Tensor calculus*, Toronto University Press, Toronto.
Thirring H (1925), Zur tensoranalytischen darstellung der elastizitätstheorie, *Phys Z*, 26, 518-522.
Truesdell C (1953), The physical components of vectors and tensors, *Z angew Math Mech*, 33, 345-356.
Truesdell C (1954), Remarks on the paper "The physical components of vectors and tensors", *Z angew Math Mech*, 34, 69-70.

Reduced constraint manifolds

Paulo Boulos and Nelson Achcar

Department of Structures and Foundation Engineering, Escola Politecnica Universidade de São Paulo, CP 61548, São Paulo, SP, Brazil

The formalization of the concept of internal constraint is usually done by means of restrictions on the deformation gradients, by imposing that they must stay on a submanifold of Lin^+. Our point of view is to impose restrictions on the right Cauchy-Green tensors, by imposing that they must stay on a submanifold of $Psym$, which we call reduced constraint manifold. We determine: all the constraint manifolds that are independent of the local reference configuration, a new formula for the reaction space, all the constraint manifolds whose reaction spaces are independent of the deformation gradient.

INTRODUCTION

An internal constraint is a limitation on the possible motions of a body point.The formalization of this concept can be achieved by specifying, for a fixed reference configuration, a regular submanifold $\mathcal{M}$ of Lin^+ (see section 2 for notation) called constraint manifold, to which must belong the deformation gradients at the point under consideration.One imposes that $\mathcal{M}$ be objective, that is, invariant under left action by the rotation group. This condition gives an equivalent way of imposing restrictions, namely, that the right Cauchy-Green tensor C must belong to a convenientely defined submanifold of $Psym$ called by us *reduced constraint manifold* (definition 3 (b)). In the present article we introduce the concept of reduced constraint manifold, we prove that there is a one to one correspondence between the set of reduced constraint manifolds and the set of the constraint manifolds and, through the new concept, we determine the constraint manifolds that are invariant relative to reference configurations (Theorem 8), and the ones whose reaction spaces are independent of the deformation imposed to the body (Theorem 15). This result uses a new formula for the reaction space (Proposition 12).

NOTATION

$\mathbf{R}, \mathbf{R}_*^+$: respectively,the field of real numbers,the set of positive reals.

$\mathbf{V}$: the vector space of translations associated to the affine space $\mathbf{E}$ of the points of Euclidean Geometry. The usual scalar product of the elements $\mathbf{v}$ and $\mathbf{w}$ of $\mathbf{V}$ will be denoted by $\mathbf{v} \cdot \mathbf{w}$.

Lin: the vector space of all (second order) tensors, viewed as linear operators of $\mathbf{V}$, provided with the following scalar product

$$A : B = tr(A^\top B)$$

($\top$ stands for transpose)

$\perp$ stands for orthogonal complement relative to the above scalar product, and $\perp_s$ stands for orthogonal complement relative to the scalar product induced on Sym.

$\mathbf{1}$ stands for the identity operator of $\mathbf{V}$.

$Lin^+ = \{F \in Lin \mid detF > 0\}$

$Sym = \{F \in Lin \mid F^\top = F\}$

$Skw = \{F \in Lin \mid F^\top = -F\}$

$Rot = \{R \in Lin^+ \mid R^\top = R^{-1}\}$

$Unim = \{F \in Lin^+ \mid detF = 1\}$

$Psym = \{C \in Sym \mid C \textit{ is positive definite}\}$

$Dev = \{C \in Sym \mid trC = 0\}$

$Sph = \mathbf{R}\mathbf{1}$

$\Sigma : Lin \to Sym$ is given by

$$\Sigma(F) = \frac{1}{2}(F + F^\top)$$

$\varphi : Lin^+ \to Psym$ is given by

$$\varphi(F) = F^\top F$$

$c_F : Lin \to Lin$, for each F in Lin, is given by

$$c_F(G) = FGF^\top$$

$u : Lin^+ \to Psym$ is given by

$$u(F) = U$$

where $F = RU$ is the right polar decomposition of F.

$dim\mathcal{N}$: the dimension of the (differentiable) manifold $\mathcal{N}$.

$\dot{\mathcal{N}}_X$: the tangent space to the manifold $\mathcal{N}$ at X.

$f_{*X} : \dot{\mathcal{M}}_X \to \dot{\mathcal{N}}_{f(X)}$: the differential at X of the differentiable mapping $f : \mathcal{M} \to \mathcal{N}$ between manifolds.

Proposition 1 *For every F in Lin^+ we have*
(i) $\varphi r_F = c_{F^T}\varphi$
(ii) $\varphi_{*F} = 2c_{F^T}\Sigma r_{F^{-1}}$
where $r_F : Lin^+ \to Lin^+$ *is given by* $r_F(G) = GF$.

Proof. From (i), whose proof is left to the reader, it follows that $\varphi = c_{F^T}\varphi r_{F^{-1}}$. By taking differentials, one obtains

$$\varphi_{*1} = (c_{F^T})_{*1}\varphi_{*1}(r_{F^{-1}})_{*F}$$

. Then (ii) follows by observing that $(c_{F^T})_{*1} = c_{F^T}$, $(r_{F^{-1}})_{*F} = r_{F^{-1}}$ and that

$$\varphi_{*1}(N) = 1^T N + N^T 1 = N + N^T = 2\Sigma(N)$$

Corollary 2 *φ is a submersion.*

Proof. It follows from (ii), since $r_{F^{-1}}$ is a diffeomorfism, and Σ and c_{F^T} are surjective.

INTERNAL CONSTRAINTS

Definition 3 *(a) A* constraint manifold *(Podio-Guidugli and Vianello, 1989) is a connected regular submanifold $\mathcal{M}$ of Lin^+ such that*

$$(i)\ Rot\mathcal{M} \subset \mathcal{M} \quad (ii)\ 1 \in \mathcal{M}$$

(b) A reduced constraint manifold *is a connected regular submanifold $\mathcal{C}$ of $Psym$ such that $1 \in \mathcal{C}$.*

Lemma 4 *If $\mathcal{M}$ is a constraint manifold then $\mathcal{M} \cap Psym$ is a reduced constraint manifold, whose dimension is $dim\mathcal{M} - 3$.*

Proof. Clearly $1 \in \mathcal{M} \cap Psym$.Now if we can prove that

$$(\ \dot{RotU}\ )_U \cap Sym = \{0\} \qquad (1)$$

for every U in $\mathcal{M} \cap Psym$, then it will follow that the sum $(\ \dot{RotU}\ )_U + Sym$ is direct, and since its dimension is 3+6=9, it must coincide with Lin.

Since

$$(\dot{RotU})_U \subset \dot{\mathcal{M}}_U,\ (\dot{Psym})_U = Sym,\ (\dot{Lin^+})_U = Lin,$$

we have

$$\dot{\mathcal{M}}_U + (\ \dot{Psym})_U\ = (\ \dot{Lin^+})_U$$

Accordingly, $\mathcal{M}$ and $Psym$ are transversal in each U of their intersection, so that (Varadarajan, 1974) such intersection is a regular submanifold of Lin^+.

To prove (1), we observe that an element of $(\dot{Rot})_U$ is of the form WU, with W in Skw. If WU is in Sym, then $-WU = UW$, so that if e is an eigenvector of U corresponding to the eingenvalue λ, one obtains

$$-\lambda W(e) = U(W(e))$$

so that W(e) must be zero, othe[illegible] would be eigenvalues of the positive de[illegible]. Since there is an ortonormal basis formed by eigenvectors of U, it follows that $W = 0$, so that (1) is proved.

The statement about the dimension follows from

$$dim\,\mathcal{M} + dim\,Psym = dim\,(\mathcal{M} \cap Psym) + dim\,Lin^+$$

Finally, since $\mathcal{M} \cap Psym = u(\mathcal{M})$, $\mathcal{M}$ is connected and u continuous, it follows that $\mathcal{M} \cap Psym$ is connected.

Proposition 5 *The mapping*

$$\mathcal{M} \mapsto \varphi(\mathcal{M})$$

is a bijection between the set of constraint manifolds and the set of reduced constraint manifolds, its inverse being given by

$$\mathcal{C} \mapsto \varphi^{-1}(\mathcal{C})$$

Forthermore, $dim\,\varphi(\mathcal{M}) = dim\,\mathcal{M} - 3$

Proof. Since $\mathcal{M}$ contains 1, and

$$\varphi(\mathcal{M}) = r^{-1}(\mathcal{M} \cap Psym) \qquad (2)$$

where $r : Psym \to Psym$ is the diffeomorphism given by $r(C) = C^{\frac{1}{2}}$, we can conclude by Lemma 4 that $\varphi(\mathcal{M})$ is a reduced constraint manifold.

On the other hand, if $\mathcal{C}$ is a reduced constraint manifold then $\varphi^{-1}(\mathcal{C})$ is a regular submanifold of Lin^+ for, according to Corollary 2, φ is a submersion.The relation

$$\varphi^{-1}(\mathcal{C}) = \bigcup_{C\in\mathcal{C}} \varphi^{-1}(C) = \bigcup_{C\in\mathcal{C}} Rot\,C^{\frac{1}{2}}$$

and the fact that $\mathcal{C}$ is connected allows us to conclude that $\varphi^{-1}(\mathcal{C})$ is connected. The same relation shows that condition(i) of Definition 3 is satisfied. Clearly condition (ii) is also satisfied, so that $\varphi^{-1}(\mathcal{C})$ is a constraint manifold.

Since φ is surjective we have $\varphi^{-1}(\varphi(\mathcal{C})) = \mathcal{C}$, and from (2)

$$\varphi^{-1}(\varphi(\mathcal{M})) = \varphi^{-1}(r^{-1}(\mathcal{M} \cap Psym)) = u^{-1}(\mathcal{M} \cap Psym) = \mathcal{M}$$

The statement about dimension follows from Lemma 4 and from (2).

CONFIGURATION INDEPENDENT CONSTRAINT MANIFOLDS

In (Podio-Guidugli and Vianello, 1989) it is proved that in order to a constraint manifold be independent of the (local) configuration at a body point it is necessary and sufficient that it be a subgroup of Lin^+. In this section we determine such constraint manifolds.

We shall need the following result, proved in (Podio-Guidugli, 1979), for which we give a new proof.

Proposition 6 *If W is a proper vector subspace of Sym invariant by c_R for all R in Rot, then W=Dev or W=Sph.*

Proof. (a) We claim that there is no proper vector subspace of Dev invariant under c_R for all R in Rot.

By a standard result of Group Representation Theory (Varadarajan, 1974), this will be proved if we can show that a linear operator T of Dev that commutes with $c_R|_{Dev}$ for all R in Rot must be a multiple of the identity. To see this, extend T to a linear operator $\tilde{T}$ of Sym by imposing it to be the identity in Sph. It is easy to see that $\tilde{T}$ commutes with c_R for all R in Rot, that is, $\tilde{T}$ is isotropic, so it is of the form (Gurtin, 1981)

$$\tilde{T}(A) = \alpha A + \beta tr A\, \mathbf{1}$$

Hence $T(A) = \alpha A$ for all A in Dev.

(b) Since c_R is an orthogonal operator of Sym, the fact that W is invariant under c_R implies that the same occurs with $W^{\perp\bullet}$. Clearly $W \cap Dev$ and $W^{\perp\bullet} \cap Dev$ are invariant under c_R. But we must have $W \cap Dev \neq \{0\}$ *or* $W^{\perp\bullet} \cap Dev \neq \{0\}$ (otherwise $dim W \leq 1$ and $dim W^{\perp\bullet} \leq 1$, which is impossible). In the former case we have by part (a) that $W \cap Dev = Dev$, so that $W \supset Dev$. Since $dim Dev = 5$ and W is a proper subspace of Sym, we must have $W = Dev$. The other case is treated similarly, to conclude that $W^{\perp\bullet} = Dev$, that is, $W = Sph$.

Lemma 7 *If $\mathcal{M}$ is a constraint manifold then*
(i) $SkwF \subset \dot{\mathcal{M}}_F$, for every F in $\mathcal{M}$.
(ii) $\varphi|_{\mathcal{M}}$ is a submersion.

Proof. (i) For W in Skw choose a curve $\alpha(t)$ in Rot such that $\alpha(0) = \mathbf{1}$, $\dot{\alpha}(0) = W$. Then the curve $\alpha(t)F$ is in $\mathcal{M}$, by Definition 3 (a)(i), passes by F at t=0, and has WF as tangent vector at this point, so that WF is in $\dot{\mathcal{M}}_F$.

(ii) By Proposition 1 (ii) we have $ker\, \varphi_{*F} = Skw\, F$, so that by part (i) $ker\, \varphi_{*F}$ is contained in $\dot{\mathcal{M}}_F$. Hence the kernels of φ_{*F} and $(\varphi|_{\mathcal{M}})_{*F}$ coincide. Using this we have

$$\begin{aligned} dim\, \mathcal{M} &= dim\, ker(\varphi|_{\mathcal{M}})_{*F} \\ &+ dim\,(\varphi|_{\mathcal{M}})_{*F}(\dot{\mathcal{M}}_F) \\ &= 3 + dim\, \varphi_{*F}(\dot{\mathcal{M}}_F) \end{aligned}$$

so that, in view of Proposition 5, we have

$$dim\, \varphi_{*F}(\dot{\mathcal{M}}_F) = dim\, \mathcal{M} - 3 = dim\, \varphi(\mathcal{M}).$$

Theorem 8 *Let $\mathcal{M}$ be a constraint manifold that is a subgroup of Lin^+. Then $\mathcal{M}$ is Rot, $\mathbf{R}^+_* Rot$, $Unim$, or Lin^+.*

Proof. Since $\mathcal{M}$ is a regular submanifold of Lin^+ as well as a subgroup, it is a Lie subgroup of Lin^+. Put $\mathcal{C} = \varphi(\mathcal{M})$. Then using Proposition 1, we have, for R in Rot,

$$c_R(\mathcal{C}) = \varphi\, r_{R^\top}(\mathcal{M}) = \varphi(\mathcal{M}) = \mathcal{C}$$

where we have used the fact that Rot is contained in the group $\mathcal{M}$.

From this relation it follows that for every R in Rot,

$$c_R(\dot{\mathcal{C}}_1) = \dot{\mathcal{C}}_1 \tag{3}$$

Case 1 : $\dot{\mathcal{C}}_1$ is a trivial vector subespace of Sym.

If $\dot{\mathcal{C}}_1 = 0$ we have $\mathcal{C} = \{\mathbf{1}\}$, and $\mathcal{M} = \varphi^{-1}\{\mathbf{1}\} = Rot$. If $\dot{\mathcal{C}}_1 = Sym$ then $\mathcal{C}$ is an open submanifold of $Psym$, so that $\mathcal{M} = \varphi^{-1}(\mathcal{C})$ is an open submanifold of Lin^+. This group is generated by any neighbourhood of $\mathbf{1}$ (Varadarajan, 1974), in particular by $\mathcal{M}$. Since $\mathcal{M}$ is a group, we have $\mathcal{M} = Lin^+$.

Case 2: $\dot{\mathcal{C}}_1$ is a non-trivial vector subspace of Sym.

By (3) and Proposition 6 we must have $\dot{\mathcal{C}}_1$ equal to Dev or Sph. Notice that

$$\varphi_{*\mathbf{1}}(\dot{\mathcal{M}}_1) = \dot{\mathcal{C}}_1, \quad \varphi_{*\mathbf{1}}(H) = H + H^\top \tag{4}$$

for every H in $\dot{\mathcal{M}}_1$, the first equality being granted by Lemma 7 (ii).

Now if $\dot{\mathcal{C}}_1 = Dev$ we must have by (4), that $H + H^\top$ belongs to Dev for every H in $\dot{\mathcal{M}}_1$, so $tr\, H = 0$. Hence $\dot{\mathcal{M}}_1$ is contained in the Lie algebra of the Lie group $Unim$. Since both are of dimension 8 ($dim\, \mathcal{M} = dim\, \mathcal{C} + 3$), they must coincide, so that $\mathcal{M}$ must be $Unim$.

Finally, if $\dot{\mathcal{C}}_1 = Sph$, we must have by (4) that $H + H^\top = \alpha\mathbf{1}$ for every H in $\dot{\mathcal{M}}_1$, where the scalar α depends on H. Noting that

$$H = \frac{\alpha}{2}\mathbf{1} + (H - \frac{\alpha}{2}\mathbf{1})$$

and that

$$\begin{aligned} (H - \frac{\alpha}{2}\mathbf{1})^\top &= H^\top - \frac{\alpha}{2}\mathbf{1} \\ &= \alpha\mathbf{1} - H - \frac{\alpha}{2}\mathbf{1} = -(H - \frac{\alpha}{2}\mathbf{1}) \end{aligned}$$

we see that $\dot{\mathcal{M}}_1$ is contained in $\mathbf{R1} + Skw$. Since both are of dimension 4, they must coincide, so $\mathcal{M}$ must equal the corresponding Lie group of the Lie algebra $\mathbf{R1} + Skw$, namely $\mathcal{M} = \mathbf{R}^+_* Rot$

REACTION SPACE

Definition 9 *(Podio-Guidugli, 1990) The* reaction space *at a point F of a constraint manifold $\mathcal{M}$ is the vector space*

$$\mathcal{R}(F) = (\dot{\mathcal{M}}_F F^{-1})^\perp$$

Clearly the dimension of $\mathcal{R}(F)$ is $9 - dim\mathcal{M}$.

Lemma 10 *(i) For any subset $\mathcal{L}$ of Lin we have*

$$\mathcal{L}^\perp \cap Sym = (\Sigma(\mathcal{L}))^{\perp\bullet}$$

(ii) For any subset $\mathcal{N}$ of Sym and any F in Lin we have

$$(F\mathcal{N}F^\top)^{\perp\bullet} = F^{-\top}\mathcal{N}^{\perp\bullet}F^{-1}$$

Proof. (i) It suffices to observe that for N in Sym and A in Lin the equality $N : A = 0$ is equivalent to $N : \Sigma(A) = 0$.

(ii) clearly $F\mathcal{N}F^\top$ is contained in Sym. Since

$$X : FNF^\top = F^\top XF : N$$

we see that a symmetric X is in $(F\mathcal{N}F^\top)^{\perp\bullet}$ if and only if $F^\top XF$ is in $\mathcal{N}^{\perp\bullet}$, that is, if and only if X is in $F^{-\top}\mathcal{N}^{\perp\bullet}F^{-1}$.

Lemma 11 *(i)* $\mathcal{R}(F) \subset Sym$
(ii) $\mathcal{R}(F) = \mathcal{D}(F)^{\perp\bullet}$ *where* $\mathcal{D}(F) = \Sigma(\dot{\mathcal{M}}_F F^{-1})$

Proof. The proof of (i) can be found in (Podio-Guidugli and Vianello, 1989), but follows easily from Lemma 7 (i), and (ii) follows from (i) and Lemma 7 (i) with $\mathcal{L} = \mathcal{M}_F F^{-1}$.

Proposition 12 *For F in the constraint manifold $\mathcal{M}$ we have*

$$\mathcal{R}(F) = F\dot{\mathcal{C}}^{\perp\bullet}_{F^\top F}F^\top$$

where $\mathcal{C} = \varphi(\mathcal{M})$.

Proof. Since $\mathcal{M}F^{-1}$ is a constraint manifold, then by Lemma 7 (ii) we can write

$$\varphi_{*1}(\dot{\mathcal{M}F^{-1}})_1 = (\dot{\varphi(\mathcal{M}F^{-1})})_1 \tag{5}$$

By Proposition 1 (ii) the left side of the above equality is equal to $\mathcal{D}(F)$ (as defined in Lemma 11). On the other hand, by part (ii) of the same proposition we have

$$\varphi(\mathcal{M}F^{-1}) = \varphi r_{F^{-1}}(\mathcal{M}) = c_{F^{-\top}}(\mathcal{C})$$

so that

$$\begin{aligned}\varphi((\dot{\mathcal{M}F^{-1}}))_1 &= (c_{F^{-\top}})_{*F^\top F}(\dot{\mathcal{C}}_{F^\top F}) \\ &= c_{F^{-\top}}(\dot{\mathcal{C}}_{F^\top F}) = F^{-\top}\dot{\mathcal{C}}_{F^\top F}F^{-1}\end{aligned}$$

(We have used the fact that $c_{F^{-\top}}|_{Psym}$ is a diffeomorphism).

Hence (5) becomes

$$\mathcal{D}(F) = F^{-\top}\dot{\mathcal{C}}_{F^\top F}F^{-1}$$

The result to be proved follows from this equality by using Lemma 11 (ii) and Lemma 10 (ii).

Examples 13

1. *Rigidity constraint*: $\mathcal{M} = Rot$, so $\mathcal{C} = \{\mathbf{1}\}$, $\dot{\mathcal{C}}_{\mathbf{1}} = \{0\}$. By using Proposition 12 we obtain $\mathcal{R}(F) = Sym$.

2. *Incompressibility constraint*: $\mathcal{M} = Unim$, $\mathcal{C} = Unim \cap Psym$, $\dot{\mathcal{C}}_{\mathbf{1}} = Dev$, $\dot{\mathcal{C}}_C = \dot{\mathcal{C}}_{\mathbf{1}}C = Dev\,C$. By proposition 12 we obtain $\mathcal{R}(F) = Sph$.

3. *Conformality constraint*: $\mathcal{M} =]\alpha, \beta[\,Rot$, with $0 \leq \alpha < 1 < \beta \leq +\infty$, so $\mathcal{C} =]\alpha^2, \beta^2[\,\mathbf{1}$, $\dot{\mathcal{C}}_C = Sph$. By using Proposition 12 we obtain $\mathcal{R}(F) = Dev$.

   The following examples appears in the litterature. They are handled in our approach by Lemma 14 to follow them.

4. *Constraint of inextensibility in diretion* e (e a unit vector):

$$\mathcal{M} = \{\, F \in Lin^+ \mid F(\mathrm{e}) \cdot F(\mathrm{e}) = 1\,\}$$

$$\mathcal{C} = \{\, C \in Psym \mid C : \mathrm{e} \otimes \mathrm{e} = 1\}$$

$$\mathcal{R}(F) = \mathbf{R}F(\mathrm{e} \otimes \mathrm{e})F^\top = \mathbf{R}F(\mathrm{e}) \otimes F(\mathrm{e})$$

5. *Constraint of inextensibility in the mean* :

$$\mathcal{M} = \{F \in Lin^+ \mid trF^\top F = 3\}$$

$$\mathcal{C} = \{C \in Psym \mid C : \mathbf{1} = 3\}$$

$$\mathcal{R}(F) = \mathbf{R}FF^\top$$

6. *Constraint that preserves area in a plane of normal* $\mathbf{n}$ ($\mathbf{n}$ a unit vector)

$$\mathcal{M} = \{F \in Lin^+ \mid F^*(\mathbf{n}) \cdot F^*(\mathbf{n}) = 1\}$$

   where $F^* = detF\, F^{-\top}$.

$$\mathcal{C} = \{C \in Psym \mid detC\, C^{-1} : \mathbf{n} \otimes \mathbf{n} = 1\}$$

$$\mathcal{R}(F) = \mathbf{R}(\mathbf{1} - F^*(\mathbf{n}) \otimes F^*(\mathbf{n}))$$

Lemma 14 *Let $\mathcal{H} = \{H \in Sym \mid H : A = a\}$ ($A \neq 0$ a fixed element of Sym) and $\zeta : Psym \to Psym$ a difeomorfism such that $\zeta(\mathbf{1}) \in \mathcal{H}$, and $\mathcal{C} = \zeta^{-1}(\mathcal{H} \cap Psym)$. Then*

$$\mathcal{R}(F) = \mathbf{R}F\zeta^\top_{*C}(A)F^\top$$

Proof. Since $\zeta(\mathcal{C}) = \mathcal{H} \cap Psym$ and ζ is a difeomorfism then

$$\zeta_{*C}(\dot{\mathcal{C}}_C) = (\dot{\mathcal{H} \cap Psym})_{\zeta(C)} = \dot{\mathcal{H}}_{\zeta(C)}$$

so that for H in $\dot{\mathcal{C}}_C$ we have $\zeta_{*C}(H) : A = 0$, that is, $H : \zeta^\top_{*C}(A) = 0$.This shows that $\zeta^\top_{*C}(A)$ is in $\dot{\mathcal{C}}^{\perp\bullet}$.Since $dim\mathcal{C} = dim\mathcal{H} = 5$, then $\dot{\mathcal{C}}^{\perp\bullet} = \mathbf{R}\zeta^\top_{*C}(A)$, and the proof follows now from Proposition 12.

Using this Lemma with ζ the identity map we obtain at once $\mathcal{R}(F)$ in the Examples 4 and 5 above. As to Example 6, where $\zeta(C) = detC\, C^{-1}$, a straightforward calculation gives

$$\zeta^\top_{*C}(\mathbf{n} \otimes \mathbf{n}) = C^{-1} - detC\, C^{-1}(\mathbf{n}) \otimes C^{-1}(\mathbf{n})$$

and $\mathcal{R}(F)$ follows from Lemma 14.

Theorem 15 *Let $\mathcal{M}$ be a constraint manifold such that $\mathcal{R}(F)$ is independent of F. Then $\mathcal{M}$ must be one of the following: a conformality constraint, the rigidity constraint, an open submanifold of Unim, an open submanifold of Lin^+.*

Proof. Put $\varphi(\mathcal{M}) = \mathcal{C}$. Since $\mathcal{R}(F)$ is independent of F, and on account of Proposition 12, we have

$$F\dot{\mathcal{C}}^{\perp\bullet}_{F^\top F}F^\top = \dot{\mathcal{C}}^{\perp\bullet}_{\mathbf{1}}$$

for every F in $\mathcal{M}$, so that, by Lemma 10 (ii) we have

$$F^{-\top}\dot{\mathcal{C}}_{F^\top F}F^{-1} = \dot{\mathcal{C}}_{\mathbf{1}} \tag{6}$$

for every F in $\mathcal{M}$.

Since $Rot \subset \mathcal{M}$ it follows that for every R in Rot we have

$$R\dot{\mathcal{C}}_{\mathbf{1}}R^\top = \dot{\mathcal{C}}_{\mathbf{1}} \tag{7}$$

so that according to Proposition 6 we are left with four possibilities for $\dot{\mathcal{C}}_1$, namely, Sph, Dev, 0, and Sym.

On the other hand, if C is in $\mathcal{C}$, choose F in $\mathcal{M}$ such that $\varphi(F) = C$. Then there is R in Rot such that the right polar decomposition of F is $F = RC^{\frac{1}{2}}$. Substituing in (6) we will obtain

$$\dot{\mathcal{C}}_C = C^{\frac{1}{2}} R^\top \dot{\mathcal{C}}_1 R C^{\frac{1}{2}} = C^{\frac{1}{2}} \dot{\mathcal{C}}_1 C^{\frac{1}{2}} \tag{8}$$

where use has been made of (7).

1. If $\dot{\mathcal{C}}_1 = Sph$ then by (8) we have $\dot{\mathcal{C}}_C = \mathbf{R}C$ It is not difficult to verify that in this case $\mathcal{C}$ is of the form $\mathcal{C} =]\gamma, \delta[\mathbf{1}$ with $0 \le \gamma < 1 < \delta \le +\infty$,so that $\mathcal{M} = \varphi^{-1}(\mathcal{C}) =]\gamma^{\frac{1}{2}}, \delta^{\frac{1}{2}}[Rot$, a conformality constraint.

2. Suppose $\dot{\mathcal{C}}_1 = Dev$. We claim that in this case $\mathcal{C}$ is contained in $Unim$. In effect, let C be in $\mathcal{C}$, and choose a differentiable curve in $\mathcal{C}$ such that $\alpha(0) = 1$ and $\alpha(1) = C$.Then

   $$\dot{\alpha}(t) \in \dot{\mathcal{C}}_{\alpha(t)} = \alpha(t)^{\frac{1}{2}}\, Dev\, \alpha(t)^{\frac{1}{2}}$$

   where use has been made of (8). Hence

   $$tr(\alpha(t)^{-\frac{1}{2}} \dot{\alpha}(t) \alpha(t)^{-\frac{1}{2}} = 0$$

   or

   $$tr(\alpha(t)^{-1} \dot{\alpha}(t)) = 0$$

   for every t in [0,1], which shows that the curve $t \mapsto \alpha(t)^{-1}\dot{\alpha}(t)$ is a curve in the Lie algebra of $Unim$. Therefore the product integration (Dollard and Friedman. 1987) of this curve is an element belonging to $Unim$, given by $\alpha(0)^{-1}\alpha(1)$, which is precisely C.

   By the above we have that $\mathcal{C}$ is contained in $Unim \cap Psym$. Since the dimensions of $\mathcal{C}$ and of $Unim \cap Psym$ are both equal to 5, $\mathcal{C}$ is an open submanifold of $Unim \cap Psym$, which in turn is equal to $\varphi(Unim)$. Hence $\mathcal{M} = \varphi^{-1}(\mathcal{C})$ is an open submanifold of $Unim$.

3. If $\dot{\mathcal{C}}_1 = \mathbf{0}$ then $\mathcal{C} = \{\mathbf{1}\}$ so that $\mathcal{M} = Rot$.

4. If $\dot{\mathcal{C}}_1 = Sym$, then $\mathcal{C}$ is an open submanifold of $Psym$, so $\mathcal{M} = \varphi^{-1}(\mathcal{C})$ is clearly an open submanifold of Lin^+.

REFERENCES

Cohen H and Wang CC , On the response and symetry of elastic materials with internal constraints, *Arch Rat Mech Anal 99*, 1987.

Dollard JD and Friedman CN , *Product integration.Encyclopedia of Mathematics and its aplications*, Addison Wesley, Massachussets, 1979.

Gurtin ME , *An introduction to continuum mechanics*, Academic Press, New York, 1981.

Podio-Guidugli P, *Constrained elasticity*, Rend Mat Acc Lincei, 1990.

Podio-Guidugli P and Vianello M , Constraint manifolds for isotropic solids,*Arch Rat Mech Anal 105*,1989.

Varadarajan VS, *Lie groups, Lie algebras and their representations*, Prentice-Hall.Inc, 1974.

A general FEM formulation of nonlinear dynamics applied to accessing the statical loading effect upon the dynamic response of planar frames

Reyolando M L R F Brasil and Carlos E N Mazzilli

Department of Structural and Foundation Engineering, Escola Politécnica
Universidade de São Paulo, CP 61548, 05424-970 São Paulo, SP, Brazil

This paper initially discusses the dynamics of discrete structural systems of geometricaly nonlinear behaviour costituted by linear elastic materials. Two formulations are derived, namely *global* and *incremental*. They are both suitable to general FE modelling, as the matrix equations of motion are written in explicit form. Matrices and vectors involved are characterized in terms of constraint equations defined within the continuum discretization. In principle, such formulations are applicable to any structural theory, as the theories of beams, plates and shells. As an example, the Bernoulli-Euler beam element is studied herewith. Both global and incremental formulations capture the effect geometrical nonlinearities have upon inertial and elastic forces alike. The ANDROS FEM program, developed by the authors, which is based upon the global formulation, has been successfully used in several nonlinear analyses. From this general background, the paper proceeds to consider the effect statical loading may have upon the free undamped vibration frequencies of a structure. It is shown that the tangent stiffness matrix of the incremental formulation should be used in the resultant eingenvalue problem. In some cases, axial forces are seen to have a strong influence on the internal resonance tuning. It is shown, in a sample structure thus tuned and subjected to dynamical loading, that a nonlinear regime may appear in the response.

A GENERAL FEM FORMULATION

Discrete structural systems of geometrically nonlinear behaviour constituted by linear elastic material are initially considered. The equations of motion in explicit form are investigated, retaining nonlinearities both in the elastic and in the inertial forces. The foregoing formulation is based on Mazzilli (1988) and is already in adequate form for application to the finite-element method, thus allowing the analysis of large engineering systems. The secant matrices of mass, equivalent damping – there included the inertial damping – and stiffness, as well as the equivalent load vector, are characterized within the global equations of motion. Alternatively, the tangent matrices of mass, damping and stiffness, and the incremental equivalent load vector are deduced within the incremental equations of motion. These latter may be eventually used for consideration of elastoplastic behaviour, interpreting it as hypoelasticity in each time increment. The formulation is able to tackle conservative and non-conservative applied loads, as well as translation and rotation support excitations.

As the starting point, the generalized Lagrange's equations are recast. For a system with n degrees of freedom $Q_1, Q_2, \dots, Q_n$, they are:

$$\frac{d}{dt}\left[\frac{\partial \mathcal{L}}{\partial \dot{Q}_r}\right] - \left[\frac{\partial \mathcal{L}}{\partial Q_r}\right] = N^r, \quad r = 1\,to\,n$$

the Lagrangian function $\mathcal{L}$ being given by the difference between the kinetic energy T and the total potential energy V. The generalized forces N^r retain the effects of the nonconservative forces. One can also define $\mathcal{L}$ as the difference between the kinetic energy and the strain energy U, so that N^r would then also include the effects of applied conservative forces. Holonomic constraints are assumed, so that the position vector of a generic volume element $d\Omega$ of the deformable system is supposed to be a known function of the generalized coordinates and the time:

$$\vec{R} = \vec{R}(Q_1, Q_2, \dots, Q_n, t)$$

If these functions are all linear in the generalized coordinates, geometrical nonlinearities will be lost. Therefore,

part of "MECHANICS PAN-AMERICA 1993" edited by MRM Crespo da Silva and CEN Mazzilli
Appl Mech Rev vol 46, no 11, part 2, November 1993

ASME Reprint No AMR134

extreme caution should be taken when the finite-element technique is introduced into the formulation. The usual hypothesis that the displacement field within a finite element is given by a linear combination of nodal displacements may be inadequate for the nonlinear analysis. Hence, at the Solid Mechanics level it is necessary that the underlying structural theory be consistently nonlinear and further that at the structural discretization level, via the finite-element technique, nonlinearities are not subtly lost within the matrix equations of motion.

The kinetic energy is:

$$T = \frac{1}{2}\int_{\Omega} \dot{\vec{R}} \cdot \dot{\vec{R}} \rho d\Omega$$

where Ω is the region occupied by the undeformed system and ρ the specific mass. The velocity vector is:

$$\dot{\vec{R}} = \frac{\partial \vec{R}}{\partial Q_r}\dot{Q}_r + \frac{\partial \vec{R}}{\partial t}$$

and consequently:

$$T = \frac{1}{2}A^{rs}\dot{Q}_r\dot{Q}_s + B^r\dot{Q}_r + \frac{1}{2}C$$

with:

$$A^{rs} = \int_{\Omega} \frac{\partial \vec{R}}{\partial Q_r} \cdot \frac{\partial \vec{R}}{\partial Q_s} \rho d\Omega;$$

$$B^{r} = \int_{\Omega} \frac{\partial \vec{R}}{\partial Q_r} \cdot \frac{\partial \vec{R}}{\partial t} \rho d\Omega;$$

$$C = \int_{\Omega} \frac{\partial \vec{R}}{\partial t} \cdot \frac{\partial \vec{R}}{\partial t} \rho d\Omega$$

Recasting Lagrange's equations, one gets:

$$\begin{aligned} A^{rs}\ddot{Q}_s + \left[\frac{\partial A^{rs}}{\partial Q_t} - \frac{1}{2}\frac{\partial A^{st}}{\partial Q_r}\right]\dot{Q}_s\dot{Q}_t \quad &+ \quad \frac{\partial A^{rs}}{\partial t}\dot{Q}_s + \\ \left[\frac{\partial B^r}{\partial Q_s} - \frac{\partial B^s}{\partial Q_r}\right]\dot{Q}_s \frac{\partial B^r}{\partial t} - \frac{1}{2}\frac{\partial C}{\partial Q_r} \quad &= \quad -\frac{\partial U}{\partial Q_r} + N^r \end{aligned}$$

A special though still rather general class of holonomic constraints is now considered. It is supposed that there exists a reference frame $Yy^1y^2y^3$, called "relative", with respect to which the system constraints are scleronomic. Support excitations are defined by rigid-body motion of the relative frame $Yy^1y^2y^3$ with respect to an inertial frame $Xx^1x^2x^3$. Calling $\vec{R}$ the position vector in the inertial frame, $\vec{r}$ the position vector in the relative frame and $\vec{S}$ the vector (Y-X), one writes:

$$\vec{R} = \vec{r} + \vec{S}; \quad \vec{S} = S^i\vec{e}_i; \quad \vec{r} = a^i_j y^j \vec{e}_i$$

where the matrix $[a^i_j]$ defines the relative frame rotation with respect to the inertial frame. It can be explicitly given in terms of the Euler angles (Mazzilli, 1988). For a planar problem, the matrix $[a^i_j]$ can be written in terms of the support rotation $\phi(t)$:

$$[a^i_j] = \begin{bmatrix} \cos\phi & -\sin\phi \\ \sin\phi & \cos\phi \end{bmatrix}$$

It was already observed that it is a feature of nonlinear structural theories to render nonlinear functions for the coordinates y^j in the variables $Q_1, Q_2, ..., Q_n$. Additionally, support excitations are defined by rotations through the matrix $[a^i_j(t)]$ or by translations through $S^i(t)$. Hence:

$$\vec{R} = [a^i_j(t)y^j(Q_1, Q_2, ..., Q_n) + S^i(t)]\vec{e}_i$$

Back into expressions for A^{rs}, B^r e C, and taking these into Lagrange's equations, one arrives at:

$$\begin{aligned} F^{rsjm}\delta_{jm}\ddot{Q}_s \quad &+ \\ \left(F^{rsjm}_{,t} - \frac{1}{2}F^{stjm}_{,r}\right)\delta_{jm}\dot{Q}_s\dot{Q}_t \quad &+ \\ (F^{rsjm} - F^{srjm})a^i_j\dot{a}^k_m\delta_{ik}\dot{Q}_s \quad &+ \\ H^{rj}a^i_j\ddot{S}^k\delta_{ik} \quad &+ \\ G^{rjm}a^i_j\ddot{a}^k_m\delta_{ik} \quad &= \quad -U_{,r} + N^r \end{aligned}$$

Notation $(.)_{,r}$ indicates partial differentiation with respect to Q_r, δ_{jm} being the Kronecker's symbol and:

$$\begin{aligned} F^{rsjm} \quad &= \quad \int_{\Omega} \frac{\partial y^j}{\partial Q_r}\frac{\partial y^m}{\partial Q_s}\rho d\Omega; \\ G^{rjm} \quad &= \quad \int_{\Omega} \frac{\partial y^j}{\partial Q_r} y^m \rho d\Omega; \\ H^{rj} \quad &= \quad \int_{\Omega} \frac{\partial y^j}{\partial Q_r}\rho d\Omega \end{aligned}$$

All terms dependent of F^{rsjm}, G^{rjm} e H^{rj} in the above equations of motion are inertial forces, there included the Coriolis forces:

$$(F^{rsjm} - F^{srjm})a^i_j\dot{a}^k_m\delta_{ik}\dot{Q}_s$$

and the centrifugal forces:

$$G^{rjm}a^i_j\ddot{a}^k_m\delta_{ik}$$

Since F^{rsjm}, G^{rjm} e H^{rj} may be functions of the generalized coordinates, it is clear that geometrical nonlinearities can in fact generate nonlinear inertial forces. The elastic force vector $U_{,r}$, on its turn, may also include nonlinear terms caused by geometrical nonlinearities, as it is well known even in Statics. It is supposed that the generalized force vector always include viscous damping:

$$N^r = P^r - \mu^{rs}\dot{Q}_s$$

The global nonlinear equations of motion can now be written in the compact form:

$$M^{rs}\ddot{Q}_s + D^{rs}\dot{Q}_s + U_{,r} = \mathcal{F}^r$$

where:

$$M^{rs} = F^{rsjm}\delta_{jm}$$

$$\begin{aligned} D^{rs} &= \mu^{rs} + (F^{rsjm} - F^{srjm})a^i_j \dot{a}^k_m \delta_{ik} \\ &+ \left(F^{rsjm}_{,t} - \frac{1}{2}F^{stjm}_{,r}\right)\delta_{jm}\dot{Q}_t \end{aligned}$$

$$\mathcal{F}^r = P^r - G^{rjm}a^i_j \ddot{a}^k_m \delta_{ik} - H^{rj}a^i_j \ddot{S}^k \delta_{ik}$$

It should be observed that the introduction of the stiffness matrix in the global equation of motion is, in some ways, arbitrary. In fact, what naturally appears there is the elastic force vector $U_{,r}$. Obviously, one could think of the secant stiffness matrix K^{rs}_S, as:

$$U_{,r} = K^{rs}_S Q_s$$

Nevertheless, several other matrices could be thought of, as the linear theory stiffness matrix, for example. Once a particular stiffness matrix K^{rs} has been chosen, one can add to both sides of the global equation of motion the term $K^{rs}Q_s$. Introducing now the definition:

$$\Delta\mathcal{F}^r = K^{rs}Q_s - U_{,r}$$

one finally gets for the global equations of motion:

$$M^{rs}\ddot{Q}_s + D^{rs}\dot{Q}_s + K^{rs}Q_s = \mathcal{F}^r + \Delta\mathcal{F}^r$$

In other words, the arbitrary choice of the stiffness matrix implies in adding to the load vector $\mathcal{F}^r$ a correcting term. It should be observed that, even in Statics, the global equilibrium equation:

$$U_{,r} = P^r$$

can well be written in the form:

$$K^{rs}Q_s = P^r + \Delta\mathcal{F}^r$$

and, in numerical nonlinear analysis, this latter suggests an iterative procedure equivalent to that of the modified Newton-Raphson method. In fact, choosing a particular matrix K^{rs} and supposing in the first iteration that $\Delta\mathcal{F}^r = 0$, one can obtain Q_s from the equilibrium equation. The new value for $\Delta\mathcal{F}^r$ would then come after its definition and so forth.

In a great number of cases it may be more convenient to work with the incremental equations of motion:

$$M^{rs}_T\delta\ddot{Q}_s + D^{rs}_T \quad \ldots \quad {}_s = \delta\mathcal{P}^r$$

where:

$$M^{rs}_T = M^{rs}$$

$$\begin{aligned} D^{rs}_T &= \mu^{rs} + (F^{rsjm} - F^{srjm})a^i_j \dot{a}^k_m \delta_{ik} \\ &+ (F^{rsjm}_{,t} + F^{rtjm}_{,s} - F^{stjm}_{,r})\delta_{jm}\dot{Q}_t \end{aligned}$$

$$\begin{aligned} K^{rs}_T &= U_{,rs} + G^{rjm}_{,s}a^i_j \ddot{a}^k_m \delta_{ik} + H^{rj}_{,s}a^i_j \ddot{S}^k \delta_{ik} \\ &+ F^{rtjm}_{,s}\delta_{jm}\ddot{Q}_t + \left(F^{rujm}_{,st} - \frac{1}{2}F^{utjm}_{,rs}\right)\delta_{jm}\dot{Q}_u\dot{Q}_t \\ &+ (F^{rtjm}_{,s} - F^{trjm}_{,s})a^i_j \dot{a}^k_m \delta_{ik}\dot{Q}_t + \mu^{rt}_{,s}\dot{Q}_t \end{aligned}$$

$$\begin{aligned} \delta\mathcal{P}^r &= \delta P^r - G^{rjm}(\delta a^i_j \ddot{a}^k_m + a^i_j \delta\ddot{a}^k_m)\delta_{ik} \\ &- H^{rj}(\delta a^i_j \ddot{S}^k + a^i_j \delta\ddot{S}^k)\delta_{ik} \\ &- (F^{rsjm} - F^{srjm})(\delta a^i_j \dot{a}^k_m + a^i_j \delta\dot{a}^k_m)\delta_{ik} \end{aligned}$$

A PLANAR STRUT FINITE ELEMENT

As an application example of the previous section general formulation, we consider now the 2-D strut finite element according to the Bernoulli-Euler theory (Mazzilli, 1990). From Figs 1a and 1b the following relations can be derived for the displacements u (local system $\bar{y}^1$ direction) and v (local system $\bar{y}^2$ direction) of the elemental mass dm situated in a cross section defined by the strut axis coordinate x and at a distance y from the cross section centroid:

$$\begin{aligned} u &= \bar{u} - y\sin\alpha \\ v &= \bar{v} + y(\cos\alpha - 1) \end{aligned}$$

where $\bar{u}$ and $\bar{v}$ are the u and v displacements of a material point on the strut axis and α is the cross-section rotation, for which rigorously:

$$\begin{aligned} \sin\alpha &= \frac{\bar{v}'}{\bar{\lambda}} \\ \cos\alpha &= \frac{1+\bar{u}'}{\bar{\lambda}} \\ \tan\alpha &= \frac{\bar{v}'}{1+\bar{u}'} \end{aligned}$$

Notation $(.)'$ denotes differentiation with respect to **x**. The axis stretching is:

$$\bar{\lambda} = \sqrt{(1+\bar{u}')^2 + (\bar{v}')^2}$$

Observe that the "local system" $Y\bar{y}^1\bar{y}^2$ is defined by a rotation θ, independent of time, with respect to the relative frame Yy^1y^2. In what follows here, the elemental

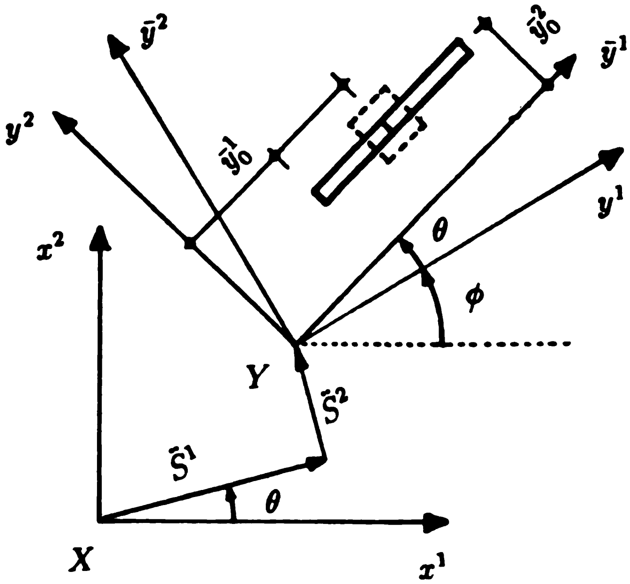

Fig 1a

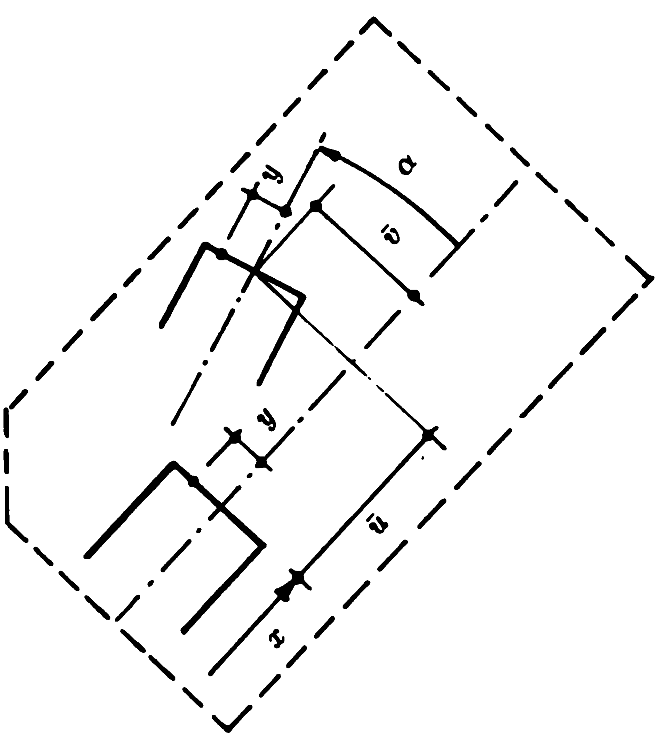

Fig 1b

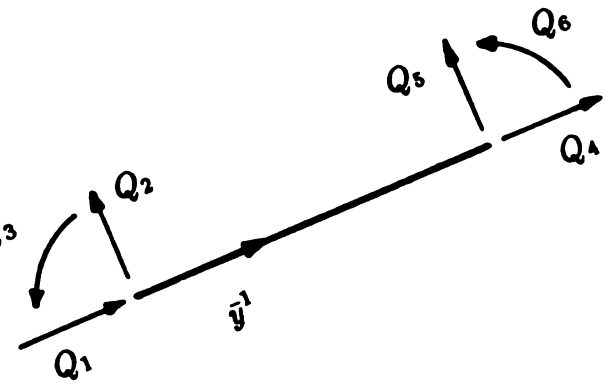

Fig 2

matrices and vectors will be defined for the local system. The constraint equations will then be:

$$
\begin{aligned}
\bar{y}^1 &= \bar{y}_0^1 + x + \bar{u} - y \sin\alpha \\
\bar{y}^2 &= \bar{y}_0^2 + \bar{v} + y \cos\alpha
\end{aligned}
$$

The following approximations will be assumed from now on:

$$\sin\alpha \approx \alpha \approx \tan\alpha \approx \bar{v}'$$

$$\cos\alpha \approx 1 - \frac{1}{2}(\bar{v}')^2$$

The Bernoulli-Euler strut does not allow for shear strain and the longitudinal strain ϵ can be defined as:

$$\epsilon = \bar{\epsilon} - y\alpha' \approx \bar{\epsilon} - y\bar{v}''$$

$$\bar{\epsilon} = \bar{\lambda} - 1 \approx \bar{u}' + \frac{1}{2}(\bar{v}')^2$$

To formulate the finite element it is necessary to introduce the discretization, that is, the displacement field within the element should be defined in terms of the nodal displacements, interpreted as generalized coordinates (Q_1 to Q_6) and indicated in Fig 2.

As in the standard applications of the finite-element method, one can think of stating that the transversal displacements $\bar{v}$ result from a **linear combination** of the nodal displacements:

$$\bar{v} = Q_i \Psi_i \text{ , } sum\ from\ 1\ to\ 6,\ where:$$

$$\Psi_1(x) = \Psi_4 = 0$$

$$\Psi_2(x) = 1 - 3\frac{x^2}{\ell^2} + 2\frac{x^3}{\ell^3}$$

$$\Psi_3(x) = x - 2\frac{x^2}{\ell} + \frac{x^3}{\ell^2}$$

$$\Psi_5(x) = 3\frac{x^2}{\ell^2} - 2\frac{x^3}{\ell^3}$$

$$\Psi_6(x) = -\frac{x^2}{\ell} + \frac{x^3}{\ell^2}$$

Nevertheless, if the longitudinal displacements $\bar{u}$ are also supposed to result from a **linear combination** of the nodal displacements, important geometrical nonlinearities will be lost. Instead, we shall follow here the simple hypothesis proposed by Souza Lima and Venancio Filho (1982) for Statics, that is, the **constancy** of normal forces N inside the element. It is interesting to remark that an equivalent hypothesis was recently proposed by Salami and Morley (1992), still in Statics.

$$\begin{aligned} N &= \frac{EA}{\ell}\int_0^\ell \bar{\epsilon}dx \\ &= \frac{EA}{\ell}\left[\bar{u}(\ell)-\bar{u}(0)+\frac{1}{2}\int_0^\ell(\bar{v}')^2dx\right] \\ &= \frac{EA}{\ell}\left[Q_4-Q_1+\frac{1}{2}\alpha_{ij}(\ell)Q_iQ_j\right] \end{aligned}$$

where EA is the axial stiffness and:

$$\alpha_{ij}(x)=\int_0^x \Psi_i'(z)\Psi_j'(z)dz$$

Therefore:

$$\bar{u}'=\frac{1}{\ell}(Q_4-Q_1)+\frac{1}{2\ell}Q_iQ_j\alpha_{ij}(\ell)-\frac{1}{2}Q_iQ_j\Psi_i'\Psi_j'$$

and, after integration in $\mathbf{x}$:

$$\bar{u}=Q_1+\left[\frac{1}{\ell}(Q_4-Q_1)+\frac{1}{2\ell}Q_iQ_j\alpha_{ij}(\ell)\right]x-\frac{1}{2}Q_iQ_j\alpha_{ij}(x)$$

or:

$$\bar{u}=Q_1\left(1-\frac{x}{\ell}\right)+Q_4\left(\frac{x}{\ell}\right)+\frac{1}{2}Q_iQ_j\left[\frac{x}{\ell}\alpha_{ij}(\ell)-\alpha_{ij}(x)\right]$$

It should be noted that the field of longitudinal displacements $\bar{u}$ has not resulted a linear function of the generalized coordinates!

The constraint equations can now be written in compact form as:

$$\bar{y}^j=\gamma^j(x,Q_1,Q_2,...,Q_6)+y\delta^j(x,Q_1,Q_2,...,Q_6)$$

where:

$$\gamma^1=\bar{y}_0^1+x+Q_i\Phi_i(x)+\frac{1}{2}Q_iQ_j\beta_{ij}(x)$$

$$\delta^1=-Q_i\Psi_i'$$

$$\gamma^2=\bar{y}_0^2+Q_i\Psi_i$$

$$\delta^2=1-\frac{1}{2}Q_iQ_j\Psi_i'\Psi_j'$$

In the above equations, $\Phi_i(x)$, $i=1,2,...,6$, are the standard interpolation functions of the linear analysis:

$$\Phi_1(x) \cdot$$

$$\Phi$$

$$\Phi_2(x)=\Phi_3(x)=\Phi_5(x)=\Phi_6(x)=0$$

and

$$\beta_{ij}(x)=\left[\frac{x}{\ell}\alpha_{ij}(\ell)-\alpha_{ij}(x)\right]$$

One is now ready to write in explicit form the elemental matrices and vectors used in the **global equations of motion**. In the local system, they are written as:

$$\bar{M}^{rs}=\rho A\int_0^\ell(\gamma^1_{,r}\gamma^1_{,s}+\gamma^2_{,r}\gamma^2_{,s})dx+\rho I\int_0^\ell(\delta^1_{,r}\delta^1_{,s}+\delta^2_{,r}\delta^2_{,s})dx$$

$$\begin{aligned} \bar{D}^{rs} &= \mu^{rs}-2\dot{\phi}\left[\rho A\int_0^\ell(\gamma^1_{,r}\gamma^2_{,s}-\gamma^1_{,s}\gamma^2_{,r})dx\right] \\ &+ \dot{Q}_i\rho A\int_0^\ell\left(\frac{1}{2}\gamma^1_{,ri}\gamma^1_{,s}+\gamma^1_{,r}\gamma^1_{,si}-\frac{1}{2}\gamma^1_{,sr}\gamma^1_{,i}\right)dx \\ &+ \dot{Q}_i\rho I\int_0^\ell\delta^2_{,si}\delta^2_{,r}dx \end{aligned}$$

$$\begin{aligned} \bar{U}_{,r} &= \frac{EA}{\ell}\left[\ell Q_i\Phi_i'+\frac{1}{2}\alpha_{ij}(\ell)Q_iQ_j\right][\ell\Phi_r'+Q_k\alpha_{kr}(\ell)] \\ &+ EIQ_i\int_0^\ell\Psi_i''(x)\Psi_r''(x)dx \end{aligned}$$

$$\begin{aligned} \bar{\mathcal{F}}^r &= \bar{K}^{rs}Q_s-\bar{U}_{,r}+\bar{P}^r \\ &+ \dot{\phi}^2\rho A\int_0^\ell(\gamma^1_{,r}\gamma^1+\gamma^2_{,r}\gamma^2)dx \\ &+ \dot{\phi}^2\rho I\int_0^\ell(\delta^1_{,r}\delta^1+\delta^2_{,r}\delta^2)dx \\ &+ \ddot{\phi}\rho A\int_0^\ell(\gamma^1_{,r}\gamma^2-\gamma^2_{,r}\gamma^1)dx \\ &+ \ddot{\phi}\rho I\int_0^\ell(\delta^1_{,r}\delta^2-\delta^2_{,r}\delta^1)dx \\ &- \rho A\ddot{S}^1\left[\cos\phi\int_0^\ell\gamma^1_{,r}dx+\sin\phi\int_0^\ell\gamma^2_{,r}dx\right] \\ &- \rho A\ddot{S}^2\left[-\sin\phi\int_0^\ell\gamma^1_{,r}dx+\cos\phi\int_0^\ell\gamma^2_{,r}dx\right] \end{aligned}$$

In the above equations $\phi(t)$ stands for the support rotation characterized by the imposed angle between the relative Yy^1 axis and the inertial Xx^1 axis.

The matrices and vectors of the **incremental formulation** are now explicitly written for the local system:

$$\bar{M}_T^{rs}=\rho A\int_0^\ell(\gamma^1_{,r}\gamma^1_{,s}+\gamma^2_{,r}\gamma^2_{,s})dx+\rho I\int_0^\ell(\delta^1_{,r}\delta^1_{,s}+\delta^2_{,r}\delta^2_{,s})dx$$

$$\begin{aligned} \bar{D}_T^{rs} &= \mu^{rs}-2\dot{\phi}\left[\rho A\int_0^\ell(\gamma^1_{,r}\gamma^2_{,s}-\gamma^1_{,s}\gamma^2_{,r})dx\right] \\ &+ 2\left[\rho A\int_0^\ell\gamma^1_{,r}\gamma^1_{,si}dx+\rho I\int_0^\ell\delta^2_{,r}\delta^2_{,si}dx\right]\dot{Q}_i \end{aligned}$$

$$
\begin{aligned}
\bar{U}_{,rs} &= \frac{EA}{\ell}[\ell\Phi'_s + \alpha_{is}(\ell)Q_i][\ell\Phi'_r + Q_j\alpha_{jr}(\ell)] \\
&+ \frac{EA}{\ell}\left[\ell Q_i\Phi'_i + \frac{1}{2}\alpha_{ij}Q_iQ_j\right]\alpha_{rs} \\
&+ EI\int_0^\ell \Psi''_r(x)\Psi''_s(x)dx
\end{aligned}
$$

$$
\begin{aligned}
\bar{K}_T^{rs} &= \bar{U}_{,rs} + \mu^{ri}_{,s}\dot{Q}_i \\
&- \dot{\phi}^2\rho A\int_0^\ell(\gamma^1_{,rs}\gamma^1 + \gamma^1_{,r}\gamma^1_{,s} + \gamma^2_{,r}\gamma^2_{,s})dx \\
&+ \dot{\phi}^2\rho I\int_0^\ell(\delta^1_{,r}\delta^1_{,s} + \delta^2_{,rs}\delta^2 + \delta^2_{,r}\delta^2_{,s})dx \\
&- \ddot{\phi}\rho A\int_0^\ell(\gamma^1_{,rs}\gamma^2 + \gamma^1_{,r}\gamma^2_{,s} - \gamma^2_{,r}\gamma^1_{,s})dx \\
&+ \ddot{\phi}\rho I\int_0^\ell(\delta^1_{,r}\delta^2_{,s} - \delta^2_{,rs}\delta^1 - \delta^2_{,r}\delta^1_{,s})dx \\
&+ \rho A\ddot{S}^1\left[\cos\phi\int_0^\ell\gamma^1_{,rs}dx + \sin\phi\int_0^\ell\gamma^2_{,rs}dx\right] \\
&+ \rho A\ddot{S}^2\left[-\sin\phi\int_0^\ell\gamma^1_{,rs}dx + \cos\phi\int_0^\ell\gamma^2_{,rs}dx\right] \\
&+ \ddot{Q}_i\rho A\int_0^\ell(\gamma^1_{,rs}\gamma^1_{,i} + \gamma^1_{,r}\gamma^1_{,si})dx \\
&+ \ddot{Q}_i\rho I\int_0^\ell(\delta^2_{,rs}\delta^2_{,i} + \delta^2_{,r}\delta^2_{,si})dx \\
&+ \left[\rho A\int_0^\ell\gamma^1_{,rs}\gamma^1_{,ij}dx + \rho I\int_0^\ell\delta^2_{,rs}\delta^2_{,ij}dx\right]\dot{Q}_i\dot{Q}_j \\
&- 2\dot{\phi}\left[\rho A\int_0^\ell(\gamma^1_{,rs}\gamma^2_{,i} - \gamma^1_{,is}\gamma^2_{,r})dx\right]\dot{Q}_i
\end{aligned}
$$

$$
\begin{aligned}
\delta\bar{P}^r &= \delta\bar{P}^r \\
&+ 2\dot{\phi}\rho A\left[\int_0^\ell(\gamma^1_{,r}\gamma^1 + \gamma^2_{,r}\gamma^2)dx\right]\delta\dot{\phi} \\
&+ 2\dot{\phi}\rho I\left[\int_0^\ell(\delta^1_{,r}\delta^1 + \delta^2_{,r}\delta^2)dx\right]\delta\dot{\phi} \\
&+ 2\rho A\left[\int_0^\ell(\gamma^1_{,r}\gamma^2_{,s} - \gamma^1_{,s}\gamma^2_{,r})dx\right]\delta\dot{\phi} \\
&+ 2\rho\left[I\int_0^\ell(\delta^1_{,r}\delta^2_{,s} - \delta^1_{,s}\delta^2_{,r})dx\right]\delta\dot{\phi} \\
&+ \rho A\left[\int_0^\ell(\gamma^1_{,r}\gamma^2 - \gamma^2_{,r}\gamma^1)dx\right]\delta\ddot{\phi} \\
&+ \rho I\left[\int_0^\ell(\delta^1_{,r}\delta^2 - \delta^2_{,r}\delta^1)dx\right[\delta\ddot{\phi} \\
&- \rho A\ddot{S}^1\left[-\sin\phi\int_0^\ell\gamma^1_{,r}dx + \cos\phi\int_0^\ell\gamma^2_{,r}dx\right]\delta\phi \\
&- \rho A\ddot{S}^2\left[-\cos\phi\int_0^\ell\gamma^1_{,r}dx - \sin\phi\int_0^\ell\gamma^2_{,r}dx\right]\delta\phi \\
&- \rho A\left[-\sin\phi\int_0^\ell\gamma^1_{,r}dx + \cos\phi\int_0^\ell\gamma^2_{,r}dx\right]\delta\ddot{S}^2 \\
&- \rho A\left[-\cos\phi\int_0^\ell\gamma^1_{,r}dx - \sin\phi\int_0^\ell\gamma^2_{,r}dx\right]\delta\ddot{S}^1
\end{aligned}
$$

Note that all matrices and vectors of both the global and the incremental equations of motion can be explicitly given in terms of the generalized coordinates, by considering the expressions for γ^1, γ^2, δ^1 and δ^2 previously written and the derivatives:

$$
\begin{aligned}
\gamma^1_{,r} &= \Phi_r + Q_i\beta_{ir} & \gamma^1_{,rs} &= \beta_{rs} \\
\gamma^2_{,r} &= \Psi_r & \gamma_{,rs} &= 0 \\
\delta^1_{,r} &= -\Psi'_r & \delta^1_{,rs} &= 0 \\
\delta^2_{,r} &= -Q_i\Psi'_i\Psi'_r & \delta^2_{,rs} &= -\Psi'_r\Psi'_s
\end{aligned}
$$

The authors implemented at the Computational Mechanics Laboratory of Escola Politécnica da Universidade de São Paulo, the ANDROS system of FEM programs to perform nonlinear dynamical analysis of structures, based upon the global formulation (Mazzilli and Brasil, 1992). It has been successfully used in several nonlinear analyses reported in a number of papers (Brasil and Mazzilli, 1991), (Brasil and Mazzilli, 1992).

INFLUENCE OF AXIAL FORCES ON UNDAMPED VIBRATION FREQUENCIES OF PLANAR FRAMED STRUCTURES

If a considerable level of static load is applied to planar framed structures, resulting in high axial forces in some members, their natural frequencies of undamped free vibration may change considerably. The undamped equation of motion for those (small) vibrations about the deformed configuration is:

$$
m_T^{rs}\,\delta\ddot{q}_s + k_T^{rs}\,\delta q_s = 0
$$

where k_T^{rs} stands for the coefficients of the tangent stiffness matrix for that level of static loading. The coefficients of the tangent mass matriz m_T^{rs} are those of m^{rs} and can usually be made equal to those of the linear theory mass matrix. These are the two matrices one should use in the eigenvalue problem solution to find the natural frequencies of free undamped vibrations for the statically loaded deformed structure.

One of the programs included in the ANDROS system performs a static nonlinear analysis of planar framed structures, via the Modified Newton-Raphson algorithm, to obtain the tangent stiffness matrix at a certain level of loading. The system also features a standard eigenvalues routine, based on Holseholder-QL algorithm, to give the frequencies of undamped free vibrations about the statically loaded deformed configuration of the structure.

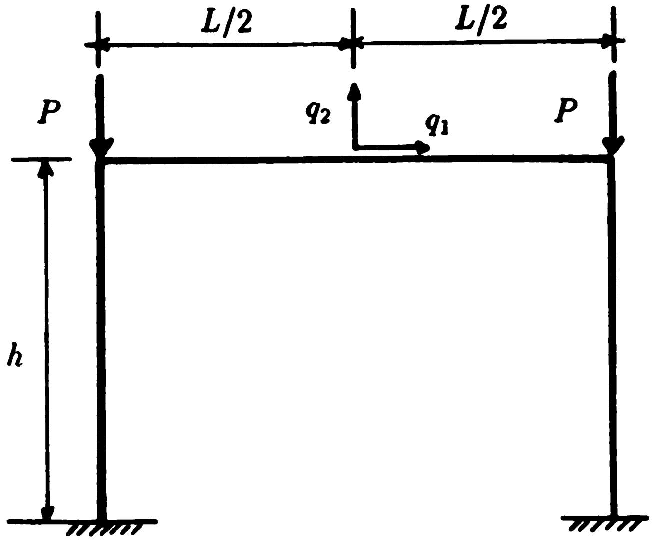

Fig 3

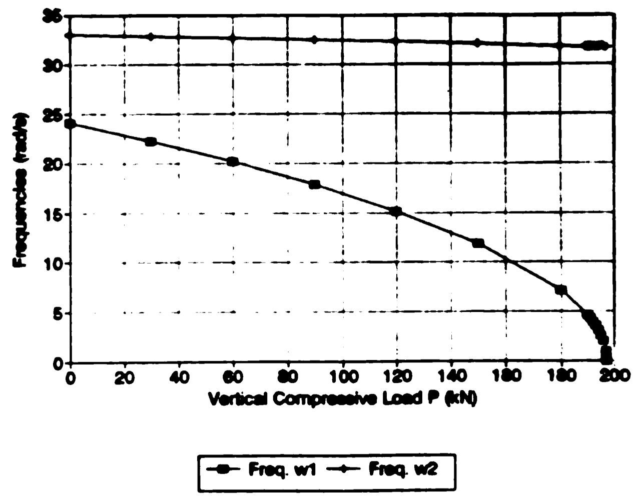

Fig 4

The simple portal frame of Fig 3 was analysed. It is constituted by a four-element horizontal beam and two three-element columns clamped in their bases. Two compressive vertical loads P are applied to the top of the columns. These forces could, as an example, be given by prestressing of the columns. The geometrical and material properties of the analysed model are:

$$A = 3.48 \times 10^{-3} m^2; \quad I = 1.55 \times 10^{-3} m^4;$$

$$L = 7.5m; \quad h = 3.0m;$$

$$E = 2.05 \times 10^{11} Pa; \quad \rho = 7.85 \times 10^3 kg/m^3$$

This structure was analysed for several levels of the P load. The values of its two lowest natural frequencies, namely: ω_1 (the sway mode frequency) and ω_2 (the first symmetrical mode frequency), are plotted in Fig 4 against the variation of P. One can see that ω_1 decreases according to a curve, reaching a zero value for the buckling load predicted by Timoshenko (1961), whereas ω_2 is nearly constant.

ANALYSIS OF A FRAME UNDER NEAR EXTERNAL AND INTERNAL RESONANCE CONDITIONS

As another example of the capabilities of the ANDROS FEM system, a full nonlinear dynamical analysis of a portal frame, with the same geometrical and material properties of the structure shown in Fig 3, is presented. When the load P is set to the value of 110 kN, one can see, in Fig 4, that the near internal resonance condition ($2\omega_1 \approx \omega_2$) is reached between the sway mode and the first symmetrical mode. It was considered a Rayleigh type viscous (linear) damping matrix to yield 0.5% damping rates for these first two modes.

In a forced motion analysis at this level of load, harmonic vertical support excitation was applied, of the form

$$\ddot{S}^2 = \ddot{S}_o \sin \Omega t$$

at near resonance with the symmetrical mode ($\Omega \approx \omega_2$).

For a better understanding of the effects of the geometrical nonlinearities, one should analyse Fig 5 where q_1 stationary amplitude is plotted. The ground acceleration amplitude $\ddot{S}_o$ is kept constant (equal to 0.25 g) while its frequency Ω varies around ω_2. These conditions of near internal and external resonances lead to the "saturation" of the symmetrical mode, through which the energy is pumped into the system, with consequent rapid growing of the lateral vibrations (which otherwise would be near null), due to transference of the surplus energy. Although these postcritical vibrations are found to be theoretically stable, the considerable amplitude of the sway movement may lead to structural damage or even to failure.

CONCLUDING REMARKS

This paper fits into a research line which starts with consistent and general formulations of analytical dynamics, having in mind a robust modelling. The next step would be its application to the finite-element method which would put at reach the analysis of complex engineering problems. Stationary basic solutions could then be surveyed, in special basic statical equilibrium configurations. It would follow a modal analysis considering small perturbations around the chosen basic state, which would give evidences of the relevant modes to be kept in a low-dimension version of the large-size problem. Here, intuitive engineering reasoning – such as the consideration of the energy imparted to the selected modes and the possibility of internal and external resonances –, together with computational techniques for location of in-

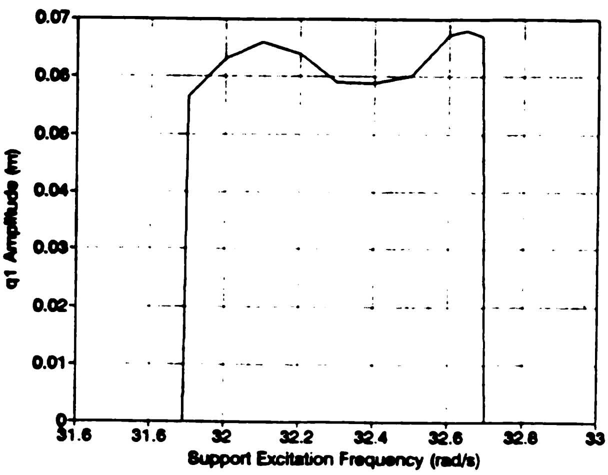

Fig 5

variant manifolds and their tangencies are required. Nonlinear parametric studies for the associated few-degree-of-freedom system would follow, supplying a valuable qualitative knowledge of alternative competing regimes. These studies would them be used to define the quantitative analysis to be performed in the original large-size system via the finite-element method. An effort in this way was made by Mazzilli and Brasil (1993). As a matter of fact, such a research line is already being pursued at LMC – Computational Mechanics Laboratory – of Escola Politécnica, University of São Paulo. At this moment, a general consistent formulation of analytical dynamics – which is part of the subject of this paper – is already available. Based upon it the ANDROS finite-element program was developed (Mazzilli and Brasil, 1992). ANDROS was capable of capturing in large systems the expected nonlinear phenomena after the study of associated simple systems.

Initial work is already under way on the condensation of multiple into few-degree-of-freedom systems, to which perturbation analyses can be applied in automatic fashion with the help of symbolic computation. So far this has been done following very much the intuitive engineering reasoning and considerable help is expected from the applied mathematicians in the more rigorous search of the invariant manifolds.

REFERENCES

Mazzilli C E N (1988), Dinâmica não-linear e estabilidade: uma formulação para sistemas submetidos a excitação de suporte ou a carregamentos não-conservativos, Associate Professor Thesis (in Portuguese) Escola Politécnica da Universidade de São Paulo, São Paulo, Brazil

Mazzilli C E N (1990), Nonlinear Finite Element Formulation in Dynamics, Tech Rep BT/PEF-9008, Escola Politécnica da Universidade de São Paulo

Souza Lima V M and Venâncio Filho F (1982), Considerações sobre a não-linearidade geométrica em estruturas reticuladas, in Proc of III Escola de Matemática Aplicada (in Portuguese), LNCC/CNPq, Rio de Janeiro, Brazil

Salami A T and Morley C T (1992), Finite element analysis of geometric non-linearity in plane frameworks, *The Structural Engineer*, 70 (15)

Mazzilli C E N and Brasil R M L R F (1992), ANDROS - A Finite-Element Program for Nonlinear Dynamics, Tech Report BT/PEF/9213, Escola Politécnica da USP, Dep. de Eng. de Estruturas e Fundações, São Paulo, Brazil

Brasil R M L F and Mazzilli C E N (1991), Dynamical Analysis of Framed Structures of Geometrical Nonlinear Behavior: a Finite Element Approach, in *Proc. of the II Pan American Congress of Applied Mechanics*, Valparaiso, Chile, 232-235

Brasil R M L F and Mazzilli C E N (1992), Nonlinear FE Analysis in Dynamics: Simplifications Aiming at Small Computers, in *Proc. of the IV International Conference on Education, Practice and Promotion of Computational Methods in Engineering using Small Computers*, Dalian, China, 531-536

Timoshenko S P (1961), *Theory of Elastic Stability*, McGraw-Hill, New York, NY

Mazzilli C E N and Brasil R M L R F (1993), Effect of Axial Forces on the Nonlinear Vibrations of a Three-Time Redundant Portal Frame: Analytical and Numerical Studies, submitted for publication to *Nonlinear Dynamics*

Geometrically exact analysis of spatial frames

Paulo M Pimenta and Takashi Yojo

Department of Structural and Foundation Engineering, Escola Politécnica
Universidade de São Paulo, CP 61548, 05424-970 São Paulo, SP, Brazil

A fully nonlinear, geometrically exact, finite strain rod model is derived from basic kinematical assumptions. The model incorporates shear distortion in bending and can take account of torsion warping. Rotation in 3D space is handled with the aid of the Euler-Rodrigues formula. The accomplished parametrization is simple and does not require update algorithms based on quaternions parameters. Weak and strong forms of the equilibrium equations are derived in terms of cross section strains and stresses, which are objective and suitable for constitutive description. As an example, an invariant linear elastic constitutive equation based on the small strain theory is presented. The attained formulation is very convenient for numerical procedures employing Galerkin projection like the finite element method and can be readily implemented in a finite element code. A mixed formulation of Hu-Washizu type is also derived, allowing for independent interpolation of the displacement, strain and stress fields within a finite element. An exact expression for the Fréchet derivative of the weak form of equilibrium is obtained in closed form, which is always symmetric for conservative loading, even far from an equilibrium state and is very helpful for numerical procedures like the Newton method as well as for stability and bifurcation analysis. Several numerical examples illustrate the usefulness of the formulation in the lateral stability analysis of spatial frames. These examples were computed with the code FENOMENA, which is under development at the Computational Mechanics Laboratory of the Escola Politécnica.

INTRODUCTION

The interest on geometrically nonlinear analysis of structures has increased in the recent few years. Besides the practical importance of nonlinear static and dynamic analysis of flexible rod and shell assemblages, the development of convenient geometrically exact models has contributed to this fact. These models show many benefits, which have been emphasized by many authors, as one can verify in a non-exhaustive list reproduced in the references.

This work derives a geometrically exact rod model from the kinematic assumption that cross sections, which are initially orthogonal to the axis, remain plane and undistorted during the deformation. The theory accommodates finite strains, large displacements and rotations, and accounts for shear distortion in bending. Torsion warping can be effortlessly acquainted for, provided elastic behavior is assumed. On the other hand, the introduction of elastic-plastic, visco-plastic and visco-elastic constitutive equations in terms of cross section generalized strains and stresses is straightforward. The consideration of cross section inertia is direct as well.

The accomplished formulation can be readily applied to the nonlinear analysis of spatial frames through the finite element method and presents the following advantages:

(a) rotations in 3D space are treated in a consistent but convenient way through the Euler-Rodrigues formula: update algorithms based on quaternion parameters are not required;
(b) there is no need of approximate strain-displacement relationships or additional assumptions like moderate rotations, small curvatures and small cross section dimensions;
(c) generalized cross section strains and stresses, which are energetically conjugate, can be consistently defined;
(d) generalized cross section displacements and external loadings, which are energetically conjugate, can be consistently defined;
(e) equilibrium and motion equations are consistently derived in weak form as well as in strong form;
(f) boundary conditions are obtained by variational arguments;

part of "MECHANICS PAN-AMERICA 1993" edited by MRM Crespo da Silva and CEN Mazzilli ASME Reprint No AMR134

(g) the issue of conservative external moments is completely elucidated;
(h) an exact expression for the Fréchet derivative of the weak form of equilibrium is obtained in closed form, which is always symmetric for conservative loadings, even far from an equilibrium state;
(i) objectivity requirements are exactly observed;
(j) conservation laws can be exactly satisfied;
(k) weak formulations of mixed type are easily obtained, that can be readily applied to formulation of reliable finite elements.

The developed rod model can be easily implemented in a nonlinear finite element code. Some simple numerical examples are shown at the end of the work as an illustration of the model usefulness.

Along the text, intensive use of vector and tensor calculus is made. Vectors are denoted by small case bold letters while tensors and matrices are denoted by bold capital letters. Summation convention over repeated Greek subscripts from 1 to 2 is adopted.

KINEMATICS

As reference configuration a straight rod with length ℓ is considered, as shown in figure 1. The domain occupied by it is denoted by $\mathcal{B}$. If needed, initial curved configurations can be mapped from $\mathcal{B}$. The boundary of $\mathcal{B}$ is here identified by $\mathcal{S} = \mathcal{S}_L \cup \mathcal{S}_E$, where $\mathcal{S}_L$ represents the lateral surface of the rod whereas $\mathcal{S}_E$ denotes its end surfaces.

A local orthogonal vector system $\{\boldsymbol{e}_1^r, \boldsymbol{e}_2^r, \boldsymbol{e}_3^r\}$, with $\boldsymbol{e}_3^r$ along the rod axis, is placed as shown in figure 1. Thus, a cross section lies on the plane defined by the vectors $\boldsymbol{e}_1^r$ and $\boldsymbol{e}_2^r$. Material points have their position in $\mathcal{B}$ given by the vector

$$\boldsymbol{\xi} = \boldsymbol{\zeta} + \boldsymbol{a}^r , \tag{1}$$

where $\boldsymbol{\zeta}$ describes the points on the rod axis while $\boldsymbol{a}^r$ describes the relative position of points on a cross section with respect to the axis. Local Cartesian coordinates are defined in the reference configuration by

$$x_\alpha = \boldsymbol{a}^r \cdot \boldsymbol{e}_\alpha^r \quad \text{and} \quad x_3 = \boldsymbol{\zeta} \cdot \boldsymbol{e}_3^r , \tag{2}$$

where the dot indicates the scalar product of two vectors. Thus, $\boldsymbol{a}^r$ can be represented by

$$\boldsymbol{a}^r = x_\alpha \boldsymbol{e}_\alpha^r . \tag{3}$$

The third local Cartesian coordinate is chosen here as the primary parameter and replaced by

$$\zeta = x_3 . \tag{4}$$

It is assumed that ζ lies in the interval $(0, \ell)$, i.e. $\zeta = 0$ at one end of the rod and $\zeta = \ell$ at the other end. Cross sections are identified by A whereas their contours are denoted by C.

During the rod motion, the position of the material points can be described by the mapping

$$\boldsymbol{x} = \hat{\boldsymbol{x}}(\boldsymbol{\xi}, t) , \tag{5}$$

where t is the time. $\boldsymbol{x}$ can be decomposed as follows

$$\boldsymbol{x} = \boldsymbol{z} + \boldsymbol{a} , \tag{6}$$

where

$$\boldsymbol{z} = \hat{\boldsymbol{z}}(\zeta, t) \tag{7}$$

describes the motion of points on the rod axis whilst $\boldsymbol{a}$ is a vector field indicated by

$$\boldsymbol{a} = \hat{\boldsymbol{a}}(\boldsymbol{\xi}, t) , \tag{8}$$

that describes the relative motion of the remaining points on a cross section.

The basic kinematic assumption states that cross sections remain plane and undistorted during the motion. Hence, $\boldsymbol{a}$ is given by

$$\boldsymbol{a} = \boldsymbol{Q}\boldsymbol{a}^r , \tag{8}$$

where

$$\boldsymbol{Q} = \hat{\boldsymbol{Q}}(\zeta, t) \tag{10}$$

is a rotation, i.e. an orthogonal tensor with positive determinant. A local orthogonal system attached to the cross sections, as displayed in the figure 1, can be defined by

$$\boldsymbol{e}_i = \boldsymbol{Q}\boldsymbol{e}_i^r , \quad (i = 1, 2, 3) . \tag{11}$$

$\boldsymbol{e}_3$ remains normal to the cross section during the rod motion while for $\boldsymbol{a}$ the following representation holds

$$\boldsymbol{a} = x_\alpha \boldsymbol{e}_\alpha , \tag{11}$$

i.e. $\boldsymbol{a}$ has constant components on the moving local basis $\{\boldsymbol{e}_1, \boldsymbol{e}_2, \boldsymbol{e}_3\}$ attached to the cross sections.

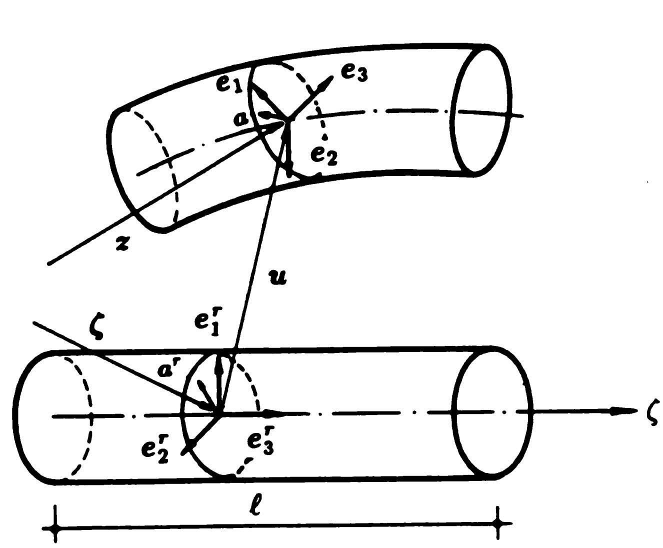

FIG 1. Rod deformation

The components of the axial displacement vector

$$u = z - \zeta\,, \tag{12}$$

are regarded as the cross section translational degrees of freedom. On the other hand, the rotation tensor Q can be expressed by the Euler-Rodrigues formula

$$Q = I + a\Theta + b\Theta^2\,, \tag{13}$$

where I is the identity tensor and Θ is a skew-symmetric tensor, whose axial vector is denoted by θ and

$$a = \frac{\operatorname{sen}\theta}{\theta} \quad \text{and} \quad b = \frac{1}{2}\frac{\operatorname{sen}^2(\theta/2)}{(\theta/2)^2} \tag{14}$$

are real continuous functions of θ. θ is the rotation angle given by the norm of θ, as follows

$$\theta = \|\theta\|\,. \tag{15}$$

We register here that $\theta = \theta e$, where e is the unit vector along the rotation axis with positive sense given by the right-hand rule. The components of θ are regarded as the cross section rotational degrees of freedom.

The deformation gradient

$$F = \hat{F}(\xi, t) \tag{16}$$

can be computed through

$$F = \frac{\partial z}{\partial x_\alpha} \otimes e^r_\alpha + z' \otimes e^r_3\,, \tag{17}$$

where the notation $(\cdot)'$ stands for the differentiation with respect to ζ and the notation $\otimes$ stands for the tensor product. After some manipulation, the deformation gradient can be expressed by

$$F = Q + (\eta + \kappa \times a) \otimes e^r_3\,, \tag{18}$$

where

$$\begin{aligned} \eta &= z' - e_3 \quad \text{and} \\ \kappa &= \Gamma\theta' \end{aligned} \tag{19}$$

can be regarded as generalized strains. In (19) the tensor

$$\Gamma = I + b\Theta + c\Theta^2 \tag{20}$$

has been introduced, where b is already defined in (14) and c is the continuous function of θ below

$$c = \frac{1-a}{\theta^2}\,. \tag{21}$$

We remark that κ is the axial ed from the skew-symmetric tensor

$$K = \tag{22}$$

where the notation $(\cdot)^T$ indicates the transposition of a tensor or matrix. Note that κ is not the curvature of the rod axis.

The generalized strains η and κ are affected by superposed rigid body motions. Hence, they are not convenient for constitutive description. The rotated strains

$$\eta^r = \hat{\eta}^r(\zeta, t) \quad \text{and} \quad \kappa^r = \hat{\kappa}^r(\zeta, t) \tag{23}$$

defined by

$$\begin{aligned} \eta^r &= Q^T\eta = Q^T z' - e^r_3 \quad \text{and} \\ \kappa^r &= Q^T\kappa = \Gamma^T\theta' \end{aligned} \tag{24}$$

are not affected by superposed rigid body motions. In $(24)_2$ the property

$$Q^T\Gamma = \Gamma^T \tag{25}$$

has been used. The deformation gradient can be expressed, with help from (24), by

$$F = Q\left[I + (\eta^r + \kappa^r \times a^r) \otimes e^r_3\right]. \tag{26}$$

Indicating the differentiation with respect to time by a superposed dot, as usual, the velocity of a material point is given by

$$\dot{z} = \dot{u} + \omega \times a\,, \tag{27}$$

where $\times$ stands for the vector product and ω is the cross section spin vector, which is the axial vector of

$$\Omega = \dot{Q}Q^T\,. \tag{28}$$

Similarly to $(19)_2$, ω can be computed through

$$\omega = \Gamma\dot{\theta}\,. \tag{29}$$

By time differentiation of (26), the following expression for the velocity gradient can be obtained

$$\dot{F} = \Omega F + Q\left[(\dot{\eta}^r + \dot{\kappa}^r \times a^r) \otimes e^r_3\right], \tag{30}$$

where

$$\begin{aligned} \dot{\eta}^r &= Q^T(\dot{u}' + z' \times \omega) \quad \text{and} \\ \dot{\kappa}^r &= Q^T\omega' \end{aligned} \tag{31}$$

are generalized strain rates. Alternative expressions for (31) are obtained by insertion of (29) in (31)

$$\begin{aligned} \dot{\eta}^r &= Q^T\left[\dot{u}' + z' \times (\Gamma\dot{\theta})\right] \\ \dot{\kappa}^r &= Q^T(\Gamma'\dot{\theta} + \Gamma\dot{\theta}') \end{aligned} \tag{32}$$

In $(32)_2$ one has, by differentiation of (20) with respect to ζ, the tensor

$$\begin{aligned} \Gamma' = b\Theta' &+ c(\Theta\Theta' + \Theta'\Theta) + \\ &+ d(\theta\cdot\theta')\Theta + e(\theta\cdot\theta')\Theta^2\,, \end{aligned} \tag{33}$$

where

$$d = \frac{a-2b}{\theta^2} \quad \text{and} \quad e = \frac{b-3c}{\theta^2} \tag{34}$$

are continuous real functions of θ.

The cross section displacement vector

$$\boldsymbol{d} = \hat{\boldsymbol{d}}(\zeta, t) \tag{35}$$

given by

$$\boldsymbol{d} = \begin{bmatrix} \boldsymbol{u} \\ \boldsymbol{\theta} \end{bmatrix} \tag{36}$$

is now introduced. The cross section strain vector

$$\boldsymbol{\epsilon} = \hat{\boldsymbol{\epsilon}}(\boldsymbol{d}) \tag{37}$$

given by

$$\boldsymbol{\epsilon} = \begin{bmatrix} \boldsymbol{\eta}^r \\ \boldsymbol{\kappa}^r \end{bmatrix}. \tag{38}$$

can also be introduced. The time differentiation of (38) leads to

$$\dot{\boldsymbol{\epsilon}} = \boldsymbol{B}\boldsymbol{\Delta}\dot{\boldsymbol{d}}, \tag{39}$$

where $\boldsymbol{\Delta}$ is the differential operator

$$\boldsymbol{\Delta} = \begin{bmatrix} \boldsymbol{I}\frac{\partial}{\partial\zeta} & \boldsymbol{O} \\ \boldsymbol{O} & \boldsymbol{I} \\ \boldsymbol{O} & \boldsymbol{I}\frac{\partial}{\partial\zeta} \end{bmatrix} \tag{40}$$

and $\boldsymbol{B}$ is the matrix given by

$$\boldsymbol{B} = \begin{bmatrix} \boldsymbol{Q}^T & \boldsymbol{O} \\ \boldsymbol{O} & \boldsymbol{Q}^T \end{bmatrix} \begin{bmatrix} \boldsymbol{I} & \boldsymbol{Z}'\boldsymbol{\Gamma} & \boldsymbol{O} \\ \boldsymbol{O} & \boldsymbol{\Gamma}' & \boldsymbol{\Gamma} \end{bmatrix}. \tag{41}$$

$\boldsymbol{O}$ and $\boldsymbol{Z}'$, that appear in (41), are the null tensor and the skew-symmetric tensor whose axial vector is

$$\boldsymbol{z}' = \boldsymbol{e}_3^r + \boldsymbol{u}'. \tag{42}$$

KINETICS

Introducing the notation : for the scalar product of two tensors, the internal power is given by

$$P_{int} = \int_0^\ell \int_A \boldsymbol{P} : \dot{\boldsymbol{F}}\, dA\, d\zeta, \tag{43}$$

where

$$\boldsymbol{P} = \hat{\boldsymbol{P}}(\boldsymbol{\xi}, t) \tag{44}$$

is the non-symmetric Piola stress tensor. $\boldsymbol{P}$ can be expressed by

$$\boldsymbol{P} = \boldsymbol{t}_\alpha \otimes \boldsymbol{e}_\alpha^r + \boldsymbol{\tau} \otimes \boldsymbol{e}_3^r. \tag{45}$$

Since the cross sections remain plane and undistorted, $\boldsymbol{\tau}$ is also the stress vector acting on them, i.e.

$$\boldsymbol{\tau} = \boldsymbol{T}\boldsymbol{e}_3, \tag{46}$$

where $\boldsymbol{T}$ is the Cauchy stress tensor. Hence, the force and moment resultants on a cross section

$$\boldsymbol{n} = \hat{\boldsymbol{n}}(\zeta, t) \quad \text{and} \quad \boldsymbol{m} = \hat{\boldsymbol{m}}(\zeta, t) \tag{47}$$

can be defined by

$$\begin{aligned} \boldsymbol{n} &= \int_A \boldsymbol{\tau}\, dA \quad \text{and} \\ \boldsymbol{m} &= \int_A \boldsymbol{a} \times \boldsymbol{\tau}\, dA. \end{aligned} \tag{48}$$

The resultants $\boldsymbol{n}$ and $\boldsymbol{m}$ are affected by superposed rigid body motions and are, for this sake, not convenient for constitutive description. On the other hand, the rotated vectors

$$\boldsymbol{n}^r = \hat{\boldsymbol{n}}^r(\zeta, t) \quad \text{and} \quad \boldsymbol{m}^r = \hat{\boldsymbol{m}}^r(\zeta, t) \tag{49}$$

defined by

$$\boldsymbol{n}^r = \boldsymbol{Q}^T\boldsymbol{n} \quad \text{and} \quad \boldsymbol{m}^r = \boldsymbol{Q}^T\boldsymbol{m} \tag{50}$$

remain invariant under superposed rigid body motions. If one introduces the rotated stress vector $\boldsymbol{\tau}^r$ given by

$$\boldsymbol{\tau}^r = \boldsymbol{Q}^T\boldsymbol{\tau}, \tag{51}$$

the rotated cross section resultants can also be defined by

$$\begin{aligned} \boldsymbol{n}^r &= \int_A \boldsymbol{\tau}^r\, dA \quad \text{and} \\ \boldsymbol{m}^r &= \int_A \boldsymbol{a}^r \times \boldsymbol{\tau}^r\, dA. \end{aligned} \tag{52}$$

At this point we recall that $\boldsymbol{a}^r$, $\boldsymbol{\eta}^r$, $\boldsymbol{\kappa}^r$, $\boldsymbol{n}^r$, $\boldsymbol{m}^r$ and $\boldsymbol{\tau}^r$ have the same components on $\{\boldsymbol{e}_1^r, \boldsymbol{e}_2^r, \boldsymbol{e}_3^r\}$ as $\boldsymbol{a}$, $\boldsymbol{\eta}$, $\boldsymbol{\kappa}$, $\boldsymbol{n}$, $\boldsymbol{m}$ and $\boldsymbol{\tau}$ on $\{\boldsymbol{e}_1, \boldsymbol{e}_2, \boldsymbol{e}_3\}$.

Introducing (30) and (45) in $\boldsymbol{P} : \dot{\boldsymbol{F}}$ and considering that $\boldsymbol{P}\boldsymbol{F}^T = \det(\boldsymbol{F})\boldsymbol{T}$ is symmetric and for this reason $\boldsymbol{P}\boldsymbol{F}^T : \boldsymbol{\Omega} = \boldsymbol{O}$, from (43) one arrives at

$$P_{int} = \int_0^\ell (\boldsymbol{n}^r \cdot \dot{\boldsymbol{\eta}}^r + \boldsymbol{m}^r \cdot \dot{\boldsymbol{\kappa}}^r)\, d\zeta. \tag{53}$$

Defining the cross section vector of stress resultants by

$$\boldsymbol{\sigma} = \begin{bmatrix} \boldsymbol{n}^r \\ \boldsymbol{m}^r \end{bmatrix}, \tag{54}$$

(53) can be written as

$$P_{int} = \int_0^\ell \boldsymbol{\sigma} \cdot \dot{\boldsymbol{\epsilon}}\, d\zeta = \int_0^\ell \boldsymbol{\sigma} \cdot \boldsymbol{B}\boldsymbol{\Delta}\dot{\boldsymbol{d}}\, d\zeta, \tag{55}$$

where use of (39) was made.

Suppose that surface and body loadings are applied along the rod. The surface loading per unit reference area is mapped from S_L and denoted by $\bar{\boldsymbol{t}}$ while the body loading per unit reference volume is mapp[illegible] B and identified by $\bar{\boldsymbol{b}}$. The external power along the rod is then given by

$$P_{ext} = \int_0^{\ell} \Big[\int_C \bar{\boldsymbol{t}} \cdot \dot{\boldsymbol{x}} dC + \int_A \bar{\boldsymbol{b}} \cdot \dot{\boldsymbol{x}} dA \Big] d\zeta . \tag{56}$$

Introducing (27) in (56), one obtains

$$P_{ext} = \int_0^{\ell} (\bar{\boldsymbol{n}} \cdot \dot{\boldsymbol{u}} + \bar{\boldsymbol{m}} \cdot \boldsymbol{\omega})\, d\zeta , \tag{57}$$

where

$$\bar{\boldsymbol{n}} = \hat{\bar{\boldsymbol{n}}}(\zeta, t) \quad \text{and} \quad \bar{\boldsymbol{m}} = \hat{\bar{\boldsymbol{m}}}(\zeta, t) \tag{58}$$

are the external force and moment resultants per unit reference length given by

$$\begin{aligned} \bar{\boldsymbol{n}} &= \int_C \bar{\boldsymbol{t}} dC + \int_A \bar{\boldsymbol{b}} dA \quad \text{and} \\ \bar{\boldsymbol{m}} &= \int_C \boldsymbol{a} \times \bar{\boldsymbol{t}} dC + \int_A \boldsymbol{a} \times \bar{\boldsymbol{b}} dA . \end{aligned} \tag{59}$$

Introducing (29) in (57), one has

$$P_{ext} = \int_0^{\ell} (\bar{\boldsymbol{n}} \cdot \dot{\boldsymbol{u}} + \bar{\boldsymbol{\mu}} \cdot \dot{\boldsymbol{\theta}})\, d\zeta , \tag{60}$$

where

$$\bar{\boldsymbol{\mu}} = \hat{\bar{\boldsymbol{\mu}}}(\zeta, t) , \tag{61}$$

given by

$$\bar{\boldsymbol{\mu}} = \boldsymbol{\Gamma}^T \bar{\boldsymbol{m}} , \tag{62}$$

is the external loading energetically conjugate with $\boldsymbol{\theta}$. We emphasize that $\bar{\boldsymbol{m}}$ is not conjugate with $\boldsymbol{\theta}$.

At this point, the following rotated external force and moment per unit reference length can be introduced

$$\bar{\boldsymbol{n}}^r = \boldsymbol{Q}^T \bar{\boldsymbol{n}} \quad \text{and} \quad \bar{\boldsymbol{m}}^r = \boldsymbol{Q}^T \bar{\boldsymbol{m}} . \tag{63}$$

Taking account of (25), one has

$$\bar{\boldsymbol{\mu}} = \boldsymbol{\Gamma}^T \bar{\boldsymbol{m}} = \boldsymbol{\Gamma} \bar{\boldsymbol{m}}^r . \tag{64}$$

Introducing now the vector of external loading per unit reference length defined by

$$\bar{\boldsymbol{q}} = \begin{bmatrix} \bar{\boldsymbol{n}} \\ \bar{\boldsymbol{\mu}} \end{bmatrix} , \tag{65}$$

the external power can be written as

$$P_{ext} = \int_0^{\ell} \bar{\boldsymbol{q}} \cdot \dot{\boldsymbol{d}}\, d\zeta . \tag{66}$$

STATICS

The virtual strains

$$\delta\boldsymbol{\eta}^r = \delta\hat{\boldsymbol{\eta}}^r \qquad \delta\hat{\boldsymbol{\kappa}}^r(\zeta) \tag{67}$$

are obtained by consistent linearization of (24). Their expressions, similar to (32), are displayed below

$$\begin{aligned} \delta\boldsymbol{\eta}^r &= \boldsymbol{Q}^T [\delta\boldsymbol{u}' + \boldsymbol{z}' \times (\boldsymbol{\Gamma}\delta\boldsymbol{\theta})] \quad \text{and} \\ \delta\boldsymbol{\kappa}^r &= \boldsymbol{Q}^T (\boldsymbol{\Gamma}'\delta\boldsymbol{\theta} + \boldsymbol{\Gamma}\delta\boldsymbol{\theta}') , \end{aligned} \tag{68}$$

where

$$\delta\boldsymbol{u} = \delta\hat{\boldsymbol{u}}(\zeta) \quad \text{and} \quad \delta\boldsymbol{\theta} = \delta\hat{\boldsymbol{\theta}}(\zeta) \tag{69}$$

are virtual displacements. Hence, with help from

$$\delta\boldsymbol{\varepsilon} = \delta\hat{\boldsymbol{\varepsilon}}(\zeta) \quad \text{and} \quad \delta\boldsymbol{d} = \delta\hat{\boldsymbol{d}}(\zeta) , \tag{70}$$

which are defined similarly to (36) and (38), one has

$$\delta\boldsymbol{\varepsilon} = \boldsymbol{B}\boldsymbol{\Delta}\delta\boldsymbol{d} . \tag{71}$$

(71) is analogous to (39). The internal virtual work can then be expressed by

$$\begin{aligned} \delta W_{int} &= \int_0^{\ell} (\boldsymbol{n}^r \cdot \delta\boldsymbol{\eta}^r + \boldsymbol{m}^r \cdot \delta\boldsymbol{\kappa}^r) d\zeta \\ &= \int_0^{\ell} \boldsymbol{\sigma} \cdot \delta\boldsymbol{\varepsilon}\, d\zeta \\ &= \int_0^{\ell} \boldsymbol{\sigma} \cdot \boldsymbol{B}\boldsymbol{\Delta}\delta\boldsymbol{d}\, d\zeta , \end{aligned} \tag{72}$$

which are similar to (53) and (55). δW_{int} is a functional of the fields $\boldsymbol{\sigma}$ and $\delta\boldsymbol{d}$ as indicated below

$$\delta W_{int} = \delta\hat{W}_{int}[\boldsymbol{\sigma}, \delta\boldsymbol{d}] . \tag{73}$$

The external virtual work is defined by

$$\begin{aligned} \delta W_{ext} &= \int_0^{\ell} (\bar{\boldsymbol{n}} \cdot \delta\boldsymbol{u} + \bar{\boldsymbol{\mu}} \cdot \delta\boldsymbol{\theta})\, d\zeta \\ &= \int_0^{\ell} \bar{\boldsymbol{q}} \cdot \delta\boldsymbol{d}\, d\zeta , \end{aligned} \tag{74}$$

which are similar to (60) and (66). δW_{ext} is a functional of the fields $\bar{\boldsymbol{q}}$ and $\delta\boldsymbol{d}$ as indicated below

$$\delta W_{ext} = \delta\hat{W}_{int}[\bar{\boldsymbol{q}}, \delta\boldsymbol{d}] . \tag{75}$$

The weak form of the equilibrium equations is given by the virtual work theorem, viz.

$$\delta W_{int} - \delta W_{ext} = 0 , \quad \forall \delta\boldsymbol{d} \mid \delta\hat{\boldsymbol{d}}(0) = \delta\hat{\boldsymbol{d}}(\ell) = 0 . \tag{76}$$

Inserting (72) and (74) in (76) and performing partial integration on terms with $\delta\boldsymbol{u}'$ and $(\boldsymbol{\Gamma}\delta\boldsymbol{\theta})'$, one obtains, after some manipulation,

$$\int_0^{\ell} \big[(\boldsymbol{n}' + \bar{\boldsymbol{n}}) \cdot \delta\boldsymbol{u} + \boldsymbol{\Gamma}^T (\boldsymbol{m}' + \boldsymbol{z}' \times \boldsymbol{n} + \bar{\boldsymbol{m}}) \cdot \delta\boldsymbol{\theta} \big]\, d\zeta = 0 .$$

Hence, by the standard argument of variational calculus, the following local equilibrium equations in $(0,\ell)$ are obtained

$$\begin{gathered} n' + \bar{n} = o \quad \text{and} \\ m' + z' \times n + \bar{m} = o , \end{gathered} \tag{77}$$

where o is the null vector. With the aid of (50) and (63), the equilibrium equations can be replaced by

$$\begin{gathered} n^{r\prime} + \kappa^r \times n^r + \bar{n}^r = o \text{ and} \\ m^{r\prime} + \kappa^r \times m^r + (e_3^r + \eta^r) \times n^r + \bar{m}^r = o . \end{gathered} \tag{78}$$

The vector

$$q = \begin{bmatrix} n \\ \mu \end{bmatrix} , \tag{79}$$

which is similar to (65), is now introduced. μ in (79) is analogous to (64), i.e.

$$\mu = \Gamma^T m = \Gamma m^r . \tag{80}$$

(76) is now extended in order to incorporate the virtual work of the external forces on the rod ends, as follows

$$\delta W_{int} - \delta W_{ext} = q^\star \cdot \delta d \Big|_{\zeta=0}^{\zeta=\ell} , \quad \forall \delta d , \tag{81}$$

where $q^\star$ are prescribed values at $\zeta = 0$ and $\zeta = \ell$. Inserting (72) and (74) in (81), performing the partial integrations done in (76) and considering (77), one obtains

$$(q - q^\star) \cdot \delta d \Big|_{\zeta=0}^{\zeta=\ell} = 0 .$$

Thus the natural boundary conditions of this model are

$$q = q^\star \qquad \text{at} \quad \zeta = 0 \quad \text{and} \quad \zeta = \ell . \tag{82}$$

We remark that the natural boundary condition involves μ at the rod ends and not m.

POTENTIALS

A rod is called elastic if there is a scalar valued function

$$\psi_{int} = \hat{\psi}_{int}(\epsilon) \tag{83}$$

such that

$$\sigma = \frac{\partial \psi_{int}}{\partial \epsilon} . \tag{84}$$

ψ_{int} is called strain energy per unit reference length.

The gradient of σ defines an operator D, given by

$$D = \frac{\partial \sigma}{\partial \epsilon} = \begin{bmatrix} \partial n^r / \partial \eta^r & \partial n^r / \partial \kappa^r \\ \partial m^r / \partial \eta^r & \partial m^r / \partial \kappa^r \end{bmatrix} . \tag{85}$$

D contains the cross section elastic tangent moduli. Regarding (84), D is also given by

$$D = \frac{\partial^2 \psi_{int}}{\partial \epsilon^2} . \tag{86}$$

Thus, D is symmetric.

For linear elastic rods D is constant. Hence, for such rods, one has

$$\psi_{int} = \frac{1}{2} \epsilon \cdot D \epsilon \quad \text{and} \quad \sigma = D \epsilon . \tag{87}$$

The functional

$$\Psi_{int} = \hat{\Psi}_{int}[d] \tag{88}$$

defined by

$$\Psi_{int} = \int_0^\ell \psi_{int} \circ \hat{\epsilon}(d) \, d\zeta \tag{89}$$

is called internal potential energy or strain energy of the rod. In (89) the notation $\circ$ stands for the composition of two functions, as usual.

The Fréchet derivative of (88) with respect to d yields

$$\delta \Psi_{int} = \int_0^\ell \sigma \cdot B \Delta \delta d \, d\zeta . \tag{90}$$

$\delta \Psi_{int}$ is a functional of two fields indicated by

$$\delta \Psi_{int} = \delta \hat{\Psi}_{int}[d, \delta d] . \tag{91}$$

Note that $\delta \Psi_{int}$ can also be expressed by

$$\delta \Psi_{int} = \delta \hat{W}_{int} \left[\frac{\partial \psi_{int}}{\partial \epsilon} \circ \hat{\epsilon}(d), \delta d \right] . \tag{92}$$

The second Fréchet derivative of (88) with respect to d can be computed through the Gateaux derivative of (91) with respect to d. The outcome is a functional of two fields indicated by

$$\delta^2 \Psi_{int} = \delta^2 \hat{\Psi}_{int}[d, \delta d] \tag{93}$$

and given by the following symmetric bilinear form

$$\begin{aligned} \delta^2 \Psi_{int} = \int_0^\ell \big[& (D B \Delta \delta d) \cdot (B \Delta \delta d) + \\ & + (G \Delta \delta d) \cdot (\Delta \delta d) \big] \, d\zeta , \end{aligned} \tag{94}$$

where D is defined in (86) and G is a symmetric operator which characterizes the geometrical effects from the internal forces. G can be expressed by

$$G = \begin{bmatrix} O & G_{u'\theta} & O \\ G_{u'\theta}^T & G_{\theta\theta} & G_{\theta\theta'} \\ O & G_{\theta\theta'}^T & O \end{bmatrix} . \tag{95}$$

With the aid of the skew-symmetric tensors N and M, whose axial vectors are n and m, and introducing the following continuous functions of θ

$$f = \frac{c - b - 4d}{\theta^2} \quad \text{and} \quad g = \frac{d - }{} \tag{96}$$

the elements of G are

$$
\begin{aligned}
\boldsymbol{G}_{u'\theta} =& -\boldsymbol{N\Gamma}\,,\\
\boldsymbol{G}_{\theta\theta'} =& \frac{1}{2}\boldsymbol{\Gamma}^T\boldsymbol{M\Gamma}\\
&-\frac{1}{2}c(\boldsymbol{M\Theta}+\boldsymbol{\Theta M})\\
&-\frac{1}{2}d(\boldsymbol{\Theta m}\otimes\boldsymbol{\theta}+\boldsymbol{\theta}\otimes\boldsymbol{\Theta m})\\
&+\frac{1}{2}e(\boldsymbol{\Theta}^2\boldsymbol{m}\otimes\boldsymbol{\theta}+\boldsymbol{\theta}\otimes\boldsymbol{\Theta}^2\boldsymbol{m})\,,\\
\boldsymbol{G}_{\theta\theta} =& \frac{1}{2}\boldsymbol{\Gamma}^T(\boldsymbol{Z}'\boldsymbol{N}+\boldsymbol{N}\boldsymbol{Z}')\boldsymbol{\Gamma}\\
&+\frac{1}{2}(\boldsymbol{\Gamma}^T\boldsymbol{M}\boldsymbol{\Gamma}'-\boldsymbol{\Gamma}'^T\boldsymbol{M}\boldsymbol{\Gamma})\\
&-\frac{1}{2}c\big[(\boldsymbol{N}\boldsymbol{Z}'-\boldsymbol{Z}'\boldsymbol{N})\boldsymbol{\Theta}\\
&\qquad+\boldsymbol{\Theta}(\boldsymbol{N}\boldsymbol{Z}'-\boldsymbol{Z}'\boldsymbol{N})\\
&\qquad+\boldsymbol{M}\boldsymbol{\Theta}'+\boldsymbol{\Theta}'\boldsymbol{M}\big]\\
&-\frac{1}{2}d\big[\boldsymbol{\Theta}(\boldsymbol{n}\times\boldsymbol{z}')\otimes\boldsymbol{\theta}+\boldsymbol{\theta}\otimes\boldsymbol{\Theta}(\boldsymbol{n}\times\boldsymbol{z}')\\
&\qquad+\boldsymbol{\Theta}'\boldsymbol{m}\otimes\boldsymbol{\theta}+\boldsymbol{\theta}\otimes\boldsymbol{\Theta}'\boldsymbol{m}\\
&\qquad+\boldsymbol{\Theta m}\otimes\boldsymbol{\theta}'+\boldsymbol{\theta}'\otimes\boldsymbol{\Theta m}\big]\\
&+\frac{1}{2}e(\boldsymbol{\Theta\Theta}'\boldsymbol{m}\otimes\boldsymbol{\theta}+\boldsymbol{\theta}\otimes\boldsymbol{\Theta\Theta}'\boldsymbol{m}\\
&\qquad+\boldsymbol{\Theta}'\boldsymbol{\Theta m}\otimes\boldsymbol{\theta}+\boldsymbol{\theta}\otimes\boldsymbol{\Theta}'\boldsymbol{\Theta m}\\
&\qquad+\boldsymbol{\Theta}^2\boldsymbol{m}\otimes\boldsymbol{\theta}'+\boldsymbol{\theta}'\otimes\boldsymbol{\Theta}^2\boldsymbol{m})\\
&-\frac{1}{2}e(\boldsymbol{\theta}\cdot\boldsymbol{\theta}')(\boldsymbol{\Theta M}+\boldsymbol{M\Theta})\\
&-\frac{1}{2}f(\boldsymbol{\theta}\cdot\boldsymbol{\theta}')(\boldsymbol{\Theta m}\otimes\boldsymbol{\theta}+\boldsymbol{\theta}\otimes\boldsymbol{\Theta m})\\
&+\frac{1}{2}g(\boldsymbol{\theta}\cdot\boldsymbol{\theta}')(\boldsymbol{\Theta}^2\boldsymbol{m}\otimes\boldsymbol{\theta}+\boldsymbol{\theta}\otimes\boldsymbol{\Theta}^2\boldsymbol{m})\,.
\end{aligned}
\tag{97}
$$

The external loading $\bar{\boldsymbol{q}}$ is called conservative if there is a scalar valued function

$$\psi_{ext}=\hat{\psi}_{ext}(\boldsymbol{d}) \tag{98}$$

such that

$$\bar{\boldsymbol{q}}=-\frac{\partial\psi_{ext}}{\partial\boldsymbol{d}}\,. \tag{99}$$

Hence, for such loadings, the gradient

$$\boldsymbol{L}=\frac{\partial\bar{\boldsymbol{q}}}{\partial\boldsymbol{d}} \tag{100}$$

is a symmetric operator given by

$$\boldsymbol{L}=-\frac{\partial^2\psi_{ext}}{\partial\boldsymbol{d}^2}\,. \tag{101}$$

$\boldsymbol{L}$ characterizes the geometrical effects from the external loading distributed along the rod.

For example, if $\bar{\boldsymbol{t}}$ and $\bar{\boldsymbol{b}}$ do r n the displacements, one has

$$\boldsymbol{L}=\frac{\partial\bar{\boldsymbol{q}}}{\partial\boldsymbol{d}}=\Big[\ (\tag{102}$$

where, with the aid of the skew-symmetric tensors $\boldsymbol{A}$, $\bar{\boldsymbol{M}}$, $\bar{\boldsymbol{T}}$ and $\bar{\boldsymbol{B}}$, whose axial vectors are $\boldsymbol{a}$, $\bar{\boldsymbol{m}}$, $\bar{\boldsymbol{t}}$ and $\bar{\boldsymbol{b}}$, respectively, $\boldsymbol{L}_{\theta\theta}$ is given by

$$
\begin{aligned}
\boldsymbol{L}_{\theta\theta} =& \frac{1}{2}\boldsymbol{\Gamma}^T\Big[\int_C(\bar{\boldsymbol{T}}\boldsymbol{A}+\boldsymbol{A}\bar{\boldsymbol{T}})dC\Big]\boldsymbol{\Gamma}\\
&+\frac{1}{2}\boldsymbol{\Gamma}^T\Big[\int_A(\bar{\boldsymbol{B}}\boldsymbol{A}+\boldsymbol{A}\bar{\boldsymbol{B}})dA\Big]\boldsymbol{\Gamma}\\
&-\frac{1}{2}c(\bar{\boldsymbol{M}}\boldsymbol{\Theta}+\boldsymbol{\Theta}\bar{\boldsymbol{M}})\\
&-\frac{1}{2}d(\boldsymbol{\Theta}\bar{\boldsymbol{m}}\otimes\boldsymbol{\theta}+\boldsymbol{\theta}\otimes\boldsymbol{\Theta}\bar{\boldsymbol{m}})\\
&+\frac{1}{2}e(\boldsymbol{\Theta}^2\bar{\boldsymbol{m}}\otimes\boldsymbol{\theta}+\boldsymbol{\theta}\otimes\boldsymbol{\Theta}^2\bar{\boldsymbol{m}})\,.
\end{aligned}
\tag{103}
$$

If $\bar{\boldsymbol{t}}$ and $\bar{\boldsymbol{b}}$ do not depend on the displacements and comply with

$$\int_C(\bar{\boldsymbol{T}}\boldsymbol{A}+\boldsymbol{A}\bar{\boldsymbol{T}})dC+\int_A(\bar{\boldsymbol{B}}\boldsymbol{A}+\boldsymbol{A}\bar{\boldsymbol{B}})dA=\boldsymbol{O}\,, \tag{104}$$

then the external moment $\bar{\boldsymbol{m}}$ is called semi-tangential. Thus, for semi-tangential external moments, one has

$$
\begin{aligned}
\boldsymbol{L}_{\theta\theta} =& -\frac{1}{2}c(\bar{\boldsymbol{M}}\boldsymbol{\Theta}+\boldsymbol{\Theta}\bar{\boldsymbol{M}})\\
&-\frac{1}{2}d(\boldsymbol{\Theta}\bar{\boldsymbol{m}}\otimes\boldsymbol{\theta}+\boldsymbol{\theta}\otimes\boldsymbol{\Theta}\bar{\boldsymbol{m}})\\
&+\frac{1}{2}e(\boldsymbol{\Theta}^2\bar{\boldsymbol{m}}\otimes\boldsymbol{\theta}+\boldsymbol{\theta}\otimes\boldsymbol{\Theta}^2\bar{\boldsymbol{m}})\,.
\end{aligned}
\tag{105}
$$

Notice that, for semi-tangential moments, $\boldsymbol{L}_{\theta\theta}$ does not depend on the application points of the external forces. Semi-tangential moments are conservative and comply with

$$\dot{\bar{\boldsymbol{m}}}=\frac{1}{2}\boldsymbol{\omega}\times\bar{\boldsymbol{m}}\,. \tag{106}$$

(106) justifies the nomenclature.

An external moment such that

$$\bar{\boldsymbol{\mu}}=\boldsymbol{\Gamma}^T\bar{\boldsymbol{m}}=\text{constant} \tag{107}$$

is also conservative and leads to

$$\boldsymbol{L}_{\theta\theta}=\boldsymbol{O}\,. \tag{108}$$

However, in practice such a moment is unlikely to occur.

The functional

$$\Psi_{ext}=\hat{\Psi}_{ext}[\boldsymbol{d}] \tag{109}$$

defined by

$$\Psi_{ext}=\int_0^{\ell}\psi_{ext}\,d\zeta \tag{110}$$

is called external potential energy of the rod.

The Fréchet derivative of (109) with respect to $\boldsymbol{d}$ yields

$$\delta\Psi_{ext}=\int_0^{\ell}\frac{\partial\psi_{ext}}{\partial\boldsymbol{d}}\cdot\delta\boldsymbol{d}\,d\zeta\,. \tag{111}$$

$\delta\Psi_{ext}$ is a functional of two fields indicated by

$$\delta\Psi_{ext} = \delta\hat{\Psi}_{ext}[\boldsymbol{d}, \delta\boldsymbol{d}]. \tag{112}$$

Note that $\delta\Psi_{ext}$ can also be expressed by

$$\delta\Psi_{ext} = -\delta\hat{W}_{ext}\left[\frac{\partial\psi_{ext}}{\partial\boldsymbol{d}}, \delta\boldsymbol{d}\right]. \tag{113}$$

The second Fréchet derivative of (109) with respect to $\boldsymbol{d}$ can be computed through the Gateaux derivative of (113) with respect to $\boldsymbol{d}$. The result is the following symmetric bilinear form

$$\delta^2\Psi_{ext} = -\int_0^\ell (\boldsymbol{L}\delta\boldsymbol{d})\cdot\delta\boldsymbol{d}\, d\zeta. \tag{114}$$

The functional

$$\Psi = \hat{\Psi}[\boldsymbol{d}] \tag{115}$$

defined by

$$\Psi = \Psi_{int} + \Psi_{ext} \tag{116}$$

is the potential energy of the rod. In view of (76), (92) and (113), one concludes that

$$\delta\Psi = 0. \tag{117}$$

Thus, Ψ is stationary at an equilibrium configuration. On the other hand, regarding (94) and (114), the second Fréchet derivative of (115) with respect to $\boldsymbol{d}$ is the following bilinear form

$$\begin{aligned}\delta^2\Psi = \int_0^\ell \big[&(\boldsymbol{DB\Delta}\delta\boldsymbol{d})\cdot(\boldsymbol{B\Delta}\delta\boldsymbol{d}) + \\ &+(\boldsymbol{G\Delta}\delta\boldsymbol{d})\cdot(\boldsymbol{\Delta}\delta\boldsymbol{d}) - (\boldsymbol{L}\delta\boldsymbol{d})\cdot\delta\boldsymbol{d}\big]\, d\zeta.\end{aligned} \tag{118}$$

We remark that the bilinear form (118) is always symmetric, even far from an equilibrium state. (118) is important in numerical procedures like the Newton method as well as in the stability and bifurcation analysis of structures.

FINITE ELEMENTS

The application of the finite element method is standard. In a pure displacement model the displacement field $\boldsymbol{d}$ is interpolated within an element through

$$\boldsymbol{d} = \boldsymbol{Np}, \tag{119}$$

where $\boldsymbol{p}$ is the vector of the element nodal displacements, which collects the vectors $\boldsymbol{d}$ from the element nodes, and $\boldsymbol{N}$ is an interpolation matrix. For linear elements with two nodes $\boldsymbol{N}$ contains linear functions of ζ, while for quadratic elements with three nodes $\boldsymbol{N}$ contains quadratic functions of ζ. In the standard Galerkin projection the virtual displacements are likewise interpolated through

$$\delta\boldsymbol{d} = \boldsymbol{N}\delta\boldsymbol{p}. \tag{120}$$

The vector of the element nodal forces $\boldsymbol{\pi}$, that collects the vectors $\boldsymbol{q}^\star$ from the element nodes, is defined, in agreement with (81), by

$$\boldsymbol{\pi}\cdot\delta\boldsymbol{p} = \int_0^\ell [\boldsymbol{\sigma}\cdot\boldsymbol{B\Delta}\delta\boldsymbol{d} - \bar{\boldsymbol{q}}\cdot\delta\boldsymbol{d}]\, d\zeta. \tag{121}$$

Introducing (119) and (120) in (121), the resulting projection is

$$\boldsymbol{\pi} = \int_0^\ell [(\boldsymbol{\Delta N})^T\boldsymbol{B}^T\boldsymbol{\sigma} - \boldsymbol{N}^T\bar{\boldsymbol{q}}]\, d\zeta. \tag{122}$$

The element tangent stiffness matrix $\boldsymbol{K}$ is defined, in harmony with (121) and (118), by

$$\begin{aligned}(\boldsymbol{K}\delta\boldsymbol{d})\cdot\delta\boldsymbol{d} = \int_0^\ell \big[&(\boldsymbol{B}^T\boldsymbol{DB} + \boldsymbol{G})(\boldsymbol{\Delta}\delta\boldsymbol{d})\cdot(\boldsymbol{\Delta}\delta\boldsymbol{d}) \\ &- (\boldsymbol{L}\delta\boldsymbol{d})\cdot\delta\boldsymbol{d}\big]\, d\zeta.\end{aligned} \tag{123}$$

Introducing (119) and (120) in (123), the resulting projection is

$$\begin{aligned}\boldsymbol{K} = \int_0^\ell \big[&(\boldsymbol{\Delta N})^T(\boldsymbol{B}^T\boldsymbol{DB} + \boldsymbol{G})(\boldsymbol{\Delta N}) \\ &- \boldsymbol{N}^T\boldsymbol{LN}\big]\, d\zeta.\end{aligned} \tag{124}$$

An advantage of the developed formulation is that all interpolations and operations can be performed in the global system of the structure. This saves numerous transformations from element local systems to the global system or vice-versa. As a matter of fact, the transformation of $\boldsymbol{D}$ from the local reference system to the global system is the only one required in the code.

It is known that exactly integrated displacement finite element models, like the one derived above, present the phenomenon of shear locking. In the one-dimensional case this can be circumvented by reduced numerical integration. For example, in the case of linear elements a one-point Gauss scheme can be adopted while for quadratic elements a two-point Gauss scheme is sufficient. At first sight this seems a rather numerical trick. However it can be justified by mixed models, which interpolate simultaneously displacements, strains and stresses. The variational basis of such models is an extended functional that includes the fields $\boldsymbol{d}$, $\boldsymbol{\varepsilon}$ and $\boldsymbol{\sigma}$. This three-field functional

$$H = \hat{H}[\boldsymbol{d}, \boldsymbol{\varepsilon}, \boldsymbol{\sigma}] \tag{125}$$

can be given by

$$H = \int_0^\ell \left\{\hat{\psi}_{int}(\boldsymbol{\varepsilon}) + \boldsymbol{\sigma}\cdot\left[\hat{\boldsymbol{\varepsilon}}(\boldsymbol{d}) - \boldsymbol{\varepsilon}\right] + \hat{\psi}_{ext}(\boldsymbol{d})\right\} d\zeta. \tag{126}$$

The Fréchet derivative of (126) with respect to $\boldsymbol{d}$, $\boldsymbol{\varepsilon}$ and $\boldsymbol{\sigma}$ conducts to

$$\begin{aligned}\delta H = &\int_0^\ell (\boldsymbol{\sigma}\cdot\boldsymbol{B\Delta}\delta\boldsymbol{d} - \bar{\boldsymbol{q}}\cdot\delta\boldsymbol{d})\, d\zeta \\ &+ \int_0^\ell \left(\frac{\partial\psi_{int}}{\partial\boldsymbol{\varepsilon}} - \boldsymbol{\sigma}\right)\cdot\delta\boldsymbol{\varepsilon}\, d\zeta \\ &+ \int_0^\ell (\hat{\boldsymbol{\varepsilon}}(\boldsymbol{d}) - \boldsymbol{\varepsilon})\cdot\delta\boldsymbol{\sigma}\, d\zeta\end{aligned} \tag{127}$$

(127) is suitable for mixed Galerkin projection or for any other generalized projection like, for example, the collocation method.

NUMERICAL EXAMPLES

Some simple numerical examples are presented in this section as an illustration for the developed formulation. A linear elastic rod was assumed. The operator $\boldsymbol{D}$ in (87) was taken from the geometrically linear theory and its matrix in the rod local system at reference configuration is

$$\boldsymbol{D} = \begin{bmatrix} GA & 0 & 0 & 0 & 0 & GS_1^* \\ \cdot & GA & 0 & 0 & 0 & GS_2^* \\ \cdot & \cdot & EA & ES_1 & ES_2 & 0 \\ \cdot & \cdot & \cdot & EJ_{11} & EJ_{12} & 0 \\ \cdot & sym. & \cdot & \cdot & EJ_{22} & 0 \\ \cdot & \cdot & \cdot & \cdot & \cdot & GJ_t^* \end{bmatrix} . \quad (128)$$

In (128), E is the Young modulus, G is the shear modulus, A is the cross section area, S_α are the cross section static moments defined by

$$S_1 = \int_A x_2 dA \quad \text{and} \quad S_2 = -\int_A x_1 dA , \qquad (129)$$

$J_{\alpha\beta}$ are the cross section inertia constants defined by

$$\begin{aligned} J_{11} &= \int_A x_2^2 dA , \\ J_{22} &= \int_A x_1^2 dA \quad \text{and} \qquad (130) \\ J_{12} &= -\int_A x_1 x_2 dA , \end{aligned}$$

J_t^* is the torsion constant given by

$$J_t^* = J_t + A s_\alpha s_\alpha , \qquad (131)$$

where J_t is the Saint-Venant torsion constant and s_α are the coordinates of the cross section shear center. Finally, S_α^* are the following constants

$$S_1^* = -A s_2 \quad \text{and} \quad S_2 = A s_1 , \qquad (131)$$

The assumed cross sections are described in figure 2 and are represented by the letters R, T, I, C, L and V. All cross sections have the same area. The assumed material Young modulus was E=210,000 M[illegible] [illegible]he assumed shear modulus was G=800,000 M[illegible] [illegible]ples were computed with linear and qua[illegible] [illegible] with at least five elements. The result[illegible] [illegible] with respect to element type and nu[illegible]

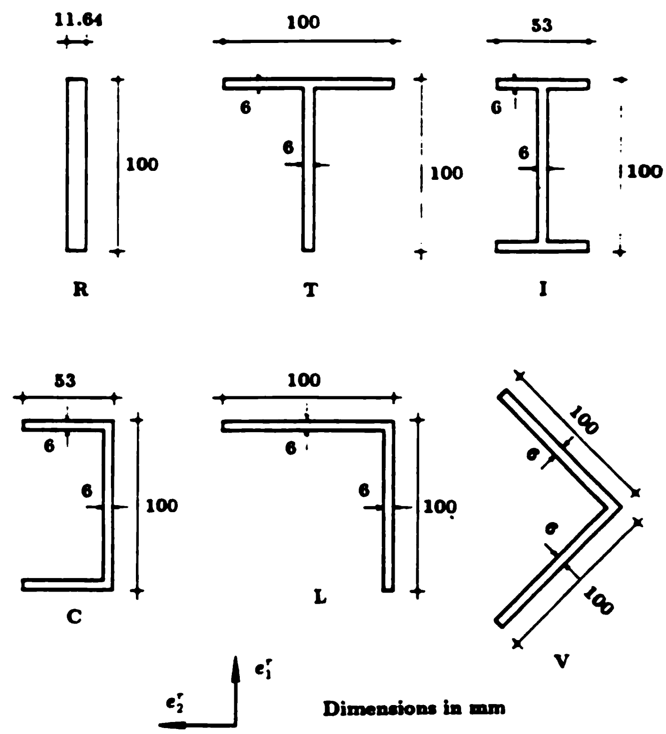

FIG 2. Cross sections

Example 1

The first example shows the lateral buckling of a cantilever beam with a concentrated load at the tip. Six cross sections were considered as displayed in the figure 2. The axis is placed along the cross section centroids and the load is applied on the axis in the direction of e_1^r, as displayed in the figure 2. Figure 3 shows the computed lateral displacements of the point of load application. Only three cases presented a symmetric stable bifurcation. Notice the large displacements and rotations. Rotation angles over 0.30 rd were observed. The Newton method for solving the nonlinear problem at each load level could be applied in exact form, showing always its characteristic quadratic asymptotic rate of convergence. The load increments were controlled by an automatic algorithm. To circumvent bifurcation points a very small geometric perturbation was introduced, when necessary. The examples were computed varying the position of the rod axis but retaining the position of the load. The results remained invariant.

Example 2

The second example, shown in figure 4, is similar to the first one, but the axis is placed along the cross section shear centers. The load at the tip is applied on the shear center of the end cross section. Notice that, this time, five cross sections have presented a symmetric stable bifurcation. Even the asymmetric C and V sections presented this time a bifurcation. Note that the T section has exhibited the highest critical load.

Example 3

This example shows the lateral buckling of a L-shaped frame with a concentrated load at the tip. Axis and load were placed on the shear centers of the cross sections. Only the frames with double-symmetric sections like the R and I section presented a stable symmetric bifurcation, as one can see in figure 5. In the other four cases a continuous nonlinear behavior was observed.

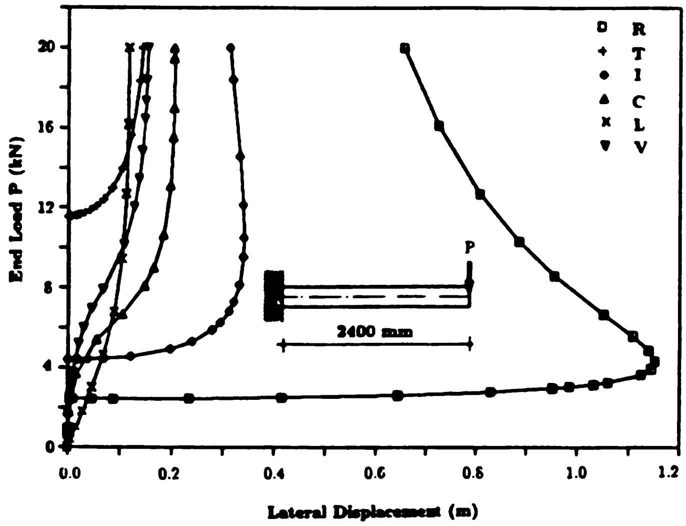

FIG 3. Example 1

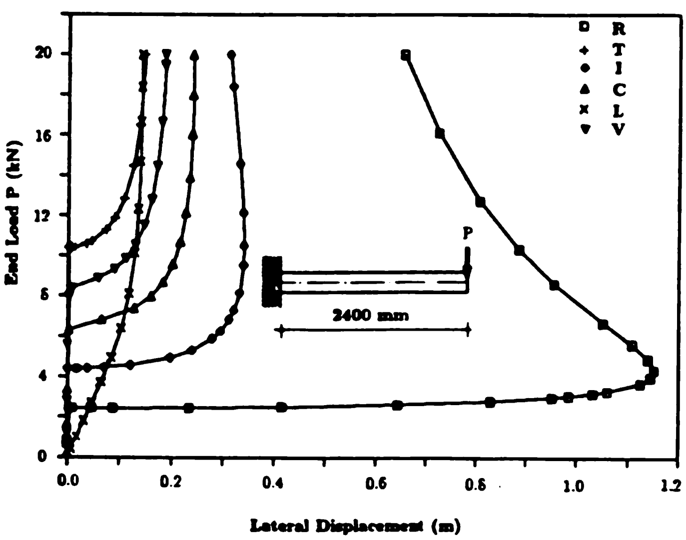

FIG 4. Example 2

Example 4

This example shows the lateral buckling of a I-beam under concentrated and uniformly distributed loading. The loadings were placed on the top and at the bottom of beam, as displayed in figure 6.

Example 5

This example, displayed in figure 7, shows the lateral buckling of a I-beam under different end moments. The first two cases correspond to quasi-tangential moments and the third case corresponds to a semi-tangential moment. The critical loads for the quasi-tangential moments coincide and are one half of the critical load for the semi-tangential moment.

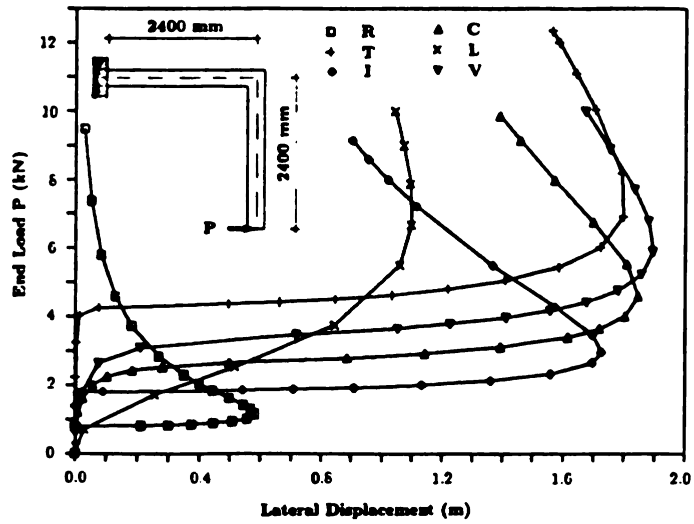

FIG 5. Example 3

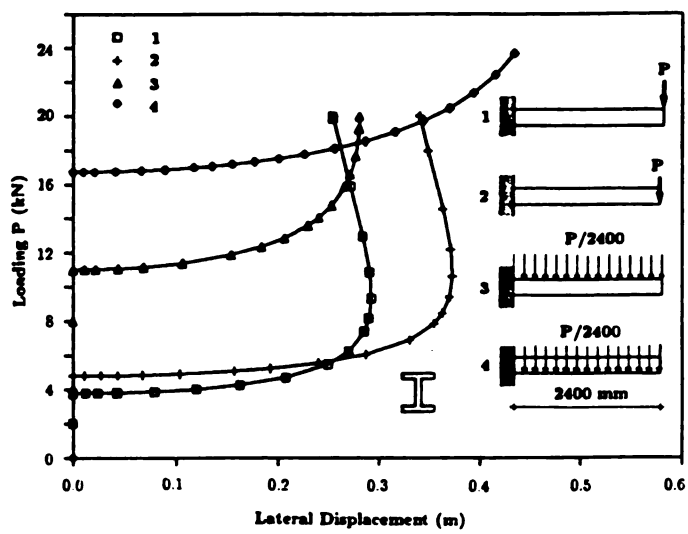

FIG 6. Example 4

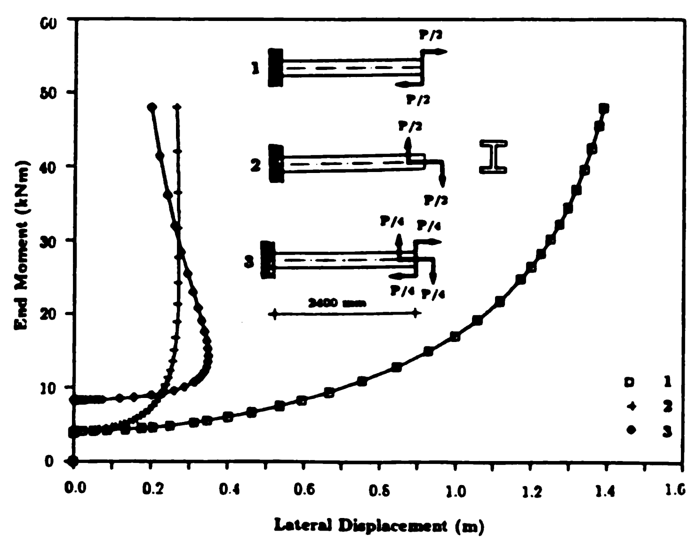

FIG 7. Example 5

CONCLUSIONS

A geometrically exact fully nonlinear rod model, which can be readily applied to finite element analysis of spatial frames, was formulated. The advantages of the model, that were pointed out by the authors in the introduction, could be corroborated along the text. Some simple numerical examples have shown the effectiveness of the developed formulation.

REFERENCES

Simo JC, A finite strain beam formulation. The three-dimensional dynamic problem. Part I, *Comput Meths Appl Mech Engrg* **49**, 55–70 (1985)

Simo JC and Vu-Quoc L, A three-dimensional finite strain rod model. Part II: computational aspects, *Comput Meths Appl Mech Engrg* **58**, 79–116 (1986)

Simo JC and Vu-Quoc L, A geometrically exact rod model incorporating shear and torsion-warping deformation, *Int J Solids Structures* **27**, 371–393 (1991)

Chang SL, Large deflection kinematics formulation for three-dimensional framed structures, *Comput Meths Appl Mech Engrg* **94**, 17–36 (1992)

Saleeb AF, Chang TYP and Gendy AS, Effective modelling of spatial buckling of beam assemblages, accounting for warping constraints and rotation-dependency of moments, *Int J Numer Meths Engrg* **33**, 469–502 (1992)

Saleeb, AF and Gendy, AS, Shear-flexible models for spatial buckling of thin-walled curved beams, *Int J Numer Meths Engrg* **31**, 729–757 (1991)

Cheng H and Blandford GE, Thin-walled space frames. Part I: Large-deformation analysis theory, *J Structural Engrg* **117**(8), 2499–2520 (1991)

Cheng H and Blandford GE, Thin-walled space frames. Part II: Algorithmic details and applications, *J Structural Engrg* **117**(8), 2521–2539 (1991)

Danielsen DA and Hodges DH, A beam theory for large global rotation, moderate local rotation and small strain, *J Appl Mech* **55**, 179–184 (1988)

Determination of stress concentration factors for shallow and sharp v-notches using a hybrid method

José LF Freire, Eduardo A Carvalho, and Marco AM Cavaco

Departamento de Engenharia Mecânica, Pontifícia Universidade Católica do Rio de Janeiro PUC/Rio, 22453, Rio de Janeiro, Brazil

Stress distributions near the root of shallow and sharp V-notches are determined through a hybrid method which associates the isochromatic photoelastic response with the analytical description of the stress state for the points studied.

INTRODUCTION

Improvements in model preparation and loading cycle procedures, together with the well-known advantages of high resolution and whole-field technique, have maintained photoelasticity as a cost-effective method for stress analysis purposes. In the design stage, reasonably accurate stress concentration factors (SCF) may be quickly measured. More accurate SCF evaluation and analysis of photoelastic data, such as stress separation, are more time consuming and so considerable amount of research has been directed to speed and to augment photoelasticity capabilities by its coupling to image analysis techniques, to micro-computers and to appropriate numerical methods.

Several computer-based algorithms have been proposed to determine accurately fringe orders and stresses at interior and surface points of photoelastic models. Berghaus fitted photoelastic data to field differential equations of elasticity in finite difference [1] and finite element [2] forms. Thompson and co-workers [3,4] determined SCF and performed stress separation in plane problems by using asymptotic analysis and least-squares.

Sanford has shown that the photoelasticity [5] and other optical method [6] responses can be associated to the least-squares technique to determine key parameters of elasticity problems if their mathematical governing equations are known. Freire and co-workers proposed that suitable approximate stress functions could be used to fit photoelasticity isochromatic data [7] and other optical technique responses [8] to solve plane elasticity problems for isotropic and orthotropic materials. A similar procedure was also presented by Huang et alii [9]. These last two approaches [7,8,9] allowed the automatic stress separation of the photoelastic response without the need for collection of isoclinic data.

The present paper associates the isochromatic optical response of plane photoelastic models to approximate polynomial stress functions in order to generate analytical expressions for stress distributions near the root of shallow notches. The paper also uses the Creager-Paris [10] equations developed for blunt cracks in order to determine SCF for sharp V-notches where the opening angle is less than 60°.

BASIC EQUATIONS FOR PLANE ELASTICITY AND SHALLOW NOTCHES

Stress distributions near the root of shallow notches can be determined through the coupling of photoelasticity data collected inside the desired region and the analytic description of the stress state for each point studied. Using the Goursat-Kolosov complex representation of the plane problem and the potential functions φ and ψ, it is possible to describe the stress state as

$$\begin{aligned}\sigma_r &= 2Re\varphi' - Re[e^{2i\theta}(\overline{z}\varphi'' + \psi')]\\ \sigma_\theta &= 2Re\varphi' + Re[e^{2i\theta}(\overline{z}\varphi'' + \psi')]\\ \tau_{r\theta} &= Im[e^{2i\theta}(\overline{z}\varphi'' + \psi')]\end{aligned} \qquad (1)$$

The functions φ and ψ can be chosen to satisfy certain boundary or special loading conditions of the photoelastic models. For example,

$$\varphi(z) = \sum^{m}(a_m + ib_m)z^m + w\ell_n z \qquad (2)$$

$$\psi(z) = \sum^{n}(p_n + iq_n)z^n + h\ell_n z \tag{3}$$

can be used to fit isochromatic data for important problems such as stress concentration near holes, V - notches, and also the brazilian disc problem.

For example, polynomial functions work well for stress concentration problems such as bars with holes and U-notches. For a hole in a infinite plane subjected to tension load, $\varphi = a_{-1}z^{-1} + a_1 z$ and $\psi = p_{-3}z^{-3} + p_1 z$ give the exact solution. For other problems envolving holes and U-notches, polynomial functions such as

$$\varphi = \sum a_m z^m \qquad \text{and} \qquad \psi = \sum p_n z^n \tag{4}$$

give good results. In general, m and n vary from -3 to +5 to fit data which can be taken relatively far from the maximum stress location and may be affected by the far field stress distributions, including the influence of free boundaries.

The constants a_m, b_m, p_n, q_n, w and h are determined through a Newton-Raphson least-squares fitting technique as proposed by Sanford [5,6] using the basic photoelasticity equation,

$$\sigma_1 - \sigma_2 = \frac{N}{t} f_\sigma \tag{5}$$

where N is the isochromatic fringe order, f_σ is the fringe calibration value and t is the specimen thickness. For stress separation purpose, boundary conditions must be given. Free boundary conditions near the stress concentration location are given by

$$\sigma_n = 0 \qquad \text{and} \qquad \tau_{nt} = 0 \tag{6}$$

where n and t are the normal and tangential directions for points at the free boundary.

Additional conditions for points located along symmetry lines can be established as

$$\tau_{j\ell} = 0 \tag{7}$$

where j and ℓ are directions parallel and perpendicular to the symmetry axes. If the isochromatic fringe orders N for points along the free boundary can be reliably measured, equations (8) below can be applied

$$\sigma_t = \frac{N}{t} f_\sigma \tag{8}$$

Coupling equations (2) and (3) or (4) with (1) and substituting into (5) gives the non-linear equation

$$(\sigma_1 - \sigma_2)^2 = \left(\frac{N}{t} f_\sigma\right)^2 = (\sigma_r - \sigma_\theta)^2 + 4\tau_{r\theta}^2 = F_1(a_m, b_m \ldots, w, r, \theta) \tag{9}$$

Linear equations are generated from the substitutions of (2), (3) or (4) into (1) and later into (6) to (8), giving

$$\sigma_n = F_2(a_m, b_m, \ldots, w, r, \theta) = 0 \tag{10}$$

$$\tau_{nt} = F_3(a_m, b_m, \ldots, w, r, \theta) = 0 \tag{11}$$

$$\sigma_t = F_4(a_m, b_m, \ldots, w, r, \theta) = \frac{N}{t} f_\sigma \tag{12}$$

$$\tau_{j\ell} = F_5(a_m, b_m, \ldots, w, r, \theta) = 0 \tag{13}$$

It is interesting to note that the solution of the problem for $a_m, b_m, \ldots, w$ will need only data collection (isochromatic fringe orders) at interior points of the models. Use of equations (12) and (13) is optional and will depend on the quality of data N that can be collected along the boundary. Data need to be collected only inside the particular region of the model that is being studied. Depending on the model geometry, loading conditions, and complexity of the aproximated stress function selected to use in the problem, the chosen region may be the entire model or just a small part of it. A total of $i + s + c$ data points is collected, where i, s and c are, respectively, the number of data taken from the interior points, from the symmetry lines and from the free boundary.

In general, $i + s + 3c$ equations (9) to (13) are solved simultaneously through a Newton-Raphson least-squares fitting technique. For this, g functions are generated such that

$$g_{1i} = F_{1i}(a_m, b_m, \ldots, w, r_i, \theta_i) - \left(\frac{N_i}{t} f_\sigma\right) \tag{14}$$

$$g_{2c} = F_{2i} \tag{15}$$

$$g_{3c} = F_{3i} \tag{16}$$

$$g_{4c} = F_{4c} - \left(\frac{N_c}{t} f_\sigma\right)^2 \tag{17}$$

$$g_{5s} = F_{5s} \tag{18}$$

The unknowns $a_m, b_m, ..., w$ are iteractively determined using initial estimations such as a_{mo}, b_{mo}, ..., w_o and the recurrence expressions such as (19) where the Δ increments are determined from the matricial equation (20) - (23).

$$a_{m_{k+1}} = a_{m_k} + \Delta a_{m_k} \tag{19}$$

$$\Delta = (A^T A)^{-1} AG \tag{20}$$

$$\Delta^T = (\Delta a_m, \Delta b_m, ..., \Delta w) \tag{21}$$

$$G^T = (-g_{1i} W_1, ..., -g_{5s} W_5) \tag{22}$$

$$A = \begin{bmatrix} W_1 \frac{\partial_{g11}}{\partial_{a_m}} & W_1 \frac{\partial_{g11}}{\partial_{b_m}} & \cdots & W_1 \frac{\partial_{g11}}{\partial_w} \\ \vdots & & & \\ W_5 \frac{\partial_{g5s}}{\partial_{a_m}} & W_5 \frac{\partial_{5s}}{\partial_{b_m}} & \cdots & W_5 \frac{\partial_{g5s}}{\partial_w} \end{bmatrix} \tag{23}$$

It was shown in [11] that about $k = 10$ iteractions are needed to reach final convergence. The weight functions W_1 to W_5 were used to equilibrate numerically the system of equations and have the following shape [11],

$$W_1 = i / \sum_{p=1}^{i} (g_{1p})^2 . S \tag{24}$$

$$W_5 = s / \sum_{p=1}^{s} (g_{5p})^2 . S \tag{25}$$

$$S = \frac{(1 + s + 3c)}{\left(\sum^i g_1^2 + \sum^c g_2^2 + \sum^c g_3^2 + \sum^c g_4^2 + \sum^s g_5^2\right)} \tag{26}$$

Problems of the plane elasticity have already been tested with success. Among them are classical problems such as bars under uniaxial tension, three, and four point bending; finite and infinite bars with holes; U-notches under bending; and the brazilian disc problem. It can be noticed that stress separations were succesfully accomplished in both cases. In one case (brazilian disc) the whole specimen was analysed [7]. In the other case (U-notch) only a small region of interest, near the stress concentration, was focused. Results for this example are shown below.

Bar with Symmetrical U-Notches Under Bending

Data for this example was collected directly from a photograph presented by Frocht in [12], page 234. Results [12] for stress separation applying the shear difference and the slope equilibrium method were also used for comparison purposes.

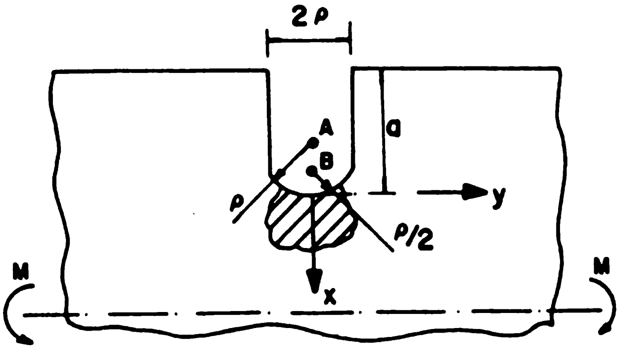

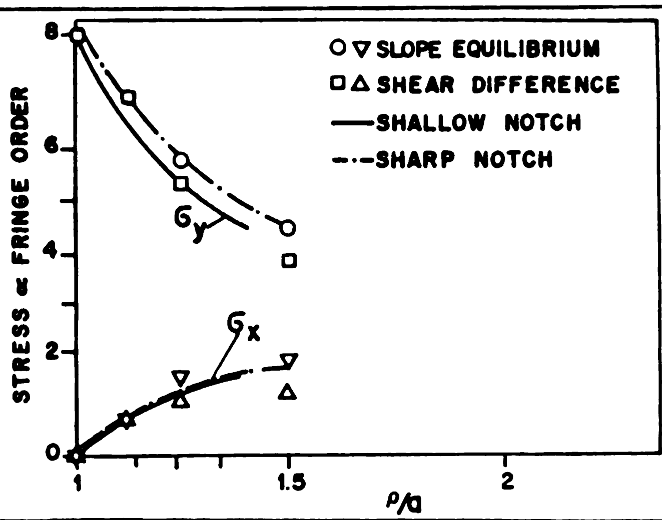

FIG. 1 - Bar with symmetrically located U-notches under bending. Comparison between stress separation results obtained from Frocht [12] and the present method. Region of data collection is shown in the Figure. A = origin for shallow notch approach. B - origin for sharp notch approach.

The region of data collection was small and is hown in Fig. 1. The coordinate system was coinided with the curvature center of the notch. Sixty ive data points were used, 45 of which were inteior points, 10 were along the symmetry line and .0 were along the notch boundary. The stress funcions φ and ψ used the terms $a(-2)$ to $a(5)$ and $p(-3)$ to $p(5)$. It should be noted that the terms $a(-1), a(1), p(-3)$, $p(-1)$ and $p(1)$ interpolate exactly the case of an infinite plane with a circular hole under tension.

Principal separated stress values obtained from equations (1) to (3) after determination of the terms a and p by the minimization scheme are presented n Fig. 1 and compared with Frocht's results. It can be seen that the agreement is very good. Results for he isochromatic fringe order fitting was also very good. Maximum fringe order determined by this nethod was 8.0, while Frocht's was 8.2.

Equations for Singular and Sharp V-Notches

After William's [1], Mahinfalah and Zachary [2] developed the following equations (27) for the stress components at points in the neighborhood of the vertex of reentrant singular corners for mixed mode I and II (Fig. 2). They used a stress function such as $\phi(z) = r^{\lambda+1} f(\theta)$. The stress equations are

$$\begin{aligned}
\sigma_r &= K_I r^{\lambda^+ -1} Q^+[f_1(\theta)] - K_{II} r^{\lambda^- -1} Q^-[f_2(\theta)] \\
\sigma_\theta &= K_I r^{\lambda^+ -1}(1+\lambda^+) Q^+[f_3(\theta)] - K_{II} r^{\lambda^- -1} \\
&\quad (1+\lambda^-) Q^-[f_4(\theta)] \\
\tau_{r\theta} &= K_I r^{\lambda^+ -1} Q^+[f_5(\theta)] + K_{II} r^{\lambda^- -1} Q^-[f_6(\theta)]
\end{aligned} \tag{27}$$

where K_I an K_{II} are defined as in expression (28) and the other terms are given in the Appendix.

$$K_{I,II} = \lim_{r\to 0} (2\pi)^{1/2} r^{\lambda - 1_{I,II}} \sigma_{I,II} \tag{28}$$

The values of λ^+ and λ^- are solutions of the eigenvalue equations

$$\lambda sin 2\alpha = \pm sin 2\lambda\alpha \tag{29}$$

and their first determinations (smaller values of $\lambda \neq 0$) are show in Fig. 2. The degree of singularity of the stress, $1-\lambda$, is maximum when the angle α of the V-notch is zero. For this case, $\lambda = 1/2$, and the notch assumes a crack shape. Freire and Carvalho [13] showed that stress intensity factors for 45° V-notches and crack-like notches ($\alpha = 0$) and their stress distributions near the notch tip are very simitar. For example, Fig. 3

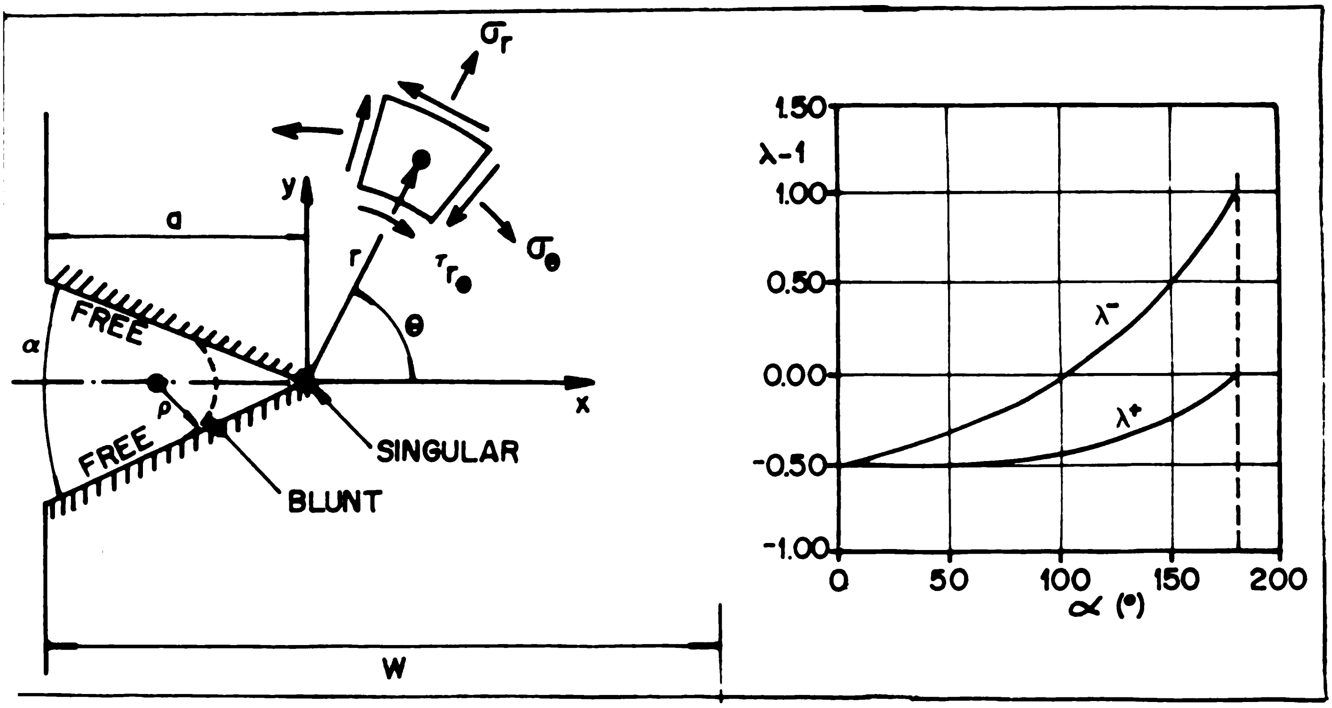

FIG. 2 - Geometry notation for singular and blunt V-notches. Degreee of singularity $(1-\lambda)$ with the angle (α) of the reentrant corner.

shows computer-plotted isochromatic fringe distributions for a crack and for a 45° V-notch specimens under tension [13]. Considering that $\lambda \simeq 1/2$ in mode I for V-notches with opening angle $0 < \alpha < 60°$, K_I for these notches and for cracks can be used indistinctly. Based on this conclusion it is possible to determine the stress field for the region near the root of blunt V-notches by coupling the isochromatic photoelastic response to the Creager-Paris equations [10] and to the Sanford's overdeterministic approach [5,6].

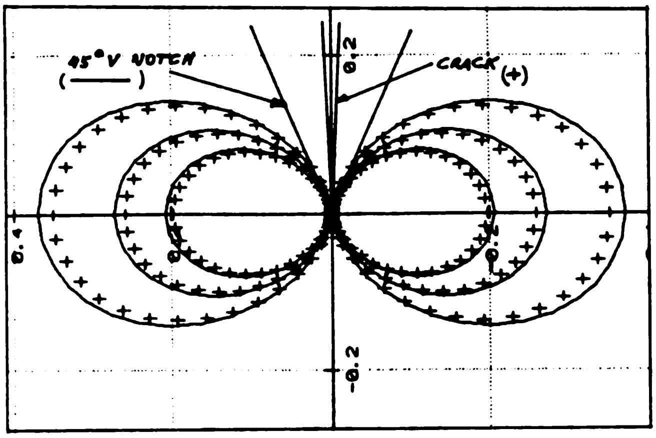

FIG. 3 - Computer-plotted isochromatic fringe distributions for a crack and for a 45° V-notch specimen under tension $a/w = 0.05$, near field.

The Creager and Paris [10] elastic stress equations for points near the root of sharp notches are presented below for mode I for blunt cracks (small ρ/a) in a form equivalent to the usual sharp crack-tip stress fields. They showed that their difference was a simple function of the curvature radius at the crack-tip. For these equations, the origin of the coordinate system (r, θ) is located $\rho/2$ away from the notch-root.

$$\begin{aligned}
\sigma_x &= \frac{K_I}{(2\pi r)^{1/2}} \cos\frac{\theta}{2}\left[1 - \sin\frac{\theta}{2}\sin\frac{3}{2}\theta\right] - \frac{K_I}{(2\pi r)^{1/2}}\frac{\rho}{2r}\cos\frac{3}{2}\theta \\
\sigma_y &= \frac{K_I}{(2\pi r)^{1/2}} \cos\frac{\theta}{2}\left[1 + \sin\frac{\theta}{2}\sin\frac{3}{2}\theta\right] + \frac{K_I}{(2\pi r)^{1/2}}\frac{\rho}{2r}\cos\frac{3}{2}\theta \\
\tau_{xy} &= \frac{K_I}{(2\pi r)^{1/2}} \sin\frac{\theta}{2}\cos\frac{\theta}{2}\cos\frac{3}{2}\theta - \frac{K_I}{(2\pi r)^{1/2}}\frac{\rho}{2r}\sin\frac{3}{2}\theta
\end{aligned} \tag{30}$$

Substitution of equations (30) into the photoelasticity equation (2) and generation of a functional G_i fort each collected i data point will give

$$G_i = (\sigma_1 - \sigma_2)_i^2 - \left(\frac{N_i}{t} f_\sigma\right)^2 = F_i(K_I, \rho, r_i, \theta_i) - \left(\frac{N_i}{t} f_\sigma\right)^2 \tag{31}$$

The application of the minimization scheme presented in the preceding section for G will lead to the determination of the K_I constant which best fit the data points in the least-squares sense. The determined K_I will be the stress intensity factor for a equivalent crack (or V-notch with $0 < \alpha < 60°$) which has its tip located at the origin of the (r, θ) coordinate system.

Two examples were chosen to demonstrate the method. The first example was a bar with symmetrical U-notches under bending. The second example envolved a bar with a sharp V-notch under tension. This U-notch geometry is equivalent to a Charpy notch used for impact tests.

Bar with Symmetrical U-Notches Under Bending

Due to its geometrical relations, this example can be considered as a limiting case, where both procedures for SCF determination for shallow and sharp notches can be applied.

Results for the sharp-notch SCF determination are also plotted in Fig. 1 for comparison purposes. It can be seen that these results agreed very well with the shallow notch procedure and also with Frocht's results. Only 25 data points were used in this case. K_I determination through the fitting procedure gave satisfactory results (10% difference from the analytical value), reminding that the effective crack length $a*$ should be determined from the origin of the system of coordinates, $a* = a - \rho/2$, for the sharp notch approach. In this case, it is not expected that the procedure furnish an accurate value for K_I since this geometry is considerably different from a crack. In this case, K_I plays the whole of an adjusting parameter for the experimental data.

Bar with Charpy V-Notch Under Tension

The second example applied the sharp notch procedure to the Charpy V-notch bar geometry under tension load (Fig. 4). The K_I determined value agreed with K_I for a crack with the same effective geometry (less than 1% difference).

The value of the maximum stress ($\sigma_y = \sigma_{max}$) at the notch-root ($\rho/2$, 0) can be determined using equations (30). In terms of the isochromatic fringe response, this value was calculated to be $N_{max} =$ 8.6 which is very close to the photoelastic direct observation ($N_{max} = 8.8$).

Using σ_{max} or N_{max} and a nominal stress or fringe order, the stress concentration factor for the Charpy V-notch can be calculated as $K_t = N_{max}/N_{nom}$. In the present case, the presence of bending in the net section was considered in the calculation of N_{nom} as suggested by Noda and Nisitani [14].

The values of K_t determined in this analysis were 3.4 and 3.5, respectively by the overdeterministic approach and by the photoelastic direct observation. Theoretical results from Noda and Nisitani [14] for $\alpha = 60°$ give $K_t = 3.7$. Recent results from Demelio et al. [15], approximated to the Charpy geometry and considering the N_{nom} calculated as in [14], give $K_t \simeq 3.6$.

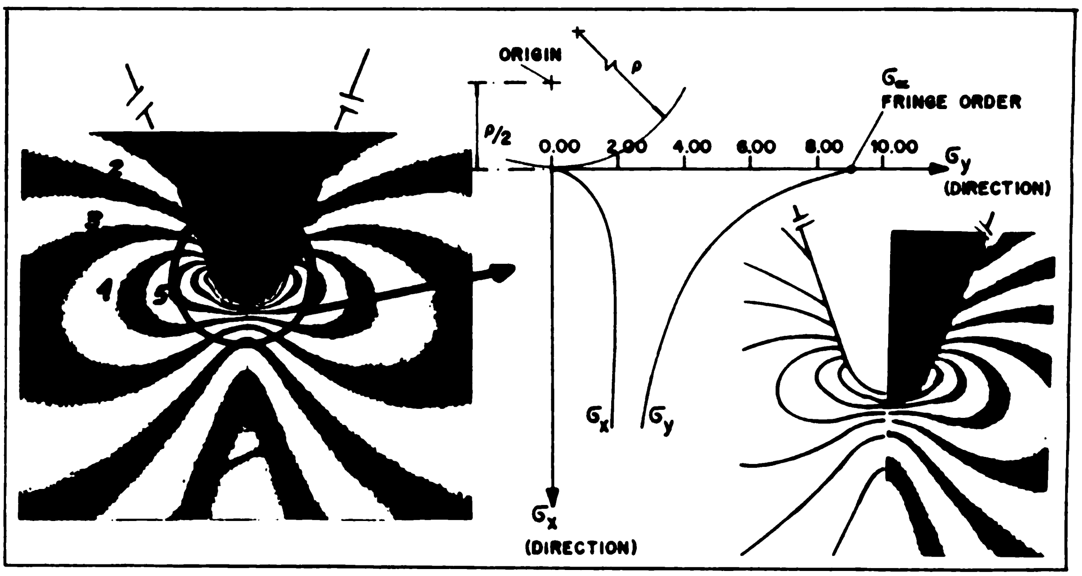

FIG. 4. Bar with a Charpy V-notch under tension. Distribution od stresses along the x axis in a region near the notch-root. Regenerated and original isochromatic distributions. Standard deviation between calculated and measured (25) data points is equal to 2.5%.

Fig. 4 gives the stress distributions for the photoelastic analysis in locations very near to the notch-root. This separation is possible if equations (30) are calculated independently for each point (r, θ) using ρ and the determined K_I value.

This Figure, also presents isochromatic fringe orders regenerated by the procedure using the calculated K_I value, equation (30) and equation (2). The calculated isochromatic fringe values and their distributions are commonly used to give a measure of how good the fitting procedure is working. This can be done visually or by comparing collected with calculated data point by point and determining their standard deviation. Good fittings generate standard deviations which are generally under 3%.

REFERENCES

[1] Berghaus, D., Stress analysis using elastic field equations, photoelasticity and least squares. *Proc. of SEM Conference on Experimental Mechanics*, 33-42, 1987.

[2] Berghaus, D., Combining photoelasticity and finite-elements methods for stress analysis using least-squares. *Proc. of SEM Spring Conference on Experimental Mechanics*, 231-237, 1989.

[3] Thompson, J. C. and Negus, K. J., Developments in least squares asymptotic analysis of isochromatic data from stress concentration regions in plane problems, *Strain*, v. 20, n. 3,

133-134, August 1984.

[4] Dhillon, J. C. Thompson, K. J. Negus, A simplified method for predicting the stress concentration in notches from experimental stress, *Strain*, v. 24, n. 23, 95-98, August 1988.

[5] Sanford, R. J. , Application of the least-squares method to photoelastic analysis, *Experimental Mechanics*, 192–197, June 1980.

[6] Sanford, R.J., "Determining fracture parameters with full-field optical methods," *Experimental Mechanics*, 29 (3), 241-247, 1989.

[7] Freire, J. L. F. , and Cavaco, M. A. M. , Analysis of photoelastic data through stress function fittings, Proceedings of the SEM Spring Conference on Experimental Mechanics, 213-217, 1992.

[8] Freire, J.L.F., Cavaco, M.A.M., Burger, C.P. and Castro, L.O.G., "*Otpical methods for experimental mechanics and image analysis*" , (In Portuguese) Proceedings of the XI Brazilian Congress on Mechanical Engineering, Braziliam Society for Mechanical Sciences, 49-52, 1991.

[9] Huang, Y.M., Lin, C.H., Suhling, J.C. and Rowlands, R.E., "Determining the three individual stress components from measured isochromatic fringes", *Experimental Mechanical*, v. 31, n.4, 310-318, 1991.

[10] Creager, M. and Paris, P.C., "Elastic Field Equations for Blunt Cracks with Reference to Stress Corrosion Cracking," *International Journal of Fracture Mechanics*, v.3, 247-252, December, 1967.

[11] Cavaco, M.A.M., *An hybrid method for stress analysis*, (in Portuguese), MSc Thesis, Catholic University of Rio de Janeiro, 1990.

[12] Frocht, M. M. , *Photoelasticity*, Vol. I e II, John Wiley & Sons, Inc. , New York, 1941.

[13] Freire, J. L. F. and Carvalho, E. A., "Stress Intensity Factors for 45° U-notches, "Proceedings of the VII SEM International Congress on Experimental Mechanics, 500-504, June 1992.

[14] Noda, N.A. and Nisitani, H., "Stress Concentration of a Strip with a Single Edge Notch," *Engineering Fracture Mechanics*, v. 28, n. 2, 233-238, 1987.

[15] Demelio, G., Papalettere, C. and Pastore, C., "Stress Concentration Factor for V-Notches," Proceedings of the 1989 Conference on Experimental Mechanics, SEM, 147-153, 1989.

APPENDIX

$$\begin{aligned}
f_1(\theta) &= [(3-\lambda^+)\,cos(\lambda^+-1)\theta - \\
&\quad -(1+\lambda^+)\beta_1 cos(\lambda^++1)\theta] \\
f_2(\theta) &= [(3-\lambda^-)\,sin(\lambda^--1)\theta - \\
&\quad -(1+\lambda^-)\beta_2 sin(\lambda^-+1)\theta] \\
f_3(\theta) &= [cos(\lambda^+-1)\theta + \beta_1 cos(\lambda^++1)\theta] \\
f_4(\theta) &= [sin(\lambda^--1)\theta + \beta_2 sin(\lambda^-+1)\theta] \\
f_5(\theta) &= [(\lambda^+-1)\,sin(\lambda^+-1)\theta + \\
&\quad +(\lambda^++1)\beta_1 sin(\lambda^++1)\theta] \\
f_6(\theta) &= [(\lambda^--1)\,cos(\lambda^--1)\theta + \\
&\quad +(\lambda^-+1)\beta_2 cos(\lambda^-+1)\theta]
\end{aligned}$$

$$\beta_1 = -\frac{(\lambda-1)\ sin\ (\lambda-1)\ \alpha}{(\lambda+1)\ sin\ (\lambda+1)\ \alpha}$$

$$\beta_2 = \frac{sin\ (\lambda-1)\alpha}{sin\ (\lambda+1)\ \alpha}$$

$$C_1 = Q_1 K_I$$
$$C_2 = -Q_2 K_{II}$$

$$Q_1 = 1/\{(2\pi)^{1/2}(1+\beta_1)(\lambda^+)(1+\lambda^+)$$
$$Q_2 = 1/(2\pi)^{1/2}(\lambda^-)[\lambda^- - 1 + \beta_2(\lambda^-+1)]$$

$$Q^+ = \lambda^+(Q_1)$$
$$Q^- = \lambda^-(Q_2)$$

Micromechanics as a basis of stochastic finite elements and differences: An overview

M Ostoja-Starzewski

Department of Materials Science and Mechanics
Michigan State University, East Lansing, MI 48824-1226

A generalization of conventional deterministic finite element and difference methods to deal with spatial material fluctuations hinges on the problem of determination of stochastic constitutive laws. This problem is analyzed here through a paradigm of micromechanics of elastic polycrystals and matrix-inclusion composites. Passage to a sought-for random meso-continuum is based on a scale dependent window playing the role of a Representative Volume Element (RVE). It turns out that the microstructure cannot be uniquely approximated by a random field of stiffness with continuous realizations, but, rather, two random continuum fields may be introduced to bound the material response from above and from below. Since the RVE corresponds to a single finite element, or finite difference cell, not infinitely larger than the crystal size, these two random fields are to be used to bound the solution of a given boundary value problem at a given scale of resolution. The window-based random continuum formulation is also employed in analysis of rigid perfectly-plastic materials, whereby the classical method of slip-lines is generalized to a stochastic finite difference scheme. The present paper is complemented by a comparison of this methodology to other existing stochastic solution methods.

1. INTRODUCTION

The necessity to account for random effects in determining the response of a mechanical system is due, in general, to three different sources: random external forcing, random boundary conditions, and random material parameters. In the last fifteen years the powerful finite element method has undergone various new developments to incorporate these random effects, and is now termed Stochastic Finite Elements (SFE), see e.g. (Contreras, 1980; Benaroya and Rehak, 1988). In this paper we focus only on the type of SFE problems which deal with randomness stemming from fluctuations in material properties. Most of the past research in that area concerned linear elastic structural responses and relied on a straightforward generalization of Hooke's law, that is

$$\underset{\sim}{\sigma} = \underset{\sim}{C}(\underset{\sim}{x}, \omega)\,\underset{\sim}{\varepsilon} \tag{1.1}$$

In equation (1.1) $\underset{\sim}{x}$ stands for a location within the body domain, ω is an index from the sample space Ω, and $\underset{\sim}{C}(\underset{\sim}{x}, \omega)$ is a continuous realization of a random tensor field of stiffnesses. Part of the assumption (1.1) is the invertibility of such a constitutive law, that is

$$\underset{\sim}{\varepsilon} = \underset{\sim}{S}(\underset{\sim}{x}, \omega)\,\underset{\sim}{\sigma} \qquad \underset{\sim}{S}(\underset{\sim}{x}, \omega) = \underset{\sim}{C}^{-1}(\underset{\sim}{x}, \omega) \tag{1.2}$$

whereby $\underset{\sim}{\varepsilon}$ and $\underset{\sim}{\sigma}$ in (1.1) and $(1.2)_1$ are uniform fields applied to a hypothetical and unspecified Representative Volume Element (RVE) of a random medium. In fact, typically, a locally isotropic form

$$\sigma_{ij} = \lambda(\underset{\sim}{x}, \omega)\,\delta_{ij}\varepsilon_{kk} + 2\mu(\underset{\sim}{x}, \omega)\,\varepsilon_{ij} \tag{1.3}$$

is adopted by simply postulating one or both elastic constants, such as the Young's modulus, to be a random field.

While the effort in SFE has been on the development of efficient numerical methods for solution of boundary value problems, the above model - equations (1.1-3) - lacks a connection to the material microstructure. It is the determination of that missing micromechanics link, which forms the main objective of this paper. Additionally, our methodolgy may also be applied to other than elastic microstructures, and used in solution of random media problems by finite differences. A very closely related issue of specification of continuum random fields approximating elastic microstructures is studied by Ostoja-Starzewski (1993b).

The paper's outline is as follows. In Section 2 we describe the passage from the level of a linear elastic microstructure to that of two random meso-continuum models $\underset{\sim}{C}_{\delta}(\underset{\sim}{x}, \omega)$, where δ indicates the scale dependence. Next follows a stochastic variational formulation of finite elements - in both dispalcement and force approaches - which illustrates the role of these meso-continuum models in bounding the actual response. The micromechanics approach is employed in Section 3, which focuses on rigid--perfectly plastic materials with random fluctuations in the yield functions. It follows here that the method of slip-lines - well known from the deterministic homogenous media problems - is now to be generalized to stochastic finite differences. Section 4 is devoted to comparisons with other existing approaches. Thus, we briefly review the classical SFE methods for elastic structures and discuss their applicability in micromechanics-based analyses. In the area of plasticity, we discuss the relation of our formulation of Section 3 to a recent study of Nordgren (1992).

2. ELASTIC MEDIA PROBLEMS

2.1 Random medium model

Fundamental role in our formulation is played by the concept of a *random medium* (or *random microstructure*), which, as is commonly done in mechanics of random media (Willis, 1981), is taken as a family $\boldsymbol{B} = \{\mathbf{B}(\omega);\ \omega \in \Omega\}$ of deterministic media $\mathbf{B}(\omega)$, where ω indicates one specimen (realization), and Ω is an underlying sample (probability) space. Formally, Ω is equipped with a σ-algebra F and a probability distribution P. In an experimental setting P may be specified by a set of stereological measurements, while in a theoretical setting P is usually specified by a chosen model of a microstructure. All specimens $\mathbf{B}(\omega)$ occupy the same domain in x_1, x_2-plane; we employ a two-dimensional setting (2-D) for the clarity of presentation.

In the following we consider two types of the random medium $\boldsymbol{B}$. In the first one, we take every specimen $\mathbf{B}(\omega)$ to be modeled by a realization of a *Voronoi tessellation* (Fig. 1.a), while in the second by a realization of a matrix-inclusion composite (Fig. 1 b). Fundamental in both cases is a planar space-homogeneous Poisson process of some given density. In case of a Voronoi tessellation each cell, centered at a Poisson point $\underline{x}$, is assumed to be occupied by a homogeneous continuum governed by a stiffness tensor $\underline{C}(x, \omega)$ following a space-homogeneous probability distribution $P(\underline{C})$. In case of the matrix-inclusion composite, we use an inhibition Poisson process to ensure that there is no overlap of inclusions shaped as round disks. We assume the disks to be occupied by a homogeneous isotropic continuum of one kind, while the matrix by a continuum of another.

In case of both models we assume all the phases to satisfy the so-called *ellipticity conditions*: $\exists\alpha, \beta > 0$ such that for any $\underline{\varepsilon}$ the following inequalities hold for all the phases

$$\alpha\underline{\varepsilon}\underline{\varepsilon} \le \underline{\varepsilon}\underline{C}\underline{\varepsilon} \le \beta\underline{\varepsilon}\underline{\varepsilon} \tag{2.1}$$

Thus, we have two realistic ergodic media models without holes and rigid inclusions described by random fields $\underline{C} = \{\underline{C}(\underline{x}, \omega);\ \underline{x} \in B; \omega \in \Omega\}$ with piecewise-constant realizations. This piecewise-constant nature of stiffness fields is an obstacle to employing the governing equations of continuum elasticity, which require that the stiffness fields be differentiable. Thus, there is a need for another continuum model - one that possibly loses some information due to a "smearing-out" procedure, but is sufficiently differentiable and grasps the meso-level behavior.

2.2 Two scale-dependent random continuum fields

First, with the help of Fig. 1, we introduce a square-shaped *window* of scale

$$\delta = \frac{L}{d} \tag{2.2}$$

Equation (2.2) defines a nondimensional parameter δ, typically greater than 1, specifying the scale L of observation (and/or measurement) relative to a typical microscale d (i.e. grain size) of the material structure. $\delta = 1$ is the smallest scale we consider: scale of a crystal or inclusion. In view of the fact that the Voronoi tessellation is a random medium, the window bounds a random microstructure $B_\delta = \{B_\delta(\omega);\ \omega \in \Omega\}$, where $B_\delta(\omega)$ is a single realization from a given specimen $\mathbf{B}(\omega)$.

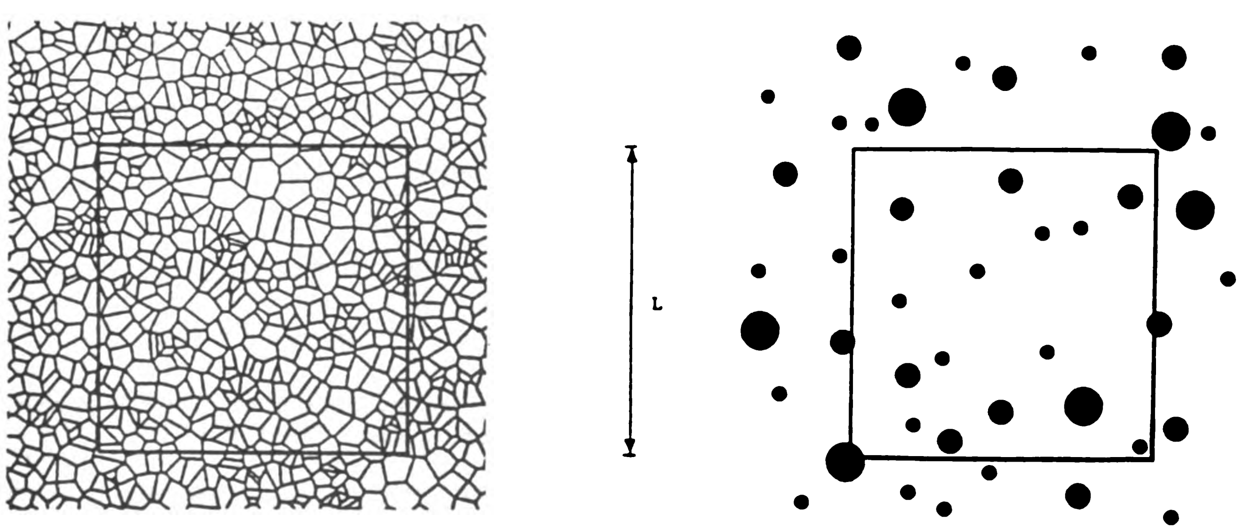

FIG 1.a) A Voronoi tessellation with an average cell size d; b) a matrix-inclusion composite with inclusions of average diameter d; in both cases a window of size L is indicated.

A continuum-type constitutive law is obtained by postulating the existence of an effective homogeneous continuum $B_\delta^{cont}(\omega)$ of the same volume V_δ (i.e. area in 2-D), whose potential energy U, or complementary energy U*, under given uniform boundary conditions equals that of a microstructure $B_\delta(\omega)$ under the same boundary conditions. These are of two basic types:

i) displacement-controlled (*essential*)

$$u(\underset{\sim}{x}) = \varepsilon_{ij}^0 x_j \qquad \text{on} \qquad \partial B_\delta \tag{2.3}$$

where $\underset{\sim}{\varepsilon}^0$ is a given constant tensor and ∂B_δ is the boundary of B_δ,

ii) stress-controlled (*natural*)

$$\underset{\sim}{t} = \sigma_{ij}^0 n_j \qquad \text{on} \qquad \partial B_\delta \tag{2.4}$$

where $\underset{\sim}{\sigma}^0$ is a given constant tensor.

Boundary condition (2.3) results in an effective random stiffness tensor $\underset{\sim}{C}_\delta^e(\omega)$, with the Hooke's law being

$$\bar{\underset{\sim}{\sigma}}(\omega) = \underset{\sim}{C}_\delta^e(\omega)\,\underset{\sim}{\varepsilon}^0 \tag{2.5}$$

which points to a random nature of the resulting stress field; overbar indicates a volume average (i.e. area average in 2-D). It has to be pointed out that the surface traction is random inhomogenous on $\partial B_\delta(\omega)$, with the fluctuations disappearing in the limit $\delta \to \infty$.

On the other hand, (2.4) results in a following random form of Hooke's law, involving a compliance tensor,

$$\bar{\underset{\sim}{\varepsilon}}(\omega) = \underset{\sim}{S}_\delta^n(\omega)\,\underset{\sim}{\sigma}^0 \tag{2.6}$$

which points to a random nature of the resulting strain field, and the presence of random fluctuations in the dispalcement u_i on the window boundary. Hereafter, superscripts ^{e} and ^{n} stand for essential and natural conditions, respectively. Also, we shall use the same type of notation for conductivity and out-of-plane elasticity, whereby $\underset{\sim}{\varepsilon}$ and $\underset{\sim}{\sigma}$ are vectors, C_{ij} is conductivity, and S_{ij} is resistivity.

Following (Ostoja-Starzewski, 1992a, 1993a, b) we list here these principal observations:

1. Due to the heterogeneity of the microstructure $B_\delta(\omega)$, the inverse

$$\underset{\sim}{C}_\delta^n(\omega) = \left[\underset{\sim}{S}_\delta^n(\omega)\right]^{-1} \tag{2.7}$$

is for any finite δ, in general, different from $\underset{\sim}{C}_\delta^e$ obtained under essential conditions.

2. $\underset{\sim}{C}_\delta^e(\omega)$ and $\underset{\sim}{C}_\delta^n(\omega)$ satisfy an inequality

$$\underset{\sim}{C}_\delta^n(\omega) \le \underset{\sim}{C}_\delta^e(\omega) \tag{2.8}$$

Hereinafter, for two fourth-rank tensors $\underset{\sim}{A}$ and $\underset{\sim}{B}$, an order relation $\underset{\sim}{B} \le \underset{\sim}{A}$ means

$$t_{ij} B_{ijkl} t_{kl} \le t_{ij} A \quad [illegible] \quad \neq 0 \tag{2.9}$$

3. In view of the spa[illegible] f microstructure's statistics, $\underset{\sim}{C}_\delta^n(\omega)$ and [illegible] as δ tends to infinity; this defines a deterministic continuum $\mathbf{B}_{det}$ for a single specimen $\mathbf{B}(\omega)$

$$\underset{\sim}{C}^{det}(\omega) = \underset{\sim}{C}_\infty^n(\omega) = \underset{\sim}{C}_\infty^e(\omega) \tag{2.10}$$

whereby the window of infinite extent plays the role of an RVE of deterministic elasticity theory; in other words, it is at $\delta \to \infty$ that the invertibility of the constitutive law is obtained.

4. Ergodicity of the microstructure implies that

$$\underset{\sim}{C}^{det}(\omega) = \underset{\sim}{C}^{eff} \qquad \forall \omega \in \Omega \tag{2.11}$$

where $\underset{\sim}{C}^{eff}$ is the effective response tensor (independent of ω) of a homogeneous medium.

5. At any finite δ both response tensors are, in general, anisotropic, with the nature of anisotropy dependent on any specific $B_\delta(\omega)$. This indicates that the model (1.3) is invalid. On the other hand, (2.8) is isotropic due to the spatial homogeneity and isotropy of the underlying Poisson point process and the spatial homogeneity of $P(\underset{\sim}{C})$.

6. Since the window may be placed arbitrarily in the domain of $\mathbf{B}(\omega)$, the essential and natural boundary conditions define two different inhomogeneous tensor fields at the scale δ with continuous realizations, which lead to two *random meso-continuum approximations*: $\boldsymbol{B}_\delta^e = \{\mathbf{B}_\delta^e(\omega)\,;\ \omega \in \Omega\}$ and $\boldsymbol{B}_\delta^n = \{\mathbf{B}_\delta^n(\omega)\,;\ \omega \in \Omega\}$, respectively. Accordingly, a window of size δ may be considered as an RVE of these two random continuum models; this calls into question the unique response law (1.1-2).

7. Our definition of two inhomogeneous tensor fields is conceptually similar - but not the same (!) - to the procedure of *local averaging* in the theory of random fields applied to a single realization $\underset{\sim}{C}(\omega)$; $\omega \in \Omega$ (Vanmarcke, 1983); it becomes the same in case of a 1-D model only when applied to compliance. In two and three dimensions computational mechanics methods have to be implemented - in a Monte Carlo sense - to find the energies and, hence, the effective moduli of finite windows and their probability distributions $P(\underset{\sim}{C}_\delta^e)$ and $P(\underset{\sim}{C}_\delta^n)$. Similarly, the autocorrelation (autocovariance) functions may be determined (see also Ostoja-Starzewski and Wang, 1989 and 1990).

8. Principles of minimum potential and complementary energies can be used to obtain a hierarchy of scale-dependent bounds on the effective stiffness tensor $\underset{\sim}{C}^{eff}$ (see also Huet, 1990)

$$\begin{gathered}(\underset{\sim}{S}^R)^{-1} \equiv \langle \underset{\sim}{S}_1^n \rangle^{-1} \le \langle \underset{\sim}{S}_{\delta'}^n \rangle^{-1} \le \langle \underset{\sim}{S}_\delta^n \rangle^{-1} \le \underset{\sim}{C}^{eff} \le \\ \langle \underset{\sim}{C}_\delta^e \rangle \le \langle \underset{\sim}{C}_{\delta'}^e \rangle \le \langle \underset{\sim}{C}_1^e \rangle \equiv \underset{\sim}{C}^V \qquad \forall \delta' < \delta\end{gathered} \tag{2.12}$$

This is equivalent, by inversion, to a hierarchy of bounds on the effective compliance $\underset{\sim}{S}^{eff} = (\underset{\sim}{C}^{eff})^{-1}$

$$\begin{gathered}\underset{\sim}{S}^R \equiv \langle \underset{\sim}{S}_1^n \rangle \ge \langle \underset{\sim}{S}_{\delta'}^n \rangle \ge \langle \underset{\sim}{S}_\delta^n \rangle \ge \underset{\sim}{S}^{eff} \ge \\ \langle \underset{\sim}{C}_\delta^e \rangle^{-1} \ge \langle \underset{\sim}{C}_{\delta'}^e \rangle^{-1} \ge \langle \underset{\sim}{C}_1^e \rangle^{-1} \equiv (\underset{\sim}{C}^V)^{-1} \qquad \forall \delta' < \delta\end{gathered} \tag{2.13}$$

9. Since two different random anisotropic continua result, a

given boundary value problem must then be solved to find the upper and lower bounds on response according as random fields $\underset{\sim}{C}_\delta^e$ and $\underset{\sim}{C}_\delta^n$ are employed, see Sections 2.3 and 2.4.

2.3 Variational approach to stochastic finite elements

2.3.1 The displacement method

We start from the principle of minimum potential energy for each $\mathbf{B}(\omega)$ of $\boldsymbol{B}$

$$\delta \Pi(\omega) = \delta (U(\omega) - W) = 0 \tag{2.14}$$

where $U(\omega)$ is the (random) strain energy and W is the work done by body forces $\underset{\sim}{f}$ and surface tractions $\underset{\sim}{t}$. More explicitly,

$$\delta \Pi(\omega) = \int_V \underset{\sim}{\sigma}(\omega)\,\delta\underset{\sim}{\varepsilon}\,dV - \int_V \underset{\sim}{f}\,\delta\underset{\sim}{u}\,dV - \int_{S_t} \underset{\sim}{t}\,\delta\underset{\sim}{u}\,dS = 0 \tag{2.15}$$

where S_t is the part of the body on which tractions are prescribed. Now, with respect to Fig. 2 showing a typical $\mathbf{B}(\omega)$, we introduce a triangulation of the body domain $\mathbf{B}$ of $\mathbf{B}(\omega)$, a closed set, into a finite number of (closed) triangles K_i (i = 1, 2, ... , N) such that

$$\mathbf{B} = \bigcup_{i=1}^{N} K_i \tag{2.16}$$

whereby (2.15) is replaced, approximately, by

$$\delta \Pi(\omega) =$$

$$= \sum_{i=1}^{N} \int_{V_i} \underset{\sim}{\sigma}(\omega)\,\delta\underset{\sim}{\varepsilon}\,dV - \sum_{i=1}^{N} \int_{V_i} \underset{\sim}{f}\,\delta\underset{\sim}{u}\,dV - \sum_{i=1}^{N} \int_{{}^iS_t} \underset{\sim}{t}\,\delta\underset{\sim}{u}\,dS = 0 \tag{2.17}$$

It is noted here, in this displacement method, that the kinematic constraints are imposed on each triangle so that the first term in (2.17) becomes

$$\sum_{i=1}^{N} \int_{V_i} \underset{\sim}{\varepsilon}\,{}^i\underset{\sim}{C}^e(\omega)\,\delta\underset{\sim}{\varepsilon}\,dV \tag{2.18}$$

where ${}^i\underset{\sim}{C}^e(\omega)$ should be the tensor $\underset{\sim}{C}_\delta^e$ determined according to Section 2.2 for the i-th particular triangular finite element. In other words, this finite element specifies a window over which the essential boundary conditions are prescribed, while δ may be chosen to be the base of an isosceles right triangle; of course some other definiton of δ may be adopted here, such as, for example, δ being an equivalent diameter of a circle of the same area as the given triangle.

An important issue concerns the choice of interpolation functions: linear ones

$$u_e(x_1, x_2) = a + bx_1 + cx_2 \tag{2.19}$$

are fully consistent with the uniform strain implied by (2.3). Observing that the uniform strain (as well as uniform stress) is *the* strain used in micromechanics to define a passage to effective constitutive law, we see an inconsistency in using micromechanical inputs for finite element methods using higher order interpolation functions. Thus, a 2-nd, and higher, order triangular elements as well as all quadrilateral elements would not be consistent with (2.3).

Returning to (2.17) and (2.18) we find

$$[K(\omega)]\{U\} = \{F\} \tag{2.20}$$

which provides the basis for a Monte Carlo solution of the finite element problem, as well as for solution in terms of moments; see Section 2.3.3 for a discussion of the ensemble average solution. The global stiffness matrix in (2.20) is synthesized from the stiffness matrices of all the elements

$$[K(\omega)] = \sum_{i=1}^{N} [{}^iK(\omega)] \tag{2.21}$$

where each $[{}^iK(\omega)]$ is obtained as follows

$$\begin{aligned}[{}^iK(\omega)] &= \int_{{}^iV} [{}^iB]^T [{}^iC(\omega)] [{}^iB]\,dV = \\ &= [{}^iB]^T [{}^iC] [{}^iB]\,{}^iV\end{aligned} \tag{2.22}$$

In the above $[{}^iC(\omega)]$ is the matrix of material moduli, given by ${}^i\underset{\sim}{C}^e(\omega)$, while $[{}^iB]$ is the gradient matrix.

2.3.2 The force method

We start from the principle of minimum complementary energy

$$\delta \Pi^*(\omega) = \int_V \delta\underset{\sim}{\sigma}\underset{\sim}{\varepsilon}(\omega)\,dV - \int_{S_u} \delta\underset{\sim}{t}\underset{\sim}{u}\,dS = 0 \tag{2.23}$$

for each $\mathbf{B}(\omega)$ of $\boldsymbol{B}$, and S_u is the part of the body on which displacements are prescribed. By employing the triangulation (2.16), we obtain (again approximately)

$$\delta \Pi^*(\omega) = \sum_{i=1}^{N} \int_{{}^iV} \delta\underset{\sim}{\sigma}\underset{\sim}{\varepsilon}(\omega)\,dV - \sum_{i=1}^{N} \int_{{}^iS_u} \delta\underset{\sim}{t}\underset{\sim}{u}\,dS = 0 \tag{2.24}$$

Since now force constraints are imposed on each triangle, the first term in (2.24) becomes

$$\sum_{i=1}^{N} \int_{{}^iV} \delta\underset{\sim}{\sigma}\,{}^i\underset{\sim}{S}^n(\omega)\,\underset{\sim}{\sigma}\,dV \tag{2.25}$$

where ${}^i\underset{\sim}{S}^n(\omega)$ should be the tensor $\underset{\sim}{S}_\delta^n(\omega)$ determined according to Section 2.2 for the i-th particular finite element. Also here the system (2.24) may now be expressed in a form.

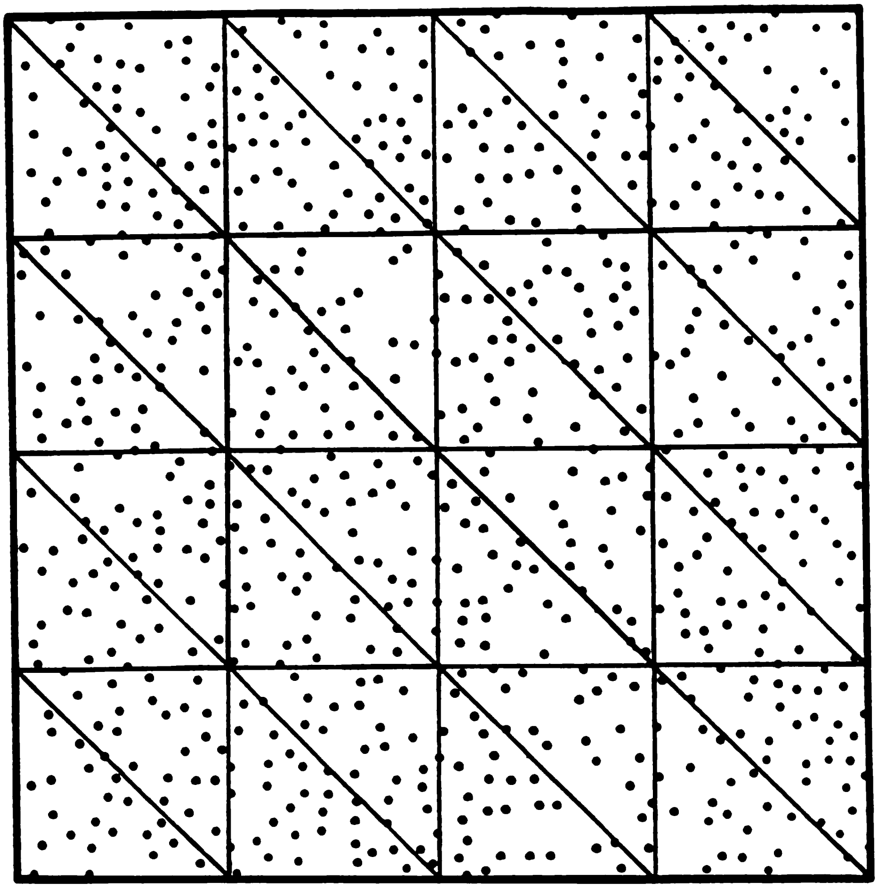

FIG 2. Showing a membrane of a matrix-inclusion composite with a finite element mesh of resolution δ.

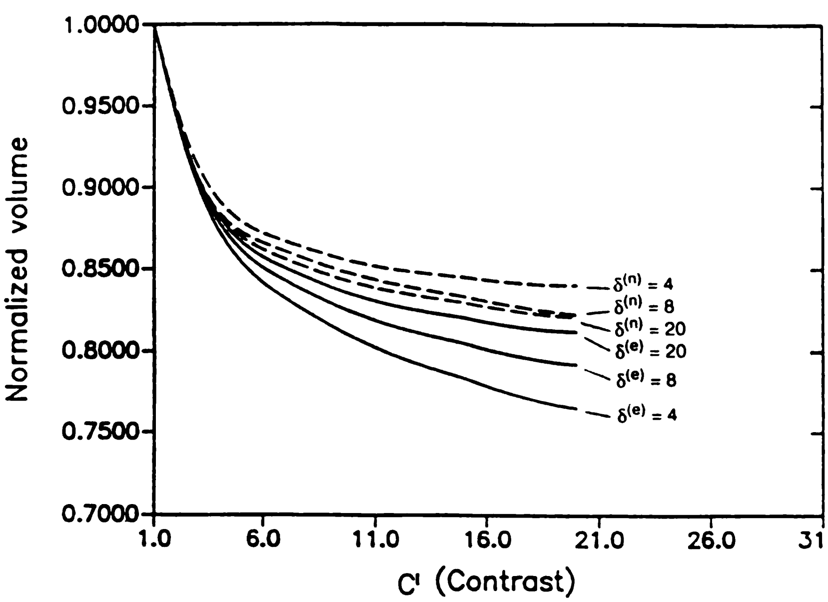

FIG 3. Graph of the ensemble average "upper" and "lower" responses, normalized over the deterministic case $C^i = C^m = 1$. $\delta^{(e)}$ and $\delta^{(n)}$ correspond to $\underline{C}^e_\delta$ and $\underline{C}^n_\delta$ in equation (2.29), respectively.

2.3.3 Ensemble average formulations

It follows from the Section 2.2 that (2.17) would provide a "stiffer" statistical solution $\{\underset{\sim}{u}^e(\omega);\omega\in\Omega\}$, while (2.24) a "softer" one $\{\underset{\sim}{u}^n(\omega);\omega\in\Omega\}$; ^{e} and ^{n} superscripts have the same meaning as defined earlier. The actual solution $\underset{\sim}{u}^{act}(\omega)$ lies between these two. However, the force method in finite element analyses has some well known drawbacks. Thus, a question arises whether a lower bound on $\underset{\sim}{u}^{act}(\omega)$ can be obtained by employing the displacement approach solely?

To this end, we carry out ensemble averaging of (2.6) to obtain

$$\langle\underset{\sim}{\varepsilon}\rangle = \langle\underset{\sim}{S}^n_\delta\rangle\underset{\sim}{\sigma}^0 \tag{2.26}$$

which results in a uniform strain field and linear displacements on the boundary of each i-th finite element. Since the surface tractions are now linear on the element boundary and there is no randomness present, this can now be used in a deterministic displacement formulation

$$\delta\langle\Pi\rangle = \sum_{i=1}^{N}\int_{V_e}\underset{\sim}{\sigma}\delta\underset{\sim}{\varepsilon}dV - \sum_{i=1}^{N}\int_{V_i}\underset{\sim}{f}\delta\underset{\sim}{u}dV - \sum_{i=1}^{N}\int_{S_t}\underset{\sim}{t}\delta\underset{\sim}{u}dS = 0 \tag{2.27}$$

providing we replace $\underset{\sim}{\sigma}$ by $\underset{\sim}{\sigma}^0 = \langle\underset{\sim}{S}^n_\delta\rangle^{-1}\langle\underset{\sim}{\varepsilon}\rangle$ and $\underset{\sim}{\varepsilon}$ by $\langle\underset{\sim}{\varepsilon}\rangle$. Of course the upper bound on $\underset{\sim}{u}^{act}(\omega)$ is obtained by either averaging $\{\underset{\sim}{u}^e(\omega);\omega\in\Omega\}$, or, more simply employing (2.22) above with an ensemble averaged form of (2.5)

$$\langle\underset{\sim}{\sigma}\rangle = \langle\underset{\sim}{C}^e_\delta\rangle\underset{\sim}{\varepsilon}^0 \tag{2.28}$$

Dually, one can set up a pair of lower/upper bound solutions by using the averaged version of the complementary energy principle of Section 2.3.2, but, in view of our observation at the top of this Section, this would seem to be of less interest.

2.4 Example results

An approximate solution method in an SFE problem has recently been implemented by Alzebdeh and Ostoja-Starzewski (1993). With respect to Fig. 2, which shows a typical realization B(ω) of $\boldsymbol{B}$, the problem was formulated and run as follows:

i) Out-of plane displacements $u(x_1, x_2)$ of a matrix-inclusion composite defined in Section 2.1 were studied. These were governed by a Poisson equation with Dirichlet boundary conditions

$$\frac{\partial}{\partial x_i}\left(C_{ij}(\underset{\sim}{x},\omega)\frac{\partial u}{\partial x_j}\right) = f \qquad u(\underset{\sim}{x}) = 0, \underset{\sim}{x}\in\partial\mathbf{B} \tag{2.29}$$

where f is constant throughout **B**, and C_{ij} are components and realizations of two conductivity random tensor fields (of second rank) of continuum approximations $\boldsymbol{B}^e_\delta$ or $\boldsymbol{B}^n_\delta$, where δ corresponds to the mesh size.

ii) Generation, in a Monte Carlo sense, of a realization **B**(ω) and calculation of the effective moduli $\underset{\sim}{C}^e_\delta$ and $\underset{\sim}{C}^n_\delta$ for each square-shaped window (recall Fig.1 b).

iii) Using of thus obtained ${}^i\underset{\sim}{C}^e(\omega)$ of any given square as ${}^i\underset{\sim}{C}^e(\omega)$ for the two (isosceles right) triangular-shaped windows making up the square-shaped one, and calculating the stiffer response using a triangular mesh.

iv) Using of ${}^i\underset{\sim}{C}^n(\omega)$ obtained in point ii) as ${}^i\underset{\sim}{C}^n(\omega)$ for the two triangular-shaped windows making up the square-shaped one, and calculating the softer response using a triangular mesh.

v) Repeating ii) - iv) a number of (say, twenty or fifty) times.

Fig. 3 gives results of the above solution method for three mesh sizes - δ = 4, 8, 20. Specifically, this figure shows the ensemble average volumes contained under the membrane - $V^{(e)}(\omega)$ and $V^{(n)}(\omega)$ versus increasing contrast, i.e. ratio of inclusion stiffness C^i to matrix stiffness C^m. In order to nondimensionalize the problem, we took $C^m = 1$. We see that, for a fixed δ, both curves are decreasing monotonically and diverging away from the homogenous medium case $C^i = C^m = 1$, with increasing C^i. In addition, for a fixed contrast, we see that the two responses (bounds) get closer with increasing δ, and have a tendency to converge to a unique value as $\delta\to\infty$, which corresponds to the deterministic case, recall (2.8). This limit, however, can only be thought of in an approximate sense (a finite element is *finite* !). In fact, in situations where a resolution of local stresses is desired, we would use rather small elements - i.e. small δ - and obtain two quite different bounds on the response, accompanied by significant fluctuations. Further discussion and results on the strength of fluctuations in $V^{(e)}(\omega)$ and $V^{(n)}(\omega)$ are given in (Alzebdeh and Ostoja-Starzewski, 1993).

3. PLASTIC MEDIA PROBLEMS

3.1 Random medium model

The basic concepts introduced in Section 2.1 - i.e. those of a random medium $\boldsymbol{B}$ of domain D defined on Ω and the x_1, x_2-plane, a window of scale δ, and a random continuum approximation $\boldsymbol{B}_\delta$ - may be applied to materials having a different constitutive response than the elastic one. Specifically, in view of the availability of an effective solution method for rigid-plastic materials - that is, the method of slip-lines - we focus on materials describable by the yield function

$$(\sigma_{11}-\sigma_{22})^2 + 4\sigma_{12}^2 = 4k_\delta^2 \tag{3.1}$$

in which k_δ is a random field, parametrized by x and y, that describes effective plastic limit of the microstructure according to the chosen resolution δ. A micromechanical basis for determination of k_δ is discussed in Section 3.2 below. At this stage we assume that the statistics of k_δ and, in particular, its average $\langle k_\delta\rangle$ and the autocorrelation distance r_c are known.

It is interesting to observe that (3.1) may be viewed as a special kind of a yield condition obtained from that of a partially cohesive granular-type medium (Sokolovskii, 1965)

$$(\sigma_{11}-\sigma_{22})^2+4\sigma_{12}^2 = (\sin\rho_\delta)^2(\sigma_{11}+\sigma_{22}+2H_\delta)^2 \tag{3.2}$$

where H_δ is the strength in uniform tension, while ρ_δ is the angle of internal friction; also here we have made the two constitutive coefficients scale-dependent. It is apparent that (3.1) may be obtained from (3.2) in the limit of H_δ going to infinity and ρ_δ going to zero. However, in the following we shall review our recent results for media governed by (3.1); plasticity of materials governed by (3.2) is studied elsewhere (Ostoja-Starzewski, 1993c).

In accordance with the foregoing developments, by $\boldsymbol{B}_\delta = \{\mathbf{B}_\delta(\omega);\ \omega \in \Omega\ \} = \{\mathbf{B}(k_\delta(\omega));\ \omega \in \Omega\ \}$ we denote a continuous random (plastic) medium specified by a scale δ with

$$k_\delta(\underline{x},\underline{\omega}) = \langle k_\delta\rangle + k_\delta'(\underline{x},\omega) \qquad \langle k'_\delta(\underline{x},\omega)\rangle = 0 \tag{3.3}$$

where k_δ' is the zero-mean noise in k_δ. In the following we assume:

- scale $\delta > r_c$, so that $k_\delta(\underline{x},\omega)$ may be treated as a white-noise random field on that scale;
- $k_\delta(\underline{x},\omega)$ is space-homogeneous, ergodic, and has a high signal-to-noise ratio

$$|k_\delta'| \ll \langle k_\delta\rangle \tag{3.4}$$

3.2 Slip-lines and stochastic finite differences

The field equations of any realization $\mathbf{B}_\delta(\omega)$ are

$$\frac{\partial\sigma_{11}}{\partial x_1}+\frac{\partial\sigma_{12}}{\partial x_2} = 0 \qquad \frac{\partial\sigma_{22}}{\partial x_2}+\frac{\partial\sigma_{12}}{\partial x_1} = 0$$
$$(\sigma_{11}-\sigma_{22})^2+4\sigma_{12}^2 = 4k_\delta^2 \tag{3.5}$$

In the above k_δ, and hence, σ_{11}, σ_{22}, σ_{12} are parametrized by ω, but for clarity of presentation we do not show this explicitly. As is usual in the theory of slip-lines (see e.g. Kachanov, 1971; Szczepinski, 1979), two functions p and φ are now introduced

$$\sigma_{11} = p+k_\delta\cos(2\varphi) \qquad \sigma_{22} = p-k_\delta\cos(2\varphi)$$
$$\sigma_{12} = k_\delta\sin(2\varphi) \tag{3.6}$$

Upon substitution of (3.6) into (3.5), and setting $\varphi = -\pi/4$ on differentiation, we get

$$\frac{\partial p}{\partial x_1}+2k_\delta\frac{\partial\varphi}{\partial x_1} = \frac{\partial k_\delta}{\partial x_2} \qquad \frac{\partial p}{\partial x_2}-2k_\delta\frac{\partial\varphi}{\partial x_2} = \frac{\partial k_\delta}{\partial x_1} \tag{3.7}$$

where the rectangular axes are now along the local slip-line directions. The above will be independent of the orientation of the axes if $\frac{\partial}{\partial x_1}$ and $\frac{\partial}{\partial x_2}$ are replaced by the tangential derivatives $\frac{\partial}{\partial s_\alpha}$ and $\frac{\partial}{\partial s_\beta}$ along the α and β characteristics, respectively. Hence,

$$dp+2k_\delta d\varphi = \frac{\partial k_\delta}{\partial s_\beta}ds_\alpha \qquad dp-2k_\delta d\varphi = \frac{\partial k_\delta}{\partial s_\alpha}ds_\beta \tag{3.8}$$

These relations represent a system of two quasi-linear hyperbolic equations driven by the random terms involving k_δ. The corresponding characteristic directions are specified by

$$\frac{dx_2}{dx_1} = \tan(\varphi+\pi/4) \qquad \frac{dx_2}{dx_1} = \tan(\varphi-\pi/4) \tag{3.9}$$

Equations (3.8) and (3.9) form the basis for a determination of the Hencky-Prandtl network of slip-lines in a given boundary value problem. In cases of Cauchy and characterisitc problems studied below this relies on the method of finite-differences for finding x, y, p, and φ at a new point N given the data $\{x_i, y_i, p_i, \varphi_i\}$ at the two preceding points i = 1, 2. As discussed by Ostoja-Starzewski (1992b), due to the randomness in k_1, k_2 and k_N, as well as the possible randomness in the initial data p_1, φ_1, p_2, and φ_2, two characteristics of the deterministic problem are replaced here by two wedges (cones) of forward dependence, which contain all the characteristics of the stochastic problem emanating from points 1 and 2. Additionally, there is randomness in p_N and φ_N at the new point N which definitely amplifies the uncertainty in the further evolution. The forward evolution from points 1 and 2 to N displays a Markov property ($x \equiv x_1$ and $y \equiv x_2$ here)

$$P\{[x,y,p,\varphi]_N | [x,y,p,\varphi]_{D^-}\} = P\{[x,y,p,\varphi]_N | [x,y,p,\varphi]_{(1,2)}\} \tag{3.10}$$

where D^- is the domain of backward dependence including points 1 and 2, see Fig. 4 a). In the finite difference discretization of the governing equations D^- consists of a system of points. The Markov property (3.10) may, in principle, be used to either solve the problem analytically by calculating the transition probability as the conditional probability specified by the right hand side above with the help of formulas (3.11-13) below. At the same time, the Markov property (3.10) also suggests two finite-difference methods of determination of the network of slip-lines: *an exact method* and a *mean field method.* The first one is based on an observation that any point of the intersection of two cones of forward dependence becomes the initial point of further evolution, and, hence, the probability distribution of $\{x_i, y_i, p_i, \varphi_i;\ i=1, 2\}$ leads to a probability distribution of $\{x_N, y_N, p_N, \varphi_N\}$, which, in turn, serves as input for calculation of the next point. On the other hand, the mean field method replaces the domain of intersection of both forward dependence cones by an average point $\langle N \rangle$, and uses it as input for further calculations. Henceforth we focus on the exact method.

Formulas of the exact method in the set-up of forward differencing follow from (3.9) as

$$
\begin{aligned}
x_N &= \frac{y_2 - y_1 + x_1 \tan\left(\varphi_1 + \frac{\pi}{4}\right) - x_2 \tan\left(\varphi_2 - \frac{\pi}{4}\right)}{\tan\left(\varphi_1 + \frac{\pi}{4}\right) - \tan\left(\varphi_2 - \frac{\pi}{4}\right)} \\
y_N &= \frac{x_2 - x_1 + y_1 \cot\left(\varphi_1 + \frac{\pi}{4}\right) - y_2 \cot\left(\varphi_2 + \frac{\pi}{4}\right)}{\cot\left(\varphi_1 + \frac{\pi}{4}\right) - \cot\left(\varphi_2 - \frac{\pi}{4}\right)}
\end{aligned}
\tag{3.11}
$$

and from (3.8) as

$$
\begin{aligned}
p_N &= p_1 - (k_N + k_1)(\varphi_N - \varphi_1) + \frac{\partial}{\partial s_\beta} ds_\alpha \\
\varphi_N &= [p_1 - p_2 + \varphi_1 (k_1 + k_N) + \varphi_2 (k_2 + k_N)] \\
&\quad \left. \frac{\partial k}{\partial s_\beta} ds_\alpha - \frac{\partial k}{\partial s_\alpha} ds_\beta \right] (k_1 + k_2 + 2k_N)^{-1}
\end{aligned}
\tag{3.12}
$$

where

$$
\begin{aligned}
ds_\alpha &= [(x_N - x_1)^2 + (y_N - y_1)^2]^{1/2} \\
ds_\beta &= [(x_N - x_2)^2 + (y_N - y_2)^2]^{1/2}
\end{aligned}
\tag{3.13}
$$

and the derivatives of k with respect to s_α and s_β are treated in the finite-difference sense.

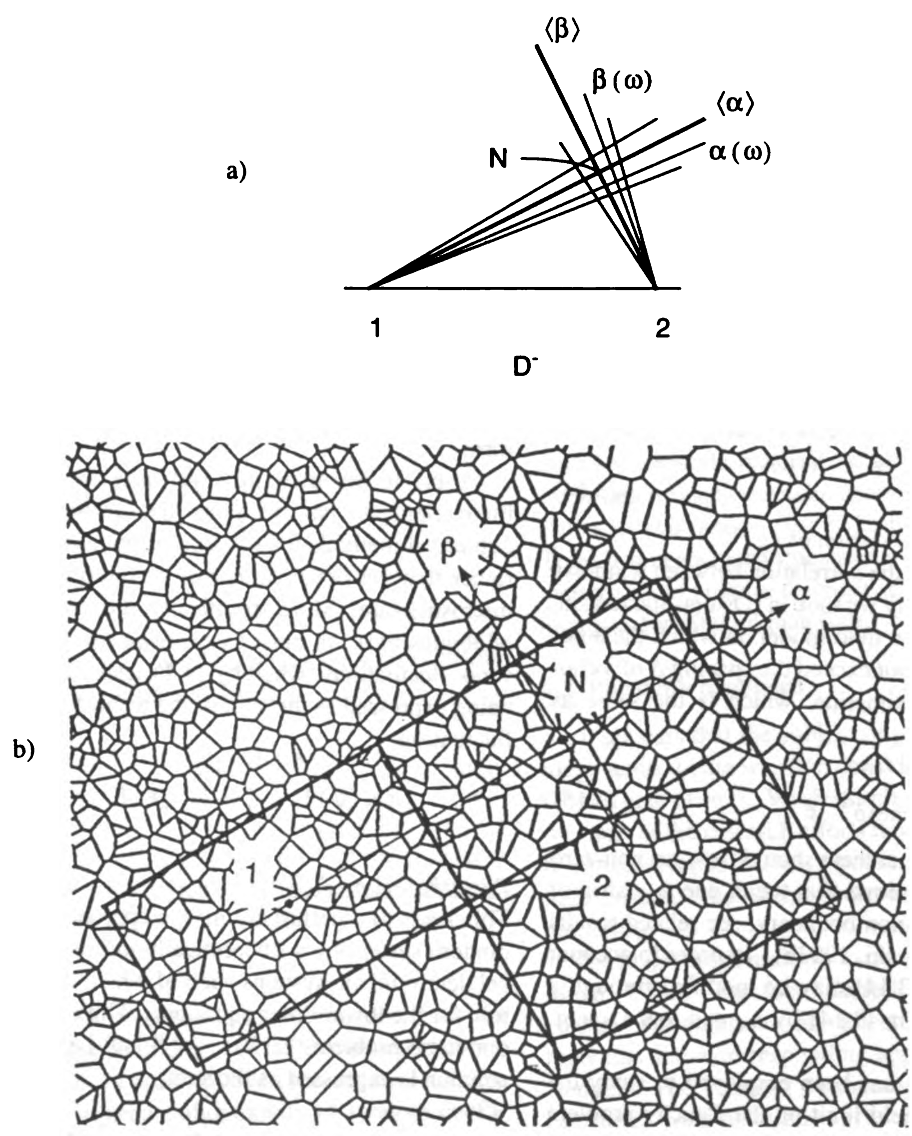

FIG 4. a) Scatter in the characteristics emanating from points 1 and 2; b) windows involved in finding the local average random field k_δ at 1, 2 and N from the microstructure.

Since the coefficients k_1, k_2 and k_N in the above are all random, the finite difference statement (3.11)-(3.12) of the field equations brings us back to the issue of choice of a random field k_δ. With reference to Fig. 4 b) we consider the random microstructure *B* to be represented by a Voronoi-type mosaic of grains, recall Fig. 1 a). Two characteristics α and β of the continuum approximation (at $\delta \cong 10$ here) are indicated as passing through points 1 and 2, respectively, and crossing at the new point N. Three rectangular shaped windows $B_1(\omega)$, $B_2(\omega)$ and $B_N(\omega)$ centered at these three particular points represent three domains of the microstructure $\mathbf{B}(\omega)$, whose effective plasticities are described by k_1, k_2 and k_N, respectively. Clearly, due to the finite crystal size, these three quantities cannot be taken as independent random variables, but should reflect the "local smearing out" in each window accounting for the correlation at their boundaries. Effective plasticity of a given window is a function of plasticities of all the crystals belonging to that window, and hence, in view of the results for elastic materials in Section 2.2, should generally be anisotropic. However, due to lack of such a model at present, we adopt here the very simple model of a moving average random field (Vanmarcke, 1983). Thus, at every location $\underset{\sim}{x}$ the value k_δ is an average of plasticities of all the crystals in the window centered at $\underset{\sim}{x}$. In other words, since all these crystals have random orientations and strengths, the average of their plasticities over a rectangular area with sides of length L_1 and L_2, respectively, is a new random field k_δ with a covariance function

$$C_{k_\delta}(\xi, \eta) = \begin{cases} \sigma_{k_\delta}^2 \left(1 - \frac{|\xi|}{L_1}\right)\left(1 - \frac{|\eta|}{L_2}\right) & |\xi| \le L_1 \\ & |\eta| \le L_2 \\ 0 & \text{elsewhere} \end{cases} \tag{3.14}$$

where σ_{k_δ} is the standard deviation of k_δ.

It is seen from (3.14) that the correlation between windows that touch is zero. This is why we took in (Ostoja-Starzewski, 1992b) a white-noise random field model, in which the autocorrelation distance r_c does not exceed the spacing Δ of a chosen finite difference approximation, which is the same as δ_{meso}

$$\Delta = \delta_{meso} \ge r_c \tag{3.15}$$

It can be argued, however, that there should be some non-zero correlation between the windows that touch due to a strip of crystals straddling the common boundary; see related results in elasticity (Ostoja-Starzewski, 1993b). In order to account for this effect, the model (3.14) may be modified through a replacement of L_1 and L_2 in (3.14) by $L_1 + d$ and $L_2 + d$, respectively.

The above formulation has been employed to study the effects of randomness in yield limit on the Cauchy problem and characteristic boundary value problems(Ostoja-Starzewski, 1992c), as well as on the load carrying capability of a pipe under internal pressure (Ostoja-Starzewski and Setyabudhy, 1992). It has been found that the averages of stochastic solutions tend to differ from the solution of a corresponding boundary value problem for a homogeneous deterministic medium when randomness in k_δ increases and is combined with the increasing inhomogeneity in boundary conditions.

4. COMPARISONS WITH OTHER THEORIES

4.1 Elasticity problems

4.1.1. A review of classical SFE methods

The need for development of finite element methods taking into account the uncertainty in structural material parameters has been recognized since the late seventies. As a result of the observation that many engineering structures are described by spatially random material properties, several theoretical methodologies were developed in the civil engineering literature. To the best of this author's knowledge all these studies in stochastic finite elements were and are being based on a simple generalization of the Hooke's law to an inhomogeneous locally isotropic continuum

$$\varepsilon_{ij} = \frac{1}{E(\underset{\sim}{x}, \omega)} [(1 + \nu(\underset{\sim}{x}, \omega))\sigma_{ij} - \nu(\underset{\sim}{x}, \omega)\delta_{ij}\sigma_{kk}] \tag{4.1}$$

where two elastic coeffiicients $E(\underset{\sim}{x}, \omega)$ and $\nu(\underset{\sim}{x}, \omega)$ are random fields. In fact, typically, the Young's modulus only has been adopted as random. In view of the micromechanical analysis of Section 2.2 it becomes evident that (4.1) is in error, since i) a unique random field of stiffness/compliance cannot be determined from the microstructure, ii) a random continuum approximation is, in general, of a locally anisotropic form.

It has to be noted, however, that the effort in stochastic finite elements has been on the development of efficient numerical methods for solution of boundary value problems, rather than on development of a connection to the material microstructure. More specifically, these classical SFE methodologies have, in most cases, been restricted to the case of weak fluctuations, whereby (4.1) leads to a stiffness matrix being expressed as the sum of the mean and the weak random fluctuation

$$[K(\omega)] = [\langle K\rangle] + \varepsilon[K'(\omega)] \tag{4.2}$$

Perturbation method

This leads to a perturbation-type approach: replacement of a random system by a (theoretically infinite) number of identical deterministic systems each of which depends on the solutoin for the lower order equations. Thus, to second order, for our static problem (2.120) - $[K(\omega)]\{U\} = \{F\}$ - the solution is expressed as the sum

$$\{U\} \cong \{U_0\} + \varepsilon\{U_1\} + \varepsilon^2\{U_2\} \tag{4.3}$$

where $\varepsilon << 1$

$$\{U_0\} = [\langle K\rangle]^{-1}\{F\}$$
$$\{U_1\} = -[\langle K\rangle]^{-1}[K'(\omega)]\{U_0\} \qquad (4.4)$$
$$\{U_2\} = -[\langle K\rangle]^{-1}[K'(\omega)]\{U_1\}$$

Neumann series method

This method, advanced by Shinozuka & Yamazaki (1988), is based on a Neumann series for the inverse of a random operator $[K(\omega)]$, which takes the following form

$$[K(\omega)] = (I - P(\omega) + P^2(\omega) - P^3(\omega) + \ldots)[\langle K\rangle]^{-1}$$
$$P(\omega) = [\langle K\rangle]^{-1}[K'(\omega)] \qquad (4.5)$$

The method was introduced as an avenue for a speedier way of solving the stochastic problem by a Monte Carlo simulation. To that end also a Cholesky decomposition of $[K(\omega)]$ is implemented.

Weigthed integral method

In contradistinction to the above two methods, this one focuses on the determination of the random stiffness matrix $[K(\omega)]$. The idea, in the setting of an elastic plate problem (Deodatis et al, 1991), is to start with a locally isotropic random field of, say, Young's modulus (recall eq (4.1) and the discussion following it) and assign it to all the finite elements according to

$${}^iE(\underline{x},\omega) = {}^i\langle E\rangle[1 + {}^if(\underline{x},\omega)] \qquad \langle {}^if(\underline{x},\omega)\rangle = 0 \qquad (4.6)$$

Next, all the elements of $[K(\omega)]$ are calculated as

$$[{}^iK(\omega)] = \int_{{}^iV} [{}^iB]^T[{}^iC(\omega)][{}^iB]\,dV = \left[{}^iK_0\right] + {}^iX_0(\omega)\left[\Delta^iK_0\right] \qquad (4.7)$$

where $\left[{}^iK_0\right]$ and $\left[\Delta^iK_0\right]$ are deterministic matrices, while ${}^iX_0(\omega)$ is a random variable given as

$${}^iX_0(\omega) = \int_{{}^iA} {}^if(\underline{x},\omega)\,d^iA \qquad (4.8)$$

From a micromechanics standpoint this approach gives a Voigt-type estimate for the effective stiffness of the i-th finite element; also, compare (4.7-8) with (2.20).

Spectral method

It is well known that in a representation of a random function by a Fourier series, the coefficients of the expansion become, in general, correlated. In order to retain the uncorrelatedness while obtaining the desired orthogonality of random coefficients, a Karhunen-Loéve expansion (see e.g. Yaglom, 1962) is introduced. This idea has been employed by Ghanem & Spanos (1991) to represent the spatial variability of random field of Young's modulus such as in (4.6). However, this method is not limited to weak fluctuations and avoids the inconsistencies between various other methods involved in the inversion of the random stiffness matrix $[K(\omega)]$. Also, it is designed to do away with the problem of dealing with a large number of random variates resulting from a pointwise representation of the random field $[E(\underline{x},\omega)]$.

While this method is elegant - recasting of the original problem in terms of a denumerable set of uncorrelated random variables - it has also suffered from a lack of good input from micromechanics. Additionally, its claim of being able to deal consistently with strong noise in material properties has to be qualified - this is discussed in Section 4.1.2 below.

4.1.2 Conclusions

The foregoing very brief review of the SFE methods leads to two principal conclusions:

i) a necessity of a correct link to micromechanics in setting up of the continuum random fields (Ostoja-Starzewski, 1993a) and of the random stiffness matrix $[K(\omega)]$,

ii) a need for a careful interpretation of the variational principles as a basis for SFE,

Thus, although an assumption such as (4.1) is generally incorrect, it follows that the classical SFE methodologies are amenable to possible modifications to incorporate the micromechanical input of the type described in Section 2.2. More precisely, once a continuum random field specification of a given material is found, an existing approach - such as perturbation, Neumann series, Karhunen-Loéve series - may be applied to determine the upper and lower bounds on response according to the stochastic variational formulation given in Section 2.3.

Presence of a strong noise in material properties requires particular attention. A valuable paradigm in the situation of strong microscale material variability is provided by studies in the deterministic *homogenization theory*, see e.g. (Sanchez-Palencia and Zaoui, 1987; Hollister and Kikuchi, 1992). Thus, it appears that a stochastic extension of homogenization theory should provide the most adequate formulation of finite elements for random materials.

4.2 Plasticity problems

It appears that the subject of plasticity of randomly inhomogeneous media was first considered in the seminal work of Olszak et al (1962). While, similar to the situation in elasticity, most of the research efforts have been on finding the effective macroscopic plastic response (see e.g. Zaoui, 1987), very little attention has been given to random meso-continuum modelling.

The major work we have to mention here is that due to Nordgren (1992). The focus there has been on an original stochastic formulation of lower-bound and upper-bound theorems and a corresponding application to the loading of a wedge. The random continuum model involves a three parameter yield function

$$f = aJ_2 + bI_1 + cI_1^2 - 1 \qquad (4.9)$$

where a, b, and c are strength parameters, and I_1 and J_2 are the (first and second) stress invariants of stress and deviatoric stress. a, b, and c are random fields obtained from an unconfined uniaxial compression test with yield stress q, for which (4.9) gives

$$\frac{1}{3}aq^2 - bq + cq^2 = 1 \tag{4.10}$$

Random nature of the field q is represented by the presence of fluctuations q' about the mean $\bar{q}$, that is

$$q(\underset{\sim}{x}, \omega) = \bar{q} + q'(\underset{\sim}{x}, \omega) \qquad \langle q'(\underset{\sim}{x}, \omega) \rangle = 0 \tag{4.11}$$

The correlation function of the random field q' is taken to be homogeneous and isotropic, and, in particular, of the following form

$$B(r) = B_0/(1 + r^2/h^2) \tag{4.12}$$

In (4.12) B_0 is the variance of fluctuations q', while h specifies their lengthscale.

We note here two differences of this model from ours assumed in Section 3:
i) no dependence on the scale δ versus such dependence implied in (3.3),
ii) the covariance in Nordgren's model goes to 0 only as the distance between two points goes to infinity - compare this with (3.14); this difference is due to taking the process of "local smearing out" as a point of departure in our approach to formulating random continuum models from micromechanics.

Solution of the boundary value problem of a wedge in (Nordgren, 1992) has been based on finding the mean of the minimum energy dissipation on the multiple branches of possible zig-zag velocity paths along the rigid-plastic boundary - an extensive computational procedure. By contrast, we propose solving a given stochastic boundary value problem directly by calculating a large number (one hundred, say) of responses in a Monte Carlo sense. Unless the mesh resolution is more than about fifty points, this is done in a matter of (at the most) a couple of minutes on a workstation or a personal computer and yields, practically, the whole range of possible behaviors - that is, the probability distributions of slip-line fields, stress fields, and velocity fields.

5. CLOSURE

In this paper we have discussed the formulation of finite element methods and differences for materials with random microstructures. The key role in this formulation is played by a window concept which, on one hand, leads to a specification of constitutive laws of a random meso-continuum, while on the other, corresponds to a single finite element or difference cell. It follows that by a relatively straightforward modification a finite element/difference program can be made to incorporate a meso-mechanical input. Such an input may, in principle by provided in three different ways:
i) a direct computational mechanics simulation of the microstructure in each window (cell), repeated n times in a Monte Carlo sense for various realizations;
ii) an assignment of medium's properties according to a random meso-continuum model (Ostoja-Starzewski, 1993b);
iii) an analytical derivation of the stochastic constitutive laws at the meso-scale.

Work is currently underway to include in our approach other constitutive responses - e.g. stochastic continuum damage mechanics (Ostoja-Starzewski, 1989) - and ideally, as mentioned at the end of Section 4.1, to integrate it with a stochastic version of the homogenization theory.

ACKNOWLEDGEMENT

This research was supported by a contract AFOSR-89-0423 and by an NSF grant No. MSS 9202772.

REFERENCES

Alzebdeh K and Ostoja-Starzewski M (1993), "Micromechanically based stochastic finite elements," *Finite Elem. Anal. Design*, in press.

Baecher GB and Ingra TS (1981), "Stochastic FEM in settlement prediction," *J Geotech Engng Div ASCE* **107**(GT4), 449-463.

Benaroya H and Rehak M (1988), "Finite element methods in probabilistic structural analysis: a selective review," *Appl Mech Rev* **41**(5), 201-213.

Contreras H (1980), "The stochastic finite-element method," *Comp & Struct* **12**, 341-348.

Deodatis G, Wall W and Shinozuka M (1991), "Analysis of two-dimensional stochstic systems by the weighted integral method," *Computational stochastic mechanics* (P.D. Spanos and C.A. Brebbia, Eds.), CMP-Elsevier, 395-406.

Ghanem R and Spanos PD (1991), *Stochastic finite elements: a spectral approach*, Springer-Verlag, Berlin.

Hollister SJ and Kikuchi N (1992), "A comparison of homogenization and standard mechanics analyses for periodic porous composites," *Comp Mech* **10**, 73-95.

Huet C (1990), "Application of variational concepts to size effects in elastic heterogeneous bodies," *J Mech Phys Solids* **38**(6), 813-841.

Kachanov LM (1971), *Foundations of the theory of plasticity*, North-Holland, Amsterdam.

Liu WK, Belytschko T and Mani A (1986), "Random field finite elements," *Int J Num Meth Engng* **23**, 1831-1845.

Nordgren RP (1992), "Limit analysis of a stochastically inhomogeneous plastic medium with application to plane contact problems," *ASME J Appl Mech* **59**, 477-484.

Olszak W, Rychlewski J and Urbanowski W (1962), "Plasticity under inhomogeneous conditions," *Adv Appl Mech* **7**, 132-214.

Ostoja-Starzewski M (1989), "Damage in a random microstructure: size effects, fractals, and entropy maximization," *Appl Mech Rev* (Special Issue: *Mechanics Pan-America 1989*), **42**(11, Part 2), S202-S212.

Ostoja-Starzewski M (1992a), "Random fields and processes in mechanics of granular materials," in *Advances in micromechanics of granular materials* (Proc. 2nd US-Japan Seminar on Micro-mechanics of Granular Materials; H. Shen et al, Eds.); *Stud ApplMech* **31**, 71-80, Elsevier; extended version in *Mech Mater* **16**, 55-64 (1993).

Ostoja-Starzewski M (1992b), "Plastic flow of random media: micromechanics, Markov property and slip-lines," *Appl Mech Rev* (Special Issue: Material Instabilities), Vol. **45**(3, Part 2), S75-S82.

Ostoja-Starzewski M (1992c), "Boundary value problems in plastic flow of random media," in *Plastic flow and creep* (H. Zbib, Ed.), AMD-Vol. 135, MD-Vol. 31, 149-158.

Ostoja-Starzewski M (1993a), "Micromechanics as a basis of random elastic continuum approximtions," *Probabilistic Engng Mech* **8**(2), 107-114.

Ostoja-Starzewski M (1993b), "Micromechanics as a basis of continuum random fields," *Appl Mech Rev* (Special Issue: *Micromechanics of Random Media*), to appear.

Ostoja-Starzewski M (1993c), "Stability of a slope of granular medium," unpublished notes.

Ostoja-Starzewski M and Setyabudhy R (1992), "Limit analysis of a cylindrical tube of a random inhomogeneous plastic material under internal pressure," in *Recent advances in structural mechanics* (YW Kwon and HH Chung, Eds.), PVP-Vol. 248 and NE-Vol. 10, 87-92.

Ostoja-Starzewski M and Wang C (1989), "Linear elasticity of planar Delaunay networks: random field characterization of effective moduli," *Acta Mech* **80**, 61-80.

Ostoja-Starzewski M and Wang C (1990), "Linear elasticity of planar Delaunay networks - II: Voigt and Reuss bounds, and modification for centroids," *Acta Mech* **84**, 47-61.

Sanchez-Palencia E and Zaoui A (Eds.) (1987), *Homogenization techniques for composite media*, Lecture Notes in Physics **272**.

Shinozuka M and Yamazaki F (1988), "Stochastic finite element analysis: an introduction," in *Stochastic Structural Dynamics: Progress in Theory and Applications* (ST Ariaratnam, GI Schuëller and I Elishakoff, Eds.), 241-291, Elsevier Applied Sci., London.

Sokolovskii VV (1965), *Statics of granular media*, Pergamon Press, Oxford.

Szczepinski W (1979), *Introduction to the mechanics of plastic forming of metals*, Sijthoff & Noordhoff Int. Publ./PWN, Alphen an der Rijn/Warsaw.

Vanmarcke EH (1983), *Random fields: analysis and synthesis*, MIT Press, Cambridge, MA.

Willis JR (1981), "Variational and related methods for the overall properties of composites," *Adv Appl Mech* **21**, 2-78.

Yaglom AM (1962), *An introduction to the theory of stationary random functions*, Dover, New York.

Zaoui A (1987), Approximate statistical modelling and applications, in *Homogenization techniques for composite media* (Sanchez-Palencia, E. and Zaoui, A., Eds.), Lecture Notes in Physics **272**.

Dynamic post-buckling behavior of thin-walled structures with flexible knife-edge supports

MA Souza

Departamento de Engenharia Civil, Pontificia Universidade Católica do Rio de Janeiro
22453-900 Rio de Janeiro, Brazil

The paper discusses the influence that changes of the simply supported boundary condition during the loading process have on the dynamic post-buckling behavior of elastic thin-walled structures. Of special interest is the knife-edge type of support which is associated to the free-to-rotate boundary condition. The results presented show how changes of the free-to-rotate condition during the loading process can dramatically alter the response of thin-walled structures. This fact is highlighted by the equilibrium paths and the characteristic curves presented. The former relate the applied compressive load and the lateral displacement, whereas, the latter relate the compressive load and the square of the corresponding natural frequency of vibration. The importance of an adquate design of the supports is stressed in view of the observed dramatic changes. The work is done in the scope of the elastic stability and damping is not included in the analysis.

INTRODUCTION

The adequate design of the support is undoubtedly a major factor of success of any experimental program. The comparison between the results theoretically predicted and those obtained in the experiment is only valid and meaningful if the actual support conditions in the laboratory and those used in the theoretical analysis are exactly the same. Different support conditions lead to different response and, therefore, theory and experiment will disagree due to the sole factor that the theoretical and the experimental analysis were carried out for different support conditions, despite the fact that all the geometric and elastic parameters might be exactly the same.

An example of carefully designed support conditions can be found in the work of Albert et al. (1992) where several situations were analyzed and reported in detail. The experimental results presented in their paper highlight the importance of correctly considering the actual support conditions in the theoretical prediction of the results.

Theoretically the simply supported boundary condition is the simplest and for this reason frequently used in analytical solutions to illustrate how a particular theory works. In practice, though, it represents the most difficult support condition to be achieved in the laboratory, the main reason for this being the free-to-rotate requirement. For cylindrical shells, for instance, the free-to-rotate boundary condition means, in practice, a knife-edge type of support. For thin-walled cylindrical shells under axial compression it is not difficult to imagine that such a boundary condition cannot last long, since as the axial load is applied the knife-edge end will behave like a spring. The contact zone between the end of the shell and the supporting plate or disk, originally a circumferential line soon becomes a contact area due to the axial load and, therefore, the free-to-rotate condition is violated. The support condition is no longer the initially free-to-rotate one and, therefore, any comparison between theoretical and experimental results is meaningless, unless such changes of the support boundary conditions are previously incorporated in the theoretical analysis. The type of support condition described above is illustrated in Figs 1a-b where a schematic knife-edge condition corresponding to a cylindrical shell is shown, Fig. 1a, together with the detail of the end of the shell wall where the knife-edge is located. The detail presented refers to the loaded situation when the end of the shell behaves like a spring and this is schematically shown in Fig. 1b. The change from a a point contact, in the case of columns, or a line contact in the case of thin-walled cylindrical shells occurs during the loading process and is due to the axial compressive loading. The present work deals with such changes of the support conditions as described in the sequel.

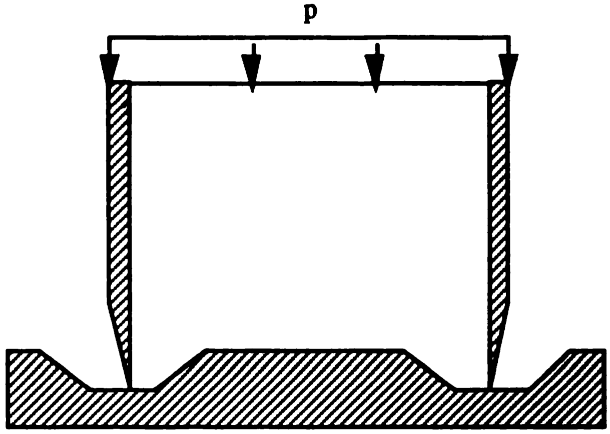

a. The cylindrical shell

part of "MECHANICS PAN-AMERICA 1993" edited by MRM Crespo da Silva and CEN Mazzilli ASME Reprint No AMR134
Appl Mech Rev vol 46, no 11, part 2, November 1993

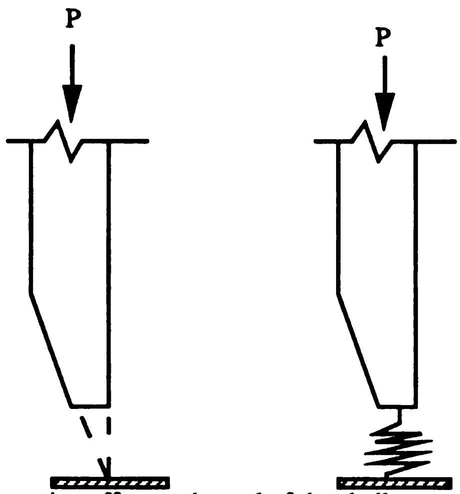

b. The spring effect at the end of the shell

FIG 1. The knife-edge support

The influence of hardening and softening of the supports on the dynamic post-buckling behavior of thin-walled structures has previously been investigated by Souza (1987a, 1988, 1989). There, the goal was to understand how changes of the boundary conditions at the supports during the loading process affect the dynamic response. In this work the objective is to understand how the changes in the knife-edge supports during the loading process affect the post-buckling dynamic response. In order to do so a simplified model is introduced and discussed in detail.

THE SIMPLIFIED MODEL

The model used in the analysis is shown in Fig. 2 below. It consists of a rigid bar of length L free at one end where the vertical load P is applied and supported at the other end by a laterally fixed support able to displace vertically, and a flexible support which consists of a linear spring of stiffness K and a rotational spring of stiffness C. In the idealized situation corresponding to the simply supported condition we have $C = 0$ and $K \to \infty$.

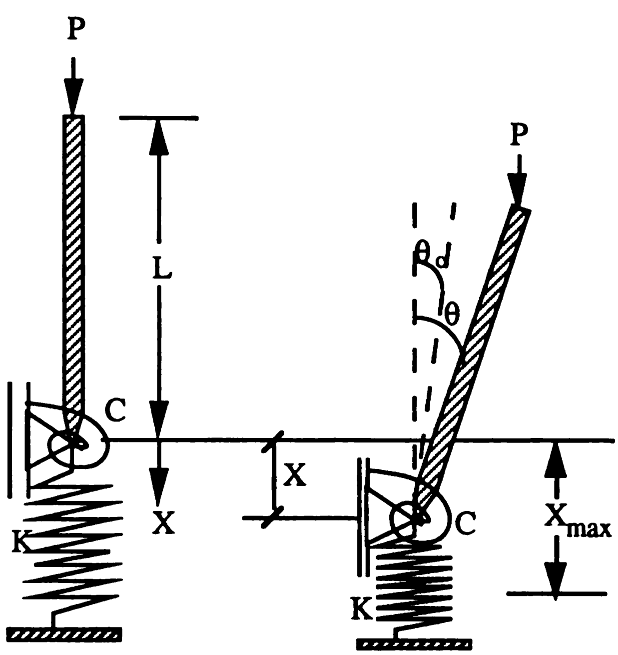

FIG 2. The simplified model

In order to model the loss of the knife-edge condition and, therefore, the loss of the free-to-rotate condition, the stiffness of the rotational spring, C, is considered as dependent on the vertical displacement X of the supported end, X_{max} being the maximum possible displacement, i.e., $0 \le X \le X_{max}$. In the unloaded situation corresponding to $P = 0$ and $X = 0$, the stiffness of the rotational spring has an initial value C_i. As the vertical load P is applied, the end support displaces of a value X and the stiffness of the rotational spring $C(X)$ increases, reaching a constant final value, C_f, when $X = X_{max}$. For the sake of simplicity a linear relationship between $C(X)$ and X is considered in the analysis. The use of the parameters ξ and γ, defined as

$$\xi = \frac{X}{X_{max}} \tag{1}$$

and

$$\gamma = \frac{C_f}{C_i} \tag{2}$$

together with the linear relationshipp between $C(X)$ and X, enables the expression of the rotational spring's stiffness as a function of ξ in the following form

$$\frac{1}{C_i} C(\xi) = \begin{cases} 1 + (\gamma - 1)\xi & \dots\ 0 \le \xi \le 1 \\ \gamma & \dots\ \xi \ge 1 \end{cases} \tag{3}$$

The free-to-rotate condition corresponds to the limiting situation $C_i \to 0$ for $P = 0$ and $X = 0$. Throughout the analysis C_i will be considered as nonzero due to the choice of the function $C(\xi)$ as defined in Eqn. (3), where the final constant value of the rotational spring's stiffness C_f, is considered to be proportional to its initial value, C_i. Therefore, $C_i \neq 0$ means that from the beginning the support is not completely free to rotate. The stiffness function of the rotational spring, $C(\xi)$, can be ilustrated as shown in Fig. 3.

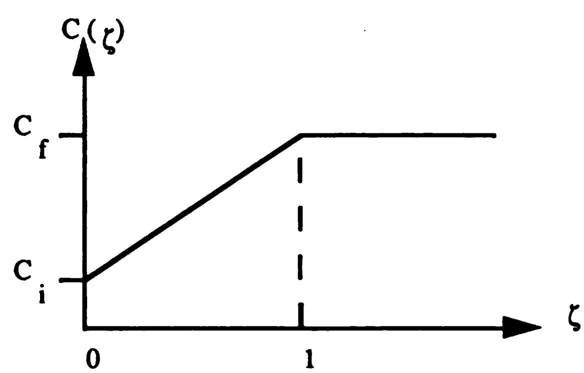

FIG 3. The stiffness function $C(\zeta)$

The model can be treated both as perfect or initially imperfect depending on the angular displacement θ_o, which corresponds to the value of θ for $P = 0$, Fig. 2. Therefore, $\theta_o = 0$ corresponds to the perfect situation, whereas, $\theta_o \neq 0$ corresponds to the initially imperfect one.

For the perfect model, $\theta_o = 0$, two situations can occur: i) the value of the critical load is greater than KX_{max}, in which case buckling occurs for $X = X_{max}$; ii) the value of the critical load is smaller than KX_{max} and, therefore, the model buckles for a value of X smaller than its maximum value X_{max}. The latter is the most interesting case since the model will buckle while still vertically displacing. This is the case chosen to be discussed in the paper.

The stability and the vibration characteristics of the model are investigated and summarized according to the procedure described by Souza (1987a). What follows is the study of such characteristics.

STABILITY CHARACTERISTICS

The stability characteristics are illustrated by the equilibrium paths which relate the applied load P and the angular displacement θ, Fig. 2. The equilibrium paths are obtained using the principle of the stationary potential energy (Souza, 1987b).

Equilibrium paths

The functional of total potential energy, V, for the most general case of initially imperfect model can be expressed in the following form

i) $0 \leq \xi \leq 1$

$$V = \frac{1}{2} KX_{max}\,\xi^2 + \frac{1}{2} C_i\left[1 + (\gamma - 1)\xi\right](\theta - \theta_o)^2 - P\left[X_{max}\,\xi + L\left(\cos\theta_o - \cos\theta\right)\right] \tag{4}$$

ii) $\xi \geq 1$

$$V = \frac{1}{2} C_i\,\gamma\,(\theta - \theta_o)^2 - PL\left(\cos\theta_o - \cos\theta\right) \tag{5}$$

where all the parameters have previously been defined.

For the first case, $0 \leq \xi \leq 1$ the equilibrium equations are

$$\frac{\partial V}{\partial \xi} = 0 \;;\; \frac{\partial V}{\partial \theta} = 0 \tag{6}$$

which lead to the following load displacement relationship:

$$p = \frac{\left[1 - \vartheta\dfrac{(\gamma - 1)}{2\beta}(\theta - \theta_o)\right]}{\left[1 - \vartheta\dfrac{(\theta - \theta_o)}{\sin\theta}\right]}\,\frac{(\theta - \theta_o)}{\sin\theta} \tag{7}$$

and

$$\xi = \frac{1}{\mu}p - \frac{\vartheta}{2\beta}(\theta - \theta_o)^2 \tag{8}$$

where p is the load parameter defined as

$$p = \frac{PL}{C_i} \tag{9}$$

and the parameters μ, ϑ and β are defined as follows:

$$\mu = \frac{KX_{max}}{C_i / L} \tag{10}$$

$$\vartheta = \frac{(\gamma - 1)}{\mu} \tag{11}$$

$$\beta = \frac{X_{max}}{L} \tag{12}$$

The value of the critical load parameter, p_{cr}, can be obtained by considering the perfect case, $\theta_o = 0$, and taking the limit of the load parameter p in Eq. (7) as $\theta \rightarrow 0$, i.e.

$$p_{cr} = \lim_{\substack{\theta \to 0 \\ (\theta_o = 0)}} p = \frac{1}{(1 - \vartheta)} \tag{13}$$

Therefore, the critical value of ξ, ξ_{cr}, can be obtained from Eqs. (8) and (13) as

$$\xi_{cr} = \frac{1}{\mu(1 - \vartheta)} = \frac{1}{\mu}p_{cr} \tag{14}$$

For the second case, $\xi \geq 1$, the equilibrium equation $\partial V / \partial\theta = 0$ leads to the following load displacement relationship

$$p = \gamma\,\frac{(\theta - \theta_o)}{\sin\theta} \tag{15}$$

It is worth noticing that in the case of a constant stiffness of the rotational spring, $C(\zeta) = C_f$, the value of the critical load parameter is $p_{cr} = \gamma$. Since we are interested in the situation in which the perfect model buckles while still vertically displacing, i.e. for $0 < \zeta < 1$ as previously mentioned, then $KX_{max} > C_f$, leading to the condition $\mu > \gamma$ according to the definition of μ and γ, Eqs. (10) and (2), respectively.

In order to illustrate the influence of the stiffness $C(\xi)$, which depends on the vertical displacement, on the equilibrium paths several situations with $\mu > \gamma$ will be considered. Initially, the influence of the various parameters will be illustrated, starting with the influence of μ on the relationship between p_{cr} and γ and shown in Fig. 4. It can be observed that μ is always greater then γ.

The linear relationship between p_{cr} and ξ_{cr}, Eq. (14), is shown in Fig. 5 for different values of γ.

Figure 6 illustrates the relationship between ξ_{cr} and μ for different values of the parameter γ, whereas, Fig. 7 shows how ξ_{cr} and γ are related.

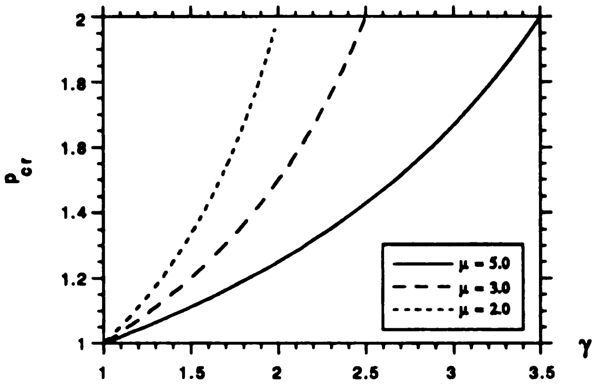

FIG 4. γ versus p_{cr}

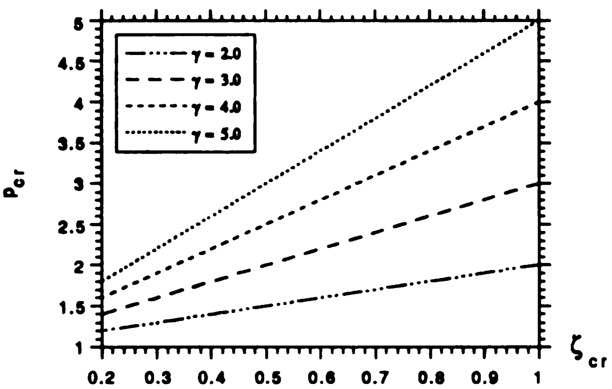

FIG. 5 ζ_{cr} versus p_{cr}

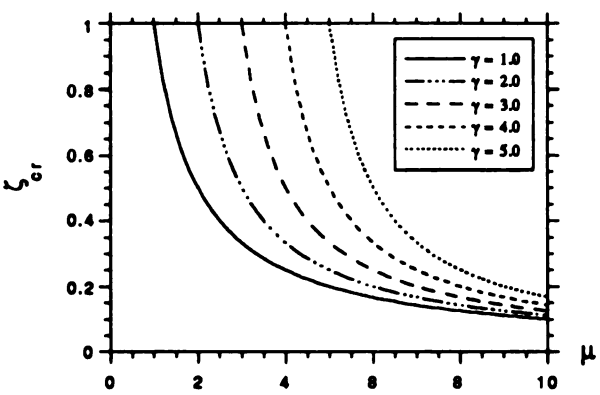

FIG. 6 ζ_{cr} versus μ

The relationship between ξ and p for $\gamma = 2$ and $\mu = 4$ and different values of the parameter β is illustrated by the curves presented in Fig. 8.

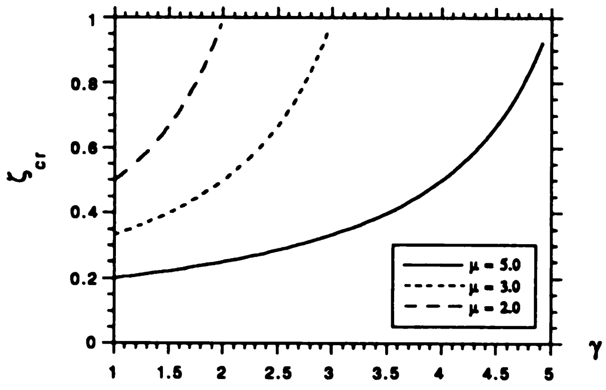

FIG. 7 ζ_{cr} versus γ

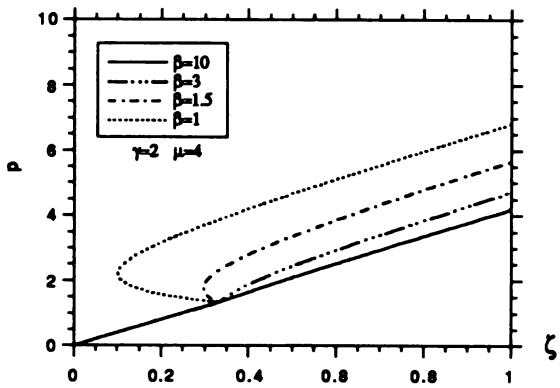

FIG. 8 ζ versus γ

Figure 9 shows how θ and ξ are related for $\gamma = 2$, $\mu = 4$ and different values of β.

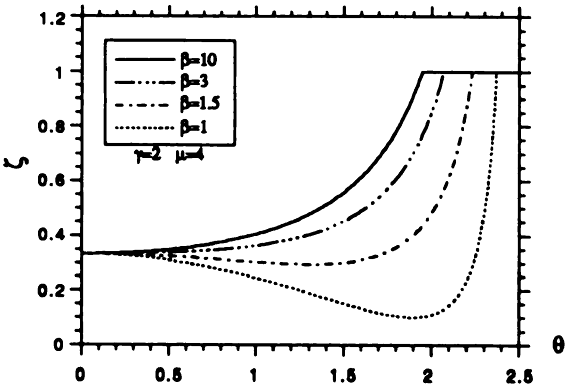

FIG. 9 θ versus ζ

The influence of β on the equilibrium paths is shown in Fig. 10 for $\gamma = 2$ and $\mu = 4$.

Figure 11 illustrates how the parameter γ affects the equiilibrium paths for $\mu = 4$ and $\beta = 10$.

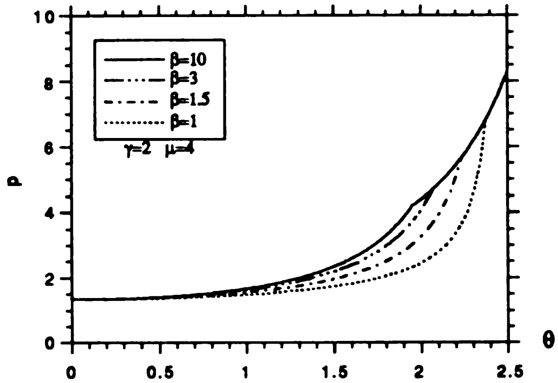

FIG. 10 Equilibrium paths - The influence of β

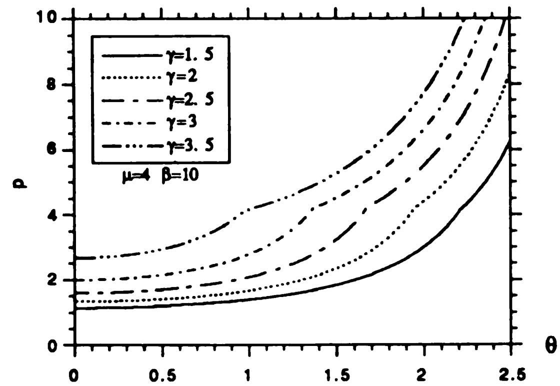

FIG. 11 Equilibrium paths - The influence of γ

The influence of γ on the relationship between θ and ζ can be observed in Fig. 12, corresponding to $\mu = 4$ and $\beta = 10$.

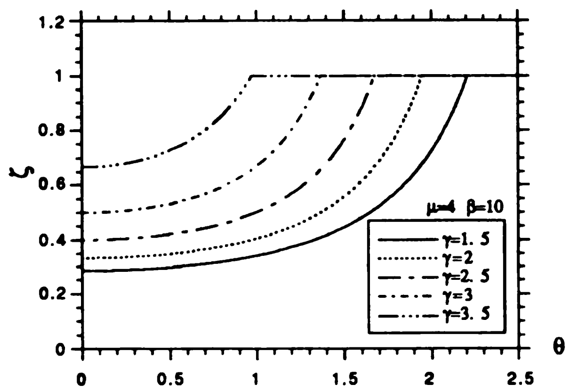

FIG. 12 θ versus ζ

Equilibrium paths for both the perfect and the imperfect model are shown in Fig. 13 for $\gamma = 4$, $\mu = 5$ and $\beta = 10$.

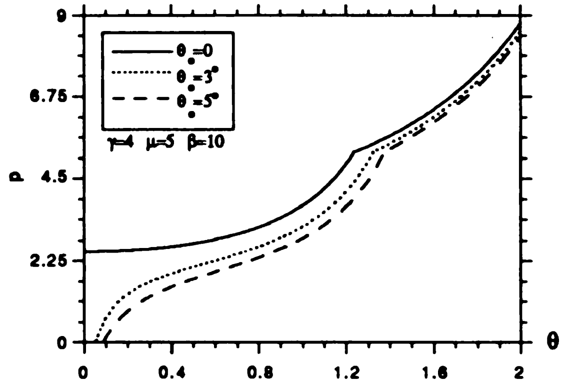

FIG. 13 Equilibrium paths

Figure 14 highlights the influence of the stiffness function $C(\zeta)$ on the equilibrium paths as compared to the case of constant stiffness C_f, for $\gamma = 4$, $\mu = 5$, $\beta = 10$ and $\theta_o = 0°$ and 3°. In brackets are indicated whether $C(\zeta)$ or C_f are considered, together with the value of θ_o, i.e. $[C(\zeta)$ or C_f, $\theta_o]$.

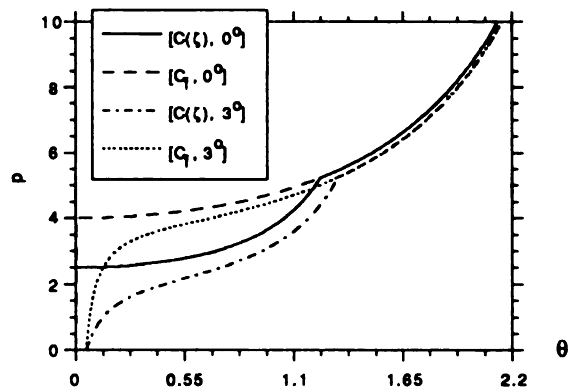

FIG. 14 Equilibrium paths (γ=4 μ=5 β=10)

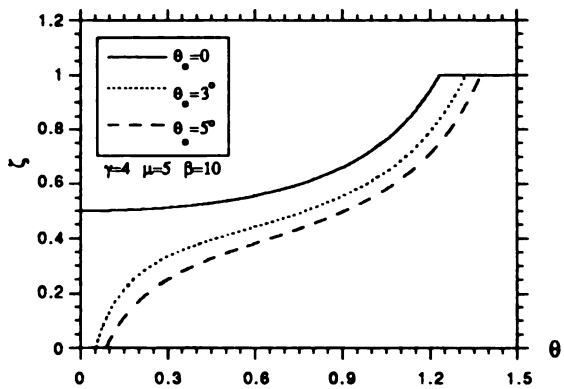

FIG. 15 θ versus ζ

Figure 15 shows the relationship between θ and ζ for $\gamma = 4$, $\mu = 5$, $\beta = 10$ and $\theta o = 0^o$, 3^o and 5^o. The relationship between ζ and p for the same parameters of Fig. 15 is shown in Fig. 16.

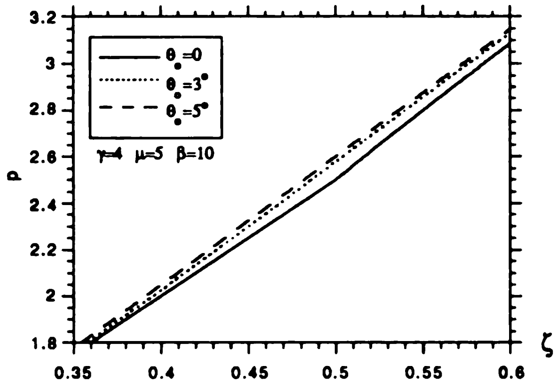

FIG. 16 ζ versus p

The results shown in Figs 4-16 illustrate how the changes of the support conditions in terms of a rotational spring's stiffness dependent on the linear displacement influence the equilibrium paths and also how the different parameters involved are related. Of special illustrative effect are the equilibrium paths of Fig. 13 where the effect of $C(\zeta)$ is clearly observed. Figure 13 should be interpretd as follows: had the system started with a constant stiffness $C(\zeta) = C_f$ then the equilibrium path would be the higher value one; since it started with $C(\zeta) = C_i$, it only reaches the same equilibrium path when $\zeta = 1$, which can be clearly observed.

The model presents equilibrium paths which are all stable: the primary path corresponding to $\theta = 0$ with $\theta_O = 0$, the scondary path corresponding to $\theta \neq 0$ with $\theta_O = 0$ and the imperfect path corresponding to $\theta_O \neq 0$. This can be proved from the second derivatives of the total potential energy functional, V.

Having discussed different aspects of the equilibrium paths of the model, what follows is the study of the characteristic curves which illustrate the vibration characteristics of the model.

VIBRATION CHARACTERISTICS

The vibration characteristics of the model are presented in terms of the characteristics curves which relate the applied load, P, and the square of the corresponding natural frequency of vibration ω.

Characteristics curves

The natural frequency of vibration corresponding to a given load level is determined by the procedure described in Souza (1987b). It consists of perturbing the equilibrium configuration and investingating the motion around such an equilibrium configuration. In order to investigate the lateral motion a small perturbation is introduced, represented by the angle ϕ shown in Fig. 17, keeping the load level constant. Therefore, the total potential energy functional V becomes a function of $(\theta + \phi)$. Such a procedure allows the determination of the natural frequency of vibration as a function of the applied compressive load.

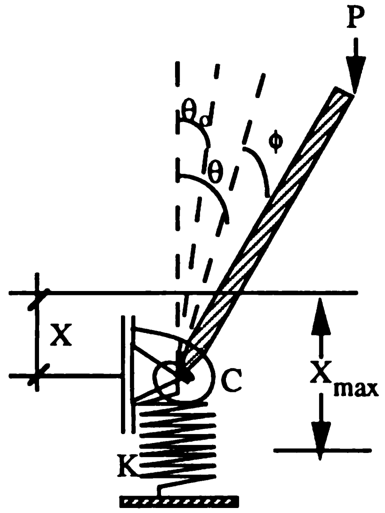

FIG. 17 The perturbed configuration

The equation of motion is obtained from the Euler-Lagrange equation (Souza, 1987b)

$$\frac{d}{dt}\frac{\partial T}{\partial \dot{\phi}} + \frac{\partial V}{\partial \phi} = 0 \tag{16}$$

where T is obtained the kinetic energy given by

$$T = \frac{1}{2} I^* \dot{\phi}^2 \tag{17}$$

I^* being the generalized moment of inertial and $\phi.dot$ is the angular velocity. It can be expressed as

$$\ddot{\phi} + \omega^2 \phi = 0 \tag{18}$$

where terms of of $O(\phi^2)$ and higher are neglected and ϕ is the natural frequency of vibration corresponding to the applied load level P. Before continuing, let us introduce the natural frequency of vibration function, f, defined as follows:

$$f^2 = \frac{C_i}{I^*} \omega^2 \tag{19}$$

The relationship between the applied load level, p, and the square of the corresponding natural frequency of vibration function, f, depends on the range of ζ and can be summarized as follows:

i) $0 \leq \zeta \leq 1$

$$f^2 = 1 - \frac{\vartheta(\gamma - 1)}{2\beta}(\theta - \theta_o)^2 + (\vartheta - cos\theta)\, p \tag{20}$$

ii) $\zeta \geq 1$

$$f^2 = \gamma - p \cos \theta \qquad (21)$$

All the parameters in Eqs (20) and (21) have previously been defined.

In order to illustrate the post-buckling dynamic response characteristic curves will be presented. Figure 18 shows characteristic curves for $\gamma = 2, \mu = 4$ and different values of β. Such characteristic curves correspond to the equilibrium paths shown in Fig. 10.

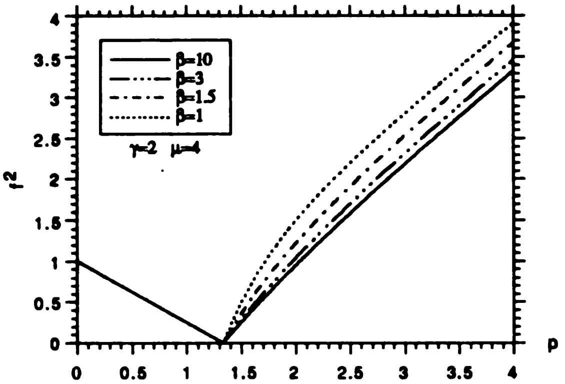

FIG. 18 Characteristic curves - The influence of β

The relationship between ζ and f^2 also for $\gamma = 2$, $\mu = 4$ and different values of β is illustrated by the curves of Fig. 19, corresponding to the ζ versus p curves of Fig. 8.

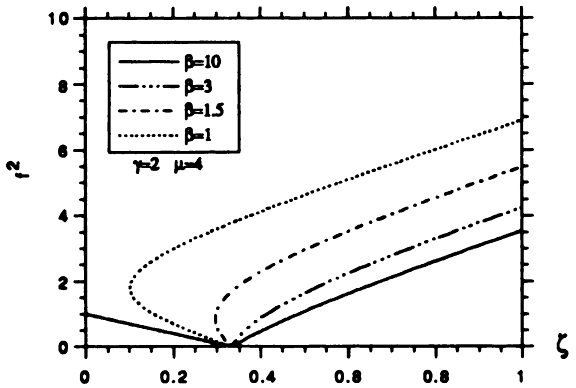

FIG. 19 ζ versus f^2

Characteristics curves corresponding to $\mu = 4, \beta = 10$ and different values of γ are shown in Fig. 20. The corresponding equilibrium paths are those shown in Fig. 11.

Figure 21 shows the characteristics curves corresponding to the equilibrium paths of Fig. 13 for $\gamma = 4$, $\mu = 5$, $\beta = 10$ and $\theta_0 = 0^o$, 3^o and 5^o.

The relationship between ζ and f^2 for the same parameters of Fig. 21 is shown in Fig. 22.

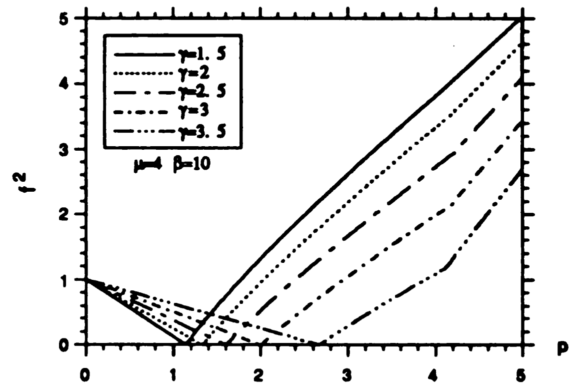

FIG. 20 Characteristic curves - The influence of γ

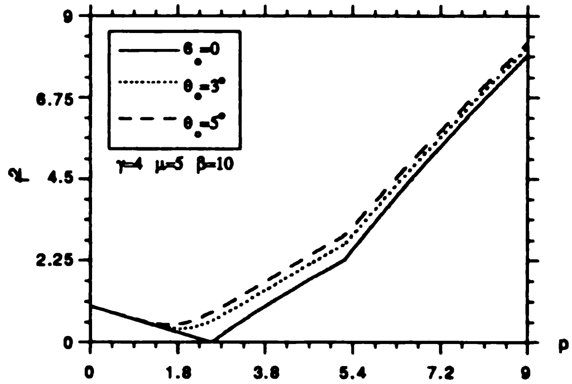

FIG. 21 Characteristic Curves

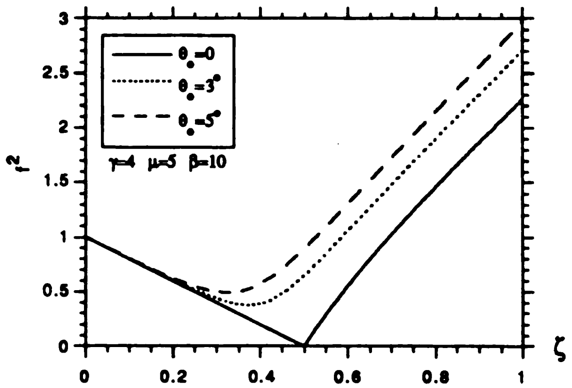

FIG. 22 Characteristic curves (ζ versus f^2)

The influence of the stiffness function $C(\zeta)$ can be observed in the characteristic curves shown in Fig. 23 for $\gamma = 4$, $\mu = 5$, $\beta = 10$ and $\theta_0 = 0^o, 3^o$ and 5^o. Figure 23 corresponds to the equilibrium paths of Fig. 14. In this case also the explanation is the same as that of Fig. 13: had the model started with a constant stiffness $C(\zeta) = C_f$, then the f^2 vs P curve would start at the value 4.0 $(= \gamma)$.

Since it starts with $C(\zeta) = C_i$, the characteristics curves only reach those corresponding to $C(\zeta) = C_f$ for $\zeta = 1$.

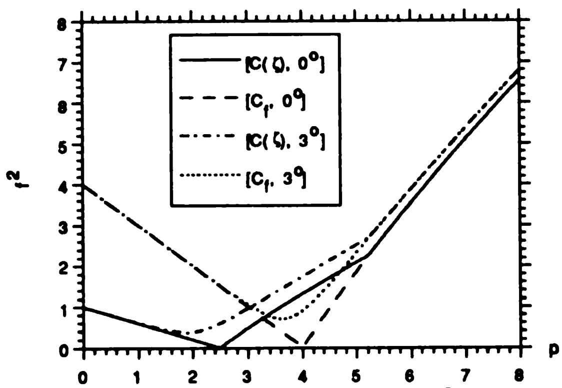

FIG. 23 Characteristic curves (γ=4 μ=5 β=10)

The results presented in Figs 18-23 illustrate how the dynamical response of the model is affected by the changes of the knife-edge support condition according to the $C(\zeta)$ function, described by Eq.(3) and illustrated in Fig. (3)..

DISCUSSION OF THE RESULTS

The results obtained illustrate how the changes in the boundary conditions of knife-edge type of supports due to the compressive loading affect the dynamic post-buckling response of thin-walled structures. As the loading process takes place the knife-edge support with the free-to-rotate capability is altered to that of a spring type of support in which the free-to-rotate condition no longer exists. Such behavior was modeled in a way that the coupling between the stiffening of the support resulting from the loss of the free-to-rotate boundary condition and the vertical displacement due to the load is incorporated.

Since the model exhibits a stable post-buckling behavior the results obtained are similar in nature to those previously obtained by the author (Souza, 1987a-b, 1988, 1989). In terms of the dynamic post-buckling behavior the main characteristic is related to the relationship between the applied load and the corresponding natural frequency of vibration: the level of the natural frequency of vibration of the initially imperfect model is always higher than the frequency level of the perfect counterpart for the same load level.

The results presented illustrate how changes of the knife-edge type of supports can alter the response of the of the structure both in terms of the equilibrium paths and the characteristic curves. It is also clear from the results obtained that unless the stiffness of the rotational spring is constant, a much more complex behavior is observed.

CONCLUSION

A careful investigation and design of the supports, in particular the knife-edge type, is a decise factor in the success of any experimental program dealing with thin-walled structures liable to buckling.

The influence of changes of the knife-edge support condition during the loading process on both the equilibrium paths and the characteristic curves was discussed. The loss of the free-to-rotate capability of the knife-edge support resulting from the increase of the load level leads to the stiffening of the support. The importance of incorporating such characteristics of the supports in the analysis is of major importance in order to allow a meaningful comparison between theoretical prediction and experimental results.

A simplified model with the capability of reproducing the behavior described above was introduced and a detailed analysis was carried out. The results obtained show how such stiffening of the support dramatically alter both the static and the dynamic post-buckling response. Knife-edge type of supports of thin-walled structures are bound to exhibit the behavior modeled in the paper. The results presented contribute for the understanding of the dynamic post-buckling behavior of thin-walled structures with flexible knife-edge supports.

REFERENCES

Albert C., Essa HS and Kennedy DJL, Distortional buckling of steel beams in cantilever - suspended span construction, *Canadian Journal of Civil Engineering* 19(5), 767-780 (1992).

Souza MA, The effects of initial imperfection and changing support conditions on the vibration of structural elements liable to buckling, *Thin-Walled Structures*, 5(6), 411-423 (1987).

Souza MA, Post-buckling vibration characteristics of structural elements, *Engineering Structures*, 9(2), 134-137 (1987).

Souza MA, The effect of softening of the supports on the stability and dynamics of structures, *Proceedings of the 2nd Conference on Non-Linear Vibrations, Stability, and Dynamics of Structures and Mechanisms*, Blacksburg, VA, (1988).

Souza MA, The influence of hardening of the supports on the stability and vibration of structures, *Applied Mechanics Reviews*, 42, S245-S248 (1989) .

Stability and bifurcations of nonlinear multibody systems

Edwin J Kreuzer

Ocean Engineering Section II, Technical University Hamburg-Harburg
D-21071 Hamburg, Germany

Many technical systems are adequately described only by means of nonlinear mathematical models. Multibody systems became the most important mechanical models for analyzing engineering dynamics problems. The long-term or steady-state behavior of such systems can have a periodic, quasi-periodic, or chaotic character. Changes of the qualitative behavior are characterized by local and global bifurcations. This paper deals with stability problems in multibody system dynamics and explains different bifurcation phenomena as well as methods for analyzing them. Results from a simple oscillator prove the applicability of the methods.

CONTENTS

INTRODUCTION

Growing demands on speed and precision make it necessary to operate closer to the dynamic limits. These increasing demands on dynamic systems such as vehicles, mechanisms, and all kinds of machinery have motivated progress in mechanical modeling. Multibody systems are among the most important models for mechanical engineering systems. Multibody system dynamics is, therefore, world wide a very active area of research for both: improving and extending modeling and simulation procedures as well as analyzing the stability with respect to variable design parameters.

Different types of nonlinearities in engineering mechanical systems cause problems in the stability analysis. Many mechanical systems consist of linear components with local nonlinearities introduced for example by nonlinear springs, nonlinear dampers, dry friction, and backlash. Such nonlinearities may be desirable to avoid excessively high responses or stresses but also undesirable because of extensive wear or noise problems. Global nonlinearities originate from geometrically or kinematically nonlinear behavior often observed in mechanism, robot, and vehicle dynamics.

The performance of a technical system depends on its dynamic behavior which can be predicted using mathematical models for the multibody system and the excitation. Local stability, in the neighborhood of a steady-state operating point, of mechanical systems has been the subject of many research projects. But, neither the system parameters nor the excitation are precisely known; both may even vary during operation. Moreover, if a structure is to require a control system, the dynamics must be well understood. While local stability studies may be used to determine whether a given operating point can be maintained, a complete stability study must involve global analysis. Furthermore, changes of systems parameters may cause smooth or drastic changes in the qualitative behavior of the nonlinear system: so-called local and global bifurcations. A common feature of nonlinear dynamic systems is that for a given set of inputs the systems possess multiple stable steady states. It is therefore concluded that local stability at an operating point does not gurantee that it can be maintained. A stable and robust engineering system must consequently account for the regions of attraction corresponding to the steady states and how they are affected by varying parameters.

The subject of this paper is to study the qualitative behavior of multibody systems with local nonlinearities, which are excited by periodic external load. The Lyapunov spectra computed from the mathematical model provides a quantitative diagnosis for the different types of behavior.

MATHEMATICAL MODEL

Equations of motion of multibody systems are given by

$$\dot{\boldsymbol{x}} = \boldsymbol{f}(\boldsymbol{x}, \boldsymbol{\mu}) \quad , \tag{1}$$

part of "MECHANICS PAN-AMERICA 1993" edited by MRM Crespo da Silva and CEN Mazzilli
ASME Reprint No AMR134
Appl Mech Rev vol 46, no 11, part 2, November 1993

where $\boldsymbol{x}, \boldsymbol{f} \in R^N$ and $\boldsymbol{\mu} \in R^P$ is a parameter vector. The formulation of analytical mathematical models (1) is nowadays convieniently performed by using computerized formalisms for the generation of symbolic equations of motion, see e.g. Daberkow et al (1993).

The governing equations of nonlinear dynamic systems show a rich and fascinating variety of qualitative behavior like periodic, quasiperiodic or chaotic solutions for various parameter sets or initial conditions. We want information about how the equilibrium or periodic orbit of a vector field described by (1) changes with perturbations. This aspect of studying how dynamics depends upon parameters is called bifurcation theory. The general approach in order to study bifurcations is based on ideas of multivariable calculus and differential topology. From an engineering point of view it is important to have some kind of toolbox which helps to locate bifurcations in parameter space. As a starting point we assume that $\boldsymbol{f}$ of (1) is periodic with a period T. Hence, instead of looking at trajectories in the time domain, we use the so-called Poincaré map

$$\boldsymbol{x}_{n+1} = \boldsymbol{g}(\boldsymbol{x}_n, \boldsymbol{\mu}) \tag{2}$$

for studying the stability of periodic solutions $\bar{\boldsymbol{x}}(t) = \bar{\boldsymbol{x}}(t+T)$. Again, $\boldsymbol{g}$ is a nonlinear vector valued function which is smooth if $\boldsymbol{f}$ is smooth; n is the discrete time. A periodic motion of the continuous system (1) corresponds to a fixed point of the discrete system (2).

LOCAL BIFURCATIONS

There is a highly developed theory that enables one to determine some types of local bifurcations of equilibria of (1) and fixed points of (2) with power series. This theory is called center manifold theory. The calculations begin with the determination of the linearized vector field at the equilibrium (fixed point) and its eigenvalues and eigenvectors. Based upon this information, we can produce a normal form for the bifurcation. The effect of such a coordinate transformation is that the computations are more easily carried out. The normal form is a parameterized power series expansion that provides simple analytic expressions of the vector field at the bifurcation point. Once the normal forms have been computed, one can investigate the dynamics of the normal forms and classify the situation under consideration.

For local codimension one bifurcations one is left with a few specific equations from which we can determine the qualitative features of each type of bifurcation, see e.g. Guckenheimer and Holmes (1986). The calculations are a combination of numeric and analytic ones. We are developing a program package based upon efficient numeric algorithms and symbol manipulation programs for analyzing local bifurcations, Kleczka and Kreuzer (1992). Symmetry properties of the vector fields are often observed in multibody system models and are therefore also considered.

GLOBAL BIFURCATIONS

Contrary to local bifurcations the situation is more difficult in the case of global bifurcations, where the global topological structure of the phase portrait changes qualitatively. Hence, the analysis of such a behavior cannot be reduced to the study of the neighborhood of an equilibrium or a fixed point of the discrete system. There may be global changes in a phase portrait associated with saddle-node bifurcations. But there are even more complex situations which result from intersections of homoclinic and heteroclinic orbits and the so-called crises phenomena.

Transverse homoclinic (heteroclinic) orbits of a Poincaré map which imply chaotic motions can be determined numerically and analytically by means of a global perturbation technique introduced by Melnikov. The analytical perturbation method invented by Melnikov can only be applied if the perturbations are small. The resulting Melnikov function is the lowest order approximation for the distance between the stable and unstable manifolds of a fixed point of (2). If the Melnikov function oscillates about zero and has simple zeros then the stable and unstable manifolds have transversal intersections. An interesting discussion of the theory can be found in Wiggens (1988).

The sudden disappearances and sudden blow-ups of chaotic attractors are called crises phenomena, e.g. Ueda (1980) or Grebogi, Ott, and Yorke (1983). An interior crisis is a sudden enlargement of a chaotic attractor (sometimes with symmetry properties) often resulting in a one piece strange attractor. An exterior crisis causes a chaotic attractor to disappear due to its collision with an unstable periodic solution.

Global bifurcations are not smooth. Consequently, the resulting changes of the dynamics are not smooth, and often the system jumps, collapses or explodes, in other words its behavior changes drastically.

The enormous value of computers for dynamical systems has been mainly as an experimental tool. With digital computers we have the ability to produce reproducible data and pictures, some of which are chaotic from simple explicit equations. A complex picture, however, does not necessarily elucidate an already complex phe-

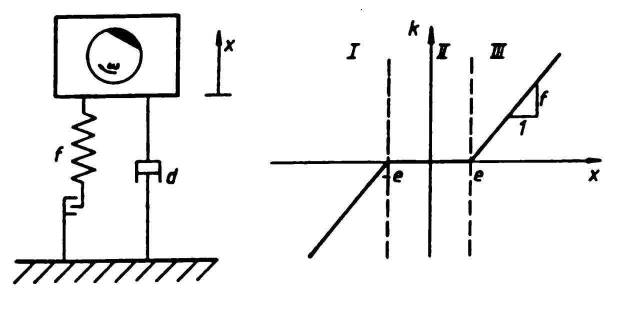

FIG 1. Model of the system and characteristic of the nonlinearity

nomenon unless we can organize the information the picture represents.

EXAMPLE

Vibrations of unloaded gears and synchronization parts within their functional backlash cause rattling noise. Increasing irregularities in shaft speed of modern engines and decreasing general sound level make this old comfort problem more important. Simultaneously, the hammering of the involved mechanical parts produces high dynamic overload. This is also a typical design problem.

A simple model of a mechanical system with backlash is a single degree-of-freedom oscillator with a piecewise linear, symmetric restoring force subjected to periodic excitations caused by an unbalanced rotor, see Fig 1 and Kleczka et al (1992). Because of its periodic time dependence, a common way to describe the dynamics is by means of an extended cylindrical state space

$$\begin{aligned} \boldsymbol{x} &= (x, y = \dot{x}\ , \quad \theta = t \bmod 2\pi) \in R^2 \times S^1, \\ & S^1 = [0, 2\pi) \quad , \end{aligned} \tag{3}$$

where x represents the position, y gives the velocity, and θ determines the circular coordinate and is to be interpreted as the phase angle of excitation. The resulting set of first order autonomous differential equations is given by

$$\begin{bmatrix} \dot{x} \\ \dot{y} \\ \dot{\theta} \end{bmatrix} = \begin{bmatrix} y \\ -2dy - k(x) + a\cos\theta \\ 1 \end{bmatrix} \tag{4}$$

with the nomalized parameters d of the damper, a of the amplitude of excitation, and the piecewise linear function $k(x)$ of the restoring force:

$$k(x) = \begin{cases} f(x-e) & , \quad x > e, \\ 0 & , \quad |x| \leq e, \\ f(x+e) & , \quad x < -e. \end{cases} \tag{5}$$

The following parameters have been kept fixed: amplitude of excitation a = 10.0, frequency of excitation $\omega = 1.0$.

This simple model shows the whole scenario of nonlinear behavior like periodic orbits, solutions of multiple period, chaotic solutions, various types of bifurcations and coexistence of even qualitatively different solutions. The global analysis of the nonlinear dynamics requires large-scale numerical investigations. Global stability analysis with respect to initial conditions leads to the problem of the determination of long-term behavior, i.e. attractors, and their domains of attraction.

A global analysis in parameter space can be carried out with a calculation of Lyapunov exponents and bifurcation diagrams. Lyapunov exponents are measures for the average exponential divergence or convergence of neighboring trajectories. Since they can be computed either from a mathematical model or from experimental data, they are widely used for the classification of attractors.

Lines in a bifurcation diagram represent periodic solutions changing under variation of the control parameter smooth or, in case of a local bifurcation, non-smooth. The corresponding Lyapunov exponent is negative, indicating stable, convergent long-term behaviour. Bifurcation points correspond to orbits of marginal stability and therefore have zero exponents. Chaotic dynamics produces non-periodic sequences of points in the bifurcation diagram leading to wide grey-patterned structures. The corresponding largest Lyapunov exponent is positive, in-

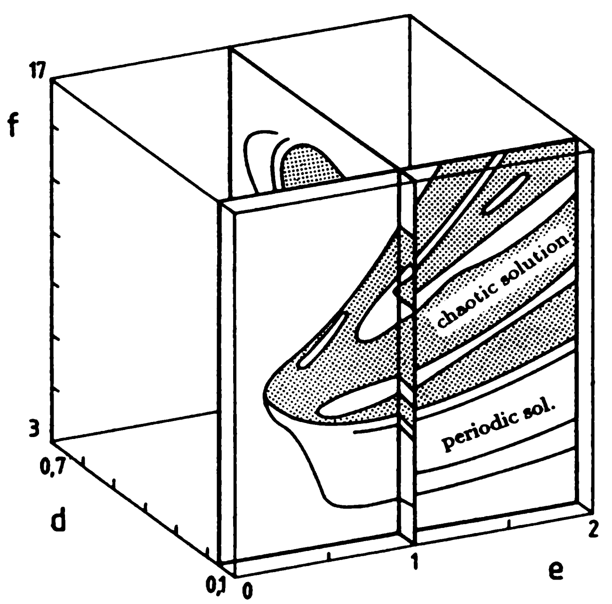

FIG 2. Stability diagram for parameters d, e, and f; solid lines indicate bifurcations.

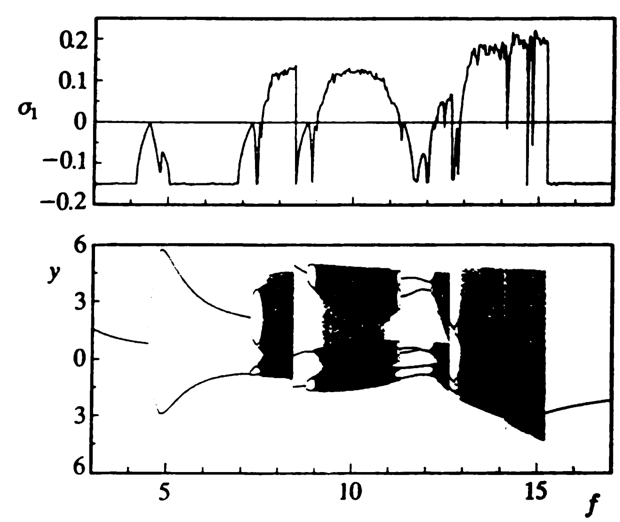

FIG 3. Bifurcation diagram and largest Lyapunov exponent σ_1 for variation of the stiffness ratio f.

dicating divergent, unpredictable dynamics. For a first overview on the dynamic behavior, the largest Lyapunov exponent was calculated for a broad range of parameter values in order to distinguish the parameter regions with regular and chaotic behavior reliable, Fig 2.

The analysis for variation of the stiffness ratio f only, all other values fixed ($d = 0.15$, $e = 1.0$, $a = 10.0$, $\omega = 1.0$), is shown in Fig 3. The stability and bifurcation analysis using center manifold theory is presented in Kleczka et al (1992).

For the backlash oscillator an unstable, saddle type, symmetric periodic orbit plays the decisive role in the global bifurcation scenario; its stable and unstable invariant manifolds intersect, leading to homoclinic structures with significant influence on the dynamics of the system, Fig 4 (a). In this case the emergence of the homoclinic intersection coincides with the emergence of a chaotic attractor. As the global topological structure of the system changes qualitatively, the system undergoes a global bifurcation.

Looking at the bifurcation diagram of Fig 3 one realizes that there are sudden disappearances and sudden blowups of the chaotic attractor: crisis phenomena.

(a)

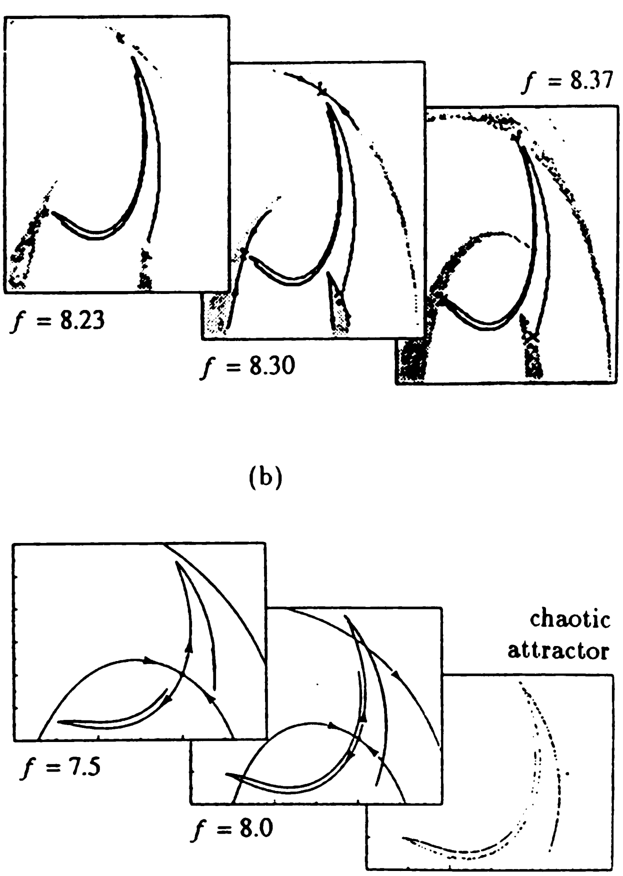

FIG 4. Poincaré maps of the backlash oscillator for demonstrating global bifurcations
(a) homoclinic bifurcation
(b) exterior crisis

An exterior crisis occurs at parameter value $f \approx 8.4$. The system abruptly terminates the chaotic behavior with a period three solution. How does the transition from chaotic to periodic occur as the parameter f is varied? The chaotic attractor vanishes, because it collides with an unstable periodic solution. Figure 4 (b) shows how basin boundary and unstable periodic orbits (fixed points) approach the chaotic attractor and finally destroy it by an exterior crisis. We observe that the chaotic attractor approaches the period three solution, the domain of attraction of the periodic solution grows towards the strange attractor in form of fingers, and the boundary crisis is triggered when the stable manifold of the saddle touches the unstable manifold.

An interior crisis can be observed at a parameter value of $f \approx 9.17$. More details may be found in Kleczka et al (1992).

CONCLUSIONS

The analysis of local and global bifurcations of mechanical systems replaced by multibody system models is discussed. The stability analysis of periodic motions is based upon Poincaré maps which have to be approximated analytically if local bifurcations are studied in a general form. Lyapunov exponents and bifurcation diagrams are helpful for the classification of the dynamic behavior of nonlinear systems. The global analysis requires normally large scale numerical simulations. By means of a combined computer aided numeric–symbolic approach a systematic analysis of bifurcation phenomena is visible.

REFERENCES

Daberkow A, Kreuzer E, Leister G, and Schiehlen W (1993), CAD Modelling, Multibody System Formalisms and Visualization – An Integrated Approach, in *Advanced Multibody System Dynamics – Simulation and Software Tools*, W Schiehlen (ed), Kluwer Academic Publisher, Dordrecht, 87 - 106.

Grebogi C, Ott E, and Yorke J (1983), Crises, sudden changes in chaotic attractors, and transient chaos, *Physica D* 7, 181 - 200.

Guckenheimer J and Holmes P (1986), *Nonlinear Oscillations, Dynamical Systems, and Bifurcations of Vector Fields*, Springer-Verlag, New York.

Kleczka W and Kreuzer E (1993), On the Systematic Analytic-Numeric Bifurcation Analysis, in *Proceedings of the Workshop on Bifurcation and Chaos in Mechanical Systems*, Special Issue of the Nonlinear Dynamics, to appear.

Kleczka M, Kreuzer E, and Schiehlen W (1992), Local and Global Stability of a Piecewise Linear Oscillator, *Phil Trans R Soc London A* 338, 533 - 546.

Ueda Y (1980), Explosion of strange attractors exhibited by Duffing's equation, *Annals of the New York Academy of Sciences 357 (12)*, 422 - 434

Wiggins S (1988), *Global Bifurcations and Chaos – Analytical Methods*, Springer-Verlag, New York.

Stability of linear mechanical systems with holonomic constraints

Peter C Müller

Safety Control Engineering, University of Wuppertal, D-42097 Wuppertal, Germany

Singular systems (descriptor systems, differential-algebraic equations) are a recent topic of research in numerical mathematics, mechanics and control theory as well. But compared with common methods available for investigating regular systems many problems still have to be solved making also available a complete set of tools to analyze, to design and to simulate singular systems. In this contribution the aspect of stability is considered. Some new results for linear singular systems are presented based on a generalized Lyapunov matrix equation. Particularly, for mechanical systems with holonomic constraints the well-known stability theorem of Thomson and Tait is generalized.

INTRODUCTION

In the last decade there was an essential progress dealing with dynamical systems described by differential-algebraic equations. In control theory descriptor systems (or singular control systems) have been investigated (Dai, 1989) and effective codes have been developed in numerical mathematics to simulate such systems, for example by Griepentrog and März (1986), Führer (1988), Hairer et al (1989), and Brenan et al (1989). But still there are many unsolved problems related to the analysis, design and simulation of descriptor systems. Here, we consider the stability behavior of differential-algebraic equations. Particularly, mechanical systems with explicit holonomic constraints are investigated. Mechanical systems with holonomic and/or nonholonomic constraints are a special class of descriptor systems which have been considered for long times in detail, for example by Neimark and Fufaev (1972), but even in this special case a lot of unsolved problems exist.

We are dealing with the stability problem of linear mechanical systems with holonomic constraints. Applying Lagrange's equation of the first kind systems with explicit constraints are governed by a set of differential equations of second order

$$\mathbf{M}\,\ddot{\mathbf{z}}(t) + (\mathbf{D}+\mathbf{G})\,\dot{\mathbf{z}}(t) + (\mathbf{K}+\mathbf{N})\,\mathbf{z}(t) = \mathbf{F}^T\,\boldsymbol{\lambda}(t) \tag{1}$$

and by algebraic equations representing the holonomic constraints

$$\mathbf{F}\,\mathbf{z}(t) = 0. \tag{2}$$

The square matrices **M**, **D**, **G**, **K** and **N** are related to inertia, damping, gyroscopic, stiffness, and circulatory forces, respectively (Müller 1977); $\mathbf{z}(t)$ denotes the f-dimensional vector of displacements and $\boldsymbol{\lambda}(t)$ is the p-dimensional vector of Lagrange's multipliers (or of the constraint forces). The $p \times f$-matrix **F** characterizes the constraints and is assumed to be row regular

$$\operatorname{rank}\mathbf{F} = p. \tag{3}$$

Usually Eq (2) is applied to eliminate redundant coordinates and to write down a set of regular equations of second order with respect to $f-p$ generalized coordinates without constraint forces. But here, the stability problem of the dynamical system (1, 2) is directly discussed without eliminating the constrained modes. Reasons for this may be the difficulties of handling large systems with some subsystems interconnected by Eq (2) or of manipulating kinematically closed-loop structures.

For a more general approach linear singular systems

$$\mathbf{E}\,\dot{\mathbf{x}}(t) = \mathbf{A}\,\mathbf{x}(t) \tag{4}$$

are considered where the matrix **E** is singular and $\mathbf{x}(t)$ denotes an n-dimensional vector of generalized state variables (or descriptor variables). The mechanical system of Eqs (1) and (2) is included into this notation by defining

$$\mathbf{x} = \begin{bmatrix} \mathbf{z} \\ \dot{\mathbf{z}} \\ \boldsymbol{\lambda} \end{bmatrix}, \quad \mathbf{E} = \begin{bmatrix} \mathbf{I} & & \\ & \mathbf{I} & \\ & & \mathbf{0} \end{bmatrix}, \tag{5}$$

part of "MECHANICS PAN-AMERICA 1993" edited by MRM Crespo da Silva and CEN Mazzilli ASME Reprint No AMR134
Appl Mech Rev vol 46, no 11, part 2, November 1993

$$\mathbf{A}=\begin{bmatrix} \mathbf{0} & \mathbf{I} & \mathbf{0} \\ -\mathbf{M}^{-1}(\mathbf{K}+\mathbf{N}) & -\mathbf{M}^{-1}(\mathbf{D}+\mathbf{G}) & \mathbf{M}^{-1}\mathbf{F}^T \\ \mathbf{F} & \mathbf{0} & \mathbf{0} \end{bmatrix}. \quad (6)$$

The dimensions are related by $n = 2f + p$.

In the following we are interested in the stability behavior of the equilibrium point $\mathbf{x} = \mathbf{0}$ and thus of the system of Eq (4). For this, first we have to define "stability" with respect to differential-algebraic systems and secondly to look for suitable criteria checking stability.

STABILITY

For regular dynamical systems the notation "stability" is well defined (even if there is not only one definition of stability but a great number of definitions related to different requirements of applications) and a related stability theory is well established (Hahn, 1967). For example, remember only the notion of stability in the sense of Lyapunov, asymptotic stability, absolute stability, and the well-known stability theory of Lyapunov.

Compared with the large amount of research related to stability problems of regular systems almost nothing has been investigated with respect to the stability behavior of singular systems. First general attempts have been presented by Bajić (1986, 1987, 1988a, 1988b), Bajić and Milić (1987), Bajić et al (1989), Griepentrog and März (1986), Dolezal (1987), Hill and Mareels (1990), März (1991). Additionally in case of linear time-invariant singular systems of Eq (4) stability has been defined by the eigenvalues of the matrix pencil $(\lambda\mathbf{E} - \mathbf{A})$.

One essential difficulty of a suitable stability definition is the problem in which (sub-) space stability has to be defined. Avoiding impulse solutions of Eq (4), initial conditions $\mathbf{x}(t_0) = \mathbf{x}_0$ must be consistent with the algebraic constraint equations. By the algebraic constraints nonimpulsive solutions belong to a consistent manifold $\mathcal{M}$ which is a subspace of the generalized state space. Restricting the stability problem to the consistent manifold $\mathcal{M}$, stability of an equilibrium point $\mathbf{x} = \mathbf{0}$ of Eq (4) can be defined in the sense of Lyapunov restricting the perturbed motion to the consistent manifold $\mathcal{M}$. Similarly asymptotic stability is defined with respect to $\mathcal{M}$.

This stability definition is useful no doubt and it corresponds exactly to the stability definition of the related regular system if the algebraic constraints are used to eliminate redundant coordinates ending in a regular set of ordinary differential equations. But this elimination procedure requires an exact description of the dynamical system and an exact elimination algorithm. If on the contrary there are some uncertain parameters in Eq (4) the above mentioned stability definition is unsatisfactory. The consistent manifold $\mathcal{M}$ is not certainly defined, and therefore the stability behavior of an uncertain system cannot be covered by this stability definition. Looking for robust stability a different definition is required.

Besides of the efforts of the group of Bajić (1986 etc.) actually there is no general stability theory available even confining ourselves to the definition of stability in the sense of Lyapunov restricted to $\mathcal{M}$. It may be expected that the method of Lyapunov functions for the stability problem of motions with respect to a part of the variables will be a helpful tool for further general stability investigations, see for example Oziraner and Rumiantsev (1972) or Müller (1982).

Contrary to the missing general theory in the special case of linear time-invariant singular systems of Eq (4) the stability behavior can be discussed in more detail as it is shown in the next sections.

LINEAR TIME-INVARIANT DESCRIPTOR SYSTEMS

Looking for the stability of the linear descriptor system (4) we use the stability definition of control theory (Dai, 1989):
Lemma: System (4) is called asymptotically stable *iff* all finite eigenvalues λ_i, $i = 1, \ldots, n_1$, of the matrix pencil $(\lambda\mathbf{E} - \mathbf{A})$ have negative real parts.

This definition assumes the existence of certain finite eigenvalues λ_i, $i = 1, \ldots, n_1$, of the matrix pencil $(\lambda\mathbf{E}-\mathbf{A})$, that is the vanishing of the characteristic polynomial

$$p(\lambda) \equiv det(\lambda\mathbf{E} - \mathbf{A}) \quad (7)$$

for some isolated values λ_i. That includes the requirements of quadratic matrices $\mathbf{E}$, $\mathbf{A}$ and additionally of

$$p(\lambda) \not\equiv 0\,. \quad (8)$$

These two requirements define a regular matrix pencil $(\lambda\mathbf{E} - \mathbf{A})$; otherwise the pencil is called singular. Therefore, the above stability definition is meaningful only for regular pencils; in case of singular pencils a stability definition does not exist. In the following regular matrix pencils are assumed in Eq (4). Mechanical systems described by Eqs (1) and (2) always define a regular matrix pencil via Eqs (5–6).

It is well-known in matrix theory that a regular matrix pencil $(\lambda\mathbf{E} - \mathbf{A})$ is strictly equivalent to the Kronecker canonical form (Dai, 1989), that is there exist two regular matrices

$$\mathbf{R} = \begin{bmatrix} \mathbf{R}_1 \\ \mathbf{R}_2 \end{bmatrix}, \qquad \mathbf{S} = \begin{bmatrix} \mathbf{S}_1 & \mathbf{S}_2 \end{bmatrix} \quad (9)$$

such that

$$\mathbf{RES} = \begin{bmatrix} \mathbf{I}_1 & \mathbf{0} \\ \mathbf{0} & \mathbf{N}_k \end{bmatrix}, \qquad \mathbf{RAS} = \begin{bmatrix} \mathbf{A}_1 & \mathbf{0} \\ \mathbf{0} & \mathbf{I}_2 \end{bmatrix}, \quad (10)$$

where the identity matrices $\mathbf{I}_1$, $\mathbf{I}_2$ are of dimen[illegible] n_2 with $n_1+n_2 = n$ and the $n_2 \times n_2$ matrix $\mathbf{N}_k$

index k ($\mathbf{N}_k^{k-1} \neq \mathbf{0}$, $\mathbf{N}_k^k = \mathbf{0}$) defining the index of the linear descriptor system (4). Introducing new coordinates

$$\begin{bmatrix} \mathbf{y}_1 \\ \mathbf{y}_2 \end{bmatrix} = \mathbf{S}^{-1}\mathbf{x}, \qquad \mathbf{x} = \mathbf{S}_1\mathbf{y}_1 + \mathbf{S}_2\mathbf{y}_2 \tag{11}$$

system (4) is decoupled in the "slow" subsystem

$$\dot{\mathbf{y}}_1 = \mathbf{A}_1\mathbf{y}_1 \tag{12}$$

and the "fast" subsystem

$$\mathbf{N}_k\dot{\mathbf{y}}_2 = \mathbf{y}_2\,. \tag{13}$$

Consistent solutions require $\mathbf{y}_2(t_0) = \mathbf{0}$ and therefore $\mathbf{y}_2(t) \equiv \mathbf{0}$. It is easily shown that the eigenvalues of the system (4) coincide exactly with the eigenvalues of the slow subsystem (12). Therefore, the asymptotic stability of Eq (4) is guaranteed *iff* the slow subsystem is asymptotically stable.

Besides the discussion of stability by eigenvalues the stability behaviour of linear regular systems can be handled by the Lyapunov matrix equation (Müller, 1977). Therefore, the stability of the slow subsystem can be investigated by definiteness properties of matrices $\mathbf{P}_1$, $\mathbf{Q}_1$ of the Lyapunov matrix equation

$$\mathbf{A}_1^T\mathbf{P}_1 + \mathbf{P}_1\mathbf{A}_1 = -\mathbf{Q}_1\,. \tag{14}$$

The question arises how to apply all the well-known results on Eq (14) to the original system matrices $\mathbf{E}$, $\mathbf{A}$. Performing the equivalence back-transformation of Eqs (10,11) the equation (14) results in a generalized Lyapunov matrix equation

$$\mathbf{A}^T\mathbf{P}\mathbf{E} + \mathbf{E}^T\mathbf{P}\mathbf{A} = -\mathbf{Q} \tag{15}$$

which includes besides of Eq (14) certain arbitrary terms with respect to the fast subsystem (13). This equation (15) may be also found by a Lyapunov function

$$v = \mathbf{x}^T\mathbf{E}^T\mathbf{P}\mathbf{E}\,\mathbf{x} \tag{16}$$

which leads in usual manner to

$$\dot{v} = \mathbf{x}^T(\mathbf{A}^T\mathbf{P}\mathbf{E} + \mathbf{E}^T\mathbf{P}\mathbf{A})\,\mathbf{x} \overset{!}{=} -\mathbf{x}^T\mathbf{Q}\,\mathbf{x}\,. \tag{17}$$

The stability requirement in Eq (17) results in Eq (15).

From Eqs (14–17) we have the first main result.

Theorem 1: If there are symmetric matrices $\mathbf{P}$, $\mathbf{Q}$ satisfying equation (15) and if

$$\mathbf{x}^T\mathbf{E}^T\mathbf{P}\mathbf{E}\,\mathbf{x} > 0 \qquad \forall \mathbf{x} = \mathbf{S}_1\,\mathbf{y}_1 \neq \mathbf{0}\,, \tag{18}$$

$$\mathbf{x}^T\mathbf{Q}\mathbf{x} \geq 0 \qquad \forall \mathbf{x} = \mathbf{S}_1\,\mathbf{y}_1 \tag{19}$$

then system (4) is asymptotically stable if

$$rank\begin{bmatrix} s\mathbf{E} - \mathbf{A} \\ \mathbf{S}_1^T\mathbf{Q} \end{bmatrix} = n \qquad \forall s \in \mathbb{C} \tag{20}$$

and marginally stable if condition (20) does not hold.

The term of marginal stability denotes stability in the sense of Lyapunov without asymptotic stability. It should be noted that Theorem 1 presents a generalization of a result by Owens and Debeljkovic (1985) where the observability condition (20) does not appear and the requirement (19) is replaced by its positive definite analogue. The weakening of inequality (20) to the positive semidefinite case requires the additional observability condition (20). In case of mechanical systems this generalization means that complete damping can be replaced by pervasive damping (Müller, 1977).

A special difficulty is the check whether the quadratic forms (18), (19) are positive (semi-) definite with respect to the states of the consistent manifold $\mathcal{M}$ only. Comparing the admissible states $\mathbf{x} = \mathbf{S}_1\mathbf{y}_1$ with the transformation (11) obviously the definiteness check is restricted to consistent states. The columns of $\mathbf{S}_1$ present a basis of $\mathcal{M}$. The condition (20) requires R-observability (Dai, 1989) of a fictitious measurement matrix $\mathbf{S}_1^T\mathbf{Q}$ with respect to the dynamic system (4). Compared with the usual observability condition in case of regular systems (Müller,1977), the projection on $\mathcal{M}$, that is ($\mathbf{S}_1^T\mathbf{Q}$), is needed instead of the full matrix $\mathbf{Q}$.

Applying Theorem 1 usually it is very difficult to find the matrix $\mathbf{S}_1$. Only if $\mathbf{S}_1$ can be calculated explicitly or if $\mathcal{M}$ can be imbedded in a subspace $\bar{\mathcal{M}} \supset \mathcal{M}$ and (18), (19) hold for all $\mathbf{x} \in \bar{\mathcal{M}}$, then Theorem 1 may lead to interesting stability results. In the following section the application of Theorem 1 to the mechanical system (1) with holonomic constraints (2) is shown.

LINEAR TIME-INVARIANT MECHANICAL SYSTEMS WITH HOLONOMIC CONSTRAINTS

Very often stability behavior of mechanical systems has been proved using the total energy, that is the Hamiltonian, as a Lyapunov function. In case of linear time-invariant mechanical systems this approach leads to the well-known theorem of Thomson and Tait which was strictly proved by Chetaev (Müller, 1977). Is it possible to generalize this theorem for mechanical systems (1) with holonomic constraints (2)?

As usual we have to restrict the problem to the non-circulatory case:

$$\mathbf{N} = \mathbf{0}\,. \tag{21}$$

Using the Hamiltonian

$$v = H = \frac{1}{2}\dot{\mathbf{z}}^T\mathbf{M}\,\dot{\mathbf{z}} + \frac{1}{2}\mathbf{z}^T\mathbf{K}\,\mathbf{z} \tag{22}$$

for the Lyapunov function (16) the Lyapunov matrix equation (15) holds for

$$\mathbf{P} = \frac{1}{2}\begin{bmatrix} \mathbf{K} & & \\ & \mathbf{M} & \\ & & \mathbf{0} \end{bmatrix}, \tag{23}$$

$$\mathbf{Q} = \begin{bmatrix} \mathbf{0} & & \\ & \mathbf{D} & -\frac{1}{2}\mathbf{F}^T \\ & -\frac{1}{2}\mathbf{F} & \mathbf{0} \end{bmatrix}. \tag{24}$$

It should be noted that neither the matrix $\mathbf{P}$ is positive definite (at best it is positive semidefinite only) nor the matrix $\mathbf{Q}$ is positive semidefinite (it is indefinite for $\mathbf{F} \neq \mathbf{0}$) but that the conditions (18), (19) are valid if the matrices $\mathbf{M}$, $\mathbf{K}$ are positive definite and $\mathbf{D}$ is positive semidefinite at least:

$$\mathbf{x}^T\mathbf{E}^T\mathbf{P}\mathbf{E}\,\mathbf{x} = H > 0, \tag{25}$$

$$\mathbf{x}^T\mathbf{Q}\,\mathbf{x} = \dot{\mathbf{z}}^T\mathbf{D}\,\dot{\mathbf{z}} \geq 0. \tag{26}$$

The main problem is the check of condition (20).

As mentioned above the essential step to check condition (20) is the calculation of the matrix $\mathbf{S}_1$ of the transformation (10,11). By Müller and Schüpphaus (1993) this transformation has been derived for mechanical systems (1) with holonomic constraints (2). The transformation matrices are given by

$$\mathbf{R} = \begin{bmatrix} \mathbf{L}(\mathbf{I}_f - \mathbf{V}^T\mathbf{F}) & \mathbf{0} & \mathbf{U}\bar{\mathbf{P}}\mathbf{V}^T \\ \mathbf{U}\bar{\mathbf{P}}\mathbf{V}^T\mathbf{F} & \mathbf{L}(\mathbf{I}_f - \mathbf{V}^T\mathbf{F}) & \mathbf{U}\mathbf{X}\mathbf{V}^T \\ \mathbf{0} & \mathbf{F} & \mathbf{0} \\ \mathbf{F} & \mathbf{0} & \mathbf{0} \\ \mathbf{0} & \mathbf{0} & \mathbf{I}_p \end{bmatrix}, \tag{27}$$

$$\mathbf{S} = \Big[\underbrace{\begin{matrix} \mathbf{L}^+ & \mathbf{0} \\ \mathbf{0} & \mathbf{L}^+ \\ \mathbf{V}\bar{\mathbf{Q}}\mathbf{L}^+ & \mathbf{V}\bar{\mathbf{P}}\mathbf{L}^+ \end{matrix}}_{\mathbf{S}_1}\ \underbrace{\begin{matrix} \mathbf{0} & \mathbf{0} & \mathbf{V}^T \\ \mathbf{0} & \mathbf{V}^T & -\mathbf{L}^+\mathbf{U}\bar{\mathbf{P}}\mathbf{V}^T \\ \bar{\mathbf{F}} & \mathbf{V}\bar{\mathbf{P}}\mathbf{V}^T & \mathbf{V}\mathbf{X}\mathbf{V}^T \end{matrix}}_{\mathbf{S}_2}\Big], \tag{28}$$

with

$$\begin{aligned} \bar{\mathbf{P}} &= \mathbf{D} + \mathbf{G}, & \mathbf{L}^+ &= \mathbf{L}^T(\mathbf{L}\mathbf{L}^T)^{-1}, \\ \bar{\mathbf{Q}} &= \mathbf{K} + \mathbf{N}, & \mathbf{V} &= \bar{\mathbf{F}}\mathbf{F}\mathbf{M}^{-1}, \\ \bar{\mathbf{F}} &= (\mathbf{F}\mathbf{M}^{-1}\mathbf{F}^T)^{-1}, & \mathbf{U} &= \mathbf{L}\mathbf{M}^{-1}(\mathbf{I}_f - \mathbf{F}^T\mathbf{V}), \\ \mathbf{L} &= (kernel\ \mathbf{F})^T, & \mathbf{X} &= (\bar{\mathbf{Q}} - \bar{\mathbf{P}}\mathbf{L}^+\mathbf{U}\bar{\mathbf{P}}). \end{aligned}$$

The dimensions of the slow and fast subsystems Eqs (12, 13) are

$$n_1 = 2(f-p), \quad n_2 = 3p. \tag{29}$$

The matrix of the slow subsystem (12) results in

$$\mathbf{A}_1 = \begin{bmatrix} \mathbf{0} & \mathbf{I}_{f-p} \\ -\mathbf{U}\bar{\mathbf{Q}}\mathbf{L}^+ & -\mathbf{U}\bar{\mathbf{P}}\mathbf{L}^+ \end{bmatrix} \tag{30}$$

and the nilpotent matrix of Eq (13) is

$$\mathbf{N}_k = \mathbf{N}_3 = \begin{bmatrix} \mathbf{0} & \mathbf{I}_p & \mathbf{0} \\ \mathbf{0} & \mathbf{0} & \mathbf{I}_p \\ \mathbf{0} & \mathbf{0} & \mathbf{0} \end{bmatrix} \tag{31}$$

From the transformation matrix $\mathbf{S}$, Eq (28), the submatrix $\mathbf{S}_1$ is available and condition (20) can be proved. From this, the second main result is obtained.

Theorem 2: If the system matrices of a non-circulatory mechanical system (1), (2), (21) satisfy

$$\mathbf{M} = \mathbf{M}^T > 0, \quad \mathbf{D} = \mathbf{D}^T \geq 0, \quad \mathbf{K} = \mathbf{K}^T > 0 \tag{32}$$

then the mechanical system is asymptotically stable if

$$rank \begin{bmatrix} \mathbf{M}s^2 + (\mathbf{D}+\mathbf{G})s + \mathbf{K} & -\mathbf{F}^T \\ \mathbf{F} & \mathbf{0} \\ (\mathbf{I} - \mathbf{F}^+\mathbf{F})\mathbf{D}s & \mathbf{0} \end{bmatrix} = f + p \tag{33}$$

for all $s \in \mathbb{C}$ holds and marginally stable if (33) does not hold.

Here, $\mathbf{F}^+$ represents the Moore-Penrose inverse matrix of $\mathbf{F}$.

Theorem 2 represents a very conservative result. It only states that if the unconstrained mechanical system is asymptotically stable and if the constraints do not block pervasive damping then the constrained mechanical system is asymptotically stable, too. But the effect of stabilization by the constraints is not included. But that can be shown very easily by a formal trick. If the holonomic constraints (2) are satisfied then the stability behavior of the mechanical system is not changed if the damping and stiffness matrices $\mathbf{D}$ and $\mathbf{K}$ are replaced by $\mathbf{D}+\alpha\mathbf{F}^T\mathbf{F}$ and $\mathbf{K}+\beta\mathbf{F}^T\mathbf{F}$. Then the third main result is immediately derived.

Theorem 3: If the system matrices of a non-circulatory mechanical system (1), (2), (21) satisfy

$$\mathbf{M} = \mathbf{M}^T > 0, \quad \mathbf{D} + \alpha\mathbf{F}^T\mathbf{F} \geq 0, \quad \mathbf{K} + \beta\mathbf{F}^T\mathbf{F} > 0 \tag{34}$$

for certain positive numbers $\alpha > 0$, $\beta > 0$ then the mechanical system is asymptotically stable if condition (33) holds and marginally stable if condition (33) does not hold.

Here, the stabilization effect of the holonomic constraints is explicitly shown. Theorem 3 represents the proper generalization of the stability theorem of Thomson, Tait, Chetaev including also the effect of pervasive damping.

CONCLUSION

This contribution deals with the stability problem of descriptor systems. It critically reviews the state of the art demonstrating problems in the kind of suitable definitions for stability of descriptor systems and indicating as well a lack of stability theory related to singular dynamical systems. It is hoped that a stability theory can be developed based on the results of partial stability. In case of linear descriptor systems some detailed stability results have been proved based on an extended Lyapunov matrix equation. But to improve the applicability of these results an effective algorithm has to be established characterizing the consistent solution subspace. This is possible in the case of constrained mechanical systems. There, the matrices of a transformation to the Kronecker canonical form can be calculated explicitly. Therefore, the general results on the stability of linear descriptor systems have been specialized to mechanical systems with holonomic constraints generalizing the famous theorem of Thomson, Tait, Chetaev.

REFERENCES

Bajić, VB (1986), Partial exponential stability of semi-state systems, *Int J Control* **44**(5), 1383-1394.

Bajić, VB (1987), Lyapunov function candidates for semi-state systems, *Int J Control* **46**(6), 2171-2181.

Bajić, VB (1988a), Equation of perturbed motions and stability of state and semi-state systems, *Int J Control* **47**(6), 1849-1860.

Bajić, VB (1988b), Generic stability and boundedness of semistate systems, *IMA J Math Control & Inform* **5**, 103-115.

Bajić, VB and Milić, MM (1987), Extended stability of motion of semi-state systems, *Int J Control* **46**(6), 2183-2197.

Bajić, VB, Zivković, MM, and Zivković, JS (1989), Nonlinearities in semistate systems and exponential stability of response, *Int J Control* **50**(4), 1559-1561.

Brenan, KE, Campbell, SL, and Petzold, LR (1989), *Numerical solution of initial value problems in differential-algebraic equations*, North-Holland, New York.

Dai, L (1989), *Singular control systems*, Lecture Notes in Control and Information Sciences 118, Springer, Berlin-Heidelberg, Germany.

Dolezal, V (1987), Some practical stability criteria for semistate equations, *Circuits Systems Signal Process* **6**(3), 335-345.

Führer, C (1988), Differential-algebraische Gleichungssysteme in mechanischen Mehrkörpersystemen: Theorie, numerische Ansätze und Anwendungen, PhD Thesis, Technische Universität München, Germany.

Griepentrog, E and März, R (1986), *Differential-algebraic equations and their numerical treatment*, Teubner, Leipzig, Germany.

Hahn, W (1967), *Stability of motion*, Springer, Berlin-Heidelberg, Germany.

Hairer, E, Lubich, C, and Roche, M (1989), *The numerical solution of differential-algebraic systems by Runge-Kutta methods*, Lecture Notes in Mathematics 1409, Springer, Berlin-Heidelberg, Germany.

Hill, DJ and Mareels, IMY (1990), Stability theory for differential-algebraic systems with application to power systems, in *Robust Control of Linear Systems and Nonlinear Control*, MA Kaashoek, JH van Schuppen and ACM Ran (eds), Birkhäuser, Basel, Switzerland, 437-445.

März, R (1991), On quasi-index 2 differential-algebraic equations, Reprint 269, Humboldt-Universität Berlin, Germany.

Müller, PC (1977), *Stabilität und Matrizen*, Springer, Berlin-Heidelberg, Germany.

Müller, PC (1982), Zum Problem der partiellen asymptotischen Stabilität, in *Festschrift Prof. Dr. rer. nat. Kurt Magnus*, Lehrstuhl B für Mechanik, Technische Universität München, Germany, 237-268.

Müller PC and Schüpphaus, R (1993), Control of linear mechanical descriptor systems, in *Proceedings of the European Control Conference (ECC'93)*, Groningen, The Netherlands, June 28 - July 1, 1993.

Neimark, JI and Fufaev, NA (1972), *Dynamics of nonholonomic systems*, Translations of Mathematical Monographs 33, American Mathematical Society, Providence RI.

Owens, DH and Debeljkovic, DL (1985), Consistency and Lyapunov stability of linear descriptor systems: a general analysis, *IMA J Math Control & Inform* **2**, 139-151.

Oziraner, AS and Rumiantsev, VV (1972), The method of Lyapunov functions in the stability problem for motion with respect to a part of the variables, *J Appl Math Mech* **36**, 341-362.

Dynamic modelling and control strategies of space manipulators

A Ercoli-Finzi and P Mantegazza

Dipartimento di Ingegneria Aerospaziale
Politecnico di Milano, via Golgi 40, 20133 Milano, Italy

In this work the dynamics of a manipulator arm is analyzed by Maggi's formulation and by automatic development of the equations of motion. Two control strategies, that is an adaptive and a standard one, are taken into account in order to satisfactory perform pick and place maneuvers. Numerical simulations emphasize performance qualities and limits of the two choices and suggest a possible implementation of mixed control strategies.

CONTENTS

INTRODUCTION

Because of the difficulties and dangers connected with space exploration, robots and space manipulators have been heavily employed since the beginning of space activity. It is merit of Vikings and Luna probes (Gatland 1980) if a specific knowledge of some celestial bodies has been acquired. Future activities will be quite similar and robots and manipulators will be utilized more and more, as it now happens for manipulator arms designed for the Space Shuttle and HERMES.

Since their repairing and servicing cannot be easily and frequently scheduled and, on the other hand, requirements on their performances are very tight, the dynamic behavior of space manipulators must be deeply understood and accurately simulated and tested on ground, to avoid mistakes and, in some cases, disasters.

Numerical simulations imply the resolution of the equations of motion, whose number can be very high, because of the many degrees of freedom. On the other hand their structure is very complex, due to the complexity of the body chain, coming from their constraints and physical properties.

For that an accurate, realistic, easily implementable (and computationally effective) dynamic model is required. To this aim the method proposed by Maggi (1896) is adopted, because it allows to take into account both holonomic and non-holonomic constraints and at the same time is characterized by the simplest equations, obtained with the least mathematical complexity (Kane and Levinson 1980).

In order to guarantee real time simulations and the capability of facing dynamic systems with different physical and geometric characteristics, the symbolic equations manipulation can be adopted by making use of ad hoc developed or already existing software. As it will be shown, Maggi's equations are also well fitted to the adoption of different control strategies, to assure the end effector prescribed motion. In this case, if rapid highly non linear maneuvers are required, the inverse dynamics must be computed to anticipate control forces. By using symbolic manipulation, it is then possible to carry out real time simulations on realistic dynamic models.

Attention will be focused both on standard and adaptive control strategies, the latter being particularly suitable in case of badly known physical and geometric parameters.

KINEMATICS

The dynamic model here developed is referred to a tree like multibody chain, both open and closed, either connected to the ground or not. If an n-rigid link system is analyzed, its 3D configuration is described by $3n$ parameters x_{ki} (k = 1,2,3 i = 1,...n), related by m holonomic constraints equations

$$f_j(x_{ki}, t) = 0 \qquad (1)$$

A p-dimensional time function configuration vector $\{q\}$ can be defined, p=3n-m, constrained by m_a non-holonomic, i.e. differential equations

$$[A]\{\dot{q}\}+\{b\}=0 \qquad (2)$$

By partitioning the vector $\{q\}$ in a (p-m_a) component vector $\{q_i\}$ and a m_a component vector $\{q_d\}$, Eq (2) takes the form

$$[A_i, A_d]\{\dot{q}_i, \dot{q}_d\}+\{b\}=0 \qquad (3)$$

If $[A_d]$ is a non singular matrix, it is possible to solve Eq (3) with respect to $\{q_d\}$

$$\{\dot{q}_d\}=[C]\{\dot{q}_i\}+\{d\} \qquad (4)$$

and to introduce a p_a dimension parameter vector $\{u\}$, $p_a = p - m_a$, defined by

$$\{u\}=[U]\{\dot{q}_i\}+\{u_t\} \qquad (5)$$

which represents the independent parameter vector of the system, to be determined by integration of the equations of motion.

Linear and angular velocities of each link and body are functions of u according to

$$\{v\}=[V_r]\{u\}+\{v_t\} \qquad (6)$$

$$\{\omega\}=[\omega_r]\{u\}+\{\omega_t\} \qquad (7)$$

in which the columns of $[V_r]$ are the partial linear velocities.

In the case of open chains, with 1 degree of freedom rotatioual or translational joints, anchored to a main body, like the Shuttle or the Space Station, the total number of degrees of freedom is the joints number N, and the joint displacements can suitably be assumed as lagrangian coordinates. If the chain is not anchored, the configuration of one body must be defined with respect to a known reference frame; by introducing Euler angles and the coordinates of one point, that is 6 new degrees of freedom, the matrix $[U]$ takes the diagonal form

$$[U]=[[E_u];[E_d];1] \qquad (8)$$

$[E_u]$ being the coordinate transformation matrix and $[E_d]$ the Euler angles derivatives transformation matrix.

Internal constraints of closed loop chains can be taken into account by assuming the same linear and rotational velocities for the two parts of broken joints; their general compact form is of the type of Eq (2) that represents a generic non holonomic constrai[illegible]

In order to describe the k[illegible] [illegible]onships between a pair of adjacent links of [illegible] [illegible]cessary to know the position and orienta[illegible] [illegible]s and bodies as function of lagrangian coordinates. To this aim a reference frame must be assigned to each link: the coordinate transformation between two adjacent links is

$$\{x_{i-1}\}=[\Lambda_{i-1,i}]\{x_i\} \qquad (9)$$

where $[\Lambda_{i-1,i}]$ is the transformation matrix that can be computed through the Denavit-Hartenberg parameters. If $\{x_i\}$ is homogeneus and its fourth coordinate is taken always with unit value, we have

$$[\Lambda_{i-1,i}]=\begin{bmatrix} c\vartheta_i & -s\vartheta_i c\alpha_i & s\vartheta_i s\alpha_i & a_i c\vartheta_i \\ s\vartheta_i & c\vartheta_i c\alpha_i & -c\vartheta_i s\alpha_i & a_i s\vartheta_i \\ 0 & s\alpha_i & c\alpha_i & d_i \\ 0 & 0 & 0 & 1 \end{bmatrix} \qquad (10)$$

ϑ, α, a and d being the Denavit-Hartenberg parameters (Paul 1981).

The absolute position of the end effector is

$$\{x_0\}=[T]\{x_N\} \qquad (11)$$

where $\{x_N\}$ is its local position and

$$[T]=[\Lambda_{0,1}][\Lambda_{1,2}]\ldots[\Lambda_{N-1,N}] \qquad (12)$$

In the case of a floating arm

$$\{x_0\}=[T']\{x_N\}=[\Lambda][T]\{x_N\} \qquad (13)$$

$[\Lambda]$ being the transformation matrix between the first reference frame and the anchored one.

Linear and angular velocities depend only on the derivatives of $[\Lambda_{i-1,i}]$ and $[\Lambda]$ and the highly non linear kinematic equations allow to compute positions and velocities when q and $\dot{q}$ are known by

$$x_i = f_i(\{q\}) \qquad (14)$$

If the inverse kinematics is required, as it frequently happens for controlled dynamics, $\{q\}$ and $\{\dot{q}\}$ must be determined as a function of $\{x\}$. In this case

$$\{\dot{q}\}=[J]^{-1}\{\dot{x}\} \qquad (15)$$

where $[J]$ is the Jacobian of Eq (14).

Since it is generally almost impossible to obtain an analytical solution, in the following a numerical procedure, based on Newton-Raphson technique, is proposed (Teukolsky et al 1986), according to which Eq (14) becomes

$$\{x\} = [J]_0 \Delta\{q\} + F(\{q_0\}) \tag{16}$$

being $\{q_0\}$ supposed to be close to its actual value. If Jacobian matrix is not singular, $\Delta\{q\}$, and consequently $\{q\}$, can be evaluated and the procedure iterated till convergence.

DYNAMICS

As already said, the dynamic equations are derived by Maggi's method, with the advantage that only the internal forces driving the joints must be taken into account. No role is played by the reaction forces, related to the constraints, and by non-working forces. Besides, as stated by Kane, who is nowadays recognized as the developer of the equations themselves (Borri et al 1986), they are particularly suitable for implementation.

To this aim, the equations of motion of an N masses system, obtained from D'Alembert principle

$$\{F_j\} - m_j\{a_j\} = 0 \qquad j=1,\dots N \tag{17}$$

is projected on the partial linear velocities, giving

$$\{F_r\} + \{F_r^*\} = 0 \tag{18}$$

where

$$\{F_r\} = \sum_{j=1}^{N}\{V_r\}_j^T\{F_j\} \tag{19}$$

are the generalized active forces and

$$\{F_r^*\} = -\sum_{j=1}^{N}\{V_r\}_j^T m_r\{a_r\} \tag{20}$$

are the generalized inertia forces.

For a fixed constrained rigid body we have

$$\{\alpha\} = [\omega_r]\{\dot u\} + \{\dot q\}^T\left[\frac{\partial\omega_r}{\partial q_s}\right]\{u\} \tag{21}$$

$$\{a\} = [V_r]\{\dot u\} + \{\dot q\}^T\left[\frac{\partial V_r}{\partial q_s}\right]\{u\} \tag{22}$$

and

$$\{F_r^*\} = -\sum_{i=1}^{N}\Bigg\{\{V_r\}_i^T m_i\left(\sum_{s=1}^{Pa}\{V_s\}_i\dot u_s\right) + \{\omega_r\}_i^T[I]_i\left(\sum_{s=1}^{Pa}\{\omega_s\}_i\dot u_s\right) +$$
$$+\{V_r\}_i^T m_i\left(\sum_{s=1}^{Pa}\sum_{t=1}^{Pa}\frac{\partial\{V_s\}_i}{\partial q_t}u_s\dot q_t\right) +$$
$$+\{\omega_r\}_i^T\left[[I]_i\left(\sum_{s=1}^{Pa}\sum_{t=1}^{Pa}\frac{\partial\{\omega_s\}_i}{\partial q_t}u_s\dot q_t\right) + [\omega x]_i[I]_i\{\omega\}_i\right]\Bigg\} \tag{23}$$

It is remarked that $\{F_r^*\}$ linearly depends from $\{\dot u\}$ in Eq(23).

By a suitable rearrangement, the equations of motion can be given the compact form

$$[M]\{\dot u\} = \{f\} + \{\tau\} \tag{24}$$

$[M]$ being a positive definite matrix

$$M_{rs} = \sum_{i=1}^{N}\{V_r\}_i^T m_i\{V_s\}_i + \{\omega_r\}_i^T[I]_i\{\omega_s\} \tag{25}$$

and $\{f\}$ is the part of $\{F^*\}$ representing the forces due to the motion, like Coriolis, centrifugal, etc., and $\{\tau\}$ the generalized active force vector. A similar, even if much more complex system, can be obtained for flexible bodies (Galli 1991), but due to the large computer memory requirements only lumped deformable elements at the joints have been modelled.

IMPLEMENTATION AND RESULTS

The equations have been automatically derived by MACSYMA and subsequently solved numerically. As a first step a double tether system was tested, proving a very good agreement with theoretical results.

As a second step, an implementation has been carried out for the 3 d.o.f. Stanford and Puma manipulators, whose equations are known (Levi and Hemati 1986, Passera 1990), by Lagrangian derivation. Numerical solutions, compared with the results obtained by DADS, a general purpose computer program for the dynamic analysis of multybodies, evidenced an excellent agreement and a significant time saving, due to the appropriate formulation and to the symbolic manipulation of the equations of motion.

The most important conclusion from the operational point of view is that translational joints highly reduce the equation complexity with respect to rotation joints, due to the simpler Denavit-Hartenberg matrices. Anyway, even in the case of rigid link manipulators, the memory requirement is dramatically large, as proved by the f_1 element of Puma equations that covers more than 190 program rows.

CONTROL STRATEGIES

In the specific case of a space manipulator, the control system is devoted to solve tracking problems, that means to assure that the end effector describes a prescribed trajectory typical of a pick and place maneuver in presence of known obstacles.

The choice has been a multybody system without redundancies, so that only a finite number of configurations turns out to be compatible with each end effector position.

In this case the joints space control is the simplest one in that it is possible to find, by inverse kinematics, the joint displacements corresponding to the desired end effector positions. To this aim the trajectories are suitably checked as time functions and the corresponding joint positions are acquired by the procedure previously recalled. The inverse dynamic problem strongly asks for a symbolic manipulation, allowing at the same time accurate modelling and real time simulations.

The control problem finds its main difficulty in the not completely known physical characteristics of manipulators, as it frequently happens when they are devoted to transportation and manipulation of target objects. To avoid design errors coming from this insufficient knowledge, adaptive control strategies are suitable (Galli 1991).

ADAPTIVE CONTROL

In order to find the control law of model reference adaptive P.D. control system, utilizing a feed-forward and a feed-back loop (Craig 1988), the error vector

$$\{e\} = \{q_d\} - \{q\} \tag{26}$$

and a suitable evolution of the generalized velocities

$$\{\dot{u}^*\} = \{\ddot{u}_d\} + [K_p]\{e\} + [K_d]\{\dot{e}\} \tag{27}$$

are introduced. In the above equations d refers to the desired values and $[K_p]$, $[K_d]$ are positive definite matrices.

By inverse dynamics control $\{\tau\}$, responsible of the desired motion, can be evaluated when physical parameters are known, by the equation of motion

$$\{\tau\} = \sum_{i=1}^{rj} m_{ij} f_{ij}(\{q\},\{u\}) + \sum_{i=1}^{sj} n_{ij} g_{ij}(\{q\},\{u\}) \tag{28}$$

in which m_{ij} and n_{ij} are physical parameters, while f and g depend on geometric parameters.

The correlation between the coordinate error vector $\{x\}$

$$\{x\}_i = \tag{29}$$

and the parameter vector $\{\varphi\}$ is

$$\{\dot{x}\} = [A]\{x\} + [B][M']^{-1}[W]\{\varphi\} \tag{30}$$

where $[M']$ is the estimated mass matrix. If $[K_p]$ and $[K_d]$ are diagonal, $[A]$ and $[B]$ are also diagonal, with

$$A_{ii} = \begin{bmatrix} 0 & 1 \\ -k_{pi} & -k_{di} \end{bmatrix} \tag{31}$$

$$[B] = [0,1]^T \tag{32}$$

Lyapunov stability criterion assure that the system is stable if parameter estimation satisfies the condition

$$\{\dot{p}\} = [\Gamma][W]^T [M']^{-1}\{e\}_1 \tag{33}$$

being

$$\{e\}_1 = \{\dot{e}\} + [\psi]\{e\} \tag{34}$$

the filtered vector.

The implementation of the proposed control strategy requires the evaluation of $[W]$, in the case of symbolic manipulation. That is feasible when the equations of motion are first order equations with respect to the parameters. That implies a suitable choice of the parameters themselves that not always is an obvious one. In this case Eq (28) can be written in the form

$$[W]\{PAR\} = \{\tau\} \tag{35}$$

$\{PAR\}$ being the vector of the physical parameters, from which $[W]$ can be obtained.

STANDARD CONTROL

Due to the complex implementation of adaptive control, also a standard control strategy has been adopted.

The adopted control system is a double PID stage with a faster internal loop on the joint speed and an outer slower loop on positions. Passing band bounds must assure that no excitation of structural frequencies of elements connected to velocity and position sensors can occur (Paul 1981).

Attention must be paid also to possible instabilities due to the coupling of the velocity and position loop, caused by different changes in physical characteristics of the manipulator.

NUMERICAL SIMULATIONS

The designed adaptive control has been first tested on the double tether system, by asking the end effector to perform a circular trajectory with a mass estimation error of 80 per cent.

Numerical results prove that controls are well behaving: the parameter identification occurs in a few seconds and the actual trajectory is the desired one, Figs 1-2.

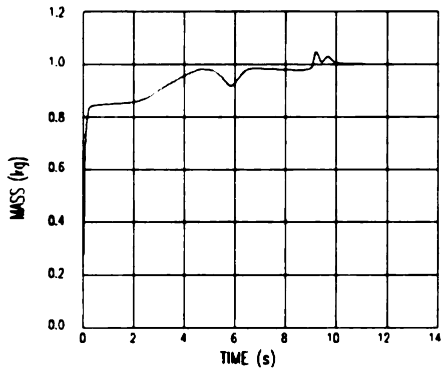

Fig 1. Double tether system: mass identification.

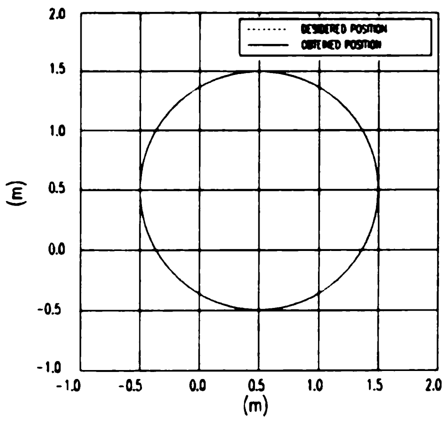

Fig 2. Adaptive double tether system: end effector trajectory.

Comparison with non adaptive control implementation making use of the same PD controller, Fig 3, enphasizes the efficiency of the adaptive law.

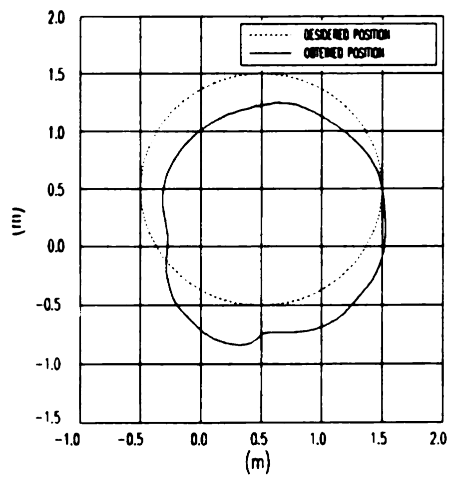

Fig 3. Non adaptive trajectory tracking.

Further simulations have been performed with the Stanford Manipulator, the physical and geometrical parameters of which are well known (Paul 1981). Identification of the inertial parameters of the third body has been carried out for a pick and place maneuver (Fig 4) of a 3 kg mass (Fig 5).

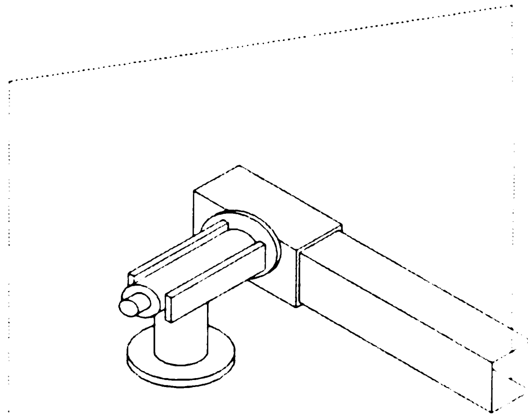

Fig 4. Pick and place trajectory.

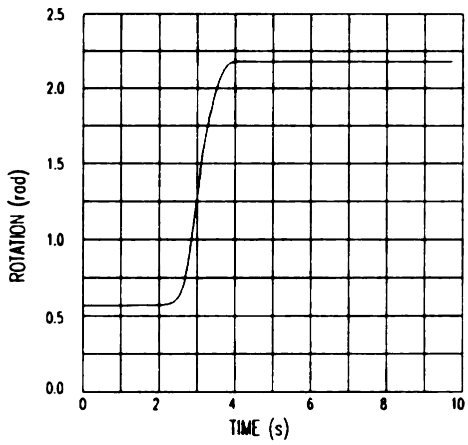

Fig 5. First coordinate behavior.

Figure 6 shows that the tracking error is quite small and anyway largely reduced with respect to non adaptive control.

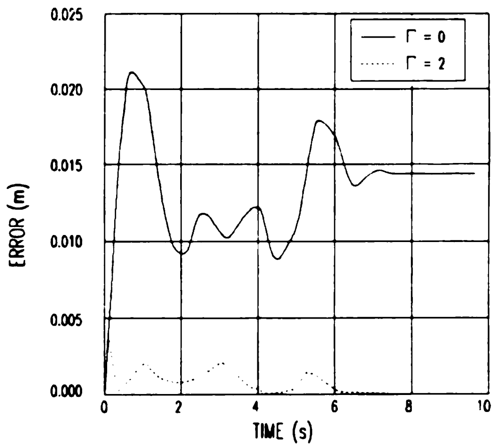

Fig 6. Tracking error with and without adaptivity.

The effect of Γ weight on the tracking is shown in Fig 7, according to which errors decrease for higher, even if bounded, Γ values.

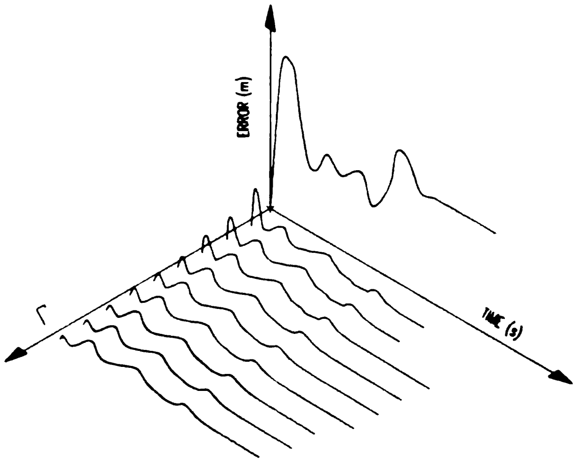

Fig 7. Tracking error for different adaptive weights.

Parameters convergence to the actual values occurs only if they can be univocally identified, otherwise their identification, even if inaccurate, corresponds to the exact values of the significant parameters in the equations of motion.

For the Stanford manipulator, the identification of the mass only brings to the fine value, Fig 8, while the mass and first order moment identification leads to incorrect values, Fig 9-10, that nevertheless imply the right weight moment on the second joint.

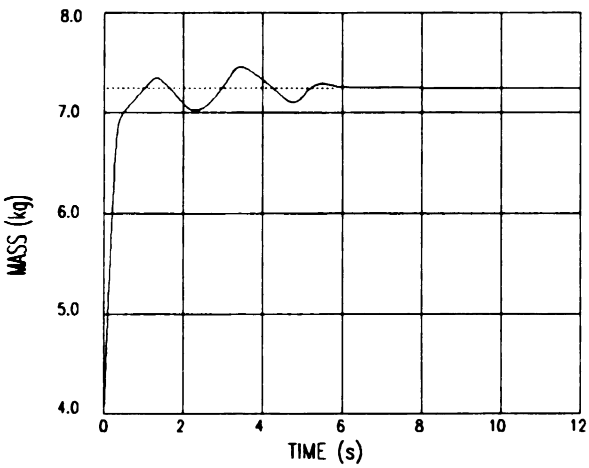

Fig 8. Mass identification.

In order to evaluate the performance of different control systems, a standard control based on the nominal characteristics of Stanford Manipulator has been implemented.

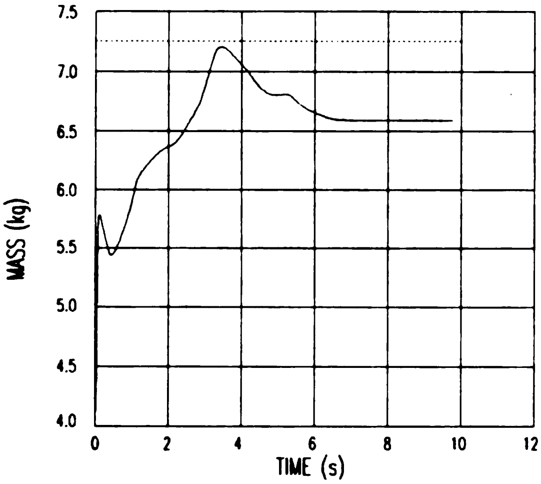

Fig 9. Mass identification.

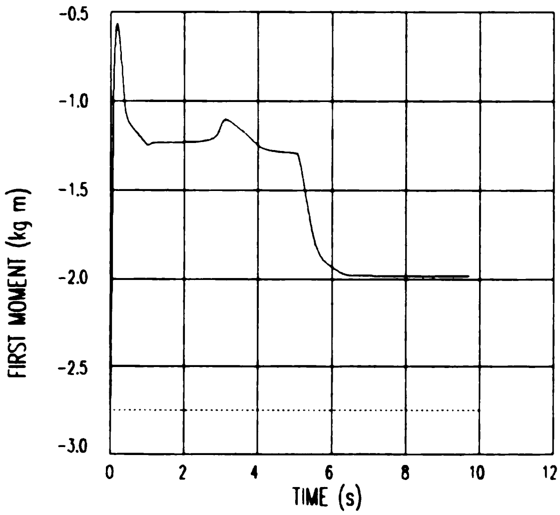

Fig 10. First moment identification.

Also in this case the errors are sufficiently small, Fig 11, and the tracking performance can be increased by feeding forward the system with the desired joint spin, Fig 12, reaching values comparable to those of the adaptive control.

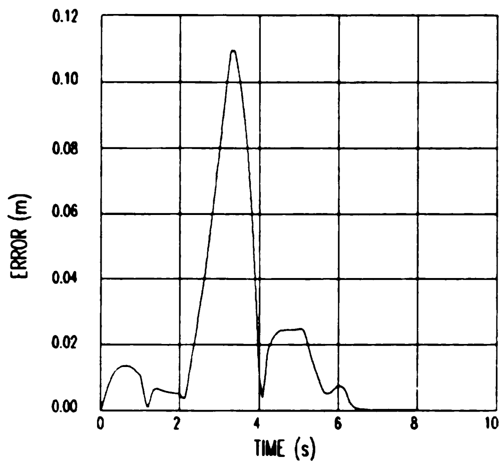

Fig 11. Tracking error with torque feed-forward.

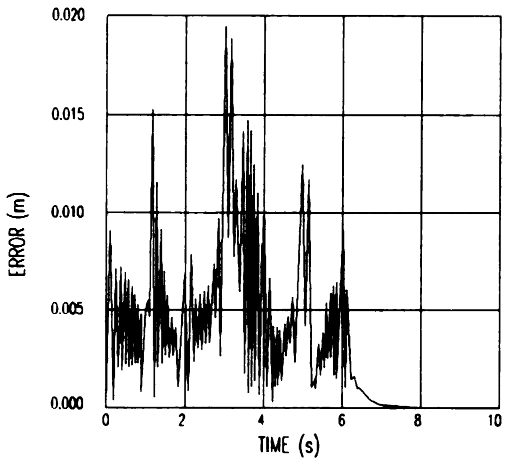

Fig 12. Tracking error with torque and velocity feed-forward.

Robustness of the control system has been tested by modelling external disturbances and actuator dynamics. In the first case viscous and Coulomb friction forces have been introduced. In this case, for the same pick and place maneuver, the adaptive controls presents errors similar to the previous ones, even if the final position is reached with major difficulty, Fig 13, due to the fact that the integration block is substituted by the adaptive block.

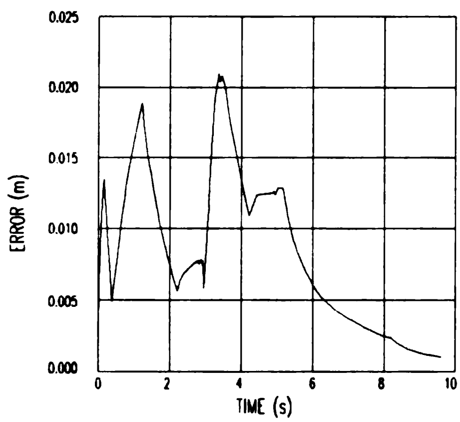

Fig 13. Adaptive control with friction: tracking error.

On the contrary standard control errors are not affected by the modelled disturb, Fig 14, on the basis of the design structure.

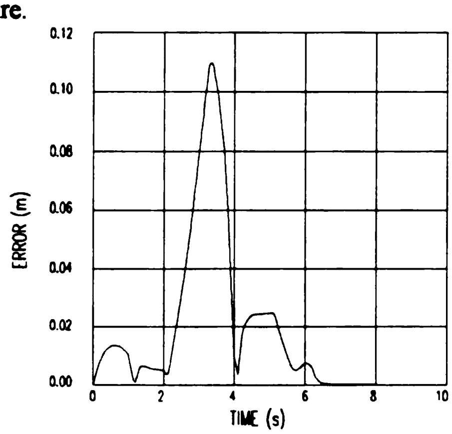

Fig 14. Standard control with friction: tracking error.

A similar behavior is noticed in the second case, when a limit torque is imposed on the DC actuator. The adaptive control becomes unstable and the end effector doesn't succeed in performing the maneuver, due to the fact that the Lyapunov function adopted is insensible to actuator dynamics.

Standard control errors instead increase, Fig 15, but only when a torque larger than the allowed is requested, otherwise the system shows a sufficiently high precision.

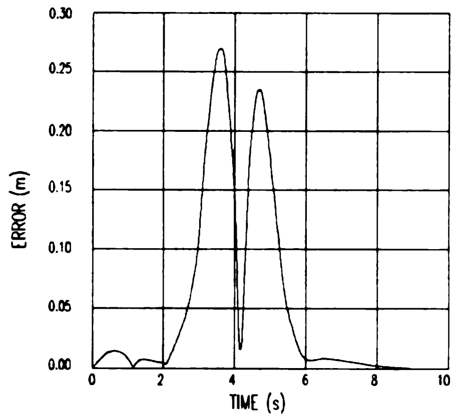

Fig 15. Standard control with torque saturation: tracking error.

CONCLUSION

The paper has shown that Maggi's method, particularly if coupled with symbolic manipulation, is suitable for the dynamic modelling of multibody systems.

Control systems, can obtain very good performances, even in case of badly known physical characteristics, if adaptive blocks are adopted.

In any case standard control systems, when accurately designed, can give excellent performances and in case of some unmodelled disturbances, e.g. saturation of the actuators, can behave even better than the adaptive ones.

The suggestion is here given that the adoption of a mixed control system, with two parallel stages, an adaptive and a standard PID, could lead to better overall results for widely varying operative conditions.

REFERENCES

Gatland K et al (1980), *Space technology*, Salamander Book.

Maggi GA (1986), *Principi della teoria matematica del movimento dei corpi*, corso di Meccanica Razionale, Hoeply, Milano, Italy.

Levi Civita T and Amaldi U (1926), *Lezioni di Meccanica Razionale*, Zanichelli, Bologna, Italy.

Kane TR and Levinson DA (1980), Formulation of equations of motion for complex spacecraft, *J. of Guidance and Control*, 3(2).

Paul RP (1981), *Robot manipulator: mathematics programming and control*, MIT Press.

Teukolsky SA and oths (1986), *Numerical recipes-The art of scientific computing*, Cambridge University Press.

Borri M, Bottasso C and Mantegazza P (1990), Equivalence of Kane's and Maggi's equations, *Journal of the Italian Association of Theoretical and Applied Mechanics*, 25(4).

Leu MC and Hemati N (1986), Automated symbolic derivation of dynamic equations of motion for robotic manipulators, *Transaction of the ASME*, 108.

Passera C (1990), Robot spaziali: un approccio per la generazione automatica delle equazioni dinamiche, Master Thesis, Politecnico di Milano, Milano, Italy.

Galli A (1991), Manipolazione simbolica e controllo adattativo di sistemi multicorpo, Master thesis, Politecnico di Milano, Milano, Italy.

Craig JJ (1988), *Adaptive control of mechanical manipulators*, Addison-Wesley.

Modal analysis of a flexible three-link system in variable configurations

JW Benner

US Army MICOM, AMSMI-RD-ST-GD, Redstone Arsenal AL 35898-5247

SC Sinha and GJ Wiens

Department of Mechanical Engineering, Auburn University, Auburn AL 36849-5341

In this paper, some experimental results of modal tests performed on a large three-link flexible system are reported. These modal tests were conducted at the NASA's LSS GTF (Large Space Structures Ground Test Facility) located at MSFC (Marshall Space Flight Center). The experimental results were obtained for various configurations and compared with those obtained using the Component Mode Synthesis technique. The mode functions were selected to keep the computation as simple as possible without compromising the accuracy. The results obtained from the dynamic software simulation package called TREETOPS have also been included for completeness. It is found that the experimental results are in excellent agreement with those obtained by the use of component mode techniques for the aforementioned structures. The average percent change in the frequencies is observed to be 6.09%, while the average mode shape correspondence is noted as 94.5%.

INTRODUCTION

In recent years, the aerospace industry has been involved in the extensive use of multibodied structures. This is evidenced by many examples, such as, the space station, the space shuttle, space robots, and the list goes on. With the incorporation of composite materials, the ability to achieve a high payload to weight ratio has been facilitated. Also, scientists and engineers have been asking large lightweight robotic manipulators to perform precise, high speed maneuvers. In consequence, these lightweight structures exhibit high flexibilities, and due to the stringent requirements demanded of them, the study of their vibration characteristics has become of paramount importance.

The complexity of the LSS (Large space structures) is such that it has become increasingly difficult to accurately model their dynamic behavior. Therefore, high speed computers have been heavily relied upon for simulation and analysis. The modeling techniques utilized in the software packages are predominantly based on the finite element method. As the size of the system increases, the model becomes too complicated and simulation time is undesirably high. Therefore, the component mode techniques are being turned to as an alternate approach in simplifying the system model.

As industry is turning to the component mode techniques, the need to verify this procedure is becoming increasingly important. Despite the generous amounts of analytical research being conducted, there is a lack of experimental data available for verification. Therefore, NASA's MSFC has embarked on creating a national testbed for such structures. This testbed will be used to explore new issues associated with large flexible structures and also provide research data for which one use is the experimental verification of component mode techniques.

The component mode technique is based on simplifying the system model by reducing the system into separate components or substructures. This reduces the system of partial differential equations of motion, which sometimes can not be solved, down to a group of component equations that have known solutions. The knowledge of the component behavior, along with how they are constrained by the system configuration, can then be used to assemble a feasible mathematical model for the entire system. This is significant when one considers that many times the major components of large systems are being built by separate contractors and analysis of the entire assembled system is often times not feasible. Therefore, the component mode techniques allow for much of the analysis to be done on the component level.

Many methods have been developed on the basis of the component mode approach. Hurty, who is considered the pioneer in this field, developed the Component Mode Synthesis technique (Hurty, 1960; Thomson, 1988). The Craig-Bampton method differs only slightly from Hurty's and the two give the same numerical results (Craig, Jr and Bampton, 1968). Gladwell also developed a variant of Hurty's method which has come to be called the Branch Mode Analysis (Gladwell, 1964). Furthermore, Benfield and Hruda developed the Component Mode Substitution technique (Benfield and Hruda, 1971). Dowell has also developed a technique where he incorporates the use of Lagrange multipliers, in a systematic approach, to permit for various system constraints (Dowell, 1972, 1979, 1980a and b, 1983, 1984; Dowell and Klein, 1974). In general, these methods tend to differ only in the selection of the various component modes. In this paper Hurty's Method is utilized. For complete reference of this method see (Hurty, 1960; Thomson, 1988; Meirovitch, 1980; Meirovitch and Hale, 1980).

THEORETICAL ANALYSIS USING COMPONENT MODE SYNTHESIS

The various component mode techniques tend to differ, in general, only in the selection of the component mode functions, all of which can be determined by solving some type of component eigenvalue problem. For further reference one may look into Benfield and Hruda (1971), Rubin (1975), and Craig and Bampton (1968). In this investigation, we will be considering a slightly new approach. The component mode techniques, as stated earlier, were introduced to simplify the computation problems associated with other methods, and still produce a reliable approximation. With this premise in mind, we suggest the use of simple polynomials as alternative mode functions. Hurty has previously suggested this (Hurty, 1960), along with Meirovitch and Hale (1980).

The first criterion placed on these polynomials, is that they qualify as admissible functions. In general, the admissible functions must be selected such that displacements and forces exist at the internal boundaries of the system. The other criteria are that the admissible functions selected form a complete set, and they should be linearly independent. A reasonable check to see if the frequencies converge will provide assurance that a given set of mode functions forms a complete set. In considering the problem associated with early truncation of the mode function set, Macneal (1971) and Rubin (1975) proposed a technique to include the effect of residual modes not retained (Meirovitch, 1980; Meirovitch and Hale, 1980).

We will now consider a three link flexible system as shown in Fig 1, and examine the undamped, free vibration problem. We will denote Fig 1 as Configuration 1.

The equation of motion for an arbitrary substructure, is given as

$$[M_s]\{\ddot{\zeta}_s(t)\} + [K_s]\{\zeta_s(t)\} = \{0\} \tag{1}$$

where $[M_s]$ and $[K_s]$ are the substructure mass and stiffness matrices respectively, $\{\zeta_s(t)\}$ is the time dependent generalized coordinate, and the ¨ represents the second derivative with respect to time, [... 'es a matrix and { } represents a column vector). ... 'ict our analysis

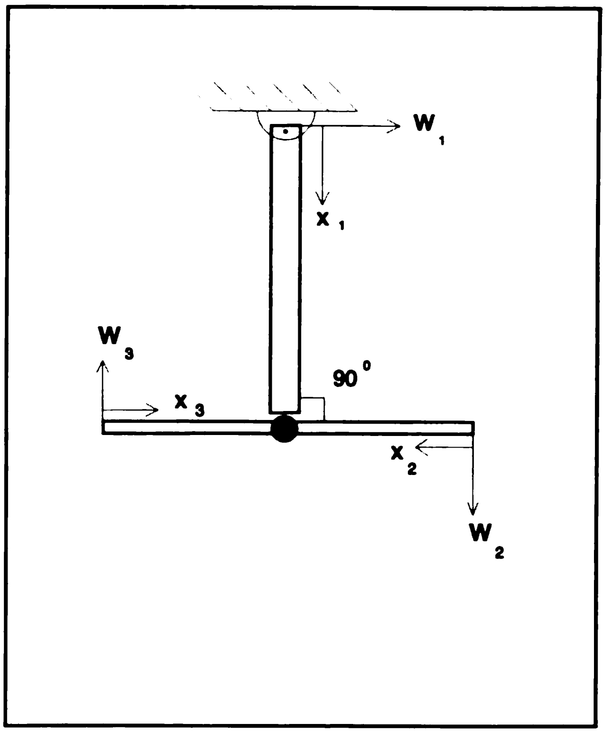

Figure 1. Configuration 1

to motions of small amplitude so that the free vibrations in longitudinal, transverse, and twisting motion are decoupled. Also, we shall assume infinite axial rigidity of all three members, which is later supported by experimentation. That is, the system considered in Fig 1 has two adjustable joints (top revolute joint at $x_1 = 0$ and bottom revolute joint between link 1 and the composite body formed by links 2 and 3). It should be noted that links 2 and 3 are rigidly clamped together at $x_2 = L_2$, $x_3 = L_3$. The other joints are locked in various configurations; hence a quasi-dynamic analysis is presented here. In addition, we are only concerned with vibration in the plane of the paper as shown by Fig 1.

Next, we will choose the transverse displacement vector for component 1 to be

$$w_1(x_1,t) = \left[\frac{x_1}{L_1}\right]^2 \zeta_1 + \left[\frac{x_1}{L_1}\right]^3 \zeta_2 + \dots + \left[\frac{x_1}{L_1}\right]^n \zeta_{n-1} \tag{2}$$

where ζ is taken to be a function of time although not explicitly shown, and n is equal to the highest power of the last spatial function. The displacement vector chosen for component 1 satisfies all geometric and force conditions at the external and internal boundaries of component 1, whereby the interface of the components is designated the internal boundary. These conditions are

$$\begin{aligned} &w_1(0) = 0,\ w_1'(0) = 0, \\ &w_1''(0) \neq 0,\ w_1'''(0) \neq 0, \\ &w_1(L_1) \neq 0,\ w_1'(L_1) \neq 0, \\ &w_1''(L_1) \neq 0,\ w_1'''(L_1) \neq 0 \end{aligned} \tag{3}$$

where the $'$ represents the derivative with respect to the spatial coordinate. Note that shear forces and moments are allowed at the interface.

We choose the displacement vectors for component 2

$$\begin{aligned} w_2(x_2,t) = 1(x_2)\zeta_n + \left[\frac{x_2}{L_2}\right]\zeta_{n+1} + \\ \left[\frac{x_2}{L_2}\right]^4 \zeta_{n+2} + \dots + \left[\frac{x_2}{L_2}\right]^m \zeta_{m+1} \end{aligned} \tag{4}$$

$$u_2(x_2,t) = 1(x_2)\zeta_{m+2} \tag{5}$$

where $u_2(x_2,t)$ is the axial displacement of component 2, and m is the highest power of the last spatial function. Here again, these displacement vectors were chosen so that they satisfy all geometric and force conditions at the boundaries of component 2. These conditions are as follows:

$$\begin{aligned} &w_2(0) \neq 0,\ w_2'(0) \neq 0, \\ &w_2''(0) = 0,\ w_2'''(0) = 0, \\ &w_2(L_2) \neq 0,\ w_2'(L_2) \neq 0, \\ &w_2''(L_2) \neq 0,\ w_2'''(L_2) \neq 0\ . \end{aligned} \tag{6}$$

In Eqs (2), (4), and (5), rigid body translation and rigid body rotation modes are represented by $1(x)$ and (x/L) respectively, whereas the remaining functions represent deformation modes. And similarly for component 3,

$$\begin{aligned} w_3(x_3,t) = 1(x_3)\zeta_{m+3} + \left[\frac{x_3}{L_3}\right]\zeta_{m+4} \\ + \left[\frac{x_3}{L_3}\right]^4 \zeta_{m+5} + \dots + \left[\frac{x_3}{L_3}\right]^m \zeta_{2m+1} \end{aligned} \tag{7}$$

$$u_3(x_3,t) = 1(x_3)\zeta_{2m+2} \tag{8}$$

where these displacement vectors satisfy similar boundary conditions as in Eq (6).

Now we compute the generalized mass matrix for each component which is derived as follows. Consider the displacement vector for a given beam

$$w_s(x_s,t) = \sum_{i=1}^{N} \phi_i(x_s)\zeta_i(t) \tag{9}$$

where ϕ is the spatial function and N is the desired number of mode functions. The velocity is

$$v_s(x_s) = \sum_{i=1}^{N} \phi_i(x_s)\dot{\zeta}_i(t) \tag{10}$$

and therefore the kinetic energy becomes

$$T_s = \frac{1}{2} \sum_{i=1}^{N}\sum_{j=1}^{N} \dot{\zeta}_i\dot{\zeta}_j \int \phi_i(x_s)\phi_j(x_s)dm \tag{11}$$

or

$$T_s = \frac{1}{2} \sum_{i=1}^{N}\sum_{j=1}^{N} m_{ij}\dot{\zeta}_i\dot{\zeta}_j \tag{12}$$

where the generalized mass is defined to be

$$m_{ij} = \int \phi_i(x_s)\phi_j(x_s)dm \tag{13}$$

and the integration is carried out over the entire system. Therefore applying Eq (13) to component 1 we obtain

$$m_{ij} = \int_0^{L_1} \rho_1(x_1)\phi_i(x_1)\phi_j(x_1)dx_1 \tag{14}$$

where ρ_1 is the mass density per unit length of component 1. For example, when n=3 in Eq (2), we obtain

$$m_{11} = \int_0^{L_1} \rho_1\phi_1\phi_1 dx_1$$

$$= \int_0^{L_1} \rho_1 \left[\frac{x_1}{L_1}\right]^4 dx_1 = \left[\frac{1}{5}\right]\rho_1 L_1 \tag{15}$$

$$m_{12} = m_{21} = \int_0^{L_1} \rho_1\phi_1\phi_2 dx_1$$

$$= \int_0^{L_1} \rho_1 \left[\frac{x_1}{L_1}\right] dx_1 = \left[\frac{1}{6}\right]\rho_1 L_1 \tag{16}$$

$$m_{22} = \int_0^{L_1} \rho_1\phi_2\phi_2 dx_1$$

$$= \int_0^{L_1} \rho_1 \left[\frac{x_1}{L_1}\right]^6 dx_1 = \left[\frac{1}{7}\right]\rho_1 L_1 \tag{17}$$

substituting in the appropriate values (Table 1)

$$[M_1] = \rho_1 L_1 \begin{bmatrix} \frac{1}{5} & \frac{1}{6} \\ \frac{1}{6} & \frac{1}{7} \end{bmatrix} . \tag{18}$$

TABLE 1. BASIC DATA *

	Component 1 (Box Beam)	Component 2 (Solid Beam)	Component 3 (Solid Beam)
Material	Aluminum	Aluminum	Aluminum
E	68.95E+9	68.95E+9	68.95E+9
Volume Density	2768	2768	2768
Base	0.0635	0.0335	0.0335
Height	0.018	0.009	0.009
Thickness	0.003175	______	______
Moment of Inertia	9.13E-8	2.04E-9	2.04E-9
Area	5.64E-4	3.02E-4	3.02E-4

* All in S.I base units (Kg,m)

In like manner, the generalized mass matrices for component 2 and 3 are computed for m=6. Noting that there is no coupling between the lateral and longitudinal displacements we obtain,

$$[M_2] = \rho_2 L_2 \begin{bmatrix} 1 & \frac{1}{2} & \frac{1}{5} & \frac{1}{6} & \frac{1}{7} & 0 \\ \frac{1}{2} & \frac{1}{3} & \frac{1}{6} & \frac{1}{7} & \frac{1}{8} & 0 \\ \frac{1}{5} & \frac{1}{6} & \frac{1}{9} & \frac{1}{10} & \frac{1}{11} & 0 \\ \frac{1}{6} & \frac{1}{7} & \frac{1}{10} & \frac{1}{11} & \frac{1}{12} & 0 \\ \frac{1}{7} & \frac{1}{8} & \frac{1}{11} & \frac{1}{12} & \frac{1}{13} & 0 \\ 0 & 0 & 0 & 0 & 0 & 1 \end{bmatrix} . \tag{19}$$

Changing subscripts 2 to 3, one obtains the definition for $[M_3]$. We arrange matrices, $[M_1]$, $[M_2]$, and $[M_3]$, into the system block diagonal matrix as

$$[M^d] = \begin{bmatrix} [M_1] & & \\ & [M_2] & \\ & & [M_3] \end{bmatrix} . \tag{20}$$

We form the generalized stiffness matrix by expressing the flexural potential energy for a- 'er-Bernoulli beam in bending.

$$U_s = \frac{1}{2} \int E_s I_s \left[\frac{dw_s}{dx_s} \right]^2 dx_s \, . \tag{21}$$

Substituting for w_s, as in Eq (9), we get

$$U_s = \frac{1}{2} \sum_i \sum_j \zeta_i \zeta_j \int E_s I_s \phi_i'' \phi_j'' \, dx_s \tag{22}$$

$$= \frac{1}{2} \sum_i \sum_j k_{ij} \zeta_i \zeta_j \tag{23}$$

where the generalized stiffness is defined to be

$$k_{ij} = \int_0^{L_s} E_s I_s \phi_i'' \phi_j'' \, dx_s \, . \tag{24}$$

Therefore, applying this Eq to component 1

$$k_{11} = E_1 I_1 \int_0^{L_1} \phi_1'' \phi_1'' \, dx_1$$

$$= E_1 I_1 \int_0^{L_1} \left[\frac{2}{L_1^2} \right] dx_1 = 4 \frac{E_1 I_1}{L_1^3} \tag{25}$$

$$k_{12} = k_{21} = E_1 I_1 \int_0^{L_1} \left[\frac{2}{L_1^2} \right] \times \left[\frac{6x_1}{L_1^3} \right] dx_1 = 6 \frac{E_1 I_1}{L_1^3} \tag{26}$$

$$k_{22} = 12 \frac{E_1 I_1}{L_1^3} \tag{27}$$

which results in

$$[K_1] = \frac{E_1 I_1}{L_1^3} \begin{bmatrix} 4 & 6 \\ 6 & 12 \end{bmatrix} . \tag{28}$$

Similarly, for component 2 we arrive at

$$[K_2] = \frac{E_2 I_2}{L_2^3} \begin{bmatrix} 0 & 0 & 0 & 0 & 0 & 0 \\ 0 & 0 & 0 & 0 & 0 & 0 \\ 0 & 0 & 28.8 & 40 & 51.43 & 0 \\ 0 & 0 & 40 & 57.143 & 75 & 0 \\ 0 & 0 & 51.43 & 75 & 100 & 0 \\ 0 & 0 & 0 & 0 & 0 & 0 \end{bmatrix} . \tag{29}$$

Again, changing subscripts 2 to 3, $[K_3]$ is similarly defined for component 3. Furthermore, assembling these matrices into the block diagonal stiffness matrix we obtain Eq (30).

Since we have formed the mass and stiffness matrix for the decoupled system, the equations must be coupled by a simple coordinate transformation. The transformation matrix

$$[K^d] = \begin{bmatrix} [K_1] & & \\ & [K_2] & \\ & & [K_3] \end{bmatrix} . \tag{30}$$

[β] is a transformation from the dependent generalized coordinate $\{\zeta(t)\}$, into a set of independent generalized coordinates $\{q(t)\}$

$$\{\zeta(t)\} = [\beta]\{q(t)\} . \tag{31}$$

This matrix, [β], is formed directly from the equations of constraint for the system, which arise due to the force and displacement compatibility requirements at the component interfaces. These constraint equations may be written in local generalized coordinates $\{\zeta(t)\}$. Upon forming all the constraint equations for each interface, we obtain a set of linear constraint equations which can be written as

$$[A]\{\zeta(t)\} = \{0\} \tag{32}$$

where $[A]$ is a (c x M) matrix of constant coefficients. Note that c is the total number of constraint equations, and M is the dimension of $\{\zeta(t)\}$. Next, the matrix may be partitioned as such

$$[A] = [A_1 \vdots A_2] \tag{33}$$

where $[A_1]$ is a square matrix of order (c x c). Furthermore, Eq (33) may now be written in the following form

$$[A_1]\{\zeta(t)\}_d + [A_2]\{q(t)\} = \{0\} \tag{34}$$

where $\{q(t)\}$ is a subset of $\{\zeta(t)\}$ which is chosen to include the independent variables, and $\{\zeta(t)\}_d$ is chosen to include the dependent variables. This is achieved by choosing $[A_1]$ to be nonsingular. Next, Eq (34) can be rewritten into the following form

$$\{\zeta(t)\}_d = -[A_1]^{-1}[A_2]\{q(t)\} . \tag{35}$$

Finally, the complete vector $\{\zeta(t)\}$ can be expressed in terms of the independent subset $\{q(t)\}$, by supplying the identity matrix where needed,

$$\{\zeta(t)\} = \begin{bmatrix} [I] \\ \hline -[A_1]^{-1}[A_2] \end{bmatrix} \{q(t)\} . \tag{36}$$

Therefore,

$$[\beta] = \begin{bmatrix} [I] \\ \hline -[A_1]^{-1}[A_2] \end{bmatrix} \tag{37}$$

which forms the coordinate transformation matrix [β] (Hurty, 1965).

Consider the case where the three link structure is in the configuration shown in Fig 1. In general, the displacement equations at the junction are

$$\begin{aligned} w_1(L_1) + u_2(L_2) &= 0 \\ w_1(L_1) - u_3(L_3) &= 0 \end{aligned} \tag{38}$$

$$\begin{aligned} w_2(L_2) &= 0 \\ w_3(L_3) &= 0 \end{aligned} \tag{39}$$

$$\begin{aligned} w_1'(L_1) - w_2'(L_2) &= 0 \\ w_1'(L_1) - w_3'(L_3) &= 0 . \end{aligned} \tag{40}$$

Equations (39) arise due to the assumption of infinite axial rigidity. Equations (40) enforce that the component rotations due to bending at the junction are equal. However, the links are modeled as Euler-Bernoulli beams and therefore, in the absence of shear deflection this rotation angle reduces to the slope. The force equilibrium equation is

$$M_1(L_1) + M_2(L_2) + M_3(L_3) = 0 \tag{41}$$

where M's are the moments. This equation is further simplified to

$$E_1I_1w_1''(L_1) + E_2I_2w_2''(L_2) + E_3I_3w_3''(L_3) = 0 . \tag{42}$$

In general, there would also be equations that would enforce the shear and axial force at the junction, but again for our assumptions these are neglected. These equations are now evaluated and expressed in terms of $\{\zeta(t)\}$ as in Eq (32), where $[A]$ is equal to the following constant matrix.

$$\begin{bmatrix} 0 & 0 & 1 & 1 & 1 & 1 & 1 & 0 & 0 & 0 & 0 & 0 & 0 & 0 \\ 1 & 1 & 0 & 0 & 0 & 0 & 0 & 1 & 0 & 0 & 0 & 0 & 0 & 0 \\ \frac{2}{L_1} & \frac{3}{L_1} & 0 & \frac{-1}{L_2} & \frac{-4}{L_2} & \frac{-5}{L_2} & \frac{-6}{L_2} & 0 & 0 & 0 & 0 & 0 & 0 & 0 \\ \left(\frac{2I_1}{I_2L_1^2}\right) & \left(\frac{6I_1}{I_2L_1^2}\right) & 0 & 0 & \frac{12}{L_2^2} & \frac{20}{L_2^2} & \frac{30}{L_2^2} & 0 & 0 & 0 & \frac{12}{L_3^2} & \frac{20}{L_3^2} & \frac{30}{L_3^2} & 0 \\ 0 & 0 & 0 & 0 & 0 & 0 & 0 & 0 & 1 & 1 & 1 & 1 & 1 & 0 \\ 1 & 1 & 0 & 0 & 0 & 0 & 0 & 0 & 0 & 0 & 0 & 0 & 0 & -1 \\ \frac{2}{L_1} & \frac{3}{L_1} & 0 & 0 & 0 & 0 & 0 & 0 & 0 & \frac{-1}{L_3} & \frac{-4}{L_3} & \frac{-5}{L_3} & \frac{-6}{L_3} & 0 \end{bmatrix} \tag{43}$$

Because there are 14 generalized coordinates and 7 constraints this means that there are 14-7=7 redundant coordinates. The $[A]$ matrix is now partitioned as indicated Eq (33). Let

$$\begin{aligned} &\zeta_1 = q_1, \ \zeta_{12} = q_{12}, \ \zeta_2 = q_2, \ \zeta_{13} = q_{13}, \\ &\quad \zeta_3 = q_3, \ \zeta_{14} = q_{14}, \ \zeta_4 = q_4 \end{aligned} \tag{44}$$

where these are chosen to ensure that $[A_1]$ is nonsingular. Therefore, $[A_1]$ is formed by taking the first four and last three columns of $[A]$, and $[A_2]$ is formed by taking columns five through eleven of $[A]$. The transformation matrix [β] can now be formed from Eq (37), and is shown in the APPENDIX.

$$[M] = [\beta]^T [M^d] [\beta] \quad and \quad [K] = [\beta]^T [K^d] [\beta] \tag{45}$$

Finally, the system matrices are formed by the transformation defined below and are listed in the APPENDIX. Once the system matrices have been constructed, the natural frequencies can be obtained from the resulting eigenvalue problem, where the first four natural frequencies are

$$\omega_{n1} = 2.5390\ Hz \quad , \quad \omega_{n2} = 3.3339\ Hz$$
$$\omega_{n3} = 3.9432\ Hz \quad , \quad \omega_{n4} = 19.6606\ Hz \qquad (46)$$

To examine the possibility of premature truncation of the mode functions in the component displacement vectors, we will consider adding more terms in Eqs (2), (4) and (7) to test for convergence of the natural frequencies. Table 2 summarizes the results. At this stage, the mode shapes can be determined as described in the following. The eigenvalue problem can be solved for the independent coordinate vector $\{q(t)\}$ with respect to an arbitrary reference. Subsequently, $\{q(t)\}$ can be transformed into the dependent coordinate vector $\{\zeta(t)\}$, which can be used to find the respective component displacement vectors defined by Eqs (2), (4), (5), (7), and (8). Therefore, these component modes can be assembled to obtain the system natural modes.

TABLE 2. CONVERGENCE OF FREQUENCIES FOR CONFIGURATION 1

Frequency (Hertz) n=3 m=6	Frequency (Hertz) n=4 m=7	Frequency (Hertz) n=5 m=8	Frequency (Hertz) n=6 m=9	Frequency (Hertz) n=7 m=10
ω_{n1}=2.5390	2.5385	2.5385	2.5385	2.5385
ω_{n2}=3.3339	3.3338	3.3338	3.3338	3.3338
ω_{n3}=3.9432	3.9399	3.9398	3.9398	3.9398
ω_{n4}=19.6606	19.5271	19.5220	19.5340	19.5246

In a similar manner, the structure is analyzed in two more configurations shown in Figs 6 and 11. The convergence of the natural frequencies was found to be similar to configuration 1 and the mode shapes are shown in Figs 2-5, 7-10 and 12-15.

EXPERIMENTAL PROCEDURE

As was stated earlier, the experimental procedure was conducted at NASA Marshall Space Flight Center and signified the advent for the Multibody Modeling Verification and Control (MMVC) project.

The test article was designed to simulate a large flexible multibody system. One of the design criteria was that the structure should exhibit dense mode concentration at low frequencies. The closely packed modes were desirable because this typifies the dynamic behavior of multibodied, flexible structures in space environments. It was also designed so that the maximum deflections would fall within the linear deflection range and that the vibration was restricted to be in the plane shown by Fig 1.

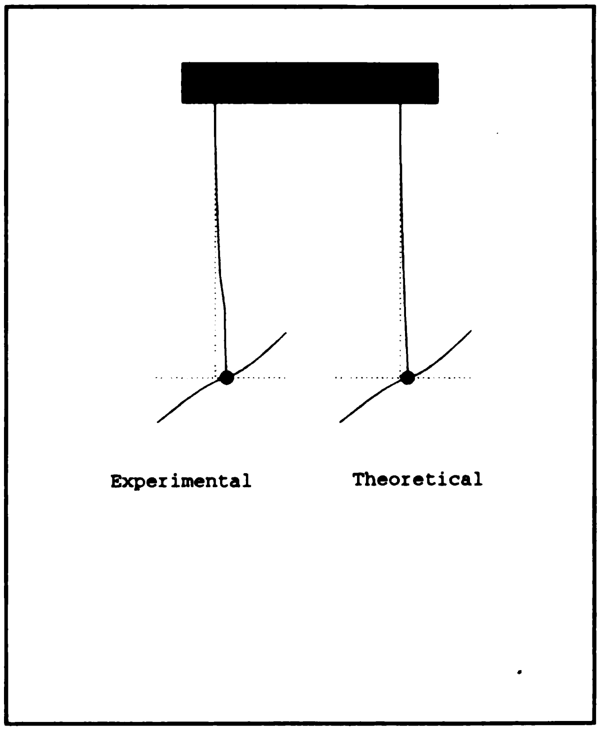

Figure 2. System Modes 1 for Configuration 1

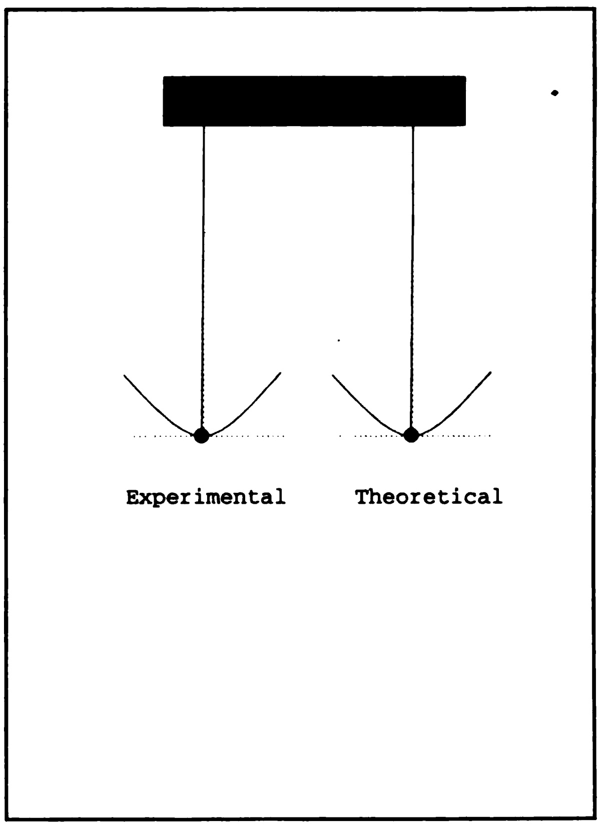

Figure 3. System Modes 2 for Configuration 1

The resulting dimensions for each component can be found in, Table 1. Essentially, the design process yielded a linear, time invariant, observable system, so that the modal analysis technique could be applied for the study.

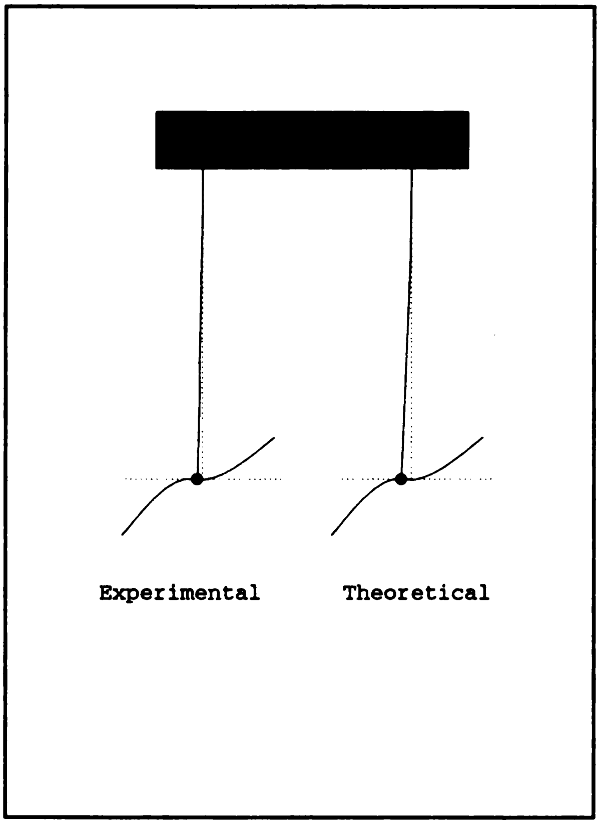

Figure 4. System Modes 3 for Configuration 1

After the system was assembled, the external boundary conditions were examined. The external joint that supported the structure was designed to facilitate the interchanging of the system components. Therefore, this fixed boundary condition was validated by testing the dynamic response of an isolated cantilever beam, which indeed closely resembled an actual cantilever beam response. Therefore, this joint closely approximated a fixed boundary. Also, each component was tested to show that the axial vibration for each respective component was negligible, and thus, the assumption of infinite axial rigidity was justified.

Each component was discretized into nine measurement response and force input points. These points were chosen to accurately excite and observe all modes of interest within the desired frequency range. The excitation was achieved by the direct impact hammer technique. This technique utilized the use of a load cell at the tip of the hammer to measure the force input. The tip of the hammer was selected to exhibit good frequency content throughout the frequency range of interest.

The piezoelectric accelerometer, or the response transducer, was located at the end of component 3. It was

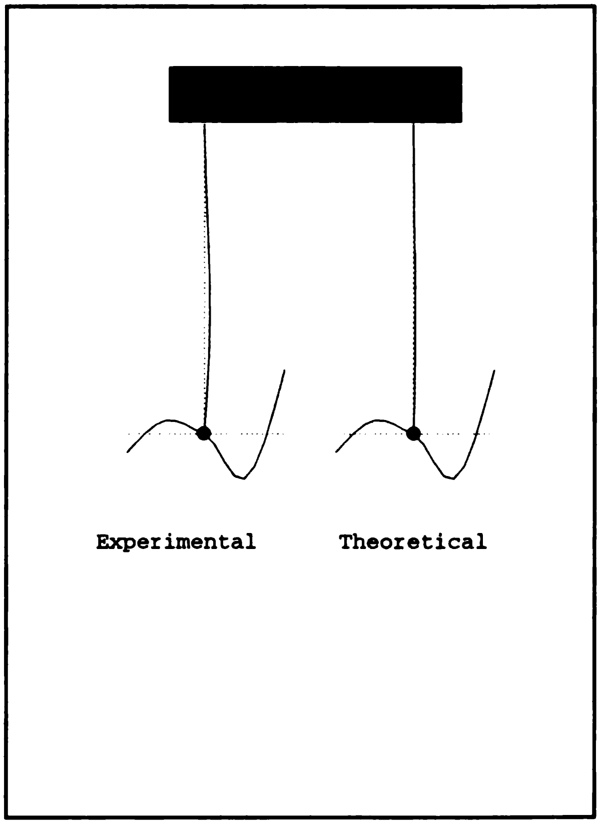

Figure 5. System Modes 4 for Configuration 1

mounted on the structure with a type of strong adhesive, and therefore, accurately described the response of the system. The structure was impacted by the hammer at all the points on each component, while frequency response data was collected. The accelerometer did not mass load the system, as was evidenced by doubling the weight of the accelerometer and noticing that there were no shifts in the frequency response function.

The system was tested in nine different configurations. It was speculated that gravity might have an effect on highly flexible, possibly nonlinear, structures. It was discovered that gravity had negligible effect on the frequencies and mode shapes of this system, and therefore, the original nine configurations reduced to three unique configurations. These configurations are depicted in Figs 1, 6, and 11. The experimental natural frequencies of the structure for all three configurations are summarized in Table 3. The experimental system mode shapes corresponding to these configurations are shown in Figs 2-5, 7-10 and 12-15.

A comparison of analytical and experimental values of frequencies are summarized in Table 4. In addition to the results from Secs 2 and 3, the results as computed by TREETOPS are also presented. As stated before, TREETOPS is a dynamic simulation software package that is based on component mode technique. The TREETOPS

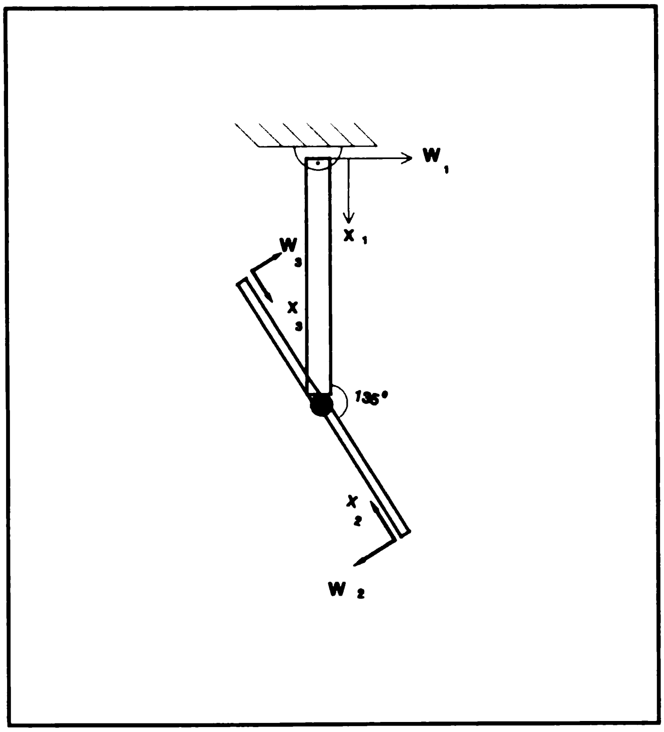

Figure 6. Configuration 2

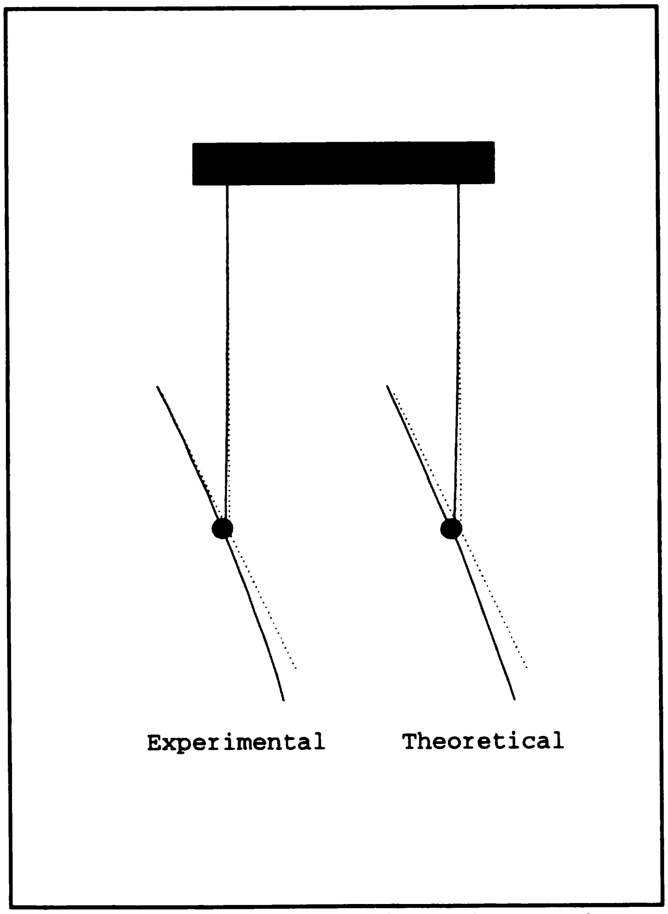

Figure 7. System Modes 1 for Configuration 2

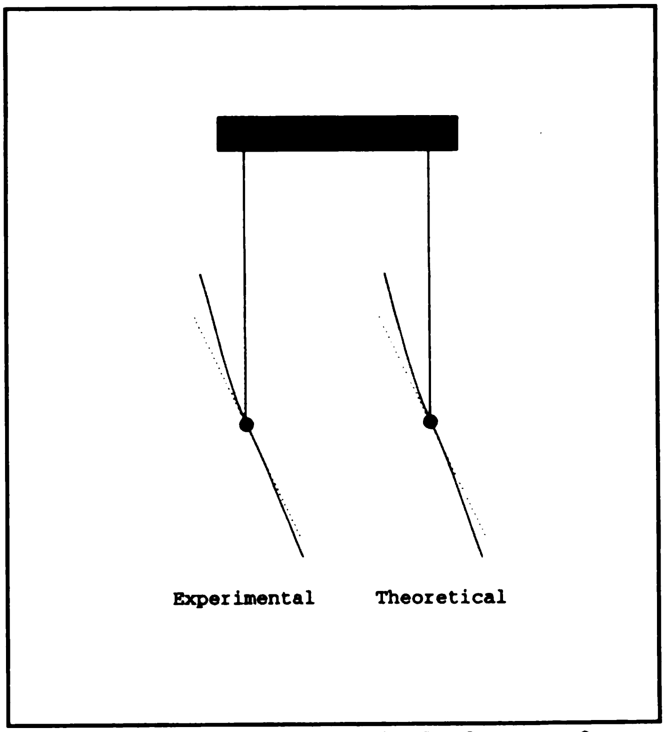

Figure 8. System Modes 2 for Configuration 2

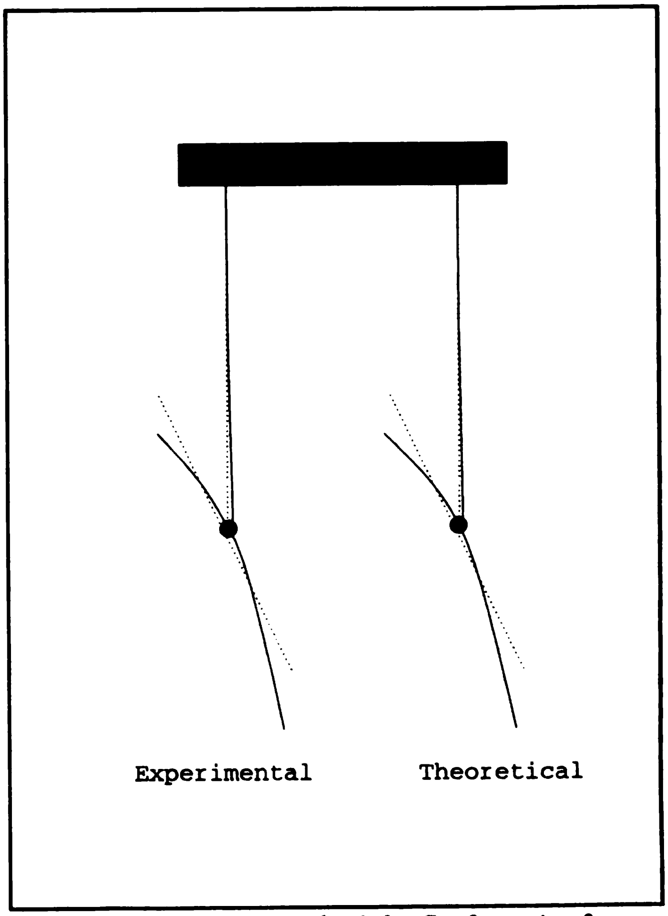

Figure 9. System Modes 3 for Configuration 2

results are based on the first five contilever beam modes selected as component modes. This flexible data was generated by another software package called TREEBEAMS.

An excellent agreement between the TREETOPS results and the experimental values was found. The detailed comparison is not included for brevity.

TABLE 3. EXPERIMENTAL FREQUENCIES

	Configuration 1	Configuration 2	Configuration 3
Mode Number	ω_n (Hz)	ω_n (Hz)	ω_n (Hz)
1	2.25	2.12	2.12
2	3.37	3.37	3.37
3	3.75	4.12	5.00
4	19.83	19.79	19.8

TABLE 4. CORRELATION OF FREQUENCIES

	Configuration 1			Configuration 2			Configuration 3		
	ω_{n1}	ω_{n2}	ω_{n3}	ω_{n1}	ω_{n2}	ω_{n3}	ω_{n1}	ω_{n2}	ω_{n3}
Hurty's Method	2.54	3.33	3.94	1.60	3.31	4.15	2.27	3.35	5.78
Experimental	2.25	3.37	3.75	2.12	3.37	4.12	2.12	3.37	5.00
TREETOPS	2.55	3.33	3.96	2.37	3.40	4.72	2.28	3.38	5.78

CORRELATION OF THEORETICAL AND EXPERIMENTAL RESULTS

The theoretical and experimental mode shapes are compared by the Modal Assurance Criterion (MAC). This condition number ranges from 0 to 1 where a 1 signifies perfect correspondence of the two modes. The MAC is defined as

$$0 \leq \frac{(v^T u)^2}{(v^T v)(u^T u)} \leq 1 \tag{47}$$

where v and u are the theoretical and experimental mode shapes, respectively. Table 5 summarizes the information for configurations.

TABLE 5. MAC FOR VARIOUS CONFIGURATIONS

Mode	Configuration 1	Configuration 2	Configuration 3
1	0.982	0.909	0.992
2	0.981	0.834	0.994
3	0.926	0.907	0.970
4	0.929	0.954	0.957

DISCUSSION AND CONCLUSIONS

For the first time, an experiment has been conducted to determine the natural frequencies and mode shapes of a large flexible three-link system and the results are compared with those obtained from a component mode synthesis technique. The theoretical results in this study show that the use of integral powers of (x/L) is an adequate approximation of the modes of vibration for Euler-Bernoulli beams in a chain-like structure. These polynomials proved to be suitable admissible functions for the system, as it is analyzed in three different configurations. The experimental evidence not only verified the use of these simple mode functions, but also validated the dynamic software simulation package, TREETOPS, which is based on the component mode technique. The influence of gravity turned out to be negligible because the cross sections of the links were relatively large. It was concluded that the gravitational forces could alter the frequencies and mode shapes only if the links are very flexible.

The results show that the average frequency difference between the experimental and the theoretical results was 6.09%. Yet this number can be misleading considering that seventy-five percent of the frequency results had an average percent difference of 2.22%. Also, the experimental and theoretical mode shapes, on the average, had 94.5% correspondence.

Although in this study the use of simple polynomials has produced good results, it is almost certain that this would not be the case for more complex systems. It would be an excellent idea to develop a library of suitable admissible functions for future use.

A major concern is how to accurately control large, flexible, multibody structures to perform precise maneuvers. In the future, as in the spirit of this research, decentralized control, or control on the component level should be investigated. Also, the nonlinear behavior of such structures undergoing large displacements and exhibiting large deflections will need to be addressed. Here again, the experimental evidence will prove to be a necessity in the exploration of these areas.

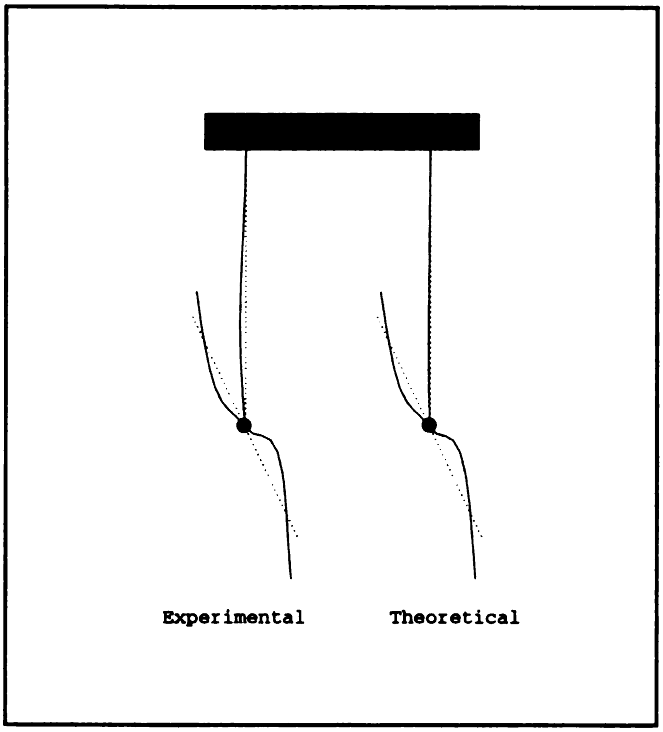

Figure 10. System Modes 4 for Configuration 2

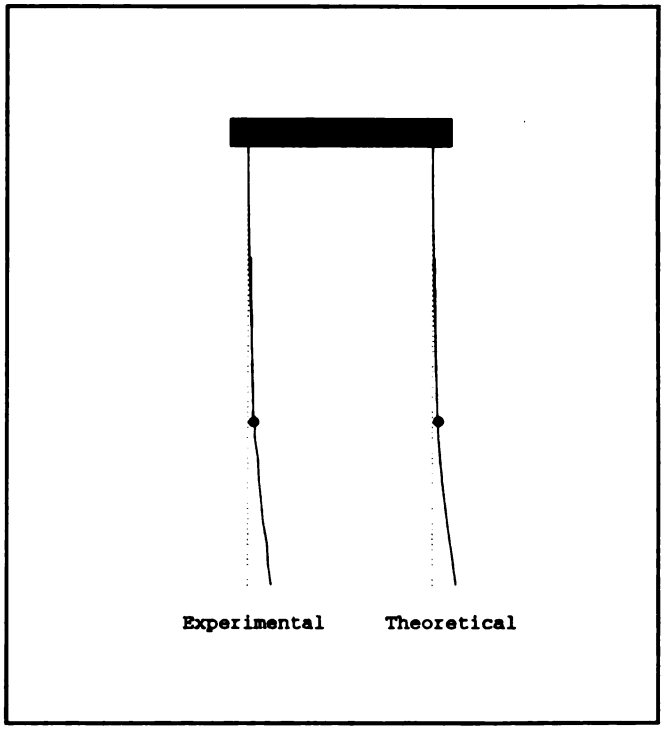

Figure 12. System Modes 1 for Configuration 3

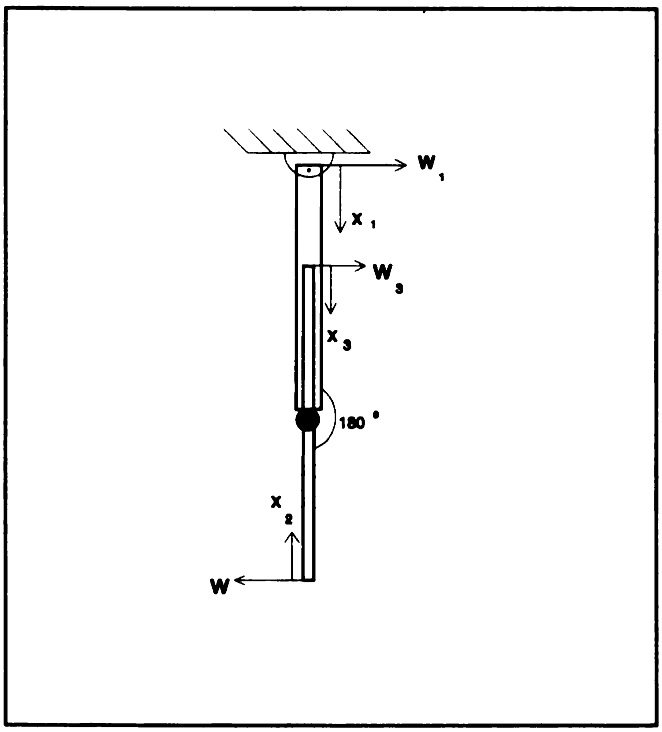

Figure 11. Configuration 3

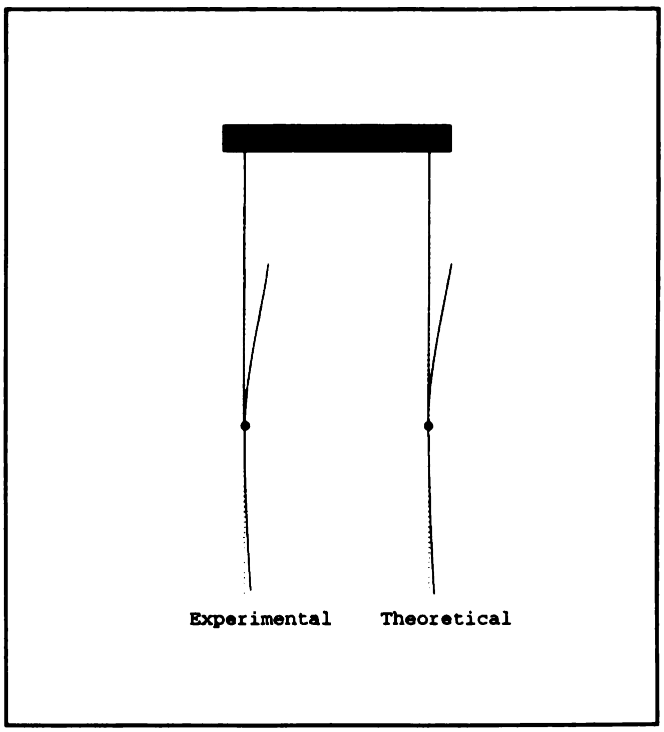

Figure 13. System Modes 2 for Configuration 3

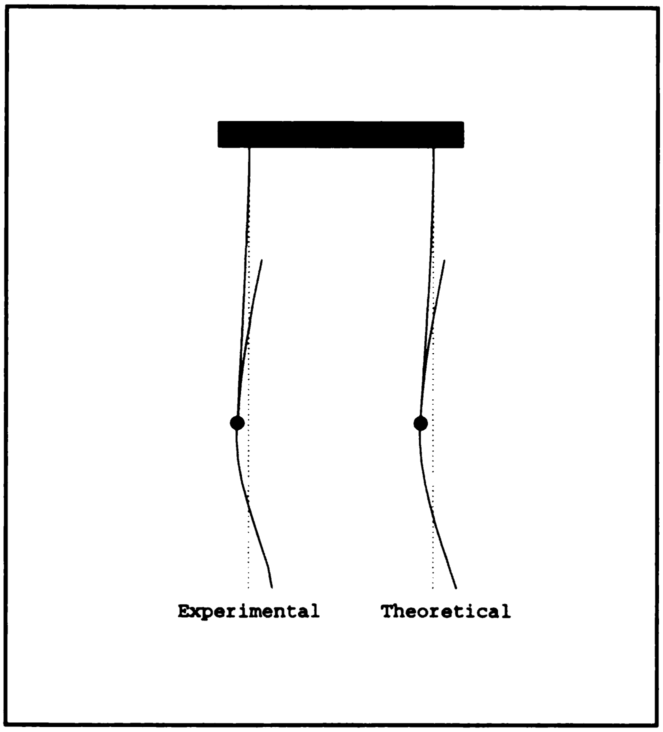

Figure 14. System Modes 3 for Configuration 3

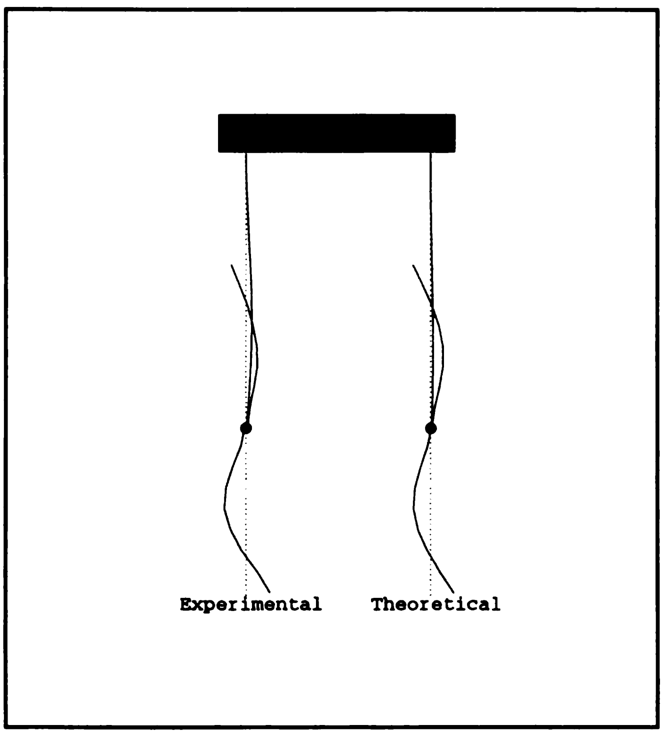

Figure 15. System Modes 4 for Configuration 3

ACKNOWLEDGEMENT

The authors would like to thank NASA for the funding of this research under Grant Numbers NGT 50567 and NAG8-123(16). Thanks are also due to Dr Henry B Waites, who, in large part, was responsible for the supervision of the experiment, and Allen Patterson and David Smart for help in the coordination of the experiment.

REFERENCES

Benfield WA and Hruda RF (1971), Vibration analysis of substructures by component mode substitution, *AIAA J*, 9(7), 1255-1261.

Craig, Jr RR and Bampton MC (1968), Coupling of substructures for dynamic analyses, *AIAA J* 6(7), 1313-1319.

Dowell EH (1972), Free vibrations of an arbitrary structure in terms of component modes, *J of Applied Mechanics*, 727-732.

Dowell EH (1979), On some general properties of combined dynamical systems, *J of Applied Mechanics* **46**, 206-209.

Dowell EH (1980a), Component mode analysis of nonlinear and nonconservative systems, *J of Applied Mechanics* **47**, 172-176.

Dowell EH (1980b), Bounds on damping by a component modes method using Lagrange multipliers, *J of Applied Mechanics* **47**, 211-213.

Dowell EH (1983), Component mode analysis of nonlinear, nonconservative systems, *J of Applied Mechanics* **50**, 204-209.

Dowell EH (1984), On the modal approach to structural modification, *J of the American Helicopter Society*, 75-77.

Dowell EH and Klein LR (1974), Analysis of modal damping by component modes method using Lagrange multipliers, *J of Applied Mechanics*, 527-528.Gladwell GM (1964), Branch mode analysis of vibrating systems, *J of Sound and Vibration* **1**, 41-59.

Hurty WC (1960), Vibrations of structural systems by component synthesis, *J of the Engineering Mechanics Division, Proceedings of ASCE*, 51-69.

Hurty WC (1965), Dynamic analysis of structural systems using component modes, *AIAA J* 3(4), 678-684.

Meirovitch L (1980), *Computational methods in structural dynamics*, Sijthoff and Noordhoff, 286-298.

Meirovitch L and Hale AL (1980), On the substructure synthesis method, *An International Conference on Recent Advances in Structural Dynamics* Southampton England, 7-11.

Macneal RH (1971), A hybrid method of component mode synthesis, *Computers and Structures J* **1**, 581-601.

Rubin S (1975), Improved component mode representation for structural dynamic analysis, *AIAA J* 13(8), 995-1006.

Thomson WT (1988), *Theory of vibration with applications*, Prentice Hall, 246-251.

APPENDIX

$$
\begin{bmatrix}
1.5245 & 2.5409 & 3.8114 & -2.7119 & 4.0787 & 2.7192 & 0.2719 \\
-1.5245 & -2.5409 & -3.8114 & 1.7119 & -4.0787 & -2.7192 & -0.2719 \\
3.9372 & 5.5620 & 7.3430 & 0.1771 & 2.5074 & 1.6716 & 0.1672 \\
-4.9372 & -6.5620 & -8.3430 & -0.1771 & -2.5074 & -1.6716 & -0.1672 \\
1 & 0 & 0 & 0 & 0 & 0 & 0 \\
0 & 1 & 0 & 0 & 0 & 0 & 0 \\
0 & 0 & 1 & 0 & 0 & 0 & 0 \\
0 & 0 & 0 & 1 & 0 & 0 & 0 \\
0 & 0 & 0 & 0 & 1 & 0 & 0 \\
0 & 0 & 0 & 0 & 0 & 1 & 0 \\
0 & 0 & 0 & 0 & 0 & 0 & 1 \\
0.9060 & 1.5100 & 2.2649 & 0.1712 & -3.5762 & -3.3841 & -1.8384 \\
-0.9060 & -1.5100 & -2.2649 & -0.1712 & 2.5762 & 2.3841 & 0.8384 \\
0 & 0 & 0 & -1 & 0 & 0 & 0
\end{bmatrix}
$$

Matrix 1. Transformation matrix β for configuration 1

$$
\begin{bmatrix}
5.3875 & 7.8156 & 10.5016 & -0.0262 & 3.9472 & 2.6300 & 0.2628 \\
 & 11.3488 & 15.2603 & -0.1001 & 5.7802 & 3.8510 & 0.3847 \\
 & & 20.5318 & -0.2096 & 7.8281 & 5.2151 & 0.5209 \\
 & \textit{SYMMETRIC} & & 3.8721 & -0.5829 & -0.3888 & -0.0389 \\
 & & & & 4.0576 & 2.4250 & 0.2266 \\
 & & & & & 1.5527 & 0.1495 \\
 & & & & & & 0.0147
\end{bmatrix}
$$

Matrix 2. System Mass Matrix for Configuration 1

$$
\begin{bmatrix}
0.5500 & 0.8833 & 1.2892 & -0.3152 & 1.0756 & 0.7220 & 0.0737 \\
 & 1.4324 & 2.1039 & -0.5253 & 1.7926 & 1.2034 & 0.1228 \\
 & & 3.1038 & -0.7879 & 2.6890 & 1.8051 & 0.1842 \\
 & \textit{SYMMETRIC} & & 0.3856 & -0.8573 & -0.5706 & -0.0568 \\
 & & & & 2.9415 & 1.9798 & 0.1970 \\
 & & & & & 1.3398 & 0.1333 \\
 & & & & & & 0.0137
\end{bmatrix}
$$

Matrix 3. System Stiffness Matrix for Configuration 1

Coupled motion in the dynamic analysis of a three block structure

A Sinopoli

Dipartimento di Scienza e Tecnica del Restauro, Istituto Universitario di Architettura, Tolentini 197, 30135 Venezia, Italy

V Sepe

Dipartimento di Ingegneria Strutturale e Geotecnica, Universita "La Sapienza" Via Eudossiana 18, 00185 Roma, Italy

A mathematical model is presented for the in-plane dynamic analysis of a structure composed of three rigid blocks, simply supported on each other, in presence of dry friction. In order to investigate the dynamics excited by a given ground motion, a Lagrangian formulation is proposed, with displacements, velocities and reactive forces restricted in bounded fields, due to the incompenetrability of the elements. Special attention is devoted to the modelling of the impacts, and to the role of Coulomb friction during the smooth dynamics. Different failure modes are obtained, characterized by a different participation factor of the degrees of freedom. Regions of coupling between rocking and sliding-displacements can be identified, as a function of the features of the excitation and of the friction coefficients. Survival domains decreasing with time can be obtained. They seem to indicate that, in presence of an earthquake, excessive relative displacements in the contact surfaces between the elements would be the most probable cause of failure of such a structure.

INTRODUCTION

The dynamic analisys of structures made of rigid blocks has been the object of many researches since the latter part of the last century. The reason of such an interest was connected in the past, to the possibility to estimate the peak acceleration of an earthquake by observing the overturning of monumental columns or tombstones; more recently, to the necessity to evaluate the seismic stability and safety of structures, ranging from nuclear plants, to elevated tanks, to monumental buildings, like the Roman and Greek temples. Particularly in Europe, the problem of mainteinance and safety of the monumental patrimony has generated a renewed interest, both theoretical and experimental, on this argument.

In spite of the fact that monumental structures are made of many blocks, very few papers tackled with the dynamic analysis of multiblock systems. Certainly, this is due to the complexity of the dynamic behaviour of such systems. In fact, many efforts have been devoted exclusively to identify a general stability criterion for the rocking response, induced by a horizontal harmonic excitation on a single block on a rigid ground (Housner 1963, Yim 1980, Spanos 1984, Hogan 1989, Sinopoli 1991). Therefore, not enough attention has been devoted to the mechanical modelling of multiblock structures.

The dynamic behaviour of a structure made of three rigid blocks, simply supported on each other (i. e. a trilith: the simplest scheme of a columnade belonging to a temple) and excited by a sine wave ground motion, has been investigated only by means of a single degree of freedom model (Allen, Oppenheim et al, 1986).

However, the main purpose of a consistent mechanical model is to identify the most relevant aspects of the response, with minimum a-priori restrictions and to recognize a "safe domain" for the given structure, i. e. a domain in the in the load space, within which the structure survives (tipically, in case of seismic excitations, the load

part of "MECHANICS PAN-AMERICA 1993" edited by MRM Crespo da Silva and CEN Mazzilli ASME Reprint No AMR134

space is the one of the parameters of the external action, and the parameters are an "intensity" and a significative "frequency")

This must be done by taking into account all the possible dynamical modes. In case of multiblock structures, the absence of connections between the elements and the consequent unilateral constraints can give rise to several possible mechanisms, so that relevant aspects of the motion can be rocking, relative rotations with consequent impacts, slidings with friction, loss of equilibrium due to excessive rotations or relative displacements; the slidings, if bounded, determine permanent changes of the geometry.

The importance of these aspects on the dynamical behaviour has been outlined since some years, so that studies have been started concerning the simulation of the impact, the role of dry friction, the coupling between the degrees of freedom, the experimental investigation and numerical simulation of the dynamics. Further, an extensive review has been presented on the mechanical models relevant in the study of the free and forced dynamics of structures made by large blocks without mortar (Augusti and Sinopoli 1992).

In spite of the active interest aroused on these themes and many studies in the last decade, some aspects still remain to be investigated, above all the interplay between dynamics and friction, particularly at the time of impact (Shenton and Jones 1991, Sinopoli 1993). Anyhow, the first results obtained by investigations on the impact between rigid bodies (Sinopoli 1989, Ageno and Sinopoli 1991) showed that the coupling between the degrees of freedom cannot be ignored after an impact, even in the case of a single block on a rigid ground.

Further, a previous work on the dynamic analysis of a trilith (Sepe and Sinopoli, 1991) showed that the assumption of a system with one degree of freedom, for standard values of the mechanical and geometrical features, is correct only in the first part of the motion, until the system either overturns or comes back to the static equilibrium configuration; in the second case, the occurring impacts can be responsible of relative slidings between the blocks, so that a general model must be defined, where all the possible degrees of freedom of the system are taken into account.

The structure dealt with in this paper is made of three blocks, rigid by assumption and simply supported by each other. The aim of the research is to verify if relative sliding displacements can induce a failure mode due to the loss of geometrical configuration (that is increasing distance between the contact points at the top of the columns) and to quantify its probability with respect to overturning; this feature of the motion has never been analyzed or taken into account in the scientific literature.

The dynamic model presented here does not take into account the sliding of the structure with respect to the plane support; this assumption reduces the complexity of the investigation.

Special attention is devoted to the modelling of the contact law. With respect to the impact, a theoretical preliminary approach proposed by one of the authors is used, formulated here as a quadratic programming problem; it neglects the role of dry friction during the impact.

THE PROBLEM

The assumptions

Let us consider the plane structure shown in Fig.1, made of three rigid blocks, simply supported with each other, in presence of dry friction. Further, assume also that the possibility of sliding displacements of the two columns with respect to the plane support is not taken into account in the evaluation of the degrees of freedom of the system; such an assumption, which reduces quantitatively the complexity of the problem, is acceptable from a pratical point of view because relative sliding motions at the top of the columns are more probable and therefore more important than the corresponding ones at the bottom, in the failure mode due to the loss of the geometrical configuration.

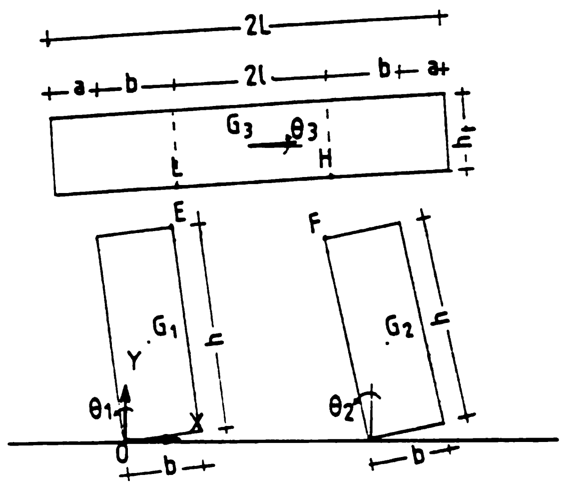

FIG 1. Geometrical features and degrees of freedom of the analyzed system.

The lagrangian coordinates q_k (with $k=1,2,..5$) describing the instantaneous configuration are: $q_1 = \theta_1$ and $q_2 = \theta_2$, that is the rotations of the left and right columns, and: $q_3 = x_3$, $q_4 = y_3$ and $q_5 = \theta_3$, respectively, the horizontal and vertical displacements, and the rotation of the architrave.

The absence of connections between the blocks and the rigidity assumption implies bounded variations for the lagrangian coordinates q_k; the boundaries of these domains depend on the instantaneous configuration and on its persistence with the time. For example, the boundaries for the rotations of the columns coincide always with the restraint of impenetrability with the ground; on the contrary, the bounded values for the coordinates of the architrave depend on the efficiency of the contacts with the columns.

During the motion, either free induced by given initial conditions or forced due to any excitation, many and different mechanisms are possible; they correspond to the many kinds of efficient contacts (see for example Fig. 2) and to the loss of any contact.

There are two kinds of loss of contact. The first one, due to excessive relative displacements along either tangent line to the blocks boundaries on the contact point, always induces the collapse of the structure, due to the gravitational field. The second one is the uplift of the lintel with respect to the columns; but, the possibility of a renewed possible contact must be checked with the time.

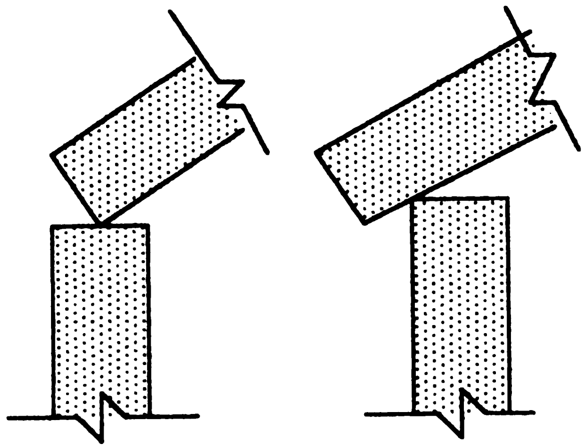

FIG 2. Different kinds of possible contacts.

During the motion the starting of each mechanism, which is governed by given differential equations, and the efficiency and the persistency of any contact depend on the geometrical and mechanical fetures of the system, and instantaneously on the values of the reactive forces in the contact points.

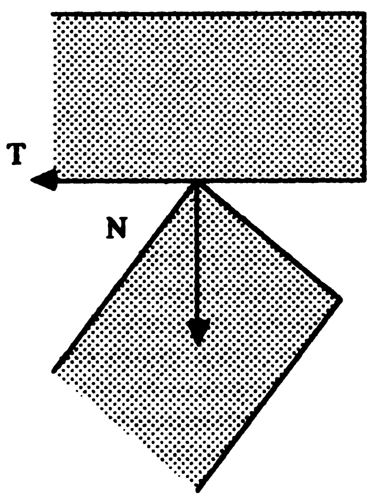

FIG 3. System of unit vectors on the contact point.

Therefore, the dynamic evolution requires a step by step control in order to check if the lagrangian coordinates, their derivatives and the contact reactions satisfy both the incompenetrability and the rigidity assumptions. That can be made by defining a contact law.

SMOOTH DYNAMICS

Let us consider any contact between the lintel and either column, involving only the point P_i belonging to both the boundaries of the blocks. Then, it is possible to define a normal system of unit vectors (T, N) such that T is parallel to the boundary of either element (Fig. 3). Let us define like u^{T}_{i}, u^{N}_{i} the tangen and normal relative position of the point P_i referred to the system (N, T) .

Normal contact law

The efficiency of the i-th contact is characterized by:

$$u^{N}_{i} = 0 \tag{1}$$

with:

$$u^{N}_{i} \geq 0 \tag{2}$$

The persistency of the same contact, on the contrary, depends on the value of the normal relative velocity $\dot{u}^{N}_{i}$; the contact is mantained if:

$$\dot{u}^{N}_{i} = 0 \tag{3a}$$

or lost, if:

$$\dot{u}^{N}_{i} > 0 \tag{3b}$$

with:

$$u^{N}_{i} \geq 0 \tag{4}$$

Then, it is expected that a reactive force:

$$F^{N}_{i} \geq 0 \tag{5}$$

acts in the contact point, in order that eq.(4) is satisfied. The loss of contact, that is eq. (3b), implies a zero value for the reactive force, the normal contact law can be expressed as:

$$\dot{u}^{N}_{i}\ F^{N}_{i} = 0 \tag{6}$$

with:

$$\left.\begin{aligned} \dot{u}^{N}_{i} &\geq 0 \\ F^{N}_{i} &\geq 0 \end{aligned}\right. \tag{6a}$$

for:

$$u^{N}_{i} = 0 \tag{6b}$$

And:

$$F^{N}_{i} = 0 \tag{7a}$$

for:

$$\dot{u}^{N}_{i} > 0 \tag{7b}$$

Equations (6) and (7) define the normal contact law like a linear complementarity problem (Jean and Moreau 1991).

Tangent contact law

In presence of dry friction, an interplay between dynamics and friction is expected, only when the contact is efficient.

Then, if eqs. (1) and (3a) are satisfied, the tangential Coulomb contact law assumes the form:

$$F^{T}_{i} \leq \mu_s \; |F^{N}_{i}| \tag{8a}$$

if and until:

$$\dot{u}^{T}_{i} = 0 \tag{8b}$$

whith μ_s static friction coefficient. On the contrary, if the tangential relative velocity is different from zero:

$$\dot{u}^{T}_{i} \neq 0 \tag{9a}$$

then:

$$F^{T}_{i} = -\,sgn(u^{T}_{i})\,\mu_k \,|F^{N}_{i}| \tag{9b}$$

where μ_k is the kinetic friction coefficient.

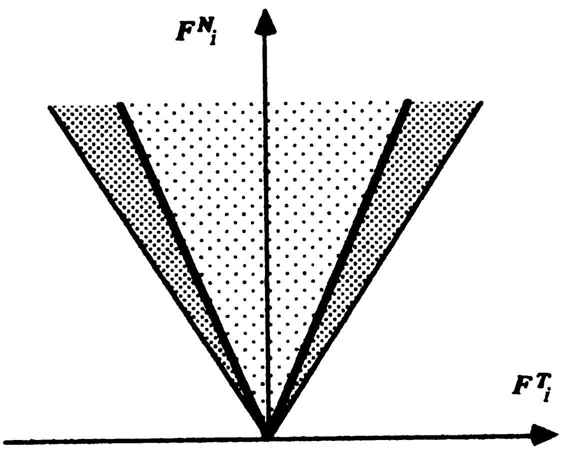

FIG 4. Coulomb cone.

Once more the reactive force disappears in correspondence to zero value of the normal relative velocity; then:

$$F^{T}_{i} = 0 \tag{10a}$$

for:

$$u^{N}_{i} > 0 \tag{10b}$$

NON - SMOOTH DYNAMICS

The impact

During the dynamic evolution, it may happen that one or more points P_i, starting from positions interior to the domain of the admissible values ($u^{N}_{i} > 0$), come suddendly in contact with the boundary of another element, but chracterized by negative values of the normal relative velocity $\dot{u}^{N}_{i}$. This situation violates the normal contact law expressed by eqs. (6); then, it is expected that at this instant an impulsive force acts on the contact, inducing a discontinuity on both the normal and tangential relative velocities.

The general analysis of the impact between rigid bodies, in presence of dry friction, when the area of the surfaces involved in the phenomenon is different from zero, is in our opinion a still open problem.

Different are the solutions proposed in the scientific literature (Housner 1963, Ishiyama 1982, Jean and Moreau 1991, Shenton and Jones 1991). A common feature of is the elimination of the apparent indetermination by means of some "a priori" assumptions.

For example, one of them concerns the "a priori" choice of the point candidate to mantain the contact after the shock; consequently, the Newton experimental law can be utilized with zero value for the restitution coefficient, typical of the inelastic shocks between rigid bodies.

One of the Authors (Sinopoli 1989) proposed, on the contrary, an approach where the inelastic impact, in absence of friction, is formulated as a problem of dynamical evolution governed by a variational principle, without reference to the restitution coefficient. The solutions is then determined the minimum value of a quadratic form R, subject to the constrains imposed to the system. After an impact, among all the admissible motions, the actual one is the closest (in the space the metric of which is the kinetic energy) to the one characterizing the system if it could become completely free.

In presence of friction, the most critical point is the evaluation of its role during the impact. Following a weak formulation, the friction performance must be expressed in terms of restraints on the velocities, which remain constant during the impact (persistent constraints); but, the character of a frictional contact is that it generally varies and depends on the instantaneous redistribution of the velocities (Augusti and Sinopoli 1992).

In this respect, two formulations have been proposed, where the friction has been either taken into account roughly (Sinopoli 1987) or neglected (Sinopoli 1989); the validity of either model depends mainly on the assumptions concerning the starting instant of the friction performance and, then, on the impact unelasticity, on the rigidity of the material and on the duration of the impact. The main point whose treatment is still unsatisfactory, is the coupling between rocking and sliding. This point is particularly relevant for actual structures, made of many blocks: slides, in fact, make loss of equilibrium possible, but at the same time dissipate energy; the prevalence of either aspect decides the safety of a structure. Another question regards the validity of the "Coulomb friction" hypothesis, or the values of static and kinetic friction coefficients: the first one can be particularly high when ancient costructions are concerned, in which the surfaces may have remained in standing contact for centuries.

For this reason, an experimental investigation has been performed (Ageno and Sinopoli 1991) on marble blocks of several sizes, impacting a marble ground. As a consequence a new theoretical model has been formulated recently (Sinopoli 1993b).

In this paper, the friction performance starts to act only after the impact; so that during the shock no restrictions must be imposed to the tangential velocities of points P_i.

If $\dot{q}^-$ is the velocity vector of the system before the impact, the velocity $\dot{q}^+$ after the shock is determined among all the admissible ones q as:

$$min \left\{ R = (\dot{q} - \dot{q}^-)^* M \ (\dot{q} - \dot{q}^-) \right\} \tag{11}$$

where $*$ means transposition and M is the mass matrix, subject to the constraint of inpenetrability:

$$\dot{u}^N{}_i \geq 0 \tag{12}$$

which must be satisfied by all the points P_i of the elements coming into contact.

DYNAMICS EQUATIONS

Let us consider the dynamics induced by a given horizontal ground motion: $x(t) = x_o \sin(\omega t + \phi)$ and represent the corresponding acceleration, in g units (where g is the garvity acceleration) as: $x(t) = K_s \, g \sin(\omega t + \phi)$.

The periodicity and then the stationarity character of such an excitation makes it very different from an earthquake. Nevertheless, it can be considered as a preliminary step toward the knowledge of the forced dynamics of the system.

During the time, the dynamics are governed by a set of differential equations, the number and the form of which change depending on the started or mantained mechanisms.

For example, if all the contacts are efficient and persistent without sliding displacements, referring to the Lagrangian formalism, the system of dynamics equations is:

$$d/dt \ (\partial L/\partial \dot{q}_k) - (\partial L/\partial q_k) = Q_k \qquad k=1,2,..5 \tag{13}$$

together to the differential kinematic relationships, expressing the constraints imposed to the normal relative velocities $\dot{u}^N{}_i$ of the contact points P_i:

$$\dot{u}^N{}_i = \sum_{k=1}^{5} a^N{}_{ik} \, \dot{q}_k = 0 \qquad i = 1, 2 \tag{14a}$$

and to the tangential relative velocities $u^T{}_i$:

$$\dot{u}^T{}_i = \sum_{k=1}^{5} a^T{}_{ik} \dot{q}_k = 0 \qquad i = 1, 2 \tag{14b}$$

In eq. (13) L is the Lagrangian of the system, which takes into account the effects of the ground motion and of the gravity, and Q_k is the generalized force, representing the effects on the k-th degree of freedom of the interactions $F^N{}_i$ and $F^T{}_i$ between the parts of the system. $F^N{}_i$ and $F^T{}_i$ are present in the expression of Q_k as a given combination of the Lagrangian multipliers corresponding to the constraints equations satisfied by the $\dot{q}_k$

The particular expression of Q_k depends on the kind of the contact (absence or presence of relative sliding motions, or uplift), in accord to the stated contact laws.

If any *i-th* contact is absent, the corresponding *i-th* constraint equation and the *i-th* term in the expression of Q_k disappear.

NUMERICAL INVESTIGATION AND RESULTS

A numerical investigation has been performed as a function of the amplitude K_S, the frequency ω of the horizontal sine wave excitation, and of the static and kinetic dry friction coefficients. The sizes of the elements of the analyzed system are shown in Fig. 5; they correspond to a columnade of the E3 Greek temple at Selinus (Sicily).

A temptative value equal to *3* has been selected for the mass ratio between the lintel and a column. Such a value is probably too large in comparison with the actual one, so that the inertial effects on the dynamics response are emphasized; but, as it will be clear in the following, the features of the dynamics and the aim of this paper allow such a choice as a preliminary investigation.

Following the dynamic evolution, it has been very difficult to give a systematic interpretation of the results obtained.

As an example, in Fig. 6 the time history of the relative displacement between the contact points at the top of the left column is shown, for different values of the frequency ω, for a given amplitude $K_S = 0.4$ and for values of friction coefficients f_s and f_k, respectively equal to 0.6 and to 0.3.

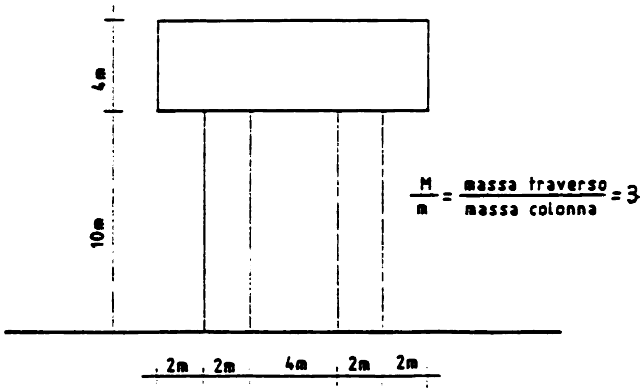

FIG 5. Sizes of the analyzed system.

An adimensionalized time has been used: $t/T = \omega t/2\pi$, in order to compare the motions in one period of the excitation.

It is evident that small variations in the features of the ground motion can induce completely different responses.

Nevertheless, something can be said by comparison with the dynamic response obtained in the previous one degree of freedom model (Sepe and Sinopoli 1991).

In fact, by analyzing the response of the same trilith in the simple rocking model, three regions were identified, if K_S was increased for a given ω in the (ω, K_S) plane, where respectively: a) there was no motion; b) the motion was orbitally stable; c) the motion was orbitally unstable (overturning).

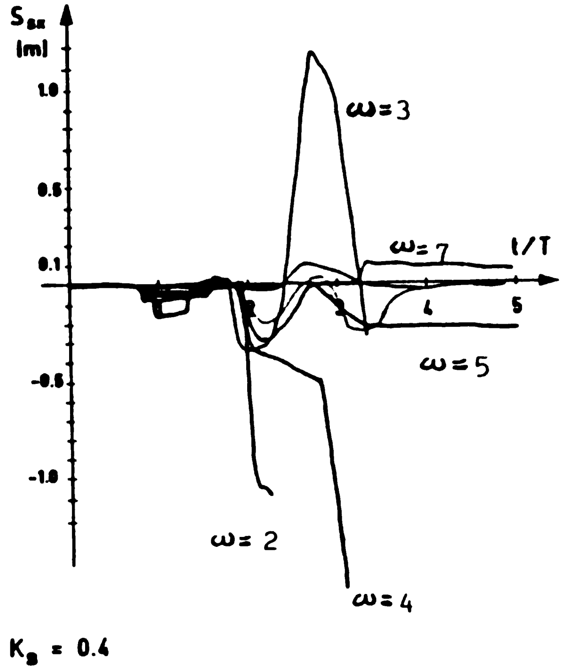

FIG 6. Time history of the relative displacement for different values of the angular frequency ω.

Only the first and the third regions remain almost unvaried in the coupled slide-rocking model.

The most important difference is in the second region, where now the motion is generally unbounded and two different failure modes can be identified: the overturning and the failure due to the loss of the geometrical configuration for either eccessive slidings or coupled effects between excessive slidings and rotation.

Therefore, as a first step, let us evaluate the sensitivity of the system to cumulate slidings in a given

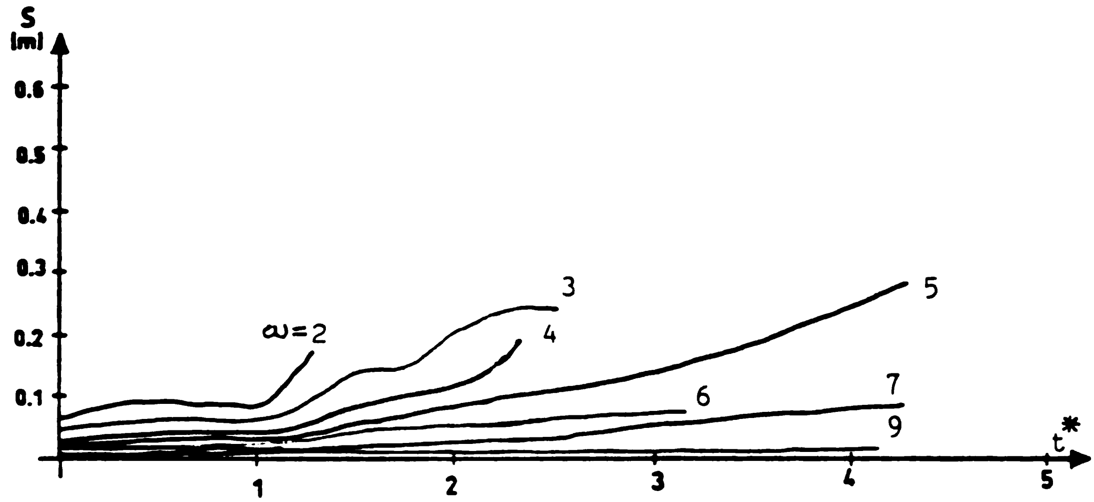

FIG 7. Mean absolute relative displacement for different values of the angular frequency ω.

time interval. To this aim let the absolute value of the mean relative displacement S, in a given time interval $(0 - t^*)$, be defined as:

$$S = \frac{1}{t^*}\int_0^{t^*} (\,|S_l| + |S_r|\,)\, dt \qquad (15)$$

where S_l and S_r are, respectively, the mean relative displacement cumulated in the time t^* at the top of the left and right column; t^* is the time measured from the first impact and adimensionalized with respect to the period T of the excitation. A better interpretation of the dynamic response is then obtained. In Fig.7, the dependence of S on the time t^* is shown for a given value of K_s ($K_s = 0.4$) and of the static and kinetic friction coefficients ($\mu_s = 0.6$ and $\mu_k = 0.3$) and for different values of ω.

Generally, S decreases with ω for a given K_s, and increases with K_s, but in a different way depending on ω; this circumstance can be observed in Figs.8, where the rate of S, as a function of the angular frequency ω, .has been measured in meters per periods T (Fig.8a) and in meters per seconds (Fig.8b).

Both S and its velocity are absolute values; therefore, they are correlated with the energy dissipated by the system due to the slidings. By observing Figs. 8 and 9, it seems that for small values of the angular frequency such an energy is large, but it tends quickly to zero with ω.

This fact alone cannot give us any information about the safety of the structutre; in the sense that a little amount of dissipated energy, either per period or per second, does not imply necessarily failure for increasing dynamic response, due to the strong non linearity of the system.

It is necessary to examine closely the features of the motion and, particularly, to investigate the effects of the coupling between the degrees of freedom.

Our parametric investigation considered a domain in the load space of the ground motion, defined by values of the angular frequency ω ranging from 1 to 12 rad/sec,

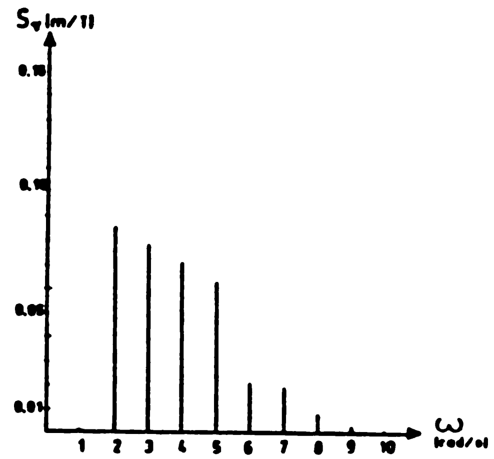

FIG 8a. Mean velocity of S (meters/ period) as a function of the angular frequency ω for $k_s = 0.4$.

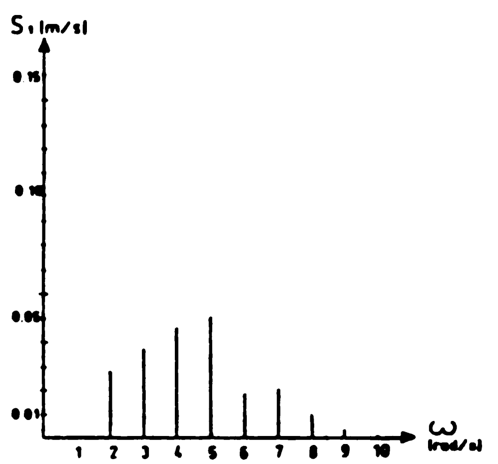

FIG 8b. Mean velocity of S (meters/ seconds) as a function of the angular frequency ω for $k_s = 0.4$.

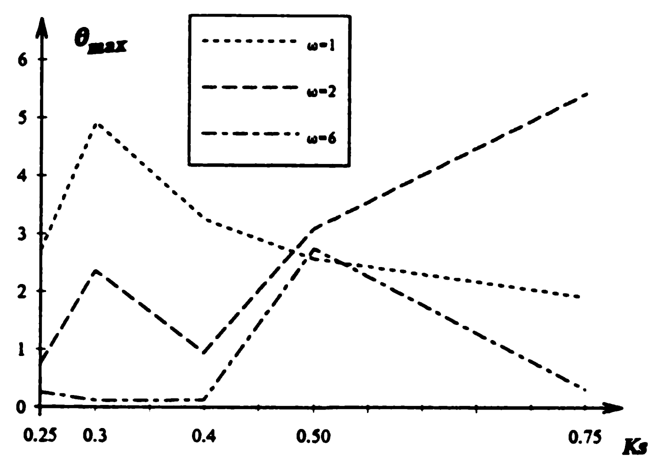

FIG 9a. Maximum rotation of either column as a function of K_s.

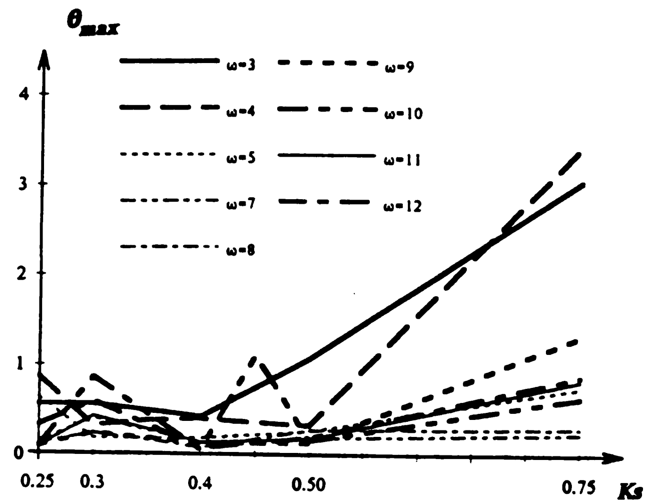

FIG 9b. Maximum rotation of either column as a function of K_s.

and of the acceleration amplitude K_S ranging from *0.2* to *0.75*, in gravity acceleration units; smaller values of K_S cannot induce motion due to the character of the equilibrium configuration (Sinopoli 1990).

Unfortunately, the dynamic responses obtained don't exhibit any periodic feature, except some isolated case which will be discussed later. Anyhow, let us show the maximum rotation of either column (adimensionalized with respect to the angle corresponding to the unstable static equilibrium configuration; i. e. center of the mass of the column along the vertical line), as a function of K_S for different values of ω (Figs. 9a and 9b), until five seconds.

The rotations shown in Fig. 9b increase on the average with K_S and reach dangerous values of the angle only for very large values of the acceleration. On the contrary, anomalous behaviours can be observed in Fig. 9a, possibly due to the coupling with the slidings.

Then, let us analyze and compare the responses of the different degrees of freedom, in order to verify the role of the coupling in the loss of the geometrical configuration responsible of the failure.

The loss of the geometrical configuration means not only the variation of the configuration due to the dynamics, but especially the increased distance between the support points of the lintel.

The variation of the geometric features of the system persists even if the dynamics stop at a given instant and the trilith comes back to the initial equilibrium configuration; then the cumulate sliding can be considered as a measure of the permanent damage induced by the excitation on the structure. Further, such loss of the geometric configuration is always present in the second region of the load plane, where the simple rocking model was characterized by periodic and bounded responses.

The maximum values of the adimensionalized rotation and of the relative displacement (adimensionalized with respect to the width of the column), are shown respectively in Fig. 10a and 10b.

The rotation for the case $K_S = 0.4$ is strictly exponentially decreasing with ω, a typical behaviour of the simple rocking model. The same occurs only on the average for the other cases (Fig. 10a), but with the exception of some evident

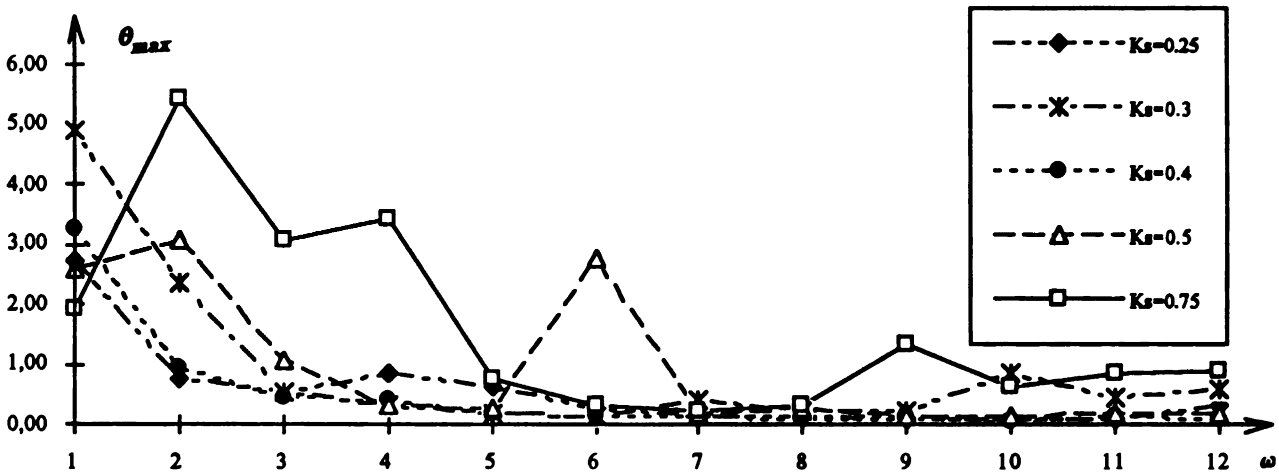

FIG 10a. Maximum adimensionalized rotation of either column until 5 sec.

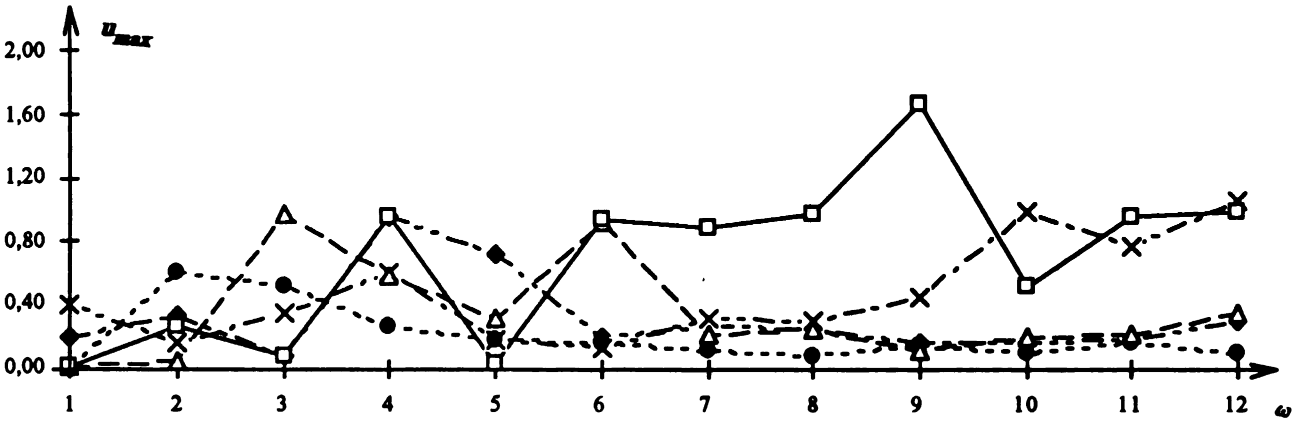

FIG 10b. Maximum adimensionalized relative displacement on either contact point until 5 sec.

peak; for example the one for $\omega = 6$ *rad/sec* and $K_s = 0.5$.

The same peaks can be observed in Fig. 10b for the relative displacement; they suggest a strong coupling influence on the dynamics response.

Furthermore, by comparison from the two figures, it can be said that for small values of ω and of K_s, on the average , the rotations and the slidings have a dual behaviour as a function of the angular frquency. Particularly, the rocking is dominant for small values of the frequency, while the sliding prevails in the remaining range.

Anyway, under a deterministic point of view, no systematic trend for the rocking can be identified by increasing the amplitude of the excitation, as can be verified by checking the corresponding values for $\omega = 1$.

Once more the rotation increases with K_s, only on the average, inducing increasing values of the slidings especially for large ω.

By following the dynamics evolution for a long time interval, the mean behaviour outlined above becomes more and more evident. In fact, the same variables of the motion of Figs. 10a and 10b are shown in Figs. 11a and 11b, after a time span equal to *1000 sec*.

For small values of the frequency, the rocking response is almost unvaried; on the contrary, the sliding is increased. Both slidings and rotations become important in the range of large frequencies, with well evident coupled peaks.

With respect to the cumulative slidings, even if in a given time interval they are not quantitatively large, it is sufficient to wait for a time long enough, in order that the failure occurs in any case.

With respect to the maximum value of the angle, the results suggest that, in correspondence to a given value of the amplitude acceleration, a value for the frequency can be determined below which a failure due to overturning is expected for the structure; such a value of the frequency is very small in comparison with the one characterizing the peak acceleration of an earthquake, so that this failure mode seems quite improbable.

On the contrary, for increasing values of the frequencies, both the dynamic responses increase with the time so that

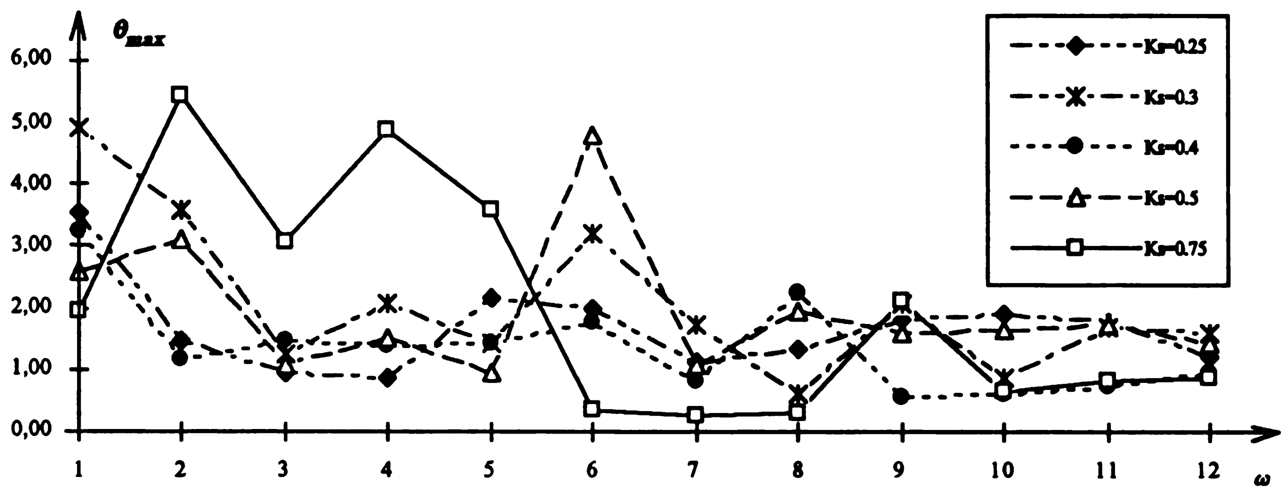

FIG 11a. Maximum adimensionalized rotation of either column until the collapse or 1000 sec.

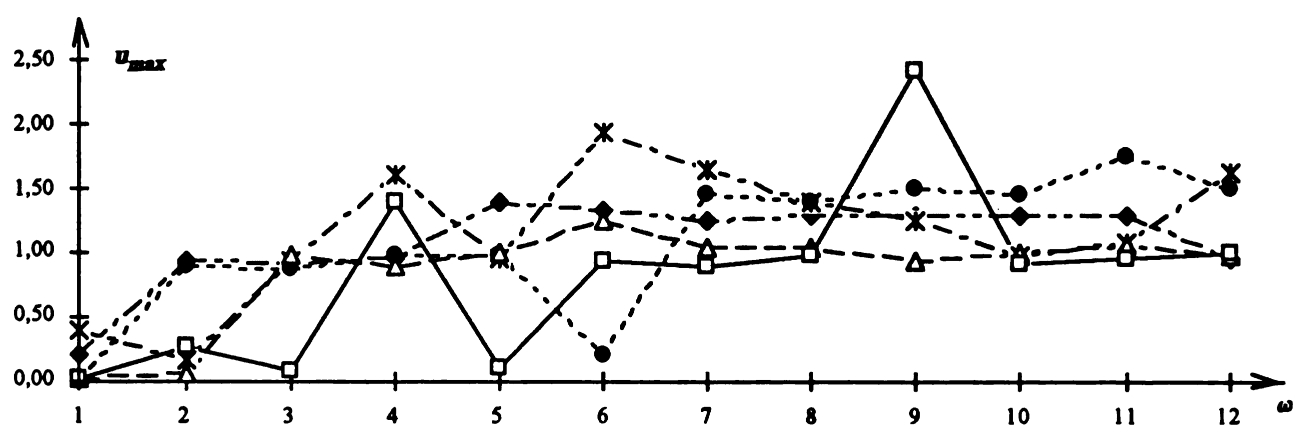

FIG 11b. Maximum adimensionalized relative displacement on either contact point until the collapse or 1000 sec.

both the failure modes, due to overturning and excessive slidings, are expected for the coupling between the degrees of freedom.

In effects, the slidings seem to be more important than the rocking; but, the coupling unpredictable in terms of dependence on the angular frequency, generates the coupled peaks mentioned above so that relative displacements and rotations must be considered as equally determinant in the coupled motion for the collapse.

Such peaks recall the parametric resonance identified as a feature of the response of a single degree of freedom model, investigated by means of an analytical approach.

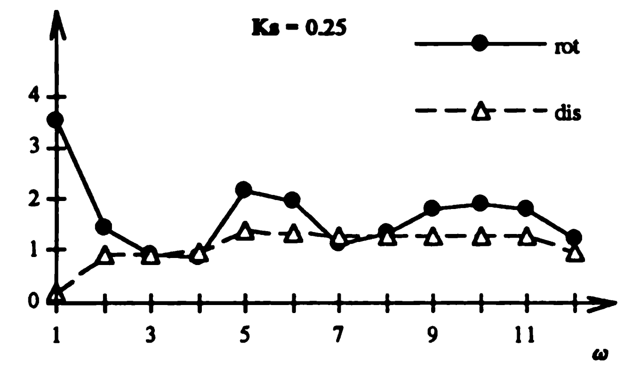

FIG 12a. Maximum rotation and sliding for *Ks=0.25.*

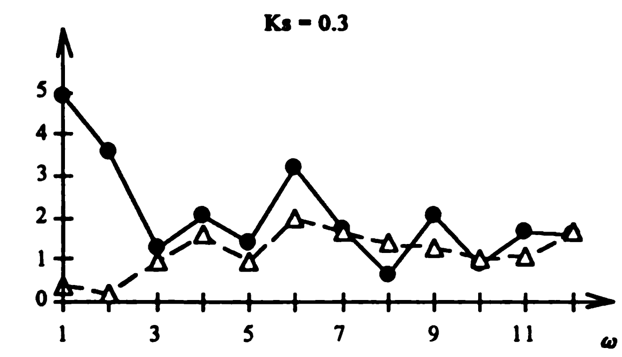

FIG 12b. Maximum rotation and sliding for *Ks=0.3.*

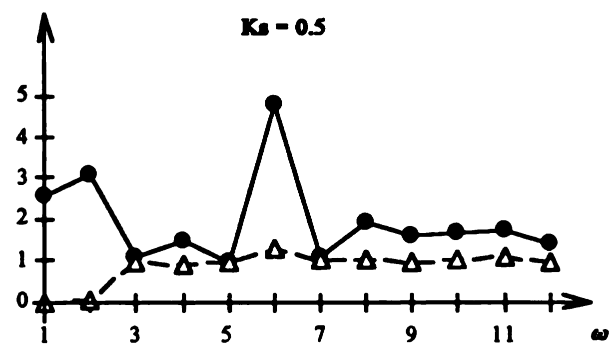

FIG 12c. Maximum rotation and sliding for *Ks=0.5.*

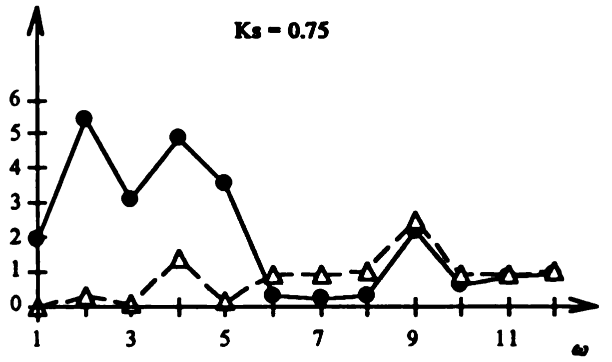

FIG 12d. Maximum rotation and sliding for *Ks=0.75.*

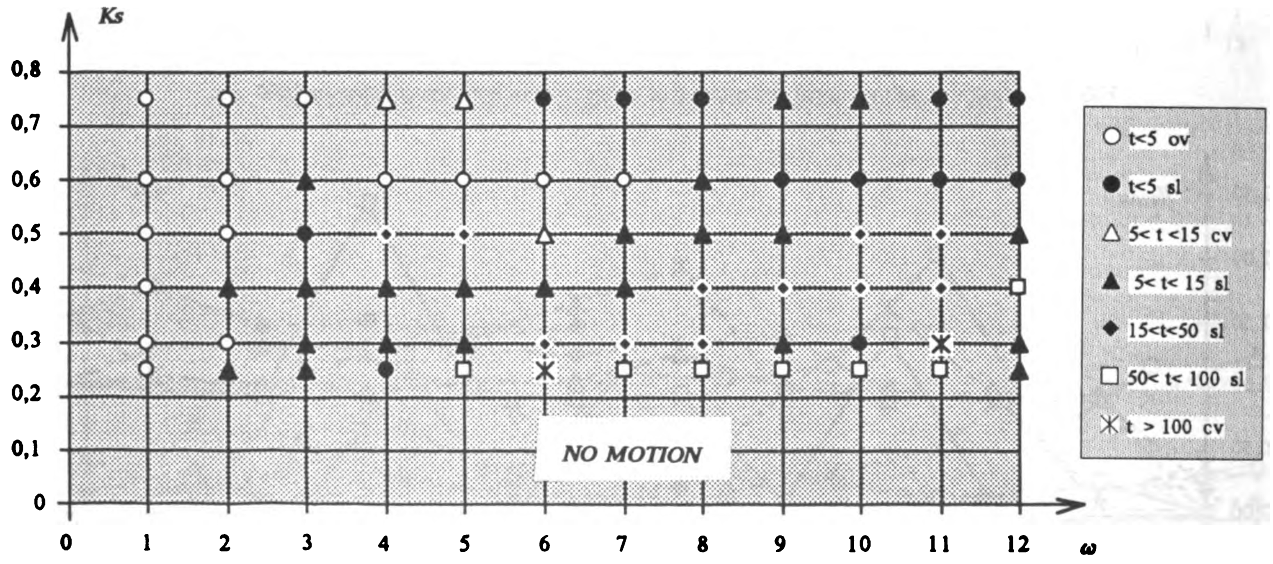

FIG 13. Survival domains for $f_s = 0.6$ and $f_k = 0.3$.

There, the character of the differential equations governing the motion were determined by matching the equation governing the motion of different mechanisms into a unique equation, able to take into account the discontinuity character of the dynamics (Sinopoli 1991)..

But, in the present model, any analytical investigation is not allowed. due to the large number of degrees of freedom and the complexity of the differential equations

In Figs. 12a-d, the strong coupling between the rocking and the sliding, for ω larger than *3 rad/sec*, can be observed in detail, after a time span of *1000 sec.*

From the considerations made until now, it follows that it is difficult to give some criterion about the safety of the structure, by analyzing the features of the motion. In fact, the response of any degree of freedom is generally increasing with the time.

Only one case has been found, for $\omega = 6$ *rad/sec* and $K_s = 0.25$, where the rotation of the right column seemed to librate around the unstable static equilibrium configuration; while, the other degrees of freedoms were oscillating with amplitude slowly increasing with time. Therefore, the global motion was unbounded in any case.

Probably, the most interesting result of this investigation is the definition of a survival domain in the load plane (ω,K_s), where many and different regions can be identified, characterized by different failure modes and by different instant into when such a collapse occurs.

Then, it is possible to follow the evolution of the boundaries of the safe region for the trilith with time; further, it is evident that, for such a kind of structure, the probability of failure is an increasing function of time, which reaches the value one with the time increasing to infinity.

The role of dry friction coefficients

Given a time interval, the position and the global area of the survival domain in the load plane depend on the geometry and on the mass ratio of the system, and moreover, on the contact law and on the performance of friction.

In fact, the main difference between the results of the present study and the ones obtained with the simple rocking model, is the loss of systematic trends of the dynamic response with respect to the parameters of the excitation, due to the presence of the slidings; therefore, it is expected that the variations of the friction coefficient can modify the features of the motion sensibly.

A further parametric investigation has then been performed for different values of the friction coefficients and of their ratio. Three cases will be presented here. The first, case a) for for values of friction coefficients f_s and f_k, respectively equal to *0.6* and to *0.3*; the second one: case b), for values equal to *0.6* and *0.6*, and the third one: case c), for values equal to *0.75* and *0.25*.

The variation of the survival domains for case c) can be observed in Fig. 14 and compared with the similar one of Fig. 13, for case a).

The areas corresponding to a long survival time have disappeared, while the area of the regions where an early collapse occrs are increased.

In order to understand the results obtained, let us observe that the values of the friction coefficients for case c) implie a decreased possibility to start the sliding during the smooth dynamics. Therefore, it is expected that the value of the maximum rotation increases with time until the first impact occurs; at this instant, relative displacements between the

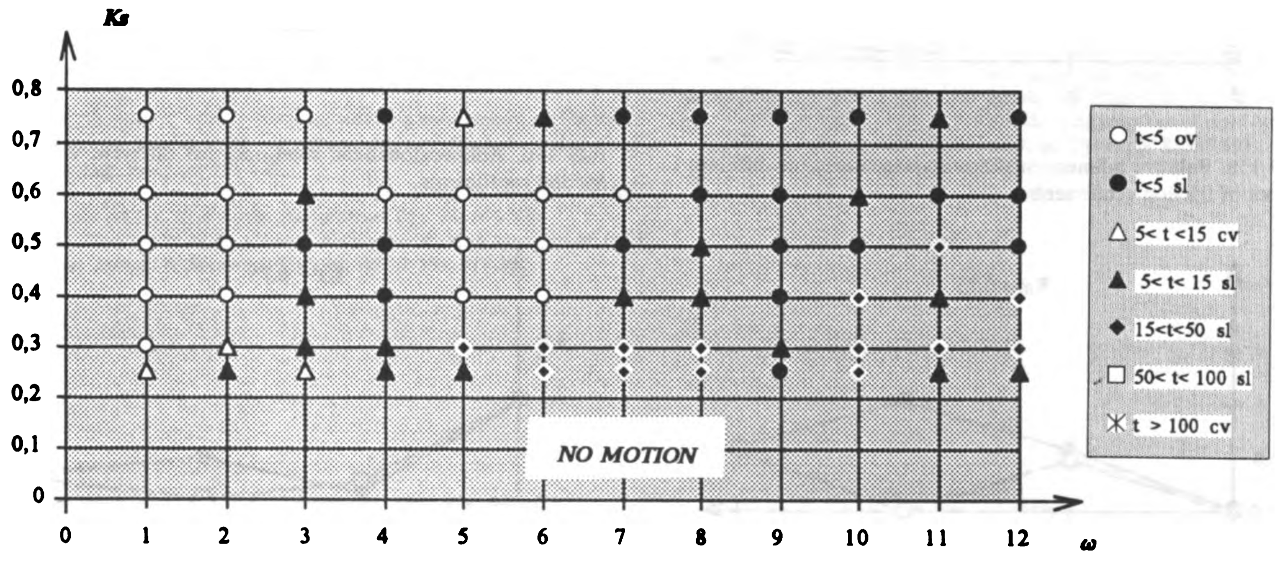

FIG 14. Survival domains for $f_s = 0.75$ and $f_k = 0.25$.

lintel and the columns can start as a consequence of the shock.

However, the small value of the kinetic friction coefficient does not allow the system to dissipate energy enough, so that it is expected that the trilith collapses earlier than in case a).

The comparison between the coupled responses, for the three cases analyzed, is shown in Fig. 15 and 16, for a time duration of five secondsGenerally, an increased value of the static friction coefficient determines larger values for both the maximum rotation and the relative displacement, except for large values of K_s $(K_s = 0.75)$.

On the contrary, the increase of the kinetic coefficient determines reduced or equal values for both rotation and sliding.

CONCLUSIONS

The dynamical behaviour of blocks structures, in particular under an earthquake-type load, is a well developed field of research, which has already given some significative results. Much less developed appear the applications of these studies to actual problems, by means of correct models able

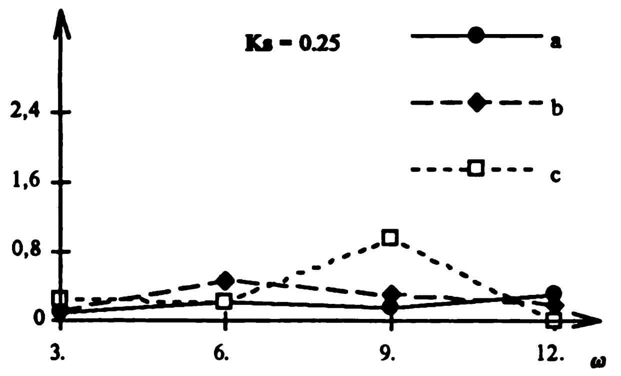

FIG 15a. Adimensionalized maximum rotation and sliding for different values of friction ceefficients.

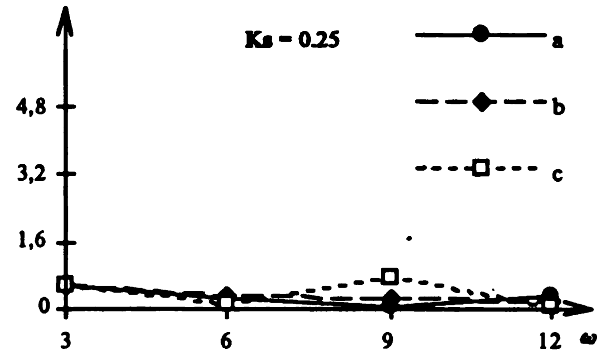

FIG 16a. Adimensionalized maximum rotation and sliding for different values of friction ceefficients.

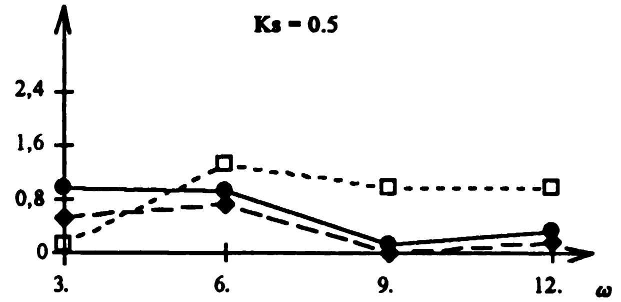

FIG 15b. Relative adimensionalized displacements for different values of friction ceefficients.

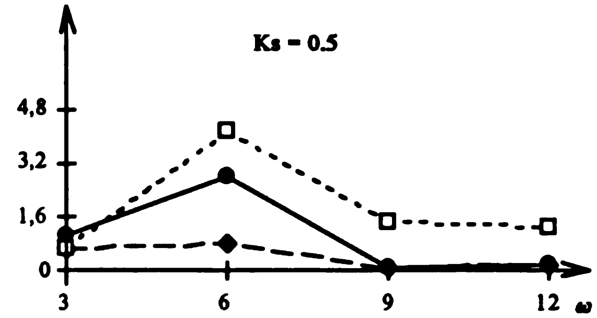

FIG 16b. Adimensionalized rotationss for different values of friction ceefficients.

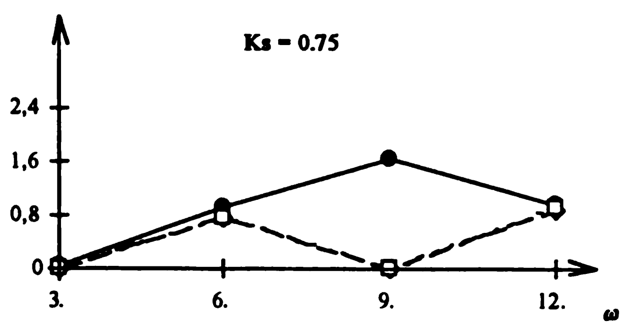

FIG 15c. Adimensionalized maximum rotation and sliding for different [illegible] friction ceefficients.

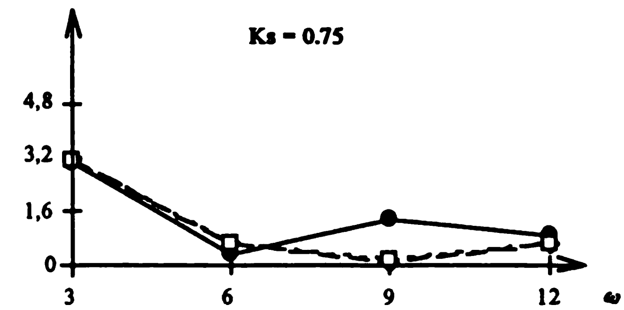

FIG 16c. Adimensionalized maximum rotation and sliding for different values of friction ceefficients.

to simulate the actual behaviour.

Even in the few cases in which the importance of the problem forced a systematic study parallel to the actual works, like the restoration of the Parthenon, the dynamic aspects have been somewhat undervalued, and the structural analysis followed the quasi-static approach.

The present paper is an attempt towards filling this gap.

A model to investigate the coupled motion of a trilith with the same geometric features of the columnade of the E3 Temple at Selinus (Sicily) has been proposed.

Special attention has been devoted to the modelling the contact law and the impact problem. Some assumptions, due both to the necessity to reduce the complexity of the study and to still open problem, have been made.

A parametric investigation has been performed as a function of the excitation parameters and of the mechanical features of the system.

Collapse by overall excessive rotation is a rather improbable failure mode under seismic loads; on the contrary, both overturning and collapse due to excessive sliding as a consequence of the coupled dynamics, seem to be a mode of collapse, which requires only a time long enough.

The effects of the variations for the values of the friction coefficients have been analyzed.

Further, survival domains in the load plane have been identified, the position and the area of which depend on the duration of the time interval analyzed.

ACKNOWLEDGEMENT

The Authors acknowledge the Ministero dell'Università e della Ricerca Scientifica e Tecnologica, and the Ministero dei Beni Culturali ed Ambientali of Italy, by which the research has been supported

REFERENCES

Ageno A, Sinopoli A, (1991), Indagine teorica e sperimentale sul problema dell'urto fra blocchi rigidi, in: *Proceedings of 5th Italian Nat. Conf. Earth. Eng.*, Palermo, 465-478.

Allen RH, Oppenheim IJ et al, (1986), On the dynamics response of rigid body assemblies, *Earthquake Engng Struct Dyn* 14, 861-876.

Aslam M, Godden W et al, (1980), Earthquake rocking response of rigid bodies', *Journal of Structural Division, ASCE*, 106, 377-392.

Augusti G, Sinopoli A, (1992), Modelling the dynamlics of large block structures, *Meccanica*, 27 (3), 195-211.

Franciosi V, Sinopoli A, (1986), The stability degree of masonry structures: the earthquake as crisis parameter, *Mechanics Research Communications*, 13 (4), 187-192.

Hogan SJ, (1989), On the dynamics of rigid block motion under harmonic forcing, *Proc Royal Soc Lond* A425, 441-476

Housner WG, (1963), The behavior of inverted pendulum structures during earthquakes, *Bul Seism. Society of America*, 53, 403-417.

Ishiyama Y, (1982), Motions of rigid bodies and criteria for overturning by earthquake excitations, *Earthquake Engr and Struc Dynamics* 10, 635-650

Jean M, Moreau JJ, (1991), Dynamics of elastic or rigid bodies with frictional contact: Numerical methods', in *Proceedings of Mecanique, modelalisation numerique et dynamique des materiaux*, LMA (ed), CNRS 124, Marseille, 9-29.

Moreau JJ, (1963), Les liaisons unilatérales et le principe de Gauss' *C. R. Acad. Sc. Paris*, 256, 871-874.

Moreau JJ, (1983), Liaisons unilaterales sans frottement et chocs inelastiques, *C. R. Acad. Sc. Paris*, 296, Serie II, 1473-1476.

Moreau JJ, (1986), Une formulation du contact à frottement sec; application au calcul numerique, *C. R. Acad. sc. Paris*, Serie II, 296, 799-801.

Sepe V, Sinopoli A, (1991), La dinamica del trilite: Modello generale e limiti di validità del modello ad un grado di libertà, in *Proceedings of 5th National Conference Earthquake Engineering*, Palermo, 567-578.

Sepe V, (1992), Comportamento dinamico di strutture costituite da blocchi rigidi sovrapposti: il trilite, PhD Thesis, Florence University.

Shenton III HW, Jones NP, (1991), Base excitation of rigid bodies. I. Formulation, *Journal of Engineering Mechanics, ASCE*, 117 (10), 2286-2306.

Sinopoli A, (1987), Dynamics and impact in a system with unilateral constraints. The relevance of dry friction, *Meccanica*, 22, 210-215.

Sinopoli A, (1989), Kinematic approach in the impact problem of rigid bodies, *Appl Mech Rev* 42(11), 233-244.

Sinopoli A, (1990), Non linear dynamic analysis of multiblock structures, in *Proceedings of European Conference on Structural Dynamics*, Kratzig (ed), Balkema, 127-134.

Sinopoli A, Ageno A, (1990), The role of dry friction in the impact problem of rigid bodies, in: *Proceedings of Euromech Colloquium 273: Unilateral Contact and Dry Friction*, Montpellier, 129-132.

Sinopoli A, (1991), Dynamic analysis of a stone column excited by a sine wave ground motion, *Applied Mechanics Reviews*, 44(10), Part 2, 246-255.

Sinopoli A, (1993a), Base excitation of rigid bodies. I. Formulation, (Discussion), *Journal of Engineering Mechanics, ASCE*, 119 (EM1).

Sinopoli A, (1993b), Theoretical and experimental investigation on the impact of a rigid block on a rigid ground, in: *Proceedings of Euromech Colloquium 306: Mechanics of Contact Impact*, Prague.

Spanos PD and Koh AS, (1984), Rocking of rigid blocks due to harmonic shaking, *Journal Eng Mech Div Am Soc Civ Engrs* 110, 1627-1642.

Yim C, Chopra AK, Penzien J, (1980), Rocking response of rigid blocks to earthquakes, *Earthquake Engr. and Struc. Dynamics*, 8, 565-587.

Knowledge-based shock-wave modeling by GENESIS

Barry Hunt and Arthur P Adamson (retired)

GE Aircraft Engines, Cincinnati OH 45215

GENESIS—GEneralized Nonlinear Extension of Surface Integral Schemes—offers the prospect of extending existing 3-D panel codes, originally developed for *linear* flows over complex configurations, to the general régime of flows governed by the unsteady Euler equation—without significant increases in computational time or resources. The boundary representation of a shock discontinuity exploits its causal link with conditions at the sonic point to suppress, non-dissipatively, the physically-impossible formation of an expansion shock. Three approaches are described, two approximate and one nominally exact, for solving the transonic Euler equation on conventional computers; some 2-D transonic results are presented, obtained on a PC in about one second.

INTRODUCTION. Panel codes for the numerical solution of aerodynamic problems expressed in the form of *integral equations* had attained a stage of relatively complete maturity, for *linear* applications, more than a decade ago (Hunt, 1982). Integral methodologies were then generally considered to have reached their limit of useful development, and attention was switched to tools offering a more complete understanding of *nonlinear* phenomena. The prime focus became the numerical solution of problems expressed in the form of *differential equations*; in particular, finite-difference and finite-element schemes became predominant. Today, almost the entire budget of both industry and government for computational tools for aerodynamic prediction is vested in differential methods, both in terms of the number of researchers addressing their refinement and the amount of computational resources attached to their solution.

Computational solutions of the *Navier-Stokes* equation (or more usually its non-dissipative approximation expressed by the Euler equation) are now starting to become commonplace even for complete airframe geometries, and for major portions of their propulsion units. Significant design improvements can be attributed in large part to the availability of such tools. However, these successes are, unquestionably, neither cost-free nor problem-free. Differential methods are making heavy and increasing demands on human and computational resources. Their application and interpretation requires specialists who are often far removed from the engineering design process. Their fidelity in the representation of certain important flow features (*e.g.* shock-waves) is sometimes dubious, as is their performance near the "linear" end of the flow spectrum. Their integration with computational schemes simulating other, *interacting* physical processes (*e.g.* heat transfer, mechanical distortion and vibration) may never be achievable for realistic configurations.

There is now a growing recognition that *integral* methodologies may remove or significantly reduce all these differential difficulties. Integral methods are *not* intrinsically linear, as was once believed — even *boundary* integral methods. It is likely, in fact, that the old generation of panel codes can be updated, relatively easily, to address most, if not all, of the same set of flow problems that differential methods are now addressing. Work is currently in hand to develop a general boundary-integral framework—**GENESIS**—for nonlinear, unsteady aerodynamic and aero-acoustic problems involving arbitrary motions of flexible 3-D bodies—*without any field integrations*. The present paper focuses on *steady-state*, transonic flows.

1 CONCEPTUAL OVERVIEW OF LINEAR AERODYNAMIC PANEL CODES

Boundary integral methods (BIM's), generally known as *panel codes*, have been a mainstream tool in the aerodynamic design of military and civil aircraft for more than a quarter of a century [Hunt, 1978, 1980a,b, 1982] Most major airframers have developed their own in-house codes, with varying degrees of sophistication. For the *linear, incompressible* flow régimes to which they apply, these codes generally offer arbitrarily high accuracy at affordable cost, in terms of both data-preparation and computation time on conventional computers. The primary reason for this economy is the fact that, for such types of flow régime, the problem reduces to the computation of certain quantities *only* on the configuration surface.

For an *irrotational* flow, the velocity vector $\vec{V}$ is the gradient of a scalar potential: $\vec{V} = \nabla\Phi$. If the flow is also *incompressible*, we have $\nabla \cdot \vec{V} = 0$, so that the potential Φ now satisfies *Laplace's Equation* : $\nabla^2\Phi = 0$. We here designate any BIM which solves the equations of incompressible, irrotational flow, subject to some prescribed set of boundary conditions, as a *Laplace BIM*.

Some Laplace BIM implementations are couched in terms of the velocity potential Φ, and some in terms of the velocity vector, $\vec{V}$ (Hunt, 1978, 1980a). We shall consider here only **velocity-based formulations**. One particular velocity-based formulation known by the acronym SAVER will be outlined in Sec 2 .

1 .1 Surface singularity types

Panel codes discretize the configuration surface into some number N of surface *panels*, each patched with one or more types of "***surface singularity***" distribution. These distributions (prescribed or unknown) relate to either the *potential-jump* $\Delta\Phi$ or the *vector velocity-jump* $\Delta\vec{V}$ across that panel, between a (fictitious) *interior* domain Ω_{int} and the (physical) *exterior* domain Ω (see Fig 1). Different implementations imply different fictitious interior fields and therefore different surface singularity distributions. The most common implementations use some combination, or just one, of the following types of singularity distribution:

- *Sources* : A locally continuous surface-source patch on each panel; the local source density σ is *defined as* the normal component of the vector velocity jump across the panel: $\sigma = \hat{n} \cdot \Delta\vec{V}$, with $\Delta\vec{V} = \vec{V}_{ext} - \vec{V}_{int}$ and where the local surface unit normal $\hat{n}$ points into the physical domain Ω;

- *Vorticity* : A locally continuous surface-vorticity patch on each panel; the (vector) vorticity $\vec{\omega}$ is *defined* to lie in the local tangent plane and be equal in magnitude and orthogonal to the in-plane component of the vector velocity jump: $\vec{\omega} = \hat{n} \times \Delta \vec{V}$;
- *Dipoles* : A locally continuous surface-dipole (doublet) patch on each panel; the axis of each elemental dipole vector is parallel to the local surface unit normal $\hat{n}$, and the local dipole density μ is *defined* as the potential jump across the panel: $\vec{\mu} = \Delta\Phi\,\hat{n}$, with $\Delta\Phi = \Phi_{ext} - \Phi_{int}$.

Note 1: A normal-dipole distribution and a vorticity distribution are in fact **equivalent.** [see Hunt (1978, 1980a), where a complete discussion of the above singularity types and their association with a variety of boundary conditions is given].

1.2 Influence matrices

The dominant part of a panel-code computation is the formation of an *influence matrix*. We here use the symbolic notation $[\vec{U}]$ to represent the vector **velocity-influence matrix**, and $\{\lambda\}$ the **singularity array** defining the values of the singularity distribution(s) at a set of *N control points*. Some of the values in $\{\lambda\}$ may be prescribed, while the remainder, generally of a different *type*, will be unknown and must be computed such that a prescribed set of boundary conditions $\{V_{nBC}\}$ is satisfied—usually at the same N control points.

In a 3-D velocity-based formulation, the *vector* element $\vec{U}(i,j)$ of the vector influence matrix $[\vec{U}]$ represents the normal component $U_n(i,j)$ and two orthogonal tangential components $U_{s1}(i,j)$, $U_{s2}(i,j)$ of the *perturbation velocity* "induced" at a specific control point on panel i by unit value of the jth singularity patch, λ_j. The vector influence matrix $[\vec{U}]$ is generally stored as its three scalar component matrices: the **normal influence matrix** $[U_n]$, and the two **tangential influence matrices** $[U_{s1}]$ and $[U_{s2}]$. If the formulation employs vorticity as a singularity type, the vorticity $\vec{\omega}$ on each patch will also be a vector, orthogonal to $\hat{n}$, and may be defined in terms of its components ω_1, ω_2 along two directions $\hat{s}_1$, $\hat{s}_2$ associated with that patch. These local (unit) tangent vectors $\hat{s}_1(i)$, $\hat{s}_2(i)$ associated with $U_{s1}(i,j)$, $U_{s2}(i,j)$, $\omega_1(i)$ and $\omega_2(i)$ are defined at control point i, relative to a coordinate system fixed in the body. [Generally, only $\hat{s}_1(i)$ needs to be stored, since usually $\hat{s}_2(i) = \hat{s}_1 \times \hat{n}$.]

In 2-D, there is again the normal influence matrix $[U_n]$, but only *one* tangential influence matrix, $[U_s]$; if the formulation employs vorticity, that vorticity $\vec{\omega}$ is then a vector oriented into the paper.

In both the 2-D *and* the 3-D case, the evaluation of each vector element $\vec{U}(i,j)$ is usually performed analytically, but sometimes numerically [Hunt, 1978, 1980a,b].

Note 2: For velocity-based implementations employing both source and vorticity distributions (such as the SAVER formulation discussed in Sec 2), the vector influence matrix $[\vec{U}]$ for only *one* of these singularity types is needed: the other matrix is obtained by simple vector rotation of each vector matrix element $\vec{U}(i,j)$.

Note 3: Some more sophisticated implementations also take account of the gradient of the boundary distribution(s) λ, and employ curved instead of planar panels—still with analytic coefficicients.

2 SAVER: SOURCE AND VORTICITY EVALUATION BY RELAXATION

2.1 Conceptual overview of SAVER

A particularly effective Laplace-BIM formulation known as SAVER (Source And Vorticity Evaluation by Relaxation) has been developed at GE Aircraft Engines. First introduced in Hunt (1991a) and inspired by a novel work by Raj and Gray (1979), SAVER has been applied successfully to a wide range of cases. The underlying model is outlined here for the 2-D case; its extension to 3-D is described in Sec 4.1 . In 2-D, the local (unit) tangent vector at the body surface is uniquely defined by $\hat{s} = \hat{j} \times \hat{n}$, with $\hat{j}$ oriented into the paper. The normal component of $\vec{V}$ is $V_n = \hat{n} \cdot \vec{V}$ and the remaining tangential part, defined in 3-D by $\vec{V}_s = \vec{V} - V_n\,\hat{n} = (\hat{n} \times \vec{V}) \times \hat{n}$, reduces in 2-D to $\vec{V}_s = \hat{s} \cdot \vec{V}\,\hat{s}$, or $V_s = \hat{s} \cdot \vec{V}$.

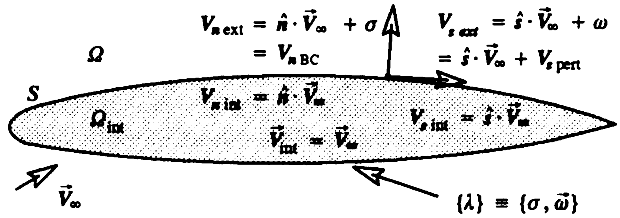

Fig 1. SAVER implies an internal field $\vec{V}_{int} = \vec{V}_\infty$ by fixing the boundary source as : $\sigma = -\hat{n} \cdot \vec{V}_\infty + V_{nBC}$ and relaxing the vorticity : $\{\omega\} = [U_s]\{\sigma, \vec{\omega}\} \equiv \{\vec{V}_{s\,pert}\}$

With SAVER (see Fig 1), the velocity field in the (fictitious) interior domain Ω_{int} inside a closed body is *implied* to be equal to the unperturbed (uniform) onset flow vector $\vec{V}_\infty$. This simple condition, equivalent to requiring that the *perturbation velocity* be zero throughout the interior of the body, is then used by SAVER to imply the required normal-velocity boundary condition, as follows:

a) The boundary singularity distribution $\{\lambda\}$ is defined to consist of *both* a source distribution σ and a vorticity distribution ω on the body boundary, S. Symbolically: $\{\lambda\} \equiv \{\sigma, \omega\}$.

b) The boundary source distribution σ [defined earlier as equal to the normal component of $\Delta\vec{V} = \vec{V}_{ext} - \vec{V}_{int}$, *i.e.* the vector velocity jump] is *fixed a priori* as being locally equal to the quantity $-\hat{n} \cdot \vec{V}_\infty + V_{nBC}$, where V_{nBC} is the prescribed normal-velocity boundary condition. If the implication is correct that the total velocity on the *inner* face of S is $\vec{V}_\infty$, then the total normal velocity on its *outer* face must therefore be equal to $\hat{n} \cdot \vec{V}_\infty + \sigma = V_{nBC}$.

c) The local boundary-vorticity vector $\vec{\omega} = \omega\hat{j}$, [defined earlier to be equal in magnitude and orthogonal to the in-plane component of the vector velocity jump, $\vec{\omega} = \hat{n} \times \Delta\vec{V} = \hat{n} \times \Delta\vec{V}_{pert}$] is then coerced to be equal in magnitude and orthogonal to the tangential component $\{V_{s\,pert}\}$ of the computed perturbation velocity $\{\vec{V}_{pert}\} = [\vec{U}]\{\lambda\}$ *induced* by the overall distribution $\{\lambda\}$ (*i.e.* by σ and ω) at the set of control points in Ω, *i.e.* on the *outer* face of S. That is, the boundary-vorticity part ω of the overall singularity distribution $\{\lambda\}$ is updated iteratively, starting from some assumed initial guess for $\{V_{s\,pert}\}$, by the ***relaxation cycle*** :

$$\{\omega\} = \{V_{s\,pert}\}$$
$$\{V_{s\,pert}\} = [U_s]\{\sigma, \omega\}$$

Note 4: This condition (coerced on the *outer* face of the boundary S) implies that the tangential component of the perturbation velocity on the *inner* face of S must be zero.

Note 5: SAVER has the option of computing the actual value V_n on the body surface S, and applying a secondary sequence to adjust σ to strictly enforce the required condition V_{nBC} (Hunt, 1991b).

Note 6: SAVER reinforces a *Kutta condition* at each cycle (Hunt, 1991b) by adding a multiple of a (pre-computed) circulatory vorticity *eigendistribution* ω_c to force equality of the trailing-edge velocities.

Once the relaxation cycle has converged (typically four or five iterations), SAVER gives the required total velocity at the boundary simply as $\vec{V} = \vec{V}_\infty + \vec{V}_{pert}$, which will be *tangential* if the solid boundary-condition $V_{nBC} = 0$ was used in step (b) above to fix σ.

SAVER in its present 2-D form employs piecewise-quadratic distributions σ and $\vec{\omega}$ on circular-arc or planar panels. All influence coefficients are evaluated analytically. For all (thick and thin) airfoils evaluated, this second-order accurate code produces results more accurately and more rapidly than any other known code. These virtues can be expected to carry across in large part to 3-D.

In a proposed variant **DESIGN SAVER**, the boundary *vorticity* ω is prescribed a priori, and the boundary *source* σ is coerced to equal the computed *normal* velocity perturbation: $\{\sigma\} = \{V_{n\,pert}\}$. In 2-D, the local vorticity ω is a unique function of the local pressure (thus allowing the pressure to be the prescribed quantity). Moreover, the resulting source σ can be interpreted directly as a local *surface transpiration function*, $V_{trn} = \sigma$, which is related (analogously to boundary-layer modeling) to an equivalent normal displacement of the body boundary. It seems likely that development of this concept could lead to a 3-D shape-design capability. It is worth noting that the numerical conditioning of this proposed "design" variant is exactly the same as that of the "analysis" form outlined above: the same matrices are used in both cases. **DESIGN SAVER** thus promises to share the computational efficiency of **SAVER**.

2.2 SAVER as the basis for generalized, nonlinear flows

Three specific features uniquely equip SAVER as the basis of a generalized solver for ***unsteady, compressible flows***: first, its foundation in the vector *velocity* field (rather than a scalar potential); second, its explicit coupling between the singularity distributions, the boundary conditions, the onset-flow vector and the perturbation velocity; and third, the remarkably low number of relaxation cycles it requires to obtain a converged tangential velocity solution, V_t.

A velocity-based approach to unsteady, *incompressible* flows was introduced in Hunt (1982). Work is underway to extend this to unsteady, compressible flows by coupling it with the GENESIS methodology first introduced in Hunt and Plybon (1990) for steady-state, compressible, rotational flows.

GENESIS converts *field* nonlinearities to equivalent *boundary* functions. These consist of:

i) a local correction to be added to the prescribed normal-velocity boundary condition V_{nBC}. The resulting sum V'_{nBC} is used by SAVER in its definition of the boundary source σ. This yields an *equivalent pseudo-Laplace problem*, with boundary condition V'_{nBC}, to be solved by SAVER for the *pseudo-Laplace tangential velocity* V'_t.

ii) a local correction to be added to the computed pseudo-Laplace tangential velocity V'_t. The resulting sum V_t is the required solution of the original nonlinear (compressible and/or rotational) problem.

These two corrections are computed from the current estimate of the local nonlinear velocity V_t on the boundary S.

The fundamental principles and current status of GENESIS for steady flows will be outlined in Section 4.1. First, we give in Sec 3 an "integral viewpoint" of the fundamentals of transonic flow.

3 COMPRESSIBLE, TRANSONIC FLOWS

We give here an overview of the steady-state modeling of real, compressible flows by the Euler equation and the so-called full-potential equation. The extension of incompressible, steady-state panel codes to such compressible flows will be discussed in Sec 4.

Real, *transonic* flows involve flow discontinuities across compression shocks. Mechanical dissipation and heat conduction in the internal structure of a physical shock (considered to be properly modeled by the Navier-Stokes equations, even in the shock interior) generally produce an overall increase in the entropy along any streamline traversing the shock. The local entropy increase depends on the interaction between these two dissipative effects. For flows of aerodynamic interest, this increase is quasi-discontinuous across the shock. The flow is usually considered to be non-conducting (adiabatic), so that (in a steady flow) the *stagnation-enthalpy* flux along any stream-tube is constant, even when the stream-tube traverses a shock. The dissipative processes, however, produce a quasi-discontinuous reduction in stagnation *pressure* across the shock. This irreversible loss is related to the entropy jump. The jumps in the various thermodynamic properties across a shock are expressed by the *Rankine-Hugoniot* (R-H) relations presented in Sec 3.1 below.

The "*full potential*" (FP) approximation of a transonic flow assumes that the entropy jump across a shock is small enough to be ignored; this is tantamount to assuming that the flow remains homentropic and irrotational in traversing a shock, so that the velocity vector can be still be expressed throughout the smooth part of the flow as the gradient of a scalar potential. This approximation implies that, even in the absence of numerical errors, the solution of the FP equation is generally incapable of giving an accurate simulation of the jump properties across a shock, and of the shock location. Numerous empirical devices have been developed in an attempt to produce numerical FP solutions which are reasonably close to physical reality. These devices are necessary not only to give a reasonable simulation of compression shocks, but also to prevent the formation of non-physical *expansion shocks* in the numerical solution.

The *Euler* equations go a step further than the potential approximation, in the sense that they do support the *presence* of field vorticity in their solution. However, the absence of mechanical and thermal dissipative effects in the equations implies that they do not support the *creation* of vorticity: this requires an extra set of dissipative terms which are modeled in the *Navier-Stokes* (N-S) equations through the presence of finite coefficients of viscosity and thermal conduction [Hunt and Plybon, 1990]. It is possible to argue that the Euler equations represent a limit of the N-S equations, in which these coefficients each go to zero while keeping the same *ratio* as that required to produce an R-H shock. Nonetheless, with *zero* coefficients in the numerical equations, it is still necessary to apply an extraneous condition (equivalent to the second law of thermodynamics) **to prevent the formation of *expansion* shocks**. If such a condition is enforced properly, *and* the compression shock is coerced to simulate an R-H shock, the solution of the Euler equations can be considered as an infinite-Re solution of the N-S equations. [Note, however, that an accurate *inviscid* solution, without numerical errors, can still deviate from physically observed flows, because of viscous effects which can be significant in traversing a shock wave at a solid boundary.]

The values of the thermodynamic variables (pressure, density, temperature, etc.) can be expressed *everywhere* purely in terms of the local velocity $\vec{V}$, both for the FP and Euler equations. This fact is one of the fundamental pillars enabling velocity-based integral methods to serve as the basis of generalized, nonlinear flow solvers.

3.1 Thermodynamic variables as functions of velocity

For a *steady, adiabatic* flow of an ideal fluid with local temperature T, the ***conservation of stagnation enthalpy*** is expressed by:

$$c_p T + \tfrac{1}{2}V^2 = c_p T_\infty + \tfrac{1}{2}V_\infty^2 = c_p T_{t\infty} = \tfrac{1}{2}V_{max}^2 \qquad (1)$$

where c_p is the specific heat at constant pressure, $T_{t\infty}$ is the freestream stagnation temperature, $c_p T_{t\infty}$ the stagnation enthalpy, and V_{max} the maximum speed thermodynamically possible :

$$V_{max} = \frac{V_\infty}{M_\infty}\sqrt{M_\infty^2 + \frac{2}{\gamma - 1}} \qquad (2)$$

We introduce a ***reference Mach number*** $M_{ref} = V_{ref}/a_\infty$ with a_∞ the freestream sonic speed defined either by $a_\infty = (\gamma \Re T_\infty)^{1/2}$ or by $a_\infty = V_\infty/M_\infty$ if $V_\infty \neq 0$. The quantity V_{ref} is any suitable ***reference speed***. The specific-heats ratio γ, gas constant $\Re$ and c_p

are related by $c_p = \gamma\Re/(\gamma-1)$. Introducing an *incompressible pressure coefficient*: $C_{pINC} = (V_\infty^2 - V^2)/V_{ref}^2$, eq (1) then gives a globally-valid expression for a ***relative temperature*** $T_r \equiv T/T_\infty$:

$$T_r = 1 + \frac{\gamma-1}{2}\frac{V_\infty^2 - V^2}{a_\infty^2} = 1 + \frac{\gamma-1}{2} M_{ref}^2 C_{pINC} . \quad (3)$$

This equation gives the local relative temperature (and hence T) in a compressible flow, once the local flowspeed V is known. The local sonic speed is then given by: $a = a_\infty T_r^{1/2}$. In order to obtain the local density and pressure, we first introduce the concept of a local ***relative stagnation pressure*** $p_{t\,r} \equiv p_t/p_{t\infty}$, where p_t is the local stagnation pressure and $p_{t\infty}$ the freestream stagnation pressure. The local ***relative pressure*** p_r and ***relative density*** ϱ_r are then :

$$p_r \equiv p/p_\infty = p_{t\,r} T_r^{\frac{\gamma}{\gamma-1}} \quad \text{and} \quad \varrho_r \equiv \varrho/\varrho_\infty = p_r/T_r . \quad (4)$$

For adiabatic, homentropic flows, p_t is constant, *i.e.* $p_{t\,r} = 1.0$. This applies everywhere if the FP approximation is used, but only upstream of shocks if the Euler equation is used.

For the Euler equation, the computation of pressure and density *downstream of a shock*, given the local flowspeed V, needs to take account of the jumps across the shock and of the reduced stagnation pressure p_t downstream of it. Let subscript 1 denote the local upstream face of a shock, and 2 its local downstream face. The stagnation temperature is constant: $r_{Tt} \equiv T_{t2}/T_{t1} = 1.0$. The jumps in the other flow properties are given by the so-called *Rankine-Hugoniot* (R-H) relations. These can be expressed purely in terms of the local *shock-normal velocity* $V_{\nu 1}$ entering the shock: $V_{\nu 1} = \hat{\nu}\cdot\vec{V}_1$, with $\hat{\nu}$ the unit normal to the shock surface, oriented downstream. It is useful to introduce the local *shock-entry normal Mach number:* $M_{\nu 1} = V_{\nu 1}/a_1$, with a_1 obtained from $V = V_1$ as above. The R-H *normal velocity ratio* $r_V \equiv V_{\nu 2}/V_{\nu 1}$ is given by:

$$r_V = [1 + \tfrac{\gamma-1}{2} M_{\nu 1}^2] / [(1 + \tfrac{\gamma-1}{2}) M_{\nu 1}^2] . \quad (5)$$

The other relevant steady-state R-H relations are then:

- *Normal-velocity jump* $\sigma_\nu \equiv V_{\nu 2} - V_{\nu 1} = (r_V - 1) V_{\nu 1}$.
- *Density ratio* $r_\varrho \equiv \varrho_2/\varrho_1 = 1/r_V$.
- *Pressure ratio* $r_p \equiv p_2/p_1 = [\gamma M_{\nu 1}^2 - \tfrac{\gamma-1}{2}] / [1 + \tfrac{\gamma-1}{2}]$
- *Stagnation pressure and density ratios* $r_{pt} \equiv p_{t2}/p_{t1}$ and $r_{\varrho t} \equiv \varrho_{t2}/\varrho_{t1}$ are both equal to $\left(r_p / r_\varrho^\gamma\right)^{-1/(\gamma-1)}$.

To compute p and ϱ at a point P further downstream of the shock, eq (4) again applies, but now with the relative stagnation pressure $p_{t\,r}$ defined by the R-H stagnation pressure ratio: $p_{t\,r} = r_{pt}$, this being computed at the shock on the same streamline on which P lies (on the boundary S, $V_{\nu 1}$ is thus the shock-entry velocity on S).

3.2 Field variables in an integral method

In addition to the local velocity vector $\vec{V}$, it is convenient with an integral method to define a flow in terms of the divergence and curl of $\vec{V}$, instead of using the thermodynamic variables. These functions are termed respectively the ***field source*** $\Sigma = \nabla\cdot\vec{V}$ and ***field vorticity*** $\vec{\Gamma} \equiv \nabla\times\vec{V}$. For the Euler equation, we denote these functions by Σ_E and $\vec{\Gamma}_E$; they can be expressed everywhere purely in terms of the flowspeed V and its derivatives, as we show below.

3.2.1 Field source in a steady, transonic "Euler" flow

For *steady, adiabatic* flows of an ideal fluid governed by the Euler equation, conservation of stagnation enthalpy is expressed by (1).

The *isentropic relation* written as $T/T_{up} = (\varrho/\varrho_{up})^{\gamma-1}$, where the subscript "up" relates to some point upstream, is valid everywhere for a shock-free flow, or everywhere upstream of shocks in a shocked flow; in these cases we can take the freestream T_∞, ϱ_∞ as the "upstream" values. For a transonic flow, this relation is also valid along any one streamline *downstream* of a shock, but the values T_2, ϱ_2 on the downstream face of the shock for that streamline (see below) then need to be taken as the "upstream" values for the downstream part of the streamline. Thus for *any* streamline in a shock-free or shocked flow of a perfect gas we can readily obtain from (1):

$$\gamma\Re T_{up}\left(\varrho/\varrho_{up}\right)^{\gamma-1} = \frac{\gamma-1}{2}(V_{max}^2 - V^2) . \quad (6)$$

Taking the streamwise derivative of (6) in any continuous region of the flow (*i.e.* applying the operator $\hat{s}\cdot\nabla$ where $\hat{s}$ is the local unit vector of the velocity), and removing a factor $\gamma - 1$, gives:

$$\gamma\Re T_{up}\left(\frac{\varrho}{\varrho_{up}}\right)^{\gamma-2}\frac{\hat{s}\cdot\nabla\varrho}{\varrho_{up}} \equiv \gamma\Re T\,\hat{s}\cdot\nabla\varrho/\varrho$$
$$\equiv \gamma\Re T\,\frac{1}{\varrho}\frac{\partial\varrho}{\partial s} = -\,\hat{s}\cdot\nabla\tfrac{1}{2}V^2 \quad (7)$$

so that, introducing the local sonic speed a defined by $a^2 = \gamma\Re T = \frac{\gamma-1}{2}(V_{max}^2 - V^2)$, we have :

$$\frac{1}{\varrho}\frac{\partial\varrho}{\partial s} = -\frac{\hat{s}\cdot\nabla\frac{1}{2}V^2}{a^2} . \quad (8)$$

The continuity equation for steady flow is $\nabla\cdot(\varrho\vec{V}) = 0$, giving $\nabla\cdot\vec{V} = -\vec{V}\cdot\nabla\varrho/\varrho = -(V/\varrho)\,\partial\varrho/\partial s$ which, using (8) and introducing the local Mach number $M = V/a$, becomes:

$$\Sigma_E \equiv \nabla\cdot\vec{V} = \frac{V}{a^2}\,\hat{s}\cdot\nabla\tfrac{1}{2}V^2 = \frac{V^2}{a^2}\frac{\partial V}{\partial s} = M^2\frac{\partial V}{\partial s} . \quad (9)$$

The field source relation $\Sigma_E = M^2\partial V/\partial s$ is valid in any ***non-dissipative*** part of a steady flow governed by the FP or Euler equation.

Note 7: The value of the steady-state Euler field source Σ_E can also be derived from the steady-state (inviscid, non-dissipative) momentum equation, which can be expressed in the form $-\nabla p/\varrho = \nabla\frac{1}{2}V^2 + \vec{V}\times(\nabla\times\vec{V})$. Taking the scalar product of this equation with the local velocity vector $\vec{V} = V\hat{s}$ gives $-(V/\varrho)\,\partial p/\partial s = \vec{V}\cdot\nabla\frac{1}{2}V^2$. Then, since p/ϱ^γ is constant along a streamline upstream of a shock and equal to a different constant downstream of the shock, we have $\partial p/\partial s = (\gamma p/\varrho)\partial\varrho/\partial s = a^2\,\partial\varrho/\partial s$, giving $\Sigma_E = -(V/\varrho)\,\partial\varrho/\partial s = \vec{V}\cdot\nabla\frac{1}{2}V^2/a^2 = M^2\partial V/\partial s$, i.e. the expression obtained in eq (9) from the (non-dissipative) equation expressing conservation of stagnation enthalpy.

Note 8: The adiabatic (non-dissipative) shock normal-velocity jump [σ_{ad}, say] can be considered to result from traversing an infinitely dense *volume*-source distribution Σ_E representing the shock discontinuity: $\sigma_{ad} = V_{\nu 2} - V_{\nu 1} = \int\Sigma_E\,ds$. Now, under the adiabatic assumption we have from eq (1): $a^2 = \frac{\gamma-1}{2}(V_{max}^2 - V^2)$; the function $M^2\partial V/\partial s$ in (9) defining the Euler source can thus be seen to be precisely the derivative w.r.t. s of a *transcendental function* F:

$$F = \frac{1}{\gamma-1}\left(V_{max}\,\ell n\,\frac{V_{max} + V}{V_{max} - V} - 2V\right) . \quad (10)$$

Note 9: It then readily follows that the non-dissipative velocity jump σ_{ad} consistent with the non-dissipative Euler (or FP) equation must be the solution, for a given entry value $V_{\nu 1}$, of the equation:

$$\sigma_{ad} = \frac{V_{max}}{\gamma+1}\,\ell n\left(\frac{V_{max} + V_{\nu 1} + \sigma_{ad}}{V_{max} - V_{\nu 1} - \sigma_{ad}}\,\frac{V_{max} - V_{\nu 1}}{V_{max} + V_{\nu 1}}\right) . \quad (11)$$

Note 10: Equation (11) can be solved numerically, for any entry speed $V_{\nu 1}$, by using a *calculus of variations* approach or by the method discussed in Sec 5.1 ; the resulting shock jump σ_{ad} is *not* equal to the R-H value $\sigma_\nu = (r_V - 1)V_{\nu 1}$, and diverges significantly from it as V_{max} decreases (i.e. as the Mach number M_∞ increases). [**Example:** For $M_\infty = 0.5$ corresponding to $V_{max} = \sqrt{21} \approx 4.58$, and a shock-entry normal velocity of $V_{\nu 1} = 2.5\,V_\infty$ corresponding to $M_{\nu 1} = 1.4555$, the solution of (11) is $\sigma_{ad} = -1.42\,V_\infty$ while the R-H jump is $\sigma_\nu = -1.10\,V_\infty$.] The reason for this discrepancy is that in the interior of a real shock, the flow process is ***dissipative***: the shock is σ_{ad} corresponding to the non-dissipative equation used in the region of the flow does *not* correspond to the R-H jump σ_v. If the computed flow solution is to exhibit a realistic jump, the R-H value $\sigma_v = (r_V - 1) V_{v1}$ corresponding to the computed local entry value V_{v1} *must be imposed extraneously*. This is analogous to coercing an inviscid flow to satisfy the physically observed Kutta condition by extraneously supplying that model with the correct amount of "vorticity" — the amount that would be produced by the (viscous) Navier-Stokes equation under the same pressure field (see Note 6).

3.2.2 *Field vorticity in a steady, transonic "Euler" flow*

For notational simplicity, we confine our attention here to the 2-D case. Upstream of shocks, the flow is irrotational, $\vec{\Gamma} = 0$, so the local vorticity jump across a shock is the value of $\nabla \times \vec{V} = \vec{\Gamma}_g = \Gamma_g \hat{j}$ on the downstream face of the shock. Using *Crocco's theorem* and the fact that the stagnation enthalpy is constant, it can be shown (Hunt and Plybon, 1990) that the ***field vorticity*** at a point on the downstream face of the shock is given by:

$$\Gamma_2 = (1 - M_{v1}^2)\mathcal{K}_1 \sigma_v \tag{12}$$

where $\mathcal{K}_1$ is the streamline curvature at shock entry. Downstream of such a shock, the flow generally remains rotational and, assuming that dissipative processes are negligible everywhere outside shocks (inviscid, adiabatic flow) the entropy remains constant along any one streamline. The vorticity Γ_g, however, varies along a streamline in proportion to the local static pressure, p. Thus $\Gamma_g / p =$ ***constant*** $= \Gamma_2 / p_2$, or, using the relative pressure defined in (4), $\Gamma_g = \Gamma_2(p_r / p_{r2}) = \Gamma_2(T_r / T_{r2})^{\gamma/(\gamma-1)}$, where the relative temperatures T_r and T_{r2} are evaluated from (3), purely in terms of the local flowspeed V and the shock-exit speed V_2 on the same streamline.

4 NEW-GENERATION PANEL CODES FOR STEADY, COMPRESSIBLE FLOWS

It was shown in Sec 3 that for an ideal gas flow governed by the steady-state *Euler* equation, the divergence of the velocity—interpreted as a local ***field source*** Σ_g—is given by (9). Expressions for the curl of the velocity vector—interpreted as local ***field vorticity***—for regions downstream of compression shocks, were given in Sec 3.2.2. In recent years, a number of *field-integral* methods (FIMs) have been developed for solving the *full potential* equation, both for steady flows and for unsteady flows [*e.g.* Hu and Chu (1990), Morino and Iemma (1993)]. In an FP approximation, the field vorticity is ignored, and the field source Σ_g in (9) is considered as a finite entity *inducing* a velocity perturbation. In all cases reported to date, the overall perturbation velocity has been evaluated by performing a ***field integration*** over the region of space where Σ_g has a finite value. This leads to a computational process with a large operation count, comparable to that of conventional (differential) CFD approaches. Like conventional CFD, FIMs have problems with non-physical, "non-dissipative" shock jumps [see Note 10 at the end of Sec 3.2.1]. They also suffer from the need to artificially modify the equation to be solved—rendering it *dissipative*—in order to suppress the formation of ***expansion shocks*** which would otherwise be just as likely to form as compression shocks in the absence of dissipation. Such expansion shocks, while mathematically valid, are not physically admissible in a dissipative (real) flow.

We now introduce a generalization of the full-potential FIM process to the complete steady-state *Euler* equation, and show how a mathematical framework known as GENESIS enables the *field* integrals for both source and vorticitv · ·ansformed first into *surface* integrals, and then into a si ' modification of the boundary conditions for an r) pseudo-Laplace problem. This sequence of li lved by the SAVER algorithm described in Sec

4.1 The GENESIS identity for a stationary body

4.1.1 *GENESIS for a field integral method (FIM)*

GENESIS—**GE**neralized **N**onlinear **E**xtension of **S**urface **I**ntegral **S**chemes—was first introduced in Hunt and Plybon (1990), and has continued to develop [Hunt (1991a,b), Hunt and Adamson (1992a,b,c)] towards a generalized methodology for the solution of unsteady, nonlinear, multidisciplinary problems. We here outline its basic principles for steady-state problems. First we introduce the vector *inverse-square operator* defined in 3-D by $\vec{K} = \vec{r}_{QP} / 4\pi r_{QP}^3$ (in 2-D the operator becomes $\vec{K} = \vec{r}_{QP} / 2\pi r_{QP}^2$), where $\vec{r}_{QP}$ is the line vector drawn from a running point Q to a fixed point P, with both points in a domain Ω external to a body with boundary S (see Fig 2). The outer boundary of Ω is denoted by S_0.

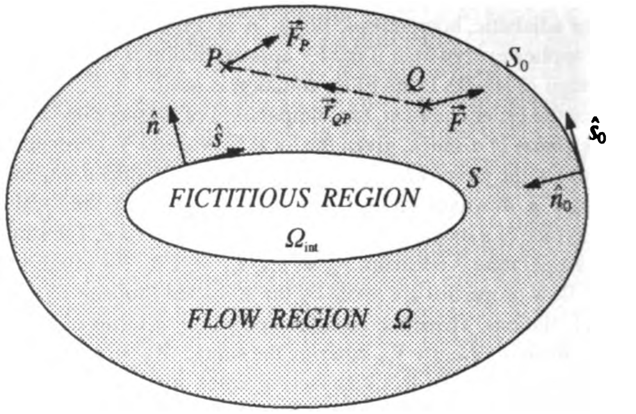

$$\vec{F}_P = \int_{S+S_0} (\hat{n}\cdot\vec{F})\,\vec{K}\,dS + \int_{S+S_0} (\hat{n}\times\vec{F})\times\vec{K}\,dS + \int_{\Omega} (\nabla\cdot\vec{F})\,\vec{K}\,d\Omega + \int_{\Omega} (\nabla\times\vec{F})\times\vec{K}\,d\Omega \tag{13}$$

Fig 2. Running point Q in Ω ; Fixed point P in Ω.

For any *arbitrary*, continuous vector field $\vec{F}$ in Ω, it can be shown [Hunt, 1977] that the ***identity*** (13) in Fig 2 holds for any point P in Ω, or lying on the face of its boundary S or S_0 belonging to Ω. In eq (13), the unit normal vector $\hat{n}$ at a running point Q on S or S_0 points into Ω, and the gradient operator ∇ is applied with respect to the coordinates of the running point Q.

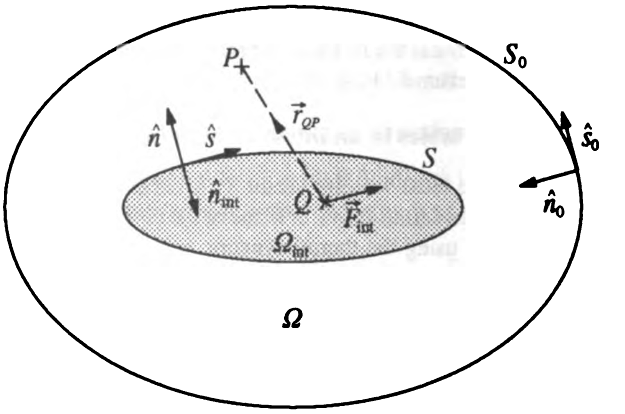

$$0 = \int_S (-\hat{n}\cdot\vec{F}_{int})\,\vec{K}\,dS + \int_S (-\hat{n}\times\vec{F}_{int})\times\vec{K}\,dS + \int_{\Omega_{int}} (\nabla\cdot\vec{F}_{int})\,\vec{K}\,d\Omega_{int} + \int_{\Omega_{int}} (\nabla\times\vec{F}_{int})\times\vec{K}\,d\Omega_{int} \tag{14}$$

Fig 3. Running point Q in Ω_{int} ; Fixed point P in Ω.

We now consider the "fictitious" domain Ω_{int} in the interior of the body, and hypothesize an arbitrary, continuous vector field $\vec{F}_{int}$ in Ω_{int} (Fig 3). We let the running point Q now range over Ω_{int} and its boundary S, but keep the fixed point P the same as above, *i.e.* P is still in Ω, or on the face of its boundary S or S_∞ belonging to Ω. It can be shown the identity (14) in Fig 3 now holds for the interior field $\vec{F}_{int}$ in Ω_{int}, relative to the fixed point P (*external* to Ω_{int}). In eq (14), the unit normal $\hat{n}_{int}$ pointing into the *interior* domain Ω_{int} at a running point Q on S or S_∞ has been replaced by $-\hat{n}$, (see Fig 3).

Suppose we first choose *both* vectors $\vec{F}$ in Ω and $\vec{F}_{int}$ in Ω_{int} to be identical to the uniform, "unperturbed" velocity $\vec{V}_\infty$. Adding (13) and (14), with all field derivatives now zero, then gives:

$$\vec{V}_\infty = \int_{S_\infty}(\hat{n}\cdot\vec{V}_\infty)\,\vec{K}\,dS + \int_{S_\infty}(\hat{n}\times\vec{V}_\infty)\times\vec{K}\,dS . \quad (15)$$

Suppose we next keep $\vec{F}_{int} = \vec{V}_\infty$ in Ω_{int}, as above, but now let the field $\vec{F}$ in Ω be equal to the overall velocity field $\vec{V}$ comprising the sum of $\vec{V}_\infty$ and the perturbation velocity $\vec{V}_{pert}$ *induced* by the presence of the body boundary S. We assume here that the body is *stationary* and that the normal velocity of the air at the boundary S is given by $\hat{n}\cdot\vec{V} = V_{nBC}$. [For a solid body we will have $V_{nBC} = 0$, and, in the general case, the total velocity field $\vec{V}$ in Ω will be both compressible and rotational.] Adding (13) and (14) now gives:

$$\begin{aligned}\vec{V}_P = & \int_{S+S_\infty}(\hat{n}\cdot\vec{V})\,\vec{K}\,dS + \int_{S+S_\infty}(\hat{n}\times\vec{V})\times\vec{K}\,dS \\ & - \int_S(\hat{n}\cdot\vec{V}_\infty)\,\vec{K}\,dS - \int_S(\hat{n}\times\vec{V}_\infty)\times\vec{K}\,dS \\ & + \int_\Omega(\nabla\cdot\vec{V})\,\vec{K}\,d\Omega + \int_\Omega(\nabla\times\vec{V})\times\vec{K}\,d\Omega . \quad (16)\end{aligned}$$

Note that $\vec{V}\rightarrow\vec{V}_\infty$ at the outer boundary S_∞, if that boundary is sufficiently far removed from the body. Thus, using (15) and the definition $\vec{V} = \vec{V}_\infty + \vec{V}_{pert}$, we obtain from (16):

$$\begin{aligned}\vec{V}_P = \vec{V}_\infty & + \int_S(\hat{n}\cdot\vec{V}_{pert})\,\vec{K}\,dS + \int_S(\hat{n}\times\vec{V}_{pert})\times\vec{K}\,dS \\ & + \int_\Omega(\nabla\cdot\vec{V})\,\vec{K}\,d\Omega + \int_\Omega(\nabla\times\vec{V})\times\vec{K}\,d\Omega . \quad (17)\end{aligned}$$

Writing the (solid-body) boundary condition on S as $\hat{n}\cdot\vec{V}_{pert} = -\hat{n}\cdot\vec{V}_\infty + V_{nBC}$ and introducing a *fixed boundary source distribution* $\sigma = -\hat{n}\cdot\vec{V}_\infty + V_{nBC}$, we finally obtain the *GENESIS identity for compressible, rotational flow over a stationary body*:

$$\begin{aligned}\vec{V}_{P\,pert} = & \int_S\sigma\vec{K}\,dS + \int_S(\hat{n}\times\vec{V}_{pert})\times\vec{K}\,dS \\ & + \int_\Omega(\nabla\cdot\vec{V})\,\vec{K}\,d\Omega + \int_\Omega(\nabla\times\vec{V})\times\vec{K}\,d\Omega . \quad (18)\end{aligned}$$

If the total field $\vec{V}$ is *incompressible and irrotational*, (18) reduces to the identity underlying the SAVER algorithm of Sec 2:

$$\vec{V}_{P\,pert} = \int_S\sigma\vec{K}\,dS + \int_S(\hat{n}\times\vec{V}_{pert})\times\vec{K}\,dS . \quad (19)$$

- If the velocity field $\vec{V}$ is *compressible but irrotational*, (18) with $\nabla\times\vec{V} = 0$ forms the basis of a *field integral method* (FIM) for the FP equation. In a FIM, the field source Σ_s is computed *on each field-mesh cell*, using $\Sigma_s = M^2\partial V/\partial s$ (see Sec 3 .2 .1).
- For the transonic Euler equation, the field vorticity $\nabla\times\vec{V}$ in (18), (see Sec 3 .2 .2), is zero upstream of shocks but not downstream of shocks. This vorticity co-exists with the "full potential" field source Σ_s to give a FIM for the Euler equation.

Note 11: If compression shocks are allowed to form spontaneously during the iterations of the FIM, *i.e.* as a dense concentration of the *field* source Σ_s, the shock will be smeared across some number of cells of the field mesh, but even in the limit of zero cell size will *not* have the R-H jump value (see Note 10 in Sec 3 .2 .1).

Note 12: It is permissible within such a FIM to *fit* a compression shock *explicitly* as a *surface* source distribution on the shock face, with strength equal to the R-H velocity jump $\sigma_v = (r_V - 1)\,V_{v1}$ [see Sec 3 .1]. We justify this (see Note 11) by hypothesizing that the shock is contained in a "thin" but finite volume Δ, of thickness δh, say, and with a linear variation of $\vec{F}$ across that thickness, with slope equal to $\sigma_v/\delta h$. The evaluation of the volume integrals for this shock volume is performed separately from those for the smooth regions outside the shock. In the limit as $\delta h\rightarrow 0$, the volume integral $\int_\Delta(\nabla\cdot\vec{V})\,\vec{K}\,d\Delta$ relating to the "Rankine-Hugoniot" *volume* source distribution within the shock can be replaced exactly by the surface integral $\int_{S_{sh}}\sigma_v\vec{K}\,dS_{sh}$ over the shock surface S_{sh}. The contribution from the volume integral $\int_\Delta(\nabla\times\vec{V})\times\vec{K}\,d\Delta$ for the shock vorticity vanishes if we assume that the velocity component tangential to the shock is continuous across the shock. [The contribution from the shock footprint, of width δh on the body surface S, also vanishes.]

4 .1 .2 *Transformation of field integrals to boundary form*

With again $\sigma = V_{nBC} - \hat{n}\cdot\vec{V}_\infty$, we can express (18) in the form:

$$\vec{V}_{P\,pert} = \vec{V}_{FP} + \int_S\sigma\vec{K}\,dS + \int_S(\hat{n}\times\vec{V}_{pert})\times\vec{K}\,dS \quad (20)$$

where $\vec{V}_{FP}$ is the *nonlinear field-induced velocity perturbation*:

$$\vec{V}_{FP} = \int_\Omega(\nabla\cdot\vec{V})\,\vec{K}\,d\Omega + \int_\Omega(\nabla\times\vec{V})\times\vec{K}\,d\Omega . \quad (21)$$

Suppose we are able to *construct* a field $\vec{F}$ such that throughout Ω:

$$\nabla\cdot\vec{F} = \nabla\cdot\vec{V} \quad \text{and} \quad \nabla\times\vec{F} = \nabla\times\vec{V} . \quad (22)$$

Then we will have, using (13):

$$\begin{aligned}\vec{V}_{FP} & = \int_\Omega(\nabla\cdot\vec{F})\,\vec{K}\,d\Omega + \int_\Omega(\nabla\times\vec{F})\times\vec{K}\,d\Omega \\ & = \vec{F}_P - \int_{S+S_\infty}(\hat{n}\cdot\vec{F})\,\vec{K}\,dS - \int_{S+S_\infty}(\hat{n}\times\vec{F})\times\vec{K}\,dS . \quad (23)\end{aligned}$$

If we choose to construct the field $\vec{F}$ such that $\vec{F}\rightarrow 0$ sufficiently quickly as the outer boundary S_∞ is approached, the contribution from the boundary integrals over S_∞ will evaluate to zero at P. Suppose further that we introduce on the body boundary S the boundary functions σ_F and $\vec{\omega}_F$ defined by:

$$\sigma_F = -\hat{n}\cdot\vec{F} \quad \text{and} \quad \vec{\omega}_F = -\hat{n}\times\vec{F} . \quad (24)$$

We designate $\vec{F}$ an "*equivalent vector field*", and σ_F and $\vec{\omega}_F$ "*equivalent boundary source and vorticity distributions*": on the basis of (21) and (23) they are *equivalent* to the actual field functions $\nabla\cdot\vec{V}$ and $\nabla\times\vec{V}$. For points P lying on S we can now write $\vec{F}_P = -\sigma_{FP}\,\hat{n} - \vec{\omega}_{FP}\times\hat{n}$. Thus (23) becomes:

$$\begin{aligned}\vec{V}_{FP} & = \int_S\sigma_F\vec{K}\,dS + \int_S\vec{\omega}_F\times\vec{K}\,dS + \vec{F}_P \\ & = \int_S\sigma_F\vec{K}\,dS + \int_S\vec{\omega}_F\times\vec{K}\,dS - \sigma_{FP}\,\hat{n} - \vec{\omega}_{FP}\times\hat{n} \quad (25)\\ & \qquad \textit{when } P \textit{ lies on } S.\end{aligned}$$

Thus the *field* integrals defining the nonlinear field-induced perturbation in (21) can be replaced by the *surface* integrals [plus local contribution $\vec{F}_P$] in (25). Putting (25) in (20) and rearranging gives:

$$\vec{V}_{P\,pert} - \vec{F}_P = \int_S(\sigma + \sigma_F)\vec{K}\,dS + \int_S(\hat{n}\times\vec{V}_{pert} + \vec{\omega}_F)\times\vec{K} \quad (26)$$

or, finally, the ***equivalent pseudo-Laplace problem***:

$$\vec{V}'_{P\,\text{pert}} = \int_S \sigma' \vec{K}\, dS + \int_S (\hat{n}\times\vec{V}'_{\text{pert}})\times\vec{K}\, dS = \int_S \sigma' \vec{K}\, dS + \int_S \vec{\omega}'\times\vec{K}\, dS \tag{27}$$

where we have introduced the notation:

$$\vec{V}'_{\text{pert}} = \vec{V}_{\text{pert}} - \vec{F}$$
(pseudo-Laplace perturbation velocity)

$$\sigma' = \sigma + \sigma_F = -\hat{n}\cdot\vec{V}_\infty + V_{nBC} + \sigma_F \tag{28}$$
(fixed, given σ_F)

$$\vec{\omega}' = \hat{n}\times\vec{V}_{\text{pert}} + \vec{\omega}_F = \hat{n}\times\vec{V}'_{\text{pert}}$$
(to be determined by relaxation).

Equation (27), representing the compressible/rotational field problem, is formally identical to the SAVER identity (19) representing the linear "Laplace" (incompressible, irrotational) problem. Thus, to summarize, in order to solve the nonlinear Euler equation:

- We *construct* a vector field $\vec{F}$ in Ω, with $\vec{F}\to 0$ sufficiently quickly as the outer boundary S_∞ is approached, and such that $\nabla\cdot\vec{F} = \nabla\cdot\vec{V}$ and $\nabla\times\vec{F} = \nabla\times\vec{V}$ throughout Ω, these field functions being defined for the nonlinear Euler equation, purely from the computed $\vec{V}$, as in Secs 3 .2 .1 and 3 .2 .2 .
- The *pseudo-Laplace problem* (27), which is a transformation of the general nonlinear form (18), is solved by first fixing the surface source on S as $\sigma' = -\hat{n}\cdot\vec{V}_\infty + V_{nBC} + \sigma_F$ [*i.e.* the normal-velocity boundary condition for the pseudo-Laplace problem is that of the physical problem augmented by the ***boundary-condition increment*** $\sigma_F = -\hat{n}\cdot\vec{F}$]. The surface vorticity $\vec{\omega}'$ is then obtained by SAVER, coercing $\vec{\omega}'$ at each iteration to be equal to the currently computed value $\hat{n}\times\vec{V}'_{\text{pert}}$.
- At convergence, the *nonlinear* velocity field is given by $\vec{V} = \vec{V}_\infty + \vec{V}'_{\text{pert}} + \vec{F}$, with $\vec{V}'_{\text{pert}}$ the solution of the pseudo-Laplace problem (27); in particular, in the 2-D case the tangential velocity at a point P on the boundary is given by :
$$V_{sP} = V'_{sP} - \omega_{FP} \,. \tag{29}$$
- During the iteration, the unconverged values V_{sP} are used to update the Euler field source $\nabla\cdot\vec{F} = \nabla\cdot\vec{V}$ and vorticity $\nabla\times\vec{F} = \nabla\times\vec{V}$ defined by (9) and (12). These values are then used to construct the next estimate of the vector field $\vec{F}$ in Ω. The overall cycle defined above is repeated to convergence.
- Three different ways of constructing $\vec{F}$, either nominally exactly or approximately, are outlined in Sec 5 below. Note that a discontinuous $\vec{F}$ can be constructed such that no explicit source-sheet representation of a shock is required: even this can be represented fully by "equivalent" surface distributions on S.
- In the case of lifting configurations, the overall surface S carrying the "equivalent" boundary source and vorticity distributions also includes the vortical wake surface(s) emanating from the body. These wakes may either be assumed to be "rigid" (pre-defined location), or they may need to be "relaxed" to their rolled-up, force-free position (Hunt, 1978).

5 CONSTRUCTION OF THE EQUIVALENT FIELD $\vec{F}$

The construction of a vector field $\vec{F}$ whose divergence and curl match those of the physical field, either approximately or nominally exactly, is fundamental to GENESIS. In the case of an *unbounded domain* Ω with outer boundary S_∞ at infinity, it is convenient to construct $\vec{F}$ such that $\vec{F}\to 0$ sufficiently quickly as S_∞ is approached; this extra condition is no[illegible] a bounded domain (internal flows). Only unbounde[illegible] considered here.

Three distinct methods have been devised for the construction of the equivalent vector field $\vec{F}$.

The **Semi-Analytic Method** is outlined in Sec 5 .1 . This method is *approximate*: it introduces a new field, called the semi-analytic field, which is "close to" but different from the Euler field. The Semi-Analytic Method reduces the flowfield problem to a set of local, multi-valued, algebraic equations with a clear distinction between subsonic and supersonic *local candidate solutions*: this enables compression shocks to be modeled as exact discontinuities, and expansion shocks to be explicitly suppressed from the solution. This method involves no field evaluations: *all* computations are performed on the body boundary. The error field (the difference between the semi-analytic field and the Euler field), can be reduced or eliminated by one of the other two methods described below.

The **Uncurling Method** evaluates the *field functions* Σ_E and $\vec{\Gamma}_E$ of Secs 3 .2 .1 and 3 .2 .2 on a *field mesh* covering the region of Ω where those functions are non-zero. "Uncurling" then reduces these to an equivalent field vector $\vec{F}$, and then to boundary source σ_F and vorticity $\vec{\omega}_F$ — no field *integrals* are evaluated. The Uncurling Method, outlined in Sec 5 .2 , is *nominally exact*: the computed result approaches the exact Euler solution as the field mesh is refined.

The **Profile Method** computes the exact Euler field values Σ_E and $\vec{\Gamma}_E$ *on the boundary* S, but *approximates* their functional variation along lines drawn outwards from S, using shape functions with pre-defined profile shape. The equivalent field vector $\vec{F}$ is evaluated on S as the solution of an *ordinary* (vector) differential equation expressed on S. This solution is formed piecewise as the sum of a particular integral and a complementary function, and is effected through the use of combined *marching* and *shooting* techniques; this forces continuity of $\vec{F}$ between the beginning and end of the marching range, but allows a shock to be treated anywhere in the range as an exact discontinuity with the physical (R-H) jump condition. With this method, *all* computations are performed on the body boundary.

Both the Profile Method and the Uncurling Method can be applied either to solve the complete Euler field, or to eliminate the error field arising from application of the Semi-Analytic Method.

5 .1 The Semi-Analytic Method

The Semi-Analytic Method for the construction of the equivalent field $\vec{F}$ was developed specifically to deal with the difficult problems associated with shock waves and the mixed elliptic/hyperbolic equation types arising in transonic flows. It is an approximate method, generally requiring correction by the Uncurling Method of Sec 5 .2 or the Profile Method of Sec 5 .3 . Numerous variants of the Semi-Analytic Method are possible (Hunt and Adamson, 1992a), all based on identifying a suitable ***perfect (vector) differential function***. The variant described here is known as the **D-Field** approximation. We consider only the 2-D case in a cartesian x, z system with unit vectors $\hat{i}, \hat{k}$; the extension to 3-D is straightforward.

In the D-Field, the local flowspeed V is replaced by its x-component $U = \hat{i}\cdot\vec{V}$, and its streamwise derivative is replaced by an x-derivative. The Euler source $\Sigma_E = M^2\partial V/\partial s$ is thus approximated by the *D-Field source* $\Sigma_D = M_D^2\partial U/\partial x$, where M_D is the *D-Mach number* defined by $M_D = U/a_D$. Here, a_D is the *D-sonic speed* defined by $a_D^2 = \frac{\gamma-1}{2}(V_{\max}^2 - U^2)$, approximating the Euler sonic speed given earlier by $a^2 = \frac{\gamma-1}{2}(V_{\max}^2 - V^2)$. Moreover, the Euler field vorticity $\vec{\Gamma}_E$ is replaced in the D-Field by a ***spurious vorticity*** $\vec{\Gamma}_D = \Gamma_D\hat{j}$, defined by $\Gamma_D = M_D^2\partial U/\partial z$. The purpose of introducing this spurious vorticity is to allow an equivalent vector field $\vec{F}_D$ to be constructed *analytically* as a perfect differential function.

5.1.1 *The perfect differential defining the D-Field*

Consider the vector field function $\vec{F}_D$ defined by:

$$\vec{F}_D = F_D(U)\,\hat{i} \qquad \text{with} \qquad F_D(U) = \lambda(U) + \lambda_\infty \tag{30}$$

$$\text{where} \quad \lambda(U) = \frac{2}{\gamma - 1}\left[V_{max}\, \ell n \sqrt{\frac{V_{max} + U}{V_{max} - U}} - U \right]$$

$$\text{and} \quad \lambda_\infty = \frac{2}{\gamma - 1}\left[V_{max}\, \ell n \sqrt{\frac{V_{max} - U_\infty}{V_{max} + U_\infty}} + U_\infty \right].$$

It is easy to show that $\partial F_D/\partial U = \partial\lambda/\partial U = M_D^2$, from which it immediately follows that the divergence and curl of $\vec{F}_D$ are respectively the functions Σ_D and $\vec{\Gamma}_D$ defined above. It can also readily be seen that $F_D(U) \to 0$ as $U \to U_\infty$, *i.e.* on the outer boundary S_∞.

For a solid body with local unit normal $\hat{n} = n_x\hat{i} + n_z\hat{k}$ and tangent $\hat{s} = \hat{j}\times\hat{n} = n_z\hat{i} - n_x\hat{k}$, the vector velocity on S must satisfy $\vec{V} = V_s\,\hat{s}$, so that $U = n_z V_s$. From (24) and (30) we have $\omega_F = -n_z F_D$. Finally, from (24) and the relation $\vec{V}'_{pert} = \vec{V}_{pert} - \vec{F}$ in (28), we deduce in the 2-D case that $V_s = V'_s - \omega_F$. Combining these equations for U, V_s and ω_F gives the following nonlinear (*transcendental*) equation at a point on S:

$$U - n_z^2 F_D(U) = U' \tag{31}$$

where U' is defined by $U' = n_z V'_s$. [This is *not* the x-component of the pseudo-Laplace velocity $\vec{V}'_s$ since the normal component V'_n in the equivalent pseudo-Laplace problem is not in general zero.]

Equation (31), giving the value of the nonlinear velocity component U as an implicit function of the pseudo-Laplace quantity U' for given values of n_z and V_{max}, is termed the ***D-equation***. The generic graph of the D-Equation for some point P is shown in Fig 4. Only the physically relevant part of this graph is shown—there are other, non-physical branches corresponding to values of U greater than the maximum possible value V_{max}. We also consider here only positive values of U, thus limiting the present discussion to *attached* flows (this is *not* a necessary assumption). One of the key processes in the GENESIS algorithm is solving (31) for U at each point on S, given the current estimate of U'. A method of solution is outlined in Sec 5.1.4, but first we need to address the problem of the *existence* or "*feasibility*" of solutions of (31) at every point on the boundary.

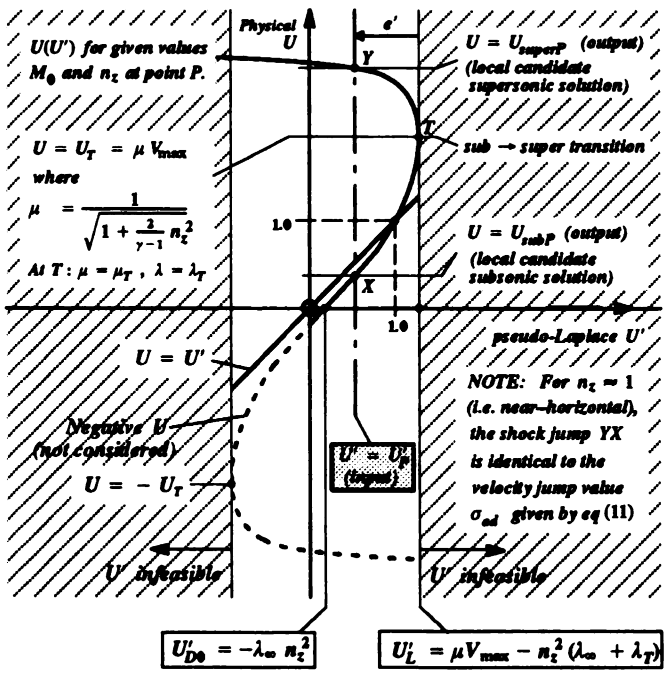

Fig 4. Generic graph of the D-Equation.

We see from Fig 4 that a solution U of the D-Equation can exist at a point P only for a pseudo-Laplace value U' which is less than a ***local limit value*** U'_L. For given values n_z and V_{max}, it can easily be shown that, at this limit value of U', the corresponding "D-critical" value U_T of U [indicated by T on Fig 4; see also Note 14 below] is given by $U_T = \mu V_{max}$, where μ is a local *geometric* constant: $\mu = \left(1 + \frac{2}{\gamma-1}n_z^2\right)^{-1/2}$. Inserting $U = U_T$ into (30) and (31) gives the *maximum feasible value* (limit value) of U' at P as:

$$U'_L = \mu V_{max} - n_z^2(\lambda_\infty + \lambda_T) \tag{32}$$

$$\text{where} \quad \lambda_T(V_{max}, n_z) = \frac{2}{\gamma - 1} V_{max}\left[\ell n \sqrt{\frac{1+\mu}{1-\mu}} - \mu \right].$$

It is convenient to consider the pseudo-Laplace tangential velocity V'_s as the sum of the "Laplace" tangential velocity and a *tangential velocity increment* associated with the nonlinearity of the D-Field, as represented by the equivalent distributions σ_F and $\vec{\omega}_F$ defined in (24). We denote by V'_{sA} the *unperturbed Laplace solution* [*i.e.* the local tangential velocity obtained by SAVER with $\sigma_F = 0$ in (24)], and by V'_{sF} the ***field-induced increment*** in the pseudo-Laplace tangential velocity when the finite ("compressible") value defined by (24) is used for σ_F:

$$V'_{sF} = V'_s - V'_{sA}. \tag{33}$$

Thus the x-component of the tangential velocity increment [*i.e.* multiplying (33) by n_z] is given by:

$$U'_F = U' - U'_A. \tag{34}$$

From the definition of the local limit value U'_L in (32), it follows that the *local maximum-feasible increment* in the pseudo-Laplace solution, *due to the boundary-condition increment* σ_F, is given by:

$$U'_{FL} = U'_L - U'_A. \tag{35}$$

Note 13: For a given "shape" of the distribution F_D evaluated on S, the local increment U'_F in (34) is *proportional* at any point P to the value of $\sigma_F = -n_x F_D$ at that point: if we scale the entire distribution F_D (and thus σ_F) by a constant factor, r_T say, the entire distribution U'_F will scale by that same factor. This follows from the linear nature of the pseudo-Laplace field. Thus, given the values F_D and U'_F at a particular point, we can write a **proportionality relation** at that point:

$$\partial U'_F/\partial F_D = K = U'_F/F_D. \tag{36}$$

Note 14: The "D-critical" value U_T defined earlier as $U_T = \mu V_{max}$, with $\mu = \left(1 + \frac{2}{\gamma-1}n_z^2\right)^{-1/2}$, reduces for a horizontal local boundary (i.e. $n_z^2 = 1$) to $U_T = \sqrt{\frac{\gamma-1}{\gamma+1}}\,V_{max}$; this is identical to the **critical speed** for the Euler equation, at which the local Mach number has unit value. This justifies the use of the term "D-critical."

5.1.2 *The exceedance parameter defining the flow state*

It is now convenient to introduce the concept of a local exceedance e', defined at a particular point by:

$$e' = U'_F - U'_{FL} \equiv U' - U'_L. \tag{37}$$

We denote by e'_T the *maximum* value of e' found on the body boundary during a particular iteration [*i.e.* the most positive value detected in the pseudo-Laplace computation: $e'_T = \mathbf{max}(e')$]. Suppose that this maximum is detected at a point P_T.

Except for P_T, there will be *two* relevant can[illegible] [illegible]lutions for U at each point P. These are a ***candidate*** [illegible] [illegible]n U_{sub}

(marked as X in Fig 4) and a ***candidate supersonic solution*** U_{sup} (marked as Y). At P_T, these two candidate solutions will coincide exactly, both being equal to the local D-sonic (D-critical) speed at that point: the point T on Fig 4 thus corresponds to a point of *continuous transition between D-subsonic and D-supersonic states.*

The value of the maximum exceedance e'_T ***defines the global state of the nonlinear flow***. Three possibilities exist for the value of the maximum exceedance: $e'_T = 0$ [*i.e.* $U' = U'_L$ at one or more points on S, implying the limit of global feasibility] ; $e'_T < 0$ [*i.e.* $U' < U'_L$ everywhere, implying global feasibility]; $e'_T > 0$ [*i.e.* $U' > U'_L$ at one or more points, implying global infeasibility].

- If $e'_T = 0$ when the subsonic candidate U_{sub} is taken at all points, the flow is ***subsonic D-critical, sonic at*** P_T. We call the unique freestream Mach number at which this condition occurs, the "*subsonic D-critical Mach number*", $M^*_{D_{sub}}$.
- If $e'_T = 0$ when the supersonic candidate U_{sup} is taken at all points, the flow is ***supersonic D-critical, sonic at*** P_T. We call the unique freestream Mach number at which this condition occurs, the "*supersonic D-critical Mach number*", $M^*_{D_{sup}}$.
- If $e'_T = 0$ when the solution has candidates of both types, arranged quasi-physically, it is a ***feasible D-transonic flow***.
- If $e'_T < 0$ when U takes its subsonic candidate value at every boundary point, the flow is ***fully D-subsonic***.
- If $e'_T < 0$ when U takes its supersonic candidate value at every boundary point, the flow is ***fully D-supersonic***.
- If $e'_T > 0$ (*i.e.* $U' > U'_L$ at one or more points), the overall flow is ***infeasible***, and some adjustment is needed to the underlying hypotheses: this is discussed in Sec 5 .1 .3 .

Note 15: The physics of a real flow requires that a transition from a subsonic state to a supersonic state be *smooth* (no expansion shock).

Note 16: A transition from a supersonic to a subsonic state will usually (but not always) occur through a discontinuity. (There is the possibility of a shock-free transonic flow.)

Note 17: The difference XY in Fig 4 between the D-subsonic and D-supersonic candidate solutions at a point with horizontal surface tangent ($n_z^2 = 1$) is equal to the "adiabatic shock jump" obtained by an alternative method in Note 10 in Sec 3 .2 .1 .

Note 18: As discussed earlier, the Euler equation lacks the dissipative mechanisms needed to suppress the formation of (non-physical) expansion shocks. The extraneous enforcement of smoothness through a D-sonic point P_T — only for a subsonic-to-supersonic transition, and the logic governing the choice of candidate (Sec 5 .1 .4), justify the use of the term "knowledge-based" for the semi-analytic GENESIS approach described here.

5 .1 .3 Scaling of infeasible flows

As indicated in Sec 5 .1 .2 , the *entire pseudo-Laplace solution* is considered to be *infeasible* if for *any* boundary point the computed field-induced increment $U'_F = n_z V'_{tF}$ exceeds its local maximum-feasible value U'_{FL} , *i.e.* if $e'_T > 0$. If this occurs, some adjustment needs to be made to the parameters defining the pseudo-Laplace problem; specifically, some adjustment to the boundary-condition increment $\sigma_F = -n_x F_D$, and thus to F_D , is needed. The required change in e'_T [*i.e.* the *reduction* required in U'_F at the maximum-exceedance (D-sonic) point P_T to make the pseudo-Laplace solution "feasible"] is clearly equal to $-e'_T$. The determination of the corresponding adjustment needed for F_D is based on the "proportionality" relation (36) presented above. At P_T, (37) and (36) become:

$$e'_T = U'_{FT} - U'_{FL} \equiv U'_T - U'_L \quad \text{and} \quad \frac{\partial U'_{FT}}{\partial F_{[illegible]}} \; [illegible] = \frac{U'_{FT}}{F_{DT}} . \tag{38}$$

For a D-transonic solution (defined in Se[illegible] [illegible]$_{max}$ fixed (*i.e.* prescribed M_∞), the only free parameters available are the unknown shock locations. We shall not consider *shock relaxation* here, except to note that a simple technique can be envisaged, determining the sensitivity of e'_T to the shock location.

If, on the other hand, we are attempting to determine a D-critical solution as defined in Sec 5 .1 .2 , or a D-transonic solution with a single, *prescribed* shock location, we can see from (30) that the only parameter available to modify F_D, given the body geometry, is V_{max} . This is related uniquely to the freestream Mach number M_∞ through (2). Differentiating the first equation in (38) w.r.t. V_{max}, then using the second equation, gives a *sensitivity relation* at P_T :

$$\frac{\partial e'_T}{\partial V_{max}} = K_T \frac{\partial F_{DT}}{\partial V_{max}} - \frac{\partial U'_L}{\partial V_{max}} . \tag{39}$$

Introducing the parameters (written here for $U_\infty = 1$) :

$$\chi_T = \frac{2}{\gamma - 1}\left(K_T + n_{zT}^2\right), \qquad Y_\infty = \frac{1}{V_{max}^2 - 1}$$
$$B_\infty = \ln\sqrt{\left(\frac{V_{max}-1}{V_{max}+1}\right)}, \qquad \mu_T = \left(1 + \frac{2}{\gamma-1} n_{zT}^2\right)^{-1/2} \tag{40}$$
$$B_{\mu T} = \ln\sqrt{\left(\frac{1+\mu_T}{1-\mu_T}\right)} , \qquad D_{\mu T} = B_{\mu T} - \mu_T ,$$

we can show from (30), (32) and (39) that the first and second derivatives of e'_T w.r.t. V_{max} are given by :

$$\partial e'_T / \partial V_{max} = \chi_T \left(B_\infty + D_{\mu T} + V_{max} Y_\infty\right) - \mu_T$$
$$\text{and} \quad \partial^2 e'_T / \partial V_{max}^2 = -2 \chi_T Y_\infty^2 . \tag{41}$$

This allows the required change in V_{max} to drive $e'_T \to 0$ to be obtained by a first- or second-order *Newton-Raphson* iteration cycle: $V_{max} = V_{max} + \delta V_{max}$, with δV_{max} at each iteration defined by:

$$\delta V_{max} = -\eta_{01}(1 + \underbrace{\eta_{01}\eta_{21}}_{\text{2nd order term}}) . \tag{42}$$

Here η_{01} and η_{21} indicate ratios of e'_T and the derivatives in (41):

$$\eta_{01} = \frac{e'_T}{\partial e'_T / \partial V_{max}} \quad \text{and} \quad \eta_{21} = \frac{\partial^2 e'_T / \partial V_{max}^2}{\partial e'_T / \partial V_{max}} . \tag{43}$$

This cycle is iterated until V_{max} converges. At convergence, the resulting *scaled* value of U'_F at the maximum-exceedance point P_T will be precisely equal to the *new*, local limit value U'_{FL} corresponding to the converged V_{max} value. The *entire* U'_F and V'_{tF} distributions, scaled in the same ratio, r_T say, will then be "feasible". The new, "feasible" freestream Mach number is obtained from (2) as:

$$M_\infty = \left(\frac{\gamma-1}{2}\left(V_{max}^2 - 1\right)\right)^{-1/2} . \tag{44}$$

To determine the scaling ratio r_T, we insert the new V_{max} into (30) to obtain the "scaled" value of F_D at the point P_T. The ratio r_T of the new F_D to its previous value is then applied to (linearly) scale the entire U'_F and V'_{tF} distributions. Added to the (Laplace) U'_A distribution, the scaled U'_F gives a *globally feasible* U' distribution.

The nonlinear D-equation (31) now needs to be re-solved for the (subsonic or supersonic) value of U at each point, given this (scaled) feasible distribution U' and the new V_{max} (*i.e.* the new M_∞).

5 .1 .4 Solution of the D-Equation at each boundary point

Given V_{max} and a *feasible* estimate of the pseudo-Laplace U' distribution (*i.e.* one which nowhere exceeds its local maximum feasible value U'_L), we need to evaluate the subsonic candidate solution U_{sub} or the supersonic candidate solution U_{sup} at every point on the body boundary. These are distinct roots of the nonlinear (transcendental) D-equation (31) at each point, with F_D defined by (30).

The choice of which root to select at each boundary point is a *knowledge-based* decision. If the flow is fully D-subsonic, as defined in Sec 5.1.2, the subsonic root should always be taken. If the flow is D-transonic, the supersonic root should be taken for points lying downstream of a D-sonic (maximum-exceedance) point P_T but upstream of a compression shock; all other points take the subsonic root. The choice of root at a particular point may vary as the iteration proceeds and the location identified for P_T varies.

GENESIS uses a 2nd-order *Newton-Raphson* scheme to solve (31) for U_{sub} or U_{sup} at each point, given the pseudo-Laplace distribution U'. The ***initial estimate*** of U to start the iteration depends on the local U' value, and is determined adaptively, as follows.

If U' is close to its local limit value U'_L [Fig 4], then U will be close to its D-sonic value $U_T = \mu V_{max}$; a function of the form $U = U_T(1+\Delta)$ is therefore used to give an initial estimate of U. Replacing U in (30) by this form and inserting in (31) allows a power-series expansion about point T in Fig 4 to be developed, relating Δ implicitly to a *proximity parameter* $\Delta' = e'/U_T$, where e' is the exceedance parameter defined by (37). The assumption that Δ is small allows the series to be inverted, giving Δ explicitly as a simple function of Δ'. We take $\Delta > 0$ to get U_{sup}, otherwise $\Delta < 0$.

If the proximity parameter Δ' is not small, the linear approximant $U = U' - U'_{D*}$ is instead used as initial estimate, with the origin shift U'_{D*} defined by $U'_{D*} = -\lambda_\infty n_\zeta^2$ as shown in Fig 4.

Starting from this initial estimate, the Newton-Raphson iteration is defined by $U = U + \delta U$, with δU defined at each iteration by:

$$\delta U = -\eta_{01}(1 + \underbrace{\eta_{01}\eta_{21}}_{\text{2nd order term}}) \tag{45}$$

with now:

$$\eta_{01} = \frac{n_\zeta^2 F_D - U + U'}{\eta_1} \quad \text{and} \quad \eta_{21} = \frac{\gamma - 1}{2}\,\frac{U}{\eta_1}\left(\frac{n_\zeta V_{max}}{a_D^2}\right)^2 \tag{46}$$

in which $\eta_1 = (n_\zeta U)^2/a_D^2 - 1$ and $a_D^2 = \frac{\gamma-1}{2}(V_{max}^2 - U^2)$, with F_D defined by (30) using the current estimate of U. The adaptive initialization described above ensures that U_{sub} or U_{sup} at each point is obtained to machine precision in two or three iterations, for a given U' distribution. At convergence, the nonlinear D-Field tangential velocity is obtained from the pseudo-Laplace solution, using (29).

5.1.5 *Example solution of the D-Field*

A transonic solution of the D-Field for a non-lifting NACA0012 airfoil, obtained numerically by the GENESIS Semi-Analytic Method, is shown in Fig 5 below. The figure also shows the subsonic D-critical solution and the linear (Laplace) solution $V'_{\zeta A}$.

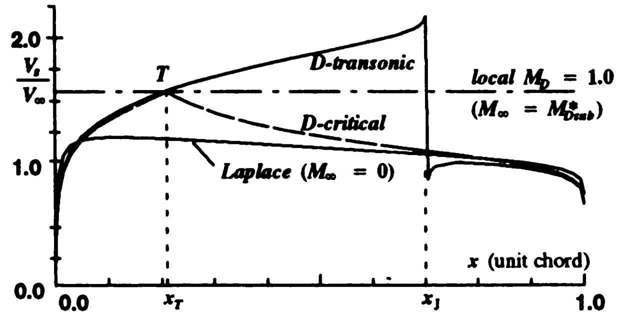

Fig 5. NACA0012, α = 0, D–Field. No correction for spurious vorticity

Note that *no correction* for the spurious vorticity $\Gamma_D = M_D^2 \partial U/\partial z$ implicitly present in the D-Field has been applied in Fig 5: without correction, this solution can therefore *not* be interpreted as an accurate Euler solution. Generally, a correction needs to be incorporated within the Semi-Analytic Method to annihilate the spurious vorticity. Two corrective methods are discussed in their own right in Secs 5.2 and 5.3, and then as part of a composite method in Sec 5.4.

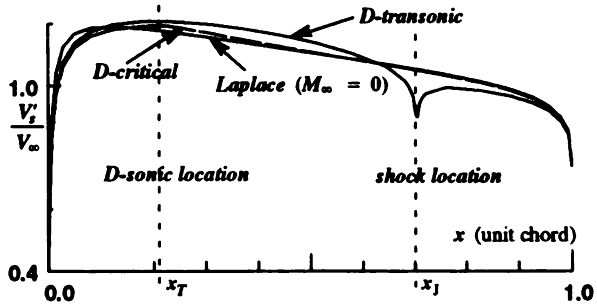

Fig 6. Pseudo–Laplace solution V'_ζ for D–Field, before application of the correction $-\omega_F$

The *pseudo-Laplace solution* corresponding to Fig 5 is shown in Fig 6. It can be seen from Fig 6 that the D-critical pseudo-Laplace solution lies close to the actual Laplace solution $V'_{\zeta A}$, and that even the transonic pseudo-Laplace solution itself is relatively close. Most of the difference between the nonlinear solutions in Fig 5 comes from (29), *i.e.* the final application of the tangential correction $-\omega_F$. The small departure of the pseudo-Laplace solution from the actual Laplace solution is responsible for the rapid convergence characteristics demonstrated by the GENESIS Semi-Analytic Method. In fact, a relatively good result is obtained for D-Field in the *first iteration* of the overall algorithm [*i.e.* starting with the *Laplace* value $U'_A = n_\zeta V'_{\zeta A}$ for U in (30)], with complete convergence generally in about three or four iterations. The results shown here were obtained in about one second of CPU time on a 486 personal computer, using a non-optimized pilot code written in ADA.

5.2 The Uncurling Method

"Uncurling" offers a ***nominally exact*** means of constructing an equivalent field $\vec{F}$, given the Euler values Σ_E and $\vec{\Gamma}_E$ of Secs 3.2.1 and 3.2.2 on a *field mesh* external to the body. The process is outlined here for the 2-D case. We suppose that Σ_E and $\vec{\Gamma}_E = \Gamma_E \hat{j}$ are known at each corner point × on the "active mesh" shown cross-shaded in Fig 7, and are numerically zero everywhere outside that mesh (*e.g.* on the "passive" and "polar" meshes shown in the figure).

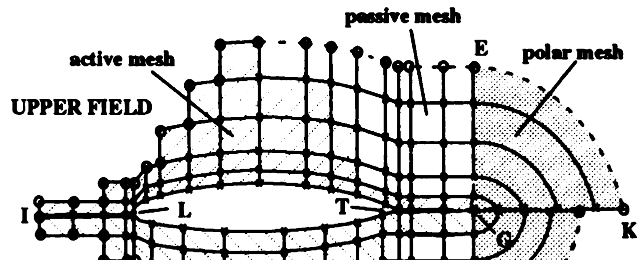

Fig 7. Active, passive and polar meshes used for the (nominally-exact) Uncurling Method.

A generic cell of *arbitrary* shape is shown in Fig 8. The values of Σ_E and Γ_E are known at its four vertices. From these eight values, *bilinear approximations* $\Sigma(\xi,\zeta)$ and $\Gamma(\xi,\zeta)$ shown in (47) can be derived for this cell, using local cartesian coordinates ξ and ζ measured from corner A [*e.g.*, a least-squares fit could be used]. These bilinear functions will *not* generally match the 8 known corner values precisely, as only 6 coefficients are available. The functions Σ

and Γ will thus display slight discontinuities across cell boundaries, but the error will decrease continuously as the cell size is reduced.

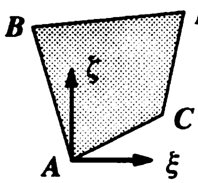

$$\Sigma(\xi,\zeta) = \Sigma_A + \Sigma_X \xi + \Sigma_Z \zeta \approx \Sigma_B(\xi,\zeta)$$
$$\Gamma(\xi,\zeta) = \Gamma_A + \Gamma_X \xi + \Gamma_Z \zeta \approx \Gamma_B(\xi,\zeta) \qquad (47)$$

Fig 8 . Generic cell from mesh in Fig 7 .

From $\Sigma(\xi,\zeta)$ and $\Gamma(\xi,\zeta)$, the uncurling process constructs an equivalent vector field $\vec{F}$ cell-by-cell on the compound mesh shown in Fig 7 (active, passive and polar meshes), such that:

- $\nabla\cdot\vec{F} = \Sigma(\xi,\zeta)$ and $\nabla\times\vec{F} = \Gamma(\xi,\zeta)\,\hat{j}$ *exactly*, on every cell;
- $\vec{F}$ is *continuous* across cell boundaries (but see Note 20 below);
- $\vec{F}$ is *zero* on the outer edge of the mesh (circles in Fig 7).

We construct $\vec{F}$ as a piecewise *bi-quadratic* vector field. For the generic cell in Fig 8 , we use the bi-quadratic vector representation:

$$\vec{F}(\xi,\zeta) = \vec{F}_A + \vec{F}_{X1}\,\xi + \vec{F}_{X2}\,\xi^2 + \vec{F}_{Z1}\,\zeta + \vec{F}_{Z2}\,\zeta^2 + \vec{F}_{XZ}\,\xi\zeta \quad (48)$$

Six vector coefficients are needed in this equation (*i.e.* the 12 scalar values F_{Ax}, F_{Az}, F_{X1x}, F_{X1z}, F_{X2x}, F_{X2z}, F_{Z1x}, F_{Z1z}, F_{Z2x}, F_{Z2z}, F_{XZx}, F_{XZz} for this cell). Now *six* scalar values defining $\vec{F}$ at three of the cell corners (say, A, B and C) will be known, either from adjacent cells computed earlier, or from $\vec{F}=\mathbf{0}$ at the outer edge of the mesh; six further scalar equations are thus needed. These are obtained by matching the coefficients of $\nabla\cdot\vec{F}$ and $\nabla\times\vec{F}$ obtained from (48) with those in (47). For example, we have:

$$\nabla\cdot\vec{F}(\xi,\zeta) = (F_{X1x} + F_{Z1z}) + (2F_{X2x} + F_{XZz})\,\xi + (2F_{Z2z} + F_{XZx})\,\zeta$$
$$\text{and } \Sigma(\xi,\zeta) = \quad \Sigma_A \quad + \quad \Sigma_X\,\xi \quad + \quad \Sigma_Z\,\zeta \qquad (49)$$

giving three of the extra six equations needed :

$$F_{X1x} + F_{Z1z} = \Sigma_A\ ; \qquad 2F_{X2x} + F_{XZz} = \Sigma_X\ ;$$
$$\text{and} \quad 2F_{Z2z} + F_{XZx} = \Sigma_Z\ . \qquad (50)$$

The three final equations result from equating the coefficients of $\nabla\times\vec{F}$ and $\vec{\Gamma}$. Solving the resulting set of 12 independent, linear equations gives the desired coefficients for (48). The value of $\vec{F}$ at the fourth corner of the cell, D say, then follows immediately.

This "cartesian uncurling" process constructs $\vec{F}$ starting from the first cell in the active mesh to the last cell in the passive mesh [in which Σ_A, Σ_X, Σ_Z, Γ_A, Γ_X, Γ_Z in (47) are all zero]. The upper and lower fields are uncurled separately. The equivalent surface source σ_F and vorticity $\vec{\omega}_F$ [eq (24)] are located on the body surface ***LT*** (Fig 7), its extensions ***IL*** and ***TG***, and the vertical plane ***EGH***.

An analogous "polar uncurling" process constructs a vector field $\vec{F}$ on the cylindrical polar mesh (shown shaded in Fig 7), starting from the values obtained on the vertical plane ***EGH*** by the cartesian uncurling process described above. In this polar mesh region both $\nabla\cdot\vec{F}$ and $\nabla\times\vec{F}$ would here be taken as zero, though finite values could also be used. This process effectively transfers the equivalent distributions σ_F and $\vec{\omega}_F$ from ***EGH*** to the horizontal surface ***GK***.

Note 19: The *symbolic matrix* defining the 12 linear equations to be solved on each cell can be inverted *analytically*, though the algebra is somewhat tedious. If this symbolic inverse is available, the computational work involved in constructing the field over the entire mesh would be relatively small. If the symbolic inverse is not available, a numerical matrix for each set of 12 equations, i.e. for each cell, would in general need to be inverted separately. However, if the mesh used has all cells geometrically identical (for example, square cells), the numerical matrix needs to be inverted only once. This would offer an efficient means of solution for the entire mesh.

Note 20: The uncurling process can be applied to solve the complete Euler equations, nominally exactly. If shock waves are present (see Note 12), they can be considered to be contained within cells of infinitesimal width, coinciding with cell boundaries. Instead of $\vec{F}$ being transmitted *continuously* from one cell to its neighbor downstream, the R-H discontinuity can then be applied at the cell interface. By this means, the shock-wave discontinuity is transmitted entirely to the body boundary, and will appear as a discontinuity in the equivalent boundary distributions — primarily $\vec{\omega}_F$.

Note 21: The uncurling process can alternatively be applied to eliminate an error field associated with the use of a less accurate method. Two such methods are the Semi-Analytic Method of Sec 5 .1 , and the Profile Method discussed below. If used in this way, a coarser mesh may suffice for the uncurling process, and this may need to extend only a short distance away from the body.

5 .3 The Profile Method

The Profile Method for the construction of the equivalent vector field $\vec{F}$ is an adaptation of the classical *separation of variables* approach (Hunt and Plybon, 1990). It is an *approximate* method, and can be used as an economic alternative to the Uncurling Method. The equivalent field functions $\Sigma = \nabla\cdot\vec{F}$ and $\vec{\Gamma} = \nabla\times\vec{F}$ (and possibly some number of their normal derivatives) are given the exact Euler-field values Σ_E and Γ_E *on the boundary S*. However, their functional variation along lines drawn outwards from S is *approximated* using ***decay functions*** of pre-defined profile shape, analogously to classical boundary-layer theory. Two variants have been developed: one (cartesian) uses exponential decay functions; the other (cylindrical polar) has inverse-power radial-decay functions. Only the polar profile method will be outlined here (Fig 9).

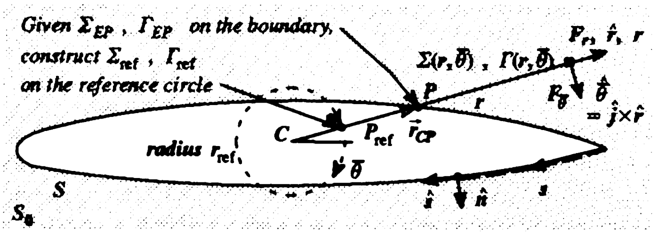

Fig 9 . Coordinate system for Polar Profile Method.

With origin C, reference radius r_{ref} and $\bar{\theta}$ measured *clockwise*, the approximating functions Σ, Γ have profiles matching Σ_E, Γ_E on S:

$$\nabla\cdot\vec{F} = \Sigma(r,\bar{\theta}) = \Sigma_{ref}(\bar{\theta})\,(r/r_{ref})^{-(p+1)}$$
$$\text{where} \quad \Sigma_{ref}(\bar{\theta}) = \Sigma_{EP}(\bar{\theta})\,(r_{CP}/r_{ref})^{(p+1)}$$
$$\text{and} \quad \nabla\times\vec{F} = \vec{\Gamma}(r,\bar{\theta}) = \vec{\Gamma}_{ref}(\bar{\theta})\,(r/r_{ref})^{-(p+1)} \qquad (51)$$
$$\text{where} \quad \Gamma_{ref}(\bar{\theta}) = \Gamma_{EP}(\bar{\theta})\,(r_{CP}/r_{ref})^{(p+1)} \quad \text{with } p = \text{constant.}$$

Suppose the equivalent field $\vec{F} \equiv F_r\,\hat{r} + F_{\bar{\theta}}\,\hat{\bar{\theta}}$ has the form :

$$F_r(r,\bar{\theta}) = F_{r\,ref}(\bar{\theta})\,(r/r_{ref})^{-p} \text{ so that } F_{rP} = F_{r\,ref}\,(r_{CP}/r_{ref})^{-p}$$
$$F_{\bar{\theta}}(r,\bar{\theta}) = F_{\bar{\theta}\,ref}(\bar{\theta})\,(r/r_{ref})^{-p} \text{ so that } F_{\bar{\theta}P} = F_{\bar{\theta}\,ref}\,(r_{CP}/r_{ref})^{-p}\ . \qquad (52)$$

The divergence and curl of $\vec{F}$ in this polar system are given by:

$$\nabla\cdot\vec{F} = \frac{1}{r}\left[\frac{\partial}{\partial r}(r\,F_r) + \frac{\partial F_{\bar{\theta}}}{\partial\bar{\theta}}\right]\ ;\ \nabla\times\vec{F} = \frac{1}{r}\left[\frac{\partial}{\partial r}(r\,F_{\bar{\theta}}) - \frac{\partial F_r}{\partial\bar{\theta}}\right]\hat{j} \quad (53)$$

Then it is easy to show that $F_{\bar{\theta}\,ref}$ and $F_{r\,ref}$ must satisfy a coupled pair of *ordinary differential equations* written on the reference circle as :

$$\frac{dF_{r\,ref}}{d\bar{\theta}} + a\,F_{\bar{\theta}\,ref} = -\,r_{ref}\,\Gamma_{ref}\ ; \quad \frac{dF_{\bar{\theta}\,ref}}{d\bar{\theta}} - a\,F_{r\,ref} = r_{ref}\Sigma_{ref} \quad (54)$$

in which we have written $a = p - 1$. It is also easy to show that the contribution from the boundary S_∞ at infinity will vanish if $p > 0$.

Equations (54) possess a *vector complementary-function* $\vec{F}_{CF}$ such that $\nabla\cdot\vec{F}_{CF} = 0$ and $\nabla\times\vec{F}_{CF} = 0$ for any constants A, B:

$$F_{CFr}(\bar{\theta}) = A\cos a\bar{\theta} + B\sin a\bar{\theta}$$
$$F_{CF\bar{\theta}}(\bar{\theta}) = A\sin a\bar{\theta} - B\cos a\bar{\theta}. \quad (55)$$

If a is non-integer (*i.e* p non-integer), $\vec{F}_{CF}$ will be *discontinuous* across $\bar{\theta} = 2\pi \to 0$; the components of the discontinuity are:

$$\Delta F_{CFr} \equiv F_{CFr}(2\pi) - F_{CFr}(0) = B\sin p2\pi - A(1-\cos p2\pi)$$
$$\Delta F_{CF\bar{\theta}} \equiv F_{CF\bar{\theta}}(2\pi) - F_{CF\bar{\theta}}(0) = A\sin p2\pi + B(1-\cos p2\pi). \quad (56)$$

Suppose we now approximate the (known) functions $r_{ref}\Sigma_{ref}(\bar{\theta})$ and $r_{ref}\Gamma_{ref}(\bar{\theta})$ on panel j by *quadratic* representations:

$$r_{ref}\Sigma_{ref} = \Sigma_0 + \Sigma_1\theta' + \Sigma_2\theta'^2; \quad r_{ref}\Gamma_{ref} = \Gamma_0 + \Gamma_1\theta' + \Gamma_2\theta'^2 \quad (57)$$

with each coefficient constant on panel j, and with θ' measured from its midpoint (positive clockwise). We next form a quadratic *vector particular integral* $\vec{F}_{PI} = F_{PIr}\hat{r} + F_{PI\bar{\theta}}\hat{\bar{\theta}}$, defined by:

$$F_{PI\bar{\theta}}(\bar{\theta}) = F_{\bar{\theta}0} + F_{\bar{\theta}1}\theta' + F_{\bar{\theta}2}\theta'^2; \quad F_{PIr}(\bar{\theta}) = F_{r0} + F_{r1}\theta' + F_{r2}\theta'^2 \quad (58)$$

We force $\vec{F}_{PI}$ to be an exact solution of (54) on panel j by inserting (58) in (53) and matching the coefficients of $r_{ref}\nabla\cdot\vec{F}_{PI}$ and $r_{ref}\nabla\times\vec{F}_{PI}$ on the reference circle with those in (57), to give:

$$\begin{aligned} F_{\bar{\theta}2} &= -\Gamma_2/a; & F_{r1} &= (2F_{\bar{\theta}2} - \Sigma_1)/a; \\ F_{\bar{\theta}0} &= -(F_{r1} + \Gamma_0)/a; & F_{r2} &= -\Sigma_2/a; \\ F_{\bar{\theta}1} &= -(2F_{r2} + \Gamma_1)/a; & F_{r0} &= (F_{\bar{\theta}1} - \Sigma_0)/a. \end{aligned} \quad (59)$$

We can now add to the particular-integral vector $\vec{F}_{PI}$, *locally* on panel j, the complementary function vector $\vec{F}_{CF}(\bar{\theta})$, with the local coefficients A, B in (55) chosen to make the resulting vector $\vec{F}_{ref} = \vec{F}_{PI} + \vec{F}_{CF}$ at entry to panel j equal to that at exit from panel $j-1$ (unless a shock is present: see Note 22 below). This process is repeated from the first to the last panel on the body, to form a vector $\vec{F}_{ref}$ which is C_0–continuous for $\bar{\theta} = 0 \to 2\pi$ but *discontinuous* across $\bar{\theta} = 2\pi \to 0$. Finally, we *globally* add the discontinuous vector $\vec{F}_{CF}(\bar{\theta})$ with global coefficients A, B in (55) now chosen to force $\Delta\vec{F}_{CF}$ in (56) to exactly cancel this remaining discontinuity in $\vec{F}_{ref}$.

Note 22: Only a slight modification is required when shocks are present. These are treated using an argument similar to that presented in Note 20 for the Uncurling Method. Suppose a shock exists at the junction of panels $j-1$ and j, with required velocity jump $\Delta\vec{V}$. Then, instead of selecting the local coefficients A, B in the additive complementary function $\vec{F}_{CF}(\bar{\theta})$ for panel j so as to make the vector $\vec{F}_{ref}$ entering panel j continuous with that exiting panel $j-1$, as above, we enforce a *vector discontinuity* $\Delta\vec{V}$ between $j-1$ and j.

Note 23: The Profile Method can be improved by constructing n vectors $\vec{F}_{ref}$, instead of only one. This enables $n-1$ normal derivatives of Σ_E and Γ_E to be matched on S, as well as their values.

5 .4 Composite GENESIS: Correction of semi-analytic fields

The Semi-Analytic Method of Sec 5 .1 provides rapid solution of an *approximation* of the Euler equation. The solution (*e.g.* the D-Field) has three errors: the *spurious vorticity* $\vec{\Gamma}_D$ differs significantly from $\vec{\Gamma}_E$, the Euler vorticity; the *field source* Σ_D differs somewhat from Σ_E; and the *shock jump* differs somewhat from the R-H value, σ_r. We can remove or significantly reduce these errors, by combining this method with the Uncurling Method or the Profile Method.

The required Euler source Σ_E and vorticity $\vec{\Gamma}_E$ can be expressed as the sum of a *semi-analytic field* and a *corrective field.* Rather than restrict ourselves to the particular case of the D-Field, we use here a more general semi-analytic field $\vec{F}_{SA} = F_{SA}(U)\hat{i}$ [Hunt and Plybon, 1990]. We use the symbol m to denote the pseudo-Mach number U/c for this field, with c a general pseudo-sonic speed [Hunt and Adamson (1992a) also define a *C-Field*, with $c = a_\infty$ = constant.] Thus we have in this more general semi-analytic case:

$$\Sigma_E = m^2\partial U/\partial x + \Sigma_{CORR} \text{ and } \quad \Gamma_E = m^2\partial U/\partial z + \Gamma_{CORR} \quad (60)$$

At a point P, where the velocity is $\vec{V} = V_s\hat{s}$ with $\hat{s} = s_x, s_z$ the local streamline unit vector, let the *streamline curvature* be $\mathcal{K}$, with $\mathcal{K} > 0$ when the local streamline is concave when viewed from the body. It can be shown that Σ_{CORR} and Γ_{CORR} at P are given by:

$$\Sigma_{CORR} = (1 - m^2 s_z^2)\Sigma_E - m^2[C_2 DV_s + S_2(\mathcal{K}V_s - \tfrac{1}{2}\Gamma_E)]$$
$$\Gamma_{CORR} = (1 - m^2 s_x^2)\Gamma_E + m^2[C_2\mathcal{K}V_s - S_2(DV_s - \tfrac{1}{2}\Sigma_E)] \quad (61)$$

where $C_2 = s_x^2 - s_z^2$, $S_2 = 2s_x s_z$, and $DV_s \equiv dV_s/ds$ is the local velocity gradient evaluated in the direction $\hat{s}$. The Euler values Σ_E, $\vec{\Gamma}_E$, and thus the corrective fields Σ_{CORR}, Γ_{CORR} in (61), can be evaluated everywhere, as before, from the current estimate of $\vec{V}$.

A corrective field vector $\vec{F}_{CORR}$ equivalent to Σ_{CORR}, Γ_{CORR} can now be constructed, either *nominally exactly* (by the Uncurling Method, Sec 5 .2), or *approximately* (by the Profile Method, Sec 5 .3). The *composite* equivalent vector $\vec{F}$ is then the sum of the semi-analytic and corrective fields: $\vec{F} = F_{SA}\hat{i} + \vec{F}_{CORR}$. The (composite) equivalent boundary distributions are thus given by:

$$\sigma_F = -n_x F_{SA} + \sigma_{CORR} \quad \text{and} \quad \omega_F = -n_z F_{SA} + \omega_{CORR} \quad (62)$$
$$\text{where} \quad \sigma_{CORR} = -\hat{n}\cdot\vec{F}_{CORR} \quad \text{and} \quad \omega_{CORR} = -\hat{s}\cdot\vec{F}_{CORR}.$$

When the Semi-Analytic Method is based on the D-Field, *i.e.* $F_{SA} \equiv F_D$ [eq (30)], the procedure is almost exactly as in Sec 5 .1 , with the exception that, given the current estimate of the pseudo-Laplace function U', the D-Equation (31) to be solved at each point for U_{sub} or U_{sup} is now replaced by the *composite D-Equation*:

$$U - n_z^2 F_D(U) + U'_{CORR} = U' \quad \text{with} \quad U'_{CORR} = n_z\omega_{CORR}. \quad (63)$$

Here we are still using the same definition of the pseudo-Laplace function $U' = n_z V_s'$, but with V_s' [*i.e.* the pseudo-Laplace tangential velocity] now computed by SAVER with the *composite* boundary condition (prescribed source) $V_n' = \sigma_F = -n_x F_{SA} + \sigma_{CORR}$. This composite D-Equation can more conveniently be written:

$$U - n_z^2 F_D(U) = U'' \quad \text{where} \quad U'' = U' - U'_{CORR}. \quad (64)$$

The generic graph of (64) is identical to that in Fig 4 , but with U' replaced by U''. Thus it is now the maximum feasible value of U'' which is defined by the function on the r.h.s. of (32). Hence the local *maximum-feasible value* (limit) of the pseudo-Laplace function U', again symbolized as U_L', is defined for the *composite* D-Field by:

$$U_L' = \mu V_{max} - n_z^2(\lambda_m + \lambda_T) + U'_{CORR}. \quad (65)$$

The *maximum feasible increment* in the pseudo-Laplace function U' due to the (composite) boundary-condition increment σ_F, again symbolized as U_{FL}', still has the same symbolic form as (35), but with U_L' now defined by (65). The local *exceedance parameter* for the *composite* field has the same form as (37).

The scaling process defined in Sec 5 .1 .3 for "infeasible" flows [*i.e.* the adjustment of M_∞ when, for at least one point on the boundary, U' exceeds its local maximum-feasible value U_L' — now defined by (65)] is still fully applicable for the *composite* field, if the function U'_{CORR} in (63) and (65) is obtained using values established at the previous iteration, and is regarded as *frozen* for the current iteration. Once a (transonic) problem has been rendered feasible, the point P_T where the maximum exceedance $e_T' = \max(e') = 0$ occurs is now the sonic point of the *composite* field, *i.e.* the Euler field.

Inserting the (scaled) pseudo-Laplace function U' and the current estimate of U'_{CORR} into the second equation in (64), gives a new estimate of the (feasible) distribution U'', which then allows the (Euler) velocity field $\vec{V}$ to be updated (Sec 5 .1 .4). The value of U for the composite field (*i.e.* for the Euler field) is obtained at every point on the body boundary as the local subsonic or supersonic candidate solution U_{sub} or U_{sup} of (64); this is done exactly as described in Sec 5 .1 .4 , but with U' in (43) now replaced by U''. At convergence, the tangential velocity in the composite (Euler) field is obtained from the pseudo-Laplace solution, using (29) with the tangential velocity correction $\vec{\omega}_F$ now defined by (62).

6 SUMMARY

We have described the current status of the evolving GENESIS methodology. The GENESIS semi-analytic method offers a totally rational, boundary-only, nominally exact solution of a field approximating the transonic Euler equation, with a precise treatment of compression shocks and explicit suppression of expansion shocks. Uncorrected 2-D transonic results have been presented for this method, demonstrating its high speed and fidelity. Two corrective methods were introduced for the annihilation of the error field resulting from this semi-analytic method: one of them is nominally exact, and involves simple computations on a field mesh; the other is itself approximate, but involves only boundary computations. A proposed composite method embeds either of these corrective methods within the iteration cycle of the semi-analytic method. This offers the prospect of accurate, 2-D transonic Euler solutions for lifting bodies, with physically correct shock treatment, in a few seconds CPU time on a personal computer.

The extension to three-dimensions appears straightforward, building upon the existing power, flexibility and ease of use of the various 3-D panel codes available to the aerospace community. GENESIS could merely modify the boundary conditions satisfied by these existing codes, but significant advantage would be gained if the SAVER methodology were used to replace their existing singularity representations and solution algorithms. The resulting code would offer transonic 3-D Euler solutions for little more CPU time than current *linear* computations, for the same configurations.

Extension to arbitrary, unsteady motions also appears achievable. The mathematical identity underlying GENESIS relates to an arbitrary vector field, and can be applied equally validly to an *instantaneous snapshot* of a time-varying vector velocity field. The field source and vorticity terms, described here for only the steady-state case, would then also involve the evaluation of instantaneous time derivatives of some of the thermodynamic variables.

It can very plausibly be conjectured that generalized boundary-integral schemes may in the relatively near future be addressing compressible, rotational flow problems for three-dimensional multi-body configurations, in the general fields of *unsteady aerodynamics* and *aero-acoustics*. The way will then be open to general *multi-disciplinary* simulations, either on conventional computer architectures, or on vector machines—for which integral methods are particularly well suited (Hunt and Adamson, 1992c).

ACKNOWLEDGMENT The first author has engaged a number of his colleagues in discussions relating to some of the innovative concepts introduced in this paper, and would like to express particular thanks to *George Converse*, *Ron Plybon* and *Jim Keith* at GE Aircraft Engines, and to *Carson Yates* (NASA LaRC).

REFERENCES

Hunt B (1977), Relationships between volume, surface and line distributions of vorticity, source and doublicity. BAC(MAD) Report Ae/384.

Hunt B (1978), The panel method for subsonic aerodynamic flows: a survey of mathematical formulations and numerical models and an outline of the new BAe scheme. *Von Karman Institute Lecture Series* 1978–4.

Raj P, Gray RB (1979), Computation of three-dimensional potential flow using surface vorticity distribution. *J Aircraft* 16(3), 162–169.

Hunt B (1980a), The mathematical basis and numerical principles of the boundary integral method for incompressible potential flow over 3D aerodynamic configurations. In *Numerical Methods in Applied Fluid Dynamics*, Hunt (ed), Academic Press, London, UK, 49–136.

Hunt B (1980b), Recent and anticipated advances in the panel method: The key to generalised field calculations? *Von Karman Institute Lecture Series* 1980–5.

Hunt B (1982), The role of computational fluid dynamics in high-angle-of-attack aerodynamics. *AGARD Lecture Series* 121, 1982, 6.1–6.28

Hunt B, Plybon RC (1990), Generalization of the boundary integral method to nonlinear problems of compressible fluid flow: The no-mesh alternative. Part I: Maths; Part II: Physics. In *Boundary Element Methods in Engineering*, (Proc. *ISBEM*–89, East Hartford, USA, Oct 1989), BS Annigeri, K Tseng (eds); Springer-Verlag, Berlin, Germany, 147–160.

Hu H, Chu Li-C (1990), Unsteady three-dimensional transonic flow computations using field element method. In *Boundary Element Methods in Engineering*, (Proc. *ISBEM*–89, East Hartford, USA, Oct 1989), BS Annigeri, K Tseng (eds); Springer-Verlag, Berlin, Germany, 140–146.

Hunt B, (1991a), GENESIS: A mesh-free, knowledge-based, nonlinear BIM for compressible, viscous flows over arbitrary bodies: Theoretical framework and basic physical principles. In *Boundary Integral Methods: Theory and Applications*, (Proc. *IABEM*–90, Rome, Italy, Oct 1990), L Morino, R Piva (eds); Springer-Verlag, Berlin, Germany, 241–250.

Hunt B, (1991b), Knowledge-based, nonlinear boundary-integral models of compressible, viscous flows over arbitrary bodies: Taking CFD back to basics. In *Mechanics Pan-America 1991* (Proc. *PACAM*-2, Valparaiso, Chile, Jan 1991). PA Kittl, DT Mook (eds). AMR 44(11) Part 2 (Nov 1991), S130–S142.

Hunt B, Adamson AP (1992a), Current status of the GENESIS methodology for knowledge-based treatment of transonic flows, with emphasis on shock fitting and non-dissipative suppression of expansion shocks. In *Boundary Element Methods: Fundamentals and Applications*, (Proc. *IABEM*–91, Kyoto, Japan, Oct 1991), S Kobayashi, N Nishimura (eds); Springer–Verlag, Berlin, Germany, 111–120.

Hunt B, Adamson AP (1992b), Knowledge-based, mesh-free transonic flow computations using GENESIS. *IABEM–92*, Boulder, Colorado, Aug. 3–6, 1992.

Hunt B, Adamson AP (1992c), Boundary-integral methods as the basis for a unified, knowledge-based approach to multi-disciplinary, nonlinear, full-configuration modeling. *Comp. Aerosci. Conf.*, NASA Ames, Aug. 18–20, 1992.

Morino L, Iemma U (1993), Boundary integral equations and conservative dissipation schemes for full potential transonic flows. To appear in *Computational Mechanics* in 1993. (Short form "BEM for transonic flows" presented at *IABEM–92* as above.)

Variational-asymptotical analysis of initially curved and twisted composite beams

Carlos ES Cesnik and Dewey H Hodges

School of Aerospace Engineering, Georgia Institute of Technology, Atlanta GA 30332-0150

An asymptotically exact methodology, based on geometrically nonlinear, three-dimensional elasticity, is presented for cross-sectional analysis of initially curved and twisted, nonhomogeneous, anisotropic beams. Through accounting for all possible deformation in the three-dimensional representation, the analysis correctly accounts for the complex elastic coupling phenomena in anisotripic beams associated with shear deformation. The analysis is subject only to the restrictions that the strain is small relative to unity and that the maximum dimension of the cross section is small relative to the wave length of the deformation and to the minimum radius of curvature and/or twist. The resulting cross-sectional elastic constants exhibit first-order dependence on the initial curvature and twist. As is well known, the associated geometrically-exact, one-dimensional equilibrium and kinematical equations also depend on initial twist and curvature. Present numerical results show that it is insufficient to account for initial twist and curvature in the beam equations only. The corrections to the stiffness model derived herein are also necessary in general for proper representation of anisotropic beams.

INTRODUCTION

When a flexible structure has one dimension that is larger than the other two, it can often be treated as a beam, a one-dimensional structure. Many engineering structures can be idealized as beams, leading to much simpler equations than would be obtained if complete three-dimensional elasticity were used to model the structure. Although dimensional reduction processes can be extremely simple for homogeneous, isotropic, prismatic beams, and especially for restricted cases of deformation, they are far less tractable for composite beams undergoing arbitrary deformation. It is known that, in general, all possible deformations of the three-dimensional structure must be included in the formulation, as decribed by Giavotto *et al.* (1983) and Atılgan and Hodges (1991).

In this paper, we refer to all three-dimensional cross-sectional deformation as "warping" – whether the displacement is in the cross-sectional plane or out of it. All the components of warping in composite beams may be coupled. Also, there may be elastic couplings among all the global deformation components. This means that instead of 6 fundamental stiffnesses (extension, bending in the 2 principal directions, torsion, and shear in the 2 principal directions), there could be as many as 21 (a fully populated, symmetric 6×6 matrix). Furthermore, simple integrals over the cross section will not suffice to determine these elastic constants for the most general case. These complexities make the determination of the elastic constants (what is termed herein as "modeling") a much more difficult task.

There have been many investigators approaching the problem of a naturally curved and twisted beams in the literature, although no one has carried this out in a general way as it is proposed in this paper. Among them, Washizu (1964) considers the problem of an initially curved and twisted rod, but restricts it only to the homogeneous and isotropic case. Note, however, that Washizu deals with restrained warping, which is beyond the scope of our present work. Whitman and Cohen (1978) present an elegant approach to the problem, including the effects of initial stress, but they do not include any kind of warping in the kinematics. Berdichevsky and Staroselsky (1983) introduce the variational-asymptotic method to this problem, but limit their analysis to isotropic materials only. More recently, there are the works of Bauchau and Hong (1988) and Kosmatka (1991). Even though both works deal with nonhomogeneous anisotropic beams, they are restricted to thin-walled cross sections. Furthermore, the first one does not take into account in-plane warping, and the second one only considers initial twist. A more complete work is presented by Borri *et al.* (1992). They deal with initial twist as well as initial curvature for anisotropic beams and the formulation correctly accounts for generalized warping. It is an extension of Giavotto *et al.* (1983) and, therefore, based on the linear Saint-Venant approach. Hodges and Atılgan (1991) offer an overview of other works in this field.

In this paper, to further explore these issues, we present an anisotropic beam theory from geometrically nonlinear, three-dimensional elasticity. The kinematics are derived for arbitrary warping based upon the general framework of Danielson and Hodges (1987). Next, the three-dimensional strain energy based on this strain field is dimensionally reduced via the variational-asymptotical method of Berdichevsky (1981), which involves taking advantage of some small parameters. We consider only geometrically nonlinear theory, so that the maximum strain, ε, is small compared to unity. For the other two small parameters, we consider three lengths: h, a cross-sectional dimension, ℓ, the wavelength of the beam (one-dimensional) deformation, and R, the maximum radius of initial curvature and/or twist. In light of the slenderness of beamlike structures, we take the other two small parameters as $\frac{h}{\ell}$ and $\frac{h}{R}$.

The resulting equations govern both sectional and global deformation, as well as provide the three-dimensional displacement and strain fields in terms of beam deformation quantities. The formulation also naturally leads to geometrically exact, one-dimensional kinematical and intrinsic equilibrium equations for the beam deformation developed in Hodges (1990).

CROSS-SECTIONAL ANALYSIS

The kinematics of the beam are based on the general formulation of Danielson and Hodges (1987). Local rotation, as defined therein, is taken to be of the order of the strain. Since only geometrically nonlinear behavior is considered, the strain can be treated as small relative to unity without imposing any explicit restrictions on the magnitudes of the displacement of the reference line or the section rotation. Subject only to these restrictions, all possible deformations of beams are taken into account in the analysis.

The objective is to derive a strain energy function in terms of one-dimensional quantities only. To proceed, we first define the geometry of the undeformed beam and the displacement field. A typical point in the undeformed beam can be located by its arclength x_1 along a reference line r and its cross-sectional Cartesian coordinates x_2 and x_3 so that the position vector to an arbitrary point in the beam can be written as

$$\hat{\mathbf{r}}(x_1,x_2,x_3) = \mathbf{r}(x_1) + x_\alpha \mathbf{b}_\alpha(x_1) \tag{1}$$

where $\mathbf{r}(x_1)$ is the position vector to an arbitrary point on r. (Roman indices vary from 1 to 3, while Greek indices vary from 2 to 3; repeated indices are summed over their range.) The unit vectors $\mathbf{b}_\alpha(x_1)$ are parallel to planar Cartesian coordinates x_α in the plane of the reference cross section at a typical value of x_1; vectors $\mathbf{b}_i(x_1)$ form an orthonormal triad with $\mathbf{b}_1$ being perpendicular to the reference cross-sectional plane and tangent to r (see Fig 1).

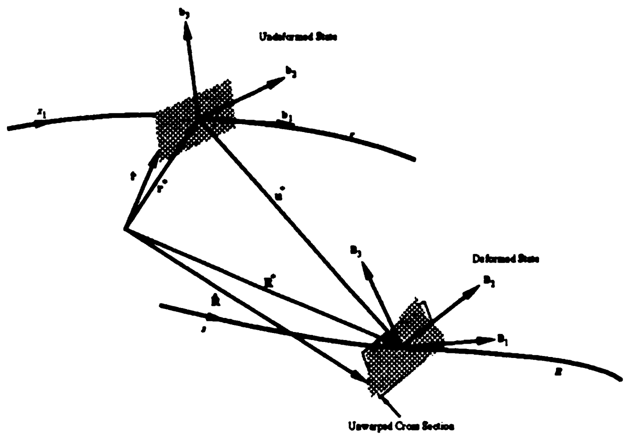

FIG 1. Schematic of beam deformation

Because of the arbitrary deformation, the material points that make up the reference cross section no longer stay exactly in a plane as the beam deforms. However, this set of points does lie very close to a plane, the orientation and displacement of which vary with the axial coordinate x_1. Since the characteristic length over which the deformation varies is assumed to be large relative to the largest cross section dimension, restrained warping (edge-zone) effects are not treated.

The position vector to an arbitrary point in the deformed beam can be then represented by

$$\begin{aligned}\hat{\mathbf{R}}(x_1,x_2,x_3) = \mathbf{R}(x_1) + x_\alpha \mathbf{B}_\alpha(x_1) \\ + w_i \mathbf{B}_i(x_1)\end{aligned} \tag{2}$$

where $\mathbf{R}(x_1) = \mathbf{r}(x_1)+\mathbf{u}(x_1)$, $\mathbf{u} = u_i\mathbf{b}_i$ is the displacement vector of points on the reference line r, and $w_i(x_1,x_2,x_3)$ is the general warping displacement of an arbitrary point in the cross section, consisting of both in- and out-of-plane components so that all possible deformations are considered. Eq (2) is six times redundant because of the manner in which warping is introduced; this redundancy is dealt with below. Note that $\mathbf{B}_1 = \mathbf{B}_2 \times \mathbf{B}_3$ is not in general tangent to the reference line of the deformed beam. The relationship between $\mathbf{B}_i$ and $\mathbf{b}_i$ is determined by

$$\mathbf{B}_i(x_1) = C_{ij}(x_1)\mathbf{b}_j(x_1) \tag{3}$$

where $C(x_1)$ is the matrix of direction cosines.

Further details of the kinematics are available in Danielson and Hodges (1987), where the three-dimensional strain field is developed in a particularly simple form when strain and local rotation are small

$$\Gamma^* = \frac{\chi + \chi^T}{2} - I \tag{4}$$

Here I is the 3×3 identity matrix, Γ^* is a 3×3 symmetric matrix with elements Γ^*_{ij}. The matrix χ is given by

$$\begin{aligned}\chi_{ij} &= \mathbf{B}_i \cdot \mathbf{G}_k \mathbf{g}^k \cdot \mathbf{b}_j \\ \mathbf{G}_i &= \frac{\partial \hat{\mathbf{R}}}{\partial x_i} \\ \mathbf{g}^i &= \frac{1}{2\sqrt{g}} e_{ijk} \frac{\partial \hat{\mathbf{r}}}{\partial x_j} \times \frac{\partial \hat{\mathbf{r}}}{\partial x_k}\end{aligned} \tag{5}$$

where $\sqrt{g} = 1 - x_2k_3 + x_3k_2 > 0$, e_{ijk} is the permutation symbol, and k_α are measure numbers in the $\mathbf{b}_i$ basis of the initial curvature of the undeformed beam. Introducing the initial twist k_1 and column matrices w, k, and ξ, containing, respectively, the components w_i, k_i, and $\lfloor 0 \ x_2 \ x_3 \rfloor^T$, one can express the strain field as a 6×1 column matrix $\Gamma = \lfloor \Gamma^*_{11} \ 2\Gamma^*_{12} \ 2\Gamma^*_{13} \ \Gamma^*_{22} \ 2\Gamma^*_{23} \ \Gamma^*_{33} \rfloor^T$ so that

$$\Gamma = \begin{bmatrix} \frac{1}{\sqrt{g}} I & -\frac{1}{\sqrt{g}}\tilde{\xi} \\ 0 & 0 \end{bmatrix} \begin{Bmatrix} \gamma \\ \kappa \end{Bmatrix} + \begin{bmatrix} \frac{1}{\sqrt{g}} I \\ 0 \end{bmatrix} w' + \begin{bmatrix} \partial_1 \\ \partial_2 \end{bmatrix} w$$

$$\partial_1 \triangleq \frac{1}{\sqrt{g}}\tilde{k} + \frac{k_1 I}{\sqrt{g}}\left(x_3\frac{\partial}{\partial x_2} - x_2\frac{\partial}{\partial x_3}\right) + \begin{bmatrix} 0 & 0 & 0 \\ \frac{\partial}{\partial x_2} & 0 & 0 \\ \frac{\partial}{\partial x_3} & 0 & 0 \end{bmatrix} \tag{6}$$

$$\partial_2 \triangleq \begin{bmatrix} 0 & \frac{\partial}{\partial x_2} & 0 \\ 0 & \frac{\partial}{\partial x_3} & \frac{\partial}{\partial x_2} \\ 0 & 0 & \frac{\partial}{\partial x_3} \end{bmatrix}$$

where $\widetilde{(\ )}_{ij} = -e_{ijk}(\ )_k$; $\gamma = \lfloor \gamma_{11} \ 2\gamma_{12} \ 2\gamma_{13} \rfloor^T$ and $\kappa = \lfloor \kappa_1 \ \kappa_2 \ \kappa_3 \rfloor^T$, the so-called force and moment strain measures. Note that γ_{11} is an extensional strain measure, $2\gamma_{1\alpha}$ are a shear strain measure, κ_1 is the elastic twist per unit length, and κ_α are the elastic components of the bending curvature. These strain measures can be expressed in matrix form as

$$\begin{aligned}\gamma &= C(e_1 + u' + \tilde{k}u) - e_1 \\ \tilde{\kappa} &= -C'C^T + C\tilde{k}C^T - \tilde{k}\end{aligned} \tag{7}$$

Here $u = \lfloor u_1\ u_2\ u_3 \rfloor^T$ and $e_1 = \lfloor 1\ 0\ 0 \rfloor^T$. The force and moment strain measures are so designated because they are conjugate to the actual section force and moment, respectively.

Since warping displacements are very small relative to the cross section dimensions, the few nonlinear terms in the strain field, which couple w and κ, are of higher order and have been neglected in Eq (6). The form of the strain field is of great importance because it is now linear in γ, κ, and w_i and its derivatives.

VARIATIONAL-ASYMPTOTICAL FORMULATION

In constructing a one-dimensional beam theory from three-dimensional elasticity, we attempt to represent the strain energy stored in a three-dimensional body by finding the strain energy which would be stored in an imaginary one-dimensional body.

This modeling process cannot be performed in an exact manner. However, due to the interest of working with a simple one-dimensional theory, researchers have turned to asymptotical methods in order to reduce the dimension of the model for bodies which contain one or more small parameters. Beams are such bodies, because the characteristic cross-sectional dimension of the beam is much smaller than its length.

Thus, in what follows we replace the three-dimensional beam problem by an *approximate* one-dimensional one in which the strain energy per unit length will be a function only of x_1. This will be done with the aid of the variational-asymptotical formulation of Berdichevsky (1981). (See Atılgan *et al.* 1991 for additional discussion of this methodology.)

The strain energy per unit length can then be written as

$$U = \frac{1}{2}\langle Z^T \Gamma \sqrt{g}\rangle \tag{8}$$

where the angle brackets signify the integral over the cross sectional area, Z is the three-dimensional Jaumann stress, which is conjugate to the Jaumann strain (Γ)

$$Z = D\Gamma \tag{9}$$

and D is the 6×6 symmetric material matrix. This functional is to be minimized with the following constraints

$$\begin{aligned}\langle w_i\rangle &= 0\\ \langle w_{2,3} - w_{3,2}\rangle &= 0\\ \langle \xi_\alpha w_1\rangle &= 0\end{aligned} \tag{10}$$

which are discussed in more detail in Hodges *et al.* (1992).

Assuming small to moderate curvatures, one can take

$$(\sqrt{g})^{-1} \approx 1 + x_2 k_3 - x_3 k_2$$

so that $O(\frac{h^2}{R^2})$ terms are neglected, where $R = (k^T k)^{-\frac{1}{2}}$.

Let us first consider the case where the strain energy is approximated so that all terms of higher order than $O(\frac{\mu \varepsilon^2 h^2}{R^2})$, as well as all $\frac{h}{l}$ contributions, are ignored. So, the strains must be developed to include all terms that are $O(\varepsilon)$ and $O(\frac{h\varepsilon}{R})$. With these considerations, the Jaumann strain can be approximated as

$$\Gamma = X\epsilon + \partial w + X_k\epsilon + \partial_k w \tag{11}$$

where

$$\begin{aligned}
X &\triangleq \begin{bmatrix} I & -\widetilde{\xi} \\ 0 & 0 \end{bmatrix} \qquad \epsilon \triangleq \lfloor \gamma\ \ \kappa \rfloor^T\\
X_k &\triangleq X(x_2k_3 - x_3k_2)\\
\partial &\triangleq \begin{bmatrix} 0 & 0 & 0\\ \frac{\partial}{\partial x_2} & 0 & 0\\ \frac{\partial}{\partial x_3} & 0 & 0\\ 0 & \frac{\partial}{\partial x_2} & 0\\ 0 & \frac{\partial}{\partial x_3} & \frac{\partial}{\partial x_2}\\ 0 & 0 & \frac{\partial}{\partial x_3} \end{bmatrix}\\
\partial_k &\triangleq \begin{bmatrix} \widetilde{k} + Ik_1\left(x_3\frac{\partial}{\partial x_2} - x_2\frac{\partial}{\partial x_3}\right)\\ 0 \end{bmatrix}
\end{aligned} \tag{12}$$

The presence of the warping in the above creates practical difficulties because it is a three-dimensional quantity. Thus, we must eliminate the warping, and we do so using a combination of the variational-asymptotical method, originally developed by Berdichevsky (1981), and the finite element method, following Hodges *et al.* (1992). First, the warping can be discretized by using the finite element technique. Let

$$w = SW \tag{13}$$

in which the matrix S contains the shape functions and W is the nodal displacement column matrix. Now the strain becomes

$$\Gamma = X\epsilon + BW + X_k\epsilon + B_kW \tag{14}$$

where

$$B \triangleq \partial S \qquad B_k \triangleq \partial_k S \tag{15}$$

In terms of energy density

$$\begin{aligned}\delta U =& \langle(\delta\epsilon^T X^T + \delta W^T B^T + \delta\epsilon^T {X_k}^T\\ &+ \delta W^T {B_k}^T)D(X\epsilon + BW + X_k\epsilon\\ &+ B_kW)\,(1 - x_2k_3 + x_3k_2)\rangle\end{aligned} \tag{16}$$

We can now rewrite the strain energy density in terms of the new matrices defined in the Appendix

$$\begin{aligned}\delta U =& \delta\epsilon^T(A\epsilon + R^TW + {C_k}^T\epsilon + {R_k}^TW\\
&+ C_k\epsilon + {L_k}^TW + G_k\epsilon + {M_k}^TW)\\
&+ \delta W^T(R\epsilon + EW + L_k\epsilon + F_kW\\
&+ R_k\epsilon + {F_k}^TW + M_k\epsilon + E_kW)\\
&+ \delta\epsilon^T(\bar{A}\epsilon + \bar{R}^TW + \bar{C}_k^T\epsilon + \bar{R}_k^TW\\
&+ \bar{C}_k^T\epsilon + \bar{L}_k^TW + \bar{G}_k^T\epsilon + \bar{M}_k^TW)\\
&+ \delta W^T(\bar{R}\epsilon + \bar{E}W + \bar{L}_k\epsilon + \bar{F}_kW\\
&+ \bar{R}_k\epsilon + \bar{F}_k^TW + \bar{M}_k\epsilon + \bar{E}_kW)\end{aligned} \tag{17}$$

Noticing that every $(\bar{\ })$ term is one order higher than the correspondent ( ), the above functional can be approximated asymptotically by

$$\begin{aligned}\delta U =& \delta\epsilon^T(A\epsilon + R^T W) \\ &+ \delta W^T(R\epsilon + EW)\end{aligned} \tag{18}$$

which is exactly the same expression obtained for the first approximation without initial twist or curvature by Hodges *et al.* (1992). Therefore,

$$W = -E^{-1}R\epsilon \tag{19}$$

which is $O(\varepsilon)$. Note here that in order to solve for the warping in this manner, the six constraints defined by Eq (10) were first applied to W in the energy.

Now, substitute Eq (19) into the original energy density functional (Eq (17))

$$\begin{aligned}\delta U =& \delta\epsilon^T[A - R^T E^{-1}R + \bar{A} + 2C_k \\ &- {R_k}^T E^{-1}R - (E^{-1}R)^T R_k \\ &- \bar{R}^T E^{-1}R - (E^{-1}R)^T\bar{R} \\ &- (E^{-1}R)^T L_k - {L_k}^T(E^{-1}R) \\ &+ (E^{-1}R)^T(F_k + {F_k}^T)(E^{-1}R) \\ &+ (E^{-1}R)^T(\bar{E})(E^{-1}R) + G_k \\ &- {M_k}^T(E^{-1}R) - (E^{-1}R)^T M_k \\ &+ (E^{-1}R)^T E_k(E^{-1}R) + 2{C_k}^T \\ &- {\bar{R}_k}{}^T E^{-1}R - (E^{-1}R)^T\bar{R}_k \\ &- (E^{-1}R)^T\bar{L}_k - {\bar{L}_k}{}^T(E^{-1}R) \\ &+ (E^{-1}R)^T(\bar{F}_k + {\bar{F}_k}{}^T)(E^{-1}R) \\ &+ \bar{G}_k - \bar{M}_k(E^{-1}R) \\ &- (E^{-1}R)^T\bar{M}_k \\ &+ (E^{-1}R)^T\bar{E}_k(E^{-1}R)]\epsilon\end{aligned} \tag{20}$$

which directly leads us to the candidate for the first approximation

$$\delta U_1 = \delta\epsilon^T(A - R^T E^{-1}R)\epsilon \tag{21}$$

The next step is to go to the second approximation with the substitution

$$W = -E^{-1}R\epsilon + V \tag{22}$$

where V is the perturbation of the previous solution. It can be shown that

$$\begin{aligned}V =& -E^{-1}[L_k + R_k - \bar{E}E^{-1}R \\ &- (F_k + {F_k}^T)E^{-1}R]\epsilon\end{aligned} \tag{23}$$

which is $O(\frac{h\epsilon}{R})$, *i.e.*, one order higher than W. This leads us to two important conclusions: (a) Eq (21) is *the* first approximation of Eq (16); and (b) all terms in the Eq (20) that include V are of order $(\frac{h}{R})^2$ or smaller relative to the leading terms. This means that they can be neglected for the level of approximation sought here. We note that W, Γ, and Z can now be calculated to first order in $\frac{h}{R}$.

Analogous to what was done above, the second approximation can be written as

$$\begin{aligned}\delta U_2 =& \delta\epsilon^T[(A - R^T E^{-1}R) + C_k \\ &+ (E^{-1}R)^T(F_k + {F_k}^T)(E^{-1}R) \\ &- (E^{-1}R)^T R_k - {R_k}^T(E^{-1}R) \\ &+ (E^{-1}R)^T\bar{E}(E^{-1}R)]\epsilon\end{aligned} \tag{24}$$

Therefore, for the second approximation, the strain energy density can be written as

$$2U = \epsilon^T\hat{S}\epsilon \tag{25}$$

where

$$\begin{aligned}\hat{S} =& A - R^T E^{-1}R + C_k \\ &+ (E^{-1}R)^T(F_k + {F_k}^T)(E^{-1}R) \\ &- (E^{-1}R)^T R_k - {R_k}^T(E^{-1}R) \\ &+ (E^{-1}R)^T\bar{E}(E^{-1}R)\end{aligned} \tag{26}$$

from where one can easily see that the initial curvature and twist do change the sectional stiffness matrix to first order in $\frac{h}{R}$.

Finally, we note that under certain circumstances $\hat{S}$ can be reduced, as noted by Hodges *et al.* (1992). This matrix is 6×6 because of the presence of shear deformation. There are also transverse shear related effects associated with slenderness, which are accounted for in higher asymptotical approximations. Thus, for slender beams one may not need to use the full 6×6 form of $\hat{S}$. Minimization of $\hat{S}$ with respect to the transverse shear measures $2\gamma_{1\alpha}$ produces a 4×4 stiffness matrix denoted by $\mathcal{S}$. This minimization is equivalent to undertaking the following operations on the stiffness matrix: (1) invert the 6×6 matrix; (2) ignore the rows and columns associated with transverse shear, leaving a 4×4 matrix; (3) invert this resulting 4×4 matrix yielding the "reduced" stiffness matrix associated with extension, torsion, and two bending measures. The result is an approximate strain energy per unit length of the form

$$2U^* = \begin{Bmatrix}\gamma_{11} \\ K\end{Bmatrix}^T [\mathcal{S}] \begin{Bmatrix}\gamma_{11} \\ K\end{Bmatrix} \tag{27}$$

Thus, the strain energy is in the same *form* as in classical theory (which has no transverse shear deformation in the one-dimensional energy). However, the appropriate coupling effects involving transverse shear, first noted by Rehfield *et al.* (1990), are present in Eq (27); and the numerical values of the resultant elastic constants can differ considerably from those of a "classical" theory, in which shear deformation is set equal to zero at the outset. This reduction is suitable for slender beams undergoing low-frequency (i.e., long wavelength) vibration.

APPLICATIONS

A cross-sectional analysis computer code called VABS (*V*ariational-*A*symptotical *B*eam *S*ectional Analysis) has been developed based upon the theoretical formulation presented herein. From it one gets a reduced, asymptotically correct stiffness matrix and warping displacements for a general, nonhomogeneous, anisotropic beam cross section. The discretization of the cross-sectional domain is made with the finite element technique. The element which has been developed is four-noded, planar, and rectangular, with three degrees of freedom per node. The algebraic operations at the element level, including element quadrature, were carried out via symbolic manipulation by using *Mathematica* (see Wolfram 1988).

VABS has been verified before for prismatic anisotropic beams and its results agree very well with experimental data as shown by Hodges *et al.* (1992). Here, the code is first verified for an isotropic square cross section with dimensions 2.0×10^{-2} m by 2.0×10^{-2} m. The material properties are assumed to be $E = 26$ MPa and $\nu = 0.3$.

To present results for initially curved and twisted beams, we examine the isotropic case for which closed-form solutions for the Saint-Venant stiffnesses are known. For small to moderate initial twist or curvature (small $\frac{h}{R}$ ratio), there is no change in the diagonal terms of the stiffness matrix (namely extension, twist and bending stiffnesses) when compared to the prismatic ones. However, there is extension-twist coupling due to initial twist and extension-bending coupling due to initial curvature. These are given in closed form by Berdichevsky and Staroselsky (1983)

$$\begin{aligned} \hat{S}_{14} &= E(I_{22} + I_{33} - J)\, k_1 \\ \hat{S}_{15} &= -\,(1+\nu)EI_{22}\, k_2 \\ \hat{S}_{16} &= -\,(1+\nu)EI_{33}\, k_3 \end{aligned} \tag{28}$$

and are used as baseline values for the present results.

Some sample results are shown here for the sake of evaluating the convergence of the finite element method for determining the stiffness constants as a function of the mesh refinement. We show the convergence only for coupling terms which arise from initial twist and curvature. The error taken is defined as

$$\text{Relative Error} = \left| \frac{S_{VABS} - S_{exact}}{S_{exact}} \right| \tag{29}$$

where S_{exact} is the exact stiffnesses for an isotropic beam.

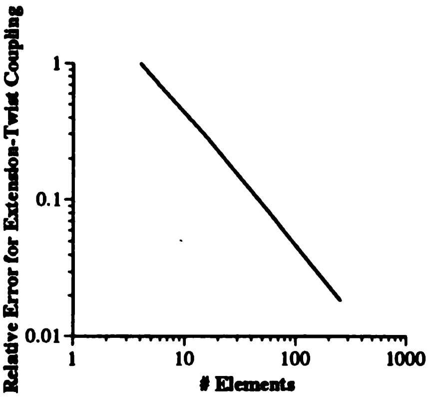

FIG 2. Convergence history of the extension-twist stiffness term due to initial twist.

Fig 2 describes the convergence behavior of the extension-twist coupling term for nonzero initial twist. Similarly, Fig 3 deals with the extension-bending coupling term for nonzero initial curvature. For these plots, S_{exact} in Eq (29) is taken from Eq (28). As one can see from the results, the relative errors decrese linearly on a logarithmic scale with respect to the number of elements. The slope of the line indicates a relative error that is approximately inversely proportional to the number of elements. The extension-twist coupling involves the torsional stiffness, which is less accurate than the bending stiffness for the same number of elements in the mesh. This is reflected in the larger error in the calculation of the extension-twist coupling. However, the relative error for all the terms is still smaller than 2% for 100 elements (a 10×10 mesh).

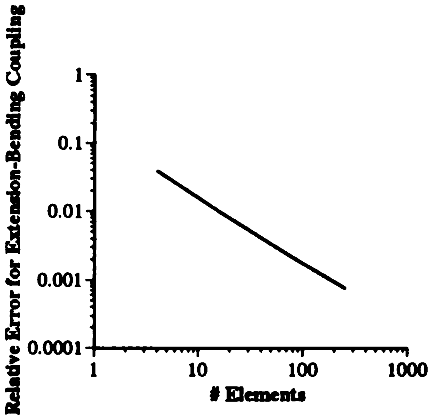

FIG 3. Convergence history of the extension-bending stiffness due to initial curvature.

Now, let us consider two composite beams studied both experimentally and theoretically by Minguet (1989). The two layups for these beams are defined as

(BT): $[45°/0°]_{3s}$

(ET): $[20°/-70°/-70°/20°]_{2a}$

where BT reflects the fact that the prismatic beam has bending-twist coupling and ET that the prismatic beam has extension-twist coupling. The beams have thin rectangular cross sections of width 30.023 mm and of thickness 1.4712 mm and 1.9215 mm, respectively. The material used is AS4/3501-6 Graphite/Epoxy, the properties of which are given in Table I.

TABLE I. Properties of AS4/3501-6 Graphite/Epoxy ("L" direction is along the fibers and "N" is normal to the laminate)

$E_{LL} = 142$ GPa	$E_{TT} = E_{NN} = 9.80$ GPa
$G_{LT} = G_{LN} = 6.00$ GPa	$G_{TN} = 4.80$ GPa
$\nu_{LT} = \nu_{LN} = 0.3$	$\nu_{TN} = 0.34$

The resulting stiffness constants are given in Tables II and III. The first column contains the results for a prismatic beam from NABSA (*N*onhomogeneous *A*nisotropic *B*eam *S*ection *A*nalysis), which is based in Giavotto *et al.* (1983). The second column contains similar results from VABS. Notice that the stiffnesses for the prismatic case are all very close to each other except the shear stiffness constants. This is already expected considering the fact that VABS ignores terms in the strain energy of first and higher orders in $\frac{h}{l}$ while NABSA treats the Saint-Venant flexure solution, equivalent to retaining terms of second order in $\frac{h}{l}$. Based on the study of the effects of these terms by Hodges *et al.* (1992) for static behavior of certain composite beams, it is believed that these differences will not make any noticeable differences in the results for static and low-frequency dynamic analysis of composite beams.

Now consider the remaining three columns. These are results from VABS for the coefficients of k_i in the stiffness constants. To get the stiffness coefficient for any given element of the stiffness matrix, multiply the value of k_i times the appropriate column, *i.e.*,

$$\hat{S} = \hat{S}^0 + k_i\,\hat{S}^\Delta \tag{30}$$

where $\hat{S}^0$ is the stiffness contribution from the prismatic solution and $\hat{S}^\Delta$ is the one correspondent to the Δ $\mathbf{VABS}_{k_i}$ column.

TABLE II. Stiffness results (N, N m, and N m^2) for (BT)
(1 extension; 2, 3 shear; 4 torsion; 5, 6 bending)

$\hat{S}$	NABSA	VABS	Δ $\mathbf{VABS}_{k_1}$	Δ $\mathbf{VABS}_{k_2}$	Δ $\mathbf{VABS}_{k_3}$
$\hat{S}_{11}$	3.6097×10^6	3.6102×10^6	–	–	–
$\hat{S}_{12}$	-2.0706×10^5	-2.0840×10^5	–	–	–
$\hat{S}_{14}$	–	–	9.8127×10^3	7.8316×10^1	1.2842×10^2
$\hat{S}_{15}$	–	–	3.5885×10^2	-6.3885×10^1	-6.6953×10^1
$\hat{S}_{16}$	–	–	–	–	-1.7436×10^4
$\hat{S}_{22}$	4.1671×10^5	4.1938×10^5	–	–	–
$\hat{S}_{24}$	–	–	-8.7215×10^2	1.5205×10^2	2.5090×10^2
$\hat{S}_{25}$	–	–	6.6052×10^2	-7.7677×10^1	-1.3465×10^2
$\hat{S}_{26}$	–	–	–	–	-6.6630×10^3
$\hat{S}_{33}$	3.0613×10^4	2.1102×10^5	–	–	–
$\hat{S}_{34}$	–	–	–	–	6.2392×10^2
$\hat{S}_{36}$	–	–	-1.3765×10^3	2.2591×10^2	-2.0692×10^1
$\hat{S}_{44}$	3.5901×10^{-1}	3.7020×10^{-1}	–	–	–
$\hat{S}_{45}$	9.9152×10^{-2}	1.0483×10^{-1}	–	–	–
$\hat{S}_{26}$	–	–	–	–	3.2658×10^{-1}
$\hat{S}_{55}$	5.3149×10^{-1}	5.3493×10^{-1}	–	–	–
$\hat{S}_{66}$	2.6339×10^2	2.6342×10^2	–	–	–

TABLE III. Stiffness results (N, N m, and N m^2) for (ET)
(1 extension; 2, 3 shear; 4 torsion; 5, 6 bending)

$\hat{S}$	NABSA	VABS	Δ $\mathbf{VABS}_{k_1}$	Δ $\mathbf{VABS}_{k_2}$	Δ $\mathbf{VABS}_{k_3}$
$\hat{S}_{11}$	3.3740×10^6	3.3780×10^6	3.3982×10^5	–	–
$\hat{S}_{12}$	–	–	–	4.0044×10^4	–
$\hat{S}_{13}$	–	–	–	–	9.1980×10^2
$\hat{S}_{14}$	-9.7020×10^2	-9.7200×10^2	9.4172×10^3	–	–
$\hat{S}_{15}$	–	–	–	-9.7921×10^1	–
$\hat{S}_{16}$	–	–	–	–	-1.1972×10^4
$\hat{S}_{22}$	5.8894×10^5	7.6509×10^5	-1.4557×10^6	–	–
$\hat{S}_{24}$	–	–	–	-4.7823×10^1	–
$\hat{S}_{25}$	4.1081×10^2	4.3770×10^2	8.8435×10^0	–	–
$\hat{S}_{33}$	4.4242×10^4	2.5711×10^5	–	–	–
$\hat{S}_{34}$	–	–	–	–	7.6086×10^2
$\hat{S}_{36}$	7.0107×10^0	2.2868×10^{-5}	-2.5669×10^3	–	–
$\hat{S}_{44}$	1.0547×10^0	1.6383×10^0	-5.0193×10^0	–	–
$\hat{S}_{45}$	–	–	–	5.6113×10^{-2}	–
$\hat{S}_{46}$	–	–	–	–	2.8158×10^0
$\hat{S}_{55}$	1.0796×10^0	1.0475×10^0	5.0080×10^{-1}	–	–
$\hat{S}_{66}$	2.4279×10^2	2.4367×10^2	3.9801×10^1	–	–

As one can see, Tables II and III show that the presence of initial twist and curvature introduces new couplings among the one-dimensional deformation measures. Beams of this size have h about 30 mm; so that $\frac{h}{R}$ does not exceed about 0.12, and, therefore, $\sqrt{k^T k}$ should not exceed about 4.0 rad/m. Even though the new terms are of lower orders of magnitude when compared to the main diagonal terms (keeping in mind the unit system used herein), their presence can have important effects when larger pretwist is considered (see Kosmatka 1991). For example, note the contribution of the extension-twist coupling due to the presence of the pretwist in Table III. Even for small pretwist, the extension-twist coupling can be increased by 10%. Not only is it possible to alter *existing* couplings, new couplings can appear where there were no couplings present at all in the prismatic beam. For example, extension-twist coupling shows up in Table II, and extension-bending coupling shows up in Table III.

The most important issue in evaluation of the contribution of the first-order correction terms to the stiffness constants is whether these terms have any noticeable effects on the predicted deformation of the beam. Consider the beams, which are essentially thin strips, with fixed-free boundary conditions and with two possible load cases: a transverse force applied perpendicular to the strip, and an axial load applied along the strip, both at the beam tip. Two levels of load are applied: one small (in the linear range) and one large (in the geometrically nonlinear range). A representative sample of the results obtained are presented herein.

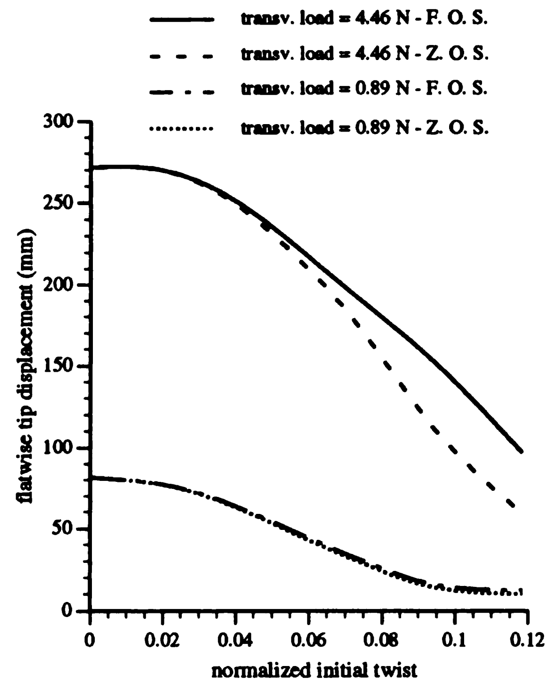

FIG 5. Flatwise tip displacement due to transverse load for BT beam.
Note: F.O.S. = first-order stiffness matrix.
Z.O.S. = zeroth-order stiffness matrix.

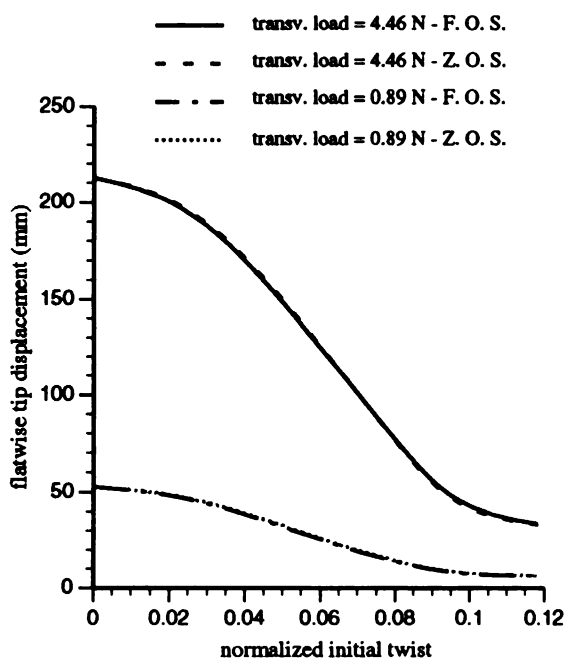

FIG 4. Flatwise tip displacement due to transverse load for ET beam.
Note: F.O.S. = first-order stiffness matrix.
Z.O.S. = zeroth-order stiffness matrix.

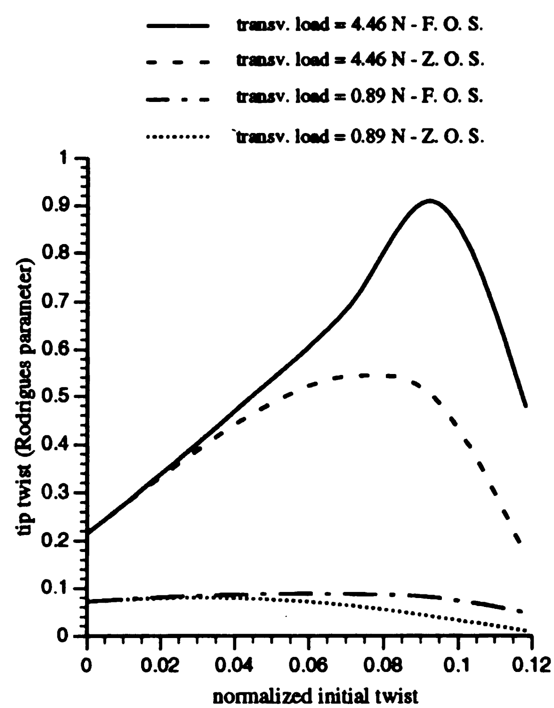

FIG 6. Rodrigues parameter corresponding to tip twist due to transverse load for BT beam.
Note: F.O.S. = first-order stiffness matrix.
Z.O.S. = zeroth-order stiffness matrix.

Figs 4 and 5 show the flatwise tip displacement for the ET and BT beams, respectively, for both transverse loads – with and without the first-order correction to the stiffness matrix – versus the normalized initial twist hk_1. According to Fig 4, the effect of the first-order correction to the stiffness model is negligibly small for both small and large loading. However, according to Fig 5, the effect of the first-order correction to the stiffness in the BT beam cannot be ignored for the large load, in the geometrically nonlinear range. The twist deformation seems to be more sensitive to these terms. In Fig 6 the Rodrigues parameter which corresponds to the twist of the tip (which is the twist angle for small deformation) is shown versus the normalized initial twist hk_1. Here we see that even small loading, in the linear range, is strongly affected by the first-order correction terms in the stiffness matrix.

In the case of initial curvature, one of the worst cases appears to be the effect of inplane curvature (k_3) on the edgewise displacement, in the presence of an axial force. In Fig 7 the edgewise displacement at the tip of the ET beam is shown for two levels of axial force applied at the tip versus the normalized initial inplane curvature of the beam hk_3. Here the error is smaller than with the initial twist, but not negligible, and is worse for the larger load.

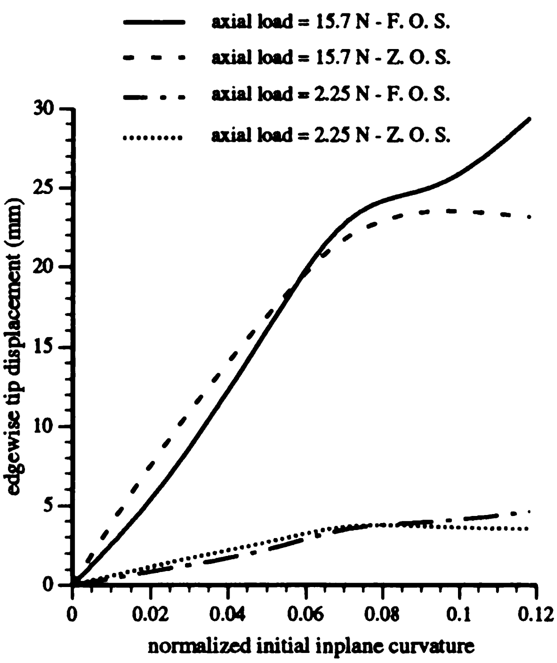

FIG 7. Edgewise tip displacement due to axial load for ET beam.
Note: F.O.S. = first-order stiffness matrix.
Z.O.S. = zeroth-order stiffness matrix.

the total energy remains less than 3% for the ET beam, while for the BT beam it reaches approximately 30%.

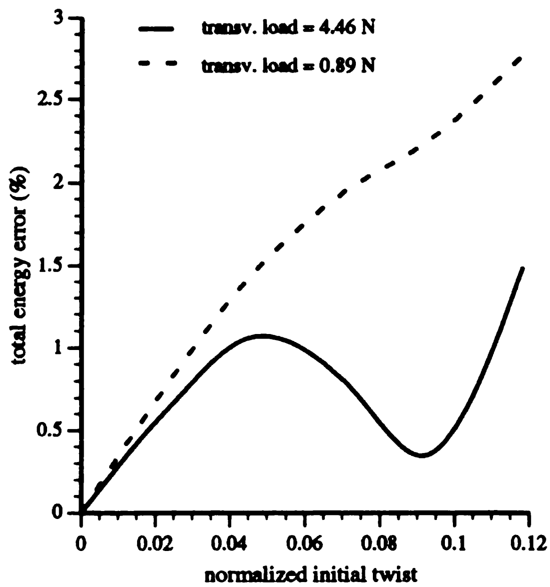

FIG 8. Total energy due to transverse load for ET beam.

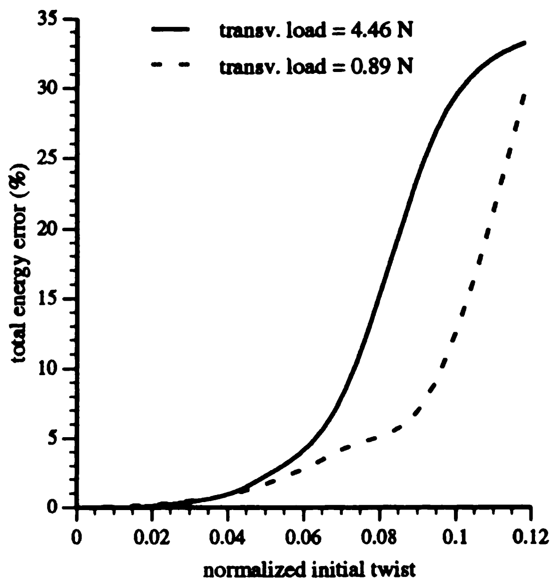

FIG 9. Total energy due to transverse load for EB beam.

The total strain and potential energy in the loaded beam is a convenient way to quantify the effects of initial curvature and twist. Figs 8 and 9 show the total energy of the ET and BT beams, respectively, versus the normalized initial twist hk_1. The error in

These results clearly show that a naïve approach in which one uses stiffness constants from a prismatic beam sectional analysis in the geometrically-exact one-dimensional equilibrium and kinematical equations for initially curved and twisted beams, the results will not be correct in general. The section constants must include the first-order correction terms due to initial curvature and twist. Judging from the size of the errors from initial twist, it is noted that second-order corrections to the stiffness may be needed for it.

CONCLUDING REMARKS

An asymptotically exact methodology, based on geometrically nonlinear, three-dimensional elasticity, is presented for analysis of initially curved and twisted, nonhomogeneous, anisotropic beams. The analysis is subject only to the restrictions that the strain is small relative to unity and that the maximum dimension of the cross section is small relative to a length parameter (thus, restrained warping effects are not considered) and to the minimum radius of curvature and/or twist. A two-dimensional functional is derived which enables the determination of sectional elastic constants, as well as relations between the beam (*i.e.*, one-dimensional) displacement and generalized strain measures and the three-dimensional displacement and strain fields. The initial twist and curvature not only appear in the equilibrium and kinematical equations, but they also influence the sectional modeling, as shown in the final form of the stiffness matrix. A cross-sectional analysis code called VABS (*V*ariational-*A*symptotical *B*eam *S*ectional Analysis) has been developed based upon the theoretical formulation presented herein, from which one gets an asymptotically correct stiffness matrix and warping displacements for a general, nonhomogeneous, anisotropic beam cross section. Numerical results were obtained first for an isotropic beam, which converge to the asymptotic closed-form solution for the stiffnesses. Then, two laminated cases were analyzed, showing the influence of the initial twist and curvature in the elastic constants. It is concluded that for any general-purpose analysis of composite beams, the effects of initial curvature and twist need to be included in all aspects of the analysis. That is, one cannot simply use the geometrically-exact equilibrium and kinematical equations for initially curved and twisted beams with sectional constants calculated from a prismatic beam.

ACKNOWLEDGEMENTS

Technical discussions with Prof. Victor L. Berdichevsky and Mr. Xiaoyang Shang of Georgia Institute of Technology and Prof. Ali R. Atılgan of Istanbul Technical University are gratefully acknowledged. The computer program of Mr. Shang was used in the generation of the one-dimensional results presented herein. This work was supported by the U.S. Army Research Office under contracts DAAL03-88-C-0003 (the Center of Excellence for Rotary Wing Aircraft Technology), by the CNPq (Conselho Nacional de Desenvolvimento Científico e Technológico), and by EMBRAER (Empresa Brasileira de Aeronáutia S.A.).

APPENDIX

The matrices used in Eq (17) are defined as

$$A \triangleq \langle X^T D X \rangle \qquad \bar{A} \triangleq \langle X^T D X \, (-x_2 k_3 + x_3 k_2) \rangle$$

$$R \triangleq \langle B^T D X \rangle \qquad \bar{R} \triangleq \langle B^T D X \, (-x_2 k_3 + x_3 k_2) \rangle$$

$$E \triangleq \langle B^T D B \rangle \qquad \bar{E} \triangleq \langle B^T D B \, (-x_2 k_3 + x_3 k_2) \rangle$$

$$E_k \triangleq \langle {B_k}^T D B_k \rangle \qquad \bar{E}_k \triangleq \langle {B_k}^T D B_k \, (-x_2 k_3 + x_3 k_2) \rangle$$

$$R_k \triangleq \langle {B_k}^T D X \rangle \qquad \bar{R}_k \triangleq \langle {B_k}^T D X \, (-x_2 k_3 + x_3 k_2) \rangle$$

$$F_k \triangleq \langle B^T D B_k \rangle \qquad \bar{F}_k \triangleq \langle B^T D B_k \, (-x_2 k_3 + x_3 k_2) \rangle$$

$$C_k \triangleq \langle {X_k}^T D X \rangle \qquad \bar{C}_k \triangleq \langle {X_k}^T D X \, (-x_2 k_3 + x_3 k_2) \rangle$$

$$G_k \triangleq \langle {X_k}^T D X_k \rangle \qquad \bar{G}_k \triangleq \langle {X_k}^T D X_k \, (-x_2 k_3 + x_3 k_2) \rangle$$

$$L_k \triangleq \langle B^T D X_k \rangle \qquad \bar{L}_k \triangleq \langle B^T D X_k \, (-x_2 k_3 + x_3 k_2) \rangle$$

$$M_k \triangleq \langle {B_k}^T D X_k \rangle \qquad \bar{M}_k \triangleq \langle {B_k}^T D X_k \, (-x_2 k_3 + x_3 k_2) \rangle$$

REFERENCES

Atılgan, A. R., and Hodges, D. H. (1991), 'A Unified Nonlinear Analysis for Nonhomogeneous, Anisotropic Beams with Closed Cross Sections,' *AIAA Journal*, **29**, 1990 – 1999.

Atılgan, A. R., Hodges, D. H., Fulton, M. V., and Cesnik, C. E. S. (1991), 'Application of the Variational-Asymptotical Method to Static and Dynamic Behavior of Elastic Beams,' *Proceedings of the 32nd Structures, Structural Dynamics, and Materials Conference*, Baltimore MD, 1078 – 1093.

Bauchau, O. A., and Hong, C. H. (1988), 'Nonlinear Composite Beam Theory,' *Journal of Applied Mechanics*, **55**, 156 – 163.

Berdichevsky, V. L. (1981), 'On the Energy of an Elastic Rod,' *PMM*, **45**, No. 4, 518 – 529.

Berdichevsky, V. L., and Staroselsky, L. A. (1983),'On the Theory of Curvilinear Timoshenko-type Rods,' *PMM*, **47**, 809 – 817.

Borri, M., Ghiringhelli, G. L., and Merline, T. (1992), 'Linear Analysis of Naturally Curved and Twisted Anisotropic Beams,' *Composites Engineering*, **2**, 433 – 456.

Danielson, D. A., and Hodges, D. H. (1987), 'Nonlinear Beam Kinematics by Decomposition of the Rotation Tensor,' *Journal of Applied Mechanics*, **54**, 258 – 262.

Giavotto, V., Borri, M., Mantegazza, P., Ghiringhelli, G., Carmashi, V., Maffioli, G. C., and Massi, F. (1983), 'Anisotropic Beam Theory and Applications,' *Computers and Structures*, **16**, 403 – 413.

Hodges, D. H. (1990), 'A Mixed Variational Formulation Based On Exact Intrinsic Equations for Dynamics of Moving Beams,' *International Journal of Solids and Structures*, **26**, 1253 – 1273.

Hodges, D. H., and Atılgan, A. R. (1991), 'Asymptotical Modeling of Initially Curved and Twisted Composite Rotor Blades,' *Proceedings of the AHS International Technical Specialists' Meeting on Rotorcraft Basic Research*, Atlanta GA, 1.1 – 1.15.

Hodges, D. H., Atılgan, A. R., Cesnik, C. E. S., and Fulton, M. V. (1992), 'On a Simplified Strain Energy Function for Geometrically Nonlinear Behavior of Anisotropic Beams,' *Composites Engineering*, **2**, 513 – 526.

the 32nd Structures, Structural Dynamics, and Materials Conference, Baltimore MD, 1037 – 1049.

Minguet, P. (1989), 'Static and Dynamic Behavior of Composite Helicopter Rotor Blades Under Large Deflection,' *Ph.D. Dissertation*, Massachusetts Institute of Technology, Cambridge MA.

Rehfield, L. W., Atilgan, A. R., and Hodges, D. H. (1990), 'Nonclassical Behavior of Thin-Walled Composite Beams with Closed Cross Sections,' *Journal of the American Helicopter Society*, **35**, 42 – 50.

Washizu, K. (1964), 'Some Considerations on a Naturally Curved and Twisted Slender Beam,' *Journal of Math. and Physics*, **43**, 111 – 116.

Whitman, A. B., and Cohen, H. (1978), 'Constitutive Equations for Curved and Twisted, Initially Stressed Elastic Rods,' *Acta Mechanica*, **30**, 237 – 257.

Wolfram, S. (1988), *Mathematica*, Addison-Wesley Publishing Company, Reading MA.

Compressive strength and failure time based on local buckling in viscoelastic composites

RA Schapery

Department of Aerospace Engineering and Engineering Mechanics
University of Texas, Austin TX 78712

The axial compressive strength and failure time of unidirectional, viscoelastic composites are investigated. Effects of nonlinear shear behavior and fiber misalignment are emphasized because they are important strength-limiting factors in those strongly anisotropic composites which fail by local buckling in the shear mode of deformation. We first describe the basic buckling model and then, neglecting hereditary effects, predict the compressive strengths of an untoughened and a rubber-toughened carbon/epoxy composite. Next, using a nonlinear viscoelastic constitutive equation for shear behavior, failure time for constant load and compressive strength for increasing load history are predicted by a numerical method. Additionally, approximate analytical formulas are developed which enable one to easily estimate buckling response as a function of initial fiber misalignment angle as well as loading and material parameters.

INTRODUCTION

Microbuckling appears to be the primary strength-limiting mechanism in modern, highly anisotropic composites (Fleck and Budiansky, 1990), such as carbon fiber-reinforced plastic. Over the past three decades, investigators have used linear theory of varying degrees of complexity in studies of failure by fiber buckling (e.g. Rosen, 1965 and Waas, et al 1990). For the commonly used levels of fiber volume fraction, the dominant deformation mode is one in which the wave length is long compared to the fiber diameter and is characterized locally by simple shearing deformation. These linear analyses predict a strength which is approximately or exactly equal to the principal shear modulus G_{12}. Measured strengths are commonly one-third to one-fifth of this modulus. Kink bands are observed in compression failed specimens and, as a result, elastic and plastic buckling analyses of kink bands have been made in an effort to resolve this discrepancy (e.g. Fleck and Budiansky, 1990 and Budiansky, 1983). Assuming a state of local, simple shear deformation, Wisnom (1990) and Schapery (1991) independently showed that the combined effects of shear nonlinearity and realistic amounts of initial fiber misalignment are sufficient to reduce the compressive strength from the linear theory value of G_{12} to observed levels. (In earlier work, Hahn and Williams (1986), among others, also demonstrated that these effects lead to a significant loss in strength.). One may interpret the shear analysis as applying to a kink band which is normal to the fibers. Alternatively, distributed shear buckling may trigger a local failure initiation event, which is followed by a kink band propagating from the site of the initial event.

The strength model used here is based on the shear stress-strain behavior of the composite, and thus it is a modified version of Wisnom's shear buckling model, which uses an approximate micromechanical prediction of shear behavior. Not only does it lead to realistic strength predictions, but it also is sufficiently simple that nonlinear viscoelastic behavior is easily taken into account.

Finally, the reader is referred to a recent review of compressive strength of composites and kink band models (Budiansky and Fleck, 1993). Also, see Slaughter et al (1993) for a study of the effects of multiaxial loading and creep of nonlinear viscous composites.

SHEAR BUCKLING MODEL

Figure 1 illustrates the shear deformation and tractions acting on a local material element. The axial force/area, σ, in the right figure is decomposed into a traction σ_t which acts in the instantaneous fiber direction, ϕ_t , and a horizontal shear traction τ. If $|\phi_t| << 1$, then

$$\tau = \sigma\phi_t \qquad (1)$$

part of "MECHANICS PAN-AMERICA 1993" edited by MRM Crespo da Silva and CEN Mazzilli ASME Reprint No AMR134

Equilibrium considerations imply the same shear traction acts parallel to the fibers and that the traction normal to the fibers, to the first order in ϕ_t, is zero. Prior to application of σ , the local fiber angle is ϕ_0 (assumed small). The shear strain due to the loading is therefore $\gamma \equiv \phi_t - \phi_0$. Combining these results we obtain

$$\sigma = \tau/(\gamma + \phi_0) \tag{2}$$

where τ is, in general, a constitutive function of the shear strain history $\gamma(t)$; we assume the fiber axial modulus is so relatively high that the effect of σ on this constitutive relation can be neglected. Wisnom (1990) used $\tau = G_m\gamma/v_m$, where G_m is the (strain-dependent) secant shear modulus of the (resin) matrix and v_m is the matrix volume fraction; this result is based on a two-dimensional layer model in which fiber shear deformation is neglected. We do not employ this idealization here. Instead, we use the composite constitutive equation to relate τ and γ , which at least implicitly accounts for three-dimensional microstresses and fiber-shear effects.

QUASI-ELASTIC STRENGTH PREDICTION

Viscoelastic effects in structural composites under constant or monotonically increasing loading are often weak enough to either neglect them or to account for them simply through a time-dependent stress-strain equation. This is the case for Hexcel's carbon/epoxy composite, T2C145/F155, characterized by Mignery and Schapery (1991); for simple shear,

$$\gamma = S_0\tau + S_m t^m \tau^q \quad \text{when } \tau > \tau_1 \tag{3}$$

where $m = 0.05, q = 2.4$, S_0 and S_m are positive constants, and t is the time under load. In the linear range, $\tau \leq \tau_1$, the equation is similar, with $q = 1$. The epoxy matrix (designated as F155) is toughened with rubber particles, and exhibits noticeable time-dependence, as reflected in the t^m factor. In contrast, Hercules' carbon/epoxy composite, AS4/3502, characterized by Schapery (1989), has an untoughened matrix (designated as 3502); its time-dependence at room temperature is very weak and is usually neglected. Figure 2 shows the shear stress-strain curves for both composites, in which we use the resin designation to identify the two composites; note that $t = 1$ second and $t = 1$ year (extrapolated) curves are shown for the F155 composite. (Although t varies for each case, a constant value was used in drawing the curves for F155 since m is so small.) The stress-strain curve for the 3502 composite is from Schapery's (1989) data; it was not possible to fit the data with a power law like that in Eq (3).

Figure 3 illustrates behavior predicted by Eq (2) for the 3502 composite. The axial stress is divided by the zero-strain shear modulus, $G_{12}(0)$, and thus linear strength theory corresponds to an ordinate value of unity. The axial compressive strength is the maximum stress on these curves, and corresponds to the onset of failure by shear buckling. Figure 4 shows how these maxima vary with the initial fiber angle ϕ_0. Although the stress-strain curves in Fig 2 are quite different, the strengths in Fig 4 are remarkably close. As mentioned previously, typically measured strength $> G_{12}(0)/5$, which implies $\phi_0 < 2^0$ (cf. Fig 4); also, if $\phi_0 \to 0$, then the strength is $G_{12}(0)$, which is the result from linear theory. (For F155, $G_{12}(0)$ is time-dependent.) Although not shown here, when $\phi_0 < 2^0$, the shear strain at which the maximum stress is reached

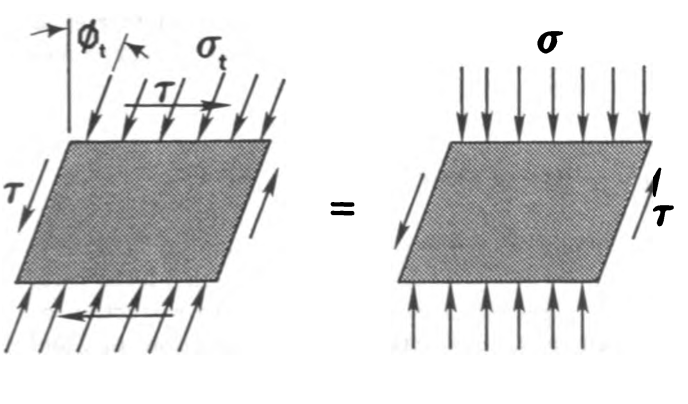

FIG 1. Representative comp... ...nt in compression and...

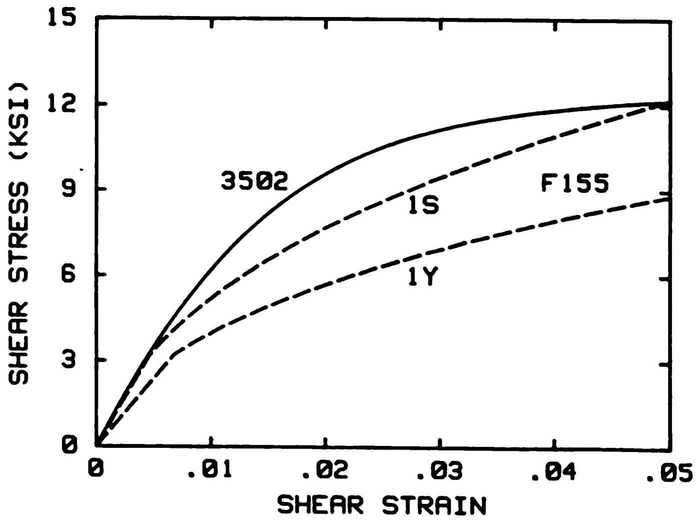

FIG 2. Stress vs strain for two composites.

is less than 0.02 for both composites; this strain is well below the ultimate strain in simple shear (cf. Fig 2).

Finally, it is readily shown that the maximum of Eq (2) is given by $\sigma_{max} = \partial\tau/\partial\gamma = (\partial\gamma/\partial\tau)^{-1}$ where $\tau = \tau(\gamma, t)$, and thus the strength is equal to the tangent modulus. The corresponding shear stress and strain may be found analytically when Eq (3) applies. Specifically, using Eqs (2) and (3) along with the condition $\partial\sigma/\partial\tau = 0$ yields

$$\tau = [\phi_0/S_m t^m (q-1)]^{1/q} \tag{4}$$

at the point $\sigma = \sigma_{max}$. Then, using this shear stress,

$$\sigma_{max} = \{S_0 + q(S_m t^m)^{1/q}[\phi_0/(q-1)]^{(q-1)/q}\}^{-1} \tag{5}$$

VISCOELASTIC MODEL

Constitutive equation

The shear stress-strain equation in the linear viscoelastic range may be written in the form

$$\gamma = \int_{0^-}^{t} S(t-t')\frac{d\tau}{d\tau'}dt' \tag{6}$$

providing that $\tau = \gamma = 0$ for $t < 0$ and the material does not age. The lower integration limit is 0^-, rather than 0, which allows for a stepwise applied stress at $t = 0$. For a creep test, $\tau = \tau_c H(t)$ (where τ_c is a constant and $H(t) \equiv 0$ when $t < 0$ and $H(t) \equiv 1$ when $t > 0$), then with the help of the Dirac delta function Eq (6) gives for $t > 0$,

$$\gamma = S(t)\tau_c \tag{7}$$

showing that $S(t)$ is the linear viscoelastic creep compliance, since this compliance is defined as γ/τ_c.

For the nonlinear range of behavior we shall use the constitutive equation

$$\gamma = S_0\tau + \int_{0^-}^{t} \Delta S(t-t')\frac{df}{dt'}dt' \tag{8}$$

where $S_0 \equiv S(0^+)$ is the initial creep compliance and $\Delta S(t) \equiv S(t) - S_0$ is the transient component of the linear viscoelastic creep compliance.

Also, $f = f(\tau)$ is an odd function of shear stress. By using $S = S_0 + \Delta S$ in (6), it is seen that it is a special case of Eq (8) if $f(\tau) = \tau$ at sufficiently low stress levels.Equation (8) was introduced by Leaderman (1943), and has met with limited success over the years (Findley et al , 1976). For some materials, including some fiber-reinforced plastics, both ΔS and f obey power laws. Specifically, with $\rho \equiv t/t_1$,

$$\Delta S = S_1\rho^m \tag{9}$$

Also,

$$f = S_2 \mid \tau \mid^q Sgn(\tau) \tag{10}$$

when $\mid \tau \mid > \tau_1$ and $f = \tau$ when $\mid \tau \mid \le \tau_1$, where t_1, S_1, S_2, m, q and τ_1 are positive constants; $Sgn(\tau)$ is

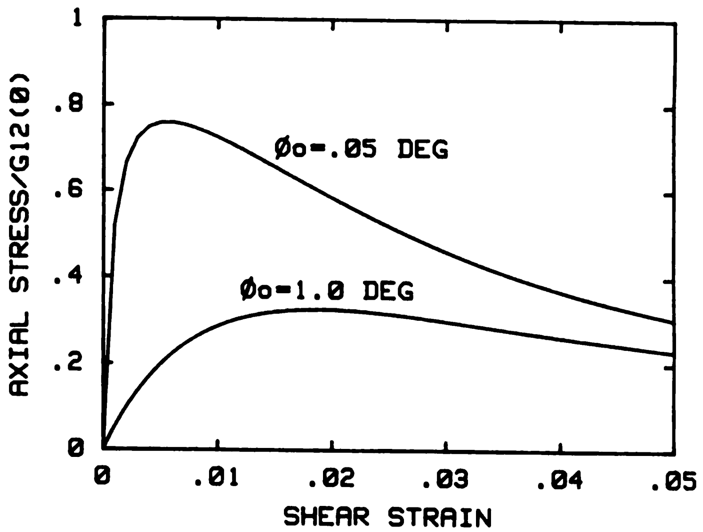

FIG 3. Effect of initial angle ϕ_0 for the 3502 composite.

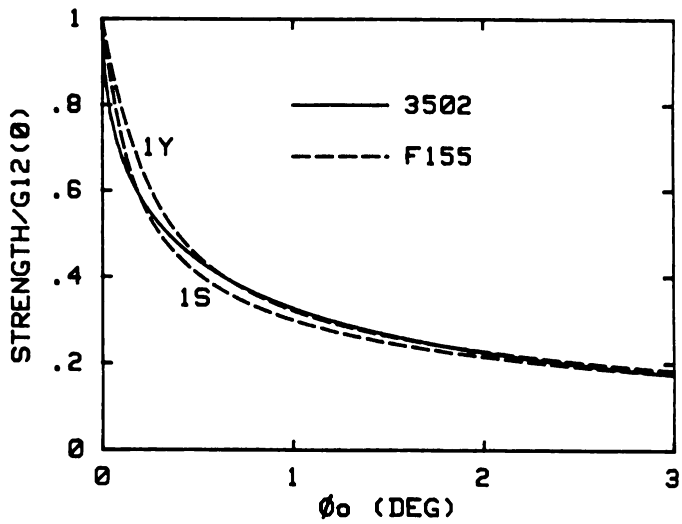

FIG 4. Effect of initial fiber angle ϕ_0 on strength.

the sign of τ and $|\ |$ denotes absolute value. For notational simplicity, we shall suppose $\tau \geq 0$ in what follows. (Observe that this formulation was used earlier in the quasi-elastic strain representation, Eq (3).) The function f will be continuous if we use

$$S_2 = \tau_1^{1-q} \tag{11}$$

On the other hand t_1 is a free constant since it may be combined with S_1; but this time constant is retained to express results in terms of a dimensionless time. Equations (9) and (10) were used by Mignery and Schapery (1991) in characterizing the behavior of a carbon fiber/rubber-toughened composite under constant and increasing loads.

For application to the fiber microbuckling problem, it will be helpful to write the constitutive equation using a normalized strain γ/ϕ_0 and other dimensionless ratios,

$$Y \equiv (S_1\tau/\phi_0)^q \quad , \quad k_0 \equiv S_0/S_1 \tag{12}$$
$$k_1 \equiv (\phi_0/S_1\tau_1)^{q-1} \quad , \quad \rho \equiv t/t_1$$

Then, with the assumption that $\tau_1 << \tau_{max}$,

$$\gamma/\phi_0 = k_0 Y^{1/q} + k_1 \int_{0-}^{\rho} (\rho - \rho')^m \frac{dY}{d\rho'} d\rho' \tag{13}$$

The linear viscoelastic case is recovered by using $q = 1$.

Buckling equation

The shear strain may be eliminated by combining Eqs (2) and (13) to obtain an integral equation for Y in terms of the applied axial stress for $\rho > 0$,

$$\frac{1 - k_0 x}{x} Y^{1/q} - k_1 \int_{0-}^{\rho} (\rho - \rho')^m \frac{dY}{d\rho'}\, d\rho' = 1 \tag{14}$$

where $x \equiv S_1\sigma$ is a dimensionless axial stress. An alternative form, which is useful when $k_0 \neq 0$, is

$$\frac{1 - \hat{\sigma}}{\hat{\sigma}}\, \hat{\tau}^{1/q} - \int_{0-}^{\hat{t}} (\hat{t} - \hat{t}')^m \frac{d\hat{\tau}}{d\hat{t}'}\, d\hat{t}' = 1 \tag{15}$$

where

$$\hat{\sigma} \equiv k_0 x = S_0\sigma \quad , \quad \hat{\tau} \equiv k_0^q Y \tag{16}$$

$$\hat{t} \equiv (k_1/k_0^q)^{1/m} t/t_1 \tag{17}$$

When the axial stress is expressed in the form $\hat{\sigma} = \hat{\sigma}(\hat{t})$, the solution $\hat{\tau} = \hat{\tau}(\hat{t})$ depends on only the exponents, m and q.

The normalized fiber misalignment angle, $\phi \equiv \phi_t/\phi_0$ may be expressed simply in terms of Y or $\hat{\tau}$ by using Eq (1),

$$\phi = Y^{1/q}/x \tag{18}$$

or

$$\phi = \hat{\tau}^{1/q}/\hat{\sigma} \tag{19}$$

If $\hat{\sigma}$ vanishes at any time, then Eq (13) may be used to predict ϕ by recognizing that

$$\phi = \gamma/\phi_0 + 1 \tag{20}$$

CREEP BUCKLING (σ = constant)

Quasi-elastic solution

For many linear viscoelasticity problems, the convolution integral may be approximated quite well by a simple product (Schapery, 1965); for example, the quasi-elastic approximation to Eq (6) is $\gamma(t) \simeq S(t)\tau(t)$. Here, we shall use this simplification in nonlinear Eq (15), and later compare the result with numerical solutions. Thus

$$\frac{1 - \hat{\sigma}}{\hat{\sigma}} \hat{\tau}^{1/q} - \hat{t}^m \hat{\tau} = 1 \tag{21}$$

or, by using Eq (19) for ϕ,

$$(1 - \hat{\sigma})\phi - \hat{t}^m \phi^q \hat{\sigma}^q = 1 \tag{22}$$

This nonlinear equation may be readily solved numerically for $\phi = \phi(\hat{t})$, given the constant stress $\hat{\sigma}$. It can be shown that the quasi-elastic solution approaches the exact solution to Eq (15) as $\hat{t} \to 0$; it is helpful to use the quasi-elastic solution at short times in developing the numerical solution to Eq (15). When $\hat{\sigma} < 1$ and $q > 1$, Eq (22) has a double-valued solution, with the lower branch providing the stable solution. Instability or failure occurs when the condition $d\hat{t}/d\phi = 0$ is satisfied; we find at this point that

$$\phi = q/(q-1)(1-\hat{\sigma}) \tag{23}$$

which, together with Eq (22), provides the quasi-elastic, normalized failure time $\hat{t}_q$,

$$\hat{t}_q = \left[\left(\frac{1-\hat{\sigma}}{\hat{\sigma}}\right)^q \left(\frac{q-1}{q}\right)^q \frac{1}{q-1}\right]^{1/m} \tag{24}$$

The effect of initial angle ϕ_0 and other parameters on the physical failure time t_q is obtained by noting that $\hat{t}_q$ is independent of ϕ_0, and thus from (12) and (17),

$$t_q = \hat{t}_q t_1 \left[\frac{k_0^q (S_1\tau_1)^{q-1}}{\phi_0^{q-1}}\right]^{1/m} \tag{25}$$

When $\hat{\sigma} = 1$ then $t_q = 0$, which corresponds to elastic buckling; certainly, for even higher loads, $\hat{\sigma} > 1$, failure occurs immediately upon loading.

Exact and numerical solutions

Equation (15) may be simplified for creep buckling by introducing one more change of variables. Specifically, use

$$S_r \equiv \tau/\tau_0 \quad , \quad t_r \equiv t/t_q \tag{26}$$

where τ_0 is the shear stress at $t = 0^+$,

$$\tau_0 \equiv \sigma\phi_0/(1 - \sigma S_0) \tag{27}$$

and t_q is given by Eq (25). Then the integral equation for $S_r = S_r(t_r)$ is

$$S_r - k\int_{0^-}^{t_r} (t_r - t_r')^m \frac{dS_r^q}{dt_r'} dt_r' = 1 \tag{28}$$

where

$$k \equiv [(q-1)/q]^{q-1}/q \tag{29}$$

Thus, $S_r(t_r)$ is independent of applied stress σ and all other parameters, except for m and q. This result is very helpful since an analytical solution to Eq (28) has not been obtained except for a Maxwell model ($m = 1$). For $m = 1$ we find that

$$S_r = [1 - (q-1)kt_r]^{1/(1-q)} \tag{30}$$

which provides a finite failure time when $q > 1$,

$$t_r = [q/(q-1)]^q \tag{31}$$

This time ratio t/t_q increases monotonically (with decreasing q) from e at $q = \infty$ to ∞ at $q = 1$. The same behavior of the failure time has been obtained from the numerical solution of Eq (28) for $0 < m < 1$. For the linear viscoelastic case, $q = 1$, the exact solution diverges exponentially in time (Schapery, 1991), so that $t_r = \infty$ for all $m > 0$.

Equation (28) was solved numerically after removing the discontinuity at $t = 0$. Noting that $S_r = 0$ when $t_r < 0$ and $S_r = 1$ at $t_r = 0^+$, Eq (28) becomes, for $t_r > 0$,

$$S_r - kt_r^m - k\int_{0+}^{t_r} (t_r - t_r')^m \frac{dS_r^q}{dt_r'} dt_r' = 1 \tag{32}$$

This integral equation was solved numerically by converting it to a matrix equation by using a piecewise linear representation of $S_r^q(t_r)$; excellent accuracy was obtained with 100 time intervals.

Figures 5 and 6 give results for $m = 0.05$ and $m = 0.5$, respectively, using $q = 2.4$; the Maxwell model solution, Eq (30), is also shown in both figures. Numerical solutions to Eq (28) are designated as *viscoelastic.*

It is seen that the quasi-elastic approximation provides a conservative solution to the failure time. Moreover, even for the extreme case of highly rate-dependent behavior ($m = 1$), the failure time is not much greater. Considering the scatter in actual failure time that one can expect (probably greater than the spread of the different cases in Figs 5 and 6) in view of its sensitivity to the initial fiber angle as inferred from Eq (25), a quasi-elastic prediction

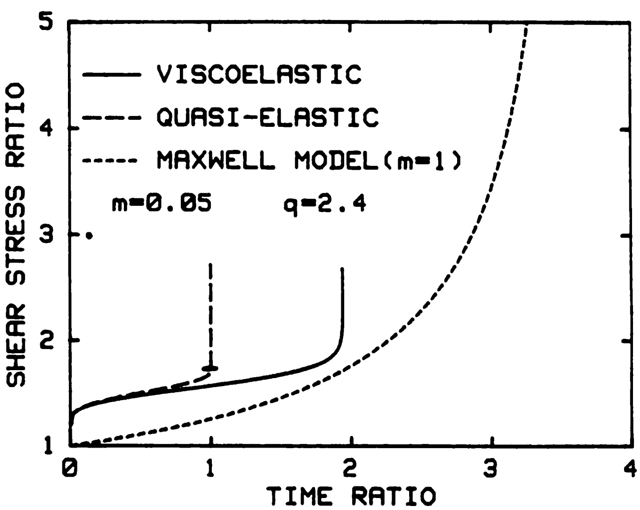

FIG 5. Shear stress ratio τ/τ_0 vs time ratio t/t_q

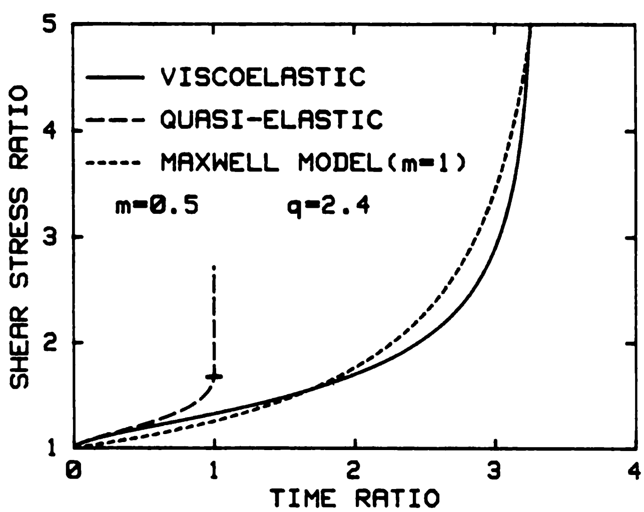

FIG 6. Shear stress ratio τ/τ_0 vs time ratio t/t_q

may be adequate for engineering applications, especially for small m.

Finally, we mention that the overall axial strain is practically independent of the amount of local shearing up to failure, and thus is not a good indicator of impending creep failure.

BUCKLING UNDER INCREASING STRESS

The axial stress is taken as a power law in time for $t > 0$,

$$\sigma = \sigma_n (t/t_1)^n \tag{33}$$

where σ_n and n are positive constants. In terms of normalized variables in Eqs (16) and (17),

$$\hat{\sigma} = k_n \hat{t}^n \tag{34}$$

where

$$k_n = S_0 \sigma_n (k_0^q / k_1)^{n/m} \tag{35}$$

In order to simplify the solution to Eq (15), it is helpful to introduce another change in dependent variable. Specifically, define a new time variable,

$$T \equiv k_n^{1/n} \hat{t} \tag{36}$$

Then

$$\hat{\sigma} = T^n \tag{37}$$

and Eq (15) becomes

$$\frac{1-\hat{\sigma}}{\hat{\sigma}} \hat{\tau}^{1/q} - k_2 \int_{0^-}^{T} (T - T')^m \frac{d\hat{\tau}}{dT'} dT' = 1 \tag{38}$$

where

$$k_2 \equiv k_n^{-m/n} = k_1 / k_0^q (S_0 \sigma_n)^{m/n} \tag{39}$$

Note that since $n > 0$ the lower integration limit may be taken as 0 since the solution will be continuous at $T = 0$. The solution $\hat{\tau} = \hat{\tau}(T)$ to Eq (38) is seen to depend on the load rate-dependent dimensionless parameter, k_2, as well as the exponents m, n and q. The higher the loading rate, as specified by increasing values of σ_n, the smaller will be k_2, and thus, as expected, the effect of viscoelasticity will decrease.

Quasi-elastic solution

For this case Eq (38) becomes,

$$\frac{1-\hat{\sigma}}{\hat{\sigma}} \hat{\tau}^{1/q} - k_2 T^m \hat{\tau} = 1 \tag{40}$$

or, in terms of normalized fiber angle using Eq (19),

$$(1-\hat{\sigma})\phi - k_2 T^m \phi^q \hat{\sigma}^q = 1 \tag{41}$$

As in the creep case, the failure (initiation) time is obtained from the condition $d\hat{T}/d\phi = 0$. The angle at failure initiation ϕ_q is the same as in Eq (23), except now $\hat{\sigma}$ depends on the failure time T_q. Denote the stress at failure by $\hat{\sigma}_q$, and then substitute Eq (23) into (41) to obtain a nonlinear algebraic equation for $\hat{\sigma}_q$,

$$\hat{\sigma}_q (1 + k_3 \hat{\sigma}_q^p) = 1 \tag{42}$$

where

$$p \equiv m/qn \quad , \quad k_3 \equiv q \left[k_2 / (q-1)^{(q-1)} \right]^{1/q} \tag{43}$$

and Eq (37) has been used to eliminate T in favor of $\hat{\sigma}$. In many cases $p << 1$; thus, as a first approximation use $\hat{\sigma}_q^p = 1$, which yields

$$\hat{\sigma}_{q1} = 1/(1 + k_3) \tag{44}$$

A better approximation may be obtained by examining the behavior of $\hat{\sigma}_q$ for small values of p and for the cases in which k_3 is very large and very small. We obtain

$$\hat{\sigma}_q \simeq \hat{\sigma}_{q1}^{\alpha} \tag{45}$$

where

$$\alpha \equiv \left(1 + \frac{k_3 p}{1 + k_3} \right)^{-1} \tag{46}$$

This result has been found to agree with numerical solutions to Eq (42) to within 3% for all cases of practical interest which were studied; for all $p, k_3 > 0$, a maximum error of only 10% was found.

An equation for $\phi = \phi(\hat{\sigma})$ prior to failure may be obtained by using Eq (37) to express (41) entirely in terms of ϕ and $\hat{\sigma}$,

$$\phi - k_2 \frac{\hat{\sigma}^{q+(m/n)}}{1-\hat{\sigma}} \phi^q = (1-\hat{\sigma})^{-1} \tag{47}$$

Numerical solution

A numerical method similar to that used for the creep problem was used to solve Eq (38). As before, it is helpful to use the quasi-elastic solution to provide the very short time response. However, in order that the short time quasi-elastic solution approach the exact solution as $T \to 0$, it is found necessary to modify the constant k_2. Specifically, replace k_2 in Eqs (40) and (41) by

$$k_2' \equiv I_r k_2 \tag{48}$$

where k_2 is given by Eq (39) and, with $r = nq$,

$$I_r \equiv \Gamma(r+1)\Gamma(m+1)/\Gamma(r+m+1) \tag{49}$$

in which $\Gamma(x)$ is the Gamma function of x. When $m << 1$ or $r << 1$, then $I_r \simeq 1$.

Figures 7 and 8 provide results for $m = 0.05$ and $m = 0.5$, respectively, using $q = 2.4$; the value of $k_2 = 10$ was used to emphasize viscoelastic effects. The Maxwell model solution ($m = 1$) was found numerically, and is shown for comparison. *Viscoelastic* in the figures refers to the numerical solution to Eq (38). The horizontal axis is the axial stress ratio $\hat{\sigma}/\hat{\sigma}_q = \sigma/\sigma_q$, where σ_q is the quasi-elastic failure stress. The k_2', Eq (48), was used in place of k_2 to predict all quasi-elastic solutions from Eqs (41) and (42). It is observed in these figures that the quasi-elastic solution for $m = 0.05$ and $m = 0.5$ is close to the numerical solution of Eq (38) for most of the time; when $m = 0.05$, the quasi-elastic strength is very close to the viscoelastic strength.

CONCLUDING REMARKS

The importance of the effect of initial fiber angle and shear nonlinearity on strength has been shown. In a previous study (Schapery, 1991) linear theory was used to predict the growth of the fiber angle under cyclic loading. One may combine the present and earlier analyses to predict the influence of low-level cyclic loading on the residual compressive strength (Schapery, 1993); specifically, the initial fiber angle in the present nonlinear analysis would be taken as the residual fiber angle following cyclic loading.

We have not accounted for the spacewise distribution of initial fiber angles, the free surfaces, and resulting nonuniform stress and strain distributions. However, it is believed that the primary factors which influence compressive strength are contained in the simple shear model. Initial fiber angles have been reported to range from about 1/3 to 3 degrees (Wisnom, 1990 and Yurgartis, 1987), depending on the composite, which through the present theory is consistent with the range of experimental strengths. What is needed at this time in order to check the theory and develop a more detailed, realistic model is experimental work which combines knowledge of initial fiber angle distributions, shear stress-strain behavior and compressive strengths, all on one or more composites. Experimental studies, in which changes in shear strain-strain behavior due to temperature, loading history, etc., are correlated with compressive strength would also be useful in assessing the model.

Acknowledgment - Sponsorship of this work by the Office of Naval Research, Solid Mechanics Program, with Dr YDS Rajapakse as scientific officer, is gratefully acknowledged.

REFERENCES

Budiansky B, Micromechanics. *Computers & Structures* **16**, 3-12 (1983).

Budiansky B and Fleck NA, Compressive failure of fibre composites, *J Mech Phys Solids* **41**, 183-211 (1993).

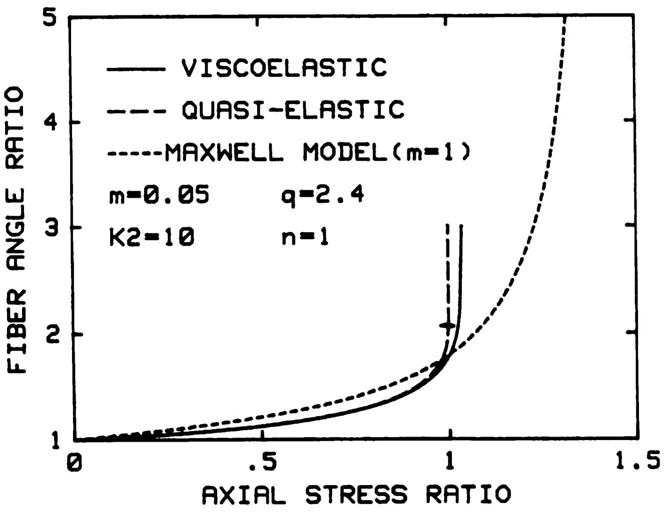

FIG 7. Fiber angle ratio ϕ_t/ϕ_0 vs axial stress ratio σ/σ_q

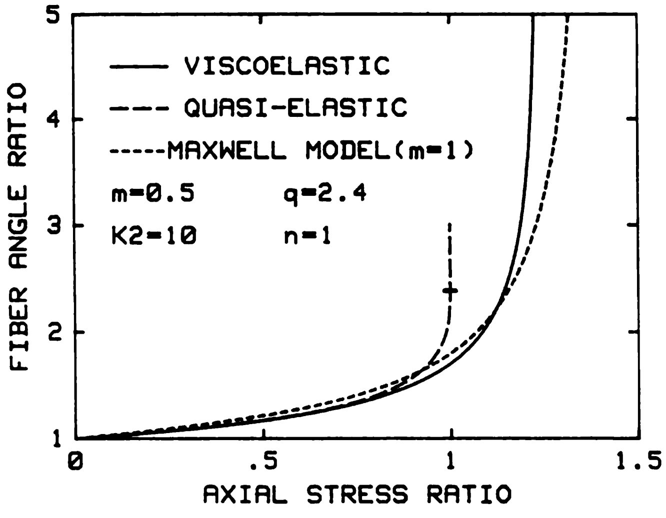

FIG 8. Fiber angle ratio ϕ_t/ϕ_0 vs axial stress ratio σ/σ_q

Findley WN, Lai JS and Onaran K, *Creep and relaxation of nonlinear viscoelastic materials*, North-Holland Pub Co, Amsterdam (1976).

Fleck NA and Budiansky B, Compressive failure of fibre composites due to microbuckling. In *Inelastic Deformation of Composite Materials*, G. J. Dvorak (Ed), Springer-Verlag, 235-273 (1990).

Hahn HT and Williams JG, Compression failure mechanisms in unidirectional composites. *Composite Materials: Testing and Design (Seventh Conference, ASTM STP 893)*, J M Whitney (Ed), American Society for Testing and Materials, Philadelphia,115-139 (1986).

Leaderman H, *Elastic and creep properties of filamentous materials*, Textile Fdn, Wash DC (1943).

Mignery LA and Schapery RA, Viscoelastic and nonlinear adherend effects in bonded composite joints. *J Adhesion* **34**,17-40 (1991).

Rosen BW, Mechanics of composite strengthening. *Fiber Composite Materials*, American Society for Metals, 37-75 (1965).

Schapery RA, A method of viscoelastic stress analysis using elastic solutions, *J Franklin Inst*, **279**, 268-289 (1965).

Schapery RA, Mechanical characterization and analysis of inelastic composite laminates with growing damage. *Mechanics of Composite Materials and Structures* **100**, American Society of Mechanical Engineering, 1-9 (1989).

Schapery R A, Analysis of local buckling in viscoelastic composites. *Local Mechanics Concepts for Composite Material Systems*, Proc IUTAM Symp, VPI and SU, 229-250, 1991.

Schapery RA, On nonlinear viscoelastic constitutive equations for composite materials. Proc. VII Int. Congr. on Exp. Mech, 9-21 (1992).

Schapery RA, Nonlinear viscoelastic effects in the compressive behavior of fiber composites, Proc First Joint ASCE-EMD, ASME-AMD, SES Meeting, (1993).

Slaughter WS, Fleck NA and Budiansky G, Compressive failure of fibre composites: The rolls of multi-axial loading and creep, *J. Eng Mat and Tech*, in press (1993).

Waas AM, Babcock CD, Jr., and Knauss WG, A mechanical model for elastic fiber microbuckling. *J Applied Mechanics* **57**, 138-149 (1990).

Wisnom MR, The effect of fibre misalignment on the compressive strength of unidirectional carbon fibre/epoxy. *Composites* **21**, 403-407 (1990).

Yurgartis SW, Measurement of small angle fiber misalignments in continuous fiber composites. *Composites Science and Technology* **30**, 279-293 (1987).

Estimation of Lyapunov exponents using a semi-discrete formulation

Josef S Török

Department of Mechanical Engineering
Rochester Institute of Technology, Rochester NY 14623

Lyaponov exponents are a generalization of the eigenvalues of a dynamical system at an equilibrium point. They are used to determine the stability of any type of steady-state behavior, including chaotic solutions. More specifically, Lyapunov exponents measure the exponential rates of divergence or convergence associated with nearby trajectories. This paper presents an efficient method of estimating the Lyapunov spectrum of continuous dynamical systems. Based on the Lie series expansion of the flow, the technique can be readily implemented to estimate the Lyapunov exponents of dynamical systems governed by ordinary differential equations.

INTRODUCTION

For periodic motion, the spectrum of exponents contains only zero or negative values, indicating convergence to a highly predictable motion. At the other extreme, a chaotic system will exhibit at least one positive exponent. A positive exponent is significant, because it gives an indication of the rate at which one loses the ability to predict the system response. This is closely related to the property of sensitive dependence on initial conditions, which is characteristic of chaotic systems. Therefore, one way to determine if a system is behaving in a chaotic manner is to calculate the Lyapunov exponents. A further motivation for calculating these exponents is that a knowledge of the entire spectrum of Lyapunov exponents can be used to calculate an approximate fractal dimension of the attractor (Holmes and Moon, 1983). Unfortunately, there is no general analytical way to determine the Lyapunov exponents for a general system of equations. The Lyapunov spectrum must be numerically approximated.

It is a simple calculation to determine the Lyapunov exponents of a linear system. Linear differential equations can in principle be solved exactly, and thus the exponents can be determined by an inspection of the solution. For example, the unforced equation

$$\ddot{q} + 5\dot{q} + 6q = 0$$

has the general solution

$$q = Ae^{\lambda_1 t} + Be^{\lambda_2 t}$$

in which the Lyapunov exponents, λ_1 and λ_2, are equal to -2 and -3, respectively.

A forced system such as

$$\ddot{q} + 5\dot{q} + 6q = F\cos(\omega t)$$

has the same exponents, but with an additional exponent that has a zero real part, i.e. purely imaginary. This fact is apparent from the general solution of the problem, which is readily computed as

$$q = Ae^{\lambda_1 t} + Be^{\lambda_2 t} + C(e^{i\omega t} + e^{-i\omega t})$$

It is interesting to note that the exponents in this example are constant, in that they do not depend on initial conditions. Furthermore, since the forcing function does not alter the complementary solution, λ_1 and λ_2 are independent of F and ω. This makes the computation of Lyapunov exponents for linear systems very easy.

There are no analytical methods available to precisely determine the Lyapunov spectrum for nonlinear systems. Nonlinearities can cause repeated stretching and folding of a small region of initial conditions as it evolves in its state space (Wolf et al, 1985). This causes the locally-determined Lyapunov exponents to vary considerably over a trajectory. Thus, it is necessary to examine the long-time average of the exponents. Furthermore, unlike the case for linear systems, the Lyapunov exponents change with forcing amplitude and frequency. This important fact is the motivation of this investigation.

Even for a relatively simple nonlinear differential equation, such as the Duffing equation, a periodic or even a chaotic response can be obtained for a given set of system parameters merely by changing the forcing amplitude and frequency. For example, the forced Duffing equation

$$\ddot{q} + 0.1\dot{q} - q + q^3 = 3.2\cos(\omega t)$$

yields a periodic response for $\omega = 0.482$, but exhibits chaotic behavior for $\omega = 0.475$. This indicates that one of the exponents has shifted from negative to positive over a very small change in the forcing frequency ω.

ESTIMATION OF LYAPUNOV EXPONENTS

In higher order systems, Lyapunov exponents are determined by examining the long-term evolution of an infinitesimal n-sphere of initial conditions, with 'n' being the order of the dynamical system. As the system evolves, the initial n-sphere will expand or contract along its n principal axes, resulting in a deformed n-ellipsoid.

The general method of numerically calculating the exponents of a dynamical system proceeds in the following manner. First, a point that lies near the steady-state attractor of the system of interest is selected. This means that the system must first be integrated well into its post-transient state. Initially, a vector of magnitude ϵ and arbitrary direction is chosen and is attached to a point on the trajectory. It is important that this ϵ be small because as pointed out above, a repeated stretching and folding can take place in the state space. Only the stretching of the space is of interest here. A small test vector is better able to avoid any effects of folding. A second vector, perpendicular to the first, but equal in magnitude, is also constructed at the test point.

Additional vectors are added in a similar fashion until the vector set forms an orthogonal basis $\{b_i\}$ for the state space in the region of the test point. The test point and nearby initial conditions determined by the vector set are then integrated ahead for a short length of time.

After integration, the largest vector is used to calculate the largest local exponent from the equation

$$\lambda_1 = (\ 1/\Delta t\ )\ \ln(\ l_f/\epsilon\ )$$

where Δt is the time interval over which the system is integrated and l_f is the length of the largest vector after integration. This vector will automatically tend toward the direction of greatest divergence (or convergence). The second vector is not free to tend toward the direction associated with the second largest exponent because of the effect of the largest exponent upon its evolution. Instead, the second exponent is determined from the calculation of the sum of the first two exponents, which measures the rate of contraction of an area in state space. This is obtained from the equation

$$\lambda_1 + \lambda_2 = (\ 1/\Delta t\ )\ \ln(A_f/\epsilon^2)$$

in which A_f is the final area of the space determined by the first two vectors. Subsequent exponent sums are computed in a similar fashion for higher dimensional systems (Wolf et al, 1985).

The largest vector is then normalized to a magnitude of ϵ, while its direction is preserved, enabling this vector to continue converging to the direction associated with the largest exponent. Additional vectors are again constructed perpendicular to the first. This is repeated over a long time in the simulation and the exponents are then calculated as a long-time average over the steaty-state motion. This long-time average is extremely important, as even very close trajectories leading to periodic motion can temporarily diverge from each other over short time intervals. This phenomenon is what characterizes transient chaos.

This procedure is based directly on the definition of the Lyapunov spectrum. The one drawback is that the collection of initial conditions must be repeatedly integrated over short time intervals. The evolution of an n-sphere must be carefully tracked to determine the divergence (convergence) rates along the attractor. In the following section, a more convenient method is proposed based on the concept of a forward-advance mapping.

COMPUTATION OF LYAPUNOV EXPONENTS

The determination of the Lyapunov exponents for ordinary differential equations will be accomplished using a semi-discrete formulation. The dynamics of the system will be discretized by the introduction of a time-advance mapping. Consequently, Lyapunov exponents can be calculated by using techniques that work well for discrete dynamical systems, as addressed below.

Consider a nonlinear point mapping defined on R^n by the equation

$$\mathbf{x}_{n+1} = \mathbf{F}(\mathbf{x}_n),\ n > 1 \tag{1}$$

Then to the first order,

$$\delta\mathbf{x}_{n+1} = \mathbf{F}\ (\mathbf{x}_n + \delta\mathbf{x}_n) - \mathbf{F}(\mathbf{x}_n) \tag{2}$$

$$= [\mathbf{DF}]_n \delta\mathbf{x}_n \tag{3}$$

in which $[\mathbf{DF}]_n$ is the Jacobian of $\mathbf{F}(\mathbf{x})$ evaluated at $\mathbf{x} = \mathbf{x}_n$. From the usual definition

$$\mathrm{DF}_{ij} = \partial F_i/\partial x_j \tag{4}$$

Thus equation (3) gives an estimate of the variation at the $(n+1)^{st}$ step of the iteration in term of the variation at the n^{th} step. Repeatedly applying equation (3) results in

$$\delta x_{n+1} = DF_n * DF_{n-1} * DF_{n-2} * \ldots\ldots * DF_1(\delta x_1) \quad (5)$$

Equation (5) represents the variation at the $(n+1)^{st}$ step in terms of the initial variation δx_1. To avoid divergence of the vector norms, due to repeated application of the Jacobian matricees, it is more convenient to express equation (5) as

$$\delta x_{n+1} = DF_n[DF_{n-1} \ldots\ldots\ldots DF_1(\delta x_1)] \quad (6)$$

In equation (6), the latest Jacobian is applied to the current set of vectors. To avoid divergence of the variations, due to stretching of orbits, a Gram-Schmidt orthonormalization procedure is applied at each step to accomplish two things:

(i) estimate the local growth rate of the vectors

(ii) replace the vectors with a renormalized set as described in the previous section.

The vector with a largest growth rate is always renormalized and used as the first replacement vector. It should be noted that the growth rate of the local basis vectors is governed by the absolute values of the eigenvalues at each iteration. Denote the eigenvalues of $[DF]_n$ at the n^{th} iteration by

$$\Lambda_1(n),\ \Lambda_2(n),\ \ldots\ldots\ ,\Lambda_n(n). \quad (7)$$

For non-degenerate cases, the magnitude of each eigenvalue can be expressed as

$$\Lambda_1(n) = \exp(\lambda_{loc,i}(n)) \quad (8)$$

so that

$$\lambda_{loc,i}(n) = \log \Lambda_i(n) \quad (9)$$

represents the local convergence (or divergence) rate.

The Lyapunov exponents are computed as a long-time average, consequently the global behavior of the mapping is determined by the eigenvalues of the product Jacobian

$$[JP] = [DF_n][DF_{n-1}] \ldots\ldots [DF_1] \quad (10)$$

as $n \to \infty$. Thus the Lyapunov exponents for mappings such as (1) are defined as

$$\lambda_i = \lim_{n\to\infty} (1/n) \textstyle\sum_{k=1} \log \Lambda_i(k) \quad (11)$$

In order to apply the above to continuous dynamical systems, the flow must be discretized. That is, the governing equations must be integrated forward, for arbitrary initial conditions, to a specified time in order to construct a time-advance mapping. The procedure is outlined as follows.

An initial value problem defined by a system of differential equations

$$\dot{x} = X(x,t),\ \ x(0) = x_0$$

is integrated from the initial condition x_o. Denote this solution as $x(t;x_0)$. Since the initial condition, x_0, is arbitrary, a sequence of points is defined inductively as

$$x_{n+1} = F(x_n) \quad (13)$$

in which

$$x_{n+1} = x(h;x_n) \quad (14)$$

At each step, the initial point x_0 in (12) is replaced by the current state vector x_n. That is, x_{n+1} is obtained by advancing the solution of (12) over a time $\Delta t = h$, from an initial point x_n.

Since most differential equations cannot be integrated analytically, the time-advance mapping must be constructed with the aid of numerical integration schemes. The drawback of using a numerical routine such as Runge-Kutta, is that an explicit form of the time-advance mapping (13) is not obtained.

The standard method of estimating local divergence (or convergence) rates entails the comparison of the time-evolution of two trajectories at neighboring points (Wolf et al, 1985). The neighboring trajectories are tracked by solving the associated variational equation

$$\frac{d}{dt}(\delta x) = [J]\ \delta x$$
$$\delta x(0) = \delta x_0 \quad (15)$$

simultaneously with the original differential equation (12). The variational equations (15) are obtained by applying the variational operator to equation (12).

Although equation (15) is linear, the coupled system is now twice the order of the original system (12). This makes the numerical integration more tedious. Essentially, the differential equations along with the coupled set of local variational equations must be numerically integrated over small displacements in the phase space. The local divergence (or convergence) are determined by analyzing the evolution of the variations δx.

A more attractive approach is to construct an approximate, yet explicit, form of the time-advance map

$$x_{n+1} = F(x_n) \tag{16}$$

The objective is to develop an explicit mapping with no worse of an error than a corresponding numerical integration scheme. Since errors are typically based on Taylor series expansions, a truncated Taylor expansion of the solution will not introduce any more errors than numerical integration of the differential equations.

Series solutions to an initial value problem can be conveniently and efficiently developed from the theory of continuous transformation groups (Torok and Advani, 1985). Briefly, the coefficients of the series expansion can be computed from the associated infinitesimal generator of the system of differential equations. Specifically, given an initial value problem

$$\begin{aligned} \dot{x}_1 &= X_1(x_1, x_2, \ldots\ldots, x_n), \;\; x_1(0) = \dot{x}_1 \\ \dot{x}_2 &= X_2(x_1, x_2, \ldots\ldots, x_n), \;\; x_2(0) = \dot{x}_2 \\ &\vdots \\ \dot{x}_n &= X_n(x_1, x_2, \ldots\ldots, x_n), \; x_n(0) = \dot{x}_n \end{aligned} \tag{17}$$

the infinitesimal generator is defined as the operator

$$U = X_1\, \partial/\partial x_1 + X_2\, \partial/\partial x_2 + \ldots\ldots + X_n\, \partial/\partial x_n \tag{18}$$

in which the coefficients in (18) are given as the right hand sides of equation (17). It can be shown that the series representation of the solution $x_i{}^t = x_i(t)$ is given by

$$x_i{}^t = x_i + (Ux_i)t + (U^2x_i)t^2/2 + \ldots + (U^kx_i)\, t^k/k! + \ldots$$

in which the variable, x_i, represents an arbitrary initial value.

Thus, the explicit time-advance mapping is developed as

$$\begin{aligned} (x_i)_{n+1} &= F((x_i)_n) \\ &= x_i{}^h \end{aligned} \tag{19}$$

That is,

$$\begin{aligned} (x_i)_{n+1} &= x_i{}^h \\ &= x_i + (Ux_i)h + (U^2x_i)h^2/2 + \ldots \end{aligned} \tag{20}$$

in which $(x_i)_n$ is substituted for the initial condition x_i.

As an example, consider the problem

$$\begin{aligned} \dot{x} &= x^2, \;\; x(0) = x_o \\ \dot{y} &= xy, \;\; y(0) = y_o \end{aligned} \tag{21}$$

The infinitesimal generator associated with this system of differential equations is given as the operator

$$U = x^2\, \partial/\partial x + xy\, \partial/\partial y \tag{22}$$

The powers of the operator U are computed successively as

$$\begin{array}{ll} Ux = x^2 & Uy = xy \\ U^2x = 2x^3 & U^2y = 2x^2y \\ U^3x = 6x^4 & U^3y = 6x^3y \\ U^4x = 24x^5 & U^4y = 24x^4y \\ \vdots & \vdots \end{array} \tag{23}$$

and the series representations of the solutions are

$$x^t = x + x^2t + 2x^3t^2/2 + 6x^4t^3/3! + 24x^5t^4/4! + .. \tag{24}$$

$$y^t = y + xyt + 2x^2yt^2/2 + 6x^3yt^3/3! + 24x^4yt^4/4! + .. \tag{25}$$

in which x and y are arbitrary initial conditions.

By inspection, the solutions (24) and (25) are found to converge to

$$x^t = x/(1-xt) \tag{26}$$

$$y^t = y/(1-xt) \tag{27}$$

As mentioned above, the variables x and y in equations (26) and (27) represent arbitrary initial conditions. Hence substitution the initial conditions from equations (21), results in the solutions

$$x(t) = x_o/(1-x_ot) \tag{28}$$

$$y(t) = y_o/(1-x_ot) \tag{29}$$

Furthermore, the time-advance solution for arbitrary h is given by

$$x^h = x_o/(1-x_oh) \tag{30}$$

$$y^h = y_o/(1-x_oh) \tag{31}$$

Alternatively, since x_o and y_o are abitrary, the time-advance mapping is explicitly deduced as

$$x_{n+1} = x_n/(1-hx_n) \tag{32}$$

$$y_{n+1} = y_n/(1-hx_n) \tag{33}$$

Hence the conti[illegible] dynamics of the system (12) are equivalently, [illegible]sely, represented by the discrete [illegible]ing [illegible] (33). Thus point mapping techniques are applicable, eliminating the cumbersome numerical tracking of trajectories.

Most nonlinear systems, however do not admit solutions which are expressible in terms of elementary functions as in (28) and (29). In such cases, a truncated series representation is used to construct the time-advance mapping. Using this discretized version of the dynamics, equations (1) through (11) are used to estimate the Lyapunov spectrum.

SUMMARY

A semi-discrete algorithm for the computation of Lyapunov exponents associated with continuous dynamical systems has been discussed. The proposed method consists of developing formal power series solutions based on Lie series expansions of the flow. The truncated power series can be used to construct forward advanced mappings, thereby converting a continuous dynamical system to a discrete one. Methods known to be reliable for discrete systems can then be utilized, eliminating the necessity of integrating the associated variational equations simultaneously with the original equations of motion.

Table 1. illustrates the results obtained by applying the proposed method to estimate the Lyapunov spectrum of the Lorenz system (Wolf et al, 1985). The complete spectrum of exponents of the Lorenz system is approximately (2.16, 0.0, -32.4) bits per second. The parameter h represents the time-advance used for the forward advance mapping. The integer N represents the number of time steps (in thousands) used for the averaging process. Excellent agreement is implied, especially for smaller time steps. It appears that the proposed algorithm is sensitive to the particular time step used, but does not vary considerably with the number of averaging steps.

TABLE 1. Estimated Lyapunov Spectrum of the Lorenz System

N	h= .01	.02	.03	.04	.05
5	2.2057 -0.0171 -32.4842	2.1600 0.0031 -32.4433	2.1669 -0.0104 -32.3526	2.1622 -0.0295 -32.0123	2.6833 -0.4543 -31.0620
6	2.2051 -0.0056 -32.4951	2.1496 0.0104 -32.4402	2.1779 -0.0149 -32.3590	2.1055 0.0232 -32.0095	2.6034 -0.4076 -31.0351
7	2.2025 -0.0101 -32.4880	2.1668 0.0056 -32.4525	2.1538 -0.0070 -32.3428	2.1252 0.0066 -32.0102	2.5766 -0.4098 -31.0233
8	2.2129 -0.0124 -32.4960	2.1702 0.0026 -32.4529	2.1543 -0.0048 -32.3452	2.1397 -0.0062 -32.0104	2.5789 -0.4055 -31.0332
9	2.2306 -0.0137 -32.5124	2.1640 0.0111 -32.4552	2.1675 -0.0119 -32.3509	2.1418 -0.0083 -32.0123	2.5734 -0.4018 -31.0380
10	2.2189 -0.0129 -32.5016	2.1675 0.0054 -32.4531	2.1623 -0.0054 -32.3528	2.1363 -0.0008 -32.0144	2.5792 -0.4150 -31.0383
15	2.2050 -0.0064 -32.4942	2.1731 0.0018 -32.4549	2.1632 -0.0030 -32.3568	2.1346 0.0039 -32.0162	2.5528 -0.4198 -31.0100

ACKNOWLEDGEMENT

The author wishes to thank Kathryn A. Playfoot for her editing and typing of this manuscript.

REFERENCES

Holmes PJ and Moon FC (1983), Strange Attractors and Chaos in Nonlinear Mechanics, *ASME J Appl Mech* **50** 1021-1032.

Wolf A, Swift JB, Swinney HL, and Vastano JA (1985), Determining Lyapunov Exponents from a Time Series, *Physica D* **16** 285-317.

Torok JS and Advani SH (1985), Continuous Transformation Groups and Series Solution of Initial Value Problems, *Int J Nonlinear Mech* **20**(4) 283-289.

Deveiopment of numericai simulations of dynamic/aerodynamic interactions

JA Luton, DT Mook, AH Nayfeh

Department of Engineering Science and Mechanics
Virginia Polytechnic Institute and State University, Blacksburg VA 24061-0219

CP Mracek

WL/MNGA, Elgin Air Force Base FL 32542-5434

A procedure for simulating aerodynamic/dynamic interactions is described. The equations of motion of the flowing air and the lifting structure are integrated numerically by an iterative technique based on Hamming's predictor-corrector method. The solution provides the flowfield and the motion of the lifting body simultaneously. The technique is modular and different models of the flow and the structure can be incorporated by simply changing subroutines. For the current examples of wingrock of highly swept delta wings and flutter of very flexible, very high-aspect-ratio wings, the flowfields are considered incompressible and modeled by vortex-lattice and continuous vorticity-panel methods. These models are inherently nonlinear and provide a force-free wake as part of the solution. It is shown that the instabilities can be easily suppressed by means of actively controlled flaps.

INTRODUCTION

In this article we discuss one aspect of the problem of modelling fluid-structure interactions, namely the numerical simulation of the motion of a lifting structure in a uniform, subsonic stream. We consider the spontaneous motion that develops as the angle of attack of a highly swept delta wing mounted on a free-to-roll sting in a uniform stream is steadily increased; the phenomenon is known as wing rock. Then we consider the spontaneous motion that develops when the speed of a uniform stream flowing past a thin, high-aspect-ratio, very flexible wing increases while the angle of attack decreases in such a way that the lift force remains constant. Both spontaneous motions are manifestations of a loss of dynamic stability, and both are forms of flutter. We refer to the former as rigid-body flutter and to the latter as aeroelastic flutter.

Wing rock can be a problem for a highly maneuverable military aircraft when it is performing tactical, high-alpha maneuvers and even when it is landing. Highly flexible, large-aspect-ratio wings are often found on the high-altitude, long-endurance (HALE) aircraft now intended for atmospheric monitoring and previously intended for observation platforms to verify some of the provisions of the strategic-arms-reduction treaty (START). Thus, both phenomena occur well within the subsonic-flow regime. We consider the flow to be incompressible.

The simulations of such phenomena involve equations of motion for both the lifting bodies and the flowing air. An apparent impasse develops: In order to integrate the equations of motion of the body, one must know the aerodynamic forces acting on the body; and in order to integrate the equations of motion of the flowing air and subsequently find the aerodynamic forces, one must know the motion of the body (for the boundary conditions on the flowfield). The difficulty can be resolved by an iteration scheme; to obtain the present results, we developed an algorithm based on Hamming's predictor-corrector method.

The remainder of the article is divided into five sections: In the second section, we describe the numerical model used to simulate the flowfield. In the third section, we discuss the simulation of wing rock and its suppression by feedback-controlled flaperons. In the fourth section, we discuss aeroelastic flutter and its suppression by feedback-controlled flaperons. Finally, in the last section, we present some concluding remarks.

AERODYNAMIC MODEL

The flowfield is modelled by either the general unsteady vortex-lattice method or the general unsteady vorticity-panel method. The basis for the methods is the definitions of incompressible flow, Div $\vec{v}=0$ (where $\vec{v}$ is the velocity), and vorticity, $\vec{\Omega}=$ Curl $\vec{v}$. These two equations can be manipulated to provide $\vec{v}$ as a function of $\vec{\Omega}$:

part of "MECHANICS PAN-AMERICA 1993" edited by M[illegible] [illegible]ilva and CEN Mazzilli ASME Reprint No AMR134
Appl Mech Rev vol 46, no 11, part 2, November 1993

$$\vec{v}(\vec{r}_p, t) = \frac{1}{4\pi} \iiint_{\text{volume}} \frac{\vec{\Omega}(\vec{r}_s, t) \times (\vec{r}_p - \vec{r}_s) d\tau(\vec{r}_s)}{|\vec{r}_p - \vec{r}_s|^2} \quad (1)$$

where $d\tau$ is the volume element at position $\vec{r}_s$ in the flowfield $\vec{v}$ is the velocity at position $\vec{r}_p$ in the flowfield, and $\times$ denotes the vector product.

There are six characteristics of the velocity given by Eq. (1) that are worth mentioning:

1. When the vorticity is confined to a straight line segment, Eq. (1) reduces to the Biot-Savart law.

2. The volume of the "flowfield", over which the integration in Eq. (1) is carried out, includes the interiors of solid objects in the actual flow.

3. The vorticity, $\vec{\Omega}$, may be zero in large parts of the flowfield, and the velocity, $\vec{v}$, is irrotational there.

4. Vorticity any where in the flowfield generates velocity everywhere.

5. The velocity, $\vec{v}$, decays as the reciprocal of the distance from the vorticity-containing regions.

6. Equation (1) is a purely kinematic relationship and, consequently, is valid for "viscous" as well as "inviscid" models of incompressible flowfields.

In the actual flow over a wing, the vorticity in the boundary layers on the upper and lower surfaces and the vorticity in the wake generate a velocity field that disturbs the freestream to the extent that the no-slip and no-penetration conditions are satisfied. We consider thin wings and merge the boundary layers on the upper and lower surfaces, into a single vortex sheet, which is called a lifting surface here. And we also consider the wake to be a vortex sheet. Because the position of the vortex sheet representing the wing is prescribed, a pressure jump across the sheet exists. The sheet representing the wake is allowed to deform freely in such a way as to eliminate the pressure jump.

To facilitate the computations in one procedure, Konstadinopoulos et al. (1985), we represent the lifting surface as a lattice of discrete vortex lines, which divides the sheet into a system of closed four-sided elements. Each discrete vortex segment of a given element is a straight line. The quadrilateral elements are not, in general, planar. To satisfy the requirement of spatial conservation of circulation, the circulations around the segments along the four sides of a given element are equal. The discrete vortex arrangement for a given element produces the same velocity field as a panel of constant-strength doublets when the panel is planar.

In the other procedure, Mracek et al. (1993) and Mracek (1988), we represent the lifting surface as a system of triangular panels over which the two in-plane components of vorticity vary linearly. This vorticity field is divergenceless. As a consequence discrete vortex lines form along the edges of the lifting surface.

To use either of the methods, one must specify where separation occurs; usually this means that one must specify the edges of the lifting surface from which the wakes emanate. The rate at which vorticity is shed into the wakes is determined by forcing the pressures on the upper and lower sides of the lifting surface to be equal along the edges where the wakes are attached. After the vorticity has been shed, it convects with the local fluid-particle velocity and the circulation around a given segment remains constant. The procedure generates a wake in the force-free position for an inviscid fluid as part of the solution. Hence, the wake is modelled as a region of rotational, inviscid flow. Two computed wakes are shown in Figs. 1 and 2.

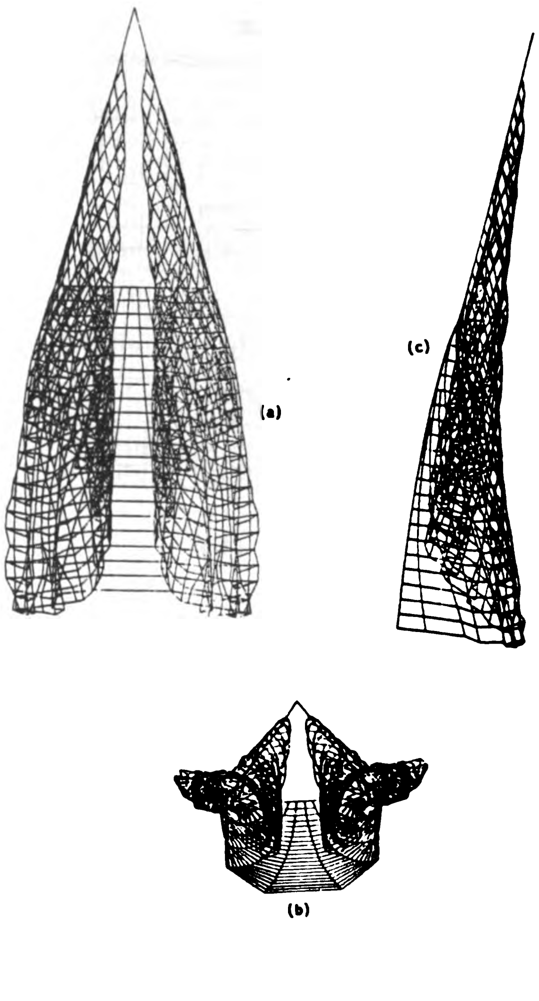

Fig. 1. Computed steady-state wake for flow past a unit-aspect-ratio delta wing at 20° angle of attack. (a) Top view, (b) rear view, and (c) side view.

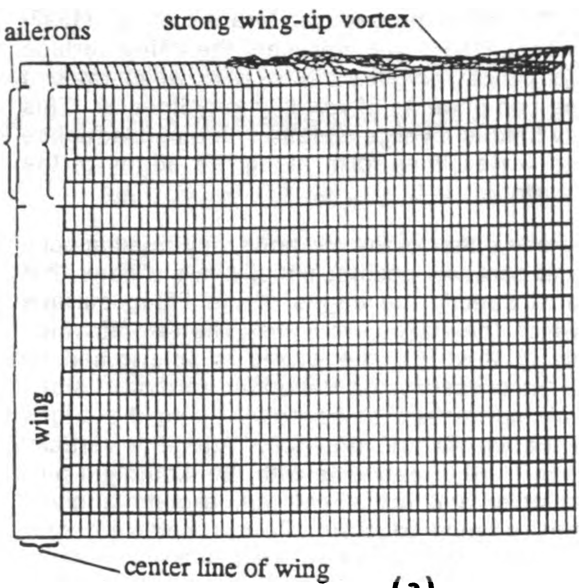

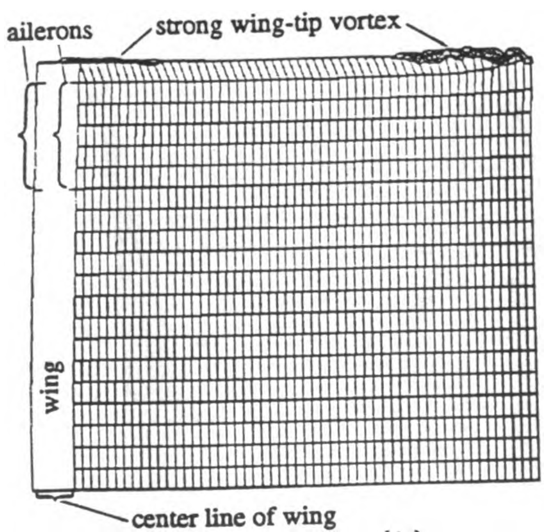

Fig. 2. Computed wake for unsteady flow past an aspect-ratio 20 rectangular wing. The wing is oscillating in bending and twist. In part (a) the wing tip is moving upward and nearly no vorticity is generated at the wing-tip. In part (b) the upward motion of the wing tip is slowing and strong wing-tip vorticity is beginning to develop.

The vorticity in the wake influences the flow over the wing. At any given instant, the vorticity in the wake was shed from the edges of the wing at an earlier time; hence, the current flowfield is influenced by what happened earlier. In other words, the current flowfield depends on the history of the flow, and the historian is the wake. Typically, the vorticity most recently shed is closest to the wing and has the strongest influence on the flow over the wing; hence, the historian has a fading memory.

In both procedures, the vorticity on the lifting surface is determined by imposing the no-penetration condition, and there is one point in each element of the lifting surface, called the control point, where this condition is imposed. In both procedures, the control point is the centroid of the corners.

The pressures are computed with the unsteady Bernoulli equation. The difference between the pressures on the two sides of the element is multiplied by the area of, and the unit vector normal to, the element to produce the elemental force. Then the elemental forces and their moments are summed.

WING ROCK

In Fig. 3, a delta wing mounted on a free-to-roll sting is shown. Here we consider the case where the distance d is zero. The equation governing the roll angle ϕ is

$$I_{xx}\ddot{\phi} = \frac{1}{2}\rho v_{\infty}^{2} S b C_R - \mu_x \dot{\phi} \tag{2}$$

where I_{xx} is the moment of inertia of the wing, ρ is the density of the air, v_∞ is speed of the freestream, S is the area of the planform, b is the span, C_R is the roll-moment coefficient which depends on the current values of ϕ and $\dot{\phi}$ and their histories, and μ_x is the damping coefficient for the roller bearing in the string.

The flaperons are operated by a servo mechanism and a feedback control law. The commanded deflections, δ_c, are given by

$$\delta_c = K_1\phi_1 + K_2\dot{\phi} \tag{3}$$

the servo-mechanism is governed by

$$\ddot{\delta} = -K_3\dot{\delta} - K_4(\delta - \delta_c) \tag{4}$$

and finally,

$$\delta_p = -\delta_s = \delta \tag{5}$$

where K_1 .and K_2 are constant gains, K_3 and K_4 are constant characteristic parameters of the servo-mechanism, δ_p is the port-side deflection, and δ_s is the starboard-side deflection. In the present examples, Eqs. (3)-(5) are linear with constant coefficients, but the method is not restricted to such equations.

We wish to integrate Eqs. (2)-(5) and the equations governing the flowfield simultaneously to produce ϕ, C_R, δ_c, and δ. The flow-chart of the algorithm is shown in Fig. 4.

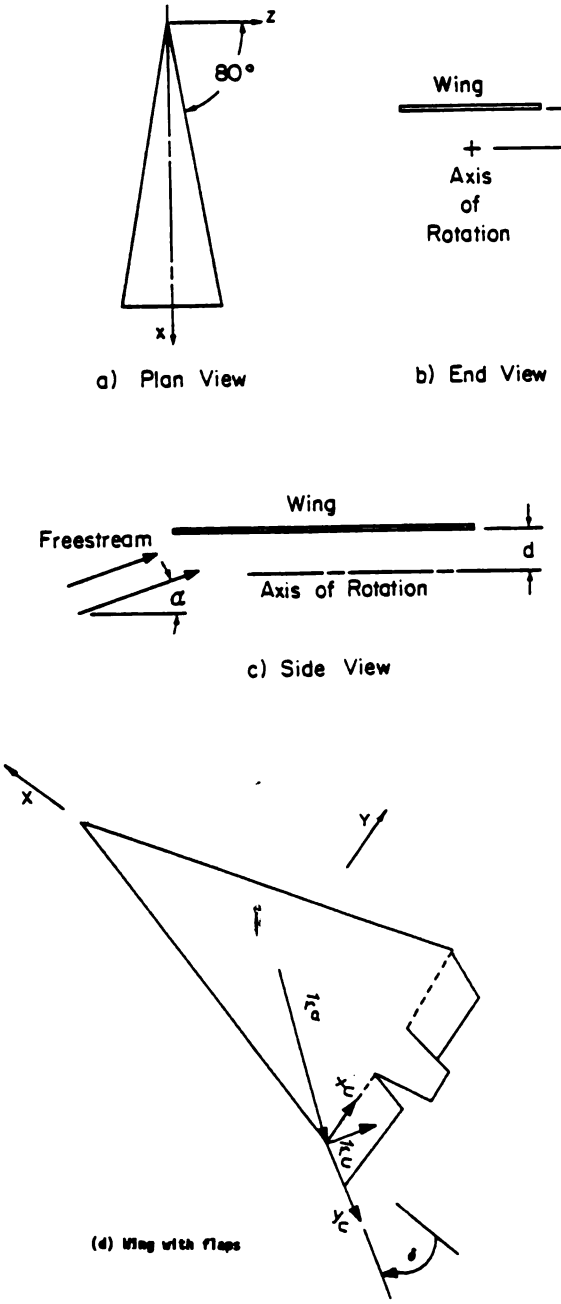

Quantity	Magnitude	Units
ρ	1.2000	kg/m³
U	15.000	m/s
S	0.0321	m²
b	0.1500	m
μ_x	0.5×10^{-4}	
I_{xx}	1.3×10^{-4}	kg-m²

(e) Physical properties

Fig. 3. A schematic drawing of the delta wing used in the numerical simulation of wing rock.

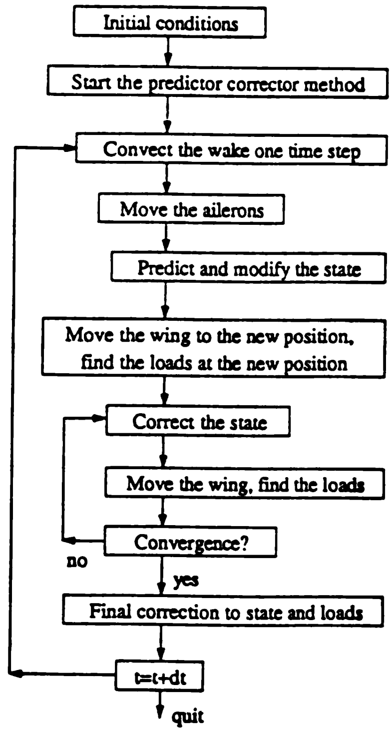

Fig. 4. Flow-chart for the predictor-corrector method.

To produce a simulation of an uncontrolled response, we first fix δ and exclude Eqs. (3)-(5); fix the wing at $\phi = 5°$ and allow a steady state to develop; and then the wing is released. When the angle of attack is below 25 degrees approximately, ϕ oscillates and decays to zero. When the angle of attack is greater than 25 degrees, ϕ grows and reaches a limit cycle. The results for 27.5 degrees angle of attack are shown in Fig. 5. The amplitude of the limit cycle is 29.6 degrees and its period is 0.3 sec; both agree well with the observations of Levin and Katz (1982).

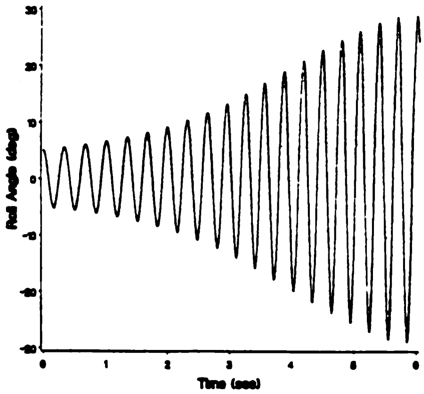

Fig. 5. The uncontrolled response in roll for a unit-aspect-ratio delta wing at 27.5° angle of attack.

Numerical simulations of wing rock were first obtained by Konstadinopoulos (1985) and

Konstadinopoulos (1984). They were able to simulate the experiments of Nguyen et al. (1983) and Levin and Katz accurately. They also were able to develop analytical expressions for the roll moment, which enabled Nayfeh et al. (1989) and Elzebda et al. (1989) to develop analytical models of wing rock. Luo and Lan (1993), working independently, also developed an analytical model.

To produce a simulation of a controlled response, we add Eqs. (3)-(5) to the system of equations being solved. The controlled response at 27.5 degrees angle of attack are shown in Fig. 6. After some trial and error, we chose $K_1 = 1.$ and $K_2 = 20$. The deflection of the port-side aileron is shown in Fig. 7. The unstable motion is quickly damped. The aileron deflection appears to decay, but if the control is shut off ϕ will begin to grow.

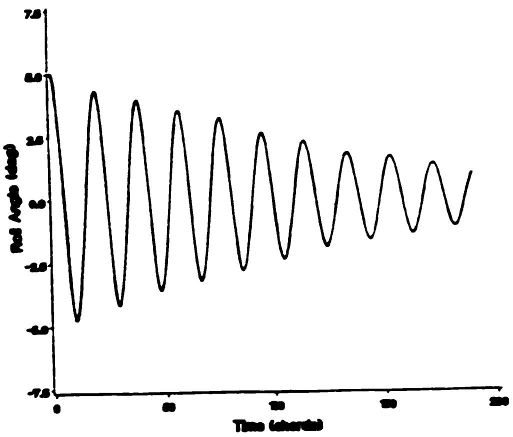

Fig. 6. The controlled response in roll for a unit-aspect-ratio delta wing at 27.5° angle of attack.

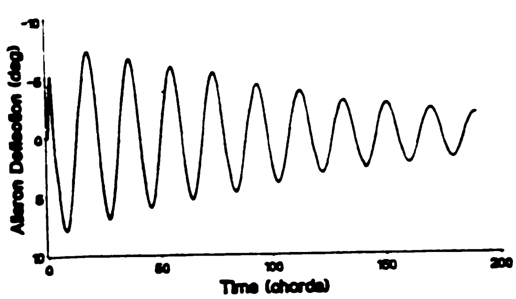

Fig. 7. Controlled aileron deflection as a function of time.

FLUTTER

In this example we consider a high-as very flexible, uniform wing, such as t presented in Fig. 8. (The method car wise variations of the properties.) H

chosen the elastic and inertial axes to be coincident. All of the twist/bending coupling is produced by the aerodynamic loads.

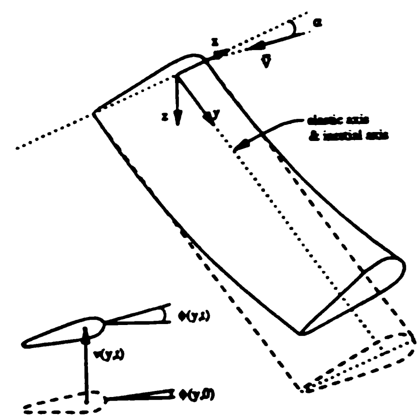

Fig. 8. A schematic of the high-aspect-ratio rectangular wing.

The dimensionless equations of motion of the wing are

$$\ddot{\phi} - D_t\phi'' = q_t Q_t \tag{6a}$$

$$\ddot{v} + D_b v'''' - D_b(2v'^2 v'''' + 10v'v''v''' + 3v''^3) = q_b Q_b - w - \frac{1}{2} q_b Q_b v'^2 \tag{6b}$$

$$u(y,t) = -\frac{1}{2}\int_0^y v'^2 dy \tag{6c}$$

where $D_b = \frac{EI}{mL_c^2V^2}$, $D_t = \frac{GJ}{V^2J_0}$, $q_b = \frac{\rho L_c^2}{2m}$,

$q_t = \frac{\rho L_c}{2J_0}$, and $w = \frac{gL_c}{V^2}$. Here EI is the flexural stiffness, GJ is the torsional stiffness, ρ is the density of the air, L_c is a characteristic length, J_0 is the mass polar moment of inertia, V is the speed of the freestream and m is the mass per unit of span. The dimensionless aerodynamic loads, Q_b and Q_t, are functions of the current shape and motion of the wing as well as the histories of these quantities. The nonlinear terms come from the curvature.

The boundary conditions are

$$\phi(0,t) = 0 \quad \phi'(L,t) = 0 \tag{7a}$$

$$v(0,t) = 0 \quad v''(L,t) = 0 \tag{7b}$$

$$v'(0,t) = 0 \quad v'''(L,t) = 0 \tag{7c}$$

Now the goal is to solve Eqs. (6) and (7) as well as those governing the flow for u, v, ϕ, Q_t, and Q_b simultaneously. The first step is to discretize, or convert, the partial-differential equations into a set of ordinary-differential equations. To this end, we represent v and ϕ as expansions in terms of the linear, free-vibration modes:

$$\phi(y,t) = \sum_{m=1}^{M} C_m(t)\chi_m(y) \tag{8a}$$

$$v(y,t) = \sum_{m=1}^{N} B_m(t)\psi_m(y) \tag{8b}$$

For the present results, four flexural and three torsional modes are used. The modes (χ_m and ψ_m) can be obtained analytically or numerically. The expansions are substituted into Eqs. (6) and Galerkin's procedure is applied to produce a set of $N+M$ second-order ordinary differential equations (see Luton, 1991) governing the time-dependent coefficients. These equations are integrated by the same algorithm used in the simulation of wing rock.

To control the anticipated flutter, we add flaps near the wing tips, a feedback-control system, and a servo-mechanism to move the flaps. The control law for the commanded flap deflection has the form:

$$\delta_c = G_1\dot{v}(0.95L, t) + G_2\dot{\phi}(0.95L,t) \tag{9}$$

and the actual flap deflection is given by

$$\ddot{\delta} = G_3(\delta_c - \delta) + G_4\dot{\delta} \tag{10}$$

where G_1, G_2, G_3, and G_4 are constants. The deflection, δ, is limited to $\pm$ 12 degrees and has zero velocity at these extreme positions. The control law and servo equation need not be linear nor have constant coefficients.

In Figs. 9-11, the responses of the uncontrolled wing to an initial disturbance are shown for three speeds near the flutter speed. The angles of attack are adjusted so that the lift forces are the same. In Fig. 9, the speed in the freestream is 75 m/s and α is 2.4 degrees; the motion of the wing decays very slowly to the static equilibrium position. In this simulation, all damping is due to the aerodynamic loads. Though the aerodynamic model is 'inviscid', there is still 'damping' as a result of the transfer of energy from the wing to the flowing air. In Fig. 11, the speed is 80 m/s and the response grows slowly. The appearance of the torsional response is similar to that of the flexural response in both cases. In Fig. 10, the speed is 77.5 m/s and the response to the initial disturbance is a limit cycle. Dong (1991) also found limit cycles near the flutter speed in his two-dimensional simulations of flutter. For a small range of speeds limit cycles exist and their amplitudes increase with the freestream speed. The nonlinear terms in the bending equation were deleted for these results, so all nonlinear effects are from the aerodynamic model.

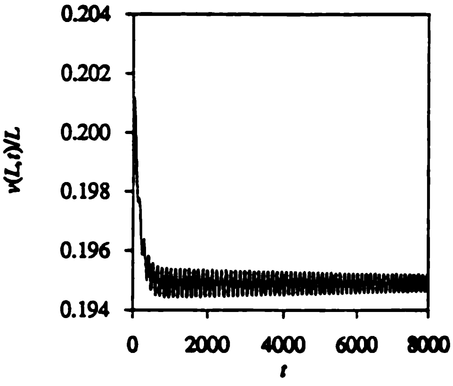

Fig. 9. Wing-tip deflection as a function of time for the rectangular wing when the speed in the freestream is 75 m/s and α is 2.4 degrees.

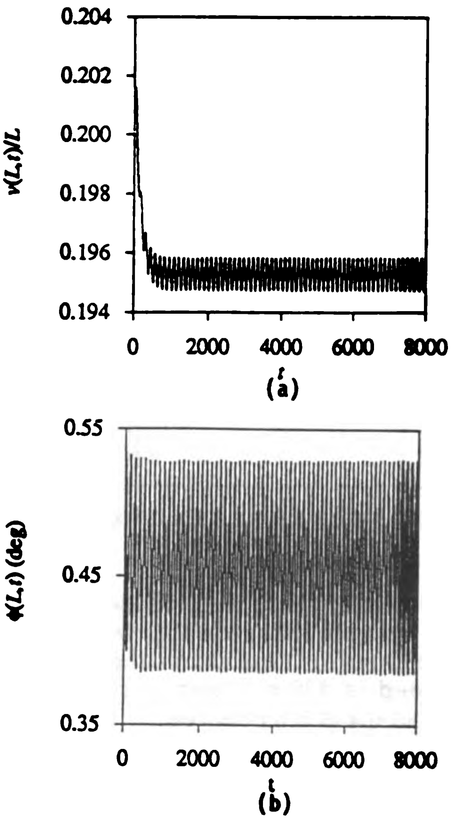

Fig. 10. (a) Wing-tip deflection and (b) wing-tip twist angle as functions of time for the rectangular wing when the speed in the freestream is 77.5 m/s.

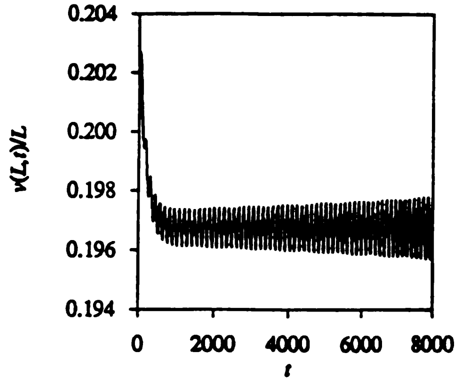

Fig. 11. Wing-tip deflection as a function of time for the rectangular wing when the speed in the freestream is 80 m/s.

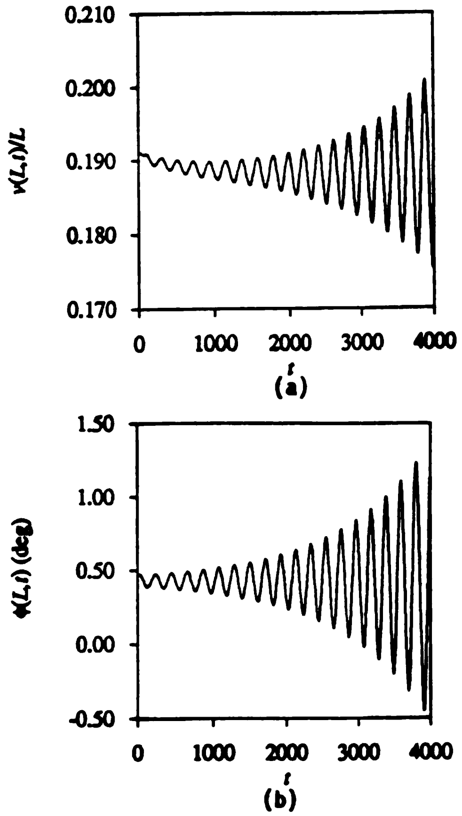

Fig. 12. (a) Uncontrolled wing-tip deflection and (b) uncontrolled wing-tip twist angle as functions of time when the freestream speed is 125 m/s and α and the angle of attack is 0.65 degree.

In Fig. 12, we show a supercritical response; here the speed is 125 m/s and α is 0.65 degree. The response oscillates while its amplitude appears to be growing exponentially. Bending and twist respond at the same frequency. In Fig. 13, we show the response under the same conditions as those used in Fig. 12 after the control system has been activated at the nondimensional time of 2000. The gains are $G_1 = -5$ and $G_2 = 500$. Although the oscillation has already developed a moderately large amplitude, the actively controlled aileron quickly suppresses the motion. When the control system is activated at a very early stage, flutter can be suppressed at speeds of 150 m/s or more, twice the critical speed.

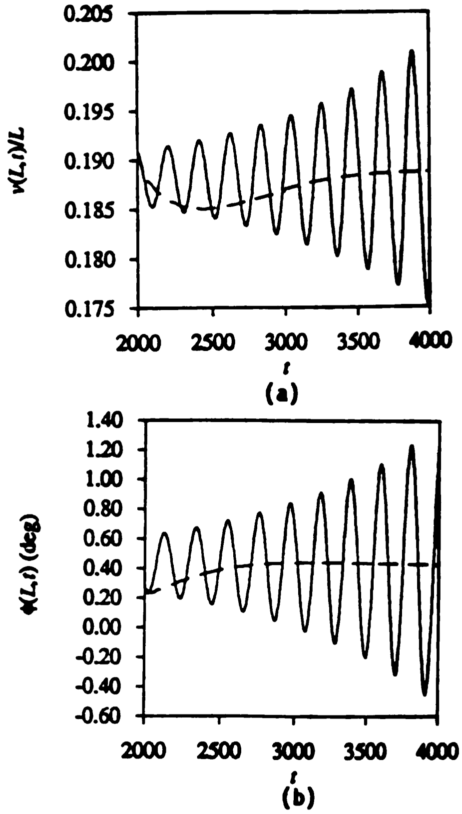

Fig. 13. (a) Controlled wing-tip deflection and b) controlled wing-tip twist angle as functions of time when the freestream speed is 125 m/s and α and the angle of attack is 0.65 degree. The control system is activated at time step 2000.

CONCLUDING REMARKS

A general formulation for simulating dynamic/aerodynamic interactions has been presented. The general formulation is modular and, consequently, different methods for simulating the flowfield and different dynamic and structural models can be used without changing the basic algorithm. Aerodynamic, material, inertial, and geometric nonlinear effects may be included. Motions in the subcritical, critical, and supercritical regimes can be simulated with no prior assumptions as to the form of the solution (e.g., periodic motions).

A relatively simple, linear feedback control system has been successfully used to suppress flutter in the present simulation. The control system consists of one or more ailerons as well as a servo motor. The present simulation is also capable of incorporating nonlinear control laws and variable gains. The gains for the current study were selected by a trial-and-error procedure. It was found that a wide range of gains is effective in the suppression of the instability. The control system can suppress flutter at almost twice the flutter speed. Although no attempt has been made to find the power requirements necessary for the aileron motion, it appears that only very small deflections and low frequencies are needed, especially when there is little or no delay in activating the control system.

ACKNOWLEDGEMENT

This work was supported by the Air Force Office of Scientific Research under Grant No. AFOSR-90-0032.

REFERENCES

Dong B, Numerical simulations of wakes, blade-vortex interaction, flutter, and flutter suppression by feedback control, PhD Thesis, Virginia Polytechnic Institute and State University, Blacksburg, VA, 1991.

Elzebda JM, Nayfeh AH, and Mook DT, Development of an analytical model of wing rock for slender delta wings, *J. Aircraft* **26**, 737-743 (1989).

Konstadinopoulos P, Mook DT, Nayfeh AH, Subsonic wing rock of slender delta wings, *J. Aircraft* **22**, 223-228 (1985).

Konstadinopoulos P, Thrasher DF, Mook DT, Nayfeh AH, and Watson L, A vortex-lattice method for general, unsteady aerodynamics, *J. Aircraft* **22**, 43-49 (1985).

Konstadinopoulos P, Numerical simulation of the subsonic wing-rock phenomenon, PhD Thesis, Virginia Polytechnic Institute and State University, Blacksburg, VA, 1984.

Levin D and Katz J, Dynamic load measurement of delta wings undergoing self-induced roll oscillation, AIAA Paper No. 82-1320 (1982).

Luo J and Lan CE, Control of wing-rock motion of slender delta wings, *J. Guid. Contr. and Dyns* **16**, 225-231 (1993).

Luton JA, Numerical simulations of subsonic aeroelastic behavior and flutter suppression by active control, PhD Thesis, Virginia Polytechnic Institute and State University, Blacksburg, VA, 1991.

Mracek C, Unsteady potential-flow solution by vortex panels coupled with dynamics and controls, PhD Thesis, Virginia Polytechnic Institute and State University, Blacksburg, VA, 1988.

Mracek CP, Kim MJ, and Mook DT, Three-dimensional potential flows by a vorticity-panel method, *Comput. & Fluids*, in press (1993).

Nayfeh AH, Elzebda JM, and Mook DT, Analytical study of the subsonic wing-rock phenomenon for slender delta wings, *J. Aircraft* **26**, 805-809 (1989).

Nguyen LT, Yip L, and Chambers JR, Self-induced wing rock of slender delta wings, AIAA Paper No. 82-1883 (1983).

Large-amplitude plate vibration in an elevated thermal environment

Jon Lee

Wright Laboratory (FIB), Wright-Patterson AFB, OH 45433

At elevated temperatures the dynamics of vibrating plate (or shell) must include the three thermal effects: (i) the global expansion by uniform plate temperature, (ii) the local expansion by temperature variation over the plate, and (iii) the thermal moment induced by temperature gradient across the plate thickness. For the single-mode prototype model of Galerkin representation, (i) and (ii) give rise to the combined stiffness that is responsible for thermal buckling, whereas (iii) contributes to the combined forcing of acoustic and thermal excitations. For the high-temperature sonic fatigue test facility at the Wright Lab, the present study is devoted to the mean square estimates on transverse displacement and normal stress/strain by the equivalent linearization technique.

1. INTRODUCTION

Transatmospheric vehicle (National Aero-Space Plane) technology presents a grand challenge of the rest of this century and the next for aerospace science and engineering communities. In contrast to the ballistic re-entry vehicles (space shuttles) piercing through the atmosphere nearly vertically, the transatmospheric vehicle will remain in the dense layer of the atmosphere for a good portion of its flight, and hence the air near the moving vehicle is heated to very high temperatures (aerodynamic heating). According to computational fluid dynamic simulations of hypersonic lifting body, the skin temperature can readily reach 2000°F and, in particular, the nose cone and external skin panels near the jet efflux are estimated to have temperatures over 3500°F (Barthelemy, 1991). At these high-temperature hypersonic flights, acoustic fatigue becomes a severe structural problem because not only are the pressure fluctuations anticipated in the range of 160-180 dB, but also the skin panels can vibrate chaotically about the thermally buckled positions whose amplitudes increase as the square root of temperature above the critical buckling temperature, i.e., the snap-through phenomena (Seide and Adami, 1983). Realizing the importance of elevated temperature on acoustic fatigue, work has begun as early as in the 70's to establish fatigue failure criteria in a combined thermal-acoustic environment (Schneider, 1974).

Sonic fatigue is a fluid-structure interaction problem requiring simultaneous solution of the Navier-Stokes equations for pressure/temperature and the structural dynamic equation for ensuing stress/strain. For large-amplitude deflections, the shape of structures defining the fluid-structure interface is not known *a priori*, hence must be determined from the solution of the fluid and structure equations. However, much progress has been made in the past by decoupling the structural part of the problem from solving the Navier-Stokes equations for pressure fluctuations. Following in this tradition, we shall in this paper investigate dynamics of a piece of hypersonic vehicle structure modeled by the so-called von Karman-Herrmann-Chu plate equation under prescribed pressure and temperature variations.

Although Bolotin (1963) derived the basic plate/shell equation for large-amplitude deflection subjected to temperature variation in the late 50's (Sec 2), the role of thermal effects has not yet been elucidated in their full generality. To exhibit the essential features, we expand the transverse displacement, Airy's stress function, and temperature distributions in trigonometric functions, and obtain the modal equations for the simply-supported and clamped plates (Sec 3).By a suitable nondimensionalization the modal equations of both the simply-supported and clamped plates are found to have three thermal terms. The first is global thermal expansion by a uniform plate temperature, the second corresponds to local thermal expansion by temperature variation over the plate, and the third term represents the thermal moment induced by temperature gradient through the plate thickness (Sec 4).

To proceed further, it is necessary to specify a typical temperature variation over the plate and temperature gradient across the plate (Sec 5). Much insight into the role of thermal terms can be gained by the prototype single-mode equation for both the simply-supported and clamped plates (Sec 6). The uniform temperature and temperature variation over the plate represent a kind of thermal stiffness which counteracts the structural stiffness. Hence, the combined thermal-structural stiffness is positive when the sum of uniform and local temperatures is less than the critical buckling temperature (pre-buckling), whereas it becomes negative when the sum exceeds the critical buckling temperature (post-buckling). In contrast, the temperature gradient gives rise to thermal moment, representing an additional loading (Boley and Weiner, 1960). Therefore, this together with external pressure constitute the combined thermal-acoustic forcing.

Under the acoustic loading, it is straightforward to estimate the mean response of a single-mode equation. However, the equivalent linearization technique (Caughey, 1963) cannot be applied when the temperature gradient

part of "MECHANICS PAN-AMERICA 1993" edited by MRM Crespo da Silva and CEN Mazzilli — ASME Reprint No AMR134
Appl Mech Rev vol 46, no 11, part 2, November 1993

represents a constant forcing. This therefore calls for reformulation to remove the constant thermal forcing. The main conclusion of this paper is that the uniform temperature, temperature variation over the plate, and temperature gradient across the plate can contribute additively to the mean square displacement (Sec 7) and also to the normal stress and strain (Sec 8). Yet, the thermal effects are felt most strongly when the acoustic loading is weak.

2. LARGE-DISPLACEMENT PLATE EQUATIONS

Let us begin with the following strain-stress relations

$$\varepsilon_x = \frac{1}{E}(\sigma_x - \mu\sigma_y) + \alpha T, \quad \varepsilon_y = \frac{1}{E}(\sigma_y - \mu\sigma_x) + \alpha T, \quad \varepsilon_{xy} = \frac{1+\mu}{E}\sigma_{xy}, \tag{1}$$

where E is the modulus of elasticity, μ Poisson's ratio, T the local plate temperature, and α the thermal expansion coefficient. In the absence of αT, Eq (1) is the usual relationship of strain (ε_x, ε_y, ε_{xy}) and stress (σ_x, σ_y, σ_{xy}). For $\alpha>0$, raising T would result in increased strain, in conformity with the physical notion of thermal expansion. The inverse relation is

$$\sigma_x = \frac{E}{(1-\mu^2)}\left[\varepsilon_x + \mu\varepsilon_y - (1+\mu)\alpha T\right],$$
$$\sigma_y = \frac{E}{(1-\mu^2)}\left[\varepsilon_y + \mu\varepsilon_x - (1+\mu)\alpha T\right], \quad \sigma_{xy} = \frac{E}{(1+\mu)}\varepsilon_{xy}. \tag{2}$$

Since the sign for αT is negative, the stress may in fact decrease as T is raised.

Following Bolotin (1963) we decompose T into

$$T(x,y,z) = \bar{T}(x,y) + z\theta(x,y), \tag{3}$$

where $\bar{T}(x,y)=h^{-1}\int_{-h/2}^{h/2}T(x,y,z)dz$ is temperature averaged over the plate thickness h, and $\theta(x,y)$ is the temperature gradient across h. Note that only the linear temperature variation in z is included in (3), according to the thin plate theory. We now summarize the compatibility, transverse displacement equation, and immovable edge and boundary conditions (see, Lee (1992) for the detail). It is however more convenient to measure x and y in units of a and b, the respective sides of plate, so that x and y now range over [0, 1]. First, the compatibility condition is

$$\hat{\nabla}^4 F + Eh\alpha b^2\hat{\nabla}^2\bar{T} = Eh\beta^2\left[\left(\frac{\partial^2 w}{\partial x\partial y}\right)^2 - \left(\frac{\partial^2 w}{\partial x^2}\right)\left(\frac{\partial^2 w}{\partial y^2}\right)\right], \tag{4}$$

where $\beta=b/a$ and $\hat{\nabla}^2=\beta^2\partial^2/\partial x^2+\partial^2/\partial y^2$. Note that the biharmonic operator applies to Airy's stress function F, and the transverse displacement w is governed by the von Karman type of large-deflection plate equation, written in the following symbolic form

$$R_1 + R_2 + R_3 + R_4 = 0, \tag{5}$$

where

$$R_1=\rho h\frac{\partial^2 w}{\partial t^2} + \rho h\xi\frac{\partial w}{\partial t} - p, \quad R_2=Db^{-4}\hat{\nabla}^4 w, \quad R_3=\alpha(1+\mu)Db^{-2}\hat{\nabla}^2\theta,$$

$$R_4=\frac{\beta^2}{b^4}\left[\left(\frac{\partial^2 w}{\partial x^2}\right)\left(\frac{\partial^2 F}{\partial y^2}\right) + \left(\frac{\partial^2 w}{\partial y^2}\right)\left(\frac{\partial^2 F}{\partial x^2}\right) - 2\left(\frac{\partial^2 w}{\partial x\partial y}\right)\left(\frac{\partial^2 F}{\partial x\partial y}\right)\right].$$

Here, ρ is the cross-sectional mass density, ξ the damping coefficient, p the external pressure, and $D=Eh^3/12(1-\mu^2)$ the flexural rigidity. The $\rho h\xi(\partial w/\partial t)$ is introduced to R_1 for viscous damping, but a more appropriate damping model would be $\xi D\hat{\nabla}^4(\partial w/\partial t)$ of Maekawa (1982). Eqs (4) and (5) are essentially Eqs (4.131) and (4.132) of Bolotin (1963), and also agree in form with Eqs (13.7.1) and (13.11.3) of Boley and Weiner (1960).

The compatibility states force balances at the mid-plate. Hence, it constrains the in-plane displacements u and v in x and y axes, respectively. Let us assume a homogeneous solution of $\hat{\nabla}^4 G=0$

$$G = P_x b^2 y^2/2 + P_y a^2 x^2/2 - P_{xy}abxy. \tag{6}$$

Here, the constants P_x, P_y, and P_{xy} representing the membrane stresses can be evaluated through the immovable edge conditions (Mei, 1980)

$$\frac{\partial^2 F}{\partial x\partial y} = 0 \text{ and } \int_0^1\int_0^1\left(\frac{\partial u}{\partial x}\right)dxdy = 0 \text{ at } x=0,\ 1$$
$$\frac{\partial^2 F}{\partial x\partial y} = 0 \text{ and } \int_0^1\int_0^1\left(\frac{\partial v}{\partial y}\right)dxdy = 0 \text{ at } y=0,\ 1 \tag{7}$$

Note that the edge displacements are suppressed only in the average sense. The integrands expressed in F and w are given by Eq (4.140) of Bolotin (1963)

$$b\beta\left(\frac{\partial u}{\partial x}\right) = \frac{1}{Eh}\left[\frac{\partial^2 F}{\partial y^2} - \mu\beta^2\frac{\partial^2 F}{\partial x^2}\right] + \alpha b^2\bar{T} - \frac{\beta^2}{2}\left(\frac{\partial w}{\partial x}\right)^2,$$
$$b\left(\frac{\partial v}{\partial y}\right) = \frac{1}{Eh}\left[\beta^2\frac{\partial^2 F}{\partial x^2} - \mu\frac{\partial^2 F}{\partial y^2}\right] + \alpha b^2\bar{T} - \frac{1}{2}\left(\frac{\partial w}{\partial y}\right)^2, \tag{8}$$

as given by Eq (4.140) of Bolotin (1963). For the boundary conditions, we first assume no transverse displacement

$$w(0,y) = w(1,y) = w(x,0) = w(x,1) = 0. \tag{9}$$

For a simply-supported plate, the tangential components of the bending moment being zero implies (Eq (12.4.2) of Boley and Weiner, 1963)

$$\beta^2\frac{\partial^2 w}{\partial x^2} + \alpha b^2(1+\mu)\theta = 0 \text{ at } x=0,\ 1$$
$$\frac{\partial^2 w}{\partial y^2} + \alpha b^2(1+\mu)\theta = 0 \text{ at } y=0,\ 1 \tag{10}$$

Whereas, we have for a clamped plate

$$\frac{\partial w}{\partial x} = 0 \text{ at } x=0,\ 1 \text{ and } \frac{\partial w}{\partial y} = 0 \text{ at } y=0,\ 1. \tag{11}$$

For an isotropic plate, the assumption that $\partial u/\partial x$, $\partial v/\partial y$, $\partial w/\partial x$, ... are constant across the plate leads to the following stress tensor

$$\sigma_x = \frac{1}{hb^2}\frac{\partial^2 F}{\partial y^2} - \frac{zE}{b^2(1-\mu^2)}\left(\beta^2\frac{\partial^2 w}{\partial x^2} + \mu\frac{\partial^2 w}{\partial y^2}\right) - \frac{zE\alpha\theta}{(1-\mu)},$$
$$\sigma_y = \frac{1}{hb^2}\frac{\partial^2 F}{\partial x^2} - \frac{zE}{b^2(1-\mu^2)}\left(\frac{\partial^2 w}{\partial y^2} + \mu\beta^2\frac{\partial^2 w}{\partial x^2}\right) - \frac{zE\alpha\theta}{(1-\mu)},$$
$$\sigma_{xy} = -\frac{\beta}{h\beta^2}\frac{\partial^2 F}{\partial x\partial y} - \frac{\beta zE}{b^2(1+\mu)}\frac{\partial^2 w}{\partial x\partial} \tag{12}$$

also given by Eqs (29-31) of Choi and Vaicaitis (1989). Inserting Eq (12) to (1) yields

$$\varepsilon_x = \frac{1}{Ehb^2}\left(\frac{\partial^2 F}{\partial y^2} - \mu\beta^2\frac{\partial^2 F}{\partial x^2}\right) - z\beta^2\frac{\partial^2 w}{\partial x^2} + \alpha T,$$

$$\varepsilon_y = \frac{1}{Ehb^2}\left(\beta^2\frac{\partial^2 F}{\partial x^2} - \mu\frac{\partial^2 F}{\partial y^2}\right) - z\frac{\partial^2 w}{\partial y^2} + \alpha T,$$

$$\varepsilon_{xy} = -\frac{(1+\mu)\beta}{Ehb^2}\frac{\partial^2 F}{\partial x\partial y} - \frac{\beta}{b^2}\frac{\partial^2 w}{\partial x\partial y}\ . \tag{13}$$

Eqs (12-13) will be used for the stress/strain computation in Sec 8.

3. THE DERIVATION OF MODAL EQUATIONS

Since $P_{xy}=0$ for the immovable edge (7), we construct F from homogeneous solution (6) and the particular solution expanded in cosines

$$F=-P_xb^2y^2/2 - P_ya^2x^2/2 + Eh\sum_{p=0}^{\infty}\sum_{q=0}^{\infty}F_{pq}\cos p\pi x\,\cos q\pi y. \tag{14}$$

And, a similar expansion is introduced for $\bar{T}$(Sunakawa and Uemura, 1960)

$$\bar{T} = t_o + \sum_{p=0}^{\infty}\sum_{q=0}^{\infty}t_{pq}\cos p\pi x\,\cos q\pi y. \tag{15}$$

Note that the term for p=q=0 is excluded from Eqs (14-15). To evaluate F_{pq} one must further assume an expansion for w.

For a simply-supported plate, it is standard to expand w in $\Psi_m(x)=\sin(m\pi x)$ with the desired properties that they are orthogonal and $\Psi_m(x)\Psi_n(y)$ is an eigenfunction of the biharmonic operator, i.e, the Helmholtz problem. We therefore adopt for a simply-supported plate

$$w(x,y)=\sum_{m=0}^{\infty}\sum_{n=0}^{\infty}w_{mn}\psi_m(x)\psi_n(y), \tag{16}$$

where $\psi_m(x)=\sqrt{2}\Psi_m(x)$ are orthonormal. On the other hand, $\Phi_m(x)=\cos(m+1)\pi x-\cos(m-1)\pi x$ have been used for the clamped plate problems (e.g., Maekawa, 1982, and Paul, 1982). However, they lack the desired properties so that the inertial and stiffness matrices become nondiagonal. Although one can readily construct orthonormal bases from $\Phi_m(x)$, as will be done shortly, the $\Phi_m(x)\Phi_n(y)$ is not an eigenfunction of the Helmholtz problem. Hence, a nondiagonal stiffness matrix is still unavoidable.

Let us rewrite $\Phi_m(x)=2S_m(x)$, where $S_m(x)=\sin(m\pi x)x\sin\pi x$, and construct the orthonormal φ_m from Φ_m by the Gram-Schmidt procedure (Luenberger, 1969). Since $S_1(x)$, $S_3(x)$, ... are even and $S_2(x)$, $S_4(x)$, ... are odd, one finds that $\varphi_m(x)$ also split into the even $\varphi_1=\sqrt{8/3}S_1(x)$, $\varphi_3=\sqrt{24/5}S_3(x)+\sqrt{8/15}S_1(x)$, ... and odd components $\varphi_2=2S_2(x)$, $\varphi_4=\sqrt{16/3}S_4(x)+\sqrt{4/3}S_2(x)$, ... Summing up, we then have

$$\varphi_m(x)=\sum_{1}^{m} \tag{17}$$

where

$$a_{mi} = \begin{bmatrix} \sqrt{8/3} & 0 & 0 & 0 & 0 & 0 & \cdots \\ 0 & 2 & 0 & 0 & 0 & 0 & \cdots \\ \sqrt{8/15} & 0 & \sqrt{24/5} & 0 & 0 & 0 & \cdots \\ 0 & \sqrt{4/3} & 0 & \sqrt{16/3} & 0 & 0 & \cdots \\ \sqrt{8/35} & 0 & 3\sqrt{8/35} & 0 & \sqrt{40/7} & 0 & \cdots \\ 0 & \sqrt{2/3} & 0 & \sqrt{8/3} & 0 & \sqrt{6} & \cdots \\ \vdots & \vdots & \vdots & \vdots & \vdots & \vdots & \vdots \end{bmatrix}$$

The expansion for a clamped plate has the form

$$w(x,y)=\sum_{m=0}^{\infty}\sum_{n=0}^{\infty}w_{mn}\varphi_m(x)\varphi_n(y), \tag{18}$$

where φ_m are orthonormal.

Simply-Supported Plate: By inserting Eqs (14-16) into (4) and collecting the coefficients for F_{pq}, we have

$$F_{pq} = \frac{\alpha b^2 t_{pq}}{\pi^2(p^2\beta^2+q^2)} + \frac{A_{pq}}{(p^2\beta+q^2/\beta)^2}\ , \tag{19}$$

where A_{pq} given in Appendix A consists of nine sums B_1-B_9 of Levy (1942). In parallel to (16), we also expand

$$\begin{pmatrix}\theta(x,y)\\ p(x,y)\end{pmatrix} = \sum_{m=0}^{\infty}\sum_{n=0}^{\infty}\begin{pmatrix}\theta_{mn}\\ p_{mn}\end{pmatrix}\psi_m(x)\psi_n(y). \tag{20}$$

Now, introduce Eqs (14), (16) and (20) into (5) and sort out the coefficients for w_{rs} by the Galerkin procedure. Because of the orthonormality, one can write down at once

$$\int_0^1\int_0^1 R_1\psi_r(x)\psi_s(y)dxdy= \rho h\frac{\partial^2 w_{rs}}{\partial t^2} + \rho h\xi\frac{\partial w_{rs}}{\partial t} - p_{rs},$$

$$\int_0^1\int_0^1 R_2\psi_r(x)\psi_s(y)dxdy= \frac{D\pi^4}{b^4}(\beta^2r^2 + s^2)^2 w_{rs},$$

$$\int_0^1\int_0^1 R_3\psi_r(x)\psi_s(y)dxdy= -\frac{\alpha(1+\mu)D\pi^2}{b^2}(\beta^2r^2 + s^2)\theta_{rs}. \tag{21}$$

On the other hand, the integral for R_4 is complicated due to the product of F and w. After some algebra, we have

$$\begin{aligned}\int_0^1\int_0^1 R_4\psi_r(x)\psi_s(y)dxdy= &-\frac{\pi^2\alpha Eht_o}{b^2(1-\mu)}(\beta^2r^2 + s^2)\,w_{rs}\\ &-\frac{\pi^2\beta^2\alpha Eh}{4b^2}B_{rs}\left(w_{mn}, \frac{t_{pq}}{(\beta^2p^2+q^2)}\right) + \frac{\pi^4\beta^2 Eh}{2b^4(1-\mu^2)}K_1 w_{rs}\\ &-\frac{\pi^4\beta^2 Eh}{4b^4}B_{rs}\left(w_{mn}, \frac{A_{pq}}{(\beta p^2+q^2/\beta)^2}\right),\end{aligned} \tag{22}$$

where

$$K_1=\sum_{m,n=1}^{\infty}\left\{r^2(\beta^2 m^2w_{mn}^2+\mu n^2w_{mn}^2)+s^2(\mu m^2w_{mn}^2+\beta^{-2}n^2w_{mn}^2)\right\}.$$

The B_{rs} is given in Appendix B. By equating the sum of four integrals in Eqs (21-22) to zero, the modal equation is obtained for w_{rs}.

Clamped Plate: Inserting Eqs (14-15) and (18) into (4), we obtain

$$F_{pq} = \frac{\alpha b^2 t_{pq}}{\pi^2(p^2\beta^2+q^2)} + \frac{C_{pq}}{(p^2\beta+q^2/\beta)^2}, \tag{23}$$

where C_{pq} is given in Appendix C. Similar to (20) we let

$$\begin{pmatrix}\theta(x,y)\\ p(x,y)\end{pmatrix} = \sum_{m=0}^{\infty}\sum_{n=0}^{\infty}\begin{pmatrix}\theta_{mn}\\ p_{mn}\end{pmatrix}\varphi_m(x)\varphi_n(y). \tag{24}$$

Because of the orthonormality, one finds at once

$$\int_0^1\int_0^1 R_1\varphi_r(x)\varphi_s(y)dxdy = \rho h\frac{\partial^2 w_{rs}}{\partial t^2} + \rho h\xi\frac{\partial w_{rs}}{\partial t} - p_{rs}. \tag{25}$$

For the biharmonic term, we obtain

$$\int_0^1\int_0^1 R_2\varphi_r(x)\varphi_s(y)dxdy = \frac{D\pi^4}{b^4}K_2, \tag{26}$$

where

$$K_2 = -\frac{\beta^4}{8}\sum_{m=1}^{\infty} w_{ms}\sum_{i=1}^{m} a_{mi}\sum_I{}' \sum_J{}' IJ a_{r(i+I+J)}(i+I)^4 - \frac{1}{8}\sum_{n=1}^{\infty} w_{rn}\sum_{j=1}^{n} a_{nj}\sum_I{}' \sum_J{}' IJ a_{s(i+I+J)}(i+I)^4$$
$$+\frac{\beta^2}{32}\sum_{m,n=1}^{\infty} w_{mn}\Big\{\sum_{i=1}^{m} a_{mi}\sum_I{}' \sum_J{}' IJ a_{r(i+I+J)}(i+I)^2\Big\} \times\Big\{\sum_{j=1}^{n} a_{nj}\sum_I{}' \sum_J{}' IJ a_{s(i+I+J)}(i+I)^2\Big\}.$$

Here, the notation $\sum_I{}' f(I)=f(1)+f(-1)$ of Maekawa (1982) is used to consolidate the shifted summands. Similarly, we find

$$\int_0^1\int_0^1 R_3\varphi_r(x)\varphi_s(y)dxdy = -\frac{\alpha(1+\mu)D\pi^2}{b^2}K_3, \tag{27}$$

where

$$K_3 = -\frac{\beta^2}{8}\sum_{m=1}^{\infty}\theta_{ms}\sum_{i=1}^{m} a_{mi}\sum_I{}' \sum_J{}' IJ a_{r(i+I+J)}(i+I)^2 - \frac{1}{8}\sum_{n=1}^{\infty}\theta_{rn}\sum_{j=1}^{n} a_{nj}\sum_I{}' \sum_J{}' IJ a_{s(i+I+J)}(i+I)^2.$$

Finally, the integral for R_4 can be put in the form

$$\int_0^1\int_0^1 R_4\varphi_r(x)\varphi_s(y)dxdy = -\frac{\pi^2\alpha Eht_o}{b^2(1-\mu)}(\beta^2K_4+K_5) - \frac{\pi^2\beta^2\alpha Eh}{4b^2}D_{rs}\Big(w_{mn}, \frac{t_{pq}}{(\beta^2p^2+q^2)}\Big)$$
$$+\frac{\pi^4\beta^2 Eh}{2b^4(1-\mu^2)}\Big\{(\beta^2K_6+\mu K_7)K_4 + (\mu K_6+\beta^{-2}K_7)K_5\Big\} - \frac{\pi^4\beta^2 Eh}{4b^4}D_{rs}\Big(w_{mn}, \frac{C_{pq}}{(\beta p^2+q^2/\beta)^2}\Big). \tag{28}$$

The D_{rs} and K_4 - K_7 are given in Appendix D. Again, the modal equations for a clamped plate are formed from the four integrals in Eqs (25-28).

4. UNIFIED MODAL EQUATIONS

For unified representation we put the modal equations in a dimensionless form by scaling the length by h, the time by $\gamma=(\rho hb^4/\pi^4 D)^{1/2}$, the force by $(\rho h^2/\gamma^2)$, and the temperature by T^*, to be defined shortly. Accordingly, the dimensionless mechanical variables are

$$\tau = t/\gamma,\ P_{rs} = (\gamma^2/\rho h^2)p_{rs},\ W_{rs} = w_{rs}/h, \tag{29}$$

and thermal variables are

$$T_o = t_o/T^*,\ T_{pq} = t_{pq}/T^*,\ \Theta_{rs} = h\theta_{rs}/T^*. \tag{30}$$

Simply-Supported Plate: The modal equation for W_{rs} follows by equating the sum of four integrals (21-22) to zero. For a simply-supported plate, the appropriate T^* is the critical buckling temperature $T_s^*=\pi^2h^2(\beta^2+1)/12\alpha b^2(1+\mu)$, at which the global thermal expansion cancels out the structural stiffness for W_{11} (Wilcox and Clemmer, 1964, and Schneider, 1974). Using the variables (29-30), the dimensionless modal equation becomes

$$\underbrace{\frac{\partial^2 W_{rs}}{\partial\tau^2}}_{\text{(SP-1)}} + \underbrace{\gamma\xi\frac{\partial W_{rs}}{\partial\tau}}_{\text{(SP-2)}} \underbrace{- P_{rs}}_{\text{(SP-3)}} + \underbrace{(\beta^2r^2+s^2)^2 W_{rs}}_{\text{(SP-4)}} + \underbrace{6\beta^2K_1W_{rs}}_{\text{(SP-5a)}}$$
$$\underbrace{-3\beta^2(1-\mu^2)B_{rs}\Big(W_{mn}, \frac{A_{pq}}{(\beta p^2+q^2/\beta)^2}\Big)}_{\text{(SP-5b)}} \underbrace{-(\beta^2+1)(\beta^2r^2+s^2)T_oW_{rs}}_{\text{(SP-6)}}$$
$$\underbrace{-\frac{(1-\mu)\beta^2(\beta^2+1)}{4}B_{rs}\Big(W_{mn}, \frac{T_{pq}}{(\beta^2p^2+q^2)}\Big)}_{\text{(SP-7)}}$$
$$\underbrace{-\frac{(\beta^2+1)(\beta^2r^2+s^2)}{12}\Theta_{rs}}_{\text{(SP-8)}} = 0. \tag{31}$$

We may interpret the terms labeled by SP (simply-supported plate) 1 - 8 as follows: SP-1 is the inertial term, SP-2 represents viscous damping, SP-3 is the external forcing, SP-4 is the usual stiffness term, and SP-5a and 5b represent the cubic stiffness. Note that SP-5a is the immovable edge contribution, whereas SP-5b is derived from the product of w and F. The thermal effects are embodied by the last three terms. That is, SP-6 is the global thermal expansion owing to uniform plate temperature, SP-7 is the local thermal expansion by temperature variation over the plate, and SP-8 represents the thermal moment induced by temperature gradient across the plate thickness.

Clamped Plate: Using $T_c^*=\pi^2h^2(\beta^4+2\beta^2/3+1)/3\alpha b^2(1+\mu)\times(\beta^2+1)$ for the clamped plate, the modal equation becomes

$$\underbrace{\frac{\partial^2 W_{rs}}{\partial\tau^2}}_{\text{(CP-1)}} + \underbrace{\gamma\xi\frac{\partial W_{rs}}{\partial\tau}}_{\text{(CP-2)}} \underbrace{- P_{rs}}_{\text{(CP-3)}} + \underbrace{[K_2(W_{mn})]_{rs}}_{\text{(CP-4)}}$$
$$\underbrace{+6\beta^2[(\beta^2K_6+\mu K_7)K_4+(\mu K_6+\beta^{-2}K_7)K_5]_{rs}}_{\text{(CP-5a)}}$$
$$\underbrace{-3\beta^2(1-\mu^2)D_{rs}\Big(W_{mn}, \frac{C_{pq}}{(\beta p^2+q^2/\beta)^2}\Big)}_{\text{(CP-5b)}}$$
$$\underbrace{-\frac{4(\beta^4+2\beta^2/3+1)}{(\beta^2+1)}T_o[\beta^2K_4(W_{mn})+K_5(W_{mn})]_{rs}}_{\text{(CP-6)}}$$
$$\underbrace{-\frac{(1-\mu)\beta^2(\beta^4+2\beta^2/3+1)}{(\beta^2+1)}D_{rs}\Big(W_{mn}, \frac{T_{pq}}{(\beta^2p^2+q^2)}\Big)}_{\text{(CP-7)}}$$

$$-\frac{(\beta^4+2\beta^2/3+1)}{3(\beta^2+1)}[K_3(\Theta_{mn})]_{rs}=0. \tag{32}$$

(CP-8)

The CP (clamped plate) 1-8 have the same meaning as SP 1-8.

The enumeration of (31) and (32) has been carried out by Lee(1992) for the lowest order W_{11}, W_{13}, W_{31}, and W_{33} to provide a comparison with Levy's (1942) simply-supported plate case and the clamped plate result of Paul (1982). Even with only four W_{rs}, the modal equations have a bewildering number of constant, linear, and cubic terms. Therefore, as a check on the internal consistency, we construct the Hamiltonian H(p,q), where $p_1=\dot{W}_{11}$, $p_2=\dot{W}_{13}$, $p_3=\dot{W}_{31}$, $p_4=\dot{W}_{33}$, $q_1=W_{11}$, $q_2=W_{13}$, $q_3=W_{31}$, $q_4=W_{33}$, from which the equations for W_{rs} have been recovered by

$$\dot{p}_i=-\frac{\partial H}{\partial q_i},\quad \dot{q}_i=\frac{\partial H}{\partial p_i}, \tag{33}$$

for the simply-supported (Lee, 1986) and clamped (Lee, 1992) plates.

5. TEMPERATURE VARIATION AND GRADIENT

To proceed further, it is necessary to specify T_{pq} and Θ_{rs} in Eqs (31-32). We split the averaged temperature into uniform t_o and variation $t_v(x,y)$

$$\bar{T}=t_o+t_v(x,y), \tag{34}$$

as in (15). Hence, Eq (3) has the form

$$T=t_o+t_v(x,y)+Z\Theta(x,y), \tag{35}$$

where $Z=z/h$ ranges over [1/2, -1/2]. Since t_o is assumed nonzero, the magnitude of (t_v, Θ) will be measured by multiples (δ_v, δ_g) of t_o

$$t_v=\delta_v t_o f_v(x,y),\quad \Theta=\delta_g t_o f_g(x,y). \tag{36}$$

In words, ($\delta_v t_o$,$\delta_v t_o$) is the magnitude of temperature (variation, gradient) with the distribution ($f_v(x,y)$, $f_g(x,y)$). Upon inserting (36) into (35) we have the dimensionless form

$$T/T^*=T_o+(\delta_v T_o)f_v(x,y)+(\delta_g T_o)Zf_g(x,y), \tag{37}$$

where $T^*=(T_s^*, T_c^*)$ for the (simply-supported, clamped) plate.

First, by comparing (37) with (15) we have

$$(\delta_v T_o)f_v(x,y)=\sum_{p=0}^{\infty}\sum_{q=0}^{\infty}T_{pq}\cos p\pi x\cos q\pi y. \tag{38}$$

Let us examine a few examples. If $f_v=\sin\pi x\sin\pi y$ we find from (38) that

$$T_{pq}=\frac{16\delta_v T_o}{\pi^2(p^2-1)(q^2-1)} \quad \text{[illegible]} q\neq 0) \tag{39}$$

For the second example $f_v=\sin\pi x^2\sin\pi y^2$, the sum in (38) reduces to a finite sum (1/4)(1-cos2πx)(1-cos2πy). Hence,

$$T_{20}=T_{02}=-T_{22}=-\delta_v T_o/4,\quad T_{pq}=0 \text{ (for other p, q)}. \tag{40}$$

Now, for the temperature gradient we write in view of (20) and (24)

$$(\delta_g T_o)f_g(x,y)=\sum_{m=0}^{\infty}\sum_{n=0}^{\infty}\Theta_{mn}\eta_m(x)\eta_n(y), \tag{41}$$

where $\eta_m=(\psi_m, \varphi_m)$ for the (simply-supported, clamped) plate. For simplicity we shall suppose $f_g=\sin\pi x\sin\pi y$ for the simply-supported plate and obtain

$$\Theta_{11}=\delta_g T_o/2,\quad \Theta_{mn}=0 \text{ (for other m, n)} \tag{42}$$

Whereas, $f_g=\sin\pi x^2\sin\pi y^2$ gives rise to

$$\Theta_{11}=3\delta_g T_o/8,\quad \Theta_{mn}=0 \text{ (for other m, n)} \tag{43}$$

for a simple temperature gradient for the clamped plate.

Although it appears at first sight that δ_v and δ_g can be chosen arbitrarily, this is not the case when the temperature variation and gradient are nonuniform. Note that a nonuniform Θ cannot exist unless t_v is also nonuniform; i.e, $\delta_v=0$ implies $\delta_g=0$. What is then the maximum value of δ_g, denoted by $(\delta_g)_{max}$, for a given δ_v? This cannot be answered in general without knowing the f_v and f_g. However, in the case $f_v=f_g$, one may infer $(\delta_g)_{max}=2\delta_v$. Sunakawa and Uemura (1960) have used a parabolic distribution for f_v and f_g, and prescribed $(\delta_g)_{max}=(4/3)\delta_v$, for which the lower plate temperature is half the upper plate temperature. In view of the recent attempts (Kehoe and Synder, 1991; Richards and Thompson, 1991) to generate various temperature profiles over a panel by radiant heating, the sorts of f_v that we have discussed here are not unphysical. Yet, to the best of our knowledge no attempt has yet been made to either measure or control f_g over a plate.

6. SINGLE-MODE EQUATION FOR W_{11}

Let us examine the simplest case of a single mode W_{11} when all others are suppressed. Under (40) and (42), the simply-supported plate equation (31) gives

$$\ddot{W}_{11}+\gamma\xi\dot{W}_{11}+(\beta^2+1)^2\left\{1-T_o\left[1+\frac{1}{8}(1-\mu)\delta_v\right]\right\}W_{11}+4e(\mu,\beta)W_{11}^3$$
$$-\left[P_{11}+\frac{1}{24}(\beta^2+1)^2\delta_g T_o\right]=0, \tag{44}$$

where $e(\mu,\beta)=(3/4)[(1-\mu^2)(\beta^4+1)+2(\beta^4+1+2\mu\beta^2)]$. Under (40) and (43) Eq (32) similarly reduces to

$$\ddot{W}_{11}+\gamma\xi\dot{W}_{11}+$$
$$+\frac{16}{3}(\beta^4+2\beta^2/3+1)\left\{1-T_o\left[1+\frac{1}{6}(1-\mu)\delta_v\left(1+\beta^2(\beta^2+1)^{-2}\right)\right]\right\}W_{11}$$
$$+\frac{128}{9}d(\mu,\beta)W_{11}^3-\left[P_{11}+\frac{1}{6}(\beta^4+2\beta^2/3+1)\delta_g T_o\right]=0, \tag{45}$$

where $d(\mu,\beta)=(3\beta^2/4)\{(\beta^2+\beta^{-2}+2\mu)+(1-\mu^2)(4/9)[17(\beta^2+$

$\beta^{-2})/8+4(\beta+\beta^{-1})^{-2}+(\beta+4\beta^{-1})^{-2}+(4\beta+\beta^{-1})^{-2}]\}$. The eight terms in Eqs (31-32) are now regrouped into five. The first two inertial and damping terms are retained intact. However, the third term of Eq (44, 45) is the combined stiffness which subsumes the stiffness (SP-6, CP-4), global thermal expansion (SP-6, CP-6), and local thermal expansion (SP-7, CP-7). And, the fourth term represents the cubic stiffness (SP-5, CP-5). Finally, the last term in Eq (44, 45) is the combined forcing of the external pressure (SP-3, CP-3) and thermal moment (SP-8, CP-8).

Since Eqs (44) and (45) are similar, we present them in a prototype form ($q=W_{11}$ and $f=P_{11}$)

$$\ddot{q} + \omega_0\xi\dot{q} + \omega_0^2(1-s)q + \kappa q^3 = f_o + f(t), \tag{46}$$

where $\omega_o=(\beta^2+1)$, $s=T_o[1+(1-\mu)\delta_v/8]$, $\kappa=4e$, $f_o=(\beta^2+1)^2\delta_g T_o/24$ for the simply-supported plate; and $\omega_o=16(\beta^4+2\beta^2/3+1)/3$, $s=T_o[1+(1-\mu)\delta_v(1+\beta^2(\beta^2+1)^{-2})/6]$, $\kappa=128d/9$, $f_o=(\beta^4+2\beta^2/3+1)\delta_g T_o/6$ for the clamped plate. Also, $\gamma=\omega_o$ is introduced. Note that the combined stiffness $\omega_0^2(1-s)$ is positive when the thermal loading is weak ($s<1$ for pre-buckling), whereas it becomes negative under a strong thermal loading ($s>1$ for post-buckling).

Without damping and forcing, the Hamiltonian $H=K+U$ for Eq (46) has the kinetic energy $K=p^2/2$ and potential (strain) energy $U=\omega_0^2(1-s)q^2/2+\kappa q^4/4-f_oq$. When $f_o=0$ the potential energy is even, $U(q)=U(-q)$. Hence, f_o has a very significant effect of destroying the symmetry property of Duffing oscillator as defined by Räty (1984). Fig 1(a) shows the symmetric U of a simply-supported plate under $f_o=0$. Note that the single well potential develops a double well as $s>1$. Although δ_vT_o has been lumped into a parameter s, one must specify δ_g and T_o for f_o. For qualitative discussions, we let $\delta_v=\delta_g=1$ and express T_o in terms of s

$$T_o=s/[1+(1-\mu)/8],\ T_o=s/[1+(1-\mu)(1+\beta^2(\beta^2+1)^{-2})/6], \tag{47}$$

for the simply-supported and clamped plates. In this way, the three thermal terms can all be quantified by s. Shown in Fig 2 are the potentials of Fig 1(a) being asymmetrized by the temperature gradient. Note that an asymmetric U has also been observed in an electrical power system model (Nayfeh et al., 1990) and imperfect structural model (Souza and Mook, 1991).

A. Thermally Buckled Modal Amplitude

The static problem of (46) is governed by

$$\kappa Q^3 + \omega_0^2(1-s)Q - f_o = 0. \tag{48}$$

For $f_o=0$ the two regimes of (48) are $Q_1=0$ for $s<1$ and

$$Q_2 = \pm\omega_o\sqrt{(s-1)/\kappa}, \tag{49}$$

for $s>1$. Since (48) is nothing but $\partial U/\partial q=0$, the Q_1 and Q_2 represent the trough of symmetric U, shown in Fig 1(b). When $f_o\neq0$ Eq (48) again has two regimes. For $s<s^*$ it has only one real root

$$Q_3=\left[\frac{f_o}{2\kappa}+\sqrt{\left(\frac{f_o}{2\kappa}\right)^2+\left(\frac{\omega_0^2(1-s)}{3\kappa}\right)^3}\,\right]^{1/3} - \left[-\frac{f_o}{2\kappa}+\sqrt{\left(\frac{f_o}{2\kappa}\right)^2+\left(\frac{\omega_0^2(1-s)}{3\kappa}\right)^3}\,\right]^{1/3}, \tag{50}$$

for the radicand is positive. In fact, the critical s^* is determined by the zero radicand

$$s^* = 1 + \left(\frac{3\kappa}{\omega_0^2}\right)\left(\frac{f_o}{2\kappa}\right)^{2/3}. \tag{51}$$

For $s>s^*$ the radicand is negative, so that the two real roots representing the trough of asymmetric double well potential are

$$Q_{4,n}=2\left(\frac{\omega_0^2(s-1)}{3\kappa}\right)^{1/2}\cos\left(\frac{\vartheta}{3}+\frac{2\pi n}{3}\right),\ (n=0,\ 1) \tag{52}$$

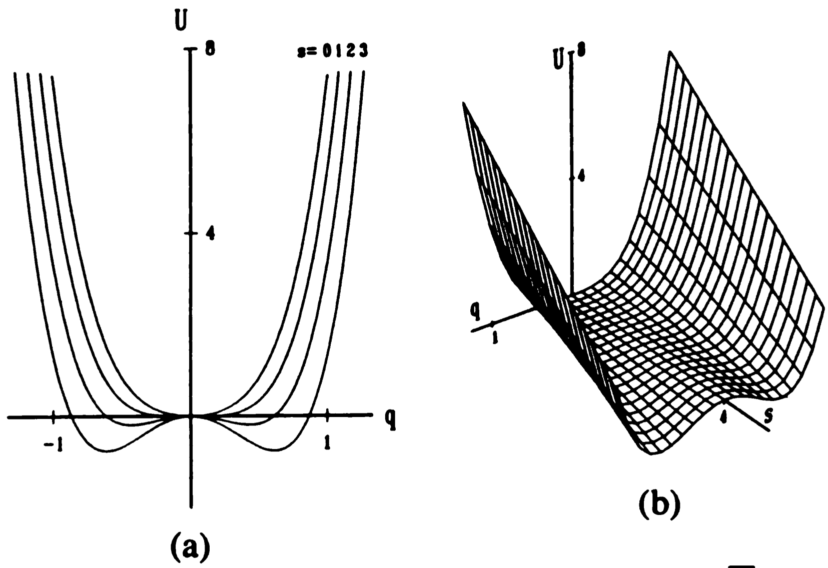

Fig 1. The potential energy U of a simply-supported plate under $\beta=1$ and $\mu=\sqrt{0.1}$. (a) Discrete increments of s =0, 1, 2, 3. (b) Single well potential developing a symmetric double well.

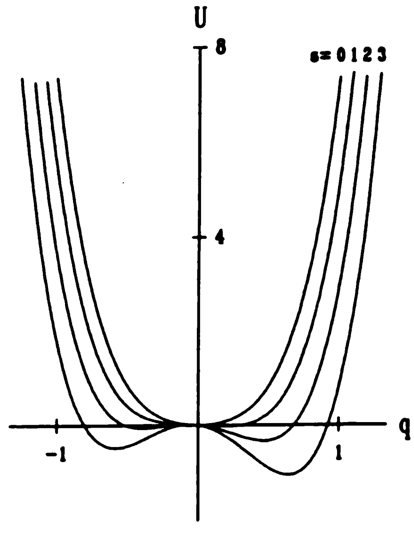

Fig 2. Asymmetrized potentials due to $f_o=s/6[1+(1-\mu)/8]$ of the simply-supported plate under $\beta=1$ and $\mu=\sqrt{0.1}$

where $\cos\vartheta = \left((f_0/2\kappa)^2/(\omega_0^2(s-1)/3\kappa)^3\right)^{1/2}$. In Fig 3 we compare the pairs (Q_1, Q_2) and (Q_3, Q_4) under the relation (47). Note that the emergence of two roots (52) is quite sudden, and Q_3 and $Q_{4,0}$ are joined smoothly at $s=s^*$. As expected, the (Q_3, Q_4) degenerate to (Q_1, Q_2) when $f_0=0$.

B. Dynamic Considerations

The equilibrium Q_3 is stable for $s<s^*$ and becomes unstable at $s=s^*$. On the other hand, the stable equilibrium states are given by Q_4 for $s>s^*$. The local dynamic can best be examined by the change of variable $q=Q+r$ in (46)

$$\ddot{r} + \omega_0\xi\dot{r} + [\omega_0^2(1-s)+3\kappa Q^2]r + 3\kappa Qr^2 + \kappa r^3 = f(t), \qquad (53)$$

by virtue of (48). Eq (53) now describes oscillations about the state Q. In fact, we have traded Eq (46) with the right-hand side f_0 term with a pair of (48) and (53). Under $f_0=0$, we have $Q_1=0$ for $s<1$, so that (48) and (53) reduce to the original equation (46). And, for $s>1$ we have, since $Q=Q_2$

$$\ddot{r} + \omega_0\xi\dot{r} + 2\omega_0^2(s-1)r + 3\kappa Q_2 r^2 + \kappa r^3 = f(t). \qquad (54)$$

This therefore has led Schneider (1974) to conclude that the natural frequency is increased by the $\sqrt{2}$ factor after thermal buckling. Although (46) and (53) are equivalent, the latter system is better suited for a local analysis about the Q (Sec 7).

For the global analysis, one must deal directly with (46). This equation, however, does not appear studied in its entirety, although there is no dearth of investigations pertaining to certain subsystems of it. Of course, the most notable is when $f_0=0$. Introducing $f(t)=M\cos\Omega t$(where M and Ω are the forcing amplitude and frequency), (46) is has the well-known Duffing's equation

$$\ddot{q} + \omega_0\xi\dot{q} + \omega_0^2(1-s)q + \kappa q^3 = M\cos\Omega t, \qquad (55)$$

with a hard ($\kappa>0$) and soft ($\kappa>0$) spring (Stoker, 1950). For $s<1$ the equilibrium $Q_1=0$ represents the trough of single well potential in Fig 1(b). As s passes through unity, Q_1 becomes unstable and Q_2 is now the stable equilibrium state. Let us rewrite (55) for $s>1$

$$\ddot{q} + \omega_0\xi\dot{q} - \omega_0^2(s-1)q + \kappa q^3 = M\cos\Omega t. \qquad (56)$$

This is the so-called buckled beam equation of Holmes (1979). The dynamics of Duffing and Holmes oscillators have been investigated extensively (see, for instance, Huberman and Crutchfield (1979), Räty et al. (1984), and Nayfeh and Sanchez (1989) for soft Duffing oscillator; Novak and Frehlick (1982) for hard Duffing oscillator; and Guckenheimer and Holmes (1983) for Holmes oscillator). The general observation is that the development of chaos in these oscillators can be ascribed to the symmetry breaking, thereby engendering even modes consistent with the period doubling scenario of Feigenbaum (Kalafati and Malakhov, 1983).

Under $f_0\neq 0$ Duffing's equation that Ueda (1981) has originally investigated is Eq (46) with $f=M\cos\Omega t$, but $s=1$ so that only the cubic stiffness term is present. On the other hand, the systems of Nayfeh et al. (1990) and Souza and Mook (1991) have a nonzero forcing term; however, their cosine potential represents a nonlinear pendulum.

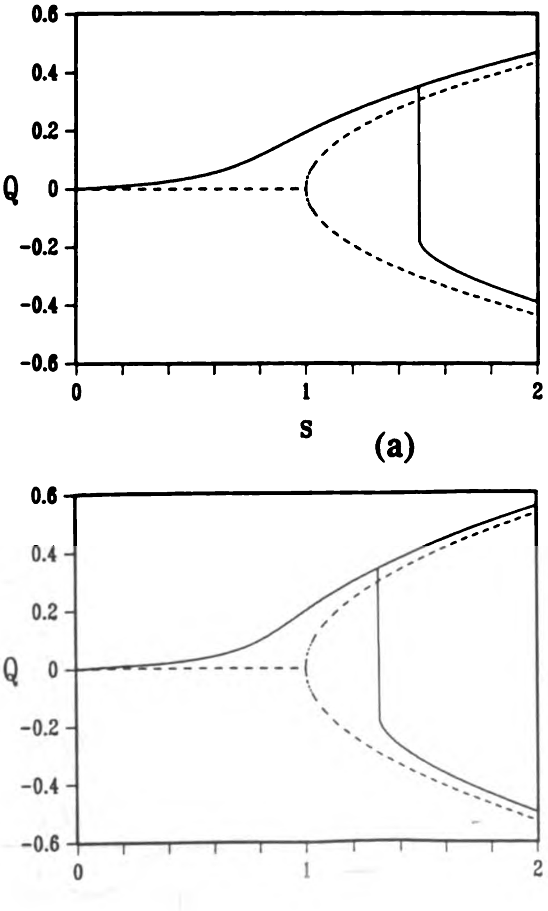

Fig 3. The trough of potential ...rmined by the real roots of Eq (48). The f_0 is rela... ...nder $\delta_v=\delta_g=1$. Q_1 and Q_2 are denoted by a broke... ...by a solid line. (a) Simply- supported plate; (b) cl...

7. RANDOM DISPLACEMENT ESTIMATION

The combined forcing $g=f_0+f$ is a nonzero-mean Gaussian process when f(t) is assumed zero-mean Gaussian. The

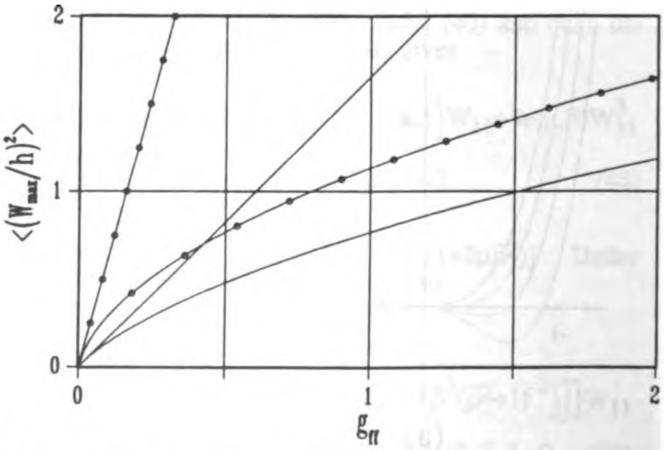

Fig 4. Linear and nonlinear estimates of the maximum mean square displacement under $\beta=1$, $\mu=\sqrt{0.1}$, $\xi=0.04$. The simply-supported plate is denoted by a line with circles, and the clamped plate without circles.

equivalent linearization technique was formulated (Caughey, 1963) for a zero-mean Gaussian excitation, hence it is necessary to reformulate the problem so that f_0 does not appear in the forcing term. We shall first consider $f_0=0$ in Sec 7A and the general case $f_0 \neq 0$ will be presented in Sec 7B.

A. Acoustic Loading ($g=f(t)$)

Pre-buckling ($s<1$): Let us denote by q_{lin} the amplitude of linearized Eq (46) under $f_0=0$. The mean square amplitude is given by Eq (E3) of Appendix E

$$<q_{lin}^2> \approx \frac{g_{ff}(f)}{2\xi\omega_0^3(1-s)}, \tag{57}$$

where < > is the statistical (time) average and $g_{ff}(f)$ is the power spectral density in frequency. Now, for (46) the equivalent linearization technique yields

$$<q^2> = \frac{\omega_0^2(1-s)}{6\kappa}\left[\sqrt{1+\frac{12\kappa<q_{lin}^2>}{\omega_0^2(1-s)}}-1\right], \tag{58}$$

as given by Eq (E9). For small κ, (58) reduces to $<q^2> \approx <q_{lin}^2>$ as expected, and $<q^2> \approx <q_{lin}^2>^{1/2}$ when κ is large.

For the nonthermal ($s=0$) reference, we have evaluated $<q_{lin}^2>$ and $<q^2>$ for $\beta=1$, $\mu^2=0.1$, $\xi=0.04$, and presented in Fig 4 the maximum displacement

$$<(W_{max}/h)^2> = c<q_{lin}^2> \text{ or } c<q^2>, \tag{59}$$

where $c=(4, 64/9)$ for the (simply-supported, clamped) plate. In the figure, the straight lines originating from the origin are linear input-output relations. However, the mean square displacement (58) increases more gradually due to a nonlinear saturation provided by the equivalent linearization. For a given g_{ff}, the simply-supported plate has a larger mean displacement than the corresponding clamped plate, as already noted by Mei (1980).

In the thermal case ($s>0$), the mean square displacement increases with s, as evidenced by the three $s=0$, 0.5 and 0.9 in Fig 5. However, the net thermal contribution diminishes as g_{ff} becomes large. This may be inferred from the limiting form of (58), $<q^2> \approx (g_{ff}/6\xi\kappa\omega_0)^{1/2}$, as $g_{ff} \to \infty$, which is independent of s. In other words, the uniform temperature and temperature variation will have no effect on the mean square displacement when the acoustic loading is large.

Post-buckling ($s>1$): Denoting by r_{lin} the amplitude of linearized Eq (54), we have in parallel to (57)

$$<r_{lin}^2> \approx \frac{g_{ff}}{4\xi\omega_0^3(s-1)}. \tag{60}$$

The equivalent linearization procedure goes through just as in the pre-buckled case, for the quadratic term in (54) has no consequence under the Gaussian assumption. Hence,

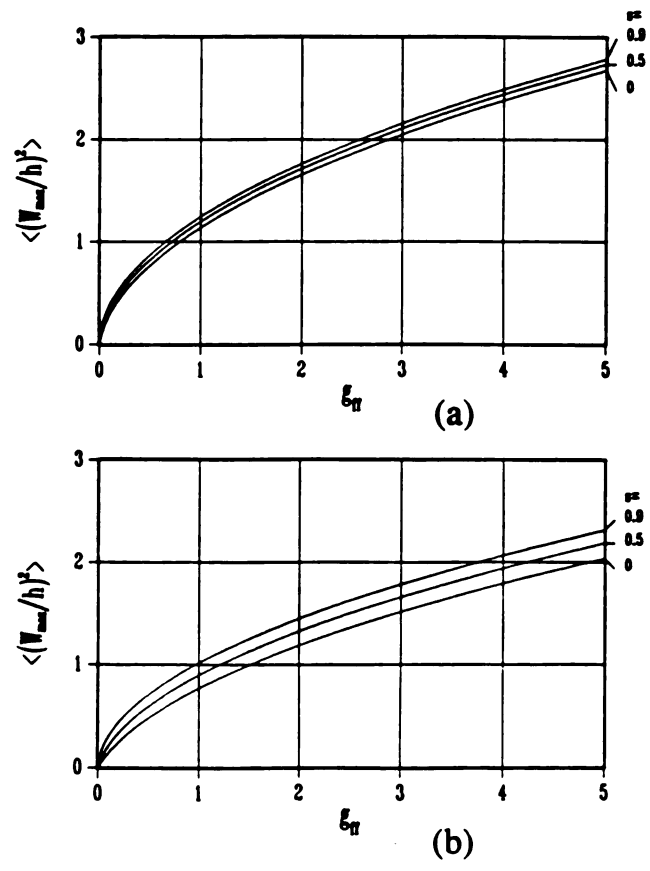

Fig 5. Maximum mean square displacement of a pre-buckled plate ($s<1$) under $\beta=1$, $\mu=\sqrt{0.1}$, $\xi=0.04$. (a) Simply-supported plate; (b) clamped plate.

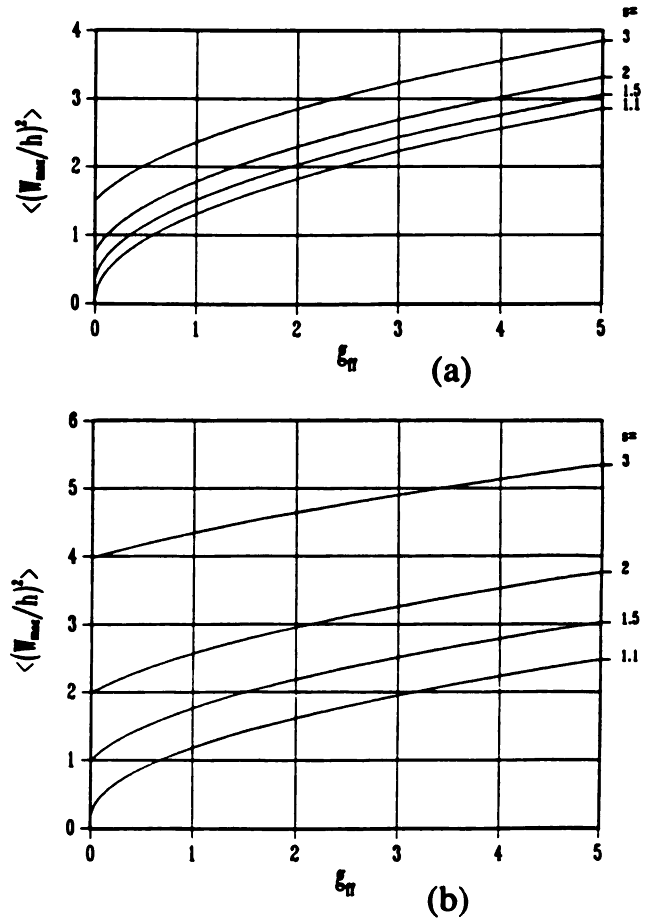

Fig 6. Total mean square displacement of a post-buck' ... under $\beta=1$, $\mu=\sqrt{0.1}$, $\xi=0.04$. (a) Simply-supported p... plate.

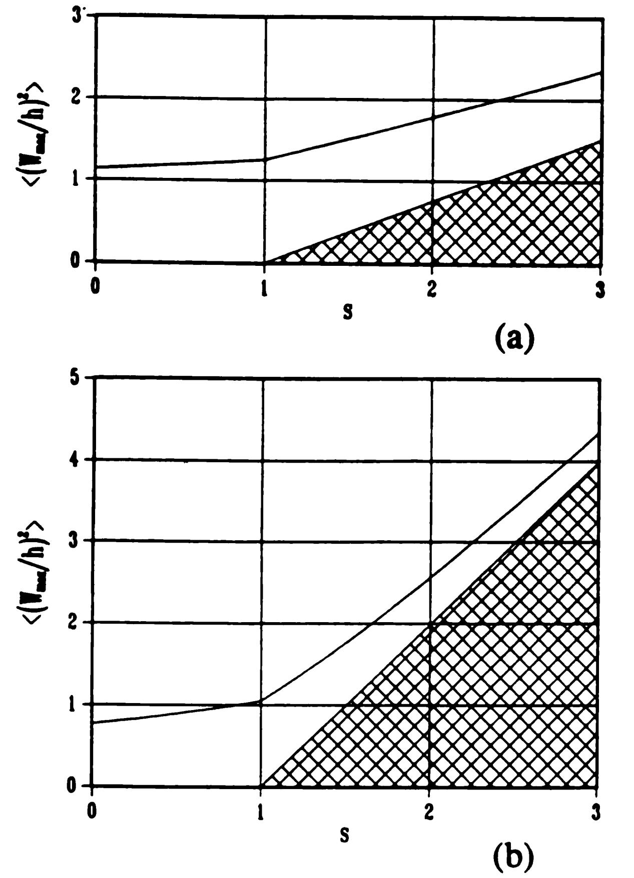

Fig 7. Maximum mean square displacement under $\beta=1$, $\mu=\sqrt{0.1}$, $\xi=0.04$, and $g_{ff}=1$. The cross-hatched triangle represents the squared buckled plate amplitude. (a) Simply-supported plate; (b) clamped plate.

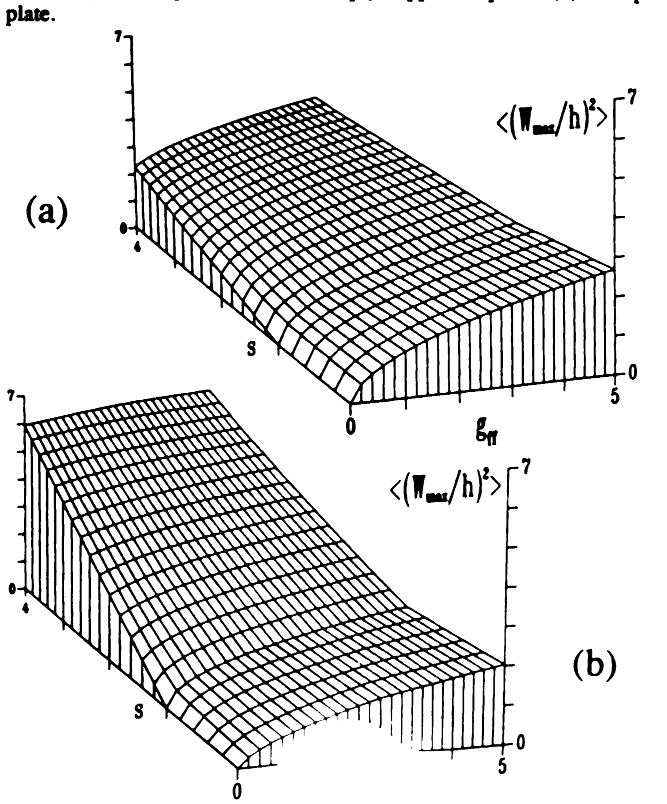

Fig 8. The composite vi[...] re displacements of Figs 5 and 6. (a) Simply-su[...] ped plate.

$$\langle r^2\rangle = \frac{\omega_0^2(s-1)}{3\kappa}\left[\sqrt{1+\frac{6\kappa\langle r_{lin}^2\rangle}{\omega_0^2(s-1)}}-1\right]. \tag{61}$$

And, the total mean square amplitude is given by

$$\langle q^2\rangle = Q_2^2 + \langle r^2\rangle, \tag{62}$$

since $\langle r\rangle=0$.

Fig 6 shows that the total mean square displacement increases greatly with s. However, the increase is largely due to the contribution of Q_2. To show this, we have presented in Fig 7 the separate contributions of Q_2 and $\langle r^2\rangle$ at $g_{ff}=1$. We see the squared Q_2 increasing linearly with (s-1), but $\langle r^2\rangle$ actually falls off with s. This is again supported by the asymptotic form of (61), $\langle r^2\rangle \propto 1/s$, as $s \to \infty$. Hence, the mean square amplitude due to fluctuations is smaller in a post-buckled state than in the pre-buckled. This has also been borne out by the Monte Carlo simulation of Choi and Vaicaitis (1989), in which the magnitude of stress fluctuations is considerably smaller whenever the stress time history shifts to buckled states. The composite of Figs 5 and 6 is shown by the surface plot of total mean displacement in Fig 8.

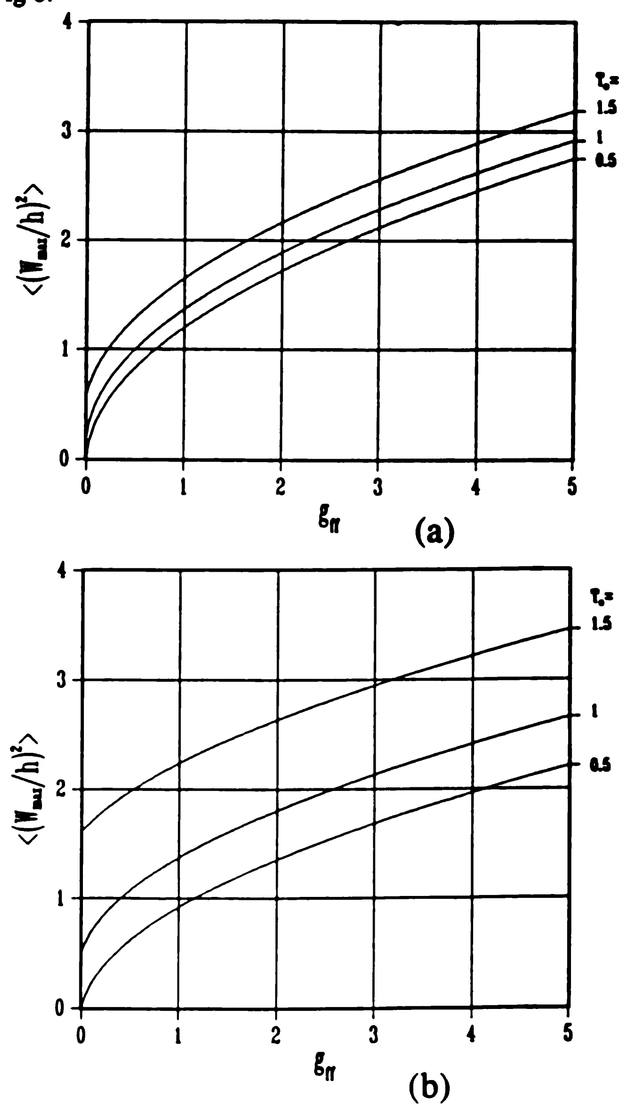

Fig 9. Total mean square displacement under the combined forcing. Here, $\beta=1$, $\mu=\sqrt{0.1}$, $\xi=0.04$, $\delta_v=\delta_g=1$. The range of T_0 includes the critical s* of (a) simply-supported plate and (b) clamped plate.

B. Combined Acoustic and Thermal Loading ($g=f_0+f(t)$)

The analysis of Sec 7A is valid when there is no heat flux through the plate thickness. This may occur, for instance, when the temperature gradient vanishes due to one side of the plate being insulated. Under a nonuniform heat flux, the temperature gradient will be neither constant nor linear over the plate. One must then retain f_0 as a nonzero-mean on which the Gaussian excitations are superposed. Instead of (46), it is more appropriate to use the local dynamical equation (53). Denoting the combined linear stiffness by $k_c=\omega_0^2(1-s)+3\kappa Q^2$, the mean square amplitude of linearized equation (53) is

$$<r_{lin}^2> = \frac{g_{ff}}{2\xi\omega_0 k_c}. \tag{63}$$

And, the equivalent linearization procedure yields

$$<r^2> = \frac{k_c}{6\kappa}\left[\sqrt{1+\frac{12\kappa<r_{lin}^2>}{k_c}} - 1\right], \tag{64}$$

together with

$$<q^2> = Q^2 + <r^2>. \tag{65}$$

Eqs (63-65) are analogous to Eqs (60-62) of the post-buckled case; however, Q is now given by Q_3 and $Q_{4,n}$.

Again, for simplicity we let $\delta_g=\delta_v=1$. We then present in Fig 9 the total mean square response computed by joining Q_3 and $Q_{4,0}$ smoothly at $s=s^*$. That Q>0 indicates that the thermal moment induced by f_0 increases the mean square displacement above the level of Fig 8. As in Fig 6, the clamped plate responds more favorably to the temperature gradient than a simply-supported plate (Fig 9).

8. RMS STRESS AND STRAIN

Let us put the normal stress (12) and strain (13) in dimensionless form, $\begin{pmatrix}\sigma_x\\ \sigma_y\end{pmatrix}=\frac{\pi^2Eh^2}{b^2}\begin{pmatrix}\hat\sigma_x\\ \hat\sigma_y\end{pmatrix}$, $\begin{pmatrix}\varepsilon_x\\ \varepsilon_y\end{pmatrix}=\frac{\pi^2h^2}{b^2}\begin{pmatrix}\hat\varepsilon_x\\ \hat\varepsilon_y\end{pmatrix}$.

For the single-mode representation, we shall present the stress and strain as a function x at y=1/2

Simply-Supported Plate:

$$\hat\sigma_x=-\frac{(\beta^2+1)T_0}{12(1-\mu^2)}\left\{1+\frac{(1-\mu)\delta_v}{4}\left[1-\frac{\cos2\pi x}{(\beta^2+1)}\right]+Z\delta_g\sin\pi x\right\}+$$
$$+\frac{2Z(\beta^2+\mu)}{(1-\mu^2)}(\sin\pi x)q+\left[\frac{(\beta^2+\mu)}{(1-\mu^2)}+\beta^2\right]\frac{q^2}{2}, \tag{66}$$

$$\hat\varepsilon_x=\frac{(\beta^2+1)\delta_vT_0}{12(1+\mu)}\left\{f_v-\frac{1}{4}\left[(1+\mu\cos2\pi x)-\frac{(1-\mu\beta^2)}{(\beta^2+1)}\cos2\pi x\right]\right\}+$$
$$+2Z\beta^2(\sin\pi x)q+(2\beta^2+\mu\cos2\pi x)q^2/2, \tag{67}$$

Clamped Plate:

$$\hat\sigma_x=-\frac{(\beta^4+2\beta^2/3+1)T_0}{3(1-\mu^2)(\beta^2+1)}\left\{1+\frac{(1-\mu)\delta_v}{4}\left[1-\frac{\cos2\pi x}{(\beta^2+1)}\right]+Z\delta_g\sin^2\pi x\right\}-$$
$$-\frac{16Z}{3(1-\mu^2)}[\beta^2\cos2\pi x+\mu\sin^2\pi x]q+\frac{32}{9}\left\{\frac{3(\beta^2+\mu)}{16(1-\mu^2)}+\frac{5\beta^2}{16}\right.$$
$$\left.+\frac{\cos2\pi x}{2(\beta+\beta^{-1})^2}-\frac{\cos2\pi x}{(\beta+4\beta^{-1})^2}+\frac{\cos4\pi x}{4(4\beta+\beta^{-1})^2}\right\}q^2, \tag{68}$$

$$\hat\varepsilon_x=\frac{(\beta^4+2\beta^2/3+1)\delta_vT_0}{3(1+\mu)(\beta^2+1)}\left\{\sin^2\pi x-\right.$$
$$\left.-\frac{1}{4}\left[(1+\mu\cos2\pi x)-\frac{(1-\mu\beta^2)}{(\beta^2+1)}\cos2\pi x\right]\right\}-\frac{16Z\beta^2}{3}(\cos2\pi x)q$$
$$+\frac{32}{9}\left\{\frac{3\beta^2}{16}+\frac{1}{4}(\beta^2+\mu\cos2\pi x)+\frac{1}{16}(\beta^2-\mu\cos4\pi x)+\frac{\cos2\pi x}{2(\beta+\beta^{-1})^2}\right.$$
$$\left.\times(1-\mu\beta^2)-\frac{\cos2\pi x}{(\beta+4\beta^{-1})^2}\left(1-\frac{\mu\beta^2}{4}\right)+\frac{\cos4\pi x}{4(4\beta+\beta^{-1})^2}\left(\frac{1}{4}-\mu\beta^2\right)\right\}q^2. \tag{69}$$

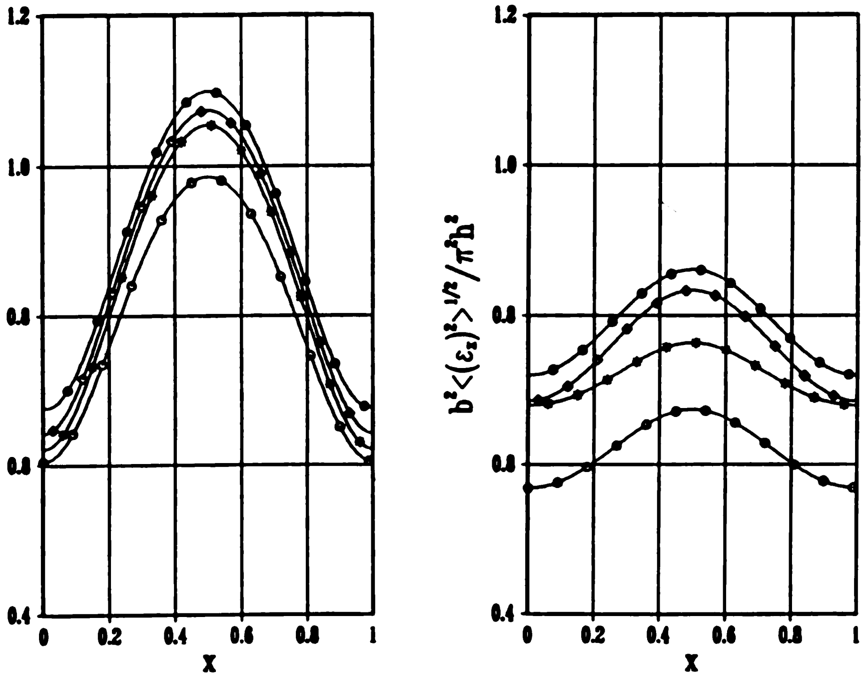

Fig 10. RMS extreme-fiber stress and strain of a simply-supported plate under $\beta=1$, $\mu=\sqrt{0.1}$, $\xi=0.04$, and $g_{ff}=1$. o for $T_0=\delta_v=\delta_g=0$; * for $T_0=1.2$, $\delta_v=\delta_g=0$; ◊ for $T_0=1.2$, $\delta_v=1$, $\delta_g=0$; • for $T_0=1.2$, $\delta_v=\delta_g=1$.

Eqs (63-66) have the symbolic form

$$\wp = C_0 + C_1q + C_2q^2, \tag{70}$$

where $\wp$ represents ($\hat\sigma_{x,y}$, $\hat\varepsilon_{x,y}$) and C's are the coefficients involving x. Under the assumption of zero-mean Gaussian, we obtain by squaring and averaging

$$<\wp^2>=C_0^2+(C_1^2+2C_0C_2)<q^2>+$$
$$+3C_3^2(<q^2>)^2. \tag{71}$$

To be specific, we consider the parameter values $T_0=1.2$, $\delta_v=\delta_g=1$, and $g_{ff}=1$. After computing the extreme-fiber stress and strain (at Z=1/2), we estimate the mean square value by (71). To quantify the thermal contributions, we have shown four plots in each of Figs 10 and 11. The first (open circle) is the nonthermal case ($T_0=\delta_v=\delta_g=0$); the second (asterisk) in[...] only the uniform tempera[...]

1.2, $\delta_v=\delta_g=0$); the third (diamond) involves both the uniform temperature and temperature variation over the plate ($T_0=1.2$, $\delta_v=1$, $\delta_g=0$); and the last (solid circle) represents the fully thermal case ($T_0=1.2$, $\delta_v=\delta_g=1$). Figs 10 and 11 show that the three thermal terms contribute additively over the entire x. Moreover, the contribution by the uniform temperature (asterisk) is at least a half the total thermal contribution for both the normal stress and strain. The parameter values of the figures are meant to be typical; however, a variant may be noticed under a different parameter choice.

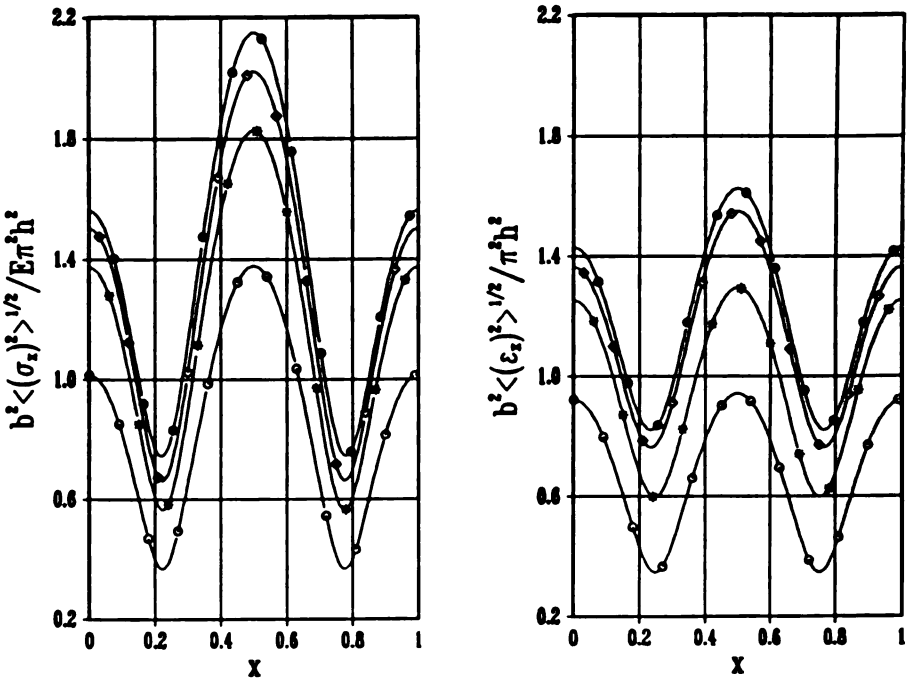

Fig 11. RMS extreme-fiber stress and strain of a clamped plate under $\beta=1$, $\mu=\sqrt{0.1}$, $\xi=0.04$, and $g_{ff}=1$. o for $T_0=\delta_v=\delta_g=0$; * for $T_0=1.2$, $\delta_v=\delta_g=0$; ◊ for $T_0=1.2$, $\delta_v=1$, $\delta_g=0$; • for $T_0=1.2$, $\delta_v=\delta_g=1$.

9. ASSESSMENT OF SINGLE-MODE DYNAMICS

The parameter reaches the critical value s=1 when thermal expansion is sufficient to induce buckling under the immovable edge condition. For a pre-buckled plate (s<1) the thermal expansion brings about increased mean square amplitude over the nonthermal (s=0) level. However, the relative increase diminishes as the acoustic loading becomes large. On the other hand, for a post-buckled plate (s>1) the total mean square displacement is sum of the square of buckled plate amplitude and mean square displacement due to the acoustic excitation only. Note that the square of buckled plate amplitude increases with (s-1), but the mean square displacement due to fluctuations falls off by 1/s, as s becomes large. Hence, the total mean square displacement is dominated by the buckled plate amplitude in the high-temperature limit.

It is important to point out that the temperature gradient across the plate introduces a qualitative change in overall dynamics. For a positive temperature gradient, there appears another critical value s=s* by which the thermal buckling is now characterized. Quantitatively, however, the thermal loading brings about additive contributions of the three thermal terms to the mean square amplitude as well as the rms normal stress and strain.

At this juncture, one may ask: How good is the random dynamics of a single-mode equation? Clearly, we cannot answer this fully without a detailed investigation of multi-mode equations. In the nonthermal case, however, Mei and Paul (1986) have shown that the single-mode analysis can provide an adequate approximation when the external forcing is weak. In fact, this is a good news in that the thermal effects show up most poignantly in the weak forcing range. Hence, the peculiarities of thermal effects might have already been captured by the single-mode analysis presented here. In any event, because of the Hamiltonian equations (33) of motion, it behooves us to investigate the multimode systems by Fokker-Planck formulation (Heuer et al., 1992).

ACKNOWLE

This work wa ... AFOSR task 2304N1.

REFERENCES

Barthelemy RR (1991), The National Aero-Space Plane program - A revolutionary concept, Structural Testing Technology at High Temperature Conference, SEM, Nov 4-6, Dayton, OH.

Boley BA and Weiner JH (1960), *Theory of thermal stresses*, Wiley, NY.

Bolotin VV (1963), *Nonconservative problems of the theory of elastic stability*, MacMillan, NY.

Caughey TK (1963), Equivalent linearization techniques, J Acoust Soc Am, 35, 1706-1711.

Choi ST and Vaicaitis R (1989), Response and fatigue of stiffened panels, Prob Engr Mech., 4, 150-160.

Guckenheimer J and Holmes P (1983), *Nonlinear oscillations, Dynamical systems, and bifurcation of vector fileds*, Appl Math Sci, No 42, Springer-Verlag, NY.

Heuer R, Irschik H, and Ziegler F (1992), Large amplitude random vibration of polygonal plates, In *Nonlinear stochastic mechanics*, Bellomo N and Casciati F (eds.), 285-296, Springer-Verlag, Berlin.

Holmes P(1979), A nonlinear oscillator with a strange attractor, Phil Trans, Roy Soc London A, 292, 419-448.

Huberman BA and Crutchfield JP (1979), Chaotic states of anharmonic systems in perioidc fields, Phy Rev Lett, 43, 1743-1747.

Kalafati YuD and Malakhov BA (1983), Dynamical chaos and spontaneous symmetry breaking in anharmonic systems excited by a periodic force, JETP Lett, 37, 577-581.

Kehoe MW and Synder HT (1991), High temperature ground vibration test technique, Structural Testing Technology at High Temperature Conference, SEM, Nov 4-6, Dayton, OH.

Lee J (1986), Free vibration of a large-amplitude deflected plate--Reexamination by the dynamical systems theory, J Appl Mech, ASME, 53, 633-640.

Lee J (1992), Large-amplitude plate vibration in an elevated thermal environment, WL-TR-92-3049, Wright-Patterson AFB, OH.

Levy S (1942), Bending of rectangular plates with large deflections, NACA Rept No 737.

Lin YK (1976), *Probabilistic theory of structural dynamics*, Robert E Krieger Pub, Huntington, NY.

Luenberger DG (1969), *Optimization by vector space methods*, Wiley, NY.

Maekawa S (1982), On the sonic fatigue life estimation of skin structures at room and elevated temperatures, J Sound Vib, 80, 41-59.

Mei C (1980), Response of nonlinear structural panels subjected to high

intensity noise, AFWAL-TR-80-3018, Wright-Patterson AFB, OH.
Mei C and Paul DB (1986), Nonlinear multimode response of clamped rectangular plates to acoustic loading, AIAA J, 24, 643-648.
Nayfeh AH and Sanchez NE (1989), Bifurcations in forced softening Duffing oscillator, Int J Nonl Mech, 24, 483-497.
Nayfeh MA, Hamdan AMA, and Nayfeh AH (1990), Chaos and instability in a power system - primary resonant case, Nonl Dyn, 1, 313-339.
Novak S and Frehlich RG (1982), Transition to chaos in the Duffing oscillator, Phy Rev A, 26, 3660-3663.
Paul DB (1982), Large deflections of clamped rectangular plates with arbitrary temperature distributions, AFWAL-TR-81-3003, Vol 1, Wright-Patterson AFB, OH.
Raty R, Von Boehm J, and Isomaki HM (1984), Absence of inversion-symmetric limit cycles for even periods and the chaotic motion of Duffing's oscillator, Phy Lett A, 103, 289-292.
Richards WL and Thompson RC (1991), Titanium honeycomb panel testing, Structural Testing Technology at High Temperature Conference, SEM, Nov 406, Dayton, OH.
Schneider CW (1974), Acoustic Fatigue of Aircraft Structures at Elevated Temperatures, AFFDL-TR-73-155, Wright-Patterson AFB, OH.
Seide P and Adami C (1983), Dynamic Stability of Beams in a Combined Thermal-Acoustic Environment, AFWAL-TR-83-3072, Wright-Patterson AFB, OH.
Souza MA and Mook DT (1991), Post-buckling nonlinear vibrations of initially imperfect structural systems, 32nd SDM Conference, AIAA-91-1228-CP, 2772-2275.
Stoker JJ (1950), *Nonlinear vibrations in mechanical and electrical systems*, Interscience, NY.
Sunakawa M and Uemura M (1960), Deformation and thermal stress in a rectangular plate subjected to aerodynamic heating, Rept. No 359, Aero Res Inst, Univ of Tokyo.
Ueda Y (1981), Explosion of strange attractors exhibited by Duffing's equation, In *Nonlinear dynamics*, Helleman RHG (ed.), 422-434, New York Academy of Sciences, NY.
Wilcox MW and Clemmer LE (1964), Large deflection analysis of heated plates, J Engr Mech Div Proc, ASCE, 90, 165-189.

APPENDIX A: A_{pq}

$A_{pq}= B_{pq}- D_{pq}$, where

$$B_{pq}=\sum_{m=0}^{\infty}\sum_{n=0}^{\infty}\sum_{r=0}^{\infty}\sum_{s=0}^{\infty} mnrs[\delta^p_{m+r} +\delta^p_{m-r} +\delta^p_{r-m}(1- \delta^o_p)]$$
$$\times[\delta^q_{n+s} +\delta^q_{n-s} +\delta^q_{s-n}(1- \delta^o_q)]w_{mn}w_{rs},$$

$$D_{pq}=\sum_{m=0}^{\infty}\sum_{n=0}^{\infty}\sum_{r=0}^{\infty}\sum_{s=0}^{\infty} m^2s^2[-\delta^p_{m+r} +\delta^p_{m-r} +\delta^p_{r-m}(1- \delta^o_p)]$$
$$\times[-\delta^q_{n+s} +\delta^q_{n-s} +\delta^q_{s-n}(1- \delta^o_q)]w_{mn}w_{rs}.,$$

APPENDIX B: B_{rs}

$B_{rs}= F_1+F_2 -2F_3$, where

$$F_1=\sum_{n=1}^{\infty}\sum_{q=0}^{\infty} q^2\left\{\sum_{m=1}^{\infty}\sum_{p=0}^{\infty} w_{mn}F_{pq}m^2(\delta^m_{r-p} -\delta^m_{p-r} +\delta^m_{p+r})\right\}$$
$$\times (\delta^n_{s-q} -\delta^n_{q-s} +\delta^n_{q+s}),$$

$$F_2=\sum_{n=1}^{\infty}\sum_{q=0}^{\infty} n^2\left\{\sum_{m=1}^{\infty}\sum_{p=0}^{\infty} w_{mn}F_{pq}p^2(\delta^m_{r-p} -\delta^m_{p-r} +\delta^m_{p+r})\right\}$$
$$\times (\delta^n_{s-q} -\delta^n_{q-s} +\delta^n_{q+s}),$$

$$F_3=\sum_{n=1}^{\infty}\sum_{q=0}^{\infty} nq\left\{\sum_{m=1}^{\infty}\sum_{p=0}^{\infty} w_{mn}F_{pq}mp(\delta^m_{r-p} -\delta^m_{p-r} +\delta^m_{p+r})\right\}$$
$$\times (\delta^n_{s-q} -\delta^n_{q-s} +\delta^n_{q+s}).$$

APPENDIX C: C_{pq}

$C_{pq}=(L_{pq}- J_{pq})/64$, where

$$L_{pq}=\sum_{n=0}^{q} K^+_{pn(q-n)} +\sum_{n=q}^{\infty} K^-_{pn(n-q)} +\sum_{n=0}^{\infty} K^-_{pn(n+q)}(1- \delta^o_q),$$

$$K^{\pm}_{pnj}=\sum_{s=n}^{\infty}\sum_{d=j}^{\infty} a_{sn}a_{dj}\, H_{psd}\, 2(nj\mp1) - \sum_{s=n-2}^{\infty}\sum_{d=j}^{\infty} a_{s(n-2)}a_{dj}\, H_{psd}$$
$$\times(n-1)(j\pm1) - \sum_{s=n+2}^{\infty}\sum_{d=j}^{\infty} a_{s(n+2)}a_{dj}\, H_{psd}\, (n+1)(j\mp1),$$

$$H_{psd}=\sum_{m=0}^{p} G^+_{m(p-m)sd} +\sum_{m=p}^{\infty} G^-_{m(m-p)sd} +\sum_{m=0}^{\infty} G^-_{m(m+p)sd}(1- \delta^o_p),$$

$$G^{\pm}_{misd}=\sum_{r=m}^{\infty}\sum_{c=i}^{\infty} w_{rs}w_{cd}a_{rm}a_{ci}\, 2(mi\mp1) -\sum_{r=m-2}^{\infty}\sum_{c=i}^{\infty} w_{rs}w_{cd}a_{r(m-2)}$$
$$\times a_{ci}(m-1)(i\pm1) - \sum_{r=m+2}^{\infty}\sum_{c=i}^{\infty} w_{rs}w_{cd}a_{r(m+2)}a_{ci}\, (m+1)(i\mp1),$$

$$J_{pq}= \sum_{j=0}^{q} O^+_{p(q-j)j} +\sum_{j=q}^{\infty} O^-_{p(j-q)j} +\sum_{j=0}^{\infty} O^-_{p(j+q)j}\, (1- \delta^o_q),$$

$$O^{\pm}_{pnj}=\pm\sum_{s=n}^{\infty}\sum_{d=j}^{\infty} a_{sn}a_{dj}N_{psd}\, 2(j^2+1) \mp\sum_{s=n}^{\infty}\sum_{d=j-2}^{\infty} a_{sn}a_{d(j-2)}N_{psd}\, (j-1)^2$$
$$\mp \sum_{s=n}^{\infty}\sum_{d=j+2}^{\infty} a_{sn}a_{d(j+2)}\, N_{psd}\, (j+1)^2,$$

$$N_{psd}=\sum_{m=0}^{p} M^+_{m(p-m)sd} +\sum_{m=p}^{\infty} M^-_{m(m-p)sd} +\sum_{m=0}^{\infty} M^-_{m(m+p)sd}(1- \delta^o_p),$$

$$M^{\pm}_{misd}=\pm\sum_{r=m}^{\infty}\sum_{c=i}^{\infty} w_{rs}w_{cd}a_{rm}a_{ci}2(m^2+1)\mp\sum_{r=m-2}^{\infty}\sum_{c=i}^{\infty} w_{rs}w_{cd}a_{r(m-2)}$$
$$\times a_{ci}(m-1)^2 \mp\sum_{r=m+2}^{\infty}\sum_{c=i}^{\infty} w_{rs}w_{cd}a_{r(m+2)}a_{ci}\, (m+1)^2 .$$

APPENDIX D: D_{rs} and K_4 - K_7

$D_{rs}= I_1+I_2 - 2I_3$, where

$$I_1= - \frac{1}{64}\sum_{m=1}^{\infty}\sum_{n=1}^{\infty} w_{mn}\sum_{p=0}^{\infty}\sum_{q=0}^{\infty} F_{pq}q^2\left\{\sum_{c=1}^{m} a_{mc}Q_{cpr}\right\}\left\{\sum_{d=1}^{n} a_{nd}\, R_{dqs}\right\},$$

$$I_2= - \frac{1}{64}\sum_{m=1}^{\infty}\sum_{n=1}^{\infty} w_{mn}\sum_{p=0}^{\infty}\sum_{q=0}^{\infty} F_{pq}p^2\left\{\sum_{c=1}^{m} a_{mc}R_{cpr}\right\}\left\{\sum_{d=1}^{n} a_{nd}\, Q_{dqs}\right\},$$

$$I_3= \frac{1}{64}\sum_{m=1}^{\infty}\sum_{n=1}^{\infty} w_{mn}\sum_{p=0}^{\infty}\sum_{q=0}^{\infty} F_{pq}qp\left\{\sum_{i=1}^{m} a_{mi}S_{ipr}\right\}\left\{\sum_{j=1}^{n} a_{nj}\, S_{jqs}\right\},$$

$$Q_{cpr}= \sum\nolimits'_J \sum\nolimits'_I JI(c+I)^2 \left\{a_{r(c+I+J-p)} +a_{r(c+I+J+p)} -a_{r(-c-I-J+p)}\right\},$$

$$R_{dqs}= -\delta^1_d \sum\nolimits'_I I(2-I)\left\{a_{s(2+I-q)} +a_{s(2+I+q)} -a_{s(-2-I+q)}\right\}$$
$$- (1-\delta^1_d) \sum\nolimits'_J \sum\nolimits'_I JI\left\{a_{s(d+I+J-q)} +a_{s(d+I+J+q)} -a_{s(-d-I-J+q)}\right\},$$

$$S_{ipr}= \sum\nolimits'_J \sum\nolimits'_I JI(i+I) \left\{a_{r(i+I+J-p)} -a_{r(i+I+J+p)} -a_{r(-i-I-J+p)}\right\},$$

$$K_4= - \frac{1}{8} \sum_{m=1}^{\infty} w_{ms} \sum_{i=1}^{m} a_{mi} \sum\nolimits'_J \sum\nolimits'_I JI\, a_{r(i+I+J)}\, (i+I)^2 ,$$

$$K_5= - \frac{1}{8} \sum_{n=1}^{\infty} w_{rn} \sum_{j=1}^{n} a_{nj} \sum\nolimits'_J \sum\nolimits'_I JI\, a_{s(j+I+J)}\, (j+I)^2 ,$$

$$K_6= - \frac{1}{8} \sum_{m=1}^{\infty}\sum_{n=1}^{\infty}\sum_{r=1}^{\infty} w_{mn}w_{rn} \sum_{i=1}^{m} a_{mi} \sum\nolimits'_J \sum\nolimits'_I JI\, a_{r(i+I+J)}\, (i+I)^2 ,$$

$$K_7= - \frac{1}{8} \sum_{m=1}^{\infty}\sum_{n=1}^{\infty}\sum_{s=1}^{\infty} w_{mn}w_{ms} \sum_{j=1}^{n} a_{nj} \sum\nolimits'_J \sum\nolimits'_I JI\, a_{s(j+I+J)}\, (j+I)^2 .$$

APPENDIX E: Equivalent Linearization Technique

Let us begin with a damped linear oscillator

$$\ddot{x} + \beta\dot{x} + kx = f(t), \tag{E1}$$

where β is the damping coefficient and k the stiffness. Assume that f(t) is a stationary Gaussian with the power spectral density $\phi_{ff}(\omega)$, where ω is the angular frequency. The mean square response is

$$<x^2> = \frac{\pi\phi_{ff}(\sqrt{k}\,)}{\beta k},$$

where $\langle\ \rangle$ denotes an ensemble (or time) average. Note the sign $\approx$ is used because $\phi_{ff}(\omega)$ is assumed constant over the narrow resonance peaks at $\omega = \pm\sqrt{k}$ (see, Fig 5.3 of Lin, 1976). Rewrite (E2) by using $\phi_{ff}(\omega) = g_{ff}(f)/2\pi$, where f is frequency

$$\langle x^2\rangle \approx \frac{g_{ff}}{2\beta k}. \tag{E3}$$

Here, the argument of g_{ff} is suppressed for a constant spectrum.

Now consider a damped Duffing oscillator

$$\ddot{x} + \beta\dot{x} + kx + \gamma x^3 = f(t), \tag{E4}$$

where γ denotes the strenght of hard spring. Rather than solving (E4) by perturbation, the aim is to replace it by a linear system of the form

$$\ddot{x} + \beta\dot{x} + k_e x + e = f(t). \tag{E5}$$

By a judicious choice of the equivalent stiffness k_e, one attempts to capture the nonlinearity in a statistical sense. And,

attempts to capture the nonlinearity in a statistical sense. And,
the degree of failure is quantified by the error $e = (-k_e + k)x + \gamma x^3$. In the equivalent linearization technique, k_e is found by minimizing the mean square error, i.e., $d\langle e^2\rangle/dk_e = 0$. When x is zero-mean Gaussian, a simple expression follows

$$k_e = k + 3\gamma\langle x^2\rangle. \tag{E6}$$

By suppressing the error term, (E5) is linear so that

$$\langle x^2\rangle \approx \frac{g_{ff}}{2\beta k_e}, \tag{E7}$$

in view of (E3). Inserting (E6) into (E7) and identifying $\langle x^2_{lin}\rangle = g_{ff}/2\beta k$, we have (Caughey, 1963)

$$\frac{3\gamma}{k}(\langle x^2\rangle)^2 + \langle x^2\rangle - \langle x^2_{lin}\rangle = 0, \tag{E8}$$

the positive root is

$$\langle x^2\rangle = \frac{k}{6\gamma}\left[\sqrt{1+\frac{12\gamma\langle x^2_{lin}\rangle}{k}} - 1\right]. \tag{E9}$$

Hybrid Padé-Galerkin technique for differential equations

James F Geer

Department of Systems Science, Watson School of Engineering and Applied Science State University of New York, Binghamton NY 13902

Carl M Andersen

Department of Mathematics, College of William and Mary, Williamsburg VA 23185

A three-step hybrid analysis technique, which successively uses the regular perturbation expansion method, the Padé expansion method, and then a Galerkin approximation, is presented and applied to some model boundary value problems. In the first step of the method, the regular perturbation method is used to construct an approximation to the solution in the form of a finite power series in a small parameter ϵ associated with the problem. In the second step of the method, the series approximation obtained in step one is used to construct a Padé approximation in the form of a rational function in the parameter ϵ. In the third step, the various powers of ϵ which appear in the Padé approximation are replaced by new (unknown) parameters $\{\delta_j\}$. These new parameters are determined by requiring that the residual formed by substituting the new approximation into the governing differential equation is orthogonal to each of the perturbation coordinate functions used in step one. The technique is applied to model problems involving ordinary or partial differential equations. In general, the technique appears to provide good approximations to the solution even when the perturbation and Padé approximations fail to do so. The method is discussed and topics for future investigations are indicated.

INTRODUCTION

We have introduced and applied a hybrid perturbation-Galerkin technique to a variety of problems involving ordinary differential equations (Andersen and Geer, 1991; Geer and Andersen, 1989b, 1990, 1991b), partial differential equations (Geer and Andersen, 1991a; Singler and Geer, 1993), and integral equations (Geer and Andersen, 1989a), which contain a parameter ϵ. For many different classes of problems, this technique appears to significantly improve the usefulness of perturbation expansions over a wide range of parameter values.

In this paper, we show how some of these hybrid ideas can be combined with Padé (or rational function) approximations to provide approximate solutions of even greater accuracy. The hybrid technique we shall describe successively uses the regular perturbation expansion method (see, e.g., Nayfeh, 1973), the Padé expansion method (see, e.g. Baker, 1975), and then a Galerkin approximation (see, e.g., Galerkin, 1915). In the first step of the method, the regular perturbation method is used to construct an approximate solution in the form of a finite power series in a small parameter ϵ associated with the problem. In the second step of the method, the series approximation obtained in step one is used to construct a Padé approximation in the form of a rational function in the parameter ϵ. In the third step, the various powers of ϵ which appear in the Padé approximation are replaced by new (unknown) parameters $\{\delta_j\}$. These new parameters are determined by requiring that the residual formed by substituting the new approximation into the original governing differential equation is orthogonal to each of the perturbation coordinate functions used in step one. This hybrid method has the potential of overcoming some of the drawbacks of the perturbation method, the Padé method, and the Galerkin method when they are applied by themselves, while combining some of the good features of each.

Padé approximants have been popular among physicists for improving the convergence of series or for obtaining information from divergent series (see, e.g., Baker, 1975; Gaunt and Guttmann, 1974; and Hunter, 1973). They are easily constructed from the first few terms of a power series representation of a function, requiring only the solution of a system of linear algebraic equations. From a mathematical point of view, the power series representation of a function fails to converge because of the presence of one or more (real or complex) singularities of

part of "MECHANICS PAN-AMERICA 1993" edited by MRM Crespo da Silva and CEN Mazzilli ASME Reprint No AMR134

CONTENTS

the function, which the series representation is unable to adequately approximate. The more general Padé, or rational function, approximation of the function can better simulate the presence, or at least the effect, of these singularities. This is accomplished through the presence of zeros in the denominator of the approximation (the simulation of poles) or the combination of zeros of the numerator and denominator at nearly the same locations (which can simulate certain branch cuts) (see, e.g., Andersen and Geer, 1982; Dadfar, et al, 1984; or Van Dyke, 1974). However, the region of convergence of a sequence of Padé approximants is, in general, not closely related to the region of convergence of the power series on which the approximations are based. In fact, the construction of Padé approximants in the usual way may lead to approximations which fail to converge at points where the Taylor series of the function does converge. Often this is due to the appearance of spurious poles or zeros in the approximants which are not present in the original function. (See, e.g., Bender and Orszag, 1978, for some simple, but very interesting, examples which illustrate this phenomena.) As we shall demonstrate below, the hybrid method we will describe appears to overcome this drawback of the Padé method by "adjusting" the location of the poles and zeros of the approximants to simulate better the true analytical structure of the function being modeled.

Some general observations about the hybrid technique we are proposing are the following. First, in many perturbation problems, much effort has to be expended to compute each additional term in a perturbation expansion. Through the use of the proposed hybrid method, the "information" contained in the known perturbation terms can be exploited more fully. In particular, more of the analytical structure of the solution can be "uncovered" using a rational function approximation. Secondly, another way of viewing the technique is to recognize that in many perturbation expansions the functional form of the higher order terms can be well approximated by a linear combination of the lower order terms. Thus, much of the effect of the higher order terms may be included by applying the technique to the lower order terms. Finally, preliminary unpublished investigations indicate that, while the use of a Taylor series expansion is frequently limited by a finite radius of convergence, the proposed hybrid method can sometimes yield good results even well outside the radius of convergence.

In Sec 2 we shall describe our method in more detail and then apply it to two model boundary value problems involving ordinary differential equations (Sec 3) and to two model problems involving partial differential equations (Sec 4). Finally, we shall discuss observations about the method in Sec 5, and also indicate topics for further investigation.

DESCRIPTION OF THE METHOD

We consider the problem of finding approximations to the solution $u(x,\epsilon)$ to the problem

$$L(u,\epsilon)=0,\ x\in D,\quad \text{with } B(u,\epsilon)=0,\quad x\in\partial D. \tag{1}$$

Here L represents a (linear or nonlinear) differential operator, x is a scalar or a vector, D is the domain in which the differential equation is to hold, ∂D denotes the boundary of D, and ϵ is a small parameter. For simplicity we shall assume that the operator B, which defines the boundary conditions of the problem, is linear and homogeneous in u.

The hybrid Padé-Galerkin technique we present can be conveniently described as the following three-step process.

Step one: For small values of the parameter ϵ, we assume that u can be expanded in a (convergent or asymptotic) perturbation series of the form

$$u(x,\epsilon)=\sum_{j=0}^{n}u_j(x)\epsilon^j+O(\epsilon^{n+1}). \tag{2}$$

Here each of the perturbation coordinate functions u_j is determined in a straightforward manner using the regular perturbation method.

Step two: We now use the functions $\{u_j\}$ determined in step one to construct the Padé approximant $P[M,N]$ defined by

$$P[M,N](x,\epsilon)\equiv\frac{\sum_{j=0}^{M}v_j(x)\epsilon^j}{\sum_{j=0}^{N}w_j(x)\epsilon^j},\quad w_0(x)\equiv 1. \tag{3}$$

Here the functions $\{v_j(x)\}$ and $\{w_j(x)\}$ are determined by the condition that $P[M,N](x,\epsilon)=u(x,\epsilon)+O(\epsilon^{M+N+1})$, as $\epsilon\to 0$. This condition leads to the requirements

$$v_j(x)=\sum_{k=0}^{j}w_k(x)u_{j-k}(x),\quad j=0,1,...,M, \tag{4}$$

$$\sum_{k=1}^{\min(p,N)} u_{p-k}(x) w_k(x) = -u_p(x), \qquad p = M+1, M+2, \ldots, M+N. \tag{5}$$

Step three: Once $P[M, N]$ has been determined, we define the hybrid Padé-Galerkin approximation $H[M, N]$ by

$$H[M, N](x, \epsilon) = \frac{\sum_{j=0}^{M} v_j(x) \delta_j}{1 + \sum_{j=1}^{N} w_j(x) \delta_{M+j}}. \tag{6}$$

Here $H[M, N]$ has the *same functional form* as $P[M, N]$ except that each power of ϵ in the definition of $P[M, N]$ (except the coefficient of w_0) has been replaced by a new (unknown) parameter, or amplitude, $\delta_j = \delta_j(\epsilon)$. The $M + N + 1$ amplitudes $\{\delta_j\}$ are determined by requiring that the residual formed by substituting $H[M, N]$ into the governing differential equation is orthogonal to each of the perturbation coordinate functions used in step one. Thus, the new amplitudes $\{\delta_j\}$ are determined from the Galerkin conditions

$$\int_D L\left(H[M, N](x, \epsilon), \epsilon\right) u_k \, dx = 0, \quad k = 0, 1, \ldots, M + N. \tag{7}$$

Conditions (7) are a system of $M+N+1$ equations for the $M + N + 1$ amplitudes $\{\delta_j\}$. In general, these equations are nonlinear and must be solved numerically. However, we note that they can be solved efficiently using Newton's method, starting with small values of ϵ, where we expect $\delta_j \cong \epsilon^j$, for $0 \le j \le M$, and $\delta_{M+j} \cong \epsilon^j$, for $1 \le j \le N$, and then incrementally proceeding to larger values of ϵ.

Before applying this technique, we make a few observations. In step one of the method, i.e., the perturbation step, the solution to a particular problem involving a small parameter is developed in terms of a series of *unknown functions* with *preassigned coefficients*, i.e. gauge functions. The unknown functions are usually determined by solving a recursive set of differential equations which are, in general, simpler than the original governing differential equation. Using these perturbation coordinate functions, a new approximation in the form of a rational function of ϵ can be constructed in a straightforward manner. (We note that the Padé approximant $P[M, 0]$ as defined above is the same as the perturbation approximation of order M, while $P[M, N]$ with $N > 0$ is a truly new approximation.) By contrast, using the Galerkin technique in the standard manner, one seeks an approximate solution to the problem in the form of a series of *specified* (known) *coordinate functions* with *unknown coefficients*. The coefficients are determined by requiring that the residual formed by substituting the trial solution into the governing differential equation is orthogonal to each of the coordinate functions. The technique we are proposing simply replaces the power series form of the approximation in the Galerkin step by a more general rational function approximation to the solution.

We also observe that the perturbation, Padé, and Galerkin methods have each been useful when applied by themselves in providing approximate solutions to a wide variety of nonlinear (and otherwise difficult) problems. However, each of these techniques has certain drawbacks. The perturbation method has at least two major drawbacks. First, as the number of terms in the perturbation expansion increases, the mathematical complexity of the equations which determine the unknown functions increases rapidly. Thus, in most practical applications, the perturbation series is limited to only a few terms. A second drawback to the perturbation method is the requirement of restricting the perturbation parameter to small values in order to obtain solutions of acceptable accuracy. (These drawbacks of the perturbation method have been recognized and several modifications or extensions have been proposed, as, e.g., in Andersen and Geer, 1982, and Van Dyke, 1974.) One of the main drawbacks of the Padé method is that it often has to be applied "blindly", with little or no assurance that the approximations obtained will converge to the solution as the number of terms is increased. Also, a rational function obviously has (real or complex) poles which may or may not improve the quality of the approximations obtained. The main shortcoming of the Galerkin method is the difficulty, from a practical point of view, of selecting a small number of good coordinate functions.

By basing our technique on a formal perturbation expansion of the solution, we should note that our particular choice of coordinate functions overcomes the main drawback of the Galerkin method (at least for the case when $N = 0$.) By the way they are constructed, the perturbation coordinate functions are (under certain assumptions) elements of a set of functions which span the space of solutions in a neighborhood of their point of generation. Thus, they should fully characterize the solution u in that neighborhood. Also, in many applications, the functions $\{u_j\}$ are determined by solving a set of linear equations, even though the original operator L may be nonlinear. The first property is necessary for the convergence of the Galerkin method, while the second property enhances the effectiveness of the proposed hybrid method for solving nonlinear problems. In addition, for $N > 0$, we shall demonstrate below that the Galerkin method appears to determine the parameters of the Padé approximants in such a manner that the poles of $H[M, N]$ tend to *improve* and not degrade the quality of the approximations obtained.

In the following sections we shall apply our method to several model boundary value problems involving ordinary or partial differential equations. These examples will serve to illustrate the application of the method, and will also provide insights into some of the mathematical properties of the method. A more thorough and detailed analysis of some of the mathematical properties of the technique, as well as the application of the method to certain singular perturbation problems, will be presented elsewhere.

APPLICATIONS TO ORDINARY DIFFERENTIAL EQUATIONS

In this section we shall apply our method to two model boundary value problems involving second order ordinary differential equations.

Example 1: We consider first the two-point boundary value problem

$$\begin{gathered} L(u,\epsilon) \equiv u''(x) - \epsilon u'(x) - \epsilon = 0, \quad 0 < x < 1, \\ \text{with } B(u,\epsilon) \equiv u = 0, \quad \text{for } x = 0 \text{ and } x = 1. \end{gathered} \tag{8}$$

To help evaluate the accuracy of our proposed hybrid method, we note that this simple problem has the exact solution

$$u = \frac{1 - e^{\epsilon x}}{1 - e^{\epsilon}} - x. \tag{9}$$

The Taylor series expansion of $u(x,\epsilon)$ about $\epsilon = 0$ converges for $|\epsilon| < 2\pi$, since the singularities of u which lie closest to the origin in the complex ϵ−plane are located at $\epsilon = \pm 2\pi i$. We also note that u develops a boundary layer at $x = 1$ as ϵ becomes large.

Step one: Using the regular perturbation method we find that each of the perturbation coefficient functions u_j in Eq (2) is a polynomial of degree $j+1$ which vanishes at $x = 0$ and $x = 1$. In particular, we find $u_0 = 0$, $u_1 = x(x-1)/2$, $u_2 = x(x-1)(2x-1)/12$, $u_3 = x^2(1-x)^2/24$, and $u_4 = x(x-1)(2x-1)(3x^2-3x-1)/720$.

Step two: We now use the perturbation coordinate functions $\{u_j(x)\}$ determined in step one to calculate Padé approximations $P[M,N]$ for various values of M and N. In particular for $M+N=2$, using Eqs (4) and (5), we find

$$P[2,0] = \epsilon\, u_1(x) + \epsilon^2 u_2(x), \tag{10}$$

which is the second order perturbation solution, and

$$P[1,1] = \frac{\epsilon\, x(x-1)/2}{1+\epsilon(1-2x)/6}, \tag{11}$$

since $v_0 \equiv 0$, $v_1 = x(x-1)/6$, and $w_1 = (1-2x)/6$. We note that $P[1,1]$ has a pole at $x = 1/2 + 3/\epsilon$, which lies *inside* the interval $[0,1]$ for $\epsilon > 6$. Thus, we do not expect $P[1,1]$ to be a good approximation to $u(x,\epsilon)$ for $\epsilon > 6$. In Figs 1 and 2, we have plotted $P[2,0]$ and $P[1,1]$, along with the exact solution, for $\epsilon = 5$ and $\epsilon = 10$, respectively. The influence of the pole of $P[1,1]$ is evident in Fig 2.

Step three: We now use the *form* of the Padé approximations determined in step two to define the hybrid approximations

$$H[2,0] = \delta_1\, u_1(x) + \delta_2\, u_2(x), \tag{12}$$

and

$$H[1,1] = \frac{\delta_1\, x(x-1)/2}{1+\delta_2\,(1-2x)/6}, \tag{13}$$

where the amplitudes $\delta_1 = \delta_1(\epsilon)$ and $\delta_2 = \delta_2(\epsilon)$ are determined from the Galerkin conditions (7), which for this example become

$$\int_0^1 \left(H''[M,N] - \epsilon H'[M,N] - \epsilon\right) u_k\, dx = 0, \text{ for } k = 1,2. \tag{14}$$

When $M = 2$ and $N = 0$, Eqs (14) are the *linear* equations

$$\begin{gathered} (1/12)\delta_1 + (\epsilon/720)\delta_2 = \epsilon/12, \\ (\epsilon/720)\delta_1 - (1/720)\delta_2 = 0, \end{gathered} \tag{15}$$

from which we find

$$\delta_1 = \frac{\epsilon}{1+\epsilon^2/60}, \quad \delta_2 = \frac{\epsilon^2}{1+\epsilon^2/60}. \tag{16}$$

When $M = 1$ and $N = 1$, from Eqs (14) we find that δ_1 and δ_2 satisfy the *nonlinear* equations

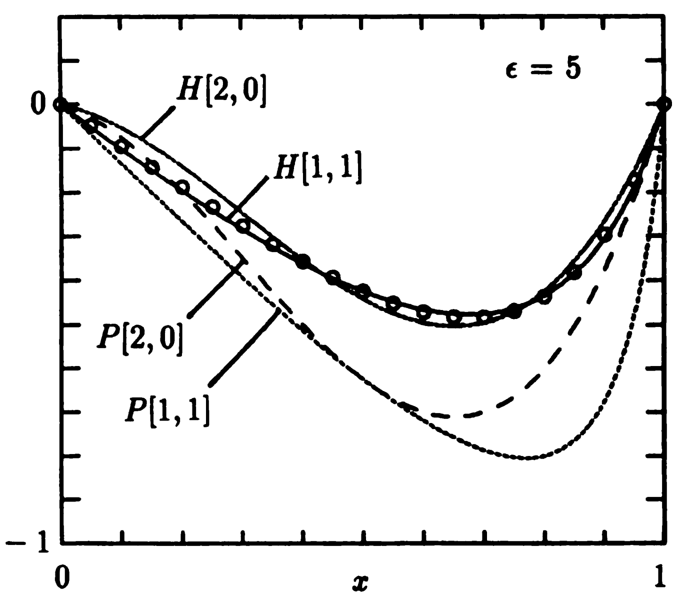

FIG 1. The Padé approximations $P[2,0]$ and $P[1,1]$, the hybrid approximations $H[2,0]$ and $H[1,1]$, and the exact solution (circles) for Ex 1 with $\epsilon = 5$.

$$\delta_1 = \frac{2\epsilon\,\delta_2^4}{9(3\epsilon+\delta_2)(36-\delta_2^2)\log(\frac{6+\delta_2}{6-\delta_2}) - 324\epsilon\,\delta_2 - 108\delta_2^2 + 6\epsilon\,\delta_2^3}, \tag{17}$$

$$\log\left(\frac{6+\delta_2}{6-\delta_2}\right) - \frac{4\,\delta_2(324\,\epsilon + 216\,\delta_2 - 9\,\epsilon\,\delta_2^2 - 4\,\delta_2^3)}{(36-\delta_2^2)(108\,\epsilon + 72\,\delta_2 - \epsilon\,\delta_2^2)} = 0. \tag{18}$$

Equation (17) expresses δ_1 in terms of δ_2, while Eq (18) is an equation for δ_2 as a function of ϵ, which must be solved numerically. In Figs 1 and 2 we have also plotted $H[2,0]$ and $H[1,1]$ for $\epsilon = 5$ and $\epsilon = 10$, respectively. As these figures illustrate, the hybrid approximations are more accurate than the Padé approximations on which they are based.

Although we shall discuss, more fully, insights about our method provided by this example (as well as our other examples) in the Discussion section, we make a few preliminary observations at this point. First, from Eqs (16) and Eqs (17)-(18) it follows that

$$\begin{aligned} &\delta_1 = \epsilon + O(\epsilon^3) \text{ and } \delta_2 = \epsilon^2 + O(\epsilon^3), \\ &\qquad \text{as } \epsilon \to 0, \text{ for } M = 2 \text{ and } N = 0, \\ &\delta_1 = \epsilon + O(\epsilon^2) \text{ and } \delta_2 = \epsilon + O(\epsilon^2), \\ &\qquad \text{as } \epsilon \to 0, \text{ for } M = 1 \text{ and } N = 1. \end{aligned} \tag{19}$$

Thus $H[2,0]$ reduces to $P[2,0]$ and $H[1,1]$ reduces to $P[1,1]$, as $\epsilon \to 0$. In addition, as $\epsilon \to \infty$, we find from Eqs (17) and (18) that, for the case $M = 1$ and $N = 1$,

$$\begin{aligned} &\delta_1 = 4 + O(\gamma(\epsilon)), \\ &\delta_2 = 6 - \gamma(\epsilon) + o(\gamma(\epsilon)), \quad \text{as } \epsilon \to \infty. \end{aligned} \tag{20}$$

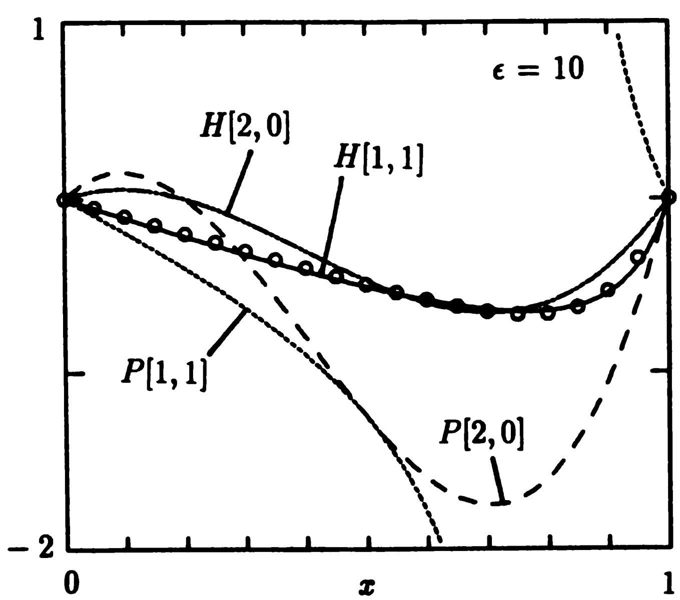

FIG 2. The Padé approximations $P[2,0]$ and $P[1,1]$, the hybrid approximations $H[2,0]$ and $H[1,1]$, and the exact solution (circles) for Ex 1 with $\epsilon = 10$. For this value of ϵ, the pole of $P[1,1]$ lies at $x = 0.8$.

Here $\gamma(\epsilon) \to 0^+$ as $\epsilon \to +\infty$ and is defined by $\gamma\log(\gamma) = -12/\epsilon$. From these results, as well as the numerical solution of Eqs (17) and (18) for "intermediate" values of ϵ, we find that the pole of $H[1,1]$, which is located at $x = 1/2 + 3/\delta_2$, lies *outside* the interval [0,1] for all positive values of ϵ. (The location of the pole approaches 1 from above as ϵ becomes large, with the pole lying, for example, at about 1.008 when $\epsilon = 50$.)

It is straightforward to use the procedure and formulas outlined above to construct Padé and hybrid approximations to $u(x,\epsilon)$ for other (larger) values of M and N. For example, we find

$$\begin{aligned} P[4,0](x,\epsilon) &= \epsilon\,u_1(x) + \epsilon^2\,u_2(x) + \epsilon^3\,u_3(x) + \epsilon^4\,u_4(x), \\ H[4,0](x,\epsilon) &= \delta_1\,u_1(x) + \delta_2\,u_2(x) + \delta_3\,u_3(x) + \delta_4\,u_4(x), \end{aligned} \tag{21}$$

where

$$\begin{aligned} \delta_1 &= \frac{15120\,\epsilon + 420\,\epsilon^3}{15120 + 420\,\epsilon^2 + \epsilon^4}, \quad \delta_2 = \epsilon\delta_1, \\ \delta_3 &= \frac{15120\,\epsilon^3}{15120 + 420\,\epsilon^2 + \epsilon^4}, \quad \delta_4 = \epsilon\delta_3; \end{aligned} \tag{22}$$

and

$$\begin{aligned} P[2,2] &= \frac{\epsilon\,v_1(x) + \epsilon^2\,v_2(x)}{1 + \epsilon\,w_1(x) + \epsilon^2\,w_2(x)}, \\ H[2,2] &= \frac{\delta_1\,v_1(x) + \delta_2\,v_2(x)}{1 + \delta_3\,w_1(x) + \delta_4\,w_2(x)}, \end{aligned} \tag{23}$$

with

$$\begin{aligned} v_1 &= \frac{x(x-1)}{2}, \\ v_2 &= -\frac{x(x-1)(2x-1)(x+1)(x-2)}{60(x^2-x+1)}, \\ w_1 &= -\frac{(2x-1)(2x^2-2x+1)}{10(x^2-x+1)}, \\ w_2 &= \frac{3x^4 - 6x^3 + 4x^2 - x + 1}{x^2 - x + 1}. \end{aligned} \tag{24}$$

In Fig 3 we have plotted the Padé approximation $P[2,2]$, the hybrid approximations $H[4,0]$ and $H[2,2]$, as well as the exact solution, for $\epsilon = 50$. Here $H[2,2]$ is clearly the "best" of the approximations shown and does a good job of simulating the boundary layer behavior of the exact solution, even at this moderately large value of ϵ where the boundary layer is well formed.

Example 2: We consider now the two-point boundary value problem

$$\begin{aligned} L(u,\epsilon) \equiv u''(x) + \epsilon\sin(2x)\,u'(x) + \\ 2\,\epsilon\cos(2x)u - 2\,\epsilon\cos(2x) = 0, \qquad 0 < x < \pi, \\ \text{with } B(u,\epsilon) \equiv u = 0, \text{ for } x = 0 \text{ and } x = \pi. \end{aligned} \tag{25}$$

The exact solution to this problem is

$$u = 1 - e^{-\epsilon \sin^2(x)}. \tag{26}$$

The Taylor series expansion of $u(x, \epsilon)$ about $\epsilon = 0$ converges for all $|\epsilon| < \infty$, since u has no singularities in the finite part of the complex ϵ−plane. For this example, u develops boundary layers at both $x = 0$ and $x = \pi$ as ϵ becomes large.

Step one: Using the regular perturbation method we find the u_j in Eq (2) are given by $u_0(x) = 0$ and $u_j(x) = (-1)^{j+1} \sin^{2j}(x)/j!$, for $j \geq 1$.

Step two: Using the perturbation coordinate functions $\{u_j(x)\}$ determined in step one, we can calculate Padé approximations $P[M, N]$ for various values of M and N. In particular for $M + N = 2$, using Eqs (4) and (5), we find

$$P[2, 0](x, \epsilon) = \epsilon \sin^2(x) - \epsilon^2 \sin^4(x)/2, \tag{27}$$

which is the second order perturbation solution, and

$$P[1, 1](x, \epsilon) = \frac{\epsilon \sin^2(x)}{1 + (\epsilon/2)\sin^2(x)}. \tag{28}$$

We note that, for $\epsilon > 0$, the poles of $P[1, 1]$ are all complex and, hence, lie *outside* the interval $D \equiv [0, 1]$. In particular, the poles which lie closest to D are at $x = \pm i \sinh^{-1}(\sqrt{2/\epsilon})$ and $x = \pi \pm i \sinh^{-1}(\sqrt{2/\epsilon})$, which approach $x = 0$ and $x = \pi$, respectively, as $\epsilon \to +\infty$. In Fig 4, we have plotted $P[2, 0]$ and $P[1, 1]$, along with the exact solution, for $\epsilon = 10$. The influence of the (complex) poles of $P[1, 1]$ in helping to simulate the steep slope of the solution near the ends of the interval is evident in Fig 4.

Step three: We now use the form of the Padé approximations determined in step two to define the hybrid approximations

$$H[2, 0] = \delta_1 \sin^2(x) - \delta_2 \sin^4(x)/2, \tag{29}$$

and

$$H[1, 1] = \frac{\delta_1 \sin^2(x)}{1 + (\delta_2/2)\sin^2(x)}, \tag{30}$$

where the amplitudes δ_1 and δ_2 are determined from the Galerkin conditions (7), which for this example become

$$\int_0^1 \{H[M, N]'' + \epsilon \sin(2x) H[M, N]' + 2\epsilon \cos(2x) H[M, N] - 2\epsilon \cos(2x)\} u_k \, dx = 0, \quad k = 1, 2. \tag{31}$$

When $M = 2$ and $N = 0$ Eqs (31) are *linear* and their solution is

$$\delta_1 = \frac{16\epsilon(2 + \epsilon)}{32 + 16\epsilon + 3\epsilon^2}, \quad \delta_2 = \frac{32\epsilon^2}{32 + 16\epsilon + 3\epsilon^2}. \tag{32}$$

When $M = 1$ and $N = 1$, Eqs (31) are *nonlinear* and must be solved numerically. In Fig 4 we have also plotted $H[2, 0]$ and $H[1, 1]$ for $\epsilon = 10$. As the figure illustrates, the hybrid approximations are again more accurate than the Padé approximations on which they are based. Using Eqs (31), we can again show that the relations (19) hold for this example as well. Also, it is straightforward to use the procedure and formulas outlined above to construct Padé and hybrid approximations to $u(x, \epsilon)$ for other (larger) values of M and N.

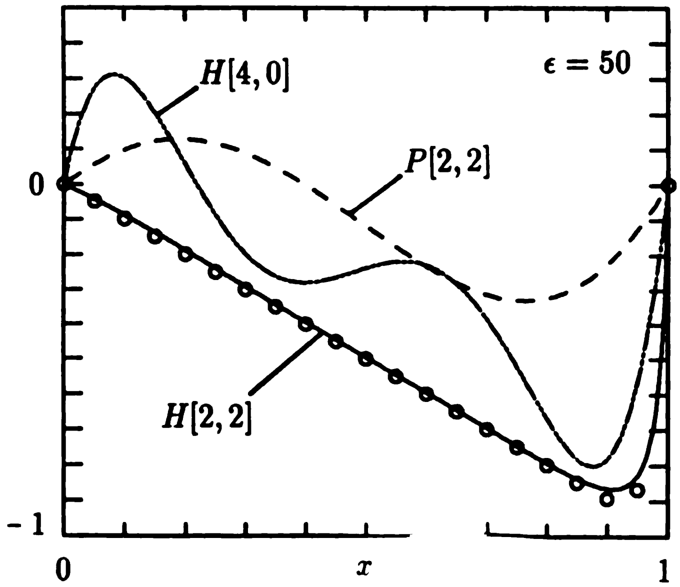

FIG 3. The Padé approxim... hybrid approximations $H[4, 0]$ and H... act solution (circles) for Ex 1 with $\epsilon = 5$...

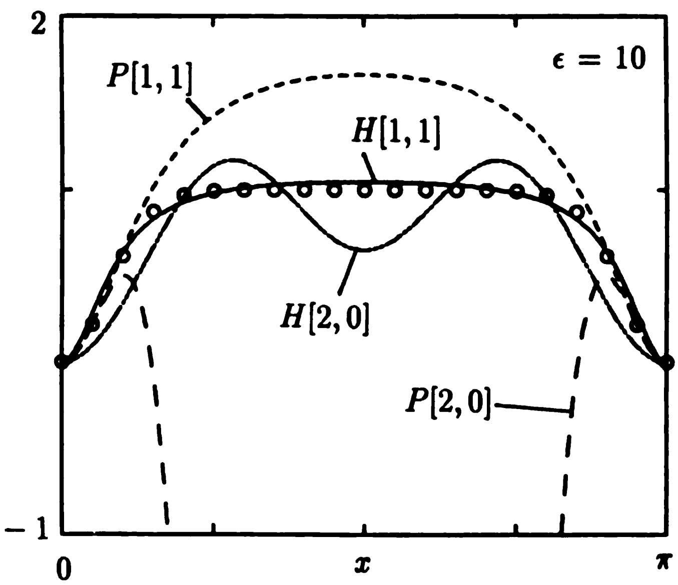

FIG 4. The Padé approximations $P[2, 0]$ and $P[1, 1]$, the hybrid approximations $H[2, 0]$ and $H[1, 1]$, and the exact solution (circles) for Ex 2 with $\epsilon = 10$.

APPLICATIONS TO PARTIAL DIFFERENTIAL EQUATIONS

In this section, we shall apply our method to two model elliptic boundary value problems in two space dimensions.

Example 3: We consider the elliptic boundary value problem

$$L(u,\epsilon) \equiv \nabla^2 u + \epsilon\cos(x)\sin(y)u_x + \epsilon\sin(x)\cos(y)u_y \\ -2\epsilon\sin(x)\sin(y)u + 2\epsilon\sin(x)\sin(y) = 0, \tag{33}$$

for $(x,y) \in D \equiv \{(x,y) : 0 < x < \pi, 0 < y < \pi\}$, with $B(u,\epsilon) \equiv u = 0$ for $(x,y) \in \partial D$. Here ∇^2 denotes the usual (two dimensional) Laplacian operator. This problem has the exact solution

$$u = 1 - e^{-\epsilon\sin(x)\sin(y)}, \tag{34}$$

and hence its Taylor series expansion about $\epsilon = 0$ converges for all $|\epsilon| < \infty$. We also note that, as $\epsilon \to +\infty$, u develops a boundary layer around the entire boundary of D, and approaches the value of 1 at each point in the interior of D. Figure 5 depicts a surface plot of the exact solution for $\epsilon = 10$.

Step one: Using the regular perturbation method we find $u_0 \equiv 0$ and

$$u_j = \frac{(-1)^{j+1}}{j!}\sin^j(x)\sin^j(y), \text{ for } j \geq 1. \tag{35}$$

Step two: Using the perturbation coordinate functions in Eqs (35) we find

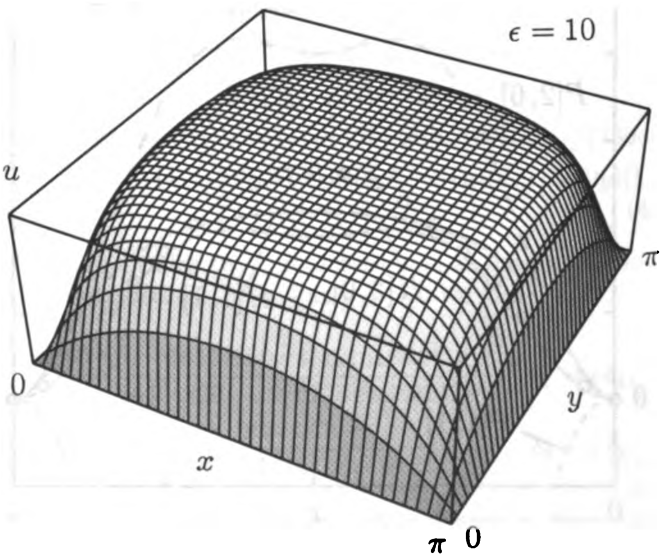

FIG 5. A surface plot of the exact solution, Eq (34), for Ex 3 with $\epsilon = 10$. Note the rather steep boundary layer around the entire boundary of D.

$$P[2,0] = \epsilon\sin(x)\sin(y) - (\epsilon^2/2)\sin^2(x)\sin^2(y), \\ P[1,1] = \frac{\epsilon\sin(x)\sin(y)}{1+(\epsilon/2)\sin(x)\sin(y)}. \tag{36}$$

We note that $P[1,1]$ has real poles for $\epsilon \geq 2$ where $\sin(x)\sin(y) = -2/\epsilon$, and hence these poles lie *outside* of D for all values of $\epsilon > 0$. In Fig 6 we have plotted a cross-section of the approximate solutions $P[2,0]$ and $P[1,1]$, along with the exact solution, at $y = \pi/2$ for $0 \leq x \leq \pi$ for $\epsilon = 10$.

Step three: Using the form of the Padé approximants above, we define

$$H[2,0] = \delta_1\sin(x)\sin(y) - (\delta_2/2)\sin^2(x)\sin^2(y), \\ H[1,1] = \frac{\delta_1\sin(x)\sin(y)}{1+(\delta_2/2)\sin(x)\sin(y)}, \tag{37}$$

where δ_1 and δ_2 are determined from the Galerkin conditions (7), which for this example become

$$\int_0^\pi\int_0^\pi L(H[M,N],\epsilon)\,u_k(x,y)\,dx\,dy = 0, \text{ for } k = 1,2. \tag{38}$$

For $N = 2$ and $N = 0$, these equations are linear and yield the solutions

$$\delta_1 = 32\epsilon(6075\pi^4 + 7632\pi^2\epsilon - 409600)/\Delta, \\ \delta_2 = 800\epsilon^2(243\pi^4 - 16384)/\Delta, \\ \Delta \equiv 194400\pi^4 - 13107200 + 244224\pi^2\epsilon \\ + (2097152 - 18225\pi^4)\epsilon^2. \tag{39}$$

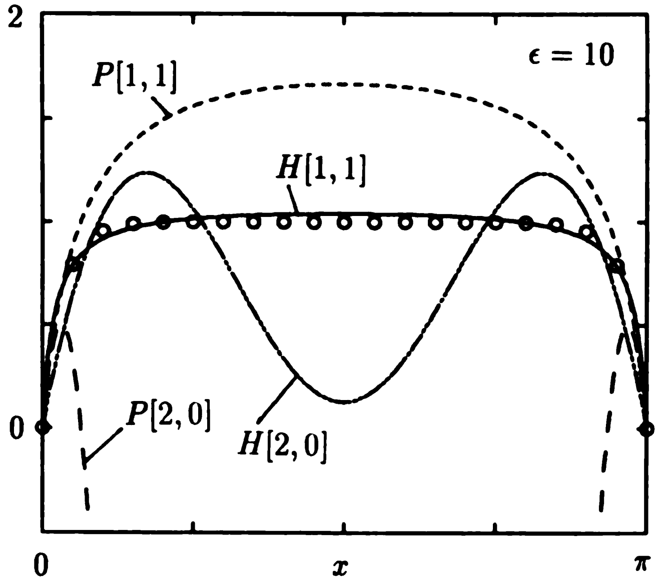

FIG 6. The Padé approximations $P[2,0]$ and $P[1,1]$, the hybrid approximations $H[2,0]$ and $H[1,1]$, and the exact solution (circles) for Ex 3 along the cross section $y = \pi/2$ with $\epsilon = 10$. Note the very "poor" quality of the perturbation solution $P[2,0]$, on which all of the other (much better!) approximations are ultimately based

From Eqs (38) and (39) it follows that δ_1 and δ_2 satisfy the conditions (19) as $\epsilon \to 0$. In Fig 6 we have also plotted the approximate solutions $H[2,0]$ and $H[1,1]$ at $y = \pi/2$ for $0 \le x \le \pi$. The improvement of the hybrid solutions over the corresponding perturbation solutions is evident from the figure.

Example 4: We consider the problem

$$L(u,\epsilon) \equiv \nabla^2 u + \epsilon \sin(x)\cos(y) u_x + 2\,\epsilon \sin(x)\sin(y) = 0, \tag{40}$$

for $(x,y) \in D \equiv \{(x,y) : 0 < x < \pi, 0 < y < \pi\}$, with $B(u,\epsilon) \equiv u = 0$ for $(x,y) \in \partial D$. Although there appears to be no closed form solution for this problem, it is straightforward to show that its solution $u(x,y)$ exhibits a number of interesting properties. The solution is positive over the entire domain D for positive values of ϵ and is invariant under the 180° rotation $x \to \pi - x$, $y \to \pi - y$. Since Eq (40) is also invariant under the transformation $\epsilon \to -\epsilon$, and $u(x,y) \to -u(x, \pi - y)$, we may focus our attention on solutions for positive ϵ. Figure 7 depicts a surface plot of the "exact" solution, obtained by purely numerical means, for $\epsilon = 12$. The solution has a regular perturbation expansion about $\epsilon = 0$, which converges for values of ϵ with $|\epsilon| < \epsilon_0 \cong 6.7$. (See Geer and Andersen, 1991a, where this equation was discussed in some detail.) In addition, as $\epsilon \to +\infty$, the solution develops a number of boundary layers over *portions* of ∂D, but not over the entire boundary.

Step one: Using the regular perturbation method, we find

$$\begin{aligned}
u_0 &\equiv 0,\\
u_1 &= \sin(x)\sin(y),\\
u_2 &= (1/32)\sin(2x)\sin(2y),\\
u_3 &= \frac{1}{128}\left\{\frac{1}{9}\sin(3x)\sin(3y) + \frac{1}{5}\sin(3x)\sin(y)\right.\\
&\quad \left. -\frac{1}{5}\sin(x)\sin(3y) - \sin(x)\sin(y)\right\},\\
u_4 &= \frac{1}{49152}\sin(4x)\sin(4y) + \frac{7}{76800}\sin(4x)\sin(2y)\\
&\quad - \frac{1}{19200}\sin(2x)\sin(4y) - \frac{1}{1920}\sin(2x)\sin(2y).
\end{aligned} \tag{41}$$

Step two: Using Eqs (41) we find

$$\begin{aligned}
P[2,0] &= \epsilon\sin(x)\sin(y) + (\epsilon^2/32)\sin(2x)\sin(2y),\\
P[1,1] &= \frac{\epsilon\sin(x)\sin(y)}{1 - (\epsilon/8)\cos(x)\cos(y)}.
\end{aligned} \tag{42}$$

We note that the poles of $P[1,1]$ lie inside D for $\epsilon > 8$. In Fig 8 we have plotted approximations to the diagonal cross-section $y = x$ of the solution at $\epsilon = 12$ using $P[2,0]$, $P[1,1]$, and the numerical solution.

Step three: Using the expressions in (42) we define

$$\begin{aligned}
H[2,0] &= \delta_1\sin(x)\sin(y) + (\delta_2/32)\sin(2x)\sin(2y),\\
H[1,1] &= \frac{\delta_1\sin(x)\sin(y)}{1 - (\delta_2/8)\cos(x)\cos(y)}.
\end{aligned} \tag{43}$$

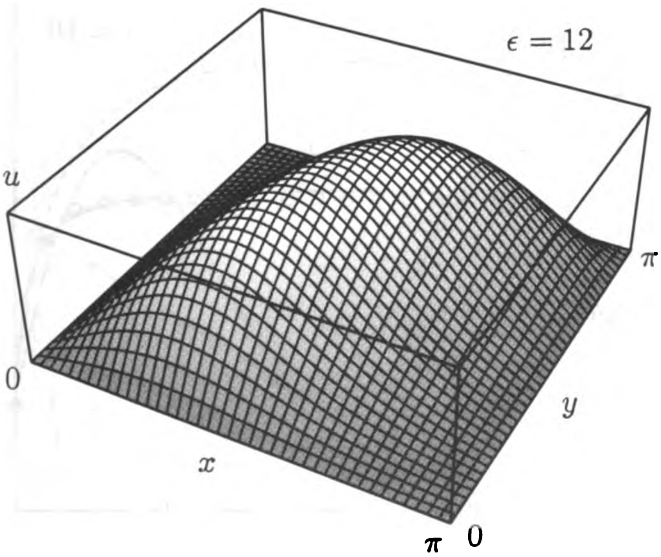

FIG 7. A surface plot of the "exact" solution for Ex 3 obtained by purely numerical means for $\epsilon = 12$. Note the boundary layers beg... to form around portions of the boundary of D ... ar $(x,y) = (0,0)$ and $(x,y) = (\pi,\pi)$, a... rnal "rise" forming near the diagonal $x =$

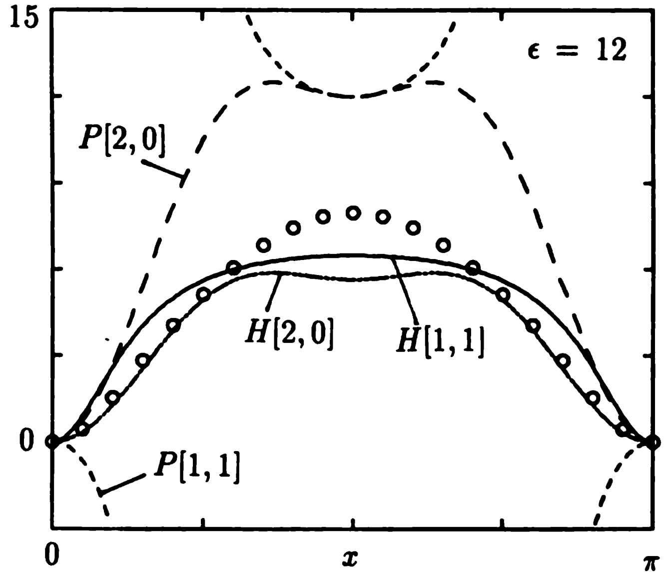

FIG 8. The Padé approximations $P[2,0]$ and $P[1,1]$, the hybrid approximations $H[2,0]$ and $H[1,1]$, and the exact solution (circles) for Ex 4 along the diagonal cross section $x = y$ with $\epsilon = 12$.

For $M = 2$ and $N = 0$, the Galerkin conditions (7) are linear and give

$$\delta_1 = \frac{\epsilon}{1+\epsilon^2/128}, \quad \delta_2 = \frac{\epsilon^2}{1+\epsilon^2/128}. \tag{44}$$

For $M = 1$ and $N = 1$, these conditions are nonlinear and must be solved numerically. Using these numerically computed solutions, it appears that the poles of $H[1,1]$ always lie outside of D. In Fig 8 we have also plotted approximations to the diagonal cross-section $y = x$ of the solution at $\epsilon = 12$ using $H[2,0]$ and $H[1,1]$.

The quality of the hybrid approximations improves as the order of the Padé approximants is increased. In particular, we find

$$P[4,0] = \sum_{j=1}^{4} \epsilon^j u_j(x,y), \quad H[4,0] = \sum_{j=1}^{4} \delta_j u_j(x,y), \tag{45}$$

and

$$P[2,2] = \frac{\epsilon\, v_1 + \epsilon^2\, v_2}{1+\epsilon\, w_1 + \epsilon^2\, w_2}, \quad H[2,2] = \frac{\delta_1\, v_1 + \delta_2\, v_2}{1+\delta_3\, w_1 + \delta_4\, w_2}, \tag{46}$$

where

$$\begin{aligned}
v_1 &= \sin(x)\sin(y),\\
v_2 &= [65 + \cos(2x) + 193\cos(2y) - 25\cos(2x)\cos(2y)]\\
&\quad \sin(2x)\sin(2y)/\{160[125 - 11\cos(2x) + 61\cos(2y)\\
&\quad + 5\cos(2x)\cos(2y)]\},\\
w_1 &= -\{1201\cos(x)\cos(y) - 31\cos(3x)\cos(y)\\
&\quad + 137\cos(x)\cos(3y) + 25\cos(3x)\cos(3y)\} \;/\; \{80\\
&\quad [125 - 11\cos(2x) + 61\cos(2y) + 5\cos(2x)\cos(2y)]\},\\
w_2 &= \{32301 - 7590\cos(2x) + 237\cos(4x)\\
&\quad + 25962\cos(2y) - 4396\cos(2x)\cos(2y)\\
&\quad + 106\cos(4x)\cos(2y) + 2109\cos(4y)\\
&\quad - 902\cos(2x)\cos(4y) + 125\cos(4x)\cos(4y)\}/\{23040\\
&\quad [125 - 11\cos(2x) + 61\cos(2y) + 5\cos(2x)\cos(2y)]\}.
\end{aligned} \tag{47}$$

The amplitudes $\{\delta_j\}$ are determined as indicated above. In particular, for $M = 4$ and $N = 0$ we find

$$\begin{aligned}
\delta_1 &= \frac{56524800\,\epsilon + 1216128\,\epsilon^3}{56524800 + 1216128\,\epsilon^2 + 2141\,\epsilon^4}, \quad \delta_2 = \epsilon\,\delta_1,\\
\delta_3 &= \frac{56524800\,\epsilon^3}{56524800 + 1216128\,\epsilon^2 + 2141\,\epsilon^4}, \quad \delta_4 = \epsilon\,\delta_3,
\end{aligned} \tag{48}$$

while the amplitudes for $M = N = 2$ must be determined numerically.

In Fig 9 we have plotted approximations to the diagonal cross-section $y = x$ of the solution at $\epsilon = 12$ using $P[4,0]$, $H[4,0]$, $P[2,2]$,and $H[2,2]$. From the figure we see that each hybrid approximation is an improvement over the Padé approximation on which it is based, while $H[2,2]$ appears to be the "best" of all of the hybrid approximations.

DISCUSSION AND OBSERVATIONS

We now make some observations concerning our method as related to the examples we have presented.

In Ex 1 we considered a simple two point boundary value problem. The hybrid solutions presented provide approximations which are consistently more accurate than the perturbation or Padé approximations on which they are based, and they appear to be converging to the exact solution as the number of terms is increased. This is true for small values of ϵ, for which the perturbation and Padé solutions give reasonable approximations to the solution, as well as for larger values of ϵ, where the perturbation and Padé solutions fail to give reasonable approximations. Part of the reason for this behavior is related to the convergence properties of the original perturbation series. The Taylor series expansion (and, hence, the regular perturbation expansion) of the solution converges only for values of ϵ with $|\epsilon| < 2\pi$. Thus, the perturbation solution, by itself, is useless for computing approximations to $u(x,\epsilon)$ for values of ϵ with $|\epsilon| > 2\pi$. However, we have shown (Andersen and Geer, 1991) that the sequence of approximations $\{H[M,0]\}$ converges to the exact solution as $M \to \infty$ for each $0 \le x \le 1$ and for each $0 \le \epsilon < \infty$. In addition, for $N \ge 1$, each Padé approximation $P[M,N]$ fails to give a reasonable approximation to the solution when one or more of its poles moves inside the domain (interval) $D = (0,1)$. The presence of a pole in a Padé approximation is undoubtedly related to the formation of the boundary layer at $x = 1$ as ϵ increases.

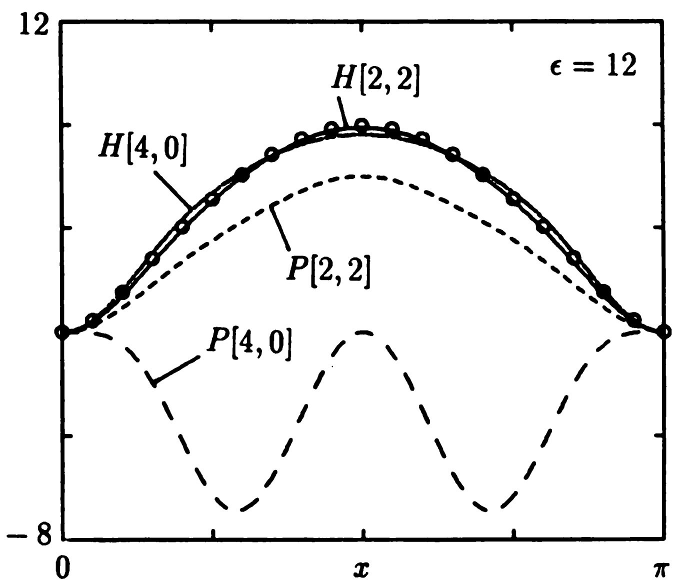

FIG 9. The Padé approximations $P[4,0]$ and $P[2,2]$, the hybrid approximations $H[4,0]$ and $H[2,2]$, and the exact solution (circles) for Ex 4 along the diagonal cross section $x = y$ with $\epsilon = 12$.

When this pole lies *outside* of D, but "close to" $x = 1$, it helps to simulate the steep slope of the solution forming within the boundary layer. When a pole moves *inside* D, however, it creates a singularity in the approximation which is not present in the exact solution. It appears that the poles of the hybrid approximations $H[M, N]$ always lie *outside* of D and hence $H[M, N]$ has the potential of providing at least a reasonable approximation to the exact solution, even when the corresponding Padé approximation cannot do so. In Fig 10 we have plotted the location of the pole of $P[1,1]$ and of $H[1,1]$ for $0 \le \epsilon \le 30$. As the figure illustrates, the pole of $H[1,1]$ asymptotically approaches 1 from *outside* of D, as $\epsilon \to \infty$.

In Ex 2, the perturbation solutions converge to the exact solution for all finite values of ϵ, as the number of terms in the approximation is increased. However, as ϵ increases, boundary layers form at each end of the domain (interval) D, and, consequently, more terms are required in the perturbation expansion to provide approximations of "acceptable" accuracy. In this case, the poles of the Padé and hybrid approximations lie in the complex plane and hence outside of D for all real values of ϵ. Some of these poles do approach the ends of the interval $D = [0, 1]$, however, as $\epsilon \to \infty$, and hence help to simulate the actual behavior of the exact solutions in these regions. In Fig 11 we have indicated the location of these poles of $P[1,1]$ and $H[1,1]$ as a function of ϵ. From the figure it is clear that the poles of $H[1,1]$ lie closer to the boundary of D than do the corresponding poles of $P[1,1]$. This helps to explain the increased accuracy of the hybrid approximations.

In our third example, we examined a two dimensional, elliptic boundary value problem involving a simple partial differential equation. As in Ex 2, the perturbation solution converges to the exact solution for all finite values of ϵ, as the number of terms in the approximation is increased. However, as ϵ increases, boundary layers now form over the *entire boundary* of the domain D. Consequently, more terms in the perturbation expansion are again required to provide approximations of "acceptable" accuracy as ϵ increases. In this case, all of the real poles of the Padé and hybrid approximations $P[1,1]$ and $H[1,1]$ lie *outside* of D for all real values of ϵ. In Fig 12 we have plotted the location of the real poles of these approximations for selected values of $\epsilon > 2$. From the figure we see that, as in Ex 2, the poles of $H[1,1]$ lie closer to the boundary of D than do the corresponding poles of $P[1,1]$.

In Ex 4 we considered another two dimensional, elliptic boundary value problem, whose exact solution develops a more complicated boundary layer structure as ϵ increases. In this case the perturbation solution has a *finite* radius of convergence, and hence the classical perturbation approximations are useless for values of ϵ with magnitude greater than the radius of convergence. However, all of the hybrid solutions appear to give reasonable approximations even for values of ϵ moderately above the radius of convergence (see Figs 8 and 9). In this case, the poles of $P[1,1]$ move inside D for values of $\epsilon > 8$. The location of these poles are indicated in Fig 13. The corresponding poles of $H[1,1]$ are purely imaginary (since $|\delta_2| < 8$) and hence they lie outside of D.

The observations we have indicated above, as well as experience we have had with the method for other examples, motivate us to make the following conjecture. It appears that, if the original perturbation expansion has a *finite* radius of convergence, then the poles of the Padé approximations constructed from this expansion will move

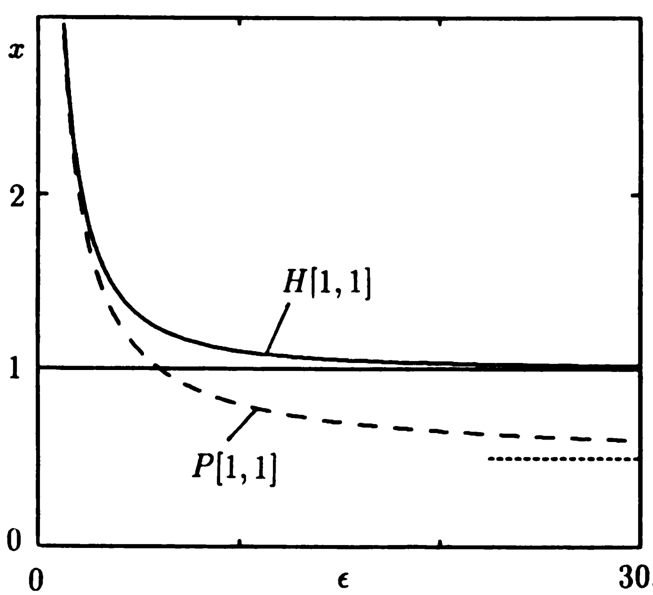

FIG 10. A plot of the location of the poles (vertical axis) of $P[1,1]$ and $H[1,1]$ for Ex 1 as ϵ (horizontal axis) varies between 0 and 30. The "critical" value of $x = 1$ is indicated, as well as the asymptotic value (short dashed line) of the pole of $P[1,1]$ as $\epsilon \to \infty$.

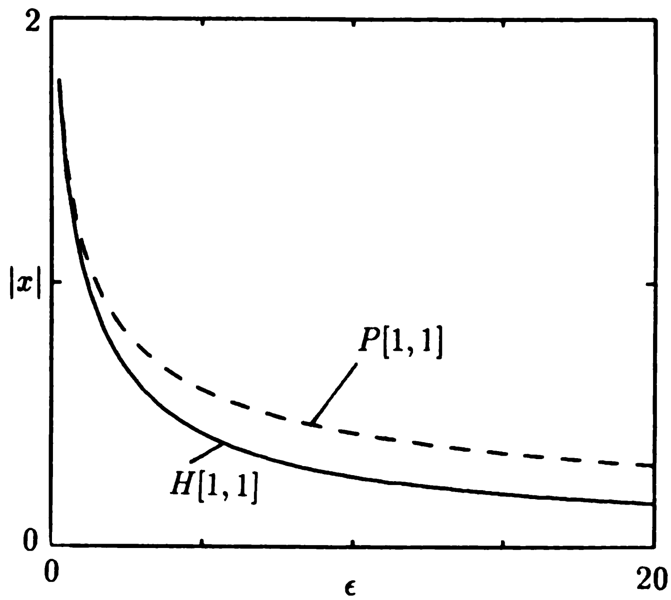

FIG 11. A plot of the magnitude (vertical axis) of the poles of $P[1,1]$ and $H[1,1]$ for Ex 2 which lie closest to $x = 0$ as ϵ (horizontal axis) varies between 0 and 20. These poles are purely imaginary and lie at $x = \pm i \sinh^{-1}(\sqrt{2/\epsilon})$ and $x = \pm i \sinh^{-1}(\sqrt{2/\delta_2})$ for $P[1,1]$ and $H[1,1]$, respectively.

inside the domain D as ϵ increases. If the original perturbation expansion has an *infinite* radius of convergence, then the poles of the Padé approximations will remain *outside* of D. In the first case, the hybrid approximations we have described appear to keep the corresponding poles outside of D for all values of ϵ, while in the second case the hybrid solutions appear to move the poles closer to the boundary of D. In either case, the hybrid technique appears to "adjust" the location of the poles in such a manner as to provide approximate solutions of greater accuracy than the corresponding Padé approximation. Obviously, this conjecture needs to be studied in more detail and is the subject of some of our current investigations.

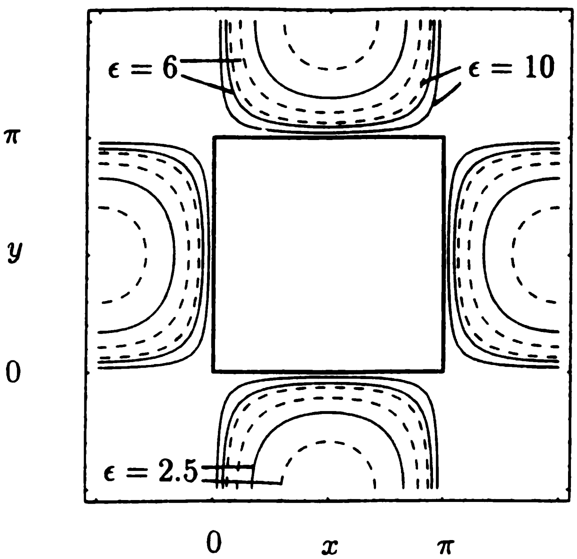

FIG 12. A plot of the locations of some of the poles of $P[1,1]$ (dashed lines) and $H[1,1]$ (solid lines) in the $x, y-$plane which lie closest to D for Ex 3 with $\epsilon = 2.5$, 6, and 10. The boundary of D is also indicated. Note that the poles of $H[1,1]$ lie closer to the boundary of D than do the corresponding poles of $P[1,1]$.

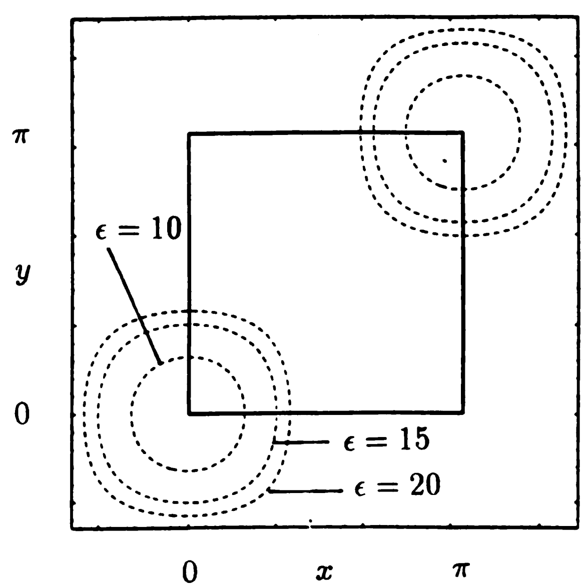

FIG 13. A plot of the locations of some of the poles of $P[1,1]$ (dashed lines) in the $x, y-$plane which lie closest to D for Ex 4 with $\epsilon = 10$, 15, and 20. The boundary of D is also indicated. The influence of the pole of $P[1,1]$ at $\epsilon = 12$ is also evident in Fig 8.

In general, the basic idea of using the original perturbation expansion to construct one or more Padé approximations seems to be justified, and, in fact, is recommended when the solution tends to exhibit some kind of boundary layer behavior as ϵ increases. The increased ability of the Padé solutions to simulate boundary layer behavior appears to provide more accurate approximations, even for "smaller" values of ϵ, for which the boundary layer is not yet well formed (see, e.g., Figs 1 and 2). For "any" value of ϵ, however, the hybrid solutions are consistently more accurate than the Padé solutions on which they are based, and it is recommended that the additional step of computing the new amplitudes $\{\delta_j\}$ be undertaken, especially when only a few perturbation coordinate functions are known.

REFERENCES

Andersen C, and Geer J (1982), Power series expansions for the frequency and period of the limit cycle of the van der Pol equation, *SIAM J Appl Math* **42**, 678-693.

Andersen C, and Geer J (1991), Investigating a hybrid perturbation Galerkin technique, ICASE Rep. No. 88-65 (NASA-Langley) and *J Symb Comp* **12**, 695-714.

Baker, G (1975), *Essentials of Padé Approximants*, Academic Press, New York.

Bender, C M, and Orszag, S A (1978), *Advanced mathematical methods for scientists and engineers*, McGraw-Hill, New York.

Dadfar M, Geer J, and Andersen C (1984), Perturbation analysis of the limit cycle of the free van der Pol equation, *SIAM J Appl Math* **44**, 881-895.

Galerkin B (1915), *Vestnik Inzhenerov, Tech* **19**, 897-908.

Gaunt D, and Guttmann A (1974), Series expansions: analysis of coefficients, *Phase Transitions and Critical Phenomena*, (Domb C and Green M, eds.) (3), Academic Press, New York.

Geer J, and Andersen C (1989a), A hybrid perturbation Galerkin technique with applications to slender body theory, *SIAM J Appl Math* **49**, 344-361.

Geer J, and Andersen C (1989b), A hybrid perturbation-Galerkin method for differential equations containing a parameter, ICASE Rep. No. 89-49 (NASA-Langley) and *Appl Mech Rev* **42**, S69-S77.

Geer J, and Andersen C (1990), A hybrid perturbation-Galerkin technique that combines multiple expansions. *SIAM J Appl Math* **50**, 1474-1495.

Geer J, and Andersen C (1991a), A hybrid perturbation-Galerkin technique for partial differential equations. *Asymptotic Analysis and the Numerical Solution of Partial Differential Equations.* Lec Notes Pure Appl Math 130, Marcel Dekker, New York, 113-134.

Geer J, and Andersen C (1991b), Resonant frequency calculations using a hybrid perturbation-Galerkin Technique, ICASE Rep. No. 91-68 (NASA-Langley) and *Appl Mech Rev* **44**(11), 2, S76-S88.

Hunter D, and Baker G (1973), Methods of series analysis I. Comparison of current methods used in the theory of critical phenomena, *Phys Rev* **B7**, 3346-3376.

Nayfeh A (1973), *Perturbation Methods*, Wiley, New York.

Singler T, and Geer J (1993), A hybrid perturbation Galerkin solution to a problem in selective withdrawal, *Phys Fluids* **A5**(5), 1156-1166.

Van Dyke, M (1974), Analysis and improvement of perturbation series, *Quart J Mech Appl Math* **27**, 423-450.

Method of virtual power applied to Cosserat surfaces with deformable directors

Boris Krajnc Alves

Department of Informatics, Federal University of Espírito Santo, Vitória ES, Brazil 29069

Jacob Lubliner

Department of Civil Engineering, University of California, Berkeley CA 94720

Following a brief outline of the method of virtual power, the local equations of motion for a Cosserat surface with inextensible directors are derived by means of this method. The model obtained coincides with the results derived from three-dimensional theory by Simo and Fox. Subsequently the model is extended so as to account for deformable directors. Besides the linear-momentum and moment-of-momentum balance equations, one additional scalar equation is derived. This equation replaces the director-momentum balance equation of Naghdi and therefore eliminates the necessity of introducing constitutive restrictions. The equivalence between the model derived by the virtual-power method and the results from the direct method of Naghdi are finally noted.

INTRODUCTION

It is the purpose of this paper to show how the method of virtual power, as introduced by Germain (1973) and modified by Lubliner (1983a), can be applied to the derivation of the local equations of motion for a Cosserat surface. Initially the application is restricted to a Cosserat surface with inextensible directors. The basic equations derived are not novel but their derivation by the virtual power method does not seem to have been proposed in the literature. In contrast with the direct approach of Naghdi (1972), where kinematics plays a fundamental role in the definition of the model, the derivation using the virtual power method is intrinsically based on the physics of the problem where meaningful forces and moments, a priori assumed, are placed in duality with velocities and rates of rotations. As a result, a physically sound model is obtained with the degree of kinematic indeterminacy as a direct consequence of its duality with the assumed forces and moments.

The restricted model is then extended to account for deformable directors. In Naghdi's direct method, the approach is to derive the basic field equations in accordance with the results of the asymptotic expansion of the three-dimensional equations. Thus Naghdi's model, besides assuming balance of linear momentum and moment of momentum, postulates an additional equation of balance of director momentum. The overdeterminacy in the theory is overcome by introducing constitutive restrictions such that the moment-of-momentum balance equation becomes identically satisfied. The physical interpretation of the equation of balance of director momentum has been a major subject of research in the works of Naghdi and co-authors. Ericksen and Truesdell (1958) also derived the basic field equations for a Cosserat surface but, not assuming balance of director momentum, obtained an incomplete theory. Green, Naghdi and Wainwright (1965) also did not postulate it but latter assumed it to hold in order to solve the indeterminacies of the model (see Naghdi, 1972, page 490, footnote 17).

As shown in the present paper, the method of virtual power is an effective way of deriving the appropriate equations. The local linear-momentum and moment-of-momentum balance equations are derived from the fundamental axiom of the method of virtual power. An additional scalar equation is derived with the help of a physically reasonable hypothesis and the principle of virtual power. The resulting set of equations eliminates the need for constitutive restrictions. It is finally shown that in the sense of the virtual-power method this model is nonetheless equivalent to that of Naghdi's direct method.

part of "MECHANICS PAN-AMERICA 1993" edited by MRM Crespo da Silva and CEN Mazzilli ASME Reprint No AMR134
Appl Mech Rev vol 46, no 11, part 2, November 1993 S266

THE METHOD OF VIRTUAL POWER

As originally proposed by Germain (1973), the method of virtual power may be summarized by the following two statements:

Axiom of virtual power of internal forces:

> *The virtual power of the internal forces on any virtual rigid-body velocity field is zero.*

Principle of virtual power:

> *For a body in equilibrium with respect to a Galilean frame, the virtual power of the internal and external forces on any virtual velocity field is zero.*

The axiom of virtual power of internal forces is simply a restatement of the laws of motion. In an alternative formulation which dispenses with the a priori introduction of internal forces, the words *internal forces* in the statement of the axiom are replaced by *external and inertial force systems* (for the definition of the inertial force system and additional considerations see Lubliner (1983a-b, 1984)). The principle of virtual power is then used to define the *internal force system* (a generalization of the notion of *stress field* in classical continuum mechanics) with the help of the *principle of localization* (for details and an application, see Lubliner (1986)). The modified axiom is referred to as the *fundamental axiom of the method of virtual power.*

In the remainder of this section the method of virtual power is formalized in a manner appropriate to its application to Cosserat surfaces.

A body is modeled as a smooth, compact, orientable manifold $\mathcal{B}$ with smooth boundary and dimension at most 3. Configurations are mappings $\kappa : \mathcal{B} \to \mathcal{M}$, where $\mathcal{M}$ is a smooth finite-dimensional affine manifold without boundary, belonging to a *configuration space* $\mathcal{C}$ which is itself a smooth infinite-dimensional manifold modeled on a Banach space (Marsden and Hughes, 1983). Following previously introduced terminology (Lubliner, 1986), we call a body model *simple* if $\mathcal{M}$ is the Euclidean affine space modeled on $\mathbf{R}^3$ (as is commonly done, the Euclidean affine space will often be denoted simply $\mathbf{R}^3$) and *generalized* otherwise. A Cosserat surface is a generalized body model where $\mathcal{B}$ is a surface or 2-manifold and $\mathcal{M} = T\mathbf{R}^3$, the tangent bundle of $\mathbf{R}^3$, which may be identified with $\mathbf{R}^3 \times \mathbf{R}^3$ and whose elements are ordered pairs of vectors in $\mathbf{R}^3$.

Motions are one-parameter families of configurations, describing curves in the space of configurations $\mathcal{C}$:

$$\tilde{\kappa} : I \to \mathcal{C}, \quad \text{for } \tilde{\kappa}(t) \in \mathcal{C} \text{ and } I \text{ an interval of } \mathbf{R}.$$

For convenience, the configuration at time t, $\tilde{\kappa}(t)$, will be denoted κ_t.

If, at a given point $p \in \mathcal{B}$, the mapping $t \to \kappa_t(p)$ is differentiable, then the derivative, denoted $\boldsymbol{v}_t(p)$, is the material velocity of $p \in \mathcal{B}$ at time $t \in I$, and is a vector tangent to the curve $t \to \kappa_t(p)$ at $\kappa_t(p)$ (that is, $\boldsymbol{v}_t(p) \in T\mathcal{C}_{\kappa_t(p)}$). A material velocity field at a configuration κ is thus a mapping $\boldsymbol{v} : \mathcal{B} \to T\mathcal{C}_\kappa$, and is in a sense a tangent vector to the curve $t \to \kappa_t$ at κ_t. The concept of a tangent to a curve in a finite dimensional manifold is thus naturally generalized. In manifold terminology, the material velocity field is an element of $T\mathcal{C}$, the tangent bundle to the configuration space $\mathcal{C}$. In the remainder it is assumed that both the configuration manifold $\mathcal{C}$ and its tangent bundle are modeled on appropriate Banach spaces (for additional definitions, see Hirsch (1976), Spivak (1979), Abraham and Marsden (1983)).

In the application of the method of virtual power it is useful to assume that all rigid-body motions from a given configuration $\kappa \in \mathcal{C}$ are a priori possible (any external constraints are applied afterwards).[1] The velocity-field space $T\mathcal{C}_\kappa$ thus contains the space of all rigid-body velocity fields as a closed finite-dimensional subspace, to be denoted $T\mathcal{C}^r_\kappa$.

A force system is naturally defined as a continuous linear functional on the space of virtual velocity fields and hence is characterized by its virtual power on a virtual velocity field. A force system is consequently an element of the topological dual of the tangent space $T\mathcal{C}$, denoted $T^*\mathcal{C}$ and denoted the cotangent bundle of $\mathcal{C}$. In the application of the method of virtual power, the crucial step is the choice of the physically meaningful force systems that describe the model being studied. Following physical intuition, at each configuration $\kappa \in \mathcal{C}$ a subspace $\mathcal{F}_\kappa$ of $T^*\mathcal{C}_\kappa$, consisting of the physically meaningful force systems at the configuration κ, is chosen, generating the subbundle $\mathcal{F}$ of $T^*\mathcal{C}$. If $\boldsymbol{f} \in \mathcal{F}_\kappa$ and $\boldsymbol{\eta} \in T\mathcal{C}_\kappa$ then the value of $\boldsymbol{f}$ at $\boldsymbol{\eta}$ will be denoted by $< \boldsymbol{f}, \boldsymbol{\eta} >$ and represents the virtual power of the force system $\boldsymbol{f}$ on the virtual velocity field $\boldsymbol{\eta}$.

We now define

$\boldsymbol{f}^e_t$: external force system exerted on $\mathcal{B}$ by other bodies at time t in a motion, $t \to \kappa_t$,

$\boldsymbol{f}^i_t$: inertial force system at time t;

then the fundamental axiom of virtual power may be written as

$$< \boldsymbol{f}^e_t + \boldsymbol{f}^i_t, \eta > = 0 \quad \forall\, \eta \in T\mathcal{C}^r_\kappa.$$

[1] In a simple body model, a rigid-body motion is one in which all configurations can be derived from one another by a Euclidean mapping. The definition must be extended appropriately for a generalized body model.

$$\begin{tikzcd} TC_\kappa \arrow[r, phantom, "< f, \eta >"] \arrow[d, "Tl_\kappa"'] & TC^*_\kappa \\ T\mathcal{D}_{l(\kappa)} \arrow[r, phantom, "\ll \sigma, \epsilon \gg"] & T\mathcal{D}^*_{l(\kappa)} \arrow[u, "Tl^*_\kappa"'] \end{tikzcd}$$

FIG 1: Commutative Diagram for a Simple Body Model

Therefore, if $(TC^r)^\perp$ denotes the orthogonal complement of (TC^r), then we may write $f^e_t + f^i_t \in (TC^r)^\perp \cap \mathcal{F}_\kappa$, the space of equilibrated force systems at the configuration κ.

The application of the principle of virtual power requires the notion of internal force system, which does work when a body is deformed. A deformed state (or *deformation*) of the body may be described by an equivalence class of configurations that differ by a (*generalized*) rigid-body displacement. If $\mathcal{R}$ denotes the corresponding equivalence relation, then the space of deformations is the quotient set $\mathcal{C}/\mathcal{R}$. Quotient sets do not, in general, inherit a manifold structure; it is also preferable not to work with quotient sets but with manifolds where an appropriate physical interpretation is possible. Thus we postulate the existence of a deformation manifold $\mathcal{D}$, modeled on a Banach space, and an injection $k : \mathcal{C}/\mathcal{R} \rightarrow \mathcal{D}$ such that if $j : \mathcal{C} \rightarrow \mathcal{C}/\mathcal{R}$ is the canonical surjection of $\mathcal{C}$ onto $\mathcal{C}/\mathcal{R}$, then the mapping

$$l = k \circ j : \mathcal{C} \rightarrow \mathcal{D},$$

is differentiable in some appropriate sense.[2] Clearly, the appropriate notion of differentiability must be determined by the specific model being studied.

If $Tl_\kappa : TC_\kappa \rightarrow T\mathcal{D}_{l(\kappa)}$ denotes the derivative of l at the configuration κ and $T\mathcal{D}_{l(\kappa)}$ the image of TC_κ by Tl_κ (by hypothesis a Banach space and in a sense the tangent space to the deformation manifold $\mathcal{D}$ at $l(\kappa)$), then the commutative diagram in Figure 1 holds. Here $\ll \sigma, \epsilon \gg$ denotes the duality pairing in $T\mathcal{D}_\kappa \times T\mathcal{D}^*_\kappa$, and Tl^*_κ is the adjoint mapping to Tl_κ, defined by

$$< Tl^*_\kappa \sigma, \eta > = \ll \sigma, Tl_\kappa \eta \gg \quad \forall \eta \in TC_\kappa.$$

The space $T\mathcal{D}_{l(\kappa)}$ is the deformation-rate space, and its dual, $T\mathcal{D}^*_{l(\kappa)}$, the internal force-system space. The linear mapping $Tl_\kappa : TC_\kappa \rightarrow T\mathcal{D}_{l(\kappa)}$ is such that Kernel $[Tl_\kappa] = TC^r_\kappa$.

Finally, the principle of virtual power defines uniquely (for the given choice of $\mathcal{D}$) the internal force system[3] σ compatible with the model being studied and associated with an equilibrated external force system $f \in F_\kappa \cap (TC^r_\kappa)^\perp$. Thus

$$\ll \sigma, Tl_\kappa \eta \gg = < Tl^*_\kappa \sigma, \eta > = < f, \eta > \quad \forall \eta \in TC_\kappa.$$

The space of internal force systems may consequently be described by $(Tl^*_\kappa)^{-1}(\mathcal{F}_\kappa)$.[4]

Finally, if $t \rightarrow \kappa_t$ is a motion and σ the internal force system acting at time t, the *deformation power* at time t is defined by

$$P^*_t = \ll \sigma, Tl_\kappa v_t \gg,$$

that is, the value of the internal virtual power at the actual velocity field v_t of the body.

COSSERAT SURFACE. BASIC DEFINITIONS

A Cosserat surface may be regarded as a smooth, compact and orientable two-dimensional manifold $\mathcal{B}$, with a smooth boundary and a vector-bundle structure associated with it. As previously indicated, the configuration manifold $\mathcal{M}$ is TR^3 (the tangent bundle of R^3), which may be identified with $R^3 \times R^3$, so that a configuration κ may be identified with the pair of mappings $(r : \mathcal{B} \rightarrow R^3, d : \mathcal{B} \rightarrow R^3)$. Here $r : \mathcal{B} \rightarrow R^3$ is an embedding, and $\mathcal{N} = r(\mathcal{B})$ is the surface occupied by $\mathcal{B}$ in the configuration κ, while the mapping $d \circ r^{-1} : \mathcal{N} \rightarrow TR^3_{r(\mathcal{B})}$ defines a *director* at each point of $\mathcal{N}$; d is called the *director field.*

In order to apply the method of virtual power to Cosserat surfaces it is necessary to provide an appropriate definition of rigid-body motions. This may be done by temporarily identifying the Cosserat surface with a shell, a three-dimensional simple body. Following this reasoning, the Cosserat surface at a given configuration $\kappa = (r, d)$ may be identified with the set

$$W_\kappa = \{X \in R^3 | X = r(p) + \zeta d(p); \;\; p \in \mathcal{B}; \zeta \in [-\tfrac{1}{2}, \tfrac{1}{2}]\},$$

while $D(p) = \| d(p) \|$, the Euclidean norm of $d(p)$, is identified with the thickness of the shell at $p \in \mathcal{B}$. To guarantee the uniqueness of the above representation, the following restrictions are imposed for all $p \in \mathcal{B}$:

(i) $d(p) \notin T\mathcal{N}_{r(p)}$,

(ii) $D(p) < 2 \times \min\{R_\alpha(p), \quad \alpha = 1, 2\}$,

where $T\mathcal{N}_{r(p)} \subset TR^3_{r(p)}$ is the tangent plane to $\mathcal{N}$ at $r(p)$, and $R_\alpha(p)$ $(\alpha = 1, 2)$ are the principal radii of curvature of the embedded surface $\mathcal{N}$ at $r(p)$.

---

[2] In general, more than one choice [illegible] possible; witness the many possible strain tensors in [illegible] um mechanics.

[3] In the work of Germain (197[illegible] [illegible] e system is the negative of the one defined here

[4] By hypothesis TC_κ is a Banach space, TC^r_κ a closed subspace and Tl_κ a linear map from TC_κ onto $T\mathcal{D}_{l_\kappa} \sim TC_\kappa / TC^r_\kappa$; it follows (Horvath, 1968) that $Tl^*_\kappa : T\mathcal{D}_{l_\kappa} \rightarrow (TC^r_\kappa)^\perp$ is a bijection.

We may now assert that two configurations $\kappa = (\boldsymbol{r}, \boldsymbol{d})$ and $\kappa^* = (\boldsymbol{r}^*, \boldsymbol{d}^*)$ of a Cosserat surface $\mathcal{B}$ are equivalent to within a rigid-body displacement if the respective sets W_κ and W_{κ^*} are so equivalent in the classical sense, that is, they are related to each other by a Euclidean mapping. This assertion leads to

$$\begin{aligned}\boldsymbol{r}^*(p) &= \boldsymbol{x}_0 + \boldsymbol{v} + \boldsymbol{Q}(\boldsymbol{r}(p) - \boldsymbol{x}_0),\\ \boldsymbol{d}^*(p) &= \boldsymbol{Q}(\boldsymbol{d}(p)),\end{aligned}$$

for $\boldsymbol{x}_0, \boldsymbol{v} \in \boldsymbol{R}^3$ and $\boldsymbol{Q} \in SO(3)$ (the rotation group on $\boldsymbol{R}^3$, that is, the set of proper orthogonal second-rank tensors).

In what follows we assume that the manifold $\mathcal{B}$ is diffeomorphic to a subset of $\boldsymbol{R}^2$ and may without loss of generality be identified with such a subset. The configuration space under this assumption may be described by mappings $(\boldsymbol{r} : \mathcal{B} \subset \boldsymbol{R}^2 \to \boldsymbol{R}^3, \boldsymbol{d} : \mathcal{B} \subset \boldsymbol{R}^2 \to \boldsymbol{R}^3)$. The mapping $\boldsymbol{r}$ induces a parametrization of the reference surface $\mathcal{N} \subset \boldsymbol{R}^3$ following the coordinate lines (θ_1, θ_2) in $\boldsymbol{R}^2$. Vectors tangent to the coordinate lines (convected coordinates) on $\mathcal{N}$ and forming a natural basis for the tangent space, at each point of $\mathcal{N}$, are given by

$$\boldsymbol{a}_\alpha = \frac{\partial \boldsymbol{r}}{\partial \theta_\alpha} \qquad \text{for } \alpha = 1, 2. \tag{1}$$

It follows from hypothesis (i) that $(\boldsymbol{a}_1, \boldsymbol{a}_2, \boldsymbol{d})$ form a basis for $T\boldsymbol{R}^3_{r(p)}$ at all $p \in \mathcal{B}$.

A physically meaningful force system in a Cosserat surface is given by force and moment distributions on $\mathcal{N}$, together with boundary forces and moments along the edge $\partial\mathcal{N}$. Since the power of a force and a moment is, respectively, on a linear and an angular velocity, the natural kinematic quantities in the Cosserat surface that may be placed in duality with the aforementioned force system are the velocity field of points in the reference surface, contributing to the power of distributed and boundary forces, and the director angular velocity field naturally contributing to the power of distributed and boundary moments.

COSSERAT SURFACE WITH INEXTENSIBLE DIRECTORS

In a two-dimensional Cosserat continuum, the physically meaningful moments form a two-dimensional fiber bundle described by the bending and twisting moments. Sufficient kinematic structure to account for those components is contained in the restricted theory of Cosserat surfaces with inextensible directors, which is treated in the present section. An extension that takes into account forces associated with changes in length of the directors is considered in the next section.

Kinematics of the restricted Cosserat Surface

Configurations of the restricted Cosserat surface are given by mappings

$$\kappa : \mathcal{B} \subset \boldsymbol{R}^2 \to \boldsymbol{R}^3, \qquad \kappa(p) = (\boldsymbol{r}(p), \boldsymbol{d}(p)),$$

where $\boldsymbol{r} : \mathcal{B} \subset \boldsymbol{R}^2 \to \boldsymbol{R}^3$ is an embedding. Without loss of generality, it is moreover assumed that

$$D(p) = \| \boldsymbol{d}(p) \| = 1,$$

for all $p \in \mathcal{B}$.[5]

If (θ_1, θ_2) defines a coordinate chart on $\boldsymbol{R}^2$ then it induces a parametrization on the surface $\boldsymbol{r}(\mathcal{B}) = \mathcal{N} \subset \boldsymbol{R}^3$. The reference configuration is represented by $\kappa_0 = (\boldsymbol{r}_0, \boldsymbol{d}_0)$, with $\boldsymbol{r}_0(\mathcal{B}) = \mathcal{N}_0$.

The base vectors tangent to the coordinate lines on $\mathcal{N}$ and $\mathcal{N}_0$ are respectively denoted by

$$\begin{aligned}\boldsymbol{a}_\alpha &= \frac{\partial}{\partial \theta_\alpha} \boldsymbol{r} \ \in T\boldsymbol{R}^3_{\mathcal{N}},\\ \boldsymbol{A}_\alpha &= \frac{\partial}{\partial \theta_\alpha} \boldsymbol{r}_0 \ \in T\boldsymbol{R}^3_{\mathcal{N}_0},\end{aligned}$$

and the components of the metric tensor by

$$\begin{aligned}a_{\alpha\beta} &= \boldsymbol{a}_\alpha \cdot \boldsymbol{a}_\beta,\\ A_{\alpha\beta} &= \boldsymbol{A}_\alpha \cdot \boldsymbol{A}_\beta\end{aligned}$$

(for additional details see Flugge (1970), Marsden and Hughes (1983)).

As indicated in the previous section, at each point $p \in \mathcal{M}$, $(\boldsymbol{a}_1, \boldsymbol{a}_2, \boldsymbol{a}_3)$, where $\boldsymbol{a}_3 = \boldsymbol{d}$, form a local curvilinear basis for $T\boldsymbol{R}^3_{r(p)}$. The dual base vectors are defined by $\boldsymbol{a}_i \cdot \boldsymbol{a}^j = \delta_i^j$ (Kronecker delta) for $1 \le i, j \le 3$ and clearly $\boldsymbol{a}^3 = (\boldsymbol{a}_1 \times \boldsymbol{a}_2)/a$, with $a = \det(a_{ij})$, $a_{ij} = \boldsymbol{a}_i \cdot \boldsymbol{a}_j$.

We assume the summation convention with repeated greek indices representing summations of indices over 1,2 and repeated latin indices over 1,2,3.

Rigid-body motions $t \to \kappa_t^* = (\boldsymbol{r}_t^*, \boldsymbol{d}_t^*)$ from a configuration $\kappa = (\boldsymbol{r}, \boldsymbol{d})$ are given by

$$\begin{aligned}\boldsymbol{r}_t^*(p) &= \boldsymbol{x}_0 + \boldsymbol{c}_t + \boldsymbol{Q}_t(\boldsymbol{r}(p) - \boldsymbol{x}_0),\\ \boldsymbol{d}_t^*(p) &= \boldsymbol{Q}_t \boldsymbol{d}(p),\end{aligned}$$

where $\boldsymbol{x}_0$ is a fixed point in $\boldsymbol{R}^3$, $t \to \boldsymbol{c}_t$ and $t \to \boldsymbol{Q}_t$ map $I \subset \boldsymbol{R}$ into $\boldsymbol{R}^3$ and $SO(3)$, respectively. If these mappings are differentiable, then the velocity field at $t \in I$ in a rigid-body motion is given by $(\dot{\boldsymbol{r}}_t^*, \dot{\boldsymbol{d}}_t^*)$, where

$$\begin{aligned}\dot{\boldsymbol{r}}_t^*(p) &= \boldsymbol{v} + \boldsymbol{w} \times (\boldsymbol{r}_t^*(p) - \boldsymbol{x}_0 - \boldsymbol{c}_t),\\ \dot{\boldsymbol{d}}_t^*(p) &= \boldsymbol{w} \times \boldsymbol{d}_t^*.\end{aligned}$$

[5]The assumption $D(p) = 1$ does not imply that the shell analyzed as a Cosserat surface has uniform thickness. It is merely a statement that the thickness plays no role at all in the two-dimensional theory of inextensible directors.

Here $\boldsymbol{v} = \dot{\boldsymbol{c}}_t$ and $\boldsymbol{w}$ is the axial vector of $\dot{\boldsymbol{Q}}_t\boldsymbol{Q}_t^{\mathrm{T}}$, where $(\cdot)^{\mathrm{T}}$ denotes the transpose operator.

If virtual velocity fields on $\mathcal{B}$ are denoted by $\delta\kappa = (\delta\boldsymbol{r}, \delta\boldsymbol{d})$, then rigid-body velocity fields or distributors — that is, the elements of $TC^r_{\kappa(p)}$ — are characterized by

$$(\delta\boldsymbol{r}, \delta\boldsymbol{d})(p) = (\boldsymbol{v} + \boldsymbol{w} \times (\boldsymbol{r}(p) - \boldsymbol{c}), \boldsymbol{w} \times \boldsymbol{d}(p)),$$

with $\boldsymbol{c}, \boldsymbol{v}, \boldsymbol{w} \in \boldsymbol{R}^3$. Clearly,

$$\delta\boldsymbol{d} \cdot \boldsymbol{d} = 0 \quad \text{for all } (\delta\boldsymbol{r}, \delta\boldsymbol{d}) \in TC^r_\kappa. \tag{2}$$

If $t \to \kappa_t = (\boldsymbol{r}_t, \boldsymbol{d}_t)$ is an arbitrary motion, then the hypothesis of inextensible directors leads to the following identities:

$$\dot{\boldsymbol{d}}_t \cdot \boldsymbol{d}_t = 0, \tag{3}$$

$$\boldsymbol{d}_t|_\alpha \cdot \boldsymbol{d}_t = 0, \tag{4}$$

$$\dot{\boldsymbol{d}}_t|_\alpha \cdot \boldsymbol{d}_t = -\boldsymbol{d}_t|_\alpha \cdot \dot{\boldsymbol{d}}_t. \tag{5}$$

where $(\cdot)|_\alpha$ denotes covariant differentiation along θ_α.

In what follows, the subscript t will be dropped from $\kappa_t = (\boldsymbol{r}_t, \boldsymbol{d}_t)$ as well as from $(\dot{\boldsymbol{r}}_t, \dot{\boldsymbol{d}}_t)$ in order to simplify the writing. Decomposing the covariant derivative of the director field with respect to the curvilinear basis $(\boldsymbol{a}_1, \boldsymbol{a}_2, \boldsymbol{a}_3)$, we define the quantities $\lambda^i_{\cdot\alpha}$ by

$$\boldsymbol{d}|_\alpha = \lambda^\mu_{\cdot\alpha}\boldsymbol{a}_\mu + \lambda^3_{\cdot\alpha}\boldsymbol{d}. \tag{6}$$

Since $\boldsymbol{d}|_\alpha \cdot \boldsymbol{d} = 0$, it follows that

$$\lambda^3_{\cdot\alpha} = -\lambda^\mu_{\cdot\alpha}a_{\mu 3}, \tag{7}$$

and

$$\boldsymbol{d}|_\alpha = \lambda^\mu_{\cdot\alpha}\tilde{\boldsymbol{a}}_\mu,$$

where $\tilde{\boldsymbol{a}}_\alpha = \boldsymbol{a}_\mu - (\boldsymbol{a}_\mu \cdot \boldsymbol{d})\boldsymbol{d}$ is the projection of $\boldsymbol{a}_\mu$ onto the plane perpendicular to $\boldsymbol{d}$.

Equations of motion

Following the method of virtual power, the basic equations of motion are obtained from the fundamental axiom of the method of virtual power,

$$< \boldsymbol{f}^e_t + \boldsymbol{f}^i_t, \boldsymbol{\eta} > = 0 \qquad \forall\boldsymbol{\eta} \in TC^r_{\kappa_t}.$$

We assume that the inertial force system consists of forces and couples that are continuously distributed over the reference surface $\mathcal{N}$, with the forces representing the classical inertia of the particles and the couples the rotatory inertia of the directors. This assumption is consistent, to the first order, with the asymptotic expansion of the shell as a three-dimensional simple body, and is also adopted by Naghdi (1972) in his direct method. Such a hypothesis leads to the following expression for the inertial force system:

$$< \boldsymbol{f}^i_t, \boldsymbol{\eta} > = -\iint_{\mathcal{N}} (\rho\dot{\boldsymbol{v}} \cdot \delta\boldsymbol{r} +$$

where $\boldsymbol{v} = \dot{\boldsymbol{r}}$ is the velocity field of points in the reference surface, $\boldsymbol{w}$ the angular velocity of the director field, ρ the mass density per unit area and I a parameter determining the contribution to the inertia of the director field. On the basis of the above assumptions, the axiom may be written as

$$< \boldsymbol{f}^e_t + \boldsymbol{f}^i_t, \boldsymbol{\eta} > = \iint_{\mathcal{N}} \rho(\boldsymbol{f} \cdot \delta\boldsymbol{r} + \boldsymbol{m} \cdot \delta\boldsymbol{d}) \; d\mathcal{N}$$
$$+ \int_{\partial\mathcal{N}} (\boldsymbol{N} \cdot \delta\boldsymbol{r} + \boldsymbol{M} \cdot \delta\boldsymbol{d}) \; d\partial\mathcal{N}$$
$$- \iint_{\mathcal{N}} \rho(\dot{\boldsymbol{v}} \cdot \delta\boldsymbol{r} + I\dot{\boldsymbol{w}} \cdot \delta\boldsymbol{d}) \; d\mathcal{N} = 0$$
$$\forall\boldsymbol{\eta} = (\delta\boldsymbol{r}, \delta\boldsymbol{d}) \in TC^r_{\kappa^t}, \tag{8}$$

where $\boldsymbol{f}, \boldsymbol{m}$ are respectively the distributed external forces and moments on $\mathcal{N}$. The boundary forces and moments $\boldsymbol{N}, \boldsymbol{M}$ are implicitly dependent on the outward unit normal $\boldsymbol{\nu}_p \in T\partial\mathcal{N}^\perp_{r(p)} \subset T\mathcal{N}_{r(p)}$ to the boundary $\partial\mathcal{N}$, i.e.

$$\boldsymbol{N} = \boldsymbol{N}(p, t, \boldsymbol{\nu}_p), \qquad \boldsymbol{M} = \boldsymbol{M}(p, t, \boldsymbol{\nu}_p).$$

Remark I: The moment $\boldsymbol{M}$ may be decomposed into:

$$\boldsymbol{M} = (\boldsymbol{M} \cdot \boldsymbol{d})\,\boldsymbol{d} + \tilde{\boldsymbol{M}},$$

where $\tilde{\boldsymbol{M}} = (\boldsymbol{1} - \boldsymbol{d} \otimes \boldsymbol{d})\boldsymbol{M}$ and $\boldsymbol{1}$ is the identity on $\boldsymbol{R}^3$. From (2) it follows that

$$\boldsymbol{M} \cdot \delta\boldsymbol{d} = \tilde{\boldsymbol{M}} \cdot \delta\boldsymbol{d} \qquad \forall\,(\delta\boldsymbol{r}, \delta\boldsymbol{d}) \in TC^r_\kappa.$$

Moreover, the component $(\boldsymbol{M} \cdot \boldsymbol{d})\,\boldsymbol{d}$ of the boundary moment is a reaction in the restricted Cosserat theory, since its virtual power in an arbitrary virtual velocity field is zero. Without loss of generality we assume that $\boldsymbol{M} \cdot \boldsymbol{d} = 0$.

Finally we define

$$\bar{\boldsymbol{M}} = \boldsymbol{d} \times \boldsymbol{M} \tag{9}$$

and note that $\boldsymbol{M} = \bar{\boldsymbol{M}} \times \boldsymbol{d}$. ■

If we assume a distributor of the form

$$\delta\boldsymbol{r} = \boldsymbol{c} \in \boldsymbol{R}^3, \qquad \delta\boldsymbol{d} = 0,$$

corresponding to a virtual rigid-body translation, then from the arbitrariness of $\boldsymbol{c}$ it follows that

$$\iint_{\mathcal{N}} \rho(\boldsymbol{f} - \dot{\boldsymbol{v}}) \; d\mathcal{N} + \int_{\partial\mathcal{N}} \boldsymbol{N} \; d\partial\mathcal{N} = 0. \tag{10}$$

Equation (10) expresses the balance of linear momentum (Naghdi, 1972). If the vector fields in (10) are smooth then it can be shown that $\boldsymbol{N}$ depends linearly on the unit normal $\boldsymbol{\nu}_p = \nu_\alpha \boldsymbol{a}^\alpha$ to the boundary $\partial\mathcal{N}$ (see Naghdi, 1972, pages 492-494) and finally that $\boldsymbol{N}$ may be decomposed into

$$\boldsymbol{N}(p, t, \boldsymbol{\nu}_p) = \boldsymbol{N}^\alpha \nu_\alpha. \tag{11}$$

Following the application of the divergence theorem for surfaces,

$$\int_{\partial\mathcal{N}} \boldsymbol{N}^\alpha \nu_\alpha \; d\partial\mathcal{N} = \iint_{\mathcal{N}} \boldsymbol{N}^\alpha|_\alpha \; d\mathcal{N}, \tag{12}$$

in Equation (10), we obtain the localized expression for the conservation of linear momentum:

$$\boldsymbol{N}^\alpha|_\alpha + \rho \boldsymbol{f} = \rho \dot{\boldsymbol{v}}. \tag{13}$$

Similarly, a distributor of the form

$$\delta \boldsymbol{r} = \boldsymbol{\Omega} \times \boldsymbol{r}, \qquad \delta \boldsymbol{d} = \boldsymbol{\Omega} \times \boldsymbol{d},$$

with $\boldsymbol{\Omega} \in \boldsymbol{R}^3$, corresponding to a virtual rigid-body rotation, when substituted in (8) yields

$$\iint_{\mathcal{N}} [\rho(\boldsymbol{f} - \dot{\boldsymbol{v}}) \cdot (\boldsymbol{\Omega} \times \boldsymbol{r}) + \rho(\boldsymbol{m} - I\dot{\boldsymbol{w}}) \cdot (\boldsymbol{\Omega} \times \boldsymbol{d})] \; d\mathcal{N} + \int_{\partial\mathcal{N}} [\boldsymbol{N} \cdot (\boldsymbol{\Omega} \times \boldsymbol{r}) + \boldsymbol{M} \cdot (\boldsymbol{\Omega} \times \boldsymbol{d})] \; d\partial\mathcal{N} = 0. \tag{14}$$

Using the vector identity $\boldsymbol{a} \cdot (\boldsymbol{b} \times \boldsymbol{c}) = \boldsymbol{b} \cdot (\boldsymbol{c} \times \boldsymbol{a})$, recalling that $\boldsymbol{N} = \boldsymbol{N}^\alpha \nu_\alpha$, $\boldsymbol{r}_{,\alpha} = \boldsymbol{a}_\alpha$, and applying the divergence theorem for surfaces, we obtain

$$\int_{\partial\mathcal{N}} (\boldsymbol{r} \times \boldsymbol{N}^\alpha) \nu_\alpha \; d\partial\mathcal{N} = \iint_{\mathcal{N}} (\boldsymbol{r} \times \boldsymbol{N}^\alpha|_\alpha + \boldsymbol{a}_\alpha \times \boldsymbol{N}^\alpha) \; d\mathcal{N}.$$

Equation (14) then reduces to

$$\iint_{\mathcal{N}} \{\boldsymbol{r} \times [\boldsymbol{N}^\alpha|_\alpha + \rho(\boldsymbol{f} - \dot{\boldsymbol{v}})] + \boldsymbol{d} \times \rho(\boldsymbol{m} - I\dot{\boldsymbol{w}})\} \; d\mathcal{N} + \iint_{\mathcal{N}} \boldsymbol{a}_\alpha \times \boldsymbol{N}^\alpha \; d\mathcal{N} = \int_{\partial\mathcal{N}} \boldsymbol{d} \times \boldsymbol{M} \; d\partial\mathcal{N}.$$

From the balance of linear momentum (13) and the definition (9), the above equation leads to the balance of moment of momentum,

$$\iint_{\mathcal{N}} (\boldsymbol{d} \times \rho(\boldsymbol{m} - I\dot{\boldsymbol{w}}) + \boldsymbol{a}_\alpha \times \boldsymbol{N}^\alpha) \; d\mathcal{N} + \int_{\partial\mathcal{N}} \bar{\boldsymbol{M}} \; d\partial\mathcal{N} = 0. \tag{15}$$

Using similar arguments to those employed in Equations (10)-(13), we conclude that

$$\bar{\boldsymbol{M}} = \bar{\boldsymbol{M}}^\alpha \nu_\alpha, \tag{16}$$

$$\int_{\partial\mathcal{N}} \bar{\boldsymbol{M}} \; d\partial\mathcal{N} = \iint_{\mathcal{N}} \bar{\boldsymbol{M}}^\alpha|_\alpha \; d\mathcal{N}, \tag{17}$$

and finally

$$\bar{\boldsymbol{M}}^\alpha|_\alpha + \boldsymbol{d} \times \rho \boldsymbol{m} + \boldsymbol{a}_\alpha \times \boldsymbol{N}^\alpha = \boldsymbol{d} \times \rho I \dot{\boldsymbol{w}}. \tag{18}$$

Equations (13) and (18) are the classical equations of motion for a Cosserat surface with inextensible directors (Naghdi, 1972; Simo and Fox, 1987).

Internal virtual power

From (9), (11), (16) and the divergence theorem for surfaces we obtain

$$\int_{\partial\mathcal{N}} (\boldsymbol{N} \cdot \delta\boldsymbol{r} + \boldsymbol{M} \cdot \delta\boldsymbol{d}) \; d\partial\mathcal{N} = \iint_{\mathcal{N}} (\boldsymbol{N}^\alpha|_\alpha \cdot \delta\boldsymbol{r} + \boldsymbol{N}^\alpha \cdot \delta\boldsymbol{r}|_\alpha + \bar{\boldsymbol{M}}^\alpha|_\alpha \times \boldsymbol{d} \cdot \delta\boldsymbol{d} + \bar{\boldsymbol{M}}^\alpha \times \boldsymbol{d}|_\alpha \cdot \delta\boldsymbol{d} + \bar{\boldsymbol{M}}^\alpha \times \boldsymbol{d} \cdot \delta\boldsymbol{d}|_\alpha) \; d\mathcal{N}. \tag{19}$$

Replacing (19) in (8), the virtual power of the external and inertial force systems reduces to:

$$< \boldsymbol{f}^e_t + \boldsymbol{f}^i_t, \eta > = \iint_{\mathcal{N}} \{[\boldsymbol{N}^\alpha|_\alpha + \rho(\boldsymbol{f} - \dot{\boldsymbol{v}})] \cdot \delta\boldsymbol{r} + \bar{\boldsymbol{M}}^\alpha \times \boldsymbol{d}|_\alpha \cdot \delta\boldsymbol{d} + [\bar{\boldsymbol{M}}^\alpha|_\alpha \times \boldsymbol{d} + \rho(\boldsymbol{m} - I\dot{\boldsymbol{w}})] \cdot \delta\boldsymbol{d} + \boldsymbol{N}^\alpha \cdot \delta\boldsymbol{r}|_\alpha + \bar{\boldsymbol{M}}^\alpha \times \boldsymbol{d} \cdot \delta\boldsymbol{d}|_\alpha\} \; d\mathcal{N}. \tag{20}$$

From the vector identity $(\boldsymbol{a} \times \boldsymbol{b}) \times \boldsymbol{c} = \boldsymbol{b}(\boldsymbol{a} \cdot \boldsymbol{c}) - \boldsymbol{a}(\boldsymbol{b} \cdot \boldsymbol{c})$ and the balance of angular momentum (18) it follows that

$$[\bar{\boldsymbol{M}}^\alpha|_\alpha + \boldsymbol{d} \times \rho(\boldsymbol{m} - I\dot{\boldsymbol{w}}) + \boldsymbol{a}_\alpha \times \boldsymbol{N}^\alpha] \times \boldsymbol{d} \cdot \delta\boldsymbol{d} = [\bar{\boldsymbol{M}}^\alpha|_\alpha \times \boldsymbol{d} + \rho(\boldsymbol{m} - I\dot{\boldsymbol{w}})] \cdot \delta\boldsymbol{d} + (\boldsymbol{N}^\alpha \cdot \boldsymbol{d})(\delta\boldsymbol{d} \cdot \boldsymbol{a}_\alpha) - (\boldsymbol{N}^\alpha \cdot \delta\boldsymbol{d})(\boldsymbol{a}_\alpha \cdot \boldsymbol{d}) = 0. \tag{21}$$

Moreover, if we define

$$\boldsymbol{M}^\alpha = \bar{\boldsymbol{M}}^\alpha \times \boldsymbol{d} \tag{22}$$

then Remark I implies that $\bar{\boldsymbol{M}}^\alpha = \boldsymbol{d} \times \boldsymbol{M}^\alpha$ and

$$\bar{\boldsymbol{M}}^\alpha \times \boldsymbol{d}|_\alpha \cdot \delta\boldsymbol{d} = (\boldsymbol{M}^\alpha \cdot \delta\boldsymbol{d})(\boldsymbol{d} \cdot \boldsymbol{d}|_\alpha) - (\boldsymbol{M}^\alpha \cdot \boldsymbol{d}|_\alpha)(\boldsymbol{d} \cdot \delta\boldsymbol{d}) = 0. \tag{23}$$

Replacing (21), (22) and the balance of linear momentum (13) in (20) yields

$$\begin{aligned} < \boldsymbol{f}^e_t + \boldsymbol{f}^i_t, \eta > &= \iint_{\mathcal{N}} \boldsymbol{N}^\alpha \cdot \delta\boldsymbol{r}|_\alpha + \boldsymbol{M}^\alpha \cdot \delta\boldsymbol{d}|_\alpha \; d\mathcal{N} \\ &\quad + \iint_{\mathcal{N}} (\boldsymbol{N}^\alpha \cdot \boldsymbol{d})(\delta\boldsymbol{d} \cdot \boldsymbol{a}_\alpha) - (\boldsymbol{N}^\alpha \cdot \delta\boldsymbol{d})(\boldsymbol{a}_\alpha \cdot \boldsymbol{d}) \; d\mathcal{N} \\ &= \iint_{\mathcal{N}} \boldsymbol{N}^\alpha \cdot \delta\boldsymbol{r}|_\alpha + \boldsymbol{M}^\alpha \cdot \delta\boldsymbol{d}|_\alpha \; d\mathcal{N} \\ &\quad - \iint_{\mathcal{N}} (\boldsymbol{a}_\alpha \times \boldsymbol{N}^\alpha) \times \boldsymbol{d} \cdot \delta\boldsymbol{d} \; d\mathcal{N}. \end{aligned} \tag{24}$$

Introduction of components

Decomposing the vector fields $\boldsymbol{N}^\alpha$ and $\boldsymbol{M}^\alpha$ with respect to the curvilinear basis $(\boldsymbol{a}_1, \boldsymbol{a}_2, \boldsymbol{a}_3)$, with $\boldsymbol{a}_3 = \boldsymbol{d}$, we define

$$\boldsymbol{N}^\alpha = N^{\beta\alpha} \boldsymbol{a}_\beta + Q^\alpha \boldsymbol{d}, \tag{25}$$

$$\boldsymbol{M}^\alpha = M^{\beta\alpha} \boldsymbol{a}_\beta + M^{3\alpha} \boldsymbol{d}. \tag{26}$$

By hypothesis $M^\alpha \cdot d = 0$, therefore

$$M^{3\alpha} = -M^{\beta\alpha} a_{3\beta}, \tag{27}$$

and consequently $M^\alpha = M^{\beta\alpha}\tilde{a}_\beta$, where

$$\tilde{a}_\beta = a_\beta - (a_\beta \cdot d)d. \tag{28}$$

Remark II: Replacing $\bar{M}^\alpha = d \times M^\alpha$ in the equation of balance of moment of momentum (18) and on taking the inner product of the above expression with d, we obtain

$$(d|_\alpha \times M^\alpha)\cdot d + (a_\alpha \times N^\alpha)\cdot d = 0. \tag{29}$$

Substituting (6), (25) and (26) in Equation (29) yields

$$\begin{aligned} & M^{\alpha\mu}\lambda^{\beta}_{.\mu} a_\beta \times a_\alpha \cdot d + N^{\beta\alpha} a_\alpha \times a_\beta \cdot d \\ &= (N^{\beta\alpha} - \lambda^{\beta}_{.\mu} M^{\alpha\mu})\, a_\alpha \times a_\beta \cdot d \\ &= (N^{\beta\alpha} - \lambda^{\beta}_{.\mu} M^{\alpha\mu}) a\, \epsilon_{\alpha\beta 3} = 0. \end{aligned}$$

Therefore $\epsilon_{\alpha\beta 3}(N^{\beta\alpha} - \lambda^{\beta}_{.\alpha} M^{\alpha\mu}) = 0$, where ϵ_{ijk} for $(1 \le i,j,k \le 3)$ denotes the permutation symbols.

Finally, if

$$N^{\beta\alpha}_{eff} = (N^{\beta\alpha} - \lambda^{\beta}_{.\mu} M^{\alpha\mu}), \tag{30}$$

then $N_{eff} = (N_{eff})^{\mathsf{T}}$, where $N_{eff} = N^{\alpha\beta}_{eff}(a_\alpha \otimes a_\beta)$. N_{eff} will be referred to as the effective membrane stress tensor and is related to the power of changes of length and distortion on the reference surface $\mathcal{N}$, measured by the metric tensor $a_{\alpha\beta}$ (see Lemma 1). ■

Remark II motivates the definition of the following deformation measures:

$$\begin{aligned} \varepsilon &= \varepsilon_{\alpha\beta} a^\alpha \otimes a^\beta, \\ \kappa &= \kappa_{\alpha\beta} a^\alpha \otimes a^\beta, \\ \gamma &= \gamma_\alpha a^\alpha, \end{aligned} \tag{31}$$

where

$$\begin{aligned} \varepsilon_{\alpha\beta} &= \frac{1}{2}(a_\alpha \cdot a_\beta - A_\alpha \cdot A_\beta), \\ \kappa_{\alpha\beta} &= (d|_\beta \cdot a_\alpha - d_0|_\beta \cdot A_\alpha), \\ \gamma_\alpha &= d \cdot a_\alpha - d_0 \cdot A_\alpha \end{aligned}$$

and A_α, d_0 are respectively the vector fields a_α, d at the reference configuration. The convected time derivatives (a special case of Lie derivatives) of the aforementioned deformation measures may be defined as follows (Marsden and Hughes, 1983; Simo and Fox, 1987):

$$\begin{aligned} \mathcal{L}_v \varepsilon &= \dot{\varepsilon}_{\alpha\beta} a^\alpha \otimes a^\beta, \\ \mathcal{L}_v \kappa &= \dot{\kappa}_{\alpha\beta} a^\alpha \otimes a^\beta, \\ \mathcal{L}_v \gamma &= \dot{\gamma}_\alpha a^\alpha. \end{aligned}$$

On the above Equations

$$\begin{aligned} \dot{\varepsilon}_{\alpha\beta} &= \frac{1}{2}(\dot{a}_\alpha \cdot a_\beta + a_\alpha \cdot \dot{a}_\beta), \\ \dot{\kappa}_{\alpha\beta} &= (\dot{d}|_\beta \cdot a_\alpha + d|_\beta \cdot \dot{a}_\alpha), \\ \dot{\gamma}_\alpha &= (\dot{d} \cdot a_\alpha + d.\dot{a}_\alpha). \end{aligned} \tag{32}$$

Component form of the internal virtual power

Lemma 1 *The deformation power is given by:*

$$\iint_{\mathcal{N}} (N^{\alpha\beta}_{eff}\dot{\varepsilon}_{\alpha\beta} + M^{\alpha\beta}\dot{\kappa}_{\alpha\beta} + Q^{\alpha}_{eff}\dot{\gamma}_\alpha)\ d\mathcal{N}, \tag{33}$$

where

$$Q^\alpha_{eff} = (Q^\alpha - \lambda^3_{.\beta} M^{\alpha\beta}). \tag{34}$$

Proof: We obtain the deformation power by replacing the virtual velocity field in the virtual power of the external and inertial force systems by the actual velocity field of the motion. Replacing $(\delta r, \delta d)$ in Equation (24) by $(\dot{r}, \dot{d})$ yields

$$\iint_{\mathcal{N}} N^\alpha \cdot \dot{a}_\alpha + M^\alpha \cdot \dot{d}|_\alpha\ d\mathcal{N} + \iint_{\mathcal{N}} (N^\alpha \cdot d)(\dot{d} \cdot a_\alpha) - (N^\alpha \cdot \dot{d})(a_\alpha \cdot d)\ d\mathcal{N}.$$

- Using (5), (6), (7) and (26) we find that

$$\begin{aligned} M^\alpha \cdot \dot{d}|_\alpha &= M^{\beta\alpha} a_\beta \cdot \dot{a}_{3,\alpha} - M^{3\alpha} a_{3,\alpha} \cdot \dot{a}_3 \\ &= M^{\beta\alpha}\dot{\kappa}_{\beta\alpha} - M^{\beta\alpha}\dot{a}_\beta \cdot a_{3,\alpha} - M^{3\alpha} a_{3,\alpha} \cdot \dot{a}_3 \\ &= M^{\beta\alpha}\dot{\kappa}_{\beta\alpha} - M^{\beta\alpha}\lambda^{\mu}_{.\alpha}\dot{a}_\beta \cdot a_\mu \\ &\quad - M^{\beta\alpha}\lambda^{3}_{.\alpha}\dot{a}_\beta \cdot a_3 - M^{3\alpha} a_{3,\alpha} \cdot \dot{a}_3. \end{aligned} \tag{35}$$

- From (25) and (35) we obtain

$$\begin{aligned} N^\alpha \cdot \dot{a}_\alpha + M^\alpha \cdot \dot{d}|_\alpha &= (N^{\beta\alpha} - M^{\alpha\mu}\lambda^{\beta}_{.\mu})\,\dot{a}_\alpha \cdot a_\beta \\ &\quad + M^{\beta\alpha}\dot{\kappa}_{\beta\alpha} + (Q^\alpha - \lambda^3_{.\beta} M^{\alpha\beta})\,\dot{a}_\alpha \cdot a_3 \\ &\quad - M^{3\alpha}\lambda^{\mu}_{.\alpha} a_\mu \cdot \dot{a}_3 - M^{3\alpha}\lambda^{3}_{.\alpha} a_3 \cdot \dot{a}_3. \end{aligned}$$

  From substituting (30), (32.a-b) and (34) in the above equation it follows that

$$\begin{aligned} N^\alpha \cdot \dot{a}_\alpha + M^\alpha \cdot \dot{d}|_\alpha &= N^{\alpha\beta}_{eff} \cdot \dot{\varepsilon}_{\alpha\beta} + M^{\alpha\beta} \cdot \dot{\kappa}_{\alpha\beta} \\ &\quad + Q^\alpha_{eff}\dot{a}_\alpha \cdot a_3 - M^{3\alpha}\lambda^{\mu}_{.\alpha} a_\mu \cdot \dot{a}_3. \end{aligned} \tag{36}$$

- Using (25) and (28) we obtain

$$\begin{aligned} & (N^\alpha \cdot d)(\dot{d} \cdot a_\alpha) - (N^\alpha \cdot \dot{d})(a_\alpha \cdot d) \\ &= [(N^{\beta\alpha} a_{\beta 3} + Q^\alpha) a_\alpha - a_{\alpha 3}(N^{\beta\alpha} a_\beta + Q^\alpha a_3)] \cdot \dot{a}_3 \\ &= [(N^{\beta\alpha} - \lambda^{\beta}_{.\mu} M^{\alpha\mu}) - (N^{\alpha\beta} - \lambda^{\alpha}_{.\mu} M^{\beta\mu}) \\ &\quad + \lambda^{\beta}_{.\mu} M^{\alpha\mu} - \lambda^{\alpha}_{.\mu} M^{\beta\mu}] a_{\beta 3} a_\alpha + Q^\alpha \tilde{a}_\alpha \cdot \dot{a}_3 \end{aligned} \tag{37}$$

From (30) and (34), the right-hand side of the above expression yields

$$\Big\{[(N^{\beta\alpha}_{eff} - N^{\alpha\beta}_{eff}) + (\lambda^{\beta}_{.\mu}M^{\alpha\mu} - \lambda^{\alpha}_{.\mu}M^{\beta\mu})]a_{\beta 3}\boldsymbol{a}_{\alpha} + (Q^{\alpha}_{eff} + \lambda^{3}_{.\beta}M^{\alpha\beta})\tilde{\boldsymbol{a}}_{\alpha}\Big\} \cdot \dot{\boldsymbol{a}}_3. \tag{38}$$

On substituting $N^{\alpha\beta}_{eff} = N^{\beta\alpha}_{eff}$, $M^{3\alpha} = -a_{3\beta}M^{\beta\alpha}$ and $\lambda^{3}_{.\beta} = -a_{3\alpha}\lambda^{\alpha}_{.\beta}$ in (38), Equation (37) reduces to

$$\begin{aligned}(\boldsymbol{N}^{\alpha} \cdot \boldsymbol{d})(\dot{\boldsymbol{d}} \cdot \boldsymbol{a}_{\alpha}) - (\boldsymbol{N}^{\alpha} \cdot \dot{\boldsymbol{d}})(\boldsymbol{a}_{\alpha} \cdot \boldsymbol{d}) &= (Q^{\alpha}_{eff} - a_{3\beta}\lambda^{\alpha}_{.\mu}M^{\beta\mu})\,\tilde{\boldsymbol{a}}_{\alpha} \cdot \dot{\boldsymbol{a}}_3. \\ &= (Q^{\alpha}_{eff} + \lambda^{\alpha}_{.\mu}M^{3\mu})\,\tilde{\boldsymbol{a}}_{\alpha} \cdot \dot{\boldsymbol{a}}_3. \end{aligned} \tag{39}$$

Note that from (3) and (28) it follows that

$$\tilde{\boldsymbol{a}}_{\alpha} \cdot \dot{\boldsymbol{a}}_3 = \boldsymbol{a}_{\alpha} \cdot \dot{\boldsymbol{a}}_3.$$

- Adding expressions (36) and (39), we finally obtain the deformation power per unit area

$$\begin{aligned}\boldsymbol{N}^{\alpha} \cdot \dot{\boldsymbol{a}}_{\alpha} + \boldsymbol{M}^{\alpha} \cdot \dot{\boldsymbol{d}}|_{\alpha} + (\boldsymbol{N}^{\alpha} \cdot \boldsymbol{d})(\dot{\boldsymbol{d}} \cdot \boldsymbol{a}_{\alpha}) \\ - (\boldsymbol{N}^{\alpha} \cdot \dot{\boldsymbol{d}})(\boldsymbol{a}_{\alpha} \cdot \boldsymbol{d}) \\ = N^{\alpha\beta}_{eff}\dot{\varepsilon}_{\alpha\beta} + M^{\alpha\beta}\dot{\kappa}_{\alpha\beta} + Q^{\alpha}_{eff}\dot{\gamma}_{\alpha}\end{aligned} \tag{40}$$

Integration of the right-hand side over the surface proves the lemma.

■

If κ is taken as the reference configuration and arbitrary motions from this configuration are considered, then the velocity fields generated by those motions at $\kappa \in \mathcal{C}$ form the tangent bundle $T\mathcal{C}_{\kappa}$. It follows that Equation (33) represents the internal virtual power if the actual deformation-rate components $\dot{\varepsilon}_{\alpha\beta}$, $\dot{\kappa}_{\alpha\beta}$, $\dot{\gamma}_{\alpha}$ are replaced by the virtual deformation rates $\delta\varepsilon_{\alpha\beta}$, $\delta\kappa_{\alpha\beta}$, $\delta\gamma_{\alpha}$.

Equations (13),(18) and appropriate constitutive relations for $N^{\alpha\beta}_{eff}$, $M^{\alpha\beta}$, Q^{α}_{eff} (and hence for $\boldsymbol{N}^{\alpha}$ and $\boldsymbol{M}^{\alpha}$) form a complete set of equations determining the motion of the Cosserat surface with inextensible directors. For elastic behavior, a strain energy function $\varphi(\boldsymbol{\varepsilon}, \boldsymbol{\kappa}, \boldsymbol{\gamma})$, whose dependence on the invariants of the reference surface is implicitly assumed (see Carroll and Naghdi, 1972, for additional details), is postulated to describe the constitutive relation in the functional form:

$$N^{\alpha\beta}_{eff} = \frac{\partial\varphi}{\partial\varepsilon_{\alpha\beta}}, \quad M^{\alpha\beta} = \frac{\partial\varphi}{\partial\kappa_{\alpha\beta}}, \quad Q^{\alpha} = \frac{\partial\varphi}{\partial\gamma_{\alpha}}.$$

For additional considerations on constitutive relations, see Naghdi (1972) and Niordson (1985).

COSSERAT SURFACE WITH DEFORMABLE DIRECTORS

Equations of motion and deformation power

An extension of the Cosserat-surface model with inextensible directors to one with deformable directors will be based on the following guidelines.

- The terms involving the force systems of the preceding model have the same physical motivation in their extension and therefore remain unchanged. Moments as physically understood are conjugate to angular velocity fields. A natural choice is given by the changes in orientation of the director field. If $\boldsymbol{d} = D\hat{\boldsymbol{d}}$, with $D^2 = \boldsymbol{d} \cdot \boldsymbol{d}$ and $\hat{\boldsymbol{d}}.\hat{\boldsymbol{d}} = 1$, then such changes in orientation are equivalently given by the variations of the unit director field $\hat{\boldsymbol{d}}$. This interpretation is at variance with the adopted by Naghdi (1972), as is seen in the next section.

- Changes in length of the directors are naturally associated with a scalar field expressing in an appropriate sense the pressure or squeezing forces applied along the director field. Such contributions may be conceived of as distributed on the surface as well as along the boundary.

- The inertia functional is assumed to have the same form as in the previous model but with additional terms due to the variations of the length of the director field.

In accordance with these guidelines, it may be assumed that the virtual power of the external and inertial force systems is given by

$$\begin{aligned}< \boldsymbol{f}^{e}_{t} + \boldsymbol{f}^{i}_{t}, \boldsymbol{\eta} > = \iint_{\mathcal{N}} \rho(\boldsymbol{f} \cdot \delta\boldsymbol{r} + \boldsymbol{m} \cdot \delta\hat{\boldsymbol{d}} + p\delta D)\ d\mathcal{N} \\ + \int_{\partial\mathcal{N}} (\boldsymbol{N} \cdot \delta\boldsymbol{r} + \boldsymbol{M} \cdot \delta\hat{\boldsymbol{d}} + P\delta D)\ d\partial\mathcal{N} \\ - \iint_{\mathcal{N}} \rho[\dot{\boldsymbol{v}} \cdot \delta\boldsymbol{r} + I\dot{\boldsymbol{w}} \cdot (D\delta\hat{\boldsymbol{d}} + \delta D\hat{\boldsymbol{d}})]\ d\mathcal{N} \\ \forall\boldsymbol{\eta} \in T\mathcal{C}_{\kappa}.\end{aligned} \tag{41}$$

The virtual velocity fields for the extended theory are conveniently denoted $\boldsymbol{\eta} = (\delta\boldsymbol{r}, \delta\hat{\boldsymbol{d}}, \delta D)$.

Because of the similarity of the virtual-power expression for the extended model with the one for the preceding model, Equation (8), most of the developments of the preceding section still hold if the director field is replaced, where appropriate, by the unit director field $\hat{\boldsymbol{d}}$. Equations (2)-(5) naturally hold for $\hat{\boldsymbol{d}}$ and definitions (6)-(7) expressing the covariant derivative of the unit director field are still valid. Thus

$$\hat{\boldsymbol{d}}|_{\alpha} = \lambda^{\mu}_{.\alpha}\boldsymbol{a}_{\alpha} + \lambda^{3}_{.\alpha}\boldsymbol{a}_3. \tag{42}$$

Clearly $\hat{d}|_\alpha \cdot \hat{d} = 0$, and again

$$\lambda^3_{.\alpha} = -\lambda^\mu_{.\alpha} a_{\mu 3}, \tag{43}$$

where by definition $a_3 = \hat{d}$.

To obtain the basic equations of motion we apply the fundamental axiom of the method of virtual power. As we shall see, one additional scalar equation is needed to describe the evolution of the length of the directors. Even though this equation is not obtained from the axiom, it has a clear and physically intuitive derivation. This aspect is indeed one of the great advantages of the method of virtual power.

The application of the fundamental axiom to the extended model leads to the linear-momentum equation,

$$N^\alpha|_\alpha + \rho f = \rho \dot{v}, \tag{44}$$

and the moment-of-momentum equation,

$$\bar{M}^\alpha|_\alpha + \hat{d} \times \rho m + a_\alpha \times N^\alpha = \hat{d} \times \rho I \dot{w}, \tag{45}$$

where by definition $N = N^\alpha \nu_\alpha$, $\bar{M} = \hat{d} \times M = \bar{M}^\alpha \nu_\alpha$ (see Remark I and Equations (11), (16) and (22) for the corresponding definitions in the restricted Cosserat theory of inextensible directors). The derivations of the above equations follow precisely the same steps as used in the preceding model and therefore will not be repeated. From Equations (44) and (45), the virtual power due to the external and inertial force systems (41) reduces to (see Equations (19-24))

$$\begin{aligned} < f^e_\iota + f^i_\iota, \eta > = & \iint_{\mathcal{N}} [N^\alpha \cdot \delta r|_\alpha + M^\alpha \cdot \delta \hat{d}|_\alpha \\ & - (a_\alpha \times N^\alpha) \times \hat{d} \cdot \delta \hat{d}]\, d\mathcal{N} \\ & + \iint_{\mathcal{N}} \rho (p - I\dot{w} \cdot \hat{d}) \delta D \; d\mathcal{N} \\ & + \int_{\partial \mathcal{N}} P \delta D \; d\partial\mathcal{N} \qquad \forall \eta \in TC_\kappa, \end{aligned} \tag{46}$$

where $M^\alpha = \bar{M}^\alpha \times \hat{d}$ and $\bar{M}^\alpha = \hat{d} \times M^\alpha$.

Assuming, for the purpose of deriving the basic equations of motion, that the Cosserat surface is in principle not subjected to constraints, we apply the virtual velocity field

$$\delta r = 0, \quad \delta \hat{d} = 0 \quad \text{and } \delta D = \delta \bar{D} \text{ (constant)},$$

corresponding to an uniform change in length of the directors, to (46). With this virtual velocity field, the power of the external and inertial force systems reduces to

$$\begin{aligned} < f^e_\iota + f^i_\iota, \eta > = \delta \bar{D} \Big\{ & \int_{\partial\mathcal{N}} P \; d\partial\mathcal{N} \\ & + \iint_{\mathcal{N}} \rho (p - I\dot{w} \cdot \hat{d}) \; d\mathcal{N} \Big\} \quad \forall \eta \end{aligned}$$

It follows from the principle of virtual [illegible] is external-cum-inertial force system the[illegible] in internal force system dual to changes in director length (that is, a linear functional in δD contributing to the internal virtual power associated with a virtual velocity field characterized by $(\delta r, \delta \hat{d}, \delta D)$). We assume a priori that this internal virtual power is given by

$$\ll \sigma, T d^*_\kappa \gg = \iint_{\mathcal{N}} H \delta D \; d\mathcal{N}.$$

Applying the principle of virtual power,

$$\ll \sigma, T d_\kappa \gg = < f^e_\iota + f^e_\iota, \eta > \qquad \forall \eta \in TC_\kappa,$$

to this particular virtual velocity field leads to

$$\iint_{\mathcal{N}} H \; d\mathcal{N} = \int_{\partial\mathcal{N}} P \; d\partial\mathcal{N} + \iint_{\mathcal{N}} \rho [p - I\dot{w} \cdot \hat{d}] \; d\mathcal{N},$$

and finally, under an appropriate smoothness hypothesis, it follows that

$$P = P^\alpha \nu_\alpha, \tag{47}$$

$$P^\alpha|_\alpha + \rho p - H = \rho I \dot{w} \cdot \hat{d}. \tag{48}$$

Moreover, applying Equations (47) and (48) to the expression for the virtual power (46), we obtain

$$\begin{aligned} < f^e_\iota + f^i_\iota, \eta > = & \iint_{\mathcal{N}} [N^\alpha \cdot \delta r|_\alpha + M^\alpha \cdot \delta \hat{d}|_\alpha \\ & - (a_\alpha \times N^\alpha) \times \hat{d} \cdot \delta \hat{d} + P^\alpha \delta D|_\alpha + H \delta D]\, d\mathcal{N}. \end{aligned} \tag{49}$$

Following the same developments as in Lemma 1, it can be shown that the deformation power is given by

$$\begin{aligned} \iint_{\mathcal{N}} (& N^{\alpha\beta}_{eff} \cdot \dot{\varepsilon}_{\alpha\beta} + M^{\alpha\beta} \cdot \dot{\kappa}_{\alpha\beta} + Q^\alpha_{eff} \cdot \dot{\gamma}_\alpha \\ & + P^\alpha \dot{\xi}_\alpha + H \dot{\Delta})\, d\mathcal{N}. \end{aligned} \tag{50}$$

The deformations ξ_α and Δ are defined by

$$\begin{aligned} \xi_\alpha &= D|_\alpha - D_0|_\alpha, & \dot{\xi}_\alpha &= \dot{D}|_\alpha, \\ \Delta &= D - D_0, & \dot{\Delta} &= \dot{D}, \end{aligned} \tag{51}$$

where $D_0 = ||d_0||$.

Equations (44), (45), (48) and appropriate constitutive relations for $N^{\alpha\beta}_{eff}$, $M^{\alpha\beta}$, Q^α_{eff}, P^α and H form a complete set of equations determining the motion of the Cosserat surface.

Note the appearance in Equation (48) of the internal force H dual to changes in director length. In the complete problem, H is constitutively determined by the motion and therefore should not be regarded as an additional unknown scalar field. As we shall see, this term is in a certain sense associated with the intrinsic director couple of Naghdi (1972) and the across-the-thickness stress resultant of Simo and Fox (1987).

The proposed theory includes essentially the same external and inertial force systems as the theory of Naghdi

(1972). Consequently, according to the principle of virtual power, they may be considered equivalent. The major differences lie in the identification of the internal forces and their corresponding constitutive relations.

Equation (48) does not follow directly from the director-momentum Equation of Naghdi (see Equation (56)). This is not surprising, in view of the intervention of internal forces in both equations and the natural differences between the internal force H and the intrinsic director couple of Naghdi. The similarities of the above model with the one proposed by Naghdi is analyzed in the next section.

NAGHDI'S COSSERAT SURFACE OF DEFORMABLE DIRECTORS

Equations of motion and internal virtual power

Naghdi's equations for a Cosserat surface with deformable directors may be obtained if the virtual power of the external and inertial force systems is assumed a priori to take the form

$$\begin{aligned} < \boldsymbol{f}_t^e + \boldsymbol{f}_t^i, \boldsymbol{\eta} > = & \iint_{\mathcal{N}} \rho(\boldsymbol{f} \cdot \delta\boldsymbol{r} + \boldsymbol{m}^* \cdot \delta\boldsymbol{d}) \; d\mathcal{N} \\ & + \int_{\partial\mathcal{N}} (\boldsymbol{N} \cdot \delta\boldsymbol{r} + \boldsymbol{M}^* \cdot \delta\boldsymbol{d}) \; d\partial\mathcal{N} \\ & - \iint_{\mathcal{N}} \rho[\dot{\boldsymbol{v}} \cdot \delta\boldsymbol{r} + I\dot{\boldsymbol{w}} \cdot \delta\boldsymbol{d}] \; d\mathcal{N} \\ & \qquad \forall \boldsymbol{\eta} = (\delta\boldsymbol{r}, \delta\boldsymbol{d}) \in TC_\kappa . \end{aligned} \tag{52}$$

Denoting

$$\tilde{\boldsymbol{m}}^* = (1 - \hat{\boldsymbol{d}} \otimes \hat{\boldsymbol{d}})\boldsymbol{m}^*, \qquad \boldsymbol{m}^* = (\boldsymbol{m}^* \cdot \hat{\boldsymbol{d}})\,\hat{\boldsymbol{d}} + \tilde{\boldsymbol{m}}^*,$$
$$\tilde{\boldsymbol{M}}^* = (1 - \hat{\boldsymbol{d}} \otimes \hat{\boldsymbol{d}})\boldsymbol{M}^*, \qquad \boldsymbol{M}^* = (\boldsymbol{M}^* \cdot \hat{\boldsymbol{d}})\,\hat{\boldsymbol{d}} + \tilde{\boldsymbol{M}}^*,$$

and observing that $\delta\boldsymbol{d} = \delta D\,\hat{\boldsymbol{d}} + D\,\delta\hat{\boldsymbol{d}}$, we may alternatively write Equation (52) as

$$\begin{aligned} < \boldsymbol{f}_t^e + \boldsymbol{f}_t^i, \boldsymbol{\eta} > = & \\ & \iint_{\mathcal{N}} \rho[\boldsymbol{f} \cdot \delta\boldsymbol{r} + (\boldsymbol{m}^* \cdot \hat{\boldsymbol{d}})\delta D + D\tilde{\boldsymbol{m}}^* \cdot \delta\hat{\boldsymbol{d}}] \; d\mathcal{N} \\ & + \int_{\partial\mathcal{N}} [\boldsymbol{N} \cdot \delta\boldsymbol{r} + D\tilde{\boldsymbol{M}}^* \cdot \delta\hat{\boldsymbol{d}} + (\boldsymbol{M}^* \cdot \hat{\boldsymbol{d}})\delta D] \; d\partial\mathcal{N} \\ & - \iint_{\mathcal{N}} \rho[\dot{\boldsymbol{v}} \cdot \delta\boldsymbol{r} + I\dot{\boldsymbol{w}} \cdot \delta\boldsymbol{d}] \; d\mathcal{N} \\ & \qquad \forall \boldsymbol{\eta} = (\delta\boldsymbol{r}, \delta\boldsymbol{d}) \in TC_\kappa . \end{aligned} \tag{53}$$

Finally, with the definitions

$$\begin{aligned} \boldsymbol{m} &= D\tilde{\boldsymbol{m}}^*, & \boldsymbol{M} &= D\tilde{\boldsymbol{M}}^*, \\ p &= \boldsymbol{m}^* \cdot \hat{\boldsymbol{d}}, & P &= \boldsymbol{M}^* \cdot \hat{\boldsymbol{d}}, \end{aligned} \tag{54}$$

Equation (53) takes the same form as (41). Hence both models account for basically the same inertial and external force systems. Note that the moment $\boldsymbol{M}^*$ in Naghdi's theory encompasses what in the present model are the distinct notions of moment and pressure, duals respectively to changes in director orientation and length.

Before invoking the fundamental axiom, we insert a virtual velocity field $\boldsymbol{\eta}^*$ such that $\delta\boldsymbol{r} = 0$ and $\delta\boldsymbol{d} = \delta\boldsymbol{d}^*$ (constant on the reference surface), into the expression (52) for the virtual power of the external and inertial force systems. By the same arguments as used in deriving Equation (48), we assume that to this virtual velocity field is associated the following internal virtual power:

$$\ll \boldsymbol{\sigma}, Td_\kappa\boldsymbol{\eta}^* \gg = \iint_{\mathcal{N}} \boldsymbol{H}^* \cdot \delta\boldsymbol{d} \; d\mathcal{N} .$$

Following the application of the principle of virtual power to this particular virtual velocity field, we obtain

$$\iint_{\mathcal{N}} \boldsymbol{H}^* \; d\mathcal{N} = \int_{\partial\mathcal{N}} \boldsymbol{M}^* \; d\partial\mathcal{N} + \iint_{\mathcal{N}} \rho(\boldsymbol{m}^* - I\dot{\boldsymbol{w}}) \; d\mathcal{N} ,$$

and, under an appropriate smoothness assumption,

$$\boldsymbol{M}^* = \boldsymbol{M}^{*\alpha}\nu_\alpha, \tag{55}$$

$$\boldsymbol{M}^{*\alpha}|_\alpha + \rho\boldsymbol{m}^* - \boldsymbol{H}^* = \rho I\dot{\boldsymbol{w}}. \tag{56}$$

Equation (56) describes the balance of director momentum. $\boldsymbol{H}^*$ is variously called the intrinsic director couple (Naghdi, 1972) or the across-the-thickness stress resultant (Simo and Fox, 1987).

From the fundamental axiom, we obtain

(i) **Balance of linear momentum**

$$\boldsymbol{N}^\alpha|_\alpha + \rho\boldsymbol{f} = \rho\dot{\boldsymbol{v}}, \tag{57}$$

(ii) **Balance of moment of momentum**

$$\begin{aligned} (\boldsymbol{d} \times \boldsymbol{M}^{*\alpha})|_\alpha + \boldsymbol{d} \times \rho\boldsymbol{m}^* + \boldsymbol{a}_\alpha \times \boldsymbol{N}^\alpha = & \\ \boldsymbol{d} \times \rho I\dot{\boldsymbol{w}}, & \end{aligned} \tag{58}$$

where by definition $\boldsymbol{N} = \boldsymbol{N}^\alpha\nu_\alpha$ and $\boldsymbol{M}^* = \boldsymbol{M}^{*\alpha}\nu_\alpha$. Substituting Equation (56) in (58) yields

$$\boldsymbol{d} \times \boldsymbol{H}^* = -(\boldsymbol{d}|_\alpha \times \boldsymbol{M}^{*\alpha} + \boldsymbol{a}_\alpha \times \boldsymbol{N}^\alpha), \tag{59}$$

and finally, replacing Equations (56) and (57) in (52), we obtain

$$< \boldsymbol{f}_t^e + \boldsymbol{f}_t^i, \boldsymbol{\eta} > = \iint_{\mathcal{N}} [\boldsymbol{N}^\alpha \cdot \delta\boldsymbol{r}|_\alpha + \boldsymbol{M}^{*\alpha} \cdot \delta\boldsymbol{d}|_\alpha + \boldsymbol{H}^* \cdot \delta\boldsymbol{d}] \; d\mathcal{N} . \tag{60}$$

Equations (56), (57) and appropriate constitutive relations for $\boldsymbol{N}^\alpha$, $\boldsymbol{M}^{*\alpha}$ and $\boldsymbol{H}^*$ form a complete set of equations determining the motion of the Cosserat surface. Equation (59) is regarded by Naghdi as a restriction on the admissible constitutive relations. Clearly, the moment-of-momentums balance Equation (58) is identically satisfied.

Relationship between the internal forces

The membrane stresses $\boldsymbol{N}^\alpha$ in both models are defined identically. From definitions (54.c-d) it follows that

$$\begin{aligned} P^\alpha &= \boldsymbol{M}^{*\alpha}\cdot\hat{\boldsymbol{d}}, \\ \boldsymbol{M}^\alpha &= D\tilde{\boldsymbol{M}}^{*\alpha} = D(\hat{\boldsymbol{d}}\times\boldsymbol{M}^{*\alpha})\times\hat{\boldsymbol{d}}, \\ \boldsymbol{M}^{*\alpha} &= \frac{1}{D}\boldsymbol{M}^\alpha + P^\alpha\hat{\boldsymbol{d}} = \frac{1}{D}M^{\beta\alpha}\tilde{\boldsymbol{a}}_\beta + P^\alpha\hat{\boldsymbol{d}}, \end{aligned} \tag{61}$$

where $\tilde{\boldsymbol{a}}_\beta = \boldsymbol{a}_\beta - (\boldsymbol{a}_\beta\cdot\hat{\boldsymbol{d}})\hat{\boldsymbol{d}}$. Equations (61) imply that once constitutive relations for $M^{\alpha\beta}$ and P^α are proposed then constitutive Equations for $\boldsymbol{M}^{*\alpha}$ may be obtained, and vice versa.

Remark III: From Equations (61) and (31), the relationship between $\boldsymbol{M}^{*\alpha}$ and the generalized deformations and internal forces of the proposed model may be readily established. Since

$$\begin{aligned} \boldsymbol{M}^{*\alpha}\cdot\boldsymbol{a}_\beta &= \frac{1}{D}M^{\mu\alpha}\tilde{\boldsymbol{a}}_\mu\cdot\boldsymbol{a}_\beta + P^\alpha a_{\beta 3} \\ &= \frac{1}{D}M^{\mu\alpha}(a_{\mu\beta} - a_{3\mu}a_{3\beta}) + P^\alpha a_{\beta 3}, \end{aligned}$$

it follows that

$$\begin{aligned} \boldsymbol{M}^{*\alpha}\cdot\boldsymbol{a}_\beta = {} & \frac{1}{\Delta + D_0}M^{\mu\alpha}[(2\epsilon_{\mu\beta} + A_{\mu\beta}) \\ & - (\gamma_\mu + \boldsymbol{A}_\mu\cdot\hat{\boldsymbol{d}}_0)(\gamma_\beta + \boldsymbol{A}_\beta\cdot\hat{\boldsymbol{d}}_0)] \\ & + P^\alpha(\gamma_\beta + \boldsymbol{A}_\beta\cdot\hat{\boldsymbol{d}}_0), \end{aligned} \tag{62}$$

where $\boldsymbol{A}_\alpha$ and $\hat{\boldsymbol{d}}_0$ are respectively the base vectors $\boldsymbol{a}_\alpha$ and the unit director field $\hat{\boldsymbol{d}}$ at the reference surface $\mathcal{N}_0$.

In general, the same conclusions hold conversely. This is clear from Equations (61) and the fact that whatever generalized deformations are defined for a Cosserat surface, the current configuration is determined, from the reference configuration, to within a Euclidean mapping. The last remark implies that $\boldsymbol{M}^{*\alpha}$, $\boldsymbol{a}_\alpha$ and $\hat{\boldsymbol{d}}$ are determined up to an orthogonal transformation, and clearly constitutive equations for P^α and $M^{\alpha\beta}$ may be established from an appropriate constitutive equation for $\boldsymbol{M}^*$ or its components. ■

From Equation (59) and the decomposition $\boldsymbol{H}^* = \tilde{\boldsymbol{H}}^* + (\boldsymbol{H}^*\cdot\hat{\boldsymbol{d}})\hat{\boldsymbol{d}}$, where $\tilde{\boldsymbol{H}}^* = (\hat{\boldsymbol{d}}\times\boldsymbol{H}^*)\times\hat{\boldsymbol{d}}$, it follows that

$$D\tilde{\boldsymbol{H}}^* = -(\boldsymbol{d}|_\alpha\times\boldsymbol{M}^{*\alpha})\times\hat{\boldsymbol{d}} - (\boldsymbol{a}_\alpha\times\boldsymbol{N}^\alpha)\times\hat{\boldsymbol{d}}. \tag{63}$$

Clearly,

$$\begin{aligned} & (\boldsymbol{d}|_\alpha\times\boldsymbol{M}^{*\alpha})\times\hat{\boldsymbol{d}} \\ &= [(D|_\alpha\hat{\boldsymbol{d}} + D\hat{\boldsymbol{d}}|_\alpha).\hat{\boldsymbol{d}}]\,\boldsymbol{M}^{*\alpha} \\ &\quad - (\boldsymbol{M}^{*\alpha}\cdot\hat{\boldsymbol{d}})(D|_\alpha\hat{\boldsymbol{d}} + D\hat{\boldsymbol{d}}|_\alpha) \\ &= D|_\alpha\tilde{\boldsymbol{M}}^{*\alpha} - (\boldsymbol{M}^{*\alpha}\cdot\hat{\boldsymbol{d}})\,D\hat{\boldsymbol{d}}|_\alpha, \end{aligned}$$

and after substituting (61.a-b) in the above equation, we obtain

$$\begin{aligned} (\boldsymbol{d}|_\alpha\times\boldsymbol{M}^{*\alpha})\times\hat{\boldsymbol{d}} &= \frac{1}{D}D|_\alpha\boldsymbol{M}^\alpha - DP^\alpha\hat{\boldsymbol{d}}|_\alpha \\ &= (\frac{1}{D}D|_\alpha M^{\beta\alpha} - DP^\alpha\lambda^\beta_{.\alpha})\tilde{\boldsymbol{a}}_\beta. \end{aligned} \tag{64}$$

From Equation (39) it follows that

$$(\boldsymbol{a}_\alpha\times\boldsymbol{N}^\alpha)\times\hat{\boldsymbol{d}} = -(Q^\beta_{eff} + \lambda^\beta_{.\alpha}M^{3\alpha})\tilde{\boldsymbol{a}}_\beta, \tag{65}$$

replacing (64) and (65) in (63) leads to

$$\begin{aligned} D\tilde{\boldsymbol{H}}^* = {} & (Q^\beta_{eff} - \frac{1}{D}D|_\alpha M^{\beta\alpha})\tilde{\boldsymbol{a}}_\beta \\ & + (DP^\alpha + M^{3\alpha})\lambda^\beta_{.\alpha}\tilde{\boldsymbol{a}}_\beta. \end{aligned} \tag{66}$$

The axial component $\boldsymbol{H}^{*\alpha}\cdot\hat{\boldsymbol{d}}$ may be obtained from the internal virtual-power expression (60) and (62). Since

$$\boldsymbol{H}^*\cdot\delta\boldsymbol{d} = D\tilde{\boldsymbol{H}}^*\cdot\delta\hat{\boldsymbol{d}} + (\boldsymbol{H}^*\cdot\hat{\boldsymbol{d}})\delta D,$$

and

$$\begin{aligned} \boldsymbol{M}^{*\alpha}\cdot\delta\boldsymbol{d}|_\alpha &= (\boldsymbol{M}^{*\alpha}\cdot\hat{\boldsymbol{d}})\,\delta D|_\alpha + (\tilde{\boldsymbol{M}}^{*\alpha}\cdot\hat{\boldsymbol{d}}|_\alpha)\,\delta D \\ &\quad + D|_\alpha\tilde{\boldsymbol{M}}^{*\alpha}\cdot\delta\hat{\boldsymbol{d}} + D\tilde{\boldsymbol{M}}^{*\alpha}\cdot\delta\hat{\boldsymbol{d}}|_\alpha \\ &\quad + D(\boldsymbol{M}^{*\alpha}\cdot\hat{\boldsymbol{d}})\hat{\boldsymbol{d}}\cdot\delta\hat{\boldsymbol{d}}|_\alpha \\ &= P^\alpha\delta D|_\alpha + \boldsymbol{M}^\alpha\cdot\delta\hat{\boldsymbol{d}}|_\alpha \\ &\quad + (\frac{1}{D}D|_\alpha\boldsymbol{M}^\alpha - DP^\alpha\hat{\boldsymbol{d}}|_\alpha)\cdot\delta\hat{\boldsymbol{d}} \\ &\quad + (\tilde{\boldsymbol{M}}^{*\alpha}\cdot\hat{\boldsymbol{d}}|_\alpha)\delta D, \end{aligned}$$

where the identity $\hat{\boldsymbol{d}}\cdot\delta\hat{\boldsymbol{d}}|_\alpha = -\hat{\boldsymbol{d}}|_\alpha\cdot\delta\hat{\boldsymbol{d}}$ was used, it follows that

$$\begin{aligned} \boldsymbol{H}^*\cdot\delta\boldsymbol{d} + \boldsymbol{M}^{*\alpha}\cdot\delta\boldsymbol{d}|_\alpha = {} & \boldsymbol{M}^\alpha\cdot\delta\hat{\boldsymbol{d}}|_\alpha + P^\alpha\delta D|_\alpha \\ & + (\boldsymbol{H}^*\cdot\hat{\boldsymbol{d}} + \tilde{\boldsymbol{M}}^{*\alpha}\cdot\hat{\boldsymbol{d}}|_\alpha)\,\delta D \\ & + (D\tilde{\boldsymbol{H}}^* + \frac{1}{D}D|_\alpha\boldsymbol{M}^\alpha - DP^\alpha\hat{\boldsymbol{d}}|_\alpha)\cdot\delta\hat{\boldsymbol{d}}. \end{aligned}$$

From Equations (63) and (64), clearly

$$\begin{aligned} & \left(D\tilde{\boldsymbol{H}}^* + \frac{1}{D}D|_\alpha\boldsymbol{M}^\alpha - DP^\alpha\hat{\boldsymbol{d}}|_\alpha\right)\cdot\delta\hat{\boldsymbol{d}} = \\ & \quad - (\boldsymbol{a}_\alpha\times\boldsymbol{N}^\alpha)\times\hat{\boldsymbol{d}}\cdot\delta\hat{\boldsymbol{d}}, \end{aligned}$$

and finally,

$$\begin{aligned} \boldsymbol{H}^*\cdot\delta\boldsymbol{d} + \boldsymbol{M}^{*\alpha}.\delta\boldsymbol{d}|_\alpha = {} & \boldsymbol{M}^\alpha\cdot\delta\hat{\boldsymbol{d}}|_\alpha + P^\alpha\delta D|_\alpha \\ & + (\boldsymbol{H}^*\cdot\hat{\boldsymbol{d}} + \tilde{\boldsymbol{M}}^{*\alpha}\cdot\hat{\boldsymbol{d}}|_\alpha)\delta D - (\boldsymbol{a}_\alpha\times\boldsymbol{N}^\alpha)\times\hat{\boldsymbol{d}}\cdot\delta\hat{\boldsymbol{d}}. \end{aligned}$$

If we define

$$H = \boldsymbol{H}^*\cdot\hat{\boldsymbol{d}} + \tilde{\boldsymbol{M}}^{*\alpha}\cdot\hat{\boldsymbol{d}}|_\alpha \tag{67}$$

then the internal virtual-power expression (60) reduces to (49). Obviously,

$$\boldsymbol{H}^*\cdot\hat{\boldsymbol{d}} = H - \frac{1}{D}\boldsymbol{M}^\alpha\cdot\hat{\boldsymbol{d}}|_\alpha, \tag{68}$$

or in components,

$$\boldsymbol{H}^* \cdot \hat{\boldsymbol{d}} = H - M^{\mu\alpha}\lambda^{\beta}_{.\alpha}(a_{\mu\beta} - a_{\mu3}a_{\beta3}). \tag{69}$$

Equations (66) and (69) finally lead to

$$\begin{aligned}\boldsymbol{H}^* &= \frac{1}{D}\left(Q^{\beta}_{eff} - \frac{1}{D}D|_{\alpha}M^{\beta\alpha}\right)\tilde{\boldsymbol{a}}_{\beta} \\ &+ \left(P^{\alpha} + \frac{1}{D}M^{3\alpha}\right)\lambda^{\beta}_{.\alpha}\tilde{\boldsymbol{a}}_{\beta} \\ &+ \left[H - M^{\mu\alpha}\lambda^{\beta}_{.\alpha}(a_{\mu\beta} - a_{\mu3}a_{\beta3})\right]\hat{\boldsymbol{d}}.\end{aligned} \tag{70}$$

Remark IV:

For a Cosserat surface of inextensible directors,

$$D = \|\boldsymbol{d}\| = 1, \qquad D|_{\alpha} = 0,$$

Equation (70) reduces to

$$\begin{aligned}\boldsymbol{H}^* &= [Q^{\beta}_{eff} + (P^{\alpha} + M^{3\alpha})\lambda^{\beta}_{.\alpha}]\,\tilde{\boldsymbol{a}}_{\beta} \\ &+ [H - M^{\mu\alpha}\lambda^{\beta}_{.\alpha}(a_{\mu\beta} - a_{\mu3}a_{\beta3})]\,\hat{\boldsymbol{d}}.\end{aligned}$$

Finally the internal force $(P^{\alpha}\hat{\boldsymbol{d}}|_{\alpha} + H\hat{\boldsymbol{d}})$ constitutes a reaction in the restricted model of inextensible directors and hence only the component $(\boldsymbol{H}^* - H\hat{\boldsymbol{d}} - P^{\alpha}\hat{\boldsymbol{d}}|_{\alpha})$ of $\boldsymbol{H}^*$ is determined from the motion of the Cosserat surface. ■

We observe that both Naghdi's and the proposed model assume essentially the same external and inertial force systems. The apparent differences should be regarded solely in terms of different physical interpretations of the vector fields involved. The fundamental fact is that both theories account for the same basic mechanisms. Regardless of the differences in definitions of the internal force systems, the internal virtual power associated with a given virtual velocity field is the same in both theories. This is consistent with the principle of virtual power and naturally follows from the equality of the external virtual power under appropriate identifications of the vector fields involved.

The relationship between the internal forces of both models was studied in detail in this section. As is seen, once constitutive equations for one model are postulated, corresponding constitutive equations for the other model may be directly obtained. This clearly shows the equivalence between both formulations.

One of the basic advantages of the proposed model is its relative simplicity compared with the developments of Naghdi. The necessity of considering restrictions on constitutive relations is completely eliminated and for elastostatic problems there is an uncoupling between the motion of the reference surface and the orientation of the director field with the deformation (changes in length) of the directors. Of course this uncoupling holds as long as the same is true with respect to the constitutive relations but clearly no such uncoupling is evident in Naghdi's equations whatever constitutive equations are used.

CONCLUSIONS

The equations of motion for a Cosserat surface were derived by means of the method of virtual power. Both the model with inextensible directors and its generalization to account for deformable directors were analyzed.

The equations derived for the Cosserat surface with inextensible directors coincides with the ones derived from the three-dimensional theory by Simo and Fox (1987). Our derivation shows the effectiveness of the method of virtual power in deriving such equations through a complete two-dimensional theory.

In the extension of the model to account for deformable directors a new set of equations is proposed. Besides the equations of linear and moment of momentum, one additional scalar equation is derived. This equation replaces the director-momentum equation of Naghdi and therefore eliminates the necessity of dealing with constitutive restrictions. One of the advantages of the proposed model is its direct connection with the constrained Cosserat surface of inextensible directors. The generalized deformations and internal forces are carried over invariantly. So far, most computer implementations of Cosserat surfaces have been restricted to the constrained model. The equations proposed here might furnish an efficient setting for the extension of those algorithms.

Clearly, some constitutive relations and a connection with the results of the asymptotic expansion of the three-dimensional equations are still needed in order to assess the usefulness of the theory presented here. The connection with the three-dimensional asymptotic expansion should be done first to identify the basic force systems in our model with equivalent resultants from the three-dimensional theory, and second to obtain constitutive relations that truly represent—to be sure, to the degree of approximation expected from a two-dimensional theory—the properties of the shell as a three-dimensional continuum. Since our objective was basically restricted to the derivation of the equations by means of the method of virtual power, this task is beyond the scope of this paper.

A final remark should be given with respect to the derivation of the equations for the Cosserat surface of deformable directors. As seen, the application of the fundamental axiom of the method of virtual power is alone not enough to solve the indeterminacies of the extended model. Even though the extension is straightforward, it does not truly reflect a pure application of the method of virtual power. The derivation should appropriately be regarded as an extension of the method of virtual power which reflects the three-dimensional nature of the additional force systems introduced in the model.

REFERENCES

Abraham R, Marsden JR, and Ratiu T (1983), *Manifolds, Tensor Analysis and Applications*, Addison-Wesley, Reading, MA.

Antman SS (1972), *The Theory of Rods*, Handbuch der Physik, volume VIa/2, Springer-Verlag, Berlin. Pages 641-703.

Carroll MM and Naghdi PM (1972), The influence of the reference geometry on the response of elastic shells, *Arch Rat Mech Anal* **48**, 302–318.

Epstein M and Segev R (1980), Differentiable manifolds and the Principle of Virtual Work in Continuum Mechanics, *J Mathematical Phys*, **21**, 1243–1245.

Ericksen JL and Truesdell C (1958), Exact theory of stress and strain in shells, *Arch Rat Mech Anal*, **1**, 295–323.

Flügge W (1970), *Tensor Analysis and Continuum Mechanics*, Springer-Verlag, Berlin.

Germain P (1973), Sur l'application de la méthode des puissances virtuelles en la mécanique des milieux continus, *CR Acad Sci Paris*, **274**, A1051–1054.

Gotteland M and Barbe M (1981), Étude comparative de la théorie des milieux micromorphiques et micropolaires et la théorie des directeurs appliquées aux surfaces, *Journal de Mechanique*, **20(4)**, 643–657.

Green AE and Naghdi PM (1974), On the derivation of shell theories by direct approach, *J Appl Mech*, **41**, 173–176.

Green AE, Naghdi PM, and Wainwright WL (1965), A general theory of a Cosserat surface, *Arch Rat Mech Anal*, **20**, 237–303.

Hirsch MW (1976), *Differential Topology*, Graduate Texts in Mathematics, volume 33, Springer-Verlag, New York.

Horvath J (1966), *Topological Vector Spaces and Distributions*, volume I, Addison-Wesley, Reading, MA.

Lubliner J (1983a), Inertia in simple body models, *Mech Research Commun*, **10(1)**, 1–7.

Lubliner J (1983b), Inertia in simple dipolar continua, *Mech Research Commun*, **10(5)**, 273–278.

Lubliner J (1984), Generalized inertia in constrained body models, *Mech Research Commun*, **11(5)**, 309–315

Lubliner J (1985), *Thermomechanics of Deformable Bodies*, Department of Civil Engineering, University of California at Berkeley, Berkeley, CA.

Lubliner J (1986), The method of virtual power and a simple multipolar rod model, *Arch Mech*, **38(1-2)**, 3–12.

Marsden JE and Hughes T (1983), *Mathematical Foundations of Elasticity*, Prentice-Hall, Englewood Cliffs, NJ.

Naghdi PM (1972), *The Theory of Shells and Plates*, Handbuch der Physik, volume VIa/2, Springer-Verlag, Berlin.

Niordson FI (1985), *Shell Theory*, Series in Applied Mathematics and Mechanics, North-Holland.

Simmonds JG and Danielson DA (1972), Non-linear shell theory with finite rotation and stress-function vectors, *J Appl Mech*, **39(4)**, 1085–1090.

Simo JC and Fox DD (1989), On a stress resultant geometrically exact shell model, part I : Formulation and optimal parametrization, *Comput Methods Appl Mech Engrg*, **72**, 267–304.

Spivak M (1979), *A Comprehensive Introduction to Differential Geometry*, volume 1, Publish or Perish, Houston, TX.

Jump phenomena, bifurcations, and chaos in a pressure loaded spherical cap under harmonic excitation

Paulo Batista Gonçalves

Department of Civil Engineering, Pontifical Catholic University
22453-900 Rio de Janeiro, Brazil

This paper investigates the dynamic non-linear behaviour of a pre-loaded shallow spherical shell under a harmonic excitation. For this, the Marguerre partial differential equations of motion for an imperfect, pre-loaded cap is reduced to a finite degree of freedom system using the Galerkin method. The displacements and stress functions are described by a linear combination of Bessel functions and modified Bessel functions that satisfy all the relevant boundary and continuity conditions. The resulting differential equations of motion are solved by the Galerkin-Urabe procedure, or, alternatively, by numerical integration. To study the response of the shallow cap under harmonic excitation, phase plane portraits, Poincaré maps, resonance curves, and bifurcation diagrams are plotted for a number of loading conditions. Results indicate that, for static load levels between the upper and lower limit point loads, the shell may display jumps due to the presence of competing potential wells and the presence of non-linear resonance curves within each well. Additionally, different physical situations are identified in which period-doubling phenomena and chaos can be observed.

INTRODUCTION

Due mainly to the discovery of chaotic motions in physical systems governed by deterministic equations, in a remarkably short time, the field of non-linear dynamics, as a topic of pure and applied mathematics, has experienced considerable development (Palis and de Melo, 1982; Arnold, 1982; Guckenheimer and Holmes, 1983; Wiggins, 1990). Engineering sciences have also benefited from these developments in that many non-linear dynamical problems have been treated and new classes of phenomena have been identified. Research in civil and mechanical engineering is well documented in the books of Thompson and Stewart (1987), Moon (1987) and Kapitaniak (1991), and in the review articles by Nayfeh and Balachandran (1989) and Holmes (1990). A detailed analysis of non-linear engineering problems, using traditional perturbation methods, can be found in Nayfeh and Mook (1979).

The consideration of non-linear effects on the modelling of structural systems is of particular concern in the static and dynamic analysis of structural elements liable to buckling. A particular feature of these systems is that, as parameters are changed, the stability of the equilibrium points can change as well as the number of equilibrium points (Thompson and Hunt, 1984). The existence of competing static equilibrium positions brings out, when the system is subjected to dynamic loads, a whole range of phenomena that are not found in linear systems. These include jumps, subharmonic and super-harmonic oscillations, period-multiplying bifurcations, co-existing small and large amplitude oscillations, combination resonances, modal interaction and chaotic motions (Nayfeh and Mook, 1979; Thompson and Stewart, 1987).

Among various non-linear problems analysed in literature, thin elastic shells have received a great deal of attention due to its complex non-linear behaviour. Analytical and experimental investigations of cylindrical and spherical shells have indicated that thin shells, when subjected to dynamic loads, may display a wealth of non-linear phenomena including chaotic motions (Chen and Babcock, 1975; Yasuda and Kushida, 1984; Nayfeh and Raouf, 1987; Raouf and Nayfeh, 1989). This is due to the presence of strong quadratic and cubic geometric non-linearities in the equations of motion. Nevertheless, the non-linear dynamic behaviour of thin shells is not completely understood and new phenomena are still coming to light.

Shallow spherical caps when subjected to static pressure loading often exhibit a highly non-linear response and may be subjected to either limit-point instability or bifurcational instability with unstable post-buckling response. As shown by Gonçalves and Croll (1992), the degree of non-linearity and the loading carrying capacity of these shell components are very sensitive to the geometric imperfections that are often induced during fabrication and installation procedures. For certain practical ranges of load levels and initial geometric imperfections, these shells may exhibit more than one point attractor. Also, the combined effects of initial geometric imperfections and compressive stresses will change substantially the natural frequencies and alter, consequently, the dynamic response and stability characteristics of these systems (Gonçalves, 1991). As a result, it is expected that pressure loaded imperfect spherical caps under dynamic loads may display complex dynamic phenomena such as those described earlier.

Although the effects of geometric imperfections on static buckling resistance of pressure loaded spherical caps have been the topic of numerous investigations in the past few decades (e. g. Budiansky, 1959; Huang, 1964, Yamada et al., 1983; Gonçalves and Croll, 1992), most of the studies of the linear and non-linear vibrations of these shells have, however, been limited to perfect (and usually unloaded) shells (e. g. Archer, 1962; Evesen and Evan-Iwanowski, 1967; Grossman et al., 1969; Yasuda and Kushida, 1984). In the present work a new non-linear modelling for the axisymmetric dynamic behaviour of clamped shallow spherical shells is presented, which considers the combined effects of pressure loading and geometric imperfections on the vibration characteristics and non-linear response of the cap. The basic approach in this work is to solve

part of "MECHANICS PAN-AMERICA 1993" edited by MRM Crespo da Silva and CEN Mazzilli
ASME Reprint No AMR134

the dynamic version of the fourth-order Marguerre equations by the Galerkin method. An accurate solution described by a linear combination of Bessel functions and modified Bessel functions based on the free vibration modes of the unloaded perfect cap is used to determine the non-linear pre-stress state of the imperfect cap and to examine its linear and non-linear vibration characteristics along the pre- and post-buckling paths. Each term of the modal expansions satisfies all the relevant boundary and continuity conditions.

Recently monographs on algorithms for simulating non-linear dynamical systems were written by Seydel (1988) and Parker and Chua (1989). Also, software packages are available for the analysis of non-linear differential equations, with emphasis on chaotic behaviour (Parker and Chua, 1989; Yorke, 1990). In order to study the non-linear behaviour of the cap, routines, based on these references, were used to integrate numerically the equations of motion and record time histories of the response, phase portraits, Poincaré maps, stable and unstable fixed points, Lyapunov exponents and bifurcation diagrams. Results show that, for static load levels between the upper and lower limit point loads, the shell may display jumps due to the presence of competing potential wells and the presence of non-linear resonance curves within each well. Additionally, different physical situations are identified in which period-doubling phenomena and chaos can be observed.

BASIC EQUATIONS

The geometry of a uniformly loaded shallow spherical cap with clamped edge conditions is presented in Fig. 1, where R, a, H and h are the principal radius of curvature of the sphere, the base radius of the cap, the rise of the mid-surface at the apex and the shell thickness, respectively. The polar co-ordinate system in the base plane is defined by r and θ, and the external uniform pressure distributed over the surface of the shell is denoted by q.

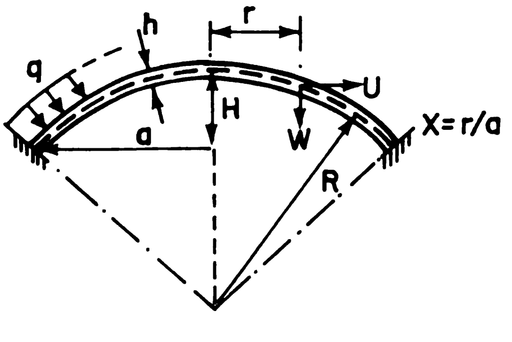

FIG 1. Shell geometry, displacements and co-ordinate system

Within the framework of shallow shell theory ($H/a < 0.25$), the tangential forces and displacements can be taken to be their projections onto the base plane of the shell. The basic equations governing large deformations, but small strains, of shallow spherical caps were formulated by Marguerre (1939). In the case of axisymmetric static deformations of a thin imperfect cap, the governing equations may be expressed in the non-dimensional form as

$$\nabla^4 w_s = \lambda^2\alpha^{1/2}\nabla^2 f_s + Q\frac{4\lambda^4}{\alpha^{1/2}} + \frac{\alpha}{x}\{f_{s,x}(w_{s,x}+\hat{w}_{,x})\} \tag{1.a}$$

$$\nabla^4 f_s = -\lambda^2\alpha^{-1/2}\nabla^2 w_s - \frac{1}{x}\{w_{s,x}w_{s,xx} + (\hat{w}_{,x}w_{s,x})_{,x}\} \tag{1.b}$$

where $()_{,x} = \partial/\partial x()$, $\alpha = 12(1-\nu^2)$ and λ is a geometrical parameter described by

$$\lambda = \alpha^{1/4}a/\sqrt{Rh} \tag{2}$$

The non-dimensional radial co-ordinate x, the vertical displacement w_s, imperfection shape $\hat{w}$, stress function f_s, and load parameter Q are related to the corresponding physical quantities by

$$x = \frac{r}{a} \qquad w_s = \frac{W_s}{h} \qquad \hat{w} = \frac{\hat{W}}{h}$$

$$f_s = \frac{F_s}{Eh^3} \qquad Q = \frac{q}{q_{cl}} \tag{3}$$

where $q_{cl} = 2E(h/R)^2/\sqrt{3(1-\nu^2)}$ is the classical buckling pressure of a complete spherical shell, E is the Young's modulus and ν is the Poisson's ratio.

The static stress resultants, couples and non-linear strain-displacement relations are given by

$$\frac{a^2N_r}{Eh^3} = \frac{1}{x}f_{s,x}$$

$$\frac{a^2N_\theta}{Eh^3} = f_{s,xx}$$

$$\frac{12(1-\nu^2)a^2M_r}{Eh^4} = \frac{1}{x}w_{s,x} + \nu w_{s,xx}$$

$$\frac{12(1-\nu^2)a^2M_\theta}{Eh^4} = w_{s,xx} + \frac{\nu}{x}w_{s,x}$$

$$\varepsilon_r = \frac{h}{a}u_{s,x} + \left(\frac{h}{a}\right)^2\left[\hat{w}_{,x}w_{s,x} + \frac{1}{2}w_{s,x}^2\right]$$

$$\varepsilon_\theta = \frac{h}{a}\frac{u_s}{x} \tag{4}$$

where $u_s(= U_s/h)$ is the non-dimensional displacement in the radial direction.

The boundary conditions at the clamped edge $x = 1$ of the shallow shell are

$$w_s = 0 \qquad w_{s,x} = 0 \qquad u_s = f_{s,xx} - \frac{\nu}{x}f_{s,x} = 0 \tag{5}$$

When a uniform static pressure is applied to the cap, it yields a basic static geometrically non-linear state of displacements and stresses. To represent the basic static axisymmetric response, the displacement w_s and the stress function f_s are assumed in the form

$$w_s(x) = \sum_{i=1}^{N} W_{0i}\phi_i(x) \tag{6.a}$$

$$f_s(x) = \sum_{i=1}^{N} F_{si}\psi_i(x) \tag{6.b}$$

where each separate generalized function

$$\phi_i(x) = J_0(K_i x) + \frac{J_1(K_i)}{I_1(K_i)} I_0(K_i x) - \left[J_1(K_i)\frac{I_0(K_i)}{I_1(K_i)} + J_0(K_i)\right] \tag{7.a}$$

$$\psi_i(x) = J_0(K_i x) - \frac{J_1(K_i)}{I_1(K_i)} I_0(K_i x) + \frac{K_i^2(\lambda^4 + K_i^4)}{4\lambda^4}\left[J_1(K_i)\frac{I_0(K_i)}{I_1(K_i)} + J_0(K_i)\right]x^2 \tag{7.b}$$

exactly satisfies the clamped boundary conditions at x=1 as well as the continuity requirements of displacements and stresses at the centre of the shell (x=0).

In equations (7.a) and (7.b) J_0 and J_1 are Bessel functions, and I_0, and I_1 modified Bessel functions of the first kind, and $K_n (0 < K_1 < K_2 < \ldots)$ are the roots of the equation

$$[J_0(K_n)I_1(K_n) + I_0(K_n)J_1(K_n)] \times K_n\left[\frac{\lambda^4 + K_n^4}{\lambda^4}\frac{(1-\nu)}{2} - 1\right] + 2J_1(K_n)I_1(K_n)(1+\nu) = 0 \tag{8}$$

It might be observed that the generalised functions (7.a) and (7.b) are also the linear vibration modes of an unloaded clamped shallow spherical shell (Yasuda and Kushida, 1984).

To facilitate a convenient representation of axisymmetric geometric imperfections of an arbitrarily specified shape and consequently allow an efficient modal analysis of the imperfect shell, a Fourier-Bessel series is used to describe the "general" imperfection, $\hat{w}(x)$. This Fourier-Bessel series may be written as

$$\hat{w}(x) = \hat{W}\left[\sum_{i=1}^{N} \hat{w}_i\phi_i(x) / \mathrm{MAX}\left(\sum_{i=1}^{N} \hat{w}_i\phi_i(x)\right)\right] \tag{9}$$

where $\hat{w}_i$ is the amplitude of the ith harmonic and $\phi_i(x)$ is the modal function given by (7.a). Note that $\{\phi_i(x)\}$ represents a complete set of orthogonal functions in [0,1] (Yasuda and Kushida, 1984).

For convenience, the expression between brackets in (9) is written in such a way that its maximum value is always equal to one. Consequently the magnitude and sign of the maximum amplitude will be given by $\hat{W}$.

Substituting expressions (6) and (9) into equations (1.a) and (1.b) and applying a Galerkin minimisation procedure one obtains a set of 2N non-linear algebraic equations characterizing the static behaviour of the cap. The expressions (7.a) and (7.b) are used as the weighting functions in this Galerkin procedure. These non-linear equations are unfortunately too long to be presented here; the interested reader will find them in Gonçalves and Croll (1990). These algebraic non-linear equations are solved by the Newton-Raphson method. The solution procedure is implemented in such a way that, without manual intervention, if convergence of the Newton-Raphson scheme fails in one step, the programme returns to the previous step and then chooses a new control parameter and modifies the Jacobian matrix accordingly.

In the further analysis the dynamic behaviour of the cap around the axisymmetric non-linear static state will be considered. For this, a dynamic perturbation is superimposed on the basic static state. In this case one has

$$W_p(x,t) = \hat{w}(x) + w_s(x) + w(x,t)$$
$$F_p(x,t) = f_s(x) + f(x,t) \tag{10}$$

where $w(x,t)$ denotes the incremental displacement component and $f(x,t)$, the corresponding incremental stress function.

Using expressions (10) and the dimensionless parameters, one obtains the following non-dimensional equation of motion

$$\nabla^4 w + w_{,\tau\tau} + \bar{c}w_{,\tau} = \lambda^2\alpha^{1/2}\nabla^2 f + \frac{\alpha}{x}\{f_{,x}(\hat{w} + w_s + w)_{,x} + f_{s,x}w_{,x}\}_{,x} + \frac{4\lambda^4}{\alpha^{1/2}}A_f\sin(\Omega\tau) \tag{11.a}$$

and the associated compatibility equation

$$\nabla^4 f = -\lambda^2\alpha^{-1/2}\nabla^2 w - \frac{1}{x}\{w_{,x}w_{,xx} + [(\hat{w}_{,x} + w_{s,x})w_{,x}]_{,x}\} \tag{11.b}$$

where $\tau = t/\gamma$, $\bar{c} = \gamma c/\rho h$, $\Omega = \gamma\omega$, $\gamma^2 = (\alpha a^4\rho/Eh^2)$, ρ is the mass density, t is time, ω is the driving frequency and c is the damping coefficient.

The incremental state is assumed in the separable form

$$w(x,t) = \sum_{i=1}^{N} W_i(t)\phi_i(x) \tag{12.a}$$

$$f(x,t) = \sum_{i=1}^{N} F_i(t)\psi_i(x) \tag{12.b}$$

The substitution of expressions (12) into equations (11.a) and (11.b), the use of the complete equations for the basic non-linear static state, and the application of the Galerkin method yields the required second-order ordinary differential equations of motion. To study the non-linear behaviour of the cap, these equations are reduced to a set of first order differential equations which are numerically integrated using the fourth-order Runge-Kutta method with double precision.

Alternatively, approximating in (12) the temporal functions $W_i(t)$ and $F_i(t)$ by

$$W_i(t) = W_i\cos(\omega t) + W_c \tag{13.a}$$

$$F_i(t) = F_{1i}\cos(\omega t) + F_{2i}(\cos(\omega t))^2 + F_c \tag{13.b}$$

substituting the resulting expressions in (11) and finally applying the Galerkin-Urabe method (Urabe, 1965), one obtains the required modal dynamic equations for the imperfect loaded cap. Neglecting non-linear terms in w and f a system of homogeneous linear algebraic equations is obtained. The solution of the resulting eigenvalue problem gives the vibration modes and the relationship between the load parameter and the square of the corresponding natural frequencies. The solution of the eigenvalue problem is obtained b[illegible] n of

Rutishauser's algorithm (Rutishauser, 1958). For the evaluation of the Bessel functions and modified Bessel functions, the polynomial expansions presented by Abramowitz and Stegun (1964) were used.

The constant terms in equations (13) are added due to the presence of quadratic non-linearity.

RESULTS AND DISCUSSION

In each of the non-linear paths reported in this section, care has been taken to achieve convergence through the use of a suitable number of terms N in the expansions (6) and (12). The number of terms N necessary to attain convergence to within 1% increases as the value of the geometrical parameter λ increase and, consequently, the waviness of the static solution and vibration modes increases.

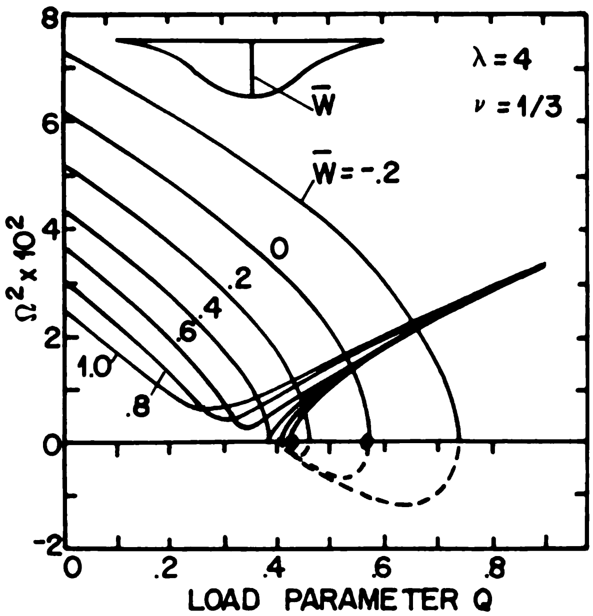

FIG 2. The square of the frequency versus applied load for the shell.

Figure 2 shows the relationship between the square of the frequency parameter Ω^2 ($\Omega = \gamma\omega$) associated with the lowest natural frequency and the load parameter Q for a shell with $\lambda = 4$ and $\nu = 1/3$. Figure 3 shows the variation of the load parameter Q with the central deflection of the cap $W_s(0)$. The dashed curves in these figures correspond to unstable regions. In Figs 2 and 3 the imperfection is taken in the form of the first vibration mode of the unloaded perfect cap (i=1, $K_1 = 4.3461$ in the modal expansion (9)). These results typify the effects of the non-linear pre-stress state and initial geometric imperfections on the axisymmetrical natural frequencies of the cap. This influence depends on the shape, magnitude and sign of the imperfections. In the pre-buckling region positive imperfections decrease the minimum frequency and the upper limit point load Q_U, whereas negative imperfections increase these two parameters. For relatively small positive and for negative values of $\hat{W}$ there is a gradual variation of the frequency parameter up to the neighbourhood of the buckling load after which the natural frequency begins to drop off sharply to zero as the buckling load is approached; similar behaviour is observed along the post-buckling path. These results and conclusions are typical of shallow caps with $\lambda \leq 5.5$ (Gonçalves, 1991; Gonçalves and Croll, 1992).

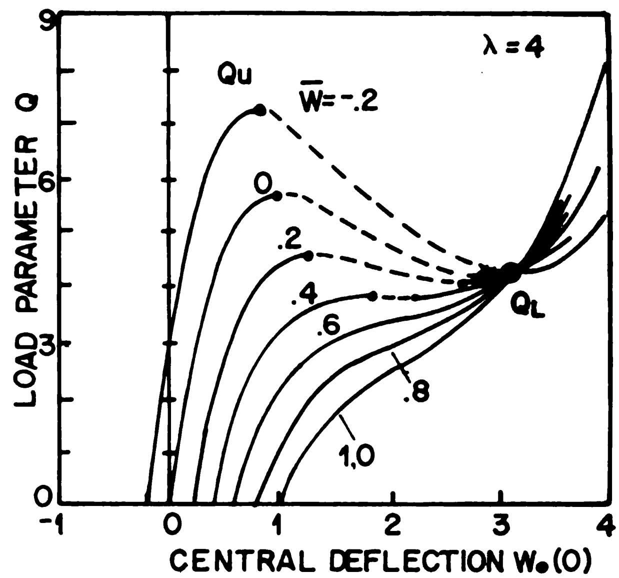

FIG 3. Non-linear equilibrium paths of perfect and imperfect caps.

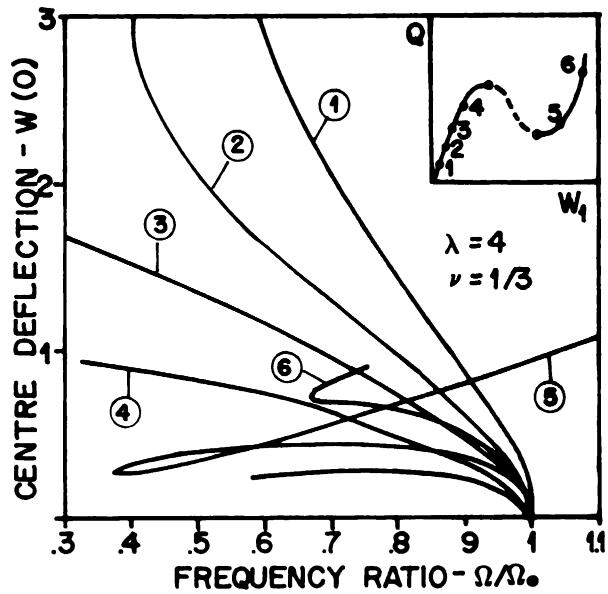

FIG 4. Influence of the static pre-stress state on the non-linear vibrations of the cap

The effect of the non-linear static stress state on the non-linear free-vibration frequencies is illustrated in Fig 4 where the displacement at the centre of the cap, $W(0)$, is plotted as a function of the frequency ratio Ω/Ω_0, for different load levels. Here Ω_0 is the fundamental free vibration frequency of the cap. Curves 1 to 4 are associated to increasing load levels along the pre-buckling path while curves 5 and 6 are related to post-buckling configurations. All response curves exhibit initial softening trends. As expected, the degree of softening increases with load along the pre-buckling path and decreases with load along the post buckling path. The curves associated with post-buckling configurations exhibit a high degree of non-linearity, presenting sometimes looping characteristics.

It is well known, both theoretically and experimentally, that for perfect and imperfect caps with $\lambda \leq 5.5$, the buckling pattern is always axisymmetric and the load-displacement curves are smooth both before and after buckling (e. g. Yamada et al., 1983). On the other hand, as shown by Huang (1964), for $\lambda > 5.5$ the perfect cap initially deforms symmetrically until it reaches a pressure slightly above $Q = 0.75$ where it bifurcates into an asymmetric mode. Whether the imperfect shell with $\lambda > 5.5$ will buckle symmetrically or asymmetrically it will depend on the imperfections. Several studies have shown that as the magnitude of the imperfection increases, the buckling pattern changes from asymmetric to axisymmetric. The value of the maximum imperfection magnitude required to produce this transition state is usually a small fraction of the shell thickness (Yamada et al., 1983). These facts indicate that the present results based on the axisymmetric formulation are particularly suited for the analysis of shallow caps with $\lambda \leq 5.5$. For higher values of λ the present analysis should be complemented by an analysis including asymmetric effects.

ONE-DEGREE-OF-FREEDOM MODEL

In a dissipative system energy is lost due to damping and the system may settle down to a final motion which can be described by only a few dimensions (Bishop et al., 1988). Numerical results have shown that for shallow spherical caps ($\lambda \leq 5.5$) the first mode is dominant and a simplified one-degree-of-freedom model is capable of describing with a reasonable degree of accuracy the non-linear behaviour of the cap. This allows one to use various mathematical and numerical tools recently developed for the investigation of the global behaviour of non-linear one-degree-of-freedom dynamical systems (Seydel, 1988; Parker and Chua, 1989; Yorke, 1990).

Using in (6) a number of terms N necessary to achieve convergence of the non-linear static state and using only one mode (i=1 in (12)) to describe the dynamic response, one obtains the following one-degree-of-freedom model for the cap

$$W_{1,\tau\tau}+\bar{c}W_{1,\tau}+\alpha_1 W_1+\alpha_2 W_1^2+\alpha_3 W_1^3=\beta A_f \sin(\Omega\tau) \qquad (14)$$

where the coefficients α_i and β are functions of the shell parameters and of the static pre-stress state.

As one can observe, Eq. (14), governing the motion of the pressure loaded cap, possesses both quadratic and cubic non-linearities.

Elimination of both damping and forcing will produce the equation

$$W_{1,\tau\tau}+\alpha_1 W_1+\alpha_2 W_1^2+\alpha_3 W_1^3=0 \qquad (15)$$

Multiplying Eq.(15) by $W_{1,\tau}$ and integrating will yield

$$\frac{1}{2}W_{1,\tau}^2+\frac{1}{2}\alpha_1 W_1^2+\frac{1}{3}\alpha_2 W_1^3+\frac{1}{4}\alpha_3 W_1^4=C \qquad (16)$$

where $T = 1/2W_{1,\tau}^2$ is recognized as the kinetic energy, $\Pi = 1\backslash 2\alpha_1 W_1^2 + 1\backslash 3\alpha_2 W_1^3 + 1\backslash 4\alpha_3 W_1^4$ is seen to be the potential energy and C is a constant.

Table 1 shows the values of the coefficients α_i for a perfect cap with $\lambda = 4$ and $\nu = 1/3$ under selected static load levels.

A schematic representation of the shell static non-linear response and of the damped unforced vibration response for representative load levels are shown in Fig. 5. For $Q < Q_L$, only one equilibrium point (a point attractor) exists. For $Q_L < Q < Q_U$ there are three equilibrium points: two stable equilibrium positions separated by a saddle. In this range one has a non-symmetric two-well potential function, as illustrated in Fig. 5.b. As the load increases from Q_L, well C, associated with the buckled state, becomes deeper, while well A, associated with the unbuckled state, becomes shallower and the corresponding basin of attraction shrinks and disappears for $Q > Q_U$. At $Q = Q_U$ and $Q = Q_L$ an attractor meets an unstable point and both are destroyed (saddle-node annihilation). As basin A shrinks the probability of occurrence of dynamic instability (jumps from well A into well C) increases greatly. The existence of these competing attractors for $Q_L < Q < Q_U$ is the main source of the complex non-linear dynamic behaviour shown herein.

Table 1

Load - Q	α_1	α_2	α_3
0.00	612.77	-581.51	154.24
0.01	552.16	-559.53	154.24
0.20	486.40	-534.34	154.24
0.30	413.34	-504.41	154.24
0.40	328.67	-466.48	154.24
0.50	219.87	-410.50	154.24

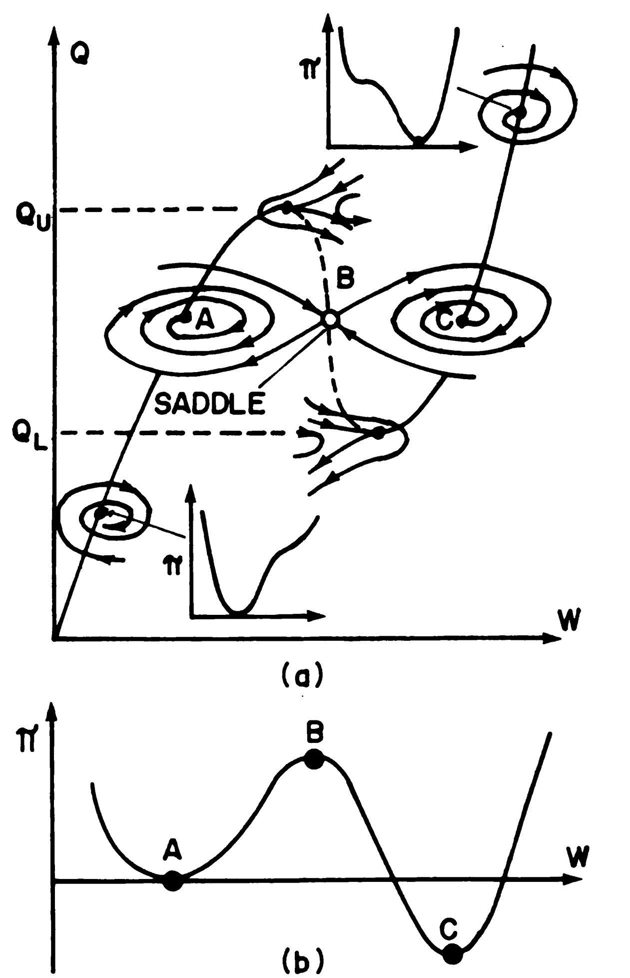

FIG 5. Schematic representation of the shell response, showing two saddle-node bifurcations

For a perfect cap with $\lambda = 4$ and $\nu = 1/3$ and $Q=0.5$, equation (14) reduces to

$$W_{1,\tau\tau}+\bar{c}W_{1,\tau}+219.87W_1-410.50W_1^2+$$

$$154.24W_1^3 = 358.88A_f\sin(\Omega\tau) \qquad (17)$$

The shape of the corresponding potential is illustrated in Fig. 6, showing two smooth minima at $W_1(0)=0$ and $W_1(0)=2.9734$ where the damped, unforced system has point attractors and a maximum at $W_1(0)=1.1518$, corresponding to a saddle point. A small external vibration converts these static equilibrium points to limit cycles in the forced system. The following results are related to this potential function.

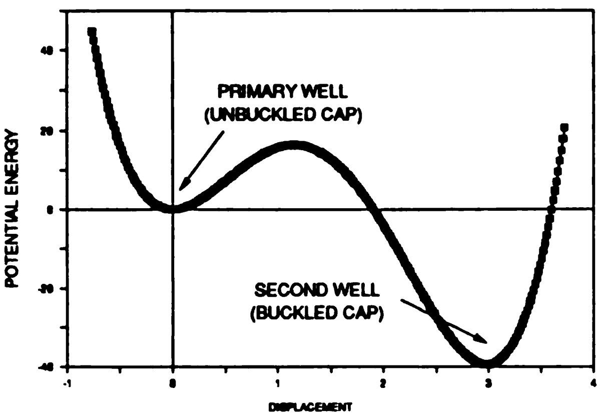

FIG 6. Non-symmetric two-well potential

One feature commonly found when modelling non-linear systems is the possibility of multiple coexisting periodic solutions. This may be due to the existence, for example, of multiple potential wells, resonance curves and competing subharmonic oscillations. In any of these cases, the final, steady state motion persisting after transients have decayed, depends crucially on the initial conditions given to the system. Here, for load levels between Q_U and Q_L and small values of the forcing amplitude A_f one has at least two stable, small amplitude periodic solutions and one unstable periodic solution which emanate from the three equilibrium points. For larger values of the forcing, other solutions may appear due to the presence of resonance curves within each well. The simultaneous presence of subharmonic oscillations is also possible. As an illustration Fig. 7 shows, for $A_f=-0.027$, $\Omega_f=12$ and $\bar{c}=1$, five stable periodic solutions, each of which is a possible long-term motion of the forced cap. Within each well there is one large amplitude period-one oscillation coexisting with a small period-one oscillation. They indicate the simultaneous presence of resonance curves, one within each well. The unbuckled cap also displays a subharmonic oscillation of order three, as shown in Fig. 7.b. The black dots are the stable fixed points of the Poincaré map. These points are calculated by a numerical scheme that combines a cell-mapping approach (Flashner and Guttalu, 1988) with the Newton-Raphson procedure.

For large forcing amplitudes there may also exist global oscillations about all three equilibria, as illustrated in Fig. 8. In addition to periodic response of various orders, the cap may display also chaotic motions.

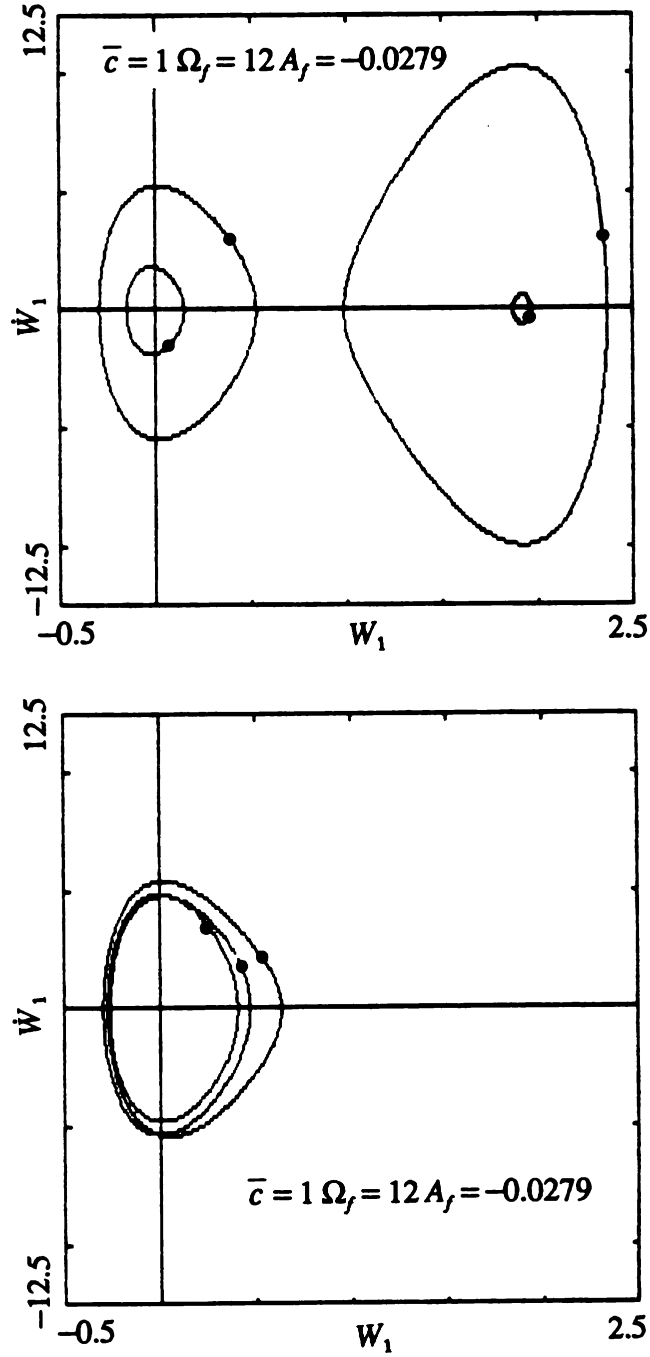

FIG 7. Phase projections of five coexisting stable periodic attractors

A detailed parametric analysis of Eq. (14) reveals that three different physical situations may arise in which the cap displays period doubling cascades leading to chaos. These are:

1- chaotic motions associated with softening spring effect in the resonance zone.

2- chaotic motions which appear just before escape from a potential well.

3- large amplitude chaotic motions in which the cap jumps back and forth between the two wells.

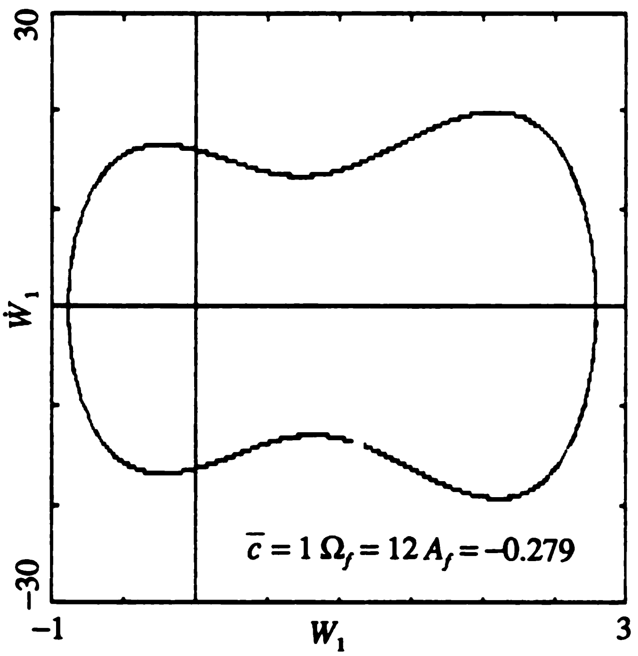

FIG 8. Large amplitude oscillations about all three equilibria

In the Duffing equation with softening type elastic characteristics, chaotic behaviour was observed by various authors at the region of the principal resonance. See, for example, Thompson and Stewart (1987) and Szemplinska-Stupnicka (1988). Taking $\bar{c}=2$ and $A_f=0.033$, using the driving frequency parameter as a control parameter, and plotting the projection of the phase curve onto the W_1 *vs*. Ω_f plane, one obtains, as Ω_f is decreased from 12 to 9, two branches of a resonance curve (see Fig. 9.a). Other stable segments of the curve can be obtained increasing Ω_f from 11 to 14, as shown in Fig. 9.b. These two pictures show clearly the softening nature of the frequency-response curves and the sudden increases and decreases in amplitude as the frequency is varied. This simple numerical procedure reveals that, instead of a smooth response as the one obtained from smooth variational equations (Nayfeh and Mook, 1979), the amplitude presents small fluctuations near the place where the upper cyclic fold should be. These fluctuations denote the region where flip bifurcations occur. A plot of the position of the Poincaré displacement co-ordinate W_1 versus the bifurcation parameter Ω_f leads to the bifurcation diagram depicted in Fig. 10. It confirms the existence of a cascade of period-doubling bifurcations leading eventually to chaos in a narrow zone of the frequency, just before the peak resonant amplitude. The zone of chaotic motion ends very sharply and is succeeded by a jump into the non-resonant, small-amplitude branch of the resonance curve. The phase portrait and the corresponding Poincaré section of a chaotic trajectory are recorded for $\Omega_f=10$in Figs. 11 and 12, respectively. The chaotic attractor exhibits the same simply-folded band structure observed by Thompson and Stewart (1987) for other softening spring oscillators. This chaotic response coexists with a smaller amplitude periodic limit cycle at the same control parameter value and within the same well. There is at least one more stable solution in the second well.

Now the behaviour of the unbuckled cap will be considered, when the amplitude of the forcing, A_f, is taken as a bifurcation parameter. For small values of A_f the motion may be confined into the shallower well, but for larger values of A_f the motion can no longer be confined into this well and the shell escapes, being trapped into the second, deeper well. With the proper choice of damping and excitation frequency, just before escape, the response goes through a cascade of period doubling bifurcations culminating in a chaotic behaviour, as illustrated by the bifurcation diagram shown in Fig. 13. Again the chaotic zone ends very sharply and the response, after some transients, jumps into the second well. This phenomenon is usually called dynamic snap-through buckling.

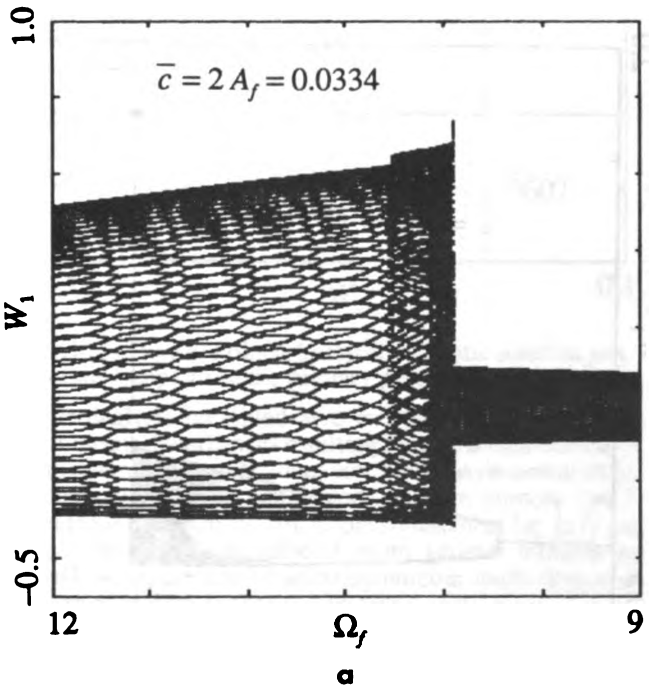

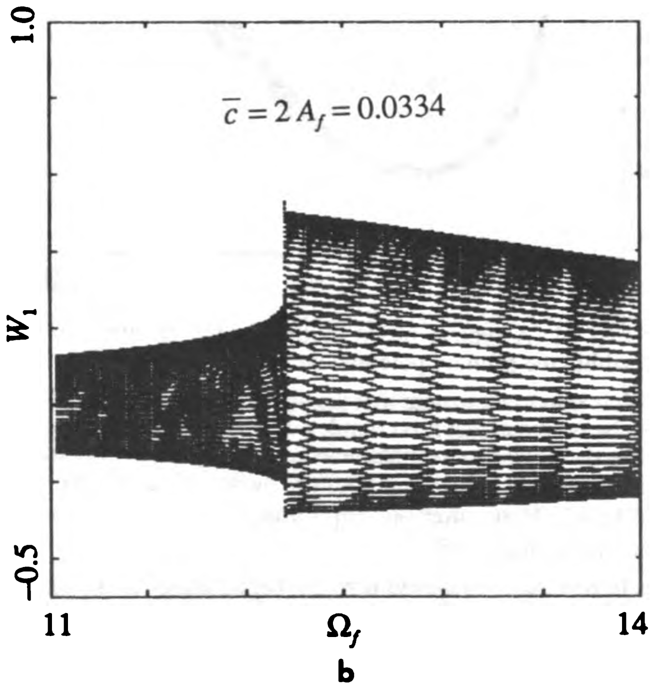

FIG 9. Numerically obtained resonance curves within the primary potential well, showing softening t

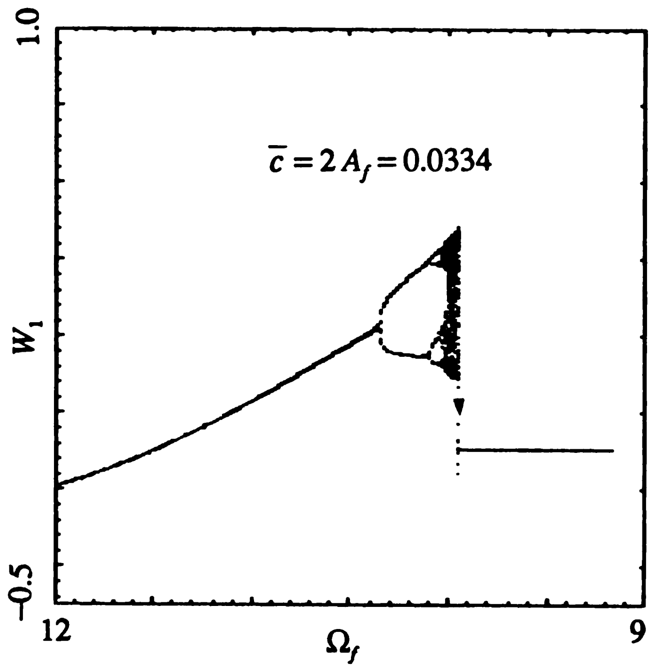

FIG 10. Bifurcation diagram. Poincaré co-ordinate, W_1, as a function of the forcing frequency.

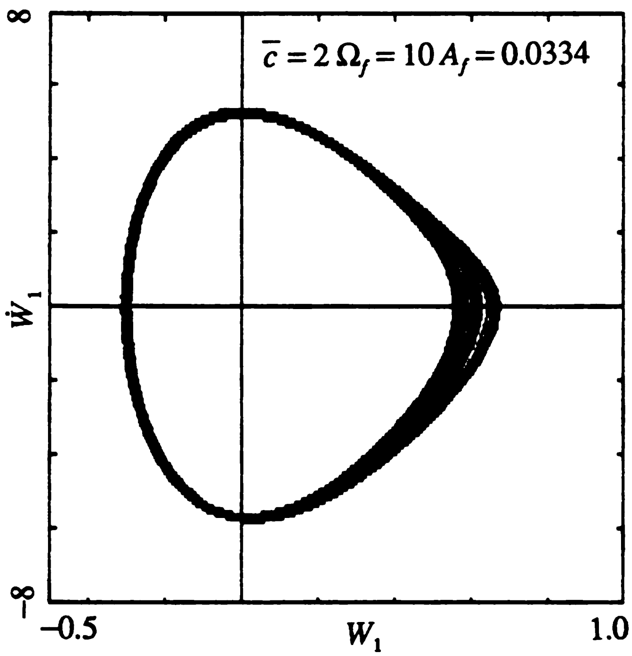

FIG 11. A typical phase portrait in the chaotic zone within the primary potential well

It is important to note that the beginning of a cascade does not always mean that it is completed; depending on the values of the shell and forcing parameters, the jump may occur after a finite number of flip bifurcations as shown in Fig. 14 for $\overline{c} = 2$ and $\Omega_f = 7$. Here, after one flip bifurcation, the cap escapes from the primary well.

In both cases analysed here the beginning of a cascade is a clear indication that an unsafe region is being approached. This fact could probably be used to control the behaviour of the structure and prevent unwanted jumps. These results also show that, for certain static load values, even low excitation vels can produce period-multiplying bifurcations and chaotic tions in the single-degree-of-freedom model.

In Fig. 15 the chaotic attractor for parameter values $\overline{c} = 3, A_f = 0.06$ and $\Omega_f = 12$ is shown. The nature of the chaotic attractors are verified by evaluating Lyapunov exponents.

In addition to the chaotic responses within one potential well, another type of chaotic response can be found in which the cap jumps back and forth between the two wells in a erratic manner. A typical chaotic attractor for large amplitude oscillations is depicted in Fig. 16. This type of chaotic response is associated with moderate to large forcing amplitudes and is well documented in literature.

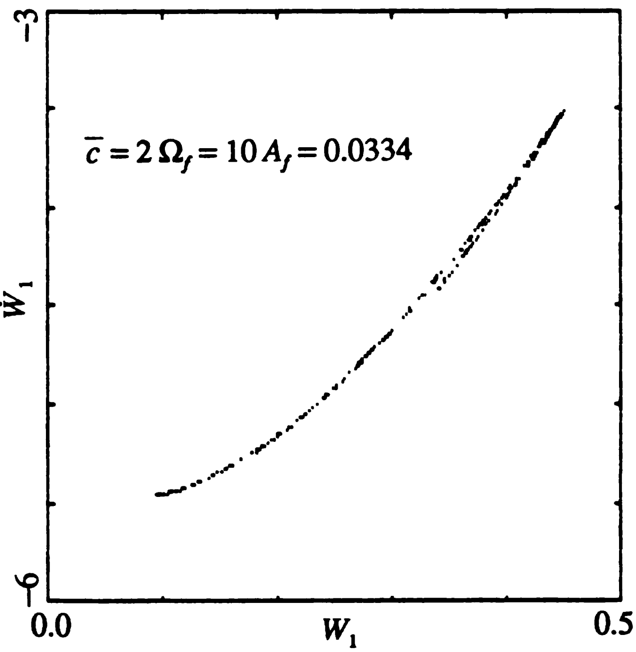

FIG 12. Poincaré map of the cap.

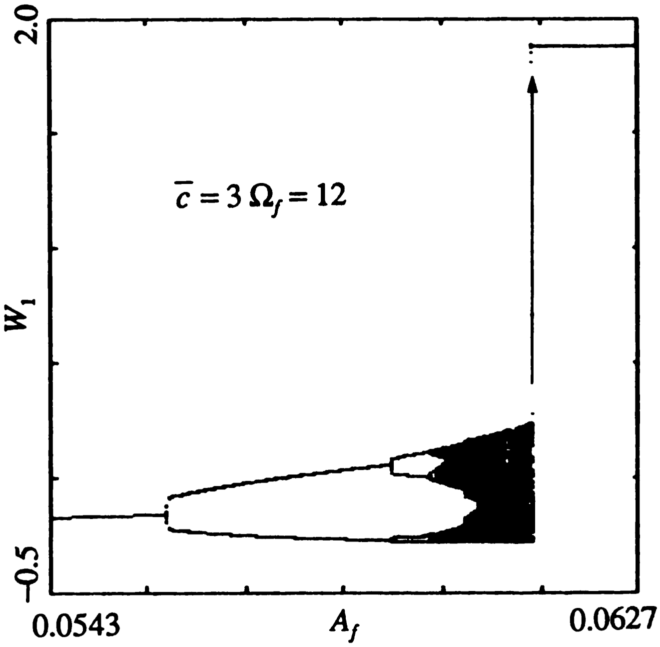

FIG 13. Period-doubling bifurcations leading to chaos and escape from the primary potential well.

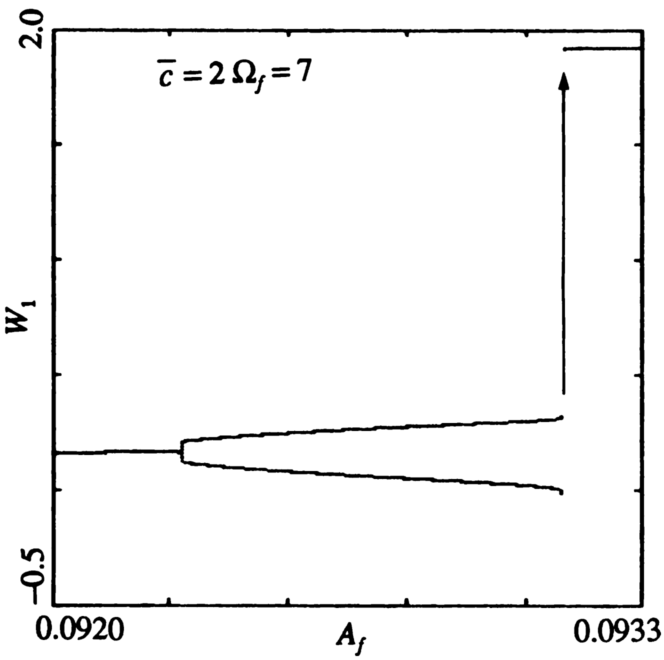

FIG 14. Bifurcation diagram.

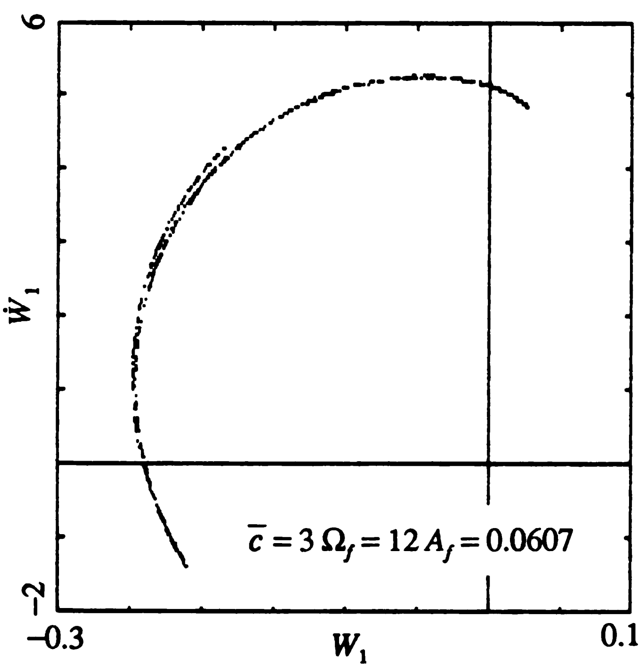

FIG 15. Typical Poincaré map of a chaotic solution just before escape from the primary potential well

The analysis presented here is with respect to spatially axisymmetric disturbances resulting in axisymmetric motions. The mathematical model does not allow asymmetric deformations and hence no conclusions on such motions can be drawn from this analysis. So, stable solutions of Eq. (17) may not be physically realizable if more general motions are allowed. Also, the use of an axisymmetric multi-degree-of-freedom model may change the parameter values at which bifurcations occur. Preliminary results using the multi-degree-of-freedom model presented at the beginning of this work have shown that, in spite of some changes in global behaviour, the basic features observed using this one-degree-of-freedom model still remains.

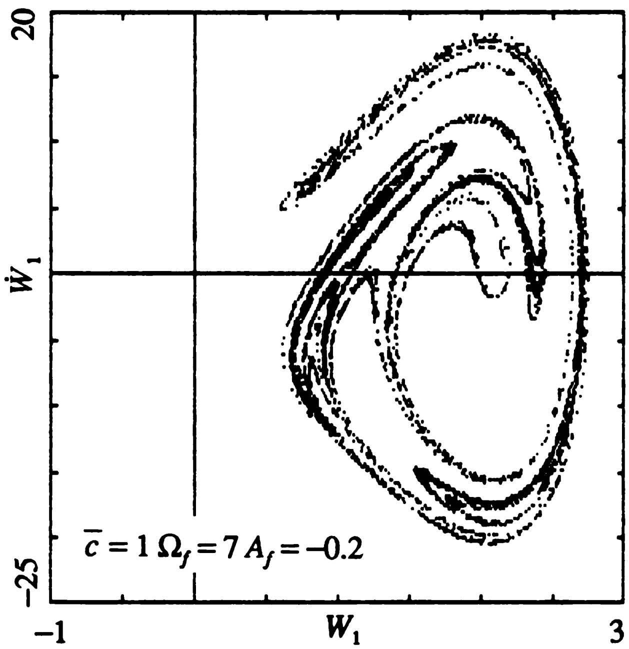

FIG 16. Chaotic attractor. Response associated with large forcing amplitudes.

CONCLUSIONS

Based on Marguerre's shallow shell equations, an accurate multi-mode solution is formulated and applied to study the non-linear vibration characteristics of a pressure-loaded geometrically imperfect spherical cap along its non-linear pre-and-post-buckling paths. It is shown both analytically and by computer simulation that pressure loaded shallow spherical shell exhibit a high degree of non-linearity and that the pre-stress state may alter significantly the natural frequencies and non-linear vibration characteristics of perfect and imperfect shells.

A detailed parametric study, using computer simulations, shows that the cap under harmonic excitation may display complex non-linear behaviour, including jumps and multiple coexisting periodic solutions due to the existence of competing potential wells and the presence of non-linear resonance curves within each well. Additionally, different physical situations are identified in which period-doubling phenomena and chaos can be observed.

Although the present analysis is restricted to clamped spherical caps, the conclusions could perhaps be extended to thin-walled structural elements liable to fold type buckling such as conical caps, cylindrical panels and shallow arches.

REFERENCES

Abramowitz M and Stegun IA, *Handbook of Mathematical Functions*. New York: Dover Publications, 1964.

Archer RR, On the influence of uniform stress states on the natural frequencies of spherical shells, *ASME J. Appl. Mech.* **29**, 502-505 (1962)

Arnold VI, *Geometrical Methods in the Theory of Ordinary Differential Equations*, Springer-Verlag, New York, 1982

Bishop SR, Virgin LN, and Leung DLM, On the computation of domains of attraction during the dynamic modelling of oscillating systems, *Appl. Math. Modelling*, **12**, 503-516 (1988)

Budiansky B, Buckling of clamped shallow spherical shells, *Proc. IUTAM Symposium on the Theory of Thin Elastic Shells*, Delft, The Netherlands, 64-94, 1959

Chen JC and Babcock CD, Nonlinear vibrations of cylindrical shells, *AIAA J.* **13**, 868-876 (1975)

Evensen HA and Evan-Iwanowski RM, Dynamic response and stability of shallow spherical shells subjected time-dependent loading, *AIAA J.* 5, 969-976 (1967)

Flashner H and Guttalu RS, A computational approach for studying domains of attraction for non-linear systems, *Int. J. Non-Linear Mechanics* 23(4), 279-295 (1988)

Gonçalves PB and Croll JGA, *Non-Linear Buckling Response of Pressure Loaded Spherical Caps*, Internal Report, Department of Civil Engineering, PUC-Rio, Brazil, 1990

Gonçalves PB, Vibration characteristics and nonlinear response of shallow spherical caps, *in Structural Dynamics: Recent Advances*, Petyt, Wolfe and Mei (ed.), Elsevier, London, 1991, 781-790

Gonçalves PB and Croll JGA, Axisymmetric buckling of pressure-loaded spherical caps, *ASCE J. Structural Engineering* 118, 970-985 (1992)

Grossman PL, Koplik B, and Yu Y, Nonlinear vibrations of shallow spherical shells, *ASME J. Appl. Mech.* 36, 451-458 (1969)

Guckenheimer J and Holmes P, *Nonlinear Oscillations, Dynamical Systems, and Bifurcations of Vector Fields*, Springer-Verlag, New York, 1983

Holmes P, Nonlinear dynamics, chaos, and mechanics, *Appl. Mech. Rev.* 43(5), Part 2, S23-S39 (1990)

Huang N, Unsymmetrical buckling of thin shallow spherical shells, *ASME J. Appl. Mech.* 31, 447-457 (1964)

Kapitaniak T, Chaotic Oscillations in Mechanical Systems, *Manchester University Press*, Manchester, UK, 1991

Marguerre K, Zur Theorie der gekrümmten platte grosser formänderung, *Jahrbuch der 1939 der deutschen Luftfahrtforschung*, 413 (1939)

Nayfeh AH and Mook DT, *Nonlinear Oscillations*, John Wiley & Sons, New York, 1979

Nayfeh AH and Raouf RA, Non-linear forced response of circular cylindrical shells, *ASME Des. Analysis Plates Shells* 105, 145 (1986)

Nayfeh AH and Balachandran B, Modal interaction in dynamical and structural systems, *Appl. Mech. Rev.* 42(11), Part 2, S175-S201 (1989)

Moon FC, *Chaotic Vibrations: An Introduction for Applied Scientists and Engineers*, John Wiley & Sons, New York, 1987

Palis J and de Melo W, *Geometric Theory of Dynamical Systems: An Introduction*, Springer-Verlag, New York, 1982

Parker ST and Chua LO, *Practical Numerical Algorithms for Chaotic Systems*, Springer-Verlag, New York, 1989

Raouf RA and Nayfeh AH, Non-linear axisymetric response of closed spherical shells to a radial harmonic excitation, *Int. J. Non-Linear Mechanics* 25(5), 475-492 (1990)

Rutishauser H, Solution of eigenvalue problems with the LR-transformations, *National Bureau of Standards Applied Mathematics Series*, 49, 47-81 (1958)

Seydel R, *From Equilibrium to Chaos: Practical Bifurcation and Stability Analysis*, Elsevier, New York, 1988

Thompson JMT and Hunt GW, *Elastic Instability Phenomena*, John Wiley & Sons, Chichester UK, 1984

Thompson JMT and Stewart HB, *Nonlinear Dynamics and Chaos: Geometrical Methods for Engineers and Scientists*, John Wiley & Sons, Chichester, UK, 1987

Urabe M, Galerkin's procedure for nonlinear periodic systems, *Archives Rational Mech. Analysis* 20, 120-152 (1965)

Wiggins S, *Introduction to Applied Nonlinear Dynamical Systems and Chaos*, Springer-Verlag, New York, 1990

Yamada S, Uchiyama K, and Yamada M, Experimental investigation of the buckling of shallow spherical shells, *Int. J. Non-Linear Mechanics* 18, 37-54 (1983)

Yasuda K and Kushida G, Nonlinear forced oscillations of a shallow spherical shell, *Bulletin of the Japanese Society of Mechanical Engineers* 27, 2233-2240 (1984)

Yorke JA, *DYNAMICS - An Iterative Program for IBM PC Clones*, University of Maryland, 1990

Transformation of liposomes: Mechanical behavior and stability

D Pamplona

Departamento de Engenharia Civil Pontifícia Universidade Católica do Rio de Janeiro
Rua Marquês de São Vicente, 225, Gávea 22453-900, Rio de Janeiro, RJ, Brazil

Liposomes are small artificial vesicles of lipid bilayer, wich enclose and are surrounded by water. Morphological transformations in liposomes, starting from a spherical shape, due to changes in the osmotic pressure, have been described in the literature. The first transformation is into a circular biconcave form, afterwards the biconcave side view is maintained, while the front view reveals transformations into elliptical or regular polygonal forms, usually triangular, square or pentagonal. Finite elasticity and the theory of thin shells were used to analyse the behavior of the liposomes under decreasing volume. The biological membrane was considered as a two dimensional fluid layer, exhibiting solid properties to some extent, e.g., elasticity. The stability of the liposmes was studied by using the method of elastic perturbation to obtain the critical pressure for the biconcave transformation and the long liposome tubes. The transformations to elliptical and regular polygonal forms were studied using the linear stability equations of elasticity.

CONTENTS

INTRODUCTION

The mechanical properties and behavior of biological membranes has been studied since 1930. In particular, Evans and Skalak (1980) were engaged in the study of their mechanics and thermodynamics, while Jenkins (1977) and others studied the red blood cells and their equilibrium configurations.

Hotani (1984) has managed to observe the morphological behavior of the liposome by means of dark-field light microscopy. He verified that the change in osmotic pressure in initially spherical liposomes leads to a steady decrease of interior volume. The first transformation is into a cirvular biconcave shape, and then transformations through striking polygonal forms occur, until the liposomes reach the stable forms of thin filaments and small spheres.

In a previous paper Pamplona and Calladine (1993), describe a constitutive law for the lipid bilayer explaining the axially symmetric transformations, which are consistent with Hotani's observed morphological transformations.

The principal aim of this work is to study the changes of the liposomes in a variety of nonsymmetric configurations, and through Donnell's stability equations show that the number of lobes around the circumference, in a form which precedes the jump into two , three or four-armed configurations, would depend on the surface-strain elasticity.

HOTANI'S ESSAYS

Hotani (1984) made small bilayer vesicles of phospholipids with diameters between 7 and 8mm, which enclose and were surrounded by water.

Using dark-field light microscopy, whose lamp heat gradually evaporates the external water, he observed the liposomes transformations. Those transformations are due to the decrease in the interior volume of the vesicles. To some extent he observed that the transformations were reversible, when small amounts of water were added to the microscope slide.

The phospholipids which constitute the observed liposomes are molecules with a hydrophilic "head" which seeks water and a hydrophobic "tail" which shuns water. In an aqueous environment these hydrophobic effects drive the molecules to construct, by self-assembly, spherical bilayers of "heads". In the space of 5 nm between layers of "heads", the "tails" can be free of the contact with the water, Fig 1.

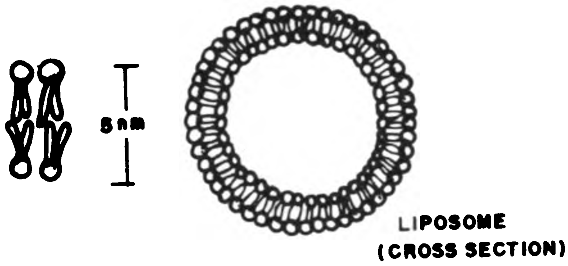

FIG 1 - Schematic representation of a liposome.

In Hotani's tests the original spherical shape first changed into a biconcave shape, after which the vesicle began to undulate in the equator until it suddenly jumped to a two, three, four or five pronged shape. As the reduction of interior volume continues, some of the arms could shrink, or eventually turn in a very long and thin tube, which could break up into a number of small spherical vesicles, as can be seen in Fig 2.

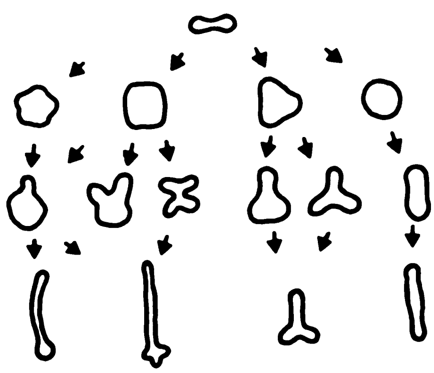

FIG 2 - Schematic of transformations of liposomes, Hotani (1984).

CONSTITUTIVE RELATIONS FOR THE BILAYER

A constitutive equation for the liposome membrane was extensively discussed by Pamplona and Calladine (1993). It is taken here as suggested in their paper.

In order to write the equations, we must consider the circumferential and meridional components of stretch λ_θ, λ_s and the curvatures k_θ^*, k_s^*. As observed by Hotani (1984), if the area of the membrane is assumed to be constant,

$$\lambda_s \lambda_\theta = 1 \,. \tag{1}$$

We assume that the constitutive relation for the stresses is

$$N_\theta^* = T^* + C^* F_1(\lambda) \tag{2}$$

$$N_s^* = T^* + C^* F_2(\lambda) \tag{3}$$

in which N_θ^* and N_s^* are the circumferential and meridional stresses, T^* is closely related to the mean of N_s^* and N_θ^*, and C^* is a constant that relates the stiffness against the change of area under equal bi-axial loading.

The bending constitutive equation is assumed such that:

$$M_s^* = M_\theta^* = B^* \left[k_s^* + k_\theta^* \right] \tag{4}$$

where,
M_s^* and M_θ^* are the meridional and circumferential bending moments and B^* is the "bending stiffness".

DIFFERENTIAL EQUATIONS OF THE PROBLEM AND BOUNDARY CONDITIONS

For the axisymmetric deformations of a liposome with an initial spherical shape of radius, a, the geometrical relations obtained from Fig 3 are

$$r = \sin s \tag{5}$$

$$z = 1 - \cos s \tag{6}$$

$$\frac{d\phi}{dS} = k \tag{7}$$

$$\frac{dR}{dS} = \cos\theta \tag{8}$$

$$\frac{dZ}{dS} = \sin\theta \tag{9}$$

By definition

$$\lambda_s = \frac{dS}{ds} \text{ and } \lambda_\theta = \frac{R}{r} = \frac{R}{\sin s},$$

The variables R, Z, r, k_s, k_θ have been made dimensionless dividing by the undeformed radius a. That is, $r = r^*/a$ etc ...

If, we consider the chain rule,

$$\frac{d()}{dS} = \frac{d()}{ds}\frac{ds}{dS} = \frac{d()}{dS}\lambda_\theta = \frac{d()}{ds}\frac{R}{\sin s} = ()' \frac{R}{\sin s} \,. \tag{10a}$$

Using Eq (1), and (10a)

$$\frac{ds}{dS} = \frac{1}{\lambda_s} = \lambda_\theta = \frac{R}{\sin s} \,. \tag{10b}$$

Considering the equilibrium equations taken directly from Flugge (1962) or Calladine (1983), where the variables have been made dimensionless by multiplying by a^2/B (for example $N_s = N_s^* a^2/B$), after some manipulation and using the constitutive relations, we obtain

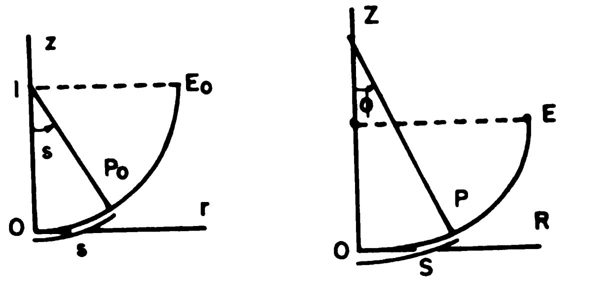

Und shape (Spherical) Def shape (Biconcave)

FIG 3 - Diagrams showing the meridians of a liposome.

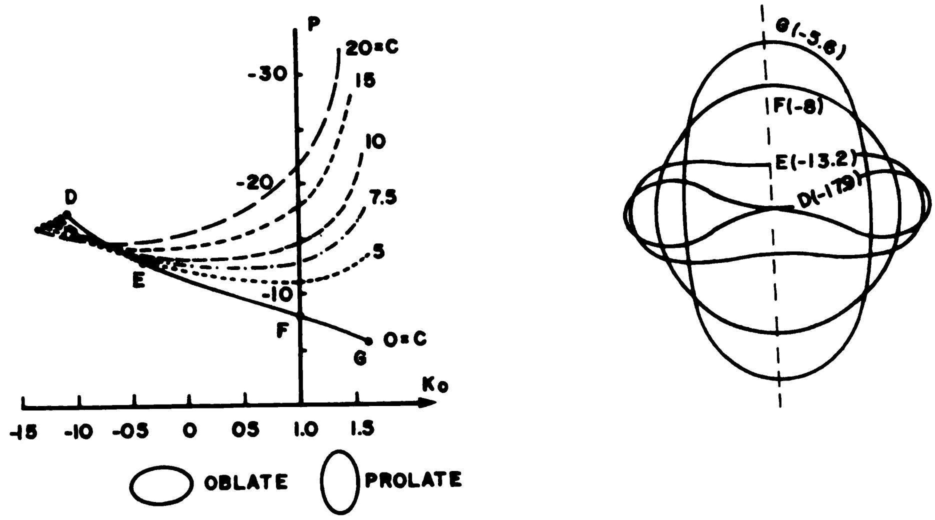

(a) (b)

FIG 4 - Plots of equilibrium paths.

$$AQ = \left[p - (T + CF_1)k - (T + CF_2)\sin\phi/R - Q\cos\phi/R\right]$$
$$Q' = AQ \operatorname{sen} s/R \tag{11}$$

$$AT = -C\,dF_1/ds + \left[C(F_2 - F_1)\cos\phi/R + kQ\right]$$
$$T' = AT \operatorname{sen} s/R \tag{12}$$

$$k' = \left[-Q + \sin\phi\cos\phi/R^2 - k\cos\phi/R\right]\sin s/R \tag{13}$$

$$R' = \cos\phi\sin s/R \tag{14}$$

$$Z' = \sin\phi\ \sin s/R \tag{15}$$

$$\phi' = k\sin s/R \tag{16}$$

Equations (11) - (16) provide us with the 6 differential equations with the 6 unknowns R, Z, ϕ, k, Q and T. Equations (14) - (16) are Eqs (7) - (9) rewritten.

The equations were solved by a standard Runge-Kutta procedure of fourth order joined with a "shooting" method, used with unknown starting values of Q' and k at $s = 0$, until the appropriate conditions at the equator namely,

$$\phi\left(\frac{\pi}{2}\right) = \frac{\pi}{2} \text{ and } Q\left(\frac{\pi}{2}\right) = 0$$

are satisfied.

SOLUTIONS OF THE EQUATIONS

The equations of the previous item where solved for several different values of C, where

$$C = \frac{C^* a^2}{B^*}. \tag{17}$$

Since C^* and B^* are constants of the biological material, we will have a different C^* for each different initial size of the liposome. Some of these solutions are shown in Fig 4.

For every solution the meridional profile of the deformed liposome was generated and Fig 4(b) shows a selection of these cases with $C = 0$.

From observations of Fig 4(a), it is possible to notice that for each C the liposome will maintain the initial spherical form, $K_0 = 1$, until a critical pressure, P_{cr} is reached, when it can assume either the biconcave (prolate) or the peanut (oblate) forms.

The $C = 0$ case, although it seems strange since $a \neq 0$ always, represents the case when the deformations are not reversible anymore. It can be interpreted as the membrane having zero in-plane surface stiffness.

STABILITY: AXIALLY - SYMMETRIC BIFURCATION

As seen in last section, the liposome bifurcates in a prolate or oblate shape at a certain critical pressure.

Performing a first-order perturbation, $\phi^* = \phi^0 - A_0 \sin 2s = s - A_0 \sin 2s$, which involves a linearisation of the Eqs (11) - (16), it is possible to obtain an analytical expression for the critical pressure, namely

$$p_{cr} = -\left(8 + \frac{2}{3} C\right), \qquad (18)$$

what confirms the numerical result shown in Fig 5.

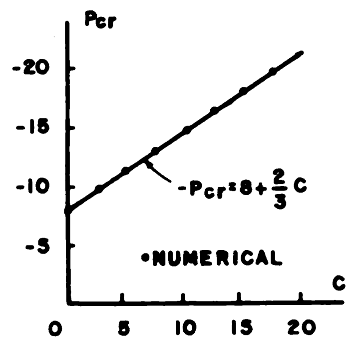

FIG 5 - Bifurcation pressures.

An extensive discussion of these results and comparison with other works done by Helfrich (1976) an Jenkins (1977) is given in Pamplona and Calladine (1993).

STABILITY: OTHER SHAPES

Lobed figures

After obtaining the path for the first bifurcation, which is when the spherical liposome buckles into a biconcave form, it is possible to observe *undulations* in the outer circumference of the deformed liposome. Eventually it formed, typically, a well-defined two-three-four or five lobed figure, Fig 6, and then rather suddenly, this figure would *jump* into a two four or five - pronged shape.

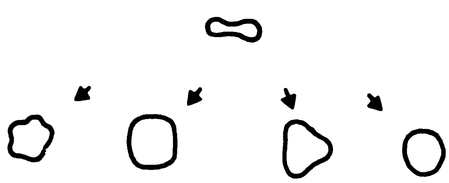

FIG 6 - Further transformations after the biconcave shape, Hotani (1984)

To study the stability at this stage, we choose to perturb the biconcave shape at several different external pressures. Donnell's stability equations, obtained by the second variation of the potential energy, in accordance with the Trefftz criterion, taken directly from Bruch and Almroth (1975), were choosed due to their simplicity. These are

$$(rN_\phi)_{,\phi} + r_\phi N_{\phi\theta,\theta} - r_\phi N_\theta \cos\phi - \qquad (19)$$

$$(rN_{\phi\theta})_{,\phi} + r_\phi N_{\theta,\theta} + r_\phi N_{\phi\theta} \cos \qquad (20)$$

$$\left[\frac{1}{r_\phi}(rM_\phi)_{,\phi}\right]_{,\phi} + 2\left[M_{\phi\theta,\phi\theta} + \frac{r_\phi}{r} M_{\phi\theta,\theta}\cos\phi\right] +$$

$$\left[\frac{r_\phi}{r} M_{\theta,\theta\theta} - (M_\theta \cos\phi)_{,\phi}\right]$$

$$-(rN_\phi + r_\phi N_\theta \sin\phi) = \left[(rN_\phi^0 \beta_\phi)_{,\phi} + (rN_\theta^0 \beta_\theta)_{,\theta}\right] \qquad (21)$$

(^{0}) are determined by the shape that is been perturbed, as the shell is not subjected to torsional loading, $N^0_{\phi\theta} = 0$.

Changing the variables, by introducing Eqs (7) - (8) into Eqs (19) - (21), gives

$$r\frac{\partial N_s}{\partial S} + \frac{\partial N_{s\theta}}{\partial \theta} + (N_s - N_\theta)\cos\phi = 0 \qquad (22)$$

$$r\frac{\partial N_\theta}{\partial S} + \frac{\partial N_{s\theta}}{\partial \theta} + 2\cos\phi\, N_{s\theta} = 0 \qquad (23)$$

$$r\frac{\partial^2 M_s}{\partial S^2} + 2\frac{\partial^2 M_\theta}{\partial\theta\partial S} + \frac{1}{2}\frac{\partial^2 M_\theta}{\partial\theta^2} + 2\cos\phi\frac{\partial M_s}{\partial S} -$$

$$\cos\phi\frac{\partial M_\phi}{\partial S} + 2\frac{\cos\phi}{r}\frac{\partial M_{S\theta}}{\partial\theta} +$$

$$+ \sin\phi\, K_s M_\theta - \sin\phi\, M_s K_s - N_{s\theta} K_s - N_\theta \sin\phi =$$

$$\cos\phi N_s^0 b_s + r\frac{\partial N_s^0}{\partial S}\beta_s + rN_s^0\frac{\partial\beta_s}{\partial S} + N_\theta^0\frac{\partial\beta_\theta}{\partial\theta} \qquad (24)$$

where

$$N_s = C\left[u_{,s} + \frac{w}{r_\phi} + \frac{\mu}{r}(v_{,\theta} + u\cos\phi + w\sin\phi)\right] \qquad (25)$$

$$N_\theta = C\left[\frac{1}{r}(v_{,\theta} + u\cos\phi + w\sin\phi) + \mu\left(u_{,s} + \frac{w}{r_\phi}\right)\right] \qquad (26)$$

$$N_{S\theta} = \frac{C(1-\mu)}{2}\left[v_{,s} - \frac{v\cos\phi}{r} + \frac{u_{,\theta}}{r}\right] \qquad (27)$$

$$M_s = -D\left[w_{,ss} + \frac{\mu}{r}\left(\frac{w_{,\theta\theta}}{r} + w_{,s}\cos\phi\right)\right] \qquad (28)$$

$$M_\theta = -D\left[\frac{1}{r}\left(\frac{w_{,\theta\theta}}{r} + w_{,s}\cos\phi\right) + \mu w_{,ss}\right] \qquad (29)$$

$$M_{S\theta} = -\frac{D(1-\mu)}{2}\left[\frac{w_{,s\theta}}{r} - w_{,\theta}\frac{\cos\phi}{r^2}\right] \qquad (30)$$

C, D are the extensional and bending stiffness parameters and μ is the Poisson's ratio. The quantities u, v and w are the incremental quantities of the middle-surface displacements components, u^*, v^* and w^*, in the meridional, circunferencial and transversal directions, namely

$$u^* = u^0 + u$$
$$v^* = v^0 + v \qquad (31)$$
$$w^* = w^0 + w .$$

The following increments, satisfying the boundary conditions, where choosen:

$$u = A_3 \sin 2\phi \sin n\theta$$
$$v = A_2 \sin \phi \cos n\theta \qquad (32)$$
$$w = A_1 \sin^2 \phi \sin n\theta$$

where n is the number of lobes in the equator.

To solve the differential problem, obtained when Eqs (25) - (30) are introduced in Eqs.(22) - (24), the Galerkin method was used. Since we are looking for non-vanishing values of A_1, A_2 and A_3, relations between the critical pressure p and the number of buckling lobes, n, can be achieved, as can be seen in Fig 7.

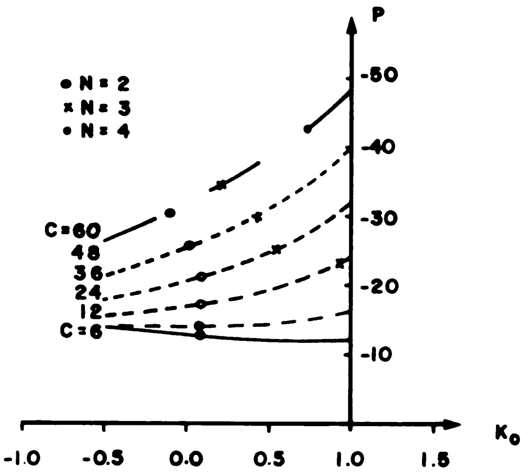

FIG 7 - Critical pressures on the plots of equilibrium paths.

As expected when Donnell's equations are used, for small values of n the critical pressure obtained is higher then it should be, as can be seem in Table 1, for the critical pressure of the liposome buckling from the spherical to the biconcave form.

C*	Numerical	Equation 18	Donnell
6	-12	-12	-15.00
12	-16	-16	-19.00
24	-24	-24	-27.15
36	-32	-32	-36.30
48	-40	-40	-43.45
60	-48	-48	-51.75

TABLE 1 - Critical pressure for the spherical liposome.

Although it is clear that the critical pressures obtained in this item are not the right ones, for the purpose of this work and for the sake of simplicity we accept the results. Since it was the intent to see if the number of lobes or undulations around the circumference, in a form which preceds the jump into a two, three or four-armed configurations, would depend on the surface - strain elasticity via constant C, it seems reasonable to us, to affirm it based in this study. For, if the value of C were to be confirmed effectively to zero, as in the studies done by Sekimura and Hotani (1989), there would be no feature on which the number of lobes could depend.

Long tubes

Performing a first-order perturbation, $\phi^* = \phi^0 + \phi = \pi/2 + A_4 \sin 2\pi x / b$, which involved the linearization of the various equilibrium equations for a cylindrical shell it was possible to observe that a long tube of liposome material, e.g.

$$M_\theta = M_s = B(k_\theta + k_s)$$

would spontaneously bifurcate. For b equal to the inital circumference of the tube, $2\pi a$, as can be seen in Fig 8.

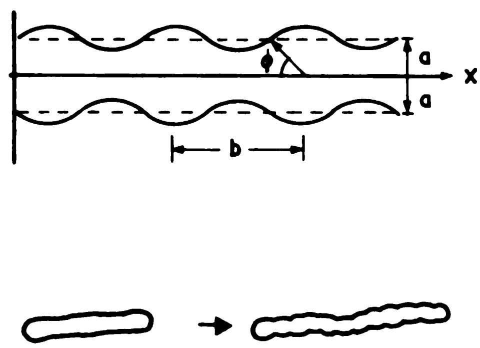

FIG 8 - Long tubes transformation.

In a subsequent paper we shall describe our studies on elongated axi-symmetric configurations of liposomes.

CONCLUSIONS

It seams desirable to develop a "physical" understanding of the shape-change of the vesicles made by lipid bilayers. In our first paper (Pamplona and Calladine, 1993) it was possible obtain a constitutive law for the lipid-bilayer and explain the axially symmetric transformations. In this paper it was possible to show that the number of lobes around the circumference, which precede the jump would depend on the surface-strain elasticity. It is concluded that if the surface strain were not considered, as has been done by other authors, the sphere would buckle in a prolate shape, not in a biconcave as it actually does. There then would be no feature on with the number of lobes would depend.

Although the cirtical pressures obtained throught Donnell's equations are higher then the correct ones, it seems reasonable to affirm a connection between the inital size of the liposome and the number of lobes of the transformation.

ACKNOWLEGMENT

The author wishes to express her appreciating to the Brazilian Government which, though the Brazilian Council for Scientific and Technical Development, provided financial support during the sabbatical leave when this work with Professor Calladine began. Expressing her gratitude for Professor Calladine, for the opportunity to work with him, which has been a very rewargidng professional experience.

REFERENCES

Hotani S (1984) Transformation Pathways of Liposomes, *J Mol Biol* **178**, 113-120.

Evans E A and Skalak R (1980) *Mechanics and thermodynamics of biomembranes*, CRC-Press.

Dueling H J and Helfrich W (1976) Red blood cell shapes as explained on a basis of curvature elasticity, *Biophysical Journal* **16**, 861-868.

Jenkins J T (1977) Static equilibrium configurations of a model red blood cell, *J Math Bilogy* **4**, 149-169.

Pamplona D and Calladine C R (1993) The Mechanics of Axially Symmetric Liposomes, *J Biomech Eng* (accepted for publication).

Flugge W (1962) *Stresses in Shells*, Springer, Berlin.

Calladine C R (1983) *Theory of Shell Structures*, University Press, Cambridge.

Bruch D O and Almroth B O (1975) *Buckling of Bars, Plates and Shells*, Itália, MacGraw-Hill.

Sekimura T and Hotani S (1989) Shape formation of liposomes and the principle of least bending energy of membranes, *Forma* **4**, 27-34.

Coupling of a state-space inflow to nonlinear blade equations and extraction of generalized aerodynamic force mode shapes

Donizeti de Andrade

Instituto Tecnológico de Aeronáutica, CTA, São José dos Campos, SP, 12228-900, Brazil

David A Peters

Washington University, St Louis MO 63130-4899

The aeroelastic stability of helicopter rotors in hovering flight has been investigated by a set of generalized dynamic wake equations and hybrid equations of motion for an elastic blade cantilevered in bending and having a torsional root spring to model pitch-link flexibility. The generalized dynamic wake model employed is based on an induced flow distribution expanded in a set of harmonic and radial shape functions, including undetermined time dependent coefficients as aerodynamic states. The flow is described by a system of first-order, ordinary differential equations in time, for which the pressure distribution at the rotor disk is expressed as a summation of the discrete loadings on each blade, accounting simultaneously for a finite number of blades and overall rotor effects. The present methodology leads to a standard eigenanalysis for the associated dynamics, for which the partitioned coefficient matrices depend on the numerical solution of the blade equilibrium and inflow steady-state equations. Numerical results for a two-bladed, stiff-inplane hingeless rotor with torsionally soft blades show the importance of unsteady, three-dimensional aerodynamics in predicting associated generalized aerodynamic force mode shapes.

LIST OF SYMBOLS

a	lift curve slope (per radian)
a_n^m, b_n^m	induced flow expansion coefficients in the rotating frame, nondimensional
$\bar{a}_1^0$	steady uniform inflow (steady-state a_1^0)
$[\mathcal{DM}], [\mathcal{C}], [\mathcal{K}], [\mathcal{M}]$, and $[\mathcal{GF}]$	coefficient matrices of blade state-variables, Fig 7
$[am], [qs], [k]$	apparent mass, quasi-steady, and inflow stiffness matrices, Fig 7
B_{nl}^m	$= (-1)^{(n+l-2m-2)/2} \sqrt{\frac{K_n^m}{K_l^m}} \sqrt{(2n+1)(2l+1)} \cdot \sum_{q=m,m+2,\ldots}^{n-1} \frac{\pi}{2} K_q^m \frac{(2q-1)}{(l-q)(l+q+1)}$
K_n^m	$= \frac{2}{\pi} \frac{(n+m-1)!!\,(n-m-1)!!}{(n+m)!!\,(n-m)!!}$
m, n	harmonic and shape function numbers, respectively
N	number of modified orthogonal Duncan polynomials in blade modal expansions for each of the elastic torsion, flap bending, and lead-lag bending deflections
Q	number of rotor blades
R	rotor radius, m
$\bar{r}$	blade radial coordinate, $\bar{r} = r/R$
$\bar{t}$	nondimensional time, $\bar{t} = \Omega t$
U_∞	free-stream velocity component of the blade section, m/s
$\left[V_n^m\right]$	matrix of momentum theory flow parameters
y', z'	blade coordinates associated with the deformed blade reference frame, along unit vectors $\mathbf{j}', \mathbf{k}'$
α	local blade angle of attack
$\bar{\lambda}$	induced flow at the rotor disk due to shed wake, positive downwards, $\bar{\lambda} = \lambda/(\Omega R)$
$\phi_n^m(\bar{r})$	$= \sqrt{(2n+1)\frac{\pi}{2}K_n^m} \sum_{q=m,m+2,\ldots}^{n-1} \bar{r}^q \frac{(-1)^{(q-m)/2}(n+q)!!}{(q-m)!!\,(q+m)!!\,(n-q-1)!!}$
$\bar{\psi}$	azimuthal position on the rotor disk for induced inflow expansion in the rotating frame, *rad*
$\hat{\psi}_q$	relative position of q-th blade, $\hat{\psi}_q = \bar{t} + \frac{2\pi}{Q}(q-1)$
Ω	rotor rotational speed, *rad/s*
$\overset{*}{(\,)}$	$= d/d\bar{t}$

part of "MECHANICS PAN-AMERICA 1993" edited by MRM Crespo da Silva and CEN Mazzilli
ASME Reprint No AMR134

INTRODUCTION

The physical environment of helicopter rotor blades has been investigated for many years. At this time, it is well known that a continuous pumping of a substantial mass of air (inflow) through the rotor disk (due to the existence of a shed wake below the helicopter rotor) implies that its aerodynamic field, in hovering or forward flight, is very different and much more complicated than its fixed-wing counterpart. For performance predictions one can rely on average values of the wake geometry corresponding to a given configuration and operating condition. When dynamics is present though, as is the case of aeroelastic investigations, the task involves strong coupling of aerodynamic and structural dynamic loads. The advent of hingeless rotors with very flexible blades has made even stronger such inherent coupling of loads acting upon helicopter rotor blades. A realistic model for the aeroelastic behavior of the helicopter rotor can be summarized as shown in the flow-chart in Fig 1.

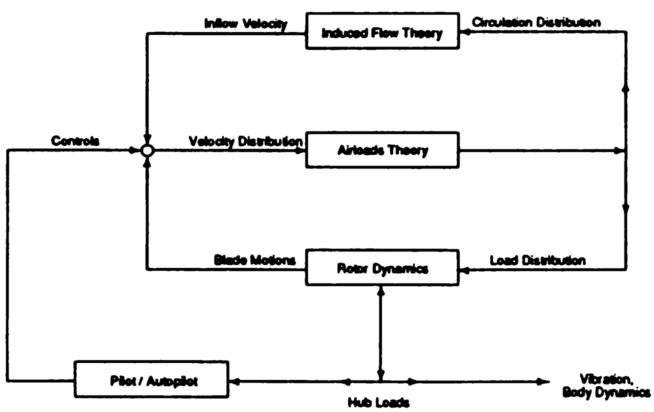

FIG 1. Aeroelastic environment of helicopter rotor.

At least three basic technology modules must be coupled within an aeroelastic analysis of the helicopter rotor (Peters and Su, 1991): 1) a structure dynamic model, 2) an induced flow model, and 3) an airloads model. The double feedback loop in Fig 1 emphasizes the important coupling between wake dynamics and rotor dynamics through the predicted airloads, that become the forcing functions for both the structure and induced flow.

In spite of this, classically, the induced flow model has often been treated with a two-dimensional, quasi-steady aerodynamics, including a uniform flow distribution (Hodges and Ormiston, 1976, and Hodges, 1976). That modeling lacks some physical information, such as three-dimensional tip relief and unsteady wake vortex alignment, which are very important in predicting aerodynamic damping. A much more realistic approach is three-dimensional vortex lattice unsteady aerodynamics, for which global effects and time history of circulation would be taken into account. These, however, are not amenable to eigenanalysis.

In the late 1980's, research work has attempted to bridge the critical gap between structural and aerodynamic operators used in aeroelastic applications such as those in Hodges and Ormiston (1976) and Hodges (1976). In Kwon (1988), and Kwon et al (1991), a panel code is formulated and coupled, respectively, with nonlinear blade models of Hodges and Ormiston (1976), and Hodges (1976), both based on the original Hodges and Dowell (1974) equations. This panel model is based on a piecewise constant distribution of sources and doublets, with a prescribed tip-vortex geometry and calculated inner wake. A Fourier analysis associated with a moving block technique is employed to obtain damping and frequency of the most lightly damping mode, which has the frequency near the fundamental lead-lag bending frequency of the rotating blade. The fact that a standard eigenanalysis is out of the question (meaning that only the damping and frequency of the most lightly damped mode can be obtained) and that excessive computer memory requirements are inevitable to accomplish convergence (since small time steps and many wake layers underneath the rotor must be suitably established) imposes innate limitations to the use of this method in aeroelastic stability investigations. Nevertheless, the method is useful, and results show the importance to the three-dimensional and unsteady effects in the prediction of lead-lag damping.

More recently, the generalized dynamic wake model developed by Peters and He (1987) and He (1989) has been coupled with Hodges (1976) nonlinear blade model. This blend is done in such a way that the aerodynamic forces and moments in the blade equations, as well as the pressure coefficients in the generalized dynamic inflow equations, are obtained as explicit nonlinear functions of the blade deformation and generalized dynamic inflow state variables, leading to standard eigenanalysis (de Andrade, 1992, and de Andrade and Peters, 1992). Consequently, reliable and computationally efficient results are expected, setting the generalized dynamic wake methodology as an appropriate alternative to use in rotor design and optimization.

As detailed in de Andrade (1992), the thick panel code (Kwon, 1988, and Kwon et al, 1991) requires large computing times and memory for coupling with Hodges-Dowell equations. This makes it difficult to perform any detailed study of the damping mechanisms with this code. On the other hand, the present state-space three-dimensional wake methodology applied to the Hodges-Dowell equations gives essentially identical answers for flap-lag-torsion damping as obtained with the panel code, but at 1/50th of the computing cost.

The generalized dynamic wake model has been extensively correlated with Kwon's thick panel aerodynamics (Kwon e al, 1991) and with the experimental results from Sharpe (1986). Complete details concerning the validation of the flap-lag-damping results obtained through this approach can be found in de Andrade and Peters (1992). Most recently, a deep investigation trying to explain the typical errors still present on both generalized dynamic wake model and panel aerodynamics flap-lag-torsion damping results with respect to experiments has been conducted (de Andrade and Peters, 1993). That research shows that correlations with experiments can be improved considerably when correct lift and drag coefficients

$$\begin{bmatrix} \ddots & & & \\ & [K_n^m] & & \\ & & \ddots & \\ & & & [K_n^m] \\ & & & & \ddots \end{bmatrix} \begin{Bmatrix} \vdots \\ \{a_n^m\} \\ \vdots \\ \cdots\cdots \\ \vdots \\ \{b_n^m\} \\ \vdots \end{Bmatrix}^{*} + \begin{bmatrix} \ddots & & \ddots & \\ [B_{nl}^m][V_n^m] & & -m[K_n^m] & \\ & \ddots & & \ddots \\ \ddots & & \ddots & \\ m[K_n^m] & & [B_{nl}^m][V_n^m] & \\ & \ddots & & \ddots \end{bmatrix} \begin{Bmatrix} \vdots \\ \{a_l^m\} \\ \vdots \\ \cdots\cdots \\ \vdots \\ \{b_l^m\} \\ \vdots \end{Bmatrix} = \frac{1}{2} \begin{Bmatrix} \vdots \\ \{\hat{\tau}_n^{mc}\} \\ \vdots \\ \cdots\cdots \\ \vdots \\ \{\hat{\tau}_n^{ms}\} \\ \vdots \end{Bmatrix}$$

FIG 2. Generalized dynamic wake equations in the rotating system.

based on the experimental Reynolds number are introduced, and when correction for recirculation in the test chamber is accounted for.

The purpose of this paper is to explore in detail the importance of unsteady three-dimensional aerodynamic effects in aeroelastic stability of helicopter rotors in hovering flight. With the present generalized dynamic wake model this task is naturally accomplished, since the solution approach leads directly to all eigenvalues and eigenvectors associated with a given rotor operating condition. Knowing the eigenvector associated with a given mode of interest, extraction of inflow distribution, blade displacements, and generalized aerodynamic force mode shapes, for example, is straighforward.

GENERALIZED DYNAMIC WAKE EQUATIONS IN THE ROTATING SYSTEM

The generalized dynamic wake equations formulated by Peters and He (1987, 1989) are derived from the basic potential flow conservation laws, where the spatial variation of pressure across the rotor is related to the variation of velocity at the disk (i.e., to the fluid flow momentum flux) and to the acceleration of the fluid flow through linear matrix operators. Particularized for hovering flight and written in the rotating system, they are given as in Fig 2.

Such a set of first-order differential equations is based on a nondimensional induced flow distribution at the rotor disk expanded in a entire set of harmonic and radial shape functions, including undetermined time dependent coefficients as aerodynamic states:

$$\bar{\lambda}(\bar{r}, \hat{\psi}, \bar{t}) = \sum_{m,n} \phi_n^m(\bar{r}) \left[a_n^m(\bar{t}) \cos(m\hat{\psi}) + b_n^m(\bar{t}) \sin(m\hat{\psi}) \right] \quad (1)$$

This induced flow representation not only offers a complete description of the flow, which is suitable to incorporate three-dimensional effects, but also handles higher harmonic dynamics, by the truncation at any harmonic of interest.

Within the first and second terms on the left-hand-side of Fig 2 one observes, respectively, the "apparent mass" and "quasi-steady" operators. The former is obtained in closed form and includes diagonal matrices as elements. In Fig 2, for the cosine part m assumes values 0, 1, 2,..., while for the sine part m has values 1, 2, 3,... The pressure distribution at the rotor disk, as seen on the right-hand-side of Fig 2, is modeled as a summation of the discrete loading on each blade, accounting simultaneously for a finite number of blades and overall rotor effects. For instance, the cosine part of the wake forcing functions has the form

$$\hat{\tau}_n^{mc} = \frac{1}{\pi} \sum_{q=1}^{Q} \left[\int_0^1 \phi_n^m(\bar{r})\, J_0(m\hat{b})\, \frac{L_S}{\rho_\infty \Omega^2 R^3}\, d\bar{r} \right] \cos(m\hat{\psi}_q) \qquad m \neq 0 \quad (2)$$

L_S is the total wake-generating circulatory lift at the blade section (Peters and Su, 1991; He, 1989, and de Andrade, 1992) which can be evaluated from a lift theory, and ρ_∞ is the air density (kg/m^3). The J_0 term arises from matching the present inflow model with Theodorsen lift theory (Peters and Su, 1991, and de Andrade, 1992). This is accomplished when a particular chordwise pressure distribution, which results in no induced flow on the airfoil due to bound vorticity, is applied with the inflow distribution defined in Peters' and He's model (1987, 1989). As discussed in Peters and Su (1991), when one deals with slender (high aspect-ratio) blades, it is reasonable to set J_0 to unity. This is equivalent to a lifting-line approximation for the lift and induced drag, with the inflow computed on the lifting-line. As a consequence, the nondimensional pressure expansion coefficients at the right-hand side of Fig 2 have their expressions simplified considerably. The present research is based on the above assumptions.

THE HINGELESS ROTOR BLADE MODEL AND THE BLADE EQUATIONS OF MOTION

Blade Configuration

The blade configuration adopted in this research is shown in Fig 3. The parameters of interest in this study are precone, β_{pc}, the inclination of the pitch bearing with respect to the plane of rotation (positive upwards); droop, β_d, the inclination (positive downwards at zero pitch angle) of the blade segment outboard of the pitch change bearing; and blade root offset, e_1, the distance between the center of rotation and the root of the blade. The blade is cantilevered in bending, and the kinematics of the pitch-link connection between the outboard segment of the blade and the swashplate control system is modeled by a torsional root spring.

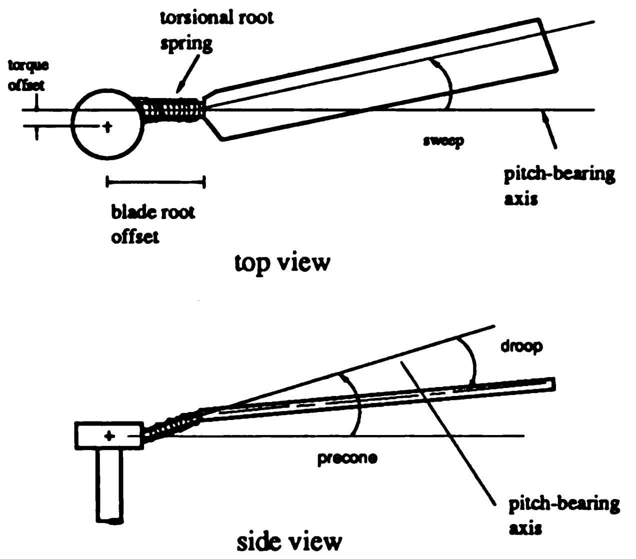

FIG 3. Rotor blade configuration.

The blade bending deflections v and w are defined parallel to and fixed to the sectional principal axes at the root end of the blade (along y and z axes), as sketched in Fig 4. This means that the lead-lag (v) and flap (w) deflections are literal inplane and out-of-plane displacements only at zero thrust condition, because they direction is established chordwise after the rigid body rotations, including collective pitch at the root (θ_0) and the pitch due to root spring deformation ($\Phi(t)$), are taken. The axial deflection u and the blade elastic torsion deformation ϕ are also shown in Fig 4.

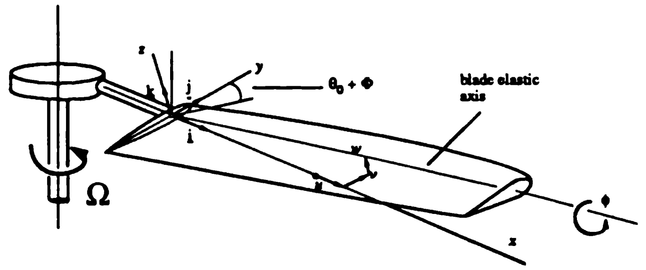

FIG 4. Orientation of blade elastic displacements.

Blade Equations of Motion

The rotor is treated in isolation; no couplings with the helicopter body degrees of freedom are accounted for. The blade equations of motion are derived from Hamilton's Principle. The cross section structural and inertial properties are assumed doubly symmetric with respect to the blade cross section principal axes and no strain energy from restrained torsional warping is considered. Furthermore, in this research, mass axis, tension axis, and aerodynamic center offsets from the elastic axis are all zero. The struc... and inertial operators are taken from Hodges and ... 1), and Hodges (1976), respectively. The aero... or is based on thin airfoil theory, in a way ... vs a time domain analysis, with a three... -induced flow governed by the generalized dynamic inflow model in Fig 2, according to the development presented in de Andrade (1992). The airfoil lift curve slope and the profile drag coefficients are assumed constant. The blade section is pivoted at an axis at its quarter-chord point (i.e., the x' axis normal to y' and z' axes in Figs 5-6; it coincides with the blade elastic axis intersection at the airfoil and is also the airfoil aerodynamic center in the context of thin airfoil theory). The deformed blade section is pitching at an angular speed $\dot{\varepsilon}$ about x' axis, as shown in those figures.

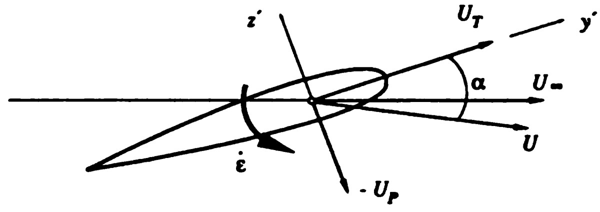

FIG 5. Unsteady motion of the blade section.

From Fig 5 it can be seen that the airfoil velocity components along the principal axes y' and z' (through the shear center of the section) are $U_T\,\underline{j}'$ and $U_P\,\underline{k}'$. α is the instantaneous angle of attack of the blade section and it is defined as the angle between the chordline and the resultant velocity at the cross section, $\underline{U} = U_T\,\underline{j}' + U_P\,\underline{k}'$. Also, the lift per unit of length (circulatory, L_C, and noncirculatory, L_{NC}) and pitching moment per unit of length (circulatory and noncirculatory) are expressed in terms of U_T, U_P and $\dot{\varepsilon}$. Since U_T, U_P and $\dot{\varepsilon}$ can be expressed in terms of the blade elastic displacements, v, w, and ϕ, the root pitch Φ, and the inflow expansion coefficients a_n^m and b_n^m, the generalized aerodynamic forces and moments, L_u, L_v, L_w, M_ϕ and the integral over the blade length of the moment due to the root spring, M_Φ, are expressed in terms of blade displacements and inflow expansion coefficients as well.

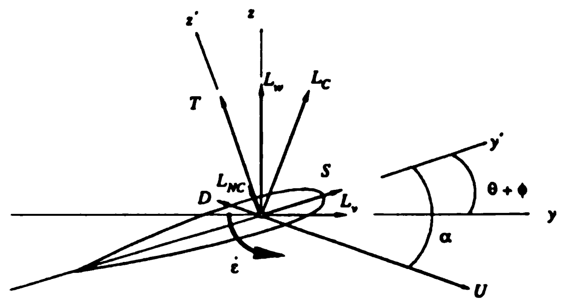

FIG 6. Orientation of aerodynamic loads.

In the derivation of the blade equations a ordering scheme is employed, based on a small parameter of the order of magnitude of the bending slopes. Resulting equations are simplified by integration of the variational equation for the blade radial displacement to obtain the blade tension and by an expression of tension and radial displacements in terms of remaining blade displacements and torsional root spring deformation. In summary, a set of nonlinear hybrid equations of motion, consisting of one integro-partial differential equation for the root pitch, and three integro-partial differential equations each for flapwise and chordwise bending and elastic torsion, is obtained.

Concerning the airloads-inflow coupling, three points should be mentioned: 1) under the assumptions of the thin airfoil theory ($U \approx U_\infty$), and up to the second order, the wake-generating circulatory lift is taken as the circulatory part of L_w in this research (rigorously, one should take the circulatory lift normal to the rotor disk, along the induced flow direction, for all operational conditions; 2) a lifting-line approximation is taken by setting J_0 to unity in the nondimensional pressure expansion coefficients (Fig 2 and Eq (2)); and 3) under thin airfoil theory, the lifting-line is placed at the blade quarter-chord, which, typically, has a constant azimuthal coordinate for a rectangular blade. Since $\widehat{\psi}_q$, the azimuthal position of the q-th blade, is defined at the blade midchord for the compatibilization with Theodorsen's lift theory (Peters and Su, 1991, and de Andrade, 1992), it would, rigorously, be a function of the radial coordinate $\bar{r}$. However, numerical results from Peters and Su (1991) show that this skewing (yawing) has a negligible effect on the inflow computation.

COUPLING INFLOW AND BLADE EQUATIONS OF MOTION - SOLUTION APPROACH

The first step towards solution is to simplify the blade nonlinear hybrid equations by the assumption of uniform mass and stiffness, and to obtain nonlinear ordinary differential equations in time by applying Galerkin's method. Before that, the blade nondimensional displacements in lead-lag, flap (both nondimensional on $(R - e_1)$), and torsion are expanded, respectively, as:

$$\left.\begin{aligned} \bar{v} &= \sum_{i=1}^{N} [V_{0i} + \Delta V_i(\bar{t})]\Psi_i(\bar{x}) \\ \bar{w} &= \sum_{i=1}^{N} [W_{0i} + \Delta W_i(\bar{t})]\Psi_i(\bar{x}) \\ \phi &= \sum_{i=1}^{N} [\Phi_{0i} + \Delta\,\Phi_i(\bar{t})]\Theta_i(\bar{x}) \end{aligned}\right\} \qquad (3)$$

Each expansion assumes small unsteady perturbation about steady equilibrium condition; the variables with "zero" indices are equilibrium generalized coordinates, and the ones with "delta" are perturbation coordinates. Modified orthogonal Duncan polynomials are taken as mode shapes ($\Psi_i(\bar{x})$ for lead-lag and flap bending and $\Theta_i(\bar{x})$ for torsion).

The pitch angle due to the root spring is expanded about the equilibrium condition as $\Phi = \Phi_0 + \Delta\,\Phi(\bar{t})$, with no dependence on the blade spanwise coordinate. Also, the inflow expansion coefficients are split into steady-state and perturbation part as:

$$a_n^m(\bar{t}) = \bar{a}_n^m + \tilde{a}_n^m(\bar{t}) \text{ and } b_n^m(\bar{t}) = \bar{b}_n^m + \tilde{b}_n^m(\bar{t}) \qquad (4)$$

Modal Equilibrium Equations

The steady-state part of the inflow equations can be expressed in the following short-hand notation:

$$\begin{bmatrix} [B_0][V_0] & -[K] \\ [K]^T & [B_1][V_1] \end{bmatrix} \begin{Bmatrix} \{\bar{a}_n^m\} \\ \{\bar{b}_n^m\} \end{Bmatrix} = \frac{1}{2} \begin{Bmatrix} \{\bar{\tau}_n^{mc}\} \\ \{\bar{\tau}_n^{ms}\} \end{Bmatrix} \qquad (5)$$

Since at steady-state the "antisymmetric" part of the pressure ($\bar{\tau}_n^{ms}$) is zero, the second row partition in Eq. (4) can be solved for the $\bar{b}$'s as:

$$\{\bar{b}_n^m\} = -[V_1]^{-1}[B_1]^{-1}[K]^T\{\bar{a}_n^m\} \qquad (6)$$

for $m = 0, Q, 2Q, 3Q, \ldots$

Then, substituting back in the first "row", a system of S nonlinear algebraic equations is obtained (S is the number of inflow steady-state expansion coefficients taken), that can be represented in the following form:

$$\bar{a}_n^m = \bar{a}_n^m(V_{0j}, W_{0j}, \Phi_{0j}, \Phi_0, \bar{a}_n^m) \qquad (7)$$

As observed in the above representation, the $\bar{a}$'s are nonlinear related to all blade equilibrium generalized coordinates, and to the $\bar{a}$'s themselves. This is a consequence of the use of the nonlinear version of the inflow equations (Peters and HaQuang, 1988), which defines the momentum theory flow parameters as function of the steady, uniform inflow as:

$$V_1^0 = V_T = \sqrt{3}\,\bar{a}_1^0; \qquad V_n^m = 2V_T = 2\sqrt{3}\,\bar{a}_1^0, \qquad (8)$$

$$(n,m) \neq (1,0)$$

Also, the steady-state lift, within the $\bar{\tau}_n^{mc}$ involves nonlinear relation between flap and lead-lag.

In the blade equations, by substituting only the equilibrium and steady-state quantities and dropping out all time derivative terms, a set of $(3N + 1)$ nonlinear equations for ($\delta V_{0i}, \delta W_{0i}, \delta\Phi_{0i}$, and $\delta\Phi_0$) is established.

Collecting altogether blade and inflow steady-state equations, a set of $((3N + 1) + S)$ nonlinear algebraic equations in terms of the equilibrium parts of the blade generalized coordinates and the inflow steady-state expansion coefficients $\bar{a}$'s is obtained.

$$\begin{Bmatrix} \{\Delta Z\} \\ \{\Delta Z^{*}\} \\ \begin{Bmatrix} \tilde{a}_n^m \\ \tilde{b}_n^m \end{Bmatrix} \end{Bmatrix}^{*} = \begin{bmatrix} 0 & I & 0 \\ -[\mathcal{M}]^{-1}[\mathcal{K}] & -[\mathcal{M}]^{-1}[\mathcal{C}] & -[\mathcal{M}]^{-1}[\mathcal{k}] \\ -[\mathfrak{am}]^{-1}[\mathfrak{QS}] & -[\mathfrak{am}]^{-1}[\mathfrak{AM}] & -[\mathfrak{am}]^{-1}[\mathfrak{qs}] \end{bmatrix} \begin{Bmatrix} \{\Delta Z\} \\ \{\Delta Z^{*}\} \\ \begin{Bmatrix} \tilde{a}_n^m \\ \tilde{b}_n^m \end{Bmatrix} \end{Bmatrix}$$

FIG 7. Linearized perturbation equations in state-variable form.

Eigenproblem for the Perturbation Variables

The perturbation equations are obtained by substituting the equilibrium (steady-state) and perturbation quantities, subtracting off the equilibrium (steady-state) equations, and discarding all nonlinear products of dynamic perturbation quantities. The coupled linearized perturbation equations can be set into a state-variable form as given in Fig 7. In that equation, the second row partition comes from the blade perturbation equations and the third row partition is from the unsteady inflow perturbation equations. At the right-hand-side of the equation, one can observe the stability matrix; its elements are constant partitioned coefficient matrices which depend on the solution of the equilibrium/steady-state equations (these matrices are defined in de Andrade (1992)). The column vector $\{\Delta Z\}$ contains the perturbation modal generalized coordinates from all blades. They are coupled through the inflow pressure functions, Eq (2), that involve summations over all the blades. The stability of small motions about the equilibrium operating condition is determined by the eigenvalues of the stability matrix. It is interesting to observe that by removing last partitioned row and partitioned column of the equations within Fig 7, one basically recovers the same stability problem obtained by Hodges and Ormiston (1976) in the 70's under a quasi-steady aerodynamic model.

Eigenproblem Solution Approach

To solve for the eigenproblem, a "harmonic-assumed approach" is adopted (de Andrade, 1992). Under this solution scheme, one takes advantage of multiblade coordinate transformation, and the equations of motion are written for a reference blade, with the blade modes of vibration (collective, differential, cyclic) assumed beforehand, by keeping selected harmonic numbers in the inflow expansion. This means that the effects of all blades are accounted automatically as the selected harmonic numbers in the inflow expansion are varied.

Taking, for example, a 2-bladed rotor, to obtain the dynamics associated with the collec[illegible]e, "even only" harmonic numbers are selected [illegible] expansion (p in the following expressions

$$\begin{Bmatrix} \tilde{a}_n^m \\ \tilde{b}_n^m \end{Bmatrix} = \left\lfloor \{\cdots(\tilde{a}_n^{2p})\cdots\},\ \{\cdots(\tilde{b}_n^{2p})\cdots\} \right\rfloor^T \tag{9}$$

and the vector of blade states takes the form

$$\{\Delta Z\} = \left\lfloor \frac{\Delta V_{j1}+\Delta V_{j2}}{2}, \frac{\Delta W_{j1}+\Delta W_{j2}}{2}, \frac{\Delta\Phi_{j1}+\Delta\Phi_{j2}}{2}, \frac{\Delta\Phi_1+\Delta\Phi_2}{2} \right\rfloor^T \tag{10}$$

$$j = 1, 2, 3, \ldots, N$$

Similarly, to obtain the dynamics of the differential (cyclic) mode, one assumes "odd only" harmonic numbers,

$$\begin{Bmatrix} \tilde{a}_n^m \\ \tilde{b}_n^m \end{Bmatrix} = \left\lfloor \{\cdots(\tilde{a}_n^{2p+1})\cdots\},\ \{\cdots(\tilde{b}_n^{2p+1})\cdots\} \right\rfloor^T \tag{11}$$

and the vector of blade states takes the form

$$\{\Delta Z\} = \left\lfloor \frac{\Delta V_{j1}-\Delta V_{j2}}{2}, \frac{\Delta W_{j1}-\Delta W_{j2}}{2}, \frac{\Delta\Phi_{j1}-\Delta\Phi_{j2}}{2}, \frac{\Delta\Phi_1-\Delta\Phi_2}{2} \right\rfloor^T \tag{12}$$

$$j = 1, 2, 3, \ldots, N$$

For a Q-bladed rotor, under the same solution method, the harmonic number varies as

$$\begin{array}{lll} \text{collective mode:} & m = j\,Q & \\ \text{differential mode:} & m = Q/2 + j\,Q & (Q \text{ even}) \\ p\text{-th cyclic mode:} & m = |\,p \pm j\,Q\,| & \end{array} \tag{13}$$

$$j = 0, 1, 2, 3, \ldots$$

RESULTS AND DISCUSSION

The rotor configuration and operational conditions for which the results are obtained in this research come from Sharpe's (1986) experimental investigations (a two-bladed, untwisted, stiff inplane, torsionally soft hingeless model rotor, including a blade root offset, tested at a nominal speed of 1,000 RPM). The hub was designed to allow variation in precone, blade droop, pitch control stiffness and blade pitch angle. Results from the present approach are denoted by GDWM (Generalized Dynamic Wake Model) in the following plots.

Values assumed for the harmonic numbers (m) are shown in the legends, where "(E)" means that "even only" harmonic numbers are taken within the inflow expansion. The total number of spatial modes (inflow states) in the inflow expansion is chosen as 15, 45, 66, and 91, leading to 6, 15, 21, and 28 expansion coefficients (S), respectively, in the steady-state (equilibrium) analysis. Such inflow expansion selections come from a mathematically consistent hierarchy presented in He (1989). The convergence of the present methodology is investigated in detail by de Andrade (1992) and de Andrade and Peters (1992). In this paper we present results for aerodynamic force mode shapes including steady-state and dynamics. All results include 5 mode shapes for each of elastic torsion, flap bending, and lead-lag bending deflections. Also, the aerodynamic loads to be presented in this section have been normalized by twice the product of the dynamic pressure at the blade tip and the blade length. It is important to mention that the theoretical approaches from which the numerical results are compared herein have the same structural, inertial, and airloads models (the first from Hodges and Dowell, 1974, and the last two from Hodges, 1976), so the differences are basically due to the differences in the inflow.

Numerical results for steady-state (equilibrium)

The effects of the present approach on general steady-state blade deflections and steady-state aerodynamic load mode shapes are presented in Fig 1-3. Results from the present methodology are correlated with two-dimensional, momentum/blade-element counterparts, which include uniform inflow distribution.

First, in Fig 8, one observes steady-state inflow distributions for rotor configurations including soft pitch flexures, zero precone and droop, for the blades at $\theta_0 = 8°$. The uniform momentum theory takes the inflow at the 3/4 blade span. It predicts too large induced flow at the root sections and to small values at the tip sections. The generalized dynamic inflow methodology shows nonuniform inflow distributions, and, as the number of expansion coefficients increases, the inflow begins to climb near the blade tip, meaning that they are converging to the Prandtl "exact" tip correction. Basically, this nonuniformity and implicit three-dimensional characteristics are the major ingredients responsible for the partial capture of the tip relief on both steady-state induced drag and lift distribution to be shown. On the other hand, since this finite-state inflow model is based on a cylindrical, undistorted wake, no upwash due tip-vortex is captured, what would happen if prescribed or free-wake models were used.

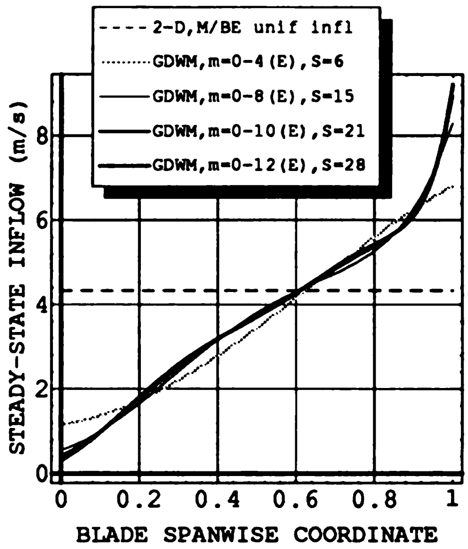

FIG 8. Spanwise steady-state inflow
SOFT PITCH FLEXURE, $\beta_{pc} = \beta_d = 0°$; $\theta_0 = 8°$

Figure 9 (a) show correlations for the steady-state induced drag. The finite-state results start capturing the three-dimensional tip-relief effects as the number of expansion coefficients increases, and show a maximum loading at 92% of the

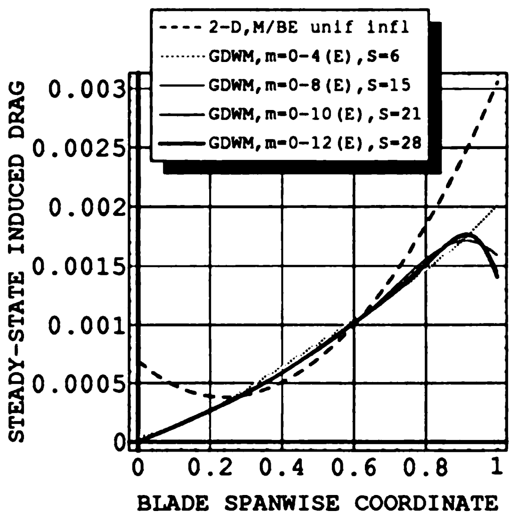

(a)

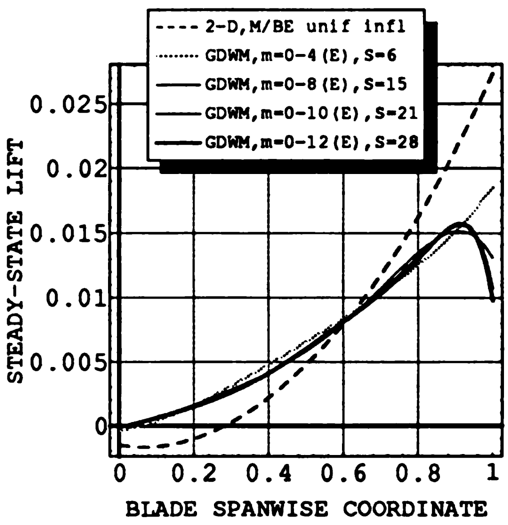

(b)

FIG 9. Spanwise distributions of steady-state aerodynamic loads
SOFT PITCH FLEXURE, $\beta_{pc} = \beta_d = 0°$; $\theta_0 = 8°$; (a) INDUCED DRAG; (b) LIFT

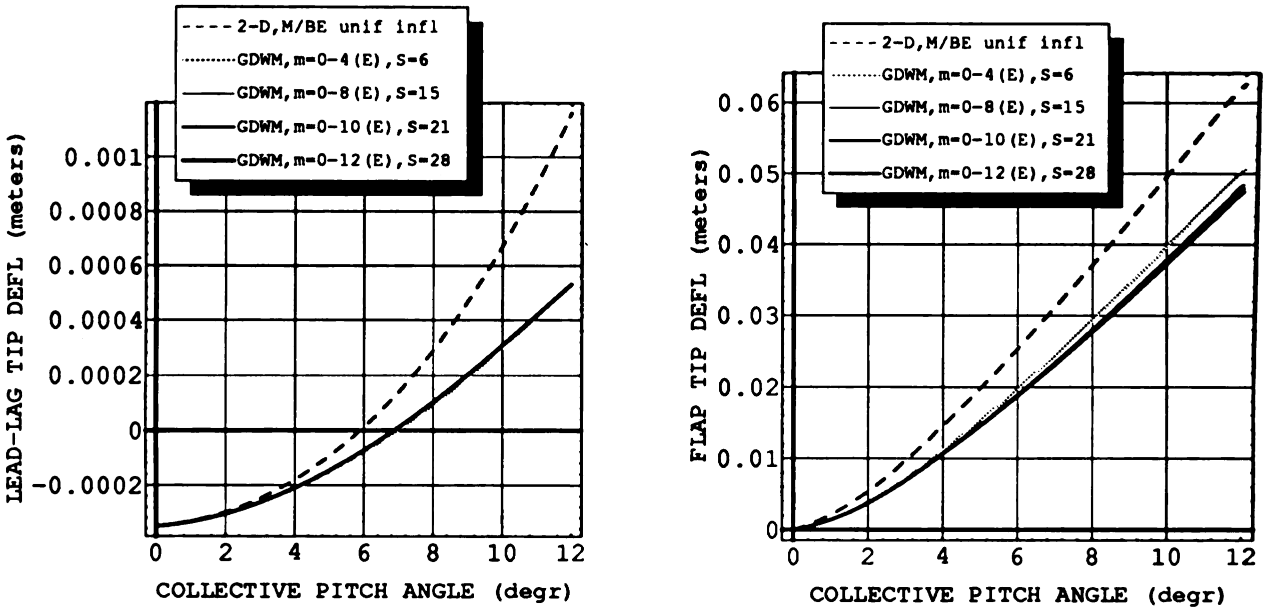

(a) (b)

FIG 10. Bending equilibrium deflections at the blade tip (*m*) in terms of the collective pitch angle (*degrees*) SOFT PITCH FLEXURE, $\beta_{pc} = \beta_d = 0°$; (a) LEAD-LAG; (b) FLAP

blade length and quickly decreasing load towards the tip. Regarding the two-dimensional uniform momentum/blade-element results, too much induced drag is obtained at both the blade root and tip sections, which is basically responsible for different sectional bending moments leading to higher lead-lag equilibrium deflections, specially near the blade tip, as shown in Fig 10 (a).

Correlations for steady-state lift distributions are presented in Fig 9 (b). Here, the two-dimensional, uniform momentum/blade-element theory predicts too little lift at the root sections and too much lift at the tip sections. The GDWM results for lift have basically the same trend a those shown for the steady-state induced drag, showing more evident drop near the tip due to three-dimensional tip relief. The differences between the two approaches are ultimately responsible for the differences shown in the flap equilibrium deflections at the blade tip as shown in Fig 10 (b).

Figure 10 shows correlations for blade bending tip deflections in lead-lag and flap in terms of the collective pitch angle. Remarkable differences are observed in the lead-lag deflections from the two theoretical approaches as seen in Fig 10 (a). It is observed that a zero thrust the blade is lagging in the rotor plane, due to the profile drag. As the thrust gets higher, the blade assumes positive chordwise displacements (the transition occurs at 6° of collective pitch as predicted by the two-dimensional aerodynamics, and at 7° by the finite-state formulation). As commented before, such differences are essentially due to the differences in the induced drag predictions (shown in Fig 9 (a)), since ... oaches have the same profile drag (the same co... rag coefficient is assumed). Similarly, consi... s are obtained for the flap equilibrium de... ade tip, as observed in Fig 10 (b), which are basically due to the differences in the lift distribution between the respective approaches (Fig 9 (b)). Interpreting the bending equilibrium displacements results just shown, for instance, the values of lead-lag and flap at the blade tip at $\theta_0 = 12°$ and computing the inplane displacement, one finds that the blade tip is lagging 0.0052 *m* and is above the rotor disk about 0.048*m*.

As detailed in de Andrade (1992), relative small differences between the two approaches are obtained for the torsion equilibrium deflections at the blade tip. The role of the pitch flexure in the steady-state results was investigated as well. Aerodynamic loads and blade equilibrium deflections remain practically the same as the stiffness of the pitch flexure is largely varied.

Numerical results for dynamics (eigenanalysis)

The dynamics results from the present approach to be shown in this paper are obtained directly from an eigenanalysis. Recall that, with the finite-state wake model eigenvector information contains not only information on structural deflections and velocities, but also contains information on the inflow oscillations. Thus, one can construct the in-phase (real) and out-of-phase (imaginary) lift associated with any given mode. Here we are concerned with the generalized aerodynamic mode shapes which can be obtained directly from the eigenvectors associated with a given rotor operating condition. For this research, the rotor mode of interest is defined as the one with frequency nearest the fundamental lead-lag frequency of the rotating blade, which is known for being lightly damped (all results here are for the rotor mode with frequency around 1.5/*rev*). Unfortunately, no experimental data involving blade displacements or aerodynamic forces are

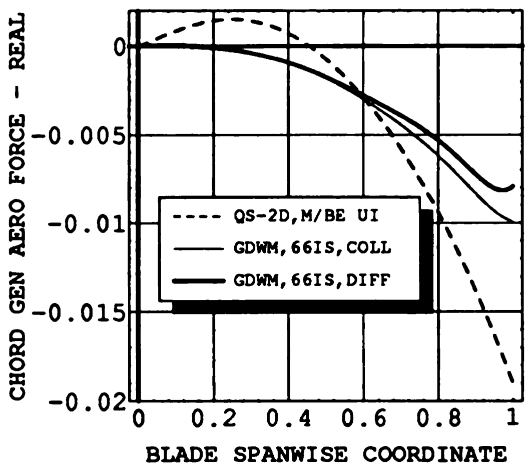

FIG 11. Spanwise distribution of chordwise generalized aerodynamic force (drag due to chordwise mode) - real part soft pitch flexure; $\theta_0 = 4°$; $\beta_{pc} = \beta_d = 0°$; diff vs. coll

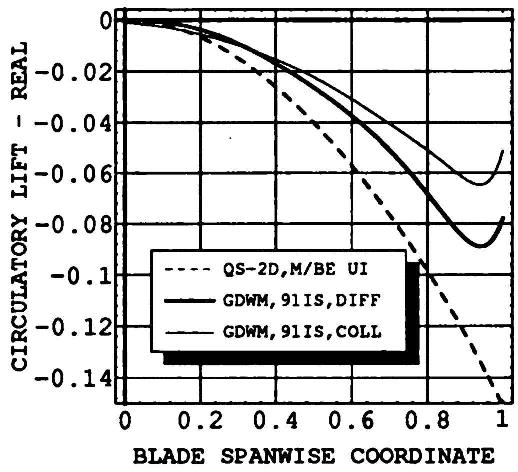

FIG 12. Spanwise distribution of circulatory lift (lift due to chordwise mode) - real part; $\beta_{pc} = \beta_d = 0°$ soft pitch flexure; $\theta_0 = 4°$; differential vs. collective

available at this point, so the correlations to be presented here include GDWM and quasi-steady two-dimensional aerodynamic techniques.

First, correlations are presented for eigenvectors associated with the "rotor mode of interest" at $\theta_0 = 4°$. With respect to the chordwise generalized aerodynamic force, the real part (which is the dominant contribution – the imaginary part is very small) is shown in Fig 11. GDWM results for the rotor differential and collective modes of vibration are presented along with the quasi-steady two-dimensional counterparts. First, we notice that the quasi-steady loads are even qualitatively correct due to assumption of uniform inflow and the neglect of unsteady induced inflow. Finite-state inflow chordwise generalized aerodynamic forces show a drop of about 50% with respect to the quasi-steady two-dimensional prediction. Due to the predominance of the first lead-lag at low values of collective pitch, a great part of that represents chordwise damping loss. This confirms the differences observed for the lead-lag damping between the two approaches (de Andrade and Peters, 1992 and 1993). Regarding the circulatory lift mode shapes, in Fig 12 the real part (in-phase) is presented (both real and imaginary parts have the same order of magnitude, due to close dependence on perturbational flap, for which real and imaginary parts have the same order of magnitude (de Andrade, 1992)). The higher level of circulatory lift associated with the differential mode (in comparison with the collective circulatory lift) is a direct consequence of the lower inflow resultant from this mode when compared to the inflow associated with the collective mode of vibration. Also, one observes a severe drop in the values for the incremental collective and differential circulatory lifts (which are the corresponding perturbation wake-generating circulatory lift, L_S, in Eq (2)) compared with the quasi-steady two-dimensional aerodynamic perturbational lift.

As the thrust increases, strong structural couplings are present. Figures 13 and 14 show generalized aerodynamic mode shapes for chordwise force and circulatory lift, respectively, for $\theta_0 = 8°$. Here the chordwise load goes along the real and imaginary part of the circulatory lift (flapwise loads) and coupled flap-lag-torsion motions to define the blade damping. The differences between generalized wake loads and the quasi-steady loads seen in Figs 13 and 14 account for the 50% improvement in damping as pointed out in de Andrade, 1992, and de Andrade and Peters (1992, 1993).

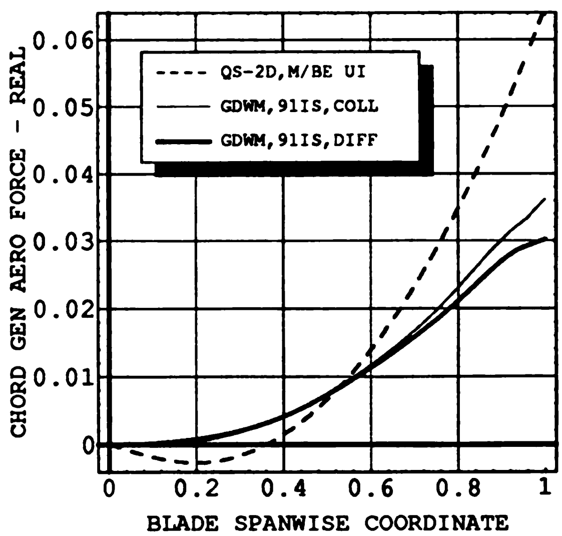

FIG 13. Spanwise distribution of chordwise generalized aerodynamic force - real part; $\beta_{pc} = \beta_d = 0°$ soft pitch flexure; $\theta_0 = 8°$; differential vs. collective

CONCLUSIONS

This research investigates the stability of helicopter rotors in hovering flight through a coupled set of generalized dynamic inflow equations and hybrid equations of motion for an elastic blade cantilevered in bending and having a torsional

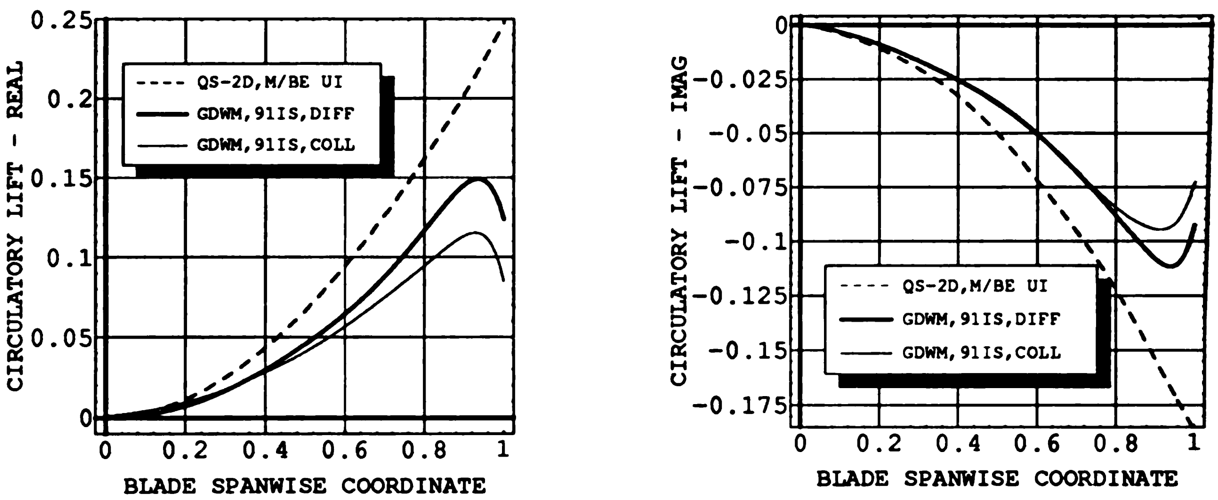

(a) (b)

FIG 14. Spanwise distribution of circulatory lift - differential vs. collective soft pitch flexure; $\theta_0 = 8°$; $\beta_{pc} = \beta_d = 0°$; (a) real part; (b) imaginary part

root spring to model pitch-link flexibility. The present approach leads to a standard eigenanalysis for the dynamic part of the problem, for which the coefficient matrices depend on the numerical solution of blade equilibrium and inflow steady-states. Results presented in this paper are for a two-bladed, untwisted stiff inplane hingeless small scale (model) rotor with torsionally soft blades, including blade root offset, precone. They confirm the importance of three-dimensional, unsteady aerodynamics for aeroelastic investigations. The major conclusions associated with this application of the generalized dynamic wake model can be summarized as: 1) numerical results show that three-dimensional tip relief effects within the nonuniform steady-state inflow are significant to predict steady-state aerodynamic loads and blade deflections, and 2) eigenvector analysis correlations reinforced qualitative and quantitative shortcomings associated with quasi-steady two-dimensional aerodynamic theory for aeroelastic applications in hover.

The treatment of the aeroelastic stability through an eigenanalysis as formulated in this work is specially convenient when helicopter integrated dynamics are involved. The elimination of time-marching and moving block analyses, present current state-of-the-art approaches to the same problem, with essentially no essential loss of accuracy for the obtained results, constitutes the primary contributions of the present methodology. The efficiency of this makes rotor optimization with aeroelastic stability a practical endeavor.

REFERENCES

Peters DA and Su A (1991), An integrated airloads-inflow model for use in rotor aeroelasticity and control analysis, in *Proceedings of the American Helicopter Society 47th Annual National Forum*, Phoenix AZ.

Hodges DH and Ormiston RA (... of elastic bending and torsion of uniform ca ... les in hover with variable structural couplin ...)2.

Hodges DH (1976), Nonlinear equations of motion for cantilever rotor blades in hover with pitch-link flexibility, twist, precone, droop, sweep, torque offset and blade root offset, NASA TM X-73,112.

Kwon OJ (1988), A technique for the prediction of aerodynamics and aeroelasticity of rotor blades, PhD Thesis, Georgia Institute of Technology, Atlanta GA.

Kwon OJ, Hodges DH, and Sankar LN (1991), Stability of hingeless rotors in hover using three-dimensional unsteady aerodynamics, *Journal of the American Helicopter Society*, **36**(2) 21-31.

Hodges DH and Dowell EH (1974), Nonlinear equations of motion for the elastic bending and torsion of twisted nonuniform rotor blades, NASA TN D-7818.

Peters DA and He CJ (1987), A closed form unsteady aerodynamic theory for lifting rotor in hover and forward flight, in *Proceedings of the American Helicopter Society 43rd Annual National Forum*, St. Louis MO.

He CJ (1989), Development and application of a generalized dynamic wake theory for lifting rotors, PhD Thesis, Georgia Institute of Technology, Atlanta GA.

de Andrade D (1992), Application of finite-state inflow to flap-lag-torsion damping in hover, PhD Thesis, Georgia Institute of Technology, Atlanta GA.

de Andrade D and Peters DA (1992), On a finite-state inflow to flap-lag-torsion damping in hover, in *Proceedings of the 18th European Rotorcraft Forum*, Avignon, France, paper No 2.

de Andrade D and Peters DA (1993), Correlations of experimental flap-lag-torsion damping - a case study, in *Proceedings of the American Helicopter Society 49th Annual National Forum*, St. Louis MO, 1011-1027.

Sharpe DL (1986), An experimental investigation of the flap-lag-torsion aeroelastic stability of a small-scale hingeless rotor in hover, NASA TP-2546.

Peters DA and HaQuang N (1988), Dynamic inflow for practical application, *Journal of the American Helicopter Society*, **33** (4) 64-68.

Damping of vibrations of layered elastic-viscoelastic beams

Richard B Hetnarski, Ray A West[1] and Joseph S Torok

Rochester Institute of Technology, Rochester NY 14623

A five-layer cantilever beam consisting of an elastic core, two symmetric viscoelastic layers, and two elastic constraining layers is considered. The viscoelastic effects are incorporated in the Euler-Bernoulli beam theory. If the contraction and extension of the constraining layers is neglecterd a fourth order differential equation of motion is received. Inclusion of contraction and extension of the constraining layers results in a more accurate sixth order differential equation. Appropriate boundary conditions are derived. Laplace transforms are used extensively. Both the analytical solution and the numerical results are presented.

INTRODUCTION

For many years there has been a substantial interest among researchers and engineers in developing effective methods of damping of beam vibrations. One such method consists of bounding to the top and the bottom of an elastic beam symmetrical layers of viscoelastic material. These layers, due to internal shear during the motion of the beam, changes a part of the kinetic energy into heat, which then is distributed to the ambient atmosphere. In order to increase the effect of shear, additional two thin elastic layers are bounded to the viscoelastic layers. In this way, we deal with a five-layer beam shown in Fig. 1.

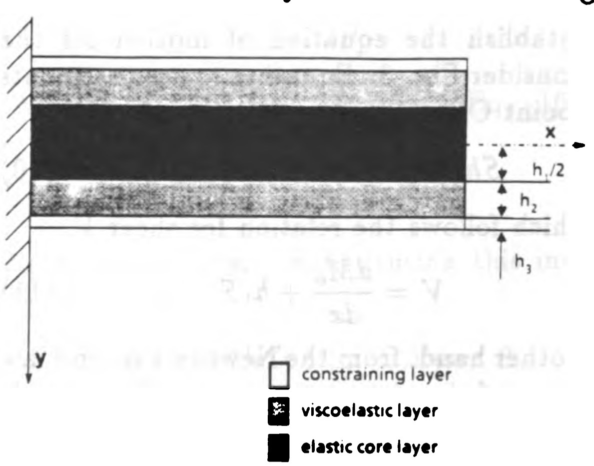

Fig. 1. Five-layer cantilever beam.

The analytical treatment of such or similar composite beams is difficult, see e.g., [1 - 4]. A short introduction to the method shown here has been presented in [5], and some other results are presented in [6] and [7].

The assumptions made in this analysis are: (1) Viscoelastic layers are characterized by a complex shear modulus $G = G^*(1 + \eta i)$. (2) The central structural element and the constraining layers and are assumed to remain in pure bending. (3) The neutral axes of the core and of the constraining layers have identical deflection lines during bending. In the next Section, it is also assumed that the lengths of constraining layers remain constant at all times during motion, and equal to the length of the central layer; this is equivalent to the assumption that the constraining layers are not stretched or shortened during bending. This assumption is waved in the subsequent Section where the sixth order differential equation of motion is derived.

FOURTH ORDER DIFFERENTIAL EQUATION OF MOTION

The analysis leading to the fourth-order equation of motion is based on the geometry of motion of the beam presented in Fig. 2 where the lower

[1] Present address: Xerox Corporation, Fairport, NY 14450.

half of the beam is shown. Segment AB lies on the line $a_1 - a_1$ normal to the deflection line of teh beam. Line segments AB' and C'D lie on a line $a_2 - a_2$ parallel to the y axis. Obviously, when the beam is not deflected, the lines $a_1 - a_1$ and $a_2 - a_2$ coinside. Segments AB' and C'D lie on the same line $a_2 - a_2$ if the constraining layer does not stretch and if deflections are small. It follows from $\triangle ABB'$ in Fig. 2 that

$$m \approx (h_1/2)y' \qquad (1)$$

where $y' = tan\angle BAB' \approx sin\angle BAB'$ for small deflections. Similarly, from $\triangle CC'D$, we have

$$n \approx -(h_3/2)y' \qquad (2)$$

It is seen, therefore, that the angle of shear $/\gamma$ in the viscoelastic layer is

$$\gamma = y' + (m-n)/2 \qquad (3)$$

or, after substitution,

$$\gamma = ay' \qquad (4)$$

where

$$a = 1 + (h_1 + h_3)/2h_2 \qquad (5)$$

A convention is used that γ is positive in the counter-clockwise direction if measured from the line $a_1 - a_1$. Therefore, the shear S acting on the surface of core per unit length of the beam and, in the opposite direction, on the surface of the constraining layer, is

$$S = \gamma G_1 b \qquad (6)$$

in units of force per units of length. Here b is the width of the beam.

In our case, the bending moment M in an arbitrary cross-section consists of two parts

$$M = M_o + M_1 \qquad (7)$$

where M_o is due to the stiffness of the beam

$$M_o = -EI\frac{\partial^2 y}{\partial x^2} \qquad (8)$$

while M_1 is due to shear S in the viscoelastic layers, see Fig. 3. Since the constr·ining layers are thin compared to the core, t[illegible] of inclusion of the bending stiffne[illegible] straining layers is very small. Ne[illegible] Eq. (8),

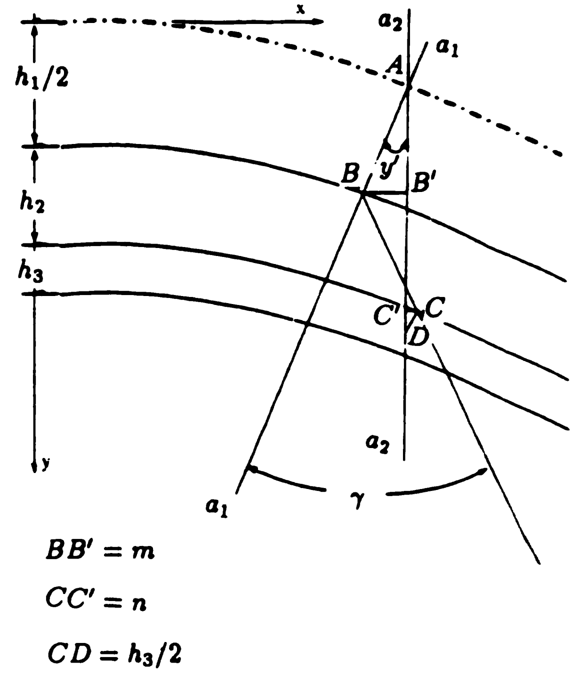

Fig. 2. Geometry of bending (fourth order eq.).

the stiffness EI of the layered beam is taken as a combination of the stiffnesses of the core and of the constraining layers:

$$EI = E_1 I_1 + 2E_3 I_3 \qquad (9)$$

It is assumed that the viscoelastic layers do not contribute to the stiffness of the beam.

To establish the equation of motion for the beam consider Fig. 3. Equating to zero moments about point O we receive

$$Sh_1 dx - Vdx + dM_o = 0 \qquad (10)$$

from which follows the relation for shear V

$$V = \frac{dM_o}{dx} + h_1 S \qquad (11)$$

On the other hand, from the Newton's second law the motion of the element in vertical direction is

$$(\rho dx)\ddot{y} = dV \qquad (12)$$

where $\rho = (\rho_1 h_1 + 2\rho_2 h_2 + 2\rho_3 h_3)b$ and ρ_i are mass densities of the materials of appropriate layers. Dividing by dx yields

$$\rho\ddot{y} = V' \qquad (13)$$

Differentiating V from Eq. (11) and substituting in Eq. (13) results in

$$\rho \ddot{y} = M_o'' + h_1 S' \qquad (14)$$

Substituting in Eq. (14) M_o from Eq. (8) and S from Eq. (6) with γ from Eq. (4) we arrive at the equation of motion

$$EIy^{IV} - abh_1 G y'' + \rho \ddot{y} = 0 \qquad (15)$$

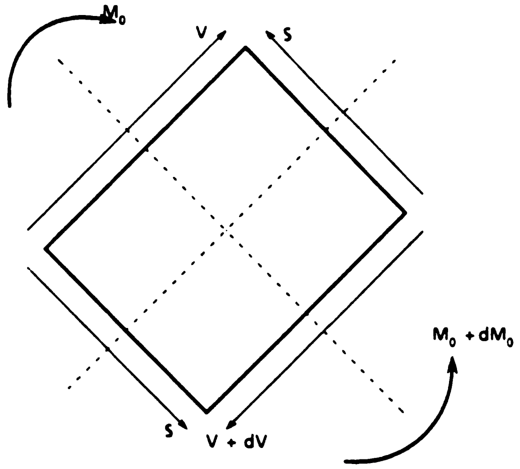

Fig. 3. Free body diagram for beam element.

or, in a simpler form,

$$y^{IV} - cGy'' + \frac{\rho}{EI}\ddot{y} = 0 \qquad (16)$$

where

$$c = \frac{abh_1}{EI} \qquad (17)$$

Assume that that the solution to Eq. (16) may be presented in the form

$$y(x,t) = w(x)e^{\omega t} \qquad (18)$$

where ω is complex. Substituting this into Eq. (16) results in

$$w^{IV} - cGw'' + (\omega/\omega_o)^2 w = 0 \qquad (19)$$

where

$$\omega_o = (EI/\rho)^{1/2} \qquad (20)$$

Applying the Laplace transform

$$\bar{w}(p) = \int_0^\infty w(x)e^{-px}dx \qquad (21)$$

to Eq. (19), we receive after simple transformation

$$\bar{w}(p) = \frac{1}{p^4 - rp^2 + s^2}(\alpha_1 p^3 + \alpha_2 p^2 + \alpha_3 p + \alpha_4) \qquad (22)$$

where $r = cG$, $s = \omega/\omega_o$, and

$$\alpha_1 = w(0), \quad \alpha_2 = w'(0)$$

$$\alpha_3 = w''(0) - cGw(0), \quad \alpha_4 = w'''(0) - cGw'(0) \qquad (23)$$

Writing the denominator in Eq. (22) in the form

$$p^4 - rp^2 + s^2 = (p^2 - u^2)(p^2 - v^2) \qquad (24)$$

we may observe that the appropriate inverse Laplace transforms are

$$L^{-1}\left\{\frac{p^3}{(p^2-u^2)(p^2-v^2)}\right\} = \frac{u^2 \cos ux - v^2 \cos vx}{u^2 - v^2} \equiv L_1 \qquad (25)$$

$$L^{-1}\left\{\frac{p^2}{(p^2-u^2)(p^2-v^2)}\right\} = \frac{u \,sh\, ux - v \,sh\, vx}{u^2 - v^2} \equiv L_2 \qquad (26)$$

$$L^{-1}\left\{\frac{p}{(p^2-u^2)(p^2-v^2)}\right\} = \frac{ch\, ux - ch\, vx}{u^2 - v^2} \equiv L_3 \qquad (27)$$

$$L^{-1}\left\{\frac{1}{(p^2-u^2)(p^2-v^2)}\right\} = \frac{v \,sh\, ux - u \,sh\, vx}{u^2 - v^2} \equiv L_4 \qquad (28)$$

Therefore,

$$w(x) = \alpha_1 L_1 + \alpha_2 L_2 + \alpha_3 L_3 + \alpha_4 L_4 \qquad (29)$$

The boundary conditions are determined from the energy approach. Utilizing the left-hand side of Eq. (19) calculate the integral

$$I = \int_0^l [w_i^{IV} - cGw_i'' + (\omega/\omega_o)^2 w_i]w_j dx \qquad (30)$$

where w_i and w_j are functions of x only, and subscripts i and j denote node numbers. Integrating Eq. (30) repeatedly by parts, the following result is obtained:

$$I = \int_0^l [w_j^{IV} - cGw_j'' + (\omega/\omega_o)^2 w_j] w_i dx$$
$$+ [w_i''' w_j - w_i'' w_j' + w_i' w_j''$$
$$- w_i w_j''' - cG(w_i' w_j - w_i w_j')]_0^l \qquad (31)$$

The boundary conditions are received when the expression in brackets in Eq. (31) is equal to zero both for $x = 0$ and for $x = l$. Observe first that $w_k(0) = w_k'(0) = 0$, $(k = i, j)$ are consistent with customary boundary conditions for a cantilever beam. Rearrange now the terms in brackets in Eq. (31) to arrive at the form

$$(w_i''' - cGw_i')w_j - (w_j''' - cGw_j')w_i - w_i'' w_j' + w_j'' w_i' \qquad (32)$$

This expression is zero when

$$w_k'''(l) - cGw_k'(l) = 0 \text{ and } w_k''(l) = 0, \quad (k = i, j) \qquad (33)$$

The first of these conditions is not intuitively obvious. A complete set of boundary conditions is then:

$$w = 0 \text{ and } w' = 0 \text{ for } x = 0 \qquad (34)$$

and

$$w''' - cGFw' = 0 \text{ and } w'' = 0 \text{ for } x = l \qquad (35)$$

SIXTH ORDER DIFFERENTIAL EQUATION OF MOTION

The results of the previous Section will lead to the derivation of a more accurate description of free vibrations of a beam. We will now assume that the extension and contraction of the constraining layers is not neglected.

Inasmuch as the angle of shear is $\gamma = ay'$ Eq. (15) is rewritten in the form

$$EIy^{IV} - bh_1G\gamma' + \rho\ddot{y} = 0 \qquad (36)$$

Because of the shear force exerted by the viscoelastic layers on the constraining layers, there exists a longitudinal deformation in the constraining layers in the form [illegible] sion and contraction. This deformati[illegible] magnitude of the angle of shear. I[illegible] olute value of the shear angle is a[illegible] n the absolute value of γ. As shown in Fig. 4, the resulting angle of shear is for a given moment of time t

$$\gamma + \delta = ay' = \frac{u(x)}{h_2} \qquad (37)$$

where $u(x)$ is the longitudinal displacement of the constraining layer on the positive side of the y-axis. Observe that u(x) in the situation shown in Fig. 4 is negative. This is consistent with the assumed convention for the sign of the angle; clock-wise direction of δ in Fig. 4 indicates a negative angle. Submitting $\gamma + \delta$ in place of γ in Eq. (36) yields

$$EIy^{IV} - bh_1G\frac{d}{dx}(\gamma + \delta) + \rho\ddot{y} = 0 \qquad (38)$$

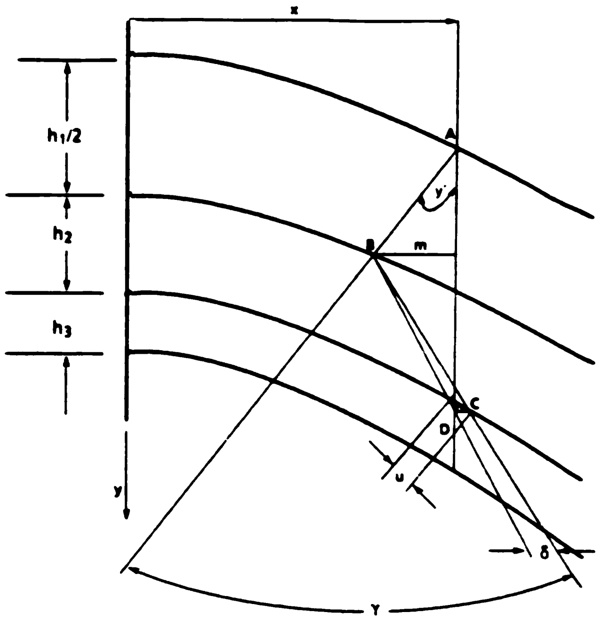

Fig. 4. Geometry of bending (sixth order eq.).

Introducing the value of $\gamma + \delta$ from Eq. (37) results in

$$EIy^{IV} - bh_1G(ay'' + u'/h_2) + \rho\ddot{y} = 0 \qquad (39)$$

The relation between the shear stress τ in the viscoelastic layer and the strain in the constraining layer at a position x is

$$E_3H_3u' = \int_x^l \tau dx \qquad (40)$$

in this relation the sign of τ is the same as the sign of u'. Differentiating Eq. (40) gives

$$E_3h_3u'' = -\tau(x) \tag{41}$$

On the other hand, the relation between τ and $\gamma+\delta$ is

$$\tau = -G(\gamma+\delta) \tag{42}$$

Combining Eqs. (41) and (42) results in

$$E_3h_3u'' - G(\gamma+\delta) = 0 \tag{43}$$

Differentiating Eq. (39) with respect to x and substituting u'' from Eq. (43) gives

$$EIy^{V} - bh_1G[ay''' + \frac{G}{h_2h_3E_3}(ay' + \frac{u}{h_2})] + \rho\ddot{y}' = 0. \tag{44}$$

Differentiating Eq. (44) with respect to x and substituting

$$\frac{u'}{h_2} = \frac{EI}{bh_1G}y^{IV} - ay'' + \frac{\rho}{bh_1G}\ddot{y} \tag{45}$$

which is obtained from Eq. (39), yields the sixth order differential equation of motion

$$y^{VI} - G(c + \frac{1}{h_2h_3E_3})y^{IV} + \frac{\rho}{EI}\ddot{y}'' - \frac{G}{h_2h_3E_3}\frac{\rho}{EI}\ddot{y} = 0 \tag{46}$$

This is the equation of motion in which the effect of the longitudinal deformation of constraining layers is included.

Assuming that

$$y(x,t) = y(x)e^{i\omega t} \tag{47}$$

we may present the equation of motion in the form

$$y^{VI} + a_4y^{IV} + a_2y'' + a_oy = 0 \tag{48}$$

where

$$a_0 = \frac{G}{h_2h_3E_3}\frac{\rho\omega^2}{EI}$$
$$a_2 = -\frac{\rho\omega^2}{EI}$$
$$a_4 = -G(c + \frac{1}{h_2h_3E_3}) \tag{49}$$

The six boundary conditions required for the solution fo the six-order equation are obtained by the variational approach (see [8])

$$\begin{aligned} y(0) &= 0 \\ y'(0) &= 0 \\ [y^{V} + a_4y''' + a_2y']_{x=l} &= 0 \\ [y^{IV} + a_4y'']_{x=l} &= 0 \\ y'''(0) &= 0 \\ y'''(l) &= 0 \end{aligned} \tag{50}$$

LENGTH CHANGES IN THE CONSTRAINING LAYERS

We present here a simple analysis in order to assess the magnitude of stretching and contraction of the constraining layers.

Observe that the longitudinal displacement in the constraining layer at any cross-section x is

$$u(x) = \int_0^x \frac{1}{E_3A_3}\int_\xi^l \tau(x)bd\zeta d\xi \tag{51}$$

where $\tau(x)$ is shear stress at the surface of the constraining layer due to shear force in the viscoelsatic layer. With $\tau = \gamma G$ and $\gamma = ay'$, this equation yields

$$u(x) = \frac{aG}{h_3E_3}[y(l)x - \int_0^x y(\xi)d\xi] \tag{52}$$

On the other hand, the displacement due to shear is $\gamma h_2 = ay'h_2$, and the ratio of u and γh_2 is therefore

$$\frac{u(x)}{\gamma h_2} = \frac{G}{h_2h_3E_3}\frac{y(l)x - \int_0^x y(\xi)d\xi}{y'(x)} \tag{53}$$

NUMERICAL ANALYSIS

The resultant sixth order differential equation is linear with constant coefficients. Such an equation admits exponential solutions. Subsequently, a general solution of the stated boundary value problem is a linear combination of six complex-valued exponential functions. Working through this approach leads to a rather complicated characteristic equation for the frequency parameter, see [8].

Again we turn to the Laplace transform method. From the transformed Eq. (46) follows:

$$L\{y(p)\}$$

$$= \frac{p^3 y''(0) + p[y^{IV}(0) + a_4 y''(0)] + y^{V}(0)}{p^6 + a_4 p^4 + a_2 p^2 + a_o} \tag{54}$$

The right-hand side of this equation is in the form

$$\frac{Ap^3 + Bp + C}{p^6 + a_4 p^4 + a_2 p^2 + a_o} \tag{55}$$

By means of partial fractions we can write

$$\frac{Ap^3 + Bp + C}{(p^2 - l^2)(p^2 - m^2)(p^2 - n^2)}$$

$$= \frac{d_1 p + d_2}{p^2 - l^2} + \frac{d_3 p + d_4}{p^2 - m^2} + \frac{d_5 p + d_6}{p^2 - n^2} \tag{56}$$

It follows that

$$d_1 = \frac{y''(0) l^2 + y^{IV}(0) + a_4 y''(0)}{(l^2 - m^2)(l^2 - n^2)} \tag{57}$$

$$d_2 = \frac{y^{V}(0)}{l(l^2 - m^2)(l^2 - n^2)} \tag{58}$$

$$d_3 = \frac{y''(0) m^2 + y^{IV}(0) + a_4 y''(0)}{(m^2 - l^2)(m^2 - n^2} \tag{59}$$

$$d_4 = \frac{y^{V}(0)}{m(m^2 - l^2)(m^2 - n^2)} \tag{60}$$

$$d_5 = \frac{y''(0) l^2 + y^{IV}(0) + a_4 y''(0)}{(n^2 - l^2)(n^2 - m^2)} \tag{61}$$

$$d_6 = \frac{y^5}{n(n^2 - l^2)(n^2 - m^2)} \tag{62}$$

CASE STUDY

Investigation to determine the effect of varying the damping of factor η on the system response was conducted. Some results are presented here, and more detailed analysis is contained in [8]. Five different values of η were selected: 0.06, 0.24, 0.36, 0.54, and 0.96. The thickness of the elastic core of the beam was taken as one inch and the thicknesses of the viscoelastic layers and the constraining layers were taken ... tenth inch and one-hundreth inch, resp... e length of the beam was taken as 2... tic core was considered steel. Th... naterial was considered rubber w... x modulus stated below together with other values:

$$c = 42.112 \times 10^{-6} 1/lb;\ E_3 = 30 \times 10^6 lb/in^2;$$

$$\rho/b = 7.4562 \times 10^{-4} lb\, sec^2/in^3;\ \Omega = 1;$$

$$G^* = 48.35(1 + i\eta);$$

$$EI/b = 2.5 \times 10^6 lb\, in;$$

$$\omega_o = [E(1 + i\eta)I/\rho]^{1/2};$$

$$\omega_j = \Omega[E(1 + i\eta)I/\rho]^{1/2}$$

Mathematica software was used to compute the various dynamic parameters, such as natural frequency. Graphical outputs depicting the real and the imaginary parts of the response functions were obtained. As the damping factor increased, the time for the response to be damped out was significantly reduced.

The parameters l, m, and n, the undamped natural frequency ω_o, and the damped natural frequency of the system ω_j, were computed for each value of the damping factor. Given the system's natural circular frequency and the parameters l, m, and n, the response of the system has been computed.

The reduction of time for the damping out of the system with the increase of the value of the damping factor is clear from the figures provided. For example, the absolute value of the amplitude of both the real and the imaginary curves shown for $\eta = 0.06$ is greater than 0.5 after 45 seconds. For $\eta = 0.36$ this is less than 0.5 after only 13 seconds, and for $\eta = 0.96$ this is less than 0.25 after only 9 seconds. Some results are shown in Figs. 5-8.

The thickness of the viscoelastic layers does not significantly affect the damping. However, its value appears in the eigenfunctions.

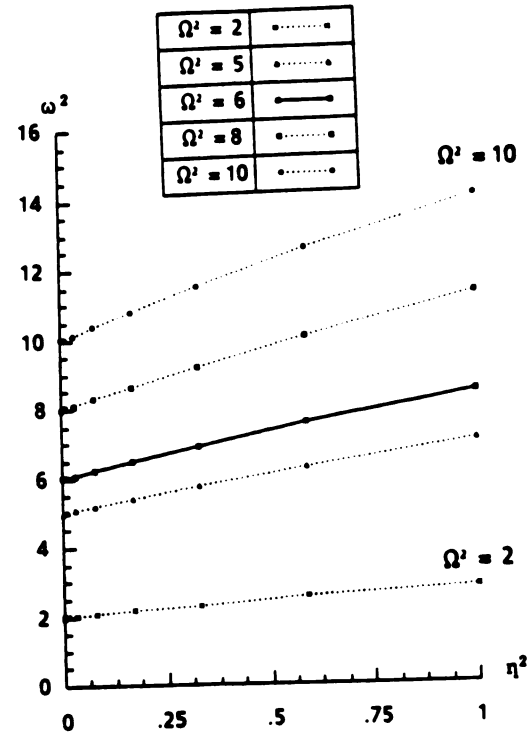

Fig. 5. Family of curves.
Frequency v. modal loss factor.

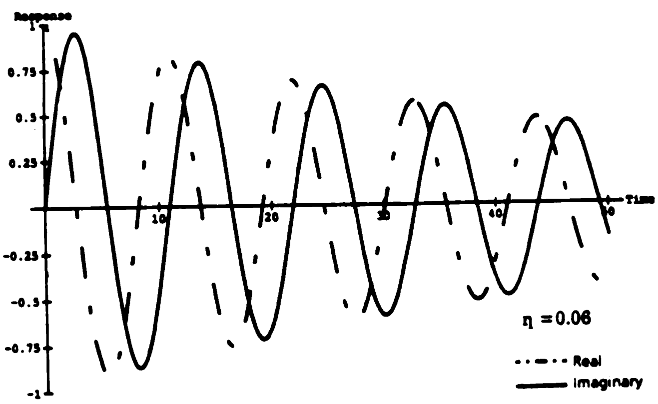

Fig. 6. Response v. time for $\eta = 0.06$.

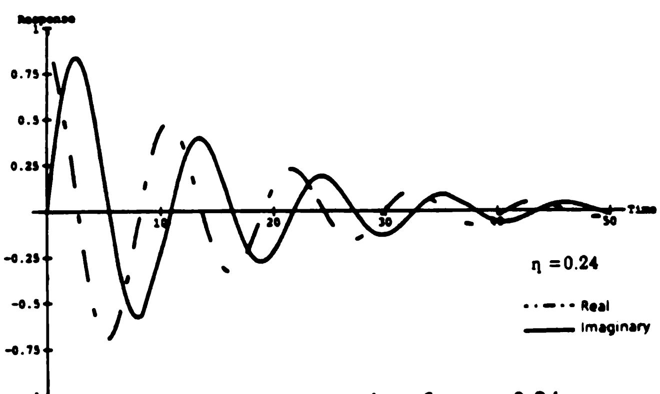

Fig. 7. Response v. time for $\eta = 0.24$.

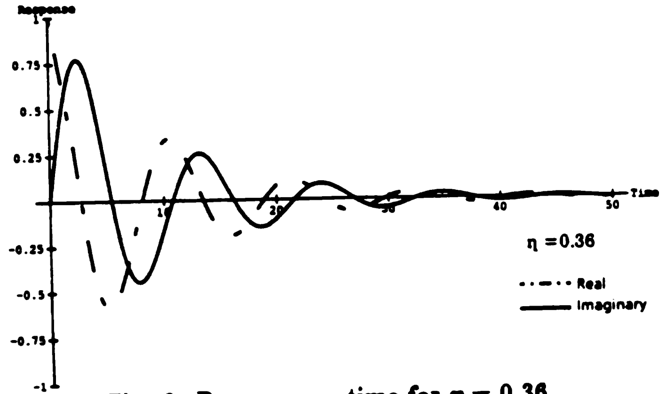

Fig. 8. Response v. time for $\eta = 0.36$.

ACKNOWLEDGEMENT

The first author (RBH) gratefully acknowledges the assistance and advice received from Dr. Christos C. Chamis and Dr. Murray S. Hirschbein, both at NASA Lewis Research Center, Cleveland, OH, during the preparation of the theoretical part of this project.

REFERENCES

[1] DiTaranto RA, Theory of vibratory bending for elastic and viscoelastic layered finite length beams, *J.Applied Mechanics*, 881-886 (1965).

[2] Mead DJ, Markus S, The forced vibration of a three-layer, damped sandwitch beam with arbitrary boundary conditions, *J. Sound Vib.*. 163-175 (1969).

[3] Sato K and Shikanai D, Damping of flexural vibration of viscoelastic sandwitch beams subjected to axial force, *Bulletin of JSME*, No. 253, vol. 29, 2204-2210 (1986).

[4] Nashif AD, *Vibration Damping*, Wiley, New York, 1985.

[5] Hetnarski RB, Hirschbein MS, and Chamis CC, Damping of free vibrations of beams with constrained viscoelastic layers, *Proc. Ninth Canadian Cong. of Appl. Mech.*, Saskatchewan, 113-114 (1983).

[6] Hetnarski RB, Messalti M, Hirschbein MS, and Chamis CC, Viscoelastic Damping in Beams, *Proc. First Pan-Am. Cong. of Appl. Mech.*, Rio de Janeiro, 659-662 (1989).

[7] Messalti M, Viscoelastic Damping of beams, MSc Thesis, Rochester Institute of Technology, Rochester, NY 1988.

[8] West RA, Damping of elastic-viscoelastic beams, MSc Thesis, Rochester Institute of Technology, Rochester, NY 1992.

Evaluation of the structural health of mechanical cables

Patricio AA Laura

Institute of Applied Mechanics, (CONICET-SENID-ACCE), Universidad Nacional del Sur, 8000 - Bahia Blanca, Argentina

Mechanical cables have long been used for towing, for remote control or for the supplying of communication or other service links between two vehicles. They also constitute the basic structural element in suspended bridges. On the other hand they are used in biomedical engineering applications; to lower men underground as deep as 16,000 ft and they are considered in superconductivity applications. Obviously the problem of evaluating the "structural health" of cables or ropes by means of non-destructive test methods is of the utmost importance. This article is concerned with a survey of the available methods.

INTRODUCTION

A cable or rope is made of natural or man-made fibers and of metallic wires. They are used extensively from transmitting electrical or optical signals to hoisting, fishing, hauling, rigging and basic structural elements of the utmost importance whenever one encounters technological applications that demand lightweight, flexible, or easily deployable structural members or conductors. On top of these uses: they are employed in many life sustaining situations: suspended bridges, elevators, ski chairlifts and gondolas, etc.

As stated by Costello (1990), "... a list of the uses of wire rope is almost endless. Recent research into the possible use of wire strands as braces for teeth is one such example.

Wire rope is used to lower men underground as deep as 16,000 ft in the gold mines of South Africa... one such rope used in a shaft that runs over several sheaves is 9.3 miles long and weighs 110 tn.... Wire rope is also being considered in superconductivity applications". Certainly, ropes made out of synthetic materials (nylon, kevlar, etc.) have become increasingly popular in the last three decades (Goeller and Laura, 1971).

Obviously, methods of detecting imminent failure in cables could prevent the loss of valuable equipment, and more important, the possible loss of human life. The nondestructive test methods available are:

- thorough visual examination and measurement of the external diameter
- X-rays
- (induced) wave propagation
- electromagnetic field (EM)
- acoustic emission (AE)

In view of the fact that the electromagnetic field method and the acoustic emission technique have been reviewed recently (Laura, 1993) the present article will only present some basic concepts which are the foundations of both methodologies.

It is generally accepted that in order to perform a rational and careful inspection in the case of ropes used in mine hoists and, in general, in any type of elevators systems, it is necessary to combine the visual and the EM method (Weischedel, 1991).

On the other hand the AE method and the (induced) wave propagation approach are certainly valid techniques for the types of applications previously mentioned. Weischedel (1991) also feels that it is an inadequate, and probably dangerous, common practice in the North American mining practice to have in-house inspectors carry out the visual inspection while outside inspection companies perform EM inspections as a service. According to Geller *et al* (1989), sole reliance on inspection results obtained by outside inspection services is probably to be blamed for many rope failures in the mining industry.

Weischedel feels (1991) that both visual and EM inspections should be performed or, at least, supervised by knowledgeable in-house personnel.

Obviously, the method of visual inspection of the rope is very simple and does not require expensive instrumentation. It requires experienced personnel to carry it out and only surface flaws can be detected. Visual inspection must be used as a supplement to other test procedures.

The extremely valuable X-ray method yields detailed information on the cable at a defined location. Once a trouble zone in the cable has been found, the X-ray approach will allow for the determination of broken inner wires, degree of damage suffered by the core, etc. This

part of "MECHANICS PAN-AMERICA 1993" edited by MRM Crespo da Silva and CEN Mazzilli
ASME Reprint No AMR134

technique can be used as a supplement to other test procedures.

INDUCED WAVE PROPAGATION METHOD

Vanderveldt and Gilheany (1970) are probably among the first researchers who have studied the propagation of a longitudinal pulse in wire ropes subjected to axial loads with the goal of generating a failure detection method.

Kwun and Burkhardt (1988 and 1990) have developed a nondestructive evaluation method based on the analysis of wave motion in a rope. The technique involves:

1. applying a transverse, impulsive force to a cable
2. detecting the resulting motion of the propagating impulse wave
3. analyzing the detected signal.

Their approach allows for the measurement of tension in the rope and detection of defects such as broken strands and damage caused by corrosion. They emphasize the fact that the propagation motion of the impulse wave, although generally following the well known classical description of the wave motion on a flexible string, is rather complicated (Kwun and Burkhardt, 1992).

This complicated behavior is caused, mainly, by wave dispersion.

The governing partial differential equation, in the case of small amplitude transverse vibrations and when a stiff string is considered, is:

$$\frac{\partial u^2}{\partial x^2} - B\frac{\partial u^4}{\partial x^4} = m\frac{\partial u^2}{\partial t^2} \tag{1}$$

where

u (x, t): transverse displacement
T: tension in the string
B: πr^4 E/4 (flexural rigidity of the string)
E: Young's modulus
r: radius of the string
m: $\rho\pi r^2$ (mass per unit length of the string)
ρ: density.

Since the stiffness term is present, a wave will propagate at a speed which is a function of its frequency. The dispersion relation is:

$$k^2 = -\frac{T}{2B} + \left[\left(\frac{T}{2B}\right)^2 + \frac{m\omega^2}{B}\right]^{1/2} \tag{2}$$

where:
k: wavenumber
ω: angular wave frequency.

When $\omega \to 0$, the phase velocity $V = \omega/k \to \left[\frac{T}{m}\right]^{1/2}$ which is the phase velocity in a flexible string. If the frequency is very high, V approaches $\left(\pi^2 E r^2 f^2 / \rho\right)^{1/4}$ which is the phase velocity in a circular bar of radius r. The dispersive effect is greater with increasing radius in view of the fact that the stiffness is proportional to the fourth power of the radius.

In the case of wire rope each strand and wire can bend individually. Hence, the stiffness of a rope having radius r is smaller than the stiffness of a rod having the same radius (Kwun and Burkhardt, 1992). These authors have shown that the dispersion relation determined experimentally agrees well with the theoretical one derived for a stiff string when proper adjustment is made in the bending stiffness for the rope and which takes into account the relative ease of movement between the individual wires or strands.

THE ELECTROMAGNETIC (EM) INSPECTION METHOD

Two approaches have been developed:

- localized fault inspection (LF)
- loss of metallic cross sectional inspection (LMA).

The first practical LF instruments (developed early in the 30's) used DC magnetization of the rope. They measure the magnetic flux leakage surrounding the rope and saturate magnetically a section of the steel rope in the longitudinal direction by strong permanent or electric magnets. In the case of a broken wire or core, corrosion or abrasion, the magnetic flux is distorted and leaks from the rope. Sense coils or Hall generators, close to the rope, sense the leakage of flux. these transducers sense only *changes* of the magnetic flux.

The LMA AC instruments were developed early in the present century (Wait, 1979).

They are based on AC magnetization of the rope which serves as a ferrous core of a coil or transformer. A variation of the cross sectional area of the rope is tranduced into a change of the impedance of the system and in turn, this change is a measure of the alteration of the cross sectional area. the modern rope evaluation equipment by the electromagnetic approach allows for a simultaneous LMA/LF determination.

Extremely thorough studies on the EM method are available in the open literature (Weischedel, 1985, 1991). In the case of mooring ropes *in-situ* inspection is now possible since a waterproof sensor head has been recently developed (Bavins, 1988)

Clearly the EM inspection method is not applicable in the case of cables made out of synthetic materials.

THE ACOUSTIC EMISSION (AE) METHOD

Acoustic emission is defined as the high frequency stress waves generated by the rapid release of strain energy that occurs within a solid. Sources of acoustic emission are: initiation and propagation of cracks, twin[illegible] [illegible]lip, sudden reorientation of grain boundaries, bubble formation during boiling or martensitic phase transformations (Liptai and Tatro, 1976).

The words "acoustic emission" mean nowadays not only the phenomenon but also a rather complex and sophisticated technology of methods and applications in many fields of engineering: nuclear reactors, structures, space vehicles, materials research, etc (Matthews and Black, 1981).

Earlier studies which made use of acoustic emission for monitoring the "state of health" of ropes employed very simple reasoning: "... in the case of continuous media when a stress wave is emitted due to the propagation of a small flaw or a crack, motion can be detected using a standard accelerometer. It seems reasonable, then, to use a similar detection system which basically consist of tightly woven strands while, in turn, each strand is made up of tightly wound wires" (Laura *et al*, 1969, 1970). Accordingly, if an increasing tensile load is applied, the individual wires fail first and strands later. Preliminary investigations showed that clearly audible stress waves were emitted at approximately 95% of the maximum load allowing then enough time to terminate any further loading of the wire rope. On the other hand, significant stress wave emissions were obtained as a loading to failure was applied to the wire rope.

The experimental investigation previously described was extended by Harris and Dunegan (1974) who employed more sophisticated and sensitive instrumentation and obtained acoustic emissions when performing tensile, fatigue and fatigue with periodic overload tests.

Extremely thorough and successful investigations have been performed at the Defense Research Establishment Pacific late in the 70's (Matthews and Black, 1981) on acoustic emission phenomena of a variable depth sonar tow cable while in operation.

The monitoring system, calibrated by having a cable system crack and fail in service while towing a concrete block, measures the peak amplitude of the transient signals and counts those which exceed IV (indication of general fatigue cracking) and 10V (gives an estimate of broken strands). There is also a unit which provides an audible sound from the acoustic emission signals. Vanderveldt and Tran (1971) were the first researchers to apply the stress wave emission monitoring method to the study of synthetic ropes. These researchers showed that an increase of at least an order of magnitude in the slope of the curve of the number of stress wave emissions vs the applied load is a good indicator of impeding catastrophic failure. No significant differences in stress wave emission characteristics were observed for the types of synthetic ropes considered.

Acoustic emissions of synthetic ropes subjected to loading have been studied by other researchers. Important results were obtained by Williams and Lee (1982). Recently the NDE technique of acoustic-ultrasonic testing has been applied to nylon ropes. (Williams *et al*, 1984)

CONCLUDING REMARKS

Cables, ropes, or yarns are among the oldest tools that man has developed and used in order to improve his living conditions. An eloquent proof of the importance of the subject matter is given by recent publications which deal with the following problems:

- stress analysis in power conductors predicting low cycle fatigue life and static overload conditions under handling and installation conditions (Owen *et al*, 1992)
- bending of spiral strands in the case of large radii of curvature analyzing bending stiffness and overall hysteresis, both being amplitude dependent (Raoof and Huang, 1992)
- prediction of cable damping under cyclic bending (Raoof and Huang, 1991).

Performing tests of the integrity of such ropes without in any way impairing their function is certainly of the utmost importance.

This paper has presented a brief survey of the methods which allow for the evaluation of the "structural health" of mechanical cables.

The obvious question is: Which is the best method? As in many other situations in engineering, there is not a unique answer. In the case of off-shore applications, a suspended bridge and similar structural situations, the EM method is more convenient. If monitoring the "state of health" of a tow cable while in operation is needed, it is necessary to make use of AE techniques. Furthermore, the EM inspection method is not applicable in the case of synthetic ropes while the AE technique gives satisfactory answers.

It appears at this point that the wave propagation approach (Kwun and Burkhard, 1992) exhibits highly promising features but additional research on the methodology is needed. On the other hand, if on adopts the philosophy of monitoring the state of structural health of a cable during its entire operation, one finds that the AE technique is the most convenient one. Obviously, the location of the transducing devices must be chosen very carefully in order to optimize the cost of the monitoring operation. It is important to point out that Malyshev and Chentsov (1989) have proposed an acoustic emission method of determining the actual bending resistance of cables. The method is potentially useful for the inspection of the quality of products and the development of new cable grades.

ACKNOWLEDGEMENT

The present study is sponsored by CONICET Research and Development Program (PID-BID, 1992).

REFERENCES

Bavins TG (1988), NDT of semi-submersible production platform mooring. Proceedings of the Symposium on the Non-Destructive Testing of Wire Rope (British Institute for Non-Destructive Testing, London, UK).

Costello GA (1990), Theory of wire rope. Springer-Verlag, New York.

Geller LE, UDD JE, Blanchard R and Daniel KE (1989), About electromagnetic wire rope testing in New Brunswick mines and related data. Report MRL 89-40. Canada Centre for Mineral and Energy Technology 51 pp.

Goeller JE and Laura PAA (1971), Analytical and experimental study of the dynamic response of segmented cable systems. *J of Sound and Vib* **18**(3) 311-324

Harris DO and Dunegan RL (1974), Acoustic emission testing of wire rope. *Mat Eval*, **15**, 1-6.

Kwun H and Burkhardt GL (1988), Feasibility of nondestructive evaluation of synthetic or wire ropes using a transverse-impulse vibrational wave. *Nondestructive Test Int* **21**, 341-343.

Kwun H and Burkhardt GL (1990), Nondestructive evaluation of ropes by using transverse - impulse vibrational wave method. US Patent N°4, 979, 125.

Kwun H and Burkhardt GL (1992), Experimental investigation of dynamics of transverse-impulse wave propagation and dispersion in steel wire ropes. *J Acoust Soc Am*, **92**(4) Pt 1, 1973-1980.

Laura PAA, Vanderveldt H and Gaffney PG (1969), Acoustic detection of structural failure of mechanical cables. *J Acoust Soc Am* **45**(3) 791-793.

Laura PAA, Vanderveldt H and Gaffney PG (1970), Mechanical behavior of stranded wire rope and feasibility of detection of cable failure. *Marine Tech Soc J* **4**(3) 19-32.

Laura PAA (1993), Non-destructive testing of mechanical cables and monitoring their structural condition. Institute of Applied Mechanics (Bahia Blanca, Argentina) Publication N° 93-15.

Liptai RG and Tatro CA 91976), Acoustic-emission inspection Metal Handbook. Non-destructive inspection, Vol 11, 234-243.

Malyshev LA and Chentsov VP (1989), Acoustic emission method of determining the bending resistance of cables. *Soviet J Nondestructive Testing* **24**, 627-630 (Translated from *Defektos Kopiya*, 1988, 9, 65-69.

Matthews JR and Black MR (1981), Acoustic emission signature of variable depth sonar tow cable. International Advances of Non Destructive Testing 181-214.

Owen DG, Reuben RL, Chen A and Feld G (1992), Some internal mechanical aspects of flexible pipes, cables and umbilicals for marine applicaitons. *Marine Structures* **5**, 387-398.

Raoof M and Huang YP (1991), Upper-bound prediction of cable damping under cyclic bending. *J of Eng Mech ASCE* **117**, 2729-2747.

Raoof M and Huang YP (1992), Free bending characteristics of axially preloaded spiral strands *Proc Instn Civ Engrs Structs and Bldgs* **94**, 469-484.

Vanderveldt H and Gilheany JJ (1970), Propagation of a longitudinal pulse in wire ropes under axial loads. *Exp Mech***10** (10) 401-407.

Vanderveldt HH and Tran Q (1971), Acoustic emission from synthetic rope, *Naval Engrs J* **83**, 65-68.

Wait JR (1979), Review of electromagnetic methods in nondestructive testing of wire ropes. *Proc IEEE* **6**(2) 892-903 *Wire Rope News and Sling Technology*

Weischedel HR (1985), The inspection of wire ropes in service: a critical review. *Mat Eval* **43**(13) 1592-1605

Weischedel HR (1991). The inspection of mine hoist ropes. *Wire Rope News and Sling Tech*, June.

Williams JR and Lee SS (1982), Acoustic emission rupture load characterizations of double-braided nylon. *Marine Tech* **19**, 268-271.

Williams JR, Hainsworth J and Lee SS (1984), Acoustic - ultrasonic nondestructive evaluation of double braided nylon ropes using the stress wave factor. *Fibre Sci Tech* **21**, 169-180.

Green's functions in generalized micropolar thermoelasticity

Ranjit S Dhaliwal and Jun Wang

Department of Mathematics and Statistics
University of Calgary, Calgary, Alberta T2N 1N4

General solution of the generalized micropolar thermoelastic equations has been obtained for arbitrary distribution of the body couples, body forces, and heat sources in an infinite body. Short time solutions have been obtained for the cases of impulsive body force and heat source acting at a point. Numerical values of the short time solutions have been displayed graphically.

INTRODUCTION

In recent years the so-called "second sound" effect in solids has been given increasing attention. This effect arises from the possible transport of heat by a wave propagation process rather than diffusion. Lord and Shulman (1967), Green and Lindsay (1972), Lebon (1982), developed various generalized theories of thermoelasticity based on different approaches to thermodynamics. Boschi and Iesan (1972), Dost and Tabarrok (1978), Chandrasekharaiah (1986) derived various generalized theories of micropolar thermoelasticity. Owing to the newness of these theories, only few problems have been studied by Dhaliwal and Sherief (1981), Sherief (1986; 1992), Ignaczak and Mrowka-Matejewska (1989), Oncu and Moodie (1992) and Wang and Dhaliwal (1993).

In this paper, we study the problem of determining the displacements, rotations, and temperature in an infinite micropolar thermoelastic medium under the action of time dependent body forces, body couples, and heat sources. In section 2, we summarize the basic equations of the generalized micropolar thermoelasticity derived by Chandrasekharaiah (1986). In section 3, we derive the general solution of these equations by using the Fourier-Laplace transforms for any arbitrary distribution of body forces, body couples, and heat sources in an infinite medium. In sections 4 and 5, respectively, we derive solutions for an impulsively applied point body force and heat source. Exact inversions have been obtained in the space domain and Laplace inversions have been obtained only for small time approximations.

PRELIMINARIES

Consider a homogeneous isotropic elastic solid occupying an infinite space. The governing equations of generalized micropolar thermoelasticity are given Chandrasekharaiah (1986) [we have changed the notations of variables in order to compare our results with that for coupled theory derived by Shanker and Dhaliwal (1975)] as

$$(\lambda + \mu - \alpha)u_{j,ji} + (\mu + \alpha)\ddot{u}_{j,ji} + 2\alpha\varepsilon_{ijk}w_{k,j} - \nu\theta_{,i} + \rho X_i = \rho\ddot{u}_i, \tag{2.1}$$

$$(\gamma + \varepsilon)w_{i,jj} + (\beta + \gamma - \varepsilon)w_{i,ji} + 2\alpha\varepsilon_{ijk}u_{k,j} - 4\alpha w_i + JY_i = J\ddot{w}_i, \tag{2.2}$$

$$k\theta_{,ii} = \dot{\theta} + \tau\ddot{\theta} + \eta_{\circ}(\dot{u}_{i,i} + \tau\ddot{u}_{i,i}) - Q - \tau\dot{Q}, \tag{2.3}$$

where

- u_i = the components of the displacement vector
- θ = the temperature deviation above the initial temperature $\theta_{\circ}$
- w_i = the components the microrotation vector
- X_i = the components of body force
- Y_i = the components of body couple
- Q = the strength of internal heat source
- k = the coefficient of heat conduction
- ρ = mass density
- τ = the relaxation time
- J = the rotational inertia
- $\eta_{\circ}$ = $\rho\nu\theta_{\circ}/C_e$
- C_e = the specific heat at constant deformation
- ε_{ijk} = the unit anti-symmetric tensor

and λ, μ, ν, α, β, γ, and ε are material constants.

In above equations, the notation of Cartesian tensor is employed, superposed dots denote the time derivatives and a comma followed by the idex i denotes the partial derivative with respect to x_i.

The basic equations (2.1)-2.3) may be rewritten in vector form as

part of "MECHANICS PAN-AMERICA 1993" edited by M and CEN Mazzilli — ASME Reprint No AMR134
Appl Mech Rev vol 46, no 11, part 2, November 1993

$$(\lambda + 2\mu)\nabla\nabla \cdot \mathbf{u} - (\mu + \alpha)\nabla \times \nabla$$
$$+ 2\alpha\nabla \times \mathbf{w} - \nu\nabla\theta + \rho X = \rho\ddot{\mathbf{u}}, \tag{2.4}$$

$$(\beta + 2\gamma)\nabla\nabla \cdot \mathbf{w} - (\gamma + \varepsilon)\nabla \times \nabla \times \mathbf{w}$$
$$+ 2\alpha\nabla \times \mathbf{u} - 4\alpha\mathbf{w} + JY = J\ddot{\mathbf{w}}, \tag{2.5}$$

$$k\nabla^2\theta = \dot{\theta} + \tau\ddot{\theta} + \eta_o(\nabla\dot{\mathbf{u}} + \tau\nabla\ddot{\mathbf{u}}) - Q - \tau\dot{Q}. \tag{2.6}$$

THE GENERAL SOLUTION OF THE BASIC EQUATIONS

In this section we shall find the displacement vector $\mathbf{u}(x_1, x_2, x_3, t)$, microrotation vector $\mathbf{w}(x_1, x_2, x_3, t)$, and temperature field $\theta(x_1, x_2, x_3, t)$, in an infinite thermoelastic body under the action of time dependent body forces **X**, body couples **Y**, and heat sources Q, ie, we shall find the solution of equations given by (2.4)-(2.6) for $-\infty < x_1, x_2, x_3 < \infty$, $t > 0$, under prescribed body forces, body couples and heat sources, with the initial conditions

$$\mathbf{u}(x_1, x_2, x_3, 0) = \dot{u}(x_1, x_2, x_3, 0) = 0,$$

$$\theta(x_1, x_2, x_3, 0) = \dot{\theta}(x_1, x_2, x_3, 0) = 0,$$

$$\mathbf{w}(x_1, x_2, x_3, 0) = \dot{\mathbf{w}}(x_1, x_2, x_3, 0) = 0,$$

and the regularity conditions

$$\mathbf{u} \to 0,\ \mathbf{w} \to 0,\ \theta \to 0 \text{ as } (x_1, x_2, x_3) \to \pm\infty.$$

To solve the equations (2.4)-(2.6), we shall first reduce them to a simpler form by decomposing the vectors **u, w, X** and **Y** into their potential and solenoidal parts, ie.

$$\mathbf{u} = \nabla\varphi + \nabla \times \Psi, \quad \mathrm{div}\Psi = 0, \tag{3.1}$$

$$\mathbf{w} = \nabla\Sigma + \nabla \times \mathbf{H}, \quad \mathrm{div}\mathbf{H} = 0, \tag{3.2}$$

$$X = \nabla\upsilon + \nabla \times \psi, \quad \mathrm{div}\psi = 0, \tag{3.3}$$

$$Y = \nabla\phi + \nabla \times \eta, \quad \mathrm{div}\eta = 0. \tag{3.4}$$

Substitution of equations (3.1)-(3.4) into the basic equations (2.4)-(2.6), yields

$$[\square_1 D - \omega_1\nabla^2\frac{\partial}{\partial t}(1 + \tau\frac{\partial}{\partial t})]\varphi = -\rho D\upsilon - \frac{q}{p}\nu Q \tag{3.5}$$

$$(\square_2\square_4 + 4\alpha^2\nabla^2)\Psi = 2\alpha J\nabla \times \eta - \rho\square_4\psi, \tag{3.6}$$

$$(\square_2\square_4 + 4\alpha^2\nabla^2)\mathbf{H} = 2\alpha\rho\nabla \times \psi - J\square_2\eta, \tag{3.7}$$

$$\square_3\Sigma + J\phi = 0, \tag{3.8}$$

$$[\square_1 D - \omega_1\nabla^2\frac{\partial}{\partial t}(1 + \tau\frac{\partial}{\partial t})]\theta$$
$$= -\rho\eta_o\nabla^2\frac{\partial}{\partial t}(1 + \tau\frac{\partial}{\partial t})\upsilon - \frac{q}{p}\square_1 Q, \tag{3.9}$$

where

$$D = \nabla^2 - \frac{1}{k}\frac{\partial}{\partial t}(1 + \tau\frac{\partial}{\partial t}), \quad \omega_1 = \eta_o\nu/k,$$

$$\square_1 = (\lambda + 2\mu)\nabla^2 - \rho\frac{\partial^2}{\partial t^2}, \quad \square_2 = (\mu + \alpha)\nabla^2 - \rho\frac{\partial^2}{\partial t^2},$$

$$\square_3 = (\beta + 2\gamma)\nabla^2 - 4\alpha - J\frac{\partial^2}{\partial t^2},$$

$$\square_4 = (\gamma + \varepsilon)\nabla^2 - 4\alpha - J\frac{\partial^2}{\partial t^2}$$

To solve these wave equations, we introduce the Laplace transform $\bar{f}(x_1, x_2, x_3, p)$ of the function $f(x_1, x_2, x_3, t)$ by the relation

$$\bar{f}(x_1, x_2, x_3, p)$$
$$= \int_0^\infty f(x_1, x_2, x_3, t)\exp\{-pt\}dt, \quad \mathrm{Re}(p) > 0, \tag{3.10}$$

and also the Fourier-Laplace transform $\hat{f}(\xi_1, \xi_2, \xi_3, p)$ of the function $f(x_1, x_2, x_3, t)$ by the relation

$$\hat{f}(\xi_1, \xi_2, \xi_3, p)$$
$$= (2\pi)^{-3/2}\int_\Omega \bar{f}(x_1, x_2, x_3, p)\exp\{ix_k\xi_k\}d\Omega \tag{3.11}$$

where $d\Omega = dx_1dx_2dx_3$ and Ω is the x_1, x_2, x_3, - space

Application of (3.10) and (3.11) to equations (3.5)-(3.9) yields the following system of algebraic equations

$$[(\xi^2 + \beta_1^2)(\xi^2 + q) + \omega q\xi^2]\hat{\varphi}$$
$$= \frac{1}{c_1^2}(\xi^2 + q)\hat{\upsilon} - \frac{\nu q}{\rho c_1^2 p}\hat{Q}, \tag{3.12}$$

$$[(\xi^2 + \beta_2^2)(\xi^2 + 2s^* + \beta_4^2) - r^*s^*\xi^2]\hat{\Psi}_i$$
$$= -i\frac{r^*}{c_4^2}\xi_j\varepsilon_{ijk}\hat{\eta}_k + \frac{1}{c_2^2}(\xi^2 + 2s^* + \beta_4^2)\hat{\psi}_i, \tag{3.13}$$

$$[(\xi^2 + \beta_2^2)(\xi^2 + 2s^* + \beta_4^2) - r^*s^*\xi^2]\hat{\mathbf{H}}_i$$
$$= -i\frac{s^*}{c_2^2}\xi_j\varepsilon_{ijk}\hat{\psi}_k + \frac{1}{c_4^2}(\xi^2 + \beta_2^2)\hat{\eta}_i, \tag{3.14}$$

$$(\xi^2+\beta_3^2)\hat{\Sigma} = \frac{1}{c_3^2}\hat{\phi}, \tag{3.15}$$

$$[(\xi^2+\beta_1^2)(\xi^2+q)+\omega q\xi^2]\hat{\theta}$$

$$= \frac{1}{c_1^2}\eta_o k q\hat{\upsilon} + \frac{q}{p}(\xi^2+\beta_1^2)\hat{Q}, \tag{3.16}$$

where

$$c_1^2 = \frac{\lambda+2\mu}{\rho}, \quad c_2^2 = \frac{\mu+\alpha}{\rho},$$

$$c_3^2 = \frac{\beta+2\gamma}{J}, \quad c_4^2 = \frac{\gamma+\epsilon}{J},$$

$$\beta_1 = \frac{p}{c_1}, \quad \beta_2 = \frac{p}{c_2},$$

$$\beta_3 = \left[\frac{p^2+4\alpha/J}{c_3}\right], \quad \beta_4 = \frac{p}{c_4},$$

$$\omega = \frac{k}{\lambda+2\mu}\omega_1 = \frac{\nu\eta_\circ}{\lambda+2\mu}, \quad q = \frac{1}{k}p(1+\tau p),$$

$$r^* = \frac{2\alpha}{\rho c_2^2}, \quad s^* = \frac{2\alpha}{Jc_4^2}.$$

and $\xi^2 = \xi_1^2+\xi_2^2+\xi_3^2$

Taking the Fourier-Laplace transform of (3.1)-(3.4), we find that

$$\hat{u}_i = -i\xi_i\hat{\varphi} - i\xi_j\epsilon_{ijk}\hat{\Psi}_k, \tag{3.17}$$

$$\hat{w}_i = -i\xi_i\hat{\Sigma} - i\xi_j\epsilon_{ijk}\hat{H}_k, \tag{3.18}$$

$$\hat{X}_i = -i\xi_i\hat{\upsilon} - i\xi_j\epsilon_{ijk}\hat{\psi}_k, \tag{3.19}$$

$$\hat{Y}_i = -i\xi_i\hat{\phi} - i\xi_j\epsilon_{ijk}\hat{\eta}_k. \tag{3.20}$$

Substituting for $\hat{\varphi}$, $\hat{\Psi}_k$, $\hat{\Sigma}$, $\hat{H}_k$ from equations (3.17)-(3.20) into equations (3.12)-(3.15) and taking into account the relation

$$\epsilon_{ijk}\epsilon_{kmn} = \delta_{jn}\delta_{mi} - \delta_{jm}\delta_{in}$$

along with the conditions div$\psi = 0$, div$\eta = 0$, where δ_{ij} is the Kronecker delta function, we obtain

$$\hat{u}_i = i\frac{\nu q\xi_i}{\rho c_1^2 p\Delta_1}\hat{Q} - i\frac{\xi^2+q}{c_1^2\Delta_1}\xi_i\hat{\upsilon} + \frac{r^*\xi^2}{c_4^2\Delta_2}\hat{\eta}_i$$
$$- i\frac{\xi_j\epsilon_{ijk}}{c_4^2\Delta_2}(\xi^2+2s^*+\beta_4^2)\hat{\psi}_k, \tag{3.21}$$

$$\hat{w}_i = -\frac{i}{c_3^2(\xi^2+\beta_3^2)}\xi_i\hat{\phi} + \frac{s^*\xi^2}{c_2^2\Delta_2}\hat{\psi}_i$$
$$- i\frac{\xi_j\epsilon_{ijk}}{c_4^2\Delta_2}(\xi^2+\beta_2^2)\hat{\eta}_k, \tag{3.22}$$

where

$$\Delta_1 = (\xi^2+\beta_1^2)(\xi^2+q)+\omega q\xi^2$$
$$= (\xi^2-\lambda_1^2)(\xi^2-\lambda_2^2), \tag{3.23}$$

$$\Delta_2 = (\xi^2+\beta_2^2)(\xi^2+2s^*+\beta_4^2) - r^*s^*\xi^2$$
$$= (\xi^2-\mu_1^2)(\xi^2-\mu_2^2), \tag{3.24}$$

and $\lambda_{1,2}^2$ and $\mu_{1,2}^2$ are the roots of the equations $\Delta_1(\xi^2) = 0$, $\Delta_2(\xi^2) = 0$, respectively. From equation (3.16), we obtain

$$\hat{\theta} = \frac{kq}{c_1^2\Delta_1}\eta_o\hat{\upsilon} + \frac{q}{p\Delta_1}(\xi^2+\beta_1^2)\hat{Q}. \tag{3.25}$$

From equation (3.19) and (3.20), we find that

$$\hat{\upsilon} = i\frac{1}{\xi^2}\xi_k\hat{X}_k, \qquad \hat{\psi}_i = -\frac{i}{\xi^2}\epsilon_{ijk}\xi_j\hat{X}_k, \tag{3.26}$$

$$\hat{\phi} = i\frac{1}{\xi^2}\xi_k\hat{Y}_k, \qquad \hat{\eta}_i = -\frac{i}{\xi^2}\epsilon_{ijk}\xi_j\hat{Y}_k. \tag{3.27}$$

Substituting from equations (3.26) and (3.27) into equations (3.21), (3.22) and (3.25), we obtain

$$\hat{u}_i = i\frac{\nu q\xi_i}{\rho c_1^2 p\Delta_1}\hat{Q} + \frac{\xi^2+q}{c_1^2\Delta_1\xi^2}\xi_i\xi_k\hat{X}_k - \frac{ir^*}{c_4^2\Delta_2}\epsilon_{ijk}\xi_j\hat{Y}_k$$
$$+ \frac{\xi^2+2s^*+\beta_4^2}{c_2^2\Delta_2\xi^2}(\xi^2\hat{X}_i - \xi_i\xi_j\hat{X}_j), \tag{3.28}$$

$$\hat{w}_i = \frac{1}{c_3^2(\xi^2+\beta_3^2)\xi^2}\xi_i\xi_k\hat{Y}_k - \frac{s^*i}{c_2^2\Delta_2}\xi_j\epsilon_{ijk}\hat{X}_k$$
$$+ \frac{\xi^2+\beta_2^2}{c_4^2\Delta_2\xi^2}(\xi^2\hat{Y}_i - \xi_i\xi_k\hat{Y}_k), \tag{3.29}$$

$$\hat{\theta} = \frac{(\xi^2+\beta_1^2)q}{p\Delta_1}\hat{Q} + \frac{\eta_\circ kq}{c_1^2\Delta_1}i\xi_k\hat{X}_k. \tag{3.30}$$

The above system of equations (3.28)-(3.30) give rise to the general solution for the determination of displacement, microrotation, and temperature field for any given body forces, body couples, and heat sources applied in the infinite medium by first inverting the Fourier transform and then inverting the Laplace transform.

If we let $\tau \to 0$, then $q \to p/k$ and the equations (3.28)-(3.30) reduce to the corresponding ones derived by Shanker and Dhaliwal (1975) for the coupled theory. If we let $\alpha \to 0$, then equations (3.28) and (3.29) give rise to the following solution for generalized thermoelasticity

$$\hat{u}_i = i\frac{\nu q\xi_i}{\rho c_1^2 p\Delta_1}\hat{Q} + \frac{\xi^2+q}{c_1^2\Delta_1\xi^2}\xi_i\xi_k\hat{X}_k$$
$$+ \frac{\xi^2\hat{X}_i - \xi_i\xi_j\hat{X}_j}{c_2^2(\xi^2+\beta_2^2)\xi^2}, \tag{3.31}$$

$$\hat{\theta} = \frac{(\xi^2 + \beta_1^2)q}{\Delta_1 p}\hat{Q} + \frac{\eta.\,kq}{c_1^2\Delta_1}i\xi_k\hat{X}_k, \tag{3.32}$$

which agree with the previous results obtained by Wang and Dhaliwal (1993), where dimensionless variables have been used.

THE EFFECT OF AN IMPULSIVELY APPLIED BODY FORCE

In this section we consider the case when a body force is applied impulsively at the origin of an infinite elastic space. For such a body force we may write

$$X = \frac{1}{\rho}\delta(x)\delta(y)\delta(z)\delta(t)\{0,\ 0,\ F\},\ Y = 0,\ Q = 0, \tag{4.1}$$

where $\delta(\cdot)$ is the Dirac delta function, F is a constant, and, for the sake of convenience, we have written (x, y, z) for (x_1, x_2, x_3).

The Fourier-Laplace transform of equation (4.1) gives

$$\hat{X} = \frac{F}{(2\pi)^{3/2}\rho}\{0,\ 0,\ 1\},\quad ,\ \hat{Y} = 0,\quad \hat{Q} = 0. \tag{4.2}$$

Substitution from equation (4.2) into equations (3.28)-(3.30) yields

$$\hat{u}_1(\xi_1,\xi_2,\xi_3,p) = \frac{F}{(2\pi)^{3/2}\rho}\Big[\frac{\xi^2 + q}{c_1^2\Delta_1\xi^2} - \frac{\xi^2 + 2s^* + \beta_4^2}{c_2^2\Delta_2\xi^2}\Big]\xi_1\xi_3, \tag{4.3}$$

$$\hat{u}_2(\xi_1,\xi_2,\xi_3,p) = \frac{F}{(2\pi)^{3/2}\rho}\Big[\frac{\xi^2 + q}{c_1^2\Delta_1\xi^2} - \frac{\xi^2 + 2s^* + \beta_4^2}{c_2^2\Delta_2\xi^2}\Big]\xi_2\xi_3, \tag{4.4}$$

$$\hat{u}_3(\xi_1,\xi_2,\xi_3,p) = \frac{F}{(2\pi)^{3/2}\rho}\Big[\frac{\xi^2 + q}{c_1^2\Delta_1\xi^2}\xi_3^2 + \frac{\xi^2 + 2s^* + \beta_4^2}{c_2^2\Delta_2} - \frac{\xi^2 + 2s^* + \beta_4^2}{c_2^2\Delta_2\xi^2}\xi_3^2\Big], \tag{4.5}$$

$$\hat{w}_1(\xi_1,\xi_2,\xi_3,p) = -\frac{s^*F}{(2\pi)^{3/2}\rho c_2^2\Delta_2}i\xi_2, \tag{4.6}$$

$$\hat{w}_2(\xi_1,\xi_2,\xi_3,p) = \frac{s^*F}{(2\pi)^{3/2}\rho c_2^2\Delta_2}i\xi_3, \tag{4.7}$$

$$\hat{w}_3(\xi_1,\xi_2,\xi_3,p) = 0, \tag{4.8}$$

$$\hat{\theta}(\xi_1,\xi_2,\xi_3,p) = \frac{\eta.\,kFq}{(2\pi)^{3/2}\rho c_1^2\Delta_1}i\xi_3. \tag{4.9}$$

On inverting the Fourier transform with respect to ξ_1, ξ_2, and ξ_3, in equations (4.3)-(4.9), we obtain

$$\bar{u}_1(x,y,z,p) = \frac{iF}{(2\pi)^3\rho}\frac{\partial}{\partial x}\Big(\frac{1}{c_1^2}I_1 - \frac{1}{c_2^2}I_2\Big), \tag{4.10}$$

$$\bar{u}_2(x,y,z,p) = \frac{iF}{(2\pi)^3\rho}\frac{\partial}{\partial y}\Big(\frac{1}{c_1^2}I_1 - \frac{1}{c_2^2}I_2\Big), \tag{4.11}$$

$$\bar{u}_3(x,y,z,p) = \frac{F}{(2\pi)^3\rho}\Big[i\frac{\partial}{\partial z}\Big(\frac{1}{c_1^2}I_1 - \frac{1}{c_2^2}I_2\Big) + \frac{1}{c_2^2}I_3\Big], \tag{4.12}$$

$$\bar{w}_1(x,y,z,p) = \frac{s^*F}{(2\pi)^3\rho c_2^2}\frac{\partial}{\partial y}I_4, \tag{4.13}$$

$$\bar{w}_2(x,y,z,p) = -\frac{s^*F}{(2\pi)^3\rho c_2^2}\frac{\partial}{\partial x}I_4, \tag{4.14}$$

$$\bar{w}_3(x,y,z,p) = 0, \tag{4.15}$$

$$\bar{\theta}(x,y,z,p) = -\frac{\eta.\,kFq}{(2\pi)^3\rho c_1^2}\frac{\partial}{\partial z}I_5, \tag{4.16}$$

where

$$I_1 = \iiint_{-\infty}^{\infty}\frac{(\xi^2 + q)\xi_3}{\xi^2(\xi^2 - \lambda_1^2)(\xi^2 - \lambda_2^2)}\exp\{-i(\xi_1 x + \xi_2 y + \xi_3 z)\}d\xi_1 d\xi_2 d\xi_3, \tag{4.17}$$

$$I_2 = \iiint_{-\infty}^{\infty}\frac{(\xi^2 + 2s^* + \beta_4^2)\xi_3}{\xi^2(\xi^2 - \mu_1^2)(\xi^2 - \mu_2^2)}\exp\{-i(\xi_1 x + \xi_2 y + \xi_3 z)\}d\xi_1 d\xi_2 d\xi_3, \tag{4.18}$$

$$I_3 = \iiint_{-\infty}^{\infty}\frac{\xi^2 + 2s^* + \beta_4^2}{(\xi^2 - \mu_1^2)(\xi^2 - \mu_2^2)}\exp\{-i(\xi_1 x + \xi_2 y + \xi_3 z)\}d\xi_1 d\xi_2 d\xi_3, \tag{4.19}$$

$$I_4 = \iiint_{-\infty}^{\infty}\frac{1}{(\xi^2 - \mu_1^2)(\xi^2 - \mu_2^2)}\exp\{-i(\xi_1 x + \xi_2 y + \xi_3 z)\}d\xi_1 d\xi_2 d\xi_3, \tag{4.20}$$

$$I_5 = \iiint_{-\infty}^{\infty}\frac{1}{(\xi^2 - \lambda_1^2)(\xi^2 - \lambda_2^2)}\exp\{-i(\xi_1 x + \xi_2 y + \xi_3 z)\}d\xi_1 d\xi_2 d\xi_3. \tag{4.21}$$

Using polar coordinates

$$\xi_1 = r_1\cos\theta_1,\ \xi_2 = r_1\sin\theta_1,\ x = r\cos\theta_2,\ y = Y\sin\theta_2,$$

we have found that

$$I_1 = \int_{-\infty}^{\infty} \xi_3 e^{-i\xi_3 z}\int_0^{\infty}\int_0^{2\pi} \frac{(\xi_3^2+r_1^2+q)\exp\{-ir_1r\cos(\theta_1-\theta_2)\}}{(\xi_3^2+r_1^2)(\xi_3^2+r_1^2-\lambda_1^2)(\xi_3^2+r_1^2-\lambda_2^2)} r_1 dr_1 d\theta_1 d\xi_3. \quad (4.22)$$

Evaluating the θ_1 integration, we get

$$I_1 = 2\pi\int_0^{\infty} r_1 J_0(r_1 r)dr_1 \int_{-\infty}^{\infty} \frac{(\xi_3^2 + r_1^2 + q)\xi_3\exp\{-i\xi_3 z\}d\xi_3}{(\xi_3^2 + r_1^2)(\xi_3^2 + r_1^2 - \lambda_1^2)(\xi_3^2 + r_1^2 - \lambda_2^2)}, \quad (4.23)$$

where $J_n(z)$ is the Bessel function of the first kind and of order n. Evaluating ξ_3 integration we find that

$$I_1 = -2\pi i\int_0^{\infty}\Big[\frac{\pi q}{\lambda_1^2\lambda_2^2}\exp\{-|z|r_1\} + \frac{\pi(\lambda_1^2 - q)}{\lambda_1^2(\lambda_1^2-\lambda_2^2)}\exp\{-|z|(r_1^2-\lambda_1^2)^{1/2}\} - \frac{\pi(\lambda_2^2 - q)}{\lambda_2^2(\lambda_1^2-\lambda_2^2)}\exp\{-|z|(r_1^2-\lambda_2^2)^{1/2}\}\Big] r_1 J_0(r_1 r)dr_1. \quad (4.24)$$

Using the known integral (Watson, 1958; p 514), we find that

$$I_1 = -2\pi^2 i\Big[\frac{2q\Gamma(3/2)}{\lambda_1^2\lambda_2^2\sqrt{\pi}}\frac{|z|r}{(z^2+r^2)^{3/2}} + \frac{\lambda_1^2 + q}{\lambda_1^2(\lambda_1^2-\lambda_2^2)}\sqrt{\frac{2}{\pi}}\frac{|z|(i\lambda_1)^{3/2}}{(z^2+r^2)^{3/4}}K_{3/2}[i\lambda_1(z^2+r^2)^{1/2}] + \frac{\lambda_2^2 + q}{\lambda_2^2(\lambda_2^2-\lambda_1^2)}\sqrt{\frac{2}{\pi}}\frac{|z|(i\lambda_2)^{3/2}}{(z^2+r^2)^{3/4}}K_{3/2}[i\lambda_2(z^2+r^2)^{1/2}]\Big], \quad (4.25)$$

where $K_n[Z]$ is the modified Bessel function of the third kind and of order n. Replacing $\lambda_{1,2}$ by $\mu_{1,2}$ and by $2s^* + \beta_4^2$ in equation (4.25), we find that

$$I_2 = -2\pi^2 i\Big[\frac{4s^*\Gamma(3/2)}{\mu_1^2\mu_2^2\sqrt{\pi}}\frac{|z|r}{(z^2+r^2)^{3/2}} + \frac{\mu_2^2+2s^*+\beta_4^2}{\mu_2^2(\mu^2-\mu_1^2)}\sqrt{\frac{2}{\pi}}\frac{|z|(i\mu_2)^{3/2}}{(z^2+r^2)^{3/4}}K_{3/2}[i\mu_2(z^2+r^2)^{1/2}]\Big], + \frac{\mu_1^2+2s^*+\beta_4^2}{\mu_1^2(\mu_1^2-\mu_2^2)}\sqrt{\frac{2}{\pi}}\frac{|z|(i\mu_1)^{3/2}}{(z^2+r^2)^{3/4}}K_{3/2}[i\mu_1(z^2+r^2)^{1/2}] \quad (4.26)$$

Adopting the above procedure, we find that

$$I_3 = (2\pi)^{3/2}(i\mu_1)^{1/2}(z^2 + r^2)^{-1/4}K_{1/2}[i\mu_1(z^2 + r^2)^{1/2}]. \quad)$$

$$I_4 = -\frac{(2\pi)^{3/2}}{\mu_1^2-\mu_2^2}\Big[(i\mu_1)^{1/2}(z^2 + r^2)^{-1/4}K_{1/2}[i\mu_1(z^2 + r^2)^{1/2}] - (i\mu_2)^{1/2}(z^2 + r^2)^{-1/4}K_{1/2}[i\mu_2(z^2 + r^2)^{1/2}]\Big]. \quad (4.28)$$

Replacing $\mu_{1,2}$ by $\lambda_{1,2}$ in equation (4.28), we find that

$$I_5 = -\frac{(2\pi)^{3/2}}{\lambda_1^2-\lambda_2^2}\Big[(i\lambda_1)^{1/2}(z^2 + r^2)^{-1/4}K_{1/2}[i\lambda_1(z^2 + r^2)^{1/2}] - (i\lambda_2)^{1/2}(z^2 + r^2)^{-1/4}K_{1/2}[i\lambda_2(z^2 + r^2)^{1/2}]\Big]. \quad (4.29)$$

It is a formidable task to find the inverse Laplace transform of the equations (4.25)-(4.29). For this reason we have resorted to the case of small time approximations. First, we note that

$$2\lambda_{1,2}^2 = -[\frac{p^2}{c_1^2} + \frac{p}{k}(1+\omega)(1+\tau p)] \pm \sqrt{[\frac{1}{c_1^2}p^2 + \frac{p}{k}(1+\omega)(1+\tau p)]^2 - \frac{4}{c_1^2}\frac{1}{k}p^3(1+\tau p)}, \quad (4.30)$$

$$2\mu_{1,2}^2 = -[(\frac{1}{c_2^2} + \frac{1}{c_4^2})p^2 + (2-\tau^*)s^*] \pm \sqrt{[(\frac{1}{c_2^2} + \frac{1}{c_4^2})p^2 + (2-\tau^*)s^*]^2 - 4p^2(p^2/c_4^2 + 2s^*)/c_2^2}. \quad (4.31)$$

Expanding the above equations binomially and retaining only the necessary terms, we obtain

$$\lambda_1 \approx -a_1 i - m_1 pi, \qquad \lambda_2 \approx -a_2 i - m_2 pi, \quad (4.32)$$

$$\mu_1 \approx n_2 pi, \qquad \mu_1 \approx n_2 pi, \quad (4.33)$$

where

$$m_{1,2} = \frac{\sqrt{2}}{2}\Big[\frac{1}{c_1^2} + \frac{\tau}{k} + \frac{\tau}{k}\omega \mp [(\frac{1}{c_1^2} + \frac{\tau}{k} + \frac{\tau}{k}\omega)^2 - 4\tau/(c_1^2 k)]^{1/2}\Big]^{1/2}, \quad (4.34)$$

$$a_{1,2} = \frac{1}{4m_1}\Big[-\frac{1+\omega}{k} \pm [(\frac{1}{c_1^2} + \frac{\tau}{k} + \frac{\tau}{k}\omega)\frac{1+\omega}{k} - 2/(c_1^2 k)]/[(\frac{1}{c_1^2} + \frac{\tau}{k} + \frac{\tau}{k}\omega)^2 - 4\tau/(c_1^2 k)]\Big], \quad (4.35)$$

$$n_{1,2} = \frac{\sqrt{2}}{2}\Big[\frac{1}{c_2^2} + \frac{1}{c_4^2} \mp [(\frac{1}{c_2^2} + \frac{1}{c_4^2})^2 - 4/(c_2^2 c_4^2)]^{1/2}\Big]^{1/2}, \quad (4.36)$$

Substituting for λ_1, λ_2, μ_1, and μ_2 from equations (4.32) and (4.33) into equations (4.25)-(4.29) and expanding the right hand sides of these equations in inverse powers of p by making use of the relation (Watson, 1958):

$$K_{n+\frac{1}{2}}(z) = \left(\frac{\pi}{2z}\right)^{1/2} e^{-z} \sum_{k=0}^{n} \frac{(n+k)!}{k!(n-k)!} \frac{1}{(2z)^k}, \tag{4.37}$$

we obtain the following expressions for I_i ($i = 1, 2, 3, 4, 5$):

$$\begin{aligned} I_1 \approx 2\pi^2 i\Big[&\frac{|z|}{R^2}e^{-(a_1+m_1 p)R}\left(r_1\frac{1}{p} + s_1\frac{1}{p^2}\right) \\ &+ \frac{|z|}{R^3}e^{-(a_1+m_1 p)R}\, r_1\frac{1}{m_1}\frac{1}{p^2} \\ &+ \frac{|z|}{R^2}e^{-(a_2+m_2 p)R}\left(r_2\frac{1}{p} + s_2\frac{1}{p^2}\right) \\ &+ \frac{|z|}{R^3}e^{-(a_2+m_2 p)R}\, r_2\frac{1}{m_2}\frac{1}{p^2}\Big], \end{aligned} \tag{4.38}$$

$$\begin{aligned} I_2 \approx 2\pi^2 i\Big[&\frac{|z|}{R^2}e^{-n_1 pR}\left(b_1\frac{1}{p} + d_1\frac{1}{p^2}\right) \\ &+ \frac{|z|}{R^3}e^{-n_1 pR}\, b_1\frac{1}{n_1}\frac{1}{p^2} \\ &+ \frac{|z|}{R^2}e^{-n_2 pR}\left(b_2\frac{1}{p} + d_2\frac{1}{p^2}\right) \\ &+ \frac{|z|}{R^3}e^{-n_2 pR}\, b_2\frac{1}{n_2}\frac{1}{p^2}\Big], \end{aligned} \tag{4.39}$$

$$I_3 = 2\pi^2 \frac{1}{R}e^{-n_1 Rp}, \tag{4.40}$$

$$I_4 = \frac{2\pi^2}{n_1^2 - n_2^2}\left[\frac{1}{R}e^{-n_1 Rp} - \frac{1}{R}e^{-n_2 Rp}\right]\frac{1}{p^2}, \tag{4.41}$$

$$I_5 = \frac{2\pi^2}{m_1^2 - m_2^2}\left[\frac{1}{R}e^{-n_1 Rp} - \frac{1}{R}e^{-n_2 Rp}\right]\frac{1}{p^2}, \tag{4.42}$$

where $R = (x^2 + y^2 + z^2)^{1/2}$ and

$$r_1 = \frac{\tau - m_1 k}{k m_1 (m_2^2 - m_1^2)}, \qquad r_2 = \frac{\tau - m_2 k}{k m_2 (m_1^2 - m_2^2)}, \tag{4.43}$$

$$s_1 = \frac{(1-a_1 k)m_1(m_2^2 - m_1^2) - (\tau - m_1 k)\left[a_1(m_2^2 - m_1^2) + 2m_1(m_2 a_2 - m_1 a_1)\right]}{k m_2^2 (m_1^2 - m_2^2)^2}, \tag{4.44}$$

$$s_2 = \frac{(1-a_2 k)m_2(m_1^2 - m_2^2) - (\tau - m_2 k)\left[a_2(m_1^2 - m_2^2) + 2m_2(m_1 a_1 - m_2 a_2)\right]}{k m_1^2 (m_2^2 - m_1^2)^2}, \tag{4.45}$$

$$b_1 = \frac{1 - n_1 c_4^2}{c_4^2 n_1 (n_2 - n_1)}, \qquad b_2 = \frac{1 - n_2 c_4^2}{c_4^2 n_2 (n_1 - n_2)}, \tag{4.46}$$

$$d_1 = \frac{2s^*}{n_1^2 (n_2 - n_1)}, \qquad d_2 = \frac{2s^*}{n_2^2 (n_1 - n_2)}. \tag{4.47}$$

Substituting the above values I_1, I_2, I_3, I_4 and I_5 into equations (4.10)-(4.16), we find that

$$\begin{aligned} \bar{u}_1(x,y,z,p)\frac{4\pi\rho}{F} \approx \frac{|z|x}{c_1^2 R^3}\Big[&\frac{1}{R}m_1 e^{-a_1 R}e^{-m_1 Rp} \\ &+ \left(a_1 r_1 + m_1 s_1 + 3\frac{1}{R}r_1\right)e^{-a_1 R}e^{-m_1 Rp}\frac{1}{p} \\ &+ \left(a_1 s_1 + \frac{2s_1 m_1 + a_1 r_1}{m_1 R} + \frac{3r_1}{m_1 R^2}\right)e^{-a_1 R}e^{-m_1 Rp}\frac{1}{p^2} \\ &+ \frac{1}{R}m_2 e^{-a_2 R}e^{-m_2 Rp} \\ &+ \left(a_2 r_2 + m_2 s_2 + 3\frac{1}{R}r_2\right)e^{-a_2 R}e^{-m_2 Rp}\frac{1}{p} \\ &+ \left(a_2 s_2 + \frac{2s_2 m_2 + a_2 r_2}{m_2 R} + \frac{3r_2}{m_2 R^2}\right)e^{-a_2 R}e^{-m_2 Rp}\frac{1}{p^2}\Big] - \frac{|z|x}{c_2^2 R^3}\Big[\frac{1}{R}n_1 e^{-n_1 Rp} \\ &+ \left(n_1 d_1 + 3\frac{1}{R}b_1\right)e^{-n_1 Rp}\frac{1}{p} \\ &+ \left[\frac{2}{R}d_1 + 3b_1/(n_1 R^2)\right]e^{-n_1 Rp}\frac{1}{p^2} + \frac{1}{R}n_2 e^{-n_2 Rp} \\ &+ \left(n_2 d_2 + \frac{3}{R}b_2\right)e^{-n_2 Rp}\frac{1}{p} \\ &+ \left[\frac{2}{R}d_2 + 3b_2/(n_2 R^2)\right]e^{-n_2 Rp}\frac{1}{p^2}\Big], \end{aligned} \tag{4.48}$$

$$\bar{u}_2(x,y,z,p) = \frac{y}{x}\bar{u}_1(x,y,z,p) \tag{4.49}$$

$$
\begin{aligned}
\bar{u}_3(x,y,z,p)\frac{4\pi\rho}{F} \approx\ & \frac{|z|z}{c_1^2R^3}\Big[\frac{1}{R}m_1e^{-a_1R}e^{-m_1Rp} \\
&+ (a_1r_1 + m_1s_1 + 3\frac{1}{R}r_1)e^{-a_1R}e^{-m_1Rp}\ \frac{1}{p} \\
&+ (a_1s_1 + \frac{2s_1m_1 + a_1r_1}{m_1R} \\
&+ \frac{3r_1}{m_1R^2})e^{-a_1R}e^{-m_1Rp}\ \frac{1}{p^2} \\
&+ \frac{1}{R}m_2e^{-a_2R}e^{-m_2Rp} \\
&+ (a_2r_2 + m_2s_2 + 3\frac{1}{R}r_2)e^{-a_2R}e^{-m_2Rp}\ \frac{1}{p} \\
&+ (a_2s_2 + \frac{2s_2m_2 + a_2r_2}{m_2R} \\
&+ \frac{3r_2}{m_2R^2})e^{-a_2R}e^{-m_2Rp}\ \frac{1}{p^2}\Big] - \frac{|z|z}{c_2^2R^3}\Big[\frac{1}{R}n_1e^{-n_1Rp} \\
&+ (n_1d_1 + 3\frac{1}{R}b_1)e^{-n_1Rp}\ \frac{1}{p} \\
&+ [\frac{2}{R}d_1 + 3b_1/(n_1R^2)]e^{-n_1Rp}\ \frac{1}{p^2} \\
&+ \frac{1}{R}n_2e^{-n_2Rp} + (n_2d_2 + \frac{3}{R}b_2)e^{-n_2Rp}\ \frac{1}{p} \\
&+ [\frac{2}{R}d_2 + 3b_2/(n_2R^2)]e^{-n_2Rp}\ \frac{1}{p^2}\Big] \\
&+ \frac{1}{c_2^2}\ \frac{1}{R}e^{-n_1Rp},
\end{aligned}
\tag{4.50}
$$

$$
\begin{aligned}
\bar{w}_1(x,y,z,p)\frac{4\pi\rho}{F} \approx\ & \frac{s^*y}{c_2^2(n_1^2-n_2^2)R^2}\Big[n_2e^{-n_2Rp}\ \frac{1}{p} \\
&+ \frac{1}{R}e^{-n_2Rp}\ \frac{1}{p^2} - n_1e^{-n_1Rp}\ \frac{1}{p} \\
&- \frac{1}{R}e^{-n_1Rp}\ \frac{1}{p^2}\Big],
\end{aligned}
\tag{4.51}
$$

$$
\bar{w}_2(x,y,z,p) = \frac{x}{y}\bar{w}_1(x,y,z,p) \tag{4.52}
$$

$$
\bar{w}_3(x,y,z,p) = 0, \tag{4.53}
$$

$$
\begin{aligned}
\bar{\theta}(x,y,z,p)\frac{4\pi\rho}{\eta.F} \approx\ & \frac{z}{c_1^2(m_1^2-m_2^2)R^2}\Big[m_1e^{-m_1Rp}\ \frac{1}{p} \\
&+ \frac{1}{R}e^{-m_1Rp}\ \frac{1}{p^2} - m_2e^{-m_2Rp}\ \frac{1}{p} \\
&- \frac{1}{R}e^{-m_2Rp}\ \frac{1}{p^2}\Big].
\end{aligned}
\tag{4.54}
$$

From equations (4.48)-(4.54), ... aplace transform with respect to p (Erd ... tain

$$
\begin{aligned}
u_1(x,y,z,t)\frac{4\pi\rho}{F} \approx\ & \frac{|z|x}{c_1^2R^3}\Big[\frac{1}{R}m_1e^{-a_1R}\delta(t-m_1R) \\
&+ (a_1r_1 + m_1s_1 + 3\frac{1}{R}r_1)e^{-a_1R}H(t-m_1R) \\
&+ (a_1s_1 + \frac{2s_1m_1 + a_1r_1}{m_1R} \\
&+ \frac{3r_1}{m_1R^2})e^{-a_1R}A(t-m_1R) \\
&+ \frac{1}{R}m_2e^{-a_2R}\delta(t-m_2R) \\
&+ (a_2r_2 + m_2s_2 + 3\frac{1}{R}r_2)e^{-a_2R}H(t-m_2R) \\
&+ (a_2s_2 + \frac{2s_2m_2 + a_2r_2}{m_2R} + \frac{3r_2}{m_2R^2}) \\
&\times e^{-a_2R}A(t-m_2R)\Big] - \frac{|z|x}{c_2^2R^3}\Big[\frac{1}{R}n_1\delta(t-n_1R) \\
&+ (n_1d_1 + 3\frac{1}{R}b_1)H(t-n_1R) \\
&+ [\frac{2}{R}d_1 + 3b_1/(n_1R^2)]A(t-n_1R) \\
&+ \frac{1}{R}n_2\delta(t-n_2R) + (n_2d_2 + \frac{3}{R}b_2)H(t-n_2R) \\
&+ [\frac{2}{R}d_2 + 3b_2/(n_2R^2)]A(t-n_2R)\Big],
\end{aligned}
\tag{4.55}
$$

$$
u_2(x,y,z,t) = u_1(y,x,z,t), \tag{4.56}
$$

$$
\begin{aligned}
u_3(x,y,z,t)\frac{4\pi\rho}{F} \approx\ & \frac{|z|z}{c_1^2R^3}\Big[\frac{1}{R}m_1e^{-a_1R}\delta(t-m_1R) \\
&+ (a_1r_1 + m_1s_1 + 3\frac{1}{R}r_1)e^{-a_1R}H(t-m_1R) \\
&+ (a_1s_1 + \frac{2s_1m_1 + a_1r_1}{m_1R} \\
&+ \frac{3r_1}{m_1R^2})e^{-a_1R}A(t-m_1R) + \frac{1}{R}m_2e^{-a_2R}\delta(t-m_2R) \\
&+ (a_2r_2 + m_2s_2 + 3\frac{1}{R}r_2)e^{-a_2R}H(t-m_2R) \\
&+ (a_2s_2 + \frac{2s_2m_2 + a_2r_2}{m_2R} \\
&+ \frac{3r_2}{m_2R^2})e^{-a_2R}A(t-m_2R)\Big] \\
&- \frac{|z|z}{c_2^2R^3}\Big[\frac{1}{R}n_1\delta(t-n_1R) + (n_1d_1 + 3\frac{1}{R}b_1)H(t-n_1R) \\
&+ [\frac{2}{R}d_1 + 3b_1/(n_1R^2)]A(t-n_1R) \\
&+ \frac{1}{R}n_2\delta(t-n_2R) + (n_2d_2 + \frac{3}{R}b_2)H(t-n_2R) \\
&+ [\frac{2}{R}d_2 + 3b_2/(n_2R^2)]A(t-n_2R)\Big] \\
&+ \frac{1}{c_2^2}\ \frac{1}{R}\delta(t-n_1R),
\end{aligned}
\tag{4.57}
$$

$$
\begin{aligned}
w_1(x,y,z,t)\frac{4\pi\rho}{F} \approx\ & \frac{s^*y}{c_2^2(n_1^2-n_2^2)R^2}\Big[n_2H(t-n_2R) \\
&+ \frac{1}{R}A(t-n_2R) - n_1H(t-n_1R) - \frac{1}{R}A(t-n_1R)\Big],
\end{aligned}
\tag{4.58}
$$

$$w_2(x,y,z,t) = -w_1(y,x,z,t), \tag{4.59}$$

$$w_3(x,y,z,t) = 0, \tag{4.60}$$

$$\theta(x,y,z,t)\frac{4\pi\rho}{\eta.F} \approx \frac{z}{c_1^2(m_1^2-m_2^2)R^2}\Big[m_1H(t-m_1R) + \frac{1}{R}A(t-m_1R) - m_2H(t-m_2R) - \frac{1}{R}A(t-m_2R)\Big]. \tag{4.61}$$

where

$$A(t-a) = \begin{cases} 0 & \text{for } 0 < t < a, \\ t-a & \text{for } t > a, \end{cases} \tag{4.62}$$

$H(t)$ is the Heaviside step function and $\delta(t)$ is the Dirac delta function.

From equations (4.55)-(4.61), we note that the displacement components have four inifinite discontinuities at $t = m_1 R$, $t = m_2 R$, $t = n_1 R$ and $t = n_2 R$, due to the presence of Dirac delta functions. The microrotation components w_1 and w_2 have only two finite discontinuities at $t = n_1R$ and $t = n R$, with the respective jumps of the magnitudes

$$\frac{F}{4\pi\rho}\frac{s^*\zeta}{c_2^2(n_2^2-n_1^2)R^2}n_1 \quad \text{and} \quad \frac{F}{4\pi\rho}\frac{s^*\zeta}{c_2^2(n_1^2-n_2^2)R^2}n_2,$$

where $\zeta = y$ for w_1 and $\zeta = x$ for w_2. The third microrotation component w_3 vanishes identically when the applied body force is in the z-direction. The temperature field has only two finite discontinuities at $t = m_1 R$ and $t = m_2 R$, with jumps of magnitudes

$$\frac{F}{4\pi\rho}\frac{\eta.zm_1}{c_1^2(m_1^2-m_2^2)R^2} \quad \text{and} \quad \frac{F}{4\pi\rho}\frac{\eta.zm_2}{c_1^2(m_2^2-m_1^2)R^2}$$

respectively. These jumps diminish with the increase of the distance of the disturbance from the origin.

THE EFFECT OF IMPULSIVELY APPLIED HEAT SOURCE

Consider when a heat source of constant strength S is applied impulsively at the origin. Then we may take

$$Q(x,y,z,t) = S\delta(x)\delta(y)\delta(z)\delta(t), \quad X = 0, \quad Y = 0. \tag{5.1}$$

In our transform notation this can be written as

$$\hat{Q}(\xi_1,\xi_2,\xi_3,p) = \frac{S}{(2\pi)^{3/2}}, \quad \hat{X} = 0, \quad \hat{Y} = 0. \tag{5.2}$$

Substituting from equation (5.2) in equations (3.28)-(3.30), we find that

$$(\hat{u}_1,\hat{u}_2\ \hat{u}_3) = \frac{\nu Sq}{(2\pi)^{3/2}\rho c_1^2 p}\frac{i}{\Delta_1}(\xi_1,\xi_2,\xi_3), \tag{5.3}$$

$$\hat{\theta}(\xi_1,\xi_2,\xi_3,p) = \frac{Sq}{(2\pi)^{3/2}p}\frac{\xi^2+\beta_1^2}{\Delta_1}, \tag{5.4}$$

$$\hat{w}_i(\xi_1,\xi_2,\xi_3,p) \equiv 0, \quad i = 1,2,3. \tag{5.5}$$

Inverting the Fourier transform with respect to ξ_1, ξ_2 and ξ_3 in the above equations, we obtain

$$(\bar{u}_1,\bar{u}_2,\bar{u}_3) = \frac{-\nu Sq}{(2\pi)^3\rho c_1^2 p}\Big(\frac{\partial}{\partial x},\frac{\partial}{\partial y},\frac{\partial}{\partial z}\Big)I_5, \tag{5.6}$$

$$\bar{\theta}(x,y,z,p) = \frac{Sq}{(2\pi)^3 p}I_6, \tag{5.7}$$

where I_5 is defined in equation (4.29) and

$$I_6 = \iiint_{-\infty}^{\infty}\frac{\xi^2+\beta^2}{(\xi^2-\lambda_1^2)(\xi^2-\lambda_2^2)}\exp\{-i(\xi_1 x + \xi_2 y + \xi_3 z)\}d\xi_1 d\xi_2 d\xi_3. \tag{5.8}$$

Integrating equation (5.8), we obtain

$$I_6 = 2\pi^2\sqrt{\frac{2}{\pi}}\Big[\frac{\lambda_1^2+\beta_1^2}{\lambda_1^2-\lambda_2^2}\frac{(i\lambda_1)^{1/2}}{R^{1/2}}K_{1/2}(i\lambda_1 R) - \frac{\lambda_2^2+\beta_1^2}{\lambda_1^2-\lambda_2^2}\frac{(i\lambda_2)^{1/2}}{R^{1/2}}K_{1/2}(i\lambda_2 R)\Big]. \tag{5.9}$$

It may be noticed that this is a spherically symmetric case and we will find the radial displacement u_R instead of u_1, u_2 and u_3. From equation (5.6), we see that

$$\bar{u}_R(R,t) = \frac{-\nu Sq}{(2\pi)^3\rho c_1^2 p}\frac{\partial}{\partial R}I_5. \tag{5.10}$$

Using equation (4.42), we find that

$$\bar{u}_R(R,p)\frac{4\pi\rho k}{\nu S} = \frac{1}{c_1^2 R}\Big[\tau n_1 e^{-n_1 R p} - \tau n_2 e^{-n_2 R p} + (n_1 + \frac{\tau}{R})e^{-n_1 R p}\frac{1}{p} - (n_2 + \frac{\tau}{R})e^{-n_2 R p}\frac{1}{p} + \frac{1}{R}e^{-n_1 R p}\frac{1}{p^2} - \frac{1}{R}e^{-n_2 R p}\frac{1}{p^2}\Big]. \quad (5.11)$$

Expanding the right hand terms of equation (5.9) in the ascending powers of $\frac{1}{p}$ and retaining only the necessary terms, we obtain

$$I_6 = 2\pi^2\frac{1}{R}\Big[(h_1 + h_2\frac{1}{p} + h_3\frac{1}{p^2})e^{-(a_1+m_1 p)R} + (l_1 + l_2\frac{1}{p} + l_3\frac{1}{p^2})e^{-(a_2+m_2 p)R}\Big], \quad (5.12)$$

where

$$h_1 = \frac{1 - m_1^2 c_1^2}{c_1^2(m_2^2 - m_1^2)}, \quad (5.13)$$

$$h_2 = 2\,\frac{a_1 m_1 c_1^2(m_1^2 - m_2^2) + (a_1 m_1 - a_2 m_2)(1 - m_1^2 c_1^2)}{c_1^2(m_2^2 - m_1^2)^2}, \quad (5.14)$$

$$h_3 = 2\,\frac{a_1^2(m_1^2 - m_2^2)c_1^2 + (a_1^2 - a_2^2)(1 - m_1^2 c_1^2)}{c_1^2(m_2^2 - m_1^2)^2} + \frac{4(a_1 m_1 - a_2 m_2)h_2}{m_2^2 - m_1^2}, \quad (5.15)$$

$$l_1 = \frac{1 - m_2^2 c_1^2}{c_1^2(m_1^2 - m_2^2)}, \quad (5.16)$$

$$l_2 = 2\,\frac{a_2 m_2 c_1^2(m_2^2 - m_1^2) + (a_2 m_2 - a_1 m_1)(1 - m_2^2 c_1^2)}{c_1^2(m_1^2 - m_2^2)^2}, \quad (5.17)$$

$$l_3 = 2\,\frac{a_2^2(m_2^2 - m_1^2)c_1^2 + (a_2^2 - a_1^2)(1 - m_2^2 c_1^2)}{c_1^2(m_1^2 - m_2^2)^2} + \frac{4(a_2 m_2 - a_1 m_1)l_2}{m_1^2 - m_2^2}. \quad (5.18)$$

Substituting from equation (5.12) into equation (5.7), we find that

$$\bar{\theta}(R, p)\frac{4\pi k}{S} = \frac{1}{R}\Big[\tau h_1 p + h_1 + \tau h_2 + (h_2 + \tau h_3)\frac{1}{p} + h_3\frac{1}{p^2}\Big]e^{-a_1 R}e^{-m_1 R p} + \frac{1}{R}\Big[\tau l_1 p + l_1 + \tau l_2 + (l_2 + \tau l_3)\frac{1}{p} + l_3\frac{1}{p^2}\Big]e^{-a_2 R}e^{-m_2 R p}. \quad (5.19)$$

On inverting the Laplace transform in equations (5.11) and (5.19), we obtain the displacement and temperature field for the case of impulsively applied heat source as

$$u_R(R,t)\frac{4\pi\rho k}{\nu S} = \frac{1}{c_1^2 R}\Big[\tau n_1\delta(t - n_1 R) - \tau n_2\delta(t - n_2 R) + (n_1 + \frac{\tau}{R})H(t - n_1 R) - (n_2 + \frac{\tau}{R})H(t - n_2 R) + \frac{1}{R}A(t - n_1 R) - \frac{1}{R}A(t - n_2 R)\Big]. \quad (5.20)$$

$$\theta(R, t)\frac{4\pi k}{S} = \Big[\tau h_1\delta'(t - m_1 R) + (h_1 + \tau h_2)\delta(t - m_1 R) + (h_2 + \tau h_3)H(t - m_1 R) + h_3 A(t - m_1 R)\Big]\frac{1}{R}e^{-a_1 R} + \Big[\tau l_1\delta'(t - m_2 R) + (l_1 + \tau l_2)\delta(t - m_2 R) + (l_2 + \tau l_3)H(t - m_2 R) + l_3 A(t - m_2 R)\Big]\frac{1}{R}e^{-a_2 R}. \quad (5.21)$$

From equations (5.20) and (5.21), we note that the radial displacement u_R and temperature field θ have two infinite discontinuities each at $t = n_1 R$, $t = n_2 R$ and $t = m_1 R$, $t = m_2 R$ respectively while in this case the microrotation vector is identically equal to zero.

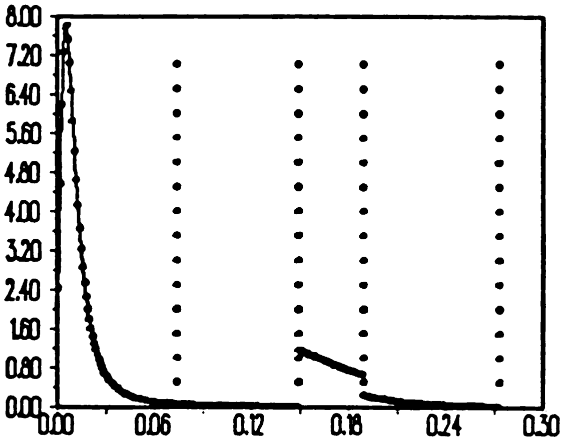

Fig 1. Numerical values of $U_r = \dfrac{4\pi\rho}{F} u_r \times 10^{-4}$ *vs* r at z = 0.01 for the case of impulsively applied body force.

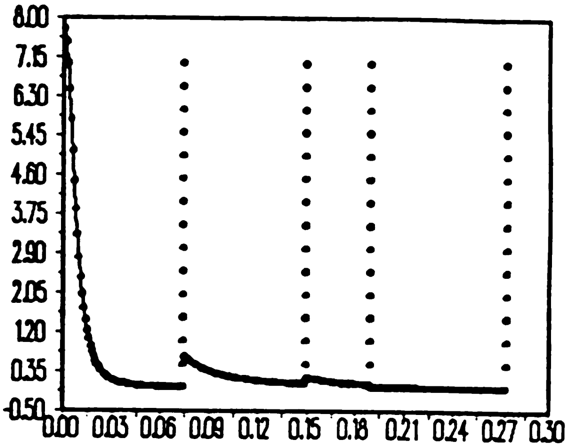

Fig 2. Numerical values of $U_z = \dfrac{4\pi\rho}{F} u_z \times 10^{-4}$ *vs* r at z = 0.01 for the case of impulsively applied body force.

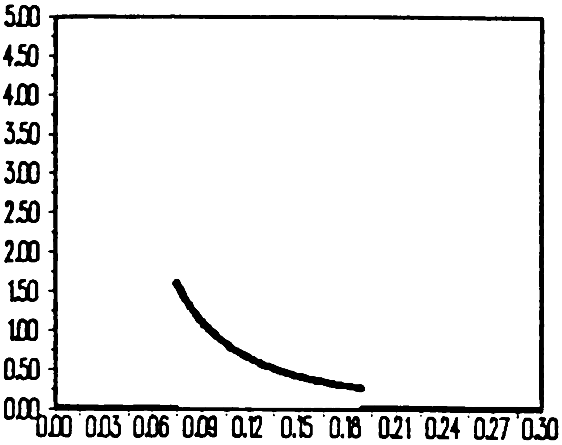

Fig 3. Numerical values of $W_r = \dfrac{4\pi\rho}{F} w_r / s^*$ *vs* r at z = 0.01 for the case of impulsively applied body force.

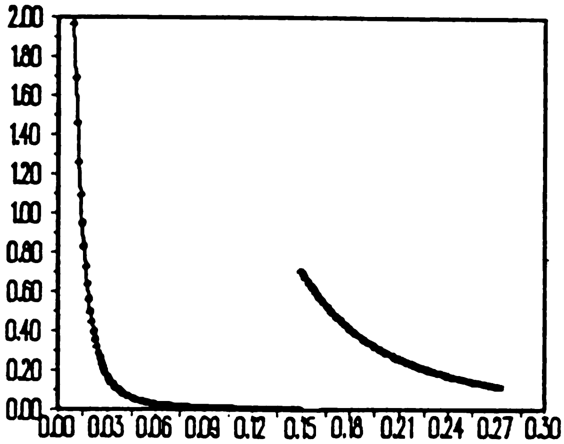

Fig 4. Numerical values of $T = \dfrac{4\pi\rho}{\eta \circ F} \theta$ *vs* r at z = 0.01 for the case of impulsively applied body force.

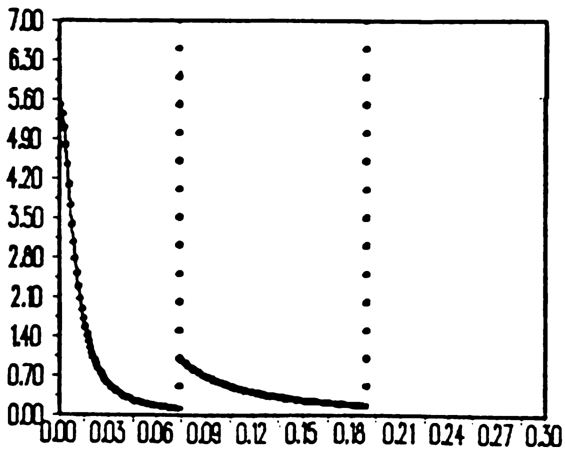

Fig 5. Numerical values of $U_r = \dfrac{4\pi\rho k}{vS} u_R$ *vs* R for the case of impulsively applied heat source.

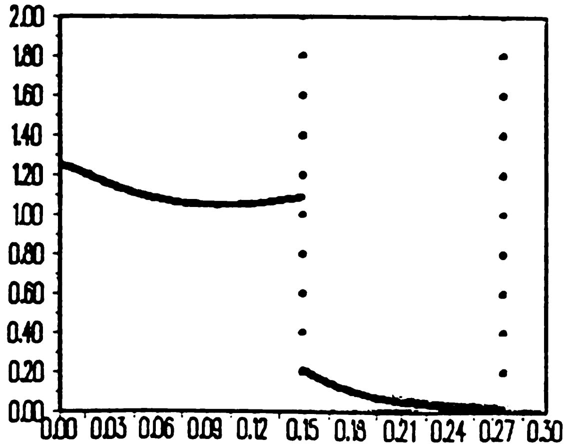

Fig 6. Numerical values of $T = \dfrac{4\pi k}{S} \theta \times 10^{-5}$ *vs* R for the case of impulsively applied heat source.

NUMERICAL RESULTS AND CONCLUSIONS

From equations (4.55)-(4.61) and equations (5.20)-(5.21), it is apparent that for the generalized problems, the displacement, microrotation and temperature fields vanish identically for $R > t/M$, where $M = \max\{m_1, m_2, n_1, n_2\}$, due to the finite supports of functions $H(t\text{-}MR)$ and $A(t\text{-}MR)$ for fixed t and constant M; hence the effect of the body force or heat source is confined to a bounded but time-dependent region of space surrounding the point where the external load is applied. This means that we have a signal propagating with a finite speed.

We have calculated the numerical values of the displacement, microrotation, and temperature field for the cases of impulsively applied body force and heat source. To obtain these numerical values, we have taken, as in Shanker and Dhaliwal (1975), $c_1 = 5.2$, $c_2 = 3.8$, $c_3 = 3.45$, $c_4 = 1.5$, $\omega = 0.0729$, $k = 1$, $\tau = 0.1$ and $t = 0.05$.

For the case of an impulsive body force, the numerical values have been calculated at a plane $z = 0.01$ along the r axis, in the cylindrical polar coordinates, and have been displayed in Figs 1-4, in which the dotted vertical lines denote the infinite discontinuities. In this case, displacements have infinite discontinuities, at r = 0.074137, 0.149528, 0.189498, and 0.273741.

The microrotation component w_r has only two finite discontinuities at r = 0.074137 and 0.189498 with jumps of magnitude 1.597888 and 0.257279, respectively. While the component w_z is identically zero.

The temperature also has two finite discontinuities at r = 0.149528 and 0.273741 with jumps of magnitude 0.699699 and 0.116881, respectively.

For the case of impulsively applied heat source, the numerical results are calculated along R axis and have been shown in Figs 5 and 6. the radial displacement, in this case, has two infinite discontinuities at R = 0.074808 and 0.189762 while the temperature has two infinite discontinuities at R = 0.149862 and 0.273924. The components of microrotation vector are identically zero.

REFERENCES

Boschi, E and Iesan, D (1972). A generalized theory of linear micropolar thermoelasticity, *Meccanica*, **3**, 154-157.

Chandrasekharaiah, DS (1986). Heat-flux dependent micropolar thermoelasticity, *Int J Engng Sci*, **24**, 1389-1395.

Dhaliwal, RS and Sherief, HH (1981). Generalized one-dimensional thermal-shock problem for small times, *J Therm Stresses*, **4**, 407-420.

Dost, S and Tabarrok, B (1978). Generalized micropolar thermoelasticity, *Int J Engng Sci*, **16**, 173-183.

Erdelyri, A (1954). Tables of integral transforms, Vol 1, 2, McGraw-Hill.

Green, AE and Lindsay, KA (1972). Thermoelasticity, *J Elasticity*, **2**, 1-7.

Ignaczak, J and Mrowka-Matejewska, E (1990). One-dimensional Green's function in temperature-rate dependent thermoelasticity, *J Therm Stresses*, **13**, 281-296.

Lebon, G (1982). A generalized theory of thermoelasticity, *J Tech Phys*, **23**, 37-46.

Lord, H and Shulman, Y (1967). A generalized dynamical theory of thermoelasticity, *J Mech Phys Solids*, **15**, 299-309.

Shanker, MU and Dhaliwal, RS (1975). Dynamic coupled thermoelastic problems in micropolar theory - I, *Int J Engng Sci*, **13**, 121-148.

Sherief, HH (1986). Fundamental solution of the generalized thermoelastic problem for short times, J Therm Stresses, **9**, 151-164.

Sherief, HH (1992). Fundamental solution for thermoelasticity with two relaxation times, *Int J Engng Sci*, **30**, 861-870.

Oncu, TS and Moodie, TB (1992). On the propagation of thermoelastic waves in temperature-rate dependent materials, *J Elasticity*, **29**, 263-281.

Wang, J and Dhaliwal, RS (1993). Fundamental solutions of the generalized thermoelastic equations, *J Therm Stresses* **16** 135-161.

Watson, GN (1958). A treatize on the theory of Bessel functions, Cambridge University Press.

Principles and the uncertainty principles of the probabilistic strength of materials and their applications to seismology

P Kittl, G Díaz and V Martínez

Departamento de Ingeniería de los Materiales, IDIEM, Facultad de Ciencias Físicas y Matemáticas, Universidad de Chile, Casilla 1420, Santiago, Chile.

The principles of Fracture-Statistics Mechanics are presented using two functional equations, namely one for the cumulative probability of fracture, and another for the local probability of fracture. These two functional equations are independent and they become compatible only when the volume considered is very small. The determination of the specific-risk function can be made by means of integral equations, without having to specify the analytical expression for this function. This two principles give two principles of uncertainty. Some applications to seismology are given where it is shown that the possibilities of predicting the instant of occurrence and the magnitude of an earthquake are null. Only the probability of occurrence of an earthquake of a given magnitude in a given place can be known. The instant of occurrence, the magnitude and the location are aleatory.

INTRODUCTION

In any discipline, it is important to know which are the hypothesis employed for its development. Thus, it is obtained a hypothetic-deductive system that, when it does not result in its applications, permits to check rapidly the hypothesis or models in order to produce a new model or a new theory that corresponds to the events occurred. In the present work, it is attempted to do this. One of the unavoidable consequences of the present theory is the impossibility of predicting that one is going to occur, which is expressed by means of the uncertainty principles. Let suppose that we have a set of fractures (earthquakes), from where we choose some of them (the earthquakes already occurred), and that we also require to know the stress (magnitude of the earthquake) and in what place of the next sample (earthquake epicenter) will occur the fracture (earthquake). In such a case, the uncertainty principles indicate that this is impossible. In the following, the above ideas anticipated will be developed.

PRINCIPLES OF THE PROBABILISTIC STRENGTH OF MATERIALS

The cumulative probability of fracture in an isotropic brittle body subjected to a constant stress field σ can be determined [1,2] using the following functional equation:

$$\tilde{F}_{12}(V = V_1 + V_2, \sigma) = \tilde{F}_1(V_1, \sigma)\tilde{F}_2(V_2, \sigma), \qquad (1)$$

where V_1 and V_2 are the volumes resulting from an arbitrary disjointed division of the body of volume V. $\tilde{F}_{12}$ is the cumulative probability of nonfracture of the whole volume V, and $\tilde{F}_1$ and $\tilde{F}_2$ are the cumulative probabilities of nonfracture of volumes V_1 and V_2, respectively. The boundary condition $\tilde{F}_{12}(0,\sigma) = \tilde{F}_1(0, \sigma) = \tilde{F}_2(0,\sigma) = 1$ yields easily $\tilde{F}_{12} = \tilde{F}_1 = \tilde{F}_2 = F$ and then functional Eq 1 has a solution already indicated by Euler:

$$F(V,\sigma) = 1 - \tilde{F}(V,\sigma) = 1 - \exp\left\{-\frac{V}{V_0}\phi_1(\sigma)\right\}, \qquad (2)$$

where V_0 is the unit volume and $\phi_1(\sigma)$ is the specific-risk-of-fracture function. This formula given by Weibull can be easily generalized for uniaxial variable-stress fields:

$$1-F(V,\sigma) = \lim_{N\to\infty}\prod_{i=1}^{N}\left[1-F(V_i,\sigma_i)\right] = \lim_{N\to\infty}\prod_{i=1}^{N}\exp\left[-\frac{V_i}{V_o}\phi_1(\sigma_i)\right] = \lim_{N\to\infty}\exp\left[-\sum_{i=1}^{N}\frac{V_i}{V_o}\phi_1(\sigma_i)\right]$$

$$\Rightarrow F(V,\sigma) = 1 - \exp\left\{-\frac{1}{V_o}\int_V \phi_1[\sigma(r)]dV\right\}, \tag{3}$$

where r is the position vector, $\sigma(r) \le \sigma$ is the stress field, and the volume is determined by the condition $\sigma(r) \ge 0$. When $F(V,\sigma)$ is experimentally known and $\sigma(r)$ is obtained from the Theory of Elasticity then integral Eq 3 can be solved in particular cases.

As regards the local probability of fracture F_L, *ie* the percentage of fractures starting in a given region of the body subjected to some stress, the proofs known so far [3,4] as obtained by a passage to the limit. The following discussion shows that it cannot be otherwise and it supplies an expression for ascertaining this percentage.

Since $F_L(V_1,\sigma) = n_1/N$ and $F_L(V_2,\sigma) = n_2/N$ where n_1 and n_2 are the numbers of the fractures that are started in V_1 and V_2, respectively, and N is the total number of test — with $n_1/n_2 = V_1/V_2$ — then the local probability of fracture is given by the following functional equation:

$$F_L(V_1,\sigma)V_2 - F_L(V_2,\sigma)V_1 = 0 \tag{4}$$

Putting $V_1 = V$ and $V_2 = V + \Delta V$, $\Delta V \longrightarrow 0$, yields:

$$F_L(V,\sigma) = F_L'(V,\sigma)V, \tag{5}$$

whose solution is:

$$0 \le F_L(V,\sigma) = \frac{V}{V_o}\phi_2(\sigma) \le 1, \tag{6}$$

in which $\phi_2(\sigma)$ must be determined.

Thus the principles of Fracture-Statistics Mechanics are represented by functional Eqs 1 and 4 (whose solutions are 2 and 6) that are independent and incompatible except in the region where $(V/V_0)\phi_1(\sigma)$ and $(V/V_0)\phi_2(\sigma)$ tend towards zero. In order that the functions become equal in that boundary then $\phi_1 = \phi_2$ and accordingly

$$F(V,\sigma) = F_L(V,\sigma) = \frac{V}{V_o}\phi(\sigma)$$
$$\frac{V}{V_o}\phi(\sigma) \to 0. \tag{7}$$

The foregoing means that the local probability of fracture can be determined only by a passage to the limit in a very small region of the total body. Hence Eq 7 becomes:

$$\frac{dn}{N} = \frac{\phi[\sigma(r)]}{V_o}dV, \tag{8}$$

where dn is the number of the fractures started in dV. The integration of Eq 8 produces:

$$\frac{n}{N} = \frac{1}{V_o}\int_V \phi[\sigma(r)]dV;\ r \in V[\sigma(r) \ge 0], \tag{9}$$

and the elimination of N from Eqs 8 and 9 yields:

$$\frac{dn}{n} = \frac{\phi[\sigma(r)]dV}{\int_{rev[\sigma(r)\ge 0]}\phi[\sigma(r)]dV}. \tag{10}$$

From Eq 10, where $\sigma(r) = \sigma$ = constant, it is easy to reobtain $n_1/n_2 = V_1/V_2$.

If the percentage of fractures in some volume $V_1 \le V$ is to be ascertained, then Eq 10 must be integrated in this volume, assuming that $\phi(\sigma)$ is known. If $dn/ndV = 1/g(r,\sigma)$ is already known then Eq 10 is converted into an integral equation allowing to obtain $\phi(\sigma)$:

$$\int_{rev[\sigma(r)\ge 0]}\phi[\sigma(r)]dV = g(r,\sigma)\phi[\sigma(r)]. \tag{11}$$

Integral equation 11 is a particular instance of integral equation 3 and it allows to obtain $\phi(\sigma)$ excepting a constant factor. Integral equation (11) becomes trivial solely when $\sigma(r) = \sigma$, *ie* when the stress field is uniform; hence the particular instances of the solutions will be dealt with in other works. As $\sigma(r) = \sigma f(r)$, where $|f(r)| \le 1$, the expression of dn/ndV tends towards a finite limit when σ tends to infinite. In the stress space the integral equation 11 is transformed into

$$\int_0^\sigma \phi(\Sigma)dV(\Sigma,\sigma) = g(\sigma)\phi(\sigma). \tag{12}$$

A great number of works supports the mentioned theories and $\phi(\sigma)$ can be expressed in the following form of Weibull:

$$\phi(\sigma)=\begin{Bmatrix}\left(\dfrac{\sigma-\sigma_L}{\sigma_0}\right)^m & \sigma\geq\sigma_L \\ 0 & \sigma<\sigma_L\end{Bmatrix} \tag{13}$$

and Kies-Kittl:

$$\phi(\sigma)=\begin{Bmatrix}K\left(\dfrac{\sigma-\sigma_L}{\sigma_S-\sigma}\right)^m & \sigma_L\leq\sigma\leq\sigma_S \\ 0 & 0\leq\sigma\leq\sigma_L \\ \infty & \sigma>\sigma_S\end{Bmatrix} \tag{14}$$

Equation 10 coincides with that one previously obtained by Kittl and Camilo [4]. It is equivalent to the one obtained by Oh and Finnie [3] solely when $\phi(\sigma)=(\sigma/\sigma_0)^m$ where σ_0 and m are real numbers greater than zero.

THE UNCERTAINTY PRINCIPLES OF PROBABILISTIC STRENGTH OF MATERIALS

In Probabilistic Strength of Materials [2], when $\phi(\sigma)$ has the expression given by formula (3), the following relationships are well known:

$$\bar{\sigma}=\int_0^\infty \sigma\frac{dF}{d\sigma}d\sigma=\sigma_0\left(\frac{V}{V_0}\right)^{-1/m}\Gamma\left(1+\frac{1}{m}\right)+\sigma_L \tag{15}$$

$$\Delta\sigma=\int_0^\infty(\sigma-\bar{\sigma})^2\frac{dF}{d\sigma}d\sigma=\sigma_0\left(\frac{V}{V_0}\right)^{-1/m}$$

$$\times\left\{\Gamma\left(1+\frac{2}{m}\right)-\Gamma^2\left(1+\frac{1}{m}\right)\right\}^{1/2} \tag{16}$$

By means of simple transformations it is obtained:

$$V\left(\frac{\bar{\sigma}}{\sigma_0}\right)^m=V_0K_1;\quad V\left(\frac{\Delta\sigma}{\sigma_0}\right)^m=V_0K_2, \tag{17}$$

where K_1 and K_2 are constant. Hence, it may be guessed that the following relationships would be valid:

$$\frac{V}{V_0}\bar{\phi}=K_1\ ;\ \frac{V}{V_0}\Delta\phi=K_2 \tag{18}$$

where $\phi(\sigma)$ is the specific risk of fracture function of Weibull without any definite analytical form and with the unique condition that it is positive. $\bar{\phi}$ and $\Delta\phi$ are the mean value and the dispersion of $\phi(\sigma)$, respectively.

The relations defined in equation 18 would constitute the uncertainty principle of probabilistic strength of materials. This principle, for the case of uniform stress field, was already enunciated previously [5,6]. In the following paragraphs it will be intended to extend this principle to the case of variable stress field.

The formulas (18) can be easily proved. In accord with equation 2 the function of frequency is:

$$\frac{dF(v,\sigma)}{d\sigma}=\frac{v}{v_0}\exp\left\{-\frac{v}{v_0}\phi(\sigma)\right\}\phi'(\sigma). \tag{19}$$

The mean value of ϕ is calculated as follows:

$$\begin{aligned}\bar{\phi}&=\int_0^\infty\phi\frac{v}{v_0}\exp\left\{-\frac{v}{v_0}\phi(\sigma)\right\}\phi'(\sigma)d\sigma\\&=\frac{v_0}{v}\int_0^\infty\xi e^{-\xi}d\xi=\frac{v_0}{v},\end{aligned} \tag{20}$$

Calculating $\overline{\phi^2}$ it is obtained:

$$\begin{aligned}\overline{\phi^2}&=\int_0^\infty\phi^2\exp\left\{-\frac{v}{v_0}\phi(\sigma)\right\}\frac{v}{v_0}\phi'(\sigma)d\sigma\\&=\left(\frac{v_0}{v}\right)^2\int_0^\infty\xi^2e^{-\xi}d\xi=2\left(\frac{v_0}{v}\right)^2,\end{aligned} \tag{21}$$

and finally the dispersion of ϕ is determined as follows:

$$\begin{aligned}\overline{\Delta\phi^2}&=\overline{\phi^2}-\bar{\phi}^2=2\left(\frac{v_0}{v}\right)^2-\left(\frac{v_0}{v}\right)^2=\left(\frac{v_0}{v}\right)^2\\\Delta\phi&=\sqrt{\overline{\Delta\phi^2}}=\frac{v_0}{v}.\end{aligned} \tag{22}$$

So the relationships guessed (18) give now exactly:

$$\bar{\phi}\frac{V}{V_0}=1\ ;\ \Delta\phi\frac{V}{V_0}=1, \tag{23}$$

where ϕ has no any analytical prefixed form. In the case when the function of cumulative probability of fracture or yielding has the following expression:

$$F(V,\sigma) = 1 - \exp\left\{ -\frac{V}{V_0} K\phi(\sigma) \right\}, \tag{24}$$

where K is a constant, it is easy to see that the expressions of equation 18 are transformed in the following ones:

$$\bar{\phi}\frac{V}{V_0} = K \; ; \; \Delta\phi\frac{V}{V_0} = K. \tag{25}$$

When the stress-field space is variable the space can be divided by means of isotensional surfaces [2] and the cumulative probability of fracture or yielding is given by the following expression:

$$F(\sigma) = 1 - \exp\left\{ -\frac{1}{V_0}\int_0^{\infty} \phi(\Sigma)\,dV(\Sigma,\sigma) \right\}. \tag{26}$$

Adopting as a new variable

$$0 \le \xi(\sigma) = \frac{1}{V_0}\int_0^{\sigma} \phi(\Sigma)\,dV(\Sigma,\sigma) < \infty, \tag{27}$$

where $dV(\Sigma,\sigma)$ depends upon the geometry of the material subjected to the variable stress field. Hence the functions of cumulative probability and frequency can be expressed in a simplified manner:

$$F(\xi) = 1 - e^{-\xi} \qquad \frac{dF}{d\xi} = e^{-\xi} \tag{28}$$

Hence, with a great simplicity the mean value and the mean square dispersion of ξ can be obtained:

$$\bar{\xi} = \int_0^{\infty} \xi e^{-\xi} d\xi = 1 \; ; \; \overline{\xi^2} = \int_0^{\infty} \xi^2 e^{-\xi} d\xi = 2. \tag{29}$$

Therefore, the dispersion of ξ is:

$$\Delta\xi = \sqrt{\overline{\xi^2} - \bar{\xi}^2} = \sqrt{2 - 1.} = 1. \tag{30}$$

So if in a variable stress field ξ is adopted as the independent variable then the uncertainty relationships have a particular simple form. Therefore, upper limits can be obtained for the equations 27 and the first of equations 29 and also a limit for the equation 30

$$\xi \le \frac{V}{V_0}\phi ; 1 = \bar{\xi} \le \frac{V}{V_0}\bar{\phi} ; \begin{cases} \frac{V}{V_0}\Delta\phi \rightarrow 1 = \Delta\xi \\ V \longrightarrow 0 \end{cases} \tag{31}$$

The relationships (Eq 31) are true relationships of uncertainty because the first relation shows that for the place of fracture or yielding to be exactly located then V-->0, since $\bar{\phi}V \ge V_0$ according to the second relation, the stress will increase indefinitely, $\bar{\phi} - - > \infty$, then the piece will not break or will not yield and σ-->∞. However, according to the last relationship, $1 = (V/V_0)\Delta\phi$, $\Delta\phi$-->∞ and then the uncertainty in the determination of the stress at which the failure occurs becomes indefinitely great. Therefore, there is a contradiction and it can be seen that the problem of the exact determination of the place and the stress wherever the fracture occurs has an impossible solution. It can be remembered that $\phi(\sigma)$ is a crescent and monotonous function [1]. These considerations can also be made from the equations 23 corresponding to uniform stress field taking a small portion of a variable stress field where the same can be considered as uniform.

For the special case when the function of Weibull takes the potential form $\phi(\sigma) = (\sigma/\sigma_0)^m$ the constants K_1 and K_2 can be calculated in an exact and simple form and the relations of uncertainty are valid for the body subjected to a variable stress field as a whole. Hence, with $\xi(\sigma)$ defined into the stress-field space, the following expression into the real space [2] is obtained:

$$\xi(\sigma) = \frac{1}{V_0}\int_V \phi[\sigma f(r)]dV = \frac{\phi(\sigma)}{V_o}\int_V f^m(r)\,dV = \frac{\phi(\sigma)KV}{V_0}, \tag{32}$$

where r is the position vector and f is a function obtained from the elasticity theory. Thus,

$$\bar{\phi} = \int_0^{\infty} \phi(\sigma) e^{-\xi(\sigma)} \frac{d\xi(\sigma)}{d\sigma} d\sigma, \tag{33}$$

therefore

$$\bar{\phi} = \int_0^\infty \frac{VK}{V_0}\phi(\sigma)e^{-\frac{V}{V_0}K\phi(\sigma)}\phi'(\sigma)d\sigma = \frac{V_0}{VK}\int_0^\infty \xi e^{-\xi}d\xi = \frac{V_0}{VK}, \tag{34}$$

and finally

$$\frac{V}{V_0}\bar{\phi} = K_1 = \frac{1}{K} = \frac{1}{\frac{\sigma_0^m}{V}\int_V \phi[f(r)]dV} = \frac{1}{\frac{1}{V}\int_V f^m(r)dV} \tag{35}$$

Likewise it is obtained:

$$\frac{V}{V_0}\Delta\phi = K_1 = K_2 \tag{36}$$

It can be seen without any difficulty that the volume is proportional to the dispersion in the position. The function of frequency of the position can be expressed in the following manner:

$$f(r) = \frac{1}{V} \quad r \in V; f(r) = 0 \quad r \notin V; \int_V f(r)dV = 1. \tag{37}$$

The mean value and the dispersion are calculated in the following form:

$$\begin{aligned} \bar{r} &= \int_V r f(r)dV \\ \overline{\Delta r^2} &= \overline{r^2} - \bar{r}^2 = \int_V r^2 f(r)dV - \bar{r}^2 \\ \Delta r &= \sqrt{\overline{\Delta r^2}}. \end{aligned} \tag{38}$$

In the case of a volume included into a parallelepiped of coordinates $(b_1-a_1, b_2-a_2, b_3-a_3)$ and considering a system of cartesian coordinates (x,y,z) the calculations give the following results:

$$\begin{aligned} \bar{x} &= \int_{a_1}^{b_1} dx \int_{a_2}^{b_2} dy \int_{a_3}^{b_3} \frac{x dz}{(b_1-a_1)(b_2-a_2)(b_3-a_3)} = \frac{b_1+a_1}{12} \\ \overline{\Delta x^2} &= \int_{a_1}^{b_1} dx \int_{a_2}^{b_2} dy \int_{a_3}^{b_3} \frac{(x-\bar{x})^2 dz}{(b_1-a_1)(b_2-a_2)(b_3-a_3)} = \frac{(b_1-a_1)^2}{12} \\ \Delta x &= (b_1-a_1)/2\sqrt{3}. \end{aligned} \tag{39}$$

Analogous results are obtained for $\bar{y}$, $\bar{z}$, Δy, Δz. Thus:

$$\Delta x \Delta y \Delta z = \frac{(b_1-a_1)(b_2-a_2)(b_3-a_3)}{24\sqrt{3}} = \frac{V}{24\sqrt{3}}, \tag{40}$$

Therefore, the equation $\Delta\phi V = 1$ is transformed into:

$$\Delta x \Delta y \Delta z \Delta\phi = \frac{V_0}{24\sqrt{3}}, \tag{41}$$

and for the case of a global rectangular body:

$$\Delta x \Delta y \Delta z \Delta\phi = \frac{V_0 K_2}{24\sqrt{3}}. \tag{42}$$

As to the local probability of fracture, the dispersion of the number of fractures n_1 starting in volume V_1 is obtained through the following group of relationships, as it is well-known from the elemental theory of Statistics:

$$\begin{aligned} n_1 &= N\frac{V_1}{V} \\ \Delta n_1 &= \sqrt{n_1} = \sqrt{N}\sqrt{\frac{V_1}{V}} \\ \frac{\Delta n_1}{n_1} &= \frac{1}{\sqrt{N}}\sqrt{\frac{V}{V_1}} = \frac{1}{\sqrt{n_1}} \end{aligned} \tag{43}$$

This group of relationships (43) represents the second principle of uncertainty of Probabilistic Strength of Materials. None of the two principles of uncertainty, relationships (31) and (43), depends on constants of the material.

APPLICATIONS TO SEISMOLOGY

An immediate application to Seismology can be made wherein probabilistic [7] or implicitly probabilistic [8] models have been introduced. The Seismic phenomenon is equivalent to a brittle fracture by a slowly gradual stress and if in a definite volume we have a definite number n of earthquakes of magnitude equal or greater than a given one, then fluctuations of order $\sqrt{n}$ may be expected, and if the mean time between earthquakes is $\bar{t}$ then stretchs of time of order $\bar{t}\sqrt{n}$ may be expected. For instance, in the closenesses of Valparaíso city (Chile, latitude 33°S) five strong earthquakes have had since 1575 with an approximate average interval of 82 years which makes possible to expect the existance of intervals of order of 200 years without earthquakes. However, another analysis can be made. If the Seismological phenomenon in front of Valparaíso Coasts consists of a constant increasing in the time of the mean space stress σ and later the fracture, then $\sigma \alpha$ t; $\Delta\sigma \alpha \Delta t$; $\bar{\sigma} \alpha \bar{t}$ t wherein $\bar{\sigma}$ is the time medium stress. If the material that is fracturing at the seism moment is of the Weibullian type, with $\phi(\sigma) = (\sigma/\sigma_0)^m$ (σ,m>0), then the equations 15 and 16 are valid.

In the case of the surrounding of Valparaíso $\bar{t}$ = 82 years, Δt = 6 years and, therefore, $\Delta t/\bar{t} = \sigma/\bar{\sigma}$ = 0.073 which implies, according to Eqs 15 and 16, m ~ 20. This last value belongs to a rock of impossible material properties. In consequence, this hypothesis of the average intervals of 82 years cannot be accepted and it must be revised. In all probability, the epicenters of old earthquakes were equivocally determined. In the case of earthquakes on the surrounding of Santiago city (Chile, latitude 33° 27'S) $\bar{t} \sim \Delta t$ = 28 years which gives us m ~ 1 and, hence, this hypothesis cannot be accepted too because the rocks have m ~ 6. Therefore the most probable hypothesis is that one of the variable volumen $V = \lambda t$ with σ = constant which was developed by Kittl and Díaz [7].

The growth of fissures that finally originate the fracture can be basically attributed to some of the following situations. The first of them implies an increasing of tension until the critical tension is reached which activates the crack causing the fracture. The second case is referred to a fatigue phenomenons, static as much as dynamic, and here is required an aggressive atmosphere in static fatigue, for example corrosion by water in ceramic materials, or in the case of metals when they are in presence of any acid in processes of static and/or dynamic fatigue. In the seismological ambit and particularly in the central coast of Chile, in front of Valparaíso, the said aggressive environments do not exist, neither aqueous nor gaseous, to the deepnesses in which the contact between the Nazca and Continental plates is verified. The creep does not exist too because if it existed then the great seisms registered would not produce there. In relation to the dynamic fatigue this does not exist in any way because of it needs approximately 10^4 cycles to be noted.

The theory of fracture of Weibull has, in the present time, a wide variety of applications because of which the simile of the chain, the most weak link, has been exceeded and the statistic is not necessary referred to bodies in which an only crack propagating activates the mechanism of fracture [2]. It is a mistake the idea concerning that since Weibull statistics is valid in an unidimensional body then it is not valid in three dimensions. This last because a body of three dimensions, where the probability of fracture is given by formula (3), can be constructed with unidimensional bars. In seismology, it deals with the fracture of a rocky material for which, in the case of granite, the Weibull function has been applied [9] where the growth of a certain number of cracks was required to fracture the material. Whichever the activation of the fracture, friction between plates, roughness [10] and so on, all of them must undergo a Weibull statistics. In the case of concrete in which the mechanism of fracture is by coalescence of cracks [11], the Weibull function even is valid there too. In a tectonic process, the failure is simply by slip at high velocity. Once the tension is annuled, since the earthquake has occurred, a new growth in the tension is initiated. When this last is verified, we are in presence of a new sample because the surrounding of the last failure is similar to that where the next one will produce. It is also worthwhile to note that this zone – where the phenomenon is produced – displaces.

It is necessary to emphasize the importance of the local probability of fracture, because in seismology a big relevance is given to the place where the earthquake occurs. Therefore, the local probability is very useful. By means of it, we may determine whether a certain number of events occurred in a determined zone correspond at the same statistical serie or not. This last may lead to decide whether events considered as concurrent in a same place, have been or not.

In the present time, the concept of seismic gap is the most widely criterion used for prediction of earthquakes [12-16]. However, according with the scarce number of events considered, such predictions fall out of the ambit of statistics, that is to say very few samples for a population evidently greater.

As a consequence of the uncertainty principles we can say that nor the place, nor the time, nor the magnitude of an earthquake can be predicted, but its probability.

ACKNOWLEDGEMENTS

The authors wish to thank the Fondo Nacional de Desarrollo Científico y Tecnológico (FONDECYT) for Grants N° 1253-91, 0516-88, 1195-91 and 056-93.

REFERENCES

1. Weibull, W, A statistical theory of the strength of materials, *Ing. Vetenskaps Akad. Handl.* **151**, 1-45 (1939).
2. Kittl, P and Díaz, G, Weibull's fracture statistics, or probabilistic strength of materials: State of the art, *Res Mech* **24**, 99-207 (1988).
3. Oh, KPL and Finnie, I, On the location of fracture in brittle solids-I, *Int J Fract Mech* **6**, 287-300 (1970).
4. Kittl, P and Camilo, GM, Local probability of failure in statistical theory of brittle fracture, *Res Mech Lett* **1**, 115-118 (1981).
5. Kittl, P, On the foundation of fracture statistics, *Latin Am J Metall Mat* **5**, 85-88 (1985).
6. Kittl, P and Díaz, G, Five deductions of Weibull's distribution function in the probabilistic strength of materials, *Eng Fract Mech* **36**, 749-762 (1990).
7. Kittl, P and Díaz, G, Earthquakes risk and fracture statistics, *Phys Earth Planet Inter* **49**, 222-224 (1987).
8. Carlson, JM and Langer, JS, Properties of earthquakes generated by fault dinamics, *Phys Rev Lett* **62**, 2632-2635 (1989).
9. Kittl, P, León, M, Díaz, G and Lillo, A, Probabilistic compressive strength of sound dry granite, *Rock Mech Rock Eng* **23**, 21-28 (1990).
10. Ruff, LJ, Fault asperities inferred from seismic body waves. In Earthquakes: Observation, Theory and Interpretation, Eds H Kanamori and E Boschi, N-Holland Publishing Co, Amsterdam (1983) 251-276.
11. Hu, X, Mai, Y-W and Cotterell, B, A statistical theory of time-dependent fracture for cementitious materials subjected to cyclic loading, *J Mat Sci* **24**, 3118-3122 (1989).
12. Comte, D, Eisenberg, A, Lorca, E, Pardo, M, Ponce, L, Saragoni, R, Singh, SK and Suárez, G, The 1985 central Chile earthquake, a repeat of previous great earthquakes in the region?, *Science* **233**, 449-453 (1986).
13. Nishenko, SP, Seismic potential for large and great earthquakes along the Chilean and southern Peruvian margins of S America: a quantitative reappraisal, *J Geophys Res* **90**, 3589-3615 (1985).
14. Nishenko, SP, Barrientos, SE and Comte, D, To catch an earthquake, USA-Chile Workshop: Geotechnical earthquake instrumentation for seismic hazard reduction in Chile, Jan. 6-10, IDIEM, Chile. Univ of Chile, Chile, Univ of N Carolina at Charlotte, USA (1992) pp 5-10.
15. Kausel, E, Near future seismological prediction of major earthquakes in Chile, USA-Chile Workshop: Geotechnical earthquake instrumentation for seismic hazard reduction in Chile, Jan 6-10, IDIEM, Chile. Univ of Chile, Chile, Univ of N Carolina at Charlotte, USA (1992) pp 11-12.
16. Ponce, L, Medium and short-term forecast of large and great earthquakes in Chile, USA-Chile Workshop: Geotechnical earthquake instrumentation for seismic hazard reduction in Chile, Jan 6-10, IDIEM, Chile. Univ of Chile, Chile, Univ of N Carolina at Charlotte, USA (1992) pp 13-15.

applied mechanics reviews

AN ASSESSMENT
OF THE WORLD LITERATURE
IN ENGINEERING SCIENCES

Applied Mechanics Reviews (ISSN 0003-6900) is published monthly by the ASME, 345 E 47th St, New York NY 10017. 2nd class postage paid at New York NY and additional mailing offices. **POSTMASTER:** Send address changes to ASME/AMR, 22 Law Drive, Box 2300, Fairfield NJ 07007-2300. **CHANGES OF ADDRESS** must be received at ASME seven weeks before they are to be effective. Send old label and new address. **SUBSCRIPTION PRICES:** $534 (incl Annual Index and Suppl.), single copies $57 (Suppl. or Index $84). Countries outside USA and Canada add $102 for postage ($156 airmail). 2nd library subscription $99. **DISCLAIMER:** "The Society shall not be responsible for statements or opinions ...printed in its publications" (ASME Bylaws B7.1.3).

The American Society of Mechanical Engineers

AUTHOR INDEX

PACAM I and II STILL AVAILABLE

Copies of

MECHANICS PAN-AMERICA 1989 (PACAM I, Rio de Janeiro, Brazil), *published as Applied Mechanics Reviews Volume 42, Number 11, Part 2 (November 1989);*

and

MECHANICS PAN-AMERICA 1991 (PACAM II, Valparaiso, Chile), *published as Applied Mechanics Reviews Volume 44, Number 11, Part 2 (November 1991)*

are still available and may be ordered at the special price of $24.00 with a copy of this form.

☐ **PACAM I: AMR vol 42, no 11, part 2, Nov 1989 - Book #800148**

☐ **PACAM II: AMR vol 44, no 11, part 2, Nov 1991 - Book #AMR106**

Unit Prices:

ASME member:	$12.00	_____
non-members:	$24.00	_____
shipping, USA and CANADA:	$6.00	_____
shipping, outside USA and CANADA:	$10.00	_____
TOTAL DUE:	**$**_____	

ASME member prices apply to the purchase of 1 copy of any reprint for the member's personal use with shipment to his or her personal attention. *Ordering information:* Advance payment required if billed outside USA or Canada. Foreign and Canadian checks not accepted unless payable in US dollars through a US bank. CA, GA, IL, TX purchasers must add sales tax, Canadians 7% GST, or furnish tax exemption certificate.

Send order to:	**ASME Marketing Dept** **22 Law Drive, PO Box 2300** **Fairfield NJ 07007-2300**
Order by ***phone***	**1-800-THE-ASME**, or **1-800-843-2763**
or ***FAX*** *form to:*	**201-882-1717**

ASME members, to receive discount you must indicate your membership no.:____________________

ASME Member Name (PRINT):____________________

Signature:____________________

SHIP TO: Name:____________________

Company:____________________

Street address:____________________

City, State, ZIP:____________________

Country:____________________

CHECK ONE:

[ ] Payment enclosed, [ ] Bill me, [ ] Bill my company

PO No.:______________ Total enclosed: $________

CHARGE MY:

[ ] Mastercard Interbank No:____________________

[ ] Mastercard/Visa Account No:____________________

[ ] American Express Account No: ____________________

Expiration date:____________________

Signature: ____________________

BILL TO: Name:____________________

Company:____________________

Street address:____________________

City, State, ZIP:____________________

Country:____________________

FOURTH PAN AMERICAN CONGRESS OF APPLIED MECHANICS

PACAM IV

January 3-6, 1995, Universidad del Salvador, Buenos Aires, Argentina

CALL FOR PAPERS

The **Fourth Pan American Congress of Applied Mechanics** will be held in **Buenos Aires, Argentina** on the campus of the **Universidad del Salvador** during **January 3-6, 1995.** The Congress is sponsored by the **American Academy of Mechanics** and the **Asociación Argentina de Mecánica Computacional,** and is open to participants from all over the world.

The purpose of PACAM IV is (1) to expose mature engineers and scientists as well as advanced graduate students to new findings, techniques, and problems, and (2) to provide opportunities for personal interactions through formal lectures and informal conversations.

Papers in all areas of applied mechanics, including computational mechanics, are solicited by the Organizing Committee, which consists of the following persons:

Patricio A.A. Laura, Bahia Blanca, Argentina, *Chairman*
Sergio R. Idelsohn, Santa Fe, Argentina and **Dean T. Mook,** Blacksburg, Virginia, USA, *Vice Chairmen*
Luis A. Godoy, Córdoba, Argentina, *Chairman of the Editorial Committee*
Gustavo Sanchez Sarmiento, Buenos Aires, Argentina, *Chairman of the Local Arrangements Committee*

P. Bainum (Washington, D.C., USA)
F. Basombrio (Bariloche, Argentina)
P. Ballesteros (Mexico City, Mexico)
M. Crespo da Silva (Troy, New York, USA)
G. Dulikravich (Univ. Park, Pennsylvania, USA)
E. Dvorkin (Buenos Aires, Argentina)
R. Feijoo (Rio de Janeiro, Brazil)
J. Geer (Binghamton, New York, USA)
P. Glockner (Calgary, Canada)
P. Hajela (Troy, New York, USA)
J. Kelly (Berkeley, California, USA)
P. Kittl (Santiago, Chile)
A. Leissa (Columbus, Ohio, USA)
H. Liebowitz (Washington, D.C., USA)
O. Manero (Mexico City, Mexico)
C. Mazzilli (Sao Paulo, Brazil)
A. Müller (Caracas, Venezuela)
E. Oñate (Barcelona, Spain)
M. Paidoussis (Montreal, Canada)
M. Pazini Brandão (São Jose dos Campos, Brazil)
J. Reddy (College Station, Texas, USA)
J. Schetz (Blacksburg, Virginia, USA)
H. Sosa (Philadelphia, Pennsylvania, USA)
M. Souza (Rio de Janeiro, Brazil)
L. Suarez (Mayagüez, Puerto Rico)
E. Taroco (Rio de Janeiro, Brazil)
G. Treviño (Houghton, Michigan, USA)
R. Villaverde (Irvine, California, USA)

Accepted four-page manuscripts will appear in the Proceedings, which will be distributed at the Congress. After the Congress, selected participants will be invited to prepare full-length articles for a special issue of **Applied Mechanics Reviews** entitled **Mechanics Pan America.**

A packet with more information about PACAM IV and the typing requirements for manuscripts to be published in the Congress Proceedings can be obtained by writing to one of the following persons:

Prof. Sergio R. Idelsohn
Grupo de Tecnologia Mecánica de INTEC
Guemes 3450
3000 Santa Fe
ARGENTINA
Tel 54-42-559181
FAX 54-42-550944/E-MAIL rnsergio@arcride.edu.ar

Prof. Dean T. Mook
Virginia Polytechnic Institute and State University
Department of Engineering Science and Mechanics
Blacksburg, Virginia 24061-0219
USA
Tel 1-703-231-6841
FAX 1-703-231-4574/E-MAIL Sally@vtvm1.cc.vt.edu

The deadline for receipt of papers for the Congress is April 30, 1994. The languages for the Congress are English, Spanish, and Portuguese; nevertheless, authors are encouraged to write and present their papers in English.

APPLIED MECHANICS REVIEWS **ISSN 0003-6900**

Volume 46, Number 11, Part **2, November 1993**

ASME Reprint No AMR 134